NEXCEL
Nonmetallic Excellence and Innovation Center for Building Materials
非金属材料创新中心

CNBM | CBMA

aramco 沙特阿美

Advancing with Nonmetallic Materials:

A Compendium of NEXCEL Publications 2022-2025

(Volume II)

Preface

It is with great pleasure that we present this collection of research, *Advancing with Nonmetallic Materials: A Compendium of NEXCEL Publications 2022-2025*. This c*ompendium* brings together 112 research papers, all published by the researchers of NEXCEL project teams over a productive four-year period. It should be noted that 26 papers of them were originally published in Chinese and are presented as such to preserve the integrity of the authors' work. Readers can refer to the English abstracts of them to grasp the key contributions and conclusions. The remaining 86 papers were kept and presented in English.

The years 2022-2025 represented a phase of intense exploration and significant advancement in nonmetallic materials for NEXCEL. In a world marked by rapid transformations and complex challenges, materials transition to higher efficiency, more resilience and more intelligence is crucial for meeting sustainability goals and construction needs. The works compiled here stand as a testament to our commitment to generating knowledge that is not only academically sound but also practically applicable.

This Compendium is more than a simple archive of publications; it is a curated map of our intellectual journey. To facilitate the readers to navigate this substantial body of work, we organized the papers into two volumes and six chapters:

VOLUME I

- Chapter 1: FRPs & Advanced Composites (48 papers)

VOLUME II

- Chapter 2: Special Mortars & Concrete (19 papers)
- Chapter 3: Pavement for Roads & Bridges (16 papers)
- Chapter 4: Construction Chemicals (10 papers)
- Chapter 5: Waterproofing & Repair Materials (5 papers)
- Chapter 6: Insulation & Composite Cladding (14 papers)

Each chapter synthesizes key findings and traces the innovation of thought within its focus area, offering readers a coherent narrative of progress and discovery across multiple projects.

The primary aim of this Compendium is twofold. First, it serves to consolidate the core outcomes of our diverse research portfolio, providing a comprehensive

overview of NEXCEL's contributions to its fields of expertise. We hope this synthesis will reveal connections between different projects, highlight emerging materials, and identify promising avenues for future nonmetallic deployment.

Second, and equally important, this Compendium is conceived as a vital channel for interaction and exchange with our valued stakeholders. To our founding sponsor Aramco, our operating archive China Building Materials Academy (CBMA), sponsors, project partners, strategic partners, and the broader academic and practitioner communities: these pages contain the tangible outputs of our shared mission. We invite you to engage with these findings, critique them, build upon them, and explore their practical application scenarios. True impact is achieved not in isolation, but through exchange and partnership. It is our sincere hope that the insights contained herein will inform policy, inspire innovation, enhance professional practice, and stimulate further collaborative ventures.

We extend our deepest gratitude to the dedicated researchers, project staff, and contributing authors whose expertise and hard work are the key foundation of this Compendium. We also acknowledge the unwavering support of our partners, and funders, whose trust and resources made this research possible.

As we look beyond, we envision this Compendium as a springboard for the next phase of our work. May it facilitate the wider dissemination and application of our collective outcomes, strengthening existing partnership and forging new ones as we continue to pursue a promising future for the construction sector.

Prof HOU Diyang

Chairman of NEXCEL Technical Advisory Committee

Feb 2026

© 2026 NEXCEL
This Compendium has been compiled from PDF files provided by the individual authors of each paper. The copyrights of all included papers in this Compendium remain with their original authors. Any questions regarding the content or intellectual property should be directed to its authors. NEXCEL is not responsible for the intellectual property or accuracy of the individual papers.

Contents

VOLUME II

Chapter 2: Special Mortars & Concrete

1. **Differences in micro grain/fiber distributions between matrix and interlayer of ce mentitious filaments affected by extrusion molding (2022SFP1-1)** 1
   Rijiao Yang, Yi Zhu, Yan Lan, Qiang Zeng, Yu Peng, Zhendi Wang
2. **Gradient distribution of slender glass microfibers in 3D printed cementitious filam ents (2022SFP1-1)** 15
   Rijiao Yang, Qiang Zeng, Zhendi Wang
3. **Rebar-matrix interface in extrusion molded cementitious filaments (2022SFP1-1)** 20
   Rijiao Yang, Qiang Zeng, Zhendi Wang
4. **Effects of polymer-cement ratio on the properties of polymer mortar (2022SFP5-1) - *in Chinese*** 27
   Wang Junwei, Li Hao, Li Wenxiu, Jia Haitao, Zhai Yanjun, Zhang Gonghui
5. **Effect of polymer modified volcanic rock coarse aggregate on properties of concrete (2022SFP5-1) - *in Chinese*** 31
   Wang Junwei, Wu Guoqi, Hong Junjie, Peng Xinyong, Zhai Yanjun
6. **Improving the interfacial properties of PVA fiber and cementitious composite: Design and characterization (2023TDA1-1)** 36
   Shun Yao, Chuanlin Hu, Fazhou Wang, Shuguang Hu
7. **A two-step synthesis of porous nitrogen-doped graphene for electrochemical capacitors (2023TDA1-1)** 46
   Jiahao Li , Zhenjia Wu, Rong Huang, Anbang Ge, Jie Ying
8. **Impact of C-F-S-H/PCE nanocomposites on hydration and mechanical properties of slag cement (2023TDA1-1) - *in Chinese*** 58
   Qin Zihao, Dong Yemin, Hu Chuanlin
9. **Effect of styrene acrylic latex on the performance of metakaolin blended cement: From hydration to mechanical properties (2023TDA6-2)** 66
   Ye Pan, Zichen Lu, Lei Wang, Xiaojie Yang, Juan Li, Ruijun Gao, Zhenping Sun
10. **Mechanical performance of polymer-modified mortar with the newly designed gradient structure: effect of polymer types and content (2023TDA6-2)** 79
    Ye Pan, Zichen Lu, Lei Wang, Yanrong Zhang, Yi Ding, Zhenping Sun
11. **Research progress on cencrete-polymer composites (2023TDA6-2) - *in Chinese*** 93
    Lu Zichen, Liu Danting, Wang Lei
12. **The influence of gradient change in polymer content on the properties of cement** 105

mortar (2023TDA6-2) - *in Chinese*

Pan Ye, Lu Zichen

13. **Research on gradient-enhanced polymer-modified concrete for structural use and comparison with conventional concrete (2023TDA6-2)** 112

Ye Pan, Zichen Lu, Lei Wang

14. **A new method to improve the crack resistance of cement-based composites: Development of magneto-responsive polymer latex and performance evaluation (2023TDA6-2)** 124

Lei Wang, Jing Wang, Zichen Lu, Xiangming Kong

15. **Modification of early-age microstructure and enhanced mechanical properties of cement paste via injecting low-dose CO_2 at fresh stage (2023PHD-6)** 133

Shuang Luo, Ming-Zhi Guo, Tung-Chai Ling

16. **Effect of CO2-mixing dose and prolonged mixing time on fresh and hardened properties of cement pastes (2023PHD-6)** 143

Minlu WANG, Shuang LUO, Ba Tung PHAM, Tung-Chai LING

17. **Recent advance of monomer in-situ polymerization modiffed cement-based materials (2024PHD-8)** 155

Kai Wu, Jiangfeng Long, Longbang Qing, Geert De Schutter

18. **Design of microwave absorbing frequency bands and selection criteria for vitreous aggregates in cement-based materials (2024PHD-10)** 174

Zihao Wu, Shuai Xie, Chao Ma, Yingxiang Wang, Ronghua Su, Jing Wang, Zhijiang Ji

19. **Effects of coal gas fine ash on electromagnetic properties of cement mortar and carbon black modification (2024PHD-10)** 196

Yingxiang Wang, Shuai Xie, Chao Ma, Zihao Wu, Jing Wang, Zhijiang Ji

Chapter 3: Pavement for Roads & Bridges

1. **Rheological properties of warm mixed asphalt (2022TDA2-4)** 232

Rong Chang, Yongchun Qin, Peng Wang

2. **Effect of warm mix agent on the chemo-mechanical performance of binder with different oil sources (2022TDA2-4)** 238

Rong Chang, Aimin Sha1, Jie Wang

3. **Performance research and engineering application of in-place recycled asphalt mixture with warm mixing technology (2022SFP3-1) - *in Chinese*** 246

Zeng Wei, Xu Jian, Wang Peng

4. **Impacts of asphalt and mineral types on interfacial behaviors: A molecular dynamic s study (2022PHD-2)** 252

Guoqing Sun, Zhenxing Niu, Jiupeng Zhang, Xiaoyong Tan, Yufei Jing, Zixuan Chen

5. **Comprehensive evaluation of ballastless-track sealants based on macro–micro tests** 271

and principal component analysis (2022PHD-2)

Guoqing Sun , Zhe Hu , Jiupeng Zhang , Hengxiao Xue

6. **Microscopic properties of asphalt and polyethylene at an extraordinary high dosage through molecular dynamics simulation (2023SFP1-2)** 280

Yuye Jin, Haoyi Li, Jie Chen, Qianqian Wang, Yanhua Bao, Shuguang Hou

7. **Preparation method and properties of high viscosity and elasticity road asphalt modified recycled low-density polyethylene plastic at a large dosage (2023SFP1-2) - *in Chinese*** 299

Jiang Jianguo, Sun Tiangan, Wang Xunzhi, Wang Qianqian, Hou Shuguang

8. **Preparation of waterborne polyurethane- modified trackless emulsified asphalt and its road performance (2024TDA-4) - *in Chinese*** 302

Wang Peng, Wang Jie, Lan Yong, Ma Qing, Geng Shuang, Xu Jian

9. **Degradation mechanism and performance of polyurethane mixture under water conditions (2024TDA-4)** 310

Li Pengfei, Wang Jie, Cao Zhilong, Xu Jian, Li Song, Wang Peng, Zhang Zhiqing

10. **Study on the road performance and development mechanism of polyurethane binder in different media solutions (2024TDA-4)** 322

Li Pengfei, Cao Zhilong, Zhang Zhiqing, Wang Jie, Xu Jian, Wang Peng

11. **A practical method for testing the properties of phase-change building materials and composites (2024SFP-3)** 335

Haijian Liabe, Yingxin Liu, Wei Zhuang,Hao Wu, Zhongcheng Ma

12. **Investigation on physical, rheological properties and VOCs emission of asphalt modified with hydrocarbon-based graphene (2024SFP-5)** 343

Yansong Fan, Meizhu Chen, Xiaoyu Yang, Jianwei Zhang, Jun He, Muyan Han

13. **Optimization design of asphalt emulsion with rejuvenator towards a uniform distribution inside the damaged porous asphalt mixture for a better ravelling resistance (2024PHD-1)** 354

Bin Yang, Jiwang Jiang, Haopeng Wang, Zhen Leng, Xin Sui, Xi Jiang

14. **Maintenance mechanisms of rejuvenator-optimized asphalt emulsion in damaged porous asphalt mixture: Morphological, physicochemical, and rheological characterizations (2024PHD-1)** 369

Bin Yang, Jiwang Jiang, Zhen Leng, Xi Jiang, Yubo Sun, Chuanqi Yan, Zhifei Tan, Gaoyang Li

15. **Investigating the role of sulfur stabilizer in modulating aging properties of SBS-modified asphalt (20245PHD-2)** 381

Junjie Zhang, Pengwei Sun, Zefeng Ma, Mingxin Dai, Rong Zhuo, Guilian Zou, Yiqiu Tan

16. **Evolution of Phase Structure and Mechanical Properties in Aged SBS-Modified Asphalt (2024PHD-2)** 395

Junjie Zhang, Yiqiu Tan

Chapter 4: Construction Chemicals

1. **Preparation and performance of EPEG-type PCE and its application in ultra-high performance concrete (2022TDA3-1)** 429

   Tong Xue，Jie Bai，Wenying Xu，Zuobao Song，Ting LiJuan Li，Ruijun Gao

2. **Research status and prospect of domestic polyether macromonomer (2022TDA3-1) - *in Chinese*** 433

   Xu Wenying, Xue Tong, Li Ting, Wang Bo, Cai Yang, Gao Ruijun, Bai Jie

3. **Research on the mix proportion of low-carbon concrete utilizing a novel polycarboxylate Superplasticizer (2022TDA3-1)** 437

   Xue Tong, Bai Jie, Li Juan, Song Zuobao, Li Ting, Gao Ruijun

4. **Research on the effect and mechanism of binder-sand ratio on UHPC performance (2022TDA3-1)** 445

   MA Qiang, ZHANG Jiangtao, XUE Tong, QU Haiyang, FAN Deke, LIU Ruichao, BAI Jie, XU Wenying, WANG Bo

5 **Research on properties of sulfoaluminate cement-based premixed fluid solidified soil curing agent (2022SFP2-1) - *in Chinese*** 456

   Li Yue, Qi Zhiyang, Lin Hui, Wang Baoliang, Zhang Chao, Guo Qiusheng

6 **Fluid solidification of construction waste soil (2022SFP2-1) - *in Chinese*** 461

   Guo Jinzhu, Wang Jian, Li Xiaoning, Li Ting

7 **Interfacial performance of asphalt-aggregate system under different conditions based on molecular dynamics simulation (2022PHD-2)** 465

   Guoqing Sun, Jiupeng Zhang, Zixuan Chen,Zhenxing Niu, Yan Li

8 **Protective and flame-retardant bifunctional epoxy-based nanocomposite coating by intercomponent synergy between modified CaAl-LDH and rGO (2023SFP4-1)** 478

   Hassan Murtaza, Jingmao Zhao, Mohammad Tabish, Jingbao Wang, Muhammad Mubeen, Jingfan Zhang, Sheng Zhang, Baomin Fan

9 **Preparation of tung oil microcapsules and their self-healing properties (2023SFP4-1) - *in Chinese*** 496

   Wang Wanling, Zhao Jingmao

10 **Preparation of graphene oxide/aluminum hypophosphite hybrids and improved flame retardancy of polycarbonate(PC)/acrylonitrile butadiene styrene(ABS) blends (2023SFP4-1) - *in Chinese*** 504

   Zhang Jingfan, Zhang Sheng, Zhao Jingmao

Chapter 5: Waterproofing & Repair Materials

1 **Performance of thermal-oxidative aging on the structure and properties of ethylene propylene diene monomer (EPDM) vulcanizates (2023TDA2-2)** 512

Quanchao Hu, Qiang Chen, Peiru Song, Xingyu Gong, Junyi Chen, and Yongxian Zhao

2 **Exploring the structure, characteristics, and thermal degradation of composites comprising thermoplastic polyolefin and graphene oxide under high-temperature dynamic shear conditions (2023TDA2-2)** 528

Quanchao Hu, Hailiang Huang, Yufei Teng, Ying Yang, Gang Wang, Junyi Chen, Yongxian Zhao

3 **Development of sustainable desulfurized waste crumb rubber modiffedasphalt with enhanced self-healing properties (2024PHD-7)** 541

Tianwei Zhang, Shanjun Gao, Yanheng He, Quantao Liu, Shi Xu, Ronghua Zhuang, Shangheng Zeng, Jianying Yu

4 **Effect of aging on structure and properties of self-healing-enhanced SBS modiffed asphalt with dual dynamic chemical bonds (2024PHD-7)** 556

Tianwei Zhang, Shanjun Gao, Yanheng He, Quantao Liu, Shi Xu, Ronghua Zhuang, Shangheng Zeng, Jianying Yu

5 **Effect of dynamic disulfide bonds on microstructure, storage stability, and self-healing performance of desulfurized waste crumb rubber–modified asphalt (2024PHD-7)** 568

Tianwei Zhang, Shanjun Gao, Yanheng He, Quantao Liu, Ronghua Zhuang, Shangheng Zeng, Hao Duan, and Jianying Yu

Chapter 6: Insulation & Composite Cladding

1 **Influence of slurry characteristics on the bubble stability in foamed concrete (2022SFP4-1)** 579

Min Xiao, Fangxian Li, Pengfei Yang, Bin Li, Jiangxiong Wei, Qijun Yu

2 **Process optimization study of encapsulation method for pre-treatment of recycled EPS particles (2022SFP4-1) - *in Chinese*** 591

LI Fangxian, FENG Ruiqi, ZHANG Zucong, YANG Pengfei, WEI Jiangxiong

3 **Experimental study on seismic performance of two-story two-bay. Precast concrete frame with UHPC-based connections (2023TDA3-2)** 595

Yanghui Li, Weichen Xue, Jiafei Jiang

4 **Out-of-plane response of prefabricated concrete shear walls connected via grouted sleeves (2023TDA3-2)** 607

Weichen Xue, Qian Huang, Zhijun Xu, Jiayin Yu, Ya Li

5 **Calculation method for heat transfer coefficient of ribbed composite insulated exterior wall panels (2023TDA3-2) - *in Chinese*** 620

CHUAN Yang, LI Junni, LI Xin, SHI Tianxiang

6 **Experimental research on shearing behavior of connectors in precast sandwich insulation wall panel (2023TDA3-2) - *in Chinese*** 627

XU Xiaotong, XIAO Ming, WANG Zan, JIANG Anwei, GU Yang, LI Wei

7 **Experimental research on anchoring performance of connectors in precast sandwich insulation wall panel (2023TDA3-2) - *in Chinese*** 634

BU Fanjie, XU Xiaotong, XIAO Ming, WANG Zan, JIANG Anwei, GU Yang, LI Wei

8 **Finite element analysis of stress performance of precast concrete multi-ribbed sandwich insulation facade panel (2023TDA3-2) - *in Chinese*** 643

SHI Tianxiang, FENG Bo, XIAO Ming, LYU Wanqing, HAN Wenlong

9 **Hydrophobic phenolic/silica aerogel composites with high fire safety and strength for efficient thermal insulation (2024TDA-2)** 649

Zhixin Wang, Yong Kong, Mengcheng Nie, Kuo Liu, Qinghua Liu, Xiaodong Shen

10 **Advances in inorganic hybrid phenolic aerogels (2024TDA-2) - *in Chinese*** 660

WANG Zhixin, KONG Yong, SHEN Xiaodong

11 **External thermal insulation composite systems (ETICS) supplier and its certification method (2024TDA-5) - *in Chinese*** 669

ZHANG Jincheng, SUN Shibing, JIN Xiaodong, GUO Hongbin, ZENG Chunyan, WU Wei, HAN Yunpeng

12 **Research on the influencing factors of the compatibility index of the exterior insulation system (ETICS) of the thin plastered exterior wall (2024TDA-5) - *in Chinese*** 673

JIN Xiaodong, ZHANG Haohao, SUN Shibing, ZHANG Jincheng, GUO Hongbin, ZENG Chunyan, WU Wei

13 **Self-assembled coatings with durable ffame retardancy for EPS foam (2024PHD-3)** 679

Xiaodong Jin, Xinyi Wu, Wufei Tang, Zheni Tan, Wanfu Wang, Shibing Sun

14 **Recycling of wind turbine blade powder into HDPE wood-plastic composites: Enhanced mechanical and flame-retardant properties via interfacial modification (2024PHD-3)** 693

YiChen Chen, Wufei Tang, Zhaozhen Zhang, Peixin Li, Shibing Sun, Wanfu Wang, Xiaodong Jin

Additive Manufacturing 60 (2022) 103236

Contents lists available at ScienceDirect

Additive Manufacturing

journal homepage: www.elsevier.com/locate/addma

Differences in micro grain/fiber distributions between matrix and interlayer of cementitious filaments affected by extrusion molding

Rijiao Yang [a,b], Yi Zhu [a,c,d], Yan Lan [a], Qiang Zeng [a,*], Yu Peng [a], Zhendi Wang [b,e,**]

[a] College of Civil Engineering and Architecture, Zhejiang University, Hangzhou 310058, China
[b] State Key Laboratory of Green Building Materials, China Building Materials Academy, Beijing 100024, China
[c] Center for Balance Architecture, Zhejiang University, Hangzhou 310058, China
[d] The Architectural Design & Research Institute of Zhejiang University Co., Ltd., Hangzhou, 310028, China
[e] School of Materials Science and Engineering, Chang'an University, Xi'an 710061, China

ARTICLE INFO

Keywords:
Extrusion
Glass fibers
Directional orientation
Interface

ABSTRACT

Extrusion molding generally causes laminar structure with obvious interfaces, however, the impacts of extrusion molding on the distributions of micro grains/fibers in the matrix and interface of filaments haven't been fully addressed. Herein, X-ray computed tomography was employed to track the cement micro particles and glass microfibers in extrusion molded cementitious composites (EMCC). Results show that small grains migrated into the interface while coarse grains stayed in the matrix of filaments. Glass microfibers in the matrix and interface were roughly parallel and perpendicular to the printing direction, respectively. The mechanisms of shearing stress gradients built in the EMCC filaments and collisions on the microfibers during pumping were proposed to account for the featured distributions and directions of the micro grains and fibers. The findings would deepen the understandings in particle redistribution in non-Newtonian liquid during extrusion molding and facilitate the design and development of 3D printing construction materials.

1. Introduction

Three-dimensional (3D) printing is a widely used automatic construction technique that builds a structure through the pattern of material addition [1,2] and shows great benefits in structure design, manpower saving, and clean construction environments [3,4]. For the scenarios of 3D printing constructions, extrusion molding is probably the most widely used technique due to its high printing efficiency, simple printing equipment and low cost [5,6]. With the unique printing pattern, extrusion molding significantly affects phases (fiber and particle) distribution during pumping. This issue has not been fully addressed especially when micro grains and microfibers with high slenderness and low stiffness are involved.

During extrusion printing, the materials, asking for a delicate balance among viscosity, flowability and thixotropy [7–9], are pumped through a pipe and then extruded though a nozzle to form uniform and controllable filaments, whose yield strength should rapidly grow to resist itself and upper gravity [10,11]. The need of material properties and formless construction strictly limit the migration of phases in cementitious composite after printing [12–14]. This is quite different from conventional cementitious materials casting, where sufficient vibrations or stirrings may cause obvious particle redistribution, so isotropic microstructures and engineering properties can be built [15,16]. For extrusion molding, however, cementitious materials are subjected to non-uniform shearing actions during the pumping process [17,18]. Specifically, less shearing forces are exerted to the core filament (plug flowing) with lower shearing rate and faster flowing speed, while larger shearing forces are exerted on the edge of the filament with higher shearing rate [19,20]. The viscosity of cementitious slurries decreases non-linearly with the increase of shearing rate, following a viscosity-shearing rate regime of non-Newtonian fluid [21,22]. The gradients of shear stress and viscosity built in the printing tube can cause the special and uneven distribution of particles after the slurries are extruded [23]. A transparent model concrete flowing test implied that, in the process of pumping, large particles move towards the core area and small particles are more likely to gather in the edge of the printing tube [24]. Similar findings were documented elsewhere [17,19]. However, when regarding to the distribution of cement grains, a main phase

* Corresponding author.
** Corresponding author at: State Key Laboratory of Green Building Materials, China Building Materials Academy, Beijing 100024, China.
E-mail addresses: cengq14@zju.edu.cn (Q. Zeng), wzhendi@163.com (Z. Wang).

https://doi.org/10.1016/j.addma.2022.103236
Received 7 August 2022; Received in revised form 19 September 2022; Accepted 15 October 2022
Available online 19 October 2022
2214-8604/© 2022 Elsevier B.V. All rights reserved.

Table 1
Physical properties and chemical composition of the cement.

Fineness (0.08 mm sieve /%)	Density (g/cm^3)	Specific surface (m^2/kg)	Standard consistency (%)	Soundness (mm)	Setting time (min)		Flexural strength (MPa)		Compressive strength (MPa)	
					Initial	Final	3 d	28 d	3 d	28 d
0.8	3.15	338	25.2	0.5	138	215	6.4	9.0	29.7	51.0
Chemical composition	SiO_2	Al_2O_3	Fe_2O_3	CaO	MgO	SO_3	Na_2Oeq	f-CaO	Loss	Cl-
Content/%	21.8	4.55	3.45	64.4	2.9	2.45	0.532	0.93	1.27	0.011

that acts as the binding material in extrusion molding cementitious composites (EMCC), the relevant research, to the best knowledge of the authors, has not been reported.

Another interesting but unaddressed issue for particle distribution in EMCC is the distribution and direction of particles with high slenderness. The highly slender particles in EMCC can be specified as fibers. Fibers in different types (e.g., carbon fiber, steel fiber, glass fiber, polymer fiber, mineral fibers) and sizes (from microns to millimeters in diameter) are often used to reinforce EMCC [25–31]. For example, wollatonite microfibers were employed to fabricate EMCC with good printing performances and mechanical strengths [30,31]. The reinforcement is greatly affected by both the spatial and directional distributions of the fibers used in EMCC. Previous studies indicated that steel fibers are difficult to stay in the interlayer zone between filaments [27, 32]. A number of studies have shown that aligned fibers help to improve compressive, flexural and tensile properties compared with randomly distributed fibers [33–35]. Fiber orientation could be influenced by extrusion parameters [15,36], flow patterns, wall effect of formworks and external electromagnetic field for steel fibers [26]. The properties of materials and printing parameters, such as viscosity [37] and yield strength [38] can also impact fiber orientation. It was demonstrated that the non-uniform shearing effect during the pumping extrusion process again contributes to the alignment of macro fibers along the printing direction [28,39,40]. Pham et al. [27] detected the directional and spatial distribution of steel fibers in EMCC by X-ray micro-computed tomography (XCT) and testified the strongly orientated distribution of the fibers in the EMCC matrix. Arunothayan et al. [15] evaluated the fiber alignment in an EMCC reinforced with steel fibers by the 2D image processing technique. It is noteworthy that steel fibers generally possess high modulus or stiffness, so the gradients of shearing forces during the extrusion process would have minor effect on the fibers themselves. For these fibers with low stiffness and high slenderness, the non-uniform shearing forces may torture the fibers in the printing process. So non-uniform fiber orientation and distribution may occur for EMCC with soft fibers. For example, 3D printed polymer composites with glass microfibers that have large slenderness (L/D= 461.5) showed that the fibers were disorderly distributed in the core area and the edge area of the pipeline, and showed strongly orientated distribution only in the non-uniform shearing area [41,42]. It is therefore greatly curious what are the orientation and spatial distribution of glass microfibers in EMCC after extrusion molding.

To address the above questions, in this work, EMCCs with two dosages of glass microfibers (0.3% and 0.6%) were fabricated and the spatial distribution and direction of the cement grains and glass microfibers were resolved by XCT. Elaborate analyses on the size and orientation distributions of cement grains and glass microfibers were performed. A layer-by-layer imaging analysis was specifically used to quantify the differences in particles' distributions and fibers' orientation between the filaments' matrix and interface. The mechanisms of extrusion molding effected particle redistribution in EMCC were profoundly discussed.

Table 2
Mix proportions of the 3D-printed EMCC.

Sample ID	Water /wt%	Cement /wt%	Accelerator /wt%	HPMC /wt%	PCE-SP /wt %	Glass fiber /wt%
EMCC-3	30	100	2.25	0.15	0.44	0.3
EMCC-6	30	100	2.25	0.15	0.44	0.6

2. Materials and methods

2.1. Raw materials

A Portland cement (Type PI 42.5 according to a Chinese standard) was used as the only binder for EMCC fabrication. No other inorganic fillers were added so that the anhydrous cement grains can be tracked after extrusion molding. For the mix proportions of EMCC, water-to-cement (w/c) ratio of 0.3, Hydroxypropyl methylcellulose (HPMC, from Renqiu Shuangcheng Chemical Products Factory, Shangdong, China) of 0.15 wt% (in reference to cement weight), polycarboxylate superplasticizer (PCE-SP, from Huawei Yinkai Building Materials Technology, Shangdong, China) of 0.44 wt%, and alkali accelerator (from Jiaozuo Xinzhuwang Material Technology Company, Henan, China) of 2.25 wt% were used. The compositions and physical properties of the cement are listed in Table 1.

Glass microfibers with 14 μm in diameter (D) and 6 mm in length (L) (L/D = 429) were used to reinforce the cementitious materials (see Appendix A). Two glass microfibers contents of 0.3 wt% and 0.6 wt% were used. The relevant low fiber contents were designed to avoid the possible agglomerations of glass microfibers that would obstruct the printing nozzle [16,28]. Details of the mix proportions are listed in Table 2.

2.2. Sample preparation

Fresh EMCC slurries were prepared according to the mix proportions shown in Table 2. First, the solids including cement, alkali accelerator and HPMC experienced a dry-mixing in a mixing bowl with low-speed stirrings of 60 r/min for 30 s. Later, a PCE-SP water solution was prepared by mixing the PCE-SP powder in water with sufficient hand stirrings, and was poured into the mixing bowl followed by high-speed stirrings of 120 r/min for 120 s. Subsequently, glass microfibers were mixed with the neat cement slurries with the high-speed stirrings of 120 r/min for 60 s to generate the slurries of glass microfiber reinforced cementitious slurries. In this work, the glass microfibers were artificially dispersed and gradually added into the cement slurries, and manual agitations were employed to randomize the distribution of the glass microfibers. After that, the flowability and viscosity of the prepared cementitious slurries were tested. The flowability of EMCC slurries was tested as follows: the slurries were poured into the truncated cone (with the upper diameter of 36 mm, lower diameter of 60 mm and height of 60 mm); then the cone was removed, the expansion of the slurries was measured after 30 s. The slump flows of EMCC3 and EMCC6 were 93.4 mm and 91.7 mm, respectively. Viskomat XL (Germany) was used to test viscosity of the EMCCs. The maximum speed of 120 rpm was obtained in 4 min and the speed slowed down to zero in next 4 min. Results showed

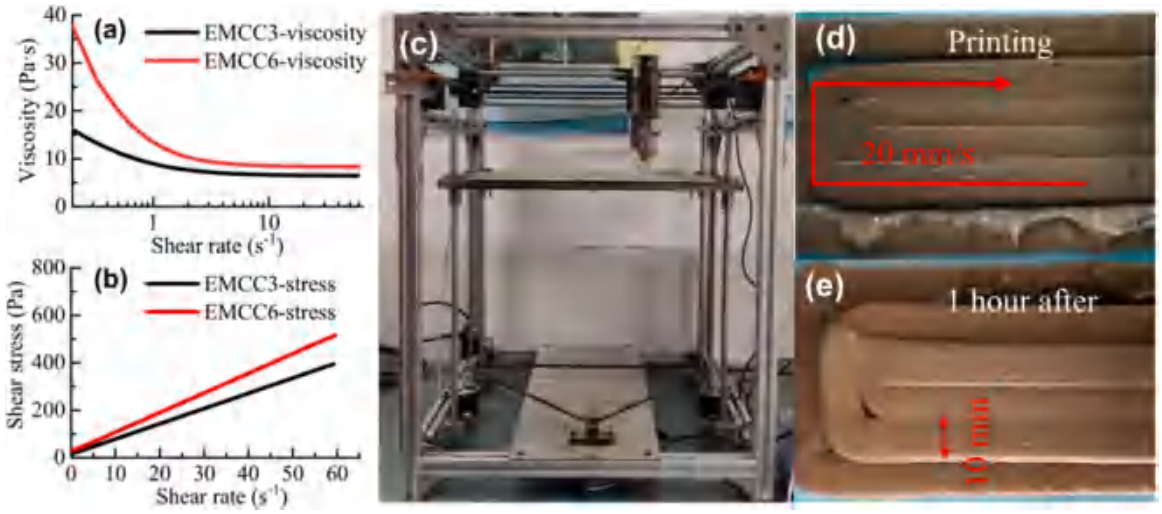

Fig. 1. Viscosity (a) and stress (b) of EMCC3 and EMCC6 slurries tested at different shear rates; (c) image of 3D cementitious composites printer; (d) in-situ extrusion molding with the printing speed of 20 mm/s, and (e) the hardened EMCC structure (after 1 h).

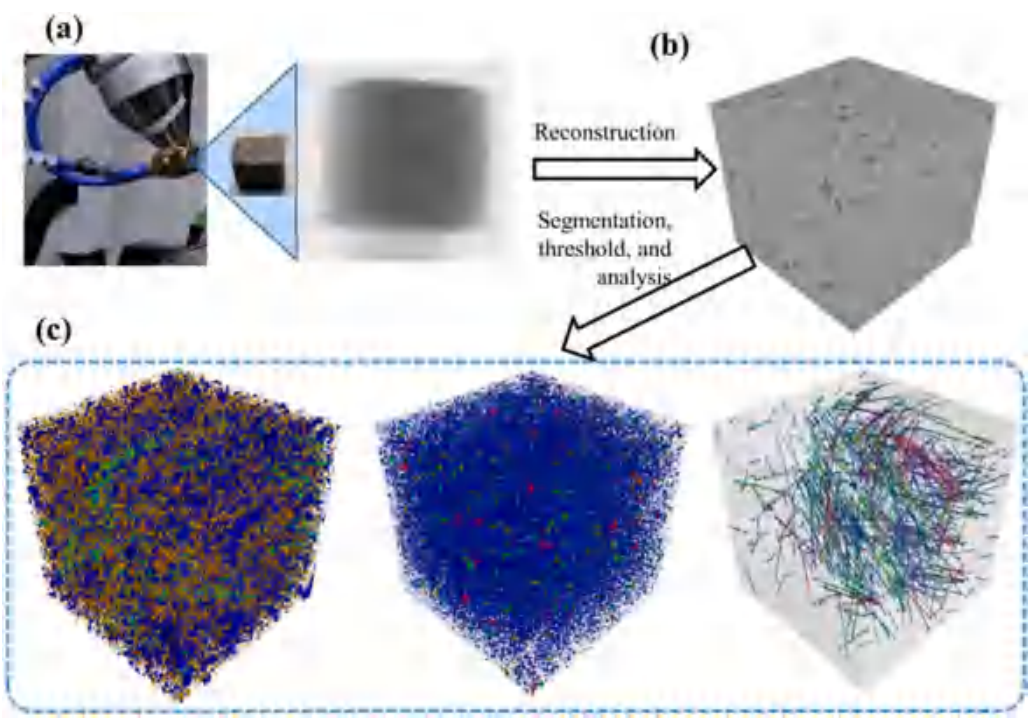

Fig. 2. Test and data processing by micro-XCT: (a) XCT scans of a 3D-printed EMCC sample; (b) image stacking and reconstruction; and (c) image of the mixed phases (left), grains (middle) and fibers (right).

that the viscosity and shear stress of EMCC6 were greater than those of EMCC3 at the same shear rate (Fig. 1a and b).

The readily prepared printable slurries mixed with glass microfibers were manually loaded into the feed bin of an automatic 3D printing machine built by China Building Materials Academy (CBMA). Fresh material was pumped through a pipe by screw extrusion (5IK60RGN-CF, 60W) and deposited in specified positions, forming a multi-layered structure. An integrated printer control system in the 3D printing machine enables the controls of coordinate (x, y, and z in 450 × 450 × 450 mm^3), moving speed of printing head (0–30 mm/s), and speed of slurries pumping (0–10 mL/s) (Fig. 1**c**). In this work, the printing parameters were set as follows: moving speed of printing head in 20 mm/s, pumping speed of the slurries in 1.57 mL/s, and filament diameter of 10 mm. The parameters were optimized according to our experiences and the results reported in the literature [12,43,44]. The freshly printed EMCC filaments and the finished EMCC units (6 filaments in width for the bottom layer, and 4 filaments for the upper 3 layers) are displayed in Fig. 1**d and e**. It is worth mentioning that the printed specimens did not undergo significant deformation within 24 h. The printed EMCC units were stored in a curing chamber (temperature of 23 ℃ and relative humidity >65%) until the testing age (after one year).

Specimens of different sizes were pre-tested. For demonstration, only representative samples were analyzed. Small cuboids (around 6 mm × 6 mm × 6 mm) including both the matrix and interface between filaments were cut from the central part of each EMCC unit. The size of the samples was selected to keep the resolution of XCT images, as a larger sample for XCT tests generally causes a coarser resolution of the obtained X-ray projections.

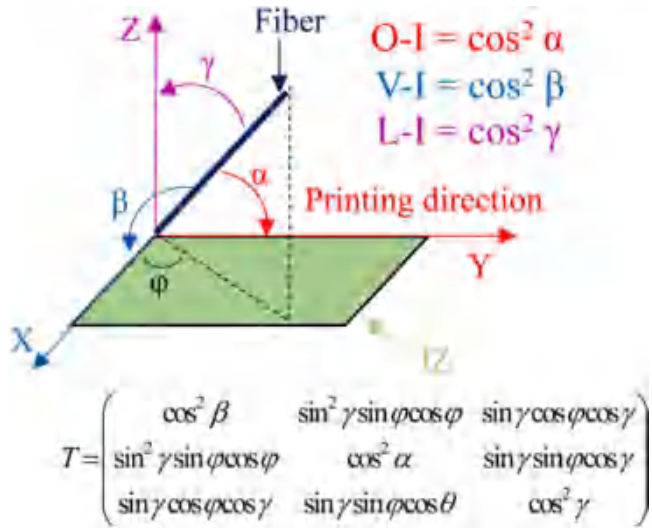

Fig. 3. Directional indexes for fiber distribution (*O-I*, *V-I* and *L-I*) and orientation tensor.

2.3. XCT test and phase analysis

XCT tests were performed in a XTH255/320 LC device (Nikon, Japan). An EMCC sample was first fixed on the sample frame between the X-ray emitter and the detector with the pixels of 2000v× 2000 h (Fig. 2**a**). The X-ray emission parameters were set as 100 kV and 60 μA. A thin Cu film (0.5 mm) was attached on the X-ray emitter to filter the X-ray noises. As X-ray beams penetrate through a material, they attenuate due to the complex interactions between the X-ray and material [45,46], such that projections with different X-ray signal intensities at different spatial positions can non-destructively provide the material information. The exposure time was set as 708 ms, and the complete scans generated 2500 X-ray projections with the resolution of 5 μm/pixel in 30 min.

The massive X-ray projections were subsequently loaded into the CT3dpro software for screening the data quality (Fig. 2**b**). Afterwards, all qualified X-ray projections were stacked for 3D structure computing [47]. Further noise filtering and X-ray attenuation corrections were performed to improve the quality of images.

Successive operations of ROI segmentation, threshold segmentation, filter treatment, fiber extraction, reconstruction and multi-pattern illustration were conducted [27]. Before rigorous 3D structure reconstruction, a region of interest (ROI) for each sample was selected to representatively demonstrate the materials' structure. Here, the ROI of

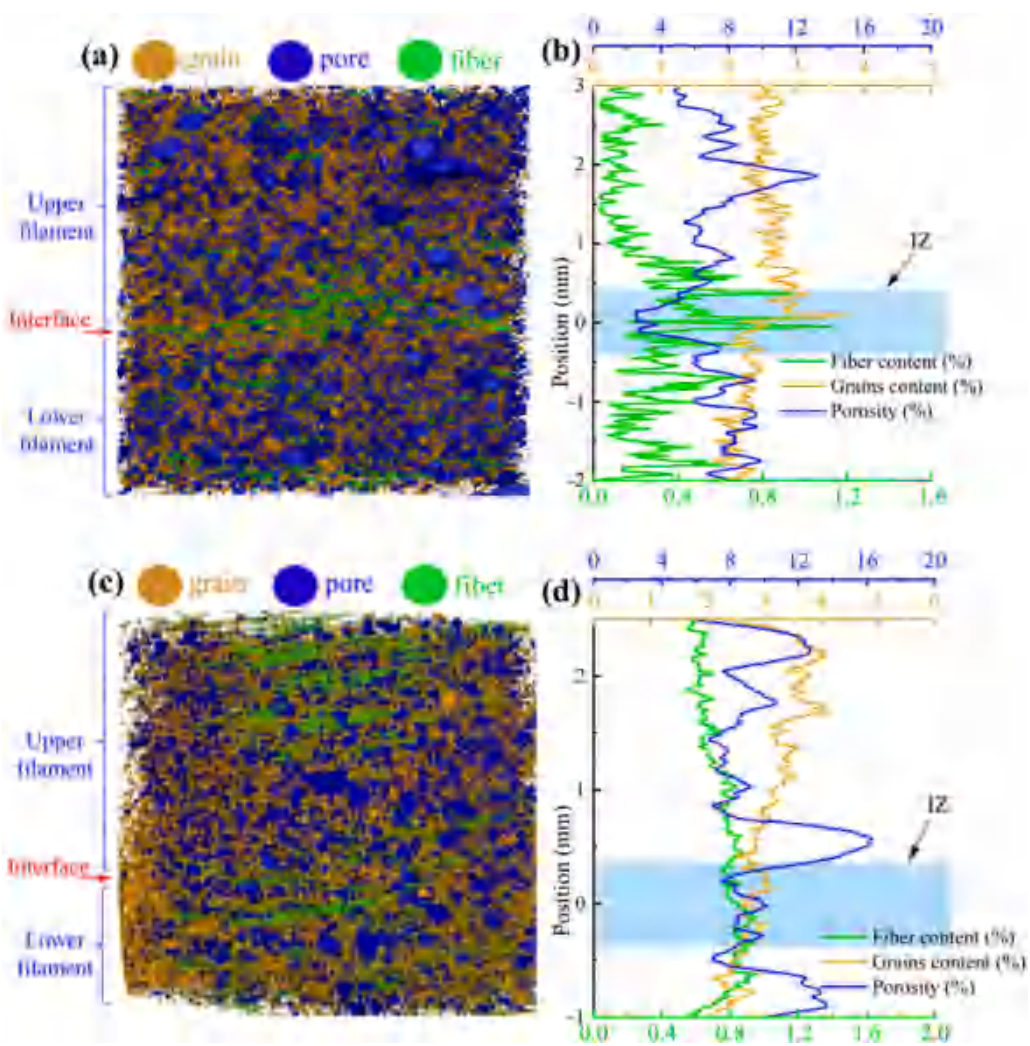

Fig. 4. 3D structure and vertical distributions of fibers, cement grains and pores in EMCC3 (a, b) and EMCC6 (c, d). The interface between the upper and lower filaments was set as 0 in the y-axis of b and d (green = glass microfibers, brown = anhydrous cement grains, blue = pores, transparent areas = the other phases including calcium silicate hydrates (CSH) and other cement hydrates).

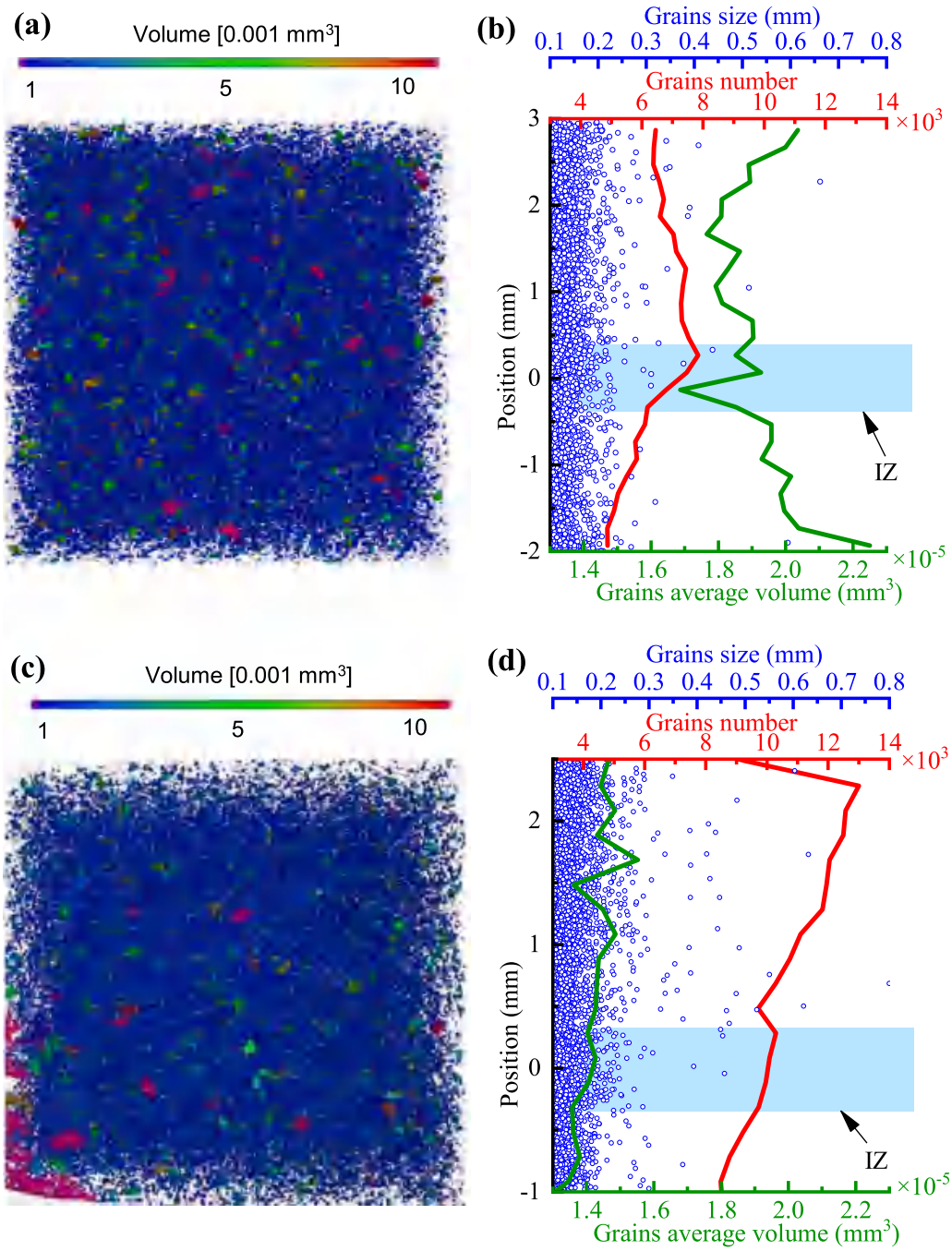

Fig. 5. 3D structure resolved by XCT and distribution (size, volume and number) of cement grains in EMCC3 (a, b) and EMCC6 (c, d).

$5 \times 5 \times 5$ mm^3 containing both the matrix and interlayer for each EMCC sample was elaborately selected (Fig. 2**c**). A geometry-and volume-based segmentation method was applied to resolve the 3D structure and distribution of glass microfibers (see Appendix B for more details of the method).

2.4. Fiber orientation assessment

For the analysis of fiber orientation distribution, traditional measurements assume that each fiber is straight, and ignore the effects of length changes and the fracture of the fibers during extrusion molding [15,16,28]. Those assumptions may be acceptable for rigid and stiff macro fibers (e.g., steel fibers) in EMCC. In this case, the high slenderness of the glass microfibers may be tortured under the shearing actions during extrusion molding. Here, each fiber was divided into the size of the voxel level, and the direction of those divided voxels in the fiber was adopted to measure the fiber orientation. In the material level, the directions of all fiber voxels in ROI were counted to statistically analyze the fiber orientation distribution [27]. When assessing the 3D orientation distributions, the print direction was set as the reference direction. The fiber module and material/pore inclusion module in the VGstudio3.0MAX software were used for fiber, pore and cement grain particle analyses.

To quantify the fiber orientation distribution, directional indexes were used to assess the orientation of fibers. Assume that the O axis is the printing direction (Y axis), the L axis is perpendicular to the interlayer plane (Z axis), and the V axis is perpendicular to the printing direction in the interlayer plane (X axis) (Fig. 3), then three indexes, i.e., the fiber

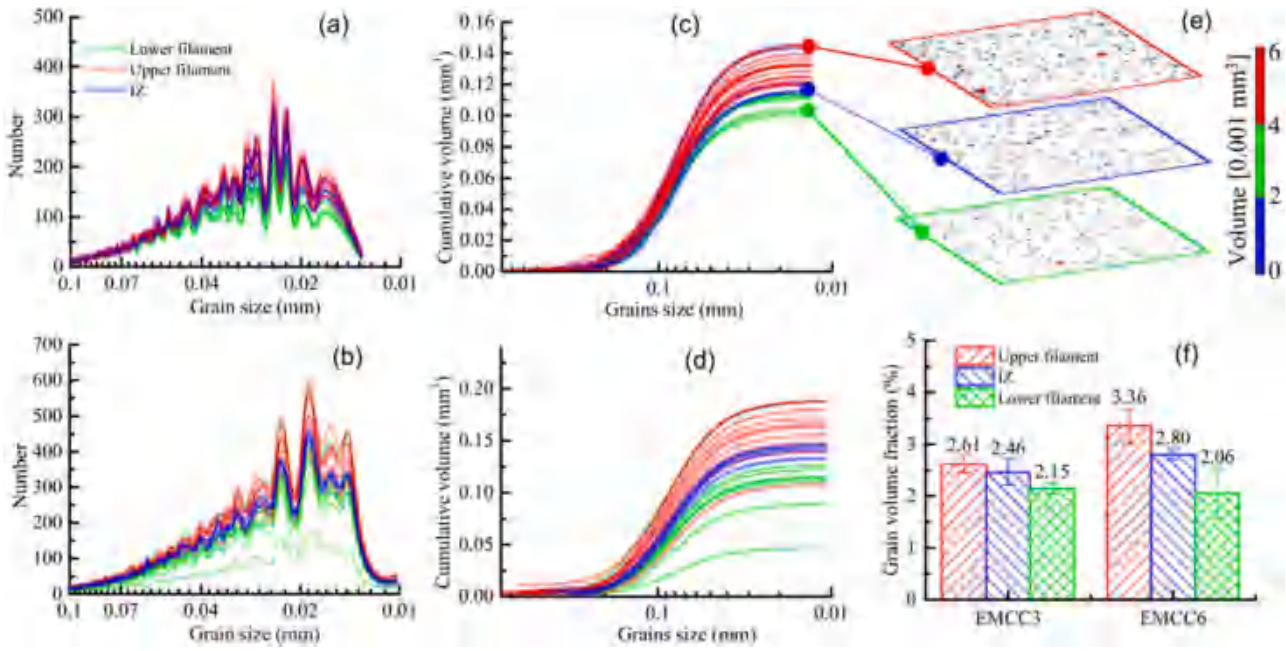

Fig. 6. PND and PSD curves for EMCC3 (a and c) and EMCC6 (b and d); (e) typical XCT images (thickness of 0.2 mm) in the upper filament, lower filament and IZ (the particle size smaller than 0.1 mm were excluded for better illustration); (f) grain volume fractions in the upper filament, IZ and lower filament in EMCC3 and EMCC6.

orientation index ($O\text{-}I = \cos^2\alpha$), stratification index or layer index ($L\text{-}I = \cos^2\gamma$) and vertical index ($V\text{-}I = \cos^2\beta$), can be obtained. The stratification index measures the deviation of a fiber from the direction L. In the case of L-I = 0, the fibers are distributed parallel to the interlayer plane. The vertical index refers to the distribution of a fiber in the horizontal plane perpendicular to the printing direction. Note that the sum of the three coefficients equals to1 ($O\text{-}I + L\text{-}I + V\text{-}L = 1$).

3. Results and discussion

3.1. General outcomes

Fig. 4 selectively and representatively displays 3D images of the EMCC ROIs containing different phases and their distributions perpendicular to the interlayer plane. An interlayer zone (IZ) between two EMCC filaments can be generally identified according to the porosity changes and the thickness of IZ is affected by printing parameters and materials with typical values of 0.2–3 mm [48,49]. In this work, a clear gap between the upper and lower filaments can be observed (Figure B.1). The changes of porosity in IZ are probably owning to the lubrication layer formed in the outer area of filaments during extrusion printing [48]. Considering the porosity variation and the lubrication, the IZ thickness was set as 0.8 mm (Fig. 4 **a and c**).

For the fiber content distribution in EMCC3, a peak of fiber content up to 1.1% was observed, heavily higher than the designed fiber content of 0.3% (Fig. 4**b**). A slight fiber rise (fiber content = 0.96%) was observed near the IZ in EMCC6 (Fig. 4**d**). The uneven distribution of fiber contents indicates the great impacts of extrusion on microstructure of EMCC. The rises of fiber content near the IZ indicated that the fibers gradually migrated to the interface of the filaments (or the inner surface of the pumping pipe) during extrusion printing owing to the uneven shearing forces. Similar observations of fiber accumulation near the filaments' surface were reported for 3D printed polymer composites [41, 42].

For the anhydrous cement grains, the content in the upper filament (3.70% for EMCC3 and 4.12% for EMCC6) was systematically higher than that in the lower filament (2.59% for EMCC3 and 3.04% for EMCC6) (Fig. 4**b and d**). This is caused by the sinking of cement grains in each filament due to the effect of gravity. A peak of the anhydrous cement grain distribution was observed near the IZ in EMCC3 (Fig. 4**b**), evidencing the gather of the anhydrous cement grains. In general, the results of Fig. 4 suggested that both the fibers and anhydrous cement particles may migrate towards the IZ between the upper and lower filaments.

3.2. Analysis of anhydrous cement grains

To understand the transport of cement grains during extrusion molding, specific analysis on thin slice with the thickness of 0.2 mm was performed on the ROIs, and the distributions of grain number, individual size and average size in each slice were output (Fig. 5). For EMCC3, along with the vertical direction from up to down, the average particle size of the cement grains decreased first and then increased, while their number increased first and then decreased. This implied that smaller cement grains were more likely to migrate into the IZ under uneven shearing forces, while larger cement grains stayed in the matrix (Fig. 5**a and b**).

For EMCC6, the trend of grain number and average size showed strong difference (Fig. 5**c and d**). Specifically, they both decreased from up to bottom and no shifts appeared at the IZ. Interestingly, the grain number density was below 8000 (in 5 mm^3) with the average grain volume higher than 1.6×10^{-5} mm^3 in all positions of EMCC3 (Fig. 5**b**). However, the grain number density was over 8000 with the average grain volume lower than 1.6×10^{-5} mm^3 at all positions of EMCC6 (Fig. 5**d**). The thinner grain size and more grain number near the IZ of EMCC3 may be associated to the particle migration under the shearing forces during pumping [17]. During concrete pumping, a water bleeding layer (or lubricate layer) containing more thin particles and water can form on the pumping tube inner surface [43,44,50], which may enhance hydration of the cement grains [51–54]. The accelerated cement hydration, in turn, decreases the size of the anhydrous cement grains.

To further demonstrate the material differences between the IZ and matrix in EMCCs, particle number distribution (PND) and particle size distribution (PSD) were analyzed (Fig. 6). The PND and PSD curves were plotted based on the data in 3–10 slices for EMCC3 (Fig. 6**a and c**) and EMCC6 (Fig. 6**b and d**), and typical layers of 0.2 mm in thickness were

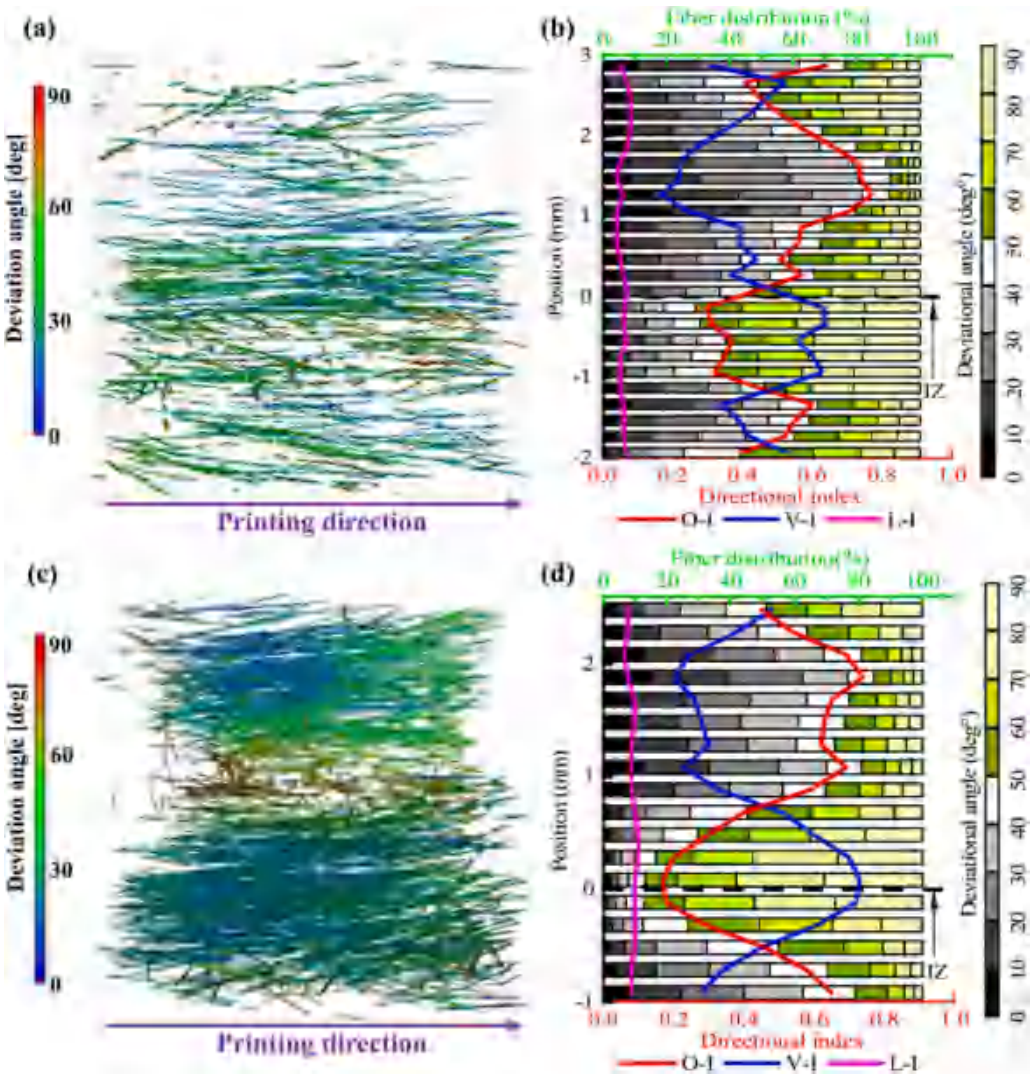

Fig. 7. 3D image resolved by XCT and directional distribution (directional index and deviational angle of printing direction) of fibers in EMCC3 (a, b) and EMCC6 (c, d).

extracted from the upper filament, lower filament and IZ for demonstration (Fig. 6**e**).

Similar PND and PSD trends in the matrix and IZ of the EMCCs were observed. Most of the number was determined by the grains with the size between 0.015 and 0.06 mm (Fig. 6**a and b**), and most of the volume was occupied by the grains with the size between 0.04 and 0.2 mm (Fig. 6**c and d**). The PND and PSD results indicated that the thin particles dominate the number distribution, while the large particles determine the volume distribution for a powder system like cement grains [55,56]. Compared with EMCC6 that showed the concentrated PND in the size range of 0.01–0.02 mm with the PND intensity of 200–700 (Fig. 6**b**), EMCC3 showed the concentrated PND in a bigger size range (0.02–0.03 mm) with a lower PND intensity (100−500) (Fig. 6**a**). When glancing at the PSD curves and typical layers (Fig. 6**e**), the cement grain volume in the upper filament was higher than that in the lower filament due to the sink of the cement grains under the gravity forces, while the cement grain volume in IZ was between them for both EMCC3 (Fig. 6**c**) and EMCC6 (Fig. 6**d**).

Statistic cement grain volume fractions in the IZ, upper filament, and lower filament are illustrated in Fig. 6**f**. Clearly, the cement grain volume fractions of the IZ and upper filament of EMCC6 were 2.802% and 3.358%, higher than those of EMCC3 (2.462% and 2.613%) by 13.81% and 28.51%, respectively. Similar cement grain volume fractions between EMCC3 (2.146%) and EMCC6 (2.060%) were observed in the lower filament (Fig. 6**f**). The grain volume fraction of the lower filament in EMCC3 was less than that of the upper filament by 17.9%, while by 38.7% in EMCC6. The results indicated that increasing fiber content would enhance the difference of cement grain volume fraction among the IZ, upper filament, and lower filament (Fig. 6**f**). This was probably owing to the fact that the higher flowability is required for the cementitious slurries with more microfibers, so cement grains are more likely to sink under the gravity actions [57,58]. Therefore, in each filament, the bottom part of the upper filament always contains more cement grains than the top part of the lower filament in our case (Fig. 6).

3.3. Analysis of glass microfibers

Fig. 7 demonstrates 3D images of the glass microfibers and their directional distributions. It can be seen that fibers generally present an obvious stratification distribution along with the printing direction (Fig. 7**a and c**). Specific analysis on thin layers with the thickness of 0.2 mm was performed. For both EMCC3 and EMCC6, the stratification coefficient (or layer index) (LI) is basically close to 0 (Fig. 7**b and d**), confirming that fibers follow the stratification distribution ($\cos^2\alpha \approx 0.1$; see Fig. 3). In other words, the glass microfibers, at any position of the specimens, are distributed parallel to the IZ, which may be caused by the

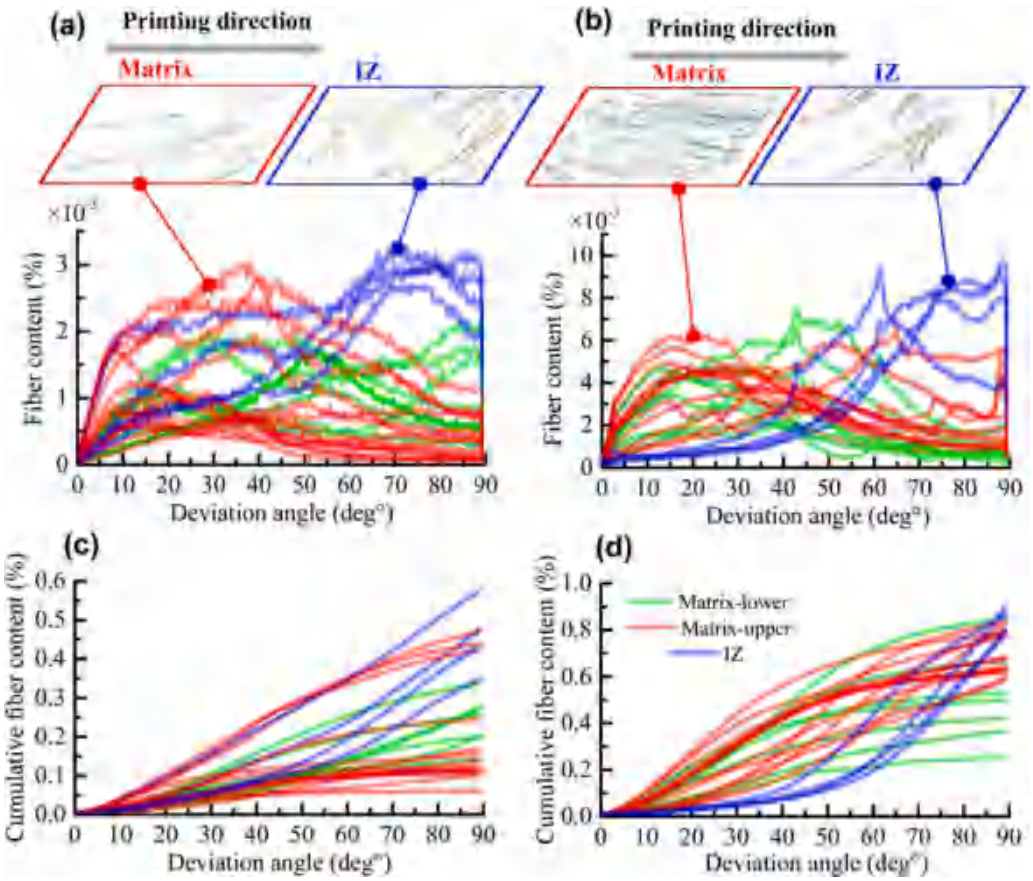

Fig. 8. Selective demonstrations and fiber directional distributions in the upper filament, lower filament and IZ in EMCC3 (a, c) and EMCC6 (b, d).

uneven shearing forces parallel to the IZ plane [42]. The stratified microfibers, in turn, would impact the distribution of shearing forces, consequently, the microfibers, like micro cement grains, may migrate to the IZ.

As *L-I* was closed to 0.1, *O-I* and *V-I* basically played the complementary roles on the determination of fiber directional distribution (*L-I*+*O-I*+*V-I*=1, Fig. 3). Here, only the results of *O-I* and the corresponding angle (α) were taken as the examples to demonstrate the results. The angle of the fibers deviating from the printing direction (α) was also plotted in Fig. 7**b and d**. From the histogram of deviational angle with position, it can be easily found that the fibers in the matrix of filaments mainly distributed within 50°, evidencing the strongly orientated distribution of the glass microfibers in EMCC3 and EMCC6 (Fig. 7**b and d**). However, the fibers in or close to the IZ between two filaments mainly possessed the deviational angles over 50°, suggesting that those fibers were not following the printing direction. The fiber orientation in IZ changed more severely for the EMCC with higher fiber content. The distribution of *O-I* showed the similar trend with that of α. High *O-I* values up to 0.77 for EMCC3 and 0.74 for EMCC6 were found in the filaments' matrices, indicating that most fibers were aligned following the printing direction. The printing-direction orientated fibers have been widely documented in 3D printed concrete with steel fibers [27,28, 59]. In the IZ between two extrusion molded filaments, sharp decreases in *O-I* values down to 0.3 for EMCC3 and to 0.17 for EMCC6 were observed (Fig. 7**b and d**), which again means that the fibers were more likely to be perpendicular to the printing direction. The reasons are due to the change of shearing force for different viscosity, see Section 3.4 for further discussion.

Fiber direction and content distributions were analyzed statistically (Fig. 8). Little differences in direction and content distributions between the upper and lower filaments were probed, while differences rose greatly between the filaments' matrix and IZ. A high proportion of the fibers in IZ emerged at high deviational angles between 50° and 90°, but the fibers in the matrices of filaments appeared at low deviational angles between 10° and 40° (Fig. 8**a and b**). So, fiber content in the matrices of filaments rose rapidly at the low deviational angles, while that in the IZ cumulated greatly at the high deviational angles (Fig. 8**c and d**). The distribution of fibers in this work was consistent with the literature [41, 60].

Selective slices of XCT images in the IZ and matrix of filaments are also demonstrated in Fig. 8. Evidently, fibers in the filament matrix of EMCC3, that mainly followed the printing direction, were less than those in the IZ that were roughly perpendicular to the printing direction (Fig. 8**a**). For EMCC6, similar trends of different directional distributions between the fibers in the matrix and those in the IZ were observed (Fig. 8**b**). Interesting, some fibers in the IZ of EMCC3 and EMCC6 were *bent and tortured* (Fig. 8**a and b**), suggesting the occurrence of non-uniform shearing forces on the fibers during extrusion molding. Fibers also agglomerated together in the IZ to form fiber bundles (Fig. 8**b**).

Some characteristic parameters that feature the orientation and content distributions are demonstrated in Fig. 9. Results of the deviation angle at the highest fiber content suggested that fibers in the IZ possessed systematically higher deviation angles (78.4° and 78.1°) than those in the matrices of filaments (41.9°and 37.2°) of EMCC3 and EMCC6 (Fig. 9**a**). Analysis of the value of C_{50} (a value of the deviational angle when the cumulative fraction of glass microfibers is 50% [41,60]) also displayed that the matrices of filaments had much higher fiber content along the printing direction (40.0° and 38.3°) than the IZ (60.1° and 68.9°) (Fig. 9**b**). The *O-I* values of the fibers decreased from 0.55 and 0.58 in the matrices of filaments for EMCC3 and EMCC6, to 0.35 and 0.21 in the IZ with the decrease extents of 36.4% and 63.8%, respectively (Fig. 9**c**). Those results, again, evidenced that the direction of the

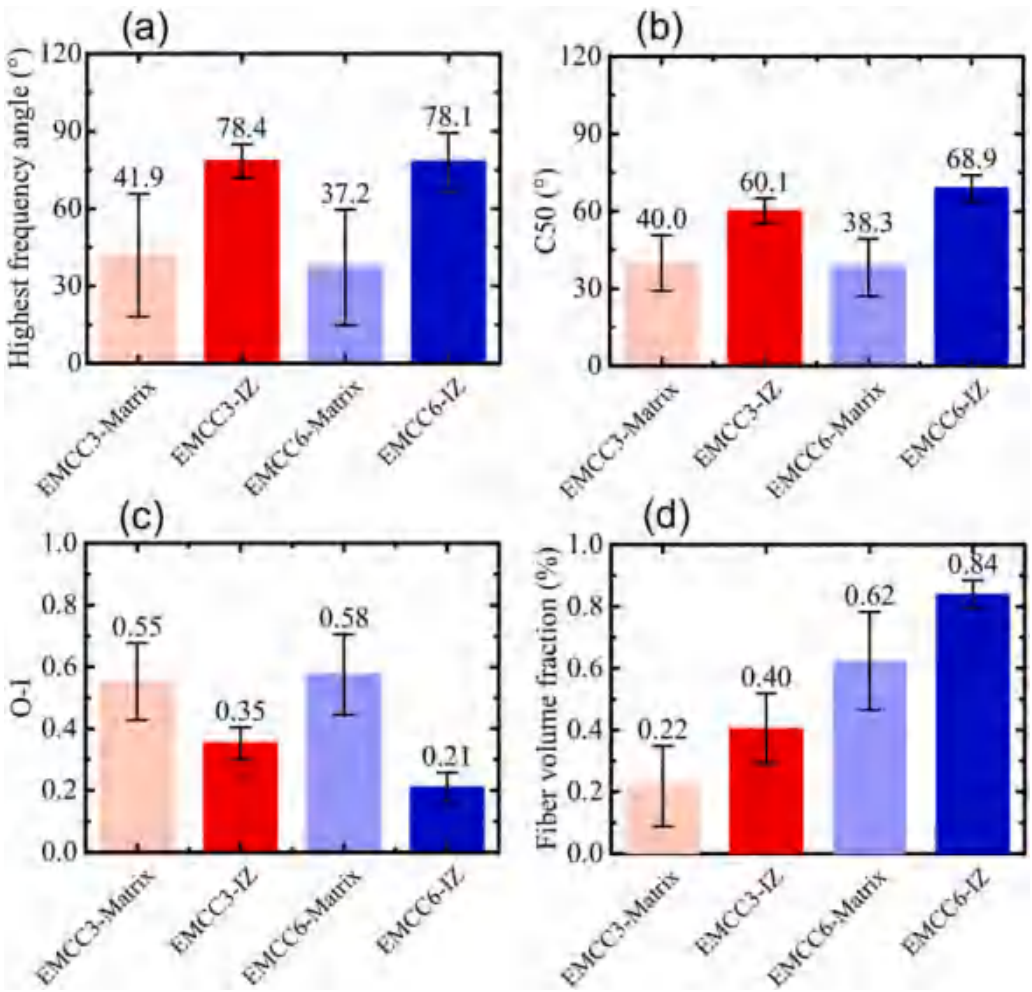

Fig. 9. Results of (a) highest frequency angle, (b) the value of the deviational angle when the cumulative fraction of glass microfibers is 50% (C_{50}), (c) orientation index (O-I) and (d) fiber volume fraction in the matrices and IZ for EMCC3 and EMCC6.

microfibers near the printing tube inner surface was changed during extrusion molding, and this orientation change was severer with the increase of fiber content.

Moreover, different total fiber contents between the matrices of filaments and IZ were obtained. In EMCC3, the total fiber content in IZ was 0.4%, higher than the designed total fiber content (0.3%) by 33.3% and that in the matrices of filaments (0.22%) by 81.8% (Fig. 9**d**). Those data indicated that microfibers may migrate from the matrix to the IZ during extrusion molding. The differences in orientation and content between fibers in the IZ and those in the matrix of extrusion molded filaments were reported for fiber reinforced polymers after 3D printing [41,42], the observations, however, to the best knowledge of the authors, have never been documented for 3D printing cementitious materials elsewhere.

3.4. Discussion on the mechanisms

In this work, the distribution information (including content and direction) of micro cement grains and glass microfibers in EMCCs were resolved with μ-XCT. Non-uniform distribution of the cement grains in filaments was reported. Coarse cement grains were detected to be in the center of the filaments while small grains were more likely to gather in the IZ between the filaments (Figs. 4 and 5). The distribution of those anhydrous cement grains, like the macro particles in concrete during pumping or 3D printing [19,23], would also be affected by the uneven shearing forces during the process of extrusion molding. When particles flow in a thin pipe during pumping, shearing force gradients build up between the central and surface slurries in the pumping pipe. Under the actions of shearing force gradients, grains begin to roll and move along the printing direction. Coarse grains would suffer large shearing force gradients, so they tend to migrate from the surface to the center of the printing pipe (Fig. 10**a**). Additionally, the high shearing forces built near the inner surface of pumping pipe would shrink grains and enhance water bleeding, and this thin bleeding surface layer may also act as the lubricant that improve the slurries' flowability [43,48,50]. Those mechanisms that account for the particle flows during concrete pumping [23] may also work for the transport of grains in EMCC during 3D printing observed in our experiments and those reported in Ref. [19]. The locally raised water content and lowered cement grain size in the IZ between filaments can enhance the hydration of the cement grains [51–54], which may, in turn, further decrease the size of the cement grains in the IZ. Therefore, different distributions of the anhydrous cement grains between the IZ and matrices of EMCC filaments were observed (Figs. 4–6).

In our experimental results, differences in grain content were observed between the upper and lower filaments. Specifically, the top part of the lower filament showed less cement grain content than the bottom part of the upper filament (Fig. 6**f**). This would be the direct consequence of particle sinking in the cementitious slurries due to the gravity actions, similar observations were reported elsewhere [57,58].

The μ-XCT analysis also demonstrated the gathering of glass microfibers in the IZ between two neighbored EMCC filaments (Fig. 9). Such

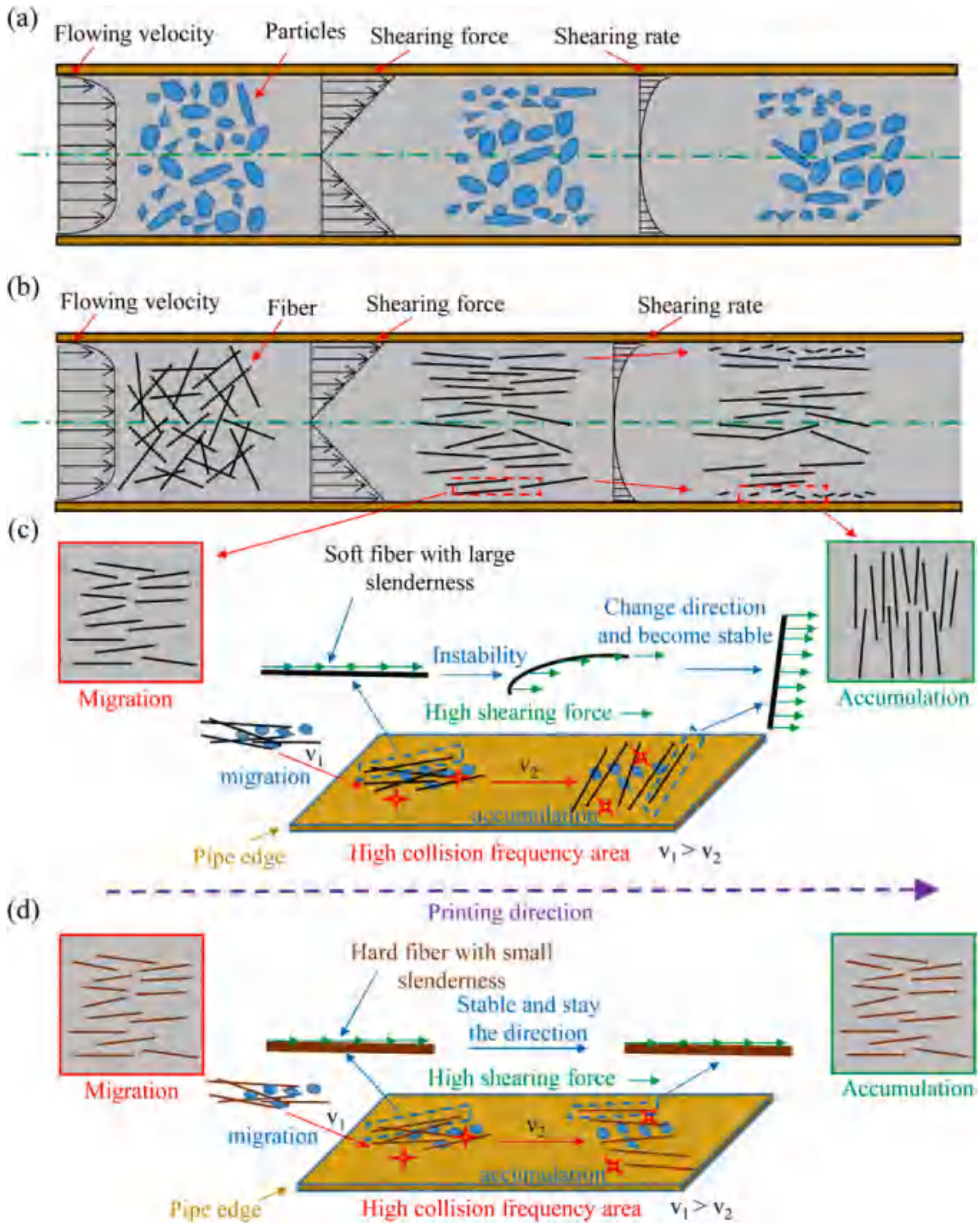

Fig. 10. Schematic diagram of the effect of non-uniform shearing on the distributions of particles (a) and fibers (b); schematic diagram of the effect of high shearing force, collision and fiber stiffness on fiber directional change in interlayer zone for soft fibers (c) and normally rigid fibers (d).

fiber gathering in the surface area was observed for the 3D printed polymer composites with fibers [41,42]. Auernhammer et al. [24] also reported the gathering of tiny glass balls in transparent model concrete. In this case, glass microfibers agglomerated together to form fiber bundles for EMCC6 (Fig. 8**b**). The growth of fiber bundles may course the obstruction of the printing pipe. This is why fiber content lower than 1% was recommended in Refs [16,28] to avoid the blockage of nozzle for EMCC printing.

Orientation analysis of the glass microfibers in EMCCs indicated that most of the glass microfibers followed the printing direction (L-$I \approx 0.1$ as demonstrated in Fig. 7**b and d**), consistent with the results documented in the literature [27,42]. During extrusion molding, the glass microfibers that were randomly mixed in the slurries suffered uneven shearing actions at different flowing rate. For example, if the two ends of a fiber were at different distances from the surface of the printing pipe, then different shearing stresses and moving speeds rose at the fiber's two

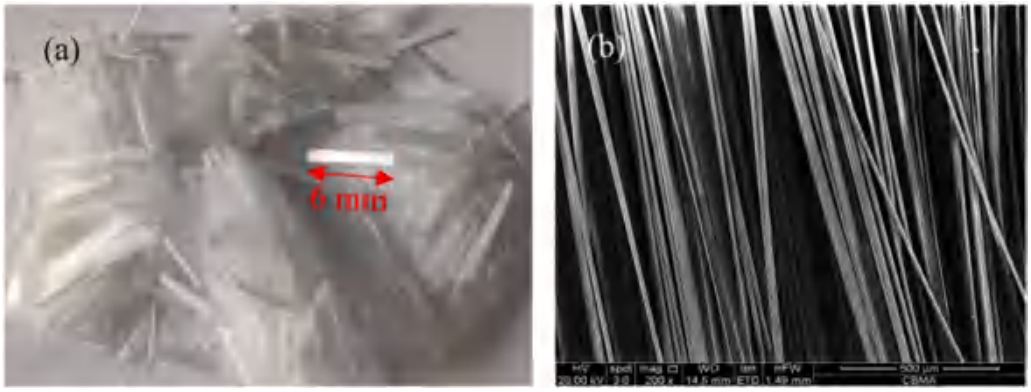

Fig. A.1. (a) Typical photo of the glass microfibers and (b) SEM image.

ends. So the fiber would rotate to diminish the shearing stress gradients, in this way, most glass microfibers were following the printing direction (Fig. 10**b**). The mechanisms also account for the orientation of steel fibers after 3D printing documented elsewhere [26,61].

In this work, however, glass microfibers showed different orientations in the IZ from those in the matrix of filaments ($O\text{-}I$ = 0.35 for EMCC3 and 0.21 for EMCC6; Fig. 9**c**). Specifically, the fibers in the IZ were perpendicular to the printing direction (Fig. 8**a and b**). This phenomenon, to the best of the authors, has not been reported elsewhere for 3D printed cementitious materials, but was occasional documented for 3D printed polymer-based composites [41,42]. This would be the consequences of the combined actions of high shearing forces on the slurries confined in the pumping pipe [19,20], large slenderness of glass microfibers with low stiffness [28], as well as high particle collision on the surface of the pumping pipe [17,62]. As illustrated in Fig. 10**c**, to balance the shearing forces, the fibers either follow or are perpendicular to the printing direction [47,63]. For the glass microfibers with high slenderness and low stiffness, the shearing forces would also bend the fibers (Fig. 8**a and b**). The high frequency of particle collisions [17,62] may cause the agglomeration of microfibers to form fiber bundles (Fig. 8**b**). In this work, it indicates that the IZ with fibers perpendicular to the printing direction possessed lower porosity, while the matrix with fibers parallel to the printing direction had higher porosity (Fig. 4). Those would have complex impacts on the mechanical properties of EMCC [48].

It is noteworthy that the premise of forming perpendicularly orientated fibers in IZ is that the fibers should possess thin diameter, large slenderness and low stiffness. Therefore, steel fibers with relatively low slenderness, high stiffness and large diameter [28] are not likely to be bent and agglomerate in the IZ (Fig. 10**d**). It is therefore reasonable that almost all tests on 3D printed steel fiber concrete reported that the fibers follow the printing direction [27,28].

While the distribution characteristics resolved by μ-XCT evidenced the changes in direction and content of cement grains and microfibers between the IZ and matrix of EMCC filaments, some issues still haven't been fully addressed in this present work. First, the resolution of the XCT used is limited (around 5 μm/pixel), therefore a certain portion of the anhydrous cement grains cannot be resolved. This would cause incomplete analysis of the anhydrous cement grains in EMCC. For example, the XCT data in this work did not directly support the hypothesis that the surface bleeding can enhance cement hydration in the IZ between filaments. Second, in this work, the influential factors (such as, printing speed and fiber size) on the distribution of cement grains and microfibers were not tested. While the printing speed was set as 20 mm/s according to the data reported in the literature [12,43,44], the changes in printing speed may change the shearing stresses on the fibers and consequently alter their direction and distribution. More rigorous investigations are wanted to fully address the problems in flows of particles (including both cement grains and fibers) and the impacts of printing patterns towards better controls in materials' structure and properties in 3D printed construction.

Overall, in this work, the changes in direction and content distributions of cement grains and glass microfibers between the IZ and matrix of filaments in EMCCs were reported for the first time. The findings would deepen the understandings in particle flows of EMCCs during 3D printing as well as the designs and controls of 3D printing construction materials.

4. Conclusion

This paper attempted to characterize the distribution of anhydrous cement grains and glass microfiber in EMCC by XCT. Conclusions were drawn as follows:

1. The anhydrous cement grains in EMCC showed a non-uniform distribution between matrix and IZ for uneven shearing force. The smaller particles tended to appear in the IZ while the larger particles were likely to gather in the matrix.
2. Gradient of micro cement grain content rose from the upper filament to the lower filaments. The grain volume fraction of the lower filament in EMCC3 was less than that of the upper filament by 17.9%, while by 38.7% in EMCC6.
3. Glass microfibers gathered in the IZ, with the maximum fiber content up to 1.10% for EMCC3 and 0.96% for EMCC6.
4. Glass microfibers in the matrix of filaments were mostly parallel to the printing direction and these in the IZ were perpendicular to the printing direction in the stratified plane. The orientation index in the matrix of filaments was 0.55 for EMCC3 and 0.58 for EMCC6, while that in the IZ was 0.35 for EMCC3 and 0.21 for EMCC6.
5. The featured distribution of glass microfibers in EMCCs was rooted to the uneven shearing forces during printing. A conceptual model was proposed to capture the mechanisms of change in fibers orientation in the IZ with high shearing stress, low flowing rate and high collision frequency. This model would specifically capture the orientation and distribution of fibers with large slenderness and low stiffness.

Moreover, the results also revealed the mechanism of migration of micro particles/fibers in cementitious slurries under uneven shearing forces during extrusion. The findings will deepen the understandings of particle flow in non-Newtonian liquid and shed much light on tuning and fabricating cementitious composites for digital construction.

CRediT authorship contribution statement

Rijiao Yang: Conceptualization, Methodology, Software, Data curation, Investigation, Writing – original draft. **Yi Zhu:** Methodology, Software. **Yan Lan:** Methodology, Software. **Qiang Zeng:**

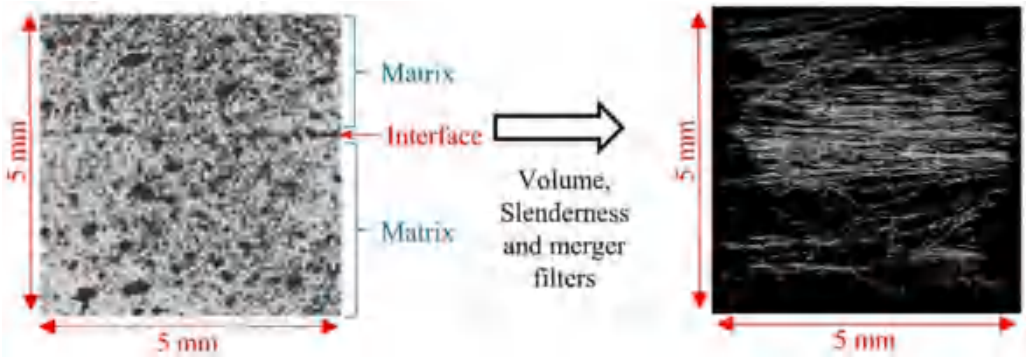

Fig. B.1. Coarse image of a ROI (left) and the resolved fibers after the treatments (right).

Conceptualization, Supervision, Funding acquisition, Methodology, Writing – review & editing. **Yu Peng:** Methodology, Software. **Zhendi Wang:** Conceptualization, Supervision, Funding acquisition, Writing – review & editing.

Declaration of Competing Interest

The authors declare that they have no known competing financial interests or personal relationships that could have appeared to influence the work reported in this paper.

Data availability

Data will be made available on request.

Acknowledgments

This work was supported by the Program Fund of Non-Metallic Excellence and Innovation Center for Building Materials (2022SFP1-1), NSFC (No. 52038004 and 51878602), and the Fundamental Research Funds for the Central Universities, CHD (No. 300102311501).

Appendix A

Glass fibers

Glass fibers with the length of 6 mm and diameter of 20 μm (Fig. A.1) were used to reinforce the cementitious slurries.

Appendix B

Fiber diagnosis and analysis

Due to the little difference of density between glass microfibers (density = 2.70 g/mL) and cement matrix (density =2.58 g/mL), they would show similar gray values in XCT images [64]. Therefore, it is not feasible to directly extract the glass microfibers from the cement matrix by the ordinary gray value thresholding method [27,65]. In this work, enhanced treatments to the XCT images were developed for the extraction of microfibers. First, a filter of volume was used for preliminary segmentation to remove the micro cement grains because their volumes are systematically lower than those of the glass microfibers (V= 0.002 mm^3). However, this filter may fail to filter out all cement grains, because some cement grains can agglomerate together to form a large "cement gain". Therefore, a filter of geometry was employed to remove the agglomerated cement grains, since the slenderness of the glass microfibers is greatly larger than those of the cement grains with and without agglomerations. Later, a smooth treatment was performed to eliminate the cement grain particles attached to or close to the glass microfibers. Those treatments allow us to clearly distinguish between the glass microfibers and the cement matrix (Fig. B.1), while they possess the similar density. Here, 25 slices in EMCC6 were tested to validate the proposed treatments. The results showed the fiber contents between 0.4% and 0.9%, with the average value of 0.66%, close to the design fiber content (0.6%). This suggested that our treatments are reliable to extract the fibers for the cement matrix with similar density. After the preliminary enhanced imaging treatments, all three main phases, i.e., glass microfibers, cement grains and pores, were readily constructed for further analyses.

References

[1] P. Shakor, S. Nejadi, S. Sutjipto, G. Paul, N. Gowripalan, Effects of deposition velocity in the presence/absence of E6-glass fibre on extrusion-based 3D printed mortar, Addit. Manuf. 32 (2020), 101069, https://doi.org/10.1016/j.addma.2020.101069.
[2] J. Xiao, H. Liu, T. Ding, Finite element analysis on the anisotropic behavior of 3D printed concrete under compression and flexure, Addit. Manuf. 39 (2021), 101712, https://doi.org/10.1016/j.addma.2020.101712.
[3] T. Ooms, G. Vantyghem, R. Van Coile, W. De Corte, A parametric modelling strategy for the numerical simulation of 3D concrete printing with complex geometries, Addit. Manuf. 38 (2021), 101743, https://doi.org/10.1016/j.addma.2020.101743.
[4] A. du Plessis, A.J. Babafemi, S.C. Paul, B. Panda, J.P. Tran, C. Broeckhoven, Biomimicry for 3D concrete printing: a review and perspective, Addit. Manuf. 38 (2021), 101823, https://doi.org/10.1016/j.addma.2020.101823.
[5] C. Vlachakis, M. Perry, L. Biondi, J. McAlorum, 3D printed temperature-sensing repairs for concrete structures, Addit. Manuf. 34 (2020), 101238, https://doi.org/10.1016/j.addma.2020.101238.
[6] L. Wang, Y. Liu, Y. Yang, Y. Li, M. Bai, Bonding performance of 3D printing concrete with self-locking interfaces exposed to compression–shear and compression–splitting stresses, Addit. Manuf. 42 (2021), 101992, https://doi.org/10.1016/j.addma.2021.101992.
[7] X. Sun, J. Zhou, Q. Wang, J. Shi, H. Wang, PVA fibre reinforced high-strength cementitious composite for 3D printing: Mechanical properties and durability, Addit. Manuf. 49 (2022), 102500, https://doi.org/10.1016/j.addma.2021.102500.
[8] Y. Zhang, Y. Zhang, W. She, L. Yang, G. Liu, Y. Yang, Rheological and harden properties of the high-thixotropy 3D printing concrete, Constr. Build. Mater. 201 (2019) 278–285, https://doi.org/10.1016/j.conbuildmat.2018.12.061.
[9] A.V. Rahul, M. Santhanam, H. Meena, Z. Ghani, 3D printable concrete: mixture design and test methods, Cem. Concr. Compos. 97 (2019) 13–23, https://doi.org/10.1016/j.cemconcomp.2018.12.014.
[10] S.A.O. Nair, G. Sant, N. Neithalath, Mathematical morphology-based point cloud analysis techniques for geometry assessment of 3D printed concrete elements, Addit. Manuf. 49 (2022), 102499, https://doi.org/10.1016/j.addma.2021.102499.
[11] X. Liu, B. Sun, The influence of interface on the structural stability in 3D concrete printing processes, Addit. Manuf. 48 (2021), 102456, https://doi.org/10.1016/j.addma.2021.102456.
[12] V.N. Nerella, S. Hempel, V. Mechtcherine, Effects of layer-interface properties on mechanical performance of concrete elements produced by extrusion-based 3D-printing, Constr. Build. Mater. 205 (2019) 586–601, https://doi.org/10.1016/j.conbuildmat.2019.01.235.
[13] T.T. Le, S.A. Austin, S. Lim, R.A. Buswell, R. Law, A.G.F. Gibb, T. Thorpe, Hardened properties of high-performance printing concrete, Cem. Concr. Res. 42 (2012) 558–566, https://doi.org/10.1016/j.cemconres.2011.12.003.
[14] B. Panda, S.C. Paul, M.J. Tan, Anisotropic mechanical performance of 3D printed fiber reinforced sustainable construction material, Mater. Lett. 209 (2017) 146–149, https://doi.org/10.1016/j.matlet.2017.07.123.
[15] A.R. Arunothayan, B. Nematollahi, R. Ranade, S.H. Bong, J.G. Sanjayan, K. H. Khayat, Fiber orientation effects on ultra-high performance concrete formed by 3D printing, Cem. Concr. Res. 143 (2021), 106384, https://doi.org/10.1016/j.cemconres.2021.106384.

[16] J. Zhou, J. Lai, L. Du, K. Wu, S. Dong, Effect of directionally distributed steel fiber on static and dynamic properties of 3D printed cementitious composite, Constr. Build. Mater. 318 (2022), 125945, https://doi.org/10.1016/j.conbuildmat.2021.125948.

[17] X. Xie, L. Zhang, C. Shi, X. Liu, Prediction of lubrication layer properties of pumped concrete based on flow induced particle migration, Constr. Build. Mater. 322 (2022), 126115, https://doi.org/10.1016/j.conbuildmat.2021.126115.

[18] B. Lu, Y. Weng, M. Li, Y. Qian, K. Fai Leong, M. Jen Tan, S. Qian, A systematical review of 3D printable cementitious materials, Constr. Build. Mater. 207 (2019) 477–490, https://doi.org/10.1016/j.conbuildmat.2019.02.144.

[19] E. Secrieru, W. Mohamed, S. Fataei, V. Mechtcherine, Assessment and prediction of concrete flow and pumping pressure in pipeline, Cem. Concr. Compos. 107 (2020), 103495, https://doi.org/10.1016/j.cemconcomp.2019.103495.

[20] D. Feys, How much is bulk concrete sheared during pumping, Constr. Build. Mater. 223 (2019) 341–351, https://doi.org/10.1016/j.conbuildmat.2019.06.224.

[21] M. Chen, L. Yang, Y. Zheng, L. Li, S. Wang, Y. Huang, P. Zhao, L. Lu, X. Cheng, Rheological behaviors and structure build-up of 3D printed polypropylene and polyvinyl alcohol fiber-reinforced calcium sulphoaluminate cement composites, J. Mater. Res. Technol. 10 (2021) 1402–1414, https://doi.org/10.1016/j.jmrt.2020.12.115.

[22] Z. Zhao, M. Chen, J. Xu, L. Li, Y. Huang, L. Yang, P. Zhao, L. Lu, Mix design and rheological properties of magnesium potassium phosphate cement composites based on the 3D printing extrusion system, Constr. Build. Mater. 284 (2021), 122797, https://doi.org/10.1016/j.conbuildmat.2021.122797.

[23] S. Fataei, E. Secrieru, V. Mechtcherine, N. Roussel, A first-order physical model for the prediction of shear-induced particle migration and lubricating layer formation during concrete pumping, Cem. Concr. Res. 147 (2021), 106530, https://doi.org/10.1016/j.cemconres.2021.106530.

[24] G.K. Auernhammer, S. Fataei, M.A. Hausteind, H.P. Patela, R. Schwarze, E. Secrieru, V. Mechtcherine, Transparent model concrete with tunable rheology for investigating flow and particle-migration during transport in pipes, Mater. Des. 193 (2020), 108673, https://doi.org/10.1016/j.matdes.2020.108673.

[25] Q. Jiang, Q. Liu, S. Wu, H. Zheng, W. Sun, Modification effect of nanosilica and polypropylene fiber for extrusion-based 3D printing concrete: printability and mechanical anisotropy, Addit. Manuf. 56 (2022), 102944, https://doi.org/10.1016/j.addma.2022.102944.

[26] H. Huang, X. Gao, L. Teng, Fiber alignment and its effect on mechanical properties of UHPC: an overview, Constr. Build. Mater. 296 (2021), 123741, https://doi.org/10.1016/j.conbuildmat.2021.123741.

[27] L. Pham, P. Tran, J. Sanjayan, Steel fibres reinforced 3D printed concrete: influence of fibre sizes on mechanical performance, Constr. Build. Mater. 250 (2020), 118785, https://doi.org/10.1016/j.conbuildmat.2020.118785.

[28] M. Hambach, M. Rutzen, D. Volkmer, Properties of 3D-printed fiber-reinforced portland cement paste, 3D Concr. Print. Technol. (2019) 73–113, https://doi.org/10.1016/B978-0-12-815481-6.00005-1.

[29] T. Ding, J. Xiao, S. Zou, J. Yu, Flexural properties of 3D printed fibre-reinforced concrete with recycled sand, Constr. Build. Mater. 288 (2021), 123077, https://doi.org/10.1016/j.conbuildmat.2021.123077.

[30] S.H. Bong, B. Nematollahi, M. Xia, S.H. Ghaffar, J. Pan, J. Dai, Properties of additively manufactured geopolymer incorporating mineral wollastonite microfibers, Constr. Build. Mater. 331 (2022), 127282, https://doi.org/10.1016/j.conbuildmat.2022.127282.

[31] J. Archez, N. Texier-Mandoki, X. Bourbon, J.F. Caron, S. Rossignol, Shaping of geopolymer composites by 3D printing, J. Build. Eng. 34 (2021), 101894, https://doi.org/10.1016/j.jobe.2020.101894.

[32] A. Singh, Q. Liu, J. Xiao, Q. Lyu, Mechanical and macrostructural properties of 3D printed concrete dosed with steel fibers under different loading direction, Constr. Build. Mater. 323 (2022), 126616, https://doi.org/10.1016/j.conbuildmat.2022.126616.

[33] M.A. Vicentea, G. Ruizb, D.C. Gonzáleza, J. Míngueza, M. Tarifac, X. Zhang, Effects of fiber orientation and content on the static and fatigue behavior of SFRC by using CT-Scan technology, Int. J. Fatigue 128 (2019), 105178, https://doi.org/10.1016/j.ijfatigue.2019.06.038.

[34] H. Huang, X. Gao, K.H. Khayat, Contribution of fiber alignment on flexural properties of UHPC and prediction using the Composite Theory, Cem. Concr. Compos. 118 (2021), 103971, https://doi.org/10.1016/j.cemconcomp.2021.103971.

[35] A. Abrishambaf, M. Pimentel, S. Nunes, Influence of fibre orientation on the tensile behaviour of ultra-high performance fibre reinforced cementitious composites, Cem. Concr. Res. 97 (2017) 28–40, https://doi.org/10.1016/j.cemconres.2017.03.007.

[36] S.T. Kang, J.K. Kim, Numerical simulation of the variation of fiber orientation distribution during flow molding of Ultra High Performance Cementitious Composites (UHPCC), Cem. Concr. Compos. 34 (2012) 208–217, https://doi.org/10.1016/j.cemconcomp.2011.09.015.

[37] W. Meng, K.H. Khayat, Improving flexural performance of ultra-high-performance concrete by rheology control of suspending mortar, Compos. Part B: Eng. 117 (2017) 26–34, https://doi.org/10.1016/j.compositesb.2017.02.019.

[38] L. Martinie, N. Roussel, Simple tools for fiber orientation prediction in industrial practice, Cem. Concr. Res. 41 (2011) 993–1000, https://doi.org/10.1016/j.cemconres.2011.05.008.

[39] J. Liu, S. Li, K. Fox, P. Tran, 3D concrete printing of bioinspired Bouligand structure: A study on impact resistance, Addit. Manuf. 50 (2022), 102544, https://doi.org/10.1016/j.addma.2021.102544.

[40] L. Dong, Y. Yang, Z. Liu, Q. Ren, J. Li, Y. Zhang, C. Wu, Microstructure and mechanical behaviour of 3D printed ultra-high performance concrete after elevated temperatures, Addit. Manuf. 58 (2022), 103032, https://doi.org/10.1016/j.addma.2022.103032.

[41] T. Kunishima, Y. Nagai, S. Nagai, T. Kurokawa, G. Bouvard, J. Abry, V. Fridrici, P. Kapsa, Effects of glass fiber properties and polymer molecular mass on the mechanical and tribological properties of a polyamide-66-based composite in contact with carbon steel under grease lubrication, Wear 462–463 (2020), 203500, https://doi.org/10.1016/j.wear.2020.203500.

[42] D. Yang, H. Zhang, J. Wu, E.D. McCarthy, Fibre flow and void formation in 3D printing of short-fibre reinforced thermoplastic composites: an experimental benchmark exercise, Addit. Manuf. 37 (2021), 101686, https://doi.org/10.1016/j.addma.2020.101686.

[43] Z. Geng, W. She, W. Zuo, K. Lyu, H. Pan, Y. Zhang, C. Miao, Layer-interface properties in 3D printed concrete: dual hierarchical structure and micromechanical characterization, Cem. Concr. Res. 138 (2020), 106220, https://doi.org/10.1016/j.cemconres.2020.106220.

[44] J.G. Sanjayan, B. Nematollahi, M. Xia, T. Marchment, Effect of surface moisture on inter-layer strength of 3D printed concrete, Constr. Build. Mater. 172 (2018) 468–475, https://doi.org/10.1016/j.conbuildmat.2018.03.232.

[45] Q. Zeng, P. Yang, Y. Peng, J. Wang, C. Zhou, Tracing mercury entrapment in porous cement paste after mercury intrusion test by X-ray computed tomography and implications for pore structure characterization, Mater. Charact. 151 (2019) 203–215, https://doi.org/10.1016/j.matchar.2019.02.014.

[46] S. Brisard, M. Serdar, P.J.M. Monteiro, Multiscale X-ray tomography of cementitious materials: a review, Cem. Concr. Res. 128 (2020), 105824, https://doi.org/10.1016/j.cemconres.2019.105824.

[47] Y. Peng, G. Zhao, Y. Qi, Q. Zeng, In-situ assessment of the water-penetration resistance of polymer modified cement mortars by μ-XCT, SEM and EDS, Cem. Concr. Compos. 114 (2020), 103821, https://doi.org/10.1016/j.cemconcomp.2020.103821.

[48] R. Yang, Q. Zeng, Y. Peng, H. Wang, Z. Wang, Anomalous matrix and interlayer pore structure of 3D-printed fiber-reinforced cementitious composites, Cem. Concr. Res. 157 (2022), 106829, https://doi.org/10.1016/j.cemconres.2022.106829.

[49] Y. Chen, C.R. Rodriguez, Z. Li, B. Chen, O. Çopuroğlu, E. Schlangen, Effect of different grade levels of calcined clays on fresh and hardened properties of ternary-blended cementitious materials for 3D printing, Cem. Concr. Compos. 114 (2020), 103708, https://doi.org/10.1016/j.cemconcomp.2020.103708.

[50] D. Feys, Interactions Between Rheological Properties and Pumping of Self-compacting Concrete, Ghent University, Gent, 2009. Ph-D dissertation.

[51] H. Mehdizadeh, X. Jia, K.H. Mo, T. Ling, Effect of water-to-cement ratio induced hydration on the accelerated carbonation of cement pastes, Environ. Pollut. 280 (2021), 116914, https://doi.org/10.1016/j.envpol.2021.116914.

[52] D.M. Kirby, J.J. Biernacki, The effect of water-to-cement ratio on the hydration kinetics of tricalcium silicate cements: testing the two-step hydration hypothesis, Cem. Concr. Res. 42 (2012) 1147–1156, https://doi.org/10.1016/j.cemconres.2012.05.009.

[53] V.T. Nguyen, S.Y. Lee, S. Chung, J. Moon, D.J. Kim, Effects of cement particle distribution on the hydration process of cement paste in three-dimensional computer simulation, Constr. Build. Mater. 311 (2021), 125322, https://doi.org/10.1016/j.conbuildmat.2021.125322.

[54] J.W. Bullard, H.M. Jennings, R.A. Livingston, A. Nonat, G.W. Scherer, J. S. Schweitzer, K.L. Scrivener, J.J. Thomas, Mechanisms of cement hydration, Cem. Concr. Res. 41 (2011) 1208–1223, https://doi.org/10.1016/j.cemconres.2010.09.011.

[55] H. Sun, B. Fan, S.A. Memon, Z. Cen, X. Gao, B. Lin, B. Liu, D. Li, F. Xing, X. Zhang, 3D particle size distribution of inter-ground Portland limestone/slag cement from 2D observations: characterization and distribution evaluation, Constr. Build. Mater. 147 (2017) 550–557, https://doi.org/10.1016/j.conbuildmat.2017.04.070.

[56] Y. Wang, Y. Li, Y. Su, X. He, B. Strnadel, Preparation of waste glass powder by different grinding methods and its utilization in cement-based materials, Adv. Powder Technol. 33 (2022), 103690, https://doi.org/10.1016/j.apt.2022.103690.

[57] Y. Peng, R.A. Lauten, K. Reknes, S. Jacobsen, Bleeding and sedimentation of cement paste measured by hydrostatic pressure and Turbiscan, Cem. Concr. Compos. 76 (2017) 25–38, https://doi.org/10.1016/j.cemconcomp.2016.11.013.

[58] Y. Peng, S. Jacobsen, Influence of water/cement ratio, admixtures and filler on sedimentation and bleeding of cement paste, Cem. Concr. Res. 54 (2013) 133–142, https://doi.org/10.1016/j.cemconres.2013.09.003.

[59] V.C. Lia, F.P. Bos, K. Yu, W. McGee, T.Y. Ng, S.C. Figueiredo, K. Nefs, V. Mechtcherine, V.N. Nerella, J. Pan, G.P.A.G. van Zijl, P.J. Kruger, On the emergence of 3D printable Engineered, Strain Hardening Cementitious Composites (ECC/SHCC), Cem. Concr. Res. 132 (2020), 106038, https://doi.org/10.1016/j.cemconres.2020.106038.

[60] T. Kunishima, Y. Nagai, T. Kurokawa, G. Bouvard, J. Abry, V. Fridrici, P. Kapsa, Tribological behavior of glass fiber reinforced-PA66 in contact with carbon steel under high contact pressure, sliding and grease lubricated conditions, Wear 456–457 (2020), 203383, https://doi.org/10.1016/j.wear.2020.203383.

[61] D. Feys, G. De Schutter, S. Fataei, N.S. Martys, V. Mechtcherine, Pumping of concrete: understanding a common placement method with lots of challenges, Cem. Concr. Res. 154 (2022), 106720, https://doi.org/10.1016/j.cemconres.2022.106720.

[62] H.S. Wong, M.K. Head, N.R. Buenfeld, Pore segmentation of cement-based materials from back scattered electron images, Cem. Concr. Res. 36 (2006) 1083–1090, https://doi.org/10.1016/j.cemconres.2005.10.006.

[63] J. Huang, Y. Zhang, Y. Sun, J. Ren, Z. Zhao, J. Zhang, Evaluation of pore size distribution and permeability reduction behavior in pervious concrete, Constr.

Build. Mater. 290 (2021), 123228, https://doi.org/10.1016/j.conbuildmat.2021.123228.
[64] L. Hong, P. Zhang, D. Liu, P. Gao, B. Zhan, Q. Yu, L. Sun, Effective segmentation of short fibers in glass fiber reinforced concrete's X-ray images using deep learning technology, Mater. Des. 210 (2021), 110024, https://doi.org/10.1016/j.matdes.2021.110024.
[65] W. Wang, A. Shen, Z. Lyu, Z. He, K.T.Q. Nguyen, Fresh and rheological characteristics of fiber reinforced concrete—A review, Constr. Build. Mater. 296 (2021), 123734, https://doi.org/10.1016/j.conbuildmat.2021.123734.

Gradient distribution of slender glass microfibers in 3D printed cementitious filaments

Rijiao Yang [1], Qiang Zeng [1], and Zhendi Wang [2]

1 College of Civil Engineering and Architecture, Zhejiang University, Hangzhou, 310058, China.
Email: 12212088@zju.edu.cn (YR), cengq14@zju.edu.cn (ZQ)
2 State Key Laboratory of Green Building Materials, China Building Materials Academy, Beijing 100024, P.R. China
Email: wzhendi@163.com

ABSTRACT
Extrusion is a widely used automatic construction technique that builds a structure through the pattern of material addition. The unique extrusion molding would greatly impact the microstructure of the printed cementitious filaments containing different particles in size, volume, and shape. Most studies reported the aligned distribution of fibers with small slenderness in extrusion molded cementitious filaments (EMCFs). However, the content and direction of highly slender microfibers in EMCFs have not been fully understood due to the gradient shearing forces acting on the cementitious slurries during printing. Here, we focus on the distribution of glass microfibers with the slenderness (length-to-diameter ratio) of 429 in EMCFs. X-ray computed tomography (XCT) was employed to track the glass microfibers in the EMCFs and provide the information of content and orientation of the fibers in different positions of EMCFs. To resolve the specific fibers' information, 25 layers of sheet (thickness of each layer = 0.2 mm) from the interface to the center of each EMCF were segmented during XCT analysis. The results show that the slender microfibers possessed the gradient distributions of orientation and content from the interface to the inner matrix of the EMCFs. Mechanisms of those behaviors are discussed in terms of particle collisions and distribution of shearing forces in the printing pipe during extrusion modeling. The findings would deepen the understandings in slender microfibers redistribution in non-Newtonian liquid during extrusion molding.

KEYWORDS: *3D printing, Microfibers, Spatial distribution, Orientation, Efficiency*

1. Introduction

Three-dimensional (3D) printing is one of the widely used automatic construction techniques showing great advantages in terms of economy and environmental benefits. There are different ways to 3D-printing concrete constructions, among which extrusion is easily accepted for low cost and simple equipment (Shakor et al 2020; Xiao et al 2021). During extrusion molding, the spatial distribution of particles in the printed cementitious filaments would be influenced by uneven shearing actions for different size, volume and shape of the particles, which would impact the mechanical properties of the materials (Fataei et al (2021) and Auernhammer et al (2020)).

Fibers that were often used as a reinforcement in cementitious materials could be regarded as a type of particle with large slenderness, so the spatial distribution of fibers would also be affected by the extrusion process. Morevoer, fiber orientation aslo plays an important role on the overall performance of the materials. It is worth noting that the spatial and directional distribution of fibers should be further concerned in extrusion molded cementitious filaments (EMCFs). The studies (Hambach et al (2019), Liu et al (2022) and Dong et al (2022)) reported that fibers with small slenderness presented the aligned distribution during printing, which greatly improved the flexure strength of EMCFs. Different from macro fibers with relatively small slenderness, high slender microfibers cannot easily keep straight under shearing forces, which makes the fiber directional distribution more complex. To fully understand the effect of the gradient shearing forces on fibers, it is meaningful to characterize the spatial and directional distribution of high slender microfibers in EMCFs.

This paper mainly focuses on the mechanism of fiber migration and distribution under gradient shearing actions. EMCFs with two dosages of glass microfibers were prepared and non-destructive XCT test was obtained to characterize the spatial and directional distribution of the fibers. A layer-by-layer imaging analysis was specifically used to measure the content and orientation of the microfibers. The particle collisions and distribution of shearing forces on the cementitious slurries during extrusion molding may account for the observed gradient content and direction distributions of the microfibers.

2. Sample and Methods

Glass microfiber reinforced cementitious materials were prepared by extrusion 3D printing using the mix proportions as shown in Table 1. Glass microfibers with the diameter of 14 μm and length of 6 mm (L/D = 429) were used with the contents of 0.3 wt% and 0.6 wt% (EMCF3 and EMCF6). Filaments with the diameter of 10 mm were printed in the speed of 20 mm/s to construct a unit with 8 layers of filaments. After printing, the samples were cured for 28 days and small cuboids (around 6 mm × 6 mm × 6 mm) containing the interlayer zone (IZ) were cut.

Table 1 Mix proportions of the 3D-printed extrusion molded cementitious filaments (EMCFs)

Sample ID	Water /wt%	Cement /wt%	Accelerator /wt%	HPMC /wt%	PCE-SP /wt%	Glass fiber /wt%
EMCF3	30	100	2.25	0.15	0.44	0.3
EMCF6	30	100	2.25	0.15	0.44	0.6

The specimens were put into XTH255/320 LC (Nikon, Japan) device for non-destructive XCT scans (Figure 1a). All X-ray projections were qualified and reconstructed by "CT 3D Pro" software, and the region of interest (ROI) of 5 mm cube was extracted by "VG Studio Max" software (Figure 1b). After fibers had been extracted using the threshold and filter tools in the visualizing software, fiber direction and content were analyzed by “fiber module”. Small ROI of 0.2 mm thickness was segmented for further orientation analysis (Figure 1c). Fiber orientation was evaluated by orientation index, OI = $cos^2\theta$, where θ is the angle between the fiber and the printing direction (Yang et al (2022b)).

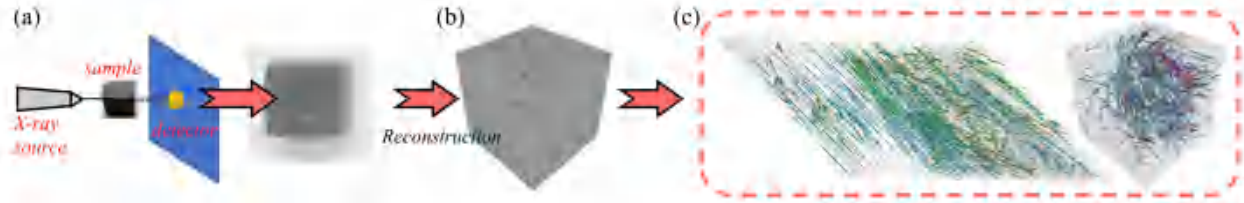

Figure 1 Test and data processing by μ-XCT: (a) XCT scans of a 3D-printed EMCF sample; (b) image stacking and reconstruction; and (c) fiber orientation analysis.

3. Results and discussion

The fiber content and directional distribution (i.e. OI) perpendicular to the interlayer plane are shown in Figure 2. The position at 0 mm denoted the center of IZ and the blue regions represented the range of IZ for both EMCF3 and EMCF6, respectively. In EMCF3, the fiber content slightly decreased from 0.3% to 0.02% and then sharply increased to 1.1% from -3 mm or 2 mm to the center of IZ (at 0 mm). The large fiber content in IZ means that the fibers migrated to IZ during extrusion, see Figure 2(a). Obviously, the fiber content changed acutely from -2 mm to 2 mm, indicating that the impact region of the uneven shearing forces on fiber spatial distribution was 4 mm in EMCF3. For EMCF6, the fiber content also increased from the matrix at -3 mm or 2 mm to the center of IZ (at 0 mm), and the impact region exceeded 5 mm. Note that the highest fiber content for EMCF6 was 0.96% (Figure 2b), less than that in EMCF3 (Figure 2a). It seems that increasing fiber dosage could enlarge the shearing impact region but lessen (limit) the fiber migration extent.

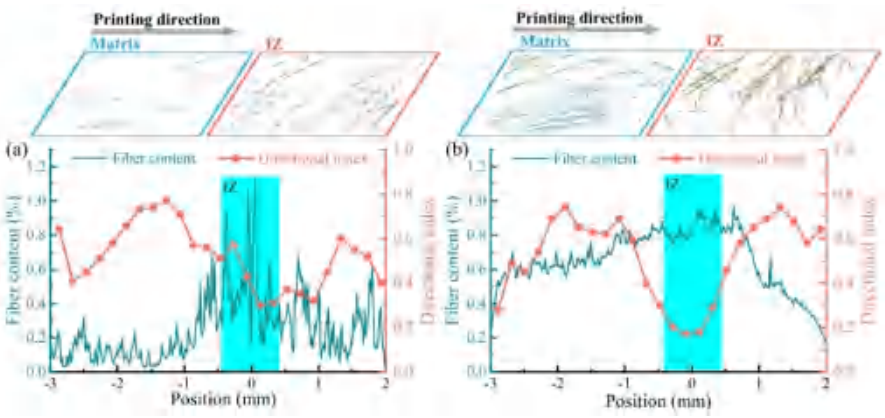

Figure 2 Fiber content and directional distributions in EMCF3 (a) and EMCF6 (b) and selective demonstrations.

The values of OI in EMCF3 increased to nearly 0.8 at 1.3 mm and then decreasd to below 0.3 around the center of IZ at 0 mm (Figure 2a). The highest OI values were recorded at 0.77 and 0.74 for ECMF3 and EMCF6, respectively, and the lowest values at the interface were found at 0.3 for EMCF3 and at 0.17 for EMCF6. Roughly, the microfibers followed the printing direction in the matrices, but were perpendicular to the printing direction in the IZ.

To evaluate the efficiency of fiber content and OI distribution, a parameter of fiber efficiency (FE) was employed (Abrishambaf et al (2017)): $f_u=C_f \cos\theta\ \tau_f\ l_f \div d_f$, where C_f is fiber content; τ_f is the bonding strength between fiber and matrix; l_f is the length of fibers and d_f is the diameter of fibers. Because other parameters were constant in this work, the relationship can be simplified as $FE=C_f \times \cos\theta$. Figure 3a displays the distribution of FE. The trend of FE in EMCF3 and EMCF6 varied greatly. In EMCF3, the trend of FE was similar with that of fiber content. But in EMCF6, the variation of FE was similar with that of OI. The FE of EMCF6 was always higher than that of EMCF3 except in the IZ. The findings in Figure 3a meant that increasing fiber dosage could strengthen the matrix but weaken the IZ. Figure 3b shows the results of FC, OI and FE. In EMCF3, the values of FC and FE in the IZ were higher than those in the matrix by 114.3% and 78.6%, respectively, while the values of OI in the IZ was less than that in the matrix by 25.9%. EMCF6 showed quite different trend, where OI and FE in the IZ were less than those in the matrix by 63.8% and 27.3%, respectively, and FC in the IZ was higher than that in the matrix by 35.5%.

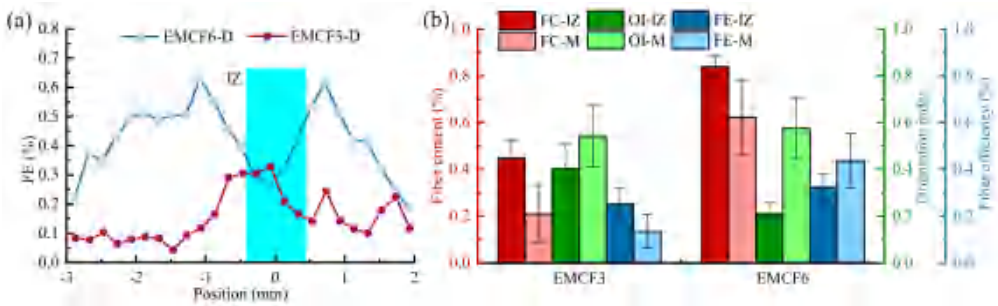

Figure 3 (a) FE distribution at different position and (b) statistical results of FC, OI and FE for both samples.

In a word, the spatial and orientation distribution of microfibers were uneven after extrusion molding. Figure 4 schematically shows the effect of non-uniform shearing actions on the gradient distribution of fibers. Our results demonstrated that the value of OI became smaller but the fiber content increased at IZ (Figure 2), indicating that microfibers were migrating to IZ with the aligned direction (Figure 4). During printing, the flowing speed of the EMCF slurries slowed down near the IZ, so the largely slender glass microfibers gradually became bent. Later, the microfibers were perpendicular to the printing direction to counterbalance the particle collisions and uneven shearing forces. The effect of gradient shearing force on the migration and orientation changes of microfibers in EMCFs has been documented in the literature (Yang et al (2022b)). It should be noted that excessively increasing fiber content would not strengthen materials, because a higher fiber dosage in cement slurries would considerably raise the gradient shearing forces, and consequently more microfibers would be perpendicular to the printing direction in IZ. However, the increased viscosity due to the increased fiber content would mitigate the migration of fibers

to IZ (Yang et al 2022a). This behavior was verified in this work as shown in Figure 2(b), where the OI values in the IZ of EMCF6 was reasonably smaller than that of EMCF3.

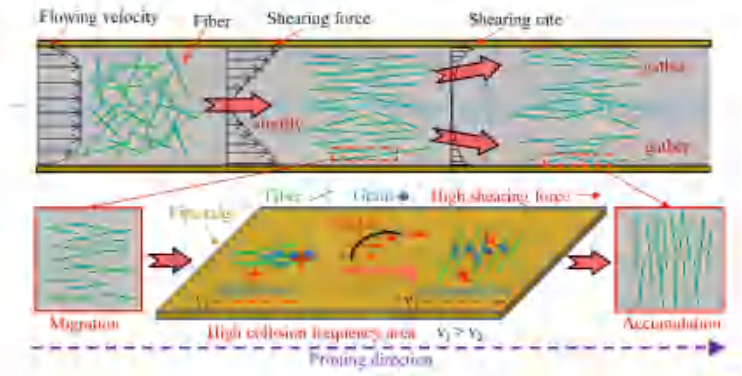

Figure 4 Schematic diagram of the effect of non-uniform shearing on the uneven distributions of fiber.

4. Conclusion

During extrusion printing, microfibers gradually migrated to IZ under gradient shearing forces leaving a matrix devoid of fibers. The large shearing forces with high fiber content and slow flowing speed resulted in bent microfibers perpendicular to the printing direction.

Acknowledgements

This work was supported by the Program Fund of Non-Metallic Excellence and Innovation Center for Building Materials (2022SFP1-1).

Reference

Abrishambaf A., Pimentel M. and Nunes S. (2017) "Influence of fibre orientation on the tensile behaviour of ultra-high performance fibre reinforced cementitious composites", *Cement and Concrete Research* 97: 28-40.

Auernhammer G. K., Fataei S., Hausteind M. A., Patela H. P., Schwarze R., Secrieru E. and Mechtcherine V. (2020) "Transparent model concrete with tunable rheology for investigating flow and particle-migration during transport in pipes", *Materials & Design* 193: 108673.

Dong L., Yang Y., Liu Z., Ren Q., Li J., Zhang Y. and Wu C. (2022) "Microstructure and mechanical behaviour of 3D printed ultra-high performance concrete after elevated temperatures", *Additive Manufacturing* 58: 103032.

Fataei S., Secrieru E., Mechtcherine V. and Roussel N. (2021) "A first-order physical model for the prediction of shear-induced particle migration and lubricating layer formation during concrete pumping", *Cement and Concrete Research* 147: 106530.

Hambach M., Rutzen M. and D. Volkmer (2019) "Properties of 3D-Printed Fiber-Reinforced Portland Cement Paste", 3D Concrete Printing Technology 73-113.

Liu J., Li S., Fox K. and Tran P. (2022) "3D concrete printing of bioinspired Bouligand structure: A study on impact resistance", *Additive Manufacturing* 50: 102544.

Shakor P., Nejadi S., Sutjipto S., Paul G. and Gowripalan N.(2020) "Effects of deposition velocity in the presence/absence of E6-glass fibre on extrusion-based 3D printed mortar", *Additive Manufacturing*. 32: 101069.

Yang R., Zeng Q., Peng Y., Wang H. and Wang Z. (2022a) "Anomalous matrix and interlayer pore structure of 3D-printed fiber-reinforced cementitious composites", *Cement and Concrete Research* 157: 106829.

Yang R., Zhu Y., Lan Y., Zeng Q., Peng Y. and Wang Z. (2022b) "Differences in micro grain/fiber distributions between matrix and interlayer of cementitious filaments affected by extrusion molding", *Additive Manufacturing* 60: 103236.

Xiao J., Liu H. and Ding T. (2021)" Finite element analysis on the anisotropic behavior of 3D printed concrete under compression and flexure", *Additive Manufacturing* 39: 101712.

The result of the review is
Accepted with Revision.

You are encouraged to revise the paper and resubmit the revised paper via the Congress website.

Please do not hesitate to contact the Scientific Committee coordinator (krittiya@siit.tu.ac.th) if you have any questions.

Thank you for your contribution to ICCC2023.

Somnuk Tangtermsirikul
Chair
ICCC2023 Scientific Committee

Rebar-matrix interface in extrusion molded cementitious filaments

Rijiao Yang [1, 2], Qiang Zeng [1]*, Zhendi Wang [2]

[1]College of Civil Engineering and Architecture, Zhejiang University, Hangzhou, 310058, China, 12212088@zju.edu.cn (Rijiao Yang), cengq14@zju.edu.cn(Qiang Zeng)

[2] State Key Laboratory of Green Building Materials, China Building Materials Academy, Beijing 100024, P.R. China,wzhendi@163.com(Zhendi Wang)

Abstract.*Extrusion molding enables automatic construction through the pattern of material addition. The unique molding would result in several features that are different from those in conventional framework molding, such as weak interlayer bonding and a laminar structure with high anisotropy. To strengthen the interlayer bonding, reinforcement is often implanted to penetrate through the extrusion molded filaments (EMF). However, different from the pre-implantation of reinforcement before concrete casting, the post-implantation of reinforcement in EMF may trigger the problems concerning the interface bonding between reinforcement and material matrix. In this work, saddle stitches, a type of U-shape rebar or fiber, are taken as an example to demonstrate the effect of the post-implantation of reinforcement on the interfacial structure between the rebar and EMF matrix. X-ray computed tomography (XCT) is employed to non-destructively probe the post-implanted saddle stitches as well as the surrounded EMF materials. Regions of interest (ROI) are set on the rebar-matrix interfaces to elaborately analyze the material or defect distributions around the saddle stitches. Results demonstrate that insufficient material filling is observed at the outboard of the U-shape rebar, while material pressing is shown at the inboard. Large defects unevenly form in the rebar-matrix interface. Mechanisms of the observations may be ascribed to the low flowability of EMF materials that can hardly migrate to the rebar-matrix interfacial gaps spontaneously. The findings would deepen the understandings in rebar-matrix interfacial structure of EMF with post-implantation of reinforcement.*

Keywords:*Extrusion;Saddle stitches;XCT; Bonding; Defects;*

1 Introduction

Concrete extrusion molding, one of the most used three-dimensional (3D) printing patterns, has brought great advances to automatic constructions [Arunothayan et al. 2021, Wang et al. 2020, Li et al. 2022]. However, the layer-by-layer addition of extrusion molding can result in anisotropic structure with weak interlayer bonding [Nerella et al. 2019, Ding et al. 2020]. To strengthen the interlayer bonding between the extrusion molded concrete filaments, many techniques have been proposed, such as adjusting printing parameters, changing mix proportions, spraying interface strengthening agency and implanting reinforcement [Lu et al. 2019, Cao et al. 2022]. The implantation of reinforcement through the extrusion molded filaments (EMFs) may be the most effective way for interface strength enhancement. In this work, we used a post-implantation method to reinforce EMFs, which is different from traditional concrete reinforcement, where the reinforcement is pre-implanted and the concrete is sufficiently vibrated after cast, so the concrete slurries fully fill the space around the reinforcement. On one hand, the reinforcement is usually implanted through several layers, which would disturb the originally printed structure [Wang et al. 2021]. On the other hand, the

EMF structure will not be vibrated to avoid the possible collapse of the 3D printed concrete [Sun et al. 2022]. In this case, concrete slurries will not flow to fill the space around the rebars. Therefore, the post-implantation of reinforcement in EMF may lead to the formation of defects between the rebars and material matrix.

This work mainly focuses on the interface structure between post-implanted rebars and cement matrix. Cementitious slurries with three viscosities were controlled to prepare the EMFs. Saddle stitches, a type of U-shape rebar, were taken as the reinforcement. X-ray computed tomography (XCT) was employed to non-destructively probe the post-implanted saddle stitches as well as the surrounded EMF materials. The defects around the saddle stitches were extracted and the mechanisms were discussed.

2 Sample and Method

Three mix proportions were designed to control the slurries' viscosity (**Table 1**). A Portland cement (Type PI 42.5) was used as the binder for EMFs fabrication. The mix proportions of EMFs were set as follows: water-to-cement (w/c) ratio of 0.3, sand-to-cement (s/c) ratio of 0.8, polycarboxylate superplasticizer (PCE-SP) of 0.3 wt%, and alkali accelerator of 1.2 wt%. To tune the EMF slurries' viscosity, hydroxypropyl methylcellulose (HPMC) of 0.2, 0.3 and 0.4 wt% (in reference to cement weight) were used.

Table 1 Mix proportions of the 3D-printed extrusion molded cementitious filaments (EMFs)

Sample ID	Cement /wt%	Water /wt%	Sand /wt%	Accelerator /wt%	HPMC /wt%	PCE-SP /wt%
EMF-02	100	30	80	1.2	0.2	0.3
EMF-03	100	30	80	1.2	0.3	0.3
EMF-04	100	30	80	1.2	0.4	0.3

EMFs were printed by a homemade 3D printing machine with the parameters shown as follows, printing speed of 30 mm/s, filament height of 20 mm, length of 200 mm. Saddle stitches with 40 mm in length, 20 mm in width and 3.0 mm in diameter were implanted into the EMFs to enhance interlayer bonding (**Figure 1a**). After two layers of EMFs were finished, the saddle stitches were manually placed in the filaments every 30 mm, and the last layer of filament was extruded to cover the saddle stitches (**Figure 1b**). After primary hardening for 24 h, the EMFs were cured for 28 d in a standard curing condition. Later, the specimens were cut into small segments containing two saddle stitches for XCT scan test.

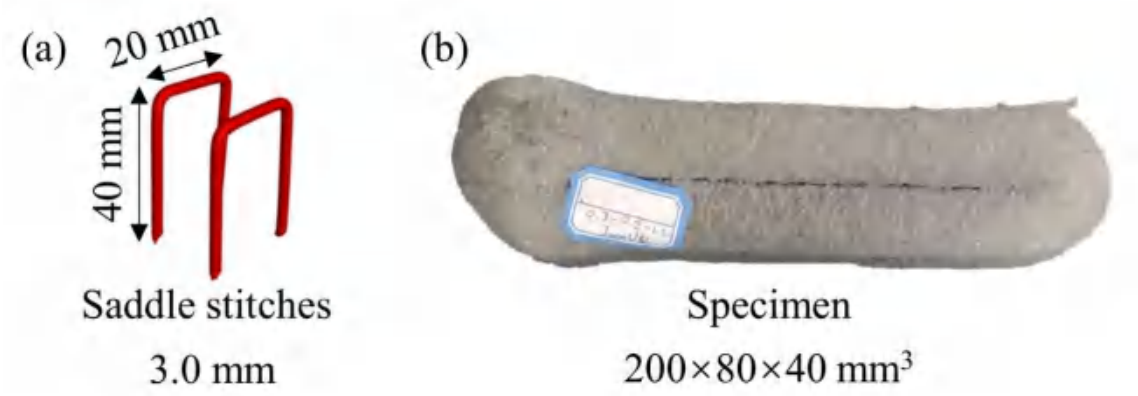

Figure 1 (a) Illustration of two saddle stitches, (b) image of an EMF specimen

The prepared EFM segments were put into a XTH255/320 LC (Nikon, Japan) device for non-destructive XCT scans (**Figure 2a**). Each segment was fixed on the sample frame between the X-ray emitter and the detector with the pixels of 2000×2000. The parameters of XCT test were set as 140 kV and 160 μA. A thin Cu film of 0.25 mm was attached on the tube to filter the noises of X-ray beams. The exposure time was set as 708 ms, and 2000 X-ray projections with the resolution of 36.5 μm/pixel were obtained in 23.6 min. All projections were qualified and reconstructed by "CT 3D Pro" software (**Figure 2b**). After reconstruction, the digital data was imported into "VG Studio" for further analysis (**Figure 2c**) [Yang et al. 2022].

A region of interest (ROI) of 8.5mm in diameter was extracted to contain the saddle stitches and the surrounding phases. A gray value threshold was applied to reconstruct the saddle stitches (**Figure 2d**). However, due to the artifacts [Aleksejev et al. 2022], the direct gray value thresholding method can not allow us to acquire the phases of low density around the saddle stiches of high density. Therefore, a specifically designed method was applied. First, the saddle stitches were first removed or set as pores, and expanded to include the region in 2 mm. Analysis based on gray value threshold was performed again to reconstruct the phases around the saddle stitches. The "pore analysis module" was used to measure the volume, and fraction of the phase identified (**Figure 2e**).

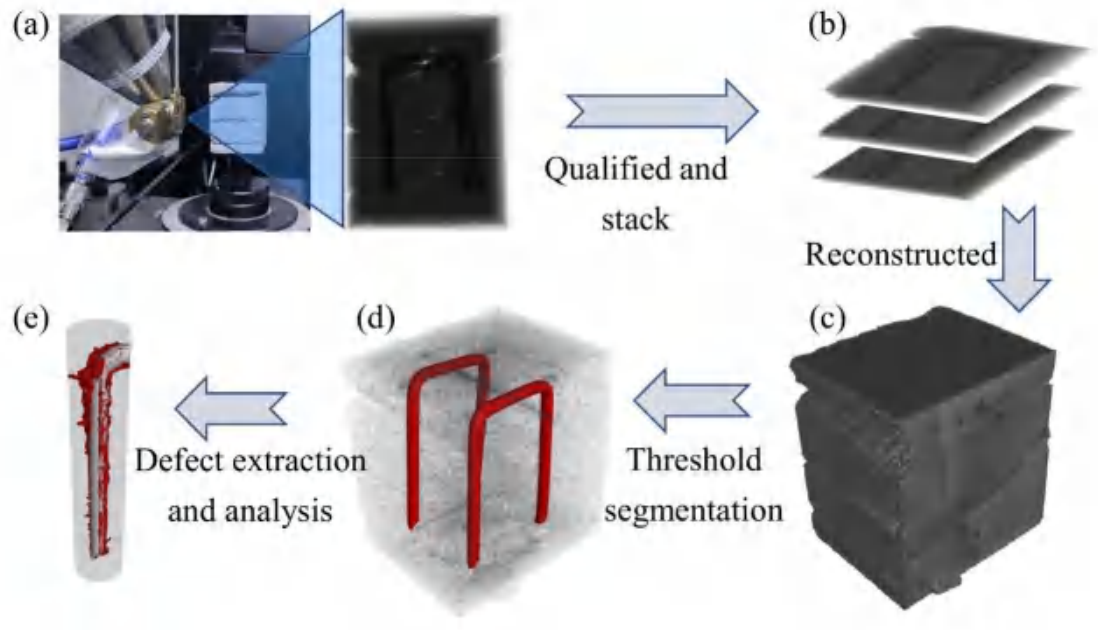

Figure 2 Test and data processing by micro-XCT: (a) XCT scans of an EMF segment with two saddle stitches; (b) image stacked in "CT3DPro" software; (c) 3D image of the sample in "VG Studio" software; (d) 3D image of the saddle stitches in the sample; (e) identification of the phase around saddle stitches.

3 Results and discussion

Figure 3a representatively shows the 3D structure of a selected ROI with three different phases in EMF-02, EMF-03 and EMF-04: rebar (gray), cement matrix (transparent), and pores (red). Those pores are large and connected, which may be diagnosed as defects. More connected defects are observed at the outboard of the U-shape rebar, while material pressing is shown at the inboard. **Figure 3b** shows the volume fraction of those defects at different positions. The volume fraction of the defects was about 10% at the bottom of the saddle stitches, and progressively increased to about 50% at the top. It can be found in **Figure 3b** that with increasing the cement slurries' viscosity, the volume fraction of defects rose, because the increased cohesive forces between cement particles enhanced the resistance against material flow.

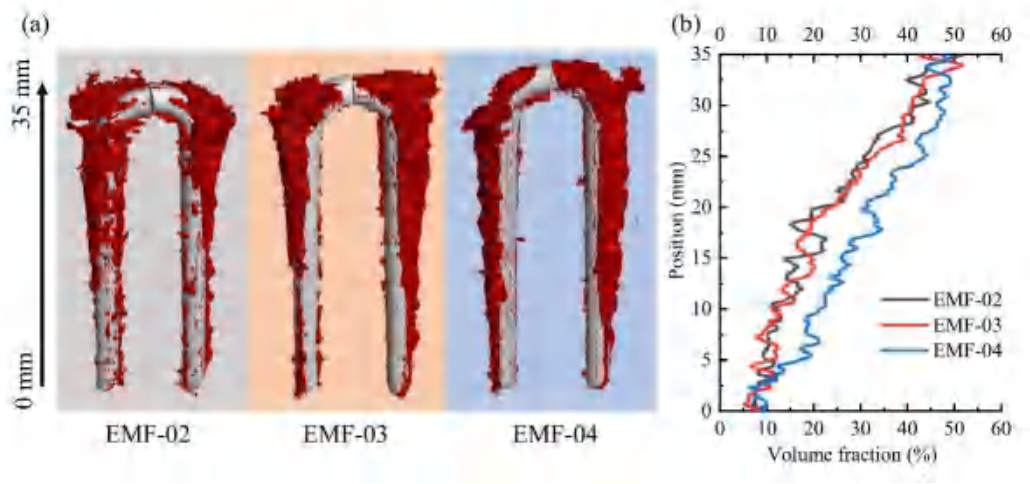

Figure 3 (a) 3D structure of a ROI containing rebar (gray), cement matrix (transparent), and pores (red); (b) changes of volume fraction of the defects in EMF-02, EMF-03 and EMF-04.

The volume and fraction of the gaps (or defects) around the saddle stitches in EMFs are shown in **Figure 4**. The volumes in each sample were above 100 mm^3. As the viscosity of the EMF slurries increased from 14 Pa·s to 20 Pa·s, the defects' volume increased from 120.60 mm^3 to 139.51 mm^3 (Figure 4a). The fraction of the defects to rebars in the same ROIs was calculated (**Figure 4b)**. The volume fractions of the defects were 23.20%, 23.81% and 30.57%, for EMF-02, EMF-03 and EMF-04, respectively.

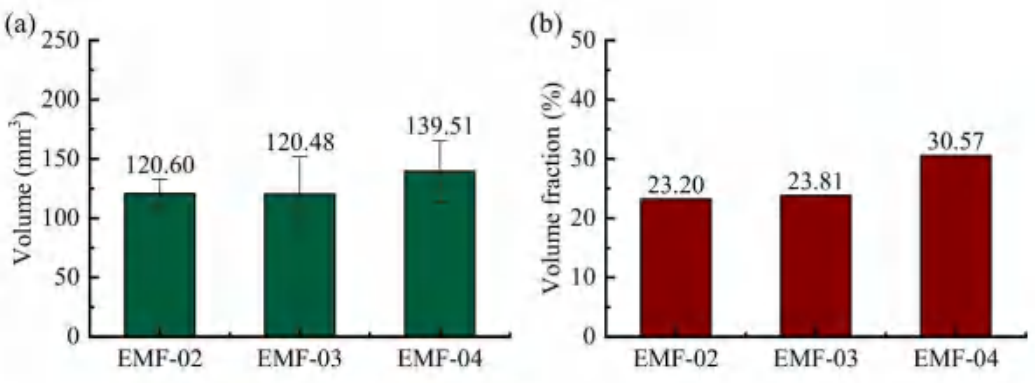

Figure 4 The result of (a) volume and (b) volume fraction of defects.

In a word, in EMFs with implanted rebars, defects were easier to form around the post-implanted saddle stitches. More defects were observed at the top of the EMFs and for the slurries with higher viscosity. The shearing action during implantation and high cohesive force of cement slurries may account for the special distribution of defects. During implantation, the surrounding cement slurries was subjected to the shearing action by the rebars and the cement slurries around the implantation path would be peeled off. Different from ordinary cement slurries, the high cohesive force of the 3D-printed slurry prevents the adjacent cement slurries from flowing and filling the gaps around the rebars. Moreover, the distance between two

branches of the saddle stitches decreases, so pressing occurred to the materials at the inboard of the U-shape rebars, and larger gaps formed at the outboard as the rebars progressively penetrated into the EMFs (Figure 3a).

4 Conclusion

In EMFs, defects were probed between post-implanted saddle stitches and cement matrix by XCT. More defects appeared at the top of the EMFs, at the outboard of the rebars, and for the cement slurries with higher viscosity.

Acknowledgements

This work was supported by the Program Fund of Non-Metallic Excellence and Innovation Center for Building Materials (2022SFP1-1).

References

Aleksejev J., Williamson M., Huber J.E., Magdysyuk O.V., Michalik S., Marrow T.J. (2022). *Use of synchrotron X-rays for direct observation of wear damage in optically-opaque contacts by means of CT imaging and X-ray diffraction*, Tribology International, 175, 107809.

Arunothayan A.R., Nematollahi B., Ranade R., Bong S.H., Sanjayan J.G., Khayat K. H. (2021) *Fiber orientation effects on ultra-high performance concrete formed by 3D printing*, Cement and Concrete Research, 143, 106384.

Cao X., Yu S., Zheng D., Cui H. (2022). *Nail planting to enhance the interface bonding strength in 3D printed concrete*, Automation in Construction, 141, 104392.

Ding T., Xiao J., Zou S., Wang Y. (2020). *Hardened properties of layered 3D printed concrete with recycled sand*, Cement and Concrete Composites, 113, 103724.

Li Z., Ma G., Wang F., Wang L., Sanjayan J. (2022). *Expansive cementitious materials to improve micro-cable reinforcement bond in 3D concrete printing*, Cement and Concrete Composites, 125, 104304.

Lu B., Weng Y., Li M., Qian Y., Leong K. F., Tan M. J., Qian S. (2019). *A systematical review of 3D printable cementitious materials*, Construction and Building Materials, 207, 477-490.

Nerella V.N., Hempel S., Mechtcherine V. (2019) *Effects of layer-interface properties on mechanical performance of concrete elements produced by extrusion-based 3D printing*, Construction and Building Materials, 205, 586–601.

Sun X., Zhou J., Wang Q., Shi J., Wang H. (2022). *PVA fibre reinforced high-strength cementitious composite for 3D printing: Mechanical properties and durability*, Additive. Manufacturing, 49, 102500.

Wang L., Tian Z., Ma G., Zhang M. (2020). *Interlayer bonding improvement of 3D printed concrete with polymer modified mortar: experiments and molecular dynamics studies*, Cement and Concrete Composites, 110, 103571.

Wang L., Ma G., Liu T., Buswell R., Li Z. (2021). *Interlayer reinforcement of 3D printed concrete by the in-process deposition of U-nails*, Cement and Concrete Research, 148, 106535.

Yang R., Zeng Q., Peng Y., Wang H., Wang Z. (2022). *Anomalous matrix and interlayer pore structure of 3D-printed fiber-reinforced cementitious composites*, Cement and Concrete Research, 157, 106829.

Yang R., Zhu Y., Lan Y., Zeng Q., Peng Y., Wang Z. (2022). *Differences in micro grain/fiber distributions between matrix and interlayer of cementitious filaments affected by extrusion molding*, Additive Manufacturing, 60, 103236.

Your full paper/extended abstract submission to XVI DBMC.

dbmc2023 发件人: 12212018@zju.edu.cn

2023-06-09 10:35:22

Dear Mr. Yang,

Your full paper/2-page extended abstract submission (Abstract/paper ID(72) "Title(Rebar-matrix interface in extrusion molded cementitious filaments)") has been reviewed. We are pleased to infrom you that the full paper/2-page extended abstract has been accepted.
The scientific committee recommends your paper to be presented orally. The guideline for oral presentation and poster preparation will be available in the coming days. If you prefer to present your paper otherwise, please let us know. The choice of the presentation mode, orally or in poster, will not have impact on your full paper, if it is provided, to be included into the conference proceedings.
Please also note that the early-bird registration for XVI DBMC remains open until June 30, 2023. We suggest you to check the registration dates and make the registration at your earliest convenience. Upon registration, you can ask the secretariart to provide a formal invitation letter in case you need to apply for a Visa to come to Beijing. Please also follow the conference website for the update on the conference venue and accommodation information.

Thank you for your interest in XVI DBMC and looking forward to seeing you in due sessions.

Best regards,
Secretariart
XVI DBMC conference
E-mail: dbmc2023@mail.tsinghua.edu.cn
Website: https://dbmc2023.civil.tsinghua.edu.cn

文章编号：2097-0846(2023)04-0030-04

聚灰比对聚合物砂浆性能影响研究

王军伟[1,2]，李 昊[1,2]，李文秀[1,2]，贾海涛[2]，翟艳军[2]，张功辉[2]

（1. 中国铁道科学研究院集团有限公司 标准计量研究所，北京100081；
2. 中铁检验认证中心有限公司，北京 100081）

摘 要：EVA乳液本身具有成膜效应与黏结作用，但添加EVA乳液易造成砂浆抗压强度降低。EVA乳液延缓水泥水化，降低水泥砂浆抗压强度。选择EVA乳液与高强水泥砂浆配制聚合物砂浆，以高强水泥砂浆为空白样品，对4种不同聚灰比（1%、2%、5%、10%）的砂浆进行试验研究。结果发现：随聚灰比增加，EVA乳液对水泥砂浆性能影响越显著。当聚合物砂浆黏结抗拉强度及抗渗性能满足要求时，应尽量降低EVA乳液用量。

关键词：聚灰比（*P/C*）；EVA乳液；抗折强度；抗压强度；黏结抗拉强度；抗渗性能

中图分类号：TQ172.1；TU528.1 **文献标志码**：A **doi**：10.3969/j.issn.2097-0846.2023.04.006

聚合物改性砂浆由水泥砂浆与聚合物进行复合改性而成，因抗折强度与黏结抗拉强度高、韧性及防水抗渗性能好等优点，广泛应用于混凝土修补、防水抗渗、防腐等领域[1]。EVA乳液是常用的聚合物之一，因本身具有脱水、成膜作用，吸附在水泥颗粒表面，可以提升与骨料间的黏结力以及砂浆的抗渗性能[2]。同时EVA乳液也阻碍水泥与水的接触及水化产物的迁移，延迟水泥凝结时间，EVA膜本身强度低，掺入水泥砂浆后会降低砂浆强度[3-5]。在聚合物改性劣质粗骨料研究过程中发现，聚合物砂浆虽然能够显著提升粗骨料的防水抗渗性能，但其凝结时间过长，不易包裹在粗骨料表面；砂浆强度低，对改性后粗骨料压碎指标、坚固性的改善造成不良影响。

聚合物与水泥浆体的质量比即聚灰比（*P/C*），对聚合物改性砂浆性能影响显著。聚灰比过小，改性砂浆防水抗渗性能偏低；过大又延长砂浆凝结时间，降低砂浆抗压强度。为提升砂浆防水抗渗性能，同时减少对砂浆强度的弱化作用，选用高强水泥砂浆为对比样品，通过试验研究不同聚灰比对聚合物砂浆性能影响，选出最佳聚灰比值，研制出适用于聚合物改性劣质粗骨料的砂浆，同时也为EVA乳液在其他聚合物砂浆中的应用提供参考。

1 试验材料

高强水泥砂浆规格为Hoja-53F，水胶比0.14，其性能指标见表1。EVA乳液牌号为BJ707，其主要性能指标见表2。

表1 高强水泥砂浆性能测试结果

出机流动度/mm	凝结时间/min		抗折强度/MPa			抗压强度/MPa		
	初凝	终凝	3 d	7 d	28 d	3 d	7 d	28 d
301	70	130	10.9	13.5	13.8	62.9	77.8	83.0

表2 EVA乳液主要性能

乳液	pH值	不挥发物/%	黏度/（MPa·s）	最低成膜温度/℃	粒径/μm
EVA	4.0~5.0	54.5	500~1 000	≤5	≤0.5

2 试验方法

试验以水泥砂浆为空白样品，4组聚合物砂浆聚灰比分别为1%、2%、5%、10%，砂浆水胶比均为0.14，EVA乳液所含水分在砂浆用水量中扣除，砂浆成型及养护参照GB/T 17671—2021《水泥胶砂强度检验方法（ISO法）》进行。

2.1 密度测试

聚合物砂浆密度依据DL/T 5126—2001《聚合物改性水泥砂浆试验规程》进行测试。

2.2 凝结时间测试

聚合物砂浆凝结时间参照GB/T 1346—2011《水泥标准稠度用水量、凝结时间、安定性检验方法》进行测试。

2.3 力学性能测试

聚合物砂浆力学性能依据DL/T 5126—2001《聚合

收稿日期：2023-05-13；修回日期：2023-06-09
基金项目：非金属材料创新中心应用示范类项目（2022SFP5-1）
第一作者：王军伟（1978—），男，副研究员，硕士。E-mail：wjwei3578@163.com

(C)1994-2023 China Academic Journal Electronic Publishing House. All rights reserved. http://www.cnki.net

物改性水泥砂浆试验规程》进行测试。

2.4　抗渗性能测试

聚合物砂浆养护至28 d,对砂浆试件进行抗渗性能测试,测试方法依据GB/T 50082—2009《普通混凝土长期性能和耐久性能试验方法标准》中的快速氯离子迁移系数法(RCM法)进行。

3　试验结果分析

3.1　聚灰比对聚合物砂浆密度的影响

不同聚合物砂浆密度测试结果如图1所示。

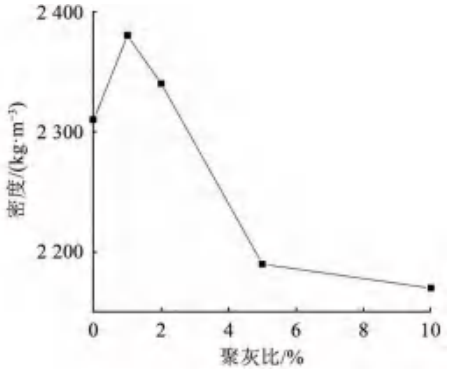

图1　聚灰比对聚合物砂浆密度的影响

EVA乳液填充到水泥砂浆孔隙中,能够改善其内部孔结构,提升水泥砂浆密实度。EVA乳液具有成膜作用,在水泥水化过程中封闭砂浆内联通孔道,减少水分流通与蒸发。在2种因素综合作用下,当聚灰比较低时(小于等于1%),随聚灰比增加,聚合物砂浆的密度也增大。如图1所示,聚灰比为1%时聚合物砂浆的密度最大,其后随聚灰比增加,密度不增反减。出现上述现象的原因是EVA乳液本身具有一定引气性能[6],在搅拌过程中引入气体,聚灰比越大引气作用越明显,砂浆中孔隙增加速度大于EVA填充速度,造成含气量增加,聚灰比大于1%后,密度随聚灰比增大而减少。

3.2　聚灰比对聚合物改性砂浆凝结时间的影响

聚合物改性砂浆凝结时间测定结果见表3。

表3　不同聚灰比聚合物改性砂浆凝结时间测定结果

聚灰比/%	凝结时间/min	
	初凝	终凝
0	70	130
1	80	140
2	100	160
5	150	230
10	170	270

有研究表明[7]EVA乳液阻碍水泥水化,随聚灰比增大凝结延迟时间变长。聚合物逐渐脱水成膜并吸附在水泥颗粒表面,在水泥水化进行过程中,水泥颗粒表面形成的聚合物膜不仅阻碍了水泥与水的接触,也阻碍了水化产物的迁移,从而延迟水泥继续水化,使凝结时间延长。另外,EVA乳液的高黏性,改变砂浆中液相离子迁移,影响水化进程,改变水化产物形态。也有研究者发现聚合物活性物质与Ca^{2+}反应,降低砂浆体系中Ca^{2+}浓度,抑制水化产物成核,同样减缓水化速度[8]。从表3可知,与空白样品相比,聚灰比为2%时,初凝、终凝时间分别增长43%、23%;聚灰比为10%时,初凝、终凝时间分别增长143%、108%。聚灰比对聚合物砂浆凝结时间延迟作用显著。

3.3　聚灰比对聚合物改性砂浆力学性能的影响

3.3.1　聚灰比对抗折强度的影响

如图2所示,相同龄期砂浆抗折强度及变化速率随聚灰比增大而减小。空白样品7 d、28 d抗折强度相比3 d分别增长24%、28%。随聚灰比增大抗折强度的增长速率减缓,聚灰比增至10%时,7 d、28 d抗折强度相比3 d只增长6%、9%,3个龄期的抗折强度相差不大。聚灰比较低时,EVA乳液呈点状分散在砂浆中,不同EVA乳液颗粒间无桥接作用,对水泥水化影响并不明显。随着聚灰比增大,EVA乳液在砂浆中呈带状或网状分布,成膜效应更显著,水泥水化产物与EVA膜相互交织,EVA膜厚度越大,越不易被水化产物穿破,形成的网状结构封堵砂浆中的孔道,抑制水化产物生长。砂浆水胶比均为0.14,水胶比在较低情况下,聚灰比延缓水泥水化作用更明显[9]。

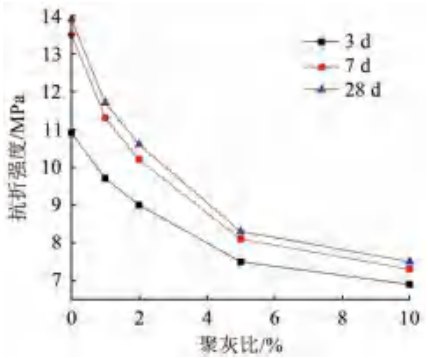

图2　聚灰比对砂浆抗折强度的影响

3.3.2　聚灰比对抗压强度的影响

虽然EVA乳液填充到砂浆内部孔隙中,能够改善砂浆孔结构,提高砂浆密实性,但EVA膜抗压强度低,在砂浆中无法起到骨架支撑作用。随聚灰比增大,EVA乳液在搅拌时引入气体增多,造成砂浆中孔隙率增加,砂浆密实度降低。如图3所示,与聚灰比对抗折强度影响类似,相同龄期砂浆抗压强度及变化速率随聚灰比增大而减小。与3 d抗压强度相比,空白样品

(C)1994-2023 China Academic Journal Electronic Publishing House. All rights reserved.　http://www.cnki.net

7 d、28 d分别增长24%、32%；聚灰比增至10%，7 d、28 d抗压强度增长率降至3%、6%。随EVA乳液用量增加，聚灰比对砂浆抗压强度的负效应越显著，且对砂浆早期水化影响大。聚灰比大于2%后，砂浆3 d抗压强度降低速率加快，聚灰比为5%时，抗压强度相比空白样品已减少约50%。

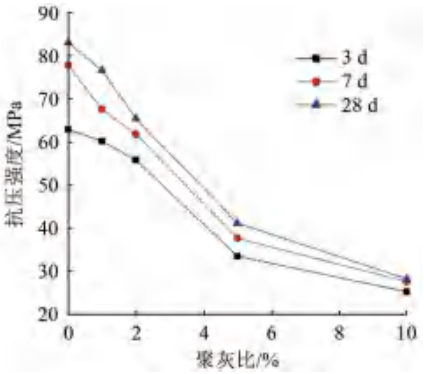

图3 聚灰比对砂浆抗压强度的影响

3.3.3 聚灰比对28 d压折比的影响

从图4可知，随聚灰比增大，28 d压折比先增加后减小，聚灰比为1%时达峰值，说明聚灰比小于1%，EVA乳液对抗压强度的弱化作用小于抗折强度。随聚灰比继续增大，EVA乳液引气效应明显，砂浆抗压强度快速下降。而EVA乳液通过渗透及表面成膜，在不同颗粒间有黏结和联接作用，抑制砂浆抗折强度降低，当聚灰比大于1%后，EVA乳液对砂浆抗压强度的弱化作用大于抗折强度，28 d压折比随聚灰比增大而减小。

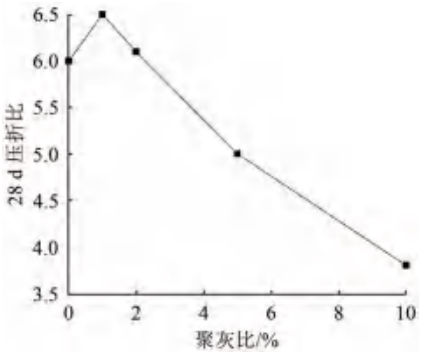

图4 聚灰比对28 d压折比的影响

3.3.4 聚灰比对黏结抗拉强度的影响

EVA乳液具有良好的黏结性能，在水泥水化产物、骨料等界面通过成膜提升黏结力。另外，EVA乳液水泥浆体渗入砂浆孔隙中，进而改善砂浆中不同颗粒之间的黏结咬合力。如图5所示，随聚灰比增加，砂浆黏结抗拉强度呈现单边增长。聚灰比大于1%后，砂浆黏结抗拉强度快速提升，聚灰比增至10%时强度值为空白样品的3倍。

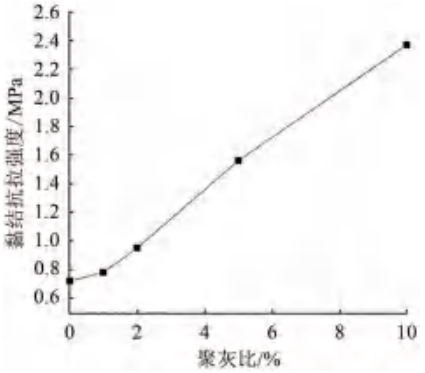

图5 聚灰比对砂浆黏结抗拉强度的影响

3.4 聚灰比对抗渗性能的影响

不同聚灰比砂浆抗渗性能测试结果见图6。

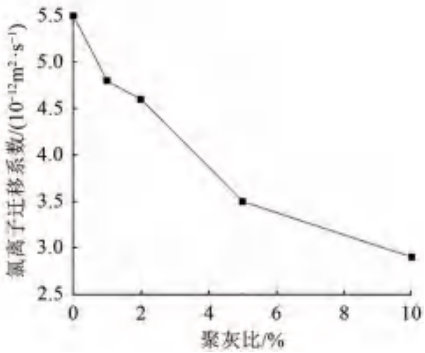

图6 聚灰比对砂浆抗渗性能的影响

随聚灰比增加，砂浆氯离子迁移系数呈现下降趋势，与空白样品相比分别降低了13%、16%、36%、47%。而氯离子迁移系数越小，砂浆抗渗性能越好，验证EVA乳液可显著提升砂浆抗渗透性能。从表2可知，EVA乳液所含的颗粒尺寸小于等于0.5 μm，在水泥浆体中主要填充10~1 000 nm的孔隙，改善过渡孔与毛细孔的结构[10]。聚灰比增加后，EVA乳液成膜效应显现，形成互联网络结构，封堵砂浆内部贯通的孔道，进而阻碍了氯离子向混凝土内部的扩散[11-12]。

4 结论

（1）当聚灰比较小时（小于1%），EVA乳液填充砂浆内孔隙，并提升砂浆密度；随聚灰比不断增加，EVA乳液引气效应显现，砂浆密度反而随聚灰比增大而减小。

（2）相同龄期砂浆抗折与抗压强度数值及变化速率随聚灰比增大而减小，聚灰比增至10%后，砂浆抗折与抗压强度随龄期增加而趋于稳定。

（3）EVA乳液明显提升聚合物砂浆黏结抗拉强度，当聚灰比大于1%后，砂浆黏结抗拉强度快速提升。

(C)1994-2023 China Academic Journal Electronic Publishing House. All rights reserved. http://www.cnki.net

（4）随聚灰比增加，砂浆氯离子迁移系数呈现下降趋势，验证EVA乳液可显著提升砂浆抗渗透性能。

（5）EVA乳液对砂浆凝结时间延迟、抗折强度与抗压强度负效应随聚灰比增加而增大，当聚合物砂浆黏结抗拉强度及抗渗性能满足要求时，应尽量降低EVA乳液用量。

参考文献：

[1] 石鑫，徐玲玲，冯涛，等.新型聚合物改性隧道防渗砂浆及工程应用研究[J].硅酸盐通报，2021，40(8)：2497-2507.

[2] 孟博旭，许金余，顾超，等.VAE乳胶粉掺量对苯丙乳液基水泥复合填缝料拉伸和剪切性能的影响[J].硅酸盐通报，2019，38(6)：1713-1718.

[3] 王世闰，杨蕊敏，李倩，等.聚合物对水泥水化进程和砂浆微观结构的影响[J].武汉轻工大学学报，2019，38(6)：34-38.

[4] 何如，徐方，綦建峰.不同聚合物乳液对水泥砂浆特性影响及作用机理[J].人民长江，2012，43(15)：54-58.

[5] 裴须强，朱玉雪，张帅.丙烯酸乳液改性水泥加固砂浆的性能研究[J].硅酸盐通报，2020，39(2)：409-415.

[6] UKRAINCZYK N, ROGINA A. Styrene-butadiene latex modified calcium aluminate cement mortar[J]. Cement and Concrete Composites，2013，41：16-23.

[7] 魏玉荣，魏茂.EVA对水泥水化影响的研究[J].中国水泥，2019(4)：87-91.

[8] 刘斯春.聚合物改性砂浆凝结时间与自由收缩变形的协调性研究[J].新型建筑材料，2017，44(6)：44-47+116.

[9] 赵文杰，张会轩，张宝砚.水灰比和聚灰比对改性砂浆性能和微观结构的影响[J].东北大学学报(自然科学版)，2010，31(2)：236-240.

[10] 张金喜，金珊珊，张江，等.聚合物乳液改性水泥砂浆基本性能研究[J].北京工业大学学报，2009，35(8)：1062-1068.

[11] 李仲玉，李奥然，李欢.聚灰比对聚合物改性水泥混凝土耐久性能研究[J].河北建筑工程学院学报，2020，38(2)：14-19.

[12] 关国英，罗红霞，赵文杰.环氧树脂乳液改性水泥基修补材料研究进展[J].硅酸盐通报，2019，38(2)：417-422.

Effects of Polymer-cement Ratio on the Properties of Polymer Mortar

WANG Junwei[1,2], LI Hao[1,2], LI Wenxiu[1,2], JIA Haitao[2], ZHAI Yanjun [2], ZHANG Gonghui[2]

(1. Standards & Metrology Research Institute, China Academy of Railway Sciences Corporation Limited, Beijing 100081, China;

2. China Railway Inspection and Certification Center Co., Ltd., Beijing 100081, China)

Abstract: EVA emulsion has film forming effect and bonding effect, but the compressive strength of polymer mortar with EVA emulsion is relatively low. It delays cement hydration and reduces the compressive strength of cement mortar. In this paper, EVA emulsion and high strength cement mortar were selected to prepare polymer mortar, and the high strength cement mortar was taken as blank sample, and four kinds of mortar with different polymer-cement ratios (1%, 2%, 5%, 10%) were tested. The results show that with the increase of polymer-cement ratio, EVA has more significant influence on the properties of cement mortar. When the bond tensile strength and impermeability of polymer mortar meet the requirements, the amount of EVA emulsion should be reduced as far as possible.

Keywords: polymer-cement ratio; EVA emulsion; flexural strength; compressive strength; bond tensile strength; impermeability

(责任编辑　问素彦)

(C)1994-2023 China Academic Journal Electronic Publishing House. All rights reserved.　http://www.cnki.net

聚合物改性火山岩粗骨料及其混凝土性能试验研究

王军伟[1,2]，吴国琦[1,2]，洪俊杰[1,2]，彭新勇[2]，翟艳军[2]
（1. 中国铁道科学研究院集团有限公司标准计量研究所，北京 100081；2. 中铁检验认证中心有限公司，北京 100081）

摘　要：火山岩粗骨料有表观密度低、孔隙率高、吸水性能强等特性，但若未经处理直接应用于混凝土中，会对新拌混凝土及硬化混凝土性能有较大影响。采用对聚合物改性的方法，对火山岩粗骨料进行表面改性，使其坚固性、吸水率、对减水剂吸附量等性能得到改善。改性后的火山岩粗骨料混凝土流变性能及和易性、抗压强度、抗氯离子渗透性能大幅提升，各项性能与普通碎石混凝土相当。

关键词：混凝土；火山岩粗骨料；聚合物改性；抗压强度；流变性能；氯离子扩散系数

中图分类号：U214.18　　**文献标识码：**A　　**文章编号：**1006-9178（2024）02-0030-05

Abstract: The volcanic rock coarse aggregate has the characteristics of low density, high porosity and strong water absorption. If the coarse volcanic aggregate is not treated, it will have a great influence on the performance of both freshly mixed concrete and hardened concrete when applied to concrete. After the volcanic rock coarse aggregate was modified by polymer modification, the properties such as soundness, water absorption and water reducing agent adsorption have been significantly improved. the rheological properties, workability, compressive strength and chloride penetration resistance of the modified volcanic rock coarse aggregate concrete are greatly improved. The properties are the same as ordinary crushed stone concrete.

Keywords: Concrete; Volcanic Rock Coarse Aggregate; Polymer Modification; Compressive Strength; Rheological Property; Chloride Diffusion Coefficient

1　概述

粗骨料约占混凝土体积的 70%，其特性直接影响混凝土各项性能。随着国内基建工程的需求增加，陆地可供开采的优质骨料资源日益减少，资源严重短缺[1]。我国火山岩资源主要分布在东南及西南地区，综合开发利用火山岩资源，利用火山岩制成粗骨料，对缓解骨料供需矛盾及环境保护具有重要意义。

火山岩粗骨料与轻质骨料类似，有表观密度低、孔隙率高、吸水性强等特性[2]。火山岩粗骨料配制的混凝土用水量大，需要更多的砂浆才能被包裹。达到相同混凝土初始流变性能，火山岩混凝土需要外加剂掺量高，保坍性能差，经时变化量大[3-4]。火山岩本身强度不高，在搅拌过程中骨料相互摩擦，骨料会破碎，改变原有粒度分布，对混凝土性能带来影响[5]。针对上述问题，选用超早强型水泥砂浆与 EVA 乳液配制聚合物砂浆，用于火山岩粗骨料聚合物改性，提升火山岩粗骨料各项性能，使其满足施工现场的应用要求。

收稿日期：2023-06-24
作者简介：王军伟，副研究员；吴国琦，高级工程师；洪俊杰，高级工程师；彭新勇，工程师；翟艳军，工程师

2　混凝土原材料及试验方法

2.1　原材料

选取产地为海南的火山岩，产地为山东临沂的普通碎石，二者均为 5 mm~25 mm 连续级配，参照 GB/T 14685—2022《建设用卵石、碎石》，测试原材料基本性能。火山岩和普通碎石物理性能见表 1。

表 1　火山岩和普通碎石物理性能

材料类型	吸水率/%	坚固性/%	表观密度/（kg/m³）	岩石抗压强度/MPa
火山岩	2.5	6	2 070	43
普通碎石	0.2	2	2 780	148
GB/T 14685—2022 规定的技术要求	≤1.0	≤5		

从表 1 可知，火山岩粗骨料表观密度略低于普通碎石；吸水率比 GB/T 14685—2022 规定的技术

(C)1994-2024 China Academic Journal Electronic Publishing House. All rights reserved.　http://www.cnki.net

要求高 150%；坚固性高于标准 20%，约为普通碎石的 3 倍；抗压强度为 43 MPa，约为普通碎石的 29%。总体而言，火山岩骨料属劣质粗骨料。火山岩粗骨料表面形貌如图 1 所示。

（a）多孔状（×20）

（b）小孔罗列（×20）

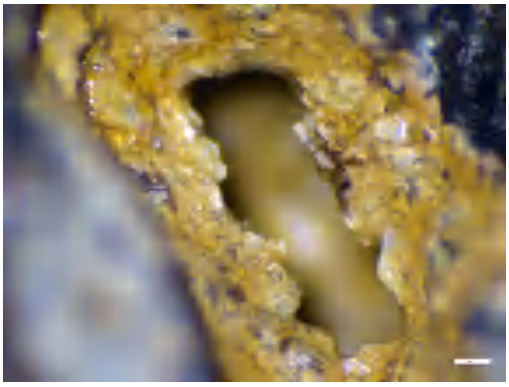

（c）孔形貌（×40）

图 1　火山岩粗骨料表面形貌

图 1（a）显示，火山岩表面呈多孔状，孔径大小不一。多孔贯穿时，凹面长达 20 mm。单孔最大孔径达 8 mm，孔深约 3 mm，孔形貌见图 1（c）。图 1（b）显示，骨料表面有孔径约为 20 μm 的小孔罗列，部分小孔内部贯穿。

水泥为普通硅酸盐水泥，规格为 P.O 42.5，比表面积为 370 m^2/kg。细骨料为山东临沂生产的天然河砂，细度模数为 3.0，含泥量为 1.5%。减水剂为江苏苏博特生产的缓凝型聚羧酸高性能减水剂，减水率为 35%（掺量 1%）。矿粉生产方为菏泽晶富矿渣粉有限公司，等级为 S95。

改性使用的 EVA 乳液牌号为 BJ707。EVA 乳液主要性能指标见表 2。

表 2　EVA 乳液主要性能指标

pH 值	不挥发物/%	粘度/（mPa·s）	最低成膜温度/℃	粒径/μm
4.0~5.0	54.5	500~1 000	≤5	≤0.5

高强水泥砂浆规格为 Hoja-53F，水胶比约为 0.14。高强水泥砂浆性能见表 3。

表 3　高强水泥砂浆性能

出机流动度/mm	凝结时间/min		抗折强度/MPa			抗压强度/MPa		
	初凝	终凝	3 天	7 天	28 天	3 天	7 天	28 天
301	70	130	10.9	13.5	13.8	62.9	77.8	83

2.2　混凝土测试方法

试验研究以普通碎石为对比样品，除粗骨料外，其他原材料均相同。通过改变减水剂掺量，使不同粗骨料混凝土坍落度达到 220 mm±10 mm，对比新拌混凝土及硬化混凝土的差异。

新拌混凝土性能主要依据 GB/T 50080—2016《普通混凝土拌合物性能试验方法标准》，测试坍落度、扩展度、含气量，以及 30 min 经时变化量。混凝土各龄期抗压强度依据 GB/T 50081—2019《混凝土物理力学性能试验方法标准》测试。氯离子扩散系数依据 GB/T 50082—2019《普通混凝土长期性能和耐久性能试验方法标准》中的氯离子扩散快速测定法测试。混凝土试件尺寸为 150 mm×150 mm×150 mm。混凝土成型后先在蒸汽养护箱中用 45 ℃蒸汽养护 10 h，然后转至标准养护室。标准养护条件下（温度 20 ℃±2 ℃，湿度不小于 95%）养护至规定龄期，测试硬化混凝土项目。

2.3　减水剂吸附量测试方法

采用总有机碳分析法（TOC）测试减水剂在粗骨料表面的吸附量，具体操作方法是：称取粗骨料颗粒 15 g，减水剂 0.15 g，水 20 g，混合搅拌 5 min。搅拌后，取适量上层液相，以 1×10^4 r/min 的转速高速离心分离 2 min，取上清液 0.5 g，加 1 mol/L 稀盐酸 1 g，加超纯水稀释至 20 g，使用

(C)1994-2024 China Academic Journal Electronic Publishing House. All rights reserved.　http://www.cnki.net

multi N/C 3100 总有机碳分析仪对试样测试。吸附量依据下式计算。

$$T = \frac{(C_0 - C_1) \times V}{m} \times 1\,000。\quad (1)$$

式（1）中：T 为吸附量，mg/g；C_0 为减水剂的初始质量浓度，mg/L；C_1 为减水剂吸附后的质量浓度，mg/L；V 为体系的体积，L；m 为细骨料质量，g。

3　火山岩粗骨料聚合物改性

火山岩粗骨料因自身特性，在未经处理前，通常只应用于强度等级为 C40 以下的混凝土。因此，需要对其进行表面改性，提升各项性能，才能拓展应用领域。依据以往的研究成果，聚合物改性剂配比为：砂浆：水：EVA=1：0.12：0.02。火山岩粗骨料改性工艺如下：将聚合物砂浆加水搅拌 2 min 后，立即将骨料加入浆体中，再搅拌 2 min，静置 10 min，分离出多余浆体，将改性后粗骨料放置于养护室养护 3 天即可。

改性后火山岩粗骨料外貌如图 2 所示。

（a）单粒改性后火山岩粗骨料外貌

（b）多粒径改性后火山岩粗骨料外貌

图 2　改性后火山岩粗骨料外貌

从图 2（a）中可以看出，火山岩粗骨料改性后，表面被聚合物改性剂包裹，已无多孔形貌。养护至 3 天后，从图 2（b）可以看出，火山岩粗骨料外观与普通碎石无异。

测试改性后火山岩粗骨料坚固性、吸水率、表观密度、对减水剂吸附量。改性前后火山岩粗骨料性能对比见表 4。

表 4　改性前后火山岩粗骨料性能对比

改性前/后	吸水率/%	坚固性/%	表观密度/（kg/m³）	对减水剂吸附量/（mg/L）
改性前	2.5	6.0	2 070	50
改性后	0.3	2.0	2 780	10

从表 4 可知，火山岩粗骨料改性后坚固性、吸水率、对减水剂吸附量分别降低 67%，88%，80%，坚固性、吸水率均达到 GB/T 14685—2022 的技术要求。火山岩粗骨料改性后，除表面包裹聚合物砂浆外，原有内部孔隙也被砂浆填充，表观密度增长约 34%，聚合物改性对火山岩粗骨料性能有显著提升。改性后火山岩粗骨料表观密度增加，缓解新拌混凝土中火山岩粗骨料上浮现象，减少混凝土离析、泌水，增强混凝土保水性能。改性后火山岩粗骨料吸附性能降低，达到相同坍落度所需减水剂掺量减少。

4　聚合物改性对火山岩混凝土性能的影响

4.1　聚合物改性对新拌混凝土性能的影响

试验选用的混凝土配合比为水泥：矿粉：粗骨料：细骨料：水=390：90：1 163：653：144。除粗骨料外，在其余材料均相同条件下，通过改变减水剂掺量使混凝土达到相同坍落度（220 mm±10 mm）。普通碎石混凝土减水剂掺量为 1%，坍落度、扩展度、含气量分别为：200 mm，680 mm，3.2%，经过 30 min 后保留值分别为：180 mm，460 mm，3.3%。改性前火山岩粗骨料混凝土减水剂掺量为 1.5%，改性后混凝土减水剂掺量为 0.8%，这表明聚合物改性显著降低了骨料对减水剂的吸附。改性前后火山岩粗骨料新拌混凝土性能见表 5。

表 5　改性前后火山岩粗骨料新拌混凝土性能

测试时间	扩展度/mm		坍落度/mm		含气量/%	
	改性前	改性后	改性前	改性后	改性前	改性后
初始值	650	740	210	220	3.5	3.3
30 min 值	480	690	120	205	2.7	3.0

(C)1994-2024 China Academic Journal Electronic Publishing House. All rights reserved.　http://www.cnki.net

从表 5 可知，相同混凝土初始坍落度条件下，与改性前相比，改性后的火山岩粗骨料混凝土初始扩展度增长 14%，30 min 扩展度和 30 min 坍落度分别增长 43% 和 71%。改性前后混凝土初始含气量相近，但改性前混凝土 30 min 含气量与初始相比降低 23%，改性后降低 9%。

火山岩粗骨料改性前表面多孔，搅拌过程中孔中空气溢出，使混凝土含气量略高，但这种气泡稳定性差、易破裂，与改性后粗骨料相比，含气量经时损失量多。通过上述分析可知，火山岩粗骨料经聚合物改性后，新拌混凝土流变性能、和易性均有明显改善。

4.2　聚合物改性对混凝土抗压强度的影响

抗压强度是混凝土力学性能的重要指标，不同强度等级混凝土应用领域或构件部位也不同。参照文中 2.2 所述试验方法，分别测试 2 天、3 天、7 天、10 天、28 天、56 天共 6 个龄期混凝土抗压强度，不同龄期混凝土抗压强度测试结果如图 3 所示。

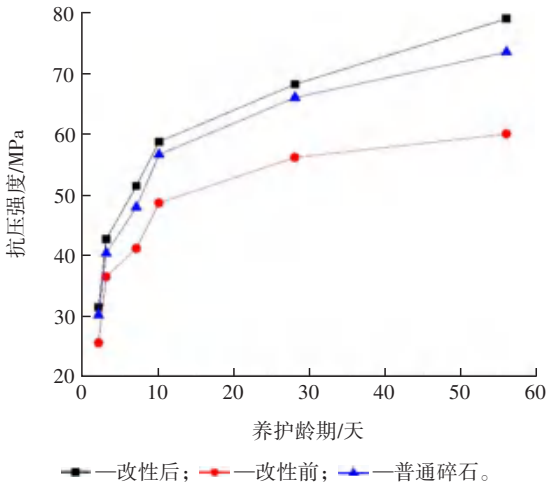

图 3　不同龄期混凝土抗压强度测试结果

从图 3 可以看出，3 种粗骨料混凝土抗压强度随龄期增加而增长，各龄期抗压强度均为改性后最大，改性前最小，表明聚合物改性促进火山岩粗骨料混凝土抗压强度增长。改性后火山岩、普通碎石粗骨料混凝土未出现离析、泌水现象，和易性优于改性前，2 天抗压强度分别高于改性前 23% 和 18%，3 种粗骨料 3 天和 7 天的抗压强度增长速率接近。改性前龄期大于 10 天的抗压强度增长速率明显慢于改性后火山岩粗骨料混凝土，整体呈现早期强度增长快，后期强度增长慢的特点[6-7]。这主要是因为改性前火山岩为多孔骨料，内部大孔较多，在混凝土搅拌过程中，水分同水泥砂浆进入孔隙中，造成局部水分布不均匀，混凝土内局部水胶比偏高。随着泥水化不断深入，多余水分蒸发遗留下的孔隙多，水化产物无法充分填充。高水胶比也造成水泥水化产物相对蓬松，水化产物结构不致密、易出现开裂情况，也降低混凝土后期抗压强度增长速率。与之相反，改性后火山岩表面包裹改性砂浆，同时封闭填充了火山岩内部孔隙，新拌混凝土中的水泥砂浆更易与改性砂浆界面结合，增强骨料与砂浆的粘结力；在粗骨料表面界面区域，形成水灰比由低至高的过渡区浆体，与未改性火山岩相比，水灰比梯度截然相反，提升了界面过渡区强度[8]。在这些因素的综合作用下，改性后的火山岩不同龄期混凝土抗压强度均高于改性前火山岩混凝土，养护后期抗压强度增速也明显加快。

4.3　聚合物改性对混凝土抗氯离子渗透性能的影响

氯离子扩散系数（DRCM）能直接反映混凝土抗氯离子渗透性能，数值越小，抗氯离子渗透性能越强。3 种粗骨料混凝土养护龄期为 10 天、28 天、56 天的氯离子扩散系数测试结果如图 4 所示。

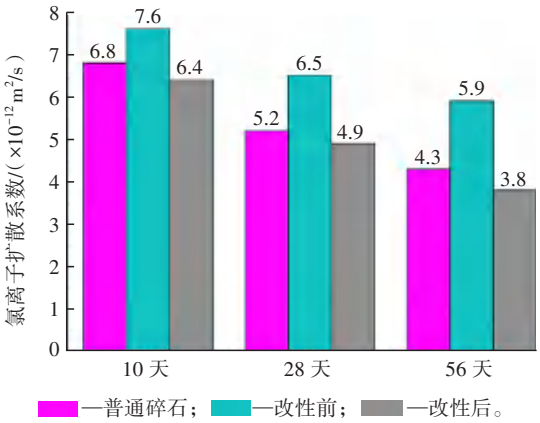

图 4　3 种粗骨料混凝土养护龄期为 10 天、28 天、56 天的氯离子扩散系数测试结果

从图 4 可以看出，相比普通碎石粗骨料混凝土，10 天、28 天和 56 天的火山岩粗骨料混凝土氯离子扩散系数分别增加 12%，25% 和 27%，改性后火山岩骨料混凝土氯离子扩散系数分别降低 6%，6% 和 12%，火山岩粗骨料改性后混凝土氯离子扩散系数显著降低。3 种粗骨料混凝土氯离子扩散系数随龄期增加而降低，改性前火山岩粗骨料混凝土氯离子扩散系数在 28 天、56 天分别比 10 天降低了 14%，22%，普通碎石粗骨料混凝土则分别降低了 23%，36%，改性后火山岩粗骨料混凝土分

(C)1994-2024 China Academic Journal Electronic Publishing House. All rights reserved.　http://www.cnki.net

别降低了 23%，41%。各个龄期均为改性后火山岩粗骨料混凝土数值最小，其次为普通碎石混凝土，最高为改性前火山岩粗骨料混凝土，改性后火山岩粗骨料混凝土 56 天氯离子扩散系数降低速率接近改性前的 2 倍。改性前火山岩粗骨料内部孔隙与贯穿传输通道较多，氯离子更容易渗透到混凝土内部；粗骨料局部水胶比高，与水泥砂浆之间形成的界面过渡区黏结力较低，水化产物结构疏松，易产生微裂缝，这些原因均使混凝土抗氯离子渗透性能降低[9]。改性后火山岩粗骨料表面包裹改性砂浆，水泥水化产物填充了骨料内部孔隙，提升混凝土密实程度，进一步改善界面过渡区，低水胶比、高强度聚合物改性砂浆本身对氯离子有迁阻作用，从而提升火山岩粗骨料混凝土抗氯离子渗透性能[10-11]。

5　结论

通过使用聚合物对火山岩粗骨料改性，获得更好的性能。通过试验和分析可以得到如下结论。

（1）火山岩粗骨料经聚合物改性后，坚固性、吸水率、对减水剂吸附量均得到显著改善。

（2）改性后火山岩粗骨料新拌混凝土的流变性能、和易性明显优于改性前。

（3）改性后火山岩粗骨料混凝土在不同龄期的抗压强度均高于改性前，10 天后抗压强度增速大于改性前。

（4）改性后火山岩粗骨料混凝土在 56 天龄期时的氯离子扩散系数降低速率接近改性前的 2 倍，混凝土抗氯离子渗透性能明显改善。

参考文献

[1] 王永海，周永祥．天然火山灰质材料及其在混凝土中的应用研究［C］//中国硅酸盐学会混凝土与水泥制品学分会，2011 年混凝土与水泥制品学术讨论会论文集．北京：中国建筑科学研究院建筑材料研究所，2011：277-286．

[2] 陈迪森．搅拌工艺对多孔类骨料混凝土性能的影响［D］．广西：广西大学，2017．

[3] 邓志恒，刘兵，盛军，等．珊瑚混凝土研究进展［J］．硅酸盐通报，2020，39（4）：1026-1034．

[4] 陈飞翔，张国志，丁沙，等．珊瑚骨料混凝土性能试验研究［J］．混凝土与水泥制品，2017（4）：17-21．

[5] 高洪波，姜宝石，谢洪波．再生火山岩骨料混凝土抗压强度及干缩性能试验［J］．山西建筑，2015，41（26）：120-123．

[6] 赵艳林，韩超，张栓柱，等．海水拌养珊瑚骨料混凝土抗压龄期强度试验研究［J］．混凝土，2011（2）：43-45．

[7] 王磊，范蕾．珊瑚碎屑混凝土的强度特性及破坏形态分析［J］．混凝土与水泥制品，2015（1）：1-4．

[8] 张栓柱．珊瑚混凝土的疲劳特性及微观机理研究［D］．广西：广西大学，2012．

[9] 黄龙．改性珊瑚骨料混凝土基本力学性能及抗渗性试验研究［D］．广西：桂林理工大学，2022．

[10] 郭曈，欧忠文，唐军务，等．PVA 改性水泥基珊瑚骨料试验研究［J］．当代化工，2017，46（11）：2213-2218．

[11] 刘军，邢锋，董必钦．混凝土孔结构和渗透性能关系研究［J］．混凝土，2007（12）：35-37，41．

（编辑　吴　磊）

2024 年全国认证认可检验检测工作会议在北京召开

2024 年 1 月 12 日，国家市场监督管理总局在北京召开 2024 年全国认证认可检验检测工作会议。会议以习近平新时代中国特色社会主义思想为指导，深入学习领会党的二十大精神和中央经济工作会议精神，深入贯彻落实习近平总书记关于高质量发展和认证认可检验检测工作系列重要指示批示精神，进一步落实全国市场监管工作会议部署要求，总结 2023 年工作，部署 2024 年重点任务。国家市场监督管理总局党组成员、副局长，国家认监委主任蒲淳出席并作工作报告。

会议强调，2024 年，要重点做好以下认证认可检验检测工作。一是着力完善认证认可检验检测“统一管理、共同实施”工作体系。健全全国认证认可工作部际联席会议制度，统筹推进质量认证“六大行动”，完善国家统一的认证制度，加强检验检测机构资质统一管理。二是加快推进认证认可检验检测“走出去”。健全完善认证认可国际合作格局，提升认证认可国际合作效能，打造合格评定国际品牌。三是积极推动认证认可检验检测服务强企强链强县。优化认证认可检验检测服务供给，服务企业降本增效提质、产业建圈强链和区域经济高质量发展。四是持续提升认证认可检验检测监管效能。夯实监管制度基础，提高智慧监管能力，压实从业机构主体责任，建立重点领域、重点环节监管长效机制，加强认证认可检验检测领域安全生产监管。五是不断提高认证认可检验检测专业化水平。加强监管队伍建设，促进从业机构和从业队伍能力提升，加快行业数字化转型发展。六是大力促进认证认可检验检测价值转化。健全采信推广机制，加强基础研究，完善评价体系，加大宣传力度。七是全面加强党对认证认可检验检测工作的领导。强化政治引领，筑牢纪律防线，深化作风建设。

天津、河北、上海、江苏、山东、湖北、广东、四川等 8 个省（市）市场监管部门进行了大会发言经验交流，北京、浙江、福建、新疆等 4 个省（区、市）市场监管部门进行了书面经验交流。总局有关司局、直属单位和特邀单位负责同志，各省、自治区、直辖市和新疆生产建设兵团市场监管局（厅、委）负责同志及有关人员参加会议。

摘编自　国家市场监督管理总局网站

(C)1994-2024 China Academic Journal Electronic Publishing House. All rights reserved.　http://www.cnki.net

Construction and Building Materials 409 (2023) 134163

Contents lists available at ScienceDirect

Construction and Building Materials

journal homepage: www.elsevier.com/locate/conbuildmat

Improving the interfacial properties of PVA fiber and cementitious composite: Design and characterization

Shun Yao [a,b], Chuanlin Hu [a,*], Fazhou Wang [a,b], Shuguang Hu [a,b]

[a] State Key Laboratory of Silicate Materials for Architectures, Wuhan University of Technology, Wuhan 430070, China
[b] School of Materials Science and Engineering, Wuhan University of Technology, Wuhan 430070, China

ARTICLE INFO

Keywords:
Fiber reinforced cementitious composites
Interfaces
Graphene oxide
Microstructure
Fracture mechanics/toughness

ABSTRACT

Poly vinyl alcohol (PVA) fiber has been widely applied to improve the ductility of cementitious materials, and the overall performance of fiber reinforced cementitious materials largely depends on the interfacial properties of the fiber and cementitious matrix. In this work, a novel design of graphene oxide (GO) modified PVA fiber is proposed to improve the interfacial properties of PVA fiber and cementitious matrix. It is found that the interaction between GO and PVA fiber forms the hydrogen bond and enables the GO to form a tight three-dimensional bonding on the surface of the PVA fiber. Meanwhile, the oxygen-containing functional groups of GO could form chemical bond with the hydration products and promote the formation of denser microstructure at the interface. Therefore, the introduction of GO prominently improves the interfacial properties of PVA fiber and cementitious matrix, which is verified by the characterizations on the microstructures and morphologies. Furthermore, it is found that GO remarkedly improves the interfacial mechanical properties and results that a zone with the enhanced mechanical properties appears near the interface, verified by the characterizations on the micro-mechanical properties including fracture toughness near the interface.

1. Introduction

Concrete is the most commonly-used construction material, and has many advantages such as wide source of raw materials, low price, good workability, etc. However, the high brittleness of concrete limited its wide application in the modern construction engineering [1–3]. The fiber has been widely used to enhance the toughness of concrete, and many studies have shown that the fiber significantly improves the crack resistance and toughness of concrete [4–8]. The mechanism is that the fiber can use its own pull-out, debonding, fracture and other processes to consume part of the energy when the concrete material fracture occurs. Among the fibers, polyvinyl alcohol (PVA) fiber has been widely used in engineering practice because of its advantages including good dispersion, strong corrosion resistance and high tensile strength [9–11]. Nowadays, with the development of nanotechnology, more and more researches have been dedicated to the application of nano-materials into cementitious composites. Some researches showed that nano-materials can improve the pore structure of concrete, and effectively prevent the development of micro-scale pores into macro-scale pores, to control the generation of cracks and prevent the brittle failure of concrete [12,13]. Carbon nanomaterials have drawn many attentions due to their superior mechanical and chemical properties [14,15]. Specially, graphene oxide (GO) is considered to be the most promising reinforced material in cementitious materials as it could form chemical bond with major hydration product of cement, i.e. C-S-H (calcium-silicate-hydrates) gel, due to the presence of carboxyl functional groups [16,17].

However, concrete is a typical multi-scale material containing heterogeneous phases. The multi-scale characteristics of concrete lead to the multi-scale failure process under load, the micro-crack in the matrix evolves with time during the whole failure process, and then it gradually develops and expands to macro-cracks. Toughening at single scale by fiber (e.g. PVA fiber) or nano-material (e.g. GO) restricts the toughing

* Corresponding author.
E-mail address: chuanlin@whut.edu.cn (C. Hu).

https://doi.org/10.1016/j.conbuildmat.2023.134163
Received 4 April 2023; Received in revised form 7 November 2023; Accepted 9 November 2023
Available online 20 November 2023
0950-0618/© 2023 Elsevier Ltd. All rights reserved.

Table 1
Chemical compositions of ASTM Type I cement.

Oxides	CaO	SiO_2	Al_2O_3	Fe_2O_3	MgO	K_2O	Na_2O	LOI
wt%	63.06	21.7	4.71	3.21	1.78	0.67	0.12	2.42

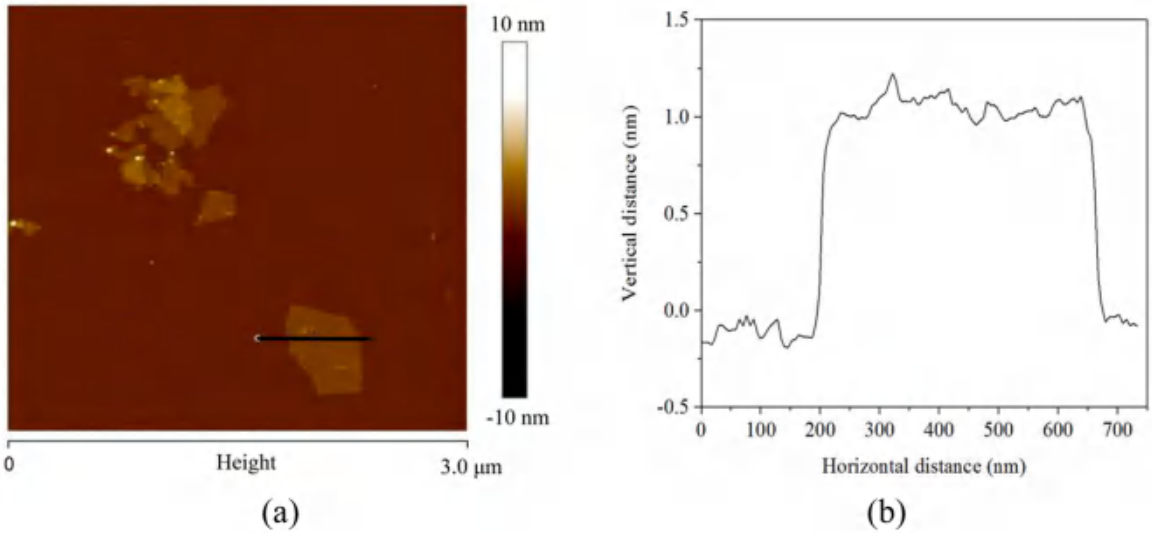

Fig. 1. (a) AFM image of GO and (b) the profile of height along the marked line.

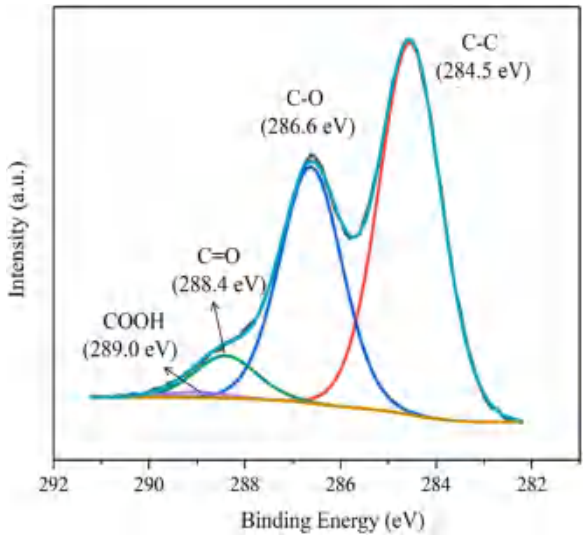

Fig. 2. XPS spectra of GO.

potential. Besides, the fiber has poor compatibility in cementitious matrix, resulting in the weak bonding between the fiber and cementitious matrix [18,19]. Moreover, GO is difficult to disperse uniformly in cementitious matrix, as it is easy to aggregate in pore solution [20,21].

In this study, a novel GO modified PVA fiber was designed by mixing PVA fibers in GO aqueous solution under heating condition. Then, GO modified PVA fiber was used in the preparation of cement paste, and the interfacial properties were characterized by various techniques including scanning electron microscopy, scanning probe microscopy, and micro-mechanical testing.

2. Materials and characterization

2.1. Materials

The chemical compositions of ASTM Type I cement used in this study were measured by X-ray fluorescence, as listed in Table 1. The fiber was commercially purchased PVA fiber with the average length of 12 mm and the average diameter of 36 μm. GO was commercially purchased, and analyzed by atomic force microscope (AFM, Bruker Dimension

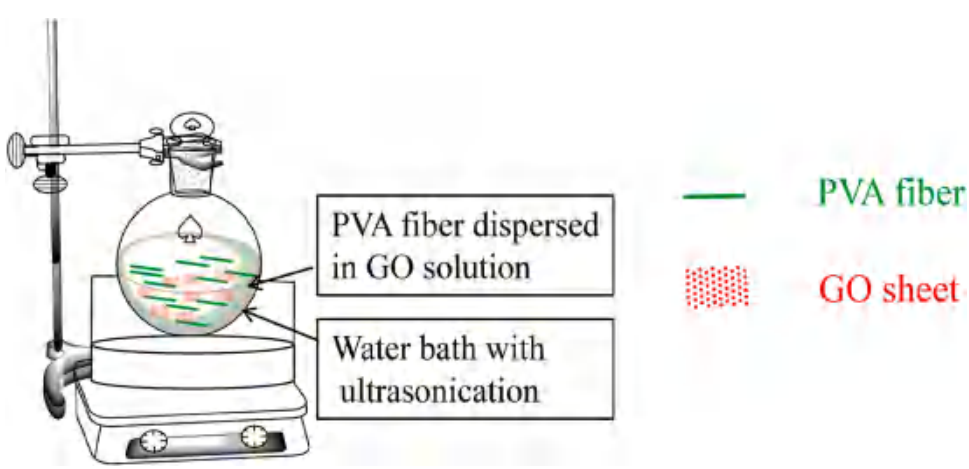

Fig. 3. The schematic diagram of reaction device for the design of the GO/PVA fiber.

Table 2
Mix proportions of cement paste samples.

Sample	w/c	Cement (g)	PVA (g)	GO/PVA (g)
1	0.35	100	4	0
2	0.35	100	0	4

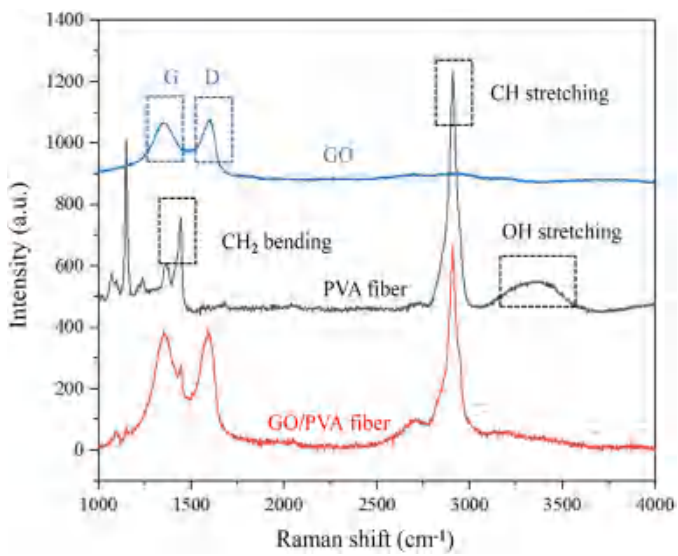

Fig. 4. Raman spectra of GO, PVA fiber and GO modified PVA fiber.

ICON) and X-ray photoelectron spectroscopy (XPS, EscaLab Xi), as shown in Fig. 1 and Fig. 2. AFM image of GO showed that the thickness of GO was around 1 nm, and the dispersed GO mainly consisted of one or two layers. Fig. 2 shows the XPS spectra of GO, the binding energies at 284.5 eV, 286.6 eV, 288.4 eV and 289.0 eV typically belonged to the C-C, C-OH, C═O, and O═C-OH functional groups, respectively [22,23]. Finally, the C/O ratio was calculated to be 2.6 according to XPS spectra.

2.2. Design of the GO modified PVA fiber

The diagram of the reaction device for the design of the GO modified PVA fiber is schematically shown in Fig. 3. The composite of GO/PVA fiber was fabricated through the following steps: First, the 0.1 g GO was dispersed in 300 ml water, and treated with ultrasonic dispersion for 10 min. Then, 300 ml GO solution and 5 g PVA fiber were added into a flask, and the solution was then continuously stirred. During the stirring, the flask was heated from 20 ℃ to 80 ℃ with a heating rate of 3 ℃/min and then maintained at 80 ℃ for another 3 h under water bath. Afterwards, the solution was filtered and the GO modified PVA fiber was collected. Finally, the GO modified PVA fiber was dried under 40 ℃ for 3 days. The mechanism GO of tightly wrapping fibers can be attributed to their different thermal expansion effects. PVA fibers will expand with increasing temperature, while GO will shrink with increasing temperature. In addition, the hydroxyl groups of the PVA fiber can react with the oxygen-containing functional groups of the GO to form the hydrogen bonding. Therefore, the surface of PVA fiber could be tightly wrapped by GO.

2.3. Preparation of cement pastes

Two cement pastes were prepared with the same water-to-cement (w/c) ratio of 0.35 and the mix proportions can be found in Table 2, where different fibers were used, i.e. PVA fiber and GO modified PVA fiber. Firstly, the cement and fiber were added into a beaker and stirred for 3 min. Then, water was added and the mixture was continuously stirred for another 3 min. After that, the fresh cement pastes were cast into 4 mm × 4 mm× 4 mm molds, and then they were cured at room condition for 24 h. Finally, the cement pastes were demoulded and cured in standard curing room (≥95% RH, 20 ℃ ± 1 ℃) for another 2 days.

For the micro-mechanical test, the small sections were cut out from the cement pastes by a low-speed diamond wheel saw. After cutting, the small sections were put in the absolute alcohol to terminate their hydrations. Then, the small sections were dried in a vacuum drying oven for one day. Before the indentation test, the samples were treated with sufficient polishing to obtain smooth and flat sample surface. Firstly, the samples were polished in a Buehler polishing machine by polishing papers for 5–10 min (240 grid, 400 grid, 600 grid, 800 grid and 1200 grid), then they were polished with different diamond suspensions for 30–60 min (3 μm, 1 μm, 0. 25 μm, and 0.05 μm).

2.4. Characterization methods

2.4.1. Morphology and structure characterization

The interaction of the GO and PVA fiber was characterized by a Raman spectrometer with a 532 nm laser source. The microstructures of the samples were characterized by scanning electron microscopy (SEM). The interface between fiber and cementitious matrix was first observed in the optical microscope and the SEM in backscattered mode. Then the 3D morphology of the interface was examined by scanning probe microscopy (SPM). The operation voltage and working distance of SEM were set to 20 kV and 10 mm respectively, and the scanning area of SPM was 40 μm × 40 μm.

2.4.2. Micro-mechanical characterization

Indentation tests and scratch tests were used to characterize the micro-mechanical properties of samples by Hysitron Triboindenter. A Berkovich tip was used for indentation test, and a spherical conical tip was used for scratch test. Before testing, the standard fused quartz

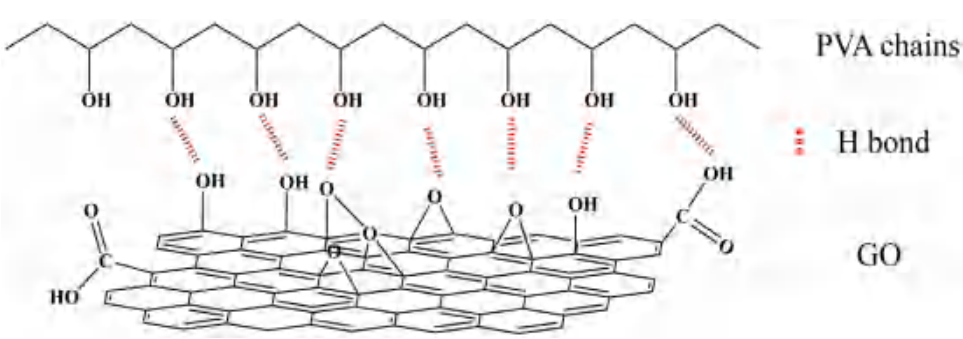

Fig. 5. The interaction mechanism between PVA fiber and GO.

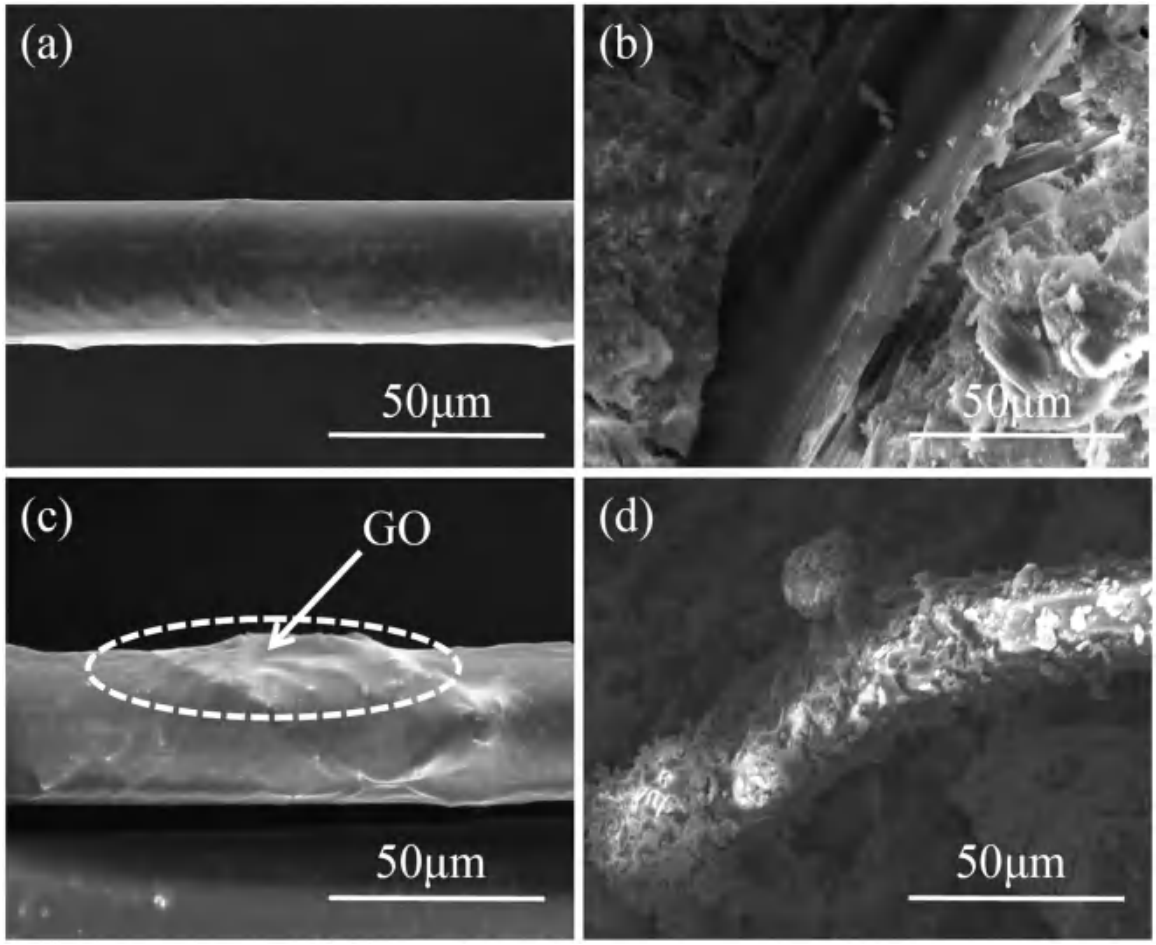

Fig. 6. Surface morphologies of (a) pristine PVA fiber, (b) pristine PVA fiber embedded in cement paste, (c) GO modified PVA fiber, and (d) GO modified PVA fiber embedded in cement paste.

sample was used to calibrate the Triboindenter. The indentation tests were carried on each sample with the following load function: the load linearly increased from 0 to 500 μN in 0.3 s, then kept constant at 500 μN for 0.3 s, and finally linearly decreased from 500 μN to 0 μN in 0.3 s 64 nano-indentation tests were performed on each sample and distributed in an 8 × 8 matrix. The indented area covered the interface between fiber and cementitious matrix. The scratch tests have been used as effective tool to investigate the interfacial properties [24]. In this study, the scratch tests were carried on each sample and each scratch passed through the fiber - cementitious matrix interface. For the scratch tests, the following load function was adopted: the vertical force (*Fv*) linearly increased with time from 0 to 100 mN at a rate of 10 mN/s, then kept constant at 100mN for 10 s, and the horizontal displacement both linearly increased with time at the rate of 15 μm/s. In the process of scratch test, the vertical displacement (*d*) was recorded automatically. From the recorded vertical displacement (*d*) value and the horizontal force (F_T) value, the fracture toughness of *Kc* of materials can be calculated according to the scheme of linear elastic fracture mechanics [25–27].

3. Results and discussion

3.1. Interaction of GO and PVA fiber

Raman spectra of GO, PVA fiber and GO modified PVA fiber are shown in Fig. 4. The Raman shifts at 1354 cm^{-1} and 1588 cm^{-1} corresponded to the G band and D band of GO. The Raman shifts of 1425 cm^{-1} and 2900 cm^{-1} corresponded to CH_2 bending and CH stretching of PVA fiber and the wide peak at 3300 cm^{-1} corresponded to OH stretching of PVA fiber. Most of Raman shifts of GO and PVA fiber were observed in Raman spectra of GO modified PVA fiber, conforming that GO was successfully bonded on the surface of PVA fibers. However, the OH stretching peak was significantly weakened and almost disappeared in GO/PVA fiber, indicating that the hydroxyl groups were consumed to form the new chemical bonds. As there were numerous oxygen-containing functional groups on the surface of GO and hydroxyl groups on the PVA molecular chain, the hydroxyl groups of the PVA fiber reacted with the oxygen-containing functional groups of the GO to form the new hydrogen bonds. Therefore, Raman spectra of GO modified PVA fiber showed that PVA fiber and GO were chemically bonded, and the interaction mechanism between PVA fiber and GO is illustrated in Fig. 5.

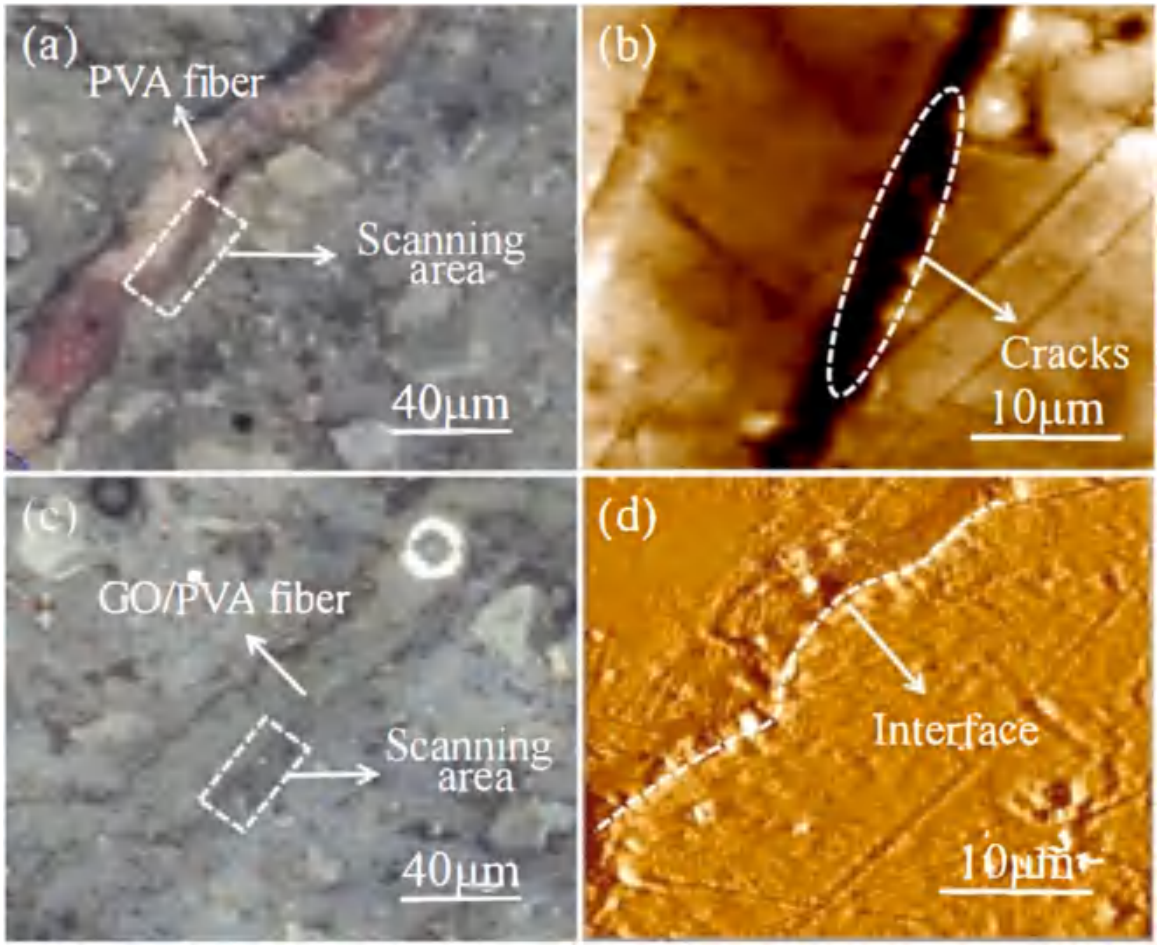

Fig. 7. Optical images of (a) pristine PVA fiber and (c) GO modified PVA fiber embedded in the cement paste, and SPM morphologies close to (b) pristine PVA fiber and (d) GO modified PVA fiber.

3.2. Surface morphology

Fig. 6 compares the surface morphologies between the pristine fiber and modified fiber. The PVA fiber presented a very smooth surface as shown in Fig. 6(a), while the GO modified PVA fiber presented a rough surface as shown in Fig. 6(c) due to the bonding on the PVA fibers by the wrinkled GO layers. Moreover, in fiber reinforced cement paste, it was found that hydration products were formed around the surface of GO/PVA fiber, while no hydration products were observed in PVA fiber in Fig. 6(b), indicating that the GO greatly promoted the formation of hydration products on the surface of GO/PVA fiber and enhanced the interaction of the PVA fiber and the cementitious matrix. The mechanism was related to the structural characteristics of GO: (1) The oxygen-containing functional groups in GO, i.e. carboxyl, hydroxyl and oxyl could attract water molecule due to their polarity and thus could promote the hydration process at the interface; (2) The carboxyl group of GO could form chemical bonding with the hydration products, especially C-S-H gel, and thus promote the formation of denser microstructure of hydration products.

3.3. Interfacial microstructure

The interfacial microstructures were firstly observed by optical microscope, and the positions of the fibers are marked in Fig. 7(a) and (c). Then SPM was used to capture an 3D morphology of the interface. There were straight cracks at the interface of the PVA fiber and the cementitious matrix as shown in Fig. 7(b), while the interface between GO modified PVA fiber and cementitious matrix was arc-shaped without any observable cracks. The result showed that GO improved the compatibility of PVA fiber and cementitious matrix, so the bonding of the PVA fiber and the cementitious matrix was significantly enhanced. Furthermore, the deformed fibers with twisted shape greatly enhanced the anchor strength which contributed to increase the energy consumption during the pulled-out process of fiber.

SEM-BSE (scanning electron microscopy-backscattered electron) imaging was used to further characterize the microstructure around the interface of the fiber and cementitious matrix. Fig. 8(a-b) show the better interfacial bonding due to the surface modification of the PVA fiber by GO, as the GO bonding on the PVA fiber promoted the formation of the hydration products which increased the quantity and density of hydration products at the interface. While Fig. 8(c-d) show weak interfacial bonding, where the micro-cracks were visible, as the fiber and cement had poor compatibility and no additional hydration products filled the interface gap. Therefore, SEM-BSE imaging illustrated that the GO bonding significantly improved the fiber-cement matrix interfacial bonding.

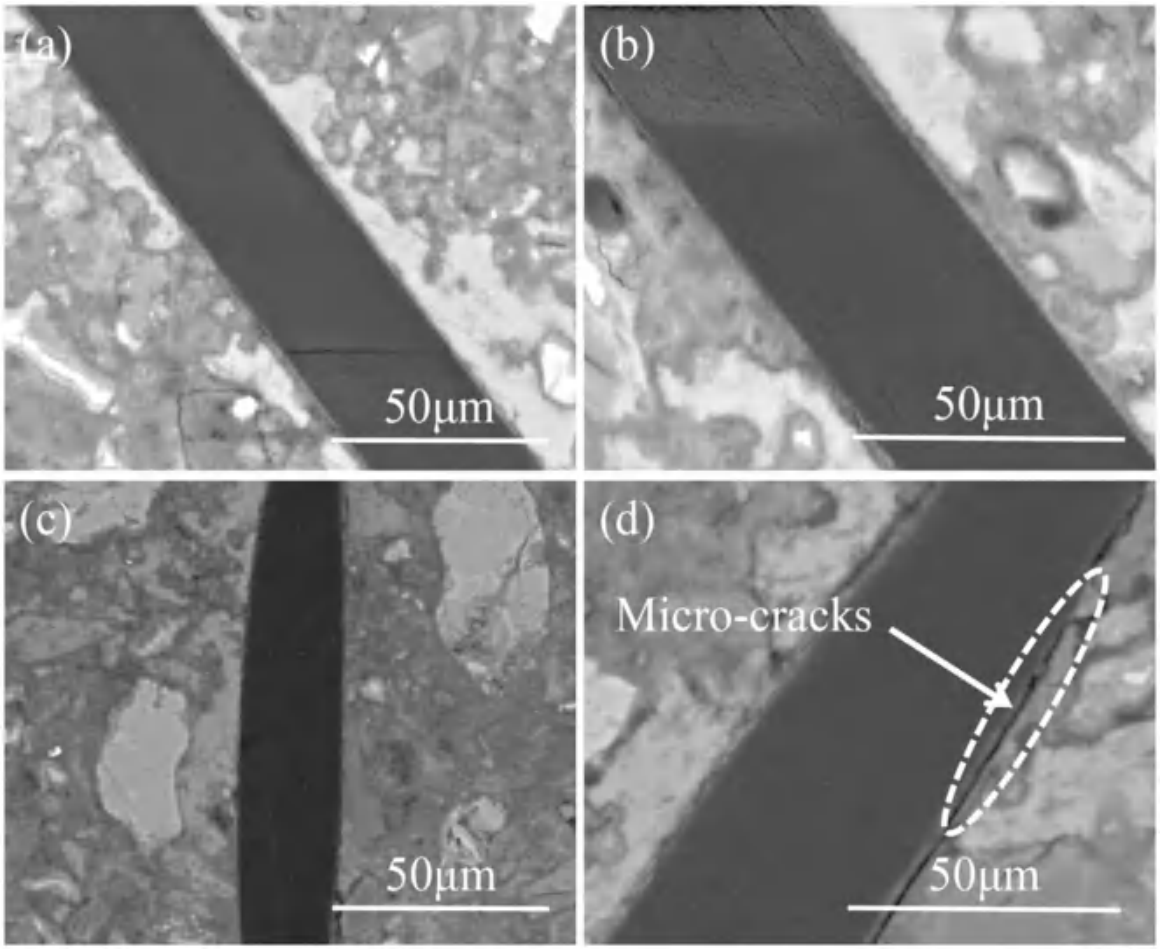

Fig. 8. SEM-BSE images of (a-b) GO modified PVA fiber and (c-d) pristine PVA fiber in the cement pastes.

3.4. Micro-mechanical properties analysis

3.4.1. Indentation analysis

Fig. 9 shows the 3D topography of indentation modulus and hardness distributions in PVA fiber reinforced cement paste. For the nano-indentation test, the indented area selected for each sample includes cementitious matrix, fiber, and their interface. According to the observation of the indentation area under an optical microscope and the distribution characteristics of micro-mechanical properties, different phases can be distinguished, which was marked in Fig. 9(a). In Fig. 9(a), the area enclosed with the white dotted line belonged to fiber, the area enclosed with the red dotted line belonged to the interface of the PVA fiber and the cementitious matrix, and the remaining area belonged to the cementitious matrix. The micro-mechanical parameters of each phase were statistically analyzed and the results are listed in Table 3. The hydration products close to the interface (denoted as "HP") had very low micro-mechanical properties and the interface had the weakest micro-mechanical properties, because the interfacial voids existed and there were no sufficient hydration products around the fiber as found through the microstructural characterization by SEM and SPM.

Fig. 10 shows the 3D topography of the indentation modulus and hardness distributions in GO/PVA fiber reinforced cement paste. Similarly, different phases in the 3D topography of micro-mechanical properties distribution can be distinguished, as marked in Fig. 10(a). The micro-mechanical parameters of each phase were statistically analyzed, and the results are listed in Table 4. Specially, a new zone with enhanced micro-mechanical properties were identified near the interface. The width of the enhanced zone is about 30 μm and the length is about 70 μm. Therefore, the area of the enhanced zone affected by GO is 2100 μm^2. Besides, the micro-mechanical properties of the interface modified by GO surpassed the hydration products in cementitious matrix, indicating that the introduction of GO significantly improved the interfacial properties. The reasons for the improvement of interfacial micro-mechanical properties by GO may include: (1) GO itself has excellent mechanical properties and enhanced the micro-mechanical properties in the interface; (2) GO can promote the rapid generation of hydration products at the interface and form the chemical bonding with the hydration products, enabling the formation of denser microstructure at the interface.

Finally, the micro-mechanical properties of various phases of the two different cement pastes are compared in Fig. 11, where the ranges of the micro-mechanical properties of various phases are plotted. The comparison in Fig. 11 clearly showed that the micro-mechanical properties of the PVA fibers were lower than those of the GO/PVA fiber, which was probably because the denser hydration products and GO around the fiber enhanced the micro-mechanical properties of fiber. Comparing to the PVA fiber reinforced cement paste, the introduction of GO remarkably increased the mean indentation modulus and the mean hardness of

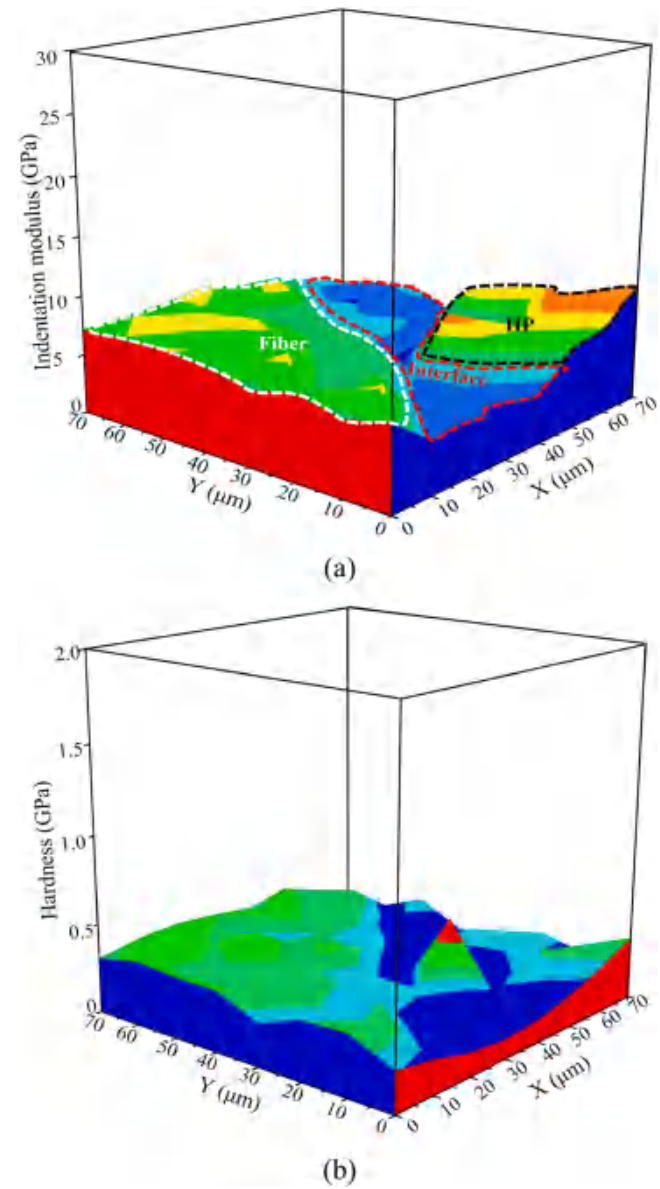

Fig. 9. 3D topographies of (a) indentation modulus and (b) hardness in PVA fiber reinforced cement paste.

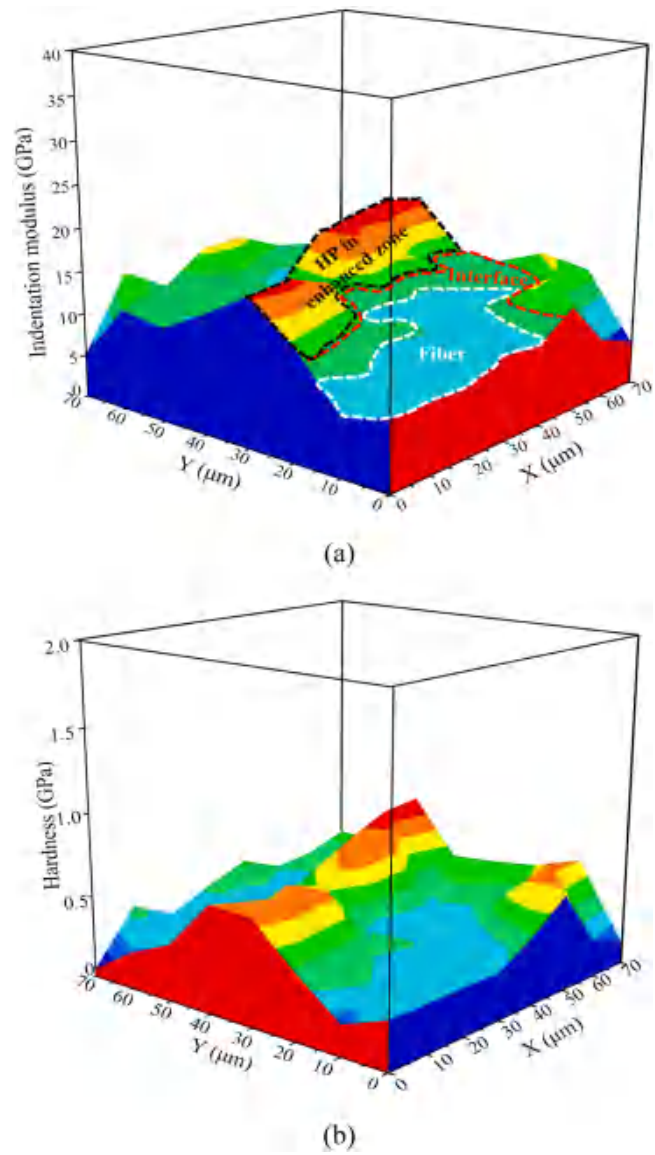

Fig. 10. 3D topographies of (a) indentation modulus and (b) hardness in GO/PVA fiber reinforced cement paste.

the interface by 151% and 318% respectively, and the mean indentation modulus and the mean hardness of the hydration products in cementitious matrix by 81% and 165% respectively. Moreover, comparing to hydration products in the PVA fiber reinforced cement paste, the indentation modulus and the hardness of the enhanced zone were increased by 139% and 435% respectively. The comparison showed that the GO not only significantly improved the interfacial properties between the PVA fiber and the cementitious matrix, but also markedly improved the micro-mechanical properties of surrounded hydration products.

3.4.2. Scratch analysis

Fig. 12 shows the scratch depth of PVA fiber reinforced cement paste and GO/PVA fiber reinforced cement paste, Fig. 13 shows the distribution of fracture toughness of fiber reinforced cement paste. During the scratch test, the scratch passed through the fiber from the right side to the left side. The load history consisted of two stages, i.e. the loading

Table 3
Summary of micro-mechanical parameters of different phases in PVA fiber reinforced cement paste.

		Fiber	Interfacial zone	HP in cementitious matrix
Indentation modulus (GPa)	Range	6.04–8.26	3.17–5.47	3.28–9.96
	Mean ± S.D.	7.07 ± 0.60	4.67 ± 0.67	6.16 ± 2.02
Hardness (GPa)	Range	0.23–0.44	0.13–0.34	0.11–0.56
	Mean ± S.D.	0.32 ± 0.05	0.22 ± 0.07	0.23 ± 0.10

Table 4
Summary of micro-mechanical parameters of different phases in GO/PVA fiber reinforced cement paste.

		Fiber	Interfacial zone	HP in enhanced zone	HP in cementitious matrix
Indentation modulus (GPa)	Range	7.67–10.86	9.35–15.64	12.22–18.29	6.77–13.90
	Mean ± S.D.	8.76 ± 1.04	11.73 ± 1.89	14.72 ± 2.16	11.15 ± 1.69
Hardness (GPa)	Range	0.49–0.66	0.71–1.05	0.93–1.54	0.37–0.87
	Mean ± S.D.	0.57 ± 0.06	0.92 ± 0.20	1.23 ± 0.18	0.61 ± 0.15

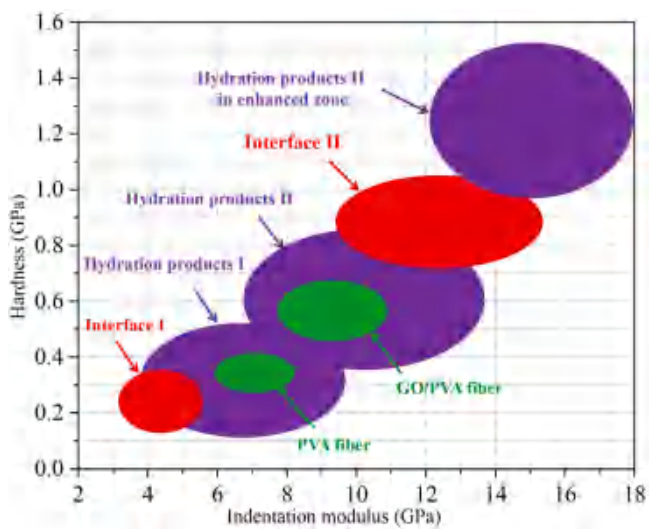

Fig. 11. The comparison of the micro-mechanical properties of different phases in PVA reinforced cement paste (denoted as "I") and GO/PVA reinforced cement paste (denoted as "II").

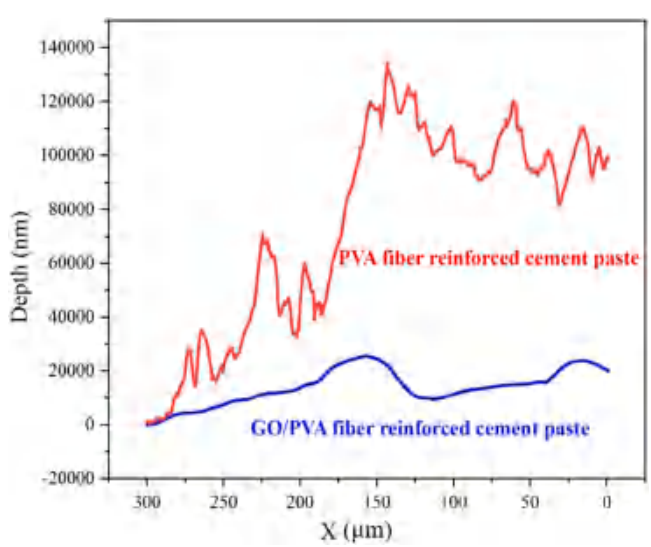

Fig. 12. The scratch depth of PVA fiber reinforced cement paste and GO/PVA fiber reinforced cement paste.

stage and holding stage. At the loading stage, when the load was low enough, the fracture toughness of individual phases was measured, while at the holding stage, the fracture toughness of the homogenized cement paste was measured. In Fig. 13, the fracture toughness distributions of the fibers in the two samples were almost identical. The fracture toughness of hydration products in PVA fiber reinforced cement paste measured from loading stage were obviously low with the mean value of 0.42 MPa·m$^{1/2}$. The fracture toughness of hydration products of GO/PVA fiber reinforced cement paste were much higher with the mean value of 0.81 MPa·m$^{1/2}$. Moreover, the average fracture toughness of the homogenized cement paste measured from loading stage of scratch test was also increased compared with that of the hydration product, indicating that the addition of fibers could improve the fracture toughness of the homogenized cement paste, as the fiber in the cementitious matrix could effectively transfer and disperse the energy. At the holding stage, the average fracture toughness of the homogenized cement paste in GO/PVA fiber reinforced cement paste was higher than in PVA fiber reinforced cement paste, which can be explained by the denser microstructure around the GO/PVA fiber and the higher efficient energy dispersion of the strong interfacial properties.

4. Conclusions

In this study, a novel GO modified PVA fiber was designed to improve the interfacial properties between PVA fiber and cementitious matrix, the improvement of interfacial properties was characterized by various techniques. The key findings are summarized as follows.

(1) The hydrogen bond between GO and PVA fiber was formed, enabling the GO to form a tight three-dimensional bonding on the surface of the PVA fiber. Moreover, a lot of oxygen-containing functional groups of GO could form chemical bond with the hydration products and promote the formation of denser microstructure at the interface. The introduction of GO significantly enhanced the interfacial properties between PVA fiber and cementitious matrix, which was verified by the characterizations on the microstructures and micro-morphologies.
(2) Due to the introduction of GO, a new zone with enhanced micromechanical properties were identified near the interface. Comparing to the PVA fiber reinforced cement paste, the introduction of GO remarkably increased the mean indentation modulus and hardness of the interface by 151% and 318% respectively, and those of the hydration products in cementitious matrix by 81% and 165% respectively. Moreover, comparing to hydration products in the PVA fiber reinforced cement paste, the mean indentation modulus and hardness of the enhanced zone were increased by 139% and 435% respectively.
(3) The micro-scratch analysis illustrated that GO improved the fracture toughness of the hydration products closed to the PVA fibers. The fracture toughness of hydration products was increased from 0.42 MPa·m$^{1/2}$ to 0.81 MPa·m$^{1/2}$. Moreover, the mean fracture toughness of the homogenized cement paste was also increased owing to the denser microstructure around the GO modified PVA fiber and the higher efficient energy dispersion of the strong interfacial properties.

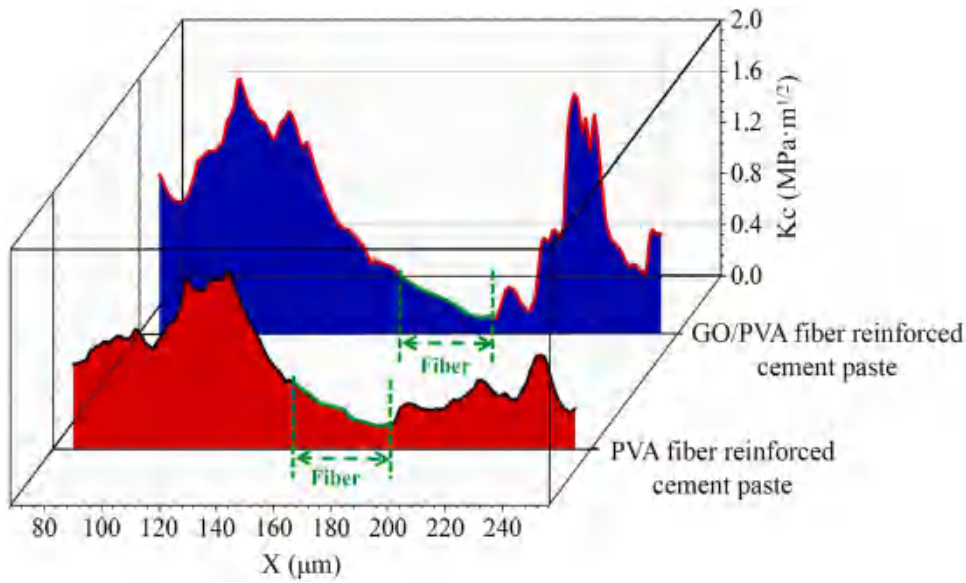

Fig. 13. The fracture toughness distributions of PVA fiber reinforced cement paste and GO/PVA fiber reinforced cement paste.

CRediT authorship contribution statement

Shun Yao: Investigation, Writing – original draft. **Chuanlin Hu:** Conceptualization, Writing – review & editing, Funding acquisition. **Fazhou Wang:** Methodology, Supervision. **Shuguang Hu:** Methodology, Supervision.

Declaration of Competing Interest

The authors declare that they have no known competing financial interests or personal relationships that could have appeared to influence the work reported in this paper.

Data Availability

Data will be made available on request.

Acknowledgments

The authors are grateful and acknowledge the support from Program Fund of Non-Metallic Excellence and innovation Center for Building Materials (Grant No.: 2023TDA1-1) and China National Natural Science Foundation (Grant No.: 51925205).

References

[1] H.G. Zhang, P.K. Sarker, Q.Y. Wang, B. He, J.C. Kuri, Z.W. Jiang, Comparison of compressive, flexural, and temperature-induced ductility behaviours of steel-PVA hybrid fibre reinforced OPC and geopolymer concretes after high temperatures exposure, Constr. Build. Mater. 399 (2023), 132560.
[2] B. Pang, Z.Q. Jin, Y.S. Zhang, L. Xu, Ultraductile waterborne epoxy-concrete composite repair material: epoxy-fiber synergistic effect on flexural and tensile performance, Cem. Concr. Comp. 129 (2022), 104463.
[3] S.M. Mousavi, M.M. Ranjbar, R. Madandoust, Combined effects of steel fibers and water to cementitious materials ratio on the fracture behavior and brittleness of high strength concrete, Eng. Fract. Mech. 216 (2019), 106517.
[4] J. Tsai, A.K. Patra, R. Wetherhold, Numerical simulations of fracture-toughness improvement using short shaped head ductile fibers, Compos Part A-Appl. S 34 (2003) 1255–1264.
[5] Z.T. Qiu, M.K. Deng, W. Zhang, Z.Y. Wu, Z.F. Dong, T. Li, Out-of-plane flexural behavior of autoclaved aerated concrete block masonry walls strengthened with high-ductility concrete, Constr. Build. Mater. 394 (2023), 132117.
[6] Y.F. Zhang, Z. Chen, F.H. Li, R.N. Jiang, Tensile behavior and failure modes of expansion anchors in high-performance steel fiber reinforced concrete, Constr. Build. Mater. 408 (2023), 133693.
[7] J.H. Muhammad, A.R. Yousif, Shear behavior of normal and high-strength concrete beams reinforced with BFRP bars and basalt macro fibers, Constr. Build. Mater. 408 (2023), 133516.
[8] M.H. Jorbat, M. Hosseini, M. Khani, Effect of polypropylene fibers on the mode I, mode II, and mixed-mode fracture toughness and crack propagation in fiber-reinforced concrete, Theor. Appl. Fract. Mec. 109 (2020), 102723.
[9] Y.L. Li, W.G. Li, D.H. Deng, K.J. Wang, W.H. Duan, Reinforcement effects of polyvinyl alcohol and polypropylene fibers on flexural behaviors of sulfoaluminate cement matrices, Cem. Concr. Comp. 88 (2018) 139–149.
[10] J.S. Qiu, X.N. Lim, E.H. Yang, Fatigue-induced in-situ strength deterioration of micro-polyvinyl alcohol (PVA) fiber in cement matrix, Cem. Concr. Comp. 82 (2017) 128–136.
[11] The effect of hydrophilic (polyvinyl alcohol) fiber content on the flexural behavior of engineered cementitious composites J Textil Inst.109 (2018) 79–84.
[12] J.X. Chen, A.T. Akono, Influence of multi-walled carbon nanotubes on the hydration products of ordinary Portland cement paste, Cem. Concr. Res 137 (2020), 106197.
[13] J.T. Liu, J.L. Fu, T.Y. Ni, Y. Yang, Fracture toughness improvement of multi-wall carbon nanotubes/graphene sheets reinforced cement paste, Constr. Build. Mater. 200 (2019) 530–538.
[14] H. Nosrati, R.S. Mamoory, D.Q.S. Le, C.E. Bünger, Enhanced fracture toughness of three dimensional graphene-hydroxyapatite nanocomposites by employing the Taguchi method, Compos Part B-Eng. 190 (2020), 107928.
[15] Z.Y. Lu, C. Lu, C.K.Y. Leung, Z.J. Li, Graphene oxide modified strain hardening cementitious composites with enhanced mechanical and thermal properties by incorporating ultra-fine phase change materials, Cem. Concr. Comp. 98 (2019) 83–94.
[16] Z. Lu, B. Chen, C.Y. Leung, Aggregation size effect of graphene oxide on its reinforcing efficiency to cement-based material, Cem. Concr. Comp. 100 (2019) 85–91.
[17] Z. Pan, L. He, L. Qiu, Mechanical properties and microstructure of a graphene oxide-cement composite, Cem. Concr. Comp. 58 (2015) 140–147.
[18] W. Zhang, X.S. Zou, F.Y. Wei, H.L. Wang, Grafting SiO_2 nanoparticles on polyvinyl alcohol fibers to enhance the interfacial bonding strength with cement, Compos Part B-Eng. 162 (2019) 500–507.
[19] Z.Y. Pi, H.G. Xiao, R. Liu, H. Li, Combination usage of nano-SiO2-coated steel fiber and silica fume and its improvement effect on SFRCC, Compos Part B-Eng. 221 (2021), 109022.
[20] L.C. Lu, P.Q. Zhao, Z.Y. Lu, A short discussion on how to effectively use graphene oxide to reinforce cementitious composites, Constr. Build. Mater. 189 (2018) 33–41.
[21] X.Y. Li, Z.Y. Lu, S. Chuah, W.G. Li, Y.M. Liu, W.H. Duan, Z.J. Li, Effects of graphene oxide aggregates on hydration degree, sorptivity, and tensile splitting strength of cement paste, Compos Part A-Appl. Sci. Manuf. 100 (2017) 1–8.
[22] R. Al-Gaashani, A. Najjar, Y. Zakaria, XPS and structural studies of high quality graphene oxide and reduced graphene oxide prepared by different chemical oxidation methods, Ceram. Int 45 (2019) 14439–14448.
[23] G. Sobon, J. Sotor, J. Jagiello, Graphene oxide vs. reduced graphene oxide as saturable absorbers for Er-doped passively mode-locked fiber laser, Opt. Express 20 (2012) 19463–19473.
[24] W.G. Li, Z.Y. Luo, Y.X. Gan, K.J. Wang, S.P. Shah, Nanoscratch on mechanical properties of interfacial transition zones (ITZs) in fly ash-based geopolymer composites, Compos Sci. Technol. 214 (2021), 109001.

[25] A.T. Akono, F.J. Ulm, Z.P. Bažant, Discussion: strength-to-fracture scaling in scratching, Eng. Fract. Mech. 119 (2014) 21–28.
[26] J.S. Lin, Y. Zhou, Can scratch tests give fracture toughness? Eng. Fract. Mech. 109 (2013) 161–168.
[27] A.T. Akono, N.X. Randall, F.J. Ulm, Experimental determination of the fracture toughness via microscratch tests: application to polymers, ceramics, and metals, J. Mater. Res 27 (2012) 485–493.

International Journal of
Molecular Sciences

MDPI

Article

A Two-Step Synthesis of Porous Nitrogen-Doped Graphene for Electrochemical Capacitors

Jiahao Li, Zhenjia Wu, Rong Huang, Anbang Ge and Jie Ying *

School of Chemical Engineering and Technology, Sun Yat-sen University, Zhuhai 519082, China; lijh255@mail2.sysu.edu.cn (J.L.); wuzhj58@mail2.sysu.edu.cn (Z.W.); huangr279@mail2.sysu.edu.cn (R.H.); geanb@mail2.sysu.edu.cn (A.G.)
* Correspondence: yingj5@mail.sysu.edu.cn

Abstract: Porous nitrogen-doped graphene (PNG) materials with high conductivity, high surface area, and chemical stability have displayed superior performance in electrochemical capacitors. However, previously reported methods for fabricating PNG render the processes expensive, hard to control, limited in production, and unsafe as well, thus largely restricting their practical applications. Herein, we present a facile two-step calcination method to prepare PNG using petroleum asphalt as the carbon source to provide the original three-dimensional porous structure directly and using environmentally friendly and high nitrogen content urea as the nitrogen source without adding any etching agent. The porous structure in PNG can largely increase its specific surface area, and the introduction of nitrogen atoms can effectively increase the degree of defects and improve the wettability of PNG. As a result, PNG displays a high specific capacitance of 157 F g^{-1} at a current density of 1 A g^{-1} and cycling stability while maintaining 98.68% initial capacitance after 10,000 cycles.

Keywords: porous nitrogen-doped graphene; petroleum asphalt; electrochemical capacitors

check for updates

Citation: Li, J.; Wu, Z.; Huang, R.; Ge, A.; Ying, J. A Two-Step Synthesis of Porous Nitrogen-Doped Graphene for Electrochemical Capacitors. *Int. J. Mol. Sci.* **2024**, *25*, 12297. https://doi.org/10.3390/ijms252212297

Academic Editor: Giovanna Iezzi

Received: 19 October 2024
Revised: 11 November 2024
Accepted: 14 November 2024
Published: 15 November 2024

Copyright: © 2024 by the authors. Licensee MDPI, Basel, Switzerland. This article is an open access article distributed under the terms and conditions of the Creative Commons Attribution (CC BY) license (https://creativecommons.org/licenses/by/4.0/).

1. Introduction

The development of high-power-density storage devices is regarded as indispensable because of the booming market of mobile and immobile electronic devices [1–3]. Electrochemical capacitors, otherwise known as supercapacitors, which offer high power density, long cycle life, and rapid charge–discharge capacity, have attracted extensive attention [4–7]. It is widely recognized that the performance of electrochemical capacitors is mainly decided by the electrode materials. Thus, the design and fabrication of high-performance electrode materials can contribute to enhancing the properties of electrochemical capacitors. Recently, a series of carbon materials with high conductivity has been investigated as efficient electrode materials for electrochemical capacitors [8–13]. Among them, porous nitrogen-doped graphene (PNG) materials display high surface area and chemical stability and thus have high electrochemical performance such as capacitance, rate capability, and cycling stability [14–19].

At present, PNG can be produced either using graphene oxide through self-assembly [20–22] and 3D printing [23–25] or by way of chemical vapor deposition [26–28]. In these configurations, pores are created between nanosheets by means of cross-linking gelation or a template drive, endowing the graphene frameworks with diverse structures and multiple functions. Moreover, it has been confirmed that introducing heteroatom dopants such as nitrogen into graphene can further modulate their electronic properties and electrochemical performance [15,29,30]. However, these methods for manufacturing PNG render the processes expensive, hard to control, limited in production, and unsafe as well, thus severely restricting their practical applications [31,32]. Therefore, the development of a simple, low-cost, and environmentally friendly approach for the fabrication of PNG is of considerable significance.

As a low-value by-product in petroleum processing, petroleum asphalt has attracted much attention because of its low cost and large quantity (over 25 million tons per year) [19,33].

The content of polycyclic aromatic hydrocarbons in petroleum asphalt is rich, and the content of ash is low, so the carbon material produced by carbonization has excellent porosity and ideal electrical conductivity [34,35]. Herein, we report the fabrication of PNG through a two-step calcination method using petroleum asphalt as a carbon source and urea as a nitrogen source without adding any etching agent. The porous structure effectively increases the specific surface area of PNG and promotes the transfer of electrolytic ions. In addition, the introduction of nitrogen atoms increases the degree of defects and improves the wettability of the material. Benefiting from this, PNG has superior specific capacitance and cycle stability, proving its good electrochemical properties as an electrode material for electrochemical capacitors.

2. Results and Discussion

The overall synthetic procedure of PNG-x (x represents the amount of urea added) is displayed in Figure 1. Asphalt, urea, and mixed salt are oxidized in the air after ball milling, and the unstable components in the mixture are decomposed into CO_2 and CO gas molecules, thus obtaining pre-PNG with mesoporous and macroporous. After high-temperature carbonization, the cross-linked oxygen-containing functional groups between the carbon layers can be removed, thereby expanding the carbon layer spacing. Then the mixed salt is removed with deionizing water, and finally, PNG-x is obtained.

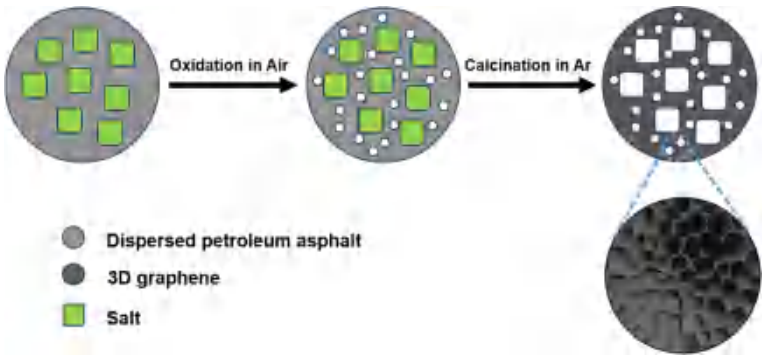

Figure 1. Scheme illustration of synthesis of PNG-x.

The morphologies of PNG-x are shown in Figure 2a–f. It can be seen that PNG-x has an obvious porous network structure, and with the increase in urea content, the morphology of PNG-x still maintains a porous structure. This proves that the two-step oxidation carbonization method can be effectively applied to the production of porous structures. In order to further confirm the mesostructure and element distribution of PNG-x, PNG-0.6 is characterized by transmission electron microscopy (TEM). Figure 3a,b are TEM images of PNG-0.6 at different magnifications. As can be seen from Figure 3a, PNG-0.6 has a clear three-dimensional porous structure. In addition, the lamellar surface of PNG-0.6 is rich in mesoporous pores (Figure 3b). Figure 3c presents the high-angle annular dark-field scanning TEM (HAADF-STEM) image of a part of PNG-0.6, and the corresponding elemental mapping images in Figure 3d–f indicate that the elements C, N, and O are homogeneously distributed throughout PNG-0.6, revealing that nitrogen obtained from urea decomposition can be effectively doped into graphene. It is worth noting that the three-dimensional porous structure of PNG-x has little effect on wettability, and PNG-x exhibits hydrophobicity only at suitable nitrogen doping levels (Figure 3g). Among them, PNG-0.6 exhibits hydrophobicity, which can avoid the adsorption of water and minimize the impact of water on the performance of the capacitor [36].

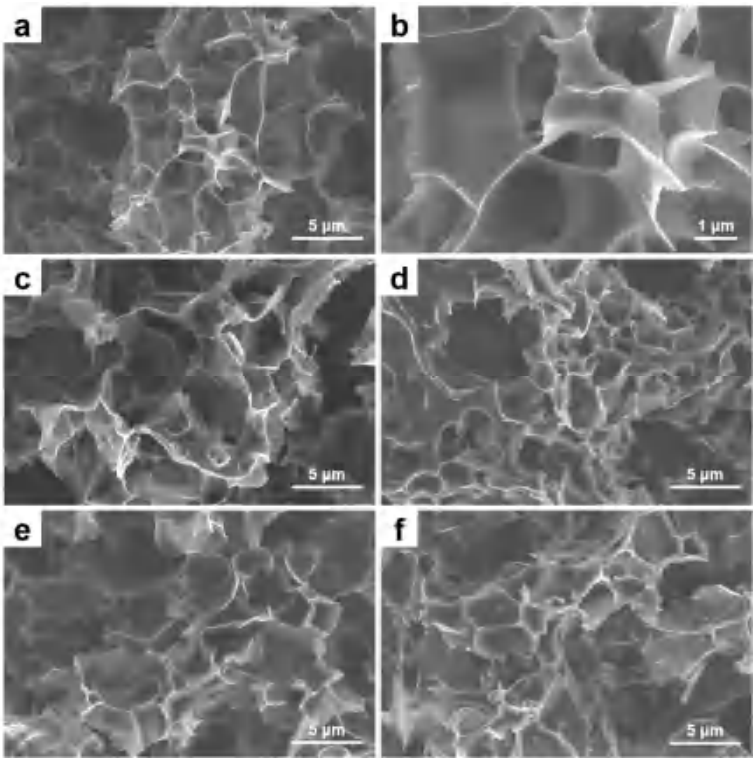

Figure 2. SEM images of (**a**,**b**) PNG-0.6, (**c**) PNG-0, (**d**) PNG-1.2, (**e**) PNG-1.5, (**f**) PNG-2.0.

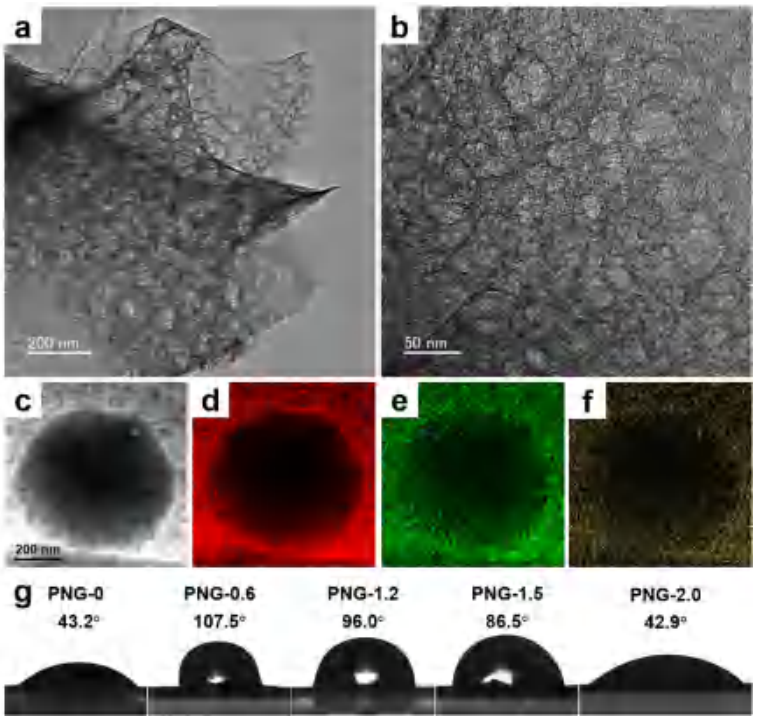

Figure 3. (**a**,**b**) TEM images of PNG-0.6, (**c**) HAADF-STEM images of PNG-0.6, (**d**–**f**) EDS elemental mappings of C, N, and O, (**g**) water drops on PNG-x.

The crystalline structure of all the samples is determined using X-ray diffraction (XRD) (Figure 4a). For all samples, two broad peaks can be observed on the XRD pattern, corresponding to the (002) and (100) crystal faces of the carbon material [18,37,38]. The diffraction angle 2θ of PNG-0.6 at the (002) plane is around 24.4°, and the average layer spacing of PNG-0.6 can be calculated as 0.358 nm according to the Bragg equation. With

the increase in urea content, the diffraction peak of PNG-x at (002) plane gradually moves to the higher angle, which proves that the increase in urea content will reduce the layer spacing of PNG-x.

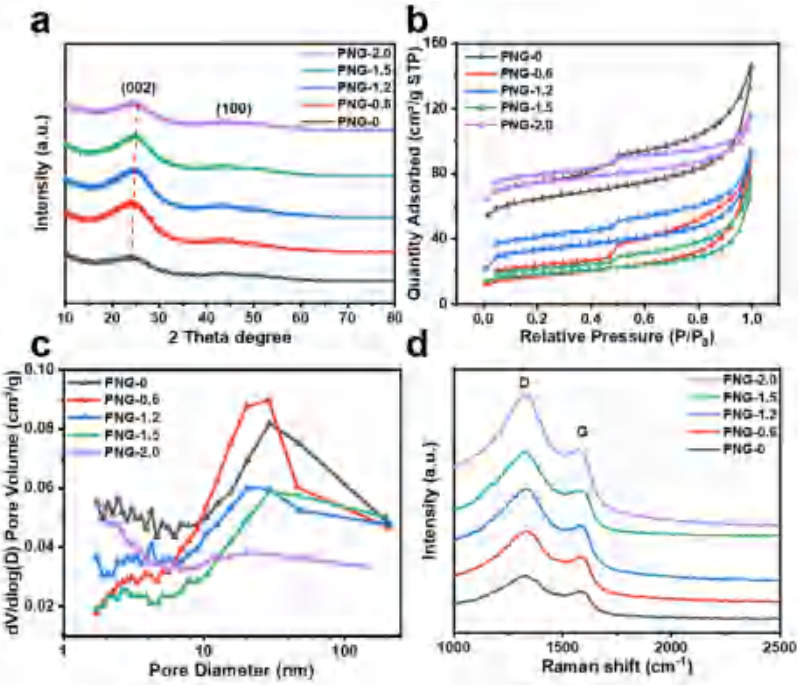

Figure 4. (**a**) XRD patterns of PNG-x, (**b**) N_2 adsorption and desorption isotherm curves of PNG-x, (**c**) diameter distribution curves of PNG-x, (**d**) Raman spectra of PNG-x.

The nitrogen adsorption/desorption isotherms of the samples are shown in Figure 4b. A typical type IV isotherm characteristic accompanied by a hysteresis loop is observed, indicating that there are a large number of mesopores in PNG-x [39,40]. As indicated in Table 1, the specific surface areas of the PNG-0, PNG-0.6, PNG-1.2, PNG-1.5, and PNG-2.0 samples, which are calculated based on the Brunauer–Emmett–Teller (BET) method, are 242, 61, 128, 67, and 283 $m^3\ g^{-1}$ respectively. The pore volumes are 0.226, 0.137, 0.146, 0.117, and 0.180 $cm^3\ g^{-1}$, respectively. The pore size of PNG-x calculated using the Barrett–Joyner–Halenda (BJH) method is mainly distributed in the mesoporous region (Figure 4c). In addition, the results in Table 1 show that adding a small amount of urea can significantly reduce the content of micropores, leading to a decrease in surface area and pore volume. With the increase in urea content, the micropore content gradually increases, and the surface area and pore volume of PNG-x will increase significantly.

Table 1. Specific surface area and pore volume of PNG-x.

Sample	S_{BET} [a] $m^2\ g^{-1}$	V_t [b] $cm^3\ g^{-1}$	V_m [c] $cm^3\ g^{-1}$
PNG-0	242	0.226	0.083
PNG-0.6	61	0.137	0.011
PNG-1.2	128	0.146	0.038
PNG-1.5	67	0.117	0.018
PNG-2.0	283	0.180	0.105

[a] BET-specific surface area; [b] total pore volume from adsorption isotherms at a relative pressure P/P_0 of 0.99; [c] t-plot micropore volume.

Raman spectroscope is a unique, non-destructive technique to investigate the structure properties of carbon materials. Figure 4d is the Raman spectrogram of PNG-x, from which peak D near 1330 cm^{-1} and peak G near 1570 cm^{-1} are observed. As shown in Table 2, the

I_D/I_G ratio of PNG-x gradually increased with the increase in urea content. The higher the I_D/I_G ratio, the higher the defect degree of PNG-x and the lower the graphitization degree, indicating that the incorporation of nitrogen atoms provided defect sites [41–43]. Moreover, the I_D/I_G ratio of PNG-x supplemented with urea is all greater than PNG-0 (1.08), which is largely due to the destruction of local symmetry by nitrogen atom doping, resulting in an increase in D-band intensity.

Table 2. I_D/I_G of PNG-x.

Sample	I_D/I_G [a]
PNG-0	1.08
PNG-0.6	1.13
PNG-1.2	1.17
PNG-1.5	1.19
PNG-2.0	1.23

[a] The intense ratio of D band and G band from Raman spectra.

X-ray photoelectron spectroscopy (XPS) is further employed to analyze the surface compositions of PNG-x. The full XPS spectra in Figure 5a clarified that all the PNG-x are composed of C, N, and O. The N 1s high-resolution peak of the PNG-0.6 in Figure 5b can be modeled into four independent peaks of 389.4 eV, 400.1 eV, 401.1 eV, and 403.1 eV, corresponding to the characteristic peaks of pyridinic-N (N-6), pyrrolic-N (N-5), graphitic-N (N-Q), and oxidized-N (N-X), respectively [44–48]. In addition, the N 1s high-resolution spectra of other samples, as shown in Figure 5c–f, can be convolved into four peaks of N-6, N-5, N-Q, and N-x. The nitrogen content of PNG-x increased from 4.18 at% to 8.96 at% with the increase in urea content (Table 3). Meanwhile, with the increase in defect nitrogen content (PNG-0 < PNG-0.6 < PNG-1.5 < PNG-1.2 < PNG-2.0), the specific surface area of PNG decreases first and then increases. This may be because the three-dimensional porous structure of PNG is first partially destroyed with the increase in urea, resulting in a decrease in the specific surface area. Then, the urea content continues to increase, which forms part of the porous carbon material, resulting in an increase in the specific surface area. Supercapacitors are classified into electrical double-layer capacitors and pseudocapacitors based on their charge storage mechanisms [49]. Among these nitrogen functional groups, N-6 and N-5 are thought to contribute more to specific capacitors by introducing pseudocapacitors, while N-Q can effectively improve the conductivity of carbon materials by promoting electron transfer, which means that PNG-0.6 has good supercapacitor performance [14].

Table 3. Nitrogen content (at%) and nitrogen binding state in PNG-x obtained by XPS.

Sample	The Ratio of Different N Groups (at%)				
	Total	Pyridinic-N	Pyrrolic-N	Graphitic-N	Oxidized-N
PNG-0	4.18	1.63	0.85	0.96	0.74
PNG-0.6	5.44	1.20	1.63	1.28	1.33
PNG-1.2	8.05	3.68	0.97	2.53	0.87
PNG-1.5	8.42	3.14	0.76	2.55	1.97
PNG-2.0	8.96	3.65	1.06	2.48	1.77

The electrochemical properties of PNG-x samples were examined in an alkaline medium. As shown in Figure 6a, cyclic voltammetry (CV) curves of different samples at a scanning rate of 100 mV s^{-1} are presented. All samples showed an approximate spindle shape, indicating the existence of electric double-layer capacitors. It is worth noting that PNG-0.6 has the largest total area. It is widely known that the specific capacitance is in proportion to the area of the CV curve, thus indicating that less nitrogen doping will increase the overall capacitance.

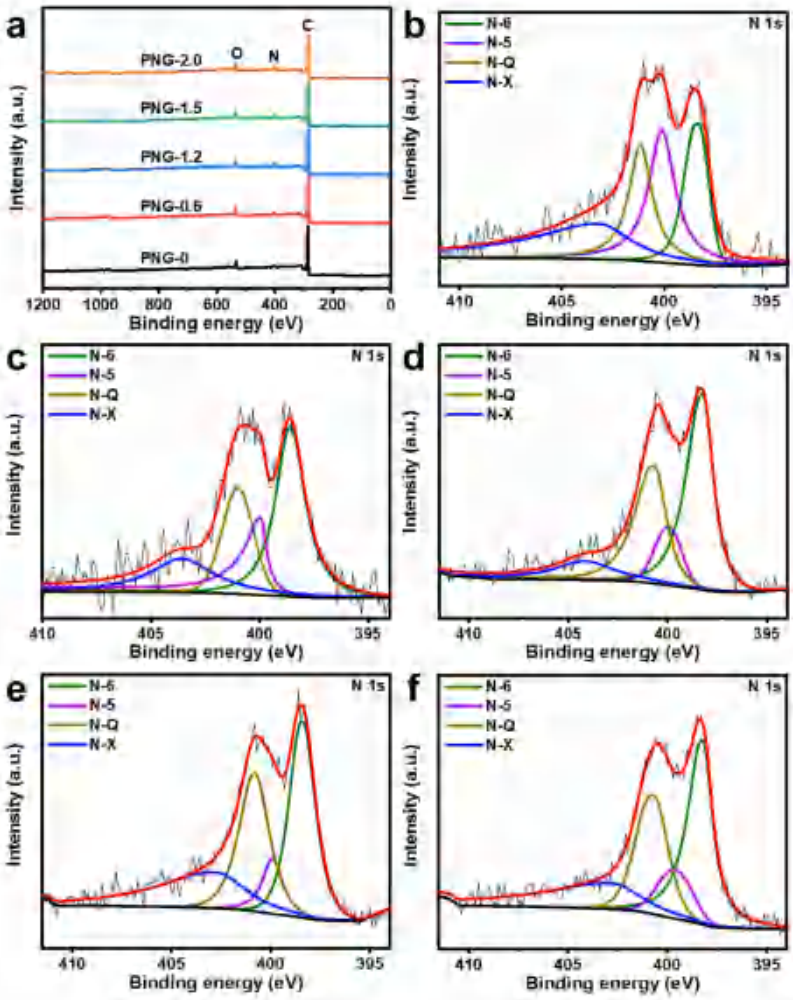

Figure 5. (**a**) XPS survey spectra of PNG-x, XPS high-resolution N 1s spectra of (**b**) PNG-0.6, (**c**) PNG-0, (**d**) PNG-1.2, (**e**) PNG-1.6, and (**f**) PNG-2.0.

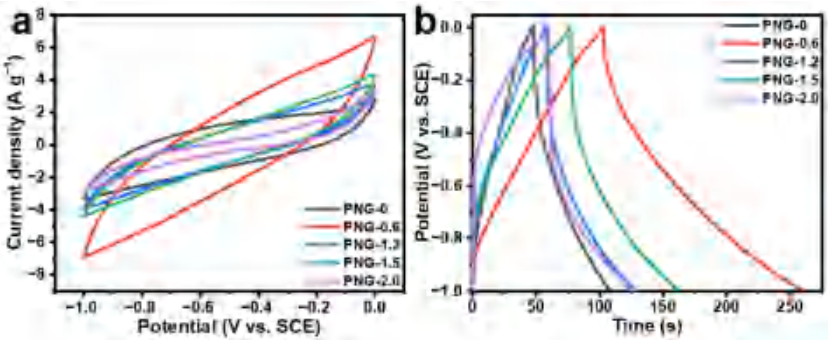

Figure 6. (**a**) CV curves of PNG-x at 100 mV s^{-1}, (**b**) GCD curves of PNG-x at 1 A g^{-1}.

The specific capacitance values of the PNG-x computed from galvanostatic charge–discharge (GCD) curves (refer to Figure 6b) were 60 F g^{-1} (PNG-0), 157 F g^{-1} (PNG-0.6), 69 F g^{-1} (PNG-1.2), 89 F g^{-1} (PNG-1.5), and 66 F g^{-1} (PNG-2.0), respectively. It can be seen that the nitrogen-doped sample has a higher specific capacitance than the sample without urea. PNG-0.6 has a high specific capacitance mainly for the following two reasons: (1) pyridinic-N and pyrrolic-N can enhance electrochemical reactivity, and (2) the rich pore structure is beneficial for improving the contact area between the electrode and the electrolyte and reducing the resistance to transfer of electrolytic ions [50,51]. Although the surface area of PNG-1.2 and PNG-2.0 is much larger than that of PNG-0.6, their high

nitrogen doping actually hinders electron transfer and reduces capacitance. PNG-1.5 also has a lower surface area than PNG-0.6, lacking enough space to transfer electrolytic ions.

Figure 7a presents the CV curves of the PNG-0.6 at different scan rates varying from 10 to 300 mV s^{-1}. With the increase in the scan rate, the CV loop maintains its spindle shape, suggesting that very little polarization occurs because of the high electronic conductivity of PNG-0.6. The GCD curves of PNG-0.6 are shown in Figure 7b. The curves are nearly triangular in shape, featuring slight curvature and no obvious potential drop at a current density ranging from 0.5 and 5 A g^{-1}, which indicates its outstanding electrochemical reversibility and rapid I–V response. Figure 7c plots the relationship between specific capacitance and current density of PNG-0.6. As the current density increases, the specific capacitance gradually decreases, which might be attributed to the limited diffusion of electrolyte ions. In addition, when the current density rises from 1 A g^{-1} to 5 A g^{-1}, about 34% of the specific capacitance scale remains unchanged, indicating that PNG-0.6 has excellent rate capability for electrochemical capacitors. This may be related to the porous structure and excellent electronic conductivity of PNG-0.6 [52].

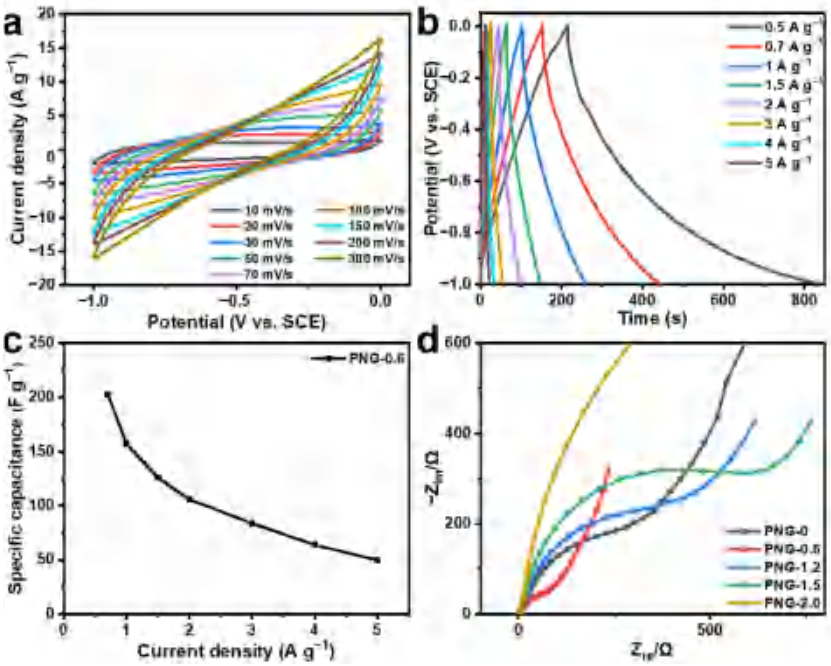

Figure 7. (**a**) CV curves at different scan rates for the PNG-0.6. (**b**) GCD curves at different current densities for PNG-0.6, (**c**) the specific capacitance versus current density for PNG-0.6, (**d**) Nyquist plots of PNG-x.

To further explore the electrochemical behavior of the PNG-x sample, electrochemical impedance spectroscopy (EIS) tests were carried out at an open-circuit voltage in the frequency range from 10^{-2} Hz to 10^{5} Hz. As shown in Figure 7d, all samples except PNG-2.0 exhibit vertical slopes in the low-frequency region, suggesting that the sample has good capacitance and low ion diffusion resistivity at the electrode/electrolyte interface. Moreover, the charge transfer impedance of PNG-0.6 is considerably lower than that of other samples, indicating that proper nitrogen doping can efficiently enhance the electrochemical properties of the material. However, too much nitrogen atom doping will lead to a decrease in resistivity and not enough to achieve fast charge transfer kinetics.

Cycling stability performance is a highly significant parameter for electrochemical capacitors. As demonstrated in Figure 8a, after 1000 cycles, the specific capacitance of PNG-0.6 began to increase, reaching a maximum of 99.92% of the initial specific capacity (3000 cycles). It may be that during the cycle, some of the graphitized carbon in PNG-0.6 degenerates to a more disordered degree, exposing more active sites and thus contributing to better contact between the electrode and the electrolyte [53]. And after 10,000 cycles, it

can still retain 98.68% of the initial specific capacitance. The results show that PNG-0.6 has excellent cyclic stability. Moreover, the first, the 2000th, 4000th, 6000th, 8000th, and 10,000th CV curves of PNG-0.6 obtained at 200 mV^{-1} are shown in Figure 8b. The CV curves are almost identical, which further indicates that PNG-0.6 is an excellent and stable electrochemical electrode material.

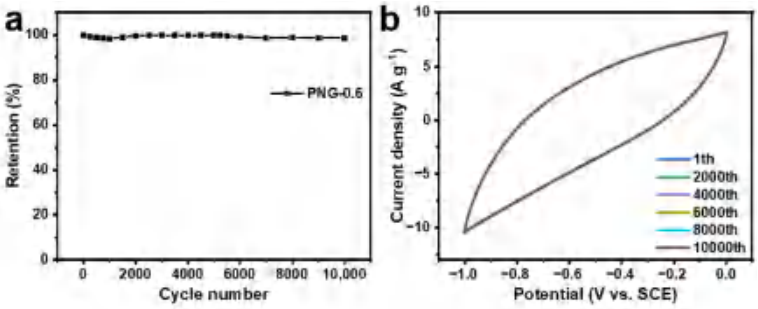

Figure 8. (**a**) Cycling stability of PNG-0.6, (**b**) The first, 2000th, 4000th, 6000th, 8000th, 10,000th CV curves of the PNG-0.6 at 200 mV s^{-1}.

3. Materials and Methods

3.1. Materials

Petroleum asphalt was purchased from Wentian New Materials Tech. Co., Ltd., Huizhou, China. Liquid aromatic petrochemical by-products were purchased from China Railway Weiye Waterproof Material Technology Co., Ltd., Jinan, China. Urea (CH_4N_2O), sodium chloride (NaCl), potassium chloride (KCl), and potassium hydroxide (KOH) were purchased from Aladdin Industrial Corporation, Shanghai, China. Nafion (5 wt%) was purchased from Sigma-Aldrich, Shanghai, China.

3.2. Synthesis of PNG-x

PNG-x was synthesized by a two-step oxidation carbonization process. In a typical procedure, 1 g petroleum asphalt was dispersed with 10 mL liquid aromatic petrochemical by-products by ultrasonic for 20 min. The above mixture was ball-milled with 20 g NaCl: KCl (mass ratio 4.5:5.5) and x (x = 0, 0.6, 1.2, 1.5, 2.0) g urea to obtain a homogeneous solid mixture. Next, the mixture was heated at a heating rate of 5 °C min^{-1} to 300 °C in a muffle furnace under air atmosphere and maintained for 2 h to obtain pre-PNG. Then, the sample was calcined at a heating rate of 3 °C min^{-1} to 700 °C under Ar atmosphere and maintained for 2 h, after which the sample was naturally cooled to room temperature. Finally, after washing and drying, PNG-x was obtained.

3.3. Characterization

Field-emission scanning electron microscopy (FESEM) was conducted on Thermoscientific Apreo 2S HiVac (Waltham, MA, USA) at the acceleration voltage of 5 kV, and TEM studies were carried out on JEOL JEM-F200 (Tokyo Japan) at the acceleration voltage of 200 kV. XRD measurements were carried out on an Ultima IV X-ray diffractometer (Tokyo, Japan) using Cu Kα radiation (λ = 1.54056 Å) with a step width of 0.05° and step time of 0.5. The specific surface area for BET measurements was conducted using a Micromeritics ASAP 2460 system (Norcross, GA, USA). The pore size distribution of each sample was computed from the adsorption isotherm branch using the BJH method. Raman analysis was performed with a confocal Raman microscope (CRM) (Alpha300R, WITec GmbH, Ulm, Germany) equipped with a TEM single-frequency laser (λ = 633nm, laser power = 2 mW, WITec GmbH, Ulm, Germany). The laser light was focused through a 50× oil immersion objective onto the sample, and the backscattered Raman signal was directed through an optic multifiber (50 μm diameter) to a spectrometer (300 g·mm^{-1} grating) and detected by the CCD camera. On the selected areas on the sample every 0.5 μm a full wavenumber range (50–2940 cm^{-1}) Raman spectrum was acquired with an integration time of 300 s. XPS

analysis was conducted on a Thermo Scientific K-Alpha X-ray photoelectron spectrometer (Waltham, MA, USA). The N 1s spectra were acquired at photon energy (hv) of 1486.6 eV and analyzer pass energies (PE) of 50 eV. The survey spectra were acquired at photon energy (hv) of 1486.6 eV and analyzer pass energies (PE) of 150 eV.

3.4. Electrochemical Measurements

Electrochemical measurements were performed on Metrohm Autolab (Herisau, Switzerland) PGSTAT 302N using a three-electrode cell. A platinum foil of 4 cm^2 was employed as a counter electrode, and a saturated calomel electrode (SCE) was utilized as a reference electrode. The slurry-coated nickel foam was used as the working electrode. To prepare the slurry, 10 mg PNG-x and 1 mg acetylene black were dispersed in a mixed solution containing 950 μL isopropanol and 50 μL nafion solution (5 wt%) under ultrasonic treatment for 30 min. In total, 100 μL of the aforementioned mixture was dropped onto nickel foam, and the coated area was approximately 1 cm × 1 cm. Subsequently, the nickel foam was left to dry overnight in the air. The mass loading of PNG-x on the nickel foam was maintained at 1 mg. All the electrochemical measurements, including CV, GCD, and EIS, were performed in 1 M KOH solution at room temperature. Generally, the CV tests were conducted at a scan rate ranging from 10 to 150 mV s^{-1} within a potential window of −1.0 V to 0 V (versus SCE). Meanwhile, the GCD measurements were performed at a current density ranging from 0.5 to 5 A g^{-1} with a potential window of −1.0 to 0 V (versus SCE). The specific capacitance of all the samples can be acquired by computing from GCD curves in accordance with the following equation:

$$C_s = \frac{\Delta t \times I}{\Delta V \times m}$$

where C_s, Δt, I, ΔV, and m represent the specific capacitance, the discharge time, the discharge current, the potential charge during discharge, and the mass of the PNG-x, respectively.

4. Conclusions

In summary, a three-dimensional porous nitrogen-doped graphene with a macro–mesoporous structure has been successfully prepared by a facile two-step calcination strategy. The macro–mesoporous structure can effectively promote the transfer of electrolytic ions. Moreover, the incorporation of nitrogen atoms also boosts the electrochemical properties of the materials. Notably, PNG-0.6 has a specific capacitance of 157 F g^{-1} when the current density is 1 A g^{-1}, which is significantly higher than that of the other samples. The initial capacitance of 98.68% can be maintained after 10,000 CV cycles, indicating that PNG-0.6 is a promising electrochemical material. Our approach provides an opportunity to design novel porous materials with low cost, high capacitance, and long-term stability in the electrochemistry field.

Author Contributions: Conceptualization, J.Y.; validation, Z.W., R.H. and A.G.; investigation, Z.W., R.H., A.G. and J.L.; data curation, J.L.; writing—original draft preparation, J.L.; writing—review and editing, J.Y.; supervision, J.Y.; project administration, J.Y.; funding acquisition, J.Y. All authors have read and agreed to the published version of the manuscript.

Funding: This research was supported by the Program Fund of Non-Metallic Excellence and Innovation Center for Building Materials (2023TDA1-1), the National Natural Science Foundation of China (52201286), and the Guangdong Basic and Applied Basic Research Foundation (2022A1515011905, 2024A1515012613).

Institutional Review Board Statement: Not applicable.

Informed Consent Statement: Not applicable.

Data Availability Statement: The original contributions presented in this study are included in the article. Further inquiries can be directed to the corresponding author.

Conflicts of Interest: The authors declare no conflicts of interest.

References

1. Beidaghi, M.; Wang, C. Micro-Supercapacitors Based on Interdigital Electrodes of Reduced Graphene Oxide and Carbon Nanotube Composites with Ultrahigh Power Handling Performance. *Adv. Funct. Mater.* **2012**, *22*, 4501–4510. [CrossRef]
2. Hwang, J.Y.; Li, M.; El-Kady, M.F.; Kaner, R.B. Next-Generation Activated Carbon Supercapacitors: A Simple Step in Electrode Processing Leads to Remarkable Gains in Energy Density. *Adv. Funct. Mater.* **2017**, *27*, e1605745. [CrossRef]
3. Pech, D.; Brunet, M.; Durou, H.; Huang, P.; Mochalin, V.; Gogotsi, Y.; Taberna, P.L.; Simon, P. Ultrahigh-power micrometre-sized supercapacitors based on onion-like carbon. *Nat. Nanotechnol.* **2010**, *5*, 651–654. [CrossRef]
4. Niu, L.; Wu, T.; Chen, M.; Yang, L.; Yang, J.; Wang, Z.; Kornyshev, A.A.; Jiang, H.; Bi, S.; Feng, G. Conductive Metal-Organic Frameworks for Supercapacitors. *Adv. Mater.* **2022**, *34*, e2200999. [CrossRef]
5. Wang, F.; Wu, X.; Yuan, X.; Liu, Z.; Zhang, Y.; Fu, L.; Zhu, Y.; Zhou, Q.; Wu, Y.; Huang, W. Latest advances in supercapacitors: From new electrode materials to novel device designs. *Chem. Soc. Rev.* **2017**, *46*, 6816–6854. [CrossRef] [PubMed]
6. Wang, G.; Zhang, L.; Zhang, J. A review of electrode materials for electrochemical supercapacitors. *Chem. Soc. Rev.* **2012**, *41*, 797–828. [CrossRef]
7. Yang, L.; Guo, X.; Jin, Z.; Guo, W.; Duan, G.; Liu, X.; Li, Y. Emergence of melanin-inspired supercapacitors. *Nano Today* **2021**, *37*, 101075. [CrossRef]
8. Chi, F.; Li, C.; Zhou, Q.; Zhang, M.; Chen, J.; Yu, X.; Shi, G. Graphene-Based Organic Electrochemical Capacitors for AC Line Filtering. *Adv. Energy. Mater.* **2017**, *7*, 1700591. [CrossRef]
9. Guo, C.; Zhang, Y.; Zeng, T.; Huang, D.; Wan, Q.; Yang, N. High-performance asymmetric supercapacitors using holey graphene electrodes and redox electrolytes. *Carbon* **2020**, *157*, 298–307. [CrossRef]
10. Heo, Y.J.; Lee, J.W.; Son, Y.R.; Lee, J.H.; Yeo, C.S.; Lam, T.D.; Park, S.Y.; Park, S.J.; Sinh, L.H.; Shin, M.K. Large-Scale Conductive Yarns Based on Twistable Korean Traditional Paper (Hanji) for Supercapacitor Applications: Toward High-Performance Paper Supercapacitors. *Adv. Energy. Mater.* **2018**, *8*, e1801854. [CrossRef]
11. Jiang, T.; Wang, Y.; Chen, G.Z. Electrochemistry of Titanium Carbide MXenes in Supercapacitor. *Small Methods* **2023**, *7*, e2201724. [CrossRef] [PubMed]
12. Liu, H.H.; Zhang, H.L.; Xu, H.B.; Lou, T.P.; Sui, Z.T.; Zhang, Y. In situ self-sacrificed template synthesis of vanadium nitride/nitrogen-doped graphene nanocomposites for electrochemical capacitors. *Nanoscale* **2018**, *10*, 5246–5253. [CrossRef] [PubMed]
13. Sahoo, G.; Polaki, S.R.; Ghosh, S.; Krishna, N.G.; Kamruddin, M.; Ostrikov, K. Plasma-tuneable oxygen functionalization of vertical graphenes enhance electrochemical capacitor performance. *Energy Storage Mater.* **2018**, *14*, 297–305. [CrossRef]
14. Liu, Z.; Qin, A.; Zhang, K.; Lian, P.; Yin, X.; Tan, H. Design and structure of nitrogen and oxygen co-doped carbon spheres with wrinkled nanocages as active material for supercapacitor application. *Nano Energy* **2021**, *90*, 106540. [CrossRef]
15. Sedajova, V.; Bakandritsos, A.; Blonski, P.; Medved, M.; Langer, R.; Zaoralova, D.; Ugolotti, J.; Dzibelova, J.; Jakubec, P.; Kupka, V.; et al. Nitrogen doped graphene with diamond-like bonds achieves unprecedented energy density at high power in a symmetric sustainable supercapacitor. *Energy Environ. Sci.* **2022**, *15*, 740–748. [CrossRef]
16. Wei, W.; Chen, Z.; Zhang, Y.; Chen, J.; Wan, L.; Du, C.; Xie, M.; Guo, X. Full-faradaic-active nitrogen species doping enables high-energy-density carbon-based supercapacitor. *J. Energy Chem.* **2020**, *48*, 277–284. [CrossRef]
17. Zhou, Q.; Chen, Q.; Xu, W.; Wang, F.; Du, X.; Zhou, Y.; Zhan, Y.; Jiang, M. Nitrogen and sulfur co-doped carbonized lignin nanotubes for supercapacitor applications. *Chem. Eng. J.* **2024**, *496*, 154126. [CrossRef]
18. Yalovega, G.E.; Brzhezinskaya, M.; Dmitriev, V.O.; Shmatko, V.A.; Ershov, I.V.; Ulyankina, A.A.; Chernysheva, D.V.; Smirnova, N.V. Interfacial Interaction in MeO_x/MWNTs (Me–Cu, Ni) Nanostructures as Efficient Electrode Materials for High-Performance Supercapacitors. *Nanomaterials* **2024**, *14*, 947. [CrossRef]
19. He, X.; Zhang, N.; Shao, X.; Wu, M.; Yu, M.; Qiu, J. A layered-template-nanospace-confinement strategy for production of corrugated graphene nanosheets from petroleum pitch for supercapacitors. *Chem. Eng. J.* **2016**, *297*, 121–127. [CrossRef]
20. Balamurugan, J.; Nguyen, T.T.; Aravindan, V.; Kim, N.H.; Lee, J.H. Flexible Solid-State Asymmetric Supercapacitors Based on Nitrogen-Doped Graphene Encapsulated Ternary Metal-Nitrides with Ultralong Cycle Life. *Adv. Funct. Mater.* **2018**, *28*, e1804663. [CrossRef]
21. Kotal, M.; Kim, H.; Roy, S.; Oh, I.-K. Sulfur and nitrogen co-doped holey graphene aerogel for structurally resilient solid-state supercapacitors under high compressions. *J. Mater. Chem. A* **2017**, *5*, 17253–17266. [CrossRef]
22. Li, Q.; Guo, X.; Zhang, Y.; Zhang, W.; Ge, C.; Zhao, L.; Wang, X.; Zhang, H.; Chen, J.; Wang, Z.; et al. Porous graphene paper for supercapacitor applications. *J. Mater. Sci. Technol.* **2017**, *33*, 793–799. [CrossRef]
23. Ma, L.; Liu, R.; Niu, H.; Xing, L.; Liu, L.; Huang, Y. Flexible and Freestanding Supercapacitor Electrodes Based on Nitrogen-Doped Carbon Networks/Graphene/Bacterial Cellulose with Ultrahigh Areal Capacitance. *ACS Appl. Mater. Interfaces* **2016**, *8*, 33608–33618. [CrossRef] [PubMed]
24. Tang, X.; Zhou, H.; Cai, Z.; Cheng, D.; He, P.; Xie, P.; Zhang, D.; Fan, T. Generalized 3D Printing of Graphene-Based Mixed-Dimensional Hybrid Aerogels. *ACS Nano* **2018**, *12*, 3502–3511. [CrossRef]
25. Yu, L.; Fan, Z.; Shao, Y.; Tian, Z.; Sun, J.; Liu, Z. Versatile N-Doped MXene Ink for Printed Electrochemical Energy Storage Application. *Adv. Energy. Mater.* **2019**, *9*, e1901839. [CrossRef]

26. Chen, J.; Han, Y.; Kong, X.; Deng, X.; Park, H.J.; Guo, Y.; Jin, S.; Qi, Z.; Lee, Z.; Qiao, Z.; et al. The Origin of Improved Electrical Double-Layer Capacitance by Inclusion of Topological Defects and Dopants in Graphene for Supercapacitors. *Angew. Chem. Int. Ed.* **2016**, *55*, 13822–13827. [CrossRef]
27. Mofokeng, T.P.; Tetana, Z.N.; Ozoemena, K.I. Defective 3D nitrogen-doped carbon nanotube-carbon fibre networks for high-performance supercapacitor: Transformative role of nitrogen-doping from surface-confined to diffusive kinetics. *Carbon* **2020**, *169*, 312–326. [CrossRef]
28. Qin, K.; Wang, L.; Wang, N.; Li, J.; Zhao, N.; Shi, C.; He, C.; He, F.; Ma, L.; Liu, E. Nitrogen and oxygen co-doped 3D nanoporous duct-like graphene@carbon nano-cage hybrid films for high-performance multi-style supercapacitors. *J. Mater. Chem. A* **2017**, *5*, 18535–18541. [CrossRef]
29. Kim, H.-K.; Bak, S.-M.; Lee, S.W.; Kim, M.-S.; Park, B.; Lee, S.C.; Choi, Y.J.; Jun, S.C.; Han, J.T.; Nam, K.-W.; et al. Scalable fabrication of micron-scale graphene nanomeshes for high-performance supercapacitor applications. *Energy Environ. Sci.* **2016**, *9*, 1270–1281. [CrossRef]
30. Xiang, X.; Deng, Z.; Zhang, H.; Gao, C.; Feng, S.; Liu, Z.; Liang, Q.; Fu, Y.; Liu, Y.; Liu, K. Polyaniline/Polydopamine-Regulated Nitrogen-Doped Graphene Aerogel with Well-developed Mesoporous Structure for Supercapacitor Electrode. *Chem. Eng. J.* **2023**, *477*, 147211. [CrossRef]
31. Chowdhury, S.; Balasubramanian, R. Three-dimensional graphene-based macrostructures for sustainable energy applications and climate change mitigation. *Prog. Mater. Sci.* **2017**, *90*, 224–275. [CrossRef]
32. Jiang, L.; Fan, Z. Design of advanced porous graphene materials: From graphene nanomesh to 3D architectures. *Nanoscale* **2014**, *6*, 1922–1945. [CrossRef]
33. Liu, J.; Liu, Y.; Li, P.; Wang, L.; Zhang, H.; Liu, H.; Liu, J.; Wang, Y.; Tian, W.; Wang, X.; et al. Fe-N-doped porous carbon from petroleum asphalt for highly efficient oxygen reduction reaction. *Carbon* **2018**, *126*, 1–8. [CrossRef]
34. Yang, W.; Li, R.; Jiang, B.; Wang, T.; Hou, L.; Li, Z.; Liu, Z.; Yang, F.; Li, Y. Production of hierarchical porous carbon nanosheets from cheap petroleum asphalt toward lightweight and high-performance electromagnetic wave absorbents. *Carbon* **2020**, *166*, 218–226. [CrossRef]
35. Yang, W.; Deng, B.; Hou, L.; Wang, T.; Tian, J.; Wang, S.; Li, R.; Yang, F.; Li, Y. Sulfur-fixation strategy toward controllable synthesis of molybdenum-based/carbon nanosheets derived from petroleum asphalt. *Chem. Eng. J.* **2020**, *380*, 122552. [CrossRef]
36. Cheng, B.; Yang, B.; Xie, X.; Wan, L.; Chen, J.; Du, C.; Zhang, Y.; Xie, M. Solvent-free mechanochemical synthesis of Mg-gallic acid complex for the fabrication of high-performance supercapacitor porous carbon. *Chem. Eng. J.* **2024**, *499*, 156672. [CrossRef]
37. Li, Z.Q.; Lu, C.J.; Xia, Z.P.; Zhou, Y.; Luo, Z. X-ray diffraction patterns of graphite and turbostratic carbon. *Carbon* **2007**, *45*, 1686–1695. [CrossRef]
38. Xiao, Y.-X.; Ying, J.; Tian, G.; Tao, Y.; Wei, H.; Fan, S.-Y.; Sun, Z.-H.; Zou, W.-J.; Hu, J.; Chang, G.-G.; et al. Highly dispersed PtPd on graphitic nanofibers and its heavy d-π effect. *Appl. Catal. B-Environ.* **2019**, *259*, 118080. [CrossRef]
39. Balgis, R.; Widiyastuti, W.; Ogi, T.; Okuyama, K. Enhanced Electrocatalytic Activity of Pt/3D Hierarchical Bimodal Macroporous Carbon Nanospheres. *ACS Appl. Mater. Interfaces* **2017**, *9*, 23792–23799. [CrossRef]
40. Xiao, Y.-X.; Ying, J.; Chen, J.-B.; Dong, Y.; Yang, X.; Tian, G.; Wu, J.; Janiak, C.; Ozoemena, K.I.; Yang, X.-Y. Confined Ultrafine Pt in Porous Carbon Fibers and Their N-Enhanced Heavy d-π Effect. *Chem. Mater.* **2022**, *34*, 3705–3714. [CrossRef]
41. Xu, J.; Wang, M.; Wickramaratne, N.P.; Jaroniec, M.; Dou, S.; Dai, L. High-performance sodium ion batteries based on a 3D anode from nitrogen-doped graphene foams. *Adv. Mater.* **2015**, *27*, 2042–2048. [CrossRef] [PubMed]
42. Kononenko, O.; Brzhezinskaya, M.; Zotov, A.; Korepanov, V.; Levashov, V.; Matveev, V.; Roshchupkin, D. Influence of numerous Moiré superlattices on transport properties of twisted multilayer graphene. *Carbon* **2022**, *194*, 52–61. [CrossRef]
43. Liu, X.; Choi, J.; Xu, Z.; Gery, C.P.; Fleischmann, S.; Forse, A.C. Raman Spectroscopy Measurements Support Disorder-Driven Capacitance in Nanoporous Carbons. *J. Am. Chem. Soc.* 2024; *accepted*. [CrossRef] [PubMed]
44. Chen, L.; Zhang, Y.; Lin, C.; Yang, W.; Meng, Y.; Guo, Y.; Li, M.; Xiao, D. Hierarchically porous nitrogen-rich carbon derived from wheat straw as an ultra-high-rate anode for lithium ion batteries. *J. Mater. Chem. A* **2014**, *2*, 9684–9690. [CrossRef]
45. Dong, Y.; Chen, J.-B.; Ying, J.; Xiao, Y.-X.; Tian, G.; Symes, M.D.; Yang, X.-Y. Efficient Water Dissociation on Confined Ultrafine Pt via Pyridinic N-Enhanced Heavy d−π Interaction. *Chem. Mater.* **2022**, *34*, 8271–8279. [CrossRef]
46. Rabchinskii, M.; Ryzhkov, S.A.; Gudkov, M.V.; Baidakova, M.V.; Saveliev, S.D.; Pavlov, S.I.; Shnitov, V.V.; Kirilenko, D.A.; Stolyarova, D.Y.; Lebedev, A.M.; et al. Unveiling a facile approach for large-scale synthesis of N-doped graphene with tuned electrical properties. *2D Mater.* **2020**, *7*, 045001. [CrossRef]
47. Brzhezinskaya, M.; Mishakov, I.V.; Bauman, Y.I.; Shubin, Y.V.; Maksimova, T.A.; Stoyanovskii, V.O.; Gerasimov, E.Y.; Vedyagin, A.A. One-pot functionalization of catalytically derived carbon nanostructures with heteroatoms for toxic-free environment. *Appl. Surf. Sci.* **2022**, *590*, 153055. [CrossRef]
48. Bulushev, D.A.; Zacharska, M.; Shlyakhova, E.V.; Chuvilin, A.L.; Gao, Y.; Beloshapkin, S.; Okotrub, A.V.; Bulusheva, L.G. Single Isolated Pd^{2+} Cations Supported on N-Doped Carbon as Active Sites for Hydrogen Production from Formic Acid Decomposition. *ACS Catal.* **2016**, *6*, 681–691. [CrossRef]
49. Khazaeli, A.; Godbille-Cardona, G.; Barz, D.P.J. A Novel Flexible Hybrid Battery–Supercapacitor Based on a Self-Assembled Vanadium-Graphene Hydrogel. *Adc. Funct. Mater.* **2020**, *30*, 1910738. [CrossRef]
50. Liu, Z.; Duan, C.; Dou, S.; Yuan, Q.; Xu, J.; Liu, W.D.; Chen, Y. Ultrafast Porous Carbon Activation Promises High-Energy Density Supercapacitors. *Small* **2022**, *18*, e2200954. [CrossRef]

51. Tian, W.; Zhang, H.; Sun, H.; Tadé, M.O.; Wang, S. Template-free synthesis of N-doped carbon with pillared-layered pores as bifunctional materials for supercapacitor and environmental applications. *Carbon* **2017**, *118*, 98–105. [CrossRef]
52. Zhang, F.; Liu, T.; Hou, G.; Kou, T.; Yue, L.; Guan, R.; Li, Y. Hierarchically porous carbon foams for electric double layer capacitors. *Nano Res.* **2016**, *9*, 2875–2888. [CrossRef]
53. Qie, L.; Chen, W.; Wang, Z.; Shao, Q.; Li, X.; Yuan, L.; Hu, X.; Zhang, W.; Huang, Y. Nitrogen-Doped Porous Carbon Nanofiber Webs as Anodes for Lithium Ion Batteries with a Superhigh Capacity and Rate Capability. *Adv. Mater.* **2012**, *24*, 2047–2050. [CrossRef] [PubMed]

Disclaimer/Publisher's Note: The statements, opinions and data contained in all publications are solely those of the individual author(s) and contributor(s) and not of MDPI and/or the editor(s). MDPI and/or the editor(s) disclaim responsibility for any injury to people or property resulting from any ideas, methods, instructions or products referred to in the content.

文章编号:1007-9629(2024)11-0969-08

C-F-S-H/PCE纳米晶核对矿粉水泥水化和力学性能的影响

秦子豪， 董烨民， 胡传林*
(武汉理工大学 硅酸盐建筑材料国家重点实验室,湖北 武汉 430070)

摘要:研究了水化铁硅酸钙/聚羧酸减水剂(C-F-S-H/PCE)纳米晶核对矿粉水泥水化和力学性能的影响.采用力学性能测试、等温量热分析、X射线衍射仪和压汞法测试了大矿粉掺量(50%、70%、90%)矿粉水泥的抗压强度、水化放热、水化产物和孔隙率.结果表明:C-F-S-H/PCE纳米晶核的掺入能够显著提升矿粉水泥的抗压强度,50%矿粉掺量的矿粉水泥1 d强度提升60%;C-F-S-H/PCE纳米晶核对矿粉水泥的水化反应具有调控作用,通过加速水泥的早期水化及氢氧化钙的形成激发了矿粉反应活性,从而推动了矿粉反应的持续进行.

关键词:矿粉水泥;C-F-S-H/PCE纳米晶核;抗压强度;水化;微观结构
中图分类号:TU528.35 **文献标志码:**A **doi:**10.3969/j.issn.1007-9629.2024.11.001

Impact of C-F-S-H/PCE Nanocomposites on Hydration and Mechanical Properties of Slag Cement

QIN Zihao, *DONG Yemin*, *HU Chuanlin**
(State Key Laboratory of Silicate Materials for Architectures, Wuhan University of Technology, Wuhan 430070, China)

Abstract: The influence of calcium-ferrite-silicate-hydrates/polycarboxylate ether (C-F-S-H/PCE) nanocomposites on the hydration and mechanical properties of slag cement were investigated. Various methods including mechanical property testing, isothermal calorimetry, X-ray diffraction, and mercury intrusion porosimeter were employed to investigate the compressive strength, hydration, and microstructure of the cement blended with large slag levels (50%, 70%, 90%). The results reveal that the C-F-S-H/PCE nanocomposites significantly enhance the compressive strength of slag cement. The 1 day compressive strength of slag cement with 50% slag content is increased by 60%. C-F-S-H/PCE nanocomposites have a regulatary effect on the hydration reaction of slag cement. By accelerating the early hydration of cement and the formation of calcium hydroxide, the reactivity of the slag is stimulated, thus promoting its continuous reaction.

Key words: slag cement; C-F-S-H/PCE nanocomposite; compressive strength; hydration; microstructure

中国水泥产量占全球总产量的55%以上[1-2],由此产生的二氧化碳约占中国碳排放总量的13%[3-6].使用矿粉、粉煤灰等矿物掺合料部分替代水泥,以降低水泥用量,是实现建材行业节能减排的最重要途径之一[7-13].然而,矿物掺合料掺量的增加导致水泥基材料早期强度发展较慢,限制了大掺量矿物掺合料水泥在实际工程中的规模化应用[10,14-16].例如,在现有研究中常用矿粉掺量通常在50%以下,而且需要通

收稿日期:2023-12-12; 修订日期:2024-04-01
基金项目:湖北省重点研发计划项目(2023BCB083);非金属材料创新中心创新基金资助项目(2023TDA1-1)
第一作者:秦子豪(1999—),男,甘肃金昌人,武汉理工大学硕士生. E-mail: 317523@whut.edu.cn
通讯作者:胡传林(1985—),男,河南商丘人,武汉理工大学研究员,博士生导师,博士. E-mail: chuanlin@whut.edu.cn

中国知网 https://www.cnki.net

过掺入早强剂、碱激发剂等促进体系的强度发展[17-18]. 由此可见,如何在提升矿粉掺量的同时保证体系强度发展仍需要进一步研究.

水化硅酸钙(C-S-H)凝胶是硅酸盐水泥主要的水化产物,也是水泥基材料强度的主要来源,因此提高早期C-S-H凝胶的生成量是提升水泥基材料早期强度的重要途径.由于C-S-H纳米晶核在组成、结构等方面与C-S-H凝胶类似,能够作为成核位点促进C-S-H凝胶的成核与生长,提升水泥基材料的早期强度发展[19-21].在矿物掺合料水泥基材料中,由于矿物掺合料中的活性元素如铝、镁和铁等的引入,使得其主要反应产物由C-S-H转变为水化(铝/铁/镁)硅酸钙(C-(A/F/M)-S-H)[22],因此,研究人员设计了新型水化铝硅酸钙/聚羧酸减水剂(C-A-S-H/PCE)纳米晶核[21]、新型水化镁硅酸钙/聚羧酸减水剂(C-M-S-H/PCE)纳米晶核[23]及新型水化铁硅酸钙/聚羧酸减水剂(C-F-S-H/PCE)纳米晶核[24],并发现相较C-S-H/PCE纳米晶核,上述3种新型纳米晶核的粒径更小,且长期分散稳定性更加优异[21, 23-27].

为了评估新型纳米晶核对大掺量矿物掺合料水泥基材料的应用潜力,本文以新型C-F-S-H/PCE纳米晶核为例,系统研究了其对大掺量矿粉取代水泥体系力学性能发展和水化进程的影响,以期为大掺量矿物掺合料复合水泥基材料的设计与应用提供新途径.

1 试验

1.1 原材料

华新水泥股份有限公司产P·I 42.5基准水泥(PC),比表面积为358 m^2/kg,密度为3.16 g/cm^3;福建金牛水泥厂产S95级粒化高炉矿渣粉(GGBFS),比表面积为430 m^2/kg,密度为2.9 g/cm^3.采用X射线荧光光谱(XRF)分析测定原材料的主要化学组成(质量分数,文中涉及的组成、水胶比等除特别注明外均为质量分数或质量比),结果如表1所示.采用X射线衍射仪(XRD)对GGBFS晶相组成进行表征,结果如图1所示.聚羧酸减水剂(PCE)由贵州皖黔建材有限公司提供,其减水率为30%,固含量为40%.

表1 原材料的化学组成

Table 1 Chemical compositions(by mass) of raw materials

Unit:%

Material	CaO	SiO_2	Al_2O_3	Fe_2O_3	MgO	Na_2O	SO_3	IL
PC	63.54	20.19	4.37	3.36	2.67	0.18	2.51	1.71
GGBFS	40.11	32.07	15.67	0.39	6.95	0.33	2.19	2.29

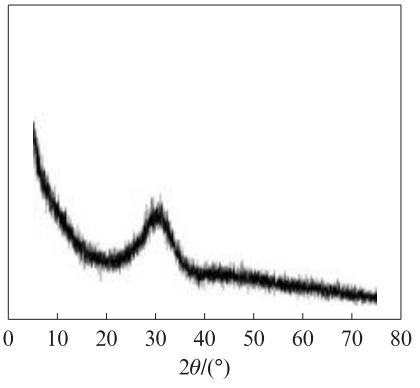

图1 GGBFS的XRD图谱

Fig. 1 XRD pattern of GGBFS

1.2 C-F-S-H/PCE纳米晶核制备

前期研究表明[24],在钙硅比(n(Ca)/n(Si))为1.00、铁硅比(n(Fe)/n(Si))为0.01~0.10条件下制备的C-F-S-H/PCE纳米晶核具有较佳性能.因此本研究以PCE为稳定剂,通过化学共沉淀法合成了n(Ca)/n(Si)和n(Fe)/n(Si)分别为1.00和0.05的C-F-S-H/PCE纳米晶核.制备C-F-S-H/PCE纳米晶核用原材料为国药集团化学试剂有限公司产四水硝酸钙($Ca(NO_3)_2·4H_2O$)、九水硅酸钠($Na_2SiO_3·9H_2O$)及九水硝酸铁($Fe(NO_3)_3·9H_2O$),三者均为分析纯试剂.C-F-S-H/PCE纳米晶核配合比如表2所示,其具体制备过程如下:按原材料配合比分别配置硝酸盐溶液(A溶液)及硅酸盐溶液(B溶液),采用蠕动泵将A溶液及B溶液滴加至PCE溶液中;滴加过程中采用磁力搅拌器进行持续搅拌,并采用30%的氢氧化钠(NaOH)溶液和65%的硝酸(HNO_3)溶液将反应pH值保持为11.7±0.1;滴加完成后继续搅拌24 h,即制备得到固含量为10%的C-F-S-H/PCE纳米晶核.

1.3 试样制备

试验采用矿粉分别替代50%、70%和90%水泥,以探究不同矿粉掺量下C-F-S-H/PCE纳米晶核对矿粉水泥早期强度及水化的影响.设置水胶比(m_w/m_b)为0.4,试验配合比如表3所示.具体制备过程如下:按配合比称取矿粉及水泥,置于搅拌器中预

中国知网 https://www.cnki.net

搅拌1 min;同时将C-F-S-H/PCE纳米晶核和去离子水混合后置于超声分散器中分散5 min,之后将其倒入搅拌器中持续搅拌3 min;接着将其浇筑于尺寸为40 mm×40 mm×40 mm模具中,先置于标准养护室(20 ℃、相对湿度RH>95%)中养护24 h后脱模,再继续置于标准养护室养护至相应龄期.

表2　C-F-S-H/PCE纳米晶核配合比

Table 2　Mix proportions of C-F-S-H/PCE nanocomposites

Unit:mmol

Solution A		Solution B
$Ca(NO_3)_2\cdot 4H_2O$	$Fe(NO_3)_3\cdot 9H_2O$	$Na_2SiO_3\cdot 9H_2O$
100.0	3.0	100.0

表3　试验配合比

Table 3　Mix proportions of experiment

Label	Sample No.	w(PC)/%	w(GGBFS)/%	w(C-F-S-H/PCE)/%
①	PC	100.0	0	0
②	S50	50.0	50.0	0
③	S70	30.0	70.0	0
④	S90	10.0	90.0	0
⑤	S50 0.5% CFSH	50.0	50.0	0.5
⑥	S70 0.5% CFSH	30.0	70.0	0.5
⑦	S90 0.5% CFSH	10.0	90.0	0.5

1.4　试验方法

(1)力学性能测试　采用TYE-300型力学性能测试机对养护龄期为1、3、28 d的试样进行抗压强度测试,加载速率为0.6 kN/s,每组试样均测试3次,取其平均值作为测试结果.

(2)水化热测试　采用TAM Air水化量热仪进行水化热分析.按配合比称取50 g矿粉和水泥的混合粉体进行预搅拌,利用超声波分散机将C-F-S-H/PCE纳米晶核与去离子水先超声分散5 min,掺入胶凝材料中再搅拌5 min,制备得到矿粉水泥浆体;随后称取15 g浆体,置于20 mL安瓿瓶中进行水化放热测试,测试温度为20 ℃,测试时间为72 h.

(3)XRD分析　采用Empyrean型X射线衍射仪对各组1 d龄期试样进行测试.预先对试样进行破碎、研磨处理,研磨过程中添加占粉体质量10%的氧化锌作为内标物.扫描速率为2(°)/min,测试范围为5°~70°.

(4)压汞法(MIP)孔结构测试　采用AutoPore IV 9500型全自动压汞仪对各组1 d龄期试样进行压汞测试.预先对试样进行破碎处理.测试压力为0.001~228 MPa,孔径测量范围为5 nm~800 μm.

2　结果和讨论

2.1　抗压强度

试样1、3、28 d抗压强度如图2所示.由图2可见:(1)C-F-S-H/PCE纳米晶核的掺入使试样S50、S70、S90的1 d抗压强度分别提升60%、75%和122%,表明C-F-S-H/PCE纳米晶核能够显著提升矿粉水泥的早强抗压强度,且提升效果随矿粉掺量提升而增强.(2)50%矿粉掺量的水泥试样(S50)1 d抗压强度显著低于普通硅酸盐水泥试样(PC);然而C-F-S-H/PCE纳米晶核的掺入使其1 d抗压强度与普通硅酸盐水泥相当,表明C-F-S-H/PCE纳米晶核的掺入有效弥补了因水泥不足造成的早期抗压强度损失.(3)C-F-S-H/PCE纳米晶核的掺入使试样S50、S70、S90的28 d抗压强度提升22%、42%和78%,表明C-F-S-H/PCE纳米晶核对于在大矿粉掺量下的矿粉潜在胶凝性激发作用更加显著.(4)与PC相比,矿粉掺量为90%时,矿粉水泥试样S90 28 d抗压强度损失57%,而C-F-S-H/PCE纳米晶核的掺入使其28 d抗压强度损失减至23%.C-F-S-H/

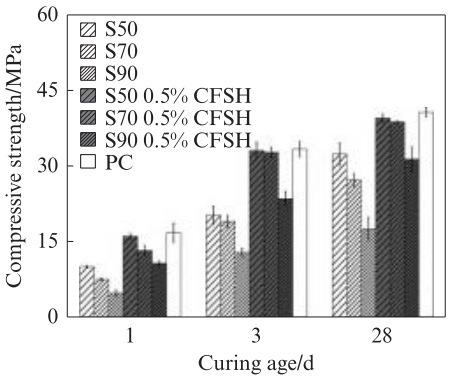

图2　试样1、3、28 d抗压强度

Fig. 2　Compressive strength of samples at 1, 3, 28 d

中国知网　https://www.cnki.net

PCE纳米晶核对于体系后期强度发展的提升作用是由于大掺量矿粉取代水泥后,纳米晶核促进了矿粉的潜在胶凝性,进而弥补了因水泥不足所导致的强度损失.

2.2 水化量热

试样72 h水化放热曲线及累计放热量曲线如图3所示.由图3(a)、(c)、(e)可见:(1)随着矿粉掺量的增加,矿粉水泥水化放热峰值显著降低,且降低幅度增加.(2)矿粉的掺入导致水泥水化放热峰出现时间由11 h提前至8 h,在C-F-S-H/PCE纳米晶核掺入后该时间提前至5 h,表明矿粉对于水泥水化具有加速作用,C-F-S-H/PCE纳米晶核的掺入进一步提升了水泥的水化速率.值得注意的是,随着矿粉的掺入,在水泥第1个水化放热峰后出现了第2个水化放热峰,其峰强随着矿粉掺量的提升而增加,该放热峰归结为矿粉的水化.(3)对于试样S70及S90,C-F-S-H/PCE纳米晶核的掺入显著提升了第2放热峰的峰强,表明C-F-S-H/PCE纳米晶核对于大掺量矿粉取代水泥中矿粉的潜在胶凝性具有提升作用.

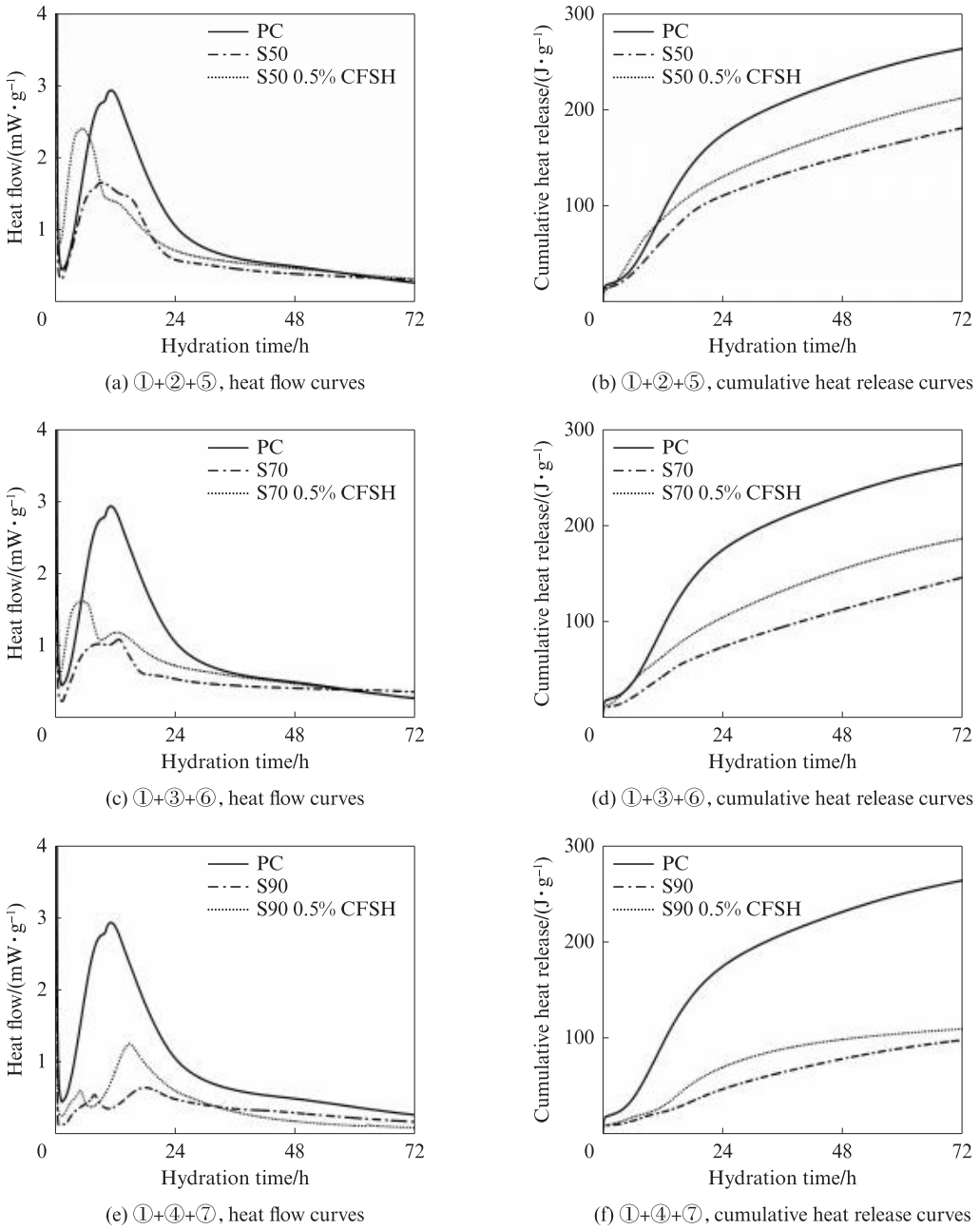

图3 试样72 h水化放热曲线及累计放热量曲线

Fig. 3 Hydration heat flow curves and cumulative heat release curves of samples within 72 h

中国知网 https://www.cnki.net

由图3(b)、(d)、(f)可见:矿粉的掺入导致矿粉水泥体系的累计水化放热量显著降低;而C-F-S-H/PCE纳米晶核的掺入,使试样S50、S70、S90的1 d累计放热量分别提升18%、42%和49%.这表明,C-F-S-H/PCE纳米晶核对于水泥及矿粉的水化反应活性具有提升作用,其中对矿粉水化反应速率的提升效果在矿粉掺量为70%及90%时更加显著.

2.3　XRD图谱

由前可知,C-F-S-H/PCE纳米晶核对矿粉水泥24 h内水化反应产生了显著的调控作用.因此针对1 d龄期矿粉水泥体系水化产物演变及微结构发展进行深入研究,各试样的XRD图谱如图4所示.其中PC0.5%CFSH表示在水泥中掺入0.5%C-F-S-H的试样.由图4可见:1 d龄期矿粉水泥的主要水化产物包括氢氧化钙(CH)及C-S-H凝胶;CH对应18°处的尖峰及30°处的宽峰,其特征峰峰强度随矿粉掺量提升而显著降低;在PC中,C-F-S-H/PCE纳米晶核的掺入导致CH特征峰增强,表明C-F-S-H/PCE纳米晶核促进了水泥的水化,从而加速了CH的形成;随着矿粉掺量的增加,对于试样S50、S70及S90,C-F-S-H/PCE纳米晶核的掺入导致CH特征峰峰强减弱.无论是否掺入C-F-S-H/PCE纳米晶核,矿粉掺量的增加均会导致CH特征峰峰强减弱;而固定矿粉掺量时,C-F-S-H/PCE纳米晶核的掺入又使得CH特征峰峰强有所增强.

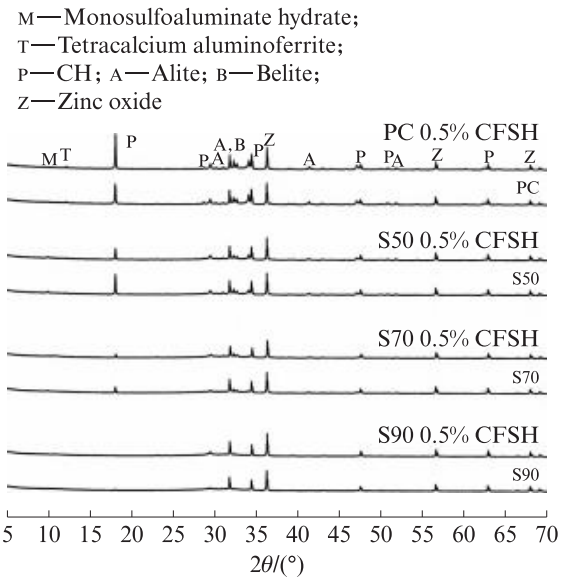

图4　1 d龄期时试样的XRD图谱

Fig. 4　XRD patterns of samples at 1 d

为进一步探究C-F-S-H/PCE纳米晶核对大掺量矿粉取代水泥体系水化的影响,采用XRD分析测试方法对1 d龄期时各试样中的CH含量进行定量计算,结果如图5所示.由图5可见:水化1 d时,C-F-S-H/PCE纳米晶核的掺入导致PC中的CH含量增加29%;然而使矿粉水泥试样S50、S70、S90中的CH含量分别降低85%、40%、32%.这表明,C-F-S-H/PCE纳米晶核虽然提高了水泥的水化反应速率,加速了CH的生成,但同时也提高了矿粉的水化反应活性,从而增加了1 d龄期时矿粉对CH的消耗量.

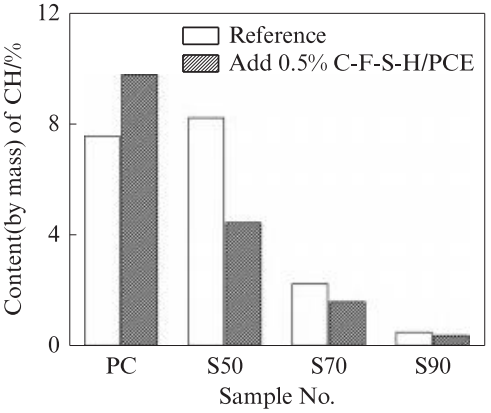

图5　1 d龄期时试样中的CH含量

Fig. 5　Content of CH in samples at 1 d

2.4　孔隙结构

水泥基材料的孔隙类型主要包括4种,分别为凝胶孔(孔径$D<10$ nm)、过渡孔(10 nm$\leqslant D<$100 nm)、毛细孔(100 nm$\leqslant D<$1 000 nm)、大孔($D\geqslant$1 000 nm)[28].各试样1 d龄期累计孔径曲线及孔径分布曲线如图6所示.由图6可见:(1)C-F-S-H/PCE纳米晶核的掺入使试样S50、S70及S90的孔体积降低(图6(a)、(c)、(e)).(2)试样S50、S70及S90的主要孔隙尺寸分布于100~1 000 nm,C-F-S-H/PCE纳米晶核掺入后,其主要孔隙尺寸小于10 nm(图6(b)、(d)、(f)),体系中的主要孔隙由毛细管孔转变为对强度无害的凝胶孔[29].(3)试样S50、S70及S90的临界孔径分别为0.35、0.55、0.67 μm,掺入C-F-S-H/PCE纳米晶核后,其临界孔径减小为0.10、0.09、0.02 μm.这表明C-F-S-H/PCE纳米晶核掺入后产生的孔径细化效果与矿粉掺量有关,在矿粉掺量为90%时细化效果最为显著.

中国知网　https://www.cnki.net

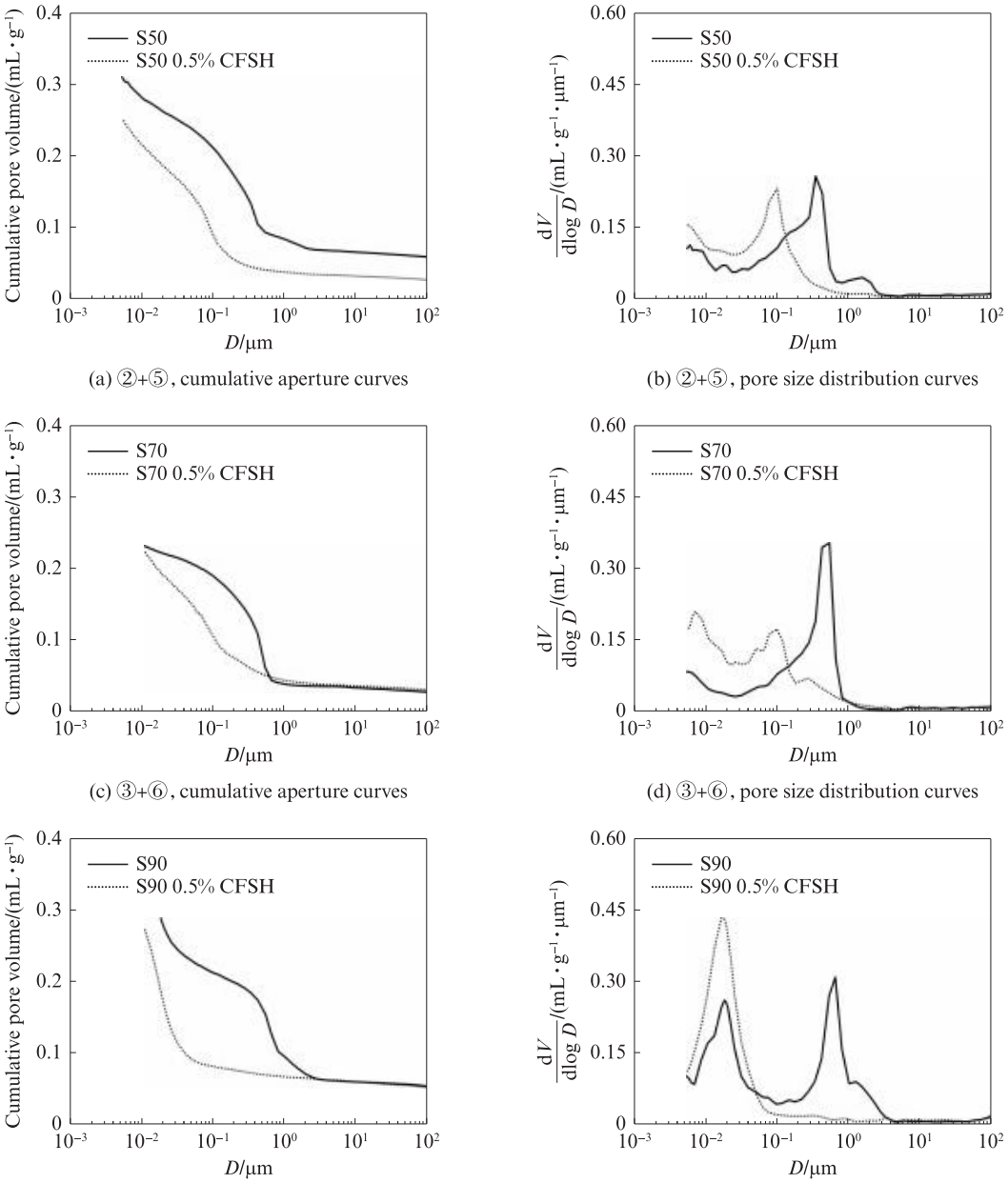

(a) ②+⑤, cumulative aperture curves

(b) ②+⑤, pore size distribution curves

(c) ③+⑥, cumulative aperture curves

(d) ③+⑥, pore size distribution curves

(e) ④+⑦, cumulative aperture curves

(f) ④+⑦, pore size distribution curves

图6 1 d龄期时试样的累计孔径曲线及孔径分布曲线

Fig. 6 Cumulative aperture curves and pore size distribution curves of samples at 1 d

3 结论

(1)C-F-S-H/PCE纳米晶核的掺入能够显著促进大掺量矿粉取代水泥体系抗压强度的提升.50%掺量的矿粉取代水泥时体系1 d强度与普通硅酸盐水泥相当,且随着矿粉掺量的增加,体系抗压强度增幅变大.这表明C-F-S-H/PCE纳米晶核对于提升大掺量矿粉取代水泥的水泥基材料强度发展具有显著优势.

(2)C-F-S-H/PCE纳米晶核能够促进矿粉水泥体系水化反应的加速进行.在矿粉掺量为50%、70%和90%时,1 d龄期时体系累计放热量分别提升18%、42%和49%.C-F-S-H/PCE纳米晶核的掺入显著提高了矿粉水化放热峰值,表明C-F-S-H/PCE纳米晶核对矿粉的潜在胶凝性有提升作用.

(3)C-F-S-H/PCE纳米晶核促进了水泥的早期水化反应速率及氢氧化钙(CH)的形成,1 d龄期时普通硅酸盐水泥中的CH含量增加29%;同时C-F-S-H/PCE纳米晶核对于矿粉早期水化反应活性的提升导致矿粉对CH的消耗速率增大,从而使得大掺量矿粉取代水泥体系中CH含量降低.

(4)C-F-S-H/PCE纳米晶核通过在早期提升矿粉水泥的水化反应程度,降低了大掺量矿粉水泥的孔体积,主要孔隙由100~1 000 nm的毛细管孔转变

中国知网 https://www.cnki.net

为小于10 nm的凝胶孔，体系微观结构致密程度得到显著提升.

参考文献：

[1] ZHUANG X Y, CHEN L, KOMARNENI S, et al. Fly ash-based geopolymer: Clean production, properties and applications[J]. Journal of Cleaner Production, 2016, 125: 253-267.

[2] 卿龙邦，喻渴来，慕儒，等. 定向钢纤维增强水泥基复合材料抗拉细观模拟[J]. 建筑材料学报，2018，21(4)：561-567.
QING Longbang, YU Kelai, MU Ru, et al. Meso-numerical simulation on fracture of aligned steel fiber reinforced cementitious composites[J]. Journal of Building Materials, 2018, 21(4): 561-567. (in Chinese)

[3] 汪保印，张洁，熊金伟，等. 废弃石粉对混凝土的性能影响及碳排放分析[J]. 建筑材料学报，2023，26(11)：1151-1157，1206.
WANG Baoyin, ZHANG Jie, XIONG Jinwei, et al. Influence of waste stone powder on properties and carbon emissions of concrete[J]. Journal of Building Materials, 2023, 26(11): 1151-1157, 1206. (in Chinese)

[4] 蒋正武，尹军. 可持续混凝土发展的技术原则与途径[J]. 建筑材料学报，2016，19(6)：957-963.
JIANG Zhengwu, YIN Jun. Technical principles and approaches for development of sustainable concrete[J]. Journal of Building Materials, 2016, 19(6): 957-963. (in Chinese)

[5] ABDALQADER A F, JIN F, AL-TABBAA A. Development of greener alkali-activated cement: Utilisation of sodium carbonate for activating slag and fly ash mixtures[J]. Journal of Cleaner Production, 2016, 113: 66-75.

[6] SCHNEIDER M. The cement industry on the way to a low-carbon future[J]. Cement and Concrete Research, 2019, 124: 105792.

[7] 侯新凯，徐德龙，薛博，等. 钢渣引起水泥体积安定性问题的探讨[J]. 建筑材料学报，2012，15(5)：588-595.
HOU Xinkai, XU Delong, XUE Bo, et al. Study on volume stability problems of cement caused by steel slag[J]. Journal of Building Materials, 2012, 15(5): 588-595. (in Chinese)

[8] 刘方华. 碱激发磷矿渣复合胶凝材料的水化特性[J]. 建筑材料学报，2020，23(5)：1038-1045.
LIU Fanghua. Hydration characteristics of alkali-activated phosphorus slag composite cementitious materials[J]. Journal of Building Materials, 2020, 23(5): 1038-1045. (in Chinese)

[9] 董烨民，钱雄，胡传林，等. 新型胶凝材料：石灰石煅烧黏土水泥研究进展[J]. 硅酸盐学报，2023，51(9)：2446-2464.
DONG Yemin, QIAN Xiong, HU Chuanlin, et al. New cementitious materials: Advances in limestone calcined clay cement[J]. Journal of the Chinese Ceramic Society, 2023, 51(9): 2446-2464. (in Chinese)

[10] RIVERA F, MARTÍNEZ P, CASTRO J, et al. "Massive volume fly-ash concrete: A more sustainable material with fly ash replacing cement and aggregates"[J]. Cement and Concrete Composites, 2015, 63: 104-112.

[11] 程子扬，陈国夫，屠艳平. 纳米$CaCO_3$对粉煤灰再生骨料混凝土性能及微结构的影响[J]. 建筑材料学报，2023，26(3)：228-235.
CHENG Ziyang, CHEN Guofu, TU Yanping. Effect of nano $CaCO_3$ on properties and microstructure of fly ash[J]. Journal of Building Materials, 2023, 26(3): 228-235. (in Chinese)

[12] 黄浩然，廖宜顺，江国喜，等. 磷建筑石膏对硫铝酸盐水泥熟料收缩特性的影响[J]. 建筑材料学报，2022，25(9)：893-900.
HUANG Haoran, LIAO Yishun, JIANG Guoxi, et al. Effect of phosphorous calcined gypsum on shrinkage characteristics of calcium sulfoaluminate cement clinker[J]. Journal of Building Materials, 2022, 25(9): 893-900. (in Chinese)

[13] 张鹏，亢洛宜，郭进军，等. 纳米SiO_2和PVA纤维增强水泥基复合材料的断裂性能[J]. 建筑材料学报，2021，24(5)：908-915.
ZHANG Peng, KANG Luoyi, GUO Jinjun, et al. Fracture properties of nano-SiO_2 and PVA fiber reinforced cementitious composites[J]. Journal of Building Materials, 2021, 24(5): 908-915. (in Chinese)

[14] LIU J Z, YU B, WANG Q. Application of steel slag in cement treated aggregate base course[J]. Journal of Cleaner Production, 2020, 269: 121733.

[15] SCRIVENER K, MARTIRENA F, BISHNOI S, et al. Calcined clay limestone cements (LC3)[J]. Cement and Concrete Research, 2018, 114: 49-56.

[16] SHARMA M, BISHNOI S, MARTIRENA F, et al. Limestone calcined clay cement and concrete: A state-of-the-art review[J]. Cement and Concrete Research, 2021, 149: 106564.

[17] 张小伟，肖瑞敏，张雄. 粉煤灰矿粉水泥胶凝体系的高效复合早强剂研制[J]. 建筑材料学报，2012，15(2)：249-254.
ZHANG Xiaowei, XIAO Ruimin, ZHANG Xiong. Preparation of high performance composites strength accelerator for cement containing fly ash and ground granulated blast-furnace slag[J]. Journal of Building Materials, 2012, 15(2): 249-254. (in Chinese)

[18] 彭饶，陈伟，李秋，等. 硫酸钠激发尾矿充填材料的性能与微观结构[J]. 建筑材料学报，2020，23(3)：685-691.
PENG Rao, CHEN Wei, LI Qiu, et al. Properties and microstructure of cemented paste tailings activated by sodium sulfate[J]. Journal of Building Materials, 2020, 23(3): 685-691. (in Chinese)

[19] OUYANG X W, KOLEVA D A, YE G, et al. Insights into the mechanisms of nucleation and growth of C-S-H on fillers[J]. Materials and Structures, 2017, 50(5): 213.

[20] LOTHENBACH B, NONAT A. Calcium silicate hydrates: Solid and liquid phase composition[J]. Cement and Concrete Research, 2015, 78: 57-70.

[21] ZOU F B, ZHANG M, HU C L, et al. Novel C-A-S-H/PCE nanocomposites: Design, characterization and the effect on cement hydration[J]. Chemical Engineering Journal, 2021, 412: 128569.

[22] DONG Y M, LIU Y D, HU C L. Towards greener ultra-high performance concrete based on highly-efficient utilization of calcined clay and limestone powder[J]. Journal of Building Engineering, 2023, 66: 105836.

中国知网 https://www.cnki.net

[23] ZHU H W, ZHANG M, ZOU F B, et al. Calcium-silicate-hydrates/polycarboxylate ether nanocomposites doped by magnesium: Enhanced stability and accelerating effect on cement hydration[J]. Journal of the American Ceramic Society, 2022, 105(7): 4930-4941.

[24] ZHU H W, QIN Z H, MA Z B, et al. Novel C-F-S-H/PCE nanocomposites with high-efficiency seeding effect on the hydration of Portland cement [J]. Cement and Concrete Composites, 2023, 140: 105077.

[25] SUN G K, YOUNG J F, KIRKPATRICK R J. The role of Al in C-S-H: NMR, XRD, and compositional results for precipitated samples[J]. Cement and Concrete Research, 2006, 36(1): 18-29.

[26] L'HÔPITAL E, LOTHENBACH B, LE SAOUT G, et al. Incorporation of aluminium in calcium-silicate-hydrates [J]. Cement and Concrete Research, 2015, 75: 91-103.

[27] L'HÔPITAL E, LOTHENBACH B, KULIK D A, et al. Influence of calcium to silica ratio on aluminium uptake in calcium silicate hydrate[J]. Cement and Concrete Research, 2016, 85: 111-121.

[28] 李克非, 罗明勇, 庞晓赟, 等. 不同养护条件下水泥基材料的孔隙结构[J]. 建筑材料学报, 2014, 17(2): 187-192, 227.
LI Kefei, LUO Mingyong, PANG Xiaoyun, et al. Pore structure of cement-based material under different curing conditions[J]. Journal of Building Materials, 2014, 17(2): 187-192, 227. (in Chinese)

[29] ANTONI M, ROSSEN J, MARTIRENA F, et al. Cement substitution by a combination of metakaolin and limestone[J]. Cement and Concrete Research, 2012, 42(12): 1579-1589.

中国知网 https://www.cnki.net

Construction and Building Materials 438 (2024) 137289

Contents lists available at ScienceDirect

Construction and Building Materials

journal homepage: www.elsevier.com/locate/conbuildmat

Effect of styrene acrylic latex on the performance of metakaolin blended cement: From hydration to mechanical properties

Ye Pan [a], Zichen Lu [a,*], Lei Wang [a], Xiaojie Yang [a], Juan Li [b], Ruijun Gao [b], Zhenping Sun [a,*]

[a] Key Laboratory of Advanced Civil Engineering Materials, Ministry of Education, School of Materials Science and Engineering, Tongji University, Shanghai 201804, China

[b] China Building Materials Academy Co., Ltd., Beijing 100024, China

ARTICLE INFO

Keywords:
SA latex
Metakaolin
Cement hydration
Mechanical property
Film formation

ABSTRACT

Effects of styrene acrylic (SA) latex on the hydration and mechanical properties of metakaolin blended cement (MKC) were systematically evaluated through the combined techniques of calorimetry, flow table test, Vicat test, mechanical measurement, QXRD, TGA and SEM. The results show that the presence of metakaolin (MK) greatly changes the interaction of SA polymer with cement grains and then modifies the properties of cement paste and mortar. Specifically, the retardation effect of SA latex on cement hydration can be alleviated through the addition of MK due to its strong adsorption ability to polymer particles, which is beneficial to shorten the setting time of cement paste. The addition of SA latex not only retards the hydration process of cement but also the pozzolanic reaction of MK with portlandite. Contrary to the adverse effect of SA latex on compressive strength, improved strength of hardened MKC mortar was observed with the increased polymer dosage from 4 % to 8 %, which is believed to be caused by the modified microstructure of the matrix through the film formation of SA polymer.

1. Introduction

Currently, about 8 % of global carbon emissions originate from the production of cement [1]. Therefore, it is of great significance to develop low-carbon and environmentally friendly cementitious materials to reduce carbon emissions. The use of supplementary cementitious materials (SCMs) to partially replace cement is a convenient and effective method of preparing low-carbon cementitious materials, such as the use of fly ash, slag, silica fume, etc. [2–4]. However, considering the large production amount of cement in the world, the reservoir of those traditional SCMs becomes limited because of the reduced production of steel [5,6] and less amount of coal used to generate electricity. Currently, a new type of low-carbon cementitious material, limestone calcined clay cement (LC3), is gradually emerging and attracts attention from all over the world. By using limestone and calcined clay with a lower carbon emission, LC3 can save nearly 50 % of conventional clinker [7,8] without depressing the mechanical properties and durability [9–11] of cement. Besides, compared to other SCMs, limestone and clay resources are abundant, which makes LC3 as a sustainable option for low-carbon cement [12].

As LC3 has proven to be a promising option for meeting carbon emission targets, many scholars studied the effect of admixtures commonly used in ordinary Portland cement (OPC) on the performance of LC3. Plank et al. [13] and Justnes et al. [14] have found that polycarboxylate (PCE) can improve the fluidity of LC3 pastes but with a significantly high PCE dosage [13,14]. Huang et al. [15] investigated the effect of alkanolamines on the properties of LC3, and the results showed that triethanolamine (TEA) improved the strength of LC3. Luan et al. [16] studied the synergic effect of TEA and C-S-H seed on the mechanical properties of LC3 used in ultra-high-performance concrete (UHPC), and the results showed that the synergic effect of the two admixtures could overcome the retardation effect of TEA on cement paste and significantly accelerate the early hydration process and improve the strength of LC3-UHPC.

As a common type of admixture used in OPC, polymer latex can greatly modify the properties of mortar or concrete, for example, the flexural and bond strength [17,18], waterproof property [19] and high toughness [20] etc. Due to those advantages, polymer latex is widely used in the construction industry, for example in ceramic tile adhesive, waterproof coating, repair mortar etc. Generally, the addition of polymer latex leads to a decrease in the compressive strength, which could be related to the retardation effect of polymer latex on cement hydration [21], the low elastic modulus of polymers film [22], and the formation of the weak interfacial zone if the excessive polymer particles were

* Corresponding authors.
E-mail addresses: luzc@tongji.edu.cn (Z. Lu), szhp@tongji.edu.cn (Z. Sun).

https://doi.org/10.1016/j.conbuildmat.2024.137289
Received 16 April 2024; Received in revised form 5 June 2024; Accepted 27 June 2024
0950-0618/© 2024 Elsevier Ltd. All rights are reserved, including those for text and data mining, AI training, and similar technologies.

agglomerated [23]. The inhibition of cement hydration by polymer latex is believed to be caused by the hindered dissolution of cement clinker or prohibited nucleation and growth process of hydration products through the adsorption of polymer particles on the surface of cement grains [24–26]. However, the addition of polymer latex can significantly improve the flexural strength of hardened cementitious materials, which is attributed to the formed polymer films to fill the pores and cracks [21] as well as the formed interlaced network structure between hydration products and polymer films [27]. Besides, these polymer films can increase the interface adhesion between hardened cementitious materials and the substrate, and thus improve the bond strength [28,29]. It was also reported that polymer latex can improve the properties of cement-based materials with the incorporation of SCMs such as fly ash [30–33], slag [34,35], and silica fume [36,37]. Rochman et al. [31] investigated the mechanical properties of Vinyl-ester (VE) based polymer concrete incorporating high-volume fly ash, and the results show that the specimen with 30 % VE and 70 % fly ash had the highest compressive strength. Yan et al. [38] studied the effect of SBR latex on the properties of silica fume blended cement and suggested that the latex struggled to offset the negative impact of silica fume on the fluidity of mortar but effectively reduced shrinkage. In addition, the incorporation of silica fume can compensate the detrimental effect of latex on compressive strength. Lho et al. [35] found that the optimal slag content for the compressive and tensile strength of the SBR-modified concrete is 40 %.

Even though a deep understanding of the interaction of polymer latex with OPC has been built, as far as the author's knowledge, limited literatures were published regarding the performance of polymer latex used in LC3. From one aspect, this topic is very important for the continuous application of polymer latex in this promising low-carbon cement. From another aspect, considering the special characteristics of calcined clay, for example, the extremely high surface area and the special nano-structure of calcined clay, it could lead to a wrong conclusion if we just follow the trend observed during the application of polymer latex in OPC. Hence, it is necessary to conduct a thorough study and clarify the performance of polymer latex in LC3.

Based on the above consideration, the performance of one commercial styrene-acrylate (SA) polymer was thoroughly investigated when it was used in the calcined clay blended cement. It should be noted that, as metakaolin (MK) is the most active component in calcined clay [39,40], MK was used in this study to simplify the research system. The hydration process, hydration products, and the corresponding mechanism were studied by varied techniques, including calorimetry, X-ray diffractometer (XRD), thermogravimetric analyzer (TGA) and scanning electron microscopy (SEM), etc. This study attempts to clarify the interaction of polymer latex with MKC. More importantly, it hopes to provide certain theoretical guidance for the application of polymer latex in low-carbon cementitious materials.

2. Experiment and methods

2.1. Raw materials

Reference cement P·I 42.5 (OPC, Fushun Orcel Technology Co., Ltd.) according to the Chinese standard GB8076–2008 was used in this study. One commercial MK was purchased from Jiaozuo Yukun Mining Co., Ltd, Henan, China. The SA latex used in this study was provided by BASF. The chemical and mineralogical composition of OPC and MK as well as the physical properties of SA latex are shown in Table 1. The chemical compositions of OPC were tested by using X-ray fluorescence (XRF), and the mineralogical compositions were measured by using XRD Rietveld refinement. The f-CaO content was measured referring to Chinese standard GB/T 176–2017.

The particle size distributions of SA latex, OPC and MK were measured by laser particle size analyzer (Mastersizer 3000, Malvern, UK) and the results were shown in Fig. 1. The measured specific surface areas of OPC and MK were 1.34 m^2/g and 16.3 m^2/g respectively through the BET method (BEISHIDE instrument, 3 H-2000, Beijing). The defoamer (AF6203) was obtained from Shanghai Guangbai New Materials Co., Ltd. Calcium hydroxide and sodium hydroxide were provided by the Sinopharm Reagent platform (all>98 % purity).

2.2. Sample preparation

First, a certain amount of MK (the specific composition is shown in Table 2) was mixed with OPC for 6 h via a rotary mixer with the rotational speed of 20 rpm (Jingcheng instrument, JC-PT-08, China) to replace 0 %, 10 % and 20 % OPC and then the MK blended cement (MKC) was prepared. Afterwards, the cement pastes or mortars were prepared by mixing the MKC with SA latex and water. The polymer dosages were fixed at 0 %, 4 %, 8 % and 12 % (by weight of MKC). The water-to-cement ratio (w/c) and sand-to-cement ratio (s/c) were kept at 0.45 and 3 respectively. In order to eliminate the air entrainment caused by the addition of latex, defoamer was used at a dosage of 0.3 wt%. Cement paste and mortar were prepared by using a laboratory planetary mixer (JJ-5, Cangzhou Yixuan Testing Instrument Co., Ltd, China) according to GB/T 17671–2021. Afterwards, the prepared cement pastes or mortars were poured into the mold and cured at 20 °C and 50 %RH for 3 d. Then they were cured under 20 °C and 95 %RH till the testing ages. The detailed composition of cement pastes or mortars prepared with different dosages of polymer is shown in Table 2, wherein, S and M represent SA latex and MK respectively, and the number behind means the dosage of polymer (for example S12) and the content of MK (for example M10).

2.3. Methods

2.3.1. Performance evaluation

The flowability of mortars was performed through a flow table test

Table 1
Chemical composition of OPC and MK (wt%) as well as physical properties of latex.

Chemical composition	OPC	MK	Mineralogical composition	OPC	MK	Physical properties	SA latex
SiO_2	20.64	44.42	C_3S	60.72		Zeta potential	-26.20 mV
Al_2O_3	5.15	50.51	C_2S	16.56		Mean size	189.20 nm
Fe_2O_3	3.76	1.51	C_3A	6.72		Solid content	50.00 wt%
CaO	63.24	0.41	C_4AF	8.28		Tg	10.40 °C
MgO	1.61	0.22	Gypsum	3.64		Charge density	-19.83 μeq/g
TiO_2	0.43	2.01	Anhydrite	0.98		Density	1.02 g/cm^3
SO_3	3.38	0.14	f-CaO	0.90			
K_2O	0.67	0.18	Other	2.20			
MnO	0.27	0.15	Quartz		6.70		
P_2O_5	0.31	0.09	Amorphous phase		84.54		
Other	0.54	0.36	Anatase		4.07		
			Hematite		3.09		
			Other		1.60		

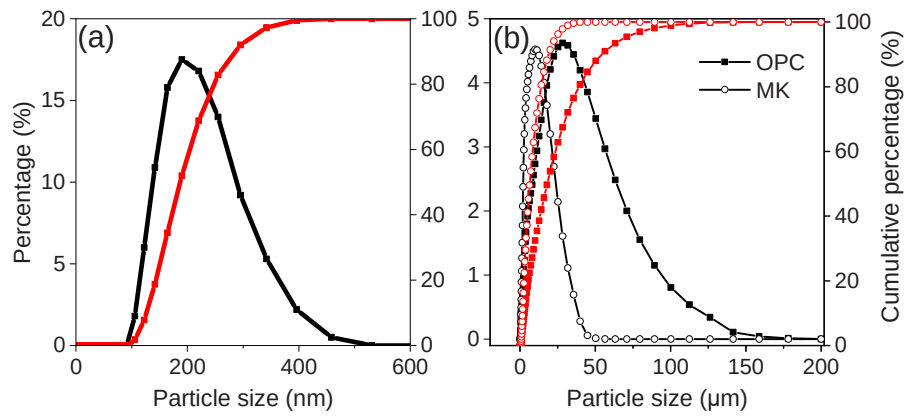

Fig. 1. Particle size distribution of SA latex (a), cement and MK (b).

Table 2
Compositions of cement pastes and mortars prepared with 100 g binder and different dosages of SA polymer (g).

Samples	SA polymer	MKC		Water	Sand*	Defoamer
		OPC	MK			
S0M0	0	100	0	45	300	0.3
S4M0	4	100	0	45	300	0.3
S8M0	8	100	0	45	300	0.3
S12M0	12	100	0	45	300	0.3
S0M10	0	90	10	45	300	0.3
S4M10	4	90	10	45	300	0.3
S8M10	8	90	10	45	300	0.3
S12M10	12	90	10	45	300	0.3
S0M20	0	80	20	45	300	0.3
S4M20	4	80	20	45	300	0.3
S8M20	8	80	20	45	300	0.3
S12M20	12	80	20	45	300	0.3

* The sand was used only for the preparation of mortar.

according to GB/T 2419–2005. The setting time of cement pastes was tested following GB/T 1346–2011 by using a Vicat apparatus. For the test of flowability and setting time, three measurements were conducted and the average value was selected as the representing data. The flexural and compressive strength of mortars were conducted according to GB/T 17671–2021. In this standard, the flexural strength was first measured to the sample with the dimension of 40 mm × 40 mm ×160 mm after curing for 3 d, 7 d, and 28 d respectively. After the measurement of flexural strength, the sample was broken into two parts with the dimensions of 40 mm × 40 mm × ~80 mm. An automatic compression test machine (WHY-300, Cangzhou Yixuan Testing Instrument Co., Ltd, China) was used for the flexural and compressive strength at a loading speed of 50 N/s and 2.4 kN/s respectively. The flexural and compressive strength were obtained through the average of 3 and 6 measurements, respectively. The bond strength of mortars (dimension of 50 mm × 50 mm × 5 mm) after curing the same age were tested through a pull-out tester (LBY-9, Hebei Guanghui Testing Instrument Co., Ltd, China) with a loading speed of 10 mm/min. The average of 8 measurements was taken as the value of bond strength.

2.3.2. Isothermal calorimetry

The hydration process of cement pastes with the addition of SA latex was monitored through a TAM-Air isothermal calorimeter (TAM Air, TA Instruments, USA) at 25 °C for 3 d. The composition of cement pastes for the calorimetric test can be referred to in Table 2 with the MKC mass of 10 g. First, a certain amount of water or SA latex was prepared and poured into an ampoule. 10 g MKC was then put into the ampoule and mixed for 1 min by using a vortex mixer (MX-S, DLAB, China). Afterwards, the ampoule was inserted into the device and the heat flow was started to record. The results were normalized based on the mass of MKC.

2.3.3. XRD

The hardened cement pastes were broken into small size after curing for 12 h, 3 d and 28 d, and then immersed in 30 mL isopropanol (5 °C) for 1 d to stop hydration. Afterwards, the prepared samples were dried in a vacuum at 40 °C for 48 h and stored in a plastic bag under the vacuum environment. Before testing, the samples were ground into powders (<75 μm). Then, the XRD analysis was performed via an X-ray diffractometer (Model D/max, RIGAKU, Japan) with a scanning range from 5° to 40° and a scanning speed of 2 °/min. Quantitative X-ray diffraction (QXRD) was used to quantitatively analyze the main hydration products in the hardened cement pastes. α-Al_2O_3 was used as an internal standard for the quantitative analysis of phases. The Rietveld refinement was conducted by HighScore software.

2.3.4. TGA

The prepared samples as described in Section 2.2.3 were also used for the thermogravimetric analysis (STA 409, Netzsch, Germany). 20 mg powder of hardened pastes was heated at a constant heating rate of 10 °C/min from room temperature to 900 °C under a nitrogen atmosphere.

2.3.5. SEM

A scanning electron microscope (Gemini 300, ZEISS, Germany) was used to study the fractured surfaces of hardened cement pastes with different dosages of SA latex under a constant MK content of 10 %. Before testing, the hardened pastes cured for 3 d were fractured into small blocks with the dimensions of 3–5 mm in length, 3–5 mm in width and 1–2 mm in thickness. Then, each sample was immersed in 30 mL cold isopropanol (5 °C) for 1 d to stop hydration. Afterwards, the prepared samples were dried in a vacuum at 40 °C for 48 h and stored in a plastic bag under the vacuum environment. Just before observation, the sample was broken into a flat shape and the fresh surface was observed. Before observation, the gold was sprayed onto the fresh surface for 60 s to obtain a better conductivity. The SEM was operated at an accelerating voltage of 5 kV.

2.3.6. Adsorption measurement

The adsorption isotherm of SA polymer on MKC was built under a constant temperature of 25 °C according to the literature [41]. 30 g MKC and 13.5 g water with different dosages of SA latex were mixed in a 50 mL centrifuge tube by a vortex mixer for 1 min and then centrifuged at 4000 rpm for 5 min. The upper suspension with polymer particles, water, and a tiny amount of cement grains was then collected with a syringe and then filtered by using a filter with a pore size of 0.45 μm to obtain the supernatant. Afterwards, the obtained supernatant was

dropped into three glass dishes and then placed in an oven at 105 °C for 8 h. Because some inorganic salts could also exist in the dried supernatant, it was further calcined at 600 °C for 1 h to decompose the polymer. At last, the solid content of polymer in the supernatant was obtained and then the adsorption amount of polymer was calculated by using the depletion method. The average of the three values was taken as the final value used in this study. In addition, the adsorption of isotherm of SA polymer on MK pastes prepared with different solutions was also tested by using the same method as described above. In order to further understand the adsorption mechanism of SA polymer on MK, DI water, NaOH solution (pH=11) and $Ca(OH)_2$ solution ((pH=11, $[Ca^{2+}]$= 25 mmol/L) were used to prepare the MK paste. The values of zeta potential of MK in those solutions were measured by using a Zetasizer (Nano ZS90, Malvern, UK).

3. Results

3.1. Flowability and setting time

Fig. 2 shows the effect of SA latex and MK on the flowability of MKC mortar. The addition of SA latex can always improve the flowability of mortar. When there is no MK, the flowability of mortar is increased by 48.8 %, 97.6 % and 140.0 % with the polymer dosage of 4 %, 8 % and 12 % respectively. However, along with the increased MK content, it is found that the flowability of MKC mortar decreased obviously, which could be caused by the high specific surface area and the irregular shape of MK particles [42,43]. Besides, the increment of the flowability of mortar caused by polymer latex was significantly decreased (to 27.6 %, 73.3 %, 129.0 % with the incorporation of 10 % MK and 21.0 %, 56.0 %, 75.0 % for that with 20 % MK). It indicates the presence of MK decreases the ability of SA latex to increase the flowability of mortar. Many publications have discussed the mechanism for the increased flowability of cement paste with the addition of polymer latex. It is believed to be caused by the adsorption of polymer particles on the surface of cement grains, which can increase the repulsive force and then break the agglomeration formed by cement grains [44,45]. Hence, the significantly decreased ability to disperse the mortar with the increased MK content indicates that there should be a strong adsorption of MK to the polymer particles.

The setting time of MKC with the varied dosages of SA latex is shown in Fig. 3. First, the addition of SA latex in MK0 (namely OPC) causes a strong delay in setting time, which matches well with results from many previous studies [24–26]. Compared to MK0, the incorporation of MK has nearly no effect on the setting time of MKC if no SA latex was added. However, it is interesting to notice that the setting times of the samples with the addition of SA latex were significantly decreased when the MK was incorporated. Besides, the increased MK content results in further

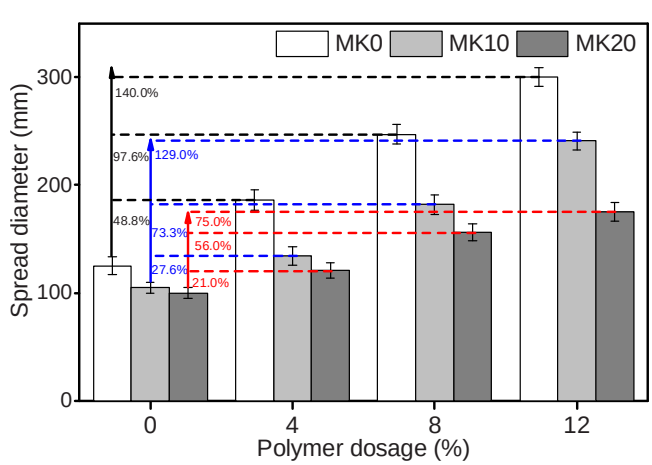

Fig. 2. The effect of SA latex on the flowability of MKC mortar.

decreased setting time. It indicates that the incorporation of MK can weaken the retardation effect of SA polymer on the setting time of cement paste.

3.2. Mechanical properties

The mechanical properties of mortars with different MK contents and SA polymer dosages were measured after curing for 3, 7, and 28 days and the results are shown in Fig. 4. To the condition without the addition of SA latex, the addition of MK has tiny effect on the flexural strength, regardless of the curing age. To the compressive strength, when the curing age is 3 d, the increased MK content leads to a decreased strength, which is believed to originate from the low reactivity of MK. When the curing age is increased to 7 d, MK10 shows a comparable strength to that of MK0, but MK20 still shows the lowest value. After curing for 28 d, a slight increase in compressive strength was observed with the increased MK content, which is believed to be caused by the MK's pozzolanic reaction [46].

To the condition with the addition of SA latex, it is found that the effect of MK depends on the dosage of SA polymer. When the polymer dosage is 4 %, generally a decreased trend in the flexural and compressive strength was observed along with the increased addition amount of MK, regardless of the curing age. When polymer dosage was increased to 8 %, a first increased and then decreased mechanical strength was found along with the increased content of MK, and the optimal content of MK was 10 %. When polymer dosage was further increased to 12 %, the flexural strength was significantly increased with the increased content of MK. A similar trend can also be found for the compressive strength but the increase was not as strong as that of flexural strength.

Regarding the effect of polymer dosages under the same MK content, a decreased trend was found in the compressive strength with the increased dosage of polymer when no MK was added, which matches well with the results in the literature [23,47,48]. However, a first decreased and then increased compressive strength was observed along with the increased polymer dosage when the MK content was 10 %. Along with the increased MK content to 20 %, the increased polymer dosage seems to have a tiny effect on the compressive strength. To the effect of SA polymer on flexural strength, a first increase and then decrease in flexural strength was found along with the increased polymer dosage when the MK content was 0 % and 10 %, which matches well with the findings shown in many literatures [49–51]. When the MK content was increased to 20 %, a continuous increase in the flexural strength can be observed.

As shown in Fig. 5, the effect of MK and SA latex on the bond strength of mortars was also evaluated. It is commonly accepted that the increased bond strength through the addition of polymer originates from the formed cross-linked network structure, which could act as an additional bond agent and increase the internal cohesion of the matrix as well as the bond force to the substrate [52,53]. Hence, regarding the effect of SA latex under the same MK content, an increased bond strength can always be found along with the increased polymer dosages to 8 %. Along with the further increased polymer dosage from 8 % to 12 %, the increased polymer dosage seems to have a limited effect on the bond strength.

The effect of MK is closely related to the polymer dosage. First, the increased content of MK can always lead to a decreased bond strength when the dosage of SA latex is 0 % and 4 %. With the increased polymer dosage to 8 % and 12 %, a first increased and then decreased bond strength was found along with the increased MK content. Again, the sample with the MK content of 10 % shows the highest strength. Obviously, a certain amount of SA polymer and MK can promote the strength of mortar, and the results show that more amount of MK is needed to obtain better mechanical properties along with the increased dosage of SA polymer. It indicates there could be a synergistic effect of SA polymer and MK on the enhancement of the strength of mortar.

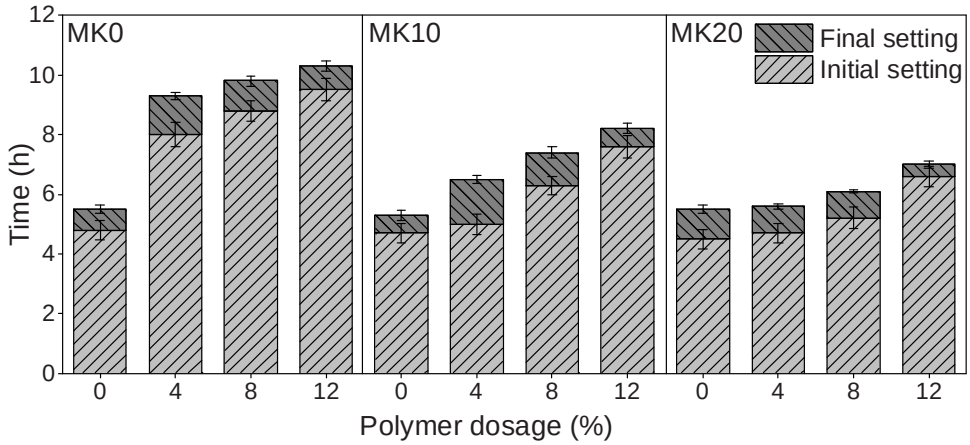

Fig. 3. The effect of SA latex on the setting time of MKC mortar.

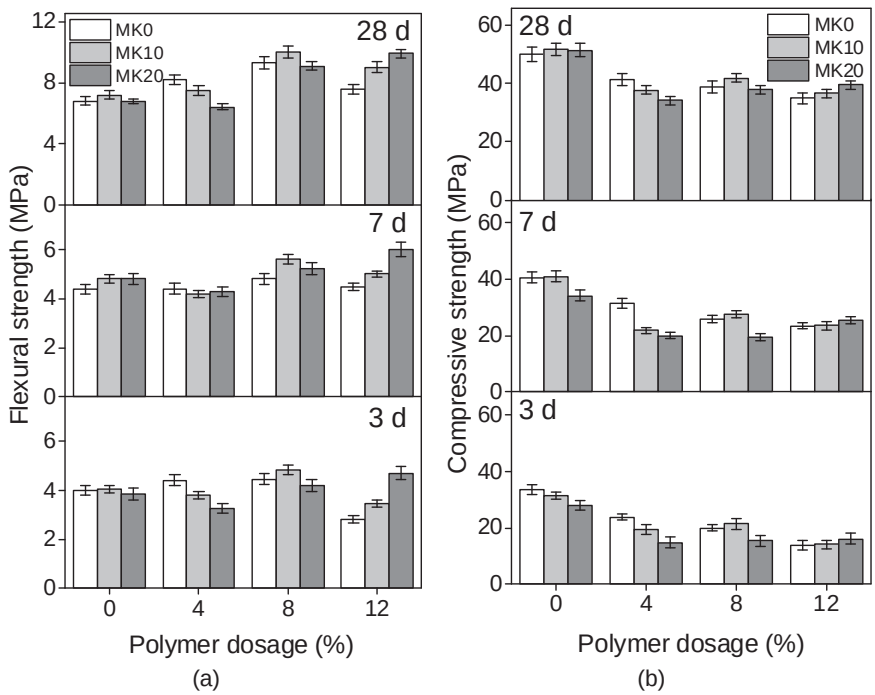

Fig. 4. The effect of SA latex on the flexural (a) and compressive (b) strength of MKC mortar.

3.3. Hydration process

The isothermal calorimetry was conducted to investigate the effect of SA latex on the hydration process of MKC, as shown in Fig. 6. Regarding the effect of SA latex on cement hydration, following our expectation, the addition of SA latex can retard the hydration process of cement by lowering the main peak of exothermic hydration, slightly delaying the induction period and reducing the cumulative heat after 70 h hydration. Regarding the effect of MK, the increased content of MK has a slight effect on the duration of the induction period but increases the height of the main peak and the cumulative heat after hydration of 70 h. Besides, along with the increased polymer dosages to 8 %, the improving capability of MK on the height of the main hydration peak was amplified. It indicates that the increased MK content is helpful to alleviate the retardation effect of SA polymer on cement hydration. With the further increased dosage to 12 %, the capability of MK to increase the peak height was decreased.

3.4. Hydration products

Comparing the results shown in Fig. 4 and Fig. 5, two interesting phenomena are observed. First, contrary to the continuous decrease in compressive strength found in MK0 with the increased polymer dosages, an increased strength can always be found for MK10 and MK20 when the polymer dosage increases from 4 % to 8 %. Second, contrary to the normally decreased mechanical strength for the sample with the increased content of SCMs, an increased mechanical strength can be found with the increased content of MK when the polymer dosage is 12 %. It indicates there should be an interaction of MK and SA polymer and then changes the properties of mortar. In order to further understand the mechanism, the hydration products were analyzed by QXRD and TGA. Corresponding to the two mentioned phenomena, samples with the increased polymer dosages under the constant content of MK (MK10) and samples with an increased MK content under the constant polymer dosage (12 %) were analyzed.

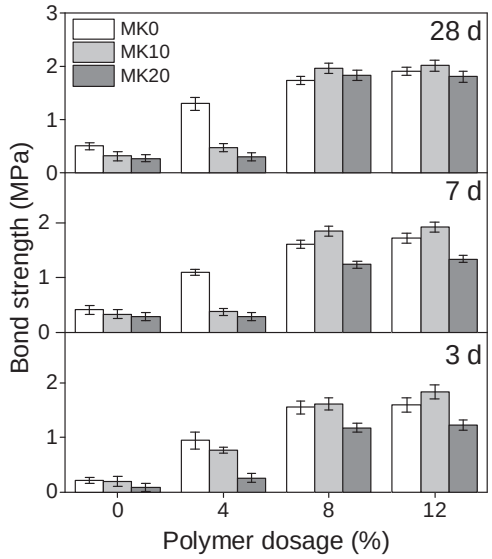

Fig. 5. The effect of SA latex on the bond strength of MKC mortar.

3.4.1. XRD/QXRD analysis

To investigate the phase composition of different samples, the XRD test was conducted and the results are shown in Fig. 7. As shown in Fig. 7, varied clinker phases (C_3S, C_2S, C_3A, and C_4AF) and hydration products (portlandite (CH), and ettringite (AFt), and monosulfate (AFm) were detected in samples.

To further determine the content of different phases, the quantitative XRD was applied for the samples after curing for 12 h, 3 d and 28 d. Because of the different initial amounts of varied clinker phases through the blending of MK to OPC, it is meaningless to directly compare the absolute content of the mineralogical phases. Therefore, the hydration degree of different clinker phases was compared, instead of their absolute amount. The calculation method of hydration degree was given by the Eq. (1).

$$W_{HD} = \frac{Q_{AC} - Q_{CC}}{Q_{AC}} \times 100\% \quad (1)$$

Wherein, W_{HD} refers to the hydration degree of clinker phases; Q_{AC} refers to the original content in anhydrous cement; Q_{CC} refers to the measured content after a certain hydration time.

Fig. 8 shows the results of the calculated hydration degree of the varied clinker phases (C_3S, C_3A, and C_4AF) and the content of hydration products (CH, and AFt) along with the increased hydration time. Regarding the effect of polymer under a constant MK content (Fig. 8(a)), normally a decreased hydration degree for the clinker phase and less formation of hydration products were observed along with the increased polymer dosages, which matches well with the calorimetric results shown in Fig. 6. When curing age was increased to 28 d, a decreased hydration degree for the varied clinker phases was found for the samples with the addition of SA polymer. However, the sample with the polymer dosage of 8 % shows a slightly higher hydration degree compared to the other two samples with the polymer dosages of 4 % and 12 %. After curing for 3 d, an increased CH content was found for the sample with the addition of polymer at the dosages of 4 % and 8 %, but not at 12 %. Considering the reduced hydration degree of C_3S with the addition of polymer, the increased CH amount could originate from the hindered pozzolanic reaction of MK.

Regarding the effect of MK content under the same polymer dosage, an increased hydration degree and more amount of hydration products (except CH in S12M20) were reached along with the increased MK content, which again proves that the addition of MK can alleviate the retardation effect of SA polymer on cement hydration. In addition, an obvious induction in the formed CH amount was found when the MK content was 20 %. It means that, under such a high MK content, the presence of SA polymer can be not enough to prohibit the pozzolanic reaction.

3.4.2. TG/DTG analysis

To further determine the effect of SA polymer on the mechanical properties of MKC, the thermogravimetric tests were carried out and the results are shown in Fig. 9. There were two main peaks in the DTG curves. The first one detected at around 100 °C is attributed to the

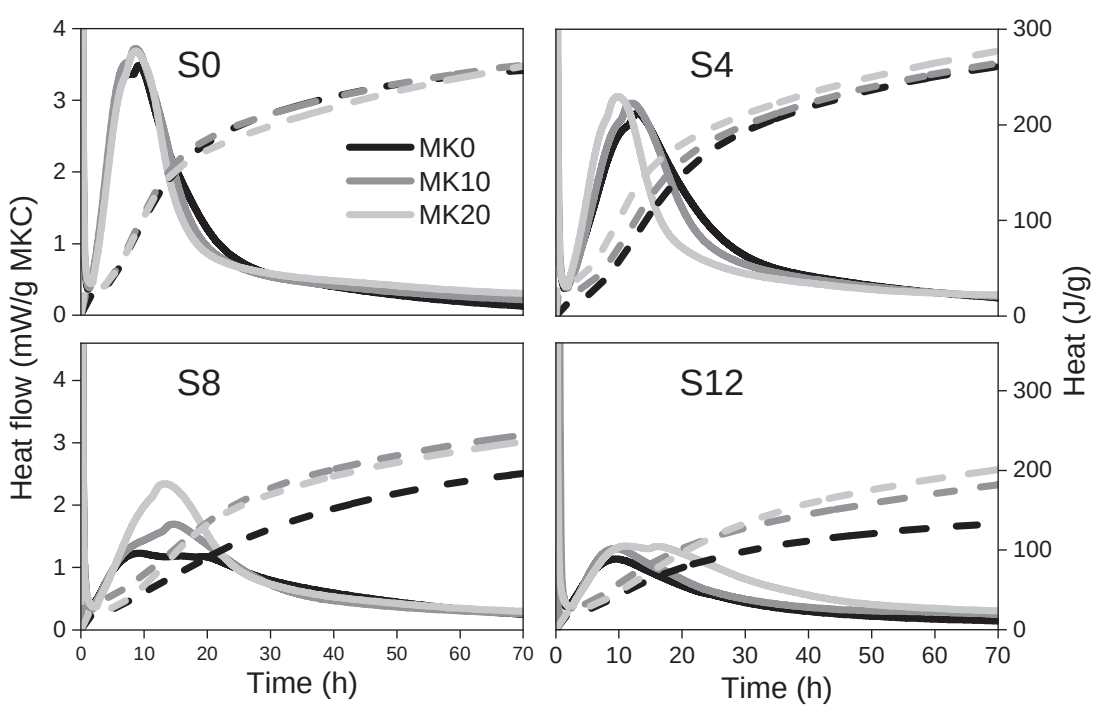

Fig. 6. The calorimetry curves of SA latex-modified MKC.

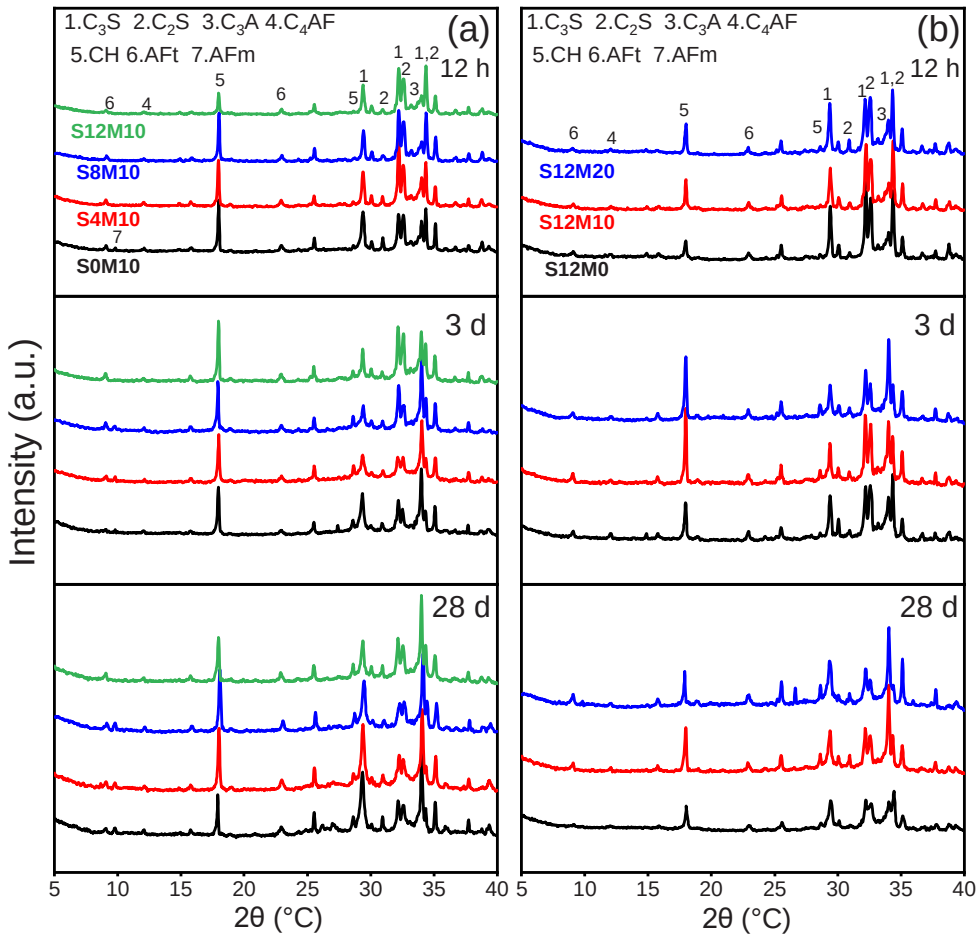

Fig. 7. XRD patterns of different samples: (a) effect of polymer dosage when MK content is 10 %; (b) effect of MK when polymer dosage is 12 %.

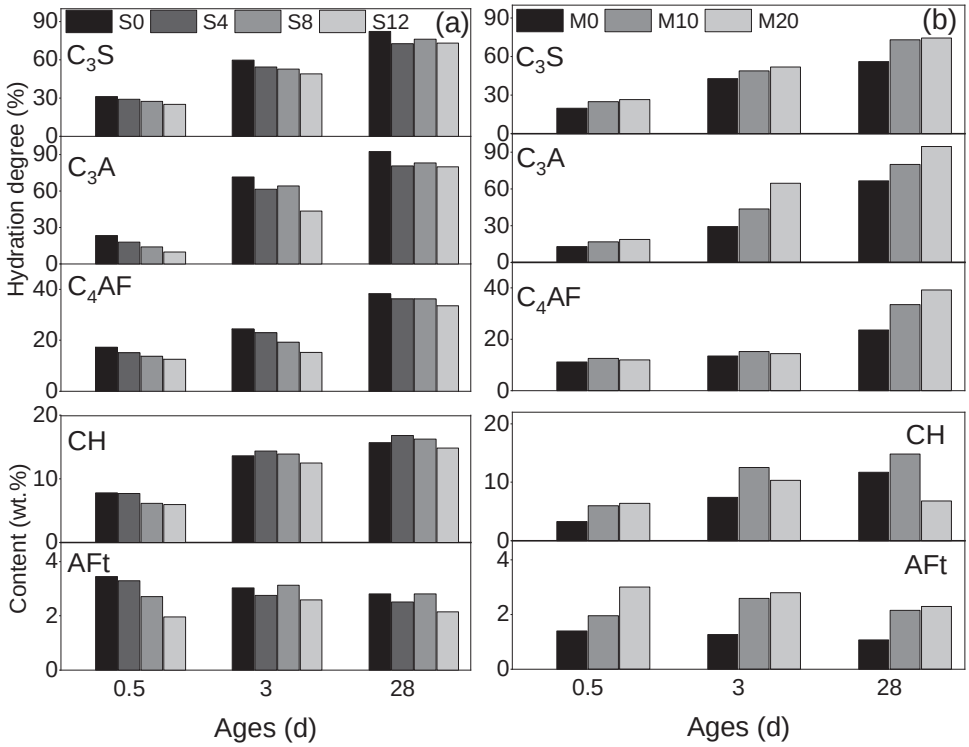

Fig. 8. Quantitative XRD results of different samples: (a) effect of polymer dosage when MK content is 10 %; (b) effect of MK when polymer dosage is 12 %.

decomposition of AFt and C-S-H gels [54]. The second one with the weight loss from 400 °C to 500 °C is related to the dehydroxylation of CH [55,56] and the decomposition of SA polymer [57]. Besides, a peak occurring at around 130°C is caused by the decomposition of AFm [56]. The weight loss in different temperature ranges for each sample was summarized in Table 3. It is noted that the weight loss caused by the SA polymer was deducted in the temperature range from 200 °C to 500 °C, which ensures that the weight loss at this temperature is mainly caused by the decomposition of hydration product, namely CH.

Regarding the effect of polymer under the constant MK content, after hydrating for 12 h, the addition of SA latex caused a reduction in the weight loss in the temperature range of 30 °C~100 °C, which indicates the formed amount of AFt and C-S-H was reduced with the increased polymer dosages. A similar trend can also be found for the calculated weight loss in the temperature range of 200 °C~500 °C. When the hydration times were 3 d and 28 d, compared to the sample without the addition of SA polymer, the weight loss caused by the decomposition of AFt and C-S-H was decreased but the CH content was increased (except S12M10), which matches well with our QXRD results shown in Fig. 8. It indicates the addition of polymer not only retards the hydration process of cement but also the pozzolanic reaction of MK. It should be noted that, compared to S4M10 and S12M10, S8M10 always shows the highest weight loss in the temperature range of 30 °C~100 °C, which could be caused by the increased amount of AFt as shown in Fig. 8. The decreased amount of CH for S12M10 could be caused by the strongly retarded cement hydration by the increased polymer dosage.

Regarding the effect of MK under the same polymer dosage, the weight loss in the temperature range of 30 °C~100 °C was increased along with the increased MK content, regardless of the curing age. It proves that the increased content of MK can alleviate the retardation effect of SA polymer on cement hydration. Besides, similar to the results shown in Fig. 8, a first increased and then decreased CH content was found when the curing ages were 3 d and 28 d, and the highest CH content was observed in S12M10. In addition, an obvious formation of monosulfate (AFm) can be found in the samples with the MK content of 20 %.

4. Discussions

As shown in the results above, the presence of MK greatly changes the interaction of cement grains with the SA polymer and then modifies the properties of cement paste or mortar. Regarding the effect of MK under the same dosage of SA polymer, without the addition of polymer, the addition of MK is harmful to the development of early compressive strength considering their low reaction activity [58] compared to that of cement. Along with the increased curing age to 28 d, the compressive strength becomes comparable to the samples with varied content of MK due to its pozzolanic reaction of MK. When the polymer dosage is 4 %, a decreased mechanical strength is found with the increased content of MK, regardless of the curing ages, which could be mainly caused by the hindered pozzolanic reaction of MK by the SA polymer. However, along with the increased polymer dosages to 8 %, an initially increased and

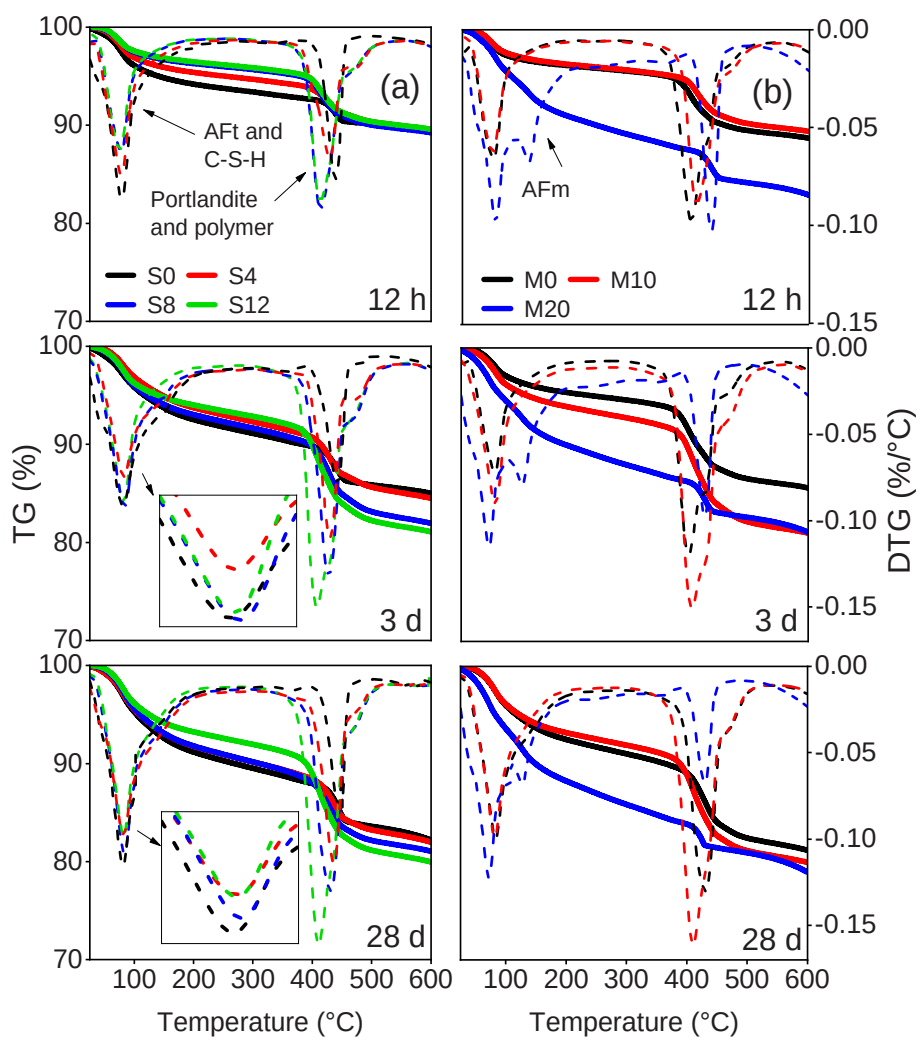

Fig. 9. TG-DTG curves of different samples: (a) the effect of polymer dosage when the content of MK is 10 %; (b) the effect of MK when polymer dosage is 12 %.

Table 3
The weight loss in different temperature ranges for each sample.

Samples		12 h		3 d		28 d	
		30–100 °C	200–500 °C	30–100 °C	200–500 °C	30–100 °C	200–500 °C
M10	S0	3.7	4.1	3.9	6.2	4.6	7.2
	S4	3.0	3.1	3.4	6.9	3.8	7.7
	S8	2.5	2.3	3.8	6.5	4.3	7.4
	S12	2.2	1.9	3.5	4.2	3.8	6.8
S12	M0	1.7	1.2	2.6	3.2	3.2	4.7
	M10	2.2	1.9	3.5	4.2	3.8	6.8
	M20	2.5	2.1	3.5	3.9	4.2	3.4

then decreased mechanical strength was observed. The sample with the MK content of 10 % shows the highest mechanical strength. Along with the increased polymer dosage to 12 %, the increased content of MK is conducive to the development of strength. The adsorption of polymer particles is an important process to affect the properties of cementitious materials, Hence, in order to better understand the interaction of SA polymer with OPC and MK, the adsorption amounts of SA polymer on the different MKCs were measured, as shown in Fig. 10.

It was found that an increased amount of SA polymer was adsorbed with the increased content of MK. The saturation adsorption was reached at 4 % for MK0. Along with the increased MK content, an increased amount of SA polymer was needed to reach saturation adsorption, namely 8 % for MK10 and nearly 12 % for MK20, respectively. The pictures shown on the right side of Fig. 9 also support that MK20 has a stronger adsorption capability than MK0 and MK10. The above results indicate that more SA polymer particles can be adsorbed by MK particles. The adsorption of SA polymer by MK can reduce the adsorption amount of polymer on the surface of cement grains, which in turn alleviates the retardation effect of SA polymer on cement hydration. Hence, a promoted hydration process and increased mechanical strength can be found with increased MK content. Furthermore, an increased content of MK was needed to reach an improved strength along with the increased dosage of polymer.

Considering the mechanism for the adsorption of SA polymer particles on MK, the adsorption amount of SA polymer on MK along with the increased polymer dosages were measured and the results are shown in Fig. 11. It was found that, the negatively charged SA polymer particles can be greatly adsorbed on MK, even though the surface charge of MK is also negative. Besides, the addition of calcium ions can decrease the absolute value of the surface charge and is beneficial to the adsorption of SA polymer particles. Regarding the adsorption of SA polymer particles on MK, one possible reason could be the formation of hydrogen bonding between the MK and the functional groups on the surface of polymer particles [59,60] or the inhomogeneous charge distribution of calcined clay [61]. Besides, the Ca^{2+} can be adsorbed on the surface of MK and then act as the anchoring sites for the negatively charged SA polymer particles [62–64].

Since the polymer plays a determinate role in promoting flexural strength and bond strength by forming a cross-linked network structure with hydration products, MK with a high specific surface area inevitably affects the modification of mortar by polymer latex. It is interesting to find that the optimal content of MK at varied polymer dosages is highly in accordance with its saturated adsorption site. Firstly, when there is no MK added, the flexural strength and bond strength of mortar can be generally improved by polymer latex. However, the excessive polymer could seriously inhibit the cement hydration and thus reduce the modulus of elasticity and overall strength [23]. Besides, a separate polymer phase within the composite will be formed by these excessive polymers, and further acts as the weak region, consequently leading to a reduction in the overall strength [65]. Then, with the addition of 10 % MK, the saturated adsorption site changes to nearly 8 %, at this time, 4 % polymer particles is not enough for the interaction with hydration products, and thus cause a relatively low strength. Further, when MK is 20 %, the saturated adsorption site changes to nearly 12 %, which is also in line with its optimal dosage of mechanical strength.

Regarding the effect of SA latex under the same MK content, even though the increased polymer dosage leads to a stronger retardation effect on cement hydration (Fig. 6), no gradual decrease in the compressive strength of mortar was found along with the increased polymer dosage when the MK content was 10 % and 20 %. On the contrary, a slight increase in both the flexural and compressive strength was observed at a polymer dosage of 8 % compared to that at a polymer dosage of 4 %. Normally, the hydration degree, amount of hydration products and the formed microstructures are three important parameters to decide the mechanical properties of hardened cementitious materials. As shown above, although S8M10 still presents a slightly stronger pozzolanic reaction at 28 d (Fig. 9), the increased dosage of SA polymer leads to a retarded hydration process of cement (Fig. 6), less

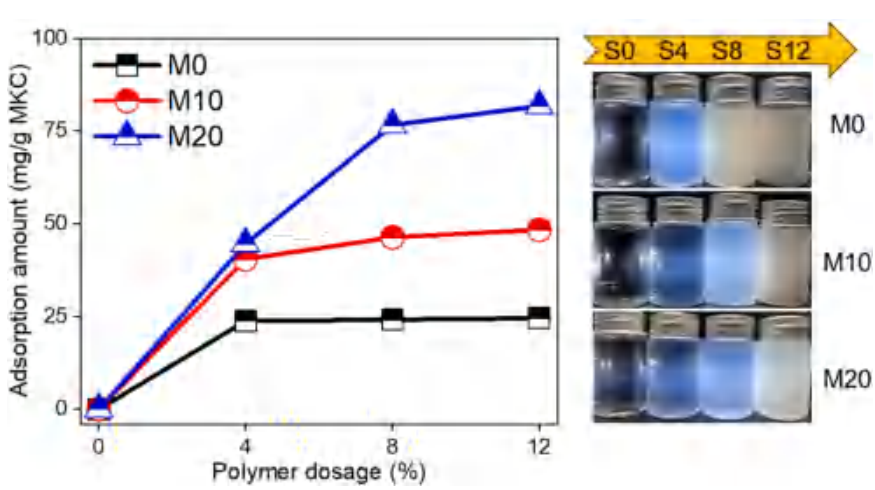

Fig. 10. The absorption isotherm of SA polymer to the different MKCs.

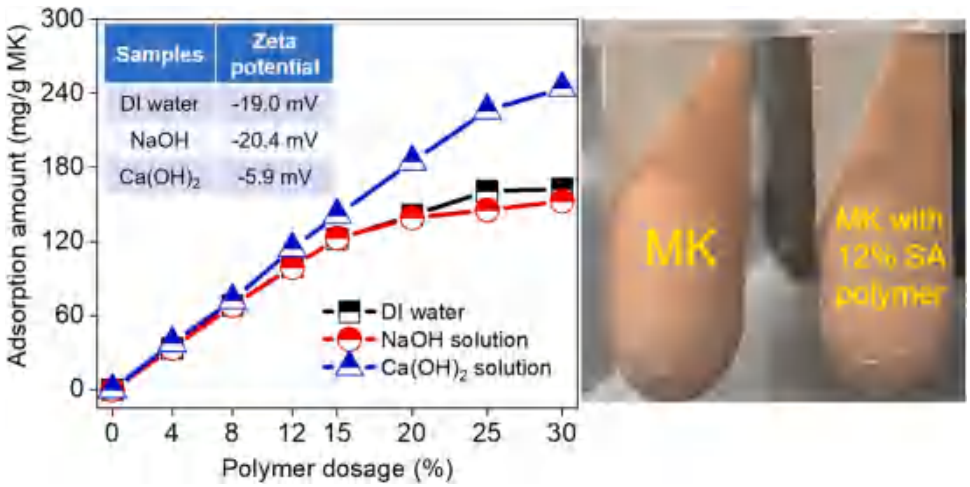

Fig. 11. The absorption amounts of SA latex on MK; (a) adsorption isotherm of SA polymer on MK prepared with different solutions (both the pH of NaOH and Ca $(OH)_2$ solution are 11); (b) pictures of centrifugated MK pastes with or without the addition of SA polymer. (Zeta potential of MK in varied solutions is shown in this figure).

amount of C_3S reacted (Fig. 8) at 3 d, Hence, from the hydration aspect, the increased polymer dosage should lead to a decrease, instead of the increase in the compressive strength at 3 d.

Considering the important role of polymer film formation on the performance of polymer-modified mortar (PMC), the microstructures of S0M10, S4M10 and S8M10 were investigated by SEM. As shown in Fig. 12, from one aspect, a large scale of AFm was observed in the sample of S0M10 after hydration for 3 d. However, in S8M10, more amount of

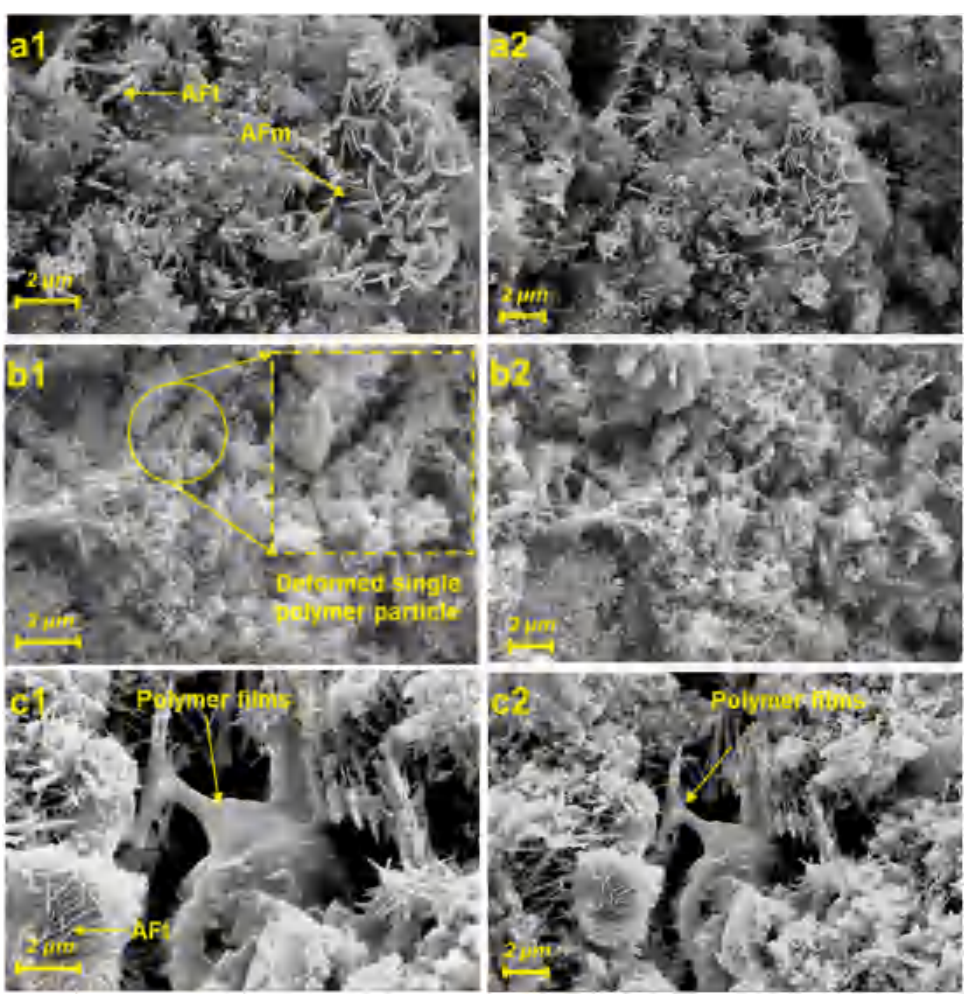

Fig. 12. SEM images of hardened cement pastes with varied polymer dosages after curing for 3 d; a, b and c mean S0, S4 and S8; 1, 2 represent magnification times of ×8000 and ×5000.

AFt was found, which matches well with the results shown in Fig. 8 and Fig. 9. Considering the negative charge property of SA polymer particles, the SA particles could be adsorbed preferentially on the surface of the aluminate-contained phase due to their positive charge property, which could impede the provision of aluminate ions through the hindrance of the dissolution of C_3A and C_4AF (Fig. 8). Under such case, the provided sulfate ions could be enough to form AFt instead of AFm. More importantly, a clear polymer film was found in S8M10, but not in S4M10. It indicates that, along with the increased adsorption surface through the addition of MK, the polymer particles could not stay close to each other under a low polymer dosage (4 %). Under such a circumstance, the polymer film cannot be formed (as indicated by the single polymer particle in Fig. 12b), which can, in turn, affect the mechanical properties of polymer-modified mortar. Along with the further increased dosage of polymer (8 %), the polymer film started to form (Fig. 12c), and then a network structure was built to densify the microstructure of the mortar, which makes it (8 %) an optimal dosage for the strength development.

Under the above consideration, the schematic diagram of the effect of SA latex under varied dosages on the mechanical performance of hardened cement paste is shown in Fig. 13. To the sample with a polymer dosage of 4 % (Fig. 13a), the polymer particles are adsorbed on the surface of cement grains. Along with cement hydration, the polymer particles tend to become packing, deformation and coalescence. Finally, the polymer film was formed, which can greatly improve the flexural and bond strength of PMC. However, when the MK was added (Fig. 13b), more polymer particles were adsorbed by the MK particles due to the high specific surface of MK. Under such circumstances, the polymer particles stayed away from each other and no obvious polymer film could be formed. Hence, the mechanical properties were decreased compared to that of S4M0. Along with the increased polymer dosage to 8 %, the polymer film not only can be formed in S8M0, but also in the sample with the addition of MK (S8M10). Besides, due to the adsorption of SA polymer particles by the MK, fewer polymer particles were adsorbed on the surface of cement grains. Hence, the retardation of SA polymer on cement hydration was alleviated and a higher mechanical strength was finally reached (Fig. 13d).

5. Conclusions

In this paper, the combined effect of SA latex and MK on the fresh and mechanical properties of MKC was systematically investigated. Based on the results above, the following conclusions can be drawn:

The presence of MK greatly changes the interaction of cement grains with the SA polymer and then modifies the properties of cement paste or

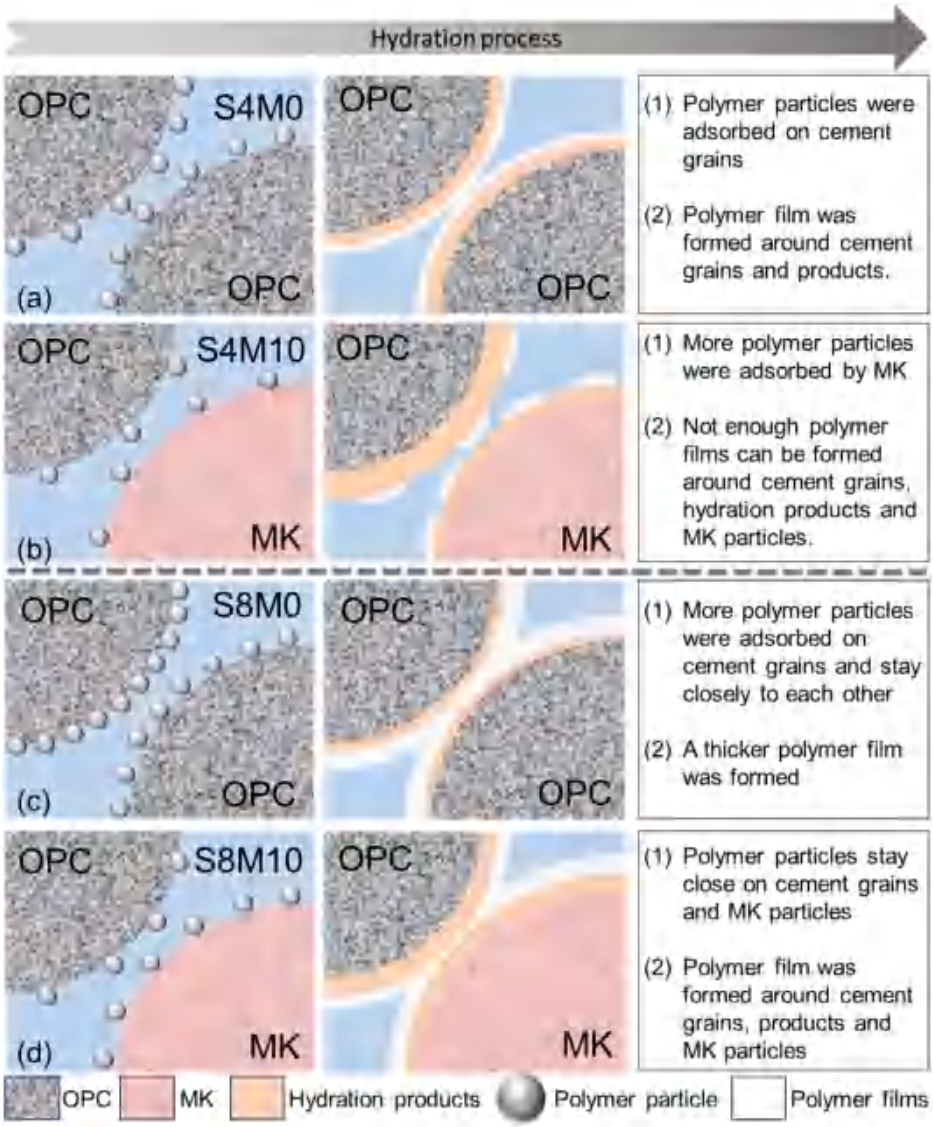

Fig. 13. Schematic diagram of the effect of SA latex under varied dosages on the mechanical performance of MKC mortar.

mortar. Specifically, the addition of SA latex improved the flowability of fresh MKC mortars. However, this improving capability was decreased with the increased MK content. Meanwhile, the setting time caused by the retardation of SA latex on cement hydration was significantly shortened by the addition of MK.

According to the results of strength measurements, the interaction of SA latex with MK can also greatly affect the mechanical properties of mortar. To the condition without the addition of polymer, the addition of MK is harmful to the development of early mechanical strength considering their low reaction activity compared to that of cement. Along with the increased curing age, a higher compressive strength was observed for the sample with the addition of MK due to the pozzolanic reaction of MK with CH. When the polymer dosage was 4 %, a decreased mechanical strength was found with the increased content of MK, regardless of the curing ages, which could be caused by the low reaction activity of MK at the early age and the hindered pozzolanic reaction of MK by the SA polymer at the late age. When the polymer dosages were increased to 8 %, the mechanical strength initially increase and then decrease with the incorporation of MK. Contrary to the normally decreased mechanical strength for the sample with the increased content of SCMs, an increased mechanical strength of mortar with 12 % SA polymer is found with the increased content of MK. It is believed to be caused by the extra adsorption of MK to SA polymer. The increased content of MK can adsorb a large amount of polymer particles and then alleviate the retarded effect of SA polymer on cement hydration. Besides, MK changes the saturated adsorption site of polymer, and affects the formation of cross-linked network by SA polymer and hydration products, and thus changes the optimal dosage of MK at varied polymer dosages.

Contrary to the continuously decreased compressive strength of mortar prepared with OPC under the increased polymer dosages, an increase in both the flexural and compressive strength of mortar with 10 % MK was observed when the polymer dosage was increased from 4 % to 8 %, which is believed to be caused by the modified microstructure of hardened cement paste through the stronger interaction between SA polymer and hydration products. It further indicates that a synergistic effect on mechanical properties can be reached with the addition of polymer latex and MK.

CRediT authorship contribution statement

Lei Wang: Methodology, Investigation. **Xiaojie Yang:** Writing – review & editing, Supervision. **Juan Li:** Methodology, Investigation. **Ruijun Gao:** Methodology, Investigation. **Zhenpin Sun:** Writing – review & editing, Supervision. **Ye Pan:** Writing – original draft, Methodology, Investigation, Data curation. **Zichen Lu:** Writing – review & editing, Supervision, Funding acquisition.

Declaration of Competing Interest

The authors declare that they have no known competing financial interests or personal relationships that could have appeared to influence the work reported in this paper.

Data availability

Data will be made available on request.

Acknowledgments

Financial support from Non-Metallic Excellence and Innovation Center for Building Materials “Research on gradient enhanced polymer modified concrete for structural use and comparison with conventional concrete” (2023TDA6-2) and the National Natural Science Foundation of China (No. 52208282) for funding this research are gratefully acknowledged.

References

[1] L. Proaño, A.T. Sarmiento, M. Figueredo, M. Cobo, Techno-economic evaluation of indirect carbonation for CO2 emissions capture in cement industry: A system dynamics approach, J. Clean. Prod. 263 (2020) 121457.
[2] A. Bicer, Effect of fly ash particle size on thermal and mechanical properties of fly ash-cement composites, Therm. Sci. Eng. Prog. 8 (2018) 78–82.
[3] E.D. Shumuye, J. Zhao, Z. Wang, Effect of fire exposure on physico-mechanical and microstructural properties of concrete containing high volume slag cement, Constr. Build. Mater. 213 (2019) 447–458.
[4] B. Ding, S. Ng, Z. Ou, Effect of sulfate on the compatibility between polycarboxylate superplasticizer and cement-based materials with or without silica fume, Constr. Build. Mater. 405 (2023) 133256.
[5] S. Barbhuiya, J. Nepal, B.B. Das, Properties, compatibility, environmental benefits and future directions of limestone calcined clay cement (LC3) concrete: A review, J. Build. Eng. 79 (2023) 107794.
[6] R. Snellings, Assessing, Understanding and Unlocking Supplementary Cementitious Materials, RILEM Tech. Lett. 1 (0) (2016) 50–55.
[7] N. Ijaz, W.-M. Ye, Zu Rehman, Z. Ijaz, M.F. Junaid, Global insights into micro-macro mechanisms and environmental implications of limestone calcined clay cement (LC3) for sustainable construction applications, Sci. Total Environ. 907 (2024) 167794.
[8] M. Antoni, J. Rossen, F. Martirena, K. Scrivener, Cement substitution by a combination of metakaolin and limestone, Cem. Concr. Res. 42 (12) (2012) 1579–1589.
[9] M. Antoni, Investigation of cement substitution by blends of calcined clays and limestone, EPFL.
[10] Y. Dhandapani, M. Santhanam, G. Kaladharan, S. Ramanathan, Towards ternary binders involving limestone additions — A review, Cem. Concr. Res. 143 (2021) 106396.
[11] K. Scrivener, F. Martirena, S. Bishnoi, S. Maity, Calcined clay limestone cements (LC3), Cem. Concr. Res. 114 (2018) 49–56.
[12] S. Bishnoi, S. Maity, A. Mallik, S. Joseph, S. Krishnan, Pilot scale manufacture of limestone calcined clay cement: The Indian experience, Indian Concr. J. 7 (7) (2014) 22–28.
[13] R. Li, L. Lei, T. Sui, J. Plank, Effectiveness of PCE superplasticizers in calcined clay blended cements, Cem. Concr. Res. 141 (2021) 106334.
[14] S. Ng, H. Justnes, Influence of dispersing agents on the rheology and early heat of hydration of blended cements with high loading of calcined marl, Cem. Concr. Compos. 60 (2015) 123–134.
[15] H. Huang, X. Li, F. Avet, W. Hanpongpun, K. Scrivener, Strength-promoting mechanism of alkanolamines on limestone-calcined clay cement and the role of sulfate, Cem. Concr. Res. 147 (2021) 106527.
[16] C. Luan, J. Wang, Z. Zhou, Synergic effect of triethanolamine and C-S-H seeding on early hydration of the limestone calcined clay cement in UHPC, Constr. Build. Mater. 400 (2023) 132675.
[17] Y. Lin, Effect of polymer to early mechanical property of the fly ash slurry, International Conference on Structures and Building Materials(ICSBM), 2012.
[18] A.A.M. Yassene, M.R. Ismail, M.S. Afify, Physicomechanical properties of irradiated SBR latex polymer-modified cement mortar composites, J. Vinyl Addit. Technol. 26 (2) (2020) 144–154.
[19] C. Jialin, L. Yixing, Performance Study on Polymer Modified Cement Mortars for Waterproof under Different Curing Conditions, China Building Waterproofing.
[20] C. Lech, S.J. Julia, Optimization of Polymer-Cement Coating Composition Using Material Model, Key Eng. Mater. 466 (2011) 191–199.
[21] M. Wang, R. Wang, H. Yao, S. Farhan, S. Zheng, Z. Wang, C. Du, H. Jiang, Research on the mechanism of polymer latex modified cement, Constr. Build. Mater. 111 (2016) 710–718.
[22] L.K. Aggarwal, P.C. Thapliyal, S.R. Karade, Properties of polymer-modified mortars using epoxy and acrylic emulsions, Constr. Build. Mater. 21 (2) (2007) 379–383.
[23] Q. Liu, W. Liu, Z. Li, S. Guo, G. Sun, Ultra-lightweight cement composites with excellent flexural strength, thermal insulation and water resistance achieved by establishing interpenetrating network, Constr. Build. Mater. 250 (2020) 118923.
[24] J. Du, Y. Bu, Z. Shen, Interfacial properties and nanostructural characteristics of epoxy resin in cement matrix, Constr. Build. Mater. 164 (2018) 103–112.
[25] Y. Tian, X. Jin, N. Jin, R. Zhao, Z. Li, H. Ma, Research on the microstructure formation of polyacrylate latex modified mortars, Constr. Build. Mater. 47 (2013) 1381–1394.
[26] X. Kong, S. Emmerling, J. Pakusch, M. Rueckel, J. Nieberle, Retardation effect of styrene-acrylate copolymer latexes on cement hydration, Cem. Concr. Res. 75 (2015) 23–41.
[27] E. Knapen, D. Van Gemert, Polymer film formation in cement mortars modified with water-soluble polymers, Cem. Concr. Compos. 58 (2015) 23–28.
[28] A. Jenni, L. Holzer, R. Zurbriggen, M. Herwegh, Influence of polymers on microstructure and adhesive strength of cementitious tile adhesive mortars, Cem. Concr. Res. 35 (1) (2005) 35–50.
[29] N. Ukrainczyk, A. Rogina, Styrene–butadiene latex modified calcium aluminate cement mortar, Cem. Concr. Compos. 41 (2013) 16–23.
[30] B.K. Varun, C.P. Anila Kumar, Strength characteristics of polymer modified high volume fly ash concrete, Mater. Today.: Proc. 46 (2021) 285–288.
[31] T. Rochman, Sumardi, S.H. Susilo, H.A. Wardhana, Vinyl-ester-based polymer concrete incorporating high volume fly ash under tensile, compressive, and flexural loads, J. King Saud. Univ. - Eng. Sci. (2023).
[32] J. Zhang, G. Pan, X. Zheng, C. Chen, Preparation and characterization of ultra-lightweight fly ash-based cement foams incorporating ethylene-vinyl acetate emulsion and waste-derived C-S-H seeds, Constr. Build. Mater. 274 (2021) 122027.

[33] T. Yaowarat, A. Suddeepong, M. Hoy, S. Horpibulsuk, T. Takaikaew, N. Vichitcholchai, A. Arulrajah, A. Chinkulkijniwat, Improvement of flexural strength of concrete pavements using natural rubber latex, Constr. Build. Mater. 282 (2021) 122704.
[34] H.-M. Kwon, T.N. Nguyen, T.A. Le, Improvement of the strength of acrylic emulsion polymer-modified mortar in high temperature and high humidity by blast furnace slag, KSCE J. Civ. Eng. 13 (1) (2009), 23-122730.
[35] B.C. Lho, M.K. Joo, K.H. Choi, J.Y. Choi, Effects of polymer-binder ratio and slag content on strength properties of autoclaved polymer-modified concrete, KSCE J. Civ. Eng. 16 (5) (2012) 803–808.
[36] H. Bilal, T. Chen, M. Ren, X. Gao, A. Su, Influence of silica fume, metakaolin & SBR latex on strength and durability performance of pervious concrete, Constr. Build. Mater. 275 (2021) 122124.
[37] A.E.Fd.S. Almeida, E.P. Sichieri, Experimental study on polymer-modified mortars with silica fume applied to fix porcelain tile, Build. Environ. 42 (7) (2007) 2645–2650.
[38] R. Yan, L. Wang, Y. Ni, S. Zhang, Z. He, B. Guan, A Study on the Properties of Composite Modified Mortar with Styrene–Butadiene Rubber Latex and Silica Fume, Polymers 16 (5) (2024) 697.
[39] X. Zhu, W. Li, Z. Du, S. Zhou, Y. Zhang, F. Li, Recycling and utilization assessment of steel slag in metakaolin based geopolymer from steel slag by-product to green geopolymer, Constr. Build. Mater. 305 (2021) 124654.
[40] J. Ambroise, M. Murat, J. Pera, Investigations on synthetic binders obtained by middle-temperature thermal dissociation of clay minerals, (1986).
[41] Z. Lu, X. Kong, C. Zhang, D. Jansen, J. Neubauer, F. Goetz-Neunhoeffer, Effects of two oppositely charged colloidal polymers on cement hydration, Cem. Concr. Compos. 96 (2019) 66–76.
[42] P. Bready, M. Chabannet, J. Pera, Microstructural and porosity of metakaolin blended cement, (1989).
[43] I.P. Sfikas, E.G. Badogiannis, K.G. Trezos, Rheology and mechanical characteristics of self-compacting concrete mixtures containing metakaolin, Constr. Build. Mater. 64 (2014) 121–129.
[44] H. Tian, X. Kong, X. Miao, L. Jiang, X. Pang, A new insight into the working mechanism of PCE emphasizing the interaction between PCE and Ca2+ in fresh cement paste, Constr. Build. Mater. 275 (2021) 122133.
[45] T. Su, X. Kong, H. Tian, D. Wang, Effects of comb-like PCE and linear copolymers on workability and early hydration of a calcium sulfoaluminate belite cement, Cem. Concr. Res. 123 (2019) 105801.
[46] Z. Li, Z. Ding, Property improvement of Portland cement by incorporating with metakaolin and slag, Cem. Concr. Res. 33 (4) (2003) 579–584.
[47] C. Shi, P. Wang, C. Ma, X. Zou, L. Yang, Effects of SAE and SBR on properties of rapid hardening repair mortar, J. Build. Eng. 35 (2) (2020) 102000.
[48] X. Zhang, M. Du, H. Fang, M. Shi, C. Zhang, F. Wang, Polymer-modified cement mortars: Their enhanced properties, applications, prospects, and challenges, Constr. Build. Mater. 299 (2021) 124290.
[49] S.H. Song, F.T. Liu, Y.B. Huang, Effect of Polymer Latex and Fiber on Properties of Sulpho Aluminate Cement Mortar, Adv. Mater. Res. 450-451 (2012) 402–406.
[50] C. Zhang, J. Liu, S. Zhang, X. Kong, Mechanical properties of polymer modified mortars using polymer latexes with varied glass transition temperature and surface charges, Cem. Concr. Compos. 150 (2024) 105573.
[51] S. Yan, H. Lu, Z. Zhou, Q. Dong, X. Chen, X. Wang, A polymer latex modified superfine cement grouting material for cement-stabilized macadam – Experimental and simulation study, Constr. Build. Mater. 413 (2024) 134893.
[52] E. Knapen, D.V. Gemert, Microstructural analysis of paste and interfacial transition zone in cement mortars modified with water-soluble polymers, Key Eng. Mater. 466 (2011) 21–28.
[53] Y. Xing, B. Wang, Effect of the chemical nature of polyvinyl alcohol on the microstructure of cement hydration products, J. Mater. Civ. Eng. (2023).
[54] J. Zhou, L. Chen, K. Zheng, G. Prateek, F. He, Z. Liu, Q. Yuan, Effect of elevated Al concentration on early-age hydration of Portland cement, Cem. Concr. Compos. 136 (2023) 104866.
[55] P.H. Borges, J.O. Costa, N.B. Milestone, C.J. Lynsdale, R.E. Streatfield, Carbonation of CH and C–S–H in composite cement pastes containing high amounts of BFS, Cem. Concr. Res. 40 (2) (2010) 284–292.
[56] K. Scrivener, R. Snellings, B. Lothenbach, C. Press, A Practical Guide to Microstructural Analysis of Cementitious Materials, Crc Press Boca Raton, FL, USA, 2016.
[57] Z.C. Lu, J.P. Merkl, M. Pulkin, R. Firdous, S. Wache, D. Stephan, A Systematic Study on Polymer-Modified Alkali-Activated Slag-Part II: From Hydration to Mechanical Properties, Materials 13 (15) (2020).
[58] S. Wild, J.M. Khatib, A. Jones, Relative strength, pozzolanic activity and cement hydration in superplasticised metakaolin concrete, Cem. Concr. Res. 26 (10) (1996) 1537–1544.
[59] H. Ouallal, Y. Dehmani, H. Moussout, L. Messaoudi, M. Azrour, Kinetic, isotherm and mechanism investigations of the removal of phenols from water by raw and calcined clays, Heliyon 5 (5) (2019) e01616.
[60] H. Chen, A. Zhong, J. Wu, J. Zhao, H. Yan, Adsorption behaviors and mechanisms of methyl orange on heat-treated palygorskite clays, Ind. Eng. Chem. Res. 51 (43) (2012) 14026–14036.
[61] R. Sposito, N. Beuntner, K.-C. Thienel, Characteristics of components in calcined clays and their influence on the efficiency of superplasticizers, Cem. Concr. Compos. 110 (2020) 103594.
[62] M. Schmid, J. Plank, Interaction of individual meta clays with polycarboxylate (PCE) superplasticizers in cement investigated via dispersion, zeta potential and sorption measurements, Appl. Clay Sci. 207 (2021) 106092.
[63] F. Zunino, K. Scrivener, The influence of the filler effect on the sulfate requirement of blended cements, Cem. Concr. Res. 126 (2019) 105918.
[64] H. Minard, S. Garrault, L. Regnaud, A. Nonat, Mechanisms and parameters controlling the tricalcium aluminate reactivity in the presence of gypsum, Cem. Concr. Res. 37 (10) (2007) 1418–1426.
[65] K. Wu, J. Long, L. Qing, G. De Schutter, Recent advance of monomer in-situ polymerization modified cement-based materials, Constr. Build. Mater. 432 (2024) 136542.

Journal of Applied Polymer Science

WILEY

Applied Polymer

RESEARCH ARTICLE

Mechanical Performance of Polymer-Modified Mortar With the Newly Designed Gradient Structure: Effect of Polymer Types and Content

Ye Pan[1] | Zichen Lu[1] | Lei Wang[1] | Yanrong Zhang[2] | Yi Ding[2] | Zhenping Sun[1]

[1]Key Laboratory of Advanced Civil Engineering Materials, Ministry of Education, School of Materials Science and Engineering, Tongji University, Shanghai, China | [2]School of Civil Engineering, Beijing Jiaotong University, Beijing, China

Correspondence: Zichen Lu (luzc@tongji.edu.cn) | Yanrong Zhang (yr.zhang@bjtu.edu.cn)

Received: 26 December 2024 | **Revised:** 6 March 2025 | **Accepted:** 19 March 2025

Funding: This study was supported by the NEXCEL Technology Development and Acceleration (TDA) Project (2023TDA6-2) "Research on gradient enhanced polymer modified concrete for structural use and comparison with conventional concrete," Science and Technology Bureau of Wanrong County (kz0050020231876), and the National Natural Science Foundation of China (52208282).

Keywords: colloids | mechanical properties | non-polymeric materials and composites | structure–property relationships

ABSTRACT

The varied damage faced by concrete in the pavement can be effectively alleviated by adding polymer latex. However, their required high dosage and prices limit their application. Hence, a new structure with the gradient distribution of polymer particles in concrete was designed. Furthermore, the performance and the corresponding mechanism of varied polymer types and contents on the mechanical performance of polymer-modified mortar (PMM) were systematically evaluated. Compared to the sample with a homogenous polymer distribution at the same dosage, a great enhancement in compressive and bond strength was found for PMM with the gradient structure. Besides, the flexural strength can also be slightly increased. Compared to styrene-acrylic (SA) and ethylene-vinyl acetate (EVA) latexes, styrene-butadiene (SB) latex with the highest charge density shows the lowest capability in modifying the mechanical performance of PMM, which could be caused by its high adsorption amount and low ductility of formed polymer film. It further indicates that, compared to the tensile stress of polymer film, its ductility is more important in determining the flexural strength of PMM. To confirm the obtained experimental results, a finite element model of mortars with different gradient structures was established, and the modeling results match well with the mechanical measurements.

1 | Introduction

Cement-based materials are commonly used for road pavement [1–4] with the advantage of high mechanical properties, long durability, and low cost. However, pavement concrete is more susceptible to the ambient environment, such as loading, rainwater, and salt attacks induced by heavy traffic and deicing salt [5]. For pavement concrete, cracking is one commonly observed damage [6]. Depending on where the cracks occur, the cracks in pavement concrete can be classified into two types: the top-down cracks, which first occur on the surface of pavement and then go deep, and the bottom-up cracks, which start at the bottom part. The first type of crack is caused by the overloaded tensile and shear stresses, while the second one is typical bending-induced cracking [3]. Hence, compared to the middle part of concrete, the upper and bottom parts of the concrete pavement play a more important role in improving the resistance ability to cracking. Furthermore, regardless of the positions where the cracks happen, they are always caused by the limitation of the flexural strength of concrete. Therefore, the reasonable way to increase

© 2025 Wiley Periodicals LLC.

the durability of concrete for pavement is to enhance its flexural strength, especially the upper and bottom parts of concrete.

Polymer latex has a wide range of applications in cement-based materials with the advantages of enhanced workability [7, 8], improved flexural and bond strength [9, 10], as well as outstanding water-proof properties [11–13]. However, unlike the admixtures used for cement-based materials with a low dosage, a much higher dosage is normally required for the polymer latex to achieve the desired properties [14]. Gholinezhad et al. [15] increased the flexural strength of mortar cured for 28 days to 11 MPa by using poly(styrene-co-ethylhexyl acrylate-co-methacrylic acid) and poly(styrene-co-butyl acrylate-co-methacrylic acid) with the dosage of 20% by weight of cement. Wang and colleagues [13] investigated the influence of polymer latex on the mechanical properties of calcium sulfoaluminate cement mortar and found that the optimal dosage is 20%. Yao and colleagues [16] also found that the flexural strength of mortar is increased by 343% when the polymer dosage reaches 30%. Considering the high price of polymer latex [17], such a high polymer dosage used in cement-based materials definitely limits the practical application in concrete for pavement.

Considering the important role of the upper and bottom parts in the concrete pavement, a new concept for modifying the performance of concrete used in pavements is put forward by designing a gradient distribution of polymer latex in cement-based materials. Namely, the polymer is enriched in the upper and bottom parts of concrete but reduced in content in the middle part of concrete. Through this method, the total dosage of polymer can be greatly reduced. However, it is still a question of how the designed gradient structure of mortar affects its overall performance. In addition, many studies have found that the performance of polymer-modified mortar (PMM) is closely related to the type of polymer latex used Xu and colleagues [18] compared the influence of styrene-acrylic (SA) latex and ethylene-vinyl acetate (EVA) latex on the mechanical properties of mortar and found that SA is more conducive to the development of flexural strength and ductility of mortar. Wang and colleagues [19] studied the influence of SA and EVA on the bond strength of mortar cured in different environments and found that the improvement in bond strength by the addition of SA is greater than that of EVA. Brien and Mahboub [20] used four different kinds of latexes to modify the performance of mortar and found that styrene-butadiene (SB) latex always has a lower ability to improve the adhesion performance of mortar. However, a deep understanding of the different effects of the varied polymer latexes on the performance of cementitious materials is still unclear considering the lack of thorough characterization of polymer particles (such as the surface charge, glass transition temperature, particle size, etc.) and the formed polymer film (such as the tensile stress, ductility, etc.).

Facing such questions, the PMM with a newly designed gradient structure was first prepared, in which the polymer particles were enriched at the upper and bottom parts, but no polymer existed in the middle part. Furthermore, the mechanical performance of PMM with the gradient structure (GPMM) after different curing ages was thoroughly evaluated and compared to that of the ordinary PMM (OPMM). In addition, the effect of different polymer types and varied dosages on the mechanical performance was also tested; three types of mainly used commercial polymer latexes, namely the SA, SB, and EVA, were used in this study. Furthermore, the corresponding mechanism to the different performances was analyzed with the combined techniques of flow table test, setting time, calorimetry, and scanning electron microscopy (SEM) with the precondition of thorough characterization on the properties of polymer particles and the formed polymer films. Finally, a finite element model of mortars with different gradient structures was established to verify the results of mechanical measurement. Based on the results shown in our study, it not only provides a thorough evaluation of the mechanical performance of the PMM with a newly designed gradient structure, but also clarifies the effect of varied polymer types and dosages, which provides a theoretical guidance on the development of polymer-modified pavement concrete.

2 | Materials and Methods

2.1 | Raw Materials

P·I 42.5 Portland cement (OPC, Fushun Orcel Technology Co. Ltd) and the ISO standard sand (Qufu Zhonglian Cement Co. Ltd.) were used in this study. SA and SB were supplied by BASF SE, and EVA was provided by Celanese (Shanghai) International Trading Co. Ltd. The zeta potential and particle size of the polymer particles were measured by Zetasizer Nano (Malvern, UK). The charge density of the polymer particles was measured by a charge titrator (BTG, Switzerland). Following the instruction from the producer of polymer latex, different deformers were used to achieve a similar density for the prepared cement paste or mortar with the addition of polymer latex. Specifically, AF6203 was used for SA (Shanghai Guangbai New Materials Co. Ltd), BASF-305 was used for SB (BASF [China] Co. Ltd.) and DNF681F for EVA (Celanese Chemical Co. Ltd.). The detailed chemical composition of OPC and the physical properties of polymer latex are shown in Table 1. The particle distribution of polymer latexes is depicted in Figure 1.

2.2 | Samples Preparation

The used water–cement ratio and sand–cement ratio were 0.45 and 3, respectively, for all of the samples. The polymer dosages were 0%, 4%, 8%, and 12% for the preparation of OPMM. The dosages of defoamer for mortar with the addition of SA, SB, and EVA at the dosage of 12% were 0.1%, 1%, and 0.6%, respectively. Under such a condition, the density of mortar modified by SA, SB, and EVA was 2.25, 2.1, and 2.23 g/cm^3, respectively, which is quite close to the theoretical density of PMM calculated under the same polymer dosage (2.26 g/cm^3, assuming the density of all polymer latexes are 1.2 g/cm^3). The similar density for the different prepared samples ensures that the difference in mechanical performance is not caused by the varied porosity. For the samples with the polymer dosage of 4% and 8%, the same dosage of defoamer was used.

As shown in Figure 2, by changing the polymer dosage at different parts, the mortar with the gradient structure was designed with the same overall dosage but different dosages at each part. Specifically, the prepared mortar with the gradient structure

10974628, 0, Downloaded from https://onlinelibrary.wiley.com/doi/10.1002/app.57075 by Tongji University, Wiley Online Library on [05/04/2025]. See the Terms and Conditions (https://onlinelibrary.wiley.com/terms-and-conditions) on Wiley Online Library for rules of use; OA articles are governed by the applicable Creative Commons License

TABLE 1 | The chemical composition of OPC and the physical properties of polymer latex.

Chemical composition	OPC	Mineralogical composition	OPC	Physical properties	SA	SB	EVA
SiO_2	20.64	C_3S	60.72	Zeta potential	−24.2 mV	−49.4 mV	−32.2 mV
Al_2O_3	5.15	C_2S	16.56	Mean size	189.2 nm	132.6 nm	224.7 nm
Fe_2O_3	3.76	C_3A	6.72	Solid content	50 wt%	50 wt%	50 wt%
CaO	63.24	C_4AF	8.28	Tg	10°C	14°C	11°C
MgO	1.61	Gypsum	3.64	Charge density	−19.83 μeq/g	−51.35 μeq/g	−27.03 μeq/g
TiO_2	0.43	Anhydrite	0.98	Density	1.02 g/cm^3	1.04 g/cm^3	1.02 g/cm^3
SO_3	3.38	f-CaO	0.9				
Other	1.12	Other	2.2				

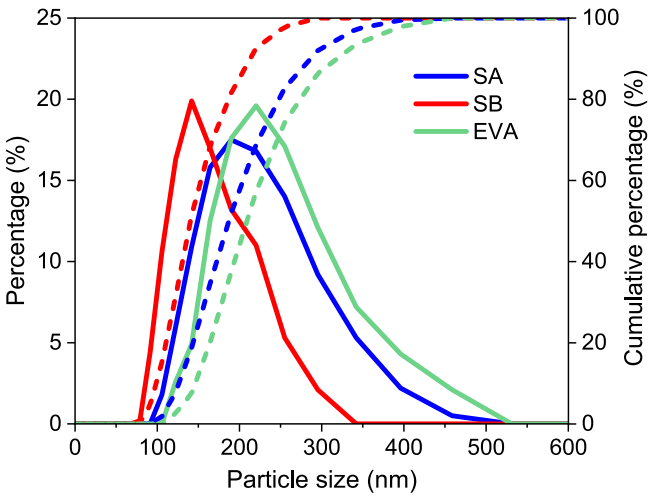

FIGURE 1 | The particle size distribution of polymer particles (the solid line and dotted line correspond to percentage curve and cumulative percentage curve, respectively). [Color figure can be viewed at wileyonlinelibrary.com]

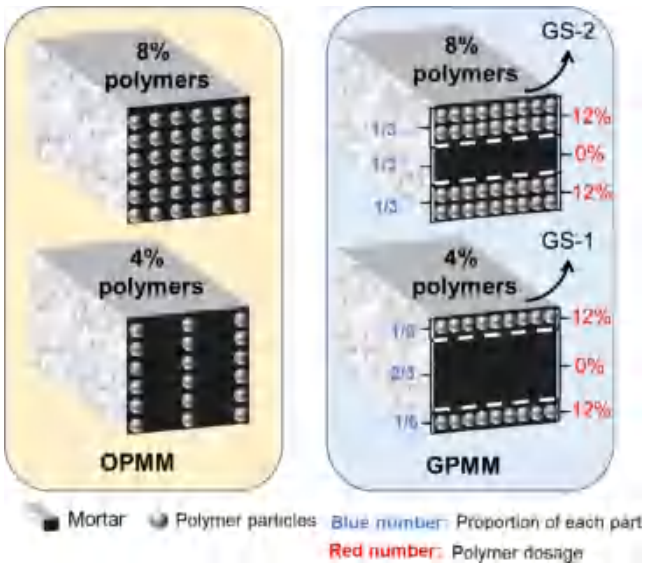

FIGURE 2 | Schematic diagram of gradient distribution of polymer inside the polymer-modified mortar. [Color figure can be viewed at wileyonlinelibrary.com]

can be divided into three parts, namely the upper part, middle part, and bottom part. In the GPMM, two structures with different thicknesses in the upper and bottom parts were designed (namely GS-1 and GS-2, as shown in Figure 2). In GS-1, the polymer dosages at the upper and bottom parts were 12% and the dosage at the middle part was zero. The middle part accounted for 2/3 of the total thickness, and the upper and bottom parts each accounted for 1/6. Hence, the overall dosage for GS-1 was 4%. In GS-2, the same dosages were kept for each part, but each part accounted for 1/3 of the total thickness. Hence, the overall dosage for GS-2 was 8%. The OPMM without the gradient structure was also prepared with the overall dosages of 4% and 8% as a comparison.

For the preparation of OPMM, as shown in Figure 3, cement, water, latex, and defoamer were mixed by a laboratory planetary mixer (JJ-5, Yixuan Testing Instrument Co. Ltd., China) for 30 s at a speed of 62 r/min at first. Then, the sand was added to the paste and mixed at the same speed for 30 s and 125 r/min for another 30 s. At last, the mortar was mixed for 60 s at 125 r/min after a break of 90 s. After mixing, the samples were cast in molds (40 mm × 40 mm × 160 mm) for flexural strength and compressive strength, as well as molds (50 mm × 50 mm × 18 mm) for bond strength. Regarding the preparation of GPMM, the mortars were cast part by part from Step 1 to 3. After the casting of each part, the molds with the mortar inside were vibrated for 30 s. It should be noted that the addition of polymer latex always leads to a high flowability and low viscosity of mortar. Hence, in order to avoid the sinking of the middle part into the bottom part, a duration of 20 min was needed before casting the middle part onto the bottom part. The upper part can be directly cast onto the middle part without waiting. After casting, the prepared samples were cured at 20°C and 50% RH for 3 days first and then changed to 20°C and 95% RH till the testing ages.

2.3 | Test Methods

2.3.1 | Mechanical Performance of PMM

In order to evaluate the mechanical performance of GPMM and compare it to that of OPMM, the mechanical properties, including the flexural strength, compressive strength, bond strength,

10974628, 0, Downloaded from https://onlinelibrary.wiley.com/doi/10.1002/app.57075 by Tongji University, Wiley Online Library on [05/04/2025]. See the Terms and Conditions (https://onlinelibrary.wiley.com/terms-and-conditions) on Wiley Online Library for rules of use; OA articles are governed by the applicable Creative Commons License

and modulus of elasticity (as shown in Figure 4) were conducted. Specifically, for the flexural strength and compressive strength, the specimens were tested with a loading speed of 50 N/s and 2.4 kN/s, respectively, by an automatic test machine (WHY-300, Cangzhou Yixuan Testing Instrument Co. Ltd., China). The flexural strength was the average of 3 measurements, and the compressive strength was the average of 6 measurements. It should be noted that the formed face of prepared specimens was used to bear the loading force, which simulates the condition of the load direction on the surface of the concrete pavement from vehicles. In order to ensure the evenness of load distribution, the forming face was gently polished until smooth by a grinder. The bond strength of mortars after curing at the same age was tested through a pull-out tester (LBY-9, Hebei Guanghui Testing Instrument Co. Ltd., China) with a loading speed of 10 mm/min. An average of eight measurements was taken as the value of bond strength. Besides, the test of the modulus of elasticity was carried out according to Standard JGJ/T 70-2009 on the mortar with the dimension of 160 mm × 40 mm × 40 mm after curing for 28 days. A program increased from 3 MPa to 1/3 compressive strength and then decreased to the initial value, which was set as a circular mode. Three measurements were conducted, and the average value was used as the representing data. The strain gauges and strain measuring instrument (DM-YB1820, Nanjing Danmo Electronic Technology Co. Ltd., China) were used in this study.

2.3.2 | Isothermal Calorimetry

The hydration process of cement pastes with the addition of different types of polymer latex at 8% was monitored by using a

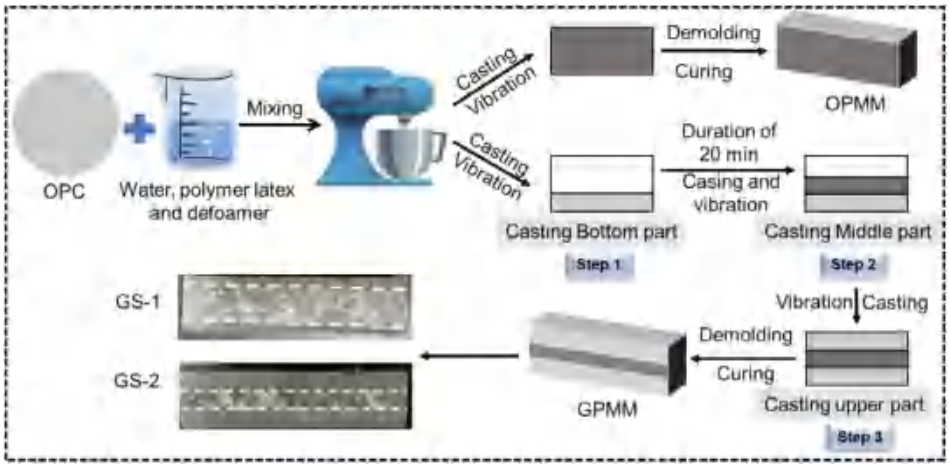

FIGURE 3 | Schematic diagram for the preparation of OPMM and GPMM. [Color figure can be viewed at wileyonlinelibrary.com]

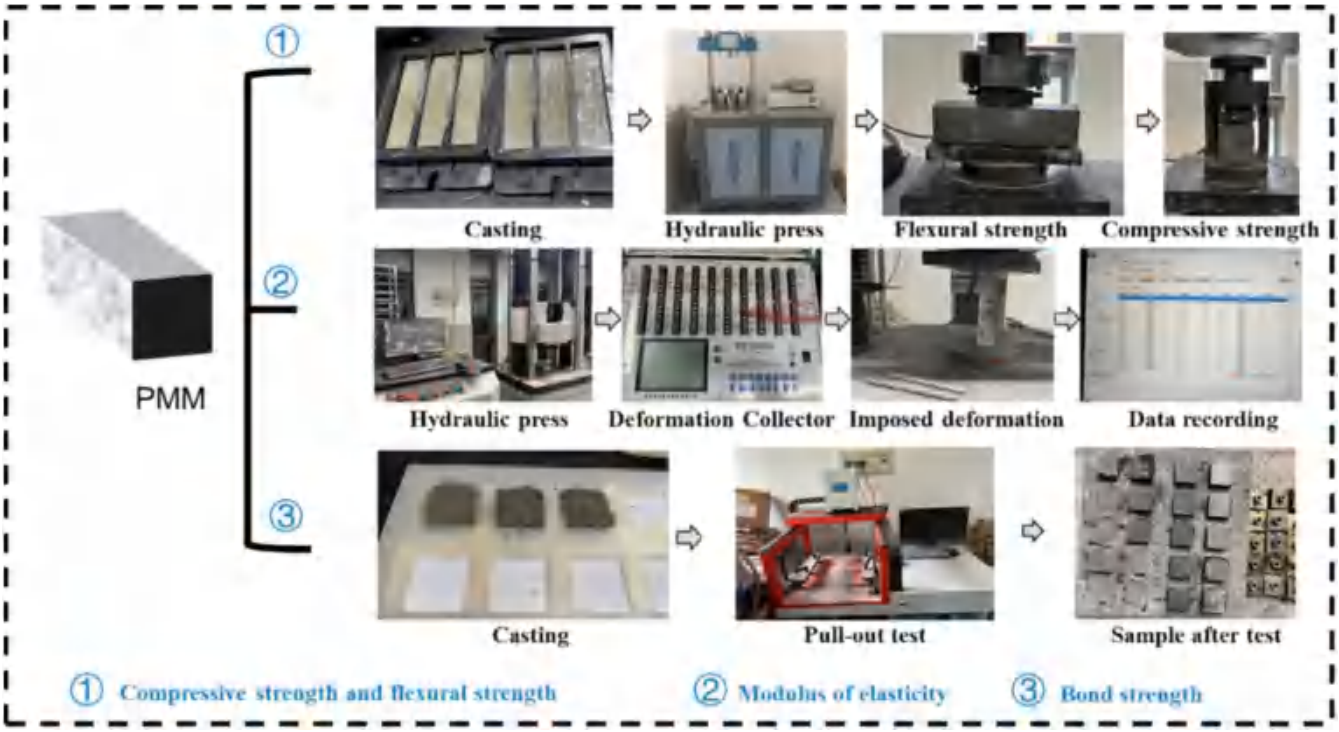

FIGURE 4 | The test methods of PMM with varied polymer dosages. [Color figure can be viewed at wileyonlinelibrary.com]

10974628, 0, Downloaded from https://onlinelibrary.wiley.com/doi/10.1002/app.57075 by Tongji University, Wiley Online Library on [05/04/2025]. See the Terms and Conditions (https://onlinelibrary.wiley.com/terms-and-conditions) on Wiley Online Library for rules of use; OA articles are governed by the applicable Creative Commons License

TAM-Air isothermal calorimeter (TAM Air, TA Instruments, USA) at 25°C for 3 days. The mixture proportion of cement pastes for the calorimetric test is shown in Table 2. First, a certain amount of water or polymer latex (calculated when the cement mass was 10 g) was prepared and poured into an ampoule. Ten gram of cement was then put into the ampoule and mixed for 1 min through a vortex mixer (MX-S, DLAB, China). Afterwards, the ampoule was inserted into the calorimeter, and then the released heat was started to record. The results of heat flow were normalized based on the mass of cement.

2.3.3 | Mechanical Performance of Polymer Films

According to the GB/T 23445-2009, the elongation at break and the tensile stress at break of three different kinds of polymer films were measured through a tensile strength tester (HY-0580, Shanghai Heng Wing Precision Instrument Co. Ltd., China). Regarding the preparation of polymer films, the viscosity of each latex was first adjusted to 1500–2000 mPa s with DI water and then cast into a 500 mm × 500 mm × 2 mm silicon rubber mold. Afterwards, each sample was placed at 20°C for 4 days and at 40°C for another 3 days in an oven to obtain a homogeneous polymer film. Finally, each polymer film was cut into the dumbbell shape with the dimensions of 13 mm × 13 mm × 2 mm (Figure 5a) for five measurements, and the averaged value was used. The tensile rate for this measurement is 2 mm/min.

2.3.4 | SEM Observation

The fractured surfaces of hardened cement pastes with different polymer dosages were observed by using a SEM (Gemini 300, ZEISS, Germany). Before testing, the hardened pastes after curing for 3 days were fractured into small blocks with a diameter of 3–5 mm by a hammer. Then, pieces of each sample were immersed in 30 mL cold isopropanol (5°C, 99.5% purity) for 1 day to stop hydration. Then, the prepared samples were dried in a vacuum drying oven at 40°C for 48 h and stored in a small plastic bag under the vacuum environment. Before observation, a fresh surface was generated by breaking the sample into a flat shape. Then, gold was sprayed onto the fresh surface under vacuum conditions for 45 s to obtain better conductivity.

2.3.5 | Adsorption Measurement

The adsorption isotherms of different polymer latexes on the surface of cement grains were established under a constant temperature of 25°C. First, 30 g OPC with different dosages (0%, 2%, 4%, 6%, 8%, 10%, 12%) of polymer latexes were mixed in a 50 mL centrifuge tube by a vortex mixer (MX-S, DLAB, China) for 1 min and centrifuged at 4000 rpm for 5 min. Then the supernatant was collected by using a syringe and filtered through a 0.45 μm filter. The obtained supernatant was dropped unevenly into three glass dishes and then placed in

TABLE 2 | The composition for the preparation of mortar with varied polymer dosages.

Latex	Samples	Structure	Polymer dosage (wt%)			Cement (g)	Sand (g)	Water (g)
			Total dosage	Upper and bottom part	Middle part			
SA, SB, EVA	OPMMs	Non-gradient distribution	0	0	0	100	300	45
			4	4	4	100	300	45
			8	8	8	100	300	45
			12	12	12	100	300	45
	GPMMs	GS-1	4	12	0	100	300	45
		GS-2	8	12	0	100	300	45

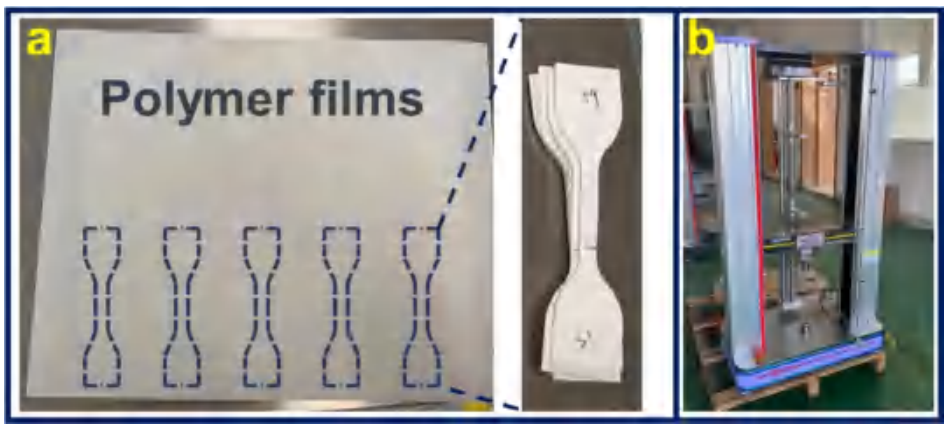

FIGURE 5 | The performance of polymer films: (a) polymer films and dumbbell-shaped molds, (b) tensile strength tester. [Color figure can be viewed at wileyonlinelibrary.com]

10974628, 0, Downloaded from https://onlinelibrary.wiley.com/doi/10.1002/app.57075 by Tongji University, Wiley Online Library on [05/04/2025]. See the Terms and Conditions (https://onlinelibrary.wiley.com/terms-and-conditions) on Wiley Online Library for rules of use; OA articles are governed by the applicable Creative Commons License

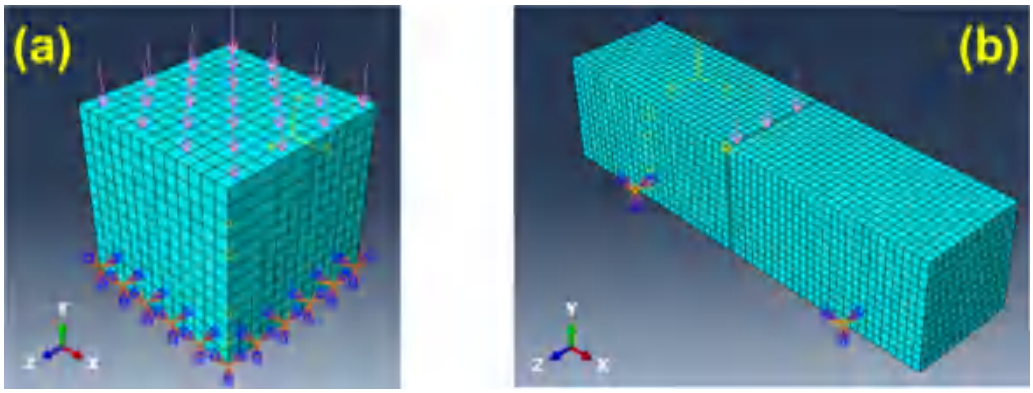

FIGURE 6 | The finite element models established for the measurement of (a) compressive strength and (b) flexural strength (a vertical force is applied in the model). [Color figure can be viewed at wileyonlinelibrary.com]

an oven at 105°C for 8 h. Then the obtained solid was further calcined at 600°C for 1 h to decompose the polymer (the decomposition temperature of polymer is about 450°C, the result is not shown here) and the solid content of the polymer in the supernatant was calculated. Finally, the adsorption amount of polymer particles on cement grains was calculated by the depletion method [21]. The average value of 3 measurements was calculated and used in this study.

2.3.6 | Finite Element Analysis of GPMM

Finite element analysis of GPMM with the different polymer dosages and distributions was conducted by using ABAQUS software to simulate the structure displacement during the measurement of compressive strength and flexural strength, which is presented in Figure 6. The modeled size and bearing load of the specimen are consistent with the parameters used in compressive and flexural strength measurements. For the analysis of compressive strength measurement, the boundary conditions are as follows: the bottom surface is fixed and the top surface is free. While for the analysis of flexural strength measurement, the bottom pivot position is fixed and the top surface is free. The modulus of elasticity used for modeling is obtained based on the test shown in Section 2.3.1. Regarding the modeling process of GPMM, six parts were created laterally from the bottom to the surface of mortar. The corresponding material properties were assigned to each part according to the designed structure of GPMM (GS-1 and GS-2). Finally, the vertical displacement of each specimen was calculated to characterize the mechanical performance of PMM with different structures.

3 | Results

3.1 | Flexural and Compressive Strength of GPMM

The effect of gradient polymer distribution on the compressive and flexural strength of mortars is presented in Figure 7a,b, respectively. Many scholars have already found that polymer latex could cause a reduction in the compressive strength of mortar, which is attributed to the inhibition of cement hydration by the addition of polymer [22] and the high porosity produced by the air-entrainment effect [23]. However, the flexural strength can be improved due to the film formation of polymer particles, which can connect the cement grains and hydration products and then form a cross-linked network structure [22].

Following the results from many publications, it can be seen that the addition of polymer latex is always beneficial to increase flexural strength, while the compressive strength shows the opposite trend. Regarding the effect of latex types on the strength of mortar, SB latex showed the greatest reduction in the compressive strength of mortar. In addition, for the flexural strength of mortar, the optimal polymer dosage for SA latex is 8%, but the optimal values for SB and EVA are 12%. Regarding the effect of gradient polymer distribution, a significant increase in the compressive strengths for the GPMMs with the overall dosages of 4% (GS-1) and 8% (GS-2) can be found compared to that of OPMMs under the same polymer dosages. However, the increase in the flexural strength for GPMM is not so obvious. A slight increase in flexural strength can be found for GPMMs modified by SB latex and EVA latex, but not for those made with SA latex. To sum up, the gradient distribution of polymer is conducive to the improvement of the compressive strength of mortars as well as the flexural strength of mortars modified by SB and EVA.

The elasticity modulus of mortar can reflect the rigidity of hardened cementitious materials. Figure 8 shows the elasticity modulus of different PMMs. The mortar without the addition of latex (Ref) has the highest modulus of elasticity. Besides, the increased addition amount of polymer leads to a significant decrease in the modulus of elasticity, which matches well with the results shown in many literatures [24, 25]. Among the three latexes, the mortar modified by SB latex has the lowest rigidity, which is consistent with the above results of compressive strength. Regarding the influence of gradient structure, an increased modulus of elasticity mortar was found for GPMM compared to that of OPMM under the same polymer dosage, and thus benefits the improvement of its compressive strength (Figure 7a).

3.2 | Bond Strength of GPMM

The bond strengths of GPMM and OPMM with varied types and dosages of polymer latexes are evaluated. As shown in

10974628, 0, Downloaded from https://onlinelibrary.wiley.com/doi/10.1002/app.57075 by Tongji University, Wiley Online Library on [05/04/2025]. See the Terms and Conditions (https://onlinelibrary.wiley.com/terms-and-conditions) on Wiley Online Library for rules of use; OA articles are governed by the applicable Creative Commons License

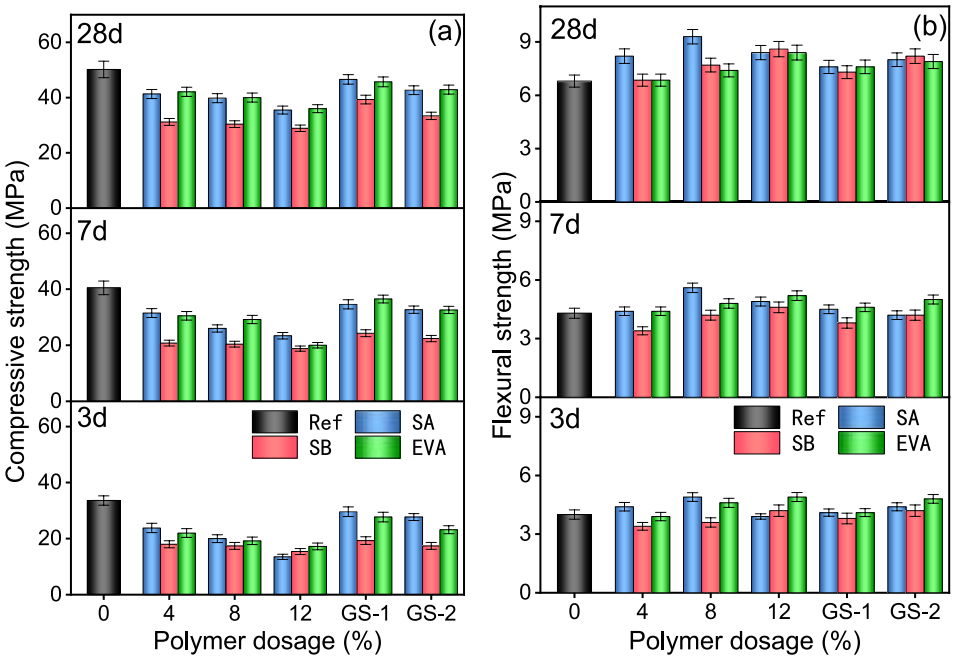

FIGURE 7 | Compressive strength (a) and flexural strength (b) of GPMM compared to that of OPMM under different polymer dosages and types. The polymer dosages of GS-1 and GS-2 are 4% and 8%, which are the same for the following figures. [Color figure can be viewed at wileyonlinelibrary.com]

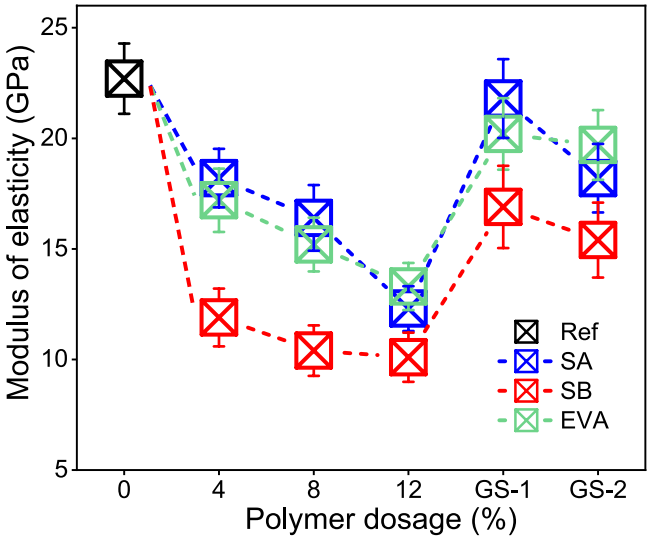

FIGURE 8 | The effect of gradient polymer distribution on the elasticity modulus of mortars. [Color figure can be viewed at wileyonlinelibrary.com]

Figure 9, an increase in the bond strength of mortar is observed along with increased polymer dosages. SA latex shows a higher effect on the improvement in the bond strength of mortars compared to that of SB latex and EVA latex. Moreover, at the same polymer dosage, the bond strengths of GPMMs are significantly higher than those of OPMMs. It suggests that the gradient distribution of polymers favors the improvement of bond strength. Considering the high correlation between bond strength and interfacial properties, the polymer in the middle part of mortar has a limited effect on the improvement of bond strength.

3.3 | Finite Element Analysis

According to the results represented above, it is found that the gradient distribution of polymer and the polymer types can greatly affect the mechanical properties of mortars. To further confirm this, a finite element analysis was adopted to simulate the effect of the gradient structure and polymer types on the vertical displacement of mortar during the compressive and flexural strength measurement.

Regarding the effect of gradient distribution of polymers, the designed gradient distribution of polymer latex can significantly increase the compressive strength of PMM and the increment is increased with the thickness of the middle part in which no polymer particles exist. Considering the high compressive strength of the Ref (without polymer, Figure 7), the middle part could act as a support structure to increase the overall compressive strength. The effect of polymer dosage (Figure 10a) and polymer distribution (Figure 10b) on the vertical displacement of mortars during the compressive strength measurement was analyzed by modeling and the results can be found in Figure 10 (taking SA latex as an example here). As shown in Figure 10a, the vertical displacement of mortar increases along with the polymer dosage, which means a decreased ability to resist compressive load. Moreover, the gradient distribution of polymer decreases the deformation during the compressive strength measurement (Figure 10b), and thus increases the compressive strength. Compared to GS-1, a high increase in the vertical displacement of the specimen with GS-2 structure was found, which further proves the key role of the middle part as a support structure.

Regarding the analysis of the deformation during the flexural strength measurement (Figure 11), an increased trend in the

10974628, 0, Downloaded from https://onlinelibrary.wiley.com/doi/10.1002/app.57075 by Tongji University, Wiley Online Library on [05/04/2025]. See the Terms and Conditions (https://onlinelibrary.wiley.com/terms-and-conditions) on Wiley Online Library for rules of use; OA articles are governed by the applicable Creative Commons License

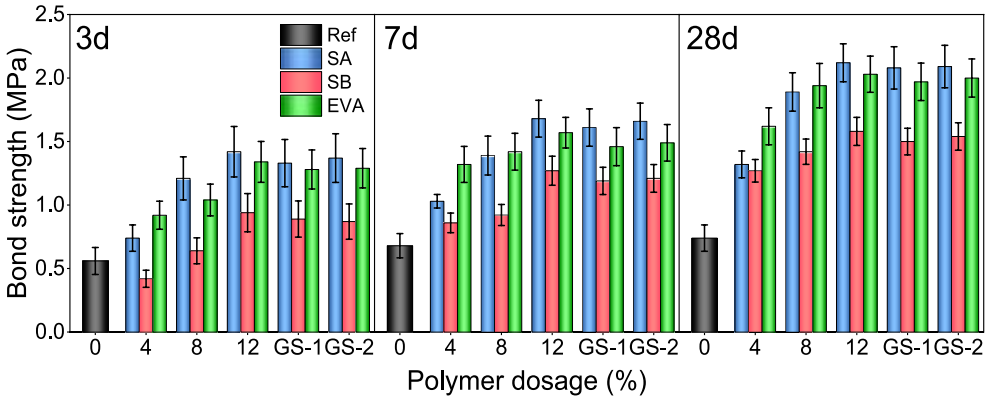

FIGURE 9 | The effect of gradient polymer distribution on the bond strength of mortars. [Color figure can be viewed at wileyonlinelibrary.com]

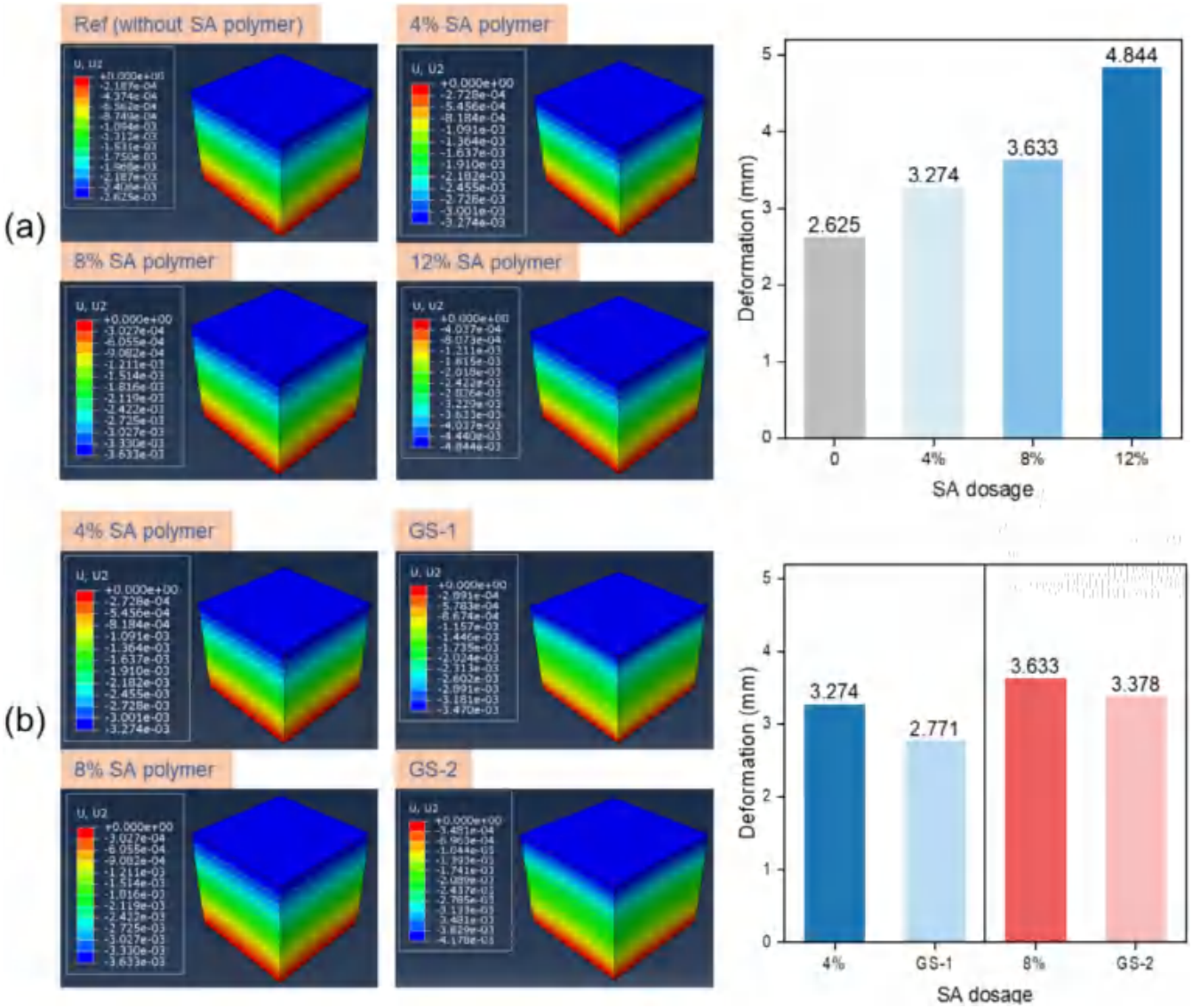

FIGURE 10 | The modeled vertical displacement of mortars during the compressive strength measurement: (a) the effect of polymer dosage and (b) the effect of gradient distribution. [Color figure can be viewed at wileyonlinelibrary.com]

deformation was found with the increased polymer content. The increase in deformation (Figure 11a) indicates that the addition of polymer improves the overall ductility of the mortar, thereby enhancing its flexural strength. In addition, it can be found that the PMM with a SA dosage of 8% shows the highest deformation, and so does the ductility. Besides, the GPMM with the gradient distribution of SA polymer shows a low deformation and thus poor ductility (Figure 11b). All of those results match well with

10974628, 0, Downloaded from https://onlinelibrary.wiley.com/doi/10.1002/app.57075 by Tongji University, Wiley Online Library on [05/04/2025]. See the Terms and Conditions (https://onlinelibrary.wiley.com/terms-and-conditions) on Wiley Online Library for rules of use; OA articles are governed by the applicable Creative Commons License

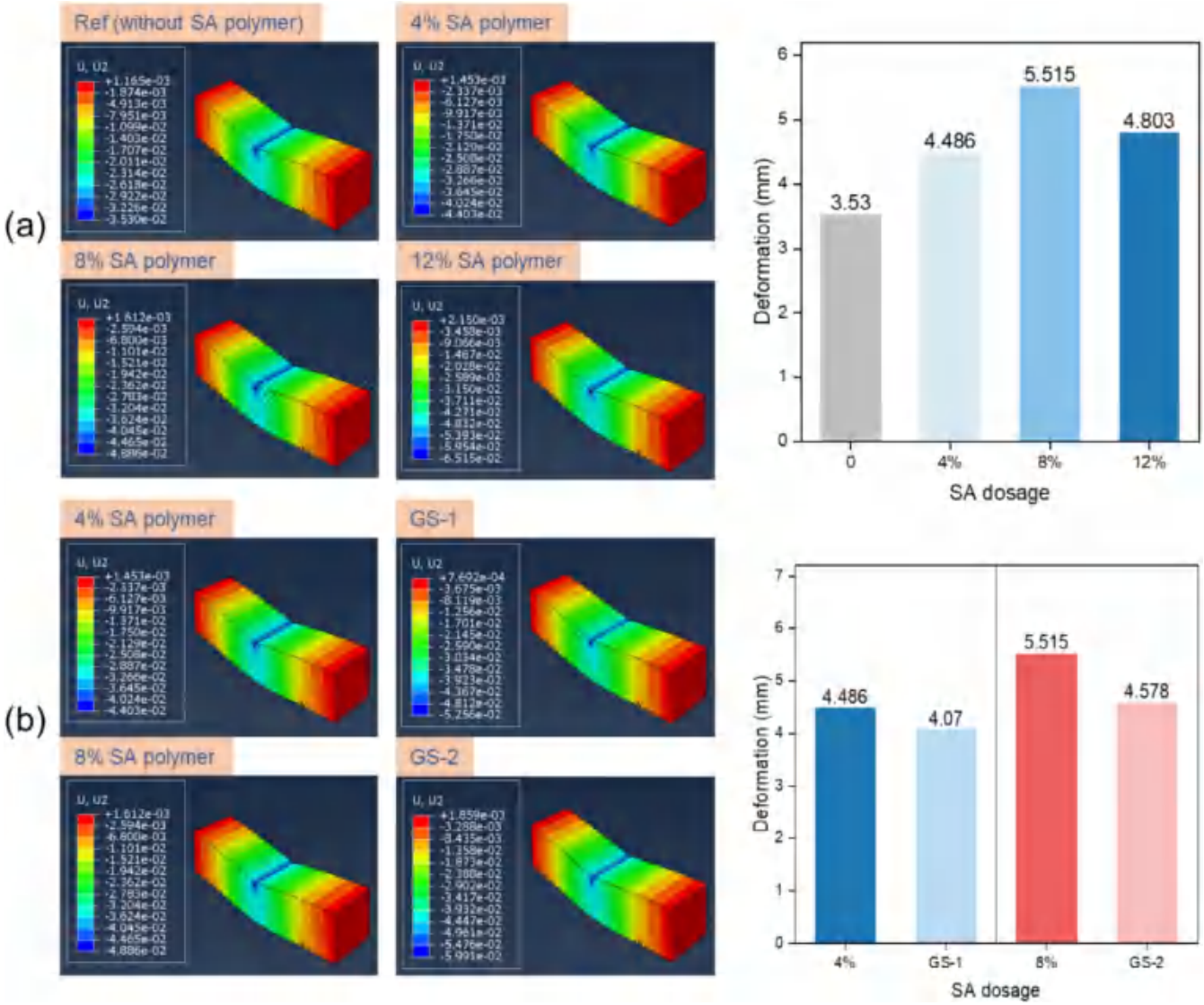

FIGURE 11 | The modeled vertical displacement of mortars during the flexural strength measurement: (a) the effect of polymer dosage and (b) the effect of gradient distribution. [Color figure can be viewed at wileyonlinelibrary.com]

the measured flexural strength and prove the reliability of the finite element analysis used in our study.

Regarding the effect of polymer types on mechanical performance (Figure 12), the addition of polymer latex can always increase the deformation of mortar under compressive load, which means a decreased compressive strength. Besides, the gradient distribution of the polymer is conducive to reducing this deformation. The displacement of mortar modified by SA latex is the smallest, followed by EVA latex, and finally SB latex. This matches well with the trend of compressive strength. Regarding the effect on the flexural strength measurement, it can be found that the deformation of mortar modified by SB and EVA latex increased along with the polymer dosage, compared to that modified by SA latex. Then, it should be pointed out that the gradient distribution can improve the ductility of PMM with the addtion of SB and EVA latex, but not that with the addition of SA latex, which is consistent with the results of flexural strength (Figure 7b).

4 | Discussion

Comparing the difference of the prepared PMM, it can be found that when the polymer dosage is the same, the effects of latex on the performance of PMM can be affected by three different factors, namely the polymer distribution, polymer types, and surface properties of polymer particles.

As seen from Figure 7, the gradient distribution of polymers increased the flexural strength of PMM with the addition of SB latex and EVA latex, but not to that with SA latex at the same polymer dosage, which could be caused by the different optimum polymer dosages for different types of polymer latexes. Clearly, for the mortar with SB latex and EVA latex, the highest flexural strength was found under the polymer dosage of 12%, but for SA latex, the optimum dosage is 8%. It indicates the further increased SA dosage to 12% is not beneficial to the flexural strength. Hence, the SA dosage of 12% at the upper and bottom part of the mortar could lead to decreased flexural

10974628, 0, Downloaded from https://onlinelibrary.wiley.com/doi/10.1002/app.57075 by Tongji University, Wiley Online Library on [05/04/2025]. See the Terms and Conditions (https://onlinelibrary.wiley.com/terms-and-conditions) on Wiley Online Library for rules of use; OA articles are governed by the applicable Creative Commons License

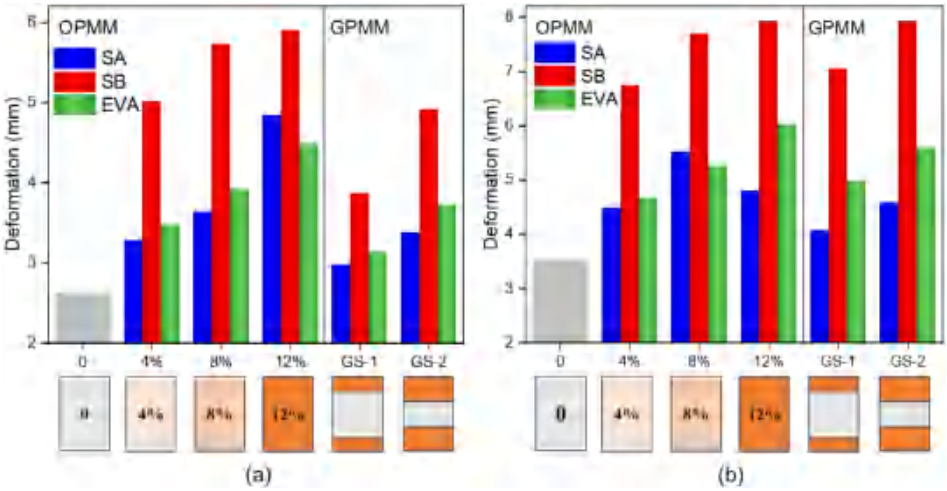

FIGURE 12 | The effect of polymer type on the vertical displacement of mortars during the: (a) compressive strength measurement and (b) flexural strength measurement. [Color figure can be viewed at wileyonlinelibrary.com]

strength compared to the sample with the same overall dosage but with a homogenous structure (4% and 8%). Actually, the first increased and then decreased flexural strength along with the increased polymer dosage is one commonly observed phenomenon [26–29]. Song et al. [26] and Wu et al. [29] proposed that the first enhancement of flexural strength can be attributed to the formed cross-linked network structure through the connection of the polymer film with hydration products. However, the excessive dosage of polymer latex could cause a decrease in the elasticity of modulus and lower the overall strength, which is harmful to the development of flexural strength. Yan et al. [28] suggested that the increased flexural strength at a low polymer dosage (< 10%) is caused by the improvement in the interface properties with cement. The further increased dosage of polymer could lead to the accumulation of polymer particles and form a weak zone, which becomes the key factor in deciding the decreased flexural strength. In addition, it is found that the bond strength of GPMM is significantly higher than that of OPMM at the same polymer dosage, which indicates that the increase in bond strength is mainly dependent on the polymer at the interface of prepared mortars.

In addition, the mortars with the addition of SA and EVA latex have a higher mechanical strength than that of SB latex. Since the polymer film plays an important role in determining the mechanical performance [30, 31], the properties of the formed polymer film, including the elongation at break and tensile stress at break, were evaluated, as shown in Figure 13. The results show that the polymer film formed by SA has the highest elongation at break, followed by EVA and SB. However, the film formed by SB has the highest tensile stress, then followed by SA and EVA. The results indicate that the elongation at break of the polymer film, namely the ductility, is more important in affecting the flexural strength of PMM compared to the tensile stress of the polymer film, which may be because the ductile films in the mortar could connect the microcracks closer and then enhance the adhesion force between the polymer film and the mortar matrix.

The adhesion between the polymer phase and matrix is not only decided by the properties of the polymer film; the surface

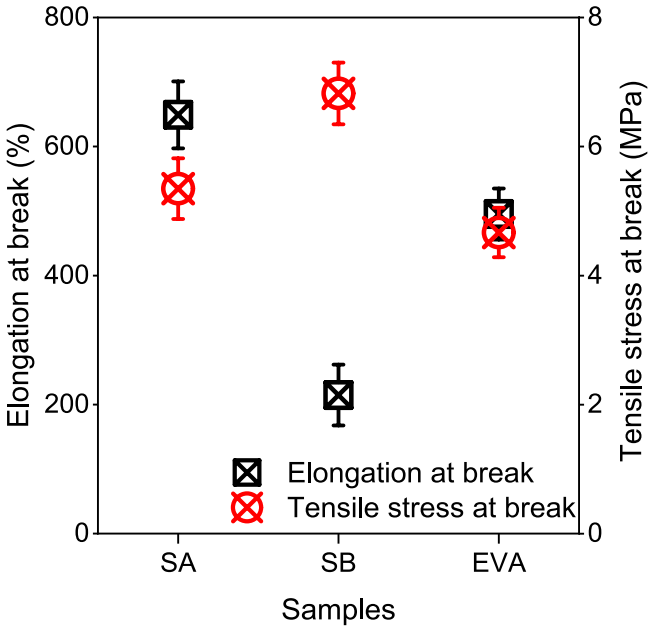

FIGURE 13 | The elongation and tensile strength at break for the polymer films prepared with different types of polymer latexes. [Color figure can be viewed at wileyonlinelibrary.com]

property, mainly including the charge density of polymer particles, should also play an important role [27]. The increased charge density normally leads to a higher adsorption amount, which could affect the microstructure of PMM. Zhang et al. [32] found that the different adsorption capabilities of polymer particles could lead to different film formation processes. If more polymer particles are left in the pore solution, more polymer particles tend to be adsorbed on the hydration products. Instead, if the polymer particles show a strong adsorption capability, it means more polymer particles are adsorbed onto the surface of cement grains, then the formed polymer films could be embedded inside hydration products. Schreiber et al. [33] pointed out the polymer particles can be continuously adsorbed onto the hydration products along with the cement hydration. In order to clarify the effect of the charge density of polymer latex on the mechanical properties of mortar, the adsorption of three varied

10974628, 0, Downloaded from https://onlinelibrary.wiley.com/doi/10.1002/app.57075 by Tongji University, Wiley Online Library on [05/04/2025]. See the Terms and Conditions (https://onlinelibrary.wiley.com/terms-and-conditions) on Wiley Online Library for rules of use; OA articles are governed by the applicable Creative Commons License

polymer latexes on the cement grains was measured, and the results are shown in Figure 14.

Clearly, following our assumption, SB latex with the highest charge density shows the highest adsorption amount, and a comparable adsorption amount was found to that of SA latex and EVA latex. It indicates that more SB polymer particles are adsorbed on the surface of cement grains and a lesser amount was left in the pore solution when the polymer dosages were 4% and 8%, respectively. Furthermore, as shown in the SEM picture (Figure 15), the different adsorption processes result in a change in the microstructure of PMM. Clearly, many deformed polymer particles, which were surrounded by hydration products, are observed in hardened cement paste with the addition of SA latex or EVA latex instead of SB latex. It indicates that more polymer particles were left in the pore solution for SA latex and EVA latex; then those polymer particles can be covered or surrounded by hydration products. Hence, the adsorption capability and adsorption process of polymer particles on the surface of cement grains or hydration products could also be one important role in determining the mechanical properties of PMM. The initially low adsorption amount on cement grains and the continuous adsorption on hydration products could, on the one hand, lower the porosity of the matrix by sealing the pores [32], and on the other hand, change the adhesion strength of the mineral matrix and the polymer films [34].

Besides, the SB latex with stronger adsorption ability seems to be more likely to reduce the formation of hydration products. To confirm this, the isothermal calorimetry was conducted, as shown in Figure 16. Clearly, the addition of polymer latexes leads

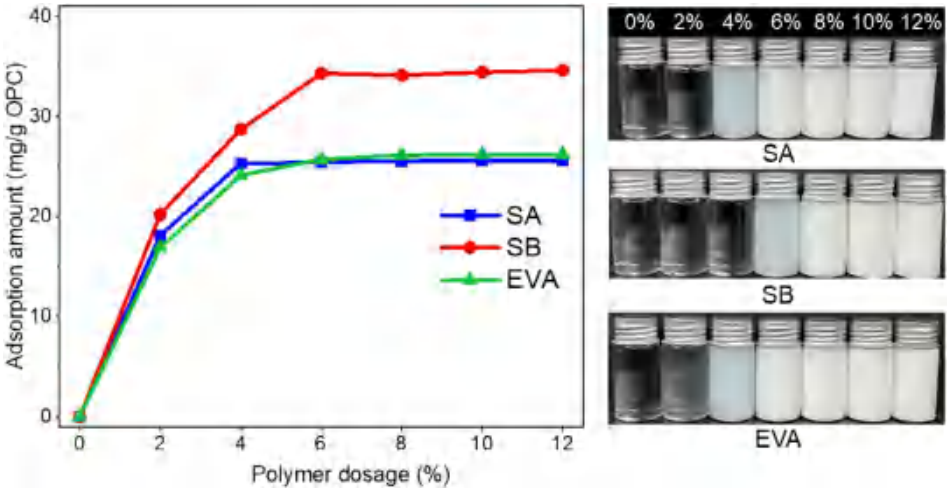

FIGURE 14 | The adsorption curves of different polymer latexes on OPC (left) and the diluted pore solutions (diluted 100 times) from the samples with different polymer dosages (right). [Color figure can be viewed at wileyonlinelibrary.com]

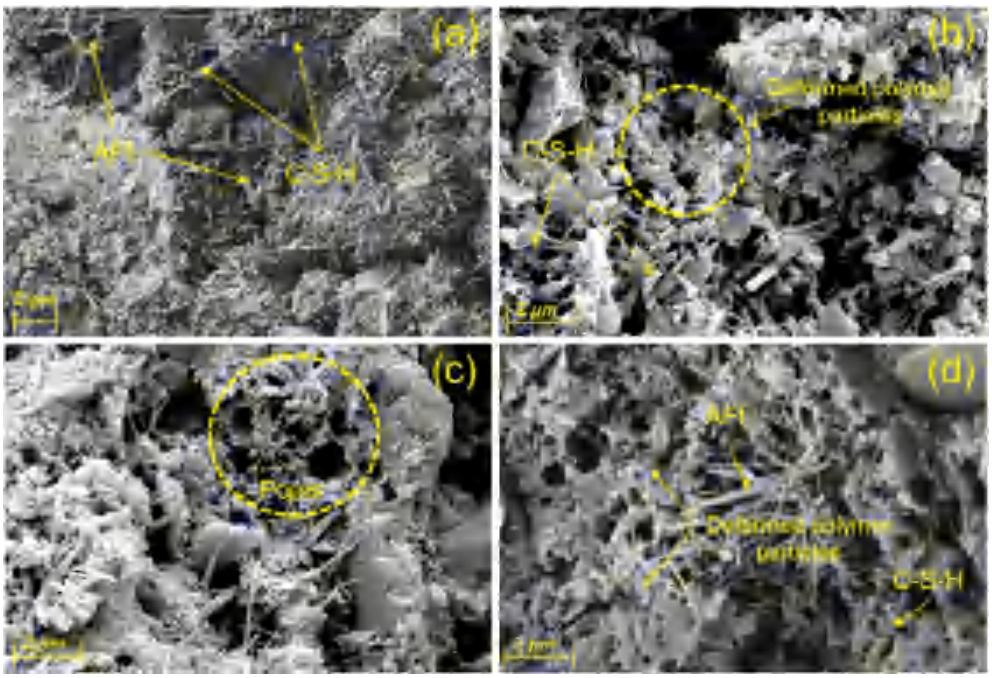

FIGURE 15 | The SEM images (Mag ×5000) of different hardened cement pastes (after curing for 3 days) modified by: (a) Ref; (b) SA; (c) SB; and (d) EVA. [Color figure can be viewed at wileyonlinelibrary.com]

10974628, 0, Downloaded from https://onlinelibrary.wiley.com/doi/10.1002/app.57075 by Tongji University, Wiley Online Library on [05/04/2025]. See the Terms and Conditions (https://onlinelibrary.wiley.com/terms-and-conditions) on Wiley Online Library for rules of use; OA articles are governed by the applicable Creative Commons License

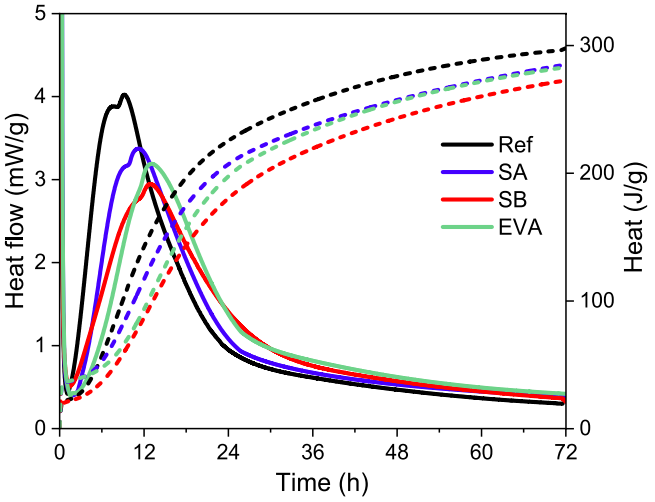

FIGURE 16 | Effect of different types of polymer latex on the hydration of cement paste (the solid line and dotted line correspond to heat flow and heat respectively). [Color figure can be viewed at wileyonlinelibrary.com]

to a strong retardation on cement hydration by slightly delaying the induction period and significantly lowering the height of the exothermic hydration peak as well as the cumulative heat, which is in accordance with the results shown in many literatures [35–37]. Comparing the three types of polymer particles, it seems that SB latex shows the strongest retardation effect on cement hydration with the lowest height in the exothermic hydration peak, then followed by EVA latex and SA latex. Based on the above analysis, it is believed that the retardation effect on cement hydration is closely related to the adsorption of polymer particles.

Hence, for PMM with the addition of SB latex, its low mechanical properties could be caused by the following three aspects. First, the high charge density of polymer particles leads to a high adsorption amount of SB latex on the surface of cement grains, which results in a strong retardation effect on cement hydration. Furthermore, the high adsorption amount on the surface of cement grains results in fewer polymer particles left in the aqueous phase to interact with the hydration products, which could affect the microstructure of the PMM. Last but not least, the polymer film formed by SB latex shows the lowest ductility, which could reduce the adhesion force between the polymer film and the mortar matrix. It further indicates that, compared to the tensile stress, the ductility of the polymer film should be more important in determining the flexural strength of PMM. SA latex and EVA latex showed a comparable adsorption amount. Compared to EVA latex, the increased flexural strength of SA-modified mortar under the dosage of 8% could be explained by the higher bonding between the polymers and cement hydrates [32].

5 | Conclusion

In this study, a gradient structure of PMM was designed and the mechanical performance was evaluated. Furthermore, the effect of polymer types and content was investigated. Based on the results above, the following conclusions can be obtained.

The addition of polymer latex causes a decrease in the compressive strength of the mortar, but favors the development of the flexural and bond strength of the mortar. Compared to the samples with the same polymer dosage, the mortar prepared with the gradient distribution of polymers shows a significant increase in compressive strength and bond strength. The increase in the flexural strength is not so obvious. The results of finite element analysis match well with the mechanical measurement. The polymer types can also greatly affect the mechanical performance of PMM. Compared to SA latex and EVA latex, SB latex with the highest charge density shows the lowest performance in modifying the mechanical performance of PMM, which could be attributed to the following three aspects: (1) low hydration degree of cement through the adsorption of SB latex; (2) loose microstructure of PMM; (3) poor ductility of polymer films. It further indicates that, compared to the tensile stress of the formed polymer film, the ductility of the polymer film should be more important in determining the flexural strength of PMM. Compared to EVA latex, SA latex with the lowest charge density shows a better performance in improving the mechanical properties of the mortar, which may be caused by the increased bonding of the SA polymer film with cement hydrates.

It should be noted that, at present, the designed gradient structure of concrete pavement reduces the efficiency of construction for the PMM with the addition of normal polymer latex. However, if one kind of responsive polymer latex can be generated and those polymer particles can be concentrated in the key area through the application of some physical stimulus, the drawback in low efficiency for the application of the gradient structure of concrete pavement can be solved. Meanwhile, the dosage of polymer latex in PMM can be greatly reduced. Definitely, it will be a great advantage to use the gradient structure in PMM under such a circumstance. That is the target for our future research, and more work is needed to reach such a goal.

Author Contributions

Ye Pan: data curation (lead), investigation (lead), methodology (lead), writing – original draft (lead). **Zichen Lu:** funding acquisition (lead), supervision (lead), writing – review and editing (lead). **Lei Wang:** investigation (equal), methodology (equal). **Yanrong Zhang:** supervision (equal), writing – review and editing (equal). **Yi Ding:** investigation (supporting), methodology (supporting). **Zhenping Sun:** supervision (equal), writing – review and editing (equal).

Acknowledgments

Financial support from the NEXCEL Technology Development and Acceleration (TDA) Project (2023TDA6-2) "Research on gradient enhanced polymer modified concrete for structural use and comparison with conventional concrete," Science and Technology Bureau of Wanrong County (kz0050020231876), and the National Natural Science Foundation of China (No. 52208282) are gratefully acknowledged.

Conflicts of Interest

The authors declare no conflicts of interest.

10974628, 0, Downloaded from https://onlinelibrary.wiley.com/doi/10.1002/app.57075 by Tongji University, Wiley Online Library on [05/04/2025]. See the Terms and Conditions (https://onlinelibrary.wiley.com/terms-and-conditions) on Wiley Online Library for rules of use; OA articles are governed by the applicable Creative Commons License

Data Availability Statement

The data that support the findings of this study are available from the corresponding author upon reasonable request.

References

1. H. Cheng, Y. Wang, J. Liu, et al., "The Long-Term Re-Cementation of Recycled Concrete Aggregate in Road Sub-base and Its Impacts on Pavement Performance," *Transportation Geotechnics* 49 (2024): 101431.

2. J. Zhao, X. Gao, S. Chen, H. Lin, Z. Li, and X. Lin, "Hydrophobic or Superhydrophobic Modification of Cement-Based Materials: A Systematic Review," *Composites Part B: Engineering* 243 (2022): 110104.

3. H. R. Karimi, E. Khedri, M. R. M. Aliha, H. Shaker, and P. Jafari Haghighatpour, "Repair Efficiency Evaluation for Cracked Asphalt Mixture Pavement in Different Ambient Temperatures Using Bitumen and Polymer Concrete as Repair Materials," *Construction and Building Materials* 369 (2023): 130556.

4. C. Yao, A. Shen, Z. Lyu, and G. Zeng, "Mitigating Freeze-Thaw Deterioration of Pavement Concrete Under Multi-Field Coupling by Superabsorbent Polymers," *Construction and Building Materials* 414 (2024): 134726.

5. Z. Lyu, A. Shen, W. Wang, S. Lin, Y. Guo, and W. Meng, "Salt Frost Resistance and Micro Characteristics of Polynary Blended Concrete Using in Frost Areas," *Cold Regions Science and Technology* 191 (2021): 103374.

6. K. Liu, X. Zhang, Y. Wang, et al., "Laboratory Investigation on Early-Age Shrinkage Cracking Behavior of Partially Continuous Reinforced Concrete Pavement," *Construction and Building Materials* 377 (2023): 131125.

7. K. T. Felekolu, B. Felekolu, A. Yalnkaya, and B. Baradan, "Influence of Styrene Acrylate and Styrene Butadiene Rubber on Fresh and Mechanical Properties of Cement Paste and Mortars," presented at 7th Asian Symposium on Polymers in Concrete, 2012.

8. N. Ukrainczyk and A. Rogina, "Styrene-Butadiene Latex Modified Calcium Aluminate Cement Mortar," *Cement and Concrete Composites* 41 (2013): 16–23.

9. Y. Lin, "Effect of Polymer to Early Mechanical Property of the Fly Ash Slurry," presented at International Conference on Structures and Building Materials (ICSBM), 2012.

10. A. A. M. Yassene, M. R. Ismail, and M. S. Afify, "Physicomechanical Properties of Irradiated SBR Latex Polymer-Modified Cement Mortar Composites," *Journal of Vinyl & Additive Technology* 26 (2020): 144–154.

11. Y. Li and X. Zhou, "Preliminary Analysis on Properties of New VAE Emulsion Used in Polymer Cement Waterproofing Coating," *China Building Waterproofing* S1 (2010): 73–76.

12. X. Zhang, M. Du, H. Fang, M. Shi, C. Zhang, and F. Wang, "Polymer-Modified Cement Mortars: Their Enhanced Properties, Applications, Prospects, and Challenges," *Construction and Building Materials* 299 (2021): 124290.

13. L. Li, R. Wang, and Q. Lu, "Influence of Polymer Latex on the Setting Time, Mechanical Properties and Durability of Calcium Sulfoaluminate Cement Mortar," *Construction and Building Materials* 169 (2018): 911–922.

14. İ. Kartal and H. Selimoğlu, "Usability of Pine Sawdust and Cotton Together as Filler in Recycled Polypropylene Composites," *International Journal of Computational Science and Engineering* 10 (2024): 244–248.

15. F. Gholinezhad, M. R. Moghbeli, A. Aghaei, and A. Allahverdi, "Effect of Organoclay Reinforced Acrylate Latex Particles on the Cement Paste Performance," *Journal of Dispersion Science and Technology* 42 (2021): 416–431.

16. Z. Xie, Q. Yuan, H. Yao, F. Zhong, and M. Jiang, "Hardened Properties and Microstructure Change of Sulphoaluminate Cement Modified With Different Doses of Styrene-Butadiene Rubber Latex," *Construction and Building Materials* 400 (2023): 132618.

17. D. Chung, "Use of Polymers for Cement-Based Structural Materials," *Journal of Materials Science* 39 (2004): 2973–2978.

18. J. Cheng, X. Shi, L. Xu, et al., "Investigation of the Effects of Styrene Acrylate Emulsion and Vinyl Acetate Ethylene Copolymer Emulsion on the Performance and Microstructure of Mortar," *Journal of Building Engineering* 75 (2023): 106965.

19. L. Li, K. Liu, B. Chen, and R. Wang, "Effect of Cyclic Curing Conditions on the Tensile Bond Strength Between the Polymer Modified Mortar and the Tile," *Case Studies in Construction Materials* 17 (2022): e01531.

20. J. V. Brien and K. C. Mahboub, "Influence of Polymer Type on Adhesion Performance of a Blended Cement Mortar," *International Journal of Adhesion & Adhesives* 43 (2013): 7–13.

21. Z. Lu, X. Kong, C. Zhang, D. Jansen, J. Neubauer, and F. Goetz-Neunhoeffer, "Effects of Two Oppositely Charged Colloidal Polymers on Cement Hydration," *Cement and Concrete Composites* 96 (2019): 66–76.

22. L. Fan, F. Xu, S. Wang, Y. Yu, J. Zhang, and J. Guo, "A Review on the Modification Mechanism of Polymer on Cement-Based Materials," *Journal of Materials Research and Technology* 26 (2023): 5816–5837.

23. H. A. Shah, Q. Yuan, and S. Zuo, "Air Entrainment in Fresh Concrete and Its Effects on Hardened Concrete—A Review," *Construction and Building Materials* 274 (2021): 121835.

24. J. P. Gorninski, D. C. Dal Molin, and C. S. Kazmierczak, "Study of the Modulus of Elasticity of Polymer Concrete Compounds and Comparative Assessment of Polymer Concrete and Portland Cement Concrete," *Cement and Concrete Research* 34 (2004): 2091–2095.

25. H. Ma and Z. Li, "Microstructures and Mechanical Properties of Polymer Modified Mortars Under Distinct Mechanisms," *Construction and Building Materials* 47 (2013): 579–587.

26. S. H. Song, F. T. Liu, and Y. B. Huang, "Effect of Polymer Latex and Fiber on Properties of Sulpho Aluminate Cement Mortar," *Advances in Materials Research* 450–451 (2012): 402–406.

27. C. Zhang, J. Liu, S. Zhang, and X. Kong, "Mechanical Properties of Polymer Modified Mortars Using Polymer Latexes With Varied Glass Transition Temperature and Surface Charges," *Cement and Concrete Composites* 150 (2024): 105573.

28. S. Yan, H. Lu, Z. Zhou, Q. Dong, X. Chen, and X. Wang, "A Polymer Latex Modified Superfine Cement Grouting Material for Cement-Stabilized Macadam—Experimental and Simulation Study," *Construction and Building Materials* 413 (2024): 134893.

29. K. Wu, J. Long, L. Qing, and G. De Schutter, "Recent Advance of Monomer In-Situ Polymerization Modified Cement-Based Materials," *Construction and Building Materials* 432 (2024): 136542.

30. M. Wang, R. Wang, H. Yao, et al., "Research on the Mechanism of Polymer Latex Modified Cement," *Construction and Building Materials* 111 (2016): 710–718.

31. E. Knapen and D. Van Gemert, "Polymer Film Formation in Cement Mortars Modified With Water-Soluble Polymers," *Cement and Concrete Composites* 58 (2015): 23–28.

32. C. Zhang, X. Kong, Z. Lu, D. Jansen, J. Pakusch, and S. Wang, "Pore Structure of Hardened Cement Paste Containing Colloidal Polymers With Varied Glass Transition Temperature and Surface Charges," *Cement and Concrete Composites* 95 (2019): 154–168.

33. J. Schreiber, J. Wang, X. Kong, J. Neubauer, and D. Jansen, "Influence of a Dialysed Polymer Latex on the Hydration of OPC—A Closer Look Into Adsorption Processes," *Cement and Concrete Research* 176 (2024): 107390.

10974628, 0, Downloaded from https://onlinelibrary.wiley.com/doi/10.1002/app.57075 by Tongji University, Wiley Online Library on [05/04/2025]. See the Terms and Conditions (https://onlinelibrary.wiley.com/terms-and-conditions) on Wiley Online Library for rules of use; OA articles are governed by the applicable Creative Commons License

34. J. Kaufmann, F. Winnefeld, and R. Zurbriggen, "Polymer Dispersions and Their Interaction With Mortar Constituents and Ceramic Tile Surfaces Studied by Zeta-Potential Measurements and Atomic Force Microscopy," *Cement and Concrete Composites* 34 (2012): 604–611.

35. J. Du, Y. Bu, and Z. Shen, "Interfacial Properties and Nanostructural Characteristics of Epoxy Resin in Cement Matrix," *Construction and Building Materials* 164 (2018): 103–112.

36. Y. Tian, X. Jin, N. Jin, R. Zhao, Z. Li, and H. Ma, "Research on the Microstructure Formation of Polyacrylate Latex Modified Mortars," *Construction and Building Materials* 47 (2013): 1381–1394.

37. X. Kong, S. Emmerling, J. Pakusch, M. Rueckel, and J. Nieberle, "Retardation Effect of Styrene-Acrylate Copolymer Latexes on Cement Hydration," *Cement and Concrete Research* 75 (2015): 23–41.

10974628, 0, Downloaded from https://onlinelibrary.wiley.com/doi/10.1002/app.57075 by Tongji University, Wiley Online Library on [05/04/2025]. See the Terms and Conditions (https://onlinelibrary.wiley.com/terms-and-conditions) on Wiley Online Library for rules of use; OA articles are governed by the applicable Creative Commons License

网络首发时间：2025-06-09 11:10:18　网络首发地址：https://link.cnki.net/urlid/37.1316.TU.20250606.1457.001

文章编号：1008-5548(2025)04-0001-12　　DOI：10.13732/j.issn.1008-5548.2025.04.003

聚合物-混凝土复合材料研究进展

卢子臣，刘丹婷，王　磊

同济大学 材料科学与工程学院，上海 200082

摘要：【目的】聚合物作为一种在水泥基材料中广泛应用的有机外加剂，能显著改善混凝土各方面性能。探讨聚合物对混凝土工作性、力学性能及耐久性的影响规律及作用机制，能够更好地指导聚合物在混凝土中的应用。**【研究现状】**综述聚合物-混凝土复合材料的种类及性能特点，分别介绍聚合物混凝土、聚合物浸渍混凝土和聚合物改性混凝土以及其他3类新型聚合物混凝土复合材料；从工作性、力学性能和耐久性3个方面的表现分析聚合物对聚合物-混凝土复合材料性能影响及作用机制。**【结论与展望】**聚合物混凝土和聚合物浸渍混凝土在力学性能和耐久性方面显示出较大优势，但高成本和复杂制备工艺限制了其大规模应用；聚合物改性混凝土虽然成本较低且应用广泛，但抗压强度随聚合物掺量的增大而下降，须通过优化骨料配比和养护条件平衡性能；新型聚合物-混凝土材料如单体原位聚合混凝土(强度高但反应难控)、纤维增强基材(延展性好但掺量敏感)、废旧塑料-橡胶混凝土(环保但强度低)各有潜力与挑战。未来需重点突破界面作用机制解析、低成本工艺及环保材料开发等瓶颈。

关键词：聚合物-混凝土复合材料；水泥基材料；作用机制

中图分类号：TU533；TU532+.1　　**文献标志码：**A

引用格式：

卢子臣，刘丹婷，王磊. 聚合物-混凝土复合材料研究进展[J]. 中国粉体技术，2025，31(4)：1-12.

LU Ziche，LIU Danting，WANG Lei. Research progress on concrete-polymer composites[J]. China Powder Science and Technology，2025，31(4)：1-12.

混凝土具有原材料广泛、价格低廉、力学性能优异等特点，已成为当今世界上使用量最大的建筑材料。普通水泥混凝土作为1种多孔且非均质的材料，抗折强度较低，脆性较大，同时耐久性也亟须进一步提高[1]。为了提高混凝土的综合性能，添加功能性材料对混凝土进行改性已成为一种常用技术手段。聚合物作为一种在水泥基材料中广泛应用的有机外加剂，在改善混凝土性能方面展现出巨大潜力[2]。

聚合物是一类由简单结构单元通过共价键重复连接而成的高分子量化合物。聚合物种类繁多，主要可分为聚合物乳液(或可再分散乳胶粉)、水溶性聚合物以及液体树脂[3]。可再分散乳胶粉是由聚合物乳液喷雾干燥而得的粉状聚合物颗粒，将聚合物乳胶粉与水再次混合时，其可以重新分散到水中，因此归入聚合物乳液。

由于水溶性聚合物掺量较小，难以在混凝土内部形成独立固相，进而不能形成复合材料，因此聚合物-混凝土复合材料中所用聚合物通常为聚合物乳液(包括可再分散乳胶粉)及聚合物树脂。研究表明，聚合物的引入可以显著改善混凝土的抗折强度、韧性和耐久性，并对其收缩和抗裂性能起到调控作用[4]。随着新材料不断涌现及施工要求多样化，聚合物-混凝土复合材料仍有一些问题须要进一步研究，如不同聚合物与水泥颗粒或水化产物之间的相互作用及微结构形成机制、聚合物对水泥基材料的增强增韧机制、复杂环境下聚合物-混凝土复合材料性能调控机制等。

针对上述问题，本文中系统综述几种聚合物-混凝土复合材料组成及性能特点，进一步讨论了聚合物在其中的作用机制与性能调控机制，对聚合物-混凝土复合材料的未来发展方向提出展望，认为未来

收稿日期：2024-10-01，**修回日期：**2025-04-19

基金项目：国家自然科学基金项目，编号：52208282；非金属材料创新中心创新基金项目，编号：2023TDA6-2；山西省万荣县2023年科技计划项目，编号：kz0050020231876。

第一作者简介：卢子臣(1987—)，男，副教授，博士，上海市海外高层次人才引进计划入选者，博士生导师，研究方向为新型混凝土外加剂、水泥基材料水化与流变、水泥基材料早期功能调控等。E-mail：luzc@tongji.edu.cn。

须重点突破界面作用机制解析、低成本工艺及环保材料开发等瓶颈。

1 聚合物-混凝土复合材料种类及组成

根据聚合物掺入混凝土的方式可将聚合物-混凝土复合材料分为3类：聚合物混凝土（polymer concrete，PC）、聚合物浸渍混凝土（polymer-impregnated concrete，PIC）和聚合物改性混凝土（polymer-modified concrete，PMC），其中聚合物改性混凝土成本较低且制作简单，应用最为广泛。各类聚合物-混凝土复合材料组成及结构示意图如图1所示。

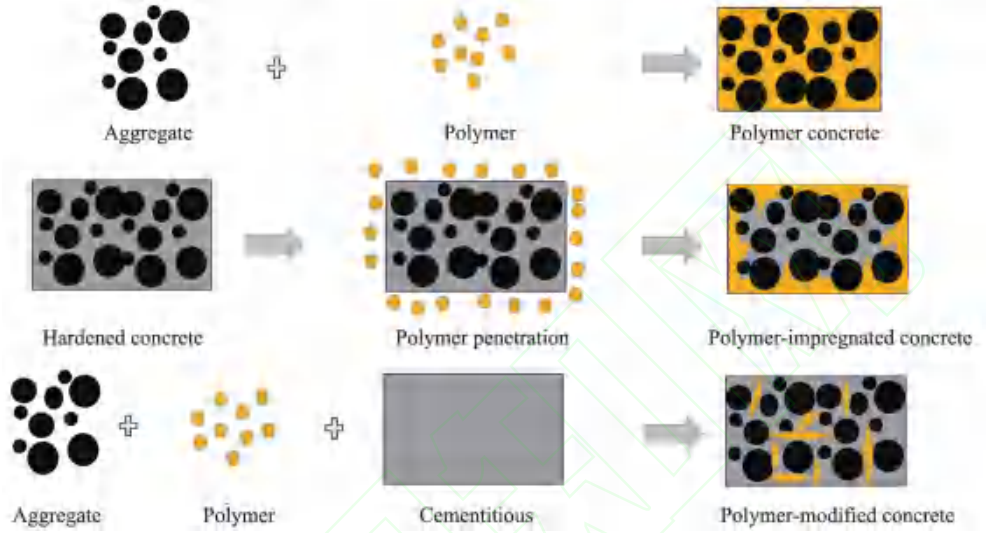

图1 几种典型聚合物-混凝土复合材料的组成及其结构示意图

Fig. 1 Schematic diagrams of composition and structure of several typical concrete-polymer composites

1.1 聚合物混凝土（PC）

聚合物混凝土中的胶凝材料为聚合物树脂，而非传统的水泥基胶凝材料。这种材料通过热固性聚合物树脂将骨料紧密结合，形成坚固的复合材料。在某些情况下，使用砂石作为填料，可进一步增强材料的性能，此时材料被称为聚合物砂浆[5]。聚酯树脂、环氧树脂和丙烯酸树脂是聚合物混凝土中常用的树脂类型[6]，以不饱和聚酯树脂和环氧树脂最为常用。不饱和聚酯树脂的掺量（质量分数，下同）通常为10%~20%，研究表明，不饱和聚酯树脂的掺量为12%~16%时，不饱和聚酯树脂混凝土的压缩强度和弯曲强度最佳，对于细骨料占比较大的混凝土体系，则须要将树脂掺量提高至15%~20%，以确保良好的黏结性能[7]。在相同掺量下，环氧树脂混凝土的抗压强度、抗弯强度和抗折强度显著高于不饱和聚酯树脂混凝土的[8]。此外，当环氧树脂掺量为30%~35%时，聚合物混凝土展现出更优越的抗弯性能[9]。与普通水泥混凝土相比，聚合物混凝土的强度高，固化快，与其他结构基体结合紧密，对液体的渗透性极低，具有更好的环境适应性和耐化学腐蚀性能，但聚合物混凝土的价格较贵，一般只用于管道制造、海洋环境等特殊工程[10]。

1.2 聚合物浸渍混凝土（PIC）

聚合物浸渍混凝土是将硬化混凝土部分或完全浸入聚合物单体中，随后在催化剂的作用下或在加热条件下引发单体聚合，实现对混凝土孔隙的填充，并在一定深度范围内形成连续相。这种处理方法显著提升了混凝土的密实性，增强了整体性能。完全浸渍的操作过程相对复杂，因此目前研究多集中在部分浸渍技术上[11]。不论是完全浸渍还是部分浸渍，均需要一定浸渍时间以确保浸渍液能够充分渗透到混凝土基材的孔隙中。在浸渍过程中，通常会要求浸渍液的黏度较低，以便更容易渗入混凝土基材内部。浸渍后，单体须要在原处聚合，这一步骤可以通过加入催化剂或加热来加速进程。常用的单体类浸渍液主要有甲基丙烯酸甲酯和丙烯腈等烯类单体及有机硅单体。常用的聚合物类浸渍液主要有环氧树脂和不饱和聚酯树脂。

研究表明，聚合物渗透增强了混凝土的抗压强度，其抗压强度为原始混凝土的2~4倍，这种渗透作用不仅增强了混凝土的密实度，还降低了透水性，同时提高了抗冻融性和耐化学侵蚀性[12]。与普通混凝土相比，在相同成本下PIC可具有更高的强度[13]。

聚合物浸渍混凝土改善了混凝土的结构和耐久性能，因此特别适合应用于高速公路、机场、地下管道和海洋结构中[14]。

1.3 聚合物改性混凝土（PMC）

聚合物改性混凝土是以水泥作为主要胶凝材料，将聚合物与骨料按一定比例与水泥混合制备而成的复合材料。聚合物以聚合物乳液（或可分散乳胶粉）的形式加入，常用的乳液类型有聚丙烯酸类、苯丙乳液、丁苯胶乳、聚醋酸乙烯酯乳液和聚乙烯醋酸乙烯酯等。基于不同的使用用途，聚合物的掺量差异较大，一般为胶凝材料总质量的2%~50%。由于聚合物改性混凝土中聚合物的用量低于聚合物混凝土，因此聚合物改性混凝土在成本上具有优势，实际应用更为广泛。

聚合物乳液是直径为0.05~5.00 μm的聚合物粒子分散在水中所形成的水分散体[15]。相较于传统的水泥混凝土，聚合物改性后的混凝土具有更高的拉伸和弯曲强度。聚合物材料不仅能提供良好的附着性能，还对机械磨损、物理冲击等结构性损伤及化学腐蚀具有显著抵抗能力。基于聚合物改性混凝土的上述优点，可将其用作修补与耐磨材料[16]。修补混凝土须满足界面过渡区相容性、施工阶段可操作性、较高的黏结强度以及与被修补结构相匹配的热膨胀系数和力学性能。

聚合物改性混凝土的另一个显著优势在于通过乳液成膜，能够在水泥基材料内部形成网状结构，有效堵塞孔隙和微裂缝，提升材料的抗渗性能，因此，聚合物乳液类外加剂也在防水工程中得到了广泛应用，如制备聚合物水泥防水砂浆和聚合物水泥防水涂料。

1.4 其他

除以上3种主要类型外，其余几类新型聚合物-混凝土复合材料因各自的优点而逐渐成为研究热点，包括单体原位聚合水泥混凝土、纤维增强水泥基复合材料和回收废旧塑料或橡胶等聚合物制成的混凝土。

1.4.1 单体原位聚合水泥混凝土

单体原位聚合水泥混凝土是在水泥水化过程中同时进行单体的聚合反应，形成连续的聚合物网络。这一聚合物网络结构均匀分布在水泥基体中，通过与水泥水化产物紧密结合，显著提升了材料的性能。单体原位聚合水泥混凝土通常采用具有活性官能团的单体，如丙烯酰胺、丙烯酸和2-丙烯酰胺-2-甲基丙磺酸。这些单体能够在水泥水化过程中通过自由基聚合反应形成聚合物网络。其中，丙烯酰胺因具有优异的化学稳定性和与水泥水化产物的协同作用而成为最常用的单体。单体原位聚合水泥混凝土的生产过程为首先将选定的单体与水泥、骨料和水混合，形成均匀的浆料，其后通过添加引发剂（例如过硫酸铵）来启动聚合反应。在整个过程中，控制聚合速率以与水泥水化速率相匹配至关重要。

1.4.2 纤维增强水泥基复合材料

根据纤维的存在形式，纤维增强水泥基复合材料可以分为工程水泥基复合材料（engineered cementitious composite，ECC）和纤维增强混凝土（fiber-reinforced concrete，FRC）。ECC中离散分布的短切纤维通过桥接裂纹与应力再分配机制，同时提升混凝土的弹性模量和断裂韧性。在拉伸荷载作用下，ECC中纤维会促进硬化混凝土产生多条细密裂缝，这一过程中吸收了大量的破坏能量，避免了贯通裂纹的形成，从而提高了材料的承载能力。ECC的极限拉应变可超过3%，展现出高延展性的特性[17]。

FRC中纤维通常是连续的，并且通常按照特定的方向排列或编织成板、布等形式。这些纤维随后与树脂基体材料胶结，形成FRC制品。常用的增强纤维材料主要包括碳纤维、芳纶纤维、玻璃纤维和玄武岩纤维[18]。

通过结合水泥基材料和纤维制成的纤维增强水泥基复合材料，不仅可以显著提高复合材料的基本力学性能，还能提升其韧性和耐久性能。这些特性使得FRC在建筑工程领域受到了广泛关注，特别是在建筑的加固补强以及作为新建建筑的功能材料等方面。

1.4.3 废旧塑料和橡胶再利用

废旧橡胶和塑料等难以自然降解的废弃物占用大量垃圾填埋场地，释放有害物质并污染土壤和水源，对环境造成了巨大的威胁。此类废弃物可作为胶凝材料、骨料或掺合料加入混凝土中，不仅促进了废弃物的再利用，同时也为聚合物-混凝土复合材料的发展开辟了新途径[19]。

废弃塑料和橡胶的利用方式主要包括2类：一类是用回收的塑料作为胶凝材料制成聚合物混凝土，另一类是将塑料和废弃橡胶代替天然骨料用作环保骨料[20]。相比于天然骨料，塑料或橡胶骨料因表面能低，表观密度小，在拌合过程中易形成弱界面过渡区与多孔结构，进而减小了基体的密度和机械强度，但可以提升混凝土的延展性。此外，塑料或橡胶骨料的热导率和声导率较低，使得它们成为制造隔热隔音混凝土的理想选择。橡胶还具有出色的抗渗性和抗裂性，以及高阻尼和低弹性模量，能够在混凝土中填补孔隙，抑制内部微裂缝的发展，并通过吸收震动来增强建筑的抗震能力[21]。混凝土的具体性能因废旧塑料-橡胶的种类和处理方式而异，在本文中不再赘述。

2 聚合物对聚合物-混凝土复合材料性能影响及作用机制

本文中主要探讨聚合物对各类聚合物-混凝土复合材料性能的影响及作用机制，重点从工作性、力学性能和耐久性3个方面进行详细分析。工作性指混凝土在拌和、运输、浇筑和成型过程中的操作便利性，主要包括流动性、黏聚性和保水性等特性。力学性能涉及材料的抗弯强度、抗折强度和抗压强度，而耐久性则涵盖耐腐蚀性、抗冻融性等关键指标。

2.1 聚合物混凝土的性能特点及作用机制

聚合物混凝土的性能主要受聚合物类型、用量、聚合度以及骨料的类型、形状和等级等因素影响[22]。

2.1.1 工作性

聚合物的种类、含量及外加剂的选择，是决定聚合物混凝土工作性的关键。通过调整这些参数可以优化混凝土的流动性、凝结时间等，以满足特定施工条件[23]。

与水泥混凝土相比，聚合物混凝土固化速度更快，具体固化时间与树脂的特性紧密相关[8]。树脂的固化速度较快时，聚合物混凝土的固化过程也相应加快。树脂的黏度是影响流动性的关键因素。使用高黏度树脂时，聚合物混凝土的铺展直径较小，而使用低黏度树脂时，铺展直径较大。

2.1.2 力学性能

树脂类型是影响混凝土抗弯性能的关键因素，树脂的物理性质对混凝土的抗弯强度产生直接影响，如凝胶时间、树脂固化过程中达到的最高温度和从树脂开始固化到达到峰值温度所需的时间[24]。树脂掺量的增加能够提升混凝土的抗弯和抗拉强度[25]。当树脂掺量从水泥质量的17%提升至20%时，聚合物混凝土的抗压强度、抗折强度和耐腐蚀性均得到显著改善；然而过高的树脂含量可能导致富树脂区的形成，这些区域缺乏足够的骨料支撑，从而降低混凝土的抗压强度，因此，除了选择高性能树脂外，优化骨料与树脂的比例对于提高聚合物混凝土的使用性能亦至关重要。最佳的骨料配比能够提高混凝土的密实度和整体性能，从而优化其弹性模量、热传导率、孔隙率以及抗弯强度和抗压强度，进而可以一定程度上平衡成本效益与力学性能。

2.1.3 耐久性

聚合物混凝土展现出优异的耐热冲击性能、隔热性、抗冻融性以及抗化学侵蚀能力，这些特性使得聚合物混凝土在冻土环境、海洋环境以及其他要求高耐久性的应用场景中成为一种理想的材料选择。

聚合物混凝土对温度变化敏感[26]，当温度从25 ℃降低到-15 ℃时，会显著提高聚合物混凝土的抗压强度、劈裂抗拉强度、抗弯强度和弹性模量[27]，但延展性、冲击性能和能量吸收能力会显著下降[28]。

聚合物混凝土具有比传统水泥混凝土更好的抗冻融耐久性[29]，尤其是聚合物含量高的混凝土。聚合物混凝土的优异耐久性主要缘于其致密的微观结构、极低的渗透性，以及骨料与聚合物基体间的高黏结强度。其不渗透特性有效阻隔了水分与腐蚀介质的侵入，而高黏结强度则显著抑制了界面裂缝的萌生与扩展，从而在腐蚀环境、冻融循环等严苛条件下表现出卓越的抗劣化能力[30]。

2.1.4　作用机制

聚合物的分子结构和交联程度对聚合物混凝土的性能有巨大的影响。聚合物作为主要的黏结剂，为混凝土提供了优异的黏结性能和化学稳定性，这些性质进一步决定了材料的抗拉强度和抗压强度[31]。与传统的水泥混凝土相比，聚合物基体与骨料之间的黏结力更大，显著提高了混凝土的整体性能。

聚合物混凝土在恶劣环境条件下往往表现出更好的耐久性，这主要得益于聚合物分子的独特结构。以环氧树脂为例，其分子链中同时存在刚性环状结构和柔性极性官能团。图 2 所示为典型环氧树脂分子结构及其交联网络示意图[32]。由图可见，环氧树脂的三维交联网络呈现出规律的空间排布，环状结构通过化学键紧密连接形成刚性骨架，而极性基团则在分子间产生强相互作用，这种特殊的结构组合赋予材料双重优势。这种结构特征使材料能够形成更稳定的交联网络，其拓扑结构可有效分散外界应力，抵御紫外线辐射、湿气渗透和化学侵蚀等多重破坏因素[33]。特别是在高温高湿环境下，交联网络中的分子键能保持较高稳定性，从而较好地维持材料的物理和机械性能[7]。

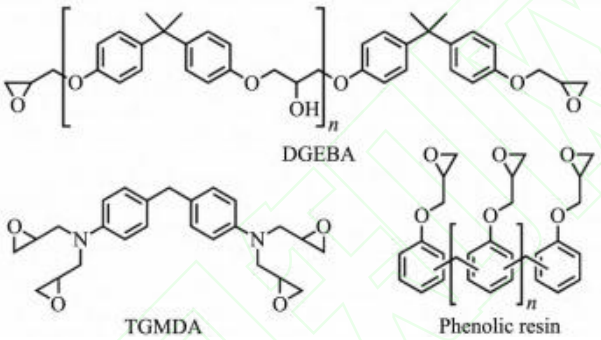

DGEBA—Diglycidyl Ether of Bisphenol A；TGMDA—Tetraglycidyl Methylene Dianiline.

图 2　典型环氧树脂分子结构[32]

Fig. 2　Molecular structures of typical epoxy resins

2.2　聚合物浸渍混凝土的性能特点及作用机制

聚合物浸渍混凝土的优点包括抗压强度、抗拉强度和抗折强度较高，同时具有优异的抗冻融性和抗酸侵蚀性，其缺点是成本较高，制备时间长以及施工复杂[16]。

由于聚合物浸渍混凝土是将已经硬化的混凝土浸入液态的有机单体或聚合物中，此时混凝土显然已经失去工作性，因此该部分只综述 PIC 的力学及耐久性等性能特点及其作用机制。

2.2.1　力学性能

相较于未处理的普通混凝土，PIC 的抗压、抗拉强度是普通混凝土的 3~4 倍，聚合物浸渍砂浆的抗压、抗拉强度提升更高，是普通混凝土的 5 倍以上[34]。PIC 的抗压强度会随着聚合物用量的增多而增大[35]。尽管 PIC 的早期抗压强度可能低于普通混凝土，但经过 28 d 养护后，其抗压强度显著超越普通混凝土。需要注意的是，尽管 PIC 极限强度较高，但其延展性较差，容易发生脆性破坏，且破坏前往往无明显征兆[14]。

2.2.2　耐久性

PIC 相较于普通混凝土具有优越的耐腐蚀性和抗冻融性。在酸性溶液的干湿循环试验中，普通混凝土的抗压强度显著降低，表面出现龟裂，而 PIC 抗压强度保持稳定，表面无明显损伤。在碱性溶液的干湿循环试验中，普通混凝土的抗压强度大幅下降，而 PIC 强度仅出现轻微下降。此外，PIC 在抗冻融循环试验中表现出优异的耐久性，可承受数百次以上的冻融循环，显示出其在极端环境下的优越性能[12]。

2.2.3　作用机制

目前对 PIC 增强机制的认识主要集中在以下几个方面：通过聚合物填充孔隙并改善水泥浆体与骨料的界面结合，显著降低了孔隙率；同时，聚合物的加入增强了水泥浆体与骨料之间的黏结强度，减少了界面处的应力集中现象。这些机制共同作用，显著提高了混凝土的力学性能和耐久性。

相比于普通混凝土，PIC具有优越的耐腐蚀性和抗冻融性的原因是，普通混凝土中存在较多孔隙，在经酸性或碱性溶液浸泡后会导致溶液进入孔隙，渗透到混凝土内部进而出现化学腐蚀，而PIC中孔隙被浸渍的单体聚合形成三维网状结构填充，腐蚀性溶液不易进入到内部，因此其耐腐蚀性较强；同样，PIC在冻融循环中能够减少水分的渗透路径，从而降低冻融循环过程中的水分膨胀压力，减少冻融损伤。同时，在聚合过程中聚合物与混凝土基材形成良好黏结，这种黏结力可以减少裂纹和孔隙产生的应力集中，从而提高混凝土的强度和耐久性。

2.3 PMC的性能特点及作用机制

聚合物乳液作为PMC的关键组分，通过成膜作用显著改善材料的黏结强度、抗折性能、抗渗性及抗裂能力。其性能提升机制与乳液中聚合物颗粒的微观形貌及化学组成密切相关。

图3所示为采用扫描电子显微镜（scanning electron microscope，SEM）观测的典型聚合物乳液粒子形貌特征。由图可见，乳液粒子呈现规整的球形结构，表面光滑的微球通过紧密堆积形成连续膜层，这种微观结构有利于在水泥水化产物中形成贯穿式聚合物网络，从而有效提升复合材料的韧性和抗渗性能[36]。图4展示了聚合物乳液的典型组成体系，其主要成分为聚合物乳液粒子，配合乳化剂构建稳定胶束结构，并含有少部分水溶性低聚物[37]。

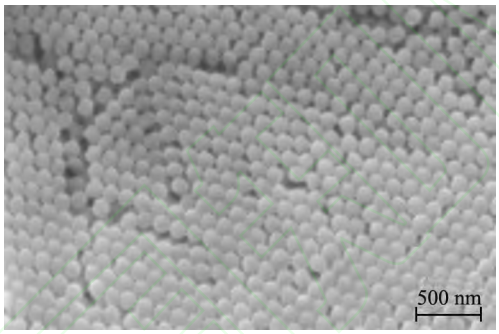

图3 聚合物乳液粒子的扫描电镜图[36]

Fig. 3 SEM image of polymer particles

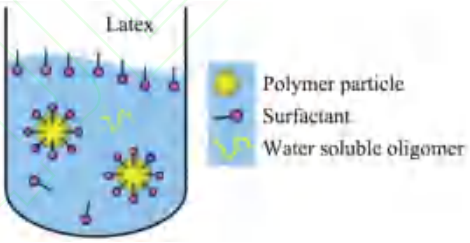

图4 聚合物乳液组成[37]

Fig. 4 Composition of polymer latex

2.3.1 工作性

一般而言，聚合物乳液的加入会提高水泥基浆体流动性，降低浆体黏度与屈服应力。进一步研究表明，聚合物乳液对水泥浆体的分散效果主要取决于乳液颗粒的表面特性及其掺量。值得注意的是，Lu等[38]研究发现，当乳液在水泥颗粒表面达到饱和吸附状态时，其分散能力反而最弱。Zhang等[39]发现，当聚合物乳液的掺量较低，浆体的流动性变差，但随着乳液掺量进一步增加，浆体的流动性开始增大，这是因为在低掺量时，硅烷乳液未能充分分散，干扰聚羧酸减水剂（polycarboxylate superplasticizer，PCE）的分散作用并轻微抑制水化反应，导致颗粒间摩擦增大，流动性下降；而在高掺量时，乳液中的表面活性剂释放充分，增强了润滑作用，且与PCE可能产生协同效应，改善颗粒分散状态，加之引气效应受到消泡剂的有效控制，从而提升了流动性。除了流动性能，聚合物乳液的加入也会显著影响水泥浆体的凝结硬化过程。聚合物乳液主要通过吸附在水泥颗粒表面抑制水化产物的成核来延缓水化，羧酸基团的络合作用影响有限。Lu等[40]在表面为羧基的乳液粒子中滴加硝酸钙与硅酸钠，使乳液粒子周围

富集生成水化硅酸钙凝胶。这种表面改性使乳液粒子表面成为水化产物的成核位点，从而消除了乳液覆盖层对水泥水化的抑制作用，使乳液对水泥基材料产生促凝效果。

2.3.2　力学性能

在抗折和抗压强度方面，随着聚合物乳液掺量的增加，PMC抗压强度整体呈现下降趋势，而抗折强度呈现先增加后下降的变化趋势[41-42]。这是因为，乳液在混合过程中会引入空气，增加内部孔隙率[43]。虽然适量的聚合物乳液可以改善混凝土的工作性；但过高的掺量会导致抗折和抗压强度下降，因此，在实际应用中，须要根据具体需求优化聚合物乳液的掺量，以平衡混凝土的强度和工作性[44]。

2.3.3　作用机制

聚合物乳液能够改善水泥基材料的黏结、抗折、抗裂、防水、防渗等各种性能的主要原因是聚合物乳液粒子可以在水泥基材料中的干燥成膜。聚合物乳液粒子的成膜过程与聚合物的玻璃化转变温度密切相关。乳液粒子的玻璃化转变温度低则最低成膜温度低，反之亦然。一般来讲，乳液聚合物的玻璃化转变温度主要取决于该聚合物的分子结构、分子量以及聚集状态等。乳液的成膜过程如图5所示。由图可见，乳液粒子的成膜一般须经历水分蒸发及粒子聚集、乳液粒子变形以及分子扩散融合这几个过程。

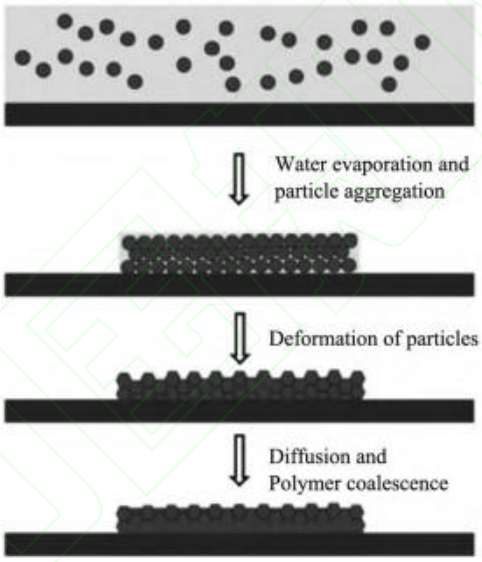

图5　乳液粒子成膜过程示意图

Fig. 5　Schematic diagram of film formation of polymer particles

将聚合物乳液拌合掺入水泥基材料中，乳液成膜后可封堵硬化水泥基材料中的孔隙与裂隙，改善水泥基材料的各种性能。水泥水化过程中聚合物乳液与水泥颗粒的相互作用如图6所示。由图可见，其微观结构演变可分为4个阶段：初始阶段，聚合物乳液掺入混凝土或砂浆后，乳液粒子均匀分散于水泥浆体基质中；随后进入吸附阶段，部分乳液粒子通过表面吸附作用附着于水泥颗粒表面或相互聚集堆积，形成物理屏障延缓水泥水化进程；随着水化反应的持续进行，体系自由水含量降低，乳液粒子在毛细管力作用下被限制于孔隙结构中，并在水泥水化产物表面形成具有黏结功能的聚合物薄膜层，有效桥接骨料界面及水化产物与未水化水泥颗粒的接触面；最终阶段，伴随水泥水化反应的深度发展，乳液粒子间残余水分被完全消耗，粒子通过融合形成三维连续聚合物网络结构。该互穿网络将水泥水化产物紧密联结，显著优化水泥石微观结构，从而提升复合材料的力学性能和耐久性[45]。

2.4　其他聚合物-混凝土复合材料的性能特点及作用机制

2.4.1　单体原位聚合水泥混凝土的性能特点及作用机制

单体原位聚合水泥混凝土的力学性能具有高度可控性，通过调节单体与水泥的比例以及引发剂与单体的比例，可优化材料的强度和韧性[46]。原位聚合技术能实现聚合物链在水泥基质中的均匀分布，

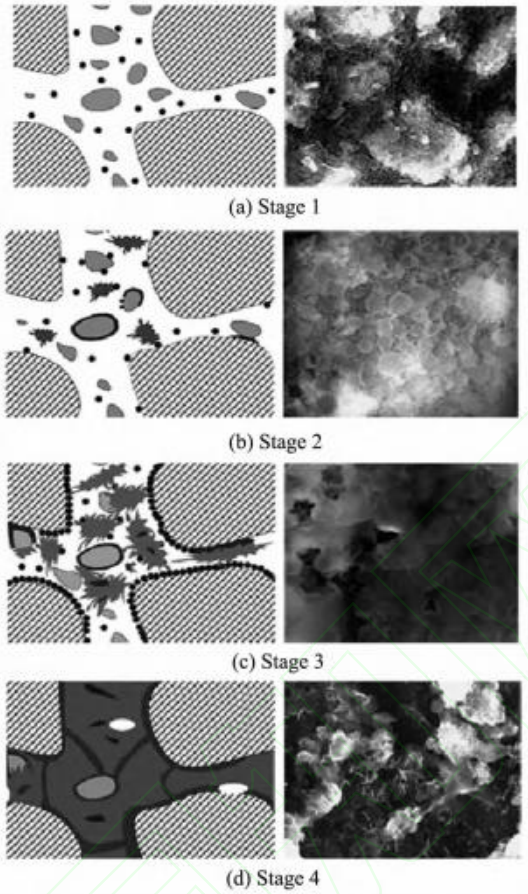

图6 水泥水化过程中聚合物乳液与水泥颗粒的相互作用[45]

Fig. 6 Interactions between polymer particles and cement during hydration

避免传统改性方法中聚合物相分离的问题,从而显著提升材料整体强度[47]。该技术对施工工艺和设备要求较高,且聚合反应速率和温度须精准控制,增加了施工复杂性与成本。此外,环境温度波动或反应速率不稳定可能导致聚合物网络形成不均匀,进而影响材料性能的稳定性,例如局部强度不足或耐久性下降。

其核心作用机制在于有机-无机协同效应:在水泥水化过程中,单体原位聚合形成的聚合物链与水泥水化产物(如C-S-H凝胶)通过化学键或物理缠绕紧密结合,增强了两相界面结合力[48]。同时,聚合物链在水泥基质中形成连续的三维网络结构,桥接水泥颗粒及水化产物,提升基体的整体性和抗裂性。聚合物链还能与C-S-H凝胶通过氢键或离子键相互作用,促进凝胶结构的致密化,进一步强化力学性能[47]。此外,水泥水化放热可为单体聚合提供能量,而聚合反应释放的热量又可能加速水化进程,形成动态协同反应机制,从而优化材料性能。

2.4.2 纤维增强水泥基复合材料的性能特点及作用机制

纤维增强水泥基复合材料的抗拉与抗折强度显著提升,尤其在短切纤维低掺量条件下,微米级纤维通过桥接微裂缝可有效提高早期抗裂性,但纤维掺量须严格控制,过量纤维可能导致基体密实性下降,抗压强度降低。此外,纤维与基体的界面黏结强度对材料性能影响敏感:黏结强度不足会导致界面脱黏,削弱荷载传递效率;黏结过强则可能引发纤维过早断裂,增加材料脆性风险[49]。纤维分散性亦是关键因素,掺量过高或分散不均会引发局部应力集中,降低复合材料整体性能。

纤维增强机制主要基于荷载传递与桥接作用:纤维通过界面黏结力将外部荷载传递至水泥基体,并在裂缝扩展时通过桥接作用延缓裂缝发展,从而提升材料韧性[50]。纤维与基体之间的粘结强度决定了纤维能否有效地将应力传递到基体中[18]。

3　结论与展望

聚合物-混凝土复合材料作为提升传统混凝土性能的重要创新方向，在材料设计、制备工艺及应用拓展方面已取得显著进展。为了满足建筑工程对高性能、环境友好及多功能材料的需求，仍须在以下方面深化研究：

1）材料优化与机制探索。须系统分析聚合物种类（如环氧树脂、聚酯树脂）、掺量梯度及界面改性对复合材料力学性能与耐久性的影响规律，结合分子动力学模拟揭示有机-无机协同增强机制。重点突破废旧塑料-橡胶表面能低、界面结合弱等瓶颈，开发高效预处理技术，提升其作为环保骨料的力学性能与稳定性。

2）工艺创新与成本控制。针对聚合物浸渍混凝土的高成本问题，优化真空浸渍与单体原位聚合工艺，实现孔隙填充率与反应速率的精准调控，降低能耗与材料损耗。推广低掺量高效益的聚合物改性混凝土，通过骨料级配设计与智能养护技术平衡抗压强度与施工便利性。

3）应用场景拓展与智能化发展。发挥聚合物混凝土耐腐蚀、抗冻融优势，扩大其在极地工程、深海设施及核废料存储等极端环境中的应用。结合人工智能技术开发自感知复合材料（如裂缝自修复、应力响应型聚合物基体），推动智能建筑与基础设施的革新。探索纤维增强基材在抗震结构中的延展性潜力，通过纤维定向排布与多尺度界面设计提升动态荷载下的能量吸收效率。

4）未来研究须以“性能-工艺-环境”协同优化为核心，深化多学科交叉融合，推动聚合物-混凝土复合材料向高性能化、功能化及绿色化方向发展，为现代建筑工程与可持续发展提供关键材料支撑。

利益冲突声明（Conflict of Interests）

所有作者声明不存在利益冲突。

All authors declare no relevant conflict of interest.

作者贡献（Authors’ Contributions）

卢子臣和刘丹婷负责综述的撰写和修改，刘丹婷和王磊负责文献资料的收集。

The review was written and revised by LU Zichen and LIU Danting. The literature was collected by LIU Danting and WANG Lei.

参考文献（References）

[1]创新驱动 主动求变 全面绿色转型 推动实现建材行业高质量发展：2024年建筑材料行业大会主旨报告[J]. 中国建材，2024，73(12)：22-29.
Innovation-driven，proactively seeking change，comprehensive green transformation，and promoting high-quality development in the building materials industry：keynote report of the 2024 building materials industry conference[J]. China Building Materials，2024，73(12)：22-29.

[2]熊剑平，申爱琴. 聚合物水泥混凝土改性机理研究[J]. 郑州大学学报(工学版)，2006，27(3)：15-20.
XIONG J P，SHEN A Q. Functional mechanism of the polymer cement concrete[J]. Journal of Zhengzhou University (Engineering Science)，2006，27(3)：15-20.

[3]OHAMA Y. Polymer-based admixtures[J]. Cement and Concrete Composites，1998，20(2/3)：189-212.

[4]衡艳阳，赵文杰. 聚合物改性水泥基材料的研究进展[J]. 硅酸盐通报，2014，33(2)：365-371.
HENG Y Y，ZHAO W J. Research development of polymer modified cement based materials[J]. Bulletin of the Chinese Ceramic Society，2014，33(2)：365-371.

[5]杨小利，王钧. 聚合物混凝土的应用及发展[J]. 玻璃钢/复合材料，1999(6)：47-48.
YANG X L，WANG J. Application and development of polymer concrete[J]. Fiber Reinforced Plastics/Composite，1999(6)：47-48.

[6] RIBEIRO M C S，TAVARES C M L，FIGUEIREDO M，et al. Bending characteristics of resin concretes[J]. Materials Research，2003，6(2)：247-254.

[7]BEDI R, CHANDRA R, SINGH S P. Mechanical properties of polymer concrete [J]. Journal of Composites, 2013, 2013(1): 1-12.

[8]ABDEL F H, MOETAZ E H. Flexural behavior of polymer concrete [J]. Construction and Building Materials, 1999, 13(5): 253-262.

[9]CAKIR F. Effects of resins on mechanical performance of polymer concrete[J]. Gradevinar, 2021, 72(10): 995-1006.

[10]廖光福, 丁志义, 袁天梦, 等. 聚合物混凝土的研究进展[J]. 胶体与聚合物, 2016, 34(2): 89-92.
LIAO G F, DING Z Y, YUAN T M, et al. Research progress of polymer concrete[J]. Chinese Journal of Colloid & Polymer, 2016, 34(2): 89-92.

[11]FOWLER D, HOUSTON J T, PAUL D R. Polymer-impregnated concrete surface treatments for highway bridge decks[J]. Journal of American Concrete Institute, 1973, 70: 93-118.

[12]CHEN C, HUANG R, WU J. Preparation and properties of polymer impregnated concrete[J]. Journal of the Chinese Institute of Engineers, 2007, 30(1): 163-168.

[13]CHEN W F, DAHL-JORGENSEN E. Polymer-impregnated concrete as a structural material[J]. Magazine of Concrete Research, 1974, 26(86): 16-20.

[14]SARDE B, PATIL Y D. Recent research status on polymer composite used in concrete: an overview [J]. Materials Today: Proceedings, 2019, 18: 3780-3790.

[15]AGGARWAL L K, THAPLIYAL P C, KARADE S R. Properties of polymer-modified mortars using epoxy and acrylic emulsions[J]. Construction and Building Materials, 2007, 21(2): 379-383.

[16]MOMTAZI A S, KOHANI K R, SABAGH M S. Polymers in concrete: applications and specifications[J]. European Online Journal of Natural and Social Sciences: Proceedings, 2015, 4(3): 62-72.

[17]GHAHSAREH F M, GUO P, WANG Y, et al. Review on material specification, characterization, and quality control of engineered cementitious composite (ECC)[J]. Construction and Building Materials, 2024, 442: 137699.

[18]于彬, 张元良, 徐一, 等. 短切玄武岩纤维增强水泥基复合材料力学性能研究[J]. 工业建筑, 2024, 54(6): 197-205.
YU B, ZHANG Y L, XU Y, et al. Mechanical properties of chopped basalt fiber-reinforced cement-based composites[J]. Industrial Construction, 2024, 54(6): 197-205.

[19]SINGH P, SINGH D N, DEBBARMA S. Macro- and micro-mechanisms associated with valorization of waste rubber in cement-based concrete and thermoplastic polymer composites: a critical review[J]. Construction and Building Materials, 2023, 371: 130807.

[20]张泽丰, 肖俊杰, 何淋, 等. 废弃塑料影响水泥基复合材料性能的研究现状[J]. 交通世界, 2021(20): 1-3.
ZHANG Z F, XIAO J J, HE L, et al. Research status of waste plastics affecting the properties of cement-based composites [J]. Transport World, 2021(20):1-3.

[21]范梦婷, 彭靖. 橡胶在建筑行业中回收利用的意义与价值[J]. 科技经济市场, 2017(9): 193-195.
FAN M T, PENG J. Significance and value of rubber recycling in construction industry[J]. Science & Technology Ecnony Market, 2017(9): 193-195.

[22]KIRLIKOVALI E. Polymer/concrete composites: a review[J]. Polymer Engineering & Science, 1981, 21(8): 507-509.

[23]NGO T, TONTM, HOA S, et al. Effect of temperature, duration and speed of pre-mixing on the dispersion of clay/epoxy nanocomposites[J]. Composites Science and Technology, 2009, 69(11/12): 1831-1840.

[24]DEHGHANI N M A, HERAS M D, SOLIMAN E, et al. Early-age strength and failure characteristics of 3D printable polymer concrete[J]. Construction and Building Materials, 2023, 394: 132119.

[25]ELALAOUI O, GHORBEL E, MIGNOT V, et al. Mechanical and physical properties of epoxy polymer concrete after exposure to temperatures up to 250 ℃[J]. Construction and Building Materials, 2012, 27(1): 415-424.

[26]VIPULANANDAN C, DHARMARAJAN N. Effect of temperature on the fracture properties of epoxy polymer concrete[J]. Cement and Concrete Research, 1988, 18(2): 265-276.

[27]HEIDARNEZHAD F, JAFARI K, OZBAKKALOGLU T. Effect of polymer content and temperature on mechanical properties of lightweight polymer concrete[J]. Construction and Building Materials, 2020, 260: 119853.

[28]SHOKRIEH M M, HEIDARI R M, SHAKOURI M, et al. Effects of thermal cycles on mechanical properties of an optimized polymer concrete[J]. Construction and Building Materials, 2011, 25(8): 3540-3549.

[29]JO B W, PARL S K, PARK J C. Mechanical properties of polymer concrete made with recycled PET and recycled concrete aggregates[J]. Construction and Building Materials, 2008, 22(12): 2281-2291.

[30]AGAVRILOAIE L, OPREA S, BARBUTA M, et al. Characterization of polymer concrete with epoxy polyurethane acryl matrix[J]. Construction and Building Materials, 2012, 37(12): 190-196.

[31]MARTINEZB G, VIGUERASS E, GENCEL O, et al. Polymer concretes: a description and methods for modification and improvement[J]. Journal of Materials Education, 2011, 33(1): 37-52.

[32]VIDIL T, TOURNILHAC F, MUSSO S, et al. Control of reactions and network structures of epoxy thermosets[J]. Progress in Polymer Science, 2016, 62(11): 126-179.

[33]FERDOUS W, MANALO A, WONG H S, et al. Optimal design for epoxy polymer concrete based on mechanical properties and durability aspects[J]. Construction and Building Materials, 2020, 232: 117229.

[34]GUPTA S, SINGH R C. Evaluation of concrete properties with impregnated different polymers [J]. International Research Journal of Engineering and Technology, 2018, 5(12): 1097-1102.

[35]谈慕华. 聚合物浸渍混凝土的增强与韧化[J]. 混凝土及建筑构件, 1980(4): 34-39.
TAN M H. Strengthening and toughening of polymer impregnated concrete[J]. Concrete, 1980(4): 34-39.

[36]PLANK J, GRETZ M. Study on the interaction between anionic and cationic latex particles and Portland cement[J]. Colloids and Surfaces A: Physicochemical and Engineering Aspects, 2008, 330(2): 227-233.

[37]KONG X M, EMMERLING S, PAKUSCH J, et al. Retardation effect of styrene-acrylate copolymer latexes on cement hydration[J]. Cement and Concrete Research, 2015, 75(9): 23-41.

[38]LU Z C, KONG X M, ZHANG C Y, et al. Effect of colloidal polymers with different surface properties on the rheological property of fresh cement pastes[J]. Colloids and Surfaces A: Physicochemical and Engineering Aspects, 2017, 520: 154-165. 5.

[39]ZHANG C Y, ZHANG S F, YU J W, et al. Water absorption behavior of hydrophobized concrete using silane emulsion as admixture[J]. Cement and Concrete Research, 2022, 154: 106738.

[40]LU Z C, KONG X M, ZHANG C Y, et al. Effect of highly carboxylated colloidal polymers on cement hydration and interactions with calcium ions[J]. Cement and Concrete Research, 2018, 113: 140-153.

[41]SHI C, ZOU X W, YANG L, et al. Influence of humidity on the mechanical properties of polymer-modified cement-based repair materials[J]. Construction and Building Materials, 2020, 261: 119928.

[42]SHI C, WANG P, MA C Y, et al. Effects of SAE and SBR on properties of rapid hardening repair mortar[J]. Journal of Building Engineering, 2021, 35: 102000.

[43]WANG R, WANG P M, LI X G. Physical and mechanical properties of styrene-butadiene rubber emulsion modified cement mortars [J]. Cement and Concrete Research, 2005, 35(5): 900-906.

[44]CHEN B, LIU J Y. Mechanical properties of polymer-modified concretes containing expanded polystyrene beads [J]. Construction and Building Materials, 2007, 21(1): 7-11.

[45]OHAMA Y. Principle of latex modification and some typical properties of latex modified mortars and concretes [J]. ACI Materials Journal, 1987, 84(6): 511-518.

[46]CHEN B M, QIAO G, HOU D S, et al. Cement-based material modified by in-situ polymerization: from experiments to molecular dynamics investigation [J]. Composites Part B: Engineering, 2020, 194: 108036.

[47]WU K, LONG J F, QING L B, et al. Recent advance of monomer in situ polymerization modified cement-based materials [J]. Construction and Building Materials, 2024, 432: 136542.

[48]YIN B, HUA X L, QI D M, et al. Performance cement-based composite obtained by in situ growth of organic-inorganic frameworks during the cement hydration[J]. Construction and Building Materials, 2022, 336: 127533.

[49]魏瑞丽, 李泽文, 刘德华, 等. 有机纤维增强水泥基复合材料研究进展[J]. 当代化工, 2024, 53(2): 460-463.
WEI R L, LI Z W, LIU D H, et al. Research progress of organic fibre reinforced cementitious composites[J]. Contemporary Chemical Industry, 2024, 53(2): 460-463.

[50]WANG Y J, BACKER S, LI V C. An experimental study of synthetic fibre reinforced cementitious composites[J]. Journal of Materials Science, 1987, 22(12): 4281-4291.

Research progress on concrete-polymer composites

LU Ziche, *LIU Danting*, *WANG Lei*

School of Materials Science and Engineering, Tongji University, Shanghai 200082, China

Abstract

Significance Concrete, a dominant construction material, often fails to achieve its designed service life and mechanical strength due to its inherent brittleness, high porosity, and susceptibility to various environmental stressors such as freeze-thaw cycles, chemical attacks, and moisture ingress. These constraints have driven continuous research on improving its durability and performance. Among various modification techniques, the incorporation of polymers into cement-based materials has emerged as a promising solution. Polymers, serving as organic additives, can significantly enhance concrete's flexibility, bonding properties, and resistance to cracking and degradation. The potential of polymers to improve the mechanical behavior and durability of concrete has attracted increasing interest from both scientific and engineering communities. Polymer-modified concrete systems are being explored for a wide range of applications, including infrastructure development, road and bridge construction, marine structures, and the rehabilitation and repair of aging facilities. A comprehensive understanding of how polymers affect the rheology, strength development, and long-term performance of concrete is essential for optimizing their use and maximizing their potential in sustainable construction.

Progress This paper comprehensively reviews the classification, preparation, and performance characteristics of concrete-polymer composites. It begins by categorizing polymer-concrete systems into four major types: polymer concrete (PC), polymer-impregnated concrete (PIC), polymer-modified concrete (PMC), and newly developed polymer-based composites. Each type exhibits unique features in terms of composition, preparation methods, and applications. For instance, PC is a composite where polymer resin entirely replaces traditional cement as the binder, achieving superior strength and chemical resistance. PIC involves the impregnation of hardened concrete with monomers that are then polymerized, enhancing impermeability and durability. PMC, the most widely used in practical applications, combines polymers with conventional cement paste to improve the overall performance at a relatively low cost. Furthermore, the paper examines how polymers influence workability, hydration behavior, mechanical properties, and durability.

Conclusions and Prospects Research findings indicate that both PC and PIC systems provide exceptional mechanical and durability performance. However, their widespread adoption is hindered by challenges such as elevated material costs, energy-intensive curing requirements, and complex fabrication techniques. In comparison, PMC offers a more viable solution for real-world applications due to its ease of implementation and cost-effectiveness. In addition to traditional systems, this review explores the potential of next-generation concrete-polymer composites. These encompass in-situ polymerized systems that achieve high strength but face challenges in reaction control, fiber-reinforced polymer composites that offer excellent toughness but are susceptible to fiber dispersion and dosage, and sustainable alternatives like waste plastic or rubber-modified concrete, which provide environmental benefits but are constrained by limitations in structural performance. Future research should prioritize addressing the interfacial interactions between polymers and cement hydrates, a critical factor influencing the composite's overall behavior. Moreover, innovation in eco-friendly and recyclable polymer materials is essential for advancing green and sustainable construction. Through interdisciplinary approaches that integrate material science, chemistry, and structural engineering, concrete-polymer composites can be further developed to meet the evolving demands of contemporary infrastructure.

Keywords: concrete-polymer composites; cementitious materials; mechanism

(责任编辑:赵雁)

聚合物掺量梯度变化对水泥砂浆性能的影响

潘晔[1,2] 卢子臣[1,2*]

(1. 同济大学 先进土木工程材料教育部重点实验室，上海 201084；2. 同济大学 材料科学与工程学院，上海 201084)

摘要：本文通过在同一水泥砂浆样品不同层深设计不同聚合物掺量，研究了聚合物掺量梯度变化对水泥砂浆的抗压强度、抗折强度、粘结强度和抗冻性能的影响。结果表明，在乳液总掺量相同的情况下，相较于普通聚合物改性水泥砂浆，水泥砂浆中聚合物梯度变化可显著提高砂浆整体的抗压、抗折和粘结强度，水泥砂浆弹性模量的变化规律与抗压强度相同。在抗冻性方面，水泥砂浆的质量损失率、强度损失率和吸水率随聚合物掺量提高而降低，聚合物掺量梯度变化使其抗冻性稍高于同掺量下普通聚合物乳液改性水泥砂浆。

关键词：土木工程材料；梯度变化；水泥砂浆；性能评价

The Influence of Gradient Change in Polymer Content on the Properties of Cement Mortar

Ye Pan[1,2] Zichen Lu[1,2*]

(1. Key Laboratory of Advanced Civil Engineering Materials of Ministry of Education, Tongji University, Shanghai 201804; 2. School of Materials Science and Engineering, Tongji University, Shanghai 201804)

Abstract: In this article, the influence of gradient changes in polymer content on the compressive strength, flexural strength, bonding strength, and frost resistance of cement mortar was investigated by designing different polymer dosages at different depths of the same cement mortar sample. The results show that when the total content of latex is the same, compared with ordinary polymer modified cement mortar, the change of polymer gradient in cement mortar can significantly improve the compressive strength, flexural strength and bonding strength of mortar as a whole. the change rule of elastic modulus of cement mortar is the same as that of compressive strength. In terms of frost resistance, the mass loss rate, strength loss rate and water absorption rate of cement mortar decrease with the increase of polymer content. The gradient change of polymer content makes its frost resistance slightly higher than that of ordinary polymer lotion modified cement mortar at the same content.

Key words: Civil engineering materials; Gradient design; Polymer cement mortar; performance evaluation

1 引言

作者简介 卢子臣，男，副教授，Email：luzc@tongji.edu.cn；潘晔，男，硕士生，Email:2130616@tongji.edu.cn

水泥基材料因其力学性能优异，价格低廉因而成为世界上应用最广泛的建筑材料之一。聚合物乳液，作为一种常用的水泥外加剂，常被用于提高水泥砂浆的抗折强度、粘结强度和抗冻性能，被广泛应用于混凝土裂缝修补，聚合物修补砂浆等领域[1,2]。

目前，对于聚合物乳液改性砂浆，国内外专家学者主要聚焦于乳液的种类和掺量对于水泥砂浆力学和耐久性能的影响及其作用机理。李建等人研究了丁苯乳液对水泥砂浆的力学性能和体积密度的影响，结果表明，丁苯乳液降低了水泥砂浆的抗压强度、体积密度和动弹性模量，但提高了其韧性[3]。王培铭等人指出，苯丙乳胶粉降低了水泥砂浆的抗压强度但明显提高了水泥砂浆的抗折和粘结抗拉强度[4]。王晓林等人认为可以显著提高砂浆的抗折强度、粘结强度，韧性和抗冻性，（醋酸乙烯－乙烯共聚物）VAE 乳胶粉改性水泥砂浆配合比的最佳掺量为 10%（质量分数）[5]。贺晓宇等人对比研究了氯丁乳液和苯丙乳液在不同掺量下对水泥砂浆 7 天和 28 天抗压、抗折以及抗冻性的影响，结果表明，苯丙乳液提高了砂浆的抗折强度，降低了其抗压强度，综合力学性能指标增加，对砂浆的改性效果明显优于氯丁乳液[6]。王茹等人研究了丁苯橡胶、苯乙烯丙烯酸酯和聚丙烯酸酯对硫铝酸盐水泥（CSA）的影响，结果表明，聚合物乳液对 CSA 水泥砂浆具有良好的减水效果和缓凝性能，SBR 胶乳改性砂浆在强度、失重、吸水性、抗渗性等方面表现最好[7]。一般认为，聚合物乳液会在水泥砂浆内成膜，形成有机-无机互穿网络结构，填充了砂浆内部的孔隙，进而改善水泥砂浆的韧性和耐久性[8,9]。

综合国内外研究来看，有关梯度结构设计对聚合物乳液改性水泥砂浆的研究较少，由于传统的制备工艺乳液掺量大，成本较高，因此本文聚焦于结构设计，通过在水泥砂浆不同层深处设计不同聚合物掺量，研究聚合物掺量梯度变化对水泥砂浆的抗压强度、抗折强度、粘结强度和抗冻性能的影响，以期能够在保证性能的同时降低掺量，提高效益，为聚合物乳液改性砂浆结构设计方面的研发提供理论指导。

2 原材料及试验方法

2.1 原材料与配合比

水泥采用曲阜中联水泥有限公司产 P・I 42.5 硅酸盐水泥，主要成分见表 1。聚合物乳液选用苯丙乳液（SA），由巴斯夫股份公司提供，固含量为 50%，Zeta 电位为-26.2mV，粒径为 189.2nm（由马尔文 Zetasizer Nano ZS 测得）。为一定程度上避免 SA 乳液在水泥浆体中的引气作用，采用 AF6203 消泡剂，掺量为 0.1%。试验水灰比为 0.45，砂灰比为 3（标准砂），非梯度乳液掺量分别为 0%（Ref），4%，8%和 12%。本试验将砂浆分为上层，中层和下层三个部分，并采用三分和六分两种梯度设计方法，具体聚合物掺量梯度示意详见图 1。其中，三分（D/3）相对应的聚合物掺量为 8%，六分（D/6）相对应的聚合物掺量为 4%。

表 1 水泥主要化学成分（wt.%）

Materials/Oxide	SiO_2	Al_2O_3	Fe_2O_3	CaO	MgO	TiO_2	SO_3	K_2O	MnO	P_2O_5
Cement	20.64	5.15	3.76	60.24	1.61	0.43	3.38	0.67	0.27	0.31

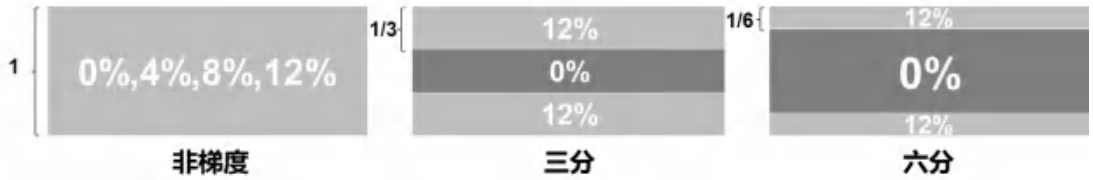

图 1 聚合物掺量梯度示意图

本试验设置 6 组样品，具体配合比如表 2 所示。

表 2 梯度聚合物改性水泥砂浆配合比

样品	水泥（克）	砂（克）	水（克）	乳液（克）	消泡剂（g）
Ref	450	1350	202.5	0	0.45
SA-04	450	1350	184.5	18	0.45
SA-08	450	1350	166.5	36	0.45
SA-12	450	1350	148.5	54	0.45
SA-D/3	450	1350	166.5	**36**	0.45
SA-D/6	450	1350	184.5	**18**	0.45

2.2 试验方法

样品制备：本试验采用符合 JJ-7 型行星式水泥砂浆搅拌机。在搅拌锅中分别依次加入水泥、乳液、水和消泡剂后，搅拌机自动完成一次低速 30 秒、再低速 30 秒同时自动加砂结束、高速 30 秒、停 90 秒、高速 60 秒后停止转动的工作程序以混匀浆体。搅拌完毕后于模具中（40 mm×40 mm×160 mm）浇注成型，其中三分样品与六分样品采用分层浇铸，每浇铸一层振动 30 次继续浇铸。样品成型 24 h 后脱模，在标准养护室中养护 3，7，28 d 后取出。

力学强度测试：通过 WHY-300 压力机，根据 GB/T17671-1999《水泥胶砂强度检验方法(ISO 法)》测定水泥砂浆强度，其中加载速度为 2.4kN/s。

拉伸粘结强度测试：通过 SLD-5000 拉拔试验机，采用根据 JGJ/T 70-2009《建筑砂浆基本性能试验方法》测定水泥砂浆拉伸粘结强度，其中加载速度为 10mm/min。

弹性模量测试：参考 JGJ/T 70-2009《建筑砂浆基本性能试验方法标准》，进行水泥砂浆弹性模量试验，试件使用 160 mm×40 mm×40 mm，程序设定为 3 MPa 到 1/3P_{max} MPa 循环三次，取最后一次形变为结果。

抗冻性测试：参考 JGJ/T 70-2009《建筑砂浆基本性能试验方法标准》，进行水泥砂浆抗冻性试验。

吸水率测试：在烘箱 40℃干燥至恒重，放入水中至规定时间，取出后擦去表面浮水，测其重量，得到吸水率。

3 结果与分析

3.1 力学强度

图 2（a）和图 2（b）分别为不同 SA 乳液掺量对水泥砂浆抗折强度和抗压强度的影响。由图可知，随着乳液的掺量增加，砂浆的抗折强度和抗压强度均有不同程度的下降。关于这一点，不同研究人员有着不同的观点。有些学者认为苯丙乳液和丁苯乳液改性水泥砂浆均会造成其力学强度的降低[3,10,11]，而孟博旭则发现苯丙乳液和 VAE 乳液提高了水泥砂浆的抗折强度[12]。一般认为，乳液对水泥砂浆抗折强度的提高源自于其在水泥中形成了具有一定强度和低模量的膜，从而形成了互穿网络结构[13]，而 SA 乳液对砂浆力学性能造成的不利影响主要是由于乳液阻碍了水泥的水化且粗化了水泥砂浆的孔隙，显著增加了硬化砂浆的孔隙率[3]。

在相同的总聚合物掺量下，SA-D/3（8%）和 SA-D/6（4%）的抗折和抗压强度均显著高于非梯度样品，这可能是由于乳液掺量的减少，梯度改性砂浆的中间层水化较为彻底，结构更为密实，因而起到了支撑整体强度的作用。

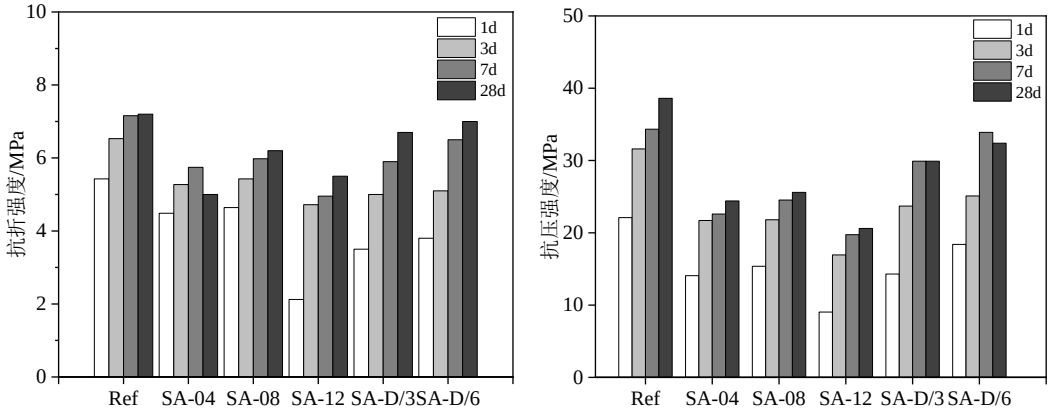

(a) (b)

图 2 梯度聚合物改性砂浆的力学性能；(a)抗折强度；(b)抗压强度

梯度聚合物改性砂浆的弹性模量如图 3 所示，弹性模量变化的规律与抗压强度类似，首先乳液的加入迅速降低了水泥的弹性模量，这是由于聚合物膜本身的低模量所致[14]，而 SA-08 的提高则可能与其形成了较多的互穿网络结构，填充了孔隙。当聚合物掺量增加到 12%时，水泥的水化被严重抑制，因而整体的弹性模量降低，这说明乳液可显著提高水泥砂浆的韧性[13]。

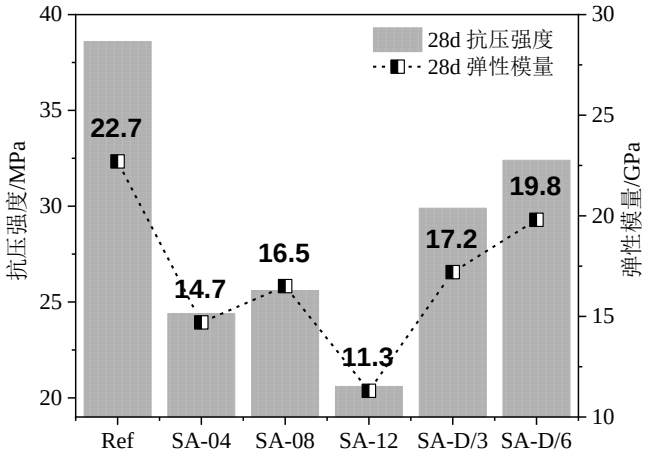

图 3 梯度聚合物改性砂浆的弹性模量

3.2 粘结强度

图 4 是梯度聚合物对砂浆拉伸粘结强度的影响。首先，SA 乳液能显著提高水泥砂浆的粘结强度，且随着聚合物掺量的提高而提高，但增加的幅度则较为减缓。乳液对粘结强度的提高主要归因于两点：一是乳液本身能在水泥产物之间形成桥接，二是乳液本身具有较好的粘附性[15]。

梯度掺量的设计几乎不会对粘结强度产生负面的影响，SA-D/3 和 SA-D/6 与 SA-12 的粘结强度相当，且显著高于同掺量下的 SA-08 和 SA-04。这是由于经过梯度聚合物掺量的设计，聚合物主要富集在上层和下层中，这是决定粘结强度的核心部分，而较为薄弱的中间层几乎成为断裂面，因此，梯度掺量不会降低砂浆的粘结强度。

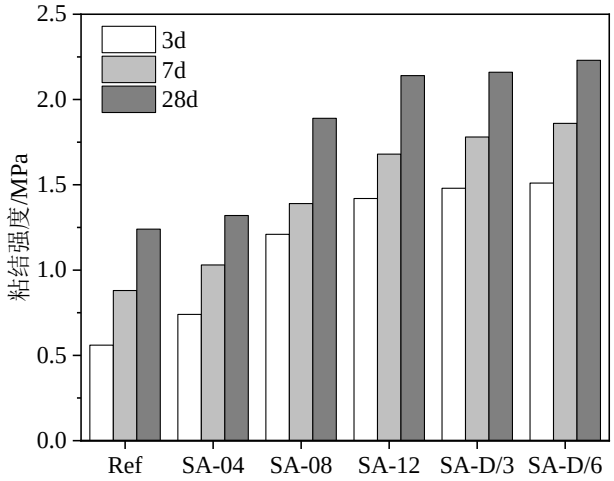

图 4 梯度聚合物改性砂浆的拉伸粘结强度

3.3 抗冻性

图 5 是梯度聚合物对砂浆抗冻性的影响。由图可知，SA 乳液显著提高了水泥砂浆在冻融循环后的强度损失率和质量损失率，且砂浆的抗冻性与砂浆中乳液的总掺量成正相关。图 6 是梯度聚合物对砂浆吸水率的影响，其规律与强度损失率的变化规律相符。

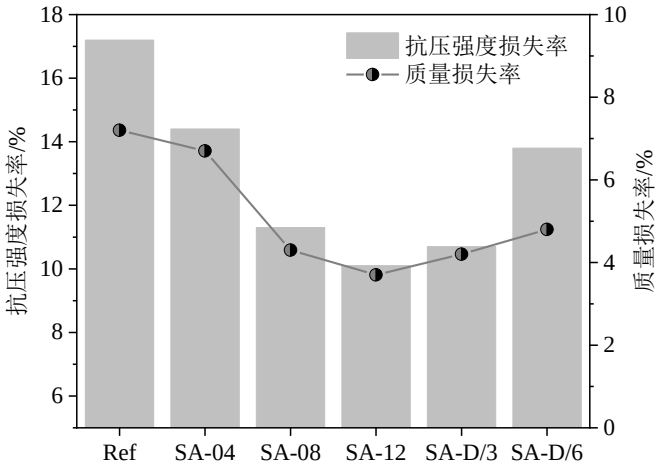

图 5 梯度聚合物改性砂浆的强度/质量损失率

乳液对于抗冻性的提高可以从三个方面解释：首先，乳液粒子的填充作用使得砂浆更密实，从而减小了砂浆孔隙可容纳的水分，结冰膨胀也随之减小，砂浆抗冻性提高；其次，乳液粒子的填充作用阻碍了水分的迁移，砂浆具有更好的耐水性；最后，互穿网络结构增加了乳液的密实性[5,16]。

当总掺量相同时，SA-D/3 和 SA-D/6 的抗冻性稍强于对应未梯度改性砂浆的抗冻性，吸水率则相反，这可能与梯度结构设计引起的不同层孔径分布有关，具体原因需要进一步研究。

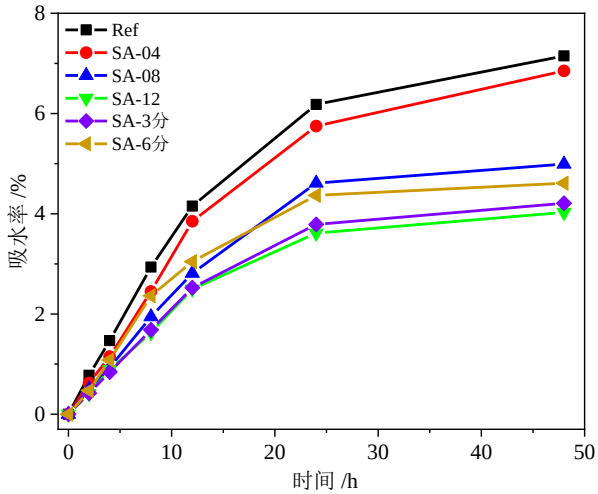

图 6 梯度聚合物改性砂浆的吸水率

4 结论

（1）SA 乳液对水泥砂浆的力学强度有不利的影响，砂浆的弹性模量与抗压强度均随乳液掺量的提高而降低。在相同的掺量下，梯度掺量聚合物改性砂浆的力学性能高于未梯度改性的砂浆。在乳液总掺量减少的情况下，砂浆的拉伸粘结强度并未出现下降，这是由于梯度聚合物掺量的设计使得乳液在基体界面处富集。

（2）水泥砂浆的抗冻性和吸水率则主要与乳液的总掺量相关，梯度设计后的聚合物改性砂浆，其抗冻性稍强于对应未梯度改性砂浆的抗冻性。

（3）聚合物掺量的梯度设计能够在保证性能的条件下有效地减少聚合物的用量，为聚合物改性砂浆的低成本高效能应用提供了一种解决方案。

5 参考文献

[1]蔡胜华,唐丽芳.聚合物水泥砂浆在混凝土修补中的应用研究[J].长江科学院院报,2007(01):44-46+60.

[2]郭浩,杭鑫坤.适于喷射的聚合物修补砂浆研究[J].新型建筑材料,2016,43(08):70-73.

[3]李建,王培铭,王茹.丁苯乳液改性水泥砂浆的力学性能与体积密度[J].建筑材料学报,2005,(06):705-709.

[4]王培铭,刘恩贵.苯丙共聚乳胶粉水泥砂浆的性能研究[J].建筑材料学报,2009,12(03):253-258+265.

[5]王晓林,冯红春,周凯.VAE 乳胶粉改性水泥砂浆的配合比优化及抗冻性研究[J].硅酸盐通报,2023,42(10):3462-3469.

[6]贺晓宇.氯丁乳液与苯丙乳液掺量对水泥砂浆性能的影响研究[J].路基工程,2017,(04):136-140.

[7] Li L, Wang R, Lu Q. Influence of polymer latex on the setting time, mechanical properties and durability of calcium sulfoaluminate cement mortar[J]. Construction and Building Materials,2018,169.

[8]王培铭,赵国荣,张国防.聚合物水泥混凝土的微观结构的研究进展[J].硅酸盐学报,2014,42(05):653-660.

[9]张娜,董文乔,王婉申等.聚合物粉末对水泥砂浆抗冻性能的影响研究[J].混凝土世界,2023,(07):32-39.

[10]姜博,郑璐.不同掺量的苯丙乳液对砂浆力学性能影响[J].北方建筑,2018,3(04):68-70.

[11]许绮,王培铭.桥面用丁苯乳液改性水泥砂浆物理性能的研究[J].建筑材料学报,2001,(02):143-147.

[12]孟博旭,许金余,顾超等.苯丙乳液和 VAE 乳液改性水泥砂浆力学性能的试验研究[J].建筑科学,2019,35(01):88-94.

[13]衡艳阳,赵文杰.苯丙乳液改性水泥基材料性能及机理研究进展[J].硅酸盐通报,2014,33(06):1431-1438

[14]王培铭,许绮,J.Stark.桥面用丁苯乳液改性水泥砂浆的力学性能[J].建筑材料学报,2001,(01):1-6.

[15]张水,于洋,宁超,李国忠.苯丙乳液改性水泥砂浆的性能研究[J].混凝土与水泥制品,2010,(02):9-12.

[16]李悦,何赫.聚合物改性水泥砂浆的研究进展[J].功能材料,2016,47(07):7038-7045.

Annex 2 : Rilem Conference paper

Research on gradient-enhanced polymer-modified concrete for structural use and comparison with conventional concrete

Ye Pan [1], Zichen Lu [1*], Lei Wang [1].

[1] Key Laboratory of Advanced Civil Engineering Materials, Ministry of Education, School of Materials Science and Engineering, Tongji University, Shanghai 201804, China
luzc@tongji.edu.cn

Abstract. The varied damage faced by concrete pavement can be effectively alleviated by adding polymer latex. However, the high dosage required and the high prices limit their application in concrete. Compared to the middle part in the concrete pavement, the top and ground parts are easier to break, and more polymers should be concentrated in these key areas. Therefore, realizing the gradient distribution of polymers in concrete pavements may be a potential option to break its technological bottleneck. In this study, a damage model for concrete pavement was constructed to investigate the effect of polymer gradient distribution on the performance of concrete. The result shows that the gradient enrichment of the polymer was favorable to the reduced interlayer loss of concrete. Based on this conclusion, a newly designed latex with great magneto-responsive property was prepared to realize the polymer gradient distribution in cement-based materials. Afterward, a device for applying an external magnetic field was designed and developed. The subsequent result indicates that the mechanical performances of mortar or concrete with a gradient structure exhibit higher mechanical properties and abrasion resistance. Besides, the local enrichment of polymer significantly reduces the cracks in concrete pavement.

Keywords: Pavement concrete, magneto-responsive polymer latex, mechanical properties, damage model.

1 Introduction

The designed service life of concrete pavement is about twice that of asphalt pavement. Still, the cost is only half that of asphalt pavement, so from the perspective of resource conservation and environmental protection, undoubtedly, concrete pavement should be greatly developed and used for high-grade roads. However, in China, the application of concrete pavement for high-grade roads only accounts for about 5% of the total pavement, which is far behind the ratio in other developed countries [1]. The reasons for the limited application of concrete pavement can be attributed to the following problems [2]: 1) fast damage and significantly reduced service life due to restrictions in pavement theory and materials; 2) difficulties in maintenance; 3) high

maintenance costs. Therefore, to promote the application of concrete pavement in high-grade roads, it is urgent to develop advanced pavement theory and new materials to greatly prolong the service life and increase the durability of the concrete pavement.

It is commonly accepted that the addition of polymer to the concrete can greatly improve the toughness and bonding strength of concrete [3,4]. Meanwhile, polymer-modified concrete (PMC) possesses many other outstanding properties, such as excellent wear resistance, corrosion resistance, freeze-thaw resistance, etc [5-7]. Therefore, the application of PMC is an important and efficient way to solve the rapid damage of concrete pavement and increase its durability. However, the high cost of polymers is a strong obstacle limiting their mass application.

Considering the stress distribution of concrete pavement under load pressure, the top part of the pavement bears strong shear stress and pressure stress, while the ground part suffers strong tensile stress [8]. Hence, compared to the middle part of the concrete pavement, the top and bottom parts are easier to break, and more polymers should be concentrated in these key areas. Based on this, it is more and more necessary to realize the local enrichment of polymer in the key areas of concrete pavement and achieve a gradient structure (a structure with a gradient distribution of polymer content) inside the pavement, which on the one hand can improve the performance of concrete pavement, and on the other hand, greatly decrease the amount of polymer admixture used and reduce the construction cost of road pavement. Unfortunately, however, limited work was done to realize the gradient distribution of polymer to enhance the properties of concrete pavement.

In this study, based on the problem above, a damage model for concrete pavement was constructed to investigate the effect of polymer distribution on the performance of concrete pavement. Besides, a newly designed magneto-responsive polymer latex and a device for applying a magnetic field were developed to reach the gradient distribution of polymer in the concrete. Finally, the comprehensive performance of mortar and concrete with the addition of magneto-responsive polymer latex have been further comprehensively evaluated. This study aims to provide a new approach for the better application of polymer latex in concrete pavement.

2 Materials and methods

2.1 Raw materials

Portland cement PI 42.5 used in this study was provided by Fushun Orcel Technology Co., Ltd. Cenosphere and silica fume in this study were purchased from Henan Zhuangwei New Material Co., Ltd. River sand with a fineness modulus of 2.5 was used as fine aggregate; basalt gravel with a maximum particle size of 25 mm was used as coarse aggregate. The water reducing agent with a solid content of 40% used in this study was provided by Shanxi Jiawei New Material Co., Ltd. The chemical composition of cement was measured via X-ray fluorescence (XRF), and its mineralogical composition was obtained by using XRD Rietveld refinement.

$FeCl_3 \cdot 6H_2O$, $FeCl_2 \cdot 4H_2O$, $NH_3 \cdot H_2O$, HCl, ethanol and sodium oleate, sodium dodecylbenzene sulfonate (SDBS), Styrene (St), n-butyl acrylate (BA), 2-acrylamido-2-methylpropane sulfonic acid (AMPS), acrylamide (AM), hexadecane (HD), azobisisobutyronitrile (AIBN) and divinylbenzene (DVB) with analytical purity were provided from Sinopharm Chemical Reagent Co., Ltd.

Table 1. The chemical and mineralogical composition of cement. (Unit: %)

Chemical composition	OPC	Mineralogical composition	OPC
SiO_2	20.64	C_3S	60.72
Al_2O_3	5.15	C_2S	16.56
Fe_2O_3	3.76	C_3A	6.72
CaO	63.24	C_4AF	8.28
MgO	1.61	Gypsum	3.64
TiO_2	0.43	Anhydrite	0.98
SO_3	3.38	f-CaO	0.9
Other	1.12	Other	2.2

2.2 Experimental methods

2.2.1 Finite element construction

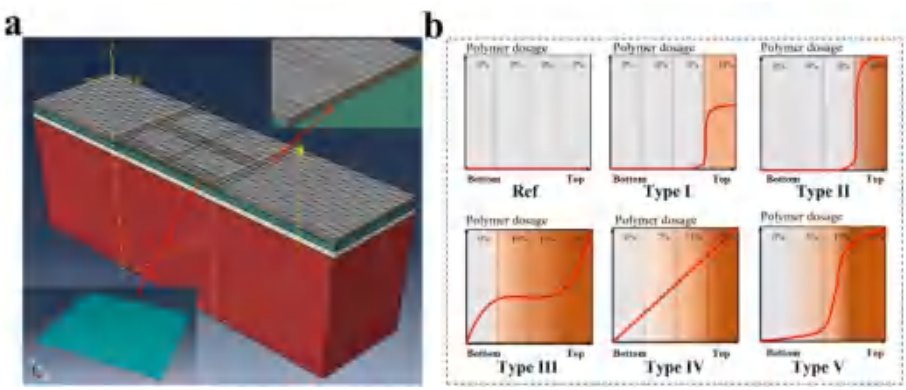

Fig. 1 (a) The finite element model of PC pavement and (b) Polymer distribution in Concrete pavement.

A finite element model of jointed plain concrete (PC) pavement incorporating contraction joints and dowel bars was established using ABAQUS simulation software, which is described by Fig. 1(a). The concrete slab was configured with standard planar dimensions of 5.00 m × 4.00 m and a thickness of 0.24 m. The overall structure of the road surface is a strip structure characterized by the direction of travel, with the vertical direction being regarded as infinite, and the lateral width is limited. A constant pavement width was kept throughout numerical simulations. The three-slab system configuration was implemented to balance computational efficiency and precision

in finite element analysis. Building upon the conventional PC pavement model, the surface layer was partitioned into four equal-depth strata with differentiated material properties.

To simulate the gradient increase in polymer content in strata from bottom to top, progressive material parameter modifications were applied across layered concrete elements. This multi-layer modeling approach enables systematic investigation of interlayer damage behavior and surface layer mechanical behavior under vehicular loading conditions corresponding to varying polymer dosage. Based on this, six types of concrete pavements with different gradient variations of latex admixture were set up.

2.2.2 Preparation and characterization of magneto-responsive polymer latex

The preparation methodology for magneto-responsive latex has been comprehensively documented in prior research. This production protocol comprises two distinct operational phases. Initially, magnetic fluids were prepared through co-precipitation techniques. Subsequently, the magneto-responsive polymer latex was synthesized via microemulsion polymerization.

Table 2. The detailed component for the polymerization of latex (Unit: g)

Magnetic fluid (60%)	Monomer				Surfactant	Initiator	DI water
	Main monomer	Functional monomer	DVB	HD			
28	St 18.86 BA 35.26	AMPS 1.16 AM 1.16	0.3	1.16	4.64	AIBN 0.56	104

During experimental execution, predetermined quantities of synthesized ferrofluid (28 g), amphiphilic stabilizers (2.32 g), and deionized water (46 g) were stirred (200 rpm, 25 °C, 2 min) and ultrasonically dispersed (30 min) to reach homogenization. The reaction system was then incorporated with monomers: styrene (3.77 g), butyl acrylate (7.05 g), AMPS (0.23 g), acrylamide (0.23 g), divinylbenzene (0.06 g), hexadecane (0.23 g), and additional water (2.4 g). This mixture underwent continuous mixing (300 rpm, 25°C, 2 h) before initiating polymerization through radical initiator introduction (0.112 g) under elevated thermal conditions (90°C, 300 rpm, 1 h).

The residual monomer fraction (46.32 g), pre-emulsified with the remaining surfactant (2.32 g) and DI water (55.6 g), was titrated within 4 h (90°C, 300 rpm). Concurrently, the remaining initiator solution (0.448 g) was gradually added within 4.5 h to complete the polymerization sequence. The detailed component for the polymerization of latex is tabulated in Table 2.

The micro morphology of prepared polymer particles was observed via transmission electron microscope (TEM, FEI Tecnai F20, USA). Specifically, a magneto-responsive polymer latex diluted to 1% is added dropwise to a carbon-covered copper grid. Imaging was performed after complete solvent evaporation under ambient conditions. Monomer copolymerization efficiency was validated through Fourier transform

infrared spectroscopic analysis (FTIR, Thermo Fisher Scientific, Nicolet iS10, USA). Quantitative analysis of magnetic properties was achieved using a vibrating sample magnetometer (VSM, LakeShore 8600, USA). Surface charge property and particle size of the prepared latex were measured by using a Zetasizer Nano system (Malvern, UK).

2.2.3 Preparation and performance evaluation of mortar or concrete containing magneto-responsive polymer latex

Table 3. The detailed compositions of prepared mortars (Unit: g).

Samples	polymer	OPC	Water	Sand	Defoamer	PCE
MRP0	0	100	45	300	0	0
MRP4	4	100	45	300	0.16	0.1
MRP8	8	100	45	300	0.32	0.2

Table 4. The detailed compositions of prepared concrete. (Unit: kg/m^3)

Sample/ Material	Cement	Cenosphere	Silica fume	Sand	Basalt gravel	Latex	Water	PCE
Ref	360	140	50	700	1015		118.5	2.75
MRP4	360	140	50	700	1015	62.85	79.25	11.0

Regarding the mortar specimen, its preparation method can refer to the national standard GB/T17671-2019, and the composition of the sample is given in Table 3. Regarding the concrete specimens, the preparation method can be referred to the national standard GB/T 50080-2016, and the composition of the samples is given in Table 4. Regarding the magnetic field-induced samples, a magnet with a maximum energy product of 52 MGOe was placed 1 cm from the top of the sample for 1 min after molding to provide a magnetic field. The prepared specimens were cured at 20 °C and 95% relative humidity for 3 d.

In order to clarify the effect of the applied magnetic field on the distribution of the polymer inside the specimen, the polymer content in different layers of the sample was quantified by using a muffle furnace. Owing to the fact that mass loss in polymer-modified mortars at 450 °C arises from not only polymer decomposition but also the decomposition of hydration products (e.g., $Ca(OH)_2$), determining the polymer content directly proves difficult. To address this, fly ash replaced cement in simulating the magnetic field-induced polymer gradient distribution within the paste. For this simulation, cylindrical specimens (height: 4 cm) were prepared under polymer dosages of 4% and 8% (by weight of fly ash), a sand-to-fly ash ratio of 3, and a water-to-fly ash ratio of 0.3. Additionally, Ca^{2+} concentration in the solution was maintained at 40 mmol/L through the addition of $Ca(NO_3)_2 \cdot 4H_2O$. Following molding, specimens underwent exposure to the magnetic field for either 1 min, with the magnet positioned 1 cm from the specimen's top. Immediately after magnetic treatment, specimens were

immersed in liquid nitrogen for 1 min before removal. Subsequently, they were sectioned into 5 layers of equal height (labeled 1 to 5, top to bottom). The segmented samples were then dried at 60 °C to constant weight, which was recorded as the initial mass. Next, samples were subjected to heating at 450 °C for 3 hours, followed by weighing of the remaining mass to calculate mass loss.

The flexural strength (160 mm × 40 mm × 40 mm) and compressive strength (40 mm × 40 mm × 40 mm) of the mortar specimens after curing for 3, 7, and 28 d were measured using a hydraulic press (WHY-300, Cangzhou Yixuan Testing Instrument Co., Ltd.). The flexural strength was measured at a loading rate of 50 N/s and the average of three measurements was taken. The compressive strength was measured at a loading rate of 2.4 kN/s and the average of six measurements was taken. The flexural strength (150 mm × 150 mm × 600 mm) and compressive strength (150 mm × 150 mm × 150 mm) of the concrete specimens after 28 d of curing were measured using a hydraulic press (DYE-2000, Hebei Rongda Road and Bridge Science and Instrumentation Equipment Factory). The flexural strength was measured at a loading rate of 0.05 MPa/s and the average of three measurements was taken. The compressive strength was measured at a loading speed of 0.5 MPa/s, and the average of three measurements was taken. In addition, the abrasion resistance of the concrete specimens was tested according to GB/T50081-2019.

2.2.4 Development of an applied magnetic field device and preparation of concrete pavements with polymer gradient distribution

To better implement the magnetic field induction for concrete pavement, a device for applying a magnetic field was designed and developed as shown in Fig. 2. The underside of the device is equipped with a 52 MGOe permanent magnet. The device can be moved using universal wheels, either manually or attached to the back of a paver. The width of the device and the magnet, as well as the distance from the pavement surface, are all adjustable and can thus be adapted to any size of concrete pavement. In this study, the distance between the magnet and the pavement surface is controlled to be 1 cm.

Fig. 2 Development of an applied magnetic field device.

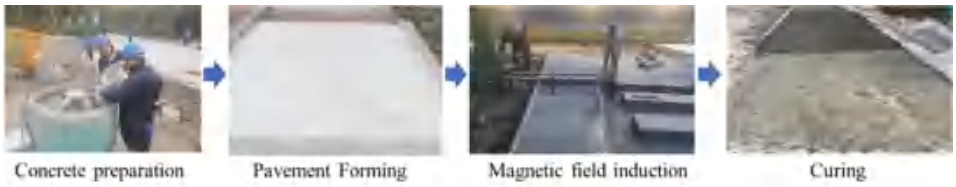

Fig. 3 Preparation of concrete pavements with polymer gradient distribution.

Fig. 3 shows a specific construction drawing of the concrete pavement, in which the specific proportion of concrete can be according to Section 2.2.3. A seven-day curing of the concrete pavement was performed after it was formed.

3 Results and discussions

3.1 Finite element analysis

The effect of gradient change of latex on the interlayer damage and surface force characteristics of concrete pavement under vehicle loading was comparatively analyzed, as shown in Fig. 4. Under vehicle loading, the trend of interlayer damage in both control and concrete pavements with gradient structure extended from the location of the slab edge to the middle of the slab. The interlayer damage and debonding area decreased with the increase of polymer dosage at the bottom of the slab. When the polymer content in the surface layer was certain, the damage area of type III pavement is similar to that of type IV pavement, and the damage of type V pavement was the smallest, which indicated that the more the polymer was enriched to the bottom of the surface layer, the more favorable it was to reduce the interlayer damage under vehicle loading.

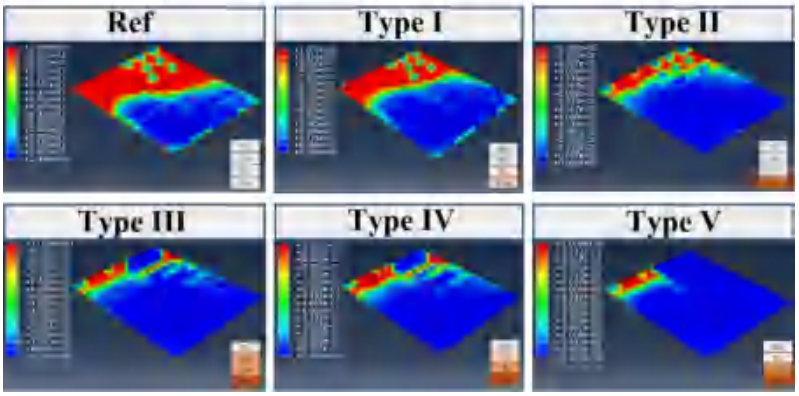

Fig. 4 Interlayer damage sprouting factor of subgrade-subgrade under vehicle loading.

3.2 Preparation of magneto-responsive polymer latex

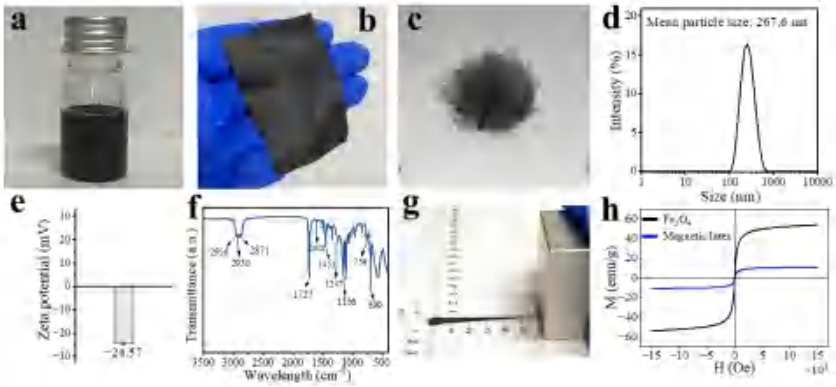

Fig. 5 Image of (a) the magneto-responsive polymer latex; (b) magnetic polymer film. (c) TEM image of magnetic polymer particles. (d) Particle size distribution of magnetic polymer particles. (e) Zeta potential of magneto-responsive polymer latex. (f) FTIR spectrum, (g) Images of the magnetic responsiveness of polymer latex:(h) Magnetic hysteresis loops of Fe_3O_4 and magnetic polymer latex.

The synthesized magneto-responsive polymer composite exhibited a black appearance (Fig. 5(a)) and demonstrated stability in forming continuous films at room temperature (Fig. 5(b)). Microscopic analysis revealed spherical magnetic polymer particles with approximate diameters of 250 nm (Fig. 5(c)). Size distribution measurements (Fig. 5(d)) indicated an average particle size of 267.6 nm, while zeta potential testing (Fig. 5(e)) recorded a value of -24.57 mV. The polymer film was analyzed by using FTIR, with results displayed in Fig. 5(f). Distinctive signals for styrene were observed at 699 cm^{-1} and 759 cm^{-1} (C-H aromatic bending), 1602 cm^{-1} (C=C stretching), and at 2871 cm^{-1}, 2930 cm^{-1}, and 2956 cm^{-1} (asymmetric stretching). For butyl acrylate, characteristic peaks appeared at 1156 cm^{-1} and 1247 cm^{-1} (C-O stretching), 1453 cm^{-1} (CH_2 stretching), and 1727 cm^{-1} (C=O stretching). The presence of these key spectral bands confirmed the successful synthesis of styrene-acrylic latex, which formed the primary component of the magneto-responsive polymer material.

Besides, the latex displayed notable magnetic responsiveness, reacting to external fields, with detectable effects observed up to 6 cm away (Fig. 5(g)). Magnetic hysteresis analysis (Fig. 5(h)) showed that both Fe_3O_4 and the polymer particles exhibited near-zero coercivity and residual magnetization, characteristic of superparamagnetic behavior. These materials achieved instantaneous magnetization under external fields while losing magnetism immediately after field removal. Comparative measurements revealed Fe_3O_4's saturation magnetization (50.2 emu/g) significantly exceeded the composite's value (14.8 emu/g). This difference arises because the copolymer shell surrounding the magnetic particles contributes negligible magnetization [9].

3.3 Performance evaluation of cementitious materials with magneto-responsive polymer latex

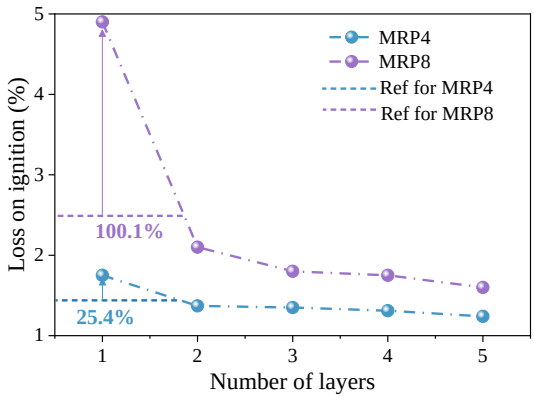

Fig. 6 The effect of an external magnetic field on the gradient distribution of the polymer

Fig. 6 illustrates the influence of an external magnetic field on the polymer gradient distribution within the specimens. In the MRP4 system, exposure to the magnetic field for 1 min resulted in a mass loss increase of approximately 25.4% in layer 1 compared to the reference specimen (Ref) without magnetic treatment. This phenomenon occurred because the magnetic polymer particles migrated towards and accumulated in layer 1 under the external magnetic field. Similarly, the MRP8 system exhibited a comparable trend following magnetic induction. A key distinction, however, was the more pronounced enrichment observed in the MRP8 system. Specifically, after 1 min of magnetic induction, the mass loss increased for MRP8, reaching 100.1% relative to Ref, markedly higher than the increase seen in MRP4.

The mechanical performance of mortar samples containing varying polymer concentrations, tested under magnetized and non-magnetized conditions after curing for 3, 7, and 28 d, is shown in Fig. 7 (a) and 7(b). Regardless of curing duration, higher polymer content consistently reduced compressive strength. This observation aligns with existing research, which indicates that polymer latex hinders cement hydration, thereby weakening compressive strength [10]. Magnetic field application produced a slight compressive strength enhancement at identical polymer concentrations, though the decreasing trend and increasing polymer content persisted across all curing stages.

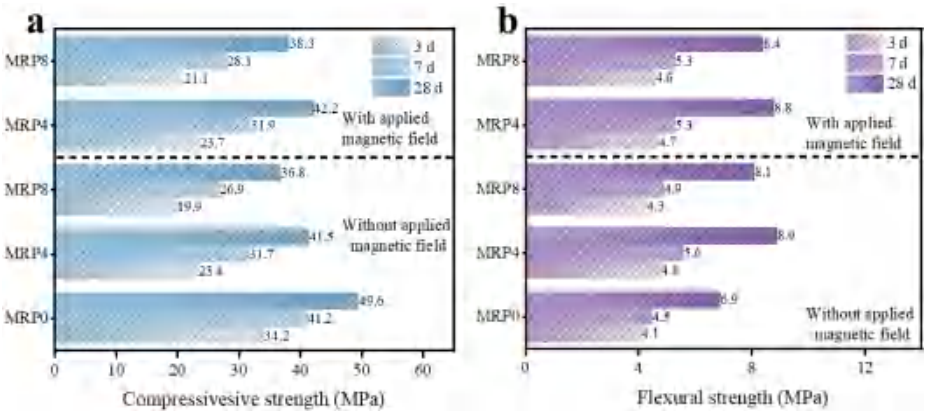

Fig. 7 The effect of magneto-responsive polymer latex on (a) compressive strength and (b) flexural strength of mortar.

For flexural strength, samples exhibited an initial rise followed by a decline as polymer concentration increased, yet all polymer-modified specimens were beyond the control group, with optimal polymer content at 4%. This improvement is attributed to polymer film formation, which binds cement particles and hydration products into cross-linked networks [10]. Notably, magnetic field exposure caused no substantial alteration in flexural strength development.

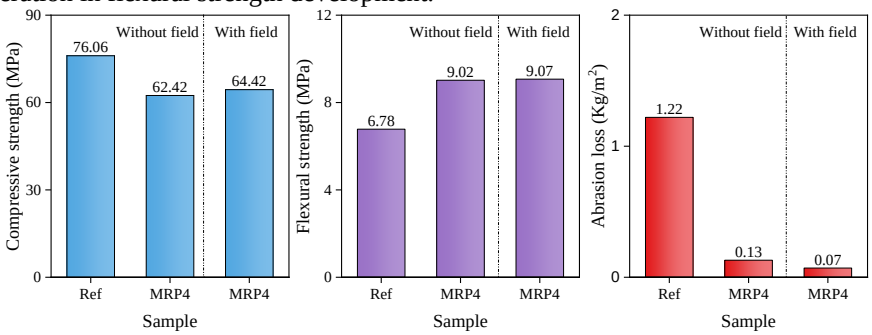

Fig. 8 Evaluation of mechanical properties and abrasion resistance of concrete containing magneto-responsive polymer latex.

The mechanical properties and abrasion amount of the magneto-responsive polymer latex-modified concrete were further measured, as shown in Fig. 8. Similar to the trend for mortar, the addition of polymer latex decreased the compressive strength of concrete but significantly increased the flexural strength and abrasion resistance of concrete. Besides, the application of a magnetic field further improved the compressive strength and abrasion resistance of concrete.

3.4 Performance evaluation of cementitious materials with magneto-responsive polymer latex

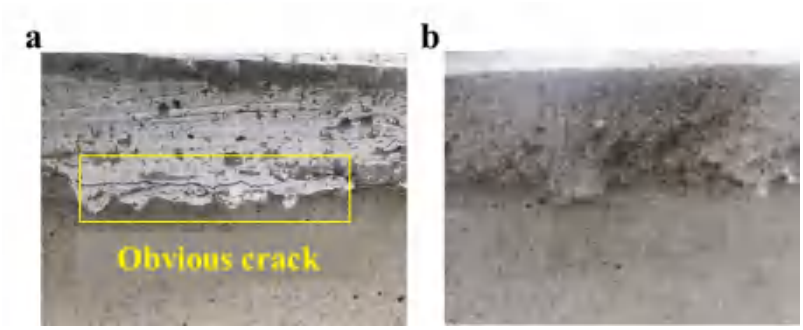

Fig. 9 Cracking of pavements (a) without and (b) with magnetic field induced.

Fig. 9 shows the observed cracks of the concrete pavement with and without a magnetic field induced after 7 d of curing. The result shows that the concrete pavement with the addition of latex significantly hinders the appearance of cracks compared to the control. This indicates that the enrichment of the polymer particles is highly favorable to the reduction of cracks in concrete pavement.

4 Conclusion

In this paper, a newly designed magneto-responsive latex and a device for applying a magnetic field were developed to realize the enrichment of polymer in cementitious materials. Then, the performance of the cement-based materials with a gradient structure was evaluated. The following conclusions were obtained:

A concrete pavement damage model was constructed to investigate the effect of the gradient distribution of the polymer on the performance of the concrete pavement, and the result shows that the gradient enrichment of the polymer was conducive to reducing the interlayer loss of concrete.

The magneto-responsive polymer latex could migrate directionally through an external magnetic field, and cause the formation of gradient structures in mortar or concrete. The result of further comprehensive evaluation of the mechanical properties of cement-based materials with magneto-responsive polymer latex added shows that the localized enrichment of polymers promotes their mechanical properties and abrasion resistance, and can impede the appearance of cracks in pavement.

References

1. J Liu, X Zhang, J Shen, et al. (2016) Current status and new countermeasures for the development of cement concrete pavements at home and abroad, Journal of China & Foreign Highway 36(04) 73-77.

2. D Feng, D Wang, J Yi, et al. (2020) Designation principle and method for functionally graded composite pavement. Science Bulletin, 65(30):3270-3286.
3. Y. Lin (2012) presented at International Conference on Structures and Building Materials (ICSBM), Effect of polymer to early mechanical property of the fly ash slurry.
4. A.A.M. Yassene, M.R. Ismail, M.S. Afify (2020) Journal of vinyl and additive technology (26) 144-154.
5. S. Zehra, R. Aslam, J. Aslam et al (2025) Chemically functionalized polymers as corrosion inhibitors: Effect of solubility, adsorption and coordination bonding, Coordination Chemistry Reviews (535) 216637.
6. I. Bozyigit, H.O. Zingil, S. Altun (2023) Performance of eco-friendly polymers for soil stabilization and their resistance to freeze–thaw action, Construction and Building Materials (379) 131-133.
7. D. Mostofinejad, H. Bahmani, A. Khorshidifar, et al. (2024) Enhancing concrete durability with polymer impregnation: A comparative study of corrosion and freeze-thaw resistance, Developments in the Built Environment (18) 100414.
8. Pang Pengfei (2015). Isotropic Layered Pavement Structure by Damage Theory [D]. Xi'an University of Architecture and Technology.
9. D. Wang, P. Yang, P. Hou, et al. (2017) Cement-based composites endowed with novel functions through controlling interface microstructure from Fe_3O_4@SiO_2 nanoparticles, Cement and Concrete Composites. (80) 268-276.
10. X.M. Kong, S. Emmerling, J. Pakusch, et al. (2015) Retardation effect of styrene-acrylate copolymer latexes on cement hydration, Cement and Concrete Research (75) 23-41.

Construction and Building Materials 505 (2025) 144665

Contents lists available at ScienceDirect

Construction and Building Materials

journal homepage: www.elsevier.com/locate/conbuildmat

A new method to improve the crack resistance of cement-based composites: Development of magneto-responsive polymer latex and performance evaluation

Lei Wang [a], Jing Wang [b], Zichen Lu [a,*], Xiangming Kong [b]

[a] Key Laboratory of Advanced Civil Engineering Materials, Ministry of Education, School of Materials Science and Engineering, Tongji University, Shanghai 201804, China

[b] Department of Civil Engineering, Tsinghua University, Beijing 100084, China

ARTICLE INFO

Keywords:
Magneto-responsive polymer latex
Cement-based composites
Mechanical properties
Crack resistance

ABSTRACT

In order to solve the cracking problem of cement-based composites in harsh environments, a magneto-responsive polymer latex was synthesized by the method of emulsion polymerization and characterized by FTIR, TEM and SEM, etc. Furthermore, the mechanical properties and crack resistance of cement-based composites modified with magneto-responsive polymer latex were evaluated by mechanical test, shrinkage measurement and anti-cracking evaluation. It was found that the application of an external magnetic field for the newly prepared polymer-modified mortar (PMM) could drag the polymer particles upward and enrich them in the top layer of PMM. Besides, the addition of magneto-responsive polymer latex can obviously increase the flexural strength and decrease the drying shrinkage of PMM compared to the reference. Under such a circumstance, the enrichment of polymer in the top layer can significantly improve the crack resistance of PMM at a low polymer dosage, which effectively solves the problem of economic burden caused by the high addition amount of polymer latex and promotes their application on a large scale.

1. Introduction

Cement-based materials are widely used in the construction industry due to their low cost and excellent mechanical properties [1–4]. However, the use of cement-based materials in harsh environments can lead to severe cracking [5]. These cracks can lead to a reduction in structural bearing capacity [6] and a decrease in durability [7]. Therefore, solving cracking problems is essential to ensure safety and extend service life. The current strategies for crack prevention can be broadly classified into two categories: surface treatment methods and internal incorporation methods. The surface treatment method primarily involves applying a protective coating to concrete, offering the advantage of a relatively simple application. Snoeck et al. [8] tried to form a calcium alginate layer through in-situ crosslinking on the surface of concrete, which effectively mitigated plastic shrinkage and reduced cracking. However, this approach often suffers from inadequate long-term durability. In contrast, the internal incorporation method introduces reinforcing components, such as steel fibers [9], nanomaterials [10,11], or various chemical admixtures [12], during the material preparation stage to enhance crack resistance and overall durability of the matrix. Among these, polymer latex shows remarkable performance in improving the flexural strength, toughness and durability of cement-based materials [13–15]. Bhogayata et al. [16] improved the mechanical properties, crack resistance, and durability of concrete by co-incorporating styrene–butadiene rubber (SBR) latex and recycled plastic fibers (RPF), and obtained the optimal dosages of 15 % SBR and 1 % RPF. However, one drawback of the application of polymer latex is the required high dosage (normally more than 10 % of the mass of cement) to achieve the desired properties [17], which significantly increases the cost of its application. Considering the fact that people normally only need the polymer-modified properties of cement-based materials in certain areas (for example the surface enrichment to modify the anti-cracking and anti-wear performance), hence, the problem of economic burden caused by the addition of polymer latex can be addressed through local enrichment of polymer latex in certain areas. An attractive approach is to endow polymer latex with responsive properties and reach polymer enrichment in certain areas.

Currently, some methods have been proposed for the active control

* Corresponding author.
E-mail address: luzc@tongji.edu.cn (Z. Lu).

https://doi.org/10.1016/j.conbuildmat.2025.144665
Received 30 April 2025; Received in revised form 30 October 2025; Accepted 24 November 2025
0950-0618/© 2025 Elsevier Ltd. All rights are reserved, including those for text and data mining, AI training, and similar technologies.

Table 1
The chemical and mineralogical composition of OPC.

Chemical composition	SiO_2	Al_2O_3	Fe_2O_3	CaO	MgO	SO_3	TiO_2	K_2O	Na_2O	Other
% by mass	20.78	4.53	3.22	62.38	3.29	3.97	0.34	0.87	0.32	0.3

Mineralogical composition	C_3S	C_2S	C_3A	C_4AF	Gypsum	Anhydrite	f-CaO	Other
% by mass	63.14	13.98	6.57	8.33	2.52	1.61	0.94	2.05

of the properties of cement-based materials through the addition of chemical admixtures with responsive properties [18–21]. That is, by actively applying external signals (such as temperature field, electric current or potential, magnetic field, microwaves, etc.) to trigger the desired response in freshly mixed or hardened cement pastes, thus achieving the target of active control of performance. Feng et al. [18] prepared a temperature-responsive suspension stabilizer, which formed a spatial network structure in the cement paste along with the increased temperature. Ezzat et al. [19] prepared a redox-responsive copolymer to achieve active rheological control of cement pastes through the activation of external electric potential. Even though many methods have been proposed to reach the actively controlled properties of cement-based materials, they still have some problems, such as the high difficulty of implementing these methods in practical engineering and their irreversible effects on cement hydration [22].

Magnetic intervention technology has been widely used in cement-based materials in recent years due to its advantages, such as precise controllability and relatively easy application [22–26]. Javahershenas et al. [23] found that the flexural strength of steel-fiber contained concrete can be increased with the prolonged treatment time in the magnetic field. Choi et al. [24] investigated the effect of an external electromagnetic field on the properties of the lubrication layer between concrete and pipe, and found that it enhanced the pumpability of concrete. Jiao et al. [25,26] investigated the structural build-up of cement pastes under magnetic fields by adding magneto-responsive particles and found that the structural build-up of cement pastes depended on the magnetizing time and magnetic field strength.

In our former investigation, a magneto-responsive polymer latex was designed [27] and its effects on the flexural strength and permeability of the polymer-modified mortar (PMM) were evaluated. The results indicated that both impermeability and flexural strength were improved through the addition of magneto-responsive polymer. However, still limited evaluation was conducted to thoroughly understand its working mechanism and the corresponding effect on the properties of PMM, especially to the anti-cracking performance. Hence, in this study, a newly designed magneto-responsive polymer latex with improved stability was first prepared and subjected to a series of characterizations. Furthermore, an external magnetic field was applied to the fresh PMM with the addition of magneto-responsive polymer, and the responsiveness of PMM was quantitatively evaluated under the effect of magnetic fields with varied intensities. Finally, the mechanical properties and crack resistance of PMM with or without an applied external magnetic field were evaluated by using mechanical, shrinkage and cracking tests. This study aims to propose a new way to increase the crack resistance of PMM. Considering that surface treatment methods often suffer from durability issues and internal incorporation methods require high material costs, we introduced a strategy that utilizes the magneto-responsive property to achieve directional migration and localized enrichment of polymer latex in specific critical regions. This novel approach not only integrates the advantages of both methods of surface protection and internal modification, but also significantly reduces the required polymer dosage, thereby effectively alleviating the economic burden associated with the application of polymer latex in cement-based materials.

2. Materials and methods

2.1. Raw materials

Portland cement PI 42.5 (OPC, Fushun Orcel Technology Co., Ltd) and ISO standard sand (Xiamen Aisio Standard Sand Co., Ltd.) were used in this study. The chemical and mineralogical composition of OPC measured by using X-ray fluorescence (XRF) and XRD Rietveld refinement are shown in Table 1. The specific surface area of OPC was measured by using BET (Micromeritics, ASAP2460, USA), and the result was 1.45 m^2/g. The polycarboxylate superplasticizer with a solid content of 40 % was synthesized in our laboratory, and its synthesis procedure and characteristic parameters have been reported in literature [28]. The defoamer (AF6230) was purchased from Shanghai Shangnan New Materials Co., Ltd. Fly ash (FA) was purchased from Anda Environmental Technology Co., Ltd. $Ca(NO_3)_2{\cdot}4\ H_2O$, ferric chloride ($FeCl_3{\cdot}6\ H_2O$), ferrous sulfate ($FeSO_4{\cdot}7\ H_2O$), ammonium hydroxide (25 wt% NH_3 in water), HCl, ethanol (C_2H_5OH), n-octane (C_8H_{18}), styrene (St), n-butyl acrylate (BA), 2-acrylamido-2-methylpropane sulfonic acid (AMPS), acrylamide (AM), divinylbenzene (DVB), hexadecane (HD), azobisisobutyronitrile (AIBN), sodium dodecylbenzene sulfonate (SDBS) of analytical purity and oleic acid of chemical purity were purchased from Sinopharm Chemical Reagent Co., Ltd. Surfactants including Co-458 and TX-50 were purchased from Nantong Aochen Chemical Co., Ltd and Jiangsu Hai'an Petrochemical Plant, respectively.

2.2. Synthesis of magneto-responsive polymer latex

The synthetic process of magneto-responsive polymer latex can be

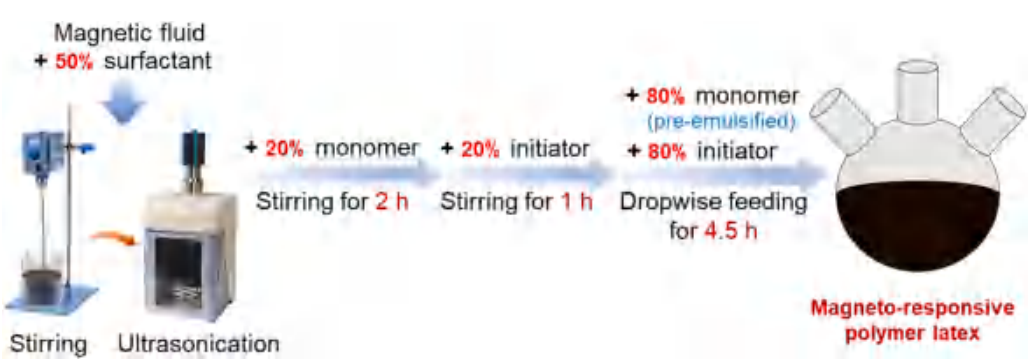

Fig. 1. The experimental process for preparing the magneto-responsive polymer latex.

Table 2
The recipe for the polymerization of latex (g).

Magnetic fluid (60 %)	Monomer						AIBN (Initiator)	Surfactant			DI water
	St	BA	AMPS	AM	DVB	HD		SDBS	Co-458	Tx-50	
28	18.86	35.26	1.16	1.16	0.3	1.16	0.56	1.4	2.28	0.96	104

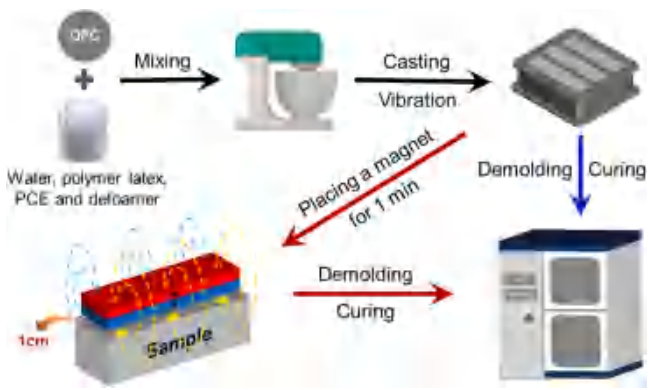

Fig. 2. The process of sample preparation.

divided into two parts. The first part was to prepare the magnetic fluid by using the co-precipitation method. $FeCl_3 \cdot 6\ H_2O$ (50 g) and $FeSO_4 \cdot 7\ H_2O$ (30 g) were first stirred thoroughly in DI water (100 g) until completely dissolved. The solution was heated to 80 °C, after which $NH_3 \cdot H_2O$ (25 wt%, 90 g) was titrated within 5 min, oleic acid (9 g) was then added immediately and stirred at a speed of 300 rpm for 2 h at 80 °C. The obtained mixture was neutralized by 1 mol/L HCl solution and then washed five times with DI water. Then, ethanol (48 g) and n-octane (12 g) were added and stirred for 10 min to extract the oleic acid-modified Fe_3O_4 particles into n-octane. The magnetic fluid with about 60 % solid content was obtained after being ultrasonicated for 30 min.

The second part was the synthesis of magneto-responsive polymer latex by using emulsion polymerization method as shown in Fig. 1. The prepared magnetic fluid (28 g), surfactants (2.32 g) including SDBS (0.7 g), Co-458 (1.14 g), and TX-50 (0.48 g) were first added into DI water (46 g) and stirred for 2 min with a speed of 500 rpm at 25°C, and then ultrasonicated at a frequency of 25 kHz for 30 min. DI water (2.4 g) and monomers (11.58 g) including St (3.772 g), BA (7.052 g), AMPS (0.232 g), AM (0. 232 g), DVB (0.06 g), HD (0.232 g) were then added to the mixture and stirred for 2 h with a speed of 300 rpm at 25 °C. Then, the mixture was warmed up to 90 °C with the same stirring speed. AIBN (0.112 g) used as the initiator was added to the mixture and stirred at a speed of 300 rpm for 1 h. The rest monomer (46.32 g), after being pre-emulsified by the rest surfactant (2.32 g) and DI water (55.6 g), was titrated within 4 h with a stirring speed of 300 rpm at 90 °C, while the rest initiator (0.448 g) was titrated within 4.5 h, and the magneto-responsive polymer latex was then prepared. The recipe for the polymerization of the latex is shown in Table 2.

2.3. Sample preparation

The polymer dosages were fixed at 0 %, 4 %, and 8 % (by weight of OPC). In order to achieve similar flowability for fresh pastes or mortars, the polycarboxylate superplasticizer (PCE) was added. In order to avoid the influence of different air void contents on mechanical properties [29], the defoamer was added to ensure a similar density for the prepared cement paste or mortar regardless of the addition of polymer latex. The dosage of defoamer was 4 % by weight of polymer. For the preparation of cement pastes, the water-to-cement mass ratio (w/c) was 0.45. Cement, latex, water, PCE, and defoamer were first stirred in a planetary mixer (NJ-160, Maifang Instrument and Equipment Co., Ltd., China) at a speed of 62 rpm for 120 s. After waiting for 15 s, the paste was then stirred at a speed of 125 rpm for 120 s. The prepared cement pastes were poured into the mold and immediately covered with plastic film. For samples to be induced by the magnetic field, a magnet with a maximum magnetic energy product of 52 MGOe was placed 1 cm away from the top of the sample after molding for 1 min. Afterwards, the prepared samples were cured at 20 °C and 95 % RH for 3 days. Then, they were cured at 20 °C and 50 % RH until the testing ages. The process of sample preparation is shown in Fig. 2. For the preparation of mortars, the water-to-cement mass ratio (w/c) was 0.45 and the sand-to-cement mass ratio (s/c) was 3. Firstly, cement, latex, water, PCE and defoamer were stirred in a planetary mixer (JJ-5, Maifang Instrument and Equipment Co., Ltd., China) at a speed of 62 rpm for 30 s. Next, sand was added to the paste and mixed at the same speed for 30 s, and then at a speed of 125 rpm for 30 s. After waiting for 90 s, the mortar was stirred at a speed of 125 rpm for 60 s, the prepared mortar was poured into the mold and immediately covered with plastic film. The subsequent treatment and curing process was the same as for cement pastes. The mixture proportions of cement pastes or mortars are shown in Table 3, wherein MRP represents magneto-responsive polymer, and the number behind represents the dosage.

Table 3
The mixture proportions of cement pastes or mortars (g).

Samples	polymer	OPC	Water	Sand*	Defoamer	PCE
MRP0	0	100	45	300	0	0
MRP4	4	100	45	300	0.16	0.1
MRP8	8	100	45	300	0.32	0.2

* The sand was only used for the preparation of mortar.

2.4. Testing and characterization

2.4.1. Characterization of magneto-responsive polymer latex

The morphology of the polymer particles was observed using a transmission electron microscope (TEM, FEI Tecnai F20, USA), where the solid content of the magneto-responsive polymer latex was first diluted to 1.0 % with deionized water, and then a drop of the diluted latex was dropped onto a carbon-coated copper mesh and observed after complete drying at room temperature. The copolymerization of the monomers was verified by Fourier transform infrared spectroscopy (FTIR, Thermo Fisher Scientific, Nicolet iS10, USA). The surface morphology and elemental distribution of the polymer films were observed by using a scanning electron microscope (SEM, Zeiss Gemini 300) equipped with an energy dispersive spectrometer (EDS). The magnetic properties of the samples were characterized by using a vibrating sample magnetometer (VSM, LakeShore 8600, USA). The zeta potential and particle size of polymer particles were measured by using Zetasizer Nano (Malvern, UK). Thermogravimetric analysis (TGA) was performed on polymer films by using STA 409 (Netzsch, Germany) at a heating rate of 10 °C/min from room temperature to 600 °C under a nitrogen atmosphere.

2.4.2. Gradient distribution of polymers induced by magnetic field

To investigate the effect of the induced magnetic field on the polymer distribution in PMM, the mass loss of PMM was measured by heating the samples at 450 °C. It should be noted that the mass loss of the samples at 450 °C included not only the decomposition of the polymer, but also the

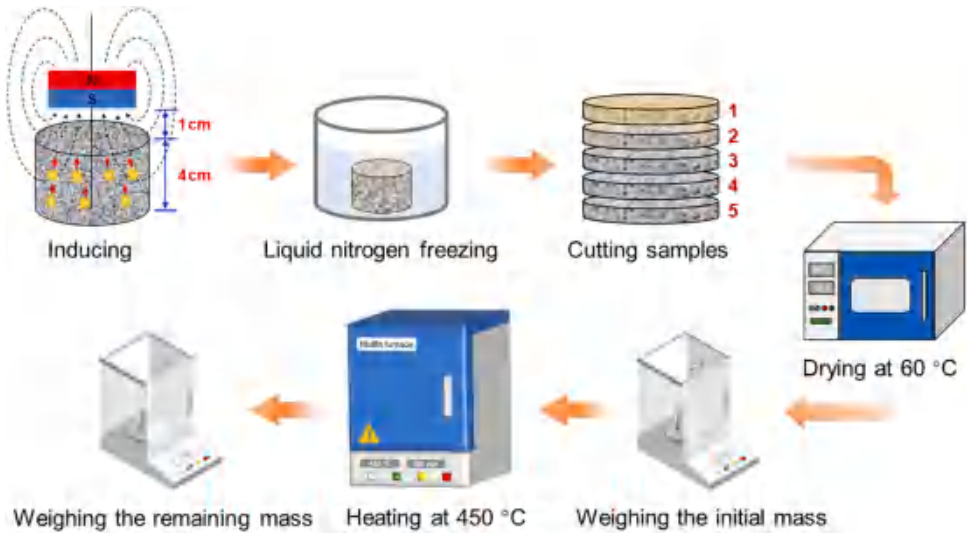

Fig. 3. The experimental process for testing the distribution of polymers induced by a magnetic field.

decomposition of the hydration product of $Ca(OH)_2$. In order to avoid the intervention of the formed $Ca(OH)_2$ on the accurate calculation of polymer content, fly ash was used instead of cement to simulate the gradient distribution of the polymer in PMM induced by the magnetic field. Cylindrical samples with a height of 4 cm were prepared in which the polymer dosages were 4 % and 8 % (by weight of fly ash), the sand-to-fly ash ratio was 3, the water-to-fly ash ratio was 0.3, and the concentration of Ca^{2+} in the solution was controlled at 40 mmol/L by adding $Ca(NO_3)_2{\cdot}4\ H_2O$ to simulate the [Ca] in the pore solution of cement pastes. The samples were molded and placed in the magnetic field for 1 or 10 min with the magnet 1 cm from the surface of the sample. Then the samples were immediately placed in liquid nitrogen for 1 min. After complete freezing, the samples were cut into 5 layers of equal height (labeled 1–5 in order from top to bottom). The cut samples were dried at 60 °C to a constant weight and recorded as the initial mass of the sample. The samples were then heated at 450 °C for 3 h and the remaining mass was weighed to present the polymer content in each layer. The experimental process is shown in Fig. 3, and the mass loss of the samples can be calculated according to Eq. (1):

$$ML = \frac{m_i - m_r}{m_i} \times 100\% \tag{1}$$

Where ML represents the mass loss of the sample originating from the polymer; m_i represents the initial mass of the sample after drying at 60 °C, g; m_r represents the remaining mass of the sample after heating at 450 °C, g.

2.4.3. Adsorption measurement

The adsorption amount of magneto-responsive polymer latex on the surface of cement particles was measured using the depletion method [30,31] at a constant temperature of 25 °C. The water-to-cement mass ratio (w/c) of cement pastes was fixed at 0.45 and the polymer dosage was gradually increased from 0 % to 20 %. First, 10 g of OPC was thoroughly mixed with DI water or polymer latex in a 25 ML centrifuge tube by using a vortex mixer (HY-2, Leici, China) for 1 min, and then centrifuged at a speed of 4000 rpm for 5 min. The supernatant was collected with a syringe and filtered through a 0.45 μm filter. The supernatant was then dried to a constant weight at 105 °C and the residual solids content, including mainly polymers and some inorganic salts in the aqueous phase, was measured. The obtained solids were sintered for 1 h at 600 °C to completely decompose the polymer (the complete decomposition temperature of the polymer is about 450 °C). Finally, the amount of polymer in the supernatant was obtained and the adsorption amount of polymer was calculated by using the depletion method. In addition, the adsorption amount of polymers on fly ash was tested by the same method as described above. The water-to-fly ash mass ratio was fixed at 0.3, and the concentration of Ca^{2+} in solution was controlled at 40 mmol/L by adding $Ca(NO_3)_2{\cdot}4\ H_2O$.

2.4.4. Mechanical properties

The mortars with and without being induced by the magnetic field were used for the testing of mechanical properties, the sample preparation was described in 2.3. The flexural strength (size 160 mm × 40 mm × 40 mm) and compressive strength (size 40 mm × 40 mm × 40 mm) of the samples after curing for 3 d, 7 d and 28 d were measured using an automatic testing machine (WHY-300, Cangzhou Yixuan Testing Instrument Co., Ltd.). The flexural strength was measured at a loading speed of 50 N/s and obtained through the average of 3 measurements. The compressive strength was measured at a loading speed of 2.4 kN/s and obtained through the average of 6 measurements. It should be noted that the tops of the samples were used to withstand the loading force due to the gradient distribution of polymer in PMM after applying the magnetic field. In order to reach a flat surface for measurement, the tops of the samples were lightly polished with sandpaper before each measurement.

2.4.5. Drying shrinkage test

For the drying shrinkage test, the mortar without being induced by the magnetic field was used, the preparation of mortar was described in 2.3. The vertical mortar shrinkage tester was used to measure the drying shrinkage of samples at different ages according to Standard JC/T 603–2004. The dimensions of the sample were 40 mm × 40 mm × 160 mm, but the effective length was 144 mm because the nail heads were pre-embedded at both ends of the samples. The samples were cured at 20 °C and 95 % RH for 24 h and then the initial length (L_0) of the samples was measured. The samples were cured at 20 °C and 50 % RH until the testing ages and the length of the samples was measured. The drying shrinkage (S_t) was calculated according to Eq. (2) and the arithmetic mean of three measurements was taken as the drying shrinkage of the samples.

$$S_t = \frac{L_0 - L_t}{144} \tag{2}$$

Where S_t represents the drying shrinkage of the sample at t d; L_0 represents the initial length of the sample after demolding, mm; L_t represents the measured length of the sample at t d, mm; 144 is the effective

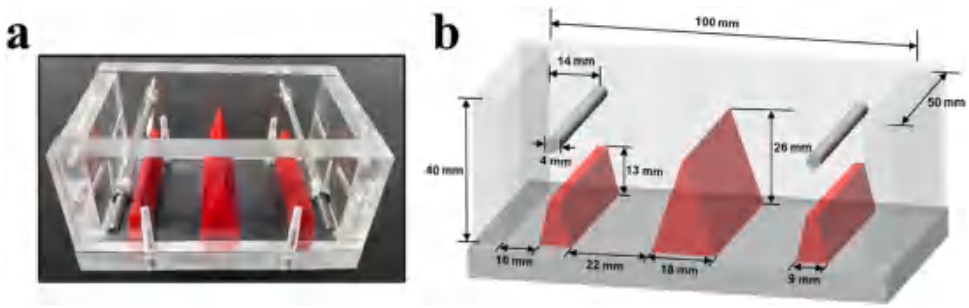

Fig. 4. The mold for cracking test: (a) Real picture, (b) Schematic drawing [32].

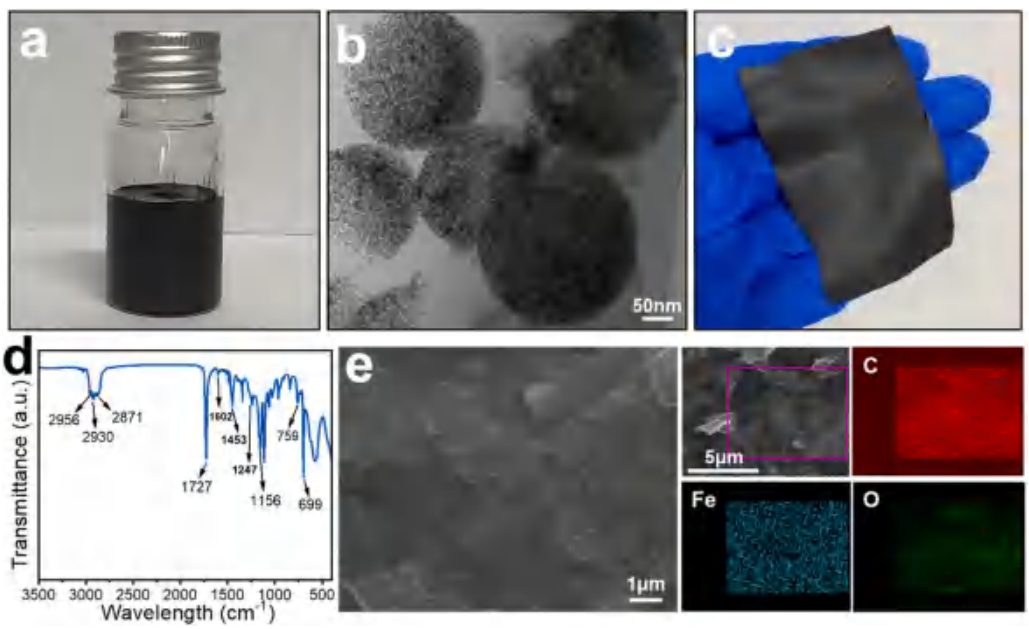

Fig. 5. (a) Image of the prepared magneto-responsive polymer latex. (b) TEM image of magnetic polymer particles. (c) Formed polymer film, (d) FTIR spectrum, (e) SEM image and EDS-mapping images of the magnetic polymer film.

length of the sample, mm.

2.4.6. Cracking test

The hardened cement paste with and without being induced by the magnetic field was used for the cracking test, the preparation of the paste was described in 2.3. The molds for the cracking test were described in detail in the literature [32], and the appearance of the mold is shown in Fig. 4. The dimensions of the samples were 100 × 50 × 40 mm. The prepared pastes were molded and placed in an artificial climate chamber. In order to simulate the real harsh environment, the temperature and relative humidity of the artificial climate chamber were set to 35 °C and 35 %, respectively. A fan which can create the wind speed of 5–8 m/s was used. Cracks appearing on the sides and tops of the samples were recorded after curing for 3 days.

3. Results and Discussion

3.1. Characterization of magneto-responsive polymer latex

The appearance of the synthesized magneto-responsive polymer latex is shown in Fig. 5a, in which the magnetic polymer particles were spherical particles with a diameter of about 250 nm (Fig. 5b). The magneto-responsive polymer latex can be stabilized to form continuous films at room temperature (Fig. 5c). The polymer film was analyzed by FTIR, and the result is shown in Fig. 5d. Peaks at 699 cm^{-1} and 759 cm^{-1} were attributed to C-H bending vibrations of styrene, while the C═C stretching vibration of the benzene ring was observed at 1602 cm^{-1}. The asymmetric stretching vibrations of C-H appeared at 2871 cm^{-1}, 2930 cm^{-1}, and 2956 cm^{-1}. The C-O stretching vibrations of the ester group were identified at 1156 cm^{-1} and 1247 cm^{-1}. The CH_2 bending vibration was found at 1453 cm^{-1} and the C═O stretching vibration of the carbonyl group was at 1727 cm^{-1}. Based on the above analysis, it could be concluded that styrene-acrylic latex was successfully synthesized as the main composition of magneto-responsive polymer latex. Furthermore, the results of SEM images and EDS-mapping images of the polymer film (Fig. 5e) showed a uniform distribution of C, Fe, and O elements, indicating that the magnetic particles were uniformly dispersed in the polymer film, which confirms the successful incorporation of the Fe_3O_4 particles in the synthesized magneto-responsive polymer latex.

The intrinsic properties of magneto-responsive polymer latex and the responsiveness of polymer-modified pastes under the effect of a magnetic field were characterized. The polymer latex showed significant magnetic responsiveness to an external magnetic field (Fig. 6a) and could be affected by a magnetic field at a distance of 6 cm (Fig. 6b). The magnetic hysteresis loops of Fe_3O_4 and magnetic polymer particles are shown in Fig. 6c. The values of coercivity and remanent magnetization of Fe_3O_4 and magnetic polymer particles were close to zero, showing a typical characteristic of superparamagnetism. When an external magnetic field was applied, they were immediately magnetized, and the

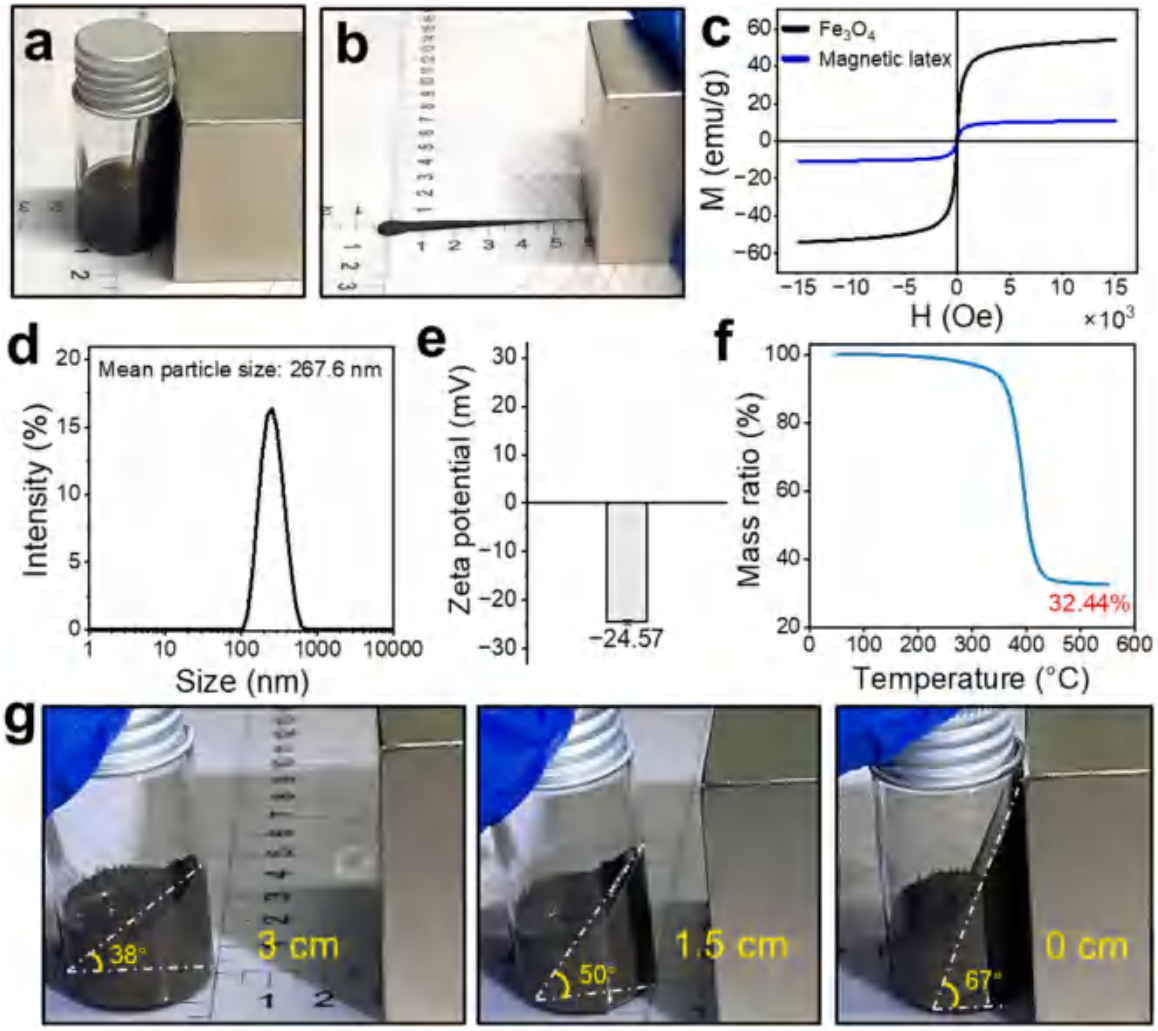

Fig. 6. Images of the magnetic responsiveness of polymer latex: (a) With external magnetic field, (b) Distance of polymer latex can be affected by the magnetic field. (c) Magnetic hysteresis loops of Fe_3O_4 and magnetic polymer particles. (d) The particle size distribution of magnetic polymer particles. (e) Zeta potential of magneto-responsive polymer latex. (f) TG curve of the polymer film. (g) Images of the responsiveness of cement pastes at different magnet distances (3/ 1.5/ 0 cm).

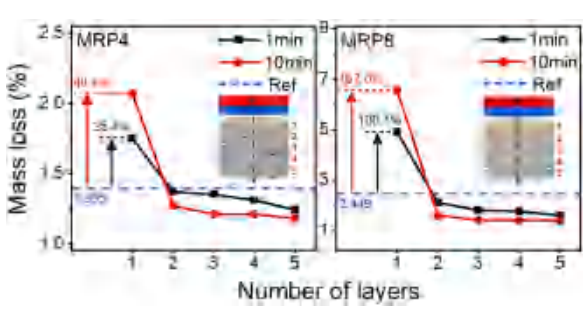

Fig. 7. The effect of external magnetic field on the gradient distribution of the polymer.

magnetization disappeared as soon as the magnetic field was removed. The saturation magnetization of Fe_3O_4 was 50.2 emu/g, much higher than that of magnetic polymer particles (14.8 emu/g), which could be caused by the low saturation magnetization of the copolymer shell of magnetic polymer particles (almost zero) [33]. The results of the particle size distribution (Fig. 6d) and zeta potential (Fig. 6e) of the polymer latex showed that the average particle size of the magnetic polymer particles was about 267.6 nm, and the zeta potential was −24.57 mV. The result of the TG curve of the polymer film was shown in Fig. 6f, and the mass loss of the sample at 450 °C was recorded as the mass of the polymer. From the TG curve, the mass of the polymer was about 67.6 % and the content of Fe_3O_4 was about 32.4 % in the magnetic polymer particles. Fig. 6g showed the responsiveness of cement pastes at different magnet distances (3/ 1.5/ 0 cm), and the magnet was placed for 1 min. The cement pastes showed magnetic responsiveness at all three different distances, and the responsiveness of the cement pastes was increased with the decreased distance. When the distance between the paste and the magnet was 3 cm, the slope angle of the paste was 38°, and the slope angle increased to 50° as the distance decreased to 1.5 cm, and increased to 67° for a distance of 0 cm.

3.2. Gradient distribution of polymers induced by magnetic field

Fig. 7 shows the effect of an external magnetic field on the gradient distribution of polymer in PMM. For the PMM with the polymer dosage of 4 % (MRP4), compared to the PMM without an applied external magnetic field (Ref), the mass loss of layer 1 increased by about 25.4 % and 48.4 % when the PMM was induced by the magnetic field for 1 min and 10 min, respectively, which clearly proved that the magnetic polymer particles moved upward by the external magnetic field and enriched in layer 1. For the PMM with the polymer dosage of 8 % (MRP8), the trend of polymer distribution was similar to the condition of MRP4 but with an increased content in the top layer after the PMM was

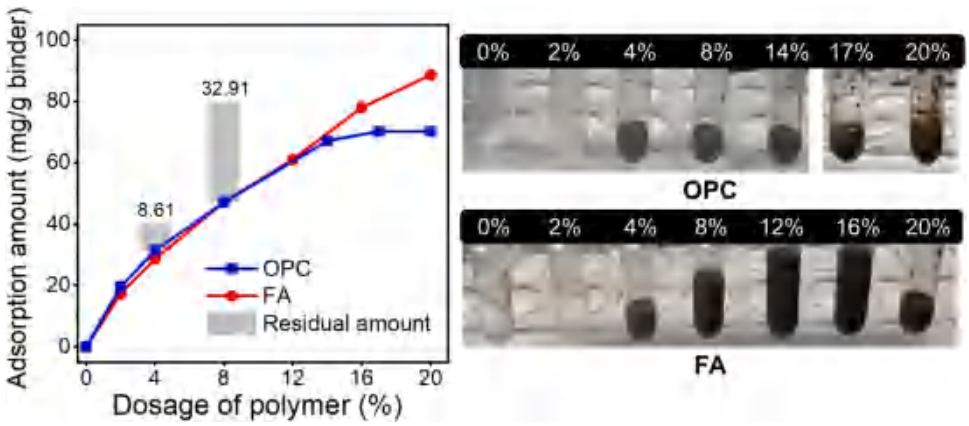

Fig. 8. The absorption isotherm of magneto-responsive polymer to OPC and fly ash (FA).

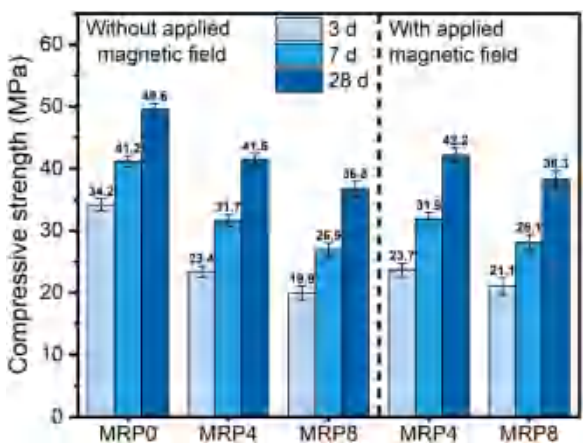

Fig. 9. The effect of magneto-responsive polymer latex on compressive strength of mortar.

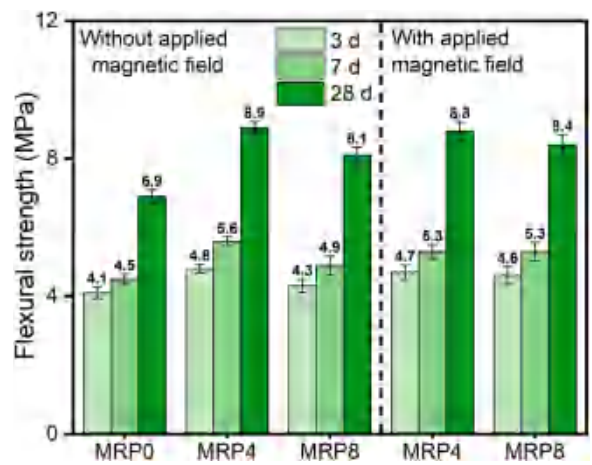

Fig. 10. The effect of magneto-responsive polymer latex on flexural strength of mortar.

induced by the magnetic field. The content of polymer in the top layer was increased along with the increased treating time by the external magnetic field. When the samples were induced by the magnetic field for 10 min, the mass loss of MRP8 was increased by 167.0 % compared to the reference, which was much higher than the 48.4 % of MRP4. It is commonly accepted that polymer particles can be adsorbed on the surface of cementitious materials [34]. When the dosage was low, most of the polymer particles could be adsorbed and only a few free polymer particles could be moved after applying the magnetic field. The increased polymer dosage resulted in more free polymer particles, which enhanced the enrichment of polymers in the top layer of the sample.

In order to verify the above assumption, the adsorption amounts of polymer on the surfaces of cement particles and fly ash were measured, as shown in Fig. 8. The results show that for the OPC system, the adsorption amount increased with increasing polymer dosage. When the polymer dosage was 2 %, a colorless and transparent pore solution (right part in Fig. 8) was obtained, indicating that the added polymer was mostly adsorbed by the cement particles. With higher polymer dosages, the adsorption amount of polymer on cement particles was increased. Meanwhile, the residual amount of polymer in the pore solution was also increased (8.61 mg/g OPC at 4 % polymer dosage and 32.91 mg/g OPC at 8 % polymer dosage). When the polymer dosage was higher than 14 %, saturation adsorption was almost reached. For the adsorption in fly ash paste, the adsorption isotherm was similar to that of OPC when the polymer dosage was lower than 12 %, which from one aspect proved the feasibility of using fly ash instead of cement for the experiment on the measurement of gradient distribution of polymers, and also provided support for the previous speculation about the different degrees of polymer enrichment at different polymer dosages.

3.3. Mechanical properties

The mechanical properties of PMM at varied polymer dosages with

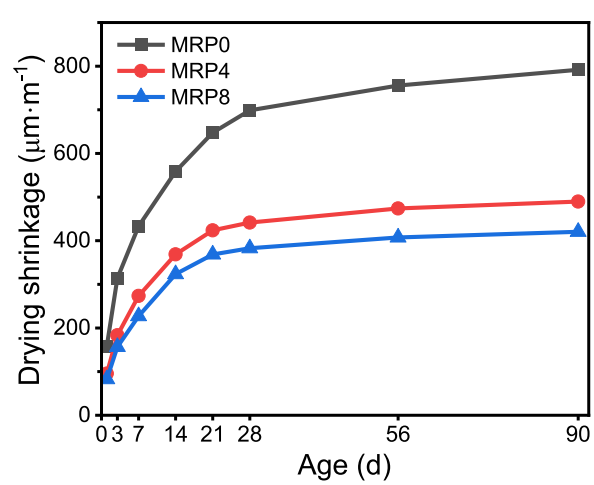

Fig. 11. The effect of magneto-responsive polymer latex on drying shrinkage of mortar.

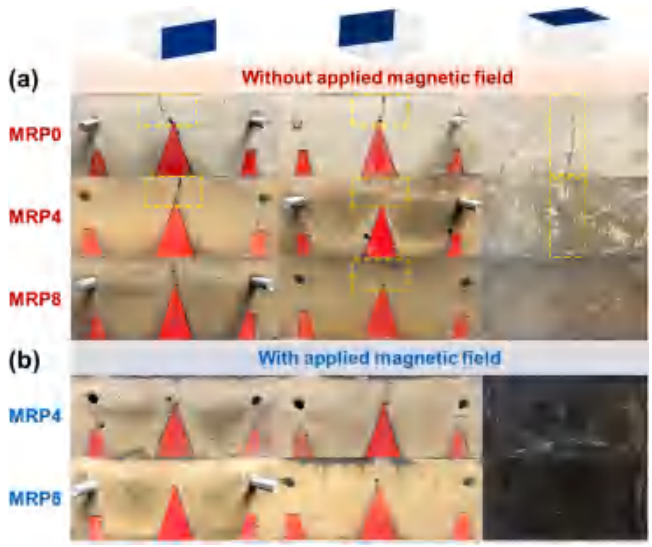

Fig. 12. Images of the samples for cracking test: (a) without an applied magnetic field; (b) with an applied magnetic field.

or without applying a magnetic field were measured after curing for 3, 7, and 28 days, and the results are shown in Fig. 9 and Fig. 10. Along with the increased polymer dosages, the compressive strength at the same curing age always showed a decreasing trend, which matched well with the results shown in literature [30]. After the PMM was induced by the magnetic field, the compressive strength increased slightly at the same polymer dosage and still showed a decreasing trend. For the flexural strength of PMM, it showed a tendency of first increase and then decrease along with the increased polymer dosage at the same curing age. In addition, all of the measured results were higher than those of the reference. The optimum polymer dosage to show the highest flexural strength was 4 %. Besides, no significant change in the flexural strength was found after applying the magnetic field.

3.4. Drying shrinkage performance

Drying shrinkage tests were conducted to evaluate the effect of the magneto-responsive polymer latex on the drying shrinkage of the mortar, as shown in Fig. 11. Clearly, the drying shrinkage increased rapidly during the first 28 d curing age regardless of the addition of polymer. The drying shrinkages were 698.7 $\mu m \cdot m^{-1}$, 441.5 $\mu m \cdot m^{-1}$ and 382.7 $\mu m \cdot m^{-1}$ for the samples of MRP0, MRP4 and MRP8 after curing for 28 d, respectively. Afterwards, the drying shrinkage showed a slow increase. The addition of polymer latex significantly reduced the drying shrinkage of the mortar in the measured ages. The drying shrinkage of MRP8 was reduced by approximately 14 % compared to that of MRP4.

3.5. Evaluation of crack resistance

Fig. 12 shows the side and top images of the samples for the cracking test. For the samples not induced by the magnetic field, cracks were observed for all the samples after curing for 3 days but to different extents. The samples without polymer latex showed obvious complete through-going cracks. When the polymer dosage was 4 %, cracks were still observed on the sides and top of the samples but with clearly reduced crack width. When the dosage of polymer reached 8 %, only a small crack was observed on one side of the sample, while no significant cracks were observed on the other surfaces. Hence, it can be concluded that the crack resistance of the samples was improved with increasing polymer dosages, which could be caused by the reduced drying shrinkage (Fig. 11) and the increased flexural strength (Fig. 10). After the samples were induced by the magnetic field, no obvious cracks were observed on the side and top of samples with the addition of MRP4 and MRP8. This indicates the applied magnetic field can lead to a significant increase in the crack resistance, which is caused by the enrichment of polymer in the top layer of samples. Besides, the dark surface of the samples after applying the magnetic field also strongly proved the enrichment of polymer latex in the top layer of samples.

4. Conclusions

In this study, the prepared magneto-responsive polymer latex was characterized, and the gradient distribution of the polymer in the mortar was evaluated. In addition, the effects of magneto-responsive polymer latex on the mechanical properties, drying shrinkage, and crack resistance of cement-based materials were studied. Based on the results of this study, the following conclusions can be drawn:

Magnetic polymer particles can move upward and enrich in the top layer of PMM after applying an external magnetic field. Both the increased polymer dosage and applying time during which the sample was exposed to the magnetic field contribute to the enrichment of the polymer in the top layer. The addition of magneto-responsive polymer latex decreased the compressive strength but significantly increased the flexural strength compared to the reference. The applied magnetic field can slightly increase the compressive strength of PMM with the addition of magneto-responsive polymer latex, but has a limited effect on the flexural strength.

Both the addition of polymer latex at the dosage of 4 % (MRP4) and 8 % (MRP8) showed strong capability to reduce drying shrinkage, and the reduction was larger for MRP8 than for MRP4. The cracks were observed in all the samples without an applied magnetic field, and the crack resistance of PMM was improved with the increased dosage of polymer latex. After applying the magnetic field, no cracks were observed on the sides and tops of samples with the addition of polymer at the dosages of 4 % and 8 %. This indicates a great improvement in crack resistance after the enrichment of polymer latex in the top layer of PMM, which is believed to be caused by the increased flexural strength and decreased drying shrinkage of PMM. This study provides one effective way to improve the anti-cracking performance of PMM and solve the problem of economic burden caused by the high addition amount of polymer latex.

CRediT authorship contribution statement

Jing Wang: Investigation. **Zichen Lu:** Writing – review & editing, Supervision, Funding acquisition, Conceptualization. **Xiangming Kong:** Writing – review & editing, Supervision. **Lei Wang:** Writing – original draft, Methodology, Investigation, Conceptualization.

Financial support

Financial support from the NEXCEL Technology Development and Acceleration (TDA) Project (2023TDA6-2) “Research on gradient enhanced polymer modified concrete for structural use and comparison with conventional concrete”, Science and Technology Bureau of Wanrong County (kz0050020231876), and the National Natural Science Foundation of China (No. 52208282) for funding this research are gratefully acknowledged.

Declaration of Competing Interest

The authors declare that they have no known competing financial interests or personal relationships that could have appeared to influence the work reported in this paper.

Acknowledgements

Financial support from the NEXCEL Technology Development and

Acceleration (TDA) Project (2023TDA6–2) "Research on gradient enhanced polymer modified concrete for structural use and comparison with conventional concrete", Science and Technology Bureau of Wanrong County (kz0050020231876), and the National Natural Science Foundation of China (No. 52208282) for funding this research are gratefully acknowledged.

Data Availability

Data will be made available on request.

References

[1] A. Dinesh, S. Indhumathi, M. Pichumani, Self-sensing cement composites for structural health monitoring: From know-how to do-how, Autom. Constr. 160 (2024) 105304, https://doi.org/10.1016/j.autcon.2024.105304.
[2] P.L. Yuan, B.D. Zhang, Y.T. Yang, T.F. Jiang, J. Li, J.L. Qiu, H.J. He, Application of polymer cement repair mortar in underground engineering: a review, Case Stud. Constr. Mater. 19 (2023) e02555, https://doi.org/10.1016/j.cscm.2023.e02555.
[3] X.M. Ma, J.L. Pan, J.M. Cai, Z.Y. Zhang, J.S. Han, A review on cement-based materials used in steel structures as fireproof coating, Constr. Build. Mater. 315 (2022) 125623, https://doi.org/10.1016/j.conbuildmat.2021.125623.
[4] W.K. Dong, J.B. Tang, K.J. Wang, Y.H. Huang, S.P. Shah, W.G. Li, Cement-based batteries for renewable and sustainable energy storage toward an energy-efficient future, Energy 315 (2025) 134382, https://doi.org/10.1016/j.energy.2025.134382.
[5] A. Azzam, M.T. Bassuoni, A. Shalaby, Performance of nano silica-modified cementitious composites reinforced with basalt fiber pellets under alkaline and salt-frost exposures, Cem. Concr. Comp. 134 (2022) 104761, https://doi.org/10.1016/j.cemconcomp.2022.104761.
[6] G.H. Lv, K. Wang, X.S. Zhang, C.Y. Ma, Q.Y. Xie, J. Liu, A characteristic model for the relationship between cracking and bearing performance of reinforced concrete, Constr. Build. Mater. 428 (2024) 136335, https://doi.org/10.1016/j.conbuildmat.2024.136335.
[7] S.L. Hou, K. Li, Z.M. Wu, F.M. Li, C.J. Shi, Quantitative evaluation on self-healing capacity of cracked concrete by water permeability test-a review, Cem. Concr. Comp. 127 (2022) 104404, https://doi.org/10.1016/j.cemconcomp.2021.104404.
[8] D. Snoeck, B. Moerkerke, A. Mignon, N. De Belie, In-situ crosslinking of superabsorbent polymers as external curing layer compared to internal curing to mitigate plastic shrinkage, Constr. Build. Mater. 262 (2020) 120819, https://doi.org/10.1016/j.conbuildmat.2020.120819.
[9] T.F. Nian, M.M. Wang, X.M. Huang, J.G. Ge, J.Q. Song, P.Y. Li, Investigating crack resistance and mechanisms of crack extension in high-content steel fibers reinforced hot recycled asphalt mixtures, Constr. Build. Mater. 450 (2024) 138717, https://doi.org/10.1016/j.conbuildmat.2024.138717.
[10] F. Maria, T. Athanasia, G. Fani, E. Anaxagoras, Carbon nanotubes' amount and type: crucial parameters in mechanical performance enhancement on cement paste nanocomposites, J. Phys. Conf. Ser. 2321 (2022) 012003, https://doi.org/10.1088/1742-6596/2321/1/012003.
[11] A.K. Thomoglou, J.G. Fantidis, M.E. Voutetaki, Z.S. Metaxa, C.E. Chalioris, Mechanical characterization of nano-reinforced mortar: X-ray Micro-CT for 3D imaging of microstructure, Eng. Proc. 41 (2023) 4, https://doi.org/10.3390/engproc2023041004.
[12] G. Yang, Y.K. Wu, H. Li, N.X. Gao, M. Jin, Z.L. Hu, J.P. Liu, Effect of shrinkage-reducing polycarboxylate admixture on cracking behavior of ultra-high strength mortar, Cem. Concr. Comp. 122 (2021) 104117, https://doi.org/10.1016/j.cemconcomp.2021.104117.
[13] C.Y. Zhang, X.M. Kong, J.W. Yu, D. Jansen, J. Pakusch, S.X. Wang, Correlation between the adsorption behavior of colloidal polymer particles and the yield stress of fresh cement pastes, Cem. Concr. Res. 152 (2022) 106668, https://doi.org/10.1016/j.cemconres.2021.106668.
[14] C.Y. Zhang, J. Liu, S.F. Zhang, X.M. Kong, Mechanical properties of polymer modified mortars using polymer latexes with varied glass transition temperature and surface charges, Cem. Concr. Comp. 150 (2024) 105573, https://doi.org/10.1016/j.cemconcomp.2024.105573.
[15] C.Y. Zhang, J. Wang, S.F. Zhang, X.W. Hou, X.M. Kong, Damping performance of hardened cement pastes containing styrene-butyl acrylate polymers with varied glass transition temperature and surface charges, Cem. Concr. Comp. 145 (2024) 105312, https://doi.org/10.1016/j.cemconcomp.2023.105312.
[16] A.C. Bhogayata, N.K. Arora, Workability, strength, and durability of concrete containing recycled plastic fibers and styrene-butadiene rubber latex, Constr. Build. Mater. 180 (2018) 382–395, https://doi.org/10.1016/j.conbuildmat.2018.05.175.
[17] L. Li, R. Wang, Q. Lu, Influence of polymer latex on the setting time, mechanical properties and durability of calcium sulfoaluminate cement mortar, Constr. Build. Mater. 169 (2018) 911–922, https://doi.org/10.1016/j.conbuildmat.2018.03.005.
[18] Q. Feng, F.J. Jia, Z.G. Peng, Y. Zheng, Development of temperature-responsive suspension stabilizer and its application in cementing slurry system, Colloids Surf. A Physicochem. Eng. Asp. 658 (2023) 130734, https://doi.org/10.1016/j.colsurfa.2022.130734.
[19] M. Ezzat, K. Lesage, R. Hoogenboom, G. De Schutter, Smart superplasticizers based on redox-responsive polymers for rheology control of cementitious materials, Cem. Concr. Res. 173 (2023) 107291, https://doi.org/10.1016/j.cemconres.2023.107291.
[20] X.Q. Wu, J.G. Dong, M.S. Tang, Microwave curing technique in concrete manufacture, Cem. Concr. Res. 17 (1987) 205–210, https://doi.org/10.1016/0008-8846(87)90103-7.
[21] H. Yazici, M.Y. Yardimci, S. Aydin, A.S. Karabulut, Mechanical properties of reactive powder concrete containing mineral admixtures under different curing regimes, Constr. Build. Mater. 23 (2009) 1223–1231, https://doi.org/10.1016/j.conbuildmat.2008.08.003.
[22] Y.Y. Zhang, K. Lesage, Y. Zhang, Y.X. Tao, K. Van Tittelboom, G. De Schutter, A comparison of magneto-responsive particles and testing protocols for active rheology control of cementitious materials, Cem. Concr. Comp. 146 (2024) 105390, https://doi.org/10.1016/j.cemconcomp.2023.105390.
[23] F. Javahershenas, M.S. Gilani, M. Hajforoush, Effect of magnetic field exposure time on mechanical and microstructure properties of steel fiber-reinforced concrete (SFRC), J. Build. Eng. 35 (2021) 101975, https://doi.org/10.1016/j.jobe.2020.101975.
[24] M.S. Choi, Y.S. Kim, J.H. Kim, J.S. Kim, S.H. Kwon, Effects of an externally imposed electromagnetic field on the formation of a lubrication layer in concrete pumping, Constr. Build. Mater. 61 (2014) 18–23, https://doi.org/10.1016/j.conbuildmat.2014.02.071.
[25] D.W. Jiao, K. El Cheikh, C.J. Shi, K. Lesage, G. De Schutter, Structural build-up of cementitious paste with nano-Fe3O4 under time-varying magnetic fields, Cem. Concr. Res. 124 (2019) 105857, https://doi.org/10.1016/j.cemconres.2019.105857.
[26] D.W. Jiao, K. Lesage, M.Y. Yardimci, K. El, C.J. Shi, G. De Schutter, Quantitative assessment of the influence of external magnetic field on clustering of nano-Fe3O4 particles in cementitious paste, Cem. Concr. Res. 142 (2021) 106345, https://doi.org/10.1016/j.cemconres.2020.106345.
[27] X.M. Kong, C.C. Wu, Y.R. Zhang, J.L. Li, Polymer-modified mortar with a gradient polymer distribution: Preparation, permeability, and mechanical behaviour, Constr. Build. Mater. 38 (2013) 195–203, https://doi.org/10.1016/j.conbuildmat.2012.07.080.
[28] L. Zhang, X. Miao, X. Kong, S. Zhou, Retardation effect of PCE superplasticizers with different architectures and their impacts on early strength of cement mortar, Cem. Concr. Comp. 104 (2019) 103369, https://doi.org/10.1016/j.cemconcomp.2019.103369.
[29] H.A. Shah, Q. Yuan, S.H. Zuo, Air entrainment in fresh concrete and its effects on hardened concrete-a review, Constr. Build. Mater. 274 (2021) 121835, https://doi.org/10.1016/j.conbuildmat.2020.121835.
[30] X.M. Kong, S. Emmerling, J. Pakusch, M. Rueckel, J. Nieberle, Retardation effect of styrene-acrylate copolymer latexes on cement hydration, Cem. Concr. Res. 75 (2015) 23–41, https://doi.org/10.1016/j.cemconres.2015.04.014.
[31] Z. Lu, X. Kong, C. Zhang, D. Jansen, J. Neubauer, F. Goetz-Neunhoeffer, Effects of two oppositely charged colloidal polymers on cement hydration, Cem. Concr. Comp. 96 (2019) 66–76, https://doi.org/10.1016/j.cemconcomp.2018.11.014.
[32] J.B. Yang, Z.P. Sun, N. De Belie, D. Snoeck, Mitigating plastic shrinkage cracking in alkali-activated slag systems by internal curing with superabsorbent polymers, Cem. Concr. Comp. 134 (2022) 104784, https://doi.org/10.1016/j.cemconcomp.2022.104784.
[33] D. Wang, P. Yang, P. Hou, L. Zhang, X. Zhang, Z. Zhou, N. Xie, S. Huang, X. Cheng, Cement-based composites endowed with novel functions through controlling interface microstructure from Fe3O4@SiO2 nanoparticles, Cem. Concr. Comp. 80 (2017) 268–276, https://doi.org/10.1016/j.cemconcomp.2017.03.017.
[34] Z.C. Lu, X.M. Kong, C.Y. Zhang, Y. Cai, Effect of highly carboxylated colloidal polymers on cement hydration and interactions with calcium ions, Cem. Concr. Res. 113 (2018) 140–153, https://doi.org/10.1016/j.cemconres.2018.08.010.

Construction and Building Materials 438 (2024) 137284

Contents lists available at ScienceDirect

Construction and Building Materials

journal homepage: www.elsevier.com/locate/conbuildmat

Modification of early-age microstructure and enhanced mechanical properties of cement paste via injecting low-dose CO_2 at fresh stage

Shuang Luo [a], Ming-Zhi Guo [b,*], Tung-Chai Ling [a,*]

[a] College of Civil Engineering, Hunan University, Changsha, Hunan Province 410082, China
[b] College of Civil Engineering, Shaoxing University, Shaoxing, Zhejiang 312000, China

ARTICLE INFO

Keywords:
CO_2-mixing
Nano-$CaCO_3$
Nano-$Ca(OH)_2$
Compressive strength
Microstructure

ABSTRACT

Most previous studies introduce high dose CO_2 (> 0.05 %) into fresh cement paste during mixing (CO_2-mixing) to sequester CO_2. However, this strategy results in poor workability and lower long-term strength. This study attempts to use a lower CO_2-mixing dose (0.017–0.083 wt.‰) to improve the performance of fresh and hardened cement pastes. The planar distribution, morphology, and evolution of the reaction products over time were investigated. The results showed that all the lower CO_2-mixing fresh pastes displayed a good workability, and the compressive strength was increased by 0.3–21.7 % at 1–28 days. The enhancement in compressive strength was attributed to the formation of monocarbonate (Mc), deriving from the reaction of nano-$CaCO_3$ covering the clinkers with the aluminum phase, which strengthened the interface bond between the clinker and the new hydration product. Moreover, the generated nano-$CaCO_3$ also resulted in local high supersaturation on the clinker surface and promoted the formation of nano-$Ca(OH)_2$ embedded in the calcium silicate hydrate (C-S-H). As a result, the compactness of the hydration products was enhanced. The refinement in the microstructures of the low-dose CO_2-mixed samples was translated into enhanced mechanical properties.

1. Introduction

As an integral component of building infrastructures, concrete has significant environmental consequences because the production of cement accounts for ~8 % of global anthropogenic CO_2 emissions [1,2]. In recent years, carbonation curing (CO_2-curing) cement-based material has been widely used to achieve sustainability in the built environment as this technology can not only sequester CO_2 but also improve the early mechanical properties of the hardened cementitious materials [3]. However, CO_2-curing is mainly applied on precast concrete under a closed chamber environment. To broaden its application in concrete industry, upcycling CO_2 during the mixing process (CO_2-mixing) of cement-based materials has been proposed [4,5].

The influencing factors of CO_2-curing and CO_2-mixing on the performance of cement-based materials are quite different, as shown in Fig. 1. In CO_2-curing, CO_2 is utilized as a curing agent, and the reaction mainly occurs in pores solution in cement matrix. Thus, CO_2-curing is greatly affected by the presence of water content (water to cement ratio, w/c), CO_2 parameters, etc. [6,7]. As carbonation proceeds, the formation of carbonation products ($CaCO_3$) can fill the pores and densify the microstructure. As a result, the mechanical properties of the CO_2-curing samples are improved with increasing carbonation time [8]. However, the improving effect of CO_2-curing is greatly limited at a higher carbonation degree. Especially, excessive precipitation of $CaCO_3$ in the outer layer of the sample could impede the CO_2 diffusion [9].

In CO_2-mixing, usually high-purity CO_2 was used during cement-based materials batching or mixing [10]. Hence, the stirring rate, w/c, and especially CO_2 dose play important roles in influencing the performance of the end products [11,12]. Unlike CO_2-curing, CO_2-mixing allows for a more readily and direct reaction of CO_2 with the clinker to form nano-$CaCO_3$. This is because the Ca^{2+} ions leached from the cement can easily react with CO_3^{2-} ions derived from the injected CO_2. Subsequently, the resulting nano-$CaCO_3$ acts as a nucleation site to promote further hydration and thereby improve the mechanical properties [11,13]. However, if excessive CO_2 is injected into the cement paste, inordinate nano-$CaCO_3$ could accumulate on the clinker surface and unfavorably impede the cement hydration [10]. Moreover, the initially generated nano-$CaCO_3$ could also directionally guide the planar distribution of the newly formed reaction products to further affect the performance of cement-based materials. Therefore, for CO_2-mixing, it is important to consider both the optimal CO_2 dose injection during such a rapid mixing process and the impact of nano-$CaCO_3$ on the subsequent

* Corresponding authors.
E-mail addresses: guo.mz.guo@connect.polyu.hk (M.-Z. Guo), tcling@hnu.edu.cn (T.-C. Ling).

https://doi.org/10.1016/j.conbuildmat.2024.137284
Received 8 April 2023; Received in revised form 10 June 2024; Accepted 27 June 2024
Available online 4 July 2024
0950-0618/© 2024 Published by Elsevier Ltd.

planar distribution of the reaction products.

Extensive efforts have been made to determine the optimal CO_2-mixing dose and elucidate the underlying mechanisms of CO_2-mixing cement-based materials [10–12,14]. Monkman et al. [10] injected 0.05–0.3 % CO_2 into the ready-mixed concrete immediately when the concrete truck paused at the wash rack for cleaning batching (an open-air environment). The results showed that the mechanical property of concrete was improved only at a 0.05 % CO_2 dose. Other studies [13, 15] reported that the formed nano-$CaCO_3$ during mixing was partly enveloped by the C-S-H gels to promote further hydration and improve the mechanical performance. To fully utilize gas and avoid the release of CO_2 into the air, Liu et al. [16] designed an airtight mixer and injected 1.76 wt.% CO_2 into the cement paste during mixing. It was found that the formation of excessive nano-$CaCO_3$ with a large specific surface area decreased the workability, which negatively affected the porosity and impaired the mechanical performance of the hardened CO_2-mixing products at 3–7 days [12,16,17]. Luo et al. [14] reported that the injection of 0.3–1.2 wt.% CO_2 into the cement paste mixed by an airtight mixer led to only a 0.4–17.6 % improvement in the carbonation degree at 1 day. This improvement was achieved at the expense of a 4.8–24.6 % decrease in fluidity and a reduction in compressive strength compared with the control group. Apparently, the injected CO_2 dose is significantly higher than the theoretical absorption capacity of the cement-based materials during such a short mixing time, resulting in a reduction in both workability and mechanical properties [10,13,18]. Therefore, it is important to study the effect of CO_2-mixing doses below 0.05 % on the properties of cement-based materials.

This study aims to study the effect of extremely low CO_2 doses (0.017, 0.033, 0.050, 0.067, and 0.083 ‰ by mass of cement, ‰ means one-thousandth part of a whole) on the performance of the cement-based materials by evaluating the workability and hardening process of CO_2-mixing cement paste over time. Furthermore, the morphological and planar distribution features of the carbonation reaction products were analyzed to dissect the underlying reaction mechanisms. Finally, the contents of the carbonation and hydration products at different times were calculated to evaluate the effect of early CO_2 injection on the subsequent hydration reactions.

2. Experimental program

2.1. Materials

P·I 42.5 Portland cement with a density of 3.12 g/cm^3 and a specific surface of 359 m^2/kg was used in this study. Its chemical compositions and mineral compositions are shown in Table 1. CO_2 gas used for mixing was an industrial-grade with a purity of 99 %. Pure deionized water was used throughout the whole experiment.

2.2. Preparation of CO_2-mixing cement paste

All the cement pastes were proportioned with a fixed w/c ratio of 0.40 in an airtight mixer, as shown in Fig. 2. Cement and water were first mixed in the airtight mixer at a speed of 140±5 r/min for approximately 30 s. Then, the mixture was remixed manually using a steel trowel within 120 s. Finally, the mixture was mechanically mixed for another 70 s at a higher speed of 285±10 r/min. At the thirtieth second, 0.017, 0.033, 0.050, 0.067, and 0.083 wt.‰ of CO_2 gas (by mass of cement) were injected into the airtight mixer to prevent air carbonation of cement pastes, demoted as C-0.017, C-0.033, C-0.05, C-0.067, and C-0.083, respectively. This translates to CO_2 volumes of approximately 8.3, 16.7, 25, 33.3, and 41.7 mL expected to react with every kg of cement in the respective mixtures. The injected CO_2 flow rates were controlled at 100, 200, 300, 400, and 500 mL/min to achieve this concentration (see Eq. 1), and the flow time of CO_2 gas was consistently set at 9 seconds for all samples. It is important to mention that the purity of the CO_2 gas used was 99 %. The control group (named as C-0) without CO_2 injection was also prepared for comparison. After mixing, the fresh pastes were cast in 40 mm × 40 mm × 40 mm cubic molds and vibrated using a vibrating table for 30 s. All samples were demolded after 24 h and then cured at 20±2 °C at a constant relative humidity of 95 % until

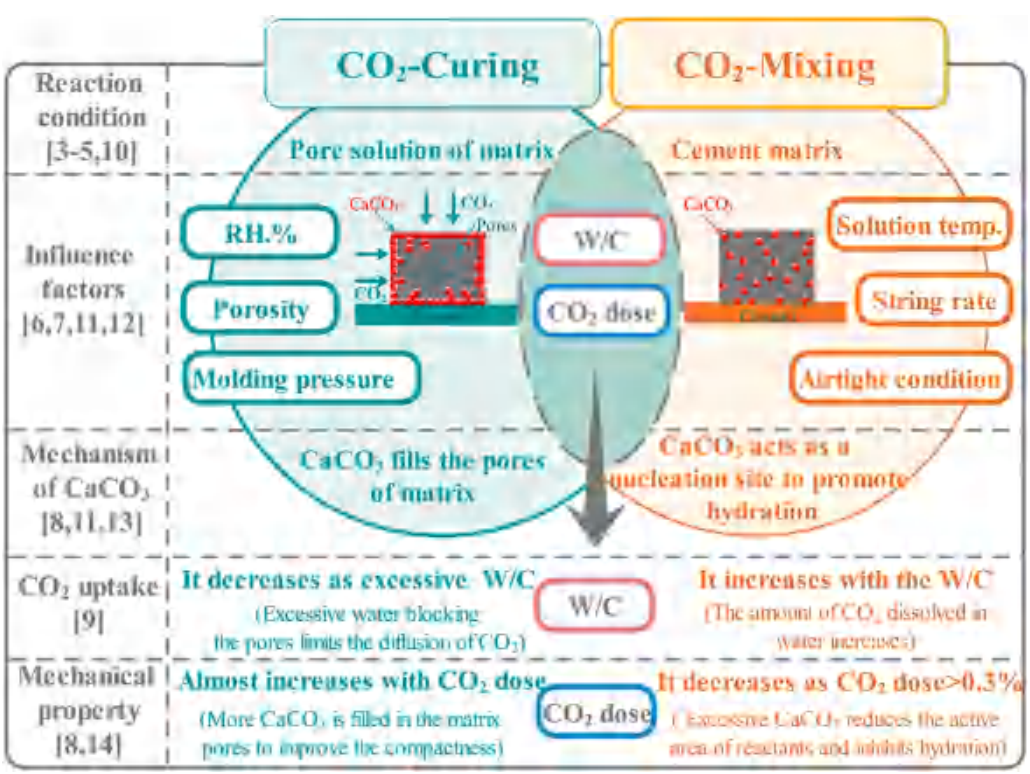

Fig. 1. The difference between CO_2-curing and CO_2-mixing on performance of cement-based materials.

Table 1
Chemical and mineral compositions of P. I 42.5 Portland cement (wt.%).

Chemical compositions									
SiO_2	Al_2O_3	Fe_2O_3	CaO	MgO	SO_3	Na_2O	f-CaO	Cl^-	LOI
20.53	4.45	3.17	62.05	2.81	2.10	0.55	0.80	0.032	1.74
Mineral compositions									
C_3S	C_2S	C_3A	C_4AF						
57.38	18.55	7.14	11.37						

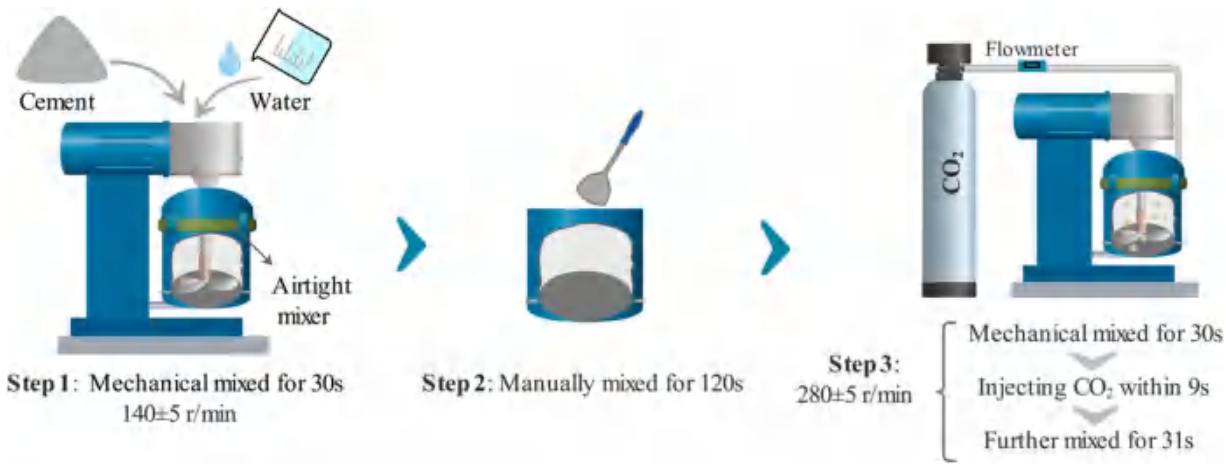

Fig. 2. Schematic diagram of airtight cement mixer (The CO_2 flow meter used has a precision of ±10 mL/min.).

the testing days.

$$v = \frac{m_{CO_2}}{\rho_{CO_2} \times t} \quad (1)$$

Where, m_{CO2} is the mass of the injected CO_2 gas (g, by mass of cement), v is the CO_2 gas flowrate (mL/min), ρ_{CO2} is the density of CO_2 gas (1.977 g/L at atmospheric pressure), and t is the CO_2-intermixing time (fixed as 9 s for all cases).

2.3. Characterization of fresh and hardened properties of CO_2-mixing paste

The presence of nano-$CaCO_3$ with a large specific surface area formed during the mixing process can promote the formation of gelling calcium silicate hydrate (C-S-H) [13], which may result in a reduction in free water and workability performance [15]. Thus, the workability of the fresh cement pastes was measured using a mini-slump flow table according to GB/T 2419–2005 [19]. The compressive strength of the hardened cement paste (three 40 mm-cubic samples) was determined using a universal compression machine with a maximum capacity of 300 kN at a fixed loading rate of 2.4 kN/s according to GB/T 17671–2021 [20]. Mineral phases of the cement pastes were determined by X-ray diffraction (XRD) with Cu Kα radiation operating at 40 mA and 45 kV, and the scanning parameters were 5–30°, 2θ scanning range, 0.02° step width, and 2°/min scan rate. The porosity of the hardened samples was determined using the software ImageJ to analyze the backscattered electron (BSE) images with a voltage of 20 kV at 500 × magnifications.

2.4. Morphology and planar distribution of reaction products

The injected CO_2 during mixing is more likely to first react with the cement clinkers to form amorphous nano-$CaCO_3$ and cover the surface of the clinkers as a nucleation site [13]. However, the excessive formation of carbonates may affect the planar distribution of reaction products surrounding the clinkers. It should be noted that some CO_3^{2-} may still remain in the paste solution after mixing due to a limited reaction rate of the clinkers [14]. The remaining CO_3^{2-} can then react with the cement hydration products (e.g., calcium hydroxide) or cement clinkers to form different crystal forms of $CaCO_3$ (calcite, aragonite, and vaterite) to affect the mechanical properties [21–24]. In order to examine the planar distribution and morphology characteristics of the reaction products, BSE images were acquired in a vacuum condition using a JEOL Ltd. equipment with 5000 × magnifications. To ensure the size comparability of the hydration products around the clinkers, all the selected clinker particle with a particle size of 25–50 μm in the BSE images. In addition, a TESCAN MIRA4 scanning electron microscope (SEM) with an energy dispersive spectrometer (EDS) was used to observe the morphology of the reaction products.

2.5. Content variation of reaction products over time

Previous studies [25,26] have shown that the presence of carbonation-generated $CaCO_3$ can react in cement composites over time. Thermogravimetric analysis (TGA) was conducted at different curing ages using a Thermo Plus EVO2 TGA (Rigaku). For each measurement, about 15 mg of powdered sample was heated at a rate of 10 °C/min from 30 to 1000°C under an N_2 flow of 30 mL/min. The content of $Ca(OH)_2$ and $CaCO_3$ at 1, 7, and 28 days was calculated according to the following Eqs. (2) and (3) [27–30].

$$\%Ca(OH)_2 = \frac{M_{400^\circ C} - M_{500^\circ C}}{M_{sample}} \times \frac{74.09}{18.01} \times 100 \quad (2)$$

$$\%CaCO_3 = \frac{M_{550^\circ C} - M_{950^\circ C}}{M_{sample}} \times \frac{100.9}{44.01} \times 100 \quad (3)$$

Where, M and M_{sample} are the relative mass loss at a given temperature and mass of samples: $Ca(OH)_2$ dihydroxylation at 400–500 °C and $CaCO_3$ decomposition at 550–950 °C.

3. Results and discussion

3.1. Fresh and hardened properties of CO_2-mixing paste

3.1.1. Workability

The workability of the fresh CO_2-mixing cement pastes reflected by mini-slump flow values is presented in Fig. 3. The workability results of all the CO_2-mixing cement pastes ranging in 114.5–119.5 mm in diameter was comparable to that of the control group (120 mm), indicating that injecting low CO_2 doses (0.017–0.083 wt.‰) exerted a negligible impact on the workability. Unlike a previous study [14], which injected a relatively higher CO_2-mixing dose (0.3–1.2 wt.%) in the fresh cement and found that the workability decreased sharply by 4.8–24.6 %. Such a neglected effect of a low CO_2-mixing dose on the workability was possibly due to the fact that the formation of a small amount of $CaCO_3$ only slightly affected the absorption of free water in the fresh matrix [18, 31].

3.1.2. Compressive strength

The compressive strength of the hardened CO_2-mixing cement pastes is shown in Fig. 4. It can be observed that samples treated with a 0.017–0.067 wt.‰ CO_2-mixing dose during the first 1–3 days of curing showed a 1.8–21.7 % increase in compressive strength compared to the control group. However, such an improvement in compressive strength became less significant with prolonging the curing age to 7–28 days. The improvement of early strength was mainly related to the formation of calcium aluminate monocarbonate (Mc, $C_3A{\bullet}CaCO_3{\bullet}11\ H_2O$) derived from the reaction between nano-$CaCO_3$ and aluminum phase in cement paste, which could effectively avoid the transformation of ettringite (AFt) [25]. The formation of Mc will be further discussed in Section 3.2.2. Another possible reason for the early age strength enhancement could be attributed to the formation of amorphous calcium carbonate (ACC) and nano-calcite, as observed in the SEM images (Fig. 9). These formations create a stronger bond with the cement hydration products [32]. In contrast, some vaterite, instead of only calcite, was detected in the later age paste samples [33] (which will be discussed in more detail in Section 3.2.3). However, it should be pointed out that the samples at a later age (7 and 28 days) suffered a relative higher strength reduction, especially for those using the highest CO_2-mixing dose (0.083 wt.‰). This was because the accumulation of excessive nano-$CaCO_3$ on the clinker surface is likely to inhibit the hydration reaction [34,35].

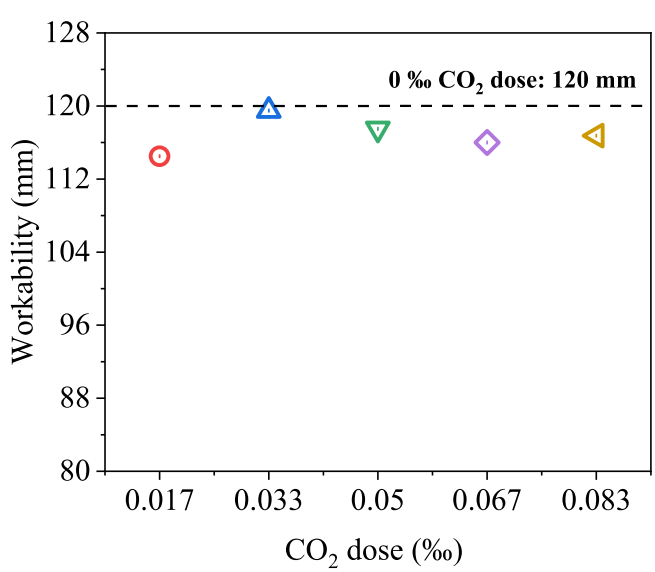

Fig. 3. Workability of fresh cement pastes intermixed with different CO_2 doses.

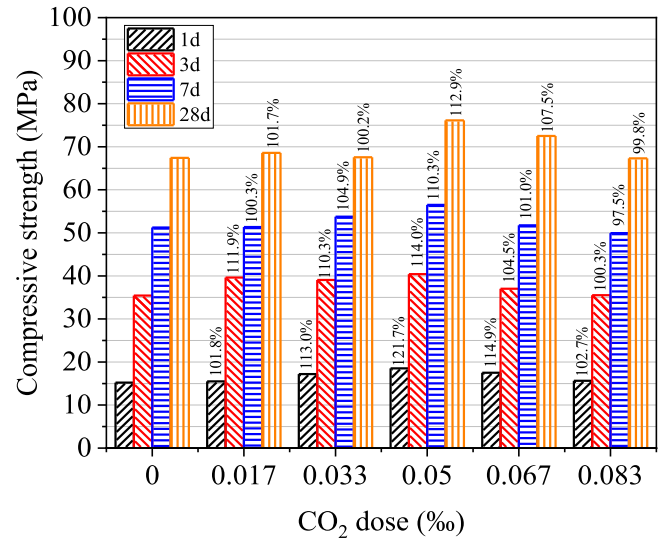

Fig. 4. Compressive strength of CO_2-mixing cement pastes.

3.1.3. Porosity

Table 2 shows the porosity results calculated by the BSE image (500×) analysis. Examples of the original BSE images, cumulative grayscalecurves and thresholded images at both 1 day and 28 days are shown in Figs. A1 and A2, respectively, in the appendix. It can be observed that C-0.05 had the lowest porosity regardless of curing ages, which corresponded to the highest compressive strength (see Fig. 4). The reduction of porosity was known to be related to pore refinement by nano-$CaCO_3$ as well as the formation of Mc which can avoid the transformation of mono sulfur hydrated calcium sulphoaluminate (AFm) into AFt. This reduced the volume shrinkage of the sample and eventually encouraged the formation of a denser structure in the matrix [36,37]. In addition, the generated nano-$CaCO_3$ could also alter the size formation of $Ca(OH)_2$ and thereby increase the amount of small-volume $Ca(OH)_2$ growth [25,38]. Small-vole $Ca(OH)_2$ was more readily overlapped with each other to efficiently fill in the gel pores (This will be discussed in more detail in Section 3.2.2). It was noteworthy that C-0.083 had a comparable porosity to the control sample. Similar findings were also observed in the cement-based materials prepared by the ex-situ addition of nano-$CaCO_3$, because the agglomeration of nano-$CaCO_3$ greatly reduced its nucleation site and hydration effects [28].

3.2. Morphology and planar distribution of reaction products

3.2.1. C-S-H

During the hydration of cement, the C-S-H formed within the boundary of the original clinkers is usually referred to as “inner products” (IP), while that formed in the initially water-filled space is designated as “outer products” (OP) [39–42]. Fig. 5 shows the BSE images of CO_2-mixing cement pastes after curing 1 and 28 days. It can be seen from Fig. 5(a) that at 1 day, IP and amount of OP were formed in the C-0 group. However, for C-0.05 and C-0.083, a relatively thicker IP rim was observed (Fig. 5(c, e)). This was probably because nano-$CaCO_3$ was formed earlier than C-S-H during cement batching and attached to the clinker surface as a “nucleation site” [13]. Furthermore, the C-S-H gels at the "nucleation site" tended to be fairly denser and underwent directional growth around the clinkers to form a thicker IP rim. The EDS 1

Table 2
Porosity (%) calculation of 1 and 28 days samples based on BSE images results.

NO.	C-0	C-0.05	C-0.083
1 day	15.66±0.9	13.02±0.82	15.07±0.58
28 days	6.74±0.8	5.67±0.32	6.75±0.34

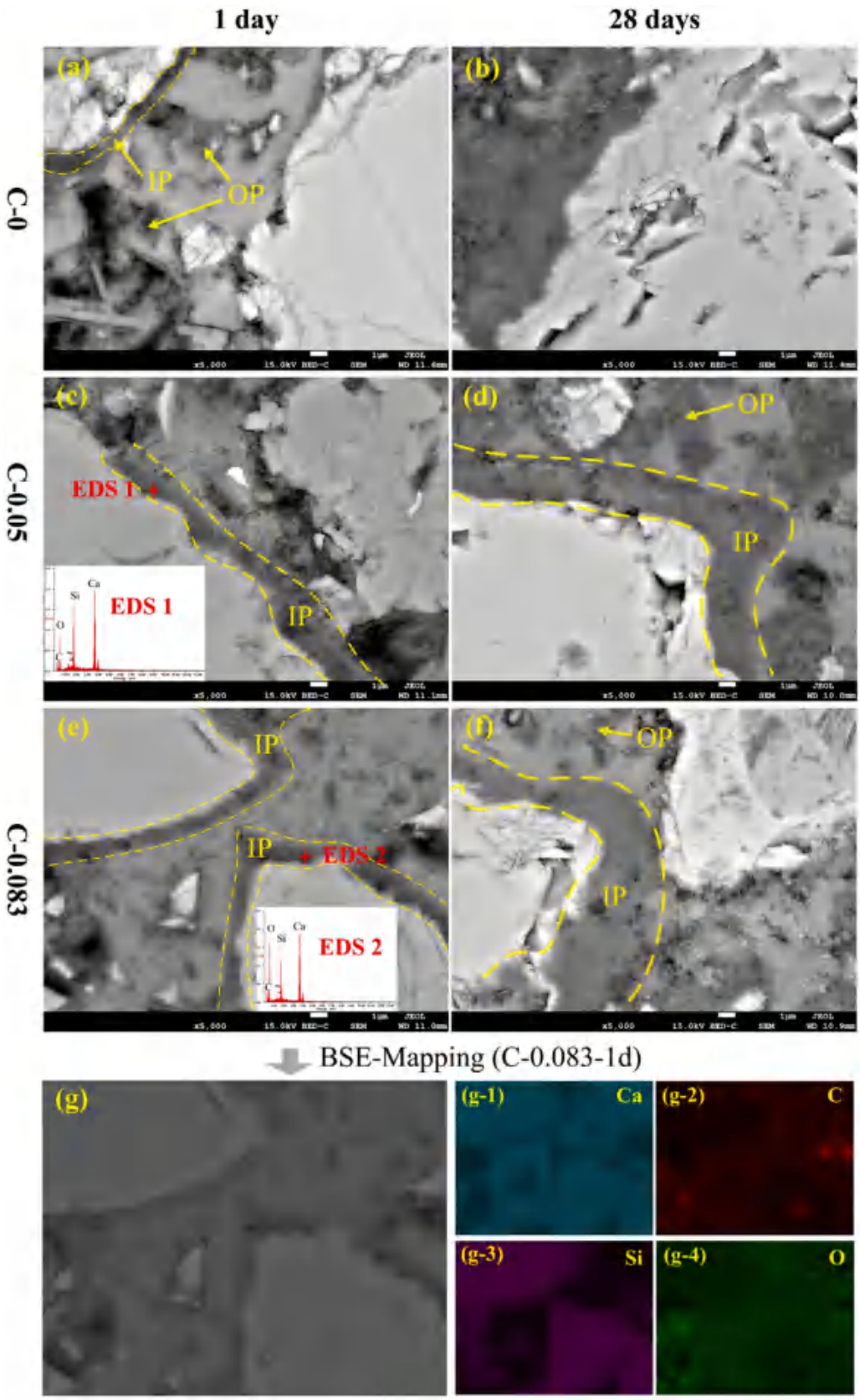

Fig. 5. BSE images of different CO_2-mixing doses cement pastes after curing for 1 and 28 days.

and 2 in Fig. 5(c) and (e) confirmed the presence of $CaCO_3$ in IP. In addition, mapping analysis was conducted to illustrate the distribution of calcium (Ca), carbon (C), silicon (Si), and oxygen (O) elements of C-0.083 at 1 day (Fig. 5(g)). A distinct IP rim was observed around the cement clinker, with a significant accumulation of C elements inside the IP, indicating the possible formation of $CaCO_3$ within the C-S-H.

At 28 days, the IP and OP in the C-0 group were morphologically indistinguishable. This "blurring" region was extended over several dozen microns, as shown in Fig. 5(b). In contrast, for the C-0.05 and C-0.083 groups, OP at 28 days was more distinct than 1 day, while the IP rim was structurally better ordered, as shown in Fig. 5(d) and (f). This may be attributed to the relatively high surface energy of nano-$CaCO_3$, which adhered to the clinker surface and adsorbed Ca^{2+} ions to serve as a nucleation site for the formation of more orderly C-S-H gels [43]. Furthermore, the IP thickness seem increased with increasing the curing age and CO_2 dose, leading to the densification of the interfacial transition region between the clinkers and the hydration products, thereby improving the mechanical properties [25,44].

3.2.2. Planar distribution of different reaction products

Figs. 6 and 7 show the backscatter SEM images and the XRD patterns of the 0.05 ‰ CO_2-mixing sample at 28 days, respectively. EDS 1 and XRD revealed the presence of Mc in the interface of clinkers and C-S-H (IP). It should be noted that hemi-carboaluminate (Hc) was normally produced before the Mc formation, but it was not observed at 28 days [45]. This observation further confirmed that nano-$CaCO_3$ was formed surrounding the clinker during cement batching. The crystal structure of the $CaCO_3$ was mainly composed of calcite and vaterite. Since Mc was harder and larger than AFm and AFt [46], the compactness and hardness of the hardened 0.05 ‰ CO_2-mixing cement paste were enhanced.

Moreover, nano-scale $Ca(OH)_2$ crystals were observed in IP, which were interlaced with nano-$CaCO_3$ (confirmed by EDS 2) to form an intimate nanoscale mixture of C-S-H and microcrystalline $Ca(OH)_2$ and $CaCO_3$. Previous studies [47–49] demonstrated that the formation of nano-$Ca(OH)_2$ was encouraged at low w/c ratios (≤0.30) because a deficiency in water in the pores of a dry cement particle resulted in local high supersaturation in the pore solution. As a result, a lack of available hydration space impeded the generation of large size $Ca(OH)_2$. Moreover, the formation of nano-$CaCO_3$ with a larger specific surface area (attached to the clinker surface) may also lead to a deficiency in free water, forming a supersaturated area (detailed reaction mechanisms are presented in Fig. 8). Some studies showed that as nucleation sites, the

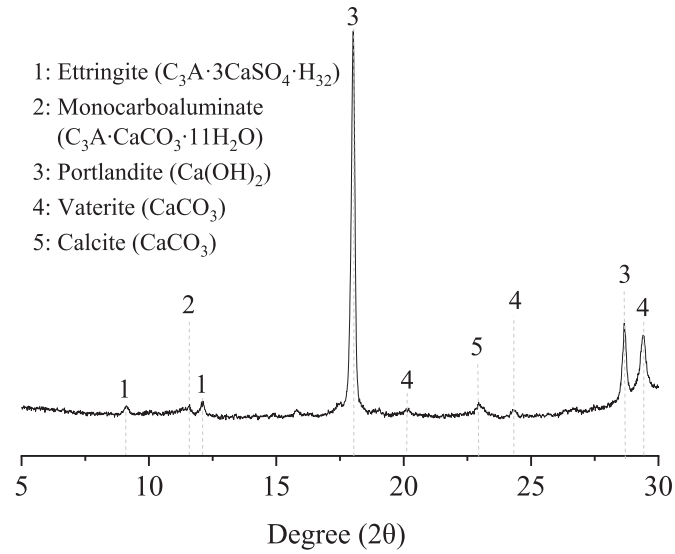

Fig. 7. XRD patterns of 0.05 ‰ CO_2-mixing sample at 28 days.

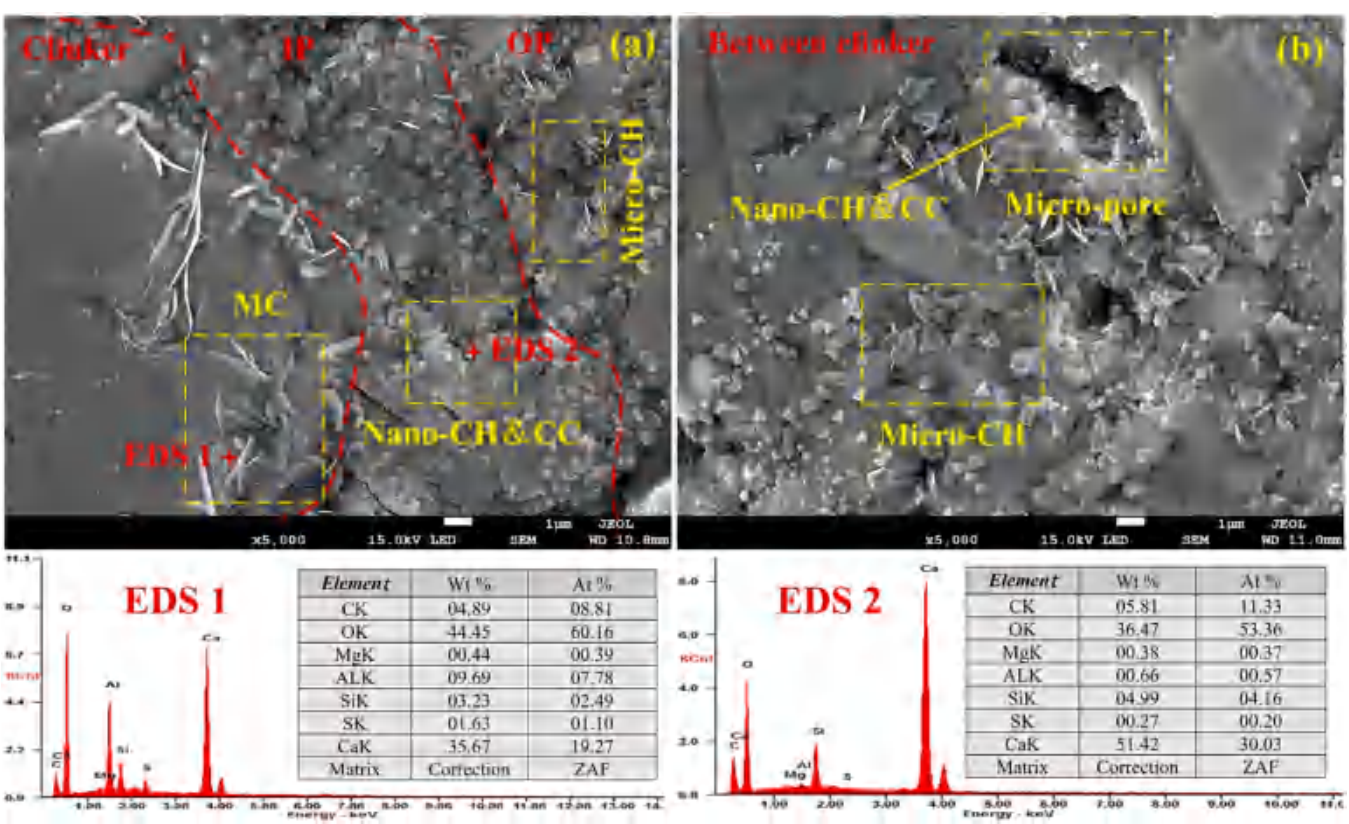

Element	Wt %	At %
CK	04.89	08.81
OK	44.45	60.16
MgK	00.44	00.39
ALK	09.69	07.78
SiK	03.23	02.49
SK	01.63	01.10
CaK	35.67	19.27
Matrix	Correction	ZAF

Element	Wt %	At %
CK	05.81	11.33
OK	36.47	53.36
MgK	00.38	00.37
ALK	00.66	00.57
SiK	04.99	04.16
SK	00.27	00.20
CaK	51.42	30.03
Matrix	Correction	ZAF

Fig. 6. Backscatter SEM images of 0.05 ‰ CO_2-mixing sample at 28 days: (a) the area around clinkers and (b) the area between clinker (CH and CC represents Ca $(OH)_2$ and $CaCO_3$, respectively).

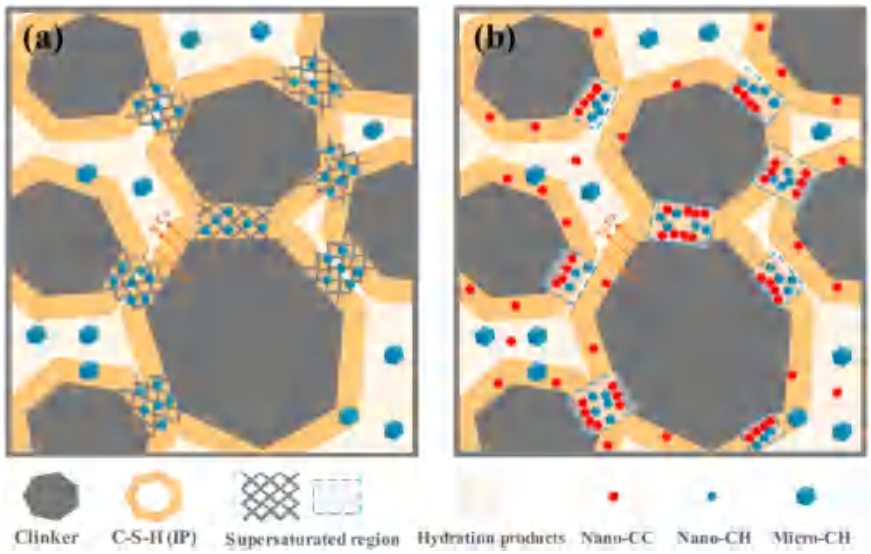

Fig. 8. Schematic of hydrated cement paste: (a) low w/c cement paste [47] and (b) CO_2-mixing cement paste.

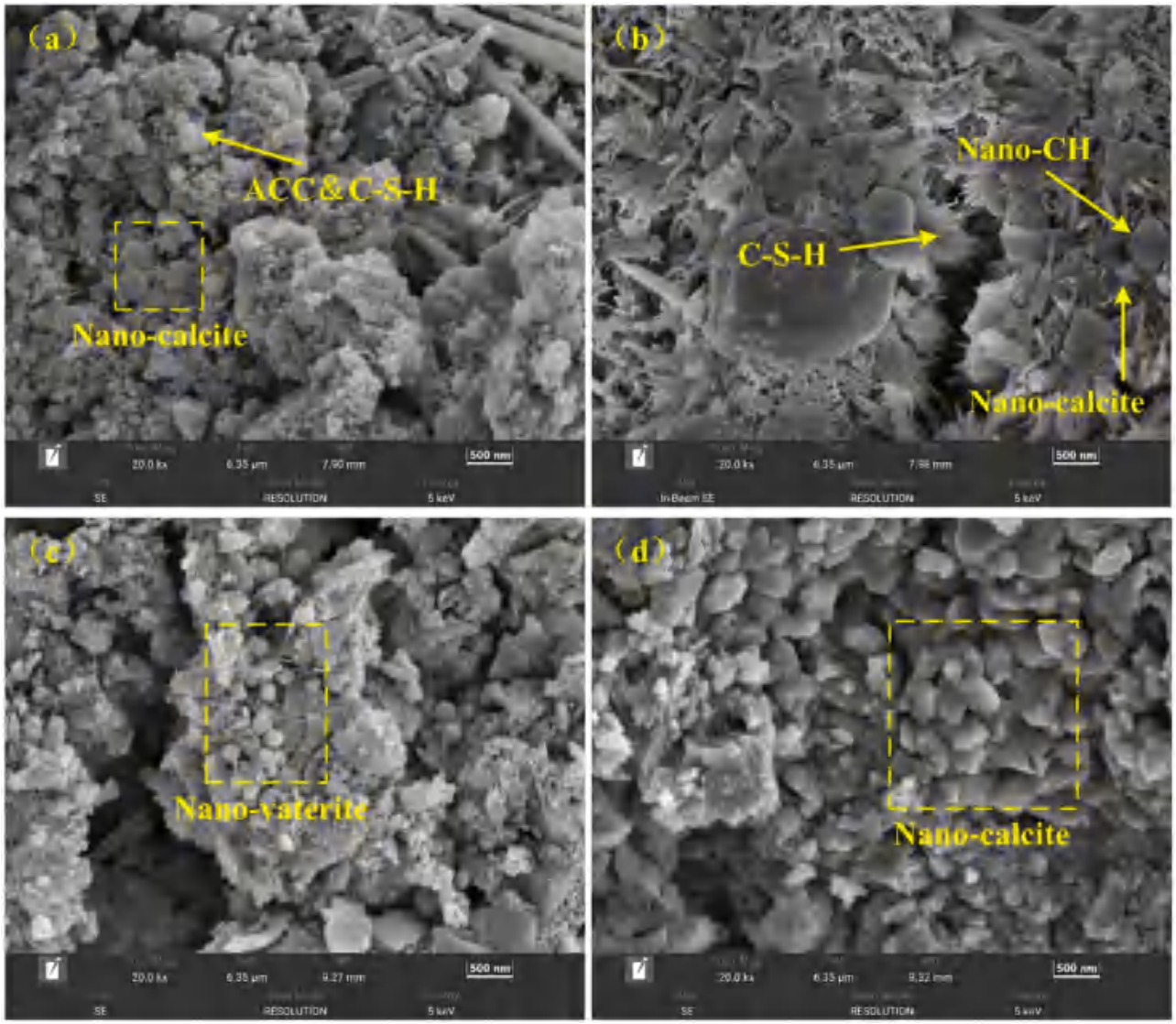

Fig. 9. SEM images of 0.05 ‰ CO_2-mixing sample: (a, b) C-0.05–1 day and (c, d) C-0.05–28 days.

generated nano-$CaCO_3$ can also function as a diffusion and support medium for crystal growth [25], which can affect the growth behavior of $Ca(OH)_2$ by reducing the growth speed of the $Ca(OH)_2$ crystal surface and thereby refine the $Ca(OH)_2$ crystal [38].

Interestingly, $Ca(OH)_2$ with a larger scale (micro-$Ca(OH)_2$) was formed in the OP area or the regions away from the clinker area (between clinkers). This was because less nano-$CaCO_3$ was produced in these areas, and sufficient free water was available for the hydration reaction. Furthermore, it can be seen from Fig. 6(b) that a large number of nano-$Ca(OH)_2$ and nano-$CaCO_3$ mixtures were filled in the micropores to reduce the porosity and thereby improve the mechanical properties [47].

3.2.3. Morphology of reaction products

Fig. 9 shows the SEM images of the 0.05 ‰ CO_2-mixing samples at 1 and 28 days. Normally, $CaCO_3$ exists in different crystal forms: amorphous calcium carbonate (ACC), calcite, aragonite, and vaterite [21–24]. It can be observed from Fig. 9(a) that at 1 day, abundant ACC was formed with the presence of nano-calcite, both of which were interlaced with the C-S-H gels. Previous studies [16,50,51] suggested that the hybrid of C-S-H and $CaCO_3$ was beneficial for the mechanical performance of cement-based materials. Besides, nano-calcite and nano-$Ca(OH)_2$ were observed in Fig. 9(b), which was consistent with the backscatter SEM results in Section 3.2.2. The generated ACC was likely to be transformed into a more stable crystalline phase in the subsequent hydration stage [52], which was confirmed by Fig. 6(b). At 28 days (Fig. 9c, d), both nano-vaterite (which appeared to lightly cover the surface of the hydrated products) and nano-calcite (which was tightly embedded in the matrix) were formed. Bentz et al. [33] suggested that compared with vaterite, calcite had a better bonding with the cement hydration products. This helped to explain why the formation of nano-calcite and ACC in the early stage contributed to a relative higher early strength. In the later stage, the conversion of some ACC into vaterite attenuated the strength improvement effect.

3.3. Content variation of reaction products over time

3.3.1. $CaCO_3$

Fig. 10 shows the $CaCO_3$ content of the CO_2-mixing samples over time. The results showed that at 1 day, the $CaCO_3$ content of all the CO_2-mixing groups (C-0.017 ~ C-0.083) was higher than that of the control group (C-0) due to the formation of ACC and nano-calcite derived from the reaction between CO_2 and Ca^{2+} leached by the clinkers in the solution. However, an inverse trend was observed at 7 and 28 days: $CaCO_3$ in the CO_2-mixing samples reacted with the aluminum phase in cement to form Mc (see Fig. 6 and Fig. 7). In addition, the denser structure of the CO_2-mixing cement pastes also decreased the CO_2 uptake from the surrounding environment at later curing ages.

3.3.2. $Ca(OH)_2$

Fig. 11 shows the $Ca(OH)_2$ content of different samples over time. It is commonly accepted that $Ca(OH)_2$ is the hydration product which can most readily react with CO_2 [53–55]. In the hardened cementitious materials, CO_2 can react with the dissolved $Ca(OH)_2$ in the pore solution, resulting in the precipitation of the almost insoluble $CaCO_3$ in the pore space or matrix [56,57]. Additionally, the CO_2 reacts with C_3S and C_2S, which correspondingly decreases the new $Ca(OH)_2$ formation (Eqn 4 and 5). Therefore, at 1 day, the $Ca(OH)_2$ content of all the CO_2-mixing groups was lower (< ~0.5 %) than that of the control group due to the injection of a certain dose of CO_2 during the batching process. However, at 7 days, the $Ca(OH)_2$ content of the CO_2-mixing groups was higher than that of the control group because there was no continuous CO_2 supply in the hardened samples, and the initially generated nano-$CaCO_3$ further promoted the cement hydration to produce more $Ca(OH)_2$. Interestingly, at 28 days, the $Ca(OH)_2$ content of the CO_2-mixing groups was comparable to that of the control group, indicating that the injected CO_2 during cement batching exerted a negligible effect on the long-term pH of the hardened cement paste. These findings were in good agreement with a previous study [10], which reported that the CO_2-mixing showed no negative effect on the durability of the ready-mixed concrete.

$$3CaO(SiO_2)+(3\text{-}x)\ CO_2+yH_2O \rightarrow xCaO(SiO_3)y(H_2O)+(3\text{-}x)CaCO_3 \quad (4)$$

$$2CaO(SiO_2)+(2\text{-}x)\ CO_2+yH_2O \rightarrow xCaO(SiO_3)y(H_2O)+(2\text{-}x)CaCO_3 \quad (5)$$

4. Conclusions

This study investigated the impact of intermixing low doses of CO_2 during cement batching on the fresh, mechanical, and microstructure properties of the end products. In general, injecting a small dose of CO_2 during cement batching led to a denser microstructure due to the formation of nano-$CaCO_3$, which can act as a nucleation site to promote the formation of a thicker and more ordered C-S-H rim around the clinker. In addition, the nano-$CaCO_3$ attached to the clinker surface can react with the aluminum phase to form Mc, which strengthened the bonding

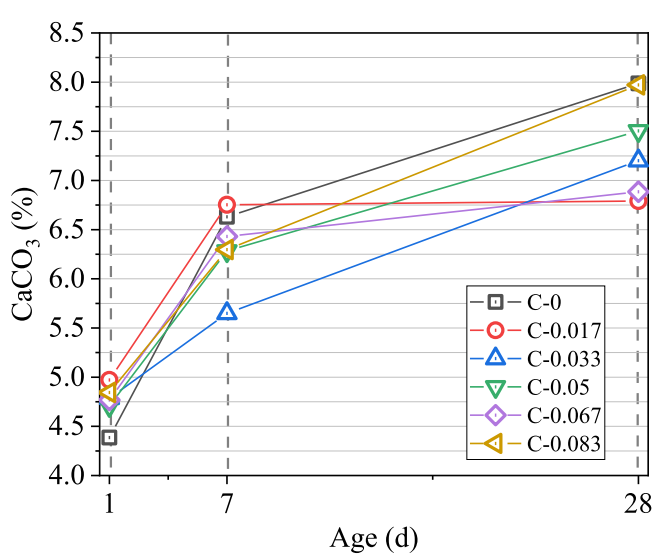

Fig. 10. $CaCO_3$ content of different CO_2-mixing samples over time.

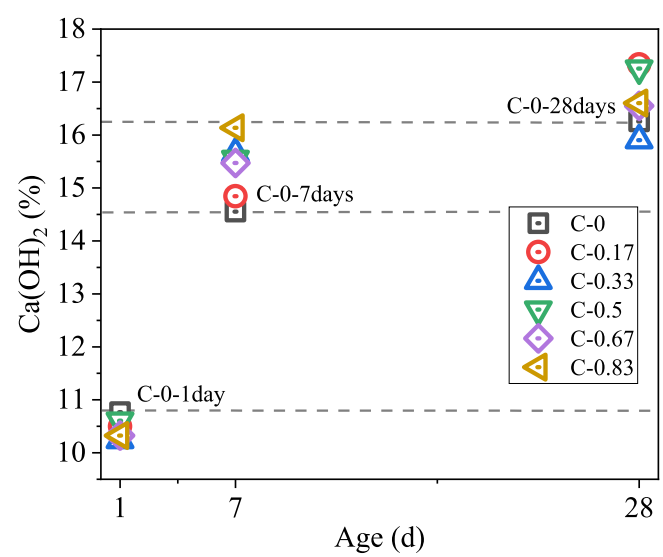

Fig. 11. $Ca(OH)_2$ content of different samples over time.

between the clinker and the C-S-H rim. Interestingly, numerous nano-Ca$(OH)_2$ particles were formed and embedded in the C-S-H gels to enhance the densification of the microstructures due to the formation of a supersaturation area on the clinker induced by the carbonation-generated nano-$CaCO_3$ with a higher specific surface area. As a result, the mechanical performance of the hardened CO_2-mixing cement matrix (0.05 ‰ dose) was improved by 10.3–21.7 % compared with the control sample cured for 1–28days. More importantly, the use of a low CO_2-mixing dose exerted a negligible influence on both the fresh properties and the durability of cementitious materials as a result of the presence of a sufficient amount of $Ca(OH)_2$ content and a denser microstructure of the cement matrix.

CRediT authorship contribution statement

Shuang Luo: Conceptualization, Data curation, Investigation, Methodology, Writing – original draft. **Tung-Chai (Bill) Ling:** Funding acquisition, Supervision, Validation, Writing – review & editing. **Ming-Zhi Guo:** Data curation, Funding acquisition, Writing – review & editing.

Declaration of Competing Interest

The authors declare that they have no known competing financial interests or personal relationships that could have appeared to influence the work reported in this paper.

Data Availability

No data was used for the research described in the article.

Acknowledgements

This work was supported by the Program Fund of Non-Metallic Excellence and Innovation Center for Building Materials (2023Ph.D-6); Natural Science Foundation of Jiangsu Province (BK20221503); Jiangsu Province Department of Science and Technology (BE2022605), Hunan Provincial Innovation Foundation for Postgraduate (CX20230390).

Appendix A. Supporting information

Supplementary data associated with this article can be found in the online version at doi:10.1016/j.conbuildmat.2024.137284.

References

[1] Z. Li, Y. Wang, Z. Li, M. Li, K. Xu, W. Liu, G. Luo, H. Yao, Limestone decomposition in an O_2 /CO_2 /steam atmosphere integrated with coal combustion, Energy Fuels 30 (2016) 5092–5100, https://doi.org/10.1021/acs.energyfuels.6b00610.
[2] T. Wu, S.T. Ng, J. Chen, Deciphering the CO_2 emissions and emission intensity of cement sector in China through decomposition analysis, J. Clean. Prod. 352 (2022) 131627, https://doi.org/10.1016/j.jclepro.2022.131627.
[3] H. El-Hassan, Y. Shao, Carbon storage through concrete block carbonation, J. Clean. Energy Technol. (2014) 287–291, https://doi.org/10.7763/JOCET.2014.V2.141.
[4] F. Xi, S.J. Davis, P. Ciais, D. Crawford-Brown, D. Guan, C. Pade, T. Shi, M. Syddall, J. Lv, L. Ji, L. Bing, J. Wang, W. Wei, K.-H. Yang, B. Lagerblad, I. Galan, C. Andrade, Y. Zhang, Z. Liu, Substantial global carbon uptake by cement carbonation, Nat. Geosci. 9 (2016) 880–883, https://doi.org/10.1038/ngeo2840.
[5] S. Monkman, Sustainable ready mixed concrete production using waste CO_2: a case study, Am. Concr. Ins. 330 (2018) 163–174. 〈https://www.concrete.org/publications/internationalconcreteabstractsportal/m/details/id/51711248〉.
[6] B.J. Zhan, D.X. Xuan, C.S. Poon, C.J. Shi, Effect of curing parameters on CO_2 curing of concrete blocks containing recycled aggregates, Cem. Concr. Compos. 71 (2016) 122–130, https://doi.org/10.1016/j.cemconcomp.2016.05.002.
[7] S. Siddique, A. Naqi, J.G. Jang, Influence of water to cement ratio on CO_2 uptake capacity of belite-rich cement upon exposure to carbonation curing, Cem. Concr. Compos. 111 (2020) 103616, https://doi.org/10.1016/j.cemconcomp.2020.103616.
[8] J.J. Chang, W. Yeih, R. Huang, J.M. Chi, Mechanical properties of carbonated concrete, J. Chin. Inst. Eng. 26 (2003) 513–522, https://doi.org/10.1080/02533839.2003.9670804.
[9] M. Chen, N. Wang, J. Yu, A. Yamaguchi, Effect of porosity on carbonation and hydration resistance of CaO materials, J. Eur. Ceram. Soc. 27 (2007) 1953–1959, https://doi.org/10.1016/j.jeurceramsoc.2006.05.101.
[10] S. Monkman, M. MacDonald, R.D. Hooton, P. Sandberg, Properties and durability of concrete produced using CO_2 as an accelerating admixture, Cem. Concr. Compos. 74 (2016) 218–224, https://doi.org/10.1016/j.cemconcomp.2016.10.007.
[11] S. Monkman, M. MacDonald, On carbon dioxide utilization as a means to improve the sustainability of ready-mixed concrete, J. Clean. Prod. 167 (2017) 365–375, https://doi.org/10.1016/j.jclepro.2017.08.194.
[12] L. Liu, Y. Ji, F. Gao, L. Zhang, Z. Zhang, X. Liu, Study on high-efficiency CO_2 absorption by fresh cement paste, Constr. Build. Mater. 270 (2021) 121364, https://doi.org/10.1016/j.conbuildmat.2020.121364.
[13] S. Monkman, B.E.J. Lee, K. Grandfield, M. MacDonald, L. Raki, The impacts of in-situ carbonate seeding on the early hydration of tricalcium silicate, Cem. Concr. Res. 136 (2020) 106179, https://doi.org/10.1016/j.cemconres.2020.106179.
[14] S. Luo, M.-Z. Guo, T.-C. Ling, Mechanical and microstructural performances of fly ash blended cement pastes with mixing CO_2 during fresh stage, Constr. Build. Mater. 358 (2022) 129444, https://doi.org/10.1016/j.conbuildmat.2022.129444.
[15] S. Monkman, M. MacDonald, Carbon dioxide upcycling into industrially produced concrete blocks, Constr. Build. Mater. 124 (2016) 127–132, https://doi.org/10.1016/j.conbuildmat.2016.07.046.
[16] X. Liu, L. Chen, A. Liu, X. Wang, Effect of nano-$CaCO_3$ on properties of cement Paste, Energy Procedia 16 (2012) 991–996, https://doi.org/10.1016/j.egypro.2012.01.158.
[17] K. Cui, D. Lau, Y. Zhang, J. Chang, Mechanical properties and mechanism of nano-$CaCO_3$ enhanced sulphoaluminate cement-based reactive powder concrete, Constr. Build. Mater. 309 (2021) 125099, https://doi.org/10.1016/j.conbuildmat.2021.125099.
[18] S. Monkman, P.A. Kenward, G. Dipple, M. MacDonald, M. Raudsepp, Activation of cement hydration with carbon dioxide, J. Sustain. Cem. Based Mater. 7 (2018) 160–181, https://doi.org/10.1080/21650373.2018.1443854.
[19] GB/T 2419, Method for Determination of Fluidity of Cement Mortar, Chinese Standards Association, China, 2005.
[20] GB/T17671, Test Method of Cement Mortar Strength (ISO method), Chinese Standards Association, China, 2021.
[21] L. Black, C. Breen, J. Yarwood, K. Garbev, P. Stemmermann, B. Gasharova, Structural features of C–S–H (I) and its carbonation in air—a Raman spectroscopic study. Part II: carbonated phases, J. Am. Ceram. Soc. 90 (2007) 908–917, https://doi.org/10.1111/j.1551-2916.2006.01429.x.
[22] A. Morandeau, M. Thiéry, P. Dangla, Investigation of the carbonation mechanism of CH and C-S-H in terms of kinetics, microstructure changes and moisture properties, Cem. Concr. Res. 56 (2014) 153–170, https://doi.org/10.1016/j.cemconres.2013.11.015.
[23] V. Rostami, Y. Shao, A.J. Boyd, Z. He, Microstructure of cement paste subject to early carbonation curing, Cem. Concr. Res. 42 (2012) 186–193, https://doi.org/10.1016/j.cemconres.2011.09.010.
[24] J. Wang, H. Xu, D. Xu, P. Du, Z. Zhou, L. Yuan, X. Cheng, Accelerated carbonation of hardened cement pastes: influence of porosity, Constr. Build. Mater. 225 (2019) 159–169, https://doi.org/10.1016/j.conbuildmat.2019.07.088.
[25] Q. Fu, Z. Zhang, X. Zhao, W. Xu, D. Niu, Effect of nano calcium carbonate on hydration characteristics and microstructure of cement-based materials: a review, J. Build. Eng. 50 (2022) 104220, https://doi.org/10.1016/j.jobe.2022.104220.
[26] G. Kakali, S. Tsivilis, E. Aggeli, M. Bati, Hydration products of C_3A, C_3S and Portland cement in the presence of $CaCO_3$, Cem. Concr. Res. 30 (2000) 1073–1077, https://doi.org/10.1016/S0008-8846(00)00292-1.
[27] W. Sha, E.A. O'Neill, Z. Guo, Differential scanning calorimetry study of ordinary Portland cement, Cem. Concr. Res. 29 (1999) 1487–1489, https://doi.org/10.1016/S0008-8846(99)00128-3.
[28] D. Xuan, B. Zhan, C.S. Poon, Assessment of mechanical properties of concrete incorporating carbonated recycled concrete aggregates, Cem. Concr. Compos. 65 (2016) 67–74, https://doi.org/10.1016/j.cemconcomp.2015.10.018.
[29] H. Mehdizadeh, Y. Meng, M.-Z. Guo, T.-C. Ling, Roles of CO_2 curing induced calcium carbonates on high temperature properties of dry-mixed cement paste, Constr. Build. Mater. 289 (2021) 123193, https://doi.org/10.1016/j.conbuildmat.2021.123193.
[30] X. Jia, T.-C. Ling, H. Mehdizadeh, K.H. Mo, Impact of CO_2 curing on the microhardness and strength of 0.35 w/c cement paste: comparative study of internal/surface layers, J. Mater. Res. Technol. 9 (2020) 11849–11860, https://doi.org/10.1016/j.jmrt.2020.08.051.
[31] CarbonCure Technologies, Canada, S. Monkman, M. MacDonald, CarbonCure Technologies, Canada, D. Hooton, University of Toronto, Canada, The durability of concrete produced using CO2 as an admixture, in: 2016: pp. 363–372. https://doi.org/10.18552/2016/SCMT4S165.
[32] S.W. Lee, Y.J. Kim, Y.H. Lee, H. Guim, S.M. Han, Behavior and characteristics of amorphous calcium carbonate and calcite using $CaCO_3$ film synthesis, Mater. Des. 112 (2016) 367–373, https://doi.org/10.1016/j.matdes.2016.09.099.
[33] D.P. Bentz, A. Ardani, T. Barrett, S.Z. Jones, D. Lootens, M.A. Peltz, T. Sato, P. E. Stutzman, J. Tanesi, W.J. Weiss, Multi-scale investigation of the performance of limestone in concrete, Constr. Build. Mater. 75 (2015) 1–10, https://doi.org/10.1016/j.conbuildmat.2014.10.042.

[34] M. Cao, X. Ming, K. He, L. Li, S. Shen, Effect of macro-, micro- and nano-calcium carbonate on properties of cementitious composites—a review, Materials 12 (2019) 781, https://doi.org/10.3390/ma12050781.
[35] L. Poudyal, K. Adhikari, M. Won, Nano calcium carbonate ($CaCO_3$) as a reliable, durable, and environment-friendly alternative to diminishing fly ash, Materials 14 (2021) 3729, https://doi.org/10.3390/ma14133729.
[36] J. Feng, F. Yang, S. Qian, Improving the bond between polypropylene fiber and cement matrix by nano calcium carbonate modification, Constr. Build. Mater. 269 (2021) 121249, https://doi.org/10.1016/j.conbuildmat.2020.121249.
[37] B. Lothenbach, G. Le Saout, E. Gallucci, K. Scrivener, Influence of limestone on the hydration of Portland cements, Cem. Concr. Res. 38 (2008) 848–860, https://doi.org/10.1016/j.cemconres.2008.01.002.
[38] T. Meng, K.L. Qian, X.Q. Qian, S.L. Zhan, Effect of the nano-$CaCO_3$ on hydrated properties and interface of cement paste, Rare Met. Mater. Eng. 37 (2) (2008) 667–669, https://doi.org/10.1134/S0033173208030156.
[39] K.O. Kjellsen, H.M. Jennings, B. Lagerblad, Evidence of hollow shells in the microstructure of cement paste, Cem. Concr. Res. 26 (1996) 593–599, https://doi.org/10.1016/0008-8846(96)00031-2.
[40] D.L. Rayment, E.E. Lachowski, The analysis of OPC pastes: a comparison between analytical electron microscopy and electron probe microanalysis, Cem. Concr. Res. 14 (1984) 43–48, https://doi.org/10.1016/0008-8846(84)90078-4.
[41] I.G. Richardson, G.W. Groves, Microstructure and microanalysis of hardened ordinary Portland cement pastes, J. Mater. Sci. 28 (1993) 265–277, https://doi.org/10.1007/BF00349061.
[42] H.F.W. Taylor, Nanostructure of C-S-H: current status, Adv. Cem. Based Mater. 1 (1993) 38–46, https://doi.org/10.1016/1065-7355(93)90006-A.
[43] Z. Wu, C. Shi, K.H. Khayat, S. Wan, Effects of different nanomaterials on hardening and performance of ultra-high strength concrete (UHSC), Cem. Concr. Compos. 70 (2016) 24–34, https://doi.org/10.1016/j.cemconcomp.2016.03.003.
[44] E. Masoero, J.J. Thomas, H.M. Jennings, A reaction zone hypothesis for the effects of particle size and water-to-cement ratio on the early hydration kinetics of C_3S, J. Am. Ceram. Soc. 97 (2014) 967–975, https://doi.org/10.1111/jace.12713.
[45] T. Runcevski, R.E. Dinnebier, O.V. Magdysyuk, H. Pollmann, Crystal structures of calcium hemicarboaluminate and carbonated calcium hemicarboaluminate from synchrotron powder diffraction data, Acta Crystallogr. Sect. B Struct. Sci. 68 (5) (2012) 493–500, https://doi.org/10.1016/j.cemconres.2007.10.006.
[46] D. Wang, C. Shi, N. Farzadnia, Z. Shi, H. Jia, Z. Ou, A review on use of limestone powder in cement-based materials: mechanism, hydration and microstructures, Constr. Build. Mater. 181 (2018) 659–672, https://doi.org/10.1016/j.conbuildmat.2018.06.075.
[47] J.J. Chen, L. Sorelli, M. Vandamme, F.-J. Ulm, G. Chanvillard, A coupled nanoindentation/SEM-EDS study on low water/cement ratio Portland cement paste: evidence for C-S-H/$Ca(OH)_2$ nanocomposites, J. Am. Ceram. Soc. (2010), https://doi.org/10.1111/j.1551-2916.2009.03599.x.
[48] G.W. Groves, Microcrystalline calcium hydroxide in Portland cement pastes of low water/cement ratio, Cem. Concr. Res. 11 (1981) 713–718, https://doi.org/10.1016/0008-8846(81)90029-6.
[49] P. Trtik, B. Münch, P. Lura, A critical examination of statistical nanoindentation on model materials and hardened cement pastes based on virtual experiments, Cem. Concr. Compos. 31 (2009) 705–714, https://doi.org/10.1016/j.cemconcomp.2009.07.001.
[50] T. Sato, F. Diallo, Seeding effect of nano-$CaCO_3$ on the hydration of tricalcium silicate, Transp. Res. Rec. J. Transp. Res. Board. 2141 (2010) 61–67, https://doi.org/10.3141/2141-11.
[51] T. Sato, J.J. Beaudoin, Effect of nano-$CaCO_3$ on hydration of cement containing supplementary cementitious materials, Adv. Cem. Res. 23 (2011) 33–43, https://doi.org/10.1680/adcr.9.00016.
[52] D. Zhang, X. Cai, B. Jaworska, Effect of pre-carbonation hydration on long-term hydration of carbonation-cured cement-based materials, Constr. Build. Mater. 231 (2020) 117122, https://doi.org/10.1016/j.conbuildmat.2019.117122.
[53] Ö. Cizer, K. Van Balen, J. Elsen, D. Van Gemert, Real-time investigation of reaction rate and mineral phase modifications of lime carbonation, Constr. Build. Mater. 35 (2012) 741–751, https://doi.org/10.1016/j.conbuildmat.2012.04.036.
[54] A.M. Neville, Properties of Concrete, 5th Ed., Pearson, Harlow, England; New York, 2011. 〈https://vdocuments.mx/properties-of-concrete-nevill-5th-edition.htmlpage=1〉.
[55] M. Thiery, G. Villain, P. Dangla, G. Platret, Investigation of the carbonation front shape on cementitious materials: effects of the chemical kinetics, Cem. Concr. Res. 37 (2007) 1047–1058, https://doi.org/10.1016/j.cemconres.2007.04.002.
[56] M.A. Peter, A. Muntean, S.A. Meier, M. Böhm, Competition of several carbonation reactions in concrete: a parametric study, Cem. Concr. Res. 38 (2008) 1385–1393, https://doi.org/10.1016/j.cemconres.2008.09.003.
[57] M. Castellote, C. Andrade, Modelling the carbonation of cementitious matrixes by means of the unreacted-core model, UR-CORE, Cem. Concr. Res. 38 (2008) 1374–1384, https://doi.org/10.1016/j.cemconres.2008.07.004.

Journal of Zhejiang University-SCIENCE A (Applied Physics & Engineering) *2023 24(10):886-897*
www.jzus.zju.edu.cn; www.springer.com/journal/11582
E-mail: jzus_a@zju.edu.cn

Research Article
https://doi.org/10.1631/jzus.A2200571

Effect of CO_2-mixing dose and prolonged mixing time on fresh and hardened properties of cement pastes

Minlu WANG, Shuang LUO, Ba Tung PHAM, Tung-Chai LING✉

College of Civil Engineering, Hunan University, Changsha 410082, China

Abstract: This study aims to investigate the influence of CO_2-mixing dose (mass fractions of 0.3%, 0.6%, and 0.9%) and prolonged mixing time on the fresh and hardened properties of cement pastes. The CO_2-mixing can act as coagulant in fresh cement mixtures, resulting in a significant reduction in workability associated with the formation of a rich calcium carbonate network on the surface of cement particles. The CO_2-mixing cement pastes were found to be much stiffer and more difficult to handle, place, and compact than the control mixture, which had a negative effect on the mechanical strength performance of the hardened pastes. However, prolonging the mixing time for 1 min (immediately after CO_2-mixing) can effectively improve the workability (by ~53%–85%) by breaking up the flocculation network of deposited calcium carbonates. As a result, the presence of detached calcium carbonate accelerated early cement hydration and densified the microstructure; this improved early-age compressive strength by ~6%–32%, depending on the CO_2-mixing dose used. Therefore, it seems that the CO_2-mixing dose should be controlled at ≤0.6% with the mixing time prolonged in order to attain satisfactory workability and mechanical strength.

Key words: CO_2-mixing; Calcium carbonate; Early cement hydration; Flowability; Microstructure

1 Introduction

Accelerated carbonation (or CO_2 curing) has been extensively studied for its potential to improve the mechanical strength of cement concrete and reduce its environmental impact (Ashraf, 2016). However, special conditions including temperature, pressure, CO_2 concentration, and sophisticated equipment are required for an accelerated carbonation process, and in general the approach can only be applied in precast production (Zhang et al., 2017). In addition, CO_2 can be sequestrated into cement-based materials and solid waste under aqueous conditions (Li et al., 2023; Mehdizadeh et al., 2023). Both dry and aqueous carbonation methods require a long process for the carbonation reaction (hours or days). Recently, the application of CO_2-mixing by directly mixing CO_2 with fresh ready-mix concrete has attracted a lot of attention due to the short reaction time (a few minutes during mixing) and its feasibility for wider application in the concrete industry. According to (Monkman and MacDonald, 2016; Monkman et al., 2016), the amount of CO_2 incorporated (~0.05%–1.5%) during concrete mixing or batching has a significant influence on compressive strength. CO_2 can convert calcium minerals into very fine calcium carbonate ($CaCO_3$) with a size of ~70 nm that acts as nucleation sites to accelerate cement hydration (Monkman et al., 2020). Monkman and MacDonald (2017) claimed that the cement consumption for a given designed concrete strength was reduced by ~5%–8%. The reaction between CO_2 and cement clinkers (including C_3S and C_2S for the precipitation of $CaCO_3$ in the presence of water) can be expressed by Eqs. (1) and (2) (Berger et al., 1972).

$$3(3CaO\cdot SiO_2)+(3-x)CO_2+yH_2O\rightarrow xCaO\cdot SiO_2\cdot yH_2O+(3-x)CaCO_3, \quad (1)$$

$$2(2CaO\cdot SiO_2)+(2-x)CO_2+yH_2O\rightarrow xCaO\cdot SiO_2\cdot yH_2O+(2-x)CaCO_3. \quad (2)$$

In terms of workability performance, Monkman and MacDonald (2016) and Liu et al. (2021) reported that CO_2-mixing of a fresh concrete mixture dramatically

✉ Tung-Chai LING, tcling@hnu.edu.cn, tcling611@yahoo.com
Tung-Chai LING, https://orcid.org/0000-0002-8276-5212

Received Nov. 28, 2022; Revision accepted Mar. 28, 2023;
Crosschecked Sept. 20, 2023

© Zhejiang University Press 2023

reduces workability. To solve this technical problem, Monkman and MacDonald (2016) used extra water to maintain equal workability of the concrete mixture and were able to successfully enhance the compressive strength by ~10%–30% compared to the control mixture. Liu et al. (2021) used superplasticizers to refine the flowability of CO_2-mixed cement paste and attained comparable strength to that of the control sample. Lippiatt et al. (2019) used a saturated aqueous CO_2 solution as mixing water for the preparation of cement pastes and found that the presence of an aqueous CO_2 solution (carbonic acid) in the paste greatly reduced flowability (Kwasny et al., 2014; Lippiatt et al., 2019; Lippiatt and Ling, 2020). In comparison to an enclosed mixing environment, the reduction of workability associated with the CO_2-mixing approach was even more pronounced (Liu, 2019). Luo et al. (2022) used fly ash to replace 10%–20% of cement in order to improve the workability of CO_2-mixed cement pastes due to the material's spherical morphology, and obtained an ~15% increase in strength. However, the mechanism of flocculation and breakup of the deposited calcium carbonate on the surface of the cement particles after subjection to prolonged mixing time was not clear.

Generally, increasing cement-mixing speed, intensity, and time enables great enhancement of the rheological behavior, hydration, and microstructure of cement concrete (Han and Ferron, 2015, 2016). According to Zhao et al. (2022), prolonging vibratory mixing helps to break down flocculation of cement particles and produce better fluidity in the concrete mixture. In fact, prolonging a short mixing period can improve the uniformity and consistency of fresh concrete, especially in the case of high-stiffness mixtures (Urban and Sicakova, 2018). In contrast to mixing at an ambient temperature (25 °C), prolonging mixing time at 40 °C for 60, 120, and 180 min can better improve the compressive strength of concrete (Hossain et al., 2018). It can be suggested that increased mixing time is anticipated to alter the fresh and hardened properties of cement pastes, in particular with additional admixture or filler, and this could also apply for the introduction of CO_2 in fresh cement paste.

This paper studies the influence of further mixing (applied immediately after CO_2-mixing with mass fractions of 0.3%, 0.6%, and 0.9%) on the fresh and hardened properties of cement pastes. All the cement pastes were prepared with a fixed water-to-cement (w/c) ratio of 0.5 in an enclosed (airtight) mixer. Calcium carbonate precipitation was confirmed by thermogravimetric analysis (TGA) and scanning electron microscope (SEM) with an energy-dispersive spectrometer (EDS). The porosity was quantified using backscattered electron microscopy (BSE) techniques. The kinetics of cement hydration with and without CO_2-mixing were investigated through isothermal calorimetry.

2 Experimental

2.1 Materials

Ordinary Portland cement (OPC) with a strength grade of P.I. 42.5 and deionized pure water were used to prepare cement pastes. The chemical and mineral compositions of OPC are given in Tables 1 and 2, respectively. CO_2 gas with an industrial-grade purity of 99% (volume fraction) was obtained from Rizhen Industrial-Gas Manufacturer in Changsha, China.

Table 1 Chemical composition of OPC

Chemical composition	Mass content (%)	Chemical composition	Mass content (%)
CaO	63.43	Fe_2O_3	3.99
SiO_2	20.30	MgO	2.03
Al_2O_3	5.42	SO_3	0.97

Table 2 Mineral composition of OPC

Mineral composition	Mass content (%)	Mineral composition	Mass content (%)
C_3S	58.99	C_4AF	12.13
C_2S	14.02	Gypsum	2.09
C_3A	7.62	Other	5.15

2.2 Mixing process and sample preparation

The CO_2-mixing cement pastes were prepared with a fixed w/c ratio of 0.5; the mix design is shown in Table 3. Based on Eq. (3), volumetric flow rates were determined for each mix design of CO_2-mixing cement pastes (mass fractions of 0.3%, 0.6%, and 0.9%).

$$v=\frac{m_{CO_2}}{\rho_{CO_2}\times t}, \tag{3}$$

where v is the CO_2 gas-flow rate (L/min), m_{CO_2} is the mass of injected CO_2 gas (g), ρ_{CO_2} is the density of CO_2

Table 3 Mix design of CO_2-mixing cement pastes

Sample	OPC mass (g)	Water mass (g)	w/c ratio	CO_2 dose* (%)	m_{CO_2} (g)	Flow rate (L/min)
AM	1500	750	0.5	0	0	0
CM/CMF-0.3	1500	750	0.5	0.3	4.5	2.28
CM/CMF-0.6	1500	750	0.5	0.6	9.0	4.55
CM/CMF-0.9	1500	750	0.5	0.9	13.5	6.83

* The CO_2 dose percentage is by weight of cement and was selected based on previous studies (Monkman and MacDonald, 2016; Monkman et al., 2016). AM: air-mixing sample; CM: CO_2-mixing samples; CMF: CO_2-mixing with further mixing samples

gas (about 1.977 g/L at atmospheric pressure), and t is the length (min) of CO_2-mixing stage (fixed at 1 min for all cases).

The mixing regime of the cement paste samples is illustrated in Fig. 1. A control sample (AM) was prepared by mixing OPC with water at 140 and 280 r/min for 1 and 2 min, respectively, to obtain a homogeneous state. As for CO_2-mixing (CM) samples, an additional mixing stage of 1 min (280 r/min) was required to allow 0.3%, 0.6%, and 0.9% CO_2 doses to be injected and mixed with the freshly prepared wet cement paste in an enclosed mixer (Fig. 2). Once the mixer was opened, the pastes were highly stiffened and not workable. To investigate the effect of prolonged mixing time, immediately after CO_2-mixing the mixture was further mixed for another 1 min at 280 r/min and labelled the samples CMF-0.3, 0.6, and 0.9. Note that before the second mixing stage, the cover of the enclosed mixer was opened in order to ensure that any unreacted CO_2 was released into the environmental air.

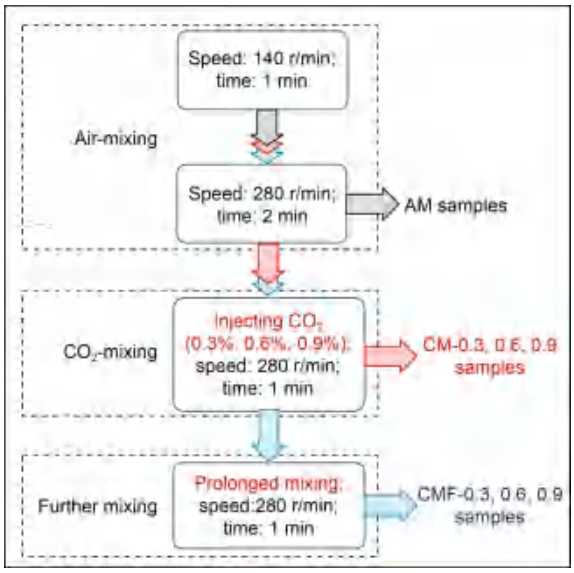

Fig. 1 Mixing regimes designed for CO_2-mixing cement pastes

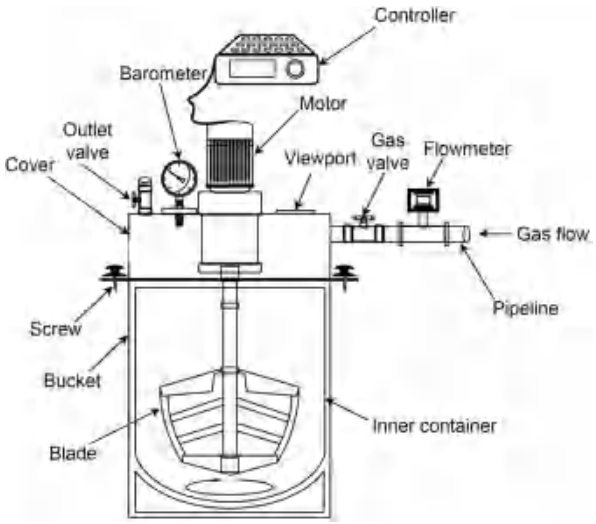

Fig. 2 Schematic diagram of the enclosed (airtight) mixer coupled with a CO_2 injector. The bucket was sealed with a rubber ring on the top and enclosed with four screws at each side. The mixer volume was 10 L, and the mixing speed and CO_2 flow rate could be controlled in the range of 0–400 r/min and 0–10 L/min, respectively

All freshly prepared mixtures were poured into 40 mm×40 mm×40 mm steel molds and vibrated for 20 s. The hardened pastes were demolded after 1 d and then further cured in a standard chamber (relative humidity of 95% and temperature (T) of 20 °C) until the testing ages.

2.3 Testing methods for fresh properties

2.3.1 Flowability

Mini-slump test was used to assess the flowability of the fresh cement paste mixture (Mehdizadeh et al., 2022). A truncated cone with a size of 36 mm×60 mm×60 mm was placed at the center of the flow table and then filled with the freshly prepared mixture. After the cone was lifted vertically, the mixture was dropped 15 times at a rate of one jolt per second. The diameter of the spread mixture in two perpendicular directions was recorded.

2.3.2 Setting time

The initial and final setting times of the fresh cement paste mixture were measured with a Vicat Apparatus in accordance with GB/T 1346 (GAQSIQ, 2012). The needle used was (1.000±0.005) mm in diameter. This test was carried out in the laboratory with a relative humidity of 60% and a room temperature of (20±3) °C.

2.3.3 Heat of hydration

The exothermal curves of samples were measured according to GB/T 12959 (GAQSIQ, 2008). The paste mixture, with a mass of 10.5 g, was placed into glass ampoules and located into channels of a TAM Air (8-channel) machine (TA Instruments, USA) at 20 °C for measurement (up to 7 d). To maintain the heat balance, the reference water was placed in the corresponding channels.

2.3.4 Thermogravimetric analysis (TGA)

The freshly prepared mixture was immersed in isopropyl alcohol to exchange the free water in order to completely stop hydration. For each sample, approximate 15 mg of the powder was used for heating from ambient temperature to 1000 °C at a rate of 10 °C/min under a nitrogen flow of 30 mL/min.

The weight loss x_C at 550–950 °C indicates the decomposition of the precipitated $CaCO_3$, as expressed in Eq. (4) (Jiang and Ling, 2020; Ma et al., 2021).

$$x_C = \frac{M_{550} - M_{950}}{M_{950}} \times \frac{100}{44} \times 100\%, \tag{4}$$

where M_{550} and M_{950} are the masses of the sample at given temperature of 550 °C and 950 °C, respectively.

2.3.5 Scanning electron microscopy (SEM)

The SEM observation was performed on oven-dried fresh paste mixture using a JSM-7900F SEM (JEOL, Japan) with an energy dispersive spectrometer (EDS). Samples were coated with a thin conductive layer of gold (Au) to minimize charging.

2.4 Testing methods for hardened properties

2.4.1 Compressive strength

Compressive strength testing was carried out at 1, 3, 7, and 28 d using a conventional compression machine with a loading rate of 2.4 kN/s, according to GB/T 17671 (SBQTS, 1999). The average values of three samples were reported.

2.4.2 Sorptivity and water absorption

The sorptivity and water absorption of samples were measured at 28 d according to ASTM C1585-04 (ASTM, 2004) and ASTM C642-13 (ASTM, 2013), respectively. Samples were first oven dried at 80 °C until a constant weight (dry weight, W_1), and then the four sides surfaces of each sample were sealed with waterproof paint (sealed weight, W_2), ensuring that water movement would take place only through the bottom surface. Plastic pipes were used to support the samples so that the water level was kept 5 mm above the bottom surface. Samples were removed from the water and weighed at intervals of 10 min, 20 min, 30 min, 1 h, 2 h, 4 h, 6 h, 12 h, 24 h, and 48 h for measurement. The sorptivity coefficient (S, mm/s$^{1/2}$) was calculated by

$$I = St_1 + b, \tag{5}$$

where I refers to the cumulative volume of absorbed water per unit of water contact area (mm^3/mm^2), t_1 is the time (s), and b is the constant which reflects the effect of initial water filling at the sample surface.

After 48 h, all samples were at constant weight (saturated surface-dry weight, W_3) to attain final water absorption values, as expressed by

$$a = \frac{W_3 - W_2}{W_1} \times 100\%, \tag{6}$$

where a is the final water absorption.

2.4.3 Backscattered electron microscopy (BSE)

Microstructure and porosity of samples at 3 and 28 d were analyzed using a BSE (JSM-IT500, JEOL, Japan). Samples were cut into size of 5 mm×10 mm×10 mm by a low-speed diamond blade. Then, moisture was removed by storing the samples in a vacuum oven at 20 °C for 5 d. After that, the samples were impregnated with a low-viscosity epoxy resin (EPO-TEK 301, BUEHLER, Germany) under vacuum conditions. After demolding, the surface of the samples was lapped using SiC papers of 400 and 1200 grit and further polished with oil-based diamond polishing fluid of 5, 2.5, and 1 μm in sequence. To calculate the microporosity, 12 BSE images at 500× magnification were

taken and analyzed with Image J software. A specific threshold with an empirical coefficient of 0.9 was chosen to avoid overestimating porosity based on the cumulative grayscale curve (Lyu et al., 2019; Peng et al., 2020).

2.4.4 Reaction products

The fractured samples derived from the compression tests at 1, 3, 7, and 28 d were immersed in isopropyl alcohol for at least 3 d to stop the hydration process and then vacuum-dried for 5 d before being ground into powder with a size of <75 μm for TGA measurement.

The degree of hydration (α) was calculated according to Eqs. (7) and (8), on the basis of the method proposed by Monteagudo et al. (2014) and Akbar and Liew (2020).

$$W_B = \mathrm{Ldh} + \mathrm{Ldx} + 0.41\mathrm{Ldc}, \tag{7}$$

$$\alpha = \frac{W_B}{0.24}, \tag{8}$$

where Ldh is the dehydration (105–400 ℃), Ldx is the dehydroxylation (400–500 ℃), and Ldc is the decarbonation (550–950 ℃). The value of 0.24 represents the maximum amount of chemically bound water required to hydrate a cement particle entirely.

3 Results and discussion

3.1 Fresh properties

3.1.1 Flowability

The appearance of the cement pastes before and after vibration on the flow table is shown in Fig. 3. As seen, CO_2 induced quick hardening of the paste mixture, which is found to be quite similar to false setting (Chung and Lee, 2011; Liu, 2019). The values of mini-slump flow of CM samples were about 31.3%, 43.1%, and 45.9% lower compared with the AM sample with increased CO_2-mixing doses of 0.3%, 0.6%, and 0.9%, respectively. This was due to the $CaCO_3$ deposited on cement particles increasing the specific surface area and thus absorbing more free water (Liu et al., 2012; Cui et al., 2021).

It is important to note that with an additional 1 min of high-speed mixing, CMF samples showed improved workability. The specific recovery rates were 52.8%, 80.6%, and 84.9% for the 0.3%, 0.6%, and

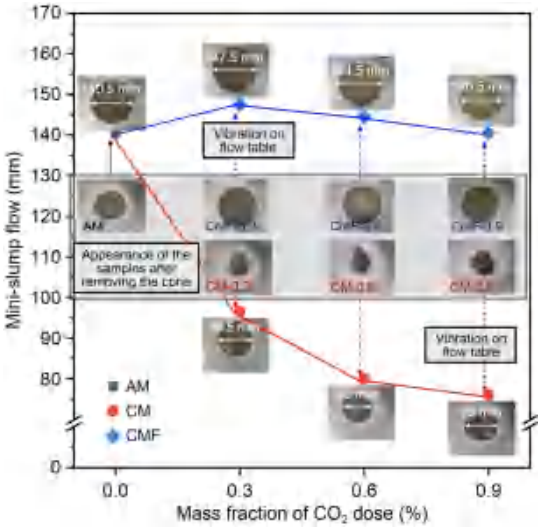

Fig. 3 Physical appearance and mini-slump flow values of the freshly prepared CO_2-mixing pastes

0.9% CO_2-mixing samples, respectively. The resulting flowability of CMF samples (140.5–147.5 mm) was even slightly higher (~5%) than that of the control AM sample. This is because the increased mixing time increases collisions between particles, inducing detachment of $CaCO_3$ which induces the balling effect and creating a lubricating layer between particles (Camiletti et al., 2013).

3.1.2 Setting time

The initial and final setting times of the cement pastes are presented in Fig. 4. The initial setting times for CM samples were 10–40 min shorter than that of the AM sample, due to the quick hardening behavior of the cement matrix. In comparison, the initial setting times for CMF samples were prolonged for 20–66 min compared to the AM sample, because of the breakup of the flocculation and release of free water.

The final setting times of CM samples and CMF samples were generally shortened compared with the AM sample, at approximately 140 min and 65 min, respectively. This was attributed to the promotion of hydration by the presence of $CaCO_3$, which led to a faster final setting time. In addition, it is worth noting that the interval between initial and final setting times of CO_2-mixing pastes was significantly shortened compared with the AM sample (from 236 min to 80–150 min), which demonstrated the potential of CO_2-mixing to provide strength for building construction in a faster and greener way (Guo et al., 2020).

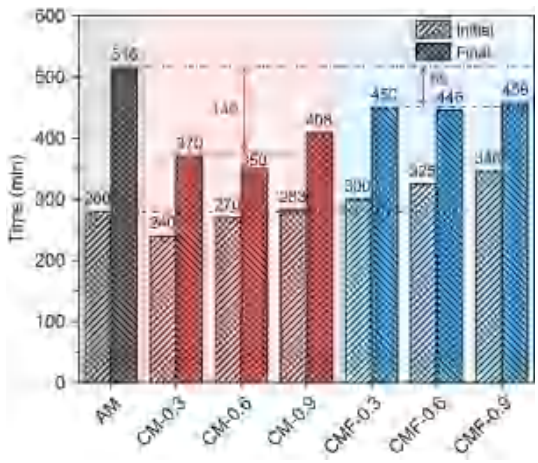

Fig. 4 Initial and final setting times of cement pastes

3.1.3 Heat of hydration

The isothermal calorimetry results of AM and CMF samples (up to 7 d) are presented in Fig. 5. The calorimetry slope increased with CO_2-mixing dose for the first 6 h, indicating an acceleration of the primary hydration peak of C_3S due to the presence of CO_2. However, the intensity of the first hydration peak was slightly lower (~6%–8%) than for the AM sample, because some of the C_3S was consumed by CO_2 during the mixing process. These results are consistent with those reported by Monkman et al. (2020), who found that C_3S was the main reactant of the CO_2-mixing process due to the absence of hydration products at the most initial hydration stage.

The second peak intensity was higher and the cumulative heat at 72 h for the higher CO_2-mixing dose samples was higher than those of the CMF-0.3 and AM samples (Fig. 5b). This was due to the formation of $CaCO_3$, which promotes aluminate hydration. However, this promotion became insignificant at a later age of 7 d. In addition, the thermal indicator of setting time reflected in the hydration heat flow (according to ASTM C1679 (ASTM, 2014)) of the CMF-0.3, 0.6, and 0.9 samples was shortened by about 29, 46, and 52 min, respectively, compared to the AM sample (Haha et al., 2010; Monkman et al., 2018). This matched the setting time measurements given in Section 3.1.2.

3.1.4 Thermogravimetric analysis

The results of the TGA for fresh cement pastes are illustrated in Fig. 6. It is notable that the peaks for hydration products (i.e., C–S–H and ettringite) are generally increased for the case of CO_2-mixing samples

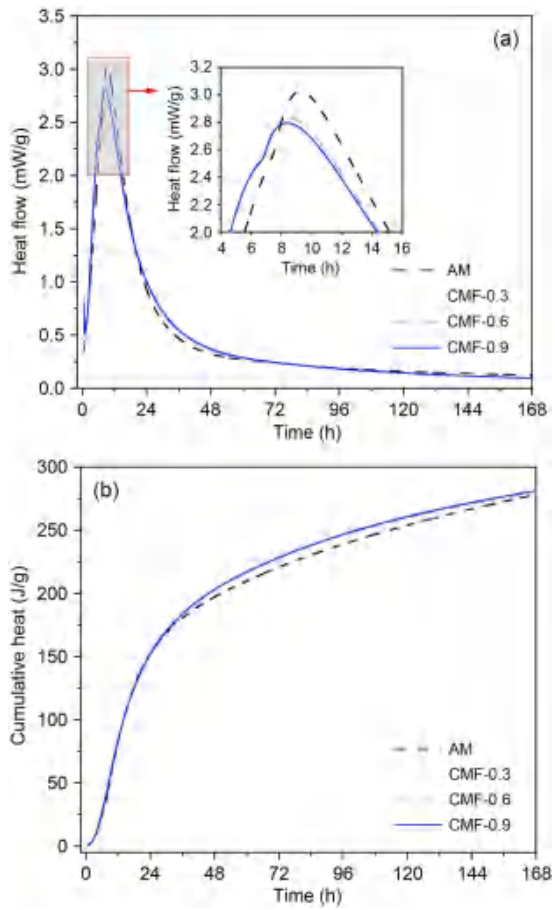

Fig. 5 Heat flow (a) and cumulative heat (b) over time for AM and CMF-0.3, 0.6, and 0.9 samples. The CM samples were excluded due to their quick hardening behavior. References to color refer to the online version of this figure

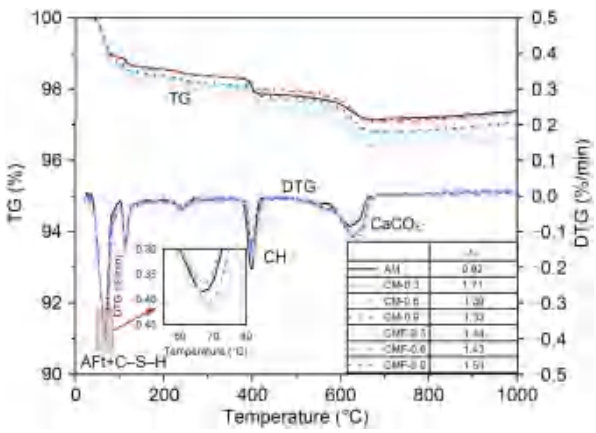

Fig. 6 Derivative thermogravimetric curve (DTG) and thermalgravimetric (TG) curves of freshly prepared cement pastes. References to color refer to the online version of this figure

due to the hydration-promotion effects of $CaCO_3$. As expected, the $Ca(OH)_2$ content in all the CO_2-mixing

cement pastes was lower than that in AM paste, because more $CaCO_3$ was precipitated. The calculation of the $CaCO_3$ content of each sample is shown in Fig. 6. It can be seen that the CM-0.3 sample had the highest $CaCO_3$ content, which may be related to the continuous dissolution of CO_2 in the water at a relative low flow rate. When the CO_2 dose was higher than 0.6%, the mixture became less workable due to the fact that most of the free water was entrapped by the flocculation networks. Moreover, CO_2 could no longer dissolve into water. Upon further mixing, the entrapped water was released and clinkers had better contact with CO_2. In addition, it can be seen that the endothermal peaks of $CaCO_3$ in all the CM and CMF samples shifted toward a slightly higher temperature compared to the AM paste, indicating that more crystalline $CaCO_3$ was formed in the pastes matrix.

3.1.5 Morphology of the fresh cement pastes

Fig. 7 compares the morphologies of AM, CM-0.6, and CMF-0.6 samples. It is clear that the surface of the AM sample was plain and neat. However, an abundance of flocculated hydration and carbonation products was deposited on the cement particles of the fresh CM-0.6 sample (Fig. 7b). The EDS spectra of spots 1 and 2 showed that the flocculated phases mainly consisted of C–S–H gels, and probably of amorphous calcium carbonate (with a relatively high content of C element). The deposited $CaCO_3$ on the surface of cement particles could interact with flowing suspended particles, which led to the so-called interlocking effect; this decreased flowability (Cao et al., 2019). Furthermore, $CaCO_3$ also acted as a nucleation site to accelerate cement hydration, leading to the formation of more reaction products on the surface layer of clinker particles (Monkman et al., 2020). As a result, more water was needed to wet the larger specific surface area of the solid particles. Upon further mixing for 1 min, the surface of these particles became smoother, with only some amorphous calcium carbonate (spot 3) instead of flocculated phases. This demonstrated that further mixing helped to destroy the flocculation network and release the entrapped free water.

3.2 Hardened properties

3.2.1 Compressive strength

The compressive strength results at 1, 3, 7, and 28 d are presented in Fig. 8. For all CM samples, the compressive strength was about 10%–20% lower than that of the control AM sample at the same curing age, which is consistent with the results found by Monkman and MacDonald (2016). This is probably due to the poor workability which caused the fresh pastes too stiffer to be fully compacted and left air pores in the matrix. Adding 1 min of mixing time immediately after CO_2 mixing resulted in distinct improvements in compressive strength compared to the corresponding CM samples. This could be primarily due to the improved workability and nucleation sites effect of the break-up deposited calcium carbonate in accelerating early hydration (He et al., 2017; Monkman et al., 2020; Dixit et al., 2021, 2022). In comparison, the rate at which strength improved (~18%–32%) was more pronounced for the cement-paste samples with low (CMF-0.3) and moderate (CMF-0.6) CO_2-mixing. At a later age (28 d), the compressive strength of CMF samples was comparable to that of AM samples because the positive effect of $CaCO_3$ as a nucleation site became less important (Luo et al., 2022). The relatively low compressive strength of the CMF-0.9 sample was attributed to the larger pore structure induced by an excessive dose of CO_2, as will be discussed in the following section.

3.2.2 Sorptivity and water absorption

Fig. 9a shows the cumulative amount of water absorbed per unit area over the square root of time; the sorptivity coefficients (i.e., the slopes of the initial line fitting) are listed in Table 4, and are useful in terms of reflecting the capillary pores of the samples (Wang et al., 2022; Zhang et al., 2022). The CMF samples had a higher water sorptivity rate than the control AM and CM samples at the first 12 h, indicating that more connected pores had formed in the paste matrix. For instance, damp patches could be clearly seen on the top surface of the CMF-0.6 sample, unlike the corresponding CM-0.6 sample. It should be noted that the CM-0.9 sample had a relatively low sorptivity coefficient compared to other samples, probably because of a larger pore size in the matrix (Fig. 10a), composed mainly of closed air pores rather than connected ones.

The final water-absorption values of CMF samples (measured at 48 h of full water immersion) were about 6%–11% lower than those of CM samples, and CMF-0.9 had the highest value. As the porosity of a paste matrix determines its compressive strength, it is

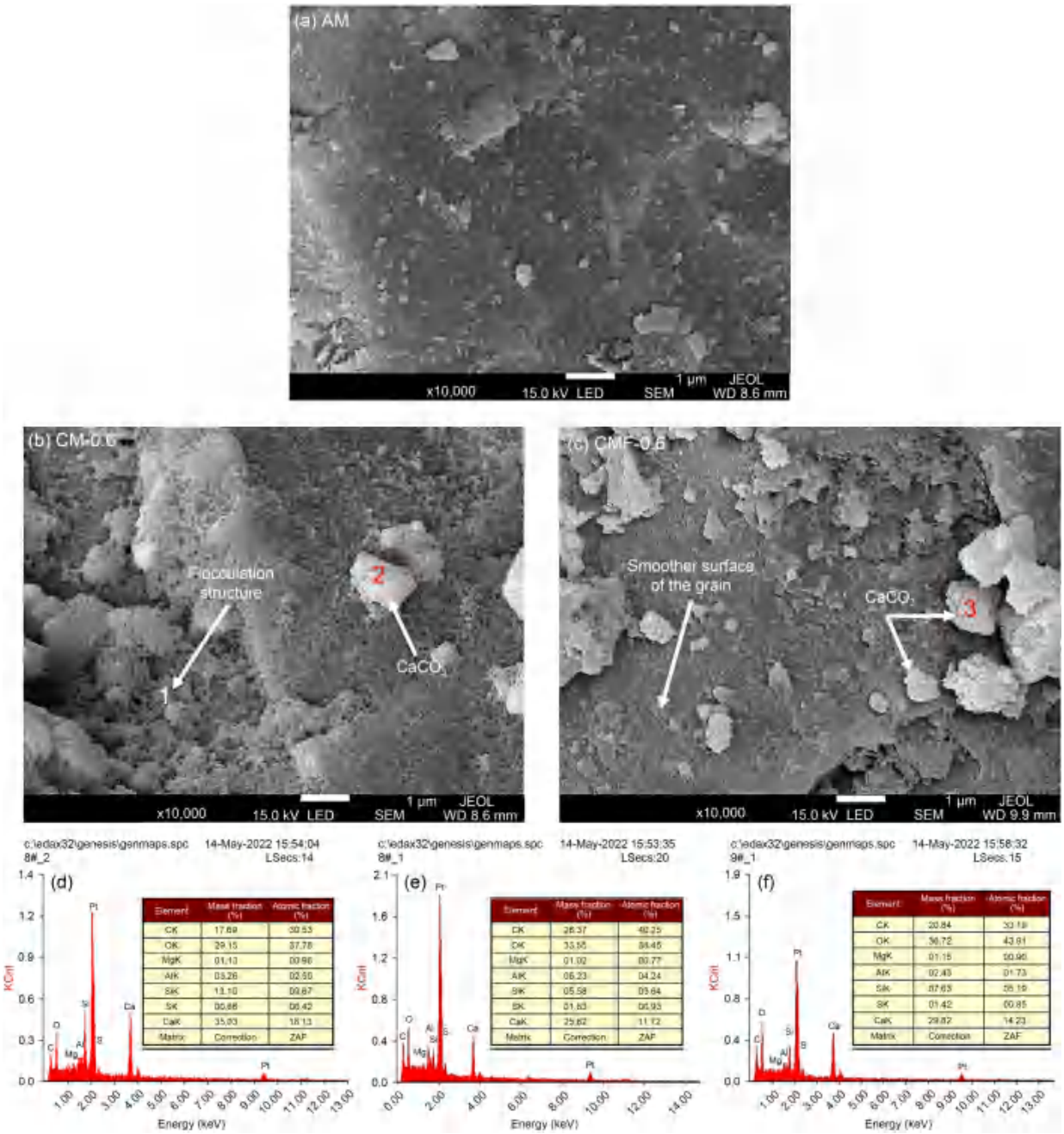

Fig. 7 Morphologies of the freshly prepared CO_2-mixing cement pastes of AM (a), CM-0.6 (b), and CMF-0.6 (c), and EDS spectra of spot 1 (d), spot 2 (e), and spot 3 (f)

of interest to plot the final water absorption as a function of compressive strength. The final water-absorption values appeared to be well correlated with the compressive strength results at 28 d (Fig. 9b). This statistical relation suggested that the lower the final water absorption, the higher the compressive strength of the samples, regardless of the CO_2-mixing dose or mixing approach.

3.2.3 Porosity analysis

An optical microscope and BSE were also used for close examination of the effects of CO_2-mixing dose and further mixing time on the pore structures of the investigated samples. Fig. 10 shows that the pore size and the amount of pores appearing on the surface of the CM samples increased with higher CO_2-mixing

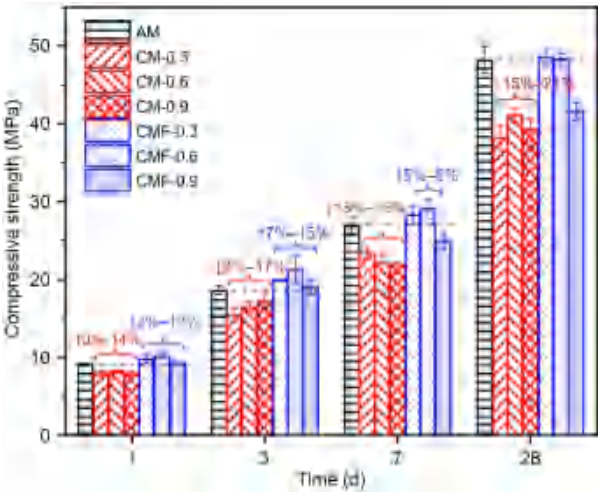

Fig. 8 Compressive strength of hardened cement pastes over time

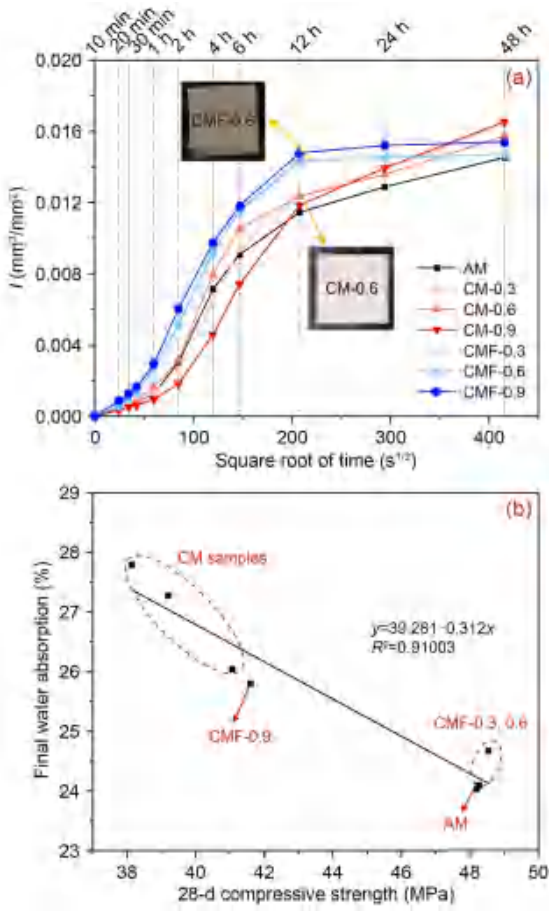

Fig. 9 Water sorptivity of CO_2-mixing cement pastes over time (a) and relationship between 28-d compressive strength and final water absorption (b)

doses. This is understandable considering their low workability, which resulted in poor compacting and

Table 4 Sorptivity coefficients (S) of the CO_2-mixing cement pastes

Sample	S ($\times10^{-5}$ mm/s$^{1/2}$)	Sample	S ($\times10^{-5}$ mm/s$^{1/2}$)
AM	6.63	CMF-0.3	8.53
CM-0.3	6.50	CMF-0.6	8.50
CM-0.6	7.56	CMF-0.9	8.76
CM-0.9	4.93		

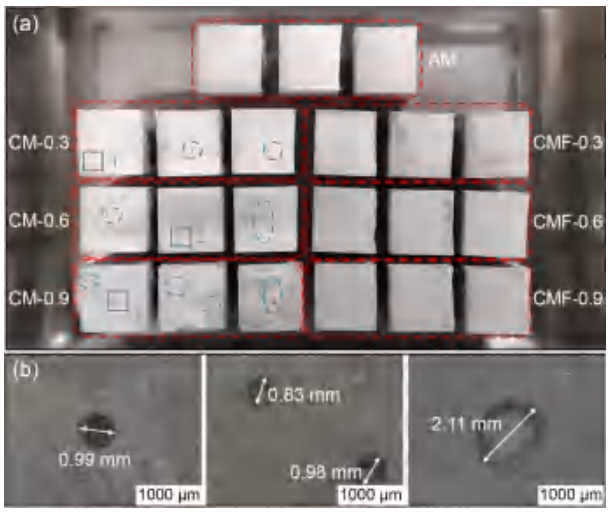

Fig. 10 Appearance of samples at 28 d (a) and pore sizes (b)

formation of cavities in the pastes. It is also congruent with the higher final water absorption and lower compressive strength of CM samples presented in Fig. 9b.

Table 5 shows the BSE porosity values of AM, CM-0.6, and CMF-0.6 samples, and the details of the porosity calculation and respective sample images are listed in Figs. S1 and S2 in the electronic supplementary materials (ESM). At 3 d, both the CM-0.6 and CMF-0.6 samples exhibited lower porosity than the control AM sample, in agreement with previous studies which reported that the presence of calcite in the cement matrix can promote early hydration and densify the microstructure (Monkman and MacDonald, 2016; Monkman et al., 2020). It is clear that the pore structure of all samples was refined over time (from 3 to 28 d) due to more complete hydration in the pastes. In comparison, the reduction of pore structure in the control sample (AM) was greater than those CO_2-mixing samples. This implies that the presence of calcite may not be beneficial for porosity refinement during hydration.

Table 5 Calculated porosity of AM, CM-0.6, and CMF-0.6 samples at 3 d and 28 d

Time (d)	Calculated porosity (%)		
	AM	CM-0.6	CMF-0.6
3	12.15	11.63	10.55
28	7.79	10.94	9.56

3.2.4 Reaction products of the hardened stage

Fig. 11a shows the evolution of $CaCO_3$ formation in CO_2-mixing cement pastes over hydration time (up to 28 d). The $CaCO_3$ content increased with time at early ages (≤7 d), possibly due to the dissolved CO_2 in the pore solution leading to precipitation of $CaCO_3$. However, $CaCO_3$ content decreased at 28 d because it reacted with tricalcium aluminate (C_3A) and/or monosulfate (AFm) to form hemi-carbonaluminate (Hc) and mono-carbonaluminate (Mc) (Zajac et al., 2014; Ren et al., 2022) (Fig. S3). In general, the CM samples had a higher content of $CaCO_3$ than the control AM and CMF samples, because part of the injected CO_2 gas was released during the further mixing of 1 min.

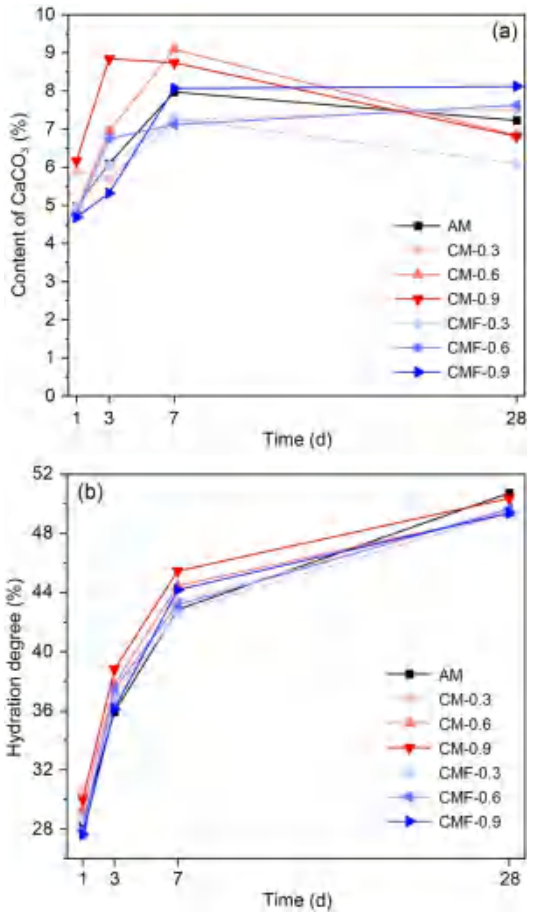

Fig. 11 The amount of $CaCO_3$ detected in CO_2-mixing cement pastes (a) and evolution of hydration degree over different hydration times (b)

The evolution of hydration degree over hydration time is plotted in Fig. 11b. At early ages (≤7 d), the hydration degree of both CM and CMF samples was generally higher than that of the control AM sample. In comparison, CM samples possessed a relatively higher hydration degree than CMF samples for a given CO_2 dose and curing age. This is due to a higher amount of actual reacted CO_2 promoting better cement hydration in CM samples. However, CM samples had a relatively low compressive strength, due to the poor compactness and larger pores associated with their lower workability. The AM sample displayed the highest hydration degree at 28 d, in line with the BSE porosity results (Table 5), proving that CO_2 mixing of the fresh cement paste only can promote early cement hydration.

4 Conclusions

In this study, the influence of CO_2 dose applied during mixing of cement pastes, as well as subsequent further mixing, on fresh and hardened properties of cement pastes was investigated. At the fresh stage, the introduction of CO_2-mixing induces quick hardening, and flowability decreases dramatically with higher CO_2 doses. This is mainly associated with the flocculation network by the formation of hydrates and carbonates on the surface of the cement clinkers. However, with 1 min of further mixing, the workability of fresh cement pastes can be improved by 52.8%–84.9% because this breaks up the flocculation network and releases entrapped free water.

In terms of compressive strength, a direct CO_2-mixing results in a ~10%–20% compressive strength loss at all curing ages, despite a higher degree of hydration. This is because of the poor compaction of the fresh cement mixture, which induces development of a more extensive pore structure in the hardened matrix. However, upon 1 min of further mixing, the overall compressive strength is enhanced by ~18%–32%, and demonstrated an early strength benefit of 3%–15% compared to the control sample. This is due to the hydration-promoting effect of the deposited $CaCO_3$ and a more densified microstructure. In addition, a strong

linear correlation between 28-d compressive strength and water absorption was observed, indicating that pore distribution plays an important role in the alteration of strength for CO_2-mixing cement pastes.

Acknowledgments

This work is supported by the Science and Technology Innovation Plan of Hunan Province (No. 2022WZ1010) and the Program Fund of Non-Metallic Excellence and Innovation Center for Building Materials (No. 2023Ph.D-6), China.

Author contributions

Minlu WANG designed the research, processed the corresponding data, and wrote the first draft of the manuscript. Shuang LUO and Ba Tung PHAM helped to organize the manuscript. Tung-Chai LING revised and edited the final version.

Conflict of interest

The authors declare that they have no known competing financial interests or personal relationships that could have influenced the work reported in this paper.

References

Akbar A, Liew KM, 2020. Influence of elevated temperature on the microstructure and mechanical performance of cement composites reinforced with recycled carbon fibers. *Composites Part B: Engineering*, 198:108245. https://doi.org/10.1016/j.compositesb.2020.108245

Ashraf W, 2016. Carbonation of cement-based materials: challenges and opportunities. *Construction and Building Materials*, 120:558-570. https://doi.org/10.1016/j.conbuildmat.2016.05.080

ASTM (American Society for Testing Materials), 2004. Standard Test Method for Measurement of Rate of Absorption of Water by Hydraulic-Cement Concretes, ASTM C1585-04. ASTM, USA.

ASTM (American Society for Testing Materials), 2013. Standard Test Method for Density, Absorption, and Voids in Hardened Concrete, ASTM C642-13. ASTM, USA.

ASTM (American Society for Testing Materials), 2014. Standard Practice for Measuring Hydration Kinetics of Hydraulic Cementitious Mixtures using Isothermal Calorimetry, ASTM C1679. ASTM, USA.

Berger RL, Young JF, Leung K, 1972. Acceleration of hydration of calcium silicates by carbon dioxide treatment. *Nature*, 240(97):16-18.

Camiletti J, Soliman AM, Nehdi ML, 2013. Effects of nano- and micro-limestone addition on early-age properties of ultra-high-performance concrete. *Materials and Structures*, 46(6):881-898. https://doi.org/10.1617/s11527-012-9940-0

Cao ML, Ming X, He KY, et al., 2019. Effect of macro-, micro- and nano-calcium carbonate on properties of cementitious composites–a review. *Materials*, 12(5):781. https://doi.org/10.3390/ma12050781

Chung CW, Lee JY, 2011. Premature stiffening of cement paste caused by secondary gypsum and syngenite formation (false set). *Architectural Research*, 13(1):25-32. https://doi.org/10.5659/aikar.2011.13.1.25

Cui K, Lau D, Zhang YY, et al., 2021. Mechanical properties and mechanism of nano-$CaCo_3$ enhanced sulphoaluminate cement-based reactive powder concrete. *Construction and Building Materials*, 309:125099. https://doi.org/10.1016/j.conbuildmat.2021.125099

Dixit A, Du HJ, Pang SD, 2021. Carbon capture in ultra-high performance concrete using pressurized CO_2 curing. *Construction and Building Materials*, 288:123076. https://doi.org/10.1016/j.conbuildmat.2021.123076

Dixit A, Geng GQ, Du HJ, et al., 2022. The role of age on carbon sequestration and strength development in blended cement mixes. *Cement and Concrete Composites*, 133: 104644. https://doi.org/10.1016/j.cemconcomp.2022.104644

GAQSIQ (General Administration of Quality Supervision, Inspection and Quarantine of the People's Republic of China), 2008. Test Methods for Heat of Hydration of Cement, GB/T 12959-2008. National Standards of the People's Republic of China (in Chinese).

GAQSIQ (General Administration of Quality Supervision, Inspection and Quarantine of the People's Republic of China), 2012. Test Methods for Water Requirement of Normal Consistency, Setting Time and Soundness of the Portland Cement, GB/T 1346-2011. National Standards of the People's Republic of China (in Chinese).

Guo JF, Wang L, Fan KP, et al., 2020. An efficient model for predicting setting time of cement based on broad learning system. *Applied Soft Computing*, 96:106698. https://doi.org/10.1016/j.asoc.2020.106698

Haha MB, de Weerdt K, Lothenbach B, 2010. Quantification of the degree of reaction of fly ash. *Cement and Concrete Research*, 40(11):1620-1629. https://doi.org/10.1016/j.cemconres.2010.07.004

Han D, Ferron RD, 2015. Effect of mixing method on microstructure and rheology of cement paste. *Construction and Building Materials*, 93:278-288. https://doi.org/10.1016/j.conbuildmat.2015.05.124

Han D, Ferron RD, 2016. Influence of high mixing intensity on rheology, hydration, and microstructure of fresh state cement paste. *Cement and Concrete Research*, 84:95-106. https://doi.org/10.1016/j.cemconres.2016.03.004

He Z, Li Z, Shao YX, 2017. Effect of carbonation mixing on CO_2 uptake and strength gain in concrete. *Journal of Materials in Civil Engineering*, 29(10):04017176. https://doi.org/10.1061/(ASCE)MT.1943-5533.0002031

Hossain M, Rashid H, Mahmud F, 2018. Effects of continuous mixing on mechanical problems of concrete. Proceedings of the 4th International Conference on Civil Engineering for Sustainable Development, article 4515.

Jiang Y, Ling TC, 2020. Production of artificial aggregates from steel-making slag: influences of accelerated carbonation during granulation and/or post-curing. *Journal of CO_2 Utilization*, 36:135-144. https://doi.org/10.1016/j.jcou.2019.11.009

Kwasny J, Basheer PAM, Russell MI, 2014. CO_2 sequestration in cement-based materials during mixing process using carbonated water and gaseous CO_2. Proceedings of the 4th International Conference on Durability of Concrete Structures, p.72-79. https://doi.org/10.5703/1288284315385

Li YS, Mehdizadeh H, Mo KH, et al., 2023. Co-utilization of aqueous carbonated basic oxygen furnace slag (BOFS) and carbonated filtrate in cement pastes considering reaction duration effect. *Cement and Concrete Composites*, 138:104988.
https://doi.org/10.1016/j.cemconcomp.2023.104988

Lippiatt N, Ling TC, 2020. Rapid hydration mechanism of carbonic acid and cement. *Journal of Building Engineering*, 31:101357.
https://doi.org/10.1016/j.jobe.2020.101357

Lippiatt N, Ling TC, Eggermont S, 2019. Combining hydration and carbonation of cement using super-saturated aqueous CO_2 solution. *Construction and Building Materials*, 229:116825.
https://doi.org/10.1016/j.conbuildmat.2019.116825

Liu LL, Ji YS, Gao FR, et al., 2021. Study on high-efficiency CO_2 absorption by fresh cement paste. *Construction and Building Materials*, 270:121364.
https://doi.org/10.1016/j.conbuildmat.2020.121364

Liu XY, 2019. Research of the Hydration and Hardening Mechanism of Cement-Based Materials after Absorbing CO_2 in Mixing Stage. MS Thesis, China University of Mining and Technology, China (in Chinese).

Liu XY, Chen L, Liu AH, et al., 2012. Effect of nano-$CaCO_3$ on properties of cement paste. *Energy Procedia*, 16:991-996.
https://doi.org/10.1016/j.egypro.2012.01.158

Luo S, Guo MZ, Ling TC, 2022. Mechanical and microstructural performances of fly ash blended cement pastes with mixing CO_2 during fresh stage. *Construction and Building Materials*, 358:129444.
https://doi.org/10.1016/j.conbuildmat.2022.129444

Lyu K, She W, Miao CW, et al., 2019. Quantitative characterization of pore morphology in hardened cement paste via SEM-BSE image analysis. *Construction and Building Materials*, 202:589-602.
https://doi.org/10.1016/j.conbuildmat.2019.01.055

Ma MT, Mehdizadeh H, Guo MZ, et al., 2021. Effect of direct carbonation routes of basic oxygen furnace slag (BOFS) on strength and hydration of blended cement paste. *Construction and Building Materials*, 304:124628.
https://doi.org/10.1016/j.conbuildmat.2021.124628

Mehdizadeh H, Cheng XF, Mo KH, et al., 2022. Upcycling of waste hydrated cement paste containing high-volume supplementary cementitious materials via CO_2 pre-treatment. *Journal of Building Engineering*, 52:104396.
https://doi.org/10.1016/j.jobe.2022.104396

Mehdizadeh H, Mo KH, Ling TC, 2023. CO_2-fixing and recovery of high-purity vaterite $CaCO_3$ from recycled concrete fines. *Resources, Conservation and Recycling*, 188:106695.
https://doi.org/10.1016/j.resconrec.2022.106695

Monkman S, MacDonald M, 2016. Carbon dioxide upcycling into industrially produced concrete blocks. *Construction and Building Materials*, 124:127-132.
https://doi.org/10.1016/j.conbuildmat.2016.07.046

Monkman S, MacDonald M, 2017. On carbon dioxide utilization as a means to improve the sustainability of ready-mixed concrete. *Journal of Cleaner Production*, 167:365-375.
https://doi.org/10.1016/j.jclepro.2017.08.194

Monkman S, MacDonald M, Hooton RD, et al., 2016. Properties and durability of concrete produced using CO_2 as an accelerating admixture. *Cement and Concrete Composites*, 74:218-224.
https://doi.org/10.1016/j.cemconcomp.2016.10.007

Monkman S, Kenward PA, Dipple G, et al., 2018. Activation of cement hydration with carbon dioxide. *Journal of Sustainable Cement-Based Materials*, 7(3):160-181.
https://doi.org/10.1080/21650373.2018.1443854

Monkman S, Lee BEJ, Grandfield K, et al., 2020. The impacts of in-situ carbonate seeding on the early hydration of tricalcium silicate. *Cement and Concrete Research*, 136:106179.
https://doi.org/10.1016/j.cemconres.2020.106179

Monteagudo SM, Moragues A, Gálvez JC, et al., 2014. The degree of hydration assessment of blended cement pastes by differential thermal and thermogravimetric analysis. Morphological evolution of the solid phases. *Thermochimica Acta*, 592:37-51.
https://doi.org/10.1016/j.tca.2014.08.008

Peng Y, Zeng Q, Xu SL, et al., 2020. BSE-IA reveals retardation mechanisms of polymer powders on cement hydration. *Journal of the American Ceramic Society*, 103(5): 3373-3389.
https://doi.org/10.1111/jace.16982

Ren PF, Ling TC, Mo KH, 2022. CO_2 pretreatment of municipal solid waste incineration fly ash and its feasible use as supplementary cementitious material. *Journal of Hazardous Materials*, 424:127457.
https://doi.org/10.1016/j.jhazmat.2021.127457

SBQTS (The State Bureau of Quality and Technical Supervision), 1999. Method of Testing Cements–Determination of Strength, GB/T 17671-1999. National Standards of the People's Republic of China (in Chinese).

Urban K, Sicakova A, 2018. The effect of mixing technique and prolonged mixing time on strength characteristics of concrete. *Proceedings*, 2(20):1290.
https://doi.org/10.3390/proceedings2201290

Wang Y, Li LS, An MZ, et al., 2022. Factors influencing the capillary water absorption characteristics of concrete and their relationship to pore structure. *Applied Sciences*, 12(4): 2211.
https://doi.org/10.3390/app12042211

Zajac M, Rossberg A, le Saout G, et al., 2014. Influence of limestone and anhydrite on the hydration of Portland cements. *Cement and Concrete Composites*, 46:99-108.
https://doi.org/10.1016/j.cemconcomp.2013.11.007

Zhang CY, Zhang SF, Yu JW, et al., 2022. Water absorption behavior of hydrophobized concrete using silane emulsion as admixture. *Cement and Concrete Research*, 154: 106738.
https://doi.org/10.1016/j.cemconres.2022.106738

Zhang D, Ghouleh Z, Shao YX, 2017. Review on carbonation curing of cement-based materials. *Journal of CO_2 Utilization*, 21:119-131.
https://doi.org/10.1016/j.jcou.2017.07.003

Zhao KY, Zhao LJ, Zhang XB, et al., 2022. An experimental study on the mixing process and properties of concrete based on an improved three-stage mixing approach. *Materials and Structures*, 55(5):134.
https://doi.org/10.1617/s11527-022-01976-y

Electronic supplementary materials

Figs. S1–S3

Construction and Building Materials 432 (2024) 136542

Contents lists available at ScienceDirect

Construction and Building Materials

journal homepage: www.elsevier.com/locate/conbuildmat

Review

Recent advance of monomer in-situ polymerization modified cement-based materials

Kai Wu [a], Jiangfeng Long [a,c,*], Longbang Qing [b,**], Geert De Schutter [c]

[a] Key Laboratory of Advanced Civil Engineering Materials of Ministry of Education, School of Materials Science and Engineering, Tongji University, Shanghai 201804, China
[b] School of Civil and Transportation Engineering, Hebei University of Technology, Tianjin 300401, China
[c] Magnel-Vandepitte Laboratory, Department of Structural Engineering and Building Materials, Ghent University, Ghent 9052, Belgium

ARTICLE INFO

Keywords:
Cement-based composite materials
Monomer in-situ polymerization
Mechanical properties
Toughening mechanism
Organic-inorganic hybrid

ABSTRACT

In recent years, in-situ polymerization has emerged as a promising technique for enhancing cementitious composites. This review examines the progress and advancements in in-situ polymerization modified cementitious composites (iPMCC), including the in-situ polymerization system, manufacturing, workability, mechanical properties, durability, microstructure, mechanism, application scenarios, and challenges. Incorporating monomers into ordinary cement-based composites (OCC) has significantly improved flexural strength (up to 203 %) while maintaining compressive strength with slight increases or minor decreases. The continuous polymer network forms strong crosslinks with cement hydrates, resulting in a more resilient polymer-cement system that effectively inhibits crack initiation and propagation under external loading conditions. iPMCC also demonstrate reduced porosity, contributing to improved durability. Lastly, this review illuminates the potential applications of iPMCC and identifies future research and challenges. It is essential for cement-based materials to demonstrate improved longevity and mechanical performance while integrating versatile applications. Overall, this review provides valuable insights into in-situ polymerization techniques for developing robust and functional cementitious materials, while also paving the way for future design, development, and utilization of organic/inorganic composite systems.

1. Introduction

Concrete stands as the most widely used construction material globally. However, the ecological downsides stemming from its production, transportation, or usage often overshadow its merits. Being a typical brittle material, concrete is susceptible to interface debonding and failure when subjected to shear stress surpassing its strength threshold [1–3]. To enhance the structural characteristics of concrete, such as its flexural strength [1,4–8], tensile strength [9–11], and interfacial bonding strength [3,12–16], researchers have explored various methods such as macro-level reinforcement [17–19], mesoscale fiber [8,20–22], micro-scale polymer [4,5,23,24–35], and nano-scale toughening C-S-H [36–39], as well as the integration of additives [40] and supplementary cementitious materials (SCMs) [41], aiming to enhance concrete's engineering performance. These approaches are geared towards cost reduction and bolstering environmental sustainability. Notably, cement production contributes to approximately 7 % of global carbon dioxide emissions [42], prompting a pressing need to curb such emissions in building material manufacturing. One potential solution involves the adoption of construction materials with heightened mechanical strength and durability [43]. As a result of this progress, it is anticipated that concrete structures will require less cementitious material for construction due to their improved mechanical properties, ultimately leading to reduced frequency of replacement and maintenance for cementitious structures. These benefits also aid in curbing cement consumption in the construction industry, presenting an ideal case for mitigating carbon dioxide emissions from the cement manufacturing process. Among these methods, the inclusion of polymers has emerged as a popular and effective approach for enhancing the engineering performance of cementitious materials [44], contributing to improved mechanical strength, prolonged lifespan of these structures,

* Corresponding author at: Key Laboratory of Advanced Civil Engineering Materials of Ministry of Education, School of Materials Science and Engineering, Tongji University, Shanghai 201804, China.
** Corresponding author.
E-mail addresses: longjfa@163.com (J. Long), qing@hebut.edu.cn (L. Qing).

https://doi.org/10.1016/j.conbuildmat.2024.136542
Received 7 March 2024; Received in revised form 28 April 2024; Accepted 5 May 2024
Available online 18 May 2024
0950-0618/© 2024 Elsevier Ltd. All rights reserved.

Nomenclature

iPMCC	In-situ polymerization modified cementitious composites
PMCC	Polymer-modified cementitious composites
OCC	Ordinary cement-based composites
PAM	Polyacrylamide
AM	Acrylamide
AA	Acrylic acid
SA	Sodium acrylate
AMPS	2-acrylanmido-2-methylpropanesulfonic acid
M/C	Monomer/cement ratio
FTIR	Fourier-transform infrared spectroscopy
ToF-SIMS	Time-of-flight secondary ion mass spectrometry
XPS	X-ray photoelectron spectroscopy
OPC	Ordinary Portland cement
C-S-H	Hydrated calcium silicate
CH	Calcium hydroxide

and significant reduction in the required consumption of concrete, thereby playing a pivotal role in minimizing environmental impact.

The amalgamation of organic and inorganic components within cementitious materials has attracted significant attention over the past five decades due to their complementary properties [44–46]. This heightened interest stems from the potential to manipulate the interaction between polymer molecules and cement hydration products at the molecular level, thereby enabling precise improvements to the concrete structure at the nanoscale. Current research underscores a growing emphasis on comprehending the nanoscale modification of cementitious materials [24,38,47,48]. Furthermore, examining the mechanical properties and microstructure of concrete constructs deepens our insight into the impact that polymer additives have on cementitious materials.

Polymer demonstrate superior tensile and bending strength, adhesive properties, and robustness against physical and chemical forces relative to inorganic substances [49,50]. Therefore, polymers are extensively utilized to bolster the comprehensive performance of cementitious materials, including cement pastes, mortars, and concretes in harsh environments [44,51,52]. Polymer-modified cementitious composites (PMCC) encompass a range of formulations, among which are: (1) Early-strength latex-modified concrete designed to inhibit cracking [1,53,54]; (2) Polypropylene-enhanced concrete aimed at augmenting water impermeability, bending strength, interfacial adhesive capacity, and contraction control [1,55,56]; (3) Water-soluble polymer modified concrete employs polymers like polyacrylamide (PAM) [1,4,23,25,32,57–71], polyvinyl alcohol (PVA) [20,33,57,72] and cellulose ether [73,74]. These water-soluble polymers possess polar and hydrophilic groups (e.g., carboxyl, hydroxyl, amide and amine), enabling them to dissolve in water without surfactants [58,75–78]. They display distinct chemical and physical characteristics, including flocculation capacity, viscosity modification, drag diminution, and adhesive qualities [65,73,79]. Among these, water-soluble polymers offer inherent advantages for application and modification, which are expected to significantly improve the performance of cement-based materials.

At present, one of the main drawbacks of most PMCC is the significant reduction in compressive strength associated with polymer incorporation [80–82], which limits its application. Previously, the common practice of incorporating polymers into cement systems involved the direct addition of high molecular weight polymers, a technique now known as the traditional method. Introducing polymers with traditional methods often result in the entanglement of polymer chains and weak interactions between polymers and cement [4]. In addition, the pronounced disparity between the polymer and cement phases [83], particularly the substantial variation in surface energies [14], frequently leads to the emergence of distinct and separated phases [4,84]. Owing to the polymer's lower compressive strength and modulus relative to cementitious materials, the isolated polymer phase emerges as the composite's vulnerability, culminating in a marked decrease in the compressive strength of PMCCs [4,85]. Additionally, the interfacial strength between polymers and cement is relatively weak [4,86,87], leading to slippage or fracture at the interface, thereby further undermining the structural integrity of the composite. For example, Liang et al. [4] enhanced the flexural strength of cement paste by 144.1 % by incorporating 5 % polymer, but the compressive strength decreased by 37.2 %. Similarly, Wang et al. [88] reported that the addition of 20 % butyl benzene latex (SBR latex) to cement increased the flexural strength by 27.1 % but led to a 34.2 % reduction in compressive strength. A notable characteristic of these modified materials is the increase in flexural strength accompanied by a significant reduction in compressive strength. Therefore, it can be inferred that incorporating polymers effectively enhances the ratio of flexural to compressive strength, indicative of improved material toughness [89]. However, the substantial decrease in compressive strength or modulus of the composites often negates this benefit, presenting challenges for the practical application of polymers.

The high viscosity and limited mobility of blended cement paste pose challenges in achieving efficient dispersion of polymer within the cementitious matrix using physical blending techniques [4,61,63,65,90]. Water-soluble monomers have high mobility and can be uniformly dispersed in the cement slurry [4,91–93]. In recent years, a novel approach has been proposed to enhance the mechanical properties and crack resistance of cement-based materials by introducing polymers through an emerging monomer in-situ polymerization method [4,27–31,34,60,94]. This composite material is termed as in-situ polymerization modified cementitious composites (iPMCC). This approach ensures the uniform distribution of polymer chains, avoiding the formation of large, separated polymer phases that could weaken the overall structural mechanics [4,30,34]. During cement hydration, the polymerization of the monomer can occur, promoting the bonding and interactions between organic and inorganic components, thereby enhancing the mechanical properties [4,34].

After conducting a comprehensive search on the Web of Science (WOS) Core Collection database for all papers related to monomer in-situ polymerization in cement-based materials, this study selected high-quality papers relevant to the field of building materials. As shown in Fig. 1, a total of 33 papers were published from 2013 to 2024. The

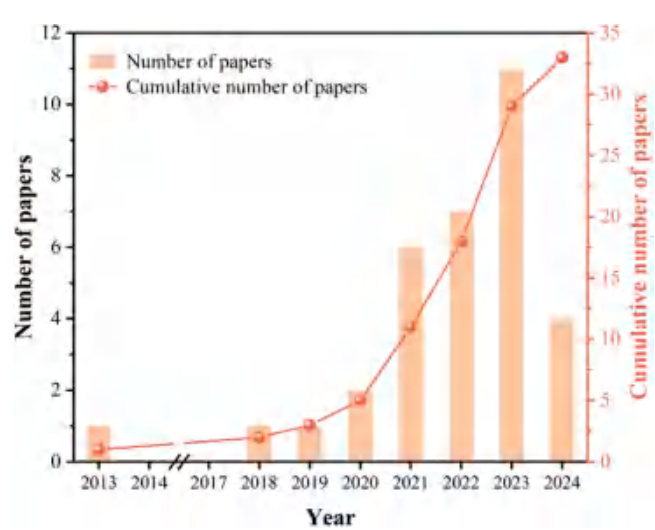

Fig. 1. Annual and cumulative number of publications on iPMCCs.

keywords for search included "in-situ polymerization" or "in situ polymerization", "monomer", and "cement/mortar/concrete". Fig. 1 illustrates a rapid increase in the number of articles in recent years.

Recent studies have investigated the application of in-situ polymerization for modifying cement-based materials. However, a comprehensive overview encompassing preparation strategies, characterization methods, and performance evaluation is currently lacking. This paper seeks to bridge this gap by presenting a state-of-the-art review on incorporating monomers through in-situ polymerization to improve the performance of cementitious materials. The cement concerned in this paper is Portland cement unless noted. The framework and content are depicted in Fig. 2, starting with an introduction to the in-situ polymerization systems and application potential, along with the manufacturing process. Emphasis is placed on analyzing and summarizing the effects of in-situ polymerization on fresh properties, mechanical properties, durability, and microstructure evolution. The underlying mechanisms are also elucidated. Each section identifies the research gaps and provides an outlook for future research. Furthermore, the discussion delves into the applications and challenges of iPMCCs, along with the emerging trends in the field. To date, a comprehensive review of the application of in-situ polymerization techniques for modifying cement-based materials is currently lacking. Thus, this review offers a comprehensive overview and valuable insights in this domain, aiming to guide the design, preparation, characterization, and development of iPMCCs, and contribute to the sustainable development of cement-based materials.

2. The potential free radical polymerization among cement hydration

Polymers in iPMCCs possess the unique capability of being generated via free radical polymerization within cement while adapting to the alkaline and temperature environment of cementitious materials. The polymerization rate can be controlled, facilitating efficient bonding between the polymers and the products of cement hydration. The primary raw materials for these polymers encompass monomers, initiators, and crosslinking agents.

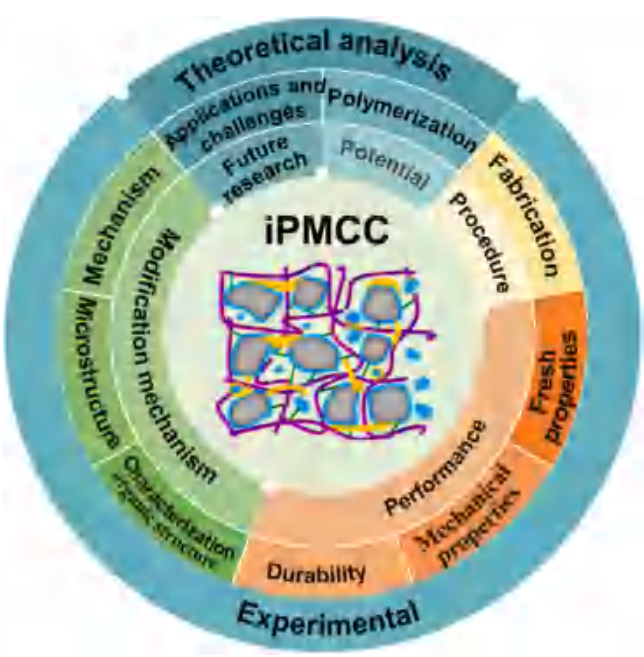

Fig. 2. Illustration of in-situ polymerization modified cementitious composites from three aspects including preparation, characterization, and properties.

2.1. Raw materials for free radical polymerization

2.1.1. Monomer

Monomers are simple compounds capable of undergoing polymerization under specific conditions to form high-molecular-weight polymers, thus serving as the low-molecular-weight precursors for polymer synthesis. Currently, monomers containing carbon-carbon double bonds and carboxyl groups, or those with carboxyl groups after hydrolysis, are often considered for in-situ polymerization modification of cementitious materials. The most involved organic monomers are acrylamide (AM) [4,26,28,30,95–97], acrylic acid (AA) [27,28,34,35,98], 2-acrylanmido-2-methylpropanesulfonic acid (AMPS) [35], 2-hydroxyethylmethacrylate (HEMA) [99], methyl methacrylate (MMA) [100], etc. The most widely used monomer is AM, which possesses amide groups and carbon-carbon double bonds, with its structural formula illustrated in Fig. 3 (a). Acrylamide is produced from acrylonitrile as raw material, and the crude product of acrylamide is formed by hydrolysis under the action of catalyst [101]. Flash evaporation and refining steps yield purified acrylamide. Polyacrylamide (PAM) is synthesized by acrylamide, and the chemical structure is shown in Fig. 3 (b). PAM is a water-soluble polymer, which is known as “ghost crystal” [102]. PAM partially hydrolyzes to form carboxylate in an alkaline environment, and presenting as a mixture of nonionic polyacrylamide (NPAM) and anionic polyacrylamide (APAM) [70] (as shown in Fig. 4). The characteristics of PAMs molecular structure are summarized in the literature [70] and show a significant impact on cement properties. Additionally, it is noteworthy that PAM exhibits high thermal stability up to 110 °C, and the softening point of solid PAM lies approximately between 220 and 230 °C. Their molecular weight typically ranges from 1×10^3 to 20×10^6 g/mol [103].

2.1.2. Initiator

Initiators are compounds that readily undergo thermal decomposition to yield free radicals (primary free radicals), which are essential for initiating the free radical polymerization and copolymerization of vinyl and divinyl monomers. In a word, the initiator and accelerator play roles in initiating and accelerating the polymerization of monomers, respectively. Ammonium persulfate (APS), potassium persulfate (KPS), and sodium bisulfate (SBS) are commonly used as initiators for the free radical polymerization of monomers [4,26], and the commonly used as accelerator is N, N, N′, N′ - tetramethyl ethylenediamine (TEMED) [4,26].

The concentration of initiator and accelerator highly affects the polymerization kinetics and polymer properties. Increasing the concentration of initiator and accelerator would reduce the length of polymer chain and gel elasticity. Excessive concentration of initiator can cause premature gelation, impeding the dispersion of polymer in cement. In contrast, reducing the amount of initiator could increase the chain length and elasticity, but slow down the polymerization rate, allowing oxygen to enter the solution and eventually producing gels with high porosity and low mechanical strength. Therefore, the catalyst concentration should be sufficient to obtain a porous gel with the required elasticity and mechanical strength. The polymerization rate of monomers directly affects the performance of iPMCCs, and the related performance regulation mechanism still needs to be further studied.

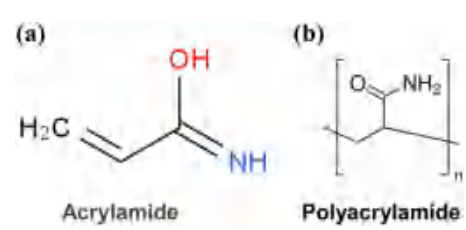

Fig. 3. Structure of acrylamide and polyacrylamide.

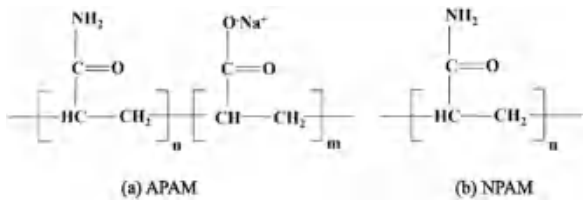

Fig. 4. Chemical molecular structures of two typical PAM.

2.1.3. Crosslinking agent

Crosslinking agents play a crucial role in forming chemical bonds between linear molecules, connecting them to create a three-dimensional, insoluble network structure that significantly enhances the strength and elasticity of polymeric materials. The crosslinking agent is employed to increase the degree of crosslinking within polymer chains, such as N, N′ -methylene diacrylamide (MBA) [97], hexamethylenetetramine / hydroquinone, polyethyleneimine, p-phenylenediamine and dimethylaminoethyl methacrylate. The commonly used crosslinking agent is MBA, which is widely available and its molecular structure is illustrated in Fig. 5.

2.2. The potential free radical polymerization

Free radical polymerization is a chemical reaction in which monomer molecules are activated by light, heat, radiation and initiator, forming reactive free radicals that subsequently polymerize with monomers to generate polymers. Table 1 and Fig. 6 illustrates the reaction mechanism. The key steps in free radical polymerization are chain initiation, growth, and termination. In an aqueous solution, the polymerization rate and molecular weight can be controlled by adjusting the initiator amount and monomer-to-solvent ratio.

Cementitious systems have demonstrated the potential for accommodating free radical polymerization [4,27,34]. However, the application of polymers in cement-based materials is relatively recent, resulting in limited studies on the polymerization kinetics in these systems. Some aspects that needs further investigation include determining and regulating polymerization rates, measuring polymerization degree and crosslink density, as well as investigating the influence of temperature, pH, and pore solution on polymerization kinetics within cementitious systems.

3. Fabrication procedure for in-situ polymerization modified cementitious composites

For iPMCCs, the monomer mass fraction, characterized by the ratio of polymer mass to that of cement, typically varies between 0.05 % and 20 % [1,62]. The form of AM incorporated into cementitious materials is mainly dry powder or solution. This substance can be directly blended it with cement, aggregate, and water, negating the requirement for additional equipment.

The poor dispersion of polymer in cement paste highly affects the PMCC performance [4,35,104,105]. Therefore, achieving the desired dispersion requires careful attention to the manufacturing process. Reference [34] refers to a method of incorporating monomer into cement using aqueous solution. Fig. 7 illustrates the schematic representation of the process for solution preparation and mixing. In the first step, the monomer was dissolved in water to form a dispersed solution,

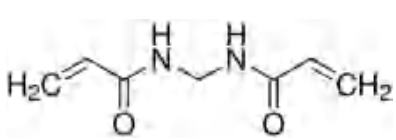

Fig. 5. Structure of N, N′ -methylene diacrylamide.

Table 1
The process of free radical polymerization.

Stage	Reaction equation
Chain raised	$I \rightarrow 2R$
	$R\cdot + M \rightarrow RM$
Chain growth	$RM\cdot + M \rightarrow RM_2$
	$RM_2\cdot + M \rightarrow RM_3$
	…
	$RM_{n-1}\cdot + M \rightarrow RM_n$
Chain termination	$RM_n\cdot \rightarrow$ Polymer

Note: Among them, I represents the initiator, $R\cdot$ represents the primary free radical, M represents the monomer, $RM\cdot$ represents the monomer radical, and $RM_n\cdot$ represents the active chain.

then adding accelerators and crosslinking agents, which facilitated them even distribution when integrated with cement particles. The solution was mixed with cement and stirred at low speed for 1 min, followed by high-speed stirring for 2 min to prepare cement slurry, which is then poured into molds (as shown in Fig. 7). Specimens were demoulded after cured at room temperature for 24 h, and then cured in a standard curing room until the test age [34]. Throughout the manufacturing process, the inclusion of ancillary additives, like superplasticizers or defoamers, is frequently necessary to preserve the material's workability and to enhance the microstructural integrity of iPMCCs [44]. Ice water can be used to slow the polymerization rate [34]. However, this is not mandatory, as monomers exhibit an induction period during free radical polymerization at room temperature [106], which prevents rapid polymerization. At present, achieving the high-performance combination of polymer and cement hydration products requires accurate controlling the polymerization rate and ensuring that it is synchronized with the cement hydration rate [27,34]. Further research is needed, including adjusting the initiator content, improving the preparation process and adding other substances to regulate the in-situ polymerization rate and hydration kinetics. Current fabrication techniques predominantly utilize traditional methods. Innovative approaches, such as ice templating [33], biomimetic brick-and-mortar structure [25], and three-dimensional vacuum-compaction-vibration techniques [107], remain underexplored and hold potential for application in iPMCCs. Furthermore, the effects of curing conditions, including variations in temperature and humidity, on the macroscopic performance and microscopic structure of the materials require further study. This will help in optimizing the material properties for broader application scopes.

4. Effect of in-situ polymerization on the performance

4.1. Fresh properties

4.1.1. Workability

Fresh cementitious materials often experience moisture loss as a portion of water migrates from the pores to the surface [73,108]. This apparent water loss decreases fluidity and hinders cement hydration, negatively impacting mechanical properties and durability [109,110]. Adding AM can enhance the water-retention capacity of cement slurry [30,96]. AM and PAM molecular chains contain amino groups (-NH_2) that can form hydrogen bonds with water molecules [111], impeding the mobility, consequently elevating the yield stress and viscosity of the system. Therefore, the addition of AM positively affects water retention in cement slurry and alleviates bleeding [70].

In general, most polymers decrease the fluidity of cement slurry [74,112], whereas the addition of AM shows the opposite effect [4,30,94,97,113]. In this study [94], the fluidity of iPMCC increased with the AM/cement ratio increasing. A 6 % AM mixture resulted in a 23.16 % increase in fluidity compared to the control group. Ref. [34] reports that adding 4 % sodium acrylate (SA) increases the fluidity of cement slurry by 35.1 %. Acrylate ions, which carry a negative charge, are adsorbed

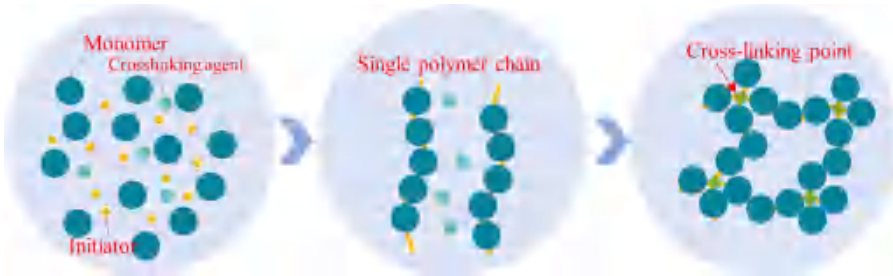

Fig. 6. The process of free radical polymerization.

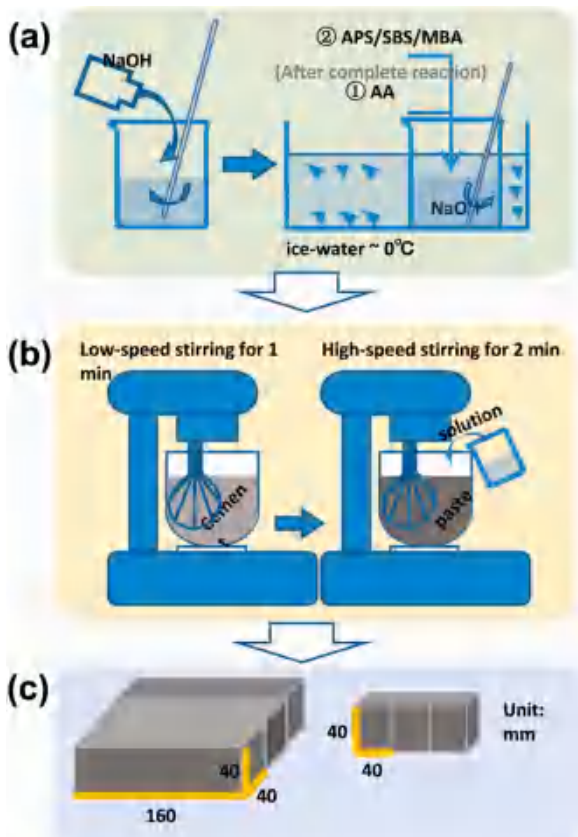

Fig. 7. Schematic diagram of the processes for (a) solution preparation, (b) mixing, and (c) casting of cement slurry in different geometries [34]. Low speed refers to a rotation of 140±2 rpm for self-rotation and 62±2 rpm for revolution. High speed refers to a rotation of 285±3 rpm for self-rotation and 125±3 rpm for revolution.

onto the positively charged surfaces of cement particles and their hydration byproducts (e.g., C_3A, C_4AF, AFt), leading to electrostatic repulsion and inhibiting flocculated structure formation [114,115]. This disperses cement particles, releases free water in the pores, and enhances slurry fluidity. Additionally, AM dissolution is an endothermic reaction, lowering the environmental temperature and slowing cement hydration, resulting in improved slurry flowability. These findings demonstrate the potential of monomers as additives for enhancing the rheological properties of cementitious materials.

However, the rheological parameters of cement slurry do not continuously increase with the monomer content. Xu et al. [34] have reported that 8 *wt.*% sodium acrylate (SA) reduces fluidity by 18.1 %, while yield stress increases significantly (4168.1 %) along with plastic viscosity (552.1 %). This rheological behavior is attributed to the interaction between monomers/polymers and cement particles. The interaction involves attractive van der Waals forces coupled with repulsive forces originating from the electrical double layer [116,117], increasing the viscosity and yield stress of fresh cement paste [63,118]. PAM reacts with calcium ions in the pore solution to form microgels, leading to rapid phase separation through gel formation or precipitation (as shown in Fig. 8) [118–120]. Microgel adsorption on cement particle surfaces amplifies van der Waals forces and increases the electrostatic repulsion among the cement particles [114]. Anionic stabilizers adversely affect the workability of fresh cement slurry, while the presence of non-ionic surfactants improves flowability through steric repulsion [44]. Increasing acrylate content enhances the adsorption of water by polymer and causing the flowability decreases [121] due to the polyacrylate (PAA, SA polymerization product) is more significant than PAM as it represents the complete hydrolysis of PAM. Thus, future research should consider the different effects of polymer characteristics on cement slurry flowability.

Sun et al. [121] explored the effects of incorporating two monomers, acrylic acid and acrylamide, into cement slurry for in-situ polymerization. Their tests on the yield stress of slurries revealed significant enhancements at high polymer concentrations, attributable to the dual functionality of polymers. Firstly, the polymers that adsorb to the cement particles create bridges, thereby strengthening the forces between particles [4,121]. Secondly, the non-adsorbed polymers remaining in the interstitial solution interact to form a robust network that effectively withstands external stresses. The in-situ polymerized PAA primarily induces flocculation, significantly enhancing inter-particle attractions [121]. Conversely, in-situ polymerized PAM, with its extended chain structure, primarily functions as a thickener, boosting interactions within the polymer matrix, while contributing less to inter-particle forces [121].

The rheological behavior of iPMCC is influenced by the synergistic effect of monomer/polymer flocculation and lubrication. Increasing monomer content improves yield stress, viscosity, and structure aggregation rate up to a saturation point. Below the optimal content, the monomer acts as a lubricant [122], dominating the lubrication effect similar to other water-soluble polymers [72]. These findings highlight

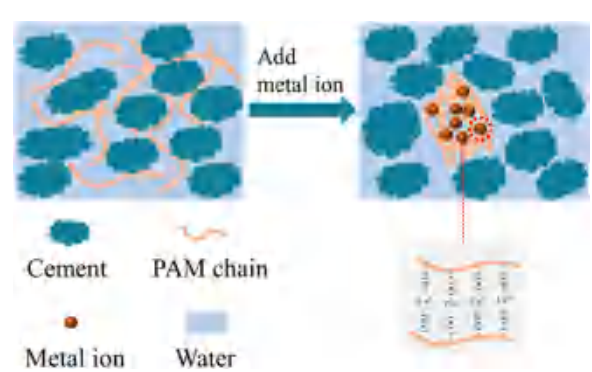

Fig. 8. The complexation of PAM chains with metal ions results in phase separation.

the importance of carefully selecting and optimizing additive content in cementitious materials since each component can have significantly different effects on overall performance.

The incorporation of polymers significantly affects the workability of PMCC as they serve multiple functions such as the reduction of water content, air entrainment, and enhancement of water retention [53]. It is important to note that incorporating monomers also yields similar effects, albeit with varying influence due to their significantly lower molecular weight compared to polymers [121]. However, during the polymerization, gradual polymer formation may alter the flowability and rheological behavior of cement slurry. Further research should explore the changes and mechanisms for flowability and rheological behavior of cement slurry during polymerization.

4.1.2. Setting time

Incorporating monomer/polymer can influence the setting time of cement [4,27,58,97,113]. The initial setting time refers to the time when the paste begins to lose its plasticity while the final setting time refers to the time when the paste has completely lost its plasticity and has started developing a certain strength. Fig. 9 depicts that as the monomer/cement (M/C) ratio increases, the initial setting time may be significantly shortened from the standard duration of 300 min to just 30 min [30]. Conversely, the time interval between the initial and final setting time gradually extends with the elevation of the M/C ratio rises since the final setting time is significantly influenced by hydration degree. The addition of polymer may serve to hinder cement hydration during the initial stages, thereby prolonging the time required to obtain adequate strength.

The in-situ polymerization of SA shortens the initial setting time [27]. During the initial stages of hydration, the monomer functions as a catalyst, expediting the process whereby the paste rapidly diminishes in fluidity by forming a three-dimensional polymer network. Additionally, the strong water adsorption capacity of sodium polyacrylate is commonly used in diapers [123]. The decrease in the amount of water available for cement hydration results in a diminished fluidity for the fresh paste. Additionally, the rapid polymerization of monomers may shorten the setting time [30]. When incorporating monomers with a M/C ratio of 0.08, the final setting time experiences a modest extension, increasing by approximately 25 %, as documented in [34]. The retarding effect mirrors the action of superabsorbent polymers (SAPs) utilized in ultra-high-performance concrete (UHPC), which not only retard the cement hydration but also mitigate the shrinkage [124]. The absorbed water in sodium polyacrylate continues to gradually release [125], prolonging the final setting time.

Zhang et al. [97] discovered that the setting time of sulphoaluminate cement (SAC) does not change remarkably when the AM content is less than 5 %. As the AM content exceeds 20 %, the initial and final setting time increases sharply. The PAM can be adsorbed onto the surface of cement particles, thereby diminishing the contact interface between the cement and water.

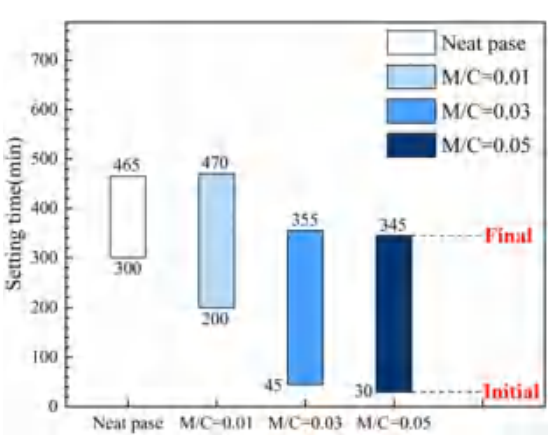

Fig. 9. Setting time of iPMCCs at different M/C ratios [30].

Ref. [1,4,126,127] have reported that carboxyl can react with calcium ions as shown in Eqs. (1) and (2), which reduces the concentration of calcium ions in pore solution and delays the precipitation of hydration products. Other ionic polymers containing carboxyl groups show similar retarding effects on cement hydration [127].

$$R-COO^{-}+Ca^{2+}\rightarrow R-COO-Ca-OOC-R \quad (1)$$

$$R-COO^{-}+Ca^{2+}\rightarrow R-COO-Ca-OH \quad (2)$$

After mixing with cement paste, the adsorption and hydrogen bonding of monomers or polymers can slow down the movement of cement particles and water molecules [59,128–130]. On the one hand, the hydrogen bond slows down the evaporation of water. On the other hand, monomer/polymer ionizes hydroxyl groups (-COO^{-}) and forms more complex compounds with cement hydration products [1,4,58,65]. These compounds will form a network that hampers the movement of water molecules and even blocks the water transmission channel among pores [63]. Currently, research primarily focuses on how monomer types and concentrations influence the setting time of cement paste. Future studies should expand their scope to examine the impact of monomers on the setting time of mortar and concrete, and explore strategies for regulating this parameter.

4.2. Mechanical properties

Strong mechanical properties are crucial for cementitious materials to ensure structural load-bearing functions. Hence, the development of iPMCCs places significant emphasis on achieving desired mechanical properties. The influences of monomer/polymer on the mechanical properties of iPMCCs from various sources are summarized in Table A1. Positive values in the table denote an increase in intensity, while negative values indicate a decrease.

4.2.1. Flexural strength and fracture toughness

Table A1 consolidates the results from laboratory tests on flexural strength, compressive strength, and the flexural-to-compressive strength ratio, which characterizes the material's brittleness, with lower values indicating increased brittleness. According to the statistical data, the relationship between the enhancement of flexural strength and compressive strength as a function of varying monomer dosages is drawn in Fig. 10. As shown in Fig. 10 (a), the addition of 1 %–8 % monomers via in-situ polymerization significantly improves the flexural

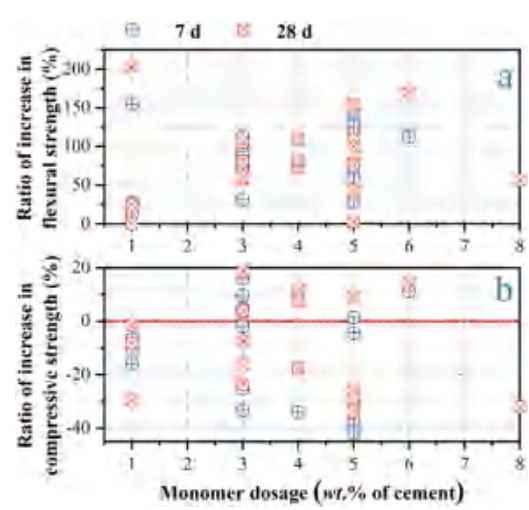

Fig. 10. The ratio of increase in (a) flexural strength and (b) compressive strength with varying monomer dosage (data is from Table A1).

strength of iPMCCs. Studies [4,28,34] have consistently shown that using - 5 % monomer content leads to a notable increase in flexural strength ranging from 50 % to 150 %, with the highest recorded increase reaching 203.1 % (in Table A1).

According to the experimental results of Liang et al. [4], compared to OPC, the optimized flexural strength of iPMCCs can be elevated from 8.5 MPa to 25.7 MPa, while the polymer dosage is only 1 %. The remarkable enhancement in flexural strength is mainly attributed to the formation of a dual interpenetrating network with chemical bonds between PAM and cement hydration products at an optimized polymer content [4,131,132]. The in-situ polymerization of AM with OPC generates a continuous interpenetrating network that effectively disperses the energy driving crack formation, consequently inhibiting the progression of cracks to a macroscopic scale [29]. The contrasting properties of hardened cement paste and soft PAM complement each other in a nuanced manner. However, a further increase in monomer dosage leads to a gradual decrease in flexural strength. This decline is attributable to the excess polymers that tend to entangle and form a separate polymer phase within the composite [4,30,34]. This phase acts as the weak region, consequently leading to a reduction in its overall strength. Meanwhile, compared with incorporating PAM, the formation of a well-dispersed polymer network through in-situ polymerization is critically important for the development of strength in iPMCCs [4].

The incorporation of monomers or polymers within cementitious composites enhances both flexural strength and tensile strength by facilitating the bridging between adjacent silicate sheets in the C-S-H and promoting hydrolytic reactions at the interfaces. This contributes to a more cohesive and interconnected microstructure, resulting in improved mechanical properties. Meanwhile, the improvement of ductility took place alongside the diminished brittleness of cementitious composites. Simulation results demonstrated the effectiveness of this hypothesis [27,29,30,133]. In addition, in-situ polymerization can significantly improve the fluidity of cement slurries [4,30,34,97], delay the cement hydration [4,5,27,28,35,97], reduce the peak exothermic temperatures [4,5,27,28,35,97], lessen the matrix cracking [28,34], and promote the formation of organic-inorganic hybrid [27,28,35,134], as well as densifying the compactness of cement matrix [4,26,34,94]. As a result, it effectively increases flexural strength, deformability, and energy dissipation capacity [4,29,34,95,96,113]. Additionally, the combination of monomers with other materials added to the cement paste has shown a synergistic toughening effect, such as fibers [29,132], limestone whiskers [29,131], zirconium phosphate [60], and liquid metals [135].

4.2.2. Compressive strength

Table A1 summarizes the compressive strength of iPMCCs in literature, and Fig. 10 (b) shows the ratio of increase in compressive strength of iPMCCs. It can be observed that adding 3 % - 6 % monomers can slightly improve the compressive strength in some experiments [26,27]. When the polymer content is less than or equal to 1 %, the compressive strength of iPMCCs approaches that of the control group. But in most cases, the compressive strength is still lower than that of the control group and decreases as the polymer dosage increases.

The traditional PMCCs have a significant drawback [80], namely the compressive strength decreasing significantly when polymer is added. The degraded compressive strength is mainly attributed to uneven polymer dispersion, poor organic-inorganic hybrid, and lower polymer stiffness. However, introducing polymer into cement matrix at an optimized ratio by in-situ polymerization method can significantly improve the flexural strength without adversely affecting the compressive strength [4]. This is because polymers can be well dispersed in cement matrix, forming an interpenetrating network. Nevertheless, as the polymer content increases, the excess polymer can unavoidably agglomerate and form separate phases, which then become the weak point and decrease the compressive strength of iPMCCs [4,30,34].

4.2.3. The ratio of flexural to compressive strength

Fig. 11 (a) presents a comparative visualization of flexural and compressive strengths as documented in various studies (the data is from Table A1). Despite some variations in mechanical properties observed across different mix proportions and specimen preparation methods, a clear demarcation line between iPMCCs and neat cement pastes is evident (indicated by the red dashed line in Fig. 11a). Incorporating monomers that polymerize within the matrix significantly improves the flexural strength and the ratio of flexural to compressive strength of iPMCCs, even at equivalent or slightly lower compressive strengths (as shown in Fig. 11b). The increase in the ratio of flexural and compressive strength implies an improvement in the brittleness of cementitious materials.

Traditional PMCCs (such as SBR, EVA, and water-based epoxy resins) have been reported that there is virtually no enhancement in compressive strength and only a modest improvement in flexural strength, often less than 50 % [136,137]. However, the statistical results indicate that over two-thirds of iPMCCs exhibit a flexural strength enhancement exceeding 50 % (Fig. 10a), and approximately one-third of iPMCCs show improved compressive strength (Fig. 10b). In terms of mechanical performance, iPMCCs present significant advantages over conventional PMCCs.

As illustrated in Fig. 12 (a), Xu et al. [34] conducted three-point bending and compressive strength tests, and found significant improvements in flexural strength and mid-span displacement with 4 % SA (MC4) (as shown in Fig. 12e). The notable improvement in mid-span displacement indicates that in-situ polymerization greatly enhances the deformability of cementitious material. As illustrated in Fig. 12 (b), the compressive load-displacement curve of MC4 exhibits a non-linear increase followed by a delayed drop, with a slow rise in displacement while maintaining the load without decreasing, indicating a decrease in stiffness (or increase in flexibility) of iPMCC specimens. Similar load-displacement behavior during bending and compression loading has been reported for PMCCs elsewhere [95]. The flexural energy and compression energy increased by 458.8 % and 161.0 %, respectively, indicating that iPMCCs possess higher energy dissipation capacity during flexural and compressive loading. Molecular dynamics simulations attribute these improvements in strength and deformability to the strengthened interface bonds between polymers and cement hydrates [27]. Furthermore, iPMCC blocks demonstrate greater structural integrity and reduced fragmentation after compression, suggesting that iPMCC concrete structures experience reduced spalling under dynamic

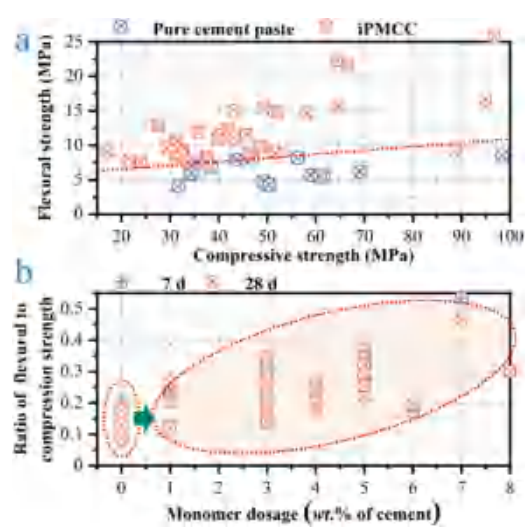

Fig. 11. (a) Comparison of flexural strength and compressive strength, (b) the ratio of flexural to compressive strength with vary monomer dosage. (The data is from Table A1.).

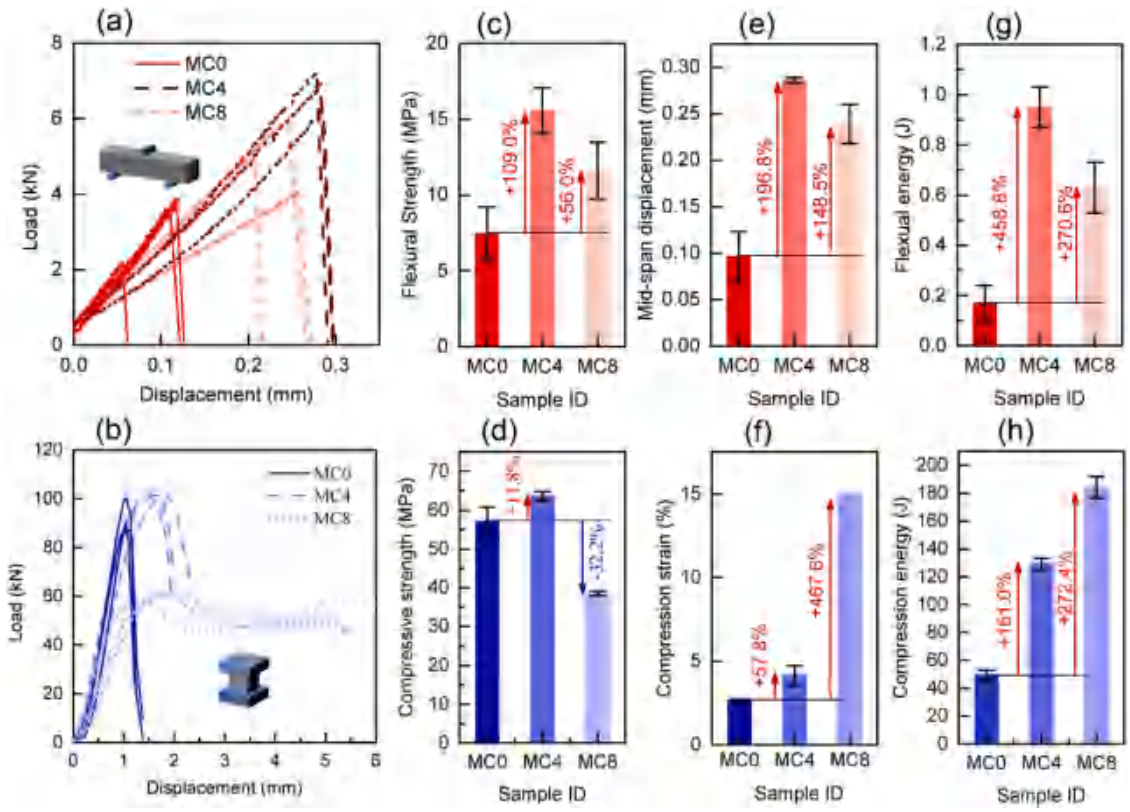

Fig. 12. Mechanical performance of iPMCCs: Load-displacement curves of (a) flexural and (b) compressive tests, (c) flexural strength, (d) compressive strength, (e) mid-span displacement, (f) compressive strain, (g, h) deformation energy of flexural and compressive tests [34]. MC0 represents neat cement paste, while MC4 and MC8 represent iPMCCs with 4 % and 8 % SA incorporation, respectively.

loads, such as seismic activity or explosions, leading to enhanced safety for humans and structures.

Based on the research findings, incorporating an appropriate amount of monomer significantly enhances the flexural strength, deformability, and energy dissipation capacity of iPMCCs, showing great potential for seismic and impact resistance in practical applications. However, the in-situ polymerization of monomer does not markedly enhance the compressive strength of iPMCCs and may even result in a reduction. This indicates that precise control measures are essential in the process of toughening and strengthening iPMCCs. Future studies can focus on adjusting the polymerization rate, enhancing bonding between organic and inorganic compounds, and improving the mechanical properties of the polymer to enhance the compressive strength of iPMCCs. Moreover, there is limited research on the mechanical properties and toughening effects of in-situ polymerization, lacking systematic evaluation methods. Future research can also explore the areas such as the long-term stability of mechanical properties, evaluation of mechanical performance when combined with fibers or steel reinforcement, and potential applications.

4.3. Durability

Liu et al. [26] found that as the content of AM in the composite increases, the coefficient of water absorption decreases markedly. The capillary water absorption coefficient of the sample containing 5 % AM is about 24 % lower than that of the control group. In another experiment, Liu et al. [5] found that as AA-AMPS increases from 0 % to 5 %, the water absorption decreases within the first 24 hours, and then increases. iPMCCs exhibited a better water resistance ability, which can be attributed to the filling effect of polymer. Once in contact with water, the polymer immediately absorbs water, causing polymer expansion, blocking pores, increasing the tortuosity and decreasing the connectivity of pores [138]. Due to those positive effects, it becomes difficult for water to penetrate into iPMCCs, resulting in a lower water permeability. However, with the further addition of 7 % AA-AMPS, the water absorption coefficient increases significantly [5]. As monomer content exceeds a critical value, the polymer could rapidly absorb water upon penetration, leading to a rapid increase in water absorption. The fuzzy structure of polymer and its increased surface area greatly enhanced water absorption capacity [139]. Consequently, the excessive addition of polymer resulted in rapid water absorption and an increased water absorption coefficient.

Liu et al. [26] found a significant decrease in chloride ion penetration depth with increasing AM content. The sample containing 5 % PAM demonstrated a chloride ion penetration depth of 1.5 cm at 28 d, which is roughly 37 % lower than that of the control group. Liu et al. [5] found that with increasing AM content, the diffusion coefficient of chloride ions decreases linearly. The enhanced resistance to chloride ion penetration observed with the addition of PAM can be attributed to the pore refinement achieved by its filling effect [140,141]. In addition, the polymer rapidly expands and blocks pores upon contact with water, inhibiting the diffusion of chloride ions. The polymer also compacts the ITZ between cement and aggregates [1], hindering the migration of chloride ions. The addition of AM has also been demonstrated to enhance the sulfate resistance of cement-based materials [141]. Thus, the formation of a protective coating by the polymer, as well as the synergistic effect between the hydrated cement phases and the corrosion-resistant polymer, greatly contributes to improve the durability of iPMCCs [58].

The durability of iPMCCs has been studied for a relatively short period, leading to limited research findings. There is a need for further investigation into the long-term aging behavior of polymers, their interactions with cementitious matrixes, as well as the durability challenges and potential improvement strategies for iPMCCs in harsh environments.

5. Modification mechanism for in-situ polymerization modified cement-based materials

5.1. Method for characterizing organic structure in cement matrix

To investigate the interaction between monomer/polymer and cementitious system, Fourier-transform infrared spectroscopy (FTIR), Raman spectroscopy, X-ray photoelectron spectroscopy (XPS), Time-of-flight secondary ion mass spectrometry (ToF-SIMS) are used to test the specimen powder.

5.1.1. Fourier-transform infrared spectroscopy (FTIR) and Raman spectroscopy

Fourier-transform Infrared Spectroscopy (FTIR) is extensively utilized in analytical laboratories for its simplicity, ease of operation, and ability of rapid, non-destructive analysis. It is particularly effective in evaluating polymer functional groups and differentiating between amorphous and crystalline matrices, generating extensive spectral data [142,143]. In the context of cement-based materials, FTIR serves as an auxiliary analytical tool for the qualitative or semi-quantitative assessment of hydration products and polymer bonding characteristics.

Fig. 13 shows the distinct differences in the infrared spectra of the cement/AM and cement/PAM composites. The peak at 1609 cm^{-1}, which represents the C═C vibration of iPMCCs with AM, is absent in the PMCCs with PAM, indicating that the polymerization was effectively completed [144]. Furthermore, the primary amide band, characterized by a C-O stretching (υ) band, is observed at a frequency of 1658 cm^{-1} in the PMCCs with PAM, and is observed at a higher frequency of 1677 cm^{-1} in the iPMCCs with AM due to the formation of O → Ca^{2+} coordination bonds and the presence of Ca^{2+}-carboxyl complexes [145]. The medium bands at 3184 cm^{-1} and 3348 cm^{-1} which correspond to the N-H symmetric and asymmetric stretching of NH_2 (υ) are absent in the PMCCs with PAM, compared to the iPMCCs with AM, indicating the hydrolysis of PAM in an alkaline environment [119,146]. Furthermore, the presence of peaks at 3645 cm^{-1} in the spectra of the samples is indicative of vibrations from hydroxyl groups and serves as evidence for the existence of calcium hydroxide (CH). The absorption bands at 972 cm^{-1} bands corresponded to υ_3(Si–O) stretching vibrations, which are characteristic of both the C_2SH_2 and the calcium silicate hydrate (C-S-H) phases present in the iPMCCs [4,27].

In the current study [4,28,34], it has been observed that the intensity of the peak at 1609 cm^{-1} in early-age samples diminishes over time and vanishes entirely once polymerization is complete. This observation confirms the polymerization's initiation and propagation mechanisms, as the free radicals generated by ammonium persulfate (APS) target and attack the carbon-carbon double bonds (C═C). In addition, the presence of a significant peak of C═C stretching vibration in the long-term samples indicates incomplete polymerization of some monomers [147]. This suggests that achieving in-situ polymerization of monomers within cement matrix requires an appropriate dosage, and excessive amounts may not be suitable for producing iPMCCs [34].

In Ref. [95], the characteristic peak of ettringite (AFt) in the SAC cement system of the infrared spectra decreased, indicating that AM polymerization inhibits the SAC hydration and AFt formation. To put it simply, the presence of acrylamide hinders the formation of AFt and slows down the hydration in the SAC cement system, which leads to the observed decrease in corresponding peak. This finding holds important implications for understanding the chemical structure and properties of cement systems.

Raman spectroscopy, a complementary vibrational spectroscopic technique to infrared spectroscopy, is employed to derive structural information from the material being analyzed. Raman shifts, related to molecular bond vibrations, provide insights into bond strengths, molecular chemical states, and local interactions such as hydrogen bonds [148]. This technique is also applied to study various silicate and sulfate phases in cement-based materials and to explore the interactions between polymers and cement [149].

Raman spectroscopy has also been employed to analyze the reduction of C═C bonds during monomer polymerization in iPMCCs [28,34,35,147], with similar analytical methods and conclusions as those obtained by FTIR. The characteristic peak near 1641 cm^{-1} indicates the existence of C═C bond, and its peak intensity gradually decreases over time, indicating the progress of monomer polymerization [147,150]. Thus, monitoring changes in the peak intensity near 1641 cm^{-1} can be used to track the progress of monomer polymerization.

In summary, the decrease in peak intensity of the C═C bond in iPMCC observed in FTIR and Raman spectra indicates the occurrence of monomer in-situ polymerization. The shift in the carboxyl group spectrum confirms the coordination between the carboxyl group and calcium ions, while some bands (such as Si-O and C═O) also shift to higher wavenumbers, potentially indicating the formation of new bonds between cement hydrates and organic phase [26]. The new bonds contribute to improve the mechanical properties, especially in terms of flexural strength. However, FTIR and Raman spectra are inadequate for quantitatively studying monomer polymerization rate and conversion degree, and alternative methods are necessary for future research.

5.1.2. Time-of-flight secondary ion mass spectrometry (ToF-SIMS)

Time-of-Flight Secondary Ion Mass Spectrometry (ToF-SIMS) analyzes elements and molecules ionized by a primary ion beam, based on their flight times from the sample surface to the detector [151]. As a scanning technique, it facilitates the mapping of element or molecule distributions [151] and is instrumental in identifying chemical bonds between polymer groups and cement hydration products.

Fig. 14 depicts the schematic diagram of PAM cross-linking with Ca^{2+} from cement [4]. The Ca^{2+} bridging both the side and end groups synergistically connects PAM and Ca^{2+}. The connection is confirmed by

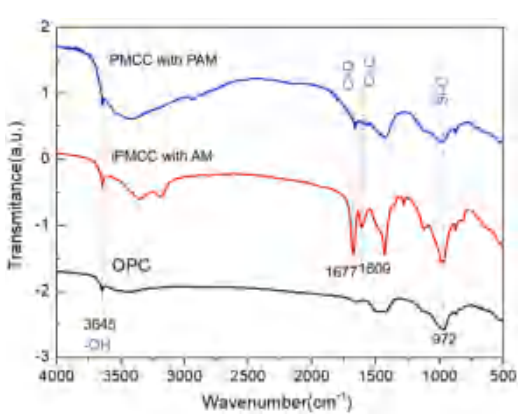

Fig. 13. Infrared spectrum analysis of OPC, PMCC with PAM, and iPMCC with AM at 28 d [4].

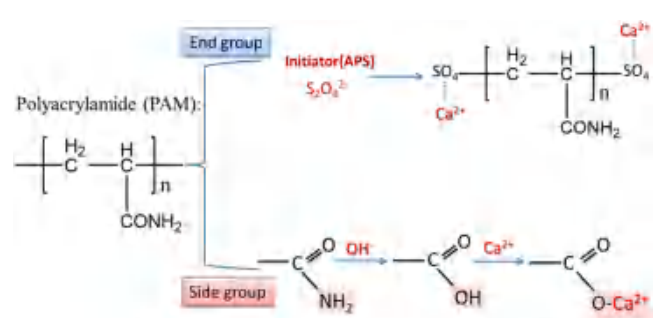

Fig. 14. Schematic diagram of the cross-linking of PAM with Ca^{2+} from cement [4].

ToF-SIMS results and shown in Fig. 15. In Fig. 15 (a), the emergence of new peaks at mass of 84.0 and 85.0 provides direct evidence of $–COOCa^+$ and $–HCOOCa^+$, confirming Ca^{2+} linking with the side groups of PAM. Additionally, the peaks of $–CaSO_4CH^-$ and $-CaSO_4CH_2$ indicate the connection between Ca^{2+} and the end group of PAM (in Fig. 14 (b)). Although the positive spectra of PMCCs with 1 *wt.*% PAM (PAM01) confirms the presence of $–COOCa^+$ and $–HCOOCa^+$ peaks, their intensity is significantly weaker than that of iPMCCs with 1 *wt.*% AM (P01). This demonstrates that the in-situ polymerization of monomers promotes the interaction between polymer and cement.

5.1.3. X-ray photoelectron spectroscopy (XPS)

X-ray Photoelectron Spectroscopy (XPS) directs X-rays, typically from Al Kα or Mg Kα sources, onto a surface, inducing the emission of photoelectrons through photon-electron interactions [152]. The kinetic energy of these photoelectrons is converted into binding energy, measured via an electron energy analyzer and detection system. XPS distinguishes the chemical compositions and oxidation states of surface elements [153], making it an invaluable surface-sensitive technique for characterizing the interactions within cement-based materials and polymers.

XPS has been employed to study the chemical interactions between cement hydrates and polymers. Fig. 16 shows the Ca 2p spectra of iPMCCs with AA-AMPS. The Ca 2p peaks exhibit variations in shape and size, indicating the involvement of Ca^{2+} in the chemical reactions within iPMCCs (Fig. 16 a). In the Ca 2p spectra of P0, four peaks are fitted, corresponding to CaO and $Ca(OH)_2$ (Fig. 16 a). The Ca 2p peak of P5 is fitted into five parts (Fig. 16 b), which are assigned to CaO, $Ca(OH)_2$, and $Ca(HCOO)_2$ (Calcium Formate) [154]. The appearance of $Ca(HCOO)_2$ demonstrates that the carboxyl groups of AA-AMPS copolymer chains react with Ca^{2+} during cement hydration to produce $Ca(HCOO)_2$ [155], contributing to the construction of a 3D interpenetrating network structure within the cement matrix. This structure enhances the flexural strength and ductility of iPMCCs.

5.2. Microstructure evolution affected by in-situ polymerization

5.2.1. Hydration

Many studies [4,5,27,28,30,35,60,96,97,135] have reported that adding monomer retards the cement hydration. Monomer could prolong the induction period and reduce the total heat release, increasing the polymer content further enhances these effects. The main influencing mechanisms include chelation [4], adsorption [127,147], and polymer film formation [147,156].

Carboxyl groups have the ability to form complexes with Ca^{2+}, which can interfere with the normal progression of cement hydration [126]. Specifically, these complexes can impede the onset of nucleation for the crystallization of hydration products by delaying the point at which the solution becomes supersaturated with respect to these products [62,104,157,158]. This delay in crystallization nucleation is a key mechanism by which the setting and hardening of cement can be retarded when carboxylic-containing compounds, such as certain monomers, are introduced into the cement mixture. This may be due to the fact that the monomer/polymer promotes the retardation effect through the chemical interaction between cement hydrates and polar functional groups of polymers [58,159]. This interaction results in the formation of amorphous materials, which are insoluble and dispersed among hydrated minerals [160].

The adsorption of monomers and polymers onto the cement grains can hinder the nucleation and growth of hydration products [4,70,96,97,161]. Adsorption interactions include electrostatic attraction, hydrogen bond and ionic bond, which depend mainly on the molecular structure of polymer [162]. Lu et al. [126] found that the electrostatic interaction drives the polymer particles to adsorb onto the surface of cement particles. C_3A is positively charged, which will adsorb negatively charged carboxyl groups, thus affecting the hydration [127,147]. The negatively charged C_3S, C_2S and C-S-H adsorb calcium ions, and then adsorb $R\text{-}COO^-$, so that the dissolution and hydration of C_3S and C_2S would be delayed [127].

Some polymer film forms on the surface of cement particles, thereby disrupting the hydration and subsequent hardening process [62]. Increasing monomer dosage results in excessive formation of multilayer polymer gel or film, the polymer film is likely to encapsulate cement particles, preventing them from coming into contact with external water and restricting their hydration [62,147]. When external free water passes through the polymer film and contact with cement particles, it triggers secondary hydration [35]. Some monomers/polymers can provide a sustained water supply capacity during the later stages of hydration, thereby leading to a slight increase in the hydration heat.

Liang et al. [4] experimentally observed that cement retards the AM polymerization. The initial temperature plays a critical role in the commencement of polymerization [35]. Higher initial temperatures provide more energy for the polymerization and shorten the time needed to reach the activation energy, leading to a quicker initiation of the polymerization. In contrast, lower initial temperatures prolong the time needed to meet the activation energy, thereby delaying polymerization startup. During the early stages, cement exhibits lower heat release, and demonstrates a weaker promoting effect on polymerization. As substantial heat is released by cement, the temperature of the system increases, thereby promoting polymerization [35]. Cement hydration provides sufficient heat to promote initiator decomposition and free radical formation, ensuring high conversion rates [4]. Currently, there is limited research on quantifying the polymerization rate of monomers in cementitious materials, and a lack of studies on controlling the in-situ polymerization rate. Future studies should focus on synchronizing the polymerization rate with the hydration rate of cement to achieve

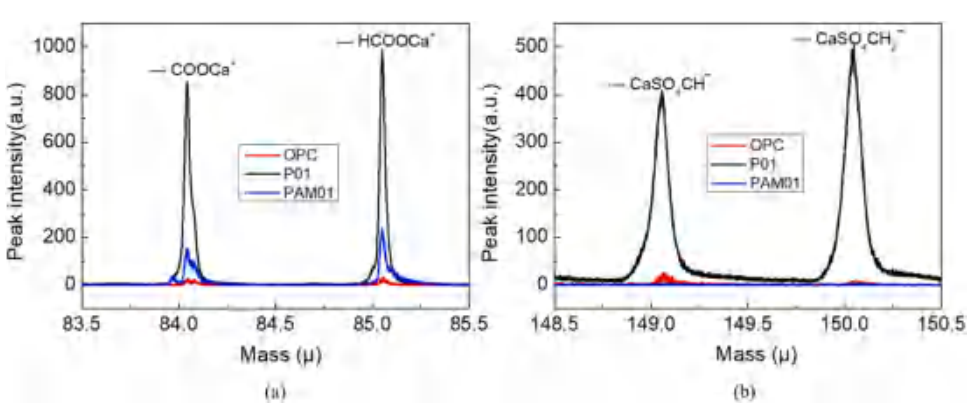

Fig. 15. ToF-SIMS tests of iPMCC with AM [4]. The cement pastes were prepared with an AM solution (P01, where AM mass is 1 *wt.*% of cement) and a PAM solution (PAM01, where PAM mass is 1 *wt.*% of cement).

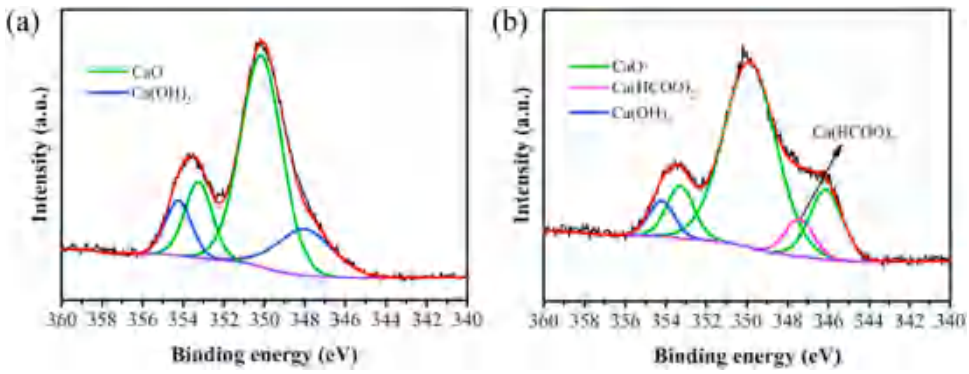

Fig. 16. The XPS results for cement pastes. (a) The Ca 2p spectra of the neat cement paste (P0), (b) the Ca 2p spectra of the cement paste with 5% AA-AMPS monomers (P5) [35].

excellent performance.

5.2.2. Phase evolution

In-situ polymerization does not change the type of phase in the hardened cement paste but affects its quantity. XRD analysis revealed that iPMCC samples contained higher amounts of anhydrous C_2S and C_3S compared to neat cement paste, suggesting that polymers caused retardation in the cement hydration. The intensity of CH peak in iPMCCs is noticeably reduced due to the significant retarding effect [4]. The amount and crystal size of CH decrease in iPMCC [4,26], leading to a further reduction in crystallinity [71].

Previous research conducted by Matsuyama et al. [163,164] focused on the intercalation of various polymers into the layer of calcium silicate hydrate (C-S-H) and observed a shift in the position of the basal peak in XRD spectrum and changes to the interlayer crystal structures. AM undergoes polymerization within the cement hydration product matrix, leading to the formation of a PAM gel that is not detectable by XRD analysis.

Thermogravimetric analysis (TGA) is a vital tool that can be used to quantify and assess the properties of hydration products based on the different stages of hydration resulting from cement. The weight loss between 400 °C and 500 °C can be attributed to the decomposition and dehydration of CH, which is linked to the hydration degree of Portland cement [165].

Liang et al. [4] found that the thermal weight loss of CH in iPMCCs with AM is lower than that of the control group. In alkaline conditions, the amine groups within PAM hydrolyze and react with Ca^{2+} from the hydrated cement. The addition of monomers such as AA [5,28,34,35] and AMPS [5,35] to OPC also leads to a decrease in CH content. Furthermore, based on the data of setting time and hydration heat release, the retarding effect of monomer/polymer also reduce the amount of CH.

In-situ polymerization of monomer further reduces CH compared to traditional PMCCs, which is attributed to the delayed hydration and the formation of Ca^{2+}–carboxylate complexes [35]. Additionally, calcium ions chelate with carboxyl groups, thereby reducing or preventing calcium ions from participating in carbonation reactions, thus increasing the carbonation resistance of hydrates [147]. Another reason is that in-situ polymerization compacts the microstructure, hindering CO_2 penetration into the layered structure of hydrates [147]. In view of the reduction of CH crystals caused by the complexation of the carboxyl group of PAM and Ca^{2+}, future research can focus on the effect of polymer on the pozzolanic reaction of mineral admixtures. In alkaline environments, amine groups hydrolyze partially, forming carboxyl that complexes with Ca^{2+} from hydrated cement, leading to calcium depletion. The decrease in CH content with increasing monomer/polymer provides qualitative evidence of the interaction between Ca^{2+} and carboxyl groups [4,26,30,35]. This provides further evidence of the chemical reaction between calcium ions and carboxyl groups.

5.2.3. Morphology feature

During the initial stage of hydration, the encapsulation effect of polymer network significantly retards cement hydration [54,166]. It is important to note that the polymer network acts as a skeleton rather than completely enclosing the hydrates [30]. As cement hydration progresses, the hydrates grow and eventually penetrate through the envelopment of polymer and interconnect with each other. Several studies have suggested that the inhibitory effect of the polymer layer gradually diminishes, with space becoming the primary controlling factor for hydration [167]. The polymer significantly retards the cement hydration in early stage but gets negligible as hydration proceeds, which is consistent with the long-term development of compressive strength.

Liu et al. [28,135] and Yin et al. [30] observed the continuous spatial polymer skeleton in the SEM image after etching the cement matrix with acid. Liang [4] reported, that the morphology of the iPMCC is different from that of neat cement paste, and increasing the AM dosage results in the formation of a polymer film on the hydrated surface of cement products. Liu et al. [26] also observed the existence of polymer films. The needle-shaped hydrates are covered with flexible PAM gel to construct fibrous products, bridging individual hydrates.

Xu et al. [34] observed the morphology of the iPMCC surfaces shown in Fig. 17 through SEM. At a low magnification, all iPMCCs samples display a relatively dense compactness. The MC4 matrix (iPMCC with 4% SA, Fig. 17 (b)) shows no significant defects or cracks, indicating improved matrix integrity and mechanical properties due to the polymer. Neat cement paste (MC0) displays the C-S-(A)-H gels bonding cement grains together and reducing the gaps between particles to a certain degree. In contrast, iPMCCs (MC4) exhibits a composite cement-polymer matrix with a less porous structure comprising cement hydration products and sodium polyacrylic. Images of iPMCC with higher polymer content (MC8) reveal cross-linked sodium polyacrylate chains bridging different hydration products. EDS analysis of Ref. [4] suggested that a higher dosage of polymer tends to cause aggregation, leading to its segregation from the cement matrix, potentially compromising the mechanical strength.

Yin et al. [30] found significant differences between the microscopic images of the iPMCC and pure cement paste. The hydrates of pure cement paste possess sharp edges and a rough surface, while the iPMCC appears as a gel-based material. This is due to the presence of the polymer as well as chemical reactions between polymer and metallic cations, resulting in a more vitrified and spherical gel-like surface morphology. Yin et al. [29] also observed significant interactions between PAM and calcium carbonate whiskers (CW) by SEM-EDS, where PAM improved the interface structure between CW and cement matrix. Liu et al. [135] discovered that the polymer adheres to the Field's metal particles, thus constructing a polymer-Field metal-cement network, which enhances the flexural strength.

In conclusion, the interweaving of a flexible polymer network with a rigid cement matrix allows the cross-linked polymer network to

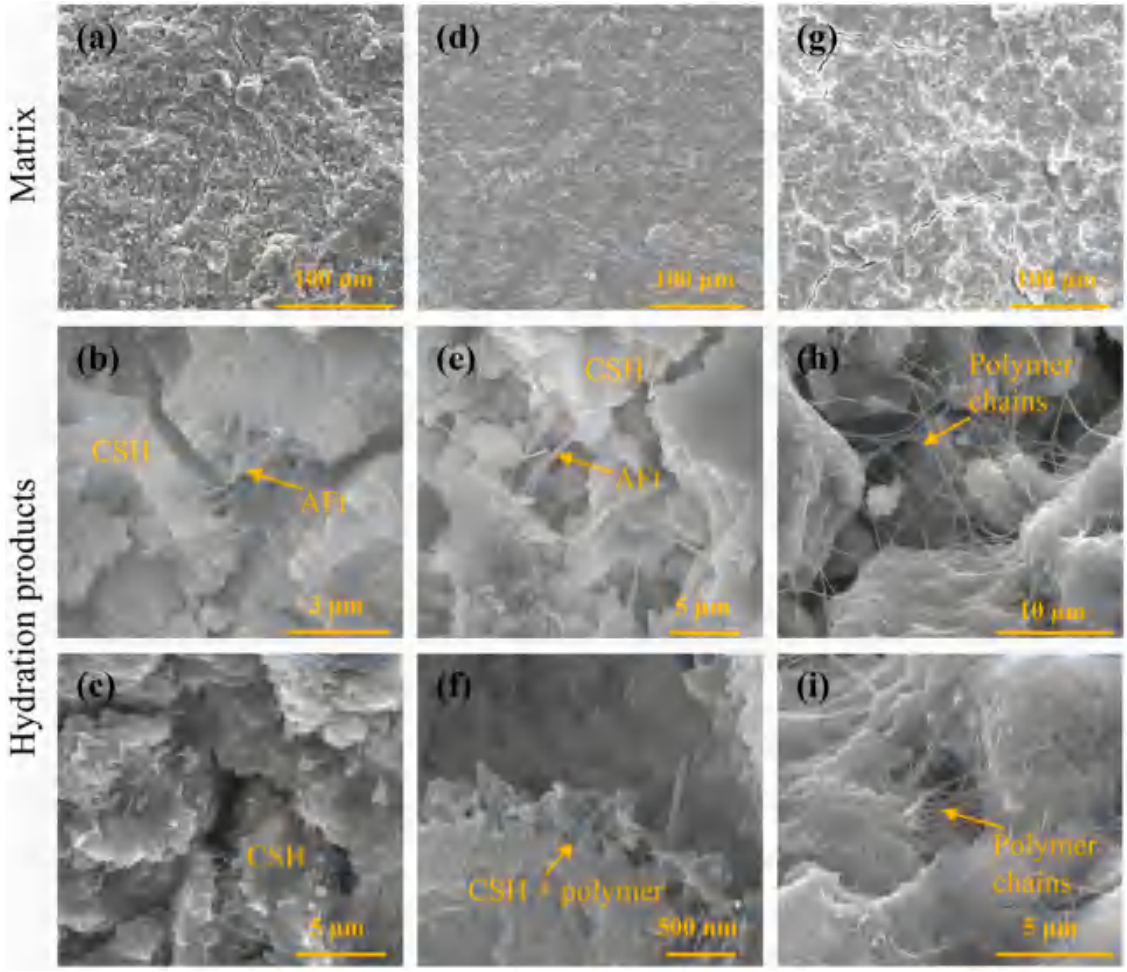

Fig. 17. SEM images for matrix and hydrated products of (a, b, c) MC0, (d, e, f) MC4, and (g, h, i) MC8 [34]. MC0, MC4, and MC8 represent the content of sodium acrylate as 0, 4 % and 8 %, respectively.

effectively dissipate crack energy by deforming the network conformation or sliding the physical entanglement points along the chain, thereby preventing macroscopic crack growth [168]. This mechanism ultimately results in enhanced mechanical properties. Future research should focus on investigating the binding forms and mechanisms between polymers and cement in greater depth.

5.2.4. Pore structure

The effect of in-situ polymerization on porosity from various sources is summarized in Table A2. Liang et al. [4] found that incorporating 1 *wt.*% AM decreases mean pore diameters, thus refining the pore structure (porosity decreased by 12.0 %). Excessive AM incorporation retards the cement hydration and decreases the hydration degree, resulting in an increase in porosity. Interestingly, compared to the in-situ polymerization of AM, the sample with 1 % PAM shows the finest pore size, yet exhibits the highest porosity [4]. This is due to the contrasting effects of pre-synthesized PAM, acting as a superabsorbent polymer (SAP), which both densifies the microstructure through internal curing and creates large voids attributed to swollen SAP particles [169]. BET results confirm that iPMCCs with AM have a smaller surface area [26], indicating PAM fills the large pores in cement matrix and compacts the internal structure. The reduction in pore diameter and cumulative porosity in cement paste is also attributed to the presence of a compacted polymer network. PAM can be absorbed onto the surface of hydrates due to the hydrolysis of amine groups [4]. This results in the pore-filling effect and consequently decreases the pore diameter and cumulative porosity.

Xu et al. [34] found that in-situ polymerization of 4 % SA can achieve more uniform distribution and smaller air void, indicating the enhanced density of cement matrix. However, using more SA (8 %) increases the size of large and anisotropic cavities, which can be considered as defects and harm mechanical strength. These studies [4,26,34,35,94] demonstrate that the in-situ polymerization of monomer in cement greatly refines the pore as cement hydration and polymerization proceed simultaneously. In addition, in-situ polymerization decreases the sphericity and density of pores [34], indicating an increase in the anisotropy of voids, and a possible change in the mechanism of pore formation. In future studies, it may be necessary to clarify the mechanism of pore structure formation during in-situ polymerization.

Liu et al. [35] found a significant decrease in total porosity as the dosage of AA-AMPS increases. The reduction in porosity and critical pore size is attributed to the filling effect of AA-AMPS copolymers within cement matrix. Larger pores are blocked, resulting in a denser matrix structure, and improving the mechanical properties.

Fig. 18 was plotted based on the porosity increase ratio and the strength increase ratio. All increase rates were calculated using the control groups from the respective literatures as references. It was observed that, although the introduction of large air bubbles increased the porosity in some groups, a decrease in porosity in most of the test samples led to an improvement in flexural strength. However, compressive strength seems to be less correlated with porosity changes. Overall, iPMCCs show a more noticeable improvement in flexural strength, while the overall compressive strength slightly decreases.

Based on the above research, it can be concluded that the polymer at

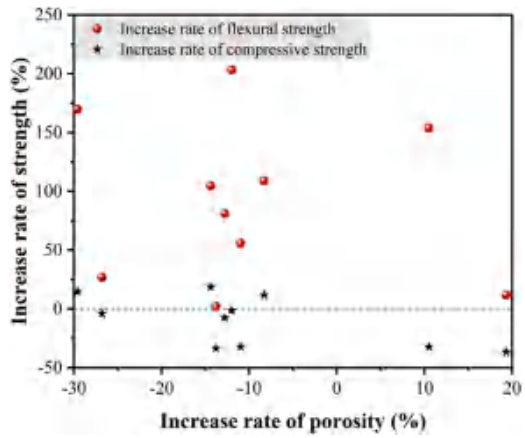

Fig. 18. Strength increase ratio via porosity increase ratio.

early stage retards cement hydration and complexing with calcium ions would affect the generation of hydrates. However, the monomer improves flowability and enhances chemical interaction between the polymer network and hydrates, bridging adjacent cement hydrates as a whole to densify the cement matrix, effectively suppressing the development of micro-cracks under external loads, and enhancing flexural strength. By introducing polymers to compact the internal structure, defects in iPMCCs can be reduced while limiting crack propagation [29]. Moreover, some monomers and initiators can generate gas during the polymerization, leaving large pores in hardened paste. Limited research has been conducted on the role of in-situ polymerization in gas evolution. The water absorption and release by polymer can also affect the pore structure [170], and further research is required to understand the mechanisms and impact on the formation of cementitious microstructures.

5.3. Modification mechanism

The monomers, initiators, and crosslinking agents are completely dissolved in water and uniformly mixed with cement (Fig. 19 (a)). Adding monomers significantly improves the fluidity of cement paste and ensures homogeneous distribution of monomers in cement matrix [4,30,34]. Then, monomers begin to polymerize and are generally completed within a few hours (Fig. 19 (b)) [4,28,35]. The formation of polymer network significantly shortens the initial setting time [27,30], but prolongs the final setting time and retards the cement hydration by enveloping cement particles [30,34,97], thus limiting water uptake. The chemical reaction between polymers and cement components forms a continuous but thin sub-stable layer [116,117], further retarding cement hydration (Fig. 19 (c)). In the later age, the polymers act as an internal curing agent, promoting cement hydration, and the hydration products fill the polymer network [28]. These hydrated products break through the polymer envelope and interconnect (Fig. 19 (d)), integrating the polymer into the cement matrix, leading to increased density and improved flexural strengths of iPMCCs. Minor differences in long-term compressive strength are observed compared to pure cement paste.

Polymerization, initiated by the initiator and facilitated by the exothermic hydration of cement, forms the polymer skeleton [4]. Cement hydration products gradually fill the voids among the polymer skeletons [28], forming a polymer-cement composite structure. Calcium released from cement hydration coordinates with carboxyl groups in the polymer, connecting adjacent C-S-H silicate sheets and activating hydrolysis reactions at the interface [4,27,29,30]. The stability of the polymer network is enhanced through hydrogen bonds and coordination bonds (Fig. 19 (e)) [171–173]. Enriched Ca-Si provides a preferred surface for C-S-H nucleation within the polymer network [30], promoting the combination of organic and inorganic components. This process constructs a spatial cement-polymer network that combines flexibility and stiffness [28]. The polymer, with its volume expansion and resistance to shear strains [173], induces compressive stress at crack tips, thereby impeding crack propagation (Fig. 19 (f)). This improves the deformation capacity, flexural strength and toughness of the cement matrix. Chemical bonding between the polymer and hydration products enhances the bond strength, compatibility, and reduces the CH content, thereby further improves the performance [4,27,29,30]. In addition, the in-situ polymerization of monomer ensures the uniform distribution of polymer within cement matrix [4,28], enhancing the synergy effect between cement and polymer. The polymer film covers cement hydrates, bridging microcracks, filling voids, dispersing and absorbing applied forces during loading, densifying the internal structure, and ultimately improving the toughness of cement matrix.

6. Application prospects and further research

6.1. Application prospects

Concrete, characterized by low tensile strength and weak crack

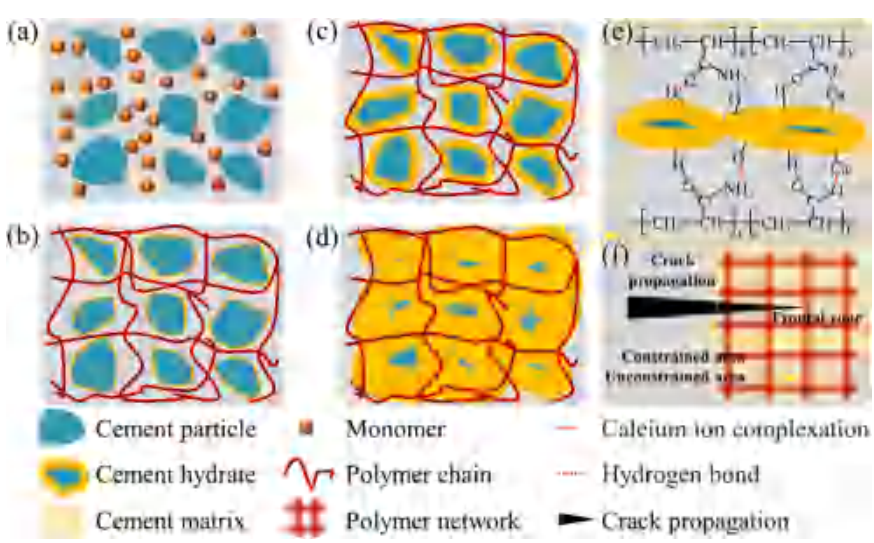

Fig. 19. Simplified illustration of polymer-cement network in cement matrix. (a) Immediately after mixing raw materials; (b) Formation of polymer skeletons; (c) Cement hydration and polymer films; (d) Hardened structure; (e) Chemical bonding between the polymer and hydrates; (f) Schematic diagram of crack propagation.

resistance, often displays brittle behavior. To address this challenge, the incorporation of polymers into these composite materials emerges as a viable solution, offering structural components with exceptional durability and mechanical strength. Polymers have witnessed extensive applications in the development of building materials and can play a crucial role in addressing various requirements of current and future constructions. They provide a solution to many limitations of cementitious materials, including resistance to acid-base corrosion, frost resistance, and bonding properties [44].

iPMCCs are a novel type of PMCCs. The unique incorporation method and easily adjustable polymer structure, coupled with simultaneous polymerization and cement hydration reactions, will facilitate the binding between the polymer and cementitious matrixes. These aspects contribute to the excellent mechanical properties of iPMCCs, particularly their toughness. This makes iPMCCs promising for applications in structural components that require high tensile strength and crack prevention. The addition of monomers toughens the matrix, and the further optimization of material systems and preparation processes can enhance the flexural and compressive strengths, making it possible for iPMCCs to be used as large span structural components, such as bridges and beams. Additionally, their workability makes them suitable for applications in 3D printing [121,174] and shotcrete, while their good toughness can be applied in marine pipeline connections.

Nowadays, many buildings suffer from aging and require repair. Cement mortar is widely utilized, yet it suffers from limitations like low flexural strength and poor toughness. Especially, its poor bond performance leads to interfacial damage and failure of repair. Since polymers can form a high-molecular film with excellent adhesion and cohesion in cement mortar, PMCCs exhibit favorable bonding characteristics and compatibility with old concrete [44]. In the restoration of aging structures, polymers can improve the bonding properties and adhesion of cement-based materials. Meanwhile, it may have a better combination effect with steel bars, enhancing the mechanical properties of reinforced concrete. Compared to pure cementitious materials, PMCC improves the durability of repair structures by combining polymers with supplementary cementitious materials (SCMs) [44]. Therefore, PMCC is more effective in repairing concrete. Due to the excellent adhesive properties of PMCC, it is widely used in the adhesive layer of tiles, stone and other exterior wall materials, as well as external wall insulation systems [44, 175,176]. iPMCCs may further enhance these functions. Building energy storage has also been preliminarily demonstrated as an important application direction [177,178].

In practical applications, certain polymers like epoxy resins are employed as protective coatings on steel [179], which not only enhances the adhesion between steel and concrete but also improves corrosion resistance. Cementitious materials exhibit significant mass loss when exposed to acidic solutions [180]. The entry of acidic solutions into Portland cement structures can cause the hydrolysis of CH. Once the hydrolysis by-products precipitate and form a porous structure, the seemingly intact material loses its internal integrity. However, adding polymer to cement demonstrates excellent stability in acidic solutions [181,182]. When the polymer reaches a certain content, it is less affected by acid solutions and prevents their penetration into the cementitious matrix. Due to their superior corrosion resistance, PMCCs have gained widespread use. iPMCCs also show promise as a corrosion barrier, and offer the benefits of straightforward application, affordability, and a brief time to completion, resulting in substantial economic and social advantages.

6.2. Challenges in the application of in-situ polymerization

PMCC is extensively employed in the construction for its excellent bonding properties, waterproof performance, and corrosion resistance compared to OCC. However, despite its excellent mechanical properties and corrosion resistance properties, PMCC does possess some drawbacks. Establishing closer collaboration among engineers specializing in building materials and polymers is essential to ensure the proper utilization of polymer materials in enhancing building products, thus making a substantial contribution to the advancement of iPMCC.

As illustrated in Fig. 1, the technique of in-situ polymerization to develop iPMCCs has recently gained attention. Despite its apparent advantages, substantial gaps and numerous challenges still exist in the research, summarized as follows:

1. One major challenge is designing an optimal mixing ratio for iPMCC, as well as determining the optimal curing conditions. The optimal ratio of material plays a crucial role in composite material preparation and determines its best performance.
2. There is the issue of thoroughly evaluating the properties of this new material. Current studies are not comprehensive, particularly concerning long-term performance, mechanical stability, volume stability, and durability. These aspects require significant enhancement in future research efforts.
3. Although iPMCCs demonstrate certain superior properties compared to PMCCs, their application in engineering projects is still limited. Future integration into practical applications will likely face challenges such as cost management and controlling the rapid rate of polymerization that can occur at high temperatures. These issues must be addressed to leverage the full potential of iPMCCs in construction and other fields.
4. Polymers offer advantages such as structural diversity and flexibility to design molecular structures [183,184]. From the viewpoint of the structure-property relationship, the performance of polymer is governed by its molecular structure. Polycarboxylate superplasticizer serves as a prime example of the flexibility and design potential inherent in molecular structure, allowing cementitious materials to possess adjustable properties to meet various application scenarios and significantly promote the progress of construction projects [185]. However, these benefits could be mitigated or neglected in engineering applications, as polymers of the same type but with different molecular structures are often overlooked. In-situ polymerization primarily forms polymer networks consisting of linear molecular chains crosslinked into a network structure. Further research is needed to understand the effect of monomers, functional groups, and different crosslinking forms on the bond with cementitious matrixes. Another limitation in current research on iPMCCs is the lack of understanding of the sequence between the polymer network and cement skeleton, as well as the ability to control their reaction rates to promote binding and achieve excellent performance.

7. Conclusions

The review on in-situ polymerization modified cement composites (iPMCC) extensively examines their development, emphasizing enhancements in flexural strength and reduced brittleness compared to ordinary cement composites (OCC). The review highlights the role of monomers, initiators, and crosslinking agents in forming polymers through free radical polymerization, adaptable to the alkaline and thermal environments of cementitious materials. This study reviews the preparation of polymer-cement interpenetrating networks starting from the dissolution of monomers in water, triggering polymerization by initiators and the facilitation of crosslinking. The continuous in-situ polymerization during cement hydration contributes to a uniform polymer distribution within the cement matrix, enhancing chemical bonding and interactions between organic and inorganic components. Additionally, the review discusses the mechanical and durability aspects of iPMCCs, noting that while flexural strength and energy absorption are significantly enhanced, compressive strength may not improve and can decrease in some experiments. The durability improvements include better water resistance and chloride ion penetration resistance due to the interaction of corrosion-resistant polymers. Technological

advancements such as FTIR, Raman spectroscopy, XPS, and ToF-SIMS have been utilized to confirm the in-situ polymerization of monomers during cement hydration, revealing important interactions like those between carboxyl groups and calcium ions. Despite these advances, challenges remain in the development and application of iPMCCs, necessitating further research to optimize their composition and performance for broader engineering applications.

CRediT authorship contribution statement

Kai Wu: Writing – review & editing, Writing – original draft, Methodology, Investigation, Funding acquisition, Conceptualization. **Jiangfeng Long:** Writing – review & editing, Writing – original draft, Validation, Software, Investigation, Data curation. **Longbang Qing:** Writing – review & editing, Project administration, Methodology, Conceptualization. **Geert De Schutter:** Supervision, Methodology, Formal analysis, Conceptualization.

Declaration of Competing Interest

The authors declare that they have no known competing financial interests or personal relationships that could have appeared to influence the work reported in this paper.

Data Availability

Data will be made available on request.

Acknowledgment

This work was financially supported by the National Natural Science Foundation of China (52278270, 52022027, 51978505), Key Technologies R&D Program of CNBM (2021HX0506), and the Program Fund of Non-Metallic Excellence and Innovation Center for Building Materials (Grants #24PHD-8).

Appendix A. Supporting information

Supplementary data associated with this article can be found in the online version at doi:10.1016/j.conbuildmat.2024.136542.

References

[1] Z. Sun, Q. Xu, Micromechanical analysis of polyacrylamide-modified concrete for improving strengths, Mater. Sci. Eng. A 490 (2008) 181–192, https://doi.org/10.1016/j.msea.2008.01.026.
[2] L. Yan, C.H. Jenkins, R.L. Pendleton, Polyolefin fiber-reinforced concrete composites: Part II. Damping and interface debonding, Cem. Concr. Res. 30 (2000) 403–410, https://doi.org/10.1016/S0008-8846(99)00268-9.
[3] S.T. Smith, J.G. Teng, FRP-strengthened RC beams. I: review of debonding strength models, Eng. Struct. 24 (2002) 385–395, https://doi.org/10.1016/S0141-0296(01)00105-5.
[4] R. Liang, Q. Liu, D. Hou, Z. Li, G. Sun, Flexural strength enhancement of cement paste through monomer incorporation and in situ bond formation, Cem. Concr. Res. 152 (2022) 106675, https://doi.org/10.1016/j.cemconres.2021.106675.
[5] Q. Liu, Z. Lu, X. Liang, R. Liang, Z. Li, G. Sun, High flexural strength and durability of concrete reinforced by in situ polymerization of acrylic acid and 1-acrylanmido-2-methylpropanesulfonic acid, Constr. Build. Mater. 292 (2021) 123428, https://doi.org/10.1016/j.conbuildmat.2021.123428.
[6] N. Abdelmelek, E. Lubloy, Flexural strength of silica fume, fly ash, and metakaolin of hardened cement paste after exposure to elevated temperatures, J. Therm. Anal. Calorim. 147 (2022) 7159–7169, https://doi.org/10.1007/s10973-021-11035-3.
[7] X. Gu, H. Tan, X. He, J. Zhang, X. Deng, Z. Zheng, M. Li, J. Yang, Improvement in flexural strength of Portland cement by lamellar structured montmorillonite, Constr. Build. Mater. 329 (2022) 127208, https://doi.org/10.1016/j.conbuildmat.2022.127208.
[8] M. Hambach, H. Möller, T. Neumann, D. Volkmer, Portland cement paste with aligned carbon fibers exhibiting exceptionally high flexural strength (> 100MPa), Cem. Concr. Res. 89 (2016) 80–86, https://doi.org/10.1016/j.cemconres.2016.08.011.
[9] Larsen Ingrid Lande, Thorstensen Rein Terje, The influence of steel fibres on compressive and tensile strength of ultra high performance concrete: a review, Constr. Build. Mater. 256 (2020) 119459, https://doi.org/10.1016/j.conbuildmat.2020.119459.
[10] W. Lokuge, T. Aravinthan, Effect of fly ash on the behaviour of polymer concrete with different types of resin, Mater. Des. 51 (2013) 175–181, https://doi.org/10.1016/j.matdes.2013.03.078.
[11] Y. Zhang, Y. Zhu, S. Qu, A. Kumar, X. Shao, Improvement of flexural and tensile strength of layered-casting UHPC with aligned steel fibers, Constr. Build. Mater. 251 (2020) 118893, https://doi.org/10.1016/j.conbuildmat.2020.118893.
[12] G. Sheng, Y. Zuo, L. Zheng, X. Li, Y. Wu, Imitating Spiders to catch flying insects: realizing high-strength bonding of bamboo scraps/magnesium oxychloride lightweight composite interface, Compos. Sci. Technol. 230 (2022) 109767, https://doi.org/10.1016/j.compscitech.2022.109767.
[13] S.-Y. Guo, X. Zhang, J.-Z. Chen, B. Mou, H.-S. Shang, P. Wang, L. Zhang, J. Ren, Mechanical and interface bonding properties of epoxy resin reinforced Portland cement repairing mortar, Constr. Build. Mater. 264 (2020) 120715, https://doi.org/10.1016/j.conbuildmat.2020.120715.
[14] N.K. Ilango, P. Gujar, A.K. Nagesh, A. Alex, P. Ghosh, Interfacial adhesion mechanism between organic polymer coating and hydrating cement paste, Cem. Concr. Compos. 115 (2021) 103856, https://doi.org/10.1016/j.cemconcomp.2020.103856.
[15] W. Zhang, X. Xu, H. Wang, F. Wei, Y. Zhang, Experimental and numerical analysis of interfacial bonding strength of polyoxymethylene reinforced cement composites, Constr. Build. Mater. 207 (2019) 1–9, https://doi.org/10.1016/j.conbuildmat.2019.02.122.
[16] I.J. Merchant, D.E. Macphee, H.W. Chandler, R.J. Henderson, Toughening cement-based materials through the control of interfacial bonding, Cem. Concr. Res. 31 (2001) 1873–1880, https://doi.org/10.1016/S0008-8846(01)00500-2.
[17] Y. Zheng, Y. Zhang, J. Zhuo, Y. Zhang, C. Wan, A review of the mechanical properties and durability of basalt fiber-reinforced concrete, Constr. Build. Mater. 359 (2022) 129360, https://doi.org/10.1016/j.conbuildmat.2022.129360.
[18] V.C. Li, M. Maalej, Toughening in cement based composites. Part II: fiber reinforced cementitious composites, Cem. Concr. Compos. 18 (1996) 239–249, https://doi.org/10.1016/0958-9465(95)00029-1.
[19] H. Yan, W. Sun, H. Chen, The effect of silica fume and steel fiber on the dynamic mechanical performance of high-strength concrete, Cem. Concr. Res. 29 (1999) 423–426, https://doi.org/10.1016/S0008-8846(98)00235-X.
[20] M. Cao, Z. Liu, C. Xie, Effect of steel-PVA hybrid fibers on compressive behavior of CaCO3 whiskers reinforced cement mortar, J. Build. Eng. 31 (2020) 101314, https://doi.org/10.1016/j.jobe.2020.101314.
[21] L. Lavagna, S. Musso, G. Ferro, M. Pavese, Cement-based composites containing functionalized carbon fibers, Cem. Concr. Compos. 88 (2018) 165–171, https://doi.org/10.1016/j.cemconcomp.2018.02.007.
[22] X. Xu, Y. Li, B. Yu, B. Zhu, Q. Liu, H. Hu, Z. Hu, B. Yu, S. Wang, J. Meng, A novelty method of multi-scale toughening cement-based materials: reactive powder concrete with endogenous whiskers, J. Build. Eng. 50 (2022) 104142, https://doi.org/10.1016/j.jobe.2022.104142.
[23] H. Pan, Z. Geng, P. Huang, Y. Zhou, J. Tang, W. She, J. Liu, A bionic solution to make cement matrix tough, Cem. Concr. Compos. 136 (2023) 104881, https://doi.org/10.1016/j.cemconcomp.2022.104881.
[24] D. Hou, J. Yu, P. Wang, Molecular dynamics modeling of the structure, dynamics, energetics and mechanical properties of cement-polymer nanocomposite, Compos. Part B Eng. 162 (2019) 433–444, https://doi.org/10.1016/j.compositesb.2018.12.142.
[25] H. Pan, W. She, W. Zuo, Y. Zhou, J. Huang, Z. Zhang, Z. Geng, Y. Yao, W. Zhang, L. Zheng, C. Miao, J. Liu, Hierarchical toughening of a biomimetic bulk cement composite, ACS Appl. Mater. Interfaces 12 (2020) 53297–53309, https://doi.org/10.1021/acsami.0c15313.
[26] Q. Liu, R. Liu, Q. Wang, R. Liang, Z. Li, G. Sun, Cement mortar with enhanced flexural strength and durability-related properties using in situ polymerized interpenetration network, Front. Struct. Civ. Eng. 15 (2021) 99–108, https://doi.org/10.1007/s11709-021-0721-0.
[27] B. Chen, G. Qiao, D. Hou, M. Wang, Z. Li, Cement-based material modified by in-situ polymerization: From experiments to molecular dynamics investigation, Compos. Part B Eng. 194 (2020) 108036, https://doi.org/10.1016/j.compositesb.2020.108036.
[28] Q. Liu, Z. Lu, J. Xu, Z. Li, G. Sun, Insight into the *in situ* copolymerization of monomers on cement hydration and the mechanical performance of cement paste, J. Sustain. Cem. Based Mater. 12 (2023) 736–750, https://doi.org/10.1080/21650373.2022.2118190.
[29] B. Yin, X. Hua, D. Qi, K. Han, P. Wang, D. Hou, C. Liu, Multi-scale synergistic modification and mechanical properties of cement-based composites based on in-situ polymerization, Cem. Concr. Compos. 137 (2023) 104945, https://doi.org/10.1016/j.cemconcomp.2023.104945.
[30] B. Yin, X. Hua, D. Qi, P. Wang, G. Qiao, F. Fan, X. Hua, X. Wang, D. Hou, Performance cement-based composite obtained by in-situ growth of organic–inorganic frameworks during the cement hydration, Constr. Build. Mater. 336 (2022) 127533, https://doi.org/10.1016/j.conbuildmat.2022.127533.
[31] L.X. Li, Y.J. Xie, Z.W. Feng, C.H. Zhu, S.M. Li, Research on toughness and modification mechanism of in situ toughening mortar, Appl. Mech. Mater. 174–177 (2012) 1380–1383, https://doi.org/10.4028/www.scientific.net/AMM.174-177.1380.
[32] Q. Liu, W. Liu, Z. Li, S. Guo, G. Sun, Ultra-lightweight cement composites with excellent flexural strength, thermal insulation and water resistance achieved by establishing interpenetrating network, Constr. Build. Mater. 250 (2020) 118923, https://doi.org/10.1016/j.conbuildmat.2020.118923.

[33] Y. Chen, Y. Zheng, Y. Zhou, W. Zhang, W. Li, W. She, J. Liu, C. Miao, Multi-layered cement-hydrogel composite with high toughness, low thermal conductivity, and self-healing capability, Nat. Commun. 14 (2023) 3438, https://doi.org/10.1038/s41467-023-39235-5.

[34] C. Xu, Y. Dai, Y. Peng, J. Wang, Z. Zhang, Q. Gui, Q. Zeng, Multi-scale structure of in-situ polymerized cementitious composites with improved flowability, strength, deformability and anti-permeability, Compos. Part B Eng. 245 (2022) 110222, https://doi.org/10.1016/j.compositesb.2022.110222.

[35] Q. Liu, Z. Lu, X. Hu, B. Chen, Z. Li, R. Liang, G. Sun, A mechanical strong polymer-cement composite fabricated by in situ polymerization within the cement matrix, J. Build. Eng. 42 (2021) 103048, https://doi.org/10.1016/j.jobe.2021.103048.

[36] L. Zhao, X. Guo, C. Ge, Q. Li, L. Guo, X. Shu, J. Liu, Mechanical behavior and toughening mechanism of polycarboxylate superplasticizer modified graphene oxide reinforced cement composites, Compos. Part B Eng. 113 (2017) 308–316, https://doi.org/10.1016/j.compositesb.2017.01.056.

[37] J. Chen, A.-T. Akono, Influence of multi-walled carbon nanotubes on the hydration products of ordinary Portland cement paste, Cem. Concr. Res. 137 (2020) 106197, https://doi.org/10.1016/j.cemconres.2020.106197.

[38] L.P. Singh, W. Zhu, T. Howind, U. Sharma, Quantification and characterization of C-S-H in silica nanoparticles incorporated cementitious system, Cem. Concr. Compos. 79 (2017) 106–116, https://doi.org/10.1016/j.cemconcomp.2017.02.004.

[39] Z. Zhang, Y. Yan, Z. Qu, G. Geng, Endowing strength to calcium silicate hydrate (C-S-H) powder by high pressure mechanical compaction, Cem. Concr. Res. 159 (2022) 106858, https://doi.org/10.1016/j.cemconres.2022.106858.

[40] G. Lai, X. Liu, S. Li, Y. Xu, Y. Zheng, J. Guan, R. Gao, Z. Wei, Z. Wang, S. Cui, Development of chemical admixtures for green and environmentally friendly concrete: a review, J. Clean. Prod. 389 (2023) 136116, https://doi.org/10.1016/j.jclepro.2023.136116.

[41] R. Snellings, P. Suraneni, J. Skibsted, Future and emerging supplementary cementitious materials, Cem. Concr. Res. 171 (2023) 107199, https://doi.org/10.1016/j.cemconres.2023.107199.

[42] Supriya, R. Chaudhury, U. Sharma, P.C. Thapliyal, L.P. Singh, Low-CO2 emission strategies to achieve net zero target in cement sector, , J. Clean. Prod. 417 (2023) 137466, https://doi.org/10.1016/j.jclepro.2023.137466.

[43] N. Makul, Advanced smart concrete - a review of current progress, benefits and challenges, J. Clean. Prod. 274 (2020) 122899, https://doi.org/10.1016/j.jclepro.2020.122899.

[44] X. Zhang, M. Du, H. Fang, M. Shi, C. Zhang, F. Wang, Polymer-modified cement mortars: Their enhanced properties, applications, prospects, and challenges, Constr. Build. Mater. 299 (2021) 124290, https://doi.org/10.1016/j.conbuildmat.2021.124290.

[45] Y. Ohama, Recent progress in concrete-polymer composites, Adv. Cem. Based Mater. 5 (1997) 31–40, https://doi.org/10.1016/S1065-7355(96)00005-3.

[46] S.S. Pendhari, T. Kant, Y.M. Desai, Application of polymer composites in civil construction: A general review, Compos. Struct. 84 (2008) 114–124, https://doi.org/10.1016/j.compstruct.2007.06.007.

[47] Z. Zhu, Z. Wang, L. Xu, Y. Zhou, Y. Chen, K. Wu, G. De Schutter, Synthesis and characterization of an intermediate for C-S-H structure tailoring, Cem. Concr. Res. 160 (2022) 106923, https://doi.org/10.1016/j.cemconres.2022.106923.

[48] Y. Zhou, W. She, D. Hou, B. Yin, H. Chang, J. Jiang, J. Li, Modification of incorporation and in-situ polymerization of aniline on the nano-structure and meso-structure of calcium silicate hydrates, Constr. Build. Mater. 182 (2018) 459–468, https://doi.org/10.1016/j.conbuildmat.2018.06.141.

[49] F.L. Maranhão, V.M. John, Bond strength and transversal deformation aging on cement-polymer adhesive mortar, Constr. Build. Mater. 23 (2009) 1022–1027, https://doi.org/10.1016/j.conbuildmat.2008.05.019.

[50] L. Agavriloaie, S. Oprea, M. Barbuta, F. Luca, Characterisation of polymer concrete with epoxy polyurethane acryl matrix, Constr. Build. Mater. 37 (2012) 190–196, https://doi.org/10.1016/j.conbuildmat.2012.07.037.

[51] H. Ma, Z. Li, Microstructures and mechanical properties of polymer modified mortars under distinct mechanisms, Constr. Build. Mater. 47 (2013) 579–587, https://doi.org/10.1016/j.conbuildmat.2013.05.048.

[52] J.A. Rossignolo, M.V.C. Agnesini, Durability of polymer-modified lightweight aggregate concrete, Cem. Concr. Compos. 26 (2004) 375–380, https://doi.org/10.1016/S0958-9465(03)00022-2.

[53] S. Boutti, M. Urvoy, I. Dubois-Brugger, C. Graillat, E. Bourgeat-Lami, R. Spitz, Influence of low fractions of styrene/butyl acrylate polymer latexes on some properties of ordinary portland cement mortars, Macromol. Mater. Eng. 292 (2007) 33–45, https://doi.org/10.1002/mame.200600316.

[54] Y. Tian, X. Jin, N. Jin, R. Zhao, Z. Li, H. Ma, Research on the microstructure formation of polyacrylate latex modified mortars, Constr. Build. Mater. 47 (2013) 1381–1394, https://doi.org/10.1016/j.conbuildmat.2013.06.016.

[55] K. Bicer, H. Yalciner, A. Pekrioglu Balkıs, A. Kumbasaroglu, Effect of corrosion on flexural strength of reinforced concrete beams with polypropylene fibers, Constr. Build. Mater. 185 (2018) 574–588, https://doi.org/10.1016/j.conbuildmat.2018.07.021.

[56] Z. Sun, Q. Xu, Microscopic, physical and mechanical analysis of polypropylene fiber reinforced concrete, Mater. Sci. Eng. A 527 (2009) 198–204, https://doi.org/10.1016/j.msea.2009.07.056.

[57] C. Negro, A. Blanco, E. Fuente, L.M. Sánchez, J. Tijero, Influence of flocculant molecular weight and anionic charge on flocculation behaviour and on the manufacture of fibre cement composites by the Hatschek process, Cem. Concr. Res. 35 (2005) 2095–2103, https://doi.org/10.1016/j.cemconres.2005.03.004.

[58] U.S. Rai, R.K. Singh, Effect of polyacrylamide on the different properties of cement and mortar, Mater. Sci. Eng. A 392 (2005) 42–50, https://doi.org/10.1016/j.msea.2004.08.050.

[59] H. Li, D. Ni, L. Li, B. Dong, Q. Chen, L. Gu, Insight into the role of polyacrylamide polymer powder on the cracking in plastic period of cement mortar, Constr. Build. Mater. 260 (2020) 119914, https://doi.org/10.1016/j.conbuildmat.2020.119914.

[60] B. Yin, D. Qi, X. Hua, F. Fan, K. Han, Y. Hou, D. Hou, B. Chen, Mechanical properties and micro-mechanism of cement-based materials strengthened by in-situ organic-inorganic polymerization, Cem. Concr. Compos. 142 (2023) 105202, https://doi.org/10.1016/j.cemconcomp.2023.105202.

[61] H. Bessaies-Bey, R. Baumann, M. Schmitz, M. Radler, N. Roussel, Effect of polyacrylamide on rheology of fresh cement pastes, Cem. Concr. Res. 76 (2015) 98–106, https://doi.org/10.1016/j.cemconres.2015.05.012.

[62] H. Yao, M. Fan, T. Huang, Q. Yuan, Z. Xie, Z. Chen, Y. Li, J. Wang, Retardation and bridging effect of anionic polyacrylamide in cement paste and its relationship with early properties, Constr. Build. Mater. 306 (2021) 124822, https://doi.org/10.1016/j.conbuildmat.2021.124822.

[63] L. Gu, T. Liu, K. Wu, Z. Yang, Z. Wen, Z. Zhang, G. De Schutter, H. Li, Comparative study on the role of PAM and PANA on the property of fresh cement paste, Cem. Concr. Compos. 133 (2022) 104701, https://doi.org/10.1016/j.cemconcomp.2022.104701.

[64] Q. Liu, Q. Jiang, M. Huang, J. Xin, P. Chen, S. Wu, Modifying effect of anionic polyacrylamide dose for cement-based 3DP materials: Printability and mechanical performance tests, Constr. Build. Mater. 330 (2022) 127156, https://doi.org/10.1016/j.conbuildmat.2022.127156.

[65] C. Negro, L.M. Sánchez, E. Fuente, Á. Blanco, J. Tijero, Polyacrylamide induced flocculation of a cement suspension, Chem. Eng. Sci. 61 (2006) 2522–2532, https://doi.org/10.1016/j.ces.2005.11.013.

[66] M.M. Ghobashy, G. Bassioni, pH stimuli-responsive poly(acrylamide- *co* -sodium alginate) hydrogels prepared by γ-radiation for improved compressive strength of concrete, Adv. Polym. Technol. 37 (2018) 2123–2133, https://doi.org/10.1002/adv.21870.

[67] F. Zhi, Y. Jiang, M.-Z. Guo, W. Jin, X. Yan, P. Zhu, L. Jiang, Effect of polyacrylamide on the carbonation behavior of cement paste, Cem. Concr. Res. 156 (2022) 106756, https://doi.org/10.1016/j.cemconres.2022.106756.

[68] F. Zhi, L. Jiang, M. Jin, P. Xu, B. Xiao, Q. Jiang, L. Chen, Y. Gu, Inhibition effect and mechanism of polyacrylamide for steel corrosion in simulated concrete pore solution, Constr. Build. Mater. 259 (2020) 120425, https://doi.org/10.1016/j.conbuildmat.2020.120425.

[69] G. Qiao, D. Hou, P. Wang, Z. Lu, Insights on failure modes of calcium-silicate-hydrate interface strengthened by polyacrylamides: structure, dynamic and mechanical properties, Constr. Build. Mater. 278 (2021) 122406, https://doi.org/10.1016/j.conbuildmat.2021.122406.

[70] Q. Yuan, Z. Xie, H. Yao, M. Fan, T. Huang, Comparative study on the early properties of cement modified with different ionic polyacrylamides, Constr. Build. Mater. 339 (2022) 127671, https://doi.org/10.1016/j.conbuildmat.2022.127671.

[71] Q. Yuan, Z. Xie, H. Yao, T. Huang, M. Fan, Hydration, mechanical properties, and microstructural characteristics of cement pastes with different ionic polyacrylamides: a comparative study, J. Build. Eng. 56 (2022) 104763, https://doi.org/10.1016/j.jobe.2022.104763.

[72] C.C. Thong, D.C.L. Teo, C.K. Ng, Application of polyvinyl alcohol (PVA) in cement-based composite materials: a review of its engineering properties and microstructure behavior, Constr. Build. Mater. 107 (2016) 172–180, https://doi.org/10.1016/j.conbuildmat.2015.12.188.

[73] L. Patural, P. Marchal, A. Govin, P. Grosseau, B. Ruot, O. Devès, Cellulose ethers influence on water retention and consistency in cement-based mortars, Cem. Concr. Res. 41 (2011) 46–55, https://doi.org/10.1016/j.cemconres.2010.09.004.

[74] Z.H. Ou, B.G. Ma, S.W. Jian, Influence of cellulose ethers molecular parameters on hydration kinetics of Portland cement at early ages, Constr. Build. Mater. 33 (2012) 78–83, https://doi.org/10.1016/j.conbuildmat.2012.01.007.

[75] Y. Ohama, Polymer-based admixtures, Cem. Concr. Compos. 20 (1998) 189–212, https://doi.org/10.1016/S0958-9465(97)00065-6.

[76] H. Paiva, L.M. Silva, J.A. Labrincha, V.M. Ferreira, Effects of a water-retaining agent on the rheological behaviour of a single-coat render mortar, Cem. Concr. Res. 36 (2006) 1257–1262, https://doi.org/10.1016/j.cemconres.2006.02.018.

[77] J. Pourchez, A. Peschard, P. Grosseau, R. Guyonnet, B. Guilhot, F. Vallée, HPMC and HEMC influence on cement hydration, Cem. Concr. Res. 36 (2006) 288–294, https://doi.org/10.1016/j.cemconres.2005.08.003.

[78] T.M. Pique, A. Vazquez, R.D. Toledo Filho, Use of simple non-destructive techniques to evaluate the hydration reactions of PVA-modified cement pastes, Constr. Build. Mater. 133 (2017) 340–347, https://doi.org/10.1016/j.conbuildmat.2016.12.013.

[79] B. Bose, C.R. Davis, K.A. Erk, Microstructural refinement of cement paste internally cured by polyacrylamide composite hydrogel particles containing silica fume and nanosilica, Cem. Concr. Res. 143 (2021) 106400, https://doi.org/10.1016/j.cemconres.2021.106400.

[80] J. Wongpa, K. Kiattikomol, C. Jaturapitakkul, P. Chindaprasirt, Compressive strength, modulus of elasticity, and water permeability of inorganic polymer concrete, Mater. Des. 31 (2010) 4748–4754, https://doi.org/10.1016/j.matdes.2010.05.012.

[81] Z. Naseem, E. Shamsaei, K. Sagoe-Crentsil, W. Duan, Antifoaming effect of graphene oxide nanosheets in polymer-modified cement composites for enhanced microstructure and mechanical performance, Cem. Concr. Res. 158 (2022) 106843, https://doi.org/10.1016/j.cemconres.2022.106843.

[82] K.-R. Wu, D. Zhang, J.-M. Song, Properties of polymer-modified cement mortar using pre-enveloping method, Cem. Concr. Res. 32 (2002) 425–429, https://doi.org/10.1016/S0008-8846(01)00697-4.

[83] J. Hot, H. Bessaies-Bey, C. Brumaud, M. Duc, C. Castella, N. Roussel, Adsorbing polymers and viscosity of cement pastes, Cem. Concr. Res. 63 (2014) 12–19, https://doi.org/10.1016/j.cemconres.2014.04.005.

[84] N. Shirshova, A. Menner, G.P. Funkhouser, A. Bismarck, Polymerised high internal phase emulsion cement hybrids: macroporous polymer scaffolds for setting cements, Cem. Concr. Res. 41 (2011) 443–450, https://doi.org/10.1016/j.cemconres.2011.01.017.

[85] J.A. Rosewitz, H.A. Choshali, N. Rahbar, Bioinspired design of architected cement-polymer composites, Cem. Concr. Compos. 96 (2019) 252–265, https://doi.org/10.1016/j.cemconcomp.2018.12.010.

[86] W. Zhang, X. Zou, F. Wei, H. Wang, G. Zhang, Y. Huang, Y. Zhang, Grafting SiO2 nanoparticles on polyvinyl alcohol fibers to enhance the interfacial bonding strength with cement, Compos. Part B Eng. 162 (2019) 500–507, https://doi.org/10.1016/j.compositesb.2019.01.034.

[87] H. Azadmanesh, S.A.H. Hashemi, S.H. Ghasemi, The effect of styrene-butadiene rubber and ethylene vinyl acetate polymers on the mechanical properties of Engineered Cementitious Composites, Compos. Commun. 24 (2021) 100656, https://doi.org/10.1016/j.coco.2021.100656.

[88] M. Wang, R. Wang, H. Yao, S. Farhan, S. Zheng, Z. Wang, C. Du, H. Jiang, Research on the mechanism of polymer latex modified cement, Constr. Build. Mater. 111 (2016) 710–718, https://doi.org/10.1016/j.conbuildmat.2016.02.117.

[89] R. Wang, P.-M. Wang, X.-G. Li, Physical and mechanical properties of styrene–butadiene rubber emulsion modified cement mortars, Cem. Concr. Res. 35 (2005) 900–906, https://doi.org/10.1016/j.cemconres.2004.07.012.

[90] Z. Su, C. Li, G. Jiang, J. Li, H. Lu, F. Guo, Rheology and thixotropy of cement pastes containing polyacrylamide, Geofluids 2022 (2022) e1029984, https://doi.org/10.1155/2022/1029984.

[91] Z. Xie, H. Yao, Q. Yuan, F. Zhong, The roles of water-soluble polymers in cement-based materials: a systematic review, J. Build. Eng. 73 (2023) 106811, https://doi.org/10.1016/j.jobe.2023.106811.

[92] N. Tarannum, Km Pooja, R. Khan, Preparation and applications of hydrophobic multicomponent based redispersible polymer powder: a review, Constr. Build. Mater. 247 (2020) 118579, https://doi.org/10.1016/j.conbuildmat.2020.118579.

[93] E. Knapen, D. Van Gemert, Cement hydration and microstructure formation in the presence of water-soluble polymers, Cem. Concr. Res. 39 (2009) 6–13, https://doi.org/10.1016/j.cemconres.2008.10.003.

[94] C. Pan, S. Liu, S. Yao, X. Gao, H. Zhang, J. Zhu, P. Shen, X. Guan, H. Li, Influence of acrylamide in-situ polymerization on the mechanical properties and microstructure of OPC-CSA-Cs-FA quaternary system, J. Build. Eng. 67 (2023) 105906, https://doi.org/10.1016/j.jobe.2023.105906.

[95] J. Wang, H. Zhang, Y. Zhu, Z. Yan, H. Chai, Acrylamide in-situ polymerization of toughened sulphoaluminate cement-based grouting materials, Constr. Build. Mater. 319 (2022) 126105, https://doi.org/10.1016/j.conbuildmat.2021.126105.

[96] H. Zhang, S. Yao, J. Wang, R. Zhou, Y. Zhu, D. Zou, Tensile properties of sulfoaluminate cement-based grouting materials toughened by in-situ polymerization of acrylamide, Constr. Build. Mater. 375 (2023) 130885, https://doi.org/10.1016/j.conbuildmat.2023.130885.

[97] H. Zhang, R. Zhou, S. Liu, Y. Zhu, S. Wang, J. Wang, X. Guan, Enhanced toughness of ultra-fine sulphoaluminate cement-based hybrid grouting materials by incorporating in-situ polymerization of acrylamide, Constr. Build. Mater. 292 (2021) 123421, https://doi.org/10.1016/j.conbuildmat.2021.123421.

[98] J. Chen, N. Gao, J. Wu, G. Shan, M. Qiao, Q. Ran, J. Liu, Effects of the charge density of anionic copolymers on the properties of fresh cement pastes, Constr. Build. Mater. 263 (2020) 120207, https://doi.org/10.1016/j.conbuildmat.2020.120207.

[99] B. Myszka, K. Hurle, K. Zheng, S.E. Wolf, A.R. Boccaccini, Mechanical improvement of calcium carbonate cements by in situ HEMA polymerization during hardening, J. Mater. Chem. B 7 (2019) 3403–3411, https://doi.org/10.1039/C9TB00237E.

[100] C.A. Anagnostopoulos, Cement–clay grouts modified with acrylic resin or methyl methacrylate ester: Physical and mechanical properties, Constr. Build. Mater. 21 (2007) 252–257, https://doi.org/10.1016/j.conbuildmat.2005.12.007.

[101] J. Li, J. Chen, Y. Wang, G. Luo, H. Yu, Hydration of acrylonitrile to produce acrylamide using biocatalyst in a membrane dispersion microreactor, Bioresour. Technol. 169 (2014) 416–420, https://doi.org/10.1016/j.biortech.2014.07.034.

[102] J.K. Koh, C.W. Lai, M.R. Johan, S.S. Gan, W.W. Chua, Recent advances of modified polyacrylamide in drilling technology, J. Pet. Sci. Eng. 215 (2022) 110566, https://doi.org/10.1016/j.petrol.2022.110566.

[103] G. Gelardi, S. Mantellato, D. Marchon, M. Palacios, A.B. Eberhardt, R.J. Flatt. Chemistry of chemical admixtures, Elsevier, 2016, pp. 149–218, https://doi.org/10.1016/B978-0-08-100693-1.00009-6.

[104] X. Kong, S. Emmerling, J. Pakusch, M. Rueckel, J. Nieberle, Retardation effect of styrene-acrylate copolymer latexes on cement hydration, Cem. Concr. Res. 75 (2015) 23–41, https://doi.org/10.1016/j.cemconres.2015.04.014.

[105] B. Pang, Y. Jia, S.D. Pang, Y. Zhang, H. Du, G. Geng, H. Ni, J. Qian, H. Qiao, G. Liu, The interpenetration polymer network in a cement paste–waterborne epoxy system, Cem. Concr. Res. 139 (2021) 106236, https://doi.org/10.1016/j.cemconres.2020.106236.

[106] A. Giz, H. Çatalgil-Giz, A. Alb, J.-L. Brousseau, W.F. Reed, Kinetics and mechanisms of acrylamide polymerization from absolute, online monitoring of polymerization reaction, Macromolecules 34 (2001) 1180–1191, https://doi.org/10.1021/ma000815s.

[107] B. Wang, X. Xing, F. Lin, S. Wang, F. Li, H. Huang, J. Wei, Q. Yu, Effect of vacuum–vibration–compaction molding on the properties and performances of polymer-modified cementitious material, Cem. Concr. Compos. 148 (2024) 105450, https://doi.org/10.1016/j.cemconcomp.2024.105450.

[108] D. Bülichen, J. Kainz, J. Plank, Working mechanism of methyl hydroxyethyl cellulose (MHEC) as water retention agent, Cem. Concr. Res. 42 (2012) 953–959, https://doi.org/10.1016/j.cemconres.2012.03.016.

[109] J. Dai, Q. Wang, X. Lou, X. Bao, B. Zhang, J. Wang, X. Zhang, Solution calorimetry to assess effects of water-cement ratio and low temperature on hydration heat of cement, Constr. Build. Mater. 269 (2021) 121222, https://doi.org/10.1016/j.conbuildmat.2020.121222.

[110] Y. Ji, Z. Sun, X. Yang, C. Li, X. Tang, Assessment and mechanism study of bleeding process in cement paste by 1H low-field NMR, Constr. Build. Mater. 100 (2015) 255–261, https://doi.org/10.1016/j.conbuildmat.2015.09.062.

[111] H. Zhang, Z. Liu, J. Mai, N. Wang, J. Zhong, X. Mai, N. Zhang, Super-elastic smart phase change material (SPCM) for thermal energy storage, Chem. Eng. J. 411 (2021) 128482, https://doi.org/10.1016/j.cej.2021.128482.

[112] F. Montes, T. Fu, J.P. Youngblood, J. Weiss, Rheological impact of using cellulose nanocrystals (CNC) in cement pastes, Constr. Build. Mater. 235 (2020) 117497, https://doi.org/10.1016/j.conbuildmat.2019.117497.

[113] H. Zhang, X. Zhang, Z. Guo, H. Chai, Optimization of the injection and physical properties of sulfoaluminate cement via the In situ polymerization of acrylamide, Buildings 12 (2022) 2237, https://doi.org/10.3390/buildings12122237.

[114] C. Zhang, X. Kong, J. Yin, X. Fu, Rheology of fresh cement pastes containing polymer nanoparticles, Cem. Concr. Res. 144 (2021) 106419, https://doi.org/10.1016/j.cemconres.2021.106419.

[115] J. Chen, M. Qiao, N. Gao, J. Wu, G. Shan, B. Zhu, Q. Ran, Acrylate based post-acting polymers as novel viscosity modifying admixtures for concrete, Constr. Build. Mater. 312 (2021) 125414, https://doi.org/10.1016/j.conbuildmat.2021.125414.

[116] T. Huang, B. Li, Q. Yuan, Z. Shi, Y. Xie, C. Shi, Rheological behavior of Portland clinker-calcium sulphoaluminate clinker-anhydrite ternary blend, Cem. Concr. Compos. 104 (2019) 103403, https://doi.org/10.1016/j.cemconcomp.2019.103403.

[117] J. Zhou, K. Zheng, Z. Liu, F. He, Chemical effect of nano-alumina on early-age hydration of Portland cement, Cem. Concr. Res. 116 (2019) 159–167, https://doi.org/10.1016/j.cemconres.2018.11.007.

[118] L. Fang, J. Zhou, Q. Yuan, Y. Que, Z. Chen, C. Zhang, Rheological Properties of Fresh Cement Paste Modified by In Situ Polymerization of Acrylamide Monomer, J. Mater. Civ. Eng. 35 (2023) 04023467, https://doi.org/10.1061/JMCEE7.MTENG-15958.

[119] Q. Ma, P.J. Shuler, C.W. Aften, Y. Tang, Theoretical studies of hydrolysis and stability of polyacrylamide polymers, Polym. Degrad. Stab. 121 (2015) 69–77, https://doi.org/10.1016/j.polymdegradstab.2015.08.012.

[120] R.D. Shupe, Chemical stability of polyacrylamide polymers, J. Pet. Technol. 33 (1981) 1513–1529, https://doi.org/10.2118/9299-PA.

[121] Z. Sun, Y. Li, X. Ming, Q. Liu, Z. Li, B. Chen, Yield stress of in-situ polymerization modified cement paste, Cem. Concr. Res. 174 (2023) 107346, https://doi.org/10.1016/j.cemconres.2023.107346.

[122] A. Soltani, A. Deng, A. Taheri, B.C. O'Kelly, Intermittent swelling and shrinkage of a highly expansive soil treated with polyacrylamide, J. Rock. Mech. Geotech. Eng. 14 (2022) 252–261, https://doi.org/10.1016/j.jrmge.2021.04.009.

[123] S. Li, J.M. Scheiger, Z. Wang, B. Huber, M. Hoffmann, M. Wilhelm, P.A. Levkin, Diapers to thickeners and pressure-sensitive adhesives: recycling of superabsorbers via UV degradation, ACS Appl. Mater. Interfaces 15 (2023) 44186–44193, https://doi.org/10.1021/acsami.3c06999.

[124] J. Justs, M. Wyrzykowski, D. Bajare, P. Lura, Internal curing by superabsorbent polymers in ultra-high performance concrete, Cem. Concr. Res. 76 (2015) 82–90, https://doi.org/10.1016/j.cemconres.2015.05.005.

[125] P. Zhong, Z. Hu, M. Griffa, M. Wyrzykowski, J. Liu, P. Lura, Mechanisms of internal curing water release from retentive and non-retentive superabsorbent polymers in cement paste, Cem. Concr. Res. 147 (2021) 106494, https://doi.org/10.1016/j.cemconres.2021.106494.

[126] Z. Lu, X. Kong, C. Zhang, Y. Cai, Effect of highly carboxylated colloidal polymers on cement hydration and interactions with calcium ions, Cem. Concr. Res. 113 (2018) 140–153, https://doi.org/10.1016/j.cemconres.2018.08.010.

[127] Z. Lu, X. Kong, C. Zhang, D. Jansen, J. Neubauer, F. Goetz-Neunhoeffer, Effects of two oppositely charged colloidal polymers on cement hydration, Cem. Concr. Compos. 96 (2019) 66–76, https://doi.org/10.1016/j.cemconcomp.2018.11.014.

[128] Y. Deng, J.B. Dixon, G.N. White, R.H. Loeppert, A.S.R. Juo, Bonding between polyacrylamide and smectite, Colloids Surf. Physicochem. Eng. Asp. 281 (2006) 82–91, https://doi.org/10.1016/j.colsurfa.2006.02.030.

[129] R. Wang, X. Chen, Y. Yang, Y. Xu, Q. Zhang, Y. Zhang, Y. Cheng, Imidazolidinyl urea reinforced polyacrylamide hydrogels through the formation of multiple hydrogen bonds, React. Funct. Polym. 172 (2022) 105183, https://doi.org/10.1016/j.reactfunctpolym.2022.105183.

[130] M.N. Rodnikova, G.M. Agayan, N.K. Balabaev, Description of the spatial networks of hydrogen bonds in liquids by topological methods, J. Mol. Liq. 283 (2019) 374–379, https://doi.org/10.1016/j.molliq.2019.03.090.

[131] J. Xu, J. Tang, C. Gao, R. Wang, W. Wang, Z. Meng, J. Liu, Synergistic toughening mechanism of concrete based on polymerization of acrylamide monomer and wollastonite whisker, Kuei Suan Jen Hsueh PaoJournal Chin, Ceram. Soc. 52 (2024) 533–544, https://doi.org/10.14062/j.issn.0454-5648.20230585.

[132] X. Hua, K. Han, Z. Lin, B. Yin, P. Wang, D. Qi, D. Hou, J. Chen, Modification of in-situ polymerization of acrylamide and synergies with fiber in enhancing cement-based composite, J. Build. Eng. 85 (2024) 108605, https://doi.org/10.1016/j.jobe.2024.108605.

[133] A.A. Bahraq, M.A. Al-Osta, O.S.B. Al-Amoudi, T.A. Saleh, I.B. Obot, Atomistic simulation of polymer-cement interactions: progress and research challenges, Constr. Build. Mater. 327 (2022) 126881, https://doi.org/10.1016/j.conbuildmat.2022.126881.

[134] Q. Liu, X. Ming, M. Wang, Z. Li, G. Sun, R. Liang, Improved mechanical strength of cement paste by polyvinylpyrrolidone and In situ polymerized acrylic acid, J. Mater. Civ. Eng. 35 (2023) 4023096, https://doi.org/10.1061/JMCEE7.MTENG-13954.

[135] Q. Liu, X. Ming, J. Xu, D. Hou, G. Sun, Z. Li, G. Geng, Robust cement composite with low hydration temperature and high mechanical performance achieved by Field's metal and acrylic acid-acrylamide copolymer, Constr. Build. Mater. 387 (2023) 131655, https://doi.org/10.1016/j.conbuildmat.2023.131655.

[136] Y. Peng, G. Zhao, Y. Qi, Q. Zeng, In-situ assessment of the water-penetration resistance of polymer modified cement mortars by μ-XCT, SEM and EDS, Cem. Concr. Compos. 114 (2020) 103821, https://doi.org/10.1016/j.cemconcomp.2020.103821.

[137] F. Moodi, A. Kashi, A.A. Ramezanianpour, M. Pourebrahimi, Investigation on mechanical and durability properties of polymer and latex-modified concretes, Constr. Build. Mater. 191 (2018) 145–154, https://doi.org/10.1016/j.conbuildmat.2018.09.198.

[138] Z. Lu, X. Zhou, J. Zhang, Study on the performance of a new type of water-repellent admixture for cement mortar, Cem. Concr. Res. 34 (2004) 2015–2019, https://doi.org/10.1016/j.cemconres.2004.02.019.

[139] X. Hu, Q. Wang, Q. Liu, Z. Li, G. Sun, Villus-like nanocomposite hydrogels with a super-high water absorption capacity, J. Mater. Chem. A 8 (2020) 12613–12622, https://doi.org/10.1039/D0TA03907A.

[140] H. Chai, H. Zhang, C. Hou, Z. Guo, S. Liu, Experimental study on chloride corrosion resistance of sulphoaluminate cement modified by acrylamide in situ polymerization, J. Build. Eng. 73 (2023) 106730, https://doi.org/10.1016/j.jobe.2023.106730.

[141] H. Chai, S. Liu, L. Zhao, Y. Tian, Z. Guo, H. Zhang, Enhancing sulfate resistance of sulfate-aluminate cement grouting material through acrylamide in-situ polymerization modification, Constr. Build. Mater. 408 (2023) 133799, https://doi.org/10.1016/j.conbuildmat.2023.133799.

[142] V.H.J.M.D. Santos, D. Pontin, G.G.D. Ponzi, A.S.D.G.E. Stepanha, R.B. Martel, M. K. Schütz, S.M.O. Einloft, F. Dalla, Vecchia, Application of fourier transform infrared spectroscopy (FTIR) coupled with multivariate regression for calcium carbonate (CaCO3) quantification in cement, Constr. Build. Mater. 313 (2021) 125413, https://doi.org/10.1016/j.conbuildmat.2021.125413.

[143] J. Higl, D. Hinder, C. Rathgeber, B. Ramming, M. Lindén, Detailed in situ ATR-FTIR spectroscopy study of the early stages of C-S-H formation during hydration of monoclinic C3S, Cem. Concr. Res. 142 (2021) 106367, https://doi.org/10.1016/j.cemconres.2021.106367.

[144] N. Jonathan, The infrared and Raman spectra and structure of acrylamide, J. Mol. Spectrosc. 6 (1961) 205–214, https://doi.org/10.1016/0022-2852(61)90243-0.

[145] R. Wang, L. Yao, P. Wang, Mechanism analysis and effect of styrene–acrylate copolymer powder on cement hydrates, Constr. Build. Mater. 41 (2013) 538–544, https://doi.org/10.1016/j.conbuildmat.2012.12.028.

[146] B. Xiong, R.D. Loss, D. Shields, T. Pawlik, R. Hochreiter, A.L. Zydney, M. Kumar, Polyacrylamide degradation and its implications in environmental systems, NPJ Clean. Water 1 (2018) 17, https://doi.org/10.1038/s41545-018-0016-8.

[147] Q. Liu, X. Ming, M. Wang, Q. Wang, Y. Li, Z. Li, D. Hou, G. Geng, Probing the hydration behavior of tricalcium aluminate under the in situ polymerization of acrylic acid, Cem. Concr. Res. 177 (2024) 107429, https://doi.org/10.1016/j.cemconres.2024.107429.

[148] M.-L. Wong, Polarizability and tensor ellipsoid in the raman effect, Vib. Spectrosc. 7 (1994) 197–199, https://doi.org/10.1016/0924-2031(94)85031-3.

[149] C. Tang, T.-C. Ling, K.H. Mo, Raman spectroscopy as a tool to understand the mechanism of concrete durability—a review, Constr. Build. Mater. 268 (2021) 121079, https://doi.org/10.1016/j.conbuildmat.2020.121079.

[150] H.G.M. Edwards, A.F. Johnson, I.R. Lewis, Applications of Raman spectroscopy to the study of polymers and polymerization processes, J. Raman Spectrosc. 24 (1993) 475–483, https://doi.org/10.1002/jrs.1250240803.

[151] L. Bernard, A. Leemann, Assessing the potential of ToF-SIMS as a complementary approach to investigate cement-based materials — applications related to alkali–silica reaction, Cem. Concr. Res. 68 (2015) 156–165, https://doi.org/10.1016/j.cemconres.2014.11.008.

[152] L.M. Haselbach, S. Ma, Potential for carbon adsorption on concrete: surface XPS analyses, Environ. Sci. Technol. 42 (2008) 5329–5334, https://doi.org/10.1021/es800717q.

[153] R.L. Vander Wal, V.M. Bryg, M.D. Hays, XPS analysis of combustion aerosols for chemical composition, surface chemistry, and carbon chemical state, Anal. Chem. 83 (2011) 1924–1930, https://doi.org/10.1021/ac102365s.

[154] Z. Lu, X. Li, A. Hanif, B. Chen, P. Parthasarathy, J. Yu, Z. Li, Early-age interaction mechanism between the graphene oxide and cement hydrates, Constr. Build. Mater. 152 (2017) 232–239, https://doi.org/10.1016/j.conbuildmat.2017.06.176.

[155] B. Demri, D. Muster, XPS study of some calcium compounds, J. Mater. Process. Technol. 55 (1995) 311–314, https://doi.org/10.1016/0924-0136(95)02023-3.

[156] E. Knapen, D. Van Gemert, Polymer film formation in cement mortars modified with water-soluble polymers, Cem. Concr. Compos. 58 (2015) 23–28, https://doi.org/10.1016/j.cemconcomp.2014.11.015.

[157] Z. Su, J.M.J.M. Bijen, J.A. Larbi, Influence of polymer modification on the hydration of portland cement, Cem. Concr. Res. 21 (1991) 242–250, https://doi.org/10.1016/0008-8846(91)90004-2.

[158] J. Cheung, A. Jeknavorian, L. Roberts, D. Silva, Impact of admixtures on the hydration kinetics of Portland cement, Cem. Concr. Res. 41 (2011) 1289–1309, https://doi.org/10.1016/j.cemconres.2011.03.005.

[159] J. Skalny, M.E. Tadros, Retardation of tricalcium aluminate hydration by sulfates, J. Am. Ceram. Soc. 60 (1977) 174–175, https://doi.org/10.1111/j.1151-2916.1977.tb15503.x.

[160] N.K. Singh, P.C. Mishra, V.K. Singh, K.K. Narang, Effects of hydroxyethyl cellulose and oxalic acid on the properties of cement, Cem. Concr. Res. 33 (2003) 1319–1329, https://doi.org/10.1016/S0008-8846(03)00060-7.

[161] J. Plank, B. Sachsenhauser, Experimental determination of the effective anionic charge density of polycarboxylate superplasticizers in cement pore solution, Cem. Concr. Res. 39 (2009) 1–5, https://doi.org/10.1016/j.cemconres.2008.09.001.

[162] K. Lewandowska, Comparative studies of rheological properties of polyacrylamide and partially hydrolyzed polyacrylamide solutions, J. Appl. Polym. Sci. 103 (2007) 2235–2241, https://doi.org/10.1002/app.25247.

[163] H. Matsuyama, J.F. Young, Synthesis of calcium silicate hydrate/polymer complexes: Part I. Anionic and nonionic polymers, J. Mater. Res. 14 (1999) 3379–3388, https://doi.org/10.1557/JMR.1999.0458.

[164] H. Matsuyama, J.F. Young, Synthesis of calcium silicate hydrate/polymer complexes: Part II. Cationic polymers and complex formation with different polymers, J. Mater. Res. 14 (1999) 3389–3396, https://doi.org/10.1557/JMR.1999.0459.

[165] P. Mounanga, A. Khelidj, A. Loukili, V. Baroghel-Bouny, Predicting Ca(OH)2 content and chemical shrinkage of hydrating cement pastes using analytical approach, Cem. Concr. Res. 34 (2004) 255–265, https://doi.org/10.1016/j.cemconres.2003.07.006.

[166] Z. Su, K. Sujata, J.M.J.M. Bijen, H.M. Jennings, A.L.A. Fraaij, The evolution of the microstructure in styrene acrylate polymer-modified cement pastes at the early stage of cement hydration, Adv. Cem. Based Mater. 3 (1996) 87–93, https://doi.org/10.1016/S1065-7355(96)90041-3.

[167] K.L. Scrivener, P. Juilland, Paulo J.M. Monteiro, Advances in understanding hydration of Portland cement, Cem. Concr. Res. 78 (2015) 38–56, https://doi.org/10.1016/j.cemconres.2015.05.025.

[168] J. Wang, C. Liu, Y. Liu, S. Zhang, Double-network interpenetrating bone cement via in situ hybridization protocol, Adv. Funct. Mater. 20 (2010) 3997–4011, https://doi.org/10.1002/adfm.201000995.

[169] S.-H. Kang, S.-G. Hong, J. Moon, The effect of superabsorbent polymer on various scale of pore structure in ultra-high performance concrete, Constr. Build. Mater. 172 (2018) 29–40, https://doi.org/10.1016/j.conbuildmat.2018.03.193.

[170] G. Zhang, H. Xia, W. Zhang, Y. Niu, L. Song, H. Chen, D. Cao, Mechanical properties, drying shrinkage, microstructure of modified cement mortar based on poly(acrylamide-co-methacrylic acid) microgel, Constr. Build. Mater. 284 (2021) 122824, https://doi.org/10.1016/j.conbuildmat.2021.122824.

[171] J. Xu, X. Wang, X. Zhang, Y. Zhang, Z. Yang, S. Li, L. Tao, Q. Wang, T. Wang, Room-temperature self-healing supramolecular polyurethanes based on the synergistic strengthening of biomimetic hierarchical hydrogen-bonding interactions and coordination bonds, Chem. Eng. J. 451 (2023) 138673, https://doi.org/10.1016/j.cej.2022.138673.

[172] L. Zheng, Y. Wu, X. Li, Y. Zuo, Molecular-level topological deep cross-fusion strategy towards organic–inorganic lightweight composites, Chem. Eng. J. 474 (2023) 145666, https://doi.org/10.1016/j.cej.2023.145666.

[173] W. Zhou, Q. Ye, J. Cao, S.Q. Shi, J. Li, Performance improvement of magnesium oxychloride cement via nanoparticles-enhanced organic–inorganic hybrid network, Constr. Build. Mater. 343 (2022) 128096, https://doi.org/10.1016/j.conbuildmat.2022.128096.

[174] P. Feng, Z. Liu, L. Shao, W. Wang, J. Hong, C. Miao, Effects of in-situ polymerization on mechanical properties of 3D printing mortars and its mechanism, Kuei Suan Jen Hsueh PaoJournal Chin, Ceram. Soc. 51 (2023) 1093–1103, https://doi.org/10.14062/j.issn.0454-5648.20220751.

[175] S. Demirdag, The effect of using different polymer and cement based materials in pore filling applications on technical parameters of travertine stone, Constr. Build. Mater. 23 (2009) 522–530, https://doi.org/10.1016/j.conbuildmat.2007.10.019.

[176] A.A.P. Mansur, D.B. Santos, H.S. Mansur, A microstructural approach to adherence mechanism of poly(vinyl alcohol) modified cement systems to ceramic tiles, Cem. Concr. Res. 37 (2007) 270–282, https://doi.org/10.1016/j.cemconres.2006.11.011.

[177] Y. Zhang, D. Zhang, Polymer/cement composite electrolyte with high strength and high ionic conductivity for structural supercapacitors, Cem. Concr. Compos. 149 (2024) 105512, https://doi.org/10.1016/j.cemconcomp.2024.105512.

[178] P. Jiao, C. Fang, D. Zhang, In-situ polymerized polyacrylamide/magnesium phosphate cement electrolyte for structural supercapacitor, J. Energy Storage 55 (2022) 105416, https://doi.org/10.1016/j.est.2022.105416.

[179] M.D. Maksimović, V.B. Mišković-Stanković, The corrosion behaviour of epoxy-resin electrocoated steel, Corros. Sci. 33 (1992) 271–279, https://doi.org/10.1016/0010-938X(92)90151-R.

[180] T. Gutberlet, H. Hilbig, R.E. Beddoe, Acid attack on hydrated cement — effect of mineral acids on the degradation process, Cem. Concr. Res. 74 (2015) 35–43, https://doi.org/10.1016/j.cemconres.2015.03.011.

[181] G. Xiong, X. Chen, G. Li, L. Chen, Sulphuric acid resistance of soluble soda glass–polyvinyl acetate latex–modified cement mortar, Cem. Concr. Res. 31 (2001) 83–86, https://doi.org/10.1016/S0008-8846(00)00426-9.

[182] W. Hua, H. Jiang, Z. Zhou, Research on nitric acid corrosion resistance of latex modified ordinary portland cement mortar, Appl. Mech. Mater. 485 (2012) 262–265, https://doi.org/10.4028/www.scientific.net/AMR.485.262.
[183] X.S. Yi, W.X. Shi, S.L. Yu, X.H. Li, N. Sun, C. He, Factorial design applied to flux decline of anionic polyacrylamide removal from water by modified polyvinylidene fluoride ultrafiltration membranes, Desalination 274 (2011) 7–12, https://doi.org/10.1016/j.desal.2010.10.019.
[184] S. Abdurrahmanoglu, V. Can, O. Okay, Design of high-toughness polyacrylamide hydrogels by hydrophobic modification, Polymer 50 (2009) 5449–5455, https://doi.org/10.1016/j.polymer.2009.09.042.
[185] D. Marchon, S. Kawashima, H. Bessaies-Bey, S. Mantellato, S. Ng, Hydration and rheology control of concrete for digital fabrication: Potential admixtures and cement chemistry, Cem. Concr. Res. 112 (2018) 96–110, https://doi.org/10.1016/j.cemconres.2018.05.014.

Construction and Building Materials 463 (2025) 140095

Contents lists available at ScienceDirect

Construction and Building Materials

journal homepage: www.elsevier.com/locate/conbuildmat

Design of microwave absorbing frequency bands and selection criteria for vitreous aggregates in cement-based materials

Zihao Wu [a,b], Shuai Xie [a], Chao Ma [a], Yingxiang Wang [a], Ronghua Su [c,*], Jing Wang [a], Zhijiang Ji [a,b,**]

[a] State Key Laboratory of Green Building Materials, China Building Materials Academy, Beijing 100024, PR China
[b] School of Materials Science and Engineering, Wuhan University of Technology, Wuhan 430070, PR China
[c] Defense Engineering Institute, AMS, Beijing 100850, PR China

ARTICLE INFO

Keywords:
Microwave absorption
Frequency band design
Vitreous aggregates
Finite element analysis
Mechanics and thermal insulation

ABSTRACT

The electromagnetic wave (EMW) absorption frequency band of cement-based materials lacks designability. Vitreous aggregates, as wave-transmitting materials, can improve the impedance matching of the cement matrix and adjust the absorption frequency band. To investigate the relationship between vitreous aggregates and absorption frequency bands, cement-based EMW absorbing materials were prepared using aggregates of varying particle sizes and volume ratios, supplemented by finite element simulations. The absorption performance and mechanisms were systematically analyzed. The results indicate that, at higher frequency bands, increasing the volume ratio or particle size of the vitreous aggregates can optimize impedance matching characteristics, enhance reflection loss (RL), and broaden the effective absorption bandwidth (EAB). Conversely, at lower frequency bands, reducing the volume ratio or particle size is necessary to improve overall performance. Throughout the entire frequency band, the average RL is minimally affected by the aggregates, with a difference of no more than −1.54 dB. When the absorption rate of EMW exceeds 90 %, effective protection is established in the high-frequency band, with the EAB reaching up to 6.57 GHz; when the absorption rate exceeds 80 %, effective protection can be achieved across the entire frequency band, with the EAB reaching up to 12.4 GHz. Finite element simulation results indicate that vitreous aggregates can alter the transmission direction and increase the loss paths of EMWs. The larger the particle size, the greater the angle of refraction for the EMWs. The strongest EM loss occurs between adjacent aggregates, followed by loss within the cement matrix. The thermal insulation performance of cement-based materials improves with increasing particle size of aggregates. Although there is a slight reduction in mechanical strength, it still exceeds the standard specifications for strength. This work provides guidance for the design of absorption frequency bands and the selection criteria for vitreous aggregates in cement-based EMW absorbing materials.

1. Introduction

The rapid development of electronic communication and radar technology has led to electromagnetic waves (EMWs) becoming a new source of pollution that threatens human living environments and poses serious risks to information security[1–3]. The demand for EMW protection in civil construction and special engineering projects is increasing, creating an urgent need for the design of EMW protection materials with higher absorption efficiency, especially for engineering materials that can provide effective protection across different frequency bands[4–6]. Cement-based materials, as the most widely used construction materials, are important raw materials in the field of engineering construction[7,8]. However, the dense structure of cement-based materials results in poor EMW impedance matching performance and only a weak ability to dissipate EMWs[9,10]. Therefore, it is possible to improve the raw materials and optimize the structure of cement-based materials to enhance their wave absorption performance and meet the needs of special engineering construction.

Introducing efficient wave-absorbing agents into cement-based materials can enhance the EMW dissipation capacity of the matrix[11–14].

* Corresponding author.
** Corresponding author at: State Key Laboratory of Green Building Materials, China Building Materials Academy, Beijing 100024, PR China.
E-mail addresses: suronghua2023@163.com (R. Su), jzj1618@126.com (Z. Ji).

https://doi.org/10.1016/j.conbuildmat.2025.140095
Received 6 December 2024; Received in revised form 15 January 2025; Accepted 19 January 2025
0950-0618/© 2025 Elsevier Ltd. All rights are reserved, including those for text and data mining, AI training, and similar technologies.

Common wave-absorbing agents include carbon materials[15–17], ferrites[6,18], and metals[19,20]. Carbon black (CB), as a typical conductive material, possesses numerous microscopic defects, high dielectric loss, a large specific surface area, good stability, and low cost, making it advantageous for use in construction materials. However, when the CB mass fraction exceeds 7.5 %, the cement-based material reaches the percolation threshold[21], resulting in a reflection loss (RL) of less than −7 dB at high frequencies[22]. Although efficient wave-absorbing agents improve the EMW dissipation capacity of cement-based materials, the density of the cement-based materials and the high conductivity of the absorbing agents lead to poor impedance matching performance. This causes a significant amount of EMWs to reflect off the surface of the cement-based material, preventing them from entering the absorbing material and achieving effective absorption.

By adding aggregates with low dielectric constants to cement-based materials, EMW reflection is effectively reduced, surface impedance is optimized, more EMWs are guided into the interior of the materials, and pathways for EMW attenuation are increased. Examples of such porous aggregates include expanded polystyrene foam particles (EPS)[23], expanded perlite (EP)[24], and expanded glass microspheres (EG)[25]. When the material is filled with 50 % EPS and 2 % CB, the effective absorbing bandwidth (EAB) can reach up to 10.6 GHz[26]. By optimizing a helical carbon fiber/cement composite system with high-strength EG, EAB can be extended to 13 GHz[10]. When EP is used to optimize a fly ash sintered aggregate/cement composite system, the wave absorption performance exhibiting an effectiveness better than −10 dB can reach a bandwidth of 14 GHz[24]. Among them, vitreous aggregates, as inorganic flame-retardant aggregates, are lightweight, have good wave transmission, and possess high mechanical strength, along with great development potential. However, these studies have only investigated the effects of single vitreous aggregates or aggregates within a narrow particle size range on the microwave absorption performance of cement-based materials, and the absorption frequency bands of cement-based materials lack designability, resulting in poor performance for specific frequency band protection. The correlation between aggregates and absorption frequency bands has not been studied, and there are no criteria for selecting aggregates in the design of absorbing frequency band adjustments.

To address the research gap, various scales and volume ratios of vitreous aggregates were selected to prepare cement-based microwave absorption materials in this work. The correlation between vitreous aggregates and absorption frequency bands within the 1.1–18 GHz frequency range was established, and the influence of aggregates on absorption performance and the absorption mechanism was studied. Additionally, finite element simulation models were employed to visualize the transmission modes of EMWs within the cement-based absorption materials. This work provides a theoretical basis for the design of absorption frequency bands and the selection of vitreous aggregates.

2. Experimental program

2.1. Raw materials, mix design and sample preparation

The raw materials used in the experiment are shown in Table 1.

The XRF and XRD analysis results of the aggregates indicate that the XRD peak patterns are similar, all exhibiting typical amorphous glass diffraction peaks. The chemical compositions obtained from XRF are consistent, varying only in the proportions of the glassy components. Therefore, it can be concluded that all three aggregates are glass media. As shown in Fig. 2, the internal morphology of the three glass media aggregates varies: HG has a hollow structure, while both EG and EP exhibit a honeycomb-like porous structure. Although all lightweight aggregates are composed of the same glass media, their internal structures differ slightly. The porous structure of the glassy phase within the aggregates, along with the gases contained inside, serves as a transparent material for EMWs. The specific effects on EM parameters are illustrated in Fig. 4. Within the frequency range of 1.1–18 GHz, the imaginary parts of the dielectric constant and magnetic permeability are approximately 0, indicating that the aggregates demonstrate no dielectric or magnetic loss. The real part of the dielectric constant is around 2.7, and the real part of the magnetic permeability is approximately 1.25, indicating that the aggregate has basically no EM storage capacity. Therefore, the three types of vitreous aggregate can be regarded as wave-transmitting materials, and the aggregate plays the role of a resonant cavity in the wave absorbing material. In the lateral comparison experiment, the volume ratio of each type of vitreous aggregate is ensured to be the same; in the longitudinal comparison experiment, four different types of vitreous aggregate with apparent volume ratios of 30 %, 40 %, 50 %, and 60 % are selected, and the mix ratios of the prepared samples (per cubic meter) are shown in Table 6, where C# represents the blank group.

Table 1
Raw materials.

Raw materials	Production Place	Property
P·I 42.5 Portland cement	China Building Materials Academy	Table 2
CB (absorbent)	Tianjin Huaran Chemical Co., Ltd., China	Table 3 and Fig. 1
Modified polyether (CB dispersant)	WinBos Chemical Materials Co., Ltd., China	pH (1 % aqueous solution): 7.0–8.0.
Re-dispersible latex powder (RLP)	Anhui Wanwei Huashan New Materials Co., Ltd., China	-
Hydroxypropyl methylcellulose (HPMC)	Qingdao Mingyue Seaweed Group, China	Viscosity: 200,000 mPa·s
Polypropylene fiber (PPF)	Jiangsu Sisi Yuan Fiber Co., Ltd., China	Length: 3–6 mm
Vitreous aggregates	-	Tables 4, 5 and Figs. 2, 3
Deionized water	China Building Materials Academy	-

From Fig. 1 and Table 3, it can be seen that the CB exhibits a chain-like agglomerated structure, with a particle size distribution ranging from 50 to 100 nm. CB is difficult to dissolve in water and tends to agglomerate, so a dispersant needs to be added to prepare a dispersion of CB in water in advance, and then the remaining raw materials are stirred and mixed to prepare the samples. The specific preparation scheme is as follows:

(1) Preparation of CB dispersion: Weighed CB, dispersant, and half of the mass of water are pre-mechanically stirred for 10 min, then ultrasound dispersed for 30 min to obtain a CB dispersion liquid.
(2) Preparation of lightweight cement EMW absorbing slurry: Cement, modifying material, vitreous aggregate, prepared CB dispersion liquid, and the remaining mass of water are uniformly stirred in a cement mortar mixer to obtain slurry with vitreous aggregate surfaces evenly wrapped by cement slurry.
(3) Preparation of test samples: The lightweight cement EMW absorbing slurry is poured into steel molds for: 1) 180 mm × 180 mm × 20 mm for RL testing using the arch method; 2) 40 mm × 40 mm × 160 mm for mechanical performance testing; 3) 300 mm × 300 mm × 30 mm for thermal conductivity testing; 4) filled into waveguide fixtures of 22.9 mm × 10.2 mm × 5.0 mm (X-band, 8.2–12.4 GHz) and 15.8 mm × 7.9 mm × 5.0 mm (Ku-band, 12.4–18 GHz) for EM parameter testing of waveguide samples.
(4) Sample curing: The prepared cement-based EMW absorbing samples are placed in a concrete standard curing box for 28 days of constant temperature and humidity curing.

2.2. Testing methods

The test method is shown in Fig. 5.

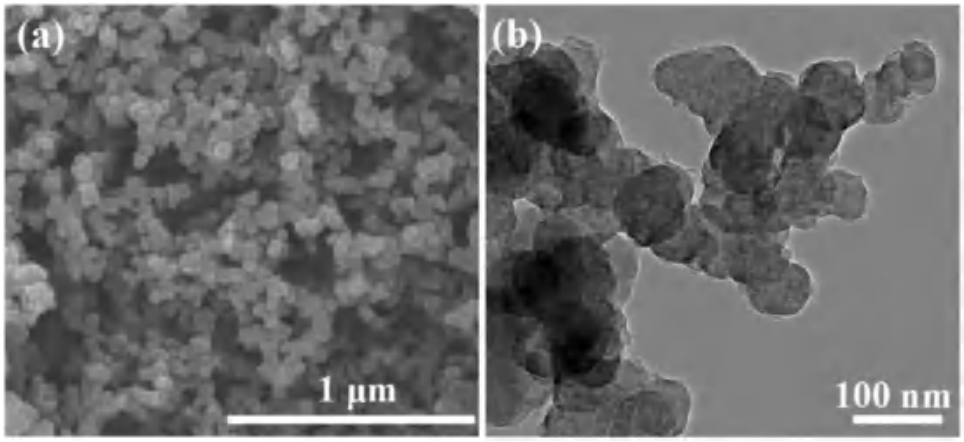

Fig. 1. SEM (a) and TEM (b) diagrams for CB.

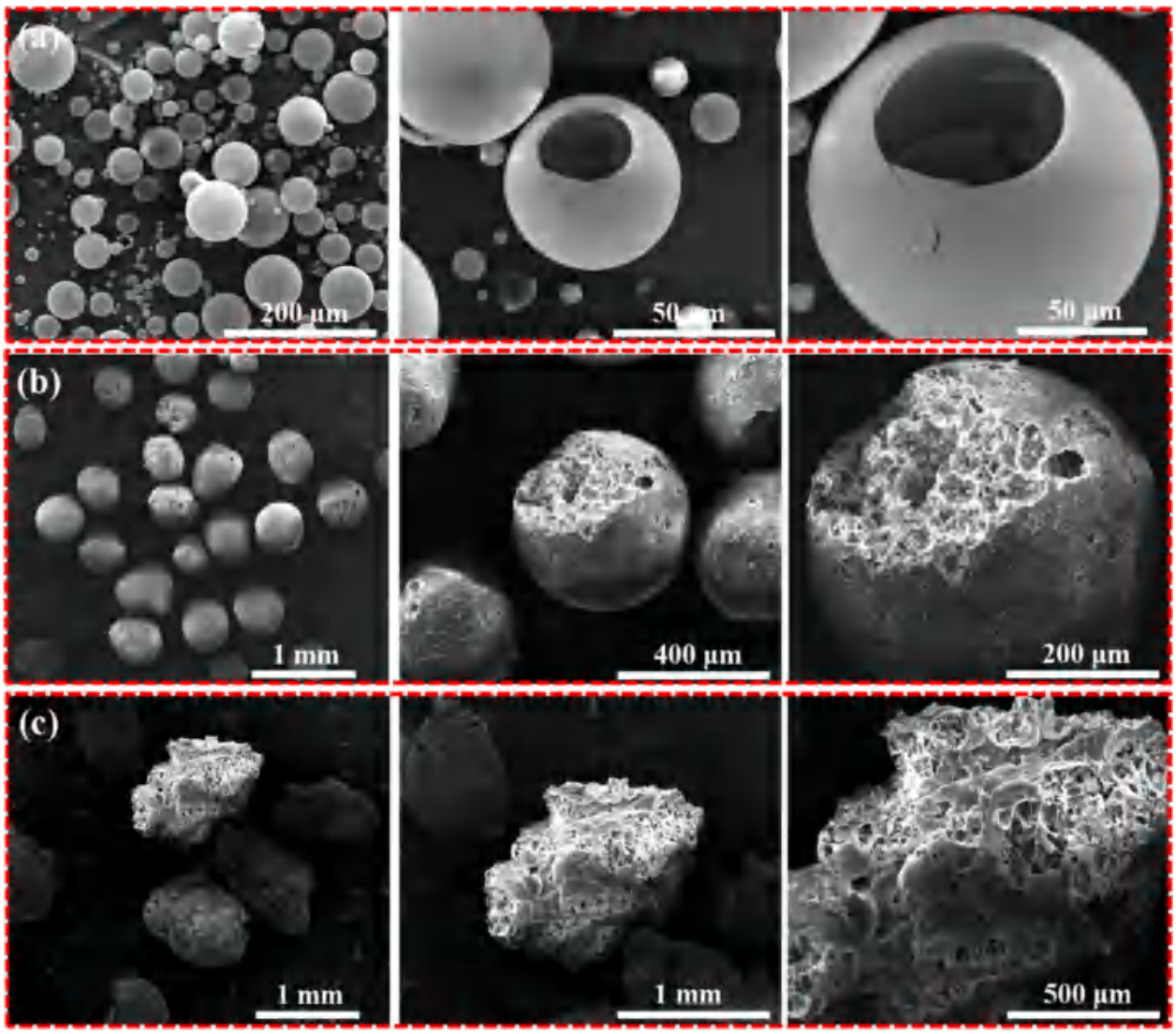

Fig. 2. SEM diagrams of HG (a), EG (b) and EP (c).

2.2.1. EM performance testing

The RL test of lightweight cement-based EMW absorbing materials is conducted using the arch reflection method in a microwave darkroom, with a test frequency range of 1.1–18 GHz. The EM parameters are measured using the waveguide method according to the Chinese standard GB/T 35679–2017 <Measuring method for electromagnetic parameters of solid materials at microwave frequencies using waveguide>, with a test frequency range of 8.2–18 GHz. The

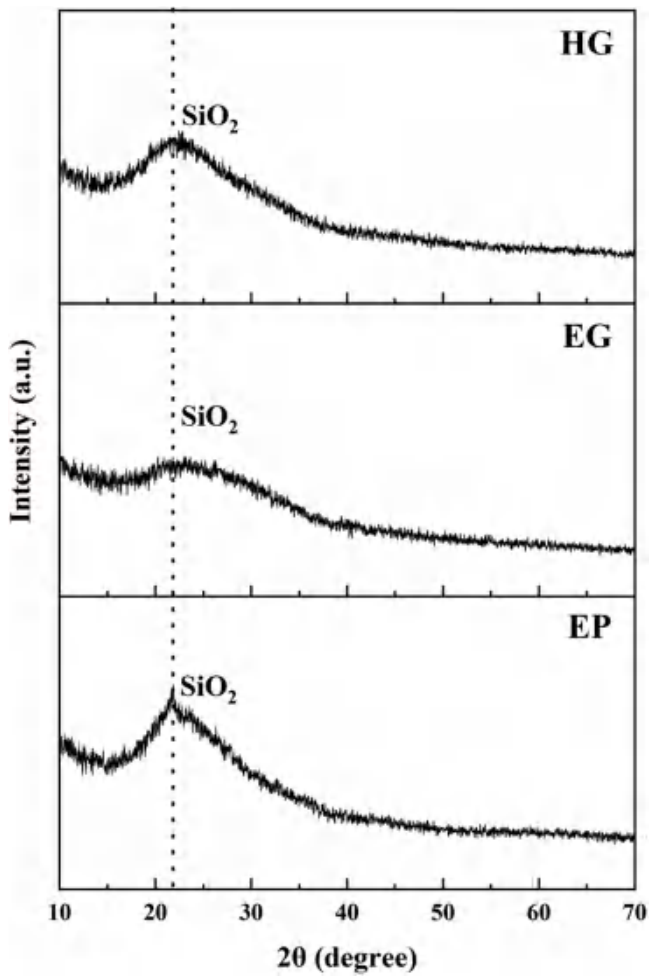

Fig. 3. The XRD characterizations of HG, EG, and EP.

conductivity is measured using the four-electrode voltammetry method, which can eliminate the contact resistance between the electrodes and the cement matrix, avoiding polarization effects[27]. The resistance (R) is calculated by $R = U/I$, where U is the voltage between the test electrodes and I is the current flowing through the sample. The electrical resistivity (ρ) is calculated by $\rho = RS/L$, where S is the contact area between the copper plate and the sample, L is the distance between two copper plates. The electrical conductivity (σ) is calculated by $\sigma = 1/\rho$.

2.2.2. Mechanical and thermal conductivity performance testing

Mechanical performance testing is conducted according to the test methods specified in the Chinese standard GB/T 17671–2021 <Test method of cement mortar strength> . Thermal conductivity is measured according to the test methods specified in the Chinese standard GB/T 10294–2008 <Thermal insulation - Determination of steady-state thermal resistance and related properties - Guarded hot plate apparatus> .

3. Results and discussion

3.1. Absorption mechanism of EMW

Based on the transmission line theory, the EMW absorbing perfor-

Table 3
Physical and chemical properties of CB.

Resistivity (Ω·cm)	Particle size (nm)	Apparent density (g/cm^3)	Ash content	Iodine adsorption (g/kg)	Specific surface area (m^2/g)
2.0	50–100	0.2–0.3	≤ 0.2 %	≥ 280	120

Table 4
Basic properties of vitreous aggregates.

Name of vitreous aggregates	Particle size	Packing density
Expanded perlite (EP)	0.8–1.9 mm	160 kg/m^3
Expanded glass beads (EG)	0.3–0.7 mm	270 kg/m^3
Hollow glass beads (HG)	20–125 μm	170 kg/m^3

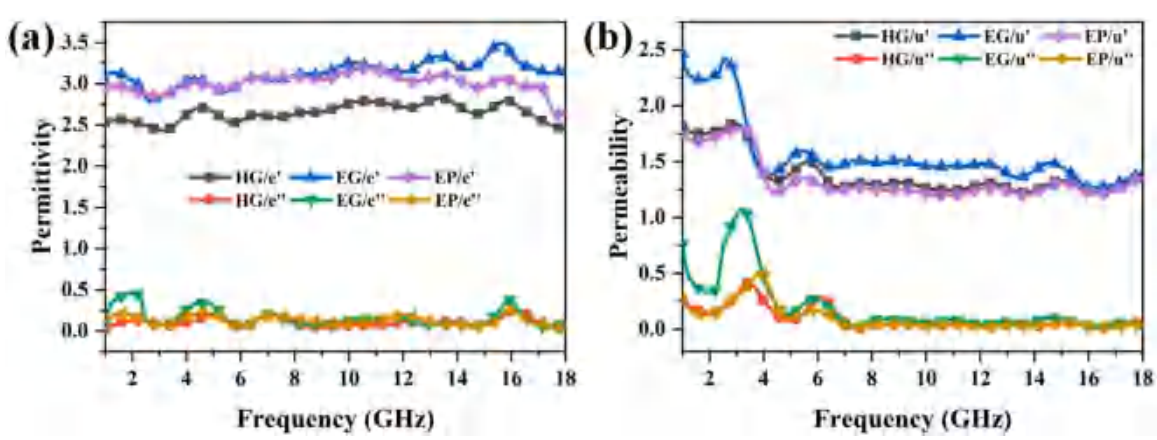

Fig. 4. Electromagnetic parameters of vitreous aggregates.

Table 2
Basal properties of Portland cement.

Fineness 0.08/%	Specific surface area/ m^2·kg^{-1}	Density/g·cm^{-3}	Initial setting time/min	Final setting time/min	Flexural strength/ MPa			Compressive strength/ MPa		
					3d	7d	28d	3d	7d	28d
0.6	358	3.11	105	168	5.4	6.6	8.3	25.8	35.2	50.5

Table 5
Chemical composition of HG, EG and EP (by mass).

Component	SiO_2	Na_2O	CaO	K_2O	Al_2O_3	MgO	Others
	Content (%)						
HG	80.572	11.897	5.701	0.02	0.382	0.108	1.32
EG	69.935	16.378	6.926	0.52	2.846	2.42	0.975
EP	74.237	4.562	0.597	3.672	15.733	0.218	0.981

Table 6
Mix design of cement-based EMW absorbing materials (per cubic meter).

Samples ID	Cement/kg	HPMC/kg	RLP/kg	Water reducer/kg	PPF/kg	CB/kg	Dispersant/kg	VR/m^3	Water/kg
C#	1850	9.2	9.2	13.8	9.2	37	7.4	0	1110
1#HG/1#EG/1#EP	1295	6.4	6.4	9.7	6.4	26	5.2	0.3	777
2#HG/2#EG/2#EP	1110	5.5	5.5	8.3	5.5	22	4.4	0.4	666
3#HG/3#EG/3#EP	925	4.6	4.6	6.9	4.6	19	3.8	0.5	555
4#HG/4#EG/4#EP	740	3.7	3.7	5.5	3.7	15	3	0.6	444

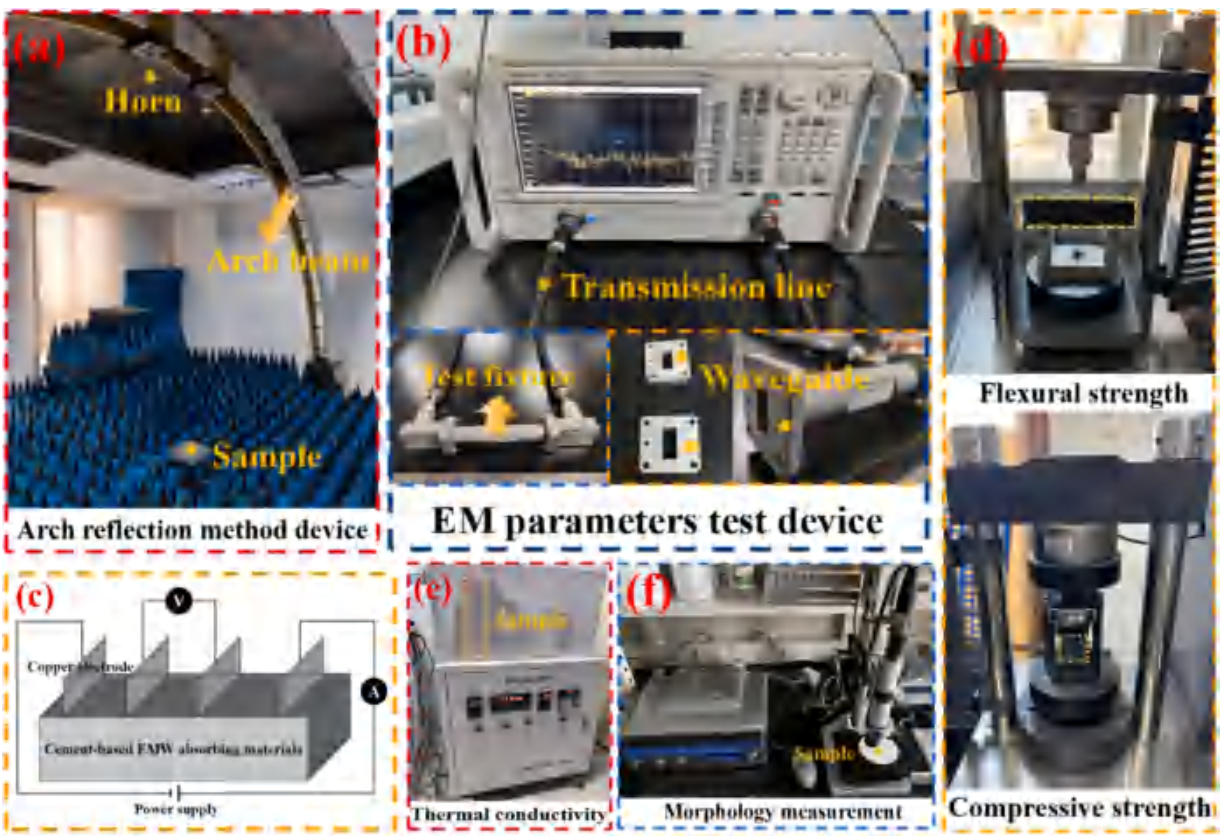

Fig. 5. Test systems of arching reflected method (a), waveguide method (b), electrical conductivity (c), mechanical properties (d), thermal conductivity (e), and morphology measurement (f).

mance of the absorbing material can be expressed by RL (dB), as shown in Eq. (1):

$$RL = 20\lg\left|\frac{Z_{in} - Z_0}{Z_{in} + Z_0}\right| \tag{1}$$

$$Z_0 = \sqrt{\frac{\mu_0}{\varepsilon_0}} \tag{2}$$

$$Z_{in} = Z_0\sqrt{\frac{\mu_r}{\varepsilon_r}}\tanh\left(j\frac{2\pi f}{c}d\sqrt{\mu_r\varepsilon_r}\right) \tag{3}$$

Where Z_o (Z_o =377 Ω) is the characteristic impedance of the free space, Z_{in} is the input impedance of the absorbing material; μ_o and ε_o stand for the complex permeability and complex permittivity of the free space, respectively; μ_r and ε_r stand for the complex permeability and complex permittivity of the absorbing material, respectively. f indicates the frequency of the incident wave, d designates the thickness of the absorbing material, c is the velocity of light, j is the imaginary unit.

According to Eqs. (1)-(3), it can be seen that the EMW attenuation loss capacity of the absorbing material is affected by the complex permeability (μ_r=μ'-$j\mu''$) and complex permittivity (ε_r=ε'-$j\varepsilon''$). The real part μ' and ε' indicate the capacity of magnetic and electric energy storage, while the imaginary part μ'' and ε'' stand for the magnetic and electric energy dissipation capacity. This can be used to define the magnetic loss factor (tan [[__]]#948;$_\mu$=μ''/μ') and dielectric loss factor

(tan [[__]]#948;$_e$=$\varepsilon''/\varepsilon'$), where the higher the values of tan [[__]] #948;$_\mu$ and tan [[__]]#948;$_e$ of the absorbing material, the stronger the EM loss capability.

The RL curve of EMW absorbing materials has many absorption peaks, which are related to the thickness and EM parameters of the material, as shown in Eq. (4). The theory of EMW interference and cancellation can also be explained using this equation, which can guide the design of the thickness of absorbing materials.

$$f_m = \frac{(2n+1)c}{4d\sqrt{\varepsilon_r \mu_r}}; \left(n = 0, 1, 2, \ldots\right) \tag{4}$$

Where f_m is the frequency corresponding to the absorption peak, d is matching thickness.

When the input impedance (Z_{in}) of the EMW absorbing material is close to the characteristic impedance (Z_o) of the free space, a large number of EMWs can enter the absorbing material and the reflectivity is reduced, indicating that the absorbing material has excellent impedance matching performance. Therefore, EMW absorbing materials with excellent performance need to satisfy both excellent impedance matching performance and high EMW loss capability. The impedance matching performance is described in Eq. (5):

$$Z = |Z_{in}/Z_0| = \sqrt{\frac{\mu_r}{\varepsilon_r}} \tanh\left(j\frac{2\pi f}{c} d\sqrt{\mu_r \varepsilon_r}\right) \tag{5}$$

When Z approaches 1, it indicates that the EMW absorbing material has optimal impedance matching performance, and almost all incident EMWs can transmit into the absorbing material.

3.2. Absorbing properties of EMW absorbing materials

3.2.1. Reflection loss

The RL of blank group and the lightweight cement-based EMW absorbing materials prepared with three types of vitreous aggregates—HG, EG, and EP—at different particle sizes and volume ratios were tested using the arch reflection method (Fig. 6a and Fig. 7). The thickness of the samples was 20 mm. According to the analysis of Fig. 6(a), when the cement paste is mixed with CB, which accounts for 2 % of the cement mass, the EMW absorbing material exhibits a significant absorption peak at a lower frequency of around 4.5 GHz, while the peak absolute value of the absorption peak at higher frequencies is relatively small. Overall, the EMW absorbing performance of the material is better at lower frequencies. The analysis reveals that the variation trend of the RL curve for lightweight cement-based EMW absorbing materials can be divided into two stages (Fig. 7), outlined by green and blue rectangles. It is evident that among the three types of lightweight EMW absorbing materials, as the volume ratio of vitreous aggregates increases, the frequency points corresponding to the absorption peaks of the RL curve generally shift towards higher frequencies. For the three different particle sizes of EMW absorbing materials, the changes in the RL curve indicate that with an increase in the volume proportion of vitreous aggregates, the variation trend of the RL curve can also be divided into two segments: 1) At lower frequencies, as the volume proportion of vitreous aggregates increases, the RL curve shifts positively along the Y-axis, indicating an increase in RL values and a decrease in wave absorption performance. As the frequency of EMWs shifts to higher values, the RL curve shows an opposite trend. At the lower frequency of 5.54 GHz, the optimal RL value is −16.1 dB. 2) At higher frequencies, as the volume proportion of vitreous aggregates increases, the RL curve shifts negatively along the Y-axis, leading to a decrease in RL values and an enhancement in wave absorption performance. At the higher frequency of 8.4 GHz, the optimal RL value is −16.3 dB. Therefore, the trends in wave absorption materials with different volume proportions of vitreous aggregates vary across different frequency ranges. To achieve excellent absorption performance at lower frequencies, the absorbent materials with low volume of light aggregate can be selected at lower frequencies; conversely, at higher frequencies, opting for materials with a higher proportion can yield better absorption results. However, there is an optimal range for the volume of vitreous aggregates, which needs to be determined in conjunction with the effective bandwidth of absorption discussed later. Comparison with the blank group shows that the inclusion of vitreous aggregates results in superior absorption performance across the entire frequency range, particularly at high frequencies where performance is significantly enhanced.

From the EM parameters shown in Fig. 4, it can be seen that the three types of vitreous aggregates are light and wave-permeable aggregates, with a complex permittivity of (2.75 ± 0.25)-0j and a complex permeability of (1.25 ± 0.2)-0j. They exhibit minimal EM loss ability for EMWs. Incorporating these aggregates into a dense cement matrix can optimize the EM parameters of the cement matrix and improve its impedance matching performance[23–25]. According to the Bruggeman's theory, the optimized equivalent permittivity is[28,29]:

$$\varepsilon_{eff} = \varepsilon_e + 3\varepsilon_{eff} f_i (\varepsilon_i - \varepsilon_e) / (\varepsilon_e + 2\varepsilon_{eff}) \tag{6}$$

In the equation: ε_{eff} represents the equivalent dielectric constant; ε_i is the dielectric constant of the aggregate; f_i denotes the volumetric fraction of the aggregate; ε_e refers to the dielectric constant of the homogeneous medium (here, the cement matrix). The EM parameters of cement slurry matrices are relatively high, indicating a capacity for electromagnetic loss. However, due to their dense structure, they exhibit poor impedance matching, making it difficult for EMWs to penetrate the interior of the cement matrix. This limitation restricts the loss ability of the cement matrix to dissipate EMWs, thus the wave-absorbing performance is limited. After the cement matrix is mixed with wave-absorbing aggregate, the Bruggeman's formula indicates that as the volume ratio of vitreous aggregates increases, the dielectric constant of the cement matrix gradually decreases. When the vitreous aggregates are evenly

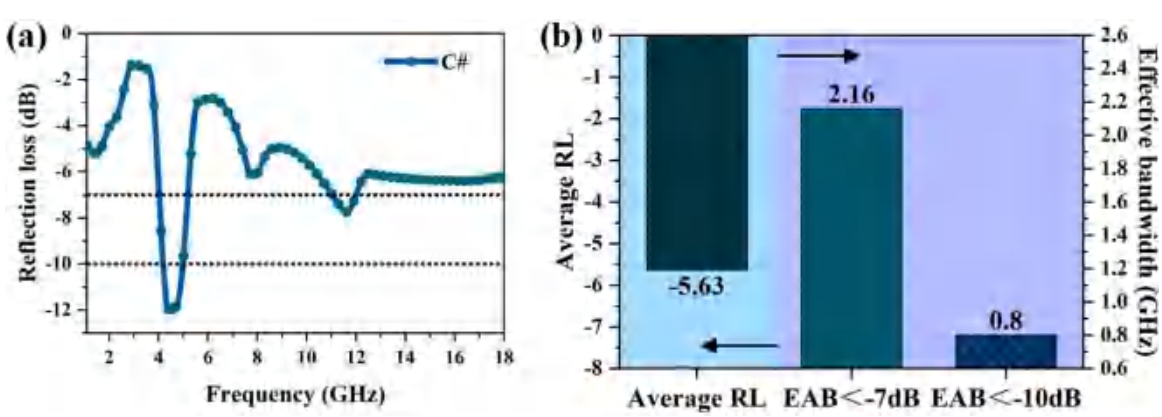

Fig. 6. EMW absorbing properties of blank group.

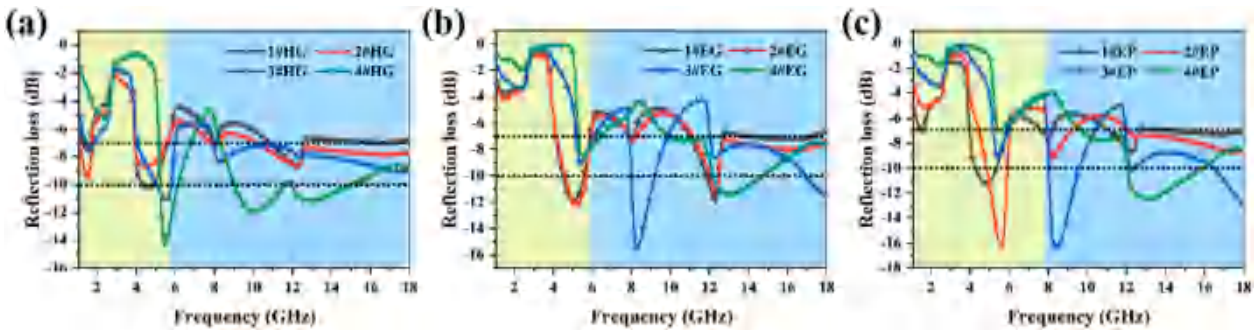

Fig. 7. RL curves of lightweight cement-based EMW absorbing materials (Different ratios).

distributed within the cement matrix, it facilitates the entry of EMWs into the cement matrix, reduces the reflection of these waves at the surface, and allows for greater absorption of EMWs within the absorbing material, thereby enhancing the wave absorption performance. According to Eq. (4), the reduction in dielectric constant resulting from the addition of vitreous aggregates leads to an increase in the absorption peak frequency f_m, which supports the observation that a higher volume ratio of vitreous aggregates shifts the absorption peak towards higher frequencies.

Fig. 8 shows that, at the same volume ratio of vitreous aggregate, as the particle size gradually increases from micrometers to millimeters, the frequency points corresponding to the RL absorption peaks shift towards higher frequencies in the 1.1–18 GHz range, and the EMW absorbing performance in the high-frequency range is enhanced. The trend of the RL curve, as the size of the vitreous aggregate increases, can be divided into two distinct stages: 1) At lower frequencies, the RL value of the EMW absorbing material made from small particle size vitreous aggregates is relatively low, indicating that EMW absorbing materials with small particle size vitreous aggregates perform better in low-frequency ranges; 2) At higher frequencies, the EMW absorbing material made from large particle size vitreous aggregates also shows a lower RL value, suggesting that EMW absorbing materials with large particle size vitreous aggregates perform better at high frequencies. Based on this, when designing and selecting EMW absorbing materials, the particle size of vitreous aggregates can be chosen based on the target frequency band for EM protection.

Due to the uniform thickness of the samples being 20 mm, it can be inferred from Eq. (4) that the trend of the frequency points corresponding to the absorption peaks is significantly related to the EM parameters of the absorbing materials, which are related to the aggregate ratio and particle size. According to the scattering mechanism of EMWs, the scattering methods are primarily categorized into Rayleigh

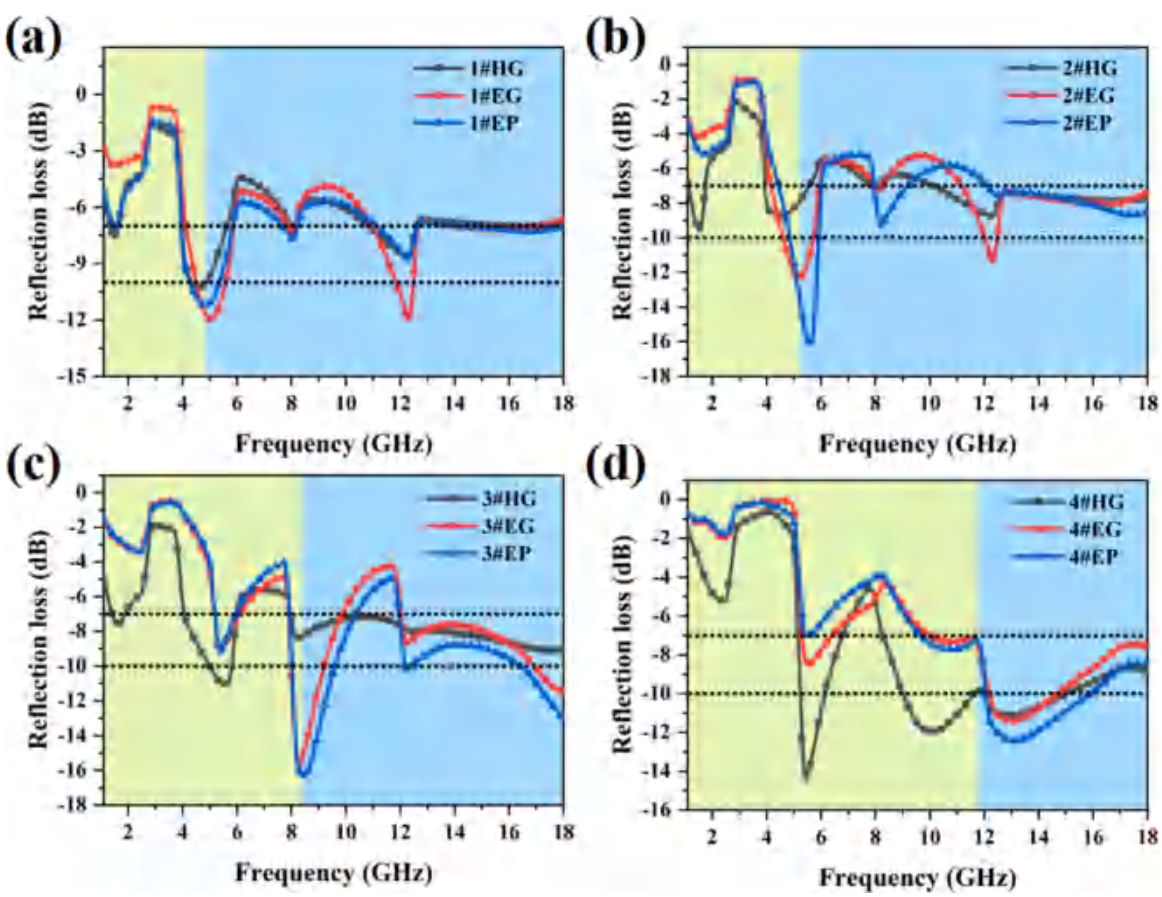

Fig. 8. RL curves of lightweight cement-based EMW absorbing materials (Different aggregates).

scattering and Mie scattering[30], with the determination formula given by $\alpha = 2\pi r/\lambda$, where α is the scattering determination factor, r is the aggregate radius, and λ represents the wavelength of electromagnetic wave. From the relationship between the radius of vitreous aggregates and frequency, it can be calculated that when in the low-frequency range, $\alpha << 0.1$, Rayleigh scattering predominates in EMW scattering. Additionally, the smaller the aggregate particle size, the more frequent the Rayleigh scattering occurs; therefore, vitreous aggregates with small particle sizes exhibit better wave-absorbing performance. Furthermore, Rayleigh scattering does not significantly affect the transmission path of EMWs[31], which is why the RL curve waveform of HG vitreous aggregate EMW absorbing materials is similar to that of the blank group. When in the high-frequency range, $\alpha > 0.1$, Mie scattering predominates in EMW scattering. As the aggregate particle size increases from the micron scale to the millimeter scale, larger particle sizes are closer to the wavelength of EMWs in the centimeter range at high frequencies, resulting in more frequent Mie scattering. Thus, vitreous aggregates with larger particle sizes demonstrate better EMW absorbing performance. Mie scattering can cause significant energy loss to EMWs, affecting their transmission path and resulting in sharper absorption peaks at high frequencies[32], which supports the observation that larger aggregate particle sizes lead to absorption peaks shifting towards the high-frequency direction.

The average RL values of the EMW absorbing materials in the frequency range of 1.1–18 GHz were statistically analyzed (Fig. 9). It can be observed that the average RL of EMW absorbing materials with different particle sizes varies little within the frequency range of 1.1–18 GHz, with discrepancies not exceeding −1.54 dB. This is due to the varying EMW protective capabilities of absorbing materials with different aggregate particle sizes and volume ratios, which emphasize either high or low-frequency performance. However, the protective efficacy is balanced across the entire EMW frequency spectrum. Consequently, a similar wave absorption protection effect is exhibited throughout the frequency range of 1.1–18 GHz. To achieve optimal protective effects at either low or high frequencies, it is necessary to select the aggregate proportions or particle sizes based on the specific EMW frequency range. Additionally, a comparison with the blank group in Fig. 6(b) indicates that regardless of the type of vitreous aggregate added, the average RL is superior to that of the blank group.

3.2.2. Effective absorbing bandwidth

The effective absorption bandwidth (EAB) reflects the actual protective frequency range of the EMW absorbing materials that meets specific absorption rates within the tested frequency band. Typically, EAB is indicated by an RL of less than −7 dB (over 80 % EMW absorption rate) or an RL of less than −10 dB (over 90 % EMW absorption rate). Therefore, the EAB is statistically analyzed for both absorption rates (Fig. 10). It can be observed that in both protective frequency ranges for different absorption rates, the overall trend shows that as the volume ratio of vitreous aggregates increases, the EAB also increases. When the RL is less than −7 dB, the EAB of the EMW absorbing materials is relatively wide at a vitreous aggregate volume ratio of 50 %, reaching a maximum of 12.4 GHz. Meanwhile, when the RL is less than −10 dB, the EAB almost consistently increases with the increase in the volume ratio of vitreous aggregates, and the widest protective frequency range can reach 6.57 GHz. Combining the EAB of the blank group in Fig. 6(b), it can be seen that the EAB of the EMW absorbing materials with the addition of vitreous aggregates is almost always greater than that of the blank group. The inclusion of vitreous aggregates can broaden the frequency range of the EMW absorbing materials at specific absorption rates, enhancing the EMW protection effect. By correlating the RL statistical results from Fig. 6 and Fig. 7, it is evident that when the RL is less than −7 dB, the EMW absorbing materials can achieve effective protection in both high and low frequency ranges, with the size and volume ratio of the aggregates having little impact on the EAB. However, when the RL is less than −10 dB, the EMW absorbing materials can only

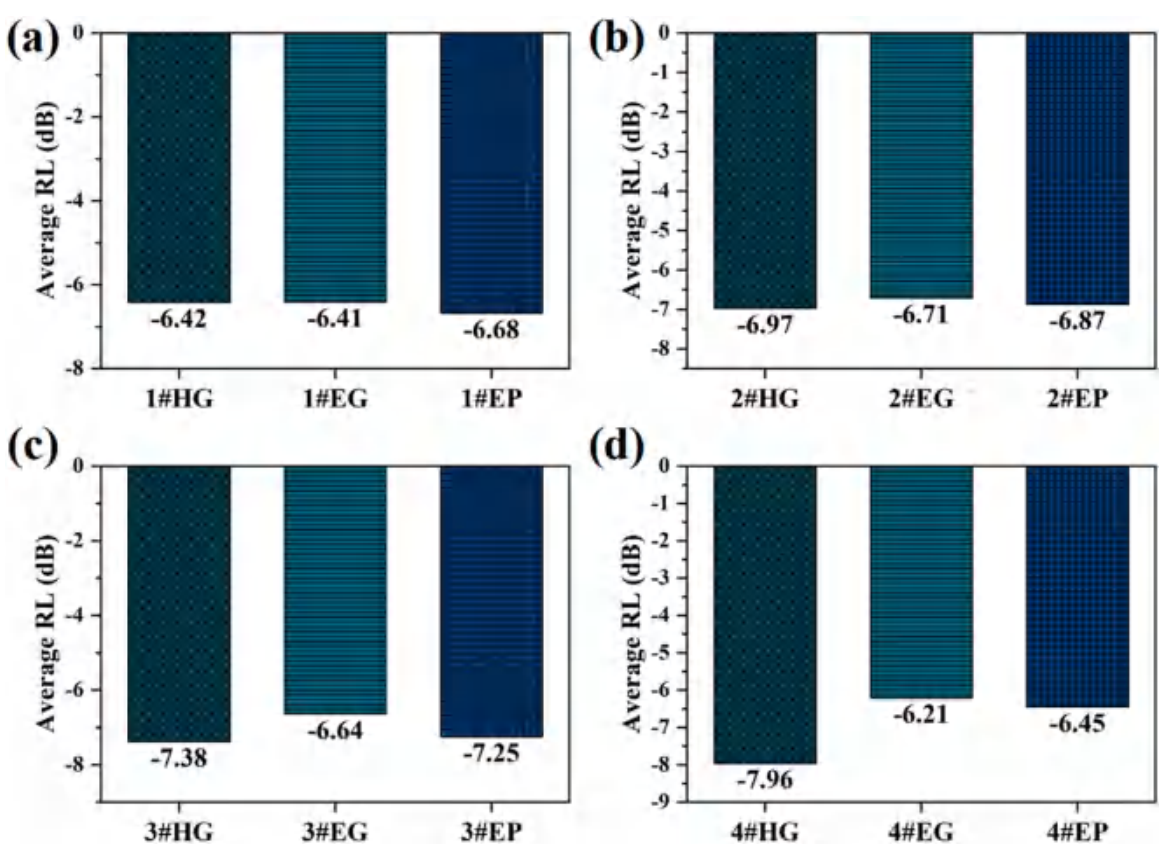

Fig. 9. Average RL of lightweight cement-based EMW absorbing materials.

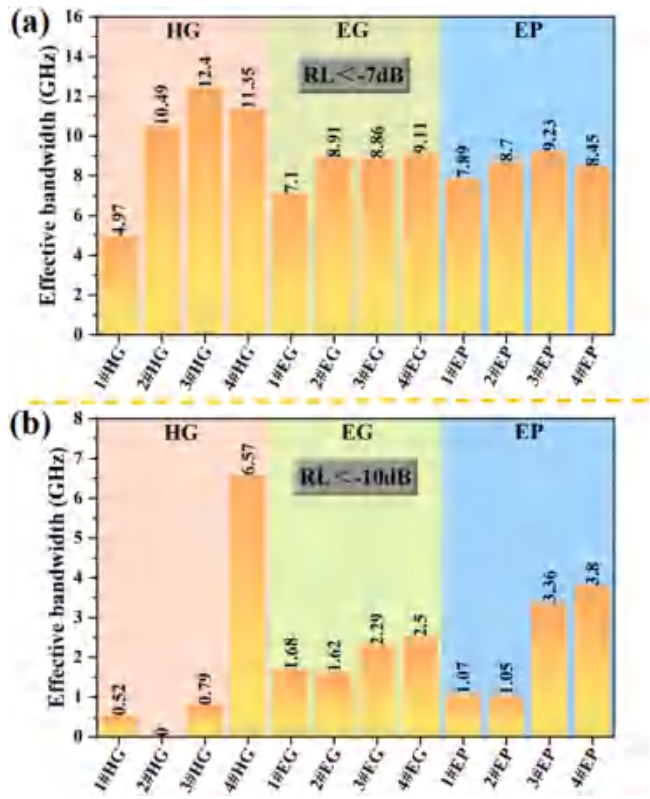

Fig. 10. EAB of lightweight cement-based EMW absorbing materials.

provide effective protection at high frequencies, while the protection effect at low frequencies is relatively weak. Moreover, the larger the aggregate particle size or the higher the volume ratio of the aggregates, the better the EMW absorbing performance at high frequencies, resulting in a wider EAB. Therefore, the selection of vitreous aggregate particle size and volume ratio can be made based on EMW protection requirements.

3.3. EM parameter of EMW absorbing materials

The complex permittivity and complex permeability primarily arise from the polarization and magnetization of the EMW absorbing medium. The tangent of the dielectric loss angle and the tangent of the magnetic loss angle reflect the energy dissipation capability of EMWs [33]. Due to the non-magnetic nature of the raw materials, the complex permeability of the EMW absorbing materials is 1–0j, and the tangent of the magnetic loss angle is 0, indicating that the material has no magnetic loss performance. The complex permittivity of the EMW absorbing materials in the X and Ku frequency bands was tested, as shown in Fig. 11. It can be observed that for the three types of EMW absorbing materials, as the volume ratio of the aggregates increases, both the real and imaginary parts of the complex permittivity decrease. The real part of the complex permittivity shows a significant decline, while the imaginary part decreases to a lesser extent. The range of variation for the complex permittivity is from 2.9–0.4j to 6.1–1.8j. It can be confirmed that with the substantial incorporation of vitreous aggregates with low dielectric constants, the overall complex permittivity of the cement-based materials is significantly reduced. The dielectric loss capability of the cement-based materials will decrease as the complex permittivity decreases. However, the impedance matching performance of the EMW absorbing materials is enhanced. Plotting the tangent of the dielectric loss angle can support the above statement, as the tangent of the dielectric loss angle gradually decreases with the increasing gradient of vitreous aggregate incorporation. From the perspective of the tangent of the dielectric loss angle alone, the dielectric loss capability of the EMW absorbing materials decreases. However, the measured RL values decrease, indicating an improvement in EMW absorbing performance. Therefore, it is necessary to consider the promoting effect of the impedance matching role of vitreous aggregates on EMW absorbing performance, which will be discussed in the next section.

The Bruggeman equivalent dielectric constant formula indicates that the complex dielectric constant of EMW absorbing materials with the same volume ratio of vitreous aggregates should theoretically be the same. However, in actual tests, although the complex dielectric constants of the three types of vitreous aggregates are essentially consistent, the complex dielectric constants of the EMW absorbing materials differ when the volume ratio of the vitreous aggregates is the same, exhibiting a consistent pattern. This discrepancy is primarily related to the radius sizes of the vitreous aggregates. When EMWs of the same wavelength pass through vitreous aggregates of different radii, the presence of Rayleigh scattering and Mie scattering causes the EMWs to undergo different paths of refraction, scattering, and reflection within the vitreous aggregates, affecting the output EMW signal. As a result, the measured EM parameters are influenced, which in turn affects the wave-absorbing performance. With a fixed volume ratio of 60 % vitreous aggregates, the measured values of the complex dielectric constants for three types of EMW absorbing materials are shown in Fig. 12. It can be observed that in the X and Ku bands, as the aggregate particle size gradually increases from the micron level to the millimeter level, the real part of the complex dielectric constant decreases, while the imaginary part shows no obvious pattern. However, by calculating the dielectric loss tangent, it can be visually observed that the aggregate particle size has combined effects on both the real and imaginary parts of the complex dielectric constant. Within a specific range of particle sizes, such as the transition from the micron level to the millimeter level, this will lead to an enhancement of the ability to dissipate dielectric losses from EMWs. This supports the observation that with a fixed volume ratio, as the aggregate particle size increases, the RL of the EMW absorbing material decreases, enhancing its EMW absorbing performance.

3.4. Impedance matching performance of EMW absorbing materials

As shown in formula (5), the impedance matching performance can be used to measure the ease with which EMWs in free space enter the interior of EMW absorbing materials. Normalized impedance is used to describe the intrinsic impedance matching between free space and the EMW absorbing materials. The closer Z is to 1, the better the impedance matching performance of the material. When Z equals 1, it indicates that EMWs can completely enter the material at this frequency point. From the normalized impedance of the EMW absorbing materials in the X and Ku bands shown in Fig. 13, it can be observed that as the volume ratio of the aggregates increases, the normalized impedance of the EMW absorbing materials approaches 1. This indicates that the impedance matching performance of the EMW absorbing materials improves, resulting in a reduction in the frequency of EMW reflections, making it easier for EMWs to enter the cement matrix and be dissipated. At the maximum volume ratio of the aggregates, perfect matching with free space is even achieved at certain frequency points, allowing EMWs to completely enter the EMW absorbing materials and be dissipated. This supports the observed trend in the RL curve. Although the tangent of the dielectric loss angle of the EMW absorbing materials decreases, the promoting effect of impedance matching enhances the macroscopic EMW absorbing performance.

The previous text mentions that the scattering mechanism of EMW is affected by aggregate particle size. At low frequencies, Rayleigh scattering predominates with small particle size aggregates, while at high frequencies, Mie scattering predominates with large particle size aggregates. Therefore, although it can be theoretically deduced from the Bruggeman equivalent dielectric constant formula that the dielectric

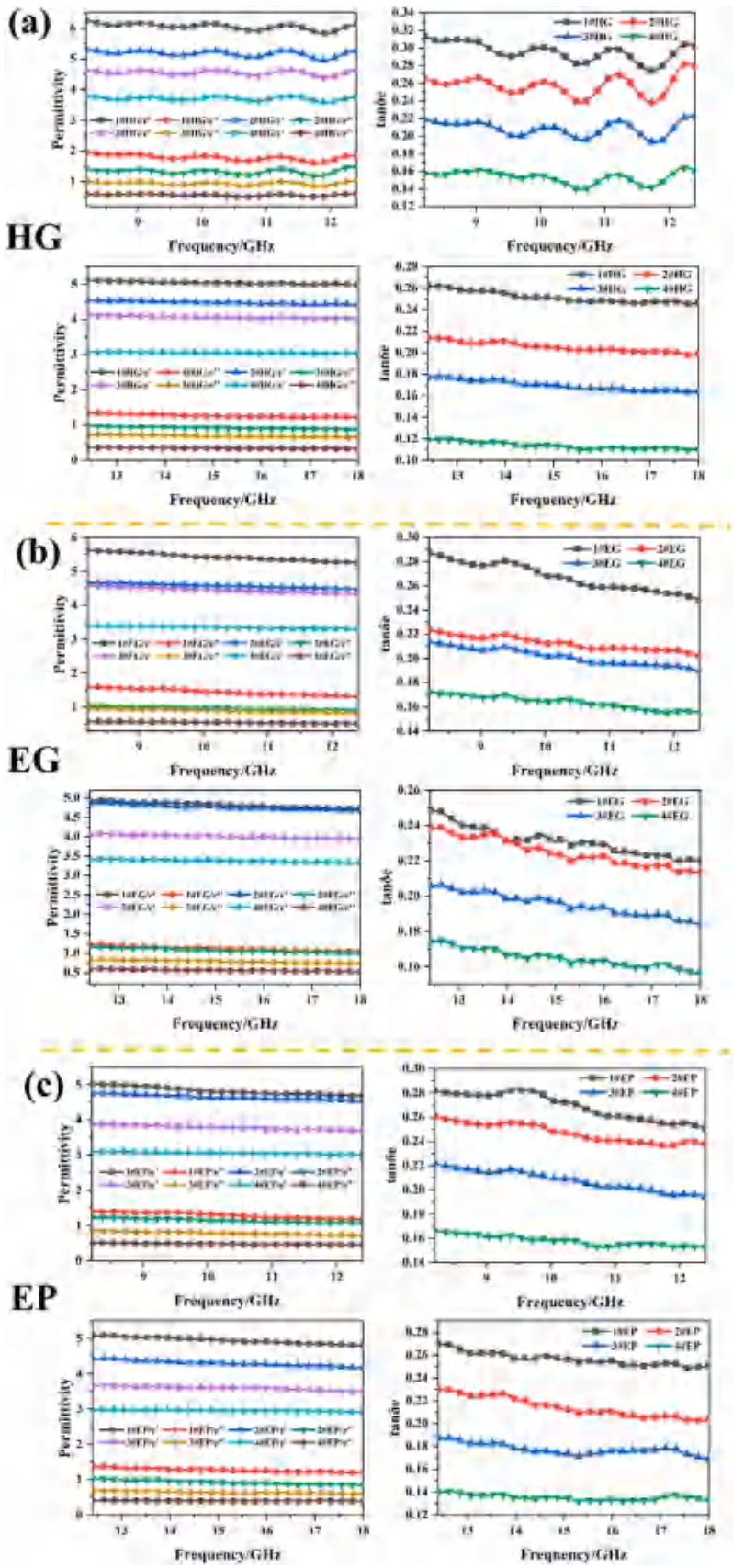

Fig. 11. Complex dielectric constants of absorbing materials in X and Ku bands.

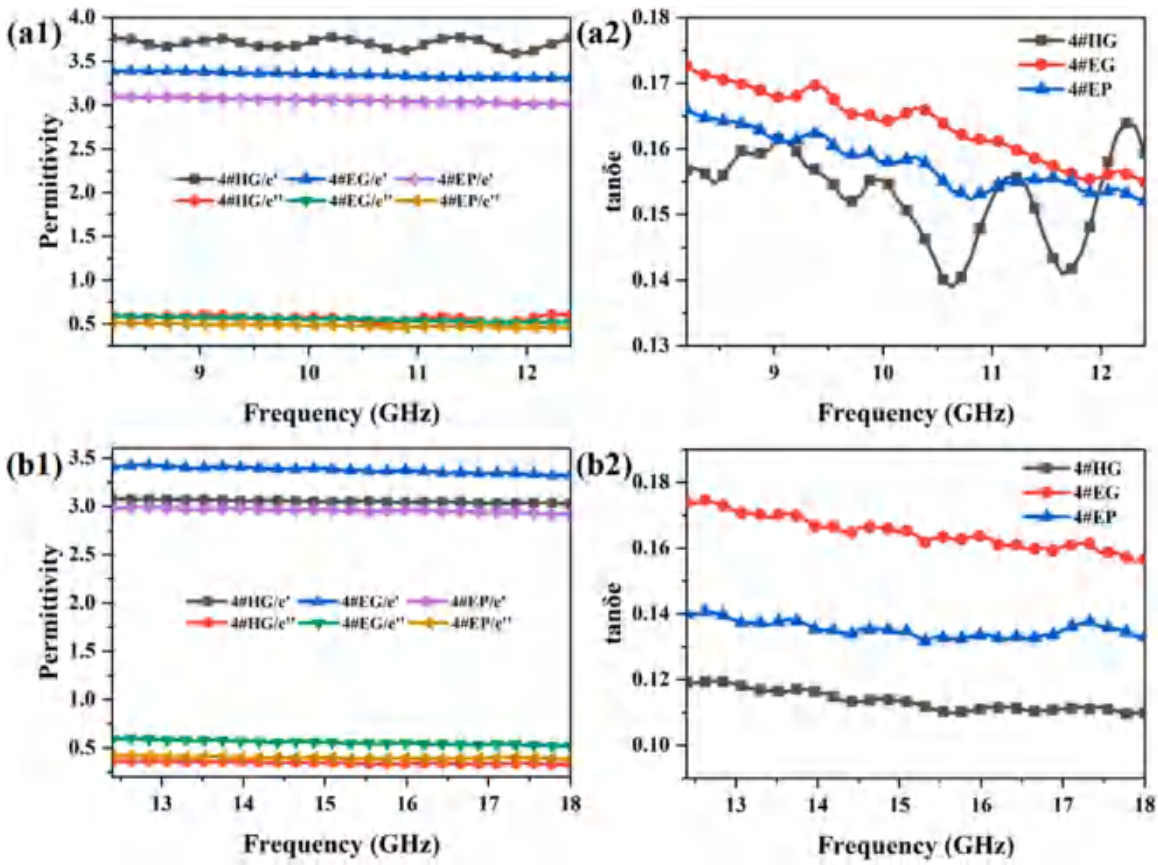

Fig. 12. Complex permittivity of absorbing materials at 60 % volume ratio.

constants of absorbing materials are consistent, leading to consistent impedance matching, in reality, the scattering mechanism of EMW is affected by the particle size of aggregate. This results in different dielectric constants, which in turn leads to varying degrees of impedance matching. From the normalized impedance in Fig. 14, with a fixed aggregate volume of 60 %, it can be observed that as the aggregate particle size increases, the peak position of the normalized impedance curve shifts towards higher frequencies. Larger aggregate sizes lead to better impedance matching at high frequencies, supporting the notion that an increase in particle size enhances high-frequency wave absorption performance. Conversely, reducing the particle size results in better impedance matching at low frequencies, thereby enhancing low-frequency wave absorption performance. The variation of the EM parameters of the measured absorbing materials is in good agreement with the RL curve changes obtained from the arc reflection method.

3.5. Cole-Cole curve of EMW absorbing materials

CB is a dielectric material, and in vitreous aggregate absorbing materials with added CB, the attenuation of EM energy is primarily due to the dielectric loss mechanism. Dielectric loss includes interfacial polarization loss and resistive loss[34]. According to Debye relaxation theory [35], the complex dielectric constant can be described as:

$$\varepsilon = \varepsilon_\infty + \frac{\varepsilon_s - \varepsilon_\infty}{1 + 2\pi f \tau \cdot j} = \varepsilon' - j\varepsilon'' \tag{7}$$

ε_s is the static dielectric constant, ε_∞ is the dielectric constant at high-frequency limits, and τ represents the polarization relaxation time. ε' and ε'' can be expressed as[36–38]:

$$\varepsilon' = \varepsilon_\infty + \frac{\varepsilon_s - \varepsilon_\infty}{1 + (2\pi f \tau)^2} \tag{8}$$

$$\varepsilon'' = \frac{2\pi f \tau(\varepsilon_s - \varepsilon_\infty)}{1 + (2\pi f \tau)^2} \tag{9}$$

For CB, a typical dielectric material, dielectric loss primarily arises from polarization effects. In a periodic EM field, the electric dipoles in CB rotate repeatedly, which can consume the energy of the incident EMWs, resulting in relaxation polarization[39]. According to the Debye relaxation theory, the relationship between ε' and ε'' can be represented by the Cole-Cole curve[36,40]:

$$\left(\varepsilon' - \frac{\varepsilon_s + \varepsilon_\infty}{2}\right)^2 + (\varepsilon'')^2 = \left(\frac{\varepsilon_s - \varepsilon_\infty}{2}\right)^2 \tag{10}$$

This formula is defined as the Cole-Cole semicircle, reflecting the Debye relaxation process. Figs. 15–17 show the Cole-Cole semicircle curves for the blank group and vitreous aggregate cement-based absorbing materials in the X and Ku frequency bands. The frequency bands in the figures correspond to the higher frequency portions of the RL curve graphs, where only the matching of the polarization loss mechanism and reflection loss at higher frequencies is analyzed. It can be observed that there are multiple semicircles in the Cole-Cole curve, indicating the presence of a significant amount of strong relaxation polarization loss mechanisms[41,42]. A horizontal comparison of the data reveals that the greater the amount of vitreous aggregate, the more semicircles appear in the Cole-Cole curve, indicating stronger relaxation polarization loss, which supports the notion that more aggregate leads to better wave absorption performance. When comparing the same aggregate content, a vertical comparison of the impact of aggregate particle size on the Cole-Cole curve shows that as the particle size of the vitreous aggregate increases, more semicircles appear in the Cole-Cole curve, indicating stronger relaxation polarization loss, which supports the notion that larger aggregate particle sizes result in better wave absorption performance.

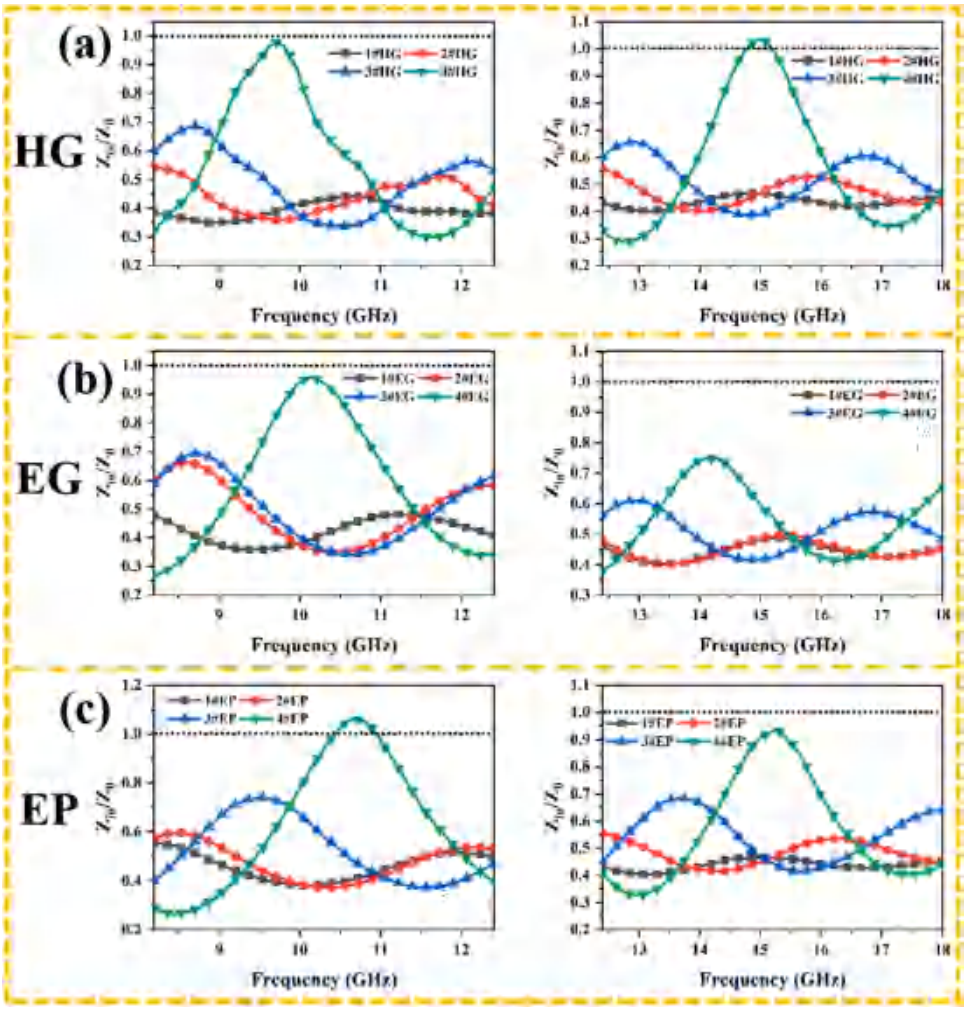

Fig. 13. Normalized impedance of absorbing materials in X and Ku bands.

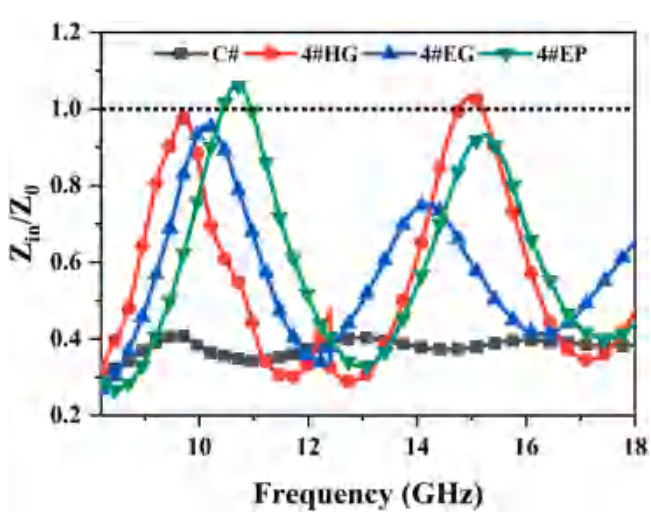

Fig. 14. Normalized impedance of absorbing materials at 60 % volume ratio in 12.4–18 GHz.

The Cole-Cole semicircle curve of vitreous aggregate cement-based absorbing materials is irregular and non-systematic, indicating that in addition to dipole relaxation polarization, there are other strong polarization processes present in the loss mechanisms[43]. CB has strong conductivity. When vitreous aggregate is incorporated into the cement matrix, a large number of interfaces with different EM parameter differences are formed between the cement matrix and the vitreous aggregate, leading to significant interfacial polarization loss under the influence of CB and periodic EM fields[44]. The electric dipoles within CB also undergo dipole polarization under the action of the EM field, accompanied by resistive loss. Therefore, interfacial polarization, dipole polarization, and resistive loss are also important forms of loss for absorbing materials under periodic EM fields.

3.6. Visual analysis of EM field transmission inside EMW absorbing materials

The arch reflection method can obtain the macroscopic RL curve of lightweight EMW absorbing materials, however, it cannot reflect the transmission of EMWs within the material and does not provide an intuitive understanding of the reflection, refraction, and scattering phenomena that occur when EMWs pass through vitreous aggregates and the cement matrix. Specifically, the presence of vitreous aggregates with varying particle sizes within the EMW absorbing material may influence the transmission pathways of EMWs. Therefore, it is essential to understand the modes of transmission and loss pathways of EMWs inside the absorbing materials as a criterion for selecting vitreous aggregates. A finite element analysis approach is employed to simulate the transmission pathways of EMWs within lightweight absorbing materials containing vitreous aggregates of different particle sizes.

The X and Ku frequency bands are widely used in current radar

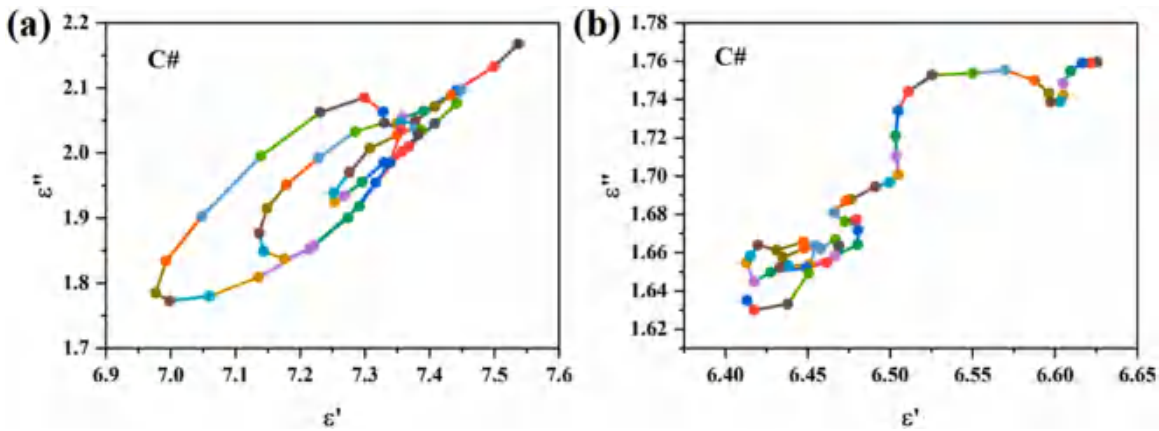

Fig. 15. Cole-Cole curves for blank groups in X and Ku bands.

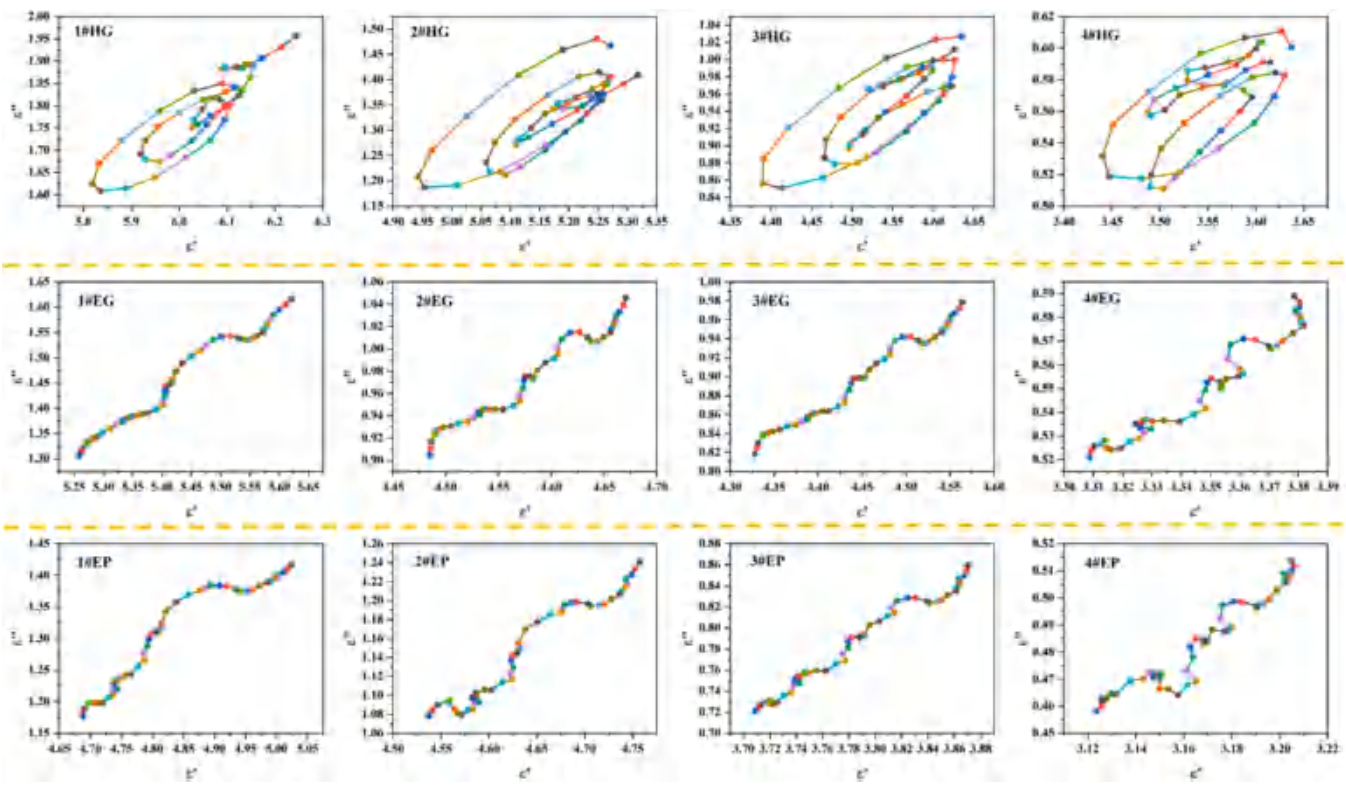

Fig. 16. Cole-Cole curves of absorbing material in X-band.

systems[45]. Therefore, the transmission of electromagnetic waves in the 8.2–18 GHz frequency range is simulated in this work. Measured EM parameters are used for the basic material parameter settings. The particle size range of vitreous aggregates includes micrometer to millimeter levels. To avoid an excessive number of small aggregate models that could affect the visualization of EMWs transmission, the simulation calculation is optimized and the model is simplified. A two-dimensional cross-section of lightweight absorbing material, with a 30 % volume ratio of different particle sizes of vitreous aggregates (HG, EG, and EP), is selected for the modeling analysis. In order to avoid shape inaccuracies of the aggregates, the aggregates are uniformly approximated as circular models of equal particle size. The distribution of particles within the model is set according to ideal conditions of uniform distribution.

The idealized two-dimensional cross-section model is illustrated in Fig. 18(a), where the metal test substrate for the arch reflection method is set as a perfect electrical conductor boundary (PEC). The EM parameters of the cement matrix and the internal cavity are derived from measured data, as seen in Fig. 18(c) and Fig. 4. The EMW excitation source is a periodic electric field polarized along the X-axis, with Floquet periodic boundaries set on both sides of the Y-axis. A perfect matching layer (PML) is used to simulate the absorption of all EMWs reflected back to the port at the external boundary. The cement matrix and the interior of the vitreous aggregates are divided into finite element meshes. As shown in Fig. 18(b), the transmission paths of EMWs are represented by vector arrows, which can be clearly illustrated within the model.

For the simulation in the X and Ku frequency bands, 8.2 GHz and 18 GHz are designated as the boundary frequency points, respectively, with the midpoint frequency of 12.4 GHz selected at the intersection of the two bands. The pink arrows represent the electric field strength vector, the red arrows represent the current density vector, and the white arrows represent the EM power loss density vector. By analyzing

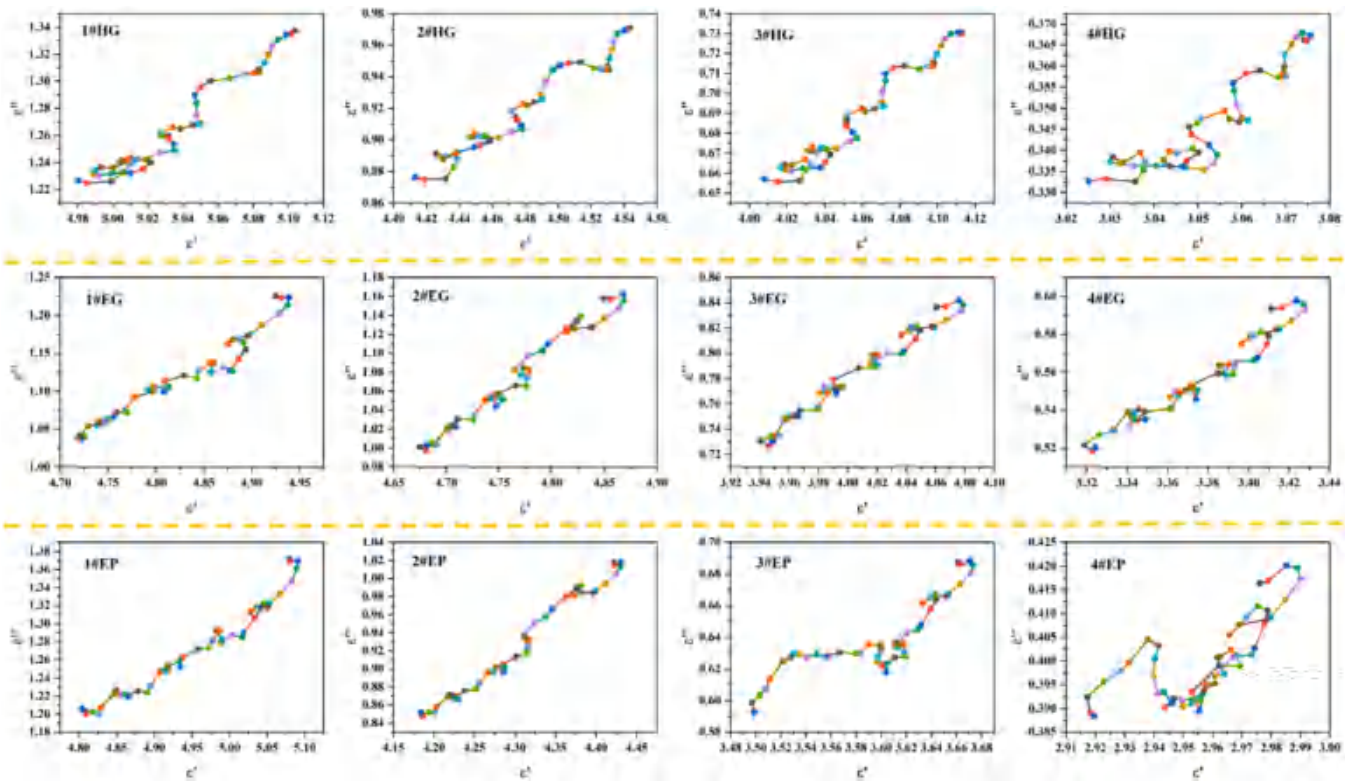

Fig. 17. Cole-Cole curves of absorbing material in Ku-band.

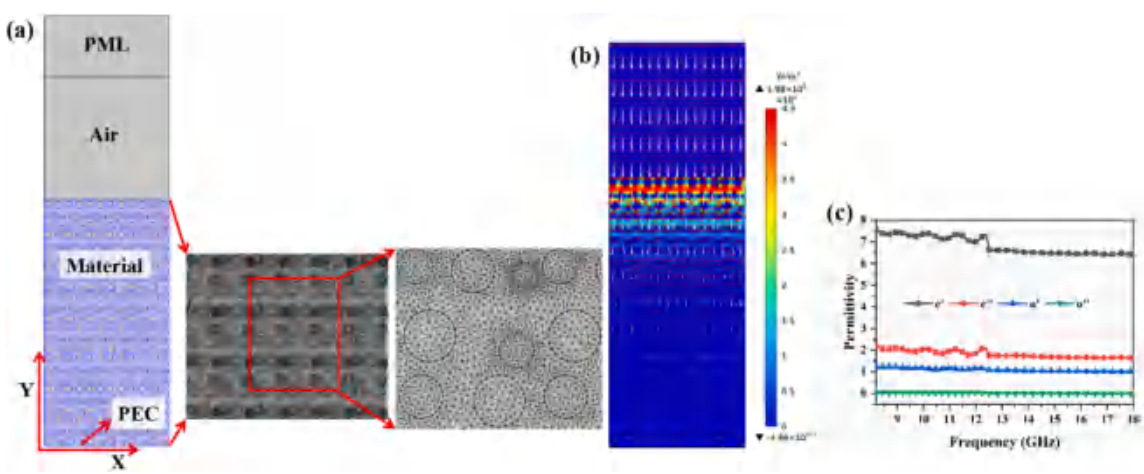

Fig. 18. Two-dimensional cross-section model and grid division diagram (a), EMW transmission diagram (b), EM parameters of cement matrix for simulation (c).

the simulation diagrams of the electric field strength distribution, current density distribution, and EM power loss density distribution of EMWs in vitreous aggregate microwave absorption materials, the loss process occurring between the vitreous aggregate and the cement matrix can be observed. The micrometer-sized HG aggregate has a particle size that is too small and overly dense for modeling, making it difficult to clearly observe the transmission of EMWs. Therefore, the HG model only includes enlarged schematic views of the upper, middle, and lower sections. All other aggregate models include schematic diagrams of the complete models.

As shown in Fig. 19, the electric field strength is primarily distributed within the vitreous aggregates and between adjacent aggregates, while the electric field strength distribution in the surrounding cement matrix is relatively weak, indicating that the vitreous aggregates have a significant impact on the distribution of electric field strength. The direction of the electric field vector changes at the surface of the aggregates, indicating that EMWs undergo reflection, refraction, and scattering at the aggregate interfaces. The superposition and interference of the incident and reflected waves alter the direction of the electric field vector. From the surface to the bottom layer of the absorption material, as the frequency of the incident EMWs increases, the number of direction changes of the electric field strength vector also increases. The electric field strength vector changes direction between adjacent vitreous aggregates, with a maximum possible deflection of 180°. At the lower frequency of 8.2 GHz, the EMWs change direction 3 times; at the boundary frequency of 12.4 GHz, the EMWs change direction 5 times; and at the higher frequency of 18 GHz, the EMWs change direction 7 times. At higher frequencies, the wavelength of EMWs is shorter, corresponding to centimeter waves that are closer in size to the aggregates. This leads to a greater number of scattering mechanisms, resulting in

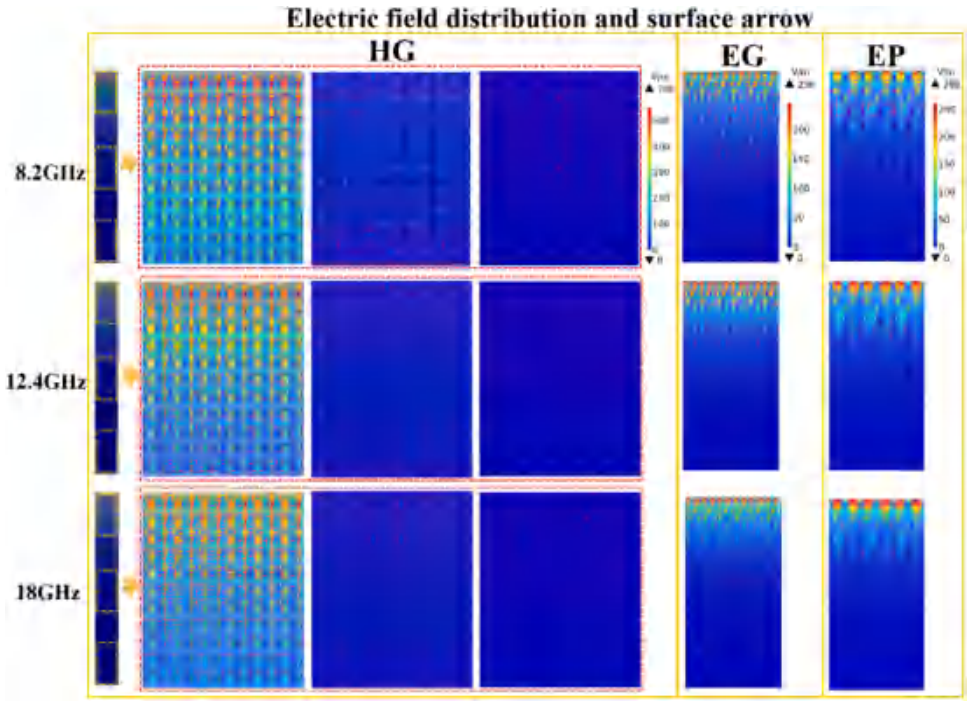

Fig. 19. Electric field intensity distribution and surface arrow.

more scattering of EMWs and increased interference with reflected and refracted waves. Consequently, the number of changes in the direction of the electric field strength vector increases, causing significant loss of EM energy. This correlates with the variations in the RL data obtained from experimental tests. It can also be observed that the refraction angle of the electric field strength vector is larger at the interfaces of larger aggregates and smaller at the interfaces of smaller aggregates. This phenomenon occurs because the EMWs in the 8.2–18 GHz frequency range are all centimeter waves, which are closer in size to larger aggregates. When EMWs pass through the vitreous aggregates, they are more likely to produce Mie scattering at the interfaces of larger aggregates, leading to an increased tendency for interference, which in turn results in a larger refraction angle for the electric field strength vector.

After the addition of CB, the conductivity of the cement matrix is enhanced. Electromagnetic induction from the EM field generates micro currents within the cement matrix, leading to conductive losses[46]. From the simulation diagram (Fig. 20) of the current density distribution, it can be seen that the current density distribution exists only within the conductive cement matrix. Along the direction of the EMW propagation, the current density distribution in the cement matrix between the aggregates is the strongest, indicating significant conduction

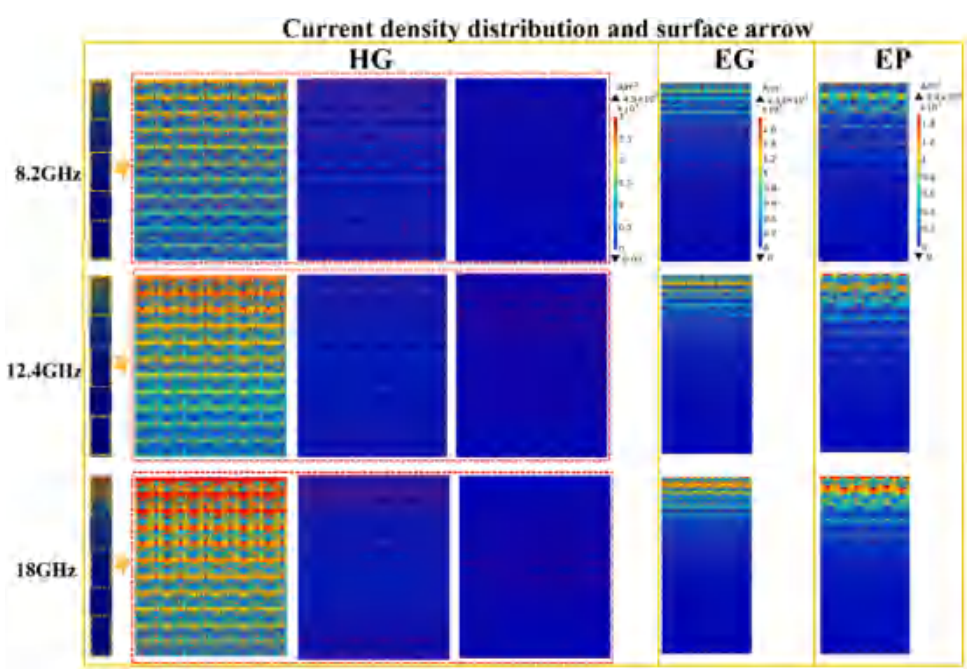

Fig. 20. Current density distribution and surface arrow.

losses. Strong conduction losses occur approximately every $\lambda/4$ distance.

The vitreous aggregate does not attenuate EMWs, rather, it increases the transmission path of the waves through scattering. The strength of conductive losses corresponds to the strength of reflection losses at that frequency point. As the penetration depth of the EMWs increases, the surface density trend of the current density distribution decreases, and the intensity of conductive losses decreases sequentially from the surface layer to the bottom layer. The phase difference between the magnetic field and electric field of a plane EMW is $\pi/2$, and the phase difference between the electric field vector and the current density vector is also $\pi/2$[21]. Therefore, as shown in the diagrams of electric field distribution and current density distribution, at the position where the electric field strength is highest, such as inside the aggregates, the current density strength is at its lowest. Unlike the distribution of electric field strength vectors, the direction of the current density vector differs by a phase of $\lambda/4$ from the direction of the electric field strength vector. However, the pattern of changes in the direction of the current density vector is consistent with that of the electric field strength vector. The direction of the current density vector is influenced by the size of the aggregates, and the pattern of refraction angles is similar to that of the electric field strength vectors, both of which are strongly affected by scattering from the aggregates.

The distribution map of EM power loss density (Fig. 21) intuitively reflects the areas of strong and weak losses of EMWs within the cement matrix. Electromagnetic power loss primarily occurs between adjacent aggregates, followed by within the cement matrix that has been doped with CB. Strong EM losses occur approximately every $\lambda/4$ distance. It can be observed that larger aggregate sizes have a greater impact on the direction of EMW transmission, with the maximum refraction angle exceeding 45°. At the interfaces of smaller aggregates, near the wavefront, the EMWs exhibit significant refraction, whereas the refraction angle decreases further away from the wavefront. In contrast, at the interfaces of larger aggregates, there can also be a significant refraction angle even away from the wavefront. In the longitudinal position of the EMW absorbing materials, the distances over which the EMWs refract are extended, resulting in greater EM loss. It is explained that in the high frequency range, larger sized aggregate EMW absorbing materials exhibit a stronger wave-absorbing effect. From the surface to the bottom layer of the absorbing material, the EM loss power decreases sequentially, with smaller RL values corresponding to greater EM loss power.

3.7. Microstructure and electrical conductivity of EMW absorbing materials

SEM was used to observe the morphology of the fracture surfaces of three types of lightweight microwave absorbing materials and the blank group (Fig. 22 a1-a4). The cement matrix doped with CB uniformly wraps around the surface of the vitreous aggregate particles. EDS-Mapping scans reveal that the carbon element from the CB is evenly distributed within the cement matrix that encapsulates the vitreous aggregates, indicating that a three-dimensional conductive network has formed in the cement matrix, connected by a large number of CB particles as conductive elements. Combining the resistivity and conductivity of the microwave absorption materials at the maximum vitreous aggregate content (Fig. 22 b1, b2), it can be observed that the conductivity of the cement matrix is the strongest, exceeding 2×10^{-3} S/m, supporting the formation of a three-dimensional conductive network by the CB in the cement matrix. As the aggregate particle size increases, the resistivity of the absorption material increases, corresponding to a lower conductivity, with a maximum resistivity exceeding 18 kΩ·m. This is because smaller aggregate particle sizes lead to smaller void structures formed within the cement matrix, resulting in tighter and more uniform connections between the aggregates and a more developed macroscopic conductive network. Conversely, larger aggregate particle sizes result in larger void structures within the cement matrix, leading to a more dispersed distribution of the cement matrix between aggregates, which affects the construction of the macroscopic conductive network, corresponding to an increase in resistivity.

From the SEM images, it can be observed that the cement matrix doped with CB has good contact with the vitreous aggregates. In the cement matrix of blank group, nano-sized CB clusters can be observed, with the CB clusters overlapping each other to form microscopic conductive pathways. The independent CB particles at the microscopic level can be equivalently considered as capacitors, while the overlapping CB clusters within the cement matrix form inductors[21]. When a periodic EM field penetrates the cement matrix, it causes energy loss. Additionally, the real part of the EM parameters of the vitreous

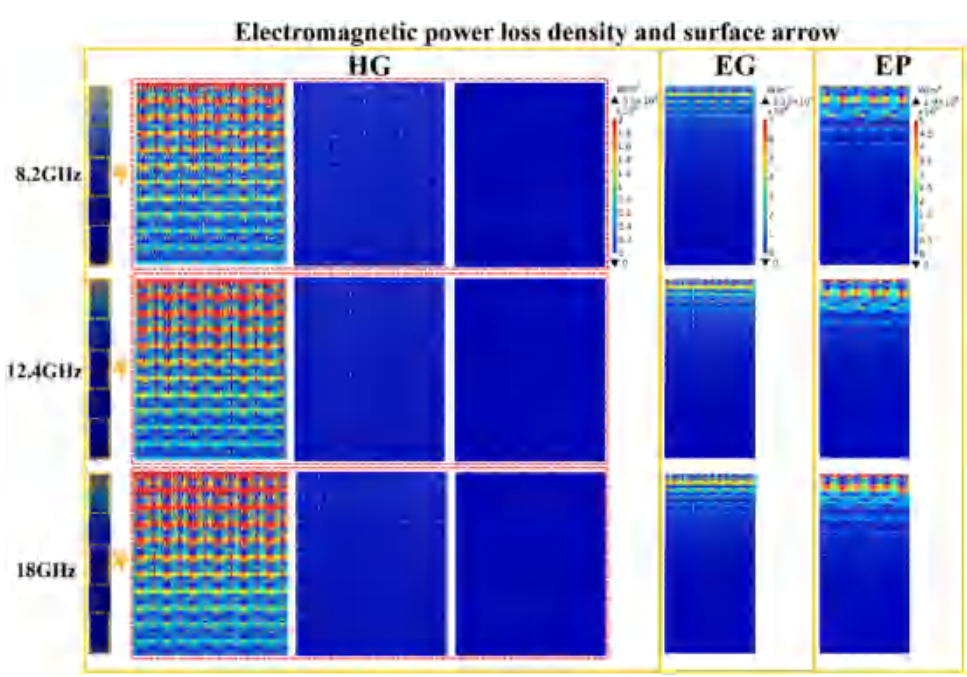

Fig. 21. EM power loss density and surface arrow.

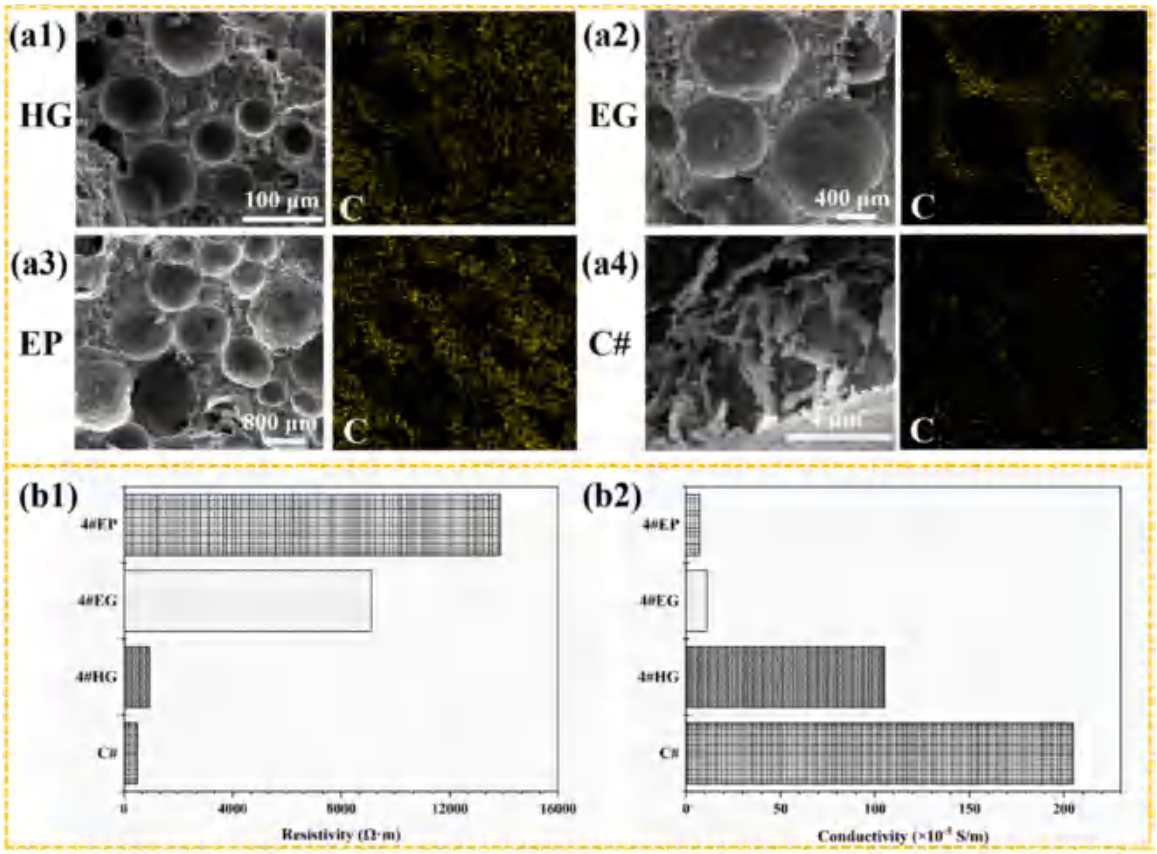

Fig. 22. SEM images and EDS-Mapping (a1-a4), resistivity and conductivity (b1, b2) of EMW absorbing materials and blank group.

aggregates is relatively low, close to that of air, while the cement matrix doped with CB has a higher conductivity, allowing it to serve as a conductive structure. Therefore, a single vitreous aggregate uniformly wrapped by the cement matrix can be regarded as a resonant cavity, where EMW can resonate within the resonant cavity structure[47]. This results in the coexistence of EM energy losses caused by the CB absorber itself and the resonant EM losses generated by the resonant cavity structure, leading to a coupled absorption effect. The resonant wavelength of the resonant cavity is related to the size of the cavity and the propagation mode of the EMW. Typically, the maximum resonant wavelength is considered. When the EMW is a transverse magnetic wave (TM wave), the resonant cavity can achieve the maximum resonant wavelength (λ_{max}). The relationship between the maximum resonant wavelength of an idealized spherical resonant cavity and the size of the cavity is shown in Formula 11[47]:

$$\lambda_{\max}=\frac{\pi\sqrt{\mu_i\varepsilon_i}}{1.372}R \tag{11}$$

Where R is the radius of the resonant cavity, ε_i and μ_i are the relative permittivity and relative permeability of the resonant cavity, respectively.

It can be seen that as the size of the resonant cavity increases, the corresponding maximum resonant wavelength becomes larger. Among the three types of vitreous aggregates, the largest λ_{max} is found in EP particles, with the maximum particle size of EP being 1.9 mm. Calculations show that the λ_{max} of EP particles is approximately 6.53 mm, corresponding to a resonant frequency of 45.94 GHz. The particle sizes of the other aggregates are all smaller than those of EP, and since the differences in EM parameters among the aggregates are relatively small, the λ_{max} of the other aggregates is less than 6.53 mm, corresponding to resonant frequencies higher than 45.94 GHz. However, the multiple reflections within a single resonant cavity and the scattering coupling between multiple resonant cavities make it difficult to accurately predict the actual resonant frequency. As a result, resonant EM losses may occur in the testing frequency range of 1.1–18 GHz. When resonant EM losses happen, the wavelengths of EMWs in the X and Ku frequency bands are less than 3 cm, approaching 1.6 cm, which are in the centimeter wave range. The wavelength is close to the resonant wavelength, and the high-frequency band is near the resonant frequency, leading to stronger resonance of high-frequency EMWs within the resonant cavity. The macroscopic representation is that as the testing frequency approaches the high-frequency range, smaller RL values correspond to enhanced wave-absorbing performance, which corresponds to the changes in RL values obtained through the arch reflection method testing.

3.8. Absorption mechanism of EMW absorbing materials

When subjected to EMW radiation, various wave absorption loss mechanisms occur within vitreous aggregate absorbing materials. A schematic diagram of the loss mechanisms is shown in Fig. 23. Impedance matching is a key factor determining whether EMWs can smoothly enter the interior of the absorbing material[48,49]. By optimizing the EM parameters of the absorbing material, good impedance matching performance can be achieved, allowing more EMWs to penetrate into the absorbing material, resulting in complex EMW losses. At the macroscopic scale of the thickness of the absorbing material, as described in Eq. (4), a phenomenon of EMW destructive interference occurs, known as the $\lambda/4$ interference cancellation effect[50]. Strong EMW losses occur approximately at every $\lambda/4$ interval within the absorbing materials.

The EMW absorbing material contains a large number of vitreous aggregates, with a cement paste containing CB wrapping around the surfaces of these vitreous aggregates, forming resonant cavities of different sizes that produce EMW resonance losses. The vitreous

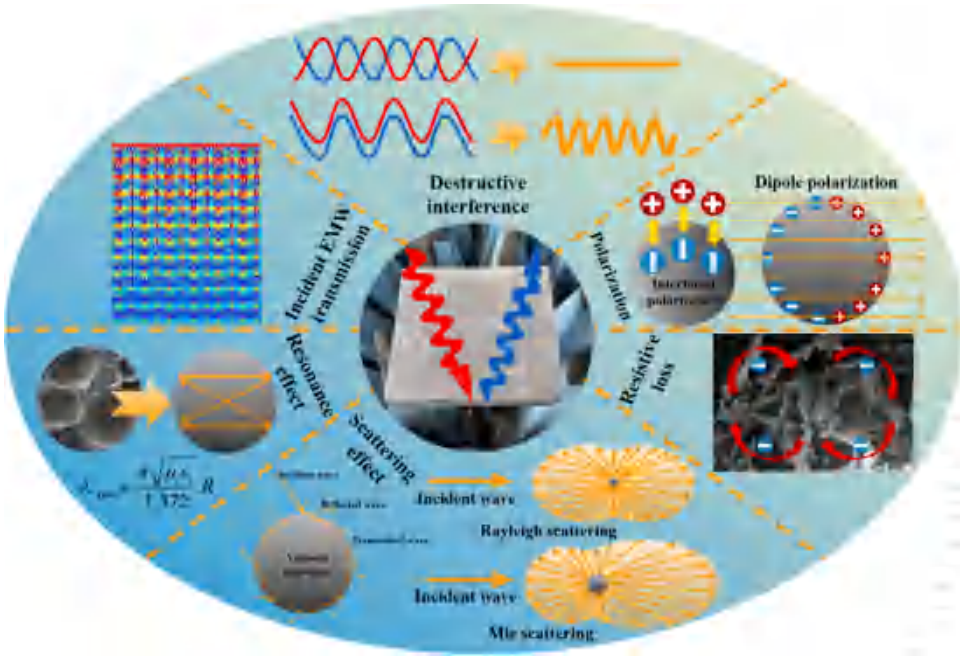

Fig. 23. Schematic diagram of EMW absorption mechanism.

aggregates induce various scattering effects on EMWs: when treated as scattering elements, different sizes of vitreous aggregates correspond to different scattering mechanisms. When the aggregate particle size is much smaller than the wavelength of the EMWs, strong Rayleigh scattering occurs, and the smaller the particle size, the stronger the Rayleigh scattering occurs. This explains why reducing the aggregate particle size results in stronger reflection losses in the low-frequency EMW range. When the aggregate particle size approaches the wavelength of the EMWs, strong Mie scattering occurs, which has a significant loss effect on the EMWs. In the high-frequency EMW range, as the aggregate particle size increases, such as with EP particles, when the size approaches the wavelength of the EMWs, the Mie scattering effect becomes stronger, leading to greater corresponding reflection losses. Additionally, when EMWs enter the interior of the aggregates, multiple reflections occur, increasing the transmission path[51,52]. On larger aggregate surfaces, EMWs will diffract, continuously generating diffracted EMWs along the tangent direction of the aggregate surface. During the diffraction process, the energy of the EMWs exhibits exponential decay[21].

In addition to the loss mechanisms associated with the resonant cavity structure, the efficient EMW absorber CB plays a significant role in EMW attenuation. As a conductive material, CB has a structure similar to grape, with conductive particles interlinked within a given volume, forming a conductive network[53]. Interface polarization occurs at the interface of heterogeneous media and is caused by the differing polarities or conductivities of the components on either side. Under the influence of electromagnetic induction, electrons or ions within the dielectric accumulate at the interface[54–56]. In this work, the substantial differences in EM parameters inside and outside the resonant cavity cause charge redistribution at the interface, resulting in interface polarization[57]. Therefore, the conductive cement matrix with a resonant cavity structure not only improves impedance characteristics to some extent but also induces interface polarization, both of which contribute to enhancing the absorption capacity of EMWs. It is believed that differences in dielectric characteristics (ability to hold charges), as well as electrical conductivities of different components, is responsible for the redistribution of charges and subsequent interfacial polarization [34]. Under the influence of an alternating EM field, the highly conductive CB particles generate dipole polarization, and when the polarization is not synchronized with the periodic changes of the EMWs, it attenuates the energy of the EMWs[2,58]. Therefore, the higher the frequency of the EMWs, the stronger the polarization loss. Additionally, in the alternating EM field, induced currents are generated within the CB, leading to eddy current losses that convert EMW energy into thermal energy. Due to the tunneling effect, electrons can jump and migrate between adjacent conductive network particles of CB, resulting in conduction losses that work synergistically to attenuate the EMWs[59]. In summary, due to various complex EMW coupling absorption mechanisms, vitreous aggregate absorbing materials exhibit excellent wave absorption performance.

3.9. Mechanical strength of EMW absorbing materials

The cross-sectional photos of samples clearly show the distribution of the vitreous aggregates within the cement matrix (Fig. 24 a). Aggregates of varying particle sizes are interspersed with each other, exhibiting a macroscopically uniform distribution within the cement matrix. The dry densities (Fig. 24 b1-b3), compressive and flexural strengths at 3d, 7d, and 28d (Fig. 25) of the lightweight EMW absorbing materials were statistically analyzed using mathematical methods. When the volume ratio of vitreous aggregates reached its maximum, the densities of the three types of lightweight EMW absorbing materials decreased from $1000 + kg/m^3$ to $780 + kg/m^3$. The density range of vitreous aggregates is large, with each type having a significant volume ratio exceeding 30 %. Therefore, the dry densities of different types of lightweight EMW absorbing materials are different. As the proportion of vitreous aggregates increases, the measured dry density of each type of lightweight EMW absorbing material shows a linear decreasing trend, indicating that the ratio of vitreous aggregate to cement matrix in the preparation of lightweight EMW absorbing materials is controllable and aligns with the expected calculated proportions.

As the proportion of vitreous aggregates gradually increases, the compressive and flexural strengths of the three types of lightweight EMW absorbing materials at 3d, 7d, and 28d gradually decrease. When the volume ratio of vitreous aggregates is fixed, the compressive and flexural strengths significantly decrease as the particle size of the aggregates increases. The wave absorption materials prepared from three types of vitreous aggregates (HG/EG/EP) achieve optimal comprehensive absorbing performance in terms of RL and EAB when the volume

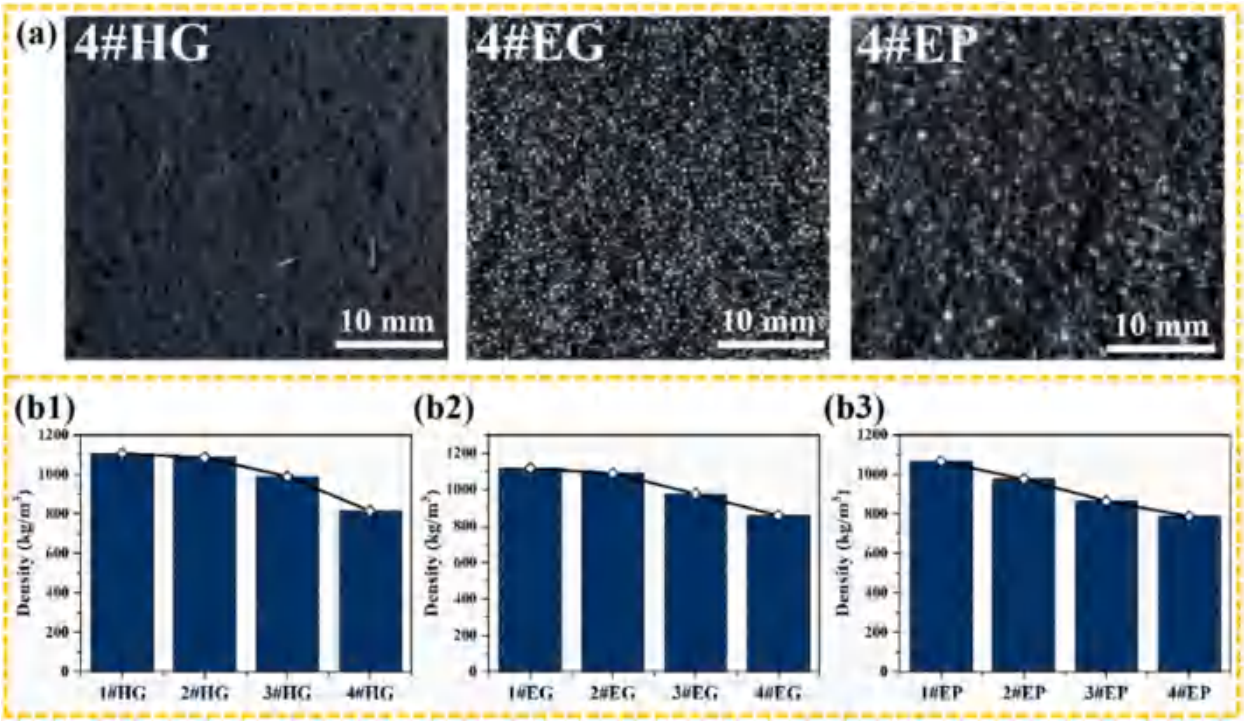

Fig. 24. Cross-section photos, and dry densities of EMW absorbing materials.

ratio of vitreous aggregates is 60 %. At this optimal ratio, the compressive strengths of the three lightweight absorption materials can reach 26.5 MPa, 14.9 MPa, and 11.6 MPa, respectively. Their flexural strengths can reach 2.1 MPa, 2.0 MPa, and 1.9 MPa, respectively, with dry densities of 813 kg/m^3 , 857 kg/m^3 , and 787 kg/m^3 . It can be seen that, at the corresponding dry density levels, the mechanical strengths of the lightweight EMW absorbing materials have exceeded the mechanical strength requirements for lightweight mortar. Therefore, the dry density of the lightweight EMW absorbing materials not only meets the requirements for lightweight usage but also satisfies the standards for mechanical strength in practical applications.

The factors contributing to the decrease in mechanical strength with the increase in the volume ratio and particle size of vitreous aggregates are as follows: 1) The lightweight EMW absorbing materials are composed of vitreous aggregates interspersed with a cement matrix that incorporates CB. Due to the lower density and strength of the vitreous aggregates, which are significantly less than those of the cement matrix, the cement matrix is the primary material determining the density and strength of the lightweight EMW absorbing materials. As the proportion of vitreous aggregates increases, the corresponding amount of cement decreases, resulting in lower compressive strength. 2) When the volume ratio of vitreous aggregates is fixed, the mechanical strength of the lightweight EMW absorbing materials is jointly provided by the strength of the cement matrix and the body strength of the vitreous aggregates. The varying mechanical strengths of the vitreous aggregates themselves also cause differences in the mechanical strength of the EMW absorbing materials. 3) Reducing the particle size of the aggregates transforms the concentrated mechanically weak areas within the cement matrix (the transition zone at the interface between the cement matrix and aggregates or the low-strength vitreous aggregate regions) into dispersed mechanically weak areas. This can hinder the propagation of cracks within the cement matrix under compressive loads and weaken the dispersive stress transfer, thereby enhancing the mechanical properties of the vitreous aggregate EMW absorbing materials. Conversely, larger aggregate particle sizes correlate with lower mechanical strengths. Under the influence of multiple factors, as the volume ratio and particle size of vitreous aggregates increase, the mechanical strength of the lightweight EMW absorbing materials decreases.

3.10. Thermal conductivity of EMW absorbing materials

The thermal conductivity of lightweight EMW absorbing materials at maximum volume ratio was measured (Fig. 26). It can be observed that as the particle size of the vitreous aggregate increases, the thermal conductivity of the EMW absorbing material decreases from 0.215 W/(m·K) to 0.168 W/(m·K), indicating good insulation performance. When the volume ratio of vitreous aggregate to cement matrix in the lightweight EMW absorbing material is fixed, the decrease in thermal conductivity with increasing aggregate particle size can be attributed to the following reasons. Lightweight EMW absorbing materials are two-phase mixtures of vitreous aggregates and cement matrices. The thermal conductivity of the cement matrix is relatively high, while the thermal conductivity of the vitreous aggregate itself is low, making it a good insulation material often used for preparing thermal insulation mortar. In EMW absorbing materials, heat flow is transferred from the cement matrix to the vitreous aggregate and then back to the cement matrix. The hindrance effect of the gas phase within the vitreous aggregate on heat flow transfer is quite significant. When the heat flow inside the EMW absorbing material is transferred from the cement matrix to the vitreous aggregate, a thermal bridging effect occurs due to the differing thermal conductivities of the two phases[60,61]. Aggregates with smaller particle sizes can create more interfaces between the cement matrix and the vitreous aggregate, resulting in a higher frequency of thermal bridging effects, which leads to an increase in thermal conductivity. Conversely, larger particle size aggregates produce fewer thermal bridging effects, effectively reducing the thermal conductivity of the EMW absorbing material. In other words, the larger size of the aggregate increases, the better the insulation performance of the EMW absorbing material.

4. Conclusion

In this work, the effects of the size and volume ratio of vitreous aggregates on the EMW absorption performance, mechanical and thermal insulation properties of cement-based materials were systematically

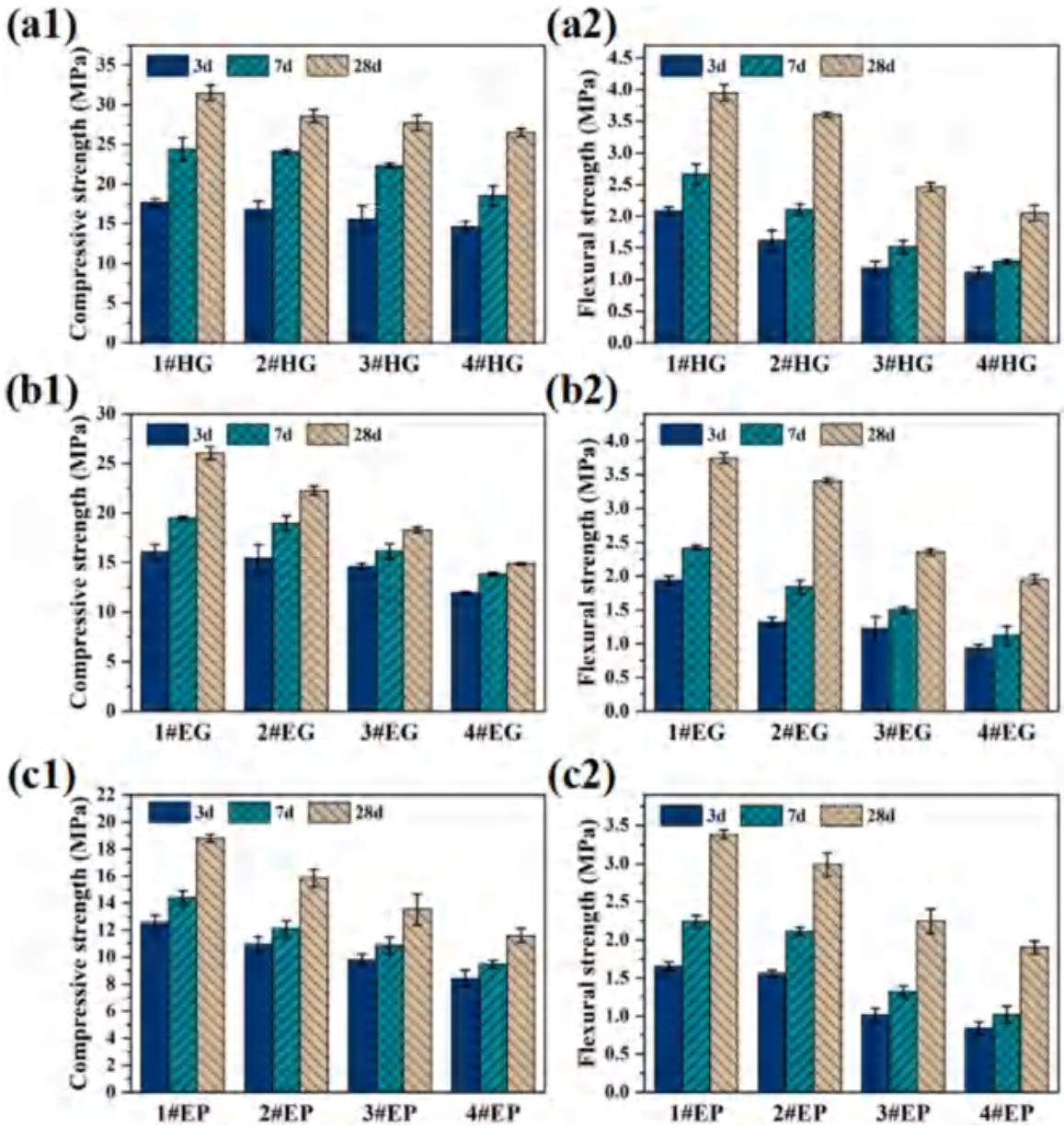

Fig. 25. Mechanical strength of EMW absorbing materials.

investigated. It provides a theoretical basis for the selection of aggregates in the design of wave-absorbing frequency bands. The main conclusions are as follows:

(1) When the frequency bands of EMWs differ, the effects of the volume ratio and particle size of vitreous aggregates on the wave-absorbing performance of lightweight absorbing materials vary. In the lower frequency range (1.1–7 GHz), decreasing the volume ratio or particle size of vitreous aggregates can achieve better wave absorption performance. In contrast, in the higher frequency range (7–18 GHz), increasing the volume ratio or particle size of vitreous aggregates is necessary to improve wave absorption performance. This is related to the changes in the EM parameters, impedance matching, and particle scattering mechanisms.

(2) Within the entire frequency range (1.1–18 GHz), the average RL is less affected by vitreous aggregate size, with differences not exceeding −1.54 dB. When the absorption rate of EMW exceeds 80 % (RL < −7 dB), the size and volume ratio of the aggregates have a minimal impact on EAB, which can achieve effective protection across the entire frequency range, with the widest EAB reaching 12.4 GHz. When the absorption rate of EMW exceeds 90 % (RL < −10 dB), effective protection can only be formed at high frequencies. The larger the particle size or the higher the volume ratio, the wider the EAB and the better the high-frequency wave-absorbing performance, with the widest EAB reaching 6.57 GHz.

(3) Finite element simulation analysis indicates that vitreous aggregates alter the transmission direction of EMWs, increasing the path of EMW loss. At the interface of the vitreous aggregates, the EMWs undergo refraction, scattering, and reflection, with the transmission behavior also influenced by the frequency band. The primary EMW power loss occurs between adjacent vitreous aggregates, followed by loss within the cement matrix containing CB. Significant EMW loss occurs at intervals of approximately $\lambda/4$. The larger the particle size, the greater the refraction angle of the EMWs.

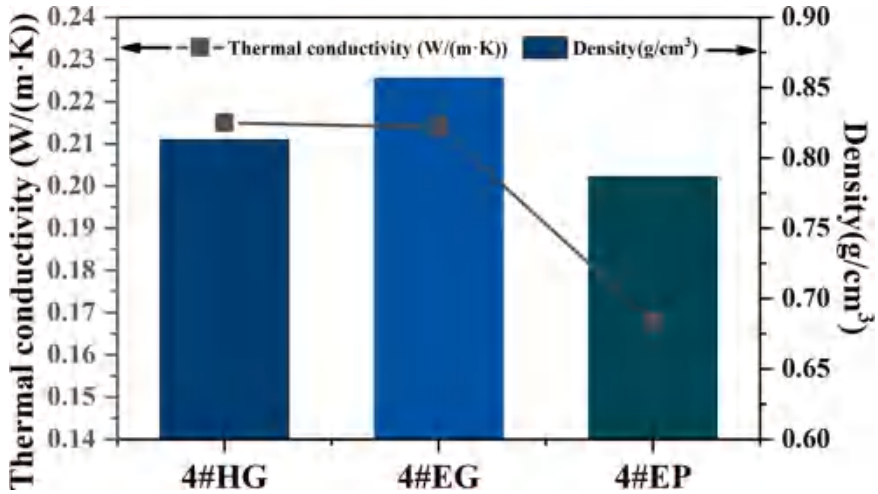

Fig. 26. Thermal conductivity of EMW absorbing materials.

(4) The thermal insulation performance of cement-based materials is enhanced by the increased particle size of vitreous aggregate. Although there is a minor reduction in mechanical strength, it still exceeds the mechanical strength of an equivalent density as per standard specifications.

CRediT authorship contribution statement

Ma Chao: Methodology, Data curation. **Xie Shuai:** Writing – review & editing, Resources, Project administration, Methodology, Data curation. **Su Ronghua:** Formal analysis, Data curation. **Wang Yingxiang:** Data curation. **Ji Zhijiang:** Supervision, Formal analysis. **Wang Jing:** Conceptualization. **Wu Zihao:** Writing – review & editing, Writing – original draft, Validation, Methodology, Investigation, Funding acquisition, Formal analysis, Data curation, Conceptualization.

Declaration of Competing Interest

The authors declare that they have no known competing financial interests or personal relationships that could have appeared to influence the work reported in this paper.

Acknowledgements

The authors would like to acknowledge the financial support provided by the National Natural Science Foundation of China (52303393); and the Nonmetallic Excellence and Innovation Center for Building Materials (No. 24PHD-10).

Data availability

Data will be made available on request.

References

[1] F.M. Idris, M. Hashim, Z. Abbas, et al., Recent developments of smart electromagnetic absorbers based polymer-composites at gigahertz frequencies, J. Magn. Magn. Mater. 405 (2016) 197–208, https://doi.org/10.1016/j.jmmm.2015.12.070.
[2] G. Ma, J. Sun, F. Aslani, et al., Review on electromagnetic wave absorbing capacity improvement of cementitious material, Constr. Build. Mater. 262 (2020) 120907, https://doi.org/10.1016/j.conbuildmat.2020.120907.
[3] A.P. Singh, B.K. Gupta, M. Mishra, et al., Multiwalled carbon nanotube/cement composites with exceptional electromagnetic interference shielding properties, Carbon 56 (2013) 86–96, https://doi.org/10.1016/j.carbon.2012.12.081.
[4] Y. Feng, S. Wang, D. Fan, et al., Coupling effects of steel slag powder and electromagnetic waves on the microstructure and hydration kinetics evolution of cementitious materials with ultra low water/binder ratio, J. Build. Eng. 58 (2022) 105036, https://doi.org/10.1016/j.jobe.2022.105036.
[5] J. Hu, Y. Liu, J. Jiang, et al., Development of electromagnetic microwave absorbers in cementitious materials, Compos. Struct. 312 (2023) 116886, https://doi.org/10.1016/j.compstruct.2023.116886.
[6] D. Stefaniuk, M. Sobótka, K. Jarczewska, et al., Microstructure properties of cementitious mortars with selected additives for electromagnetic waves absorbing applications, Cem. Concr. Compos. 134 (2022) 104732, https://doi.org/10.1016/j.cemconcomp.2022.104732.
[7] M.-Q. Cao, T.-T. Liu, Y.-H. Zhu, et al., Developing electromagnetic functional materials for green building, J. Build. Eng. 45 (2022) 103496, https://doi.org/10.1016/j.jobe.2021.103496.
[8] X. Liu, N. Wang, Z. Wang, Effects of the absorber, thickness and surface roughness on the electromagnetic wave absorption characteristics of magnesium phosphate cement, Constr. Build. Mater. 344 (2022) 128149, https://doi.org/10.1016/j.conbuildmat.2022.128149.
[9] P. Bian, B. Zhan, P. Gao, et al., Investigation on the electromagnetic wave absorption properties of foamed cement-based materials, Constr. Build. Mater. 364 (2023) 129903, https://doi.org/10.1016/j.conbuildmat.2022.129903.
[10] S. Xie, Z. Ji, B. Li, et al., Electromagnetic wave absorption properties of helical carbon fibers and expanded glass beads filled cement-based composites, Compos., Part A 114 (2018) 360–367, https://doi.org/10.1016/j.compositesa.2018.08.034.
[11] M. Jung, Y.-s Lee, S.-G. Hong, et al., Carbon nanotubes (CNTs) in ultra-high performance concrete (UHPC): Dispersion, mechanical properties, and electromagnetic interference (EMI) shielding effectiveness (SE), Cem. Concr. Res. 131 (2020) 106017, https://doi.org/10.1016/j.cemconres.2020.106017.
[12] D. Micheli, R. Pastore, A. Vricella, et al., Electromagnetic characterization and shielding effectiveness of concrete composite reinforced with carbon nanotubes in the mobile phones frequency band, Mater. Sci. Eng. B. 188 (2014) 119–129, https://doi.org/10.1016/j.mseb.2014.07.001.
[13] I.W. Nam, J.H. Choi, C.G. Kim, et al., Fabrication and design of electromagnetic wave absorber composed of carbon nanotube-incorporated cement composites, Compos. Struct. 206 (2018) 439–447, https://doi.org/10.1016/j.compstruct.2018.07.058.
[14] M. Ozturk, M. Karaaslan, O. Akgol, et al., Mechanical and electromagnetic performance of cement based composites containing different replacement levels of ground granulated blast furnace slag, fly ash, silica fume and rice husk ash, Cem. Concr. Res. 136 (2020) 106177, https://doi.org/10.1016/j.cemconres.2020.106177.
[15] S.K. Ghosh, K. Nath, S. Nath Chowdhury, et al., Combination effect of functionalized high aspect ratio carbonaceous nanofillers and carbon black on electrical, thermal conductivity, dielectric and EMI shielding behavior of co-continuous thermoplastic elastomeric blend composite films, Chem. Eng. J. Adv. 15 (2023) 100505, https://doi.org/10.1016/j.ceja.2023.100505.
[16] D. Shuang, A. Hongmei, W. Baomin, Research on the electromagnetic wave absorption properties of GNPs/EMD cement composite, Constr. Build. Mater. 321 (2022) 126398, https://doi.org/10.1016/j.conbuildmat.2022.126398.
[17] H. Zhang, T. Liu, Z. Huang, et al., Engineering flexible and green electromagnetic interference shielding materials with high performance through modulating WS_2 nanosheets on carbon fibers, J. Mater. 8 (2022) 327–334, https://doi.org/10.1016/j.jmat.2021.09.003.
[18] Y. He, L. Lu, K. Sun, et al., Electromagnetic wave absorbing cement-based composite using Nano-Fe_3O_4 magnetic fluid as absorber, Cem. Concr. Compos. 92 (2018) 1–6, https://doi.org/10.1016/j.cemconcomp.2018.05.004.
[19] J. Cheng, Y. Li, H. Raza, et al., Cross-Scale Synergistic Manipulation of Dielectric Genes in Polymetallic Sulfides from Micropolarization to Macroconductance Toward Wide-Band Microwave Absorption, Adv. Funct. Mater. n/a 2405643. https://doi.org/10.1002/adfm.202405643.
[20] J. Wang, Y. Wang, J. Cheng, et al., Abundant vacancies induced high polarization-attenuation effects in flower-like WS_2 microwave absorbers, J. Mater. Sci. Technol. 194 (2024) 193–202, https://doi.org/10.1016/j.jmst.2024.01.085.

[21] C. Ma, S. Xie, Z. Wu, et al., Research and simulation of three-layered lightweight cement-based electromagnetic wave absorbing composite containing expanded polystyrene and carbon black, Constr. Build. Mater. 393 (2023) 132047, https://doi.org/10.1016/j.conbuildmat.2023.132047.

[22] Y. Dai, M. Sun, C. Liu, et al., Electromagnetic wave absorbing characteristics of carbon black cement-based composites, Cem. Concr. Compos. 32 (2010) 508–513, https://doi.org/10.1016/j.cemconcomp.2010.03.009.

[23] H. Guan, S. Liu, Y. Duan, et al., Investigation of the electromagnetic characteristics of cement based composites filled with EPS, Cem. Concr. Compos. 29 (2007) 49–54, https://doi.org/10.1016/j.cemconcomp.2006.08.001.

[24] Z. Wang, Z. Wang, M. Ning, Optimization of electromagnetic wave absorption bandwidth of cement-based composites with doped expanded perlite, Constr. Build. Mater. 259 (2020) 119863, https://doi.org/10.1016/j.conbuildmat.2020.119863.

[25] B. Li, Z. Ji, S. Xie, et al., Electromagnetic wave absorption properties of carbon black/cement-based composites filled with porous glass pellets, J. Mater. Sci.: Mater. Electron. 30 (2019) 12416–12425, https://doi.org/10.1007/s10854-019-01600-w.

[26] L. Baoyi, D. Yuping, Z. Yuefang, et al., Electromagnetic wave absorption properties of cement-based composites filled with porous materials, Mater. Des. 32 (2011) 3017–3020, https://doi.org/10.1016/j.matdes.2010.12.017.

[27] B. Han, L. Zhang, J. Ou, Influence of water content on conductivity and piezoresistivity of cement-based material with both carbon fiber and carbon black, J. Wuhan. Univ. Technol. -Mater. Sci. Ed. 25 (2010) 147–151, https://doi.org/10.1007/s11595-010-1147-z.

[28] I.V. Ciuchi, C.S. Olariu, L. Mitoseriu, Determination of bone mineral volume fraction using impedance analysis and Bruggeman model, Mater. Sci. Eng. B. 178 (2013) 1296–1302, https://doi.org/10.1016/j.mseb.2013.04.001.

[29] A.H. Sihvola, E. Alanen, Studies of mixing formulae in the complex plane, IEEE Trans. Geosci. Remote Sens. 29 (1991) 679–687, https://doi.org/10.1109/36.135831.

[30] X. Li, L. Xie, X. Zheng, The comparison between the Mie theory and the Rayleigh approximation to calculate the EM scattering by partially charged sand, J. Quant. Spectrosc. Radiat. Transf. 113 (2012) 251–258, https://doi.org/10.1016/j.jqsrt.2011.09.020.

[31] M. Chekroun, L. Le Marrec, O. Abraham, et al., Analysis of coherent surface wave dispersion and attenuation for non-destructive testing of concrete, Ultrasonics 49 (2009) 743–751, https://doi.org/10.1016/j.ultras.2009.05.006.

[32] Y.-l Xu, Radiative-scattering signatures of an ensemble of nonspherical particles, J. Quant. Spectrosc. Radiat. Transf. 89 (2004) 385–419, https://doi.org/10.1016/j.jqsrt.2004.05.037.

[33] Y. Rao, X. Qi, Q. Peng, et al., Mixed-dimensional conductive network heterostructures: An effective interfacial strategy to aggrandize dielectric loss for designing microwave absorbers, J. Alloy. Compd. 910 (2022) 164974, https://doi.org/10.1016/j.jallcom.2022.164974.

[34] M. Qin, L. Zhang, H. Wu, Dielectric Loss Mechanism in Electromagnetic Wave Absorbing Materials, Adv. Sci. 9 (2022) 2105553, https://doi.org/10.1002/advs.202105553.

[35] X. Zhang, Y. Fan, J. Wang, et al., Enhanced microwave absorption performance of nitrogen-doped porous carbon dodecahedrons composite embedded with ceric dioxide, Adv. Powder Technol. 33 (2022) 103527, https://doi.org/10.1016/j.apt.2022.103527.

[36] L. Yue, Y. Yang, Q. Zhou, et al., Broadband electromagnetic wave absorbing performance by designing the foam structure and double-layer for cement-based composites containing MWCNTs, Cem. Concr. Compos. 131 (2022) 104595, https://doi.org/10.1016/j.cemconcomp.2022.104595.

[37] Y. Gao, C. Wang, J. Li, et al., Adjustment of dielectric permittivity and loss of graphene/thermoplastic polyurethane flexible foam: Towards high microwave absorbing performance, Compos., Part A 117 (2019) 65–75, https://doi.org/10.1016/j.compositesa.2018.10.036.

[38] B. Kuang, W. Song, M. Ning, et al., Chemical reduction dependent dielectric properties and dielectric loss mechanism of reduced graphene oxide, Carbon 127 (2018) 209–217, https://doi.org/10.1016/j.carbon.2017.10.092.

[39] S. Xie, Y. Zhang, Z. Ji, et al., Electromagnetic wave absorption of periodic cylindrical structured gypsum composites incorporate with different carbonaceous materials, J. Mater. Sci.: Mater. Electron. 32 (2021) 9208–9222, https://doi.org/10.1007/s10854-021-05586-2.

[40] L. Tan, M. Zhu, X. Li, et al., Lightweight excellent microwave absorption properties based on sulfur doped graphene, J. Saudi Chem. Soc. 24 (2020) 9–19, https://doi.org/10.1016/j.jscs.2019.08.005.

[41] G. Deng, Y. Yang, Q. Zhou, et al., Lightweight and broadband electromagnetic wave absorbing foamed cement-based composites incorporated with hybrid dielectric fibers, Constr. Build. Mater. 327 (2022) 126931, https://doi.org/10.1016/j.conbuildmat.2022.126931.

[42] W. Xing, P. Li, H. Wang, et al., The similar Cole-Cole semicircles and microwave absorption of Hexagonal Co/C composites, J. Alloy. Compd. 750 (2018) 917–926, https://doi.org/10.1016/j.jallcom.2018.04.051.

[43] C. Ma, S. Xie, Z. Ji, et al., Electromagnetic wave absorbing properties of pyramidal engineered cement mortar containing carbon black, J. Build. Eng. 84 (2024) 108618, https://doi.org/10.1016/j.jobe.2024.108618.

[44] Z. Wu, S. Xie, Z. Ji, et al., Novel lightweight cement-based materials foaming by secondary aluminum ash: microwave absorption, mechanical and thermal insulation properties, Constr. Build. Mater. 413 (2024) 134328, https://doi.org/10.1016/j.conbuildmat.2023.134328.

[45] J. Cheon, S.J. Lim, M. Kim, A composite RAS with an enhanced uniformity of absorbing performance using a MWCNT-anchored aramid fiber, Compos. Sci. Technol. 200 (2020) 108442, https://doi.org/10.1016/j.compscitech.2020.108442.

[46] D.D.L. Chung, A Review of Microwave Absorption and Reflection by Cement-Based Materials, With Emphasis on Electromagnetic Interference Shielding and Admixture Effects, Adv. Funct. Mater. n/a 2408220. https://doi.org/10.1002/adfm.202408220.

[47] D.P. Yadav, M.K. Maurya, R.A. Yadav, et al., Resonant and normal modes behavioral studies of shielded dielectric spherical shell resonator, Optik 127 (2016) 5520–5533, https://doi.org/10.1016/j.ijleo.2016.03.056.

[48] H. Rao, P. Wang, Y. Chen, et al., Tailoring electromagnetic responsiveness of Tremella-like multi-dimensional heterostructures through a self-decomposition strategy, Chem. Eng. J. 500 (2024) 157121, https://doi.org/10.1016/j.cej.2024.157121.

[49] Y. Fu, Y. Wang, J. Cheng, et al., Manipulating polarization attenuation in NbS_2–NiS_2 nanoflowers through homogeneous heterophase interface engineering toward microwave absorption with shifted frequency bands, Nano Mater. Sci. 6 (2024) 794–804, https://doi.org/10.1016/j.nanoms.2024.05.003.

[50] T. Si, S. Xie, C. Ma, et al., Microwave absorption properties of double-layer structured basalt fiber/resin composites containing carbon black and nano-Fe_3O_4, Compos. Interfaces 30 (2023) 959–981, https://doi.org/10.1080/09276440.2023.2179257.

[51] Y. Zhang, W. Hao, B. Li, et al., Electromagnetic Wave Absorbing Properties of Double-Layer Cement Composite and Theory Analysis, Asian J. Chem. 26 (2014) 5563–5566, https://doi.org/10.14233/ajchem.2014.18155.

[52] P. Xu, J. Fang, H. He, et al., In situ growth of globular MnO_2 nanoflowers inside hierarchical porous mangosteen shells-derived carbon for efficient electromagnetic wave absorber, J. Alloy. Compd. 903 (2022) 163826, https://doi.org/10.1016/j.jallcom.2022.163826.

[53] S. Xie, C. Ma, Z. Ji, et al., Electromagnetic wave absorption and heat storage dual-functional cement composites incorporated with carbon nanotubes and phase change microcapsule, J. Build. Eng. 67 (2023) 105925, https://doi.org/10.1016/j.jobe.2023.105925.

[54] N. Wang, Y. Chen, H. Rao, et al., Hierarchical core-shell transitional metal chalcogenides Co9S8/ CoSe2@C nanocube embedded into porous carbon for tunable and efficient microwave absorption, Carbon 232 (2025) 119824, https://doi.org/10.1016/j.carbon.2024.119824.

[55] W. Wang, K. Nan, H. Zheng, et al., Heterostructure design of hydrangea-like Co_2P/Ni_2P@C multilayered hollow microspheres for high-efficiency microwave absorption, J. Mater. Sci. Technol. 181 (2024) 104–114, https://doi.org/10.1016/j.jmst.2023.09.023.

[56] D. Zhang, J. Cheng, X. Yang, et al., Electromagnetic and microwave absorbing properties of magnetite nanoparticles decorated carbon nanotubes/polyaniline multiphase heterostructures, J. Mater. Sci. 49 (2014) 7221–7230, https://doi.org/10.1007/s10853-014-8429-3.

[57] Y. Yang, X. Shi, Q. Zhou, et al., Structural design and electromagnetic wave absorbing performance optimization of lightweight foam cement-based metamaterials, Constr. Build. Mater. 438 (2024) 137191, https://doi.org/10.1016/j.conbuildmat.2024.137191.

[58] J. Cheng, Y. Jin, J. Zhao, et al., From VIB- to VB-Group Transition Metal Disulfides: Structure Engineering Modulation for Superior Electromagnetic Wave Absorption, Nano-Micro Lett. 16 (2023) 29, https://doi.org/10.1007/s40820-023-01247-7.

[59] R. Peymanfar, E. Selseleh-Zakerin, A. Ahmadi, Tailoring energy band gap and microwave absorbing features of graphite-like carbon nitride (g-C_3N_4), J. Alloy. Compd. 867 (2021) 159039, https://doi.org/10.1016/j.jallcom.2021.159039.

[60] G. Chen, F. Li, J. Geng, et al., Identification, generation of autoclaved aerated concrete pore structure and simulation of its influence on thermal conductivity, Constr. Build. Mater. 294 (2021) 123572, https://doi.org/10.1016/j.conbuildmat.2021.123572.

[61] N.A. Jaya, L. Yun-Ming, H. Cheng-Yong, et al., Correlation between pore structure, compressive strength and thermal conductivity of porous metakaolin geopolymer, Constr. Build. Mater. 247 (2020) 118641, https://doi.org/10.1016/j.conbuildmat.2020.118641.

Effects of Coal Gas Fine Ash on Electromagnetic Properties of Cement Mortar and Carbon Black Modification

Yingxiang Wang[a,b], Shuai Xie[a,b,*], Chao Ma[a,b], Zihao Wu[a,b,c], Jing Wang[a,b], Zhijiang Ji[a,b]

([a] China Building Materials Academy, Beijing 100024, People's Republic of China; [b] State Key Laboratory of Green Building Materials, Beijing 100024, People's Republic of China; [c] School of Materials Science and Engineering, Wuhan University of Technology, Wuhan 430070, People's Republic of China)

Abstract: The high-value utilisation of coal gas fine ash (CGFA) continues to represent a core issue in the domain of coal gasification technology. Presently, the utilisation of unburned carbon in CGFA in conventional building materials remains challenging. However, given its excellent electromagnetic properties, it demonstrates significant potential for development in the field of electromagnetic protection. The present study explores the relationship between CGFA content and the electromagnetic performance of cement-based composites, and the modification effects of carbon black (CB), with particular focus on the electromagnetic property evolution in CB-CGFA systems at different formulation ratios. The experimental findings demonstrate that CGFA has a substantial impact on enhancing the electrical conductivity and complex permittivity of the composite material. The cement mortar demonstrates enhanced low-

First author: WANG Yingxiang(王英翔): E-mail: 1061203750@qq.com

* Corresponding author: Shuai Xie(解帅): Ph D; E-mail: xieshuai@cbma.com.cn

Funded by the National Natural Science Foundation of China (52303393) and the Nonmetallic Excellence and Innovation Center for Building Materials (No. 24PHD-10).

frequency (1-8 GHz) wave-absorbing characteristics. The numerical value of reflection loss (RL) exhibited a positive correlation with CGFA content, reaching an optimal value of -11.9 dB at 1.1 GHz for 2% CGFA content. The addition of CB to CGFA cement mortar has been shown to enhance its electromagnetic performance through synergistic effects within the cement matrix. This addition exhibits enhanced complex permittivity, characterised by combined polarization and resistive loss mechanisms. The absorbing performance exhibited a non-monotonic relationship with CB content, achieving an optimal RL of -18.95 dB at 4.24 GHz for 2% CGFA with 0.75% CB.

Key words: Coal gas fine ash, electromagnetic characteristic, electromagnetic wave absorption, cement mortar, electrical resistivity

1 Introduction

China is the world's leading consumer of coal, with coal-related CO_2 emissions accounting for 75% of its greenhouse gas output in 2021[1,2]. In order to reduce its environmental impact, China has focused on coal gasification technology, which is a key part of the transition to clean energy[3-5]. However, advancing gasification also increases gas ash emissions, particularly coal gas fine ash (CGFA)[6-9]. Traditional treatment methods, such as landfills or open piles, pollute the environment and cause huge wastage of land, financial and material resources[10]. Therefore, the effective treatment and utilisation of CGFA has become a key area of research in coal gasification technology development and solid waste reuse[11-13].

CGFA is a fine, black powder containing volcanic ash-like components, which

give it hydration activity. Some researchers have started using it as a supplementary cementitious material to partially replace cement. This offers a valuable use for coal gasification fine ash and reduces demand for cement resources[13-15]. The addition of chemical activators enhances both cement hydration and the dissolution of CGFA's active minerals, thereby improving strength development. Additionally, reducing the particle size activates the pozzolanic components in ultrafine coal gangue, shortening the hydration induction period and accelerating the exothermic peaks of geopolymers, ultimately boosting mechanical strength[16,17]. Beyond the reactivity of silicon and aluminium oxides, the unburned carbon in CGFA undergoes thermal and pressure treatments in the gasifier, promoting physicochemical transformations[18-20]. These processes induce the partial graphitisation of the carbon matrix, transforming it into an ordered crystalline structure and enhancing its electrical conductivity[21-23]. Recent studies have demonstrated the potential of CGFA as an effective carbon source for electromagnetic wave absorption applications, with experimental results indicating superior absorption performance characteristics.[24-29]. Gao[30] prepared a CGFA/paraffin absorber and found that it demonstrated a wide effective absorption bandwidth and a certain level of reflection loss intensity even at a thin thickness. Specifically, when the matching thickness is 1.7 mm, the absorber achieves optimal absorbing properties at 15.6 GHz, reaching an absorption level of -17.6 dB.

The rapid advancement of electronic technologies has led to widespread electromagnetic wave (EMW) pollution, thereby rendering effective protective measures essential for contemporary society. Cement-based electromagnetic protection

materials have emerged as promising candidates due to their inherent wave attenuation capabilities and structural functionality. Conventional preparation of cement-based protective materials relies on the uniform dispersion of conductive or magnetic fillers within the cement matrix to enhance EMW reflection and internal energy dissipation. [31-36], Due to its superior electromagnetic properties along with excellent cost-effectiveness, Carbon Black (CB) is commonly employed as a conductive filler.[37-41]. Notably, CB demonstrates optimal cost-effectiveness while maintaining superior electromagnetic performance. Ma et al[42]. investigated the use of geometric gradient structures in cement-based materials, employing CB as the wave-absorbing agent. They found that a CB content of over 1% achieved an EAB of over 12 GHz (RL of less than -5 dB) and a minimum RL of -19.4 dB in flat mortar. Conical specimens with a height of 30 mm and 3% CB content showed full-band absorption (RL <-5 dB), with a minimum RL of -40.26 dB. Wu et al.[43] developed a foamed cement-based EMW absorber using secondary aluminium ash and CB. Optimal CB content improved impedance matching, reducing RL. Higher CB content and thickness shifted the absorption peak to lower frequencies, thereby enhancing low-frequency performance and EAB. The optimised composite achieved an EAB of 14.46 GHz (RL <-10 dB) and a minimum RL of -36.34 dB (1.1-18 GHz).

Currently, CGFA is primarily regarded as a supplementary cementitious material in academic research, while its high unburned carbon content has not been effectively utilized in building material studies. Nevertheless, these unburned carbon components demonstrate remarkable electromagnetic properties, granting this industrial byproduct

significant application potential in capacitors, electromagnetic shielding and related fields. This discovery opens new possibilities for high-value utilization of CGFA, however, there are few studies on the electromagnetic properties of CGFA in the field of building materials so far. Focusing on the electromagnetic properties of unburned carbon, the effect of CGFA content on the conductivity, electromagnetic parameters, wave absorbing properties and underlying electromagnetic response mechanism of expanded perlite cement mortar were investigated in this study. Building upon this foundation, CB was introduced as a modifying agent into the CGFA cement mortar system. This modification strategy serves a dual purpose: first, it enables more in-depth investigation into the fundamental mechanisms governing electromagnetic behavior of CGFA through altering the matrix environment; second, it concurrently enhances the overall performance characteristics of the CGFA mortar by this way.

2 Materials and methods

2.1 Materials

The reference cement used in this experiment was produced by China Building Materials Academy *Co., Ltd.*. Its chemical composition and basic properties are listed in Table 1 and Table 2, respectively. The expanded perlite (EP), purchased from Xinyang Yongxin Perlite Application *Co., Ltd.*, has a packing density of 170 kg/m^{3}and a particle size range of 0.6-1.4 mm. CGFA is provided by Luoyang Ruichang Environmental Engineering *Co., Ltd.*, and its chemical composition is listed in Table 3, Fig.1 shows the microscopic morphology and particle size of CGFA, featuring spherical

microbeads (SiO_2-Al_2O_3) that resemble fly ash, as well as irregular, unburned carbon particles that are fragmentary, honeycomb-like or flaky in shape, and $D_{0.5}$ is 17.84 μm. Carbon black (CB) is purchased from Tianjin Jinqiushi Chemical *Co., Ltd.*, Fig.2 shows the microscopic morphology and particle size of CB, undispersed carbon black particles cluster together to form grape-like chains, and $D_{0.5}$ is 386.3 nm. The dispersant was purchased from China Weifang Wenbosi New Material *Co., Ltd.*. Fig.3 shows the electromagnetic parameters of the CGFA and the CB, data were measured by the coaxial method in this study, and the mass ratio of CGFA to both CB and paraffin was 3:7. Both materials exhibit high complex permittivity, indicating high dielectric loss and conductivity. However, their low permeability values suggest that electromagnetic energy dissipation occurs primarily through resistive and polarisation losses, rather than magnetic effects.

Table 1 Cement chemical compositions

Component	SiO_2	Al_2O_3	Fe_2O_3	CaO	SO_3	Na_2O	f-CaO	Loss	Cl^-
Content(%)	20.84	4.68	3.56	63.43	2.30	0.55	0.78	1.48	0.046

Table 2 Basal properties of cement

Density (g/cm^3)	Specific surface area	Initial setting time (min)	Final setting time (min)	Flexural Strength (MPa)	Compressive strength (MPa)

	(m^2/kg)			3d	28d	3d	28d
3.11	358	105	168	5.4	8.3	25.8	50.5

Table 3 CGFA chemical compositions

Component	SiO_2	Al_2O_3	Fe_2O_3	CaO	MgO	Na_2O	P_2O_5
Content(%)	41.34	23.75	11.14	10.01	2.83	3.86	2.23

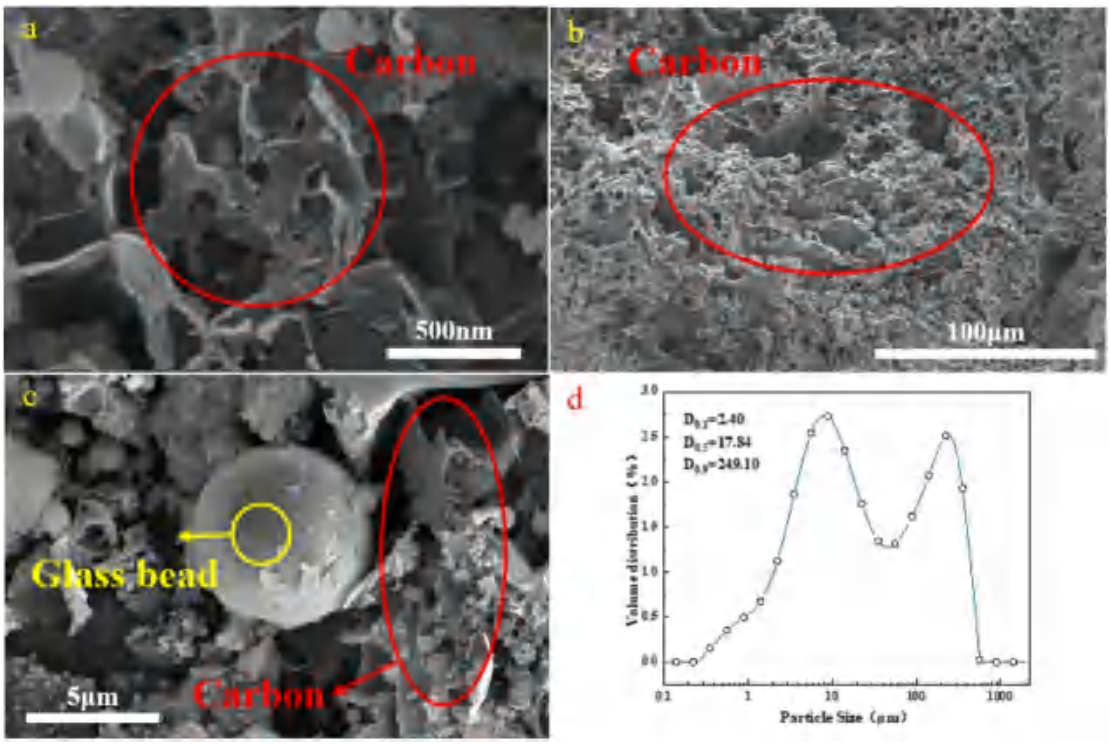

Fig.1 (a-c) Micromorphology, (d) particle size distribution of CGFA

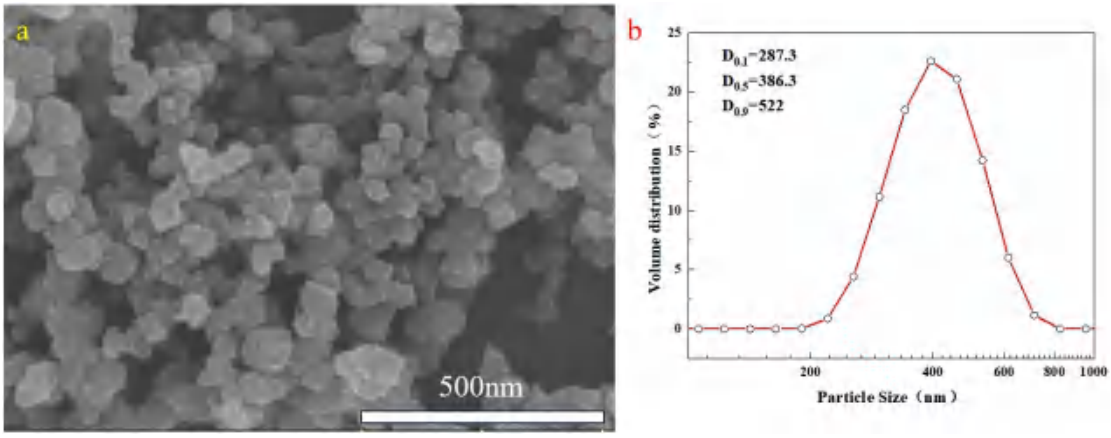

Fig.2 (a) Micromorphology and (b) particle size distribution of CB

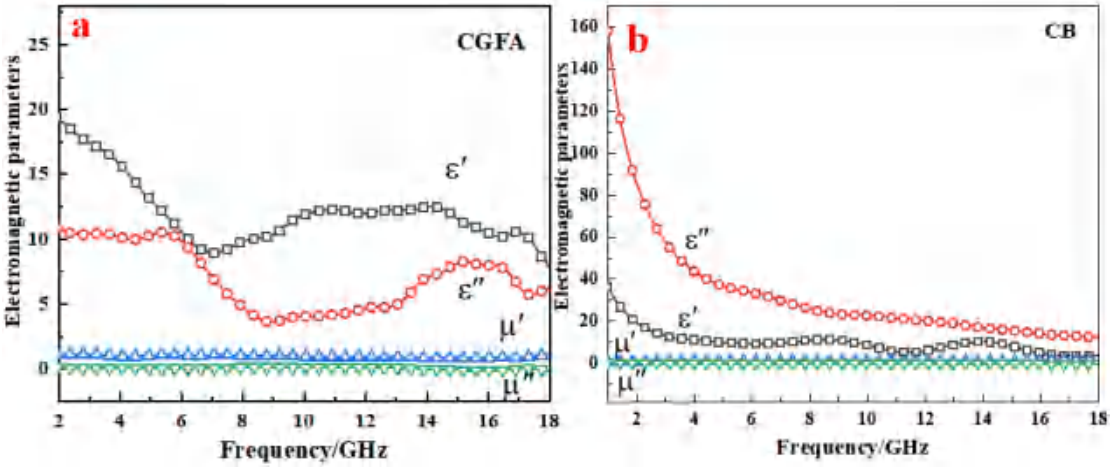

Fig.3 Electromagnetic parameters of (a) CGFA and (b) CB

2.2 Sample preparation

As detailed in Table 4, experimental specimens were prepared with CGFA replacing 0-10% of cement mass (in 2% increments) and CB content ranging from 0-1% of cement mass (in 0.25% increments). Both CGFA and CB exhibit significant water absorption. Therefore, to maintain similar fluidity in the cement mortar, the water content should be appropriately increased as the proportion of CGFA and CB is raised. The preparation process initiated with dry-mixing predetermined CGFA quantities with

reference cement in a mortar mixer at low speed for 5 min to ensure homogeneous dispersion. Subsequently, CB was ultrasonically dispersed in an aqueous solution containing dispersant (CB: dispersant = 5:1) to form a stable suspension. This CB suspension was then incorporated into the CGFA-cement mixture along with the remaining water, followed by 30 seconds mechanical mixing. Expanded perlite was added to the mixture, which underwent additional mixing for 90 seconds. The fresh mortar was cast into oil-coated steel molds with dimensions of 180 × 180 × 20 mm^3 (reflectivity testing) and 160 × 40 × 40 mm^3 (mechanical and resistivity testing). For resistivity measurements, four copper electrodes were embedded at standardized intervals using the four-probe method. Specimens were demolded after 24h and cured under standard conditions (20 ± 2 °C, RH >95%) for 28 days. Prior to testing, specimens were oven-dried at 60°C to constant mass and equilibrated to room temperature.

Table 4 Mix ratio of experimental sample

Samples	Cement/g	EP/g	Gas Fine Ash/g	CB/g	Water/g
BLANK	1300	204	0	0	468
CGFA2	1274	204	26	0	507
CGFA4	1248	204	52	0	546
GFA6	1222	204	78	0	585
GFA8	1196	204	104	0	624
GFA10	1170	204	130	0	663

CB0.25CGFA2	1274	204	26	3.25	507
CB0.25CGFA4	1248	204	52	3.25	546
CB0.25CGFA6	1222	204	78	3.25	611
CB0.25CGFA8	1196	204	104	3.25	624
CB0.25CGFA10	1170	204	130	3.25	663
CB0.5CGFA2	1274	204	26	6.5	507
CB0.5CGFA4	1248	204	52	6.5	546
CB0.5CGFA6	1222	204	78	6.5	611
CB0.5CGFA8	1196	204	104	6.5	624
CB0.5CGFA10	1170	204	130	6.5	663
CB0.75CGFA2	1274	204	26	9.75	507
CB0.75CGFA4	1248	204	52	9.75	572
CB0.75CGFA6	1222	204	78	9.75	611
CB0.75CGFA8	1196	204	104	9.75	650
CB0.75CGFA10	1170	204	130	9.75	676
CB1CGFA2	1274	204	26	13	520
CB1CGFA4	1248	204	52	13	572
CB1CGFA6	1222	204	78	13	624
CB1CGFA8	1196	204	104	13	663
CB1CGFA10	1170	204	130	13	689

2.3 Characterization method

The phase morphology and structure of CGFA, CB, and the prepared composite mortar were observed with a scanning electron microscope (Thermo Fisher Scientific-Quanta FEG 250, USA). The samples were ultrasonically dispersed in an anhydrous ethanol solution, and particle size analysis was conducted using a laser particle size analyzer (Mastersizer 3000+ Ultra, Malvern, UK). The resistivity of the sample was tested using the voltammetry method (Fig.4a). Due to the limitation of test equipment, the electromagnetic parameters of the prepared cement composite lightweight mortar can only be measured by the rectangular waveguide method (Fig.4b). The instrument used is a vector network analyzer (Agilent N5234A), and the test frequency bands are the X band (8.2-12.4 GHz) and the Ku band (12.4-18 GHz). The sample sizes were 22.9 mm × 10.2 mm × 5.0 mm and 15.8 mm × 7.9 mm × 2.0 mm, respectively. According to the Chinese national standard GJB 2038A-2011, the reflection loss (RL) of the sample within the 1.1-18 GHz band is measured by the Arch reflection method (Fig.4c). A mechanical testing machine was used to test the mechanical strength of cement mortar containing fine ash and CB, in accordance with the Chinese national standard GB/T 17671-2021 (Fig.4d). The loading rates for the compressive strength and flexural strength tests were 24 kN/s and 0.02 kN/s, respectively.

Fig.4 (a) Characterization process of resistivity, (b) electromagnetic characteristics, (c) absorbing performance, (d) and mechanical test

3 Results and discussion

3.1 Microscopic morphology

Fig.5 shows the microstructural characteristics of CGFA and CB-CGFA cement mortar. The low-magnification micrograph in Fig.5a reveals a composite structure consisting of a dense C-S-H gel matrix and expanded perlite aggregates. The mechanical integrity of the cementitious system is primarily maintained by the continuous C-S-H gel network. The abundant pores within the expanded perlite reduce the complex permittivity of the mortar, optimising impedance matching.

Fig.5b and Fig.5c show the microstructural characteristics of unburned carbon in the CGFA10 and CB0.75CGFA10 samples, respectively. Elemental analysis revealed that carbon was predominantly concentrated in the honeycomb-structured regions, whereas silicon, aluminium, calcium and oxygen were uniformly distributed in the surrounding matrix. This indicates that the honeycomb structure consists mainly of unburned carbon, which is consistent with SEM characterisation of the raw material. However, the large particle size and irregular morphology of these carbon particles restrict their uniform dispersion within the cementitious matrix. This necessitates a higher content to establish a well-developed conductive network.

Fig.6 shows the microstructure of the CB0.75CGFA10 composite. The micrograph reveals extensive CB deposition on unburned carbon surfaces, with individual CB

particles dispersed across the surfaces and CB aggregates forming grape-like chain structures. These CB particles form conductive bridges between unburned carbon particles of different sizes, which effectively supplements incomplete conductive pathways and enhances the composite's electrical conductivity. Furthermore, nano-sized CB particles can act as micro-nucleation sites, offering extra attachment points for C_3S and C_2S hydration. This mechanism accelerates hydration kinetics, enhances early strength development and improves the mechanical properties of the mortar.

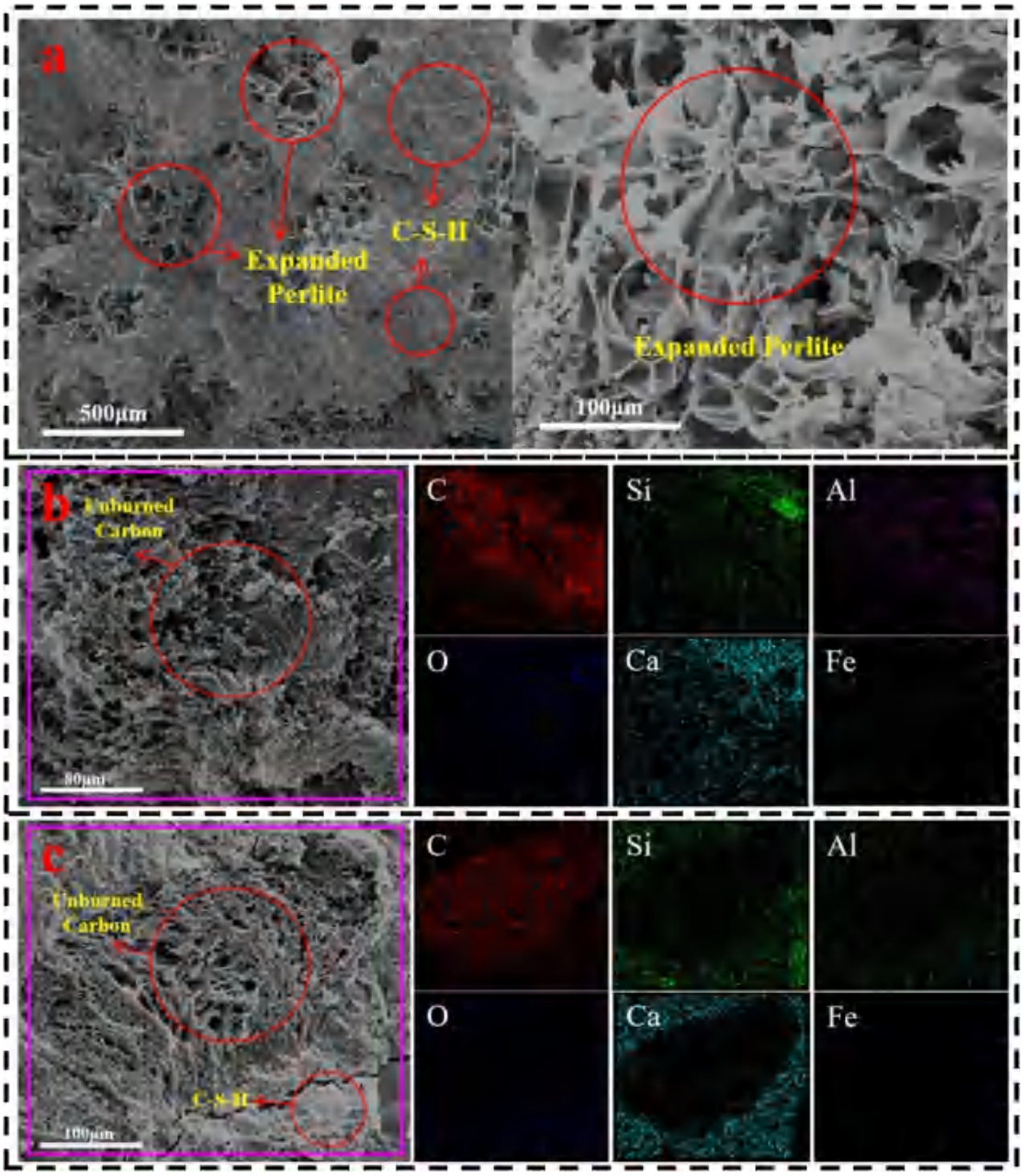

Fig.5 Microstructure: (a) 500 μm CGFA10, (b) 100 μm CGFA10,

(c) 100 μm CB0.75 CGFA10

Fig.6 Bonding morphology of CB0.75 CGFA10 (a)unburned carbon, (b)CB, (c)Element mapping.

3.2 Electromagnetic Characteristics

3.2.1 Electrical resistivity

Fig.7 shows the resistivity characteristics of cement mortar with different amounts of CGFA and CB. As can be seen from the figure, incorporating CGFA significantly enhances the mortar's electrical conductivity. The resistivity decreases progressively with increasing CGFA content, dropping from 1484.77 Ω • m to 531.54 Ω • m as the CGFA content increases from 2% to 10%. This phenomenon is due to the excellent conductivity of unburned carbon in CGFA. As particle concentration increases, improved interparticle contact facilitates electron transport and establishes fundamental conductive pathways. Incorporating CB significantly reduces the resistivity of CGFA mortar. When the CGFA content was held constant, resistivity decreased progressively with increasing CB content. Conversely, when the CB content was fixed, the resistivity gradually declined as the percentage of CGFA increased. Increasing the CB content to 1% reduced the resistivity further, from 531.54 Ω • m to 167.8 Ω • m. Compared to micrometre-sized unburned carbon particles, nano-scale CB particles demonstrated superior uniformity of dispersion. In this conductive system, the unburned carbon

particles formed the primary conductive framework and the dispersed CB nanoparticles acted as microscopic conductive units within it. This configuration provided more efficient pathways for electron hopping, thereby optimising the overall conductive network structure.

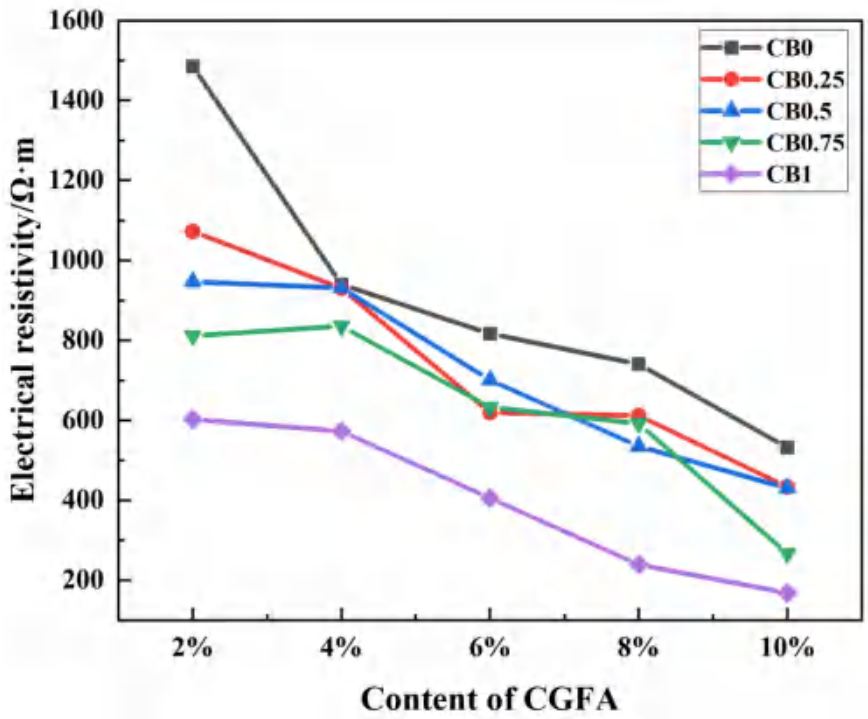

Fig.7 Resistivity of CGFA and CB-CGFA cement mortar

3.2.2 Electromagnetic Parameters

Fig.8 presents the electromagnetic parameters of cement mortar incorporating CGFA across the 8.2–18 GHz frequency range. The complex permittivity (ε' and ε") and the dielectric loss tangent (tan δe) show a positive correlation with CGFA content and frequency. Specifically, increasing the CGFA content from 0% to 10% enhanced the real part of the complex permittivity (ε') from 4.19 to 5.24, the imaginary part (ε") from 0.30 to 1.21 and the dielectric loss tangent (tan δe) from 0.07 to 0.23. These enhancements are attributed to dipole and interfacial polarization mechanisms coupled

with improved electrical conductivity[44]. The dielectric behaviour observed suggests that CGFA primarily contributes to EMW attenuation through dielectric loss mechanisms, as supported by resistivity data in Fig.6 and Cole–Cole analysis in Fig.9. In contrast, the complex permeability parameters (μ' and μ") demonstrate an inverse relationship with CGFA content and frequency. The maximum μ' value declined from 1.17 to 1.04, the μ" value reduced from 0.09 to -0.12 and the magnetic loss value decreased from 0.09 to 0.012. This suggests that the EM wave absorption mechanism in CGFA-modified mortar is predominantly governed by dielectric and resistive losses rather than magnetic losses.

Fig.9 presents the electromagnetic parameters of CGFA cement mortar containing 0.75% CB across the 8.2–18 GHz frequency range. The complex permittivity and dielectric loss tangent of the CB-CGFA system exhibit similar trends to those of the CGFA system, with increased values observed at higher CGFA contents. However, the CB-CGFA system demonstrates enhanced dielectric stability at 2%-6% CGFA content across the 8.2-18 GHz range, followed by frequency-dependent increases at 8%-10% CGFA content. Specifically, increasing the CGFA content from 0% to 10% resulted in an increase in ε' from 4.19 to 5.68, an increase in ε" from 0.30 to 1.33, and an improvement in tan δe from 0.07 to 0.23. These enhancements are superior to those of the CGFA system and are attributed to the intrinsic dielectric properties of CB, indicating significant EMW attenuation potential. The complex permeability parameters exhibit mixed trends in the CB-CGFA system. The maximum values decreased from 1.17 to 1.04 for μ', from 0.09 to -0.001 for μ", and from 0.09 to 0.02 for

magnetic loss. While these reductions are less pronounced than in the CGFA system, this suggests that CB partially mitigates permeability loss. Nevertheless, the overall magnetic properties remain relatively unaffected. The electromagnetic loss mechanism in CB-CGFA cement mortar is primarily governed by dielectric and resistive losses, with minimal contribution from magnetic loss mechanisms.

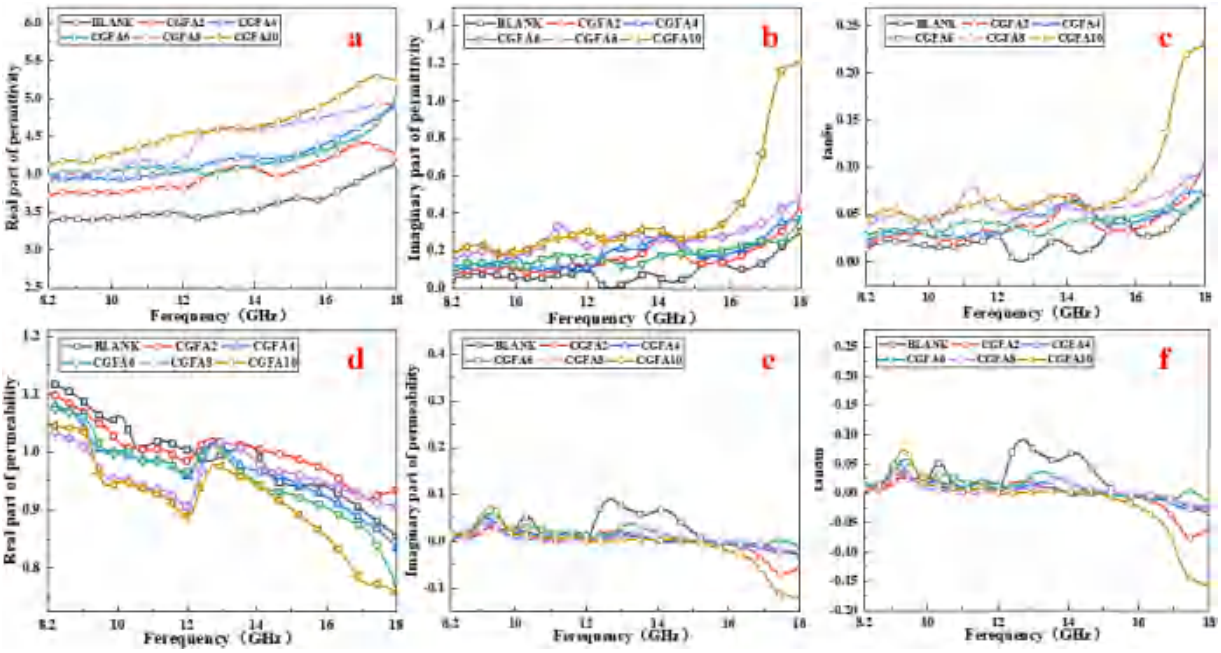

Fig.8 Electromagnetic parameters of CGFA cement mortar:

(a)Real part of permittivity, (b)Imaginary part of permittivity, (c)dielectric loss factor,

(d)Real part of permeability, (e)Imaginary part of permeability,

(f)permeability loss factor.

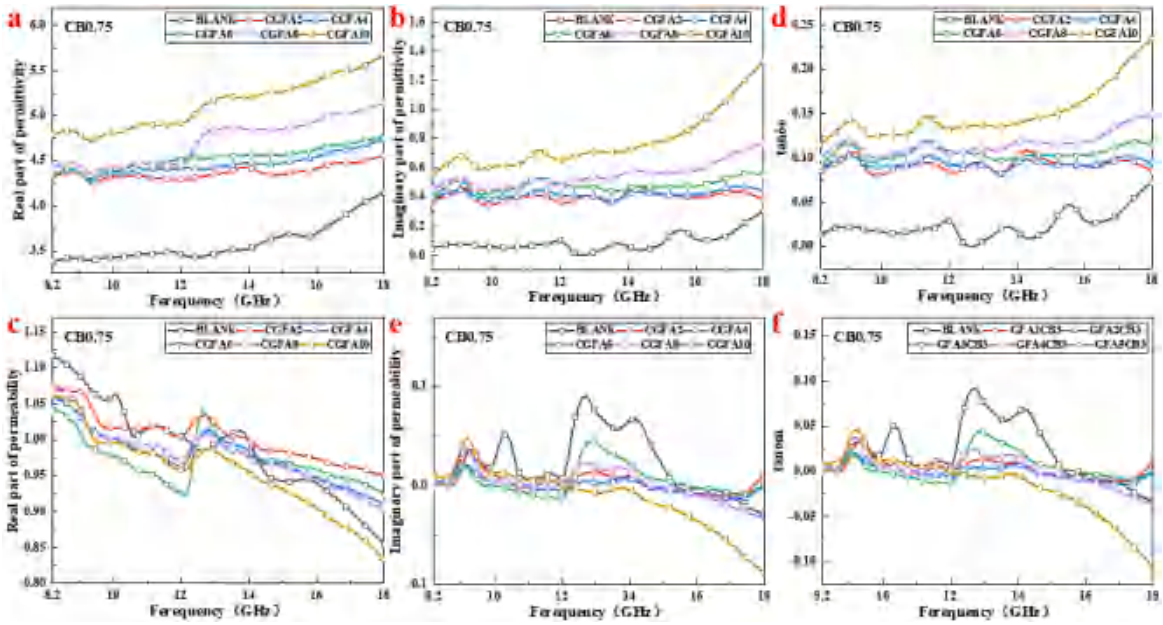

Fig.9 Electromagnetic parameters of CB-CGFA cement mortar:

(a)Real part of permittivity, (b)Imaginary part of permittivity, (c)dielectric loss factor,

(d)Real part of permeability, (e)Imaginary part of permeability,

(f)permeability loss factor.

3.2.3 Cole-Cole curve

Fig.10 shows the Cole-Cole semicircle plots of CGFA cement mortar across the 8.2-18 GHz frequency range. The Cole-Cole analysis, derived from the complex permittivity spectrum, provides critical insights into dielectric relaxation processes through the relationship[45,46].

$$\left(\varepsilon' - \frac{\varepsilon_s + \varepsilon_\infty}{2}\right)^2 + (\varepsilon'')^2 = \left(\frac{\varepsilon_s - \varepsilon_\infty}{2}\right)^2 \tag{1}$$

Where ε_s is the static dielectric constant, ε_∞ is the dielectric constant at high-frequency limits, ε' is the real part of the complex dielectric constant, ε'' is the imaginary part of the complex dielectric constant. The original electromagnetic parameter data presented in this paper were directly obtained from Fig.8 and Fig.9.

The Cole-Cole analysis provides critical insights into dielectric relaxation mechanisms. The presence of semicircular arcs in the complex permittivity plot indicates dominant polarization effects and associated dielectric loss characteristics. Multiple distinct semicircles correspond to various polarization processes, while the absence or distortion of semicircular features indicates that the main loss mechanism is resistive loss. The control group consisting of pure cement mortar exhibits several well-defined Cole-Cole semicircles, indicating substantial polarization capability primarily attributed to interfacial polarization at micron-scale particle boundaries within the cement matrix[47,48]. Low CGFA content (2%-4%) demonstrates minimal alteration in Cole-Cole behavior compared to pure cement. However, at higher CGFA concentrations (6%-10%), the semicircular features become less pronounced and morphologically distinct, revealing reduced polarization capability relative to pure cement and a transition to resistive loss-dominated mechanisms. This phenomenon can be attributed to two main factors. Firstly, CGFA has relatively weak polarisation capabilities. Secondly, the excessive electrical conductivity resulting from elevated CGFA content is an additional contributing factor.

Fig.11 shows the Cole-Cole semicircle analysis of CB-CGFA cement mortar across the 8.2-18 GHz frequency range. The analysis reveals a substantial increase in the number of semicircular arcs compared to CGFA systems, indicating enhanced polarization capability through CB incorporation. This enhancement originates from CB's nanoscale dimensions and associated multi-interface characteristics, which significantly promote interfacial polarization effects. However, the CB-CGFA system

demonstrates a more pronounced reduction in semicircle count with increasing CGFA content compared to the CGFA system. At 8% CGFA content, the polarization characteristics of CB-CGFA and CGFA systems begin to converge. This behavior stems from the distinct particle size distributions: while cement particles typically range in the tens of micrometers, CGFA spans several to hundreds of micrometers, and CB exists at the nanoscale (hundreds of nanometers). The significant size disparity between CGFA and CB particles, compared to the Cement-CGFA system, leads to more substantial reduction in polarization capability as CGFA content increases.

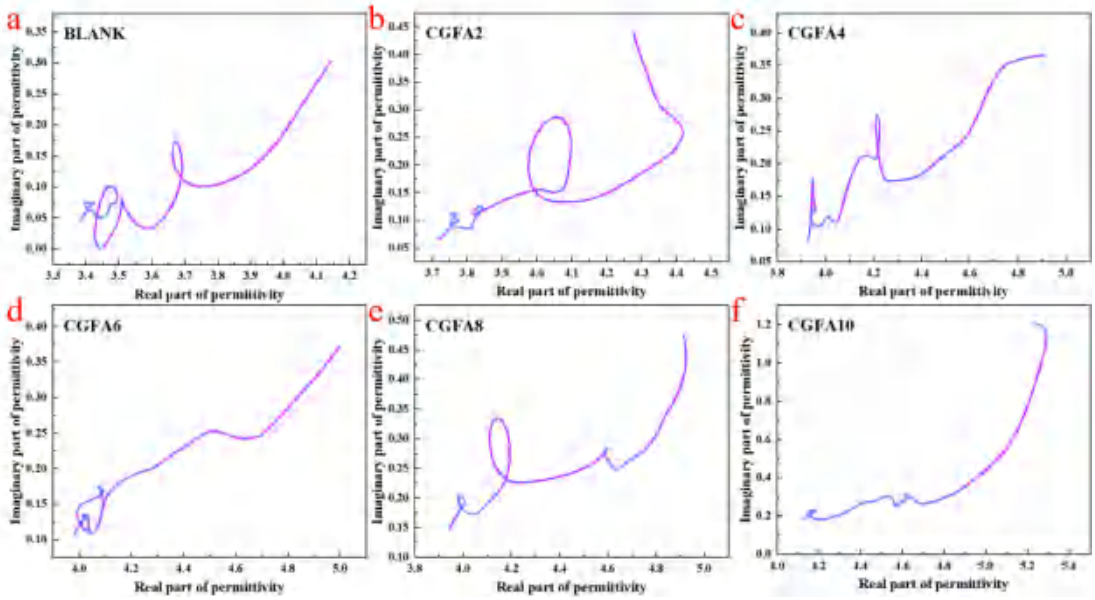

Fig.10 Cole-Cole curve of CGFA cement mortar: (a)BLANK, (b)CGFA2, (C)CGFA4, (d)CGFA6, (e)CGFA8, (f)CGFA10.

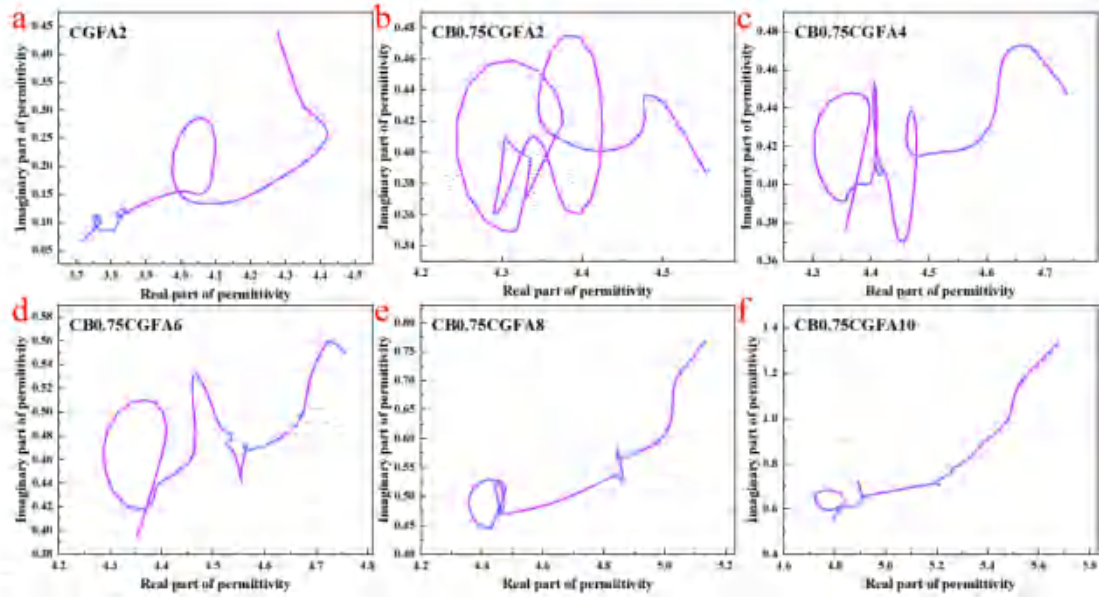

Fig.11 Cole-Cole curve of CB-CGFA cement mortar: (a)CGFA2, (b)CB0.75CGFA2, (C)CB0.75CGFA4, (d)CB0.75CGFA6, (e)CB0.75CGFA8, (f)CB0.75CGFA10.

3.3 EMW absorbing performance

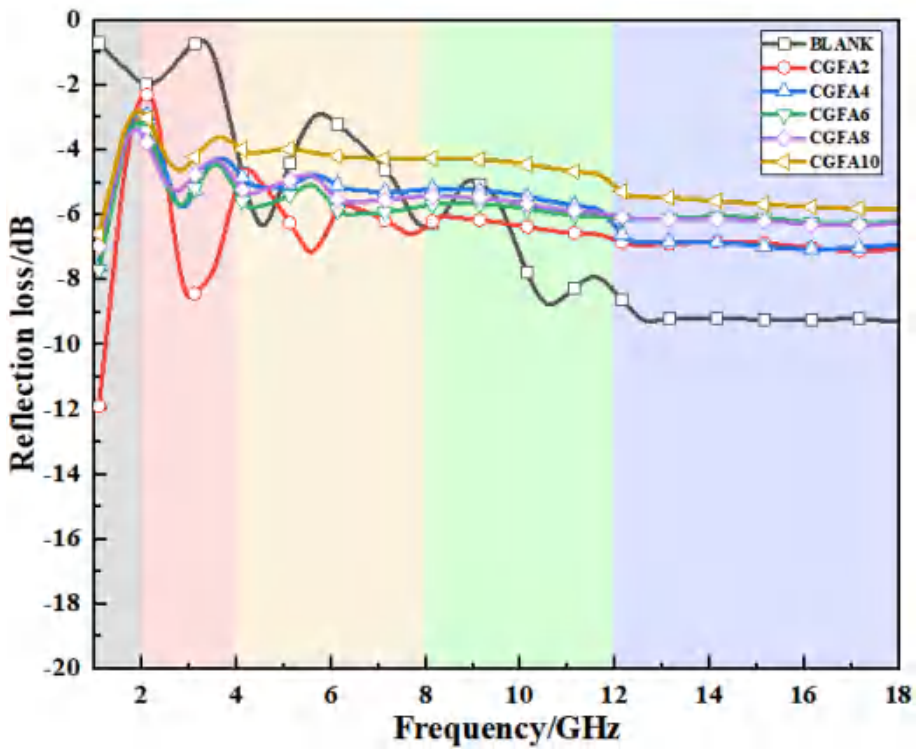

Fig.12 EMW absorbing performance of CGFA cement mortar

Fig.12 curves demonstrate the EMW absorbing performance of cement mortar with varying CGFA contents. This performance exhibits frequency-dependent behaviour. CGFA incorporation reduces absorption efficiency within the 8-18 GHz range, while enhancing performance at 1-8 GHz. Notably, the minimum RL of -11.9 dB is reached at 1.1 GHz, which is attributed to resistive loss mechanisms from residual carbon in the CGFA. The interference absorption peak shifts towards lower frequencies as the CGFA content increases, which is consistent with quarter-wavelength theory (Eq.2) [49,50]. RL analysis shows that increasing CGFA content leads to a progressive increase in RL. This is due to reduced polarization capability, as evidenced by Cole-Cole analysis in Fig.9, and consequent dielectric loss reduction. Simultaneously, impedance mismatch occurs due to the increasing complex permittivity and electrical conductivity of higher CGFA contents. This impedance mismatch promotes the reflection of EMW at the surface, thereby diminishing absorption efficiency.

$$f_m = \frac{(2n+1)c}{4d\sqrt{\varepsilon_r \mu_r}}, (\mathrm{n} = 1,2,3,.) \tag{2}$$

Where f_m is corresponding matching frequency, d is matching thickness, ε_r is the relative complex permittivity and μ_r is the relative permeability.

Fig.13 shows the EMW absorbing performance of CB-CGFA cement mortar. Incorporating CB significantly enhances the absorption characteristics, particularly within the 0.5-0.75% CB range, where distinct absorption peaks emerge at 4.2 and 7.8 GHz. Optimal performance is achieved with 2% CGFA and 0.75% CB, with a minimum RL of -18.95 dB at 4.24 GHz. However, adding more CB beyond this optimal concentration causes the RL value to rise. This phenomenon results from multiple

interacting mechanisms. The addition of CB increases interfacial polarization within the CGFA mortar, thereby enhancing the dielectric loss effects. This improves low-frequency impedance matching, facilitating greater EMW penetration and subsequent energy dissipation. As shown in Fig.6, forming a percolative conductive network at 1% CB significantly increases electrical conductivity, promoting the reflection of incident waves from the surface and consequently raising RL values[51].

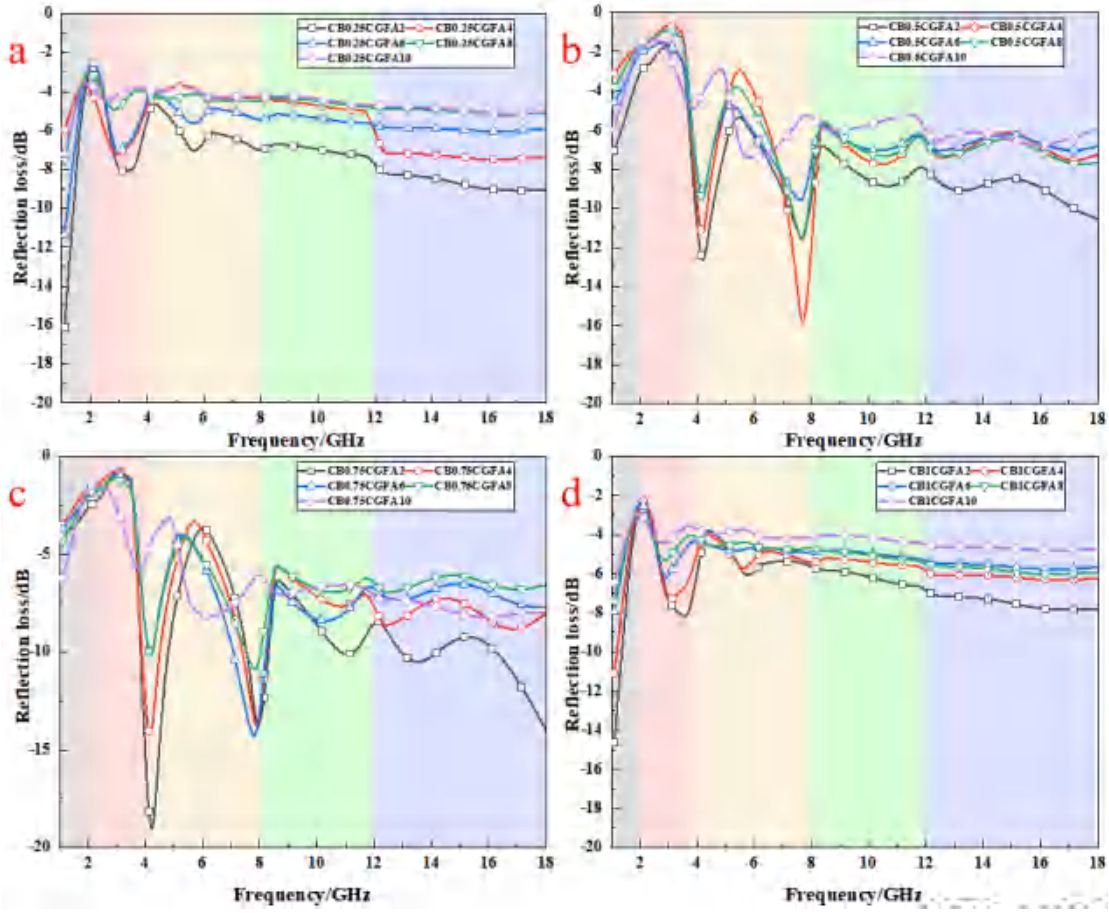

Fig.13 EMW absorbing performance of CB-CGFA cement mortar:

(a)CB0.25CGFA2-10, (B)CB0.5CGFA2-10, (B)CB0.75CGFA2-10, (B)CB1CGFA2-10.

3.4 Strength

As illustrated in Fig.14, the impact of CGFA and CB on the mechanical strength of cement mortar is demonstrated, the compressive and flexural strengths of the mortar both gradually decrease as the CGFA content increases. This phenomenon is attributed to the presence of substantial quantities of unburned carbon within the CGFA. SEM images demonstrate that the carbon particles are substantial in size and possess a porous nature, thereby forming weak zones within the mortar and thereby diminishing its localised strength. Furthermore, CGFA exhibits a notable propensity for water absorption, and an augmented level of CGFA incorporation has been demonstrated to elevate the water content, thereby impeding C-S-H hydration. However, when the CGFA content is 2%, corresponding to the sample with the best wave-absorbing performance, the reduction in compressive strength is only 3.2% compared to the pure cement control group. The incorporation of 0.75% CB did not have a significant effect on the flexural strength of the mortar, but it did have a notable effect on its compressive strength. This phenomenon can be attributed to the nanoscale nature of CB, which provides additional micro-hydration sites for cementitious materials and thereby promotes hydration. However, as the CGFA content increases, the effectiveness of this strengthening mechanism decreases. It is interesting to note that when the CB content is set at 0.75% and the CGFA content is 2%, corresponding to the sample with optimal wave-absorbing performance, the compressive strength is recorded at 43.9 MPa, which is 15.47% higher than that of the pure cement mortar control group.

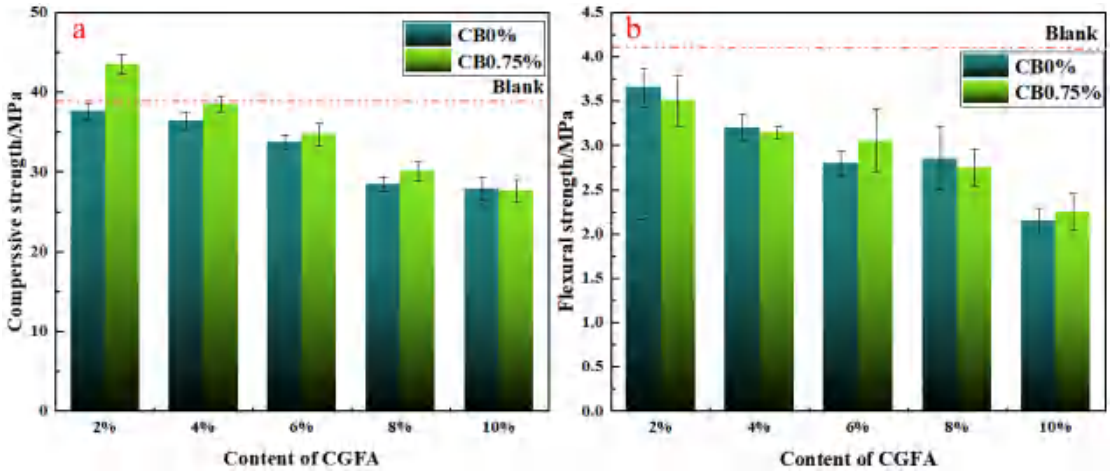

Fig.14 (a) Compressive strength and (b) Flexural strength of cement mortar

4 Conclusion

To summarise, the present study systematically investigated the electrical conductivity and electromagnetic shielding properties of CGFA in cement mortar. The findings indicate that CGFA efficiently reduces the electrical resistivity of cement mortar, substantially enhances its composite dielectric constant, and improves the wave absorption performance in low-frequency ranges. The RL value was found to be positively correlated with CGFA content, with the electromagnetic wave loss mechanism being dominated by resistive loss. When the CGFA content reached 2%, the optimal RL value of -11.9 dB was achieved at 1.1 GHz.The incorporation of CGFA was observed to result in a gradual decrease in both the flexural and compressive strengths of cement mortar. However, when compared to the control group, the specimen with optimal wave absorption performance exhibited a mere 3.2% reduction in strength.

The incorporation of CB has been demonstrated to enhance the electrical conductivity and EMW absorption performance of CGFA mortar. The incorporation of CB into CGFA mortar has been demonstrated to enhance its polarization loss capability.

In the absence of any alteration to the content of CGFA, the RL exhibited an initial decrease followed by an increase in conjunction with rising CB concentrations. Conversely, under conditions of constant CB levels, the RL maintained a positive correlation with CGFA content. The optimal absorption performance was achieved at a CGFA content of 2% and a CB dosage of 0.75%, with a peak RL value of -18.95 dB at 4.24 GHz. In addition, the incorporation of CB was found to enhance the mechanical strength of CGFA mortar. When the CB content was 0.75%, the CB-CGFA specimen with the best EMW absorbing performance exhibited a 15.47% increase in strength compared to the control group. Consequently, CGFA exhibits considerable promise for advancement in the domain of electromagnetic wave absorption within cement-based materials, with its performance susceptible to enhancement through synergistic combinations with other carbon-based materials.

Reference

[1] JIA W, LI L, LEI Y, *et al*. Synergistic effect of CO2 and PM2.5 emissions from coal consumption and the impacts on health effects [J]. *Journal of Environmental Management*, 2023. DOI: 10.1016/j.jenvman.2022.116535

[2] GUAN Y, SHAN Y, HUANG Q, *et al*. Assessment to China's Recent Emission Pattern Shifts [J]. *Earth's Future*, 2021, 9: 11. DOI: 10.1029/2021ef002241

[3] SHI J, WAN N, LI L, *et al*. Review on treatment technologies of coal gasification wastewater in China [J]. *Journal of Cleaner Production*, 2022, 333: 130166. DOI: 10.1016/j.jclepro.2021.130166

[4] XIAO J, WANG S, YE S, *et al*. Thermo-economic optimization of gasification

process with coal water slurry preheating technology [J]. *Energy*, 2020, 199. DOI: 10.1016/j.energy.2020.117354

[5] ZHENG S, SHI Y, WANG Z, *et al*. Development of new technology for coal gasification purification and research on the formation mechanism of pollutants [J]. *International Journal of Coal Science & Technology*, 2021, 8: 335-348. DOI: 10.1007/s40789-021-00420-w

[6] LIU W, OUYANG Z, CAO X, *et al.* The influence of air-stage method on flameless combustion of coal gasification fly ash with coal self-preheating technology [J]. *Fuel*, 2019, 235: 1368-1376. DOI: 10.1016/j.fuel.2018.08.127

[7] XIE W, ZHANG Z, WANG Y, *et al*. Research on grinding and flotation decarbonization of coal gasification fine slag [J]. *Fuel*, 2024, 365. DOI: 10.1016/j.fuel.2024.131136

[8] JIAO Y, YANG Z, HAN X, *et al.* Ultrasonication Improves the Flotation of Coal Gasification Fine Slag Residue [J]. *Minerals*, 2024, 14: 4. DOI: 10.3390/min14040363

[9] MIELKE K, WU G, EBERHARD M, *et al.* Optimization of Slag Mobility of Biomass Fuels in a Pilot-scale Entrained-Flow Gasifier [J]. *Chemical Engineering & Technology*, 2021, 44: 1302-1310. DOI: 10.1002/ceat.202000531

[10] LI J, FAN S, ZHANG X, *et al.* Investigation on co-combustion of coal gasification fine ash and raw coal blends: Thermal conversion, gas pollutant emission and kinetic analyses [J]. *Energy*, 2022, 246. DOI: 10.1016/j.energy.2022.123368

[11] JIA W, GUO Y, GUO F, *et al*. Co-combustion of carbon-rich fraction from coal

gasification fine slag and biochar: Gas emission, ash sintering, heavy metals evolutions and environmental risk evaluation [J]. *Chemical Engineering Journal*, 2023, 471. DOI: 10.1016/j.cej.2023.144312

[12] LIU D, WANG W, TU Y, *et al*. Flotation specificity of coal gasification fine slag based on release analysis [J]. *Journal of cleaner production*, 2022. DOI: 10.1016/j.jclepro.2022.132426

[13] LUO F, JIANG Y, WEI C. Potential of decarbonized coal gasification residues as the mineral admixture of cement-based material [J]. *Construction and Building Materials,* 2021, 269. DOI: 10.1016/j.conbuildmat.2020.121259

[14] LI Z, ZHANG Y, ZHAO H, *et al*. Structure characteristics and composition of hydration products of coal gasification slag mixed cement and lime [J]. *Construction and Building Materials*, 2019, 213: 265-274. DOI: 10.1016/j.conbuildmat.2019.03.163

[15] LUO F, WEI C. Effects of Decarbonized Coal Gasification Coarse Slag and Fine Ash on Properties of Cement Paste as Supplementary Cementitious Materials [J]. *Journal of Materials in Civil Engineering*, 2022. DOI: 10.1061/(asce)mt.1943-5533.0004439

[16] MAO X, ZHAO J, LIU J, *et al*. Use of coal chemical industry by-product coal gasification fine ash as supplementary cementitious materials in cement: Chemical excitation, hydration and hardening characteristics [J]. *Construction and Building Materials*, 2024, 426. DOI: 10.1016/j.conbuildmat.2024.136147

[17] XIANG J, QIU J, ZHAO Y, *et al.* Rheology, mechanical properties, and hydration

of synergistically activated coal gasification slag with three typical solid wastes [J]. *Cement and Concrete Composites*, 2024, 147. DOI: 10.1016/j.cemconcomp.2023.105418

[18] MIAO Z, CHEN L, CHEN K, *et al.* Physical properties and microstructures of residual carbon and slag particles present in fine slag from entrained-flow coal gasification [J]. *Advanced Powder Technology*, 2020, 31: 3781-3789. DOI: 10.1016/j.apt.2020.07.019

[19] LÜ D-P, BAI Y-H, WANG J-F, *et al.* Structural features and combustion reactivity of residual carbon in fine slag from entrained-flow gasification [J]. *Journal of Fuel Chemistry and Technology*, 2021, 49: 129-136. DOI: 10.1016/s1872-5813(21)60011-7

[20] WANG Q, BAI Y, LV P, *et al*. Separation and characterization of different types of residual carbon in fine slag from entrained flow coal gasification [J]. *Fuel*, 2023, 339. DOI: 10.1016/j.fuel.2023.127437

[21] DAI G, ZHENG S, WANG X, *et al*. Combustibility analysis of high-carbon fine slags from an entrained flow gasifier [J]. *Journal of Environmental Management*, 2020, 271. DOI: 10.1016/j.jenvman.2020.111009

[22] XU S, ZHOU Z, GAO X, *et al*. The gasification reactivity of unburned carbon present in gasification slag from entrained-flow gasifier [J]. *Fuel Processing Technology*, 2009, 90: 1062-1070. DOI: 10.1016/j.fuproc.2009.04.006

[23] GUO F, CHEN L, LI Y, *et al*. Review on the attribute cognition and carbon-ash-water separation of coal gasification fine slag [J]. *Separation and Purification*

Technology, 2023, 320. DOI: 10.1016/j.seppur.2023.124121

[24] GAO S, CHEN L, ZHANG Y, *et al*. FeOx Nanoparticle/Coal Gasification Fine Slag Hybrids for Electromagnetic Wave Absorbers [J]. *ACS Applied Nano Materials*, 2022, 5: 7767-7677. DOI: 10.1021/acsanm.2c00781

[25] HE J, GAO S, ZHANG Y, *et al*. Nanoferric tetroxide decorated N-doped residual carbon from entrained-flow coal gasification fine slag for enhancing the electromagnetic wave absorption capacity [J]. *Journal of Alloys and Compounds*, 2021, 874. DOI: 10.1016/j.jallcom.2021.159878

[26] GAO S, ZHANG Y, LI H, *et al*. The microwave absorption properties of residual carbon from coal gasification fine slag [J]. *Fuel*, 2021, 290. DOI: 10.1016/j.fuel.2020.120050

[27] C S G A B, A L C, C Y Z, *et al.* Fe nanoparticles decorated in residual carbon from coal gasification fine slag as an ultra-thin wideband microwave absorber [J]. *Composites Science and Technology*, 2021. DOI: 10.1016/j.compscitech.2021.108921

[28] ZHANG X, ZHANG Y, HE J, *et al*. ZnFe2O4 nanospheres decorated residual carbon from coal gasification fine slag as an ultra-thin microwave absorber [J]. *Fuel*, 2023, 331. DOI: 10.1016/j.fuel.2022.125811

[29] ZHANG Y, GAO S, ZHANG X, *et al*. Structural and microwave absorption properties of CoFe2O4/residual carbon composites [J]. *International Journal of Minerals, Metallurgy and Materials*, 2024, 32: 221-232. DOI: 10.1007/s12613-024-2849-0

[30] GAO ST, Z Y. Physicochemical properties and electromagnetic wave absorption performance of coal gasification fine ash [J]. *Acta Materiae Compositae Sinica*, 2024, 41: 2559-2574. DOI: 10.13801/j.cnki.fhclxb.20231026.001

[31] XIE S, WANG J, WANG W, *et al*. Electromagnetic wave absorption properties of cement based composites using helical carbon fibers as absorbent [J]. *Materials Research Express*, 2018, 5. DOI: 10.1088/2053-1591/aaae51

[32] PARK G, KIM S, PARK G-K, *et al*. Influence of carbon fiber on the electromagnetic shielding effectiveness of high-performance fiber-reinforced cementitious composites [J]. *Journal of Building Engineering*, 2021, 35. DOI: 10.1016/j.jobe.2020.101982

[33] ZHANG L, HAN B, OUYANG J, *et al*. Multifunctionality of cement based composite with electrostatic self-assembled CNT/NCB composite filler [J]. *Archives of Civil and Mechanical Engineering*, 2017, 17: 354-364. DOI: 10.1016/j.acme.2016.11.001

[34] ZHANG W, ZHENG Q, WANG D, *et al*. Electromagnetic properties and mechanisms of multiwalled carbon nanotubes modified cementitious composites [J]. *Construction and Building Materials*, 2019, 208: 427-443. DOI: 10.1016/j.conbuildmat.2019.03.029

[35] SACHDEV V K, SHARMA S K, BHATTACHARYA S, *et al*. Electromagnetic Shielding Performance Of Graphite In Cement Matrix For Applied Application [J]. *Advanced Materials Letters*, 2015, 6: 965-972. DOI: 10.5185/amlett.2015.5935

[36] BHATTACHARYA S, SACHDEV V K, CHATTERJEE R, *et al*. Decisive

properties of graphite-filled cement composites for device application [J]. *Applied Physics A*, 2008, 92: 417-420. DOI: 10.1007/s00339-008-4544-9

[37] LI B, JI Z, XIE S, *et al*. Electromagnetic wave absorption properties of carbon black/cement-based composites filled with porous glass pellets [J]. *Journal of Materials Science: Materials in Electronics*, 2019, 30: 12416-12425. DOI: 10.1007/s10854-019-01600-w

[38] WU J, XIE S, JI Z, *et al*. Effect of carbon black dispersion on cement mortar properties: Microstructure and electromagnetic properties [J]. *Mechanics of Advanced Materials and Structures*, 2024: 1-16. DOI: 10.1080/15376494.2024.2401635

[39] WU J, XIE S, JI Z, *et al*. Effect of nano carbon black content and dispersibility on the properties of cement paste [J]. *Proceedings of the Institution of Civil Engineers - Transport*, 2024: 1-13. DOI: 10.1680/jtran.24.00026

[40] LEE N, KIM S, PARK G. The Effects of Multi-Walled Carbon Nanotubes and Steel Fibers on the AC Impedance and Electromagnetic Shielding Effectiveness of High-Performance, Fiber-Reinforced Cementitious Composites [J]. *Materials*, 2019, 12. DOI: 10.3390/ma12213591

[41] PAPACHRISTOFOROU M, PAPAYIANNI I. Radiation shielding and mechanical properties of steel fiber reinforced concrete (SFRC) produced with EAF slag aggregates [J]. *Radiation Physics and Chemistry*, 2018, 149: 26-32. DOI: 10.1016/j.radphyschem.2018.03.010

[42] MA C, XIE S, JI Z, *et al*. Electromagnetic wave absorbing properties of pyramidal

engineered cement mortar containing carbon black [J]. *Journal of Building Engineering*, 2024, 84. DOI: 10.1016/j.jobe.2024.108618

[43] WU Z, XIE S, JI Z, *et al*. Novel lightweight cement-based materials foaming by secondary aluminum ash: microwave absorption, mechanical and thermal insulation properties [J]. *Construction and Building Materials*, 2024, 413. DOI: 10.1016/j.conbuildmat.2023.134328

[44] QIN H, LIAO Q, ZHANG G, *et al.* Microwave absorption properties of carbon black and tetrapod-like ZnO whiskers composites [J]. *Applied Surface Science*, 2013, 286: 7-11. DOI: 10.1016/j.apsusc.2013.08.078

[45] YUE L, YANG Y, ZHOU Q, *et al*. Broadband electromagnetic wave absorbing performance by designing the foam structure and double-layer for cement-based composites containing MWCNTs [J]. *Cement and Concrete Composites*, 2022. DOI: 10.1016/j.cemconcomp.2022.104595

[46] TAN L, ZHU M, LI X, *et al.* Lightweight excellent microwave absorption properties based on sulfur doped graphene [J]. *Journal of Saudi Chemical Society*, 2020, 24: 9-19. DOI: 10.1016/j.jscs.2019.08.005

[47] XING W, LI P, WANG H, *et al.* The similar Cole-Cole semicircles and microwave absorption of Hexagonal Co/C composites [J]. *Journal of Alloys and Compounds*, 2018, 750: 917-926. DOI: 10.1016/j.jallcom.2018.04.051

[48] LI D, LIANG X, LIU W, *et al*. Adjustable 3-D structure with enhanced interfaces and junctions towards microwave response using FeCo/C core-shell nanocomposites [J]. *Journal of Colloid and Interface Science*, 2017, 507: 131-138.

DOI: 10.1016/j.jcis.2017.07.118

[49] DENG G, YANG Y, ZHOU Q, *et al*. Lightweight and broadband electromagnetic wave absorbing foamed cement-based composites incorporated with hybrid dielectric fibers [J]. *Construction and Building Materials*, 2022, 327. DOI: 10.1016/j.conbuildmat.2022.126931

[50] SI T, XIE S, MA C, *et al*. Microwave absorption properties of double-layer structured basalt fiber/resin composites containing carbon black and nano-Fe3O4 [J]. *Composite Interfaces*, 2023, 30: 959-981. DOI: 10.1080/09276440.2023.2179257

[51] DAI Y, SUN M, LIU C, *et al.* Electromagnetic wave absorbing characteristics of carbon black cement-based composites [J]. *Cement and Concrete Composites*, 2010, 32: 508-513. DOI: 10.1016/j.cemconcomp.2010.03.009

PAPER • OPEN ACCESS

Rheological Properties of Warm Mixed Asphalt

To cite this article: Rong Chang *et al* 2023 *J. Phys.: Conf. Ser.* **2553** 012009

View the article online for updates and enhancements.

You may also like

- Low-temperature Performance and its Microstructure of SBS Modified Asphalt under Condition of Aging
Yunlian Song, Ning Zhao, Yang Zhang et al.
- Marshall immersion test of warm mix asphalt polymer using Bayat natural zeolite
A T Handayani, S N Peni and H Pandita
- Physical properties of warm cup lump modified bitumen
S Abdulrahman, M R Hainin, M K Idham et al.

This content was downloaded from IP address 223.70.210.76 on 14/12/2023 at 01:42

Rheological Properties of Warm Mixed Asphalt

Rong Chang, Yongchun Qin*, Peng Wang

Research Institute of Highway Ministry of Transport, Beijing 100088, China

Corresponding author: Yongchun Qin E-mail: yc.qin@rioh.cn

Abstract. Adding a warm mixing agent to asphalt can lower the working temperature of asphalt construction by 20–40 ℃. It is difficult to evaluate the impact of the existing warm mixed agent on the quality and effect of asphalt due to its wide variety. In this study, 70 # asphalt and 3 kinds of surfactants were selected to prepare warm mix asphalt. The result of different warm mix agents on the rheological properties of asphalt was evaluated through a rheological experiment. The results explained that the warm mixing agent could lower the Brookfield viscosity of asphalt. With the increase in asphalt temperature, the viscosity difference of different types of asphalt binder becomes smaller and smaller. A warm mixing agent will also reduce the creep stiffness of asphalt. In the multiple stress creep recovery test, the average recovery rate of asphalt and the average value of irrecoverable creep compliance have obvious stress dependence.

1. Introduction

There are many kinds of warm mixing agent products on the market, which have different effects on the quality of asphalt after being mixed with asphalt [1-3]. It is hard to predict the impact of warm mixture on the quality and effect of asphalt binder, which restricts the development of warm mix asphalt in transportation.

The existing research focuses on comparing the performance of asphalt mixture and corresponding warm mix asphalt mixture [4-5]. Hurley and Prowell showed through laboratory tests that adding Aspha-min or Sasobit or Evotherm can raise the compaction of asphalt mixture, and the compaction temperature can be as lower as 88 ℃, which cannot affect the rebound modulus of asphalt mixture [6-7]. The test results of APA (Asphalt Pavement Analyzer) show that adding Aspha-min, Sasobit, or Evotherm has no contrary influence on the rutting resistance of the asphalt mixture [8-9].

To sum up, the study on the rheological properties of warm mix asphalt binder has not been fully, comprehensively, and thoroughly. Nevertheless, it is critical to study the rheological properties of warm mix asphalt binder in depth [10-11]. This not only helps to determine the difference between warm mixed asphalt binder and base asphalt binder but also helps to determine the research and development direction of warm mix agent and the selection of warm mixing agent in engineering applications [11-12].

2. Preparation and properties of warm mixed asphalt

In this study, 70 # asphalt (A for short), 2 surfactants (Evotherm M1&Evotherm H5,) and 1 domestic warm mix additive were selected.

70 # asphalt was heated to about 145 ℃. The amount of warm mixture is calculated (M1 is 0.6% of the mass of asphalt, the ratio of H5 to asphalt is 1:9, and the ratio of domestic additives to asphalt is 2:98). After accurate weighing, the warm mixture is slowly poured into the asphalt and mixed for

Content from this work may be used under the terms of the Creative Commons Attribution 3.0 licence. Any further distribution of this work must maintain attribution to the author(s) and the title of the work, journal citation and DOI.
Published under licence by IOP Publishing Ltd

about 10 min in the mixing state. Warm mix asphalt prepared by surfactant M1, H5, and domestic organic additives is hereinafter referred to as M, H, and R, respectively. The basic physical properties of four asphalt binders, A, M, H, and R are displayed in Table 1.

Table 1. Property of asphalt binder A, M, H, and R

Index	Asphalt A	M	H	R
Original asphalt				
Penetration /0.1 mm (25 ℃)	72	112	69	119
Soften point /℃	48.5	44.5	49.0	43.5
Ductility /cm (15 ℃)	>100	>100	>100	>100
Ductility /cm (5 ℃)	7	16	6	17
Viscosity /Pa. s (135 ℃)	0.450	0.312	0.437	0.295
Flash point (℃)	290	288	294	288
G*/sinδ/kPa (64 ℃)	2.43	1.23	3.07	1.79
RTFOT				
Mass loss /%	0.28	-0.44	-0.03	-0.28
Penetration /0.1 mm (25 ℃)	49	61	48	72
Soften point /℃	53.5	57.0	54.0	51.0
G*/sinδ/kPa (64 ℃)	3.67	3.15	1.99	2.83
PAV				
G*sinδ/kPa (25 ℃)	2297	1768	2961	2102
Stiffness(60s)/MPa (-12 ℃)	161	141	111	157
m (60s) (-12 ℃)	0.354	0.390	0.381	0.355

3 Rheological property test of warm mixed asphalt

3.1 Viscosity

The viscosity of four kinds of asphalt binders A, M, H, and R at 110 ℃, 135 ℃, 155 ℃, and 175 ℃ was tested by Brookfield viscometer. The results are displayed in Table 2.

Table 2. Viscosity of asphalt A, M, H, and R

Temperature /℃	110	135	155	175
		A		
Viscosity /cp	1725	400	162	81
		M		
Viscosity /cp	1140	285	120	61.5
		H		
Viscosity /cp	1650	385	159	78.5
		R		
Viscosity /cp	1190	295	120	63.5

Adding a warm mixing agent could reduce the viscosity of the asphalt binder. The viscosity of warm mix asphalt binder R is close to that of A, and the viscosity of M and R prepared by a surfactant is the same but less than that of binder A and R. As the temperature increases, the viscosity difference of the four binders becomes smaller.

*3.2 Rutting factor (G */sin δ)*

The rutting factor of four asphalt binders A, M, H, and R are shown in Table 3.

Table 3. Rutting factor of asphalt A, M, H, R

A				M			
	Original asphalt				Original asphalt		
Temperature\ ℃	G*/kPa	G*/sinδ/kPa	δ/°	Temperature\ ℃	G*/kPa	G*/sinδ/kPa	δ/°

64	2.42	2.43	85.8	64	1.23	1.23	88.1
70	1.2	1.20	86	70	0.608	0.61	88.5
	TFOT				TFOT		
Temperature\	G*/kP	G*/sinδ/k		Temperature\	G*/kP	G*/sinδ/k	
℃	a	Pa	δ/°	℃	a	Pa	δ/°
70	1.83	1.83	85.3	70	1.26	1.26	86.9
64	3.65	3.67	84.1	64	3.15	3.17	83.3
	H				R		
	Original asphalt				Original asphalt		
Temperature\	G*/kP	G*/sinδ/k		Temperature\	G*/kP	G*/sinδ/k	
℃	a	Pa	δ/°	℃	a	Pa	δ/°
64	3.04	3.07	82.8	64	1.78	1.79	85.6
70	1.59	1.60	81.9	70	0.95	0.95	85.4
76	0.88	0.89	80.4	-	-	-	-
	TFOT				TFOT		
Temperature\	G*/kP	G*/sinδ/k		Temperature\	G*/kP	G*/sinδ/k	
℃	a	Pa	δ/°	℃	a	Pa	δ/°
70	1.98	1.99	85.5	70	1.43	1.43	86.5
64	3.99	4.01	84.2	64	2.82	2.83	85.3

The rutting factor of warm mix asphalt H produced by H5 is the highest. Warm mix asphalt H has excellent resistance to high-temperature deformation.

3.3 Creep test

Creep is a slow deformation behavior of materials under fixed stress [13]. The creep test applies a fixed stress to the specimen and tests the strain at a predetermined time. In this study, the shear stress of 10 Pa is used to test the strain of 300 s [14].

The magnitude of strain depends on the applied stress, so the compliance ratio should be changed as a measure of creep. Compliance is the ratio of strain to stress [15]. Under the given stress level, the more flexible the material is, the more likely it is to deform. Figure 1 shows the compliance results of three asphalt binders A, M, and R. Asphalt binders M and R have higher flexibility values than A, which indicates that the stiffness is reduced after adding a warm mixing agent.

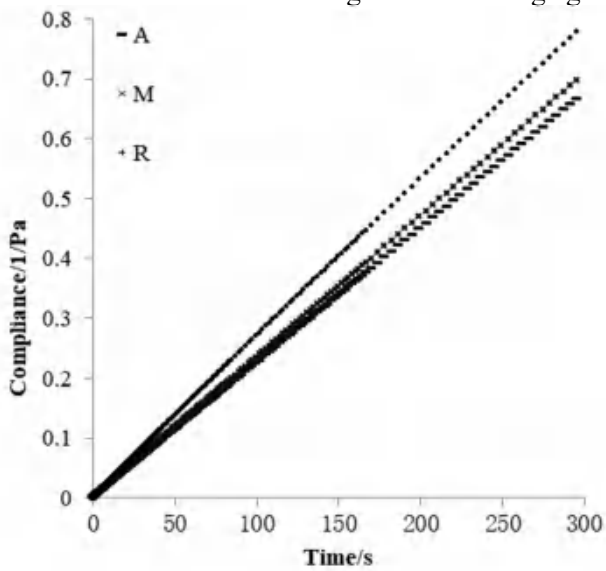

Figure 1. Creep curve of asphalt binder A, M and R

3.4 Multiple stress creep recovery

The repeated creep recovery test better simulates the site conditions. First, the material was loaded for a short time, then it was unloaded to make the material recover for a long time, and so on.

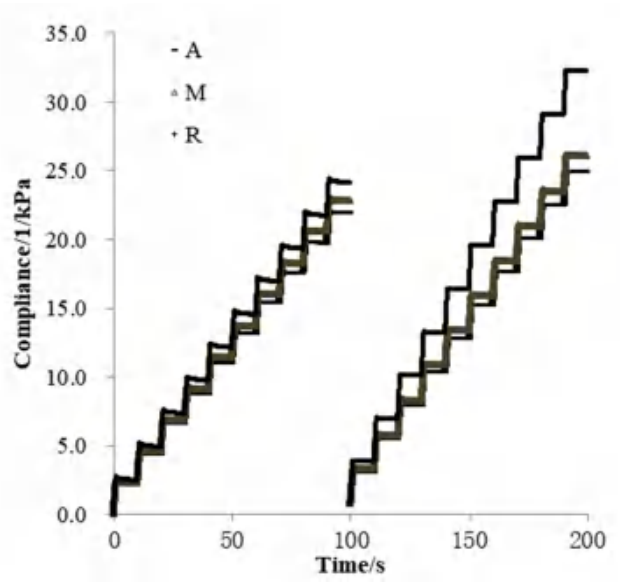

Figure 2. Compliance curve of multiple stress creep recovery

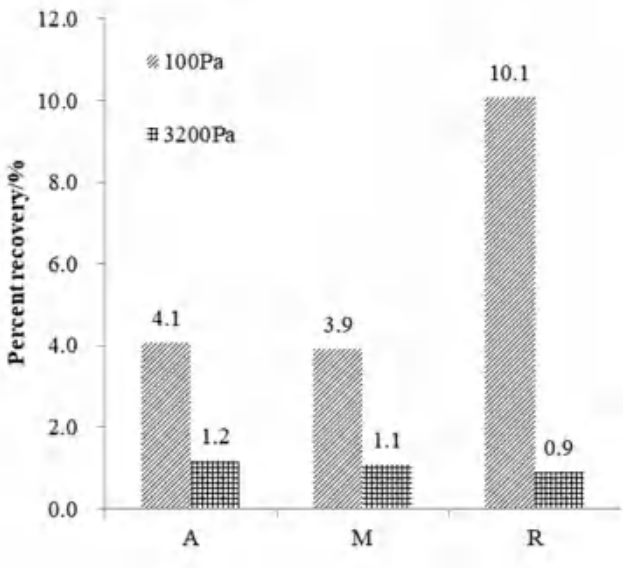

Figure 3. Average recovery rate

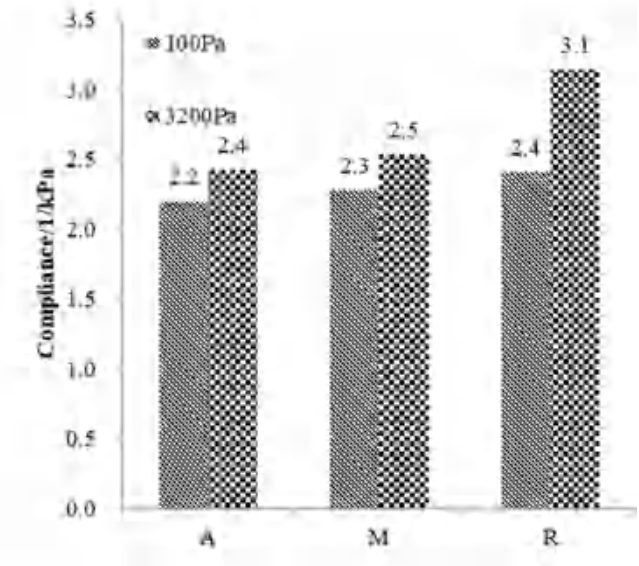

Figure 4. Unrecoverable creep compliance

Figure 2 shows the compliance curve of multiple stress creep recovery tests for three kinds of asphalt. The final strain at the creep and recovery stages of each cycle under the action of 100 Pa and 3200 Pa is calculated, respectively. Then the average recovery rate of each 10 cycles and the average value of irrecoverable creep compliance is calculated. The calculation values are shown in Figures 3 and 4.

The flexibility of M & R is higher than A, which indicates that adding a warm mixing agent reduces the stiffness of asphalt. The average recovery rate of warm mixed asphalt has obvious stress dependence, in which R is more susceptible to the influence of stress level. The average recovery rate difference between 100 Pa and 3200 Pa is 91.2%, and the average value difference of irrecoverable creep compliance is 23.5%. The average recovery rate of A and M is basically equivalent to the irrecoverable creep compliance value.

4. Conclusions

(1) Warm mixing agent will reduce Brookfield viscosity. The viscosity of R is close to A. The viscosity of M and R prepared by a surfactant is basically the same but less than that of binder A and R. With the increased temperature, the viscosity difference of different types of asphalt binder becomes smaller.

(2) The warm mix asphalt H made of surfactant H5 has the highest rutting factor and excellent resistance to high-temperature deformation.

(3) Warm mixing agents will reduce creep stiffness. In the multiple stress creep recovery test, the average recovery rate of asphalt binder and the average value of irrecoverable creep compliance have obvious stress dependence.

(4) In the future, further research will be conducted on the fatigue performance of warm mixed asphalt.

Acknowledgments

Supported by the Program Fund of Non-Metallic Excellence and Innovation Center for Building Materials, 2022TDA2-4.

References

[1] Wang H, Li X, Xiao J, et al.: (2020) High-Temperature Performance and Workability of Crumb Rubber-Modified Warm-Mix Asphalt. Journal of Testing and Evaluation 48(4), 2946-2962.

[2] Wang H, Liu X, Zhang H, et al.: (2020) Asphalt-rubber interaction and performance evaluation of rubberised asphalt binders containing non-foaming warm-mix additives. Road Materials and Pavement Design 21(6), 1612-1633.
[3] Yu H, Leng Z, Gao Z.: (2016) Thermal analysis on the component interaction of asphalt binders modified with crumb rubber and warm mix additives. Construction and Building Materials 125, 168-174.
[4] Fan P, Cheng P.: (2014) Influencing Factors Research on High Temperature Performance of Warm Mix Rubber Asphalt Mixture. Journal of Wuhan University of Technology 36(1), 62-67.
[5] He L, He Z, Ling T, et al.: (2015) Research on construction workability of asphalt-rubber mixture with warm mix additives. Journal of Functional Materials 46(20), 20102-20107.
[6] Guo N, Jing H, Lv S, et al.: (2015) Pavement performance of warm mix open graded friction course mixtures with asphalt rubber. Journal of Dalian Maritime University 41(4), 108-114.
[7] Cao W, Liu S.: (2013) Performance Evaluation of Asphalt-Rubber Stone Matrix Asphalt Mixtures with Warm Mix Asphalt Additives. Journal of Testing and Evaluation 41(1), 141-147.
[8] Cao W, Liu S.: (2013) Performance Evaluation of Asphalt-Rubber Stone Matrix Asphalt Mixtures with Warm Mix Asphalt Additives. Journal of Testing and Evaluation 41(1), 141-147.
[9] Yu Chun-rong, Ma Zai-hong, Huang Yi, et al.: (2020) Experimental Study on Compaction Temperature of Foam Warm-Rubber Asphalt Mixture. Shanghai Highways (03), 81-84+102.
[10] Chen J, Xuan Wa, Xiong Jp, et al.: (2020) High temperature stability index of Asphalt Mixture. Journal of China & Foreign Highway 40(02), 268-272.
[11] Zhou J, Wang Zn.: (2013) Study on the high temperature performance of asphalt mixes evaluated by penetration shear test. Communications Science and Technology Heilongjiang 36(10), 16-17.
[12] Wang Qz, Chen Zd, Lin Kp, et al.: (2018) Estimation and Analysis of Energy Conservation and Emissions Reduction Effects of Warm-Mix Crumb Rubber-Modified Asphalts during Construction Period. Sustainability10(12).
[13] Yu H, Leng Z, Xiao F, et al.: (2016) Rheological and chemical characteristics of rubberized binders with non-foaming warm mix additives. Construction and Building Materials 111, 671-678.
[14] Chen X, and Huang B. (2008) "Evaluation of moisture damage in hotmix asphalt using simple performance and Superpave indirect tensile tests." Constr. Build. Mater., 22(9), 1950–1962.
[15] Yu Jm, Yu Xs, et al.: (2018) Fatigue Resistance Characterization of Warm Asphalt Rubber by Multiple Approaches. Applied Sciences-Basel 8(9).

frontiers | Frontiers in Energy Research

TYPE Original Research
PUBLISHED 29 December 2023
DOI 10.3389/fenrg.2023.1337846

Check for updates

OPEN ACCESS

EDITED BY
Di Wang,
University of Ottawa, Canada

REVIEWED BY
Peng Lin,
Delft University of Technology,
Netherlands
Fan Zhang,
Aalto University, Finland

*CORRESPONDENCE
Aimin Sha,
ams@chd.edu.cn
Jie Wang,
j.wang@rioh.cn

RECEIVED 13 November 2023
ACCEPTED 30 November 2023
PUBLISHED 29 December 2023

CITATION
Chang R, Sha A and Wang J (2023), Effect of warm mix agent on the chemo-mechanical performance of binder with different oil sources.
Front. Energy Res. 11:1337846.
doi: 10.3389/fenrg.2023.1337846

COPYRIGHT
© 2023 Chang, Sha and Wang. This is an open-access article distributed under the terms of the Creative Commons Attribution License (CC BY). The use, distribution or reproduction in other forums is permitted, provided the original author(s) and the copyright owner(s) are credited and that the original publication in this journal is cited, in accordance with accepted academic practice. No use, distribution or reproduction is permitted which does not comply with these terms.

Effect of warm mix agent on the chemo-mechanical performance of binder with different oil sources

Rong Chang[1,2], Aimin Sha[1]* and Jie Wang[2]*

[1]Key Laboratory for Special Area Highway Engineering of Ministry of Education, Chang'an University, Xi'an, China, [2]Research Institute of Highway Ministry of Transport, Beijing, China

In this study, three typical oil source asphalt binders, Karamay asphalt A, CNOOC 36-1 asphalt B, Qinhuangdao CNPC asphalt C, were selected to prepare asphalt binders together with the warm mix agent Evotherm M1. The effects of warm mix agents on asphalt from different oil sources were experimentally studied via dynamic shear rheological (DSR), thermogravimetric analysis (TG), and Raman spectroscopy tests. The asphalt binders with different oil sources exhibit different properties. The rheological test results indicate that the addition of warm mix agent can slow down the decrease of asphalt viscosity during the aging process and the aging of asphalt. The results of the thermogravimetric test showed that the residual mass of asphalt with the addition of a warm mix agent significantly decreased after aging. Warm mixing agents can slow down the conversion of lightweight components to heavy components during the aging process of asphalt. By calculating the reflectivity of asphalt in Raman spectroscopy, it can be concluded that the reflectivity of asphalt decreases after adding a warm mix agent. The warm mixing agent reduces the degree of thermal evolution of asphalt. Warm mixing agents can make the chemical components in asphalt relatively stable and less prone to further pyrolysis or cracking reactions.

KEYWORDS

warm mixed asphalt, chemical additives, oil source, rheological properties, peak temperature, saddle index, asphalt reflectance

1 Introduction

Building a low-carbon society has become a strategic focus worldwide. The construction temperature of hot mix asphalt mixture is generally 160°C~180°C (Qiu et al., 2012; Zhang et al., 2023). The mixing temperature of rubber asphalt and special modified asphalt can even reach over 190°C. This not only requires a large amount of heating fuel, but also generates a large amount of harmful and toxic substances such as greenhouse gases and asphalt smoke. The working temperature of Warm Mix Asphalt (WMA) is usually between 90°C and 130°C. It can be divided into chemical process, foam process and organic additive process (Guo et al., 2017; Hou et al., 2017).

Chemical additives such as warm mix asphalt can reduce the working temperature by up to 35°C~55°C. Additives can reduce the surface tension of the aggregate asphalt interface, improve low-temperature coating and construction workability (Xu and Huang, 2010; Sun et al., 2011; Bowers et al., 2014). At present, there are various types of asphalt on the market, and the performance of asphalt after adding warm mix agents shows diversity. This results in varying quality and implementation effects of warm mix asphalt, making it difficult to estimate the impact on the final pavement performance (Dong et al., 2017).

By studying the warm mixing characteristics of asphalt from different oil sources, it is beneficial to choose the compatibility between asphalt and warm mixing agents. Further explore the impact mechanism of additives on the chemical components of asphalt, and ultimately improve the application effect of warm mix asphalt in road engineering.

This article selects three representative oil sources of road petroleum asphalt and uses dynamic shear rheological test (DSR), thermogravimetric analysis test (TG), and Raman spectroscopy test to study the characteristics of warm mixed asphalt from different oil sources. The article explores the influence of warm mixing agents on the performance and chemical composition of asphalt. It can guide the selection and analysis of warm mixed asphalt.

2 Materials and testing methods

2.1 Materials

According to the type of asphalt oil source, we selected three representative 70 # road asphalt as samples, which are labeled as: Karamay asphalt (A), CNOOC 36-1 asphalt (B), and Qinhuangdao CNPC asphalt (C).

Karamay asphalt is made from high quality naphthenic base heavy oil in Block 9. The process of blending vacuum residue with deoiled asphalt is used to produce road petroleum asphalt (Badre et al., 2006; Menapace et al., 2016). Karamay asphalt belongs to naphthenic base crude oil, which has the characteristics of low solidifying point, low wax content, low sulfur content and high resin content. It is currently the only road petroleum asphalt with a density less than 1 g/cm^3, which has the characteristics of high dynamic viscosity and high ductility after aging. Mainly used in areas with large temperature differences between day and night, long exposure to sunlight, and strong ultraviolet radiation.

CNOOC 36-1 asphalt is made from rare crude oil from the Suizhong 36-1 oilfield. Suizhong crude oil is a low sulfur cycloalkyl, high acid heavy oil with high density, low wax content, and high gum content. It has the characteristics of high low-temperature ductility, good low-temperature crack resistance, and good water stability.

Qinhuangdao China Petroleum Asphalt is mainly composed of Venezuelan Persian Cane crude oil. This crude oil has high acid value, heavy metal content, and residual carbon, while it has low saturated hydrocarbon content, high gum and asphaltene content, and low wax content.

In this study, three different original asphalt recorded as AO, BO, CO. Three types of asphalt added with warm mix agents are respectively recorded as AP, BP, CP.

The performance index test results of three types of asphalt are shown in Table 1. The test method refer to the “Test Specification for Asphalt and Asphalt Mixtures in Highway Engineering” (JTG E20).

The warm mixing agent Evotherm M1 is a surface active dosage form developed by Meadwestvaco in the United States. The warm mixing agent is a dark brown liquid at room temperature.

2.2 Preparation for warm mix asphalt binder

The preparation method of warm mixed asphalt binder: Heat the asphalt to 135°C. Calculate the amount of warm mix additives added (based on 0.6% of asphalt mass). Slowly pour the weighed warm mixing agent into the asphalt in a mixed state, with a speed of 200-300 r/min and a mixing time of 20–30 min.

2.3 Test and evaluation method

In this study, the rheological properties, thermal stability, and molecular structure information of three representative oil sources

TABLE 1 Asphalt performance indicators.

Project		Unit	A	B	C	Method
Penetration 100 g, 5 s, 15°C, 25°C, 30°C		0.1 mm	22	21	24	T0604
		0.1 mm	72	68	71	
		0.1 mm	112	113	116	
Penetration index, PI		-	−1.14	−1.27	−0.81	T0604
Softening point, $T_{R\&B}$		°C	46.0	46.5	47.5	T0606
Dynamic viscosity, 60°C		Pa·s	223.5	232.5	256.9	T0620
Ductility 5 cm/min, 10°C		Cm	>100	>100	49	T0605
Wax content		%	1.9	1.8	1.3	T0615
Flash point, COC		°C	278	287	312	T0611
Solubility		%	99.5	99.7	99.71	T0607
Density, 15°C		g/cm^3	0.977	1.011	1.049	T0603
RTFOT	Quality change	%	0.060	−0.070	−0.070	T0609
	Residual penetration ratio	%	67.4	64.8	64.8	T0604
	Residual ductility, 10°C	cm	12	9	9	T0605

of asphalt before and after warm mixing were studied. Dynamic shear rheological test, thermogravimetric analysis test, and Raman spectroscopy test were used.

2.3.1 Rheological performance tests

This study used the dynamic mechanical analysis method ASTM D7175 to test and analyze the rheological properties of asphalt. Test the high-temperature rheological properties of warm mixed asphalt as a function of temperature. Using a frequency of 10 rad/s. Scan with a temperature range of 58°C~82°C, and test at 6°C intervals (Qian et al., 2001). The constant temperature curing time at each temperature point is 10 min. Through rheological analysis, the viscoelastic indicators of asphalt before and after warm mixing, such as high temperature domain modulus of elasticity (G′) and phase angle, are obtained through testing(δ), Viscous modulus (G″), rutting factor (G*/sin δ) Etc.

2.3.2 Thermogravimetric analysis test

Thermogravimetric analysis is an analytical technique that measures the mass changes of samples at different temperatures under program-controlled temperature conditions. Warm mixed asphalt undergoes corresponding chemical changes, decomposition, and composition changes at a certain temperature, accompanied by changes in quality (Abo-Qudais and Al-Shweily, 2007; Hsu et al., 2011; Wang et al., 2022). This study uses thermogravimetric analysis to evaluate the thermal stability of warm mixed asphalt binder. In thermogravimetric analysis, test conditions are set based on the physical and chemical properties of warm mix asphalt, and appropriate sample quality and heating rate are selected. Excessive heating speed can lead to significant errors or reaction delays in obtaining real-time quality and other information of the sample. If the heating rate is too slow, it may not reflect the true state of thermal decomposition of warm mixed asphalt. In this study, METTLER TOLEDO's TGA/DSC 2 1600HT was used to test the thermal gravimetric analysis of asphalt before and after the addition of a warm mix agent and the aging effect. The test temperature was selected from 0°C to 800°C, and the heating rate was 10°C/min.

2.3.3 Raman spectra

Raman spectroscopy, as a scattering spectrum, can obtain information on molecular vibration and rotation (Wang et al., 2015). In this study, Horiba LabRAM HR Evolution was used to measure the changes in molecular structure of asphalt before and after warm mixing. Identify the size, intensity, and shape of Raman shifts in warm mix asphalt.

Asphalt samples can exhibit typical D and G peaks (Curtis et al., 1993). There may be interference from background signals in the original spectrogram, and it is necessary to perform background removal and peak splitting processing on the spectrogram to obtain effective spectral information.

The parameters of the Raman spectrum are shown in the Figure 1: H is the peak height, W is the half peak width, S is the lowest point between the D and G peaks, and H '/S is defined as the saddle index (Tan and Guo, 2014).

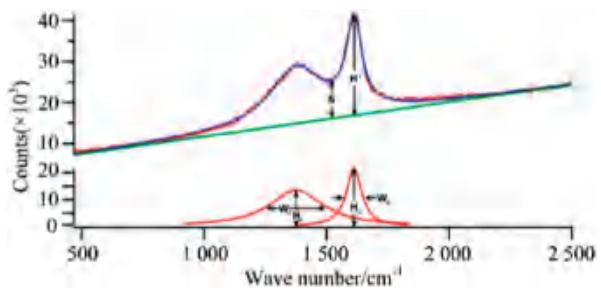

FIGURE 1
Raman spectral parameters.

3 Results and discussions

3.1 Rheological properties of warm mix asphalt

Temperature scanning experiments were conducted on three typical asphalt samples before and after adding warm mix agents under three conditions: original asphalt, RTFOT, and PAV after RTFOT. An available DSR was used for rheological testing to obtain the changes in rutting factor and phase angle under different aging conditions.

The elastic modulus of warm mixed asphaltvaries with different oil sources, mainly determined by the interaction forces between its components and asphalt molecules. The rutting factor and phase angle of different asphalt before and after warm mixing under different aging conditions are shown in Figure 2.

From the scanning results, it can be seen that as the temperature increases, the rutting factor of asphalt decreases and the phase angle increases. This means that the viscosity of asphalt decreases and the resistance to rutting decreases. The rutting factors are as follows: AO+RFTOT+PAV>AO+RFTOT>AO. After experiencing short-term and long-term aging, the modulus of asphalt continues to increase. The rutting factor of warm mixed asphalt is: AP + RFTOT + PAV>AP + RFTOT>AP. The rutting factor of warm mixed asphalt gradually increases with the deepening of aging degree. Comparing the rutting factors of asphalt and warm mix asphalt under the same aging state, it can be seen that the rutting factor of warm mix asphalt is slightly greater than the rutting factor of the original asphalt. The addition of warm mix agents makes asphalt have stronger resistance to deformation. After RTFOT, the rutting factor of warm mix asphalt is the same as that of the original asphalt. After experiencing both short and long-term aging, the rutting factor of asphalt in its original state is greater than that of warm mix asphalt. From this, it can be seen that the addition of warm mix agents can slow down the aging and hardening degree of the base asphalt.

Phase angle δ As the aging state changes, there is a continuous increasing trend within the scanning temperature range. The phase angle of the original asphalt sample is in descending order: AO>AO+RTFOT>AO+RTFOT+PAV.

As the aging degree deepens, the phase angle gradually decreases and the viscosity of asphalt gradually decreases. The phase angle of

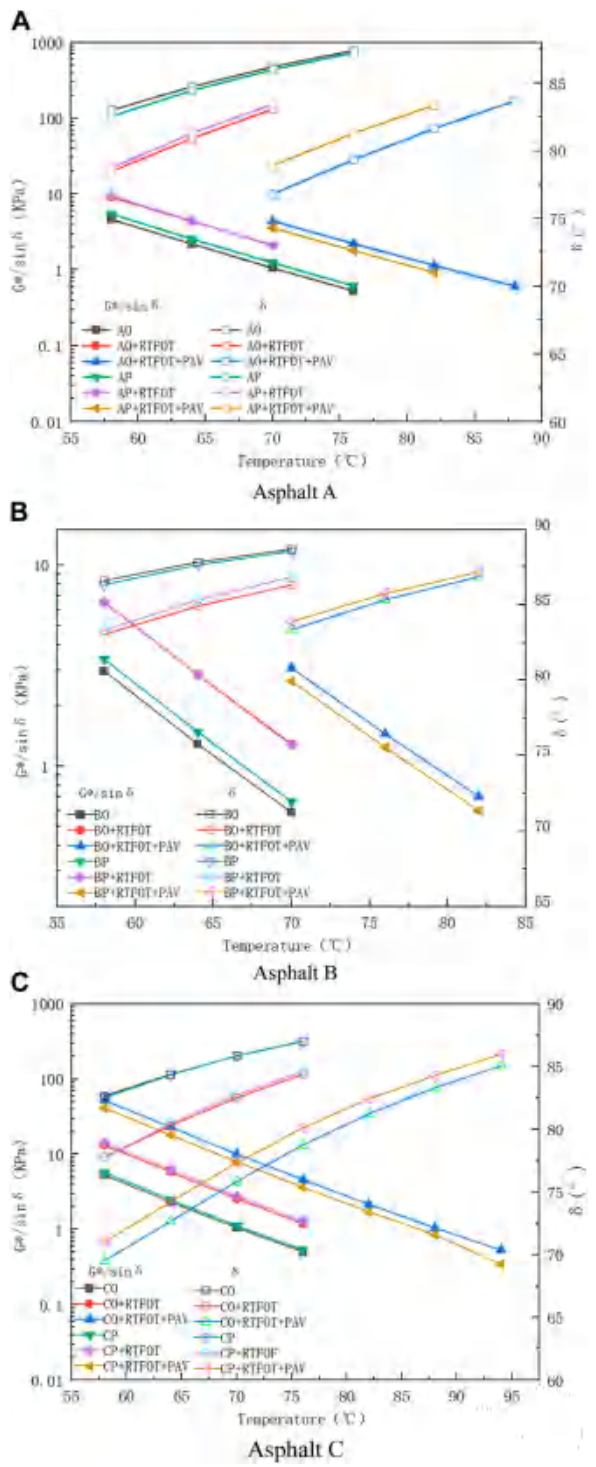

FIGURE 2
Rheological properties of warm mixed asphalt with different oil sources. (A) Asphalt A, (B) Asphalt B, (C) Asphalt C.

warm mixed asphalt is in the order of AP>AP+RTFOT>AP+RTFOT+PAV, which is consistent with the phase angle variation of the original asphalt sample.

Comparing the phase angles of asphalt and warm mix asphalt under the same aging effect, it can be seen that the phase angle of warm mix asphalt is slightly smaller than the phase angle of the original asphalt. The addition of warm mix agent slightly reduces the viscosity of asphalt, further explaining the principle that warm mix agent can mix at low temperature. After RTFOT, the phase angle of warm mixed asphalt is slightly greater than that of the original asphalt. After short and long-term aging, the phase angle of warm mix asphalt is much greater than that of the original asphalt. The phase angle characterizes the viscosity of asphalt, and the smaller the phase angle, the smaller the viscosity of asphalt. The addition of warm mix agents can delay the decrease in viscosity of asphalt under aging and alleviate its aging.

In the lower temperature scanning stage, the deeper the aging degree of asphalt, the better the content of high molecular weight components in asphalt. Asphalt binders exhibit better elastic properties, resulting in lower phase angles compared to other aging stages. As the temperature increases, the asphalt material gradually softens and tends towards viscous flow dynamics. The asphalt samples with deeper aging degree show a faster increase in viscosity composition and a significant increase in phase angle with the increase of temperature.

B asphalt and C asphalt exhibit similar rheological properties as A asphalt. The delaying effect of warm mix agent on B asphalt is not as good as A asphalt. The performance is better when mixed with asphalt A.

3.2 Thermal stability of warm mixed asphalt

This study controls the temperature rise and fall rate of the sample, and then measures the mass change of the sample at different temperatures. Determine the thermal decomposition of asphalt at different temperatures. Test the mass loss rate of the sample before and after warm mixing at different temperatures. Analyze the influence of warm mixing agents on the thermal stability of asphalt.

The quality of asphalt remains basically unchanged between 0°C and 214.46°C, and its performance remains stable. The quality of asphalt will not be lost during the heating and mixing process of asphalt and aggregates at 214°C. Asphalt begins to experience mass loss from 296°C. The thermal decomposition process is basically completed at around 500°C. Asphalt materials are basically completely carbonized.

The thermal decomposition process of asphalt after PAV basically ends at around 543°C, and the thermogravimetric curve remains stable. After adding a warm mixing agent to asphalt, there is basically no effect on the inflection point temperature and residual quality of the original asphalt sample. After long-term aging, the residual mass of the original sample increases, while the residual mass of the warm mixing agent decreases.

As the temperature increases, each component in asphalt begins to decompose. The original small molecules and decomposed small molecules in asphalt gradually break free from intermolecular forces and escape from the asphalt material (Hou et al., 2015; Hou et al., 2016). Therefore, the thermal stability of asphalt before and after warm mixing is evaluated by analyzing the inflection point temperature and residual mass ratio of the thermogravimetric curve of asphalt materials.

The inflection point temperature and residual mass data of three types of asphalt are shown in the Table 2.

TABLE 2 Thermal weight loss data of different asphalt under different aging conditions.

Asphalt	Peak temperature (°C)	Residual mass (%)	Asphalt	Peak temperature (°C)	Residual mass (%)
AO	468.17	8.88	AO-PAV	467.83	10.71
AP	472.33	8.67	AP-PAV	468.0	6.47
BO	468.33	9.6	BO-PAV	468.00	11.29
BP	470.67	10.32	BP-PAV	464.33	10.62
CO	464.00	13.6	CO-PAV	464.33	14.62
CP	459.83	13.13	CP-PAV	459.83	11.34

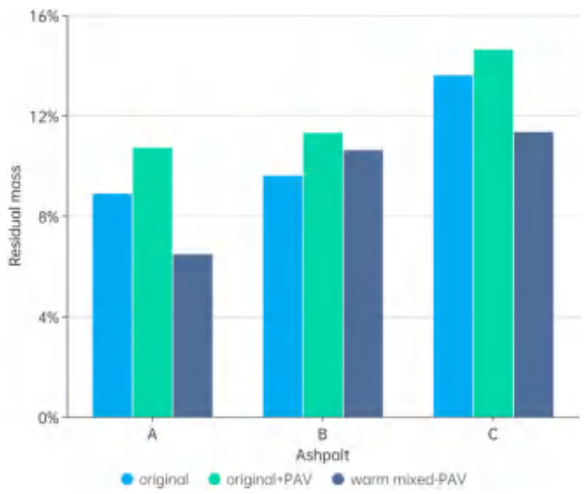

FIGURE 3
Different residual qualities of asphalt.

Analyze the residual quality changes of three types of asphalt samples, long-term aging PAV, and warm mix asphalt after long-term aging PAV, as shown in Figure 3.

The residual mass of asphalt from different oil sources gradually increases with long-term aging. Aging can cause the association and aggregation of asphalt molecules. The addition of warm mix agents will have a certain impact on the composition and microstructure of asphalt components. After the aging of warm mix asphalt binder, the residual quality significantly decreases, indicating that the warm mix agent will slow down the conversion of light components to heavy components in the aging process of asphalt. Warm mix agents can reduce the molecular association of asphalt during aging and slow down the aging of asphalt.

By comparing the residual quality of different types of asphalt, A asphalt has the smallest residual quality after thermogravimetric analysis, followed by B asphalt. C asphalt has more carbonized components that have not been decomposed. The residual mass of asphalt with more asphaltene content after thermogravimetric analysis is greater. Asphalt has a high content of asphaltene and is prone to carbonization. The higher the content of non decomposable components at high temperatures, the higher the residual mass ratio of thermogravimetry. Generally, components that cannot be decomposed above 460°C have larger molecular weights, more condensed aromatic rings, and are prone to carbonization. Therefore, there will be significant differences in the residual quality of asphalt from different oil sources.

3.3 Molecular structure changes of warm mixed asphalt

This study used Raman spectroscopy to test the changes in molecular structure and chemical bond information of warm mixed asphalt from different oil sources. Raman spectroscopy is a non-destructive spectroscopy technique that uses laser irradiation of asphalt samples to measure the changes in photon energy scattered by asphalt, thereby obtaining molecular structure and composition information before and after warm mixing of asphalt (Shan et al., 2010).

This study used HORIBA Scientific LabRAM HR Evolution for Raman spectroscopy testing. Raman spectroscopy is a surface test with a detection depth of about 10 nm and a spot size of 1um.The Raman spectra of three different types of warm mixed asphalt were shown in Figure 4.

Based on the Raman spectra of each asphalt, determine the positions of the D and G peaks and perform peak fitting. Obtain quantitative characterization parameters for the D and G peaks, mainly including: (Zhang et al., 2023) Peak position: W_D and W_G represent the positions of D and G peaks, respectively; (Qiu et al., 2012) Half height width: $FWHM_D$ and $FWHM_G$; (Guo et al., 2017) Peak height: H; (Hou et al., 2017) Half peak width: W; (Sun et al., 2011) S is the lowest point between the D and G peaks; (Bowers et al., 2014) Saddle index: H ’/S.

Wilkins et al. [*] proposed a method for peak separation of asphalt Raman spectra through extensive experimental data analysis, and provided a formula for calculating asphalt reflectance using Raman spectral parameters. The formula for calculating the reflectance of asphalt Raman spectroscopy parameters is:

$$R_0\%(\text{cal}) = -3.291 + 7.432\log(VG - VD) - 0.306\log(\text{saddle index}) - 2.935\log FWHMG - 3.118\log FWHMD$$

In the formula, v_D and v_G are the peak positions of D and G peaks, with peak spacing of (v_G-v_D). The half width at half height of D and G peaks is FWHM-D and FWHM-G and the saddle index. Calculate the Raman spectral parameters of different types of asphalt in the Table 3.

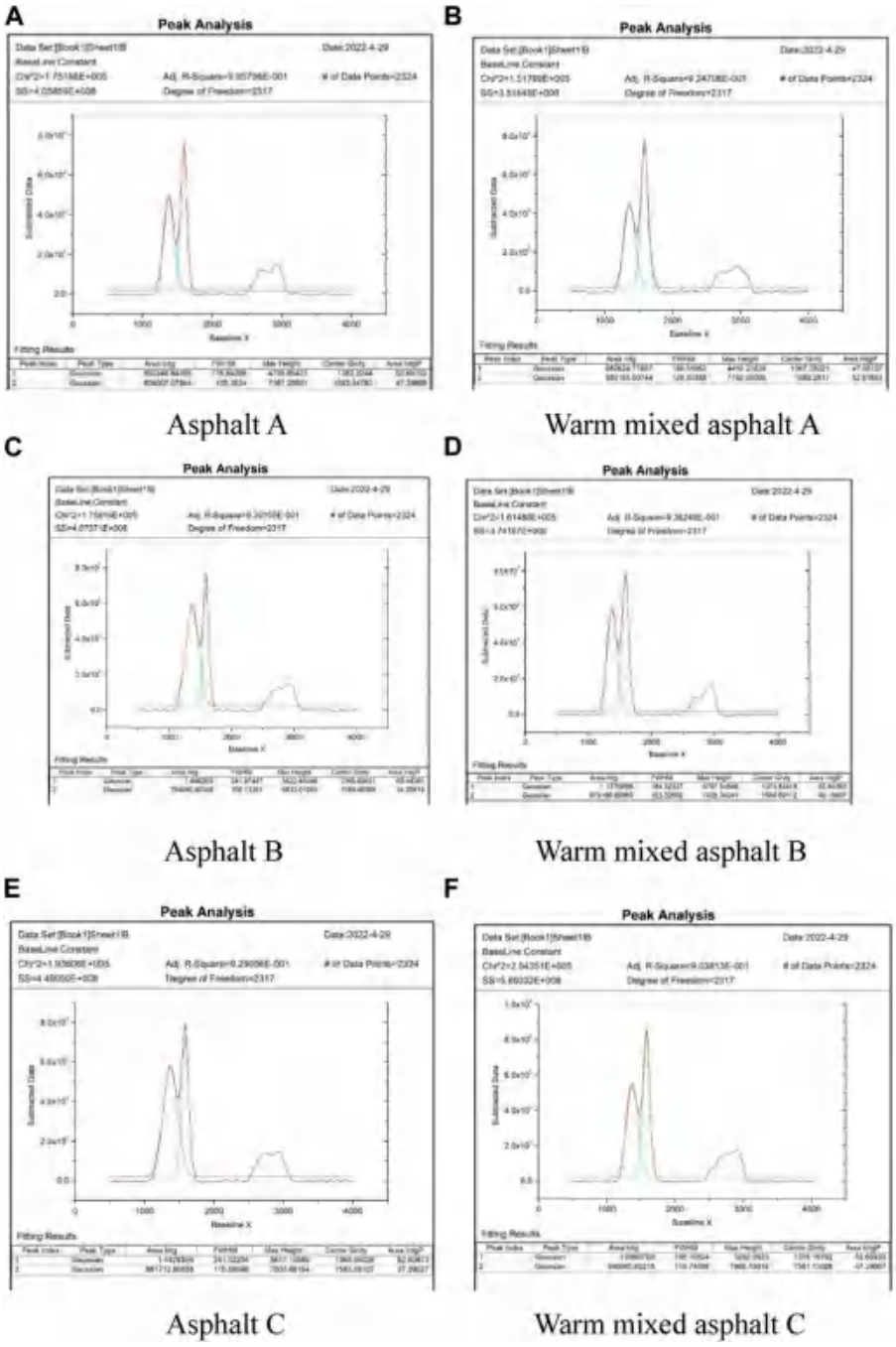

FIGURE 4
Raman spectra of three different types of warm mixed asphalt. (A) Asphalt A, (B) Warm mixed asphalt A, (C) Asphalt B, (D) Warm mixed asphalt B, (E) Asphalt C, and (F) Warm mixed asphalt C.

Raman spectroscopy parameters can better characterize the maturity of asphalt. By using the Lorentz peak fitting method to process the original test results, effective characteristic parameters of Raman peaks can be obtained. The saddle index and reflectance changes of asphalt before and after warm mixing can be analyzed as shown in the Figure 5.

As the degree of thermal evolution gradually increases, the alkane structure in asphalt gradually decreases. Due to the association effect, the spacing between aromatic ring structures decreases, resulting in an increase in reflectivity. The warm mix agent reduces the degree of thermal evolution of asphalt. The reflectivity of different types of asphalt decreases after adding warm mix agents. The decrease in thermal evolution indicates that the components in asphalt are relatively stable and less prone to further thermal decomposition.

TABLE 3 Raman spectroscopic parameters of asphalt.

Asphat	FWHM (D)/cm^{-1}	Area(D)/cm^{-1}	FWHM (G)/cm^{-1}	Area (G)/cm^{-1}	V_G-V_D/cm^{-1}	Saddle index/S	Reflectivity/%
AO	188.011	882625	128.034	980187.7	218.88	2.33	0.71
AP	176.84	892246.8	105.38	804007.1	211.32	2.90	0.90
BO	241.97	1448200	105.13	764690.8	220.85	1.91	0.68
BP	184.32	1137590	123.32	975166.7	209.86	2.10	0.67
CO	241.322	1442930	115.58	861712.7	214.46	1.67	0.48
CP	195.1	1099070	116.74	990045.9	205.94	2.19	0.59

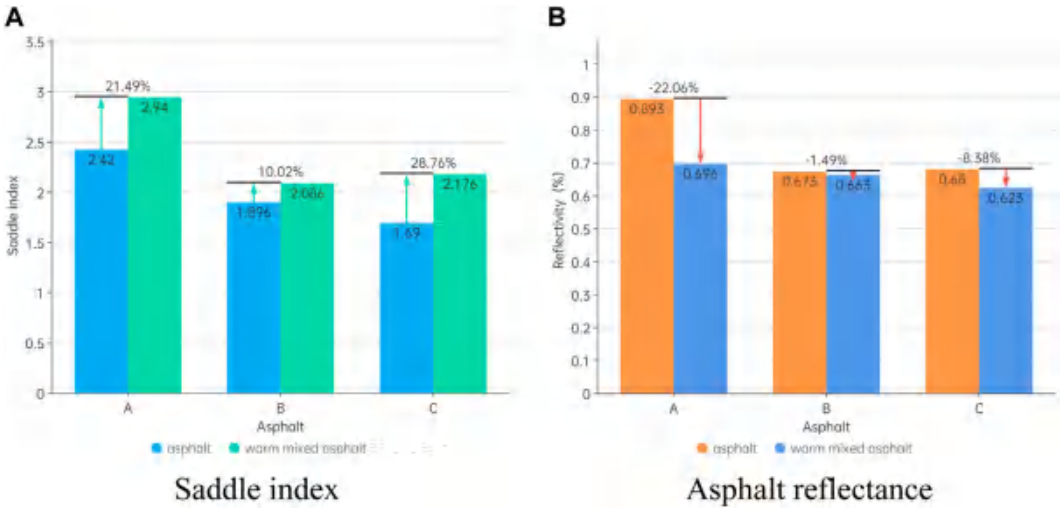

FIGURE 5
Asphalt Raman parameters. (A) Saddle index. (B) Asphalt reflectance.

4 Conclusion

Through dynamic shear rheological test, thermal weight loss test, and Raman spectroscopy test, the rheological properties, thermal decomposition stability, and the influence of temperature mixing agents on the microstructure of three typical oil source asphalt were studied. The results indicate that asphalt binders with different oil sources exhibit different warm mix properties.

(1) The addition of warm mix agents can delay the decrease in viscosity of asphalt under aging and alleviate the aging of asphalt.
(2) Asphalt with high asphaltene content has a large residual mass after thermal decomposition. Warm mix agents can slow down the molecular association of asphalt during the aging process. The residual mass of warm mixed asphalt after thermal decomposition has decreased.
(3) The reflectivity of different types of asphalt decreases after adding warm mix agents, indicating that warm mix agents reduce the degree of thermal evolution of asphalt. Warm mixing agents can make the components in asphalt relatively stable and less prone to further pyrolysis or cracking reactions.

Data availability statement

The original contributions presented in the study are included in the article/supplementary material, further inquiries can be directed to the corresponding authors.

Author contributions

RC: Writing–original draft. AS: Writing–review and editing. JW: Writing–review and editing.

Funding

The author(s) declare financial support was received for the research, authorship, and/or publication of this article. Supported by the Program Fund of Non-Metallic Excellence and Innovation Center for Building Materials, 2022TDA2-4.

Conflict of interest

The authors declare that the research was conducted in the absence of any commercial or financial relationships that could be construed as a potential conflict of interest.

Publisher's note

All claims expressed in this article are solely those of the authors and do not necessarily represent those of their affiliated organizations, or those of the publisher, the editors and the reviewers. Any product that may be evaluated in this article, or claim that may be made by its manufacturer, is not guaranteed or endorsed by the publisher.

References

Abo-Qudais, S., and Al-Shweily, H. (2007). Effect of aggregate properties on asphalt mixtures stripping and creep behavior. Constr. Build. Mater. 21 (9), 1886–1898. doi:10.1016/j.conbuildmat.2005.07.014

Badre, S., Goncalves, C. C., Norinaga, K., Gustavson, G., and Mullins, O. C. (2006). Molecular size and weight of asphaltene and asphaltene solubility fractions from coals, crude oils and bitumen. Fuel 85 (1), 1–11. doi:10.1016/j.fuel.2005.05.021

Bowers, B. F., Huang, B., Shu, X., and Miller, B. C. (2014). Investigation of reclaimed asphalt pavement blending efficiency through GPC and FTIR. Constr. Build. Mater. 50, 517–523. doi:10.1016/j.conbuildmat.2013.10.003

Curtis, C. W., Ensley, K., and Epps, J. (1993). Fundamental properties of asphalt-aggregate interactions including adhesion and absorption[R]. No. SHRP-A-341. Washington, DC: National Research Council.

Dong, Z., Liu, Z., Wang, P., and Gong, X. (2017). Nanostructure characterization of asphalt-aggregate interface through molecular dynamics simulation and atomic force microscopy. Fuel 189, 155–163. doi:10.1016/j.fuel.2016.10.077

Guo, M., Tan, Y., Wang, L., and Hou, Y. (2017). Diffusion of asphaltene, resin, aromatic and saturate components of asphalt on mineral aggregates surface: molecular dynamics simulation. Road Mater. Pavement Des. 18 (3), 149–158. doi:10.1080/14680629.2017.1329870

Hou, Y., Sun, W., Das, P., Song, X., Wang, L., Ge, Z., et al. (2016). Coupled Navier–Stokes phase-field model to evaluate the microscopic phase separation in asphalt binder under thermal loading. J. Mater. Civ. Eng. 28 (10), 04016100. doi:10.1061/(asce)mt.1943-5533.0001581

Hou, Y., Wang, L., Pauli, T., and Sun, W. (2015). Investigation of the asphalt self-healing mechanism using a phase-field model. J. Mater. Civ. Eng. 27 (3), 04014118. doi:10.1061/(asce)mt.1943-5533.0001047

Hou, Y., Wang, L., Wang, D., Guo, M., Liu, P., and Yu, J. (2017). Characterization of bitumen micro-mechanical behaviors using AFM, phase dynamics theory and MD simulation. Materials 10 (2), 208. doi:10.3390/ma10020208

Hsu, C. S., Hendrickson, C. L., Rodgers, R. P., McKenna, A. M., and Marshall, A. G. (2011). Petroleomics: advanced molecular probe for petroleum heavy ends. J. mass Spectrom. 46 (4), 337–343. doi:10.1002/jms.1893

Menapace, I., Masad, E., Papavassiliou, G., and Kassem, E. (2016). Evaluation of ageing in asphalt cores using low-field nuclear magnetic resonance. Int. J. Pavement Eng. 17 (10), 847–860. doi:10.1080/10298436.2015.1019503

Qian, K., Robbins, W. K., Hughey, C. A., Cooper, H. J., Rodgers, R. P., and Marshall, A. G. (2001). Resolution and identification of elemental compositions for more than 3000 crude acids in heavy petroleum by negative-ion microelectrospray high-field Fourier transform ion cyclotron resonance mass spectrometry. Energy and Fuels 15 (6), 1505–1511. doi:10.1021/ef010111z

Qiu, J., Van de Ven, M., Wu, S., Yu, J., and Molenaar, A. (2012). Evaluating self healing capability of bituminous mastics. Exp. Mech. 52 (8), 1163–1171. doi:10.1007/s11340-011-9573-1

Shan, L., Tan, Y., Underwood, S., and Kim, Y. R. (2010). Application of thixotropy to analyze fatigue and healing characteristics of asphalt binder. Transp. Res. Rec. 2179 (1), 85–92. doi:10.3141/2179-10

Sun, D. Q., Zhang, L. W., and Zhang, X. L. (2011). Quantification of SBS content in SBS polymer modified asphalt by FTIR. Trans. Tech. Publ. 287, 953–960. doi:10.4028/www.scientific.net/amr.287-290.953

Tan, Y., and Guo, M. (2014). Micro-and nano-characteration of interaction between asphalt and filler. J. Test. Eval. 42 (5), 20130253–20131097. doi:10.1520/jte20130253

Wang, D., Baliello, A., Poulikakos, L., Vasconcelos, K., Kakar, M. R., Giancontieri, G., et al. (2022). Rheological properties of asphalt binder modified with waste polyethylene: an interlaboratory research from the RILEM TC WMR. Resour. Conservation Recycl. 186, 106564. doi:10.1016/j.resconrec.2022.106564

Wang, P., Dong, Z., Tan, Y., and Liu, Z. y. (2015). Investigating the interactions of the saturate, aromatic, resin, and asphaltene four fractions in asphalt binders by molecular simulations. Energy and Fuels 29 (1), 112–121. doi:10.1021/ef502172n

Xu, T., and Huang, X. (2010). Study on combustion mechanism of asphalt binder by using TG–FTIR technique. Fuel 89 (9), 2185–2190. doi:10.1016/j.fuel.2010.01.012

Zhang, F., Sha, A., Cao, Y., Wang, W., Song, R., and Jiao, W. (2023). Characterization of self-healing properties of asphalt pavement materials containing carbon nanotubes: from the binder and mix level based on grey relational analysis. Constr. Build. Mater. 404, 133323. doi:10.1016/j.conbuildmat.2023.133323

·生产与应用·

就地温拌再生沥青混合料性能研究及工程应用

曾蔚，徐剑，王鹏

（交通运输部公路科学研究所 道路结构与材料交通运输行业重点实验室，北京 100088）

摘要：针对就地热再生在施工过程中对原路面加热温度较高、能耗大、烟气污染严重的问题，研究将表面活性剂类温拌剂与再生剂进行复配生成新型添加剂，并用于就地热再生沥青混合料中。采用车辙试验、低温小梁弯曲试验、残留稳定度试验及冻融劈裂试验，测试并分析就地温拌再生沥青混合料和就地热再生沥青混合料性能差异。结果表明：就地温拌再生沥青混合料各项性能满足规范要求，冻融劈裂（TSR）有小幅提高，因此，就地热再生沥青混合料中掺加温拌剂并未对其性能产生不利影响，反之对水稳定性有所提高。通过试验路验证，摊铺温度降低 20 ℃后，压实度、渗水系数均与就地热再生沥青混合料相当。

关键词：就地热再生　温拌技术　沥青混合料　路用性能　冻融劈裂

我国公路总里程于 2022 年底达到 535×10^4 km，其中高速公路 17.7×10^4 km，运营期道路的大中修任务不断攀升。在资源环境刚性约束下，如何将运营期道路维修养护产生的废旧路面材料进行高效再生利用，为道路使用者提供安全便捷的服务，同时减少废旧路面材料堆放占用的土地资源和环境污染，对公路交通基础设施与自然生态系统协调可持续发展意义重大。

废旧沥青路面再生技术在国际上是一项较为成熟的技术，并在欧美发达国家已得到普遍应用，我国也已广泛推广，并得到大规模的应用，但与发达国家 90% 以上的再生利用率相比还有较大的差距。就地热再生技术是一种连续式的现场热再生作业方式，具有高效、快速、经济等特点[1-2]。但在就地热再生施工过程中对原路面加热温度较高、能耗大、烟气污染严重、沥青混合料老化严重，路用性能较厂拌热再生差等问题，严重制约了该技术的推广应用。

沥青混合料温拌技术是一种绿色铺面技术，通过掺加温拌剂或机械发泡方式降低施工温度，可达到减少能耗，降低温室气体以及有害物质排放的目的，此外还可改善现场压实，在我国逐渐受到重视，其应用已初具规模[3]。将温拌技术运用到就地热再生中，可以显著降低路表加热温度，防止表层沥青碳化，可以实现沥青路面高效清洁的就地再生。

国内目前对就地热再生的性能、再生剂、经济效益等方面做了很多研究。研究表明，旧沥青混合料中掺入再生剂能提高混合料的路用性能。厂拌热再生沥青混合料引入温拌技术也是近几年的研究热点[4-5]，但将温拌技术引入就地热再生施工过程国内外鲜有研究。

本文采用车辙试验、低温小梁弯曲试验、残留稳定度试验及冻融劈裂试验，测试并分析就地温拌再生沥青混合料和热拌沥青混合料性能，研究二者的性能差异，并铺筑试验路段，对比二种混合料的路用性能。

1　试验方案

1.1　再生剂与温拌剂复配

就地热再生技术由于施工流程及再生机组的构造，要实现就地热再生沥青混合料的温拌，必须将再生剂与温拌剂的添加在同一步骤中完成。本文选择三种常用的再生剂 A、B、C 及二种表面活性剂类温拌剂 M、X 进行复配。温拌剂 M 为胺类表面活性剂，广泛应用于厂拌热再生中，

收稿日期：2023－03－22。
作者简介：曾蔚（1973—），女，副研究员，硕士毕业于同济大学道路与铁道工程专业，从事道路沥青路面养护技术及材料研究。电子邮箱：635924774@qq.com
基金项目：非金属材料创新中心应用示范类项目（编号：2022SFP3－1）

(C)1994-2023 China Academic Journal Electronic Publishing House. All rights reserved.　http://www.cnki.net

与再生剂 A、B、C 混合搅拌时均出现絮状不容物；温拌剂 X 主要成分为改性硅氧烷，与三种再生剂均有较好的相容性。选择再生效果较好的再生剂 A，将温拌剂 X 与再生剂 A 按照比例进行复配，生成新型添加剂，并将此新型添加剂按照再生剂的掺加方式进行后续的混合料试验。

1.2 原材料及试验级配

本试验中使用的 RAP 为某省高速公路现场旧料；粗集料、细集料选用试验室备用集料；沥青为 70 号基质沥青，技术要求见表 1。

本文采用试配法确定回收沥青的再生剂掺量，将再生剂按照 3%、6% 的质量比加入到回收沥青中，测定再生沥青的三大指标，即针入度、软化点、延度，通过试验研究确定再生剂用量，试验结果见表 2。确定再生剂用量为 5.0%。

沥青混合料级配采用 AC－13C，各档集料的级配及混合料合成级配如表 3 所示。

表 1 70 号沥青的技术要求

指标	试验结果
针入度（25 ℃）/（10^{-1} mm）	70
软化点/℃	51.5
延度（15 ℃）/cm	>100
溶解度/%	99.6
闪点/℃	268
密度（15 ℃）/（g·cm^{-1}）	1.040
RTFOT	
质量损失/%	－0.17
针入度（25 ℃）/（10^{-1} mm）	46
残留针入度比（25 ℃）/%	66
延度（15 ℃）/cm	27

表 2 RAP 中回收沥青及再生沥青试验结果

试验材料	再生剂掺量/%	针入度（25 ℃）/（10^{-1} mm）	软化点/℃	延度（15 ℃）/cm
老化沥青	0	25	64.5	10
老化沥青＋再生剂	3	38.8	57.5	24.8
老化沥青＋再生剂	6	55.1	56.0	37.9

表 3 AC－13C 再生沥青混合料各档集料级配及合成级配

筛孔尺寸/mm	原材料级配通过百分率/%					合成级配/%	设计级配范围/%
	RAP 矿料	10～15 mm	5～10 mm	0～3 mm	矿粉		
16	100.0	100.0	100.0	100.0	100.0	100.0	100～100
13.2	93.8	69.4	100.0	100.0	100.0	95.4	90～100
9.5	68.2	13.1	99.0	100.0	100.0	70.9	68～85
4.75	37.1	1.2	7.1	99.2	100.0	40.3	38～68
2.36	26.6	0.9	0.4	79.5	100.0	31.2	24～50
1.18	19.0	0.7	0.4	53.2	100.0	20.9	15～38
0.6	15.0	0.7	0.4	37.1	98.7	16.5	10～28
0.3	11.7	0.6	0.4	24.5	92.8	12.2	7～20
0.15	9.0	0.5	0.4	17.1	76.4	10.0	5～15
0.075	7.0	0.5	0.4	13.8	65.0	7.9	4～8
掺配比例/%	90	1	2	7	0		

1.3 试件制备

根据前期试验结果，确定再生剂掺加量为老化沥青质量比的 5%，温拌剂用量为总沥青质量 1.0‰。

本文采用等空隙率法进行沥青混合料配合比设计，确定就地热再生沥青混合料及就地温拌再生沥青混合料的最佳油石比为 4.9%，按照标准规范试验方法进行车辙、低温弯曲、浸水马歇尔、冻融劈裂试验。

2 试验结果与分析

2.1 高温性能

沥青混合料高温稳定性主要通过车辙试验进行评价。车辙试验按照《公路工程沥青及沥青混合料试验规程》中 T0719－2011 试验方法成型标准板式试件，测定试件在 60 ℃、轮胎压力 0.7 MPa 条件下的变形值。试验结果见表 4 所

(C)1994-2023 China Academic Journal Electronic Publishing House. All rights reserved. http://www.cnki.net

示。

由表 4 可知，就地热再生混合料及就地温拌再生混合料的动稳定度均满足规范的要求。由于在就地热再生中 90% 使用原路面材料，沥青混合料经过了长期使用，沥青发生老化，黏度变大，动稳定度明显优于新拌沥青混合料。

表 4　就地再生沥青混合料车辙试验结果

类型	45 min 变形/mm	60 min 变形/mm	变形差/mm	动稳定度/（次·mm^{-1}）	均值/（次·mm^{-1}）
	1.653	1.729	0.076	8 289	
再生剂 A	1.704	1.781	0.077	8 182	8 183
	1.623	1.701	0.078	8 077	
	1.847	1.929	0.082	7 683	
再生剂 A + 温拌剂 X	2.148	2.234	0.086	7 326	7 503
	2.009	2.093	0.084	7 500	

再生剂 A 加入温拌剂 X 后，动稳定度降低 8.3%；试验数据表明：就地热再生沥青混合料掺加温拌剂 X 未对其抗车辙能力造成不利影响。

2.2　低温性能

再生沥青混合料中由于沥青老化较为严重，影响其低温条件下的松弛能力和延展性。国内学者研究认为，再生沥青混合料中 RAP 含量低于 40% 时，即使不使用再生剂，其低温抗裂性能较普通沥青混合料无明显差别；当 RAP 掺量超过 50% 时，再生沥青混合料的低温抗裂性能明显降低[6-8]。因此，对于就地热再生路面，评价其低温抗裂性能尤为重要。低温弯曲试验是国内外较为常用的评价沥青混合料低温抗裂性能的试验方法。

低温弯曲试验按照《公路工程沥青及沥青混合料试验规程》JTG E20－2011 中 T0715 中沥青混合料弯曲试验方法的规定，试验温度选择为 －10 ℃，加载速率设定为 50 mm/min。测定其弯拉强度、最大弯拉应变、破坏劲度模量，试验结果见表 5 所示。

表 5　就地再生沥青混合料低温弯曲试验结果

类型	最大荷载/N	跨中挠度/mm	抗弯拉强度/MPa	劲度模量/MPa	破坏应变/με
再生剂 A	1 535.2	0.42	12.5	5678.7	2 201.2
再生剂 A + 温拌剂 X	1 452.9	0.43	12.2	5411.9	2 254.3

（1）低温条件下，沥青混合料的刚度变大，变形能力主要依靠沥青本身的黏弹性，就地热再生沥青混合料 RAP 占比达到 90%，新沥青用量相对较少，沥青的弹性降低，造成低温条件下抗变形能力减弱。

（2）由表 5 试验结果可知：就地温拌再生沥青混合料与热拌再生沥青混合料低温性能相当，温拌剂 X 的添加对低温性能改善不明显。

（3）根据规范规定，添加再生剂 A、再生剂 A + 温拌剂 X 再生沥青混合料破坏应变满足冬冷区及冬温区的大于 2 000 με 要求。由试验结果可知，可满足我国大部分地区低温性能要求。

2.3　水稳性能

沥青路面经过长期使用，沥青中轻质组分丧失，与集料的黏附性降低。由于水分的侵入，使集料表面沥青膜逐渐脱落，集料之间失去连接，造成路面松散，出现坑槽等病害，影响路面的正常使用和行车[9]。就地热再生沥青混合料中由于 90% RAP 料的存在，即使使用再生剂，沥青与集料的黏附性依然低于新沥青。因此，抗水损害性能对于就地热再生沥青混合料由为重要，本文选择浸水马歇尔试验和冻融劈裂试验评价就地再生沥青沥青混合料的水稳定性能。试验结果见表 6～7。

表 6　就地再生沥青混合料浸水马歇尔试验结果

类型	浸水 30 min 稳定度/kN	浸水 48 h 稳定度/kN	残留稳定度/%
再生剂 A	10.7	9.4	87.9
再生剂 A + 温拌剂 X	11.4	10.4	91.2

(C)1994-2023 China Academic Journal Electronic Publishing House. All rights reserved.　http://www.cnki.net

表 7 就地再生沥青混合料冻融劈裂试验结果

类型	未经冻融劈裂强度/MPa	经冻融循环后劈裂强度/MPa	冻融劈裂强度比/%
再生剂 A	1.078	0.962	89.2
再生剂 A + 温拌剂 X	1.110	1.022	92.1

从试验数据看出:

(1) 就地温拌再生沥青混合料的残留稳定度和冻融劈裂强度比均满足规范要求，并较就地热再生沥青混合料有小幅提高。

(2) 相比于热拌再生沥青混合料，就地温拌再生沥青混合料增强了抗水损能力。表面活性剂类温拌剂在沥青与集料界面的反应过程是一个复杂的液固表面物理化学过程。首先，表面活性剂类温拌剂的黏度及表面张力低，浸润能力强，与集料表面形成的接触角较小，能定向地排列在其表面，使集料表面被温拌剂润湿; 其次，表面活性剂类温拌剂由极性和非极性基团组成，二种基团分别向沥青和集料表面扩散，由于集料表面吸附着一层薄薄的水分子，极性基团的烷氧基发生水解反应生成硅羟基，取向于集料表面，同时与集料表面的羟基发生水解缩聚反应; 非极性基团则取向于沥青表面，二者发生化学反应，完成不同材料之间的反应过程[10]。

(3) 新沥青、老化沥青、再生剂在表面活性剂的调合作用下对集料的裹覆更加紧密，从而使得水稳定性能提升。

3 试验路段铺筑

就地温再生沥青混合料施工在沪陕高速 K1096 + 880 - K1108 + 000 上行车道实施，对比就地热再生与温再生沥青混合料施工质量控制，并验证掺加新型添加剂沥青混合料的路用性能。

就地温再生沥青路面施工前期按照室内试验掺配比例准备新型添加剂。本次施工通过不断调整提温器、拌和器的加热温度，控制混合料的出料和摊铺温度。施工过程中首先按照就地热再生沥青路面正常施工温度施工，各台设备运行平稳后，逐步降温，并采用无核密度仪及时关注试验路段的压实密度，用以了解路面压实度，控制降温幅度。施工期间重点关注施工各环节温度的测试，具体测试结果见表 8。

表 8 就地再生施工过程中的温度控制

检验项目	就地热再生沥青路面	就地温再生沥青路面
原路面温度/℃	16.6	15.4
路面加热温度/℃		
第一台加热机	109.5	111.1
第二台加热机	155.8	151.4
第三台加热机	197.3	174.1
路面翻松后裸露面温度/℃	79.2	71.3
耙松后料垄内温度/℃	117.4	97.2
新添加沥青混合料温度/℃	99.4	98.7
再生沥青混合料摊铺温度/℃	141.5	126.6
初压开始温度/℃	132.3	115.1

通过施工中各个环节温度测试，对比就地温再生沥青混合料与就地热再生沥青混合料: 摊铺温度降低 14.9 ℃、初压温度降低 17.2 ℃。施工过程中密切关注沥青含量、添加剂的掺加量，每天现场取料进行马歇尔稳定度及流值试验。施工完成后，分别进行就地热再生及温再生沥青混合料工后现场检测，主要测试压实度、渗水系数，具体结果见表 9。

表 9 就地再生沥青路面检测

检测项目	就地热再生沥青路面			就地温再生沥青路面		
	1	2	3	1	2	3
马歇尔指标						
稳定度/kN	15.96	13.28	15.68	16.63	15.23	15.3
流值/mm	3.29	2.92	4.35	3.48	3.63	3.64
最大理论密度	2.601	2.633	2.584	2.611	2.622	2.615
毛体积相对密度	2.506	2.531	2.501	2.529	2.536	2.529
压实度/%	96.3	96.1	96.8	96.9	96.7	96.7
渗水系数/(mL·min^{-1})	20	10	66	0	0	10

(C)1994-2023 China Academic Journal Electronic Publishing House. All rights reserved. http://www.cnki.net

压实度检测是对面层路面进行钻芯取样，测试其压实度。由于路面压实功与实验室马歇尔击实功的不同，因此就地温再生沥青路面的压实度不宜采用马歇尔密度，而是利用最大理论密度的指标进行计算。根据《公路沥青路面施工技术规范》要求，采用最大理论密度计算压实度时，压实度≥92%时可满足要求。

从表 9 现场检测数据看来:

(1) 马歇尔稳定度指标温拌与热拌相当，温拌剂的加入未对其产生不利影响。

(2) 就地温拌再生沥青混合料钻芯压实度试验结果表明，与就地热再生沥青混合料相比，压实度提升 0.4%。说明掺加此新型添加剂后，温拌再生沥青混合料在拌和压实过程中有效提升了施工和易性，在降低 15～20 ℃左右施工温度条件下，沥青混合料仍能取得与就地热再生沥青混合料相当的压实效果。

(3) 从渗水系数试验结果看，就地温再生沥青路面基本不渗水，满足规范和设计要求。

4　结论

本文通过车辙试验、低温小梁弯曲试验、残留稳定度试验及冻融劈裂试验，测试并分析就地温拌再生沥青混合料和热拌再生沥青混合料性能，并铺筑试验路段，得出如下结论:

(1) 将温拌剂与再生剂复配形成新的添加剂，此添加剂既有温拌功能又有再生功能，使用此新型添加剂生产的就地温再生沥青混合料的高温、低温性能满足规范要求，并提高其水稳定性。

(2) 通过试验路铺筑，验证就地温拌再生沥青混合料在降低 20 ℃左右施工温度条件下，沥青混合料仍能取得与就地热再生沥青混合料相当的压实效果。

(3) 就地温拌再生沥青混合料施工可降低施工温度，节约施工机械的能耗，减少沥青烟等有害气体排放，对推广就地热再生技术具有积极意义。

参考文献

[1] 王敬飞，展宏图．沥青混凝土路面就地热再生试验段全寿命周期技术评价分析［J］．公路，2017，62（11）：262－265.

[2] 牛文广．沥青路面就地热再生技术现状与发展历程［J］．中外公路，2019，39（05）：50－59.

[3] 段鹏鹏，徐肖龙，曹巍巍，等．沥青混合料温拌技术的应用研究进展［J］．上海公路，2022（03）：90－94.

[4] 闵敏，江传勇，郭旭东．大掺量 RAP 温拌沥青混合料研究及应用［J］．山西建筑，2022，48（10）：97－100.

[5] 王玄同．高 RAP 掺量下温拌再生沥青混合料性能研究［D］．大连：大连理工大学，2020.

[6] 彭文耀，李婷玉，陈宇亮，等．高掺量厂拌热再生改性沥青混合料路用性能研究［J］．公路工程，2022，47（04）：155－159.

[7] 宁世凯．RAP 掺量对沥青混凝土路用性能影响试验［J］．桂林理工大学学报，2020，40（03）：542－545.

[8] 李泉，韩庆奎，张继森，等．高废旧料掺量厂拌热再生技术性能研究［J］．中外公路，2018，38（06）：301－304.

[9] 王维营．大比例温拌再生沥青及混合料性能研究［D］．大连：大连理工大学，2018.

[10] 沈玺，高雅男，徐政．硅烷偶联剂的研究与应用［J］．上海生物医学工程，2006，26（01）：14－17.

Performance Research and Engineering Application of In－place Recycled Asphalt Mixture with Warm Mixing Technology

ZENG Wei，XU Jian，WANG Peng

(*Research Institute of Highway Ministry of Transport Key Laboratory of Transport Industry of Road Structure and Material*，*Beijing* 100088)

Abstract: During the construction process of asphalt pavement in－place recycling，the heating tempera－

(下转第 52 页)

(C)1994-2023 China Academic Journal Electronic Publishing House. All rights reserved.　http://www.cnki.net

Applicability Analysis of Hot in – Place Recycling in Expressway Maintenance in Plateau Area

YI Shouchun[1], **ZHANG Dengke**[2]

(1. *Sichuan Highway Planning, Survey, Design and Research Institute Co., Ltd. ChengDu* 610000;
2. *Sichuan Panzhihua – Xichang Expressway Co., Ltd. XiChang* 610051)

Abstract: The applicability of hot in – place Recycling of asphalt pavement regeneration in plateau areas was studied, which was conducive to the promotion and application of this technology in highway maintenance in plateau areas. Through the detection of the three major indicators of asphalt recovered before and after the hot in – place recycling regeneration of asphalt pavement of expressways in the plateau area, the applicable conditions of hot in – place thermal recycling in the plateau area were determined. Then, by analyzing the compaction situation at different paving temperatures, the compaction temperature control range in the plateau area was obtained. Finally, after tracking and testing the operation of the hot in – place regeneration section after three years of operation, it showed that the hot in – place regeneration technology can be popularized and applied in highway maintenance projects in plateau areas under certain conditions.

Keywords: asphalt pavement; hot in – place Recycling; plateau area; applicability

(上接第 47 页)

ture of the original pavement was relatively high, resulting in high energy consumption and serious smoke pollution. In this paper, a surfactant type warm mixing agent and a rejuvenating agent were mixed and used in the in – place recycled asphalt mixture. The in – place recycled asphalt mixture performance differences between warm mixing technology and conventional mixing were tested and analyzed by rutting test, low – temperature beam bending test, residual stability test, and freeze – thaw splitting test, and a test section was paved on site. The results showed that the properties of the in – place recycled asphalt mixture warm mixing technology meet the specification requirements, and the freeze – thaw splitting (TSR) has been slightly improved. Therefore, the addition of warm mixing agent does not have a negative impact on the performance of in – place recycled asphalt mixture, and conversely, it improves the water stability of pavement. Through the verification of the trial road sections, the paving temperature was reduced by 20 ℃, the compactness and water permeability coefficient were equivalent to those of the in – place recycled asphalt mixture without warm mixing technology.

Keywords: in – place recycling; warm mixing technology; asphalt mixture; road performance; freeze – thaw splitting;

·短讯·

京秦高速公路全线贯通

记者从河北省交通运输厅获悉，2023 年 2 月 4 日，随着北京至秦皇岛高速公路遵化至秦皇岛段正式运营，京津冀交通一体化重点项目京秦高速公路实现全线贯通。

京秦高速公路全长约 264 km，是京津冀协同发展交通一体化“四纵四横一环”骨架的重要组成部分。其中，京秦高速遵秦段全长约 165 km，总投资约 314 亿元，项目起点是下院寺枢纽互通，途经唐山市遵化、迁西、迁安和秦皇岛市卢龙、抚宁、海港、山海关 7 个县(市、区)，终于秦皇岛市山海关区。设有桥梁 47 座，隧道 13 座，采用双向六车道高速公路标准建设，设计时速 100 km。

(转自中国公路网)

(C)1994-2023 China Academic Journal Electronic Publishing House. All rights reserved. http://www.cnki.net

Case Studies in Construction Materials 17 (2022) e01581

Contents lists available at ScienceDirect

Case Studies in Construction Materials

journal homepage: www.elsevier.com/locate/cscm

Impacts of asphalt and mineral types on interfacial behaviors: A molecular dynamics study

Guoqing Sun, Zhenxing Niu, Jiupeng Zhang *, Xiaoyong Tan, Yufei Jing, Zixuan Chen

Key Laboratory for Special Area Highway Engineering of Ministry of Education, Chang'an University, Xi'an 710064, China

ARTICLE INFO

Keywords:
Asphalt-mineral interface
Molecular dynamics (MD) simulations
SARA components
Diffusion coefficient
The adhesion work
Relative concentration distribution

ABSTRACT

In order to analyze the interfacial interaction mechanism between the types of mineral and asphalt at the molecular scale, molecular dynamics (MD) simulations were conducted to study the interfacial behavior of three asphalt binders (AS-1, AS-2, AS-3) with five minerals (SiO_2, CaO, MgO, Al_2O_3, Fe_2O_3). Thermodynamic properties of asphalt binder were used to evaluate the rationality of MD simulations, such as density, glass transition temperature, cohesive energy density and solubility parameter. The mean square displacement (MSD), diffusion coefficient and relative concentration distribution were employed to analyze the diffusion regularity of asphalt SARA (saturate, aromatic, resin and asphaltene) components on the mineral surface, and the bonding strength between asphalt and different minerals was evaluated by calculating the adhesion work. The simulation results show that Van der Waals energy and Coulomb electrostatic energy play critical role in the adhesion of asphalt-mineral. The diffusivity of asphalt on the surfaces of five minerals was ranked as CaO > MgO > Al_2O_3 > Fe_2O_3 > SiO_2. It is enhanced with the increase of alkaline strength of minerals, and then the adhesion work of asphalt-mineral increases. The interfacial adhesion strength of the asphalt binders and minerals are directly related to the proportion of asphaltene and resin components, and the molecular mass of asphalt will affect asphalt-mineral adhesion strength, which can also be reflected by the relative concentration distribution of SARA components on mineral surface.

1. Introduction

Asphalt mixture was a multi-phase composite material, and the interface was an important factor affecting its bonding strength [1–3]. Traditional experiments were devoted to evaluating asphalt-aggregate adhesion effect through direct or indirect evaluation methods. The direct evaluation included immersion heat method [4], ultrasonic measurement [5]and surface free energy theory [6,7], and the indirect methods were mainly water stability tests [8,9]. These test methods can be used to characterize the adhesive performance, but none of them can quantify adhesion. Bitumen Bonding Strength (BBS) [10,11] and Pneumatic Adhesion Tensile Testing Instrument (PATTI) [12] were conducted to macroscopically evaluate asphalt-aggregate bonding characteristics. It found that the bonding strength was related to the thickness of asphalt film and the types of asphalt binders. However, these test methods can only evaluate the interfacial adhesion of asphalt mixture intuitively, and can't explain the adhesion mechanism between asphalt and aggregate. The interfacial adhesion can be easily obtained by observing the microstructure of asphalt binder and asphalt mixture with

* Corresponding author.
E-mail address: jiupengzhang@chd.edu.cn (J. Zhang).

https://doi.org/10.1016/j.cscm.2022.e01581
Received 13 August 2022; Received in revised form 28 September 2022; Accepted 15 October 2022
Available online 17 October 2022
2214-5095/© 2022 The Authors. Published by Elsevier Ltd. This is an open access article under the CC BY-NC-ND license (http://creativecommons.org/licenses/by-nc-nd/4.0/).

modern testing instruments. The scanning electron microscope (SEM) was employed to observe the microstructure of asphalt materials [13]. Fourier-transform infrared spectroscopy (FTIR) test can be used to study the proportion and distribution of asphalt components [14], and atomic force microscope (AFM) can be conducted to test asphalt-aggregate adhesion mechanism and the microstructure of asphalt binder [15,16]. These microscopic techniques can be helpful to further explore the adhesion mechanism of asphalt mixture.

Although the test method can effectively provide a method to measure the adhesive strength of asphalt mixture from different scales, it can't deeply explore the influence regularity of asphalt infiltration and diffusion on aggregate surface, thus unable reveal the adhesive mechanism of asphalt-aggregate interface. Molecular dynamics (MD) simulation was an effective way to study the interfacial behaviors of asphalt-aggregate from the molecular scale, and to explore the diffusion behavior of asphalt on the aggregate surface by establishing the molecular model of asphalt and aggregate [17–19]. MD simulation was to describe the movement details of each particle/atom during dynamic calculation. It can be used to perfect some material mechanism problems. For example, it can independently study the specific properties of materials by changing the proportion of components, and can be used for basic research and function prediction of a new material. In addition, MD simulation avoids the experimental time and labor consuming by using high-performance computation simulation method [20–22].

The fundament of MD simulation required to provide detailed information on atomic/molecular composition of materials, so a reasonable molecular model of asphalt and aggregate was the prime factor for effective MD simulation. Asphalt has been widely studied due to the complexity and diversity of the molecule structure. Researchers have been applying various testing methods and micro-analysis techniques to explore the thermodynamic properties of asphalt in order to pursue the representative molecular structure [23,24]. At present, there were three types of asphalt molecular models with high application recognition: three-component (asphaltene, maltenes and saturate) molecular structure proposed by Zhang and Greenfield [25], four-component (asphaltene, saturate, aromatic and gelatine) method of asphalt was put forward by Corbett, which was also known as the 'SARA' method [26]. And Li et al. [27] proposed the twelve-component molecular structure. Dong et al. [28] observed the self-aggregation state of polar components asphaltene and resin on aggregate surface by MD and atomic force microscope. The mean square displacement of SARA components on different aggregate surfaces was analyzed to explore the diffusion speed of asphalt on aggregate surfaces [29]. These previous results on asphalt-aggregate interface from the molecular scale showed good agreement with the experimental results, which further proved that MD simulation can reveal nano-scale research that was difficult to observe in macro experiments.

Previous studies mainly focused on the influence of asphalt materials or asphalt components on the aggregate surface due to the complexity and diversity of asphalt materials. The quartz and calcite were the main models for aggregate [30,31]. However, there was little research on the effect of mineral composition of aggregate on the interface. Some documents showed that the chemical and mineralogical composition of aggregate has a significant influence on the asphalt-aggregate interface [32,33]. Lyne et al. [34] considered that the elemental composition of minerals will affect its dispersed adhesion to asphalt. The research showed that the main components of minerals were composed of five oxides: SiO_2, CaO, MgO, Al_2O_3, Fe_2O_3. Therefore, the influence of mineral components on interface adhesion can be explored by MD simulation. Guo et al. [35] studied the distribution characteristics of asphalt on the five oxide surfaces of by MD simulation, and it indicated that the diffusion speed of asphalt on the surface of Al_2O_3 was faster than that of other mineral components. However, few studies considered the effects of SARA component proportion and total asphalt molecular mass on the interfacial energy of different minerals. Tan et al. [36,37] put forward that the adhesion of asphalt on alkaline aggregate is obviously better than that of acid aggregate. Therefore, it's necessary to simulate and analyze the mineral components of aggregate to explore the adhesion mechanism with different SARA components and molecular mass.

Therefore, the objective of this study is to analyze the interfacial adhesion mechanism between asphalt and five different minerals (SiO_2, CaO, MgO, Al_2O_3, Fe_2O_3), and consider the influence of three asphalts (AS-1, AS-2, AS-3) with different SARA components and

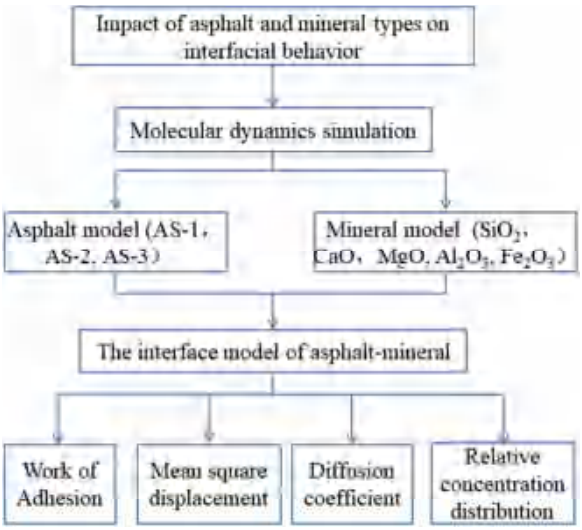

Fig. 1. Research framework.

molecular mass. The interfacial adhesion strength is evaluated by calculating the adhesion work between asphalt and different minerals, and the contribution value of SARA components to adhesion work is analyzed. The diffusion law of asphalt-aggregate interface was revealed by calculating mean square displacement (MSD) and diffusion coefficient. In addition, the adsorption and infiltration regularity of asphalt on different mineral surfaces were acquired by analyzing the relative concentration distribution of asphalt in the Z-axis direction. The research framework of this study is illustrated in Fig. 1.

2. Molecular model and simulation method

2.1. Molecular model of asphalt binder

Asphalt material was a complex chemical mixture, which the residue of petroleum refining, thus the composition of molecular structure changed with the source and batch of crude oil used to produce asphalt binder [26]. It was found that asphalt binder was mainly composed of hydrocarbons, it also contained a small amount of heterocyclic substances with similar structures and functional groups containing sulfur, nitrogen and oxygen atoms. Due to twelve different molecular structures can explain the complexity of asphalt molecular, more molecular structures can also represent different chemical components, and can characterize the physical, rheological and mechanical properties of asphalt binder. Therefore, the twelve-component molecular structure of asphalt binder was adopted in this study. That was constituted by three asphaltene components with strong viscosity and polarity, two non-polar saturate components composed of branched alkanes and cycloalkanes, two aromatic components composed of the least polar light molecular weight hydrocarbons, and five resin components with high polarity containing fused ring and heterocyclic compound, as shown in Fig. 2.

Previous studies have shown that SARA components will have great influence on the interfacial adhesion between aggregate [38–41]. Therefore, three different asphalt binders (AS-1, AS-2 and AS-3) were constructed in this study by changing the proportional difference of 12-component molecule. The detailed molecular composition was shown in Table 1. Three models with different molecular proportions can be conducted to characterize different asphalt properties, and the proportions of SARA components in the three asphalts were detailed in Table 2.

A confined asphalt layer model was constructed by using the amorphous cell module in Material Studio (MS) software. The initial density of the asphalt model was set at 0.1 g/cm^3, in order to obtain a reasonable configuration with less atomic overlap with a larger volume box under the same mass. Then, the energy optimization was performed by Forcite module, and the smart algorithm was conducted to optimize the structure. The system performed 500 ps in the isothermal-isocratic (NVT ensemble) to make the system

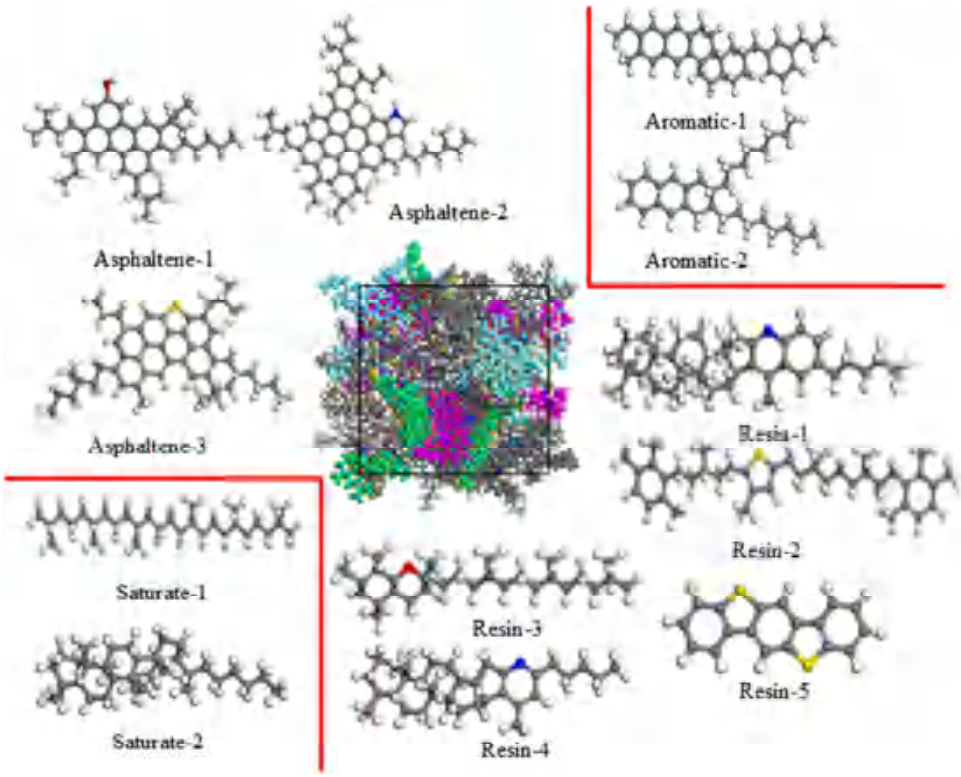

Fig. 2. Molecular structures of 12-components AS-1 asphalt (Carbon atoms are grey, hydrogen atoms are white, sulfur atoms are yellow, Nitrogen atoms are blue, and red is oxygen).

Table 1
Detailed composition of three representative asphalt models.

Chemical fractions	Molecular label	Chemical formula	AS-1		AS-2		AS-3	
			Molecular number	Fractions (%)	Molecular number	Fractions (%)	Molecular number	Fractions (%)
Saturate	Sat1	$C_{30}H_{62}$	4	11.1	2	6.5	1	2.1
	Sat2	$C_{35}H_{62}$	4		2		1	
Asphaltene	Asp1	$C_{42}H_{54}O$	3	17.3	3	20.2	1	5.1
	Asp2	$C_{66}H_{81}N$	2		2		1	
	Asp3	$C_{51}H_{62}S$	3		3		1	
Resin	Re1	$C_{40}H_{59}N$	4	39.7	4	42.0	10	50.8
	Re2	$C_{40}H_{60}S$	4		4		10	
	Re3	$C_{29}H_{50}O$	5		4		10	
	Re4	$C_{36}H_{57}N$	4		4		10	
	Re5	$C_{18}H_{10}S_2$	15		12		4	
Aromatic	Aro1	$C_{35}H_{44}$	11	31.9	10	31.3	20	41.9
	Aro2	$C_{30}H_{46}$	13		10		21	

Table 2
Proportions of SARA components of three asphalt binders.

Asphalt binders	Proportions of SARA components of asphalt binders				Total mass of molecular
	Saturate	Asphaltene	Resin	Aromatic	
AS-1	3622.9	5622.8	12,952.6	10,399.2	32,597.5
AS-2	1811.4	5622.8	11,666.7	8714.4	27,815.3
AS-3	905.7	2170.4	21,616.4	17,835.5	42,528.0

reach equilibrium at the target temperature of 453 K. Then, isothermal-isobaric (NPT ensemble) simulation was carried out at 500 ps under 1 atmosphere, and the temperature was also set at 453 K to relax the system. The optimized asphalt molecular model can be achieved by adjusting the temperature to 298.15 K and implementing NVT of 500 ps. In the process of kinetic optimization, Nose-Hoover thermostat and Andersen barometer were employed to control constant temperature and constant pressure respectively. The time step of all dynamic equilibrium based on MD simulation was 1 fs, and the cut-off distance was 15.5 Å. A flow chart can reveal the procedure of MD simulation more intuitively in Fig. 3. The temperature of 453 K was to simulate the mixing temperature of asphalt mixture in construction. In addition, the initial optimization temperature was set to 453 K to optimize the molecular structure of asphalt. The purpose was to increase the initial kinetic energy of the molecular structure, so the final molecular model can reach the most stable structural state.

When the asphalt model was dynamically optimized, an initial atomic velocity should be given to the constituent molecules, which was randomly generated according to Boltzmann distribution. Non-uniform initial speed led to the difference of asphalt molecular distribution. Therefore, three models were established for each asphalt (AS-1, AS-2, AS-3) in this study, and then the kinetic structure of asphalt models were optimized. By taking the parallel dynamics simulation method to average the three model parameters, the influence of randomness of initial velocity was eliminated during MD simulation.

2.2. Molecular model of minerals

Different types of aggregate are constituted by complex mineral components, which lead to different chemical and physical

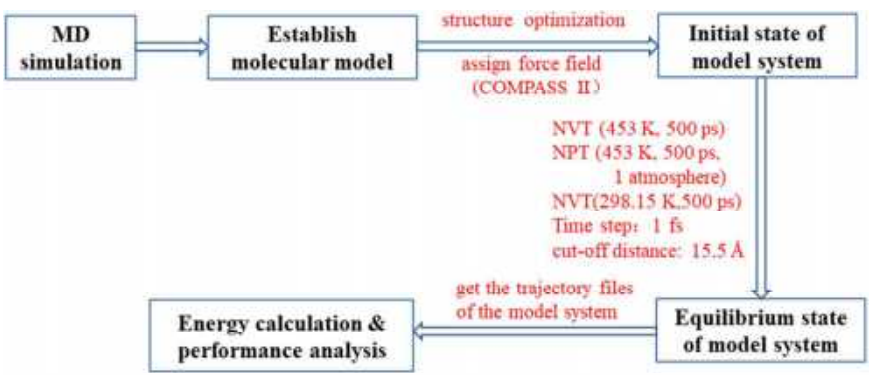

Fig. 3. Flow chart of MD simulation.

properties of asphalt mixture. In order to know the composition of aggregates, researchers systematically analyzed the chemical composition of aggregates used in roads. The results showed that the mineral components in aggregates mainly included SiO_2, CaO, MgO, Al_2O_3, Fe_2O_3 and other minerals with less content [42]. The influence on the performance of asphalt mixture can be effectively analyzed from the aspect of mineral compositions. Different mineral models were imported from the structural database in Materials Studio. The unit cells of minerals were cleaved along the [h,k,l] direction, and the detailed structural dimensions of the mineral models are shown in Table 3.

In the cleaving mineral model, 10,000 iterations of geometric optimization were demanded. Usually, when performing Forcite calculation, the atomic type will be automatically calculated before each calculation. However, for CaO, MgO, Al_2O_3 and Fe_2O_3 metal oxides, there were ionic bonds between oxygen atoms and metal atoms, and these chemical bonds were not parameterized. Therefore, it was necessary to assign forcefield types in advance to prevent them from being recalculated in the simulation process. Thus it was necessary to delete the ionic bond between oxygen atoms and metal atoms. In addition, only a few atoms in the upper layer of the mineral surface will interact with the polymer, while other atoms were only considered as a part of the bulk phase, and their influence was slight. This means that these bulk atoms can be fixed without optimization.

After the structure optimization, the two-dimensional mineral surface was produced by establishing the supercell to produce the same size as the asphalt model. Then, a vacuum plate with a thickness of 0 was added to form minerals with three-dimensional periodic boundary conditions. For the purpose of constructing the asphalt-aggregate interface model and further calculation, orthogonal geometry was preferred. Fig. 4 shows the optimized mineral models of CaO and SiO_2. At the same time, due to the hydrophilicity of SiO_2, hydroxyl (OH) groups with a density of 4.5 OH groups /nm^2 were added to represent fully hydrated silica film [43]. The reason was that the surface SiO_2 was very active, and it will be hydroxylated in the presence of water [44]. Fig. 4(b) shows the final hydrated SiO_2 model.

2.3. The molecular model of asphalt-mineral interface

The optimized confined asphalt layer was attached to the mineral surface through the build layers module to form the asphalt-

Table 3
Detailed structural dimensions of the mineral models.

Mineral types	Cleave plane (h k l)	Lattice parameters		Structure of mineral
SiO_2	(0 0 1)	a=b= 4.91 Å c= 5.402 Å	$\alpha = \beta = 90°$, $\gamma = 120°$	
MgO	(0 0 1)	a=b=c= 4.2112 Å	$\alpha = \beta = \gamma = 90°$	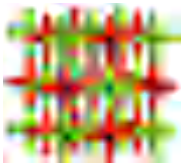
CaO	(0 0 1)	a=b=c= 4.8105 Å	$\alpha = \beta = \gamma = 90°$	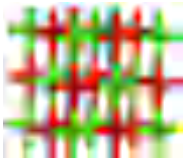
Al_2O_3	(0 0 1)	a=b= 4.759 Å c= 12.991 Å	$\alpha = \beta = 90°$, $\gamma = 120°$	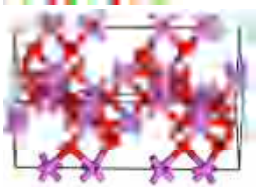
Fe_2O_3	(0 0 1)	a=b= 5.035 Å c= 13.720 Å	$\alpha = \beta = 90°$, $\gamma = 120°$	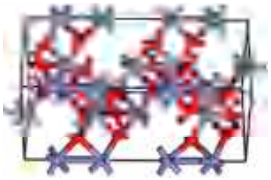

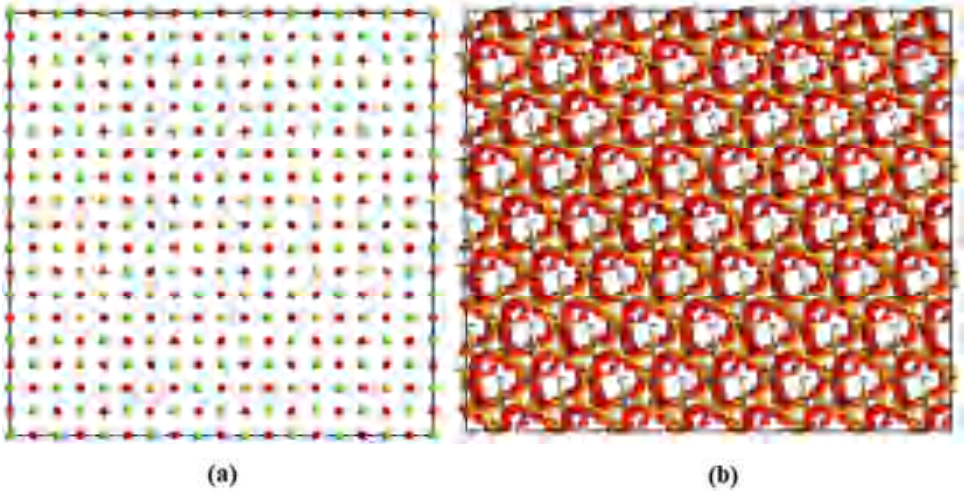

Fig. 4. Molecular model of minerals a) CaO b) SiO_2.

mineral interface model. In order to eliminate the influence of three-dimensional periodic boundary conditions in Z-axis direction, a 30 vacuum plate was added on the top of the asphalt-mineral interface model, so that the asphalt molecular model will not appear on both sides of the mineral due to the boundary periodic effect, and the simulation will be closer to reality. Fig. 5 shows the interface molecular models of AS-1 with CaO and SiO_2, respectively. The geometric optimization of the interface model was carried out, and then the dynamic calculation of the NVT ensemble of 500 ps continued to be implemented, in order to achieve sufficient dynamic optimization of the interface model. Detailed model parameters of asphalt -mineral interface were summarized as shown in Table 4.

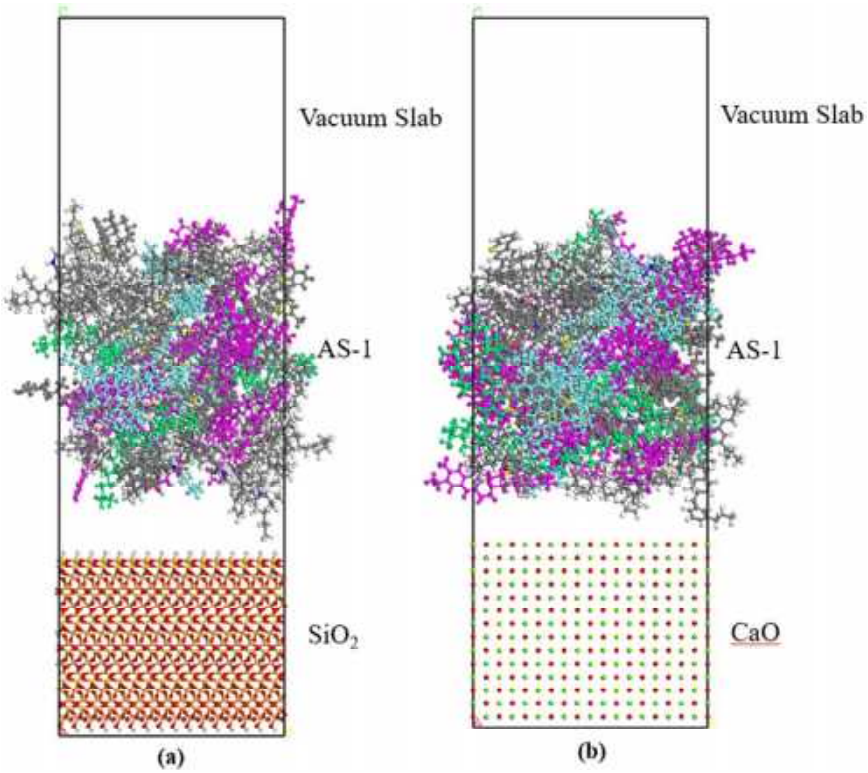

Fig. 5. Molecular model of asphalt-mineral interface: a) AS-1-SiO_2 b) AS-1-CaO.

Table 4
Detailed parameters of interface molecular model.

Molecular model		Paramaters of interface model					
Asphalt	Mineral	a (Å)	b (Å)	c (Å)	α (°)	β (°)	γ (°)
AS-1	SiO_2	35.923	38.554	114.207	90	90	90
	CaO	38.156	38.156	118.834	90	90	90
	MgO	37.864	37.864	113.999	90	90	90
	Al_2O_3	39.658	37.950	118.658	90	90	93.3
	Fe_2O_3	36.356	39.054	115.346	90	90	90
AS-2	SiO_2	34.948	37.580	118.759	90	90	90
	CaO	37.182	37.182	113.607	90	90	90
	MgO	36.890	36.890	114.517	90	90	90
	Al_2O_3	38.684	36.976	116.452	90	90	93.3
	Fe_2O_3	35.381	38.080	113.262	90	90	90
AS-3	SiO_2	42.069	40.307	128.191	90	90	90
	CaO	39.909	39.909	126.793	90	90	90
	MgO	41.723	41.723	124.036	90	90	90
	Al_2O_3	41.411	39.703	120.474	90	90	93.3
	Fe_2O_3	42.614	40.807	119.607	90	90	90

2.4. Force field

The force field is an energy function, which provides parameters for each atom type in MD simulation to calculate the energy of the system. The atomic and molecular interactions in this study were described by Condensed-phase Optimized Molecular Potentials for Atomistic Simulation Studies (COMPASS II) force field. COMPASS force field was the first ab initio force field in MD simulation, and COMPASS II was an important development extension of COMPASS force field, which helped to accurately predict the material properties of various isolated and condensed phase compounds [45].

3. MD simulation results and discussion

3.1. Density of asphalt molecule

It's worth noting that the density of asphalt was one of the important physical properties. As the thermodynamic performance parameter of asphalt molecules, density was an index to evaluate whether the size of asphalt molecular model can produce reasonable and accurate simulation results. NPT ensemble of 500 ps was implemented in the optimized asphalt molecular model in Section 2.2, and the density of three different asphalt molecules at 298.15 K temperature was calculated. The final density of asphalt molecules was the average of the results. The results were shown in Fig. 6, and it showed that the density error of the three calculation results was not significant. The density of three different asphalt was in the area of 1.00 ± 0.02 g/cm^3. Among them, asphalt AS-2 possessed the highest density, followed by AS-1 and AS-3 was the least. The experimental result of AS-1 asphalt in American SHRP at 333.15 K was 1.02–1.03 g/cm^3 [27]. The density of AAA-1 asphalt obtained by MD simulation at 298.15 K was about 1.005 g/cm^3, and the difference between experimental and simulation results was about 0.02 g/cm^3. The experimental densities of 70# and 90# asphalt were 1.009 and 1.075 g/cm^3, respectively [46]. This was also very approach to the results of simulated asphalt AS-1 and AS-2. The density of

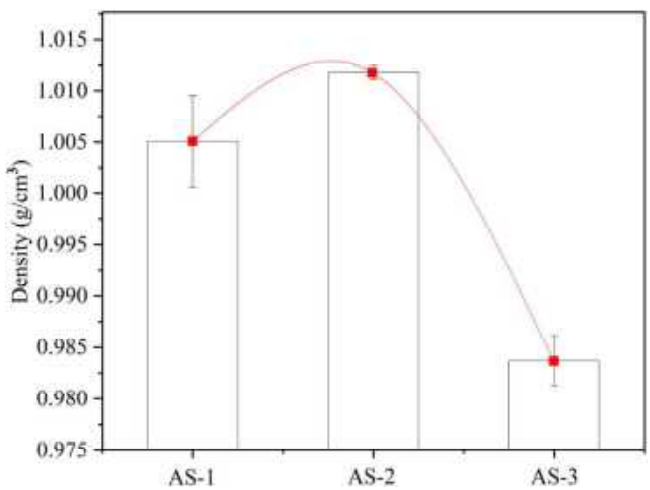

Fig. 6. Density of three asphalt molecules.

AS-3 asphalt was about 0.985 g/cm^3. In previous studies, the density of asphalt obtained by MD simulation was about 0.95–1.08 g/cm^3 [47]. And the molecular model of 12-component asphalt could better satisfy the performance requirements of actual asphalt. In fact, the density of simulated asphalt was generally lower than that of experimental asphalt. This deviation may be due to the fact that the simulated molecular model of asphalt employed a large number of carbon and hydrogen atoms, but it possessed low consideration of heteroatoms except sulfur, nitrogen and oxygen, which contributed to the simulated value being slightly lower than the experimental value.

3.2. Glass transition temperature of asphalt molecule

Asphalt, a viscoelastic material, its performance was closely related to temperature. According to the mechanical state at different temperatures, it can be divided into three states: Newtonian liquid state, viscoelastic state and glassy polymer [48]. The transition from viscoelastic state to glass state was defined as glass transition, and the temperature at this time was called glass transition temperature, which was marked as Tg. Glass transition temperature directly affected the service performance and technological performance of materials, and it was also of great significance to analyze and predict the low-temperature performance of asphalt mixture [49]. The process of asphalt glass transition was not the change of component or composition, but the change of molecular chain movement, so the Tg can be determined by the change of specific volume of asphalt molecules at different temperatures [50]. In this study, the change of molecular specific volume of three different asphalt binders at different temperatures was simulated, as shown in Fig. 7. With the increase of temperature, the specific volume of asphalt molecules was gradually increasing, which also corresponded to the decrease of the density of asphalt molecules. The reason for this phenomenon was that the increase of temperature will accelerate the movement of asphalt molecules and made it disperse more evenly, so the specific volume of asphalt molecules was gradually increasing, which was consistent with the previous experimental research phenomenon. The glass transition temperature of three kinds of asphalt (AS-1, AS-2, AS-3) obtained by MD simulation were 336 K, 323 K and 322 K, respectively. However, previous

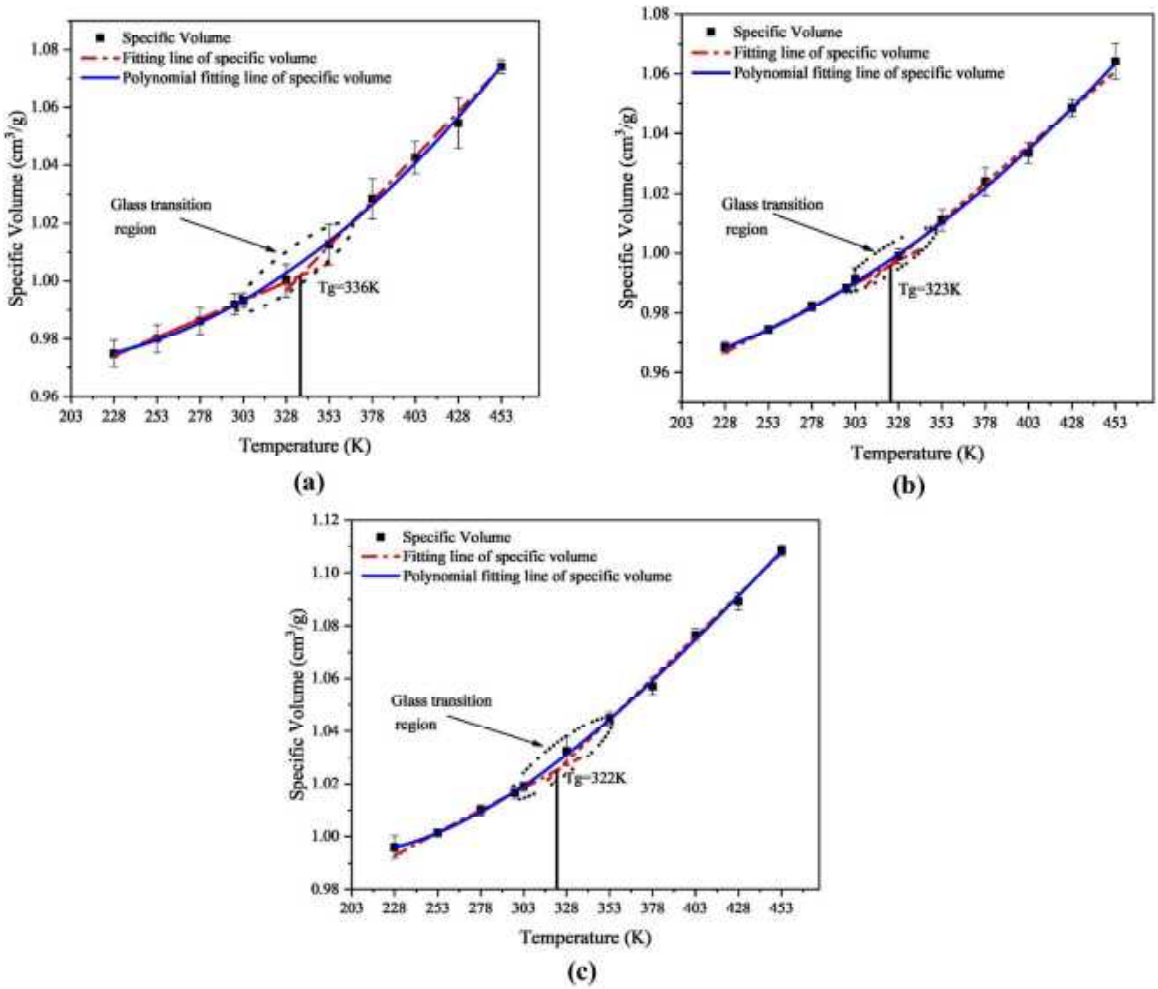

Fig. 7. The specific volume curve of asphalt at different temperatures: a) AS-1 b) AS-2 c) AS-3.

experimental results showed that the glass transition temperature of asphalt was 223–303 K [25,26,51]. The results of MD simulation were obtained on a short time scale (1 s = 10^{10} ps), so compared with the long-time scale in the experiment, higher temperature may be required in the dynamics simulation to meet the system requirements due to the superposition of time-temperature, so the glass transition temperature was increased. In addition, the cross-scale study of interface performance between asphalt and aggregate at molecular scale and macro scale will inevitably lead to differences in actual results.

3.3. Cohesive energy density and solubility parameters of asphalt molecule

Compatibility was another important property of asphalt binder, and great compatibility was beneficial to the performance of asphalt. There were many methods to study polymer compatibility, among which cohesive energy density (CED) and solubility parameters were widely accepted and reasonable methods. Solubility parameters can be used to evaluate the colloidal stability in asphalt binder. By analyzing their interaction, solvent and solute molecules can be separated effectively and independently, which was conducted to study the molecular attraction characteristics in asphalt model system. In MD simulation, because the interaction between asphalt molecules was evaluated by Van der Waals force δ_{vdw} and electrostatic force δ_{ele}, the obtained solubility parameters can be evaluated by these two components as shown in Eq. (1). CED was the square of the solubility parameter extracted from Eq. (2), which was used as a measure of mutual attraction to evaluate the intermolecular interaction within the asphalt molecular model. Table 5 showed the CED and solubility parameters of three different asphalt binders (AS-1, AS-2, AS-3) obtained by MD simulation at 298.15 K. The simulation results were basically consistent with the previous results of simulation test, and they were within the range of test results, further indicating the reliability of asphalt model.

Temperature has a great influence on asphalt performance, the changes of CED and solubility parameters of three different asphalt molecular models at different temperatures were obtained by MD simulation as shown in Fig. 8. The results indicated that CED and solubility parameters of all asphalt showed a decreasing trend with the increase of temperature. The simulation results showed that the Van der Waals component was much larger than the electrostatic component. This means that cohesion depended largely on Van der Waals force that bound asphalt molecules together. In addition, the results showed that the CED and solubility parameters of AS-2 model were the largest, while AS-3 model possessed the least. It shows that AS-2 has stronger intermolecular attraction and better cohesion. The reason might be the proportion of asphaltene and resin in asphalt which was 62.2% in AS-2, while the AS-3 was 55.9%, AS-1 was 57.0%, as shown in Table 1. For AS-2 asphalt, when the temperature increased from 228 K to 453 K, its solubility parameter also decreased from 18.45 to 16.06$(J/cm^3)^{1/2}$, which was about 14.9% lower. The reason for this phenomenon was the mobility among asphalt molecules increased when the temperature increased, which made the asphalt molecules disperse more evenly and increased the distance between asphalt molecules, and finally attributed to the weakening of the intermolecular interaction between asphalt molecules. Therefore, the solubility parameter value decreased with the increase of temperature. The CED was related to the solubility parameter value, so it also showed a similar trend with the temperature change.

$$\delta = \sqrt{CED} \tag{1}$$

$$\delta = \sqrt{\delta_{vdw}^2 + \delta_{ele}^2} \tag{2}$$

Where, CED was the cohesive energy density of asphalt molecule. δ was the solubility parameter, δ_{vdw} was the van der Waals force component of solubility parameter, and δ_{ele} was the electrostatic force component of solubility parameter.

3.4. Adhesion work between asphalt and mineral

In order to evaluate the influence of adhesion energy between different minerals and asphalt, this study quantified the adhesion strength between asphalt and mineral surface by calculating adhesion energy. Adhesion energy was defined as the energy required to divide an interface model into two independent volumetric models, so the calculated adhesion energy was generally negative and has been successfully applied to the bonding strength of interface models in the previous studies [44]. The sizes of different asphalt-mineral interface models constructed by MS were not the same, therefore the adhesion work W between asphalt and mineral was evaluated by using the ratio of adhesion energy to interface contact area, as shown in Eqs. (3) and (4).

$$\Delta E_{adhesion\text{-}energy} = -(E_{total} - (E_{asphalt} + E_{mineral})) \tag{3}$$

$$W_{total} = \Delta E / A \tag{4}$$

Table 5
Cohesive energy density and solubility parameter of asphalt binder.

Properties	AS-1	AS-2	AS-3	Experiment or previous simulation values
CED (10^8 J/m^3)	3.22	3.25	3.09	3.19–3.22[52]
Solubility parameter δ ($(J/cm^3)^{1/2}$)	17.93	18.02	17.58	13.30–22.50[52,53]
Van der Waals δ ($(J/cm^3)^{1/2}$)	17.87	17.97	17.53	N/A
Electrostatic δ ($(J/cm_3)^{1/2}$)	1.49	1.33	1.19	N/A

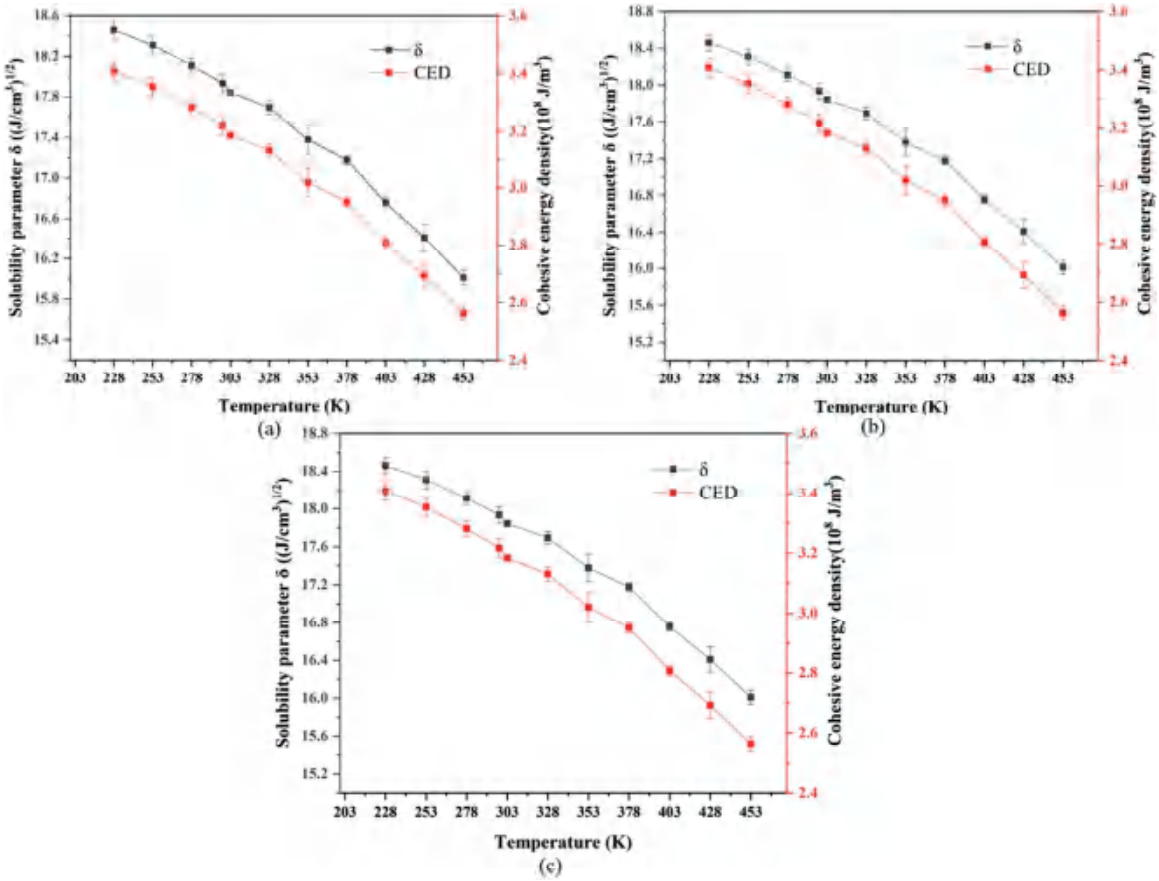

Fig. 8. Cohesive energy density and solubility parameter of three asphalt binder: a) AS-1 b) AS-2 c) AS-3.

Where, $\Delta E_{adhesion\text{-}energy}$ was the adhesion energy of asphalt and mineral. $E_{asphalt}$ and $E_{mineral}$ were the potential energy of asphalt and mineral respectively. E_{total} was the total potential energy of the whole asphalt-mineral system. W was the adhesion work of asphalt-mineral and A was the contact area between asphalt and mineral.

Fig. 9 showed adhesion work between different asphalt and minerals, and it can be seen that there was slight difference in the adhesion work by the results of three MD calculations. When the size of asphalt-aggregate model was too small, the asphalt components will diffuse unevenly on the mineral surface, and finally led to great fluctuation for the calculation results of adhesion energy between asphalt and aggregate [30]. Therefore, the calculation error was small, which further proved that the parameters and

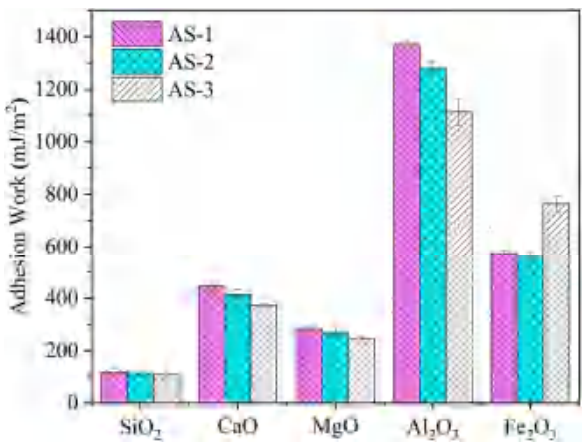

Fig. 9. Adhesion work between asphalt and mineral.

simulation time of MD simulation were reasonable. In addition, adhesion work between three asphalt and minerals was ranked as: AS-1 >AS-2 >AS-3. Although the CED of AS-2 asphalt was the maximum calculated in Section 3.3, it manifested the intermolecular interaction of AS-2 was optimum. But in fact, the molecular mass of asphaltene and resin in AS-1 asphalt was higher than that of AS-2, so AS-1 asphalt had higher interfacial adhesion work with minerals. The influence of mineral types on adhesion work was more significant compared with asphalt types. For five different minerals, the adhesion work was Al_2O_3 >Fe_2O_3 >CaO>MgO>SiO_2. Fig. 10 showed the composition form of asphalt-mineral adhesion work, indicating that the adhesion work between asphalt and mineral was mainly composed of Van der Waals energy and Coulomb electrostatic energy. Among them, for SiO_2, CaO and MgO minerals, the adhesion work was mainly contributed by van der Waals energy, which accounts for more than 90%. While for Al_2O_3 and Fe_2O_3, Coulomb electrostatic energy accounted for more than 70% of the total adhesion work. The reason for this phenomenon was that when cleaving the mineral surface, the bottom atoms Al and Fe appeared on the upper surface due to the periodic effect, which changed the atomic sequence in the Z-axis direction as shown in Fig. 11. The metal atoms Al and Fe were in closer contact with the asphalt, so the asphalt and the metal atoms generated a larger Coulomb electrostatic interaction. It eventually led to unnecessary calculation results. Therefore, the Coulomb electrostatic energy finally calculated was stronger than Van der Waals energy. This was little mentioned in the previous literature. However, if Van der Waals energy was only considered and Coulomb electrostatic effect was ignored, the calculation result of adhesion work of asphalt-minerals was ranked as: CaO>MgO>Al_2O_3 > Fe_2O_3 > SiO_2, which also accorded with the theory that there was the stronger adhesion work between asphalt and alkaline minerals.

3.5. Adhesion work between SARA components and mineral

Asphalt binder was composed of SARA components, and the influence of SARA components can be quantitatively evaluated by calculating the contribution value of adhesion work between SARA components and mineral, as shown in Eqs. (5)–(7).

$$E_{asphalt}=E_{Asp}+E_{Rc}+E_{Aro}+E_{Sat} \tag{5}$$

$$E_{Asp}=E_{total(Asp+mineral)}-(E_{Asp}+E_{mineral}) \tag{6}$$

$$W_{Asp}=E_{Asp}/A \tag{7}$$

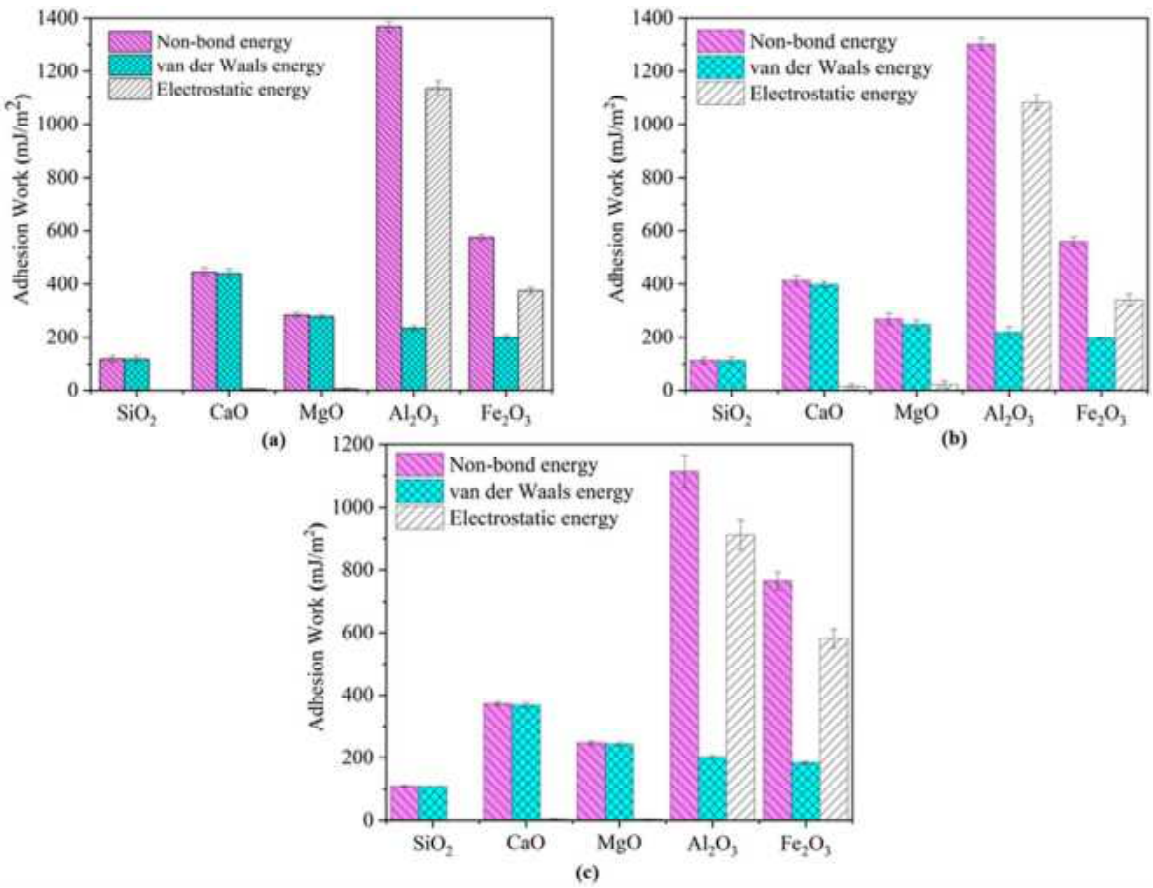

Fig. 10. Composition form of asphalt-mineral adhesion work: a) AS-1 b) AS-2 c) AS-3.

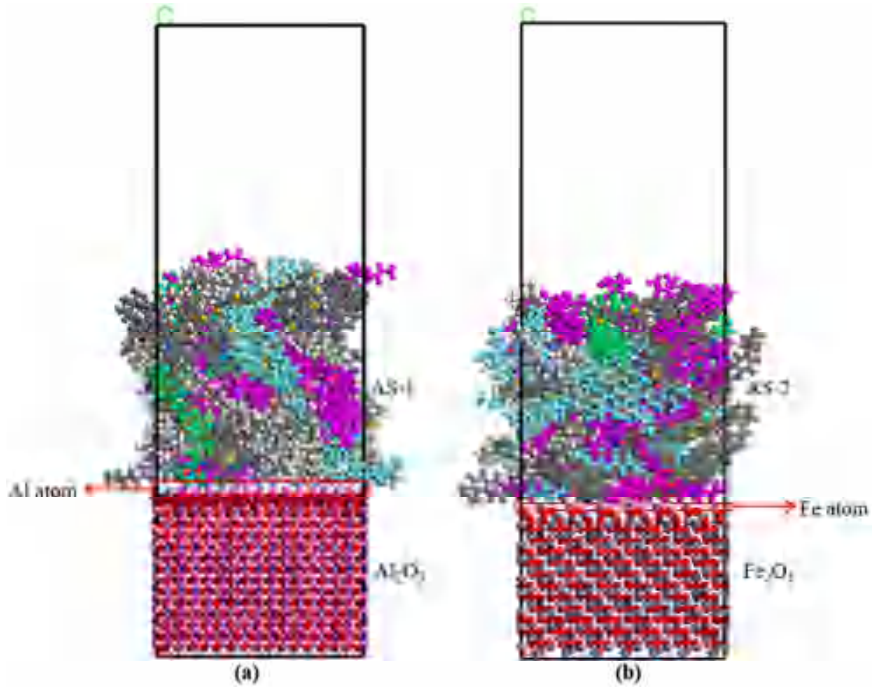

Fig. 11. Final simulation state of asphalt-mineral interface: a) AS-1-Al_2O_3 b) AS-2-Fe_2O_3.

Where, E_{Asp}, E_{Re}, E_{Aro}, E_{Sat} represented the adhesion energy between asphaltene, resin, aromatic, saturate and minerals, respectively. W_{Asp} was the adhesion work between asphaltene and mineral.

Fig. 12 showed the adhesion work of SARA components with minerals, in which (a)-(c) represented the adhesion work of three different asphalt binders with five different minerals respectively. Three groups of MD parallel simulation calculation results of each asphalt showed that the calculation error was small. For AS-1 and AS-2 asphalt, resin, aromatic and asphaltene components produced significant influence on the adhesion work, while saturate component, as a non-polar component, had the smallest contribution value to the energy. Asphaltene has always been considered as an important factor affecting the interfacial adhesion. However, due to the small proportion of asphaltene in AS-1 and AS-2, it only accounted for nearly 20%, while the aromatic component accounted for about 40%, as shown in Table 1. Therefore, aromatic components also had a great contribution to the adhesion work. It can be seen that apart from polar components such as asphaltene and resin, the proportion of components will also directly determine its contribution to the interfacial adhesion work. For AS-3 asphalt, resin and aromatic components accounted for more than 95% of the total adhesion work. This was due to resin and aromatics accounted for 92.7% in AS-3, while asphaltene only accounted for 5.1% as shown in Table 1. Although AS-3 asphalt has the highest molecular mass as shown in Table 2, its interfacial adhesion work with minerals was the least. This was also the reason for the adhesion work between three asphalt and mineral was ranked as: AS-1 > AS-2 >AS-3. It further proved that asphaltene, as the strangest polarity component in asphalt, has a great influence on the adhesion energy.

3.6. Mean square displacements and diffusion coefficients

The diffusion characteristics of asphalt on mineral surface were analyzed by mean square displacement (MSD), which can be used to characterize the change regularity of molecular mobility of asphalt components on mineral surface with time, as shown in Eq. (8). Fig. 13 showed the MSD of three different asphalt binders on five mineral surfaces at 298.15 K respectively. It indicated that the MSD value was constantly expanding with the increase of time. There were differences in the diffusion speed of asphalt on different minerals, among which the diffusion speed of CaO on asphalt was the fastest and that of SiO_2 was the slowest. In addition, the MSD values of five minerals were increasing sharply after 450 ps. At the position of 0–400 ps, for three different asphalt molecular model, the diffusion speed of asphalt on the five mineral surfaces basically met the regularity of CaO>MgO>Al_2O_3 >Fe_2O_3 >SiO_2.

According to Einstein's diffusion law, the diffusion coefficient of a particle can be determined by calculating the slope of the MSD curve as a function of time when the three-dimensional particle undergoes random Brownian motion during the simulation [54]. However, for a complex molecular model with high molecular mass like asphalt, the molecular paths were inevitably affected by abnormal diffusion [55]. As shown in Fig. 13, the molecular mobility of asphalt at the mineral surface increases exponentially after 400 ps, Therefore, in this case, the slope of log (MSD) versus log (t) curve was not always equal to 1.0 to determine the diffusion coefficient (D) of the molecule model. Fig. 14 showed the logarithmic relationship curve for AS-1 asphalt and mineral CaO. It can be seen that the logarithmic relationship curve was divided into three parts, with a slope of 0.4 at 0–100 ps and a slope of 3.28 at 380–500 ps, which all showed abnormal molecular diffusion. At 100–380 ps, the slope was 1, which satisfied Einstein's diffusion law.

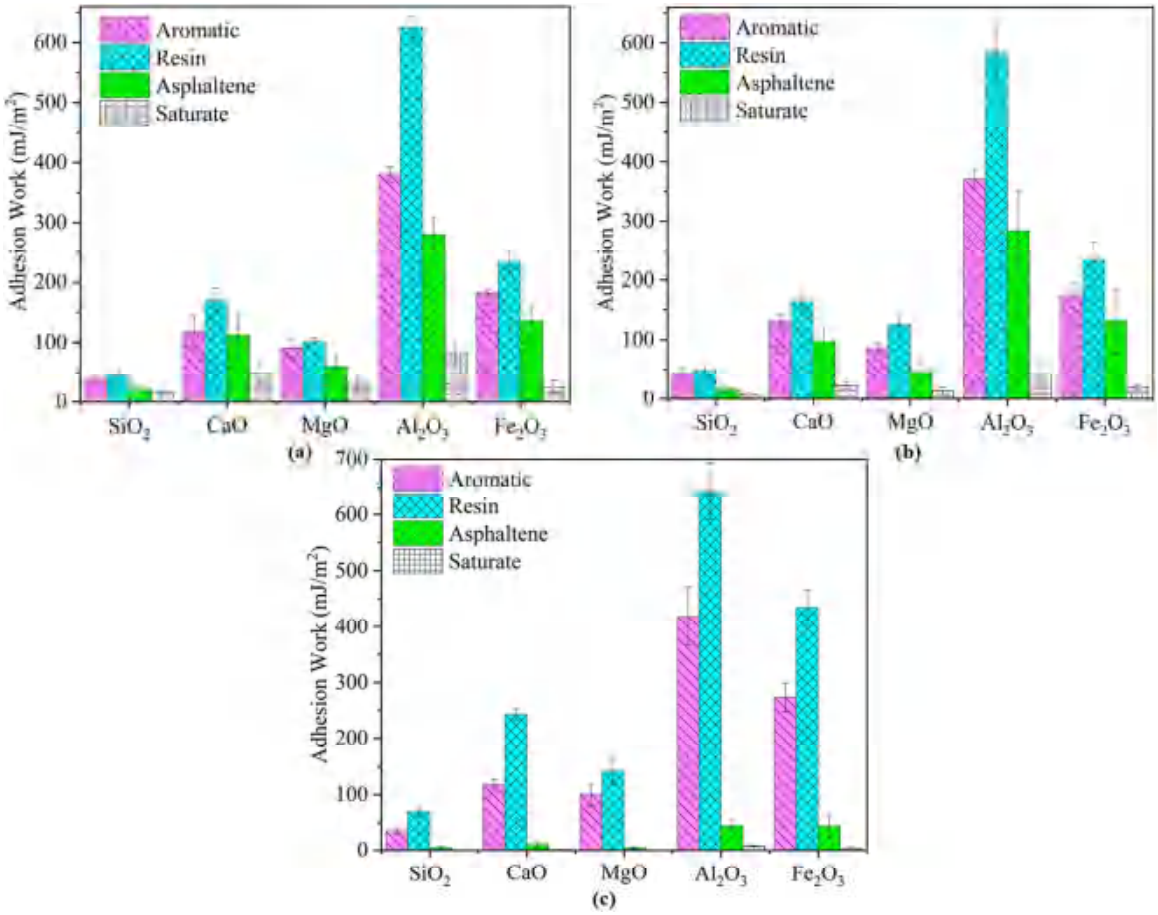

Fig. 12. Adhesion work between SARA components and mineral: a) AS-1 b) AS-2 c) AS-3.

Therefore, the trajectory between 100 and 380 ps was extracted to calculate the asphalt-aggregate diffusion coefficient. As shown in Eq. (9), the diffusion coefficient D of asphalt was 1/6 of MSD slope.

$$MSD(t) = \left\langle |r_i(t) - r_i(0)|^2 \right\rangle \tag{8}$$

$$\mathrm{D} = \frac{1}{6\mathrm{t}} \lim_{t\to\infty} \mathrm{MSD(t)} \tag{9}$$

Where , $r_i(0)$ was the initial position of molecule, $r_i(t)$ was the position of molecule i at time t, < > was the average value of all atoms in the system, and D was the diffusion coefficients of asphalt on minerals.

The diffusivity of asphalt on mineral surface was reflected by calculating the diffusion coefficient D of asphalt and different minerals as shown in Fig. 15. For three types of asphalt (AS-1, AS-2 , AS-3), the diffusion coefficients of five minerals basically showed the regularity of CaO>MgO>Al_2O_3 >Fe_2O_3 >SiO_2. The results showed that the diffusivity of asphalt on the surfaces of five minerals was positively correlated with the acidity and alkalinity of minerals. The stronger the alkalinity of minerals, the greater the diffusivity of asphalt on the surfaces of minerals, which was beneficial to the adhesion between asphalt and mineral surface, and further proves the regularity of adhesion between asphalt and minerals. In addition, AS-3 asphalt has the largest diffusion coefficient on the mineral surface, while AS-2 asphalt has the least.

To evaluate the diffusion capacity of SARA components on mineral surfaces, the diffusion coefficient of SARA on mineral surfaces was calculated in this study as shown in Fig. 16. Fig. 16 (a)-(c) showed the diffusion coefficients of three different asphalts SARA on the surfaces of five minerals respectively. The SARA components all showed the same regularity on the mineral surface: saturate > aromatic > resin > asphaltene. It can be seen that the diffusion coefficient of saturate components on the mineral surface was significantly higher than that of other components, which was due to that saturate had non-polarity and less molecular mass, so its diffusion ability was the strongest. While asphaltene, a component with strong polarity and high molecular mass, caused it to diffuse slowly at the interface. Therefore, it can explain the reason that the diffusion coefficient of AS-2 on mineral surface was the smallest and AS-3 was the largest in Fig. 15, which was directly related to the proportion of asphaltene and resin in asphalt.

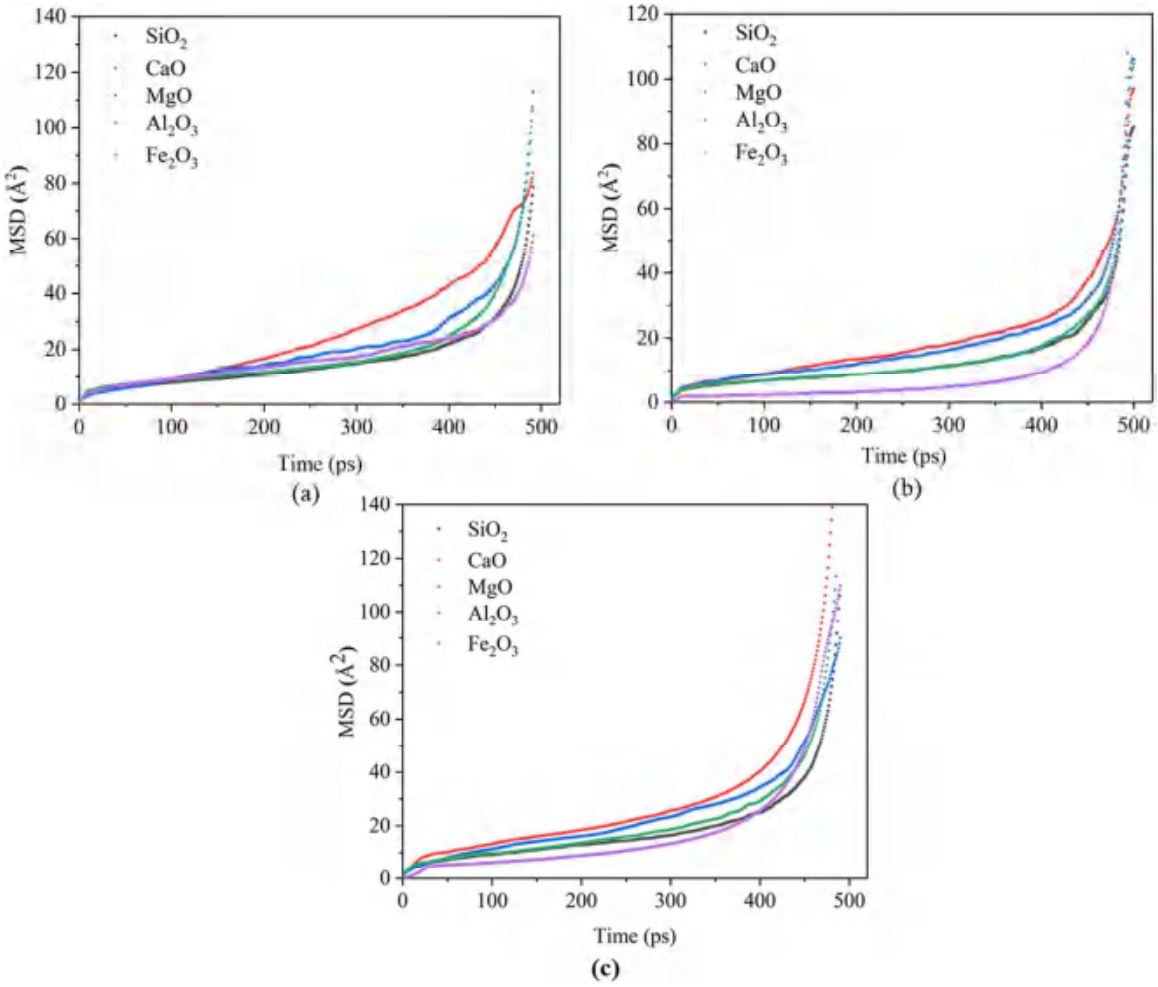

Fig. 13. Mean square displacement between asphalt and different minerals: a) AS-1 b) AS-2 c) AS-3.

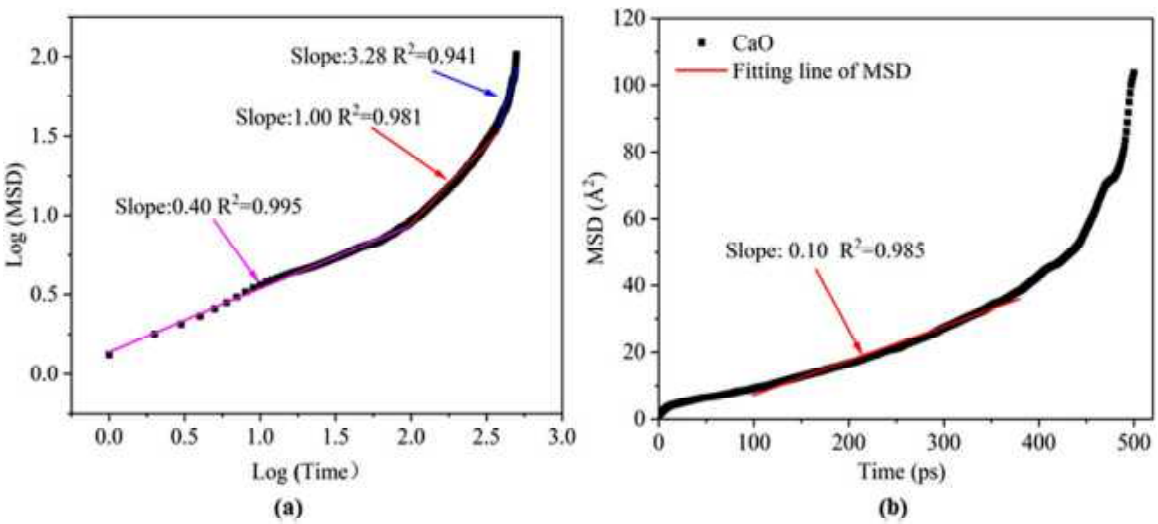

Fig. 14. Mean square displacement of AS-1 asphalt on CaO surface: a) Log (MSD) vs Log (Time) b) MSD vs Time.

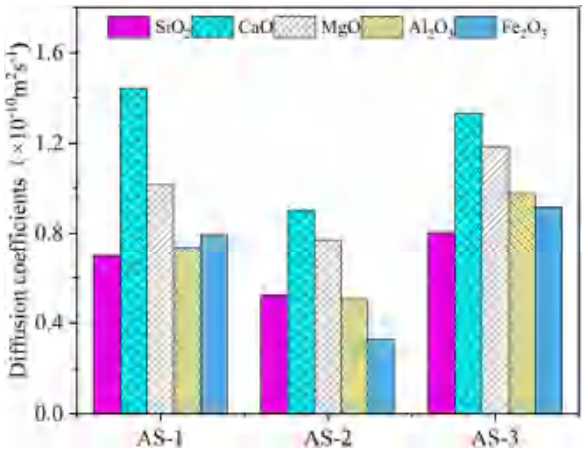

Fig. 15. Diffusion coefficient between asphalt and different minerals.

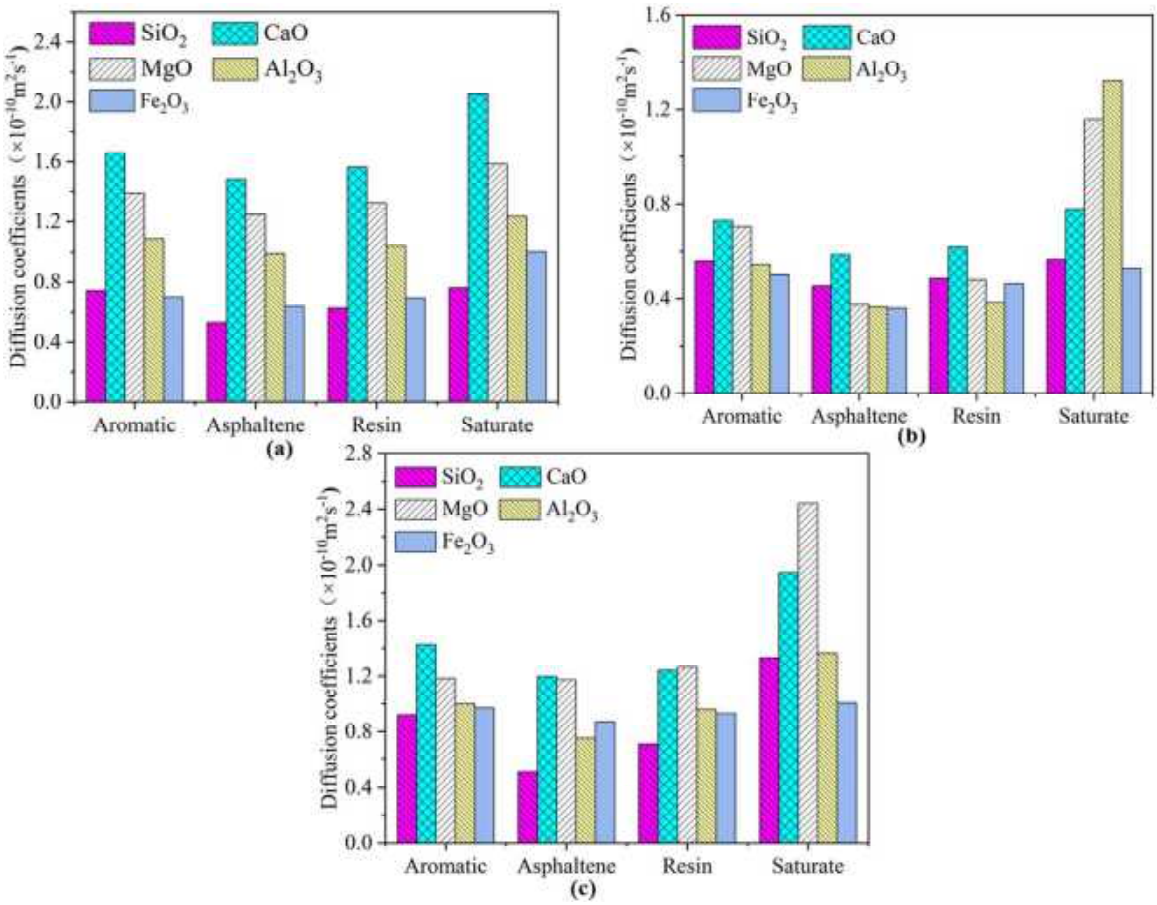

Fig. 16. Diffusion coefficients of SARA components and different oxides: a) AS-1 b) AS-2 c) AS-3.

3.7. Relative concentration distribution of SARA components on mineral surface

The diffusion coefficient calculated by MSD can only reflect the activity of asphalt molecules in the asphalt-mineral interface system, but it cannot directly evaluate the movement direction of molecules. In order to make up for this gap, the relative distribution concentration of SARA components in the Z-axis direction of the mineral surface was calculated and analyzed. Fig. 17 depicted the relative distribution concentration of SARA components on five mineral surfaces. Among them, for AS-1 asphalt and AS-2 asphalt,

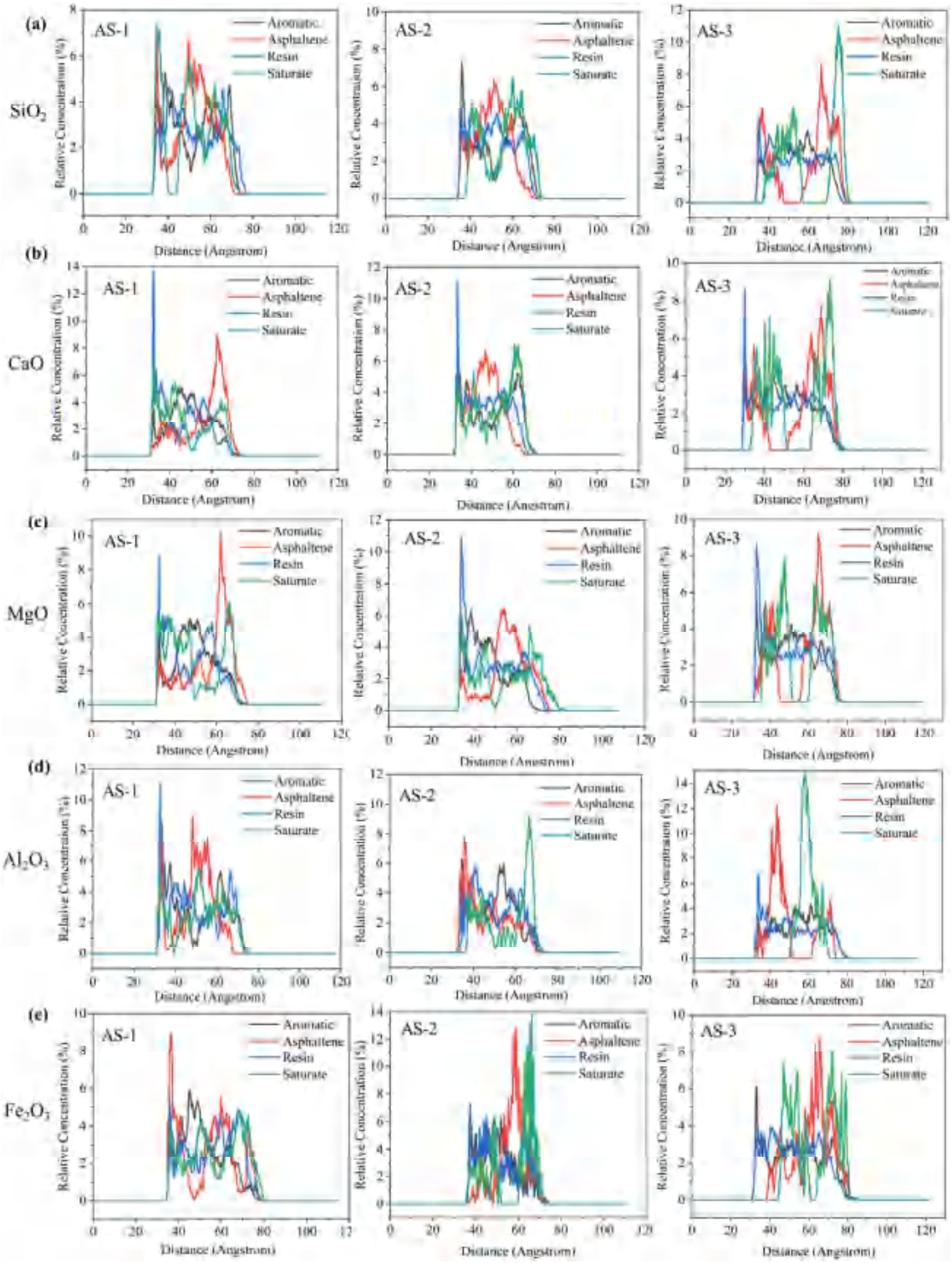

Fig. 17. Relative concentration distribution of SARA components on mineral surface: a) asphalt-SiO_2 b) asphalt-CaO c) asphalt-MgO d) asphalt-Al_2O_3 e) asphalt-Fe_2O_3.

asphaltene components were mainly concentrated near the mineral surface, but some asphaltenes were far away from the mineral surface. This is because asphaltene, as a component with the strongest polarity and large molecular mass, can adsorb the mineral surface well, and as a skeleton structure of asphalt molecules, it required to bear the stability of the overall asphalt structure, so this

may be the reason why some asphaltene components will appear far away from the mineral surface. As for AS-3 asphalt, asphaltene was mainly concentrated far away from the mineral surface. The proportion of asphaltene in AS-3 was low, so it mainly played a role in the overall stability of asphalt, which further showed that the proportion of components was also an important factor affecting the interfacial adhesion between asphalt and mineral. Resin component, as another component with strong polarity, was mainly distributed on the mineral surface, which also proved that it can generate a supernal contribution value to the adhesion energy. As for the aromatic component, its concentration distribution on the mineral surface was relatively uniform, which was due to its high content in asphalt. This was also the reason for its high contribution to the adhesion work of minerals, even more than that of asphaltene components, as shown in Section 3.4. However, as a non-polar and low proportion component, the saturate produced a more random concentration distribution, mainly away from the mineral surface.

4. Conclusions

The interfacial interaction between three types of asphalt and five types of minerals was studied by MD simulation. The MD models are reasonably verified by thermodynamic parameters such as asphalt density, glass transition temperature, cohesive energy density and solubility parameters. The adhesion mechanism between asphalt and mineral surface is revealed by calculating the adhesion work, the diffusivity, and the relative concentration distribution of asphalt on aggregate surface. The following conclusions can be drawn from the above preliminary results.

(1) The interfacial adhesion strength of the three types of asphalt and minerals are ranked as AS-1 >AS-2 >AS-3, and the order of intermolecular interaction of asphalt binder is AS-2 >AS-1 >AS-3. This is mainly related to the proportion of asphaltene and resin components in asphalt binder, and the energy is also affected by the mass of asphalt molecule.
(2) The contribution values of SARA components and minerals to the interfacial adhesion work are mainly related to the types and proportion of asphalt components. For AS-1 and AS-2, the interfacial adhesion work between minerals is mainly contributed by resin, asphaltene and aromatic components, while for AS-3, it is mainly composed of resin and aromatic components. This can be reflected by the relative concentration distribution of SARA components on the mineral surface. In addition, the diffusivity of SARA components on mineral surface is ranked as saturate> aromatic > resin > asphaltene.
(3) The diffusivity of asphalt on the five minerals surfaces was ranked as CaO> MgO > Al_2O_3 > Fe_2O_3 > SiO_2. It is enhanced with the increase of alkaline strength of minerals, and then the interfacial adhesion strength of asphalt-mineral increases.

MD simulation is an effective method to analyze the adhesion mechanism of asphalt-mineral interface from the molecular perspective of molecular model. However, the cross-scale study of interface performance between asphalt and aggregate will inevitably lead to differences in actual results such as the glass transition temperature, which may be caused by simulation time and size effect of molecules. That will need to be further explored. In addition, the failure mechanism of the asphalt-mineral interface will be the issue under the coupling effect of external factors such as asphalt aging and moisture.

Declaration of Competing Interest

The authors declare that they have no known competing financial interests or personal relationships that could have appeared to influence the work reported in this paper.

Data availability

No data was used for the research described in the article.

Acknowledgments

This work was supported by the Program Fund of Non-Metallic Excellence and Innovation Center for Building Materials (2022SFP6–5), National Natural Science Foundation of China (No. 51978068), Natural Science Foundation of Shaanxi Province (No. 2020JM-217), and Fundamental Research Funds for the Central Universities, CHD (Grant No. 310821173501, No. 300102211301). The authors gratefully acknowledge their financial support.

References

[1] A. Arshadi, H. Bahia, Development of an image-based multi-scale finite element approach to predict mechanical response of asphalt mixtures, Asph. Paving Technol. 84 (2015) 439–458.
[2] G. Sun, J. Zhang, X. Tan, D. Guo, Y. Guan, Evaluation of conventional technical properties and self-healing ability of bitumen-based sealants containing sunflower-oil microcapsules for pavement cracks, Constr. Build. Mater. 254 (2020), 119299.
[3] S. Adhikari, Z. You, K. Peterson, Multi-phase characterization of asphalt concrete using x-ray microfluorescence, Int. J. Pavement Res. Technol. 6 (2) (2013) 117.
[4] H.A. Scholz, An investigation of aggregate-asphalt adhesion by measurements of heats of immersion, Highw. Res. Rec. (1970).
[5] M. Khalili, M. Karakouzian, Feasibility of ultrasonic measurements for characterizing rheological properties of asphalt binders, Constr. Build. Mater. 75 (jan.30) (2015) 220–226.
[6] C. Guo, S. Han, R.R. Han, Evaluation of asphalt-aggregate adhesion using surface free energy theory, Appl. Mech. Mater. 686 (2014).

[7] P. Guo, B.M. Tang, M. Feng, Z.H. Yang, Warm mix recycled asphalt-aggregates adhesion based on surface free energy theory, J. Chang. Univ. 34 (4) (2014) 38–44.
[8] X. Cheng, Z. Zhang, S. Yang, L.U. Zhongshan, Experimental study of the water stability of asphalt mixture, J. Hef Univ. Technol. (Nat. ence) (2003).
[9] G. Sun, J. Zhang, Q. Liu, X. Tan, Y. Guan, Effects of microcapsules on self-healing performance of asphalt materials under different loading modes, J. Transp. Eng. Part B Pavements 147 (2) (2021), 04021010.
[10] W. Huang, Q. Lv, F. Xiao, Investigation of using binder bond strength test to evaluate adhesion and self-healing properties of modified asphalt binders, Constr. Build. Mater. 113 (jun.15) (2016) 49–56.
[11] R. Moraes, R. Velasquez, H.U. Bahia, Measuring the effect of moisture on asphalt-aggregate bond with the bitumen bond strength test, Transp. Res. Rec. J. Transp. Res. Board 2209 (1) (2011) 70–81.
[12] J. Zhang, G.D. Airey, J. Grenfell, Experimental evaluation of cohesive and adhesive bond strength and fracture energy of bitumen-aggregate systems, Mater. Struct. 49 (7) (2016) 2653–2667.
[13] A. Mokhtari, H. David Lee, R.C. Williams, C. Guymon, J.P. Scholte, S. Schram, A novel approach to evaluate fracture surfaces of aged and rejuvenator-restored asphalt using cryo-SEM and image analysis techniques, Constr. Build. Mater. 133 (2017) 301–313.
[14] M. Pérez-Martínez, P. Marsac, T. Gabet, E. Chailleux, Prediction of the mechanical properties of aged asphalt mixes from FTIR measurements, 8th RILEM International Symposium on Testing and Characterization of Sustainable and Innovative Bitumonous Materials, 2017.
[15] Y. Liu, J. Shen, An investigated review on the microstructure and micromechanical properties of asphalt based on AFM, Pet. Asph. (2017).
[16] X. Lv, W. Fan, J. Wang, M. Liang, C. Qian, H. Luo, G. Nan, B. Yao, P. Zhao, Study on adhesion of asphalt using AFM tip modified with mineral particles, Constr. Build. Mater. 207 (MAY 20) (2019) 422–430.
[17] M. Xu, J. Yi, D. Feng, Y. Huang, D. Wang, Analysis of adhesive characteristics of asphalt based on atomic force microscopy and molecular dynamics simulation, Acs Appl. Mater. Interfaces (2016) 12393.
[18] F. Guo, J. Zhang, J. Pei, B. Zhou, Z. Hu, Study on the mechanical properties of rubber asphalt by molecular dynamics simulation, J. Mol. Model. 25 (12) (2019) 1–8.
[19] J. Zhang, Z. Chen, H. Du, R. Li, J. Pei, Study on Interface Behavior Between Asphalt and Silica in Aggregate Based on Molecular Dynamics, 2016.
[20] H. Yao, J. Liu, M. Xu, A. Bick, J. Zhang, Generation and properties of the new asphalt binder model using molecular dynamics (MD), Sci. Rep. 11 (1) (2021) 9890.
[21] Z. Chen, J. Pei, L. Rui, F. Xiao, Performance characteristics of asphalt materials based on molecular dynamics simulation – A review, Constr. Build. Mater. 189 (2018) 695–710.
[22] G. Sun, Y. Yang, J. Zhang, Y. Cao, X. Tan, J. Pei, Modeling and optimization of pavement scale-model for magnetically coupled resonant in wireless power transmission systems, Constr. Build. Mater. 319 (2022), 126066.
[23] W.H. Daly, I. Negulescu, Implementation of GPC characterization of asphalt binders at louisiana materials laboratory, Crumb Rubber (2013).
[24] M. Shakirullah, I. Ahmad, M. Ishaq, A.A. Shah, H. Khan, FTIR analysis of whole asphalt and some crackates, J. - Chem. Soc. Pak. 29 (5) (2007) 468–475.
[25] L. Zhang, M.L. Greenfield, Analyzing properties of model asphalts using molecular simulation, Energy Fuels 21 (3) (2007) 1712–1716.
[26] R.E. Robertson, J.F. Branthaver, P.M. Harnsberger, J.C. Peterson, S.M. Dorrence, Fundamental properties of asphalts and modified asphalts, vol II: final report, new methods, properties of materials, 2001.
[27] D.D. Li, M.L. Greenfield, Chemical compositions of improved model asphalt systems for molecular simulations, Fuel 115 (1) (2014) 347–356.
[28] Z. Dong, Z. Liu, P. Wang, X. Gong, Nanostructure characterization of asphalt-aggregate interface through molecular dynamics simulation and atomic force microscopy, Fuel 189 (feb.1) (2017) 155–163.
[29] M. Huang, H. Zhang, Y. Gao, L. Wang, Study of diffusion characteristics of asphalt–aggregate interface with molecular dynamics simulation, Int. J. Pavement Eng. 22 (3) (2021) 319–330.
[30] L. Chu, L. Luo, T.F. Fwa, Effects of aggregate mineral surface anisotropy on asphalt-aggregate interfacial bonding using molecular dynamics (MD) simulation, Constr. Build. Mater. 225 (2019) 1–12.
[31] Meng Guo, Yiqiu Tan, Jianming Wei, Using molecular dynamics simulation to study concentration distribution of asphalt binder on aggregate surface, J. Mater. Civ. Eng. (2018).
[32] J. Zhang, A.K. Apeagyei, G.D. Airey, J. Grenfell, Influence of aggregate mineralogical composition on water resistance of aggregate–bitumen adhesion, Int. J. Adhes. Adhes. 62 (2015) 45–54.
[33] W. Sun, H. Wang, Moisture effect on nanostructure and adhesion energy of asphalt on aggregate surface: A molecular dynamics study, Appl. Surf. Sci. 510 (2020).
[34] Å.L. Lyne, P. Redelius, M. Collin, B. Birgisson, Characterization of stripping properties of stone material in asphalt, Mater. Struct. (2013).
[35] M. Guo, Y. Tan, L. Wang, Y. Hou, Diffusion of asphaltene, resin, aromatic and saturate components of asphalt on mineral aggregates surface: molecular dynamics simulation, Road. Mater. Pavement Des. 18 (2017) 149–158.
[36] Y.Q. Tan, M. Guo, Interfacial thickness and interaction between asphalt and mineral fillers, 2013.
[37] M. Horgnies, E. Darque-Ceretti, H. Fezai, E. Felder, Influence of the interfacial composition on the adhesion between aggregates and bitumen: Investigations by EDX, XPS and peel tests, Int. J. Adhes. Adhes. 31 (4) (2011) 238–247.
[38] W. Hao, L. Enqiang, X. Guangji, Molecular dynamics simulation of asphalt-aggregate interface adhesion strength with moisture effect, Int. J. Pavement Eng. 18 (5) (2017) 414–423.
[39] G. Meng, T. Yiqiu, W. Jianming, Using molecular dynamics simulation to study concentration distribution of asphalt binder on aggregate surface, J. Mater. Civ. Eng. 30 (5) (2018), 04018075 (6 pp.)-04018075 (6 pp.).
[40] S. Wei, W. Hao, Moisture effect on nanostructure and adhesion energy of asphalt on aggregate surface: A molecular dynamics study, Appl. Surf. Sci. 510 (2020) 558–568.
[41] M. Xinyuan, W. Jiantao, L. Quan, W. Ren, M. Oeser, Molecular dynamics simulation of the bitumen-aggregate system and the effect of simulation details, Constr. Build. Mater. 285 (2021) 12. -12 pp.
[42] S. Xu, F. Xiao, S. Amirkhanian, D. Singh, Moisture characteristics of mixtures with warm mix asphalt technologies – A review, Constr. Build. Mater. 142 (2017) 148–161.
[43] T.L. Zhuravlev, Concentration of hydroxyl groups on the surface of amorphous silicas, Langmuir 3 (3) (1987) 316–318.
[44] G. Xu, W. Hao, Study of cohesion and adhesion properties of asphalt concrete with molecular dynamics simulation, Comput. Mater. Sci. 112 (2016) 161–169.
[45] H. Sun, Z. Jin, C. Yang, R.L.C. Akkermans, S.H. Robertson, N.A. Spenley, S. Miller, S.M. Todd, COMPASS II: extended coverage for polymer and drug-like molecule databases, J. Mol. Model. 22 (2) (2016).
[46] M. Huang, H.L. Zhang, Y. Gao, L. Wang, Study of diffusion characteristics of asphalt-aggregate interface with molecular dynamics simulation, International Journal Of Pavement Engineering.
[47] X. Qu, Q. Liu, M. Guo, D. Wang, M. Oeser, Study on the effect of aging on physical properties of asphalt binder from a microscale perspective, Constr. Build. Mater. 187 (OCT.30) (2018) 718–729.
[48] M. Marateanu, D. Anderson, Time-temperature dependency of asphalt binders – an improved model (with discussion), J. Assoc. Asph. Paving Technol. 65 (1996).
[49] G. Adam, J.H. Gibbs, On the temperature dependence of cooperative relaxation properties in glass-forming liquids, J. Chem. Phys. 43 (1) (1965) 139–146.
[50] H.A. Tabatabaee, R. Velasquez, H.U. Bahia, Modeling thermal stress in asphalt mixtures undergoing glass transition and physical hardening, Transp. Res. Rec. J. Transp. Res. Board 2296 (2296) (2012) 106–114.
[51] H.A. Tabatabaee, R. Velasquez, H.U. Bahia, Predicting low temperature physical hardening in asphalt binders, Constr. Build. Mater. 34 (2012) 162–169.
[52] P. Wang, Z.-j Dong, Y.-q Tan, Z.-y Liu, Investigating the interactions of the saturate, aromatic, resin, and asphaltene four fractions in asphalt binders by molecular simulations, Energy Fuels 29 (1) (2015) 112–121.

[53] B. Cui, X. Gu, D. Hu, Q. Dong, A multiphysics evaluation of the rejuvenator effects on aged asphalt using molecular dynamics simulations, J. Clean. Prod. 259 (2020), 120629.
[54] A. Einstein, On the movement of small particles suspended in stationary liquids required by the molecular-kinetic …, Ann. der Phys. 17 (549) (1905).
[55] G. Wu, H. Lin, D. Chen, Sorption and distribution of asphaltene, resin, aromatic and saturate fractions of heavy crude oil on quartz surface: Molecular dynamic simulation, Chemosphere 92 (11) (2013) 1465–1471.

Construction and Building Materials 400 (2023) 132708

Contents lists available at ScienceDirect

Construction and Building Materials

journal homepage: www.elsevier.com/locate/conbuildmat

Comprehensive evaluation of ballastless-track sealants based on macro–micro tests and principal component analysis

Guoqing Sun, Zhe Hu, Jiupeng Zhang, Hengxiao Xue *

Key Laboratory for Special Area Highway Engineering of Ministry of Education, Chang'an University, Xi'an 710064, China

ARTICLE INFO

Keywords:
Ballastless-track sealants
Surface roughness
Surface adhesion
Chemical bonding rate of SiO_2
Principal component analysis (PCA)

ABSTRACT

In order to establish a comprehensive evaluation system of ballastless-track sealants, a method is put forward based on macro–micro tests and principal component analysis(PCA). In this study, the performance parameters of four different ballastless-track sealants (SE, NI, WQ, SY) were obtained by low-temperature performance test, atomic force microscope (AFM) and X-ray photoelectron spectroscopy (XPS) test. Then the PCA method was conducted to reveal the complex relationship between macro and micro performance parameters of sealants, such as the maximum tensile force, the maximum failure displacement, the surface roughness, the surface adhesion, the chemical bonding rate with SiO_2, and the principal component contribution rate was calculated. Finally, the comprehensive score was utilized to evaluate the performance of different sealants. The results show that the macroscopic properties of the sealant are closely related to the microscopic parameters roughness, surface adhesion and chemical bonding rate of SiO_2. The macro–micro performance parameters of sealant are comprehensively evaluated through PCA, and the results are as follows: NI > SE > WQ > SY. The PCA can comprehensively evaluate the performance of sealant intuitively and accurately, avoiding the subjective influence of evaluating the material performance only through macro-tests or micro-tests.

1. Introduction

Chinese high-speed railways mainly adopted ballastless-track structures and set expansion joints in their base plates, which can locally control the deformation under dynamic load [1,2]. Polyurethane joint sealant was widely used in the expansion joint of ballastless-track base plate because of its good adhesion, stability and high strength [3,4]. However, the adhesive failure of ballastless-track sealants will occur under the action of environment and load, which was also the main failure reason of sealant [5–7]. As for the main failure modes of sealants, there was still a lack of a set of practical evaluation methods for adhesion. How to establish an evaluation method effectively and quantitatively for adhesion was of great engineering significance. At present, the evaluation method of sealants' adhesion performance did not adjust the test method and parameters according to the real working conditions, and it was difficult to predict the service performance of sealant efficiently and accurately because of the long test period and poor reproducibility [8]. Because there were few literatures on the research and evaluation methods of adhesion properties of sealant for ballastless-track, the research methods in related fields can be used.

Common sealants adhesive test methods in road engineering included surface energy method [9,10], destruction test [11] and direct tensile test [12–15]. To quantitatively evaluate the adhesion force between sealants and aggregates, Sun et al [16] determined and calculated the adhesion work between different types of sealants and aggregates using the sessile drop method based on the surface energy theory. Fini et al [17] studied the adhesion of various hot-poured sealants to aggregates by interfacial parameters such as contact angles and surface tensions. Zhang et al [18] measured the adhesive property between sealants and the targeted substrates by peel test. Al-Qadi [13] et al recorded the load and displacement at failure based on direct tensile test, which was utilized to evaluate adhesion performance of different sealants. In order to prepare a polyurethane waterproof binding material for bridge decks with good bonding strength and flexibility, Yang et al [19] used tensile test and determined the optimum composition based on tensile strength and elongation at breaking. Sawalha et al [20] used modified direct tensile tester and analyzed the effect of temperature changes and ageing on the adhesive property of sealants.

The above-mentioned evaluation method of sealant's adhesion performance was mainly based on macroscopic test phenomena, with the

* Corresponding author.
E-mail address: xhx1570@126.com (H. Xue).

https://doi.org/10.1016/j.conbuildmat.2023.132708
Received 3 April 2023; Received in revised form 15 May 2023; Accepted 30 July 2023
Available online 4 August 2023
0950-0618/© 2023 Published by Elsevier Ltd.

aim of optimizing the material. The direct tensile test method can most effectively simulate and restore the stress state of sealant for ballastless-track, but the test conditions and parameters need to be closely related to the actual working conditions [21,22]. Furthermore, it's more subjective to analyze the relationship between the macroscopic phenomena of sealants' adhesive failure and the experimental data through laboratory tests, and hard to evaluate their performance intuitively and comprehensively [23]. It was difficult to clarify the mechanism of adhesion failure only through macroscopic tests, microscopic testing methods should be supplemented to verify for the sake of achieving a comprehensive evaluation of the adhesive property of sealants.

Multi-scale research methods can further study the adhesion mechanism of materials and analyze the influencing factors of properties [24,25]. AFM can be exploited to quantitatively evaluate the mechanical properties of phase separated polyurethanes as a function of molecular structure [26,27]. Xue et al [8] utilized differential scanning calorimetry (DSC) and XPS to study the adhesive mechanism of the sealants, and analyzed the chemical interaction between the sealant and the joint wall materials. Galvez et al [28] used scanning electron microscope (SEM) and optical microscope for the evaluation of the adhesion failure characteristics of specimens prepared from two structural polyurethane adhesives. Tan et al [29] prepared a novel waterborne UV-curable polyurethane and studied the effects of modifier content and chain length on its surface energy, surface composition and morphology by contact angle measurement, XPS and AFM. Ma et al [30] added ethylene–vinyl acetate (EVA) to polyurethane, and studied the relationship between water and EVA content on the bonding strength of modified polyurethane materials by SEM and AFM. Among them, AFM and XPS can quantitatively test the surface roughness, surface adhesion and chemical bonding rate of the sealants, which were suitable for establishing a relationship with the macroscopic adhesion characteristics of sealants. Selecting multiple macro–micro indicators can evaluate the adhesion performance of the sealants from different aspects.

Therefore, the objective of this study is to utilize the self-developed low-temperature tensile test to obtain the macroscopic outcomes of the maximum tensile force and maximum failure displacement of the sealants, and exploit AFM and XPS to test microscopic parameters of surface roughness, surface adhesion force and chemical bonding rate with SiO_2. PCA is used to evaluate the adhesive properties of the sealants by combining the macroscopic and microscopic results.

2. Materials and methods

2.1. Materials

In this study, four different polyurethane sealants were used for ballastless-track, namely SE, NI, WQ and SY. Because the low-temperature environment has great influence on the interface performance of ballastless-track, sealants suitable for low temperature environment were selected. According to the Provisional Technical Regulations for Joint Sealing Materials for Ballastless Track of High-speed Railway TJ/GW119-2013, these materials were tested and the results are shown in Table 1 [8]. Polyurethane sealant was made by polymerizing a component containing isocyanate group (–NCO) and a component containing alcohol hydroxyl group (–OH). When the sealant contained many –NCO groups with strong polarity, it will have a better adhesion at the interface. The molar ratio of –NCO to –OH groups in sealant was defined as isocyanate index, also known as R value. Therefore, a large R value indicated that the adhesion of the sealant was great.

2.2. Low-temperature performance test of sealant

In order to quantitatively evaluate the low temperature performance of sealants, low-temperature tensile test (LTTT) was conducted to assess the maximum tensile force and maximum failure displacement of materials [22]. LTTT in this study was a self-developed test device, which was used to evaluate the low-temperature performance of the sealants. The obtained test parameters and results were convenient to establish a relationship with the real working conditions of the sealant. The fixture of adhesive specimens was composed of stainless steel strips, substrates and blocking blocks respectively. When preparing the specimens, 10 × 20 mm pre-debonding areas were sprayed on both sides of one substrate with release agents. Then the pre-debonding test piece and the blocking block were surrounded into a 50 × 5 × 20 mm pouring groove for sealants on the horizontal operating platform, weighed an appropriate amount of sealants, and mixed the sealant with high-speed shearing machine for 3 min, poured the mixed sealant into the pouring tank slowly, as shown in Fig. 1. After placing the poured specimen in a cool and ventilated place for 7 days, then installed the prepared specimen on the LTTT loading system for test, and the maximum tensile force and maximum failure displacement of the sealants were obtained at the temperature of −25°C and the loading rate of 100 mm/h.

Table 1
Performance parameters of four different sealants [8].

Performance parameters	Specification	SE	NI	WQ	SY
Tensile properties	GB/T13477.10-2017	60%,24 h pass	60%,24 h pass	150%,24 h pass	150%,24 h pass
Surface drying time (h)	GB/T16777-2008	≤12			
Hard drying time (h)	GB/T16777-2008	≤24			
Elongation at break (%)	GB/T16777-2008	≥700%	≥600%	≥700%	≥800%
Tensile strength (MPa)	GB/T16777-2008	≥1.0	≥1.5	≥0.8	≥0.8
Isocyanate index (R)	–	2.8	3.5	2.5	1.7

2.3. Surface roughness test

Atomic force microscope (AFM) can be used to test the micro-surface roughness of four different sealants, and further analyze the properties of sealants from the micro-level. Before the test, the sealant was fully mixed through a high-speed shearing machine in a mixing dish for 3 min.Then, the evenly mixed sealant was slowly poured on the glass slide placed on the horizontal table. After standing for 7 days in a well-ventilated environment without sunlight, the prepared specimen was shown in Fig. 2. The probe material used in AFM test was silicon, and the scanning range of the probe was 10 × 10 μm. During the test, the peak force mode was used for observation. In this mode, the force between the probe and the sample was always kept at a low level. Therefore, it can be used to observe polymer materials and biological materials with soft surface texture and high viscosity. In addition, the model would not damage the surface of measured material and get abundant micro-mechanical information. So it can capture the high-resolution micro-image of the sample, and the roughness R_a of different sealant materials can be calculated according to the micro-morphology data of the sample as shown in Eq. (1) [31,32].

$$R_a = \frac{1}{N}\sum_{i=1}^{n} R_i \tag{1}$$

where R_a was the roughness and R_i was the absolute value of the elevation from the contour point to the centerline within the sampling length.

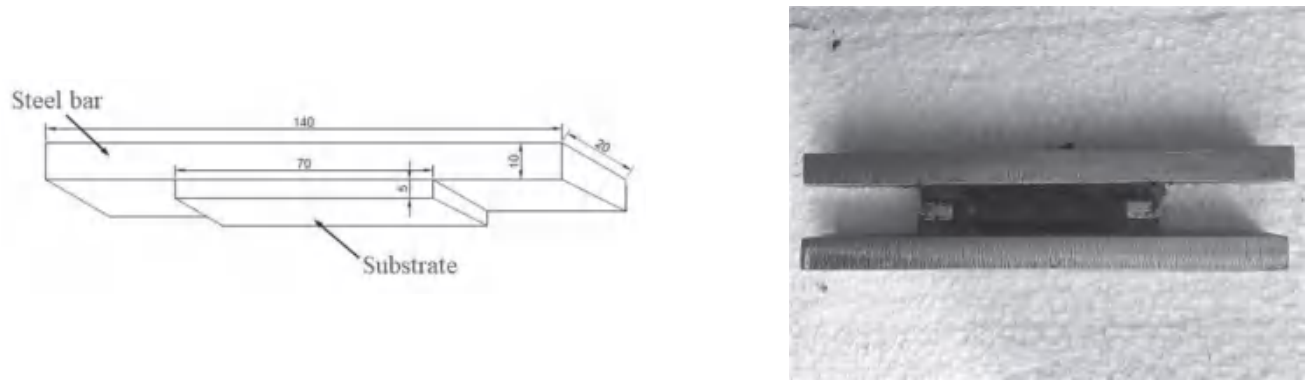

(a) (b)

Fig. 1. Composition of the sealant specimen a) specimen size b) The prepared sample.

Fig. 2. AFM test specimen.

2.4. Surface adhesion test

When observing the micro-morphology of the sealant in the peak force mode, it can also quantitatively observe the adhesion force of the sealant surface by AFM probe. The probe pressure was an important test parameter. If the pressure was too small, the probe can't touch the surface of the sample, and if the pressure was too high, it will easily lead to the probe falling into the sample. Especially for polyurethane polymer materials, which have high viscosity and soft surface texture, a reasonable probe pressure was important. Previous research results showed that too high or too low probe pressure will lead to deviation of test results, and the probe pressure was determined as 20nN [33,34].

In the data processing of different peak forces, the scanning points were classified according to respective elevations. The scanning points were distributed in five sections with 0–20%, 20–40%, 40–60%, 60–80% and 80–100% of the contour elevation difference, and achieved the surface adhesion of sealants in different intervals.

2.5. Chemical bonding rate between sealant and SiO_2

For the ballastless-track sealant, the chemical adhesion was mainly dominated by the reaction between isocyanate groups (–NCO) in polyurethane prepolymer and hydroxyl groups (–OH) on the surface of silicon elements in inorganic compounds, which indicated that SiO_2 and polyurethane sealants were chemically crosslinked [35]. Therefore, the interfacial adhesion effect between sealants and trackless materials can be evaluated by studying the chemical bonding rate between sealants and SiO_2.The chemical bonding characteristics between sealants and joint wall were tested by X-ray photoelectron spectroscopy (XPS) scanning, and the chemical interaction characteristics of sealant adhesion interface were studied. Before the test, the prepared sealant was fully mixed with 98% pure SiO_2 powder by the mass ratio of 1:1, ventilated and direct sunlight-free environment for seven days. After it was completely cured, the samples were put into disposable test tubes for testing, as shown in Fig. 3. Before of the XPS test, the pure SiO_2 powder was compared by X-ray scanning, and then the prepared sealant-SiO_2 mixed sample was scanned and tested, and the measured Si peaks were fitted according to the different valence Si peaks of pure SiO_2 and sealant-SiO_2. In order to accurately and quantitatively characterize the bonding characteristics between sealant and SiO_2, Eq.(2) was introduced to calculate the bonding rate between sealant and SiO_2 [8]:

$$r = \frac{A_{PU-SiO_2}}{A_{PU-SiO_2} + A_{SiO_2}} \tag{2}$$

where r was the bonding rate between the sealant and SiO_2 (%), A_{PU-SiO_2} was the peak area of Si atoms bonded with the sealant in XPS, A_{SiO_2} was the peak area of SiO_2 in XPS.

2.6. Principal component analysis (PCA)

Principal component analysis (PCA) was to utilize the idea of dimensionality reduction to transform many related indexes into several

Fig. 3. Mixed sample of sealant and SiO_2.

unrelated comprehensive indexes through mathematical transformation. These comprehensive indexes were the principal components of many original variables, they can be used quantitatively, intuitively and quickly to evaluate the main factors affecting the properties of materials. All data analysis was carried out in Statistical Products and Services Solution (SPSS). By implementing PCA model, the dimension of data and the number of variables were reduced, and more details of PCA can be seen in the [36–38]. In the performance analysis of four different sealants, the surface roughness, surface adhesion and chemical bonding rate with SiO_2 were obtained through micro-tests. In addition, the maximum tensile force and maximum tear displacement of sealants were obtained through macro-tests, and the complex relationship between them was analyzed and the principal components were extracted. Finally, the performance of the sealant was expressed by the comprehensive score of principal components. The flow chart of the PCA method was shown in Fig. 4.

3. Results and discussion

3.1. Low-temperature performance test of sealant

According to the LTTT test method, the adhesive properties of different sealants were tested, and the measured maximum tensile force and maximum failure displacement of sealant were shown in Fig. 5-Fig. 6 respectively.

For four different sealants, the order of maximum tensile index was NI > SE > WQ > SY. Compared with the parameters shown in Table 1, the traditional test method has a strong correlation with the adhesion test of sealant, and the tensile strength and R value were positively correlated with the maximum tensile. The reason for the analysis was that the hard segment content of the materials with larger R value was higher, and they were adsorbed to each other under the action of hydrogen bonds, forming a compact large-scale hard segment phase region, thus increasing the molecular weight and having stronger Van der Waals force with the joint wall materials. Macroscopically, the adhesion strength between materials with larger R value and substrate materials was higher. However, R value of sealant was negatively correlated with failure displacement as shown in Fig. 6. That is, a small R value will lead to a large failure displacement. The reason for this phenomenon may be that when the R value was small, the soft segment content of the sealant was high, the molecular chain was flexible, and the macroscopic performance was stronger deformation ability.

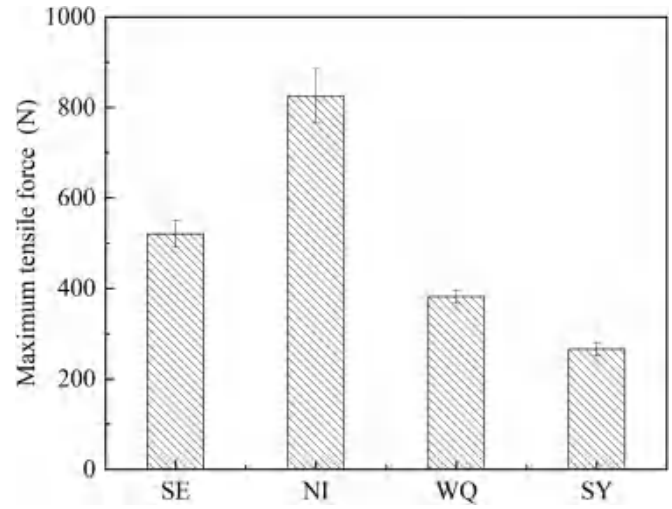

Fig. 5. Maximum tensile force of four different sealants.

3.2. Surface roughness test

Based on the peak force mode, the micro-morphology of four different sealants was scanned, and the results were shown in Fig. 7. The results showed that the micro-morphology of different sealants showed great differences. In the micro-morphology, the high and sharp place was the hard segment of sealant, and the low and smooth place was the soft segment of sealant [26]. It can be seen from the Fig. 7 that the

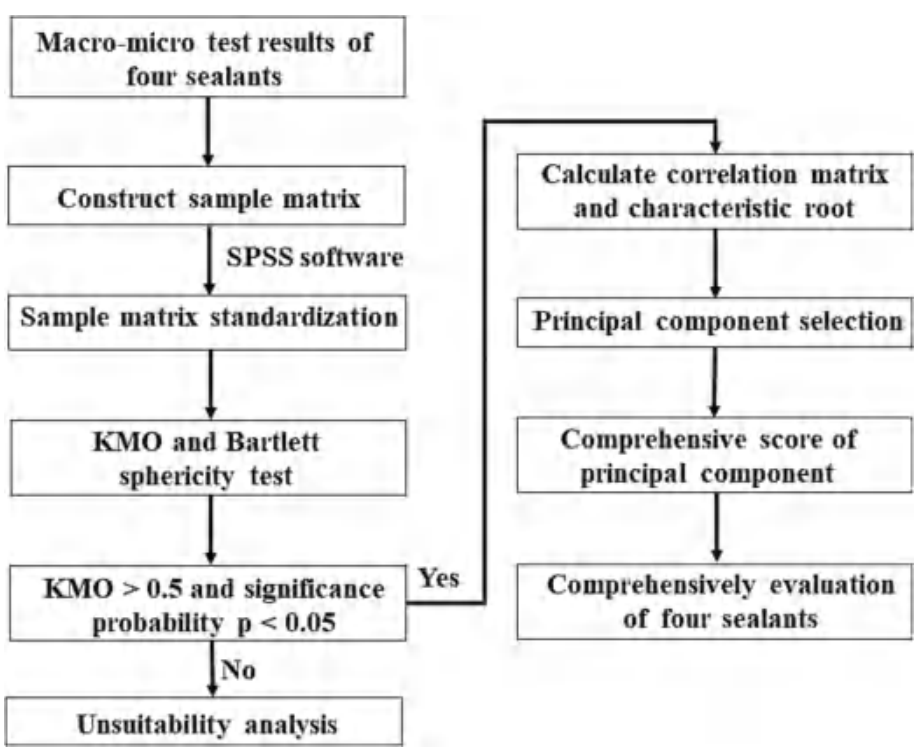

Fig.4. A flow chart of the PCA method.

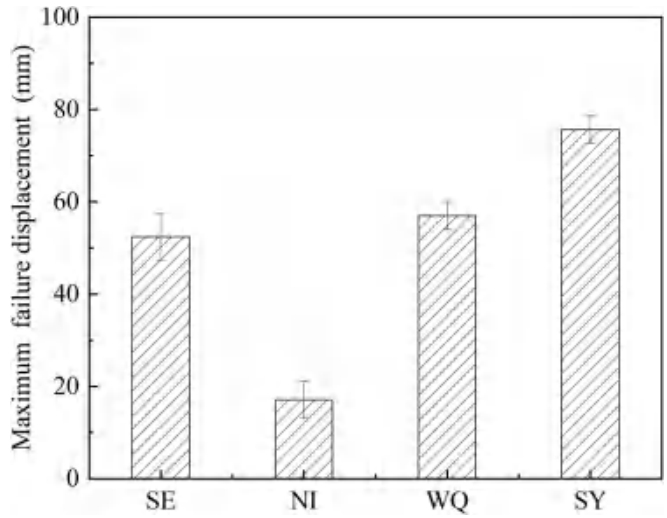

Fig. 6. Maximum failure displacement of four different sealants.

surface of the sealant NI was the roughest and the hard segment content was the highest; The SY had the smoothest surface and contained hard segments without phase region, and the content of hard segments was the lowest.

The roughness of four different sealants can be achieved according to the parameters of the micromorphology diagram. As shown in Fig. 8, the order of the roughness was NI > SE > WQ > SY. This has a good correlation with the surface morphology of the sealant measured in Fig. 7, which showed that the sealant has a large content of hard segments, and the hard segment phase region was formed by the interaction of hydrogen bonds, which made the measured roughness increase. By analyzing the results of macro-adhesion test with Fig. 5 and Fig. 6, it can be known that the interfacial adhesion strength generated by the sealant with large surface roughness was high. Based on the theory of mechanical bonding, the physical engagement and anchoring effect between liquid adhesive and adherend will significantly affect the interfacial adhesion performance. The higher the surface roughness, the more obvious the engagement and anchoring effect were, thus improving the adhesive strength of sealant.

3.3. Surface adhesion test

Considering the microphase separation characteristics of polyurethane material, it contained many transition regions of soft and hard segments besides soft and hard segments. In order to analyze the adhesion characteristics of sealant accurately and quantitatively at different points, in the peak force scanning data processing, the scanning points were classified and distributed in five intervals according to respective elevations. The average adhesion force distribution of four sealant materials at different elevation points was shown in Fig. 9. As the elevation was lower, the soft segment content of sealant was higher.

As shown in Fig. 9, the adhesive force at the lower elevation was less than that at the higher elevation, and the greater the R value, the greater the adhesive force of the sealant with higher hard segment content. The

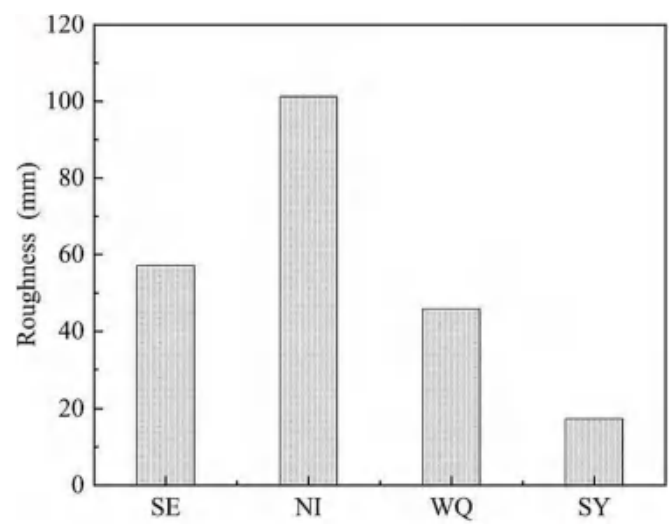

Fig.8. Surface roughness of four different sealants.

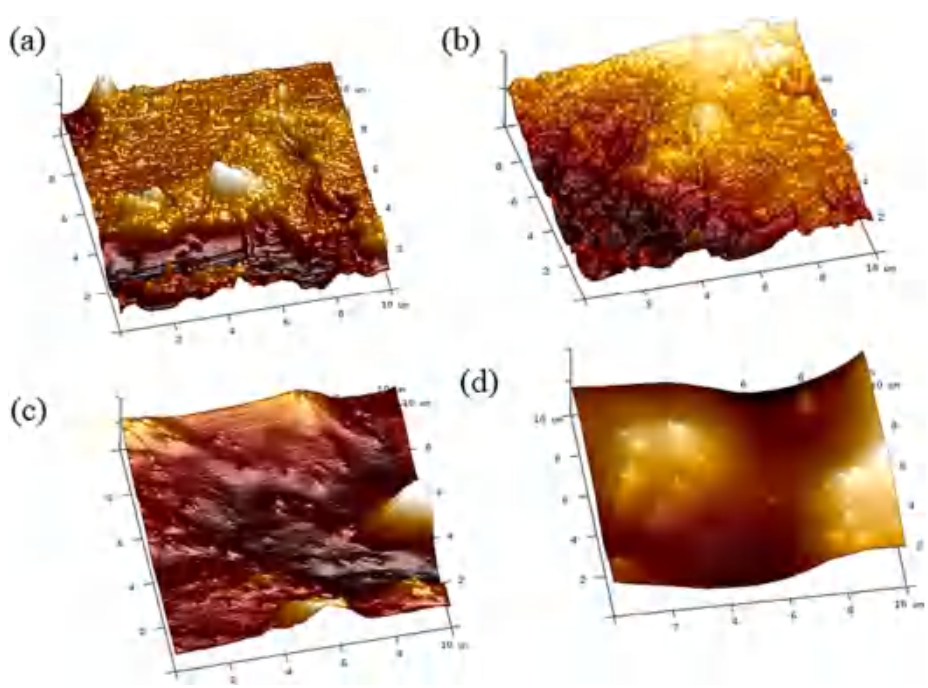

Fig. 7. Surface topography of four different sealant materials (a)SE (b)NI (c)WQ (d)SY.

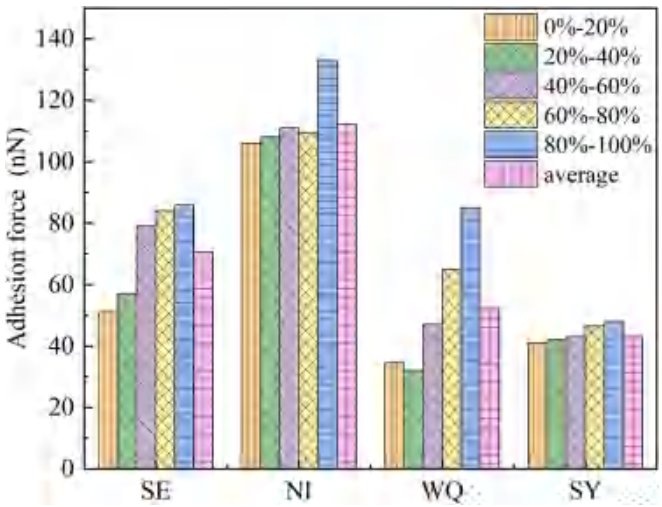

Fig. 9. Average adhesion force distribution at different elevation points.

order of the average adhesion of four different sealants was NI > SE > WQ > SY. The adhesion distribution characteristics have a good correlation with roughness results. The analysis reason was that the hard segment molecular chain was long, the molecular weight was large, and the molecular chain was closely combined. However, the molecular chain of soft segment was short and the structure was loose, which contributed to the high content of hard segment possessed great adhesion. In addition, the results of NI in the range of 60 ~ 80% elevation and WQ in the range of 20 ~ 40% elevation were inconsistent with the overall adhesion distribution characteristic. The reasons for this phenomenon may be the fact that there lacked of data samples in the transitional area, and the average was greatly affected by accidental errors. In addition, the two abnormal points were located in the transition zone between soft and hard segments. When the probe scanned this area, the attractive force was not only from the point to be measured, but also from the higher position nearby, which may affect the test results. The internal molecular weight of the sealant with higher R value was larger, and the molecular chains were more closely arranged, thus improving the intermolecular force inside the material, and also enhancing the effect between the sealant and the joint wall. This was reflected in the improvement of adhesive strength from a macro perspective.

3.4. Chemical bonding rate between sealant and SiO_2

In order to analyze the chemical bonding characteristics between sealants and SiO_2, the mixed samples of sealant-SiO_2 and pure SiO_2 powder were scanned by XPS, and the measured Si peaks were fitted according to the different valence Si peaks of pure SiO_2 and sealant-SiO_2. The results were shown in Fig. 10.

The chemical bonding characteristics of sealant and SiO_2 were analyzed, and the bonding rates of four sealant materials were calculated as shown in Fig. 11. The order of the chemical bonding rate was SE > NI > WQ > SY, which can be found in our previous studies [8]. It can be known that the R value was closely related to the chemical bonding rate, but the R value of SE with the highest bonding rate was not the largest. The research results of chemical bond theory showed that the prerequisite for the formation of chemical bond was that the contact between two substances required to reach the molecular scale, but not all the contact points that satisfied the scale requirements can form chemical bonds. Combined with the test results in Fig. 7 and Fig. 8, the roughness of NI was much higher than that of other three materials. Therefore, too rough micro-morphology made it difficult for NI to fully contact with SiO_2 powder to form bonds, so that the bonding rate in the scanning area was lower than that of SE. By comparing the bonding rate of the four sealant materials, the bonding ability between the sealant with larger R value and SiO_2 was stronger, which also explained the macro-adhesion test results from the perspective of chemical bonding.

3.5. Principal component analysis (PCA)

Four different sealants (SE, NI, WQ, SY) were tested by five macro–micro testing techniques, and the micro-performance parameters and macro-performance parameters were obtained. The results were shown in Table 2.

From Table 2, it can be concluded that the performance indexes of four sealant materials were quite different. The three indexes of NI in micro-test and the maximum tensile force in macro-test were great, but the maximum failure displacement was relatively low. In addition, SY with the largest failure displacement was not as good as the other sealant materials in other indexes. According to each index, it was obviously difficult to evaluate the type of sealant with the best adhesion. Therefore, the PCA was used to comprehensively evaluate four different sealant materials.

According to the PCA, the sample matrix X was constructed from the macro and micro test results of sealant materials, as shown in Eq. (3), and standardized by SPSS software. The applicability of the standardized matrix was tested by KMO test and Bartlett sphericity test. Finally, it was calculated that KMO = 0.607 > 0.5, approximate chi-square value of Bartlett sphericity was 37.693, significance probability $p < 0.05$. which indicated that the sample data has structural validity, indicating that PCA can be applied to this sample data.

$$X = \begin{bmatrix} 520.3 & 57.2 & 71.4 & 58.2 & 52.38 \\ 825.6 & 101.2 & 113.5 & 51.1 & 17.09 \\ 381.9 & 45.8 & 52.7 & 48.6 & 56.98 \\ 265.7 & 17.3 & 44.1 & 46.2 & 75.64 \end{bmatrix} \tag{3}$$

According to the PCA, the results of PCA were calculated. As shown in Table 3, two principal components, PCA1 and PCA2, can be obtained from the Table 3, in which the characteristic root value of the first principal component was 4.148, its variance interpretation rate was 82.965%, the characteristic root value of the second principal component was 0.807, and the cumulative variance interpretation rate of the two principal components was 99.31%>95%. Therefore, the first two components can be selected as the main components.

In addition, the principal component value of each sealant material was calculated according to the component score coefficient matrix. The expressions of PCA1 and PCA2 were calculated and output by SPSS software, such as Eqs. (4)-(5).

$$\mathrm{PCA1} = 0.24 \times X_1 + 0.237 \times X_2 + 0.239 \times X_3 + 0.117 \times X_4 - 0.237 \times X_5 \tag{4}$$

$$\mathrm{PCA2} = -0.084 \times X_1 - 0.142 \times X_2 - 0.096 \times X_3 + 1.071 \times X_4 + 0.203 \times X_5 \tag{5}$$

where X_1, X_2, X_3, X_4, X_5 respectively represent the numerical values in the matrix X, and they were the performance parameters of the sealant material.

According to the principal component score relation and the weight coefficient of each principal component, the principal component comprehensive score PCA was calculated as Eq. (6).

$$\mathrm{PCA} = \frac{82.965\%}{99.31\%} \times \mathrm{PCA1} + \frac{16.345\%}{99.31\%} \times \mathrm{PCA2} \tag{6}$$

According to the formula of principal component comprehensive score PCA, the adhesion properties of different sealants were evaluated, and the results were shown in Table 4.

By using the principal component analysis method, the complex relationship among the maximum tensile force, the maximum failure

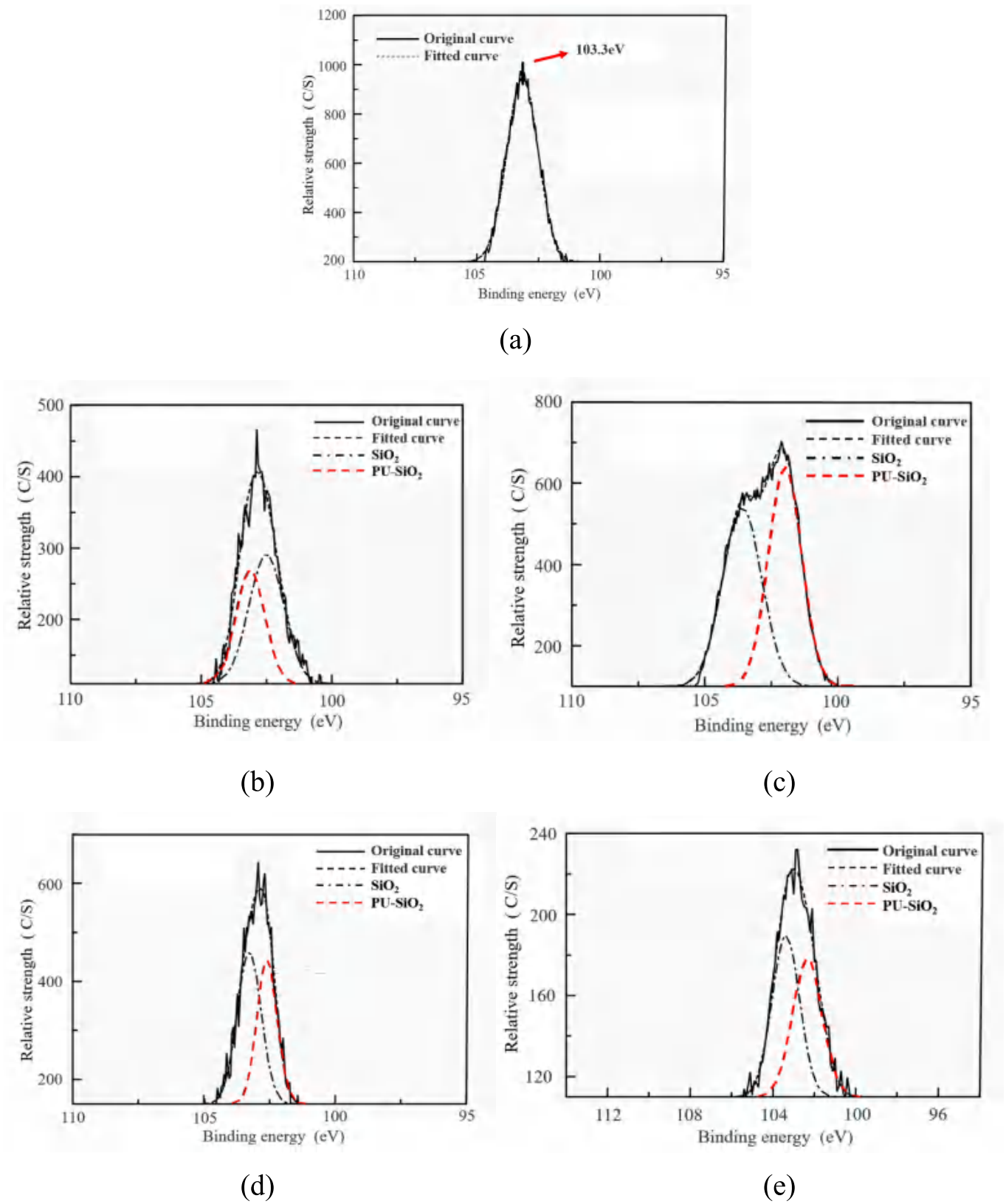

Fig.10. Chemical bonding between sealants and SiO2: (a)pure SiO_2 powder (b)SE (c)NI (d)WQ (e)SY [8].

displacement, the surface roughness, the surface adhesion, the chemical bonding of the sealant was analyzed and the principal component was extracted. Finally, the comprehensive score of the principal component was used to express the performance of the sealant. Among them, the comprehensive score of principal components was used as the evaluation index of the performance of sealant.

This method combined the microscopic test parameters (roughness, surface adhesion and chemical bonding ability with SiO_2) with the

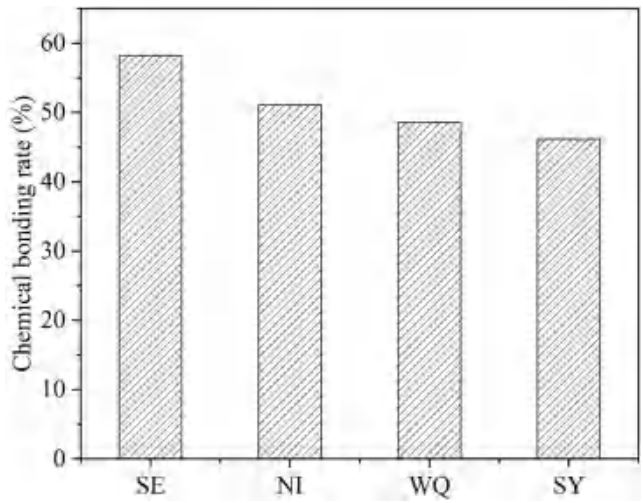

Fig.11. Chemical bonding rate between sealant and SiO_2.

Table 2
Micro-test and Macro-test results of sealants.

The types of sealants	Micro-test			Macro-test	
	Roughness (mm)	Surface adhesion (nN)	Chemical bonding rate (%)	maximum tensile force (N)	maximum failure displacement (mm)
SE	57.2	71.4	58.2	520.3	52.38
NI	101.2	113.5	51.1	825.6	17.09
WQ	45.8	52.7	48.6	381.9	56.98
SY	17.3	44.1	46.2	265.7	75.64

Table 3
The results of PCA.

Components	Characteristic root	Variance interpretation rate (%)	Cumulative variance interpretation rate (%)
1	4.148	82.965	82.965
2	0.807	16.345	99.31
3	0.034	0.69	100
4	–	–	100

Table 4
Comprehensive score of principal components.

Ranking	The types of sealants	Comprehensive score PCA	PCA1	PCA2
1	NI	0.968	1.296	−0.7
2	SE	0.398	0.185	1.48
3	WQ	−0.412	−0.435	−0.299
4	SY	−0.954	−1.047	−0.481

macroscopic test results (maximum tensile force and maximum failure displacement) to evaluate the adhesive properties of the sealants, and finally obtained the comprehensive properties of the sealant in the order of NI > SE > WQ > SY. This method can replace the existing evaluation methods for analyzing the adhesive properties of the sealant through some macroscopic tests, and avoid the influence of the macroscopic test on the material properties due to environmental factors. The macro–micro test results can be used to comprehensively evaluate the performance of sealant more accurately.

4. Conclusion

In this study, the maximum tensile force and maximum failure displacement of the ballastless-track sealants are analyzed by macro-test methods, the roughness, surface adhesion and chemical bonding rate with SiO_2 of the sealants are analyzed by micro-test method, and the macro–micro properties of the sealing adhesive are comprehensively evaluated by PCA. From the above preliminary results, the following conclusions can be drawn.

(1) Self-developed low-temperature performance tester (LTTT), combined with the actual working conditions and main failure modes of the sealant, developed an evaluation test of the adhesive performance of the sealant. The test shows that the maximum tensile force of the sealant is NI > SE > WQ > SY, and the maximum failure displacement is SY > WQ > NI > SE.
(2) The peak force mode is selected to characterize the micro-properties of the sealant, and it is found that the surface morphology of the sealant with higher R value is coarser due to a large number of hard segments coalesced, and the order of roughness and micro-adhesion is NI > SE > WQ > SY, and the corresponding adhesion of hard segments is larger.
(3) XPS analysis shows that the bonding rate between sealant and SiO_2 is SE > NI > WQ > SY, and the micro-surface morphology of sealant is too rough, which will lead to its failure to fully contact with SiO_2, thus affecting the chemical bonding rate.
(4) The macro–micro tests and analysis results of sealants are linked by PCA, and the performance of sealant is evaluated by the comprehensive score of principal components, and the comprehensive performance of sealant is ranked as NI > SE > WQ > SY. This method can replace the current evaluation method of analyzing the sealants' adhesion characteristics through some macro tests, and avoid the influence of macro tests on the material performance due to environmental factors. The macro–micro test results can be used to comprehensively evaluate the performance of sealant more accurately.

CRediT authorship contribution statement

Guoqing Sun: Conceptualization, Data curation, Formal analysis, Methodology, Writing – original draft, Writing – review & editing. **Zhe Hu:** Data curation, Investigation, Resources, Visualization. **Jiupeng Zhang:** Funding acquisition, Investigation, Supervision, Validation, Writing – review & editing. **Hengxiao Xue:** Data curation, Funding acquisition, Methodology, Supervision, Writing – review & editing.

Declaration of Competing Interest

The authors declare that they have no known competing financial interests or personal relationships that could have appeared to influence the work reported in this paper.

Data availability

Data will be made available on request.

Acknowledgements

This work was supported by the Program Fund of Non-Metallic Excellence and Innovation Center for Building Materials (2022SFP6-5), the National Natural Science Foundation of China (No. 51978068), the National Natural Science Foundation of China (No. 51908055), Natural Science Foundation of Shaanxi Province (No. 2020JM-217), and Fundamental Research Funds for the Central Universities, CHD (No. 300102219103, No.310821173501). The authors gratefully acknowledge their financial support.

References

[1] L.L. Liu, L.Z. Jiang, W.B. Zhou, J. Yu, K. Peng, Y.J. Zuo, Study on the restoring force model for the high-speed railway CRTS III slab ballastless track, Arch. Civ. Mech. Eng. 22 (3) (2022).

[2] H. Li, Z. Yi, G. Cheng, H. Wen, Y. Xie, Effects of ultraviolet radiation, high temperature and alkaline chemicals on ageing of silicone sealants used in ballastless track expansion joints, J. Wuhan Univ. Technol.-Mater. Sci. Ed. 33 (5) (2018) 1015–1021.

[3] L. Cong, F. Yang, G. Guo, M. Ren, J. Shi, L. Tan, The use of polyurethane for asphalt pavement engineering applications: a state-of-the-art review, Constr. Build. Mater. 225 (2019) 1012–1025.

[4] X. Bian, X. Duan, W. Li, J. Jiang, Track settlement restoration of ballastless high-speed railway using polyurethane grouting: full-scale model testing, Transp. Geotech. 26 (2021) 100381.

[5] H. Xue, Y. Tan, A. Sha, Developing rules of adhesive properties and mechanism of ballastless-track sealants in shear-fatigue loading, J. Mater. Civ. Eng. 32 (12) (2020).

[6] G. Sun, J. Zhang, Q.i. Liu, X. Tan, C. Zhu, Y. Guan, Effects of microcapsules on self-healing performance of asphalt materials under different loading modes, J. Transp. Eng. Part B. Pavements 147 (2) (2021) 04021010.

[7] G. Sun, J. Zhang, X. Tan, D. Guo, Y. Zhou, Y. Guan, Evaluation of conventional technical properties and self-healing ability of bitumen-based sealants containing sunflower-oil microcapsules for pavement cracks, Constr. Build. Mater. 254 (2020) 119299.

[8] H. Xue, Y. Tan, A. Sha, Test method on adhesive property of joint sealant in supporting layer of ballastless slab track, J. Mater. Civ. Eng. 32 (10) (2020).

[9] S. Wu, Q. Liu, J. Yang, R. Yang, J. Zhu, Study of adhesion between crack sealant and pavement combining surface free energy measurement with molecular dynamics simulation, Constr. Build. Mater. 240 (2020) 117900.

[10] Z. Sun, S. Li, J. Zhang, Y.i. Zeng, Adhesion property of bituminous crack sealants to different asphalt mixtures based on surface energy theory, Constr. Build. Mater. 261 (2020) 120006.

[11] S.Q. Zhang, J.S. Andre, L. Hsu, A. Toolis, S.L. Esarey, B.L. Li, Z. Chen, Nondestructive in situ detection of chemical reactions at the buried interface between polyurethane and isocyanate-based primer, Macromolecules 53 (22) (2020) 10189–10197.

[12] T. Yao, S. Han, X. Gong, J. Zhang, X. Chang, Z. Zhang, Performance evaluation of a polyurethane-urea binder for asphalt pavement groove-filling, Constr. Build. Mater. 315 (2022) 125734.

[13] M.R. Mitchell, R.E. Link, I.L. Al-Qadi, E.H. Fini, Development of a crack sealant adhesion test (CSADT) specification for hot-poured bituminous sealants, J. Test. Eval. 39 (2) (2011) 103108.

[14] M.O. Hamzah, T.S. Yee, B. Golchin, J. Voskuilen, Use of imaging technique and direct tensile test to evaluate moisture damage properties of warm mix asphalt using response surface method, Constr. Build. Mater. 132 (2017) 323–334.

[15] M. Pauletta, F. Pinzano, G. Frappa, G. Russo, Tensile tests for the improvement of adhesion between rubber and steel layers in elastomeric isolators, Appl. Sci.-Basel 10 (22) (2020) 8063.

[16] Z.L. Sun, S.T. Li, J.H. Zhang, Y. Zeng, Adhesion of bituminous crack sealants to aggregates using surface energy theory, J. Mater. Civ. Eng. 32 (10) (2020).

[17] E.H. Fini, I.L. Al-Qadi, T. Abu-Lebdeh, J.F. Masson, Use of surface energy to evaluate adhesion of bituminous crack sealants to aggregates, Am. J. Eng. Appl. Sci. 4 (2) (2011) 244–251.

[18] S.Q. Zhang, L. Hsu, A. Toolis, B.L. Li, J.K. Zhou, T. Lin, Z. Chen, Investigation of the atmospheric moisture effect on the molecular behavior of an isocyanate-based primer surface, Langmuir 37 (43) (2021) 12705–12713.

[19] G.L. Yang, C.H. Wang, H. Fu, Z.B. Yan, W.Y. Yin, Waterborne epoxy resin-polyurethane-emulsified asphalt: preparation and properties, J. Mater. Civ. Eng. 31 (11) (2019).

[20] M. Sawalha, H. Ozer, I.L. Al-Qadi, H. Xue, Development of a modified adhesion test for hot-poured asphalt crack sealants, Transp. Res. Rec. 2612 (1) (2017) 85–95.

[21] H. Xue, Y. Tan, Low-temperature adhesive properties of sealant applied in ballastless track under shear fatigue loading, J. Harbin Inst. Technol. 50 (3) (2018) 33–38.

[22] H. Xue, Y. Tan, A. Sha, Adhesive characteristic and mechanism of ballastless track sealant in hydrolysis condition, Front. Mater. 7 (2020).

[23] S. Poovaneshvaran, M.R.M. Hasan, A. Sani, R.K. Shuib, in: Alternative Testing Protocol to Assess the Bonding and Shear Resistance of Pavement Bituminous Crack-Sealant Material, AWAM International Conference on Civil Engineering (AICCE), Malaysia, 2019, pp. 1187–1200.

[24] G. Sun, Z. Niu, J. Zhang, X. Tan, Y. Jing, Z. Chen, Impacts of asphalt and mineral types on interfacial behaviors: a molecular dynamics study, Case Stud. Constr. Mater. 17 (2022) e01581.

[25] G. Sun, J. Zhang, Z. Chen, Z. Niu, Y. Li, Interfacial performance of asphalt-aggregate system under different conditions based on molecular dynamics simulation, J. Mater. Civ. Eng. 35 (6) (2023) 04023116.

[26] P. Schon, K. Bagdi, K. Molnar, P. Markus, B. Pukanszky, G.J. Vancso, Quantitative mapping of elastic moduli at the nanoscale in phase separated polyurethanes by AFM, Eur. Polym. J. 47 (4) (2011) 692–698.

[27] G. Sun, Y. Yang, J. Zhang, Y. Cao, X. Tan, J. Pei, Modeling and optimization of pavement scale-model for magnetically coupled resonant in wireless power transmission systems, Constr. Build. Mater. 319 (2022) 126066.

[28] P. Galvez, J. Abenojar, M. Angel Martinez, Durability of steel-CFRP structural adhesive joints with polyurethane adhesives, Compos. Part B-Eng. 165 (2019) 1–9.

[29] J. Tan, W. Liu, Z. Wang, Preparation and performance of waterborne UV-curable polyurethane containing long fluorinated side chains, J. Appl. Polym. Sci. 134 (8) (2017).

[30] W. Ma, C. Hu, S. Guo, Z. Zhao, T. Huang, Flexural and shear bond performance of polyurethane-mortar interface under micro- and macroscale, J. Mater. Civ. Eng. 31 (7) (2019).

[31] Z. Long, N. Guo, X. Tang, Y. Ding, L. You, F.u. Xu, Microstructural evolution of asphalt induced by chloride salt erosion, Constr. Build. Mater. 343 (2022) 128056.

[32] M. Wang, L. Liu, Investigation of microscale aging behavior of asphalt binders using atomic force microscopy, Constr. Build. Mater. 135 (2017) 411–419.

[33] A. Chau, S. Regnier, A. Delchambre, P. Lambert, Theoretical and experimental study of the influence of AFM tip geometry and orientation on capillary force, J. Adhes. Sci. Technol. 24 (15–16) (2010) 2499–2510.

[34] W. Wang, Q. Xu, S. Zhou, Y. Qin, Q. Yan, A review on evaluation methods of asphalt-aggregate adhesion, Mater. Rev. 33 (7A) (2019) 2197–2205.

[35] J.H. Tan, X.P. Wang, J.J. Tai, Y.F. Luo, D.M. Jia, Novel blends of acrylonitrile butadiene rubber and polyurethane-silica hybrid networks, Express Polym Lett 6 (7) (2012) 588–600.

[36] L.I. Bo, H.A.N. Sen, X.U. Ou-ming, T. Xu-qiu, Evaluation of asphalt pavement performance based on principal component analysis, J. Chang'An Univ. Nat. Sci. Ed. 29 (3) (2009) 15–18.

[37] T. Peng, Z. Gaofeng, N. Lei, Comprehensive evaluation of asphalt-mixture performance based on principal component analysis, Adv. Mat. Res. 1095 (2015) 280–283.

[38] R. Ren, K. Han, P. Zhao, J. Shi, L. Zhao, D. Gao, Z. Zhang, Z. Yang, Identification of asphalt fingerprints based on ATR-FTIR spectroscopy and principal component-linear discriminant analysis, Constr. Build. Mater. 198 (2019) 662–668.

buildings

MDPI

Article

Microscopic Properties of Asphalt and Polyethylene at an Extraordinary High Dosage through Molecular Dynamics Simulation

Yuye Jin [1], Haoyi Li [2], Jie Chen [3], Qianqian Wang [2], Yanhua Bao [2] and Shuguang Hou [1,*]

[1] College of Transportation Engineering, Nanjing Tech University, Nanjing 211816, China; jinyuye5341@163.com
[2] College of Materials Science and Engineering, Nanjing Tech University, Nanjing 211816, China; haoyili@njtech.edu.cn (H.L.); qqwang@njtech.edu.cn (Q.W.); 13611574066@139.com (Y.B.)
[3] Yunnan Infrastructure Investment Co., Ltd., Kunming 650000, China; jiechenyn@163.com
* Correspondence: houshuguang@njtech.edu.cn

Abstract: Using waste plastics in asphalt mixtures could be an exploratory way to dispose of waste plastics. This study aims to investigate the microscopic properties between asphalt and polyethylene (PE) at an extraordinary dosage of 20 wt.%. Various types of PE with different degrees of polymerization (DP) and structural configurations were considered. Molecular dynamics simulations were used to calculate the mechanical parameters, free volume ratio (*FVR*), and Flory–Huggins parameter of the resulting PE-modified asphalt (PEA). Two types of PEA were made and characterized by fluorescence microscopy. The simulation results indicate that the addition of PE reduces the density of modified asphalt by less than 5%, and a higher density of PEA is associated with a lower *FVR*. When the *FVR* is close, the mechanical properties are greatly influenced by the DP and configuration. The DP and the number of chains are the main parameters impacting the compatibility between PE and asphalt, based on the Flory–Huggins parameter analysis. Decreasing the DP of PE (e.g., 50, with a minimum Flory–Huggins parameter and a relative molecular mass of 1300) will significantly increase the compatibility between asphalt and PE. LDPE−2 has better compatibility with asphalt, possibly because LDPE−2 has higher purity. These findings provide valuable insights into plastic thermal cracking and industrial modification practices.

Keywords: PE-modified asphalt; extraordinary dosage; configuration; degree of polymerization; mechanical properties; compatibility

check for updates

Citation: Jin, Y.; Li, H.; Chen, J.; Wang, Q.; Bao, Y.; Hou, S. Microscopic Properties of Asphalt and Polyethylene at an Extraordinary High Dosage through Molecular Dynamics Simulation. *Buildings* **2024**, *14*, 164. https://doi.org/10.3390/buildings14010164

Academic Editor: Bjorn Birgisson

Received: 11 December 2023
Revised: 30 December 2023
Accepted: 6 January 2024
Published: 9 January 2024

Copyright: © 2024 by the authors. Licensee MDPI, Basel, Switzerland. This article is an open access article distributed under the terms and conditions of the Creative Commons Attribution (CC BY) license (https://creativecommons.org/licenses/by/4.0/).

1. Introduction

According to the Organization for Economic Co-operation and Development (OECD) research report released in 2022 [1], plastic production has increased to 460 Mt and plastic waste reached 353 Mt in 2019. Even during the COVID-19 pandemic and stagnation period, global plastic production increased to 390.7 million tons in 2021 [1]. However, only 15% of plastic waste was collected for recycling, and just 9% was recycled [2,3]. Millions of tons of recycled plastic waste are either landfilled or incinerated, causing secondary pollution to the environment and emitting significant amounts of carbon dioxide [3,4]. Microplastic particles also have a wide-ranging negative impact on human health, soil ecosystems, and aquatic ecosystems [5]. Plastic pollution has become the world's second-largest environmental pollution problem after climate change.

Biodegradation is an environmentally friendly and promising method for plastic pollution control, such as using marine microalgae [6] and nematocyst venom protein [7]. The synergistic effect between microorganisms and their enzymes has been shown to enhance the efficiency of plastic degradation [8]. In the road industry, polymers have been widely used in the modification of asphalt since the second half of the twentieth century to

decrease pavement deformation and premature rutting in heavy truck roads, especially in high-temperature areas [9]. Polyethylene (PE) is the most abundant and cost-effective recycled plastic, which can be melted and blended with asphalt materials at a standard mixing temperature. In essence, PE is expected to increase the rigidity of asphalt in high-temperature areas [10]. PE-modified asphalt (PEA) mixtures exhibit improved resistance to permanent deformation at high temperatures as well as thermal cracking under low temperatures [10–15].

PE is classified as a polyolefin in polymer and asphalt chemistry. Due to its nonpolar nature and high level of crystallinity, it can only be swelled by the maltenes of asphalt, resulting in the presence of a polymer-rich phase and an asphaltene-rich phase in PEA as observed through fluorescence microscopy [10,16–20]. The biphase nature of PEA blends always results in phase segregation due to differences in density, which poses a significant challenge to the storage stability of the binder during transportation to the application site. Early research has determined that incorporating 5% PE content is the optimal dosage to achieve outstanding performance of PEA [21–25], indicating that there are great difficulties in the large-scale application of PE in asphalt materials. The terminal effect has an important effect on the rheological properties of polymers [26]. To address this issue, researchers have employed chain group modification methods, such as NH_2-terminated PE [27], epoxy-terminated PE [28], or maleic anhydride grafted PE [29,30], to improve the storage stability of PEA. Additionally, the modification of polymer molecular architecture has been explored to promote the compatibility of PEA to some extent, including the molecular weight (MW) [31–33] and branch distribution [34,35] from experimental work. Despite numerous experimental efforts to modify PE, phase segregation and storage stability problems still limit the large-scale loading of PE in modified asphalt materials.

A key factor in improving the properties of PEA is understanding the microscopic interactions between polyolefins and asphalt. Previous studies suggested that intermolecular interactions within PEA primarily stem from PE and the aromatic phase of asphalt, as evidenced by direct fluorescent observation [9]. However, saturates, the least polar phase among the four components, also exhibit significant potential for miscibility with polyolefins. Classic atomic-level molecular simulation has become one of the commonly used methods to enhance our understanding of molecular processes in materials science [36]. With the aid of molecular dynamics simulation (MD) techniques, scholars can explore the microscopic mechanisms of polymer-modified asphalt at a molecular scale, following the construction of asphalt four-component models [37–39]. Recently, Hu et al. [40] demonstrated that graphene can effectively reduce the binding energy of asphaltenes to non-polar molecules (saturate and aromatic) and elevate the diffusion coefficient of non-polar molecules by approximately 8%. However, the diffusion coefficient of polar molecules is decreased by about 2% in modified asphalt systems with the addition of 5.8% PE. Yu et al. [41] utilized cohesive energy density (*CED*) as a crucial indicator to determine the degree of polymerization (DP) of PE molecules in natural rubber-modified asphalt. However, the best DP of PE found was only 12, which poses challenges for industrial applications.

In reality, PE or recycled PE typically has a high DP, with several thousand polymer chains splitting into an infinite number of short chains with different branches during utilization. Consequently, the use of PE or recycled PE is essential for modifying asphalt properties, and many researchers are currently exploring its large-scale collaborative utilization with other solid wastes, such as waste tire rubber [42]. Therefore, it is necessary to comprehend different PE configurations and DP using a large simulation system as a theoretical guide for PE thermal cracking or modification to enhance storage stability in modified asphalt.

To achieve large-scale use of waste plastic in road construction and consume more waste plastic products to reduce environmental pollution, an extraordinary high loading (20 wt.%) of PE was mixed with asphalt by using molecular dynamics simulation methods in this work. Different PE models were constructed with varying DP and branch arrangements for the first time to shed light on the influence of DP and molecular architecture on the performance development of PEA. The density, mechanical properties, free volume ratio (*FVR*), and mean squared displacement (*MSD*) of various types of PEAs were calculated. Their relationships were further analyzed. The compatibility between PE and asphalt was evaluated by calculating the Flory–Huggins parameter (χ), which provided a theoretical basis for the chemical engineering modification of PE to improve its compatibility with asphalt in the future.

2. Computational Parameters and Experimental Methods

2.1. Molecule Models of Asphalt

The AAA-1 type asphalt in the Strategic Highway Research Program's Materials Reference Library [43] was used in this study. Its molecular model was constructed with twelve component molecules based on Li and Greenfield's study [37]. Materials Studio 2019 was employed for both model construction and MD simulation in this research. The molecular structures and component fractions of AAA-1 asphalt were described in our previous work [44]. The base asphalt in this work was composed of four component fractions, namely 16.6%, 10.7%, 30.7%, and 42.0%, which closely matched the experimental results [43].

2.2. Molecule Models of PE

PE is a high MW compound with a chemical formula of $(C_2H_4)_n$, ranging from several thousand to several million. In this work, 20 wt.% of PE was incorporated into the asphalt model. An AAA-1 asphalt conventional model has a relative MW of approximately 33,840.811, and the MW of the added PE was estimated to be around 8460. Therefore, according to this study, the added PE should have a DP of 300 in a conventional model.

The first parameter to consider is MW distribution, as it can affect the penetration, ductility, and softening point of modified asphalt [33]. Subsequently, different DP, number of branches (BN), and their arrangement in PE chains were taken into account during the model construction and labeled differently. Five chain types of PE were designed and labeled in Table 1, which are: single chain (SC), one branch (1B), two branches (2B), six branches distributed non-staggered (6BI), and six branches distributed staggered (6BII). Branched polymers can be visualized as linear polymers with side chains of the same polymer attached to the main chain. All the side chains were unified to have a DP of 10 and were distributed at 1/2, 1/3, or 1/4 of the main chain. Even though the DP and distribution of side chains in PE are more complex, this study can serve as a theoretical guide for modifying PE in real-world scenarios, as it explores the impact of different chain types on the compatibility between the PE chains and asphalt.

Afterward, a PEA model was created by adding 20 wt.% of PE compounds to predict its performance evolution. The structural properties of the PE compounds, including DP, CN, and BN, were taken into account shown in Table 2. A total of 17 types of PE compounds with a combined DP of 300 were designed in a single conventional cell. Additionally, a long PE chain with a DP of 600 or 900 was also constructed using two or three conventional cells to investigate the size effect and the case of a long PE chain.

Table 1. Diagram for five chain types of PE.

Chain Type	Label	Chain Type
Single chain	SC	
One branch	1B	
Two branches	2B	
Six branches distributed non-staggered	6BI	
Six branches distributed staggered	6BII	

Table 2. The combination of PE compounds with different DP, CN, and BN.

Combination	Degree of Polymerization (DP)	Number of Chains (CN)	Number of Branches (BN)	Branch Chain Ratio (%)
900-SC	900	1	0	0
600-SC	600	1	0	0
300-SC	300	1	0	0
300-1B			1	3.3
300-2B			2	6.6
300-6BI			6	20
300-6BII			6	20
150-SC	150	2	0	0
150-1B			1	6.6
150-2B			2	13.3
150-6BI			6	40
150-6BII			6	40
100-SC	100	3	0	0
100-1B			1	10
100-2B			2	20
100-6BI			6	60
50-SC	50	6	0	0
50-1B			1	20
50-2B			2	40

2.3. Construction of PEA Models and Simulation Process

The research methodology is summarized in Figure 1. The simulation steps and parameter settings of PEA are described below:

(1) Firstly, 19 types of PEA models were constructed using the COMPASS II force field through the 'Amorphous cell module, and the initial density of models was set at 0.1 g/cm^3. It should be noted that to create 600-SC or 900-SC modified asphalt, the conventional cell of asphalt was expanded to 2 or 3 to achieve a loading content of 20 wt.% of PE in the modified asphalt.

(2) Then, the constructed PEA models were optimized by the Geometric optimization module with the following parameters: the energy convergence criterion was set as 1.0×10^{-4} kcal/mol, and the maximum force, maximum stress, and maximum displacement were set as 0.005 kcal/mol/Å, 0.005 GPa, and 0.001 Å, respectively.

(3) Afterward, annealing was carried out under an NVT ensemble with an initial temperature of 298 K and a maximum temperature of 500 K, completing 10 cycles to release the energy generated during the modeling process for 1 ns.
(4) In the dynamic simulation process, the 19 types of PEA models were simulated under an NPT ensemble for 500 ps at 298 K with a step of 1.0 fs to obtain a more stable structure. The pressure was set at 1.0×10^{-4} GPa. Finally, MD simulation in the NVT ensemble was performed at 298 K for 500 ps for each model, and all the analyzed data were based on these trajectories. The configuration of the 300-SC model is shown in Figure 2 after dynamic simulation.

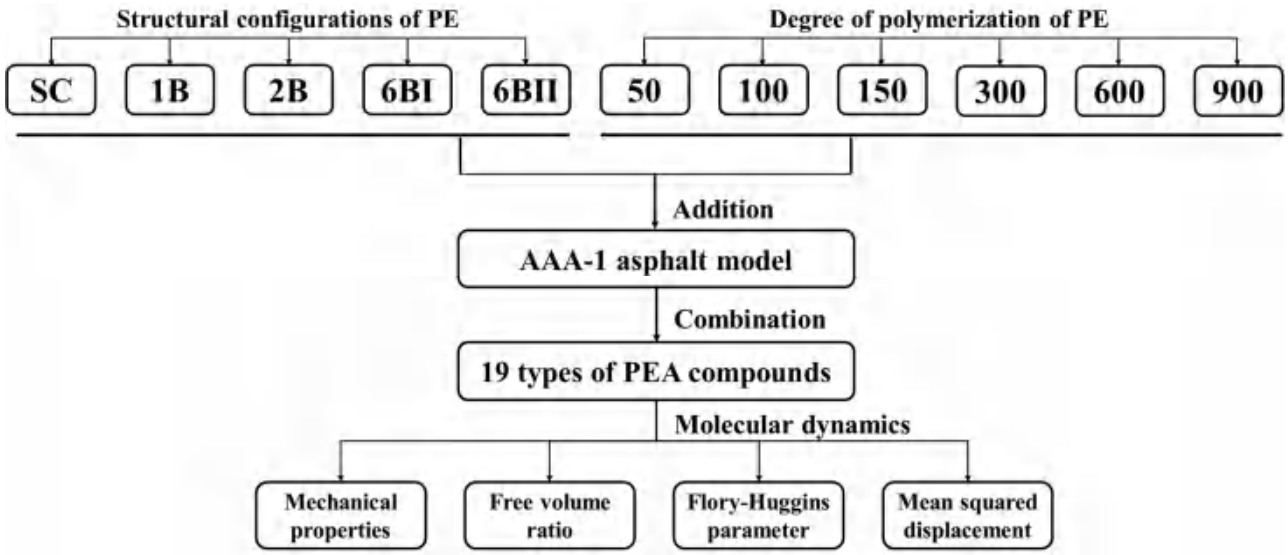

Figure 1. Diagram of research methodology.

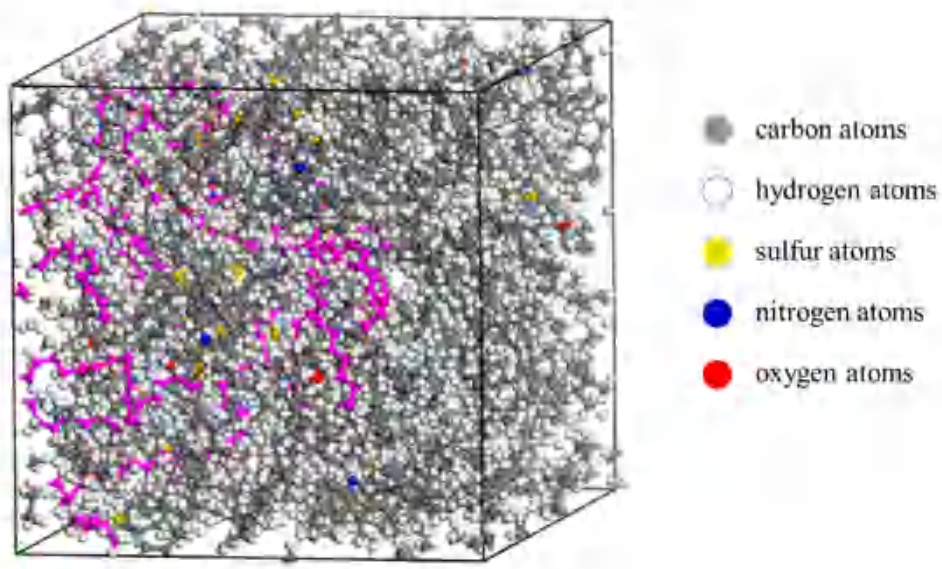

Figure 2. The configurations of the 300-SC model after dynamic simulation (PE chains shown in Pink color).

2.4. Properties Calculation and Analysis

To further study the influence of DP and configuration of PE on the microscopic properties of modified asphalt, the mechanical properties, free volume ratio (*FVR*), Flory–Huggins parameter (χ), and mean squared displacement (*MSD*) of the PEA models were calculated and the relationships among these parameters were discussed.

(1) Mechanical properties

The Bulk modulus, shear modulus, and Young's modulus of PEA were calculated to evaluate the resistance of PEA models to compressive deformation, shear strain, and tensile deformation. The Forcite module and constant strain method were used to calculate the mechanical properties of the models. The number of steps for each strain and the maximum strain amplitude were set as 4 and 0.003. The energy convergence criterion was set as 1.0×10^{-4} kcal/mol and the maximum force, maximum stress, and maximum displacement were set as 0.005 kcal/mol/Å, 0.005 GPa, and 0.001 Å. The Hill method was applied to compute the three parameters based on the elastic stiffness matrix and elastic compliance matrix of the modified asphalt models [45].

(2) Free volume ratio (FVR)

Based on the Connolly surface method [46], the FV and OV were calculated using a Connolly probe with a radius of 1.00 Å. The Van der Waals scale factor was set to 1.00, and the grid interval was 0.75 Å. The FV on the side of the atom volume surface is free of atoms, indicating the volume enclosed by the outside (blue-colored side) of the isosurface, as shown in Figure 3. The FVR represents the ratio of the free volume to the total volume of the PEA models and can be calculated by Equation (1).

$$FVR = \frac{FV}{FV + OV} * 100\% \tag{1}$$

where FVR, FV, and OV are free volume ratio, free volume (Å^3), and occupied volume (Å^3).

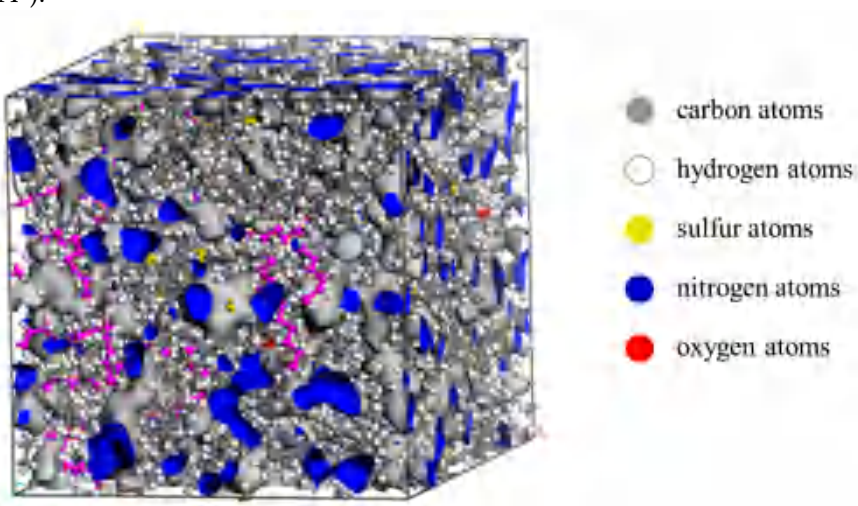

Figure 3. FV enclosed by the outside (blue colored side) of the isosurface (e.g., 300-SC modified asphalt, PE chains were shown in Pink color).

(3) Flory–Huggins parameter (χ)

Two materials with similar solubility parameter values and low χ value may be miscible [47]. The Flory–Huggins parameter (χ) was used to evaluate the compatibility of PE with asphalt systems in this study. CED is the energy required by a unit volume of condensate to overcome the intermolecular forces, which is a measure used to evaluate the strength of intermolecular interaction [48]. The solubility parameter is the square root of the CED. CED and δ were calculated using Equations (2) and (3). The Flory–Huggins parameter (χ) was calculated by Equations (4) and (5) [49,50].

$$CED = \frac{E_{coh}}{V} \tag{2}$$

$$\delta = \sqrt{CED} \tag{3}$$

$$\Delta E_{mix} = \varphi_A \left(\frac{E_{\text{coh}}}{V}\right)_A + \varphi_B \left(\frac{E_{coh}}{V}\right)_B - \left(\frac{E_{coh}}{V}\right)_{mix} \tag{4}$$

$$\chi = \left(\frac{\Delta E_{mix}}{RT\varphi_A\varphi_B}\right) V_m = \frac{V_m}{RT}(\delta_A - \delta_B)^2 = \frac{M_n}{\rho RT}(\delta_A - \delta_B)^2 \tag{5}$$

where E_{coh} is the cohesive energy (J), V is the volume of the system (m^3), ΔE_{mix} is the mixing energy of the mixture, φ_A and φ_B are the volume fractions of A and B in the mixed system, V_m is the molar volume of asphalts, R is the molar gas constant (8.314 J/mol/K), T is the temperature of the system, M_n is average molecular weight, ρ is the density.

(4) Mean squared displacement (*MSD*)

MSD is a parameter used to measure the deviation of the position of the particle with respect to the reference position after moving over time. The *MSD* ($Å^2$) of each component in the PEA was calculated using the analysis function in the Forcite module, as shown in Equation (6).

$$MSD\ (t) = \frac{1}{N} < \sum_i^N |r_i(t) - r_i(0)|^2 > \tag{6}$$

where N is the number of diffused molecules in the system, $r_i(t)$ is the position of the particle at time t, $r_i(0)$ is the position of the particle at time 0, < > is the average of all atoms in the group.

2.5. Experimental Part: Synthesis of PEA and Microscopic Tests

Two types of recycled low-density polyethylene (LDPE), namely LDPE−1 and LDPE−2, reproduced by sound-absorbing materials and packaging film, were used to synthesize PEA. These recycled plastics are produced by a qualified company and fulfilled with GB/4006-Plastics-Recycled plastic and SB/T 11149-2015-Technical specifications of waste plastics collection and sorting [51]. A Fourier transform infrared spectrometer, FTIR, (Nicolet 380, Attenuated Total internal Reflectance) and thermogravimetric-differential scanning calorimetry analysis, TG-DSC, (STA 449F5, 10 K/min under a nitrogen gas atmosphere) were used to characterize them. Base asphalt $70^{\#}$ (Sinopec Zhenhai Refining & Chemical Company, Ningbo, China) was selected as the starting material to make LDPE-modified asphalt. The asphalt was heated to 150 °C and mixed with 20% LDPE using a high shear dispersing emulsifier (FM300) for 30 min, resulting in the production of PEA samples as shown in Figure 4. The microstructure of PEA was observed using a fluorescence microscope (OLYMPUS CKX53) with blue and green excitation light sources.

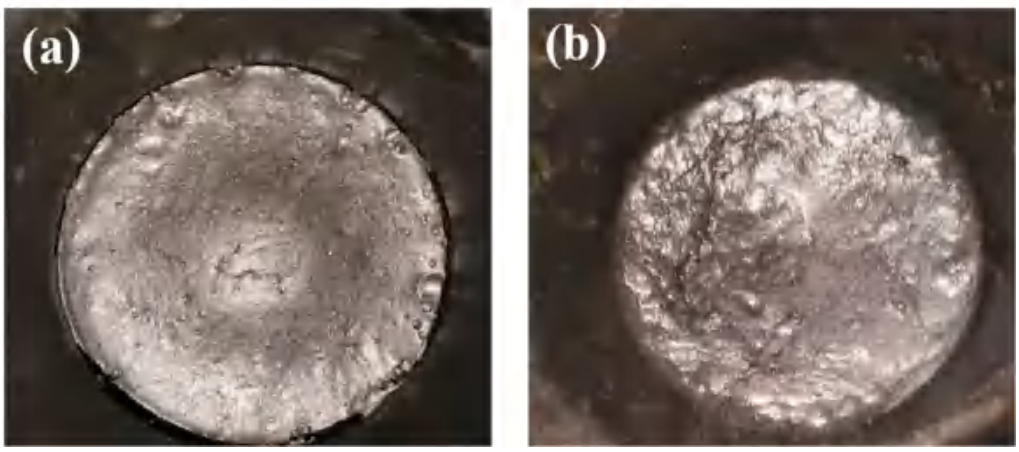

Figure 4. PEA samples: (**a**) LDPE−1; (**b**) LDPE−2.

3. Results and Discussion

3.1. Density of PEA Models

After conducting a molecular dynamics simulation, the densities of 20 different asphalt models, including AAA-1, were compiled. As illustrated in Figure 5, the density of the AAA-1 asphalt model was the highest, and the densities of all PEA models were lower than that of AAA-1. The density of the LDPE modifier typically ranges from 0.91 to 0.94 g/cm^3 [52,53], while the density of asphalt at room temperature is approximately 1.0 g/cm^3 [44]. Therefore, the addition of 20 wt.% PE content will decrease the density of modified asphalt. Longer chain lengths of PE can further reduce the density of asphalt, with the density of PE at 900 DP and 600 DP being 0.91 and 0.95 g/cm^3, respectively. The average density of PEA's shorter chain lengths is similar to that of AAM-1, as calculated in our previous work using MD simulations [44]. This indicates that the composition has a significant impact on fundamental physical parameters. The densities of PEA samples with 300 DP, 150 DP, 100 DP, and 50 DP are 0.965 ± 0.004 g/cm^3, 0.960 ± 0.004 g/cm^3, 0.966 ± 0.006 g/cm^3, and 0.959 ± 0.002 g/cm^3, respectively. Generally, there is no significant correlation between densities and configurations in different types of PEAs with the same DP of PE. Among them, the density of 300-SC, 300-6BII, and 100-1B is relatively high.

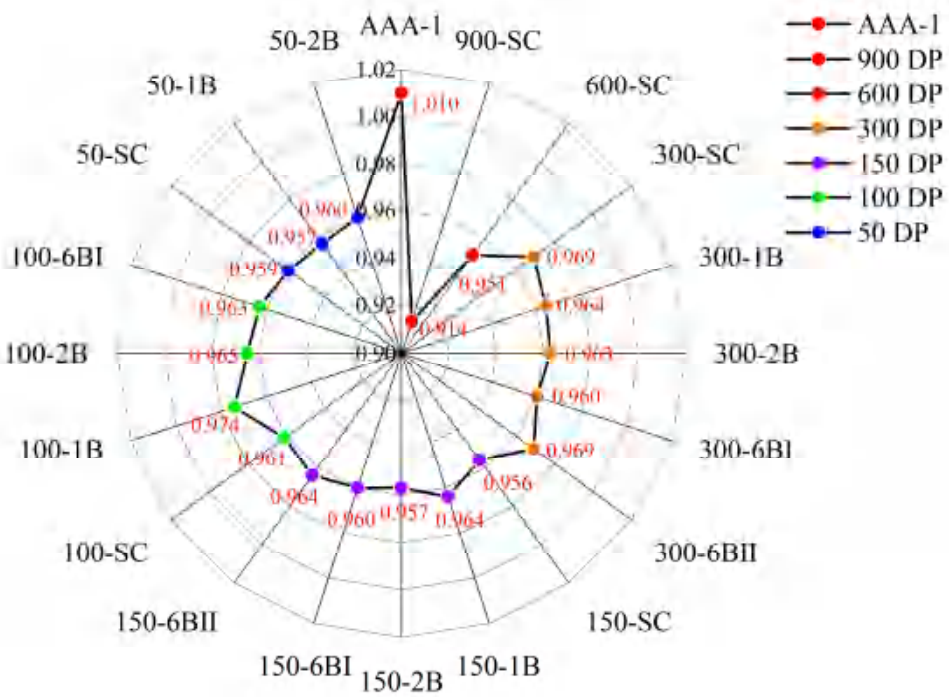

Figure 5. Densities of AAA-1 and PEA models with different DP and chain types.

3.2. Mechanical Properties of PEA Models

Table 3 presents the mechanical properties of the 20 types of PEA models at a temperature of 298 K. Additionally, the mechanical properties of two pure PE models with a total DP of 900, namely 900PE and 300PE-3B, were calculated and compared with those of PEA. Generally, among the 19 types of PEA models, only the bulk moduli of 300-SC, 300-2B, 300-6BII, and 100-1B are higher than that of AAA-1. The shear moduli and Young's moduli of 10 types of PEA models are higher than those of AAA-1, indicating that the addition of PE can improve the shear and Young's modulus of PEA to some extent. Xia et al. [14] have previously demonstrated that PE with high crystallinity can enhance the stiffness of asphalt, thereby improving its rutting resistance through rheological temperature ramp tests and multiple stress creep recovery tests. This could be attributed to the high shear modulus and Young's modulus of pure PE, which improves the mechanical properties of PEA, as shown in Table 3.

Table 3. Mechanical properties of pure PE, AAA-1, and PEA models with different chain types at 298 K.

Pure PE, AAA-1 and PEA Models with Different Chain Types	Bulk Modulus, B (GPa)	Shear Modulus, G (GPa)	Young's Modulus, E (GPa)
900PE	2.844	0.715	1.979
300PE-3B	2.827	0.724	2.001
AAA-1	3.103	0.666	1.864
900-SC	2.509	0.570	1.589
600-SC	3.006	0.531	1.505
300-SC	3.165	0.779	2.159
300-1B	2.947	0.651	1.819
300-2B	3.110	0.731	2.035
300-6BI	2.992	0.726	2.014
300-6BII	3.172	0.833	2.297
150-SC	3.044	0.650	1.822
150-1B	2.947	0.736	2.038
150-2B	2.732	0.692	1.914
150-6BI	2.824	0.529	1.495
150-6BII	2.983	0.600	1.688
100-SC	3.048	0.545	1.542
100-1B	3.139	0.803	2.220
100-2B	3.062	0.680	1.898
100-6BI	3.014	0.649	1.817
50-SC	2.983	0.734	2.035
50-1B	3.087	0.755	2.095
50-2B	2.843	0.631	1.763

In general, four types of PEA, namely 300-SC, 300-2B, 300-6BII, and 100-1B exhibit better mechanical properties than AAA-1. Compared with AAA-1, the bulk modulus, shear modulus, and Young's modulus of 300-6BII are increased by 2.22%, 25.08%, and 23.23%, respectively. Conversely, the bulk modulus of 900-SC is the worst, while the shear modulus and Young's modulus of 150-6BI modified asphalt model are the worst. A low bulk modulus indicates that the model is less rigid and more prone to deformation, and 900-SC has the highest volume and lowest density (as shown in Figure 5) due to the incorporation of the longest chain length of PE with 900 DP.

Furthermore, data analysis from Table 3 reveals that the mechanical properties of 300-SC modified asphalt are superior to those of 600-SC and 900-SC modified asphalt when considering the same size ratio. This suggests that a smaller DP leads to greater stability in a system with the same MW ratio. In a single-chain combination, DP may be the primary parameter affecting the mechanical properties. When considering chain type analysis, except for the 300-DP combination, PEA with one PE branch chain exhibits the best shear modulus and Young's modulus.

However, in general, the DP has a greater impact on the mechanical properties than the molecular architecture. Other factors, such as the length and location of branch chains, and the number of chains could also have some effects on the mechanical properties of asphalt with the same DP. The fundamental law governing these effects requires further study in the future.

3.3. Relationship between FVR *and Mechanical Properties of PEA Models*

According to Equation (1), the *FVR* for the 20 types of asphalt models were calculated and listed in Table 4. Among the PEA models, 100-1B, 300-6BII, and 300-SC exhibit the smallest *FVR*. *FVR* has a low correlation with the DP and configuration of PE. Figure 6 illustrates a negative linear relationship (R^2 = 0.9784) between density and *FVR*, indicating that a higher density of PEA is associated with lower *FVR*.

Table 4. *FVR* of AAA-1 and PEA models with different chain types.

AAA-1 and PEA Models with Different Chain Types	Occupied Volume (Å^3)	Free Volume (Å^3)	Free Volume Ratio (%)
AAA-1	45,096.22	8521.84	15.89
900-SC	175,207.85	48,425.93	21.65
600-SC	117,243.81	25,963.81	18.13
300-SC	58,714.22	11,571.54	16.46
300-1B	58,756.04	11,908.56	16.85
300-2B	58,888.77	11,868.92	16.77
300-6BI	58,792.02	12,181.74	17.16
300-6BII	58,847.59	11,463.19	16.30
150-SC	58,832.58	12,398.53	17.41
150-1B	58,630.93	12,060.54	17.06
150-2B	58,910.91	12,260.21	17.23
150-6BI	58,736.90	12,188.74	17.19
150-6BII	58,722.66	11,901.67	16.85
100-SC	58,713.87	12,131.01	17.12
100-1B	58,660.03	11,251.54	16.09
100-2B	58,899.58	11,715.55	16.59
100-6BI	58,702.49	12,054.54	17.04
50-SC	59,035.95	11,969.21	16.86
50-1B	58,638.13	12,540.28	17.62
50-2B	58,901.69	12,055.43	16.99

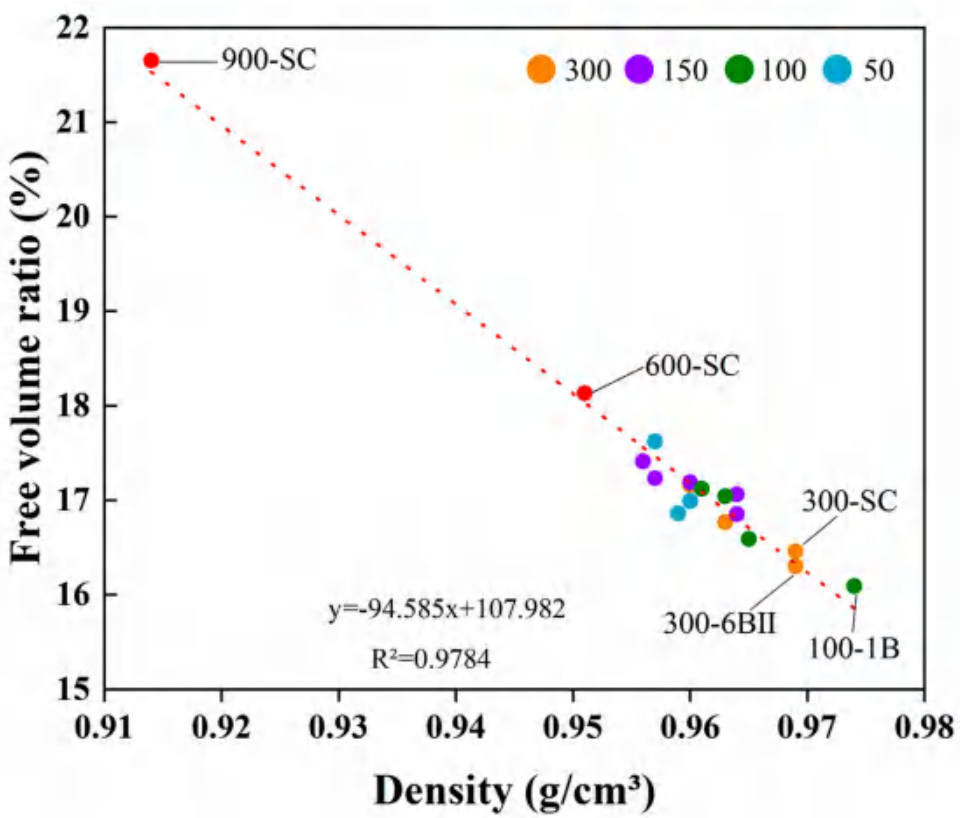

Figure 6. The relationship between *FVR* and density of the PEA models.

Figures 7–9 show the relationship between the *FVR* and bulk modulus, shear modulus, and Young's modulus of different types of PEAs. Compared to other PEA models, 300-6BII, 300-SC, and 100-1B, which have the smallest *FVR*, exhibit better mechanical properties, suggesting that a smaller *FVR* leads to better resistance to compression deformation and shear strain. In the same size ratio of PEA combinations, 300-SC has a lower *FVR* and better mechanical properties than 600-SC and 900-SC. From the gray shaded area in Figures 7–9, it can be seen that under similar *FVR* conditions, the bulk modulus, shear modulus, and Young's modulus of different combinations are greatly affected by the DP and configuration of PE.

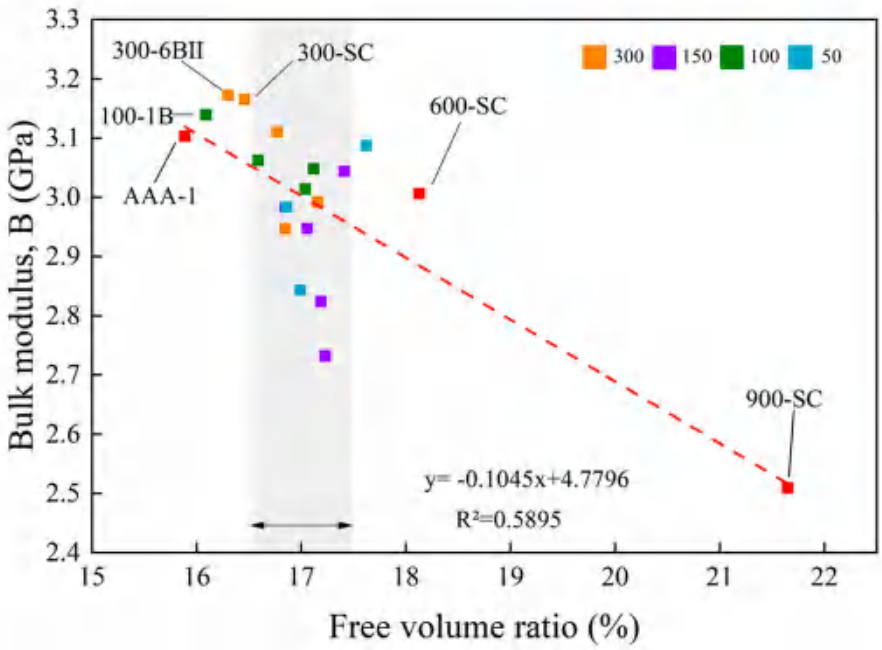

Figure 7. The relationship between the *FVR* and bulk modulus.

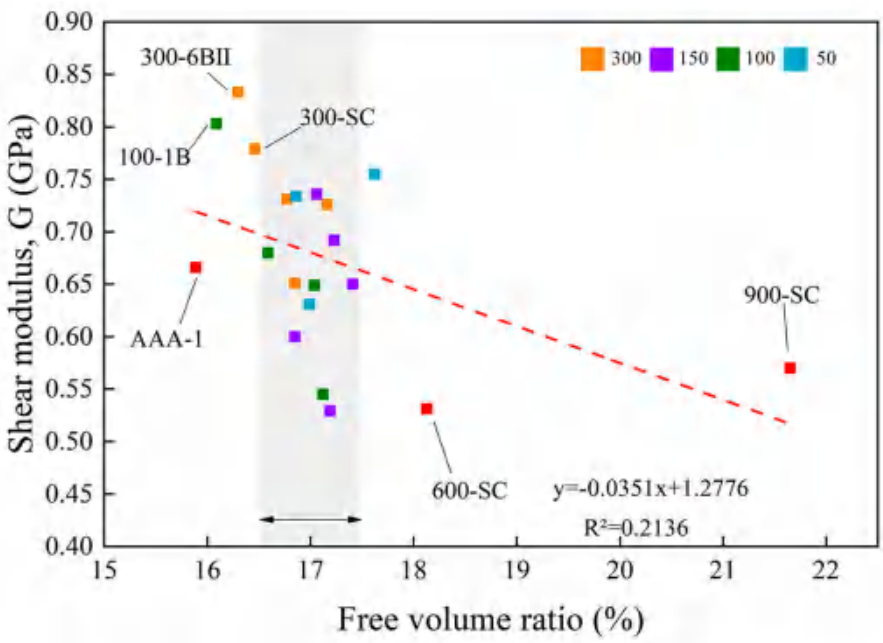

Figure 8. The relationship between the *FVR* and shear modulus.

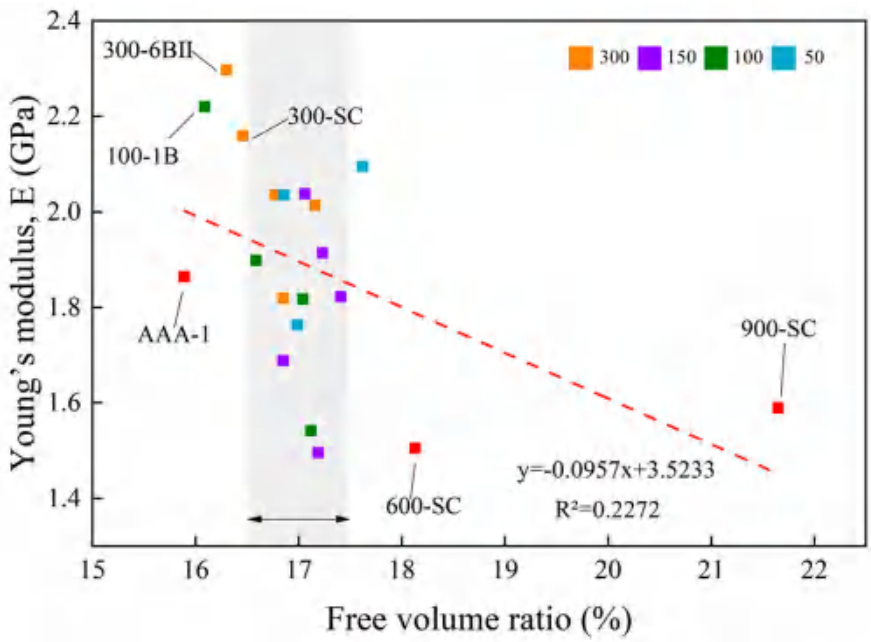

Figure 9. The relationship between the *FVR* and Young's modulus.

3.4. Compatibility Evaluation of PEA Models

The Flory–Huggins parameters were calculated to analyze the compatibility between PE and asphalt systems in different combinations. Figures 10 and 11 show the Flory–Huggins parameters of PE and asphalt systems with different PD and the number of chains at 298 K. According to Figure 10, the smaller the DP, the relative MW of one PE molecule is closer to that of the four components of asphalt, and the compatibility between PE and asphalt is better. Meanwhile, Figure 11 shows that the more chains there are, the better the compatibility between PE chains and asphalt.

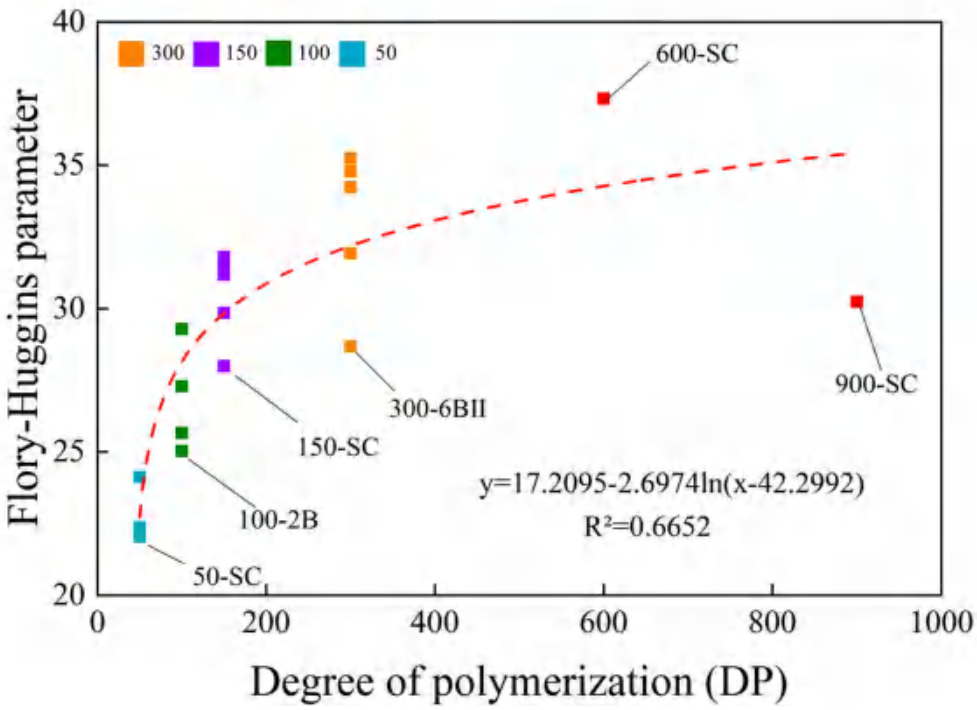

Figure 10. The Flory–Huggins parameter of PEA models with different DP.

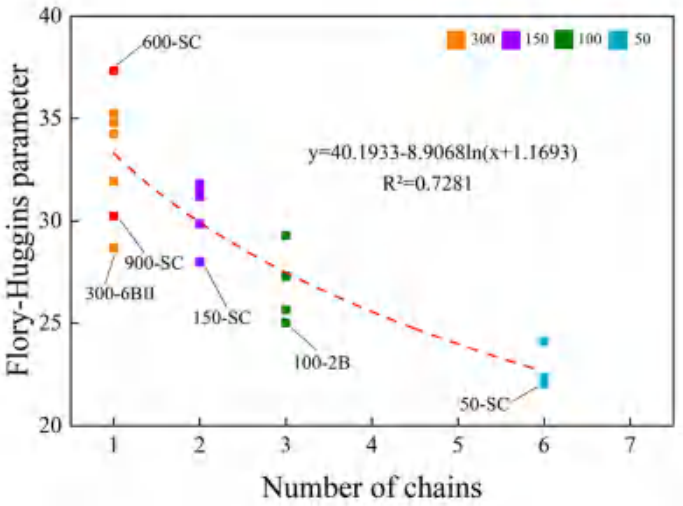

Figure 11. The Flory–Huggins parameter of PEA models with different number of chains.

When a single PE chain with 300 DP is added, the compatibility between PE and asphalt in 300-6BII is the best, which corresponds to the result of mechanical properties. Although the χ value is large at 300 DP, the PE component in PEA plays a dominant role in resisting compression deformation and shear strain with a relatively small *FVR*. When two PE chains with 150 DP are added, the compatibility of PE chains with asphalt components is improved. The 150-SC has the best compatibility. After 100-SC, the compatibility of PE chains with asphalt components further improved, among which 100-2B and 50-SC have the best compatibility.

The above results show that the compatibility of different PEA combinations was not significantly affected by the configuration. The DP and number of chains are the main parameters impacting the compatibility between PE and asphalt.

3.5. Mean squared Displacement (MSD) Analysis of PEA Models

The *MSD* of PE in the PEA models is plotted in Figure 12. The *MSD* of 100-SC is the largest, while that of 150-6BI is the smallest. As a whole, the red lines are higher than the blue lines, indicating that the displacement of SC and 1B is greater than that of 6BI and 6BII. PE with fewer branch chains is more likely to move.

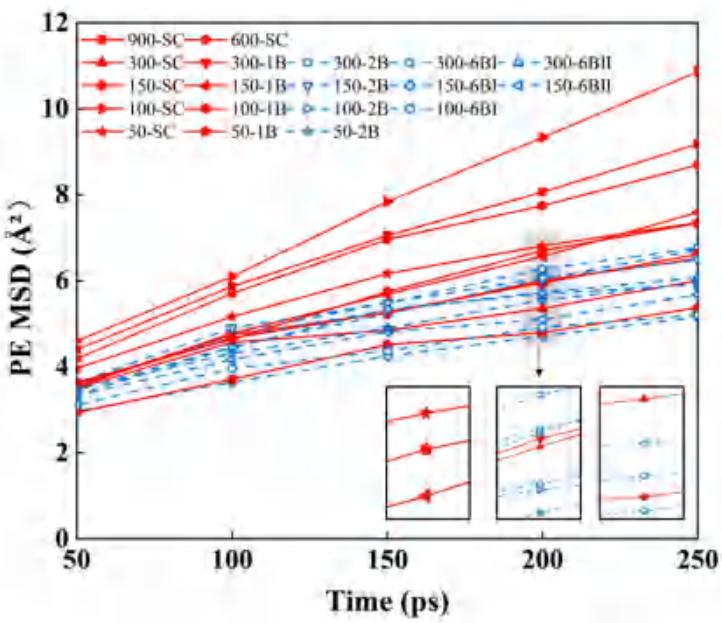

Figure 12. *MSD* of PE in 19 PEA models.

The *MSD* of five components of PEA models with polymerization degrees of 300 and 150 was calculated, as shown in Figures 13 and 14. When the DP is 300, the *MSD* of PE in PEA is the highest, and saturates rank second. The saturates are a light component and are easily moved in the system. When the DP changes from 300 to 150, the *MSD* of PE is closer to that of saturates than others in asphalt, indicating that the displacement of PE and saturation fraction is close. At this time, the compatibility between the PE and the components in the asphalt system improves.

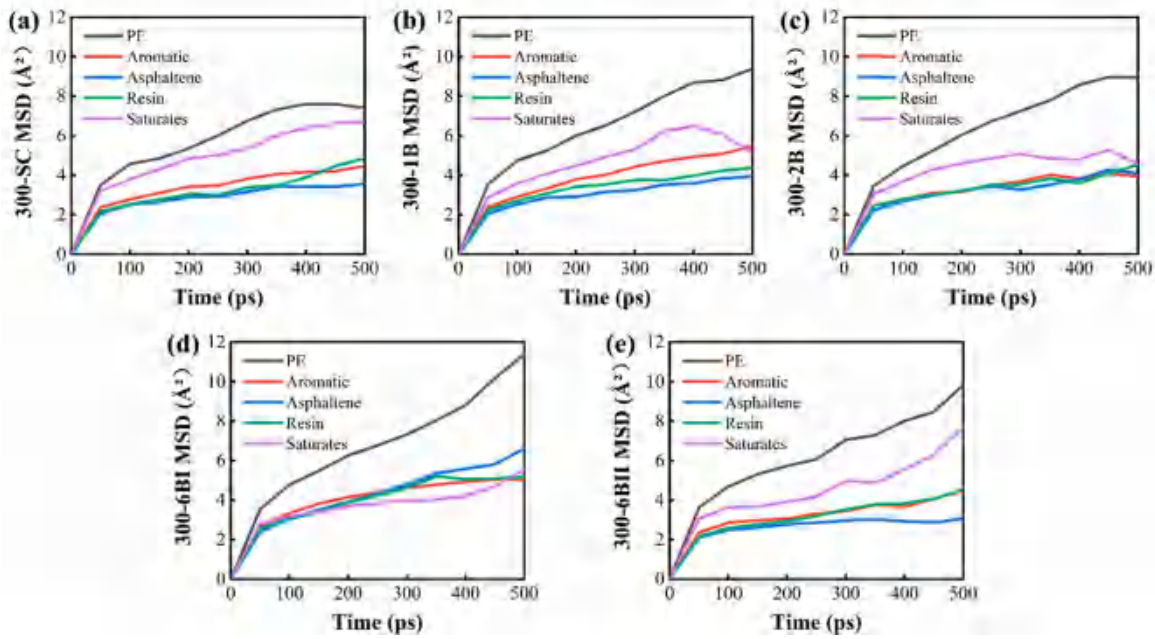

Figure 13. *MSD* of five components of PEA models with 300 DP: (**a**) 300-SC, (**b**) 300-1B, (**c**) 300-2B, (**d**) 300-6BI and (**e**) 300-6BII.

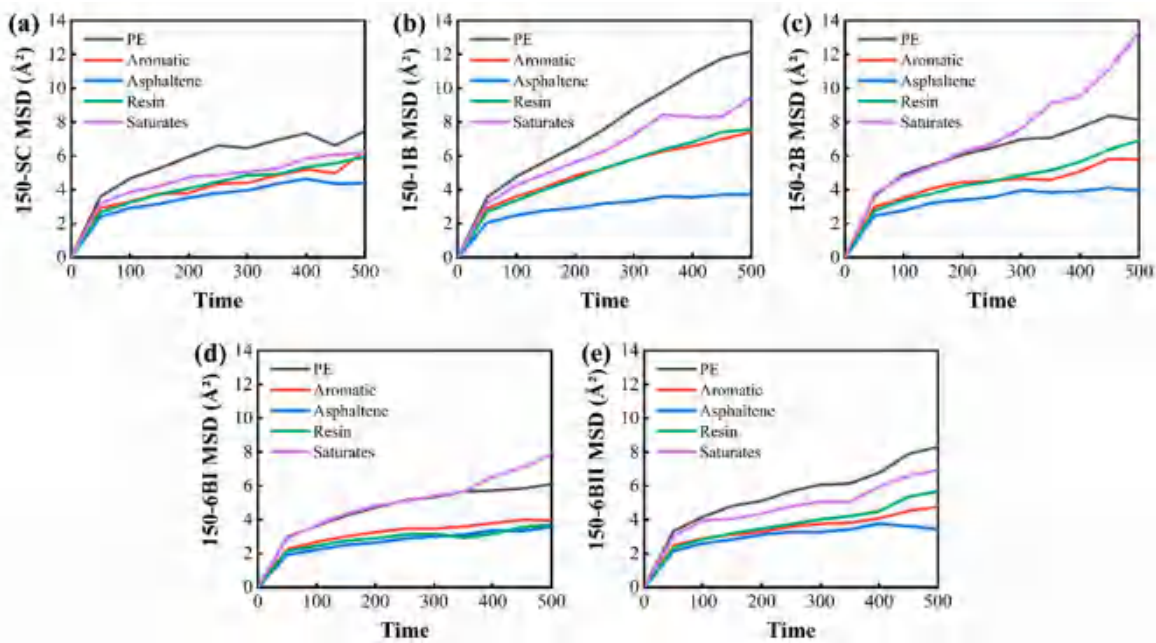

Figure 14. *MSD* of five components of PEA models with 150 DP: (**a**) 150-SC, (**b**) 150-1B, (**c**) 150-2B, (**d**) 150-6BI, and (**e**) 150-6BII.

3.6. Experimental Part: Microscopical Analysis of LDPE and PEA

Figure 15 shows the FTIR spectrum of the two LDPE samples. The functional groups of LDPE-1 and LDPE-2 samples are similar and consistent with previous spectral results [6,54,55]. All the spectra showed the presence of main group peaks at 2915 cm^{-1}, 2848 cm^{-1}, 1472 cm^{-1}, and 717 cm^{-1}. It is worth noting that LDPE-1 has small protrusions at 1262 cm^{-1}, 1098 cm^{-1}, and 1026 cm^{-1}, suggesting the presence of C-O bonds in the sample. In LDPE-2, the vibration peak of the C-O bond is at 1020 cm^{-1}. The LDPE samples were prepared with recycled plastic particles, which suggested that they are oxidized at different levels.

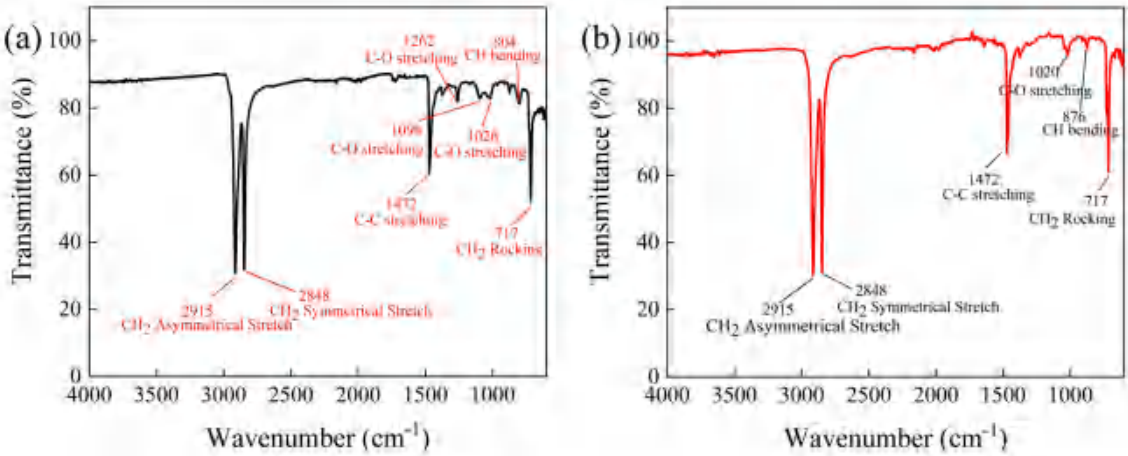

Figure 15. FTIR spectroscopy: (**a**) LDPE−1, (**b**) LDPE−2.

The TG/DSC curves of LDPE-1 and LDPE-2 are shown in Figure 16. The melting point of LDPE is approximately 108–126 °C. Both LDPE-1 and LDPE-2 samples initially have an endothermic peak at 111.86 °C and 125.37 °C, which fall within the melting point range of LDPE. Comparing these two temperatures, the crystallinity of LDPE-2 is greater than that of LDPE-1. There is a significant exothermic peak at 450 °C of LDPE-2, indicating a secondary polycondensation reaction. The mass loss of LDPE-2 is higher at more than 500 °C, implying a higher purity of LDPE-2.

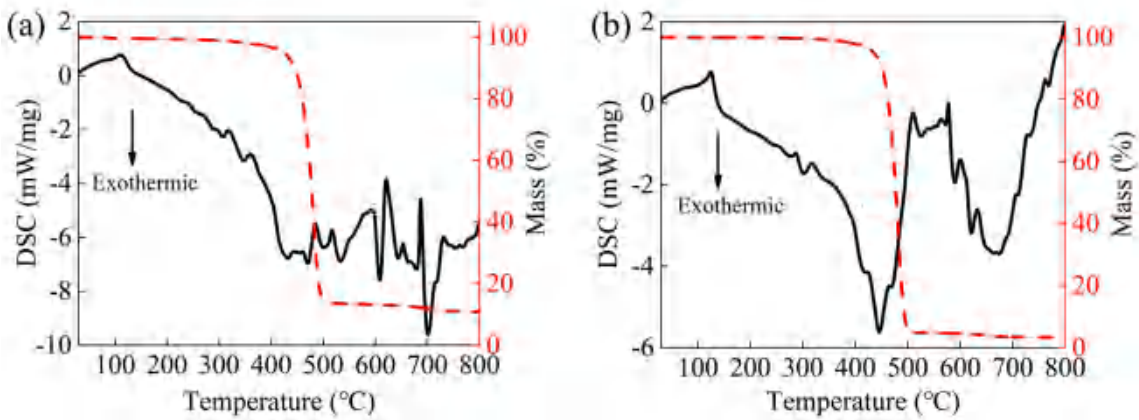

Figure 16. TG/DSC curves: (**a**) LDPE−1, (**b**) LDPE−2.

Two PEA samples amplified 10 times by fluorescence microscopy are shown in Figure 17. The π electrons in aromatic or double bond-containing compounds have conjugation, which can absorb light and enter the excited state, thus producing fluorescence [9,56]. In the mixed PEA sample, PE was excited after adsorbing aromatic or double bond-containing components in asphalt, resulting in a fluorescence effect. From Figure 17a,c, PE is dispersed with long chains stacked, while part component of asphalt

is distributed on the PE surface. Phase boundaries between the polymer-rich phase and asphaltene-rich phase are clear. The Image J software 2021 [57] was used to analyze the mean fractal diameters of Figure 17b,d as 22.15 Å and 14.2 Å, respectively. A smaller mean fractal diameter indicates better compatibility, thus LDPE−2 has better compatibility with asphalt. The reason could be that LDPE−2 has higher purity.

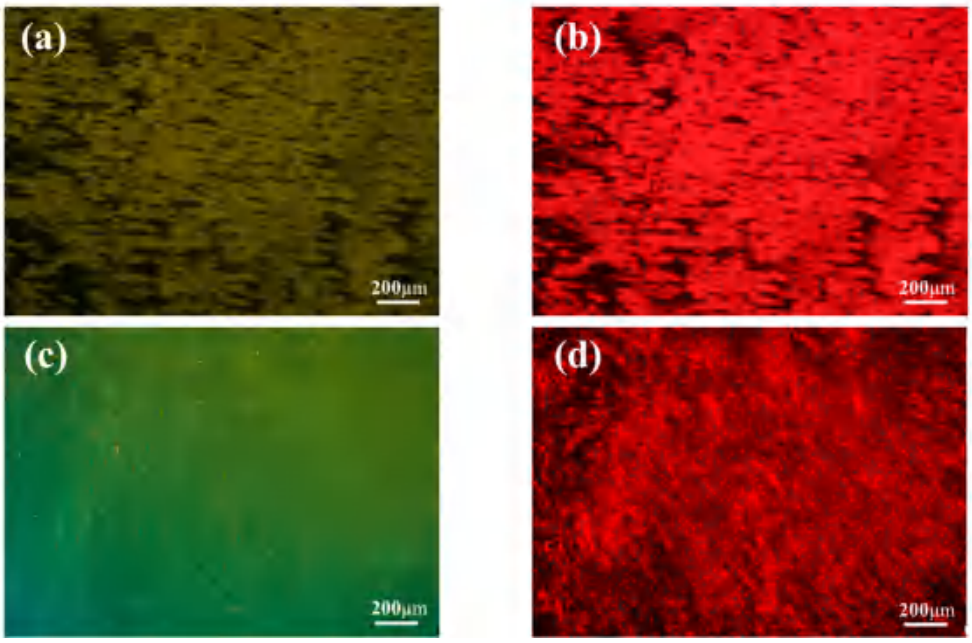

Figure 17. Fluorescence microscopy of PEA samples excited under different lights (Cold color: blue light; warm color: green light.): (**a**,**b**) LDPE−1; (**c**,**d**) LDPE−2.

Furthermore, different components in asphalt can be excited under different excitation light sources with various energies (blue or green light in this work). From Figure 17a–d, different fluorescence effects were observed in the same sample with blue or green light, showing that the PEA can be excited under green light more easily. Green light has a longer wavelength than blue light. It has been stated that the aromatic phase is more easily excited while the other components are more difficult. The characterization of asphalt with fluorescence microscopy is still progressing [56]. Figure 17b,d show the significant emission characteristics of the aromatic component and the PE mixed with the other components. Figure 17a,c further indicates that blue light with shorter wavelengths can excite the other components of asphalt, which brings a new method to distinguish different components of asphalt with fluorescence microscopy. But more work should be done in future. In summary, it is evident that PE and asphalt are still in a state of partial miscibility at the microscale from fluorescence microscopy observation.

4. Conclusions

This study aims to determine the microscopic properties of asphalt modified with PE at an extraordinary high dosage of 20 wt.% both from molecular dynamics and experimental works. Different DP and structural configurations (the number of branches and their arrangement in the main chains) of PE were designed and mixed with asphalt to build PEA molecular models. The density, mechanical properties, free volume ratio (*FVR*), mean squared displacement (*MSD*), and Flory–Huggins parameter (χ) of various types of PEAs were calculated to analyze their relationships. Two types of PEA were made and characterized by fluorescence microscopy. Based on the results and analysis, it can be concluded that:

(1) The addition of PE can reduce the density of modified asphalt by less than 5%, and a higher density of PEA is associated with lower *FVR*;

(2) When the *FVR* is close, the mechanical properties are greatly influenced by the DP and configuration of PE.
(3) The DP and the number of chains are the main parameters impacting the compatibility between PE and asphalt based on the Flory–Huggins parameter analysis. Decreasing the DP of PE (e.g., 50, with a minimum Flory–Huggins parameter and a relative molecular mass of 1300) significantly increases the compatibility between asphalt and PE.
(4) LDPE-2 has better compatibility with asphalt, possibly because LDPE−2 has higher purity.

From this work, the mechanical properties of PE, the compatibility between asphalt and PE, and intermolecular interaction in the PEA blend system should have relationships, thus affecting the storage stability. Decreasing the DP of PE increases the compatibility between asphalt and PE, which could provide theoretical guidance for chemical engineering synthesis. Further research is needed to modify the PE chains to improve their blending ability with the four components of asphalt, thus increasing the storage stability of PEA. Their mechanical properties and binding ability with aggregates should also be investigated in the future. Furthermore, microplastic pollution generated by the widespread use of PEA in road engineering cannot be ignored.

Author Contributions: Y.J.: Investigation, Methodology, Writing—original draft. H.L.: Investigation. J.C.: Investigation. Q.W.: Conception, Investigation, writing—review & editing, Supervision. Y.B.: Investigation. S.H.: Investigation, Writing—review & editing, Supervision. All authors have read and agreed to the published version of the manuscript.

Funding: This research was funded by the Program Fund of Non-Metallic Excellence and Innovation Center for Building Materials (2023SFP1-2) and the Postgraduate Research & Practice Innovation Program of Jiangsu Province (SJCX23-0505).

Data Availability Statement: Data will be made available on request.

Acknowledgments: The authors thank for the computational resources generously provided by the High-Performance Computing Center of Nanjing Tech University.

Conflicts of Interest: Author Jie Chen was employed by the company Yunnan Infrastructure Investment Co., Ltd. The remaining authors declare that the research was conducted in the absence of any commercial or financial relationships that could be construed as a potential conflict of interest.

References

1. OECD. *Global Plastics Outlook: Economic Drivers, Environmental Impacts and Policy Options*; OECD: Paris, France, 2022.
2. Nairobi. *From Pollution to Solution: A Global Assessment of Marine Litter and Plastic Pollution*; United Nations Environment Programme: Nairobi, Kenya, 2021.
3. Geyer, R.; Jambeck, J.R.; Law, K.L. Production, use, and fate of all plastics ever made. *Sci. Adv.* **2017**, *3*, e1700782. [CrossRef] [PubMed]
4. Pathak, G.; Nichter, M.; Hardon, A.; Moyer, E.; Latkar, A.; Simbaya, J.; Pakasi, D.; Taqueban, E.; Love, J. Plastic pollution and the open burning of plastic wastes. *Glob. Environ. Change* **2023**, *80*, 102648. [CrossRef]
5. Behera, S.; Das, S. Environmental impacts of microplastic and role of plastisphere microbes in the biodegradation and upcycling of microplastic. *Chemosphere* **2023**, *334*, 138928. [CrossRef] [PubMed]
6. Gowthami, A.; Syed Marjuk, M.; Raju, P.; Nanthini Devi, K.; Santhanam, P.; Dinesh Kumar, S.; Perumal, P. Biodegradation efficacy of selected marine microalgae against Low-Density Polyethylene (LDPE): An environment friendly green approach. *Mar. Pollut. Bull.* **2023**, *190*, 114889. [CrossRef] [PubMed]
7. Nisa, S.A.; Vasantharaja, R.; Supriya, S.; Inbakandan, D.; Dharani, G.; Govindaraju, K. Biodeterioration of polyethylene by jellyfish nematocyst protein. *Mar. Pollut. Bull.* **2023**, *188*, 114682. [CrossRef] [PubMed]
8. Amobonye, A.; Bhagwat, P.; Singh, S.; Pillai, S. Plastic biodegradation: Frontline microbes and their enzymes. *Sci. Total Environ.* **2021**, *759*, 143536. [CrossRef] [PubMed]
9. Polacco, G.; Filippi, S.; Merusi, F.; Stastna, G. A review of the fundamentals of polymer-modified asphalts: Asphalt/polymer interactions and principles of compatibility. *Adv. Colloid. Interface Sci.* **2015**, *224*, 72–112. [CrossRef] [PubMed]
10. Alsolieman, H.A.; Babalghaith, A.M.; Memon, Z.A.; Al-Suhaibani, A.S.; Milad, A. Evaluation and Comparison of Mechanical Properties of Polymer-Modified Asphalt Mixtures. *Polymers* **2021**, *13*, 2282. [CrossRef]

11. Alghrafy, Y.M.; Abd Alla, E.S.M.; El-Badawy, S.M. Rheological properties and aging performance of sulfur extended asphalt modified with recycled polyethylene waste. *Constr. Build. Mater.* **2021**, *273*, 121771. [CrossRef]
12. Radeef, H.R.; Hassan, N.A.; Mahmud, M.Z.H.; Abidin, A.R.Z.; Ismail, C.R.; Abbas, H.F.; Al-Saffar, Z.H. Characterisation of cracking resistance in modified hot mix asphalt under repeated loading using digital image analysis. *Theor. Appl. Fract. Mech.* **2021**, *116*, 103130. [CrossRef]
13. Abed, A.H.; Bahia, H.U. Enhancement of permanent deformation resistance of modified asphalt concrete mixtures with nano-high density polyethylene. *Constr. Build. Mater.* **2020**, *236*, 117604. [CrossRef]
14. Xia, T.; Zhang, A.; Xu, J.; Chen, X.; Xia, X.; Zhu, H.; Li, Y. Rheological behavior of bitumen modified by reclaimed polyethylene and polypropylene from different recycling sources. *J. Appl. Polym. Sci.* **2021**, *138*, 50435. [CrossRef]
15. Kakar, M.R.; Mikhailenko, P.; Piao, Z.; Bueno, M.; Poulikakos, L. Analysis of waste polyethylene (PE) and its by-products in asphalt binder. *Constr. Build. Mater.* **2021**, *280*, 122492. [CrossRef]
16. Polacco, G.; Berlincioni, S.; Biondi, D.; Stastna, J.; Zanzotto, L. Asphalt modification with different polyethylene-based polymers. *Eur. Polym. J.* **2005**, *41*, 2831–2844. [CrossRef]
17. Naskar, M.; Chaki, T.K.; Reddy, K.S. Effect of waste plastic as modifier on thermal stability and degradation kinetics of bitumen/waste plastics blend. *Thermochim. Acta* **2010**, *509*, 128–134. [CrossRef]
18. Fang, C.Q.; Zhang, Y.; Yu, Q.; Zhou, X.; Guo, D.G.; Yu, R.E.; Zhang, M. Preparation, Characterization and Hot Storage Stability of Asphalt Modified by Waste Polyethylene Packaging. *J. Mater. Sci. Technol.* **2013**, *29*, 434–438. [CrossRef]
19. Genet, M.B.; Sendekie, Z.B.; Jembere, A.L. Investigation and optimization of waste LDPE plastic as a modifier of asphalt mix for highway asphalt: Case of Ethiopian roads. *Case Stud. Chem. Environ. Eng.* **2021**, *4*, 100150. [CrossRef]
20. Vasiljevic-Shikaleska, A.; Popovska-Pavlovska, F.; Cimmino, S.; Duraccio, D.; Silvestre, C. Viscoelastic properties and morphological characteristics of polymer-modified bitumen blends. *J. Appl. Polym. Sci.* **2010**, *118*, 1320–1330. [CrossRef]
21. Hong, Z.; Yan, K.; Wang, M.; You, L.; Ge, D. Low-density polyethylene/ethylene–vinyl acetate compound modified asphalt: Optimal preparation process and high-temperature rheological properties. *Constr. Build. Mater.* **2022**, *314*, 125688. [CrossRef]
22. Poulikakos, L.D.; Pasquini, E.; Tusar, M.; Hernando, D.; Wang, D.; Mikhailenko, P.; Pasetto, M.; Baliello, A.; Falchetto, A.C.; Miljkovic, M.; et al. RILEM interlaboratory study on the mechanical properties of asphalt mixtures modified with polyethylene waste. *J. Clean. Prod.* **2022**, *375*, 134124. [CrossRef]
23. Panda, M.; Mazumdar, M. Utilization of reclaimed polyethylene in bituminous paving mixes. *J. Mater. Civil. Eng.* **2002**, *14*, 527–530. [CrossRef]
24. Pe'rez-Lepe, A.; Martı'nez-Boza, F.J.; Gallegos, C. Influence of Polymer Concentration on the Microstructure and Rheological Properties of High-Density Polyethylene (HDPE)-Modified Bitumen. *Energy Fuels* **2005**, *19*, 1148–1152. [CrossRef]
25. Hınıslıoglu, S. Use of waste high density polyethylene as bitumen modifier in asphalt concrete mix. *Mater. Lett.* **2004**, *58*, 267–271. [CrossRef]
26. Zhang, S.-Q.; Wang, W.-Q.; Lin, J.-P.; Wang, L.-Q. Rheological Behaviors of Polymers with Nanoparticles Tethered at Each End. *Chin. J. Polym. Sci.* **2023**. [CrossRef]
27. Li, M.; Chen, X.; Cong, P.; Luo, C.; Zhu, L.; Li, H.; Zhang, Y.; Chao, M.; Yan, L. Facile synthesis of polyethylene-modified asphalt by chain end-functionalization. *Compos. Commun.* **2022**, *30*, 101088. [CrossRef]
28. Li, M.R.; Luo, C.J.; Zhu, L.Y.; Li, H.Y.; Cong, P.L.; Feng, Y.Y.; Yan, L.K. A novel epoxy-terminated polyethylene modified asphalt with low-viscosity and high storage stability. *Constr. Build. Mater.* **2022**, *335*, 127473. [CrossRef]
29. Ma, D.C.; Zhao, D.J.; Zhao, J.Z.; Du, S.J.; Pang, J.Y.; Wang, W.; Fan, C.X. Functionalization of reclaimed polyethylene with maleic anhydride and its application in improving the high temperature stability of asphalt mixtures. *Constr. Build. Mater.* **2016**, *113*, 596–602. [CrossRef]
30. Vargas, M.A.; Vargas, M.A.; Sánchez-Sólis, A.; Manero, O. Asphalt/polyethylene blends: Rheological properties, microstructure and viscosity modeling. *Constr. Build. Mater.* **2013**, *45*, 243–250. [CrossRef]
31. Li, M.; Luo, C.; Zhu, L.; Cong, P.; Li, H.; Chen, X.; Zhang, Y.; Chao, M.; Yan, L. Polyethylene based on molecular weight design for eco-friendly asphalt. *J. Appl. Polym. Sci.* **2023**, *140*, 53994. [CrossRef]
32. González, O.; Muñoz, M.E.; Santamaría, A. Bitumen/polyethylene blends: Using m-LLDPEs to improve stability and viscoelastic properties. *Rheol. Acta* **2006**, *45*, 603–610. [CrossRef]
33. Yan, L.K.; Li, M.R.; Li, Q.; Li, H.Y. Modified asphalt based on polyethylene with broad molecular weight distribution. *Constr. Build. Mater.* **2020**, *260*, 119707. [CrossRef]
34. Liang, M.; Xin, X.; Fan, W.; Zhang, J.; Jiang, H.; Yao, Z. Comparison of rheological properties and compatibility of asphalt modified with various polyethylene. *Int. J. Pavement Eng.* **2021**, *22*, 11–20. [CrossRef]
35. González-Aguirre, P.; Medina-Torres, L.; Schrauwen, C.; Fonteix, C.; Pla, F.; Herrera-Nájera, R. Morphology and rheological behavior of maltene–polymer blends. I. Effect of partial hydrogenation of poly(styrene-block-butadiene-block-styrene-block)-type copolymers. *J. Appl. Polym. Sci.* **2009**, *112*, 1330–1344. [CrossRef]
36. Xu, D.; Wan, H.-X.; Yao, X.-R.; Li, J.; Yan, L.-T. Molecular Simulations in Macromolecular Science. *Chin. J. Polym. Sci.* **2023**, *41*, 1361–1370. [CrossRef]
37. Li, D.D.; Greenfield, M.L. Chemical compositions of improved model asphalt systems for molecular simulations. *Fuel* **2014**, *115*, 347–356. [CrossRef]

38. Dan, H.-C.; Zou, Z.-M.; Zhang, Z.; Tan, J.-W. Effects of aggregate type and SBS copolymer on the interfacial heat transport ability of asphalt mixture using molecular dynamics simulation. *Constr. Build. Mater.* **2020**, *250*, 118922. [CrossRef]
39. Li, R.; Leng, Z.; Yang, J.; Lu, G.; Huang, M.; Lan, J.; Zhang, H.; Bai, Y.; Dong, Z. Innovative application of waste polyethylene terephthalate (PET) derived additive as an antistripping agent for asphalt mixture: Experimental investigation and molecular dynamics simulation. *Fuel* **2021**, *300*, 121015. [CrossRef]
40. Hu, K.; Yu, C.H.; Yang, Q.L.; Li, Z.W.; Zhang, W.G.; Zhang, T.L.; Feng, Y. Mechanistic study of graphene reinforcement of rheological performance of recycled polyethylene modified asphalt: A new observation from molecular dynamics simulation. *Constr. Build. Mater.* **2022**, *320*, 126263. [CrossRef]
41. Chen, P.; Hu, K.; Caihua, Y.; Yuan, D.; Ban, X. Study of the Microscopic Mechanism of Natural Rubber (Cis-1, 4-Polyisoprene, NR)/Polyethylene (PE) Modified Asphalt from the Perspective of Simulation. *Polymers* **2022**, *14*, 4087. [CrossRef]
42. Ge, D.D.; Yan, K.Z.; You, Z.P.; Xu, H.B. Modification mechanism of asphalt binder with waste tire rubber and recycled polyethylene. *Constr. Build. Mater.* **2016**, *126*, 66–76. [CrossRef]
43. Jones, D.R. *SHRP Materials Reference Library: Asphalt Cements: A Concise Data Compilation*; Strategic Highway Research Program, National Research Council: Washington, DC, USA, 1993.
44. Du, J.; Jin, Y.; Hou, S.; Jin, R.; Wang, Q. Effect of component characteristics on mechanical properties of asphalt: A molecular dynamics study. *Case Stud. Constr. Mater.* **2023**, *18*, e02007. [CrossRef]
45. Hill, R. The Elastic Behaviour of a Crystalline Aggregate. *Proc. Phys. Soc. A* **1952**, *65*, 349–354. [CrossRef]
46. Connolly, M.L. Analytical molecular surface calculation. *J. Appl. Crystallogr.* **1983**, *16*, 548. [CrossRef]
47. Long, Z.; Zhou, S.; Jiang, S.; Ma, W.; Ding, Y.; You, L.; Tang, X.; Xu, F. Revealing compatibility mechanism of nanosilica in asphalt through molecular dynamics simulation. *J. Mol. Model.* **2021**, *27*, 81. [CrossRef]
48. Luo, L.; Chu, L.; Fwa, T.F. Molecular dynamics analysis of oxidative aging effects on thermodynamic and interfacial bonding properties of asphalt mixtures. *Constr. Build. Mater.* **2021**, *269*, 121299. [CrossRef]
49. Martinez de Arenaza, I.; Meaurio, E.; Coto, B.; Sarasua, J.-R. Molecular dynamics modelling for the analysis and prediction of miscibility in polylactide/polyvinilphenol blends. *Polymer* **2010**, *51*, 4431–4438. [CrossRef]
50. Jawalkar, S.S.; Raju; Halligudi, S.B.; Sairam, M.; Aminabhavi, T.M. Molecular Modeling Simulations to Predict Compatibility of Poly(vinyl alcohol) and Chitosan Blends: A Comparison with Experiments. *J. Phys. Chem. B* **2007**, *111*, 2431–2439. [CrossRef]
51. *SB/T 11149-2015*; Technical specifications of waste plastics collection and sorting. Ministry of Commerce: Beijing, China, 2015.
52. Zhang, F.; Hu, C. The research for crumb rubber/waste plastic compound modified asphalt. *J. Therm. Anal. Calorim.* **2015**, *124*, 729–741. [CrossRef]
53. Du, Z.; Jiang, C.; Yuan, J.; Xiao, F.; Wang, J. Low temperature performance characteristics of polyethylene modified asphalts—A review. *Constr. Build. Mater.* **2020**, *264*, 120704. [CrossRef]
54. Sridharan, R.; Krishnaswamy, V.G.; Kumar, P.S. Analysis and microbial degradation of Low-Density Polyethylene (LDPE) in Winogradsky column. *Environ. Res.* **2021**, *201*, 111646. [CrossRef]
55. Taghavi, N.; Singhal, N.; Zhuang, W.-Q.; Baroutian, S. Degradation of plastic waste using stimulated and naturally occurring microbial strains. *Chemosphere* **2021**, *263*, 127975. [CrossRef] [PubMed]
56. Evdokimov, I.N.; Fesan, A.A.; Losev, A.P. New Answers to the Optical Interrogation of Asphaltenes: Monomers and Primary Aggregates from Steady-State Fluorescence Studies. *Energy Fuels* **2016**, *30*, 4494–4503. [CrossRef]
57. Schneider, C.A.; Rasband, W.S.; Eliceiri, K.W. NIH Image to ImageJ: 25 years of image analysis. *Nat. Methods* **2012**, *9*, 671–675. [CrossRef] [PubMed]

Disclaimer/Publisher's Note: The statements, opinions and data contained in all publications are solely those of the individual author(s) and contributor(s) and not of MDPI and/or the editor(s). MDPI and/or the editor(s) disclaim responsibility for any injury to people or property resulting from any ideas, methods, instructions or products referred to in the content.

大掺量再生低密度聚乙烯塑料改性制备高粘高弹道路沥青及性能

蒋建国　孙天庚　王训芝　王倩倩　侯曙光

（南京工业大学　江苏　211816）

摘要：塑料污染已成为危害全球环境安全主的要问题之一，突破和实现大掺量再生塑料制备高粘高弹改性沥青并规模化利用，具有可观经济和环境效益。通过化学与物理复合改性方法，提升 20% 掺量再生低密度聚乙烯（LDPE）塑料与基质沥青相容性及储存稳定性，实现高粘高弹道路沥青制备，并通过性能测试评估其路用价值，为再生塑料改性沥青在路面材料中规模化应用提供指导。

关键词：再生塑料；改性沥青；相容性；储存稳定性；高粘高弹道路沥青

中图分类号：U414　　**文献标识码**：A

DOI：10.20087/j.cnki.1672-8114.2025.02.033

Preparation Method and Properties of High Viscosity and Elasticity Road Asphalt Modified Recycled Low-density Polyethylene Plastic at a Large Dosage

Jiang Jianguo, Sun Tiangeng, Wang Xunzhi, Wang Qianqian, Hou Shuguang*

(Nanjing University of Technology, Jiangsu, 211816)

Abstract：*Plastic pollution has become one of the major issues threatening global environmental security. Breaking through and achieving the preparation of high viscosity and elasticity modified asphalt with a high content of recycled plastic, and then scaling up its utilization, can bring significant economic and environmental benefits. By employing chemical and physical composite modification methods, the compatibility and storage stability between 20% recycled low-density polyethylene (LDPE) plastic and the base asphalt can be improved. This will allow the production of high viscosity and elasticity road asphalt, and its roadworthiness can be evaluated through performance testing in order to provide guidance for the large-scale application of modified asphalt with recycled plastic in road materials.*

Key words：*recycled plastics*；*modified asphalt*；*compatibility*；*storage stability*；*high viscosity and elasticity road asphalt*

全球塑料污染问题严峻，1950 年至 2021 年间累计生产约 92 亿吨塑料，回收利用率不足 10%，预计未来塑料垃圾遗弃量将大幅增长。为应对塑料污染并满足基础设施建设需求，我国正积极探索废塑料在道路建筑领域的回收利用。近年来，废塑料在道路交通领域的回收利用得到了广泛研究[1]，证明了再生热塑性塑料在道路建筑领域应用的可行性，提高再生塑料在道路建筑领域应用掺量，可极大推动塑料垃圾的材料化再生利用。现有再生塑料改性沥青中再生塑料的最佳掺量一般仅为 5% 左右[2]。

在再生塑料改性沥青中，塑料微粒能吸收沥青中的饱和分和芳香分而溶胀[3]，这种改性沥青为部分相容体系，不能完全相容成为制约再生塑料大规模应用的主要原因之一，近年来，为解决此问题，研究方向从单一改性向复合改性方向发展[4]。研究表明，共聚物可改善改性沥青的相容性[5]；交联剂可使聚合物与沥青发生反应，在两者间形成化学连接，提高沥青的相容性[6]；分子链嫁接也是提高相容性、增加储存稳定性的有效方法，马来酸酐（MA）、甲基丙烯酸（MAA）和甲基丙烯酸缩水甘油酯（GMA）用于接枝一些目前使用的聚合物改性剂[7]。

因此，拟通过物理化学相结合的方法对产量大、来源稳定的汽车隔音棉（GYM）及大棚膜（DPL）再生料进行基本物性研究，寻找再生塑料改性沥青相容性差、易离析的解决方法，以实现 20% 掺量下再生低密度聚乙烯（LDPE）改性沥青（PEA）的路用价值，旨在探索通过道路建筑领域大宗量消纳可再生塑料垃圾，变废为宝的方法。

1. 试验部分

（1）试验材料。所用基质沥青为克拉玛依 90# 沥青（VA）；再生塑料为汽车隔音棉和大棚膜的再生料；增容剂选择乙烯-丙烯酸甲酯共聚物（EMA）、乙烯-丙烯酸乙酯共聚物（EEA）、乙烯-丙烯酸丁酯共聚物（EBA）和马来酸酐；复合改性剂为糠醛抽出油。

（2）测试内容与方法。试验项目及所用方法和仪器型号，如表 1 所示。

（3）化学与物理复合改性。将 644 g 沥青加入 1000 mL 烧杯中置于烘箱中加热至 170 ℃后将烧杯移至已升温至 170 ℃的油浴锅中，将沥青与 200 g 再生塑料及 6 g 增容剂混合、溶胀，期间用弗鲁克 FW30 搅

中国知网 https://www.cnki.net

拌机以 20 r/min 不间断搅拌 30 min；混合结束后将油浴锅温度参数设置为 170 ℃，并把搅拌机换成弗鲁克 FM300 剪切机，将机器放入烧杯中共热 30 min 后进行第一次剪切，剪切转速为 3000 r/min、剪切时间为 5 min，首次剪切结束后静置 30 min，在此期间缓慢加入 150 g 糠醛抽出油；第二次剪切，剪切转速设置为 3000 r/min、剪切时间为 5 min，至此两次剪切结束；将剪切机再次换为搅拌机，以 20 r/min 的转速不间断搅拌发育 3 h[6]。

表 1 试验内容、主要试验仪器及方法汇总表

试验项目	试验仪器	方法	试验项目	试验仪器	方法
热重分析（TG/DSC）	TG-DSC 同步综合热分析仪	GB/T 19466	软化点	软化点试验仪	T 0606
熔体流动速率（MFR）	熔体流动速率仪	GB/T 3682	弹性恢复	延度仪	T 0662
拉伸性能试验	电子万能拉力试验机	GB/T 1040	相容性	倒置相差荧光显微镜	-
红外光谱（FTIR）	傅里叶红外光谱仪	GB/T 6040	储存稳定性	软化点试验仪	T 0661
针入度	针入度仪	T 0604	布氏黏度	布洛克菲尔德黏度计	T 0625
延度	延度仪	T 0605	动力黏度	真空减压毛细黏度计	T 0620

2. 结果与讨论

(1) 再生塑料基本物性

① FTIR 分析。FTIR 结果如图 1 所示，在图 1（a）GYM 中 1261 cm^{-1} 为醇的 $\delta_{(OH)}$ 峰，1095 cm^{-1}、1016 cm^{-1} 分别为仲醇、伯醇中 C-O 的 $\nu_{(CO)}$ 振动峰；717 cm^{-1} 为 $-CH_2-$ 面内摇摆振动峰（$\rho_{(-CH_2-)}$）；在图 1（b）DPL 中 1714 cm^{-1} 为羰基的伸缩振动峰 $\nu_{(C=O)}$，且无 C-O 吸收峰存在，证明此处为酮；1261 cm^{-1} 为醇的 $\delta_{(OH)}$ 峰，1095 cm^{-1} 为仲醇 C-O 的 $\nu_{(CO)}$ 振动峰；637 cm^{-1}、618 cm^{-1} 为聚氯乙烯的结晶和非结晶吸收带，1430 cm^{-1}、1340 cm^{-1}、1250 cm^{-1} 为 C-Cl 键的吸收峰。经分析，GYM 中含有醇类物质，DPL 中含有酮类物质和聚氯乙烯（PVC），可能是由于回收的老化塑料产生了氧化与分拣不完善导致。

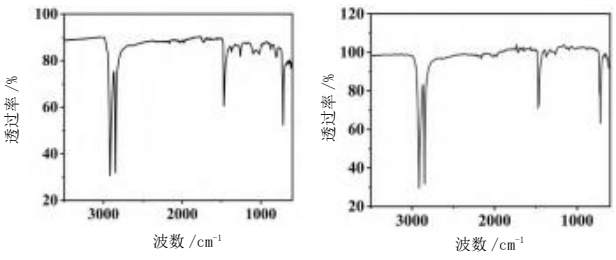

（a）GYM;（b）DPL
图 1 红外光谱分析图

② TG/DSC 分析。两种再生塑料样品的 TG/DSC 曲线如图 2 所示。LDPE 的 T_m 为 108～126 ℃。由图中 DSC 曲线可知，GYM、DPL 样品开始的结晶熔融峰的温度分别为 111.86 ℃、123.11 ℃，符合 LDPE 的熔点范围。对比图 2（a）、（b）结晶熔融峰的峰高及峰宽，结晶熔融峰及结晶度 DPL ＞ GYM。DPL 在 300 ℃出现一个较为平缓的吸热峰，与 PVC 热解过程中 HCl 脱除的主要温度范围基本吻合，进一步证明含有少量 PVC。

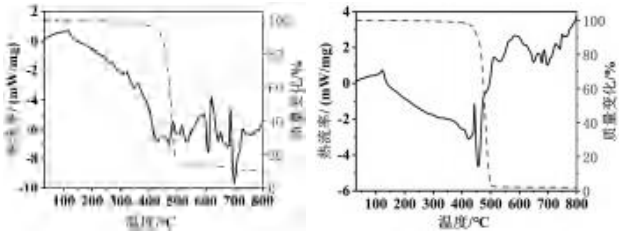

（a）GYM;（b）DPL
图 2 热重分析图

研究表明，试验所用两种再生塑料与沥青拥有相近的熔融温度窗口区，且在沥青改性过程中两种再生塑料均不会因为温度发生明显变质。

③ MFR 和力学分析。塑料 MFR 和其分子质量之间存在着强有力的联系[7]，其熔融指数越小，分子量就越大，伴随着指数减小的过程，热塑性塑料的拉伸强度、韧性等性能都逐渐增高，相反则说明分子量越小。样品 MFR 和力学性能测试结果如图 3 所示，GYM 和 DPL 的 MFR 依次递减，拉伸强度和断裂伸长率均递增，推测 PE 材料中分子量大小关系为 GYM ＜ DPL。

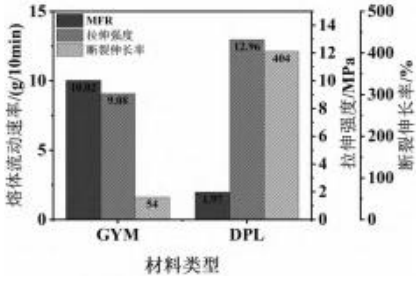

图 3 MFR 和力学性能

(2) 相容性研究

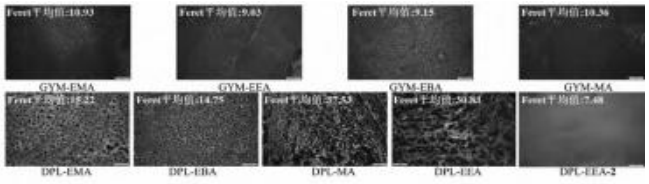

图 4 增容剂与复合改性剂对 PEA 相容性的影响

对荧光显微图像用 Image Pro Plus 软件处理图像并计算 Feret 平均值，结果如图 4 所示。相容性测试结果表明，不同增容剂的加入对于分子量较小的 GYM 类 PEA 相容性影响不明显，但是对于相对分子量较大

中国知网 https://www.cnki.net

的 DPL 类 PEA 影响显著，数据分析表明 4 种增容剂中 EBA 与 EMA 可显著提升 DPL 类 PEA 的相容性。

DPL-EEA-2 为对 DPL-EEA 进一步加入糠醛抽出油复合改性的 PEA，由图 4 可见，糠醛抽出油的加入使得样品在改性过程中发生充分的混容，混合物中的网状结构由明显变为无法具体标注，Feret 平均值从 30.83 降至 7.48。糠醛抽出油的加入会补充沥青与再生塑料溶胀过程中丧失的油分，并让溶胀继续进行，且增进各组分间的相互分散。

(3)PEA 储存稳定性试验

经试验测试，GYM 与任意增容剂混溶均会出现改性剂析出、凝聚现象；DPL-EMA 与 DPL-EEA-2 无改性剂析出、凝聚现象，图 5 为 DPL-EMA 及 DPL-EEA-2 样品的上下软化点及软化点差，两种 PEA 软化点差仅为 1 ℃，而 GYM 和 DPL-PEA 的 PEA 软化点与两种再生塑料的结晶熔融峰显示的温度接近。表明在 DPL-EMA 及 DPL-EEA-2 样品具有再生塑料和基质沥青的复合性能，储存稳定性较好。进一步对比 DPL-EEA 与 DPL-EEA-2 软化点差，表明糠醛抽出油可降低 PEA 软化点，显著提升 PEA 储存稳定性。

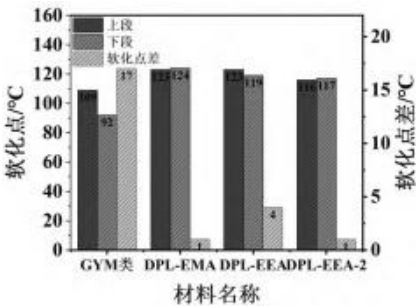

图 5 不同增容剂与复合改性剂的 PEA 软化点及软化点差

(4)PEA 路用价值分析

选择对 DPL-EMA 及 DPL-EEA-2 进一步测试其路用价值，测试结果如表 2 所示，两者技术参数均符合《高粘高弹道路沥青》（GB/T 30516—2014）要求，这两类 PEA 可应用于道路应力吸收层、桥面铺装和排水性路面等，尤其软化点达到 123 ℃，该结果表明了 PEA 优越的高温性能；离析（软化点差）仅为 1 ℃，表明所用物理、化学改性方法对提高 PEA 的相容性与储存稳定性有帮助。

表 2 PEA 路用性能技术参数

试验项目	单位	技术要求	DPL-EMA	DPL-EEA-2
针入度（25 ℃）	1/10 mm	40～80	40.2	40.8
软化点	℃	≮ 70	123.2	116.3
延度（5 ℃）	cm	≮ 20	21.3	22.4
离析（软化点差）	℃	≯ 2.5	1.0	1.1
弹性恢复（25 ℃）	%	≮ 85	96.5	95.8
布氏黏度（135 ℃）	Pa · s	报告	72.6	48.7
动力黏度（60 ℃）	mm^2/s	≮ 20000	556000	418000

3. 结论

红外、热重及 MFR 测试结果表明 GYM 与 DPL 的主要成分为 LDPE，且 DPL 的分子量大于 GYM。在 20% 再生 LDPE 掺加制备改性沥青过程中，通过化学和物理复合改性制备 PEA，表明分子量更小的 GYM 与沥青在荧光显微镜下表现出更好的相容性，但是软化点差大，储存稳定性差。DPL-EMA、DPL-EEA-糠醛抽出油组合制备的 PEA 基本指标均满足高粘高弹道路沥青规范，可应用于道路应力吸收层、桥面铺装和排水性路面等。研究结果表明 20% 掺量再生 LDPE 塑料改性沥青具有路用价值，突破了再生塑料改性沥青最佳掺量仅为 5%～8% 的壁垒。

【参考文献】

[1]CHEN S, CHE T, MOHSENI A, et al. Preliminary study of modified asphalt binders with thermoplastics: The Rheology properties and interfacial adhesion between thermoplastics and asphalt binder[J]. Construction and Building Materials,2021,301:124373.

[2]HONG Z, YAN K, WANG M, et al. Low-density polyethylene/ethylene-vinyl acetate compound modified asphalt: Optimal preparation process and high-temperature rheological properties[J]. Construction and Building Materials,2022,314:125688.

[3]POULIKAKOS L D, PASQUINI E, TUSAR M, et al. RILEM interlaboratory study on the mechanical properties of asphalt mixtures modified with polyethylene waste[J]. Journal of Cleaner Production,2022,375:134124.

[4]POLACCO G, FILIPPI S, MERUSI F, et al. A review of the fundamentals of polymer-modified asphalts: Asphalt/polymer interactions and principles of compatibility[J]. Adv Colloid Interface Sci,2015,224:72-112.

[5]MA Y, WANG S, ZHANG M, et al. Weather aging effects on modified asphalt with rubber-polyethylene composites [J]. Sci Total Environ,2023,865:161089.

[6]陆明强,蒲旭斌,黄靖坚.SBS改性沥青生产过程中的质量控制因素[J].当代化工研究,2018(02):73-74.

[7]RADEEF H R, HASSAN N A, MAHMUD M Z H, et al. Fracture resistance of polymeric wastes modified asphalt using R-curve and digital image correlation[J]. Theoretical and Applied Fracture Mechanics,2023,123:103691.

【基金项目】

非金属材料创新中心小额研发类项目“再生塑料对沥青混合料性能的影响及应用研究”（项目编号：2023SFP1-2）

【作者简介】

蒋建国（1996-），男，汉族，甘肃定西人，硕士研究生在读，研究方向：道路建筑材料。

【通信作者】

侯曙光（1977-），男，汉族，甘肃定西人，博士，教授，研究方向：道路工程。

中国知网 https://www.cnki.net

引用格式: 王鹏,王杰,兰勇,等. 水性聚氨酯改性不黏轮乳化沥青制备及其路用性能研究[J]. 北京化工大学学报(自然科学版),2024,51(6):71-78.

WANG Peng, WANG Jie, LAN Yong, et al. Preparation of waterborne polyurethane-modified trackless emulsified asphalt and its road performance[J]. Journal of Beijing University of Chemical Technology (Natural Science),2024,51(6):71-78.

水性聚氨酯改性不黏轮乳化沥青制备及其路用性能研究

王　鹏[1]　王　杰[1*]　兰　勇[2]　马　庆[1]　耿　爽[1]　徐　剑[1]

(1. 交通运输部公路科学研究所,北京 100088; 2. 上海公路投资建设发展有限公司,上海 202150)

摘　要: 为了解决沥青路面施工中黏层黏轮和服役中层间黏结不足的问题,制备了一种具有自迁移功能的水性聚氨酯改性不黏轮乳化沥青。通过针入度、软化点及不黏轮效果等实验评价了不黏轮乳化沥青路用性能,研究了水性聚氨酯改性不黏轮乳化沥青黏层微观形貌和流变特性。研究结果表明:水性聚氨酯改性剂在乳化沥青黏层养生过程中自主迁移至黏层表面;水性聚氨酯在不黏轮乳化沥青最佳掺量为3%;在35 ℃时,水性聚氨酯改性不黏轮乳化沥青黏层养生时间不大于30 min;水性聚氨酯改性不黏轮乳化沥青黏层在60 ℃时剪切强度大于1 MPa,在70 ℃时未发生黏轮现象,具有解决沥青路面施工中黏层黏轮和服役中层间黏结不足难题的潜力。水性聚氨酯改性不黏轮乳化沥青路用性能突出和施工过程环境友好,因此其有望在公路建设和养护工程中得到大规模应用,并可提高沥青路面服役寿命,助力公路交通高质量的发展。

关键词: 沥青路面; 乳化沥青; 黏层; 不黏轮; 水性聚氨酯

中图分类号: TQ323. 8　　**DOI:** 10. 13543/j. bhxbzr. 2024. 06. 007

引　言

沥青路面是一种典型的多层结构体系,黏层将各层沥青混合料黏结形成一个有机的受力整体,降低了应力集中导致沥青路面局部损坏的风险。提高层间黏层质量是延长沥青路面服役寿命重要且有效的途径[1-3]。

现阶段沥青路面黏层常采用普通乳化沥青,当夏季施工旺季阳光直射到路面时,路面温度可达60 ℃,甚至局部超过70 ℃[4]。在高温下运输和摊铺混合料施工车辆行驶在已成型的黏层上,黏层被大面积剥离带走,受到严重破坏,起不到层间黏层应有的作用,并易造成施工现场污染[5-6]。沥青路面铺筑迫切需要一种高性能不黏轮乳化沥青黏层材料。

不黏轮乳化沥青由于具有施工方便、环境友好、使用安全等优势被工程技术人员所重视。郭婷婷等[7]采用50#基质沥青制备乳化沥青,而后向乳化沥青掺加8%(质量分数,下同)增强增韧剂和8%弹性体改性剂制备不黏轮乳化沥青,所得不黏轮乳化沥青黏层层间拉拔强度高于苯乙烯-丁二烯-苯乙烯嵌段共聚物(SBS)改性乳化沥青,并表现出较好的不黏轮效果。赵阳等[8]采用30#基质沥青制备乳化沥青,并在乳化沥青中掺加4%的丁二烯-苯二烯共聚物(SBR)改性剂制备不黏轮乳化沥青,在50 ℃具有较好的不黏轮效果,且层间黏结性能好于SBR改性乳化沥青,但当60 ℃时仍有部分黏轮现象。杨闯等[9]通过乳化30#硬质沥青制备不黏轮乳化沥青,其黏层抗剪切强度明显高于普通乳化沥青黏层,但不黏轮乳化沥青延度仅有5.2 cm(实验温度为15 ℃),对黏层低温抗开裂性能有一定的影响。Fu等[10]通过掺加乳化沥青20%的水性环氧树脂

收稿日期:2024-03-15

基金项目:非金属材料创新中心创新基金(24TDA-4);交通运输部公路科学研究所成果转移转化项目(0223KF10ZY1010)

第一作者:男,1991年生,助理研究员

*通信联系人

E-mail:wang. j@rioh. cn

中国知网　https://www.cnki.net

(WER)制备了水性环氧改性乳化沥青,WER显著提高了黏层的耐高温性和层间的黏附性能。

乳化沥青黏层实现“不黏轮”主要是通过使用硬质沥青和掺加改性剂,这两种方式均可提高乳化沥青黏层软化点和不黏轮效果。但采用标号过低的沥青影响黏层低温抗裂性能,且增加乳化沥青加工和施工难度[11-12]。另外掺加少量改性剂对不黏轮效果改善有限,但大比例掺加改性剂会使不黏轮乳化沥青黏层成本过高,致使工程使用受限[7,10,13]。

为了解决沥青路面施工中黏层黏轮和服役中层间黏结不足的行业关键问题,本文提出一种新型的水性聚氨酯改性不黏轮乳化沥青,水性聚氨酯在不黏轮乳化沥青黏层养生过程中能够自主迁移至黏层表面[14]。由于聚氨酯具有较好的热稳定性,且聚氨酯改性剂富集于黏层表面,掺加少量水性聚氨酯即可显著提高黏层不黏轮效果和抗剪性能。本研究成果可提高沥青路面层间黏结质量,为沥青路面的延寿和耐久性的提升发挥积极作用。

1 实验部分

1.1 实验原料和仪器

1.1.1 实验原料

制备水性聚氨酯改性不黏轮乳化沥青(trackless emulsified asphalt,TEA)所用原材料基本性能如表1所示。SBR胶乳为苯乙烯与丁二烯经乳液聚合的产物,黏层用普通乳化沥青(PC-3)性能符合《公路沥青路面施工技术规范》(JTG F40)相关的技术要求[15]。

1.1.2 实验仪器

SYD-2801E型针入度仪、SYD-2806G型软化点实验仪,中科路达试验仪器公司;WHY-500型万能实验机,上海华龙仪器设备有限公司;Z2型正置电子显微镜,卡尔蔡司光学(中国)有限公司;CVOR-ADS型沥青动态流变仪,英国Malvern公司。

1.2 水性聚氨酯改性不黏轮乳化沥青制备

1.2.1 乳化沥青

将50#基质沥青加热至150 ℃,并向其中加入抗车辙母料,在150 ℃下加热搅拌混合沥青至均匀,然后将乳化剂和SBR胶乳分散至50 ℃去离子水中,以获得皂液。随后将皂液加入预热胶体磨中,并将混合沥青缓慢加入皂液中进行乳化,在胶体磨中循环1~2 min得到乳化沥青。

表1 实验材料基本性能

Table 1 Basic properties of experimental materials

材料	性能	数值	来源
50#基质沥青	针入度/0.1 mm	56.3	中国石油化工集团公司
	延度/cm	≥100	
	软化点/℃	50.4	
抗车辙母粒	针入度/0.1 mm	<5	杭州光华路桥有限公司
	软化点/℃	105.2	
水性聚氨酯乳液	固含量/%	35±2	一臻新材料科技有限公司
	断裂伸长率/%	≥400	
	拉伸强度/MPa	≥8	
	分子量	14 000	
	熔点/℃	135~145	
乳化剂	破乳速度	快裂	英杰维特投资有限公司
	电荷	阳离子	
SBR胶乳	型号	1469	英杰维特投资有限公司
	电荷	阳离子	
PC-3乳化沥青	针入度/0.1 mm	69.4	实验室自制
	延度/cm	≥100	

1.2.2 水性聚氨酯改性不黏轮乳化沥青

将0%、1%、2%、3%、4%(聚氨酯改性剂占乳化沥青的质量分数)水性聚氨酯改性剂加入至乳化沥青中,并搅拌均匀,制成TEA-0、TEA-1、TEA-2、TEA-3、TEA-4这5种不黏轮乳化沥青,然后将其倒入模具中,放置于35 ℃烘箱中形成不黏轮乳化沥青黏层(厚约1 mm)。

1.3 乳化沥青(黏层)路用性能测试

1.3.1 针入度、软化点及储存稳定性

不黏轮乳化沥青针入度、软化点和储存稳定性分别按《公路工程沥青及沥青混合料试验规程》(JTG E20—2011)中T0604、T0606和T0655测试[16]。

1.3.2 不黏轮效果分析

将乳化沥青涂布在水泥混凝土试块上(100 mm×100 mm×50 mm)并完成养生。采用万能实验机施加0.8 MPa压力(橡胶压头)于黏层上,保持5 s位移不变,随后以10 mm/min将压头从黏层表面拉开,分析黏层破损率(S)和拉拔强度。实验温度为70 ℃(PC-3实验温度为40 ℃)。计算黏层破损率,如式(1)所示。

$$S=A_1/A_0\times100\% \tag{1}$$

其中:S为黏层破损率,%;A_1为橡胶压头黏附沥青面

中国知网 https://www.cnki.net

积,mm^2;A_0为橡胶压头与黏层接触面积,mm^2。

1.3.3　不黏轮干燥时间

不黏轮干燥时间为乳化沥青养护的最短时间,实验方法基于《路面标线涂料》(JT/T 280—2004)不黏轮干燥时间改进[17]。实验采用 35 kg 钢制压实器,乳化沥青洒布在油毛毡上,洒布量为 0.5 kg/m^2。

1.3.4　黏层抗剪能力

通过万能实验机在 20 ℃、40 ℃和 60 ℃测试双层沥青混合料(AC-13)试件中黏层抗剪强度。实验加载速度 10 mm/min,乳化沥青洒布量 0.6 kg/m^2。

1.4　乳化沥青黏层微观形貌和流变性能

1.4.1　黏层微观形貌

通过正置电子显微镜(Z2)观察乳化沥青黏层纵断面和表面微观形貌(荧光)。

1.4.2　黏层流变性能

通过沥青动态流变仪(CVOR-ADS)测试乳化沥青黏层复数模量(|G*|)和相位角(δ),测试频率范围 1~100 rad/s。

2　结果与讨论

2.1　不黏轮乳化沥青(黏层)路用性能影响

2.1.1　针入度及软化点

针对不同掺量水性聚氨酯(乳化沥青质量分数)的不黏轮乳化沥青(TEA)测试针入度和软化点,结果如图 1 所示。

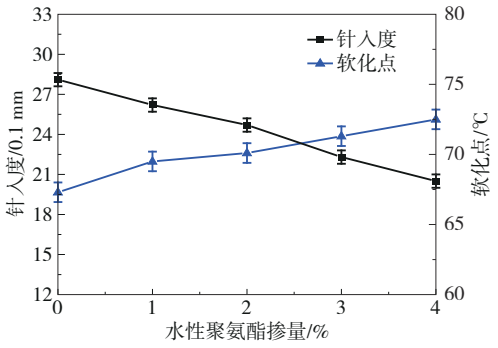

图 1　TEA 蒸发残留物针入度及软化点

Fig. 1　Penetration and softening point of TEA residue

如图 1 所示,随着水性聚氨酯用量增加,TEA 蒸发残留物针入度逐渐下降,软化点则逐渐上升。相比于未掺加水性聚氨酯,掺加乳化沥青 4% 的水性聚氨酯改性 TEA 蒸发残留物针入度降低了 8.2 (0.1 mm),而软化点却增加了 5.3 ℃。这表明水性聚氨酯有利于提高不黏轮乳化沥青黏层的高温稳定性,降低高温条件下不黏轮乳化沥青黏层出现黏轮破坏的风险。

2.1.2　储存稳定性

针对不同掺量水性聚氨酯的不黏轮乳化沥青,测试了 1 d 和 5 d 的储存稳定性,结果如图 2 所示。

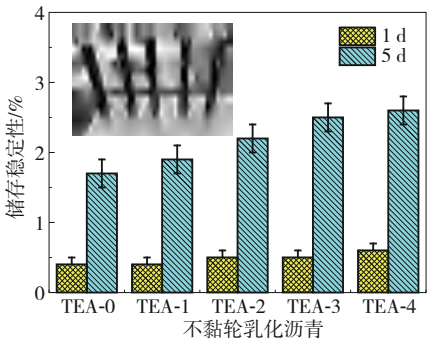

图 2　不黏轮乳化沥青储存稳定性

Fig. 2　Storage stability of TEA

如图 2 所示,随着水性聚氨酯掺量逐渐增加,实验管上下端不黏轮乳化沥青残留物含量差值缓慢增大,存储稳定性逐渐下降,当水性聚氨酯掺量达到 4% 时,1 d 和 5 d 的储存稳定性为 0.6% 和 2.6% (规范要求分别小于 1% 和 5%),不黏轮乳化沥青具有较好的储存稳定性,满足《公路沥青路面施工技术规范》(JTG F40)相关的技术要求[15]。

2.1.3　不黏轮干燥时间

为了分析水性聚氨酯对不黏轮乳化沥青不黏轮干燥时间的影响,实验测试了掺加不同水性聚氨酯不黏轮乳化沥青的沥青黏附率,实验结果如图 3 所示。

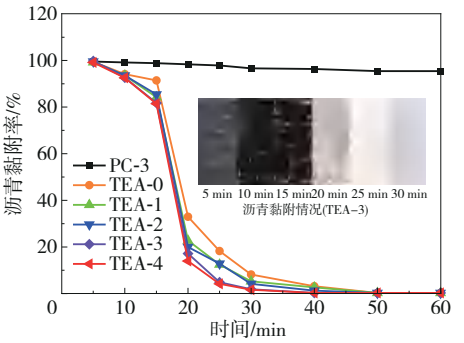

图 3　不黏轮乳化沥青不黏轮干燥时间

Fig. 3　Trackless time of TEA

如图 3 所示,通过图像分析软件(Image Pro Plus)分析测试纸上沥青黏附面积(沥青黏附率),沥青黏附率随着养生时间延长而逐渐减小。当养生

中国知网　https://www.cnki.net

5 min时,测试纸完全被沥青覆盖,乳化沥青黏层处于液态。当养生25 min时,TEA-3黏层沥青黏附率仅为3.8%,测试纸上只有少量沥青,但TEA-0和PC-3黏层的沥青黏附率分别为18.2%和97.8%。结果表明,水性聚氨酯有利于缩短不黏轮乳化沥青不黏轮干燥时间,TEA-3在35 ℃下的不黏轮干燥时间不超过30 min,大大减少了乳化沥青黏层养生时间,提高了沥青路面施工效率。

2.1.4　不黏轮效果

为了评价TEA黏层的不黏轮效果,在70 ℃下测试不同水性聚氨酯掺量的黏层破损率,其中PC-3型乳化沥青的测试温度为40 ℃,实验结果如图4所示。

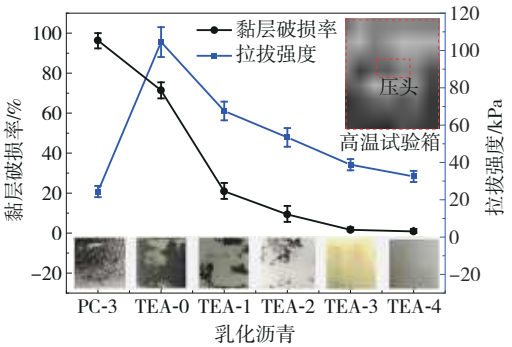

图4　不黏轮乳化沥青黏层不黏轮效果

Fig. 4　Trackless nature of TEA

如图4所示,不黏轮乳化沥青黏层破损率随水性聚氨酯掺量增加而逐渐降低,当水性聚氨酯掺量达到4%时,TEA-3黏层破坏率为1.1%,相比于TEA-0,TEA-3黏层破损率降低了98.5%,结果表明水性聚氨酯显著改善了黏层在高温下的不黏轮效果。另外从黏层破损率曲线可知,当掺量达3%时,黏层破坏率趋于稳定,黏层具有较好的不黏轮效果。由图4拉拔强度曲线可知,不黏轮乳化沥青黏层拉拔强度随掺量增加而逐渐降低,当掺量达3%时,拉拔强度为38.8 kPa,相比于TEA-0,拉拔强度降低了62.9%,结果表明水性聚氨酯降低了橡胶与黏层之间黏附力,使黏层具有更好的不黏轮效果。从不黏轮效果实验结果考虑,水性聚氨酯最佳掺量为3%。

2.1.5　黏层抗剪能力

不同乳化沥青黏层层间抗剪能力通过斜剪实验评价,实验结果如图5(a)所示,剪切破坏后的界面如图5(b)所示。

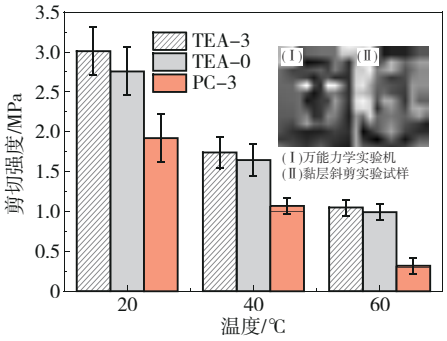

(a) 层间抗剪切强度

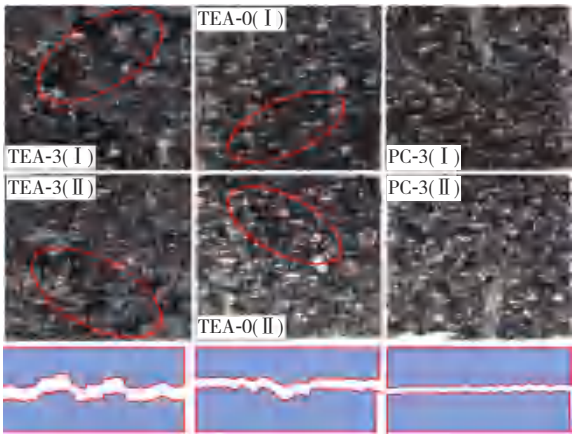

(b) 剪切破坏界面(40 ℃)

图5　乳化沥青层间剪切强度及剪切破坏界面

Fig. 5　Interlayer shear strength and shear failure interface of emulsified asphalt

从图5(a)可知,在20 ℃、40 ℃和60 ℃下,水性聚氨酯改性不黏轮乳化沥青(TEA-3)黏层剪切强度略高于TEA-0黏层,明显高于PC-3黏层。TEA-3和TEA-0黏层在60℃下的剪切强度分别为1.05 MPa和1.01 MPa,TEA-3黏层在40 ℃时的剪切强度达到1.6 MPa。TEA-3黏层在高温下具有良好的剪切强度。

如图5(b)所示,层间剪切破坏后,TEA-3和TEA-0黏层界面不规则,在40 ℃时剪切,TEA-3黏层附近沥青混合料损坏最严重(其中,(Ⅰ)(Ⅱ)分别代表剪切实验后试件的上面一块和下面一块)。PC-3黏层剪切破坏后界面光滑,沥青混合料基本未损坏。这主要是由于TEA-3黏层层间黏结力部分超过了沥青混合料集料之间的作用力(黏结力和嵌挤力),使沥青混合料发生破坏,而部分黏层保持较好状态。通过收集3种黏层试件破坏界面附近的沥青材料(三氯乙烯溶解),并涂布于溴化钾薄片上,分析3种收集的沥青材料红外特征吸收峰,结果如图6所示。

中国知网　https://www.cnki.net

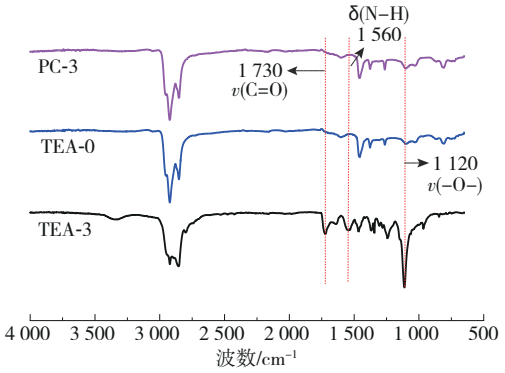

图6　剪切破坏界面材料红外光谱

Fig. 6　FT-IR spectra of shear failure of interface material

PC-3 和 TEA-0 具有相似的沥青材料红外光谱曲线(图 6),但 TEA-3 红外光谱曲线有明显不同的特征吸收峰,在 1 730 cm^{-1} 和 1 560 cm^{-1} 处有明显的特征吸收峰,分别是 v(C═O)和 δ(N—H),1 120 cm^{-1} 处特征吸收峰 v(—O—)来自于水性聚氨酯合成使用的聚醚多元醇。这表明 TEA-3 黏层剪切样品在破坏界面附近含有聚氨酯材料,聚氨酯相比于沥青具有更好的力学强度和温度稳定性,能够为沥青混合料层间提供更优异的黏结效果。斜剪实验结果表明水性聚氨酯不黏轮乳化沥青黏层(TEA-3)具有良好的剪切性能,与 TEA-0 相比,水性聚氨酯可提高高温下不黏轮乳化沥青黏层层间黏结能力。

2.2　乳化沥青黏层微观形貌及流变性能

2.2.1　黏层微观形貌

3 种乳化沥青(TEA-3、TEA-0 和 PC-3)黏层纵断面和表面微观形貌如图 7 所示。

如图 7(a)所示,TEA-3 黏层在其纵断面分为上表层(棕黄色)和底层(黑色),两层之间有过渡区,但 TEA-0 和 PC-3 黏层纵断面呈均匀状态,未有分层现象。从图 7(b)中可以看出,水性聚氨酯改性剂球形颗粒分布在 TEA-3 黏层表面,粒径为 1~10 μm,在 TEA-0 和 PC-3 黏层表面未有球形颗粒。另外,水性聚氨酯改性剂的掺加量仅为 3%,但水性聚氨酯颗粒在 TEA-3 黏层表面上的覆盖率远高于 3%。结果表明水性聚氨酯改性剂在乳化沥青养生过程中自主迁移至黏层表面,形成聚氨酯富集层和沥青层,水性聚氨酯改性乳化沥青(TEA-3)黏层呈“双层”结构特征。

2.2.2　流变性能

采用动态剪切流变仪(DSR)频率扫描分析 3 种乳化沥青(TEA-3、TEA-0 和 PC-3)黏层流变性能,

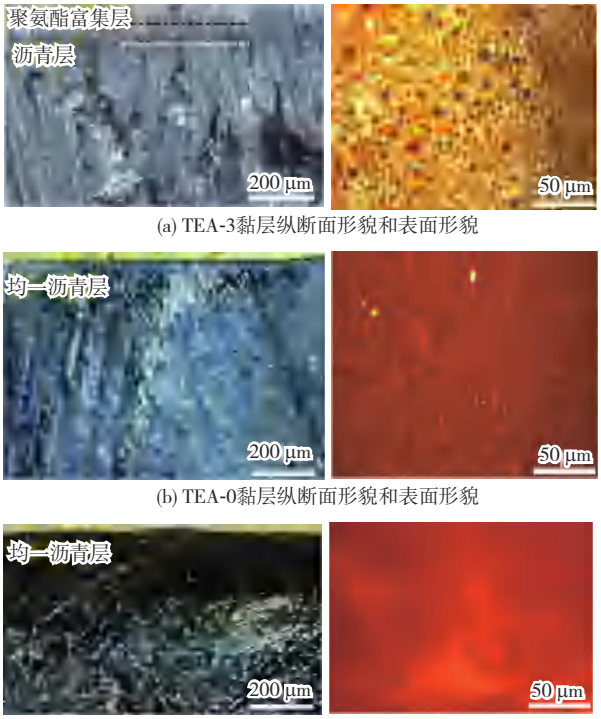

(a) TEA-3黏层纵断面形貌和表面形貌

(b) TEA-0黏层纵断面形貌和表面形貌

(c) PC-3黏层纵断面形貌和表面形貌

图7　乳化沥青黏层微观形貌

Fig. 7　Microscopic morphology of emulsified asphalt tack coat

实验结果如图 8 所示。

如图 8(a)所示,随着 TEA-3 黏层温度升高,同一频率其复数剪切模量(|G*|)逐渐降低,表明随温度升高黏层材料抵抗切应变能力下降。在图 8(b)中,同一频率 TEA-3 黏层的相位角(δ)随着温度的升高而增加,这表明随着温度升高 TEA-3 黏层弹性恢复能力下降,黏层材料逐渐表现出黏性特征。如图 8(c)和图 8(d)所示,3 种乳化沥青(TEA-0、TEA-3 和 PC-3)黏层相比,相同频率下 TEA-3 黏层复数剪切模量(|G*|)明显大于 TEA-0 和 PC-3 黏层,相同频率下 TEA-3 的 δ 明显小于 TEA-0 和 PC-3 黏层。结果表明,在相同温度下 TEA-3 黏层比 TEA-0 和 PC-3 黏层具有更好的高温抗切应变能力和弹性恢复能力,能够为沥青路面层间提供更优异的层间抗剪和黏结性能。

2.3　黏层黏轮现象分析

施工车辆轮胎对黏层的作用是一个复杂的过程,该过程主要包括 3 种作用力,轮胎与黏层的黏附力($\delta_{黏附力Ⅰ}$),黏层本体内聚力($\delta_{黏聚力Ⅱ}$),黏层与原路面黏附力($\delta_{黏附力Ⅲ}$),当 $\delta_{黏附力Ⅰ}$ 超过 $\delta_{黏聚力Ⅱ}$ 和/或 $\delta_{黏附力Ⅲ}$ 时,黏层将发生黏轮破坏[18]。轮胎与黏层的黏轮现象分析如图 9 所示。

中国知网　https://www.cnki.net

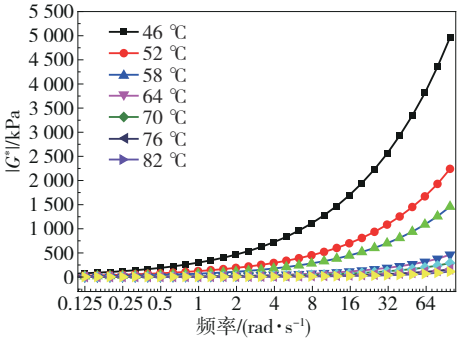

(a) TEA-3黏层复数剪切模量

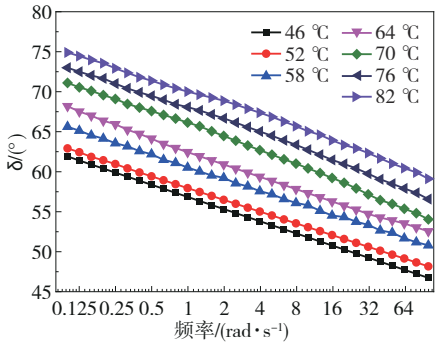

(b) TEA-3黏层相位角

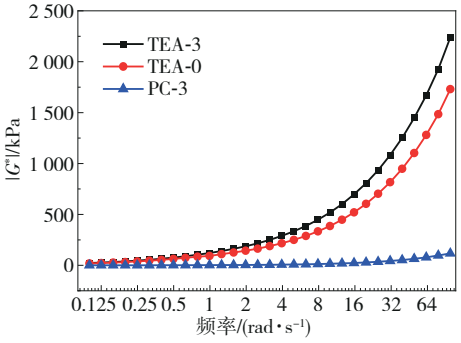

(c) 不同黏层复数剪切模量(52 ℃)

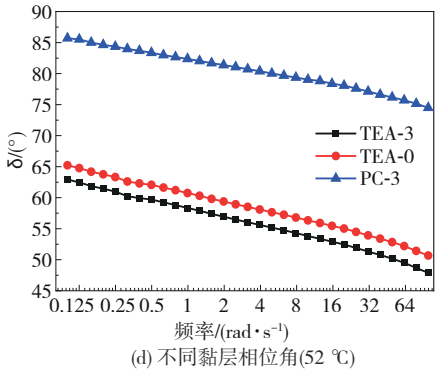

(d) 不同黏层相位角(52 ℃)

图8　乳化沥青黏层流变性能

Fig. 8　Rheological properties of emulsified asphalt tack coat

如图9所示，TEA-0黏层的$\delta_{黏附力Ⅰ}$随温度升高而增大，$\delta_{黏聚力Ⅱ}$和$\delta_{黏附力Ⅲ}$则随温度升高而减小，当$\delta_{黏附力Ⅰ}$小于$\delta_{黏聚力Ⅱ}$和$\delta_{黏附力Ⅲ}$时，黏层不会发生黏轮，但当$\delta_{黏附力Ⅰ}$大于$\delta_{黏聚力Ⅱ}$和/或$\delta_{黏附力Ⅲ}$时，黏层将发生

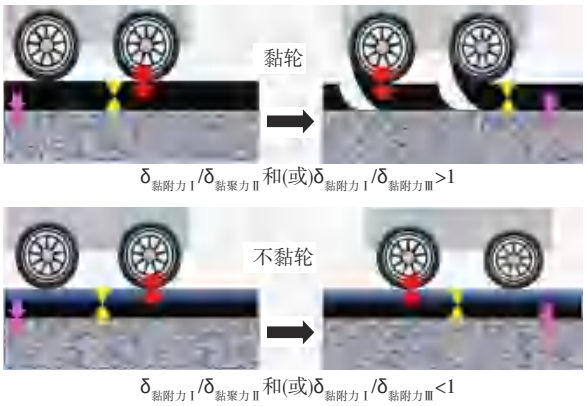

图9　黏轮现象受力分析

Fig. 9　Force analysis of the tracking phenomenon

黏轮现象。水性聚氨酯改性不黏轮乳化沥青黏层养生后形成“双层”结构，由于上层聚氨酯富集层具有较高的热稳定性，在70 ℃时，$\delta_{黏附力Ⅰ}$仍然很小。另外，采用抗车辙母粒和硬质沥青，提高了$\delta_{黏聚力Ⅱ}$和$\delta_{黏附力Ⅲ}$。在高温(70 ℃)条件下，水性聚氨酯改性不黏轮乳化沥青黏层$\delta_{黏附力Ⅰ}$也低于$\delta_{黏聚力Ⅱ}$和$\delta_{黏附力Ⅲ}$，聚氨酯改性不黏轮乳化沥青黏层具有较好的不黏轮效果。当沥青路面在夏季(尤其是60 ℃以上)施工时，掺加水性聚氨酯改性剂能够降低乳化沥青黏层发生黏轮的风险。

3　结论

(1)通过在乳化沥青中掺加水性聚氨酯改性剂成功制备出具有自迁移功能的不黏轮乳化沥青，其在养生过程中水性聚氨酯能够自主向黏层表面迁移；水性聚氨酯改性剂在乳化沥青中最佳掺加量为3%。

(2)水性聚氨酯改性不黏轮乳化沥青(TEA-3)黏层(水性聚氨酯掺量为3%)在60 ℃时层间剪切强度大于1.0 MPa，在70 ℃时黏层仍表现出较好的不黏轮效果；在35 ℃下TEA-3黏层养生时间不超过30 min。

(3)水性聚氨酯改性不黏轮乳化沥青黏层能够较好地解决沥青路面夏季施工中黏轮及服役中层间黏结不足的行业关键问题，有利于延长沥青路面服役寿命。

参考文献：

[1]　WANG J Y, XIAO F P, CHEN Z, et al. Application of tack coat in pavement engineering[J]. Construction and Building Materials, 2017, 152: 856-871.

中国知网　https://www.cnki.net

[2] ZHANG W G. Effect of tack coat application on interlayer shear strength of asphalt pavement: a state-of-the-art review based on application in the United States[J]. International Journal of Pavement Research Technology, 2017, 10(5): 434-445.

[3] 王佳, 蒲昌瑜, 吴迪. 不粘轮乳化沥青的制备及其性能评价[J]. 公路交通科技, 2022, 39(10): 9-16.
WANG J, PU C Y, WU D. Preparation and performance evaluation of non-stick wheel emulsified asphalt[J]. Journal of Highway and Transportation Research and Development, 2022, 39(10): 9-16. (in Chinese)

[4] SHI X J, REW Y, IVERS E, et al. Effects of thermally modified asphalt concrete on pavement temperature[J]. International Journal of Pavement Engineering, 2019, 20(6): 669-681.

[5] HOU D H, HAN M Z, MUHAMMAD Y, et al. Performance evaluation of modified asphalt based trackless tack coat materials[J]. Construction and Building Materials, 2018, 165: 385-394.

[6] SEO A Y, SAKHAEIFAR M S, WILSON B T. Evaluating tack properties of trackless tack coats through dynamic shear rheometer[J]. Transportation Research Record, 2017, 2632(1): 119-129.

[7] 郭婷婷, 江凯, 冯雯雯, 等. 不黏轮乳化沥青的制备及其作用机理研究[J]. 中外公路, 2021, 41(1): 242-248.
GUO T T, JIANG K, FENG W W, et al. Study on preparation and mechanism of non-stick wheel emulsified asphalt[J]. Journal of China & Foreign Highway, 2021, 41(1): 242-248. (in Chinese)

[8] 赵阳, 周启伟, 王庆珍, 等. 非黏轮改性硬质乳化沥青性能评价[J]. 重庆交通大学学报(自然科学版), 2017, 36(7): 29-32.
ZHAO Y, ZHOU Q W, WANG Q Z, et al. Performance evaluation of non-stick wheel modified hard emulsified asphalt[J]. Journal of Chongqing Jiaotong University (Natural Science), 2017, 36(7): 29-32. (in Chinese)

[9] 杨闯, 张敬义, 黄婉利. 乳化硬质沥青的制备及其在黏层油中的性能评价[J]. 石油沥青, 2017, 31(1): 64-67.
YANG C, ZHANG J Y, HUANG W L. Preparation of emulsified hard asphalt and its performance evaluation in tack coat[J]. Petroleum Asphalt, 2017, 31(1): 64-67. (in Chinese)

[10] FU H, WANG C H, NIU L L, et al. Composition optimization and performance evaluation of waterborne epoxy resin emulsified asphalt tack coat binder for pavement[J]. International Journal of Pavement Engineering, 2022, 23(1): 4034-4048.

[11] GINGRAS J P, TANGUY P A, MARIOTTI S, et al. Effect of process parameters on bitumen emulsions[J]. Chemical Engineering and Processing: Process Intensification, 2005, 44(9): 979-986.

[12] SHENG X H, WANG M, XU T, et al. Preparation, properties and modification mechanism of polyurethane modified emulsified asphalt[J]. Construction and Building Materials, 2018, 189: 375-383.

[13] LI J, DUAN S C, MUHAMMAD Y, et al. Synthesis and performance evaluation of modified asphalt-based trackless tack coat material[J]. Journal of Materials in Civil Engineering, 2019, 31(9): 04019202.

[14] HU Y Y, ZHANG C C, CHEN Y J, et al. Preparation and structure of fluorinated/non-fluorinated polyacrylate gradient emulsion blend film[J]. Materials Letters, 2010, 64(19): 2091-2093.

[15] 中华人民共和国交通运输部. 公路沥青路面施工技术规范: JTG F40—2004[S]. 北京: 人民交通出版社, 2004.
Ministry of Transport of the People's Republic of China. Technical specification for construction of highway asphalt pavements: JTG F40—2004[S]. Beijing: China Communications Press, 2004. (in Chinese)

[16] 中华人民共和国交通运输部. 公路工程沥青及沥青混合料试验规程: JTG E20-2011[S]. 北京: 人民交通出版社, 2011.
Ministry of Transport of the People's Republic of China. Standard test methods of bitumen and bituminous mixtures for highway engineering: JTG E20-2011[S]. Beijing: China Communications Press, 2011. (in Chinese)

[17] 中华人民共和国交通运输部. 路面标线涂料: JT/T 280—2004[S]. 北京:人民交通出版社, 2011.
Ministry of Transport of the People's Republic of China. Pavement marking paint: JT/T 280—2004[S]. Beijing: China Communications Press, 2011. (in Chinese)

[18] SEO A Y. Quantitative measurement of tackiness and bonding potential of trackless tack coat[D]. Texas: Texas A&M University, 2019.

中国知网 https://www.cnki.net

Preparation of waterborne polyurethane-modified trackless emulsified asphalt and its road performance

WANG Peng[1] WANG Jie[1*] LAN Yong[2] MA Qing[1] GENG Shuang[1] XU Jian[1]

(1. Research Institute of Highway Ministry of Transport, Beijing 100088;

2. Shanghai Highway Investment and Construction Development Co., Ltd, Shanghai 202150, China)

Abstract: To solve the problems resulting from tack coat tracking in the construction of asphalt pavement and its poor bonding in service, a new type of trackless emulsified asphalt (TEA) with self-migration functionality has been prepared. The road performance of the TEA was evaluated by means of penetration, softening point and tracking resistance tests. The micro-morphology and rheological properties of waterborne polyurethane-modified TEA tack coat were studied. The results showed that the waterborne polyurethane migrated to the surface of the emulsified asphalt tack coat during the curing process. The optimal content of waterborne polyurethane modifier in TEA was 3%. The curing time of the waterborne polyurethane-modified TEA tack coat at 35 ℃ was less than 30 min. The shear strength of the polyurethane-modified TEA tack coat was greater than 1 MPa at 60 ℃, and the tack coat showed no tracking phenomenon at 70 ℃. This has the potential to solve the problems of tack coat tracking in the construction of asphalt pavement and its poor bonding in service. The polyurethane-modified TEA has an outstanding road performance and an environmentally friendly construction process. Therefore, it can be expected to be employed on a large scale in highway construction and maintenance projects, improving the service life of asphalt pavement, affording highway traffic with high quality.

Key words: asphalt pavement; emulsified asphalt; tack coat; trackless; waterborne polyurethane

(责任编辑:李 蕾)

中国知网 https://www.cnki.net

Construction and Building Materials 490 (2025) 142467

Contents lists available at ScienceDirect

Construction and Building Materials

journal homepage: www.elsevier.com/locate/conbuildmat

Degradation mechanism and performance of polyurethane mixture under water conditions

Li Pengfei [a,2], Wang Jie [b,*,1,3], Cao Zhilong [a,2], Xu Jian [b,3], Li Song [a,2], Wang Peng [b,3], Zhang Zhiqing [a,*,1,2]

[a] College of Urban Transportation, Beijing University of Technology, Beijing, China
[b] Research Institute of Highway, Ministry of Transport, Beijing, China

ARTICLE INFO

Keywords:
Polyurethane mixture
Deterioration mechanism
Water environmental conditions
Polyurethane/aggregate interface
Multiscale analysis

ABSTRACT

Polyurethane mixtures exhibit improved mechanical properties and low-carbon construction characteristics, which make them gradually popularized and applied in pavement. However, their high water sensitivity is a major shortcoming in road performance. In this study, the evolution patterns of polyurethane mixture properties were first investigated under water conditions. Furthermore, the variation characteristics of the polyurethane-aggregate interface strength were explored under immersion conditions. Simultaneously, the deterioration mechanisms of polyurethane binder were analyzed through microscopic morphology, chemical structure and hydrogen bonding degree. The experimental results show that the water's erosive effect induces rapid interfacial strength loss (52.5 %-68.8 %) and key mechanical properties degradation (37.2 %-48.4 %) in polyurethane mixture during the initial 4 days of immersion. Prolonged inundation (4–16d) comparatively mitigates these effects, with interfacial strength reduction decreasing by 33.6 %-38.4 % and key mechanical properties decline slowing by 19.9 %-34.9 %. This two phases deterioration pattern (rapid decline in the early stage and moderate decline in the later stage) was observed at all three temperatures (-18℃,25℃ and 60℃), and the high temperature (60℃) exhibited the most pronounced deterioration effect. Further analyses revealed that degradation of the polyurethane binder's surface hydrophobicity directly weakens the interfacial adhesion effect with aggregates. Furthermore, the high temperature promotes the simultaneously occupation of hydrogen-bonding sites in soft-hard and hard-hard segments by water molecules, increasing the proportion of disordered hydrogen bonding from 29.0 % to 47.5 %. This process exacerbates water-induced microphase separation and reduces crosslinking density in the polyurethane binder, ultimately leading to multi-pathway deterioration of the polyurethane mixture's water stability.

1. Introduction

Asphalt mixtures are common paving materials for road surfaces, but because of the increasing complexity of the climatic environment and traffic loads, asphalt pavements are subject to cracking, rutting, and other types of road distresses [1]. Also, asphalt and asphalt mixtures generate large quantities of toxic and hazardous gases during production and preparation, which adversely affect both the environment and the workers [2]. Because of this, polyurethane mixtures began to be gradually applied in road construction. Polyurethane mixtures are pavement materials consisting of polyurethane as a binder mixed with specific graded aggregates [3]. That enables polyurethane mixtures to be constructed at room temperature due to the active chemical reaction properties of the polyurethane reaction materials [4]. Polyurethane mixtures can save much energy compared to asphalt mixtures, which require heated production and construction processes. Moreover, the production and paving processes of polyurethane mixtures do not generate harmful gases, making it an environmentally friendly

* Corresponding authors.
E-mail addresses: lpengfei20140207@163.com (L. Pengfei), j.wang@rioh.cn (W. Jie), zhilongcao@bjut.edu.cn (C. Zhilong), j.xu@rioh.cn (X. Jian), 17865155725@163.com (L. Song), wang.peng@rioh.cn (W. Peng), zhangzhiqing@bjut.edu.cn (Z. Zhiqing).
[1] There are two equally contributing corresponding authors in the paper
[2] Present address: No. 100 Pingleyuan, Chaoyang District, Beijing,China.
[3] Present address: No.8 Xitucheng Road,Haidian District, Beijing, China.

https://doi.org/10.1016/j.conbuildmat.2025.142467
Received 26 April 2025; Received in revised form 3 June 2025; Accepted 25 June 2025
Available online 27 June 2025
0950-0618/© 2025 Published by Elsevier Ltd.

pavement material.

Polyurethane mixtures have significant advantages over asphalt mixtures in terms of mechanical properties, high-temperature stability, and fatigue resistance performance. Yang has found that a polyurethane mixture had more than 3 times the tensile strength of an asphalt mixture [5]. Zhong found that polyurethane mixtures were particularly good at high temperatures, with dynamic stability up to 12,000 times/mm, which was 10 times the specification value for asphalt mixtures [6]. Cong concluded that the fatigue life of porous polyurethane mixtures was more than an order of magnitude greater than that of porous asphalt mixtures [7]. In addition, polyurethane mixtures are superior to asphalt mixtures in other roadway performance characteristics. Liao and Chen both found that polyurethane mixtures had better antiskid performance, durability, and noise reduction than asphalt mixtures; however, the water stability of polyurethane mixtures was relatively poor [8,9]. Therefore, water stability is a shortcoming of polyurethane mixture's road performance.

The high-water sensitivity of polyurethane mixtures has been extensively studied. Xu studied polyurethane mixtures and found that the Marshall stability of water immersion was only 38 % residual, and a freeze–thaw cycle could reduce the split strength by up to 75 % [10]. Sun found that freeze–thaw cycles and water immersion could reduce the strength of polyurethane mixtures to 65.7 % and 68.4 % respectively [11]. Cong took Cantabro loss as an indicator and found that most of the mass losses of water-soaked polyurethane mixtures exceeded 20 %, whereas those of asphalt mixtures were only approximately 10 % [12]. It can be seen that the deteriorating effect of water on polyurethane mixture performance is very significant, and its water sensitivity is significantly higher than that of asphalt mixtures [13,14].

Hong found that because of polyurethane mixtures' higher water sensitivity, at the mixture scale, the molding production method could affect the polyurethane mixtures' water stability [15]. At the interfacial scale, the water-induced decrease in the van der Waals force, plasticization, and hydrolysis all led to decreased interfacial properties [16]. At the binder scale, Guo concluded that film thickness had a greater influence on the water stability and stripping resistance of polyurethane mixtures [17]. However, most of the existing researches stays at the level of phenomenon description and macroscopic performance degradation patterns. Not only is there a lack of analysis of the deep deterioration mechanism of the water stability of polyurethane mixtures [18, 19], but there is also a lack of understanding of the synergistic deterioration paths among the scales. Therefore, the degradation mechanism of polyurethane mixtures under water environments must be further investigated.

In summary, to describe the investigation of the deterioration mechanism of water on polyurethane mixtures, the effects of a water environment on the key mechanical properties, volumetric properties, and abrasion loss are summarized in this paper. At the polyurethane–aggregate interface scale, the influence law of a water environment on the tensile and shear strengths of the interface was analyzed. Furthermore, at the polyurethane scale, the mechanism of the water environment on a polyurethane binder was explored from the perspectives of microscopic morphology, water resistance, temperature sensitivity, and chemical structure. The research results provide important guidance for improving the water stability of polyurethane mixtures.

2. Raw materials and test design

2.1. Raw materials

The performance indicators of a polyurethane adhesive are shown in the Table 1. In this paper, the polyurethane adhesive consists of the isocyanate compounds, the polyether-based isocyanate prepolymer, and the diluent. That adhesive contained a certain amount of oily solvent, which gradually precipitated out after curing. The properties of the coarse aggregate, fine aggregate, and mineral powders met the requirements of current technical specifications.

Table 1
Basic performance indicators of polyurethane adhesives.

Indicator	Test value
Viscosity (25℃)/ mPa·s	1600
Density (25℃)/g·cm^{-3}	1.08
Isocyanate (-NCO) content /%	11.1
Surface drying time (25°C, 50 % humidity)/h	4.0

2.2. Mix ratio design

In this study, a polyurethane mixture was prepared with reference to the Marshall design method. The gradation was determined to be AC-13, and is shown in Fig. 1. Polyurethane adhesive was added to be 5.5 % of all minerals. The polyurethane mixture mixing times and the material addition sequence were consistent with those of asphalt mixtures. After the mixing, the specimens were molded by the Marshall compaction method.

2.3. Specimen preparation

2.3.1. Polyurethane mixture

The polyurethane mixture preparation process was consistent with that of traditional asphalt mixtures. First, the aggregates and polyurethane adhesive were weighed according to the ratios in Section 2.2. Throughout the preparation of the polyurethane mixture, neither the aggregate nor the polyurethane adhesive needs to be heated. Then, the aggregates and polyurethane adhesive are mechanically mixed at ambient temperature for 90 s. After adding mineral powder and mixing for another 90 s, the Marshall compaction molding is carried out immediately. The Marshall specimens were made, and the polyurethane mixture specimens were transferred to a controlled environment at 70°C and 80 % relative humidity for 2 days of curing. This curing process is distinguished from the natural cooling and shaping process of asphalt mixtures. The fully cured polyurethane mixture specimens could be obtained after completion of this curing stage.

2.3.2. Polyurethane/aggregate interface

In this study, the interface of the stone was adhesive bonded using polyurethane adhesive, and the interface bonding efficacy was evaluated through tensile strength and shear strength measurements. As the mix design of polyurethane mixture precisely matches conventional the film thickness of polyurethane on aggregate surfaces is similar to that of asphalt mixture. standard asphalt binder (15μm - 30μm). For tensile and shear strength specimens, polyurethane binder was applied at coating areas of 1 cm^2 and 8 cm^2 respectively, with a thickness of both 20μm. From this calculation, the applied mass was calculated to be 2 mg and 16 mg for tensile strength and shear strength specimens, respectively.

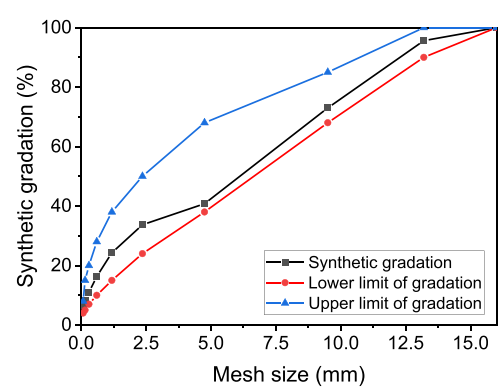

Fig. 1. Mineral gradation of polyurethane mixture.

The interlayer bonding specimens and polyurethane mixture were maintained under identical conditions.

2.3.3. Polyurethane binder

The polyurethane adhesive was uniformly coated on the surface of the substrate (polytetrafluoroethylene plates). The substrate geometry and dimensions were not special requirements provided surfaces remained planar. The film thickness of the polyurethane adhesive was set to 0.5 mm. Then the adhesive was subsequently cured at 70°C and 80 % relative humidity. Full curing was achieved within 12 h, after which the polyurethane binder was sectioned into dumbbell-shaped specimens for subsequent testing. The specific steps of different specimens are shown in Fig. 2.

2.4. Sample conditioning

The polyurethane mixture specimens, polyurethane–aggregate specimens, and polyurethane binder specimens were simultaneously immersed in high-temperature (60°C), ambient-temperature (25°C), and low-temperature (–18°C) water environments [20,21]. For the high and ambient-temperature tests, it was necessary to ensure that the specimens were completely submerged in the water solution. For the low-temperature test, the specimens were completely submerged in a room-temperature water solution, then placed in a vacuum environment for 15 min, and finally placed in a –18℃ environment for storage. The polyurethane mixtures were tested for gross bulk density, void ratio, Marshall stability, splitting strength, and Cantabro abrasion loss. The polyurethane–aggregate specimens were tested for interlayer tensile strength and interlayer shear strength. The test durations were set to 0, 1, 2, 4, 8, and 16d. The polyurethane binder was tested for its glass transition point, mass loss at elevated temperatures, contact angle, chemical structure, and microscopic morphology. Those test durations were 0 and 16d.

Fig. 2. Flow of specimens preparation.

3. Test methods

3.1. Polyurethane mixture

3.1.1. Marshall stability test

That test was conducted using a Marshall stability testing apparatus. The loading rate was 50 mm/min. There were 5 groups of parallel specimens. The test results were the average of the 5 sets of test values. The experimental procedure was conducted in compliance with the standard test method T0709 specified in JTG E20–2011.

3.1.2. Splitting strength test

The splitting strength test was also loaded at a rate of 50 mm/min, and the test results were also the average of the 5 sets of test values. The test was conducted in accordance with T0716 of JTG E20–2011.

3.1.3. Gross bulk density and void ratio

The gross bulk densities of the polyurethane mixture specimens were determined in accordance with the surface-dry method. After combining the maximum theoretical densities obtained from the vacuum method test [22]. On this basis the void ratios of the polyurethane mixtures were calculated. The experimental procedure was performed in accordance with the standardized testing method T0705 in JTG E20–2011.

3.1.4. Cantabro abrasion test

In this study, the polyurethane mixtures were placed in a Los Angeles abrasion meter and rotated at 30 rpm for 10 min. The Cantabro mass loss was calculated as the percentage of weight lost by a specimen after rotation, relative to its original weight. The test results were also the average of the 5 sets of test values. The experimental procedure was conducted in compliance with the standard test method T0733 specified in JTG E20–2011.

3.2. Polyurethane/aggregate interface

3.2.1. Interface tensile test

Interfacial tensile tests were done to evaluate the tensile performance between the polyurethane and aggregate interfaces in terms of maximum tensile strength. The tensile rate was 2.54 cm/min [23,24], and the test results were also the average of the 5 sets of test values.

3.2.2. Interface shear test

The shear performance of the polyurethane–aggregate interfaces were evaluated in terms of maximum shear strength. The shear rate was 2.54 cm/min, and the test results were also the average of the 5 sets of test values.

3.3. Polyurethane binder

3.3.1. Contact angle

Contact angles of polyurethane binder with water were measured using a goniometer. The liquid for the contact angle tests was distilled water, and the upper surfaces of the polyurethane binder films were selected as the test surfaces. All tests were conducted at a controlled temperature of 25°C. Five replicate measurements were performed for every sample. The data were averaged by excluding 15 % deviation values.

3.3.2. Interfacial stability test

The surface energy of the polyurethane binders and their components were calculated by the OWRK method [25]. On that basis, the adhesion work of basalt and limestone to polyurethane was further calculated by combining the surface energy data of basalt and limestone [26]. At the same time, the energy rate (ER) index characterizing the water stability of the polyurethane–aggregate interface was obtained. The interfacial stability assessment employs the work of adhesion and ER index. Higher values for both metrics indicate superior interfacial stability.

3.3.3. Scanning electron microscopy (SEM)

The fracture characteristics were determined by observing the fracture cross-sections of the polyurethane binder films. The magnifications were 400 × and 2000 × .

3.3.4. Thermogravimetry (TG)

The TG test environment was air, whose temperature was raised from 30 to 600°C at the rate of 10 °C/min.

3.3.5. Differential scanning calorimetry (DSC)

The DSC test environment was also air, whose temperature was raised from –60–60°C at the rate of 10 °C/min.

3.3.6. Fourier transform infrared spectroscopy (FTIR)

The test determined the ATR test mode. The test interval was 400–4000 cm^{-1}. The C═O peaks were categorized into a hard segment–hard segment C═O peak, a hard segment–soft segment C═O peak, and a disordered C═O peak [27]. The corresponding degree of hydrogen bonding was obtained by calculating the ratio of different peak areas to the 3-peak area summation, where the higher degree of hydrogen bonding between hard segments corresponded to a greater degree of microphase separation of the polyurethane [28].

4. Results and discussion

4.1. Deterioration patterns in polyurethane mixture

4.1.1. Key mechanical properties

The splitting strength and stability were chosen to characterize the key mechanical properties of the polyurethane mixtures. The splitting strengths and stabilities are shown in Fig. 3a and Fig. 3b respectively.

As shown in Fig. 3a, the splitting strengths of the polyurethane mixtures decreased gradually with the increase in water immersion duration, but all of them showed an obvious degree of deterioration in the early stage that diminished in the later stage. In the 60°C water environment, the splitting strengths decreased up to 37.2 % from 0 to 4d and by 34.9 % from 4 to 16d. A similar trend was observed at −18°C in the 0–4d and 4–16d intervals and was also observed at 25°C in the 0–8d and 8–16d intervals, which both showed greater deterioration effects on the splitting strengths during the early stage of water immersion. The degradation rates of performance in the 3 environments showed some differences due to the influence of temperature. In the 0–4d stage of immersion, the low-temperature water environment caused more damage to the mixtures. That was because the swelling effect of water gradually changing to ice during the early stage of the test quickly destroyed the internal structures of the mixtures. However, the swelling effect exceeded its peak with the increase in the immersion duration to 8–16d. The sustained damage to the mixtures from the high-temperature water environment gradually increased, and long-term water immersion (16d) decreased the splitting strengths up to 59.1 %.

As shown in Fig. 3b, the polyurethane mixtures' stabilities also decreased gradually with the increase in water immersion duration. The performance retentions were more stable at 25°C for the same immersion duration, which was similar to the splitting strength. However, the deterioration trends of specimens in the 25°C water environment tended to exceed those in the –18°C condition as the immersion duration extended to 4 to 16d. The high-temperature water environment always had the greatest deteriorating effect on the stabilities, which reached a maximum decrease of 58.9 %. The stabilities were also similar to the splitting strengths in terms of evolutionary trends. The stabilities in the 60°C water environment deteriorated more from 0 to 4d (48.4 %) than from 4–16d (19.9 %). The –18 and 25°C environments also caused more stability deterioration in the early period (0d to 4d) than in the late

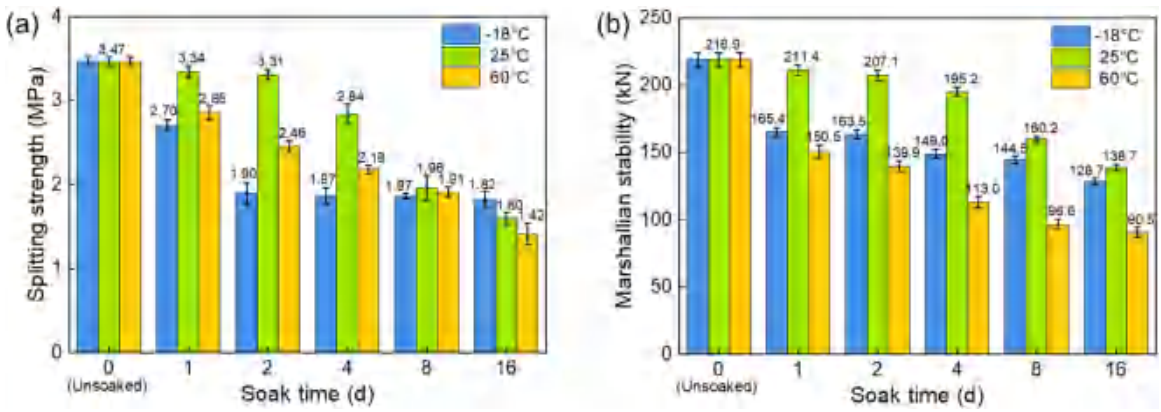

Fig. 3. Splitting strengths and stability of polyurethane mixtures.

period (4d to 16d). Therefore, the damage effect on polyurethane pavements should receive more attention during the initial stage of precipitation.

4.1.2. Volume characteristics

The road performance of polyurethane mixtures is influenced to some extent by volumetric properties. The gross bulk density and void ratio were chosen to characterize the mixes' volume characteristics. The gross bulk density and void ratio are shown in Fig. 4a and Fig. 4b respectively.

As shown in Fig. 4a, the gross bulk densities of the polyurethane mixtures in all 3 environments decreased gradually with the increase in the water immersion duration. Also, the gross bulk densities corresponding to all 3 temperatures had a more distinct decreasing trend in the 4–16d immersion period than in the 0–4d period. Meanwhile, the void ratios of all polyurethane mixtures gradually increased with the increase in water immersion duration, as shown in Fig. 4b. In the case of the 25°C environment, the void ratios increased by 7.7 % in the 0–4d period, whereas the void ratios increased by 14.6 % in the 4–16d period. That also indicated that the void ratios had a more pronounced upward trend in the late stage of water immersion than in the early stage. The long-term (greater than 4d) damaging effects of water on the polyurethane mixtures were more significant, and prolonging the water immersion duration would lead to a gradual decrease in the volumetric properties of the polyurethane mixtures. For the same immersion duration, the gross bulk densities were ranked as 60°C < 25°C < –18°C, and the void ratios were ranked as –18°C < 25°C < 60°C. The evolutionary trends of the 2 sets of indicators corresponded exactly. That not only verified that the increases in internal voids were the main cause of the decreases in densities of the polyurethane mixtures but also showed that a water temperature increase would lead to increases in the void ratios. That made the high-temperature water environment have the most significant deterioration effect on the volume properties of the polyurethane mixtures.

4.1.3. Cantabro mass loss

Cantabro mass loss could have characterized the bonding effect of the binder and the interface in some way. The mass losses of the polyurethane mixtures are shown in Fig. 5.

As shown in Fig. 5, for example at 25°C, the mass-loss rates of the polyurethane mixtures increased by 80.8 % as the water immersion duration grew from 0 to 16d. The –18 and 60°C temperatures also increased those mass-loss rates by 80.3 % and 126.9 % respectively. That suggested that the stabilization of the polyurethane binder and

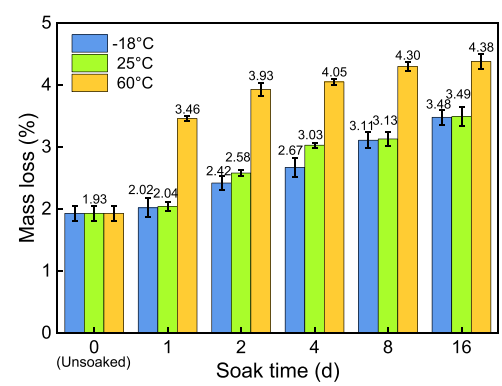

Fig. 5. Mass losses of the polyurethane mixtures.

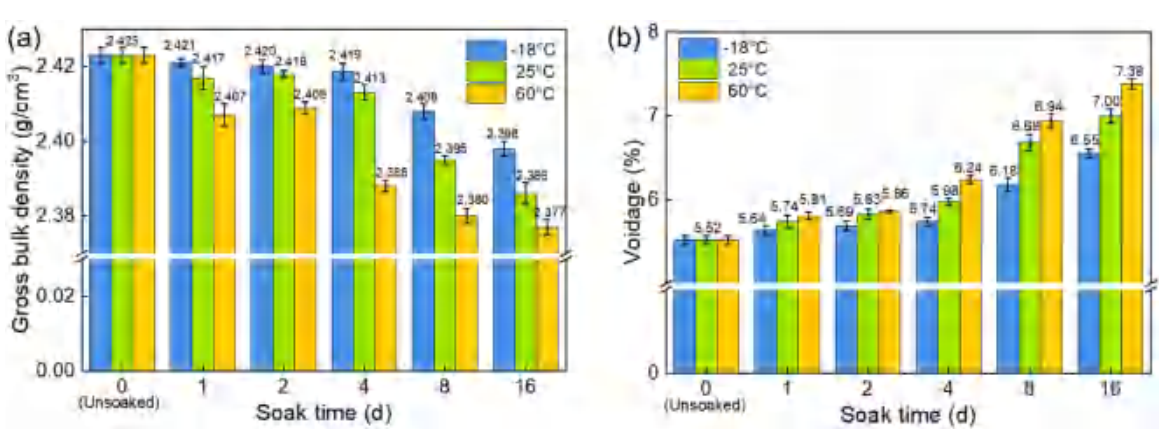

Fig. 4. Gross bulk density and void ratio of the polyurethane mixtures.

interface decreased gradually with increasing water immersion duration, and the early period of immersion (0–4d) also showed a greater tendency of deterioration than the later period. At the same immersion duration, the mass-loss rankings were all –18°C < 25°C < 60°C, showing that higher water temperature reduced the bonding effect of the interface. Specifically, the mass-loss rates in the –18°C and 25°C environments were close to each other, whereas the 60°C environment consistently had higher mass-loss rates than the former two. As the immersion duration increased, the difference in mass-loss rates between the high-temperature water environment and the low and ambient environments gradually decreased from 71.29 % and 69.61 % at 1d to 25.86 % and 25.50 % at 16d. That also suggested that the increase in immersion duration counteracted the deteriorating effect of temperature on the mixtures to some extent, but the damaging effects of the high-temperature water environment on the interfaces of the polyurethane mixtures were always the most significant.

4.2. Evolution of polyurethane/aggregate interfacial properties

4.2.1. Interface tensile test

An interface tensile test is consistent with the force characteristics of a split strength test [29]. This section focuses on describing the relationship between interfacial tensile strength and splitting strength. The results of the interfacial tensile strength tests of the polyurethane binder and the aggregate are shown in Fig. 6.

As shown in Fig. 6, the interface tensile strength of the polyurethane binder and the aggregate gradually decreased with the increase in water immersion duration. For example, the interfacial tensile strength for a water immersion of 16d decreased from 7.43 MPa to 1.56 MPa, and the performance retention rate was only 21.0 % at 60℃. That value was lower than 24.0 % and 40.8 % for 25°C and –18°C respectively, which was the reason for the greatest degradation of the splitting strengths of the polyurethane mixtures in the high-temperature water environment. To be specific, the degradation of interface tensile strengths could be divided into 2 stages. Again, taking 60°C as an example, the decrease in interface tensile strengths was 68.8 % in the early stage (0 to 4d). That was consistent with the decreasing trend in the splitting strengths of the polyurethane mixes from 0–4d, indicating that the interfacial debonding caused by water ingress dominated the damage to the mixtures at that stage.

In the late stage (4–16d), the decrease in interfacial tensile strengths was 33.6 %. The drop was significantly smaller than that of the early stage, which indicated that the water erosion effect on the interfacial tensile strengths became progressively smaller with the increase in immersion duration. It was speculated that both the polyurethane binder and the stone had high water absorption rates during the initial stage of immersion. However, the materials tended to be saturated with the extension of the immersion duration. That would have caused the effect of water on the interface to diminish. The high temperature exacerbated the erosive effect of water on the interfaces of the polyurethane mixes. Therefore, high-temperature water environments in the summer can have a more pronounced deteriorating effect on polyurethane mixtures.

4.2.2. Interface shear test

Interface shear test forces are closely related to mixture in stability tests [30]. This section focuses on the relation between interface shear strength and stability. The test results of the interfacial shear strengths of the polyurethane binder and the aggregate are shown in Fig. 7.

As is shown in Fig. 7, the interfacial shear strengths of the polyurethane binder and the aggregate also decreased gradually with the increase in water immersion duration. For instance, the interfacial shear strengths decreased from 4.00 MPa to 1.17 MPa for 16d of water immersion, and the performance retention rate was only 29.3 % at 60℃. It was also lower than 37.5 % and 56.0 % at 25°C and –18°C respectively, which also accounted for the greatest reduction in mixture stability observed in the high-temperature water environment.

The evolution of interfacial shear strengths could also be divided into 2 stages from the perspective of the deterioration process. For example, the interface shear strengths decreased by 52.5 % in the 0–4d stage at 60℃. In the 4–16d stage, the interfacial shear strengths decreased by 38.4 %. That indicated that the attenuation efficiency of interfacial shear strength decreased gradually with the increase in immersion duration. That phenomenon might have been related to the water-absorbing and swelling properties of the polyurethane binder. In the early stage of water immersion, the swelling behavior might have exacerbated the tendency of local stress to concentrate. It was speculated that as the water immersion duration increased, the potential decrease in the cross-linking network density of the polyurethane molecules might have contributed to the gradual release of part of the stresses. Such dynamic changes might have mitigated the stress concentration effect to some extent. Therefore, the initial stage of water immersion had a significant deterioration effect on the interface's tensile and shear strengths.

4.3. Degradation mechanisms of polyurethane binder

According to the previous test results, the properties of the polyurethane mixes and polyurethane–aggregate interfaces stabilized after 8d of water immersion. To investigate the intrinsic deterioration mechanism at the level of the polyurethane binder in this study, the specimens soaked at –18, 25, and 60°C for 16d were selected and compared with the unsoaked specimens.

4.3.1. Contact angle

The contact angles of water on the surfaces of the polyurethane binders measured in this study are shown in Fig. 8.

As shown in Fig. 8, the contact angle of the unsoaked polyurethanes was 85.89°, and the contact angle of the specimens immersed at –18°C for 16d was 73.89°. That showed some decrease in the contact angle of

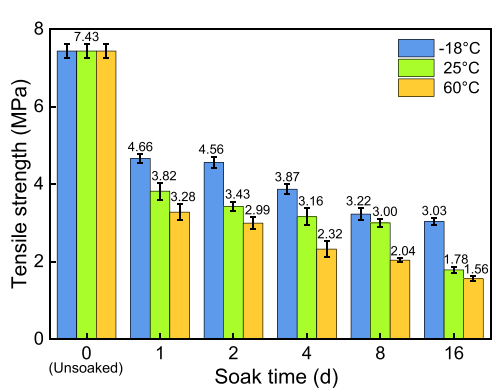

Fig. 6. Interface tensile strength of polyurethane binder and aggregate.

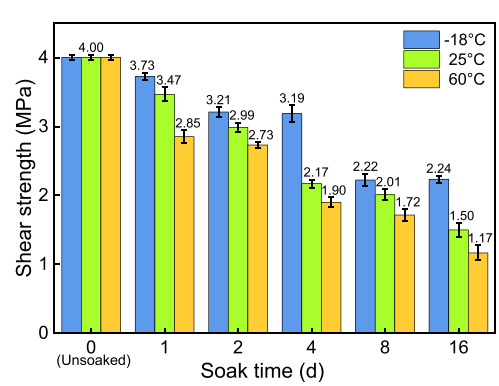

Fig. 7. Interface shear strengths of polyurethane binders and aggregate.

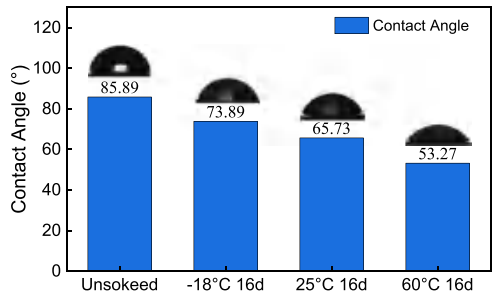

Fig. 8. Contact angles of water on the polyurethane binders.

the specimens after immersion in water. The hydrolysis of polyurethane can cause a gradual decrease in the cross-link density of its molecules, exposing the internal hydrophilic groups [31]. That process reduced the hydrophobic properties of the polyurethane binder surfaces, inducing more water to enter the interior of the binders and the mixtures, which increased the degree of interaction between the water and the stone interface. The contact angles of specimens immersed at 25°C and 60°C for 16d were 65.73° and 53.27° respectively. That showed that the higher water temperature corresponded to lower contact angles. That would be because as the water temperature increased, the cross-link density of the binder surfaces would be gradually reduced, and the destruction of the surfaces by water would be more significant. The increased water temperature also further exacerbated the water–aggregate interaction. That also contributed to the greater degradation of the polyurethane mixtures and the polyurethane–aggregate interfacial properties in high-temperature water environments.

4.3.2. Adhesion work

In this study, the adhesion work and water stability ER index of limestone and basalt with the polyurethane binder were calculated separately, and the results are shown in Fig. 9.

From Fig. 9a, as an example of basalt, the adhesion work of unsoaked polyurethane binder was 97.21 mJ/m^2. The adhesion work after water immersion showed a decreasing trend, and the decreasing degree was in the order of –18℃ < 25℃ < 60℃. That indicated that the effect of water immersion decreased the adhesive effect of the interface, and the higher water temperature corresponded to a greater degree of decrease. According to Fig. 9b, the water stability of the interface was evaluated by the ER index, and the ER of the unsoaked polyurethane binder was 0.61 in basalt. In a similar way to the adhesion work, the ER after water immersion showed a decreasing trend, and the order of decreasing degree was still –18℃ < 25℃ < 60℃. That indicated that the degree of decrease in the interfacial stability of the polyurethane binder and basalt gradually increased with the increase in water temperature.

Therefore, the high-temperature water environment had the greatest weakening effect on the shear and tensile strengths of the polyurethane–aggregate interface. That not only corroborated the contents of Section 3.2 but also indicated why the performance of the mixtures deteriorated most significantly in high-temperature environments. The polyurethane binder had the same effect as limestone. However, basalt had approximately 22 % and 6 % higher adhesion and ER index respectively than limestone. It was found that basalt and the polyurethane binder had a better interaction effect. To ensure the water stability of a polyurethane mixture, it is recommended that the polyurethane binder be used with basalt.

4.3.3. SEM

In this study, the fracture cross-section of the polyurethane binder was observed. The unsoaked specimens, –18°C, 25°C, and 60°C, are shown in Fig. 10a to Fig. 10d respectively.

As shown in Fig. 10a, the cross-sections of the un-immersed specimens showed poor flatness and many bending-like streaks, indicating that the specimens had ductile fractures. The specimens' cross-sections treated with the water environment showed better flatness and less surface texture, as shown in Fig. 10b to Fig. 10d respectively. It can be seen that the specimens under the action of the water environment had brittle fractures. At the same time, the cross-sections of the specimens contained many spheres, which were presumably formed during the curing phase of the polyurethane. Therefore, the spheres were observed by enlarging the magnification of the observation. The unsoaked specimens and the –18°C, 25°C, and 60°C soaked specimens are shown in Fig. 11a to Fig. 11d respectively.

As shown in Fig. 11a to Fig. 11d, the spheres in the 4 specimens had similar densities but were damaged to varying degrees in various environments. Specifically, the unsoaked specimens' spheres were generally intact and showed no visible damage. The spheres of the specimen immersed in water at –18°C showed a small amount of breakage. In contrast, the number of spheres damaged by immersion in water at 25 and 60°C increased significantly. In the 60°C specimen, some of the damaged spheres connected to cracks. Therefore, the order of damage was –18°C < 25°C < 60°C, which indicated that the increase in the immersion temperature led to the damage increase in the spheres. That was because the polyurethane binder surface had the worst hydrophobicity at high water temperatures. That could have encouraged more water to enter the binder, increasing the water damage. That also exacerbated the detrimental effects of water erosion on the interface. On that basis, the superimposed high-temperature effect ultimately also caused the polyurethane mixes to deteriorate more in high-temperature water environments. Therefore, increasing the stability of spheres might also be a strategy to improve water resistance performance.

4.3.4. TG

The full process mass-change curve for the thermogravimetric test is shown in Fig. 12. The mass-change curve of polyurethane could be categorized into stage I (30–290°C), stage II (290–400°C), and stage III

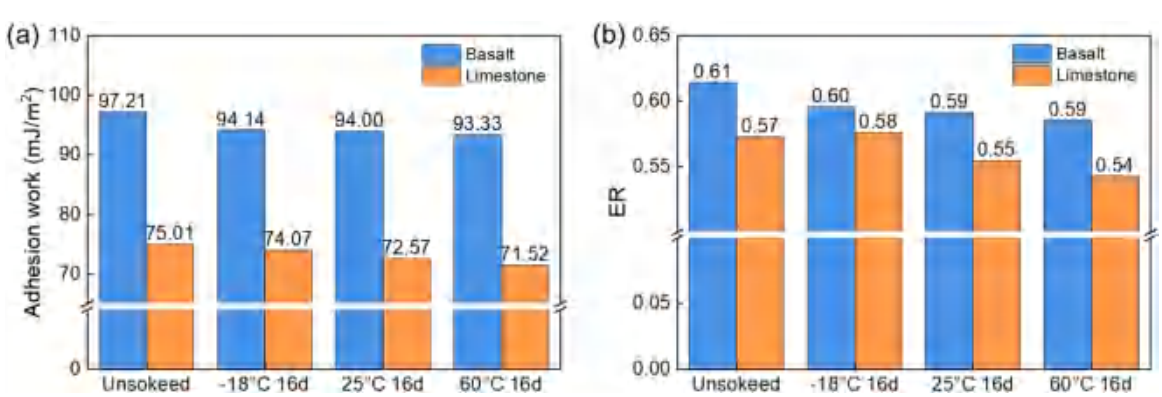

Fig. 9. Adhesion work and ER for polyurethane binder with limestone and basalt.

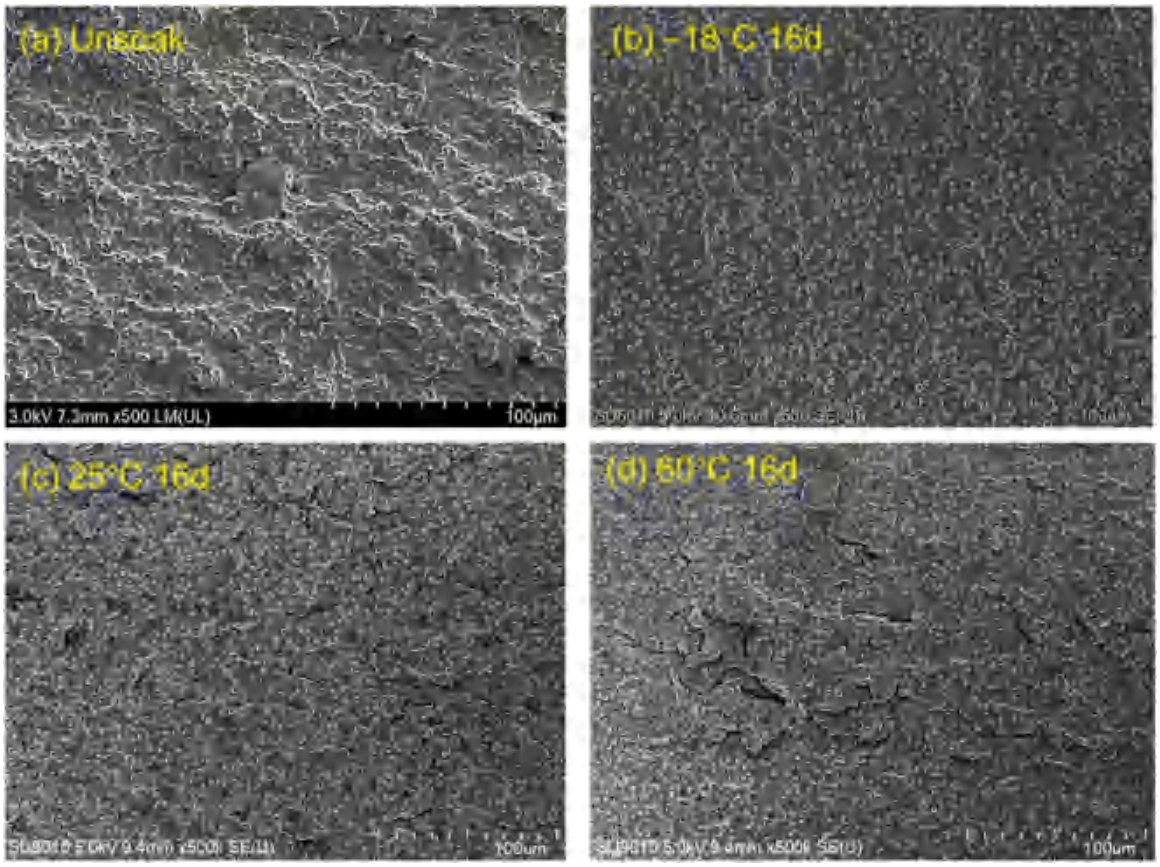

Fig. 10. Magnification of fracture section of polyurethane binder (500 ×).

(400–600°C), which corresponded to the loss of small molecule mass, decomposition of hard-segmented molecules, and the decomposition process of soft-segmented molecules respectively [32].

As shown in Fig. 12, the thermogravimetric mass-loss curves of the immersed specimens as a whole shifted in the low-temperature direction after water immersion. In the vicinity of 400°C, the mass curve of the polyurethane binder shifted from stage II to stage III in advance after water immersion. Moreover, the decomposition temperature of the polyurethane binder was ranked as 60°C < 25°C < −18°C < original condition in stage II. That showed that the higher water immersion temperature had a more significant destructive effect on the molecules of the polyurethane binder's hard segments. That phenomenon was attributed to the hard segments containing unstable polar functional groups such as carbamate bonds [33], making the hard segments weak in the molecular chain segments.

At the same time, the hydrogen bonds between the hard segments gradually decomposed with the increase in water temperature, which resulted in less aggregation of the hard segments in the high-temperature water environment. The stability of the system was reduced for both of those reasons, leading to an early decomposition of the soft section also, which made the mass-loss curve shift sooner to stage III. Furthermore, the above reasons might have also reduced the stability of the polyurethane binder, reducing the mixture's water resistance performance and increasing the water sensitivity of the polyurethane mixture. Therefore, securing the stability of the molecules within the polyurethane binder might be one way to maintain the mixture's water-stable performance.

4.3.5. DSC

The heat flow curve is shown in Fig. 13a. The glass transition temperature differences were shown in Fig. 13b. $\Delta T_{(g)}$ was soft-hard segments glass transition temperature differences under one constant condition. $\Delta T_{(sg)}$ and $\Delta T_{(hg)}$ are the difference between the glass transition temperatures of the soft and hard segments of the immersed specimens and the corresponding soft and hard segments of the unsoaked specimen, respectively. The hard-segmented molecule consisted of carbamate and aromatic chain segments with a rigid molecular structure and restricted molecular chain movement, which resulted in an insignificant $T_{(hg)}$ [34].

As shown in Fig. 13a, $T_{(sg)}$ and $T_{(hg)}$ of the unsoaked polyurethane binder appeared at −27.9°C and 58.6°C respectively. After water immersion, the 2 glass transition points showed a declining trend. In several sets of tests, the most significant decrease was observed after treatment in the 60°C water environment, which indicated that the high-temperature water environment had the most significant effect on the molecular chain segments. As shown in Fig. 13b, $\Delta T_{(sg)}$ and $\Delta T_{(hg)}$ gradually increased with the increase in water temperature. It was speculated that water molecules caused some degree of decomposition of both the soft and hard segments, making the molecules more pliable and lowering $T_{(sg)}$ and $T_{(hg)}$. Therefore, the more significant destructive effect of the water environment on the molecular chain segments (flexibility increasing) corresponded to a larger $\Delta T_{(sg)}$ and $\Delta T_{(hg)}$. Also, at the same temperature, $\Delta T_{(hg)}$ were all higher than $\Delta T_{(sg)}$. That showed that the hard segments all decomposed more than the soft segments, indicating that the hard segment interval was the weak region of the polyurethane binder.

In addition to that, the glass transition point difference ($\Delta T_{(g)}$) of the soft and hard segments could characterize the degree of microphase separation of the polyurethane binder [35]. As shown in Fig. 13b, the $\Delta T_{(g)}$ after water immersion all decreased, with the order of decrease being −18°C < 25°C < 60°C. That indicated that increasing the water temperature led to a decrease in the degree of microphase separation. That was due to water disrupting the physical cross-linking among the chain segments. In particular, the dispersion of hard segments increased,

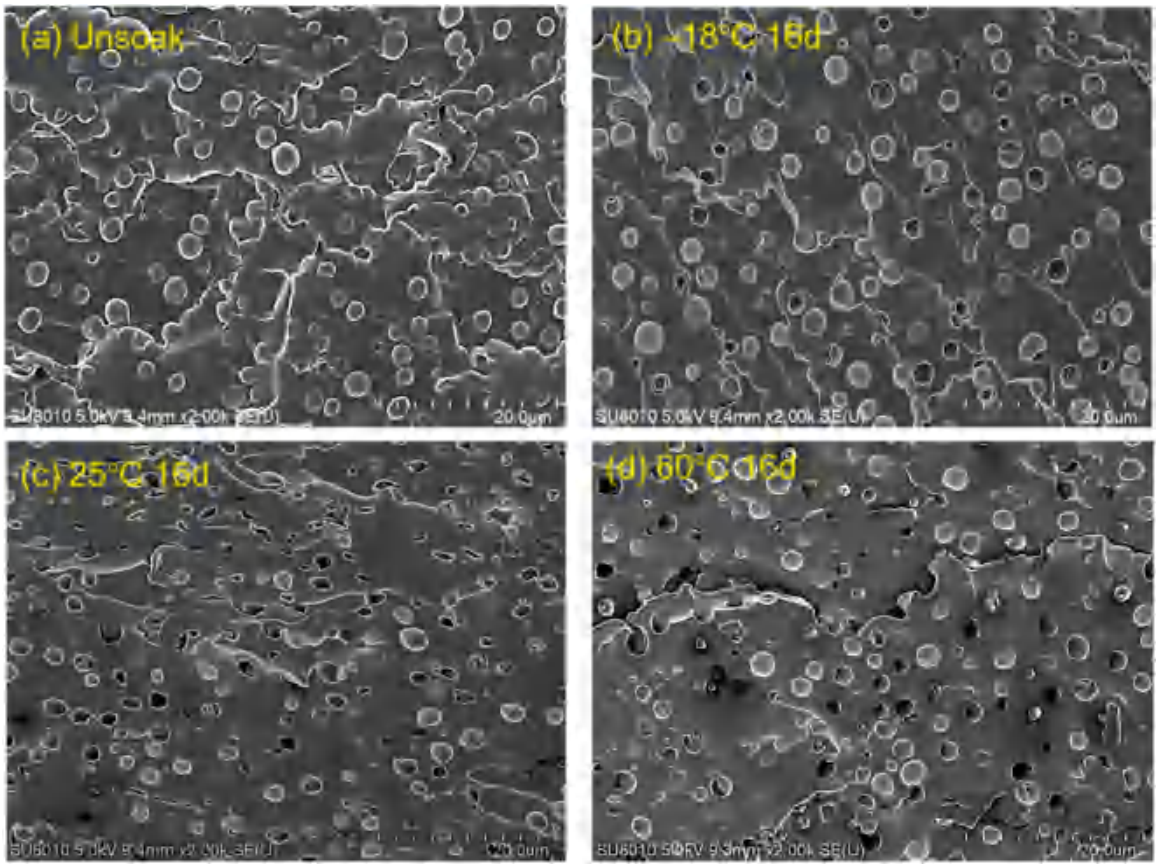

Fig. 11. Magnification of fracture sections of polyurethane binders (2000 ×).

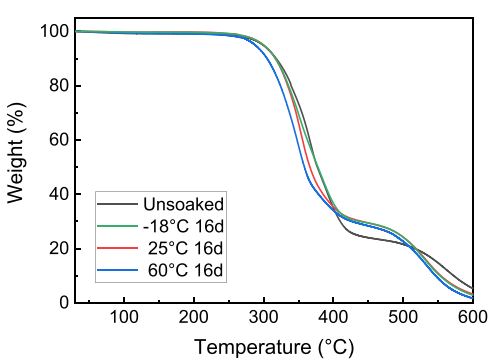

Fig. 12. Curve of the entire process of thermogravimetric test.

decreasing the strength of the molecular system and further weakening the potential road performance of the binder and the mixture. Therefore, ensuring the stability of the degree of microphase separation in water environments might be a research objective to find a way to maintain the performance of polyurethane mixtures.

4.3.6. FTIR

The FTIR further validated the hard segments' decomposition level and assessed the polyurethane binder's microphase separation [36]. The full-spectrum scanning results of the polyurethane binder are shown in Fig. 14a. The C═O peaks after the Fourier deconvolution process are shown in Fig. 14b. The C═O peak of the unsoaked polyurethane was taken as an example, and the result after peak splitting is shown in Fig. 14c. The calculated hydrogen bonding degree is shown in Fig. 14d.

As shown in Fig. 14a, the full-spectrum scans of the polyurethane binder did not show significant differences in results. In particular, the hard segments, which constituted the carbamate groups, contained N–H peaks (3300 cm^{-1}), C═O peaks (1700 cm^{-1}), and amide II bands (1530 to 1560 cm^{-1}) that showed no significant changes. At the same time, the heat flow curve of the DSC environment in Section 4.3.5 showed no significant changes. Therefore, it was speculated that the chemical hydrolysis of the hard segments was at a low level, while physical changes, such as microphase separation, were the main cause of the polyurethane binder's performance degradation.

As shown in Fig. 14d, the hydrogen bonding degree between hard segments–hard segments under the influence of water molecules decreased gradually with the increase in immersion temperature. The order of decreasing degree was –18°C < 25°C < 60°C, while the degree of disordered hydrogen bonding continued to increase. It was found that water molecules seized mainly the hydrogen bonding positions in the hard segment–hard segment, which led the hard intersegment hydrogen bonding to be converted into disordered hydrogen bonding. That further reduced the degree of microphase separation of the polyurethane binder [37]. It also verified the previous analysis that the microphase separation was the main reason for the performance deterioration.

Also, the hydrogen bonding degree between the soft and hard segments was essentially stable, and only an approximately 10 % decrease was observed at 60°C. That indicated that the high-temperature water environment simultaneously reduced the hard segment–hard segment and hard segment–soft segment hydrogen bonding degree. That hydrogen bonding degree also enabled the disordered hydrogen bonding degree to reach its maximum value. Therefore, it was found that the water molecules in a high-temperature environment broke the hydrogen bonds in both hard-segment hard hard-segment and hard-segment soft-segment areas, reducing the physical cross-linking degree within the molecules. The evolution mechanism is shown in Fig. 15. This also caused the greatest deterioration in polyurethane mixture performance in high-temperature environments. Therefore, the important research

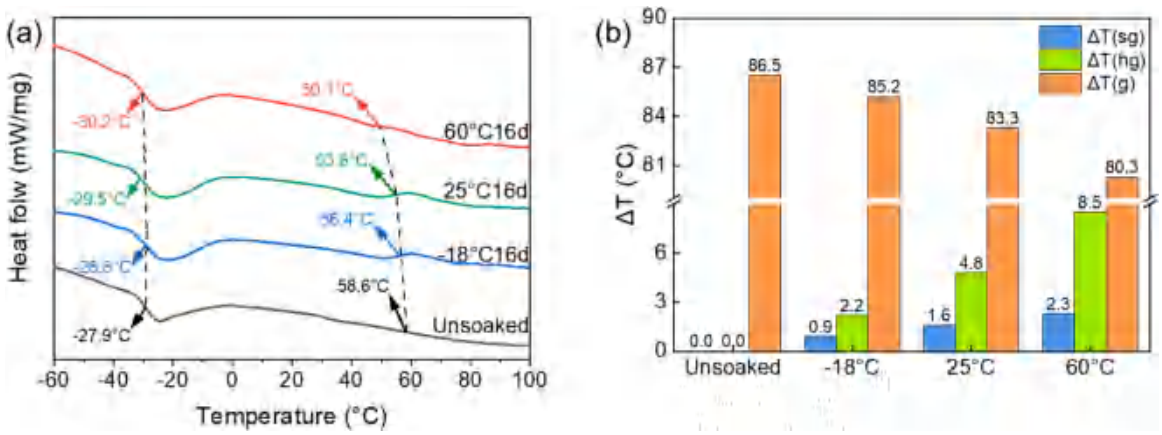

Fig. 13. Heat flow curves and glass transition point temperature differences.

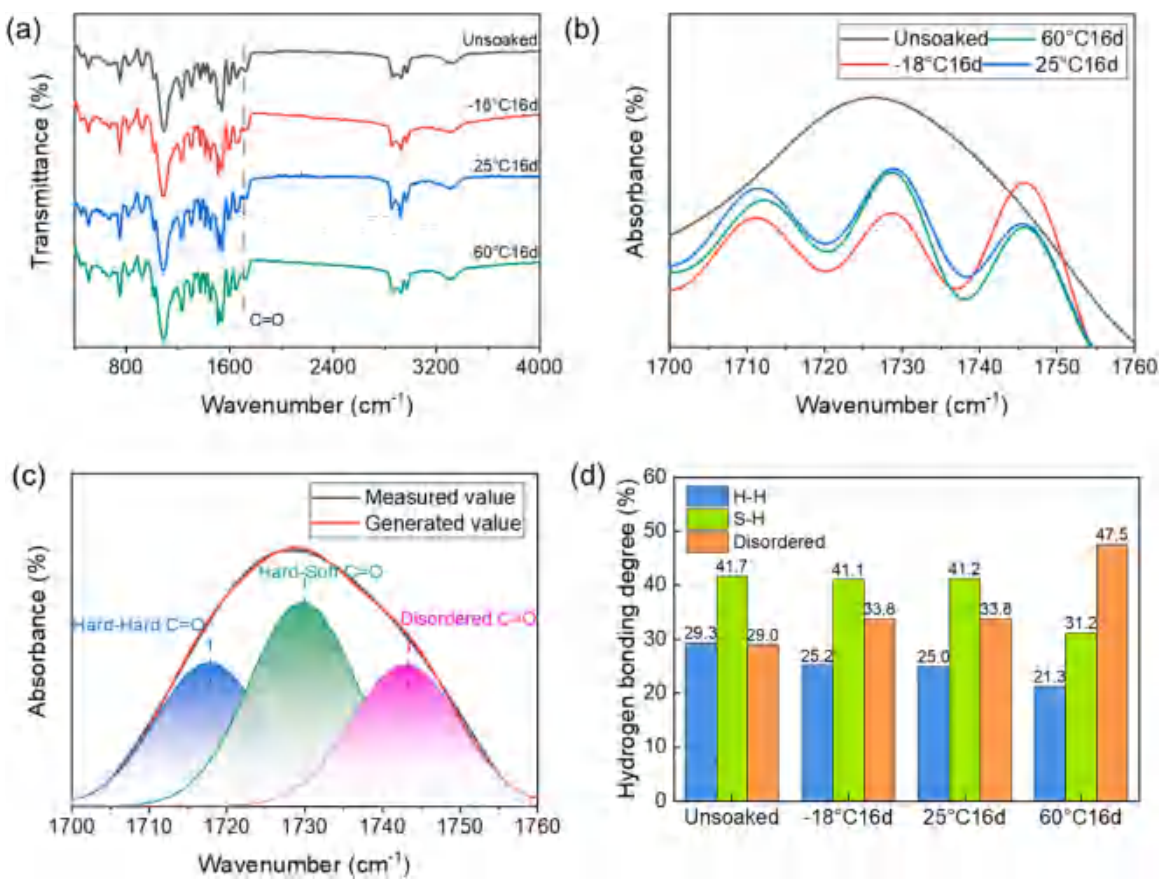

Fig. 14. Infrared spectroscopy test results and hydrogen bonding degree results.

focus would be on how to ensure stability among chain segments within the polyurethane binder to improve the water resistance of a polyurethane mixture.

5. Conclusions

In this study, the influence of water environments on the road performance of polyurethane mixture and the degradation characteristics of tensile and shear strengths at the polyurethane–aggregate interface were analyzed. The degradation mechanism of the polyurethane binder by water was studied from the perspectives of micromorphology, water resistance, and chemical structure. The conclusions are as follows:

(1) Deteriorations of the mechanical and abrasion loss resistance properties of polyurethane mixtures occur mainly at the beginning of the immersion period (0–4d), followed by a gradual stabilization at a later stage (4–16d). High temperatures can accelerate the deterioration process, causing an approximately 60 % reduction in Marshall stability and splitting strength and an approximately 80 % decrease in raveling resistance.

(2) The interface tensile and shear strengths of polyurethane mixture both have two-stage degradation trends with water immersion duration. For 0–4d of water immersion, the interfacial strength decreases by up to approximately 60 %. The decrease in interfacial strength is approximately 35 % for 4–16d of water immersion, and its deterioration slows substantially.

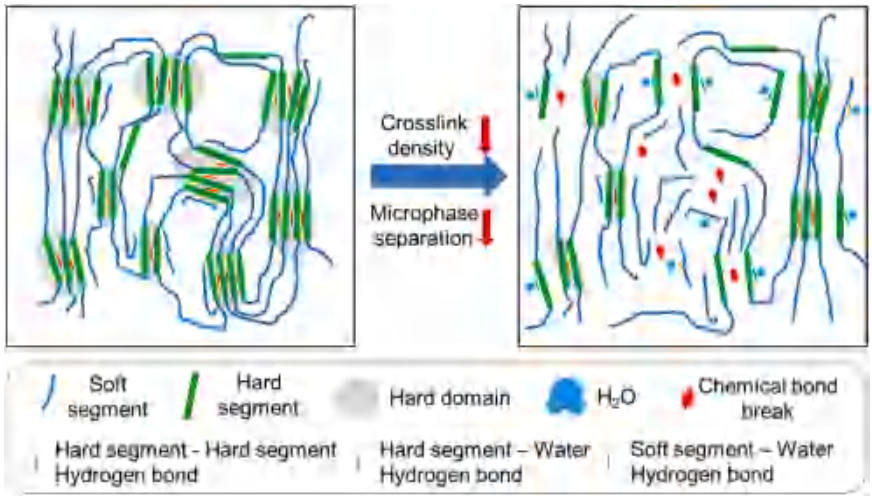

Fig. 15. Deterioration effect mechanism of water on the polyurethane binder.

(3) Water immersion would reduce the hydrophobicity of the polyurethane binder surface, leading to internal breakage in the binder and reducing the interface's adhesion effect and water stability performance. The basalt aggregate and polyurethane binder form a mixture with greater interfacial bonding performance.
(4) Water molecules would preferentially seize the hydrogen bonding positions among the hard segments, which weakens the microphase separation and cross-linking degree among the chain segments. That ultimately leads to a reduction in the road performance of binders and mixes. The temperature rise can accelerate the degradation level of a polyurethane mixture's road performance.

CRediT authorship contribution statement

Zhang zhiqing: Writing – original draft, Resources, Project administration, Methodology. **Wang Peng:** Validation. **Li Song:** Validation. **Xu Jian:** Resources, Project administration. **Cao Zhilong:** Investigation, Formal analysis, Data curation. **Wang Jie:** Resources, Project administration, Methodology. **Li Pengfei:** Writing – original draft, Methodology, Investigation, Data curation.

Declaration of Competing Interest

The authors declare that they have no known competing financial interests or personal relationships that could have appeared to influence the work reported in this paper

Acknowledgments

The authors would like to thank National Natural Science Foundation of China (Grant No.52178403, 51578027 and 52208411). The National Key R&D Program Winter Olympics Special (Grant No. 2018YFF0300305-03). The Nonmetallic Excellence and Innovation Center for Building Materials (NEXCEL) Innovation Fund (Grant No. 24TDA-4). Their assistance is sincerely appreciated.

Data availability

Data will be made available on request.

References

[1] F. Gong, X. Cheng, B. Fang, et al., Prospect of 3D printing technologies in maintenance of asphalt pavement cracks and potholes, J. Clean. Prod. 397 (2023) 136551, https://doi.org/10.1016/j.jclepro.2023.136551.
[2] Y. Xu, Y. Li, M. Duan, et al., Compaction characteristics of single-component polyurethane mixtures, J. Mater. Civ. Eng. 33 (9) (2021) 04021221, https://doi.org/10.1061/(ASCE)MT.1943-5533.0003808.
[3] B. Hong, G. Lu, J. Gao, et al., Green tunnel pavement: polyurethane ultra-thin friction course and its performance characterization, J. Clean. Prod. 289 (2021) 125131, https://doi.org/10.1016/j.jclepro.2020.125131.
[4] L. Cong, G. Guo, M. Yu, et al., The energy consumption and emission of polyurethane pavement construction based on life cycle assessment, J. Clean. Prod. 256 (2020) 120395, https://doi.org/10.1016/j.jclepro.2020.120395.
[5] F. Yang, L. Cong, J. Shi, et al., Laboratory evaluation on pavement performance of polyurethane mixture for thin overlay, J. Mater. Civ. Eng. 33 (8) (2021) 04021212, https://doi.org/10.1061/(ASCE)MT.1943-5533.0003927.
[6] K. Zhong, G. Luo, B. Zhai, et al., Deterioration of the noise reduction performance of polyurethane porous elastic mixture under void clogging and thermal-oxidative aging conditions, J. Mater. Civ. Eng. 35 (12) (2023) 04023468, https://doi.org/10.1061/JMCEE7.MTENG-16232.
[7] L. Cong, T. Wang, L. Tan, et al., Laboratory evaluation on performance of porous polyurethane mixtures and OGFC, Constr. Build. Mater. 169 (2018) 436–442, https://doi.org/10.1016/j.conbuildmat.2018.02.145.
[8] J. Chen, X. Ma, H. Wang, et al., Experimental study on anti-icing and deicing performance of polyurethane concrete as road surface layer, Constr. Build. Mater. 161 (2018) 598–605, https://doi.org/10.1016/j.conbuildmat.2017.11.170.
[9] G. Liao, H. Wang, J. Xiong, et al., Mechanical properties of poroelastic road surface with different material compositions, J. Mater. Civ. Eng. 32 (9) (2020) 04020253, https://doi.org/10.1061/(ASCE)MT.1943-5533.0003345.
[10] Y. Xu, L. Wu, X. Lv, et al., Improvement of water stability of macroporous polyurethane mixture, J. Mater. Civ. Eng. 34 (11) (2022) 04022285, https://doi.org/10.1061/(ASCE)MT.1943-5533.0004449.
[11] M. Sun, Y. Bi, M. Zheng, et al., Performance of polyurethane mixtures with skeleton-interlocking structure, J. Mater. Civ. Eng. 32 (2) (2020) 04019358, https://doi.org/10.1061/(ASCE)MT.1943-5533.0003015.
[12] L. Cong, G. Guo, F. Yang, et al., The effect of hard segment content of polyurethane on the performances of polyurethane porous mixture, Int. J. Transp. Sci. Technol. 10 (3) (2021) 254–265, https://doi.org/10.1016/j.ijtst.2020.07.003.
[13] L. Cong, F. Yang, G. Guo, et al., The use of polyurethane for asphalt pavement engineering applications: a state-of-the-art review, Constr. Build. Mater. 225 (2019) 1012–1025, https://doi.org/10.1016/j.conbuildmat.2019.07.213.
[14] L. Xu, Z. Zhao, X. Li, et al., Cracking investigation on fog seal technology with waterborne acrylate and polyurethane as a clean modification approach, J. Clean. Prod. 329 (2021) 129751, https://doi.org/10.1016/j.jclepro.2021.129751.
[15] B. Hong, G. Lu, J. Gao, et al., Evaluation of polyurethane dense graded concrete prepared using the vacuum assisted resin transfer molding technology, 121340, Constr. Build. Mater. 269 (2021) 269, https://doi.org/10.1016/j.conbuildmat.2020.121340.
[16] B. Hong, J. Wang, B. Zhang, et al., Study on the water stability of polyurethane concrete from perspective of polyurethane-aggregate interface, J. Mater. Civ. Eng. 34 (9) (2022) 04022237, https://doi.org/10.1061/(ASCE)MT.1943-5533.0004391.
[17] G. Guo, L. Cong, F. Yang, Analysis of influencing factors on water stability and stripping resistance of paving polyurethane mixture, J. Mater. Civ. Eng. 35 (3) (2023) 04022485, https://doi.org/10.1061/(ASCE)MT.1943-5533.0004469.

[18] X. Li, J. Li, J. Wang, et al., Recent applications and developments of polyurethane materials in pavement engineering, Constr. Build. Mater. 304 (2021) 124639, https://doi.org/10.1016/j.conbuildmat.2021.124639.
[19] G. Lu, L. Renken, T. Li, et al., Experimental study on the polyurethane-bound pervious mixtures in the application of permeable pavements, Constr. Build. Mater. 202 (2019) 838–850, https://doi.org/10.1016/j.conbuildmat.2019.01.051.
[20] A. Mardani, D. Hatungimana, S. Yazici, et al., Use of recycled mortar as fine aggregates in pavement concrete applications, Heliyon 10 (2024) e24264 http://creativecommons.org/licenses/by-nc-nd/4.0/.
[21] D. Jin, L. Yin, L. Malburg, et al., Laboratory evaluation and field demonstration of cold in-place recycling asphalt mixture in Michigan low-volume road, Case Stud. Constr. Mater. 20 (2024) e02923, https://doi.org/10.1016/j.cscm.2024.e02923.
[22] T. Yan, K. Cash, M. Turos, et al., High-compactability asphalt mix design framework based on binary aggregate packing, Constr. Build. Mater. 383 (2023) 131315 https://doi.org /10.1016/j.conbuildmat.2023.131315.
[23] AASHTO T 407-23, 2023, Standard Method of Test for Determining the Interlayer Shear Strength (ISS) of Asphalt Pavement Layers, American Association of State Highway and Transportation Officials, Developed by Subcommittee: 2c.
[24] AASHTO TP 114–18(2021)1, 2021, Standard Method of Test for Determining the Interlayer Shear Strength (ISS) of Asphalt Pavement Layers, American Association of State Highway and Transportation Officials, Developed by Subcommittee: 2c.
[25] M. Somani, S. Mukhopadhyay, B. Gupta, et al., Surface features and patterning in hydrolytic functionalization of polyurethane films, Polym. Bull. 79 (2022) 2305–2319, https://doi.org/10.1007/s00289-021-03601-4.
[26] S. Yan, C. Zhou, J. Ouyang, et al., Rejuvenation effect of waste cooking oil on the adhesion characteristics of aged asphalt to aggregates, Constr. Build. Mater. 327 (2022) 126907, https://doi.org/10.1016/j.conbuildmat.2022.126907.
[27] B. Wang, W. Tang, F. Zou, et al., Foaming behavior regulation of silicone rubber via evolution of crosslinked structure, Sustain. Mater. Technol. 38 (2023) e00764, https://doi.org/10.1016/j.susmat.2023.e00764.
[28] Y. Wang, Q. Sun, S. Leng, et al., Effect of dry-wet cycles on mechanical properties of polyurethane porous mixture, Int. J. Pavement Eng. 24 (2023) 2212315, https://doi.org/10.1080/10298436.2023.2212315.
[29] B. Lei, L. Yu, J. Chen, et al., Sustainable asphalt mixtures reinforced with basic oxygen furnace steel slag: multi-scale analysis of enhanced interfacial bonding, Case Stud. Constr. Mater. 22 (2025) e04198, https://doi.org/10.1016/j.cscm.2024.e04198.
[30] Y. Pei, P. Li, S. Jiang, et al., Mix design optimization of high-viscosity asphalt mixtures for ultra-thin pavement considering geometric properties and interface slip behavior for aggregate system, Constr. Build. Mater. 464 (2025) 140085, https://doi.org/10.1016/j.conbuildmat.2025.140085.
[31] K. Shi, Y. Zhang, Y. Gao, et al., Effects of adhesives on properties and mechanism of the ultra-thin pavement, Road. Mater. Pavement Des. 22 (5) (2021) 1140–1159, https://doi.org/10.1080/14680629.2019.1668289.
[32] X. Tang, Z. Chen, J. Liu, et al., Dynamic pyrolysis behaviors, products, and mechanisms of waste rubber and polyurethane bicycle tires, J. Hazard. Mater. 402 (2021) 123516, https://doi.org/10.1016/j.jhazmat.2020.123516.
[33] B. Cheng, W. Gao, X. Ren, et al., A review of microphase separation of polyurethane: characterization and applications, Polym. Test. 107 (2022) 107489, https://doi.org/10.1016/j. polymertesting.2022.107489.
[34] K. Shi, X. Li, L. Lei, et al., Influence of dangling chains on the microphase separation and damping properties of polyurethane, J. Appl. Polym. Sci. 141 (34) (2024) e55867, https://doi.org/10.1002/app.55867.
[35] F. Dong, S. Maganty, J. Meschter, et al., Effects of curing conditions on structural evolution and mechanical properties of UV-curable polyurethane acrylate coatings, Prog. Org. Coat. 114 (2018) 58–67, https://doi.org/10.1016/j.porgcoat.2017.09.018.
[36] J. Jiang, H. Gao, M. Wang, et al., Effect of fillers on the microphase separation in polyurethane composites: a review, Polym. Eng. Sci. 63 (12) (2023) 3938–3962, https://doi.org/10.1002/pen.26507.
[37] C. Wang, Z. Xu, Y. Xia, et al., Water transport mechanism and performance evaluation in polyurethane materials: a state-of-the-art review, Polym. Test. 138 (2024) 108554, https://doi.org/10.1016/j.polymertesting.2024.108554.

Construction and Building Materials 495 (2025) 143675

Contents lists available at ScienceDirect

Construction and Building Materials

journal homepage: www.elsevier.com/locate/conbuildmat

Study on the road performance and development mechanism of polyurethane binder in different media solutions

Li Pengfei [a,1], Cao Zhilong [a,1], Zhang Zhiqing [a,*,1,2], Wang Jie [b,*,2,3], Xu Jian [b,3], Wang Peng [b,3]

[a] College of Urban Transportation, Beijing University of Technology, China
[b] Research Institute of Highway, Ministry of Transport, China

ARTICLE INFO

Keywords:
Polyurethane binder
Pavement erosion environments
Road performance
Crosslink density
Hydrogen bond

ABSTRACT

Polyurethane pavements are significantly impacted by complex water environments, including acid rain, road alkalization, engine oil, and de-icing salts. This study quantified the performance loss and elucidated the degradation mechanisms of polyurethane binder under these solutions conditions. The solution soaking tests simulating environmental exposure were conducted, followed by characterization of surface morphology, mechanical properties, thermal stability and other performances. The degradation mechanisms were further elucidated through microstructure, hydrogen bonding, and crosslinking density. Finally, polyurethane binder's adaptability to road environments was comprehensively evaluated by the radar chart-based composite suitability index. The results indicated that exposure to acid, alkali, oil, salt, and water solutions reduced the polyurethane binder's toughness by 15.8 %-28.1 % and caused visible surface alterations attributed to chemical changes. The water solution has been proven to reduce the polyurethane binder's macroscopic properties by weakening hydrogen bonds and cross-linking density. Acidic and alkaline solutions could accelerate hydrolysis of the polyurethane binder, reducing cross-linking chain proportion by 5.4 %-8.4 %. Chloride ions in salt solution deteriorated properties by breaking chemical bonds, reducing crosslinking density by 5.1 %. The oil solution degradation to polyurethane binder primarily resulted from swelling effects. Overall, the deteriorating severity of water, alkali, oil, acid, and salt solutions on polyurethane binder intensify sequentially. The research findings hold significant implications for assessing the environmental adaptability of polyurethane pavements.

1. Introduction

To meet the service requirements of pavement, the current pavement is mainly paved with modified asphalt as a binder [31]. However, the asphalt must be heated at high temperatures in both the production and paving phases, which not only consumes much fossil energy, but also produces additional toxic and hazardous gas emissions [7]. However, the reactive materials of polyurethane have active chemical properties and excellent adhesion to aggregates. It can not only act as a binder to form a polyurethane mixture, but also endow the polyurethane mixture with the capability of normal temperature construction, which significantly reduces asphalt fume emissions of traditional asphalt mixtures in the production and construction processes [6,42].

Polyurethane mixtures offer a significant improvement in performance over traditional asphalt pavements. Specifically, polyurethane mixture had 5 times the high temperature performance of epoxy asphalt mixtures at 60℃ [15]. The low-temperature flexural strength of polyurethane mixtures has been found to be twice that of SBS-modified asphalt mixtures [36]. Yang has tested polyurethane mixtures and asphalt mixtures with the same gradation and found that the former had more than 3 times the tensile strength of the latter [38]. However, the water stability of polyurethane mixes is the weakness of the road performance. Liao prepared the residual Marshall stability of the polyurethane mixtures after immersion was significantly lower compared to

* Corresponding authors.
E-mail addresses: LPengfei20220823@emails.bjut.edu.cn (L. Pengfei), zhilongcao@bjut.edu.cn (C. Zhilong), zhangzhiqing@bjut.edu.cn (Z. Zhiqing), j.wang@rioh.cn (W. Jie), j.xu@rioh.cn (X. Jian), wang.peng@rioh.cn (W. Peng).
[1] Present address: No. 100 Pingleyuan, Chaoyang District, Beijing, China.
[2] There are two equally contributing corresponding authors in the paper.
[3] Present address: No.8 Xitucheng Road, Haidian District, Beijing, China.

https://doi.org/10.1016/j.conbuildmat.2025.143675
Received 22 January 2025; Received in revised form 13 August 2025; Accepted 16 September 2025
0950-0618/© 2025 Elsevier Ltd. All rights are reserved, including those for text and data mining, AI training, and similar technologies.

that of asphalt mixtures [19]. Hong conducted a study from the perspective of polyurethane and aggregate adhesion that found a 65 % decrease in interfacial tensile strength after only 1d of water immersion [12]. Gao developed porous polyurethane mixes with freeze-thaw splitting strength ratios of only 51.4–62.6 % [10]. It can be seen that polyurethane mixtures treated with water environment show the significant decrease in performance.

However, the actual service environment of pavement is complex and varied. On the basis of the effects of ordinary precipitation, acid rain has a certain adverse effect on a road surface [13]. At the same time, because the pavement basic layer contains alkaline substances, that are gradually precipitated under the action of moisture, it can cause the pavement appear alkalization phenomenon [17]. In addition, snowmelt salt is often used to reduce icing, but the saline in the salt–snow solution can affect the roadway [11]. Also, vehicles might leave a certain amount of oil on the road surface [25]. Therefore, actual pavement conditions are complex, and when considering the water environment, it is necessary to also consider the effects of acid rain, alkalization phenomenon, snowmelt salt, engine oil and other media on the performance of pavement.

The research on asphalt and asphalt mixtures has been more extensive concerning the action of different media solutions on pavements [39]. Meng found that acid rain reduces the low-temperature performance of SBS-modified asphalt and its mixtures [22]. Feng believes that a salt erosion environment can increase asphalt mixture voids, further degrading the service performance of asphalt mixtures [8]. Pang found that acid, alkali, and salt solutions reduce road performance by accelerating the dissolution of asphalt's soluble substances [24]. It can be seen that different media solutions can reduce the road performance of asphalt and asphalt mixtures. Although both asphalt and polyurethane can be used as binders, their molecular structures, adhesion characteristics and service performances are significantly different [43,44]. Therefore, the effects of different media solutions on asphalt do not apply to polyurethane binders. So, it is necessary to further investigate the effect of different media solutions on the performance of polyurethane binders.

There has been some research on the effect of different media solutions of the mechanical properties of polyurethane. Fu found that the mechanical properties of polyurethane were weakened by oil, salt, alkali and acid solutions in increasing rank order through tensile and flexural tests [9]. Chen compared 4 road pollutants including acid, alkali, salt and gasoline and found that the polyurethane's tensile and tear properties were reduced by 20–25 % in acid solution environments [1]. Zheng found no significant difference in the appearance of polyurethane cement composites under acid and alkali solutions, but alkali solutions caused a more significant mass loss [45]. Wang found that acid solutions had more significant deterioration effects on the properties of polyurethane grouting materials than alkali solutions [30,32].

The subsequent research has deepened insights into solution effects on polyurethanes. Liu confirmed that polyurethane-modified resins for repairing potholes in pavements had the greatest loss of strength in acidic environments [20]. Skuodis demonstrated salt solution's dominant weakening effect on elastic modulus through comparative assessments of gasoline, diesel, oil, and saline solutions [28]. Xie further established that both acidic and alkaline solutions induce substantially greater property degradation than aqueous solutions [35]. It can be seen that the existing studies mainly compare the effects of different solutions on the mechanical properties of polyurethane through macroscopic tests, and lack not only the assessment of other key properties (e.g., thermal stability, surface morphology), but also the systematic analysis of the degradation mechanism of polyurethane in different solutions. There is still a significant gap in the comprehensive understanding of the degradation mechanism of polyurethane binder properties.

To address these critical research gaps, this study quantifies the effects of acid, alkali, oil, salt, and water environments on polyurethane binder pavement performance while elucidating the associated deterioration mechanisms. Transcending conventional mechanical properties comparisons, the research integrates scanning electron microscopy (SEM), Fourier transform infrared spectroscopy (FTIR), and low-field nuclear magnetic resonance (LF NMR) for decoding degradation pathways through micro-morphology, hydrogen-bonding, and molecular network integrity. The performance radar charts were subsequently generated to visually assess pavement service characteristics of polyurethane binder across exposure conditions. These research results bridge knowledge gaps regarding polyurethane binder's service behavior under diverse media environments, establishing essential theoretical foundations for durable polyurethane pavement design.

2. Experiment and method

2.1. Raw materials

The polyurethane reaction material used in this study contained a certain number of oily solvents, and the polyurethane reaction raw materials basic performance parameters are shown in Table 1.

2.2. Preparation of polyurethane binder specimens

Firstly, the polyurethane reaction material was placed on the surface of a substrate. Then, the reaction material was applied at a uniform thickness with a film scraper. Subsequently, the polyurethane reaction material and the substrate were placed in an environmental chamber. After curing, the thickness of the polyurethane film was measured. After selecting the appropriate position, the sample was cut into a dumbbell-shaped specimen. The specimen length was 115 mm, width was 25 mm, thickness was 0.5 mm. The specimen preparation process is specifically shown in Fig. 1.

2.3. Experimental design

In this study was planned to investigate the role of water environmental media in influencing polyurethane by placing it in acidic, alkaline, saline, oily and neutral solutions respectively. For solution pH properties, the acidic medium was a sulfuric acid solution at a 2 % concentration. The alkaline medium was a sodium hydroxide solution at a 2 % concentration [27,3]. Because the actual service environment of winter snowmelt salt was difficult to spread evenly, to simulate the effect of high salt concentrations on a road surface, the salinity medium was a potassium chloride solution at a 10 % concentration [18]. The actual service environment of pavement is also influenced by vehicle oil, so the oily medium was automotive engine oil. The neutral medium was a pure aqueous solution. The test temperature was to 25 ℃, and the group's previous research showed that the results of the 4d immersion test were more stable, so this paper determined that the test time was 4d. The specific test plan is shown in Fig. 2.

2.4. Test and characterization

2.4.1. Mechanical properties

The specimens treated in Section 2.3 were tested for tensile strength and elongation at break, which were used as evaluation indices. Parallel specimens of 5 groups were set up, and the results were calculated by

Table 1
The basic performance of polyurethane reaction raw materials.

Indicator	Test value
Level of NCO / %	10.8
Viscosity /mPa•s (25℃)	1619.0
Surface drying time /min (30℃/90 %)	93.0
Ratio of hard and soft segments	1.0
Density /g•cm^{-3}	1.07–1.08

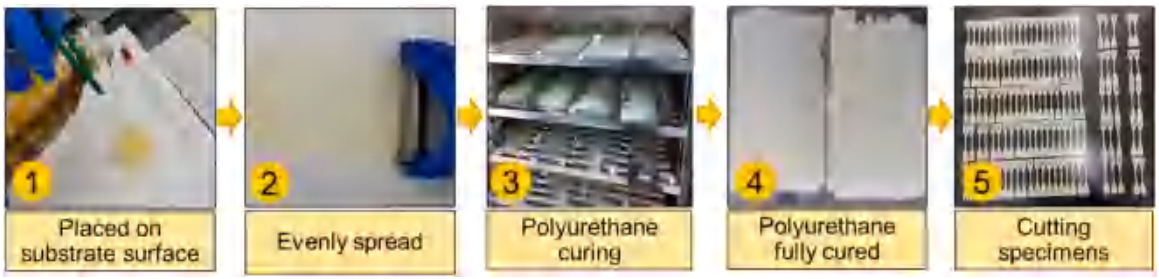

Fig. 1. The flow charts for specimen preparation.

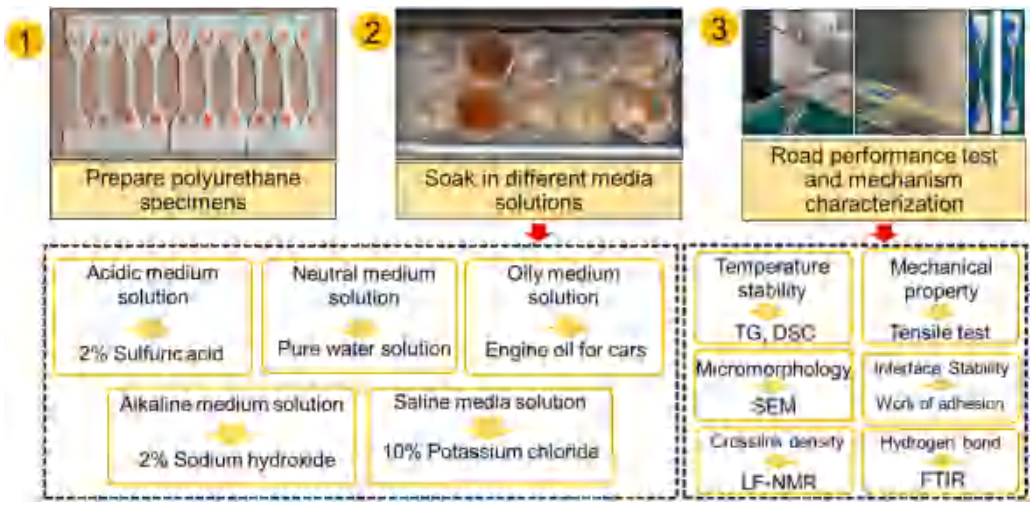

Fig. 2. The schematic of the experimental design.

equations (1) and (2):

$$T = Q/S \tag{1}$$

Where: T is tensile strength, MPa; Q is peak tensile load, N; S is section fracture area, mm^2.

$$A = (A_1 - A_0)/A_0 \times 100 \tag{2}$$

Where: A is elongation at break, %; A_0 is measurement scale (25 mm in this paper), mm; A_1 is maximum tensile length of the scale, mm.

2.4.2. Thermogravimetry (TG)

The high temperature stability of the polyurethane was characterized by a temperature corresponding to a 5 % mass loss (T_5) in thermogravimetric tests. That test started at 30°C and the temperature was increased by 10°C per minute until 620 °C was reached.

2.4.3. Differential scanning calorimeter (DSC)

The low-temperature properties of polyurethane were characterized by the glass transition temperature (T_g) tested by DSC test. The test started at −60°C and the temperature was increased by 10°C per minute until 60 °C was reached. The molecular structures of the soft and hard segments of the polyurethane were quite different, which gave those segments significant thermodynamic differences. They resulted in the soft segment's glass transition temperature (T_{sg}) differing from that of the hard segment (T_{hg}). The evolutionary difference between soft and hard segments could be characterized by comparing T_{sg} and T_{hg}.

2.4.4. Interface stability

The interfacial stability was characterized in the adhesion work and spalling work of the polyurethane-aggregate interface. In this paper, the contact angles of water and diiodomethane on polyurethane surfaces were determined. On this basis, the surface energy and its components of polyurethane were calculated by OWRK method.

The adhesion work and spalling work with polyurethane and aggregates were calculated according to Eq. (3)-(4) with reference to the aggregates surface energy parameters [37].

$$W_{sl} = 2\sqrt{\sigma_s^{LW}\sigma_l^{LW}} + 2\sqrt{\sigma_s^{-+}\sigma_l^{-+}} \tag{3}$$

Where: W_{sl} is adhesion work at the polyurethane and aggregate interface, mJ/m^2; σ_s^{LW} is polar component of the aggregate surface energy, mJ/m^2; σ_l^{LW} is polar component of the surface energy of polyurethane, mJ/m^2; σ_s^{-+} is dispersive component of the surface energy of aggregate, mJ/m^2; σ_l^{-+} is dispersive component of the surface energy of polyurethane, mJ /m^2.

$$W_p = 2\sigma_{wl} + 2\sigma_{ws} - W_{sl} \tag{4}$$

Where: W_p is spalling work at the polyurethane-aggregate interface, mJ/m^2; σ_{wl} is polyurethane-water adhesion work, mJ/m^2; σ_{ws} is aggregate-water adhesion work, mJ/m^2.

The water stability index energy ratio (ER) could be calculated based on the adhesion and spalling functions to evaluate the stability of the polyurethane-aggregate interface under the action of moisture. A larger ER index indicated to better interfacial stability and less water sensitivity. The calculation is based on Eq. (5).

$$ER = \left|\frac{W_{sl}}{W_p}\right| \tag{5}$$

2.4.5. Water absorption rate

Polyurethane specimens treated with the solutions listed in Section 2.3 had some water absorption. The water absorption rate could be

obtained by calculating the mass difference between the solution before and after immersing the specimen with the mass ratio of the original sample specimen.

2.4.6. Scanning electron microscope (SEM)

To visually compare the effects of various media solutions on the microscopic morphology of the polyurethane, the specimens cross-sections were observed by SEM. The observation magnifications were set to 400 × and 3000 × . The fracture specimen cross-section described in Section 2.4.1 was selected for testing to ensure the test results' continuity.

2.4.7. FTIR

The ATR mode was selected to test the upper surface of the polyurethane. The test range was 400–4000 cm^{-1}. To quantitatively analyse the hydrogen bonding content of the polyurethane, the C═O near 1730 cm^{-1} was divided into the free and hydrogen bonding peaks [15, 34]. The degree of hydrogen bonding could be obtained from the peak area after peak division Eq. (6):

$$H = \frac{S_{(1)}}{S_{(1)} + S_{(2)}} \tag{6}$$

Where: H is the degree of hydrogen bonding, %; $S_{(1)}$ is the hydrogen bonding peak area; $S_{(2)}$ is the freeing peak area.

2.4.8. Low-field nuclear magnetic resonance (LF NMR)

LF NMR techniques can characterize the ratio of polyurethane chain segments (content of crosslinked, dangling and free chains) and crosslink density. The test temperature was 90°C and the sequence is CPMG [33]. The test first measured the relaxation signal of polyurethane, based on which the ratio of the chain segments and the corresponding relaxation time could be calculated by Eq. (7).

$$M(t) = A \times Exp(-\frac{t}{T_{2A}})^{1.357} + B \times Exp(-\frac{t}{T_{2B}}) + C \times Exp(-\frac{t}{T_{2c}}) + A_0 \tag{7}$$

Where: $M(t)$ is the test relaxation signal, a.u; t is the test time, s; A is the crosslinked signal proportion, %; T_{2A} is the crosslinked chain signal relaxation time, us; B is the dangling-tailed signal proportion, %; T_{2B} is the dangling-tailed chain signal relaxation time, us; C is the free signal proportion, %; T_{2C} is the free signal relaxation time, us; A_0 is the correction factor.

The crosslink density was calculated using Eqs. (8)-(9):

$$\frac{1}{T_2^{av}} = \sum A^i / (A + B + C) \times T_2^i \tag{8}$$

Where: T_2^{av} is the chemical and physical crosslinking parameter, us.

$$XLD = \frac{\rho \times a \times T_2^{rl} \times n}{2f \times \xi \times T_2^{av} \times C_\infty \times M_u} \tag{9}$$

Where: ρ is the density, g/cm^3; f is the network cross-linking parameter; ξ is the transition parameter; a is the coefficient of rotational primary bonding in the statistical chain segments; C_∞ is the proton spacing and the local chain segment kinematics parameter; T_2^{rl} is the rigidity limit, us; M_u is the average molecular mass, g/mol; and n is the average number of primary bonds in the basic chain units.

3. Results and discussion

3.1. Analysis of the macroscopic road performance

3.1.1. Apparent morphology

In this study, the original (unsoaked) specimens and specimens soaked in different media were selected for comparison. The apparent morphologies of the specimens are shown in Fig. 3(a)- Fig. 3(f).

As shown in Fig. 3(a), the original (unsoaked) polyurethane specimens were generally light yellow and flat. Also, in Fig. 3(b) shows that after immersion in the acid solution, the color became darker and the specimen remained flat. That might be attributed to the oxidation of the macromolecular primary valence bonds within the polyurethane by the acid. Chemical bonds were broken and cracked, resulting in a darker color. Fig. 3(c) shows that the polyurethane's color became lighter after immersion in alkali solution and the specimen remained flat. The hydroxide in the solution attacked the carbonyl group of the polyurethane and reacted with water to form a salt that adhered to the surface of the polyurethane, which whitened the specimen after treatment with the alkaline solution. As show in Fig. 3(d), after immersion in the salt solution, the specimen showed some degree of bending, the surface was slightly yellowed, and a large amount of white material appeared. It was formed due to the adsorption of salts from the salt solution on the surface of the specimen. Fig. 3(e) shows that after immersion in the oil solution, the specimen became slightly yellow, but was no longer flat, and a certain degree of curl occurred. The oil solution might have invaded the interior of the polyurethane, changing its molecular state. Fig. 3(f) shows that the polyurethane underwent a certain degree of aging after immersion in the water solution, and the surface of the specimen turned yellow, but the specimen remained flat. Therefore, acid, alkali and water solutions changed only the color of the polyurethane. Salt and oil solutions could cause the polyurethane to turn yellow and bend. Those who apply the proposed pavement should be alert to the unfavorable effects of salt and oil solutions on polyurethane pavements.

3.1.2. Mechanical propertied

The tensile strength and elongation at break were selected as evaluation indices to investigate the effects of solution media on the mechanical properties of polyurethane. The tensile strength and elongation at break are shown in Fig. 4(a)-Fig. 4(b), respectively.

As can be seen from Fig. 4(a) to Fig. 4(b), five media (acid, alkali, salt, oil and water) have different degrees of deterioration on the tensile strength and elongation at break of polyurethane. They could cause the toughness to decrease by 15.8–28.1 %. The deterioration degrees ranked from more to less are salt > acid > oil > alkali > water. Specifically, the tensile strength and elongation at break of the original (unsoaked) specimen were 22.48 MPa and 232.4 % respectively. The degradation of polyurethane by the water solution was the least, with the tensile strength and elongation at break decreasing to 18.93 MPa and 223.2 % respectively. The water molecules that play a role in plasticization and hydrolysis. The mechanical strength of polyurethane decreased most significantly after immersion in the salt solution, with tensile strength and elongation at break decreasing to 16.17 MPa and 194.2 % respectively. That was because the high concentration of chloride ions in the salt solution broke the chemical bonds within the polyurethane binder [21].

The deterioration effects of both acid and alkali solutions were more evident than those of water solutions, and the mechanical indices in the 2 environments decrease to 16.98 MPa, 203.3 % and 18.39 MPa, 217.2 % respectively. It meant that both acids and alkalis accelerated the process of hydrolysis. Because the chemical bonds within polyurethanes are more susceptible to decomposition in acidic environments, acid solutions had a more pronounced effect on the deterioration of polyurethanes than alkaline solutions. The immersion oil solution decreases the two mechanical indicators to 17.46 MPa and 210.5 % respectively. That resulted from the diffusion of small molecules from the oily solution into the polyurethane interior, which caused swelling phenomenon [16]. Therefore, salt, acid, oil and alkali solutions all had a more significant degrading effect on the mechanical properties of polyurethane than aqueous solutions. The mechanical indicators were most sensitive to the action of salt solutions, so those who apply polyurethane pavements should be alert to the effects of snowmelt salts.

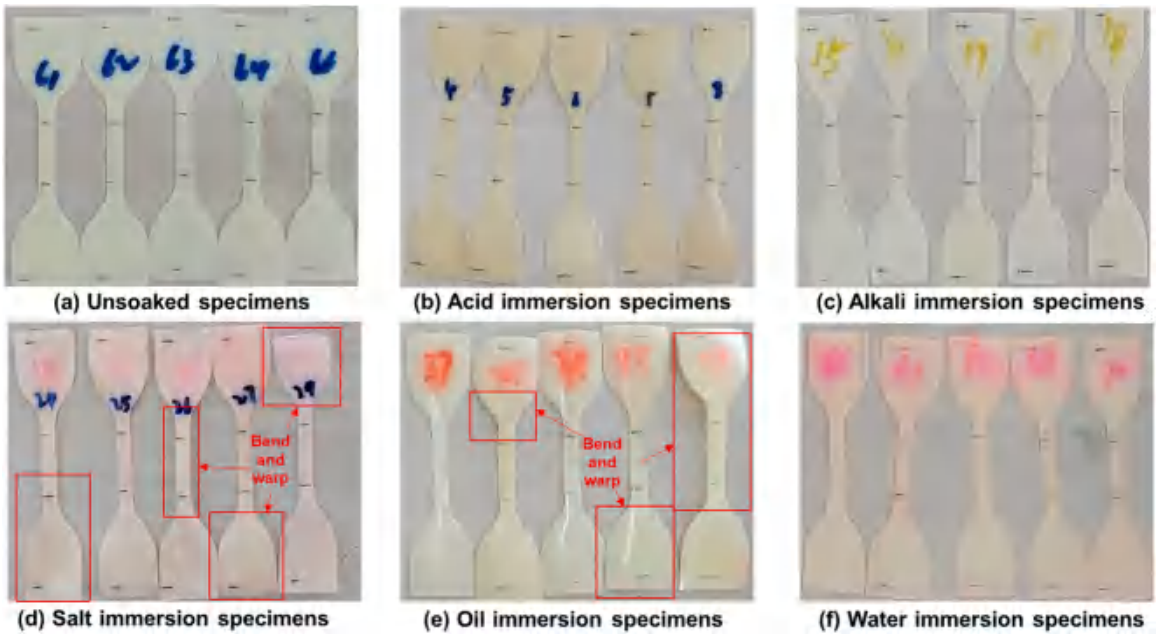

Fig. 3. Apparent morphologies of polyurethane specimens.

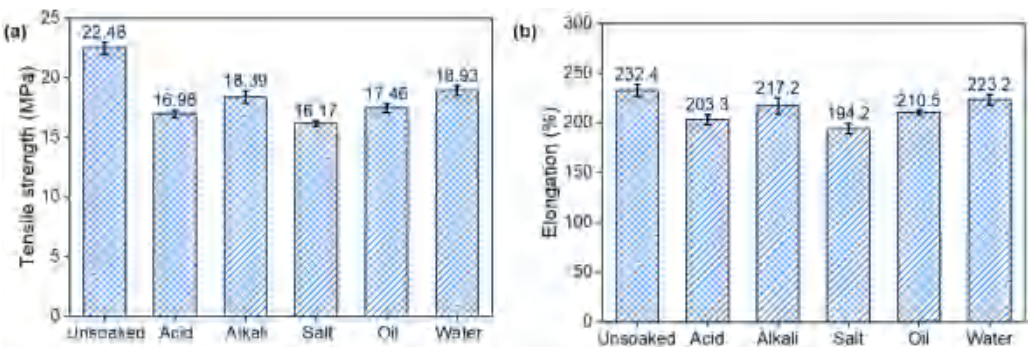

Fig. 4. The tensile strength and elongation at break of polyurethane in various media environments.

3.1.3. High temperature stability

The thermogravimetric test evaluated the high-temperature performance of polyurethane in terms of the rate of mass change. The mass change curves for the entire process of test heating and the mass change curves for the 30°C to 90°C intervals are shown in Fig. 5(a) and Fig. 5(b). The corresponding derivative thermogravimetric (DTG) test results are shown in Fig. 5(c). In this study, the temperature corresponding to a 5 % loss of mass (T_5) was selected to evaluate the high temperature stability of polyurethane. The test results are shown in Fig. 5(d). From the entire process curve in Fig. 5(a), it can be seen that the decomposition process of the original polyurethane was divided mainly into 3 temperature intervals. The 3 intervals were 30°C-300°C, 300°C-420°C and 420°C-620°C. The mass loss in the 3 intervals corresponded to the volatilization of small molecules, the decomposition of hard segments and the decomposition of soft segments, respectively.

From the overall change curve in Fig. 5(a), all temperature intervals after treatment with the media solutions moved toward lower temperatures, which indicated that all media solutions caused the polyurethane to decompose prematurely. In the second interval, the mass losses of the polyurethane treated with the media solutions were less than those of the original (unsoaked) specimens. That showed that acid, alkali, oil, salt and water solutions all reduced the polyurethane hard segment content. In addition, the 5 media solutions decreased the decomposition temperatures from 423°C to 386°C, 389°C, 372°C, 383°C, and 393°C respectively, during the shift to the third stage of decomposition. The third stage had similar changes, which indicated that all media solutions disrupted the cross-linking structure of the polyurethane molecules. It caused the hard segments of the chain to decompose prematurely, reducing the temperature stability of the polyurethane.

In regard to common temperature intervals for pavements, as shown in Fig. 5(b) for 30°C-90°C, the specimens treated with salt, acid, oil, alkali, and water solutions all showed greater mass loss than the original specimen. It meant that salts, acids, alkalis and water could destroy the molecular structure of polyurethane and reduce the stability of the corresponding crosslinking system. The swelling reaction of the oil solution also made the specimen contain more light-component oils, which would volatilize and decompose at elevated temperatures, reducing the stability of the polyurethane. Therefore, the mass loss in that temperature interval also further validated the finding that various media solutions reduced the high-temperature stability of polyurethanes. From the DTG results in Fig. 5(c), it can be seen that all tested media solutions induced an 8–17°C decrease in the peak decomposition temperature of polyurethane binder. Concurrently, the decomposition temperature range narrowed significantly in treated specimens, accompanied by an elevated maximum mass loss rate. These phenomena collectively indicate compromised high temperature performance of polyurethane binder across all exposure conditions. Notably, oil-treated polyurethane binder exhibited the most severe degradation, with its maximum

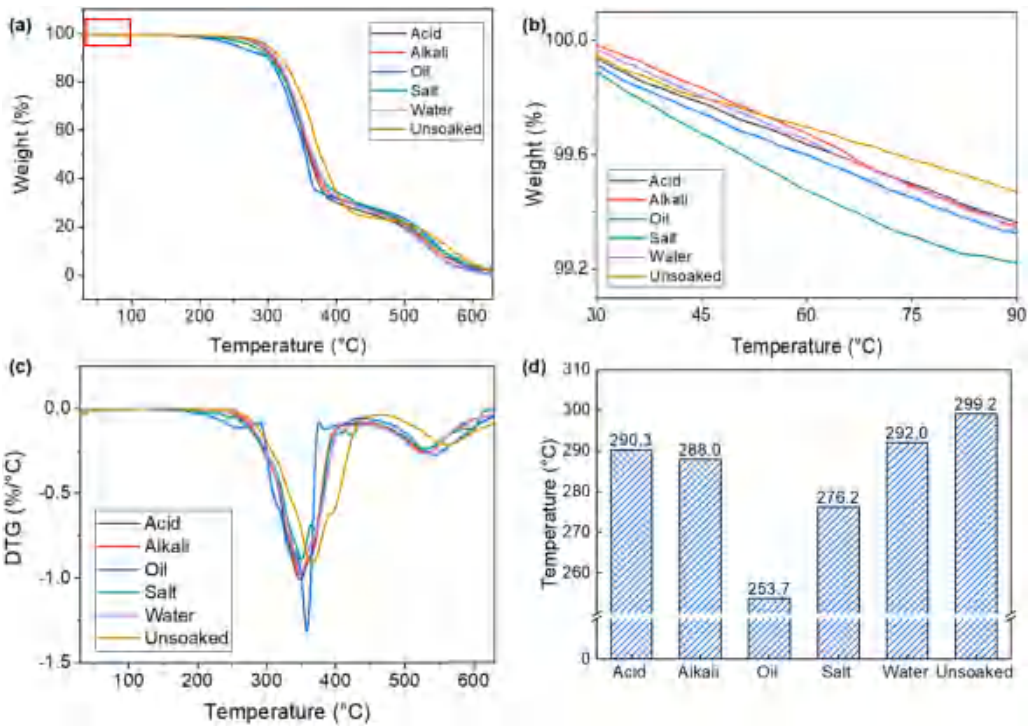

Fig. 5. The thermogravimetric test of polyurethane binder.

decomposition rate increasing by 41 % (expanded from 0.92°C/% to 1.30°C/%).

From the T_5 decomposition temperature in Fig. 5(d), the temperature of the original polyurethane was 299.2°C. The T_5 temperatures corresponding to water, alkali, acid, salt and oil solutions decrease in turn, which showed that those solutions decreased the thermal stability of polyurethane binder. In particular, the oil solution lowered the T_5 temperature the most. This phenomenon could be attributed to the swelling effect caused by the oil solution, which resulted in a higher adsorption capacity of the solution. During the heating process, the oil solvent and the adsorbed oil within the polyurethane matrix initially underwent volatilization and decomposition, leading to an earlier attainment of the T_5 temperature for the polyurethane binder treated with the oil solution. The salt solution also had the pronounced destructive effect on the molecular structure of polyurethane, which caused the large molecules to break down into more small molecules. Therefore, after the actual application of the pavement, more attention should be paid to the deterioration effects of oily and salty solutions on the temperature stability of polyurethane mixtures.

3.1.4. *Low-temperature performance*

This study evaluated evaluates the low-temperature performance of polyurethane materials with the glass transition point as an indicator. Heat flow change curves of the test process after treatment with various media solutions are shown in Fig. 6(a). The differences between the glass transition temperatures of the soft and hard sections of the polyurethane are shown in Fig. 6(b).

As shown in Fig. 6(a), The T_{sg} and T_{hg} of polyurethane occurs at approximately −30°C and 35°C, respectively. After treatment with acid, alkali, oil, salt and water solutions, the T_{sg} and T_{hg} decreased. The result of various media solutions breaking down the cross-linking structure among the polyurethane molecules and increasing the flexibility of the soft and hard segments [26]. It was a decrease in the glass transition point of the solution-treated specimens, which changed the low-temperature properties of the polyurethane. From the Fig. 6(b), acid, alkali, oil, salt and water solutions decreased the T_{sg} by 1.4°C, 1.0°C, 1.6°C, 1.2°C and 0.6°C respectively. The T_{hg} under the same conditions decreased by 4.1°C, 3.4°C, 4.7°C, 3.7°C, and 2.5°C respectively. It was found that hard segments had a greater drop than soft segments. That also showed that the hard segments were more susceptible to damage by the various media solutions. That was because the

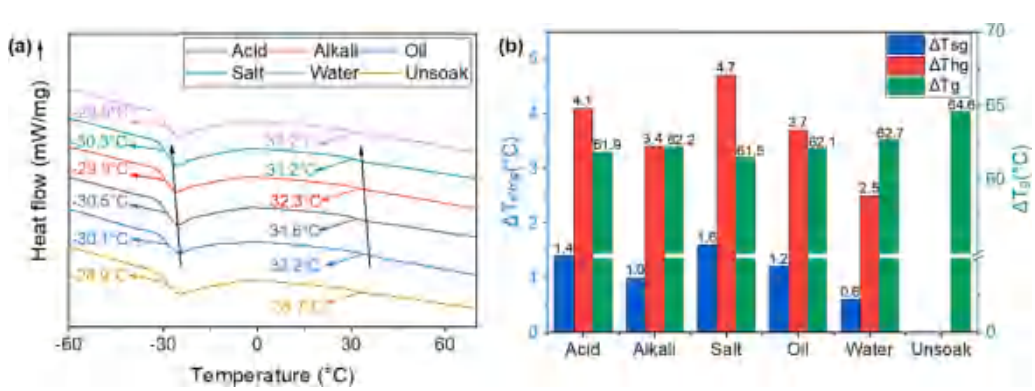

Fig. 6. Heat flow change curve and glass transition temperature differences of polyurethane.

hard segments contained decomposable functional groups such as urethanes, which made the hard segments the weak nodes of the polyurethane.

Also, the degree of microphase separation of polyurethanes significantly affected their properties. That degree could be characterized by calculating the difference between the glass transition temperatures of the soft and hard segments. As shown in Fig. 6(b), the differences in temperatures of the glass transition points of the specimens treated with acid, alkali, oil, salt and aqueous solutions were smaller than those of the original specimens. It indicates that every media solution weakened the degree of microphase separation of the polyurethane [2].

In the interior of the polyurethane, the hard segments were usually distributed in the middle of the soft segments. Therefore, it was inferred that the hard segments were fractured, resulting in increased mixing level of the hard and soft segments. That also made it difficult for the molecular chains to fully function, reducing the polyurethane's service performance. The overall ranking of the differential temperatures of the glass transition points was original > water > alkali > oil > acid > salt, indicating that the salt solution had the greatest effect on the degree of microphase separation of the polyurethane. It also corresponded to the results of the mechanical property tests mentioned above. Therefore, it is recommended that attention be paid to the effects of winter snowmelt salts after polyurethane pavement has been put into in service.

3.1.5. Interface stability

To evaluate the interfacial stabilization properties of polyurethane and stone, the adhesion work and interfacial stability index ER of polyurethane with the 3 types of stone were calculated from the surface energies of basalt, limestone, granite, polyurethane and its components. Fig. 7(a) shows the adhesion work of polyurethane with stone, and Fig. 7 (b) shows the interfacial stability index ER of polyurethane with stone.

From Fig. 7(a), as an example, the work of adhesion of the original (unsoaked) polyurethane and basalt was 97.2 mJ/m^2. The adhesion work of polyurethane and basalt treated in the water environment decreased to 94.0 mJ/m^2, and their adhesion work in acid, alkali, salt and oil solution environments further decreased to 90.5 mJ/m^2, 91.5 mJ/m^2, 71.4 mJ/m^2 and 93.6 mJ/m^2. That suggested that salt, acid, alkali, oil and water solution environments all broke the adhesion between polyurethane and basalt. The salt solution corresponded to the largest percentage decrease, which was 26.5 % compared to the original polyurethane sample. A similar phenomenon was observed for limestone and granite, which showed that all medium solutions reduced the adhesion effects at the interface of polyurethane and stone more than the water solution. The destruction of the adhesive work of the limestone and granite with polyurethane by the salt solution was also the most pronounced. There was a decrease of 24.9 % and 28.5 % respectively, relative to the original polyurethane. Therefore, all solutions weakened the adhesion effect at the interface between the polyurethane and the 3 stones. However, the work of adhesion of basalt to polyurethane was consistently approximately 22 % and 28 % respectively higher than that of limestone and granite.

The Fig. 7(b) shows that, in the case of basalt, the interface stability index ER of the original polyurethane and basalt was 0.65. This contrasts with conventional modified asphalt systems where ER values typically range 0.85–1.30 [40], indicating superior water stability in asphalt-stone interfaces. The polyurethane-basalt ER values declined significantly to 0.61, 0.63, 0.46, 0.63, and 0.63 in acid, alkali, salt, oil, and water solutions respectively. That showed that the interfacial stability of polyurethane with basalt after treatment in acid, alkali, oil and water environments all decreased to some extent compared to the original polyurethane.

In Fig. 7(b), the test results for limestone and granite ranged from 0.37 to 0.62, consistent with the 0.34–0.49 range reported in previous study [5]. The change patterns observed in limestone and granite resemble those in basalt. This indicates that various media solutions also deteriorated the interfacial stability of these two stones. From the overall point of view, the interfacial stability index ER of basalt to polyurethane was slightly larger than that of limestone, and granite's ER is significantly less than that of basalt and limestone. In combination with the adhesion work, the basalt and polyurethane had the best interfacial stability against different media solutions. In addition, that showed that the salt solution was the most obvious medium to decrease the stability of the interface between polyurethane and basalt. It might have been that the surface molecules of the polyurethane were damaged by the high concentration of chloride ions. The result was the exposure of more hydrophilic groups, making the polyurethane more readily to combine with water. It further led to a significant decrease in the interfacial stability at the interface of polyurethane and stone. Therefore, it is necessary to guard against the deteriorating effect of the interfacial stability of polyurethane pavements after winter snowmelt salts have dissolved.

3.1.6. Water-absorbent property

In this study, the mass change rates under various media solutions were measured and the specific test results are shown in Fig. 8.

As shown in Fig. 8, the rate of mass change (water absorption) of polyurethane in the water solution was 1.491 %. The corresponding rates of change for acid, alkali, salt and oil solutions were 2.065 %, 1.622 %, 2.519 % and 1.742 % respectively. Therefore, the ranking of the rate of change in the mass of polyurethane by the media solutions was salt > acid > oil > alkali > water. That was because polyurethanes were hydrolyzed in water solutions, increasing the free volume among the molecular chains, which enabled water molecules to enter more readily.

Acid and alkali could both promote the hydrolysis of polyurethane and increase the probability of water molecules entering the specimen. However, the urethane chemical bond was more easily hydrolyzed under acidic conditions. Therefore, the acid solution had a greater water absorption than the alkali solution. High concentrations of chloride ions and metal cations in salt solutions could have promoted the interaction

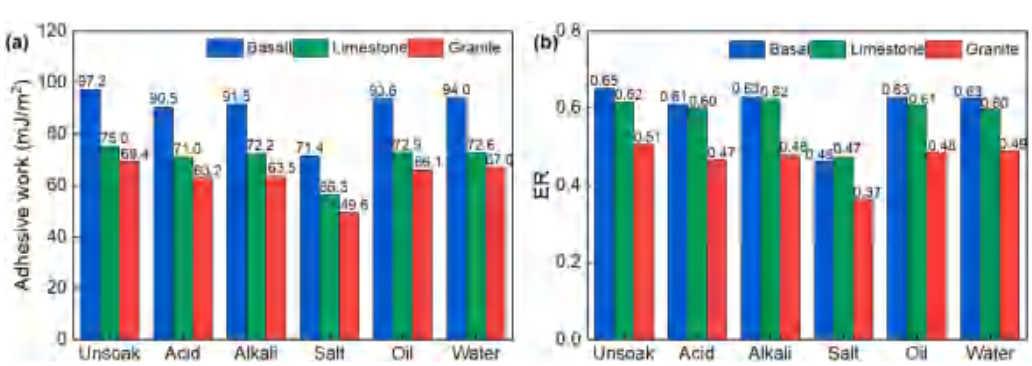

Fig. 7. Polyurethane binder and stones adhesion work and interfacial stability indicator ER.

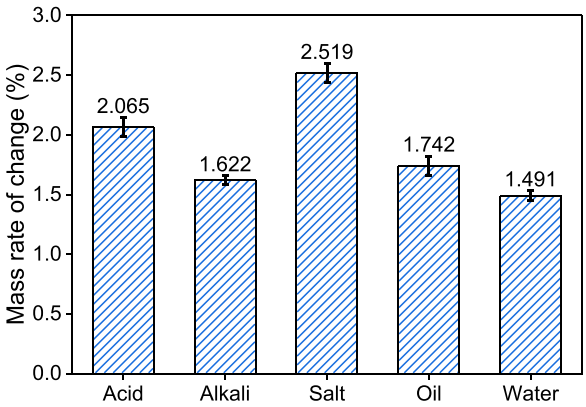

Fig. 8. The change pattern of the mass change rate of polyurethane.

of polyurethanes with water molecules [23]. It also followed that the specimens treated with the salt solution had a greater rate of mass change on a macroscopic scale, which is consistent with findings that salt solutions accelerate water absorption in polyurethane materials [41].

In contrast to the former, the oil solution had a swelling effect on the polyurethane. It could increase the internal space of the polyurethane and store a certain mass of oil inside, which increased the rate of change in the polyurethane's mass. Therefore, acid, alkali, salt and oil solutions all had a greater rate of mass change than polyurethane treated with the water solution. The change rate in the polyurethane mass was greater with salt solutions, and installers of polyurethane pavements should be alert to the effects of snowmelt salt.

3.2. Analysis of the performance deterioration mechanism

3.2.1. Micro-morphological characteristics

The morphological characteristics of the polyurethane cross-section can reflect its fracture characteristics to some extent. In this study, the specimens in original (unsoaked), acid, alkaline, salt, oil and water environments were observed with the help of SEM technology. The 400 × morphology is shown in Fig. 9.

Fig. 9(a) shows that the flatness of the original (unsoaked) specimen's fracture cross-section was poor. The surface fracture texture is generally flexural, which suggested it belonged to the ductile fracture mode. It can be seen from Fig. 9(b)-Fig. 9(f) that the specimen cross-sections treated with various media solutions showed different degrees of improvement in surface flatness. The fracture textures also all showed a significant decrease in the flexural degree, which was a characteristic cross-section of the brittle fracture mode. Therefore, all the medium solutions caused polyurethane to change from a ductile fracture mode to a brittle fracture mode. That showed that the toughness of polyurethane decreased after treatment with the media solutions. At the same time, Fig. 9(a)-Fig. 9(f) shows that the unimmersed specimen did not have significant holes. However, the interfaces treated with acid, alkali, oil, salt and water solutions all had many holes. That could have been closely related to the disruption of the crosslinked structure of the polyurethane and the detachment of small molecules [4]. Thereby, the observation magnitude was enlarged further. The results of the 3000 × morphological characterization scans are shown in Fig. 10.

As shown in Fig. 10(a), the original (unsoaked) polyurethane specimen had many "round spheres" with a smooth morphology and no damage. However, Figure10(b)- Figure10(f) show that holes, cracks and faults appeared in the specimens after treatment with acid, alkali, salt, oil and water solutions. The overall degree of breakage of the specimen was ranked as salt > acid > oil > alkali > water. The microscopic holes, cracks and faults in polyurethanes binder significantly compromise its performance. These defects act as stress concentration sites, facilitating

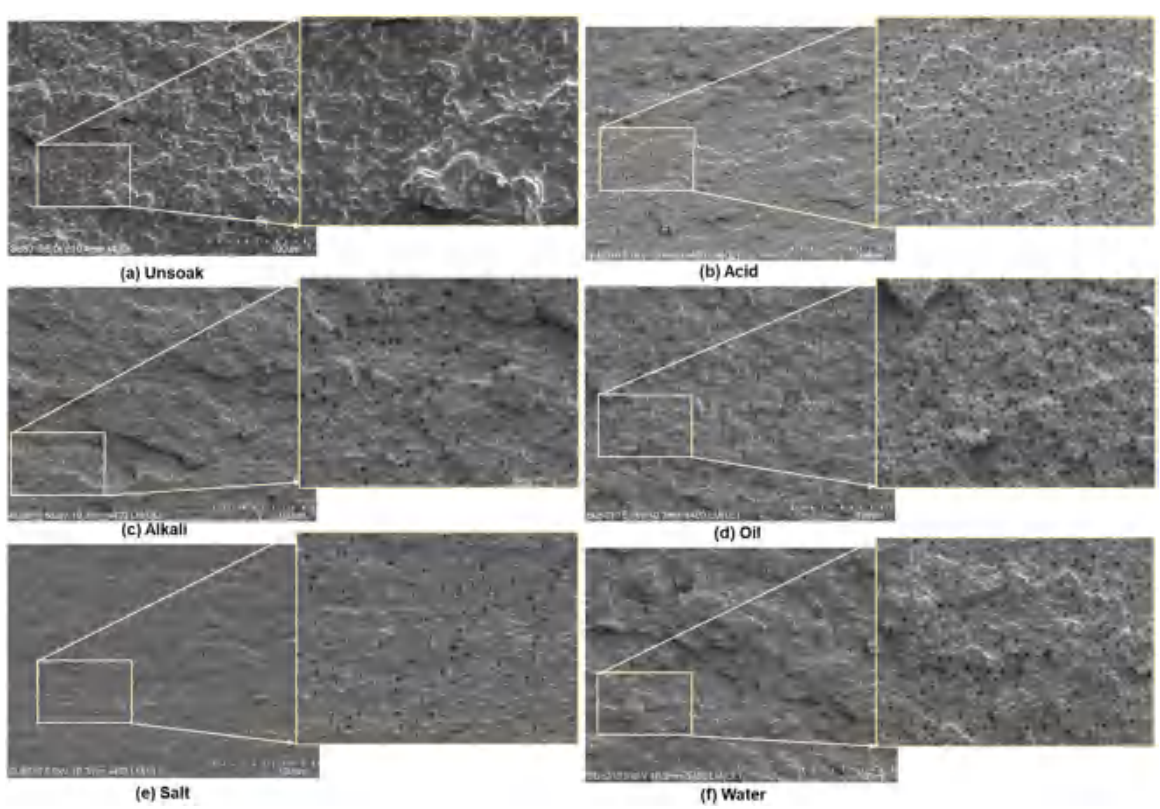

Fig. 9. Morphology of polyurethane cross-section (400 ×).

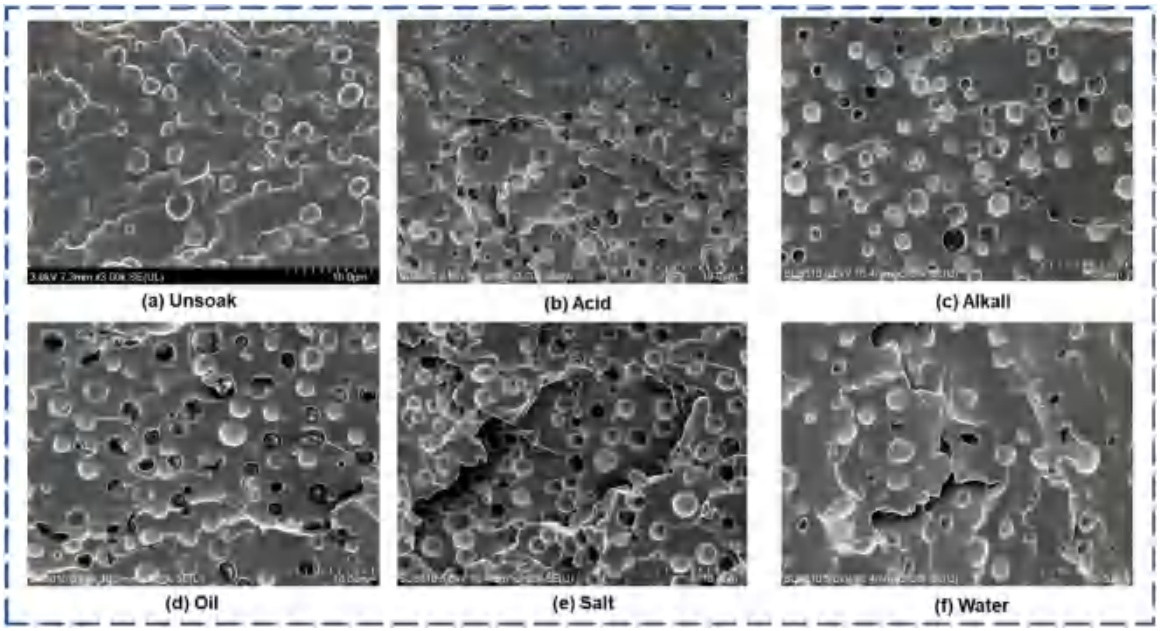

Fig. 10. Morphology of polyurethane cross-section (3000 ×).

crack propagation, while simultaneously reducing the effective load-bearing cross-section. This dual reasons substantially diminishes mechanical property. Concurrently, the cracks create pathways for water ingress, increasing absorption capacity and accelerating hydrolytic degradation. This damage also undermines both molecular integrity and thermal stability. Furthermore, these holes, cracks and faults weaken the interfacial bonding between polyurethane binder and aggregates, ultimately degrading the overall performance of the mixture. This also explains, the degradation of pavement performance after treatment of polyurethane binder with various solution media from the microstructural point of view.

3.2.2. *Crosslink density*

The crosslink density of a polymer can significantly affect its fundamental properties. In this study, polyurethane chain segment ratios and crosslink densities were tested in original, acid, alkali, salt, oil and water environments. The results of the test signals for LF NMR are shown in Fig. 11(a). The inversion results combined with Eq. (7) are shown in Fig. 11(b). All of the results in Fig. 11(b) have a fit of more than 0.99, indicating that the inversion calculations are reliable. Fig. 11(c)

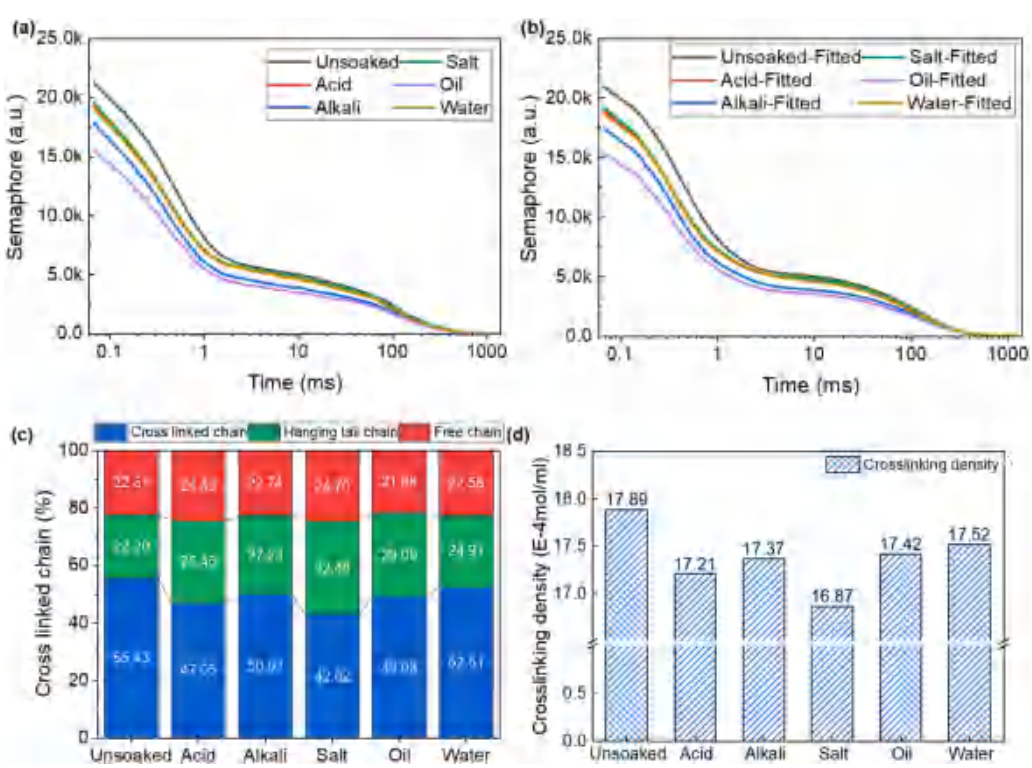

Fig. 11. Results of polyurethane chain segment ratio and cross-linking density tests.

shows the chain segment ratio of the polyurethane and Fig. 11(d) shows the crosslink density of the polyurethane.

As shown in Fig. 11(c), the proportions of crosslinked, dangling and free chains of polyurethane in the original sample were 55.43 %, 22.20 % and 22.37 % respectively. The proportions of the 3 chain segments of the water-soaked polyurethane were 52.51 %, 24.91 % and 22.58 % respectively. That showed that the proportion of crosslinked chains of polyurethane decreased and the proportion of both dangling and free chains increased slightly after treatment with the water environment. That was because hydrolysis broke down the cross-linked chains into dangling and free chains. Acid, alkali, salt and oil solutions had the same effect, and all of them were more obvious than the water solution on the chain segment decomposition of polyurethane. Acidic and alkaline solutions could reduce cross-linking chain proportion by 5.4 %-8.4 %. In particular, the decomposition of the salt solution was the most pronounced. The proportions of crosslinked, dangling and free chains of polyurethane in the salt solution were 42.82 %, 32.48 % and 24.70 % respectively. Therefore, in terms of the ratio of chain segments, all medium solutions could accelerate the decomposition of the cross-linked chains of polyurethane into dangling and free chains.

As show in Fig. 11(d), the crosslink density of polyurethane in the original sample was 17.89 E-4mol/ml, and the crosslink density of polyurethane after treatment in the aqueous environment was 17.52 E-4mol/ml. After acid, alkali, salt and oil treatments the crosslink density of polyurethane further decreased to 17.21 E-4mol/ml, 17.37 E-4mol/ml, 16.87 E-4mol/ml and 17.42 E-4mol/ml. So, the ranking by crosslink density was original specimen > water > oil > alkali > acid > salt. That suggested that acid, alkali, salt and oil environments all decrease crosslink density more than water solution environments. Therefore, acid, alkali, salt and oil environments had a more significant deterioration effect than water solution environments in terms of macroscopic properties. The salt solution remained the water environment factor with the most pronounced deterioration effect, which could reduce crosslinking density by 5.1 %

3.2.3. Hydrogen bonding

Hydrogen bonding had an important effect on the macroscopic properties of the polyurethane. The full infrared spectrum of polyurethane after treatment with various media solutions is shown in Fig. 12(a). In this study, the C═O peak was selected to analyse the hydrogen bonding interaction, and the C═O peak after the Fourier deconvolution process is shown in Fig. 12(b). As an example, the C═O peak of unsoaked polyurethane is shown in Fig. 12(c) after a peak splitting process. Based on that, the degree of hydrogen bonding in various environments was calculated in conjunction with Eq. (6), as shown in Fig. 12(d).

The degree of hydrogen bonding of polyurethane in the original (not immersed in water) environment was 47.45 %, as shown in Fig. 12(d). After treatment in the water solution the hydrogen bonding of the polyurethane decreased to 42.39 %. That was because the water molecules seized the hydrogen bonding positions within the polyurethane, leading to a decrease in the degree of hydrogen bonding [29]. Acid, alkali, salt and oil solutions had a more significant degrading effect on the degree of hydrogen bonding than the water solution. In particular, the deterioration was more pronounced in salt and acid solutions, corresponding to the decrease in the degree of hydrogen bonding to 36.85 % and 35.55 % respectively.

The decrease in the degree of hydrogen bonding can led to a decrease in the microphase separation of polyurethane. It also changed the distribution of soft and hard segments into a more chaotic one, leading to a degradation of macroscopic performance. The fundamental deterioration mechanism involves water intrusion displacing hydrogen bonding sites within polyurethane binder, thereby disrupting the original cross-linked network. This structural degradation simultaneously reduces crosslinking density (diminishing hydrophobicity and increasing water absorption), while promoting disordered hard segment and soft segment distribution that further suppresses microphase separation. Concurrently, the compromised network enhances molecular chain mobility, making the binder mechanically weaker and more prone to fracture at equivalent temperatures. These interdependent effects ultimately

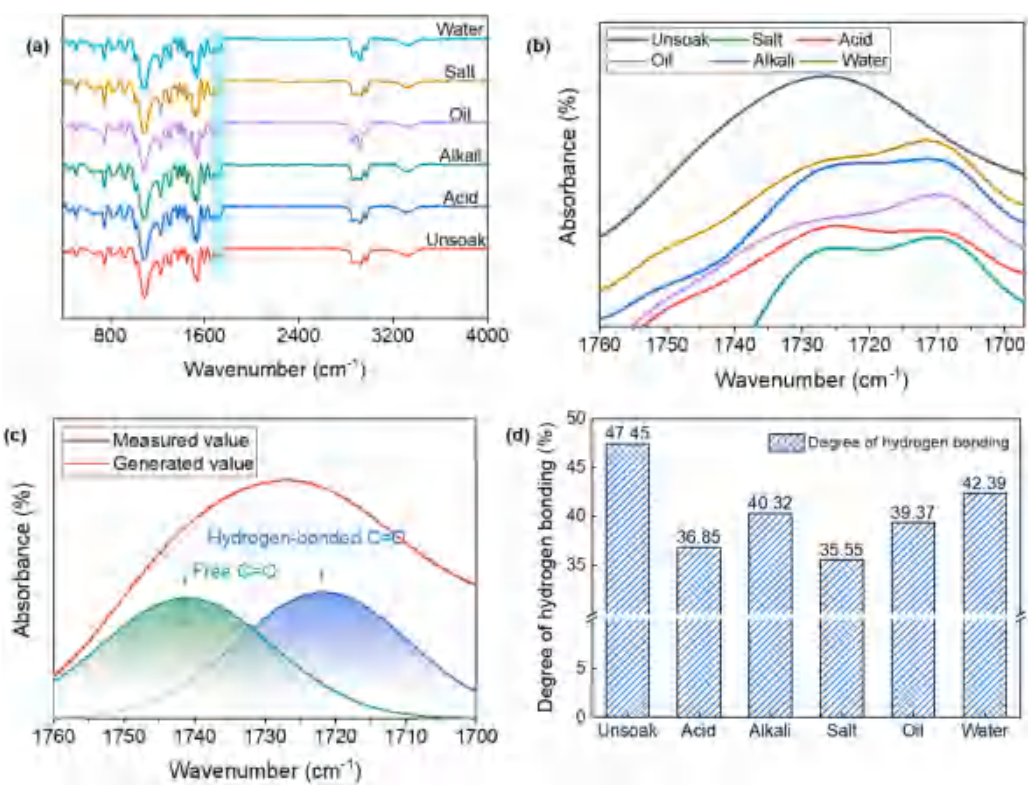

Fig. 12. The FTIR test results and degrees of hydrogen bonding of polyurethane.

degrade both thermal stability and mechanical properties. Therefore, hydrogen bond attenuation underlies microphase separation reduction under water environments, while the greater microphase separation induced by acid, alkali, salt, and oil solutions accounts for their accelerated macroscopic property deterioration.

The deteriorating effects of salt and acid solutions on polyurethane were the most prominent. The hydrogen bonding principle shows that the formation of hydrogen bonds between the amino ester amino group (N-H) of the urethane bond and the amino ester carbonyl group (-O-) of the hard segment in polyurethanes is favourable for microphase separation [14]. Based on the results, it was speculated that acid and salt solutions would reduce the number of hydrogen bonding receptors by destroying the structure of the hard segments based on the hydrolysis and plasticising effect of the water solution. It can be seen that the hard-segment content had a direct effect on the degree of hydrogen bonding in the polyurethane. That was because the hard segment contained many polar groups such as carbamates. Those groups were more likely to interact with other molecules, leading to the fracture of the hard segments, as shown in Fig. 13. Therefore, improving the stability of hard segments might be a research idea to improve the water damage resistance of polyurethane mixtures.

3.2.4. Environmental service characteristics

According to the above experimental data, the radar charts of polyurethane road indices under original, acid, alkali, oil, salt and water solutions were plotted as shown in Fig. 14(a)-Fig. 14(f), respectively. The adhesion work and ER indices were selected from basalt data. This study evaluated polyurethane's environmental adaptability by using the radar plot' areas in various environments as the 'composite suitability index'.

As shown in Fig. 14(a)-Fig. 14(f), the original (unsoaked) polyurethane was optimal in all performance indicators. The different media solutions had different effects on polyurethane properties. The composite suitability indices were ranked as original > water > alkali > oil > acid > salt. Those reflected the fact that the salt solution had the most significant weakening effect on the overall road performance of polyurethane. Specifically, it showed that except for the high and low temperature performance indicators, all other performance indicators were significantly reduced by the salt solution. That indicated that the salt solution reduced mainly polyurethane's mechanical properties, interfacial stability and water absorption properties of polyurethane. Acid, alkali, oil and water solutions also weakened polyurethane's mechanical and interfacial stability properties to a much greater extent than other properties. For that reason, the adverse effects of acid rain, pavement alkali flooding, engine oil and water solutions on the road performance of polyurethane mixtures should be noticed, such as load bearing capacity and interfacial stability. In particular, there is a requirement to focus on preventing the deteriorating effects of winter snowmelt salts on polyurethane pavements.

4. Conclusion

In this paper, acid, alkali, oil, salt and water solution effects on the road properties of polyurethane binder were investigated. Furthermore, the influence mechanism of different media solutions on polyurethane binder was also analyzed. The conclusions are as follows:

(1) Exposure to acid, alkali, salt, oil, and water solutions consistently degrades polyurethane binder toughness (reduction by 15.8–28.1 %) and increases micropore density, directly impairing pavement performance.
(2) Water infiltration serves as the fundamental factor of polyurethane binder degradation, compromising mechanical properties, thermal stability, and interfacial adhesion through hydrolysis that cleaves cross-linked chains into dangling and free segments.
(3) Acidic, alkaline, salt, and oil solutions significantly accelerate this water-driven degradation pathway, evidenced by a 12.6 %-2.9 % reduction in cross-linked chains and a corresponding 5.1 %-11.9 % weakening of hydrogen bonding, which suppresses microphase separation and amplifies macroscopic property deterioration.
(4) Salt solutions exhibit the most pronounced acceleration effect among solutions (contaminants), highlighting a critical vulnerability for polyurethane binder in environments exposed to deicing salts or coastal conditions.

The long-term durability of polyurethane binder primarily depends on its water resistance, with common environmental pollutants (especially salts) acting as accelerating degradation. Temperature and exposure duration also significantly impact the pavement performance of polyurethane binders. Therefore, the effects of different solution concentrations, immersion times and temperatures on the polyurethane binders could be further investigated in the future.

CRediT authorship contribution statement

Cao Zhilong: Software, Methodology, Investigation. **Li Pengfei:** Methodology, Investigation, Formal analysis, Data curation, Conceptualization. **Wang Peng:** Writing – review & editing. **Xu Jian:** Resources, Investigation, Funding acquisition. **Wang Jie:** Supervision, Resources, Project administration, Data curation. **Zhang Zhiqing:** Supervision, Resources, Project administration.

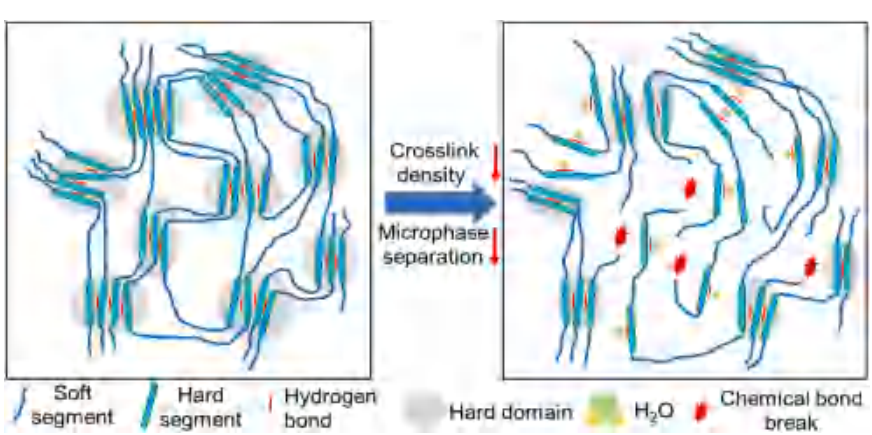

Fig. 13. Schematic diagram of the mechanism of degradation of polyurethane binder properties.

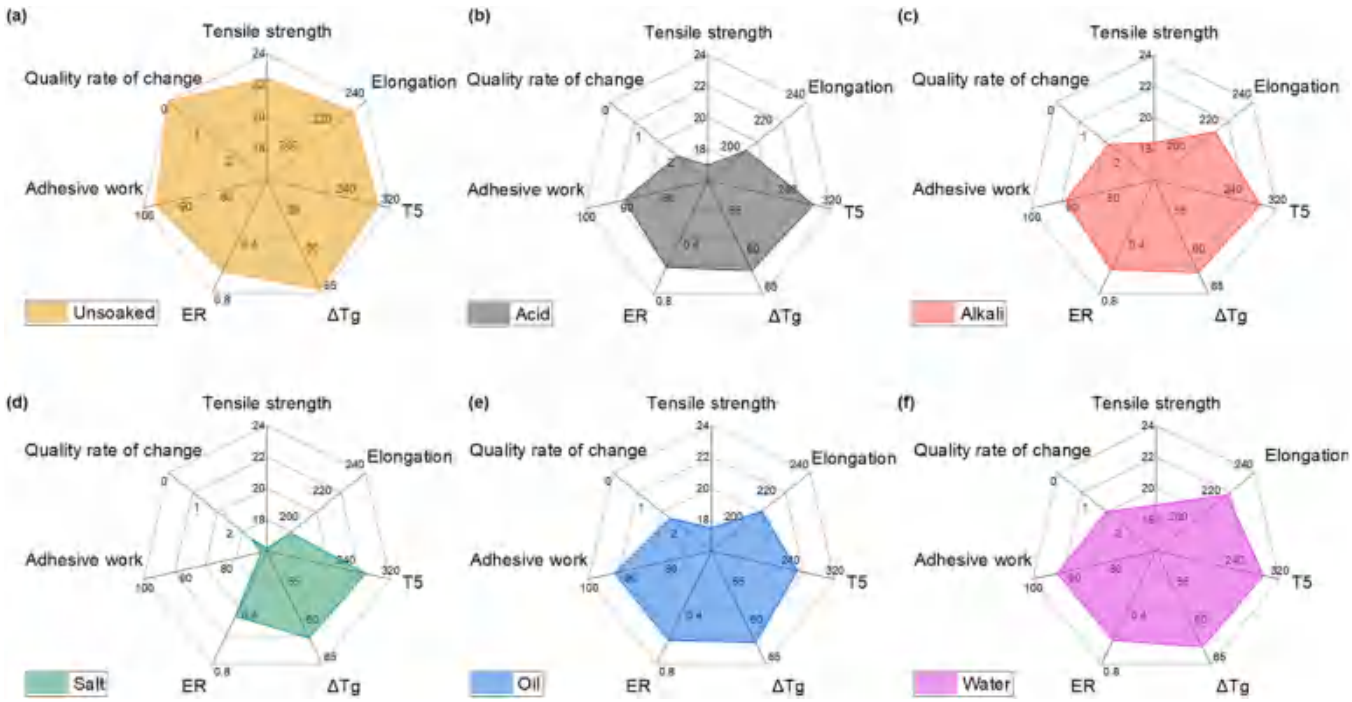

Fig. 14. The schematic representation of polyurethanes in different solution environments.

Declaration of Competing Interest

The authors declare that they have no known competing financial interests or personal relationships that could have appeared to influence the work reported in this paper.

Acknowledgments

The authors would like to thank Fundamental Research Funds for the Central Research Institutes (Grant No. 2024–9012). The National Natural Science Foundation of China (Grant No. 52178403, 51578027 and 52208411). The National Key R&D Program Winter Olympics Special (Grant No. 2018YFF0300305–03). The Nonmetallic Excellence and Innovation Center for Building Materials (NEXCEL) Innovation Fund (Grant No. 24TDA-4). Their assistance is sincerely appreciated.

Data availability

Data will be made available on request.

References

[1] Q. Chen, Y. Li, C. Wang, et al., Degradation of mechanical properties of polyurethane elastomer coatings under different pavement pollution conditions, Constr. Build. Mater. 409 (2023) 134181, https://doi.org/10.1016/j.conbuildmat.2023.134181.
[2] B. Cheng, W. Gao, X. Ren, et al., A review of microphase separation of polyurethane: characterization and applications, Polym. Test. 107 (2022) 107489, https://doi.org/10.1016/j.polymertesting.2022.107489.
[3] S. Chowdhury, S. Roy, S. Singh, Performance assessment of three alkali-treated Fly ashes as a pavement base-course material, Constr. Build. Mater. 365 (2023) 130110, https://doi.org/10.1016/j.conbuildmat.2022.130110.
[4] Z. Dai, P. Jiang, W. Luo, et al., Preparation of degradable vegetable oil-based waterborne polyurethane with tunable mechanical and thermal properties, Eur. Polym. J. 139 (2020) 109994, https://doi.org/10.1016/j.eurpolymj.2020.109994.
[5] S. Duan, J. Cui, J. Hu, et al., Research on the adhesion mechanism and compatibility of acrylate composite polyurethane binder aggregate based on surface free energy theory, Constr. Build. Mater. 438 (2024) 137236, https://doi.org/10.1016/j.conbuildmat.2024.137236.
[6] S. Duan, X. Wu, H. Wang, et al., Design and evaluation of semi self-compacting cold mix polyurethane mixture for steel bridge deck pavement, Constr. Build. Mater. 419 (2024) 135490, https://doi.org/10.1016/j.conbuildmat.2024.135490.
[7] A. Farina, M.E. Kutay, A. Anctil, Environmental assessment of asphalt mixtures modified with polymer coated rubber from scrap tires, J. Clean. Prod. 418 (2023) 138090, https://doi.org/10.1016/j.jclepro.2023.138090.
[8] B. Feng, H. Wang, S. Li, et al., The durability of asphalt mixture with the action of salt erosion: a review, Constr. Build. Mater. 315 (2022) 125749, https://doi.org/10.1016/j.conbuildmat.2021.125749.
[9] H. Fu, C. Wang, D. Wang, et al., Durability evaluation of mechanical and bonding properties of polyurethane-modified waterborne epoxy resin for road, Int. J. Pavement Eng. 24 (2023) 2027419, https://doi.org/10.1080/10298436.2022.2027419.
[10] J. Gao, H. Wang, J. Chen, et al., Laboratory evaluation on comprehensive performance of polyurethane rubber particle mixture, Constr. Build. Mater. 224 (2019) 29–39, https://doi.org/10.1016/j.conbuildmat.2019.07.044.
[11] R. Guo, H. Zhang, Y. Tan, Influence of salt dissolution on durable performance of asphalt and Self-ice-melting asphalt mixture, Constr. Build. Mater. 346 (2022) 128329, https://doi.org/10.1016/j.conbuildmat.2022.128329.
[12] Hong, B., Wang, J., Zhang, J., et al. Study on the water stability of polyurethane concrete from perspective of polyurethane-aggregate interface. J Mater Civ Eng. 34, 04022237 https://doi.org/10.1061/(ASCE)MT.1943-5533.0004391.
[13] C. Hu, Z. Zhou, Y. Luo, Study on damage evolution and mechanism of semi-flexible pavement under acid rain erosion, Case Stud. Constr. Mater. 19 (2023) e02286, https://doi.org/10.1016/j.cscm.2023.e02286.
[14] J. Jiang, H. Gao, M. Wang, et al., Effect of fillers on the microphase separation in polyurethane composites: a review, Polym. Eng. Sci. 63 (2023) 3938–3962, https://doi.org/10.1002/pen.26507.
[15] Z. Jiang, C. Tang, J. Yang, et al., A lab study to develop polyurethane concrete for bridge deck pavement, Int. J. Pavement Eng. 23 (2022) 1404–1412, https://doi.org/10.1080/10298436.2020.1804063.
[16] E. Kalkornsurapranee, C. Nakason, C. Kummerlöwe, et al., Development and preparation of high-performance thermoplastic vulcanizates based on blends of natural rubber and thermoplastic polyurethanes, J. Appl. Polym. Sci. 128 (2013) 2358–2367, https://doi.org/10.1002/app.38201.
[17] W. Li, D. Wang, C. Xiong, et al., Mechanism, prevention and remedy of alkali-pumping in new constructed asphalt pavement, Int. J. Pavement Eng. 23 (2022) 2689–2702, https://doi.org/10.1080/10298436.2020.1869237.
[18] Y. Li, H. Li, S. Nie, et al., Negative impacts of environmental factors (UV radiation, water and different solutions) on bitumen and its mechanism, Constr. Build. Mater. 265 (2020) 120288, https://doi.org/10.1016/j.conbuildmat.2020.120288.
[19] G. Liao, H. Wang, J. Xiong, et al., Mechanical properties of poroelastic road surface with different material compositions, J. Mater. Civ. Eng. 32 (2020) 04020253, https://doi.org/10.1061/(ASCE)MT.1943-5533.0003345.
[20] Q. Liu, M. Yang, H. Jing, et al., Preparation and performance of cementing materials for rapid maintenance of pavement potholes, Dyna 98 (4) (2023) 426–432, https://doi.org/10.6036/10914.
[21] P. Lyu, W. Li, X. Jing, et al., Study on chloride resistance of polyurethaneurea-coated mortar, Paint Coat. Ind. 49 (2019) 1–6, https://doi.org/10.12020/i.issn.0253-4312.2019.2.1.

[22] Y. Meng, Q. Yao, S. Mo, et al., The influence of acid rain on asphalt and its mixture performance, simulation and micro-mechanism exploration, Fuel 379 (2025) 133010, https://doi.org/10.1016/j.fuel.2024.133010.
[23] Z. Pan, G. Feng, Y. Xue, et al., A novel Green polyurethane adhesive based on castor oil and tannic acid with excellent water, salt, acid, alkali and antibacterial properties, Ind. Crops Prod. 204 (2023) 117325, https://doi.org/10.1016/j.indcrop.2023.117325.
[24] Y. Pang, P. Hao, A review of water transport in dense-graded asphalt mixtures, Constr. Build. Mater. (2017), https://doi.org/10.1016/j.conbuildmat.2017.08.092.
[25] G. Qian, X. Zhu, H. Yu, et al., The oil pollution and nitric oxide photocatalytic degradation evaluation of composite nanomaterials for asphalt pavement, Constr. Build. Mater. 314 (2022) 125497, https://doi.org/10.1016/j.conbuildmat.2021.125497.
[26] K. Shi, X. Li, L. Lei, et al., Influence of dangling chains on the microphase separation and damping properties of polyurethane, J. Appl. Polym. Sci. 141 (2024) e55867, https://doi.org/10.1002/app.55867.
[27] B. Shu, S. Wu, L. Dong, et al., Self-healing capability of asphalt mixture containing polymeric composite fibers under acid and saline-alkali water solutions, J. Clean. Prod. 268 (2020) 122387, https://doi.org/10.1016/j.jclepro.2020.122387.
[28] S. Skuodis, N. Dirgeliene, M. Zakarka, et al., Determination of degradation and compressive strength of polyurethane resin applied for bridge abutment, Balt. J. Road. Bridge E 19 (4) (2024) 96–118, https://doi.org/10.7250/bjrbe.2024-19.650.
[29] C. Wang, Z. Xu, Y. Xia, et al., Water transport mechanism and performance evaluation in polyurethane materials: a state-of-the-art review, Polym. Test. 138 (2024) 108554, https://doi.org/10.1016/j.polymertesting.2024.108554.
[30] F. Wang, X. Wang, Y. Xi, et al., Electrostatic spinning based on aqueous polyurethane block-modified polycaprolactone and its hydrophilicity study, Macromol. Mater. Eng. 306 (2021) 2100573, https://doi.org/10.1002/mame.202100573.
[31] W. Wang, L. Sun, M. Li, et al., Mechanical properties and micromechanisms of sbs-modified asphalt binder under multiple aging and regeneration effects, J. Mater. Civ. Eng. 36 (2024) 04024284, https://doi.org/10.1061/JMCEE7.MTENG-17561.
[32] Z. Wang, M. Du, H. Fang, et al., Influence of different corrosion environments on mechanical properties of a roadbed rehabilitation polyurethane grouting material under uniaxial compression, Constr. Build. Mater. 301 (2021) 124092, https://doi.org/10.1016/j.conbuildmat.2021.124092.
[33] Y. Wei, F. Wang, X. Gao, et al., Microstructure and fatigue performance of polyurethane grout materials under compression, J. Mater. Civ. Eng. 29 (2017) 04017101, https://doi.org/10.1061/(ASCE)MT.1943-5533.0001954.
[34] X. Jiang, M. Xu, M. Wang, et al., Preparation and molecular dynamics study of polyurethane damping elastomer containing dynamic disulfide bond and multiple hydrogen bond, Eur. Polym. J. 162 (2022) 110893, https://doi.org/10.1016/j.eurpolymj.2021.110893.
[35] F. Xie, T. Zhang, P. Bryant, et al., Degradation and stabilization of polyurethane elastomers, Prog. Polym. Sci. 90 (2019) 211–268, https://doi.org/10.1016/j.progpolymsci.2018.12.003.
[36] L. Xu, J. Wang, X. Xiao, et al., Performance investigation and internal-structure analysis of polyurethane bonded mixture on highway steel bridge, J. Mater. Civ. Eng. 35 (2023) 04023397, https://doi.org/10.1061/JMCEE7.MTENG-16068.
[37] S. Yan, C. Zhou, J. Ouyang, Rejuvenation effect of waste cooking oil on the adhesion characteristics of aged asphalt to aggregates, Constr. Build. Mater. 327 (2022) 126907, https://doi.org/10.1016/j.conbuildmat.2022.126907.
[38] F. Yang, L. Cong, J. Shi, et al., Laboratory evaluation on pavement performance of polyurethane mixture for thin overlay, J. Mater. Civ. Eng. 33 (2021) 04021212, https://doi.org/10.1061/(ASCE)MT.1943-5533.0003927.
[39] H. Yang, L. Pang, Y. Zou, et al., The effect of water solution erosion on rheological, cohesion and adhesion properties of asphalt, Constr. Build. Mater. 246 (2020) 118465, https://doi.org/10.1016/j.conbuildmat.2020.118465.
[40] J. Yang, Z. Zhang, J. Shi, et al., Comparative analysis of thermal aging behavior and comprehensive performance of high viscosity asphalt (HVA) from cohesion, adhesion and rheology perspectives, Constr. Build. Mater. 317 (2022) 125982, https://doi.org/10.1016/j.conbuildmat.2021.125982.
[41] M. Yu, C. Fan, Feng Ge, et al., Anticorrosion behavior of organic offshore coating systems in UV, salt spray and low temperature alternation simulated Arctic offshore environment, Mater. Today Commun. 28 (2021) 102545, https://doi.org/10.1016/j.mtcomm.2021.102545.
[42] X. Yu, Y. Yuan, Z. Deng, Experimental investigation on the water stability of castable high-capacity polyurethane bearing, Constr. Build. Mater. 398 (2023) 132485, https://doi.org/10.1016/j.conbuildmat.2023.132485.
[43] M. Zhang, Z. Hu, J. Zhao, et al., Components optimization of polyurethane-modified asphalt binder towards compatibility: insight from molecular dynamics simulations, Constr. Build. Mater. 448 (2024) 138229, https://doi.org/10.1016/j.conbuildmat.2024.138229.
[44] Z. Zhang, Z. Wang, S. Zhang, et al., Experimental studies and molecular dynamics simulation of the compatibility between thermoplastic polyurethane elastomer (TPU) and asphalt, Constr. Build. Mater. 411 (2024) 134316, https://doi.org/10.1016/j.conbuildmat.2023.134316.
[45] X. Zheng, J. Yan, Y. Wang, et al., Mechanics and durability of polyurethane cement composite (PUC) material, Mater. Plast. 61 (2024) 63–74, https://doi.org/10.37358/MP.24.2.5719.

A practical method for testing the properties of phase-change building materials and composites

Haijian Li[*a,b,c], Yingxin Liu[d], Wei Zhuang[e], Hao Wu[*a,b], Zhongcheng Ma[a,b]
[a]China Building Materials Academy Co., Ltd, Beijing 100024, China; [b]State Key Laboratory of Green Building Materials, Beijing 100024, China; [c]Non-Metallic Excellence and Innovation Center for Building Materials, Beijing, 100024, China; [d]China University of Geosciences (Beijing), Beijing,100083, China; [e]China Testing & Certification International Group Co. Ltd, Beijing, 100024, China

ABSTRACT

In this paper, a testing method special for phase change building materials was designed for testing the phase change temperatures, latent heat of phase change, specific heat of solid/liquid phase change materials and so on. The weight of the testing sample could be 5 Kg or even more. Even if the amount of the testing samples was huge, the testing samples can still be homogenous during the test, avoiding of the test data errors caused by sample preparation. Moreover, in this test method, any contrast samples were not used. The heat related to the testing sample could be calculated directly from the testing records, which eliminated the errors caused by the difference between the test conditions and the test process of the contrast samples and the testing samples. Therefore, the results based on the test method are more scientific, accurate and effective. Three typical phase change materials are selected for verifying the testing results. When compared with the results from existing literatures, the results obtained by the designed testing method showed high accuracy and repeatability. It turned out that the method could be generally used for testing the phase change properties of the phase change building materials.

Keywords: phase-change building materials, phase-change temperature, latent heat

1. INTRODUCTION

Clean and renewable energy, such as solar and wind energy, are increasingly replacing fossil fuel energy to decrease environmental pollution. However, these energy forms have fluctuations and intermittency, making it difficult to provide a steady energy supply. Researchers have addressed these issues using the energy storage technology by storing heat in phase-change materials (PCMs), which are highly efficient in this regard. Accordingly, PCM products, including phase-change building materials (PCBMs), have been developed and introduced to the market for utilization. Evaluating the properties of PCBMs and related products remains a crucial problem. Many researchers have developed different approaches and apparatuses to test the performance of PCBMs. Conventional methods, such as differential thermal analysis and differential scanning calorimetry (DSC), are commonly used to determine the phase-change temperature, latent heat, and heat capacity of PCBMs [1-5]. However, these methods have notable drawbacks: the sample size used is very small and cannot represent the practical performance of bulk materials and the equipment used are expensive and complex. Another effective testing method is the T-history approach, which can simultaneously determine the melting point, supercooling degree, fusion heat, specific heat, and thermal conductivity of several PCM samples [6-11]. However, this method has a limitation, i.e. the temperature differences between the testing sample and reference material, which introduce obvious errors. In this study, we have developed a practical method that is easy to operate. Also, it saves a lot of time and cost to perform the test. Most importantly, this test method is suitable for evaluating large-volume or large-weight PCBMs.

2. PROCEDURE OF THE METOD

This test method is based on the principle of energy conservation. According to this fundamental principle of physics, the total energy of an isolated system remains constant despite internal changes. In other words, the heat absorbed by a substance at a low temperature equals to the heat released by that substance at a high temperature. Based on the principle,

[*]Correspondence: lhj.1002@163.com (H J Li); wuhao@cbma.com.cn (H Wu)

Fifth International Conference on Mechanical Engineering and Materials (ICMEM 2024),
edited by Gupta Manoj, Jinyang Xu, Proc. of SPIE Vol. 13547, 1354736
© 2025 SPIE · 0277-786X · doi: 10.1117/12.3059786

we designed a home-made apparatus, which could help us to record some important temperature-related parameters. In the below, we have tried to explain how to obtain the critical properties of PCMs according to the experimental and calculated results. Table 1 lists some nomenclatures and some abbreviated forms used in the method.

Table 1. The abbreviation expressions in this work.

Nomenclature		***Subscript***	
T_{wH}	High temperature of water [°C]	*w*	water
T_{wL}	Low temperature of water [°C]	*wH*	high temperature of water
T_{sH}	High temperature of sample [°C]	*wL*	low temperature of water
T_{sL}	Low temperature of sample [°C]	*s*	sample or solid sample
T_{am}	Ambient temperature [°C]	*sH*	high tempersture of sample
T_P	Phase change temperature [°C]	*sL*	low temperature of sample
ΔT	Difference between T_{wL} and T_{am} [°C]	*am*	ambient temperature
Q_w	Heat released from water [kJ]	*P*	phase change
Q_s	Heat absorbed by sample [kJ]	*c*	specific heat capacity
Q_m	Heat absorbed by container of sample [kJ]	*en*	environment
Q_{en}	Heat dispersed into environment [kJ]	*sen*	sensible
Q_{sen}	Sensible heat absorbed by sample [kJ]	*l*	liquid
H	Latent heat of sample [kJ/kg]	*m*	metallic container
m_w	Mass of water [kg]	*begin*	time of the beginning of the testing
m_s	Mass of sample [kg]	*balance*	the time when the the temperature is stable
m_m	Mass of container [kg]	*end*	time of the ending of the testing
c_w	Specific heat capacity of water [kJ/(kg·°C)]		
c_c	Specific heat capacity of container[kJ/(kg·°C)]		
c_s	Specific heat capacity of solid sample[kJ/(kg·°C)]		
c_l	Specific heat capacity of liquid sample[kJ/(kg·°C)]		
t	Time[s]		

2.1 First step of the test

The apparatus used is shown in Figure 1. Before the test, the sample was placed in a thermostat for 24 h. The sample container is special designed for building materials of which the size is usually much larger than micron-materials. The size of the sample container is adjustable. The testing samples could be powders or bulk. Usually, the sample container could load samples weighing 5 Kg or above. Hot water was preheated to ~80 °C before being poured into a heat insulation box. After 30 min, a metallic container with the weighed sample was removed from the thermostat, where the temperature was maintained at $T_{sL1} \approx 10$ °C, and placed in hot water at temperature T_{wH1}. The ambient temperature was kept below 16 °C. Throughout the testing process, the temperatures of the sample and hot water were automatically recorded using a temperature recorder.

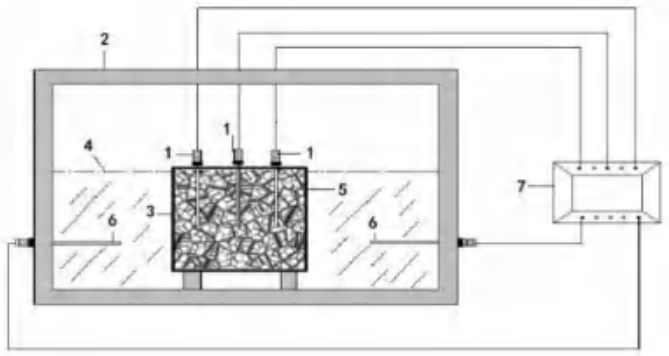

Figure 1. Schematic of the experimental apparatus: 1- digital temperature probe for sample; 2- heat insulation box; 3- metallic sample container; 4- hot water; 5- sample; 6- digital temperature probe for hot water; 7- temperature recorder.

Here, we emphasize the actual meaning of the fitting curve in our case. The fitting curve corresponds to the temperature drop of water assuming that no sample is placed in the heat insulation box. Compared to the temperature curve of water,

the only reason for temperature decrease in the fitting curve is heat loss to the environment. The fitting curve is derived from the water temperature data recorded from $t_{balance}$ to t_{end} using the following formula:

$$T = T_{am} + \Delta T \times e^{-t/k} \tag{1}$$

where T_{am} is the ambient temperature and ΔT is the difference between the initial temperature of hot water and T_{am}. Further, t is the testing time and k is a constant related to the water volume and the performance of the heat insulation box.

Figure 2 shows that the temperatures of water and the sample are the same at $T_{balance}$. Before $T_{balance}$, the temperature of water drops from T_{wH1} to T_{sH1}. Heat released by the water (Q_{w1}) includes two components: one component is transferred to the sample (Q_{s1}) and the metallic sample container (Q_{m1}) while the other component is lost to the environment (Q_{en}), with heat transfer to the heat insulation box being negligible.

$$Q_{w1} = m_{w1} \times c_w \times (T_{wH1} - T_{sH1}) \tag{2}$$

or

$$Q_{w1} = Q_{s1} + Q_{en1} + Q_{m1} \tag{3}$$

$$Q_{en1} = m_{w1} \times c_w \times (T_{wL1} - T_{sH1}) \tag{4}$$

$$Q_{m1} = m_m \times c_m \times (T_{sH1} - T_{sL1}) \tag{5}$$

where m_{w1}, m_m, c_w and c_m are the mass and specific heat of the water and container, respectively.

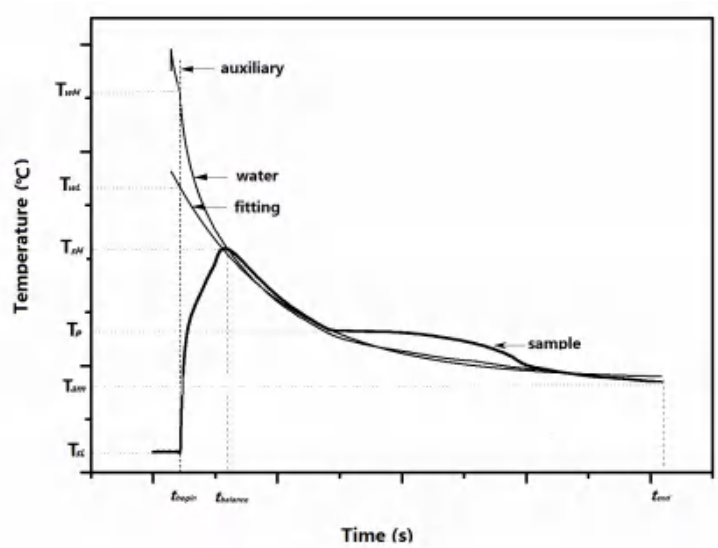

Figure 2. Temperatures as a function of time.

We can obtain Q_{s1} by combining equations (2), (3), (4), and (5):

$$Q_{s1} = m_{w1} \times c_w \times (T_{wH1} - T_{wL1}) - m_m \times c_m \times (T_{sH1} - T_{sL1}) \tag{6}$$

Furthermore, Q_{s1} can be calculated based on the rise in temperature of the sample. Q_{s1} includes the latent heat H and sensitive heat Q_{sen1} of the sample:

$$Q_{s1} = m_s \times H + Q_{sen1} \tag{7}$$

$$Q_{sen1} = m_s \times c_s \times (T_p - T_{sL1}) + m_s \times c_l \times (T_{sH1} - T_p) \tag{8}$$

where m_s is the mass of the sample, c_s is the specific heat capacity of the solid sample, and c_1 is the specific heat capacity of the liquid sample.

We can also obtain Q_{s1} by combining equations (7) and (8):

$$Q_{s1} = m_s \times H + m_s \times c_s \times (T_p - T_{sL1}) + m_s \times c_l \times (T_{sH1} - T_p) \quad (9)$$

2.2 Second step of the test

The procedure described in the first step is repeated, with the only difference being that the constant temperature T_{sL1} is changed to a new temperature T_{sL2}, which satisfies two conditions: $(T_{sL2} - T_{sL1}) \geq 10$ °C and $T_{sL2} \leq (T_p - 5$ °C). This yields the following two equations:

$$Q_{s2} = m_{w2} \times c_w \times (T_{wH2} - T_{wL2}) - m_m \times c_m \times (T_{sH2} - T_{sL2}) \quad (10)$$

or

$$Q_{s2} = m_s \times H + m_s \times c_s \times (T_p - T_{sL2}) + m_s \times c_l \times (T_{sH2} - T_p) \quad (11)$$

From equation (6), (9), (10), and (11), we can derive equation (12) for c_s:

$$c_s = \frac{m_{w1} \times c_w \times (T_{wH1} - T_{wL1}) - m_m \times c_m \times (T_{sH1} - T_{sL1} - T_{sH2} + T_{sL2}) - m_{w2} \times c_w \times (T_{wH2} - T_{wL2}) - m_s \times c_l \times (T_{sH2} - T_{sL1})}{m_s \times (T_{sL2} - T_{sL1})} \quad (12)$$

In this equation, the specific heat of the liquid sample c_l is the only uncertain value, which is determined in the next step.

2.3 Third step of the test

The procedure of the first step is repeated, and the temperature T_{sL1} is changed to a new temperature T_{sL3}, with $T_{sL3} \geq (T_p +$ 5 °C). The test results are shown in Figure 3.

The heat absorbed by the sample from hot water Q_{s3} is only because of the specific heat of the liquid sample and is unrelated to the phase-change process, which is completed before this step.

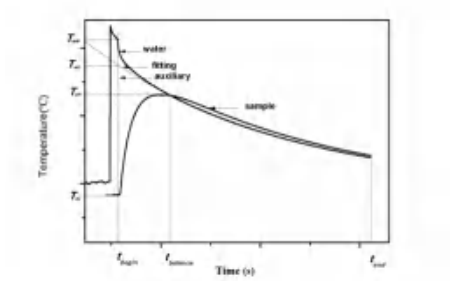

Figure 3. Temperature as a function of time when testing the specific heat of a liquid sample.

From Figure 3, we have

$$Q_{s3} = m_{w3} \times c_w \times (T_{wH3} - T_{wL3}) \quad (13)$$

$$Q_{s3} = Q_{sen3} + Q_m \quad (14)$$

$$Q_{sen3} = m_s \times c_l \times (T_{sH3} - T_{sL3}) \quad (15)$$

$$Q_m = m_m \times c_m \times (T_{sH3} - T_{sL3}) \quad (16)$$

Using equations (13)–(16), we can determine the value of c_l:

$$c_l = \frac{m_{w3} \times c_w \times (T_{wH3} - T_{wL3}) - m_m \times c_m \times (T_{sH3} - T_{sL3})}{m_s \times (T_{sH3} - T_{sL3})} \quad (17)$$

This value of c_l is substituted in equation (9) to obtain c_s.

Finally, based on equations (6), (9), (12), and (17) or (10), (11), (12), and (17), the latent heat of the sample H can be calculated:

$$H = \frac{m_{w1} \times c_w \times (T_{wH1} - T_{wL1}) - m_c \times c_c \times (T_{sH1} - T_{sL1})}{m_s} - c_s \times (T_p - T_{sL1}) - c_l \times (T_{sH1} - T_p) \quad (18)$$

or

$$H = \frac{m_{w2} \times c_w \times (T_{wH2} - T_{wL2}) - m_c \times c_c \times (T_{sH2} - T_{sL2})}{m_s} - c_s \times (T_p - T_{sL2}) - c_l \times (T_{sH2} - T_p) \quad (19)$$

3. RESULTS

Three typical phase change materials including $CaCl_2 \cdot 6H_2O$, $CH_3COONa \cdot 3H_2O$ and $Na_2SO_4 \cdot 10H_2O$ were selected as testing samples. The phase change temperatures, the latent heat of phase change and the specific heat were calculated and listed in Table 2. The maximum errors for these results are less than 5%, which indicates the high accuracy and the repeatability of the designed testing method.

Table 2. The testing results of three typical phase change materials (PCMs).

PCMs	No. of the test	T_p (°C)	H (kJ kg^{-1})	c_s (kJ kg^{-1} K^{-1})	c_l (kJ kg^{-1} K^{-1})
$CaCl_2 \cdot 6H_2O$	1	27.3-29.2	167	1.74	2.68
	2	27.2-29.6	158	1.85	2.57
	3	26.8-28.4	169	1.81	2.55
	Average	27-29	165	1.8	2.6
	Max error	2.0%	4.2%	3.3%	3.1%
$CH_3COONa \cdot 3H_2O$	1	58.2	228.5	2.35	3.33
	2	58.4	230.4	2.27	3.45
	3	58.3	236.8	2.32	3.46
	Average	58.3	232	2.3	3.4
	Max error	0.2%	2.1%	2.2%	2.1%
$Na_2SO_4 \cdot 10H_2O$	1	29.5-34.1	218.4	2.18	3.29
	2	28.7-33.2	236.7	2.31	3.16
	3	28.9-32.5	225.3	2.15	3.18
	Average	29-33	226	2.2	3.3
	Max error	3.3%	3.4%	5%	2.8%

Table 3 presents the testing results of the thermophysical properties of three typical PCMs obtained using the proposed test method and from literatures.

Compared to the properties reported in the literatures, the deviations in the measured thermophysical properties of PCMs are <10%. This indicates that the proposed method is reliable for testing the properties of PCMs.

Table 3. Thermophysical properties of some typical PCMs.

PCMs	T_p (°C)	H (kJ kg^{-1})	c_s (kJ kg^{-1} K^{-1})	c_l (kJ kg^{-1} K^{-1})	Test method	Ref.
$CaCl_2 \cdot 6H_2O$	27-29	165	1.8	2.6	Present	
	27.6-29.6	158.97-172.26			DSC	[12]
	28	200	1.25	2.13		[13]
	27-30	161			DSC	[14]
	23	130			DSC	[15]
	29.8	174			DSC	[16]
	29	190.8			DSC	[17]
	27-30.2				Self-designed	[18]
	24	140	1.4	2.1	DSC	[19]
	28	190		2.13		[20,21]
$CH_3COONa \cdot 3H_2O$	58.3	232	2.3	3.4	present	
	58	265			DSC	[16]
	58	249	2.14	2.98	DSC	[22]
	58	226-248	2.26-2.79	3.33	T-history	[6,23]
	58	245±9	2.26±0.13	3.74±0.59	T-history	[8,24]
	58	267	2.79	4.53		[23,24]
Na_2SO_4. $10H_2O$	29-33	226	2.2	3.2	present	
	34.5-35	205.82-233.35	1.92	3.26	DSC	[25]
	32.4	254			DSC	[16]
	32	251.1				
	29-30	227	3.4	4.6(gel)	DSC	[26]
	24.6-26.2				DSC	[27]
	21	198				[28]
	28-32	253(10%gel)			T-history	[29]
		235			DSC	

4. CONCLUSION

The testing method presented herein is more applicable than DSC and uses less expensive instruments. It is particularly suitable for testing bulk PCM composites used in building materials and heat-storage equipment, overcoming the limitations of DSC, which only tests small samples. Meanwhile, compared to the T-history method, this method does not require a reference sample, reducing errors associated with it. The proposed test method is easier to handle and operate and the measured results are more practical than previous methods. The thermophysical properties of common PCMs and composites can be measured using this method, and the obtained results are consistent with those reported in the literature. Testing precision can be improved if water used in the heat insulation box is replaced by oil or any other liquid with a low specific heat.

ACKNOWLEDGEMENTS

Financial support by the Program Fund of Non-Metallic Excellence and Innovation Center for Building Materials (No. 24SFP-3), Project of China National Building Material Group Co., Ltd (No. 2023SJYL0403), and Self-reliance Project of State Key Laboratory of Green Building Materials (No. ZA-118) are gratefully acknowledged.

REFERENCES

[1] Gmelin, E., Sarge, S. M., "Calibration of differential scanning calorimeters," Pure Appl. Chem. 67(11), 1789-1800 (1995).
[2] Gmelin, E., Sarge, S. M., "Temperature, heat and heat flow rate calibration of differential scanning calorimeters," Thermochim. Acta 347, 9-13 (2000).
[3] Schubnell, M., "Temperature and heat flow calibration of a DSC-Instrument in the temperature range between -100 and 160°C," J. Therm. Anal. Calorim. 61, 91-98 (2000).
[4] Schneker, B., Stäger. F., "Influence of the thermal conductivity on the Cp-determination by dynamic methods," Thermocim. Acta 304/305, 219-228 (1997).
[5] Wunderlich, B., Boller, A., Okazaki, I., Ishikiriyama, K., Chen, W., Pyda, M., Pak, J., Moon, I., Androsch, R., "Temperature-modulated differential scanning calorimetry of reversible and irreversible first-order transitions," Thermochim. Acta 330, 21-38 (1999).
[6] Zhang, Y., Jiang, Y., Jiang, Y., "A simple method, the T-history method, of determining the heat of fusion, specific heat and thermal conductivity of phase-change materials," Meas. Sci. Technol. 10, 201-205 (1999).
[7] Hong, H., Park, C. H., Choi, J. H., Peck, J. H., "Improvement of the T-history method to measure heat of fusion for phase change materials," Int. J. Air-Conditioning and Refrigeration 11(1), 32-39 (2003).
[8] Hong, H., Kim, S. K., Kim Y. S., "Accuracy improvement of T-history method for measuring heat of fusion of various materials," Int. J. Refrig. 27, 360-366 (2004).
[9] Günther, E., Hiebler, S., Mehling, H., "Determination of the heat storage capacity of PCM and PCM-objects as a function of temperature," Proc. of ECOSTOCK, 10th International Conference on Thermal Energy Storage, Stockton, USA (2006).
[10] Lázaro, A., Zalba, B., Marín, J. M., Cabeza, L. F., "Phase Change Materials and plastics compatibility," Presented at 8th Workshop IEA ECES Annex 17 "Advanced thermal energy storage techniques – Feasibility studies and demonstration projects", Kizkalesi, Turkey, (18-20 April 2005).
[11] Marin, J. M., Zalba, B., Cabeza, L., Mehling, H., "Determination of the enthalpy temperature curves of phase change materials with the T-history method – improvement to temperature dependent properties," Meas. Sci. Technol. 14, 184 -189 (2003).
[12] Xiang, L., Yuan, Z., Hongen Nian, N., "Phase change behavior of latent heat storage media based on calcium chloride hexahydrate composites containing strontium chloride hexahydrate and oxidation expandable graphite," Appl. Therm. Engin. 102, 38-44 (2016).
[13] Bilen, K., Takgil, F., Kaygusuz, K., "Thermal Energy Storage Behavior of CaCl2.6H2O during Melting and Solidification," Energy Sources, Part A 30, 775-787 (2008).
[14] Hasnain, S. M., "Review on sustainable thermal energy storage technologies, Part I: Heat storage materials and techniques," Energy Convers. Mgmt. 39(11), 1127-1138 (1998).
[15] Kimura, H., Kau., J., "Mixtures of calcium chloride hexahydrate with some salt hydrates or anhydrous salts as latent heat storage materials" Energy Convers. Mgmt. 28(3), 197-200 (1988).
[16] Sharma, A., Tyagi, V. V., Chen, C. R., Buddhi, D., "Review on thermal energy storage with phase change materials and applications," Renew. Sustain. Energy Rev. 13, 318-345 (2009).
[17] Farid, M. M., Khudhair, A. M., Razack, S., "A review on phase change energy storage: materials and applications," Energy Convers. Mgmt. 45, 1597-1615 (2004).
[18] Carlsson, B., "Phase change behavior of some latent heat storage media based on calcium chloride hexahydrate," Sol. Energy 83, 485-450 (2009).
[19] Tyagi, V.V., Buddhi, D., "Thermal cycle testing of calcium chloride hexahydrate as a possible PCM for latent heat storage," Sol. Energy Mater Sol. Cells 92, 891-899 (2008).
[20] Vakilaltojjar, S. M., Saman, W., "Analysis and modeling of a phase change storage system for air conditioning applications," Appl. Therm. Engin. 21, 2 49-263 (2001).

[21] Al-Abidi, A. A., Mat, S. B., Sopian K., Sulaiman, M. Y., Lim, C. H., Th, A., "Review of thermal energy storage for air conditioning systems," Renew. Sust. Energ. Rev. 16(8), 5802-5819 (2012).
[22] Araki, N., Futamura, M., Makino, A., Shibata, H., "Measurements of Thermophysical Properties of Sodium Acetate Hydrate," International Journal of Thermophys. 16 (6), 1455-1466 (1995).
[23] Kenisarin, M., Mahkamov, K., "Solar energy storage using phase change materials," Renew. Sust. Energ. Rev. 11, 1913-1965 (2007).
[24] Freitag, T., "A latent heat storage procedure based on super cooled salt solutions," In Proceedings of the 4th workshop IEA annex, Bendiktbeuern, Germany (10 April 1999).
[25] Purohit, B. K., Sistla, V. S., "Studies on solution crystallization of Na2SO4·10H2O embedded in porous polyurethane foam for thermal energy storage application," Thermochim. Acta 668, 9-18 (2018).
[26] Shin, B. C., Kim, S. D., Won-Hoon, P., "Phase separation and supercooling of a latent heat-storage material," Energy14(12), 921-930 (1989).
[27] Garcia-Romero, A., Diarce, G., Ibarretxe, J., Urresti, A., Sala J. M., "Influence of the experimental conditions on the subcooling of Glauber's salt when used as PCM," Sol. Energy Mater Sol. Cells 102, 189-195 (2012).
[28] Turnpenny, J. R., Etheridge, D. W., Reay, D. A., "Novel ventilation cooling system for reducing air conditioning in buildings. Part I: Testing and theoretical modelling," Appl. Therm. Eng. 20, 1019-1037 (2000).
[29] Gok, O., Yilmaz, M. O., Paksoy, H. O., "Stabilization of Glauber's salt for latent heat storage," Proceedings of the 10th International Conference on Thermal Energy Storage—Ecostock Conference (2006).

Construction and Building Materials 469 (2025) 140474

Contents lists available at ScienceDirect

Construction and Building Materials

journal homepage: www.elsevier.com/locate/conbuildmat

Investigation on physical, rheological properties and VOCs emission of asphalt modified with hydrocarbon-based graphene

Yansong Fan [a], Meizhu Chen [a,*], Xiaoyu Yang [b], Jianwei Zhang [a], Jun He [a], Muyan Han [a]

[a] State Key Laboratory of Silicate Materials for Architectures, Wuhan University of Technology, Wuhan 430070, China
[b] State Key Laboratory of Advanced Technology for Materials Synthesis and Processing, Wuhan University of Technology, Wuhan 430070, China

ARTICLE INFO

Keywords:
Modified asphalt
Hydrocarbon-based graphene
Physical properties
Rheological properties
VOCs emission

ABSTRACT

Hydrocarbon-based graphene (HG), derived from petrochemical by-products, can be economically produced in large-scale quantities needed for asphalt pavement application requirements. With the intention of exploring the application feasibility of HG in asphalt materials, the properties of HG were elucidated firstly. Basic properties and storage stability of hydrocarbon-based graphene modified asphalt (HGMA) were evaluated while its rheological behaviors and functional group were characterized. In addition, the concentrations of volatile organic compounds (VOCs) in HGMA containing different dosages of HG were assessed. The experimental results indicate that HG possesses a lamellar and pore structure, which is conducive to fusion with asphalt molecules and adsorption capacity. HGMA is harder and expresses weaker sensitivity to temperature than petroleum asphalt. The dispersion of HG in asphalt is uniform when the dosage does not exceed 1.5 % by mass of petroleum asphalt. Incorporation of HG improves the elastic recovery and anti-rutting abilities of asphalt while fatigue resistance is weakened and embrittlement is prone to occurrence. Modification of HG on asphalt belongs to a physical process. The inhibition effect of HG on VOCs emission of asphalt is positively correlates with its dosage, and the maximum concentration and stable concentration of VOCs are reduced by 58 % and 60 % respectively when the dosage of HG reaches 1.5 %. The experimental results provide a foundation for future application and development of HG in asphalt materials.

1. Introduction

As a vital part of the modern transportation system, the construction quality of asphalt pavement has a direct bearing on the overall economic development of the country [1,2]. Asphalt pavement occupies a crucial position relying on the advantages of smooth drive, quick service and convenient maintenance. However, traditional petroleum asphalt is liable to flow and crack under the impact of temperature while aging also frequently occurs during service [3,4]. As a result, rutting, cracking and other pavement diseases appear which will seriously affect road traffic safety and shorten service life [5]. Therefore, the performance of existing asphalt materials requires further enhancement to meet the application requirements in increasingly harsh service environments.

At present, styrene butadiene styrene (SBS) asphalt and rubber asphalt, as typical representatives, have been widely applied in the construction of high-grade asphalt pavement and achieve excellent effects [6–8]. Whereas, SBS modified asphalt has a high application cost and rubber powder exhibits terrible compatibility with asphalt and produces large quantities of fumes [9–11]. It is an urgent necessity to adopt a strategy for asphalt modification. Nanomaterials provide a novel research approach to strengthen the quality of asphalt materials [12–14]. Relevant researches demonstrate that nanomaterials can effectively enhance the properties of asphalt materials [15–17].

Graphene has been selected as a critical nano-modifier depending on particular two-dimensional structure, excellent mechanical strength, remarkable specific surface area and adsorption characteristic [18–20]. These properties create new possibilities for asphalt modification. Abbas et al. [21] revealed that graphene enhances the rheological properties and compatibility of rubber asphalt. Li et al. [22] found that the nano-scale graphene effectively contributed to the anti-aging properties and temperature sensibility of asphalt. Wang et al. [23] suggested that graphene is able to improve the basic properties of asphalt and absorb asphalt fumes. Huang et al. [24] demonstrated that vacancy defects promote the improvement of thermal-mechanical and anti-aging

* Corresponding author.
E-mail addresses: fys@whut.edu.cn (Y. Fan), chenmzh@whut.edu.cn (M. Chen), xyyang@whut.edu.cn (X. Yang), zhangjianwei@whut.edu.cn (J. Zhang), hejun0607@whut.edu.cn (J. He), myhan@whut.edu.cn (M. Han).

https://doi.org/10.1016/j.conbuildmat.2025.140474
Received 20 November 2024; Received in revised form 21 January 2025; Accepted 17 February 2025
0950-0618/© 2025 Elsevier Ltd. All rights are reserved, including those for text and data mining, AI training, and similar technologies.

properties. Nie et al. [25] concluded that functionalized graphene exhibits advantages on shear resistance of asphalt. These research results demonstrated graphene expressed obvious advantages to enhance the properties and inhibit fumes of asphalt materials.

However, traditional graphite-based graphene is scarce on raw materials, expensive in cost, and difficult to large-scale production for application demand of bulk asphalt materials. In addition, the development of petrochemical industry has produced large quantities of by-products which have complex composition, and dense polycyclic aromatic hydrocarbons, making it difficult to deeply process and comprehensively utilize. Fortunately, the economic and environmental value of petrochemical by-products can be drastically enhanced when it is employed as raw material to prepare hydrocarbon-based graphene (HG) [26]. Moreover, HG is liable to achieve volume production for large-scale application requirements of asphalt materials. The emergence of HG compensates for the deficiency of traditional graphite-based graphene. However, there is no research focuses on the application of HG in asphalt materials.

The aim of this research is to explore the effect of HG on properties of asphalt and evaluate its application feasibility in asphalt. For this purpose, the dispersion liquid of HG was pretreated first to obtain powder, scanning electron microscope (SEM), Raman spectrum and laser particle analyzer were employed to analyze the properties of HG powder. Subsequently, HG with 0 %, 0.5 %, 1.0 %, 1.5 % and 2.0 % by the mass of petroleum asphalt were set to prepare modified asphalt. Basic properties of modified asphalt were measured. Storage stability of hydrocarbon-based graphene modified asphalt (HGMA) and microcosmic distribution of HG in asphalt were evaluated. Moreover, rheological behaviors and functional group before and after modifying were investigated. Finally, the volatile organic compounds (VOCs) of HG asphalt were analyzed. And the experimental process is shown in Fig. 1. The experimental results will promote the application of HG in asphalt and make a great contribution to the sustainable development of the transportation industry.

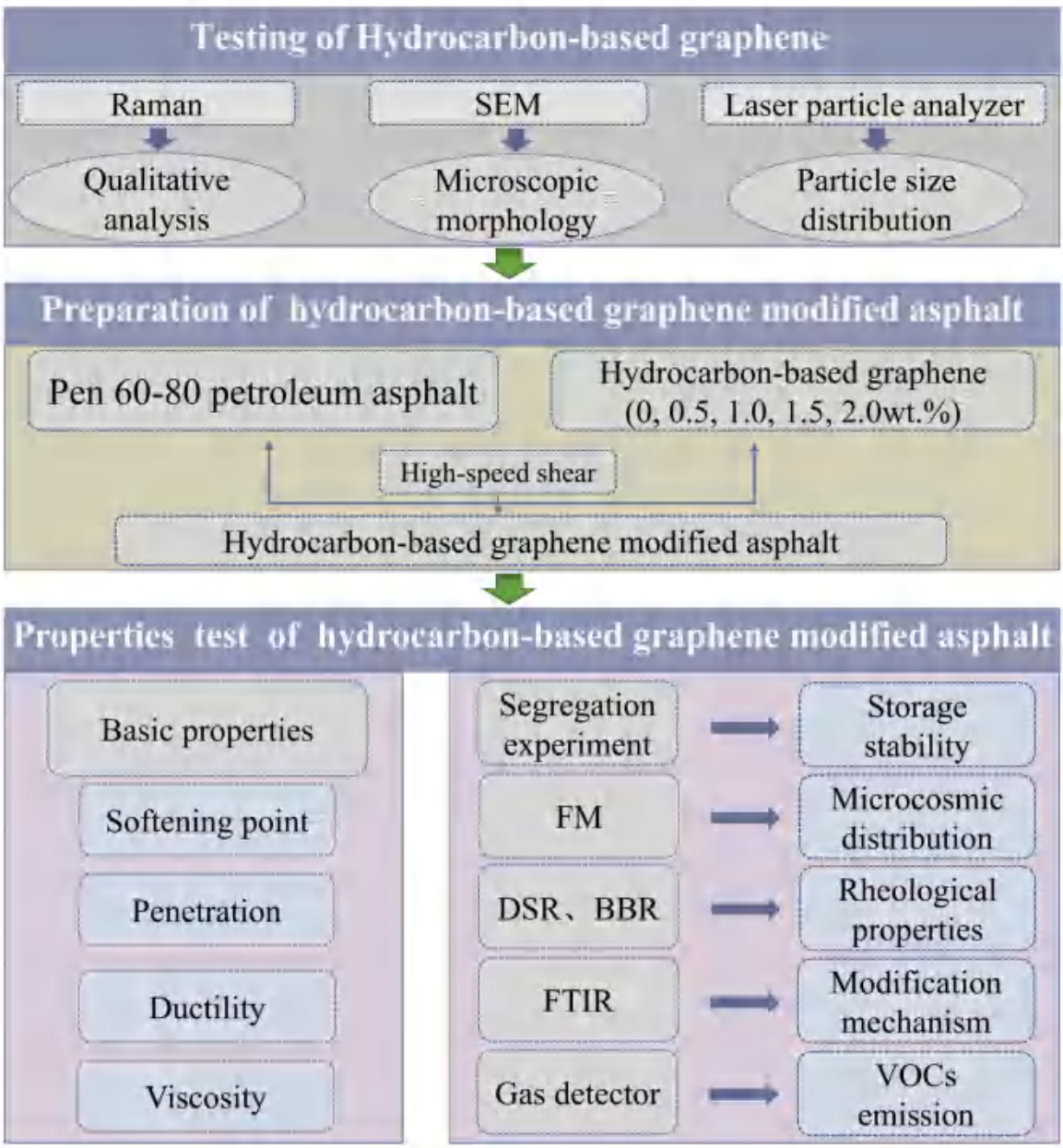

Fig. 1. Technical route of this research.

2. Materials and experimental methods

2.1. Raw materials

2.1.1. Petroleum asphalt

In this research, the asphalt optioned was 70# petroleum asphalt, whose specific properties parameters were shown in Table 1. It can be seen in Table 1 that the requirements of asphalt's properties comply with Chinese specification JTG F40-2004 [27].

2.1.2. Hydrocarbon-based graphene (HG)

HG was employed as a modifier which derived from petrochemicals, and its related performance indicators of HG is provided in Table 2. The original state of HG is dispersion liquid and requires pretreatment to obtain powder, which is conducive to controlling the solid content effectively and mixing with asphalt. Firstly, the HG dispersion liquid was filtered, and then dried at 100 °C for 2 h. Subsequently, the HG solid was ground with mortar to obtain powder. The molecular structure and appearances of dispersion liquid and obtained powder of HG are shown in Fig. 2, and a schematic of the pretreatment process is shown in Fig. 3.

2.2. Preparation of hydrocarbon-based graphene modified asphalt (HGMA)

The mass percentages of HG in asphalt were preset to 0 %, 0.5 %, 1.0 %, 1.5 % and 2.0 % by mass of petroleum asphalt, respectively. The detailed procedures for preparation of HGMA are displayed schematically in Fig. 4 and described in detail as follows. Relevant experimental parameters were selected based on Chinese specification JTG F40-2004 [27] and JTG E20-2011 [28].

(1) The 70# petroleum asphalt was heated to liquid condition in oven with the temperature of 135 ℃.
(2) The weighed HG powder was pre-mixed with asphalt manually to avoid powder splashing and form HGMA mixture.
(3) The formed HGMA mixture were sheared applying a high-speed shearing machine and subjected to the temperature at 150 ℃. The shear process was divided to three stages, shear speeds and times of three stages were set to 2000 r/min, 20 min; 3000 r/min, 30 min; and 5000 r/min, 10 min, respectively.
(4) After heat preservation in oven for half an hour to reach a stable state, the HGMA was obtained.

2.3. Properties test of hydrocarbon-based graphene (HG)

The qualitative analysis, microscopic morphology and particle size distribution of HG powder were carried out employing Raman spectrum (LabRAM Odyssey), SEM (Zeiss Ultra Plus) and laser particle analyzer (Mastersizer 2000), respectively.

Table 1
Properties parameters of 70# petroleum asphalt.

Properties	Units	Results	Requirements	Test methods
Penetration (25 ℃, 5 s, 100 g)	0.1 mm	71.2	60–80	T 0604-2011
Softening point	℃	47	≥ 46	T 0606-2011
Ductility (15 ℃)	cm	> 100	≥ 100	T 0605-2011
Density (15 ℃)	g/cm^3	1.022	/	T 0603-2011
Viscosity (135 ℃)	Pa·s	0.4	/	T 0625-2011
Flash point (COC)	℃	308	≥ 260	T 0611-2011
Mass loss (TFOT)	%	− 0.05	± 0.8	T 0609-2011

Table 2
Properties indicators of hydrocarbon-based graphene.

Properties		Units	Results
Dispersion liquid	State	/	Black liquid
	Solid content	%	4.8
Powder	State	/	Black powder
	Density	g/mL	0.2
	Specific surface area	m^2/g	207

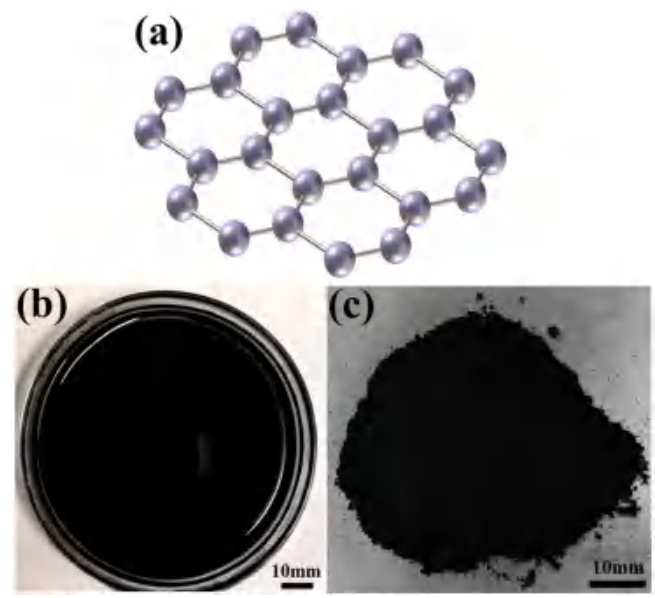

Fig. 2. Molecular structure and images of hydrocarbon-based graphene (a) Molecular structure; (b) Dispersion liquid; (c) Powder.

2.4. Experimental method of hydrocarbon-based graphene modified asphalt (HGMA)

2.4.1. Basic properties test

Based on Chinese standard JTG E20-2011 [28], main routine properties including softening point, viscosity, penetration and ductility of HGMA containing different dosages of HG were determined.

2.4.2. Storage stability test

Storage stability of HGMA were evaluated by utilizing the segregation experiment of Chinese specification JTG E20-2011 [28]. The HGMA with flow condition was weighed 50 g to inject into an aluminum tube (D = 25 mm, L = 140 mm). Subsequently, tube filled with asphalt was vertically placed in oven at 163℃. After standing for 48 h, the tube was removed and placed in a refrigerator until the sample was completely cooled and solidified. The solidified sample was divided into three equal parts and melted in an oven at 163℃. The softening point difference of top and bottom asphalt was determined and employed to elucidate storage stability.

2.4.3. Fluorescence microscope (FM) test

The dispersion state of HG powder in asphalt, which should be a crucial factor affecting the performance of modified asphalt, was observed employing FM. For this purpose, the prepared HGMA was taken and evenly distributed on the glass slide. The sample was as thin as possible in order to avoid affecting the judgment of the observation of HG powder. Finally, the FM was applied to observe the microcosmic distribution condition of HG which is magnified 100 times.

Fig. 3. Schematic for conversion of hydrocarbon-based graphene dispersion liquid to powder.

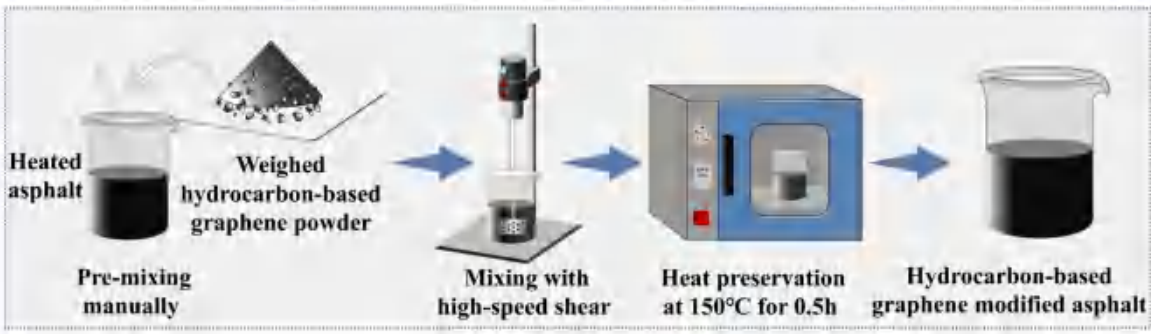

Fig. 4. Preparation of hydrocarbon-based graphene modified asphalt.

2.4.4. Rheological properties test

(1) **Dynamic shear rheometer (DSR) test**

The rheological behaviors of HGMA were characterized through dynamic shear rheometer (DSR) temperature scanning test in compliance with the Chinese specification JTG E20-2011 [28]. A rotor diameter of 25 mm and a sample thickness of 1 mm were employed to carry out high temperature scanning test in the range of 30–80 ℃. A rotor with a diameter of 8 mm and a sample thickness of 2 mm were selected to conduct low temperature scanning test at − 10 ℃ to 30 ℃. The complex shear modulus (G^*) and phase angle (δ) at high temperature were employed to evaluate the viscoelasticity at high temperature. $G^*/\sin\delta$ was selected to characterize the rutting resistance ability. The fatigue resistance was characterized through $G^* \cdot \sin\delta$ at medium temperature. The behaviors of HGMA at low temperature was determined through evaluating the relative changes between storage modulus (G') and loss modulus (G'').

(2) **Bending beam rheometer (BBR) test**

The rheological properties of HGMA at low temperatures were evaluated by BBR test according to Chinese specification JTG E20-2011 [28]. Experimental temperatures were set to − 12 ℃ and the load was 980mN ± 50 mN. The stiffness modulus (S) and creep rate (m) at 60 s were recorded which were employed to evaluate crack resistance of HGMA at low temperature.

2.4.5. Fourier transform infrared spectroscopy (FTIR) test

FTIR was applied to evaluate the functional group present in petroleum asphalt and HGMA and determine if chemical reactions occurred between HG and asphalt. The range of wave number was 400–4000 cm^{-1}, resolution was 4 cm^{-1}, scanning frequency was set to 32 times. The carbon disulfide solution was applied to dissolve asphalt, and the experiment was conducted subsequently.

2.4.6. VOCs emission test

In this research, a GT-1000 pump-suction intelligent gas detector with a built-in VOCs sensor, which exhibits high portability and accuracy, was selected to measure the emission of VOCs from asphalt. In the procedure, an asphalt sample with a weight of 50 g was taken and placed in an airtight container which was heated to the set temperature and kept for 1 h in an electric heating mantle. Then, the gas detector was connected with one end of the exhaust port of the airtight container to measure the maximum concentration and stable concentration of VOCs released by the asphalt at the high temperature. The maximum value of VOCs emission is defined as maximum concentration, and stable value of VOCs emission is stable concentration. Because the highest temperature of sample preparation in this research was 150 ℃, therefore, the set temperature for measuring VOCs was 150 ℃. The collection and detection device of VOCs is shown in Fig. 5.

3. Results and discussion

3.1. Properties of hydrocarbon-based graphene (HG)

The images of Raman spectrum, SEM and particle size distribution of HG powder are shown in Figs. 6–8, respectively. It can be seen in Fig. 6 that there are two peaks, occurred in Raman spectrum image, which are G peak at 1573 cm^{-1} and D peak at 1347 cm^{-1}. The former is the main characteristic peak of graphene which is attributed to the sp^2 hybridization of carbon atoms, and the latter is decided by the defects in graphene [29–31].

The SEM images in Fig. 7 show that HG powder exhibits a lamellar and pore structure, which is conducive to fusion with asphalt molecules. In addition, the pore structure may be related to adsorption capacity of HG. The particle size distribution data found in Fig. 8 demonstrates that 10 %, 50 % and 90 % of the particle in HG has diameters less than 0.507 μm, 1.735 μm and 20.002 μm, respectively.

3.2. Basic properties of hydrocarbon-based graphene modified asphalt (HGMA)

The softening point is a measure to characterize the consistency of asphalt and an important indicator reflecting the temperature sensitivity of asphalt. The penetration is utilized to represent the hardness degree of

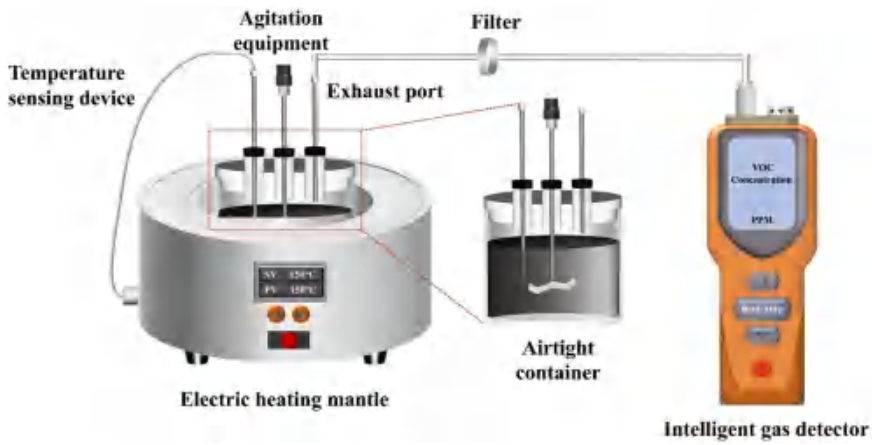

Fig. 5. Device for collection and detection device of VOCs from asphalt.

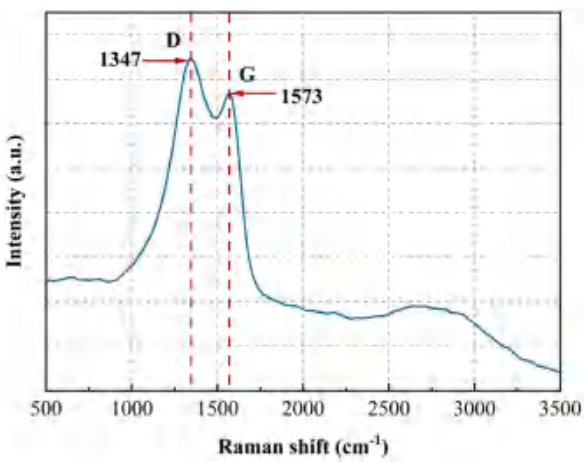

Fig. 6. Raman spectrum image of hydrocarbon-based graphene powder.

asphalt. And the plastic deformation ability and resistance of flow deformation are characterized by ductility and viscosity, respectively. In this research, these four indicators are applied to evaluate basic properties of HGMA, as shown in Fig. 9.

It can be found in Fig. 9 that softening point and viscosity of HGMA are enhanced as the increasing dosage of HG while both penetration and ductility are reduced. Specifically, the change rate of softening point and viscosity appears significant increase when the dosage of HG reaches 1.5 %. In contrast, the change rate of ductility declines sharply when the dosage of HG is changed from 1.5 % to 2.0 %, and the change trend of penetration is relatively stable. In other words, the consistency and hardness are enhanced while the fluidity, flexibility and sensitivity to temperature are weakened. In general, HG additive exhibits advantages in enhancing the high temperature performance, whereas, low temperature performance of asphalt is weakened.

The reasons could be explained that HG is filled in asphalt in the form of powder and readily combines with asphalt which impede the movement of asphalt to a certain degree. Furthermore, the flow of asphalt becomes difficult, as a result, the viscosity increases. As a layered nanomaterial, HG appears high surface activity, large surface energy and binding energy which contribute to combine with asphalt molecules. Moreover, the interlayer binding of HG mainly depends on van der

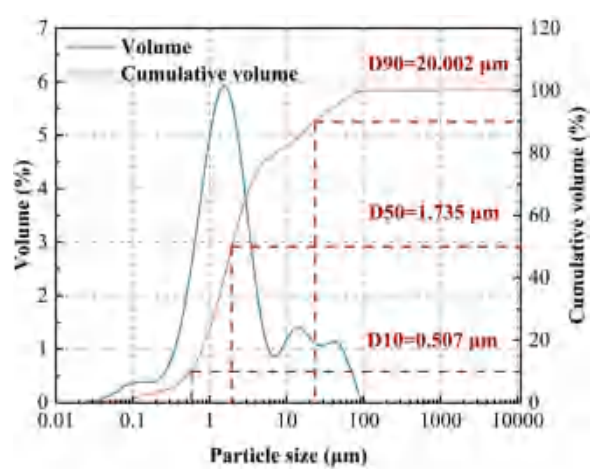

Fig. 8. Particle size distribution of hydrocarbon-based graphene powder.

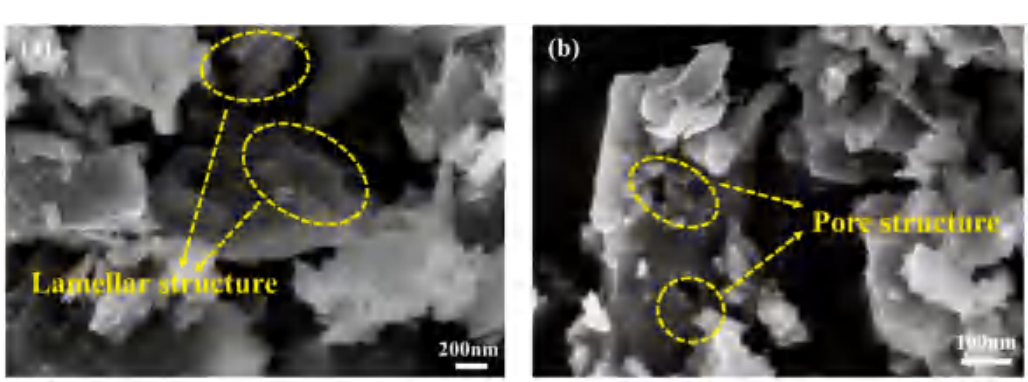

Fig. 7. SEM images of hydrocarbon-based graphene powder.

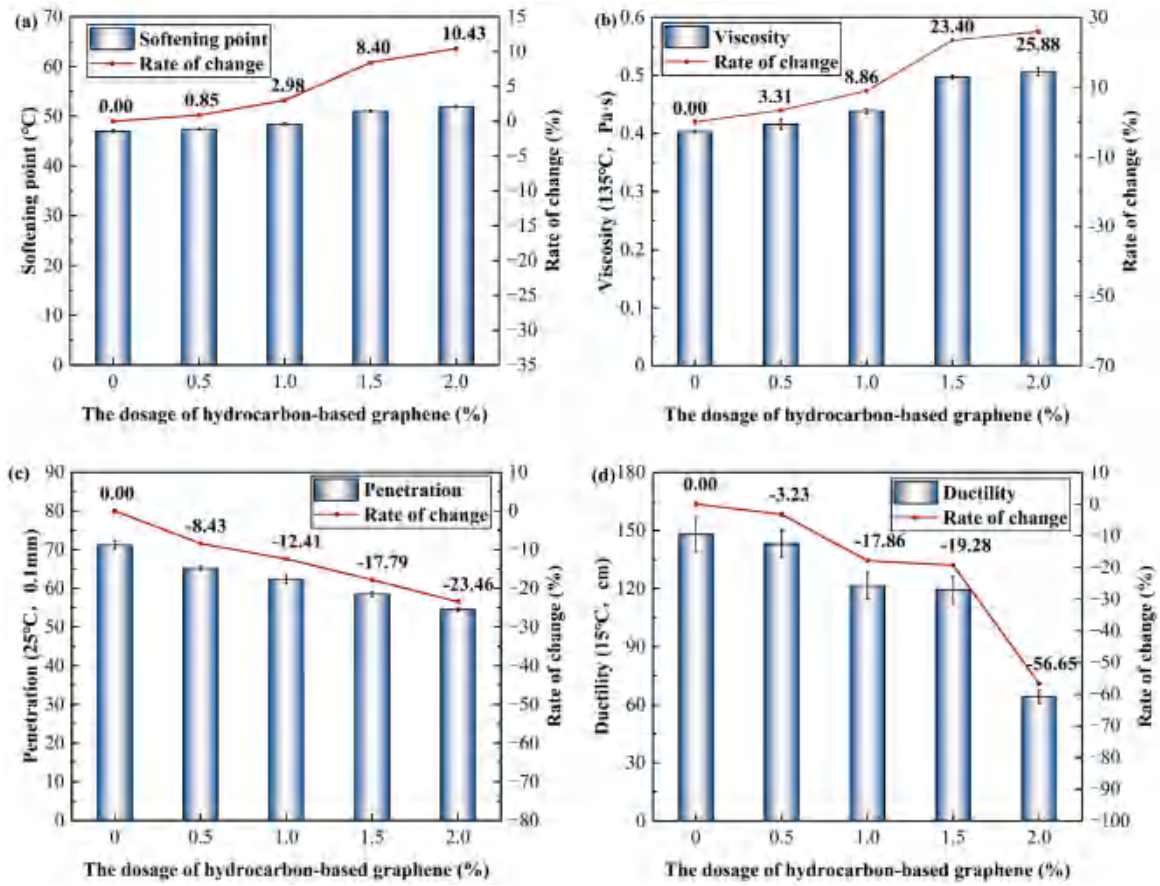

Fig. 9. Basic properties of hydrocarbon-based graphene modified asphalt.

Waals force which is relatively weak [32]. Following, the asphalt molecules are easy to form a crosslinking with HG, leading to an increase in the consistency of the asphalt [33,34]. In addition, boundary group and planar defects exist in HG which exert influence on structure stability [35]. Coupled with the large specific surface area of HG, asphalt molecules are adsorbed easily, resulting in hardening of asphalt, and consequently flexibility and malleability decrease. The reason for the sharp ductility reduction of modified asphalt with 2.0 % HG may be attributed to the serious agglomeration of HG powder in petroleum asphalt.

3.3. Storage stability of hydrocarbon-based graphene modified asphalt (HGMA)

The corresponding softening point and its difference of all samples are shown in Fig. 10. HGMA exhibits better storage stability when the difference of softening point is narrow. The Chinese standard [27] requires that the difference of softening point is less than 2.5 ℃ which suggests the modified asphalt exhibits excellent storage stability. What can be observed in Fig. 10 is that the softening point difference are 0.2 ℃, 0.4 ℃, 0.6 ℃, 0.9 ℃, 1.7 ℃, when the dosage is 0 %, 0.5 %, 1.0 %, 1.5 %, 2.0 %, respectively. The difference of softening point rises with the increase of graphene dosage. When the dosage is 2.0 %, the difference of softening point is most apparent, which may be due to the more serious agglomeration phenomenon of HG. However, the softening point difference all comply with Chinese specification requirements which demonstrates the tendency of phase separation between HG and asphalt is infrequent, and segregation occurs hardly. In other words, the storage stability performs well and HG expresses good compatibility with asphalt. It may be attributed to the layered structure and adsorption properties of HG, and full blending of HG powder and asphalt is promoted by high-speed shear.

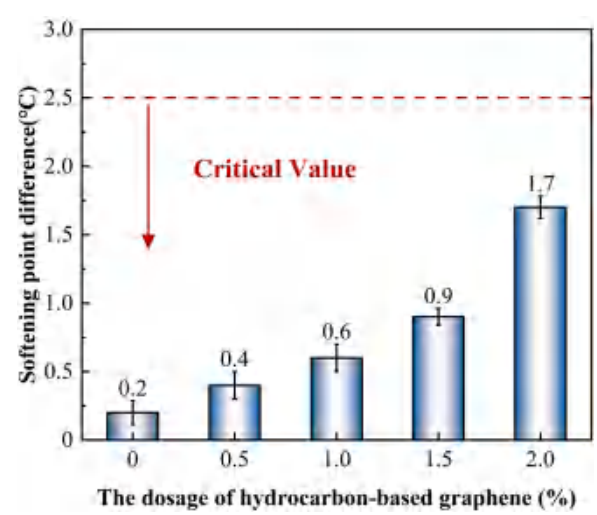

Fig. 10. Softening point difference of hydrocarbon-based graphene modified asphalt.

3.4. Microcosmic distribution of hydrocarbon-based graphene (HG) in asphalt

FM images of HGMA containing different dosage HG are shown in Fig. 11, in which asphalt is displayed as green area and the black spots correspond to HG dispersed in asphalt. When the dosage is 0.5 %, it is obvious that the HG is not scattered evenly in asphalt due to insufficient incorporation. There is extensive asphalt that has not been filled with HG and agglomeration phenomenon occurs hardly at this moment. The

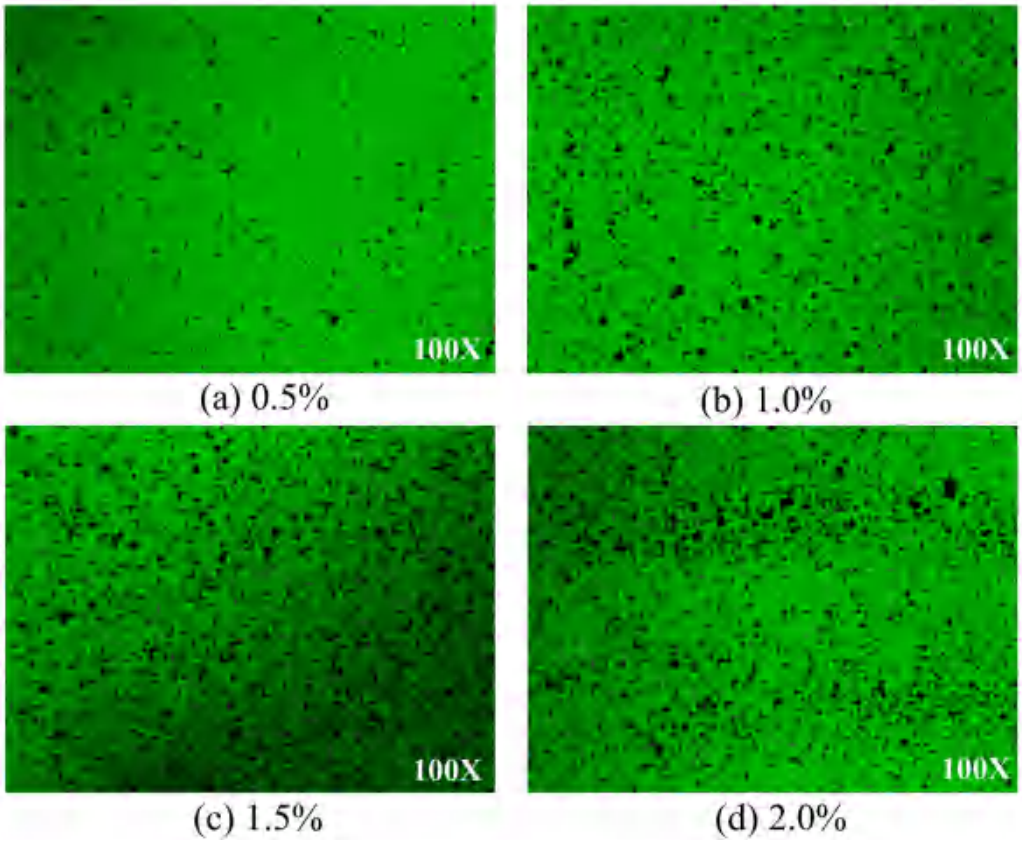

Fig. 11. FM images of hydrocarbon-based graphene modified asphalt.

distribution of HG is relatively homogeneous when the dosage is 1.0 %. Whereas, there is still a part of asphalt that is not covered by HG. The HG is the most uniform dispersed in asphalt when the dosage reaches 1.5 %. Although the agglomeration phenomenon is slightly evident than dosage of 1.0 %, there is no large agglomeration, which not exerts significant effect on the uniformity. The large aggregation appears individually and the distribution in asphalt arises regional aggregation when the dosage is 2.0 %. At this time, the distribution of HG is extremely uneven, which will exert influence on the storage stability of HGMA in Section 3.3. It is attributed to the large specific surface area of HG, and the distance between particles is closer with the increasing dosage of HG. Therefore, the electrostatic interaction and van der Waals force strengthen and consequently agglomeration takes place more extensively. And the regional distribution state results in stress concentration and is consistent with the analysis of ductility. Therefore, the reasonable content of HG is 1.5 % according to the above results.

3.5. Rheological properties of hydrocarbon-based graphene modified asphalt (HGMA)

3.5.1. Complex modulus (G^*) and phase angle (δ)

G^* and δ can be employed to characterize the viscoelasticity of asphalt materials. Asphalt, which has a high G^* exhibits advantages in elasticity, is easy to resist flow deformation at high temperatures. The relative proportion of elastic and viscous components can be reflected through δ, and asphalt which has small δ represents large proportion of elastic components and great elastic recovery property. On the contrary, the proportion of viscous components increases and permanent deformation is prone to occur. The experimentally determined G^* and δ for each HGMA samples are shown in Fig. 12 and 13, respectively.

G^* of petroleum asphalt and HGMA all declines while δ increases accordingly when temperature is elevated. Asphalt is softened and the motion state of asphalt molecules is changed by the reason of increased temperature which also results in weak intermolecular binding force. Therefore, asphalt transforms from viscoelasticity to viscosity at the high temperature which is difficult to resist deformation. The data in Fig. 12 and 13 show that G^* has a growing trend with the added dosage of HG while δ is opposite. It can be attributed to the excellent elastic properties and strong deformation ability of graphene, which means that the addition of graphene is equivalent to adding elastic components to the system. Furthermore, the relative ratio of elastic and viscous components is changed, the rate of transition from elasticity to viscosity slows down and promotes the elastic recovery ability of asphalt at high temperature. In general, HG exerts a positive effect on improving the rheological properties of asphalt at the high temperature.

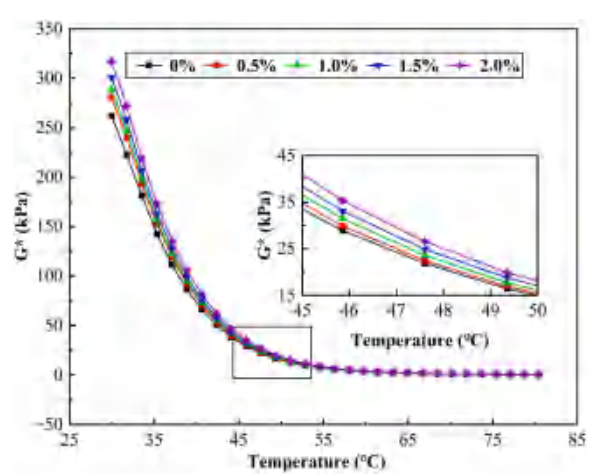

Fig. 12. G^* of hydrocarbon-based graphene modified asphalt.

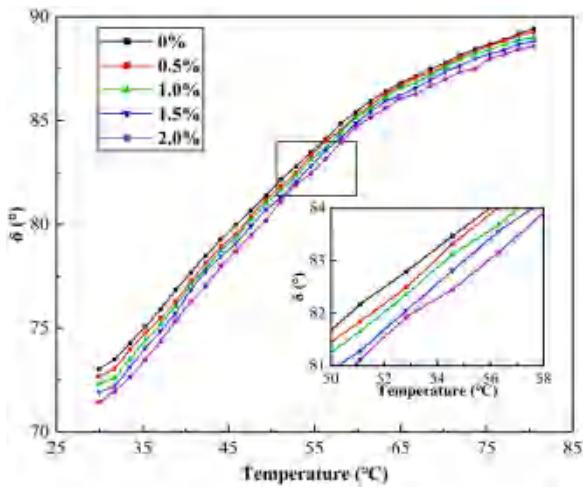

Fig. 13. δ of hydrocarbon-based graphene modified asphalt.

3.5.2. Rutting factor ($G^*/sin\ \delta$)

$G^*/sin\ \delta$ is selected to assess the deformation resistance of asphalt materials at high temperatures. The larger $G^*/sin\ \delta$ means stronger deformation resistance, and the result of $G^*/sin\ \delta$ is shown in Fig. 14.

As shown in Fig. 14, with the increase of temperature, $G^*/sin\ \delta$ shows a decreasing trend which is in accord with the observed softening at high temperatures. Compared with petroleum asphalt, $G^*/sin\ \delta$ of all HGMA samples are enhanced and appear obvious advantages as the increased dosage of HG. Therefore, the presence of HG has a better weakening effect on the generation of pavement rutting at high temperatures. The reason may be that graphene, as a powder material, adsorbs the components in asphalt. At the same temperature, HGMA is harder compared with petroleum asphalt. In other words, the rutting resistance of HGMA is enhanced to a certain extent.

Besides, the $G^*/sin\ \delta$ of asphalt is supposed to be higher than 1.0 kPa based on regulations of SHRP [36], and the temperature corresponding to 1.0 kPa is defined as failure temperature. When the temperature exceeds failure temperature, asphalt material does not meet the requirements to serve. The failure temperature of petroleum asphalt is 68.96 ℃ which is apparent in Fig. 14. It is noteworthy that failure temperature of asphalt gradually increases on account of the incremental HG dosage. This observation is consistent with the finding that HG enhances rutting resistance of asphalt at high temperatures.

3.5.3. Fatigue factor ($G^* \cdot sin\ \delta$)

$G^* \cdot sin\ \delta$ was selected to evaluate the fatigue resistance of HGMA at medium temperature. The smaller $G^* \cdot sin\ \delta$ possesses more significant fatigue resistance. The result of $G^* \cdot sin\ \delta$ is shown in Fig. 15.

Fig. 15 shows that increasing temperature results in decrement of $G^* \cdot sin\ \delta$. Because asphalt exhibits more obvious viscous state and anti-fatigue cracking characteristic is improved at high temperature. $G^* \cdot sin\ \delta$ of HGMA are enhanced as the addition of HG which indicates that fatigue resistance is impaired by HG. The fluidity of asphalt molecule is weakened and the addition of HG as an elastic component will make it difficult for asphalt to resist fatigue cracking caused by cycling load. $G^* \cdot sin\ \delta$ of asphalt is supposed to less than 5000kPa according to the specification of SHRP [36]. Under this condition, the fatigue critical temperatures of HGMA are 18.08 ℃, 18.53 ℃, 19.02 ℃, 19.30 ℃ and 20.34 ℃ when the dosages of HG are 0 %, 0.5 %, 1.0 %, 1.5 % and 2.0 %, respectively.

3.5.4. Storage modulus (G') and loss modulus (G'')

G' represents the measurement of the elastic energy which can be stored when a material is subjected to external forces. This parameter is related to the elastic deformation ability of the material, reflecting the stiffness and elasticity. G'' corresponds to the loss of energy resulting from viscous deformation, which is associated with the viscosity and softness of a material. Accordingly, G' and G'' are selected to jointly characterize the viscoelastic behavior of the asphalt, as shown in Fig. 16.

As can be seen by inspecting Fig. 16, G' and G'' values for petroleum asphalt and HGMA all appear decreasing tendency as the temperature rises. These trends are attributed to the enhanced thermal motion of asphalt molecules as the rise of temperature, leading to the weakness of intermolecular attraction. As a result, the internal structure becomes loose, and the fluidity is enhanced. However, the decrease rate of G' is greater than that of G''. In other words, the elastic component reduces more rapidly than viscous components, which indicates that the proportion of elastic components in asphalt decreases with the rising temperature, and the asphalt changes from dominantly elastic to mainly viscous. There is an intersection existing in G' and G'', and the temperature corresponding to the intersection is the temperature at which the viscoelasticity changes relatively [37]. The asphalt's viscoelastic behavior can be identified by variation of intersection temperature. Asphalt exhibits more remarkable viscosity behavior and there is less elastic component existing in asphalt when the intersection temperature falls, which demonstrates advantages at low temperatures. The intersection temperature rises with the increasing dosage of HG. It can be explained that each carbon atom in graphene owns an unpaired electron connecting with the surrounding carbon atoms to form a honeycomb grid structure which has stable structure, and can be quickly restored to

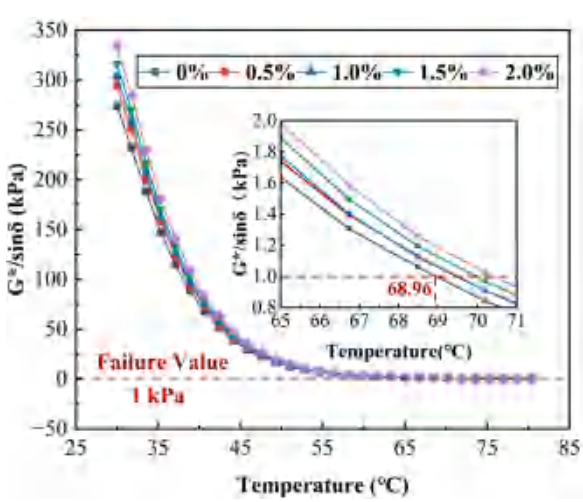

Fig. 14. $G^*/sin\ \delta$ of hydrocarbon-based graphene modified asphalt.

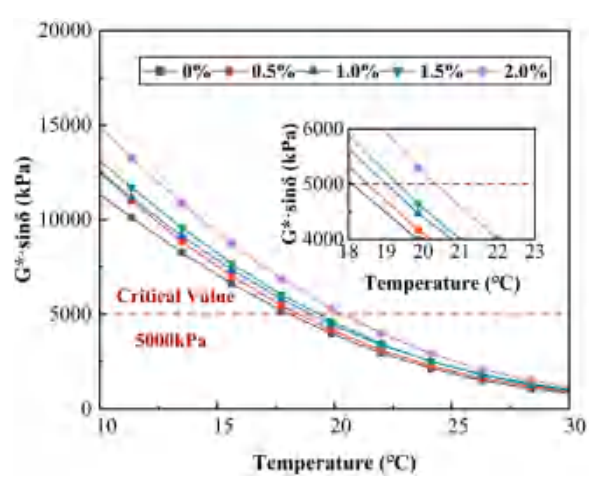

Fig. 15. $G^* \cdot sin\ \delta$ of hydrocarbon-based graphene modified asphalt.

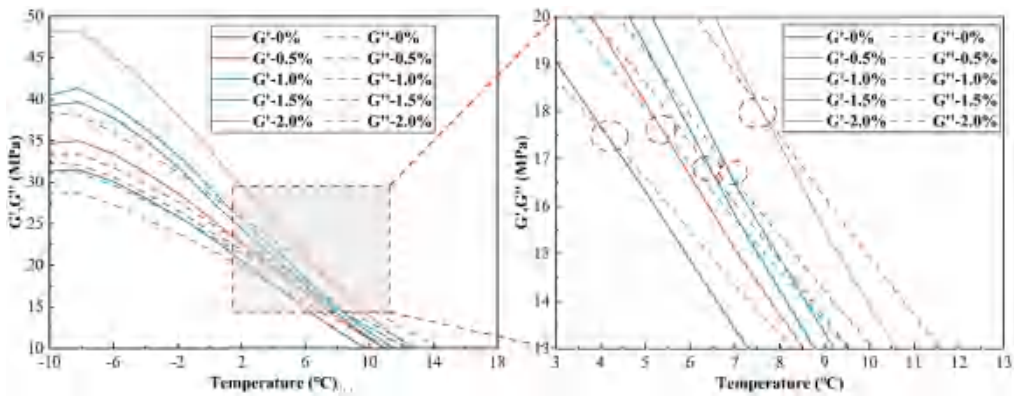

Fig. 16. *G'* and *G''* of hydrocarbon-based graphene modified asphalt.

the original state when subjected to external force. Therefore, the addition of HG increases the proportion of elastic components in asphalt, making it more difficult and slower to change to viscosity, resulting in poor performance at low temperatures. The drop of intersection temperature is least when the HG content is 1.0–1.5 %. Combined with the results of basic properties and FM, the preferred dosage of HG can be taken as 1.5 %.

3.5.5. Stiffness modulus (S) and creep rate (m)

S corresponds to the flexibility of asphalt at low temperatures while *m* value reflects the relaxation ability. Generally, asphalt with lower *S* and higher *m* value performs better at low temperature. The experimental results of *S* and *m* value of HGMA at − 12 ℃ are illustrated in Fig. 17.

It can be observed from Fig. 17 that *S* becomes larger as the increasing dosage of HG and *m* appears opposite trend. The flexibility and relaxation ability are weakened because the addition of HG. The asphalt components which have low molecular weight are adsorbed by HG, leading to the hardening of asphalt. In addition, the cross-linking of asphalt molecular chain and HG powder leads to the obstruction of movement and the reduction of flexibility. Moreover, the HG powder in asphalt will produce stress concentration. As a result, asphalt material is difficult to resist crack at low temperature. The conclusion that HG generates the deterioration of low temperature performance of HGMA is consistent with Section 3.5.4. *S* should be less than 300 MPa and *m* value is more than 0.3. All the samples meet the requirements at − 12 ℃.

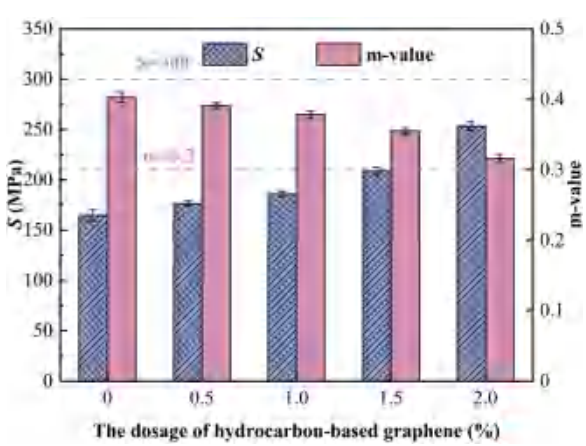

Fig. 17. *S* and *m value* of hydrocarbon-based graphene modified asphalt.

3.6. Modification mechanism of hydrocarbon-based graphene (HG) on asphalt

The reaction and modification mechanism between HG and asphalt can be further analyzed by FTIR due to special infrared characteristic peaks of various functional groups. The infrared spectra of petroleum asphalt and HGMA are shown in Fig. 18. The characteristic peak mainly occurs in the range of 700–3000 cm^{-1}. It is noticeable that the location of characteristic peaks almost same before and after modifying, and the peak intensity is differential merely. The most intense adsorption peaks correspond to asymmetrical stretching vibration and symmetrical stretching of C-H, existing at 2924 cm^{-1} and 2853 cm^{-1}, respectively. The weaker adsorption peak at 1603 cm^{-1} is associated to C═C vibration of benzene. Moreover, characteristic peaks observed at 1460 cm^{-1} and 1376 cm^{-1} are related to the in-plane bending vibration of C-H, and the stretching vibration of sulfoxide group is 1032 cm^{-1}. Finally, peaks in the 700–900 cm^{-1} region are associated with the out-of-plane wagging vibration of benzene [38–40]. In summary, no new peaks were observed in the infrared spectrum, only the peak strength occurs difference. Therefore, the chemical reaction is absent in the mixing process, and the interaction between HG and asphalt is physical mixing.

3.7. Inhibition effect of hydrocarbon-based graphene (HG) on asphalt VOCs emission

VOCs are produced during the production, storage and service process of asphalt materials. The various compositions of asphalt result in the complexity and diversity of asphalt VOCs components [41]. The

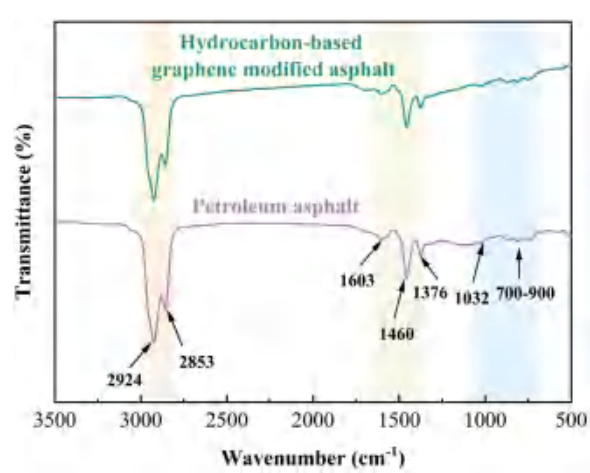

Fig. 18. FTIR images of petroleum asphalt and hydrocarbon-based graphene modified asphalt with dosage of 1.5 %.

harm of asphalt VOCs pollution to the atmospheric environment and human health should not be underestimated. Therefore, the inhibition effect of different HG dosages on the total VOCs emission of asphalt at preparation temperature is investigated. The maximum and stable values of VOCs emission under experimental conditions are recorded, as shown in Fig. 19.

What can be observed from Fig. 19 is VOCs concentration of the petroleum asphalt is the highest. The maximum concentration and stable concentration of asphalt VOCs emissions show slight difference at the same dosage of HG. Moreover, HG has a significant inhibition effect on asphalt VOCs emissions at different dosages. Specifically, the maximum concentration is reduced by 13 %, 36 %, 58 % and 73 %, the stable concentration decreased by 16 %, 37 %, 60 % and 74 % when the dosage of HG is 0.5 %, 1.0 %, 1.5 %, 2.0 %, respectively. This result is based on the large specific surface area of graphene which results in adsorption effect. Besides, the pore structure of HG also exerts beneficial effects on inhibition of asphalt VOCs emission. Combined with the FTIR result, physical adsorption is the main pattern of inhibition on VOCs. It is worth noting that the dosage of HG varies equally, but the reduction rate of VOCs concentration does not, as shown in Table 3. When the HG dosage reaches 1.0 % and 1.5 %, change rates of maximum concentration reduction are 23 % and 22 %, respectively, and the reduction effect is nearly the same and performs excellent. However, the change rates of stable concentration reduction are 21 % and 23 %, respectively, when the dosage reaches 1.0 % and 1.5 %. Therefore, the dosage of 1.5 % is preferred.

4. Conclusions

In this research, the HG prepared by petrochemical by-products was employed to modify asphalt innovatively. The characteristics of HG and its effect on properties of asphalt were investigated. Meanwhile, the modification mechanism and inhibition effect on VOCs emission were further explored. The following conclusions can be drawn.

(1) HG exhibits a lamellar and pore structure which is conducive to cross-linking and fusion with asphalt molecules. In addition, the pore structure may improve the adsorption capacity of HG and contribute to inhibiting asphalt fumes.
(2) Combined with petroleum asphalt, the consistency and hardness of HGMA are enhanced, while the fluidity and sensitivity to temperature are weakened. HG disperses evenly and there is no severe agglomeration when dosage is not more than 1.5 %.
(3) HGMA has more significant elastic recovery ability and anti-rutting ability, which is conducive to resisting deformation at the high temperature. However, fatigue resistance is weakened and embrittlement of asphalt materials is prone to occurrence at the low temperature, because the addition of HG increases the proportion of elastic components.
(4) The characteristic peaks of asphalt are consistent before and after modifying, only the peak strength occurs difference. In other words, there are no additional functional groups generated during interaction process between asphalt and HG, which belongs to physical mixing.
(5) The maximum concentration of asphalt VOCs is reduced by 13 %, 36 %, 58 % and 73 % while the stable concentration decreased by 16 %, 37 %, 60 % and 74 % when the dosage of HG is 0.5 %, 1.0 %, 1.5 %, 2.0 %, respectively. The adsorption rate was positively correlated with the increasing dosage of graphene. Combined with the change of VOCs concentration reduction rate, the dosage of 1.5 % is preferred. The inhibition effect on asphalt VOCs depends on physical adsorption.

The observations and conclusions described above clearly demonstrate that HG has beneficial effects on improving asphalt properties and pollutant inhibition. In the future, the application of HG in asphalt mixture will be explored, and the possibility of its practical application will be evaluated.

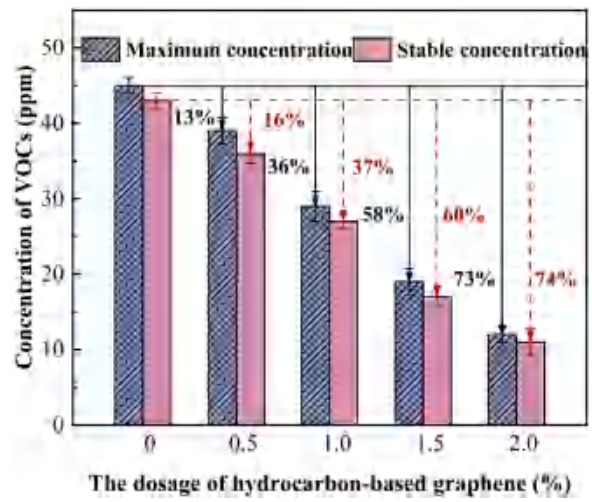

Fig. 19. VOCs emission of hydrocarbon-based graphene modified asphalt.

Table 3
Change of VOCs concentration reduction rate.

Scope of HG (%)	Change of VOCs concentration reduction rate (%)	
	Maximum concentration	Stable concentration
0–0.5	13	16
0.5–1.0	23	21
1.0–1.5	22	23
1.5–2.0	15	14

CRediT authorship contribution statement

Fan Yansong: Writing – original draft, Investigation. **Chen Meizhu:** Writing – review & editing, Supervision, Formal analysis. **Yang Xiaoyu:** Writing – review & editing, Project administration. **Zhang Jianwei:** Methodology, Investigation. **He Jun:** Methodology, Investigation. **Han Muyan:** Investigation, Conceptualization.

Declaration of Competing Interest

The authors declare that they have no known competing financial interests or personal relationships that could have appeared to influence the work reported in this paper.

Acknowledgements

This research was supported by the Program Fund of Non-metallic Excellence and Innovation Center for Building Materials (24SFP-5). The authors appreciate the assistance provided by the project, research group, and Dr. Mohammed Al Mehthel.

Data availability

Data will be made available on request.

References

[1] Y. Lv, S. Wu, N. Li, P. Cui, H. Wang, S. Amirkhanian, Z. Zhao, Performance and VOCs emission inhibition of environmentally friendly rubber modified asphalt with UiO-66 MOFs, J. Clean. Prod. 385 (2023) 135633, https://doi.org/10.1016/j.jclepro.2022.135633.
[2] X. Gong, Q. Liu, H. Wang, P. Wan, S. Chen, J. Wu, S. Wu, Synthesis of environmental-curable CO2-based polyurethane and its enhancement on properties

of asphalt binder, J. Clean. Prod. 384 (2023) 135576, https://doi.org/10.1016/j.jclepro.2022.135576.
[3] Y. Lv, S. Wu, P. Cui, Q. Liu, Y. Li, H. Xu, Y. Zhao, Environmental and feasible analysis of recycling steel slag as aggregate treated by silicone resin, Constr. Build. Mater. 299 (2021) 123914, https://doi.org/10.1016/j.conbuildmat.2021.123914.
[4] Z. He, T. Xie, H. Yu, J. Ge, W. Dai, Evaluation of quantum dot composite graphene /titanium oxide enhanced UV aging resistance modified asphalt, Constr. Build. Mater. 408 (2023) 133732, https://doi.org/10.1016/j.conbuildmat.2023.133732.
[5] L. Yao, Z. Leng, F. Ni, G. Lu, J. Jiang, Adaptive maintenance strategies to mitigate climate change impacts on asphalt pavements, Transp. Res. Part Transp. Environ. 126 (2024) 104026, https://doi.org/10.1016/j.trd.2023.104026.
[6] Z. Cao, M. Chen, J. Yu, X. Han, Preparation and characterization of active rejuvenated SBS modified bitumen for the sustainable development of high-grade asphalt pavement, J. Clean. Prod. 273 (2020) 123012, https://doi.org/10.1016/j.jclepro.2020.123012.
[7] Y. Qiu, Y. Gao, X. Zhang, Y. Wei, J. Cao, X. Wang, S. Wang, Conventional properties, rheological properties, and storage stability of crumb rubber modified asphalt with WCO and ABS, Constr. Build. Mater. 392 (2023) 131987, https://doi.org/10.1016/j.conbuildmat.2023.131987.
[8] G. Aziz, A. Ahmad, Md Muslim Ansari, Utilization of nanocenospheres a waste material to improve the physical and rheological properties of SBS asphalt binders, Fuel 374 (2024) 132378, https://doi.org/10.1016/j.fuel.2024.132378.
[9] N. Baldino, Y.M. Marchesano, O. Mileti, F.R. Lupi, D. Gabriele, Thermo-rheological behaviour of styrene-butadiene-styrene, hard plastics with or without graphene oxide modified bitumens, Case Stud. Constr. Mater. 20 (2024) e03354, https://doi.org/10.1016/j.cscm.2024.e03354.
[10] Y. Li, C. Zhao, R. Li, H. Zhang, Y. He, J. Pei, L. Lyu, Dry-process reusing the waste tire rubber and plastic in asphalt: Modification mechanism and mechanical properties, Constr. Build. Mater. 458 (2025) 139759, https://doi.org/10.1016/j.conbuildmat.2024.139759.
[11] N. Tang, C. Xue, G. Hao, W. Huang, H. Zhu, R. Li, Sustainable production of eco-friendly rubberized asphalt binders through chemically crosslinking with polymer modifier, J. Clean. Prod. 422 (2023) 138633, https://doi.org/10.1016/j.jclepro.2023.138633.
[12] A.M. Adnan, J. Wang, Investigation of the effects of nano-Al2O3 addition on compatibility, rutting and fatigue properties of styrene-butadiene-rubber modified asphalt, Constr. Build. Mater. 416 (2024) 135267, https://doi.org/10.1016/j.conbuildmat.2024.135267.
[13] N. Kamboozia, S.A. Saed, S.M. Rad, Rheological behavior of asphalt binders and fatigue resistance of SMA mixtures modified with nano-silica containing RAP materials under the effect of mixture conditioning, Constr. Build. Mater. 303 (2021) 124433, https://doi.org/10.1016/j.conbuildmat.2021.124433.
[14] Z. Wu, Y. Huang, L. Gui, L. Liang, J. Ying, W. Li, P. Kang Shen, Z. Qun Tian, 3D porous graphene nanosheets as efficient additives for high-performance styrene–butadiene–styrene/crumb rubber blend-modified asphalt, Mater. Des. 232 (2023) 112157, https://doi.org/10.1016/j.matdes.2023.112157.
[15] A. Zahid, S. Ahmed, M. Irfan, Experimental investigation of nano materials applicability in hot mix asphalt (HMA), Constr. Build. Mater. 350 (2022) 128882, https://doi.org/10.1016/j.conbuildmat.2022.128882.
[16] R. Li, F. Xiao, S. Amirkhanian, Z. You, J. Huang, Developments of nano materials and technologies on asphalt materials – a review, Constr. Build. Mater. 143 (2017) 633–648, https://doi.org/10.1016/j.conbuildmat.2017.03.158.
[17] L. Sun, X. Xin, J. Ren, Asphalt modification using nano-materials and polymers composite considering high and low temperature performance, Constr. Build. Mater. 133 (2017) 358–366, https://doi.org/10.1016/j.conbuildmat.2016.12.073.
[18] Y. Lu, X. Yang, B. Su, Self-assembly to monolayer graphene film with high electrical conductivity, J. Energy Chem. 22 (2013) 52–57, https://doi.org/10.1016/S2095-4956(13)60006-6.
[19] C. Feng, Y. Lu, Y. Liu, X. Yang, G. Tian, A facile synthesis of hierarchically porous graphene for high-performance lithium storage, New J. Chem. 46 (2022) 9999–10003, https://doi.org/10.1039/D2NJ02047E.
[20] H. Liu, Z. Tian, C. Huang, P. Wang, S. Huang, X. Yang, H. Cheng, X. Zheng, H. Tian, Z. Liu, A novel 3D Co/Mo co-catalyzed graphene sponge-mediated peroxymonosulfate activation for the highly efficient pollutants degradation, Sep. Purif. Technol. 301 (2022) 122035, https://doi.org/10.1016/j.seppur.2022.122035.
[21] A.M. Adnan, J. Wang, Enhancement of rheological performance and compatibility of tire rubber-modified asphalt binder with the addition of graphene, Constr. Build. Mater. 402 (2023) 133038, https://doi.org/10.1016/j.conbuildmat.2023.133038.
[22] X. Li, Y. Wang, Y. Wu, H. Wang, M. Chen, H. Sun, L. Fan, Properties and modification mechanism of asphalt with graphene as modifier, Constr. Build. Mater. 272 (2021) 121919, https://doi.org/10.1016/j.conbuildmat.2020.121919.
[23] C. Wang, M. Wang, Q. Chen, L. Zhang, Basic performance and asphalt smoke absorption effect of environment-friendly asphalt to improve pavement construction environment, J. Clean. Prod. 333 (2022) 130142, https://doi.org/10.1016/j.jclepro.2021.130142.
[24] Y. Huang, Z. Wu, L. Liang, J. Ying, L. Gui, L. Mo, P. Shen, Z. Tian, Critical role of vacancy defects in graphene nanosheets for enhancing asphalt binder, Constr. Build. Mater. 438 (2024) 137139, https://doi.org/10.1016/j.conbuildmat.2024.137139.
[25] F. Nie, W. Jian, D. Lau, An atomistic study on the thermomechanical properties of graphene and functionalized graphene sheets modified asphalt, Carbon 182 (2021) 615–627, https://doi.org/10.1016/j.carbon.2021.06.055.
[26] X. Yang, Y. Lu, C. Feng, A method for preparing graphene using heavy aromatic hydrocarbons as raw materials (in Chinese), CN202110575175.5, 2021.
[27] Highway Science Research Institute of the Ministry of Transport, JTG-F40, Technical Specifications for Construction of Highway Asphalt Pavements, 2004.
[28] Highway Science Research Institute of the Ministry of Transport, JTG-E20, Standard Test Methods of Bitumen and Bituminous Mixtures for Highway Engineering, 2011.
[29] G. Cao, F. An, Effectiveness of the elastic moduli characterization of graphene or other 2D materials via Raman spectroscopy, Diam. Relat. Mater. 146 (2024) 111201, https://doi.org/10.1016/j.diamond.2024.111201.
[30] W. Wu, J.C. Ranasinghe, A. Chatterjee, S. Huang, Recent advances on Raman spectroscopy of graphene: towards biosensing applications, Mater. Chem. Phys. 318 (2024) 129281, https://doi.org/10.1016/j.matchemphys.2024.129281.
[31] H. Guo, X. Yang, Q. Xu, W. Lu, J. Li, H. Dai, H. Ohmori, M. Kosinova, J. Yan, S. Li, T. Goto, R. Tu, S. Zhang, Epitaxial growth and electrical performance of graphene/3C-SiC films by laser CVD, J. Alloy. Compd. 826 (2020) 154198, https://doi.org/10.1016/j.jallcom.2020.154198.
[32] S. Fan, Y. Chen, J. Wu, S. Xiao, G. Chen, P. Chu, Structure, superlubricity, applications, and chemical vapor deposition methods of graphene solid lubricants, Tribol. Int. 198 (2024) 109896, https://doi.org/10.1016/j.triboint.2024.109896.
[33] Y. Wang, P. Polaczyk, J. He, H. Lu, R. Xiao, B. Huang, Dispersion, compatibility, and rheological properties of graphene-modified asphalt binders, Constr. Build. Mater. 350 (2022) 128886, https://doi.org/10.1016/j.conbuildmat.2022.128886.
[34] K. Liu, K. Zhang, X. Shi, Performance evaluation and modification mechanism analysis of asphalt binders modified by graphene oxide, Constr. Build. Mater. 163 (2018) 880–889, https://doi.org/10.1016/j.conbuildmat.2017.12.171.
[35] Z. Wu, L. Zhang, F. Chen, K. Liu, Q. Cao, Revealing the effect of defects on the interfacial interactions of pristine graphene modified asphalt via molecular dynamic simulations and DFT calculations, J. Mol. Liq. 409 (2024) 125497, https://doi.org/10.1016/j.molliq.2024.125497.
[36] S. Li, Q. Liu, H. Wang, J. Wang, L. He, S. Wu, Effect of kaolin and sepiolite on fume emissions of rubber modified asphalt, Constr. Build. Mater. 416 (2024) 135276, https://doi.org/10.1016/j.conbuildmat.2024.135276.
[37] Y. Zhao, M. Chen, J. Shen, P. Shi, S. Wu, D. Chen, J. Zhang, Z. Zhao, Aging behaviors of asphalt binders rejuvenated by different chemical fractions from waste cooking oil, Constr. Build. Mater. 435 (2024) 136867, https://doi.org/10.1016/j.conbuildmat.2024.136867.
[38] Z. Li, R. Zhou, Y. Zhao, Q. Cao, W. Qin, Discriminating wavenumbers selection of ATR-FTIR spectra for identifying graded asphalt, Constr. Build. Mater. 214 (2019) 565–573, https://doi.org/10.1016/j.conbuildmat.2019.04.068.
[39] R. Ren, K. Han, P. Zhao, J. Shi, L. Zhao, D. Gao, Z. Zhang, Z. Yang, Identification of asphalt fingerprints based on ATR-FTIR spectroscopy and principal component-linear discriminant analysis, Constr. Build. Mater. 198 (2019) 662–668, https://doi.org/10.1016/j.conbuildmat.2018.12.009.
[40] Y. Lv, S. Wu, N. Li, H. Wang, P. Cui, H. Xu, Y. Zhao, C. Yang, X. Zhou, S. Amirkhanian, Environmental hazard reduction and anti-aging enhancement of steel slag powder-asphalt mastic based on TiO2@UiO-67 composites, J. Clean. Prod. 419 (2023) 138331, https://doi.org/10.1016/j.jclepro.2023.138331.
[41] H. Wang, Q. Liu, S. Wu, Y. Lv, P. Wan, X. Gong, G. Liu, Study of synergistic effect of diatomite and modified attapulgite on reducing asphalt volatile organic compounds emission, Constr. Build. Mater. 400 (2023) 132827, https://doi.org/10.1016/j.conbuildmat.2023.132827.

Case Studies in Construction Materials 21 (2024) e03747

Contents lists available at ScienceDirect

Case Studies in Construction Materials

journal homepage: www.elsevier.com/locate/cscm

Optimization design of asphalt emulsion with rejuvenator towards a uniform distribution inside the damaged porous asphalt mixture for a better ravelling resistance

Bin Yang [a], Jiwang Jiang [b], Haopeng Wang [c], Zhen Leng [a,*], Xin Sui [a], Xi Jiang [a]

[a] Department of Civil and Environmental Engineering, The Hong Kong Polytechnic University, Kowloon, Hong Kong
[b] School of Transportation, Southeast University, Nanjing, Jiangsu, China
[c] Department of Civil and Environmental Engineering, University of Liverpool, Liverpool, United Kingdom

ARTICLE INFO

Keywords:
Porous asphalt (PA)
Surface treatment (ST) emulsion
Rejuvenator
Optimization
Ravelling resistance

ABSTRACT

Porous asphalt (PA) pavements usually meet the ravelling disease after opening to traffic for several years. Spraying surface treatment (ST) emulsion to PA pavement is a feasible preventive maintenance technology to alleviate this problem. However, the void clogging, nonuniform distribution and low diffusion efficiency of ST residue might hinder its widespread application. Therefore, this study aims to optimize the ST emulsion formula to improve the ravelling resistance of damaged PA. Usages of adding rejuvenators into ST emulsions were discussed. The orthogonal design method was used to determine the appropriate parameter values for preparing rejuvenator emulsions. The viscosity, contact angle and water boiling tests were then conducted to determine the optimal dosage of rejuvenator emulsion within ST emulsion. Cantabro abrasion test was performed to verify the ravelling resistance of damaged PA mixtures treated with optimized ST. Results showed that a stable and homogeneous rejuvenator emulsion could be produced by precisely controlling the PH value, emulsified temperature and emulsifier dosage. Adding rejuvenator emulsions to ST emulsions significantly improved the wettability. The optimal dosages of aromatic oil and tall oil emulsions are 10 % and 5 % by mass of ST emulsions. Optimized ST containing rejuvenator emulsions showed better ravelling resistances than pure asphalt emulsion.

1. Introduction

Porous asphalt (PA) pavement usually has a large air void content (>15 %) compared with conventional dense-graded and gap-graded asphalt pavements [1–4]. Due to the rough pavement surfaces and a large number of interconnected voids, PA pavement has been widely used in the field as a multifunctional pavement, such as enhancing skidding resistance [5], promoting seepage of rainwater [6], reducing tire-road noise [7] and alleviating the heat island effect [8]. However, attributing to the fast oxidation and ultraviolet aging of asphalt binder, the ravelling problem has become one of the main distresses for PA pavement at the early operation stage. Although many measures have been proposed and applied in the pavement construction phase to solve this problem, such as using the high viscosity asphalt binders [9,10], adding anti-stripping additives [11], and substituting the conventional asphalt binder

* Corresponding author.
E-mail address: zhen.leng@polyu.edu.hk (Z. Leng).

https://doi.org/10.1016/j.cscm.2024.e03747
Received 9 April 2024; Received in revised form 2 September 2024; Accepted 8 September 2024
Available online 14 September 2024
2214-5095/© 2024 The Author(s). Published by Elsevier Ltd. This is an open access article under the CC BY-NC license (http://creativecommons.org/licenses/by-nc/4.0/).

with epoxy resin [12,13], the ravelling distress still often occurred. Therefore, effective maintenance materials and technologies need to be developed for current PA pavements to alleviate this problem.

Recently, field experience in the Netherlands showed that before the dislodgement of aggregate particles from PA mixtures, timely spraying surface treatment (ST) emulsions to PA road could fill some micro-cracks inside PA mixture and replenish fresh asphalt binders to aged asphalt binders, which could effectively alleviate the ravelling distress [14–16]. Also, some indoor test results showed that the PA specimens treated with ST emulsions presented better mechanical behaviors concerning the anti-rutting property at a high temperature, fatigue resistance at a medium temperature and anti-cracking performance at a low temperature [17–19].

However, as a relatively new preventive maintenance material for PA pavements, several properties still need to be carefully clarified and optimized before widely promoting this technology. First, some voids of PA mixtures might be blocked by ST emulsion residue, leading to water penetration deterioration and noise absorption property attenuation [20,21]. Therefore, the material optimization towards a low viscosity and a reasonable construction technique (such as blasting at a high temperature or spraying with a high air pressure) are expected to be developed to preserve the pore structures to a large extent. Besides, the distribution of ST emulsion residues inside voids varies from each other. Jiang, et al. [22] found that a high percentage of coating area and a uniform coating film thickness helped improve the ravelling resistance. When the usage of ST emulsion is a certain value, a good wettability means the standard deviation of coating film thickness is small and more aged asphalt binder areas can be coated by ST emulsion residues. Therefore, a good wettability of ST emulsion is important to reach its potential. Third, the main demulsified component of the ST emulsion is fresh asphalt binder. The diffusion phenomenon between new asphalt binders and aged asphalt binders is very slow at room temperature, which may restrict the recovery efficiency of the mechanical performance of ST treated PA pavement. Several studies proposed incorporating recycling agents into ST emulsion to enhance diffusion efficiency and alleviate the ravelling problem [23–25]. However, the maintenance effects are quite different in different studies. Because they didn't present how to determine the dosage of rejuvenator and some even didn't indicate the dosage of rejuvenator, but directly introduced it as basic information in their papers, which makes it difficult to compare their findings. Lin, et al. [26] found that the rejuvenating agent could permeate the asphalt mixture and soften the aged binder based on the penetration test results. Xu, et al. [27] used the single-sided Cantabro abrasion test to evaluate the effects of different emulsions on ravelling resistance. They found that specimens treated with rejuvenators could decrease the mass loss ratios of PA specimens. By contrast, Zhang, et al. [28] found that aged PA mixture specimens treated with and without rejuvenators showed no difference in stiffness moduli and indirect tensile strengths, indicating no rejuvenation phenomenon was observed. The above inconsistent findings show that the application of rejuvenators as a preventive maintenance material for PA pavements is still in the preliminary exploration stage, which needs systematic investigations on the appropriate rejuvenator-adding methods, the optimal rejuvenator dosage and the reasonable evaluation indicators.

To satisfy the three demands mentioned above for optimizing the ST emulsion, rejuvenators are considered as the promising modifiers in this study. Because most rejuvenators generally have lower viscosities than asphalt binders at room temperature, which is expected to improve the penetration depth of ST emulsion in PA mixture. Besides, rejuvenators may promote the coating efficiency of newly added asphalt binders due to their better wettability than pure asphalt binders [29]. Furthermore, adding rejuvenators could enhance the diffusion efficiency between new and aged asphalt binders [30]. Therefore, this study aims to 1) investigate the feasible preparation process and appropriate production parameters of adding rejuvenators; 2) determine the optimal formula of ST emulsion containing rejuvenators; 3) verify the effectiveness of optimized ST emulsion on the ravelling resistance of PA specimen. Fig. 1 shows the flow chart of this study. Two kinds of rejuvenators were selected to add in asphalt emulsion. According to the orthogonal design table, eighteen rejuvenator emulsions were prepared after considering different compositions of PH values, emulsified temperatures and emulsifier dosages. Their storage abilities and particle size distribution properties were tested and compared as the crucial control indicators. Then, the appropriate parameter values for rejuvenator emulsion production were determined. Modified ST emulsions with different rejuvenator contents were prepared by mixing the asphalt emulsion and rejuvenator emulsion. The contact angle test was conducted to evaluate the wettability of various modified ST emulsions. Meanwhile, the shear viscosity test was conducted to

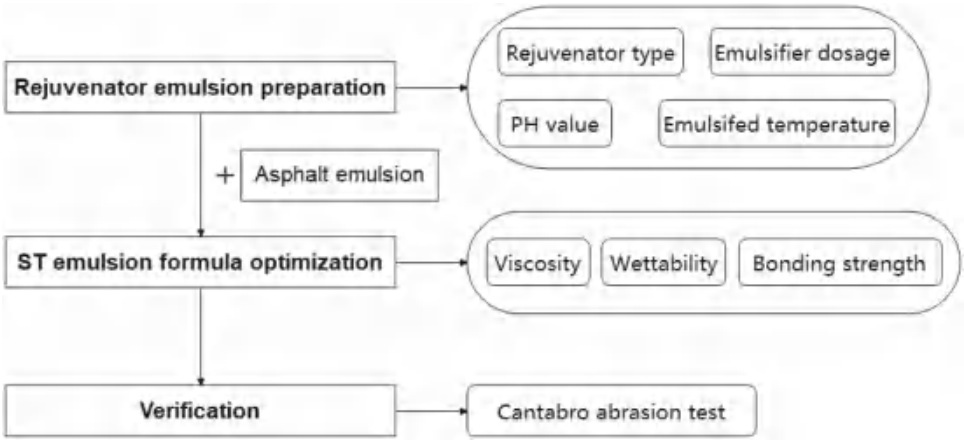

Fig. 1. Flowchart of this study.

investigate the viscosities of different ST emulsions. The water boiling test was also carried out to explore the bonding strength between ST emulsion residue and aggregate. The optimized dosage of rejuvenator emulsion was obtained based on the workability of modified ST emulsion. Lastly, the Cantabro abrasion test was conducted to investigate the ravelling resistance of damaged PA specimens and verify the optimized effectiveness.

2. Materials and Methodology

2.1. Materials and specimen preparation

2.1.1. Emulsion preparation

Asphalt emulsion usually consists of asphalt binder, distilled water, cationic emulsifier and stabilizer, where their mass percentages in this study are 60 %, 36.8 %, 3 % and 0.2 %, respectively. The main components of cationic emulsifier are lignin amine and its derivatives. Calcium chloride ($Cacl_2$) was used as the stabilizer to improve the storability of asphalt emulsion. The basic properties of asphalt emulsion are given in Table 1. The asphalt emulsion preparation process is shown as follows. Cationic emulsifiers are first dissolved in warm distilled water at 60 °C, followed by adding $Cacl_2$ powders to the solution. Then, concentrated hydrochloric acids were dripped into the aforementioned solution until the PH value reached around 2.5 to prepare the emulsifying soap. Then, the virgin asphalt binder with a penetration grade of 60/70 was emulsified by the emulsifying soap at 135 °C in the colloid mill machine. The asphalt emulsion was acquired after milling for 2 minutes. Besides, the rejuvenator emulsion preparation process is similar to that of asphalt emulsion except for several specific emulsifying parameters. The reasons why the rejuvenator needs to be emulsified and why it is recommended separately emulsification will be discussed as follows.

Fig. 2 shows that there may be three ways to add a rejuvenator into asphalt emulsion. In method one, the asphalt emulsion is first prepared, and then a certain mass of rejuvenators is directly added to the asphalt emulsion to prepare the ST emulsion containing the rejuvenator. Although this method is easy to conduct, there is an obvious problem: the rejuvenator is generally an oil-based material, which is difficult to homogeneously disperse in the oil-in-water (O/W) system of asphalt emulsion without the emulsifier's help. Thus, the ST emulsion prepared according to method 1 tends to be unstable and gradually stratified. In method two, the asphalt binders and rejuvenators are emulsified separately by the colloid mill. The stable asphalt emulsion and rejuvenator emulsion are well prepared and then stored. One may artificially mix those two emulsions in the field at an appropriate mass ratio to prepare the final ST emulsion when the old PA pavements need maintenance. In method three, the rejuvenator and asphalt binder are first blended and then the mixtures are emulsified together to prepare the ST emulsion. Compared with method three, one advantage of method two is that the rejuvenator could be emulsified at an optimal condition, which might differ from the emulsifying parameters designed for the asphalt binder. The emulsified rejuvenator can stabilize and distribute uniformly in solvent, which will be discussed later in Section 3.1. Another advantage of method two is that the worker can precisely control the mix ratio of asphalt emulsion and rejuvenator emulsion to prepare various ST emulsions with different material compositions towards different functional needs. For example, suppose an old pavement surface has been used for many years and the asphalt binders were severely aged. In that case, the dosage of rejuvenator emulsion in ST emulsion should increase to ensure that aged asphalt binders are substantially rejuvenated. Therefore, the method two, in which the rejuvenator was first emulsified and then mixed with asphalt emulsion, was adopted to prepare the ST emulsion in this study.

Fig. 3(a) shows that two kinds of rejuvenators were used in this study. And their basic properties were summarized in Table 2. One is a petrol-based rejuvenator named aromatic oil (AO), which is also the main light component in asphalt binders. The other one is a bio-based rejuvenator named tall oil (TO), which is produced from a purified pine feed stock and is expected to soften aged asphalt binder. Rejuvenators usually have significantly lower viscosities than asphalt binders at room temperature, making it easier to emulsify without such high temperatures. Besides, rejuvenators have different physical and chemical properties from asphalt binders. The optimal emulsifier dosage and the appropriate PH value of emulsified soap should also be determined to prepare a stable and homogeneous rejuvenator emulsion. Fig. 3**(b)** shows examples of AO and TO rejuvenator emulsions.

2.1.2. PA mixture preparation

A commonly used PA mixture with a nominal maximum aggregate size of 13.2 mm, named PA-13, was selected in this study. The SBS modified asphalt with a Superpave performance grade of 76–16 (PG76–16) and aggregate type of granite were used. The designed asphalt content was 4.1 % by weight of aggregates and the target air void content of PA mixture was 23±0.5 %. Limes were used to improve the anti-stripping property of the PA mixture.

Table 1
The basic properties of asphalt emulsion.

	Evaporated residue				PSD		
	Residue content (%)	Penetration (25 °C, 0.1 mm)	Softening point (°C)	Ductility (5 °C, cm)	D_{50} (μm)	*Span*	*D* [3,4] (μm)
ST emulsion	60	64	50	67.2	1.55	1.26	1.82

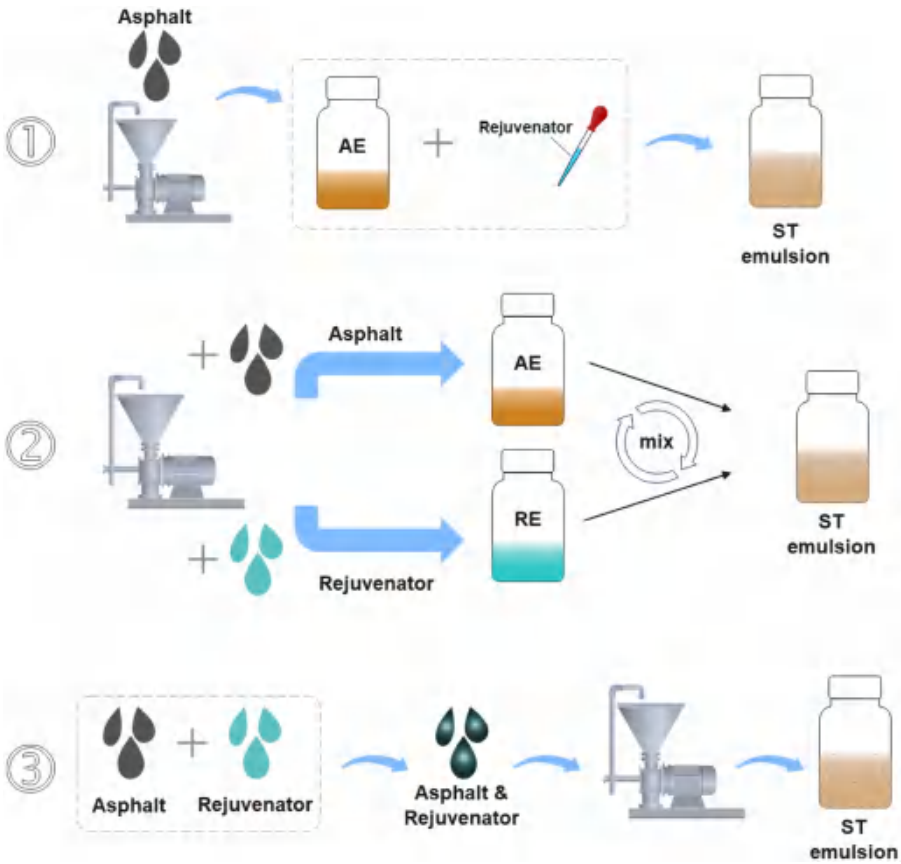

Fig. 2. Three potential methods to prepare ST emulsion containing rejuvenator.

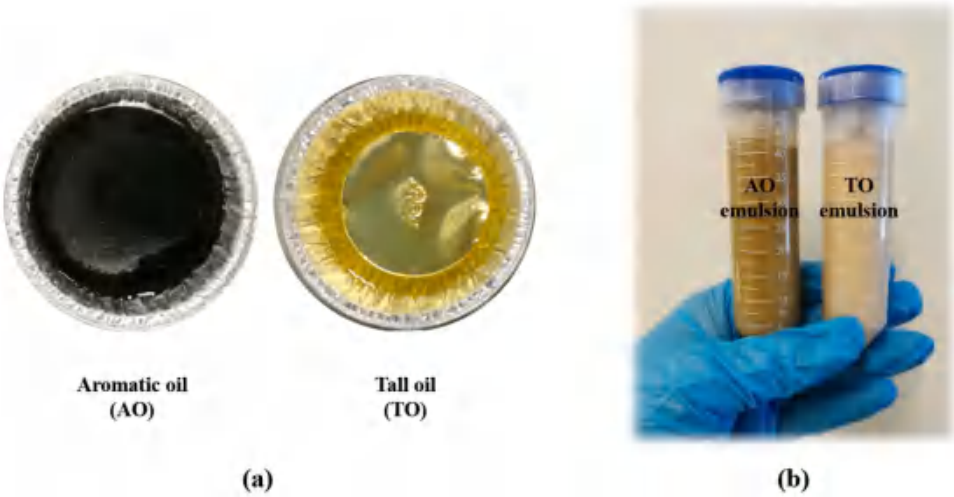

Fig. 3. Schematic graphs of (a) rejuvenators and (b) their emulsions used in this study.

2.2. Orthogonal experimental design

The orthogonal experimental design method is an efficient and fast experimental design method considering multivariate and multilevel factors. Several representative test points were selected based on the orthogonality. The features of those test points were uniformly distributed and neatly comparable, which is helpful in understanding the significance and interactions of different factors in

Table 2
The basic properties of rejuvenators.

Type	Appearance	Color	Odour	Relative density @ 20°C	Flash point (°C)
Aromatic oil	Liquid	Brown	Mild	1.006	240
Tall oil	Liquid	Yellow	Mild	0.927	279.4

a few experiments. Therefore, this statistical analysis method was used to optimize the preparation conditions of the rejuvenator emulsion.

A typical orthogonal array L9 was used to evaluate the emulsifying effects of various factors on rejuvenator emulsion. Table 3 shows a total of 9 experiments considering three factors (A/B/C) and three levels (1/2/3) for each factor. The meanings of test factors and values for each level are shown in Table 4. Factors of A, B and C represent the PH value, emulsified temperature, and emulsifier dosage, respectively. The PH value is acidic and cationic rejuvenator emulsions were prepared in this study. The emulsifier dosage means the mass ratio of the emulsifier to the whole emulsion. The emulsified temperatures for those two rejuvenators are different as the viscosities of AO and TO vary from each other.

2.3. Test methods

2.3.1. Zeta potential test

One of the main concerns about rejuvenator emulsion's workability is storage stability. Owing to its convenience and high accuracy, Zeta potential is a useful indicator for describing the stability of an unknown colloidal dispersion. The electrical potential at the slipping plane describes the potential difference between the dispersion phase and the stationary layer of fluid attached to the dispersed particle. High Zeta potential means this interface could separate mobile fluid from slipping and keep attaching to the surface. It is recognized that a solution sample is stable when the absolute value of Zeta potential is higher than 30 mV [31]. The Zetasizer with a type of Nano ZS90 manufactured by Malvern was used to conduct the Zeta potential test. All samples were diluted one thousand-fold with deionized water before testing. Three replicates were measured for each rejuvenator emulsion.

2.3.2. Particle size distribution (PSD) test

Appropriate particle size and a uniform PSD curve are crucial to the storage stability of rejuvenator emulsion. The Malvern Mastersizer 3000 was selected to measure the PSD of rejuvenator emulsion based on the laser diffraction technique. The PSD tests were performed in triplicate for each sample. D_{50} is calculated by Eq. (1), which means the average particle size of the whole colloidal dispersion system. Span indicates the concentration of PSD range, which is calculated by Eq. (2). The volume-weighted mean diameter of D [3,4] is calculated by Eq. (3).

$$D_{50} = \sum_{i=1}^{n} d_i \Big/ n \tag{1}$$

$$Span = (D_{90} - D_{10})/D_{50} \tag{2}$$

$$D[3,4] = \sum\nolimits_i^n n_i X_i^4 \Big/ \sum\nolimits_i^n n_i X_i^3 \tag{3}$$

Where d_i is the diameter of ith droplet, μm; D_{10} represents that droplet diameter such that 10 % of the total liquid volume is in drops of smaller diameter, μm; D_{50} is the volume median diameter, μm; D_{90} represents that droplet diameter such that 90 % of the total liquid volume is in drops of smaller diameter, μm; X_i is the center value of a size class, μm; n_i is the total particle number of each size class.

Table 3
L9 orthogonal array for preparing rejuvenator emulsion.

No.	Control factors and their levels		
	A	B	C
1	1	1	1
2	1	2	3
3	1	3	2
4	2	1	3
5	2	2	2
6	2	3	1
7	3	1	2
8	3	2	1
9	3	3	3

Table 4
Meanings of test factors and their corresponding levels.

Rejuvenator	Factors	Levels		
		1	2	3
AO	A. PH value	3	2	1
	B. Emulsified temperature,°C	75	90	60
	C. emulsifier dosage, %	2	3	4
TO	A. PH value	3	2	1
	B. Emulsified temperature,°C	40	60	20
	C. emulsifier dosage, %	2	3	4

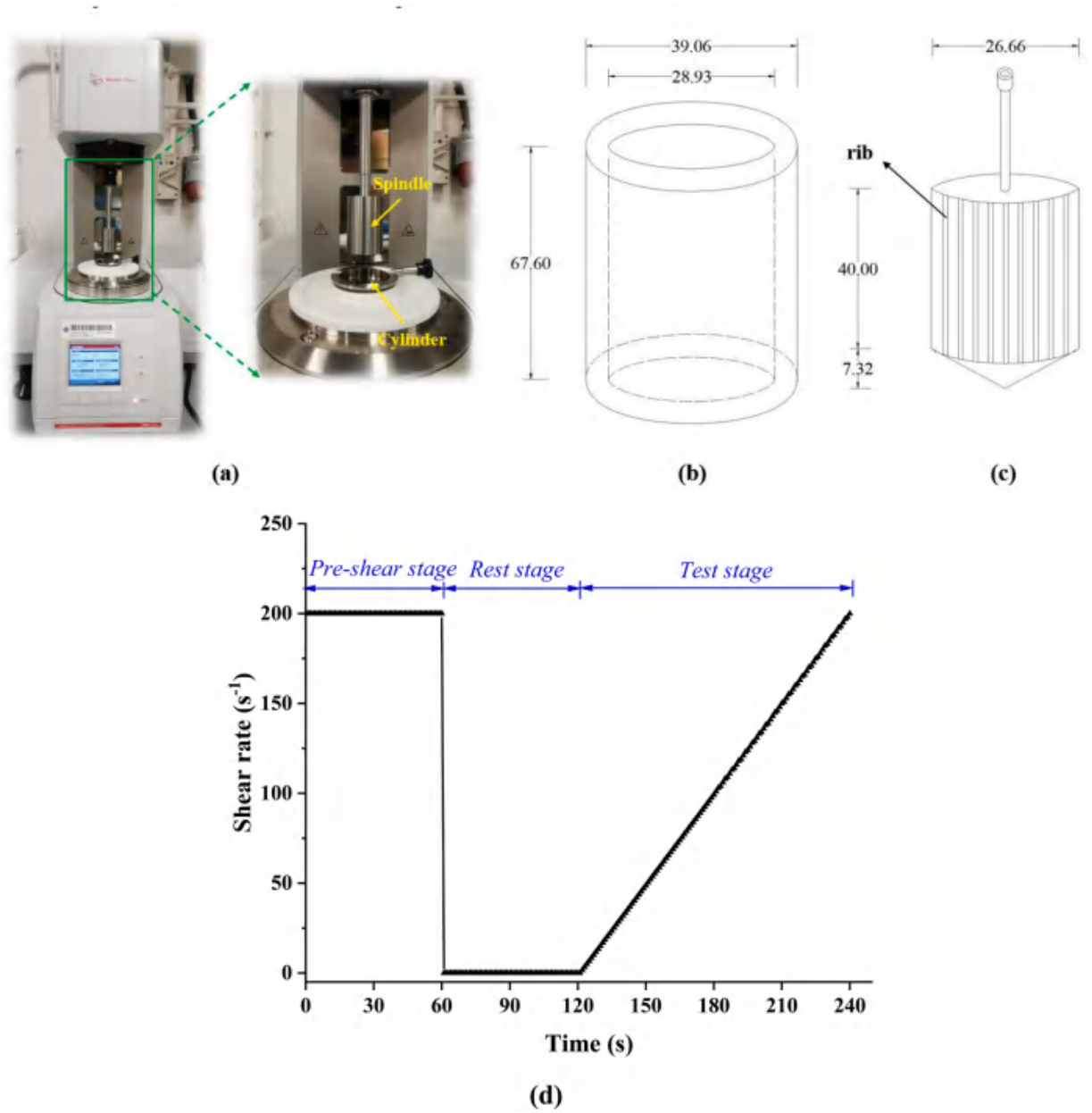

Fig. 4. Shear viscosity test: (a) DSR device set-up; (b) the cylinder; (c) the ribbed rotational spindle (unit: mm); (d) the protocol of shear viscosity test.

2.3.3. Shear viscosity test

The viscosity of ST emulsion can affect its penetration depth in the PA pavement. The shear viscosity test was conducted by a dynamic shear rheometer (DSR, model MCR 302, Anton Paar) as shown in Fig. 4**(a)**. A concentric cylinder measuring system was used due to the liquid state of the rejuvenator emulsion. The test temperature is controlled at 23 ± 0.5 °C. The rotational spindle geometry is ribbed to alleviate the slippage phenomenon (Fig. 4**(c)**). The inner diameter of the cylinder is 28.93 mm (Fig. 4**(b)**), and the diameter of the outer contour of the spindle is 26.66 mm. Thus, the radial gap between the cylinder and spindle is 2.27 mm during the measurement. The protocol of the shear viscosity test is presented in Fig. 4**(d)**. Firstly, a 60 s pre-shear with a shear rate of 200 s^{-1} is conducted following by a 60 s rest to achieve a homogeneous emulsion. Then, the shear rate linearly increased from 0 s^{-1} to 200 s^{-1} within 2 minutes to obtain the shear viscosity curve of the rejuvenator emulsion. Two replicates were tested for each emulsion.

2.3.4. Contact angle test

When the ST emulsion is sprayed to the aged PA pavement as a preventive maintenance material, most ST emulsions penetrate along the pore structure of PA pavement. Aged asphalt mastics, especially aged asphalt binders, are mainly distributed around the voids of PA mixtures. Consequently, penetrated ST emulsions will tightly contact aged asphalt binders and mastics. The wettability between ST emulsion and aged asphalt binder is of vital importance to the penetration depth of ST emulsion and distribution uniformity of ST emulsion residue thickness. Therefore, the contact angle of ST emulsion on aged asphalt binder is tested to compare the wettabilities of different ST emulsions. The long-term aged asphalt binders were first prepared according to the AASHTO R28. Then, some aged asphalt binders were dripped on the top surface of the hot glass slide. Afterward, the glass slide coated with asphalt binders was moved into the oven and cured at 150 °C for self-leveling coating. A finished specimen is shown in Fig. 5. During each contact angle test, a ST emulsion drop with 5.0 μL was dripped on the surface of aged asphalt binder. Three replicates were tested for each kind of ST emulsion. The test was conducted at room temperature with a humidity of around 70 % in the lab.

2.3.5. Water boiling test

When adding rejuvenators into fresh asphalt binders to prepare the ST emulsion, although the rejuvenator is expected to replenish light components of aged asphalt binder so as to rejuvenate it, too many rejuvenators might weaken the bonding strength of ST emulsion residue. Therefore, the water boiling test was conducted to investigate the bonding strength of ST emulsion residue according to the Chinese standard of JTG E20–2011-T0654. Several granite coarse aggregates with a size larger than 19 mm were washed and dried at first (Fig. 6**(a)**). The color of the prepared aggregate is greyish-white. Aggregates were dipped into distilled water for 1 minute and then moved to different ST emulsions for another 1 minute (Fig. 6**(b)**). After the emulsion coated aggregates were cured for 24 hours at room temperature, those specimens were separately put into boiling water for 3 minutes. Finally, the boiled aggregates were dried and then photographed by a digital camera. Instead of conventional visual observation as described in JTG E20–2011-T0654, a grayscale-based image processing was performed by the Image Pro Plus software as shown in Fig. 6**(c)**. The coating ratio can be calculated by Eq. (4). Four coarse aggregates were prepared for each kind of ST emulsion to evaluate its bond strength to aggregate.

$$Coating\ ratio = Residual\ area/(Aggregate\ area + Residual\ area) \times 100\% \tag{4}$$

2.3.6. Cantabro abrasion test

The ravelling resistance of the PA specimen treated with ST emulsion was evaluated by the cantabro abrasion test. PA mixtures were first subjected to long-term aging and followed by several freeze-thaw conditioning to prepare the damaged specimens. Subsequently, different ST emulsions were applied to PA specimens with an application rate of 0.6 kg/m^2. Then, those emulsion treated PA specimens were cured at room temperature for 14 days before the cantabro abrasion test. It should be noted that dry specimens were prepared for the Cantabro abrasion test according to the Chinese standard of JTG/T 3350–03 2020. More details about the sample preparation process can be found in our previous study [21]. Four duplicate specimens were tested in each scenario. The mass loss ratios and lost masses were calculated.

Fig. 5. Glass slide coated with asphalt binder for contact angle test.

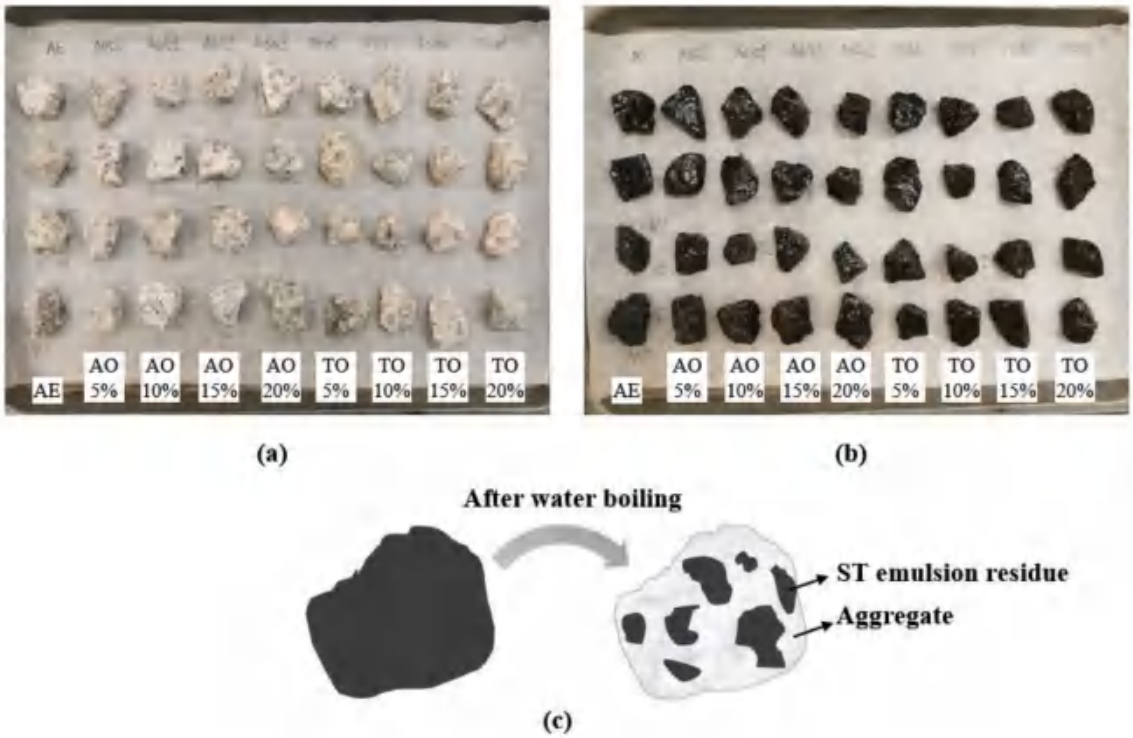

Fig. 6. Water boiling test: (a) uncoated aggregates; (b) ST emulsion coated aggregates; (c) grayscale-based image processing.

3. Results and Discussions

3.1. Design and selection of rejuvenator emulsion

3.1.1. Particle size distribution

Particle size distribution of rejuvenator droplets in the aqueous phase is an important characteristic related to the storage stability of rejuvenator emulsion. Except for the fourth composition of AO emulsion, almost all kinds of AO emulsions have a similar D_{50} around 1.50 μm as shown in Table 5. It should be noted that the fourth kind of AO emulsion quickly coalesced, leading to the micro flocs, which is inapplicable for the PSD test. Besides, all TO emulsions have no significant differences of D_{50}, which is around 1.67 μm. Compared with the D_{50} of asphalt emulsion given in Table 1, both AO and TO emulsions have similar average particle sizes with the asphalt emulsion used in this study. Therefore, preparing a stable ST emulsion by mixing rejuvenator emulsion with asphalt emulsion is feasible based on their similar PSD conditions.

The indexes of *Span* and *D* [3,4] were also calculated, and their results are summarized in Table 5. It was found that the AO emulsions have higher *Span* values than TO emulsions, meaning that AO emulsion usually has a wider PSD range than TO emulsion. In other words, the particle size of TO emulsion distributes more uniformly than that of AO emulsion. Therefore, due to the relatively high proportions of coarse droplets in the AO emulsion, its *D* [3,4] values generally exhibited slightly bigger volume-weighted mean diameters than that of the TO emulsion.

Table 5
PSD of different AO and TO emulsions.

No.	AO emulsion			TO emulsion		
	D_{50}, μm	*Span*	*D* [3,4], μm	D_{50}, μm	*Span*	*D* [3,4], μm
1	1.49	7.78	4.32	1.68	3.30	2.68
2	1.49	6.38	3.50	1.67	3.21	2.62
3	1.53	10.22	5.45	1.67	3.07	2.59
4	-	-	-	1.67	3.05	2.43
5	1.49	6.21	3.66	1.68	3.07	2.56
6	1.50	5.80	3.86	1.68	2.77	2.84
7	1.49	5.56	3.59	1.67	2.52	2.50
8	1.49	5.86	3.55	1.68	2.80	2.70
9	1.50	4.41	3.04	1.67	3.01	2.43

3.1.2. Storage stability

Good storage stability of emulsion facilitates production in large quantities and is ready for use in need. The zeta potential test results of different AO and TO emulsions are shown in the orthogonal experiment Table 6 and Table 7. k_i, (i=1,2 and 3) mean the average values at each factor level. R value represents the maximum variation range among k_i. The effect of each factor on the storage stability of the emulsion was evaluated by the k_i and R. A higher k_i value at one experimental level of a specific factor means better storage stability of the emulsion. A higher deviation of R for one factor means that its effect on the storage stability is more significant. Thus, k_i with the maximum values are considered the optimal conditions for preparing stable emulsions. The rankings of the effect of three factors on the zeta potential for AO emulsion and TO emulsion were B > A > C and A > C > B, respectively. That is to say, the critical factor affecting the stability of AO emulsion was the emulsifying temperature, while that for TO emulsion was the PH value of emulsified soap. The inconsistent critical factors for two kinds of emulsions might be attributed to their differences in thermophysical properties. The optimal experimental condition for preparing the AO emulsion was $A_3B_2C_2$, in which the PH value, emulsifying temperature and emulsifier dosage are 1, 90 °C and 3 %, respectively. And the optimal experimental condition for preparing the TO emulsion was $A_3B_2C_3$, where the PH value, emulsifying temperature and emulsifier dosage are 1, 60 °C and 4 %, respectively.

3.1.3. Determination of optimal production conditions for rejuvenator emulsion

The orthogonal experiments were conducted to determine the optimal production parameters for the AO and TO emulsion. As discussed earlier, there are no significant differences in average particle size among AO, TO and asphalt emulsions, which lays the foundation for their homogeneous mixing to prepare the ST emulsion as depicted in Fig. 2. The optimal parameters of AO emulsion and TO emulsion were determined based on the orthogonal statistical analysis of zeta potential data, which will be verified in this section. Table 8 shows the zeta potential and PSD results of the asphalt emulsion and two optimized rejuvenator emulsions. It was found that both the optimized AO emulsion and TO emulsion have the highest Zeta potential values after orthogonal experiments, indicating that their storage stabilities are significantly improved. Meanwhile, two kinds of optimized rejuvenator emulsions have similar average particle sizes with asphalt emulsions, indicating that the emulsifying conditions are appropriate for the AO and TO rejuvenators. Therefore, a stable and homogeneous ST emulsion is expected to be acquired by directly mixing AO or TO emulsion with asphalt emulsion.

3.2. ST emulsion formula optimization

3.2.1. Apparent viscosity

To ensure that as many ST residues as possible can alleviate the ravelling distress of PA pavement, the solid content of ST emulsion was fixed at 60 % based on previous studies [18,22]. Different ST emulsions were prepared by mixing AO or TO emulsions with asphalt emulsions. This study selected eight kinds of mixing proportions by mass of the whole ST emulsion, ranging from 0 % to 50 %. Fig. 7 **(a)** and **(c)** show the apparent viscosity versus shear rate of different ST emulsions. The apparent viscosity rapidly declined in a narrow range at first when the shear rate increased from 0 s^{-1} to around 25 s^{-1}. And then, it slowly decreased as the shear rate increased from 25 s^{-1} to 200 s^{-1}. It is obvious that the apparent viscosities of all ST emulsions exhibited the shear-thinning behavior, indicating that those ST emulsions belong to the Bingham plastic fluid. Specifically, as the dosage of AO emulsion increased, the apparent viscosity of ST emulsion gradually decreased. It was reported that an emulsion with a wider PSD range usually has a relatively lower apparent viscosity [32]. Compared with asphalt emulsion, the AO emulsion has a similar mean particle size and a slightly higher *Span* value. Thus, the ST emulsions containing AO emulsions had a relatively lower apparent viscosity than that of the pure asphalt emulsion. However, another kind of ST emulsion presented an opposite trend, where its apparent viscosity gradually thickened as the proportion of TO emulsion increased. One possible explanation was that the AO mainly contains fatty acids and polyol esters [33]. Large amounts of acid ions and carboxyl groups came from AO, which would combine with the heavy metal ions originating from asphalt binder,

Table 6
Zeta potential results of different AO emulsions.

No.	A (PH value)	B (Emulsifying temperature,°C)	C (Emulsifier dosage, %)	Zeta potential, mV
1	1 (3)	1 (75)	1 (2)	60.3
2	1 (3)	2 (90)	3 (4)	70.2
3	1 (3)	3 (60)	2 (3)	63.5
4	2 (2)	1 (75)	3 (4)	18.9
5	2 (2)	2 (90)	2 (3)	66.9
6	2 (2)	3 (60)	1 (2)	72.2
7	3 (1)	1 (75)	2 (3)	70.7
8	3 (1)	2 (90)	1 (2)	67.8
9	3 (1)	3 (60)	3 (4)	67.4
$k1$	64.7	50.0	66.8	
$k2$	52.7	68.3	67.1	
$k3$	68.7	67.7	52.2	
R	16.0	18.3	14.9	
Factor ranking		B > A > C		
Optimal scheme		A3B2C2		

Table 7
Zeta potential results of different TO emulsions.

No.	A (PH value)	B (Emulsifying temperature,°C)	C (Emulsifier dosage, %)	Zeta potential, mV
1	1 (3)	1 (40)	1 (2)	43.2
2	1 (3)	2 (60)	3 (4)	52.6
3	1 (3)	3 (20)	2 (3)	49.9
4	2 (2)	1 (40)	3 (4)	56.8
5	2 (2)	2 (60)	2 (3)	55.9
6	2 (2)	3 (20)	1 (2)	39.3
7	3 (1)	1 (40)	2 (3)	61.4
8	3 (1)	2 (60)	1 (2)	60.0
9	3 (1)	3 (20)	3 (4)	58.7
k1	48.6	53.8	47.5	
k2	50.7	56.2	55.7	
k3	60.0	49.3	56.0	
Range	11.4	6.9	8.5	
Factor ranking		A > C > B		
Optimal scheme		A3B2C3		

Table 8
Zeta potential and PSD results of optimized rejuvenator emulsions.

Type	Zeta potential, mV	PSD		
		D_{50}, μm	*Span*	*D* [3,4], μm
AO emulsion	75.02	1.48	5.91	3.33
TO emulsion	62.00	1.63	2.11	2.29
Asphalt emulsion	64.12	1.55	1.26	1.82

leading to the increase of apparent viscosity.

The shear stress versus shear rate results of different ST emulsions are shown in Fig. 7 **(b)** and **(d)**. Initially, ST emulsions didn't exhibit flow until the shear stress exceeded yield stress. Then the shear stress linearly increased with the shear rate, which corresponds with the characteristics of Bingham plastic fluid. As mentioned above, the more AO emulsions mixed with asphalt emulsions, the more apparent viscosity of ST emulsion decreased, which was consistent with the descending trend of shear stress as shown in Fig. 7 **(b)**. By contrast, Fig. 7 **(d)** shows that the shear stress of ST emulsion gradually increased as the addition of TO emulsion augmented, which accounts for the thickening of apparent viscosity.

3.2.2. Wettability

The wettability of the ST emulsion was evaluated by the contact angle test. The contact angles of pure asphalt emulsion, AO emulsion and TO emulsion droplets on the aged asphalt binder were 71.5°, 47.5° and 44.6°, respectively, indicating that both AO and TO emulsion have a better wettability on the surface of aged asphalt binder than asphalt emulsion. Fig. 8 shows that when adding AO emulsion or TO emulsion into asphalt emulsion to prepare the ST emulsion, the contact angle of mixed ST emulsion first rapidly decreased and then remained stable as the addition of rejuvenator emulsion increased. Especially, when the addition of rejuvenator emulsion was only 5 % by the weight of ST emulsion, the contact angles of AO-5 % and TO-5 % emulsions declined to 55.8 ° and 51.4°, which were reduced by 21.95 % and 28.11 % compared with pure asphalt emulsion. The incorporation of AO or TO emulsion in ST emulsion significantly improved the wettability, which is expected to help emulsion residue penetrate deeper and distribute more uniformly. Besides, it was observed that the TO emulsion has a lower contact angle than the AO emulsion, so the ST emulsion containing the TO emulsion always has a slightly better wettability than the ST emulsion containing the AO emulsion in each scenario.

3.2.3. Bonding strength

The coating ratio results of the water boiling test are depicted in Fig. 9. The bonding strength between original aggregates and asphalt binders generally consists of two parts, which are the adhesive strength of asphalt to aggregate and cohesive strength in asphalt binders. Results showed that the coating ratio decreased with the increase of rejuvenator emulsion, indicating the adhesive strength of composite emulsion residue to aggregate decreased. Meanwhile, it is well known that the cohesive strength of composite emulsion residues decreased with the increase of soft rejuvenating components. So, the more rejuvenator emulsions were added into ST emulsion, the worse the bonding strength of ST residue it was, which is similar to others' findings [34,35]. As the Chinese standard of JTG E20–2011-T0654 stipulated, the minimum coating ratio should not be lower than 2/3 to ensure the bonding strength between ST residue and aggregate. Therefore, it was recommended that the dosages of AO or TO emulsion used in this study should be controlled within 10 % and 5 %, respectively.

3.2.4. Determination of ST emulsion composition

The primary goal of adding rejuvenating agents into asphalt emulsion is to improve the wettability and permeability of ST emulsion

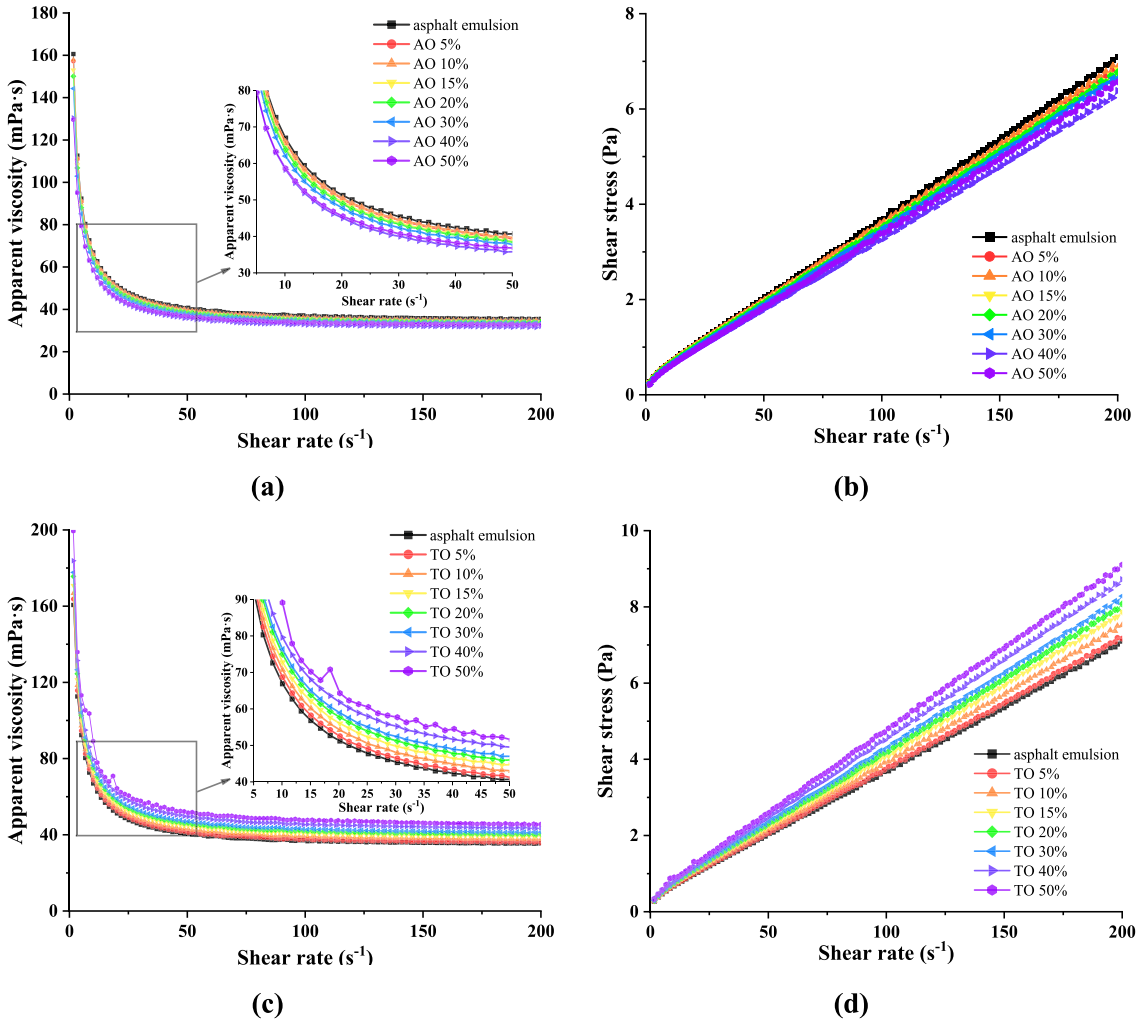

Fig. 7. Shear viscosity test results: (a) apparent viscosity curves of AO emulsions; (b) shear stress curves of AO emulsions; (c) apparent viscosity curves of TO emulsions; (d) shear stress curves of TO emulsions.

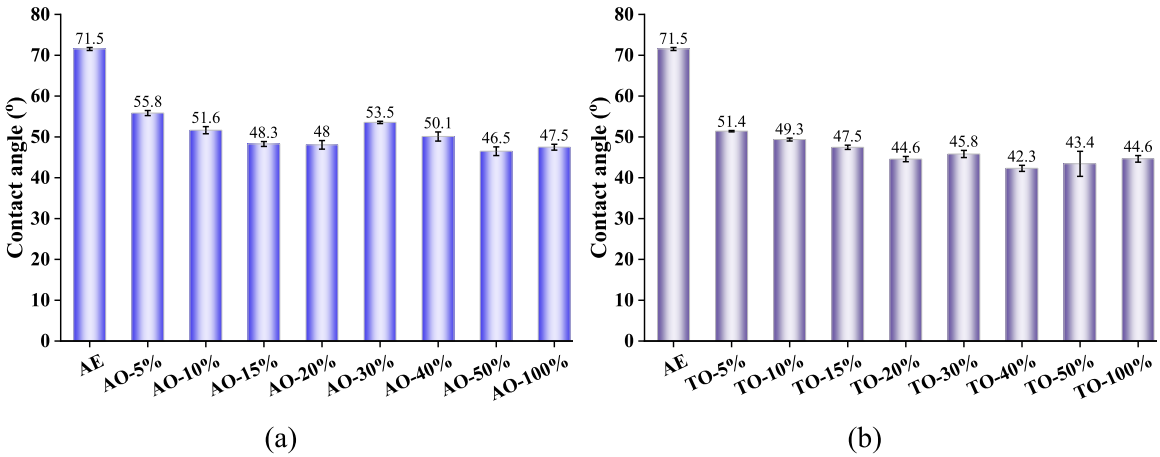

Fig. 8. Contact angles of (a) AO emulsion or (b) TO emulsion droplets on aged asphalt binder.

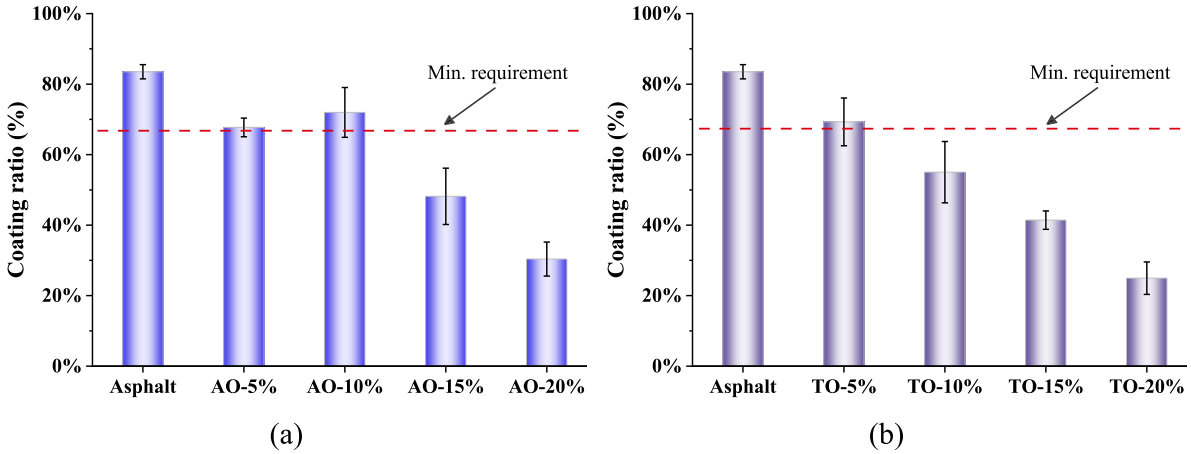

Fig. 9. Coating ratios of (a) AO emulsion or (b) TO emulsion residues on aggregate.

in PA mixture. Then, under the premise of guaranteeing the bonding strength of ST emulsion residue, rejuvenators can be added more to help revitalize more aged binders in the long term. Here comes a frequently asked question related to the ST emulsion formula. How do we determine the optimal dosage of rejuvenator emulsion in ST emulsion? Three points need to be considered for the ST emulsion formula optimization.

First, the apparent viscosity variation of ST emulsion should be controlled in a reasonable range. A sticky emulsion with a high viscosity might be difficult to penetrate inside PA pavement, leading to the accumulation of emulsion residue on the pavement surface. In contrast, the ST emulsion with a low viscosity could account for the quick draindown and the waste of emulsion residue. It was found that the apparent viscosities of ST emulsions containing different proportions of AO or TO emulsion did not show significant statistical differences. Thus, the incorporation of rejuvenator emulsion to asphalt emulsion could not change the apparent viscosity of ST emulsion.

Second, the wettability of ST emulsion is expected to be improved to deepen the penetration depth and make the ST emulsion distribute uniformly. Previous studies found that the sprayed unmodified ST emulsion had a nonuniform distribution of ST residue film [22], which not only increased the risk of blocking micro-voids to some extent, but also didn't coat the aged asphalt binder areas as much as possible. Therefore, a good wettability of ST emulsion is needed. Here, both AO and TO emulsions can significantly reduce the contact angles of ST emulsions, even at small addition amounts.

Third, the bonding strength of ST residue is a vital important performance as a preventive maintenance material. One of the motivations for using rejuvenators was replenishing light components of aged asphalt binders to rejuvenate them. If rejuvenator usage was calculated based on the effective penetration depth of emulsion and asphalt content of aged PA mixture, it was found that the needed rejuvenator content is too high to provide enough bonding strength of ST emulsion residue. However, different from the conventional hot recycling asphalt mixture, in which rejuvenators can effectively blend with and diffuse in aged asphalt binders of reclaimed asphalt pavement (RAP) at a high mixing temperature within several minutes [36,37], this study sprayed the ST emulsions containing fresh asphalt binder and rejuvenators to aged PA pavement without external heating. The diffusion behaviors between rejuvenators and aged asphalt binders are slow at outdoor temperatures. Rejuvenators were mixed with fresh asphalt binders in ST residues after the demulsification of ST emulsion, which could sacrifice the initial strength of ST residue. Take the micro-cracks in PA mixtures filled with ST residues as an example, the dosage of AO or TO rejuvenator should be carefully controlled within a certain range to ensure the bonding strength of ST residue.

To sum up, after comprehensively considering the apparent viscosity, wettability and bonding strength performances of the ST emulsion, the optimal dosages of AO and TO emulsions in ST emulsions were 10 % and 5 % in our scenarios, which were denoted by AO-10 % and TO-5 %, respectively.

3.3. Ravelling resistance verification

Three kinds of ST emulsions, named pure asphalt emulsion, asphalt emulsion containing AO emulsion (AO-10 %) and asphalt emulsion containing TO emulsion (TO-5 %), were sprayed to the top surface of damaged PA specimens to investigate their recovery efficiencies of the ravelling resistance. Specimens without emulsion treatment were also tested as a control group. Fig. 10 shows the lost masses and mass loss ratios after conducting the cantabro abrasion test. All PA specimens treated with ST emulsions exhibited significantly lower lost masses and mass loss ratios than those of the control group, indicating a better recovery effectiveness of ravelling resistance. Furthermore, compared with the results of damaged PA specimens treated with asphalt emulsion, the lost masses of specimens treated with AO-10 % and TO-5 % reduced 25.4 % and 11.2 %, respectively, indicating that the AO-10 % and TO-5 % showed better recovery efficiencies than asphalt emulsion. This phenomenon can be explained by the fact that the incorporation of AO

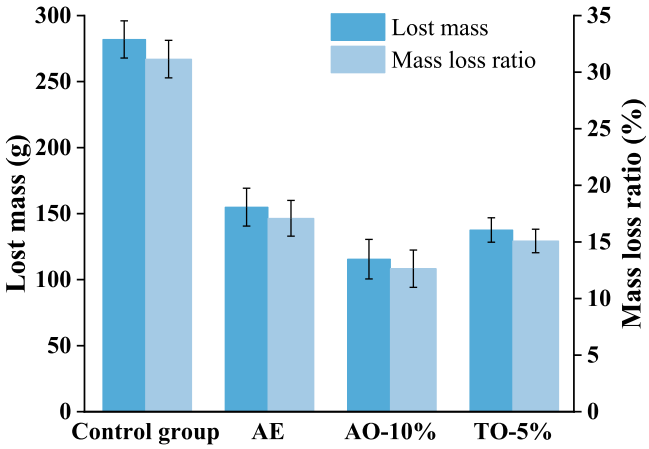

Fig. 10. Cantabro abrasion test results.

emulsion or TO emulsion could significantly improve the wettability of the ST emulsion as discussed above, which helps the emulsion penetrate deeper and distribute more uniformly inside a specimen as well as coat on more areas of aged binders surrounding the internal voids. Besides, AO-10 % and TO-5 % emulsion residues might have better diffusion efficiencies than asphalt emulsion residues due to the occurrence of rejuvenators, which is helpful in rejuvenating aged binders. Therefore, it is verified that the optimized ST emulsion containing rejuvenators could improve the ravelling resistance than pure asphalt emulsion in our cases.

In addition, compared with pure AE treated specimens, the TO-5 % treated PA specimens showed slightly lower mass loss ratios, while the AO-10 % treated PA specimen showed relatively lower mass loss ratios than the TO-5 % treated specimens, which could be explained by the following two aspects. On the one hand, Fig. 7 shows that the AO-10 % emulsion has a slightly lower apparent viscosity than that of TO-5 % emulsion. Although the addition of rejuvenator emulsion into pure asphalt emulsion didn't cause an order of magnitude change of apparent viscosity, the slight difference may affect the penetration depth of emulsion residues in PA mixture, which will further influence the recovery efficiency of ravelling resistance of PA mixture. On the other hand, the rejuvenator contents of AO-10 % and TO-5 % emulsions are different. Assuming the rejuvenating ability of AO and TO are similar, emulsion residues containing more rejuvenators theoretically could diffuse in and revitalize more aged asphalt binders, which benefits the recovery of the bonding strength of aged asphalt binders.

4. Findings and Conclusions

In this study, feasible methods of adding rejuvenators in ST emulsions were discussed at first. The appropriate parameter values were determined by the orthogonal design method to prepare stable and homogeneous rejuvenator emulsions. The viscosities, wettability and bonding strengths of different ST compositions were analyzed to determine the optimal formula. The ravelling resistances of damaged PA specimens treated with optimized ST emulsions were verified. The main findings and conclusions are summarized as follows:

1) It is recommended that the rejuvenator be emulsified at first to achieve better compatibility with asphalt emulsion.
2) Based on the PSD and zeta potential results, the appropriate PH values, emulsified temperatures and emulsifier dosages to prepare stable and homogeneous AO and TO emulsions were 1, 90 °C, 3 % and 1, 60 °C, 4 %, respectively.
3) Mixing AO or TO emulsion with asphalt emulsion didn't obviously change the apparent viscosity of the modified ST emulsion. Both AO and TO emulsions significantly improved the wettability of modified ST emulsions. The bonding strength of ST residue rapidly degraded as the dosage of rejuvenator emulsion increased. The optimal dosages of AO and TO emulsions are 10 % and 5 % by mass of the ST emulsion.
4) AO-10 % and TO-5 % emulsions ultimately reduced the lost masses of PA mixtures by 25.4 % and 11.2 % compared with the cantabro abrasion test results of damaged PA specimens treated with asphalt emulsion, demonstrating that incorporation of AO and TO emulsion into asphalt emulsion could further improve the ravelling resistance of PA.

The outcomes of this study hope to shed more light on improving the ravelling resistance of ST emulsion to prolong the lifespan of PA roads. It is worth noting that only two rejuvenators and one asphalt emulsion were selected in this study. More kinds of rejuvenators from different sources and modified/unmodified emulsions should be considered to verify the findings and conclusions above. Also, the effects of ST emulsions containing rejuvenators on the functional performances and the other mechanical properties, such as anti-rutting and anti-cracking performances, should be elaborately investigated.

Declaration of Competing Interest

The authors declare that they have no known competing financial interests or personal relationships that could have appeared to influence the work reported in this paper.

Data Availability

Data will be made available on request.

Acknowledgments

This work was supported by the Hong Kong Research Grant Council through the GRF projects (No. 15209920, 15220621); and the Nonmetallic Excellence and Innovation Center for Building Materials (No. 24PHD-1). The authors also thank the Ingevity Corp. for providing emulsifiers and thank the Kraton Corp. for providing rejuvenators for this study.

CRediT authorship contribution statement

Bin Yang: Writing – original draft, Methodology, Investigation, Data curation, Conceptualization. **Jiwang Jiang:** Methodology, Data curation. **Haopeng Wang**: Writing – review & editing. **Zhen Leng:** Writing – review & editing, Supervision, Conceptualization. **Xin Sui:** Methodology, Investigation. **Xi Jiang:** Methodology, Investigation.

References

[1] G. Lu, P. Liu, Y. Wang, S. Faßbender, D. Wang, M. Oeser, Development of a sustainable pervious pavement material using recycled ceramic aggregate and bio-based polyurethane binder, J. Clean. Prod. vol. 220 (2019) 1052–1060.
[2] D. Lu, X. Jiang, Z. Tan, B. Yin, Z. Leng, J. Zhong, Enhancing sustainability in pavement engineering: A-state-of-the-art review of cement asphalt emulsion mixtures, Clean. Mater. (2023) 100204.
[3] X. Jiang, et al., Full-scale accelerated testing of geogrid-reinforced inverted pavements, Geotext. Geomembr. vol. 52 (4) (2024) 511–525.
[4] J. Ji, T. Ma, Z. Zhang, M. Ling, X. Xu, J. Wei, Evaluation of benzaldehyd and dioctyl phthalate modified direct coal liquefaction residue asphalt binder based on rheology and microscopic mechanisms, Clean. Mater. vol. 12 (2024) 100238.
[5] D. Wang, et al., Suitability of PoroElastic road surface (PERS) for urban roads in cold regions: mechanical and functional performance assessment, J. Clean. Prod. vol. 165 (2017) 1340–1350.
[6] H. Li, H. Xu, F. Chen, K. Liu, Y. Tan, B. Leng, Evolution of water migration in porous asphalt due to clogging, J. Clean. Prod. vol. 330 (2022) 129823, https://doi.org/10.1016/j.jclepro.2021.129823.
[7] H. Wang, Y. Ding, G. Liao, C. Ai, Modeling and optimization of acoustic absorption for porous asphalt concrete, J. Eng. Mech. vol. 142 (4) (2016) 04016002.
[8] Y. Liu, T. Li, H. Peng, A new structure of permeable pavement for mitigating urban heat island, Sci. Total Environ. vol. 634 (2018) 1119–1125.
[9] C. Yan, W. Huang, P. Lin, Y. Zhang, Q. Lv, Chemical and rheological evaluation of aging properties of high content SBS polymer modified asphalt, Fuel vol. 252 (2019) 417–426.
[10] Q. Yang, J. Lin, X. Wang, D. Wang, N. Xie, X. Shi, A review of polymer-modified asphalt binder: Modification mechanisms and mechanical properties, Clean. Mater. (2024) 100255.
[11] Z. Zhang, et al., State-of-the-art of porous asphalt pavement: experience and considerations of mixture design, Constr. Build. Mater. vol. 262 (2020) 119998.
[12] G. Liao, X. Fang, H. Wang, J. Tang, P. Szary, J. Chen, Durability improvement of poroelastic road surface with treated rubber: Molecular dynamics simulation and experimental observations, J. Clean. Prod. vol. 369 (2022) 133334.
[13] G. Liao, Y. Sheng, H. Wang, Y. Li, J. Zha, W. Zhang, Polyurethane-based composite binder for poroelastic road surface: composition, preparation and properties, Constr. Build. Mater. vol. 409 (2023) 134089.
[14] Y. Zhang, M.F.C. Ven, A.A. Molenaar, S. Wu, Increasing the service life of porous asphalt with rejuvenators, Sustain. Constr. Mater. (2012) 318–330.
[15] Y. Zhang, "Extending the Lifespan of Porous Asphalt Concrete," Delft University of Technology, Delft University of Technology, 2015. [Online]. Available: ⟨http://resolver.tudelft.nl/uuid:f9860e45-e28b-477b-8df9-a094b00fd703⟩.
[16] Y. Zhang, Z. Leng, Quantification of bituminous mortar ageing and its application in ravelling evaluation of porous asphalt wearing courses, Mater. Des. vol. 119 (2017) 1–11, https://doi.org/10.1016/j.matdes.2017.01.052.
[17] M. Van de Ven, J. Qiu, and Y. Zhang, "Increasing the functional service life of porous surfacings: Development of test methods to study the effect of rejuvenating binders," in *Proceeding of 15th International Flexible Pavements Conference of AAPA,* Australian Asphalt Pavement Association, Queensland, Australia, 2013.
[18] B. Yang, Z. Leng, J. Jiang, R. Li, M. Han, Investigation of bituminous emulsion's impact on the mechanical durability of damaged porous asphalt mixture. Advances in Functional Pavements, CRC Press, 2024, pp. 273–277.
[19] B. Xu, M. Li, S. Liu, J. Fang, R. Ding, D. Cao, Performance analysis of different type preventive maintenance materials for porous asphalt based on high viscosity modified asphalt, Constr. Build. Mater. vol. 191 (2018) 320–329, https://doi.org/10.1016/j.conbuildmat.2018.10.004.
[20] Y. Zhang, Q. Liu, M. Van de Ven, A. Molenaar, S. Wu, Identification of rejuvenators on porous-asphalt concrete using optical microscopy and nanoindentation technology, J. Mater. Civ. Eng. vol. 27 (8) (2015) C4014008.
[21] B. Yang, Z. Leng, J. Jiang, Z. He, D. Li, Recovery efficiency of the damaged porous asphalt mixture with emulsion-based surface treatment: material optimization and performance verification, Constr. Build. Mater. vol. 347 (2022) 128530, https://doi.org/10.1016/j.conbuildmat.2022.128530.
[22] J. Jiang, et al., Penetration mechanism of the emulsion-based rejuvenator in damaged porous asphalt mixture: microstructure characterization and 3D reconstruction, Mater. Des. vol. 221 (2022) 111014, https://doi.org/10.1016/j.matdes.2022.111014.
[23] J. Lee, S. Li, Y. Kim, J. Lee, Effectiveness of asphalt rejuvenator, J. Test. Eval. vol. 41 (3) (2013) 433–440.
[24] C.K. Estakhri and H. Agarwal, *Effectiveness of fog seals and rejuvenators for bituminous pavement surfaces*. Texas Transportation Institute, Texas A & M University, 1991.
[25] C.-T. Chiu, M.-G. Lee, Effectiveness of seal rejuvenators for bituminous pavement surfaces, J. Test. Eval. vol. 34 (5) (2006) 390–394.
[26] J. Lin, J. Hong, C. Huang, J. Liu, S. Wu, Effectiveness of rejuvenator seal materials on performance of asphalt pavement, Constr. Build. Mater. vol. 55 (2014) 63–68.
[27] B. Xu, et al., Experimental investigation of preventive maintenance materials of porous asphalt mixture based on high viscosity modified bitumen, Constr. Build. Mater. vol. 124 (2016) 681–689, https://doi.org/10.1016/j.conbuildmat.2016.07.122.
[28] Y. Zhang, M.F.C. van de Ven, A.A.A. Molenaar, S.P. Wu, Assessment of effectiveness of rejuvenator on artificially aged porous asphalt concrete, Constr. Build. Mater. vol. 110 (2016) 286–292, https://doi.org/10.1016/j.conbuildmat.2016.02.042.

[29] Y. Fang, Z. Zhang, H. Zhang, W. Li, Analysis of wetting behavior and its influencing factors of rejuvenator/old asphalt interface based on surface wetting theory, Constr. Build. Mater. vol. 314 (2022) 125674.
[30] J. Yi, Y. Wang, Z. Pei, M. Xu, D. Feng, Mechanisms and research progress on biological rejuvenators for regenerating aged asphalt: Review and discussion, J. Clean. Prod. (2023) 138622.
[31] I. Pinto, A. Buss, Potential as a measure of asphalt emulsion stability, Energy Fuels vol. 34 (2) (2020) 2143–2151.
[32] F. Goodarzi, S. Zendehboudi, A comprehensive review on emulsions and emulsion stability in chemical and energy industries, Can. J. Chem. Eng. vol. 97 (1) (2019) 281–309.
[33] S. Ren, X. Liu, S. Erkens, P. Lin, Y. Gao, Multi-component analysis, molecular model construction, and thermodynamics performance prediction on various rejuvenators of aged bitumen, J. Mol. Liq. vol. 360 (2022) 119463.
[34] J. Ji, et al., Effectiveness of vegetable oils as rejuvenators for aged asphalt binders, J. Mater. Civ. Eng. vol. 29 (3) (2017) D4016003.
[35] B. Cui, X. Gu, D. Hu, Q. Dong, A multiphysics evaluation of the rejuvenator effects on aged asphalt using molecular dynamics simulations, J. Clean. Prod. vol. 259 (2020) 120629.
[36] J.-F. Su, J. Qiu, E. Schlangen, Y.-Y. Wang, Investigation the possibility of a new approach of using microcapsules containing waste cooking oil: in situ rejuvenation for aged bitumen, Constr. Build. Mater. vol. 74 (2015) 83–92.
[37] D. Li, et al., Investigation of rejuvenation mechanisms of reclaimed asphalt rubber pavement through mortar tests, Int. J. Pavement Eng. vol. 24 (1) (2023) 2235631.

Construction and Building Materials 464 (2025) 140185

Contents lists available at ScienceDirect

Construction and Building Materials

journal homepage: www.elsevier.com/locate/conbuildmat

Maintenance mechanisms of rejuvenator-optimized asphalt emulsion in damaged porous asphalt mixture: Morphological, physicochemical, and rheological characterizations

Bin Yang [a], Jiwang Jiang [b], Zhen Leng [a,*], Xi Jiang [a], Yubo Sun [a], Chuanqi Yan [a,c], Zhifei Tan [a], Gaoyang Li [a]

[a] Department of Civil and Environmental Engineering, The Hong Kong Polytechnic University, Kowloon, Hong Kong
[b] School of Transportation, Southeast University, Nanjing, Jiangsu, China
[c] School of Civil Engineering, Southwest Jiaotong University, Chengdu, Sichuan, China

ARTICLE INFO

Keywords:
Preventive maintenance
Porous asphalt
Rejuvenator emulsion
Asphalt emulsion
Ravelling distress

ABSTRACT

Spraying surface treatment asphalt emulsion to old porous asphalt (PA) pavement is a feasible preventive maintenance technique to alleviate the ravelling distress of PA. However, the insufficient penetration depth and non-uniform distribution of conventional asphalt emulsion in PA pavement restrict its maintenance effectiveness. Inspired by the good wettability and diffusion capacity of rejuvenator, it was innovatively used to optimize asphalt emulsion. The maintenance mechanism of rejuvenator-optimized asphalt emulsion in damaged PA was comprehensively investigated from morphological, physicochemical, and rheological perspectives, respectively. One petrol-based rejuvenator named aromatic oil, and one bio-based rejuvenator named tall oil were selected to optimize conventional asphalt emulsion. Computed tomography (CT) scanning results showed that the penetration depth of the two rejuvenator-optimized asphalt emulsions in PA was about 40 mm, which is twice the depth of conventional asphalt emulsion. Rejuvenator-optimized asphalt emulsion uniformly distributed in PA with a better coating efficiency, which improves the ravelling resistance of damaged PA. Gel permeation chromatography (GPC) analysis revealed that adding rejuvenator emulsion to asphalt emulsion significantly softened aged asphalt and reduced its molecular weight. Rheological analysis indicated that rejuvenator-optimized asphalt emulsion enhanced stress relaxation property and cracking resistance of aged asphalt binders in PA. The findings of this study hope to postpone the road rehabilitation work and prolong the service life of old PA pavement.

1. Introduction

Porous asphalt (PA) pavement has been widely used in “Sponge City” [1] due to its numerous merits including improved water drainage [2–4], reduced noise [5], and enhanced skid resistance [6]. However, compared with conventional dense- and gap-graded asphalt pavements, PA roads are susceptible to ravelling distress after they were opened to traffic for several years, primarily due to the relatively faster aging rate of asphalt binders and the high air void content [7,8]. Pavement performance of PA could rapidly deteriorate if no appropriate preventive maintenance measure (PMM) is timely taken [9]. Furthermore, the end-of-life asphalt pavement as a construction waste produces a huge burden for urban green and sustainable development. Even though the hot/cold in-place mix recycling technology could partially reuse reclaimed asphalt pavements (RAPs) for saving scarce fossil and mineral resources [10–12], a considerable amount of disposed asphalt pavement wastes faces limited landfill areas and environmental pollution dilemmas. Compared with frequently milling old pavements and re-paving new pavements, regularly applying PMM to the existing asphalt pavement can effectively reduce the consumption of mineral and asphalt resources and prolong its service life. A short construction period of PMM minimizes the negative effect of road closure on surrounding residents’ rural activities. Moreover, the relevant studies of the life cycle assessment (LCA) and life cycle cost analysis (LCCA) implied that PMM could decrease greenhouse gas (GHG) emissions and save transport expenditure in the long run [13–18].

* Corresponding author.
E-mail address: zhen.leng@polyu.edu.hk (Z. Leng).

https://doi.org/10.1016/j.conbuildmat.2025.140185
Received 5 September 2024; Received in revised form 2 January 2025; Accepted 24 January 2025
Available online 30 January 2025
0950-0618/© 2025 Published by Elsevier Ltd.

Previous studies showed that spraying surface treatment (ST) emulsion to old PA pavement could be an effective PMM to improve the ravelling distress without significantly compromising the functional performances of PA [19,20]. Generally, the main component of ST emulsion is asphalt emulsion, in which asphalt binders are homogeneously and stably dispersed in water with the help of emulsifiers [21]. ST emulsion is often seen as a sustainable maintenance material in road engineering because it can be directly sprayed to the old PA pavement surface without any external heating and mechanical agitation process. ST emulsion is known for its time-dependent phase transition behavior: when sprayed onto the surface of aged PA pavement, it initially acts as a liquid, penetrating the PA mixture through void structures. Following the evaporation of water and the demulsification of the ST emulsion, the remaining ST residue transitions into a solid phase, filling microcracks and replenishing the aged asphalt binders. In the long term, the newly added soft asphalt binder is expected to gradually soften the aged asphalt binder, decreasing its stiffness through diffusion [22].

However, three major concerns arise when applying conventional ST emulsion to old PA pavement: 1) the shallow vertical penetration depth of ST emulsion, 2) the non-uniform distribution of the ST emulsion, and 3) the slow diffusion efficiency of ST residues in aged asphalt binders. Previous study found that the penetration depth of ST emulsion in PA mixture did not exceed 20 mm when the solid content of ST emulsion is 60 % and its application rate is 0.6 kg/m^2 [23]. Whereas the design thickness of the upper layer of PA pavement in China is typically around 40 mm, a deeper penetration of ST emulsion is necessary to effectively improve the ravelling distress of aged PA pavement. Although reducing the solid content of ST emulsion and increasing the application rate could enhance the penetration depth of ST emulsion, the former scenario usually dilutes the ST emulsion with water to obtain a low asphalt content, thereby reducing the viscosity but sacrificing part of maintenance effects [24], while the latter scenario increases the risk of pore blockage without significantly improving ravelling resistance of PA [25]. So, here comes the first question: how to optimize the ST emulsion composition to enhance the penetration depth without significantly changing the solid content and the application rate of ST emulsion? The second concern of the current ST emulsion technique relates to its residue's distribution morphology inside PA pavement. Computed tomography (CT) image scanning results suggested that the average thickness of ST residue was somewhat thick, and the coating efficient was insufficient [23]. In other words, for ST residues which already penetrated in air voids, they haven't covered the aged asphalt binders around air voids as many as possible. By contrast, the accumulations of some residues in pores increased the average thickness of ST residues. The heterogeneous distribution phenomenon of ST residue indicated that some aged asphalt binders remained uncovered by new asphalt binders. Theoretically, for a given application rate of ST emulsion, the more uniformly the ST residue coats the aged asphalt binder, the better the ravelling resistance of aged PA pavement. Thus, how to optimize the material design of ST emulsion to achieve a more homogeneous distribution of ST residue in PA mixture is the second question need to be carefully considered. Thirdly, the diffusion efficiency of conventional ST residue in aged mortar of PA mixture at ambient temperature is slow, which restricts the recovery efficiency of bonding strength of asphalt binder.

Rejuvenator, a novel softening oil, contains a high proportion of light components, which has been widely applied in sustainable pavement construction with recycling use of reclaimed asphalt mixtures [26,27]. It can be categorized into two types based on their origins. One is the by-product of crude petroleum refinery, named petrol-based rejuvenator, like aromatic oil and waste engine oil. The other type is the bio-based rejuvenator derived from plant or animal waste, like the waste vegetable oil and waste cooking oil. Rejuvenator has a strong regenerating ability for aged asphalt binder to restore its properties [28], which inspires the optimization of conventional ST emulsion. Besides, rejuvenator usually has a better wettability and a higher diffusion efficiency than asphalt binder [29,30], which could be an alternative additive to optimize ST emulsion towards a better maintenance effectiveness for old PA.

Recent studies found that the ST emulsion containing rejuvenator ingredients may have a better recovery efficiency of ravelling resistance for old asphalt pavement than conventional asphalt emulsion [31–33]. These studies claimed that the incorporation of rejuvenating agent improved the rejuvenation ability of ST emulsion to efficiently revitalize aged asphalt binders. The National Center for Asphalt Technology (NCAT) in Alabama released a report on the effects of adding rejuvenators into ST emulsions to investigate their maintenance effects on old PA roads [34]. Two PA pavements were sprayed with two ST emulsions containing two different rejuvenators separately. Irrespective of the application rates of ST emulsions, both PA pavements exhibited higher mean profile depth (MPD) values compared to the same road section treated with pure asphalt emulsion, minimizing the negative effects of pore clogging. Additionally, it also indicated that the rejuvenator could help ST emulsion penetrate deeper instead of accumulation on the road surface of PA compared with the pure asphalt emulsion. Another technical report released by the Florida Department of Transportation pointed out that although the addition of rejuvenator into ST emulsion reduced the high-temperature Performance Grade (PG) of old asphalt binders by 5–7 °C [35], the Hamburg Wheel Track test results showed that the occurrence of rejuvenator could improve the anti-rutting and moisture susceptibility of PA when the application rate was well controlled [36]. Based on the above discussions, adding rejuvenators to ST emulsions appears to make the ST emulsions penetrate deeper and distribute more uniformly in PA pavements. However, quantitative evidence regarding the distribution morphology of rejuvenator-optimized ST emulsion in old PA mixtures was still missing. Little information is available regarding the working mechanisms of rejuvenator in ST emulsion as a preventive maintenance material for old PA pavement.

Thus, this study aims to comprehensively investigate the maintenance mechanisms of rejuvenator-optimized ST emulsion in old PA mixture from the morphological, physicochemical, and rheological perspectives. As the flowchart shown in Fig. 1, the distribution of ST residues in PA mixtures was first identified using X-ray CT. Penetration depth of ST residues was calculated based on the variations in air voids before and after the ST emulsion. Two indicators, thickness (T_c) and percentage of coating area (P_c) of emulsion residues, were developed to evaluate the distribution uniformity of ST residues in the PA mixture. Then, the same PA specimen was cut into four slices, and their binders, including asphalt binders and rejuvenators, were extracted using the solvent extraction method. Subsequently, the molecular weight compositions of extracted binders from different layers of the PA specimen were analyzed by the gel permeation chromatography (GPC) test. Meanwhile, Fourier Transform Infrared Spectroscopy (FTIR) was used to detect the penetration depth of rejuvenator-optimized ST emulsion based on the unique functional groups of the selected rejuvenator. In addition, relevant rheological tests were carried out to investigate the maintenance effects of rejuvenator-optimized ST residues on the anti-rutting and anti-cracking performances of old asphalt binders. Master curves were built to further analyze the rheological properties of extracted binders. The outcomes of this study hope to shed more light on the understanding of maintenance mechanisms of rejuvenator-optimized emulsion in damaged PA mixture, ultimately guiding the material design of ST emulsions and extending the service life of old PA pavement.

2. Materials and methodology

2.1. Materials and specimen preparation

2.1.1. ST emulsion preparation

A pure asphalt emulsion (AE) was prepared to serve as the control group. One petrol-based rejuvenator named aromatic oil (AO), and one

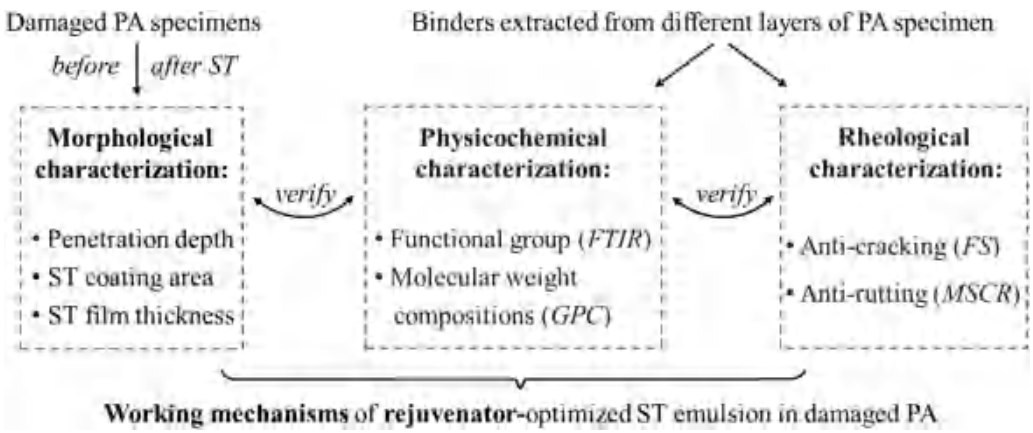

Fig. 1. Flowchart of this study.

bio-based rejuvenator named tall oil (TO) were separately emulsified to prepare two rejuvenator emulsions. The mass compositions and production conditions for those three kinds of emulsions are summarized in Table 1. Then, the AO emulsion, with a mass content of 10 %, was directly added into AE to prepare the aromatic oil optimized asphalt emulsion (AOAE). Similarly, the TO emulsion, with a mass percentage of 5 %, was mixed with AE to prepare the tall oil optimized asphalt emulsion (TOAE). So, three kinds of ST emulsions, designated as AE, AOAE, and TOAE, were used in this study. The optimization dosage of rejuvenator emulsion in asphalt emulsion was determined based on the workability (viscosity, wettability and bonding strength) of rejuvenator-optimized ST emulsion, which can be found more details in this previous study [37].

2.1.2. PA mixture preparation

The SBS modified asphalt fulfilled with the Superpave performance grading of 76–16 (PG76–16) was used in this study. The target air void is 22.5 % and the nominal maximum aggregate size is 13.2 mm. The designed asphalt content of PA mixture was 4.1 % by weight of aggregates. Fig. 2 shows the schematic diagram of this study including the sample preparations and experimental methods. The pressure aging vessel (PAV) was used to prepare the PAV aged asphalt binders. They were mixed with aggregates to prepare the PA specimen. Firstly, the same PA specimen was scanned by X-ray CT for morphological characterization before and after the application of ST emulsion. It should be noted that the second scan was conducted only after the water had completely evaporated and the emulsion had fully demulsified. Three kinds of ST emulsions were tested, and two specimens were prepared for each kind of ST emulsion. Then, the ST treated specimens were cut into 4 slices with thicknesses of 10 mm, 10 mm, 20 mm, and 20 mm from the top surface to the bottom. Later on, each slice of PA mixture was immersed in dichloromethane (DCM) solvent to dissolve the asphalt binders and rejuvenators. Given that the boiling point of DCM is 39.6 °C at 1 atm, the solutions were placed in an oven at 45 °C for 24 hours to ensure thorough evaporation of the DCM. The extracted binder mixture, including asphalt binders and rejuvenators, was then used for physicochemical and rheological tests.

Table 1
Basic information about emulsions.

Item	Weight composition				Production condition	
	Solid content	Emulsifier	Stabilizer	Water	Heating temperature for binder (°C)	pH value
AE	60 %	3 %	0.2 %	36.8 %	135	2.5
AO	60 %	3 %	0.2 %	36.8 %	90	1
TO	60 %	4 %	0.2 %	35.8 %	60	1

2.1.3. Ravelling resistance evaluation

The loose asphalt mixtures were first heated in an oven at 135 °C for 8 hours to simulate the long-term aging effect on the asphalt pavement [38,39]. Then, several cylindrical PA mixture specimens with a diameter of 100 mm and a height of 60 mm were fabricated by the Superpave gyratory compactor. Subsequently, three cycles of freezing and thawing conditioning were applied to all PA specimens to add some micro-cracks into PA mixtures. Finally, different ST emulsions were sprayed onto the surfaces of damaged PA specimens for maintenance purposes. The binder content and spraying rate of ST emulsion are 60 % and 0.6 kg/m^2, respectively [25].

The Cantabro Abrasion test was performed to evaluate the maintenance effects of different ST emulsions on the ravelling resistance of damaged PA specimens. The mass loss ratio (M_r) is calculated by Eq. (1) and the results are shown in Table 2. The damaged PA specimen without ST presented the highest M_r value than that of ST treated specimen, demonstrating the effectiveness of ST emulsions in enhancing the anti-ravelling property of damaged PA. In particular, incorporating rejuvenator emulsion into AE helped decrease the M_r values of damaged PA specimens, so the damaged PA mixtures treated with either AOAE or TOAE exhibited slightly better ravelling resistance than those only treated with AE. Reasons why adding rejuvenator emulsion to AE can help further improve the anti-ravelling property of PA specimens will be explained in the following sections of this study.

$$M_r = \frac{m_1 - m_2}{m_1} \times 100\% \tag{1}$$

where the damaged PA specimens before and after the Cantabro Abrasion test were weighed and denoted as m_1 and m_2, g.

2.2. Test methods

2.2.1. X-ray CT test

Image processing technology has been widely used in the identification and characterization of mesoscopic structures in civil engineering field [40–42]. Cross-sectional images of PA specimens, both untreated and treated with ST emulsions, were obtained using the X-ray CT machine of Nikon XT H225, which is an effective and high-precision equipment to recognize the penetration status of ST residues in PA mixture. The scanning system operated at a working voltage of 120 kV and a current of 105 μA. The horizontal resolution of CT images varied slightly between 36.873 and 37.175 μm/pixel, due to the minor placement differences among different scanning operations. The minimum vertical interval of CT images is 100 μm, and a total of 600 pieces of images were exported for analyzing volumetric characteristics from the

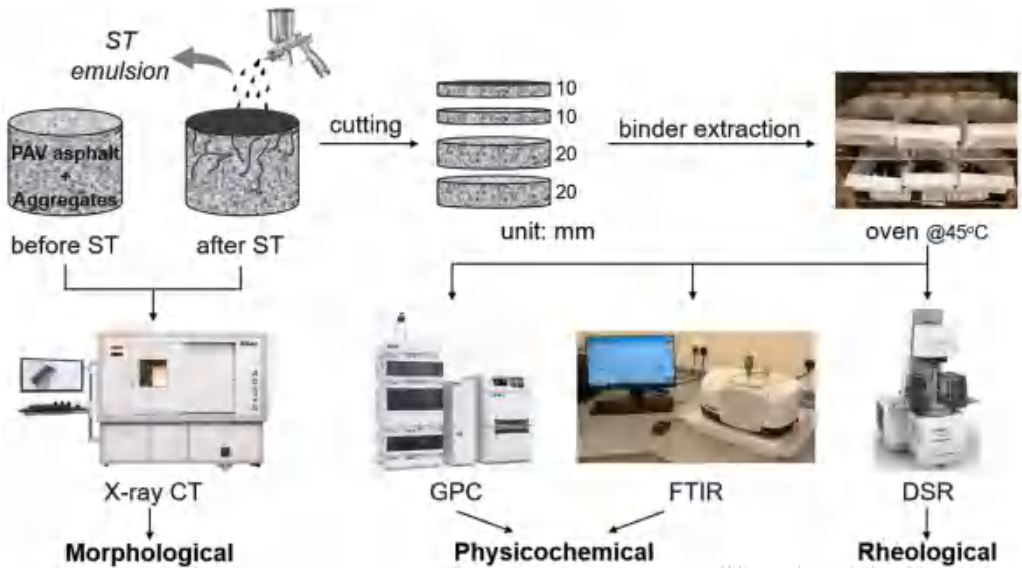

Fig. 2. Sample preparations and test methods in this study.

Table 2
Mass loss ratios of damaged PA before and after ST application.

	Without ST	AE	AOAE	TOAE
Mass loss ratio, %	31.2	17.1	12.6	15.1
St.d, %	1.7	1.6	1.7	1.0

mesoscopic perspective. After conducting the smooth, denoising, and thresholding processes for CT images, the air voids and asphalt mixtures can be easily distinguished based on their gray values from the scanning images due to their significant density differences. Then, the images were rescaled, centered, and rotated to precisely match two groups of CT images for the same PA specimen before and after the application of ST emulsion. Thereafter, the newly added ST residues could be identified through the Boolean operation. In other words, the distribution of ST residues within a PA specimen can be recognized by subtracting the CT images of the PA specimen without ST from the corresponding slice images of the same PA specimen containing ST. All CT image processing was performed using a series of customized MATLAB algorithms.

Take Fig. 3 **(a)** as an example, the black, gray, and yellow colors represent the air void, aggregate, and ST residue, respectively. The newly added ST residues are generally distributed around the air voids and the coated boundary is marked in red. The percentage of coating area (P_c) refers to the average ratio of the length of the coated boundary of ST to the perimeters of all air voids before ST in several CT images. It was proposed to evaluate the coating efficiency of ST residue, which is calculated by Eq. (2). Besides, Fig. 3 **(b)** shows a binary picture of ST residue. The droplet of each ST residue was recognized, and its center line was extracted via the skeletonization process. The thickness of ST residue at each pixel on its center line is equal to twice the distance of the center line to the nearest edge, which was depicted with different

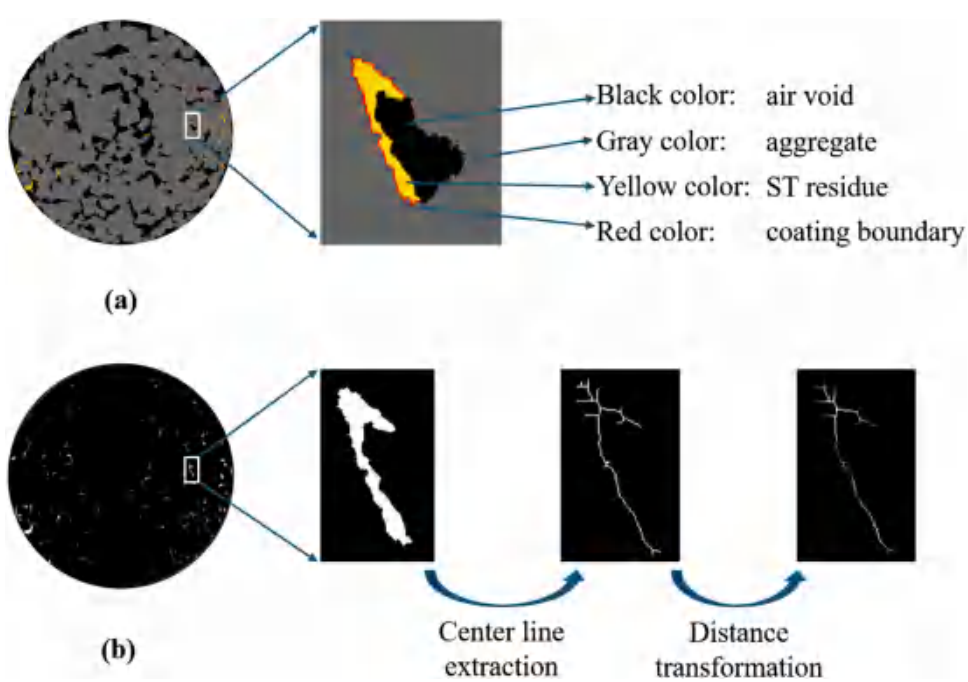

Fig. 3. CT images of PA mixture: (a) Different components of ST treated PA mixture; (b) ST residue recognition and its thickness calculation.

gray values after the distance transformation process. The average thickness of ST residues (T_c) and its standard deviation (Sd_c) were proposed to evaluate the uniformity of ST residue within PA mixture.

$$P_c = \frac{\sum_{i=1}^{i=n} L_c^i}{\sum_{i=1}^{i=n} L_a^i} \times 100 \tag{2}$$

where n is the number of CT images; L_c^i means the total lengths of the coated boundaries of ST at the number i image, mm; and L_a^i is the total perimeters of all air voids without ST condition at the number i image, mm.

2.2.2. Gel permeation chromatography (GPC) test

A GPC assembled a refractive index differential detector was used to measure the molecular weight composition of the binder extracted from ST treated PA mixture. Each binder sample with a mass of 0.05 g ± 0.002 g was dissolved in 50 ml of tetrahydrofuran (THF) solvent to prepare the binder solution. The injection volume was 20 μl for each test, with a 1 ml/min flow rate of the mobile phase. This test was performed at 30 °C. The molecular weight corresponding to the highest percentage of the total molecular composition (M_p) and the number average molecular weight (M_n) are two representative statistical parameters, which are widely used in the GPC analysis [43]. The calculation equation for M_n is shown below.

$$M_n = \frac{\sum n_i M_i}{N} \tag{3}$$

where i represents a molecular with a specific molecular weight; n_i is the total weight and the total number of molecular i in each test; N means the sum number of all kinds of molecules; M_i is the molecular weight of molecular i.

2.2.3. Fourier-transform infrared spectroscopy (FTIR) test

A PerkinElmer FTIR spectrometer operating in attenuated total reflectance (ATR) mode was selected to analyze the binders extracted from different layers of ST treated PA mixtures. Rejuvenators may contain some unique functional groups that respond with specific absorbance bands, allowing for differentiation from the asphalt binders used in this study. Theoretically, these distinct absorbance bands can serve as tracers to investigate the penetration depth of rejuvenator-optimized asphalt emulsions within PA specimens.

2.2.4. Dynamic shear rheometer (DSR) test

Asphalt binder acts as the important bonding material between aggregates in mixture. Its rheological property significantly affects the mechanical property of asphalt mixture [44,45]. Different ST emulsions may produce different maintenance effectiveness on the mechanical properties of damaged PA mixture. So, the frequency sweep (FS) test and multiple stress creep recovery (MSCR) test were conducted using a DSR to investigate the rheological property of extracted binder from PA. Two replicates were prepared for each kind of extracted binder.

2.2.4.1. FS test. The phase angles (δ) and complex shear moduli (G^*) of different binder samples extracted from different ST treated PA specimens were measured in the FS test with a frequency range of 100–0.01 Hz. The test temperatures are set from 10 °C to 60 °C with an increasing interval of 10 °C. The test strain was controlled at 0.1 % to ensure that the asphalt-based binder was within its linear viscoelastic range. The 25 mm parallel plate with a 1 mm gap and the 8 mm parallel plate with a 2 mm gap were used at test temperature ranges of 40–60 °C and 10–30 °C, respectively. Based on the time-temperature superposition principle, the shift factor was calculated using the Williams-Landel-Ferry (WLF) formula as given in Eq. (4). The reference temperature was set at 10 °C.

$$\log a_T = \frac{-C_1(T - T_0)}{C_2 + (T - T_0)} \tag{4}$$

where a_T is the shift factor; T and T_0 are the experimental temperature and the reference temperature, respectively; C_1 and C_2 are constants.

The viscoelastic response of asphalt binder can be fitted by the Modified Huet-Sayegh (MHS) model [46], which mathematical expression is shown in Eq. (5). The MHS model is optimized from Huet-Sayegh (HS) model by adding a linear dashpot in series, which can improve the goodness of fit of the master curve data at the low frequency region and help to describe the viscous behavior.

$$j^*(\omega) = \frac{G'}{|G^*(\omega)|^2} - i\left[\frac{G''}{|G^*(\omega)|^2} + \frac{1}{\eta\omega}\right] = J'(\omega) - ij''(\omega) \tag{5}$$

where $j^*(\omega)$, $J'(\omega)$ and $J''(\omega)$ represent the complex creep compliance, storage creep compliance and loss creep compliance of the MHS model, respectively; ω and η mean the reduced frequency and the linear dashpot parameter, respectively; $G^*(\omega)$, G' and G'' are the complex shear modulus storage shear modulus and loss shear modulus of the original HS model, respectively.

Besides, the Glover-Rowe parameter (G-R) is calculated by Eq. (6). The G^* and δ values at 0.005 s^{-1} and 15 °C directly obtain from the constructed master curve. G-R parameter was used to evaluate the ductility and cracking resistance of asphalt binders at a low temperature [47,48].

$$G - R = \frac{G^*(\cos\delta)^2}{\sin\delta} \tag{6}$$

2.2.4.2. Multiple stress creep recovery (MSCR) test. It is proved that MSCR test can effectively assess the anti-rutting performance of asphalt binder [49,50]. According to the standard of AASHTO M 332–23, specimens with a thickness of 1 mm and a diameter of 25 mm underwent the creep test at 60 °C and two different stress levels of 0.1 kPa and 3.2 kPa. In each stress level, a constant stress creep of 1 s duration followed by a recovery period lasting 9 s was applied to the specimen and ten cycles were repeated. $J_{nr0.1}$ and $J_{nr3.2}$ represent the average non-recoverable creep compliances at two stress levels, which can be calculated by Eq. (7). In addition, the average percent recovery of strain at both stress levels, $R_{0.1}$ and $R_{3.2}$, was calculated to evaluate the resilience of the binder after repeated stretching and relaxation.

$$J_{nr,\sigma} = \frac{\varepsilon_{nr}}{\sigma} \tag{7}$$

where $J_{nr,\sigma}$ is the nonrecoverable creep compliance at a specific stress level, kPa^{-1}; ε_{nr} is the average nonrecoverable strain of ten cycles; σ is the stress level, kPa.

3. Results and discussions

3.1. Morphological analysis

3.1.1. Air void variations of different ST emulsions treated specimens

The air void contents along the depth direction within PA mixtures before and after applying different ST emulsions were depicted in Fig. 4 with blue and red colors, respectively. It was found that the vertical profile of air voids within a PA mixture before and after ST showed a bath shape, which was consistent with other studies [51,52]. Besides, after the water evaporation of ST emulsion, the newly added ST residues partially filled the air voids and accounted for the reduction of air voids. This change was identified by conducting the Boole operation on the CT images of PA mixture obtained before and after ST emulsion. The volume distribution of ST residues is depicted in Fig. 4 in black color. It showed a vertical gradient decreasing profile in PA, with a relatively

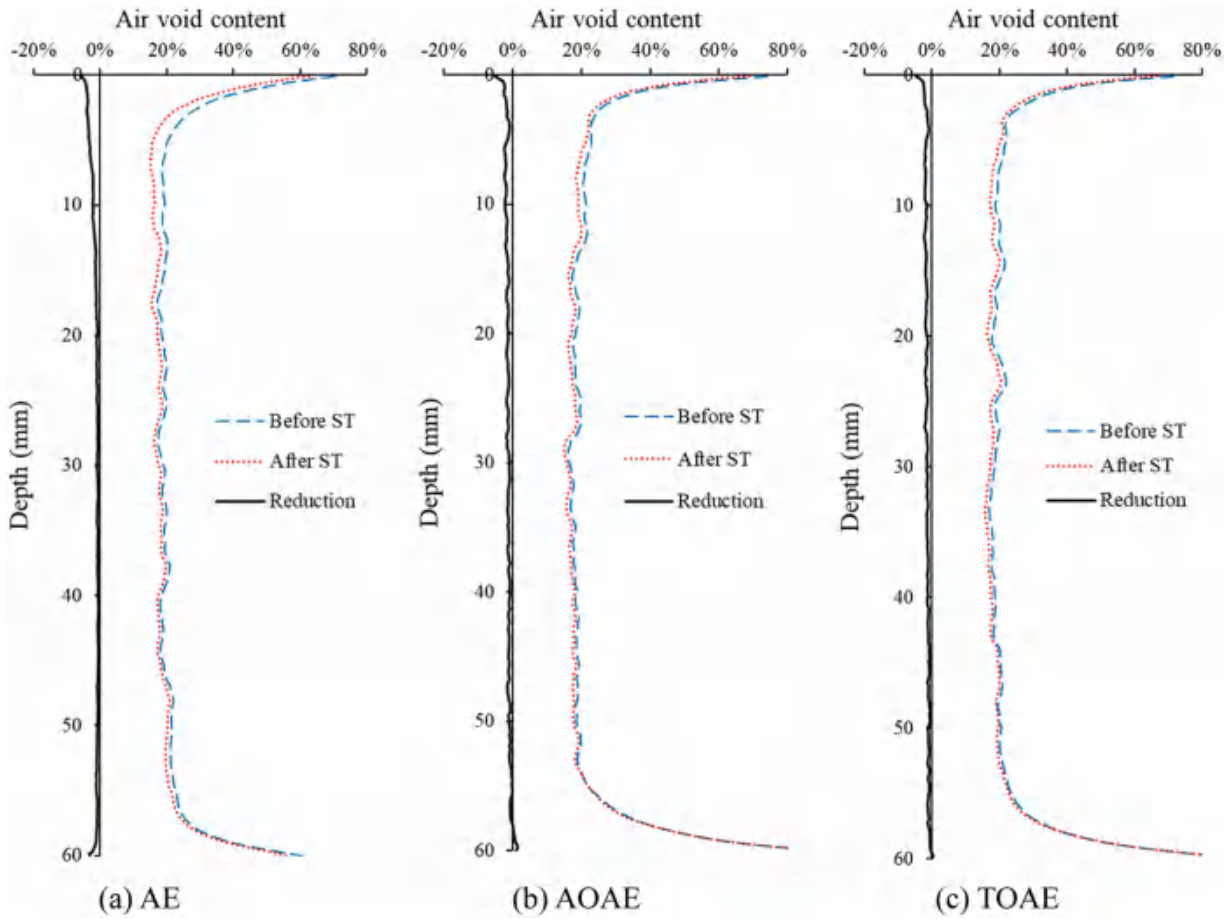

Fig. 4. The air void contents along the depth direction within a PA specimen before and after the application of ST emulsions.

higher ST value near the top surface of PA due to the accumulation effect. Despite the same application rate and solid content of three different ST emulsions, their distributions within PA specimens exhibited different characteristics. Specifically, most AE residues penetrated approximately 20 mm into the PA specimen, while the other two rejuvenator-optimized ST residues could penetrate around 40 mm with relatively smoother profiles.

An indicator, named the reduction percentage of air voids (P_{ra}), was introduced to further describe the penetration status of ST residues in PA. It refers to the ratio of the area occupied by ST residues within air voids to the entire void regions before ST in each cross-section image, which can be calculated by Eq. (8). Fig. 5 shows average P_{ra} values with a depth interval of 5 mm in PA. It indicated that all ST residues mainly accumulated near the top surface of PA specimens at first with a peak value observed in the 5–10 mm depth region. Then the P_{ra} of ST residues gradually decreased as the vertical depth increased. Interestingly, both the rejuvenator-optimized ST residues (AOAE and TOAE) showed a relatively gentle declining trend along the vertical depth direction compared to the AE residues. Due to the good wettability and permeability of the AOAE and TOAE emulsions, rejuvenator-optimized emulsions penetrated deeper into PA than the pure asphalt emulsion under the same spraying conditions. If using a P_{ra} value greater than 5 % as a reference indicator for penetration depth, AE penetrated nearly 25 mm into the PA specimen, while the penetration depths of AOAE and TOAE

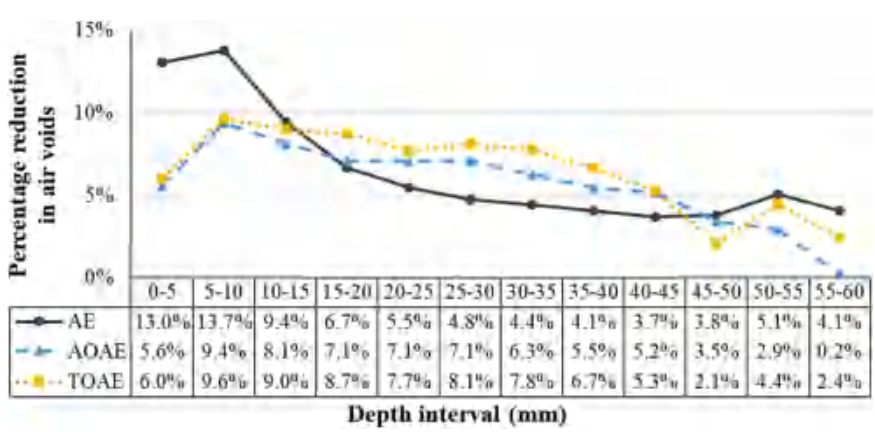

	0-5	5-10	10-15	15-20	20-25	25-30	30-35	35-40	40-45	45-50	50-55	55-60
AE	13.0%	13.7%	9.4%	6.7%	5.5%	4.8%	4.4%	4.1%	3.7%	3.8%	5.1%	4.1%
AOAE	5.6%	9.4%	8.1%	7.1%	7.1%	7.1%	6.3%	5.5%	5.2%	3.5%	2.9%	0.2%
TOAE	6.0%	9.6%	9.0%	8.7%	7.7%	8.1%	7.8%	6.7%	5.3%	2.1%	4.4%	2.4%

Fig. 5. The percentage reduction in air voids along the vertical depth of the ST treated PA specimen.

in PA mixtures are around 45 mm.

$$P_{ra} = \frac{V^i_{ST}}{V^i_{AV-b}} = \frac{V^i_{AV-b} - V^i_{AV-a}}{V^i_{AV-b}} \times 100\% \quad (8)$$

where i means the number i of the processed cross-section slice; V^i_{ST} is the volume of ST residue which is calculated by subtracting the volume of air voids in PA after ST (V^i_{AV-a}) from the volume of air voids in PA before ST (V^i_{AV-b}).

3.1.2. Distribution of ST residues

When ST emulsions penetrated PA mixtures along the air void, their residues coated on the aged asphalt mortar areas, potentially revitalizing the aged asphalt binders in the long term. Theoretically, the more boundaries of air voids were coated by ST residues, the more aged binders surrounding the air voids could be covered and rejuvenated by new ST residues. Fig. 6 illustrates the percentage of ST coating areas (P_c) in PA specimens at a 5 mm depth interval. Considering the vertical gradient distribution characteristic of ST residues in the PA specimen, it is reasonable to observe that the P_c value gradually decreased as the depth increased. Interestingly, when the P_c is no less than 10 %, the penetration depth is no more than 20 mm for the AE-treated PA specimen, but 35 mm for AOAE- and TOAE-treated PA specimens. This difference indicated that the rejuvenator-optimized ST emulsion can penetrate deeper and coat more air voids' boundaries within the PA specimen, which benefits to the replenishment of fresh asphalt binders and the recovery of bonding strength of aged asphalt binder. This finding also explains why the mass loss ratio of rejuvenator-optimized ST emulsion-treated PA specimens exhibited lower values than that of AE-treated PA specimens as shown in Table 2.

3.1.3. Thickness of ST residue

The sprayed ST emulsions mainly coated on the interfaces between aged asphalt mortars and air voids, forming new binder films after the demulsification of ST emulsions. The morphologies of ST residues in PA mixtures are complex. The average thickness of all ST residue droplets in each CT image was elaborately collected and a total of 600 data points were obtained from all CT slices of each PA specimen. These data points were summarized in a probability graph as illustrated in Fig. 7. Both the film thickness curves of AOAE and TOAE residues displayed a single peak pattern with a relatively narrow distribution range. By contrast, the AE residues exhibited a double peak pattern with a slightly wider distribution range. In particular, approximately 37 % of the AOAE and TOAE residues had a film thickness around 0.3 mm, while the AE curve exhibited the first and second peak values at film thicknesses around

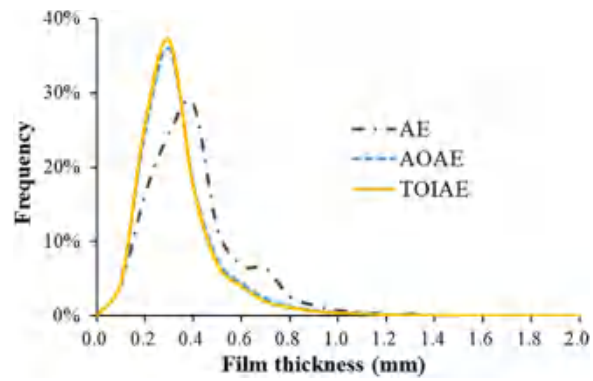

Fig. 7. Probability graphs of film thickness of three different emulsion residues.

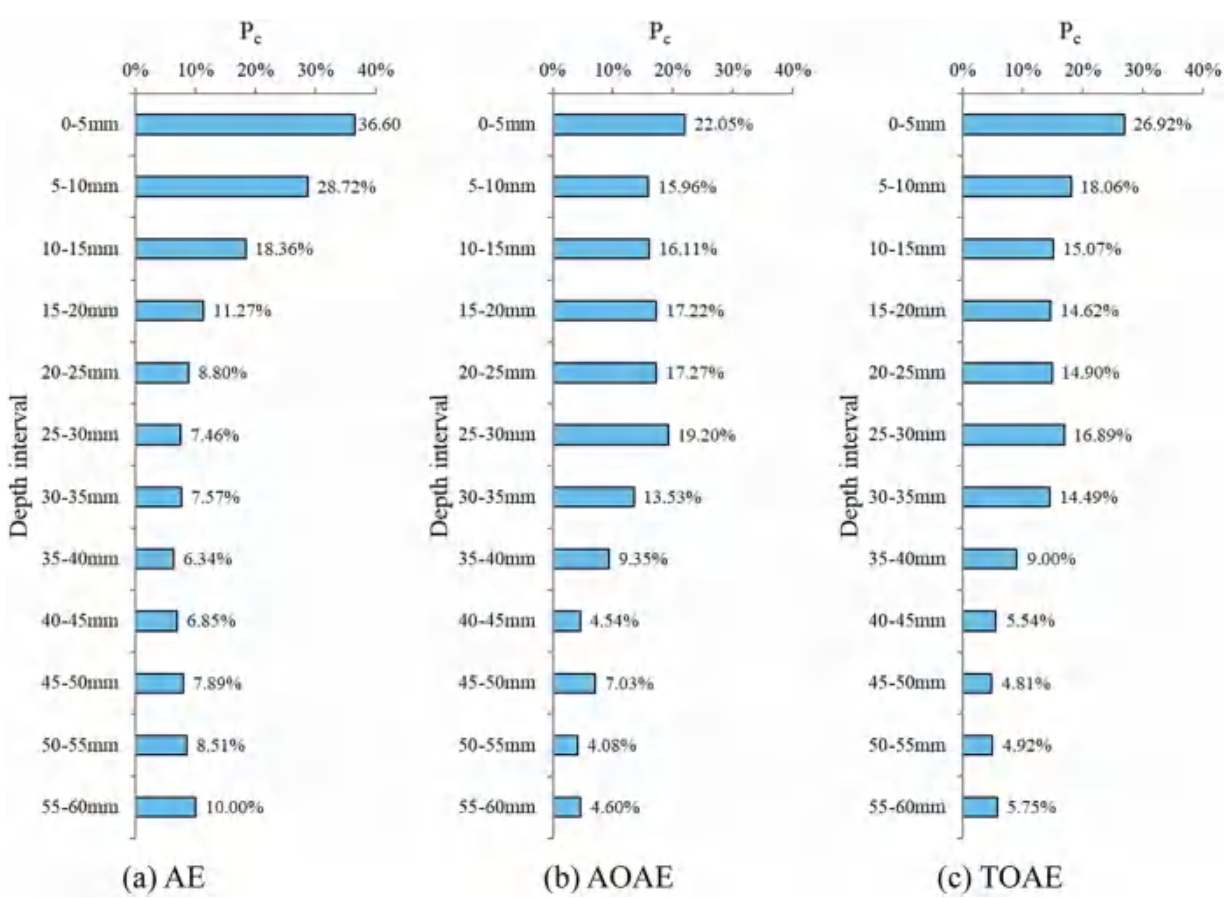

Fig. 6. The percentage of ST coating areas on air voids along the vertical depth of PA specimens.

0.4 mm and 0.7 mm, with a frequency of around 28 % and 7 %, respectively. Therefore, compared to the film thickness curve of AE residues, the peak values of curves for AOAE and TOAE residues moved to the low film thickness zone, and their frequencies of peak value significantly increased.

Furthermore, Table 3 shows the average thickness (T_c) of three different ST residues and their standard deviations (SD_c). The T_c values of AOAE and TOAE residues are around 0.280 mm, which were at least 22.5 % lower than the T_c value of AE residues. This suggests that the rejuvenator-optimized ST emulsion used in this study formed thinner film thickness than the conventional AE. That is to say, when the application rate of ST residue is constant, the rejuvenator-optimized ST residues could coat more aged binder areas surrounding air voids compared to conventional AE residues, thereby rejuvenating aged asphalt binders as much as possible. Besides, the SD_c values of AOAE and TOAE residues are 0.162 and 0.158 mm, respectively. Both are smaller than the SD_c value of AE residues, which is 0.179 mm in this study, indicating that the AOAE and TOAE residues have a more uniform film thickness distribution than conventional AE residues.

3.2. Physicochemical characterizations of asphalt binders from different layers of PA

3.2.1. GPC data analysis

The GPC test results are shown in Fig. 8, where the first row and second row of stacked plots showed the M_p and M_n values of PA specimens treated with three different ST emulsions, respectively. Each plot includes four data points corresponding to depths of 5, 15, 30, and 50 mm, representing the average molecular weight compositions of binders extracted from four layers (0–10 mm, 10–20 mm, 20–40 mm, and 40–60 mm) within a PA mixture. All stacked plots of M_p and M_n values showed obvious vertical gradient trends. A turning point, marked by a red hollow circle in each plot, indicates where both indicators show smaller values before this point, followed by slight fluctuations thereafter. A smaller M_p value means that the new asphalt binders and rejuvenators diffused into and softened aged asphalt binders, breaking down the long and convoluted molecular chains into smaller molecules. Consequently, the percentage of small molecular weight increased, resulting in the lower M_n value in the upper layer of the emulsion-treated PA specimen. Therefore, based on the GPC test results, it was reasonable to speculate that the penetration depths of AE, AOAE, and TOAE are more than 20, 40, and 20 mm, respectively.

Here are two phenomena that need to be further discussed. On the one hand, although the CT scanning results showed that TOAE emulsion penetrated deeper than pure AE, Fig. 8 shows that the turning points for AE and TOAE occurred in the third layer, which seems not support this finding. After carefully comparing the variation trends of GPC results of AE- and TOAE-treated PA specimens, it was found that both the increase rates of M_p and M_n values of the AE-treated specimen gradually slowed down before the turning points, but the growth rates for the TOAE-treated specimen kept unchanged and even higher than the AE treated specimen at the same layer level. It suggests that the TOAE emulsion has a better permeability than AE, especially in the third layer at a depth ranging from 20 to 40 mm. To concisely describe the vertical gradient curve of M_p and M_n in future studies, it is recommended to increase the number of layers and reduce the thickness of each layer. On the other hand, the AOAE-treated specimen showed higher increase rates of M_p and M_n values in third layer than the TOAE-treated specimen, indicating that the AOAE has better softening effectiveness on aged asphalt binders than TOAE, which benefits the recovery of bonding strength of aged asphalt binders. This also explains why the mass loss ratio of the treated PA mixture is lower than that of the TOAE-treated PA mixture as shown in Table 2.

Table 3
Average film thickness and standard deviation of different emulsion residues in PA.

ST residue type	T_c (mm)	SD_c (mm)
AE	0.373	0.179
AOAE	0.289	0.162
TOAE	0.272	0.158

3.2.2. FTIR data analysis

The FTIR tests were carried out to investigate the penetration depths of different ST emulsions in PA mixtures from a chemical character perspective. The main effective components of three different ST emulsions contain asphalt binders, AO (if any) and TO (if any) materials. Their FTIR spectra are depicted in Fig. 9. It was found that the rejuvenator TO has several significantly different functional groups from the asphalt binder used in this study. For example, a distinct peak at 1740 cm^{-1} in TO is attributed to the C═O stretching vibration of esters. However, another rejuvenator AO showed a similar FTIR spectrum to the asphalt binder. It is not unexpected because both AO and asphalt binder are usually derived from crude oil processing. And they generally have similar chemical compositions, which accounts for insignificant differences in FTIR spectra between AO and asphalt binder.

Fig. 10 shows the FTIR spectra of different binders extracted from different layers of TOAE-treated PA specimen. The peak observed at 1740 cm^{-1} gradually decreased as the layer level increased from layer 1 to layer 4. The binders extracted from layer 4 of PA behaved at a slight peak around 1740 cm^{-1} compared with pure asphalt binder, indicating that the TOAE penetrated the fourth layer and its penetration depth at least 40 mm. This finding is also consistent with CT images analysis.

3.3. Rheological evaluations of asphalt binders from different layers of PA

3.3.1. FS analysis

To comprehensively evaluate and compare the maintenance effects of different ST emulsions on aged PA mixtures, the rheological performances of AE-, AOAE- and TOAE-treated PA specimens were investigated through the FS test. Master curves of binders extracted from four different layers of three different ST emulsions treated PA specimens are shown in Fig. 11. The PG 76 asphalt binder, processed by the pressure aging vessel (PAV) to prepare the long-term aged asphalt binder, was also included as a control group. It was found that the binders extracted from layer 4 showed very similar rheological behaviors (G^* and δ master curves) with aged asphalt binders. This similarity indicates that either almost no ST emulsion penetrated to the fourth layer of the PA specimen, or maybe the quantity of penetrated ST emulsion in this layer was too low to have a noticeable impact on the rheological properties of the aged binders. Meanwhile, no matter which kind of ST emulsion was sprayed on the PA mixture, the G^* master curve consistently decreased from layer 4 to layer 1, and these differences are more significant in the low frequency range. This means that the newly added fresh asphalt binders and rejuvenators significantly softened the aged asphalt binders. Besides, all δ master curves shown in Fig. 11 **(a)-(c)** presented an upward trend from the fourth layer to the first layer across the whole frequency range, suggesting that the newly added different ST residues contributed to recovering the viscous characteristic of aged asphalt binders. A higher viscous component means a better stress relaxation property of asphalt binder, especially at a low service temperature.

The G-R parameter was calculated to further quantify the differences in rheological properties among three different ST emulsions treated PA specimens. As shown in Fig. 12, the application of ST residues to the aged PA mixture indeed decreased the G-R values of extracted binders, especially in the first two layers of the PA specimen, which improved the ductility and cracking resistance of treated binders at a low temperature. Overall, most G-R values of extracted binders gradually increased from the first layer to the fourth layer, and the G-R values of three different emulsions treated specimens at the fourth layer were similar to the G-R value of aged asphalt binder after considering the experimental errors.

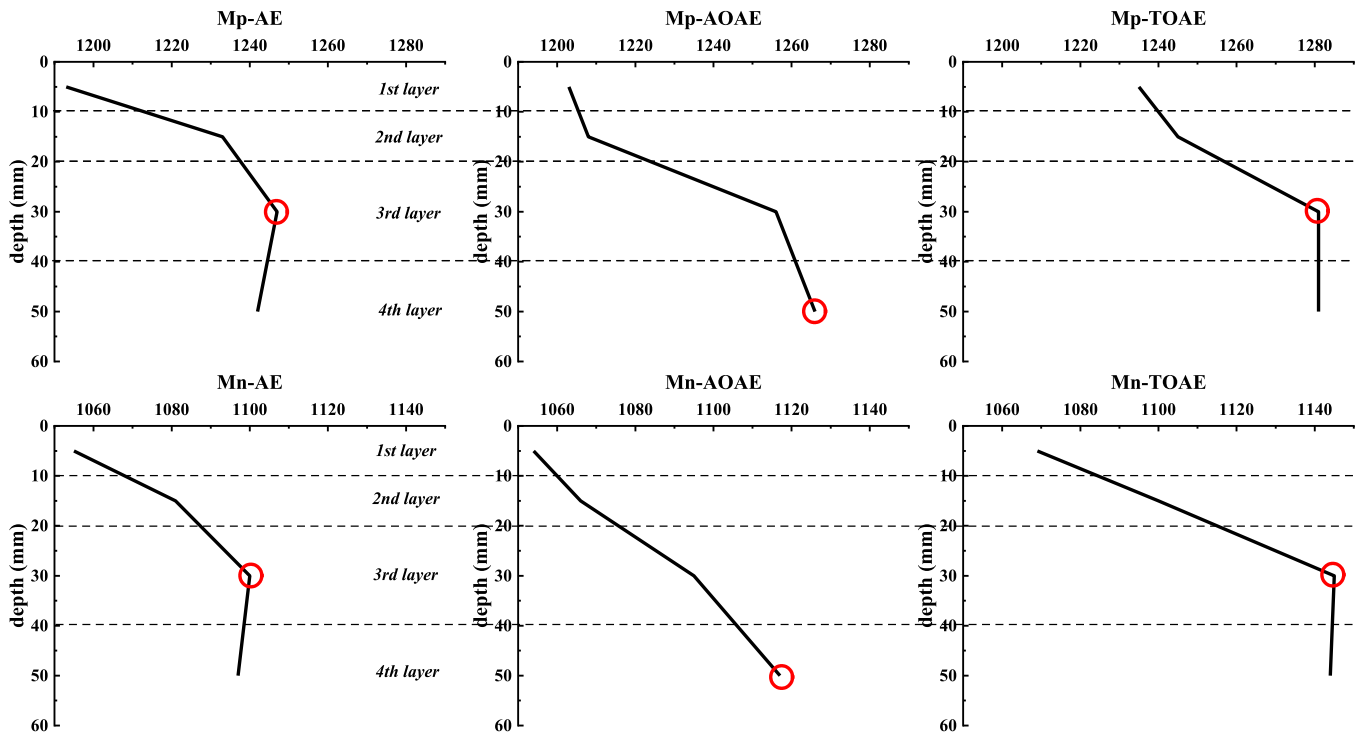

Fig. 8. GPC test results of different layers of PA specimens treated with different ST emulsions.

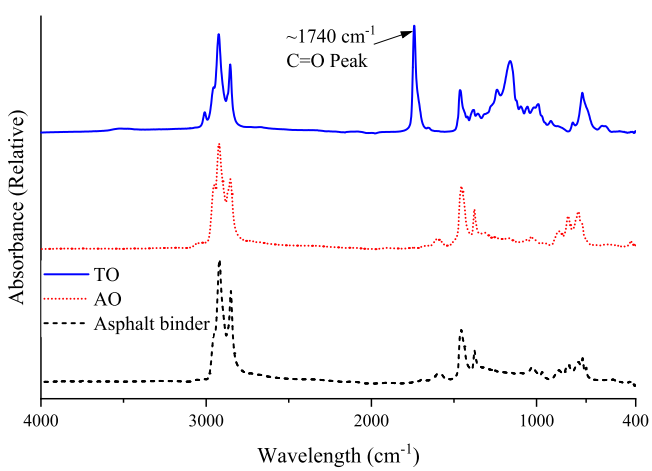

Fig. 9. FTIR spectra of the asphalt binder and two rejuvenators.

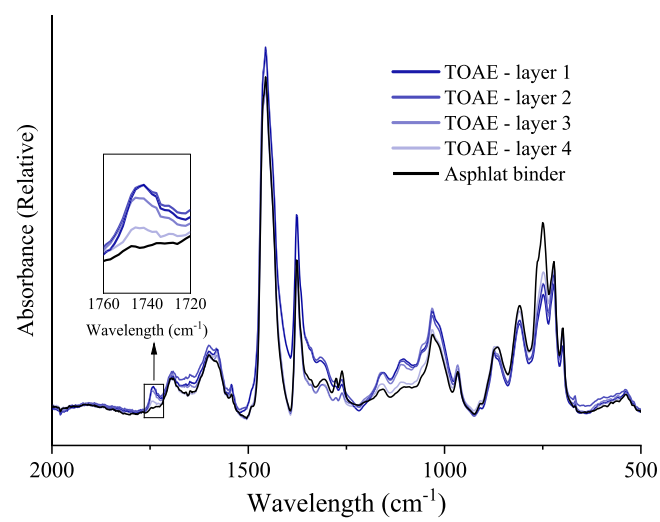

Fig. 10. FTIR spectra of different binders extracted from different layers of TOAE-treated PA specimen.

Besides, both the AOAE- and TOAE-treated specimens showed relatively lower G-R values than AE-treated ones at the same layer level in most cases, suggesting that the addition of rejuvenator emulsion into pure asphalt emulsion could further enhance the low-temperature cracking resistance of aged asphalt binders.

3.3.2. MSCR analysis

MSCR test results of the nonrecoverable creep compliance (J_{nr}) and percent recovery of strain (R) at two stress levels are depicted in Fig. 13. The long-term aged asphalt binder was also tested as a reference. For the tested binder from each layer, a high stress level at 3.2 kPa usually produced a higher J_{nr} and a lower R than the low stress level at 0.1 kPa. Overall, due to the penetration of ST emulsion in PA specimen, almost all PA mixtures treated with three different emulsions showed a gradient descending trend of J_{nr} and a gradient augment trend of R from the first layer to the fourth layer. A higher J_{nr} value means the plastic deformation and viscous flow are more significant, and a lower R value represents the recoverable elastic deformation is smaller. The addition of fresh asphalt binders and rejuvenators not only replenished light components (e.g., naphthene aromatics, saturated hydrocarbons) and softened aged asphalt binders but also enhanced the risk of rutting disease of PA pavement to some extent. Besides, after making a comparison of the J_{nr} and R values between the aged asphalt binder and other binders extracted from different layers of PA, it was found that the conventional AE residues mainly changed the viscoelastic characteristics of binders extracted from the first layer, while the other two rejuvenator-optimized emulsion residues significantly changed the viscoelastic responses of tested binders from the first two layers and even the third layer. This enhanced rejuvenating effectiveness is consistent with the findings from the GPC and FS analyses, demonstrating that the incorporation of a rejuvenator into conventional AE not

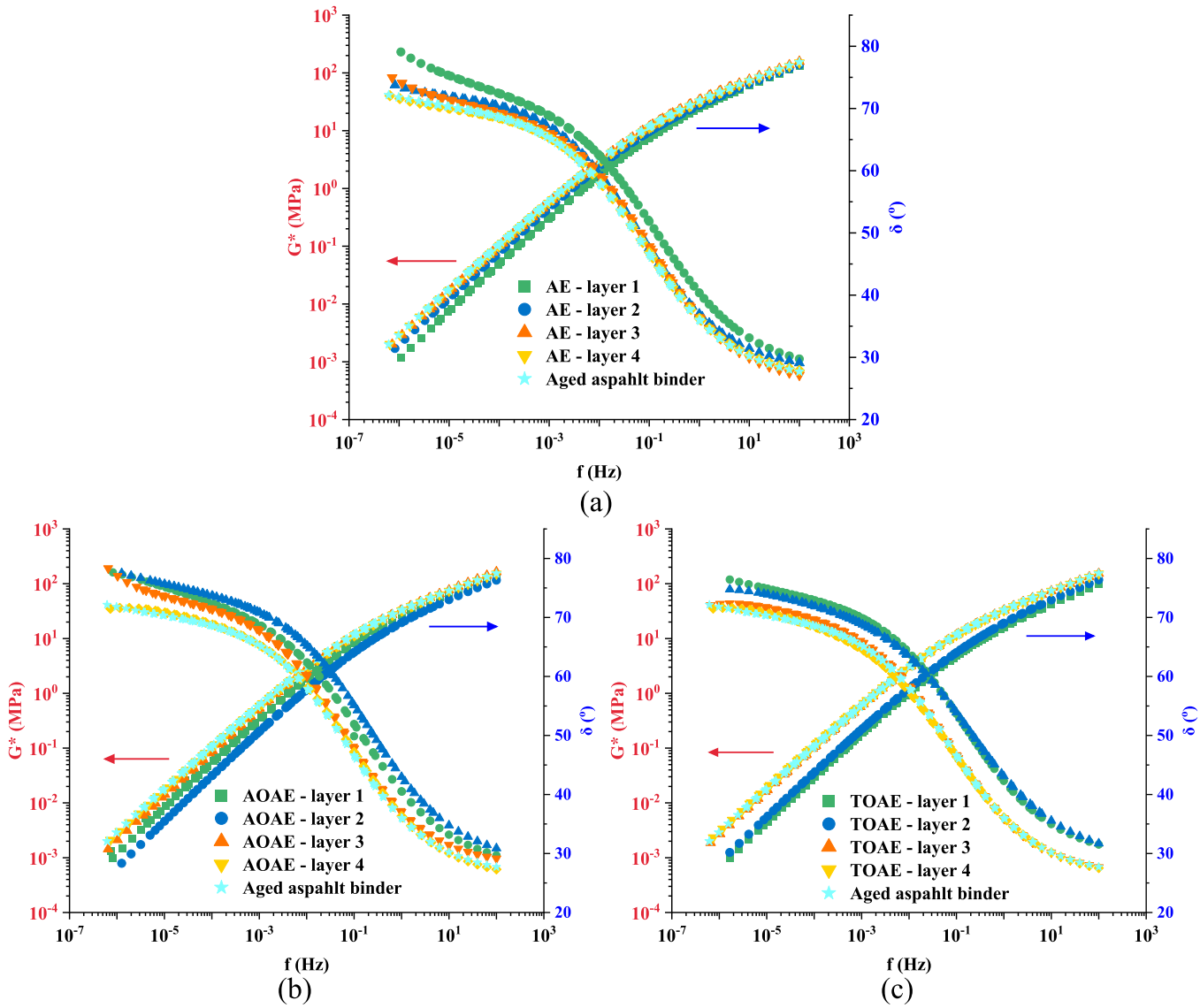

Fig. 11. G^* and δ master curves of binders extracted from different layers of different emulsions treated PA mixtures: (a) AE; (b) AOAE; (c) TOAE.

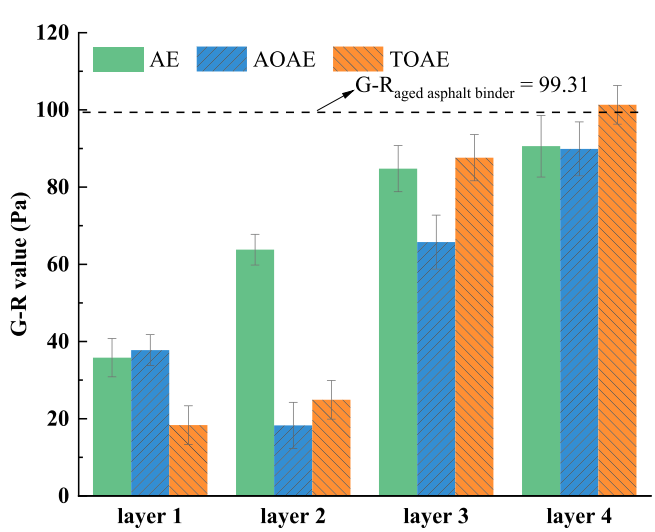

Fig. 12. G-R values of binders extracted from different layers of different emulsion treated PA mixtures.

only increased the penetration depth but also promoted the maintenance effectiveness of aged asphalt binders.

4. Findings and conclusions

In this study, three kinds of ST emulsions, including a conventional asphalt emulsion (AE) and two kinds of rejuvenator-optimized AEs, were selected to evaluate their maintenance effectiveness for damaged PA mixtures. The working mechanisms of rejuvenator-optimized AE in PA were systematically investigated from morphological, rheological, and physicochemical perspectives. The relevant findings and conclusions were summarized as follows:

1) All tests used in this study found that the distributions of different ST emulsion residues along the vertical depth of PA mixtures showed gradient decreasing trends, indicating that not all emulsion residues accumulated on the surface of PA mixture.
2) From a morphological perspective, the penetration depth of rejuvenator-optimized AEs was twice that of conventional AE, approaching 40 mm. P_c results showed that both AOAE and TOAE emulsions demonstrated better coating efficiencies and wettabilities by coating more aged asphalt areas. So, the rejuvenator-optimized

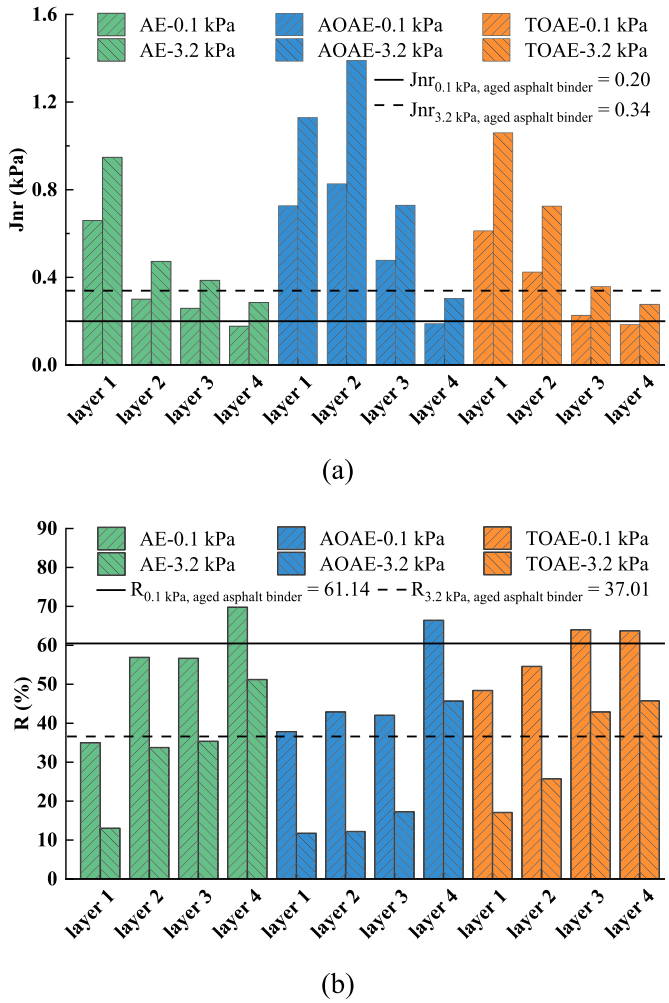

Fig. 13. MSCR test results of binders extracted from different layers of different emulsions treated PA mixtures: (a) J_{nr}; (b) R.

AEs distributed more uniformly, which promotes the ravelling resistance of damaged PA mixture.

3) From a physicochemical perspective, the penetrated emulsion residues replenished new asphalt binders as well as light components, and soften aged asphalt binders, resulting in decreases of M_p and M_n. AOAE emulsion has a better maintenance effectiveness than TOAE emulsion due to its lower M_p and M_n values. Besides, utilizing a unique functional group as a tracer to qualitatively detect the penetration of rejuvenator-optimized AE in PA mixture is feasible. FTIR spectra showed the penetration of TOAE is at least 40 mm, which is consistent with the CT image results.
4) From a rheological perspective, compared with the conventional AE residue, the rejuvenator-optimized AE residue further improved the viscoelastic property, especially the viscous aspect, of the aged asphalt binder. The AOAE and TOAE residues helped aged asphalt binder obtain a good stress relaxation property and cracking resistance at a low temperature, but they might enhance the rutting risk of PA pavement to some extent.

It should be noted that all findings are based on the indoor tests of self-prepared ST emulsions and PA specimens. Due to the limitations of cutting space and blade thickness, the PA specimen used in this study was cut into only four layers. To more accurately assess the penetration depth of the emulsions and their maintenance effects, it is recommended to equally divide the PA specimen with a height of 60 mm into five to six pieces. Besides, further evaluations of the mechanical (e.g., anti-cracking and anti-rutting …) and functional (e.g., water permeability, noise reduction, and skid-resistance …) of damaged PA mixtures treated with the rejuvenator-optimized AE is necessary. Also, the asphalt aging level and the pore structure of asphalt mixtures might affect the penetration depth of rejuvenator-optimized ST emulsion in PA mixture, which should be investigated in the future study.

CRediT authorship contribution statement

Sun Yubo: Methodology, Investigation, Data curation. **Jiang Xi:** Methodology, Investigation, Conceptualization. **Yan Chuanqi:** Methodology, Data curation. **Yang Bin:** Writing – original draft, Methodology, Investigation, Data curation, Conceptualization. **Leng Zhen:** Writing – review & editing, Supervision, Conceptualization. **Jiang Jiwang:** Methodology, Data curation, Conceptualization. **Li Gaoyang:** Methodology, Investigation. **Tan Zhifei:** Writing – review & editing, Methodology.

Declaration of Competing Interest

The authors declare that they have no known competing financial interests or personal relationships that could have appeared to influence the work reported in this paper.

Acknowledgment

This work was supported by the Hong Kong Research Grant Council through the GRF projects (No.15220621, No.15209920); and the Nonmetallic Excellence and Innovation Center for Building Materials (No. 24PHD-1). The authors also thank Kraton Corp. for providing rejuvenators and Ingevity Corp. for providing emulsifiers for this study.

Data availability

Data will be made available on request.

References

[1] E.-J. Elizondo-Martínez, V.-C. Andres-Valeri, D. Jato-Espino, J. Rodriguez-Hernandez, Review of porous concrete as multifunctional and sustainable pavement, J. Build. Eng. 27 (2020) 100967.
[2] H. Li, H. Xu, F. Chen, K. Liu, Y. Tan, B. Leng, Evolution of water migration in porous asphalt due to clogging, J. Clean. Prod. 330 (2022) 129823.
[3] X. Wang, Z.-Y. Yin, W. Wu, H.-H. Zhu, Neural network-augmented differentiable finite element method for boundary value problems, Int. J. Mech. Sci. (2024) 109783.
[4] X. Wang, W. Wu, H.-H. Zhu, Solving fluid flow in discontinuous heterogeneous porous media and multi-layer strata with interpretable physics-encoded finite element network, J. Rock. Mech. Geotech. Eng. (2024).
[5] H. Wang, Y. Ding, G. Liao, C. Ai, Modeling and optimization of acoustic absorption for porous asphalt concrete, J. Eng. Mech. 142 (4) (2016) 04016002.
[6] D. Wang, X. Chen, M. Oeser, H. Stanjek, B. Steinauer, Study of micro-texture and skid resistance change of granite slabs during the polishing with the Aachen Polishing Machine, Wear 318 (1-2) (2014) 1–11.
[7] H. Zhang, H. Li, Y. Zhang, D. Wang, J. Harvey, H. Wang, Performance enhancement of porous asphalt pavement using red mud as alternative filler, Constr. Build. Mater. 160 (2018) 707–713.
[8] K. Zhang, Y. Liu, S. Nassiri, H. Li, K. Englund, Performance evaluation of porous asphalt mixture enhanced with high dosages of cured carbon fiber composite materials, Constr. Build. Mater. 274 (2021) 122066.
[9] R.G. Hicks, J.S. Moulthrop, J. Daleiden, Selecting a preventive maintenance treatment for flexible pavements, Transp. Res. Rec. 1680 (1) (1999) 1–12.
[10] F. Xiao, L. Xu, Z. Zhao, X. Hou, Recent applications and developments of reclaimed asphalt pavement in China, 2010–2021, Sustain. Mater. Technol. (2023) e00697.
[11] A. Albayati, Y. Wang, Y. Wang, J. Haynes, A sustainable pavement concrete using warm mix asphalt and hydrated lime treated recycled concrete aggregates, Sustain. Mater. Technol. 18 (2018) e00081.
[12] Y. Fan, H. Chen, X. Yi, G. Xu, X. Cai, Y. Zhou, S. Huang, Y. Wu, H. Wang, J. Yang, Cracking resistance evaluation of epoxy asphalt mixtures with 100% reclaimed asphalt pavement (RAP), Constr. Build. Mater. 395 (2023) 132320.
[13] L. Yao, Q. Dong, J. Jiang, F. Ni, Deep reinforcement learning for long-term pavement maintenance planning, Comput. -Aided Civ. Infrastruct. Eng. 35 (11) (2020) 1230–1245.

[14] J.T. Harvey, A. Rezaei, C. Lee, Probabilistic approach to life-cycle cost analysis of preventive maintenance strategies on flexible pavements, Transp. Res. Rec. 2292 (1) (2012) 61–72.
[15] Q. Zhou, H. Ozer, I.L. Al-Qadi, Pavement preservation and maintenance schedule evaluation using a life-cycle assessment tool, in: Pavement, Roadway, and Bridge Life Cycle Assessment, 2020, CRC Press, 2020, pp. 190–199.
[16] F. Kamran, L. Hashemian, Evaluation of asphaltenes a potential alternative for cement in stabilized base courses using asphalt emulsion, Clean. Mater. 10 (2023) 100208.
[17] D. Lu, X. Jiang, Z. Tan, B. Yin, Z. Leng, J. Zhong, Enhancing sustainability in pavement Engineering: a-state-of-the-art review of cement asphalt emulsion mixtures, Clean. Mater. (2023) 100204.
[18] N.S.A. Yaro, M.H. Sutanto, N.Z. Habib, M. Napiah, A. Usman, A.H. Jagaba, A.M. Al-Sabaeei, Modeling and optimization of asphalt content, waste palm oil clinker powder and waste rice straw ash for sustainable asphalt paving employing response surface methodology: a pilot study, Clean. Mater. 8 (2023) 100187.
[19] Y. Zhang, Extending the Lifespan of Porous Asphalt Concrete, Delft University of Technology, Delft University of Technology, 2015.
[20] Y. Zhang, W. Verwaal, M. Van de Ven, A. Molenaar, S. Wu, Using high-resolution industrial CT scan to detect the distribution of rejuvenation products in porous asphalt concrete, Constr. Build. Mater. 100 (2015) 1–10.
[21] C. Chen, L. Lin, T. Ma, Effects of oil/asphalt emulsion formulation on particle size and stability, Transp. Res. Rec. 2677 (1) (2023) 587–598.
[22] B. Yang, Z. Leng, J. Jiang, R. Chen, G. Lu, Diffusion characteristics of surface treatment emulsion in aged asphalt mortar of porous asphalt mixture through SEM/EDS analysis, Int. J. Pavement Eng. 25 (1) (2024) 2290093.
[23] J. Jiang, Z. Leng, B. Yang, G. Lu, Z. Tan, M. Han, Z. Dong, Penetration mechanism of the emulsion-based rejuvenator in damaged porous asphalt mixture: microstructure characterization and 3D reconstruction, Mater. Des. 221 (2022) 111014.
[24] J. Ouyang, Y. Sun, S. Zarei, Fabrication of solvent-free asphalt emulsion prime with high penetrative ability, Constr. Build. Mater. 230 (2020) 117020.
[25] B. Yang, Z. Leng, J. Jiang, Z. He, D. Li, Recovery efficiency of the damaged porous asphalt mixture with emulsion-based surface treatment: material optimization and performance verification, Constr. Build. Mater. 347 (2022) 128530.
[26] A. Behnood, Application of rejuvenators to improve the rheological and mechanical properties of asphalt binders and mixtures: a review, J. Clean. Prod. 231 (2019) 171–182.
[27] T.B. Moghaddam, H. Baaj, The use of rejuvenating agents in production of recycled hot mix asphalt: a systematic review, Constr. Build. Mater. 114 (2016) 805–816.
[28] Y. Lu, R.S. Maia, R. Hajj, Multiscale evaluation of asphalt binder rejuvenation dosing and efficacy, Constr. Build. Mater. 408 (2023) 133813.
[29] Y. Fang, Z. Zhang, H. Zhang, W. Li, Analysis of wetting behavior and its influencing factors of rejuvenator/old asphalt interface based on surface wetting theory, Constr. Build. Mater. 314 (2022) 125674.
[30] Y. Fang, Z. Zhang, J. Yang, Y. Wang, Research on interfacial fusion characteristics of rejuvenator-aged asphalt system: wettability, permeability and molecular simulation, Constr. Build. Mater. 443 (2024) 137646.
[31] B. Xu, J. Chen, M. Li, D. Cao, S. Ping, Y. Zhang, W. Wang, Experimental investigation of preventive maintenance materials of porous asphalt mixture based on high viscosity modified bitumen, Constr. Build. Mater. 124 (2016) 681–689.
[32] B. Xu, M. Li, S. Liu, J. Fang, R. Ding, D. Cao, Performance analysis of different type preventive maintenance materials for porous asphalt based on high viscosity modified asphalt, Constr. Build. Mater. 191 (2018) 320–329.
[33] C.K. Estakhri, A.E. Alvarez, A.E. Martin, Guidelines on Construction and Maintenance of Porous Friction Courses in Texas, Texas Transportation Institute, 2008.
[34] N. Tran, D.E. Watson, N. Anwer, Effect of using fog seals without sanding on surface friction and durability of open-graded friction course, Transportation Research Board 91st Annual Meeting, Transportation Research Board, Washington DC, United States, 2012, p. 18.
[35] S. Kim, J. Musselman, G. Sholar, Evaluation of Fog Seal Preservation Technique on US-17 and US-27, Tallahassee, FL: Florida DOT (2014).
[36] N.A. Qureshi, N.H. Tran, D. Watson, S.M. Jamil, Effects of rejuvenator seal and fog seal on performance of open-graded friction course pavement, Maejo Int. J. Sci. Technol. 7 (2) (2013) 189.
[37] B. Yang, J. Jiang, H. Wang, Z. Leng, X. Sui, X. Jiang, Optimization design of asphalt emulsion with rejuvenator towards a uniform distribution inside the damaged porous asphalt mixture for a better ravelling resistance, Case Stud. Constr. Mater. 21 (2024) e03747.
[38] H.U. Bahia, H. Sadek, M.Z. Rahaman, Z. Lemke, D. Swiertz, S. Reichelt, L. Bitumix Solutions, Field aging and oil modification study, Wisconsin Deptament of Transportation, 2018.
[39] C. Yan, Y. Zhang, H.U. Bahia, Predicting rutting performance of asphalt mixture from binder properties and mixture design variables, Road. Mater. Pavement Des. 23 (1) (2022) 62–79.
[40] X. Wang, Z.-Y. Yin, W. Wu, H.-H. Zhu, Differentiable finite element method with Galerkin discretization for fast and accurate inverse analysis of multidimensional heterogeneous engineering structures, Comput. Method. Appl. Mech. Eng. 437 (2025) 117755.
[41] H. Zhang, Q. Liang, M. Shao, N. Jiang, W. Ma, Z. Ge, B. Šavija, Optimization of low-carbon lightweight foamed concrete using ground circulating fluidized bed fly ash, J. Clean. Prod. (2025) 144697.
[42] Y. Li, Z. Zhao, L. Sun, T. Guo, B. Yang, A geometrical morphology-enhanced computer vision approach for structural health assessment, Struct. Health Monitor. (2025) 14759217241307575.
[43] J. Ma, G. Sun, D. Sun, F. Yu, M. Hu, T. Lu, Application of gel permeation chromatography technology in asphalt materials: a review, Constr. Build. Mater. 278 (2021) 122386.
[44] Q. Lv, W. Huang, H. Sadek, F. Xiao, C. Yan, Investigation of the rutting performance of various modified asphalt mixtures using the Hamburg wheel-tracking device test and multiple stress creep recovery test, Constr. Build. Mater. 206 (2019) 62–70.
[45] C. Xing, G. Zheng, L. Zhang, Y. Tan, Thermoregulation performance and mechanical properties of phase change asphalt mortars, J. Mater. Civ. Eng. 36 (8) (2024) 04024213.
[46] M. Woldekidan, M. Huurman, A. Pronk, A modified HS model: Numerical applications in modeling the response of bituminous materials, Finite Elem. Anal. Des. 53 (2012) 37–47.
[47] G. Rowe, G. King, M. Anderson, The influence of binder rheology on the cracking of asphalt mixes in airport and highway projects, J. Test. Eval. 42 (5) (2014) 1063–1072.
[48] D. Li, Z. Leng, F. Zou, H. Yu, Effects of rubber absorption on the aging resistance of hot and warm asphalt rubber binders prepared with waste tire rubber, J. Clean. Prod. 303 (2021) 127082.
[49] L. Zhang, C. Xing, F. Gao, T.-s Li, Y.-q Tan, Using DSR and MSCR tests to characterize high temperature performance of different rubber modified asphalt, Constr. Build. Mater. 127 (2016) 466–474.
[50] H. Wang, X. Liu, P. Apostolidis, M. van de Ven, S. Erkens, A. Skarpas, Effect of laboratory aging on chemistry and rheology of crumb rubber modified bitumen, Mater. Struct. 53 (2020) 1–15.
[51] A. Meng, C. Xing, Y. Tan, S. Xiao, J. Li, G. Li, Investigation on clogging characteristics of permeable asphalt mixtures, Constr. Build. Mater. 264 (2020) 120273.
[52] H. Li, H. Shi, H. Xu, Y. Tian, Y. Tan, K. Liu, Exploring freeze-thaw damage distribution of asphalt mixture through DIC in combination with CT, Int. J. Damage Mech. (2024), 10567895241245750.

Construction and Building Materials 425 (2024) 136045

Contents lists available at ScienceDirect

Construction and Building Materials

journal homepage: www.elsevier.com/locate/conbuildmat

Investigating the role of sulfur stabilizer in modulating aging properties of SBS-modified asphalt

Junjie Zhang [a,b], Pengwei Sun [a], Zefeng Ma [c], Mingxin Dai [a], Rong Zhuo [d], Guilian Zou [b], Yiqiu Tan [a,e,*]

[a] School of Transportation Science and Engineering, Harbin Institute of Technology, Harbin, China
[b] School of Civil Engineering and Transportation, South China University of Technology, Guangzhou, China
[c] Poly Changda Overseas Engineering Co., Ltd, Guangzhou, China
[d] Guangzhou Metro Design and Research Institute Co., Ltd, Guangzhou, China
[e] State Key Laboratory of Urban Water Resource and Environment, Harbin Institute of Technology, Harbin, China

ARTICLE INFO

Keywords:
Sulfur stabilizer
Aging behavior
Molecular weight
Chemical structure
Rheology and morphology

ABSTRACT

Stabilizers are commonly employed in SBS-modified asphalt, yet their specific impact on aging behavior remains ambiguous. Past studies have not agreed on their role and have primarily examined effects on the SBS polymer phase, neglecting asphalt phase influences. Understanding these interactions is essential for aging mechanisms and rejuvenation strategies. To solve this issue, this study compared three types of asphalt to analyze their properties during aging. Microscopic tests comprising morphology, chemical structure, and molecular weight analyses with nine quantitative indicators were conducted, and the distinct influences of stabilizers on asphalt and SBS polymer phases were elucidated. The results revealed that the change rate in the physical properties of SBS-modified asphalt during aging decreases with sulfur addition, rheological parameters indicated that sulfur predominantly protects the polymer network structure from degradation during short-term aging. Furthermore, stabilizers had no explicit impact on the carbonyl index but could delay the generation of asphaltene molecules during aging, the change rates of asphaltene% were 1.65% without stabilizers and 12.36% with them after TFOT (Thin film oven test) aging. Stabilizers also notably mitigated polymer degradation and exhibited beneficial effects even during PAV (Pressure aging vessel) aging. The overall findings contribute to a clearer understanding of the complex interplay among the various components of SBS-modified asphalt, such as base asphalt, SBS modifiers, and stabilizers, providing theoretical insights into aging mechanisms and rejuvenation strategies involving stabilizers.

1. Introduction

Styrene-butadiene-styrene (SBS) triblock copolymers are widely employed worldwide to enhance asphalt performance [1]. The incorporation of SBS into asphalt creates a crosslinked network through the polystyrene segments [2], while the polybutadiene segments, as soft segments, add flexibility and elasticity [3]. Despite these benefits, SBS-modified asphalt faces storage stability issues due to thermodynamic incompatibility. Dynamic vulcanization has been demonstrated to be one of the most effective methods for improving compatibility and is commonly employed in practical engineering applications [4]. However, the exact vulcanization mechanism remains not fully elucidated. Simultaneously, the existence of sulfur stabilizers and polymers makes the aging mechanism of SBS-modified asphalt more complex compared to conventional asphalt [5,6]. Although enhancing aging resistance can prolong pavement lifespan and reduce pavement distress [7], the aging complexity of SBS/Sulfur-modified asphalt hinders this aim. After aging, both physical and chemical changes occur in asphalt components, SBS polymers, and stabilizers. Currently, the precise function of the stabilizer during the aging process remains ambiguous. Understanding the contribution of the stabilizer during aging is crucial for unraveling the aging mechanism of SBS-modified asphalt containing stabilizers and providing rejuvenation methods.

To overcome this issue, previous research has extensively evaluated the influence of stabilizers on SBS-modified asphalt, such as: Wen et al. [8] evaluated how sulfur content affects rheological properties, while

* Corresponding author at: School of Transportation Science and Engineering, Harbin Institute of Technology, Harbin, China.
E-mail address: tanyiqiu@hit.edu.cn (Y. Tan).

https://doi.org/10.1016/j.conbuildmat.2024.136045
Received 18 December 2023; Received in revised form 11 March 2024; Accepted 27 March 2024
Available online 1 April 2024
0950-0618/© 2024 Elsevier Ltd. All rights reserved.

Liang et al. [9] explored polymerized sulfur's influence on morphology and storage stability. Geng et al. [10] demonstrated a bio-based stabilizer's efficacy compared to a sulfur stabilizer. Huang et al. [11] assessed the high-temperature performance of SBS/Sulfur modified asphalt at different SBS content and noted sulfur's favorable effect, especially at low SBS levels. However, rare studies have focused on the influence of stabilizers on SBS-modified asphalt under different aging processes. Several studies suggest that sulfur stabilizers can refine SBS polymer size and promote uniform dispersion, forming a denser network [12], but aging also leads to the degradation of SBS copolymers and the disruption of the three-dimensional network. It remains unclear whether the stabilizer maintains its strengthening effect on the polymer network after aging.

Several studies have explored the impact of stabilizers on the aging behavior of SBS-modified asphalt. For instance, Zhang et al. [13] indicated a more pronounced degradation of SBS polymers during aging after the addition of stabilizers, concluding a negative impact during aging. Conversely, Tang et al. [14], examining aging in high-content SBS-modified asphalt, suggested that stabilizer inclusion could enhance aging resistance. In the study conducted by Hao et al. [15], although the introduction of stabilizers led to more severe SBS polymer degradation during aging, it resulted in improved rheological performance. It is evident that there is no consensus regarding how stabilizers impact the aging behavior of SBS-modified asphalt, and the precise mechanisms of stabilizers during aging remain unclear. Moreover, most current research has primarily addressed the impact of stabilizers on the SBS polymer phase, while the impact on the asphalt phase has received less attention. Previous studies have indicated that, on one hand, sulfur stabilizers engage in addition reactions with unsaturated carbon-carbon double bonds in the PB segment of SBS copolymers [16] or substitution reactions with hydrogen atoms adjacent to double bonds [17]. On the other hand, asphaltene and polycyclic aromatic compounds can react with stabilizers to form C-S bonds at 140°C [18]. At temperatures exceeding 140°C, hydrogen in the aromatic nuclei or side chains is replaced, leading to the generation of sulfides [19]. These reactions suggest that stabilizers also chemically interact with the asphalt phase. Nevertheless, aging leads to variations in asphalt components, and the influence of stabilizers on the alterations in asphalt components remains undetermined.

Apart from sulfur stabilizers, the effects of many additives on the aging performance of asphalt have been more deeply elucidated. For example, the addition of imidazoline in asphalt can reduce oxygen absorption and disassociate larger molecules [20]; The interlayer structure of montmorillonite can suppress oxygen diffusion within asphalt [21]; the presence of layer-structured double hydroxides (LDHs) enhances asphalt's resistance to aging due to their multi-layered structure [22], and nanomaterials bolster asphalt's antioxidative potential by augmenting its UV absorption or reflection capacity [23]. However, the precise mechanisms underlying the effects of sulfur stabilizers on aging performance remain inadequately explored. Moreover, in contrast to the interaction patterns between other additives and asphalt, the multi-component polymer system involving asphalt components, SBS modifiers, and stabilizers demonstrates intricate interplays among its constituents, leading to complex mechanisms during aging, it is still uncertain whether sulfur enhances the aging resistance of SBS-modified asphalt. Thus, the roles and contributions of SBS polymers, base asphalt, and stabilizers in aging remain to be studied further.

Overall, this paper aims to analyze the role and contributions of stabilizers in the aging process of SBS-modified asphalt and discuss the distinct influence of stabilizers on the SBS polymer phase and the asphalt phase during aging. To achieve this objective, three types of asphalt, including base asphalt, SBS-modified asphalt, and SBS/Sulfur-modified asphalt, were selected for testing conventional physical properties and rheological behavior. Fourier transform infrared spectroscopy, fluorescence microscopy, and gel permeation chromatography were utilized to respectively examine the evolution of phase morphology, chemical structure, and molecular weight during aging. Microscopic indicators were used to assess the effects of stabilizers on both the asphalt and polymer phases. Ultimately, this study can help to better understand the function and contributions of stabilizers in the aging process of SBS-modified asphalt and provide a foundation for developing ideal phase structures for asphalt modification.

2. Objectives and scope

The objectives of this paper are:

1) Investigate the role and contributions of stabilizers in the aging process of SBS-modified asphalt.
2) Explore the degradation mechanisms within the multi-phase system, involving base asphalt, modifiers, and stabilizers, throughout the entire aging process.
3) Establishing distinct indicators to characterize the effects of stabilizers on the SBS polymer phase and asphalt phase during aging.

3. Materials and experimental schedule

3.1. Materials

This paper aims to examine the impact of sulfur stabilizers on the aging behavior of SBS-modified asphalt. Thus, a comparative investigation was performed involving both SBS-modified asphalt and SBS/Sulfur-modified asphalt, control studies were carried out by introducing 90# base asphalt to better differentiate the distinct influences of SBS polymer and sulfur during the aging process. SBS-modified asphalt and SBS/Sulfur-modified asphalt were produced using 90# base asphalt, linear-shaped SBS 1301, and stabilizer. SBS 1301 is supplied by Yanshan Petrochemical Co., Ltd, which is a linear copolymer with an average molecular weight of 100,000 g/mol and 30 wt% styrene. Elemental sulfur derived from a commercial product was employed as a stabilizer to add to SBS-modified asphalt so that chemical crosslinking can be achieved. The technical characterization of 90# base asphalt is shown in Table 1, and the main properties of copolymer SBS 1301 listed are in Table 2.

3.2. Sample preparation

In this paper, 90# base asphalt, SBS-modified asphalt, and SBS/Sulfur-modified asphalt were tested and analyzed. 90# based asphalt was used to prepare both SBS-modified asphalt and SBS/Sulfur-modified asphalt by a high-speed emulsification shearing machine and a mechanical stirrer. Currently, the SBS content in asphalt used for roads is generally around 5%, and the sulfur content accounts for 3% of the SBS content, which equates to 0.15% of the total. This choice ensures relevance to practical applications. Thus, 5% SBS content and 0.15% sulfur content were determined in this paper. Initially, the polymer is processed through high-speed shearing to attain a specific fineness and ensure dispersion within the asphalt. Following high-speed shearing, the stabilizer is incorporated during low-speed stirring, consistent with the previous series of experiments [24].

Table 1
Characterization of 90# base asphalt.

Property		Unit	Results
Penetration at 25°C (0.1 mm)		0.1 mm	91.4
Softening point (R&B)		℃	47.2
Ductility at 15°C		cm	> 100
Density at 15℃		g/cm^3	1.013
Viscosity at 60°C		Pa·s	156
RTFOT	Mass loss	%	0.08
(163℃ , 85 min)	Residual penetration ratio	%	81.2
	Residual ductility at 15℃	cm	35

Table 2
Properties of SBS 1301.

Property	Unit	Results
Structure	-	Linear
Styrene–butadiene ratio	-	3:7
Average molecular weight	g/mol	100000
Shore hardness	A	70
Tensile strength	MPa	27
Breaking elongation	%	921
Ash content	%	0.2

The specific steps are as follows: 1) To produce SBS-modified asphalt with physical crosslinking, 90# base asphalt, and 5 wt% liner-shaped SBS 1301 were sheared at a speed of 4000 rpm for 0.5 hours at 180°C. 2) After dividing the samples into two groups, the first group was stirred in a mechanical stirrer for 2 hours at 180°C, so that SBS-modified asphalt could be produced. 3) The samples in the second group were different for SBS/Sulfur-modified asphalt, the materials in this group were stirred mechanically at 180°C for 1 hour. 4) After that, adding 0.15 wt% sulfur and mixing continuously for 1.5 hours at 180°C. This creates chemical crosslinking that strengthens the asphalt.

Fig. 1 illustrates the preparation procedure of samples.

3.3. Experimental schedule

"Short-term aging and long-term aging were conducted on three types of asphalt through the thin film oven test (TFOT) and the pressure aging vessel (PAV) methods. The specific procedures were following ASTM D1754 [25] and ASTM D6521 [26]. Conventional physical properties and rheological characteristics represent the macroscopic changes during aging for the three asphalt types. Microscopic tests, including fluorescence microscope (FM) test, Fourier transform infrared spectroscopy (FTIR) test, and gel permeation chromatography (GPC) test, were conducted to quantify microscopic parameters characterizing the asphalt. To quantify the entirety of the aging process, three characterization parameters were suggested for each microscopic test, and the impact of stabilizers on the SBS polymer phase and the asphalt phase during aging was assessed based on the quantitative parameters. The change rate of each parameter during aging was calculated using the formula mentioned.

$$Changerate = \frac{Parameterofagedsample - Parameterofunagedsample}{Parameterofunagedsample} \quad (1)$$

The research framework of this study is illustrated in Fig. 2.

4. Methods

4.1. Conventional test

The physical property tests were conducted on three types of asphalt binder, including asphalt samples before and after aging. These tests covered penetration, softening point, low-temperature ductility, and 135°C rotational viscosity tests, the rotational viscosity test was exclusively applied to assess polymer-modified asphalt. All four tests were conducted in strict accordance with ASTM standards, specifically ASTM D5 [27], ASTM D36 [28], ASTM D113 [29], and ASTM D4402 [30].

4.2. Fluorescence microscope (FM) test

A fluorescence microscope test was used to analyze the morphology characterization of SBS-modified asphalt and SBS/Sulfur-modified asphalt. To collect fluorescence images at various aging stages, a CSM-900E series fluorescence microscope was chosen. The dispersity, continuous, and discontinuous phases of SBS copolymer can be evaluated. SBS/Sulfur-modified asphalt was observed under a fluorescence microscope with 400 ×magnification. To minimize experimental uncertainties, the asphalt samples were melted and mixed uniformly in the beaker, and three parallel tests were conducted at equidistant positions from the bottom, middle, and top of the beaker, hot-drop coverslips were used to manufacture the test samples. To further investigate the morphological changes during the aging process, three quantitative parameters including phase size, phase dispersion, and phase ratio were proposed. Phase size indicates the average particle diameter of the SBS polymer phase, representing the degradation degree of the SBS polymer during aging. Phase dispersion characterizes the consistency among varying particle sizes within the SBS polymer, while the phase ratio illustrates the proportion of the SBS phase compared to the asphalt phase. Both phase dispersion and phase ratio can describe the polymer network structure.

$$Phasesize = \frac{\sum_{i=1}^{n} \sqrt{\frac{4 \times Polymer_{area}^{i}}{\pi}}}{n} \quad (2)$$

$$Phasedispersion = \frac{\sum_{i=1}^{n} (Polymer_{area}^{i+1} - Polymer_{area}^{i})}{n} \quad (3)$$

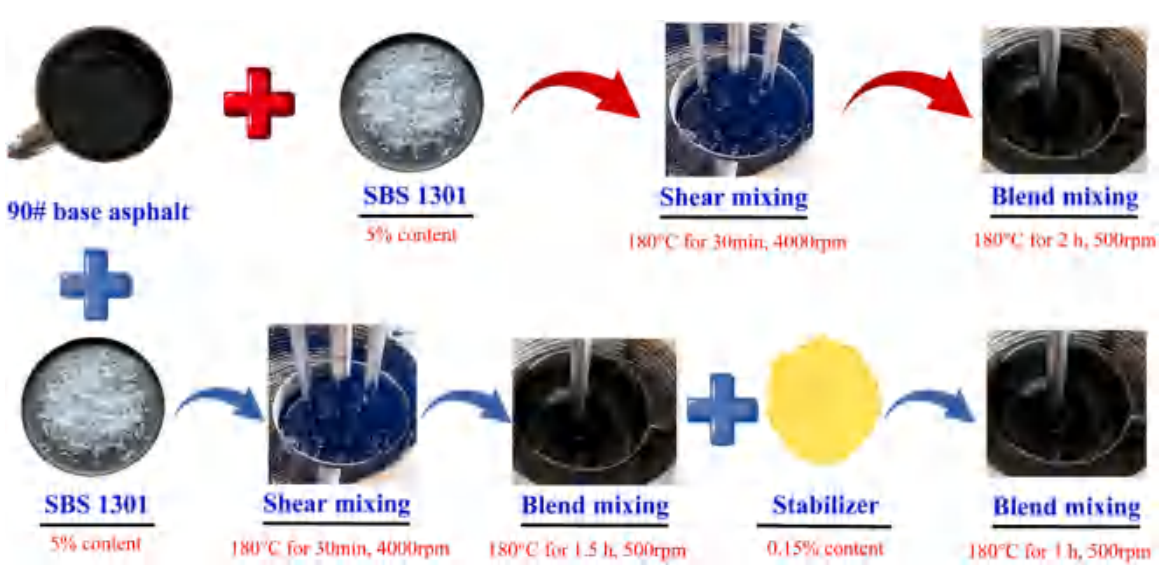

Fig. 1. The process of sample preparation.

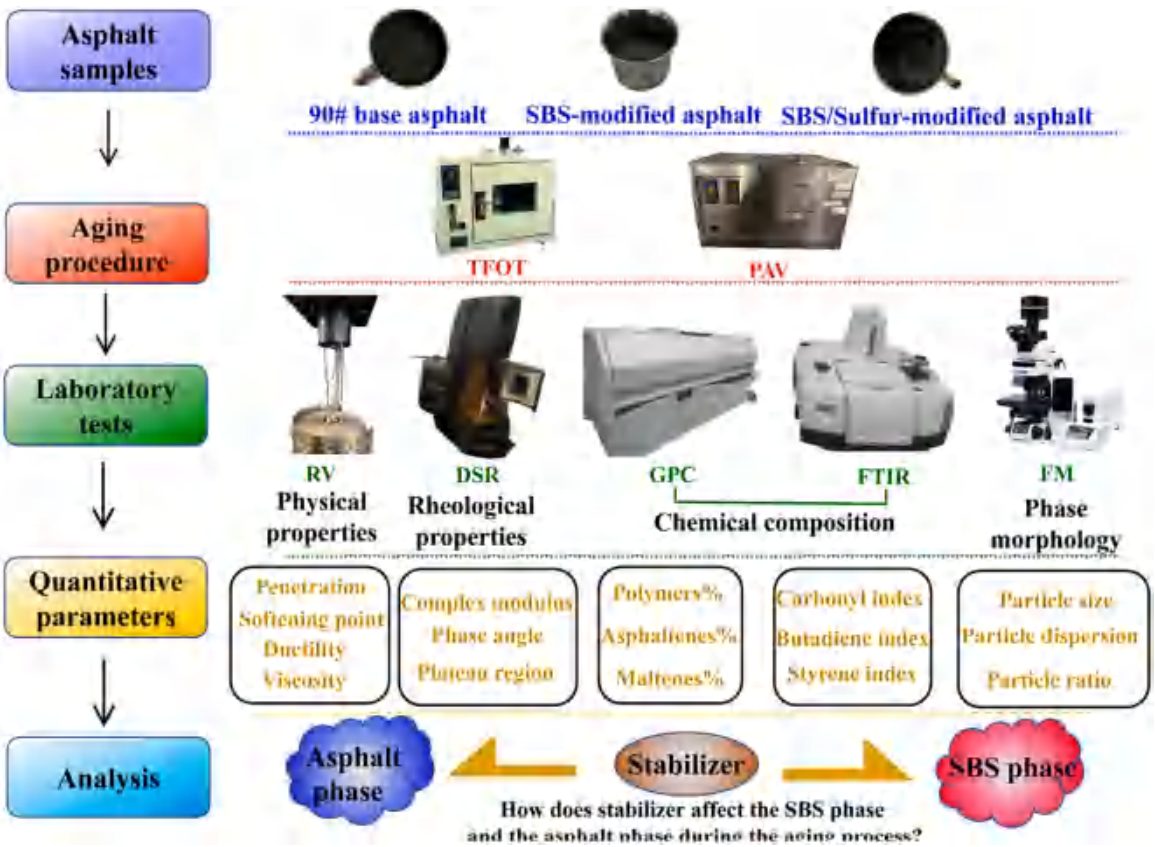

Fig. 2. The framework of this study.

$$Phaseratio = \frac{\sum_{i=1}^{n} Ploymer^{i}_{area}}{Asphalt_{area}} \tag{4}$$

where n is the quantity of SBS polymer particles in the fluorescence image; i represents the ith SBS polymer;$Polymer^{i}_{area}$ represents the area of the SBS polymer phase within the fluorescence image;$Asphalt_{area}$ is the area of the asphalt phase in the fluorescent image.

4.3. Fourier transform infrared spectroscopy (FTIR) test

In this paper, the infrared spectra were analyzed by the Bruker VERTEX70 series Fourier transform infrared spectroscopy (FTIR). FTIR test was employed to analyze the chemistry characterization of phase evolution of SBS/Sulfur-modified asphalt, the samples were tested with a wavenumbers range of 4000 cm^{-1} to 400 cm^{-1}, with a resolution of 0.4 cm^{-1}. All test samples were prepared by the membrane process. The carbonyl index (*CI*) is commonly used as an aging index to characterize the oxidation level of the asphalt phase [31], the effect of sample thickness was eliminated by the reference peak. Butadiene index (*BI*) and styrene index (*SI*) were selected to monitor the deterioration degree of SBS copolymer. Three types of indexes can be computed by the following formulas:

$$Carbonyl\ index(CI) = \frac{Carbonyl\ areaaround\ 1700cm^{-1}}{\sum Area\ between\ the\ spectral\ 1800cm^{-1} and\ 650cm^{-1}} \tag{5}$$

$$Butadieneindex(BI) = \frac{ButadieneAreaaround\ 966cm^{-1}}{\sum Areabetween\ the\ spectral\ 1800cm^{-1}\ and\ 650cm^{-1}} \tag{6}$$

$$Styreneindex(SI) = \frac{StyreneAreaaround699cm^{-1}}{\sum Areabetween\ the\ spectral\ 1800cm^{-1}\ and\ 650cm^{-1}} \tag{7}$$

4.4. Gel permeation chromatography (GPC) test

To assess the molecular weight distribution of the three types of asphalt during aging, about 20 mg of each asphalt was weighed and dissolved in a mobile phase to create a 2 mg/mL solution. After complete dissolution, the samples were filtered into 2 mL vials using sample filters. Tetrahydrofuran (THF) was employed as the mobile phase, and polystyrene served as the standard reference. The GPC analysis was conducted using an Agilent 1260 Infinity II High-Pressure Liquid Chromatography (HPLC) equipped with a refractive index (RI) detector. The injection volume was 200 μL, and the elution was conducted at a flow rate of 1.0 mL/min for 30 minutes. According to Daly et al.'s research, the chromatogram of modified asphalt can be divided into three components based on molecular weight: polymers, asphaltene, and maltene [32]. As shown in Fig. 3, the critical molecular weights for these components are 19,000 and 3000, respectively. The proportions of these three components can be calculated using the following formula.

$$Polymers\% = \frac{Area_{polymers}}{Totalarea\ under\ chromatogram} \times 100\% \tag{8}$$

$$Asphaltenes\% = \frac{Area_{asphaltenes}}{Totalarea\ under\ chromatogram} \times 100\% \tag{9}$$

$$Maltenes\% = \frac{Area_{maltenes}}{Totalarea\ under\ chromatogram} \times 100\% \tag{10}$$

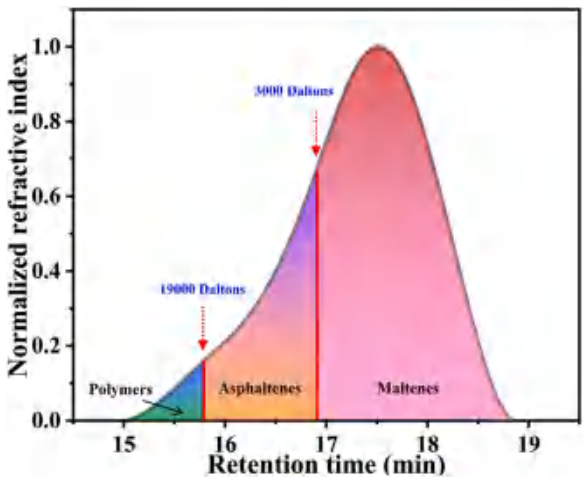

Fig. 3. The Molecular weight distribution of SBS-modified asphalt.

4.5. Dynamic shear rheometer (DSR) test

Dynamic shear rheometer was employed to investigate the rheological properties of both SBS-modified asphalt and SBS/Sulfur modified asphalt. Frequency sweeps were conducted between 0.01 and 100 Hz at a temperature range from 34°C to 82°C so that the master curve could be constructed to analyze the complex modulus and phase angle at a wider frequency range. 25 mm parallel plate geometry with a gap of 1 mm were determined from 34°to 82°C A fixed strain of 0.1% was selected within the linear viscoelastic. 25°C was chosen as the reference temperature to establish the master curve of asphalt binder. In this paper, the sigmoidal model was employed to fit the data of the complex modulus master curve [33]. The sigmoidal model was developed from Project 1–37 A under the National Highway Cooperative Research Program [34]. It is primarily used for constructing complex modulus master curves. the same shift factor was also used to construct the phase angle master curve. Fig. 4 illustrates the shifting process of the complex modulus master curve. Previous research has demonstrated the formation of a polymer network structure in SBS-modified asphalt, resulting in the emergence of a plateau region in the phase angle curve [35,36]. The plateau region does not manifest under all conditions but rather appears selectively under specific temperature or frequency parameters. As per the findings by Chen et al. [37], the plateau region in base asphalt typically occurs under either high temperatures or low frequencies.

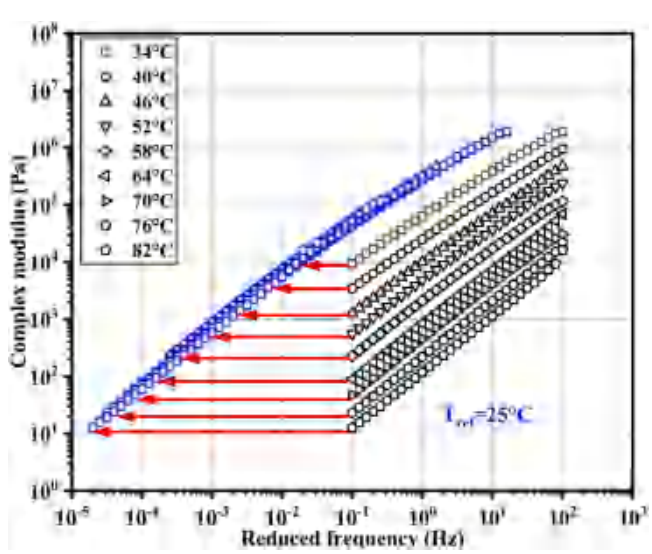

Fig. 4. The schematic diagram of the shifting process.

Conversely, in SBS-modified asphalt, the plateau region appears in the mid-temperature mid-frequency range.

To quantify the features of the plateau region in the phase angle of the master curve, a parameter for the plateau region was proposed. Within the plateau region, the phase angle exhibits stability, showing no variation or minimal fluctuation as the frequency changes. Thus, the first derivative curve was plotted by the fitted master curve, as illustrated in Fig. 5, when the first derivative reaches zero, it indicates three distinct frequencies, with the frequencies positioned in the middle range being designated as the left and right frequencies of the plateau region, respectively. The parameter of the plateau region can be calculated using the following formula:

$$\lambda = \lg(f_{rp}) - lg(f_{lp}) \tag{11}$$

where λ is the plateau region parameter of the phase angle curve; f_{lp} represents the frequency corresponding to the left side of the plateau region; f_{rp} represents the frequency corresponding to the right side of the plateau region.

5. Results and discussion

5.1. Physical properties

Table 3 presents the physical properties of three asphalt samples before and after aging. It is noticeable that the addition of sulfur has led to an elevation in both the softening point and viscosity of SBS-modified asphalt, accompanied by a decrease in penetration, which indicates that adding sulfur has effectively enhanced the high-temperature performance. Previous research has also confirmed that the introduction of sulfur enhances the asphalt's elasticity [38], the addition of sulfur can form chemical cross-linking, reinforcing the polymer network structure. However, the strengthened network structure restricts the movement of SBS molecules during stretching, leading to a reduction in low-temperature ductility after sulfur incorporation.

To better illustrate the impact of aging on the physical properties of three asphalt types, the change rate in various indicators during the aging process was also computed. It is conspicuous that base asphalt displays the most significant change rate following both short-term and long-term aging. This can primarily be ascribed to the aging process within base asphalt, which leads to the formation of asphaltenes with higher molecular weight. Conversely, aging in SBS-modified asphalt not only induced the oxidation of the base asphalt but also accompanied the degradation of the SBS modifier. The oxidation of base asphalt gives rise to larger molecules and enhanced asphalt elasticity, while the degradation of the SBS modifier produces smaller molecules and softens the asphalt. As depicted in Table 3, the change rate in softening points for

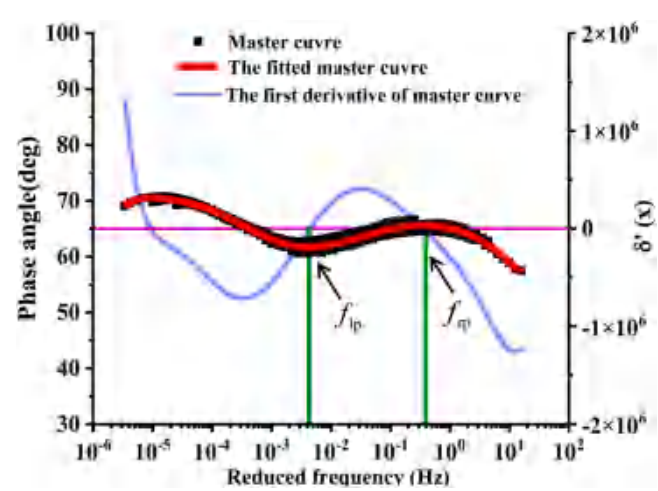

Fig. 5. The methods to determine the frequency of the plateau region.

Table 3
The physical properties of three asphalt samples at different aging times.

Asphalt type		Penetration (25°C, 0.1 mm)		Softening point (°C)		Ductility (5°C /15°C, cm)		Viscosity (135°C, Pa·s)	
		Value	Change rate	Value	Change rate	Value	Change rate	Value	Change rate
Base	Origin	91.4	0.00%	47.2	0.00%	>150	–	–	–
	TFOT	74.2	-18.82%	52.1	10.38%	35.0	–	–	–
	PAV	31.1	-65.97%	56.7	20.13%	12.7	–	–	–
SBS	Origin	75.2	0.00%	72.4	0.00%-	40.1	0.00%	1.548	0.00%
	TFOT	72.0	-4.26%	69.0	-4.7%	23.5	-41.40%	1.515	-2.13%
	PAV	51.7	-31.25%	81.1	12.0%	3.2	-92.02%	2.134	37.86%
SBS/ Sulfur	Origin	73.1	-0.00%	78.5	0.00%	31.0	0.00%	1.631	0.00%
	TFOT	71.3	-2.46%	76.1	-3.06%	17.4	-43.87%	1.607	-1.47%
	PAV	53.8	-26.40%	82.2	4.71%	2.1	-93.23%	2.016	23.61%

the three asphalt types are as follows: 10.4% and 20.1% for the base asphalt, −4.7% and 12.0% for the SBS-modified asphalt, and −3.0% and 4.7% for the SBS/Sulfur-modified asphalt. After short-term aging, SBS-modified asphalt experiences a decline in its softening point, which subsequently shows a gradual increase after PAV aging. This trend signifies that the degradation of the SBS modifier takes precedence in the initial phases of aging. In comparison, base asphalt typically exhibits a more pronounced change rate, consistent with previous research findings [39,40]. Moreover, the inclusion of a stabilizer leads to a lower rate of change during aging, reflecting enhanced stability in its physical properties throughout the aging process.

5.2. Rheological properties

To further analyze the impact of the stabilizer on performance during aging, Fig. 6 displays the master curves of complex modulus and phase angle for three types of asphalt. It can be observed that the complex modulus of the three asphalt types increases while the phase angle decreases as aging time increases. Compared to SBS-modified asphalt, base asphalt exhibits a smaller complex modulus and a larger phase angle during aging, and this distinction becomes particularly pronounced at a lower frequency (High temperature). Another noteworthy dissimilarity lies in the curve shape of the phase angle, base asphalt generally lacks a rubbery plateau region, and plateau region indicates the minimal variation of phase angle from one point to another. Prior research has established that neither pure asphalt nor pure modifier gives rise to a plateau region [37]. The formation of such a plateau region is typically attributed to the network structure forged by the modifier within the asphalt [41]. With the addition of sulfur, the complex modulus of SBS-modified asphalt increases, and the higher complex modulus in the high-temperature (low-frequency) region indicates that SBS/Sulfur-modified asphalt has better high-temperature performance. Phase angle also decreases across the entire frequency range, indicating better elastic response with lower phase angle. It can be observed that whether sulfur is added or not, the phase angle master curve will exhibit a plateau region. However, with the introduction of sulfur, the plateau region becomes more gradual, indicating the enhancement of the polymer network structure by the stabilizer.

The impact of the stabilizer becomes evident after short-term aging. From the phase angle curve, it can be observed that SBS-modified asphalt no longer exhibits a plateau region after short-term aging. Simultaneously, the results of phase angle at different temperatures show a deviation, and the mater curve of phase angle becomes less smooth, indicating the absence of temperature dependence. According to the viscoelasticity theory of polymer homogeneous systems [42], the deviation degree from the curve reflects the extent of polymer phase separation. Thus, this suggests that phase separation occurs between the SBS and asphalt phases at this stage. In contrast, SBS/Sulfur-modified asphalt after TFOT aging exhibits relatively minor distinctions from the unaged samples, the plateau region persists, and the value of phase angle experiences a slight reduction. After PAV aging, neither SBS-modified asphalt nor SBS/Sulfur-modified asphalt retains a plateau region, which indicates that the severe degradation of the SBS modifier has also disrupted the polymer network structure.

To compare the aging of three asphalt types, the complex modulus and phase angle were listed in Table 4, both of the levels which were measured at 64°C and a frequency of 100 rad/s (15.9 Hz). The temperature of 64°C closely represents the practical temperature of the road surface. The frequency of wheel load impact on the road surface is closely related to the vehicle speed and wheel size. With wheel sizes ranging from 14 to 18 in. and vehicle speeds ranging from 20 to 120 km/h, the frequency of road surface impact falls within the range of 3–30 Hz. Thus, the median frequency (100 rad/s, 15.9 Hz) as the representative value was selected. The rubbery plateau parameter was also calculated to evaluate the plateau region, which can describe the length of the rubbery plateau. The change rate of three parameters was rigorously computed at various aging times. As illustrated in Table 4, compared to the base asphalt, both SBS-modified asphalt and SBS/Sulfur-modified asphalt exhibit a lower change rate in complex modulus and phase angle during aging. This implies the introduction of the SBS modifier into the asphalt leads to a decreased susceptibility to aging. The SBS modifier absorbed light components from the asphalt, leading to swelling and a reduction in the rate of oxidation reactions during aging, thus protecting the asphalt phase [43]. With the introduction of the stabilizer, SBS/Sulfur-modified asphalt experiences a pronounced increase in complex modulus and a corresponding decrease in phase angle, signifying enhanced elasticity. Moreover, the addition of the stabilizer further reduces the change rate during aging, after PAV aging, the change rate in complex modulus is 324.91% and 203.54% for the two types of modified asphalt, while the change rate of phase angle is −4.51% and −3.05%. This data emphasizes that the addition of the stabilizer enhances the aging resistance of SBS-modified asphalt. From the plateau region parameter, it can be observed that short-term aging has a minor impact on SBS/Sulfur-modified asphalt, with a change from 2.1 to 1.9, and the plateau region shifts towards lower frequency with aging. After PAV aging, the plateau region parameters become zero in both types of asphalt. Nevertheless, it is evident that even after PAV aging, the phase angle curve of SBS/Sulfur-modified asphalt still exhibits distinct differences compared to the other two types of asphalt, at frequencies as low as 10^{-3} Hz and lower, the phase angle curve of SBS/Sulfur-modified asphalt remains relatively stable. Previous studies have already demonstrated a strong correlation between the plateau region and the crosslinking degree of the polymer network [15]. The addition of stabilizers contributes to the formation of the denser crosslinking network in SBS/Sulfur-modified asphalt. The chemical crosslinking bonds possess significantly higher bond energy levels, typically 1–2 orders of magnitude greater than van der Waals forces and also more stable [44]. Consequently, the polymer network becomes less susceptible to deterioration during aging.

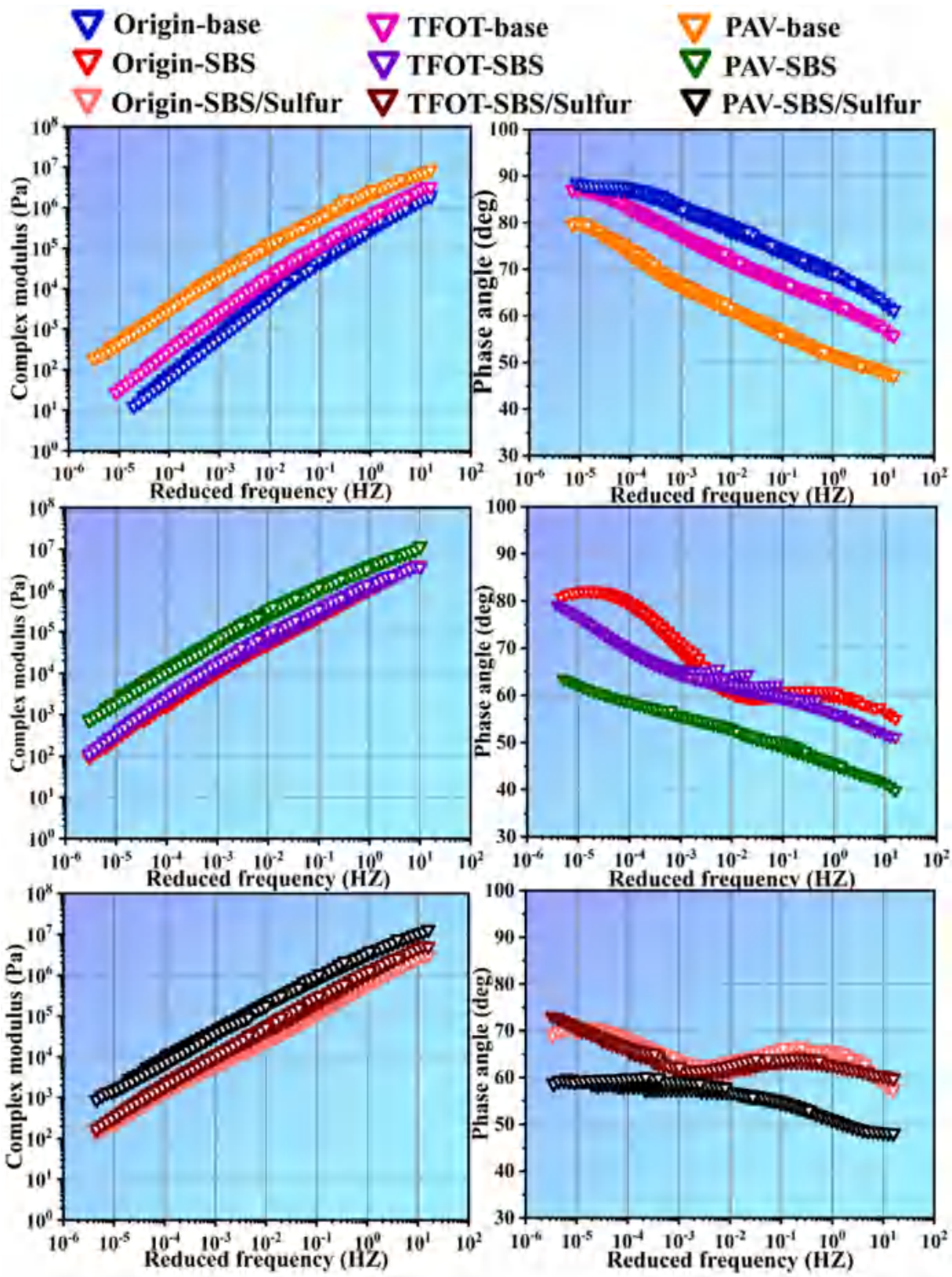

Fig. 6. Master curve of both SBS- and SBS/Sulfur-modified asphalt.

5.3. Chemical composition

5.3.1. FTIR results

To analyze the changes in the chemical structure of the three types of asphalt, Figs. 7 and 8 depict the infrared spectra of the functional group region (4000–1200 cm^{-1}) and the fingerprint region (1200–500 cm^{-1}), respectively. As shown in Fig. 7, the absorption peaks of the three asphalt types closely resemble each other in the functional group region.

Table 4
The rheological properties at different aging time.

Asphalt type		Complex modulus (Pa)		Phase angle (°C)		Plateau region (Hz)	
		Value	Change rate	Value	Change rate	Value	Change rate
Base	Origin	11398.4	0.00%	77.3	0.00%	0.0	0.00%
	TFOT	26242.6	130.23%	76.7	-0.78%	0.0	0.00%
	PAV	91085.7	699.11%	66.8	-13.58%	0.0	0.00%
SBS	Origin	41766.6	0.00%	62.1	0.00%	1.2	0.00%
	TFOT	52296.1	25.21%	65.4	5.31%	0.0	-100.00%
	PAV	177470.0	324.91%	59.3	-4.51%	0.0	-100.00%
SBS/ Sulfur	Origin	45962.1	0.00%	59.1	0.00%	2.1	0.00%
	TFOT	57011.5	24.04%	61.8	4.57%	1.9	-9.52%
	PAV	139512.0	203.54%	57.3	-3.05%	0.0	-100.00%

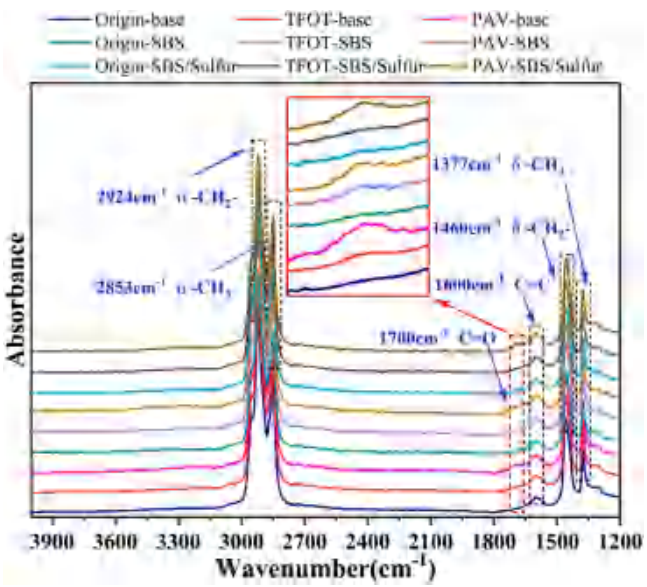

Fig. 7. FTIR results of both SBS- and SBS/Sulfur-modified asphalt.

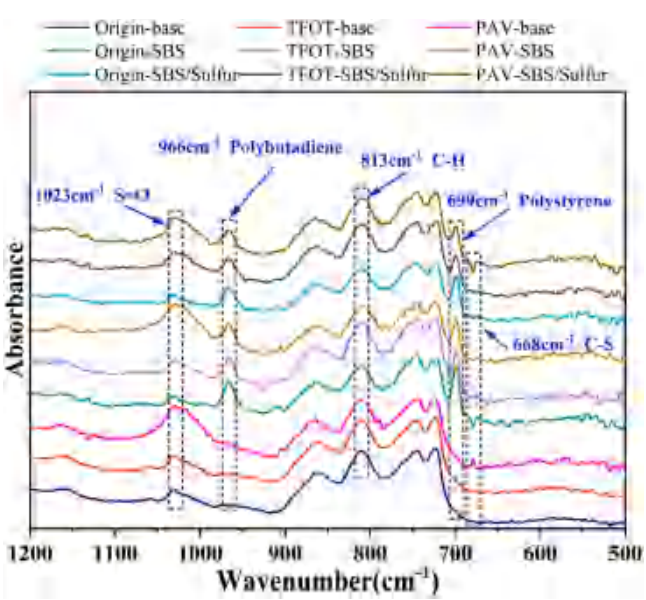

Fig. 8. FTIR results of SBS-modified asphalt in different aging stages.

The peaks at 2924 cm^{-1} and 2853 cm^{-1} are attributed to C-H vibrations in the asphalt, while the 1700 cm^{-1} peak corresponds to the stretching vibration of C═O in carbonyl groups, and the 1600 cm^{-1} peak is linked to C═C vibrations. Carbonyl (the absorption peaks at 1700 cm^{-1}) is the most common oxidation functional group during asphalt aging and is widely used to characterize asphalt oxidation [45]. The absorption peak at 1700 cm^{-1} for all three asphalt types increases, particularly after PAV aging. Both modified asphalts exhibit smaller absorption peaks compared to the base asphalt. However, whether a stabilizer is added or not, there is no clear distinction between the two modified asphalts. Previous research has similarly confirmed that the incorporation of the SBS modifier hinders the formation of carbonyl groups during aging [46]. Furthermore, the presence of an SBS modifier in the base asphalt, due to its absorption of lighter components, shifts the overall molecular size distribution towards larger dimensions [44], which may contribute to the reduced aging rate in SBS-modified asphalt. In SBS/Sulfur-modified asphalt, carbonyl compounds, such as ketones and aldehydes, belong to the resins. While sulfurization reactions mainly react with aromatic rings in asphalt to produce sulfurized asphaltene [18]. This can explain why stabilizers have no significant effect on the carbonyl index.

Fig. 8 displays the spectral changes within the wavenumber range of 1200–500 cm^{-1} for the three asphalt types. The peak at 1023 cm^{-1} corresponds to the stretching vibration of S═O in sulfoxide groups, whereas the peaks at 966 cm^{-1} and 699 cm^{-1} are ascribed to the trans-C═C vibration in polystyrene and the bending vibration of the benzene ring in polybutadiene, respectively. The peaks at 966 cm^{-1} and 699 cm^{-1} are distinctive features of the SBS-modified asphalt, absent in the base asphalt. Sulfoxide groups exhibit a similar variation trend to carbonyl groups, with the base asphalt maintaining a higher absorption peak. However, sulfoxide groups are susceptible to decomposition at elevated temperatures [47], making it challenging to attribute the reduction in peak intensity solely to aging. Thus, this study refrains from considering the sulfoxide index as a quantitative indicator. Furthermore, the introduction of a stabilizer did not result in the emergence of new absorption peaks. Prior research indicated that stabilizers primarily undergo cross-linking reactions to form additional cross-linking bonds [9], predominantly manifested by the absorption peak at 688 cm^{-1}, attributed to C-S bonds. Nevertheless, Fig. 8 provides evidence that C-S bonds do not follow a distinct pattern of change. An increase in the absorption intensity at 668 cm^{-1} was also observed in the aging of base asphalt. Due to the concurrent occurrence of cross-linking and degradation, it is challenging to derive reliable information from C-S bonds. Additionally, there is a more pronounced decrease at 699 cm^{-1} and 966 cm^{-1} after adding the stabilizer, confirming that the stabilizer primarily reacts with SBS copolymer, especially with the double bonds in polybutadiene.

To conduct a more detailed analysis, Table 5 presents the parameters *CI*, *BI*, and *SI*, along with their change rates. *CI* represents the oxidation level within the asphalt phase, and *BI* and *SI* indicate the degradation

Table 5
The Functional group indexes at different aging time.

Asphalt type		*CI*		*BI*		*SI*	
		Value	Change rate	Value	Change rate	Value	Change rate
Base	Origin	0.00712	0.00%	0.0000	0.00%	0.0000	0.00%
	TFOT	0.01081	51.83%	0.0000	0.00%	0.0000	0.00%
	PAV	0.10007	1300.00%	0.0000	0.00%	0.0000	0.00%
SBS	Origin	0.00550	0.00%	0.21435	0.00%	0.14925	0.00%
	TFOT	0.00842	53.1%	0.18436	-13.9%	0.13477	-9.70%
	PAV	0.02706	392.00%	0.13793	-35.7%	0.11244	-24.66%
SBS/Sulfur	Origin	0.00439	0.00%	0.15529	0.00%	0.13184	0.00%
	TFOT	0.00668	52.16%	0.14183	-8.67%	0.12124	-8.04%
	PAV	0.02105	379.50%	0.12493	-19.55%	0.10206	-22.59%

degree of SBS copolymers. After PAV aging, the *CI* change rates for the three asphalts are 1300.0%, 392.0%, and 379.5%, indicating the base asphalt exhibits a higher level of asphalt oxidation. However, there are no significant differences observed between the two modified asphalts. Before and after adding the stabilizer, the *BI* and *SI* values for the two modified asphalts are 0.21435 and 0.14183, and 0.14925 and 0.13184, respectively. *BI* displays a more prominent change than *SI*, indicating that stabilization primarily involves reactions related to butadiene. Typically, sulfur undergoes addition reactions on the double bonds of butadiene or substitution reactions on hydrogen atoms adjacent to the double bonds [17]. Therefore, the unsaturated carbon-carbon double bonds in butadiene are considered the primary sites for vulcanization reactions. Although both *BI* and *SI* decrease after adding the stabilizer, SBS/Sulfur-modified asphalt shows a lower degradation rate for *BI* during aging, implying a reduced rate of degradation with stabilizer incorporation. *BI* exhibits a lower rate of change compared to *SI*, as polybutadiene demonstrates higher reactivity in chemical reactions than polystyrene, leading to faster degradation in the former [47]. Ideally, the stabilizer attaches to both ends of the C-S bonds in SBS and asphalt molecules. Some studies propose that when the SBS modifier is initially dispersed in the asphalt before the stabilizer is introduced, most cross-linking occurs between SBS molecules, with fewer linkages to the asphalt [48]. This might explain why the stabilizer has no significant effect on the oxidation changes in the asphalt phase.

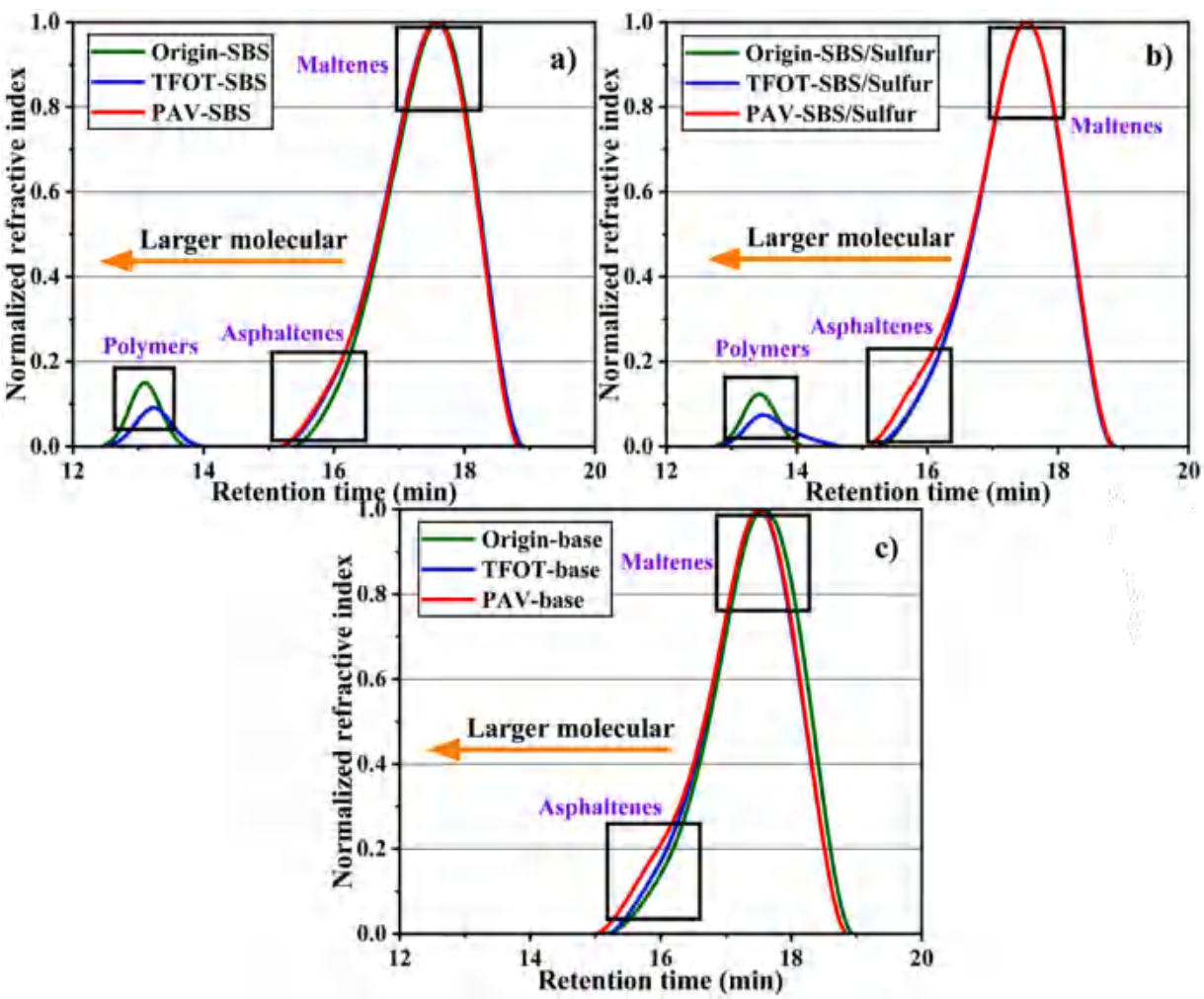

Fig. 9. The GPC results of three types of asphalt.

5.3.2. GPC results

Regarding the GPC results, shorter retention times correspond to higher molecular weights. The highlighted regions in Fig. 9 represent the sequential elution of polymers, asphaltene, and maltene according to their molecular weights. The presence of the SBS modifier introduces a unique feature to the GPC curve of both modified asphalts, and the addition of the stabilizer results in a reduction in size and a rightward shift of the SBS characteristic peak, signifying a decrease in the molecular weight of the SBS copolymer. The characteristic peak of SBS copolymer decreases and shifts to the right after aging. In short-term aging, SBS/Sulfur asphalt exhibits a lower SBS characteristic peak, indicating a reduced molecular weight, and the SBS characteristic peak disappears in both asphalt types after PAV aging, signifying severe degradation of the SBS modifier.

Additionally, it is noteworthy that the maltene peaks of the modified asphalts largely overlap before and after aging, while the peak in the base asphalt shifts to the left. This implies a greater molecular weight change in the base asphalt after aging, consistent with the FTIR results. Another detail is the asphaltene peak between 15 and 16 minutes: the short-term and long-term aging curves overlap in SBS-modified asphalt, while the curves for unaged and short-term aging overlap in SBS/Sulfur-modified asphalt, which will be discussed in detail below.

It can be observed from Table 6 that after PAV aging, the change rate in asphaltene and maltene in the base asphalt were 21.86% and −4.96%, respectively, significantly higher than those in the two modified asphalts. This further supports the idea that the addition of SBS modifier can retard the oxidation rate of asphalt. While the stabilizer notably impacts polymer degradation, its effect on maltene remains minimal. Polymer changes in the two types of asphalt after short-term aging were −53.10% and −18.94%, respectively. Lin et al. discussed the effect of stabilizers on component distribution, suggesting that it affects the absorption of light components by SBS copolymers [49]. In Table 6, the maltene change in the two modified asphalts after aging showed no significant difference, and the change rate of asphaltene during aging decreased with the addition of stabilizers. Generally, the sulfurization reaction primarily involves the reaction of sulfide with SBS modifiers and asphalt binders. In the sulfurization of SBS copolymers, sulfur easily undergoes addition reactions with double bonds in polybutadiene or substitution reactions at allylic hydrogen atoms. This explains the reduction in the molecular weight of SBS copolymers. Regarding the sulfurization of asphalt binders, sulfur is believed to react mainly with naphthenic aromatic compounds at 140°C to form sulfide asphaltenes [50], while at temperatures above 140°C, it substitutes hydrogen in aromatic rings or side chains to produce thioethers [51]. Thus, the reduction of reactive sites in asphaltene after sulfurization leads to a lower rate of asphaltene generation during aging in the presence of stabilizers. Compared to FTIR results, carbonyl compounds, such as ketones and aldehydes, are part of the resin, which in turn belongs to the maltenes%, This elucidates why there is no significant difference in maltenes% and CI between the two types of modified asphalt before and after stabilizer addition. This implies that stabilizers primarily exert a positive influence on asphalt phase aging by impacting asphaltene.

5.4. Phase morphology

To visually comprehend the changes occurring in the SBS copolymer, Fig. 10 exhibits the fluorescence images of both SBS-modified asphalt and SBS/Sulfur-modified asphalt during aging. It can be revealed that the addition of stabilizer resulted in a thinner filamentous polymer network and a smaller size of the SBS copolymer phase, as well as the appearance of a more complex and densely crosslinked network. These findings indicate that the addition of stabilizer led to the formation of a homogeneous system. The polymer network is magnified and depicted in the upper right corner for better observation. After short-term aging, SBS/Sulfur-modified asphalt retains a relatively intact polymer network with reduced SBS polymer size, whereas SBS-modified asphalt exhibits no apparent polymer network, and SBS polymers transform from fibrillar to punctate distribution after TFOT aging. PAV aging results in severe degradation of the SBS polymer network in both types of asphalt, further reducing the polymer size.

In SBS-modified asphalt, the essential morphological change revolves around the distribution of SBS polymer particle sizes. These sizes increase by absorbing light asphalt constituents but decrease during aging. Also, the polymer network exhibits a close connection to these size shifts. To further discuss the morphological changes in both types of asphalt, the fluorescent images were analyzed to quantify the particle size and distribution of SBS copolymers, and three quantitative parameters including phase size, phase dispersion, and phase ratio calculated using the software Image-Pro-Plus, the results are listed in Table 7. It can be observed that after adding the stabilizer, the phase size of SBS/sulfur-modified asphalt noticeably decreases, along with reduced phase dispersion and increased phase ratio. Abigail et al. reported sulfur functions as a plasticizer, aiding in the dispersion and swelling of the polymer at the initial stage, subsequently, sulfur facilitates crosslinking reactions, resulting in the formation of finer particles that continue to develop into a filamentous network [52]. After aging, the SBS polymer phase size in both types of asphalt notably decreases. However, unlike the reduction in particle size due to sulfurization, aging is accompanied by a decrease in the phase ratio. This suggests that sulfurization leads to a reduction in particle size along with an increase in the particle number, whereas aging results in a reduction in both particle size and particle number due to polymer degradation. Hence, it indicates that the aging level of the two types of asphalt cannot be solely judged based on particle size. The change rate of phase ratio for the two types of asphalt after TFOT aging is −48.38% and 7.13%, respectively, which signifies that the addition of stabilizers has strengthened the polymer network, further refining it without disruption during aging. After PAV aging, although SBS polymer in SBS/Sulfur-modified asphalt displays smaller particle sizes, it exhibits a reduced change rate of phase size. The change rates for phase dispersion and phase ratio in both types of asphalt are −61.84% and −36.41%, −98.15% and −97.67%, respectively. This implies that even after PAV aging, SBS/Sulfur-modified asphalt

Table 6
The Functional group indexes at different aging time.

Asphalt type		*Polymers%*		*Asphaltenes%*		*Maltenes%*	
		Value	Change rate	Value	Change rate	Value	Change rate
Base	Origin	0.00%	0.00%	18.48%	0.00%	81.52%	0.00%
	TFOT	0.00%	0.00%	19.73%	6.76%	80.27%	-1.53%
	PAV	0.00%	0.00%	22.52%	21.86%	77.48%	-4.96%
SBS	Origin	5.16%	0.00%	17.47%	0.00%	77.37%	0.00%
	TFOT	3.51%	-53.10%	19.63%	12.36%	76.86%	-0.65%
	PAV	0.00%	-100.00%	20.46%	17.12%	79.54%	2.80%
SBS/Sulfur	Origin	4.54%	0.00%	19.43%	0.00%	76.03%	0.00%
	TFOT	3.68%	-18.94%	19.75%	1.65%	76.67%	0.84%
	PAV	0.00%	-100.00%	21.76%	11.99%	78.24%	2.91%

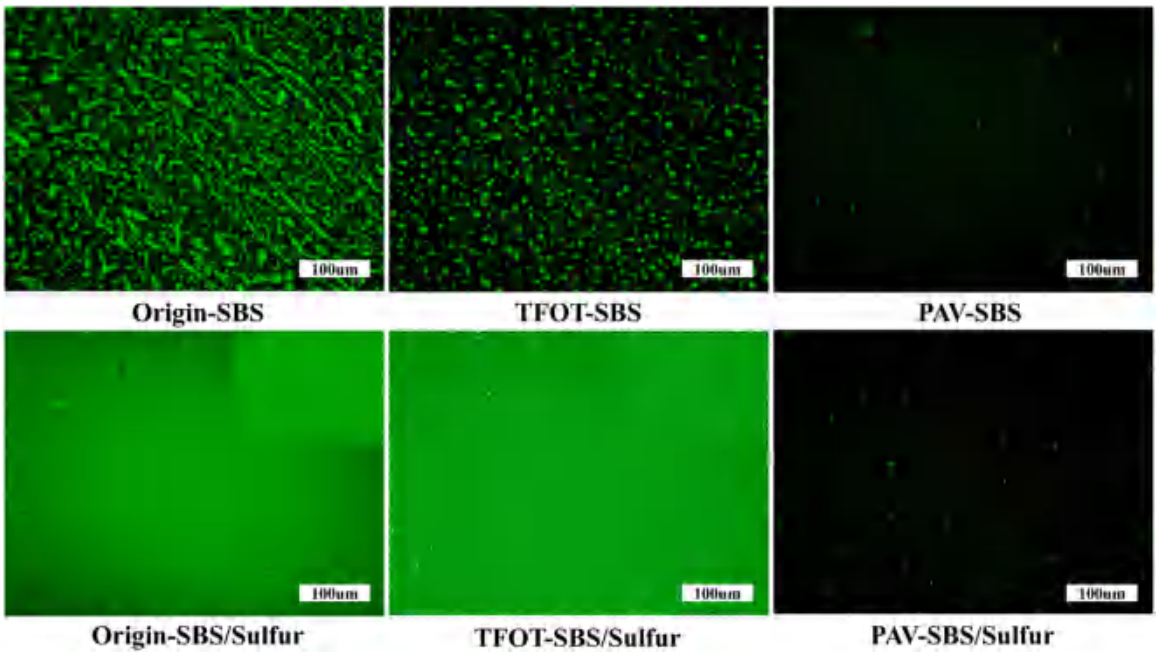

Fig. 10. Fluorescence images at different aging processes.

Table 7
The phase size at different aging times.

Asphalt type		Phase size (um)		Phase Dispersion		Phase ratio%	
		Value	Change rate	Value	Change rate	Value	Change rate
SBS	Origin	5.91	0.00%	4.35	0.00%	24.31%	0.00%
	TFOT	5.76	-2.54%	3.54	-18.62%	12.55%	-48.38%
	PAV	3.38	-42.81%	1.66	-61.84%	0.45%	-98.15%
SBS/Sulfur	Origin	4.25	0.00%	2.06	0.00%	34.77%	0.00%
	TFOT	4.18	-1.65%	1.47	-28.64%	37.25%	7.13%
	PAV	2.82	-33.64%	1.31	-36.41%	0.81%	-97.67%

maintains more polymer phase. This indicates that the stabilizer strengthened the polymer network, making it more resistant to aging.

Among these 16 characterization parameters mentioned in Fig. 2, the methods for testing the ductility and the 135°C rotation viscosity differ between base asphalt and modified asphalt, while the applicability of the remaining 14 parameters remains relatively consistent across all three types of asphalt. The results displaying the standardized variations of these 14 parameters are presented in Table 8.

The lower the change rate, the better the aging resistance of asphalt. From Table 8, it can be seen that except for the parameters in the plateau region and those related to the polymer phase, all parameters for base asphalt after PAV aging are 1.00. Since the parameters in the plateau region and those related to polymers are associated with polymer properties rather than base asphalt properties, it can be inferred that the

Table 8
The change rate after standardization.

Characterization parameters		Change rate					
		Base		SBS		SBS/Sulfur	
		TFOT	PAV	TFOT	PAV	TFOT	PAV
Macroscopic performance parameter	Penetration	0.29	1.00	0.06	0.47	0.04	0.40
	Softening point	0.52	1.00	0.23	0.60	0.15	0.23
	Complex modulus	0.19	1.00	0.04	0.46	0.03	0.29
	Phase angle	0.06	1.00	0.39	0.72	0.33	0.56
	Plateau region	0.00	0.00	1.00	1.00	0.10	1.00
Polymer phase Parameters	Butadiene index	0.00	0.00	0.39	1.00	0.24	0.55
	Styrene index	0.00	0.00	0.39	1.00	0.33	0.92
	Polymers%	0.00	0.00	0.53	1.00	0.19	1.00
	Phase size	0.00	0.00	0.06	1.00	0.04	0.79
	Phase dispersion	0.00	0.00	0.30	1.00	0.46	0.59
Asphalt phase Parameters	Carbonyl index	0.04	1.00	0.04	0.30	0.04	0.29
	Asphaltenes%	0.31	1.00	0.57	0.78	0.08	0.55
	Maltenes%	0.31	1.00	0.13	0.56	0.17	0.59
Parameters for both phase	Phase ratio	0.00	0.00	0.49	1.00	0.07	0.99

base asphalt exhibits the poorest aging resistance performance. Regarding the characterization parameters of the two modified asphalts, quantitative parameters such as BI, Polymers%, and phase dispersion are more indicative of stabilizer properties in terms of polymer phase. As for the parameters of the asphalt phase, the quantitative parameter Asphaltenes% characterizes the influence of stabilizers more prominently. Therefore, radar chart analysis was conducted using the above five performance parameters and four micro-scale parameters with clear distinctions for stabilizers, so that the impact of stabilizers on the SBS polymer phase and asphalt phase can be further refined, as well as the comprehensive performance during aging.

According to Table 8, these nine change rates were divided into three groups, Macroscopic Performance Parameters: Penetration, softening point, complex modulus, phase angle, plateau region; Polymer Phase Parameters: Butadiene index, polymers%, phase dispersion; Asphalt Phase Parameters: Asphaltenes%. Fig. 11 presents the radar chart results, the base asphalt showed zero values in polymer-related parameters on the radar chart due to the absence of polymers, while the other parameters indicated noticeable growth during aging. Moreover, distinct differences were observed between the two modified asphalts after both short-term and long-term aging. In comparison to SBS-modified asphalt, SBS/Sulfur-modified asphalt exhibited lower values in asphaltenes%, butadiene index, and phase dispersion after PAV aging, which indicated stabilizers primarily affect the generation of asphaltene molecules and the degradation of polymers during the aging process. In terms of the comprehensive performance during aging, the radar chart areas (absolute areas) of both modified asphalts after short-term and long-term aging were 0.383 and 0.074, 1.649 and 0.825, respectively. This indicates that the addition of stabilizers has a positive contribution to the aging of SBS-modified asphalt.

6. Conclusions

This study ultimately conducted a comprehensive analysis of the aging process of 90# base asphalt, SBS-modified asphalt, and SBS/Sulfur-modified asphalt, utilizing five macroscopic performance parameters and four microscopic characterization parameters. The effects of stabilizers on both the asphalt phases and polymer phases during aging were meticulously investigated. and the distinct roles played by asphalt, SBS polymer, and stabilizers throughout the aging process were explored. The main findings can be described as follows:

1) The change rate in the physical properties of SBS-modified asphalt during aging decreases with the addition of stabilizers, which signifies enhanced stability of the physical properties in SBS/Sulfur-modified asphalt. Rheological parameters not only demonstrate reduced changes but also indicate that sulfur predominantly protects the polymer network structure from degradation during short-term aging, consistent with the FM test results.
2) The stabilizers primarily react with the carbon-carbon double bonds in the butadiene, resulting in different degradation rates for the butadiene index and styrene index during aging. It is evident that the stabilizers initially reduce the degradation rate of SBS polymers when combined with GPC test results, both types of modified asphalt

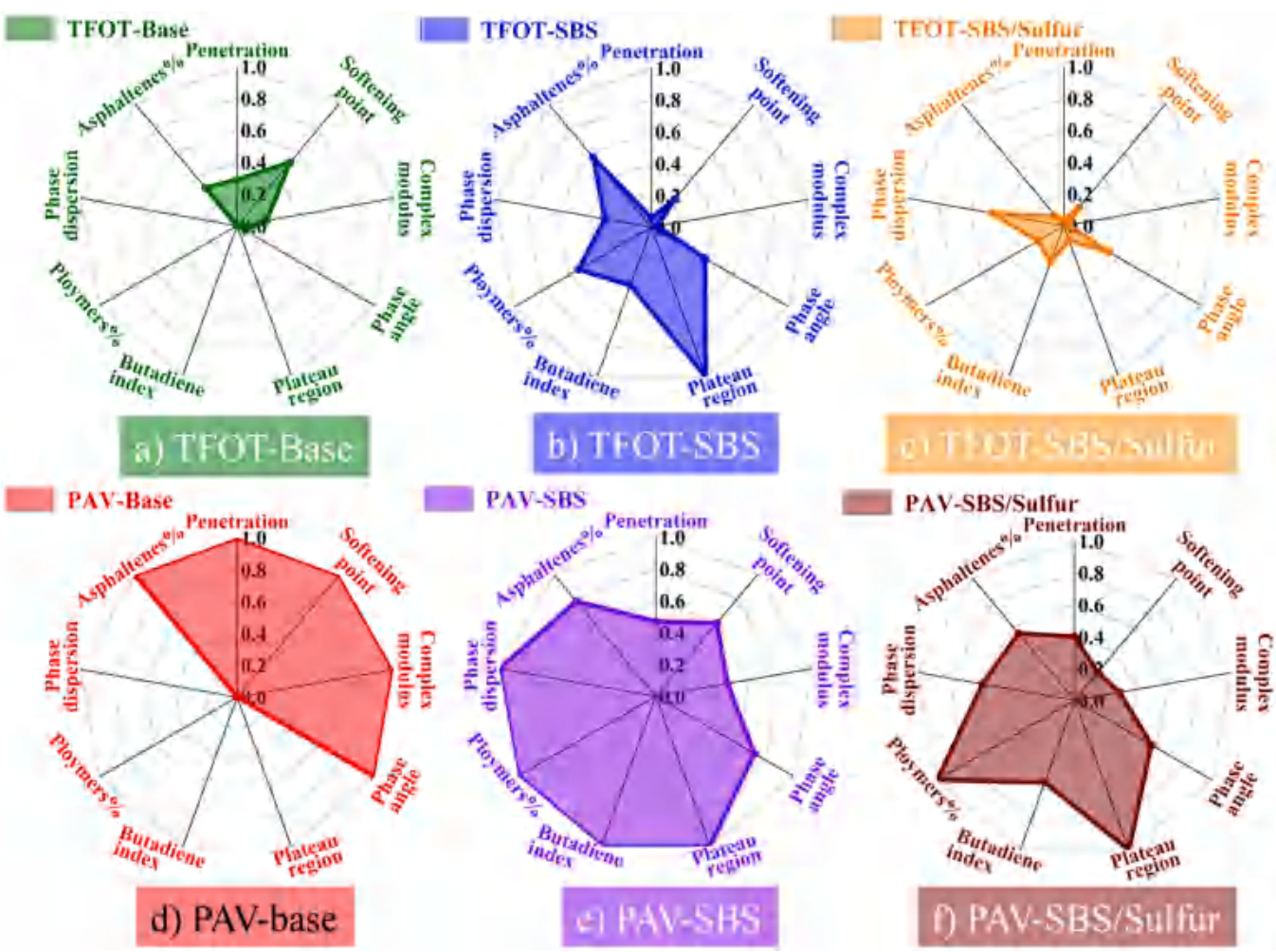

Fig. 11. The radar charts of three types of asphalt.

exhibit the disappearance of polymer peaks in the GPC curves after PAV aging.

3) The addition of the SBS modifier noticeably reduces the carbonyl index after aging, while stabilizers do not exhibit a similar impact on this index. According to the GPC test results, the change rate of asphaltenes% declines with stabilizer incorporation during the aging process, which implies that stabilizers primarily influence asphaltene molecules within the asphalt phase.
4) After aging, SBS/Sulfur-modified asphalt exhibits smaller SBS copolymer particle sizes compared to SBS-modified asphalt, while this reduction in particle size is partly attributed to the sulfurization reaction. After the addition of stabilizer, the change rate of the phase size of the SBS/Sulfur-modified asphalt during aging remains relatively low.

This study reveals the positive contribution of sulfur stabilizers in the aging process of SBS-modified asphalt, and it meticulously examines the diverse effects of the stabilizer on the asphalt phase and the SBS polymer phase throughout aging. The sulfur stabilizer primarily functions positively during aging by reducing the degradation rate of SBS copolymer and retarding the formation of asphaltene molecules. This contributes to a better understanding of the complex interplay within the multiphase system of SBS-modified asphalt, encompassing base asphalt, SBS modifiers, and stabilizers. providing theoretical underpinnings for intricate aging mechanisms and rejuvenation methods involving stabilizers. Additional research could involve examining the specific reaction pathways of sulfur and its more nuanced effects on other components of asphalt. Furthermore, a broader inquiry into the generalizability of the research findings could be undertaken, including the exploration of different stabilizer concentrations and the utilization of multiple stabilizers.

CRediT authorship contribution statement

Junjie Zhang: Writing – review & editing, Writing – original draft, Visualization, Investigation. **Zefeng Ma:** Methodology, Investigation. **Pengwei Sun:** Writing – original draft, Methodology, Investigation. **Guilian Zou:** Validation, Software. **Mingxin Dai:** Investigation, Formal analysis. **Yiqiu Tan:** Writing – review & editing, Methodology, Funding acquisition, Conceptualization. **Rong Zhuo:** Validation, Software.

Declaration of Competing Interest

The authors have declared that no conflict of interest exists.

Data Availability

Data will be made available on request.

Acknowledgements

This study was mainly supported by the National Natural Science Foundation of China joint fund for regional innovation and development (U20A20315). This study was also supported by the Non-metallic Materials Innovation Center Project (24PHD-2). Thanks to the anonymous reviewers for many comments that have notably helped us improve the manuscript.

References

[1] N. Nciri, N. Kim, N. Cho, New insights into the effects of styrene-butadiene-styrene polymer modifier on the structure, properties, and performance of asphalt binder: the case of AP-5 asphalt, Mater. Chem. Phys. 193 (2017) 477–495.
[2] A. Schaur, S. Unterberger, R. Lackner, Impact of molecular structure of SBS on thermomechanical properties of polymer modified bitumen, Eur. Polym. J. 96 (2017) 256–265.
[3] J. Zhu, B. Birgisson, N. Kringos, Polymer modification of bitumen: Advances and challenges, Eur. Polym. J. 54 (2014) 18–38.
[4] A. Behnood, M. Modiri Gharehveran, Morphology, rheology, and physical properties of polymer-modified asphalt binders, Eur. Polym. J. 112 (2019) 766–791.
[5] S. Wang, W. Huang, A. Kang, Laboratory evaluation of the properties of high-cured crumb rubber modified asphalt containing sulfur and polymer after the oxidative aging procedure, Constr. Build. Mater. 304 (2021) 124611.
[6] L. Zhang, M. Shan, C. Xing, Y. Cui, P. Wang, M. Liu, Mechanism of physical hardening on the fracture characteristics of polymer-modified asphalt binder, Constr. Build. Mater. 409 (2023) 134091.
[7] X. Xiong, A. Meng, J. Lu, Y. Tan, B. Chen, J. Tang, C. Zhang, S. Xiao, J. Hu, Automatic detection and location of pavement internal distresses from ground penetrating radar images based on deep learning, Constr. Build. Mater. 411 (2024) 134483.
[8] G. Wen, Y. Zhang, Y. Zhang, K. Sun, Y. Fan, Rheological characterization of storage-stable SBS-modified asphalts, Polym. Test. 21 (2002) 295–302.
[9] M. Liang, X. Xin, W. Fan, S. Ren, M. Liang, J. Shi, Effects of polymerized sulfur on rheological properties, morphology and stability of SBS modified asphalt, Constr. Build. Mater. 150 (2017) 860–871.
[10] L. Geng, Y. Liu, Q. Xu, F. Han, X. Yu, T. Qin, Development of bio-based stabilizers and their effects on the performance of SBS-modified asphalt, Constr. Build. Mater. 271 (2021) 121889.
[11] W. Huang, N. Tang, Characterizing SBS modified asphalt with sulfur using multiple stress creep recovery test, Constr. Build. Mater. 93 (2015) 514–521.
[12] J.S. Chen, C.C. Huang, Fundamental characterization of SBS-modified asphalt mixed with sulfur, J. Appl. Polym. Sci. 103 (2007) 2817–2825.
[13] F. Zhang, J. Yu, S. Wu, Effect of ageing on rheological properties of storage-stable SBS/sulfur-modified asphalts, J. Hazard. Mater. 182 (2010) 507–517.
[14] N. Tang, W. Huang, G. Hao, Effect of aging on morphology, rheology, and chemical properties of highly polymer modified asphalt binders, Constr. Build. Mater. 281 (2021) 122595.
[15] G. Hao, W. Huang, J. Yuan, N. Tang, F. Xiao, Effect of aging on chemical and rheological properties of SBS modified asphalt with different compositions, Constr. Build. Mater. 156 (2017) 902–910.
[16] F. Dong, P. Yang, X. Yu, M. Jiang, S. Wang, Y. Zu, B. Chen, J. Wang, Morphology, chemical reaction mechanism, and cross-linking degree of asphalt binder modified by SBS block co-polymer, Constr. Build. Mater. 378 (2023) 131204.
[17] L. Shao, Z.Y. Ji, J.Z. Ma, C.H. Xue, Z.L. Ma, J. Zhang, The synergy of double cross-linking agents on the properties of styrene butadiene rubber foams, Sci. Rep. 6 (1) (2016) 15.
[18] J. Zhang, M.S. Sakhaeifar, D.N. Little, Characterisation of rheological properties of sulfur-extended asphalt with/without crumb rubber, Int. J. Pavement Eng. 23 (2022) 1491–1499.
[19] Y. Zhang, G. Richard S, C. Kookheon, P. Jeffrey, Recent advances in the polymerization of elemental sulphur, inverse vulcanization and methods to obtain functional Chalcogenide Hybrid Inorganic/Organic Polymers (CHIPs), Polym. Chem. 10 (2019) 4078–4105.
[20] I. Gawel, F. Czechowski, J. Kosno, An environmental friendly anti-ageing additive to bitumen, Constr. Build. Mater. 110 (2016) 42–47.
[21] J. Yu, P. Feng, H. Zhang, S. Wu, Effect of organo-montmorillonite on aging properties of asphalt, Constr. Build. Mater. 23 (2009) 2636–2640.
[22] Z.J. Zhao, S. Xu, W.F. Wu, J.Y. Yu, S.P. Wu, The Aging Resistance of Asphalt Containing a Compound of {LDHs} and Antioxidant, Pet. Sci. Technol. 33 (2015) 787–793.
[23] R. Li, F. Xiao, S. Amirkhanian, Z. You, J. Huang, Developments of nano materials and technologies on asphalt materials – A review, Constr. Build. Mater. 143 (2017) 633–648.
[24] Y. Tan, J. Zhang, G. Zou, H. Qin, Aging characterization of rheology and morphology evolution of SBS-modified asphalt, Constr. Build. Mater. 342 (2022) 128027.
[25] ASTM D1754, Standard Test Method for Effects of Heat and Air on Asphaltic Materials (Thin-Film Oven Test),ASTM International, West Conshohocken, PA, 2020.
[26] ASTM D6521, Standard Practice for Accelerated Aging of Asphalt Binder Using a Pressurized Aging Vessel (PAV), ASTM International, West Conshohocken, PA, 2022.
[27] ASTM D5, Standard Test Method for Penetration of Bituminous Materials, ASTM International, West Conshohocken, PA, 2006.
[28] ASTM D36, Standard Test Method for Softening Point of Bitumen (Ring-and-Ball Apparatus),ASTM International, West Conshohocken, PA, 2006.
[29] ASTM D113, Standard Test Method for Ductility of Asphalt Materials, ASTM International, West Conshohocken, PA, 2017.
[30] ASTM D4402, Standard Test Method for Viscosity Determination of Asphalt at Elevated Temperatures Using a Rotational Viscometer, ASTM International, West Conshohocken, PA, 2006.
[31] M.R. Islam, D. Salomon, N.M. Wasiuddin, Investigation of oxidative aging of field-extracted asphalt binders at various conditions using carbonyl index, Constr. Build. Mater. 415 (2024) 134969.
[32] W.H. Daly, I. Negulescu, S.S. Balamurugan, Implementation of GPC characterization of asphalt binders at Louisiana materials laboratory, Department of Chemistry,Louisiana State University, Baton Rouge, LA, 2013.
[33] N.I. Nur, E. Chailleux, G.D. Airey, A comparative study of the influence of shift factor equations on master curve construction, Int. J. Pavement Res. Technol. 4 (2011) 324–336.

[34] N.I.M. Yusoff, M.T. Shaw, G.D. Airey, Modelling the linear viscoelastic rheological properties of bituminous binders, Constr. Build. Mater. 25 (2011) 2171–2189.
[35] S.M. Asgharzadeh, N. Tabatabaee, K. Naderi, M.N. Partl, Evaluation of rheological master curve models for bituminous binders, Mater. Struct. 48 (2015) 393–406.
[36] J. Zhang, F. Guo, H. Lv, R. Zhuo, Y. Tan, Characterization of Phase Structure and Performance Degradation of Aged SBS-Modified Asphalt, J. Mater. Civ. Eng. 36 (2024) 4024061.
[37] Z. Chen, H. Zhang, H. Duan, C. Wu, Determination of time-temperature superposition relationship of SBS modified asphalt based on special rheological phenomenon caused by SBS-formed structure in asphalt matrix, Constr. Build. Mater. 260 (2020) 119835.
[38] J. Zhang, Y. Tan, Rheology, morphology and phase behavior of SBS/sulfur modified asphalt based on experimental assessment and molecular dynamics, Int. J. Pavement Eng. (2022) 1–13.
[39] J. Lin, J. Hong, J. Liu, S. Wu, Investigation on physical and chemical parameters to predict long-term aging of asphalt binder, Constr. Build. Mater. 122 (2016) 753–759.
[40] F. Wang, Y. Xiao, P. Cui, J. Lin, M. Li, Z. Chen, Correlation of asphalt performance indicators and aging Degrees: A review, Constr. Build. Mater. 250 (2020) 118824.
[41] W. Hong, L. Mo, C. Pan, M. Riara, M. Wei, J. Zhang, Investigation of rejuvenation and modification of aged asphalt binders by using aromatic oil-SBS polymer blend, Constr. Build. Mater. 231 (2020) 117154.
[42] H.A. Khonakdar, U. Wagenknecht, S.H. Jafari, R. Hässler, H. Eslami, Dynamic mechanical properties and morphology of polyethylene/ethylene vinyl acetate copolymer blends, Adv. Polym. Technol. 23 (2004) 307–315.
[43] Y.L. Zhao, F. Gu, X.M. Huang, Analysis on SBS modified asphalt aging characterization based on fourier transform infrared spectroscopy, J. Build. Mater. 14 (2011) 620–623.
[44] Z. Li, B. Li, Y. Zhang, C. Fa, Z. Zhao, Y. Yu, Rheological Property and Surface Structure of SBS Compound Modified Asphalt with Nano Sulfur, J. Mater. Sci. Eng. 38 (2020) 425–430.
[45] P.R. Herrington, B. James, T.F.P. Henning, Effect of concentration on the rate of formation of carbonyl compounds during oxidation of roading bitumen, Fuel 322 (2022) 124133.
[46] L. Sun, Y. Wang, Y. Zhang, Aging mechanism and effective recycling ratio of SBS modified asphalt, Constr. Build. Mater. 70 (2014) 26–35.
[47] C. Yan, W. Huang, J. Ma, J. Xu, Q. Lv, P. Lin, Characterizing the SBS polymer degradation within high content polymer modified asphalt using ATR-FTIR, Constr. Build. Mater. 233 (2020) 117708.
[48] X. Ye, Study on compatibility systems and related rheological behaviors in the preparation process of high content SBS modified asphalt (In Chinese), East China University of Science and Technology, Shanghai, 2020.
[49] P. Lin, W. Huang, Y. Li, N. Tang, F. Xiao, Investigation of influence factors on low temperature properties of SBS modified asphalt, Constr. Build. Mater. 154 (2017) 609–622.
[50] M. Mousavi, E.H. Fini, Phenolic compounds to amplify the effect of sulfur on Bitumen's thermomechanical properties, Fuel 287 (2021) 119532.
[51] J.J. Griebel, R.S. Glass, K. Char, J. Pyun, Polymerizations with elemental sulfur: A novel route to high sulfur content polymers for sustainability, energy and defense, Prog. Polym. Sci. 58 (2016) 90–125.
[52] A. Martínez-Estrada, A.E. Chávez-Castellanos, M. Herrera-Alonso, R. Herrera-Nájera, Comparative study of the effect of sulfur on the morphology and rheological properties of SB- and SBS-modified asphalt, J. Appl. Polym. Sci. 115 (2010) 3409–3422.

Evolution of Phase Structure and Mechanical Properties in Aged SBS-Modified Asphalt

Junjie Zhang, Yiqiu Tan*

The authors' information is shown as follows.

Junjie Zhang: School of Transportation Science and Engineering, Harbin Institute of Technology, Huanghe Road, Nangang District, Harbin 150001, China; School of Civil Engineering and Transportation, South China University of Technology, Wushan Road, Tianhe District, Guangzhou 510000, China; junjiezhang@hit.edu.cn

Yiqiu Tan*: School of Transportation Science and Engineering, Harbin Institute of Technology, Huanghe Road, Nangang District, Harbin 150001, China; State Key Laboratory of Urban Water Resource and Environment, Harbin Institute of Technology, Huanghe Road, Nangang District, Harbin 150001, China; tanyiqiu@hit.edu.cn

ABSTRACT: Although previous studies have broadly explored the aging process of Styrene-Butadiene-Styrene (SBS)-modified asphalt, there is still a lack of understanding regarding the precise evolution patterns of its phase structure during aging, and whether aged SBS-modified asphalt retains its modified properties. or reverts to conventional asphalt. To fill these gaps, this paper focused on key performance characteristics that differentiate SBS-modified asphalt from conventional asphalt, including viscosity, elasticity, and toughness properties, evaluated how aging influences mechanical properties, and examined morphological changes at different aging stages. The effective method for phase structure characterization was ultimately established. Based on the results, it was found that mechanical property variations, especially in the toughness curve, effectively indicate the phase structure. The fracture strength σ_B and fracture elongation ε_B of SBS-modified asphalt after RTFOT aging 8 h closely match those of 70# base asphalt after RTFOT aging 8 h, with values of 1364.32 and 0.005, compared to 1421.07 and 0.007, respectively. This curve helps determine whether aged SBS-modified asphalt remains modified or reverts to conventional asphalt. Aging primarily affects instantaneous elastic deformation, with minimal impact on delayed elastic deformation. Morphological analysis supports

these findings, showing that SBS polymer degradation precedes significant network disruption, and increased toughness results mainly from SBS polymer presence.

KEYWORDS: SBS-modified asphalt; phase structure; mechanical properties; toughness and tenacity; aging behavior.

1 INTRODUCTION

Although SBS-modified asphalt performs better excellent properties compared to conventional asphalt, such as better elasticity **(Behnood et al. 2016)**, greater ductility **(Kök et al. 2012)**, and better high- and low-temperature performance **(Mokhtari and Nejad 2012)**, etc., there is still a question mark over whether SBS-modified asphalt can maintain such excellence after aging. In other words, it remains uncertain whether aged SBS-modified asphalt retains its characteristics as a modified asphalt or reverts to conventional asphalt. Even though past studies largely discussed the aging behavior of SBS-modified asphalt **(Chen et al. 2022)**, the performance degradation patterns and phase evolution behavior of SBS-modified asphalt during aging remain inadequately explained. Generally, the phase behavior dominates the macroscopic properties of polymer-modified asphalt, different phase structures can endow materials with different mechanical properties **(Wu et al. 2016)**. It is crucial to understand the transformation of phase behavior in SBS-modified asphalt during the aging time.

Understanding the changes in the phase structure of aged SBS-modified asphalt aids in recognizing different aging states, revealing degradation patterns, and providing practical guidance for pavement maintenance and asphalt rejuvenation. Although past studies broadly discussed the phase structure of SBS-modified asphalt **(Airey 2002)**, it is still uncertain evolution patterns of phase structure during the aging process, one major concern revolves around the confusion regarding the concept of phase structure. Phase structure is often regarded as a multidimensional concept with multiple dimensions and aspects **(Jiang et al. 2018)**, encompassing morphological structure, material structure, chemical structure, mechanical properties, rheological characteristics, etc., these aspects have been extensively studied in many researches. For instance, Zhao et al. **(2011)** investigated phase structure change by chemical analysis and discovered that the aging rate of SBS-modified asphalt was much lower than the aging rate of both SBS

copolymer and base asphalt individually. Wang et al. **(2017)** evaluated the phase structure of SBS-modified asphalt by phase morphology. They concluded that the existing rejuvenation method could not restore the initial phase structure of SBS-modified asphalt. Kaya et al. **(2019)** analyzed the phase structure after long-term aging through the perspective of viscoelastic behavior. It can be found that different testing methods have been employed to investigate the phase structure, however, there has been a lack of comprehensive explanations regarding the evolution of phase structure during aging and its corresponding relationship with performance degradation. For instance, Phase morphology can directly reflect phase structure but does not provide any information regarding performance variations. Rheological methods have a strong correlation with phase structure, but there is still a lack of direct indicators specifically related to phase structure among the numerous rheological parameters. Currently, there is a lack of well-established and highly discriminating phase structure characterization methods for SBS-modified asphalt that can effectively capture the degradation patterns of its properties during aging.

The incorporation of SBS copolymer into asphalt leads to a more diverse and complex phase structure in SBS-modified asphalt **(Chen et al. 2021a)**. Hence, in contrast to the examination of aging in base asphalt, many research efforts have focused on SBS modifier degradation or the interaction between SBS and asphalt when investigating the aging of SBS-modified asphalt, such as Wei et al. **(2019)** attempted to extract SBS modifier from aged SBS-modified asphalt for separate study. Chen et al. **(2021b)** analyzed the aging mechanism of SBS-modified asphalt, proposing multi-dimensional nanomaterials to enhance thermo-oxidative and UV aging resistance. Yu et al. **(2021)** confirmed intensified competition between asphaltenes constituents and SBS polymers during aging through molecular simulations. These studies highlight the unique aging process of SBS-modified asphalt, However, they have not definitively addressed whether aged SBS-modified asphalt eventually becomes akin to base asphalt, the timing of this transition, and its dynamic evolution. From a rheological perspective, Wu et al. **(2009)** demonstrated that ultimately, aged SBS-modified asphalt aligns closely with base asphalt characteristics. Apart from rheological behavior, SBS-modified asphalt shows significant differences from base asphalt in other aspects such as higher viscosity **(Jasso et al. 2015)**, better elasticity, and more excellent toughness **(Xu et al. 2022a)**.

The challenge lies in selecting suitable methods for characterizing phase transitions to precisely capture distinct attributes during various aging phases. Based on the yield and fracture theories of polymers **(Ward and Sweeney 2012)**, the stress-strain curve of polymer materials can be classified into six categories (**Figure 1**), such as: a) brittle and weak; b) soft and weak; c) soft and tough; d) brittle and hard; e) strong and hard; f) tough and hard, different stress-strain curve shapes can provide insights into various mechanical properties of polymers, including high/low modulus, high/low strength, high/low toughness, etc., such as brittle plastics (small strain) **(Guan et al. 2020)**, elastic rubber (large strain) **(Diab and You 2017),** and ductile materials (high stress and strain) **(Seiler et al. 2020)**. The mechanical curve can visually describe the mechanical failure criteria of SBS-modified asphalt after service and degradation, such as stress fractures, hysteresis, etc., In our prior research **(Tan et al. 2022)**, a strong correlation has been established between the mechanical response and the performance deterioration behavior of SBS-modified asphalt during the aging process. Therefore, it is a feasible approach by mechanical curves to depict the evolution of phase structure and performance degradation.

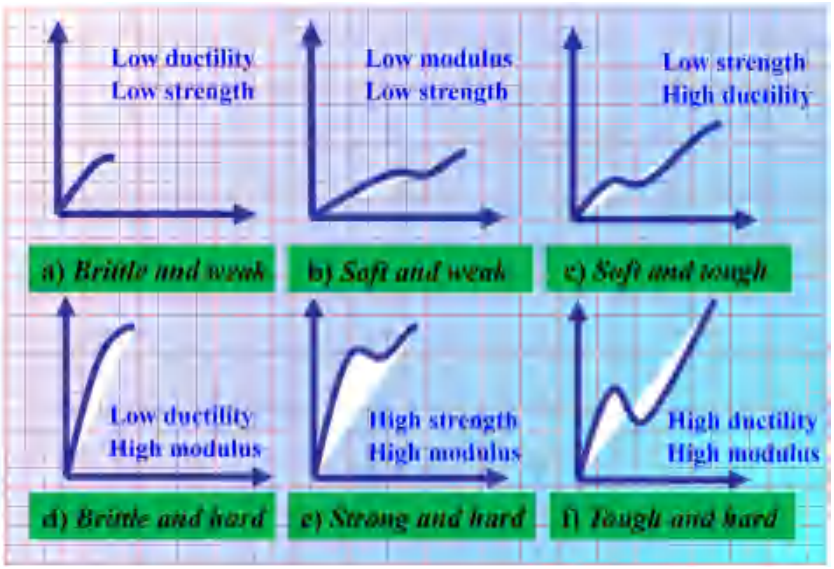

Figure 1 Stress-strain curve of polymer materials

In summary, many questions regarding SBS-modified asphalt's aging process remain unresolved. The precise transformation patterns of phase structure and the degradation trends of performance during aging remain unclear. Whether SBS-modified asphalt reverts to its original state akin to conventional asphalt or undergoes distinct degradation patterns in properties like viscosity, elasticity, and toughness is yet to be fully ascertained. These property changes vary based on aging

conditions. Moreover, a lack of precise methods for characterizing phase structure transformations exists. To address these issues, this study comprehensively examined the impact of aging on various viscoelastic properties, mechanical failure, and morphological changes at different aging stages. The outcomes contribute to a better comprehension of phase evolution in aged SBS-modified asphalt and foster the development of a stable phase structure.

2 OBJECTIVES AND SCOPE

The objectives of this paper are:

1) Propose a simple, accurate, and distinguishable characterization method for tracking the phase structure transitions of SBS-modified asphalt during aging.
2) Differentiate between diverse mechanical states of SBS-modified asphalt as it ages, encompassing viscous flow, viscoelasticity, and viscous-toughness states.
3) Combine morphological changes to analyze the reasons behind the transitions in different mechanical states of SBS-modified asphalt during aging.

3 MATERIALS AND EXPERIMENTAL SCHEDULE

3.1 Materials

70# base asphalt and SBS-modified asphalt (I-D) were used in this paper so that the performance of aged SBS-modified asphalt can be compared with 70# base asphalt. SBS-modified asphalt (I-D) was produced using 70# base asphalt, linear-shaped SBS 1301, and stabilizer. SBS 1301 is supplied by Yanshan Petrochemical Co., Ltd, a linear copolymer with an average molecular weight of 100,000 g/mol and 30 wt.% styrenes. Elemental sulfur derived from a commercial product was employed as a stabilizer to add to SBS-modified asphalt to achieve chemical cross-linking. The technical characterization of 70# asphalt is shown in **Table 1**, and the main properties of SBS-modified asphalt (I-D) are listed in **Table 2**.

Table 1 Characterization of 70# base asphalt

Property	Results	Limit value	Specification
Penetration at 25°C (0.1mm)	65	60~80	ASTM D5 **(ASTM 2005)**
Softening point (R&B, °C)	48	⩾43	ASTM D36 **(ASTM 2006a)**

Ductility at 15°C (cm)		> 100	⩾40	ASTM D113 **(ASTM 2017a)**
Viscosity at 60°C (Pa·s)		310	⩾160	ASTM D4402 **(ASTM 2006b)**
RTFOT (163℃, 85min)	Mass loss (%)	-0.05	±0.8	ASTM D6 **(ASTM 2018a)**
	Residual penetration ratio (%)	78.6	⩾54	ASTM D243 **(ASTM 2008)**
	Residual ductility at 10℃ (cm)	9	⩾4	ASTM D113 **(ASTM 2017a)**
SARA fractions	Saturate (%)	17.62	/	AASHTO T164 **(AASHTO 2014)**
	Aromatics (%)	41.25		
	Resin (%)	25.73		
	Asphaltene (%)	15.41		

Table 2 The main properties of SBS-modified asphalt (I-D)

Property		Results	Limit value	Specification
Penetration at 25°C (0.1mm)		59	40~60	ASTM D5 **(ASTM 2005)**
Softening point (R&B, °C)		78	⩾60	ASTM D36 **(ASTM 2006a)**
Ductility at 5°C (cm)		44	⩾20	ASTM D113 **(ASTM 2017a)**
Elastic restitution at 25°C (%)		92	⩾75	ASTM D6084 **(ASTM 2010)**
Kinematic viscosity (Pa·s)	165℃	0.517	/	ASTM D2170 **(ASTM 2007)**
	135℃	1.931	⩽3	
RTFOT (163℃, 85min)	Mass loss (%)	-0.212	±1.0	ASTM D6 **(ASTM 2018)**
	Residual penetration ratio (%)	82	⩾65	ASTM D243 **(ASTM 2018)**
	Residual ductility at 5℃ (cm)	32	⩾15	ASTM D113 **(ASTM 2017a)**

3.2 Sample preparation

In practical engineering applications, SBS-modified asphalt typically contains 5% SBS content. Therefore, 5% SBS content was also employed in this study to match practical conditions. SBS-modified asphalt was prepared by a high-speed

emulsification shearing machine and a mechanical stirrer. High-speed shearing is applied to achieve optimal particle size for SBS modification and swelling, while mechanical mixing ensures even dispersion, preventing segregation. The preparation process of SBS-modified asphalt aligns with our previous team research **(Tan et al. 2022; Zhang and Tan 2022)**.

The specific steps are as follows:

1) 70# base asphalt, and 5 wt.% liner-shaped SBS 1301 were sheared at a speed of 4000 rpm for 0.5 hours at 180°C so that the SBS copolymer could achieve the desired particle.

2) After that, the materials were stirred mechanically with a stirring rate of 500 rpm at 180°C for 1 hour. The mechanical stirring aids in further swelling and dispersing the SBS copolymer within the asphalt, enhancing the modification effect.

3) Adding 0.15 wt.% stabilizers and mixing continuously for 1.5 hours at 180°C, the addition of stabilizers demands adequate time to facilitate cross-linking reactions between the SBS modifier and the base asphalt binder.

Figure 2 represents the preparation process.

Figure 2 The process of sample preparation

3.3 Experimental schedule

The rolling thin film oven test (RTFOT) and pressure aging vessel (PAV) test are commonly used to simulate short-term and long-term aging. This paper focuses on the influence of the aging process on the viscoelasticity phase behavior of SBS-modified asphalt and does not refer to the comparison of different aging methods. According to Tian et al.'s research, RTFOT and 5 h PAV can achieve the same aging effect **(Tian et al. 2021)**. Therefore, the RTFOT delayed aging method was developed to simulate the

aging process in the study. The specific information can be described as follows: The samples were placed in the rolling thin film oven at 180°C for 2 h, 4 h, 6 h, and 8 h, respectively. The airflow was 5000 ml/min ± 200ml/min, so the specimens with a different aging degree were produced.

Traditionally, SBS-modified asphalt has been recognized for its higher viscosity, improved elasticity, and greater tenacity compared to conventional asphalt. Thus, phase structure evolution was evaluated from those prominent features to establish a connection between microstructure and mechanical properties. The transformations of viscous, viscoelastic, and viscosity-toughness states at different aging times were analyzed and characterized.

4 METHODS

4.1 Rotational viscosity test

The rotational viscosity was tested to evaluate the viscous behavior of SBS-modified asphalt at different aging stages by a rotational viscometer (RV). Six test temperatures (115°C, 125°C, 135°C, 145°C, 155°C, 165°C) were determined to explore the high-temperature phase behavior and temperature susceptibility of SBS-modified asphalt. The test was conducted following ASTM D 4402 **(ASTM 2015a)**, and the torque measures rotational viscosity at a fixed temperature. The viscosity-temperature curve can also be obtained by a modified Refutas curve **(ASTM 2017b)**. The equation can be described as follows:

$$\log\log(\eta) = n - VTS\log(T) \tag{1}$$

Where: η is the viscosity of SBS modified asphalt; n is the regression coefficient; VTS is the slope of the regression line, represents the temperature sensitivity; T means the test temperature, °C.

4.2 Elastic recovery test

The elastic recovery test was employed to investigate the change of elongation and elastic recovery rate of SBS-modified asphalt in different aging times, which was conducted by ductilimeter according to ASTM D 6084 **(ASTM 2010).** To better evaluate and distinguish the elastic recovery properties at the different aging times, the asphalt samples were soaked in water at 25°C for 1 h. Then the specimens were pulled at a constant speed of 5 cm/min to 10 cm distance and held for 10 min. After

that, the asphalt binders were cut in the middle of the samples and selected 14 points in time (1 min, 2 min, 5 min, 10 min, 15 min, 20 min, 25 min, 30 min, 35 min, 40 min, 45 min, 50 min, 55 min, 60 min) to measure the elastic recovery properties. The elongation and elastic recovery rate were calculated by the following equations:

$$ER = \frac{10 - x}{10} \times 100\% \tag{2}$$

Where x represents the remaining length of the asphalt sample, cm; ER (elastic recovery) is the elongation, which means the percentage of return to initial condition after elongation, %.

$$ERR = \frac{ER_2 - ER_1}{t_2 - t_1} \tag{3}$$

Where ERR (elastic recovery rate) is the average rate of elastic recovery change in the times of t_1 to t_2, %/min; ER_1, ER_2 are the corresponding elongation to the measurement time of t_1 and t_2, %, respectively; t_1, t_2 are the selected time points, min.

4.3 Dynamic shear rheometer (DSR) test

Dynamic shear rheometer test was employed to investigate the viscoelastic phase behavior of SBS-modified asphalt by dynamic mechanical analysis. Temperature sweeps were conducted at a constant frequency of 1.592 Hz at a temperature range from -10°C to 70°C with an interval of 10°C, a fixed strain of 0.1% was selected within the linear viscoelastic, and 8 mm parallel plate geometry with a gap of 2 mm were used from -10°C to 30°C, 25 mm parallel plate geometry with a gap of 1 mm were determined from 40° to 70°C, the detailed test procedures were based on ASTM D 7175 **(ASTM 2015b)**.

4.4 Multiple stress creep recovery test

A dynamic shear rheometer was also employed to perform the multiple stress creep recovery (MSCR) tests. The test was conducted at 64°C, and two types of stress (0.1, 3.2 kPa) were used for the test. The loading process contained 20 cycles (10 cycles at 0.1 kPa, 10 cycles at 3.2 kPa), and every cycle included 1 s creep and 9 s recovery by ASTM D 7405 **(ASTM 2015c)**. Traditionally, the MSCR test was used to evaluate the high-temperature performance of asphalt binder and two parameters, including the percent recovery and non-recoverable creep. As shown in **Figure 3**, two parameters can be calculated by equations (1) and (2). In this paper, Burger's model was also used to fit the test results for better evaluating the elastic

recovery properties.

$$R = \frac{\varepsilon_p - \varepsilon_u}{\varepsilon_p} \times 100\% \tag{4}$$

$$J_{nr} = \frac{\varepsilon_u}{\sigma} \tag{5}$$

Where R is the percent recovery, %; J_{nr} is non-recoverable creep, kPa^{-1}; ε_p, ε_u represents the peak and unrecovered strain in each cycle, and σ means the stress level, 0.1 or 3.2 kPa in the test.

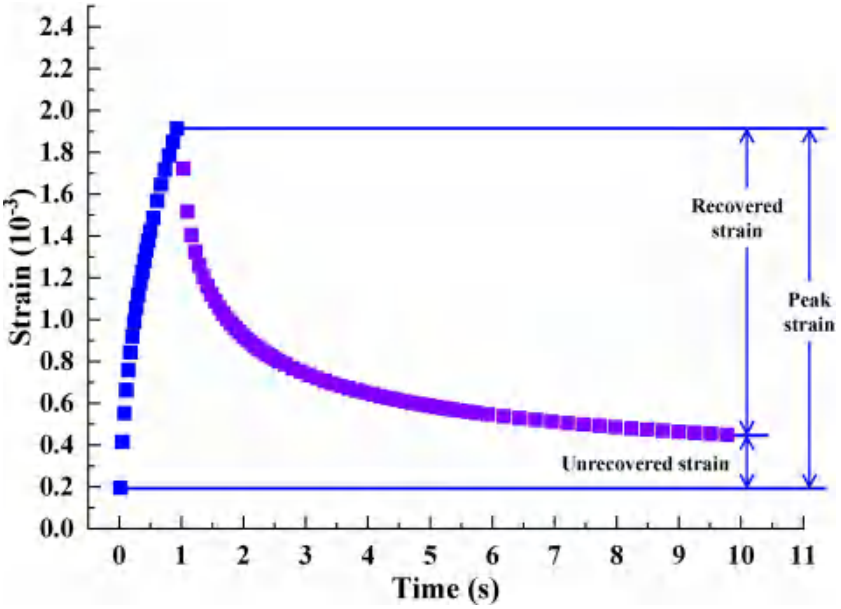

Figure 3 creep and recovery in one cycle

Burger's model can be expressed as follows:

$$\frac{\varepsilon(t)}{\sigma_0} = \frac{1}{E_1} + \frac{t}{\eta_1} + \frac{1}{E_2}(1 - e^{-E_2 t/\eta_2}) \tag{6}$$

Where $\varepsilon(t)$ is cumulative strain; σ_0 is the stress level, kPa; t is the loading time, s; E_1, η_1 are the elastic and damping coefficient in the Maxwell model; E_2, η_2 are the elastic and damping coefficient in the Kelvin model;

The total deformation in the creep test can be divided into three types: 1) instantaneous elastic deformation; 2) delayed elastic deformation; and 3) viscous deformation; which can be described as:

$$J(t) = J_e + J_v + J_{de} = \frac{1}{E_1} + \frac{t}{\eta_1} + \frac{1}{E_2}(1 - e^{-E_2 t/\eta_2}) \tag{7}$$

$$J_e' = \frac{J_e}{J_e + J_v + J_{de}} \tag{8}$$

$$J_v' = \frac{J_v}{J_e + J_v + J_{de}} \tag{9}$$

$$J_{de}' = \frac{J_{de}}{J_e + J_v + J_{de}} \tag{10}$$

$$V_r = \frac{J_v}{J_e + J_{de}} \tag{11}$$

Where $J(t)$ is the total creep compliance, kPa^{-1}; J_e, J_v, J_{de} are the instantaneous elastic compliance, the viscous compliance, and the delayed elastic compliance, kPa^{-1}, $J_e = 1/E_1$, $J_v = t/\eta_1$, $J_{de} = (1 - e^{-E_2 t/\eta_2})/E_1$; J_e', J_v', J_{de}' are the instantaneous elastic component, the viscous component, and the delayed elastic component, represents the percentage of total deformation, %; V_r is the ratio of the viscous compliance to the elastic compliance.

4.5 Toughness and tenacity test

A toughness and tenacity test was performed to analyze the viscosity-tenacity phase behaviors of SBS-modified asphalt during the different aging times. The experiment steps were conducted in line with the specification ASTM D 5801 **(ASTM 2017c)**. The details can be described as follows: the asphalt samples were conditioned in the oven at 80°C for 1 h, and then the samples (50g ± 1g) were poured into the test vessel for preparation. The samples (with the test vessel) were placed in a water bath at 25°C for 1.5 h. After that, the samples were stretched at 25°C with a 500 mm/min loading rate. The region area in the load-deformation curve can obtain two parameters: toughness and tenacity. As shown in **Figure 4**, the toughness and tenacity can be calculated by the following equations.

$$T_o = SA + SB \tag{12}$$

$$T_e = SB \tag{13}$$

Where T_o and T_e are the toughness and tenacity of the asphalt binder, respectively, N•m; SA and SB are the corresponding areas to the white part and shaded part in Figure 4, N•m;

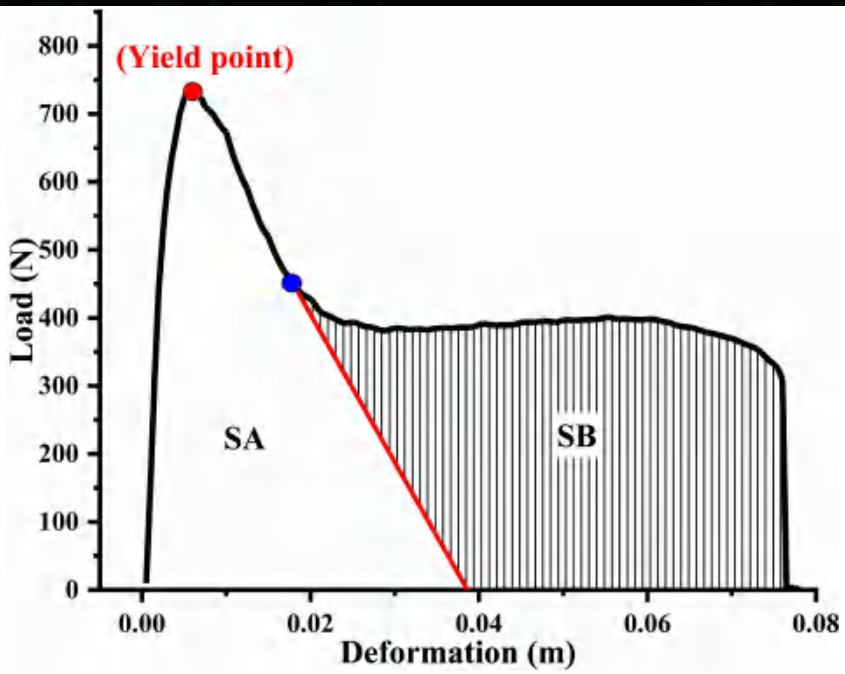

Figure 4 The load-deformation curve

4.6 Fluorescence microscope (FM) test

A fluorescence microscope test was used to analyze the morphology characterization of the phase structure of SBS-modified asphalt. To collect fluorescence images at various aging stages, a CSM-900E series fluorescence microscope was chosen. The dispersity, continuous, and discontinuous phases of SBS copolymer can be evaluated. SBS-modified asphalt was observed under a fluorescence microscope with 400 ×magnification, and hot-drop coverslips were used to manufacture the test samples.

Figure 5 shows the flowchart of experimental methods in this study.

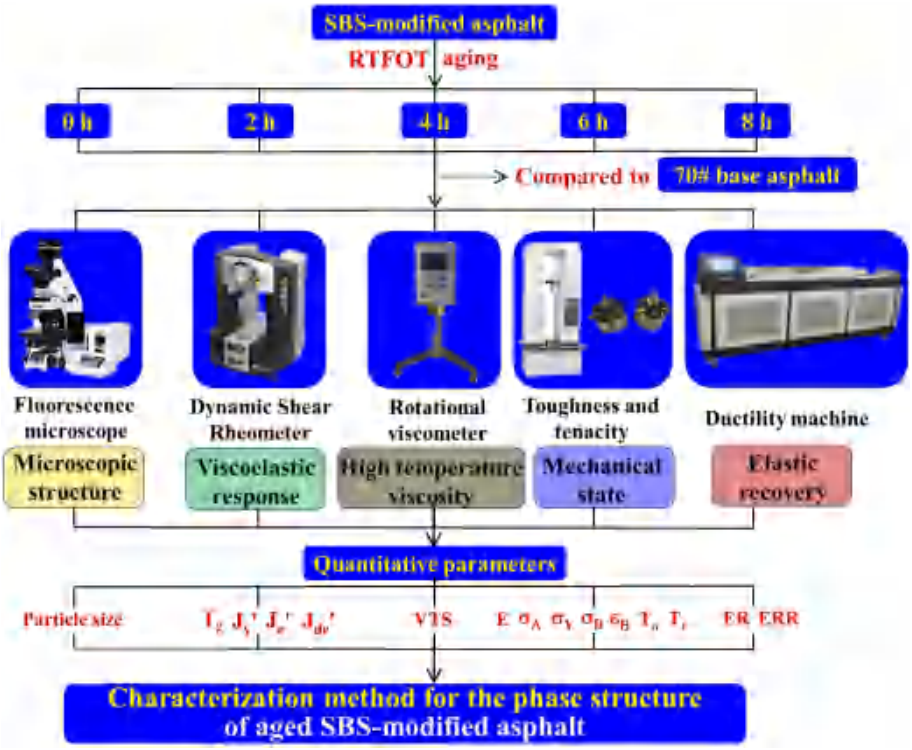

Figure 5 The flowchart of experimental methods

5 RESULTS AND DISCUSSION

5.1 Effect of aging behavior on the viscous flow properties

Viscosity plays a critical role in assessing the viscous flow properties of asphalt materials **(Ding et al. 2019)**. The viscosity-temperature curve significantly impacts asphalt paving, as demonstrated in **Figure 6**. It can be seen the viscosity decreases with the increased temperature, at the temperatures below 155°C, there were significant viscosity differences among various aging times, indicating a viscous state at temperatures exceeding 155°C or 165°C. The temperature susceptibility was also assessed in Figure 6b. VTS value (the scope of regression line) represented the temperature sensitivity of asphalt viscosity. Higher VTS values, represents by gentle lines, suggest lower temperature sensitivity in SBS-modified asphalt. Liang et al. **(2022a)** also reported a similar finding, they analyzed the viscosity behavior of aged SBS-modified asphalt at various temperatures using the Arrhenius equation to calculate activation energy (E_a). The increasing E_a with aging indicates reduced temperature sensitivity, signifying the need for more energy to overcome heightened polarity and intermolecular forces among asphalt molecules due to aging. Besides the reduced temperature sensitivity after aging, examining the specific VTS values

reveals further details. VTS values at aging times of 0 h, 2 h, and 4 h were -1.191, -1.192, and -1.188, respectively, while the VTS values after 6 h are much higher than those at earlier aging times. The results showed distinct aging stages in SBS-modified asphalt in terms of the viscosity-temperature curve.

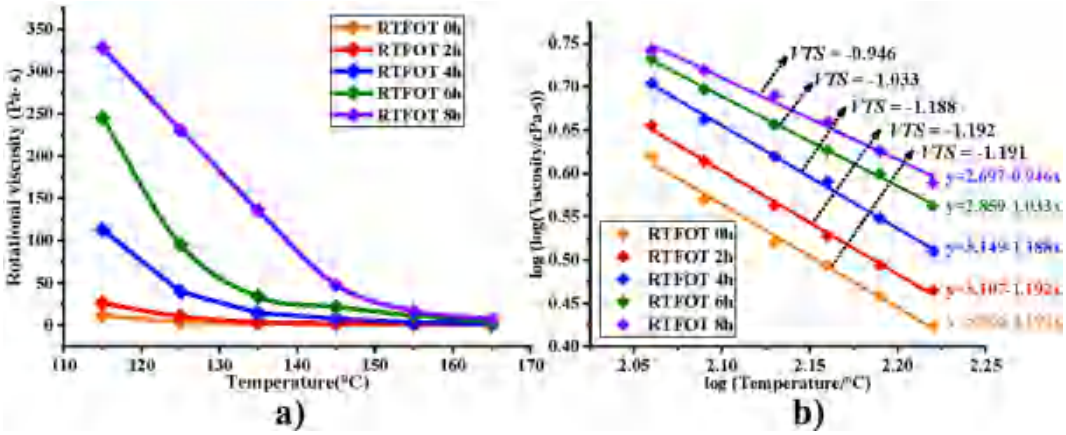

Figure 6 Rotational viscosity test: a) viscosity; b) temperature susceptibility

Generally, the viscosity change of SBS-modified asphalt after aging can be attributed to two main reasons **(Zhang et al. 2010)**: the changes in asphalt composition and the degradation of SBS copolymer. More asphaltenes and resins after aging can increase the viscosity, while the lower molecular weight caused by the degradation of SBS copolymer will decrease the viscosity results. The VTS values enhanced considerably after RTFOT 6h, which indicated the degradation of SBS copolymer could not show a predominant role at this aging stage. These results can also be gained elsewhere **(Yan et al. 2019)**. Although SBS copolymer and asphalt binder can protect each other under aging behavior **(Wei et al. 2019)**, the degradation of SBS copolymer might exist in the early aging stage.

5.2 Effect of aging behavior on the viscoelastic properties

To investigate the difference in viscoelastic properties of SBS-modified asphalt at various aging time, **Figure 7** represent the black diagrams (G* vs δ) and cole-cole diagrams (G'' vs G') of aged SBS-modified asphalt, both the black and cole-cole diagrams can well describe the viscoelastic response without the effect of temperature or frequency. It can be seen from **Figure 7a** that when the phase angle falls below 35°, the differences in complex modulus among different aging stages are not distinct, lower phase angles indicate better elasticity and worse viscosity. A lower phase angle corresponds to lower testing temperatures. As the phase angle increases, which indicates high-temperature testing, the specimen shows higher viscosity and a smaller

complex modulus, making the distinction more pronounced. Additionally, there is an obvious "plateau region" of SBS-modified asphalt before aging, which can be ascribed to the contribution of a polymer network in SBS-modified asphalt **(Airey 2002)**. With the increase of aging time, the curve shows the left shifts in black diagrams. The plateau region initially exists but becomes blurry gradually after RTFOT 2 h, and the shifting degree after RTFOT 2 h is also more significant, which indicates there exist different aging rates in aged SBS-modified asphalt. **Figure 7b** illustrates the results of cole-cole diagrams, The loss modulus (viscous modulus) is higher than the storage modulus (elastic modulus) at most of the test temperature range, which indicates the loss modulus has the leading function at this temperature range, and SBS-modified asphalt primarily shows viscosity. When the ratio of G'' to G' is less than 1, which represents SBS-modified asphalt has excellent deformation recovery properties **(Shi et al. 2022)**, on the contrary, SBS-modified asphalt is close to a viscous flow state when the ratio is more than 1. The curve shifts to the dividing line with the increasing aging time, which indicates that aging behavior improved the elasticity and decreased the viscosity, and the deformation capacity and stress relaxation were diminished.

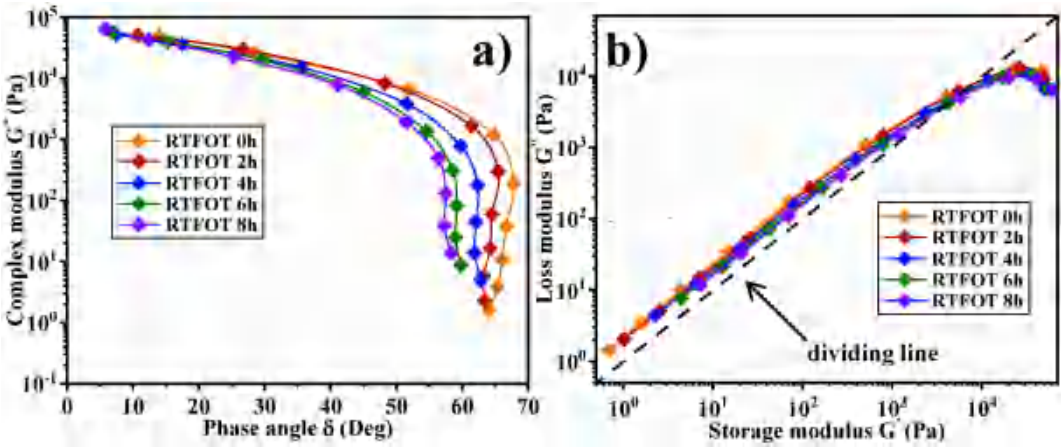

Figure 7 The rheological results: a) black diagram; b) cole-cole diagram

The high-temperature phase behavior has been described by the viscous flow properties, while the low-temperature phase behavior of SBS-modified asphalt after aging also equally deserves our attention. The glass transition temperature (T_g) is the critical temperature during the transformation of the viscoelastic state with temperature, which has rich physicochemical significance and can characterize the low-temperature performance of asphalt materials **(Laukkanen et al. 2018)**. Below the temperature (T_g), SBS-modified asphalt loses its viscoelastic properties and

behaves as a brittle material with high modulus., According to ASTM E1640 **(ASTM 2018b),** three methods including the storage modulus G', the loss modulus G'', and the loss factor tanδ can be employed to determine the T_g temperature by the dynamic mechanical analysis (DMA), and the peak value of storage modulus was most popularly used and greater clarity. **Figure 8** shows the dynamic mechanical temperature spectrum at different aging times, both the storage modulus G' and loss modulus G'' increased with the raising aging time, and the curve of loss modulus shifts to the right. The loss factor tanδ can be regarded as the ratio of the viscous modulus G'' to elastic modulus G', so the decreased loss factor indicates the worse viscosity and the better elasticity.

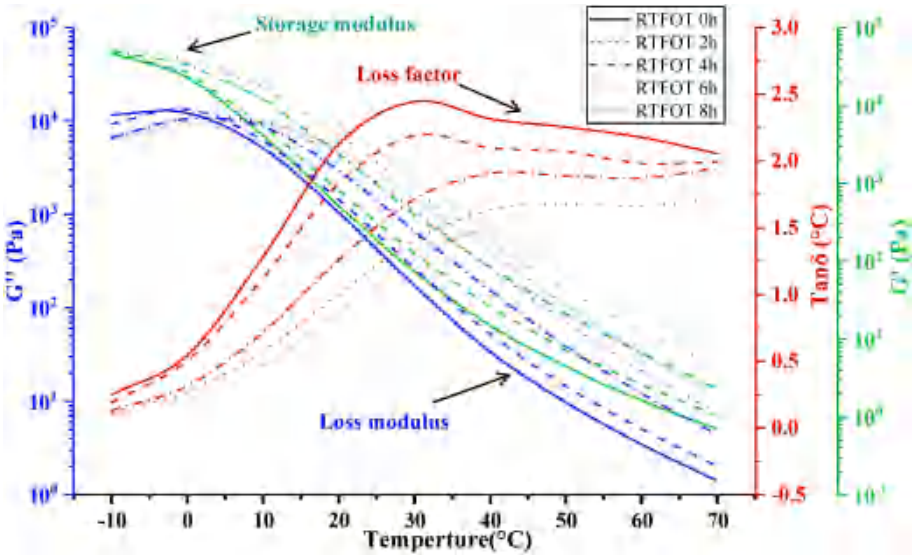

Figure 8 Dynamic mechanical temperature spectra

Figure 9 represents the T_g temperature at different aging times by the loss modulus, the rising T_g temperature indicated the decrease of stiffness and toughness, accompanied by the deterioration of low-temperature performance. Past studies reported that T_g temperature of SBS-modified asphalt reduced after adding rubber processing oil due to the replenishment of saturate and aromatic **(Lin et al. 2017)**. Thus, one of the primary reasons for the decline in the T_g temperature during aging can be attributed to the diminished presence of lighter components. It can be seen from **Figure 9** that the values of T_g temperature at different aging times (RTFOT 0 h ~ 8 h) are -3.2°C, -1.1°C, 3.1°C, 5.2°C and 6.8°C, the values of the T_g temperature exhibits significant jumps at the range of RTFOT 4 h to 6 h. According to the mixing rule ($T_g^{new} = W^A T_g^A + W^B T_g^B$, W represents the weight, %) **(Lin et al. 2021)**, the application of SBS copolymer into asphalt could decrease the T_g temperature due to

the absorption of maltene, while the SBS copolymer dissociated and failed under aging behavior. That is, both the failure of the SBS copolymer and the decline in the light components of the asphalt binder will increase the T_g temperature. In Luo's research, the incorporation of an oil-based rejuvenator can restore the T_g temperature of SBS-modified asphalt that has undergone long-term aging, however, its efficacy is not applicable in the case of short-term aging **(Luo 2020)**. In conclusion, the degradation of SBS copolymer primarily affects the T_g temperature during the early aging stage, while the reduction of light components becomes a factor in the long-term aging process.

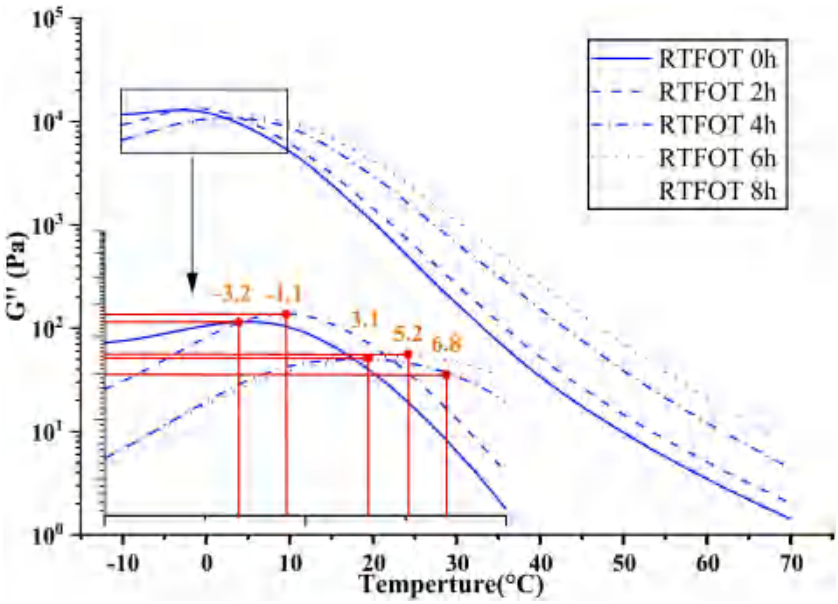

Figure 9 The glass transition temperature at different aging time

5.3 Effect of aging behavior on the elastic recovery properties

As a mechanical indicator, the elastic recovery properties correlate well with the high- and low-temperature performance, fatigue, and durability of SBS-modified asphalt **(Cong et al. 2020)**. The elastic recovery represents the self-healing ability of asphalt after deformation. This paper used two typical tests to evaluate the residual elastic recovery after aging: the elastic recovery test and the multiple stress creep recovery test. **Figure 10** shows the elastic recovery test results, and the ER and ERR were calculated by the previous formulas (2) and (3). It can be seen that the ER decreases with the rising aging time. The period of 0 ~ 10 min presents the fastest deformation of elastic recovery. Generally, SBS-modified asphalt has better elastic recovery performance than base asphalt due to the incorporation of SBS modifier, but the ER results can still reach 63% after RTFOT 8 h, significantly higher than the base

asphalt, which indicates that aging behavior has an insignificant influence on the elastic recovery properties. To address the limitations of the ER results in assessing aging effects, we introduced the calculation of the elastic recovery rate (ERR), which represents the average rate of elastic recovery change.

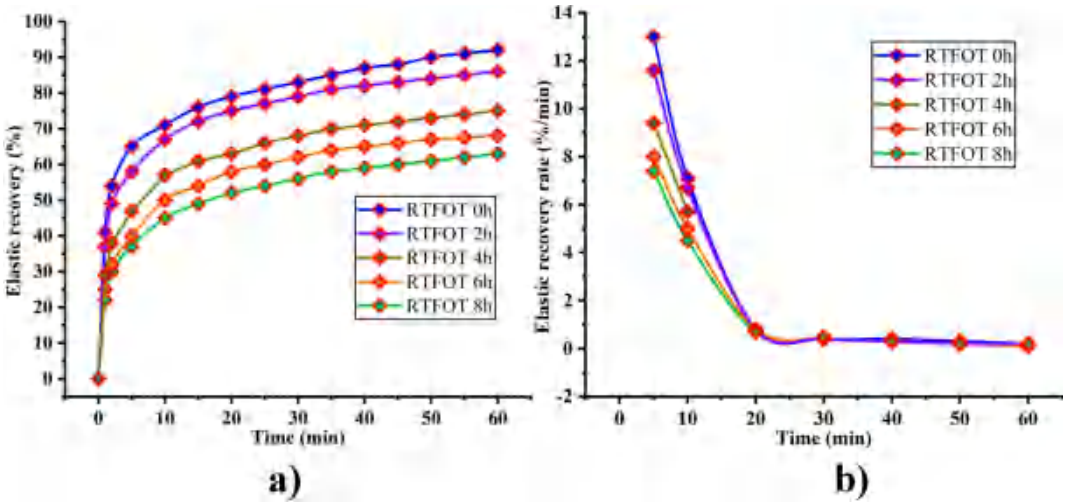

Figure 10 The test results of elastic recovery: a) ER; b) ERR

It can be observed that the samples under different aging times have striking differences in ERR (**Figure 10b**), the ERR is entirely consistent when the period time exceeds 20 min, and the aging behavior primarily influences the early stage (0 ~ 20 min), the ERR of different aging times at the first 5 mins were 13, 11.6, 9.4, 8, 7.4 %/min, respectively. Considering the first few minutes as the instantaneous elastic stage and the subsequent time as the delayed elastic stage, it becomes apparent that aging has a more pronounced effect on instantaneous elasticity. This can be explained as follows: During stretching, SBS polymers align along the stretch direction, with the elastic component aiding in stress absorption and dissipation within the asphalt. Initially, the asphalt retains significant stored recovery stress. Upon load removal, the elastic component releases stored energy, akin to the rebound effect seen in rubber **(Le Cam 2017)**. This helps the asphalt regain its original shape. As the recovery value increases, internal stress within the sample diminishes, leading to a gradual stabilization of the elastic recovery rate.

To further investigate the elastic recovery properties, **Table 3** represents the MSCR results of both SBS-modified asphalt and 70# base asphalt. With the increased aging time, SBS-modified asphalt presents lower deformation and weaker recovery capabilities. The percent recovery and accumulated deformation decreased with the rising aging time. In contrast, the percent recovery at 0.1 and 3.2 kPa after RTFOT 8 h

are 55.7% and 48.5%, respectively, which are still much more than the percent recovery of base asphalt and indicate the elastic recovery of SBS-modified asphalt after serious aging are still better than base asphalt. It is worth noting that the percent recovery reflected the proportion and relative deformation, and the total deformation of aged SBS-modified asphalt is also still lower than the unaged samples. Thus, those indicators are not sensitive to aging time and cannot sufficiently represent the elastic recovery properties.

Table 3 The results of the MSCR test

Asphalt type	Stress level			
	0.1 kPa		3.2 kPa	
	$R_{0.1}$	$J_{nr\,0.1}$	$R_{3.2}$	$J_{nr\,3.2}$
RTFOT 0 h	85.1%	0.254	83.2%	0.316
RTFOT 2 h	68.2%	0.312	63.5%	0.434
RTFOT 4 h	65.3%	0.376	61.1%	0.475
RTFOT 6 h	59.2%	0.634	53.4%	0.721
RTFOT 8 h	55.7%	0.696	48.5%	0.779
70# base asphalt	0.3%	1.469	0.2%	6.815

Burger's model has been widely employed to describe the viscoelastic characteristics of asphalt-based materials **(Saboo and Mudgal 2018)**. In this paper, Burger's model was used to fit the first cycle of the creep-recovery curve by equation (6). **Figure 11** shows the fitted results and the first cycle at 0.1 kPa. It was clear that the experimental results at different aging times and the fitted curve are in a strong agreement. The J_e, J_v, J_{de} were calculated by four fitted parameters according to equation (7), and J_e', J_v', J_{de}' and were computed based on equations (8~11). As illustrated in Figure 11b, the J_e, J_v, and J_{de} decreased with the increasing aging time. That is, the resist deformation ability of SBS-modified asphalt was improved after aging.

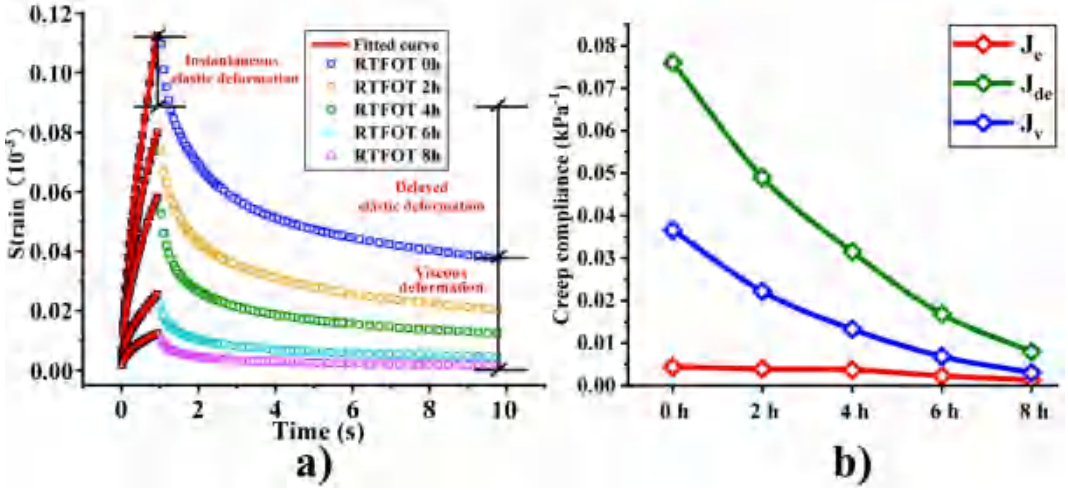

Figure 11 The results based on Burger's model: a) the fitted curve; b) three deformations

However, the proportion of instantaneous elastic deformation, delayed elastic deformation, and viscous deformation in the total deformation has a significant difference at the different aging times (**Figure 12**). J_e' and V_r raised and J_v' declined with the rising of aging time, The proportion of viscous deformation in the total deformation only remained 24.68%, which indicated the aged SBS-modified asphalt shows the lower viscosity proportion and more excellent elasticity. The percentage of delayed elastic deformation in total deformation (J_{de}') has no noticeable difference at various aging times, which is consistent with the results of the elastic recovery test.

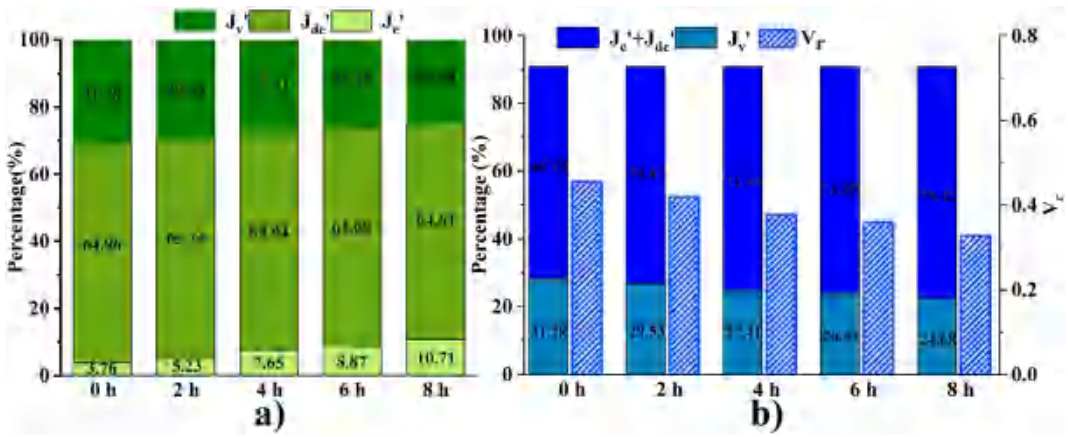

Figure 12 The proportions of three deformations: a) three components; b) viscoelastic ratio

Past studies have reported that the instantaneous elastic and viscous deformation can reflect the rigidity and viscosity of asphalt binder, respectively **(Cao et al. 2020)**.

It also can be seen from the results that the viscous component J_v' decreased and the instantaneous elastic component J_e' enhanced after aging. It is commonly acknowledged that the aging process improves the elastic behavior and leads to the worse viscosity of SBS-modified asphalt. In contrast, the delayed elastic component presents insignificant changes during the aging process, which indicates that the aging behavior has little influence on the delayed elastic deformation. According to Qin's research, the instantaneous elastic recovery capability can be mainly ascribed to the elastomer in the SBS copolymer structure **(Qin et al. 2018)**. The delayed elastic recovery capability is predominantly affected by the polymer network in SBS-modified asphalt **(Słowik 2015)**. Thus, the different situations between instantaneous and delayed elastic after aging also demonstrate the sequential order under aging behavior, which suggests the elastomer was primarily degraded before the destruction of the crosslinking network structure in SBS-modified asphalt.

5.4 Effect of aging behavior on the toughness properties

The toughness and tenacity test can describe the unique characteristics of SBS-modified asphalt, which also has a strong correspondence with viscoelastic mechanics **(Liang et al. 2022b)**. Toughness represents the tensile and cohesive strength of asphalt binder, and tenacity reflects the resistance to deformation and fracture. Generally, the toughness curve of conventional asphalt presents an unimodal curve shape, while SBS-modified asphalt's toughness curve has a bimodal shape. The most apparent difference between the two shapes is the presence or absence of delayed fracture and considerable deformation. As illustrated in **Figure 13**, the toughness curve of SBS-modified asphalt changed from a bimodal to an unimodal curve shape with the increase of aging time. The unimodal curve shape indicates the shortfall of tenacity in SBS-modified asphalt. It can be seen that SBS-modified asphalt after RTFOT 6 h has no tenacity but still retains the yield strength. **Figure 13b** presents the results of 70# base asphalt before aging and after RTFOT 8 h, it is evident that the yield strength of SBS-modified asphalt is approximately three times higher than unaged 70# base asphalt, while the SBS-modified asphalt exhibits a curve profile that closely resembles that of the 70# base asphalt, with a unimodal curve shape. After RTFOT 8 h, both SBS-modified asphalt and 70# base asphalt exhibited brittle fracture before reaching the yield point, and the toughness curve of SBS-modified asphalt after RTFOT 8 h has no tenacity and yield phenomenon.

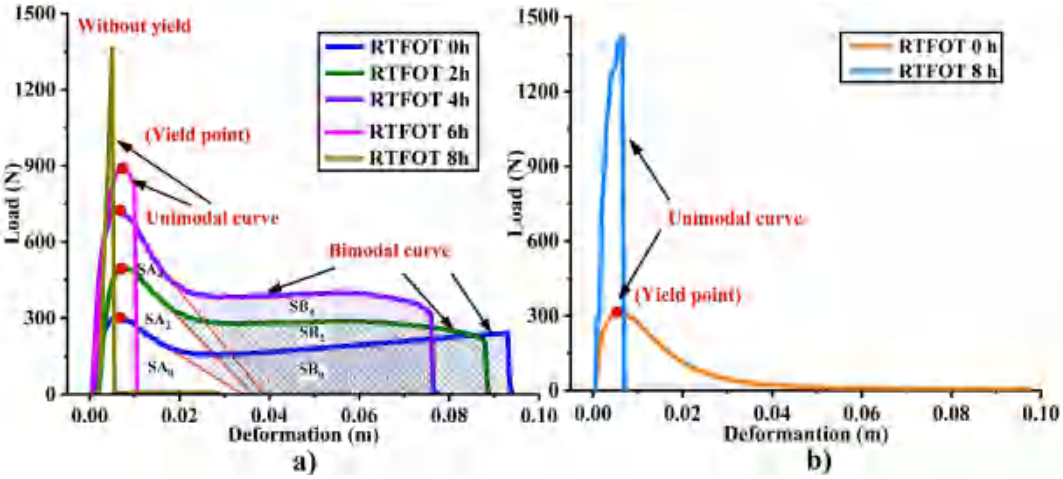

Figure 13 The shape of the toughness curve: a) SBS-modified asphalt; b) 70# base asphalt

Following the theory of polymer yield and fracture **(Kinloch 2013)**, the stress-strain curve can be divided into different regions (**Figure 14**). The OA segment represents the elastic deformation region, with point A being the elastic limit point, and the deformation in this segment can be fully recovered. The yield point, also known as the Y point, polymer materials undergo a strain softening stage after yielding, the stress exhibits a decrease instead of further increment as the strain increases, and the necking exists in the specimen cross-section. And then a cold drawing phenomenon occurs, a uniform thinning throughout the entire working section, the strain continues to increase while the stress remains relatively constant in this stage. In the final stage, called strain hardening, the polymer material undergoes significant deformation, and with the progression of strain, the stress experiences a subsequent increase. At point B, which corresponds to the fracture point, the stress reaches the fracture strength of the polymer materials. Once the stress surpasses the fracture strength, the material undergoes fracture. Therefore, the variation in the aging process of SBS-modified asphalt can be further quantitatively analyzed through mechanical parameters. For instance, the elastic modulus E serves as an indicator of the material's stiffness or flexibility; The fracture strength σ_B provides a measure of the material's tensile strength, indicating its relative strength or weakness; The fracture elongation ε_B is an indicator of the material's ductility or ability to undergo plastic deformation; The integral of the curve, T_e, is indicative of the material's toughness or resistance to fracture.

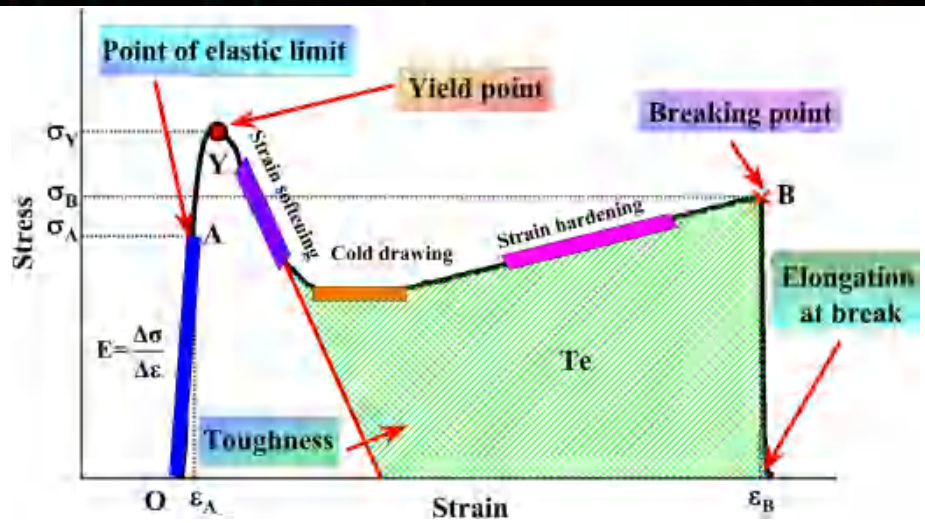

Figure 14 The different stages of the stress-strain curve

Table 4 shows the quantitative parameters in the toughness curve, it can be observed that both SBS-modified asphalt and 70# base asphalt demonstrate an increase in elastic modulus (E) and elastic limit strength (σ_A) after aging, while the fracture strength (σ_B) also experiences an augmentation. However, the fracture elongation (ε_B) gradually diminishes. Aging typically leads to asphalt becoming harder and more brittle, in accordance with common experience (Liu et al. 2022). The yielding strength (σ_Y) grows, and then the yield point rises but does not shift after aging. After RTFOT 8 h, both types of asphalt show no yield strength, indicating that the material has reached a brittle fracture state before yielding. The toughness parameter T_o first increases and then decreases as the aging time advances, while the tenacity parameter T_e continues to decline. Generally, toughness includes two aspects: bonding ability and impact resistance, and tenacity primarily has to do with plastic deformation after yielding (Zhang and Hu 2015). Thus, the higher bonding strength caused by aging behavior leads to the initial increase in toughness parameter T_o.

Table 4 The mechanic's parameters of the toughness curve

Aging time	SBS-modified asphalt					70# base asphalt	
	0 h	2 h	4 h	6 h	8 h	0 h	8 h
E	73.77	90.62	155.65	154.91	253.86	81.45	327.31
σ_A	258.20	362.47	700.43	852.024	1142.36	173.44	262.13
σ_Y	297.83	494.61	732.62	888.91	\	315.10	\
σ_B	239.36	215.57	337.07	811.61	1364.32	4.31	1421.07

ε_B	0.094	0.089	0.076	0.010	0.005	0.09	0.007
T_o	25.7	29.6	32.4	9.3	2.2	11.7	13.6
T_e	15.1	13.4	11.1	0.0	0.0	0.3	0.0

As depicted in **Figure 14**, the comprehensive stress-strain curve encompasses four distinct stages: the elastic deformation phase, the strain softening phase, the cold drawing phase, and the strain hardening phase. It becomes evident that SBS-modified asphalt no longer undergoes strain hardening after 2 h, and after 8 h, it loses its yield strength, leaving only the elastic deformation phase. Past research reported that the two rigid polystyrene blocks in SBS polymer significantly increase the tensile deformation resistance of SBS-modified asphalt **(Harper 2002)**, and the complex crosslinking network in polymer-modified asphalt is also one of the reasons for the increased toughness **(Zhang et al. 2018)**. In the early stage, the light components in the asphalt binder decrease, and the bonding strength grows with the aging time. Subsequently, the SBS copolymer relaxes but the polymer network remains, and the SBS-modified asphalt still has certain toughness, tenacity, and large deformation. With the increase of aging time, the split and dissociation of the SBS copolymer emerge, and the reduced particle size leads to the gradual failure of the polymer network. Ultimately, the tenacity completely disappears. It can be found that the shape of the toughness curve has a very obvious distinction for the aging behavior of SBS-modified asphalt. From the perspective of toughness, the curve shape of SBS-modified asphalt after RTFOT 6 h is identical to the conventional asphalt. The parameter of the toughness curve can be used to judge whether aged SBS-modified asphalt can be treated as modified asphalt or conventional asphalt.

5.5 Effect of aging behavior on the morphological structure

Figure 15 presents fluorescence images depicting the five aging stages of SBS-modified asphalt, offering a more intuitive depiction of the morphological structure, dispersibility, and particle size of SBS polymers within the asphalt. **Figure 15f** represents the unaged 70# base asphalt, and its fluorescence image appears black due to the absence of SBS polymer. It is noticeable that SBS-modified asphalt exhibits distinct morphological structures at different aging times, while unaged SBS-modified asphalt exhibits an approximate network-like structure. However, only a few residual

filamentous structures can be observed after RTFOT 2 h. The majority of the SBS polymers are dispersed in a punctate manner after 4 h, and the filamentous structure becomes absent. The SBS polymers adopt a granular distribution with reduced particle sizes. The dissolution of SBS polymer during aging may be a contributing factor to the reduction in particle size **(Zhang et al. 2017)**. After 6 h and 8 h, there is a further reduction in the number of SBS polymer particles, although they persist compared to the 70# base asphalt. In another study examining the aging of SBS-modified asphalt **(Zhang et al. 2023)**, fluorescence results revealed varying degrees of degradation. After 5 years of field aging, 8 days of UV aging, and 20 hours of PAV aging, SBS showed distinct levels of deterioration. Notably, the most severe degradation occurred after 20 hours of PAV aging, resulting in only tiny specks visible in the fluorescence images. In this study, RTFOT aging 8 h surpasses PAV aging 20 h in terms of asphalt deterioration. Some literature suggests that RTFOT aging for 4.8 hours produces a degradation level equivalent to 20 hours of PAV aging **(Yao et al. 2021)**. Hence, the results showing the degradation of SBS modifiers in fluorescence microscopy also explain the varying rates of performance decline in aged SBS-modified asphalt, which will be discussed further in the upcoming correlation heatmaps. Hence, the results showing the degradation of SBS modifiers in fluorescence microscopy also explain the varying rates of performance decline in aged SBS-modified asphalt.

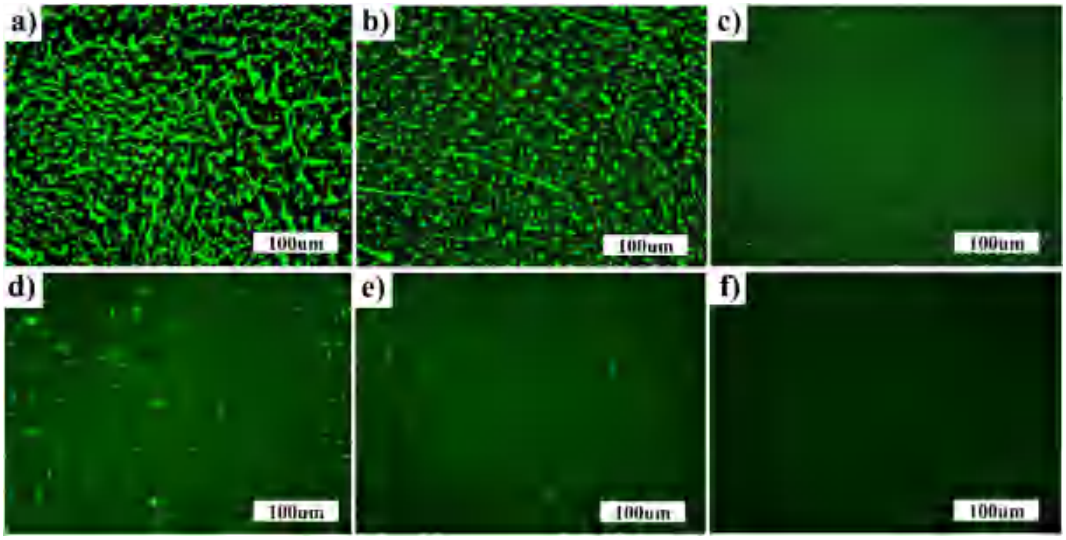

Figure 15 Fluorescence images: a) and b) 0 and 2 h; c) and d) 4 and 6 h; e) and f) 8 h and 70# base asphalt

To achieve a more refined quantification analysis of the fluorescence results, the

software Image-Pro Plus was employed to compute the range and proportion of particle sizes in each fluorescent image. **Figure 16** illustrates the particle size and distribution of SBS polymers at different aging times. It can be observed that the size of SBS polymers continuously decreases during the aging process, starting from a maximum particle diameter of 50 μm initially and reaching 17 μm after RTFOT 8 h. After RTFOT 2 h, the fluorescent images continue to exhibit persistent filamentous structures, which comprise the polymer network. This observation suggests an ongoing degradation process of the SBS polymer, eventually leading to the disappearance of the polymer network. This finding provides support and serves as an explanation for the experimental results of elastic recovery. After the dissolution of the polymer network structure, the toughness of SBS-modified asphalt persists, signifying that the increased toughness is primarily attributable to the presence of SBS polymer, this finding aligns with prior research **(Jiang et al. 2017)**. Nevertheless, the toughness abruptly diminishes after aging 4 h, and currently, a satisfactory explanation remains elusive, apart from the observed decrease in both the size and quantity of SBS particles. Besides the decrease in particle size, another consequence of aging is the emergence of an irregular particle size distribution. As depicted in **Figure 16**, there is a discernible increase in distinct peaks after aging, indicating a fragmented and dispersed particle size distribution, intensifying the degree of heterogeneity.

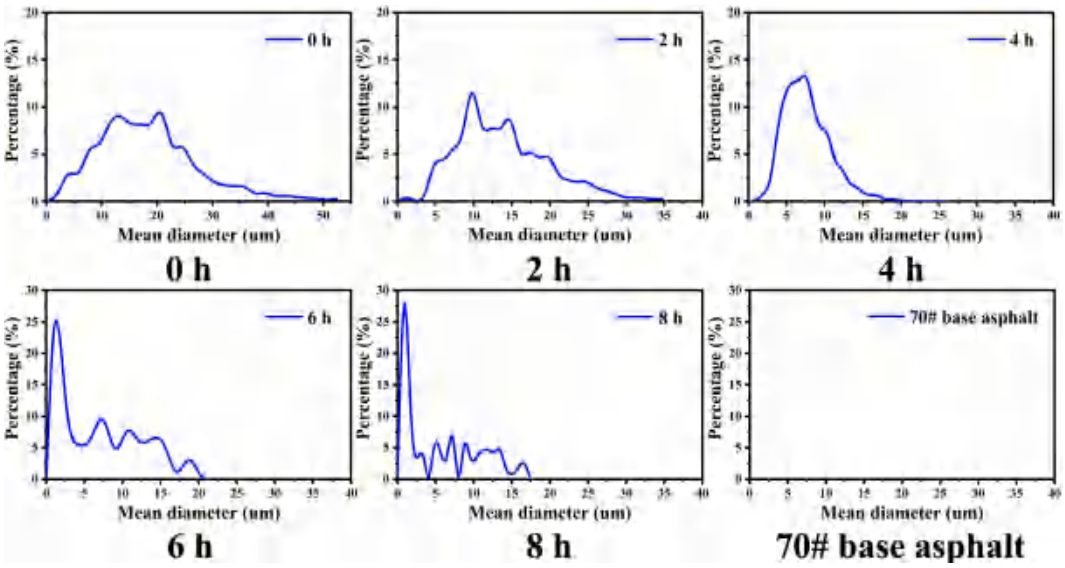

Figure 16 The size distribution of SBS copolymer at different aging times

To further analyze the characterization of aged SBS-modified asphalt's phase structure and assess the suitability of the mentioned quantitative parameters in

describing phase evolution and performance degradation during aging, we conducted correlation analysis using the most relevant parameters from the aforementioned tests. The results are depicted in the correlation heatmap shown in **Figure 17**, where -1 and 1 respectively represent strong negative and positive correlations, and values closer to 0 indicate no correlation. The heatmap revealed robust correlations between many indicators and aging time, indicating significant linear trends during aging. However, toughness parameters T_o, which exhibit non-linear behavior with an initial increase followed by a decrease, display weaker correlations. Other quantifiable parameters within the toughness curve show strong correlations with aging. Moreover, ERR and the related parameters in the MSCR test exhibit a strong correlation, confirming the reliability of evaluating the elastic recovery performance of aged SBS-modified asphalt in the test. Compared to different properties, the toughness curve not only provides a comprehensive set of parameters but also effectively distinguishes the critical state between modified and unmodified asphalt during aging, with clear physical significance. Therefore, it is well-suited for characterizing the phase structure evolution in aged SBS-modified asphalt.

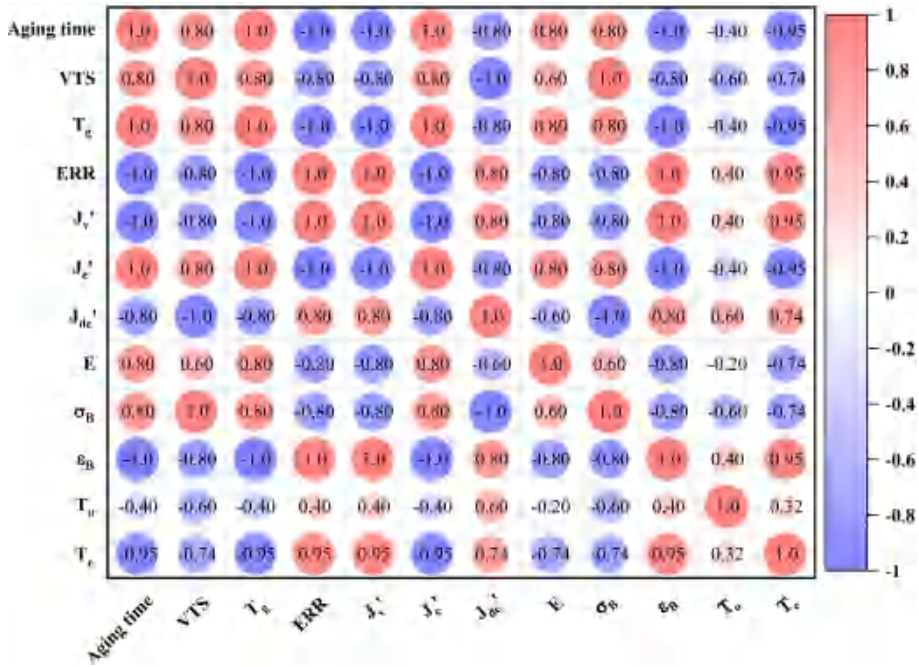

Figure 17 The correlation heatmap of different indicators

6 CONCLUSIONS

In this paper, the effect of the aging process on the different viscoelastic properties including viscous flow properties, viscoelastic properties, elastic recovery properties,

and toughness properties were analyzed. The morphological structure under different aging stages was investigated, and the characterization methods for discerning the phase structure have been definitively identified. Based on the test results, the primary conclusions can be generalized as follows:

1) Based on the low- and high-temperature phase behavior results, it can be concluded different aging stages were observed in SBS-modified asphalt, the degradation of SBS copolymer exists in the early-stage aging, and the reduction of light components becomes a factor in the long-term aging process.

2) Aging primarily influenced instantaneous elastic deformation, with limited impact on delayed elastic deformation. The instantaneous and delayed elastic recovery capability can be mainly ascribed to the elastomer and polymer network, respectively, the different situations indicated the elastomer degraded before the destruction of the crosslinking network.

3) Toughness and tenacity test effectively characterized fracture and deformation resistance. SBS-modified asphalt lost tenacity after RTFOT 6 h but retains yield strength, and the toughness curve shape resembled that of conventional asphalt, and both the tenacity and yield phenomenon completely disappear after RTFOT 8 h.

4) The heatmap revealed robust correlations between many indicators and aging time. Compared to different properties, toughness properties were firstly deteriorated with the aging times, followed by the elastic properties and viscous properties. Elastic recovery properties remained significantly better in SBS-modified asphalt even after RTFOT 8 h. The phase structure can be effectively delineated by the distinct mechanical property variations observed in the toughness curve.

5) Fluorescence results showed decreasing size and number of SBS polymers during aging, leading to a fragmented particle size distribution. SBS polymer degradation preceded the disruption of the polymer network. Toughness remains even without the polymer network, suggesting that increased toughness is mainly due to the presence of SBS polymer.

In summary, this study explored the influence of aging on the transformation among different phase behaviors. The toughness properties exhibit distinctive characteristics and has a clear degree of differentiation at different aging times, the toughness curve can effectively characterize the transformations in phase structure. Additional factors will be considered to verify the effectiveness of this findings in the future study, such

as the type of modifier, the presence or absence of stabilizer, different crude oils and photo-oxidative aging.

DATA AVAILABILITY STATEMENT

Some or all data, models, or code that support the findings of this study are available from the corresponding author upon reasonable request.

ACKNOWLEDGEMENTS

This study was mainly supported by the National Natural Science Foundation of China joint fund for regional innovation and development (U20A20315). This study was also supported by the Non-metallic Materials Innovation Center Project (24PHD-2). Thanks to the anonymous reviewers for the comments that have notably helped us improve the manuscript.

REFERENCE

AASHTO. 2014. Standard method of test for quantitative extraction of asphalt binder from hot mix asphalt (HMA). AASHTO T164. American Association of State Highway and Transportation Officials.

Airey, G. D. 2002. "Use of Black Diagrams to Identify Inconsistencies in Rheological Data." Road Mater. Pavement Des., 3 (4): 403–424.

ASTM. 2005. Standard test method for penetration of bituminous materials. ASTM D5. West Conshohocken, PA: ASTM.

ASTM. 2006a. Standard test method for softening point of bitumen (ring-and-ball apparatus). ASTM D36. West Conshohocken, PA: ASTM.

ASTM. 2006b. Standard test method for viscosity determination of asphalt at elevated temperatures using a rotational viscometer. ASTM D4402. West Conshohocken, PA: ASTM.

ASTM. 2007. Standard test method for kinematic viscosity of asphalts (bitumens). ASTM D2170. West Conshohocken, PA: ASTM.

ASTM. 2008. Standard test method for test method for residue of specified penetration. ASTM D243. West Conshohocken, PA: ASTM.

ASTM. 2010. Standard test method for elastic recovery of bituminous materials by ductilometer. ASTM D6084. West Conshohocken, PA: ASTM.

ASTM. 2015a. Standard test method for viscosity determination of asphalt at elevated temperatures using a rotational viscometer. ASTM D4402. West Conshohocken, PA: ASTM.

ASTM. 2015b. Standard Test Method for Determining the Rheological Properties of Asphalt Binder Using a Dynamic Shear Rheometer. ASTM D7175. West Conshohocken, PA: ASTM.

ASTM. 2015c. Standard Test Method for Multiple Stress Creep and Recovery (MSCR) of Asphalt Binder Using a Dynamic Shear Rheometer. ASTM D7405. West Conshohocken, PA: ASTM.

ASTM. 2017a. Standard test method for ductility of asphalt materials. ASTM D113. West Conshohocken, PA: ASTM.

ASTM. 2017b. Standard viscosity-temperature chart for asphalts. ASTM D2493. West Conshohocken, PA: ASTM.

ASTM. 2017c. Standard test method for toughness and tenacity of asphalt materials. ASTM D5801. West Conshohocken, PA: ASTM.

ASTM. 2018a. Standard test method for loss on heating of oil and asphaltic compounds. ASTM D6. West Conshohocken, PA: ASTM.

ASTM. 2018b. Standard test method for assignment of the glass transition temperature by dynamic mechanical analysis. ASTM E1640. West Conshohocken, PA: ASTM.

Behnood, A., A. Shah, R. S. McDaniel, M. Beeson, and J. Olek. 2016. “High-Temperature Properties of Asphalt Binders: Comparison of Multiple Stress Creep Recovery and Performance Grading Systems.” Transp. Res. Rec., 2574: 131–143.

Le Cam, J.-B. 2017. “Energy storage due to strain-induced crystallization in natural rubber: The physical origin of the mechanical hysteresis.” Polymer., 127: 166–173.

Cao, Z., M. Chen, J. Yu, and X. Han. 2020. “Preparation and characterization of active rejuvenated SBS modified bitumen for the sustainable development of high-grade asphalt pavement.” J. Clean. Prod., 273: 123012.

Chen, H., H. Qiu, Y. Wu, D. Kuang, and M. Xing. 2022. “Aging resistance of SBS–SBR composite modified asphalt materials for high altitude and cold regions.” Mater. Struct., 55 (7): 187.

Chen, M., J. Geng, C. Xia, L. He, and Z. Liu. 2021a. "A review of phase structure of SBS modified asphalt: Affecting factors, analytical methods, phase models and improvements." Constr. Build. Mater., 294: 123610.

Chen, Z., D. Zhang, Y. Zhang, H. Zhang, and S. Zhang. 2021b. "Influence of multi-dimensional nanomaterials composite form on thermal and ultraviolet oxidation aging resistances of {SBS} modified asphalt." Constr. Build. Mater., 273: 122054.

Cong, P., X. Guo, and L. Mei. 2020. "Investigation on rejuvenation methods of aged SBS modified asphalt binder." Fuel, 279: 118556.

Diab, A., and Z. You. 2017. "Small and large strain rheological characterizations of polymer-and crumb rubber-modified asphalt binders." Constr. Build. Mater., 144: 168–177.

Ding, Z., J. Zhang, P. Li, X. Yue, and H. Bing. 2019. "Analysis of viscous flow properties of styrene–butadiene–styrene-modified asphalt." Constr. Build. Mater., 229: 116881.

Guan, K., W. Zhu, X. Liu, and J. Wei. 2020. "Finite strain analysis of squeezing response in an elastic-brittle-plastic weak rocks considering the influence of axial stress." Tunn. Undergr. Sp. Technol., 97: 103254.

Harper, C. A. 2002. Handbook of plastics, elastomers, and composites. McGraw-Hill Education.

Jasso, M., R. Hampl, O. Vacin, D. Bakos, J. Stastna, and L. Zanzotto. 2015. "Rheology of conventional asphalt modified with SBS, Elvaloy and polyphosphoric acid." Fuel Process. Technol., 140: 172–179.

Jiang, Y., Y. Liu, J. Gong, C. Li, Z. Xi, J. Cai, and H. Xie. 2018. "Microstructures, thermal and mechanical properties of epoxy asphalt binder modified by SBS containing various styrene-butadiene structures." Mater. Struct., 51: 1–13.

Jiang, Z., C. Hu, S. M. Easa, X. Zheng, and Y. Zhang. 2017. "Evaluation of physical, rheological, and structural properties of vulcanized EVA/SBS modified bitumen." J. Appl. Polym. Sci., 134 (21).

Kaya, D., A. Topal, and T. McNally. 2019. "Relationship between processing parameters and aging with the rheological behaviour of SBS modified bitumen." Constr. Build. Mater., 221: 345–350.

Kinloch, A. J. 2013. Fracture behaviour of polymers. Springer Science & Business

Media.

Kök, B. V., M. Yilmaz, and A. Geçkil. 2012. "Evaluation of Low-Temperature and Elastic Properties of Crumb Rubber– and SBS-Modified Bitumen and Mixtures." J. Mater. Civ. Eng., 25 (2): 257–265. American Society of Civil Engineers.

Laukkanen, O., ; Ville, H. ; Soenen, H. Winter, and S. J. 2018. "Low-temperature rheological and morphological characterization of SBS modified bitumen." Constr. Build. Mater., 179: 348–359.

Liang, B., Y. Chen, F. Lan, and J. Zheng. 2022a. "Evaluation of rheological and aging behavior of modified asphalt based on activation energy of viscous flow." Constr. Build. Mater., 321: 126347.

Liang, X., X. Yu, C. Chen, G. Ding, and J. Huang. 2022b. "Towards the low-energy usage of high viscosity asphalt in porous asphalt pavements: A case study of warm-mix asphalt additives." Case Stud. Constr. Mater., 16: e00914.

Lin, P., W. Huang, Y. Li, N. Tang, and F. Xiao. 2017. "Investigation of influence factors on low temperature properties of SBS modified asphalt." Constr. Build. Mater., 154: 609–622.

Lin, P., X. Liu, P. Apostolidis, S. Erkens, S. Ren, S. Xu, T. Scarpas, and W. Huang. 2021. "On the rejuvenator dosage optimization for aged SBS modified bitumen." Constr. Build. Mater., 271: 12913.

Liu, J., L. Qi, X. Wang, M. Li, and Z. Wang. 2022. "Influence of aging induced by mutation in temperature on property and microstructure development of asphalt binders." Constr. Build. Mater., 319: 126083.

Mokhtari, A., and F. M. Nejad. 2012. "Mechanistic approach for fiber and polymer modified SMA mixtures." Constr. Build. Mater., 36: 381–390.

Qin, X., S. Zhu, X. He, and Y. Jiang. 2018. "High temperature properties of high viscosity asphalt based on rheological methods." Constr. Build. Mater., 186: 476–483.

Saboo, N., and A. Mudgal. 2018. "Modelling creep and recovery response of asphalt binders using generalized burgers model." Pet. Sci. Technol., 36 (20): 1627–1634.

Seiler, M., T. Linse, P. Hantschke, and M. Fracture. 2020. "An efficient phase-field model for fatigue fracture in ductile materials." Eng. Fract. Mech., 224: 106807.

Shi, K., F. Ma, J. Liu, R. Song, Z. Fu, J. Dai, and Y. Wen. 2022. "Development of a

new rejuvenator for aged SBS modified asphalt binder." J. Clean. Prod., 380: 134986.

Słowik, M. 2015. "Assessment of the viscoelastic properties of modified bitumens containing styrene-butadiene-styrene copolymer." Balt. J. Road Bridg. Eng., 10 (4): 299–308.

Tan, Y., J. Zhang, G. Zou, and H. Qin. 2022. "Aging characterization of rheology and morphology evolution of SBS-modified asphalt." Constr. Build. Mater., 342: 128027.

Tian, Y., H. Li, H. Zhang, B. Yang, X. Zuo, and H. Wang. 2021. "Comparative investigation on three laboratory testing methods for short-term aging of asphalt binder." Constr. Build. Mater., 266: 121204.

Wang, J., W. Zeng, Y. Qin, S. Huang, and J. Xu. 2017. "Laboratory evaluation of rejuvenating agent on reclaimed SBS modified asphalt pavement." Appl. Sci., 7 (7): 743.

Ward, I. M., and J. Sweeney. 2012. Mechanical properties of solid polymers. John Wiley & Sons.

Wei, C., H. Duan, H. Zhang, and Z. Chen. 2019. "Influence of SBS Modifier on Aging Behaviors of SBS-Modified Asphalt." J. Mater. Civ. Eng., 31 (9): 04019184.

Wu, H., V. K. Thakur, and M. R. Kessler. 2016. "Novel low-cost hybrid composites from asphaltene/SBS tri-block copolymer with improved thermal and mechanical properties." J. Mater. Sci., 51 (5): 2394–2403.

Wu, S., L. Pang, L. Mo, Y. Chen, and G. Zhu. 2009. "Influence of aging on the evolution of structure, morphology and rheology of base and SBS modified bitumen." Constr. Build. Mater., 23 (2): 1005–1010.

Xu, P., Z. Zhu, Y. Wang, P. Cong, D. Li, J. Hui, and M. Ye. 2022. "Phase structure characterization and compatibilization mechanism of epoxy asphalt modified by thermoplastic elastomer (SBS)." Constr. Build. Mater., 320: 126262.

Yan, C., W. Huang, P. Lin, Y. Zhang, and Q. Lv. 2019. "Chemical and rheological evaluation of aging properties of high content SBS polymer modified asphalt." Fuel, 252: 417–426.

Yao, X., Y. Wang, and T. Xu. 2021. "Development on recycling, aging simulation and regeneration methods of reclaimed styrene-butadiene-styrene modified asphalt."

J. Clean. Prod., 312: 127767.

Yu, C., K. Hu, Q. Yang, and Y. Chen. 2021. "Multi–scale observation of oxidative aging on the enhancement of high–temperature property of SBS modified asphalt." Constr. Build. Mater., 313: 125478.

Zhang, D., H. Zhang, and C. Shi. 2017. "Investigation of aging performance of SBS modified asphalt with various aging methods." Constr. Build. Mater., 145: 445–451.

Zhang, D., Y. Zheng, G. Yuan, H. Guo, Q. Zhou, G. Qian, and B. Liang. 2023. "Comparative analysis of rheological and microscopic performance of SBS modified asphalt based on field aging and laboratory aging." Fuel, 352: 128933.

Zhang, F., and C. Hu. 2015. "The research for high-elastic modified asphalt." J. Appl. Polym. Sci., 132 (25).

Zhang, F., C. Hu, and Y. Zhang. 2018. "The research for SIS compound modified asphalt." Mater. Chem. Phys., 205: 44–54.

Zhang, F., J. Yu, and S. Wu. 2010. "Effect of ageing on rheological properties of storage-stable SBS/sulfur-modified asphalts." J. Hazard. Mater., 182 (1–3): 507–517.

Zhang, J., and Y. Tan. 2022. "Rheology, morphology and phase behavior of SBS/sulfur modified asphalt based on experimental assessment and molecular dynamics." Int. J. Pavement Eng., 1–13.

Zhao, Y. L., F. Gu, and X. M. Huang. 2011. "Analysis on SBS modified asphalt aging characterization based on fourier transform infrared spectroscopy." J. Build. Mater., 14 (5): 620–623.

Preparation and performance of EPEG-type PCE and its application in ultra-high performance concrete

Tong Xue[1]，Jie Bai[1*]，Wenying Xu[1]，Zuobao Song[2]，Ting Li[2]，Juan Li[3*]，Ruijun Gao[3]

[1] *China Building Materials Academy(CBMA), Beijing, China*
Email: xuetongcbma@163.com
[2] *CNBM Zhongyan Technology Co., Ltd., Beijing, China*
Email: zhongyankeji@chinasccm.com
[3] *Nonmetallic Excellence and Innovation Center for Building Materials, CBMA, Beijing, China*
Email: lijuan@cbma.com.cn

ABSTRACT: To improve the workability and mechanical properties of ultra-high performance concrete (UHPC), a novel EPEG-type ultra-high dispersion polycarboxylate superplasticizer (EPEG-type PCE) was developed by radical copolymerization reaction, and the effect of EPEG-type PCE on the workability, mechanical properties and durability of UHPC was investigated in this paper. The results show that the EPEG-type PCE can improve the workability and mechanical properties of UHPC at an appropriate dosage. However, there is a critical dosage for the effect of EPEG-type PCE on the early compressive strength and fluidity of UHPC, which is 1.5% (by mass of cement). The fluidity of UHPC does not improve any more when the dosage of EPEG-type PCE increases continuously after exceeding the critical point. The compressive strength decreases with the increase of EPEG-type PCE dosage when exceeding the critical point. The long-term drying shrinkage and electric flux of UHPC increased significantly with the increase of EPEG-type PCE dosage. The higher the dosage of EPEG-type PCE, the faster the increase of electric flux value of UHPC, and the worse the chloride ion penetration resistance of UHPC.

KEYWORDS: *UHPC, EPEG-type PCE, dosage, workability, compressive strength, shrinkage*

1. Introduction

UHPC is a kind of cement-based composite material born in the 1990s, which is characterized by extremely low water-binder ratio, dense accumulation of multiple fine particles and toughening with steel fiber[1]. It is widely used in strengthening and repairing bridges, building curtain walls, prefabricated buildings and other fields[2-4]. However, the shortcomings of UHPC are also very prominent. The workability of UHPC has become very poor due to the ultra-low water-binder ratio and ultra-high amount of cementitious materials, it is usually necessary to add a large amount of polycarboxylate superplasticizer (PCE) to improve its fluidity[5-6], and the role of superplasticizer becomes very critical. In this paper, a novel EPEG-type PCE with a high water reducing rate was synthesized, which successfully realized the ultra-high dispersion of cementitious particles under the condition of low water to binder ratio. The influence of EPEG-type PCE on the workability, mechanical properties and durability of UHPC was studied, and provide reference for the application of UHPC engineering.

2.Experiment

2.1 Materials

Ethylene glycol monovinyl polyethylene glycol ether (EPEG), self-developed; Acrylic acid (AA), hydrogen peroxide, ascorbic acid, and 3-mercaptopropanoic acid (3-MPA) purchased from Hongyan reagent factory of China.
Cement: PO 52.5, Tangshan Jidong Cement Co., LTD; Superfine mineral powder (SMP): 1250 mesh; Sand: quartz sand, 20~40 mesh and 40~80 mesh, Hebei; Silica fume (SF):,amorphous SiO_2 content is 95.8% and specific surface area greater than 20 m^2/g was purchased from Gansu Sanyuan Silicon Materials Co., Ltd; Steel fiber: copper-plated fiber with a diameter of 0.22 mm and a length of 13~15 mm. Polycarboxylate superplasticizer: EPEG-type PCE, solid content is 40%.

2.2 Synthesis of PCE

330 g EPEG, 3 g hydrogen peroxide and 210 g water were added to a four-necked flask with a stirring device. 60 g AA aqueous solution as A solution, and 103 g 3-MPA and ascorbic acid aqueous solution as B solution were dripped respectively into the flask at 20℃ for 1h. and then continued reaction at a constant temperature for 1h to obtain EPEG-type PCE.

2.3 UHPC mix design

The mix design of UHPC is shown in Table 1.

Table 1 Mix ratio of UHPC

Cement	SF	SMP	Sand 20~40 mesh	Sand 40~80 mesh	Steel fiber	Water
800	150	150	630	420	150	198

2.4 Test Methods

2.4.1 Structure characterization of EPEG-type PCE

Fourier transform infrared (FT-IR) measurements were performed by FT-IR spectrometer (TENSOR 27, BRUKER, Germany) and relative molecular mass was characterized by Gel Permeation Chromatography (GPC, BI-Molecular weight Analyzer, USA).

2.4.2 UHPC performance test

UHPC fluidity test: The test was carried out according to Chinese standard of GB/T 2419-2005 'Cement mortar fluidity determination method' without vibration.

Drying shrinkage and electric flux test of UHPC: refer to Chinese standard of GB/T 50082-2009 'Test method for long-term performance and durability of ordinary concrete'.

3.Results and discussion

3.1 Characterization of EPEG-type PCE

Fig.1 is the infrared spectrum of EPEG-type PCE. There is an obvious peak at 3442 cm^{-1}, indicating the stretching vibration absorption of -OH. A strong peak at 2889 cm^{-1} and multiple peaks suggest the stretching vibration absorption of alkyl saturated carbon ($-CH_3$, $-CH_2$, etc.). 1469 cm^{-1} is the stretching vibration absorption peak of saturated carbon C-H. 1243 cm^{-1} should be the stretching vibration absorption peak of C-O in the alcohol or ether structure, a strong absorption peak at 1109 cm^{-1} should be the stretching vibration absorption peak of -O- in the ether structure. The strong peak at 842 cm^{-1} should be the trans vibration absorption peak of enyne, and the out-of-plane bending vibration absorption peak of olefin C-H at 962 cm^{-1}. The above analysis results show that the polyether molecule includes the characteristic functional groups C=C, C-O, and -OH. According to the GPC data (Fig.2), the average molecular weight of the EPEG-type PCE is 36856 $g \cdot mol^{-1}$, the molecular weight distribution value (PDI) is 1.72, and the conversion rate is 96.34%.

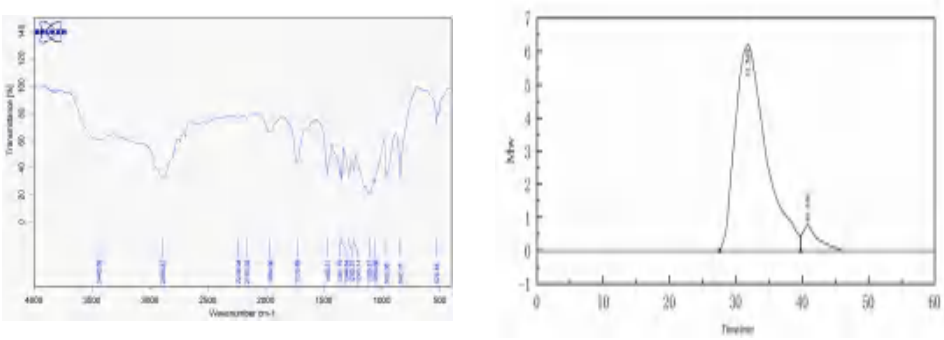

Fig.1 FT-IR of EPEG-type PCE

3.2 The effect of EPEG-type PCE dosage on the fluidity of UHPC

Table 2 shows the fluidity test results of UHPC with different EPEG-type PCE dosages. It can be seen from Table 2 that when the dosage of EPEG-type PCE is less than 1.5%, the amount of EPEG-type PCE

is positively correlated with the fluidity of UHPC. However, when the dosage of EPEG-type PCE is higher than 1.5%, this relationship is significantly changed. When the dosage of EPEG-type PCE is increased, the fluidity of the slurry remains stable and basically unchanged. Even when the dosage of EPEG-type PCE is very high, the fluidity tends to decrease slightly.

Table 2 Influence of dosage of EPEG-type PCE on fluidity of UHPC

PEC dosage %	0.5	1	1.5	2.0	2.5
Fluidity/mm	115	225	267	266	262

The dispersion mechanism of EPEG-type PCE on cement is the dual mechanism of adsorption, electrostatic repulsion and steric hindrance, which is dominated by steric hindrance, thus ensuring the good dispersion of EPEG-type PCE on cement particles. When the amount of water reducing agent exceeds the saturation point (Fig.3), the adsorption vacancies on the surface of cement particles are gradually occupied and saturated. At this time, the adsorption amount of EPEG-type PCE is almost no longer increased with the dosage of EPEG-type PCE, and the fluidity of paste is no longer increased as well. When the amount of water reducing agent is too high, the free molecules of EPEG-type PCE in the pore solution will crosslink with the molecules adsorbed on the surface of the rubber particles, thus reducing the slump flow of UHPC.

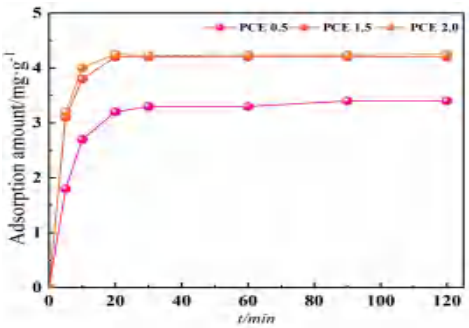

Fig.3 Adsorption capacity of EPEG-type PCE in binding material at different dosages

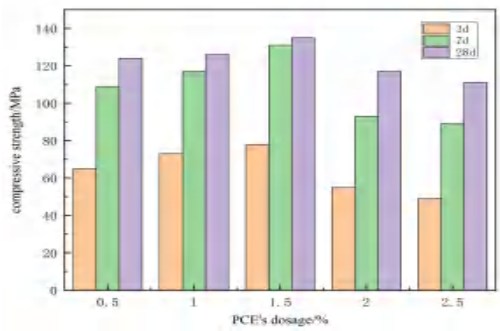

Fig.4 Compressive strength of UHPC with different dosage of EPEG-type PCE

3.3 Influence of dosage of EPEG-type PCE on compressive strength of UHPC

As shown in Fig.4. It can be seen that the dosage of EPEG-type PCE has a significant effect on the early strength of UHPC. Within a certain range, the early strength of concrete increases with EPEG-type PCE dosage, and the later strength develops steadily. When the dosage increased to 1.5%, the 3 d and 28 d compressive strength of UHPC increased to 78.6 MPa and 135.8 MPa respectively. While the water reduction dosage was 2.5%, the 3d and 28d compressive strength of UHPC decreased to 49.2 MPa and 111.9 MPa respectively. Before the saturated dosage point, the addition of EPEG-type PCE can release the flocculation water in the flocculation group of cement particles in the low water-binder ratio system and promote the hydration of cement particles. However, when the dosage of EPEG-type PCE exceeds the saturation point, EPEG-type PCE reacts with the free Ca^{2+} in the interstitial solution to form an unstable complex, which inhibits the hydration process and leads to the decrease of early strength. As the hydration process progresses, this unstable complex will decompose by itself, and hydration will continue normally.

3.4 Effect of EPEG-type PCE on durability of UHPC

3.4.1 Drying shrinkage

As shown in Table 3, The long-term drying shrinkage of UHPC increases significantly with higher PCE dosage, When the dosage of PCE increased from 1.0% to 1.5%, the drying shrinkage of UHPC increased by 9.4%. When the dosage of PCE increased to 2.0%, the drying shrinkage of UHPC reached 511×10^{-6}. The drying shrinkage of UHPC is due to the evaporation of water in the capillary pores and the gel. After the addition of PCE, the water in the system is relatively increased, and the size of the capillary pores is reduced. The greater the negative pressure generated due to the evaporation of water in the capillary pores, the more pronounced is the increase in negative pressure acting on the capillary pore wall, leading to enhanced drying shrinkage of UHPC[7].

Table 3 Drying shrinkage of UHPC with different EPEG-type PCE dosage

Age		Drying shrinkage/ $\times 10^{-6}$						
		1d	3d	7d	14d	28d	56d	90d
EPEG-type PCE dosage	1.0	93	154	276	331	402	431	443
	1.5	103	165	299	356	428	478	485
	2.0	132	209	324	376	444	501	511

3.4.2 Chloride penetration resistance

As Fig.5 shown, When EPEG-type PCE dosage is 1.0%, 1.5% and 2.0%, the electric flux values of UHPC are 100.3 C, 121.5 C and 145.7 C respectively. Compared to the electric flux at 1.0% dosage, it increases by 21.1% and 44.6% at dosage of 1.5% and 2% respectively, which indicates chloride ion penetration resistance decreases with the increase of dosage of EPEG-type PCE. This can be attributed to the low water to binder ratio, small porosity of hardened system, less internal interface defects and more active mineral admixtures in UHPC. The pozzolanic effect and secondary hydration reaction can effectively improve the pore structure of concrete.

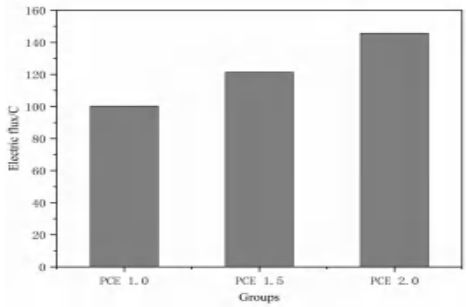

Fig.5 EPEG-type PCE on the electric flux of UHPC

4.Conclusions

A novel EPEG-type PCE was developed which can improve the workability and mechanical properties of UHPC at an appropriate dosage. When the dosage exceeds 1.5%, The slump of UHPC no longer increases with the increase of dosage of EPEG-type PCE and the compressive strength of UHPC gradually decreases. The drying shrinkage and electric flux of UHPC increase significantly with the increase of dosage of EPEG-type PCE, which indicates that the excessive addition of EPEG-type PCE will be detrimental to the durability of UHPC.

Acknowledgements

This study is sponsored by the program fund of NEXCEL, Non-Metallic Excellence and Innovation Center for Building Materials (Project No. 2022TDA3-1).

References

[1] Shi, C.J., Wu, Z., M, Xiao., J.F, et al. (2015) “review on ultra-high-performance concrete: Part I. Raw materials and mixture design”. Construction and Building Materials, (101): 741-751.

[2] Hao L W. (2013) “Preparation of polycarboxylic acid water-reducing agent for ultra-high strength RPC”, New Building Materials, (3): 27-28.

[3] Shao, Z.C, Guo, K.Y, Liu, S.W, et al. (2020) “Study on synthesis of high performance polycarboxylic acid water-reducing agent”. Chemical Industry and Engineering, 37(6): 30-37.

[4] Li F, Kong W Y, Luo J, et al. (2019) “Preparation and application of ultra-high performance concrete (UHPC)”, Concrete and Cement Products, (7): 26-29.

[5] Huang Z, Yang Y, Ran Q, et al. (2018) “Preparing hyperbranched polycarboxylate superplasticizers possessing excellent viscosity-reducing performance through in situ redox initialized polymerization method”. Cement and Concrete Composites, 93: 323-330.

[6] Shu X, Ran Q, Liu J, et al., (2016) “Tailoring the solution conformation of polycarboxylate superplasticizer toward the improvement of dispersing performance in cement paste”. Construction and Building Materials, 116: 289-298.

[7] TAM, C.M., TAM, V.W.Y., NG, K.M. (2012) “Assessing drying shrinkage and water permeability of reactive powder concrete produced in Hong Kong”. Construction and Building Materials, 26(1): 79-89.

国内聚醚大单体的研究现状及展望

许文英[1] 薛 童[1] 李 婷[2] 王 博[1] 蔡 阳[1] 高瑞军[1] 白 杰[1]
1. 中国建筑材料科学研究总院有限公司 北京 100024
2. 中建材中岩科技有限公司 北京 100024

摘 要：近些年，随着现代工程对混凝土性能要求的提高，混凝土外加剂技术及产品研究也在随之进步，其中混凝土外加剂最主要的原料——聚醚对外加剂技术的发展起着重要作用。本文介绍甲氧基聚乙二醇醚、烯丙基聚氧乙烯醚、甲基烯丙基聚氧乙烯醚、异戊烯基聚氧乙烯醚及环氧封端聚乙二醇的制备技术现状及存在的问题，并对传统聚醚合成聚羧酸减水剂的工艺进行简要说明；针对传统聚醚大单体化学改性潜力低的缺点，补充阐述了具有不同拓扑结构聚醚单体的研究现状，并对聚醚大单体的化学改性及其在未来减水剂市场的发展提出展望，对聚醚大单体未来的应用具有一定借鉴作用。

关键词：聚醚大单体；超支化；研究现状；分子结构

Research Status and Prospects of Polyether Macromonomer in China

Abstract: In recent years, with the increasing requirements for concrete performance in modern engineering, research on concrete admixture technology and products has also been progressing. Among them, the main raw material of concrete admixture — polyether macromonomer plays an important role in the development of admixture technology. This paper introduces the current situation and existing problems of the preparation technology of MPEG, APEG, HPEG, TPEG, EPEG, and briefly describes the process of synthesizing polycarboxylate superplasticizer from traditional polyether macromonomer. In response to the shortcomings of low chemical modification potential of traditional polyether macromonomer, the current research status of polyether macromonomer with different topological structures is supplemented. The chemical modification of polyether macromonomer and their development in the future water reducing agent market are proposed, which has a certain reference value for the future application of polyether macromonomer.

Key words: Polyether macromonomer; hyperbranched; research status; molecular structure

引言

聚醚大单体作为合成聚羧酸减水剂的重要原料，其分子结构是影响聚羧酸减水剂性能的关键因素。近年来，国内聚醚大单体市场持续发展，产品结构发生了明显的变化，具有功能化的新型聚醚大单体产品层出不穷，充分反映了国内聚羧酸系减水剂大单体产业链的快速发展和产品质量的不断提高[1]。市场上原材料的质量越来越差，但是对聚羧酸减水剂的性能要求却越来越高，目前的聚醚大单体尽管能满足大部分要求，但仍有缺陷和不足，如抗泥性较差，因此需要进一步提高聚羧酸减水剂性能；且对具有特殊分子结构的聚醚大单体研究较少，难以满足需求，如超高性能混凝土等。因此，有必要对聚醚大单体的研究现状进行系统的梳理、总结和评述，以期给后续研究者提供借鉴和启示。

1 普通结构聚醚大单体的发展概况

国内早期使用的聚羧酸减水剂为酯类大单体，如甲氧基聚乙二醇醚（MPEG），其分子结构式如图1所示。酯类大单体的合成通常分为2步，第一步制备一定长度的聚乙二醇链，第二步在催化剂作用下与丙烯酸发生脱水酯化反应而制备。由于在合成过程中加入苯、甲苯等有毒

收稿日期：2023-6-21
第一作者：许文英，1985年生，高级工程师，硕士，主要从事聚羧酸减水剂的研究工作，E-mail：wenying2000@126.com
项目信息：非金属材料创新中心基金资助项目（2022TDA3-1）

(C)1994-2023 China Academic Journal Electronic Publishing House. All rights reserved. http://www.cnki.net

溶剂，合成需要经过聚合、酯化，过程繁琐且不符合绿色环保要求，因此逐渐被醚类大单体取代[2]。

聚醚大单体主要是由不饱和醇起始剂与催化剂混合，通入氮气置换后，再通入环氧乙烷进行乙氧基化反应，最后脱水、过滤制备末端有双键的聚乙二醇醚，直接聚合而成，不需要进行酯化反应[3]。早期使用的醚类大单体为烯丙基聚氧乙烯醚（APEG），其分子结构式如图2所示。APEG在一定的反应温度（40～80℃）下通过水溶液聚合5～8h便可制备性能优良的聚羧酸高性能减水剂[4-6]，由此可见，APEG相对早期的酯类大单体来说，是技术上的一个重大突破。但随着技术的不断发展，APEG的缺点也逐渐显现，其聚合活性相对较低，合成得到的聚羧酸减水剂（PCEs）单体残留量大，性能较差，因此APEG逐渐退出市场。

目前较常用的聚醚大单体为甲基烯丙基聚氧乙烯醚（HPEG）、异戊烯基聚氧乙烯醚（TPEG），它们的化学结构特点是在双键上增加了一个甲基，其分子结构式如图3所示。由于甲基的供电子作用使得双键活性更强，因此与APEG相比，HPEG和TPEG的聚合活性更高，制备的PCEs性能更好，且随着起始剂原料的逐步国产化，该类聚醚大单体的价格大幅下降，已成为市场主流产品。HPEG和TPEG的聚合活性与丙烯酸等小单体一般在30～60℃进行合成，并降低丙烯酸浓度，控制滴加时间为3～4h，与APEG相比，使用HPEG和TPEG提高了制备PCEs的生产效率[7-8]。

近几年新推广的乙二醇单乙烯基聚乙二醇醚（VEPEG，2+2或2+2+2结构）和4-羟丁基乙烯基聚乙二醇醚（VBPEG，2+4结构），最早由德国巴斯夫公司在1996年提出，其分子结构式如图4所示。VEPEG和VBPEG因其不饱和双键直接与一个氧原子相连，双键链增长，反应活性大幅提高，从而大幅缩短反应时间，提高生产效率；结构中的C-O键使聚氧乙烯链摆动更加自由、活动空间更大，提高了PCE侧链的柔性，使其与混凝土原材料具有更高的适应性。张少敏[9]采用VPEG作为大单体，丙烯酸作为小单体，在双氧水-甲醛次硫酸氢钠组成的氧化还原体系中，合成聚羧酸减水剂PCE-E，通过正交试验得到最佳反应起始温度为15℃，滴加时间45min。聚醚大单体从APEG过渡到VPEG，其反应温度逐渐降低，反应时间逐渐缩短，反应效率越来越高。

张建锋等[10]研究大单体分子结构的变化，在合成的聚羧酸减水剂中所表现的性能差异，明确了合成条件等方面的差异，以及所表现出的分散性和保持性方面的不同。因此，大单体的分子结构对聚羧酸减水剂生产工艺及产品性能的影响较大[11]。

2 特殊结构聚醚大单体的发展概况

新型高活性聚醚大单体的成功研发及产业化，促进了国内聚醚大单体行业的发展，同时使得聚羧酸减水剂

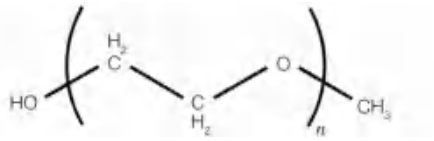

图 1　MPEG分子结构式

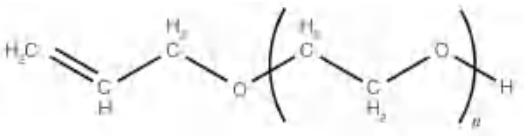

图 2　APEG分子结构式

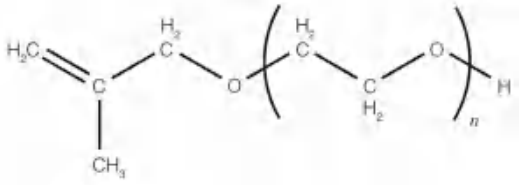

(a) HPEG

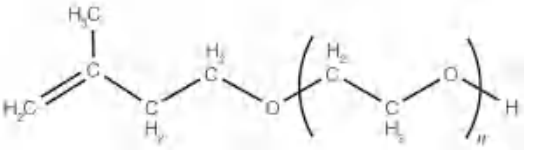

(b) TPEG

图 3　HPEG和TPEG分子结构式

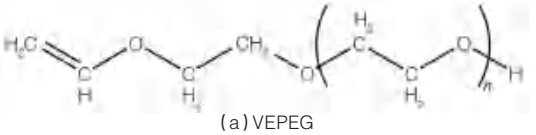

(a) VEPEG

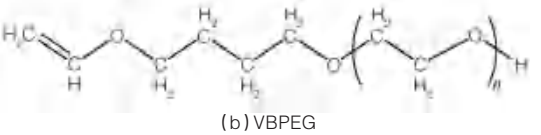

(b) VBPEG

图 4　VEPEG和VBPEG分子结构式

(C)1994-2023 China Academic Journal Electronic Publishing House. All rights reserved.　http://www.cnki.net

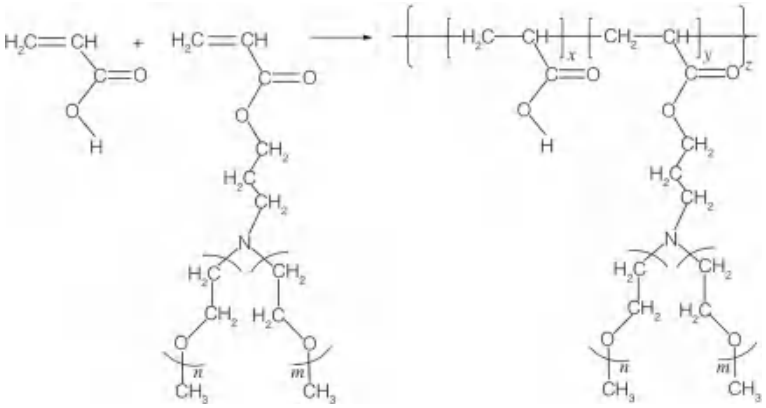

图 5　TAHB-PCEs的合成路线

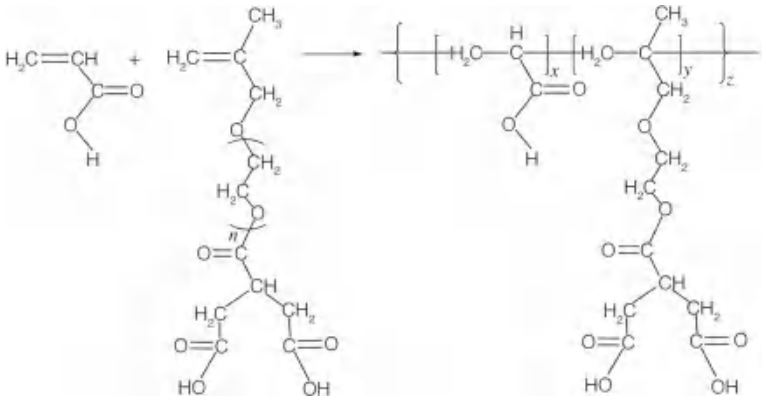

图 6　mY-PEG型聚羧酸减水剂的合成路线

的生产技术得到了提升，推动了聚羧酸减水剂的发展[12]。下面介绍不同结构的聚醚大单体的研究情况。

2.1 超支化聚醚大单体

超支化聚醚大单体以其独特的分子结构与性能成为高分子研究的热点。超支化聚合物具有不同于线性聚合物的高度支化结构，大多呈三维球形分子结构，并且含有很多的活性基团，利用这些活性基团可以制备超支化聚合物[13]。超支化聚羧酸减水剂拥有线性聚羧酸和超支化聚合物的共同性能，相比普通聚羧酸有更大的空间位阻效应和更好的分散性，所以很多学者对超支化聚醚大单体进行了研究。

姚方[14]以MPEG和氯化亚砜为原料，合成中间体氯代聚乙二醇单甲醚（Cl-MPEG），然后以乙醇胺为核心进行（PEG）长链接枝得到中间体MPEG-ETA，最后通过丙烯酰氯引入碳碳双键，合成二臂超支化聚氧乙烯醚大单体（TAHBPE），其合成路线如图5所示。

金宇等[15]以HPEG和丙三酸（TA）为原料，通过酯化反应制备一种Y型中间体（mY-PEG），然后以mY-PEG与MPEG为原料再进行酯化反应得到一种Y型大单体（Y-PEG），其合成路线如图6所示。

2.2 不同封端聚醚大单体

刘海[16]以HPEG和丁二酸酐为原料，4-二甲氨基吡啶（DMAP）为催化剂，通过酯化制备了单羧基封端型聚氧乙烯醚大单体（HPES），其合成如图7所示，用红外光谱、核磁共振氢谱对其进行表征，并探究了反应温度、时间和催化剂用量对酯化产率的影响；以HPEG和丙三酸为原料，DMAP为催化剂，通过酯化制备了分子量不同的双羧基封端型聚氧乙烯醚大单体（HPET、HPET500），其合成如图8所示，用红外光谱、核磁共振氢谱对其进行表征，并探究了反应温度、时间和催化剂用量对酯化产率的影响。

李祥河等[17]研究了一种含双羟基封端的聚醚大单体，其结构式如图9所示，选用单甲基烯丙基乙二醇醚和丙二醇单烯丙基醚为起始剂制聚醚大单体，并利用环氧丙醇对聚醚单体封端，制得端基含双羟基的新型聚醚大单体。和常规的聚醚大单体相比，制备的含双羟基封端

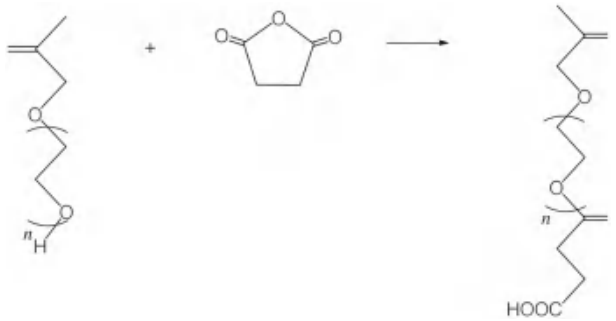

图 7　HPES大单体的合成

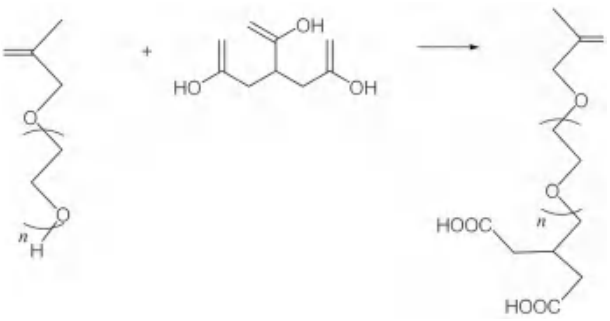

图 8　HPET大单体的合成

(C)1994-2023 China Academic Journal Electronic Publishing House. All rights reserved.　http://www.cnki.net

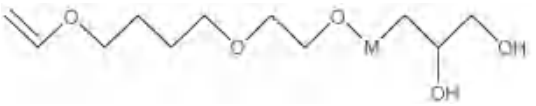

图 9　含双羟基封端的聚醚大单体结构式
（M–环氧乙烷和/或环氧丙烷聚合制得的聚醚链）

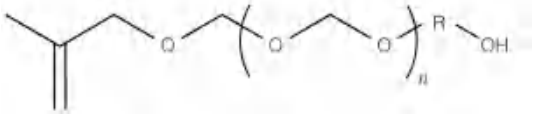

图 10　新型聚醚的分子结构式

的聚醚大单体对反应温度的敏感度低，能够实现不同环境温度的聚合，使用该聚醚大单体制备的混凝土保坍剂具有更优异的保坍性能。

2.3 改性聚醚大单体

ZHENG等[18]利用分子改性的方法将TPEG单体接入木质素分子上，制备了一种木质素聚醚大单体，再将其与TPEG及小单体进行自由基聚合，形成了一种以木质素为核的聚羧酸减水剂。

王雪敏等[19]研究了一种新型聚醚的制备方法，采用石墨烯对聚醚进行改性，利用石墨烯本身可改造性强的特点，将其接枝到聚醚结构中去，其分子结构式如图10所示，该新型聚醚大单体的化学反应惰性使其在水泥体系中不会影响水泥水化反应以及其他性能，同时利用其强大的空间位阻效应可以阻止黏土的吸附。

展望

国内聚醚大单体市场持续发展，产品结构发生了巨大变化，功能化的新型聚醚大单体成为市场的焦点，聚醚大单体产业研发水平的不断提高，反映了下游减水剂生产厂家对聚醚产品性能要求的不断提高。随着国内新建扩建乙氧基化项目的投产及生产技术的不断升级，聚醚大单体产业的产能进一步扩大，企业间的竞争将更加激烈。因此，国内的聚醚大单体生产厂家除了不断提升现有产品质量、优化生产工艺外，还应着眼于新型结构聚醚大单体的研发与应用，以适应不同减水剂产品的应用需求。

另外，随着我国“碳达峰”“碳中和”目标的不断迫近，上至起始剂的生产厂家，下至减水剂的生产厂家，都需要不断改进生产工艺，以保证产品更加低碳、环保、绿色。而具有支化结构的聚醚大单体的出现为国内大单体生产厂家提供了新的方向，目前已有不少学者开展了超支化结构聚醚大单体的研发，并成功合成出具有超高分散性能的减水剂，此外特殊结构类聚醚大单体在产品性能方面的突出优点，也使其成为未来聚醚大单体发展的主要趋势。

参考文献

[1] 金福和. 和氏璧化工集团聚羧酸减水剂产品竞争战略研究[D]. 济南: 山东大学, 2013.

[2] 李晓春, 司宏振. 聚醚大单体合成工艺的研究进展[J]. 化工技术与开发, 2020, 49(8):39–41.

[3] 刘冠杰, 王自为, 任建国, 等. 聚羧酸减水剂聚醚大单体的应用研究进展[J]. 日用化学品科学, 2018, 41(10):13–16.

[4] 王子明, 李慧群. 聚羧酸系减水剂研究与应用新进展[J]. 混凝土世界, 2012(8):50–56.

[5] 孙振平, 杨辉. 国内聚羧酸系减水剂的研究进展与展望[J]. 混凝土世界, 2013(3):31–35.

[6] 李慧群, 韩光, 梁超静, 等. 聚羧酸与萘系减水剂的相互作用机理研究[J]. 混凝土世界, 2022(8):5–9.

[7] J PLANK, H LI, M ILG, et al. A microstructural analysis of isoprenol ether–based polycarboxylates and the impact of structural motifs on the dispersing effectiveness[J]. Cement and Concrete Research, 2016, 84:20–29.

[8] C CHOMYN, J PLANK. Impact of different synthesis methods on the dispersing effectivenessof isoprenol ether–based zwitterionic and anionic polycarboxylate (PCE) super–plasticizers[J]. Cement and Concrete Research, 2019, 119:113–125.

[9] 张少敏. 新型聚醚大单体低温制备聚羧酸减水剂及其性能研究[J]. 硅酸盐通报, 2020, 39(9):2844–2848.

[10] 张建锋, 宋永良, 王政伟, 等. 大单体结构对聚羧酸减水剂性能的影响[J]. 新型建筑材料, 2014, 41(4):68–71.

[11] LEI L, PLANK J. Synthesis and properties of a vinyl ether–based polycarboxylate superplasticizer for concrete possessing clay tolerance[J]. Industrial and Engineering Chemistry Research, 2014, 53:1048–1055.

[12] H TAHARA, H ITO, Y MORI, et al. Cement additive method for producing the same, and cementcomposition:5476885[P]. 1995–12–19.

[13] MAI Y, ZHOU Y, YAN D. Real–time hierarchical self–assembly of large compound vesicles from an amphiphilic hyperbranched multiarm copolymer [J]. Small, 2007, 3(7):1170–1173.

[14] 姚方. 侧链超支化聚羧酸减水剂的合成、表征及性能[D]. 海口: 海南大学, 2022.

[15] 金宇. 聚羧酸Y型大单体及其混凝土减水剂的合成研究[D]. 广州: 华南理工大学, 2020.

[16] 刘海. 羧基封端的聚醚大单体及新型聚羧酸高性能减水剂的制备与性能[D]. 广州: 华南理工大学, 2023.

[17] 李祥河, 官梦芹, 杜可禄, 等. 一种含双羟基封端的聚醚大单体及其制备方法与应用: CN115850682A[P]. 2023–03–28.

[18] ZHENG T, ZHENG D F, QIU X Q, et al. A novel branched claw–shape lignin–based polycarboaylate superplasticizer: preparation, performance and mechanism [J]. Cement and Concrete Research, 2019, 119:89–101.

[19] 王雪敏, 吴志刚, 刘伟, 等. 一种聚醚及其制备方法和应用: CN111363138B[P]. 2022–08–02.

(C)1994-2023 China Academic Journal Electronic Publishing House. All rights reserved.　http://www.cnki.net

Research on the mix proportion of low-carbon concrete utilizing a novel polycarboxylate superplasticizer

Xue Tong[1], Bai Jie[1], Li Juan[1], Song Zuobao[2], Li Ting[2], Gao Ruijun[1*]

[1] China Building Materials Academy Co., Ltd, No.1 Guanzhuangdongli, Beijing, China
[2] CNBM Zhongyan Technology Co., Ltd, No.1 Guanzhuangdongli, Beijing, China
gao_423@163.com

Abstract: In recent decades, with the significant increase in CO_2 concentrations, global warming has brought about an abundance of extreme climate disasters. As the most widely used building material in the world, the technical concept and direction of low carbonization and sustainable production of concrete are of great significance. Cement is the primary source of CO_2 emissions throughout the entire life cycle of concrete, as the production of 1MT of cement releases approximately 0.87MT CO_2 into the atmosphere. The cement industry alone contributes to approximately 8% of global anthropogenic emissions. Hence, decreasing the cement content in concrete is a crucial step towards achieving low-carbon concrete. In this work, the feasibility of applying a novel polycarboxylate superplasticizer in the mix proportion of low-carbon concrete has been discussed. The study found that when preparing concrete of grades C30 and C50, it is feasible to increase the dosage of the superplasticizer, reduce cement and water consumption, ensure the workability of concrete, and improve its mechanical properties and durability. Through a detailed analysis of concrete's pore size distribution, the link between enhancing the macroscopic performance of concrete and improving its microscopic pore structure is elucidated. With regards to cost analysis of the proposal based on the present research work, the cost reduction resulting from the decrease in cement is more significant compared to the cost increase of the polycarboxylate superplasticizer beyond the optimal dosage. This holds significant importance for concrete production enterprises.

Keywords: Low-Carbon Concrete, Polycarboxylate Superplasticizer, Mix Proportion, Workability, Durability, gel pore.

1 Introduction

Global warming has become the focus of attention of all countries. The Paris Agreement signed in 2015 proposed that the global average temperature rise should be controlled at 2℃ below the pre-industrial level. To this end, countries have put

forward more stringent measures to reduce carbon footprint. On October 26, 2021, the Chinese government issued the Action Plan for Carbon Peak by 2030, and proposed to strengthen the research and development and application of new cementation materials, low-carbon concrete and other sustainable building materials and products. Therefore, it is of great significance to clarify the technical concept and direction of low-carbon concrete.

Cement contributes the largest carbon footprint throughout the life cycle of concrete[2]. By optimizing the concrete mix ratio, the consumption of cement can be reduced, thereby indirectly promoting the low-carbon production of concrete[3-4]. In order to ensure the engineering quality of low-carbon concrete, in the mix design, often use excellent performance of water reducer to fully disperse the cement particles, while reducing the amount of mixing water, that is to follow the principle of "under the premise of ensuring the construction of small slumps, do not pursue the premise of high fluidity and large expansion, in order to ensure the uniformity and compaction of concrete"[5].In this paper, based on the mix ratio of C30 grades commonly used in the concrete industry, the mix ratio was optimized by using ultra-high dispersive polycarboxylic superplasticizer(PCE). The workability, mechanical properties and durability of each group of concrete were compared, and the internal porosity and pore size distribution of concrete were studied. The feasibility of low-carbon concrete preparation technology based on ultra-high dispersive water reducing agent is expounded.

2 Experiment

2.1 Raw materials

Table 1. Physical and Chemical analysis of cement

SL No	Test parameter		Unit	Test Results
1	Blaine fineness		m^2/Kg	357
2	Sp gravity		-	3.19
3	C_3S		%	68.23
4	C_3A		%	5.16
5	C_4AF		%	11.63
6	45 micron retain		%	4.95
7	Setting time	Iinitial	*minute*	149
		Final	*minute*	265
8	Compressive strength	3d	*MPa*	21
		28d	*MPa*	43.9
9	Bending strength	3d	*MPa*	4.2
		28d	*MPa*	7.3

Synthetic raw materials: Ethylene glycol monovinyl polyethylene glycol ether (EPEG), self-made; Acrylic acid (AA), hydrogen peroxide(H_2O_2), ascorbic acid, and 3-mercaptopropanoic acid (3-MPA), purchased from Hongyan reagent factory of China.

Concrete raw material: Cement: P.O 42.5, SUNNSY Group; Fly Ash: Class 1 in Type F; Mineral powder: Grade S95; Coarse aggregate: Basalt, continuous gradation from 5 to 20mm, in accordance with JTG/T 3650-2020. Fine aggregate: River sand. Grade II in GB/T 14684-2022. The following details the distinct properties of various materials utilized in the experimental.

Table 2. Physical and Chemical analysis of fly ash

SL No	Test parameter	Unit	Test Results
1	Fineness	%	9.8
2	Loss on lgnition	%	2.14
3	Water demand ratio	%	95
4	Free calcium oxide	%	0.39
5	SO_3 content	%	0.44
6	Alkali content	%	0.91
7	Water content	%	0.51
8	Activity index	%	84

Table 3. Physical and Chemical analysis of mineral powder

SL No	Test parameter		Unit	Test Results
1	Loss on lgnition		%	0.62
2	Chloride content		%	0.013
3	Fluidity ratio		%	98
4	Blaine Fineness		m^2/kg	419
5	Activity index	7d	%	84
		28d	%	97

Table 4. Physical and Chemical analysis of Superplasticiser

SL No	Test parameter	Unit	Test Results
1	Relative Density	g/cm^3	1.096
2	pH	-	6.25
3	Chloride content	%	0.027
4	Total alkali (Na_2O_{eq})	%	0.085
5	Water Reduction	%	43
6	Dry material content	%	39.87

2.2 Synthesis of EPEG-type PCE

330g EPEG, 3g hydrogen peroxide and 210g water were added to a four-necked flask with a stirring device. 60g AA aqueous solution as A solution, and 103g 3-MPA and ascorbic acid aqueous solution as B solution were dripped respectively into the flask at 20℃ for 1h. and then continued reaction at a constant temperature for 1h to obtain EPEG-type PCE.

2.3 Mixture design

Considering the practical application value of the research results,the mix proportions of only cement as a cementitious material was abandoned. This study uses the mix proportions of C30 grade concrete, which is commonly used by commercial concrete producers, as a reference. It utilize three cementitious materials: cement, fly ash, and slag. Undoubtedly, cement has the highest carbon emissions and cost among the three. Furthermore, increasing the use of fly ash and mineral powder, which are industrial by-products, also benefits carbon reduction and cost lowering.In addition to the reference mix ratio, we carried out 20 groups of optimization schemes. In order to clearly illustrate the conclusions of the experiment, 5 groups of representative samples were selected to show in Table 5 below. The research experiment was conducted on two part like analysis of fresh concrete properties and hardened concrete properties. The rheological behaviors and workability of fresh concrete were evaluated through slump tests conducted at different time intervals: immediately, 30 minutes, 60 minutes, and 90 minutes. The mechanical properties of hardened concrete were evaluated using the compressive strength and flexural strength of concrete at different ages. The test sample sizes and methods were in accordance with the standard GB/T 50081-2019. The durability of concrete was evaluated using the Test Method for rapid chloride ions migration Coefficient(RCM), resistance of concrete to freczing and thawing in standard GB/T 50082-2009. In addition, the critical pore size and pore size distribution of each sample were analyzed by LF-NMR.

Table 5. Low carbon C30 concrete mix proportion design scheme

Sample ID	Quantity of different concrete ingredient,kg/m^3							
	Cement	Fly Ash	Mineral powder	Coarse aggregate	Fine aggregate	Water	PCE	PCE content
T-0	200	112	48	1002	860	158	1.82	0.51%
T-1	180	129	51	1007	865	145	1.98	0.55%
T-2	165	136	59	1013	870	137	2.12	0.59%
T-3	165	136	59	1013	870	137	2.25	0.62%
T-4	150	149	61	1019	875	126	2.56	0.71%
T-5	130	161	69	1024	879	119	2.88	0.80%
T-6	130	161	69	1024	879	119	3.21	0.89%

3 Results and Discussion

3.1 Characterization of PCE molecular structure

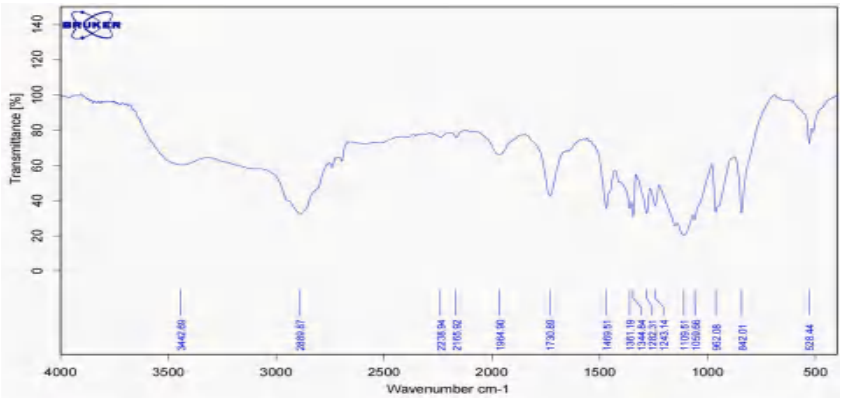

Fig.1. FT-IR spectra of EPEG-type PCE

Fig.1 is the infrared spectrum of EPEG-type PCE. There is an obvious peak at 3442cm^{-1} , indicating the stretching vibration absorption of -OH. A strong peak at 2889cm^{-1} and multiple peaks suggest the stretching vibration absorption of alkyl saturated carbon (-CH3, -CH2, etc.). 1469cm^{-1} is the stretching vibration absorption peak of saturated carbon C-H. 1243cm^{-1} should be the stretching vibration absorption peak of C-O in the alcohol or ether structure, a strong absorption peak at 1109cm^{-1} should be the stretching vibration absorption peak of -O- in the ether structure. The strong peak at 842cm^{-1} should be the trans vibration absorption peak of enyne, and the out-of-plane bending vibration absorption peak of olefin C-H at 962cm^{-1}. The above analysis results show that the polyether molecule includes the characteristic functional groups C=C, C-O and -OH.According to the GPC data (Fig.2), the average molecular weight of the EPEG-type PCE is 36856g · mol^{-1}, the molecular weight distribution value(PDI) is 1.72, and the conversion rate is 96.34%.

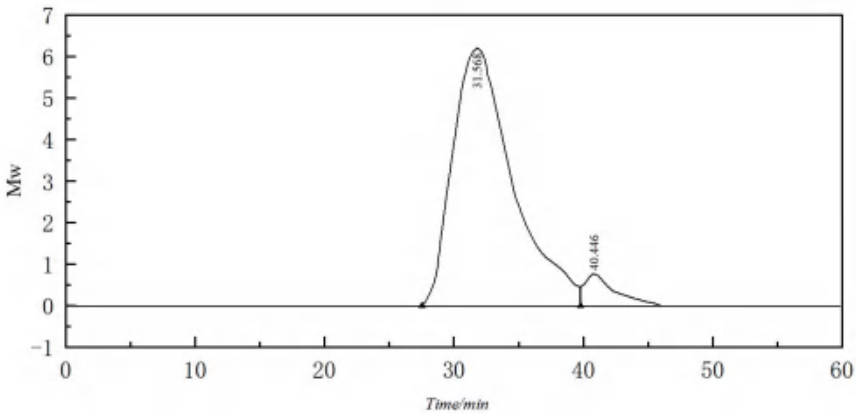

Fig.2 GPC of EPEG-type PCE

3.2 Performance evaluation of fresh concrete

In the low-carbon concrete design scheme, we used more mineral admixtures to compensate for the friction between aggregate particles caused by the lower cement content, as this would make the working performance of the fresh mixed concrete lower. It is worth noting that due to the decrease in the amount of cement and mixing water, the PCE content needs to be increased to ensure the working performance of concrete, but the increase of PCE content is not linear, as can be easily seen from Figure 3.

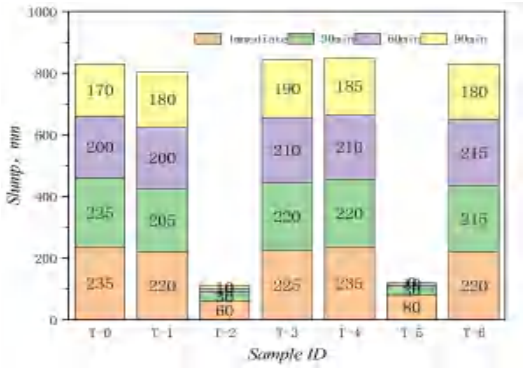

Fig.3 The slump test of fresh concrete

3.3 Mechanical properties evaluation

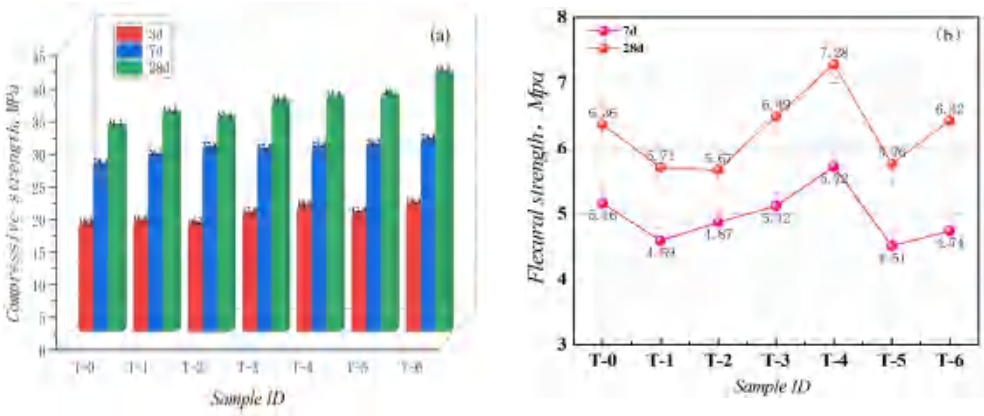

Fig.4 The mechanical properties test of concrete.(a) compress (b) Flexural

As the fig.4 shown, concrete with excellent mechanical properties can be prepared by increasing the dosage of PCE in concrete and reducing the dosage of cement and the ratio of water to cement. This may be because the cement particles with poor dispersion effect will appear agglomeration, which will affect the hydration process of cement and the morphology of hydration products. In addition, the high hydration heat caused by cement hydration will also lead to the more fragile interfacial transition zone (ITZ) between aggregate and cement hydration products, further increasing the risk of internal defects in concrete.

3.4 Evaluation of durability

As the Fig.5a shown, the electric flux values of concrete are 2364C, 2004C , 2156C, 1738C, 1584C, 2049C and 1347C, respectively.The electric flux is reduced by 43.3% when the cement dosage is reduced from 200kg to 130kg and the water-binder ratio is reduced by 0.33 from 0.44. This means that the optimized concrete has fewer internal pores, a more compact internal structure, and better durability. This is because cement only needs 23% of its weight of water to complete hydration, and the excess water will occupy the volume of fresh concrete. Once the concrete begins to harden, the excess water evaporates, leaving pores of different sizes. The more moisture in this part, the greater the internal porosity of hardened concrete, which is also an important reason for the performance of concrete.This conclusion is also confirmed in the results of concrete frost resistance(Fig.5b). This conclusion is also confirmed in the results of concrete frost resistance. After 200 freezing-thawing cycles, concrete with high electric flux shows a large loss of strength. But there are differences, which may be related to the pore size and connectivity inside the concrete.

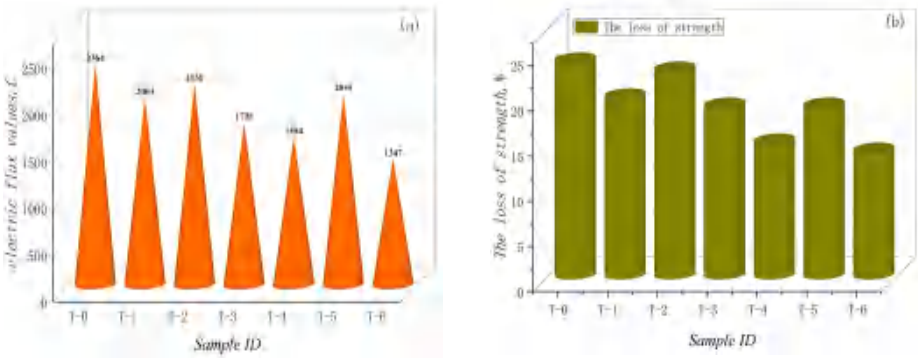

Fig.5 The evaluation of different concrete,(a) RCM, (b) freezing-thawing cycles.

3.5 Pore structure

As we all know, The microstructure of cement paste is typically characterized by two types of pores: capillary pores, created by excess water not participating in the hydration process, and gel pores, formed by the fibrous calcium silicate hydrate (C-S-H) gel during hydration[6].

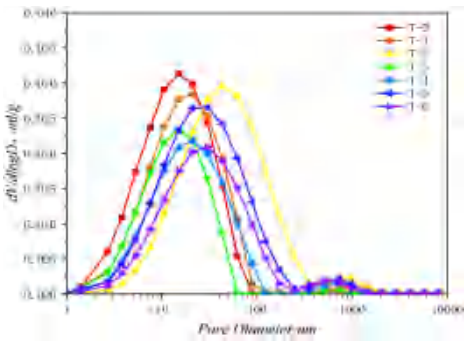

Fig.6 PSD of different concrete

As shown in Fig.6, The first and higher wave crest corresponds to the gel pore, while the second wave crest corresponds to the capillary pore[7]. The peak value of gel pores gradually decreases with a reduction in the water-to-gel ratio. As the mineral admixture content increases, the position of the gel pore peak tends to shift to the right. This trend highlights the significant impact of a low water-to-binder ratio on concrete porosity. Increasing the PCE content while reducing cement and mixing water amounts can effectively enhance the compactness and durability of concrete.

4 Conclusion

Based on the present research work & interpretation of results based on the various facts. The following are the key outcome of the present research works.

(1) The introduction of PCE can reduce the water requirement of concrete by about 39% and the cement consumption by 35%. Therefore, It is feasible to reduce the carbon footprint of concrete by increasing the dosage of PCE.

(2) Reducing the amount of cement will not reduce the properties of concrete. The main idea of low carbon concrete mix design is to fully disperse cement particles, make it fully hydrated, and reduce the existence of free water.

(3) Water-binder ratio is the main factor to determine the porosity of concrete, while the incorporation of fly ash will make the corresponding peak position of gel pores shift to the right. Porosity has a strong correspondence with the durability of concrete, which will be our next research direction.

(4)Based on the market’s raw material cost analysis, the optimized mix ratio results in a cost saving of 9.94 yuan per ton of concrete per cubic meter and a reduction in carbon emissions by 61.25 kg.

Acknowledgements

This work were financially supported by the program fund of non-metallic excellence and innovation center for building materials (Project No. 2022TDA3-1).

References

1. ZHENG C Y,ZHANG H R,CAI X R,et al.Characteristics of CO2 and atmospheric pollutant emissions from China's cement industry:A life-cycle perspective [J]. Journal of Cleaner Production, 282:124533 (2020).
2. JIANG Zhengwu, YIN Jun.Technical principles and approaches for development of sustainable concrete[J]. Joural of Building Materials, 19(6):957-963.(2016).(in Chinese)
3. ESMAEILKHANIAN B.KHAYAT K H.WALLEVIK O H. Mix design approach for low-powder self-consolidating concrete: Eco-SCC-Content optimization and performance [J]. Materials and Structures,50:124 (2017).
4. DOMONE P L.Self-compacting concrete:An analysis of 11 years of case studies [J]. Cement and Concrete Composites, 28 (2):197-208 (2006) .
5. HUSKEN G,BROUWERS H J C.A new mix design concept for earth-moist concrete:A theoretical and experimental study [J]. Cement and Concrete Research, 38(10):1246-1259(2008).
6. S.Bhattacharja, M.Moukwa, F.D'Orazio, et al., Microstructure determination of cement pastes by NMR and conventional techniques.Adv.Cem.Based Mater. 1(2)67-76(1993).
7. Q Zhang.G.Ye, E.Koenders, Investigation of the structure of heated Portland cement paste by using various techniques, Constr.Build.Mater. 38 (2) 1040-1050(2013)

Research on the effect and mechanism of binder-sand ratio on UHPC performance

MA Qiang[1,2], ZHANG Jiangtao[1,2*], XUE Tong[1*], QU Haiyang[1,2], FAN Deke[1,2], LIU Ruichao[1,2], BAI Jie[1], XU Wenying[1], WANG Bo[1]
[1]China Building Materials Academy Co.,Ltd, No.1 Guanzhuangdongli, Beijing, China
[2]CNBM Zhongyan Technology Co.,Ltd, No.1 Guanzhuangdongli, Beijing, China
xuetongcbma@163.com

Abstract: This paper focuses on the working and mechanical properties of UHPC under the conditions of different binder sand ratios. Mercury-in-pressure (MIP) was used to characterize the effect of different binder sand ratios on the pore structure evolution of UHPC hydrated slurry, and the types of hydration products and microstructure change rules in the slurry were analyzed with the help of thermal analysis (TG-DTG) and SEM. The results showed that the extensibility of UHPC decreased with the increase of the binder-sand ratio(0.9~1.2), and when the binder sand ratio was 1.1, the mix flowed relatively well and had the best mechanical properties at all ages. With the increase of the rubber-sand ratio, the flow index of the mix is getting larger and larger, and the hydrated slurry all shows the trend of slurry thickening. When the binder-sand ratio is 1.0 and 1.1, the hydration process of the slurry is faster, the generation of hydration products is high, there are more gelling pores and mesopores, relatively few macropores, and the slurry densification is higher, resulting in the best mechanical properties of the hardened slurry, especially when the binder-sand ratio is 1.1.

Keywords: Ultra-high performance concrete, Binder-sand ratio, Porosity.

1 Introduction

Ultra-high performance concrete (UHPC) is a new type of cementitious composite material with ultra-high strength, good toughness and excellent durability[1, 2] . UHPC is composed of cement, auxiliary cementitious materials, fine sand, steel fibers and water reducing agent, with ultra-low water-cementitious ratio (0.15~0.25) and ultra-high densification[2] . The ultra-high toughness of UHPC depends on the type of fibers and the amount of fiber admixture, and among the many kinds of fibers (fibers, including steel fibers, carbon fibers, glass fibers, synthetic fibers etc.), steel fibers are the most effective in increasing the toughness of UHPC . including steel fiber, carbon fiber, glass fiber, synthetic fiber, etc.), steel fiber is the most effective in improving the toughness of UHPC[3] . Due to its excellent performance, UHPC is widely used in large-span bridges, plate structures, thin-shell structures, nuclear power, etc.[4-6] .

Achieving a dense structure is crucial for preparing UHPC. Researchers employ the Fuller, Andreasen, and Dinger-Funk models to optimize particle grading and form

a dense matrix[7-9]. A well-graded aggregate can significantly decrease the porosity of UHPC and enhance its compactness to achieve the best workability and mechanical properties. The design of UHPC mixing ratio typically relies on the particle close-packing model. The close-packing state of the cementitious material is altered by adjusting the binder sand ratio (B/S), thereby changing the optimal ratio of each component of the cementitious material accordingly[10]. A low B/S results in a low content of cementitious material in the matrix, which is unfavorable for the strength development of the UHPC matrix[11]. According to Shi Chengjie et al., the optimal overall performance of UHPC was observed when the B/S ranged from 1.0 to 1.3[12]. Zhou Min et al. found that as the B/S increased from 0.8 to 1.2, the fluidity and wet packing density increased progressively, and the 7-day compressive strength also increased gradually. However, the highest 28-day compressive strength was achieved at the B/S of 1.0[10].

The total pore volume and size of UHPC are significantly lower than those of ordinary concrete. Given the dense nature of this material, the appropriateness of the cement-sand ratio is vital for UHPC performance. This study systematically investigated the impact of various cement-sand ratios (0.9-1.2) on the workability, mechanical properties, and durability of UHPC from a proportion design standpoint. Through analyzing the evolution of pore structure in hydrated UHPC slurry, its rheological properties, and the changes in type and microstructure of hydration products under various B/Ss, this study aims to offer theoretical insights for optimizing the design of UHPC materials.

2 Raw materials and test methods

2.1 Raw materials

P·II 52.5 silicate cement with a specific surface area of 385m2/kg S105 grade mineral powder with a density of 2.85g/cm3. Silica fume had a specific surface area of 22.45m2/g. The chemical compositions of the three raw materials are shown in Table 1. Aggregate was coarser quartz sand ranging from 0.3 to 0.65mm and finer quartz sand ranging from 1.5 μ m to 0.30mm, respectively. The steel fibers were end-hooked steel fibers with a diameter of 0.22mm and a length of 13mm and flat steel fibers with a diameter of 0.22mm and a length of 13mm. A homemade polycarboxylate superplasticizer(PCE) was used with a solid content of 30%. Swellers and polyether defoamers were introduced.

Table 1 Chemical composition of cement, mineral powder and silica fume

-	CaO	Al_2O_3	SiO_2	Fe_2O_3	SO_3	MgO	NaO_2	KO_2
Cement	64.49	4.05	20.65	3.22	2.53	0.60	0.04	0.68
Mineral powder	39.24	21.45	32.68	0.43	0.36	1.23	0.56	0.26
Silica fume	0.56	0.25	97.23	0.35	0.05	0.26	0.18	0.15

2.2 Preparation methods

The ingredients are blended in a mixer based on their respective mixing ratios. After thorough mixing, the UHPC premix was blended with water in a single horizontal shaft forced mixer for 240 seconds. Subsequently, steel fibers were uniformly incorporated within 120 seconds, followed by an additional 240-second stirring before shaping. The blended UHPC was poured into a steel test mold and vibrated for 20 seconds. Additionally, the extent of expansion and the 2-hour loss of UHPC were evaluated. The molded specimens are then placed in a standard curing room and allowed to cure until the specified testing age.

2.3 Mixture design

Table 2 mix proportion of UHPC

Name of the ingredient / Other concrete parameter		Quantity of different UHPC ingredient of different sample ID					
		B/S-0.9	B/S-1.0	B/S-1.1	B/S-1.2	B/S-1.1$_S$	B/S-1.1$_T$
Cement		960	960	960	960	960	960
Fly ash		150	150	150	150	150	150
Mineral powder		130	130	130	130	130	130
Quartz sand	Coarser	1160	1043	940	855	930	930
	Finer	207	186	178	170	188	188
Expansive agent		0.5	0.5	0.5	0.5	0.5	0.5
Defoaming agent		1.6	1.6	1.6	1.6	1.6	1.6
PCE		28	28	28	28	28	28
water-material ratio		0.09	0.09	0.09	0.09	0.09	0.09
Steel fiberbas	End-hooked	/	/	/	/	/	2.5
	Straight	2	2	2	2	2.5	/

Note: Datas for steel fiber are its volume percentage.

2.4 Test methods

Macroscopic properties: The extensibility and time loss of UHPC were tested in accordance with GB/T 50080-2016 Standard Test Methods for Properties of Ordinary Concrete Mixes.The mechanical properties of UHPC were tested with reference to GB/T 50081-2019 Standard Test Methods for Physical and Mechanical Properties of Concrete.The size of compressive test specimen was 100mm×100mm ×100mm, and the size of flexural test specimen was 100 mm × 100 mm × 400 mm.The flexural and compressive strength tests of UHPC were conducted by universal testing machine with loading rates of 0.8MPa/s and 0.2mm/min, respectively.The tensile properties of UHPC were tested according to T/CCPA7-2018 "Basic Properties and Test Methods of Ultra-High Performance Concrete". The rheological behavior of UHPC was tested using a Viskomat XL rheometer from Schleibinger, Germany.

Microscopic properties: The hydrated specimens of UHPC at various ages were selected after the mechanical property tests, and the internal intact samples were soaked in ethanol for 24h to abort hydration, and the samples were dried in a vacuum oven at 40℃ before microscopic tests. Thermogravimetric (TG-DTG) analysis was

carried out using a NETZSCH STA 449C synchronous thermal analyzer with a heating rate of 20℃/min and a temperature range of 30~1000℃. A Quanta 250FEG scanning electron microscope was used to test the morphology of the hydrated products, and the samples were in the form of thin sheets, and the morphology SEM was carried out after gold spraying.The porosity and pore structure (MIP) test of the hydrated samples was carried out by Autopore III 9510 mercuric piezometer with the sample size of about 20mm and the working pressure of 410MPa.

3 Results and Discussion

3.1 Effect of different grit ratios on UHPC extensibility

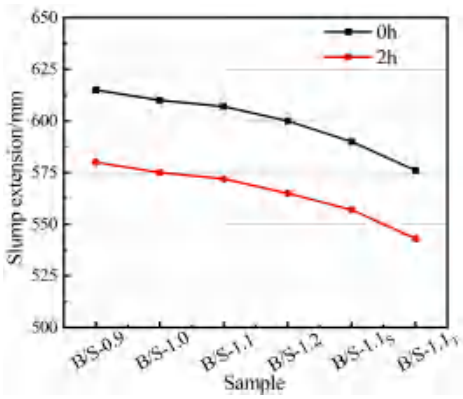

Fig. 1 Effect of different binder sand ratios on UHPC extensibility

Fig.1 shows the effect of different grit ratios on the extensibility of UHPC. In the range of 0.9~1.2, the extensibility of UHPC decreased to different degrees with the increase of the B/S. Due to the same water to material ratio, the B/S increases, the water to ash ratio decreases, the frictional resistance and cohesion between the particles of cementitious materials increases, the mixture is more viscous, and the extension degree decreases. When the B/S is between 0.9 and 1.1, the fluidity of the mix decreases to a lesser extent, and when the B/S increases to 1.2, the decrease increases significantly. Due to the low B/S, the residual water in the matrix is less, the interface transition zone between steel fiber and matrix is difficult to form a structurally loose water film, and the hydrated slurry aggregation leads to a viscous slurry with poor fluidity[13].

When the volume admixture of flat steel fibers was increased from 2% to 2.5% at a B/S of 1.1, the extensibility of the UHPC mix decreased and the flowability deteriorated under the same conditions. This may be due to the fact that the dispersion of steel fibers becomes more and more heterogeneous (agglomerated distribution) as the dosage increases, resulting in poorer flowability of the mix. When the flat steel fibers were replaced with end-hook shaped steel fibers, the extensibility continued to decrease. The initial extensibility and the 2 h warp time loss presented the same pattern.

3.2 Different binder sand ratios on the mechanical properties of UHPC

The effects of different binder sand ratios and steel fibers on the mechanical properties of UHPC are shown in Figure 2. The compressive strength, flexural strength and tensile strength of UHPC were the lowest when the sand ratio was 0.9. With the increase of the ratio of silica sand, the mechanical properties of UHPC increased, and when the ratio of silica sand was 1.1, the strength was the highest, the 28d compressive strength was 147 MPa, the flexural strength was 18.3 MPa, and the tensile strength was 8.3 MPa. However, with the increase of the ratio of silica sand to 1.2, the mechanical properties of UHPC began to decrease again. Since the water to material ratio is the same, the binder sand ratios increases and the water to ash ratio decreases. When the water-cement ratio is larger, the residual water in the mix is more, the transition zone of the aggregate interface forms a structurally loose water film, and the densification of the matrix is reduced, thus affecting the strength[14] . When the binder sand ratio is 1.2, due to little residual moisture in the matrix pores, the hydration reaction mainly occurs on the surface of the cementitious material, and the cementitious material is completely wrapped in the hydration products, which affects further hydration and leads to a reduction in strength.

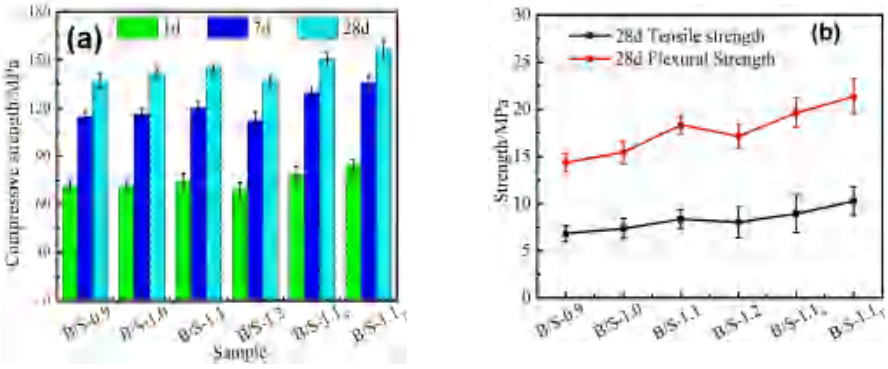

Fig. 2 Effect of different binder sand ratios on (a) compressive strength and (b) flexural and tensile strength of UHPC

The mechanical properties of UHPC increased when the volume doping of flat steel fibers was increased from 2% to 2.5% at a binder sand ratio of 1.1. When the volume dosage is 2.5%, after replacing the flat steel fibers with the same dosage of end-hooked steel fibers, the hardened body of UHPC has the best mechanical properties, with a 28d compressive strength of 155MPa, a flexural strength of 21.3MPa, and a tensile strength of 10.2MPa. It shows that increasing the dosage of the steel fibers or changing the shape of the steel fibers (end-hooked shape) can improve the mechanical properties of UHPC.

3.3 Different binder sand ratios on the rheological properties of UHPC

The Herschel~Bulkley model (H~B model) can be fitted to the rheological behavior of cementitious materials with the model equation shown in Eq. 1~1[15].

$$\tau = \tau_0 + k \times r^n \tag{1-1}$$

where τ is the shear stress(Pa); τ_0 is the yield stress(Pa); k (Pa-s); r is the shear rate (s^{-1}); and n is the flow index.

In order to investigate the effect of different binder sand ratios on the working performance of UHPC, the rheological properties of UHPC hydrated slurry with different binder sand ratios were tested. Table 3 shows the rheological parameters of different slurries fitted according to the H~B model, and R^2 is the correlation coefficient, which represents that this model can well characterize the change process of shear stress with shear rate of UHPC hydrated slurry with different binder sand ratios[16].

Table 3 Rheological parameters of UHPC hydrated slurry

Sample	τ_0 /Pa	K/Pa-s	n	R^2
B/S-0.9	8.39	1.20	1.39	0.999
B/S-1.0	11.54	1.18	1.42	0.999
B/S-1.1	11.46	0.94	1.45	0.998
B/S-1.2	9.80	0.41	1.53	0.998

The adhesion and friction between the particles inside the UHPC hydrated slurry produces a yield stress τ_0 , which the hydrated slurry needs to overcome in order to produce plastic deformation. When the shear rate r is 0, the shear stress is the yield stress τ_0 . As seen in Table 3, the yield stress of the hydrated slurry shows a trend of increasing and then decreasing when the binder sand ratio is increased from 0.9 to 1.2, and the yield stress is the lowest when the binder-sand ratio is 0.9 at 9.80Pa, and similarly at around 11.50Pa when the binder sand ratios are 1.0 and 1.1. The flow index of the hydrated slurry showed an increasing and then decreasing trend with the increase of the binder-sand ratio. When the flow index is greater than 1, the hydrated slurry shows a tendency of slurry thickening. From Tab.3, it can be seen that the flow index of all the hydrated slurries is higher than 1, which indicates that the cement-sand ratio is in the range of 0.9~1.2, the hydrated slurries show the tendency of slurry thickening, and the flow index is also increasing, which indicates that with the increase of the cement-sand ratio, the tendency of slurry thickening is more and more obvious, and the increase of the content of cementitious material makes the slurry more and more thick.

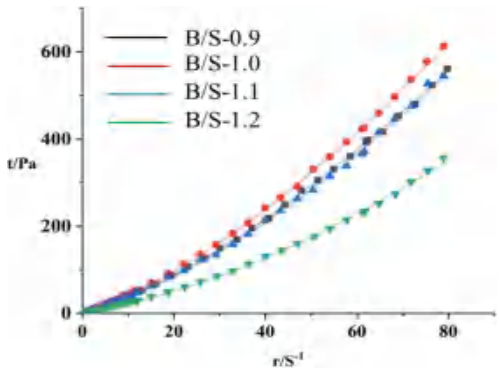

Fig 2 Rheological curves of UHPC hydrated slurry

3.4 Effect of different binder sand ratios on porosity of UHPC hydrated slurry

The pore size distribution and porosity of UHPC hydrated 28d slurries under different binder sand ratios are shown in Fig. 4, where the pore sizes range from about 0.01 nm to 200 μm. As can be seen from Fig. 4(a), the pore size distribution of all hydrated samples shows a single peak, and the pore sizes at the peaks of dv/dlog(d) curves are in the range of about 0.02 to 0.1100 nm[17] . The dv/dlog(d) curves of the prepared UHPC hydrated slurries were similar at the binder sand ratio of 0.9~1.1, and the dv/dlog(d) curves shifted to the left at the binder sand ratio of 1.2, which implied that the critical pore size decreased and the pore distribution was refined. Fig. 4(b) shows the porosity of the samples, which is about 26% for the hydrated samples with a binder sand ratio of 0.9 and 1.0, and about 31% for the hydrated samples with a binder sand ratio of 1.1 and 1.2.

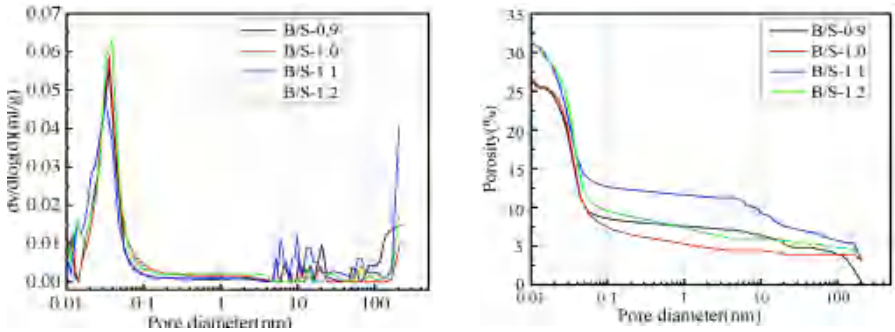

Fig. 4 (a) pore size distribution and (b) porosity of different samples

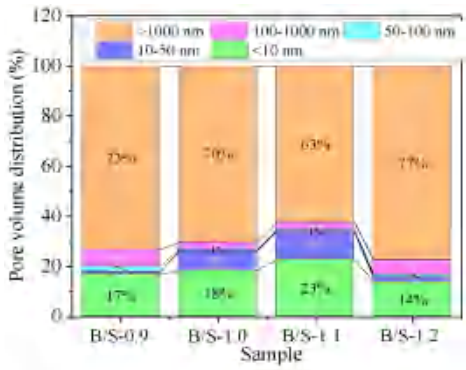

Fig 5 Pore volume distribution of different samples.

The pores of cement-based materials are categorized as follows: gel pores(d<10nm), mesoporous pore(10nm<d<50nm), medium pores(50nm<d<100nm), Large pores(100nm<d<1000nm), and macropores (d>1000nm)[18]. As can be seen from Fig.5, the pores in all hardened slurries are mainly macropores larger than 1000nm, followed by gelatinous pores with diameters less than 10nm[19] . Among them, at the binder sand ratio of 1.1, the gelatinized pores and mesopores were the most (23%) and the macropores were the least (63%). At 1.2, the cementitious pores are the least

and the macropores are relatively more. This result indicates that at a binder sand ratio of 1.0, the UHPC hydrated slurry has more small pores and fewer macropores, the slurry has the highest densification, and all mechanical properties are relatively high. When the binder sand ratio is 0.9 and 1.0, the compactness of the slurry is relatively low. When the binder sand ratio is 1.2, the pores are the most, and the density of the slurry is small, so the mechanical properties are the worst.

3.5 TG-DTA of hydration products

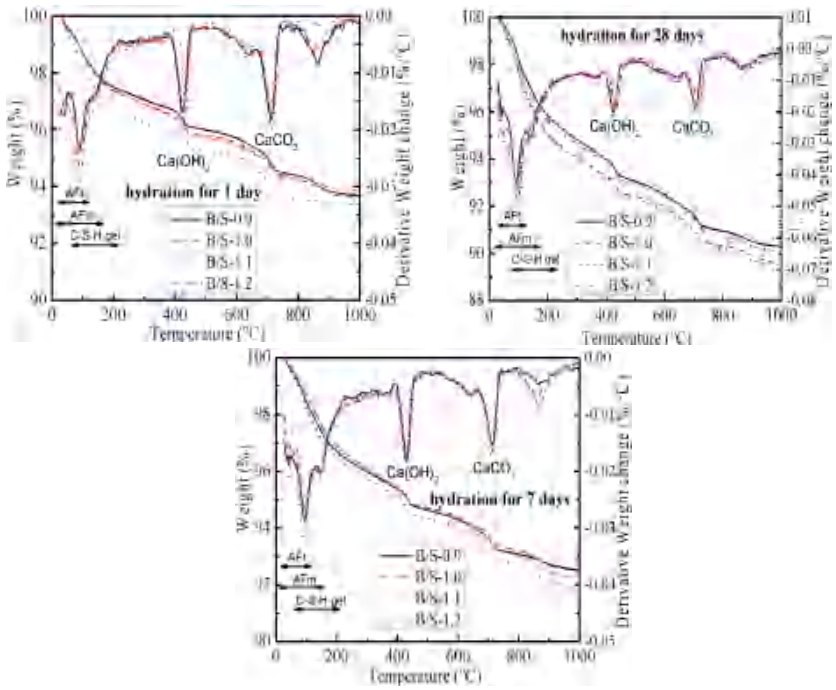

Fig. 6 Thermal analysis curves of different hydrated samples

The thermal analysis curves of UHPC hydrated slurry under different binder sand ratios are shown in Fig. 6, and the dehydration peaks of C-S-H gel[20] , AFt, $Ca(OH)_2$ and the decomposition peak of $CaCO_3$ appeared in the thermal analysis curves at around 100 °C, 150 °C, 400 °C and 700 °C. The thermal analysis curves of UHPC hydrated slurry under different binder sand ratios are shown in Fig. 6, and the thermal analysis curves of UHPC hydrated slurry under different binder sand ratios are shown in Fig. 6. From the heat loss curves, the binder sand ratio had almost no effect on the types of hydration products of UHPC hydrated slurry, and the heat loss peaks of the above hydration products appeared in each sample, but it affected the amount of hydration product generation, and the heat loss weight of each hydration product was different. At 1d of hydration, the weight of heat loss of hydration products was significantly higher than that of other samples when the binder sand ratios was 1.1. It shows that under the condition of this binder sand ratio, the water in the hydrated slurry is uniformly distributed, and the cementitious material is fully hydrated, with a

high degree of hydration. At 7d of hydration, the weight of heat loss of hydration products showed the same pattern as that of 1d of hydration, but the gap gradually narrowed. After 28d of hydration, the weight of heat loss of hydration products is similar when the binder sand ratio is 1.0 and 1.1, which is much higher than that of hydration products in the other two groups of slurries. This indicates that the hydration process of the hydrated slurry is faster and the product generation is higher when the binder sand ratio is 1.0 and 1.1. Combined with the results obtained from MIP, the relatively higher densities of the hydrated slurries at the binder sand ratios of 1.0 and 1.1 indicate that the mechanical properties of UHPC prepared under these conditions are superior.

3.6 SEM analysis of hydration products

The microscopic morphology of the hydration products in UHPC hydrated slurries under different binder sand ratios is shown in Fig. 7, where clustered AFm and hexagonal platelets of Ca(OH)2 interspersed with needle-and-rod AFt were observed in all samples within the same field of view. The morphology of the hydration products was similar in different samples, but more hydration products were observed in the hydrated slurries at the binder sand ratios of 1.0 and 1.1. In the hydrated slurry with a binder sand ratio of 1.0, the size of the hydration products was relatively large, with the lamellar distribution of platelet Ca(OH)2 and the flake AFm in the form of flower clusters, and the relative distributions of the two products in the slurry were relatively several. The cluster-like AFm and hexagonal plate-like Ca(OH)2 cross each other in the hydrated slurry with a binder sand ratio of 1.1, and the whole slurry has a high degree of compactness. This result is consistent with the results obtained from pore structure and thermal analysis.

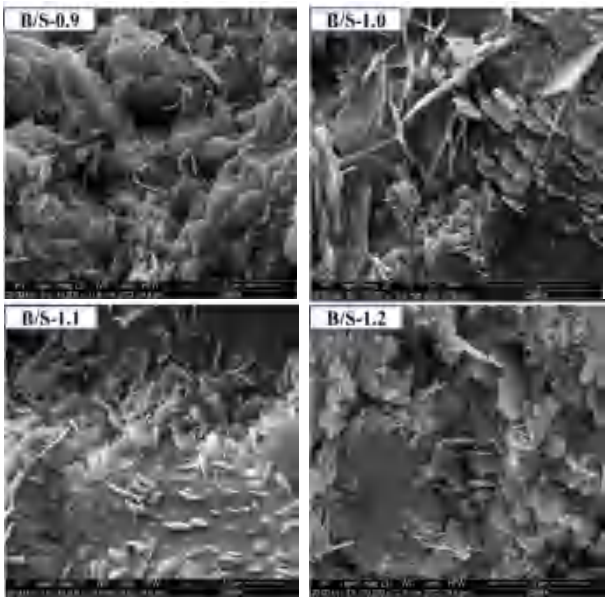

Fig. 7 Microscopic morphology of products hydrated for 7d in different samples

4 Conclusion

Based on the present research work & interpretation of results based on the various facts. The following are the key outcome of the present research works.

(1) Through the analysis of rheological properties, the flow index of UHPC binder sand ratio is greater than 1 in the range of 0.9~1.2, and the hydrated slurries all show the trend of slurry thickening. The extension degree decreased less with the increase of the binder sand ratio (0.9~1.1), and when the binder sand ratio increased to 1.2, the hydrated slurry aggregation resulted in a viscous slurry with poorer flowability.

(2) When the binder sand ratio is 1.1, the pulp has the most gelatinous pores and mesopores (23%) and the least macropores (63%), and the density of the hydrated pulp is relatively high. When the binder sand ratio is 1.2, the gelatinous pores and mesopores in the slurry are the least, the macropores are the most, and the density of the slurry is poor.

(3) When the binder sand ratio is 1.1, the water in the hydrated slurry is uniformly distributed, the cementitious material is fully hydrated, the degree of hydration is higher, and the amount of product generation is higher, and the mechanical properties such as compressive, flexural and tensile strength of UHPC prepared under these conditions are better.

Acknowledgements

This work were financially supported by the program fund of non-metallic excellence and innovation center for building materials (Project No. 2022TDA3-1).

References

1. K Khayat, W Meng, K Vallurupalli, et al. Rheological properties of ultra-high-performance concrete - An overview [J]. Cement and Concrete Research, (124): 105828 (2019).
2. D Fan, J Zhu, M Fan, et al. Intelligent design and manufacturing of ultra-high performance concrete (UHPC) - A review [J]. Construction and Building Materials, (385): 131495 (2023).
3. Z Wu, C Shi, W He, et al. Effects of steel fiber content and shape on mechanical properties of ultra high performance concrete [J]. Construction and Building Materials,(103): 8-14 (2016).
4. Z Wu, K H Khayat, C Shi. Effect of nano-SiO2 particles and curing time on development of fiber-matrix bond properties and microstructure of ultra-high strength concrete [J]. Cement and Concrete Research,(95): 247-256 (2017).
5. J Xue, B Briseghella, F Huang, et al. Review of ultra-high performance concrete and its application in bridge engineering [J]. Construction and Building Materials,(260): 119844 (2020).
6. G Habert, D Arribe, T Dehove, et al. Reducing environmental impact by increasing the strength of concrete: quantification of the improvement to concrete bridges [J]. Journal of Cleaner Production,(35): 250-262 (2012).

7. Xinpeng Wang. Design and evaluation of ecological ultra-high performance concrete based on the theory of tightest stacking [D]. Wuhan University of Technology, 2018.
8. HUANG Xinghao, ZHANG Xin, LI Zhe et al. Research on particle grading of mechanism sand based on Fuller and Tebb theory[J]. Concrete, (4): 97-101 (2019).
9. YU Rui, FAN Dingqiang, SHUI Zhonghe, WANG Xinpeng. Design of ultra-high performance concrete proportion based on the theory of closest packing of particles[J]. Journal of Silicates, 48(8): 1145-1153 2020.
10. Zhou M, Wu Zemei, Ouyang Xue et al. Effects of composition and aggregate properties on the fluidity and compressive strength of UHPC matrix[J]. Materials Guide, 37(18): 22060073 2023.
11. S Khan, Hao Y, et al. Effects of curing conditions and sand-to-binder ratios on compressive strength development of fly ash geopolymer.[J]. Journal of Materials in Civil Engineering, 30(2): 04017267 (2018).
12. SHI Cheng-Jie, QIU Wen-Jun. Design of quartz sand grading and optimum mixing amount in ultra-high performance concrete[J]. Roadbed Engineering, 5: 114-119 (2021).
13. Gong Zhiyuan, Gu Bingwei, Zou Jinli et al. Study on the early performance of UHPC with different mixing ratios[J]. New Building Materials, 6: 27-35 (2023).
14. Akaolu T, Tokyay M, elik T. Assessing the ITZ microcracking via scanning electron microscope and its effect on the failure behavior of concrete [J]. Cement and Concrete Research, 35(2): 358-363 (2005).
15. Li Bin. Synthesis and performance of side chain end-grafted β-cyclodextrin polycarboxylic acid water reducing agents [D]. China General Research Institute of Building Materials, 2022.
16. B. Wu. Influence of rheological properties on the stability of fresh concrete [D]. China General Research Institute of Building Materials Science, 2019.
17. Z Cheng, J Zhao, L Cui. Exploration of hydration and durability properties of ferroaluminate cement with compare to Portland cement [J]. Construction and Building Materials,(319): 126138 (2022).
18. M Oltulu,R Şahin. pore structure analysis of hardened cement mortars containing silica fume and different nano-powders [J]. Construction and Building Materials,(53): 658-664 (2014).
19. Z Wu, C Shi, K H Khayat. Influence of silica fume content on microstructure development and bond to steel fiber in ultra-high strength cement-based materials (UHSC) [J]. Cement and Concrete Composites,(71): 97-109 (2016).
20. H F W Taylor,A B Turner. Reactions of tricalcium silicate paste with organic liquids [J]. Cement and Concrete Research, 17(4): 613-623 (1987).

硫铝酸盐水泥基预拌流态固化土固化剂性能的研究

李悦[1]，齐帜飏[1]，林辉[1]，王保亮[2]，张超[2]，郭秋生[3]

（1.北京工业大学 城市与工程安全减灾教育部重点实验室，工程抗震与结构诊治北京市重点实验室，北京 100124；

2.中铁河北投资开发建设有限公司，河北 廊坊 065000；3.北京财贸职业学院 建筑工程管理学院，北京 101101）

摘要：以硫铝酸盐水泥和二水石膏为原材料制备了预拌流态固化土固化剂，以强度、体积膨胀率和成本为指标进行同化剂配选。以胶土比 1:9 制备固化土试样，进一步研究了硫铝酸盐水泥与二水石膏的比例对固化土抗压强度和体积稳定性的影响。结果表明，固化剂胶砂的抗压和抗折强度均随硫铝酸盐水泥掺量的增加先提高后降低再提高。硫铝酸盐水泥掺量的增加有利于固化土试样抗压强度和体积稳定性的改善。硫铝酸盐水泥与二水石膏最优配比为 7:3，采用该固化剂制备的固化土试样 28 d 体积收缩率为 0.08%，抗压强度为 1.3 MPa。

关键词：土壤固化剂；固化土；抗压强度；体积稳定性；多指标评价

中图分类号：TU528.044 **文献标识码：**A **文章编号：**1001-702X（2023）03-0042-04

Research on properties of sulfoaluminate cement-based premixed fluid solidified soil curing agent

LI Yue[1], *QI Zhiyang*[1], *LIN Hui*[1], *WANG Baoliang*[2], *ZHANG Chao*[2], *GUO Qiusheng*[3]

（1.Key Laboratory of Urban Security and Disaster Engineering of Ministry of Education，Beijing Key Laboratory of Earthquake Engineering and Structural Retrofit，Beijing University of Technology，Beijing 100124，China；

2.China Railway Hebei Investment Development and Construction Co. Ltd.，Langfang 065000，China；

3.School of Civil Engineering Management，Beijing College of Finance and Commerce，Beijing 101101，China）

Abstract: The premixed fluid-solidified soil curing agent was prepared with sulfoaluminate cement and gypsum dihydrate as the raw materials，whose proportion is selected with strength，volume expansion rate and cost as the inolices. The solidified soil sample is prepared with the ratio of cement to clay 1:9. The effect of the relative ratio of sulphoaluminate cement and gypsum dihydrate on the compressive strength and volume stability of the solidified soil sample is further studied. The results show that the compressive strength and flexural strength of curing agent mortar increase first，then decrease and then increase with the increase of sulfoaluminate cement content. The increase of sulphoaluminate cement content is beneficial to improve the compressive strength and volume stability of solidified soil samples. The optimal ratio of sulfa-aluminate cement to gypsum dihydrate is 7:3，and the volume shrinkage rate and compressive strength of solidified soil samples prepared with this curing agent are 0.08% and 1.3 MPa respectively.

Key words: soil curing agent，cured soil，compressive strength，volume stability，multi-index evaluation

0 引 言

随着城市化进程的快速推进，地下空间得到越来越广泛的利用和开发，基坑或基槽的回填是地下空间开发过程中不可避免的工程问题。对于较大的浅基坑，回填土分层夯实是一种简单有效的施工技术，但是对于深基坑、狭窄或异形基槽，回填土分层夯实技术不仅不能保证高压实度，而且施工效率较低。为了提高特殊部位回填的质量，预拌流态固化土处理技术越来越受到关注。预拌流态固化土处理技术主要是以水泥、石膏、粉煤灰、矿渣或地聚物等胶凝性材料作为固化剂，利用固化剂的胶结作用将土粒胶结在一起，从而显著提高松散土体的物理力学性能，使之成为相对强度高、密度大、孔隙小、压实度高且可泵送的工程材料[1]。

常见的流态土固化剂有普通硅酸盐水泥、复合水泥或碱激发地聚物等[1-6]。杜衍庆等[2]在土中掺入 15%的普通硅酸盐

基金项目：中铁河北投资开发建设有限公司委托项目；非金属材料创新中心应用示范类项目（2022SFP2-1）

收稿日期：2022-06-29

作者简介：李悦，男，1972 年生，博士，教授，博士生导师，主要从事建筑材料方向的研究，E-mail：liyue@bjut.edu.cn。通讯作者：齐帜飏，硕士研究生，E-mail：744755907@qq.com。

(C)1994-2023 China Academic Journal Electronic Publishing House. All rights reserved. http://www.cnki.net

水泥，所得固化土试样的 28 d 无侧限抗压强度达 500 kPa 左右。李建望[3]在调整淤泥含水量的基础上，掺入 160 g/L 的普通硅酸盐水泥，制备的淤泥质固化试样符合相应的施工要求，其 28 d 无侧限抗压强度为 70~100 kPa。范猛[4]以水与固体材料的质量比（水固比）作为非压实回填土的配合比设计参数之一，其研究结果表明，以普通硅酸盐水泥作为固化剂时的最佳水固比为 0.42。刘成龙[1]使用矿渣水泥和粉煤灰复合胶凝材料作为固化剂对土壤进行固化，研究发现，矿渣水泥与粉煤灰的最佳质量比为 2:1，当 m（砂土）:m（黏土）:m（固化剂）:m（水）=7.5:7.5:1.5:2.6 时，预拌流态固化土的 28 d 无侧限抗压强度为 2.08 MPa。易富等[5]采用碱激发地聚物对工程渣土进行固化，结果表明，掺入 5%~15%的稻壳灰可以使固化土强度提高 10%~15。赵高飞[6]以钢渣、矿渣等固废基碱激发地聚物作为土壤固化剂对土体进行固化，正交试验的结果表明，全固废预拌固化剂的最佳配比为 m（钢渣）:m（矿渣）:m（脱硫石膏）=0.10:0.78:0.12，当最优固化剂掺量为 40%、水料比控制为 0.35 时，预拌流态固化土的 28 d 无侧限抗压强度高达 18.2 MPa。Do 和 Kim[7]使用赤泥部分替代普通硅酸盐水泥制备可控低强材料（Controlled low strength material，简称 CLSM），结果表明，以赤泥为主要原料的 CLSM 的抗压强度均符合强度要求（≥800 kPa）。Jamali 和 Naganathan[8] 采用粉煤灰、石灰和 NaOH 制备 CLSM，所得 CLSM 的抗压强度为1.10~3.35 MPa，掺入石灰和 NaOH 有助于 CLSM 强度的发展。早期对流态固化土的研究更多的是关注其工作性能和力学性能，随着研究的深入和工程应用的扩展，发现其收缩性能不容忽视。Qian 等[9]的研究表明，水泥含量高、砂土比低的试样收缩应变明显较大，其收缩应变一般在 1389 με~6612 με，且在 13~15 d 时达到稳定。高强[10]在预拌流态固化土中掺入少量的硫铝酸盐水泥，研究发现，水泥水化产物钙矾石（AFt）膨胀填充固化土中的孔隙是提高固化土强度和体积稳定性的主要因素。

从上述研究可以看出，硫铝酸盐水泥与二水石膏混合制备流态土固化剂的研究较少，关于考虑成本的固化剂配合比优化设计方法未见报道。为了弥补研究存在的不足以及进一步促进预拌流态土固化剂技术在回填工程中的推广和应用，本文研究了硫铝酸盐水泥与二水石膏的比例对流态土固化剂抗压强度、抗折强度和体积膨胀率的影响，同时以强度、体积膨胀率和成本为评价指标，采用综合评分法对硫铝酸盐水泥基流态土固化剂的性能进行综合评估，旨在获得高强、高体积膨胀率和低成本的流态土固化剂配合比。然后利用优选的 3 组流态土固化剂，以胶土比 1:9 制备固化土试样，进一步研究了硫铝酸盐水泥与二水石膏的比例对固化土试样抗压强度和体积稳定性的影响。

1 试 验

1.1 原材料

硫铝酸盐水泥（SAC）：42.5 级，唐山北极熊建材有限公司生产，比表面积为 334 m^2/kg；石膏：焦作华岩水泥厂生产的二水石膏，密度为 2.3 g/cm^3。硫铝酸盐水泥和石膏的化学成分见表 1。土：黏土，含水率为 12.1%，塑限为 15.4%，液限为 22.9%。

表 1 硫铝酸盐水泥和石膏的化学成分 %

项目	CaO	SO_3	Al_2O_3	SiO_2	Fe_2O_3	MgO	TiO_2	SrO	Loss
SAC	52.17	21.10	15.44	5.89	1.72	1.35	1.43	0	0.90
石膏	48.19	50.97	0.12	0.29	0.07	0.08	0	0.24	0.04

1.2 试样制备

1.2.1 固化剂试样的制备

石膏用量按 0、10%、20%、25%、30%、35%、40%、45%、50%、60%、70%，其余为硫铝酸盐水泥，配合成固化剂，再与石英砂以 1:3 的质量比搅拌均匀，水胶比为 0.6，试模尺寸为 4 cm×4 cm×16 cm，在室温下养护 6 h 后脱模，并在（20±2）℃、相对湿度 95%环境中继续养护至规定龄期测试抗压和抗折强度。

按上述水泥与石膏配比制备固化剂净浆试样，水胶比为 0.6，将搅拌均匀的水泥净浆缓慢倒入直径 30 mm，高 30 mm 的硅胶模具和 4 cm×4 cm×16 cm 的钢模具中，在室温下养护 6 h 后脱模，随后将试样放入（20±2）℃，相对湿度 95%环境中继续养护至规定龄期测试体积稳定性和抗压强度。

1.2.2 固化土试样的制备

在黏土中加入过量的水，充分搅拌后静置 24 h 使土自然沉淀，过滤掉上层清水，得到液限状态下的饱和土。然后按胶土比 1:9 将两者混合，水固比 0.2，最后将搅拌均匀的流态固化土缓慢倒入 4 cm×4 cm×16 cm 钢模具中，在室温下养护 24 h 后拆模，脱模试样置于室内干燥环境下继续养护至 7 d 和 28 d，分别测试其抗压强度和体积稳定性。

1.3 测试方法

1.3.1 力学性能测试

固化剂胶砂试样和净浆试样的力学性能按照 GB/T 17671—2021《水泥胶砂强度检验方法（IOS 法）》进行测试；预拌流态固化土的力学性能按照团体标准 T/BGEA 001—2019《预拌流态固化土填筑工程技术标准》进行测试。

1.3.2 膨胀性能测试

使用雷氏夹膨胀测定仪测试固化剂净浆试样的膨胀性能，将圆柱形净浆试样夹至雷氏夹圆口处，然后水平放置在测定仪上，分别测量试样在 6 h、3 d 和 7 d 时雷氏夹的开口大

(C)1994-2023 China Academic Journal Electronic Publishing House. All rights reserved. http://www.cnki.net

小，并通过式(1)计算得到相应的膨胀率。

$$3\ d/(7\ d)\ 膨胀率=\frac{3\ d/(7\ d)\ 开口大小-6\ h\ 开口大小}{6\ h\ 开口大小}\times 100\% \tag{1}$$

1.3.3 流动性能测试

预拌流态固化土的流动度按照 GB/T 2419—2005《水泥胶砂流动度测定方法》进行测试。

1.3.4 体积收缩率测试

预拌流态固化土的体积收缩率测试方法：用游标卡尺测量试块 7 d 或 28 d 的长、宽、高，并计算其体积。试模体积 4 cm×4 cm×16 cm=256 cm^3 与试块体积实测值之差除以试模体积定义为体积收缩率。

2 结果与讨论

2.1 硫铝酸盐水泥基固化剂

2.1.1 硫铝酸盐水泥与二水石膏比例对固化剂胶砂试样力学性能的影响(见表 2)

表 2 硫铝酸盐水泥基固化剂胶砂试样的力学性能

硫铝酸盐水泥掺量/%	石膏掺量/%	抗压强度/MPa		抗折强度/MPa	
		7 d	28 d	7 d	28 d
30	70	20.6	24.1	4.5	5.4
40	60	22.5	29.5	4.9	6.2
50	50	26.2	37.7	5.0	8.5
55	45	31.1	38.7	5.8	8.0
60	40	30.3	47.0	7.7	8.9
65	35	28.8	42.6	7.0	8.3
70	30	31.5	48.8	6.8	8.1
75	25	38.5	49.1	6.6	8.0
80	20	39.2	51.2	6.8	8.4
90	10	45.3	55.6	8.8	9.6
100	0	53.8	58.7	11.0	12.3

由表 2 可知，随着硫铝酸盐水泥与二水石膏相对比例的增大，固化剂胶砂试样的抗压和抗折强度均呈现先提高后降低再提高的趋势，表明适当增加硫铝酸盐水泥掺量可显著改善固化剂试样的力学性能。当硫铝酸盐水泥掺量为 55%~60%时，钙矾石 AFt 的生成量较高，AFt 在形成过程中会产生约 125%的体积膨胀[11]，导致胶砂抗压和抗折强度有所降低。当硫铝酸盐水泥掺量超过 65%后，其抗压或抗折强度随水泥掺量的增加又逐渐提高，这是因为此时参与反应的二水石膏不足，导致钙矾石生成量减少，试块膨胀性逐渐降低。除此之外，养护龄期的延长有利于固化剂胶砂试样力学性能的发展，但是 28 d 比 7 d 强度的最大提高幅度仅为 36%，这也说明硫铝酸盐水泥基固化剂具有早期强度发展快的特点。

2.1.2 硫铝酸盐水泥与二水石膏比例对固化剂净浆试样膨胀性能和力学性能的影响(见表 3)

表 3 固化剂的膨胀率和 7 d 抗压强度

硫铝酸盐水泥掺量/%	石膏掺量/%	3 d 膨胀率/%	7 d 膨胀率/%	7 d 净浆抗压强度/MPa
30	70	2.7	7.7	12.84
40	60	5.6	8.3	13.47
50	50	7.2	10.1	14.32
55	45	10.7	12.5	11.34
60	40	8.1	9.7	13.57
65	35	11.1	15.3	11.39
70	30	10.3	16.2	14.66
75	25	7.4	10.8	15.40
80	20	5.4	7.1	13.45
90	10	5.3	7.0	16.31
100	0	0	2.2	24.57

由表 3 可知，固化剂净浆膨胀率随硫铝酸盐水泥掺量的增加呈先增大后减小的趋势，当硫铝酸盐水泥掺量为 65%~70%时，3 d 和 7 d 膨胀率均较大。此外，7 d 抗压强度的发展规律也是硫铝酸盐水泥水化增强和钙矾石膨胀削弱作用的综合结果。

2.1.3 固化剂配合比优选

预拌流态土固化剂的选择受很多因素的影响，如力学性能、工作性能、膨胀性能和成本等。为确定固化剂配合比的优劣，本文将固化剂胶砂的 28 d 抗压强度、固化剂净浆的 7 d 膨胀率和材料价格 3 个因素作为评价指标，采用综合评分法进行多方案优选，旨在摆脱单一评价方法的局限性，从而优选出性能和成本综合优化的预拌流态固化土固化剂。

综合评分法是一种常见的多指标方案优选方法，主要包括排队评分法和公式评分法。排队评分法是根据试验结果在指标中的排名，对试验结果进行评分，然后将每组试验的分数总和作为该组的最终得分，从而把多指标问题转化为单指标问题[12-13]。本文的做法为将单一指标中的最优值记为满分10，最差值记为最低分 1，其余的试验结果依照最优值与最差值进行等差换算。

公式评分法是一种根据实际情况为各个指标进行分配权重并整合的方法。每个指标下所对应的数据大小和极差会对评分结果造成很大影响，为了消除这种影响，唐佳军和裴长春[13]根据各个指标的极差进行权值分配，将权重分配系数大小设定为相对极差大与相对极差小的极差比值。如对于膨胀性指标，其极差相对强度指标较小，则将其权重系数分配为强度极差与膨胀率极差的比值，强度与修正后膨胀率之和再除以价格

(C)1994-2023 China Academic Journal Electronic Publishing House. All rights reserved. http://www.cnki.net

指标，进行计算后得出评分结果，计算公式见式(2)。

$$S=\frac{f+\lambda s}{t} \tag{2}$$

为消除极差对评分结果带来的影响，也可以将强度和膨胀率分别除以其最大值变成无量纲数据，再将修正后数据之和除以价格评分得到评分结果，得到无量纲公式，见式(3)。考虑到强度与膨胀率呈负相关，可以采用二者的乘积来消除极差所带来的影响，再除以价格评分得到评分结果，得到有量纲公式，见式(4)。

$$S=\frac{f/f_{max}+s/s_{max}}{t} \tag{3}$$

$$S=\frac{f\times s}{t} \tag{4}$$

式中：S——最终评分；

f——强度；

s——膨胀率；

t——价格评分；

λ——权重分配系数(强度极差与膨胀极差的比值)。

胶砂28 d抗压强度及净浆7 d膨胀率由试验测得，价格的高低由市场价决定。2021年9月市场价硫铝酸盐水泥约为1200元/t，二水石膏约为600元/t，二者价格比为2:1，因此将某种配比的价格定义为：

价格=0.66×硫铝酸盐水泥掺量+0.33×二水石膏掺量

多指标评价结果如表4所示。

表4　多指标评价结果

硫铝酸盐水泥掺量/%	石膏掺量/%	排队评分法	公式评分法		
			公式(2)	公式(3)	公式(4)
30	70	15.54	108.61	1.97	4.33
40	60	15.82	116.34	2.09	5.30
50	50	17.50	135.77	2.43	7.69
55	45	18.62	147.05	2.67	9.46
60	40	18.00	142.69	2.50	8.63
65	35	19.99	160.33	2.94	11.97
70	30	21.29	171.35	3.12	14.09
75	25	17.76	143.55	2.53	9.40
80	20	15.52	127.51	2.16	6.57
90	10	15.27	128.31	2.16	6.70
100	0	12.00	108.22	1.72	2.17

由表4可知，当硫铝酸盐水泥掺量分别为55%、65%、70%时的3种固化剂评分最高。

2.2　预拌流态固化土的性能

选用上述3组固化剂，并选用P·O42.5水泥作为对照。以胶土比为1:9、水固比为0.2制备预拌流态固化土试样，性能如表5所示。

表5　预拌流态固化土的性能

P·O42.5水泥/%	SAC/%	石膏/%	体积收缩率/%		抗压强度/MPa	
			7 d	28 d	7 d	28 d
0	55	45	0.07	0.09	0.4	1.1
0	65	35	0.09	0.10	0.6	1.1
0	70	30	0.06	0.08	0.9	1.3
100	0	0	1.20	1.40	0.8	0.9

由表5可知，以SAC和石膏为固化剂的预拌流态固化土的7 d抗压强度均大于0.3 MPa、28 d抗压强度均大于1.0 MPa。当硫铝酸盐水泥掺量从55%增加至70%，固化土的抗压强度有所提高，这说明硫铝酸盐水泥掺量的增加有利于固化土力学性能的改善。作为对比，普通硅酸盐水泥固化土的28 d抗压强度比硫铝酸盐水泥-石膏基固化土低，并且收缩显著增大，其28 d抗压强度小于1.0 MPa。

GB 50202—2018《建筑地基基础工程施工质量验收标准》规定，回填后土体抗压强度应高于0.3 MPa，交通工程的台背、涵背和墙背等部位回填要求28 d抗压强度≥0.8 MPa，一般道路路基要求28 d抗压强度≥1.0 MPa。因此本研究提出的3种固化剂均满足上述要求，测得预拌流态固化土的扩展度均在(23±5) cm，具有较好的流动性，其中硫铝酸盐水泥掺量55%时的固化剂价格最便宜。

3　结　论

(1)系统研究了以硫铝酸盐水泥和石膏为组成的流态土固化剂的综合性能，固化剂和固化土力学性能随着固化剂中硫铝酸盐水泥掺量的增加而提高，但膨胀率和成本并不符合此规律，而是存在最优值。

(2)提出了考虑成本的多指标综合评价方法，确定当水泥掺量分别为55%、65%、70%时的3种固化剂评分最高。

(3)采用3组最优的固化剂配合比，以胶土比1:9和水固比0.2制备的预拌流态固化土流动性良好，体积收缩率不大于0.10%，28 d抗压强度均大于1.0 MPa，符合GB 50202—2018的要求。

参考文献：

[1] 刘成龙.新型预拌流态固化土性能及回填施工工艺[J].山东交通学报，2021，29(4)：91-98.

[2] 杜衍庆，王新岐，曾伟，等.道路用流态固化土的基本性质与工程实践[J].天津建设科技，2021，31(3)：12-15.

[3] 李建望.河道淤泥流动化处理及其稳定性研究[D].苏州：苏州科技学院，2009.

(下转第55页)

(C)1994-2023 China Academic Journal Electronic Publishing House. All rights reserved.　http://www.cnki.net

study on autogenous volume deformation of RCC mixed with MgO，proceedings of the IOP Conference Series：Materials Science and Engineering，F，2020[C].IOP Publishing.

[4] ZHAO H，JIANG K，YANG R，*et al*.Experimental and theoretical analysis on coupled effect of hydration，temperature and humidity in early-age cement-based materials [J].International Journal of Heat and Mass Transfer，2020，146：118784.

[5] BARLUENGA G，HERNáNDEZ-OLIVARES F.Cracking control of concretes modified with short AR-glass fibers at early age. Experimental results on standard concrete and SCC [J].Cement and Concrete Research，2007，37（12）：1624-1638.

[6] BOUASKER M，MOUNANGA P，TURCRY P，*et al*.Chemical shrinkage of cement pastes and mortars at very early age：Effect of limestone filler and granular inclusions [J].Cement and Concrete Composites，2008，30（1）：13-22.

[7] 邹弘雨，刘岳辉，成慧，等.新型氧化镁膨胀剂对混凝土性能的影响[J].重庆建筑，2021，20（S1）：21-23.

[8] FERNANDES F，MANARI S，AGUAYO M，*et al*.On the feasibility of using phase change materials（PCMs） to mitigate thermal cracking in cementitious materials[J].Cement and Concrete Composites，2014，51：14-26.

[9] GUO J，ZHANG S，GUO T，*et al*.Effects of UEA and MgO expansive agents on fracture properties of concrete[J].Construction and Building Materials，2020，263：120245.

[10] COLLEPARDI M，BORSOI A，COLLEPARDI S，*et al*.Effects of shrinkage reducing admixture in shrinkage compensating concrete under non-wet curing conditions[J].Cement and Concrete Composites，2005，27（6）：704-708.

[11] MCPOLIN D，BASHEER P，LONG A，*et al*.New test method to obtain pH profiles due to carbonation of concretes containing supplementary cementitious materials [J].Journal of Materials in Civil Engineering，2007，19（11）：936-946.

[12] ZHANG J.Recent advance of MgO expansive agent in cement and concrete [J].Journal of Building Engineering，2022，45：103633.

[13] CAO F，MIAO M，YAN P.Hydration characteristics and expansive mechanism of MgO expansive agents [J].Construction and Building Materials，2018，183：234-242.

[14] DUNG N，UNLUER C.Sequestration of CO_2 in reactive MgO cement-based mixes with enhanced hydration mechanisms[J]. Construction and Building Materials，2017，143：71-82.

[15] JIANG F，DENG M，MO L，*et al*.Effects of MgO expansive agent and steel fiber on crack resistance of a bridge deck[J]. Materials，2020，13（14）：3074.

[16] 陈志城，阎培渝.补偿收缩混凝土的自收缩特性[J].硅酸盐学报，2010，38（4）：568-573.

[17] 宋春香，娄宗科，闫宁霞，等.膨胀混凝土在渠道衬砌设计中的应用研究[J].混凝土，2007，212（6）：92-94，98.

[18] 李承木.外掺氧化镁混凝土快速筑坝技术综述[J].水利水电科技进展，2013，33（5）：82-88.

（上接第 45 页）

[4] 范猛.非压实回填土基本性能及应用研究[D].北京：北京工业大学，2009.

[5] 易富，管茂成，李军，等.稻壳灰-地聚物固化土力学特性及机理分析[J].水文地质工程地质，2022，49（2）：94-101.

[6] 赵高飞.全固废预拌固化剂制备基坑回填料的研究[D].邯郸：河北工程大学，2021.

[7] Do T M，Kim Y S.Engineering properties of controlled low strength material（CLSM） incorporating red mud[J].International Journal of Geo-Engineering，2016，7（1）：1-17.

[8] Jamali S，Naganathan S.Performance Assessment of Cementless Controlled Low-Strength Material（CLSM） Utilizing Coal Ashes [J].Jordan Journal of Civil Engineering，2015，9（1）：102-116.

[9] Qian Jinsong，Hu Yiyun，Zhang，Jiake，*et al*.Evaluation the performance of controlled low strength material made of excess excavated soil[J].Journal of Cleaner Production，2019，214：79-88.

[10] 高强.水泥基流态土固化剂的试验研究[J].中国建材科技，2021，30（4）：68-73.

[11] 王硕.硫铝酸盐水泥的膨胀性能[D].大连：大连理工大学，2018.

[12] 张子建，范利丹，余永强，等.多指标混凝土正交试验的分析方法研究[J].科技通报，2017，33（11）：47-51，99.

[13] 唐佳军，裴长春.基于排队评分法与矩阵分析法的多指标再生混凝土力学性能的优选研究[J].延边大学学报（自然科学版），2019，45（3）：279-282.

(C)1994-2023 China Academic Journal Electronic Publishing House. All rights reserved. http://www.cnki.net

建筑垃圾土流态固化研究*

国金珠[1,2]　王　健[1,2]　李晓宁[1,2]　李　婷[1,2]

（1.中国建筑材料科学研究总院，北京　100024；2.中建材中岩科技有限公司，北京　100024）

摘　要：为拓展建筑垃圾土工程应用前景，实现建筑垃圾资源化再利用，研究了建筑垃圾土流态固化性能。采用水泥基土壤固化体系，设计了不同土壤固化剂配比，测试建筑垃圾土与工程常用素土强度性能、流动性能、水稳性能区别，并观察其微观形貌，分析其固化反应情况，研究发现，固化剂可激发建筑垃圾土中活性组分，建筑垃圾土3 d固化强度可达3 MPa以上，7 d固化土强度可达4.2 MPa以上，28 d强度可达4.6 MPa以上，有优秀的流动效果，初始坍落度可达280 mm，扩展度可达600 mm，且可以保持30~90 min的流动效果，水稳系数可达105%以上，建筑垃圾土具备优良流态固化性能。

关键词：建筑垃圾；土壤固化；流态固化土；强度；流动性能

建筑垃圾是一种工程废弃物，是指建设、施工单位或个人对各类建筑物等进行建设、拆除等过程中产生的废弃物，主要包括建筑废土、废砖石、废混凝土等。我国每年建筑垃圾增量在35亿t左右[1]，是我国城市排放量最大、最集中的单一品种固体废弃物，占用大量土地资源，污染大气及水体，对环境危害较大[2-3]。建筑垃圾资源化再生利用成为了解决建筑垃圾固废问题的研究重点，其中建筑垃圾破碎混合形成的建筑垃圾土再生利用技术简单，操作方便，处理效率高，对环境影响小，具有良好应用前景。杨德生等[4]研究了建筑垃圾土的物理力学特性，验证了其压缩固结性能，提出建筑垃圾土挤压后可大大提高抗剪强度。建筑垃圾土固化后可广泛应用于路基加固、夯扩桩、基坑回填等各类工程[5-8]，可消耗大量建筑垃圾，大大缓解建筑垃圾处理压力，减轻土地资源及环境负担。

土壤固化技术是指通过物理化学方法改变土壤力学性质，使其具备良好工程应用性能的一种方法，在道路、基础、污泥处理等工程领域有广泛的应用前景[9-11]。土壤固化剂可以改变土壤颗粒间性质，增强土壤粘聚性与密实度[12-13]，从而使土具备强度、抗渗性能等一些列工程技术性能。土壤固化通常采用原位固化，即将固化剂与土壤翻搅拌和，使其与土壤充分混合，经过一系列物理化学作用如夯实、水化反应等，使土壤固化[14]。但原位固化通常面临匀质性差、施工工序繁琐，施工空间要求大等一系列问题。针对这些问题，预拌流态固化技术成为了近些年来新的研究方向，即类似预拌混凝土，采用预拌流态土固化剂，与土壤一起加水搅拌，使其具有较大流动性，可以改善固化土匀质性，并可实现现场浇筑及远距离运输，极大扩展了固化土的工程应用范围。周永祥等[15]提出了预拌流态土固化剂的开发与配置原则，提出了预拌流态固化土的基本性能指标，认为坍落度达到90 mm以上的拌合固化土可称为流态固化土，坍落度达到160 mm以上的拌合固化土可满足泵送施工要求；刘成龙[16]进行了预拌流态固化土的回填施工工艺研究。

建筑垃圾土做预拌流态固化土可大大拓展建筑垃圾土工程应用前景，加大建筑垃圾处理效率，有助于解决我国建筑垃资源化处理效力不足等问题，减轻环保负担，助力节能减排。但与工程应用中最常见的素土不同，建筑垃圾土组成复杂，含土量少，土质不均匀，结构松散团聚性差，压缩变形大[17]，其作为流态固化土的工程性能还有待研究。

本文采用水泥基土壤固化体系，设计了5种土壤固化剂配比，采用两种建筑垃圾土及素土进行流态固化研究，测试其流动性能、强度性能及水稳性能，并通过电镜扫描测试其微观性能，观察其水化情况，分析其固化机理，分析建筑垃圾土流态固化性能，为建筑垃圾土的工程应用适用性研究提供参考依据。

1　试验材料与方法

1.1　材　料

本文设计5种不同土壤固化剂，固化剂成分见表1。选用不同厂家的两种建筑垃圾处理土与取自北京地区的普通素土，对土样进行水洗筛分烘干后分析土样组成见表2。

表1　土壤固化剂组成　g

配比	水泥	矿粉	硫酸钠	膨胀剂	磺酸盐减水剂	萘系减水剂
固化剂G1	40	50	4	3	3	—
固化剂G2	90	—	4	3	3	—
固化剂G3	97	—	—	—	3	—
固化剂G4	40	50	4	3	—	6
固化剂G5	40	50	4	3	—	—

注：水泥为普通硅酸盐水泥，矿粉为S95矿粉，膨胀剂为Ⅱ型膨胀剂。

表2　土样组成　%

土样	泥<75 μm	砂<5 mm	石≥5 mm
建筑垃圾土T1	36.5	13.95	49.55
建筑垃圾土T2	51.31	25.23	23.46
素土T3	91.04	4.56	4.40

*非金属材料创新中心应用示范类项目（2022SFP2-1）

第一作者：国金珠，女，1994年出生，硕士，工程师。

电子信箱：983555961@qq.com

收稿日期：2022-10-21

(C)1994-2023 China Academic Journal Electronic Publishing House. All rights reserved.　http://www.cnki.net

1.2 试验方法

1.2.1 强度试验

为分析建筑垃圾土固化效果,成型了强度试块,分别测试了固化剂强度与固化土强度。

1)固化剂强度。取固化剂 G1、G3,加水拌和(水胶比 0.35),成型 70 mm×70 mm×70 mm 抗压强度试块,在 20 ℃,相对湿度 90%条件下养护至 3,7,28 d,参照标准 GB/T 17671—2021《水泥胶砂强度检验方法》测试其无侧限抗压强度。

2)固化土强度。取固化剂 G1、G2、G3,按照掺量为干土质量 5%、10%、20%掺加(外掺),与土样 T1、T2、T3 拌和,水土(干土)质量比为 0.35,成型 70 mm×70 mm×70 mm 抗压强度试块,在 20 ℃,相对湿度 90%条件下养护至 3,7,28 d,参照标准 JTJ/T233—2011《水泥土配合比设计规程》测试其无侧限抗压强度。

1.2.2 流动性能测试

测试了建筑垃圾土与固化剂拌和后的流动情况。取固化剂 G1、G4、G5 按照掺量为干土质量 10%掺加(外掺),与土样 T1、T2、T3 拌和,水土(干土)质量比为 0.35,参照标准 GB/T 50080—2016《普通混凝土拌合物性能试验方法标准》测试其坍落度与扩展度。

1.2.3 水稳性试验

建筑垃圾土结构松散,为分析建筑垃圾土固化后的稳定性,参照标准 CJT 486—2015《土壤固化外加剂》进行了水稳性测试。

1)试验组。取固化剂 G1、G2、G3 按照掺量为干土质量 10%掺加(外掺),与土样 T1、T3 拌和,水土(干土)质量比为 0.4,成型70 mm×70 mm×70 mm 抗压强度试块,在 20 ℃,相对湿度 90%条件下养护 6 d 后,放入水中湿养 1 d 后测定其抗压强度 $F1$。

2)对照组。取固化剂 G1、G2、G3 按照掺量为干土质量 10%掺加(外掺),与土样 T1、T3 拌和,水土(干土)质量比为 0.4,成型70 mm×70 mm×70 mm 抗压强度试块,在 20 ℃,相对湿度 90%条件下养护至 7 d 龄期后测定其抗压强度 $F2$,水稳系数为:$F1/F2$。

1.2.4 扫描电子显微镜测试

为观察固化土微观形态,分析其水化情况,采用美国 FEI Nova Nano SEM 场发射电子显微镜进行电子扫描显微镜分析(SEM)。取固化剂 G1、G3,按照掺量为干土质量 10%掺加(外掺),与土样 T1、T3 拌和,水土(干土)质量比为 0.35,成型养护至 7 d 后取出,去除表面碳化层,采用无水乙醇反复浸泡冲洗终止水化后放入真空烘箱中烘干,研磨过 75 μm 筛后,进行 SEM 测试。

2 结果与讨论

2.1 强度性能

图 1 为各配比固化剂及固化土强度,由图 1a 固化剂强度结果可知,包含水泥、矿粉、激发剂、膨胀剂以及减水剂的 G1 固化剂强度低于只包含水泥与减水剂的 G3 固化剂强度,表明在胶材中掺入矿粉、激发剂及膨胀剂代替水泥后会导致强度降低,即激发剂与膨胀剂构成的硫酸盐激发体系对水泥、矿粉的激发作用无法弥补矿粉与水泥的强度差距。

由图 1b、c、d 可知,两种建筑垃圾土均有较好的固化强度,与素土强度差别不大,且均随固化剂掺量提升强度提高,当掺入 20%固化剂 G1 时建筑垃圾土 T1、T2 的 3 d 固化强度均可达到 3 MPa 以上,7 d 固化土强度可大于 4.2 MPa,28 d 强度可大于 4.6 MP,表明建筑垃圾土具有优秀的可固化性。

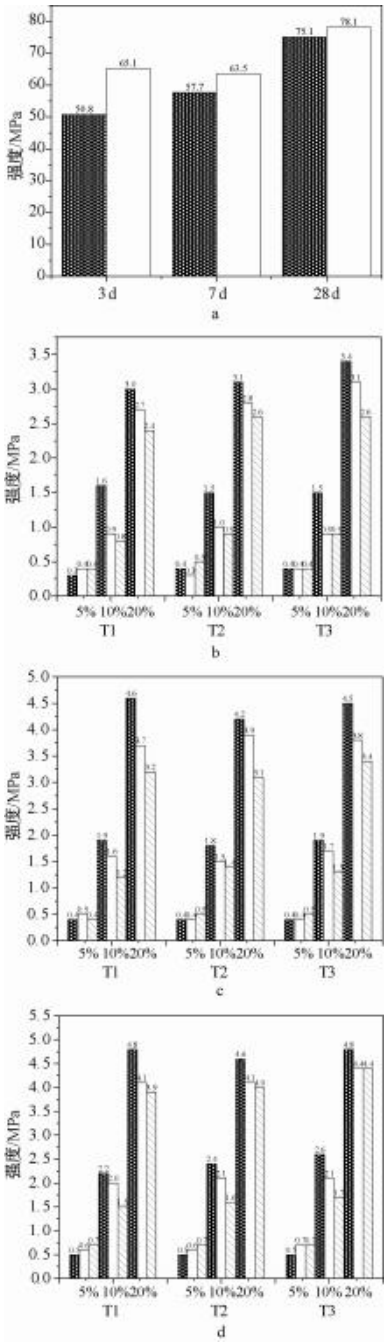

a—固化剂 3d 强度;b—固化土 3d 强度;
c—固化土 7d 强度;d—固化土 28 d 强度。
G1; G2; G3。

图 1 固化剂强度、固化土强度

在建筑垃圾土 T1、T2 及素土 T3 中均表现出固化剂 G1 的固化强度大于 G2 固化强度大于 G3 固化强度,这表明建筑垃圾土中的活性成分同普通素土一样,都可被激发。固化剂中的水泥水化后生成的碱性产物如氢氧化钙(CH),成功激发了土壤中的活性硅铝等组分,使其与硫酸钠及膨胀剂中的含铝成分反应,生成硅酸钙凝胶及钙矾石,一方面形成固化土的骨架,一方面增强土壤颗粒的胶结力,提供强度,使原本

(C)1994-2023 China Academic Journal Electronic Publishing House. All rights reserved. http://www.cnki.net

强度低于 G3 固化剂的 G1 固化剂的固化强度超过了 G3 固化剂;此外,由固化土强度结果可知,低掺量 5%时,G1 与 G3 固化剂固化强度差别不大,即可知低掺量时,激发体系及膨胀体系效果还不显著,当固化剂掺量达到 10%及 20%,G1 固化剂固化土强度均明显大于 G3 固化剂固化土强度,即激发体系及膨胀体系可有效发挥效果提供强度;

固化剂 G1 固化强度大于固化剂 G2 固化强度,即 G1 固化效果优于水泥含量更高的不含矿粉 G2 固化剂,这是因为土壤结构松散,G1 中的矿粉可起到填充作用,使固化基体更密实,提高固化强度。

2.2 流动性

掺入固化剂的拌合固化土的流动性能如表 4 所示,由测试结果可知,与素土 T3 相比,建筑垃圾土 T1、T2 坍落度、扩展度相对较大,有较好的流动效果,同时,素土的经时损失相对更小。

表 4 拌合固化土流动性能

土样	固化剂	流动	初始	30 min	60 min	90 min
T1	G1	坍落度	280	270	250	230
		扩展度	600	555	475	440
	G4	坍落度	260	220	220	120
		扩展度	580	400	370	250
	G5	坍落度	170	120	—	—
		扩展度	290	245	—	—
T2	G1	坍落度	270	250	240	210
		扩展度	550	530	495	420
	G4	坍落度	260	230	225	160
		扩展度	570	430	395	270
	G5	坍落度	160	150	—	—
		扩展度	285	295	—	—
T3	G1	坍落度	265	250	250	200
		扩展度	520	490	470	410
	G4	坍落度	250	230	225	185
		扩展度	510	425	400	265
	G5	坍落度	160	120	—	—
		扩展度	260	240	—	—

掺入 G1、G4 固化剂的拌合土,均有较好的初始流动度,且掺入固化剂 G1 的拌合固化土扩展度、坍落度、经时流动度均优于掺入固化剂 G4 的拌合固化土,且均优于掺入无减水剂的 G5 固化剂的拌合固化土,这表明,磺酸盐减水剂与奈系减水剂在建筑垃圾土及素土中均有减水效果,且磺酸盐减水剂的减水效果优于奈系减水剂的减水效果。

2.3 水稳性

图 2 为固化土的水稳系数。由测试结果可知,建筑垃圾土与素土水稳性能相差不大。且水稳系数均在 100%以上,G1、G2 水稳系数均在 105%以上。即标准养护 6 d 后水养 1 d 有助于强度增长,;从固化剂种类来看,整体呈现出固化剂 G1、G2 的固化土水稳系数略高于固化剂 G3 固化土的水稳系数,即 G1、G2 固化土的水稳性能更佳。

2.4 微观结构分析

图 3 为固化土养护 7 d 的电镜照片,由电镜结果可知,建筑垃圾土 T1 与素土 T3 在固化剂 G1、G3 的作用下均可见明显的细针状钙矾石晶体,且钙矾石在固化土基体中分布较为分散,与水泥基体中的钙矾石分布状态明显不同,钙矾石在

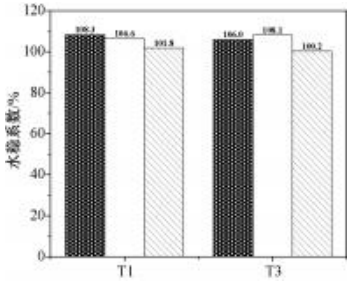

G1; G2; G3。

图 2 固化土水稳系数

水泥中为簇状生长,且较易分布于裂缝处。钙矾石主要来源于水泥水化反应及土壤激发后的固化反应,这说明有水化反应与激发固化反应进行。其中,与素土 T3 相比,掺同种固化剂的建筑垃圾土中钙矾石纤维明显尺寸更大且更多,表明建筑垃圾土中的土壤激发效果更好,固化反应产生的钙矾石更多,反应更充分。

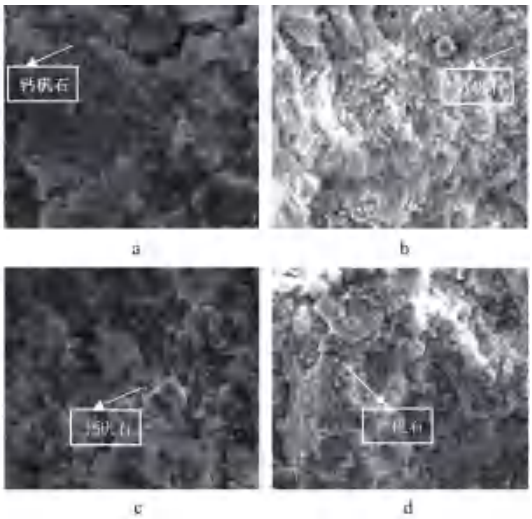

a—G1-T1;b—G1-T3;c—G3-T1;d—G3-T3。

图 3 7 d SEM 结果

与固化剂 G3 相比,掺入固化剂 G1 的固化土反应产物更多更明显,虽然 G3 中水泥含量高,但 G1 中的激发组分与膨胀组分的二元体系的激发固化效果较好,产生的固化产物更多,这也解释印证了 G1 的固化土强度高于 G3 的固化土强度。

3 结 论

建筑垃圾土的流态固化处理符合低碳环保要求,可助力于建筑垃圾固废消纳及环境治理,且可满足基坑回填,边坡加固、路基加固等各种工程,可解决施工空间小、回填空间复杂、回填质量不均等各种问题,对于建筑垃圾土的流态固化的各项性能,通过试验研究,现有如下结论:

1)建筑垃圾固化土与素土均可见明显的细针状钙矾石晶体,即建筑垃圾土与素土中的活性成分可被有效激发,有水化反应与激发固化反应进行,提供强度;与工程常用的素土相比,建筑垃圾土反应产物更多,固化强度相当;固化剂中的矿粉可填充空隙,有助于提高固化土强度。

2)建筑垃圾土在流态土壤固化剂的作用下有优秀的流动效果,初始坍落度可达 280 mm,扩展度可达 600 mm,且可

(下转第 728 页)

(C)1994-2023 China Academic Journal Electronic Publishing House. All rights reserved. http://www.cnki.net

$[\tau_{th}]=160\ MPa^2$，焊缝最大允许承载力：$F=0.7f_h\sum L[\tau_{th}]=0.7\times25\times160\times3\ 600=10\ 080\ kN>1\ 459.9\ kN$，故安全。

5.2 变形复核

滑移、牵引、卸落过程需密切监测主桁架、门型框架变形、挠度，实施前整体计算采用 3D3S 程序的空间杆系有限元方法，结构采用 Frame 单元，计算桁架与门式刚架结构在滑移过程中的内力、变形以及各个支点反力，滑移时门式钢架最不利工况最大变形值为 13 mm，结构强度和刚度均满足要求，见图 15。

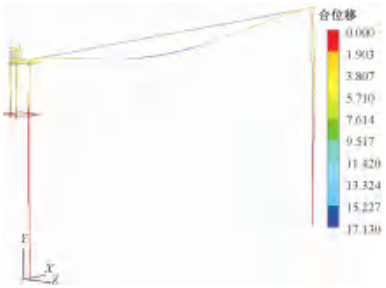

图 15 滑移时门式钢架最不利工况变形 mm

5.3 千斤顶校核

小坦克与轨道槽钢之间为钢对钢滚动摩擦，摩擦系数 $\mu=0.2$，摩擦力 $f=\mu P_0=0.2\times191=382\ kN$，采用 2 台 100 t 液压千斤顶，牵引能力满足要求。

6 结束语

通过采用焦炉单侧双机抬吊钢桁架高空临时就位、再水平牵引滑移的方式，焦炉焦侧超重、超大跨度钢桁架顺利安装，实现了焦侧钢桁架施工不占用焦侧场地，焦侧的管道系统、熄焦车系统、焦炉顶部设备管道系统均正常同步施工，实现了焦炉提前一个月投产的目标。与采用焦侧 750 t 履带吊抬吊方案相比，还节省履带吊与汽车吊进出场及台班费用，使用单台履带吊成本 60 万元，使用单台汽车吊成本 9 万元，滑移成本 30 万元，共降低成本 2×(2×60-2×9-30)= 162 万元。

通过该单侧吊装及滑移技术，吊装过程中抬吊机具投入少，滑移、顶升、卸落施工连续，自动控制可靠、精确，安全性高，为焦炉顶部增加环保屋盖钢桁架施工提供了安全可靠、经济实用、工期最短的解决方案，可在以后的类似工程推广应用。

参考文献

[1] 刘智，王光武，李铉诚，等. 大型体育馆钢桁架大跨度滑移技术[J]. 施工技术，2021，50(6)：43-46.
[2] 张家国，赵祖芳，高启博. 等. 某大跨度钢结构滑移施工监测和施工建议[J]. 钢结构，2018，33(10)：120-125.
[3] 王军杰，邱峰，王显博，等. 受限空间大跨度屋面钢结构施工技术[J]. 施工技术，2019，48(10)：68-71.
[4] 龙驭球，包世华. 结构力学(上册)[M]. 北京：高等教育出版社，1987.
[5] 杨文渊. 起重吊装常用数据手册[M]. 北京：人民交通出版社，2001.
[6] 卜一德 . 起重吊装计算机安全技术[M]. 沈阳：辽宁省劳动保护科学研究所，2008.
[7] 中华人民共和国住房和城乡建设部. 钢结构设计标准：GB 50017—2017[S]. 北京：中国建筑工业出版社，2018.
[8] 钢结构滑移施工技术标准：T/CSCS 009—2020[S]. 北京：中国建筑工业出版社，2020.

(上接第 697 页)

以保持 30~90 min 的流动效果，除此之外，磺酸盐减水剂在土壤中的减水效果优于萘系减水剂的减水效果。

3)建筑垃圾土水稳性与素土差别不大，水稳系数可达 105%以上。综上，建筑垃圾土具有优良的流态固化性能。

参考文献

[1] 张一伟，王章琼，石钊，等. 国内外建筑垃圾资源化利用现状及对策分析[J]. 山西建筑，2022，48(16)：173-176，188.
[2] 王欣玉，任雅琪，王丽丽，等. 不同类型建筑垃圾堆场大气降尘中水溶性离子污染特征[J]. 环境科学学报，2021，41(11)：4415-4422.
[3] 杨军芳. 建筑垃圾与环境保护举措[J]. 清洗世界，2022，38(8)：92-94.
[4] 杨德生，张孟喜，崔振清，等. 含建筑垃圾土的物理力学特性[J]. 上海大学学报(自然科学版)，2011，17(6)：792-798.
[5] 肖田，张俊峰，陈明，等. 石灰稳定建筑垃圾土修筑基层的适用性研究[J]. 低温建筑技术，2022，44(5)：19-21，33.
[6] 张好奇. 碱激发粉煤灰稳定建筑垃圾土力学特性与微观机理研究[D]. 武汉：湖北工业大学，2020.
[7] 尤忆，CHEW B C. 建筑垃圾在公路路基填筑中的有效应用[J]. 工业建筑，2021，51(10)：258.
[8] 周志清，王定鹏. 建筑垃圾改良膨胀土填筑路基可行性研究[J]. 西安建筑科技大学学报(自然科学版)，2021，53(5)：716-722.
[9] 董博闻，王修山，周恒宇. 应用 NS-SL 型土壤固化剂固化淤泥的路用性能试验研究[J]. 公路，2021，66(8)：13-17.
[10] 倪西海，黎海波，杨正武. 土壤固化剂在富流滩船闸改扩建工程中的应用研究[J]. 四川水利，2021，42(5)：40-42，128.
[11] 王晓晖，张辉，周逸民. 浅析土壤固化剂在道路中的应用[J]. 江西建材，2022(4)：163-164，167.
[12] 樊恒辉，高建恩，吴普特，等水泥基土壤固化剂固化土的物理化学作用[J]. 岩土力学，2010，31(12)：3741-3745.
[13] 刘世皎，樊恒辉，史祥，贺智强. BCS 土壤固化剂固化土的耐久性研究[J]. 西北农林科技大学学报(自然科学版)，2014，42(12)：214-220.
[14] 王京伟，贾存威，毛利. 就地固化技术在化工污泥路基处置中的研究及应用[J]. 中国水运(下半月)，2022，22(8)：134-136.
[15] 周永祥，王继忠. 预拌固化土的原理及工程应用前景[J]. 新型建筑材料，2019，46(10)：117-120.
[16] 刘成龙. 新型预拌流态固化土性能及回填施工工艺[J]. 山东交通学院学报，2021，29(4)：91-98.
[17] 陈宝玉，左辉，王建权. 建筑垃圾土工程特性研究[J]. 水科学与工程技术，2008(6)：65-67.

(C)1994-2023 China Academic Journal Electronic Publishing House. All rights reserved. http://www.cnki.net

Interfacial Performance of Asphalt-Aggregate System under Different Conditions Based on Molecular Dynamics Simulation

Guoqing Sun[1]; Jiupeng Zhang[2]; Zixuan Chen, Ph.D.[3]; Zhenxing Niu[4]; and Yan Li[5]

Abstract: The interface between asphalt and aggregate directly determines the performance of asphalt mixtures but unavoidable weaknesses can be easily found at the interfacial bonding region. In order to evaluate the interfacial adhesion behavior between asphalt and aggregate at the atomic scale, asphalt binders and two mineral aggregates (quartz and calcite) were selected to build molecular models and molecular dynamics (MD) simulations were conducted. The interfacial energy between asphalt and aggregate was calculated and the mineral aggregate has a more significant influence on the energy compared to the binder types. Also, the simulation result indicates that saturate, aromatic, resin, and asphaltene (SARA) components have different interfacial energies with respect to the aggregates. This result can also be derived from the relative concentration of SARA components on the aggregate surface. Additionally, oxidation of the asphalt binder results in increased interfacial energy due to the enhanced intermolecular bonding generated by oxidized functional groups. The intrusion of water greatly reduces the interfacial energy, but the energy increases under the coupling effect of oxidation and moisture, especially for calcite. The grey relational grade theory was conducted to evaluate the factors affecting the adhesive energy, and the results show that the energy of the asphalt-aggregate is more sensitive to the asphaltene index than other factors. DOI: 10.1061/JMCEE7.MTENG-15083. © 2023 American Society of Civil Engineers.

Author keywords: Molecular dynamics (MD) simulation; Saturate, aromatic, resin, and asphaltene (SARA) component; Oxidized asphalt; Moisture; Interfacial energy; Grey relational analysis.

Introduction

The asphalt mixture is a multiphase composite material mainly composed of filler, aggregate, and asphalt binder (Visintine et al. 2013; Aigner et al. 2009). The bonding strength between asphalt and mineral aggregate directly affects the performance of the asphalt mixture, due to the natural weakness occurring at the interfacial bond of the multiphase composites (Tan and Guo 2014; Li et al. 2020; Sun et al. 2021). Previous studies have also elaborated that the micro-cracks at the asphalt-aggregate interface enhance this evolution, which eventually leads to the adhesive failure of the asphalt mixture (Zhang et al. 2014; Sun et al. 2020; Wang et al. 2014). The excellent interfacial strength contributes to the favorable performance of the asphalt mixture (Xu et al. 2014; Sun et al. 2022). Therefore, it is of great significance to study the interfacial structure and performance.

The adhesive strength of the asphalt-aggregate interface plays a vital role in the performance of asphalt pavement due to the heterogeneity of the asphalt mixture. Previous literature has indicated that interfacial failure of asphalt mixtures are derived from three aspects: cohesive failure of the asphalt binder, adhesive failure of the asphalt-aggregate interface, and the failure caused by aggregate strength loss (Curtis et al. 1993). Therefore, the failure behavior of the asphalt-aggregate interface has been characterized by macro-micro tests in previous studies. The Bitumen Bonding Strength (BBS) test (Huang et al. 2016; Moraes et al. 2011) and Pneumatic Adhesion Tensile Testing Instrument (PATTI) (Tan and Guo 2014; Zhang et al. 2016; Kim et al. 2012) can be conducted to determine the tensile strength of asphalt and mineral aggregate. Some microscopic testing technologies, such as Atomic Force Microscopy (AFM) and Nano Indentation, have been used to test the adhesion mechanism of asphalt-aggregate and the microstructure of the asphalt binder and identify the phase system of asphalt binder and matrix (Tarefder and Zaman 2011; Khan et al. 2018). This has made it possible to further analyze the performance of asphalt mixtures by studying the chemical composition of asphalt and aggregate. The problems between the chemical composition and mechanical properties of asphalt-aggregate and its interface properties need to be solved (Yu et al. 2015; Hou et al. 2017). However, these micro-test techniques and macro-test methods could not directly acquire the interaction information of the asphalt-aggregate interface, and could not interpret the phenomenon of how different chemical compositions of asphalt binder absorbed aggregate and permeated and diffused on the aggregate surface (Sultana and Bhasin 2014). The limitation can be overcome using MD simulation, namely, the interaction behavior between atoms used by

[1]Ph.D. Candidate, School of Highway, Chang'an Univ., Middle Section of South Erhuan Rd., Xi'an, Shaanxi 710064, China. Email: sunguoqing@chd.edu.cn

[2]Professor, School of Highway, Chang'an Univ., Middle Section of South Erhuan Rd., Xi'an, Shaanxi 710064, China. Email: jiupengzhang@chd.edu.cn

[3]Lecturer, School of Highway, Chang'an Univ., Middle Section of South Erhuan Rd., Xi'an, Shaanxi 710064, China (corresponding author). Email: zixuanchen@chd.edu.cn

[4]Master's Candidate, School of Highway, Chang'an Univ., Middle Section of South Erhuan Rd., Xi'an, Shaanxi 710064, China. Email: niuzhenxing@chd.edu.cn

[5]Ph.D. Candidate, School of Highway, Chang'an Univ., Middle Section of South Erhuan Rd., Xi'an, Shaanxi 710064, China. Email: liyan@chd.edu.cn

Note. This manuscript was submitted on June 21, 2022; approved on September 27, 2022; published online on March 24, 2023. Discussion period open until August 24, 2023; separate discussions must be submitted for individual papers. This paper is part of the Journal of Materials in Civil Engineering, © ASCE, ISSN 0899-1561.

Downloaded from ascelibrary.org by CHANG'AN UNIVERSITY on 03/25/23. Copyright ASCE. For personal use only; all rights reserved.

establishing an atomic-scale model (Guo et al. 2020; Chen et al. 2018, 2022). It has also been widely used in the fields of chemical physics, biomolecular simulation, and material properties.

MD simulation is a method that can simulate the mechanical properties of composite materials, which can simulate the evolution process of interfacial damage and failure of heterogeneous materials and study the chemical structure and engineering properties of materials by atomic modeling. Asphalt binder is a material with very complex chemical components. Actually, it is impossible and unnecessary to generate the detailed information of its chemical composition. Therefore, the construction of a reasonable asphalt molecular model has always been a difficult point that needs to be continuously explored. Zhang and Greenfield (2007) first put forward a three-component asphalt molecular model, which mainly includes asphaltene, maltenes, and saturate. The development of micro-technology is also favorable to the observation of asphalt composition. The microstructure of asphalt was observed by AFM, and then the maltene in asphalt binder was further subdivided into resin and aromatic components (Xu and Wang 2016b). Jäger et al. (2004) determined the ratio of SARA components in asphalt by AFM. Therefore, the constructed four-component asphalt was applied in MD simulation instead of the three-component model (Chu et al. 2019; Lu and Wang 2010). Asphalt binder in Nigeria was characterized by microscopic technology. It was found that there were various organic substances in the asphaltene composed of high molecular weight polycyclic components, which were composed of nitrogen, sulfur, and oxygen heteroatoms, rather than a single molecular model (Adebiyi and Thoss 2015). Therefore, to further characterize the influence of different chemical components in the SARA components of asphalt binder, Li and Greenfield (2014) proposed the molecular model of 12-component asphalt. The thermodynamic properties, including density, cohesive energy density, diffusivity and viscosity, were calculated by MD simulation, which was more in line with the engineering properties of asphalt. Thus, the molecular structure of 12-component asphalt has been widely used in the study of asphalt-aggregate interface. Xu and Wang (2016a) used MD to simulate the tensile strength of the asphalt-aggregate interface and the adhesive and cohesive failure forms of the asphalt-aggregate interface. The effect of loading rate on adhesive strength was simulated by MD, which showed a trend consistent with the experimental results. The results of MD further showed that the attraction of asphaltene and resin components to the aggregate interface was stronger than that of the saturate and aromatic components.

As a material in constant contact with the atmospheric environment, environmental factors will produce an overwhelming effect on the performance degradation of asphalt mixture. For example, the oxidation and the intrusion of water into the asphalt-aggregate interface are also critical factors that cause the adhesive failure of the asphalt mixture. Xiao and Amirkhanian (2009) derived the conclusion that the indirect tensile strength of the asphalt mixture in wet conditions first increased and then decreased with increasing recycled asphalt binder content. However, Yi et al. (2018) found that the adhesion between asphalt binder and granite degrades with the aging process. The reason for this phenomenon can be attributed to the different asphalt mixtures used in different tests. Via MD simulation, Gao et al. (2018, 2019) found that the oxidative aging of asphalt is the main cause of the strengthening of the interfacial bonding between asphalt and strongly alkaline minerals. In addition, the moisture and asphalt aging significantly reduce the interfacial bonding strength. The coupling effect of moisture and asphalt aging on the performance of the asphalt mixture exhibits a complex mechanism.

The interface between asphalt and aggregate is mainly influenced by internal factors such as asphalt components, the types of asphalt binder and aggregate, and external factors such as oxidation and moisture. These challenges always exist in how to understand the influence of these factors on the interfacial performance via MD simulation. Therefore, the objective of this paper is to construct a molecular model of asphalt binders (AS-1, AS-2, and AS-3) and two mineral aggregates (quartz and calcite), and to study the interfacial performance of the asphalt-aggregate system under different conditions based on MD simulation. The influence of the properties of asphalt and aggregate on the adhesive energy of the asphalt mixture is analyzed by calculating the interfacial energy. The contribution of SARA components in the asphalt binder to aggregate interfacial energy and the distribution of asphalt components on the aggregate surface are analyzed to further explore the effects of SARA components. MD is conducted to study the coupling effect of moisture and oxidation on the interfacial performance of the asphalt mixture. Finally, grey relational analysis was conducted to evaluate the significant factors affecting the adhesive energy of the asphalt-aggregate system.

Molecular Models and Simulation Methods

Molecular Model for 12-Component Virgin Asphalt

Asphalt material is a complex chemical mixture that is produced in the process of petroleum refining. The elemental composition of asphalt mainly depends on its crude oil source. Preliminary analysis of asphalt produced by various crude oils shows that most asphalt contains 82%–88% carbon, 8%–11% hydrogen, 0%–6% sulfur, 0%–1.5% oxygen, and 0%–1% nitrogen (Lu and Wang 2010). The molecules are mainly composed of more than 90% hydrocarbons and contain a small amount of heterocyclic substances with similar structures and functional groups containing sulfur, nitrogen, and oxygen atoms. In this study, the 12-component asphalt molecular structure proposed by Li and Greenfield (2014) was applied, as shown in Fig. 1.

Molecular Model for 12-Component Oxidized Asphalt

The asphalt mixture is subjected to aging during its application to pavement. The main reason of asphalt aging is the chemical reaction between asphalt and oxygen in the atmosphere, which leads to changes in the molecular functional groups and component proportions of the asphalt binder. Documents show that some types of carbon atoms and sulfides in the asphalt binder were easily oxidized by studying the mechanism of asphalt aging. Among them, carbonyl and sulfoxide were considered to be the most important functional groups formed after oxidative aging (Petersen 2009; Lesueur 2009). It has been fully proved that the carbonyl group was formed by the oxygen atom replacing the hydrogen atom connected to the first carbon of the alkyl chain connected to the aromatic ring, and the sulfur element in asphaltene or the resin component was oxidized to form sulfoxide, as shown in Fig. 2. However, saturate components in the asphalt molecule have no sensitive functional groups, so its molecular structure remained unchanged after oxidation. The molecular structure of the oxidized SARA in the asphalt binder is shown in Fig. 3.

Previous studies have shown that SARA components of asphalt will greatly influence the interfacial adhesion between aggregates (Guo et al. 2018; Wang et al. 2017; Sun et al. 2020; Ma et al. 2021). Therefore, three different asphalt binders (AS-1, AS-2, and AS-3) were constructed in this study by changing the proportional differences of the 12 components. The detailed molecular composition is

Downloaded from ascelibrary.org by CHANG'AN UNIVERSITY on 03/25/23. Copyright ASCE. For personal use only; all rights reserved.

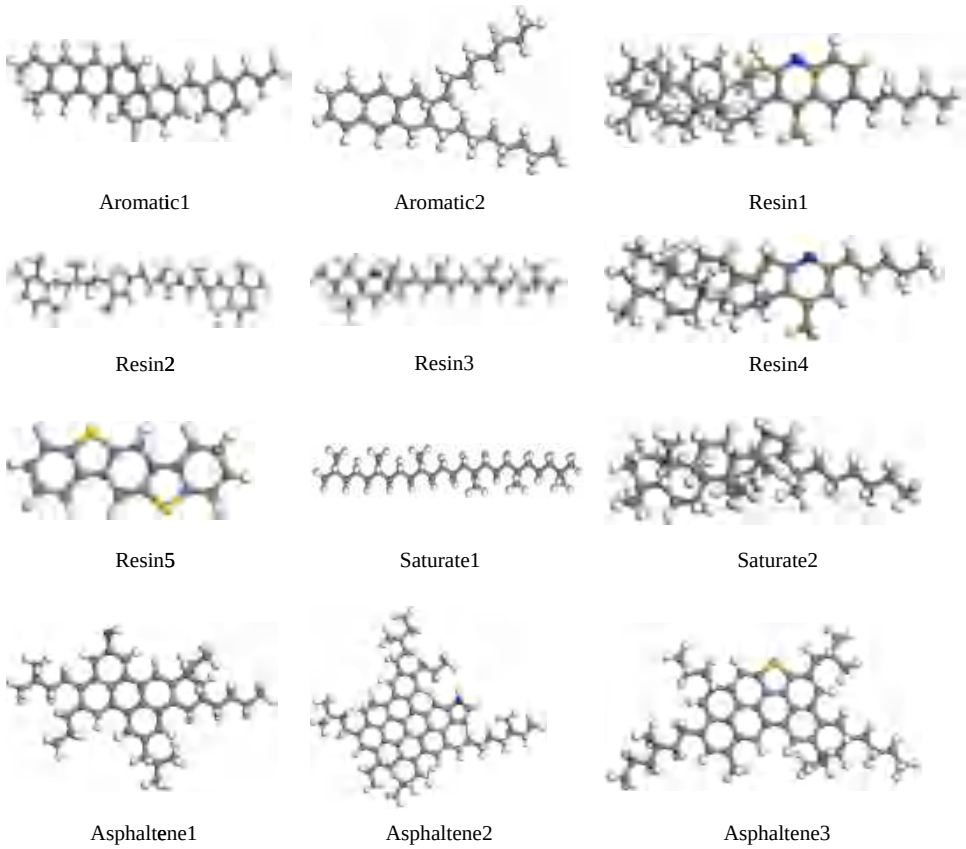

Fig. 1. Molecular structures of 12-component virgin asphalt.

shown in Table 1. The numbers represent the corresponding quantity of the 12 components of different types of asphalt. There are great differences in the SARA components of three asphalt molecules as shown in Table 2. AS-2 asphalt possesses the highest proportion of asphaltene and resin components, but its molecular mass is the lowest, while AS-3 asphalt has the lowest proportion of asphaltene and resin components, and its molecular mass is the highest. The parameters of AS-1 are between them. The main factors affecting the interface performance of asphalt can be effectively analyzed by comparing three different asphalt molecules with different SARA components. Furthermore, the AS-1 molecular models of virgin asphalt (VA), lightly oxidized asphalt (LOA), and heavily oxidized asphalt (HOA) were constructed according to different proportions of oxidized and virgin asphalt components, as shown in Figs. 4(a–c). These are three types of asphalt with different degrees of oxidation. Therefore, the difference between them is that the number of oxygen atoms due to oxidation was achieved by adding oxygen atoms.

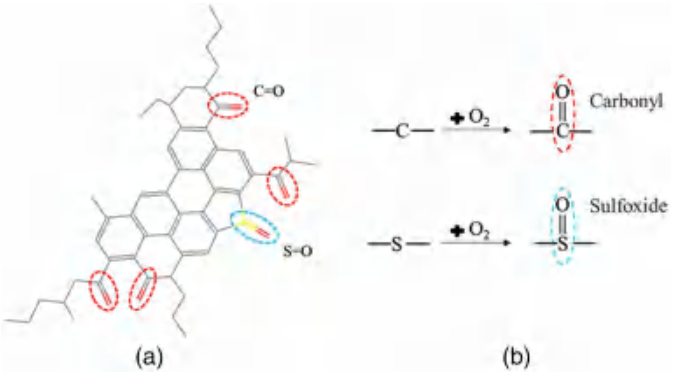

Fig. 2. Oxidized functional groups of asphalt component molecules: (a) oxidized Asphaltene; and (b) oxidized functional groups.

Force Field and Verification of Asphalt Molecular Model

The force field is an energy function that provides parameters for each atom type in the MD simulation to calculate the energy of the system. The parameters of the energy function can be derived from physical and chemical experiments and the calculation results of quantum mechanics. A suitable force field should be able to simulate the nature of atomic interaction in the material system and accurately describe the whole molecular category. The atomic and molecular interactions in this study were described by the Condensed-phase Optimized Molecular Potentials for Atomistic Simulation Studies (COMPASS II) force field. The COMPASS force field is the first ab initio force field in MD simulation, and COMPASS II is an important development extension of the COMPASS force field, which helped to accurately predict the material properties of various isolated and condensed-phase compounds. MD endowed each atom of a molecule an initial velocity, and the velocity was randomly generated according to a Boltzmann distribution. Therefore, in this study, three models were constructed for asphalt binder, and then the asphalt model was optimized in structure and kinetics. The average value of the three models was adopted to eliminate the influence of randomness of the initial velocity in the MD simulation.

Downloaded from ascelibrary.org by CHANG'AN UNIVERSITY on 03/25/23. Copyright ASCE. For personal use only; all rights reserved.

Downloaded from ascelibrary.org by CHANG'AN UNIVERSITY on 03/25/23. Copyright ASCE. For personal use only; all rights reserved.

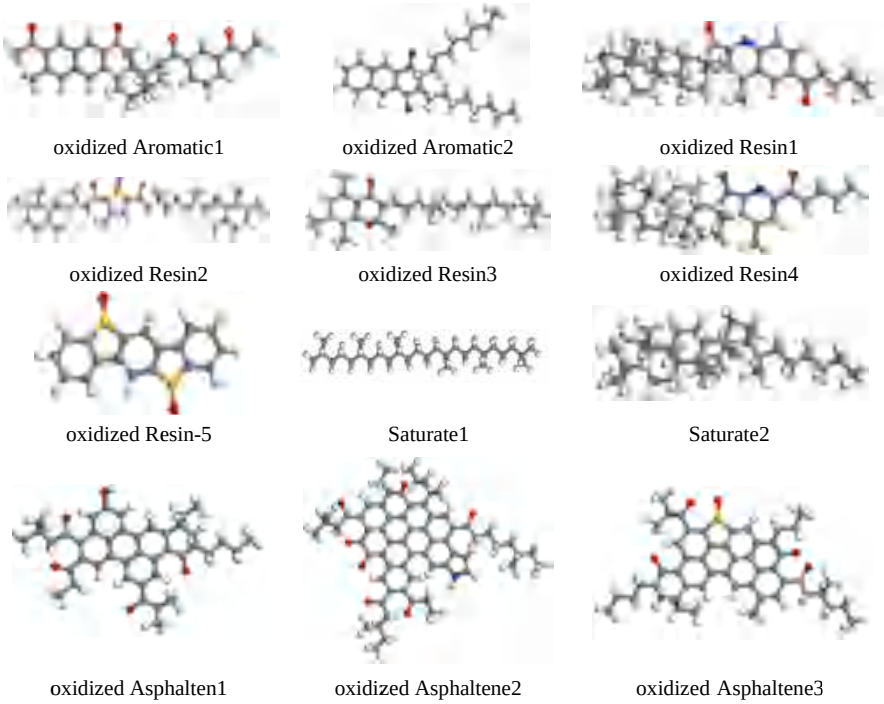

Fig. 3. Molecular structures of 12-component oxidized asphalt.

Table 1. Detailed composition of three asphalt models

			Number of molecules								
			AS-1			AS-2			AS-3		
Chemical fractions	Molecular label	Chemical formula	VA	LOA	HOA	VA	LOA	HOA	VA	LOA	HOA
Saturate	Saturate1	$C_{30}H_{62}$	4	4	4	2	2	2	1	1	1
	Saturate2	$C_{35}H_{62}$	4	4	4	2	2	2	1	1	1
Asphaltene	Asphaltene1	$C_{42}H_{54}O$	3	2	0	3	2	0	1	1	0
	Oxidized Asphaltene1	$C_{42}H_{46}O_5$	0	1	3	0	1	3	0	0	1
	Asphaltene2	$C_{66}H_{81}N$	2	1	0	2	1	0	1	1	0
	Oxidized Asphaltene2	$C_{66}H_{67}NO_7$	0	1	2	0	1	2	0	0	1
	Asphaltene3	$C_{51}H_{62}S$	3	2	0	3	2	0	1	0	0
	Oxidized Asphaltene3	$C_{51}H_{54}O_5S$	0	1	3	0	1	3	0	1	1
Resin	Resin1	$C_{40}H_{59}N$	4	2	0	4	2	0	10	5	0
	Oxidized Resin1	$C_{40}H_{55}NO_2$	0	2	4	0	2	4	0	5	10
	Resin2	$C_{40}H_{60}S$	4	2	0	4	2	0	10	5	0
	Oxidized Resin2	$C_{40}H_{56}O_3S$	0	2	4	0	2	4	0	5	10
	Resin3	$C_{29}H_{50}O$	5	3	0	4	2	0	10	5	0
	Oxidized Resin3	$C_{29}H_{48}O_2$	0	2	5	0	2	4	0	5	10
	Resin4	$C_{36}H_{57}N$	4	2	0	4	2	0	10	5	0
	Oxidized Resin4	$C_{36}H_{53}NO_2$	0	2	4	0	2	4	0	5	10
	Resin5	$C_{18}H_{10}S_2$	15	8	0	12	6	0	4	2	0
	Oxidized Resin5	$C_{18}H_{10}O_2S_2$	0	7	15	0	6	12	0	2	4
Aromatic	Aromatic1	$C_{35}H_{44}$	11	6	0	10	5	0	20	10	0
	Oxidized Aromatic1	$C_{35}H_{36}O_4$	0	5	11	0	5	10	0	10	20
	Aromatic2	$C_{30}H_{46}$	13	7	0	10	5	0	21	10	0
	Oxidized Aromatic2	$C_{30}H_{42}O_2$	0	6	13	0	5	10	0	11	21

Note: VA = virgin asphalt; LOA = lightly oxidized asphalt; and HOA = heavily oxidized asphalt.

Fig. 5 reveals the process of constructing the molecular model more intuitively. The initial density of all asphalt models was set at 0.1 g=cm^3, where a reasonable configuration with less atomic overlap can be achieved by a larger volume box under the same mass. Then, the energy optimization was performed by the Forcite module, and the Smart algorithm was used to optimize the structure. After this, an NVT ensemble (the atomic number, volume and temperature of the system were unchanged) of 500 ps was performed at

Table 2. The proportions of SARA components of asphalt binders

Asphalt binders	Fraction of SARA components				Molecular mass
	Aromatic	Asphaltene	Resin	Saturate	
VA AS-1	0.319	0.173	0.397	0.111	32,597.510
VA AS-2	0.313	0.202	0.419	0.065	27,815.330
VA AS-3	0.419	0.051	0.508	0.021	42,528.000
LOA AS-1	0.321	0.173	0.398	0.107	33,768.373
LOA AS-2	0.316	0.203	0.419	0.063	28,880.262
LOA AS-3	0.424	0.051	0.505	0.021	44,072.227
HOA AS-1	0.324	0.177	0.396	0.103	35,105.027
HOA AS-2	0.318	0.206	0.416	0.060	30,073.063
HOA AS-3	0.427	0.052	0.500	0.020	45,726.310

453 K to promote the system to reach equilibrium. Then, an NPT ensemble (atomic number, pressure, temperature of the system were unchanged, box size was changed) was carried out at 500 ps under 1 atmosphere to relax the system. The temperature of 453 K was to simulate the mixing temperature of the asphalt mixture in construction. In addition, the initial optimization temperature was set to 453 K to optimize the molecular structure of asphalt. The purpose was to increase the initial kinetic energy of the molecular structure, so the final asphalt molecular model can reach the most stable structural state. The optimized asphalt molecular model can be achieved by adjusting the temperature to 298.15 K and implementing the NVT of 500 ps. To validate the model, the density at 298.15 K was calculated to compare with experimental values, as shown in Fig. 6. The densities of the three kinds of asphalt was in the area of 1.00 ± 0.02 g=cm^3. The density of AAA-1 asphalt was 1.02–1.03 g=cm^3 in previous tests (Robertson et al. 2001), and the asphalt density was actually closer to the experimental density and previous MD simulation results (Xu and Wang 2016b). In addition, the density of asphalt in the molecular model significantly increased with increasing asphalt oxidation degree (Diab et al. 2019; Byzyka et al. 2021). These oxidized functional groups will contribute to the enhancement of polymerization ability between asphalt molecules, thus increasing the density of oxidized asphalt. It further proved that the molecular model and the force field can produce reasonable and accurate simulation results.

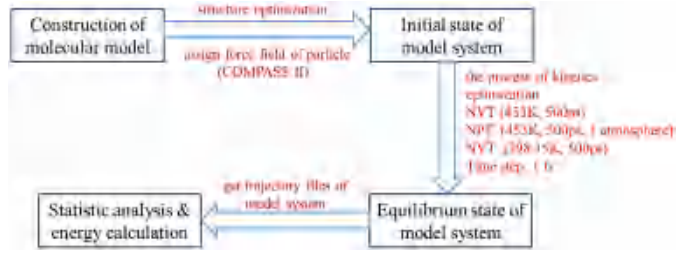

Fig. 5. A flow chart of constructing the molecular model.

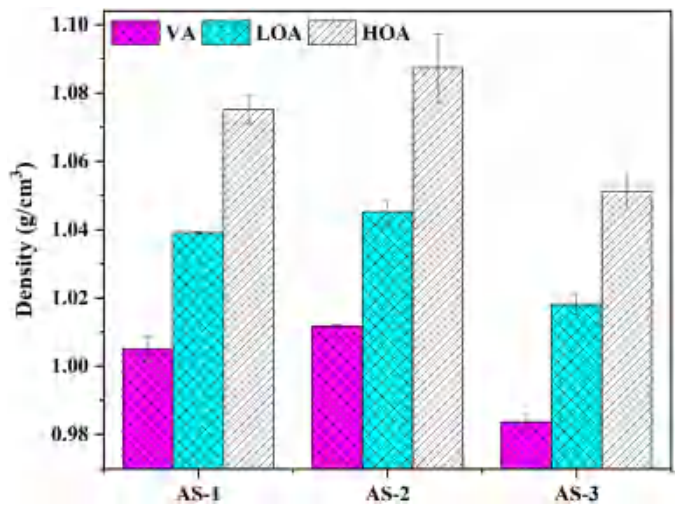

Fig. 6. The density of three representative asphalt binders.

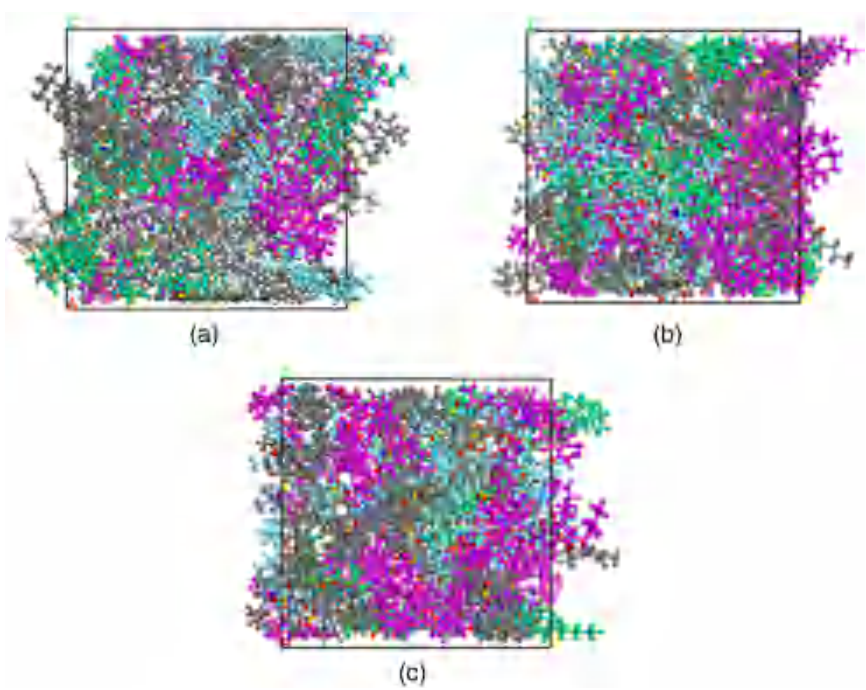

Fig. 4. The asphalt model of AS-1: (a) virgin asphalt (VA); (b) lightly oxidized asphalt (LOA); and (c) heavily oxidized asphalt (HOA).

Downloaded from ascelibrary.org by CHANG'AN UNIVERSITY on 03/25/23. Copyright ASCE. For personal use only; all rights reserved.

Table 3. Details of the mineral aggregate

Mineral types	Cleave plane (h k l)	Lattice parameters					
		a (Å)	b (Å)	c (Å)	α (degrees)	β (degrees)	γ (degrees)
A-quartz(SiO_2)	(0 0 1)	4.910	4.910	5.402	90	90	120
Calcite($CaCO_3$)	(1 0 4)	4.990	4.990	17,061	90	90	120

Molecular Model of Mineral Aggregate

The composition of mineral aggregate is complex, and different aggregate types are composed of different chemical components, which leads to different chemical and physical properties of asphalt mixture. Notably, mineral aggregate usually consists of several inorganic components. Quartz and calcite, as typical mineral components in aggregate, were selected as representative minerals in this study. The reason is that quartz and calcite are mainly composed of SiO_2 and $CaCO_3$, respectively. Studying the relationship between asphalt binder and single-component minerals can effectively provide insights for the chemical composition of aggregate on the interface performance of asphalt mixture. Quartz and calcite aggregate composition models from the structural database in Materials Studio 8.0 were imported, and the unit cells were first cut along the (h,k,l) direction. The detailed structural dimensions of the model are shown in Table 3. Then, geometric optimization was carried out for the mineral aggregate.

After optimization, the aggregate supercell was constructed to produce a size similar to that of the asphalt model, resulting in a two-dimensional aggregate surface. Then, an aggregate with three-dimensional periodic boundary conditions was formed by adding a vacuum plate with 0 Å. Orthogonal geometry was preferred for the purpose of construction and further calculation of the asphalt-aggregate interface model. For the non-orthogonal structure model of SiO_2 and $CaCO_3$, it can be transformed into an orthogonal structure model of $a = b = c = 90°$ by a redefinition lattice. Meanwhile, a fully hydroxylated silica surface with 8.28OH=nm^2 was produced to represent the aggregation layer due to the hydrophilicity of silica as shown in Fig. 7. Fig. 5 revealed the process of constructing molecular model more intuitively, and the model parameters of asphalt and aggregates are summarized, as shown in Table 4.

Interface Model of Asphalt-Aggregate under Moisture Conditions

The optimized restricted asphalt layer was attached to the aggregate base through the build layers module to form the asphalt-aggregate interface model. A 30-Å vacuum plate was added at the top of each asphalt-mineral interface model to eliminate the influence of three-dimensional periodic boundary conditions in the Z direction, which can make the simulation more realistic (Byzyka et al. 2021), as shown in Fig. 8(a). Moisture is a critical factor that can cause the adhesive failure of the asphalt mixture, and water wets aggregates more easily than asphalt and can replace asphalt wrapped on dry aggregates (Tarrer and Wagh 1991). Therefore, in this study, thin layers of 300 water molecules were inserted into the asphalt-aggregate interface to build the asphalt-H_2O-aggregate system to simulate the influence of moisture as shown in Fig. 8(b). Once the interface model was obtained, geometric optimization was performed, followed by a 500 ps canonical ensemble (NVT) to ensure further optimization of the model configuration. Three sets of asphalt-aggregate mineral models were also built and the results were averaged to eliminate the effect of randomness of the initial velocity during the dynamic simulation.

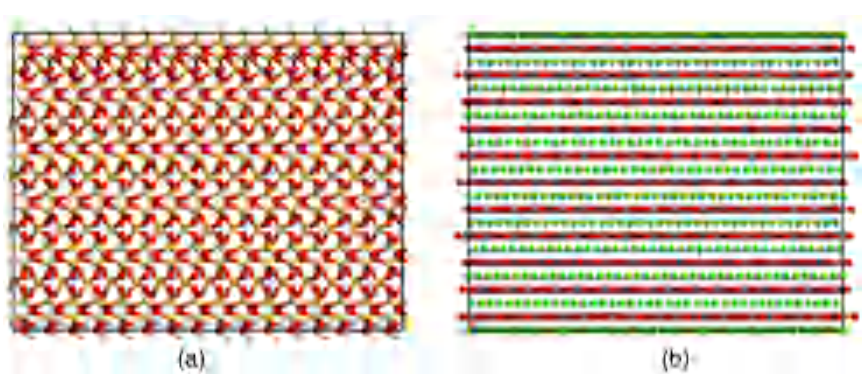

Fig. 7. The models of mineral aggregate for (a) quartz; and (b) calcite.

Table 4. The details parameters of the optimized molecular model

Molecular model	Parameters of the molecular model					
	a (Å)	b (Å)	c (Å)	α (degrees)	β (degrees)	γ (degrees)
AS-1	37.699	37.699	37.699	90.0	90.0	90.0
AS-2	35.879	35.879	35.879	90.0	90.0	90.0
AS-3	41.334	41.334	41.334	90.0	90.0	90.0
Quartz	42.804	32.280	30.524	90.0	90.0	90.0
Calcite	40.479	39.920	25.845	90.0	90.0	90.0

Downloaded from ascelibrary.org by CHANG'AN UNIVERSITY on 03/25/23. Copyright ASCE. For personal use only; all rights reserved.

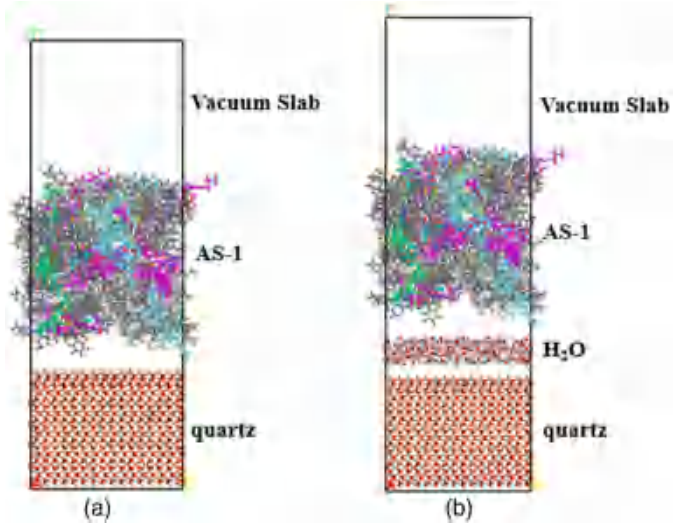

Fig. 8. The models of representative asphalt and mineral: (a) asphalt-quartz interface model; and (b) asphalt-H_2O-quartz interface model.

Evaluation Indexes for Asphalt-Aggregate Interfacial Properties

Interfacial Adhesion Energy of the Asphalt-Aggregate System

In order to evaluate the influence of adhesive energy between asphalt and minerals, this study quantified the adhesive energy between asphalt and aggregate mineral surfaces by calculating the interfacial energy. Adhesive energy is defined as the energy required to divide an interface model into two independent models, so the calculated adhesion energy was generally negative (Chen et al. 2018; Sun and Wang 2020). The interfacial adhesion energy was calculated by Eqs. (1) and (2)

$$\Delta E_{\text{interaction-energy}} = -(E_{\text{total}} - (E_{\text{asphalt}} + E_{\text{aggregate}})) \quad (1)$$

$$W_{\text{adhesion}} = \Delta E_{\text{interaction-energy}} = A \quad (2)$$

where $\Delta E_{\text{interaction-energy}}$ represents the interaction energy between asphalt and aggregate, E_{asphalt} and $E_{\text{aggregate}}$ represents the potential energy of asphalt and aggregate, respectively, and E_{total} represents the total potential energy of the asphalt-aggregate system. W_{adhesion} is the adhesive energy of asphalt binder and aggregate. A is the contact area of the interface between asphalt and aggregate.

Asphalt is composed of SARA components as shown in Eq. (3), and the contribution values of different components to aggregate can be respectively calculated. The interfacial adhesion energy calculation of asphaltene components and aggregate is shown in Eq. (4)

$$E_{\text{asphalt}} = E_{\text{Aromatic}} + E_{\text{Resin}} + E_{\text{Asphaltene}} + E_{\text{Saturate}} \quad (3)$$

$$W_{\text{adhesion-Asp}} = (E_{\text{total(Asp+aggregate)}} - -(E_{\text{Asp}} + E_{\text{aggregate}})) = A \quad (4)$$

where E_{Aromatic}, E_{Resin}, $E_{\text{Asphaltene}}$, and E_{Saturate} represent the potential energies of aromatic, resin, asphaltene, and saturate components in asphalt, respectively, and $W_{\text{adhesion-Asp}}$ represents the interfacial adhesive energy between asphaltene components and aggregate. $E_{\text{total(Asp+aggregate)}}$ represents the total potential energy of the asphaltene-mineral aggregate system.

Ratio of Interfacial Energy Loss, R_E

Water showed a great influence on the interfacial adhesive energy of the asphalt-aggregate system. When water invaded the asphalt-aggregate interface, the asphalt binder in the asphalt mixture tended to separate from the interface. The reduction of free energy in this process is defined as debonding energy in Eq. (5), which can also be conducted to analyze the influence of asphalt oxidation and moisture coupling on the adhesive energy of the asphalt-aggregate interface. By calculating the ratio of adhesion work from dry to wet conditions to adhesion work under dry conditions, as shown in Eq. (6), it can be used to evaluate the sensitivity of different asphalt-aggregate mixtures to moisture and further analyze the influence of moisture on the interface of the asphalt mixture

$$W_{\text{debonding}} = W_{\text{adhesion-asphalt}} + W_{\text{adhesion-aggregate}} - W_{\text{adhesion-energy}} \quad (5)$$

$$R_E = (W_{\text{adhesion}} - W_{\text{debonding}}) = W_{\text{adhesion}} \quad (6)$$

where $W_{\text{adhesion-asphalt}}$ and $W_{\text{adhesion-aggregate}}$ represent the energies of asphalt and aggregate at wet conditions. W_{adhesion} and $W_{\text{debonding}}$ represent the adhesive energy of the asphalt-aggregate system under dry and wet conditions, respectively.

Grey Relational Analysis

To more intuitively compare which factors had greater influence or closer correlation on the interfacial adhesive energy between asphalt and aggregate, the grey relational grade theory was conducted to evaluate the influencing factors in this study. Grey relational analysis can capture the relationship between the main factors and other factors in the system and determine the main factors affecting the adhesive energy of asphalt-aggregate. The detailed process of grey relational analysis can be found in other references (Du and Kuo 2011; Sun et al. 2017).

Results and Discussion

Interfacial Adhesive Energy of the Asphalt-Aggregate System

The interfacial adhesive energy calculated by MD simulation was determined to be a direct index to evaluate the adhesion characteristics of asphalt and aggregate. Fig. 9 revealed the interfacial adhesion energy between different asphalt and aggregate systems. In the process of simulation, three groups of parallel experiments were carried out for each asphalt-aggregate system model to eliminate the randomness of the initial velocity of the molecular model. The value indicates that the error of the asphalt-aggregate energy was small. In addition, the simulation results showed that the interfacial adhesive energy between asphalt and aggregate was completely composed of non-bonding energy, which indicated that there was no chemical bonding in the process of combining asphalt with aggregate. Furthermore, the energy was mainly composed of van der Waals energy and Coulomb electrostatic energy.

The calculation results further show that mineral aggregates have a more significant influence on the interfacial energy compared to binder types. For three types of AS-1, AS-2, AS-3, the interfacial adhesive energies of calcite were 35.0%, 22.9%, and

Downloaded from ascelibrary.org by CHANG'AN UNIVERSITY on 03/25/23. Copyright ASCE. For personal use only; all rights reserved.

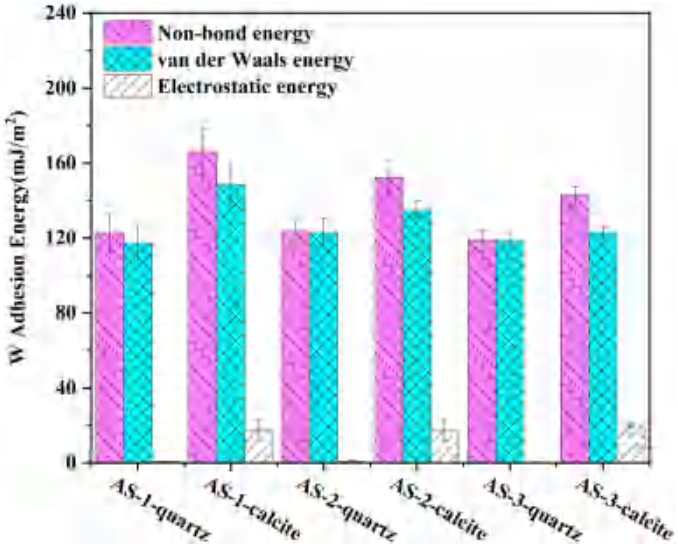

Fig. 9. Interfacial adhesive energy of several asphalt-aggregate systems.

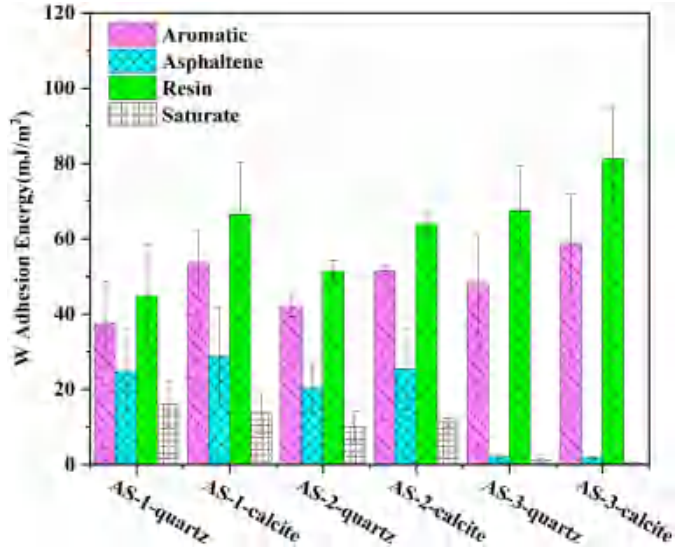

Fig. 10. Interfacial adhesive energy of SARA components-aggregate.

20.2% higher than that of quartz, respectively, in which interfaces constructed of alkaline aggregate have greater interfacial energy than those of acidic aggregate. For quartz, the interfacial energy was almost entirely composed of van der Waals energy, and Coulomb electrostatic energy could be neglected. The reason for this phenomenon can be attributed to the fact that quartz is an electrically neutral mineral and produces very weak or no electrostatic interaction with any materials. However, the interfacial adhesive energy between calcite and asphalt was mostly driven by van der Waals energy, and Coulombic electrostatic energy also played an important role. Certainly, asphalt types also influenced the energy of asphalt-aggregate. These results showed that AS-1 had the largest interfacial energy with the aggregate, followed by AS-2, and AS-3 was the least. Three types of asphalt were composed of different SARA components, so it was necessary to further study the interfacial adhesive energy of SARA components and aggregate by MD simulation.

Interfacial Adhesion Energy between SARA Components and Aggregate

The essence of asphalt-aggregate interface interaction is the adsorption behavior of asphalt components on the aggregate surface. Therefore, the adsorption of SARA components in asphalt binder on different aggregate surfaces was also the focus issue in this study, as shown in Fig. 9.

The simulation results still clearly show that there was a conspicuous difference in the energy between SARA components and aggregate in Fig. 10. For AS-1 and AS-2 asphalt, the aromatic and resin components contributed a lot to the energy, followed by asphaltene, and saturate occupying the least. This result also compares well with previous simulation results (Sun and Wang 2020). It had been documented that the main components of asphalt-aggregate interfacial adhesion energy were polar components. The colloidal structure of asphalt binder was composed of asphaltene and resin components, which directly determined the interfacial bonding strength of the asphalt mixture (Shan et al. 2019). However, the energy between AS-3 and aggregates was occupied by aromatic hydrocarbon and resin components at over 97%, where the contribution of asphaltene and saturate components to the total energy was slight and deemed to be negligible. The reason for this phenomenon might be the contributions to the different proportions of SARA components in three asphalt binders, where the fraction of asphaltene and resin in AS-3 asphalt was the least. Therefore, it may be the reason for the lowest adhesive energy between AS-3 and aggregate among the three asphalt binders in the section "Interfacial Adhesive Energy of the Asphalt-Aggregate System." According to the proportion of SARA components and total molecular mass of the three asphalt molecules in Tables 1 and 2, it can be deemed that besides the proportion of asphaltene and resin components, the interfacial energy will also be affected by the molecular mass.

Relative Concentration of Asphalt Components on the Aggregate Surface

Fig. 11 shows the relative concentrations of SARA components and aggregates in the Z direction. It can be observed that the distribution of SARA components on the aggregate was inconsistent, and the peak value of resin components appeared earlier in the Z-axis direction than other components, indicating that resin components could more easily approach the aggregate interface. However, the peak positions of asphaltene components were inconsistent, some were near the aggregate interface, as shown in Figs. 11(b, e, and f), some were far away from the aggregate interface such as Fig. 11(a), and others appeared in the middle position in Figs. 11(c and d). This phenomenon showed that polar components were more likely to be attracted by the aggregates. However, some asphaltene and resin components were far away from the aggregate interface. This reason may be attributed to the fact that only limited polar components will converge and adsorb at the aggregate interface, while others needed to shoulder the stability of the asphalt colloid structure (Dong et al. 2017). Furthermore, the peak concentrations of aromatic components were concentrated near the aggregate interface, so the simulation results also showed that the aromatic components had pretty good interfacial bonding strength with the aggregate. The saturate components, non-polar in nature, were less distributed near the aggregate interface. This further indicated that the proportion of SARA components in asphalt and the distribution characteristics of components on the aggregate surface had a significant influence on the asphalt-aggregate system.

Downloaded from ascelibrary.org by CHANG'AN UNIVERSITY on 03/25/23. Copyright ASCE. For personal use only; all rights reserved.

Downloaded from ascelibrary.org by CHANG'AN UNIVERSITY on 03/25/23. Copyright ASCE. For personal use only; all rights reserved.

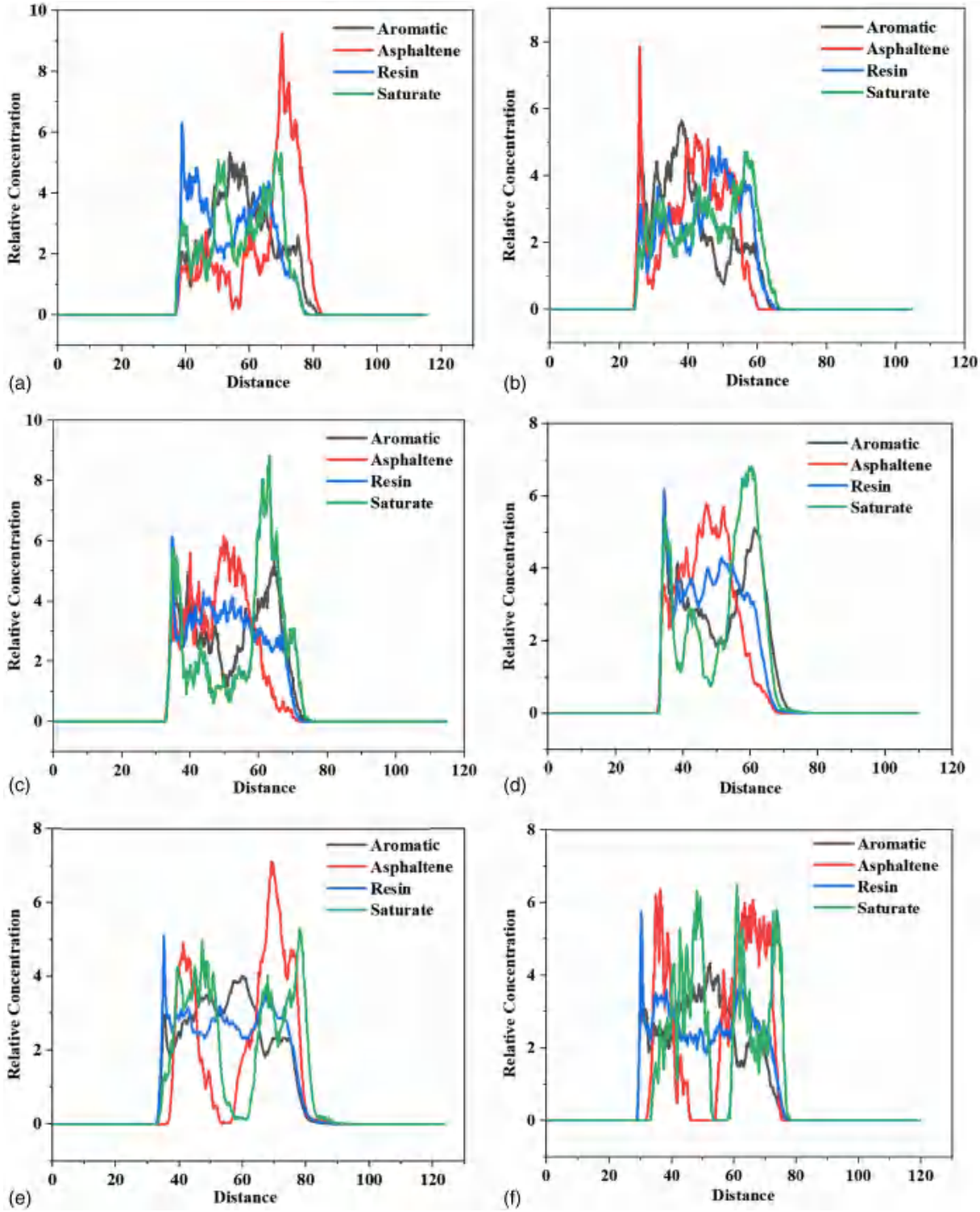

Fig. 11. Relative concentration curve of SARA components on the aggregate surface: (a) AS-1-quartz; (b) AS-1-calcite; (c) AS-2-quartz; (d) AS-2-calcite; (e) AS-3-quartz; and (f) AS-3-calcite.

Effects of Oxidized Asphalt on the Asphalt-Aggregate Interfacial Energy

Asphalt binder will suffer from different degrees of aging due to ultraviolet aging or oxidative aging of asphalt pavement. Therefore, in this study, asphalt with different oxidation degrees was considered to study the effect of aging on the interfacial bond strength of asphalt mixtures. Fig. 12 shows the interfacial adhesive energy between virgin, lightly oxidized, and heavily oxidized asphalt and aggregate. The illustration shows that oxidation can improve the interfacial energy between asphalt and aggregate. The reason for this phenomenon can be attributed to the oxidation functional groups (namely carbonyl and sulfoxide) formed after oxidation, which enhanced the intermolecular bonding of asphalt, including van der Waals forces and electrostatic interaction. However, previous test results show that aging will reduce the interfacial

Downloaded from ascelibrary.org by CHANG'AN UNIVERSITY on 03/25/23. Copyright ASCE. For personal use only; all rights reserved.

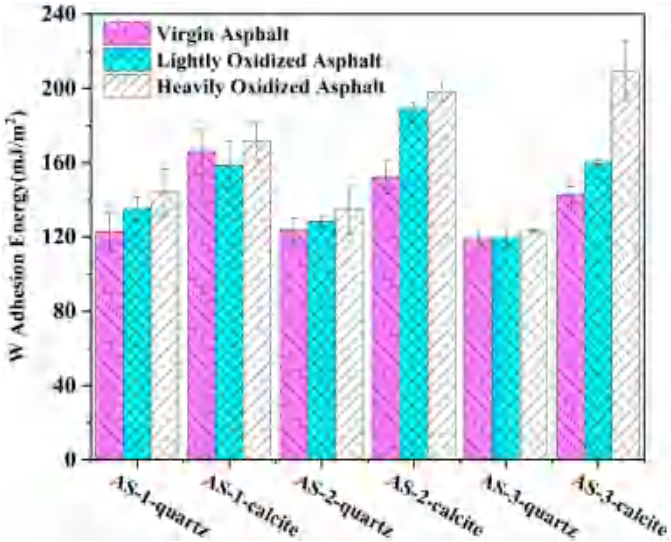

Fig. 12. Effects of oxidized asphalt on asphalt-aggregate interfacial energy.

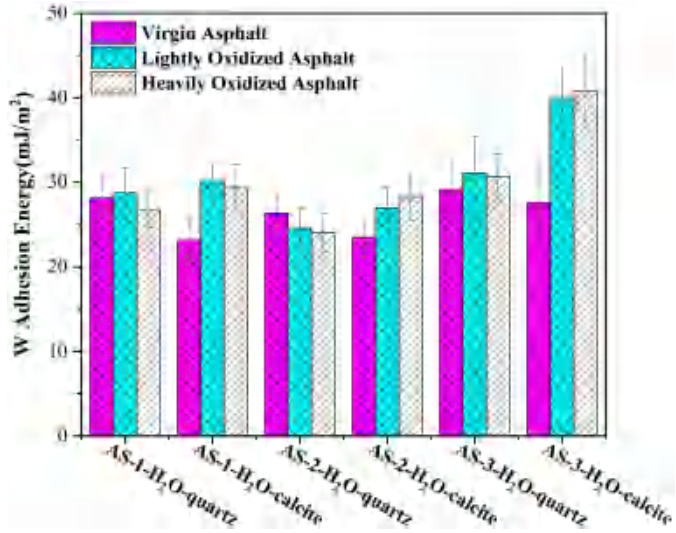

Fig. 13. Interfacial energy of the oxidized asphalt-water-aggregate.

adhesion between asphalt and aggregate, mainly because asphalt will harden after aging, but the MD simulation cannot truly simulate the phenomenon that asphalt will harden and become brittle after aging.

The energy between different aggregates and aged asphalt was also different. The interfacial energy between different oxidized asphalt and quartz was approximately the same. For alkaline aggregate calcite, the energy can be significantly improved with an increased degree of oxidation, especially for AS-2 and AS-3. The reason for this phenomenon may be attributed to the increase of molecular mass and polarity caused by oxidation, which would increase the Coulombic electrostatic energy. However, quartz is an electrically neutral structure and only affected by van der Waals energy, while Coulombic electrostatic energy was neglected, as discussed in section 4.1.

Effects of Moisture on Asphalt-Aggregate Interfacial Adhesion Energy

Water, as an important factor affecting the adhesive energy of asphalt mixtures, has always been considered as the focus index leading to the debonding of the asphalt-aggregate interface (Luo et al. 2020). Therefore, the effect of moisture was also considered in this study. Fig. 13 shows the interfacial adhesive energy of the oxidized asphalt-water-aggregate. The results show that the energy can be significantly reduced after adding a thin layer of water molecules to the asphalt-aggregate interface. The simulation further indicated that moisture was indeed a focal factor causes debonding failure of the asphalt-aggregate interface. The results also showed that the interfacial adhesion energy between asphalt and alkaline aggregate was better than that of acidic aggregate in dry condition, but the result was reversed in wet conditions for the virgin asphalt (Gao et al. 2018). This indicates that the aggregate type was not important to the damage caused by moisture when the water content was high enough to invade the interface. In addition, the interfacial energy between oxidized asphalt and aggregate was still higher than that of virgin asphalt even at wet conditions. It showed that the oxidation and moisture coupling can improve the interfacial adhesion energy. The reason can be explained that water molecules blocked the interfacial contact between asphalt and aggregate, but aging can enhance the intermolecular bonding of asphalt.

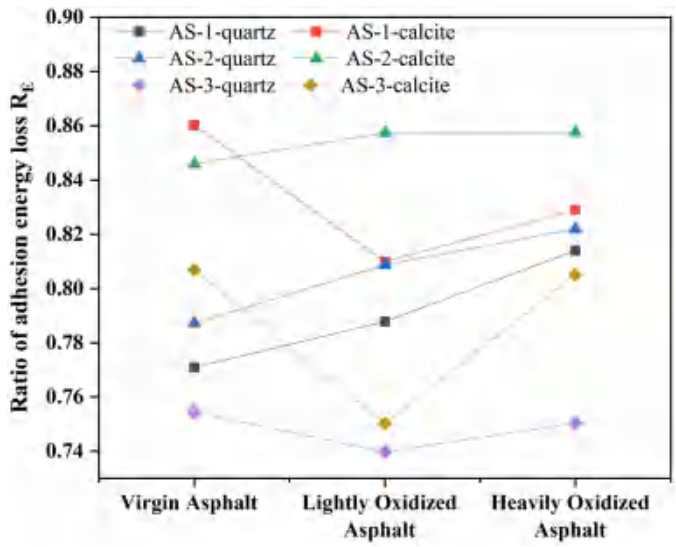

Fig. 14. Ratio of interfacial energy loss of the asphalt-aggregate system.

In addition, the ratio of energy loss, R_E, was conducted to evaluate the moisture sensitivity of asphalt-aggregate interface, and the calculation results are shown in Fig. 14. It can be observed that R_E was between 0.74 and 0.88, which is close to 1, indicating that the energy loss of the asphalt-aggregate interface was great at wet conditions. Moreover, the R_E of oxidized asphalt to calcite was larger than that of quartz, which indicated that the adhesive energy between asphalt and alkaline aggregate was excellent in dry conditions, and calcite was more susceptible to moisture damage than quartz when the water content was high enough.

Grey Relational Analysis of the Adhesive Energy between Asphalt and Aggregate

According to the results of MD simulation and previous experiments, the adhesive energy between asphalt and aggregate mainly depends on the types of asphalt and aggregate. The simulation results further proved that the influence of mineral types on the

Table 5. The parameters of different factors on the adhesive energy of an asphalt-aggregate system

Asphalt	Adhesion energy, W (mJ=m^2)		Fraction of SARA components				I_A	Molecular mass
	Quartz	Calcite	Aromatic	Asphaltene	Resin	Saturate		
VA-AS-1	122.703	165.589	0.319	0.173	0.397	0.111	1.325	32,597.510
LOA-AS-1	135.331	158.498	0.321	0.173	0.398	0.107	1.334	33,768.373
HOA-AS-1	144.074	171.565	0.324	0.177	0.396	0.103	1.340	35,105.027
VA-AS-2	123.641	152.005	0.313	0.202	0.419	0.065	1.643	27,815.330
LOA-AS-2	128.424	189.117	0.316	0.203	0.419	0.063	1.639	28,880.262
HOA-AS-2	134.786	198.256	0.318	0.206	0.416	0.060	1.646	30,073.063
VA-AS-3	118.572	142.506	0.419	0.051	0.508	0.021	1.269	42,528.000
LOA-AS-3	119.360	159.688	0.424	0.051	0.505	0.021	1.251	44,072.227
HOA-AS-3	122.956	209.040	0.427	0.052	0.500	0.020	1.236	45,726.310

Note: VA = virgin asphalt; LOA = lightly oxidized asphalt; and HOA = heavily oxidized asphalt.

Table 6. The results of grey relational analysis

Aggregates	Aromatic	Asphaltene	Resin	Saturate	I_A	Molecular mass
Quartz	0.769	0.650	0.789	0.535	0.809	0.721
Calcite	0.812	0.758	0.832	0.619	0.857	0.774

interface of asphalt mixture is more significant than that of asphalt binder. For asphalt binder, the fraction of SARA component, and the distribution and mass of the molecules had great effects on the interfacial adhesive energy between asphalt and aggregate, as shown in sections 4.2–4.3. In addition, asphaltene and resin, as polar components in asphalt binder, had always been considered as important factors in determining the interfacial adhesion between asphalt and aggregate. Previous studies have also proposed the asphaltene index $I_A = (\text{asphaltene} + \text{resin})/(\text{saturate} + \text{aromatic})$ as an index to judge its relationship with the interfacial adhesive energy between asphalt and aggregate (Xu and Wang 2016; Oyekunle 2006). Therefore, to capture the relationship between the main factors and other factors in the asphalt-aggregate interface system and determine the main factors affecting the adhesive energy, the grey relational analysis method was conducted to explore the influence of these different factors on the adhesive energy. The parameters of different factors on the adhesive energy of asphalt-aggregate system are shown in Table 5.

The grey relational grade was calculated between the adhesive work of two aggregates and different influencing factors, and then the influence grade of different factors was compared. The calculation results are shown in Table 6. For quartz and calcite, the decreasing order of the grey relational grades was: I_A > Resin > Aromatic > Mass of Molecular > Asphaltene > Saturate. Furthermore, the grey relational grade between calcite and different factors was higher than that of quartz, which indicated that alkaline aggregate has stronger correlation with SARA components and the molecular mass of asphalt binder. In addition, the relational grades between asphaltene index and interfacial adhesive energy of the two aggregates were the highest, and resin was higher than that of aromatic, which further showed the superior effect of asphaltene and resin components on adhesive energy. The reason for the increase of interfacial adhesive energy between asphalt and aggregate at different aging degrees was that the aging will generate more functional groups, and the increased molecular mass of asphalt will also provide a positive effect for the increase of adhesion energy. Saturate, as the component with the weakest polarity and less fraction, has the lowest correlation with adhesive energy. However, for the two aggregates, the grey relational grade of asphaltene was also low. The reason for that may be due to the low fraction of asphaltene, which leads to the low relational grade between asphaltene components and adhesive energy as described in section 4.3, and the interfacial adhesion energy between asphaltene and aggregates was lower than that of aromatic and resin components. Further research is needed to quantify the relationship between the SARA component ratio of asphalt and aggregate to the interfacial adhesion energy.

Conclusions

In this study, the MD simulation method was utilized to analyze the interfacial effects of the asphalt-aggregate system. It calculates the interfacial adhesive energy between asphalt and aggregate and further explores the coupling effect of oxidation and moisture on the asphalt-aggregate system. Future research will attempt to capture the long-term evolution of material structure by combining a coarse-grained model and mesoscale Monte Carlo with parallel calculation. The following conclusions can be drawn from the above preliminary results.

1. Mineral aggregate has a more significant influence on the energy compared with binder types, in which interfaces constructed by alkaline aggregate have greater energy than that of acidic aggregate. Besides the proportion of asphaltene and resin components, the interfacial energy will also be affected by the mass of molecular asphalt.
2. SARA components in asphalt binder have different interfacial energies with the aggregate, and aromatic and resin components contribute a lot, followed by asphaltene and saturate. The polar components of resin and asphaltene are more likely to attract aggregates, where the aromatic components are concentrated near the aggregate interface and the saturate components are mainly distributed far from the aggregate.
3. Oxidation of asphalt binder can improve the interfacial energy of asphalt-aggregate, especially for the interface built by calcite. MD simulation cannot truly simulate the phenomenon that asphalt will become hard and brittle after aging, but oxidized

Downloaded from ascelibrary.org by CHANG'AN UNIVERSITY on 03/25/23. Copyright ASCE. For personal use only; all rights reserved.

asphalt can form some functional groups to enhance its intermolecular bonding. The existence of water can significantly reduce the interfacial adhesion of asphalt mixture. However, the oxidation and moisture coupling can improve the interfacial energy of asphalt-aggregate in comparison with wet conditions only.

4. The grey relational analysis shows that the interfacial adhesion energy of asphalt-aggregate is more sensitive to the asphaltene index than other factors. Also, the interfacial adhesive energy between aggregate containing more calcite and asphalt is more significantly affected by asphalt properties than quartz.

Data Availability Statement

All data, models, and code generated or used during the study appear in the published article.

Acknowledgments

This work was supported by National Natural Science Foundation of China (No. 51978068), the Program Fund of Non-Metallic Excellence and Innovation Center for Building Materials (2022SFP6-5), Natural Science Foundation of Shaanxi Province (Nos. 2020JM-217 and 2021 JQ-268), and Fundamental Research Funds for the Central Universities, CHD (Nos. 310821 173501 and 300102211305). The authors gratefully acknowledge their financial support.

References

Adebiyi, F., and V. Thoss. 2015. "Spectroscopic characterization of asphaltene fraction of Nigerian bitumen." Pet. Sci. Technol. 33 (2): 245–255. https://doi.org/10.1080/10916466.2014.961609.

Aigner, E., R. Lackner, and C. Pichler. 2009. "Multiscale prediction of viscoelastic properties of asphalt concrete." J. Mater. Civ. Eng. 21 (12): 771–780. https://doi.org/10.1061/(ASCE)0899-1561(2009)21:12(771).

Byzyka, J., M. Rahman, and D. A. Chamberlain. 2021. "A laboratory investigation on thermal properties of virgin and aged asphalt mixture." Constr. Build. Mater. 305 (Oct): 124757. https://doi.org/10.1016/j.conbuildmat.2021.124757.

Chen, P., X. Luo, Y. Gao, and Y. Zhang. 2022. "Modeling percentages of cohesive and adhesive debonding in bitumen-aggregate interfaces using molecular dynamics approaches." Appl. Surf. Sci. 571 (Jan): 151318. https://doi.org/10.1016/j.apsusc.2021.151318.

Chen, Z., J. Pei, R. Li, and F. Xiao. 2018. "Performance characteristics of asphalt materials based on molecular dynamics simulation—A review." Constr. Build. Mater. 189 (Nov): 695–710. https://doi.org/10.1016/j.conbuildmat.2018.09.038.

Chu, L., L. Luo, and T. Fwa. 2019. "Effects of aggregate mineral surface anisotropy on asphalt-aggregate interfacial bonding using molecular dynamics (MD) simulation." Constr. Build. Mater. 225 (Nov): 1–12. https://doi.org/10.1016/j.conbuildmat.2019.07.178.

Curtis, C. W., K. Ensley, and J. Epps. 1993. Fundamental properties of asphalt-aggregate interactions including adhesion and absorption. Washington, DC: Strategic Highway Research Program.

Diab, A., M. Enieb, and D. Singh. 2019. "Influence of aging on properties of polymer-modified asphalt." Constr. Build. Mater. 196 (Jan): 54–65. https://doi.org/10.1016/j.conbuildmat.2018.11.105.

Dong, Z., Z. Liu, P. Wang, and X. Gong. 2017. "Nanostructure characterization of asphalt-aggregate interface through molecular dynamics simulation and atomic force microscopy." Fuel 189 (Feb): 155–163. https://doi.org/10.1016/j.fuel.2016.10.077.

Du, J. C., and M. F. Kuo. 2011. "Grey relational-regression analysis for hot mix asphalt design." Constr. Build. Mater. 25 (5): 2627–2634. https://doi.org/10.1016/j.conbuildmat.2010.12.011.

Gao, Y., Y. Zhang, F. Gu, T. Xu, and H. Wang. 2018. "Impact of minerals and water on bitumen-mineral adhesion and debonding behaviours using molecular dynamics simulations." Constr. Build. Mater. 171 (May): 214–222. https://doi.org/10.1016/j.conbuildmat.2018.03.136.

Gao, Y., Y. Zhang, Y. Yang, J. Zhang, and F. Gu. 2019. "Molecular dynamics investigation of interfacial adhesion between oxidised bitumen and mineral surfaces." Appl. Surf. Sci. 479 (Jun): 449–462. https://doi.org/10.1016/j.apsusc.2019.02.121.

Guo, F., J. Pei, J. Zhang, B. Xue, G. Sun, and R. Li. 2020. "Study on the adhesion property between asphalt binder and aggregate: A state-of-the-art review." Constr. Build. Mater. 256 (Sep): 119474. https://doi.org/10.1016/j.conbuildmat.2020.119474.

Guo, M., T. Yiqiu, and W. Jianming. 2018. "Using molecular dynamics simulation to study concentration distribution of asphalt binder on aggregate surface." J. Mater. Civ. Eng. 30 (5): 04018075. https://doi.org/10.1061/(ASCE)MT.1943-5533.0002258.

Hou, Y., L. Wang, D. Wang, M. Guo, P. Liu, and J. Yu. 2017. "Characterization of bitumen micro-mechanical behaviors using AFM, phase dynamics theory and MD simulation." Materials 10 (2): 208. https://doi.org/10.3390/ma10020208.

Huang, W., Q. Lv, and F. Xiao. 2016. "Investigation of using binder bond strength test to evaluate adhesion and self-healing properties of modified asphalt binders." Constr. Build. Mater. 113 (Jun): 49–56. https://doi.org/10.1016/j.conbuildmat.2016.03.047.

Jäger, A., R. Lackner, C. Eisenmenger-Sittner, and R. Blab. 2004. "Identification of four material phases in bitumen by atomic force microscopy." Road Mater. Pavement Des. 5 (Sup1): 9–24. https://doi.org/10.1080/14680629.2004.9689985.

Khan, Z. H., H. M. Faisal, and R. A. Tarefder. 2018. "Phase identification and characterization of aging effects in asphaltic materials by nanoindentation testing." Transp. Geotech. 17 (Dec): 154–164. https://doi.org/10.1016/j.trgeo.2018.10.002.

Kim, Y.-R., I. Pinto, and S.-W. Park. 2012. "Experimental evaluation of anti-stripping additives in bituminous mixtures through multiple scale laboratory test results." Constr. Build. Mater. 29 (Apr): 386–393. https://doi.org/10.1016/j.conbuildmat.2011.10.012.

Lesueur, D. 2009. "The colloidal structure of bitumen: Consequences on the rheology and on the mechanisms of bitumen modification." Adv. Colloid Interface Sci. 145 (1–2): 42–82. https://doi.org/10.1016/j.cis.2008.08.011.

Li, D. D., and M. L. Greenfield. 2014. "Chemical compositions of improved model asphalt systems for molecular simulations." Fuel 115 (Jan): 347–356. https://doi.org/10.1016/j.fuel.2013.07.012.

Li, F., Y. Yang, and L. Wang. 2020. "Evaluation of physicochemical interaction between asphalt binder and mineral filler through interfacial adsorbed film thickness." Constr. Build. Mater. 252 (Aug): 119135. https://doi.org/10.1016/j.conbuildmat.2020.119135.

Lu, Y., and L. Wang. 2010. "Nanoscale modelling of mechanical properties of asphalt–aggregate interface under tensile loading." Int. J. Pavement Eng. 11 (5): 393–401. https://doi.org/10.1080/10298436.2010.488733.

Luo, L., L. Chu, and T. Fwa. 2020. "Molecular dynamics analysis of moisture effect on asphalt-aggregate adhesion considering anisotropic mineral surfaces." Appl. Surf. Sci. 527 (Oct): 146830. https://doi.org/10.1016/j.apsusc.2020.146830.

Ma, X., W. Jiantao, L. Quan, W. Ren, and M. Oeser. 2021. "Molecular dynamics simulation of the bitumen-aggregate system and the effect of simulation details." Constr. Build. Mater. 285 (May): 122886. https://doi.org/10.1016/j.conbuildmat.2021.122886.

Moraes, R., R. Velasquez, and H. U. Bahia. 2011. "Measuring the effect of moisture on asphalt–aggregate bond with the bitumen bond strength test." Transp. Res. Rec. 2209 (1): 70–81. https://doi.org/10.3141/2209-09.

Oyekunle, L. 2006. "Certain relationships between chemical composition and properties of petroleum asphalts from different origin." Oil Gas Sci. Technol.-Revue de l'IFP 61 (3): 433–441. https://doi.org/10.2516/ogst:2006043a.

Petersen, J. C. 2009. "A review of the fundamentals of asphalt oxidation: Chemical, physicochemical, physical property, and durability relationships." In Transportation research circular. Washington, DC: National Academies Press. https://doi.org/10.17226/23002.

Downloaded from ascelibrary.org by CHANG'AN UNIVERSITY on 03/25/23. Copyright ASCE. For personal use only; all rights reserved.

Robertson, R. E., J. F. Branthaver, P. M. Harnsberger, J. Peterson, S. M. Dorrence, J. F. McKay, F. Turner, T. Pauli, S.-C. Huang, and J.-D. Huh. 2001. Fundamental properties of asphalts and modified asphalts, Volume 1: Interpretive report. Washington, DC: Federal Highway Administration.

Shan, L., R. Xie, N. J. Wagner, H. He, and Y. Liu. 2019. "Microstructure of neat and SBS modified asphalt binder by small-angle neutron scattering." Fuel 253 (Oct): 1589–1596. https://doi.org/10.1016/j.fuel.2019.05.087.

Sultana, S., and A. Bhasin. 2014. "Effect of chemical composition on rheology and mechanical properties of asphalt binder." Constr. Build. Mater. 72 (Dec): 293–300. https://doi.org/10.1016/j.conbuildmat.2014.09.022.

Sun, D. Q., F. Yu, L. H. Li, T. B. Lin, and X. Y. Zhu. 2017. "Effect of chemical composition and structure of asphalt binders on self-healing." Constr. Build. Mater. 133 (Feb): 495–501. https://doi.org/10.1016/j.conbuildmat.2016.12.082.

Sun, G., Y. Yang, J. Zhang, Y. Cao, X. Tan, and J. Pei. 2022. "Modeling and optimization of pavement scale-model for magnetically coupled resonant in wireless power transmission systems." Constr. Build. Mater. 319 (Feb): 126066. https://doi.org/10.1016/j.conbuildmat.2021.126066.

Sun, G., J. Zhang, Q. Liu, X. Tan, C. Zhu, and Y. Guan. 2021. "Effects of microcapsules on self-healing performance of asphalt materials under different loading modes." J. Transp. Eng. Part B Pavements 147 (2): 04021010.

Sun, G., J. Zhang, X. Tan, D. Guo, Y. Zhou, and Y. Guan. 2020. "Evaluation of conventional technical properties and self-healing ability of bitumen-based sealants containing sunflower-oil microcapsules for pavement cracks." Constr. Build. Mater. 254 (Sep): 119299. https://doi.org/10.1016/j.conbuildmat.2020.119299.

Sun, W., and H. Wang. 2020. "Moisture effect on nanostructure and adhesion energy of asphalt on aggregate surface: A molecular dynamics study." Appl. Surf. Sci. 510 (Apr): 145435. https://doi.org/10.1016/j.apsusc.2020.145435.

Tan, Y., and M. Guo. 2014. "Interfacial thickness and interaction between asphalt and mineral fillers." Mater. Struct. 47 (4): 605–614. https://doi.org/10.1617/s11527-013-0083-8.

Tarefder, R. A., and A. Zaman. 2011. "Characterization of asphalt materials for moisture damage using atomic force microscopy and nanoindentation." In Nanotechnology in civil infrastructure, 237–256. Berlin: Springer.

Tarrer, A., and V. Wagh. 1991. The effect of the physical and chemical characteristics of the aggregate on bonding. Auburn, AL: Auburn Univ.

Visintine, B., N. P. Khosla, and A. Tayebali. 2013. "Effects of higher percentage of recycled asphalt pavement on pavement performance." Road Mater. Pavement Des. 14 (2): 432–437. https://doi.org/10.1080/14680629.2013.779310.

Wang, H., L. Enqiang, and X. Guangji. 2017. "Molecular dynamics simulation of asphalt-aggregate interface adhesion strength with moisture effect." Int. J. Pavement Eng. 18 (5): 414–423. https://doi.org/10.1080/10298436.2015.1095297.

Wang, H., J. Wang, and J. Chen. 2014. "Micromechanical analysis of asphalt mixture fracture with adhesive and cohesive failure." Eng. Fract. Mech. 132 (Dec): 104–119. https://doi.org/10.1016/j.engfracmech.2014.10.029.

Xiao, F., and S. N. Amirkhanian. 2009. "Laboratory investigation of moisture damage in rubberised asphalt mixtures containing reclaimed asphalt pavement." Int. J. Pavement Eng. 10 (5): 319–328. https://doi.org/10.1080/10298430802169432.

Xu, G., and H. Wang. 2016a. "Molecular dynamics study of interfacial mechanical behavior between asphalt binder and mineral aggregate." Constr. Build. Mater. 121 (Sep): 246–254. https://doi.org/10.1016/j.conbuildmat.2016.05.167.

Xu, G., and H. Wang. 2016b. "Study of cohesion and adhesion properties of asphalt concrete with molecular dynamics simulation." Comput. Mater. Sci. 112 (Feb): 161–169. https://doi.org/10.1016/j.commatsci.2015.10.024.

Xu, T., H. Wang, Z. Li, and Y. Zhao. 2014. "Evaluation of permanent deformation of asphalt mixtures using different laboratory performance tests." Constr. Build. Mater. 53 (Feb): 561–567. https://doi.org/10.1016/j.conbuildmat.2013.12.015.

Yi, J., X. Pang, D. Feng, Z. Pei, M. Xu, S. Xie, and Y. Huang. 2018. "Studies on surface energy of asphalt and aggregate at different scales and bonding property of asphalt–aggregate system." Road Mater. Pavement Des. 19 (5): 1102–1125. https://doi.org/10.1080/14680629.2017.1300597.

Yu, X., N. A. Burnham, and M. Tao. 2015. "Surface microstructure of bitumen characterized by atomic force microscopy." Adv. Colloid Interface Sci. 218 (Apr): 17–33. https://doi.org/10.1016/j.cis.2015.01.003.

Zhang, J., G. D. Airey, and J. R. Grenfell. 2016. "Experimental evaluation of cohesive and adhesive bond strength and fracture energy of bitumen-aggregate systems." Mater. Struct. 49 (7): 2653–2667. https://doi.org/10.1617/s11527-015-0674-7.

Zhang, L., and M. L. Greenfield. 2007. "Analyzing properties of model asphalts using molecular simulation." Energy Fuels 21 (3): 1712–1716. https://doi.org/10.1021/ef060658j.

Zhang, Y., X. Luo, R. Luo, and R. L. Lytton. 2014. "Crack initiation in asphalt mixtures under external compressive loads." Constr. Build. Mater. 72 (Dec): 94–103. https://doi.org/10.1016/j.conbuildmat.2014.09.009.

Downloaded from ascelibrary.org by CHANG'AN UNIVERSITY on 03/25/23. Copyright ASCE. For personal use only; all rights reserved.

ACS APPLIED MATERIALS & INTERFACES

www.acsami.org Research Article

Protective and Flame-Retardant Bifunctional Epoxy-Based Nanocomposite Coating by Intercomponent Synergy between Modified CaAl-LDH and rGO

Hassan Murtaza, Jingmao Zhao,* Mohammad Tabish, Jingbao Wang, Muhammad Mubeen, Jingfan Zhang, Sheng Zhang, and Baomin Fan*

Cite This: *ACS Appl. Mater. Interfaces* 2024, 16, 13114−13131 Read Online

ACCESS | Metrics & More | Article Recommendations | Supporting Information

ABSTRACT: Extensive utilization in various settings poses extra requirements of coatings beyond just anticorrosion properties. Herein, 8-hydroxyquinoline (8-HQ) intercalated CaAl-based layered double hydroxide (CaAl-8HQ-LDH) was loaded on reduced GO (rGO) through a one-pot hydrothermal reaction, which was employed as the nanofiller endowing the epoxy (EP/CaAl-8HQ LDH@rGO) with excellent flame-retardancy while ensuring efficient protection for mild steel. Results of electrochemical impedance spectroscopy (EIS) demonstrated the durability of the EP/CaAl-8HQ LDH@rGO-coated specimen, with the impedance at the lowest frequency ($|Z|_{0.01Hz}$) maintained as 1.84×10^{10} Ω cm^2 after 120 days of immersion in a 3.5 wt % NaCl solution. Even for the scratched EP/CaAl-8HQ LDH@rGO system, only a slight decline in $|Z|_{0.01Hz}$ was observed during 180 h of exposure to the NaCl solution, indicating a self-healing feature supported by salt spray tests. UL-94 burning tests revealed the V-0 rating for EP/CaAl-8HQ LDH@rGO with improved thermostability. Strong physical barrier from two-dimensional rGO and the release of 8-HQ from LDH interlayers accounted for the anticorrosive and self-healing properties. However, O_2-concentration dilution and charring-layer promotion governed the flame-retardant behavior of the nanocomposite coating. The intercomponent synergy of nanofillers achieved in this work may provide a useful reference for designing multifunctional coatings.

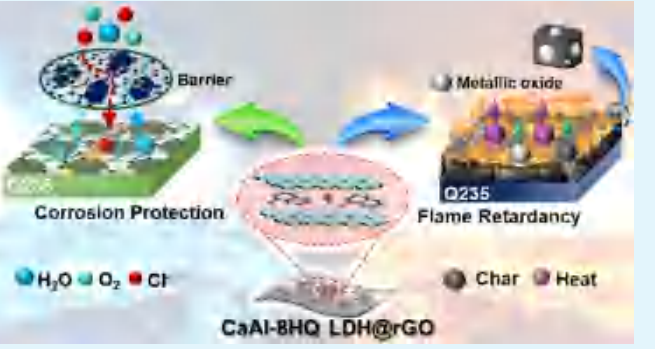

KEYWORDS: *layered double hydroxide, rGO, nanocomposites, corrosion inhibition, pristine epoxy (EP), flame-retardant*

1. INTRODUCTION

Corrosion and unplanned fire cause catastrophic consequences in various infrastructures.[1] Therein, corrosion inevitably occurs for metals in diverse aggressive media, necessitating urgent solutions. Continuous endeavors have been devoted to preventing metals from corroding, including rational design of materials,[2] electrochemical protection,[3] applying corrosion inhibitors,[4] and coatings.[5] Among these measures, organic, inorganic, and hybrid coatings are frequently employed to isolate the underlying metals from ambient corrodents due to their salient advantages such as facile preparation, high efficiency, and durability.[6] Cost-effective polymer coatings, in particular, have been favored as the physical barrier to protect metals in diverse environments due to their sufficient adhesion strength and hydrophobicity.[7] Epoxy resin (EP) is one of the most commonly utilized coating materials owing to its superior mechanical properties, dimensional stability, tunable components, and structures. However, inherent defects such as micropores and crevices, inherited from the curing procedure, allow the infiltration of corrosive species, significantly compromising its protective efficacy. Additionally, a critical concern is the flammability of a majority of polymer coatings, leading to hazardous emissions such as CO, CO_2, and smoke dust. Given the large consumption of polymer coatings in various applications like architectures, automobiles, and decorations, their flammability poses a direct threat to humans and the environment.[8] Therefore, beyond enhancing the anticorrosive efficiency, the demand for imparting flame-retardancy to EP layers has emerged as a crucial requirement in the domain of protective coatings.

Nanoscience and nanotechnology open new avenues to improve the overall performance of protective coatings, especially those based on EP. Various nanofillers, nano-

Received: December 25, 2023
Revised: January 27, 2024
Accepted: February 19, 2024
Published: March 1, 2024

Downloaded via BEIJING UNIV OF CHEMICAL TECHNOLOGY on March 26, 2024 at 07:36:56 (UTC).
See https://pubs.acs.org/sharingguidelines for options on how to legitimately share published articles.

ACS Publications © 2024 American Chemical Society

SiO_2,[9] halloysite,[10] and nano-TiO_2[11] have been incorporated into the EP matrix to seal the intrinsic defects and enhance the anticorrosive efficiency through the "labyrinth effect".[12] However, merely micropore-sealing or warping the diffusion path for corrosive species can hardly solve the long-lasting issue of EP coatings. Recent advancements have introduced nanocontainers that can accommodate anticorrosive constituents (e.g., corrosion inhibitors), serving as intelligent fillers to render active protection or self-healing functionalities to composite coatings.[13] Examples include metal−organic frameworks,[14] two-dimensional (2D) transition-metal carbonitrides,[15] and graphitic carbon nitride (g-C_3N_4),[16] which have been developed to accommodate corrosion inhibitors. For instance, Li et al.[6] embedded 2-mercapto benzimidazole into graphene oxide (GO)-loaded zeolitic imidazolate framework-8 (M-ZIF-8/GO) and incorporated this nanofiller into the EP matrix, achieving pH-response and self-healing composite coating. Mohammadkhah et al.[17] utilized glutamate/zinc ion-decorated ZIF-8 and combined it with MoS_2 (ZIF-8@MS) by an *in situ* synthesis approach. EP coating with ZIF-8@MS exhibited a pH-responsive behavior and maintained robust corrosion resistance during 21 days of immersion in 3.5 wt % NaCl corrosion. In our previous work,[18] benzotriazole was successfully incorporated into mesostructured CeO_2 and loaded on g-C_3N_4 to create a nanocomposite (BTA@ mCeO_2/g-C_3N_4). EP coating functionalized by BTA@ mCeO_2/g-C_3N_4 efficiently suppressed filiform corrosion of Zn−Mg−Al-coated steel in saline water. Despite the substantial improvement in the protective efficacy of EP-based coatings achieved by the incorporation of nanocontainers loaded with anticorrosive ingredients, limited attention has been given to enabling other desirable functions of coatings, such as flame-retardancy, in practical applications through the introduction of nanofillers.

As a burgeoning class of 2D materials, layered double hydroxides (LDHs) have gained increasing interest in protective coatings due to their chemical stability, potent barrier effect, and loading propensity.[19] Typically, Chen et al.[20] fabricated MgAl-LDH from a microarc oxidation coating on AZ31 alloy and subsequently doped 8-hydroxyquinoline (8-HQ)-modified GO into LDH interlayers, achieving robust corrosion resistance and self-healing properties for the Mg alloy. Su et al.[21] developed an ionic cross-linking strategy to combine sulfonated polyaniline-functionalized GO and LDH, which imparted long-term stability to EP-based composite coating in a 3.5 wt % NaCl solution. Notably, the flame-retardant behavior of LDH was gradually realized by researchers owing to the effect of the O_2 dilution on its structural disintegration under ambient combustion. For instance, Sui et al.[22] decorated polyphosphazene microspheres with FeCo-LDH (PHDT@FeCo-LDH), incorporating it into the EP matrix for flame-retardancy. Relying on catalytic charring, free-radical scavenging, and barrier effects, the EP sample including 4% PHDT@FeCo-LDH exhibited a high limited oxygen index (LOI) of 29.7 with a UL-94 V-0 rating. Dong et al.[23] anchored Zn−Al LDH onto reduced GO (rGO) to create a nanohybrid, which was used as the nanoflame-retardant for waterborne EP. The specimen with 1.5% nanohybrid possessed a low backside temperature (154.3 °C) but a high expansion ratio (12.13) and char residue rate (32.2%). However, the above-mentioned EP coatings with an excellent flame-retardant property lack the characterizations for anticorrosive efficiency, which is a crucial requirement in practical applications. Furthermore, the scientific understanding of the concurrent protection and flame-retardancy for coatings is still in its infancy and deserves in-depth clarification.

On that account, we developed a facile one-pot hydrothermal strategy to prepare a CaAl-8HQ LDH@rGO nanocomposite, which was incorporated into the EP matrix (EP/CaAl-8HQ LDH@rGO). This nanocomposite aims to simultaneously realize favorable protection for mild steel and flame-retardancy. The superior anticorrosive performance of EP/CaAl-8HQ LDH@rGO was assessed by electrochemical impedance spectroscopy (EIS) on unscratched and scratched specimens in a 3.5 wt % NaCl solution. The self-healing ability of this composite coating was demonstrated through salt spray tests. Besides, the flame-retardant behavior of EP/CaAl-8HQ LDH@rGO was evidenced by UL-94 and cone calorimeter measurements. An intercomponent synergetic mechanism was established to comprehensively interpret the excellent protection and flame-retardancy performances of the as-prepared nanocomposite coating.

2. MATERIALS AND METHODS

2.1. Materials. All compounds utilized in this work were analytically pure and used as received. Calcium nitrate tetrahydrate ($Ca(NO_3)_2{\cdot}4H_2O$), sodium chloride (NaCl), sodium hydroxide (NaOH), and anhydrous sodium carbonate (Na_2CO_3) were delivered by Beijing Tongguang Fine Chemical Co., Ltd. Aluminum nitrate nonahydrate ($Al(NO_3)_3{\cdot}9H_2O$) was supplied by Tianjin Damao Chemical Reagent Factory. 8-HQ (C_9H_7NO) was acquired from Shanghai Macklin Biochemical Co. Ltd. Epoxy resin (E44) and curing agent (650) were obtained from Shenzhen Mingde Chemical Co., Ltd. GO powder was sourced from Sichun Kenye Science and Technology Development Co., Ltd. Q235 steel coupons of 25 × 25 × 2 mm^3 were used as the substrate, which were mechanically abraded with SiC waterproof paper until 1600# grade, rinsed with deionized (DI) water, sonicated in ethanol solution, and finally dried.

2.2. Protocol for Fabricating the Nanocomposite. *2.2.1. Synthesis of CaAl-LDH.* The coprecipitation method was adopted to prepare CaAl-LDH, involving two solutions labeled as A and B. Specifically, Ca $(NO_3)_2{\cdot}4H_2O$ (0.30 M) and Al $(NO_3)_3{\cdot}9H_2O$ (0.10 M) were dissolved in deionized (DI) water under stirring to form solution A (60 mL), which was charged in a three-necked flask in a thermostat oil bath at 80 °C. Meanwhile, a mixed solution of Na_2CO_3 (0.20 M) and NaOH (0.67 M), labeled as solution B (40 mL), was prepared, which was decanted into the flask containing solution A. Afterward, the premixed slurry was continuously stirred for 2 h under nitrogen protection, maintaining a pH value of 10−10.5 through the addition of NaOH solution (0.5 M). Then, the homogeneous slurry was poured into a hydrothermal reactor and treated at 120 °C for 24 h. The residue powder was centrifuged at 3800 rpm for 25 min, rinsed with by DI water/ethanol until reaching a neutral pH, and oven-dried at 35 °C for 36 h, yielding the CaAl-LDH products.

2.2.2. Intercalation of 8HQ into CaAl-LDH. To acquire 8-HQ intercalated CaAl-LDH (CaAl-8HQ LDH), the Na_2CO_3 component in solution B was substituted by 8-HQ anions with an equivalent content, which can be transformed via the reaction with NaOH at 45 °C for 40 min. Solution B with 8-HQ anions was then poured into solution A to facilitate the intercalation of 8-HQ under the previously mentioned hydrothermal conditions. Of note, N_2 protection was maintained throughout the reaction to prevent the undesirable CO_3^{2-} (derived from CO_2) intercalation.

2.2.3. Loading with rGO. A GO dispersion (0.5 mg/mL) of 20 mL was mixed with 8-HQ (0.50 g) solution with an equivalent concentration. The pH value of the mixture was still maintained at 10−10.5 with the aid of a droplet of NaOH solution (0.5 M). After stirring for 1 h at 25 °C, the mixture was poured into solution A. Following the aforementioned hydrothermal procedure, the precipitate was collected, redispersed in DI water, and centrifuged five times

https://doi.org/10.1021/acsami.3c19245
ACS Appl. Mater. Interfaces 2024, 16, 13114−13131

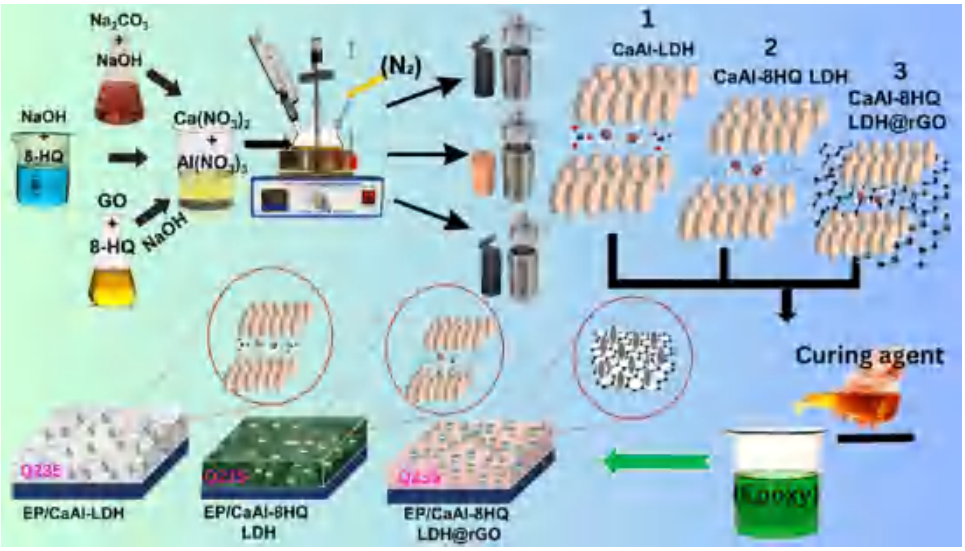

Figure 1. Schematic diagram for synthesizing the designed nanocomposites and associated coatings.

with DI water and two times with ethanol. As observed, GO underwent a reduction process, turning into the reduced form (rGO). Consequently, 8-HQ intercalated LDH decorated with rGO (CaAl-8HQ LDH@rGO) was prepared.

2.3. Coating Fabrication. EP-based nanocomposite coatings were prepared by a mechanical mixing method. Initially, CaAl-8HQ LDH@rGO (0.60 wt %) was dispersed in toluene and ultrasonicated for 30 min. EP resin (3 g) was injected into the dispersion with continuous ultrasonication for 15 min; subsequently, the low-molecular-weight polyamide 650 curing agent (1.5 g) was introduced and blended for 15 min. After degassing, an EP-based composite slurry was painted on Q235 steel using a coating roller. The coated samples were cured at 35 °C in an oven for 72 h, and the resulting coated specimen was named EP/CaAl-8HQ LDH@rGO. Employing the same painting protocol, pristine epoxy (EP), EP matrix with individual LDH (EP/CaAl-LDH), and EP matrix with CaAl-8HQ LDH (EP/CaAl-8HQ LDH) were also prepared for comparison, as illustrated in Figure 1. The thicknesses of cured coatings were gauged as 70 ± 5 μm.

2.4. Characterization. Structural properties of nanofillers were resolved by an X-ray diffractometer (XRD, Ultima IV, Rigaku, Japan) with a 2θ range of 5−90° using Cu Kα radiation (λ = 0.154 nm) at 40 kV. Fourier transform infrared spectroscopy (FTIR, Bruker, Tensor-27, Germany) was recorded in a wavenumber from 4000 to 400 cm^{-1}. Ultraviolet (UV) spectra of solutions were scanned by a AuCy-1700 PC spectrophotometer (China) between 190 and 400 nm of wavelength. Prior to analysis, CaAl-LDH and CaAl-8HQ LDH powder were dispersed in a 3.5 wt % NaCl solution for the specified duration. X-ray photoelectron spectroscopic (XPS, Kratos AXIS SUPRA, U.K.) analysis was performed using an Al Kα radiation source (1486.7 eV) with a correction at 284.8 eV for C 1s. The obtained spectra were deconvoluted by using XPSpeak 4.1 software with a Shirley background. Morphologies and the elemental components were examined via a scanning electron microscope (S-4800, HITACHI, Japan) equipped with an energy-dispersive X-ray spectroscopy (EDS) attachment. Adhesive strengths of different coatings on steel substrates were determined before and after 7 days of immersion in a 3.5 wt % NaCl solution, employing a Posi Test pull-off adhesion tester (DEFELSKO). Each coating underwent five successive parallel pull tests, and the average strength was reported. Dumbbell-shaped specimens with dimensions of 100.0 × 10.0 × 2 mm^3 were fabricated using a poly(tetrafluoroethylene) (PTFE) mold. Tensile properties of the pristine coating layers were characterized by a microcomputer-controlled universal testing machine (SHIMADZU, Japan) at a cross-head speed of 2 mm min^{-1}. The microhardness of the as-prepared layers was measured with a microhardness tester (LECO LM-700AT, Germany). For each sample, three randomly chosen spots were subjected to the test, applying a force of 100 g on the sample surfaces with a dwell time of 20 s. The hardness, denoted by Vicker's hardness, H_v, was calculated using eq 1:[24]

$$H_v = 1.854L/d^2 \quad (1)$$

where L represents the applied load in grams and d is the diagonal dimension of the diamond indentation in millimeters.

2.5. Anticorrosive Evaluations. *2.5.1. Electrochemical Test.* Electrochemical assays were carried out through a Gamry Interface1000 workstation in a classical three-electrode configuration, comprising coated steel (unscratched), a platinum sheet, and a saturated calomel electrode as the working, auxiliary, and referencing electrodes, respectively. In addition, artificial scratches were made by a metallic knife, creating an exposed area of 10 × 4 mm^2 (length × width) on the EP/CaAl-8HQ LDH@rGO-coated matrix, which was subject to subsequent measurements. Preferentially, the working electrode was immersed in 3.5 wt % NaCl solution for 2 h at 25 °C to achieve a steady state. EIS was conducted at the open circuit potential over a frequency range from 100 kHz to 10 mHz, using 10 mV amplitude fluctuation. Each measurement was fulfilled in triplicate for reproducibility. Impedance parameters were derived using the given circuit by ZSimpWin software.

2.5.2. Salt Spray Test. EP, EP/CaAl-LDH, EP/CaAl-8HQ LDH, and EP/CaAl-8HQ LDH@rGO-coated specimens, subjected to the same scratched procedure as mentioned above, were positioned in the salt spray chamber (YWX/Q-150, Guangzhou Handi Company, China). Following the protocol outlined in ASTM B117, salt spray tests were conducted with 5 wt % NaCl fog on four scratched samples.

2.6. Flame-Retardant Verification. Each EP-based coating was directly obtained by curing the formulated slurry in a mold for flame-retardant and thermal analyses. The resulting CaAl-LDH, CaAl-8HQ LDH, and CaAl-8HQ@rGO nanocomposite powders (556 mg) were mixed with EP (5 g), toluene (1.3 mL), and ammonium polyphosphate (277 mg) through mechanical stirring for 30 min. Polyamide 650 (2.5 g) was added to formulate the flame-retardant matrix. Following the procedure outlined in ISO-4589, limiting oxygen index (LOI) values were determined for pristine EP, EP/CaAl-LDH, EP/CaAl-8HQ LDH, and EP/CaAl-8HQ LDH@rGO specimens with dimensions of 100 × 6.5 × 3 mm^3 using a JF-3 oxygen index instrument (Nanjing Jingping Analytical Instruments, China). Five parallel measurements were performed for each coating, and the average LOI value was reported. The thermal stability of four coatings was investigated using a TA-Q50 apparatus in the temperature range from 25 to 800 °C with a ramp of 10 °C in an open (air) atmosphere. Combustion performance was evaluated using a cone calorimeter with

https://doi.org/10.1021/acsami.3c19245
ACS Appl. Mater. Interfaces 2024, 16, 13114−13131

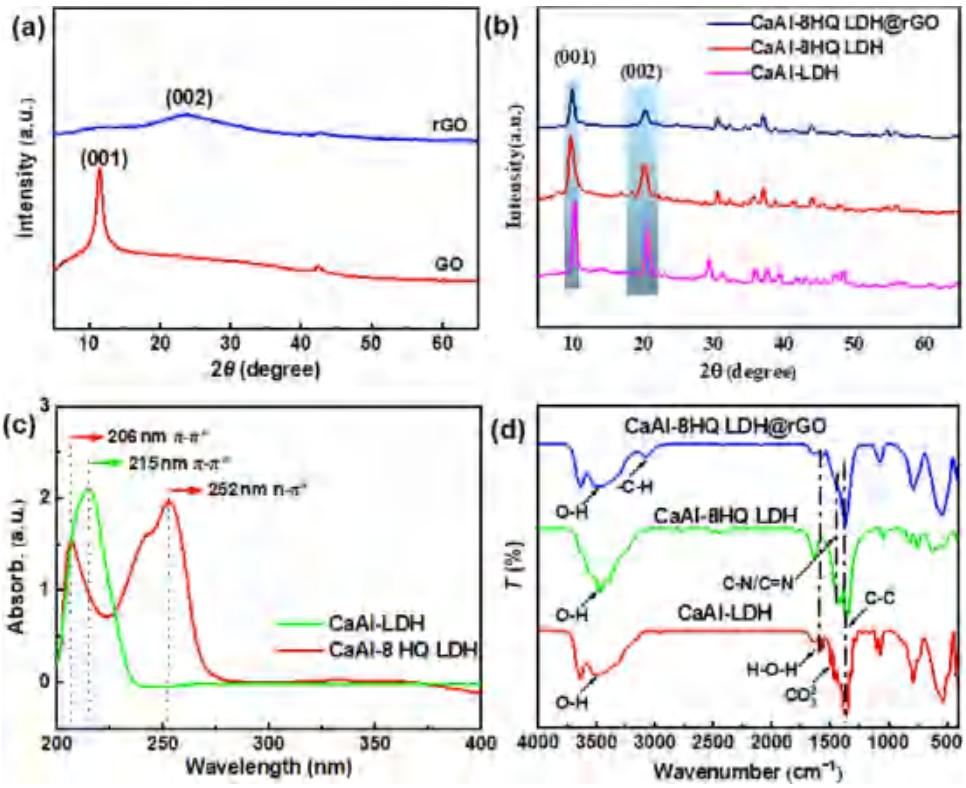

Figure 2. XRD patterns of GO before and after the hydrothermal reaction (a), CaAl-LDH, CaAl-8HQ LDH, and CaAl-8HQ LDH@GO (b). UV spectra of CaAl-LDH and CaAl-8HQ LDH aqueous dispersions (c) along with FTIR spectra of CaAl-LDH, CaAl-8HQ LDH, and CaAl-8HQ LDH@rGO (d).

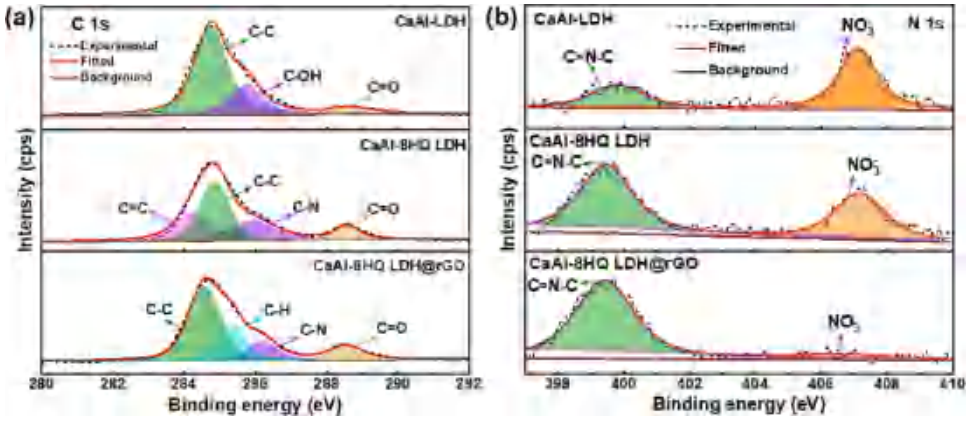

Figure 3. Deconvoluted XPS spectra of CaAl-LDH, CaAl-8HQ LDH, and CaAl-8HQ LDH@rGO nanocomposites focusing on C 1s (a) and N 1s (b).

a sample dimension of 100 × 100 × 3 mm^3 and a heat flow of 35 kW/m^2, following the ISO 5660 standard.

3. RESULTS AND DISCUSSION

3.1. Structural Confirmation of Nanocomposite. XRD patterns of raw materials and the resulting nanocomposites are shown in Figure 2a,2b. In Figure 2a, a sharp diffraction peak appears at an angle of 10.50° (2θ), indexing to the (001) plane of GO. The gauged *d*-spacing using Bragg's law is 0.84 nm, coinciding well with the reported eigenvalue.[25] Notably, GO was reduced and transformed into rGO during the loading of intercalated LDH, as indicated by the broad peak associated with the (002) plane at 23.87° (*d*-spacing of 0.37 nm). The exposure of GO to the high-temperature hydrothermal ambience likely accounts for this reduction process.[26] The decreased *d*-spacing further supports the reduction of GO during the hydrothermal reaction.[27] In Figure 2b, the XRD pattern of CaAl-LDH exhibits diffraction peaks at 10.21 and 20.60° corresponding to (001) and (002) planes of LDH, respectively.[28] For the pattern of CaAl-8HQ LDH, both peaks for typical lattice planes shift toward lower angles at 10.11° for (001) and 20.49° for (002), indicating enlarged *d*-spacings due to the intercalation of 8-HQ.[29] A similar pattern between CaAl-8HQ LDH@rGO and CaAl-8HQ LDH implies effective wrapping of rGO by inhibitor-intercalated LDH. The successful intercalation of 8-HQ into LDH interlayers is also evidenced by UV spectra, illustrating the inhibitor-release profile (Figure 2c). The prominent peaks at 215 nm for both

https://doi.org/10.1021/acsami.3c19245
ACS Appl. Mater. Interfaces 2024, 16, 13114−13131

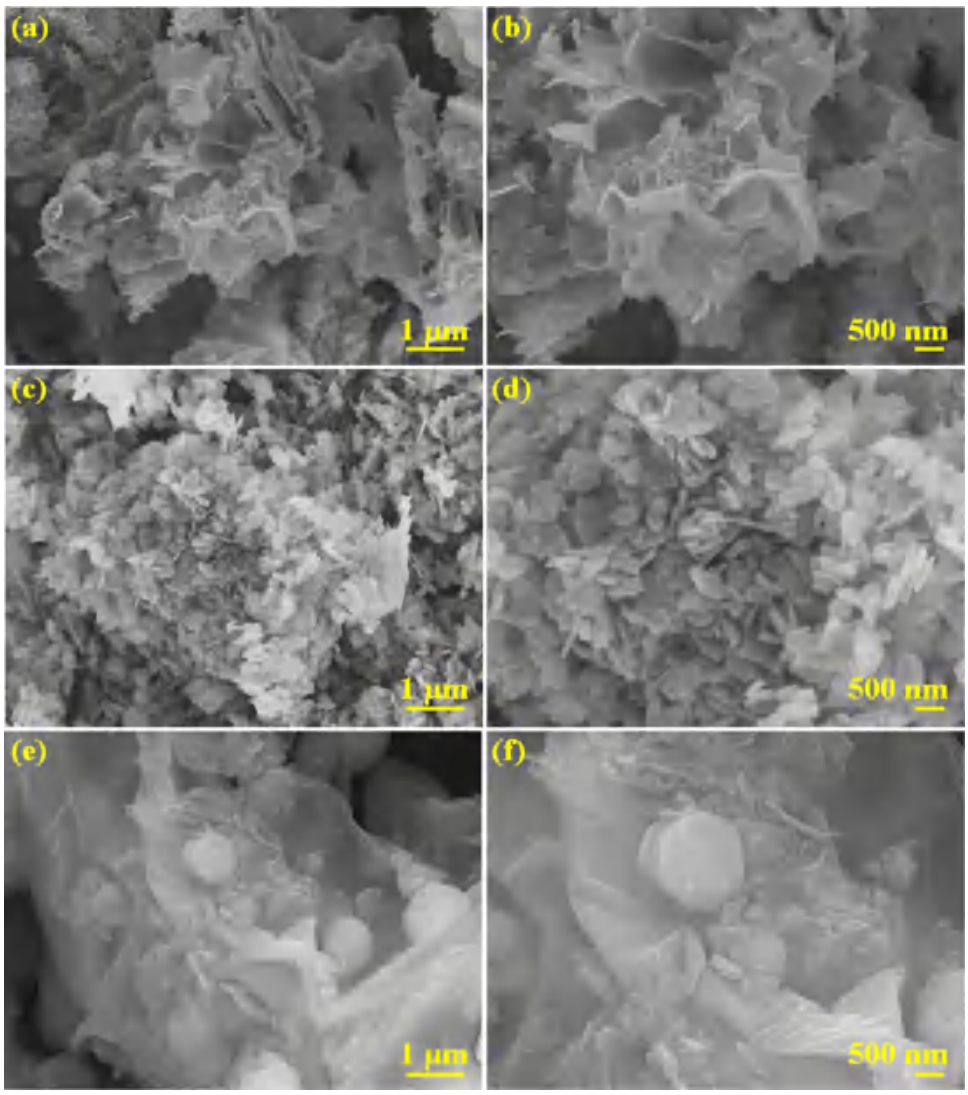

Figure 4. SEM images of CaAl-LDH (a, b), CaAl-8HQ LDH (c, d), and CaAl-8HQ LDH@rGO (e, f) at the general (left) and magnified (right) scales.

curves are attributed to the electronic transition of LDH species.[28] New peaks at 206 and 250 nm are found for the spectrum of CaAl-8HQ LDH, corresponding to the respective $\pi-\pi^*$ and $n-\pi^*$ excitations of the quinoline ring on 8-HQ.[30] In other words, the presence of 8-HQ in the solution demonstrates its effective intercalation during preparation and the ability to release an inhibitor from LDH upon exposure to the corrosive solution.

FTIR spectra of CaAl-LDH, CaAl-8HQ LDH, and CaAl-8HQ LDH@rGO are displayed in Figure 2d. The broad band in the range of 3420−3570 cm^{-1} is assigned to the stretching of −OH of CaAl-LDH accompanied by the other fingerprint at 1628 cm^{-1}.[23] In the absence of intercalators, CO_3^{2-} is inevitably sandwiched among LDH interlayers, as affirmed by the peaks at 1490 and 1377 cm^{-1}. For CaAl-8HQ LDH, a C−N/C═N characteristic vibration appears at 1424 cm^{-1},[2] evidencing the efficient intercalation of 8-HQ into LDH. In the spectrum of CaAl-8HQ LDH@rGO, the peak at 3000 cm^{-1} is assigned to C−H stretching, besides the characteristic adsorption of −OH on CaAl-LDH.[31] Of note, the stretching vibration of C−N/C═N marked at 1452 cm^{-1}, along with the C−H stretching at 3085 cm^{-1}, serves as another criterion for confirming the presence of 8-HQ in CaAl-LDH interlayers anchored on rGO.

XPS spectra in Figure 3 further distinguish the binding behaviors among the different components in the as-prepared nanocomposites. The survey spectra (Figure S1, Supporting Information, SI) reveal that Ca, Al, O, and C are the main elements for each sample, underscoring the supporting function of the LDH backbone. The three photoelectronic contributions at 284.7, 285.8, and 288.7 eV in Figure 3a (C 1s) can be ascribed to C−C, C−OH, and C═O, respectively, for each sample.[28,32] In the spectrum of CaAl-8HQ LDH, the increased enveloped area for C−N at 285.9 eV implies the intercalation of 8-HQ. Moreover, an extra peak identified at 285.4 eV (graphitic C−H) in the spectrum of CaAl-8HQ LDH@rGO demonstrates the existence of rGO in the nanocomposite.[33] Deconvoluted spectra on N 1s in Figure 3b further support the intercalation of 8-HQ into LDH. Peaks at 399.8 and 407.2 eV in the spectrum of CaAl-LDH are attributed to C═N−C and NO_3^-, respectively,[34] indicating the dominant anions embedded in the lamellar structure. In contrast, the dominant contributions of C═N−C in the spectra of CaAl-8HQ LDH and CaAl-8HQ LDH@rGO

https://doi.org/10.1021/acsami.3c19245
ACS Appl. Mater. Interfaces 2024, 16, 13114−13131

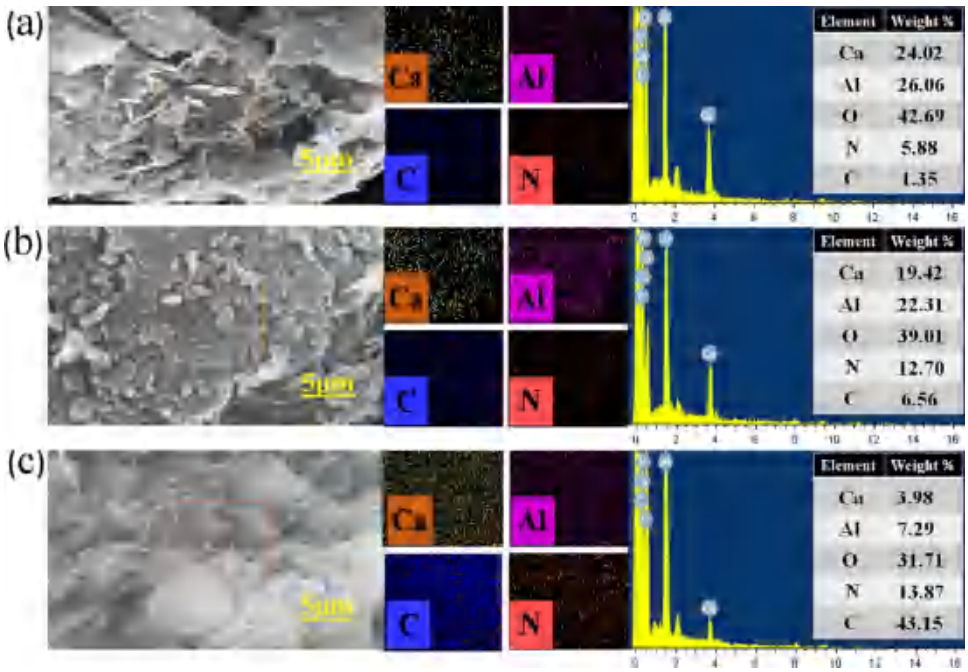

Figure 5. SEM images (left) of CaAl-LDH (a), CaAl-8HQ LDH (b), and CaAl-8HQ LDH@rGO (c) along with the corresponding EDS mapping (middle) and spectra (right) focusing on typical elements.

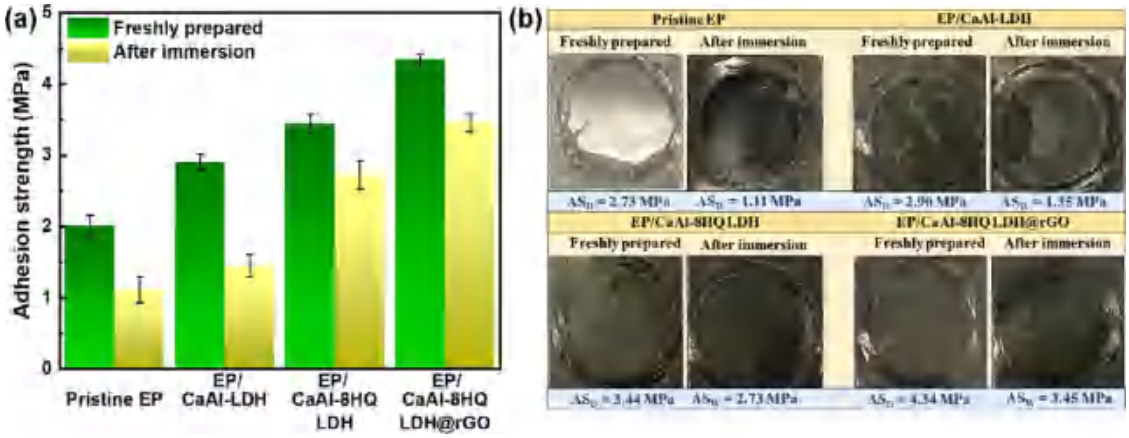

Figure 6. Adhesive strengths (a) of pristine EP, EP/CaAl-LDH, EP/CaAl-8HQ LDH, and EP/CaAl-8HQ LDH@rGO coatings on steel substrates before and after 7 days of immersion in a 3.5 wt % NaCl solution at 25 °C, along with the corresponding digital graphs of adhesion losses (b).

articulate the intercalation of 8-HQ. Especially in the spectrum of CaAl-8HQ LDH@rGO, the negligible peak for NO_3^- reveals its extremely low content, in turn, signifying a high amount of intercalated 8-HQ in the nanocomposite.[35]

Scanning electron microscopy (SEM) images of CaAl-LDH, CaAl-8HQ LDH, and CaAl-8HQ LDH@rGO are presented in Figure 4 at different magnifications. The morphology in Figure 4a displays a flower-like shape for CaAl-LDH, distinguished as the aggregation of numerous nanosheets. This is further magnified in Figure 4b. The intercalation of 8-HQ facilitates the isolation of LDH sheets, resulting in hexagonal slices for the CaAl-8HQ LDH shown in Figure 4c,4d. Figure 4e,4f clearly evidences the growth of LDHs on rGO sheets. Moreover, EDS mappings in Figure 5, selected area on images of CaAl LDH, CaAl-8HQ LDH, and CaAl-8HQ LDH@rGO, intuitively evidence the inhibitor intercalation and subsequent loading on rGO. Compared with the elemental contents of CaAl LDH (Figure 5a), a higher N content (12.70%) along with an increased C element (24.56%) is detected on CaAl-8HQ LDH in Figure 5b, suggesting the effective intercalation of 8-HQ among LDH sheets. By comparison, the overwhelming C content (41.15%) in Figure 5c results from the rGO substrate accommodating 8-HQ intercalated LDH.

A preliminary summary of the structural resolution of the as-prepared nanocomposite reveals that 8-HQ molecules are effectively intercalated among CaAl LDH interlayers. Subsequently, the modified LDH nanoparticles with a high content of 8-HQ are anchored onto the rGO during the hydrothermal reaction. This can be deemed as a promising nanofiller in coating systems to highly impede the infiltration of aggressive species and inhibit the dissolution of the metal substrate.

3.2. Mechanical Characteristics. *3.2.1. Adhesiveness.* Adhesive strengths were gauged for freshly prepared EP, EP/CaAl-LDH, EP/CaAl-8HQ LDH, and EP/CaAl-8HQ LDH@rGO coatings on steel substrates, immediately and after 7 days of immersion in a 3.5 wt % NaCl solution. Figure 6a,6b

https://doi.org/10.1021/acsami.3c19245
ACS Appl. Mater. Interfaces 2024, 16, 13114−13131

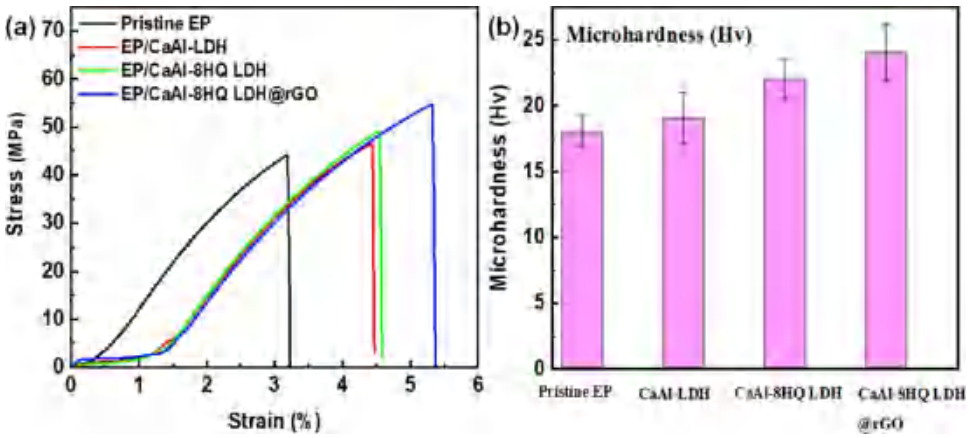

Figure 7. Stress−strain curve (a) and microhardness graphs (b) of the pristine EP, EP/CaAlLDH, EP/CaAl-8HQ LDH, and EP/CaAl-8HQ LDH@rGO composites.

Table 1. Microhardness and Tensile Strengths of the Pristine EP, EP/CaAl-LDH, EP/CaAl-8HQ LDH, and EP/CaAl-8HQ LDH@rGO Composites

samples	microhardness (Hv)	Young's modulus (MPa)	tensile strength (MPa)	maximum stress elongation (%)
pristine EP	18 ± 1	978 ± 5	42.5 ± 4.7	1.9
EP/CaAl-LDH	19 ± 3	1185 ± 1	46.5 ± 3.9	2.1
EP/CaAl-8 HQ LDH	21 ± 2	1205 ± 5	48.5 ± 5.7	2.3
EP/CaAl-8HQ LDH@rGO	24 ± 1	1454 ± 5	55.5 ± 5.7	5.6

summarizes the adhesive strengths of different coatings along with the corresponding macroscopic features. The strengths of freshly prepared EP, EP/CaAl-LDH, EP/CaAl-8HQ LDH, and EP/CaAl-8HQ LDH@rGO coatings are 2.73, 2.90, 3.44, and 4.34 MPa, respectively. Introducing nanofillers inevitably affects the physicochemical properties of the EP matrix by heterogeneous nucleation, which reinforces the interaction between the coating and the substrate.[36] As reported,[37] nanofillers with a large specific area are effective at improving the coating adhesion. By virtue of inhibitor intercalation and rGO loading, CaAl-8HQ LDH@rGO reasonably earns the largest specific area among other analogues, thus exhibiting the strongest adhesion-promoting effect for EP on the surface. Apparently, the adhesive strength of freshly prepared EP/CaAl-8HQ LDH@rGO reaches 4.34 MPa, which thereby is the most durable specimen against external aggression. The adhesion loss of specimens after exposure to the saline environment is determined by the following expression[38]

$$\text{adhesion loss (\%)} = \frac{AS_D - AS_W}{AS_D} \times 100 \quad (2)$$

where AS_D and AS_W denote adhesion strengths before and after exposure to saline water, respectively. After 7 days of immersion in NaCl solution, the adhesion strength decreases for each coating, which are 1.11 MPa (59.34%, adhesion loss, hereinafter), 1.45 MPa (53.44%), 2.73 MPa (20.64%), and 3.45 MPa (20.50%) for pristine EP, EP/CaAl-LDH, EP/CaAl-8HQ LDH, and EP/CaAl-8HQ LDH@rGO, respectively. Due to the presence of micropores and crevices in the coating, corrosive species inevitably diffuse across the pure EP layer, destroy the polar−polar binding between the coating and the steel substrate, and ultimately lower the congenitally inferior adhesive strength after immersion in the 3.5 wt % NaCl solution. In contrast, the incorporation of an arbitrary nanofiller reinforces the adhesion of the composite coating on the steel surface. Specifically, the presence of LDH in EP (EP/CaAl-LDH) densifies the EP matrix due to the heterogeneous nucleation effect,[39] effectively retarding the infiltration of the corrosive solution, in turn, partially preserving its binding strength on the substrate. When intercalating 8-HQ among LDH layers, the penetration of corrosive ions is further arrested, depending on the reinforced corrosion inhibition efficacy. EP/CaAl-8HQ LDH@rGO exhibits the minimum decline in adhesive strength, attributed to the high specific area and strong barrier effect of rGO.[40]

3.2.2. Tensile Strength and Microhardness Analysis. Tensile strength assessments were conducted to evaluate the mechanical properties of the EP-based composite coatings. Figure 7a illustrates the stress−strain curves of pristine EP, EP/CaAl-LDH, EP/CaAl-8HQ LDH, and EP/CaAL-8HQ LDH@rGO composites. Compared with pristine EP, EP/CaAl-LDH and EP/CaAl-8HQ LDH exhibit improved tensile strengths, achieving tensile strengths of 46.5 and 48.5 MPa, respectively, as tabulated in Table 1. The highest tensile strength is observed for EP/CaAl-8HQ LDH@rGO (55.5 MPa), corresponding to the largest Young's modulus (1454.0 MPa). The abundant active sites on rGO in the nanocomposite promote cross-linking among EP chains, thereby densifying the coating matrix and improving its tensile strength.[41] In addition, the introduced LDH-based nanofillers exert a strong heterogeneous nucleation effect on the EP matrix,[42] further enhancing the mechanical performance of EP/CaAL-8HQ LDH@rGO. The microhardness of different coatings is shown in Figure 7b. As expected, adding nanofillers into the EP matrix effectively enhances the microhardness of the coating. The observed microhardness values for EP/CaAl-LDH and EP/CaAl-8HQ LDH are 19 and 21 Hv, respectively. Compared with EP/CaAl-8HQ LDH, the microhardness of EP/CaAl-8HQ LDH@rGO (24 Hv) is the highest due to the proper combination of LDH with rGO sheets.[43]

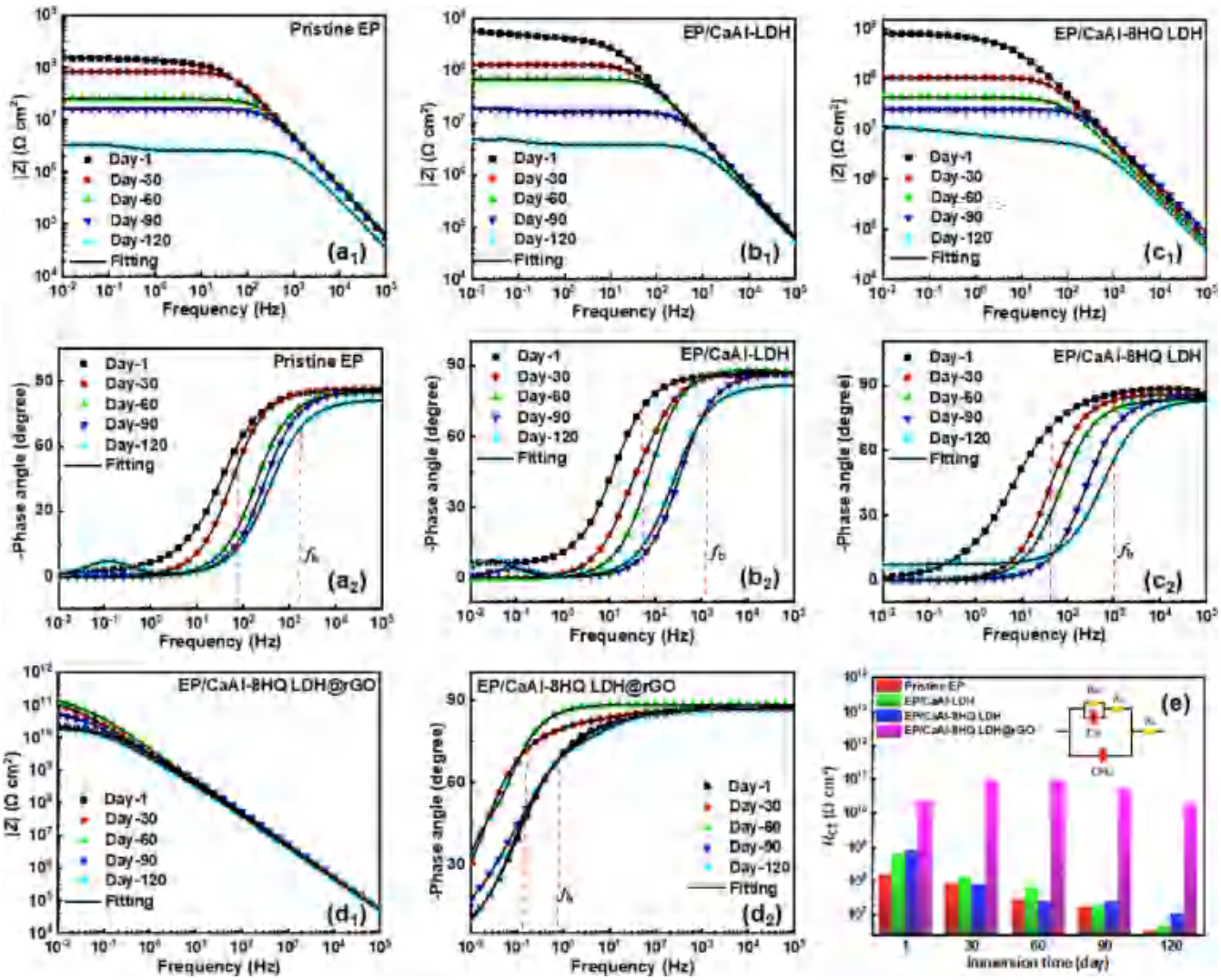

Figure 8. Bode plots of pristine EP (a_1, a_2), EP/CaAl-LDH (b_1, b_2), EP/CaAl-8HQ LDH (c_1, c_2), and EP/CaAl-8HQ LDH@rGO (d_1, d_2)-coated specimens after the allocated immersion periods in 3.5 wt % NaCl solution at 25 °C (subscript 1: modulus; subscript 2: phase angle). Summarized variation of R_{ct} values during immersion and the corresponding equivalent circuit (e).

3.3. Anticorrosive Effect of Composite Coatings. *3.3.1. EIS of Unscratched Coating.* The EIS technique was utilized to analyze the protective performance of EP coatings with different nanofillers. Figure 8 depicts the Bode spectra of EP/CaAl-LDH, EP/CaAl-8 HQ LDH, and EP/CaAl-8 HQ@rGO systems after the allocated immersion periods in a 3.5 wt % NaCl solution at 25 °C. In general, the corrosion resistance of coatings is frequently inferred from the lowest-frequency impedance value ($|Z|_{0.01Hz}$) in Bode-modulus spectra. For the spectra of pristine EP in Figure 8a_1, the $|Z|_{0.01Hz}$ value reaches 1.52×10^8 Ω cm^2 after 1 day of immersion in NaCl solution, which is close to the eigenvalue for EP systems reported elsewhere.[4] However, $|Z|_{0.01Hz}$ progressively declines for pristine EP with an increase in immersion time. At the end of 120 days of immersion, the $|Z|_{0.01Hz}$ value sharply lowers to 3.24×10^6 Ω cm^2. For the pristine EP coating, numerous micropores and crevices, inherited from the volatilization of byproducts in the curing process, provide sufficient infiltration paths for aggressive ions (e.g., Cl^-), which would migrate across the coating and ultimately corrode the substrate. Moreover, the breakpoint frequency (f_b) identified at −45° in Bode-phase angle spectra is the other iconic feature to distinguish coating resistance against corrosion.[44] Generally, the smaller value of f_b is associated with the higher corrosion resistance of coatings.[6] As seen in Figure 8a_2, f_b for pristine EP gradually shifts toward the high-frequency region as the immersion time prolongs, implying the attenuated barrier effect due to the permeation of the corrosive solution. The incorporation of CaAl-LDH in the EP matrix moderately addresses coating defects, which elevates $|Z|_{0.01Hz}$ to 5.78×10^8 Ω cm^2 after a one-day immersion period (Figure 8b_1). Unfortunately, the limited barrier effect of sole LDH can hardly sustain the long-lasting protection of EP/CaAl-LDH for steel in the saline medium.[45] Thus, $|Z|_{0.01Hz}$ largely decreases with the increase of the immersion time, which is determined as 4.79×10^6 Ω cm^2 after 120 days of exposure to the NaCl solution. Accordingly, f_b labeled in Figure 8b_2 gradually shifts to the high-frequency region due to the shortened relaxation time accompanied by the infiltration of the electrolyte. In Figure 8c_1, loading 8-HQ into LDH and the ensuing EP/CaAl-8 HQ LDH slightly increase the $|Z|_{0.01Hz}$ value to 8.11×10^8 Ω cm^2, while the decline of $|Z|_{0.01Hz}$ with the ongoing immersion exhibits a distinct behavior. Specifically, in the initial 30 days of immersion, an apparent decrease in the $|Z|_{0.01Hz}$ value is

https://doi.org/10.1021/acsami.3c19245
ACS Appl. Mater. Interfaces 2024, 16, 13114−13131

Table 2. Impedance Parameters of the Coated Specimens after the Allocated Immersion Periods in 3.5 wt % NaCl Solution at 25 °C

samples	immersion time (d)	CPE_c (S s^n cm^{-2})				CPE_{dl} (S $s^n cm^{-2}$)			
		Y_c	n_c	C_c (F cm^2)	R_c (Ω cm^2)	Y_{dl}	n_{dl}	C_{dl} (F cm^2)	R_{ct}(Ω cm^2)
EP	1	2.26×10^{-10}	0.88	1.31×10^{-10}	7.94×10^{7}	1.02×10^{-9}	0.58	2.74×10^{-10}	1.60×10^{8}
	30	5.46×10^{-10}	0.90	3.61×10^{-10}	4.45×10^{7}	7.29×10^{-9}	0.54	4.87×10^{-9}	8.55×10^{7}
	60	4.22×10^{-9}	0.87	2.77×10^{-9}	1.44×10^{7}	1.03×10^{-8}	0.59	4.34×10^{-9}	2.80×10^{7}
	90	8.63×10^{-9}	0.89	6.26×10^{-9}	8.65×10^{6}	3.27×10^{-8}	0.56	2.21×10^{-8}	1.85×10^{7}
	120	1.36×10^{-8}	0.86	7.27×10^{-9}	1.58×10^{6}	1.13×10^{-7}	0.55	5.34×10^{-8}	3.49×10^{6}
EP/CaAl LDH	1	1.82×10^{-10}	0.88	1.10×10^{-10}	1.43×10^{8}	4.02×10^{-10}	0.74	2.53×10^{-10}	6.67×10^{8}
	30	3.89×10^{-10}	0.93	2.98×10^{-10}	7.64×10^{7}	8.29×10^{-10}	0.69	2.99×10^{-10}	1.25×10^{8}
	60	6.22×10^{-10}	0.91	4.31×10^{-10}	4.02×10^{7}	1.68×10^{-9}	0.63	4.67×10^{-10}	6.76×10^{7}
	90	3.63×10^{-9}	0.86	2.10×10^{-9}	9.77×10^{6}	7.79×10^{-9}	0.65	2.77×10^{-9}	1.89×10^{7}
	120	7.36×10^{-9}	0.88	4.24×10^{-9}	2.39×10^{6}	2.39×10^{-8}	0.68	8.78×10^{-9}	4.98×10^{6}
EP/CaAl-8HQ LDH	1	1.54×10^{-10}	0.93	1.26×10^{-10}	4.53×10^{8}	3.13×10^{-10}	0.77	2.08×10^{-10}	8.18×10^{8}
	30	4.38×10^{-10}	0.91	3.02×10^{-10}	5.35×10^{7}	7.27×10^{-10}	0.71	2.25×10^{-10}	7.81×10^{7}
	60	1.35×10^{-9}	0.90	8.90×10^{-10}	1.75×10^{7}	2.17×10^{-9}	0.73	7.61×10^{-10}	2.72×10^{7}
	90	5.46×10^{-9}	0.89	3.75×10^{-9}	8.74×10^{6}	4.42×10^{-9}	0.68	1.62×10^{-9}	2.70×10^{7}
	120	9.53×10^{-9}	0.86	5.50×10^{-9}	3.61×10^{6}	1.26×10^{-8}	0.65	4.32×10^{-9}	1.09×10^{7}
EP/CaAl-8HQ LDH@rGO	1	6.38×10^{-11}	0.94	6.15×10^{-11}	8.76×10^{9}	8.05×10^{-11}	0.89	8.75×10^{-11}	2.45×10^{10}
	30	4.12×10^{-11}	0.97	4.01×10^{-11}	1.04×10^{10}	5.64×10^{-11}	0.83	7.89×10^{-11}	9.18×10^{10}
	60	3.57×10^{-11}	0.96	3.44×10^{-11}	1.13×10^{10}	4.83×10^{-11}	0.87	6.09×10^{-11}	9.78×10^{10}
	90	5.24×10^{-11}	0.98	5.16×10^{-11}	8.99×10^{9}	6.71×10^{-11}	0.84	8.40×10^{-11}	4.85×10^{10}
	120	7.47×10^{-11}	0.95	7.29×10^{-11}	8.58×10^{9}	1.24×10^{-10}	0.80	1.50×10^{-10}	1.74×10^{10}

observed; thereafter, the downward trend of $|Z|_{0.01Hz}$ is decelerated in the extended immersion period. This may be credited to the deintercalation of 8-HQ from LDH interlayers during the long-term exposure to NaCl solution. During the initial 30 days of immersion, the corrosive medium would permeate and ultimately be saturated in EP/CaAl-8 HQ LDH coating. Meanwhile, the intercalated 8-HQ molecules can be activated, released from LDH, approach the coating/steel interface with solution permeation, and thus inhibit metal dissolution. Relying on the corrosion inhibition capacity of the released 8-HQ, the $|Z|_{0.01Hz}$ value for the EP/CaAl-8 HQ LDH-coated specimen reaches 1.12×10^{7} Ω cm^2 after 120 days of immersion despite the increased f_b value (Figure 8c_2). In stark contrast, an extremely high $|Z|_{0.01Hz}$ (1.37×10^{11} Ω cm^2) is seen in Figure 8d_1 for the EP/CaAl-8HQ LDH@rGO-coated specimen at 60 days of immersion. Subsequently, a mild decline of $|Z|_{0.01Hz}$ occurs as the immersion time prolongs, indicating the durability of the EP/CaAl-8HQ LDH@rGO composite. Besides the intrinsic corrosion inhibition effect, loading CaAl-8HQ LDH on rGO assuredly enhances the physical barrier of the yielded nanocomposite, which elevates the entire protection power of this coating system. The highly stable rGO also contributes to the long-term tolerance of the EP/CaAl-8HQ LDH@rGO system against the aggression of corrosive species. Thereby, the f_b value (Figure 8d_2) locates in the low-frequency region during 120 days of immersion in the NaCl solution.

Impedance parameters were further derived as per the equivalent circuit depicted in Figure 8e to quantitatively describe the corrosion resistances of different coatings. The fitted parameters including coating (R_c) and charge transfer (R_{ct}) resistances are tabulated in Table 2. Considering the heterogeneous electrode surface, constant phase angle elements (CPEs) were employed to compensate for the frequency dispersion, whose impedance (Z_{CPE}) could be expressed as follows[46]

$$Z_{CPE} = \frac{1}{Y_0(j\omega)^n} \tag{3}$$

where Y_0 is the numerical amount of admittance (with the unit S s^n cm^{-2}), j is the image root ($j^2 = -1$), ω is the angular frequency, and n is the phase shift index. In particular, the coating (C_c) and double layer (C_{dl}) capacitances can be derived from the respective CPE_c and CPE_{dl}:[28]

$$C_c = (Y_0)^{1/n_c}\left(\frac{1}{R_s} + \frac{1}{R_c}\right)^{1-n_c/n_c} \tag{4}$$

$$C_{dl} = (Y_0)^{1/n_{dl}}\left(\frac{1}{R_s} + \frac{1}{R_{ct}}\right)^{1-n_{dl}/n_{dl}} \tag{5}$$

where R_s is the solution resistance and n_c and n_{dl} are phase shift indices for CPE_c and CPE_{dl}, respectively. As observed in Table 2, at 1 day of immersion in a 3.5 wt % NaCl solution, the EP/CaAl-8HQ LDH@rGO system exhibits the highest R_c value (1.3×10^{10} Ω cm^2), which is 3 orders of magnitude larger than the pristine EP counterpart (7.94×10^{7} Ω cm^2). Even after 120 days of immersion, the R_c of EP/CaAl-8HQ LDH@rGO still retains a relatively high level of 8.58×10^{9} Ω cm^2. Both phenomena rationally reveal the superior barrier effect of EP coating with the CaAl-8HQ LDH@rGO nanocomposite, which efficiently isolates the substrate from deterioration. Owing to the strong physical barrier, the permeation of corrosive media inward EP/CaAl-8HQ LDH@rGO is extremely retarded and thus inhibited the charge transfer at the coating/steel interface, yielding a high R_{ct} value of 1.74×10^{10} Ω cm^2. The pronounced R_{ct} for the EP/CaAl-8HQ LDH@rGO-coated specimen is explicitly displayed in Figure 8e, which also remains relatively stable during 120 days of immersion in the NaCl solution. Less electrolyte infiltration favors the maintenance of interface capacitances (i.e., C_c and C_{dl}) at a lower level.[47] Hence, C_c and C_{dl} values for the EP/

https://doi.org/10.1021/acsami.3c19245
ACS Appl. Mater. Interfaces 2024, 16, 13114−13131

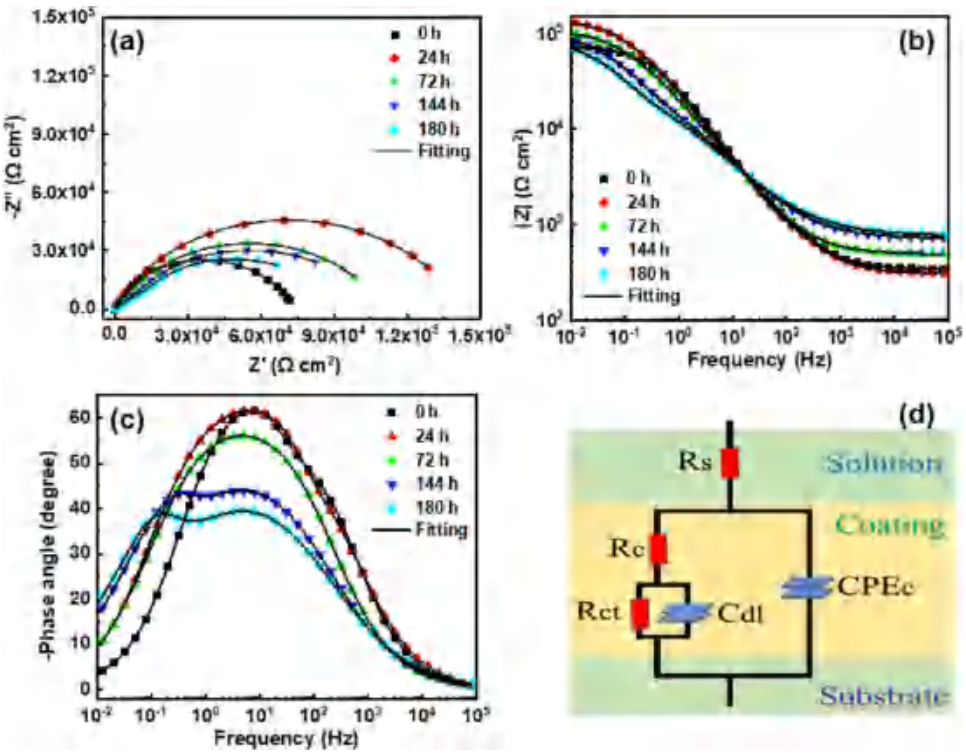

Figure 9. Nyquist (a), Bode modulus (b), and phase angle (c) plots for the specimen coated with scratched EP/CaAl-8HQ LDH@rGO after the allocated immersion periods in 3.5 wt % NaCl solution at 25 °C along with the employed equivalent circuit (d).

Table 3. Impedance Parameters of the Specimen with Scratched EP/CaAl-8HQ LDH@rGO after the Allocated Immersion Periods in 3.5 wt % NaCl Solution at 25 °C

		CPE_c (S s^n cm^{-2})				CPE_{dl} (S s^n cm^{-2})			
sample	immersion time (h)	Y_c	n_c	C_c (F cm^2)	R_c (Ω cm^2)	Y_{dl}	n_{dl}	C_{dl} (F cm^2)	R_{ct} (Ω cm^2)
scratched EP/CaAl-8HQ LDH@rGO	0	2.71×10^{-5}	0.65	9.18×10^{-6}	4.95×10^3	1.25×10^{-5}	0.57	8.19×10^{-6}	4.57×10^4
	24	1.07×10^{-5}	0.70	6.78×10^{-6}	3.23×10^4	6.79×10^{-6}	0.58	5.24×10^{-6}	1.03×10^5
	72	1.67×10^{-5}	0.66	3.13×10^{-5}	1.62×10^4	8.57×10^{-6}	0.59	6.66×10^{-6}	8.12×10^4
	144	6.63×10^{-5}	0.64	5.47×10^{-5}	1.07×10^4	1.16×10^{-5}	0.55	9.79×10^{-6}	7.03×10^4
	180	8.72×10^{-5}	0.68	7.12×10^{-5}	7.45×10^3	2.02×10^{-5}	0.56	2.24×10^{-5}	5.62×10^4

CaAl-8HQ LDH@rGO system in Table 2 are the lowest among all of the coating analogues.

3.3.2. EIS of the Specimen with the Scratched EP/CaAl-8HQ LDH@rGO. Motivated by the satisfactory protection efficacy, we conducted EIS measurements on the scratched EP/CaAl-8HQ LDH@rGO coating to further examine its tolerance against the aggression of the 3.5 wt % NaCl solution at 25 °C. Figure 9 displays the Nyquist and Bode diagrams for the specimen with the scratched EP/CaAl-8HQ LDH@rGO after the allocated immersion periods in a saline medium. Likewise, the equivalent circuit in Figure 9d was employed to derive the impedance parameters, as listed in Table 3. Nyquist spectra in Figure 9a illustrate the evolution of the capacitive loop with exposure time, in which an expansion of the curve dimension is explicit after 24 h of immersion in NaCl solution. This indicates the release of intercalated 8-HQ in LDH and the ensuing adsorption at the scratched defects. In addition to the accumulated corrosion products, the interfacial charge transfer is temporarily inhibited corresponding to the enlarged capacitive loop. Concurrently, the $|Z|_{0.01Hz}$ value recorded in Figure 9b rises for the composite coating in the initial 24 h of immersion, along with the broadened phase angle peak shown in Figure 9c.

However, the pH value of local scratch sites would be lowered, accompanied by the continuous anodic dissolution.[48] As a result, the radius of the Nyquist curve (Figure 9a) gradually shrinks with a prolonged immersion time. Accordingly, the $|Z|_{0.01Hz}$ value in Figure 9b and the phase angle maximum in Figure 9c monotonously decrease for the composite coating with an exposure time of over 24 h. Notably, the R_{ct} value of the specimen with scratched EP/CaAl-8HQ LDH@rGO still reaches 5.62×10^4 Ω cm^2 after 180 h of immersion (Table 3), which is comparable to that of the freshly scratched counterpart (4.57×10^4 Ω cm^2). On the one hand, the inhibitory film resulting from the adsorption of 8-HQ restores the corrosion-susceptible sites on the exposed steel. On the other hand, the wrapped nanocomposite exerts a strong barrier effect owing to the rGO constituent, which blocks the further infiltration of saline electrolyte through the scratch. Depending on the synergism between 8-HQ and rGO, the impedance of the coated specimen is relatively stable during 180 h of immersion in the NaCl solution despite the occurrence of artificial scratches.

https://doi.org/10.1021/acsami.3c19245
ACS Appl. Mater. Interfaces 2024, 16, 13114−13131

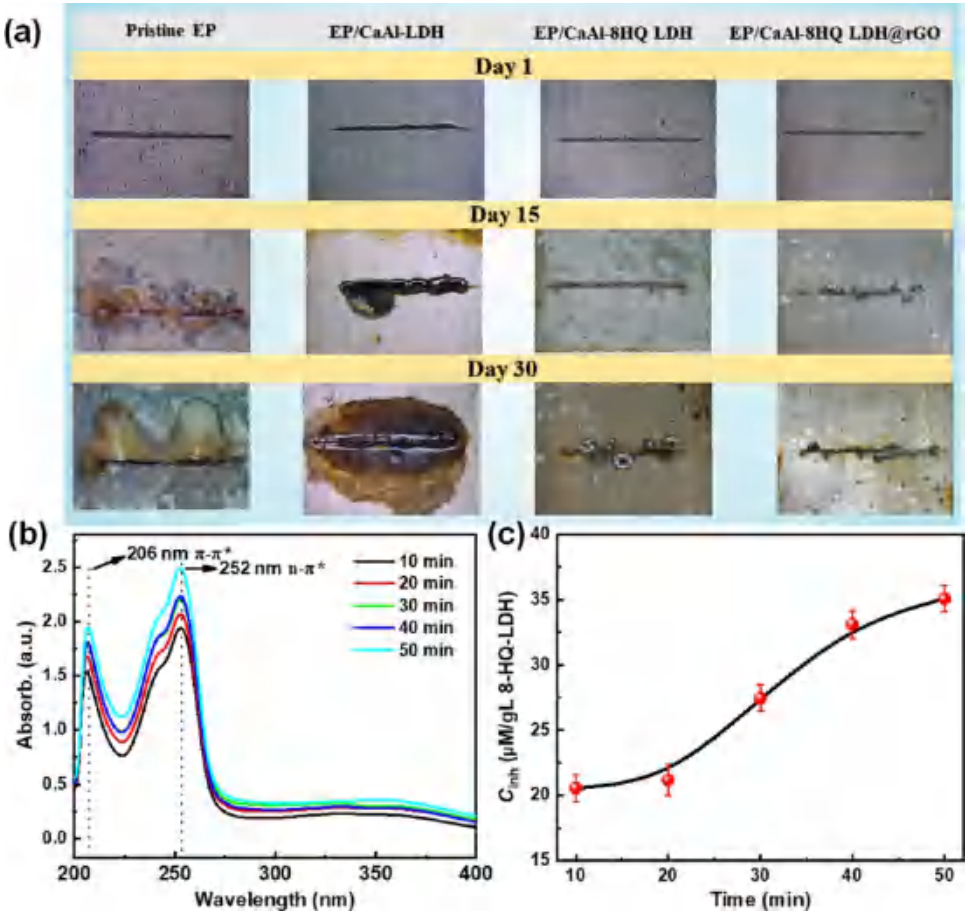

Figure 10. Digital graphs of pristine EP, EP/CaAl-LDH, EP/CaAl-8HQ LDH, and EP/CaAl-8HQ LDH@rGO-coated specimens captured at the allocated exposure time in salt spray tests (a). UV spectra of the 3.5 wt % NaCl solution containing CaAl-8HQ LDH with different periods (b), along with the release profile of 8-HQ (c).

3.3.3. Salt Spray Analysis of Scratched Specimens. To consolidate the superior anticorrosion performance of the as-designed nanocomposite coating, salt spray tests were conducted on specimens with scratched EP, EP/CaAl LDH, EP/CaAl-8HQ LDH, and EP/CaAl-8HQ LDH@rGO coatings, and the outcomes are summarized in Figure 10a. Clearly, severe damage is observed around the scratch for the pristine EP-coated specimen just after 15 days of exposure to the salt spray, which persistently deteriorates in the remaining time. Due to the local cathodic delamination,[49] apparent bulges alongside numerous corrosion products are seen for the pristine EP-coated specimen. For the EP/CaAl LDH system, the limited protection efficacy of sole LDH hardly retards the initiation and development of corrosion at the scratched site. Serious deterioration around the scratch of the EP/CaAl LDH-coated specimen is observed after 30 days of exposure. In contrast, the intercalation of 8-HQ promotes the anticorrosive feature of the entire modified LDH, which elevates the protective efficiency of the scratched EP/CaAl-8HQ LDH coating for the largely sustained surface morphology during 30 days of exposure to salt spray. As expected, the EP/CaAl-8HQ LDH@rGO-coated specimen shows the most protected appearance among the four systems, although rusty spots sparsely distribute along the scratch after 15 days of exposure. Increasing the exposure time barely aggravates the degree of corrosion at the scratched sites of EP/CaAl-8HQ LDH@rGO.

Based on electrochemical and salt spray measurements, the assumption of 8-HQ release from LDH plays a crucial role in maintaining the protective ability of the relevant coatings (i.e., EP/CaAl-8HQ LDH and EP/CaAl-8HQ LDH@rGO systems). Therefore, it is necessary to study this inhibitor-release phenomenon to unveil the anticorrosive mechanism of the composite coating. Figure 10b depicts the UV spectra of the CaAl-8HQ LDH@rGO powder dispersed in a 3.5 wt % NaCl solution at the allocated standing time. Similar to the spectrum in Figure 2c, typical absorbances at 206 and 250 nm are assigned to $\pi-\pi^*$ and $n-\pi^*$ transitions for the functional groups on 8-HQ.[50] Moreover, the intensity of both peaks increases with time, implying the increased 8-HQ concentration in the solution. This directly evidences the release of preintercalated 8-HQ from LDH interlayers. According to the established calibration curve (Figure S2, SI), the release profile of 8-HQ is shown in Figure 10c. This finding affirms that the release of 8-HQ occurs at a faster rate in the early stage due to the quick penetration of chloride (Cl^-) ions toward LDH galleries. At the same time, the concentration's dynamic equilibrium appears to be suppressing the release rate after a few minutes.[51] Due to the anion exchange capacity of LDH, the release of 8-HQ in response to contact with corrosive media enhances the self-healing ability of EP/CaAl-8HQ LDH@rGO.

3.4. Flame Retardant and Thermal Stability of the Nanocomposite Coating. Table 4 displays the UL-94

Table 4. Limiting Oxygen Index (LOI) and UL-94 Rating of EP-Based Coatings

samples	LOI (%)	UL-94			
		av-t_1 (s)	av-t_2 (s)	ratings	dripping
pristine EP	20.25			nr	burn
EP/CaAl-LDH	21.11	1.5×10^1	1.1×10^1	V-2	No
EP/CaAl-8HQ LDH	23.35	1.3×10^{-1}	9.0×10^{-1}	V-2	No
EP/CaAl-8HQ LDH@rGO	25.52	0.0	3.0×10^{-1}	V-0	No

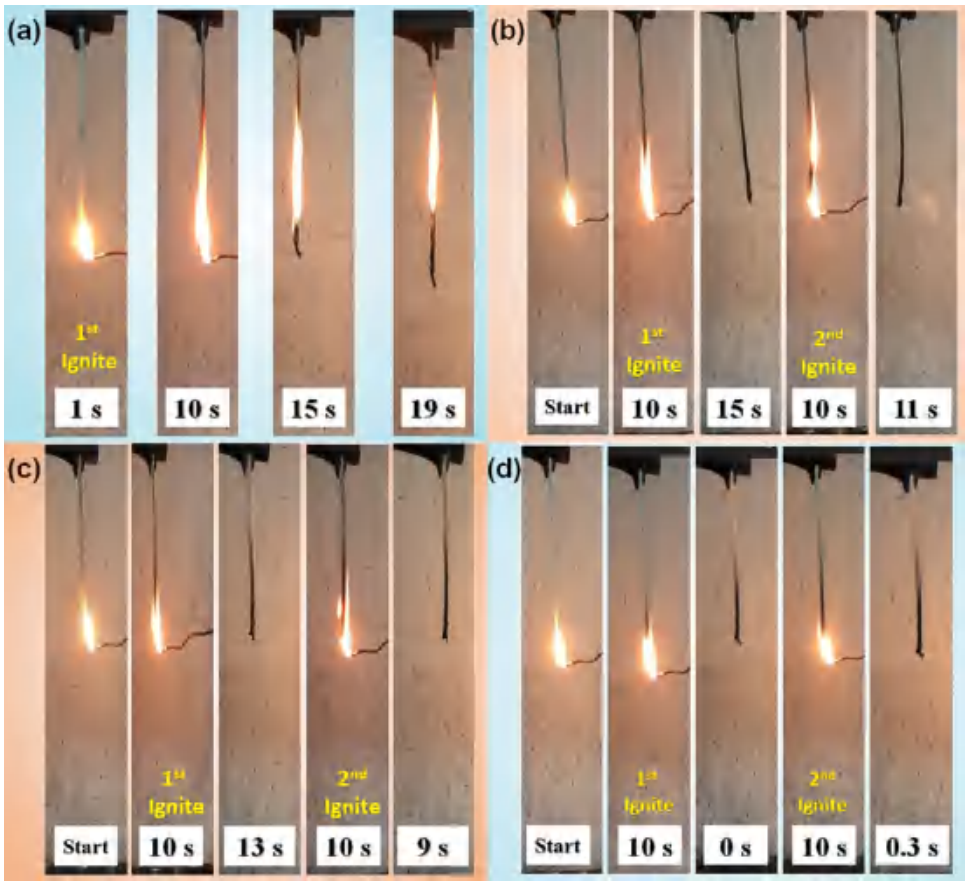

Figure 11. UL-94 burning tests of pristine EP (a), EP/CaAl-LDH (b), EP/CaAl-8HQ LDH (c), and EP/CaAl-8HQ LDH@rGO nanocomposites (d).

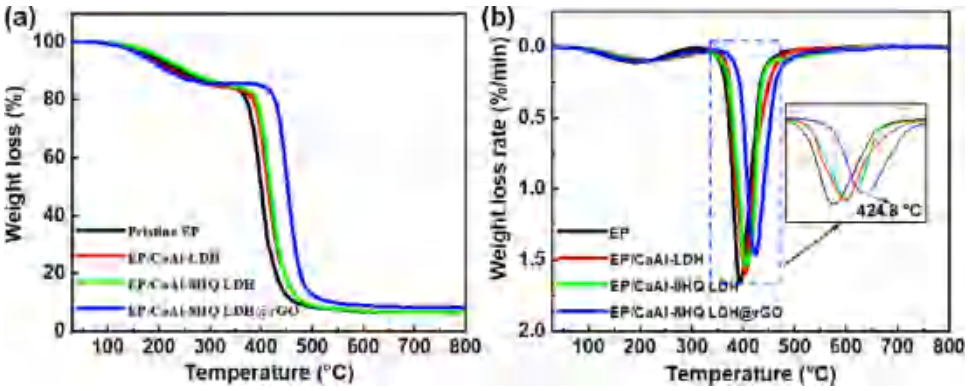

Figure 12. TGA and DTG (a, b) of the pristine EP, EP/CaAl-LDH, EP/CaAl-8HQ LDH, and EP/CaAl-8HQ LDH@rGO nanocomposites.

ratings and LOI values for the as-prepared coatings along with video snapshots during the vertical burning test. The associated eigenvalues are tabulated in Table 4 along with video snapshots during the vertical burning test, given in Figure 11. Pristine EP is rapidly burned with an LOI value of 20.25% and unrated in the UL-94 test, confirming the inflammability of the polymer matrix. The incorporation of CaAl-LDH into the EP matrix elevates the LOI value to

https://doi.org/10.1021/acsami.3c19245
ACS Appl. Mater. Interfaces 2024, 16, 13114−13131

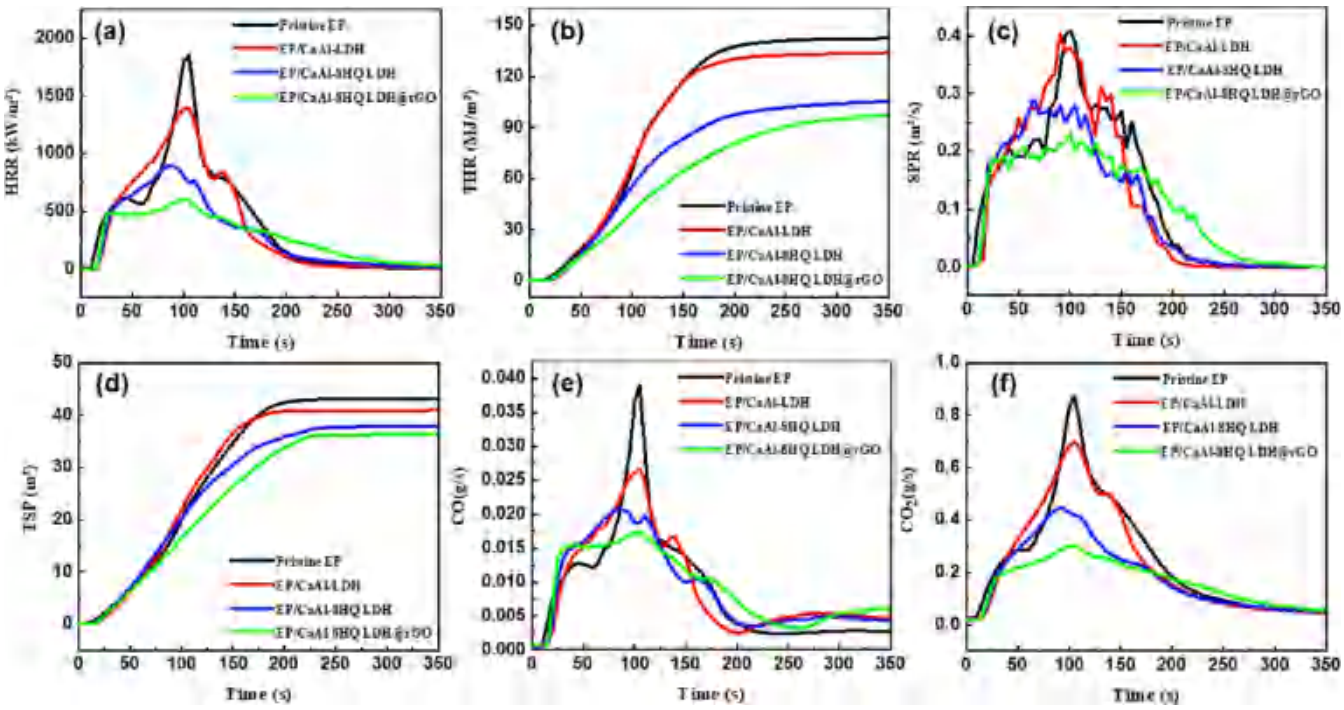

Figure 13. pHRR (a), THR (b), SPR (c), TSP (d), CO (e), and CO_2 yielded rates (f) of the pristine EP, EP/CaAL-LDH, EP/CaAl-8HQ LDH, and EP/CaAl-8HQ LDH@rGO.

21.11%, resulting in a UL-94 V-2 rating. As previously evidenced,[23] LDH decomposes into CO_2 and H_2O, which can dilute the flammable gas and O_2, retarding the development of combustion. In addition, metallic oxides derived from LDH under high temperatures are conducive to the generation of a surface char layer by the nucleation effect, isolating heat and O_2, and thus mitigating the further degradation of the EP matrix.[52] However, introducing CaAl-8HQ LDH sequentially increases the flame-retardant grade to V-2 with an elevated LOI value of 23.35%. Similar to the release behavior in the solution phase, 8-HQ would escape from LDH interlayers and moderately promote the entire flame-retardance of EP/CaAl-8HQ LDH due to the presence of a N-possessing heterocycle.[53] The excellent barrier effect and thermostability of rGO endow CaAl-8HQ LDH@rGO with strong flame-retardant and smoke-depression features toward the EP matrix. In particular, the rGO also densifies the char layer at the combustion boundary, efficiently restricting the progression of burning. Consequently, the EP/CaAl-8HQ LDH@rGO coating achieves a V-0 flame-retardant grade with a satisfactory LOI value of 25.52%.

The superiority of the CaAl-8HQ LDH@rGO nanocomposite over other analogues in flame-retardance for the EP matrix is further verified by its pyrolysis behaviors, as shown in Figure 12. In Figure 12a, all coatings exhibit the first weight-loss stage between 100 and 300 °C, resulting from the evaporation of trapped water or volatilizable compounds (e.g., oligomers). Thereafter, four coatings show distinct thermal decompositions as the temperature exceeds 300 °C. In detail, pristine EP exhibits the lowest thermal decomposition temperature, which is observed at 394.1 °C in the DTG curve in Figure 12b. The introduction of as-prepared nanofillers steadily improves the thermostability of composite coatings. As a prominent prototype, the EP/CaAl-8HQ LDH@rGO system shows the largest pyrolysis temperature at 424.8 °C compared to the EP/CaAl-8HQ LDH (406.7 °C) and EP/CaAl-LDH (404.1 °C) counterparts. Also worthy of note, the highest char residue is observed for the EP/CaAl-8HQ LDH@rGO sample, which can be assigned to the extremely stable metallic oxides and rGO at the end of the temperature increase.

Cone calorimetry measurement is an essential tool for investigating the fire behavior of composite coatings, providing insights into the flame retardancy of pristine EP, EP/CaAl-LDH, EP/CaAl-8HQ LDH, and EP/CaAl-8HQ@rGO. In Figure 13a, pristine EP is identified as a flammable polymer, exhibiting an elevated peak heat release rate (pHRR) of 1852 kW/m^2 and a relatively high total heat release rate (THR) of 140 MJ/m^2. For EP/CaAl-LDH, the realized pHRR decreases to 1395 kW/m^2, corresponding to a declining rate in contrast to pristine EP. This reduction is attributed to the endothermic reaction, catalytic impact of the metal oxides, and the dilution effect of CaAl-LDH.[54] Besides, the pHRR value of the EP/CaAl-8H LDH composite further decreases to 895 kW/m^2 compared to those of pristine EP and EP/CaAl-8HQ, which is mainly due to the presence of nitrogen on 8-HQ. EP/CaAl-8HQ LDH@rGO demonstrates a pHRR value of 598 kW/m^2 due to the synergistic effect of the LDH and rGO sheets.[55] In Figure 13b, the EP/CaAl-LDH and EP/CaAl-8HQ LDH nanocomposites exhibit THR values of 131.0 and 100.0 MJ/m^2, respectively, both lower than those of pristine EP. As expected, for EP/CaAl-8HQ LDH@rGO, the THR value considerably decreases to 88.26 MJ/m^2. This reduction in THR and pHRR values of EP/CaAl-8HQ LDH@rGO results from the catalytic carbonization action, promoting the transformation of EP into a condensed state rather than a "fuel" role for ignition and exothermic reactions.[56]

The emission of smoke during incineration is regarded as the other metric for evaluating fire safety given its significant impact on escape and evacuation.[56] The detailed data of smoke

https://doi.org/10.1021/acsami.3c19245
ACS Appl. Mater. Interfaces 2024, 16, 13114−13131

Table 5. Related Date of Cone Calorimeter Test for Pristine EP and EP Composites

samples	pHRR (kW/m^2)	THR (MJ/m^2)	PSPR (m^2/s)	TSP (m^2)	PCO (g/s)	PCO$_2$ (g/s)	Char yield (%)	FRI
Pristine EP	1852	140.0	0.40	42.74	0.038	0.87	2.47	1.00
EP/CaAl-LDH	1395	131.0	0.35	40.89	0.026	0.69	4.41	2.12
EP/CaAl-8HQ LDH	895	100.7	0.29	37.29	0.020	0.44	5.80	4.34
EP/CaAl-8HQ LDH@rGO	598	88.26	0.22	35.86	0.012	0.30	6.17	7.41

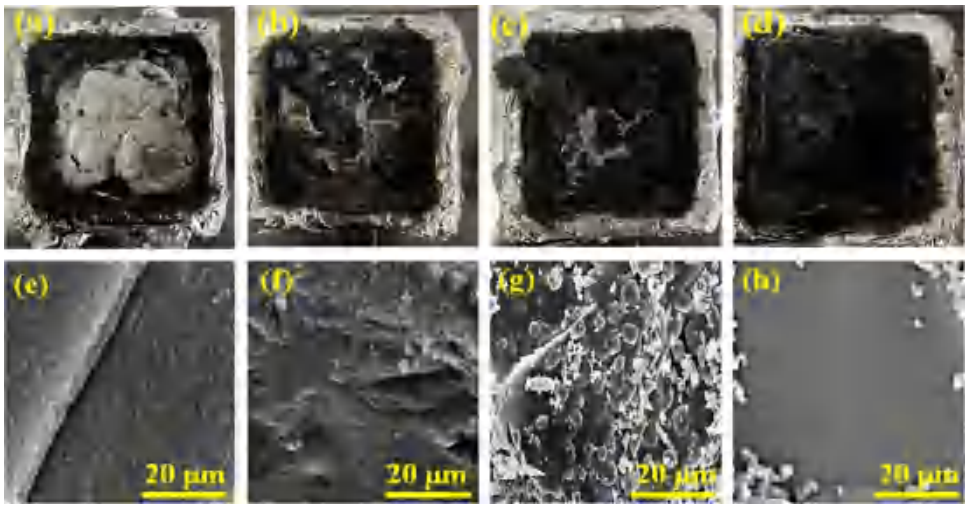

Figure 14. Macroscopic photos (upper) and SEM images (lower) of char residues for pristine EP (a, e), EP/CaAl-LDH (b, f), EP/CaAl-8HQ LDH (c, g), and EP/CaAl-8HQ LDH@rGO (d, h) after cone calorimeter tests.

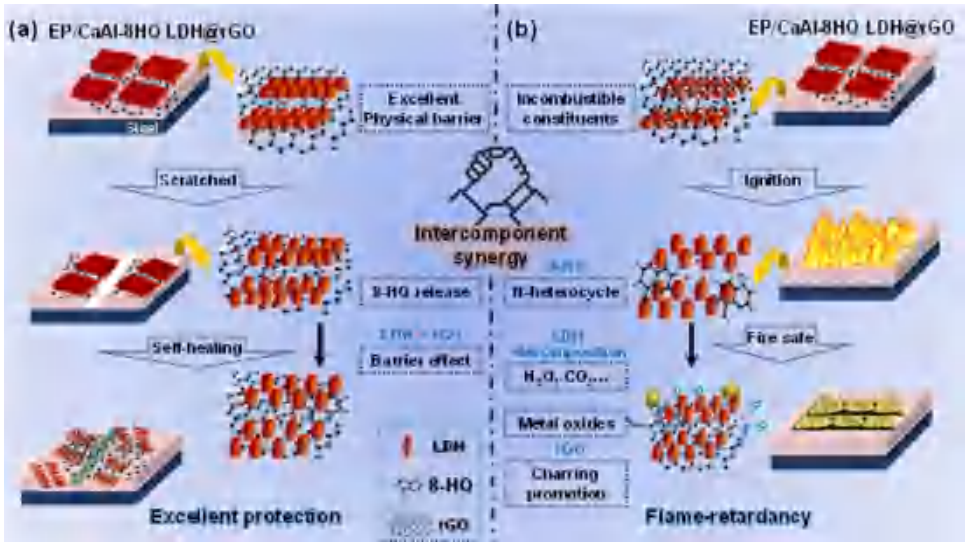

Figure 15. Schematic illustration of the corrosion self-healing and flame-retardant mechanism (a, b).

production rate (SPR), total smoke production (TSP), and CO and CO_2 yielded rates are shown in Figure 13c−f, respectively, along with the detailed eigenvalues tabulated in Table 5. Pristine EP exhibits a higher SPR value of 0.40 m^2/s and a TSP of 42.74 m^2, indicating elevated smoke generation. Moreover, it shows a peak CO yielding rate of 0.038 g/s and a peak CO_2 yielding rate of 0.87 g/s. Nevertheless, the introduction of the nanofillers substantially mitigates smoke release, as evidenced by a reduction in the SPR observed for EP/CaAl-LDH (0.35 m^2/s) and EP/CaAl-8HQ LDH (0.29 m^2/s). Meanwhile, the TSP rates of EP/CaAl-LDH, EP/CaAl-8HQ LDH, and EP/CaAl-8HQ LDH@rGO composites decrease to 40.89, 37.29, and 35.86 m^2, respectively.

Hence, the EP containing CaAl-8HQ LDH@rGO hybrids demonstrate effective smoke suppression behavior, attributed to synergistic effects such as the char layer's barrier effect and the dispersion of water molecules in the gas phase resulting from LDH decomposition. CO and CO_2 (Figure 13e,f) illustrate the lowest yield rates, attributed to the inclusion of EP/CaAl-8HQ LDH@rGO.[57]

According to cone calorimeter statistics, the flame-retardant index (FRI) serves as a primary criterion for assessing the fire retardancy of polymers,[58] which was computed using the following equation[59]

$$FRI = \frac{\left(\frac{1}{2}THR \times \left(\frac{PHRR}{TTI}\right)\right)_{neat\ EP}}{\left(\frac{1}{2}THR \times \left(\frac{PHRR}{TTI}\right)\right)_{nanocomposites}} \quad (6)$$

In summary, FRI < 1 was considered indicative of a lower degree of fire retardancy, while 1 < FRI < 10 was evaluated as having an excellent level of flame-retardant capability. The FRI value for EP/CaAl-8HQ LDH@rGO was determined to be 7.41, indicating its superior flame-retardant capability.

After conducting cone calorimeter tests, the char developments of different coatings are depicted in Figure 14 along with the corresponding SEM images. In Figure 14a, pristine EP incurs almost complete combustion, leaving minimal residual carbon and underscoring its flammability. The residual carbon of EP in Figure 14e displays low continuity and a porous structure, attributed to the release of organic fragments and volatiles during sample combustion, resulting in chars with limited heat and an O_2 insulation. For EP/CaAl-LDH given in Figure 14b, the amount of residual carbon increases, still with pinholes existing in the char layer (Figure 14f). In Figure 14c, the residual carbon of EP/CaAl-8HQ LDH is comparable to that of EP/CaAl-LDH, yet the char layer still remains discontinuous, as observed in Figure 14g. In contrast, the EP/CaAl-8HQ LDH@rGO composite displays substantial char with high continuity as evident in Figure 14h. Accordingly, a compact char layer is seen in Figure 14h, which imparts a superior shielding effect throughout the pyrolysis process, preventing the uninhibited transfer of combustible volatile molecules.[60] The thermal decomposition of LDH is an endothermic procedure, and the chemically attached water molecules generated during heating exert a diluting effect in the gas phase, reducing the combustion rate. Moreover, phenol rings and N-heterocyclic rings on 8-HQ further enhance the thermal stability of the EP composite. In addition to the strong barrier and heat resistance of rGO,[61] EP/CaAl-8HQ LDH@rGO coating exhibits an optimal flame-retardant property.

3.5. Anticorrosive and Flame-Retardant Mechanisms.

As per the documented anticorrosion and flame-retardant capacities of the EP/CaAl-8HQ LDH@rGO coating, the corresponding mechanisms are proposed in Figure 15. The favorable ion exchangeability afforded by lamellar LDH makes it readily accommodate 8-HQ,[62] whose barrier effect is undoubtedly reinforced after being loaded with the impermeable rGO (i.e., CaAl-8HQ LDH@rGO). Hence, well-dispersed CaAl-8HQ LDH@rGO nanocomposites in the EP matrix establish a strong labyrinth effect for the infiltrated corrosion media, impeding the charge transfer at the coating/steel interface. In addition, this nanocomposite could densify the coating body and promote the adhesion grade on the steel surface via its benign compatibility with EP and the heterogeneous nucleation effect, which further enhances the physical barrier of EP/CaAl-8HQ LDH@rGO, expelling the saline water. Even if the undesirable coating rupture occurs, the permeation and the ensuing accumulation of Cl^- propel the release of 8-HQ from LDH interlayers.[63] Thereupon, 8-HQ molecules adsorb on the exposed steel surface, repair the corrosion-susceptible sites, and thus exert self-healing functions. Hence, the synergy of the potent barrier effect from the LDH-on-rGO architecture and the 8-HQ release upon the initiation of coating failure accounts for the efficient protection of EP/CaAl-8HQ LDH@rGO toward the underlying steel in a 3.5 wt % NaCl solution.

Another aspect, besides the volatilization water, is that the residual carbonates embedded in CaAl-LDH can be converted into CO_2 under the ignition of EP/CaAl-8HQ LDH@rGO. LDH loaded on the surface of rGO quickly participates in the flame-retardant process due to the higher thermal conductivity of rGO sheets. The thermal decomposition of LDH is an endothermic procedure, and the chemically attached water molecules generated during heating exert a diluting effect in the gas phase, reducing the rate of combustion. The phenol rings of the 8-HQ molecules enhance the flame retardancy and improve the solubility of the polymer in organic solvents without sacrificing its inherent thermal stability. Active radicals are scavenged in the gas-phase mechanism by incorporating oxygen dilution. The release of nitrogen gas results in the dilution of combustible gases during the gaseous phase of the combustion cycle. Moreover, partial CaAl-LDH nanosheets decompose to metallic oxides (e.g., Al_2O_3) under high temperatures, which facilitates the formation and densification of the char layer at the combustion boundary.[23] An integrated and compact surface char layer isolates the EP matrix from the diffusion of O_2 and heat. The carbonizing agent in the condensed-phase mechanism induces the substrate's surface to generate a thick, compact char. This char, in turn, can restrict the substrate's interaction with heat and oxygen, while the blowing agent releases gases that cause the formed char to swell. This shielding capability is further supported by the two-dimensional rGO constituent, largely retarding the spread of flame. Hence, the combination of char formation and O_2 concentration dilution governs the flame-retardant mechanism of the EP/CaAl-8HQ LDH@rGO system.

4. CONCLUSIONS

On the basis of preparing CaAl-LDH, 8-HQ was intercalated into LDH interlayers, which were further loaded on rGO through the one-pot hydrothermal process. The resulting nanocomposite, i.e., CaAl-8HQ LDH@rGO, along with CaAl-LDH and CaAl-8HQ LDH counterparts, was incorporated into the EP matrix as nanofillers to generate composite coatings. The remarkable conclusions are listed as follows.

1. GO was reduced to rGO during the hydrothermal reaction, which accommodated 8-HQ intercalated CaAl-LDH. The successful intercalation of 8-HQ into LDH's lamellar spacing was intuitively supported by morphological, elemental, and XPS analyses. However, the release of 8-HQ from LDH in response to the saline medium was evidenced by UV spectra for the typical absorbance at 206 and 250 nm.
2. Introducing CaAl-8HQ LDH@rGO into the EP matrix largely elevated the adhesion strength on the steel substrate in both dry (4.34 MPa) and wet (3.45 MPa) states with the least adhesion loss. The specimen coated with EP/CaAl-8HQ LDH@rGO realized an excellent corrosion resistance in the 3.5 wt % NaCl solution for a long time. Specifically, a $|Z|_{0.01Hz}$ value of 1.84×10^{10} Ω cm^2 was achieved for the unscratched coating after 120 days of immersion in the saline medium. Even for the scratched EP/CaAl-8HQ LDH@rGO-coated sample, the $|Z|_{0.01Hz}$ value still kept stable and maintained the value of 1.31×10^5 Ω cm^2 after 180 h of exposure to the NaCl solution. Salt spray tests consolidated the tolerance

https://doi.org/10.1021/acsami.3c19245
ACS Appl. Mater. Interfaces 2024, 16, 13114−13131

and self-healing feature of the EP/CaAl-8HQ LDH@rGO system by virtue of the effective release inhibitor from LDH galleries. 8-HQ plays a vital role in corrosion resistance, chelating formation and promoting passivation to increase the life span of the coated metal.

3. The EP/CaAl-8HQ LDH@rGO bulk also exhibited a favorable flame-retardant performance, yielding a V-0 rating and an LOI value of 26.8%. Accordingly, this composite coating was the most thermostable with a decomposition temperature of 424.8 °C.
4. Depending on the superb physical barrier of the LDH-on-rGO nanofiller and the triggered release of 8-HQ upon coating failure, EP/CaAl-8HQ LDH@rGO afforded the best protection efficiency as compared to the as-prepared analogues. Besides, the diluted O_2 concentration by the emitted CO_2/H_2O and the promoted charring layer from the generated metallic oxide/rGO constituent collectively accounted for the flame-retardant property of the composite coating. This work may pave the way for the development of LDH-based nanofillers for protective coatings, offering self-healing properties and flame-retardant capabilities. The prepared composite can be effectively utilized in coating applications for walls and various industrial products. This application proves instrumental in safeguarding human lives by providing enhanced protection against flammability. Incorporating this composite into coating systems not only ensures improved fire resistance but also contributes to the overall safety and longevity of structures and industrial equipment.

■ ASSOCIATED CONTENT

Supporting Information

The Supporting Information is available free of charge at https://pubs.acs.org/doi/10.1021/acsami.3c19245.

Survey spectra of CaAl-LDH, CaAl-8HQ LDH, and CaAl-8HQ LDH@rGO; UV spectra of 3.5 wt % NaCl solutions with a known concentration of 8-HQ and the derived standard curve; comparison of $|Z|_{0.01Hz}$ values for different epoxy-based composite coatings at different immersion times; and comparison of HRR (kW/m^2) values for different epoxy-based composite coatings (PDF)

■ AUTHOR INFORMATION

Corresponding Authors

Jingmao Zhao − *College of Materials Science and Engineering, Beijing University of Chemical Technology, Beijing 100029, China; Beijing Key Laboratory of Electrochemical Process and Technology for Materials, Beijing 100029, China;* orcid.org/0000-0002-9197-4868; Email: jingmaozhao@126.com

Baomin Fan − *College of Chemical and Materials Engineering, Beijing Technology and Business University, Beijing 100029, China;* orcid.org/0000-0002-0430-5712; Email: fanbaomin@btbu.edu.cn

Authors

Hassan Murtaza − *College of Materials Science and Engineering, Beijing University of Chemical Technology, Beijing 100029, China*

Mohammad Tabish − *College of Materials Science and Engineering, Beijing University of Chemical Technology, Beijing 100029, China*

Jingbao Wang − *College of Materials Science and Engineering, Beijing University of Chemical Technology, Beijing 100029, China*

Muhammad Mubeen − *College of Materials Science and Engineering, Beijing University of Chemical Technology, Beijing 100029, China*

Jingfan Zhang − *State Key Laboratory of Organic−Inorganic Composites, Beijing University of Chemical Technology, Beijing 100029, China*

Sheng Zhang − *State Key Laboratory of Organic−Inorganic Composites, Beijing University of Chemical Technology, Beijing 100029, China;* orcid.org/0000-0001-7131-6246

Complete contact information is available at: https://pubs.acs.org/10.1021/acsami.3c19245

Notes

The authors declare no competing financial interest.

■ ACKNOWLEDGMENTS

This work was supported by the Program Fund of Non-Metallic Excellence and Innovation Center for Building Materials (Grant No. 2023SFP4-1).

■ REFERENCES

(1) Sykam, K.; Sivanandan, S.; Basak, P. 1, 2, 3-Triazole mediated, non-halogenated phosphorus containing protective coatings from castor oil: Flame retardant and anti-corrosion applications. *Prog. Org. Coat.* **2023**, *178*, No. 107475.

(2) Anjum, M. J.; Zhao, J.; Asl, V. Z.; Yasin, G.; Wang, W.; Wei, S.; Zhao, Z.; Khan, W. Q. In-situ intercalation of 8-hydroxyquinoline in Mg-Al LDH coating to improve the corrosion resistance of AZ31. *Corros. Sci.* **2019**, *157*, 1−10.

(3) Danaee, I.; Darmiani, E.; Rashed, G. R.; Zaarei, D. Self-healing and anticorrosive properties of Ce (III)/Ce (IV) in nanoclay−epoxy coatings. *Iran. Polym. J.* **2014**, *23*, 891−898.

(4) Zhong, F.; He, Y.; Wang, P.; Chen, C.; Xie, P.; Li, H.; Chen, J. One-step hydrothermal synthesis of reduced graphene oxide/aspartic acid intercalated layered double hydroxide for enhancing barrier and self-healing properties of epoxy coating. *React. Funct. Polym.* **2019**, *145*, No. 104380.

(5) Tabish, M.; Zhao, J.; Kumar, A.; Yan, J.; Wang, J.; Shi, F.; Zhang, J.; Peng, L.; Mushtaq, M. A.; Yasin, G. Developing epoxy-based anti-corrosion functional nanocomposite coating with CaFe-Tolyl-triazole layered double hydroxide@g-C_3N_4 as nanofillers on Q235 steel substrate against NaCl corrosive environment. *Chem. Eng. J.* **2022**, *450*, No. 137624.

(6) Li, H.; Qiang, Y.; Zhao, W.; Zhang, S. 2-Mercaptobenzimidazole-inbuilt metal-organic-frameworks modified graphene oxide towards intelligent and excellent anti-corrosion coating. *Corros. Sci.* **2021**, *191*, No. 109715.

(7) Ye, Y.; Yang, D.; Zhang, D.; Chen, H.; Zhao, H.; Li, X.; Wang, L. POSS-tetraaniline modified graphene for active corrosion protection of epoxy-based organic coating. *Chem. Eng. J.* **2020**, *383*, No. 123160.

(8) Cao, Y.; Wang, J.; Chen, K.; Zhang, X.; Zhang, B.; Fang, S.; Liang, Y.; Huang, C.; Wang, X. A Comparative Study of Chloride Adsorption Ability and Corrosion Protection Effect in Epoxy Coatings of Various Layered Double Hydroxides. *Coatings* **2022**, *12*, No. 1631, DOI: 10.3390/coatings12111631.

(9) Maia, F.; Tedim, J.; Lisenkov, A. D.; Salak, A. N.; Zheludkevich, M. L.; Ferreira, M. G. S. Silica nanocontainers for active corrosion protection. *Nanoscale* **2012**, *4*, 1287−1298.

(10) Dong, C.; Zhang, M.; Xiang, T.; Yang, L.; Chan, W.; Li, C. Novel self-healing anticorrosion coating based on L-valine and MBT-loaded halloysite nanotubes. *J. Mater. Sci.* **2018**, *53*, 7793−7808.
(11) Skorb, E. V.; Skirtach, A. G.; Sviridov, D. V.; Shchukin, D. G.; Möhwald, H. Laser-controllable coatings for corrosion protection. *ACS Nano* **2009**, *3*, 1753−1760.
(12) Situ, Y.; Ji, W.; Liu, C.; Xu, J.; Huang, H. Synergistic effect of homogeneously dispersed PANI-TiN nanocomposites towards long-term anticorrosive performance of epoxy coatings. *Prog. Org. Coat.* **2019**, *130*, 158−167.
(13) Cheng, L.; Liu, C.; Zhao, H.; Wang, L. Hierarchically self-reporting and self-healing photothermal responsive coatings towards smart corrosion protection. *Chem. Eng. J.* **2023**, *467*, No. 143463.
(14) Ramezanzadeh, M.; Ramezanzadeh, B.; Bahlakeh, G.; Tati, A.; Mahdavian, M. Development of an active/barrier bi-functional anti-corrosion system based on the epoxy nanocomposite loaded with highly-coordinated functionalized zirconium-based nanoporous metal-organic framework (Zr-MOF). *Chem. Eng. J.* **2021**, *408*, No. 127361.
(15) Liu, T.; Li, W.; Zhang, C.; Wang, W.; Dou, W.; Chen, S. Preparation of highly efficient self-healing anticorrosion epoxy coating by integration of benzotriazole corrosion inhibitor loaded 2D-COF. *J. Ind. Eng. Chem.* **2021**, *97*, 560−573.
(16) Lv, Y.; Zheng, Y.; Zhu, H.; Wu, Y. Designing a dual-functional material with barrier anti-corrosion and photocatalytic antifouling properties using g-C_3N_4 nanosheet with ZnO nanoring. *J. Mater. Sci. Technol.* **2022**, *106*, 56−69.
(17) Mohammadkhah, S.; Ramezanzadeh, M.; Mohammadloo, H. E.; Ramezanzadeh, B.; Ghamsarizade, R. Construction of a nano-micro nacre-inspired 2D-MoS_2-MOF-glutamate carrier toward designing a high-performance smart epoxy composite. *J. Ind. Eng. Chem.* **2023**, *121*, 358−377.
(18) Wang, J.; Zhao, J.; Tabish, M.; Shi, F.; Fan, B.; Peng, L.; Cheng, Q. Intelligent anticorrosion coating based on mesostructured BTA@mCeO$_2$/g-C_3N_4 nanocomposites for inhibiting the filiform corrosion of Zn-Mg-Al coated steel. *Corros. Sci.* **2023**, *221*, No. 111331.
(19) Cao, Y.; Zheng, D.; Li, X.; Lin, J.; Wang, C.; Dong, S.; Lin, C. Enhanced corrosion resistance of superhydrophobic layered double hydroxide films with long-term stability on Al substrate. *ACS Appl. Mater. Interfaces* **2018**, *10*, 15150−15162.
(20) Chen, Y.; Wu, L.; Yao, W.; Chen, Y.; Zhong, Z.; Ci, W.; Wu, J.; Xie, Z.; Yuan, Y.; Pan, F. A self-healing corrosion protection coating with graphene oxide carrying 8-hydroxyquinoline doped in layered double hydroxide on a micro-arc oxidation coating. *Corros. Sci.* **2022**, *194*, No. 109941.
(21) Su, Y.; Qiu, S.; Wei, J.; Zhu, X.; Zhao, H.; Xue, Q. Sulfonated polyaniline assisted hierarchical assembly of graphene-LDH nano-hybrid for enhanced anticorrosion performance of waterborne epoxy coatings. *Chem. Eng. J.* **2021**, *426*, No. 131269.
(22) Sui, Y.; Sima, H.; Shao, W.; Zhang, C. Novel bioderived cross-linked polyphosphazene microspheres decorated with FeCo-layered double hydroxide as an all-in-one intumescent flame retardant for epoxy resin. *Composites, Part B* **2022**, *229*, No. 109463.
(23) Dong, S.; Xiao, G.; Chen, C.; Chen, C.; Yang, Z.; Zhong, F.; Wang, M.; Zou, R. Zn-Al layered double metal hydroxide anchored reduced graphene oxide for enhancing the fire performance of composite coatings. *Colloid Surf., A* **2022**, *632*, No. 127736.
(24) Lau, K.-T.; Shi, S.-Q.; Zhou, L.-M.; Cheng, H.-M. Micro-hardness and flexural properties of randomly-oriented carbon nanotube composites. *J. Compos. Mater.* **2003**, *37*, 365−376.
(25) Bian, X.; Lu, X.; Xue, Y.; Zhang, C.; Kong, L.; Wang, C. A facile one-pot hydrothermal method to produce SnS_2/reduced graphene oxide with flake-on-sheet structures and their application in the removal of dyes from aqueous solution. *J. Colloid Interface Sci.* **2013**, *406*, 37−43.
(26) Lv, Z.; Zhong, Q.; Bu, Y. In-situ conversion of rGO/Ni_2P composite from GO/Ni-MOF precursor with enhanced electrochemical property. *Appl. Surf. Sci.* **2018**, *439*, 413−419.
(27) Zhou, S.; Yan, J.; Yan, H.; Zhang, Y.; Huang, J.; Zhao, G.; Liu, Y. ZrO_2-anchored rGO nanohybrid for simultaneously enhancing the wear resistance and anticorrosion performance of multifunctional epoxy coatings. *Prog. Org. Coat.* **2022**, *166*, No. 106795.
(28) Tabish, M.; Zhao, J.; Wang, J.; Anjum, M. J.; Qiang, Y.; Yang, Q.; Mushtaq, M. A.; Yasin, G. Improving the corrosion protection ability of epoxy coating using CaAl LDH intercalated with 2-mercaptobenzothiazole as a pigment on steel substrate. *Prog. Org. Coat.* **2022**, *165*, No. 106765.
(29) Mishra, G.; Dash, B.; Sethi, D.; Pandey, S.; Mishra, B. K. Orientation of organic anions in Zn-Al layered double hydroxides with enhanced antibacterial property. *Environ. Eng. Sci.* **2017**, *34*, 516−527.
(30) El Faydy, M.; Galai, M.; Touhami, M. E.; Obot, I. B.; Lakhrissi, B.; Zarrouk, A. Anticorrosion potential of some 5-amino-8-hydroxyquinolines derivatives on carbon steel in hydrochloric acid solution: gravimetric, electrochemical, surface morphological, UV−visible, DFT and Monte Carlo simulations. *J. Mol. Liq.* **2017**, *248*, 1014−1027.
(31) Rajasekaran, M.; Anbusrinivasan, P.; Mojumdar, S. C. Growth, spectral and thermal characterization of 8-hydroxyquinoline. *J. Therm. Anal. Calorim.* **2010**, *100*, 827−830.
(32) Chen, L.; Hu, Z.; Liu, L.; Huang, Y. A facile method to prepare multifunctional PBO fibers: simultaneously enhanced interfacial properties and UV resistance. *RSC Adv.* **2013**, *3*, 24664−24670.
(33) Shakeel, M.; Arif, M.; Yasin, G.; Li, B.; Khan, H. D. Layered by layered Ni-Mn-LDH/g-C_3N_4 nanohybrid for multi-purpose photo/electrocatalysis: morphology controlled strategy for effective charge carriers separation. *Appl. Catal., B* **2019**, *242*, 485−498.
(34) Huang, Z.; Chen, H.; Zhao, L.; Fang, W.; He, X.; Li, W.; Tian, P. In suit inducing electron-donating and electron-withdrawing groups in carbon nitride by one-step NH_4Cl-assisted route: A strategy for high solar hydrogen production efficiency. *Environ. Int.* **2019**, *126*, 289−297.
(35) Alman, V.; Singh, K.; Bhat, T.; Sheikh, A.; Gokhale, S. Sunlight Assisted improved photocatalytic degradation of rhodamine B using Pd-loaded g-C_3N_4/WO_3 nanocomposite. *Appl. Phys. A* **2020**, *126*, No. 724, DOI: 10.1007/s00339-020-03914-7.
(36) Bahramnia, H.; Semnani, H. M.; Habibolahzadeh, A.; Abdoos, H. Epoxy/polyurethane hybrid nanocomposite coatings reinforced with MWCNTs and SiO_2 nanoparticles: Processing, mechanical properties and wear behavior. *Surf. Coat. Technol.* **2021**, *415*, No. 127121.
(37) Randis, R.; Darmadi, D. B.; Gapsari, F.; Sonief, A. A.; Akpan, E. D.; Ebenso, E. E. The potential of nanocomposite-based coatings for corrosion protection of metals: A Review. *J. Mol. Liq.* **2023**, *390*, No. 123067.
(38) Motamedi, M.; Ramezanzadeh, M.; Ramezanzadeh, B.; Saadatmandi, S. Enhancement of the active/passive anti-corrosion properties of epoxy coating via inclusion of histamine/zinc modified/reduced graphene oxide nanosheets. *Appl. Surf. Sci.* **2019**, *488*, 77−91.
(39) Alibakhshi, E.; Ghasemi, E.; Mahdavian, M.; Ramezanzadeh, B.; Farashi, S. Active corrosion protection of Mg-Al-PO_4^{3-} LDH nanoparticle in silane primer coated with epoxy on mild steel. *J. Taiwan Inst. Chem. Eng.* **2017**, *75*, 248−262.
(40) Keshmiri, N.; Najmi, P.; Ramezanzadeh, M.; Ramezanzadeh, B. Designing an eco-friendly lanthanide-based metal organic framework (MOF) assembled graphene-oxide with superior active anti-corrosion performance in epoxy composite. *J. Cleaner Prod.* **2021**, *319*, No. 128732.
(41) Selim, M. S.; Fatthallah, N. A.; Shenashen, M. A.; Higazy, S. A.; Madian, H. R.; Selim, M. M.; El-Safty, S. A. Bioinspired graphene oxide−magnetite nanocomposite coatings as protective superhydrophobic antifouling surfaces. *Langmuir* **2023**, *39* (6), 2333−2346.
(42) Gojny, F. H.; Wichmann, M. H. G.; Fiedler, B.; Schulte, K. Influence of different carbon nanotubes on the mechanical properties of epoxy matrix composites − A comparative study. *Compos. Sci. Technol.* **2005**, *65*, 2300−2313.
(43) Wu, Y.; He, Y.; Chen, C.; Li, H.; Xia, Y.; Zhou, T. MoS_2-CNFs composites to enhance the anticorrosive and mechanical performance of epoxy coating. *Prog. Org. Coat.* **2019**, *129*, 178−186.

(44) Dehghani, A.; Bahlakeh, G.; Ramezanzadeh, B.; Mofidabadi, A. H. J. 2D reduced-graphene oxide (rGO) nanosheets decorated with l-histidine loaded-β-cyclodextrin for efficient epoxy nano-composite anti-corrosion properties; DFT-D modeling/experimental assessments. *FlatChem* **2021**, *30*, No. 100309.
(45) Rodriguez, J.; Bollen, E.; Nguyen, T. D.; Portier, A.; Paint, Y.; Olivier, M.-G. Incorporation of layered double hydroxides modified with benzotriazole into an epoxy resin for the corrosion protection of Zn-Mg coated steel. *Prog. Org. Coat.* **2020**, *149*, No. 105894.
(46) Brug, G. J.; van den Eeden, A. L. G.; Sluyters-Rehbach, M.; Sluyters, J. H. The analysis of electrode impedances complicated by the presence of a constant phase element. *J. Electroanal. Chem.* **1984**, *176*, 275−295.
(47) Liu, Y.; Fan, B.; Xu, B.; Yang, B. Ambient-stable polyethyleneimine functionalized $Ti_3C_2T_x$ nanohybrid corrosion inhibitor for copper in alkaline electrolyte. *Mater. Lett.* **2023**, *337*, No. 133979.
(48) Tang, X.; Cheng, Y. F. Micro-electrochemical characterization of the effect of applied stress on local anodic dissolution behavior of pipeline steel under near-neutral pH condition. *Electrochim. Acta* **2009**, *54*, 1499−1505.
(49) Liu, Z.; Fan, B.; Zhao, J.; Yang, B.; Zheng, X. Benzothiazole derivatives-based supramolecular assemblies as efficient corrosion inhibitors for copper in artificial seawater: Formation, interfacial release and protective mechanisms. *Corros. Sci.* **2023**, *212*, No. 110957.
(50) Nejad, S. A. T.; Ramezanzadeh, M.; Alibakhshi, E.; Ramezanzadeh, B.; Olivier, M. G.; Mahdavian, M. Fabrication of 8-hydroxyquinoline loaded in an aluminum-based metal-organic framework for strengthening anti-corrosion behavior of silane primer coating. *Prog. Org. Coat.* **2023**, *174*, No. 107280.
(51) Su, Y.; Qiu, S.; Yang, D.; Liu, S.; Zhao, H.; Wang, L.; Xue, Q. Active anti-corrosion of epoxy coating by nitrite ions intercalated MgAl LDH. *J. Hazard. Mater.* **2020**, *391*, No. 122215.
(52) Chen, M.-J.; Wang, X.; Li, X.-L.; Liu, X.-Y.; Zhong, L.; Wang, H.-Z.; Liu, Z.-G. The synergistic effect of cuprous oxide on an intumescent flame-retardant epoxy resin system. *RSC Adv.* **2017**, *7*, 35619−35628.
(53) Vothi, H.; Nguyen, C.; Pham, L. H.; Hoang, D. Q.; Kim, J. Novel nitrogen−phosphorus flame retardant based on phosphonamidate: Thermal stability and flame retardancy. *ACS Omega* **2019**, *4*, 17791−17797.
(54) Lv, L.-Y.; Cao, C.-F.; Qu, Y.-X.; Zhang, G.-D.; Zhao, L.; Cao, K.; Song, P.; Tang, L.-C. Smart fire-warning materials and sensors: Design principle, performances, and applications. *Mater. Sci. Eng., R* **2022**, *150*, No. 100690.
(55) Guo, Y.; Bao, C.; Song, L.; Yuan, B.; Hu, Y. In Situ Polymerization of Graphene, Graphite Oxide, and Functionalized Graphite Oxide into Epoxy Resin and Comparison Study of On-the-Flame Behavior. *Ind. Eng. Chem. Res.* **2011**, *50*, 7772−7783.
(56) Hong, N.; Song, L.; Wang, B.; Stec, A. A.; Hull, T. R.; Zhan, J.; Hu, Y. Co-precipitation synthesis of reduced graphene oxide/NiAl-layered double hydroxide hybrid and its application in flame retarding poly(methyl methacrylate). *Mater. Res. Bull.* **2014**, *49*, 657−664.
(57) Chu, F.; Xu, Z.; Zhou, Y.; Zhang, S.; Mu, X.; Wang, J.; Hu, W.; Song, L. Hierarchical core−shell TiO_2@LDH@$Ni(OH)_2$ architecture with regularly-oriented nanocatalyst shells: Towards improving the mechanical performance, flame retardancy and toxic smoke suppression of unsaturated polyester resin. *Chem. Eng. J.* **2021**, *405*, No. 126650.
(58) Vahabi, H.; Kandola, B. K.; Saeb, M. R. Flame retardancy index for thermoplastic composites. *Polymers* **2019**, *11*, No. 407, DOI: 10.3390/polym11030407.
(59) Dai, Y.; Cao, H.; Yu, X.; Han, D.; Tian, H.; Guo, L.; Zhou, X. Ammonium Polyphosphate Intercalated Yttrium-Doped Layered Double Hydroxides to Enhance the Thermal Stability and Flame Retardancy of Poly(Lactic Acid). *Adv. Polym. Technol.* **2022**, *2022*, No. 9205119.
(60) Yin, L.; Gong, K.; Zhou, K.; Qian, X.; Shi, C.; Gui, Z.; Qian, L. Flame-retardant activity of ternary integrated modified boron nitride nanosheets to epoxy resin. *J. Colloid Interface Sci.* **2022**, *608*, 853−863.
(61) Wang, M.; Xiao, G.; Chen, C.; Yang, Z.; Zhong, F.; Chen, C.; Zou, R.; Li, Y.; Li, R. Combining layered double hydroxides and carbon nanotubes to synergistically enhance the flame retardant properties of composite coatings. *Colloid Surf., A* **2022**, *638*, No. 128315.
(62) Chen, Y.; Wu, L.; Yao, W.; Zhong, Z.; Chen, Y.; Wu, J.; Pan, F. One-step in situ synthesis of graphene oxide/MgAl-layered double hydroxide coating on a micro-arc oxidation coating for enhanced corrosion protection of magnesium alloys. *Surf. Coat. Technol.* **2021**, *413*, No. 127083.
(63) Wang, X.; Li, L.; Xie, Z.-H.; Yu, G. Duplex coating combining layered double hydroxide and 8-quinolinol layers on Mg alloy for corrosion protection. *Electrochim. Acta* **2018**, *283*, 1845−1857.

引用格式: 王晚玲,赵景茂. 桐油微胶囊的制备及其自修复性能[J]. 北京化工大学学报(自然科学版),2024,51(4):51-58.
WANG WanLing, ZHAO JingMao. Preparation of tung oil microcapsules and their self-healing properties[J]. Journal of Beijing University of Chemical Technology (Natural Science), 2024,51(4):51-58.

桐油微胶囊的制备及其自修复性能

王晚玲 赵景茂*
(北京化工大学 材料科学与工程学院,北京 100029)

摘 要: 采用吐温-20 作为乳化剂成功合成以桐油为芯材、脲醛树脂为壁材的微胶囊;研究了乳化剂的含量、乳化转速和芯壁比对微胶囊表面形貌、粒径、壁厚和芯材含量的影响。最后,将微胶囊添加至环氧涂层进行红外、热稳定性、自愈性、电化学、附着力、耐水性测试,实验结果表明涂层表现出良好的自愈性能和耐水性;同时通过电化学分析发现,在添加质量分数 10% 微胶囊的环氧涂层的损伤区域,桐油在氧气的作用下聚合形成新的保护膜,表现出良好的物理阻隔性能。

关键词: 桐油; 脲醛树脂; 微胶囊; 自修复
中图分类号: TB381 **DOI:** 10.13543/j.bhxbzr.2024.04.006

引 言

自修复涂料因其可自我修复,既可防止裂纹扩展,又可延长材料使用寿命而备受关注。其中,自修复微胶囊由于合成工艺简单、无需额外人工维护成本,在防护涂层领域具有广阔的应用前景和发展潜力。

微胶囊的自愈机制是当涂层出现裂纹时,微胶囊会因外力的作用而破裂,内部具有愈合作用的芯材会流出,填补裂缝,从而达到自修复的效果。目前微胶囊常用的愈合剂芯材有双环戊二烯(DCPD)[1]、异氰酸酯[2]、环氧树脂[3]、桐油[4]、亚麻籽油[5]等,其中桐油因无需催化剂、成本低且绿色环保,是绝佳的芯材选择之一。

在微胶囊制备过程中,乳化剂的种类的选择影响着芯材的乳化效果、乳液的分散性和稳定性,从而对微胶囊的粒径和表面形貌造成影响。这是由于在乳化过程中,乳化剂分子两端的亲油基和亲水基分别插入油相和水相,在芯材液滴表面的油水界面处吸附排布形成一层牢固的乳化膜,从而降低液滴表面自由能,可有效防止液滴聚合,得到稳定分散的乳液。在此基础上,将预聚体加入乳液中,预聚体会逐渐在芯材液滴表面沉积并发生缩聚反应,形成致密的脲醛树脂外壳,最终得到粒径均匀的微胶囊。目前文献中大多使用离子型乳化剂,如十二烷基硫酸钠(SDS)[6]、十二烷基苯磺酸钠(SDBS)[7]和非离子型乳化剂,如聚(乙烯-alt-马来酸酐)(EMA)[8]、聚乙烯醇(PVA)[9]、吐温-80[10]、OP-10[11]等。还有研究者为了提高乳液的稳定性以制备出形貌良好的微胶囊,将两种乳化剂复配进行使用[12]。

本文在使用上述乳化剂合成桐油微胶囊时,发现离子型乳化剂在高速搅拌下容易产生大量泡沫,影响微胶囊的包覆率;复配型乳化剂需要探讨两种乳化剂的含量,比较复杂。因此,本文尝试寻找一种单一的非离子型乳化剂,既能完全乳化桐油,又能形成稳定乳液。在采用目前文献中大多采用的非离子型乳化剂后,发现乳化效果不佳或乳液稳定性不好。随后尝试选用非离子型吐温-20 作为乳化剂,该乳化剂有很好的热稳定性和水解稳定性,可使桐油形成稳定的乳液,从而制备出分散性良好、粒径均匀、芯材含量较高的微胶囊。通过单频电化学阻抗测试发现,添加了微胶囊的环氧涂层在划伤后 24 h 内进行了自修复过程;同时,电化学阻抗谱也表明新膜已经形成并且具有很好的物理阻隔性。

收稿日期: 2023-09-25
基金项目: "非金属材料创新中心"创新基金(2023SFP4-1)
第一作者: 女,2000 年生,硕士生
* 通信联系人
E-mail: jingmaozhao@126.com

中国知网 https://www.cnki.net

1 实验部分

1.1 实验材料

桐油,工业级,武汉国漆涂料有限公司;尿素,分析纯,上海麦克林生化科技股份有限公司;间苯二酚,分析纯,北京迈瑞达科技有限公司;甲醛溶液(质量分数 37%),分析纯,天津市大茂化学试剂厂;环己烷、盐酸、氯化铵、三乙醇胺(TEA)、氯化钠,均为分析纯,北京市通广精细化工公司生产;吐温-20,分析纯,天津百伦斯生物科技有限公司生产;正辛醇,分析纯,天津市光复精细化工研究所生产;双酚 A 型环氧树脂(牌号:E-44)及其固化剂,工业级,深圳明德化工有限公司生产;去离子水,实验室自制。

1.2 实验仪器

OES20M 型电动搅拌器,上海秋佐科学仪器有限公司;TENSOR27 型傅里叶红外光谱仪(FT-IR),德国布鲁克公司;STA449F5 型热重分析仪(TGA),德国耐驰公司;Regulus 8230 型扫描电子显微镜(SEM),日本日立公司;Better size 2000E 型激光粒度分析仪,丹东百特仪器有限公司;JT-1600B 型光学显微镜(OM),深圳市精拓优诚科技有限公司;Interface 1000 型电化学工作站,美国 Gamry Instrument 公司;Posi Test AT-M 型附着力测试仪,美国狄夫斯高公司。

1.3 微胶囊的制备

采取原位聚合两步法,具体步骤如下。

(1)将 2.5 g 尿素全部溶于 6.4 g 甲醛溶液(质量分数 37%),滴加 TEA 控制 pH 为 8~9,在 70 ℃下搅拌反应 1 h,得到脲醛预聚体。

(2)将一定量的桐油缓慢加入到盛有吐温-20 溶液的三颈烧瓶中,在室温下机械搅拌 30 min 后,加入 1~2 滴消泡剂(正辛醇),继续加入 0.25 g 间苯二酚、0.25 g 氯化铵和脲醛预聚体,然后缓慢滴加 1 mol/L 稀盐酸调节乳液 pH 至 3~5,升温至 55~60 ℃,反应 3 h 后冷却抽滤、洗涤干燥,获得以桐油为芯材,脲醛树脂为壁材的微胶囊。

1.4 自修复涂层的制备

选用 120 mm×25 mm×0.28 mm 的马口铁作为基板,先用乙醇超声清洗,除去表面的灰尘及油脂。将不同质量分数的微胶囊(0%、5%、10%、15%)用 1.2 g 二甲苯和正丁醇混合液(二甲苯和正丁醇的质量比为 7∶3)超声分散均匀,加入 2 g E-44 环氧树脂,充分搅拌。然后加入 0.56 g 聚酰胺 651 固化剂和 0.14 g T31 固化剂,继续搅拌均匀,制备成自修复涂料。利用涂覆棒将环氧混合物涂覆在马口铁基板上,涂层厚度约为 150 μm,然后在室温下固化 3~4 d。

1.5 测试与表征

1.5.1 微胶囊化学成分

采用傅里叶红外光谱仪进行分析,波数范围在 4 000~500 cm^{-1}内。将适量干燥的微胶囊粉末和脲醛外壳与 KBr 混合,研磨压片,进行分析。将桐油直接涂在压好的 KBr 片上对芯材进行化学结构分析。

1.5.2 微胶囊热重分析

采用热重分析仪研究微胶囊的热行为,在 N_2保护下以 10 ℃/min 的升温速率从室温加热至 800 ℃。

1.5.3 微胶囊形貌、壳厚和粒径分布

采用扫描电子显微镜在 3 kV 的加速电压下分析微胶囊的表面形貌。使用激光粒度分析仪(丹东百特 2000E)测定微胶囊的平均粒径和粒径分布。

1.5.4 微胶囊芯材含量和包覆率

取干燥后一定质量的微胶囊,质量记为 m_1。充分研磨并用环己烷浸泡超声,萃取出桐油后,抽滤干燥后称量,记为 m_2,按式(1)计算出微胶囊的芯材含量 ω。

$$\omega = \frac{m_1 - m_2}{m_1} \times 100\% \tag{1}$$

桐油利用率 U,即包覆率的计算公式[13]如下。

$$U = \frac{M \times \omega}{m} \times 100\% \tag{2}$$

其中:M 为合成的微胶囊总质量,g;ω 为微胶囊的芯材含量,%;m 为所用的桐油质量,g。

1.5.5 涂层自愈测试

在完全固化后的自修复涂层表面用小刀划出交叉划痕,以验证自修复效果。利用光学显微镜(OM)观察划痕区域,并对划痕表面进行镀金处理,然后在 5 kV 加速电压下使用扫描电镜观察划痕区域。

1.5.6 电化学测试

将涂层划伤后在质量分数为 3.5% 的 NaCl 溶液中浸泡 24 h,采用美国 Gamry Instrument 公司的 Interface1000 型电化学工作站进行单频阻抗测试,测试频率为 0.1 Hz,测试时间为 24 h;分别浸泡 24 h、48 h、72 h 和 96 h 进行电化学阻抗测试(EIS),测量频率范围为 100 kHz~0.01 Hz。

中国知网 https://www.cnki.net

1.5.7　涂层附着力测试

根据 GB/T 5210—2006 进行拉脱试验，以研究微胶囊对涂层附着力的影响。用黏合剂将测试柱直接黏到涂层表面，室温下固化 48 h。利用附着力测试器，将垂直、均匀的拉力施加到涂层的胶结面上，从而确定破坏涂层和基底之间的黏合所需要的附着力。

1.5.8　涂层耐水性测试

根据 GB/T 1733—93 进行涂层耐水性测定。采用质量比为 1∶1 的石蜡和松香对底板进行封边处理，然后将试板长度的 2/3 浸于水中，浸泡 200 h，观察涂层是否出现变色、起泡、生锈等现象。

2　结果与讨论

2.1　微胶囊形貌及芯材含量的影响因素

2.1.1　乳化剂含量

如图 1、图 2 所示，当乳化剂含量(乳化剂与芯材的质量比)为 10% 时，由于乳化剂含量过低，桐油不能充分乳化，导致微胶囊表面粗糙、相互黏连、容易发生团聚，因此芯材含量和包覆率都较低; 当乳化剂含量增加到 12% 时，桐油被充分乳化，微胶囊表面更加光滑紧密，形貌变得更规则，微胶囊的芯材含量和包覆率都随之升高。但当乳化剂含量提高到 15% 后，由于乳化剂用量过多，乳液黏度增大，在搅拌时会形成大量的泡沫，致使微胶囊形貌不规则，包裹不完全，容易破裂，导致微胶囊的芯材含量和包覆率下降。

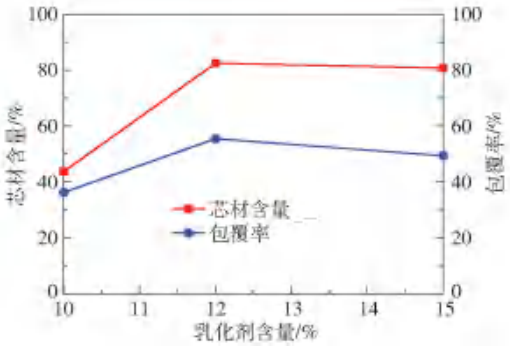

图 1　不同乳化剂含量对微胶囊芯材含量和包覆率的影响

Fig. 1　Effect of different emulsifier contents on the microcapsule core material content and coating ratio

2.1.2　乳化转速

乳化转速决定了乳液液滴的大小，微胶囊的粒径尺寸取决于乳液液滴的大小[14]。因此乳化转速的不同，将会改变微胶囊的粒径大小及分布。如

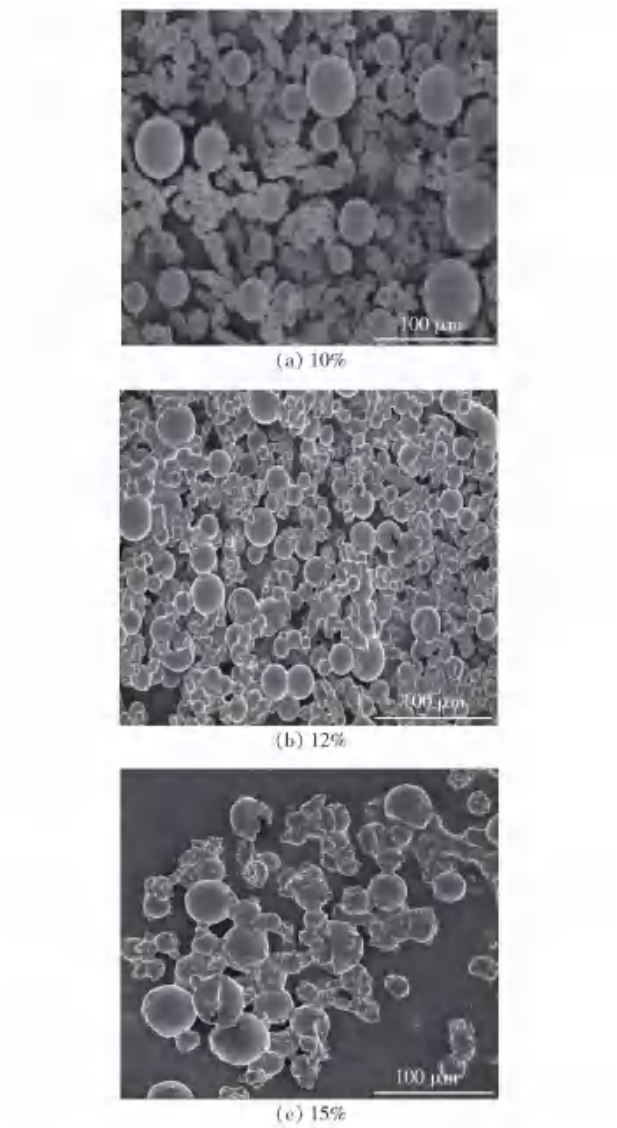

图 2　不同乳化剂含量对微胶囊表面形貌的影响

Fig. 2　Effect of different emulsifier contents on the surface topography of microcapsules

图 3 所示，由于乳液各处所受剪切力不同，在同一搅拌速度下，微胶囊的粒径呈现正态分布。随着乳化转速增大，乳液会在搅拌叶片的高速转动下被剪切成更小的液滴，导致微胶囊的粒径减小，并且分布也会更加集中。但当转速过大时，微胶囊的粒径变得更小，更容易发生团聚。另外，微胶囊的粒径大小会影响涂层的力学性能和自修复能力[15]。根据实际生产的需要，本文选择 1 200 r/min 的乳化转速，在此转速下所形成的微胶囊平均粒径为 75.56 μm，粒径大小均匀。

2.1.3　芯壁比

当体系 pH 下降时，脲醛预聚体会逐渐在乳液液滴表面沉积，随后发生聚合反应形成高分子量脲

中国知网　https://www.cnki.net

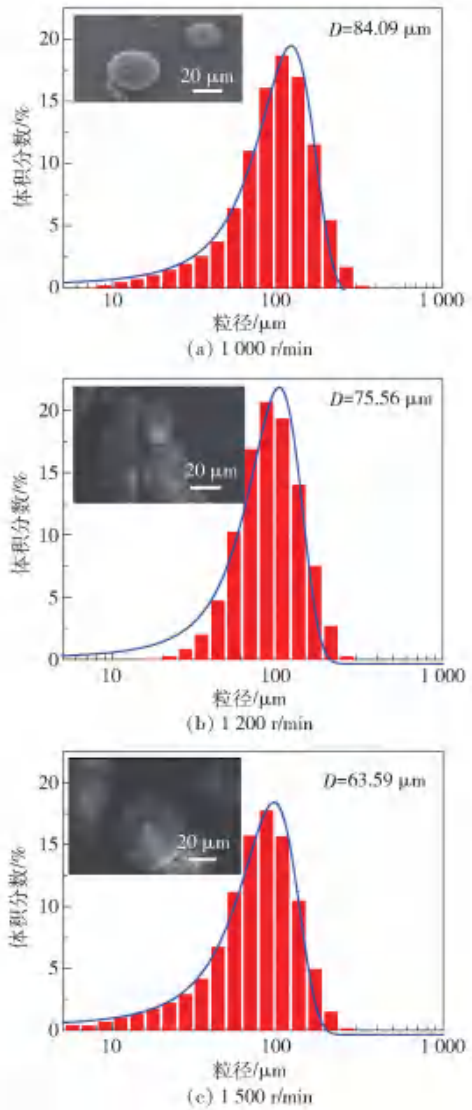

图 3　不同乳化转速对微胶囊粒径的影响

Fig. 3　Effect of different emulsification speeds on capsule size

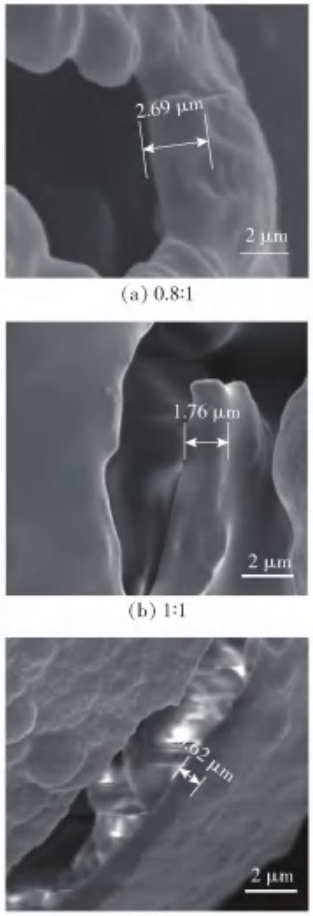

图 4　不同芯壁比对微胶囊壁厚的影响

Fig. 4　Effect of different core-to-wall ratios on the microcapsule wall thickness

醛树脂外壳。如图 4 所示,当芯壁比(芯材与壁材的质量比)为 0.8∶1 时,由于芯材桐油用量较少,多余的脲醛预聚体继续在微胶囊的表面沉积缩聚,层层包覆下使得微胶囊的壁厚增加。增大芯壁比,相当于增加桐油的用量,乳液液滴增多,脲醛预聚体的量不变,因而微胶囊的壁厚会有所减小。如果继续增大芯壁比,增大桐油的用量,则有可能使微胶囊的包覆不完全,或囊壁过薄,将导致微胶囊在实际应用中容易破裂。

同时,芯壁比也影响着微胶囊的芯材含量,芯材含量影响着涂层的自修复性能。从表 1 可知,当芯壁比增大时,壁材用量一定,芯材桐油的用量增多,微胶囊芯材含量变大,当芯壁比为 1.2∶1 时,芯材含量达 84.98%,包覆率为 72.27%,且壁厚约为 0.62 μm,结构致密,故选择 1.2∶1 的芯壁比。

表 1　不同芯壁比所制备微胶囊的芯材含量和包覆率

Table 1　Core material content and coating ratio of microcapsules prepared with different core-to-wall ratios

芯壁比	芯材含量/%	包覆率/%
1.2∶1	84.98	72.27
1∶1	69.56	46.79
0.8∶1	62.30	71.20

2.2　微胶囊的红外测试

采用红外光谱仪分别分析桐油、脲醛外壳和微胶囊的化学结构,如图 5 所示。

脲醛树脂壁材在以下位置出现特征峰:在 3 369 cm^{-1} 处的宽峰表示 O—H 和 N—H 伸缩振动,1 637 cm^{-1} 和 1 542 cm^{-1} 处分别是 C═O 和 C—N 伸缩振动峰。桐油芯材在 2 933 cm^{-1} 和 2 852 cm^{-1} 表现出 C—H 对称和反对称伸缩振动的特征峰,在

中国知网　https://www.cnki.net

1 747 cm^{-1}和 1 153 cm^{-1}处是 C═O 和 C—O 伸缩振动峰。

图 5 中的虚线区域证明，在微胶囊的红外光谱中可以检测到脲醛外壳和桐油的特征峰。实验结果表明，桐油被包封在脲醛树脂壁材中，微胶囊成功合成。

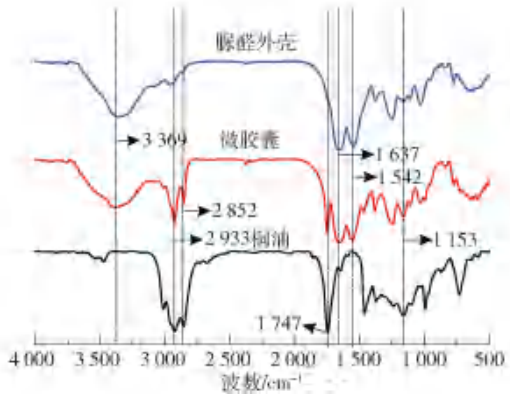

图 5　桐油、脲醛外壳和微胶囊红外光谱图

Fig. 5　FT-IR spectra of tung oil, UF and microcapsules

2.3　微胶囊热稳定性

微胶囊的热稳定性关乎微胶囊的保存和实际应用。图 6 是桐油、脲醛外壳和微胶囊的 TGA 曲线。如图 6 所示，微胶囊的热分解过程主要分为 3 个阶段：(1) 在 220 ℃左右，微胶囊开始出现质量损失，说明脲醛树脂外壳开始分解；(2) 280 ℃左右时，桐油开始分解，此时脲醛树脂已经大部分分解，曲线斜率变得稍微平缓；(3) 350 ℃左右，桐油开始大部分分解，微胶囊质量损失变大；在 480 ℃左右，桐油分解完全，曲线趋于平缓。由此可见，所制备的微胶囊热稳定性良好，可以在 220 ℃以下的温度保持稳定。

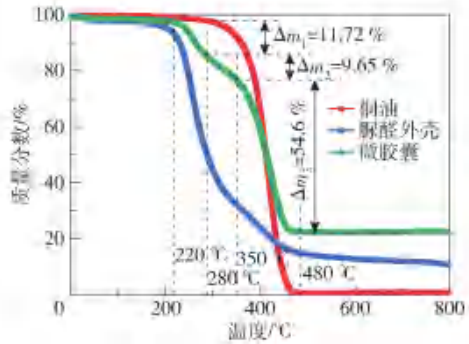

图 6　桐油、脲醛外壳和微胶囊的 TGA 曲线

Fig. 6　TGA curves of tung oil, UF shell and microcapsules

2.4　微胶囊自愈性测试

用小刀划伤涂层，划痕周围的微胶囊因受外界应力破裂，里面的桐油流出，与空气中的氧气接触，发生交联聚合反应，实现自修复。观察涂层光学显微镜照片(图 7)，可以看出，对比纯环氧涂层，含微胶囊的自修复涂层在划伤后立即有桐油流出，填补裂纹，划痕明显变浅。

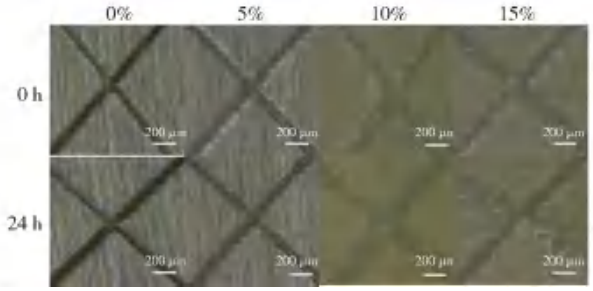

图 7　不同含量微胶囊的环氧涂层光学显微镜图

Fig. 7　OM diagram of epoxy coating of microcapsules with different contents

进一步通过 SEM 观察，如图 8 所示纯环氧涂层存在无法愈合的划痕，而含微胶囊质量分数为 5%、10%、15% 的自修复涂层随着微胶囊含量的逐渐增加，自修复效果会越好。当微胶囊添加质量分数为 5% 时，新形成的膜层无法完整填充划痕区域，当微胶囊添加质量分数达到 10% 和 15% 时，有充足的桐油被释放，填补划痕，在氧气作用下发生聚合反应，在损伤区域形成新的保护膜。

2.5　电化学测试

为了进一步评估涂层的自愈效果，将纯环氧涂层和添加 10% 微胶囊的环氧涂层划伤后浸泡在 3.5 wt% NaCl 溶液中，分别使用单频电化学阻抗和电化学阻抗进行了测试。图 9 是两种涂层在浸泡期间的单频阻抗图，可以看出，与不添加微胶囊的纯环氧涂层相比，添加微胶囊的自修复环氧涂层的阻抗值在 5 h 内有着明显的上升趋势。原因在于涂层中的微胶囊破裂，芯材桐油流出，在裂缝处形成新的保护膜，对涂层提供额外保护，阻止了溶液往基体的渗透。但由于修复尚未完成，仍有部分电解液渗入涂层内部，对涂层产生破坏。因此，涂层阻抗值在达到一定峰值后开始下降，在此过程中，芯材仍在不断流出，继续修复涂层，故接下来涂层阻抗值又表现出明显上升趋势；此外，电化学阻抗谱(图 10) 也反映了添加微胶囊的涂层的自修复性能。纯环氧涂层的阻抗值下降趋势明显，说明电解液渗入内部，基底开始腐蚀，而添加含微胶囊质量分数为 10% 的涂层阻抗值下降缓慢，经过 24 h 后阻抗值有一定的上升，这是由于在损伤区域形成了新的保护膜，表现出良好的物理阻隔性。

中国知网　https://www.cnki.net

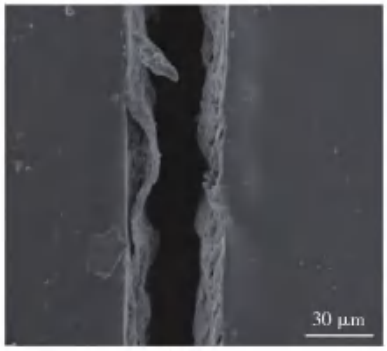

(a) 0%

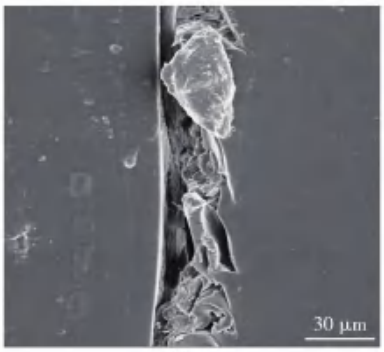

(b) 5%

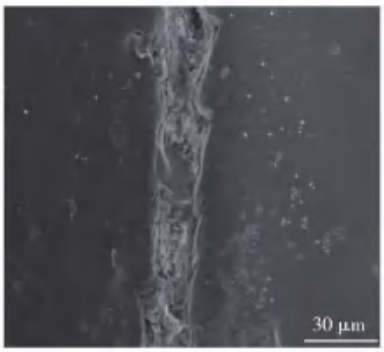

(c) 10%

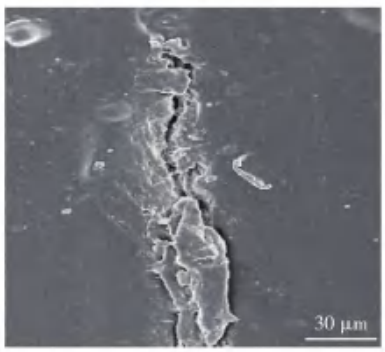

(d) 15%

图 8　不同含量微胶囊的环氧涂层划伤 24 h 后的 SEM 图

Fig. 8　SEM micrographs of epoxy coatings with different contents of microcapsules after scratching for 24 h

2.6　微胶囊附着力测试

附着力是影响涂层使用寿命的重要因素。理论上,微胶囊的加入会降低涂层的附着强度,因为脲醛

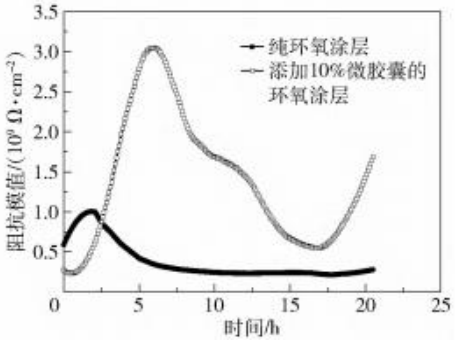

图 9　纯环氧涂层和添加质量分数为 10% 微胶囊的环氧涂层划伤样品的单频阻抗图

Fig. 9　Single frequency impedance diagrams of scratched EP coating with and without 10 wt% microcapsules

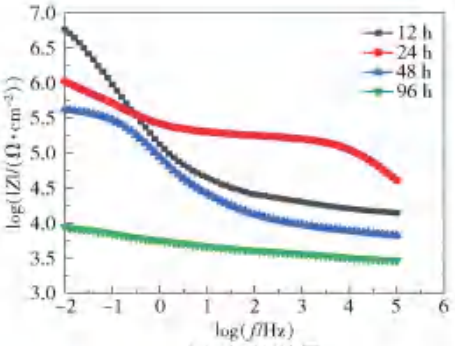

(a) 纯环氧涂层

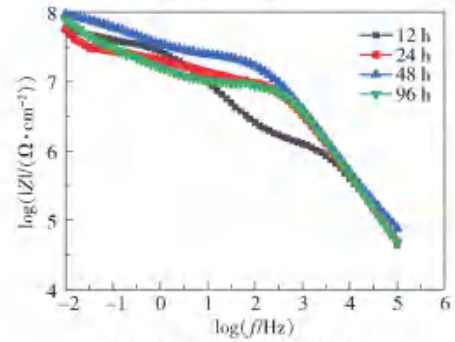

(b) 添加10%微胶囊的环氧涂层

图 10　纯环氧涂层和添加质量分数为 10% 微胶囊的环氧涂层划伤样品的 EIS 图

Fig. 10　EIS of scratched EP coatings samples with and without 10 wt% microcapsules

树脂与环氧树脂基体之间的黏结性不好,将脲醛树脂微胶囊加入环氧树脂涂层中会影响涂层的力学性能[16]。如图 11 所示,随着微胶囊含量的增加,涂层附着力会逐渐减小。当微胶囊添加量质量分数为 10% 时,涂层附着力从 5.86 MPa 降低到 4.36 MPa,而当添加量增加到质量分数为 15% 时,附着力下降到了 3.38 MPa。相比之下,添加质量分数为 10% 的微胶囊对涂层的粘合强度的影响较小,因此在保证涂

中国知网　https://www.cnki.net

层具有良好自愈性能的前提下，又要避免涂层的粘合强度大大降低，故最终选择添加质量分数为 10% 的微胶囊。

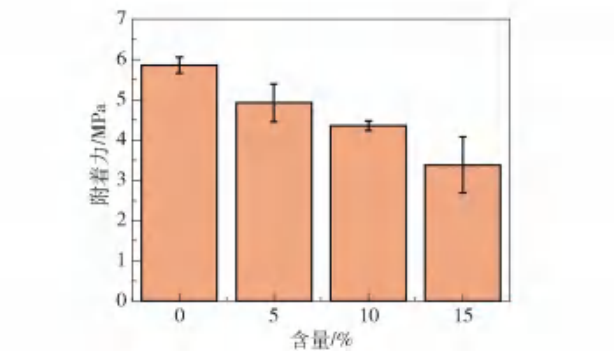

图 11　不同含量微胶囊对涂层附着力的影响

Fig. 11　Effect of different contents of microcapsules on coating adhesion

2.7　微胶囊涂层耐水性测试

由于外界因素的影响，涂层耐水性是材料在一些特定应用场合中的必要性能，如建筑材料、地下管道等。从图 12 可知，在常温耐水性试验检测后，将涂层浸泡 200 h 发现，涂层并未出现起泡、脱落、生锈等现象，表明涂层耐水性良好，且加入不同含量的微胶囊对环氧涂层的耐水性无明显影响。

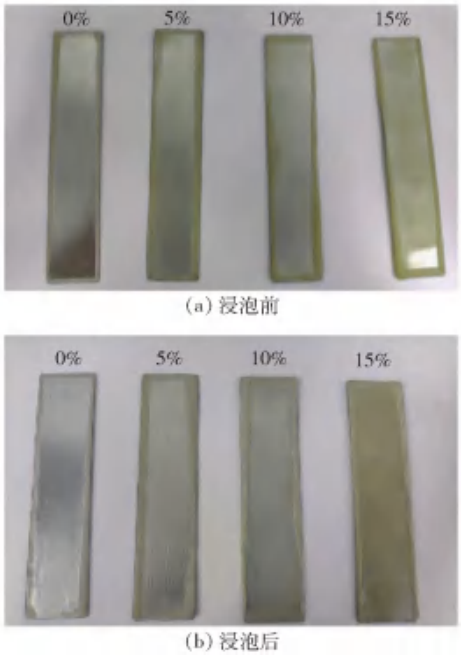

图 12　环氧涂层耐水性

Fig. 12　Water resistance of epoxy coatings

3　结论

利用原位聚合两步法，成功合成桐油微胶囊，通过探究不同的实验条件对微胶囊的影响得出最佳反应条件，即当乳化剂含量为 12%、乳化转速为 1 200 r/min、芯壁比为 1.2∶1时，可制备出粒径均匀，形貌良好的微胶囊。通过 FT-IR 和 TGA 测试表明微胶囊成功合成，并具有良好的热稳定性。将不同含量的微胶囊加入环氧涂层，通过光学显微镜和扫描电子显微镜观察探究加入不同含量微胶囊对涂层自修复性能的影响，发现加入质量分数为 10% 和质量分数为 15% 的微胶囊的涂层在 24 h 内修复效果较好，表现出良好的自愈性能。综合附着力和自愈性两种因素，最终确定添加质量分数为 10% 的微胶囊，并且进一步进行单频电化学阻抗和电化学阻抗测试，结果表明添加微胶囊的环氧涂层有着较好的自修复性能，对涂层可起一定的保护作用。

参考文献：

[1]　李海燕，王晴，崔业翔. 聚砜包覆双环戊二烯微胶囊的制备 [J]. 中国塑料，2015，29(9)：27-31.
LI H Y，WANG Q，CUI Y X. Preparation of polysulfone-coated dicyclopentadiene microcapsules [J]. China Plastics，2015，29(9)：27-31. (in Chinese)

[2]　王继永，李伟，郑春扬，等. 异氰酸酯自修复微胶囊水泥基材料的制备与性能研究 [J]. 新型建筑材料，2023，50(5)：61-67.
WANG J Y，LI W，ZHENG C Y，et al. Preparation and properties of cementitious materials of isocyanate self-healing microcapsules [J]. New Building Materials，2023，50(5)：61-67. (in Chinese)

[3]　YAO J L，YANG C P，ZHU C F，et al. Preparation process of epoxy resin microcapsules for self-healing coatings [J]. Progress in Organic Coatings，2019，132：440-444.

[4]　LI H Y，CUI Y X，LI Z K，et al. Fabrication of microcapsules containing dual-functional tung oil and properties suitable for self-healing and self-lubricating coatings [J]. Progress in Organic Coatings，2018，115：164-171.

[5]　ÇÖMLEKÇI G K，ULUTAN S. Acquired self-healing ability of an epoxy coating through microcapsules having linseed oil and its alkyd [J]. Progress in Organic Coatings，2019，129：292-299.

[6]　汪婷，王鸿博，傅佳佳，等. MUF/十八烷相变微胶囊的制备与性能研究 [J]. 化工新型材料，2020，48(6)：211-215.
WANG T，WANG H B，FU J J，et al. Preparation and properties of MUF/octadecane phase change microcapsules [J]. New Chemical Materials，2020，48(6)：

中国知网　https://www.cnki.net

211 – 215. (in Chinese)

[7] 闫小星，彭文文. 脲醛树脂包覆水性涂料微胶囊的制备及对木器裂纹涂层性能的影响[J]. 林产工业，2020，57(8)：47 – 52.
YAN X X, PENG W W. Preparation of urea-formaldehyde resin coated waterborne coating microcapsules and its effect on the performance of wood crack coating [J]. Forest Products Industry, 2020, 57(8): 47 – 52. (in Chinese)

[8] NETO A G C, PELLANDA A C, JORGE A R, et al. Preparation and evaluation of corrosion resistance of a self-healing alkyd coating based on microcapsules containing tung oil [J]. Progress in Organic Coatings, 2020, 147: 105874.

[9] LI J Y, SHI H W, LIU F C, et al. Self-healing epoxy coating based on tung oil-containing microcapsules for corrosion protection [J]. Progress in Organic Coatings, 2021, 156: 106236.

[10] PAN P, YAN X X, PENG W W. Tung oil microcapsules prepared with different emulsifiers and their effects on the properties of coating film [J]. Coatings, 2022, 12(8): 1166.

[11] 赵鹏. 乳化剂对一步原位聚合法制备自修复微胶囊的影响[J]. 广东化工，2013，40(18)：3 – 4.
ZHAO P. Effect of emulsifier on the preparation of self-healing microcapsules by one-step in situ polymerization [J]. Guangdong Chemical Industry, 2013, 40(18): 3 – 4. (in Chinese)

[12] MA Y X, JIANG D, YANG Y P, et al. The effect of complex emulsifier on the structure of tung oil and phenolic amides containing microcapsules and its anti-fouling and anti-corrosion performances [J]. Coatings, 2022, 12(4): 447.

[13] LI M Z, CAO B, SHANG R Q, et al. Synthesis of poly (urea-formaldehyde) microcapsules for the self-healing system of silicone rubber insulating material [J]. Journal of Applied Polymer Science, 2022, 139(45): e53021.

[14] SAFAEI F, KHORASANI S N, RAHNAMA H, et al. Single microcapsules containing epoxy healing agent used for development in the fabrication of cost efficient self-healing epoxy coating [J]. Progress in Organic Coatings, 2018, 114: 40 – 46.

[15] JIANG Y H, YAO J L, ZHU C F. Improving the dispersibility of poly (urea-formaldehyde) microcapsules for self-healing coatings using preparation process [J]. Journal of Renewable Materials, 2022, 10(1): 135.

[16] 倪卓，林煜豪，郭震，等. 自修复环氧树脂微胶囊合成及其反应机理[J]. 深圳大学学报(理工版)，2019，36(3)：339 – 346.
NI Z, LIN Y H, GUO Z, et al. Synthesis of microcapsules of self-healing epoxy resin and its reaction mechanism [J]. Journal of Shenzhen University (Science and Engineering Edition), 2019, 36(3): 339 – 346. (in Chinese)

Preparation of tung oil microcapsules and their self-healing properties

WANG WanLing ZHAO JingMao*

(College of Materials Science and Engineering, Beijing University of Chemical Technology, Beijing 100029, China)

Abstract: With the continuous development of self-healing intelligent functional materials, microencapsulated self-healing materials have received increasing attention in many fields. In this study, Tween-20 was used as an emulsifier to successfully synthesize microcapsules with tung oil as the core material and urea-formaldehyde resin as the wall material, and the effects of varying the emulsifier content, emulsification speed and core-to-wall ratio on the surface morphology, particle size, wall thickness and core content of the microcapsules were studied. Finally, the microcapsules were added to the epoxy coatings. The resulting coatings showed good self-healing properties and water resistance. Electrochemical analysis showed that the tung oil polymerized under the action of oxygen to form a new protective film in the damaged area of the epoxy coating with 10 wt. % microcapsules, resulting in good physical barrier properties.

Key words: tung oil; urea-formaldehyde resin; microcapsules; self-healing

(责任编辑：李 蕾)

中国知网 https://www.cnki.net

引用格式:张竞帆,张胜,赵景茂. 氧化石墨烯/次磷酸铝杂化物的制备及其对PC/ABS合金阻燃性能的改善[J]. 北京化工大学学报(自然科学版),2024,51(5):46-53.

ZHANG JingFan, ZHANG Sheng, ZHAO JingMao. Preparation of graphene oxide/aluminum hypophosphite hybrids and improved flame retardancy of polycarbonate (PC)/acrylonitrile butadiene styrene (ABS) blends[J]. Journal of Beijing University of Chemical Technology (Natural Science),2024,51(5):46-53.

氧化石墨烯/次磷酸铝杂化物的制备及其对PC/ABS合金阻燃性能的改善

张竞帆 张 胜 赵景茂*

(北京化工大学 材料科学与工程学院,北京 100029)

摘 要: 聚碳酸酯(PC)/丙烯腈-丁二烯-苯乙烯(ABS)合金作为用量最大的塑料合金之一,在使用过程中其易燃性对人民的生命财产安全造成了严重的威胁,因此对其进行阻燃改性十分必要。通过自组装方法,制备了聚乙烯亚胺(PEI)接枝氧化石墨烯纳米片(PEI-GO)来修饰次磷酸铝(AHP)。制备的PEI-GO@AHP杂化物,作为PC/ABS(质量比为70/30)合金的阻燃剂。引入质量分数为8%的PEI-GO@AHP,可确保PC/ABS达到UL-94 V-0等级和29.1%的极限氧指数(*LOI*)。其最大热释放速率(*PHRR*)和总热释放量(*THR*)分别降低了41.0%和19.6%。本研究提供了一种简单而有效的方法来制备阻燃PC/ABS合金。

关键词: 阻燃; 聚碳酸酯(PC)/丙烯腈-丁二烯-苯乙烯(ABS)合金; 次磷酸铝(AHP)

中图分类号: TB381 **DOI:** 10.13543/j.bhxbzr.2024.05.006

引 言

聚碳酸酯(PC)是一种高性能的工程塑料,具有高强度、高韧性和尺寸稳定性等优点。然而,其加工温度高、抗应力开裂能力不足以及对湿度的敏感一直限制着它的实际应用[1]。丙烯腈-丁二烯-苯乙烯(ABS)是一种三元共聚物,具有出色的光泽度、韧性和电绝缘性[2]。PC/ABS合金具有较高的冲击强度、抗应力开裂性能和耐候性,广泛应用于电子产品、汽车工业和建筑材料等领域[3]。

PC的极限氧指数(*LOI*)为25%,在垂直燃烧测试中达到了UL-94 V-2等级,但是仍需要对其进行阻燃改性,以减少燃烧中的烟气释放和抑制熔滴。ABS的阻燃性较差,其*LOI*仅为18%,无法通过UL-94垂直燃烧测试[4],并且ABS在燃烧时会释放大量致命的烟雾和毒气。因此有必要对PC/ABS合金进行阻燃改性,以提高其火安全性能[5]。

溴系阻燃剂(FRs)[6]是PC/ABS合金中的常用阻燃剂,但由于卤素具有生物累积性和毒性已经逐渐被禁用。聚磷酸铵(APP)和次磷酸铝(AHP)等磷系阻燃剂[7]已成为其替代品。Soo-Tueen等[8]发现,添加聚磷酸铵25%(质量分数,下同)和蒙脱土6%后,PC/ABS(质量比50/50)合金的*LOI*达到了31.5%。Wu等[9]研究发现,15%的AHP使PC/ABS(质量比50/50)达到了UL-94 V-0级,*LOI*为26.0%。但是APP和AHP与PC/ABS基体的相容性较差,在基体中分散不均匀,会降低自身的阻燃效率。

氧化石墨烯(GO)[10]是一种具有高比表面积的二维纳米片。在引入有机官能团如$-NH_2$、-OH和环氧基团后,GO纳米片与聚合物相容性提高,能够实现在聚合物基体中的均匀分散[11]。通过此方法能够显著改善聚合物/GO复合材料的阻燃性能。此外,研究还发现,在阻燃方面GO纳米片[12]能够起到物理屏障的作用,提高炭层的致密程度和连续性,从而隔绝燃烧过程中所产生的热

收稿日期:2023-11-06

基金项目:"非金属材料创新中心"创新基金(2023SFP4-1)

第一作者:男,1997年生,博士生

*通信联系人

E-mail:jingmaozhao@126.com

量和氧气的交换。

在本研究中,聚乙烯亚胺(PEI)通过表面接枝的方法被引入到GO纳米片上。通过静电自组装,得到PEI-GO@AHP杂化物。PEI-GO@AHP被用于PC/ABS(70/30)合金中。本文详细研究了PEI-GO@AHP杂化物对PC/ABS合金的阻燃性能的影响。

1　实验部分

1.1　主要原料

聚碳酸酯(PC, 2505,熔融指数为15)由Markrolon公司提供。丙烯腈-丁二烯-苯乙烯(ABS, 0215A)购自吉林石化股份有限公司。氧化石墨烯水溶液(GO, 2 mg/mL)由中国科学院煤炭化学研究所提供。次磷酸铝(AHP, ≥98%)、聚乙烯亚胺(PEI, ≥99%)、1-乙基-3-(3-二甲基氨基丙基)碳二亚胺盐酸盐(EDC-HCl, ≥98.5%)和N-羟基琥珀酰亚胺(NHS, ≥98%)均购自上海麦克林生化科技有限公司。

1.2　阻燃PC/ABS合金的制备

1.2.1　聚乙烯亚胺(PEI)接枝GO

首先,将250 mL PEI水溶液(10 mg/mL)和300 mL 1-乙基-3-(3-二甲基氨基丙基)碳二亚胺盐酸盐(EDC-HCl)/N-羟基琥珀酰亚胺(NHS)水溶液(12 mg/mL, EDC与NHS质量比为1/5)在烧杯中混合,然后在30 min内将300 mL GO分散液(1 mg/mL)滴加到上述溶液中,然后将混合物在室温下搅拌24 h。最后,通过透析法除去未反应的PEI。

1.2.2　PEI-GO@AHP杂化物的制备

如图1所示,将100 mL PEI-GO分散液(约0.4 mg/mL)加入到50 mL的AHP的水分散液(0.08 g/mL)中,剧烈搅拌15 min。然后过滤沉淀物,将上述沉淀物冷冻干燥24 h,最后在研磨后得到约2.5 g灰色粉末,产率约为62.5%。

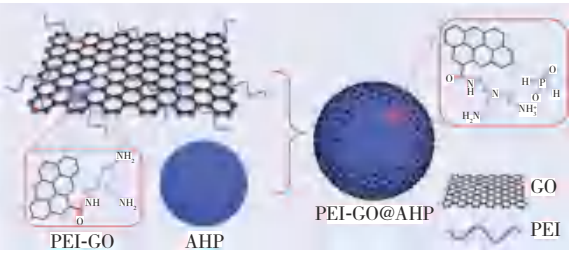

图1　PEI-GO@AHP的制备示意图

Fig. 1　The preparation route of PEI-GO@AHP

1.2.3　阻燃PC/ABS合金的熔融加工

首先,将所有原料(PC、ABS、AHP和PEI-GO@AHP)在80 ℃下干燥12 h,然后使用转矩流变仪(RM-200C,中国哈普电气技术有限公司),在220 ℃下熔融共混制备阻燃PC/ABS合金。其中,PC与ABS的质量比为7/3。制备了含有不同质量分数AHP和PEI-GO@AHP的PC/ABS复合材料,分别命名为PC/ABS/xAHP和PC/ABS/xPEI-GO@AHP(其中,x代表AHP或PEI-GO@AHP质量分数)。

1.3　测试与表征

1.3.1　AHP与PEI-GO@AHP形貌以及化学成分表征

采用德国蔡司公司的GeminiSEM 300型扫描电子显微镜(SEM)对PEI-GO@AHP杂化物的表面形貌以及锥形量热测试后材料的残炭形貌进行表征,加速电压为100 kV,测试前样品表面喷金。

采用德国蔡司公司的GeminiSEM 300型X射线能谱分析仪(EDS)检测PEI-GO@AHP的相对元素百分比,加速电压为100 kV,测试前样品表面喷金。

1.3.2　热稳定性测试

采用美国TA公司的Q50热重分析仪(TGA)在N_2氛围中对阻燃PC/ABS的热稳定性进行分析,测试温度为25~800 ℃,升温速率为10 ℃/min。

1.3.3　阻燃性能测试

根据ASTM D2863标准,采用德国Netzsch Taurus仪器公司的LOI 901极限氧指数(*LOI*)测试仪对阻燃PC/ABS合金的*LOI*值进行了测量。样品尺寸为130 mm×6.5 mm×3.2 mm,所有样品进行5次测试,结果取算术平均值。

根据ASTM D3801—2010标准,采用中国江宁分析仪器有限公司的CZF-3垂直燃烧仪对阻燃PC/ABS进行了垂直燃烧测试(UL-94)。样品尺寸为130 mm×13 mm×3.2 mm,所有样品进行5次测试,结果取算术平均值。

根据ASTM E1354标准,采用英国Fire Testing Technology公司的FTT0007锥形量热仪对阻燃PC/ABS进行了锥形量热测试。样品尺寸为100 mm×100 mm×3.0 mm。每个样品都用铝箔包裹,水平暴露在50 kW/m^{2}的外部热通量下,所有样品进行5次测试,结果取算术平均值。

采用美国霍尼韦尔的BW MCXL-4有毒气体检测仪检测阻燃PC/ABS在密闭空间(30 cm×30 cm×45.0 cm)燃烧过程中的磷化氢(PH_3)浓度。

2　结果与讨论

2.1　AHP 和 PEI-GO@AHP 杂化物的形貌

通过扫描电镜观察 AHP 和 PEI-GO@AHP 的表面形貌,并用 EDS 记录了元素图谱。结果如图 2 所示。从图 2(a)和 2(b)中可以看出,AHP 粉末为白色,PEI-GO@AHP 为棕色粉末。单个 AHP 粒子的直径约为 5 μm,表面粗糙。引入 PEI-GO 杂化后,颗粒直径无变化,但表面变得光滑,呈现出鳞片状。此外,根据图 2(c)和 2(d)中的 EDS 结果,AHP 和 PEI-GO@AHP 颗粒表面的相对元素百分比不同。AHP 中的 P、Al 和 C 元素的质量分数为 57.8%、17.2% 和 25.0%,而 PEI-GO@AHP 中的 P、Al 和 C 元素的质量分数分别为 25.0%、7.1% 和 67.9%,这表明 PEI-GO@AHP 杂化物的成功制备。

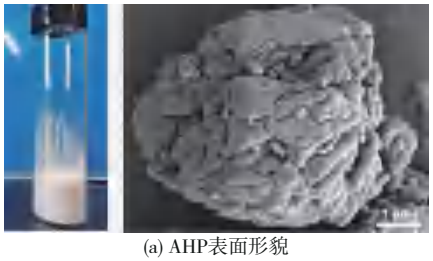

(a) AHP表面形貌

(b) PEI-GO@AHP杂化物表面形貌

元素	质量分数/%
P	57.8
Al	17.2
C	25.0

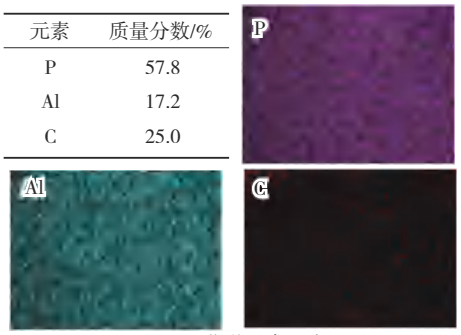

(c) AHP化学元素组成

元素	质量分数/%
P	25.0
Al	7.1
C	67.9

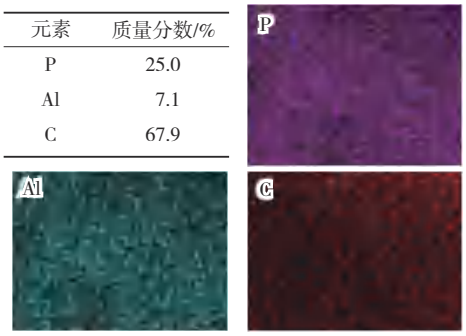

(d) PEI-GO@AHP杂化物化学元素组成

图 2　AHP 和 PEI-GO@AHP 杂化物的表面形貌和化学元素组成

Fig. 2　The morphology and elemental content of AHP and PEI-GO@AHP

2.2　PEI-GO@AHP 在基体中的分散

一般来说,阻燃剂与聚合物基体之间的相容性差,会导致阻燃剂在基体中分散不均匀,从而降低其阻燃效率[13]。

图 3 展示了 PC/ABS 中 AHP 和 PEI-GO@AHP 分布形式。如图 3 所示,可以发现 AHP 的聚集现象,但这种现象在 PC/ABS/PEI-GO@AHP 中很少见。此外,在断面处还发现 AHP 与基体之间存在明显的裂缝。而 PEI-GO@AHP 则嵌入了基体中,在阻燃剂和基体的界面上没有发现明显的裂缝或间隙,这表明 PC/ABS 与 PEI-GO@AHP 之间的相容性得到了改善[14]。

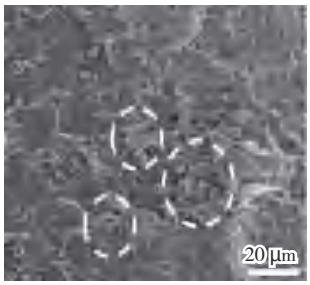

(a) PC/ABS/AHP复合材料断面

(b) AHP材料断面

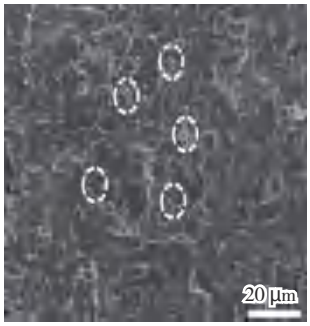

(c) PC/ABS/PEI-GO@AHP 复合材料断面

(d) PEI-GO@AHP复合材料断面

图 3　阻燃 PC/ABS 复合材料的断面 SEM 图像

Fig. 3　SEM images of the fracture surfaces for flame-retardant PC/ABS composites

2.3　热稳定性

通过 TGA 评估了 PC/ABS 及其阻燃复合材料在氮气环境下的热稳定性,结果如图 4 和表 1 所示。PC/ABS 的降解过程分为两个阶段,第一阶段是 ABS 的分

解,第二阶段是PC的分解。PC/ABS的初始分解温度($T_{5\%}$)为427.3 ℃,残炭量(Residue)为15.2%。添加AHP后,PC/ABS/8AHP的$T_{5\%}$降低,残炭量增至18.0%。当用PEI-GO@AHP代替AHP后,PC/ABS/8PEI-GO@AHP的$T_{5\%}$变得更低,残炭量略微增加到18.4%。这一现象是由于AHP和PEI-GO@AHP的初始分解温度较PC/ABS低。AHP和PEI-GO@AHP的$T_{5\%}$分别为346.5 ℃和324.1 ℃。PC/ABS/8PEI-GO@AHP的第一段最大分解速率对应温度(T_{max1})低于PC/ABS/8AHP,但PC/ABS/8GO@AHP的第二段最大分解速率对应温度(T_{max2})高于PC/ABS/8AHP,且PC/ABS/8PEI-GO@AHP的最大分解速率(DTG_{max})最低,这表明PEI-GO的参与能有效抑制基体的分解[15]。

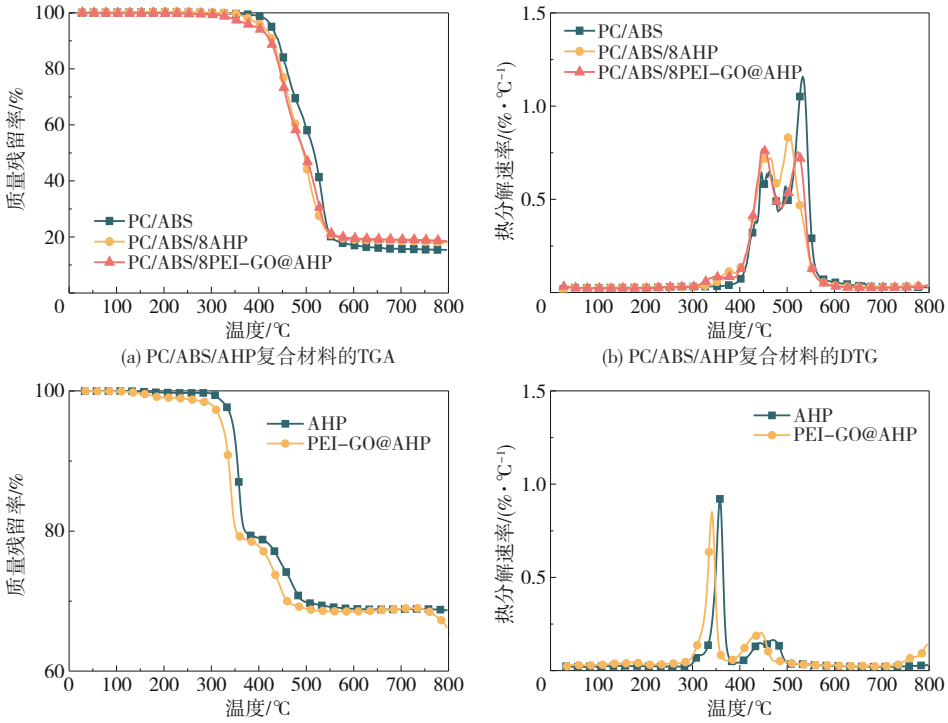

(a) PC/ABS/AHP复合材料的TGA　(b) PC/ABS/AHP复合材料的DTG

(c) AHP和PEI-GO@AHP的TGA　(d) AHP和PEI-GO@AHP的DTG

图4　PC/ABS合金、AHP和PEI-GO@AHP在氮气氛围下的热稳定性

Fig. 4　The thermal stability in a N_2 atmosphere of PC/ABS blends, AHP and PEI-GO@AHP

表1　PC/ABS复合材料的TGA和DTG主要数据

Table 1　Key data for TGA and DTG of PC/ABS, AHP and PEI-GO@AHP

样品	$T_{5\%}$/℃	T_{max1}/℃	T_{max2}/℃	DTG_{max}/(%/℃)	Residue/%
PC/ABS	427.3	462.4	533.1	1.13	15.2
PC/ABS/8AHP	410.5	454.5	504.2	0.81	18.0
PC/ABS/8PEI-GO@AHP	392.1	447.2	523.4	0.73	18.4
AHP	346.5	357.9	468.8	0.91	68.8
PEI-GO@AHP	324.1	341.5	431.8	0.79	66.3

2.4　阻燃性能

通过UL-94和LOI测试评估了PC/ABS合金的阻燃性,见表2。PC/ABS的*LOI*为23.7%,在垂直燃烧测试中完全烧毁,因此该样品未达到任何UL-94等级。加入质量分数为6 %的AHP后,PC/ABS合金的*LOI*达到了26.5%,样品通过了UL-94 V-1等级。当AHP的添加量增加到质量分数8 %时,*LOI*达到了28.6%,并通过了UL-94 V-0等级。PC/ABS/8PEI-GO@AHP也能在4 s内自熄且能通过UL-94

表2　阻燃PC/ABS合金的UL-94和*LOI*数据

Table 2　The data of UL-94 and *LOI* for the flame-retardant PC/ABS composites

样品	*LOI*/%	UL-94			
		第一次点燃自熄时间/s	第二次点燃自熄时间/s	熔滴	等级
PC/ABS	23.7	>30	–	NO	NR
PC/ABS/6AHP	26.5	3.2	14.2	NO	V1
PC/ABS/7AHP	26.7	2.0	12.1	NO	V1
PC/ABS/8AHP	28.6	1.2	3.8	NO	V0
PC/ABS/8PEI-GO@AHP	29.1	1.0	3.9	NO	V0

V-0等级,*LOI*略微提高到29.1%。

锥形量热仪是一种根据耗氧量评估材料燃烧行为的仪器。从图5和表3可以看出通过锥形量热仪评估的PC/ABS合金的阻燃和抑烟性能的相关数据。如图5(a)和5(b)所示,由于ABS本身的易燃性,PC/ABS合金的热释放速率峰值(*PHRR*)为598.8 kW/m^2,总热释放量(*THR*)为121.2 MJ/m^2。引入AHP后,由于磷酸催化基体提前分解的作用,所有含有AHP试样的点燃时间(*TTI*)均低于PC/ABS。PC/ABS/8AHP的*PHRR*和*THR*分别降低了43.8%和14.9%。PC/ABS/8PEI-GO@AHP的*PHRR*和*THR*分别降低了41.0%和19.6%。

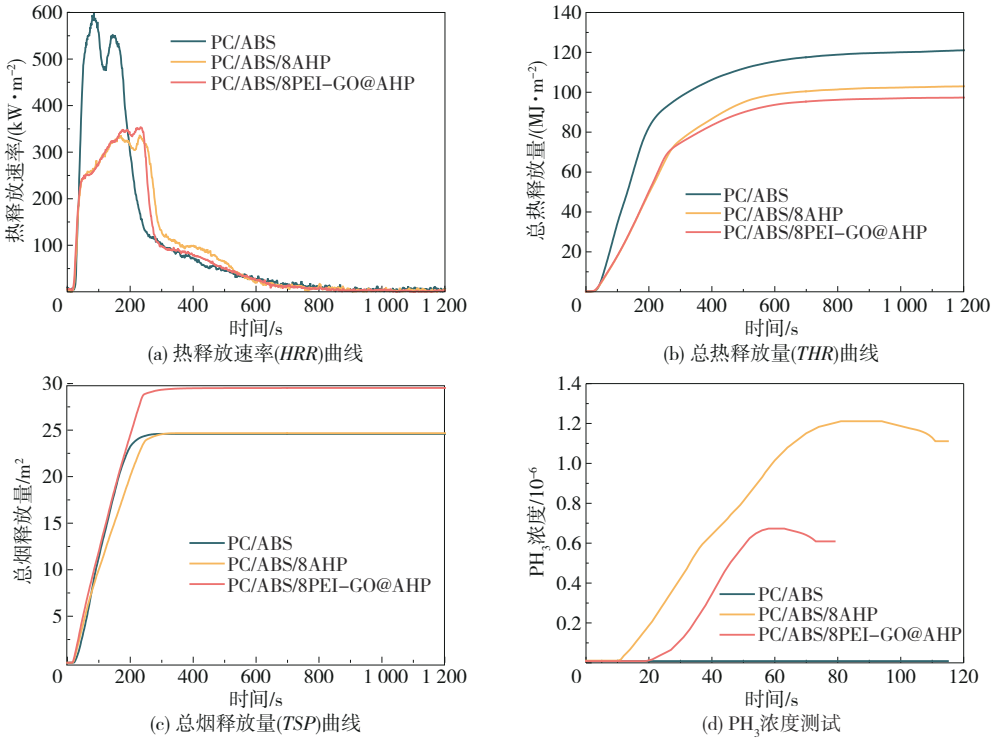

图5　阻燃PC/ABS合金锥形量热测试结果

Fig. 5　Results for the CCT for PC/ABS blends

引入了基于锥形量热测试(CCT)数据的通用无量纲标准*FRI*(阻燃指数),用于评估真实火灾情况下的逃生时间。

$$FRI = \frac{\left[THR \times \left(\frac{PHRR}{TTI}\right)\right]_{\text{PC/ABS}}}{\left[THR \times \left(\frac{PHRR}{TTI}\right)\right]_{\text{Flame - retardant PC/ABS}}} \tag{1}$$

*FRI*由公式(1)计算得出,表3列出了相应的数据。加入8% AHP后,PC/ABS/8AHP的*FRI*上升到4.2,使用8% PEI-GO@AHP后,*FRI*进一步上升到5.7,表明加入PEI-GO后阻燃性增强。然而,由于PEI-GO的阻隔效应导致PC/ABS基体燃烧不完全,总烟释放量(*TSP*)有所增加[16]。

AHP是一种高效磷系阻燃剂,但在热分解过程中会释放出磷化氢(PH_3),这是一种高毒性气体。根据相关规定,在一般工作条件下,PH_3的最大浓度

表3　PC/ABS复合材料的锥形量热测试的关键数据

Table 3　Key data for PC/ABS composites from CCT

物理量	PC/ABS	PC/ABS/8AHP	PC/ABS/8PEI-GO@AHP
TTI/s	21±0.5	16±1.0	16±1.1
PHRR/(kW·m^{-2})	598.8±8.5	336.0±10.9	353.7±9.7
THR/(MJ·m^{-2})	121.2±2.2	103.0±3.2	97.3±1.8
FRI	1.0	4.2	5.7
TSP/m^2	24.6±0.6	24.7±0.7	29.5±0.8
Residue/%	0.23±0.18	3.85±0.05	5.08±0.10

在0.31×10^{-6} g/L以内,当人暴露在1.0×10^{-6} g/L的浓度下10 min,就会致命[17]。因此,有必要关注AHP的PH_3释放量。如图5(d)所示,在PC/ABS合金燃烧过程中进行了自制PH_3检测实验,以检测密闭空间中的PH_3浓度。在点燃前,PC/ABS/8AHP检测到的PH_3浓度较低,随后浓度迅速上升到约1.2×10^{-6} g/L的峰值。然而,对于PC/ABS/8PEI-GO@AHP,点燃

前未检测到PH_3,加热20 s后PH_3浓度开始增加,但增加速度和最大浓度均低于PC/ABS/8AHP,PH_3最大浓度仅为0.6×10^{-6} g/L,这表明PEI-GO具有抑制PH_3释放的能力[18]。

2.5　阻燃机理分析

为了进一步研究PEI-GO对阻燃性能和PH_3释放的影响,通过SEM和EDS分析,观察了残炭的形貌和元素分布。如图6所示,PC/ABS被完全烧毁,只剩下0.23%的残炭。添加8.0%的AHP后,PC/ABS/8AHP的残炭增加到3.85%,但炭层看起来破碎多孔,膨胀高度为7.1 cm。而PC/ABS/8PEI-GO@AHP的炭层紧密且连续,残炭量为5.08%,膨胀高度最高,为9.2 cm。由EDS显示的结果可知,PC/ABS/8AHP和PC/ABS/8PEI-GO@AHP炭层的元素组成存在一定差异。PC/ABS/8PEI-GO@AHP中P元素的质量分数从PC/ABS/8AHP的22.4%增加到29.1%,这意味着有更多的P元素残留在凝聚相,促进了成炭。

(a) PC/ABS残炭形貌数码照片

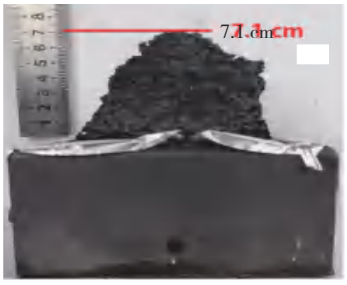

(b) PC/ABS/AHP残炭形貌数码照片

(c) PC/ABS/PEI-GO@AHP残炭形貌数码照片

(d) PC/ABS/AHP残炭形貌SEM图像

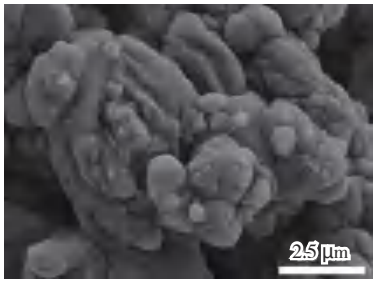

(e) PC/ABS/PEI-GO@AHP残炭形貌SEM图像

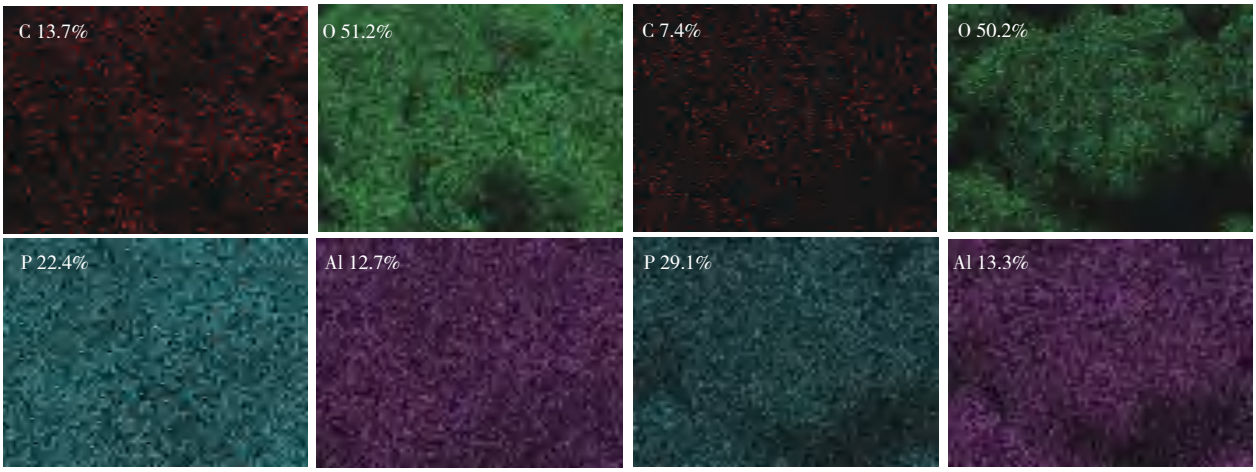

(f) PC/ABS/AHP残炭化学元素组成　　(g) PC/ABS/PEI-GO@AHP残炭化学组成

图6　阻燃PC/ABS复合材料的残炭形貌和元素组成

Fig. 6　The morphology and elemental content of the char residue after CCT for flame-retardant PC/ABS composites

图7概述了可能的阻燃机制。如图7所示的阻燃机理,首先,AHP分解成$Al_2(HPO_4)_3$和PH_3。PH_3作为有毒气体释放,$Al_2(HPO_4)_3$作为酸源催化成炭。由于“曲折路径”效应,PEI-GO在最初的分解阶段将减缓PH_3释放速率[19]。同时,PEI-GO的$-NH_2$能够通过氧化反应吸收PH_3,形成$-NH-PH_2{=}O$结构,减少PH_3的释放。从这两方面来看,PH_3释放时间延迟,PH_3浓度降低。其次,在$Al_2(HPO_4)_3$的催化作用

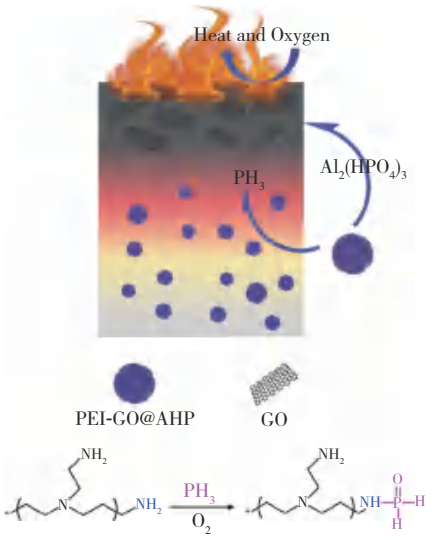

图7　阻燃机理

Fig. 7　Proposed flame-retaradant mechanism

下,PEI-GO参与成炭过程,提高了炭层的密度和强度。

3　结论

通过将PC/ABS与PEI-GO@AHP熔融共混,制备了阻燃PC/ABS合金。结果表明,与AHP相比,PEI-GO@AHP在PC/ABC中分散得更加均匀。与PC/ABS相比,加入8%的PEI-GO@AHP后,PC/ABS复合材料获得了UL-94 V-0等级,*LOI*为29.1%,*PHRR*降低41.0%,*THR*降低19.6%。在烟雾和有毒气体释放方面,PEI-GO纳米片材抑制了燃烧过程中PH_3的释放。PH_3的最大浓度降低了50%。这种阻燃PC/ABS合金拓展了PC/ABS合金在汽车外饰、建筑材料和充电桩等众多领域的应用。

参考文献:

[1] 李湘,方松刚,殷洁,等. TPP与倍半硅氧烷阻燃剂对PC/ABS的性能影响[J]. 高分子通报,2021(11):30-34.
LI X, FANG S G, YIN J, et al. Effect of TPP and sesquisiloxane flame retardants on PC/ABS performacnes[J]. Polymer Bulletin, 2021(11): 30-34. (in Chinese)

[2] 沈玉海,吴锡忠. PC/ABS阻燃增韧改性技术进展[J]. 广东化工, 2016,43(2):69,73-74.
SHEN Y H, WU X Z. Research progress on flame retardant and toughened PC/ABS alloy[J]. Guangdong Chemical Industry, 2016 ,43(2): 69,73-74. (in Chinese)

[3] 王百年,吴波,王朋辉,等. PC/ABS合金膨胀型无卤阻燃配方体系开发[J]. 塑料科技,2022,50(9):30-35.
WANG B N, WU B, WANG P H. et al. Development of PC/ABS alloy expansion halogen-free flame retardant system[J]. Plastics Science and Technology, 2022, 50(9): 30-35. (in Chinese)

[4] 李湘,殷洁,方松刚,等. PC/ABS/VMT/倍半硅氧烷阻燃性能研究[J]. 工程塑料应用,2021,49(9):135-138.
LI X, YIN J, FANG S G, et al. Study on flame retardant properties of PC/ABS/VMT/sesquisiloxane [J]. Engineering Plastics Application, 2021, 49(9): 135-138. (in Chinese)

[5] 高顺,郭正虹. PC/ABS合金的气相/凝聚相协同阻燃作用[J]. 浙江大学学报(工学版),2020, 54(12):2321-2328.
GAO S, GUO Z H. Synergistic flame retardancy of gas phase and condensed phase of PC/ABS alloy[J]. Journal of Zhejiang University (Engineering Science), 2020, 54(12): 2321-2328. (in Chinese)

[6] 苑娜娟. 高流动耐热阻燃PC/ABS合金的研制[J]. 广东化工, 2023, 50(8): 38-40.
YUAN N J. Development of high-flow heat-resistant and flame-retardant PC/ABS alloy[J]. Guangdong Chemical Industry, 2023, 50(8): 38-40. (in Chinese)

[7] 邵静波,王宇韬,张师军,等. 二苯基磷酸酯阻燃PC/ABS合金的制备[J]. 合成树脂及塑料, 2022, 39(4): 18-21.
SHAO J B, WANG Y T, ZHANG S J. et al. Preparation of diphenyl phosphate flame retardant PC/ABS alloys[J]. China Synthetic Resin and Plastics, 2022, 39(4): 18-21. (in Chinese)

[8] SOO-TUEEN B, KIEN-SIN L, LEE T S, et al. Interactive effect of ammonium polyphosphate and montmorillonite on enhancing flame retardancy of polycarbonate/acrylonitrile butadiene styrene composites[J]. Iranian Polymer Journal, 2018, 27: 899-911.

[9] WU N J, LANG S G. Flame retardancy and toughness modification of flame retardant polycarbonate/acrylonitrile-butadiene-styrene/AHP composites[J]. Polymer Degradation and Stability, 2016, 123: 26-35.

[10] XIN H, CHEN Y, LI X Q, et al. Fabrication of inorganic coatings incorporated with phosphorus-nitrogen-functionalized graphene oxide nanosheets to improve waterborne polyurethanes fire retardancy[J]. Polymer Testing, 2023, 128: 108219.

[11] JING J, ZHANG Y, FANG Z P, et al. Core-shell

flame retardant/graphene oxide hybrid: a self-assembly strategy towards reducing fire hazard and improving toughness of polylactic acid[J]. Composites Science and Technology, 2018, 165: 161-167.

[12] YUAN B H, WANG B B, HU Y X, et al. Electrical conductive and graphitizable polymer nanofibers grafted on graphene nanosheets: improving electrical conductivity and flame retardancy of polypropylene[J]. Composites Part A: Applied Science and Manufacturing, 2016, 84: 76-86.

[13] ZHAO X, CHEN L, LI D F, et al. Biomimetic construction peanut-leaf structure on ammonium polyphosphate surface: improving its compatibility with poly (lactic acid) and flame-retardant efficiency simultaneously[J]. Chemical Engineering Journal, 2021, 412: 128737.

[14] 王亮,蓝荣肇,吴俊,等. 阻燃ABS多相聚酯合金的制备与性能研究[J]. 广东化工, 2023, 50(3): 18-20.
WANG L, LAN R Z, WU J, et al. Study on preparation and properties of flame retardant ABS multi-phase polyester alloy[J]. Guangdong Chemical Industry, 2023, 50(3): 18-20. (in Chinese)

[15] 赵涛涛,宋文朋,杨桂春. 双层倍半硅氧烷物线性共聚物阻燃剂的合成及对PC/ABS合金的阻燃性能研究[J]. 粘接, 2021,45(2):7-9.
ZHAO T T, SONG W P, YANG G C. Synthesis of double-decker silsesquioxane linear polymeric flame retardant and its flame retardant properties for PC/ABS alloy[J]. Adhesion, 2021,45(2):7-9. (in Chinese)

[16] 严敏仪,刘述梅,赵建青. 滑石粉和间苯二酚双(二苯基磷酸酯)协效阻燃PC/ABS合金的研究[J]. 广东化工, 2020, 40(8): 1-4.
YAN M Y, LIU S M, ZHAO J Q. Study on synergistic effect of talcum powder and resorcinol bis(diphenyl phosphate) on the flame-retardant properties of PC/ABS alloy[J]. Guangdong Chemical Industry, 2020, 40(8): 1-4. (in Chinese)

[17] TUET W Y, RACINE M C, LAURA J, et al. A sex-balanced rodent model for evaluating phosphine inhalation toxicity[J]. Annals of the New York Academy of Sciences, 2020, 1479(1): 168-179.

[18] LI Y Y, LI X M, PAN Y T, et al. Mitigation the release of toxic PH_3 and the fire hazard of PA6/AHP composite by MOFs[J]. Journal of Hazardous Materials, 2020, 395: 122604.

[19] QU Z C, XU C A, LI X B, et al. Facile preparation of BP-MoS_2/GO composite films with excellent flame retardancy and ultrasensitive response for smart fire alarm[J]. Chemical Engineering Journal, 2021, 426: 130717.

Preparation of graphene oxide/aluminum hypophosphite hybrids and improved flame retardancy of polycarbonate (PC)/acrylonitrile butadiene styrene (ABS) blends

ZHANG JingFan　ZHANG Sheng　ZHAO JingMao*

(College of Materials Science and Engineering, Beijing University of Chemical Technology, Beijing 100029, China)

Abstract: As one of the most used plastic alloys, the flammability of polycarbonate (PC)/acrylonitrile butadiene styrene (ABS) (70/30 mass ratio) blend (PC/ABS) alloys is a threat to the safety of people's lives and property during its service, so it is necessary to improve the flame retardancy of the PC/ABS alloys. Herein, poly-ethylenimine (PEI)-grafted graphene oxide nanosheets (PEI-GO) were fabricated to decorate aluminum hypophosphite (AHP) through a self-assembly strategy. PEI-GO@AHP hybrids were prepared as a flame retardant for PC/ABS blends. The addition of 8% mass ratio PEI-GO@AHP to PC/ABS resulted in a material with a UL-94 V-0 rating and a limiting oxygen index (*LOI*) of 29.1%. The peak heat release rate (*PHRR*) and total heat release (*THR*) were decreased by 41.0% and 19.6%, respectively. Furthermore, the PEI-GO nanosheets reduced the phosphine (PH_3) concentration during combustion. This work provides a simple but effective way to fabricate flame-retardant PC/ABS blends.

Key words: flame retardancy; PC/ABS; aluminum hypophosphite

(责任编辑:李　蕾)

polymers

MDPI

Article

Performance of Thermal-Oxidative Aging on the Structure and Properties of Ethylene Propylene Diene Monomer (EPDM) Vulcanizates

Quanchao Hu [1,2], Qiang Chen [1], Peiru Song [1], Xingyu Gong [2], Junyi Chen [1,*] and Yongxian Zhao [1,*]

[1] Key Laboratory of Rubber-Plastics, Ministry of Education, Shandong Provincial Key Laboratory of Rubber-Plastics, School of Polymer Science and Engineering, Qingdao University of Science and Technology, Qingdao 266042, China
[2] Keshun Waterproof Technology Co., Ltd., Foshan 528303, China
* Correspondence: chenjunyi@qust.edu.cn (J.C.); zhaoyongxian@qust.edu.cn (Y.Z.)

Abstract: A thermal-oxidative aging test at 120 °C was conducted on ethylene propylene diene monomer (EPDM) vulcanizates of the semi-efficient vulcanization system. The effect of thermal-oxidative aging on EPDM vulcanizates was systematically studied by curing kinetics, aging coefficient, crosslinking density, macroscopic physical properties, contact angle, Fourier Transform Infrared Spectrometer (FTIR), Thermogravimetric analysis (TGA) and thermal decomposition kinetics. The results show that the content of hydroxyl and carbonyl groups as well as the carbonyl index increased with increasing aging time, indicating that EPDM vulcanizates were gradually oxidized and degraded. As a result, the EPDM vulcanized rubber chains were crosslinked with limited conformational transformation and weakened flexibility. The thermogravimetric analysis demonstrates that the thermal degradation of EPDM vulcanizates had competitive reactions of crosslinking and degradation, and the thermal decomposition curve can be divided into three stages; meanwhile, the thermal stability of EPDM vulcanizates gradually decreased with increasing aging time. The introduction of antioxidants in the system can promote the crosslinking speed and reduce the crosslinking density of EPDM vulcanizates while inhibiting the surface thermal and oxygen aging reaction. This was attributed to the fact that the antioxidant can reduce the thermal degradation reaction level, but it is not conducive to the formation of a perfect crosslinking network structure and reduces the activation energy of thermal degradation of the main chain.

Keywords: EPDM vulcanizates; thermal-oxidative aging; thermal decomposition kinetics; antioxidant

check for updates

Citation: Hu, Q.; Chen, Q.; Song, P.; Gong, X.; Chen, J.; Zhao, Y. Performance of Thermal-Oxidative Aging on the Structure and Properties of Ethylene Propylene Diene Monomer (EPDM) Vulcanizates. *Polymers* **2023**, *15*, 2329. https://doi.org/10.3390/polym15102329

Academic Editors: Ivana Salopek Čubrić, Goran Čubrić and Abhijit Majumdar

Received: 12 April 2023
Revised: 6 May 2023
Accepted: 11 May 2023
Published: 16 May 2023

Copyright: © 2023 by the authors. Licensee MDPI, Basel, Switzerland. This article is an open access article distributed under the terms and conditions of the Creative Commons Attribution (CC BY) license (https://creativecommons.org/licenses/by/4.0/).

1. Introduction

Ethylene propylene diene copolymer rubber (EPDM) not only shows excellent flexion resistance, resilience, and low-temperature resistance but also has suitable chemical structure stability. It is widely used in the automotive industry, wire and cable, sealing materials and waterproof coiled materials, and other fields. Although EPDM possesses excellent stability in chemical structure, it will still age to a certain extent under the action of external factors such as light, oxygen, heat, and chemical media in the actual service and life process, which will degrade its performance and shorten the service life of products. Therefore, it is important to study the aging law of EPDM.

The degradation process of EPDM is a complex and multi-stage mechanism that can be separated into several different steps [1]. It can lead to changes in material properties, which are caused by physical and irreversible chemical processes, such as polymer chain breaking and crosslinking [2,3]. These processes substantially affect the technically relevant properties of polymer materials, such as strength, stiffness, toughness, and modulus [4]. Generally, the extent of aging-related changes is dependent on temperature and other aging

conditions [5]. For example, the crosslinking density depends mainly on the material-dependent oxygen absorption capacity, rate of diffusion, and oxygen permeability [6], as well as the vulcanization temperature, pressure, and time. The aging of vulcanized rubber was shown to be related to a conversion of poly-sulfidic sulfur bridges to mono- and di-sulfidic sulfur bridges [7].

EPDM rubber has been studied in thermal oxygen aging [8–11], photo-oxygen aging [12,13], artificial weathering aging [14], radiation aging [15,16], and medium aging [17,18]. Its research methods and characterization methods are diverse, such as dynamic mechanical property analysis, spectral analysis (Fourier infrared spectroscopy, Raman spectroscopy), energy spectrum analysis (X-ray electron spectroscopy, nuclear magnetic resonance), and thermal analysis (differential scanning calorimetry, thermogravimetric analysis), etc. However, most of them are limited to the research of EPM and EPDM rubber. The research on the thermal oxygen aging of EPDM vulcanizates with antioxidant content and semi-efficient vulcanization system is few.

The most common aging type was thermal oxygen, which has a great effect on the performance of EPDM rubber. Therefore, the antioxidants that could delay aging and prolong the service life of rubber products by inhibiting oxidation and heat play a vital role in maintaining the property of rubber. The commonly used antioxidants include N-isopropyl-N′-phenyl-p-phenylene diamine (4010-NA) [19,20], 2-sulfur-benzimidazole (MB) [21], N-4(phenylephenyl)-maleimide (MC) [22] and 2,2,4-thrimethyl-1,2-dihydroquinoline polymer (RD) [23,24]. Here, EPDM vulcanized rubber with a semi-effective vulcanization system was subjected to thermal and oxygen aging tests at 120 °C (Scheme 1). The effects of thermal oxygen aging on the structure and properties of EPDM vulcanizates were studied in detail through physical properties, aging coefficient, surface properties, crosslinking density, microstructure, thermodynamic property, and vulcanization characteristics of EPDM vulcanizates.

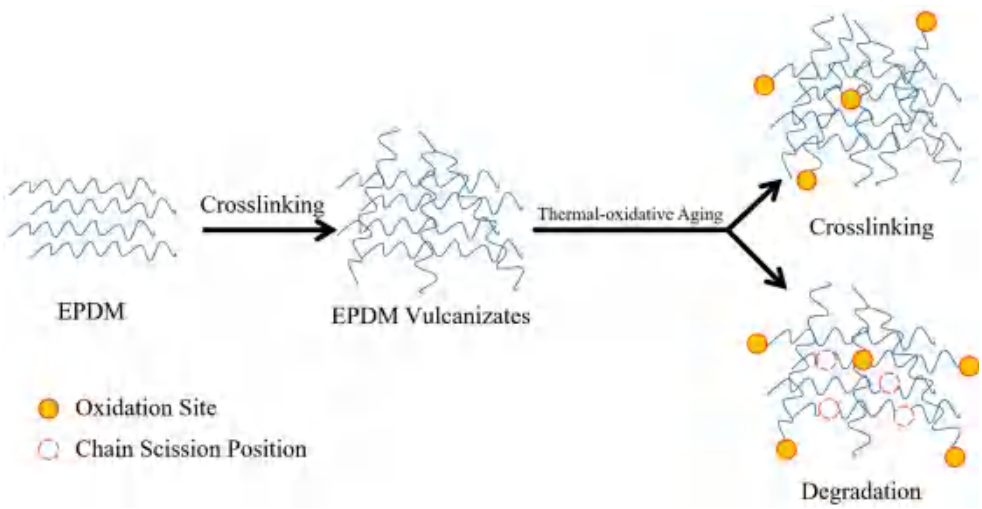

Scheme 1. The crosslinking and thermal-oxidative aging process of EPDM vulcanizates.

2. Experimental

2.1. Materials

EPDM rubber (3760P) was purchased from Dow Chemical of the United States; carbon black (N330) was purchased from Cabot Corporation; naphthenic oil (KN4006) was purchased from China National Petroleum Corporation. Sulfur, zinc oxide (ZnO), stearic acid (SA), tetramethylthiuram disulfide (TMTD), Poly(1,2-dihydro-2,2,4-trimethylquinoline) (RD), and N-Isopropyl-N′-phenyl-p-phenylenediamine (4010-NA) were all commercial industrial products.

2.2. Method

2.2.1. Preparation of EPDM Vulcanizates

A two-stage mixing process was applied to EPDM vulcanizates by a Haake torque rheometer (Thermo Fisher Scientific, Poly Lab OS, Waltham, MA, USA) in this experiment. The speed of the internal mixer was set at 60 r/min, and the initial temperature was 90 °C. EPDM, ZnO, SA, carbon black (N330), and naphthenic oil were added in sequence. After dumping and pouring into the mixing mill, the two-stage mixing process was carried out. Later, sulfur and accelerator were added while the second temperature was 50 °C. After storage for more than 16 hours, the EPDM compound was vulcanized to the required samples with a plate vulcanizer (Huzhou Dong-fang Rubber Machinery Co., Ltd., XLB-400 × 400, Huzhou, China) under the pressure of 15–20 MPa and temperature of 170 °C. The formulation of EPDM vulcanizates is listed in Table 1.

Table 1. Formulation of EPDM vulcanizates.

Samples	EPDM phr	N330 phr	Sulfur phr	TMTD phr	ZnO phr	SA phr	KN4006 phr	RD phr	4010-NA phr
#1	100	100	1.5	1.5	5	1	70	-	-
#2	100	100	1.5	1.5	5	1	70	1	2

2.2.2. Thermal-Oxidative Aging

According to ISO 188:2011 standard, the thermal-oxidative aging test was carried out on samples in the thermal oxygen aging test chamber (GOTECH TESTING MACHINES Inc., GT-7017-E, Taipei, Taiwan, China). The settings of the apparatus were as follows: temperature of 120 °C, temperature deviation of ±2 °C, air flow rate of 0.5–1.5 m/s, and air exchange rate of 3–10 times/h. The aging times were 0 h, 24 h, 72 h, 120 h, 168 h, and 336 h, respectively.

2.3. Measurements

2.3.1. Vulcanization Characteristics

The vulcanization characteristics are tested using a vulcanizer (GOTECH TESTING MACHINES Inc., GT-M2000-A, Taipei, Taiwan, China) according to GB/T 16584–1996 with a specimen weight of approximately 5 g in 170 °C for 30 min.

2.3.2. The Crosslinking Density

The rubber only swells and does not dissolve in the solvent, the mixing entropy increases and the swelling equilibrium is reached when the Gibbs free energy ΔG_s is zero (Formula (1)).

$$\Delta G_s = \Delta G_m + \Delta G_{el} = 0 \tag{1}$$

where ΔG_m, ΔG_{el} are mixing free energy and elastic free energy change, respectively. In this experiment, the equilibrium swelling method was used to determine the crosslink density of EPDM vulcanized rubber. Assuming uniform deformation of the rubber in the solvent, the Flory–Rehner equation yields Equation (2). Cyclohexane was chosen as the solvent to determine the mass and density of EPDM before swelling, then put into the cyclohexane solvent, fully swelling, and test the mass after swelling every 24 h until the difference between the two measurements was less than 0.01 g, and calculate the crosslink density according to the following Equation (2).

$$\upsilon_e = -\frac{1}{V}\left[\frac{\ln(1-v_2)+v_2+Xv_2{}^2}{v_2{}^{\frac{1}{3}}}\right] \tag{2}$$

$$v_2 = \frac{v_1}{v_1+v_3} \tag{3}$$

$$v_3 = \frac{m_2 - m_1}{\rho_3} \tag{4}$$

$$v_1 = \frac{m_3}{\rho_1} \tag{5}$$

where v_e is the crosslink density (mol/kg); V is the molar volume of solvent (L/mol); v_1 is the volume of the rubber phase (m^3); v_2 is the volume fraction of the rubber phase in vulcanizate (%); v_3 is the volume of solvent in the rubber phase after swelling (m^3); $X_{cyclohexane}$ is the interaction parameter between rubber and solvent: ($X_{cyclohexane}$: 0.35144524); ρ is the density of rubber (g/cm^3); ρ_1 is the density of reagent for swelling (g/cm^3); m_1 is the mass of vulcanized rubber before swelling (g); m_2 is the mass of vulcanized rubber after swelling (g); m_3 is the mass of the rubber phase (g).

2.3.3. Physical Property

Tensile properties and hardness are measured using an AI-7000S electronic tension machine (GOTECH TESTING MACHINES Inc., Taipei, Taiwan, China) and shore A hardness tester (GOTECH TESTING MACHINES Inc., Taipei, Taiwan, China) according to ISO 37: 2005 and ISO 7619-2: 2004, respectively. The rate of change of performance is calculated according to the following Equation (6).

$$P(\%) = \frac{X_a - X_0}{X_0} \times 100 \tag{6}$$

where P is the rate of change of performance, %; X_a is the measured value of the performance of the specimen after aging; X_0 is the measured value of the performance of the specimen before aging.

2.3.4. Water Contact Angle Test

The water contact angle is measured with contact angle meter (Shanghai Zhongchen Digital Technology Equipment Co., Ltd., JC2000D2, Shanghai, China). The measured liquid is distilled water, and the test temperature and humidity are 15 °C and 50%, respectively.

2.3.5. Aging Coefficient

The aging coefficient (AC) [25] is the standard for evaluating the thermal aging performance of rubber and can be expressed as:

$$\mathrm{AC} = \frac{\sigma_2 \times \varepsilon_2}{\sigma_1 \times \varepsilon_1} \tag{7}$$

In Equation (7), AC refers to the aging coefficient of rubber; σ_1 and σ_2 refer to the tensile strength (MPa) before and after aging; ε_1 and ε_2 represent the elongation at break (%) before and after aging, respectively.

2.3.6. Attenuated Total Reflection Fourier Transform Infrared Spectrometer (ATR-FTIR) Analysis

The FTIR spectra of samples were obtained by using a Nicolet IS 10 FTIR spectrometer (Thermo Fisher Scientific, Waltham, MA, USA) with an ATR accessory. The measurements were made with a signal average of 10 co-added scans with the resolution of 4 cm^{-1} and a range of 600~4000 cm^{-1}.

2.3.7. Thermogravimetric Analysis

The thermogravimetric test was carried out in a N_2 atmosphere. The samples were heated from 30 °C to 600 °C at the rate of 20 °C/min, and the samples were kept at 600 °C for 10 min. Then, the atmosphere was switched to air with the same rate and a 10 min constant temperature after heating to 800 °C.

2.3.8. Thermal Degradation Kinetics

The thermogravimetric analysis plays an important role in the structure and thermal stability of polymers. The relationship between quality and temperature or time is tested under a certain flow rate atmosphere, so as to analyze the thermal stability and thermal decomposition of samples.

The degradation reaction equation is usually used to describe its kinetics.

$$\frac{d_\alpha}{d_t} = kf(\alpha) \tag{8}$$

$$G(\alpha) = kt \tag{9}$$

where α refers to the conversion rate, k refers to the rate constant, and $f(\alpha)$ depends on the reaction mechanism. The relationship between the rate constant k and the reaction temperature T can be expressed by the Arrhenius equation:

$$k = Aexp\left(\frac{-E}{RT}\right) \tag{10}$$

where A is pre-factor (min^{-1}); β is heating rate (°C/min); T is temperature (K); E is the activation energy (kJ/mol); n is reaction order; and R is molar gas constant (8.314472 J/(mol.k)). For the simple reaction equation $f(\alpha)$.

$$f(\alpha) = (1-\alpha)^n \tag{11}$$

Equation (12) can be obtained by substituting Equations (10) and (11) into Equation (8):

$$\frac{d_\alpha}{d_t} = \text{Ae}^{\left(\frac{-E}{RT}\right)}(1-\alpha)^n \tag{12}$$

The Freeman–Carroll method [26] is a method to calculate the activation energy by obtaining the difference between two points according to the reciprocal of the weight-loss rate and temperature at several points on a thermogravimetric curve (TG curve). Assuming the heating rate at a constant $\beta = \frac{d_T}{d_t}$, Equation (13) can be obtained from the dynamic equation and Arrhenius equation:

$$\frac{d_\alpha}{d_T} = \frac{\text{A}}{\beta}\text{e}^{\left(\frac{-E}{RT}\right)}(1-\alpha)^n \tag{13}$$

By taking logarithms on both sides of Equation (13) and dividing them by $\Delta lg(1-\alpha)$, Equation (14) can be obtained:

$$\frac{\Delta lg\left(\frac{d_\alpha}{d_T}\right)}{\Delta lg(1-\alpha)} = -\frac{E}{2.303R} \times \frac{\Delta\left(\frac{1}{T}\right)}{\Delta lg(1-\alpha)} + n \tag{14}$$

Adopting a temperature range of 450–480 °C and a temperature interval of 2 °C, this paper performed the Freeman–Carroll operation. The activation energy E and the reaction order n were obtained respectively according to the slope and intercept of the fitting line of $\Delta lg(da/dT)/\Delta lg(1-\alpha)$ for $\Delta(1/T)/\Delta lg(1-\alpha)$.

3. Results and Discussion

3.1. Vulcanization Characteristics

The vulcanization characteristics curve of EPDM is shown in Figure 1. The formulation of a semi-effective vulcanization system was used in this article (accelerator to sulfur dosage ratio of 1, which is between CV and EV). Both polysulphide bonds and a moderate amount of single and double sulfur crosslinked bonds existed in the resulting EPDM

vulcanized rubber. The resulting EPDM vulcanized rubber has both polysulphide bonds and a moderate amount of single and double sulfur crosslinked bonds. This combines the characteristics of both CV and EV vulcanization systems to improve the thermal and oxygen aging and fatigue resistance of the vulcanized rubber. The change in torque during rubber vulcanization is proportional to the change in crosslinking density, and the rate of change in torque can be used to characterize the rate of vulcanization. The equation for the rate of vulcanization can be expressed as in Equation (15).

$$V = \frac{dln(M_H - M_t)}{dt} = K(M_H - M_t)^n \tag{15}$$

where M_H is the maximum torque (Nm); M_t (Nm) is the torque at vulcanization time t (min); K is the rate constant; n is the number of reaction stages.

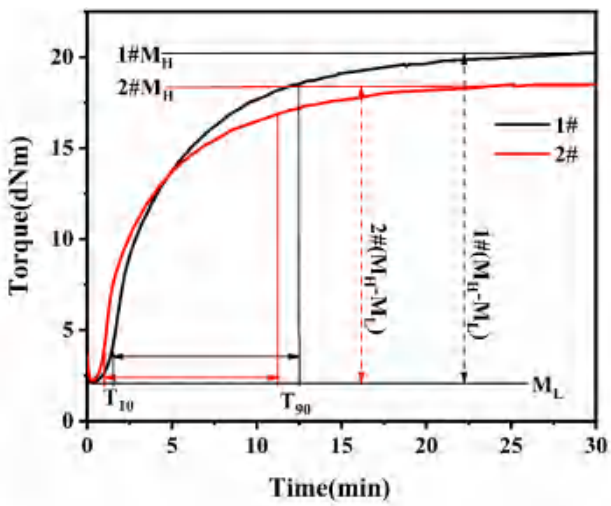

Figure 1. Vulcanization curves of EPDM vulcanizates: (#1) without antioxidant; (#2) with antioxidant.

According to the reaction model for the coking phase derived by Coran [27], the reaction equation for the vulcanization phase can be expressed as in Equation (16).

$$V_{ut} = V_{u\infty}\left[1 - e^{-K_2(t-t_i)}\right] \tag{16}$$

In addition, the reaction during the scorch period is not a primary reaction, but rather the true primary reaction begins when the rate of change of the torque reaches a maximum, and the sulfation kinetics can be expressed as

$$ln(M_H - M_t) = lnA - K(t - t_{dis}) \tag{17}$$

In this case, t_{dis}, the moment when the rate of change of torque reaches its maximum, is plotted against $(t - t_{dis})$ by $ln(M_H - M_t)$ (Figure 2). K and lnA can be obtained from the slope and intercept, respectively.

As the sulfidation process after coking was usually divided into two stages. After linear fitting the data, it was found that the result was a smooth straight line, which was consistent with a first-order kinetic reaction. Therefore, this sulfidation process can be divided into two first-order kinetic reactions.

EPDM vulcanization rubber characteristics data are shown in Table 2. Due to the addition of antioxidant, T_{10}, T_{dis} were shortened, indicating that the start reaction time was earlier. The reaction difficulty was lower than Sample 1 with increasing vulcanization rate K, CRI value, and vulcanization speed. However, the crosslink density was lower than in Sample 1.

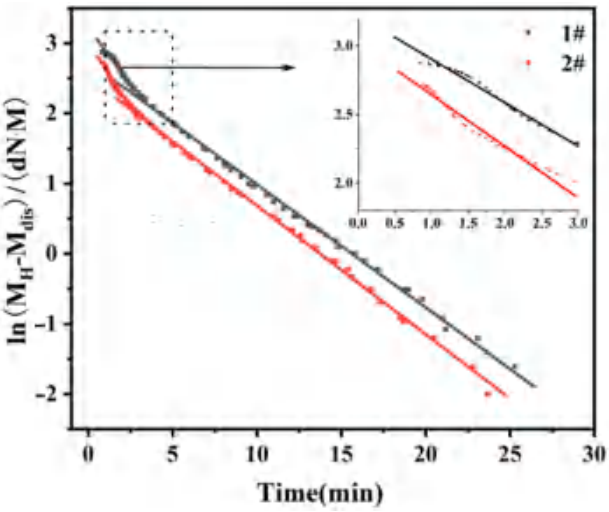

Figure 2. Relationship between $\ln(M_H - M_t)$ and t of EPDM vulcanizates: (#1) without antioxidant; (#2) with antioxidant.

Table 2. The data of vulcanization characteristics.

Sample	M_H/(N·M)	M_L/(N·M)	M_H-M_L/(N·M)	T_{10}/(min)	T_{90}/(min)	*CRI*/(min^{-1})	T_{dis}/(min)	*K*	*R*
#1	20.29	2.09	18.2	1.46	12.23	9.07	1.89	0.23 */0.17	0.990 */0.998
#2	18.55	2.25	16.3	0.98	11.32	9.57	1.19	0.27 */0.18	0.987 */0.997

Note: T_{10} is the time corresponding to a torque of 10%. T_{90} is the time corresponding to a torque of 90%. *CRI* is the sulfur addition index, $CRI = 100/(T_{90} - T_1)$, reflecting the speed of vulcanization, the larger the *CRI* value, the faster the speed of vulcanization. *: First stage fitted data.

3.2. Physical Properties and Crosslinking Density

The physical properties and crosslinking density changes of EPDM vulcanizates after aging are shown in Figure 3. It can be seen that the tensile strength, hardness, and crosslinking density of two EPDM vulcanizates gradually increase with increasing aging time. However, the elongation at break decreased with increasing aging time. Basically, EPDM vulcanizates would continue to be crosslinked at 120 °C, the conformation transition of the polymer chain was constrained, and the flexibility was weakened, which led to the increase in tensile strength and surface hardness [4]. The polarity would increase, and the flexibility would decrease due to the oxidative degradation of the carbon–carbon backbone during the thermal-oxidative aging of EPDM vulcanizates, leading to lower elongation at break.

The elongation at break of Sample #2 was higher than that of Sample #1, while the tensile strength, crosslinking density, and hardness were slightly lower than that of Sample #1. It indicated that antioxidants had an effect on the vulcanization characteristics, which can inhibit the generation of crosslinking network structure and a larger free volume of the macromolecular chain. The degradation reaction and crosslinking reaction of EPDM vulcanizates were competitive reactions during thermal-oxidative aging. Antioxidants increase the imperfection degree of crosslinking structure. At the same time, chain breaking and oxidation reactions play a leading role in increasing thermal oxygen aging time. Therefore, both the crosslinking and degradation are quick as the crosslinking density rapidly increases in 72 h, the hardness increases, and flexibility decreases rapidly. After 72 h, both crosslinking and degradation speed are reduced, and the hardness and flexibility change slowly, which is caused by the disappearance of free radicals.

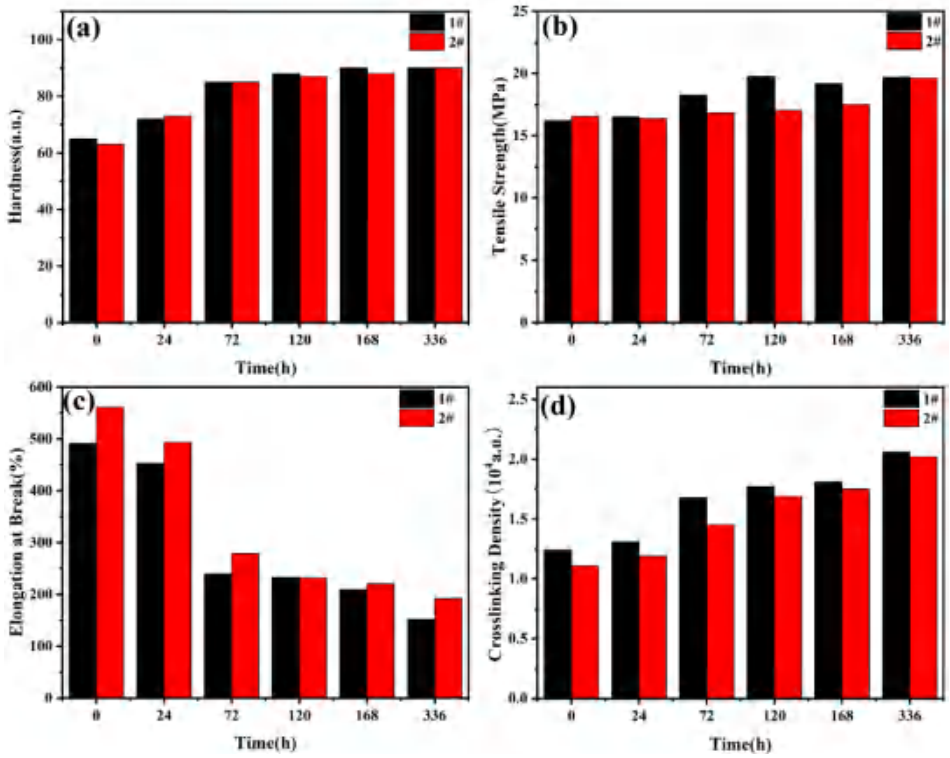

Figure 3. Changes in performance of EPDM vulcanizates after aging: (#1) without antioxidant; (#2) with antioxidant. (**a**) Hardness; (**b**) Tensile strength; (**c**) Elongation at break and (**d**) Crosslinking density.

3.3. Aging Coefficient and Retention

The aging coefficient (*AC*) was obtained from the relationship between physical and mechanical properties (e.g., tensile strength, elongation) before and after thermal and oxygen aging. It was usually a key indicator to evaluate the overall performance of rubber aging. The changes in the aging coefficient and tearing elongation retention at the break of EPDM vulcanizates with aging time are shown in Figure 4. The aging coefficient and elongation retention rate of Sample #2 were larger than those of Sample #1. It meant that the retention rate of the macro physical properties of EPDM vulcanized rubber with thermal and oxygen aging was improved because of the addition of antioxidants.

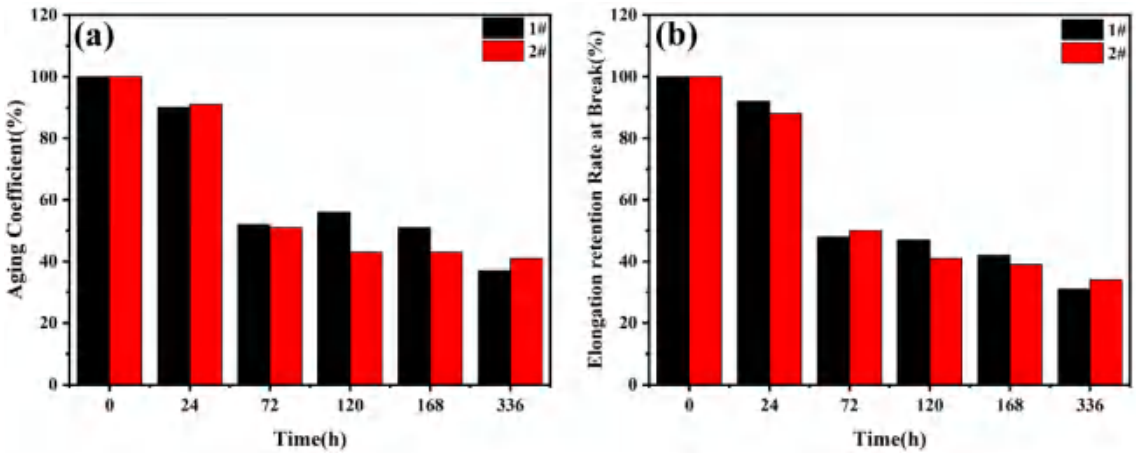

Figure 4. Elongation retention at break and AC of EPDM vulcanizates after aging: (#1) without antioxidant; (#2) with antioxidant. (**a**) Aging coefficient; (**b**) Elongation retention rate at break.

3.4. Attenuated Total Reflection Fourier Transform Infrared Spectrometer (ATR-FTIR) Analysis

In this paper, the structure of EPDM vulcanizates was analyzed by the ATR-FTIR method after aging. The change of the infrared spectrum of EPDM vulcanizates is shown in Figure 5 with aging time. The same change rule of infrared absorption peaks can be observed at different wavelengths for two samples.

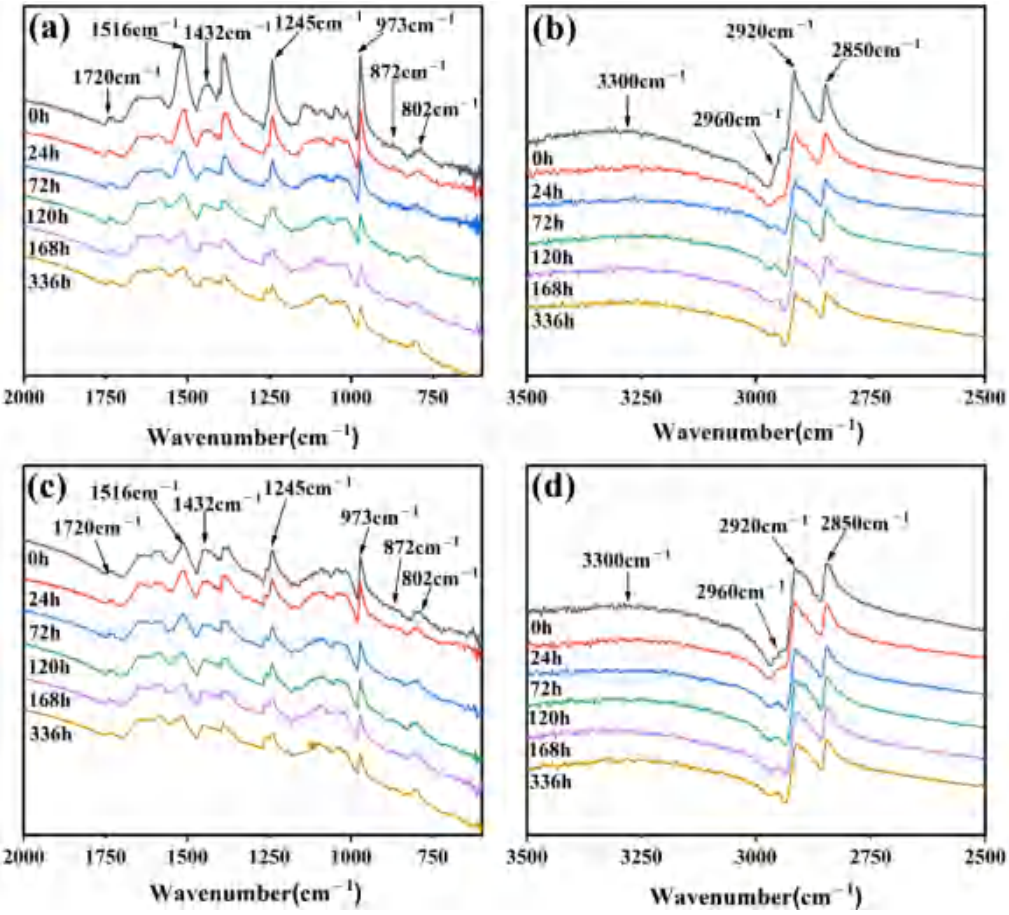

Figure 5. ATR-FTIR spectra of sample EPDM vulcanizates: (#1) without antioxidant; (#2) with antioxidant. (**a**) ATR-FTIR spectra of Sample #1 with range of 600–2000 cm^{-1}; (**b**) ATR-FTIR spectra of Sample #1 with range of 2500–3500 cm^{-1}; (**c**) ATR-FTIR spectra of Sample #2 with range of 600–2000 cm^{-1} and (**d**) ATR-FTIR spectra of Sample #2 with range of 2500–3500 cm^{-1}.

The peak at 3300 cm^{-1} was the stretching vibration peak of the hydroxyl group, which was attributed to the extended oxidation group of -OH (alcohol, hydroperoxide, and carboxylic acid) [28]. As a result of thermal-oxidative degradation, which content increased with increasing aging time. For pure EPDM, the peaks between 2800 cm^{-1} and 3000 cm^{-1} were related to CH_3, CH_2, and CH [29]. The peak at 2850 cm^{-1} and 2920 cm^{-1} belonged to the symmetric stretching vibration and asymmetric stretching vibration of the (-CH_2-) group, respectively [30], which decreased with aging time. The peak at 2960 cm^{-1} reflects the asymmetric stretching vibration of methyl [31–34]. Its content increased with the extension of the aging time, indicating a chain-rupturing reaction of the EPDM structure.

The peak at 1720 cm^{-1} was the characteristic peak of carbonyl, in which the peak area was a measure of the oxidative degradation degree of the polymer [35–37]. As carbonyl was the main product of oxidative degradation of EPDM vulcanizates, the carbonyl index can be determined, namely, the value of carbonyl sulfide line strength at 1720 cm^{-1} divided by methylene line strength at 1432 cm^{-1} [38]. Carbonyl content and carbonyl index were shown in Table 3. The upward trend of carbonyl content and carbonyl index with increasing aging time implied that EPDM vulcanizates were gradually oxidized and degraded.

Table 3. Changes in the peak area of different groups of EPDM vulcanizates after aging.

Aging Time/h	3300 cm^{-1}	2960 cm^{-1}	1720 cm^{-1}	1516 cm^{-1}	1432 cm^{-1}	1245 cm^{-1}	#1 [1]	#2 [1]
0	200.17	1.46	2.42	40.59	1.16	24.75	2.086	0.638
24	204.51	2.11	2.71	33.6	1.13	25.14	2.398	0.638
72	209.6	3.12	3.07	34.39	1.28	23.04	2.398	0.728
120	213.87	3.17	3.19	21.46	1.32	19.97	2.417	0.815
168	220.48	3.39	3.77	21.06	1.48	18.62	2.547	0.867
336	231.69	5.12	4.67	18.66	1.67	17.04	2.796	0.969

[1] carbonyl index.

The carbonyl content and carbonyl index of Sample #2 with the addition of antioxidants were smaller than those of Sample #1, indicating that the addition of RD and 4010NA antioxidants can reduce the oxidation reaction on the surface of EPDM vulcanized rubber to a certain extent and improve the resistance of heat and oxygen aging.

In the absorption region of 1500–800 cm^{-1}, the peak at 1432 cm^{-1} was the -CH_2- shear vibration mode of the propylene unit of EPDM and CH band loss due to oxidative degradation [39]. The peak at 1245 cm^{-1} was caused by macromolecular skeleton vibration, and the content decreased with increasing aging time also implies that thermal oxygen aging would lead to the fracture of the macromolecular skeleton.

The peaks at 872 cm^{-1} and 802 cm^{-1} were the deformation vibration of the typical unsaturated zone C=C-H of the diene part, and 973 cm^{-1} was the shear deformation vibration of C-H in the third monomer with double bond C=C-H. These content increased first and then decreased with the increasing aging time, which was due to crosslinking firstly, and then breakage loss of double bonds caused by the thermal-oxidative aging degradation [40,41]. The carbonyl and ester groups were formed, and the unsaturation of the third monomer decreased rapidly, which indicated that chain branching [42] and crosslinking reactions [43] occur simultaneously during the aging process of EPDM vulcanizates. Therefore, thermal-oxidation aging of EPDM vulcanizates can be seen as a process of breaking the main chain and oxidation.

3.5. Surface Property

The contact angle is an important parameter to measure the wetting performance of the liquid on the surface of the material and can express the change of polarity, hydrophilicity, and surface energy of the material surface.

Variations in the contact angle of EPDM vulcanized rubber with various aging times are shown in Figure 6, with the specific data in Table 4. The gradual decrease in contact angle for two types of EPDM vulcanized rubber can be seen with the increase in aging time.

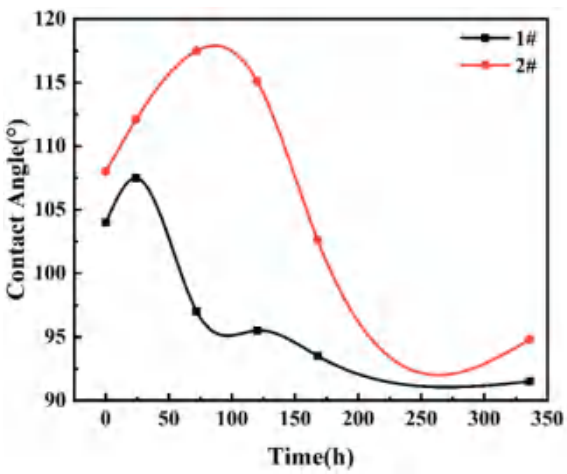

Figure 6. Contact angle of EPDM vulcanizates after aging: (#1) without antioxidant; (#2) with antioxidant.

Table 4. Contact angle of EPDM vulcanizates after aging.

Samples	0 h	24 h	72 h	120 h	168 h	336 h
#1	104.0	105.5	97.0	95.5	93.5	91.5
#2	108.0	108.1	107.5	105.1	102.6	94.8

The reason was that the main chain of EPDM vulcanized rubber was broken and oxidized with increasing oxygen-containing groups (such as carbonyl and carboxyl groups on the surface). As a result, the number of carbon atoms in the main chain would decrease with increasing water solubility, indicating the hydrophilic energy gradually increased with decreasing contact angle. As the aging time is further prolonged, the aging reaction of ethylene propylene diene monomer would intensify, and the oxidative degradation of the main chain of EPDM would further intensify, leading to an increase in the carbonyl index, resulting in the decreased contact angle.

The contact angle of Sample #2 with the addition of antioxidants was larger than Sample 1. It was probably due to the fact that the addition of the antioxidant affects the crosslinking reaction and network of the EPDM vulcanized rubber while reducing the oxidation reaction during the vulcanization process. Further, the oxidative degradation of the EPDM vulcanized rubber surface was more intense as the aging time increased. It was suggested that the addition of antioxidants RD and 4010-NA could significantly reduce the generation of oxidation groups on the surface with an increasing carbonyl index.

3.6. Thermal Degradation Behavior and Kinetic

The thermal stability of materials can be analyzed by TGA, which can reveal the relationship between the mass of the sample and temperature or time under a certain flow rate atmosphere. The TGA test was the change of sample quality at the same heating rate and isothermal time. Different stages of thermal decomposition of the sample can be seen in the TG curve with the quantitative analysis and qualitative analysis of the composition change after aging. The DTG curve represents the weight-loss rate, which can be derived from the TG curve, and the two curves correspond. The decomposition stage, decomposition temperature, decomposition rate, thermal stability, and thermal decomposition activation energy of polymer materials can be obtained by thermogravimetric analysis. The TG/DTG curve of EPDM vulcanizate after aging is shown in Figure 7.

According to the TG/DTG curve in Figure 7, the thermal weightlessness of EPDM vulcanizates can be divided into three stages. The specific data are listed in Table 5. It can be seen that the changing trend of the initial weight-loss temperature in the first stage gradually reduced with increasing aging time. However, no change can be seen with time in the second and third stages. The initial weight-loss temperature in the first stage also represents that its thermal stability gradually decreases. The weight-loss rate of EPDM vulcanizates in the first stage was gradually reduced with increasing aging time. The major losses were highly volatile substances (plasticizers, accelerators, water vapor, etc.), whose aging was accompanied by quality degradation in the first stage at 120 °C. In the second stage, medium volatile substances (EPDM rubber) lost away largely. Some scholars [4] tracked the degradation and pyrolysis process of EPDM by gas chromatography to confirm that the main products were CO_2, H_2O, CO, CH_4, and C_2H_6. These combustible substances (carbon black, etc.) were burned slowly in the third stage. The remaining materials were some mineral additives, such as ZnO.

The peak of the first weight-loss temperature increased with increasing aging time, while the peak of weight-loss temperature in the second and third stages did not change significantly. It was attributed to the loss of plasticizers, crosslinking, and degradation (the competitive reaction), which were caused by the decomposition of the carbon main chain, affecting the free volume of the material during the thermal-oxidative aging process of EPDM vulcanizates. The degradation was attributed to the oxidative degradation of the main chain of crosslinked EPDM in the second stage [44].

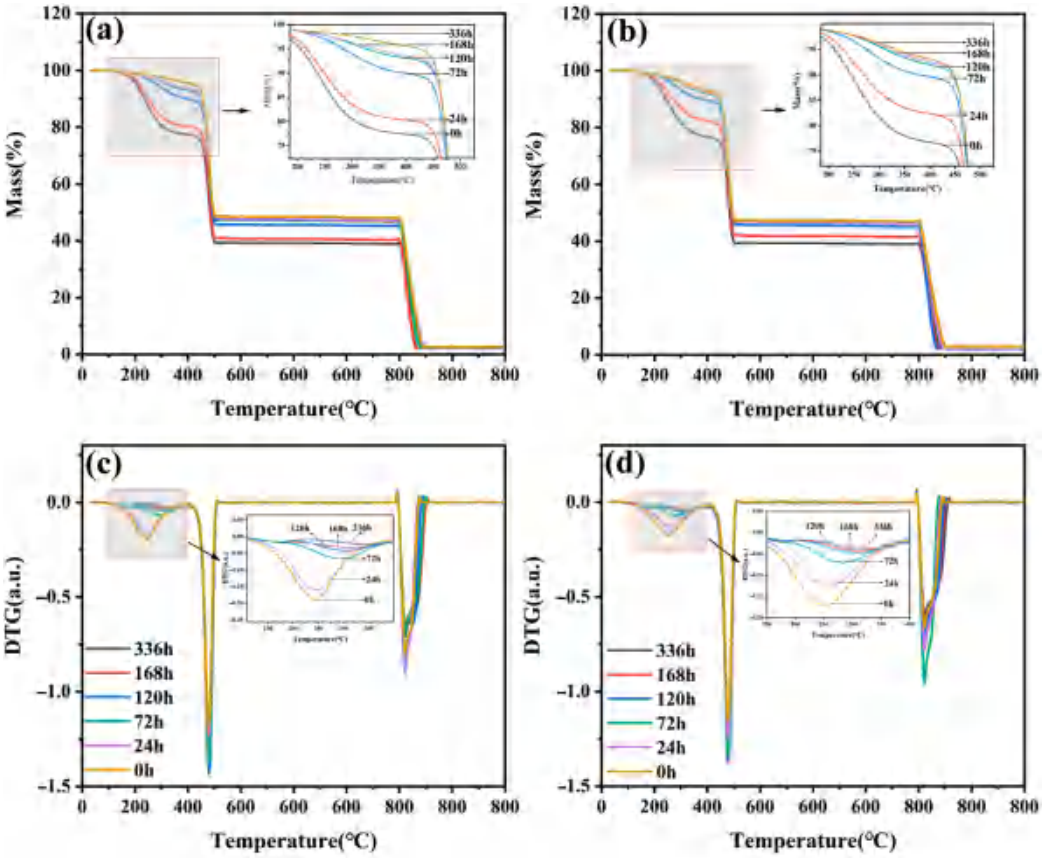

Figure 7. TG/DTG curves of EPDM vulcanizates after aging: (#1) without antioxidant; (#2) with antioxidant. (**a**) TG curves of Sample #1; (**b**) TG curves of Sample #2; (**c**) DTG curves of Sample #1 and (**d**) DTG curves of Sample #2.

Table 5. TG/DTG curve data of EPDM vulcanizates after aging.

Aging Time/h	Initial Weight-Loss Temperature/°C				Maximum Weight-Loss Temperature/°C			
	First Stage		Second Stage	Third Stage	First Stage		Second Stage	Third Stage
	#1	#2	#1, #2	#1, #2	#1	#2	#1, #2	#1, #2
0	93	101	393	800	245.67	253.33	479.33	1222.33
24	89	100	393	800	244.30	257.00	479.33	1222.33
72	89	107	393	800	298.00	283.00	479.33	1222.33
120	89	97	393	800	300.00	313.67	480.33	1222.33
168	86	89	393	800	318.67	306.67	480.33	1222.33
336	84	87	393	800	325.00	327.67	479.67	1222.33

In this paper, the temperature interval 450–480 °C was chosen to calculate the heat drop activation energy. This interval was mainly attributed to the EPDM main chain structure, where the weight-loss reaction was relatively intense. The activation energy E and the number of reaction steps n can be obtained from the slope and intercept of the straight line by the Freeman–Carroll method for graphing, respectively (Figure 8). The data of the thermal analysis of the TG/DTG curve of EPDM vulcanization rubber aging can be seen in Table 6.

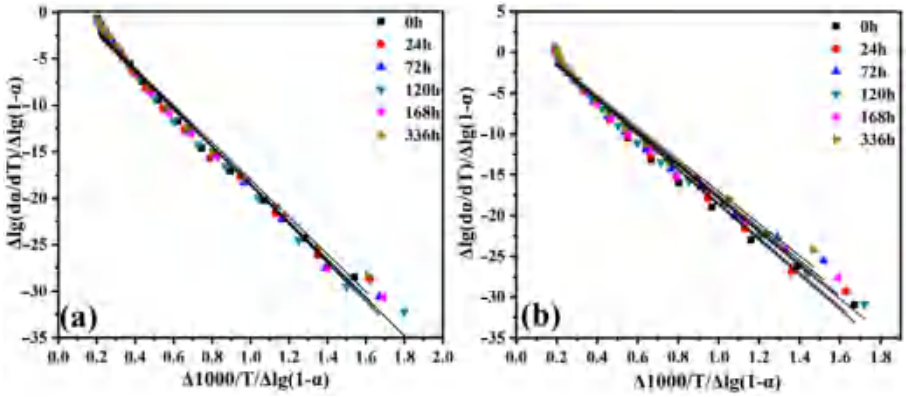

Figure 8. Relationship between $\Delta lg(d\alpha/dT)/\Delta lg(1-\alpha)$ and $\Delta 1000/T/\Delta lg(1-\alpha)$ of EPDM vulcanizates after aging: (#1) without antioxidant; (#2) with antioxidant. (**a**) Relationship of Sample #1; (**b**) Relationship of Sample #2.

Table 6. Thermal analysis data of TG/DTG curve of EPDM vulcanizates after aging.

Aging Time/h	Activation Energy E/kJ·mol^{-1}		The Number of Reaction Stages		R	
	#1	#2	#1	#2	#1	#2
0	440.111	434.951	4.4084	4.0562	0.96104	0.96488
24	434.981	431.557	4.1105	3.9756	0.95935	0.9649
72	426.952	411.185	4.0395	3.9283	0.97098	0.94975
120	420.865	413.527	3.9563	3.7456	0.9716	0.97406
168	424.908	412.543	3.9393	3.8535	0.97151	0.96355
336	418.352	405.043	3.9443	3.7375	0.96546	0.95589

It can be seen in these results that the degradation process of EPDM was complex, and which degradation reaction was not a simple stepwise reaction but a random degradation process [45]. The degradation of EPDM follows the Avrami-Erofeev two-dimensional nucleation model or random chain-breaking mechanism [46]. The activation energy E of thermal degradation of the EPDM vulcanized rubber backbone structure tends to decrease with increasing thermal and oxygen aging time. This is due to the dual effect of chain breakage and crosslinking occurring simultaneously during thermal oxygen aging with the continuous crosslinking reaction of EPDM vulcanized rubber at 120 °C under thermal oxygen [39]. The increase in crosslinking density leads to a downward trend in the activation energy of thermal degradation.

However, as the aging time increases, the oxidative degradation reaction of the EPDM backbone dominates, and the activation energy continuously decreases [44,47].

It can be seen in the comparison of the results from the #2 (with antioxidant) and #1 (without antioxidant) samples that the EPDM vulcanization starting weight-loss temperature and the first-stage weight-loss peak temperature was risen because of the addition of antioxidants.

At the same time, the number of reaction stages was reduced, indicating that the thermal degradation reaction and the oxidation effect were weakened due to the existence of antioxidants in Sample 2. This was generally consistent with the macroscopic physical and mechanical properties. The activation energy of thermal degradation of Sample 2 was smaller than that of Sample 1. It was attributed to the competition between degradation and crosslinking of the EPDM backbone. The antioxidant enhanced the crosslinking rate without help to the complete crosslinking network of the EPDM curing rubber, reducing the stability of the carbon–carbon backbone. Herein, the degradation reaction played a major role in reducing the thermal degradation activation energy.

4. Conclusions

The structure and properties of EPDM vulcanizates with two kinds of semi-efficient vulcanization systems before and after thermal-oxidative aging were investigated in detail, including vulcanization characteristics, macroscopic physical properties, surface properties, thermogravimetric behavior and kinetics, and so on.

The vulcanization characteristics showed that the vulcanization process of EPDM vulcanizates consisted of two first-order kinetic reaction stages. Antioxidants can promote the crosslinking reaction and improve the crosslinking speed but cannot form perfect crosslinking network structures. With increasing aging time, EPDM vulcanizates can continue to crosslink so that the conformational transformation of the polymer chain is constrained and the flexibility is weakened. Finally, the macroscopic physical properties (such as strength, elongation, hardness, etc.) were affected. The antioxidant can significantly improve the aging coefficient and macroscopic physical retention of EPDM vulcanizates, which can lower (reduce or decrease is OK) crosslinking density to produce larger free volume, promoting the retention of elongation and hardness.

The same change of the infrared absorption peaks of two EPDM vulcanizates at different wavelengths was shown in FTIR, which implied that the oxidation and degradation of the surface intensify as the aging time increases. Moreover, the carbonyl content and carbonyl index gradually increase with increasing aging time. This phenomenon is demonstrated macroscopically as an increase in contact angle. The degree of oxidation and degradation of the surface of EPDM vulcanizates can be reduced by antioxidants. Moreover, the thermal oxygen aging properties of the surface can be improved due to the addition of antioxidants.

Three stages of the thermal decomposition of two EPDM vulcanizates can be seen in TGA results. Sample #2, with the addition of the high boiling-point antioxidant, effectively increased the initial weight-loss temperature and the peak of the first weight-loss temperature in the first degradation stage. It can be seen in the kinetic study of the backbone of EPDM vulcanizates under the temperature range of 450–480 °C that the addition of antioxidants can reduce the reaction order and promote the formation of incomplete crosslinked network structure, which intensifies the degradation reaction and reduces the thermal degradation activation energy of the backbone.

Author Contributions: All authors contributed to the study's conception and design. Material preparation, data collection, and analysis were performed by Q.H., Q.C., P.S., X.G., J.C. and Y.Z.; the first draft of the manuscript was written by Q.H.; and all authors commented on previous versions of the manuscript. All authors have read and agreed to the published version of the manuscript.

Funding: The authors are grateful for the financial support from the Shandong Province Key Research and Development Plan of China (Public Welfare Project 2019GGX102068) and the Program Fund of Non-Metallic Excellence and Innovation Center for Building Materials, 2023TDA2-2, and Natural Science Foundation of Shandong Province (ZR2020MB041).

Institutional Review Board Statement: Not Applicable.

Informed Consent Statement: Not applicable.

Data Availability Statement: Available data are presented in the manuscript.

Conflicts of Interest: The authors declare no conflict of interest.

References

1. Torrejón, Y.N.; Giese, U.; Hannover. Consumption and reaction mechanisms of antioxidants during thermal oxidative aging. *KGK Rubberpoint* **2012**, *65*, 25–31.
2. Azura, A.R.; Ghazali, S.; Mariatti, M. Effects of the filler loading and aging time on the mechanical and electrical conductivity properties of carbon black filled natural rubber. *J. Appl. Polym. Sci.* **2008**, *110*, 747–752. [CrossRef]
3. Nakazono, T.; Ozaki, A.; Matsumoto, A. Phase separation and thermal aging behavior of styrene-butadiene rubber vulcanizates using liquid polymers as plasticizers studied by differential scanning calorimetry and dynamic mechanical spectroscopy. *J. Appl. Polym. Sci.* **2011**, *120*, 434–440. [CrossRef]

4. Tomer, N.; Delor-Jestin, F.; Singh, R.; Lacoste, J. Cross-linking assessment after accelerated ageing of ethylene propylene diene monomer rubber. *Polym. Degrad. Stab.* **2007**, *92*, 457–463. [CrossRef]
5. Osswald, S.L.B. Influence of different types of antioxidants on the aging behavior of carbon-black filled NR and SBR vulcanizates. *Polym. Test.* **2019**, *79*, 106053. [CrossRef]
6. Baldwin, J.M.; Bauer, D.R.; Ellwood, K.R. Rubber aging in tires. Part 1: Field results. *Polym. Degrad. Stab.* **2007**, *92*, 103–109. [CrossRef]
7. Chakraborty, S.; Kar, S.; Dasgupta, S.; Mukhopadhyay, R.; Chauhan, N.P.; Ameta, S.C.; Bandyopadhyay, S. Effect of Ozone, Thermo, and Thermo-oxidative Aging on the Physical Property of Styrene Butadiene Rubber-Organoclay Nanocomposites. *J. Elastomers Plast.* **2010**, *42*, 443–452. [CrossRef]
8. Wen, H.; Wang, M.; Luo, S.; Zhou, Y.; Liu, T. Aramid fiber reinforced EPDM microcellular foams: Influence of the aramid fiber content on rheological behavior, mechanical properties, thermal properties, and cellular structure. *J. Appl. Polym. Sci.* **2021**, *138*, 50531. [CrossRef]
9. Blivet, C.; Larché, J.-F.; Israëli, Y.; Bussière, P.-O.; Gardette, J.-L. Thermal oxidation of cross-linked PE and EPR used as insulation materials: Multi-scale correlation over a wide range of temperatures. *Polym. Test.* **2021**, *93*, 106913. [CrossRef]
10. Bhattacharya, A.B.; Chatterjee, T.; Naskar, K. Dynamically vulcanized blends of UHM-EPDM and polypropylene: Role of nano-fillers improving thermal and rheological properties. *Mater. Today Commun.* **2020**, *25*, 101486. [CrossRef]
11. Ma, H.; He, J.; Li, X.; Yang, R. High thermal stability and low flammability for Ethylene-Vinyl acetate Monomer/Ethylene-Propylene-Diene Monomer by incorporating macromolecular charring agent. *Polym. Adv. Technol.* **2021**, *6*, 32. [CrossRef]
12. Nordin, R.; Latiff, N.; Yusof, R.; Nawawi, W.I.; Salihin, M.Z.; Ishak, Z.A.M. Effect of several commercial rubber as substrates for zinc oxide in the photocatalytic degradation of methylene blue under visible irradiation. *Express Polym. Lett.* **2020**, *14*, 838–847. [CrossRef]
13. Wang, W.; Qu, B. Photo-and thermo-oxidative degradation of photocrosslinked ethylene–propylene–diene terpolymer. *Polym. Degrad. Stab.* **2003**, *81*, 531–537. [CrossRef]
14. Aimura, Y.; Wada, N. Reference materials for weathering tests on rubber products. *Polym. Test.* **2006**, *25*, 166–175. [CrossRef]
15. Barala, S.S.; Manda, V.; Jodha, A.S.; Meghwal, L.R.; Ajay, C.; Gopalani, D. Ethylene-propylene diene monomer-based polymer composite for attenuation of high energy radiations. *J. Appl. Polym. Sci.* **2020**, *138*, 50334. [CrossRef]
16. Zaharescu, T.; Mateescu, C.; Dima, A.; Varca, G.H.C. Evaluation of thermal and radiation stability of EPDM in the presence of some algal powders. *J. Therm. Anal. Calorim.* **2020**, *147*, 327–336. [CrossRef]
17. Yue, T.; Liu, P.; Zhao, H.; Li, S.; Zhang, L.; Liu, J. Chain dynamics evolution of ethylene-propylene-diene monomer in response to hot humid and salt fog environment. *J. Appl. Polym. Sci.* **2021**, *138*, 50742. [CrossRef]
18. Mokhtari, S.; Mohammadi, F.; Nekoomanesh-Haghighi, M. Surface modification of PP-EPDM used in automotive industry by mediated electrochemical oxidation. *Iran. Polym. J.* **2016**, *25*, 309–320. [CrossRef]
19. Rivaton, A.; Cambon, S.; Gardette, J.L. Radiochemical ageing of ethylene-propylene-diene elastomers. 4. Evaluation of some anti-oxidants. *Polym. Degrad. Stab.* **2006**, *91*, 136–143. [CrossRef]
20. Ning, N.; Ma, Q.; Zhang, Y.; Zhang, L.; Wu, H.; Tian, M. Enhanced thermo-oxidative aging resistance of EPDM at high temperature by using synergistic antioxidants. *Polym. Degrad. Stab.* **2014**, *102*, 1–8. [CrossRef]
21. Li, J.; Zhou, C.; Cao, M.S.D.; Liu, H. Synergistic Effects of Amine-Containing Antioxidants on the Aging Performances of Ethylene Propylene Diene Rubber. *Chem. Sel.* **2020**, *5*, 4961–4966. [CrossRef]
22. El-Wakil, A.E.-A.A.; El-Mogy, S.; Halim, S.F.; Abdel-Hakim, A. Enhancement of aging resistance of EPDM rubber by natural rubber-g-N (4-phenylenediamine) maleimide as a grafted antioxidant. *J. Vinyl Addit. Technol.* **2022**, *2*, 367–378. [CrossRef]
23. Liu, Y.; Gao, Q.; Liu, L.; Shi, G. Study on the Industrial Process of Rubber Anti-oxidant RD. *J. Korean Chem. Soc.* **2011**, *55*, 830–834. [CrossRef]
24. Li, Z.H.; Chen, S.J.; Zhang, J.; Shi, D.Q. Influence of different antioxidants on cure kinetics and aging behaviours of ethylene propylene diene rubber/low density polyethylene blends. *Plast. Rubber Compos.* **2013**, *38*, 187–194. [CrossRef]
25. Zhao, Z.; Tang, Q.; Zeng, S.; Yang, S.; Sun, J.; Liang, J. Effect of Sepiolite on Thermo-oxidative Stability Performance of Reinforced EPDM. *J. Mater. Res.* **2017**, *31*, 867–873.
26. Freeman, E.S.; Carroll, B. The Application of Thermoanalytical Techniques to Reaction Kinetics: The Thermogravimetric Evaluation of the Kinetics of the Decomposition of Calcium Oxalate Monohydrate. *J. Phys. Chem.* **1958**, *62*, 394–397. [CrossRef]
27. Albano, C.; Marianella, H.; Ichazo, M.N.; González, J.; DeSousa, W. Characterization of NBR/bentonite composites: Vulcanization kinetics and rheometric and mechanical properties. *Polym. Bull.* **2011**, *67*, 653–667. [CrossRef]
28. Hacıoğlu, F.; Özdemir, T.; Çavdar, S.; Usanmaz, A. Possible use of EPDM in radioactive waste disposal: Long term low dose rate and short term high dose rate irradiation in aquatic and atmospheric environment. *Radiat. Phys. Chem.* **2013**, *83*, 122–130. [CrossRef]
29. Chen, W.L.; Chen, H.C.; Tan, J.Z.; Chao, Y.J.; Van Zee, J.W. Chemical degradation of five elastomeric seal materials in a simulated and an accelerated PEM fuel cell environment. *J. Power Sources* **2011**, *196*, 1955–1966.
30. Boukezzi, L.; Boubakeur, A.; Laurent, C.; Lallouani, M. Observations on structural changes under thermal ageing of cross-linked polyethylene used as power cables insulation. *Iran. Polym. J.* **2008**, *17*, 611–624.
31. Zhao, Y.; Ma, Y.; Yao, W.; Huang, B. Styrene-Assisted Grafting of Maleic Anhydride Onto Isotactic Poly butene-1. *Polym. Eng. Sci.* **2011**, *51*, 2483–2489. [CrossRef]

32. Zhao, Y.; Du, Y.; Han, L.; Liu, Z.; Chen, J. Study on DTBP initiated MAH onto polybutene-1 with melt-grafting. *J. Polym. Eng.* **2012**, *32*, 567–574. [CrossRef]
33. Zhao, Y.; Zhou, Y.; Chen, J.; Han, L. Grafting of glycidyl methacrylate onto isotactic polybutene-1 initiated by di-tert-butyl peroxide. *J. Elastomers Plast.* **2015**, *47*, 262–276. [CrossRef]
34. Zhao, Y.; Chen, J.; Han, L.; Zhao, L. Nonisothermal crystallization kinetics of polybutene-1 containing nucleating agent with acid amides structure. *J. Polym. Eng.* **2014**, *34*, 53–58. [CrossRef]
35. Kumar, A.; Commereuc, S.; Verney, V. Ageing of elastomers: A molecular approach based on rheological characterization. *Polym. Degrad. Stab.* **2004**, *85*, 751–757. [CrossRef]
36. Zhao, Q.; Li, X.; Gao, J. Surface degradation of ethylene-propylene-diene monomer (EPDM) containing 5-ethylidene-2-norbornene (ENB) as diene in artificial weathering environment. *Polym. Degrad. Stab.* **2008**, *93*, 692–699. [CrossRef]
37. Zhao, Q.; Li, X.; Gao, J. Aging of ethylene-propylene-diene monomer (EPDM) in artificial weathering environment. *Polym. Degrad. Stab.* **2007**, *92*, 1841–1846. [CrossRef]
38. Snijders, E.A.; Boersma, A.; van Baarle, B.; Gijsman, P. Effect of dicumyl peroxide cross-linking on the UV stability of ethylene-propylene-diene (EPDM) elastomers containing 5-ethylene-2-norbornene (ENB). *Polym. Degrad. Stab.* **2005**, *89*, 484–491. [CrossRef]
39. Sun, Y.; Luo, S.; Watkins, K.; Wong, C. Electrical approach to monitor the thermal oxidation aging of carbon black filled ethylene propylene rubber. *Polym. Degrad. Stab.* **2004**, *86*, 209–215. [CrossRef]
40. Ozdemir, T. Gamma irradiation degradation/modification of 5-ethylidene 2-norbornene (ENB)-based ethylene propylene diene rubber (EPDM) depending on ENB content of EPDM and type/content of peroxides used in vulcanization. *Radiat. Phys. Chem.* **2008**, *77*, 787–793. [CrossRef]
41. Delor, F.; Teissedre, G.; Baba, M.; Lacoste, J. Ageing of EPDM-2. Role of hydroperoxides in photo-and thermo-oxidation. *Polym. Degrad. Stab.* **1998**, *60*, 321–331. [CrossRef]
42. Bhowmick, A.K.; Konar, J.; Kole, S.; Narayanan, S. Surface properties of EPDM, silicone rubber, and their blend during aging. *J. Appl. Polym. Sci.* **1995**, *57*, 631–637. [CrossRef]
43. Palmas, P.; Le Campion, L.; Bourgeoisat, C.; Martel, L. Curing and thermal ageing of elastomers as studied by 1H broadband and 13C high-resolution solid-state NMR. *Polymer* **2001**, *42*, 7675–7683. [CrossRef]
44. Zaharescu, T.; Podină, C. Radiochemical stability of EPDM. *Polym. Test.* **2001**, *20*, 141–149. [CrossRef]
45. Gamlin, C.; Dutta, N.; Roy-Choudhury, N.; Kehoe, D.; Matisons, J. Influence of ethylene–propylene ratio on the thermal degradation behaviour of EPDM elastomers. *Thermochim. Acta* **2001**, *367*, 185–193. [CrossRef]
46. Gamlin, C.D.; Dutta, N.K.; Choudhury, N.R. Mechanism and kinetics of the isothermal thermodegradation of ethylene-propylene-diene (EPDM) elastomers—ScienceDirect. *Polym. Degrad. Stab.* **2003**, *80*, 525–531. [CrossRef]
47. Assink, R.A.; Gillen, K.T.; Sanderson, B. Monitoring the degradation of a thermally aged EPDM terpolymer by 1H NMR relaxation measurements of solvent swelled samples. *Polymer* **2002**, *43*, 1349–1355. [CrossRef]

Disclaimer/Publisher's Note: The statements, opinions and data contained in all publications are solely those of the individual author(s) and contributor(s) and not of MDPI and/or the editor(s). MDPI and/or the editor(s) disclaim responsibility for any injury to people or property resulting from any ideas, methods, instructions or products referred to in the content.

Polymer Degradation and Stability 225 (2024) 110797

Contents lists available at ScienceDirect

Polymer Degradation and Stability

journal homepage: www.journals.elsevier.com/polymer-degradation-and-stability

Exploring the structure, characteristics, and thermal degradation of composites comprising thermoplastic polyolefin and graphene oxide under high-temperature dynamic shear conditions

Quanchao Hu [a,b], Hailiang Huang [b], Yufei Teng [a], Ying Yang [a], Gang Wang [b], Junyi Chen [a,*], Yongxian Zhao [a]

[a] Key Laboratory of Rubber-Plastics, Ministry of Education, School of Polymer Science and Engineering, Qingdao University of Science and Technology, Qingdao 266042, PR China

[b] Keshun Waterproof Technology Co., Ltd., Foshan 528303, PR China

ARTICLE INFO

Keywords:
Thermoplastic polyolefin
Graphene oxide
Thermal degradation
Structure and properties
Dynamic shear

ABSTRACT

Dynamic high-temperature shear aging tests were conducted on thermoplastic polyolefin (TPO)/graphene oxide (GO) composite materials using a Hakke torque rheometer. The study employed ATR-FTIR, DSC, SEM, oxygen performance testing, and TGA to analyze the structure, properties, thermal degradation behavior, kinetics, and mechanisms of TPO/GO composites. The results demonstrated that the high-temperature dynamic shear thermal oxidative aging of TPO/GO composite materials establishes a dual protective mechanism, incorporating physical (intercalation oxygen resistance) and chemical (inorganic oxygen resistance) effects. This can be attributed to the polar surface and honeycomb structure of GO, as well as the shear-induced more uniform physical distribution of GO within TPO. Consequently, TPO/GO composite materials exhibit significantly enhanced resistance to dynamic shear thermal oxidative aging compared to TPO alone.

1. Introduction

Thermoplastic polyolefin (TPO) is a recently developed polymer material which involves the random copolymerization of ethylene and propylene that exhibits exceptional performance due to the Catalloy synthesis technology [1,2]. Thermoplastic polyolefin possesses the benefits of both traditional plastics and rubber, making it suitable for a wide range of applications. These applications include roof waterproofing membranes [3,4], automotive interior parts [5], and various other fields . During the process of production and application, heat, exposure to oxygen, the presence of dynamic stress and strain may lead to alterations in the characteristics of TPO, resulting in a reduced lifespan. Hence, it is very important to investigate the response mechanism of the thermo-oxidative degradation of thermoplastic polyolefin materials.

Graphene oxide (GO) is a recently discovered material with a unique structure consisting of a single-layer two-dimensional honeycomb lattice and several advantages such as high strength, good toughness, and high thermal conductivity. Due to these properties, GO has been extensively studied for its potential to modify various polymers. It has also become a major focus of research in several fields because of its exceptional physicochemical properties [6]. In recent years, GO had emerged as a prominent functional filler in the fields of materials science and physics research. It has been extensively employed in the research of various polymers, encompassing the analysis of mechanical properties [7–9], electrical properties (conductivity [10], electrochemical properties [11], electromagnetic properties [12]), thermal conductivity [13], barrier properties [14,15], and nano-sensors [16], among numerous other applications.

The ageing process of polymer is a complex mechanism that consists of several stages, which may be categorized into various sections [17]. The material can undergo structural and property modifications due to physical and/or irreversible chemical processes, such as breakage of polymer chain, (post-) cross-linking, breakage and re-formation of covalent bond [18,19]. The polymer-related properties, including strength, hardness, polarity, and toughness, can be influenced by these processes [19,20]. The degree of performance changes related to product aging significantly depends on temperature and other aging conditions [21].

TPO waterproofing membranes are widely used in exposed waterproofing projects, such as industrial plants, airports, and sports venues.

* Corresponding author.
E-mail address: chenjunyi@qust.edu.cn (J. Chen).

https://doi.org/10.1016/j.polymdegradstab.2024.110797
Received 29 January 2024; Received in revised form 29 April 2024; Accepted 30 April 2024
Available online 1 May 2024
0141-3910/© 2024 The Authors. Published by Elsevier Ltd. This is an open access article under the CC BY-NC license (http://creativecommons.org/licenses/by-nc/4.0/).

With the development of the photovoltaic industry, the usage of TPO waterproofing membranes will significantly increase, posing higher demands on their physical properties and service life. Studying the structure and properties of graphene oxide modified TPO materials has important theoretical and application value. This article studied the changes in physical properties, crystallinity properties, rheological property, oxygen permeability, and thermal degradation of TPO/GO composite materials during dynamic high-temperature shear aging process using a Hakke torque rheometer [22–26]. The structure, properties, and thermal degradation mechanism of TPO/GO composite materials were carefully studied. The protective mechanism of GO on the thermal oxidative aging of composite materials was a dual effect of physical (intercalation oxygen resistance) and chemical (inorganic oxygen resistance).

2. Experimental

2.1. Materials

The TPO resin, specifically grade CA10A, is a thermoplastic polyolefin made from an ethylene-propylene random copolymer with a propylene concentration of 68.4 %. It is produced by LyondellBasell, a company based in Basel, the Netherlands. The GO used is characterized by a D50 particle size ranging from 7 to 12 μm and consists of 1 to 3 layers. The monolayer rate of the GO is more than 80 %. The GO is purchased from TuLing JinHua KeJi.

2.2. Sample preparation

A quantity of 200.0 g of TPO resin, specifically Sample #1, was introduced into a Hakke torque rheometer (Thermo Fisher Scientific, Poly Lab OS, Waltham, MA, USA) operating at 180 °C & 40 rpm. The resin was subjected to dynamic shearing for durations of 10 min (Sample #2) and 30 min (Sample #3) using a Banbury rotor. A total of 200 g of TPO resin was combined with 2.0 g of graphene oxide using a Hakke Torque Rheometer operating at a consistent temperature and rotating speed of 180 °C and 40 rpm for of 10 min (Sample #4) and 30 min (Sample #5), respectively. The precise procedures for preparing the TPO/GO composite sample are detailed in Table 1.

The selected formula and process conditions for the experiment were based on the following considerations.

(a) The temperature of 180 °C for the torque rheometer was based on the extrusion temperature setting of the twin-screw extruder in the actual production process. The speed and 40 rpm were set according to the conventional working speed of the torque rheometer, which was also equivalent to the working speed of the extruder.
(b) The high-temperature dynamic shear aging time is selected as 10 min and 30 min respectively. Because the torque rheometer operates in an open mode, the melt was subjected to rotor shear and severe oxidation with air. Therefore, by selecting the two time points of 10 min and 30 min, the difference in shear processing time on the overall structure can be reflected.
(c) When exploring the effect of GO content on the oxygen transmittance of materials (Fig. 6A), it was found that the composite material with 1.0 % GO content had the lowest oxygen transmittance. As a result, a composite material with 1.0 % GO addition was selected for the experiment.

2.3. Characterization

2.3.1. Physical property

Different samples with a thickness of 1.00 mm were prepared using an XH-406B flat plate vulcanizing machine (manufactured by Xihua Testing Machines Co., Ltd, Dongguan, Guangdong, China) with a pressure of 10 MPa and a temperature of 180 ± 0.5 °C.

The mechanical performance testing of the sample material partially referred to the performance indicators of the waterproof membrane.

According to the ISO 188:2011, the thermal oxidation aging tests of samples were conducted in a thermal oxidation aging test chamber (GOTECH Testing Machines INC., GT-7017-E, Taiwan, China). The setting of the device was as follows: temperature was 115 °C, temperature deviation was ±2 °C, air flow rate was 0.5–1.5 m/s, and air exchange frequency was 3–10 times/h. The aging time was 28 days.

According to GB/T 27789-2011, the acid medium treatment method is as follows: the sample is treated for 28 days in (5 ± 0.01 %) concentration of H_2SO_4.

The AI-7000S electronic universal testing machine (manufactured by GOTECH TESTING MACHINES INC., Taipei, Taiwan, China) was used to evaluate the physical and mechanical qualities of the samples, following the guidelines stated in ISO 37: 2005.

The impact resistance (0.5 kg m) and low-temperature bending resistance (−45 °C) of the sample were tested according to GB/T 27789-2011.

The hardness of samples was assessed using a Shore D hardness tester (GOTECH TESTING MACHINES INC., Taipei, Taiwan, China) in accordance with ISO 7619-2: 2004.

The melt mass flow rate (MFR) was measured in accordance with the GB/T 3682.1-2018 (ISO 1133-1:2011, MOD) standard at a temperature of 230 °C and a load of 2.16 kg.

The right-angled tearing strength was measured by the AI-7000S electronic universal testing machine in accordance with the GB/T 529-2008 (ISO 34-1:2004, MOD) standard.

2.3.2. Infrared spectrometer

The materials were analyzed using a Nicolet IS 10 Fourier transform infrared spectrometer (Thermo Fisher Scientific, Waltham, MA, USA) and infrared reflectance-reflectance absorption spectroscopy (ATR-FTIR) in the range of 4000 to 450 cm^{-1}, with a scanning rate of 5 cm^{-1}/s and 20 scans.

2.3.3. Differential scanning calorimeter

A DSC 3+ differential scanning calorimeter (METTLER TOLEDO, Zurich, Switzerland) was employed to subject the samples to a temperature range of 30 °C to 200 °C for 5 min, with a heating rate of 10 K/min, in order to remove any previous thermal effects. Subsequently, the temperature was decreased to 30 °C at a rate of 10 K/min, followed by a final increase to 200 °C at the same rate, to generate the DSC ramping curve.

Table 1
Preparation conditions of different TPO/GO composites.

No.	TPO (g)	GO (g)	Time (min)	Temperature (°C)	Rotating speed (rpm)
Sample #1	200.0	0	0	0	0
Sample #2	200.0	0	10	180	40
Sample #3	200.0	0	30	180	40
Sample #4	200.0	2.0	10	180	40
Sample #5	200.0	2.0	30	180	40

2.3.4. Rotational rheometer

Rheological experiments were conducted at a temperature of 180 °C using an MCR302 rotating rheometer manufactured by Anton Paar in Graz, Austria. The specimen has a diameter of 25 mm. There is a 1 mm gap between the rotor and the stage. The frequency ranges from 1×10^{-2} to 100 Hz, and the strain is 1 per cent.

2.3.5. Oxygen permeability

The oxygen transmission rate of all samples was measured using the OX-TRAN 2/22H Oxygen Transmission Rate Tester (AMETEK MOCON, Minneapolis, USA) at a temperature of 23.0 °C. The samples had a surface area of 5.54 cm^2, a thickness of 100 μm, and the test was conducted for a duration of 6 h. The samples underwent testing using a sample area of 5.54 cm^2 and a thickness of 100 μm.

2.3.6. Water contact angle

The samples underwent testing utilizing an SDC200S contact angle tester (Aojin Industrial Automation System Co., Ltd, Guangzhou, Guangdong, China) using distilled water as the test liquid at a temperature of 15 °C and a humidity level of 50 %.

2.3.7. Scanning electron microscope

The samples were analyzed by using a TM3030Plus scanning electron microscope (Hitachi Corporation, Tokyo, Japan) at an operating voltage of 15 kV and a magnification of 5000X. The samples were directly viewed without the use of gold spraying.

2.3.8. Thermogravimetic analysis

The samples were analyzed by using a Thermal Weight Loss Analyzer model TGA2/SDTA851 (METTLER TOLEDO, Zurich, Switzerland) under controlled circumstances. The temperature range was set from 30 °C to 600 °C in nitrogen with the airflow rate of 50 ml/min, and a temperature rise rate of 2.5 k/min.

2.3.9. Thermal degradation kinetics analysis

The samples were analyzed using a TGA2/SDTA851 thermal weight loss analyzer (METTLER TOLEDO, Zurich, Switzerland) with consistent conditions. The temperature range was set from 30 °C to 600 °C in nitrogen. The airflow rate was 50 ml/min, and the ramp rates were 1 K/min, 2.5 K/min, 5 K/min, 10 K/min, 15 K/min, and 20 K/min, respectively. The thermal analysis results were analyzed on a computer using a custom-designed software package.

3. Results and discussion

3.1. Physical property

As shown in Fig. 1, the TPO without GO gradually turned yellow with increasing shear processing time, mainly due to the degradation of macromolecular chains. And the appearance color of the sample with GO was not obvious with various shear processing time.

It can be seen in Table 2, as the shear processing time was extended, the tensile strength, hardness, right-angled tearing strength and elongation at break of TPO without GO gradually decrease with increasing melt flow rate as the shear processing time is extended. It can be attributed to the oxidative degradation of the TPO macromolecular chains due to high temperature dynamic shear, resulting in chain breakage. A simultaneous increase in the tensile strength, right-angled tearing strength and elongation at break of TPO with graphene oxide can be seen as the shear processing time increased. This can be attributed to two factors. Firstly, the addition of GO improved the viscosity of the composite with enhanced the uniform dispersion of GO, resulting in a reinforcing effect. Secondly, the high temperature dynamic shear thermo-oxidative aging of the TPO/GO nanocomposites were slowed down because of the addition of GO. The reduction in hardness and the rise in MFR were a result of the oxidative degradation of the macromolecular chains of the TPO/GO nanocomposites.

Cracks can be seen in the sample without GO as the shear processing time increased according to low-temperature bending test, which was caused by the breakage of macromolecular chains during high-temperature dynamic shear. The cracking of TPO with added GO was caused by the uneven dispersion and aggregation of GO. With the extension of shear processing time, GO dispersion becomes more uniform with no cracks appear can be seen in the sample.

Meanwhile, the samples with the 115 °C hot oxygen treatment and the 5 % sulfuric acid medium treatment showed the same aging pattern.

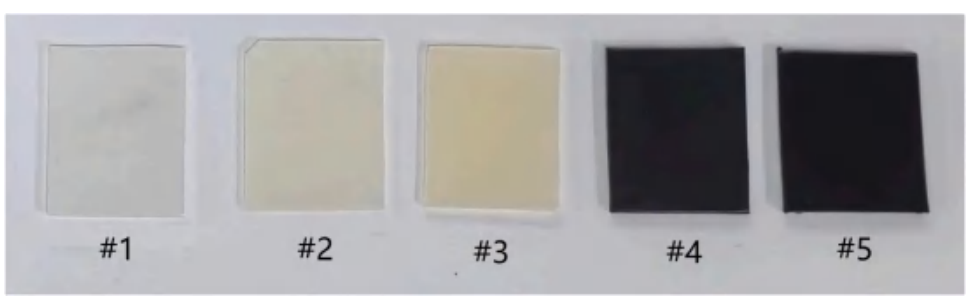

Fig. 1. Appearance of different TPO/GO nanocomposites.

Table 2
Physical properties of TPO/GO nanocomposites.

Test items	Sample #1	Sample #2	Sample #3	Sample #4	Sample #5
Tensile strength (MPa)	19.75	18.82	18.25	21.58	22.98
Elongation at break (%)	798.13	777.22	755.38	725.15	805.76
Hardness (Shore D, 15 s)	28.40	28.20	27.30	28.80	28.40
MFR,(230 °C,2.16 kg)/(g/10 min)	0.44	0.52	0.65	0.47	0.54
Right-angled tearing strength (N)	64.34	63.21	62.14	66.75	68.89
Tensile strength (115 °C-28d) (Mpa)	18.67	17.36	16.27	20.98	21.08
Elongation at break (115 °C-28d) (%)	746.41	709.06	680.82	668.15	737.55
Tensile strength (5 %H_2SO_4-28d) (Mpa)	18.87	17.53	16.34	20.19	21.98
Elongation at Break (5 %H_2SO_4-28d) (%)	758.38	722.81	691.25	675.58	778.12
Impact resistance(0.5 kg m)	no water seepage	no water seepage	no water seepage	no water seepage	no water seepage
low-temperature bending resistance (−45 °C)	no crack	no crack	crack	crack	no crack

As the shear processing time increased, the tensile strength and elongation at break of TPO without GO gradually decreased, while the tensile strength and elongation at break of TPO with GO added slightly increased. This indicated that the addition and more uniform dispersion of GO have improved the thermal oxidative aging resistance and acid resistance of TPO/GO nanocomposites.

The impact performance of 5 samples tested according to GB 328.10-2007 can meet the requirements without water seepage.

3.2. Differential scanning calorimetry analysis

This study presented the acquisition of DSC spectra by analyzing the relationship between temperature and heat flow during thermal transitions in various TPO/GO nanocomposites, as seen in Fig. 1. The particular DSC data can be found in Table 3.

The melting curves were shown in Fig. 2A. It was evident that TPO exhibits large overlapping melt peaks about 143 °C, along with two further peaks at around 134 °C and 155 °C. Due to the dynamic shear at high temperature and chain breakage, the overall regularity would decreased, increasing the difficulty of crystallization and resulting in a decrease in melting temperature for different samples (including the TPO with GO and the TPO without GO). When comparing Sample #1 with the TPO without GO at the same processing period, it was observed that the melting peak temperature of the TPO with graphene oxide changed towards higher temperatures due to the unique single-layer two-dimensional cellular network structure of GO.

From the crystallization curve in Fig. 2B, it was obvious that there were two peaks of crystallization for TPO. The first peak was labeled as No. 1, representing the primary crystallization peak of the regular chain segment of polypropylene homopolymer. The second peak was labeled as No. 2, which was attributed to the formation of the regular chain segment of polyethylene during the process of ethylene-propylene copolymerisation, which proved the homogeneous nucleus of ethylene exist in the ethylene-propylene rubber phase with a high content.

As the shear processing time increases, the crystallization peak temperature of all samples shifts to a lower temperature. This shift was accompanied by a decrease in crystallinity (*Xc*). The decrease in *Xc* was caused by the oxidative degradation of TPO macromolecular chains, which slowed down the formation of a regular lattice [27]. Incorporating GO into TPO enhanced the crystallinity of TPO/GO nanocomposites via the heterogeneous nucleation effect [28–31].

Surprisingly, as compared with the sample without GO, the temperature of second crystallization peak in TPO with GO was lower than in TPO without GO, even when processed for the same time. This was likely due to the increased number of nucleation points in the GO-added TPO, which enhanced the ability of crystallization for the polypropylene chain segments. As a result, a large number of crystals form and collide within the limited space available for polyethylene crystallization in the rubbery phase of ethylene-propylene, resulting in the lower temperature of the second crystallization peak.

3.3. Rheological analysis

The complex viscosity curve in Fig. 3A demonstrated that when the angular frequency (ω) with increasing shear force, a significant amount of molecular chain entanglement was disrupted, leading to a quick reduction in η^* with obvious shear thinning behavior.

At angular frequencies below $10^{-0.5}$ rad/s, the complex viscosity (η^*) of samples decreased over time with or without GO. However, even after processing, the η^* of TPO remained lower than the unprocessed TPO (Sample #1). This decrease in viscosity could be attributed to the degradation of the macromolecular chains caused by the high-temperature dynamic shear and the reduction in molecular weight due to oxidative chain-breaking. The η^* of TPO with GO was higher than that of TPO without GO. It could be attributed to the layered structure of GO, which was beneficial for increasing the viscosity of the TPO matrix and created more frictional resistance for the molecular chains in the TPO/GO nanocomposites. As a result, the movement of the molecular chains was limited to some extent [32,33].

It was demonstrated that a clear correlation between the ω and the energy storage modulus (G′) of TPO, indicating a rise in G′ as ω increases (Fig. 3B). When the ω was less than $10^{-0.5}$ rad/s, the G′ of TPO decreased over time during shear processing, regardless of whether GO was added or not. However, the G′ of TPO were lower than Sample #1 after processing. Because the oxidative chain breakage lead to a higher capacity for entangling short knots in the molecular chains, resulting in more pronounced viscous behavior.

The viscosity of the TPO system could be enhanced according to the addition of GO, resulting in increased number of entanglement points of molecular chains and friction between phases (interfaces). This friction partially restricted the mobility of TPO molecular chains, enhancing the rigidity of TPO/GO nanocomposites [34,35].

3.4. Fourier transform infrared spectrometer (ATR-FTIR) analysis

The ATR-FTIR technique was used to analyze the structure of several TPO/GO composites in this study. Fig. 4 displays the diverse infrared spectra of several TPO/GO composites.

The attenuated total reflectance type infrared spectra (ATR-FTIR) of various TPO/GO nanocomposites can be seen in Fig. 4. As the shear processing time increased, the distinctive carbonyl peak at 1730 cm^{-1} was can been seen with increasing intensity.

And its area can be regarded as an indicator of the extent of oxidative degradation of the polymer [36,37]. The temperature and dynamic shear during the process lead to the oxidative degradation of the TPO macromolecular chain, resulting in the formation of additional carbonyl groups with more obvious absorption peak. The increased spectral peaks in the range of 3000–3700 cm^{-1} for TPO/GO were caused by the absorption peaks of hydroxyl groups (—OH) on the surface of GO. The absorption peak at 1620 cm^{-1} was due to the bending vibration of the water molecule [30], which likely caused by the water molecules in graphite(olefin) oxide.

Interestingly, as the shear processing time increased, the peak intensities at 1620 cm^{-1} and 3000–3700 cm^{-1} decreased with increasing shear processing time. This could be attributed to two reasons. On the one hand, it could be attributed to the dehydration reaction of water molecules absorbed by graphene oxide. On the other hand, it may be due to the termination reaction (ROOH) between the hydroxyl groups (—OH) on the surface of GO and the macromolecular peroxide radicals (ROO*) under multiple aging conditions of high temperature dynamic

Table 3
Data of DSC spectra.

	Sample #1	Sample #2	Sample #3	Sample #4	Sample #5
T_m/ °C	143.20	143.00	142.70	144.30	143.40
T_{c1}/ °C	99.50	99.50	96.30	100.50	98.70
T_{c2}/ °C	75.50	75.00	74.00	74.30	72.20
ΔHm/(J g^{-1})	44.58	43.46	40.12	39.03	37.86
Xc/%	21.33	20.79	19.20	18.67	18.11

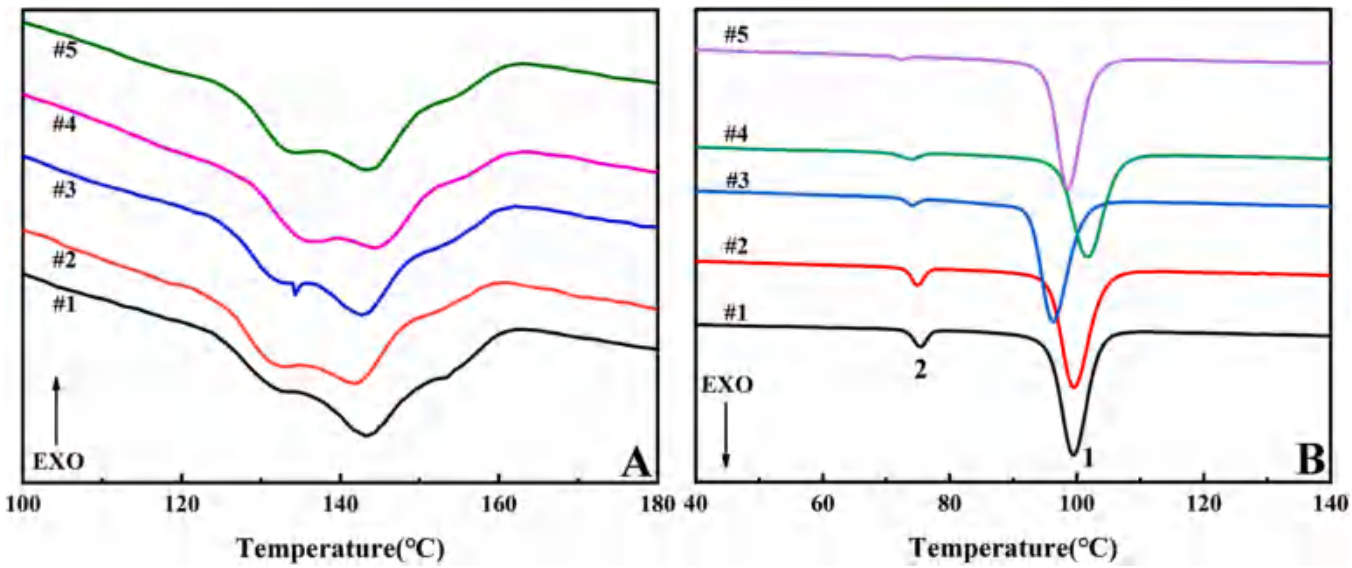

Fig. 2. DSC spectra of different TPO/GO nanocomposites: (A) Melting curves; (B) Crystallization curves.

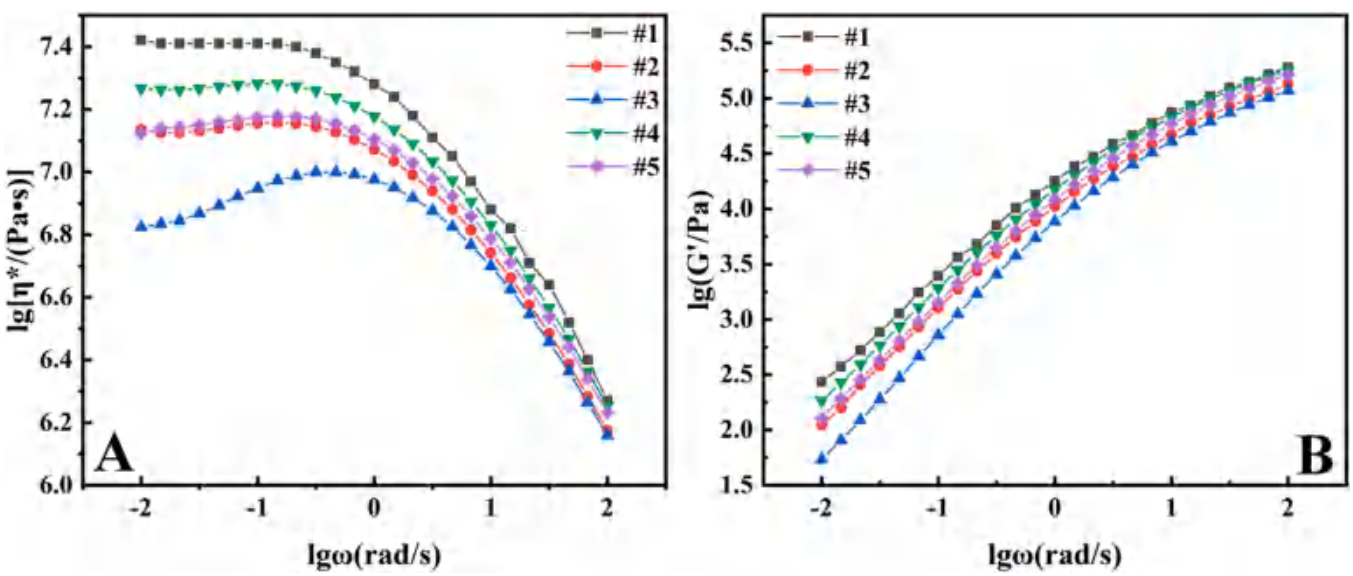

Fig. 3. Rotation rheological diagram of different TPO/GO composites: (A) complex viscosity; (B) storage modulus.

shear (oxygen, dynamic shear, temperature), which could lower the intensity of the hydroxyl group peak.

3.5. Dispersion and surface property

Scanning electron microscopy (SEM) was used to examine various TPO/GO composites at a magnification of 5000 times, as shown in Figs. 5 and 6A.

The results indicated that as the shear processing time increases, the dispersion uniformity of graphene oxide in composite materials continuously improved, resulting in a reduction in the ``agglomeration'' phenomenon of GO in TPO matrix. When the shear processing time was 30 min, the GO with a well dispersed state exist in TPO/GO composite materials. Further extension of shear processing time has little effect on the uniform dispersion of graphene oxide. This paper studies composite materials with a processing time of 30 min.

The contact angle mechanism of several TPO/GO composites was illustrated in Fig. 6.

A gradual decrease in the contact angle of TPO with and without GO addition as the shear processing time increases was demonstrated in Fig. 6B. This could be attributed to the oxidative degradation of TPO macromolecules, resulting in the breakdown of the molecules, and the gradual increase in oxygen-containing groups on the surface, such as carbonyl and carboxyl groups. The polarity of the TPO surface could be enhanced by these groups enhance, leading to an improvement in hydrophilicity. The surface roughness increased due to the addition of GO in TPO/GO composites, as predicted by Wenzel equation. It was established that the augmentation of surface roughness leads to an elevation in the contact angle on surface [38,39]. Consequently, the contact angle of TPO/GO nanocomposites surpassed the same parameter of TPO without graphene oxide.

3.6. Oxygen permeability

The diffusion of gas across a film is a process of individual molecule movement, which is classified under the mass transfer process. The gas

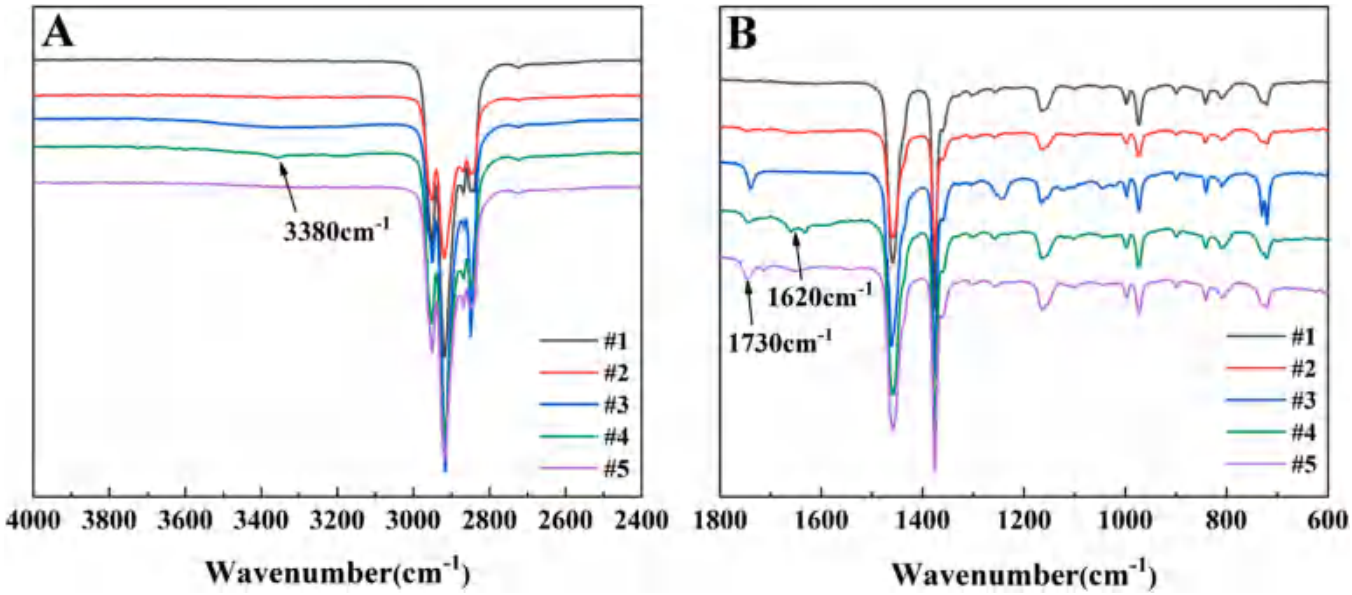

Fig. 4. Fourier Transform infrared spectrum of different TPO/GO composites: (A) ATR-FTIR spectra with range of 2400–4000 cm^{-1}; (B) ATR-FTIR spectra with range of 600–1800 cm^{-1}.

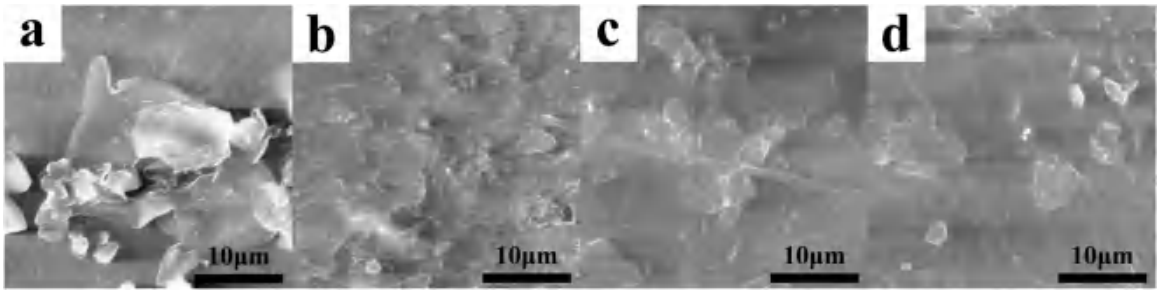

Fig. 5. SEM of TPO/GO composites (1.0 % GO) with different shear processing time: (a) 10 min; (b) 20 min; (c) 30 min; (d) 40 min.

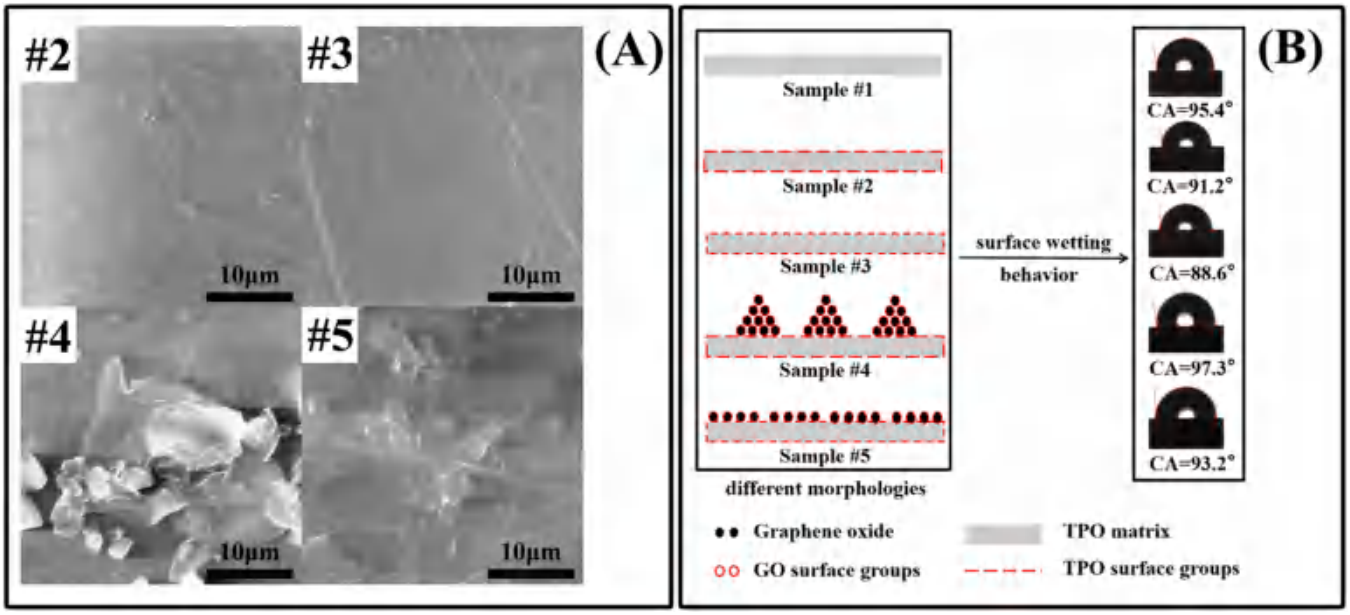

Fig. 6. Surface properties of different TPO/GO composites: (A) SEM microtopography; (B) Contact angle.

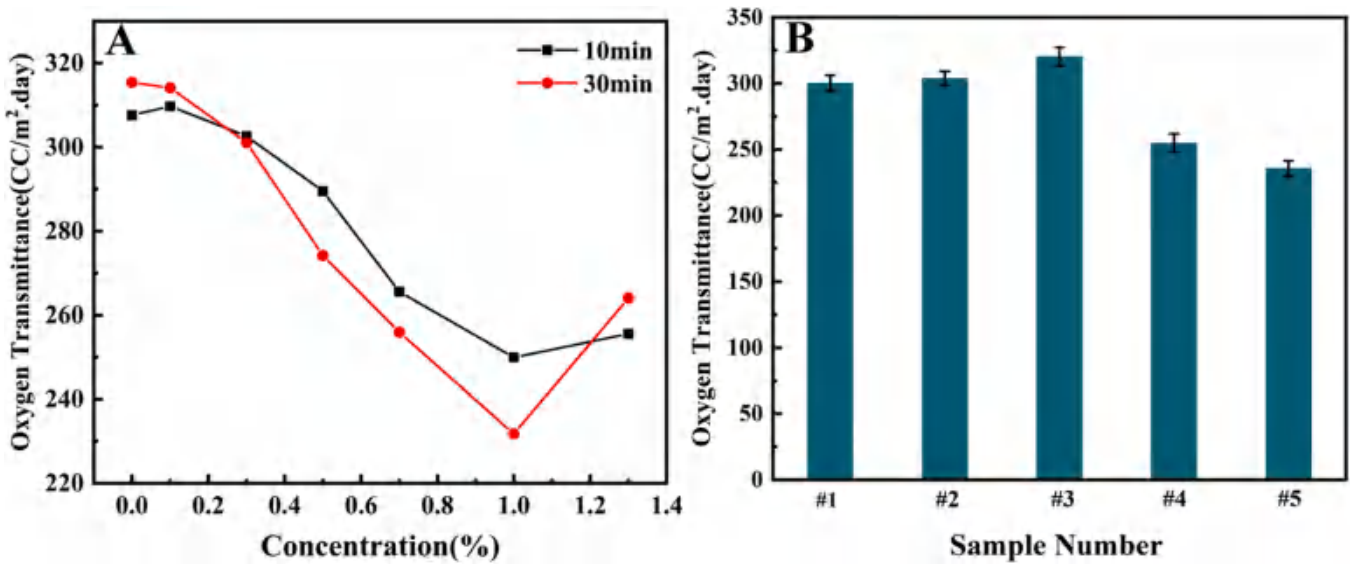

Fig. 7. Oxygen Transmittance of TPO/GO composite and TPO. Influence of shearing time and GO content on the oxygen transmittance of TPO/GO composites; (B) Oxygen Transmittance of different TPO/GO composites in this article.

penetration into the film is the result of the individual molecules permeating through the film in large numbers. Oxygen permeability refers to the amount of oxygen that passes through a certain area of a material (such as a film) over a 24-h period under a constant temperature and pressure difference. It is an important technical metric to indicates the extent of oxygen to pass through samples, as shown in Fig. 7.

A significant downward trend of the oxygen transmittance of TPO/GO composite materials can be seen in Fig. 7A with the increase of GO content. The lowest point of oxygen transmittance can be seen in the TPO/GO composite materials with 1.0 % GO. When the amount of GO added was 1.3 %, the oxygen transmittance TPO/GO composite materials increased, indicating that more GO content is not better, indicating that more GO cannot continue to reduce the oxygen transmittance. When the GO content is between 0.3 % and 1.0 %, the oxygen transmittance of TPO/GO composite material decreases with increasing shear time, indicating that shear was more effective in uniformly distributing GO within this content range. When the content exceeds 1.0 %, the viscosity increase caused by the addition of GO exacerbates shear degradation and uneven distribution, resulting in an increase of oxygen transmittance of TPO/GO composite material with 1.3 % GO content. As a result, the TPO/GO composite material with 1.0 % GO was selected for research in this paper.

It could be seen in Fig. 7B, the oxygen permeability of TPO increased as increasing shear processing time. This was primarily caused by the degradation of macromolecular chains in TPO matrix, resulting in a reduction in molecular weight. Additionally, the shear oxidation of the carbonyl group also contributes to the decrease in activation energy for oxygen permeability, thereby enhancing the overall oxygen permeability of TPO. Graphene oxide is a two-dimensional honeycomb lattice structure made of inorganic material. Its oxygen permeability was lower than TPO. Additionally, the addition of GO to the TPO/GO composite system boosts viscosity and reduces oxygen permeability [40,41]. Furthermore, the dispersion of graphene oxide was more uniform with the progress of high-temperature dynamic shearing, resulting in a further reduction in the oxygen permeability of the TPO/GO nanocomposites.

The diagram illustrating the physical distribution and chemical antioxidant activity mechanism under the previous circumstances of high temperature dynamic shear can be seen in Fig. 8. As the duration of dynamic high-temperature shear processing increases, the oxidation degradation of TPO macromolecular chains becomes more intense, leading to chain-breaking reactions. This allows for a more uniform insertion of the physical layer of GO into the TPO matrix. Additionally, the presence of oxygen, shear forces, and high temperature causes the

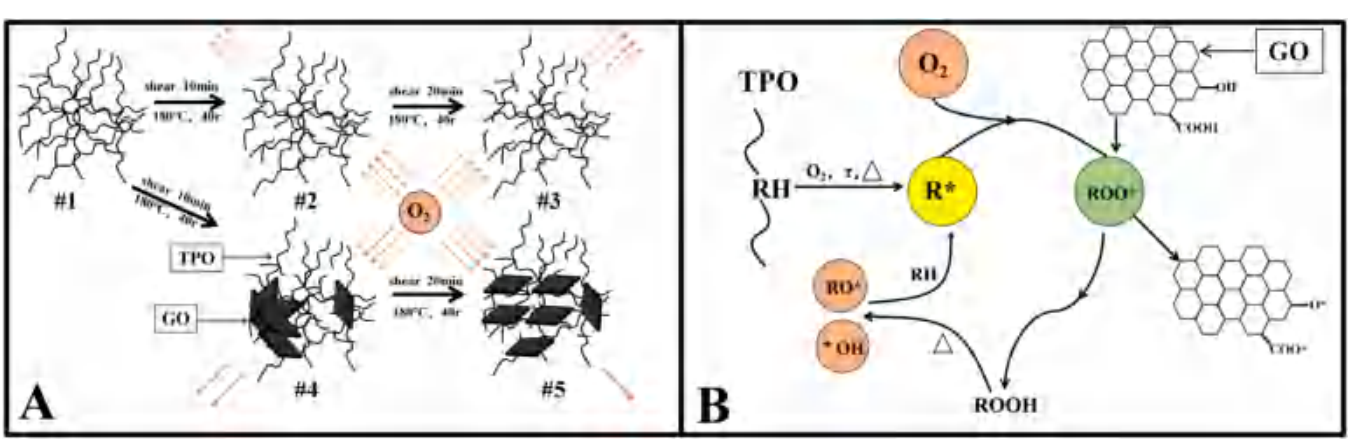

Fig. 8. Mechanism diagram of TPO/GO composites with high-temperature dynamic-shear aging: (A): Physical micro-state distribution; (B) chemical antioxidant mechanism.

TPO macromolecular chains to break and form R* radicals. These radicals then react with oxygen to generate ROO* radicals. The laminated graphene oxide acts as a barrier, preventing the penetration of oxygen. Furthermore, the -OH groups on the surface of GO and the ROO* radicals undergo a free radical chain termination reaction, resulting in the formation of ROOH. This process may hinder the aging effects caused by dynamic high temperature shear.

3.7. Thermal degradation behavior

Thermal weight loss analysis involves examining the thermal stability of a sample by measuring the its mass in relation to temperature or time, while subjecting it to a certain flow rate environment. Thermogravimetric (TG) testing measures the change in the mass of a specimen as a result of either a gradual rise in temperature or a constant temperature over time. Different phases of thermal degradation of the specimen can be seen in TG curve, providing a qualitative and quantitative analysis of the changes in its components during the aging process. DTG curve can be derived from TG curve, which depicts the mass loss rate. These two curves are directly related to each other. The TG/DTG curves for several TPO/GO composites were displayed in Fig. 9, while the individual TG/DTG data were presented in Table 4.

As shown in Fig. 8, a single step change was exhibited in the TG curves of TPO, regardless of the presence or absence of added graphene oxide. It was revealed that each sample undergoes a sequence of consecutive reactions during the degradation process, resulting in the production of a small molecule without stable intermediate product. In Table 4, the onset degradation temperature ($T_{5\ \%}$), degradation temperature at maximum rate (T_{max}), and termination degradation temperature (T_{end}) of TPO without graphene oxide decrease slightly as increasing shear processing time, indicating that high-temperature dynamic shear negatively affects the thermal degradation behavior of TPO. On the other hand, the $T_{5\ \%}$, T_{max}, and T_{end} of the TPO/GO composites increased compared to those of the TPO without GO, which may be attributed to the capacity of GO to enhance the thermal stability of TPO/GO composites. As the shear processing time increased, the $T_{5\ \%}$, T_{max}, and T_{end} of TPO/GO composites shifted towards higher temperatures. This indicated that the dispersion of graphene oxide became more uniform and the oxygen barrier effect became more pronounced with longer shear processing time. Consequently, the thermal stability of TPO/GO composites was improved.

Table 4
Basic thermogravimetric data of different TPO/GO composites.

Sample no.	$T_{5\ \%}$ (°C)	T_{max} (°C)	T_{end} (°C)	Residual percentage/%
#1	388.88	435.83	464.17	0.21
#2	388.25	434.79	464.88	0.18
#3	387.42	434.58	464.92	0.24
#4	395.79	436.04	465.54	1.10
#5	402.04	437.75	466.30	1.06

3.8. Thermal degradation kinetics

As we all know, the corresponding temperature for achieving the same conversion rate continuously increases as the heating rate increases for the same sample. This phenomenon occurs due to the direct correlation between the rate of heating and the time required to reach the final temperature of thermal deterioration. As the heating rate increases, the time to reach the endpoint temperature of thermal degradation becomes shorter with worse degree of reaction progress, resulting in a temperature shift to reach the maximum thermal degradation rate. Consequently, there was a shift back in the temperature at which this maximum rate is achieved [42], as shown in Fig. 10.

The Flynn-Wall-Ozawa formula was introduced in this research [43] to study the activation energy of thermal degradation processes of various TPO/GO composites. This approach is a dynamic integration technique, represented by the equation in Eq. (1):

$$\log(\beta) = \log\left[\frac{AE_a}{g(\alpha)}R\right] - 2.31 - 0.4567\left[\frac{E_a}{RT}\right] \quad (1)$$

The variables in the equation are as follows: α is the rate at which decomposition occurs, T is the temperature in Kelvin, β is the rate at which the temperature increases each minute, A and E are factors in the Arrhenius formula that determine the rate of reaction, and g(α) is the integral form of the function that describes the reaction mechanism. The same conversion rate α was chosen for various heating rates β. A linear regression analysis was conducted using the equation −10,000/RT, using the variable $lg\beta$ at various values of α. The straight lines, which were fitted to the data, were displayed in Fig. 11. The link between the degradation activation energy E and the varied conversion rates α were demonstrated in Fig. 12.

The average activation energy for thermal degradation (E_a) was determined by computing the activation energy (E) at various conversion rates (α). The E_a of TPO without GO declined progressively as the shear processing time increased, which may be attributed to the reduction in thermal stability resulting from the shear-induced oxidative

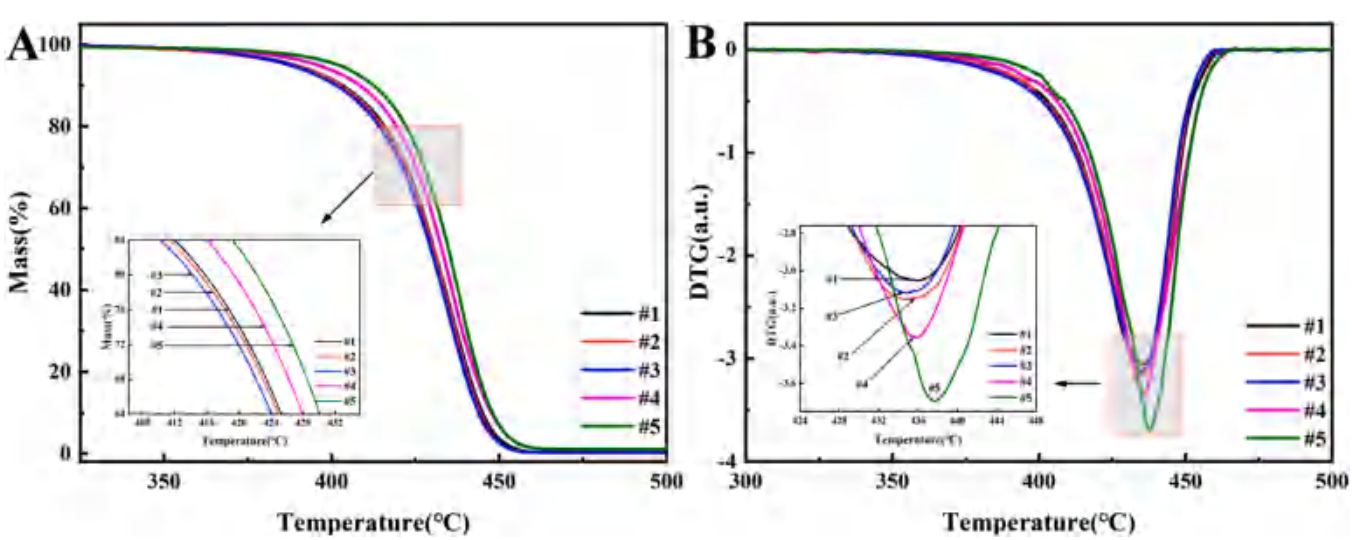

Fig. 9. TG/DTG curves of different TPO/GO composites.

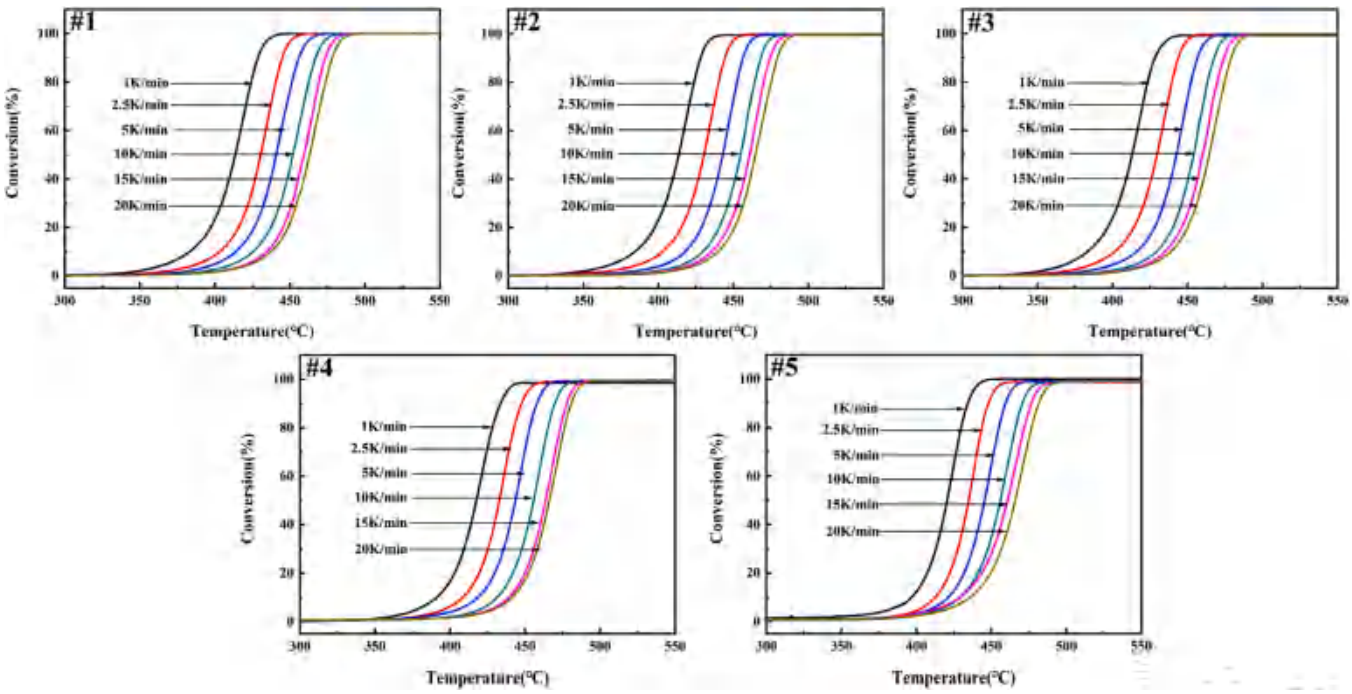

Fig. 10. Dependence of conversion (in percentage) vs. Temperature of different sample which obtained at various heating rates.

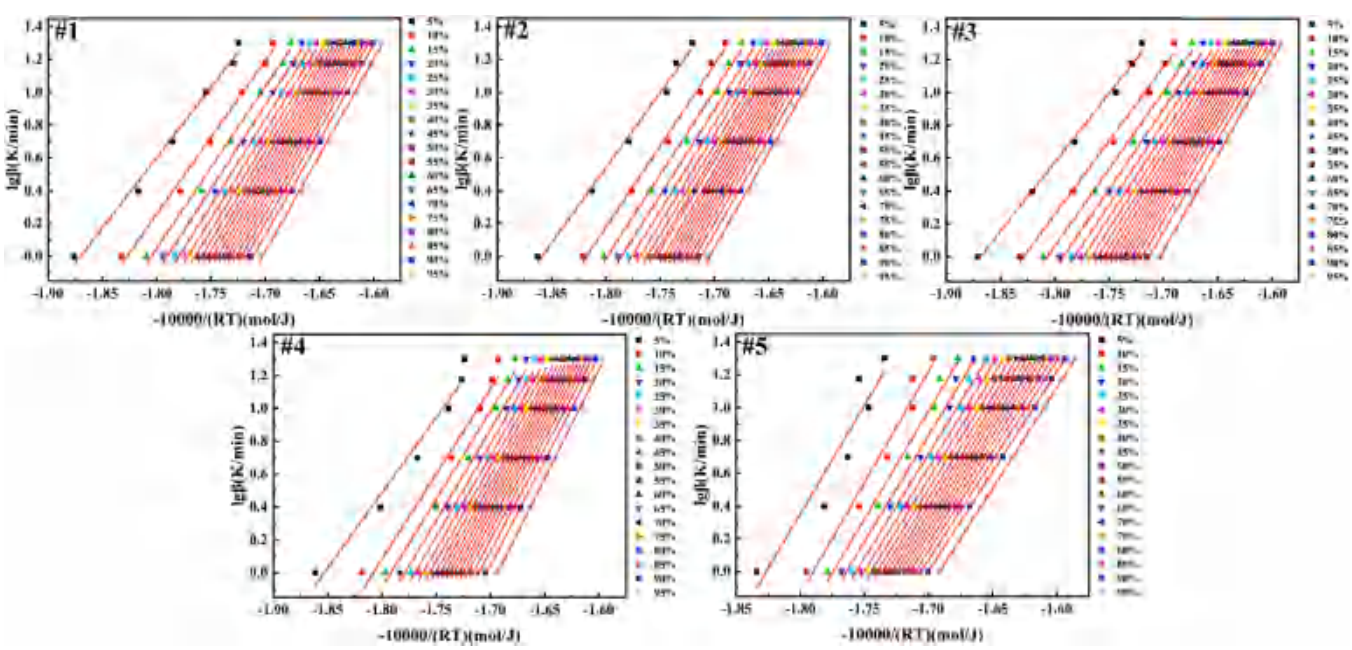

Fig. 11. Flynn–Wall–Ozawa plots of lgβ vs. −10,000/(RT) at various extents of conversion.

degradation of the macromolecular chains. The addition of graphene oxide to the thermoplastic polyolefin matrix resulted in an increase of E_a. This increase can be attributed to two factors. Firstly, the oxygen transmission rate of TPO/GO composites can be reduced because of GO. Secondly, the high-temperature shear thermo-oxidative aging process was slowed down because of the chemical antioxidant effect of GO. As a result, the overall thermal stability of the TPO/GO composites was improved.

In addition, a more evenly distributed layer of GO was incorporated into the TPO matrix because of the increasing shear processing time, resulting in reduced oxygen permeability. Furthermore, the lower oxygen permeability and chemical antioxidant effect of GO protect the structure of the TPO/GO composite matrix, increasing the average activation energy for thermal degradation.

3.9. Thermal degradation mechanism

The most used research approaches for studying thermal degradation mechanisms are the Achar equation [22–24] and the Coast–Redfern equation [25,26]. These equations are written as Eqs. (2) and (3), respectively.

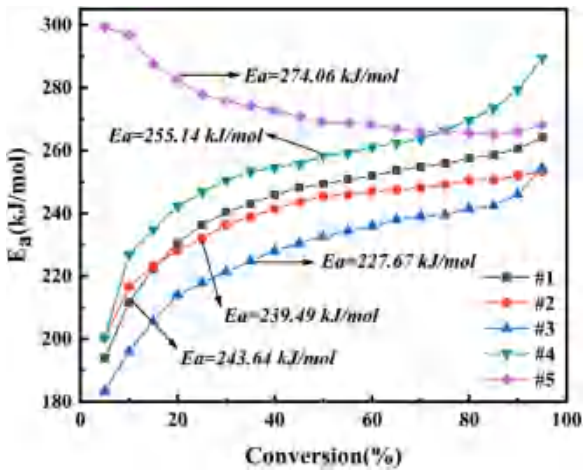

Fig. 12. Variations of the activation energies as calculated by the Flynn-Wall-Ozawa method.

Table 5
Dynamic functions.

No.	Dynamical model	$f(\alpha)$	$g(\alpha)$	Reaction order, n
1	D1, 1-D diffusion	$(\alpha/2)^{-1}$	α^2	2
2	R2, Contracting area	$(1-\alpha)^{1/2}$	$2[1-(1-\alpha)^{1/2}]$	2
3	R3, Contracting volume	$(1-\alpha)^{2/3}$	$3[1-(1-\alpha)^{1/3}]$	3

$$\ln\left[\frac{d\alpha/dT}{f(\alpha)}\right] = \ln\left(\frac{A}{\beta}\right) - \frac{E}{RT} \tag{2}$$

$$\ln\left[\frac{g(\alpha)}{T^2}\right] = \ln\left(\frac{AR}{\beta E}\right) - \frac{E}{RT} \tag{3}$$

The variables in the equation are as follows: α represents the rate at which decomposition occurs, T represents the thermodynamic temperature in Kelvin, β represents the rate at which temperature increases in Kelvin per minute, A and E represent the finger-forward factor and the apparent activation energy (kJ/mol) respectively. Additionally, $f(\alpha)$ and $g(\alpha)$ represent the differential and integral forms of the potential mechanism function. Three kinetic models were chosen from the literature [44,45], which were shown in Table 5.

The statistics in Table 6 were acquired by analyzing the raw data of thermal degradation reactions of various TPO/GO composites in 10 K/min.

The values of $d\alpha/dT$, β, and T were determined by substituting them into the mechanism functions $f(\alpha)$ and $g(\alpha)$ from Table 5, using the data provided in Table 6. The resulting data was then used in linear regression Eqs. (2) and (3), which used the linear regression of $\frac{1}{T}$ with $\ln\left[\frac{d\alpha/dT}{f(\alpha)}\right]$ and $\ln\left[\frac{g(\alpha)}{T^2}\right]$ respectively. The thermal analysis data was plotted using Achar's formula and Coats-Redfern's formula at various heating rates. The resulting linear plots can be seen in Figs. 13 and 14. The activation energy calculated by different kinetic models and the correlation coefficient of the fitting formula can be expressed by E and R, as shown in Table 7.

To ascertain the most suitable mechanism function for various samples, several established bases can be documented in the literature [46].

(1) The observed activation energy E is nearly identical to the value obtained from the Flynn-Wall-Ozawa formula.
(2) The correlation coefficient R has an absolute value close to 1.0.
(3) When using the Achar formula and the Coats-Redfern formula with different heating rates, the calculated values of activation energy E and frequency factor A for the same mechanism function are similar.
(4) The thermal breakdown of most solid compounds typically requires an activation energy (E) between 63.0 and 300.0 kJ/mol. The natural logarithm of the pre-exponential factor (lnA) normally falls between the range of 16.91 to 69.01.

From the information provided, it can be deduced that R2 serves as the most suitable mechanism function for Samples #1-4, while R3 was the most suitable mechanism function for Sample #5. The corresponding data were shown in Table 8.

GO is a type of material that has a high aspect ratio and specific surface area. It has a distinct single-layer two-dimensional honeycomb lattice structure that has low oxygen permeability. Additionally, GO can enhance the viscosity of the TPO matrix, resulting in a zigzagging pathway for gas molecule diffusion in the TPO/GO composite. This leads to a significant reduction in oxygen permeability [47,48] and improves thermal stability of the TPO/GO composites. Simultaneously, the chain termination reaction will occur between he reactive functional groups present on the surface of GO (such as hydroxyl groups and carboxyl groups) and the peroxide macromolecular radicals of the composite materials. This reaction produces hydroperoxides, slowing down the process of high-temperature dynamic shear thermo-oxidative aging, effectively. As the shear time increases, the distribution of GO in the TPO matrix becomes more uniform. Because the thermal degradation of TPO/GO composites can be caused by shearing, resulting in the formation of a physical barrier against oxygen (due to the unique honeycomb structure of GO) and a chemical antioxidant effect (due to the presence of surface polar groups on GO). This dual role of protection mechanism leads to different functional effects. It should be noted that our study primarily focuses on conventional processing conditions, which may not be suitable for extreme environments or complex graphene oxide treatments.

4. Conclusion

In the high-temperature dynamic shear aging experiment, the aging law of TPO materials is the same as that of traditional polyolefins. The

Table 6
Basic data of thermal decomposition reaction (10 k/min).

α (%)	Sample #1		Sample #2		Sample #3		Sample #4		Sample #5	
	T (K)	$d\alpha/dT$	T (K)	$d\alpha/dT$	T (K)	$d\alpha/dT$	T (K)	$d\alpha/dT$	T (K)	$d\alpha/dT$
10	698.65	0.54	702.15	0.59	702.32	0.64	703.48	0.61	702.32	0.59
20	710.48	1.24	713.32	1.37	716.48	1.38	713.65	1.42	714.32	1.23
30	716.98	1.81	719.32	2.10	719.32	2.07	719.48	2.06	720.82	1.87
40	721.65	2.38	723.32	2.89	723.48	2.80	723.82	2.67	725.32	2.39
50	725.15	2.73	726.98	2.86	727.32	2.91	727.15	3.19	729.15	2.90
60	728.82	3.14	730.32	3.12	730.15	4.15	730.32	3.17	732.48	3.04
70	732.15	2.89	733.48	3.24	733.32	3.03	733.48	3.21	735.82	2.96
80	735.82	2.49	736.65	2.81	736.32	2.82	736.65	2.82	739.32	2.65
90	740.48	1.69	740.82	1.93	740.82	1.90	740.98	1.87	743.82	1.66

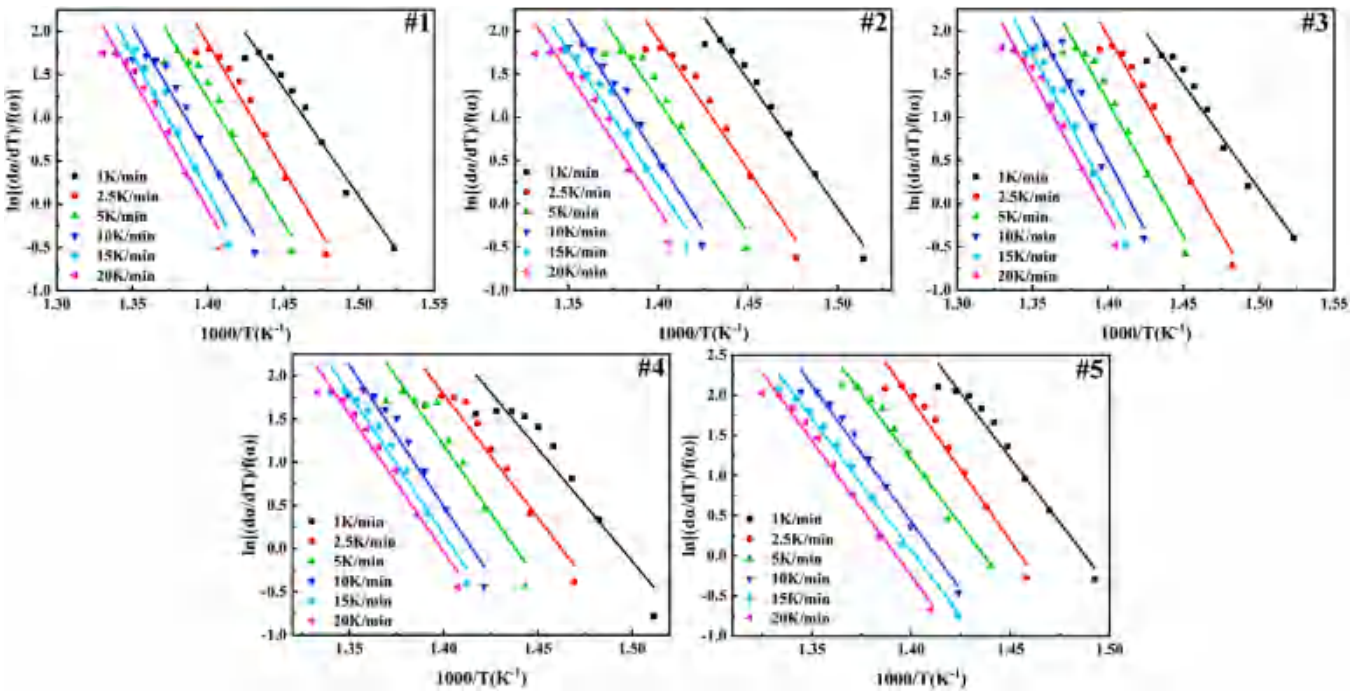

Fig. 13. Fitting line corresponding to Achar formula of mechanism function.

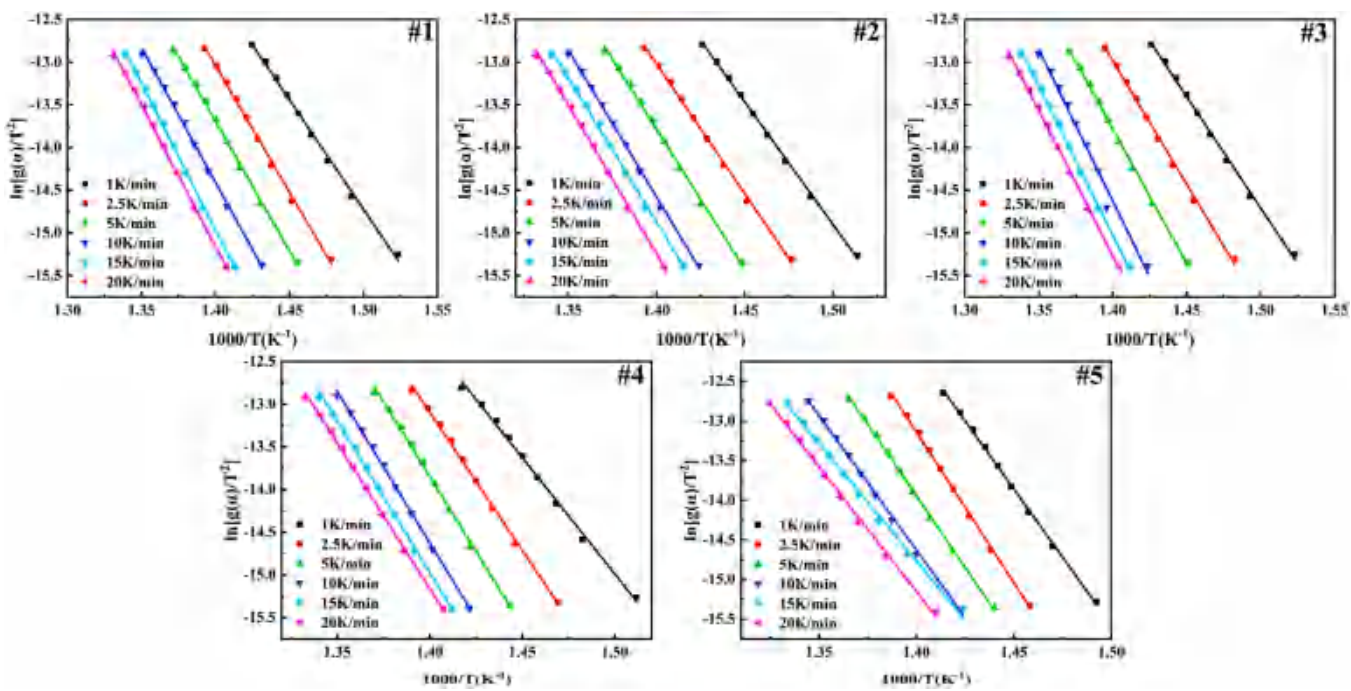

Fig. 14. The fitting line of the Coats-Redfern formula of mechanism function.

relative molecular weight, complex viscosity and physical properties of TPO materials decrease as the shear time increased. The characteristic peaks of surface polar groups (such as carbonyl and hydroxyl groups) become more obvious with decreasing contact angle. The tensile strength, hardness, complex viscosity, crystallization peak, and melting peak temperature of TPO/GO composite were increased, and the thermal degradation $T_{5\ \%}$, T_{max}, T_{end}, and E_a of TPO/GO composite were higher than those of TPO materials without GO. Because GO was a single-layer two-dimensional honeycomb lattice structure material with high specific surface area and low oxygen permeability, creating a tortuous path for gas molecule diffusion in TPO/GO composite materials, thereby significantly reducing the oxygen permeability and improving the thermal stability of TPO/GO composites.

GO was more evenly dispersed in the TPO matrix with increasing high-temperature dynamic shear time. The content of GO and processing time can affect the viscosity of composite materials and uniform dispersion of GO. When the GO content was1.0 %, the oxygen transmittance of TPO/GO composite materials reaches the lowest, and their physical and mechanical properties and aging resistance were both good. And the protective mechanism of physical (intercalation

Table 7
Thermal decomposition reaction kinetic analysis results of different TPO/GO composites.

	Sample #1				Sample #2				Sample #3				Sample #4				Sample #5			
	Achar		Coats-Redfern		Achar		Coats-Redfern		Achar		Coats-Redfern		Achar		Coats-Redfern		Achar		Coats-Redfern	
	E	*R*	*E*	*R*	*E*	*R*	*E*	*R*	*E*	*R*	*E*	*R*	*E*	*R*	*E*	*R*	*E*	*R*	*E*	*R*
D1	376.72	0.87	457.57	0.99	410.51	0.89	497.80	0.99	419.63	0.85	514.49	514.49	415.77	0.86	512.99	0.98	379.61	0.87	466.07	0.99
R2	246.75	0.94	262.36	0.99	269.02	0.94	285.74	0.99	273.34	0.91	295.36	295.36	271.11	0.93	294.94	0.99	246.62	0.93	267.09	0.99
R3	281.68	0.97	277.37	0.99	306.82	0.98	302.00	0.99	312.32	0.95	312.11	312.11	310.39	0.97	311.82	0.99	281.97	0.975	282.30	0.99

Table 8
Derivation results of non-isothermal degradation mechanism.

	$f(\alpha)$	$g(\alpha)$	Mechanism
Sample #1	$(1-\alpha)^{1/2}$	$2[1-(1-\alpha)^{1/2}]$	R2, cylindrically symmetric phase-boundary reaction, number of reaction stages $n = 2$
Sample #2	$(1-\alpha)^{1/2}$	$2[1-(1-\alpha)^{1/2}]$	R2, cylindrically symmetric phase-boundary reaction, number of reaction stages $n = 2$
Sample #3	$(1-\alpha)^{1/2}$	$2[1-(1-\alpha)^{1/2}]$	R2, cylindrically symmetric phase-boundary reaction, number of reaction stages $n = 2$
Sample #4	$(1-\alpha)^{1/2}$	$2[1-(1-\alpha)^{1/2}]$	R2, cylindrically symmetric phase-boundary reaction, number of reaction stages $n = 2$
Sample #5	$(1-\alpha)^{1/2}$	$[1-(1-\alpha)^{1/3}]$	R3, spherically symmetric phase-boundary reaction, number of reaction stages $n = 3$

inhibition of oxygen) and chemical (inorganic antioxidant effect) dual effects formed by shear thermal degradation was more obvious. The thermal stability of TPO/GO composite materials was further improved. The non isothermal degradation mechanism of TPO/GO composite materials subjected to high-temperature dynamic shearing has shifted from a cylindrical symmetric phase boundary reaction to a spherical symmetric phase boundary reaction. It should be noted that our study primarily focuses on conventional processing conditions, which may not be suitable for extreme environments or complex graphene oxide treatments.

CRediT authorship contribution statement

Quanchao Hu: Writing – original draft, Methodology, Investigation, Formal analysis, Conceptualization. **Hailiang Huang:** Formal analysis, Data curation. **Yufei Teng:** Formal analysis. **Ying Yang:** Formal analysis. **Gang Wang:** Investigation. **Junyi Chen:** Writing – review & editing, Visualization, Supervision, Conceptualization. **Yongxian Zhao:** Writing – review & editing, Supervision, Funding acquisition, Conceptualization.

Declaration of competing interest

The authors declare the following financial interests/personal relationships which may be considered as potential competing interests:

Yongxian Zhao reports financial support was provided by Shandong Province Key Research and Development Plan of China. Junyi Chen reports financial support was provided by National Natural Science Foundation of China. Quanchao Hu reports financial support was provided by Non-Metallic Excellence and Innovation Center. If there are other authors, they declare that they have no known competing financial interests or personal relationships that could have appeared to influence the work reported in this paper.

Data availability

Data will be made available on request.

Acknowledgments

The authors are grateful for the financial support from the Shandong Province Key Research and Development Plan of China (Public Welfare Project 2019GGX102068) the National Natural Science Foundation of China (Grant no. 52103118) and the Program Fund of Non-Metallic Excellence and Innovation Center for Building Materials, 2023TDA2-2.

References

[1] G. Abbas, J.-N. Sadat, H. Seyyed, A.-A. Mohammad, N. Mohammadreza, Mechanical properties of extruded glass fiber reinforced thermoplastic polyolefin composites, Polym. Compos. 41 (2020) 3748–3757, https://doi.org/10.1002/pc.25672.

[2] J. Shi, H. Dong, Y.-W. Quan, C. Chen, S.-Z. Yan, Evaluation of thermoplastic polyolefin materials for the hard shed of composite insulators, J. Appl. Polym Sci. 137 (2020) 49080, https://doi.org/10.1002/app.49080.
[3] S.-H. Wang, Y.-C. Jiang, Y.-J. Meng, Y.-C. Li, Z.-Q. Han, X.-D. Liu, H.-F. Li, J. Sun, B. Fei, X.-Y. Gu, S. Zhang, The encapsulation of intumescent flame retardants by poly-siloxane for thermoplastic polyolefin: fire safety and water resistance, Polym. Degrad. Stabil. 188 (2021) 109561, https://doi.org/10.1016/j.polymdegradstab.2021.109561.
[4] K.-N. Rovenska, M. Jiranek, P. Kokes, R. Wasserbauer, V. Kacmarikova, Does long term exposure to radon gas influence the properties of polymeric waterproof materials? Radiat. Phys. Chem. 94 (2014) 58–61, https://doi.org/10.1016/j.radphyschem.2013.05.054.
[5] S.-G. Kim, J.-W.-S. Lee, C.-B. Park, M. Sain, Enhancing cell nucleation of thermoplastic polyolefin foam blown with nitrogen, J. Appl. Polym. Sci. 118 (2010) 1691–1703, https://doi.org/10.1002/app.32294.
[6] H. Huang, Z.-X. Zhang, X.-T. Zhang, L. Yan, S.-K. Yang, L.-X. Xiao, H.-L. Lin, J. Bian, D.-Q. Chen, A facile strategy to improve the mechanical and thermal conductivity of PA6 nanocomposites by introducing graphene oxide/sodium benzoate compounding nucleator, J. Appl. Polym. Sci. J 139 (2022) 51761, https://doi.org/10.1002/app.51761.
[7] B. Dong, C. Liu, L.-Q. Zhang, Y.-P. Wu, Preparation, fracture, and fatigue of exfoliated graphene oxide/natural rubber composites, RSC Adv. 5 (2015) 17140–17148, https://doi.org/10.1039/C4RA17051B.
[8] J.-P. Long, S.-X. Li, B. Liang, Z.-G. Wang, Investigation of thermal behaviour and mechanical property of the functionalised graphene oxide/epoxy resin nanocomposites, Plast. Rubber Compos. 48 (2019) 1–10, https://doi.org/10.1080/14658011.2019.1577027.
[9] T.-Y. Yung, Y.-C. Lu, J.-S. Chen, Y.-W. Cheng, T.-Y. Liu, P.-T. Chen, Reinforcement of epoxy resin by additives of amine functionalized graphene nanosheets, Coatings 11 (2021) 1–11, https://doi.org/10.3390/coatings11010035.
[10] J.-R. Potts, O. Shankar, L. Du, R.-S. Ruoff, Processing-morphology-property relationships and composite theory analysis of reduced graphene oxide/natural rubber nanocomposites, Macromolecules 45 (2012) 6045–6055.
[11] Z.-Y. Ji, J.-L. Wu, X.-P. Shen, H. Zhou, H.-T. Xi, Preparation and characterization of graphene/NiO nanocomposites, J. Mater. Sci. 46 (2010) 1190–1195, https://doi.org/10.1007/s10853-010-4892-7.
[12] M. Ujihara, M.M.M. Ahmed, T. Imae, Y. Yamauchi, Massive-exfoliation of magnetic graphene from acceptor-type GIC by long-chain alkyl amine, J. Mater. Chem. A 2 (2014) 4244–4250, https://doi.org/10.1039/C3TA14117A.
[13] Z.-H. Wu, C. Xu, C.-Q. Ma, Z.-B. Liu, H.-M. Cheng, W.-C. Ren, Synergistic effect of aligned graphene nanosheets in graphene, foam for high-performance thermally conductive composites, Adv. Mater. 31 (2019) 1900199, https://doi.org/10.1002/adma.201900199.
[14] T.R. Aswathy, B. Dash, P. Dey, S. Nair, K. Naskar, Synergistic effect of graphene with graphene oxide, nanoclay, and nanosilica in enhancing the mechanical and barrier properties of bromobutyl rubber/epoxidized natural rubber composites, J. Appl. Polym.Sci. 138 (2021) 50746, https://doi.org/10.1002/app.50746.
[15] S.-Y. Zhou, B. Yang, Y. L, X.-R. Gao, J. Xu, G.-J. Zhong, Z.-M. Li, Realization of ultra-high barrier to water vapor by 3D-inter-connection of super-hydrophobic graphene layers in polylactide films, J. Mater. Chem. A 5 (2017) 4386–14377, https://doi.org/10.1039/c7ta03901h.
[16] Q.-Q. Guo, Y.-Y. Luo, J.-Z. Liu, X.-X. Zhang, C.-H. Lu, A well-organized graphene nanostructure for versatile strain-sensing application constructed by covalently bonded graphene/rubber Interface, J. Mater. Chem. C 6 (2018) 2139–2147, https://doi.org/10.1039/C7TC05758J.
[17] Y.-N. Torrejón, U. Giese, Consumption and reaction mechanisms of antioxidants during thermal oxidative aging, Kgk-Kaut. Gummi Kunst. 65 (2012) 25–31.
[18] A.-R. Azura, S. Ghazali, M. Mariatti, Effects of the filler loading and aging time on the mechanical and electrical conductivity properties of carbon black filled natural rubber, J. Appl. Polym. Sci. 110 (2008) 747–752, https://doi.org/10.1002/app.28517.
[19] T. Nakazono, A. Ozaki, A. Matsumoto, Phase separation and thermal aging behavior of styrene-butadiene rubber vulcanizates using liquid polymers as plasticizers studied by differential scanning calorimetry and dynamic mechanical spectroscopy, J. Appl. Polym. Sci 120 (2011) 434–440, https://doi.org/10.1002/app.33165.
[20] N.-S. Tomer, F. Delor-Jestin, R.-P. Singh, J. Lacoste, Cross-linking assessment after accelerated ageing of ethylene propylene diene monomer rubber, Polym. Degrad. Stabil. 92 (2007) 457–463, https://doi.org/10.1016/j.polymdegradstab.2006.11.013.
[21] K. Osswald, K. Reincke, M. Schossig, S. Sökmen, B. Langer, Influence of different types of antioxidants on the aging behavior of carbon-black filled NR and SBR vulcanizates, Polym. Test. 79 (2019) 106053, https://doi.org/10.1016/j.polymertesting.2019.106053.
[22] Y. Bai, C. Wu, F. Wu, J.-H. Yang, L.-L. Zhao, L. Fei, B.-L. Yi, Thermal decomposition kinetics of light-weight composite NaNH2-NaBH4 hydrogen storage materials for fuel cells, Int. J. Hydrogen Energy 37 (2012) 12973–12979, https://doi.org/10.1016/j.ijhydene.2012.05.069.
[23] Q. Zhou, J. Bian, G. Wang, F. He, H. Lin, Preparation and property of functionalized nano graphene oxide/POE-g-MAH/polystyrene composites, Acta Mater. Compos. Sin. 33 (2016) 240–248, https://doi.org/10.13801/j.cnki.fhclxb.20150707.003.
[24] X.-B. Li, F.-L. Yue, W.-C. Pang, J.-L. Wu, B.-B. Kong, Mechanical and wear properties of GO-enhanced irradiated UHMWPE with good oxidation resistance, Fuller., Nanotub. Carbon Nanostruct. 27 (2019) 459–467, https://doi.org/10.1080/1536383X.2019.1608437.
[25] P.-P. Lu, Z.-F. Ni, G.-M. Chen, M.-P. Wu, Influence of SBF-induced degradation on surface and tribological properties of irradiated GO/UHMWPE nanocomposites, Iran. Polym. J. 30 (2021) 247–255, https://doi.org/10.1007/s13726-020-00886-6.
[26] G.-Q. Zhang, X.-Q. Zeng, T.-H. Ren, E.-V.-D. Heide, Tribological properties of graphene oxide sheets as water-based lubricant additive, Ind. Lubr. Tribol. 70 (2018) 1025–1036, https://doi.org/10.1108/ILT-03-2017-0074.
[27] Y. Sun, C.-B. He, Synthesis and stereocomplex crystallization of poly(lactide)–graphene oxide nanocomposites, ACS Macro Lett. 1 (2012) 709–713, https://doi.org/10.1021/mz300131u.
[28] N. Sukhonthamethirat, V. Vao-Soongnern, S. Okamoto, S. Sakurai, Morphology and crystallization kinetics of G-resins and isotactic polypropylene, Polym. Eng. Sci. 62 (2022) 1775–1785, https://doi.org/10.1002/pen.25963.
[29] S.-H. Jafari, A.-K. Vahid, H.-A. Khonakdar, D.-D. Jehnichen, Crystallization and melting behavior of nanoclay-containing polypropylene/poly (trimethylene terephthalate) blends, Express Polym. Lett. 6 (2012) 148–158, https://doi.org/10.3144/expresspolymlett.2012.16.
[30] J.-R. Liu, H.-W. Liang, Enhancement of crystallization and mechanical properties in isotactic polypropylene via adding liquid-phase exfoliated graphene, Thermochim. Acta 699 (2021) 178916, https://doi.org/10.1016/j.tca.2021.178916.
[31] P. Sowinski, S. Veluri, E. Piorkowska, Crystallization of isotactic polypropylene nanocomposites with fibrillated poly(tetrafluoroethylene) under elevated pressure, Polymers 14 (2021) 88, https://doi.org/10.3390/polym14010088.
[32] I.-O. Navas, M. Arjmand, U. Sundararaj, Effect of carbon nanotubes on morphology evolution of polypropylene/polystyrene blends: understanding molecular interactions and carbon nanotube migration mechanisms, RSC Adv. 7 (2017) 54222–542234, https://doi.org/10.1039/C7RA11390K.
[33] M. Bertolino, D. Battegazzore, R. Arrigo, A. Frache, Designing 3D printable polypropylene: material and process optimisation through rheology, Addit. Manuf. 40 (2021) 101944, https://doi.org/10.1016/j.addma.2021.101944.
[34] Y. Zhang, P. Soo-Jin, Influence of the nanoscaled hybrid based on oxide architecture on the rheological and thermo-physical performances of carboxylated-polymeric composites, Compos. Part A 112 (2018) 356–364, https://doi.org/10.1016/j.compositesa.2018.06.020.
[35] C.-Y. Tsai, C.-S. Chang, H.-J. Sue, Quantification of long-chain branching molar fraction in polypropylene, Ind. Eng. Chem. Res. 60 (2021) 3770–3778, https://doi.org/10.1021/acs.iecr.0c05899.
[36] A. Kumar, S. Commereuc, V. Verney, Ageing of elastomers: a molecular approach based on rheological characterization, Polym. Degrad. Stabil. 85 (2004) 751–757, https://doi.org/10.1016/j.polymdegradstab.2003.11.014.
[37]] Q.-L. Zhao, X.-G. Li, G. Jin, Surface degradation of ethylene-propylene-diene monomer (EPDM) containing 5-ethylidene-2-norbornene (ENB) as diene in artificial weathering environment, Polym. Degrad. Stabil. 93 (2008) 692–699, https://doi.org/10.1016/j.polymdegradstab.2007.12.009.
[38] J.-F. Ou, W.-H. Hu, M.-S. Xue, F.-J. Wang, W. Li, Superhydrophobic surfaces on light alloy substrates fabricated by a versatile process and their corrosion protection, ACS Appl. Mater. Interfaces 5 (2013) 3101–3107, https://doi.org/10.1021/am4000134.
[39] J.-F. Ou, W.-H. Hu, S. Liu, M.-S. Xue, F.-J. Wang, W. Li, Superoleophobic textured copper surfaces fabricated by chemical etching/oxidation and surface fluorination, ACS Appl. Mater. Interfaces 5 (2013) 10035–10041, https://doi.org/10.1021/am402531m.
[40] L.-X. Du, H.-N. Yu, B.-H. Zhang, R.-L. Tang, Y. Zhang, C.-S. Qi, M.-P. Wolcott, Z.-M. Yu, J.-W. Wang, Transparent oxygen barrier nanocellulose composite films with a sandwich structure, Carbohyd. Polym. 268 (2021) 118206, https://doi.org/10.1016/j.carbpol.2021.118206.
[41] J.-Y. Li, G.-V. Ewijk, D.-J.-V. Dijken, J.-V.-D. Gucht, W.-M.-D. Vos, Single-step application of polyelectrolyte complex films as oxygen barrier coatings, ACS Appl. Mater. Interfaces 13 (2021) 21844–21853, https://doi.org/10.1021/acsami.1c05031.
[42] H. Mahmood, A. Shakeel, A. Abdullah, M.-I. Khan, M. Moniruzzaman, A comparative study on suitability of model-free and model-fitting kinetic methods to non-isothermal degradation of lignocellulosic materials, Polymers 13 (2021) 2504, https://doi.org/10.3390/polym13152504.
[43] R.-F. Zhou, X.-T. Wu, X.-H. Bao, F.-Y. Wu, X.-S. Han, J.-B. Wang, The effect of polyepoxyphenylsilsesquioxane and diethyl bis(2-hydroxyethyl) aminomethylphosphonate on the thermal stability of epoxy resin, ACS Omega 8 (2023) 2077–2084, https://doi.org/10.1021/acsomega.2c05817.
[44] X. Gao, D. Dollimore, The thermal decomposition of oxalates: part 26. A kinetic study of the thermal decomposition of manganese (II) oxalate dihydrate, Thermochim. Acta 215 (1993) 47–63, https://doi.org/10.1016/0040-6031(93)80081-K.
[45] F.-J. Gotor, J.-M. Criado, J. Malek, N. Koga, Kinetic analysis of solid-state reactions: the universality of master plots for analyzing isothermal and nonisothermal experiments, J. Phys. Chem. A 104 (2000) 10777–10782, https://doi.org/10.1021/jp0022205.
[46] J.-J. Zhang, R.-F. Wang, J.-H. Bai, Studies on the thermal decomposition non-isothermal kinetics of binuclear europium benzoate ternary complex with 1,10-phenanthroline, Chin. J. Anal. Chem. 32 (2004) 1371, https://doi.org/10.0000/cddc777412b04c738be1ff47cf9c9f9b.
[47] T.-Y. Yung, Y.-C. Lu, J.-S. Chen, Y.-W. Cheng, Y.-T. Liu, P.-T. Chen, Reinforcement of epoxy resin by additives of amine-functionalized graphene nanosheets, Coatings 11 (2021) 1–11, https://doi.org/10.3390/coatings11010035.
[48] Y. Grohens, K.-K. Sadasivunia, D. Ponnammaa, S. Thomas, Evolution from graphite to graphene elastomer composites, Prog. Polym. Sci. 39 (2013) 49–780, https://doi.org/10.1016/j.progpolymsci.2013.08.003.

Construction and Building Materials 451 (2024) 138792

Contents lists available at ScienceDirect

Construction and Building Materials

journal homepage: www.elsevier.com/locate/conbuildmat

Development of sustainable desulfurized waste crumb rubber modified asphalt with enhanced self-healing properties

Tianwei Zhang [a], Shanjun Gao [b], Yanheng He [a], Quantao Liu [c], Shi Xu [d], Ronghua Zhuang [a], Shangheng Zeng [a], Jianying Yu [a,*]

[a] State Key Laboratory of Silicate Materials for Architectures, Wuhan University of Technology, Wuhan 430070, PR China
[b] School of Material Science and Engineering, Wuhan University of Technology, Wuhan 430070, PR China
[c] Wuhan University of Technology Advanced Engineering Technology Research Institute of Zhongshan City, Zhongshan 528400, PR China
[d] Hubei Key Laboratory of Roadway Bridge and Structure Engineering, Wuhan University of Technology, Wuhan 430070, PR China

ARTICLE INFO

Keywords:
Waste crumb rubber modified asphalt
Disulfide bonds
Self-healing performance
Rheological properties

ABSTRACT

Developing waste crumb rubber modified asphalt (CRMA) with enhanced self-healing properties can improve the crack-healing ability of asphalt, which is conducive to extending the service life of asphalt pavements. The objective of this study is to introduce dynamic disulfide bonds into desulfurized waste crumb rubber and to prepare two types of intrinsic self-healing waste crumb rubber modified asphalt by the breakage-rearrangement effect of dynamic disulfide bonds. Chemical structure analysis revealed that through the esterification reaction between -COOH in dithiodipropionic acid (DPA) and dithiosalicylic acid (DTSA) and -OH in desulfurized waste crumb rubber, DPA/CRMA with aliphatic disulfide bonds and DTSA/CRMA with aromatic disulfide bonds were successfully prepared. The results of the healing tests showed that DPA/CRMA and DTSA/CRMA exhibited better healing properties due to the breakage-rearrangement effect of dynamic disulfide bonds. The fatigue healing indices of DPA/CRMA and DTSA/CRMA were 31.3 % and 36.3 % higher than those of CRMA. The fracture healing rates of DPA/CRMA and DTSA/CRMA were enhanced by 67.6 % and 79.9 % compared to CRMA. The rheological test results revealed that DPA/CRMA exhibited better cracking resistance both before and after aging compared to DTSA/CRMA. Overall, the DTSA/CRMA exhibited better self-healing performance due to the lower bond energies and stronger breakage-rearrangement effect of the aromatic disulfide bonds, while the DPA/CRMA had better cracking resistance.

1. Introduction

As a kind of hazardous solid waste, the recycling and disposal of waste crumb rubber has always been a challenge [1,2]. The use of waste crumb rubber for asphalt modification and pavement construction is an effective solution to alleviate its environmental pressure [3] and can improve the skid resistance and temperature sensitivity of asphalt pavement [4]. However, waste crumb rubber modified asphalt undergoes aging under the influence of heat, ultraviolet radiation, oxygen, and load during service, resulting in the formation of micro-cracks in asphalt pavement. If micro-cracks are not repaired in time, they will develop into visible and macroscopic cracks, which result in the maintenance of asphalt pavement [5] and consume a large amount of resources [6]. Based on the efficient recycling [7] and sustainable development [8] of waste crumb rubber modified asphalt pavement, improvement of the self-healing properties of asphalt pavement can effectively delay the generation of microcracks, thus improving its service life.

Self-healing is the inverse process of breakage, which refers to the capability of a material to repair cracks and restore certain mechanical properties. Asphalt is a visco-elastic material. When microcracks appear in asphalt, it can often spontaneously flow to some microcracks to realize self-healing. However, self-healing ability of asphalt is extremely limited, which mainly requires a long resting time and a high healing temperature [9]. Hence, there is a demand for the development of healing technologies to improve the self-healing performance of asphalt.

In recent years, intrinsic self-healing polymer modified asphalt technology (disulfide bonds basis [10], disulfide and hydrogen bonds basis [11] and oxime urethane bonds basis self-healing polyurethane modified asphalt [12]) based on dynamic chemical bonds intensively

* Corresponding author.
E-mail address: jyyu@whut.edu.cn (J. Yu).

https://doi.org/10.1016/j.conbuildmat.2024.138792
Received 7 July 2024; Received in revised form 23 September 2024; Accepted 16 October 2024
Available online 22 October 2024
0950-0618/© 2024 Elsevier Ltd. All rights are reserved, including those for text and data mining, AI training, and similar technologies.

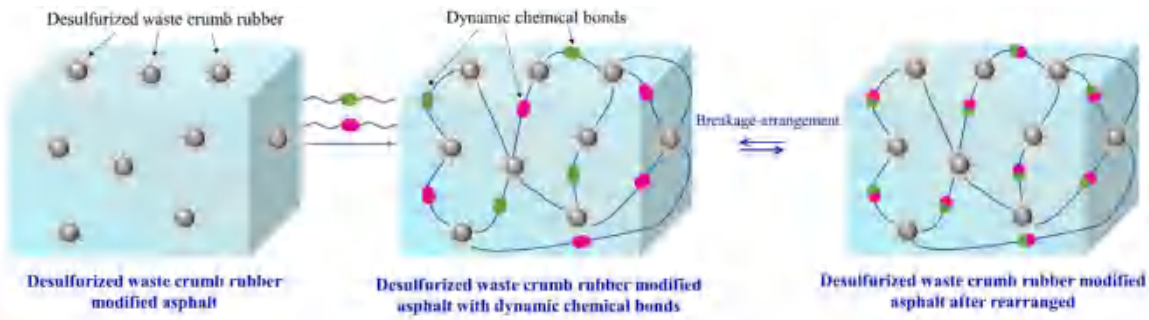

Fig. 1. Breakage-rearrangement mechanism of self-healing desulfurized waste crumb rubber modified asphalt.

investigated. The healing mechanism is to introduce dynamic chemical bonds into the polymer and to utilize the breakage-rearrangement property of dynamic chemical bonds to improve the healing capability of polymer modified asphalt. Common dynamic chemical bonds include diselenide bonds [13], acylhydrazone bonds [14] and disulfide bonds [15], etc. In 2023, Wei et al. [11] prepared a self-healing polyurethane and its modified asphalt based on disulfide bonds and hydrogen bonds. The results showed that the self-healing polyurethane modified asphalt has not only the physical self-healing ability of asphalt diffusion, but also the chemical self-healing ability based on the breakage-rearrangement effect of disulfide bonds and hydrogen bonds, which leads to a significant enhancement of the healing ability of the polyurethane modified asphalt. In 2024, Zhang et al. [16] prepared a self-healing styrene-butadiene-styrene (SBS) modified asphalt through introducing disulfide bonds into the C═C bonds position of SBS by the free radical reaction. This self-healing SBS modified asphalt exhibited better fatigue healing and fracture healing performance. Subsequently, He et al. [17] introduced acylhydrazone bonds into the C═C bonds position of SBS to prepare a self-healing SBS modified asphalt. It was found that the dynamic acylhydrazone bonds not only healed the surface microcracks of SBS modified asphalt, but also dramatically restored the fracture elongation of SBS modified asphalt. The above research utilized reactive functional groups in polyurethanes and SBS to introduce dynamic chemical bonds into polymer modified asphalt to endow it with self-healing capability. At present, there is no research on introducing dynamic chemical bonds into waste crumb rubber modified asphalt.

To develop novel intrinsic self-healing waste crumb rubber modified asphalt, dynamic chemical bonds can be introduced into the waste crumb rubber modified asphalt. Nevertheless, there are no reactive functional groups in waste crumb rubber, which makes it difficult to introduce dynamic chemical bonds into waste crumb rubber and achieve self-healing. In the research on waste crumb rubber modified asphalt, to solve the problems of poor storage stability [18] and low tensile strength [19], researchers destroyed the crosslinking structure of waste crumb rubber by chemical desulfurizer [20], microwave, etc. [21] to get a desulfurized waste crumb rubber with reactive functional groups (-OH, -NH_2, etc.) [22]. As a result, dynamic chemical bonds containing -COOH can be introduced into reactive functional groups of desulfurized waste crumb rubber for the first time through esterification reaction to prepare novel intrinsic self-healing desulfurized waste crumb rubber modified asphalt.

Table 1
Physical properties and components of asphalt.

	Properties/ Components	Results	Value	Test methods
Physical property	softening point (°C)	49.3	≥ 45	ASTM D36 [24]
	Penetration (25°C, dmm)	67	60–80	ASTM D5 [25]
	Ductility (cm)	> 100	> 100	ASTM D113 [26]
	Viscosity (60°C, Pa·s)	330	≥ 180	ASTM D4402 [27]
Chemical components	Saturates (%)	15.82		
	Aromatics (%)	40.74		
	Resins (%)	27.26		
	Asphaltenes (%)	16.18		

The breakage-rearrangement mechanism of self-healing desulfurized waste crumb rubber modified asphalt is shown in Fig. 1. Dynamic chemical bonds are connected between the desulfurized waste crumb rubber particles. When the desulfurized waste crumb rubber modified asphalt encounters external force and microcracks appear, the dynamic chemical bonds with low bond energies break first. When the external force is removed, the rearrangement of the dynamic chemical bonds occurs, which allows the microcracks of the desulfurized waste crumb rubber modified asphalt to be healed and certain properties restored. On the other hand, the dynamic chemical bonds between the desulfurized waste crumb rubber can act as a "bridge" structure, which will affect the performance of the desulfurized waste crumb rubber modified asphalt.

Herein, through the esterification reaction between -OH in desulfurized waste crumb rubber and -COOH in dithiodipropionic acid (DPA) and dithiosalicylic acid (DTSA), two types of intrinsic self-healing desulfurized waste crumb rubber modified asphalt (DPA/CRMA with aliphatic disulfide bonds and DTSA/CRMA with aromatic disulfide bonds) were prepared. The effects of disulfide bonds on the chemical structure and microstructure of self-healing desulfurized waste crumb rubber modified asphalt were investigated by Fourier Transform Infrared spectrometer (FTIR) and Fluorescence Microscopy (FM). The rheological properties of self-healing desulfurized waste crumb rubber modified asphalt were studied by Dynamic Shear Rheometer (DSR) and Bending Beam Rheometer (BBR). The effect of dynamic disulfide bonds on the healing properties of self-healing desulfurized waste crumb rubber modified asphalt was investigated by fatigue healing test and fracture healing test. Furthermore, aging may damage the disulfide bonds in self-healing desulfurized waste crumb rubber modified asphalt. Therefore, Thin Film Oven Test (TFOT) and Pressurized Aging Vessel (PAV) aging tests were conducted to investigate the effects of aging on the chemical structure, rheological properties, and healing performance of self-healing desulfurized waste crumb rubber modified asphalt.

The objectives of this study are: 1) Develop novel intrinsic self-healing desulfurized waste crumb rubber modified asphalt based on dynamic disulfide bonds. 2) Investigate the effects of aliphatic and aromatic disulfide bonds on the structure and properties of desulfurized waste crumb rubber modified asphalt. 3) Explore the effects of aging on the structure and properties of self-healing desulfurized waste crumb rubber modified asphalt. This study provided a new perspective for the development of self-healing desulfurized waste crumb rubber modified asphalt.

Table 2
Properties of DPA and DTSA.

Properties	DPA	DTSA
Molecular structure	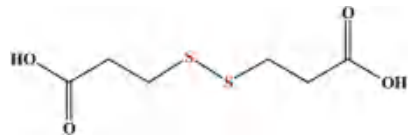	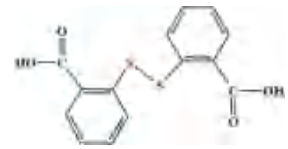
Molecular weight (g/mol)	210.27	306.36
Molecular formula	$C_6H_{10}O_4S_2$	$C_{14}H_{10}O_4S_2$
Boiling point (℃)	431.1	252.0
Purity (%)	98	99

2. Experiment

2.1. Materials and methods

2.1.1. Materials

The physical characteristics of asphalt (AH-70#) were shown in Table 1, which was sourced from Foshan Gaofu PetroChina Fuel Asphalt Co., Ltd in China. Table 2 outlined the properties of 2,2′-dithiosalicylic acid (DTSA) and 3, 3′-dithiodipropionic acid (DPA), which were procured from Bide Pharmatech Co., Ltd in China. The disulfide bonds in DPA have aliphatic hydrocarbon structure and exhibit better flexibility, while the disulfide bonds in DTSA have lower bond energies and are easier to undergo breakage-rearrangement effect [23]. The desulfurized waste crumb rubber was supplied by Hubei Hairui Environmental Protection New Material Technology Co., Ltd in China, which was obtained by processing the waste crumb rubber with chemical desulfurizer. The properties of the desulfurized waste crumb rubber were listed in Table 3. The appearance and SEM images of the desulfurized waste crumb rubber were shown in Fig. 2.

2.1.2. Preparation of self-healing desulfurized waste crumb rubber modified asphalt

The connection between desulfurized waste crumb rubber and DPA, DTSA is based on esterification reactions. The preparation process of self-healing desulfurized waste crumb rubber modified asphalt (DPA/CRMA and DTSA/CRMA) is shown in Fig. 3. The asphalt was poured into the reaction vessel and the temperature was elevated to 180 °C. Then, the desulfurized waste crumb rubber (25 % of the asphalt mass) was incorporated into the reaction vessel. The blend of desulfurized waste crumb rubber and asphalt underwent high-speed shear mixing for 1 h at 5000 rpm. Subsequently, DPA and DTSA (0.5 %、1 %、1.5 %、2.0 % and 2.5 % of the crumb rubber mass) were added and stirred at 5000 rpm for 2 h to obtain DPA/CRMA and DTSA/CRMA. Finally, the chemical structure, microstructure, rheological properties and self-healing performance of CRMA, DPA/CRMA and DTSA/CRMA were systematically investigated.

Table 3
Properties of desulfurized waste crumb rubber.

Properties	Particle size (mm)	Density (g/cm^{-3})	Ash content (%)	Metal content (%)
Results	0.45–2	1.18	6.5	< 0.05

2.1.3. Aging method

To investigate the effect of aging on the structure and properties of self-healing desulfurized crumb rubber modified asphalt, short-term and long-term aging tests were conducted, respectively. The short-term aging test of CRMA was conducted in accordance with ASTM D1754 [28]. The (50 ± 0.5 g) of CRMA was poured into a circular iron disc, then the disc was placed in a TFOT aging oven and aged for 5 h at 163 °C. The long-term aging test of CRMA was conducted by a PAV test according to ASTM D 6521 [29]. CRMA after TFOT aging was transferred to a pressure aging vessel and heated for 20 h at 100 ℃ and 2.1 MPa pressure.

2.2. FTIR

In order to characterize the chemical structure of CRMA, the changes in its functional groups were analyzed using FTIR. Dissolve 0.2 g of CRMA in 4 mL of CS_2 to get the CRMA solution, and the solution was

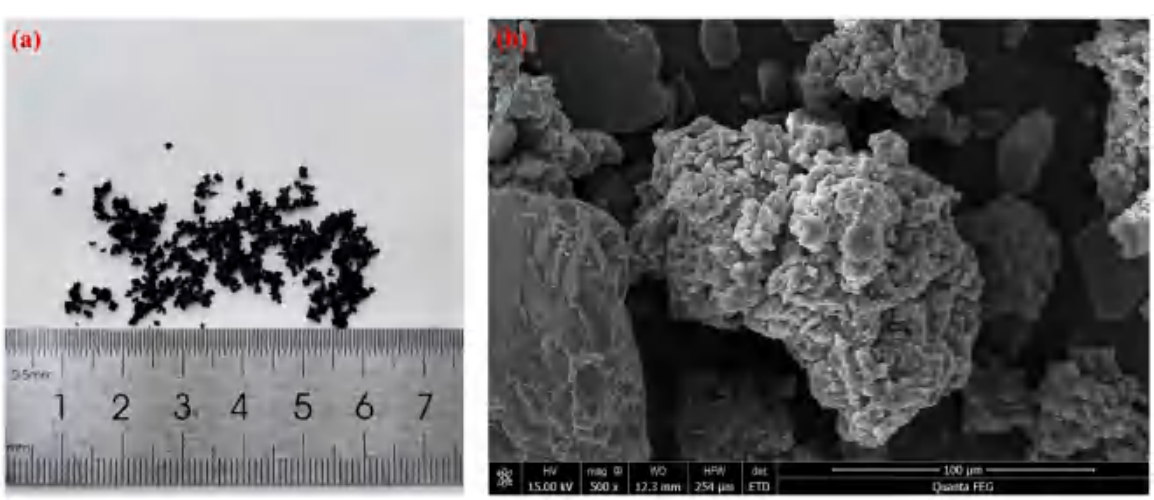

Fig. 2. (a) Appearance and (b) SEM images of desulfurized waste crumb rubber.

Fig. 3. Methodology and experimentation plan of DPA/CRMA and DTSA/CRMA.

dropped on a KBr chip. After the CS_2 evaporated, the KBr chip was placed in the FTIR spectrometer for testing. Three times tests were conducted for each CRMA sample to obtain reliable experimental results.

2.3. Fluorescence microscopy

Fluorescence microscopy is often used to explore the microstructure of asphalt binders. In this study, the microstructure of CRMA before and after aging was observed by fluorescence microscopy. The magnification of the fluorescence microscope was 100 ×.

2.4. Physical properties

Physical properties are important indicators for crumb rubber modified asphalt, which can evaluate its stability and plasticity. The softening point and ductility of CRMA were measured in accordance with ASTM D36 [24] and ASTM D113 [26]. Each crumb rubber modified asphalt sample was tested three times and the average of the data was obtained.

The softening point increment and ductility retention rate of CRMA after TFOT and PAV aging were evaluated using Eqs. (1) and (2), respectively [30]. SPI and DRR were softening point increment and ductility retention rate, respectively.

$$SPI = Aged\ softening\ point - Unaged\ softening\ point \tag{1}$$

$$DRR = \frac{Aged\ ductility}{Unaged\ ductility} \tag{2}$$

2.5. Rheological properties test

2.5.1. High-temperature rheological properties

According to the Strategic Highway Research Program (SHRP), DSR is used to evaluate the rheological properties of asphalt binders [31], which correlate with high-temperature fatigue cracking performance. The DSR test was conducted according to AASHTO T 315 [32]. The high-temperature rheological properties of CRMA were investigated by DSR (MCR-102, Antonpa Co., Ltd, Austria). The test parameters of DSR were shown in Table 4. Three times tests were conducted for each sample to obtain reliable experimental results.

2.5.2. Multiple stress creep recovery test

According to AASHTO T 350 [33], multiple stress creep recovery (MSCR) test can be used to determine the elastic response and stress dependence of asphalt binders, therefore, MSCR test was performed for CRMA in this study. The schematic diagram of the multiple stress creep recovery (MSCR) test is shown in Fig. 4. CRMA was subjected to multiple loading-recovery cycles at stress level, and each cycle consisted of 1 s of loading stage and 9 s of recovery stage. The test temperature was chosen to be 58 °C, with 20 cycles at 0.1 kPa stress level and 10 cycles at 3.2 kPa stress level. Finally, the average recovery (R), and the unrecoverable creep (J_{nr}) were calculated using Eqs. (3) and (4) [34]. CRMA was subjected to three times tests and the average of the R and J_{nr} was obtained.

$$R = \sum_{k=1}^{10} \frac{\varepsilon_c - \varepsilon_r}{\varepsilon_c - \varepsilon_0} \Big/ 10 \tag{3}$$

$$J_{nr} = \sum_{k=1}^{10} \frac{\varepsilon_r - \varepsilon_0}{\sigma} \Big/ 10 \tag{4}$$

Where R is the average recovery rate of the 10 times loading-recovery cycles. J_{nr} is the average unrecoverable creep of the 10 times loading-recovery cycles. ε_c is the strain after each loading stage. ε_0 is the

Table 4
Test parameters of DSR.

Temperature (℃)	Diameter of parallel plates (mm)	Distance between parallel plates (mm)	heating rate (rad/s)	Scan frequency (℃/min)
30–80	25	1	10	2

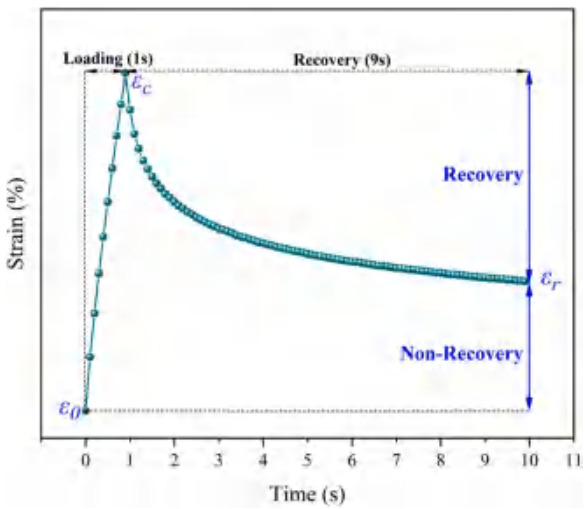

Fig. 4. Schematic diagram of MSCR test.

strain before each loading stage. ε_r is the strain after each recovery. σ is the stress level.

2.5.3. Low-temperature rheological properties

The low-temperature rheological properties are used to evaluate the low-temperature crack resistance of asphalt binders. In this study, the low-temperature rheological properties of CRMA were estimated by bending beam rheometer (BBR). The BBR test was conducted according to ASTM D6648 [35]. CRMA was made into bending beams of certain sizes and then placed in the BBR to obtain the creep rate (m) and creep stiffness (S) at a loading time of 60 s. Each CRMA sample was subjected to three times tests and the average of the S and m was obtained.

2.6. Self-healing performance test

2.6.1. Fatigue healing test

The healing properties of CRMA were investigated by fatigue healing test, which is currently the most commonly used evaluation method based on reported tests [36]. Fatigue healing test was performed through the time-scan mode of the DSR. The test was conducted at temperature of 25 °C and strain of 3 %, and complex modulus was obtained every second during the loading process. The loading process of the fatigue healing test was shown in Fig. 5 and was divided into three stages. In stage (I), The CRMA was subjected to fatigue loading to obtain the initial complex modulus (G_i^*) and fatigue complex modulus (G_f^*), and the loading was stopped when G_f^* decreased to 70 % of G_i^*. In stage (II), the CRMA was standing at 25 ℃ in a DSR insulated jacket to allow it to heal. In stage (III), the CRMA underwent fatigue loading again to get the healed complex modulus (G_h^*). The fatigue healing index of the CRMA was evaluated by (5) [37]. Three times tests were conducted for each CRMA to obtain reliable test results.

$$H_I = \frac{G_h^* - G_f^*}{G_i^* - G_f^*} \times 100\% \tag{5}$$

Where H_I is the healing index of CRMA; G_i^* is the initial complex modulus of CRMA. G_h^* is the healed complex modulus of CRMA. G_f^* is the complex modulus of CRMA after stage (I).

2.6.2. Fracture healing test

In this study, the healing performance of macroscopic cracks in CRMA was investigated through the ductility ratio before and after healing [38]. The ductility specimens of CRMA were classified into two groups. The first group ductility specimens of CRMA were subjected to a ductility test to obtain the initial ductility (D_1). The second group ductility specimens of CRMA were placed in a refrigerator for 2 h, and then the ductility specimen was cut through the middle of the ductility mold with a hot knife. The ductility specimen was assembled in the middle and stood in the oven at 25℃ for 10 h, and the ductility test was carried out to obtain the ductility (D_2) of CRMA after healing. Finally, the fracture healing rate of CRMA was calculated using (6) [39]. Each CRMA sample was conducted three times tests and the average of the H_R was obtained.

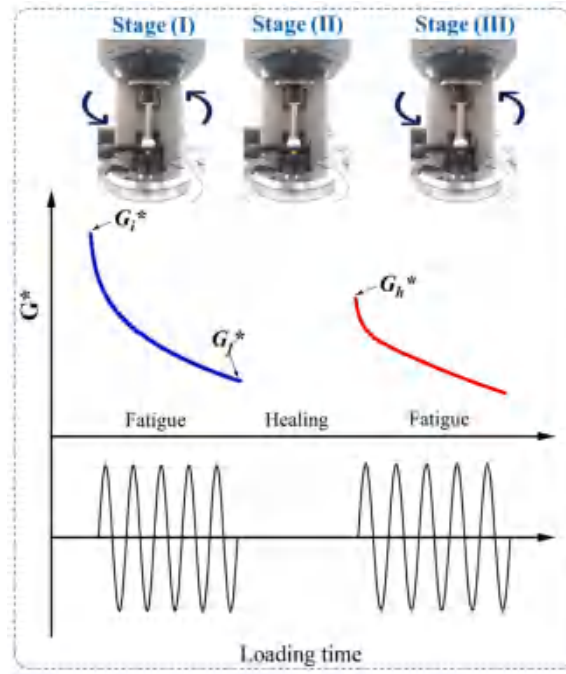

Fig. 5. Fatigue healing test.

$$H_R = D_2/D_1 \times 100\% \tag{6}$$

Where H_R represents the fracture healing rate of CRMA; D_1 represents the initial ductility of CRMA; and D_2 represents the ductility of CRMA after healing.

3. Results and discussion

3.1. Optimal dosage of DPA/CRMA and DTSA/CRMA

Fig. 6 shows the physical properties of DPA/CRMA and DTSA/CRMA with different dosages. From Fig. 6, it was observed that the softening point and ductility of CRMA were 64.5 ℃ and 6.0 cm, respectively. With the increase of DPA and DTSA dosage, the softening point and ductility of DPA/CRMA and DTSA/CRMA gradually improved, which demonstrated that dynamic chemical bonds is beneficial for improving the physical properties of modified asphalt [17]. When the dosage of DPA and DTSA was 2.5 %, the softening points of DPA/CRMA and DTSA/CMA increased to 69.4 ℃ and 70.1 ℃, and the ductility of DPA/CRMA and DTSA/CRMA improved to 9.0 and 8.7 cm. It was notable that when the dosage of DPA and DTSA exceeds 1.5 %, the increment of softening point and ductility for DPA/CRMA and DTSA/CMA significantly decreased, indicating that 1.5 % was the optimal dosage for DPA/CRMA and DTSA/CRMA. Therefore, DPA/CRMA and DTSA/CRMA with a dosage of 1.5 % were selected for subsequent experiments.

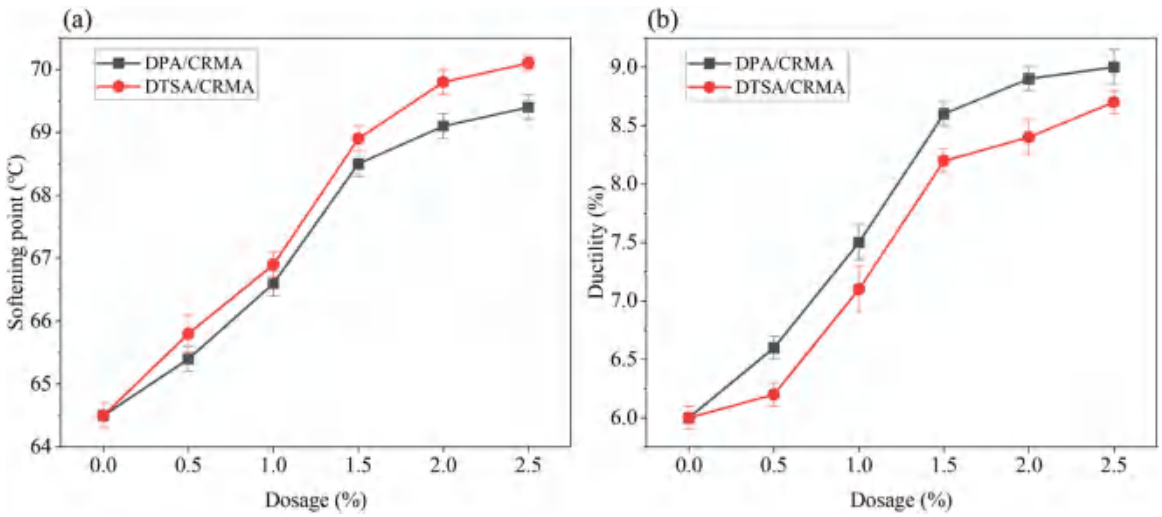

Fig. 6. Physical properties of the DPA/CRMA and DTSA/CRMA.

3.2. Chemical structure of DPA/CRMA and DTSA/CRMA before and after aging

Fig. 7 displays the FTIR spectra of the CRMA, DPA/CRMA and DTSA/CRMA. In the infrared spectra of the desulfurized waste crumb rubber (CR), the characteristic peak of -OH was at 3631–3318 cm^{-1} [40]. The characteristic peaks of C-H, methylene (-CH_2), benzene ring and methylene chain segment (CH_2)n (n $\geq$ 4) in alkanes were at 2930 cm^{-1}, 1430 cm^{-1}, 871 $cm^{-1}$and 723 cm^{-1}, respectively [41]. In the infrared spectra of CRMA, the characteristic peaks of asymmetrically substituted benzene ring appeared at 1600 cm^{-1}, and the characteristic peak of -OH was still observed at 3631–3318 cm^{-1}. In the FTIR spectra of DPA/CRMA and DTSA/CRMA, the characteristic peaks of -OH disappeared, and the characteristic peaks of -COOH in DPA and DTSA were not detected, which demonstrated the DPA and DTSA successfully connected between the desulfurized waste crumb rubber particles and formed a "bridge" structure.

Fig. 8 shows the infrared spectrum of the base asphalt (BA), CRMA, DPA/CRMA and DTSA/CRMA after aging. It was observed from Fig. 8 that the characteristic peaks of the carbonyl group (C═O) and sulfoxide group (S═O) for asphalt and all CRMA were found at 1700 cm^{-1} and 1030 cm^{-1}. The reason is that asphalt undergoes oxygen absorbing polymerization reaction during the aging process, resulting in intermolecular contractions and changes in chemical composition. This reaction generates carbonyl group and sulfinyl group [42]. The carbonyl index ($I_{C=O}$) and sulfoxide index ($I_{S=O}$) were used to characterize the aging degree of asphalt binders. The $I_{C=O}$ and $I_{S=O}$ were calculated according to Eqs. (7) and (8), where the $A_{1700cm^{-1}}$ and $A_{1030cm^{-1}}$ were the area of the characteristic peak of the carbonyl group and the sulfoxide group. $A_{2000-600cm^{-1}}$ was the peak area of all the characteristic peaks with a wavenumber between 2000 and 600 cm^{-1} [43].

$$I_{C=O} = \frac{A_{1700cm^{-1}}}{A_{2000-600cm^{-1}}} \tag{7}$$

$$I_{S=O} = \frac{A_{1030cm^{-1}}}{A_{2000-600cm^{-1}}} \tag{8}$$

The functional group indices are shown in Fig. 9. It was observed that the $I_{C=O}$ and the $I_{S=O}$ of the asphalt increased significantly after aging. The reason is that with the extension of the aging time, the components of the asphalt are transformed, in which the asphaltene content increases causing more carbonyl and sulfinyl groups to be generated [44]. The $I_{C=O}$ of asphalt after TFOT and PAV aging increased from 2.62 % to 6.14 % and 11.55 %, and the $I_{S=O}$ increased from 3.46 % to 5.63 % and 10.92 %. In CRMA, the $I_{C=O}$ and $I_{S=O}$ increased gradually after aging, and the $I_{C=O}$ and $I_{S=O}$ after aging were 5.56 % and 4.16 % after TFOT aging, and 9.22 % and 6.3 % after TFOT aging. In DPA/CRMA and DTSA/CRMA, the $I_{C=O}$ and $I_{S=O}$ gradually increased after aging. The $I_{C=O}$ of DPA/CRMA and DTSA/CRMA after TFOT aging were 3.62 % and 3.8 %, which were 34.9 % and 31.7 % lower than those of CRMA, which illustrated that dynamic disulfide bonds improve the anti-aging performance of crumb rubber modified asphalt. And the $I_{S=O}$ of DPA/CRMA and DTSA/CRMA were higher than that of CRMA, which might be due to the fact that the disulfide bonds in DPA/CRMA and DTSA/CRMA were broken and reacted with oxygen to form part of the sulfinyl group. After PAV aging, the $I_{C=O}$ of DPA/CRMA and DTSA/CRMA were 22.8 % and 19.9 % lower than those of CRMA. The $I_{S=O}$ of DPA/CRMA and DTSA/CRMA were 6.5 % and 10.3 % higher than those of CRMA. In summary, compared to CRMA, DPA/CRMA and DTSA/CRMA containing dynamic disulfide bonds had better anti-aging performance. In addition, DPA/CRMA had lower carbonyl index and sulfoxide index compared with DTSA/CRMA.

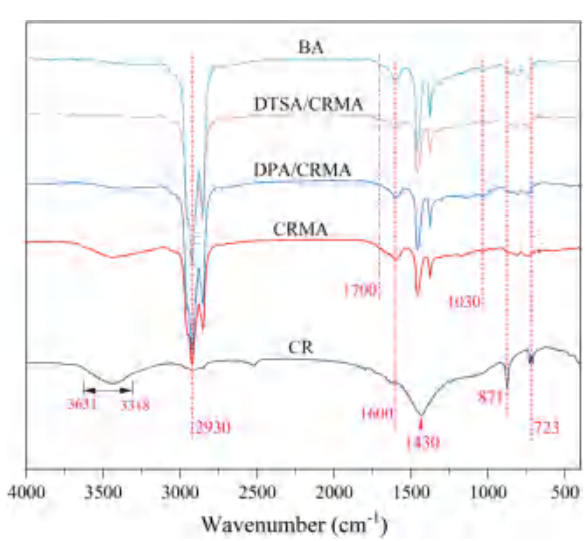

Fig. 7. Infrared spectra of the CRMA, DPA/CRMA and DTSA/CRMA.

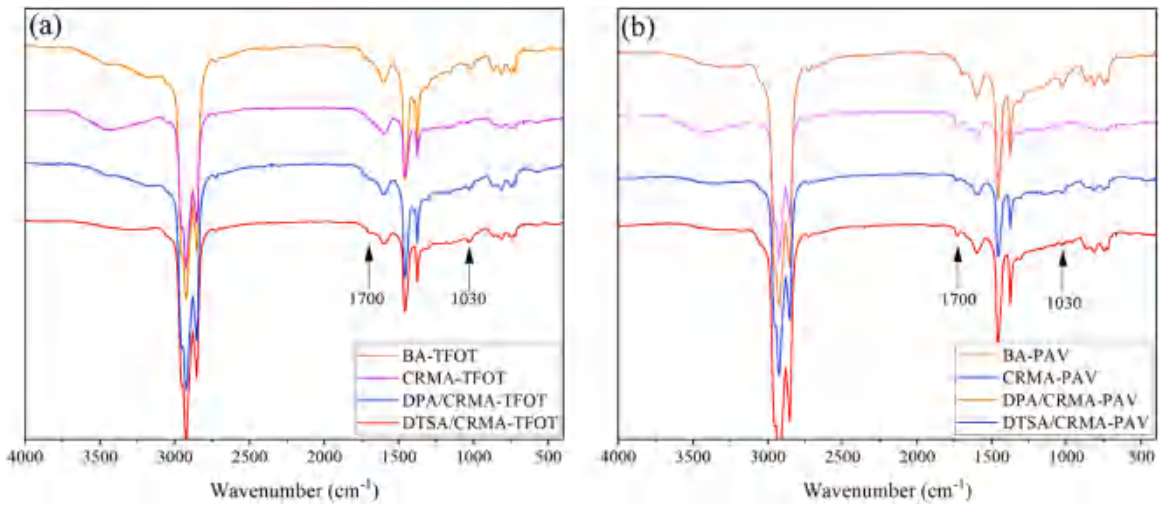

Fig. 8. Infrared spectrum of the CRMA, DPA/CRMA and DTSA/CRMA.

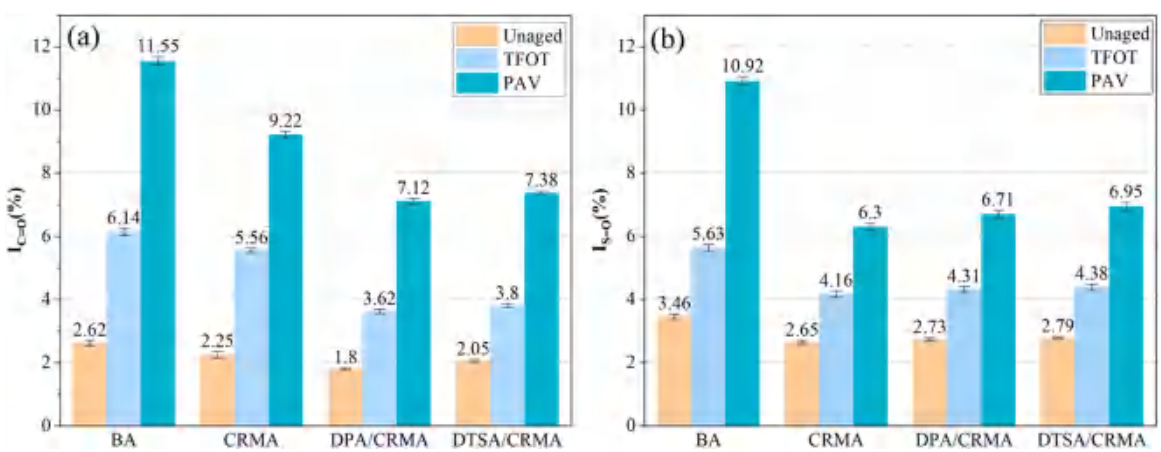

Fig. 9. Functional group indices of the CRMA, DPA/CRMA and DTSA/CRMA.

3.3. Microstructure of DPA/CRMA and DTSA/CRMA before and after aging

Fig. 10 displays the fluorescence microscope image of the CRMA, DPA/CRMA and DTSA/CRMA. It was clear from Fig. 10 that the crumb rubber in the CRMA dissolved and agglomerated. The crumb rubber of DPA/CRMA and DTSA/CRMA had better dispersibility, and the crumb rubber particles in them all had smaller sizes, indicating the dynamic disulfide bonds in DPA/CRMA and DTSA/CRMA improved the dispersion of the crumb rubber. After TFOT aging, the crumb rubber particles in CRMA, DPA/CRMA and DTSA/CRMA were agglomerated, the reason is that aging damaged the structure of the crumb rubber particles [45]. After PAV aging, the agglomeration of crumb rubber particles in CRMA became more serious, which had a negative impact on its performance. In DPA/CRMA and DTSA/CRMA, the dynamic disulfide bonds were broken after long-term aging, which caused the agglomeration of the crumb rubber particles. Compared to CRMA, the microstructures of DPA/CRMA and DTSA/CRMA after PAV aging were better, with the typical "island" structure, which indicated that the dynamic disulfide bonds improved the aging resistance of the crumb rubber modified asphalt. Furthermore, the microstructure of DPA/CRMA after aging is better than that of DTSA/CRMA, which is attributed to the fact that aromatic disulfide bonds have lower bond energies [46] and are more sensitive to aging compared to aliphatic disulfide bonds, which are more easily destroyed during aging.

3.4. Physical properties of DPA/CRMA and DTSA/CRMA before and after aging

Fig. 11 and Fig. 12 display the physical properties and aging indices of the base asphalt (BA) and all CRMA before and after aging. It was observed that due to the high elasticity of desulfurized waste crumb rubber [47], the softening point and ductility of asphalt were increased. Compared to CRMA, the softening point and ductility of DPA/CRMA and DTSA/CRMA are improved, which is because disulfide bonds form a "bridge" structure between the desulfurized waste crumb rubber and thereby enhance the performance of the desulfurized waste crumb rubber modified asphalt [48]. The softening point of DPA/CRMA and DTSA/CRMA improved by 3.7 ℃ and 4.6 ℃, respectively, and the ductility improved by 2.2 cm and 1.6 cm. The softening point and ductility of asphalt and all CRMA deteriorated after TFOT and PAV aging. After TFOT aging, the softening point increment (SPI) and ductility retention rate (DRR) of CRMA were 3.3℃ and 46.7 %, respectively. The SPI of DPA/CRMA and DTSA/CRMA were 2.7℃ and 3.0℃, and the DRR was 64.6 % and 59.2 %, which indicated that the dynamic disulfide bonds in DPA and DTSA both improved the short-term aging resistance of the crumb rubber modified asphalt. After PAV aging, the SPI of asphalt and all CRMA increases, while the DRR significantly decreases. It is noteworthy that compared with CRMA, DPA/CRMA and DTSA/CRMA showed smaller softening point increment and higher ductility retention rates. The SPI of DPA/CRMA and DTSA/CRMA were

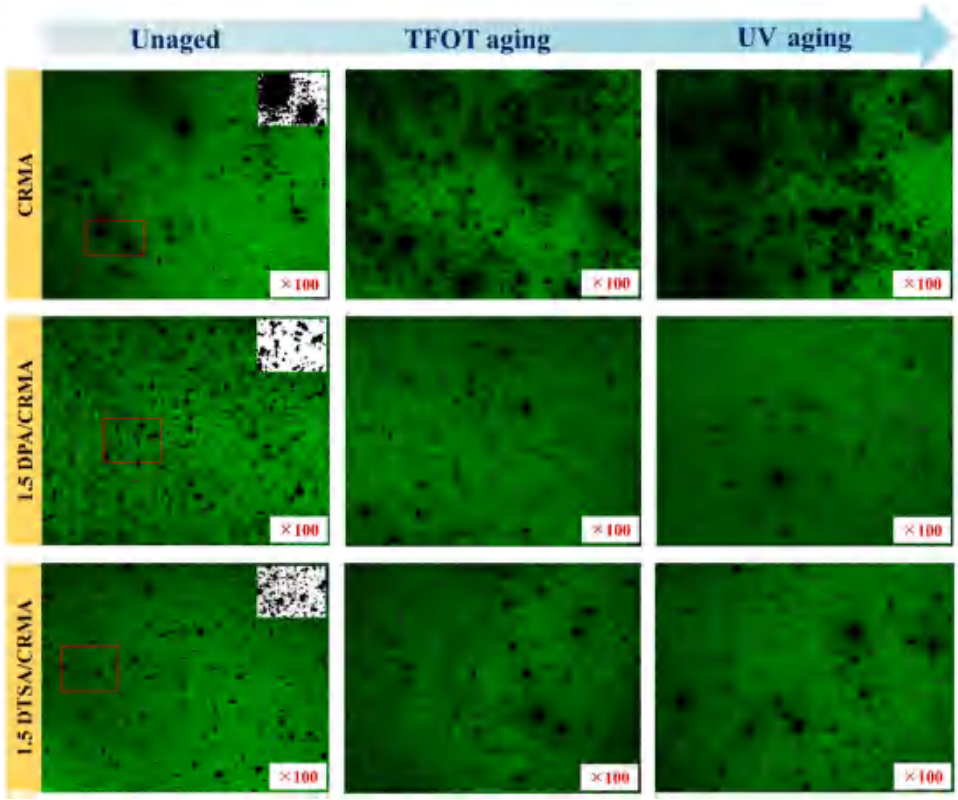

Fig. 10. Fluorescence microscopy images of the CRMA, DPA/CRMA and DTSA/CRMA.

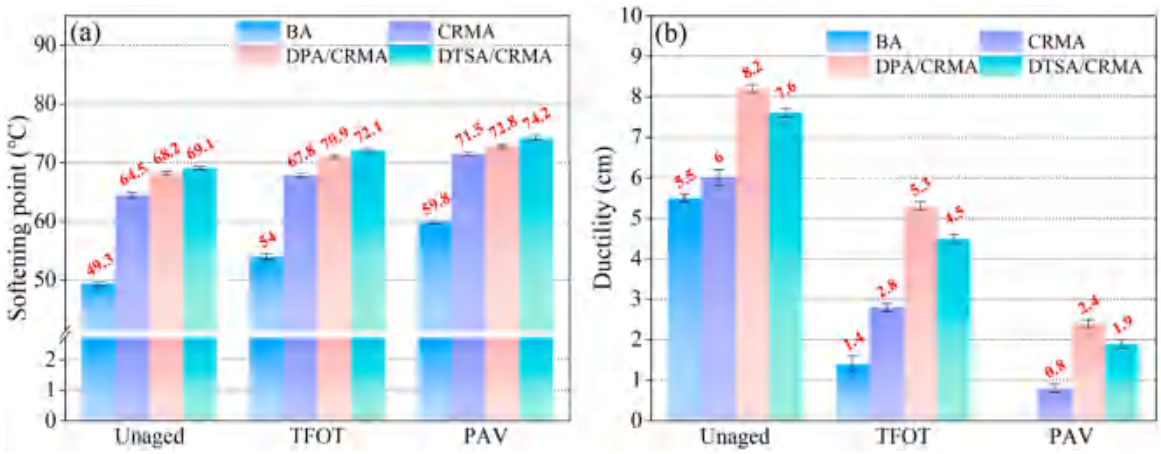

Fig. 11. Physical properties of CRMA, DPA/CRMA and DTSA/CRMA before and after aging.

reduced to 4.6℃ and 5.1℃, the DRR was 29.3 % and 25.0 %, and DPA/CRMA containing aliphatic disulfide bonds had better anti-aging performance. In conclusion, DPA/CRMA and DTSA/CRMA containing disulfide bonds had superior physical properties before and after aging, and the physical properties of DPA/CRMA were better than those of DTSA/CRMA.

3.5. Rheological properties of DPA/CRMA and DTSA/CRMA before and after aging

3.5.1. High-temperature rheological properties

Fig. 13 shows the high-temperature rheological properties of the CRMA, DPA/CRMA and DTSA/CRMA. It was observed from Fig. 13 (a)–(c) that the desulfurized waste crumb rubber improved the complex modulus of the asphalt. Compared with CRMA, DPA/CRMA and DTSA/CRMA had higher complex modulus, indicating that dynamic disulfide bonds enhanced the rheological properties of polymer modified asphalt and enabled its display elastic properties [10]. The initial complex modulus of DTSA/CRMA and DPA/CRMA were improved by 31.6 % and 38.1 % than that of CRMA, respectively. The initial complex modulus of DPA/CRMA was slightly higher than that of DTSA/CRMA. After TFOT aging, due to the asphaltene content of the asphalt increased, the asphalt exhibits hardening and brittleness, and its complex modulus increases significantly [49]. As a result, the complex modulus of asphalt and all CRMA increased. In DPA/CRMA and DTSA/CRMA, a certain degree of "bridge structure" was formed through dynamic disulfide bonds, and the change in complex modulus was small, with the smallest change in DPA/CRMA. After PAV aging, the complex modulus of all CRMA further

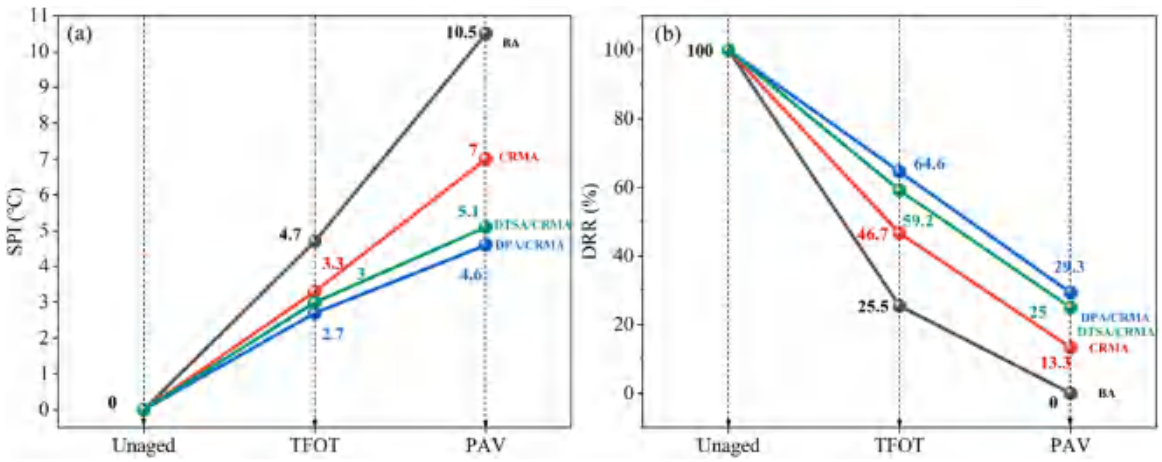

Fig. 12. SPI and DRR of CRMA, DPA/CRMA and DTSA/CRMA before and after aging.

increased. The complex modulus of asphalt after PAV aging increased by 598.0 % than that of unaged asphalt. The complex modulus of CRMA increased by 286.0 % than that of unaged, while the modulus of DPA/CRMA and DTSA/CRMA increased by 113.2 % and 125.0 %, which revealed that dynamic disulfide bonds enhance the aging resistance of the desulfurized waste crumb rubber modified asphalt, with the DPA/CRMA had better aging resistance.

As shown in Fig. 13 (d)–(f), the desulfurized waste crumb rubber improved the elastic properties of asphalt, resulting in a marked decrease of the phase angle. The phase angle was further reduced in DPA/CRMA and DTSA/CRMA due to the introduction of dynamic disulfide bonds. The phase angles of the asphalt and all CRMA increased as the test temperature rose, while the phase angle of the DPA/CRMA was the smallest. It was worth noting that a plateau region appeared in the desulfurized crumb rubber modified asphalt at 38–60℃, where the phase angle of crumb rubber modified asphalt decreased or slowly increased, which was because the desulfurized waste crumb rubber in this temperature range had better elastic deformation [50]. In DPA/CRMA and DTSA/CRMA, the temperature range in the plateau region of 30–60 ℃ was wider than that in CRMA, suggesting that dynamic disulfide bonds between the crumb rubber particles enhanced the elasticity of CRMA. After TFOT aging, the phase angles of CRMA, DPA/CRMA, and DTSA/CRMA all reduced, and the temperature range of the platform region gradually narrowed. After PAV aging, the platform area of CRMA, DPA/CRMA, and DTSA/CRMA was further reduced compared to TFOT aging, and the phase angle was also further reduced. In summary, DPA/CRMA and DTSA/CRMA with dynamic disulfide bonds exhibited excellent high temperature rheological properties. Compared with DTSA/CRMA, DPA/CRMA had better rheological properties.

3.5.2. MSCR

The multiple stress creep recovery curves of the CRMA, DPA/CRMA and DTSA/CRMA are shown in Fig. 14. It was observed that the unaged asphalt had the highest cumulative strain and exhibited significant viscous fluid properties at 0.1 stress level. The cumulative strain of the desulfurized waste crumb rubber modified asphalt was smaller, which was attributed to the fact that the desulfurized waste crumb rubber could absorb the light components in the asphalt and limit the slippage of the asphalt [51]. The cumulative strains of DPA/CRMA and DTSA/CRMA were 22.1 % and 24.6 %, which were reduced by 20.8 % and 18.3 % than CRMA, respectively. The cumulative strains of DPA/CRMA and DTSA/CRMA were significantly lower, indicating that the dynamic disulfide bonds between the desulfurized waste crumb rubber enhance the elastic properties of CRMA. The cumulative strain of asphalt and all CRMA gradually increased after TFOT aging. After PAV aging, the cumulative strain of asphalt and all CRMA significantly increased. The cumulative strain of asphalt and CRMA increased by 122.5 % and 75.8 % after PAV aging compared to unaged. The cumulative strain increments of DPA/CRMA and DTSA/CRMA after PAV aging were lower than those of asphalt and CRMA, demonstrating that dynamic disulfide bonds improved the aging resistance of desulfurized waste crumb rubber modified asphalt. At a 3.2 kPa stress level, the cumulative strains of asphalt and all CRMA were significantly increased and their cumulative strains were further increased after TFOT and PAV aging. Importantly, the cumulative strains of both DPA/CRMA and DTSA/CRMA were significantly lower than those of BA and CRMA.

The J_{nr} and R for the CRMA, DPA/CRMA and DTSA/CRMA are displayed in Fig. 15. It was clear from Fig. 15 that the asphalt had a weak recovery capacity with an R of 15.8 % at the 0.1 kPa level. The R of CRMA increased to 68.1 %, while the R of DPA/CRMA and DTSA/CRMA increased to 95.3 % and 92.2 %, respectively. This further indicated that dynamic disulfide bonds significantly improved the elasticity of crumb rubber modified asphalt. The asphalt had the highest J_{nr} values, with J_{nr} decreasing to 0.12 for CRMA and DPA/CRMA and DTSA/CRMA decreasing to 0.026 and 0.036. After TFOT and PAV aging, the light component content in asphalt decreased, resulting in its poor fluidity [52]. As a result, its J_{nr} gradually increased and R gradually reduced. The trend of increasing J and decreasing R after aging was also observed for all CRMA. However, the R of DPA/CRMA and DTSA/CRMA were higher than those of CRMA before and after aging. The R of DPA/CRMA and DTSA/CRMA after TFOT aging were 42.6 % and 41.5 % higher than CRMA. The R of DPA/CRMA and DTSA/CRMA after PAV aging were 66.5 % and 58.9 % higher than CRMA, showing that the self-healing desulfurized waste crumb rubber modified asphalt maintained better elasticity after aging. The R of asphalt and desulfurized waste crumb rubber modified asphalt decreased significantly and J_{nr} increased significantly when the stress level was increased from 0.1 kPa to 3.2 kPa. However, the R of DPA/CRMA and DTSA/CRMA remained high. In conclusion, the successful introduction of dynamic disulfide bonds enhanced the high-temperature elastic response capacity of desulfurized waste crumb rubber modified asphalt before and after aging, which is beneficial for improving its cracking resistance.

3.5.3. Low-temperature rheological properties

Fig. 16 shows the creep rate (m) and creep stiffness (S) of the CRMA, DPA/CRMA and DTSA/CRMA. It is evident from Fig. 16 that the S of asphalt at − 18 °C was higher while the m was lower because the asphalt exhibits stiffening and brittleness at low temperatures, which is unfavorable for low-temperature cracking resistance [53]. The desulfurized waste crumb rubber improved the low-temperature rheological properties of the asphalt, with the S of CRMA decreasing to 233 MPa and m

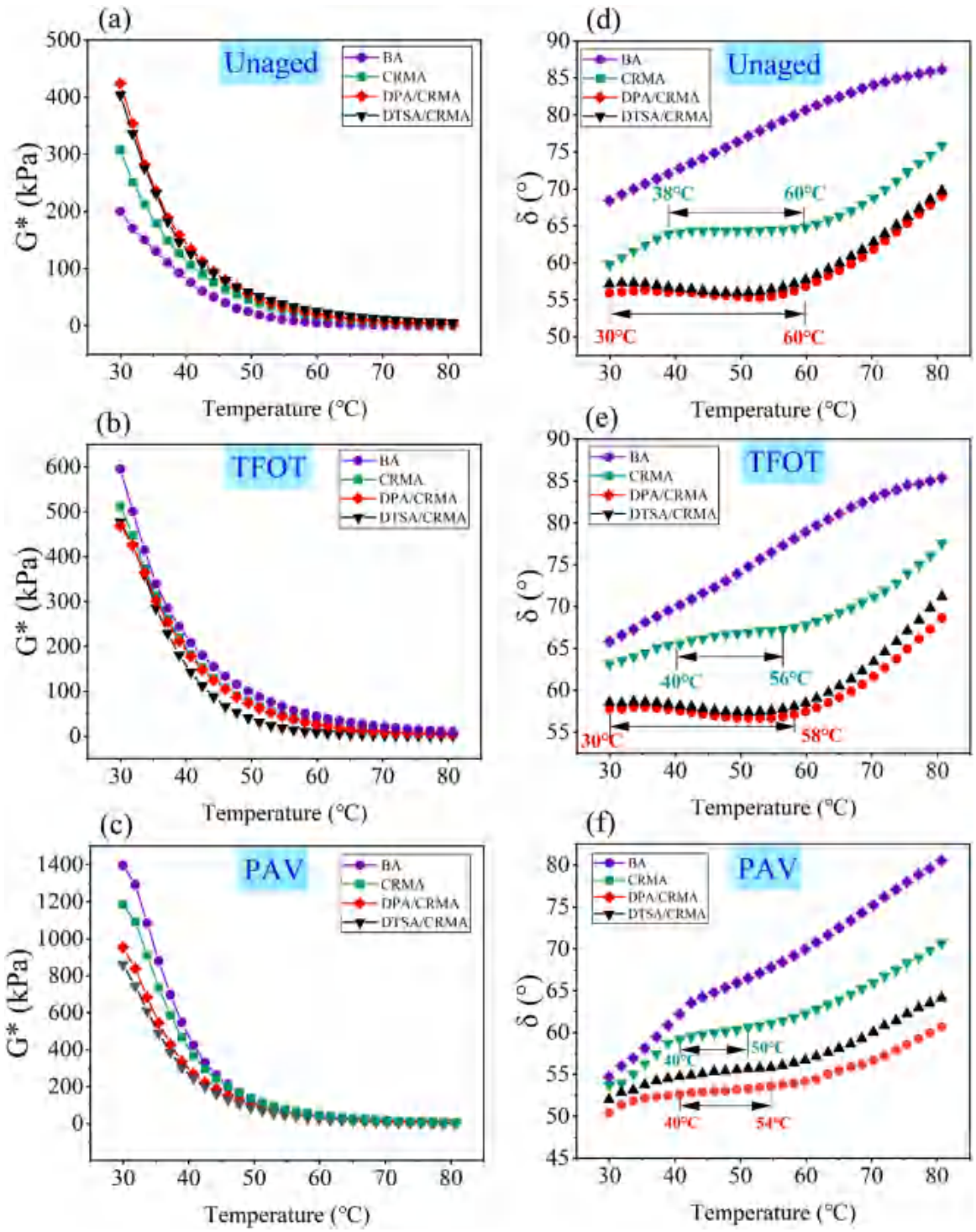

Fig. 13. High-temperature rheological properties of CRMA, DPA/CRMA and DTSA/CRMA.

increasing to 0.37. The addition of DPA and DTSA containing dynamic disulfide bonds further enhanced the rheological properties of the crumb rubber modified asphalt, with the S decreasing to 206 MPa and 215 MPa and the m increasing to 0.43 and 0.41 for DPA/CRMA and DTSA/CRMA. The reason for the enhanced low-temperature cracking resistance of DPA/CRMA and DTSA/CRMA is that on one hand, the "bridge" of dynamic disulfide bonds improves the dispersion of the crumb rubber modified asphalt [48], and on the other hand, the dynamic disulfide bonds increase its flexibility at low temperature. The low-temperature rheological properties of DPA/CRMA were better to those of DTSA/CRMA. After TFOT aging, the S of asphalt and CRMA increased and the m decreased. The reason is that the content of light components in the asphalt decreases after aging, and it becomes hard and brittle at low temperatures. The S of asphalt increased by 7.3 % and m decreased by 28.6 % compared to unaged. The S of CRMA increased by 9.9 % and m decreased by 21.6 %, while the m of DPA/CRMA and DTSA/CRMA decreased by 16.0 % and m decreased by 13.0 %. Compared to CRMA, the dynamic disulfide bonds in DPA/CRMA and DTSA/CRMA can endow desulfurized waste crumb rubber modified asphalt with a certain degree of flexibility at low temperatures, resulting in great anti-aging

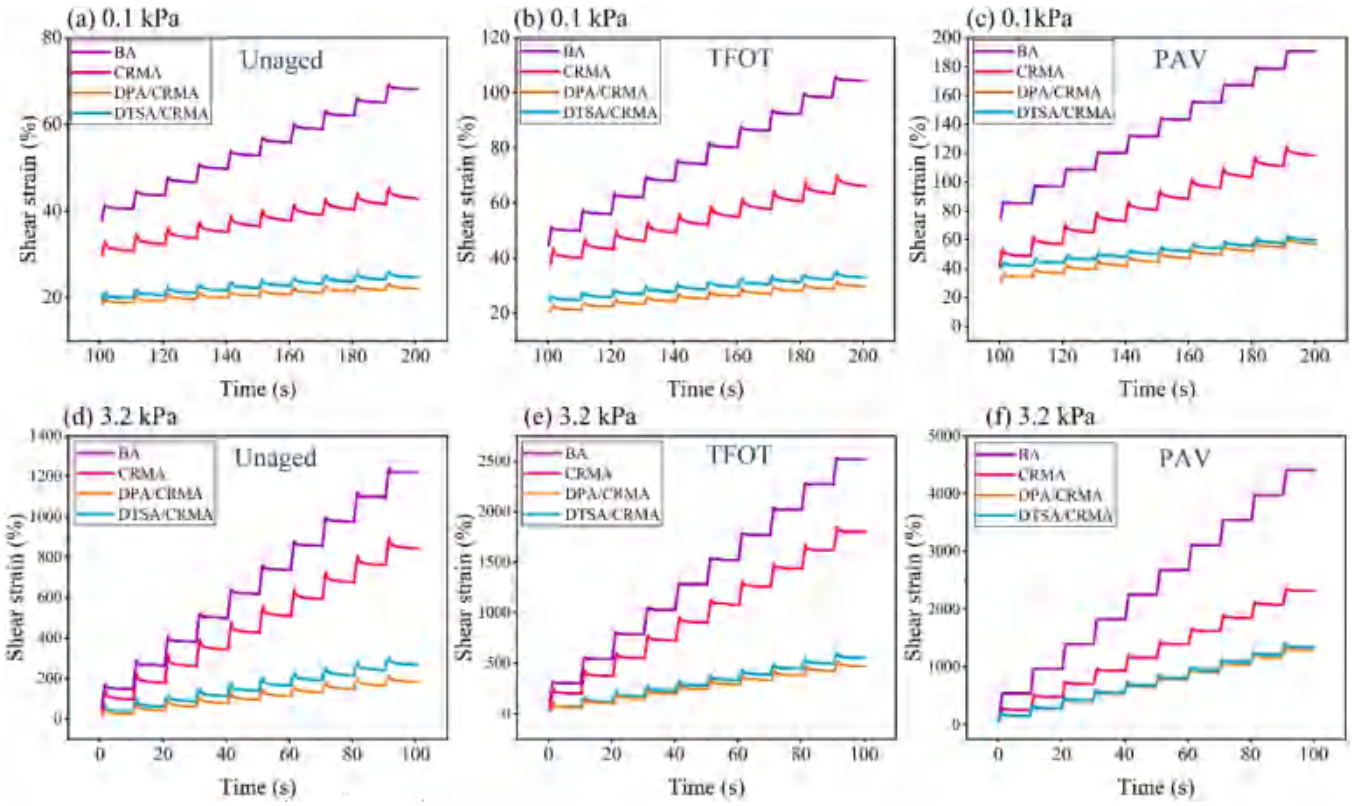

Fig. 14. MSCR curves of CRMA, DPA/CRMA and DTSA/CRMA.

capability. However, due to the fact that DPA has a more flexible disulfide bond with a straight chain hydrocarbon structure, its creep rate was the highest. After the PAV aging, the S of BA and all CRMA increased while the m decreased. The low-temperature crack resistance of BA and CRMA was markedly reduced, and the low-temperature crack resistance of DPA/CRMA and DTSA/CRMA was also significantly reduced due to the destruction of dynamic disulfide bonds. Nevertheless, compared to CRMA, DPA/CRMA and DTSA/CRMA both have higher m and lower S after PAV aging. In conclusion, DPA/CRMA and DTSA/CRMA with dynamic disulfide bonds had excellent low temperature cracking resistance. The low temperature cracking resistance of DPA/CRMA was relatively better due to the better flexibility of the aliphatic disulfide bonds.

3.6. Self-healing performance of DPA/CRMA and DTSA/CRMA before and after aging

3.6.1. Fatigue healing performance

Fig. 17 shows the fatigue healing curves and healing indices of the CRMA, DPA/CRMA and DTSA/CRMA. From Fig. 17, it was observed that asphalt had a certain self-healing ability and its fatigue healing index was 64.9 %. The fatigue healing index of CRMA was 51.8 %, which was smaller than that of asphalt, suggesting that the polymer had an adverse effect on the healing capability of asphalt [54]. The fatigue healing indices of DPA/CRMA and DTSA/CRMA reached to 83.1 % and 88.1 %, which suggested the dynamic disulfide bonds in DPA and DTSA significantly improved the healing capability of the crumb rubber modified asphalt. Among them, the DTSA/CRMA had a higher healing index, which was attributed to the fact that aromatic disulfide bonds have smaller bond energies, and are more susceptible to breakage-rearrangement effect than the aliphatic disulfide bonds [15]. The fatigue healing indices of both aged asphalt and all CRMA were reduced because aging makes asphalt and crumb rubber modified asphalt less fluid and less capable of self-healing. After TFOT aging, the healing indices of asphalt and CRMA decreased to 37.4 % and 36.1 %, respectively. The healing indices of DPA/CRMA and DTSA/CRMA decreased to 56.1 % and 54.9 %, which demonstrated that dynamic disulfide bonds can still endow crumb rubber modified asphalt with a better self-healing performance after short-term aging. The fatigue healing indices of asphalt and all CRMA decreased significantly after PAV aging. The healing indices of asphalt and CRMA decreased to 17.8 % and 21.4 % after PAV aging. The healing indices of DPA/CRMA and DTSA/CRMA showed a significant decrease, which was attributed to the destruction of dynamic disulfide bonds during PAV aging. The fatigue healing indices of DPA/CRMA and DTSA/CRMA were 38.8 % and 35.6 %. In conclusion, both DPA/CRMA and DTSA/CRMA with disulfide bonds had better fatigue healing performance before and after aging compared to CRMA and BA.

3.6.2. Fracture healing performance

Fig. 18 shows the fracture healing performance of the CRMA, DPA/CRMA and DTSA/CRMA. From Fig. 18, it was observed that the fracture healing capability of asphalt is poor [55], and the fracture healing rate was 35.3 %. The fracture healing rate of CRMA was 33.3 %, while the fracture healing rates of DPA/CRMA and DTSA/CRMA reached 55.8 % and 59.9 %, respectively. This is due to the fact that when a crack occurs, the broken disulfide bonds at the crack are able to undergo a rearrangement effect, enabling healing and strength restoration of the crack [56]. The reason for the higher self-healing rate of DTSA/CRMA is that the aromatic dynamic disulfide bonds have a stronger breakage-rearrangement effect due to the low bond energies. The fracture healing rate of both asphalt and all CRMA decreased gradually after aging. The healing rate of asphalt decreased to 12.2 % due to the transformation of the light component to the heavy component of the asphalt during aging, which reduces the fluidity and self-healing capability of the asphalt. The fracture healing rate of CRMA decreased by 11.8 % after TFOT aging. The healing rates of DPA/CRMA and DTSA/CRMA decreased by 10.3 % and 11.3 %. The healing rates of all

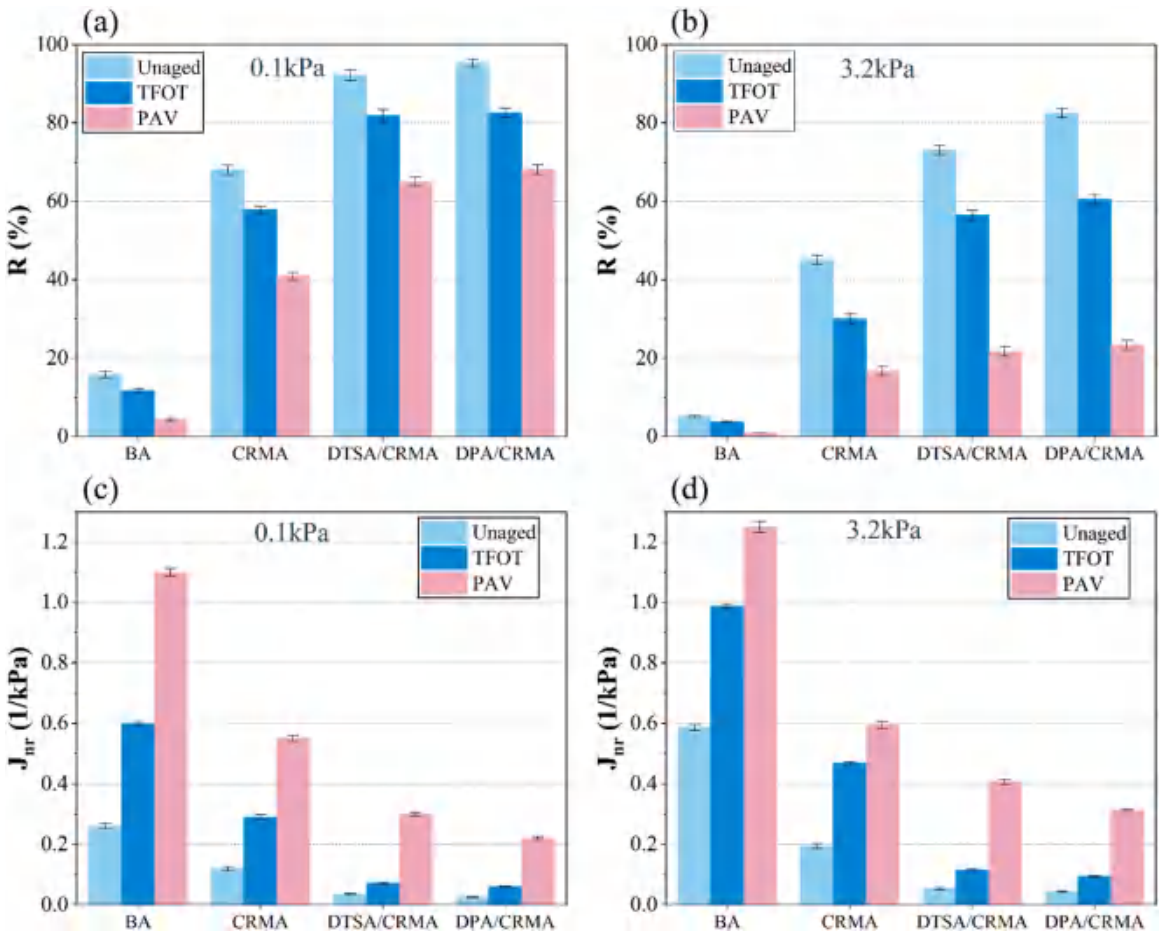

Fig. 15. R and J_{nr} of CRMA, DPA/CRMA and DTSA/CRMA.

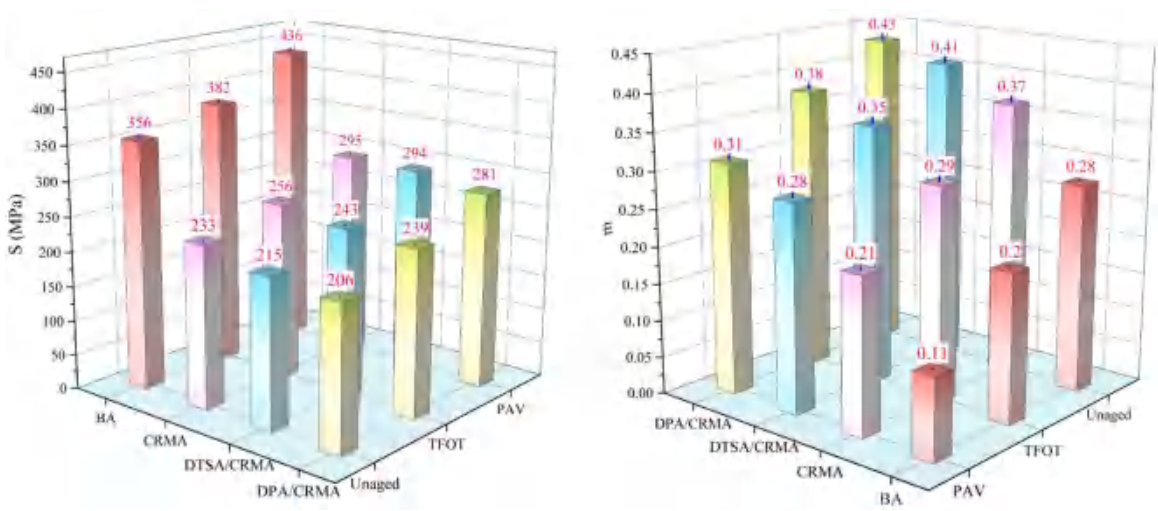

Fig. 16. S and m of the CRMA, DPA/CRMA and DTSA/CRMA.

asphalt binders decreased significantly after PAV aging. The fracture healing rate of CRMA significantly decreased to 10.5 %. The fracture healing rate of DPA/CRMA and DTSA/CRMA significantly decreased to 24.6 % and 23.3 %, indicating that the long-term aging broke the dynamic disulfide bonds in DPA and DTSA, which agreed with the fatigue healing test results. In summary, the disulfide bonds enhanced the fracture healing performance of the self-healing desulfurized waste crumb rubber modified asphalt, and the healing ability of the DPA/CRMA and DTSA/CRMA was reduced after aging due to the destruction of the dynamic disulfide bonds.

4. Conclusion

It is essential to develop intrinsic self-healing waste crumb rubber modified asphalt based on dynamic chemical bonds and to investigate the effect of aging on its structure and properties, which is conducive to

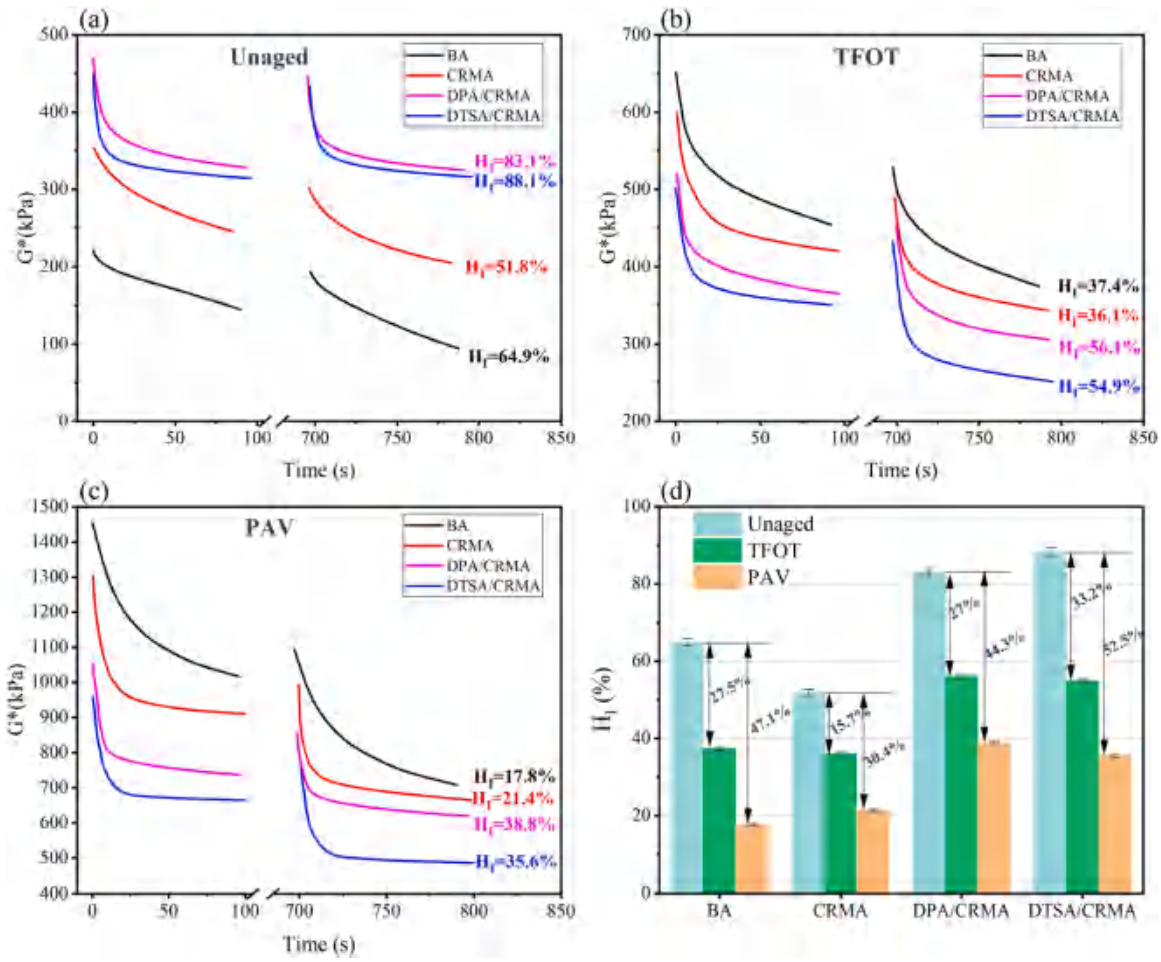

Fig. 17. Fatigue healing curves and healing indices of the CRMA, DPA/CRMA and DTSA/CRMA.

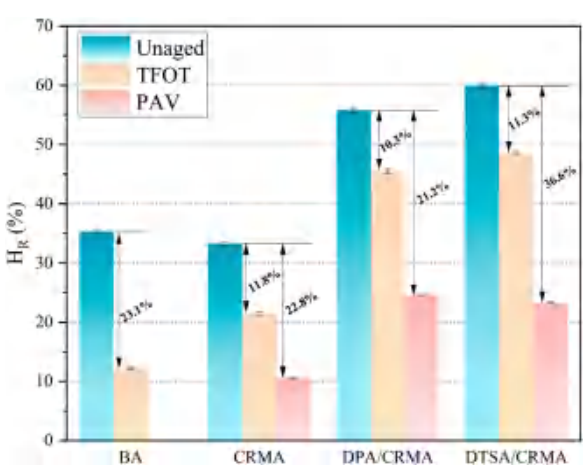

Fig. 18. Fracture healing rates of the CRMA, DPA/CRMA and DTSA/CRMA.

extending the service life of asphalt pavements. Therefore, in this study, two types of self-healing desulfurized waste crumb rubber modified asphalts (DPA/CRMA with aliphatic disulfide bonds and DTSA/CRMA with aromatic disulfide bonds) were prepared. The chemical structure, microstructure, physical properties, rheological properties and healing performance of DPA/CRMA and DTSA/CRMA before and after aging were systematically investigated. The main conclusions are summarized as below:

(1) Chemical structure analysis showed that self-healing desulfurized waste crumb rubber modified asphalts (DPA/CRMA and DTSA/CRMA) containing dynamic aliphatic and aromatic disulfide bonds were successfully prepared. After aging, the dynamic disulfide bonds in DPA/CRMA and DTSA/CRMA broke and formed sulfoxide groups, resulting in $I_{S=O}$ for DPA/CRMA and DTSA/CRMA increased by 6.5 % and 10.3 % compared to CRMA. Furthermore, the $I_{S=O}$ of DTSA/CRMA was higher than that of DPA/CRMA due to the fact that DTSA/CRMA containing aromatic disulfide groups had lower bond energies and was more sensitive to aging.

(2) Fluorescence microscopy images revealed that self-healing desulfurized waste crumb rubber modified asphalt (DPA/CRMA and DTSA/CRMA) had better dispersion due to dynamic disulfide bonds in the “bridge” structure between the desulfurized waste crumb rubber particles. After TFOT and PAV aging, the microscopic morphology of DPA/CRMA and DTSA/CRMA deteriorated and some agglomerations appeared. The microstructure of DPA/CRMA was better to that of DTSA/CRMA.

(3) Self-healing desulfurized waste crumb rubber modified asphalt had better physical properties owing to the more uniform dispersion of crumb rubber in asphalt. Compared to CRMA, the softening points of DPA/CRMA and DTSA/CRMA were improved by 3.7 °C and 4.6 °C, and the ductility was increased by 36.6 % and 26.7 %. After aging, the softening point increment of CRMA, DTSA/CRMA and DPA/CRMA was 7.0 ℃, 5.1 ℃ and 4.6 ℃ , and their ductility retention rates were 13.3 %, 25.0 %, and 29.3 %, respectively. Since aliphatic disulfide bonds had better flexibility,

the physical properties of DPA/CRMA are better than those of DTSA/CRMA.

(4) Self-healing DPA/CRMA and DTSA/CRMA exhibited superior rheological properties, which is conducive to the improvement of the crack resistance of crumb rubber modified asphalt. The high-temperature rheological test revealed that the complex modulus of DPA/CRMA and DTSA/CRMA was improved by 38.1 % and 31.6 % compared to CRMA. The low-temperature rheological test showed that the creep rate of DPA/CRMA and DTSA/CRMA was greater than 0.3 and the creep stiffness was less than 300 MPa, which demonstrated better low-temperature crack resistance. After aging, DPA/CRMA had better high and low-temperature rheological properties and crack resistance capability than DTSA/CRMA.

(5) Self-healing DPA/CRMA and DTSA/CRMA had superior healing performance under the breakage-rearrangement effect of dynamic disulfide bonds, exhibiting better healing capacity of macro- and micro-cracks. The fatigue healing indices of DPA/CRMA and DTSA/CRMA were 31.3 % and 36.3 % higher than those of CRMA, and their fracture healing rates were 22.6 % and 26.6 % higher than those of CRMA, respectively. While DTSA/CRMA had a better self-healing ability than DPA/CRMA because of its more intense breakage-rearrangement effect. In addition, DTSA/CRMA and DPA/CRMA remained better self-healing ability after aging.

In this study, intrinsic self-healing desulfurized waste crumb rubber modified asphalts containing aliphatic and aromatic dynamic disulfide bonds were prepared and their healing performance, rheological properties and physical properties were systematically investigated. However, the limitation of this study is that the effect of dynamic disulfide bonds on the properties of asphalt binders was investigated, while the effect of dynamic disulfide bonds on the properties of asphalt mixtures was not explored. Further research should focus on investigating the effects of aliphatic and aromatic dynamic disulfide bonds on the performance of desulfurized waste crumb rubber modified asphalt mixtures.

CRediT authorship contribution statement

Shangheng Zeng: Resources, Investigation. **Ronghua Zhuang:** Software, Resources. **Shi Xu:** Writing – review & editing. **Quantao Liu:** Writing – review & editing. **Yanheng He:** Methodology, Investigation. **Shanjun Gao:** Writing – review & editing. **Tianwei Zhang:** Writing – original draft, Methodology, Investigation, Formal analysis, Data curation. **Jianying Yu:** Writing – review & editing, Supervision, Project administration.

Declaration of Competing Interest

The authors declare that they have no known competing financial interests or personal relationships that could have appeared to influence the work reported in this paper.

Acknowledgement

The authors are grateful for the financial assistance from the National Key R&D Program of China (No: 2022YFC3801600) and the Program Fund of Non-Metallic Excellent and Innovation Center for Building Materials (Grants #24PHD-7).

Data availability

Data will be made available on request.

References

[1] S. Faisal Kabirb, M. Zakertabrizi, E. Hosseini, E.H. Fini, Effects of amide-based modifiers on surface activation and devulcanization of rubber, Comput. Mater. Sci. 188 (2021) 110175, https://doi.org/10.1016/j.commatsci.2020.110175.
[2] S.O. Mohaved, A. Ansarifar, S.K. Nezhad, S. Atharyfar, A novel industrial technique for recycling ethylene-propylene-diene waste rubber, Polym. Degrad. Stab. 111 (2015) 114–123, https://doi.org/10.1016/j.polymdegradstab.2014.11.003.
[3] F. Guo, J. Zhang, J. Pei, W. Ma, Z. Hu, Y. Guan, Evaluation of the compatibility between rubber and asphalt based on molecular dynamics simulation, Front. Struct. Civ. Eng. 14 (2020) 435–445, https://doi.org/10.1007/s11709-019-0603-x.
[4] S. Poovaneshvaran, L.W. Zheng, M.R.M. Hasan, X. Yang, A. Diab, Workability, compactibility and engineering properties of rubber-modified asphalt mixtures prepared via wet process, Int. J. Pavement Res. Technol. 14 (2021) 560–569, https://doi.org/10.1007/s42947-020-1006-z.
[5] Z. Liu, Preparation of microcapsule and its influence on self-healing property of asphalt, Pet. Sci. Technol. 37 (2019) 1025–1032, https://doi.org/10.1080/10916466.2019.1570253.
[6] B.R. Anupam, U.C. Sahoo, A.K. Chandrappa, A methodological review on self-healing asphalt pavements, Constr. Build. Mater. 321 (2022) 126395, https://doi.org/10.1016/j.conbuildmat.2022.126395.
[7] T. Wang, F. Xiao, X. Zhu, B. Huang, J. Wang, S. Amirkhanian, Energy consumption and environmental impact of rubberized asphalt pavement, J. Clean. Prod. 180 (2018) 139–158, https://doi.org/10.1016/j.jclepro.2018.01.086.
[8] A. Milad, A.G.F. Ahmeda, A.M. Taib, S. Rahmad, M. Solla, N.I.M. Yusoff, A review of the feasibility of using crumb rubber derived from end-of-life tire as asphalt binder modifier, J. Rubber Res. 23 (2020) 203–216, https://doi.org/10.1007/s42464-020-00050-y.
[9] L. Lyu, D. Li, Y. Chen, Y. Tian, J. Pei, Dynamic chemistry based self-healing of asphalt modified by diselenide-crosslinked polyurethane elastomer, Constr. Build. Mater. 293 (2021) 123480, https://doi.org/10.1016/j.conbuildmat.2021.123480.
[10] L. Lyu, Z. Wang, J. Ji, Y. Li, Y. Wen, J. Zhang, R. Li, Z. Chen, J. Pei, Investigating rheological and healing properties of asphalt binder modified by disulfide-crosslinked poly(urea-urethane) elastomer, Constr. Build. Mater. 347 (2022) 128546, https://doi.org/10.1016/j.conbuildmat.2022.128546.
[11] K. Wei, Y. Wu, X. Cao, X. Yang, B. Tang, B. Shan, Dual dynamic bonds approach for polyurethane recycling and self-healing of emulsified asphalt, Sci. Total Environ. 885 (2023) 163915, https://doi.org/10.1016/j.scitotenv.2023.163915.
[12] Z. Cao, L. Yuan, J. Yi, Preparation and characterization of polyurethane-modified asphalt containing dynamic covalent bonds, Constr. Build. Mater. 404 (2023) 133303, https://doi.org/10.1016/j.conbuildmat.2023.133303.
[13] X. An, R.H. Aguirresarobe, L. Irusta, F. Ruipérez, J.M. Matxain, X. Pan, N. Aramburu, D. Mecerreyes, H. Sardon, J. Zhu, Aromatic diselenide crosslinkers to enhance the reprocessability and self-healing of polyurethane thermosets, Polym. Chem. 8 (2017) 3641–3646, https://doi.org/10.1039/C7PY00448F.
[14] X. Wang, Y. Wei, D. Chen, Y. Bai, Synthesis and properties of room-temperature self-healing polyurethane elastomers, J. Macromol. Sci. Part A 54 (2017) 956–966, https://doi.org/10.1080/10601325.2017.1387483.
[15] S.-M. Kim, H. Jeon, S.-H. Shin, S.-A. Park, J. Jegal, S.Y. Hwang, D.X. Oh, J. Park, Superior toughness and fast self-healing at room temperature engineered by transparent elastomers, Adv. Mater. 30 (2018) 1705145, https://doi.org/10.1002/adma.201705145.
[16] T. Zhang, S. Gao, Y. He, R. Zhuang, X. Han, Z. Zou, J. Yu, Investigation of microstructure, rheological property and self-healing performance of SBS modified bitumen with dynamic disulfide bonds prepared by one-step method, Constr. Build. Mater. 416 (2024) 135158, https://doi.org/10.1016/j.conbuildmat.2024.135158.
[17] Y. He, S. Mao, T. Zhang, S. Zeng, H. Duan, R. Zhuang, J. Yu, Preparation and properties of self-healing SBS modified bitumen with dynamic acylhydrazone bonds, Eur. Polym. J. 210 (2024) 112932, https://doi.org/10.1016/j.eurpolymj.2024.112932.
[18] F. Xiao, Q. Zong, J. Wang, J. Chen, J. Liu, Storage stability characterization and improvement of SBS and crumb rubber composite modified asphalt, Road Mater. Pavement Des. 23 (2022) 509–526, https://doi.org/10.1080/14680629.2020.1830151.
[19] J. Li, F. Xiao, S.N. Amirkhanian, Storage, fatigue and low temperature characteristics of plasma treated rubberized binders, Constr. Build. Mater. 209 (2019) 454–462, https://doi.org/10.1016/j.conbuildmat.2019.03.136.
[20] C. Jiang, Y. Zhang, L. Ma, L. Zhou, H. He, Tailoring the properties of ground tire rubber/high-density polyethylene blends by combining surface devulcanization and in-situ grafting technology, Mater. Chem. Phys. 220 (2018) 161–170, https://doi.org/10.1016/j.matchemphys.2018.08.040.
[21] M. Sienkiewicz, K. Borzędowska-Labuda, A. Wojtkiewicz, H. Janik, Development of methods improving storage stability of bitumen modified with ground tire rubber: a review, Fuel Process. Technol. 159 (2017) 272–279, https://doi.org/10.1016/j.fuproc.2017.01.049.
[22] J. Li, F. Xiao, S.N. Amirkhanian, Rheological and chemical characterization of plasma-treated rubberized asphalt using customized extraction method, Fuel 264 (2020) 116819, https://doi.org/10.1016/j.fuel.2019.116819.
[23] L. Ling, J. Li, G. Zhang, R. Sun, C.-P. Wong, Self-healing and shape memory linear polyurethane based on disulfide linkages with excellent mechanical property, Macromol. Res. 26 (2018) 365–373, https://doi.org/10.1007/s13233-018-6037-9.
[24] ASTM-D36, American Society for Testing and Materials, Standard Test Method for Softening Point of Bitumen (Ring-And-Ball Apparatus), New York, 2006.
[25] ASTM-D5, American Society for Testing and Materials, Standard Test Method for Penetration of Bituminous Materials, New York, 2013.

[26] ASTM-D113, American Society for Testing and Materials, Standard Test Method for Ductility of Asphalt Materials, New York, 2007.
[27] ASTM-D4402, American Society for Testing and Materials, Standard Test Method for Viscosity Determination of Asphalt at Elevated Temperatures Using a Rotational Viscometer, New York, 2006.
[28] ASTM-D, American Society for Testing and Materials, Standard Test Method for Effect of Heat and Air on Asphaltic Materials (Thin-Film Oven Test), New York, 2009.
[29] ASTM-D6521, American Society for Testing and Materials, Standard practice for accelerated aging of asphalt binder using a pressurized aging vessel (PAV), New York, 2003.
[30] X. Han, S. Mao, S. Zeng, H. Duan, Q. Liu, L. Xue, J. Yu, Effect of reactive flexible rejuvenators on thermal-oxidative aging resistance of regenerated SBS modified asphalt, J. Clean. Prod. 380 (2022) 135027, https://doi.org/10.1016/j.jclepro.2022.135027.
[31] M. Liang, P. Liang, W. Fan, C. Qian, X. Xin, J. Shi, G. Nan, Thermo-rheological behavior and compatibility of modified asphalt with various styrene–butadiene structures in SBS copolymers, Mater. Des. 88 (2015) 177–185, https://doi.org/10.1016/j.matdes.2015.09.002.
[32] AASHTO, Standard Method of Test for Determining the Rheological Properties of Asphalt Binder Using a Dynamic Shear Rheometer (DSR) (AASHTO T315-12), AASHTO, Washington, DC, 2012.
[33] AASHTO, Standard Method of Test for Multiple Stress Creep Recovery (MSCR) – Test of Asphalt Binder Using a Dynamic Shear Rheometer (DSR) (AASHTO T350-14), AASHTO, Washington, DC, 2014.
[34] L. Lyu, P. Mikhailenko, Z. Piao, E.H. Fini, J. Pei, L.D. Poulikakos, Unraveling the modification mechanisms of waste bio-oils and crumb rubber on asphalt binder based on microscopy and chemo-rheology, Resour. Conserv. Recycl. 185 (2022) 106447, https://doi.org/10.1016/j.resconrec.2022.106447.
[35] ASTM-D6648, American Society for Testing and Materials, Standard test method for determining the flexural creep stiffness of asphalt binder using the bending beam rheometer (BBR), New York, 2001.
[36] D. Sun, Q. Pang, X. Zhu, Y. Tian, T. Lu, Y. Yang, Enhanced self-healing process of sustainable asphalt materials containing microcapsules, ACS Sustain. Chem. Eng. 5 (2017) 9881–9893, https://doi.org/10.1021/acssuschemeng.7b01850.
[37] D. Sun, T. Lin, X. Zhu, Y. Tian, F. Liu, Indices for self-healing performance assessments based on molecular dynamics simulation of asphalt binders, Comput. Mater. Sci. 114 (2016) 86–93, https://doi.org/10.1016/j.commatsci.2015.12.017.
[38] D. Sun, G. Sun, X. Zhu, A. Guarin, B. Li, Z. Dai, J. Ling, A comprehensive review on self-healing of asphalt materials: mechanism, model, characterization and enhancement, Adv. Colloid Interface Sci. 256 (2018) 65–93, https://doi.org/10.1016/j.cis.2018.05.003.
[39] Y. Tian, M. Zheng, P. Li, J. Zhang, R. Qiao, C. Cheng, H. Xu, Preparation and characterization of self-healing microcapsules of asphalt, Constr. Build. Mater. 263 (2020) 120174, https://doi.org/10.1016/j.conbuildmat.2020.120174.
[40] P. Kong, X. Chen, G. Xu, W. Wei, Preparation and characterization of maleic anhydride-grafted desulfurization rubber powder by free-radical polymerization, Polym. Eng. Sci. 61 (2021) 2567–2575, https://doi.org/10.1002/pen.25783.
[41] L. Yang, L. Tao, T. Zenglin, P. Jianzhong, Z. Mingliang, W. Zhenguo, Research on self-healing behavior of asphalt modified by polyurea elastomer containing dynamic disulfide/diselenide bond, Eur. Polym. J. 189 (2023) 111990, https://doi.org/10.1016/j.eurpolymj.2023.111990.
[42] R. Tauste, F. Moreno-Navarro, M. Sol-Sánchez, M.C. Rubio-Gámez, Understanding the bitumen ageing phenomenon: a review, Constr. Build. Mater. 192 (2018) 593–609, https://doi.org/10.1016/j.conbuildmat.2018.10.169.
[43] H. Liu, Z. Zhang, J. Xie, Z. Gui, N. Li, Y. Xu, Analysis of OMMT strengthened UV aging-resistance of Sasobit/SBS modified asphalt: its preparation, characterization and mechanism, J. Clean. Prod. 315 (2021) 128139, https://doi.org/10.1016/j.jclepro.2021.128139.
[44] B. Li, J. Han, D. Wei, H. Ji, T. Yao, H. Wang, J. Han, Y. Zhang, A molecular dynamics simulation study on the recovery performance of aged asphalt binder by waste vegetable oil rejuvenators, J. Clean. Prod. 442 (2024) 140796, https://doi.org/10.1016/j.jclepro.2024.140796.
[45] W. Zhang, Y. Luan, T. Ma, S. Wang, J. Chen, J. Li, M. Wu, Multilevel analysis of the aging mechanisms and performance evolution of rubber-modified asphalt, J. Mater. Civ. Eng. 33 (2021) 04021365, https://doi.org/10.1061/(ASCE)MT.1943-5533.0004000.
[46] G. Zhang, J. Pei, R. Li, P. Li, B. Zhou, The preparation and characterization of a novel self-healing based on the dynamic translocation of disulfide bonds, Mater. Res. Express 5 (2018) 105301, https://doi.org/10.1088/2053-1591/aad9d6.
[47] L. Xu, Z. Cao, M. Alae, X. Li, F. Xiao, Chemical component and low-temperature characteristics of modified asphalt composite with styrene–butadiene rubber and liquid nitrile rubber, Int. J. Pavement Eng. 25 (2024) 2362874, https://doi.org/10.1080/10298436.2024.2362874.
[48] X.-K. Li, G.-S. Chen, M.-W. Duan, W.-C. Yang, S.-C. Tang, Y.-D. Cao, Y. Luo, Branched hydroxyl modification of SBS using thiol-ene reaction and its subsequent application in modified asphalt, Ind. Eng. Chem. Res. 56 (2017) 10354–10365, https://doi.org/10.1021/acs.iecr.7b02280.
[49] D. Hu, X. Gu, Q. Dong, L. Lyu, B. Cui, J. Pei, Investigating the bio-rejuvenator effects on aged asphalt through exploring molecular evolution and chemical transformation of asphalt components during oxidative aging and regeneration, J. Clean. Prod. 329 (2021) 129711, https://doi.org/10.1016/j.jclepro.2021.129711.
[50] B. Li, H. Li, Y. Wei, X. Zhang, D. Wei, J. Li, Microscopic properties of hydrogen peroxide activated crumb rubber and its influence on the rheological properties of crumb rubber modified asphalt, Materials 12 (2019) 1434, https://doi.org/10.3390/ma12091434.
[51] D. Dong, X. Huang, X. Li, L. Zhang, Swelling process of rubber in asphalt and its effect on the structure and properties of rubber and asphalt, Constr. Build. Mater. 29 (2012) 316–322, https://doi.org/10.1016/j.conbuildmat.2011.10.021.
[52] Z. Pei, M. Xu, J. Cao, D. Feng, W. Hu, J. Ren, R. Jing, J. Yi, Analysis of the microcharacteristics of different kinds of asphalt based on different aging conditions, Mater. Struct. 55 (2022) 250, https://doi.org/10.1617/s11527-022-02088-3.
[53] A.M. Mohammed, A.H. Abed, Enhancing asphalt binder performance through nano-SiO_2 and nano-$CaCO_3$ additives: rheological and physical insights, Case Stud. Constr. Mater. 19 (2023) e02492, https://doi.org/10.1016/j.cscm.2023.e02492.
[54] B. Liang, F. Lan, K. Shi, G. Qian, Z. Liu, J. Zheng, Review on the self-healing of asphalt materials: mechanism, affecting factors, assessments and improvements, Constr. Build. Mater. 266 (2021) 120453, https://doi.org/10.1016/j.conbuildmat.2020.120453.
[55] I. Gonzalez-Torre, J. Norambuena-Contreras, Recent advances on self-healing of bituminous materials by the action of encapsulated rejuvenators, Constr. Build. Mater. 258 (2020) 119568, https://doi.org/10.1016/j.conbuildmat.2020.119568.
[56] T. Zhang, S. Gao, J. Yu, Y. He, X. Han, R. Zhuang, Preparation and performance of self-healing SBS modified bitumen based on dynamic disulfide bonds, Constr. Build. Mater. 397 (2023) 132394, https://doi.org/10.1016/j.conbuildmat.2023.132394.

Materials Today Communications 42 (2025) 111303

Contents lists available at ScienceDirect

Materials Today Communications

journal homepage: www.elsevier.com/locate/mtcomm

Effect of aging on structure and properties of self-healing-enhanced SBS modified asphalt with dual dynamic chemical bonds

Tianwei Zhang [a], Shanjun Gao [b], Yanheng He [a], Quantao Liu [c], Shi Xu [d,*], Ronghua Zhuang [a], Shangheng Zeng [a], Jianying Yu [a,*]

[a] State Key Laboratory of Silicate Materials for Architectures, Wuhan University of Technology, Wuhan 430070, PR China
[b] School of Material Science and Engineering, Wuhan University of Technology, Wuhan 430070, PR China
[c] Wuhan University of Technology Advanced Engineering Technology Research Institute of Zhongshan City, Zhongshan 528400, PR China
[d] Hubei Key Laboratory of Roadway Bridge and Structure Engineering, Wuhan University of Technology, Wuhan 430070, PR China

ARTICLE INFO

Keywords:
Self-healing
Dynamic chemical bonds
SBS modified asphalt
Aging

ABSTRACT

The introduction of dynamic chemical bonds (disulfide bonds, hydrogen bonds, etc.) into the network structure of SBS modified asphalt (SMA) can notably improve its healing properties. However, aging may break the dynamic chemical bonds in self-healing SMA, thereby deteriorating its healing ability. Therefore, it is crucial to investigate the effects of aging on the structure and properties of self-healing SMA with dynamic chemical bonds. Herein, self-healing SBS modified asphalts (SD/SMA and DDH/SMA) containing single disulfide bonds (SD) and dual disulfide bonds and hydrogen bonds (DDH) were prepared by free radical reaction, respectively. The SD/SMA and DDH/SMA were subjected to Thin Film Oven Test (TFOT) aging and Pressurized Aging Vessel (PAV) aging. Chemical structure analysis showed that the disulfide bonds underwent partial break after PAV aging. Nevertheless, the results of the healing tests indicated that compared to SMA, SD/SMA and DDH/SMA maintained superior healing properties after aging under the break-reorganization effect of dynamic chemical bonds. The fatigue healing indices of SD/SMA and DDH/SMA were 51.9 % and 95.8 % higher than those of SMA after PAV aging. The rheology tests revealed that SD/SMA and DDH/SMA had higher recovery rates and low-temperature cracking resistance than SMA before and after aging. Compared with SMA, SD/SMA and DDH/SMA had superior anti-aging performance. After PAV aging, the ductility retention rate of SD/SMA and DDH/SMA was 72.9 % and 98.9 % higher than that of SMA. Furthermore, compared to SD/SMA, DDH/SMA containing dual disulfide and hydrogen bonds had better healing capability, rheological properties and anti-aging performance.

1. Introduction

Styrene-butadiene-styrene (SBS) modified asphalt (SMA) is widely employed in pavement engineering because of its excellent high- and low-temperature performance [1–3]. However, SMA is susceptible to aging due to the effects of heat, ultraviolet radiation and oxygen, ultimately leading to cracking of asphalt pavement [4–6]. This situation leads to irregular maintenance of pavement, which consumes huge quantities of fossil energy [7]. With the development of engineering technology and the promotion of environmentally friendly road infrastructures, increasingly high requirements of the performance for SMA have been put forward. To meet the requirements of longer service life, less post-maintenance and higher safety for pavements, there is an urgent demand to develop self-healing SMA with superior anti-aging properties [8–10].

Due to the development of self-healing polymer in recent years, the technology of self-healing polymer modified asphalt is gradually drawing the focus of researchers and has been proven to significantly enhance healing capability of asphalt [11,12]. The mechanism is to introduce dynamic chemical bonds with break-reorganization effect into the polymer modified asphalt. When the asphalt binder is damaged by external forces, the dynamic chemical bonds at the cracks can be rearranged to heal the cracks and restore certain mechanical properties [13,14]. Dynamic chemical bonds include arylhydrazone bonds, diselenide bonds, disulfide bonds, hydrogen bonds, etc [15–17]. Wei et al. [18] developed a self-healing polyurethane modified asphalt based on

* Corresponding authors.
E-mail addresses: xushi@whut.edu.cn (S. Xu), jyyu@whut.edu.cn (J. Yu).

https://doi.org/10.1016/j.mtcomm.2024.111303
Received 26 September 2024; Received in revised form 25 November 2024; Accepted 12 December 2024
Available online 13 December 2024
2352-4928/© 2024 Elsevier Ltd. All rights are reserved, including those for text and data mining, AI training, and similar technologies.

disulfide and hydrogen bonds. The results showed that the self-healing polyurethane modified asphalt has the self-healing ability based on the break-reorganization effect of disulfide chemical bonds, which leads to remarkable enhancement of the healing ability for the polyurethane modified asphalt. Li et al. [19] prepared a self-healing polyurea elastomer by the reaction between amino groups of disulfides and isocyanate groups of prepolymers and blended them into SBS modified asphalt. The results indicated that the incorporation of the self-healing polyurea elastomer enhanced the healing ability and cracking resistance of SBS modified asphalt. Wei et al. [20] developed a self-healing polyurethane modified asphalt containing acylhydrazone bonds. The results revealed that the fatigue healing ability of self-healing polyurethane modified asphalt was notably enhanced. Our team prepared self-healing SBS modified asphalt by introducing the acylhydrazone bonds and disulfide bonds into the C═C bonds position of SBS by free radical reaction, respectively [21,22]. It was found that both self-healing SMA with acylhydrazone bonds and disulfide bonds had superior self-healing properties.

However, aging is inevitable for self-healing polymer modified asphalt during service, and aging may disrupt dynamic chemical bonds. Currently, there is no research about the effect of aging on the healing performance for self-healing polymer modified asphalt. Hence, it is essential to investigate the effect of aging on the dynamic chemical bonds of self-healing polymer modified asphalt and evaluate its deterioration degree of healing properties after aging.

This research aims to investigate the effects of aging on the structures and performance of self-healing SMA containing different kinds of dynamic chemical bonds. Single disulfide bonds (SD) and dual disulfide bonds and hydrogen bonds (DDH) were introduced into SBS modified asphalt through free radical reactions to develop self-healing SMA (SD/SMA and DDH/SMA). The SD/SMA and DDH/SMA were subjected to Thin Film Oven test (TFOT) aging and Pressure Aging Vessel (PAV). The chemical structures and microstructures of SD/SMA and DDH/SMA were characterized by Fourier Transform Infrared (FTIR) Spectroscopy and Fluorescence Microscopy (FM). The physical properties of SD/SMA and DDH/SMA before and after aging were explored. The rheological properties of SD/SMA and DDH/SMA were characterized by Dynamic Shear Rheometer (DSR) and Bending Beam Rheometer (BBR). The healing properties of SD/SMA and DDH/SMA before and after aging were investigated by fatigue healing and fracture healing tests.

2. Objectives and scope

The objectives of the research are:

(1) Investigate the effects of TFOT and PAV aging on the structure of dynamic chemical bonds in self-healing SMA.
(2) Explore the effects of TFOT and PAV aging on the physical performance and rheological properties of self-healing SMA.
(3) Evaluate the deterioration degree of the healing properties for self-healing SMA after TFOT and PAV aging.

3. Experiment

3.1. Materials

The specific properties of 70 # asphalt are presented in Table 1. The block ratio of butadiene and styrene in linear SBS is 70:30, with molecular weights ranging from 140,000 to 160,000 g/mol. The tensile strength and elongation of SBS are 26 MPa and 760 %, respectively. The 3,3′-dithiobispropionic acid was bought from China Bide Pharmatech Co., Ltd. The properties of the 3,3′-dithiobispropionic acid are shown in Table 2. The acrylamidamide with a purity of 99 %, hydroxypropyl methacrylate with a purity of 97 % and cumene hydroperoxide (initiator) were bought from Aladdin Biochemical Technology Co., Ltd. The characteristics of acrylamidamide and hydroxypropyl methacrylate are outlined in Table 3.

Table 1
Physical properties and components of asphalt.

	Properties/ Components	Results	Test methods
Physical property	softening point (℃)	49.3	ASTM D36
	Penetration (25℃, dmm)	67	ASTM D5
	Ductility (cm)	> 100	ASTM D113
	Viscosity (60℃, Pa· s)	330	ASTM D4402
Chemical components	Saturates (%)	15.82	
	Aromatics (%)	40.74	
	Resins (%)	27.26	
	Asphaltenes (%)	16.18	

Table 2
Properties of 3,3′-dithiobispropionic acid.

Index	Value
Structure	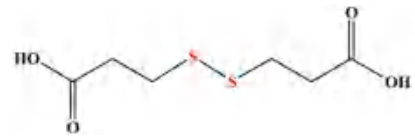
Molecular weight (g/mol)	210.27
Molecular formula	$C_6H_{10}O_4S_2$
Boiling point (℃)	431.1

3.2. Synthesis of SD and DDH

Based on our preliminary studies [22], the disulfide containing single disulfide bonds (SD) was synthesized successfully, and the synthetic reaction schema was presented in Fig. 1. The synthetic route of SD was as follows: 1) The hydroxypropyl methacrylate and 3,3′-dithiobispropionic acid (2:1 molar ratio) were mixed into a test tube. 2) 2–3 drops of concentrated sulfuric acid were added to the test tube and the reaction was carried out for 50 min at 85°C to obtain the disulfide solution. 3) The SD was obtained after leaving the solution at room temperature for 3 days. The synthetic line of the disulfide containing dual disulfide bonds and hydrogen bonds (DDH) was as follows: 1) The 3,3′-dithiobispropionic acid and acrylamidamide (1:2 molar ratio) were mixed into a test tube. 2) 5 mL of toluene and 2 drops of concentrated sulphuric acid was added to the test tube. 3) The test tube was attached to a condensing tube and reacted at 90°C for 1 h to gain the DDH solution. 4) The DDH was obtained by heating the DDH solution to 60°C for 2 h in drying oven.

3.3. Preparation of SD/SMA and DDH/SMA

Through free radical reactions [21–23], the C═C bonds of SD and DDH can be linked to the C═C bonds position of SBS to obtain self-healing SD/SMA and DDH/SMA. The reaction route is presented in Fig. 2. The flowed asphalt was added to a reactor. A specific percentage

Table 3
Characteristics of acrylamide and hydroxypropyl methacrylate.

Index	Acrylamidamide	Hydroxypropyl methacrylate
Molecular formula	C_3H_5NO	$C_7H_{12}O_3$
Molecular structure	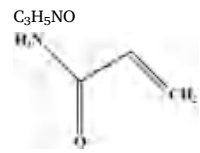	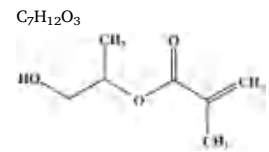
Molecular weight (g/mol)	71.07	144.17

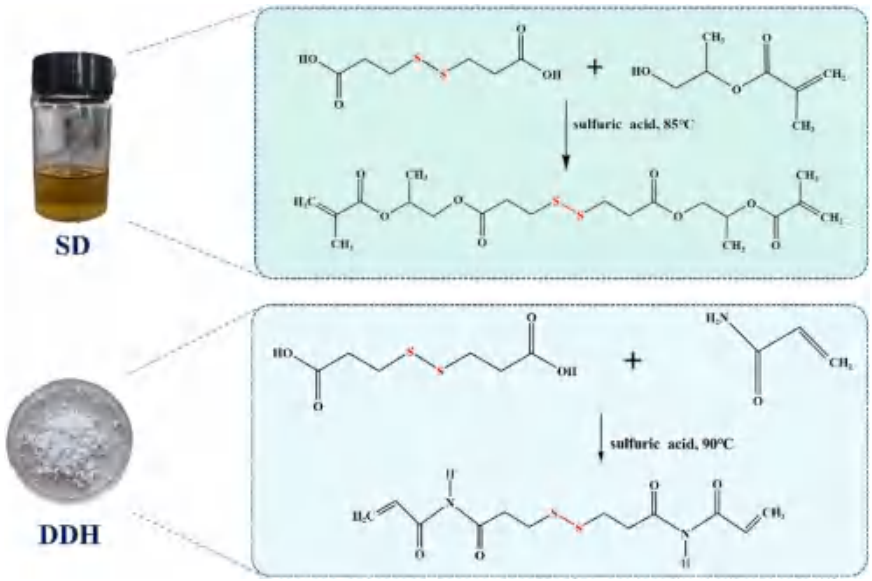

Fig. 1. Synthesis routes of the SD and DDH.

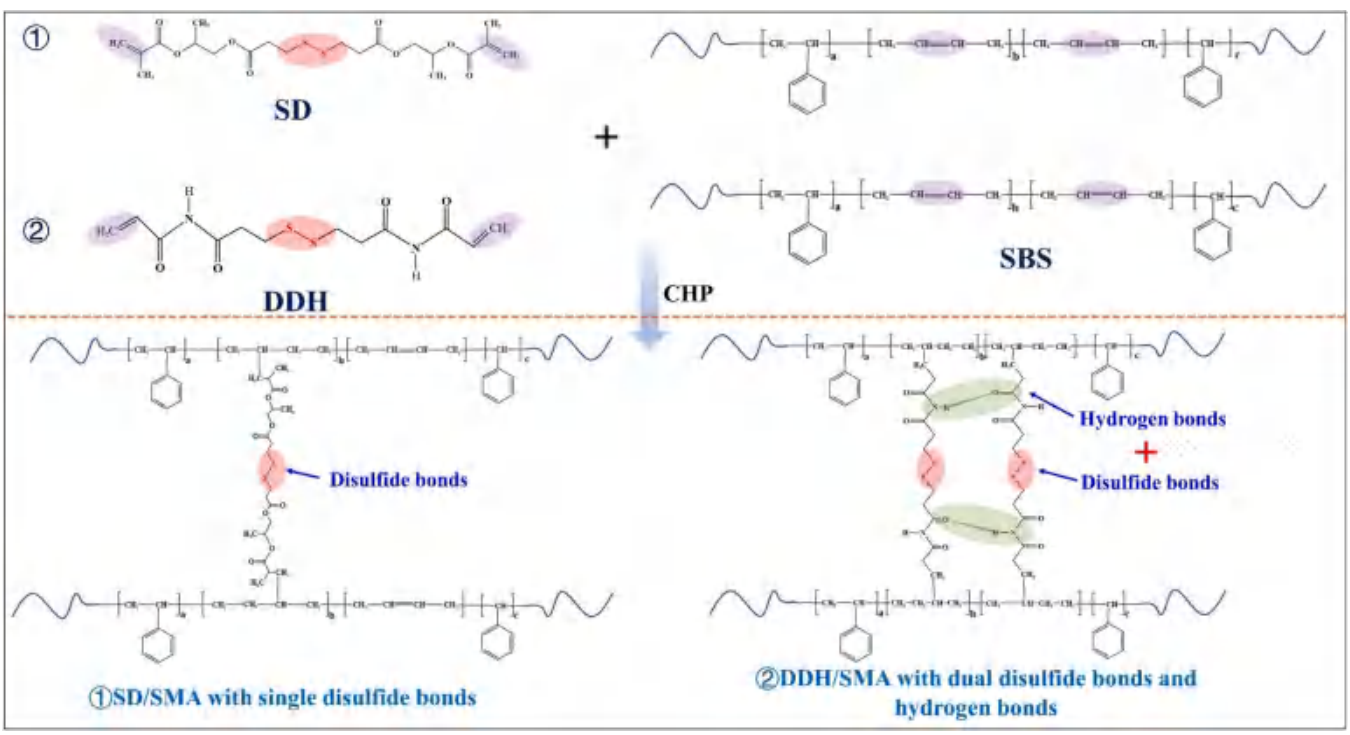

Fig. 2. Synthetic routes of the SD/SMA and DDH/SMA.

of SBS (8 % of asphalt mass) was added to the reactor and stirred with a high-speed shear machine at 4000 rpm for 30 min at 180 ℃ to obtain SBS modified asphalt for drainage pavement. Subsequently, transfer the reactor to a conventional stirrer and set the temperature to 180°C, a specific percentage of SD and DDH (0.6 % of asphalt mass) and cumyl hydroperoxide (catalyzer, 0.3 % of SBS mass) were added. Finally, the SD/SMA and DDH/SMA were obtained after stirring for 2 h at 180 °C.

3.4. Aging method

According to the ASTM D1754, the TFOT was to evaluate the short-term aging property of SMA. The (50 ± 0.5 g) of SMA was poured into a circular iron disc, then the disc was placed in a TFOT aging oven and aged for 5 h at 163°C. Based on the ASTM R28, the PAV test was to evaluate the long-term aging property of SMA. The SMA after TFOT aging is transferred to a pressure aging chamber (pressure of 2.1 MPa) and heated at 100 ℃ for 20 h.

3.5. FTIR test

The chemical structure of SMA was characterized by FTIR spectrometer. 0.2 g of SMA was dissolved in 4 mL of CS_2 solution to make SBS modified asphalt solution, and the solution was dropped on a KBr sheet. After the CS_2 evaporated, the KBr sheet was placed in the FTIR

spectrometer for testing.

3.6. Physical properties

The softening point and ductility of SMA were measured following ASTM D36 and ASTM D113. Three samples were selected for each physical properties test and averaged to obtain reliable data.

The aging properties of TFOT and PAV aged SBS modified asphalt were evaluated by Eq. (1) ~ (2), respectively. *SPI* and *DRR* are softening point increments and ductility retention rates, respectively.

$$\mathrm{SPI} = \text{Aged softening point} - \text{Unaged softening point} \tag{1}$$

$$\mathrm{DRR} = \frac{\text{Aged ductility}}{\text{Unaged ductility}} \tag{2}$$

3.7. Fluorescence microscopy (FM)

Fluorescence microscopy images are the commonly used method for evaluating the microstructure of SBS modified asphalt [24,25]. Herein, the microstructure of self-healing SMA was observed using fluorescence microscope. The resolution of a fluorescence microscope is 100×. Firstly, 1–2 drops of flowing SBS modified asphalt were put on the slide. Then the slide was put into a 120℃. The coverslips were placed on the slide after the SMA was softened. Finally, the slide was put into the fluorescence microscope platform area for observation.

3.8. Rheological properties

3.8.1. Multiple stress creep recovery test

The MSCR test program is presented in Fig. 3. According to the AASHTO T 350, the MSCR test includes two stages. The first stage is the loading stage with a time of 1 s. The second stage is the recovery stage with a time of 9 s. For the test, the stress level of 0.1 kPa was cycled for 20 times, and the stress level of 3.2 kPa was cycled for 10 times. The test temperature of MSCR is 58℃. According to the MSCR curve, the non-recoverable creep (J_{nr}) and deformation recovery rate (R) can be obtained, and the calculation formulas are Eqs. (3) and (4), respectively. R denotes the elasticity of SMA, and the higher the deformation recovery rate, the better the elasticity.

$$R = \sum_{k=1}^{10} \frac{\varepsilon_c - \varepsilon_r}{\varepsilon_c - \varepsilon_0} \Big/ 10 \tag{3}$$

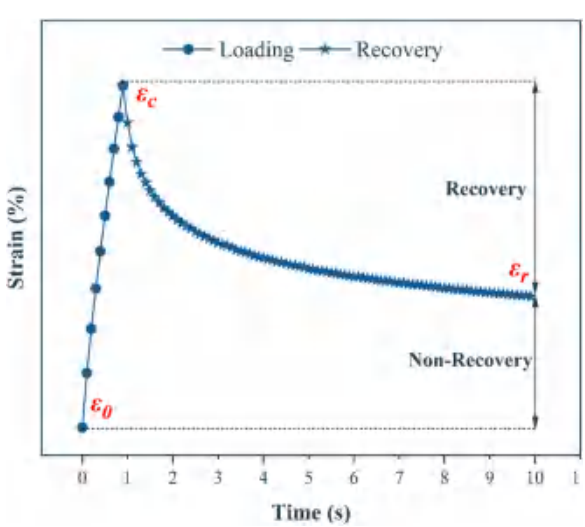

Fig. 3. MSCR test.

$$J_{nr} = \sum_{k=1}^{10} \frac{\varepsilon_r - \varepsilon_0}{\sigma} \Big/ 10 \tag{4}$$

Where *R* is the average recovery rate of the 10 times loading-recovery cycles. J_{nr} is the average unrecoverable creep of the 10 times loading-recovery cycles. ε_c is the strain after each loading stage. ε_0 is the strain before each loading stage. ε_r is the strain after each recovery. σ is the stress level.

3.8.2. Low-temperature rheological properties

The Bending Beam Rheometer (BBR) was utilized to analyze the rheological properties of SBS modified asphalt under low-temperature conditions. According to ASTM D6648, SBS modified asphalt was made into bending beams of certain sizes and then placed in the BBR to gain the creep rate (m-value) and the creep stiffness (S). The S reflects the deformation resistance of the SMA, and the m indicates the stress relaxation of the SMA stiffness [26]. The smaller the S and the larger of m-value, the better the crack resistance of SBS modified asphalt.

3.9. Self-healing performance

3.9.1. Fatigue healing test

Herein, fatigue healing test based on DSR were adopted to investigate the healing properties of SMA. The fatigue healing test includes the initial fatigue test, healing test, and secondary fatigue test. The test process is displayed in Fig. 4. Step 1: SBS modified asphalt was subjected to fatigue test to gain the initial complex modulus (G_i^*). The strain of DSR was 3 %, the frequency was 10 Hz, and the temperature of fatigue test was 25°C. When the modulus reached 70 % of the G_i^*, the fatigue test was suspended to obtain the fatigue healing modulus (G_f^*). Step 2: The SBS modified asphalt was left at 25℃ for 1 h to allow the SBS modified asphalt to self-heal. Step 3: The SBS modified asphalt underwent secondary fatigue test to obtain the healed complex modulus (G_h^*). The fatigue healing performance of SBS modified asphalt was evaluated using Eq. (5).

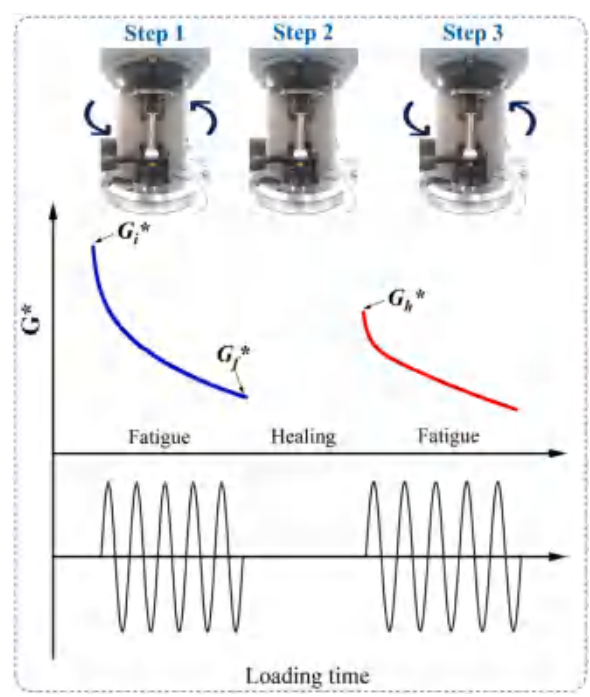

Fig. 4. Fatigue healing test.

$$HI = \frac{G_h^* - G_f^*}{G_i^* - G_f^*} \times 100\% \quad (5)$$

Where *HI* represents the healing indices of SMA; G_h^*, G_f^* and G_i^* denotes the complex modulus after self-healing, the complex modulus after the first fatigue and initial complex modulus of SMA, respectively.

3.9.2. Fracture healing test

The fracture healing property of asphalt binders is a critical indicator [27,28]. Herein, the fracture healing capability of SMA was evaluated based on ductility test through the ductility ratio before and after healing. The specific process is as follows. The ductility specimens of SMA were classified into two groups. The one group ductility specimens of SMA were subjected to a ductility test to obtain the initial ductility (D_i). Another group ductility specimen of SMA were kept in a refrigerator for 2 h, and then the ductility specimen was cut through the middle of the ductility mold with a hot knife. The ductility specimen was assembled in the middle and stood in the oven at 50°C for 20 h, and the ductility test was carried out to obtain the ductility (D_h) of SMA after healing. Lastly, the healing rate of SMA was obtained by Eq. (6) to evaluate its fracture self-healing performance.

$$HR = \frac{D_h}{D_i} \times 100\% \quad (6)$$

Where *HR* represents the healing rate of SMA; D_i and D_h represents the initial ductility and ductility after self-healing of SMA.

4. Results and discussion

4.1. Chemical structure of self-healing SMA before and after aging

Fig. 5 shows the FTIR spectra of base asphalt (BA) and all SMA before and after aging. Our previous study demonstrated successful synthesis of SD [29]. As can be seen in Fig. 5, in the FTIR spectrum of DDH, the absorption peak for hydrogen bonds was observed at 3564–3305 cm^{-1}. In the FTIR spectrum of SMA, the absorption peaks of the benzene ring and C═C bonds were found at 699 cm^{-1} and 966 cm^{-1}. In SD/SMA and DDH/SMA, the C═C bonds content in SBS was reduced due to the successful attachment of SD and DDH on the C═C bonds of SBS, leading to a decrease in the peak area at 966 cm^{-1} [22]. The C═C bonds content of self-healing SBS modified asphalt was quantitatively analyzed by Eq. (6). The $N_{C=C}$ results are shown in Table 6. It can be seen that the $N_{C=C}$ of self-healing SD/SMA and DDH/SMA was significantly decreased, indicating a significant reduction in the C═C bonds content and the successful preparation of SD/SMA and DDH/SMA. Importantly, in DDH/SMA, the absorption peak of hydrogen bonds was observed at 3564–3305 cm^{-1}, suggesting the successful development of hydrogen bonds in DDH/SMA, which is conducive to enhancing the properties of SBS modified asphalt [30]. (Table 4)

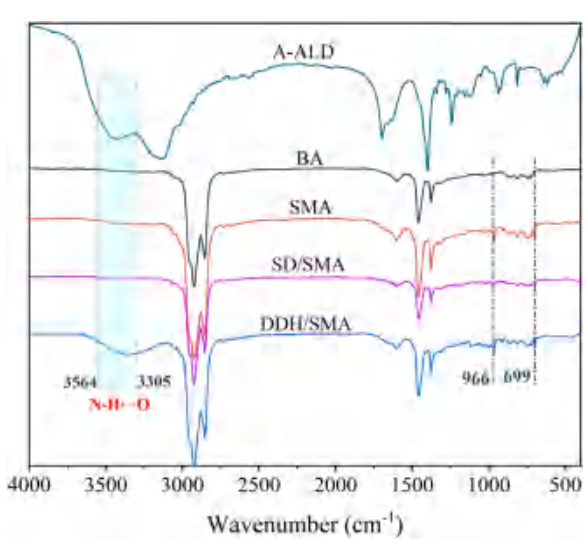

Fig. 5. Chemical structure of BA and SMA.

$$N_{C=C} = \frac{A_{966}}{A_{699}} \quad (7)$$

Where $N_{C=C}$ is the C═C index; A_{966} is the peak area of the characteristic peak of C═C bonds; A_{699} is the peak area of the characteristic peak of benzene ring, which does not change during the preparation of self-healing SBS modified asphalt.

Fig. 6 shows the infrared spectrum of the BA, CRMA, DPA/CRMA and DTSA/CRMA after aging. In Fig. 6(a) and (b), it was observed that the aging decreased the C═C bonds content in all SMA, and the absorption peaks of sulfoxide and carbonyl groups appear at 1030 cm^{-1} and 1700 cm^{-1}. For the DDH/SMA after TFOT and PAV aging, the absorption peaks of hydrogen bonds were still observed. To characterize the changes in the chemical functional groups of asphalt and SMA before and after aging, the C═C index ($I_{C=C}$), sulfoxide index ($I_{S=O}$) and carbonyl index ($I_{C=O}$) were calculated using Eqs. (7)–(10). Where $A_{1700cm^{-1}}$, $A_{1030cm^{-1}}$ and $A_{966cm^{-1}}$ was the area of the absorption peak of the carbonyl group, sulfoxide group and C═C bonds. $A_{2000-600cm^{-1}}$ was the peak area of all absorption peaks with a wavenumber between 2000 and 600 cm^{-1}.

$$I_{C=C} = \frac{A_{966cm^{-1}}}{A_{2000-600cm^{-1}}} \quad (8)$$

$$I_{S=O} = \frac{A_{1030cm^{-1}}}{A_{2000-600cm^{-1}}} \quad (9)$$

$$I_{C=O} = \frac{A_{1700cm^{-1}}}{A_{2000-600cm^{-1}}} \quad (10)$$

The functional group indices are displayed in Table 5, from which it was observed that the $I_{C=C}$ of asphalt and all SMA decreases, while the $I_{C=O}$ and $I_{S=O}$ significantly increase after aging. The $I_{C=C}$ of SMA decreased from 10.5 % to 1.76 % after PAV aging, which was attributed to the fact that aging destroyed the unsaturated C═C bonds in SBS. The $I_{C=C}$ of SD/SMA and DDH/SMA before aging were lower than those of SMA, and the $I_{C=C}$ of SD/SMA and DDH/SMA after PAV aging decreased to 3.22 % and 4.03 %, respectively. The $I_{S=O}$ of both asphalt and SMA gradually increased. It is noteworthy that the $I_{S=O}$ of SD/SMA and DDH/SMA are slightly higher than those of SMA after PAV aging, which may be due to the breakage and oxidation of disulfide bonds in SD and DDH, which result in the formation of sulfoxide groups. The $I_{C=O}$ of asphalt and SMA gradually increased after aging, and the $I_{C=O}$ of asphalt and SMA increased to 11.55 % and 10.16 % after PAV aging. While the $I_{C=O}$ of SD/SMA and DDH/SMA increased to 6.57 % and 5.63 %, respectively. In conclusion, SD/SMA and DDH/SMA had better anti-aging performance, while the disulfide bonds in SD/SMA and DDH/SMA underwent partial breakage during aging.

4.2. Microstructure of self-healing SMA before and after aging

Fig. 7 illustrates the fluorescence images of self-healing SMA before

Table 4
$N_{C=C}$ of self-healing SBS modified asphalt.

SBS modified asphalt	$N_{C=C}$
SMA	1.62
SD/SMA	1.21
DDH/SMA	1.12

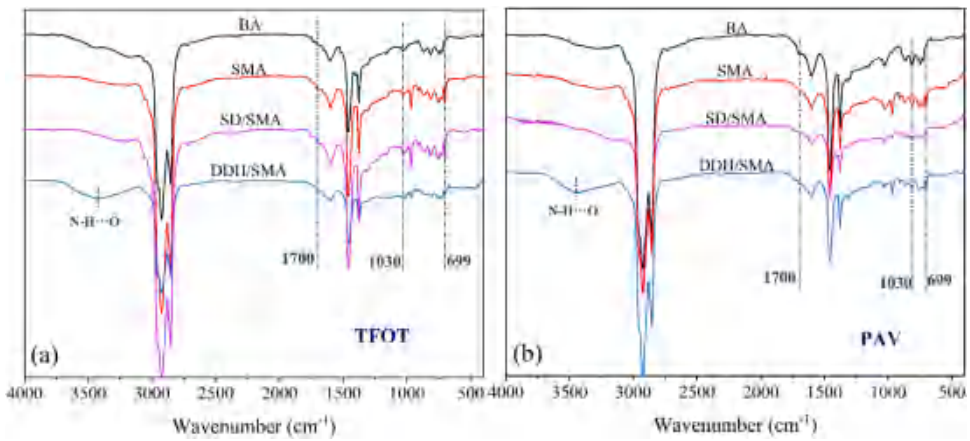

Fig. 6. Chemical structure of BA and SMA after aging.

Table 5
Functional group indices of BA and SMA.

Asphalt binder	$I_{C=C}$ (%)			$I_{S=O}$ (%)			$I_{C=O}$ (%)		
	Unaged	TFOT	PAV	Unaged	TFOT	PAV	Unaged	TFOT	PAV
BA	0	0	0	3.46	6.63	10.92	2.62	6.14	11.55
SMA	10.52	7.65	1.76	2.02	4.02	6.13	2.18	5.62	10.16
SD/SMA	6.53	5.61	3.22	1.65	3.65	6.49	1.57	3.26	6.57
DDH/SMA	6.18	5.57	4.03	1.39	3.43	6.35	1.31	2.52	5.63

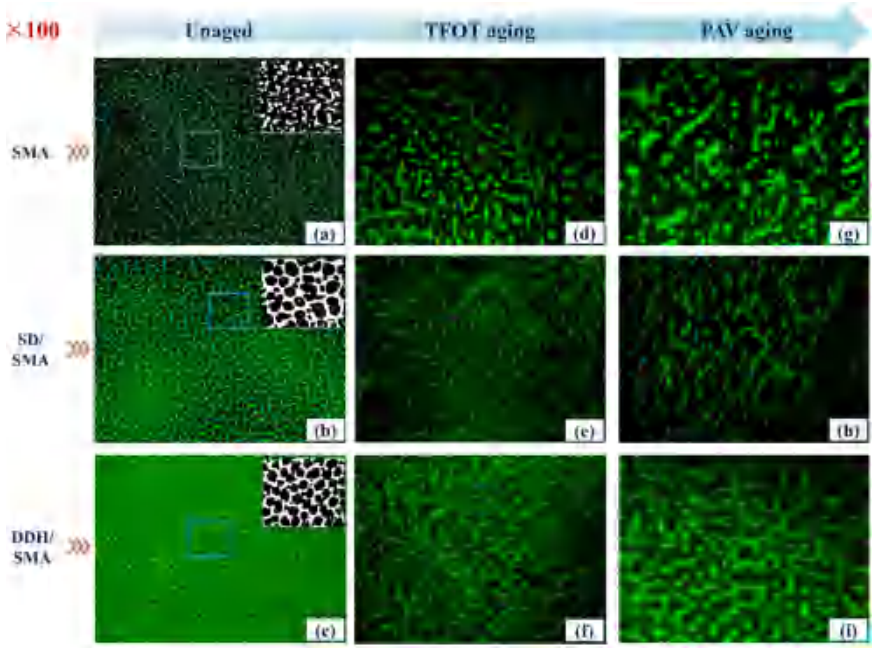

Fig. 7. Fluorescence microscope images of all SMA.

and after aging. From Fig. 7(a)~(c), it was observed that there is reunification in the images of SMA, and significant network structures appear in the images of both SD/SMA and DDH/SMA, which is conducive to enhancing the performance of SMA. This phenomenon revealed that the dynamic chemical bonds in SD and DDH can enhance the chemical cross-linking level of SBS, thereby improving the network structure of SMA. After aging, the structure of all SMA suffered deterioration. The SBS in SMA was transformed into a granular shape and the existence of localized network structures, indicating that aging made the chain of SBS broken, which is due to the destruction of C═C bonds in SBS upon aging, which was consistent with previous studies [31]. In SD/SMA and DDH/SMA, the obvious network structure of SBS can still be observed after TFOT aging, which indicates that disulfide bonds and hydrogen bonds improve the short-term anti-aging performance of SMA. Among them, DDH/SMA has a complete network structure, which is due to the existence of dual disulfide bonds and hydrogen bonds in DDH/SMA. The complete network structure of self-healing SBS modified asphalt can not only hinder the oxygen and ultraviolet light into the asphalt, but also the complete network structure is not susceptible to damage in the aging process. After PAV aging, the degradation of SBS

was more severe, SBS in SMA was almost completely degraded into granular form, while some SBS crosslinked network structures still existed in SD/SMA and DDH/SMA. In conclusion, TFOT and PAV aging damaged the network structure of SMA, while the introduction of dynamic disulfide bonds and hydrogen bonds improved the anti-aging property of SMA, which still maintained a certain degree of network structure in SD/SMA and DDH/SMA after TFOT and PAV aging. Among them, the anti-aging property of DDH/SMA is better than that of SD/SMA.

To further analyze the network structure of self-healing SBS modified asphalt before and after aging, Image software was used to calculate the area percentage of SBS (green part in fluorescence microscope images) in self-healing SBS modified asphalt. The area percentage of self-healing SBS network structure before and after aging is shown in Table 6. As can be seen from Table 6, the area percentage of SBS network structure in both self-healing SD/SMA and DDH/SMA is significantly higher than that of SMA. The reason is that the dynamic chemical bonds in the self-healing SBS modified asphalt increased the chemical cross-linking degree of SBS, which remarkably improved the network structure of SBS modified asphalt. After TFOT aging, the area percentage of self-healing SBS modified asphalt gradually decreased, indicating that aging destroyed the network structure of SBS and caused its fracture and degradation. The area percentages of SMA, SD/SMA, and DDH/SMA decreased to 24.3 %, 29.4 %, and 45.3 %, respectively. Among them, the area percentage of DDH/SMA containing dual disulfide bonds and hydrogen bonds was the highest. After PAV aging, the area percentage of self-healing SBS modified asphalt significantly decreased, indicating that PAV aging causes more severe damage to the network structure of SBS modified asphalt. The area percentage of DDH/SMA remained the highest, which showed superior anti-aging performance.

4.3. Physical properties of self-healing SMA before and after aging

Table 7 shows the physical properties of self-healing SMA before and after aging. It was observed from Table 7, the disulfide bonds and hydrogen bonds increased the softening points and ductility of SMA, and the softening point and ductility of SD/SMA and DDH/SMA are better than those of SMA. The softening points of SD/SMA and DDH/SMA were 4.5°C and 5.7°C higher than those of SMA, and the ductility was increased by 17.5 % and 21.5 % compared with that of SMA. After aging, the softening point of asphalt increased while its ductility decreased. This is due to the transformation of the light component of the asphalt into the heavy component during aging. The softening point and ductility decreased of SMA, which is due to the fact that the network structure of SBS was destroyed after aging [32]. The softening point increment (SPI) of asphalt increases significantly after aging, while the ductility retention ratio (DRR) decreases dramatically. After TFOT aging, the SPI and DRR of asphalt were 4.7°C and 15.7 %. After PAV aging, the SPI and DRR of asphalt were 10.5 °C and 0 %, respectively. In all SBS modified asphalt, the softening point showed a decreasing trend after aging. After PAV aging, the SPI and DRR of SMA were −9.5 °C and 17.7 %. In SD/SMA and DDH/SMA, the softening point increment was smaller and ductility retention was higher than that of SMA, the SPI and DRR of DDH/SMA were −4.9 °C and 35.2 % after PAV aging, respectively. It was revealed that dynamic chemical bonds significantly improved the anti-aging performance of SMA. On the one hand, the successful linkage of SD and DDH at the C═C bonds position in SBS reduced the C═C bonds content in SBS, thereby enhancing the anti-aging performance of SMA. On the other hand, dynamic chemical bonds enhanced the chemical cross-linking degree of SBS, making the network structure of SBS more complete and less susceptible to damage during aging. Remarkably, under the effect of dual dynamic disulfide and hydrogen bonds in DDH, the anti-aging performance of DDH/SMA was better than that of SD/SMA.

Table 6
Area percentage of SBS network structure in SBS modified asphalt.

Asphalt binders	Area percentage of SBS network structure (%)		
	Unaged	TFOT	PAV
SMA	28.4	24.3	19.2
SD/SMA	34.3	29.4	24.8
DDH/SMA	58.1	45.3	34.5

4.4. Rheological properties of self-healing SMA before and after aging

4.4.1. MSCR

Fig. 8 shows the MSCR curves of asphalt and all SMA before and after aging. It can be seen in Fig. 8, at the stress level of 0.1 kPa, the cumulative strain of asphalt was higher, whereas the cumulative strain of SMA was significantly lower since the network structure of SBS hinder the asphalt movement. Compared to SMA, the cumulative strains of SD/SMA and DDH/SMA were reduced by 25.0 % and 34.8 %, respectively, indicating that the dynamic chemical bonds in SD and DDH further improved the network structure of SBS and increased the elasticity of SMA. It was noticeable that the cumulative strain of DDH/SMA is lower than that of SD/SMA, which is due to the existence of dual disulfide and hydrogen bonds in DDH, making the network structure in DDH/SMA more complete than that of SD/SMA. After aging, the cumulative strain of asphalt and all SMA gradually increased. This is attributed to the fact that aging causes a reduction in the light component content of the asphalt and the breakage of the SBS chain, which leads to a transformation from elasticity to viscosity in the SMA [33,34]. After TFOT aging, the cumulative strains of asphalt and SMA increased by 36.18 % and 25.31 % than those of unaged asphalt and SMA, while the cumulative strains of SD/SMA and DDH/SMA increased by 8.59 % and 8.37 % compared to the unaged ones, which indicated that disulfide bonds and hydrogen bonds improved the anti-aging property of SBS modified asphalt. The cumulative strains of asphalt and SMA were significantly increased after PAV aging. The cumulative strains of asphalt and SMA were increased by 122.31 % and 71.32 % compared to unaged asphalt and SMA, respectively. The cumulative strains of SD/SMA and DDH/SMA after PAV aging were increased by 36.48 % and 30.41 % compared to the unaged SD/SMA and DDH/SMA. At a stress level of 3.2 kPa, the cumulative strains of both asphalt and SMA were significantly higher than those at a stress level of 0.1 kPa. The cumulative strains of both SD/SMA and DDH/SMA were also significantly lower than those of asphalt and SMA.

Table 8 shows the R and the J_{nr} of asphalt and all SMA before and after aging. From Table 8, it was observed that the asphalt had a certain degree of elasticity at 0.1 kPa level with R and J_{nr} of 15.8 % and 0.26 kPa^{-1}, respectively. The network structure of the elastomer SBS in SMA resulted in better elasticity [32], and its R increased to 80.3 %. The addition of SD and DDH enabled the elasticity of SMA to be further enhanced, and the R of SD/SMA and DDH/SMA increased to 91.3 % and 96.7 %, respectively. After aging, the R of asphalt and all SMA gradually decreases while the J_{nr} gradually increases, which is mainly due to the fact that aging decreases the elasticity and increases the viscosity of SMA. After TFOT aging, the R decreased to 11.7 % and 61.0 % for asphalt and SMA, and the R for SD/SMA and DDH/SMA was 77.7 % and 80.1 %, respectively. The R of asphalt and all SMA were significantly reduced after PAV aging. The R of asphalt and SMA decreased to 4.3 % and 37.5 %, and those of SD/SMA and DDH/SMA decreased to 52.9 % and 57.1 %. Among them, the R of SD/SMA and DDH/SMA decreased significantly after PAV aging, which was attributed to the disruption of the disulfide bonds of SD/SMA and DDH/SMA by PAV aging. Notably, SD/SMA and DDH/SMA still had higher R after aging, and DDH had better elastic recovery ability than SD/SMA. At a stress level of 3.2 kPa, the R values of asphalt and all SMA decreased while J_{nr} increased, and the R of SD/SMA and DDH/SMA remained higher than that of asphalt and SMA. In conclusion, SD/SMA and DDH/SMA had better high-temperature rheological properties before and after aging. The

Table 7
Physical properties of BA and all SMA before and after aging.

Asphalt binders	Softening point (℃)					Ductility (cm)				
	Unaged	TFOT	SPI	PAV	SPI	Unaged	TFOT	DDR	PAV	DDR
BA	49.3	54.0	4.7	59.8	10.5	41.3	6.5	15.7	0	0
SMA	88.5	84.5	−5	79.0	−9.5	47.5	20.2	42.5	8.4	17.7
SD/SMA	93.0	90.1	−2.9	86.2	−6.8	55.8	33.7	60.4	17.1	30.6
DDH/SMA	94.2	92.4	−1.8	89.3	−4.9	57.7	37.8	65.5	20.3	35.2

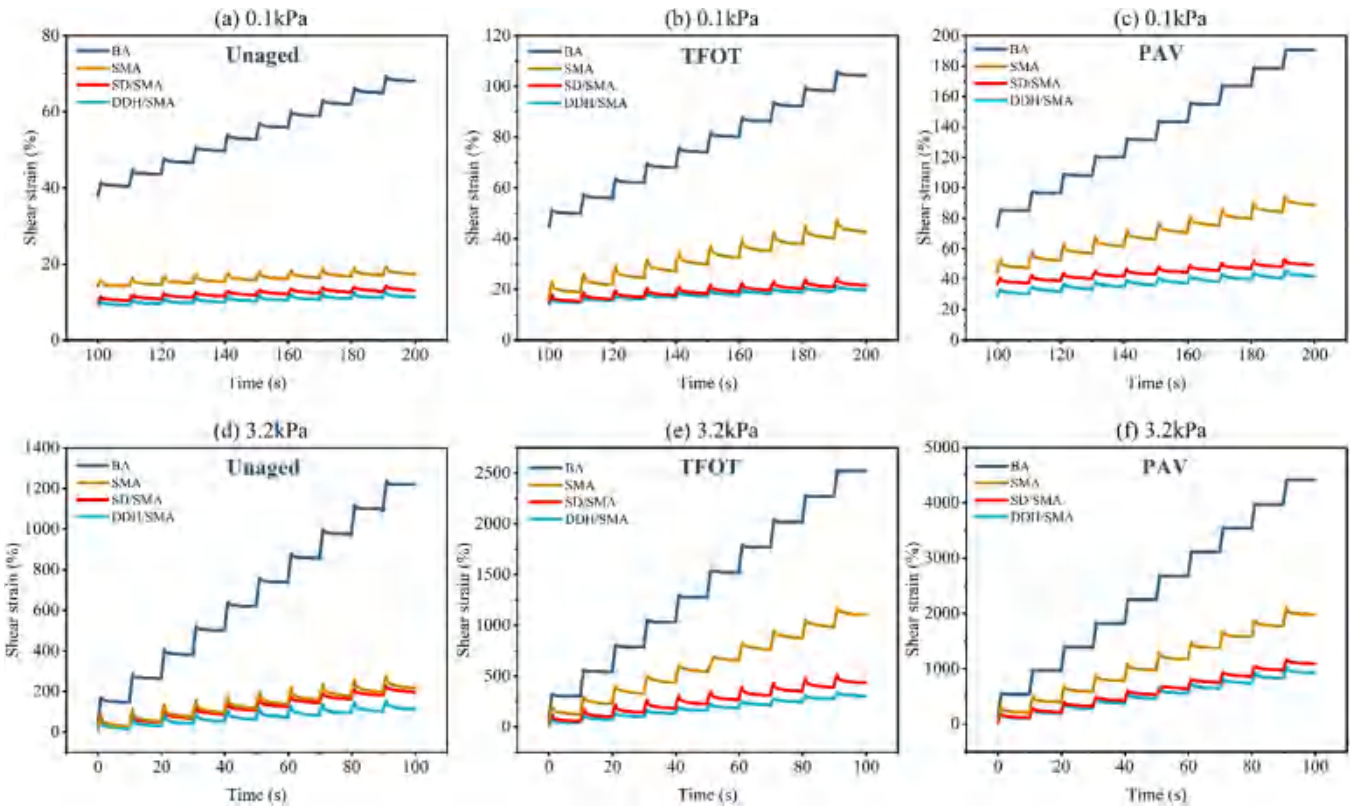

Fig. 8. MSCR curves of BA and all SMA.

Table 8
R and J_{nr} of BA and all SMA.

Asphalt binder	$R_{0.1}$ (%)			$R_{3.2}$ (%)			$J_{nr}^{0.1}$ (kPa^{-1})			$J_{nr}^{3.2}$ (kPa^{-1})		
	Unaged	TFOT	PAV	Unaged	TFOT	PAV	Unaged	TFOT	PAV	Unaged	TFOT	PAV
BA	15.8	11.7	4.3	5.2	3.8	0.9	0.26	0.6	1.1	0.486	0.887	1.25
SMA	80.3	61	37.5	62.5	48	27.5	0.041	0.13	0.35	0.069	0.226	0.525
SD/SMA	91.3	77.7	52.9	76.5	60.4	38	0.026	0.065	0.153	0.036	0.101	0.261
DDH/SMA	96.7	80.1	57.1	83.3	65.4	43.5	0.02	0.044	0.13	0.032	0.071	0.207

rheological properties of DDH/SMA were superior to those of SD/SMA due to the combination of dual disulfide bonds and hydrogen bonds in the DDH/SMA.

4.4.2. *Low-temperature rheological properties*

Fig. 9 shows the S and m-value of self-healing SMA before and after aging. From Fig. 9, it was observed that the m-value was small and the S was high since asphalt exhibit hardening at low temperatures. The low-temperature rheological properties of SMA were improved due to a certain network structure formed by SBS in the asphalt. The SD/SMA and DDH/SMA had higher m-value and smaller S compared to SMA, which is attributed to the fact that the introduction of dynamic chemical bonds increased the chemical cross-linking degree of SBS, leading to SBS modified asphalt with a more complete cross-linking network structure. Notably, both the S of SD/SMA and DDH/SMA were less than 300 MPa, while the m-value were higher than 0.3. Compared to SD/SMA, DDH/SMA containing dual disulfide bonds and hydrogen bonds had smaller S and larger m-value, suggesting better low-temperature rheological properties of DDH/SMA. After TFOT aging, the m-value and S had a relatively large variation due to the fact that the asphalt became hardened and brittle. The S of SMA after TFOT aging was 166 MPa and the m-value decreased by 16.1 %. While the change in S and m-value of SD/SMA and DDH/SMA was relatively small. The S of SD/SMA and DDH/SMA were 110 MPa and 101 MPa, and the m-value of SD/SMA and DDH/SMA were reduced by 5.7 % and 8.8 %, indicating that the dynamic chemical bonds improved the short-term aging resistance of SBS

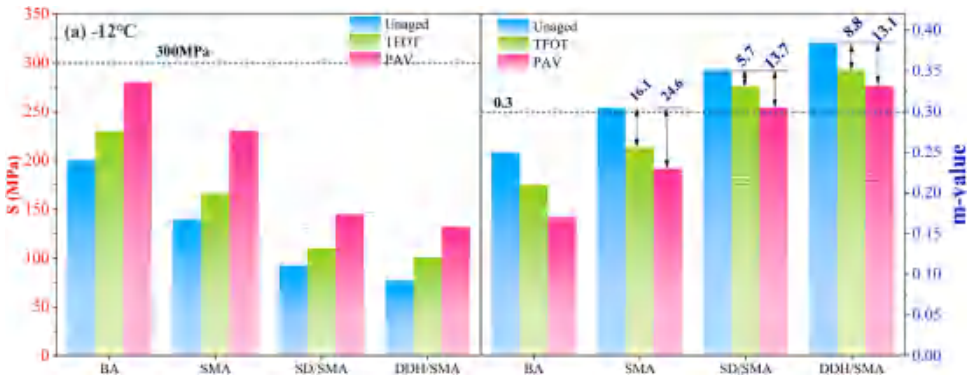

Fig. 9. S and m-value of BA and all SMA.

modified asphalt. After TFOT aging, the m-value of DDH/SMA was higher than that of SD/SMA, which indicated that DDH/SMA retained better low-temperature rheological properties than SD/SMA after aging. After PAV aging, the S of SMA increased to 230 MPa and m decreased to 0.23, while the S of SD/SMA and DDH/SMA increased to 145 MPa and 132 MPa, and m-value decreased to 0.305 and 0.332. This demonstrated that DDH/SMA still retained the best low-temperature rheological properties after PAV aging. After TFOT and PAV aging, SMA exhibited poor low-temperature cracking resistance because the m-value was reduced to below 0.3. While the m-value of both SD/SMA and DDH/SMA was higher than 0.3, which demonstrated the better low-temperature cracking resistance of both SD/SMA and DDH/SMA after aging. In addition, under the influence of dual dynamic disulfide bonds and hydrogen bonds, the local network structure of DDH/SMA after aging is better than that of SD/SMA, which leads to better low-temperature rheological properties of DDH/SMA than that of SD/SMA. In conclusion, both SD/SMA and DDH/SMA had better low-temperature rheological properties before and after aging. Furthermore, the low-temperature cracking resistance of DDH/SMA was better than that of SD/SMA because of the dual dynamic disulfide and hydrogen bonds contained in DDH/SMA.

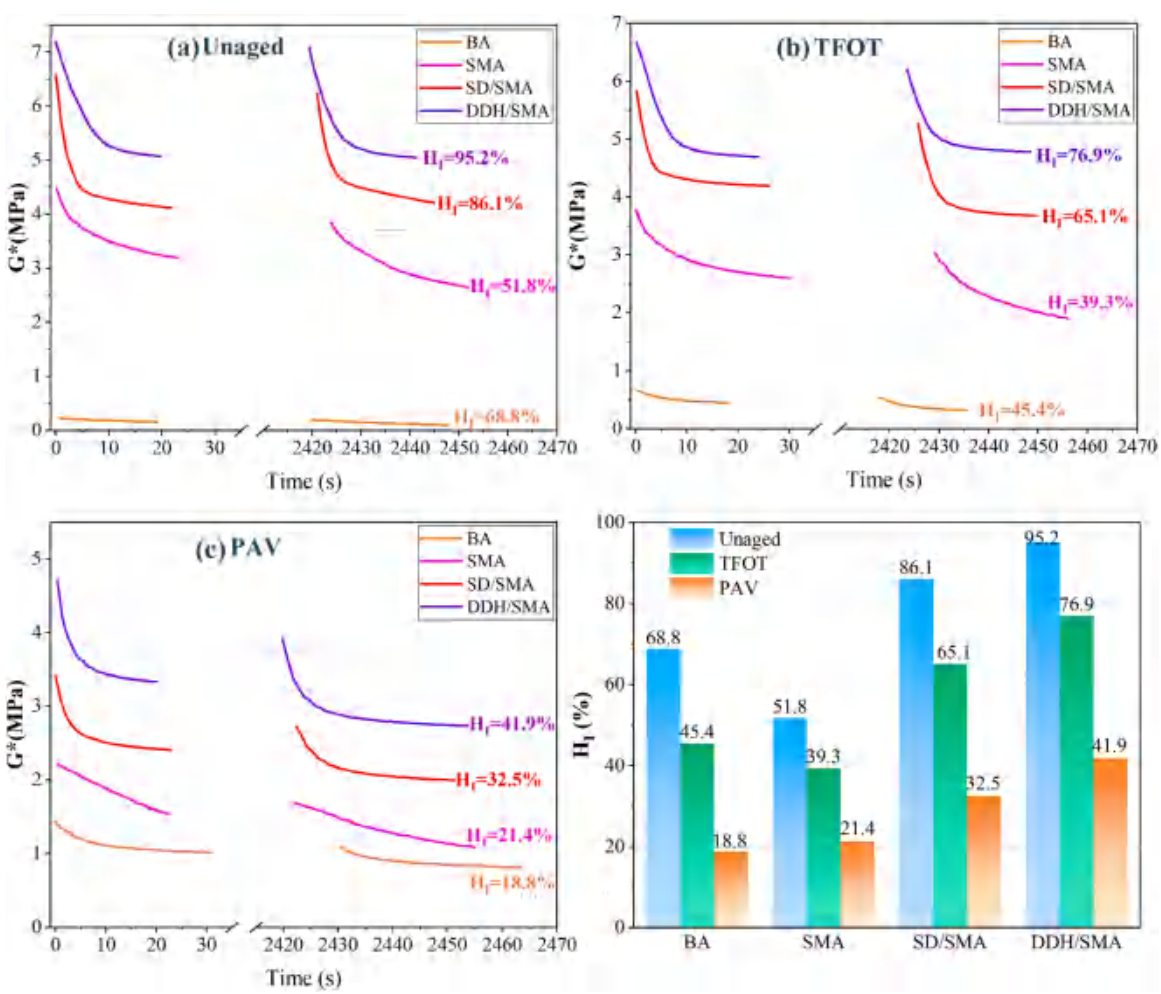

Fig. 10. Fatigue healing curves and indices of BA and SMA.

4.5. Healing performance of self-healing SMA before and after aging

4.5.1. Fatigue healing performance

Fig. 10 shows the fatigue healing curves and indices of asphalt and all SMA before and after aging. It was evident from Fig. 10 (a)~(c) that the complex modulus of asphalt and all SMA decreased after fatigue loading, and the complex modulus were restored after healing. The complex modulus of SMA was higher than that of asphalt because of the network structure formed by SBS in the asphalt. The introduction of disulfide bonds and hydrogen bonds made the complex modulus of SD/SMA and DDH/SMA higher than that of SMA. Among them, the complex modulus of DDH/SMA was superior to that of SD/SMA, which is owing to the fact that the double disulfide bonds and hydrogen bonds in DDH/SMA improve the chemical cross-linking degree of SBS modified asphalt, endowing DDH/SMA with a more complete network structure. After aging, the complex modulus of asphalt gradually increased because of the transformation of the light component into the heavy component in asphalt, which is manifested as hardening and brittleness [35]. In all SMA, the chain of SBS was broken after aging, which caused the network structure of SMA to be damaged. Consequently, the complex modulus of SMA, SD/SMA and DDH/SMA were notably reduced.

In Fig. 10 (d), both asphalt and SMA have some fatigue self-healing properties. The H_I of asphalt and SMA were 68.8 % and 51.8 %, and the SBS had some adverse impact on the healing capability of asphalt [36]. The H_I of DDH/SMA and SD/SMA increased to 95.2 % and 86.1 % under the break-reorganization effect of dynamic chemical bonds. After TFOT aging, the H_I of BA and SMA decreased to 45.4 % and 39.3 %, respectively. The reason is that the light component in the asphalt is transformed into a heavy component and the fluidity is greatly reduced, thus its healing index decreased significantly. After TFOT aging, the H_I of SD/SMA and DDH/SMA were reduced to 65.1 % and 76.9 % which were 65.6 % and 95.7 % higher than that of SMA. This suggests that disulfide bonds and hydrogen bonds improve the short-term anti-aging performance of SMA, and SD/SMA and DDH/SMA still had better healing ability after TFOT aging. In addition, the healing index of DDH/SMA containing dual dynamic disulfide and hydrogen bonds was higher than that of SD/SMA. The healing ability of asphalt and all SMA decreased dramatically after PAV aging. The H_I of asphalt and SMA decreased to 18.8 % and 21.4 % after PAV aging. The H_I of SD/SMA and DDH/SMA decreased to 32.5 % and 41.9 %, respectively, which were 51.9 % and 95.8 % better than those of SMA. This revealed that the dynamic chemical bonds in self-healing SBS modified asphalt can still undergo breakage-rearrangement effect after PAV aging. Compared to SD/SMA, DDH/SMA had a higher fatigue healing index after PAV aging. Overall, the SD/SMA and DDH/SMA had superior fatigue healing properties before and after aging, and the fatigue healing ability of DDH/SMA was better than that of SD/SMA because of the stronger break-reorganization effect of the dual disulfide bonds and hydrogen bonds.

4.5.2. Fracture healing performance

Fig. 11 shows the fracture healing rates (H_R) of asphalt and all SMA. From Fig. 11, it was observed that asphalt has a certain self-healing ability, and its H_R was 73.5 %. The H_R of SMA was reduced to 35.8 %, while the H_R of SD/SMA and DDH/SMA significantly increased. Compared with SMA, the H_R of SD/SMA and DDH/SMA increased by 85.2 % and 115.6 %, respectively. This is because the disulfide bonds and hydrogen bonds of SD/SMA and DDH/SMA can be rearranged at the fracture surface, which remarkably improves the fracture healing capability of SMA. The H_R of DDH/SMA was higher than that of SD/SMA, the reason is that the DDH/SMA contains dual disulfide and hydrogen bonds, which can undergo a more intense breakage-rearrangement effect. After aging, the H_R of both asphalt and all SMA gradually decreased. The H_R of asphalt and SMA after TFOT aging decreased to 45.6 % and 26.5 %. While the H_R of SD/SMA and DDH/SMA were 48.5 % and 59.6 %, respectively. It showed that SD/SMA and DDH/SMA still had better self-healing properties after TFOT aging. The

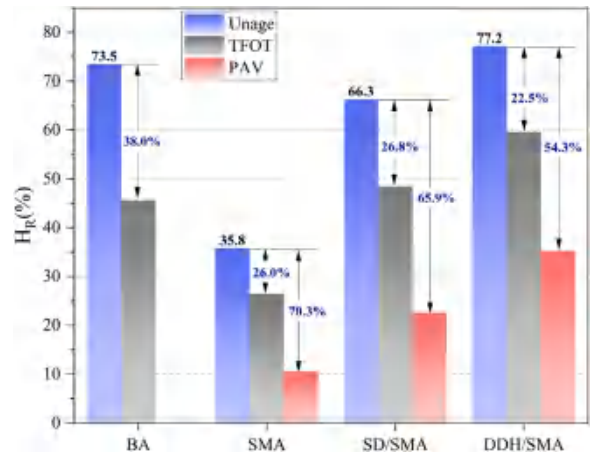

Fig. 11. Fracture healing rates of BA and SMA.

H_R of SD/SMA and DDH/SMA after TFOT aging were 83.0 % and 124.9 % higher than those of SMA. The self-healing ability of SMA was significantly reduced after PAV aging, and the H_R of SMA was 10.6 %. The SD/SMA and DDH/SMA remained with a superior healing ability after PAV aging, with H_R of 22.6 % and 35.3 %, respectively. The H_R of SD/SMA and DDH/SMA after PAV aging were 120.0 % and 253.0 % higher than those of SMA. Under the dual breakage-rearrangement effect of dynamic disulfide bonds and hydrogen bonds, DDH/SMA maintained a higher fracture healing rate after PAV aging compared to SD/SMA. In conclusion, SD/SMA and DDH/SMA had better fracture healing ability after TFOT and PAV aging. Furthermore, the fracture healing properties of DDH/SMA were superior to those of SD/SMA under the effect of break-reorganization effect of dual disulfide bonds and hydrogen bonds.

5. Self-healing mechanism

The breakage-rearrangement mechanism of the SD/SMA and DDH/SMA is shown in Fig. 12. The SD containing single disulfide bonds and the DDH containing dual disulfide bonds and hydrogen bonds are connected in the network structure of SBS modified asphalt. When microcracks appear in the SD/SMA, the low-bond energy dynamic disulfide bonds will first break into a sub-stable state. When the microcracks begin to heal, the disulfide bonds will be rearranged to achieve healing and recovery of properties in the SD/SMA. In DDH/SMA, the disulfide bonds and hydrogen bonds will first be broken into sub-stable states when microcracks occur. During the crack healing stage, the disulfide bonds and hydrogen bonds with low bond energies will be rearranged to achieve the healing of microcracks and the recovery of properties in SBS modified asphalt. Compared to SD/SMA containing single disulfide bonds, DDH/SMA containing dual disulfide and hydrogen bonds can undergo a more intense break-rearrangement effect, thus exhibiting superior fatigue healing and fracture healing performance.

6. Conclusion

Herein, two types of self-healing SMA (SD/SMA with single disulfide bonds and DDH/SMA with dual disulfide bonds and hydrogen bonds) were developed. The structure and properties of SMA, SD/SMA and DDH/SMA before and after TFOT and PAV aging were investigated. The main conclusions are as below:

(1) FTIR analysis revealed that carbonyl and sulfoxide groups were generated in SMA, SD/SMA and DDH/SMA after TFOT and PAV aging, in which the $I_{C=C}$ of SD/SMA and DDH/SMA were smaller than those of SMA. The $I_{S=O}$ of SD/SMA and DDH/SMA increased compared to SMA, indicating a partial breakage of the dynamic

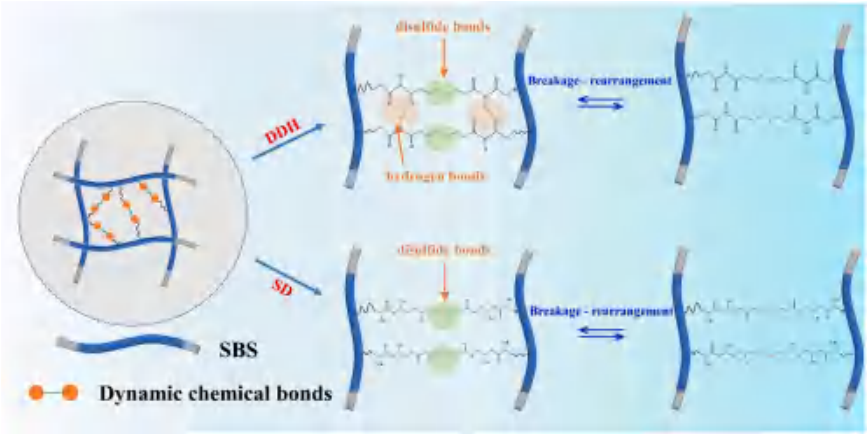

Fig. 12. Breakage-rearrangement mechanism of the SD/SMA and DDH/SMA.

disulfide bonds in SD/SMA and DDH/SMA. Among them, the $I_{C=C}$ and $I_{S=O}$ of DDH/SMA were lower than those of SD/SMA, which suggested that the anti-aging performance of DDH/SMA was better than that of SD/SMA.

(2) Microstructure analysis indicated that the network structure of SMA, SD/SMA and DDH/SMA was damaged after TFOT and PAV aging. SMA formed a dispersed granular structure, while SD/SMA and DDH/SMA remained localized network structure after aging. Among them, the network structure of DDH/SMA before and after aging is better than that of SD/SMA.

(3) The physical properties results showed that compared with SMA, SD/SMA and DDH/SMA had smaller softening point increments and larger ductility retention rates, showing better anti-aging performance. Compared to SMA, the softening point increment of SD/SMA and DDH/SMA was reduced by 28.4 % and 48.4 %, and the ductility retention rate was improved by 72.9 % and 98.8 % after PAV aged. Among them, DDH/SMA with dual disulfide bonds and hydrogen bonds had better anti-aging performance.

(4) The results of the MSCR showed that compared with SMA, SD/SMA and DDH/SMA had higher creep recovery rates after aging. The BBR results revealed that the S of both SD/SMA and DDH/SMA was less than 300 MPa, and m was higher than 0.3, which demonstrated better low-temperature crack resistance after aging. Furthermore, the rheological properties of DDH/SMA with dual disulfide bonds and hydrogen bonds were better than those of SD/SMA after aging.

(5) It was revealed that SD/SMA and DDH/SMA had superior healing properties after aging. After PAV aging, the fatigue healing indices of SD/SMA and DDH/SMA were 51.9 % and 95.8 % higher than those of SMA. Furthermore, under the break-reorganization effect of dual chemical bonds, the self-healing ability of DDH/SMA was superior to that of SD/SMA. After PAV aging, the fatigue healing index and fracture healing rate of DDH/SMA were 28.9 % and 56.2 % higher than those of SD/SMA.

7. Future research

In this study, the structure and properties of self-healing SBS modified asphalt containing dual dynamic chemical bonds before and after aging were investigated, and focuses on a systematic evaluation of its fatigue healing and fracture healing performance. Further research should investigate the effect of dual dynamic chemical bonds on the structure and properties of SBS modified asphalt mixtures.

CRediT authorship contribution statement

Tianwei Zhang: Writing – original draft, Methodology, Investigation, Formal analysis, Data curation. **Shi Xu:** Writing – review & editing. **Quantao Liu:** Writing – review & editing. **Yanheng He:** Formal analysis, Data curation. **Shanjun Gao:** Writing – review & editing, Conceptualization. **Shangheng Zeng:** Resources. **Ronghua Zhuang:** Resources. **Jianying Yu:** Writing – review & editing, Supervision, Formal analysis, Data curation.

Declaration of Competing Interest

The authors declare that they have no known competing financial interests or personal relationships that could have appeared to influence the work reported in this paper.

Acknowledgements

The authors gratefully acknowledge the financial assistance from the National Key R&D Program of China (No: 2022YFC3801600) and the Program Fund of Non-Metallic Excellent and Innovation Center for Building Materials (Grants #24PHD-7).

Data Availability

Data will be made available on request.

References

[1] Y. Meng, G. Fang, Y. Hu, Y. Qin, R. Xu, F. Yang, J. Lei, C. Zhang, Study on the effect of different aldehyde modifiers on the fume suppression effect, mechanism and road performance of SBS modified asphalt, Sci. Total Environ. 912 (2024) 169162, https://doi.org/10.1016/j.scitotenv.2023.169162.

[2] A. Fawcett, T. McNally, Polystyrene and asphaltene micelles within blends with a bitumen of an SBS block copolymer and styrene and butadiene homopolymers, Colloid Polym. Sci. 281 (2003) 203–213, https://doi.org/10.1007/s00396-002-0762-4.

[3] M. Dai, Y. Du, J. Jin, T. Wei, Design and experimental evaluation of reflective grouting asphalt concrete for durable cooling asphalt pavement, Energy Build. 294 (2023) 113262, https://doi.org/10.1016/j.enbuild.2023.113262.

[4] T. Lu, B. Li, D. Sun, M. Hu, J. Ma, G. Sun, Advances in controlled release of microcapsules and promising applications in self-healing of asphalt materials, J. Clean. Prod. 294 (2021) 126270, https://doi.org/10.1016/j.jclepro.2021.126270.

[5] W. Xia, Z. Xu, T. Xu, Self-healing behaviors and its effectiveness evaluations of fiber reinforced shape memory polyurethane/SBS modified asphalt mortar, Case Stud. Constr. Mater. 18 (2023) e01784, https://doi.org/10.1016/j.cscm.2022.e01784.

[6] B. He, Y. Xiao, Y. Li, M. Fu, J. Yu, L. Zhu, Preparation and characterization of lignin grafted layered double hydroxides for sustainable service of bitumen under ultraviolet light, J. Clean. Prod. 350 (2022) 131536, https://doi.org/10.1016/j.jclepro.2022.131536.

[7] M. Guo, H. Liu, Y. Jiao, L. Mo, Y. Tan, D. Wang, M. Liang, Effect of WMA-RAP technology on pavement performance of asphalt mixture: A state-of-the-art review,

J. Clean. Prod. 266 (2020) 121704, https://doi.org/10.1016/j.jclepro.2020.121704.
[8] K.M. Nalbandian, M. Carpio, Á. González, Analysis of the scientific evolution of self-healing asphalt pavements: toward sustainable road materials, J. Clean. Prod. 293 (2021) 126107, https://doi.org/10.1016/j.jclepro.2021.126107.
[9] Z. Cao, M. Chen, J. Yu, X. Han, Preparation and characterization of active rejuvenated SBS modified bitumen for the sustainable development of high-grade asphalt pavement, J. Clean. Prod. 273 (2020) 123012, https://doi.org/10.1016/j.jclepro.2020.123012.
[10] D. Sun, T. Lin, X. Zhu, Y. Tian, F. Liu, Indices for self-healing performance assessments based on molecular dynamics simulation of asphalt binders, Comput. Mater. Sci. 114 (2016) 86–93, https://doi.org/10.1016/j.commatsci.2015.12.017.
[11] L. Yang, L. Tao, T. Zenglin, P. Jianzhong, Z. Mingliang, W. Zhenguo, Research on self-healing behavior of asphalt modified by polyurea elastomer containing dynamic disulfide/diselenide bond, Eur. Polym. J. 189 (2023) 111990, https://doi.org/10.1016/j.eurpolymj.2023.111990.
[12] L. Lyu, D. Li, Y. Chen, Y. Tian, J. Pei, Dynamic chemistry based self-healing of asphalt modified by diselenide-crosslinked polyurethane elastomer, Constr. Build. Mater. 293 (2021) 123480, https://doi.org/10.1016/j.conbuildmat.2021.123480.
[13] S.-M. Kim, H. Jeon, S.-H. Shin, S.-A. Park, J. Jegal, S.Y. Hwang, D.X. Oh, J. Park, Superior toughness and fast self-healing at room temperature engineered by transparent elastomers, Adv. Mater. 30 (2018) 1705145, https://doi.org/10.1002/adma.201705145.
[14] X. An, R.H. Aguirresarobe, L. Irusta, F. Ruipérez, J.M. Matxain, X. Pan, N. Aramburu, D. Mecerreyes, H. Sardon, J. Zhu, Aromatic diselenide crosslinkers to enhance the reprocessability and self-healing of polyurethane thermosets, Polym. Chem. 8 (2017) 3641–3646, https://doi.org/10.1039/C7PY00448F.
[15] J. Liu, X. Ma, Y. Tong, M. Lang, Self-healing polyurethane based on ditelluride bonds, Appl. Surf. Sci. 455 (2018) 318–325, https://doi.org/10.1016/j.apsusc.2018.05.159.
[16] M. Xu, B. Cheng, Y. Sheng, J. Zhou, M. Wang, X. Jiang, X. Lu, High-performance cross-linked self-healing material based on multiple dynamic bonds, ACS Appl. Polym. Mater. 2 (2020) 2228–2237, https://doi.org/10.1021/acsapm.0c00154.
[17] M. Liu, J. Zhong, Z. Li, J. Rong, K. Yang, J. Zhou, L. Shen, F. Gao, X. Huang, H. He, A high stiffness and self-healable polyurethane based on disulfide bonds and hydrogen bonding, Eur. Polym. J. 124 (2020) 109475, https://doi.org/10.1016/j.eurpolymj.2020.109475.
[18] K. Wei, Y. Wu, X. Cao, X. Yang, B. Tang, B. Shan, Dual dynamic bonds approach for polyurethane recycling and self-healing of emulsified asphalt, Sci. Total Environ. 885 (2023) 163915, https://doi.org/10.1016/j.scitotenv.2023.163915.
[19] Y. Li, Y. Meng, J. Pei, L. Lyu, D. Hu, Self-healing performance and rheological properties of styrene-butadiene-styrene block copolymer modified asphalt promoted by polyurea elastomers containing disulfide bonds, Constr. Build. Mater. 421 (2024) 135747, https://doi.org/10.1016/j.conbuildmat.2024.135747.
[20] K. Wei, Y. Wu, X. Cao, X. Yang, B. Tang, L. Deng, Preparation and characterization of vanillin-based self-healing polyurethane-modified asphalts based on acylhydrazone chemistry, Eur. Polym. J. 211 (2024) 113010, https://doi.org/10.1016/j.eurpolymj.2024.113010.
[21] Y. He, S. Mao, T. Zhang, S. Zeng, H. Duan, R. Zhuang, J. Yu, Preparation and properties of self-healing SBS modified bitumen with dynamic acylhydrazone bonds, Eur. Polym. J. 210 (2024) 112932, https://doi.org/10.1016/j.eurpolymj.2024.112932.
[22] T. Zhang, S. Gao, Y. He, R. Zhuang, X. Han, Z. Zou, J. Yu, Investigation of microstructure, rheological property and self-healing performance of SBS modified bitumen with dynamic disulfide bonds prepared by one-step method, Constr. Build. Mater. 416 (2024) 135158, https://doi.org/10.1016/j.conbuildmat.2024.135158.
[23] P. Cong, S. Chen, H. Chen, Preparation and properties of bitumen modified with the maleic anhydride grafted styrene-butadiene-styrene triblock copolymer, Polym. Eng. Sci. 51 (2011) 1273–1279, https://doi.org/10.1002/pen.21934.
[24] X. Han, S. Mao, S. Xu, J. Yu, Z. Cao, R. Wang, P. He, S. Zeng, Effects of reactive chain extension rejuvenation systems on the viscosity–temperature characteristics, rheological properties, and morphology of aged styrene–butadiene–styrene-modified bitumen, ACS Sustain. Chem. Eng. 9 (2021) 16474–16484, https://doi.org/10.1021/acssuschemeng.1c06717.
[25] X. Yao, T. Xu, Fatigue fracture and self-healing behaviors of cold recycled emulsified asphalt mixture containing microcapsules based on semicircular bending test, J. Clean. Prod. 410 (2023) 137171, https://doi.org/10.1016/j.jclepro.2023.137171.
[26] S. Ren, X. Liu, H. Wang, W. Fan, S. Erkens, Evaluation of rheological behaviors and anti-aging properties of recycled asphalts using low-viscosity asphalt and polymers, J. Clean. Prod. 253 (2020) 120048, https://doi.org/10.1016/j.jclepro.2020.120048.
[27] J. Qiu, M.F.C. van de Ven, S. Wu, J. Yu, A.A.A. Molenaar, Investigating the self healing capability of bituminous binders, Road. Mater. Pavement Des. 10 (2009) 81–94, https://doi.org/10.1080/14680629.2009.9690237.
[28] Y. Tian, M. Zheng, P. Li, J. Zhang, R. Qiao, C. Cheng, H. Xu, Preparation and characterization of self-healing microcapsules of asphalt, Constr. Build. Mater. 263 (2020) 120174, https://doi.org/10.1016/j.conbuildmat.2020.120174.
[29] T. Zhang, S. Gao, J. Yu, Y. He, X. Han, R. Zhuang, Preparation and performance of self-healing SBS modified bitumen based on dynamic disulfide bonds, Constr. Build. Mater. 397 (2023) 132394, https://doi.org/10.1016/j.conbuildmat.2023.132394.
[30] M. Liu, J. Zhong, Z. Li, J. Rong, K. Yang, J. Zhou, L. Shen, F. Gao, X. Huang, H. He, A high stiffness and self-healable polyurethane based on disulfide bonds and hydrogen bonding, Eur. Polym. J. 124 (2020) 109475, https://doi.org/10.1016/j.eurpolymj.2020.109475.
[31] Y. Ruan, R.R. Davison, C.J. Glover, The effect of long-term oxidation on the rheological properties of polymer modified asphalts☆, Fuel 82 (2003) 1763–1773, https://doi.org/10.1016/S0016-2361(03)00144-3.
[32] G. Cuciniello, P. Leandri, S. Filippi, D. Lo Presti, M. Losa, G. Airey, Effect of ageing on the morphology and creep and recovery of polymer-modified bitumens, Mater. Struct. 51 (2018) 136, https://doi.org/10.1617/s11527-018-1263-3.
[33] J. Xu, A. Zhang, T. Zhou, X. Cao, Z. Xie, A study on thermal oxidation mechanism of styrene–butadiene–styrene block copolymer (SBS), Polym. Degrad. Stab. 92 (2007) 1682–1691, https://doi.org/10.1016/j.polymdegradstab.2007.06.008.
[34] G. Cuciniello, P. Leandri, S. Filippi, D. Lo Presti, M. Losa, G. Airey, Effect of ageing on the morphology and creep and recovery of polymer-modified bitumens, Mater. Struct. 51 (2018) 136, https://doi.org/10.1617/s11527-018-1263-3.
[35] L. Lyu, J. Pei, N.A. Burnham, E.H. Fini, L.D. Poulikakos, Nanoscale evolution of rubber-oil modified asphalt binder after thermal and UV aging, J. Clean. Prod. 426 (2023) 139098, https://doi.org/10.1016/j.jclepro.2023.139098.
[36] M. Sugano, Y. Iwabuchi, T. Watanabe, J. Kajita, K. Iwata, K. Hirano, Relations between thermal degradations of SBS copolymer and asphalt substrate in polymer modified asphalt, Clean. Tech. Environ. Policy 12 (2010) 653–659, https://doi.org/10.1007/s10098-010-0301-9.

Effect of Dynamic Disulfide Bonds on Microstructure, Storage Stability, and Self-Healing Performance of Desulfurized Waste Crumb Rubber–Modified Asphalt

Tianwei Zhang[1]; Shanjun Gao, Ph.D.[2]; Yanheng He[3]; Quantao Liu, Ph.D.[4]; Ronghua Zhuang[5]; Shangheng Zeng[6]; Hao Duan[7]; and Jianying Yu, Ph.D.[8]

Abstract: Endowing waste crumb rubber–modified asphalt (CRMA) with superior self-healing capability can extend the service life of asphalt pavement. In this study, 3,3'-dithiodipropionic acid (DPA) with dynamic disulfide bonds was introduced into waste crumb rubber particles through esterification reaction to prepare a novel self-healing crumb rubber–modified asphalt (DPA/CRMA). Fourier-transform infrared spectroscopy results revealed that the dynamic disulfide bonds were successfully connected between crumb rubber particles in DPA/CRMA. With the increase of DPA dosage, the softening point and ductility of DPA/CRMA were gradually increased. The fluorescence microscope images indicated that DPA/CRMA had better dispersibility compared to CRMA. The results of the segregation test showed that the dynamic disulfide bonds in DPA significantly enhanced the storage stability of DPA/CRMA. The results of healing tests showed that DPA improved the self-healing properties of the waste CRMA. The fatigue–healing index and fracture healing rate of DPA/CRMA increased to 96.2 and 69.8%, while those of CRMA were only 67.5 and 46.7%. In addition, dynamic disulfide bonds markedly improved the multiple fatigue–healing capacity of DPA/CRMA, and the number of fatigue–healing cycles for DPA/CRMA was 7, whereas it was only 4 cycles for CRMA. This study provided a new method to extend the service life of waste CRMA pavement. DOI: 10.1061/JMCEE7.MTENG-19412.
© 2025 American Society of Civil Engineers.

Author keywords: Crumb rubber–modified asphalt; Dynamic disulfide bonds; Healing properties; Storage stability.

Introduction

With the rapid expansion of the global automotive industry, a large amount of waste crumb rubber has been produced (Ding et al. 2019; Xu et al. 2021). How to dispose of waste crumb rubber has become an important research issue. The full utilization of waste crumb rubber is very important to solve the shortage of natural resources and reduce environmental pollution (Sun et al. 2024; Wang et al. 2018b). Since the 1960s, waste crumb rubber has gradually been used for asphalt modification and has been proven to be a high performance modifier (Bressi et al. 2019; Wang et al. 2018a). However, crumb rubber–modified asphalt (CRMA) is susceptible to cracking under environmental factors and external loads during service, greatly reducing the durability of pavement engineering and causing safety hazards.

Endowing waste CRMA with superior self-healing capability is conducive to extending the service life of asphalt pavement. Previous studies have shown that asphalt has a limited self-healing capacity and can repair cracks on its own (Li et al. 2020a; Tang et al. 2021), which has promoted the rapid development of self-healing technologies of asphalt materials. The asphalt self-healing technologies mainly include the microcapsules self-healing technology and the heat-induced self-healing (microwave heating and induction heating) technology (Lastra-González et al. 2019; Yalcin 2021; Zhang et al. 2024a). Micaelo et al. (2016) prepared a new type of microcapsule by encapsulating sunflower oil in calcium alginate as the core material and epoxy resin–cement composite as the wall material and used it to modify asphalt. It was found that the microcapsules were easy to rupture and successfully repaired the microcracks near the microcapsules. Li et al. (2018) added steel slag to asphalt and found that under the action of microwave heating equipment, steel slag in asphalt can quickly release a large amount of heat, thereby softening the asphalt and enhancing its self-healing ability. However, the applications of the microcapsule self-healing method and the heat-induced healing method are limited by the restricted repair times and external heating equipment intervention,

[1]Ph.D. Candidate, State Key Laboratory of Silicate Materials for Architectures, Wuhan Univ. of Technology, Luoshi Rd. 122, Wuhan 430070, PR China. Email: tianweizhang@whut.edu.cn

[2]Professor, School of Material Science and Engineering, Wuhan Univ. of Technology, Luoshi Rd. 122, Wuhan 430070, PR China. Email: sjgao@whut.edu.cn

[3]Ph.D. Candidate, State Key Laboratory of Silicate Materials for Architectures, Wuhan Univ. of Technology, Luoshi Rd. 122, Wuhan 430070, PR China. Email: yanhenghe@whut.edu.cn

[4]Professor, Advanced Engineering Technology Research Institute of Zhongshan City, Wuhan Univ. of Technology, Xiangxing Rd. 6, Zhongshan 528400, PR China. Email: liuqt@whut.edu.cn

[5]Ph.D. Candidate, State Key Laboratory of Silicate Materials for Architectures, Wuhan Univ. of Technology, Luoshi Rd. 122, Wuhan 430070, PR China. Email: RHzhuang@whut.edu.cn

[6]Ph.D. Candidate, State Key Laboratory of Silicate Materials for Architectures, Wuhan Univ. of Technology, Luoshi Rd. 122, Wuhan 430070, PR China. Email: shanghengzeng@whut.edu.cn

[7]Ph.D. Candidate, State Key Laboratory of Silicate Materials for Architectures, Wuhan Univ. of Technology, Luoshi Rd. 122, Wuhan 430070, PR China. Email: duanhao@whut.edu.cn

[8]Professor, State Key Laboratory of Silicate Materials for Architectures, Wuhan Univ. of Technology, Luoshi Rd. 122, Wuhan 430070, PR China (corresponding author). ORCID: https://orcid.org/0000-0002-4096-3907. Email: jyyu@whut.edu.cn

Note. This manuscript was submitted on May 17, 2024; approved on September 27, 2024; published online on March 17, 2025. Discussion period open until August 17, 2025; separate discussions must be submitted for individual papers. This paper is part of the Journal of Materials in Civil Engineering, © ASCE, ISSN 0899-1561.

Downloaded from ascelibrary.org by Jianying Yu on 03/17/25. Copyright ASCE. For personal use only; all rights reserved.

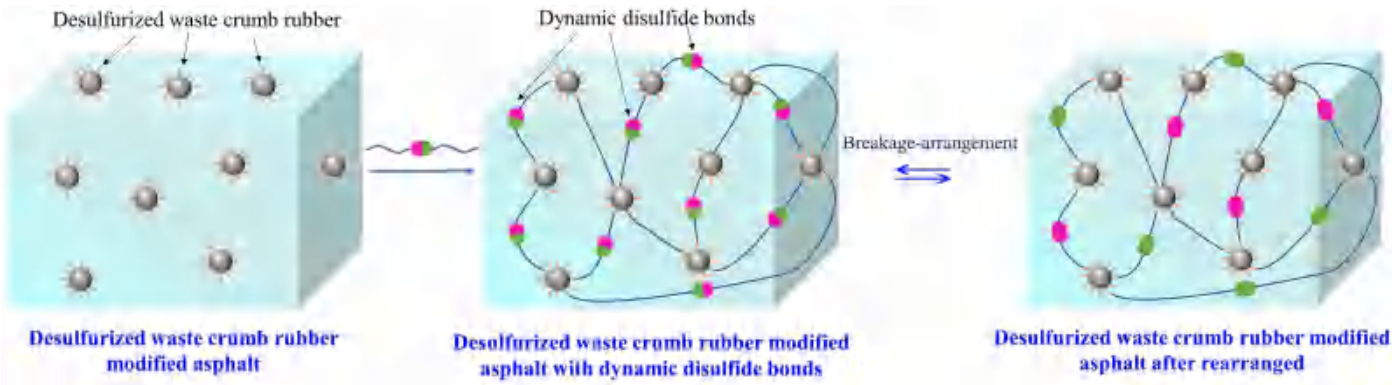

Fig. 1. Self-healing mechanism of CRMA with dynamic disulfide bonds.

respectively (Li et al. 2023; Sun et al. 2018; Grossegger et al. 2018). Thus, it is essential to develop an asphalt self-healing technology that can enable multiple healing and does not require heating equipment.

At present, self-healing polymer technology has gradually attracted the attention of researchers (He et al. 2024; Shirzad et al. 2020). The healing mechanism of the self-healing polymer technology is mainly based on the breakage–rearrangement effect of dynamic chemical bonds. The commonly used reversible chemical bonds mainly include disulfide bonds (Li et al. 2020b), acylhydrazone bonds (Kuhl et al. 2015), imine bonds (Min et al. 2022), and so on. Hu et al. (2020) introduced imine bonds into the polyurethane chain. It was found that the imine bond is beneficial to the ordered arrangement of the chain segments of the polyurethane, and the high dynamic exchange property of the imine bond ensures its effective self-healing performance at high temperatures. Chang et al. (2016) introduced acylhydrazone bonds into self-healing polymer hydrogels. The results showed that the prepared hydrogels can be self-healed in an acidic environment based on the formation and exchange mechanism of dynamic acylhydrazone bonds. de Luzuriaga et al. (2016) prepared epoxy resins containing aromatic disulfide bonds and found that disulfide bonds can undergo breakage–rearrangement to enable the mechanical properties of epoxy resins to be fully restored after damage.

Furthermore, dynamic disulfide bonds have also been used in self-healing polymer–modified asphalt. Yang et al. (2023) synthesized a polyurethane elastomer containing disulfide bonds and found that the elastomer formed a cross-linking structure in asphalt binder, significantly improving its self-healing ability at room temperature. Lyu et al. (2022) found that polyurethane containing dynamic disulfide bonds enhanced the healing capacity for fatigue cracking of asphalt in a short time based on the breakage–rearrangement effect of dynamic disulfide bonds. Wei et al. (2023) revealed that polyurethanes containing disulfide bonds form a complete physical crosslinking structure in asphalt and endow the modified asphalt with a certain dynamic reversible healing ability. Zhang et al. (2024b) introduced dynamic disulfide bonds into the network structure of SBS-modified asphalt and found that disulfide bonds markedly enhanced the healing ability of the asphalt. In conclusion, dynamic disulfide bonds are currently mainly introduced into polyurethane elastomers and SBS-modified asphalt, but there has been no research on the introduction of dynamic disulfide bonds into waste CRMA.

As desulfurized waste crumb rubber contains a large number of reactive functional groups (such as —OH), the introduction of dynamic disulfide bonds between the crumb rubber particles through the esterification reaction of —OH and —COOH is expected to endow CRMA with superior self-healing capability. The self-healing mechanism of CRMA is shown in Fig. 1. Crumb rubber particles in asphalt are linked by disulfide bonds to develop a "bridge" structure. When CRMA is suffered from external forces, the disulfide bonds in the crumb rubber will break first. After the external forces are removed, the broken disulfide bonds are restructured to enable healing and performance recovery of CRMA.

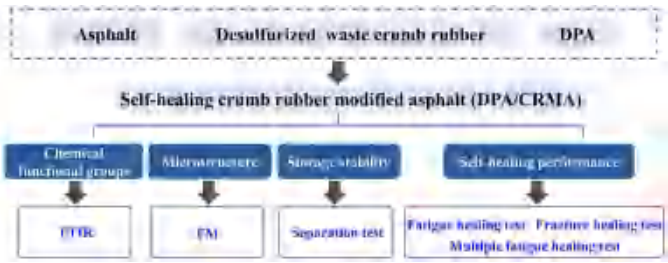

Fig. 2. Design of experiments and testing.

Herein, to develop a self-healing crumb rubber–modified asphalt (DPA/CRMA), the 3,3′-dithiodipropionic acid (DPA) with dynamic disulfide bonds was added to CRMA. Through the esterification reaction between the —OH of crumb rubber and the —COOH of DPA, the "bridge" structure with dynamic disulfide bonds between the crumb rubber particles was formed. The microstructure and chemical structure of DPA/CRMA were evaluated by fluorescence microscopy (FM) and Fourier-transform infrared (FTIR) spectroscopy, respectively. The storage stability of DPA/CRMA was evaluated by the aluminum tube segregation test. The self-healing performance of DPA/CRMA was investigated through the fatigue–healing test, multiple fatigue–healing test, and fracture healing test. The design of experiments and testing are presented in Fig. 2.

Experiment

Materials

The properties of asphalt (AH-70#) are displayed in Table 1, which were provided by Foshan Gaofu PetroChina fuel asphalt Co., Ltd (China). The reason we chose 70# asphalt is that its softening point is relatively high, making it more suitable for the warm areas, such as Wuhan, China. The properties of 3, 3'-dithiodipropionic acid (DPA) are listed in Table 2, which was purchased from Bide Pharmatech Co., Ltd (China). The crumb rubber used in this study was desulfurized waste crumb rubber (particle size of 0.45–1 mm), which was provided by Hubei Hairui Environmental Protection New Material

Downloaded from ascelibrary.org by Jianying Yu on 03/17/25. Copyright ASCE. For personal use only; all rights reserved.

Table 1. Physical properties of asphalt

Project	Value	Test methods
Penetration (25°C, 0.1 mm)	67	ASTM D5
Softening point (°C)	49.3	ASTM D36
Ductility (15°C, cm)	>100	ASTM D113

Table 2. Properties of DPA

Properties	Value
Molecular formula	$C_6H_{10}O_4S_2$
Purity (%)	98
Molecular weight (g=mol)	210.27

Technology Co., Ltd (China). The waste crumb rubber and chemical desulfurizer are added into a high-temperature closed container, where air is intermittently introduced to disrupt the network structure of the waste crumb rubber, and subsequently, an oxidation treatment is performed to obtain desulfurized waste crumb rubber. Compared to the waste crumb rubber, the cross-linking bonds and network structure in the desulfurized waste crumb rubber are disrupted, enabling it to have higher surface activity. The appearance and scanning electron microscopy (SEM) images of the desulfurized waste crumb rubber are shown in Fig. 3, it exhibited a fluffy flocculent appearance. The density and ash content of desulfurized waste crumb rubber were 1.18 g=cm^{-3} and 6.5%, respectively.

Preparation of DPA/CRMA

The melt asphalt was added to the reaction pot and the temperature was raised to 180°C. The crumb rubber (25% of asphalt mass) was added to the reaction pot. The mixture of asphalt and crumb rubber was subjected to high-speed shear mixing for 1 h at a speed of 5,000 rpm. Subsequently, a certain amount of DPA (0.5, 1, 1.5, 2, and 2.5% of the crumb rubber mass, respectively) was added and stirred at a speed of 5,000 rpm for 2 h to gain DPA/CRMA. The preparation procedure of DPA/CRMA is given in Fig. 4. DPA/CRMA with DPA content of 0.5, 1, 1.5, 2, and 2.5% were named 0.5 DPA=CRMA, 1 DPA=CRMA, 1.5 DPA=CRMA, 2 DPA=CRMA, and 2.5 DPA=CRMA, respectively. The "bridge" structure of DPA/CRMA shown in Fig. 4 was prepared.

FTIR Test

FTIR spectroscopy was used to analyze the chemical structure changes of CRMA and DPA/CRMA. The asphalt solution was made by dissolving 0.2 g of CRMA or DPA/CRMA in 4 mL of CS_2, and the solution was dropped on a KBr tablet. After the CS_2 evaporated, the KBr tablet was placed in the FTIR spectrometer for testing.

Fluorescence Microscope

The microstructure of CRMA and DPA/CRMA was observed by a fluorescence microscope (BXF-150, Shanghai Bingyu Optical Instrument Co., Ltd., China). The resolution of the fluorescence microscope was 100×. First, 1–2 drops of flowing CRMA or DPA/CRMA were put on the slide and a coverslip was put on. Then the slide was put into a 120°C oven and taken out after the hot asphalt leveled off. Finally, the slide was put into the fluorescence microscope platform area for observation. It should be noted that CRMA on the slide is as thin as possible for better observation.

Physical Property Tests

The physical property of CRMA and DPA/CRMA, including softening point, penetration, and ductility were measured following the standards of ASTM D36 (ASTM 2006), ASTM D5 (ASTM 2013), and ASTM D113 (ASTM 2007).

Storage Stability

According to ASTM D7173, 50 ± 0.5 g of CRMA or DPA/CRMA was poured into an aluminum tube, which was then placed vertically in an oven for 48 h at 163°C ± 5°C. Then, the aluminum tubes were removed and placed in the freezer at −10°C for 4 h. After taking out the aluminum tubes from the refrigerator, CRMA or DPA/CRMA was cut into three equal portions and the softening points of the bottom and top were tested. Finally, the difference of softening point between the bottom and top of CRMA or DPA/CRMA was calculated using Eq. (1) to evaluate its storage stability

$$\Delta S = S_b - S_t \tag{1}$$

where ΔS represents the difference of softening points between the bottom and top of CRMA or DPA/CRMA, °C; and S_b and S_t represents the softening point of the bottom and top for CRMA or DPA/CRMA, °C.

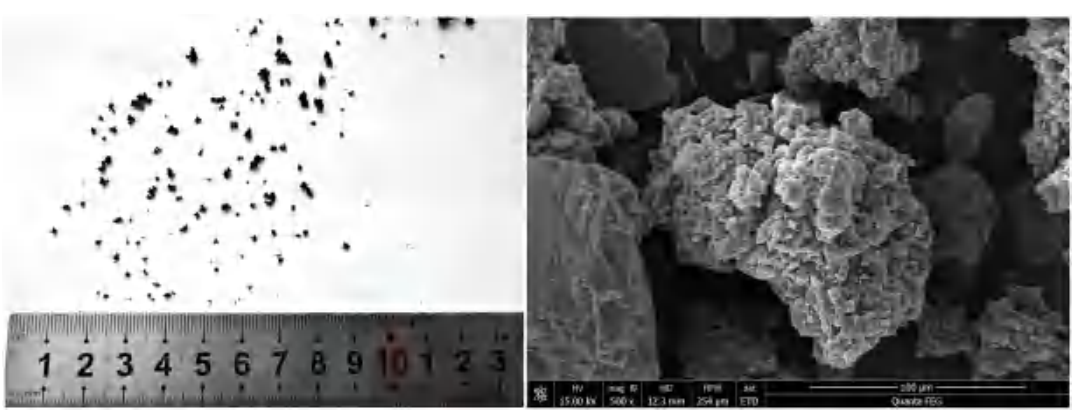

Fig. 3. Appearance and SEM images of desulfurized waste crumb rubber.

Downloaded from ascelibrary.org by Jianying Yu on 03/17/25. Copyright ASCE. For personal use only; all rights reserved.

Downloaded from ascelibrary.org by Jianying Yu on 03/17/25. Copyright ASCE. For personal use only; all rights reserved.

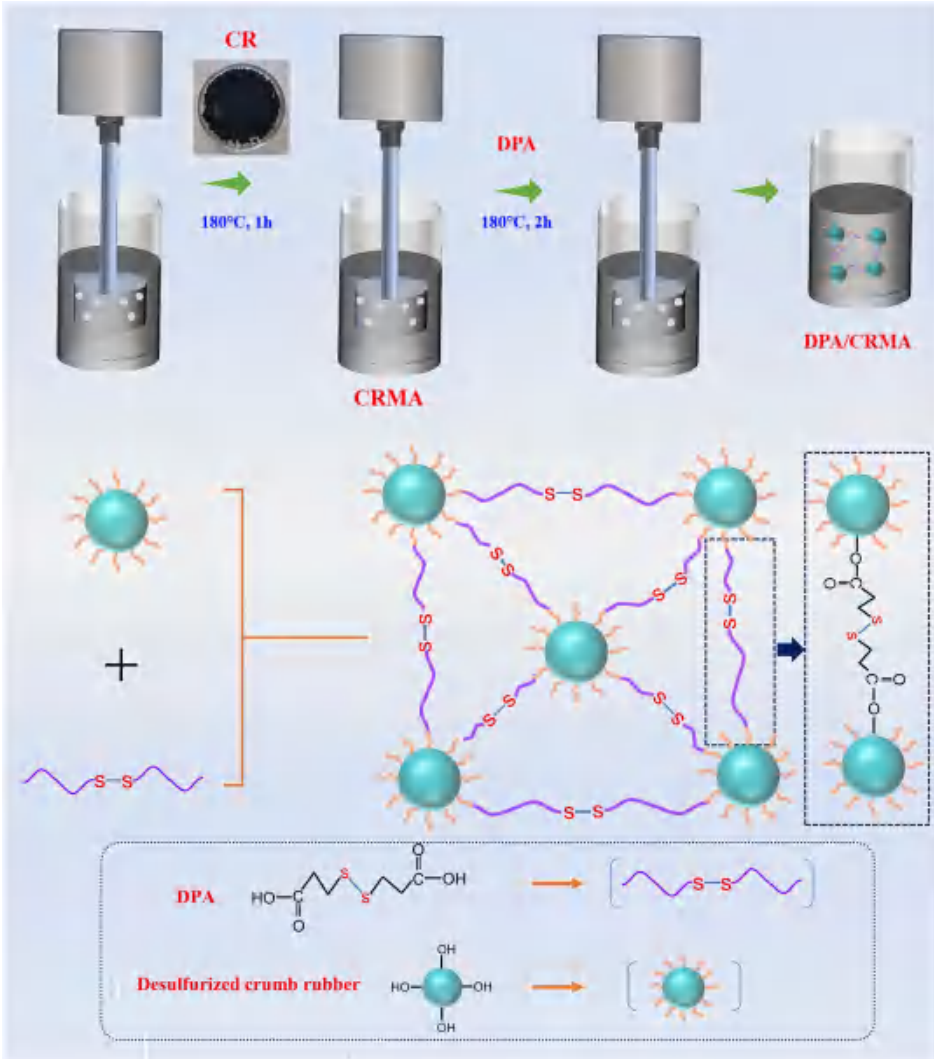

Fig. 4. Preparation procedure and structure of DPA/CRMA.

Self-Healing Performance

Fatigue–Healing Test

The fatigue–healing test based on the DSR time-scan test is commonly used to evaluate the self-healing performance of asphalt binder (Sun et al. 2018; Zhang et al. 2018). Herein, the plate diameter of DSR was 8 mm and the plate gap was 2 mm. The test frequency and strain were 10 Hz and 3%. The detailed flowchart of the fatigue–healing test is presented in Fig. 5. First, CRMA or DPA/CRMA was subjected to a time-scan test at 25°C to obtain the initial complex modulus (G_i^*). The time-scan test halted when the complex modulus (G_f^*) dropped to 70% of the G_i^*. Subsequently, CRMA or DPA/CRMA was healed for 10 min at 25 and 40°C, respectively. Lastly, the time-scan test at 25°C was repeated to obtain the healed complex modulus (G_h^*) of CRMA or DPA/CRMA. The healing index of CRMA or DPA/CRMA was calculated by Eq. (2)

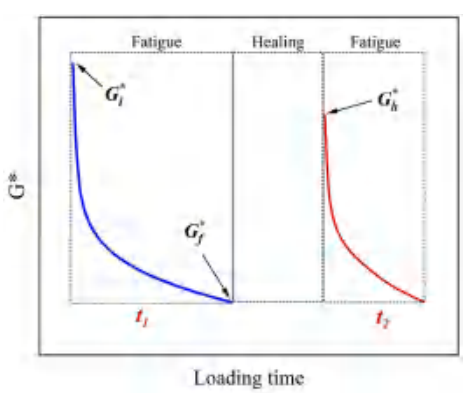

Fig. 5. Fatigue–healing test.

$$HI = \frac{(G_h^* - G_f^*) = t_2}{(G_i^* - G_f^*) = t_1} \times 100\% \quad (2)$$

where HI represents the healing index in the fatigue–healing test of CRMA or DPA/CRMA, %; G_i^*, G_f^*, and G_h^* represents the initial complex modulus, complex modulus after the first fatigue and complex modulus after self-healing of CRMA or DPA/CRMA, Pa; t_1 represents the time required for the complex modulus of CRMA or DPA/CRMA to reach 70% of the initial modulus in the first fatigue stage, s; and t_2 represents the time required for the complex modulus of CRMA or DPA/CRMA to reach 70% of the initial modulus after healing, s.

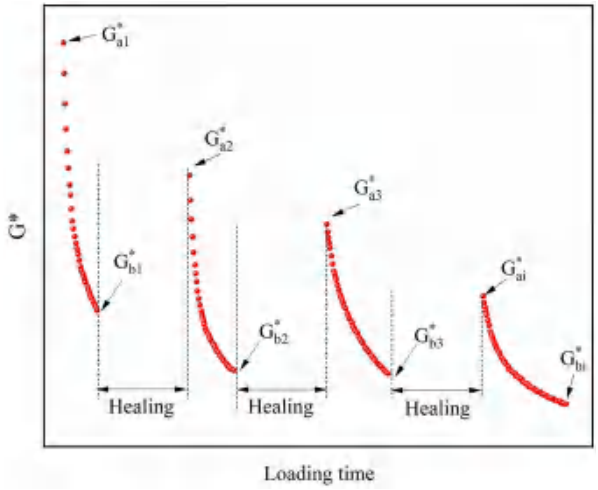

Fig. 6. Multiple fatigue–healing test.

Multiple Fatigue–Healing Test

The multiple healing performance of CRMA and DPA/CRMA is an important healing indicator. In this study, the multiple fatigue–healing performance of CRMA and DPA/CRMA was investigated by DSR. As shown in Fig. 6, the detailed steps were as follows:

1. CRMA or DPA/CRMA was subjected to a DSR time-scan test, and the test was stopped when the complex modulus (G^*_{b1}) was reduced to 70% of the initial complex modulus (G^*_{a1}).
2. CRMA or DPA/CRMA was healed for 30 min at 25°C.
3. The time-scan test was performed again to gain the healed complex modulus (G^*_{a2}), and the test was stopped when G^*_{b2} was reduced to 70% of G^*_{a2}.
4. CRMA or DPA/CRMA continued to heal for 30 min and then underwent a DSR time-scan test to obtain G^*_{a3} and G^*_{b3}.
5. The test steps were repeated until the complex modulus G^*_{bi} reduced to 50% of the initial modulus G^*_{a1} after healing, and the test was completed. The multiple fatigue–healing index (MFI, %) of CRMA or DPA/CRMA was calculated after each self-healing stage by Eq. (3)

$$\mathrm{MFI} = \frac{G^*_{a(i)} - G^*_{b1}}{G^*_{a1} - G^*_{b1}} \times 100\% \tag{3}$$

where $G^*_{a(i)}$ represents the complex modulus of CRMA or DPA/CRMA after the $i-1$ healing, Pa; G^*_{a1} represents the initial complex modulus of CRMA or DPA/CRMA, Pa; and G^*_{b1} represents the complex modulus of CRMA or DPA/CRMA after the first time-scan test, Pa.

Fracture Healing Test

The fracture healing test based on the ductility experiment can be utilized for evaluating the fracture healing performance of asphalt binder (Sun et al. 2017). In this study, the fracture healing ability of CRMA and DPA/CRMA was evaluated by the ductility ratio before and after healing. The test steps are presented in Fig. 7. The melt CRMA or DPA/CRMA samples were filled into the ductility molds. One set of the CRMA or DPA/CRMA ductility specimens was tested to obtain the initial ductility (D_i). Other sets of the CRMA or DPA/CRMA ductility specimens were stood in a freezer for 2 h at −20°C and then the CRMA or DPA/CRMA specimens were broken in the center. Then, CRMA or DPA/CRMA were assembled together at the fracture surface and then placed on the baseplate of the ductility mold and fixed by the locating pin on the baseplate, which enabled CRMA and DPA/CRMA to be in complete contact at the fracture surface. Afterward, CRMA or DPA/CRMA was healed in an oven at 25 and 40°C for 2, 4, 6, 8, and 10 h. Finally, the healed CRMA or DPA/CRMA was tested to obtain the healed ductility (D_h). The fracture self-healing performance of CRMA or DPA/CRMA was evaluated by Eq. (4)

$$\mathrm{HR} = \frac{D_h}{D_i} \times 100\% \tag{4}$$

where HR represents the fracture healing rate of CRMA or DPA/CRMA, %; D_h represents the ductility of CRMA or DPA/CRMA, cm; and D_i represents the initial ductility of CRMA or DPA/CRMA, cm.

Results and Discussion

Chemical Structure

Fig. 8 displays the infrared spectra of CRMA and DPA/CRMA. In the infrared spectra of the desulfurized crumb rubber, the characteristic peak of —OH was at 3,452 cm^{-1} (Kong et al. 2021). The characteristic peaks of C-H, methylene ($-CH_2$), benzene ring, and

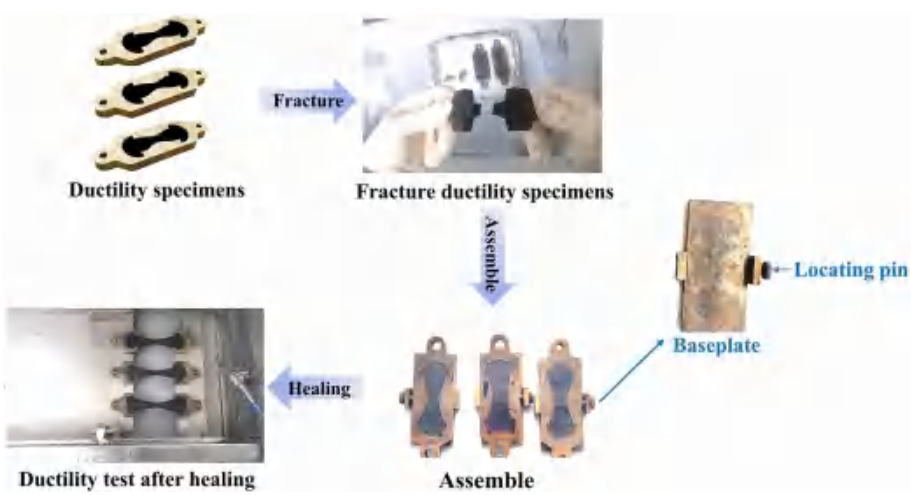

Fig. 7. Fracture healing test.

Downloaded from ascelibrary.org by Jianying Yu on 03/17/25. Copyright ASCE. For personal use only; all rights reserved.

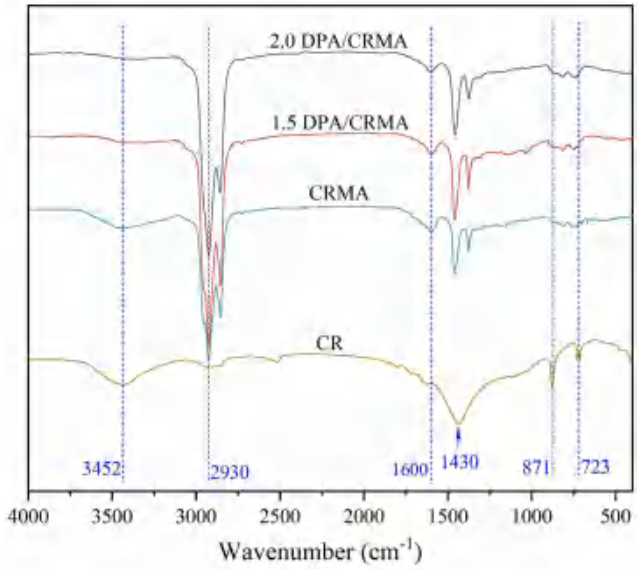

Fig. 8. Infrared spectra of CRMA and DPA/CRMA.

methylene chain segment $(CH_2)n$ ($n \geq 4$) in alkanes were at 2,930, 1,430, 871, and 723 cm^{-1}, respectively (Yang et al. 2023). In the infrared spectra of CRMA, the characteristic peaks of asymmetrically substituted benzene ring appeared at 1,600 cm^{-1}, and the characteristic peak of —OH was still observed at 3,452 cm^{-1}. In the infrared spectra of DPA/CRMA, the characteristic peaks of —OH gradually disappeared with the addition of DPA, indicating that —COOH at both ends of DPA reacted with —OH of desulfurized crumb rubber.

Microstructure

Fig. 9 displays the fluorescence microscope images of CRMA and DPA/CRMA. Fig. 9 shows that there was an agglomeration phenomenon of crumb rubber particles in CRMA. Crumb rubber absorbed the light components in asphalt and expanded, which is consistent with previous studies (Ghavibazoo and Abdelrahman 2013). Due to the fluffy and flocculent surface of desulfurized crumb rubber, its surface energy is relatively high; thus, some crumb rubber attracts each other to agglomerate. This phenomenon would deteriorate the performance of CRMA (Xu et al. 2021). The addition of DPA improved the dispersion of crumb rubber in asphalt, due to the fact that DPA can connect desulfurized crumb rubber particles at both ends, resulting in the desulfurized crumb rubber and asphalt having great compatibility and uniform dispersion. When the DPA content was 0.5%, the agglomeration phenomenon in DPA/CRMA weakened. As the DPA dosage increased, the crumb rubber in asphalt gradually existed in a more uniform dispersion structure. When the dosage of DPA was 1.5%, there was no agglomeration phenomenon in DPA/CRMA, and a better powder dispersion structure was formed, which is beneficial for improving the performance of CRMA.

To further analyze the dispersibility of the crumb rubber particles, the spots number of crumb rubber in the asphalt was calculated using the ImageJ and Photoshop software. In CRMA, the spots number was only 502 due to the agglomeration phenomenon of the crumb rubber. While the addition of DPA improved the dispersing ability of the crumb rubber, which makes CRMA have better compatibility. The spots number of crumb rubber particles in the asphalt remarkably improved with the increase of the DPA dosage. When the DPA dosage was 0.5%, the spots number of the crumb rubber increased to 718, and the spots number in DPA/CRMA reached 1,154 when the DPA dosage was 1.5%, which was 129.9% higher than that of CRMA. It should be noted that when the dosage of DPA exceeded 1.5%, the increment of spots number decreased, which might be due to the fact that part of the DPA was not connected between the crumb rubber particles. In conclusion, the DPA markedly improved the dispersion of CRMA.

Physical Properties

Table 3 shows the physical properties of CRMA and DPA/CRMA. From Table 3, it was observed that the DPA increased the softening point and ductility of DPA/CRMA and decreased its penetration. Crumb rubber in asphalt presents a granular dispersion state and forms a certain degree of swelling; thus, it can improve the physical properties of asphalt (Airey et al. 2003; Sienkiewicz et al. 2017). DPA formed a certain degree of connection between the crumb rubber particles, thereby further improving the physical properties of DPA/CRMA. With the increased of DPA dosage, the physical properties of DPA/CRMA gradually enhanced. The softening point and ductility of DPA/CRMA reached the maximum when the DPA dosage was 2.5%, which increased by 4.9°C and 3.0 cm compared to those of CRMA. It was noteworthy that the variations of softening

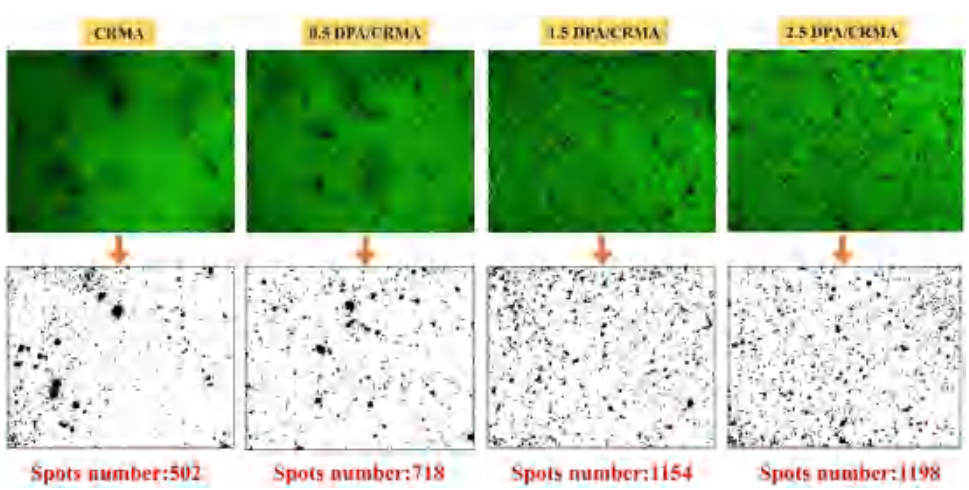

Fig. 9. Fluorescence microscopic images of CRMA and DPA/CRMA.

Downloaded from ascelibrary.org by Jianying Yu on 03/17/25. Copyright ASCE. For personal use only; all rights reserved.

Table 3. Physical properties of CRMA and DPA/CRMA

Asphalt binders	Softening point (°C)	Ductility (cm)	Penetration (dmm)
CRMA	64.5	6.0	63
0.5 DPA=CRMA	65.4	6.6	58
1 DPA=CRMA	66.6	7.5	52
1.5 DPA=CRMA	68.5	8.6	46
2 DPA=CRMA	69.1	8.9	44
2.5 DPA=CRMA	69.4	9.0	43

point, ductility, and penetration of DPA/CRMA were small when the dosage of DPA exceeded 1.5%. The reason may be that when the dosage of DPA exceeded 1.5%, the —OH on the surface of the crumb rubber was consumed, and a part of the excess DPA was not connected between the crumb rubber particles. Therefore, the optimum dosage of DPA in CRMA was 1.5%.

Storage Stability

The separation of crumb rubber and asphalt is an important challenge for CRMA (Xie et al. 2023; Zhou et al. 2020). In this study, the "bridge" formed by dynamic disulfide bonds between the crumb rubber particles will have a certain impact on the storage stability of CRMA. Table 4 shows the softening points differences (ΔS) of the bottom and top of CRMA and DPA/CRMA. It can be observed from Table 4 that the storage stability of CRMA was poor, and the softening points difference between the bottom and top layers reached 8.5°C after the segregation test. The addition of DPA reduced the softening points difference of DPA/CRMA. The reason is that DPA formed a "bridge" in the desulfurized waste crumb rubber, which led to the formation of a certain network structure of the desulfurized waste CRMA This structure made DPA/CRMA more stable at high temperatures compared to CRMA, which enables the crumb rubber particles to be less susceptible to segregation in the storage stability test, thereby reducing the softening point difference of CRMA. When the DPA dosage was 0.5%, the difference between the softening point of DPA/CRMA was reduced to 6.3°C. The softening point difference of DPA/CRMA decreased significantly with the increased DPA dosage. Critically, the softening point difference of DPA/CRMA decreased to 2.4°C when the DPA dosage was 1.5%. When the DPA dosage exceeded 1.5%, the change in the softening point difference of DPA/CRMA decreased. The reason may be that when the DPA dosage exceeds 1.5%, a portion of the DPA reacts with the polarity groups in the asphalt and is not attached to the crumb rubber particles.

Self-Healing Performance

Fatigue–Healing Performance

The fatigue–healing indices of the base asphalt (BA), CRMA, and DPA/CRMA at 25 and 40°C are displayed in Fig. 10. It can be observed from Fig. 10 that the BA had a certain self-healing ability at room temperature, and its healing index was 64.9%. The fatigue–healing index of CRMA was 51.8% at 25°C. Among all DPA/CRMA, their fatigue–healing indices at 25°C were higher than that of CRMA, indicating that the dynamic disulfide bonds endowed CRMA with higher room temperature self-healing ability. When the DPA content was 1.5%, the fatigue–healing index of DPA/CRMA was 84.6%, which was enhanced by 63.3% compared to CRMA. The reason is that crumb rubber particles were connected through dynamic disulfide bonds to form a "bridge" structure, making the

Table 4. Softening point difference of CRMA and DPA/CRMA

Parameter	CRMA	0.5 DPA=CRMA	1 DPA=CRMA	1.5 DPA=CRMA	2 DPA=CRMA	2.5 DPA=CRMA
S_b	67.8	67.1	68.8	69.5	70.5	70.9
S_t	59.3	60.8	64.2	67.1	68.3	68.9
ΔS	8.5	6.3	4.6	2.4	2.2	2.0

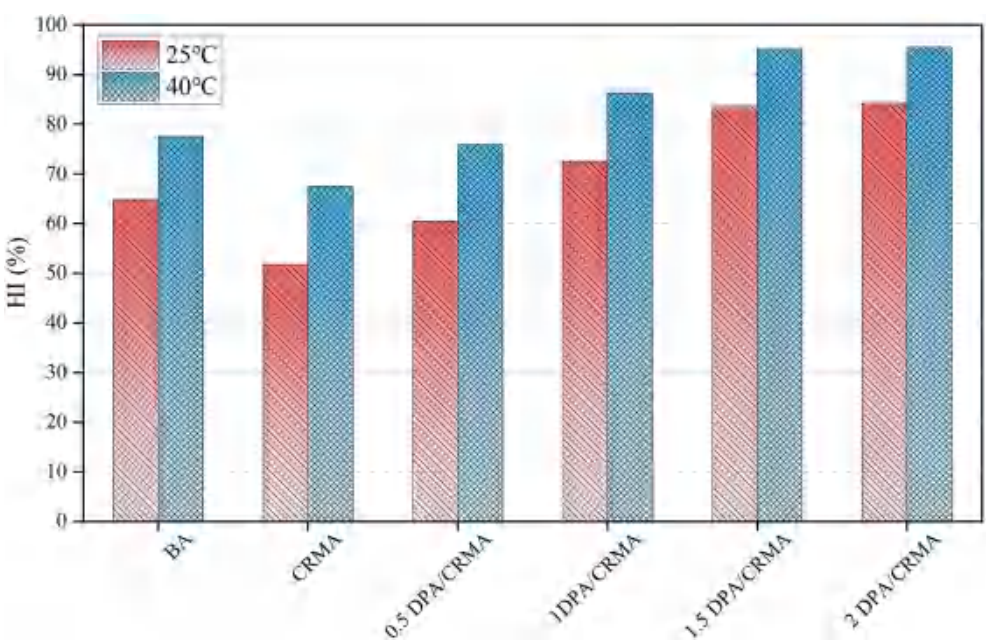

Fig. 10. Healing indices of BA, CRMA, and DPA/CRMA at 25 and 40°C.

Downloaded from ascelibrary.org by Jianying Yu on 03/17/25. Copyright ASCE. For personal use only; all rights reserved.

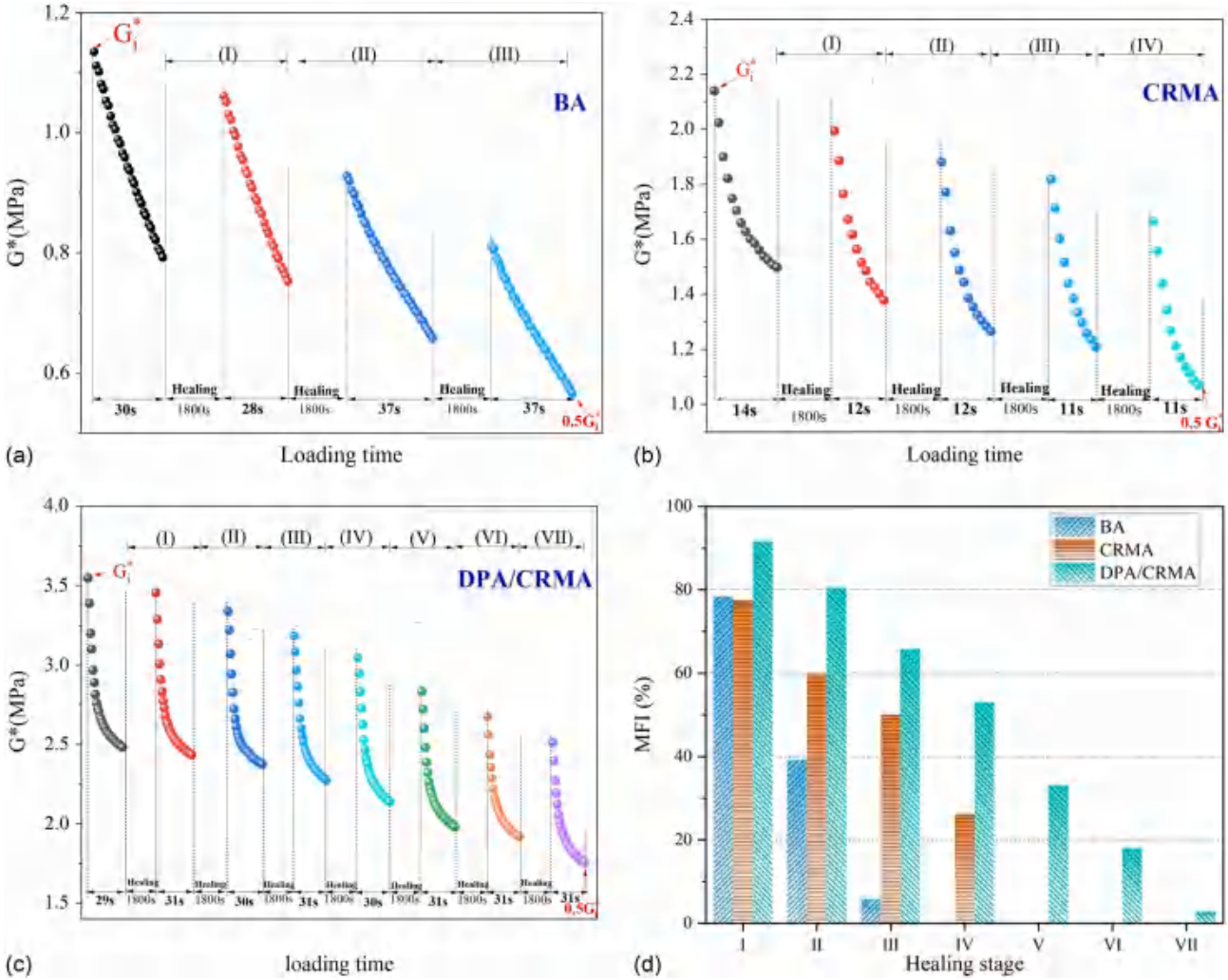

Fig. 11. Multiple fatigue–healing curves of: (a) BA; (b) CRMA; (c) DPA/CRMA; and (d) healing indices.

crumb rubber particles in asphalt relatively stable. In addition, dynamic disulfide bonds have the characteristic of breakage–rearrangement, and when microcracks occur in CRMA, the dynamic disulfide bonds can undergo breakage–rearrangement to achieve the healing of the microcracks. The fatigue–healing indices of BA, CRMA, and DPA/CRMA at 40°C were higher than those at 25°C, owing to the fact that increasing the healing temperature can accelerate the molecular movement of CRMA and DPA/CRMA, thus improving its healing ability. The self-healing index of DPA/CRMA gradually enhanced with the increase of dosage for DPA. When the dosage of DPA was 1.5%, the fatigue–healing index reached 96.2%. It was worth noting that when the DPA content exceeds 1.5%, the change of the fatigue–healing indices of DPA/CRMA at 25 and 40°C was smaller. The fatigue–healing indices of DPA/CRMA at 25 and 40°C were 85.2 and 96.8% when the DPA dosage was 2.5%. It was indicated that 1.5% was the optimal dosage of DPA in DPA/CRMA.

Multiple Fatigue–Healing Performance

The multiple fatigue–healing curves of the BA, CRMA, and 1.5 DPA=CRMA are shown in Fig. 11. It was observed that compared with CRMA, DPA/CRMA takes a longer loading time for the modulus to reach 70% of the initial complex modulus, with CRMA and ALD/CRMA taking 14 and 29 s, respectively. The reason is that the dynamic disulfide bonds between the crumb rubber particles improved the cohesion of CRMA, thus increasing its ability to resist deformation. From Fig. 11, it was observed that the number of fatigue–healing cycles in which the complex modulus of DPA/CRMA reached 50% of the initial modulus was 7, whereas it was only 4 cycles and 3 cycles for CRMA and BA. The results showed that dynamic disulfide bonds noticeably enhanced the multiple fatigue–healing capability of CRMA.

As shown in Fig. 11, DPA/CRMA had a higher self-healing index in each fatigue–healing cycle compared to CRMA and BA. In stage (I), the self-healing indices of BA, CRMA, and DPA/CRMA were 78.4, 77.4, and 91.6%, respectively. As the number of fatigue–healing cycles increased, the self-healing indices of BA, CRMA, and DPA/CRMA gradually decreased. When the number of fatigue–healing cycles was 3, the healing index of BA was dramatically reduced to 5.7%. When the fatigue–healing cycle reached 4, the self-healing index of CRMA was only 26.1%, while that of DPA/CRMA was 53.0%, which was attributed to the fact that the dynamic disulfide bonds can still undergo a breakage–rearrangement effect after several fatigue–healing cycles. When the number of fatigue–healing cycles reached 5, the complex modulus of CRMA reached half of the initial complex modulus. It was worth noting that when the number of fatigue–healing cycles reached 7, DPA/CRMA still had a certain self-healing ability. In conclusion, DPA/CRMA had a better multiple fatigue–healing capability compared to CRMA, which was due to the breakage–rearrangement effect of dynamic disulfide bonds between the crumb rubber particles.

Downloaded from ascelibrary.org by Jianying Yu on 03/17/25. Copyright ASCE. For personal use only; all rights reserved.

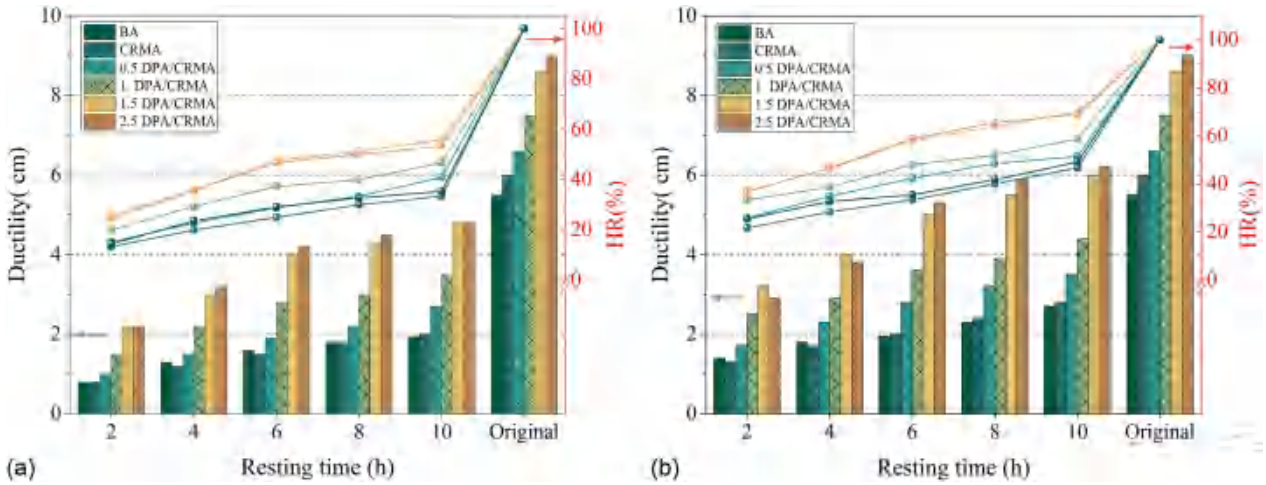

Fig. 12. Healing rate and ductility of different CRMAs: (a) 25°C; and (b) 40°C.

Fracture Healing Performance

The fracture healing rates of the BA, CRMA, and DPA/CRMA at 25 and 40°C are displayed in Fig. 12. In Fig. 12, we can see that after a certain period of healing at 25°C, the ductility of BA has been restored to a certain extent, mainly due to the limited self-healing ability of the asphalt itself. The healing rate of CRMA was slightly lower than that of BA. With the addition of DPA, the healing rate of DPA/CRMA was improved significantly, indicating that the disulfide bonds enhanced the self-healing capability of CRMA. The healing rates of BA, CRMA, and DPA/CRMA gradually increased with a prolonged resting time at 25°C. When the resting time was 10 h, the self-healing rates of both BA, CRMA, and DPA/CRMA reached the maximum. Among all DPA/CRMA, 1.5 DPA=CRMA showed the highest healing rate. When the resting time was 10 h, the self-healing rate of 1.5 DPA=CRMA reached 55.8%, which was 22.5% higher than that of CRMA. It was notable that the healing rate of 1.5 DPA=CRMA was higher at an early stage, reaching 47.6% when the resting time was 6 h. While the healing rate of CRMA increased slowly with the extension of resting time, and the healing rate of CRMA changed less when the resting time exceeded 8 h.

When the healing temperature was 40°C, the healing rate of BA, CRMA, and DPA/CRMA was improved compared to the healing rate at 25°C, indicating the importance of healing temperature in improving the self-healing capability of CRMA. For all DPA/CRMA, the healing rates at 40°C were higher than at 25°C. The reason was that increasing temperature can accelerate the dynamic exchange of disulfide bonds. It was worth noting that during the short-term healing time, the healing rate of DPA/CRMA increased rapidly. When the resting time was 4 h, the healing rate of 1.5 DPA=CRMA reached 46.5%. With the extension of resting time, the increase in healing rate of DPA/CRMA was relatively small. In summary, DPA enhanced the fracture healing capability of CRMA, especially at the early healing stage and room temperature. When the healing temperature was 40°C, the self-healing ability of DPA/CRMA was significantly improved due to the intense breakage–rearrangement effect of dynamic disulfide bonds.

According to the capillary diffusion theory, the self-healing of asphalt binder is divided into two stages: wetting healing and diffusion healing (Bommavaram et al. 2009; Wool and O'Connor 1981). The wetting healing of asphalt binder is completed within a short period after the appearance of cracks, while the diffusion healing stage takes place in the subsequent time, which is affected by factors such as healing temperature and resting time. Herein, a self-healing equation [Eq. (5)] was introduced to more accurately analyze the effect of dynamic disulfide bonds on the healing capability of CRMA. According to Eq. (5), it is evident that there is a linear relationship between the $HR(T_h; t_h)$ and the $t_h^{0.25}$

$$HR(T_h; t_h) = HR_0 + \emptyset(T_h)t_h^{0.25} \tag{5}$$

where $HR\ (T_h; t_h)$ represents the healing rate for a certain healing temperature and resting time, %; HR_0 represents the healing rate during the wetting healing stage, %; and $\emptyset(T_h)$ is a temperature-related indicator that denotes the rate at which molecules diffuse across the fracture surface to gain ductility at temperature T during the diffusion healing stage.

Fig. 13 shows the fitting results of the resting time and healing rates of different CRMA. It can be observed from Fig. 13(a) that when the healing temperature was 25°C, the correlation coefficients of BA, CRMA, 0.5 DPA=CRMA, and 1.5 DPA=CRMA were 0.986, 0.995, 0.975, and 0.985, respectively, indicating a strong relationship between the resting time and healing rate of CRMA. In the fitted curves, the higher slope indicates a greater improvement in the healing rate with an increasing resting time, which suggests a higher improvement in the fracture healing performance of CRMA. The slope of 0.5 DPA=CRMA was higher than that of CRMA, suggesting that dynamic disulfide bonds enhanced the healing capability of CRMA. The slope of 1.5 DPA=CRMA was higher than that of 0.5 CRMA, which is attributed to the fact that 1.5 DPA=CRMA contains more dynamic disulfide bonds that can undergo breakage–rearrangement compared to 0.5 DPA=CRMA. Notably, the slopes of the fitted curves for all asphalt binders at 40°C in Fig. 13(b) were higher than the slopes at 25°C, suggesting that an increase in the healing temperature is favorable for improving the healing ability of the asphalt binders. The slopes of the fitted curves for 1.5 DPA=CRMA at 40°C were higher than those of CRMA and 0.5 DPA=CRMA, indicating that the healing ability of 1.5 DPA=CRMA was higher to that of CRMA and 0.5 DPA=CRMA.

Conclusions

In this study, a novel self-healing crumb rubber–modified asphalt (DPA/CRMA) based on breakage–rearrangement properties of dynamic disulfide bonds was prepared. The physical properties, microstructure, fatigue–healing performance, multiple fatigue–healing

Downloaded from ascelibrary.org by Jianying Yu on 03/17/25. Copyright ASCE. For personal use only; all rights reserved.

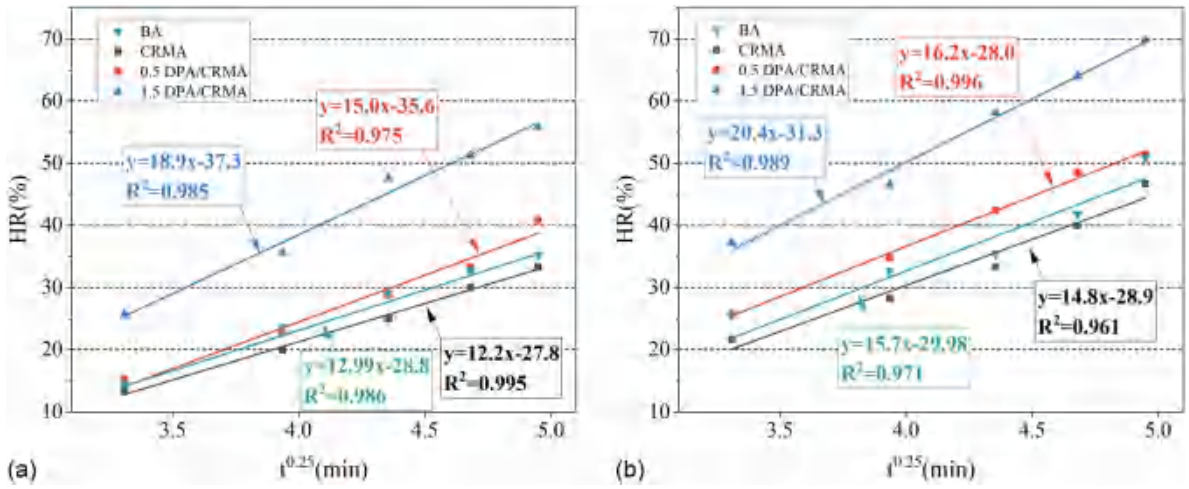

Fig. 13. Self-healing fitting curves of different CRMAs: (a) 25°C; and (b) 40°C.

performance, and fracture healing performance of DPA/CRMA were investigated. The main conclusions were as follows:

1. The chemical structure analyses of DPA/CRMA revealed that the crumb rubber particles in asphalt were successfully connected by dynamic disulfide bonds. Dynamic disulfide bonds formed a "bridge" structure between the crumb rubber particles, which improved the dispersion of crumb rubber in asphalt and thus enhanced the physical properties of CRMA. In addition, the storage stability of DPA/CRMA has also been significantly improved. The optimum dosage of DPA was 1.5%.
2. DPA/CRMA had better self-healing properties due to the breakage–rearrangement properties of dynamic disulfide bonds. Compared to CRMA, the fatigue–healing index of 1.5 DPA=CRMA increased by 32.8 and 28.7% at 25 and 40°C, respectively. While the increment of the fatigue–healing index for DPA/CRMA was small when the DPA dosage exceeded 1.5%.
3. DPA improved the multiple fatigue–healing ability of CRMA. The multiple fatigue–healing index of DPA/CRMA was superior to that of CRMA at each stage of fatigue–healing cycles. In addition, the number of fatigue–healing cycles of self-healing CRMA was 7, whereas it was only 4 cycles for CRMA.
4. DPA markedly enhanced the fracture healing capability of CRMA. The fracture healing rates of 1.5 DPA=CRMA were 22.5 and 23.1% higher than those of CRMA when the healing temperatures were 25 and 40°C, respectively. Furthermore, DPA enhanced the early-stage healing capability of CRMA, and better self-healing ability was obtained in a shorter period.

Herein, a novel self-healing crumb rubber–modified asphalt (DPA/CRMA) based on the breakage–rearrangement property of dynamic disulfide bonds was prepared. The study showed that DPA/CRMA had superior self-healing performance, which is conducive to extending the service life and reducing the maintenance cost of waste CRMA pavements. In the future, we will prepare a novel type of self-healing CRMA and its mixture, and conduct a field validation on some construction sections in Wuhan, China.

Data Availability Statement

Some or all data, models, or code that support the findings of this study are available from the corresponding author upon reasonable request.

Acknowledgments

The authors gratefully acknowledge financial support from the National Key R&D Program of China (No. 2022YFC3801600) and the Program Fund of Non-Metallic Excellent and Innovation Center for Building Materials (24PHD-7).

References

Airey, G. D., M. M. Rahman, and A. C. Collop. 2003. "Absorption of bitumen into crumb rubber using the basket drainage method." Int. J. Pavement Eng. 4 (2): 105–119. https://doi.org/10.1080/1029843032000158879.

ASTM. 2006. Standard test method for softening point of bitumen (ring-and-ball apparatus). ASTM D36. West Conshohocken, PA: ASTM.

ASTM. 2007. Standard test method for ductility of asphalt materials. ASTM D113. West Conshohocken, PA: ASTM.

ASTM. 2013. Standard test method for penetration of bituminous materials. ASTM D5. West Conshohocken, PA: ASTM.

Bommavaram, R. R., A. Bhasin, and D. N. Little. 2009. "Determining intrinsic healing properties of asphalt binders: Role of dynamic shear rheometer." Transp. Res. Rec. 2126 (1): 47–54. https://doi.org/10.3141/2126-06.

Bressi, S., N. Fiorentini, J. Huang, and M. Losa. 2019. "Crumb rubber modifier in road asphalt pavements: State of the art and statistics." Coatings 9 (6): 384. https://doi.org/10.3390/coatings9060384.

Chang, R., X. Wang, X. Li, H. An, and J. Qin. 2016. "Self-activated healable hydrogels with reversible temperature responsiveness." ACS Appl. Mater. Interfaces 8 (38): 25544–25551. https://doi.org/10.1021/acsami.6b08279.

de Luzuriaga, A. R., R. Martin, N. Markaide, A. Rekondo, G. Cabañero, J. Rodríguez, and I. Odriozola. 2016. "Epoxy resin with exchangeable disulfide crosslinks to obtain reprocessable, repairable and recyclable fiber-reinforced thermoset composites." Mater. Horiz. 3 (3): 241–247. https://doi.org/10.1039/C6MH00029K.

Ding, X., L. Chen, T. Ma, H. Ma, L. Gu, T. Chen, and Y. Ma. 2019. "Laboratory investigation of the recycled asphalt concrete with stable crumb rubber asphalt binder." Constr. Build. Mater. 203 (Apr): 552–557. https://doi.org/10.1016/j.conbuildmat.2019.01.114.

Ghavibazoo, A., and M. Abdelrahman. 2013. "Composition analysis of crumb rubber during interaction with asphalt and effect on properties of binder." Int. J. Pavement Eng. 14 (5): 517–530. https://doi.org/10.1080/10298436.2012.721548.

Grossegger, D., B. Gomez-Meijide, S. Vansteenkiste, and A. Garcia. 2018. "Influence of rheological and physical bitumen properties on heat-induced self-healing of asphalt mastic beams." Constr. Build. Mater. 182 (Sep): 298–308. https://doi.org/10.1016/j.conbuildmat.2018.06.148.

Downloaded from ascelibrary.org by Jianying Yu on 03/17/25. Copyright ASCE. For personal use only; all rights reserved.

He, Y., S. Mao, T. Zhang, S. Zeng, H. Duan, R. Zhuang, and J. Yu. 2024. "Preparation and properties of self-healing SBS modified bitumen with dynamic acylhydrazone bonds." Eur. Polym. J. 210 (Apr): 112932. https://doi.org/10.1016/j.eurpolymj.2024.112932.

Hu, J., R. Mo, X. Sheng, and X. Zhang. 2020. "A self-healing polyurethane elastomer with excellent mechanical properties based on phase-locked dynamic imine bonds." Polym. Chem. 11 (14): 2585–2594. https://doi.org/10.1039/D0PY00151A.

Kong, P., X. Chen, G. Xu, and W. Wei. 2021. "Preparation and characterization of maleic anhydride-grafted desulfurization rubber powder by free-radical polymerization." Polym. Eng. Sci. 61 (10): 2567–2575. https://doi.org/10.1002/pen.25783.

Kuhl, N., S. Bode, R. K. Bose, J. Vitz, A. Seifert, S. Hoeppener, S. J. Garcia, S. Spange, V. D. Z. Sybrand, and M. D. Hager. 2015. "Acylhydrazones as reversible covalent crosslinkers for self-healing polymers." Adv. Funct. Mater. 25 (22): 3295–3301. https://doi.org/10.1002/adfm.201501117.

Lastra-González, P., I. Indacoechea-Vega, M. A. Calzada-Pérez, D. Castro-Fresno, and A. Vega-Zamanillo. 2019. "Mechanical assessment of the induction heating as a method to accelerate the drying process of cold porous asphalt mixtures." Constr. Build. Mater. 208 (May): 646–650. https://doi.org/10.1016/j.conbuildmat.2019.03.053.

Li, B., P.-F. Cao, T. Saito, and A. P. Sokolov. 2023. "Intrinsically self-healing polymers: From mechanistic insight to current challenges." Chem. Rev. 123 (2): 701–735. https://doi.org/10.1021/acs.chemrev.2c00575.

Li, C., S. Wu, Z. Chen, G. Tao, and Y. Xiao. 2018. "Enhanced heat release and self-healing properties of steel slag filler based asphalt materials under microwave irradiation." Constr. Build. Mater. 193 (Dec): 32–41. https://doi.org/10.1016/j.conbuildmat.2018.10.193.

Li, J., S. Yang, Y. Muhammad, M. Sahibzada, Z. Zhu, T. Liu, and S. Liao. 2020a. "Fabrication and application of polyurea formaldehyde-bioasphalt microcapsules as a secondary modifier for the preparation of high self-healing rate SBS modified asphalt." Constr. Build. Mater. 246 (Jun): 118452. https://doi.org/10.1016/j.conbuildmat.2020.118452.

Li, Z.-J., J. Zhong, M.-C. Liu, J.-C. Rong, K. Yang, J.-Y. Zhou, L. Shen, F. Gao, and H.-F. He. 2020b. "Investigation on self-healing property of epoxy resins based on disulfide dynamic links." Chin. J. Polym. Sci. 38 (Sep): 932–940. https://doi.org/10.1007/s10118-020-2406-x.

Lyu, L., Z. Wang, J. Ji, Y. Li, Y. Wen, J. Zhang, R. Li, Z. Chen, and J. Pei. 2022. "Investigating rheological and healing properties of asphalt binder modified by disulfide-crosslinked poly(urea-urethane) elastomer." Constr. Build. Mater. 347 (Sep): 128546. https://doi.org/10.1016/j.conbuildmat.2022.128546.

Micaelo, R., T. Al-Mansoori, and A. Garcia. 2016. "Study of the mechanical properties and self-healing ability of asphalt mixture containing calcium-alginate capsules." Constr. Build. Mater. 123 (Oct): 734–744. https://doi.org/10.1016/j.conbuildmat.2016.07.095.

Min, J., Z. Zhou, H. Wang, Q. Chen, M. Hong, and H. Fu. 2022. "Room temperature self-healing and recyclable conductive composites for flexible electronic devices based on imine reversible covalent bond." J. Alloys Compd. 894 (Feb): 162433. https://doi.org/10.1016/j.jallcom.2021.162433.

Shirzad, S., M. Hassan, and L. N. Mohammad. 2020. "Rheological and mechanical evaluation of polyurethane prepolymer-modified asphalt mixture with self-healing abilities." J. Mater. Civ. Eng. 32 (8): 04020231. https://doi.org/10.1061/(ASCE)MT.1943-5533.0003307.

Sienkiewicz, M., K. Borzędowska-Labuda, A. Wojtkiewicz, and H. Janik. 2017. "Development of methods improving storage stability of bitumen modified with ground tire rubber: A review." Fuel Process. Technol. 159 (May): 272–279. https://doi.org/10.1016/j.fuproc.2017.01.049.

Sun, D., Q. Pang, X. Zhu, Y. Tian, T. Lu, and Y. Yang. 2017. "Enhanced self-healing process of sustainable asphalt materials containing microcapsules." ACS Sustainable Chem. Eng. 5 (11): 9881–9893. https://doi.org/10.1021/acssuschemeng.7b01850.

Sun, D., G. Sun, X. Zhu, A. Guarin, B. Li, Z. Dai, and J. Ling. 2018. "A comprehensive review on self-healing of asphalt materials: Mechanism, model, characterization and enhancement." Adv. Colloid Interface Sci. 256 (Jun): 65–93. https://doi.org/10.1016/j.cis.2018.05.003.

Sun, G., W. Ning, X. Jiang, K. Qiu, Z. Cao, and Y. Ding. 2024. "A comprehensive review on asphalt fume suppression and energy saving technologies in asphalt pavement industry." Sci. Total Environ. 913 (Feb): 169726. https://doi.org/10.1016/j.scitotenv.2023.169726.

Tang, Z., Y. Hu, and W. Hua. 2021. "Investigation of self-healing properties of dense-graded asphalt mixture containing microcapsule." IOP Conf. Ser.: Earth Environ. Sci. 768 (1): 012099. https://doi.org/10.1088/1755-1315/768/1/012099.

Wang, H., X. Liu, P. Apostolidis, and T. Scarpas. 2018a. "Review of warm mix rubberized asphalt concrete: Towards a sustainable paving technology." J. Cleaner Prod. 177 (Mar): 302–314. https://doi.org/10.1016/j.jclepro.2017.12.245.

Wang, T., F. Xiao, X. Zhu, B. Huang, J. Wang, and S. Amirkhanian. 2018b. "Energy consumption and environmental impact of rubberized asphalt pavement." J. Cleaner Prod. 180 (Apr): 139–158. https://doi.org/10.1016/j.jclepro.2018.01.086.

Wei, K., Y. Wu, X. Cao, X. Yang, B. Tang, and B. Shan. 2023. "Dual dynamic bonds approach for polyurethane recycling and self-healing of emulsified asphalt." Sci. Total Environ. 885 (Aug): 163915. https://doi.org/10.1016/j.scitotenv.2023.163915.

Wool, R. P., and K. M. O'Connor. 1981. "A theory crack healing in polymers." J. Appl. Phys. 52 (Oct): 5953–5963. https://doi.org/10.1063/1.328526.

Xie, J., X. Zhao, Y. Zhang, F. Yu, H. Luo, X. Chen, and W. He. 2023. "Preparation of terminal blend/grafting activated crumb rubber composite modified asphalt based on response surface methodology." Front. Mater. 10 (May): 1193225. https://doi.org/10.3389/fmats.2023.1193225.

Xu, P., J. Gao, J. Pei, Z. Chen, J. Zhang, and R. Li. 2021. "Research on highly dissolved rubber asphalt prepared using a composite waste engine oil addition and microwave desulfurization method." Constr. Build. Mater. 282 (May): 122641. https://doi.org/10.1016/j.conbuildmat.2021.122641.

Yalcin, E. 2021. "Effects of microwave and induction heating on the mechanical and self-healing characteristics of the asphalt mixtures containing waste metal." Constr. Build. Mater. 286 (Jun): 122965. https://doi.org/10.1016/j.conbuildmat.2021.122965.

Yang, L., L. Tao, T. Zenglin, P. Jianzhong, Z. Mingliang, and W. Zhenguo. 2023. "Research on self-healing behavior of asphalt modified by polyurea elastomer containing dynamic disulfide/diselenide bond." Eur. Polym. J. 189 (May): 111990. https://doi.org/10.1016/j.eurpolymj.2023.111990.

Zhang, F., D. Wang, A. Cannone Falchetto, and Y. Cao. 2024a. "Microwave deicing properties and carbon emissions assessment of asphalt mixtures containing steel slag towards resource conservation and waste reuse." Sci. Total Environ. 912 (Feb): 169189. https://doi.org/10.1016/j.scitotenv.2023.169189.

Zhang, H., Y. Bai, and F. Cheng. 2018. "Rheological and self-healing properties of asphalt binder containing microcapsules." Constr. Build. Mater. 187 (Oct): 138–148. https://doi.org/10.1016/j.conbuildmat.2018.07.172.

Zhang, T., S. Gao, Y. He, R. Zhuang, X. Han, Z. Zou, and J. Yu. 2024b. "Investigation of microstructure, rheological property and self-healing performance of SBS modified bitumen with dynamic disulfide bonds prepared by one-step method." Constr. Build. Mater. 416 (Feb): 135158. https://doi.org/10.1016/j.conbuildmat.2024.135158.

Zhou, T., S. F. Kabir, L. Cao, H. Luan, Z. Dong, and E. H. Fini. 2020. "Comparing effects of physisorption and chemisorption of bio-oil onto rubber particles in asphalt." J. Cleaner Prod. 273 (Nov): 123112. https://doi.org/10.1016/j.jclepro.2020.123112.

Downloaded from ascelibrary.org by Jianying Yu on 03/17/25. Copyright ASCE. For personal use only; all rights reserved.

Journal of Building Engineering 71 (2023) 106500

Contents lists available at ScienceDirect

Journal of Building Engineering

journal homepage: www.elsevier.com/locate/jobe

Influence of slurry characteristics on the bubble stability in foamed concrete

Min Xiao [a], Fangxian Li [a,*], Pengfei Yang [b], Bin Li [c], Jiangxiong Wei [a], Qijun Yu [a]

[a] School of Materials Science and Engineering, South China University of Technology, 510640, Guangzhou, China
[b] Guangzhou Guangjian Construction Engineering Testing Center Co., Ltd, 510699, Guangzhou, China
[c] Institute of Materials and Surface Engineering, University of Lisbon, 1049-001, Lisbon, Portugal

ARTICLE INFO

Keywords:
Foamed concrete
Bubble film strength
Viscosity
Bubble stability

ABSTRACT

Foamed concrete is a porous material widely used in construction, but its production remains challenging due to bubble stability issues. To address these problems, this study analyzed the influence of bubble characteristics and paste viscosity on bubble stability in foamed concrete, specifically examining pore diameter distribution, collapse depth, and density deviation. Results showed that increasing the strength of the bubble film led to a decrease in the collapse depth of foamed concrete, along with a more uniform distribution of pores and a smaller average pore diameter, indicating improved bubble stability. Adequate viscosity in the cement paste was crucial for limiting the collapse and decreasing density deviation of foamed concrete, as well as ensuring a uniform distribution of early strains. Furthermore, the bubble duration remained unruptured for longer than the setting time of foamed concrete, which was necessary for bubbles to stay stable. A theoretical model of paste viscosity and bubble film strength, based on force analysis of bubbles in foamed concrete, was developed and can predict the required paste viscosity for bubble stability. This study provides important insights into the production of stable foamed concrete and offers a theoretical basis for future research in this area.

1. Introduction

Foamed concrete is a lightweight porous material formed by introducing a precast aqueous foam into cement paste or mortar. Foamed concrete is widely used in many engineering applications, such as precast or cast-in-situ wall elements, insulation screeds, facades, slabs, and the core of lightweight sandwich panels [1–3]. The advantages of the porous structure in insulation and filling applications are its low density, self-leveling ability, low cost, low thermal conductivity, and fire-resistant properties [4,5]. However, an improper pore structure can negatively affect foamed concrete's strength, density, permeability, and insulation properties, which severely limits the application of the foamed concrete [6,7]. As a result, the bubble stability that determined pore structure has become the focus of foamed concrete.

The bubble stability depends on the properties of the bubbles in the precursor foam and their subsequent stability during the fresh foamed cement [8]. The properties of the bubbles in the precursor foam are mainly controlled by the foaming agent, while the main factor influencing the subsequent stability of the bubbles is the slurry's characteristics [8]. The properties of foamed concrete slurries that affect the bubble stability mainly include the fresh foamed concrete slurry viscosity, particle adsorption, setting time, and other factors [9,10]. The resulting morphology of the foam tends to evolve with time due to the downward flow of the interstitial fluid caused

* Corresponding author.
E-mail address: msfxli@scut.edu.cn (F. Li).

https://doi.org/10.1016/j.jobe.2023.106500
Received 11 January 2023; Received in revised form 3 April 2023; Accepted 6 April 2023
Available online 11 April 2023
2352-7102/© 2023 Published by Elsevier Ltd.

by gravity (drainage), air exchange between bubbles (ripening), and film breakage (coalescence) [11–13]. After the bubbles are mixed with the cementitious matrix, the bubbles transfer into a liquid-solid suspension system, where the component substances of the bubble film are exchanged with the components of the surrounding suspended liquid (cementitious matrix) via interpenetration, which mainly include cement particles and their hydration products, admixture particles, and superplasticizers [14]. Together with the original foaming agent component, the substances can form a new bubble film, changing the thickness and strength of the bubble film and enhancing the bubble stability [15,16]. During the foamed concrete preparation process, the bubbles are subjected to various forces, including extrusion of the material particles and buoyancy provided by the paste. When the force acting on a bubble exceeds the bubble's ability to withstand, the bubble will coalesce and ripen [17]. The collapse of fresh foamed concrete is expected to be observed, resulting in a range of instabilities. However, few studies have focused on the process of foam dispersion in a cementitious matrix, a process that plays a key role in enhancing the bubble stability in foamed concrete. If the bubble can withstand various external forces before hardening, it can form homogeneous pores in the hardened foamed concrete [1]. However, the influences of individual rheological parameters on bubble stability are not widely understood.

To reduce the risks associated with foamed concrete in engineering applications, it is necessary to develop a suitable method to prevent the collapse of the foamed concrete. Therefore, this study investigated the effects of the surface tension and strength of the bubble film, the paste viscosity, and the setting time of foamed concrete slurry, on the foamed concrete stability. The appropriate viscosity of the cement paste estimated by the force analysis of bubbles in the mixing and hardening process was compared with experimental results and the estimation equation of the most suitable viscosity for bubble stability was identified. Finally, methods to improve the foamed concrete stability were discussed.

2. Materials and methods

2.1. Materials

2.1.1. Cementitious material

This study used ordinary Portland cement and fly ash (FA) as cementitious materials. FA was used in the content range of 5–20% as a cement replacement to increase the setting time. Table 1 shows the chemical compositions.

2.1.2. Surfactants

Several foaming agents were used to produce premade foams, including composite protein foaming agent, rosin foaming agent, dodecyl foaming agent, and lauric acid foaming agent. Table 2 shows the basic technical parameters of each foaming agent. The foaming agent was diluted with regular tap water at a volumetric ratio of 1:40. Then the solution was poured into a foaming generator to produce foam through compressed air.

To evaluate the effect of the setting time on the bubble stability, the accelerator provided by BSDI was used to adjust the setting time of the foamed concrete.

2.2. Foamed concrete preparation

The preparation of foamed concrete involved two steps: preparation of cement paste and mixture with premade foam. First, the cementitious material was dry mixed at low speed for 2 min by a planetary mixer. Then, water was added and mixed at a high speed for another 3 min to produce cement paste. Finally, cement paste and foam were mixed at a low speed for 0.5 min to prepare foamed concrete. The mix proportions of foamed concrete with a density of 600 kg m^{-3} were summarized in Table 3.

2.3. Experimental methods

2.3.1. Bubble stability in foamed concrete

To characterize the bubble stability, both the collapse depth and density deviation were measured.

(1) Experimental method for measuring collapse depth [18]: After mixing, the fresh foamed concrete was poured into a cylindrical beaker, and the initial height of the foamed concrete column was set to 100 mm. After 24 h, the foamed concrete column's final height was measured. The collapsed height was measured from the difference between the initial poured height (100 mm) and the height of the hardened sample. Measurement for collapse depths of foamed concrete is shown in Fig. 1.

(2) Experimental method of density deviation of foamed concrete: The foamed concrete was cut into upper and lower layers along the direction parallel to the forming surface (the thickness of the lower layer was always specified as 50 mm). In a water-saturated state, the volume of foamed concrete was measured by drainage, and the mass was measured after 24 h in an oven at 50 °C. Finally, the mass and volume of foamed concrete were used to calculate its density. The density deviations between the upper layer and the lower layer were compared. The smaller the deviation between the two densities was, the more stable the foamed concrete slurry was [19].

Table 1
Chemical characteristics of the cementitious materials w/%.

Material	SiO_2	Al_2O_3	Fe_2O_3	CaO	MgO	K_2O	Na_2O	SO_3	TiO_2	LOI	Other
Cement	21.80	4.97	2.36	62.69	1.67	0.62	0.21	2.90	0.11	1.73	0.93
Fly ash	48.14	34.63	4.01	2.83	0.95	0.41	0.85	0.33	1.44	5.97	0.44

Table 2
Technical parameters of foaming agents.

Types of foaming agent	Active ingredient formula	pH value	Bleeding for 1 h (ml)	Sedimentation distance for 1 h (mm)	Half-time for foam evolution (min)	Full-time for foam evolution (h)
Composite protein		7.9	66	8	86	6.5
Rosin		8.2	113	30	43	4.5
Dodecyl		8.0	116	31	46	4.0
Lauric acid		8.1	120	34	40	3.5

Table 3
Mix proportions of the 600 kg m^{-3}foamed concrete.

Design plastic density (kg m^{-3})	OPC (kg)	FA (kg)	Water/cement ratio	Foam (L)
600	720	0	0.4	50.7
	684	36		50.4
	648	72		50.2
	612	108		49.9
	576	144		49.7

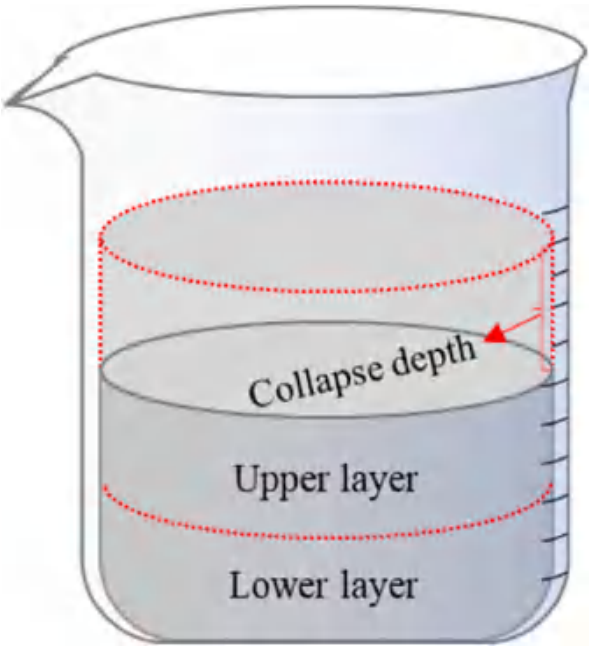

Fig. 1. Foamed concrete collapse depth measurement.

2.3.2. Surface tension

The bubble's surface tension was measured with a William Meter plate surface tension tester (model number DCAT21, Dataphsic, Germany).

2.3.3. Defoaming rate of foam

The foam was filled into a glass container and smoothed the surface within 30 s. The defoaming rate of the foam was obtained after 1 h by dividing the measured defoaming depth by the container height.

2.3.4. Strength of the bubble film

The tensile strength of the bubble film was measured using a self-made micro force tester at a displacement rate of 0.01 mm/min. A sample volume of 10 ml was used for the test, and the tensile fracture area was calculated by multiplying the fracture length by the

slurry thickness. The micro force tester had a range of 300 m • N with an accuracy of 0.1 m • N. The tensile strength device (self-made) is shown in Fig. 2.

2.3.5. Viscosity of the cement paste

The Brookfield RS-SST Viscosity Tester was used to measure the shear stress vs shear rate curves of the cement paste. The tester was outfitted with four rotors to obtain a wide range of the rheological parameters, with a 2% measurement accuracy. During the tests, the shear rate was ramped linearly from 0 to 300 s^{-1} over 60 s and then back to 0 s^{-1} at the same rate. The yield stress and viscosity values were obtained by fitting the shear stress vs shear rate curves to a suitable rheology model.

2.3.6. Strain behavior in plastic stage

Digital image correlation (DIC) is a robust, contact-free, and non-destructive technique used to measure displacements on the surface of an object [20]. Two high-resolution digital cameras were used to capture digital images of the sample deformation, and software was used to process these images and calculate the corresponding deformation distributions. This system consisted of two four-mega-pixel cameras with a maximal image resolution of 1.05 Mpx (1024 × 1024 pixels), and the relative angle of the cameras was 30°.

2.3.7. Setting time of foamed concrete

No standard method is available for determining the setting time of the foamed concrete. Some traditional test methods generally yield unstable measurement results and are difficult to repeat. The absence of free water inside the concrete is a sign of slurry setting, and the electrodeless resistivity measurement method is regarded as the best method for determining the free water consumption in the mixture. Therefore, the setting time of the foamed concrete was measured using a CCR-II electrodeless resistivity meter in the present research work. The resistivity curve of the foamed concrete is generally U-shaped, as shown in Fig. 3. When the U-shaped resistivity curve of foamed concrete reaches its lowest point, it is assumed that the free water in the slurry has been consumed and the foamed concrete has been set [21].

3. Results and discussion

3.1. Influence of surface tension and bubble film strength on the bubble stability

After the bubbles were uniformly mixed with the cement paste, the foaming agent component was adsorbed on the bubble films, influencing the surface tension of the bubbles. According to the bubble burst principle [22], for the bubble to be stable, the bubble film strength P must be greater than the pressure applied to it, $\Delta P > 2\sigma/r_0$; that is, $P_{wall} > 2\sigma/r_0$. In other words,

$$r_0 > \frac{2\sigma}{P_{wall}} \tag{1}$$

where P_{wall} represents bubble film strength, σ is the surface tension of the bubble and r_0 is the minimum stable bubble radius. Equation (1) shows that reducing the surface tension or strengthening the bubble film will result in a smaller limiting radius r_0 to ensure the bubble stability, which will decrease the defoaming tendency and make the bubbles more stable. Different foams made of four foaming agents were added to the cement paste separately, mixed, and stirred to prepare a fresh foamed concrete slurry with a plastic density of 600 kg • m^{-3}. The surface tension and the tensile strength of the cement paste were measured. Table 4 displays the surface tension values of the different foaming agents, the tensile strength of thin-layer cement paste, the minimum radius of the stable bubble, and the defoaming rate of the foam corresponding to different foaming agents.

The foamed concrete slurries prepared with four foaming agents had a maximum surface tension of 57.883 m • N/m, much lower than the cement paste's surface tension of 68.809 m • N/m, indicating that surfactants contained in the foaming agent could

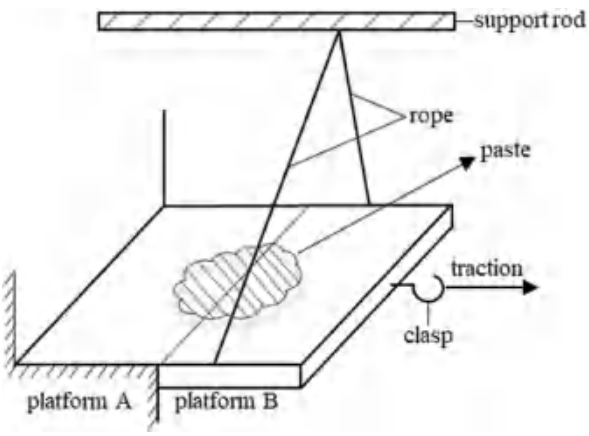

Fig. 2. Tensile testing device for thin layer cement paste.

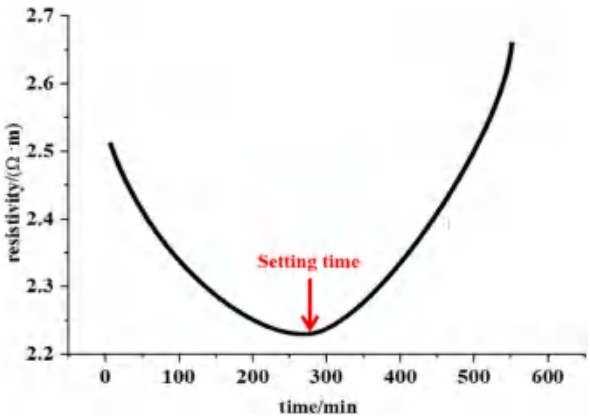

Fig. 3. U-shaped resistivity curve.

Table 4
Performance parameters of the foams prepared with different foaming agents.

Foaming agent type	Surface tension (m • N/m)	Bubble film strength (Pa)	Minimum stable bubble radius (mm)	Defoaming rate (%)
Lauric acid	41.977	305.4	0.27	42.5
Dodecyl	33.113	321.6	0.21	33.3
Rosin	35.406	340.8	0.21	29.6
Composite protein	57.883	682.5	0.17	22.1

significantly reduce the surface tension of the cement paste. The cement paste with the dodecyl group agent had the lowest surface tension. In contrast, the cement paste with the composite protein foaming agent had the highest surface tension and bubble film strength. The paste was prepared with lauric acid foaming agents, which had the lowest bubble film strength. According to a previous study [23], active substances with higher molecular weight are more favorable for bubble film strength. However, the result showed that although the molecular weight of lauric acid was greater than that of dodecyl, the film strength of the bubbles prepared from lauric acid was smaller. This phenomenon was thought to be caused by lauric acid has fewer side chains and a lack of adsorbable sites in the bubble film [24]. The composite protein foaming agent had the largest molecular weight and a complex molecular structure, which allowed it to effectively adsorb on the surface of the bubble film to enhance the strength of the bubble film. This could explain why the foam prepared with the composite protein foaming agent had the highest bubble film strength.

Table 4 shows the influence of surface tension and bubble film strength on the bubble stability. As a result of the composite protein foaming agent's strong strengthening effect on the bubble film, even with the highest surface tension, the foam exhibited high stability, with the smallest stable bubble radius of 0.17 mm and the lowest defoaming rate of 22.1%. As surface tension and bubble film strength increased together, bubble stability could still be improved, indicating that bubble film strength was more critical than the surface tension for bubble stability. Fig. 4 shows that the foamed concrete prepared with the composite protein foaming agent had more regular and uniform pores, with pore sizes mainly between 0.3 mm and 0.5 mm. In contrast, most of the pore diameters of the foamed concrete samples prepared using the other three foaming agents were greater than 0.5 mm, indicating that the foam prepared with the composite protein foaming agent was more stable against draining and ripening.

3.2. *Effect of paste viscosity on bubble stability*

To weaken the negative effects of foaming agents on bubble stability, foamed concrete prepared from composite protein foaming agents was used in the subsequent experiment. The density deviation between the upper and the lower foamed concrete layer, and the collapse depth were tested for different paste viscosities, as shown in Fig. 5. Increasing the paste viscosity from 0.2104 to 0.7662 Pa • s resulted in a gradual decrease in the collapse depth of the foamed concrete, and an increase in collapse depth was observed when the viscosity increased from 0.7662 to 2.1542 Pa • s. In cases where the viscosity was 0.7662 Pa • s, there was almost no collapse. Lowering the paste viscosity resulted in a greater density deviation between the upper and the lower foamed concrete layers (see Fig. 5). The low viscosity resulted in weak viscous resistance, allowing bubbles to easily float in foamed concrete slurry, which caused an increase in the density of the lower layer and a decrease in the density of the upper layer. The density deviation between the upper and the lower foamed concrete layers tended to vary less and stayed stable when the paste viscosity exceeded 0.7662 Pa • s. As can be seen from Fig. 5, when the paste viscosity was within a range of 0.7662–1.35 Pa • s, the density deviation of the upper and lower layers was small, and both met the design grade requirements of foamed concrete. Furthermore, the collapse depth was less than 10 mm, indicating more stability of the bubble.

During the hardening process, the strain distribution and pore structures in the foamed concrete were noticeably affected by the drainage and ripening of the bubble [25]. After 8 h of hardening, the strain distribution diagram of the foamed concrete with different paste viscosities was obtained by the DIC method, as shown in Fig. 6. When the paste viscosity was 1.8743 Pa • s, the strain direction in

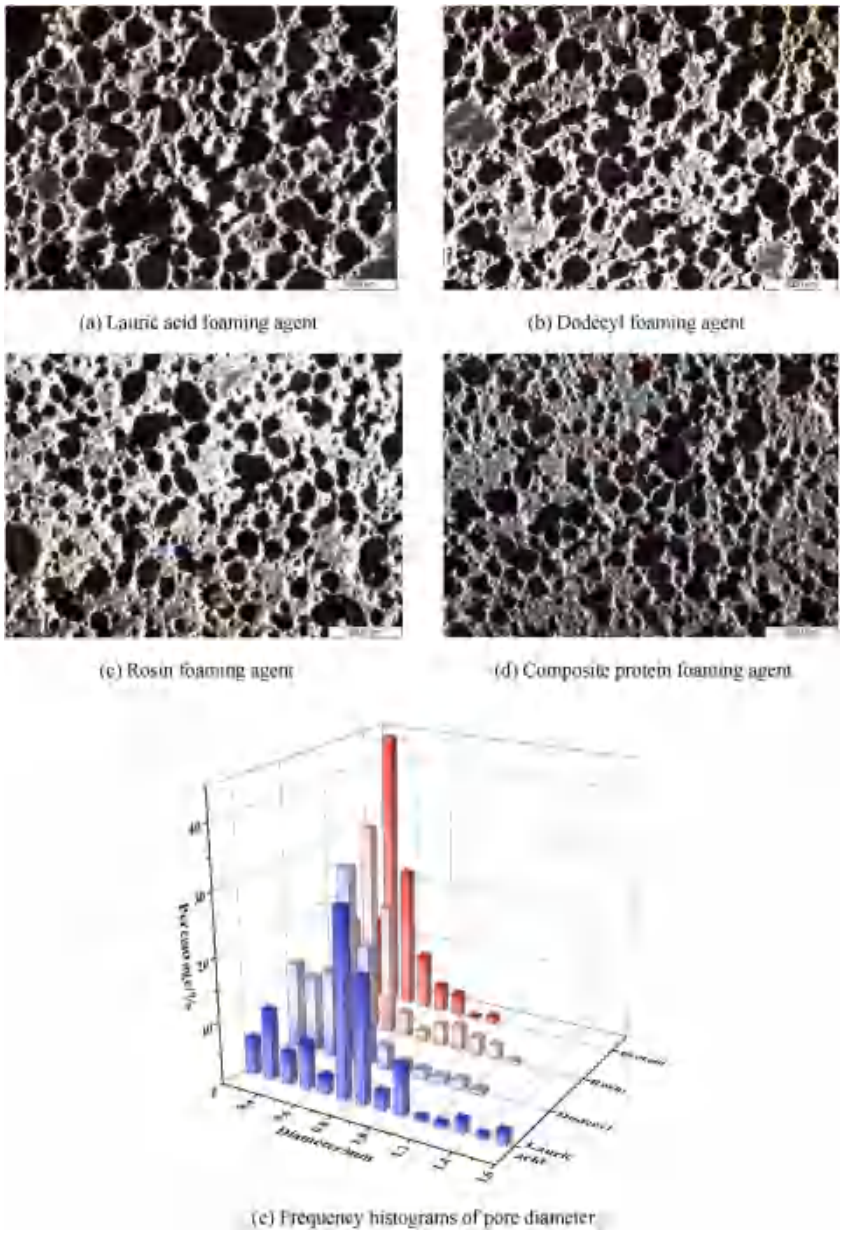

Fig. 4. Pore distribution observation of the foamed concrete prepared by different foaming agents.

the observation region was disordered and inhomogeneous, indicating an irregular change in the morphology and distribution of the bubbles. With a viscosity of 0.7662 Pa • s, the strain direction in the observation region of the specimen was consistent and homogeneous, indicating that bubbles were homogeneously distributed throughout the sample. The strain directions were upward in the upper observation region and downward in the lower observation region when paste viscosity was 0.4613 Pa • s. The viscous force of a low-viscosity paste cannot resist the buoyancy of the bubbles, resulting in the bubbles floating up and the cement paste sinking. As a result, the strain directions were inconsistent, and the distribution was inhomogeneous.

According to the bubble liquid film discharge rate equation $V = \rho g h^2/(8\eta)$ (where ρ, g, h, and η represent the density of the liquid phase, the gravitational acceleration constant, the liquid film thickness, and the liquid phase viscosity, respectively), the viscosity of the liquid phase affected the discharge rate of the liquid film and determined the stability of bubbles. Increasing the viscosity of the liquid phase will slow the discharge rate of the liquid film and make the bubbles more stable. However, if the paste viscosity is too high, the bubbles must overcome massive viscosity resistance during dispersion, resulting in severe defoaming. As a result, the paste should be adjusted to an appropriate viscosity to ensure that the bubbles are uniformly dispersed and stable.

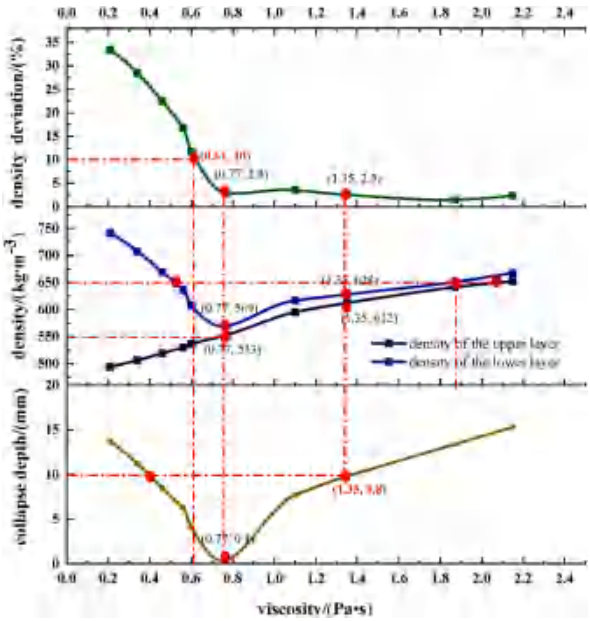

Fig. 5. Effect of viscosity on the stability of foamed concrete density deviation.

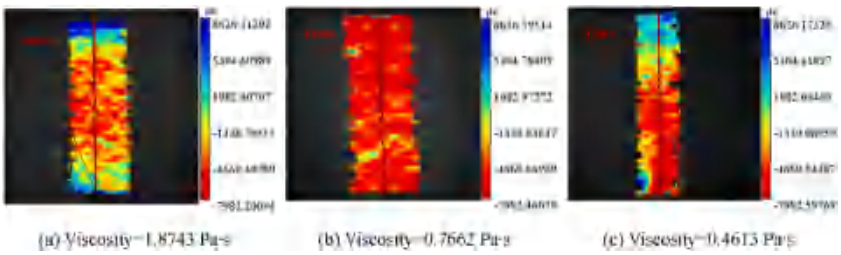

Fig. 6. Effect of the paste viscosity on the strain in the Y-direction of foamed concrete measured using digital image correlation.

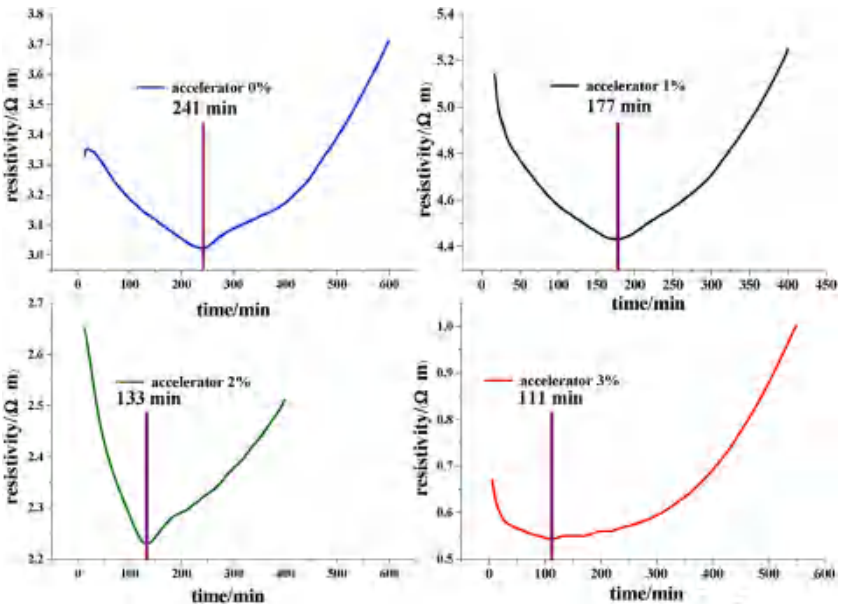

Fig. 7. Resistivity curves of foamed concrete with different dosages of accelerator.

3.3. Effect of setting time on the bubble stability

A variety of setting times were achieved by adjusting the contents of accelerator and FA in the foamed concrete. As a result of measuring the collapse depth of the foamed concrete under different setting times, the effect of the setting time on the bubble stability was investigated.

3.3.1. Effect of the accelerator and FA contents on the setting time

The resistivity curves of the foamed concrete slurry with 0%, 1%, 2%, and 3% accelerator content were shown in Fig. 7. The lowest points of the resistivity U-shaped curve were at 241, 177, 133, and 111 min. The initial setting time of the foamed concrete was determined to be the lowest point of the U-shaped resistivity curve. The foamed concrete sets faster with an increased accelerator content.

The resistivity curves of the foamed concrete with 5%, 10%, 15%, and 20% FA contents are shown in Fig. 8. The lowest points of the resistivity U-shaped curve were at 259, 283, 317, and 393 min. Increasing the FA content from 5% to 20% delayed the setting time of foamed concrete from 259 to 393 min.

3.3.2. Relationship between setting time and bubble stability

A comparison of depths of the foamed concrete at different setting times is shown in Fig. 9. The collapse depth was less than 10 mm when the setting time was less than 133 min, and the collapse depth increased with the increase in the setting time. Thus, a long setting time did not promote bubble stability. The necessary condition for the stable existence of bubbles in foamed concrete is that the time bubbles remain unburst is not less than the setting time of slurry. Bubble stability can be improved by accelerating the setting time through various methods, such as using rapid-hardening cement or adding the accelerator to the foamed concrete.

3.4. Theoretical analysis for bubble stability in foamed concrete

3.4.1. Force analysis of bubbles

The force analysis of bubbles in foamed concrete is based on the following assumptions:

1) The paste is a uniform liquid; 2) the bubble in the slurry is perfectly spherical elastomers and the external force is uniformly transmitted to the gas through the bubble wall; 3) the internal pressure of the bubbles is uniform everywhere. Based on the above assumptions, the force model schematic of a bubble under the hardening and mixing processes is presented in Fig. 10.

Each bubble in the slurry acts like an inflated balloon during the hardening process, which is subjected to the following forces: 1) a gravitational force G_0 (mainly bubble wall weight), 2) slurry buoyancy force F_{slurry} ,3) a viscous force of the slurry on a static bubble $F_{\eta 1}$ and a viscous resistance force of the slurry on a bubble in motion $F_{\eta 2}$, 4) atmospheric pressure F_{atm}. When these forces reach an equilibrium state, the bubbles stabilize at a certain depth in the slurry. A change in the equilibrium state may cause bubbles to rise and expand or even burst. Therefore, the bubbles' suspension state is very important for their stability at a given depth. The following equation can be used to calculate the gas pressure in a bubble:

$$P_{internal} = P_{atm} + \frac{2\sigma}{r_1} + \rho_{slurry} gh. \tag{2}$$

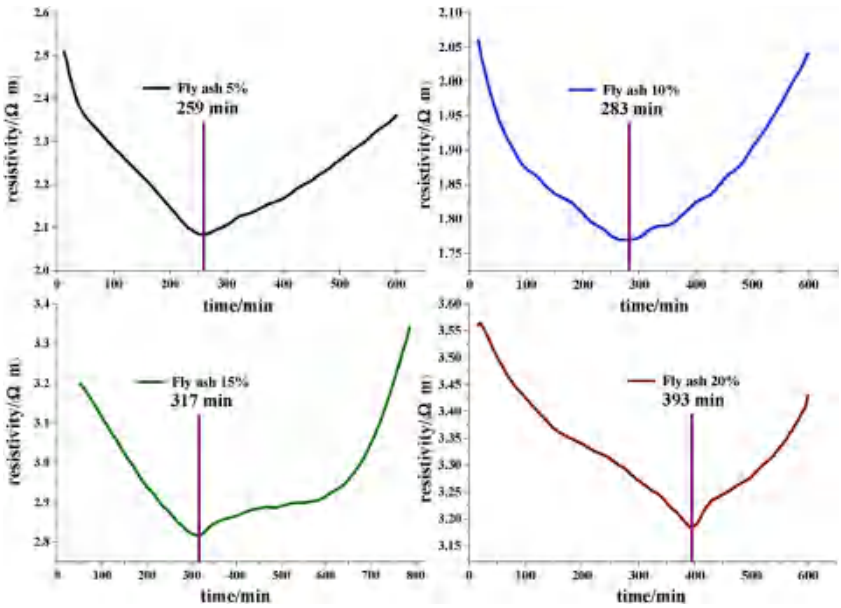

Fig. 8. Resistivity curves of foamed concrete with different dosages of fly ash.

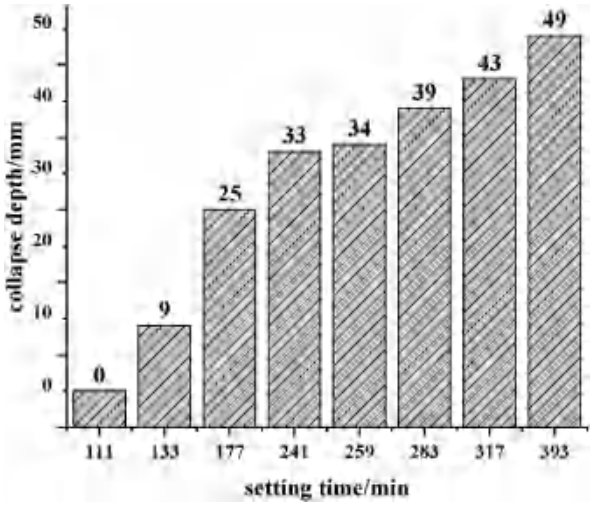

Fig. 9. Relationship between the collapse depth and the setting time of the slurry.

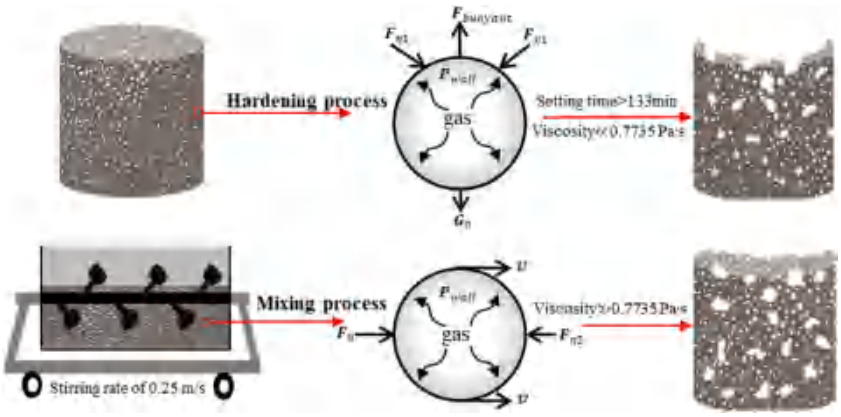

Fig. 10. Two-dimensional schematic representations of the instability mechanism of foamed concrete.

where σ represents the surface tension of the cement paste, r is the bubble radius, ρ_{slurry} refers to the density of foamed concrete slurry, and h represents the depth of the bubble in the slurry. Equation (2) shows that as the depth h of the bubbles in the slurry increases, the pressure of the gas inside the bubble will increase, causing the bubbles at this depth to become unstable. Larger bubbles will form by merging bubbles at depth h to prevent the bubbles from collapsing. However, larger bubbles have greater buoyancy, which makes them more likely to float. The bubble's floatability is independent of atmospheric pressure at a certain depth in the slurry, as expressed by the following equation:

$$F_{buoyant} = F_{\eta 1} + G_0. \tag{3}$$

Inserting the bubble radius and the density into Equation (3) yields the following equation:

$$\left(\rho_{slurry} - \rho_{bubble}\right) \bullet \frac{4\pi g r^3}{3} = F_{\eta 1}. \tag{4}$$

It can be seen from Equation (3) that, the greater the self-weight G_0 of the bubbles, or the greater the $F_{\eta 1}$ of slurry, the less likely the bubbles are to float. Whether bubbles float in foamed concrete with the same density is primarily determined by the paste viscosity. The viscous force on the bubble is related to the viscosity of the cement paste. By increasing the viscosity, the viscous force increases, preventing the rising of bubbles (buoyancy) and ripening. The forces will be in nonequilibrium if the sum of the viscous force and the bubble's gravitational force is less than the buoyancy force. The bubble's rising velocity V_T is consistent with the Stokes motion equation [26].

$$V_T = \frac{2gr^2\left(\rho_{slurry} - \rho_{bubble}\right)}{9\eta}. \tag{5}$$

where r is the bubble radius; ρ_{slurry} represents the density of the paste; ρ_{bubble} represents the density of the bubble (including the bubble film), and η refers to the paste viscosity. Based on the Stokes motion equation, a larger bubble radius results in a faster bubble rise. After the bubbles begin rising, the force acting on them gradually decreases, causing them to expand and grow in radius. Equation (4) indicates that as the bubble radius increases, the buoyancy force also increases, and the bubbles will rise faster until they are sufficiently buoyant to float to the surface and burst. Ultimately, foamed concretes is destroyed by this process.

Equation (5) shows that a higher paste viscosity (viscosity resistance) means a slower bubble rise and a more stable slurry. Moreover, it demonstrates that the bubble stability depends heavily on the paste viscosity.

$$6\pi\eta vr = F_{\eta 2} \leq P_{wall} \bullet \pi r^2, \tag{6}$$

$$\eta \leq \frac{r \bullet P_{wall}}{6v}. \tag{7}$$

When bubbles are mixed with the cementitious paste, the bubble stability is mainly determined by the viscous resistance of the base mix ($F_{\eta 2}$) and the stirring thrust of the mixing machine (F_0). The force model of the bubble is shown in Fig. 10. Considering that the bubble's force section is circular, the slurry's viscous resistance and bubble wall strength should satisfy Equation (6) to ensure that the bubble is evenly dispersed and unruptured. In the above equation, v is the shear rate of the agitator blades during the mixing process. By combining Equations (1) and (6), it is determined that the bubbles will be uniformly dispersed when the paste viscosity satisfies Equation (7). Based on the assumption that the bubbles are evenly distributed, the higher the paste viscosity is, the better the bubble stability becomes. Therefore, we can calculate the most suitable viscosity for improving the bubble stability.

Foamed concrete prepared by a composite protein foaming agent as an example. The agitator blade's shear rate was 0.25 m/s, and the bubble film strength was 682.5 Pa. The most suitable viscosity was determined to be 0.7735 Pa • s based on Equation (7) and Table 3, which was in general agreement with the measured result of the critical viscosity to prevent collapse in the studied slurry.

3.4.2. Condition of bubbles stability

The ability of a bubble to float depends on its gravitational force G_0 (mainly the bubble film weight), the paste buoyancy (hydrostatic pressure) $F_{buoyant}$, and the paste's viscous resistance F_η. When the self-weight of the bubbles was larger, the paste viscosity was greater. The bubble had more difficulty floating and hence was more stable in a certain depth of the slurry. The buoyancy was determined by the density of the paste and the bubble diameter. A higher-density paste and a larger bubble diameter would have a higher buoyancy, making the bubbles float more easily. However, an increase in paste density led to an increase in paste viscosity, making it more excellent resistance to bubble floating. This suggests that whether the increase in the slurry density will cause the bubbles to float is determined by a comprehensive competition effect between the buoyancy and viscosity resistance acting on the bubbles.

However, bubbles do not always burst when floating. While bubbles rise and expand, the bubble films can resist external forces regardless of the bubble size. Meanwhile, as the bubbles float slowly, the base mix begins to set. However along with the hydration, the hydration products continuously overlap to form a gel structure, enhancing the bubble wall strength. Furthermore, the paste viscosity increases, and the viscous resistance slows the speed of the floating bubbles and improves their stability. A stable existence of bubbles in the slurry means that the time bubbles remain unburst is not less than the setting time of the slurry. Therefore, the shorter setting time benefits the stability of the foamed concrete.

The bubble stability was influenced by the paste viscosity. As the paste viscosity increased, the bubble film became stronger, and the bubbles were less likely to burst and spread. However, an excessive paste viscosity prevented the bubbles and cementitious materials from dispersing, which resulted in loose (buoyancy) structures and higher densities than designed, as shown in Fig. 11a. A slurry with a lower viscosity was more conducive to the dispersion of bubbles, but the bubbles were prone to merging and migrating during the setting and hardening of the slurry. Merging and migration caused the bubble size to vary, resulting in an uneven distribution of the bubble sizes. It was evident from Fig. 11c that the bubbles on the upper parts of the foamed concrete sample were larger than those in the lower parts. The above analysis indicated that there was a threshold for the paste viscosity at which the material was uniformly dispersed and bubbles had difficulty merging and migrating. Therefore, the paste viscosity could be adjusted to a threshold, as shown in Fig. 11b, to produce foamed concrete with small and uniform pores.

4. Conclusion

The study investigated the factors affecting bubble stability in foamed concrete and found that bubble properties, paste viscosity, and setting time all play critical roles. Four different foaming agents were employed to create foams with varying characteristics, and the impact of these characteristics on bubble stability was analyzed. To better characterize bubble stability, we measured the pore size distribution, collapse depth, density deviation, and strain distribution of the foamed concrete. Moreover, we compared the density deviation and strain distribution of foamed concrete to analyze the effects of paste viscosity and setting time on bubble stability. Additionally, a theoretical model for paste viscosity and bubble film strength was established through force analysis of the bubbles in the foamed concrete. The main conclusions are as follows:

(1) Foams prepared with the composite protein foaming agent were more stable than those prepared with the other foaming agents, including rosin, dodecyl, and lauric acid foaming agent. The minimum stable bubble radius can be determined by the surface tension and the bubble film strength. Reducing the surface tension or strengthening the bubble film will decrease defoaming

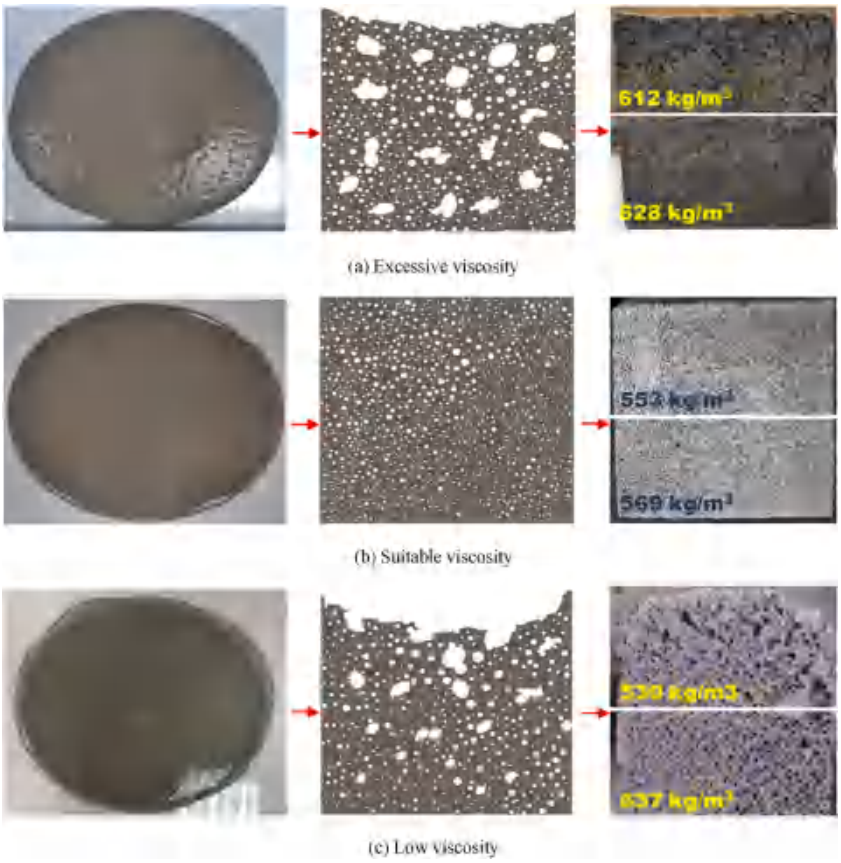

Fig. 11. Effect of viscosity on the pore state of foamed concrete.

tendency and make the bubbles more stable. The collapse depth of foamed concrete decreases as the strength of the bubble film increases, with a more uniform distribution of pores and a smaller average pore diameter, indicating better bubble stability.

(2) Adequate viscosity in the cement paste is crucial to achieving bubble stability in foamed concrete. During the bubble dispersion stage, a lower slurry viscosity is conducive to promoting bubble dispersion, while higher slurry viscosity during the hardening stage prevents the bubble from floating. As a result, a critical viscosity threshold exists to ensure bubble stability in foamed concrete. In this study, when the paste viscosity was in the range of 0.61–1.35 Pa • s, the collapse of foamed concrete and the density deviation at various heights were within 10%, and the early strains were evenly distributed.

(3) The bubble duration remained unruptured for longer than the setting time of foamed concrete, which is essential for bubble stability in foamed concrete. Assuming an appropriate setting time, the required paste viscosity for stabilizing bubbles in foamed concrete can be predicted using Equation $\eta \leq \frac{r \bullet P_{wall}}{6v}$, which agrees with the critical viscosity measured experimentally. These findings have important implications for the design of foamed concrete and the development of new foaming agents.

Credit author statement

Original draft preparation, experimentation and data analysis, Min Xiao; reviewing and editing, Fangxian Li; experimentation, Pengfei Yang, Bin Li; conceptualization and supervision, Jiangxiong wei and Qijun Yu.

All authors have read and agreed to the published version of the manuscript.

Declaration of competing interest

The authors declare that they have no known competing financial interests or personal relationships that could have appeared to influence the work reported in this paper.

Data availability

Data will be made available on request.

Acknowledgments

The authors would like to thank the financial support by the Program Fund of Non-Metallic Excellence and Innovation Center for Building Materials (2022SFP4-1), the Natural Science Foundation of Guangdong Province [grant number 2021A1515010719]. The authors would also like to thank Mr. Zhangmin Zhang for its linguistic assistance during the preparation of this manuscript.

References

[1] K. Dhasindrakrishna, S. Ramakrishnan, K. Pasupathy, et al., Collapse of fresh foam concrete: mechanisms and influencing parameters, Cem. Concr. Compos. 122 (2021), 104151, https://doi.org/10.1016/j.cemconcomp.2021.104151.
[2] M.R. Jones, A. McCarthy, Preliminary views on the potential of foamed concrete as a structural material, Mag. Concr. Res. 57 (2005) 21–31, https://doi.org/10.1680/macr.2005.57.1.21.
[3] P.J. Tikalsky, J. Pospisil, W. MacDonald, A method for assessment of the freeze–thaw resistance of preformed foam cellular concrete, Cement Concr. Res. 34 (2004) 889–893, https://doi.org/10.1016/j.cemconres.2003.11.005.
[4] Y.H.M. Amran, N. Farzadnia, A.A. Abang Ali, Properties and applications of foamed concrete; a review, Construct. Build. Mater. 101 (2015) 990–1005, https://doi.org/10.1016/j.conbuildmat.2015.10.112.
[5] E.P. Kearsley, P.J. Wainwright, The effect of porosity on the strength of foamed concrete, Cement Concr. Res. 32 (2002) 233–239, https://doi.org/10.1016/S0008-8846(01)00665-2.
[6] M.R. Jones, K. Ozlutas, L. Zheng, Stability and instability of foamed concrete, Mag. Concr. Res. 68 (2016) 542–549, https://doi.org/10.1680/macr.15.00097.
[7] E.K.K. Nambiar, K. Ramamurthy, Air-void characterisation of foam concrete, Cement Concr. Res. 37 (2007) 221–230, https://doi.org/10.1016/j.cemconres.2006.10.009.
[8] B. Feneuil, N. Roussel, O. Pitois, Optimal cement paste yield stress for the production of stable cement foams, Cement Concr. Res. 120 (2019) 142–151, https://doi.org/10.1016/j.cemconres.2019.03.002.
[9] A. Bagheri, S.A. Samea, Parameters influencing the stability of foamed concrete, J. Mater. Civ. Eng. 30 (2018), 04018091, https://doi.org/10.1061/(asce)mt.1943-5533.0002290.
[10] K. Dhasindrakrishna, K. Pasupathy, S. Ramakrishnan, et al., Effect of yield stress development on the foam-stability of aerated geopolymer concrete, Cement Concr. Res. 138 (2020), 106233, https://doi.org/10.1016/j.cemconres.2020.106233.
[11] C. Krämer, M. Schauerte, T.L. Kowald, Three-phase-foams for foam concrete application, Mater. Char. 102 (2015) 173–179, https://doi.org/10.1016/j.matchar.2015.03.004.
[12] I. Lesov, S. Tcholakova, N. Denkov, Drying of particle-loaded foams for production of porous materials: mechanism and theoretical modeling, RSC Adv. 4 (2014) 811–823, https://doi.org/10.1039/c3ra44500c.
[13] F.G. Gandolfo, H.L. Rosano, Interbubble gas diffusion and the stability of foams, J. Colloid Interface Sci. 194 (1997) 31–36, https://doi.org/10.1006/jcis.1997.5067.
[14] K. Ramamurthy, E.K. Kunhanandan Nambiar, G. Indu Siva Ranjani, A classification of studies on properties of foam concrete, Cem. Concr. Compos. 31 (2009) 388–396, https://doi.org/10.1016/j.cemconcomp.2009.04.006.
[15] M. Jones, A. McCarthy, Utilising unprocessed low-lime coal fly ash in foamed concrete, Fuel 84 (2005) 1398–1409, https://doi.org/10.1016/j.fuel.2004.09.030.
[16] S. Guignot, S. Faure, M. Vignes-Adler, et al., Liquid and particles retention in foamed suspensions, Chem. Eng. Sci. 65 (2010) 2579–2585, https://doi.org/10.1016/j.ces.2009.12.039.
[17] J.B. Joshi, K. Nandakumar, G.M. Evans, et al., Bubble generated turbulence and direct numerical simulations, Chem. Eng. Sci. 157 (2017) 26–75, https://doi.org/10.1016/j.ces.2016.03.041.
[18] S. Ghorbani, S. Ghorbani, Z. Tao, Effect of magnetized water on foam stability and compressive strength of foam concrete, Construct. Build. Mater. 197 (2019) 280–290, https://doi.org/10.1016/j.conbuildmat.2018.11.160.
[19] W. She, Y. Du, C. Miao, Application of organic- and nanoparticle-modified foams in foamed concrete: reinforcement and stabilization mechanisms, Cement Concr. Res. 106 (2018) 12–22, https://doi.org/10.1016/j.cemconres.2018.01.020.
[20] Y.F. Niu, H.L. Huang, J.X. Wei, Investigation of fatigue crack propagation behavior in steel fiber-reinforced ultra-high-performance concrete (UHPC) under cyclic flexural loading, Compos. Struct. 282 (2022), 115126, https://doi.org/10.1016/j.compstruct.2021.115126.
[21] S. Wei, Y.S. Zhang, M.R. Jones, Using the ultrasonic wave transmission method to study the setting behavior of foamed concrete, Construct. Build. Mater. 51 (2014) 62–74, https://doi.org/10.1016/j.conbuildmat.2013.10.066.
[22] P.G. Ashmpre, E.B. Smith, G.C. Bond, Annual reports on the progress of chemistry: general and physical chemistry, Annu. Rep. Prog. Chem. 63 (1966) 11–128, https://doi.org/10.1039/AR9666300011.
[23] K. Ramamurthy, Relative assessment of density and stability of foam produced with four synthetic surfactants, Mater. Struct. 38 (2010) 621–626, https://doi.org/10.1617/s11527-010-9582-z.
[24] A.H. Martin, K. Grolle, M.A. Bos, et al., Network forming properties of various proteins adsorbed at the air/water interface in relation to foam stability, J. Colloid Interface Sci. 254 (2002) 175–183, https://doi.org/10.1006/jcis.2002.8592.
[25] B. Feneuil, P. Aimedieu, M. Scheel, Stability criterion for fresh cement foams, Cement Concr. Res. 125 (2019), 105865, https://doi.org/10.1016/j.cemconres.2019.105865.
[26] D. Kd, R. H, D. F, et al., Stokes flow caused by the motion of a rigid sphere close to a viscous interface, Chem. Eng. Sci. 53 (1998) 3413–3434, https://doi.org/10.1016/S0009-2509(98)00137-7.

包裹法预处理再生 EPS 颗粒的工艺优化研究★

李方贤[1]，冯瑞琦[1]，张祖聪[1]，杨鹏飞[2]，韦江雄[1]

（1. 华南理工大学材料科学与工程学院，广州 510640）

（2. 广州广检建设工程检测中心有限公司，广州 510699）

摘　要：针对再生 EPS 颗粒与水泥基材料界面结合较差、容易上浮现象的问题，本研究提出了裹浆复合二次裹颗粒预处理再生 EPS 颗粒的方法。制备不同环氧树脂掺量的水泥浆对 EPS 颗粒进行包裹，分散颗粒选用粉煤灰、分散颗粒与 EPS 体积比为 1:18、环氧树脂掺量为 1%-2%、料浆的流动度在 120-180mm、包裹层厚度在 0.12-0.16mm 时具有较佳的包裹效果，包裹层与再生 EPS 颗粒间界面过渡区结合紧密；相比未包裹的再生 EPS 颗粒，裹浆复合二次裹颗粒预处理再生 EPS 颗粒掺入水泥基材料，抗压强度可提升 30%以上。

关键词：再生 EPS 颗粒；包裹法；环氧树脂；流动度

中图分类号：TU528.2　　**文献标识码：A**　　**文章编号：**1671-2439(2023)05-089-04

作者简介：李方贤（1979—），男，博士研究生，副教授，主要从事水泥基复合材料方面的研究，E-mail：msfxli@scut.edu.cn。

Process Optimization Study of Encapsulation Method for Pre-treatment of Recycled EPS Particles

LI Fang-xian[1]，FENG Rui-qi[1]，ZHANG Zu-cong[1]，YANG Peng-fei[2]，WEI Jiang-xiong[1]

（1. College of Materials Science and Engineering, South China University of Technology, Guangzhou 510640)

（2. Guangzhou Guangjian Construction Engineering Testing Center Co., Ltd, Guangzhou 510699)

Abstract: The inadequate interface bonding and tendency to float of recycled EPS (Expanded Polystyrene) particles in cementitious materials are significant challenges. To address these issues, a method involving the pre-encapsulation of recycled EPS particles with a dual coating was proposed. The encapsulation process involved the preparation of cement slurry with different epoxy resin dosages for wrapping the EPS particles. The dispersed particles used were fly ash, with a volume ratio of dispersed particles to EPS of 1:18. Optimal encapsulation effectiveness was achieved with epoxy resin dosages ranging from 1% to 2%, slurry flowability maintained between 120 and 180mm, and an encapsulation layer thickness of 0.12-0.16mm. The encapsulation layer exhibited a tight interface transition zone between the coating and the recycled EPS particles. Compared to non-encapsulated recycled EPS particles, Incorporation of pre-encapsulated secondary coated recycled EPS particles into cementitious materials resulted in a significant increase of over 30% in compressive strength.

Keywords: recycled EPS particles; encapsulation method; epoxy resin; flowability

聚苯乙烯(EPS)泡沫是一种高分子聚合物，在保温隔热、包装减震、装修、饮食等众多领域受到广泛运用[1-2]。然而，大量 EPS 颗粒在使用完后都被丢弃，造成极大的资源浪费和环境污染。因此，回收和资源化利用废弃 EPS 泡沫成为了当务之急。目前，国内外针对废弃 EPS 的处理方法包括焚烧法、填埋法、热分解制油法、塑料再生法等[3]。焚烧法和填埋法会对环境造成二次污染。而利用其作为燃料回收热能或采用塑料再生法等方式则成本高，缺乏实际可行性。因此，寻找更有效、环保且可行的废弃 EPS 泡沫处理方法具有重要意义。将废弃 EPS 回收，经破碎处理使其变成直径小于 5mm 的颗粒，掺入到水泥基材料中可制备成水泥基轻质保温材料应用于建筑保温工程中，不仅成本低且制备工艺简单，开辟再生 EPS 的建材资源化途径具有重要意义[4-6]。但目前的研究发现，随着 EPS 的掺入，水泥基材料保温隔热性能得到了较好的提升，但力学性能有大幅度降低[7-9]。由于 EPS 颗粒表面憎水，与水泥基材料结合较差，而且 EPS 在水泥基材料中容易产生上浮现象，导致分布不均匀，影响了掺 EPS 水泥基材料的力学性能。当前研究的主要方向是通过

基金项目：非金属材料创新中心应用示范类项目（2022SFP4-1）

(C)1994-2023 China Academic Journal Electronic Publishing House. All rights reserved.　http://www.cnki.net

对再生 EPS 改性或预包裹处理，以提高其与水泥基材料粘结性和分布的均匀性，确保其性能和应用的可靠性[10-11]。

本研究提出了裹浆复合二次裹颗粒预处理再生 EPS 颗粒的方法，采用撒小粒径的分散颗粒方法，在新包裹 EPS 颗粒的外层二次包裹上一层分散颗粒，避免相互粘结；采用环氧树脂改性水泥基材料，提升包裹层料浆的性能。研究了裹浆复合二次裹颗粒预处理再生 EPS 颗粒工艺条件，以及裹浆复合二次裹颗粒预处理再生EPS颗粒对水泥基材料抗压强度的影响。

1 试验原材料与方法

1.1 原材料

水泥为 PO42.5 普通硅酸盐水泥，基本性能如表 1 所示；粉煤灰为Ⅱ级粉煤灰，化学组成见表 2；树脂为普通环氧树脂；砂为白色石英砂，325 目；再生 EPS 颗粒为佛山市亿腾贸易有限公司生产，为 A-2 型号，颗粒粒径为 4-5mm，密度为 20kg/m^3；减水剂为聚羧酸减水剂，固含量为 33.4%。

表 1 P.O425 普通硅酸盐水泥基本性能

水泥品种	比表面积 /m^2·kg^{-1}	标准稠度用水量/%	凝结时间/min		抗折强度/MPa		抗压强度/MPa	
			初凝	终凝	3d	28d	3d	28d
OPC	360.0	26.2	217	272	5.7	8.1	28.9	44.6

表 2 粉煤灰的化学组成（wt.%）

种类	SiO_2	Al_2O_3	Fe_2O_3	K_2O	CaO	MgO	烧失量
含量	49.18	28.49	6.84	1.43	9.45	0.68	0.66

1.2 试验原材料配合比

包裹浆体的基础配合比（质量比）为水泥:水:减水剂:再生 EPS=42:17:0.04:5，环氧树脂掺量为水泥质量的 1%～3%。再生 EPS 水泥基材料设计容重为 1000kg/m^3，基础配比（质量比）为水泥:水:减水剂:再生 EPS=70:28:0.07:0.73。由于包裹后 EPS 外有一层水泥壳，在计算时需要扣除这部分质量。

1.3 性能表征

使用 SEM 观察包裹层与 EPS 的界面粘结效果。采用排水法测量包裹层厚。成型 100mm×100mm ×100mm 的试块，测试样品 3d、7d、28d 强度。

2 试验结果与讨论

2.1 裹浆复合二次裹颗粒预处理 EPS 颗粒工艺过程

借助于“包水饺时在水饺外层撒面粉防止水饺粘在一起”的思路，本研究提出了裹浆复合二次裹颗粒预处理再生 EPS 颗粒的方法。具体工艺为：先将环氧树脂与固化剂、水和水泥混合搅拌均匀，调整减水剂掺量使包裹浆体粘度和流动度适宜，再向浆体中加入再生 EPS 颗粒，继续搅拌使浆体均匀覆盖在 EPS 颗粒上且无富余料浆，随后撒入分散颗粒继续搅拌使EPS颗粒表面被分散颗粒二次覆盖且相互不粘黏。自然陈化 12h 后，将预处理 EPS 颗粒掺入水泥基材料制备轻质保温材料。裹浆复合二次裹颗粒预处理 EPS 颗粒类似于“芝麻团子状”的颗粒，如图 1 所示，由内层再生 EPS 颗粒、中间层水泥环氧浆体、外层分散粒组成的多层结构。

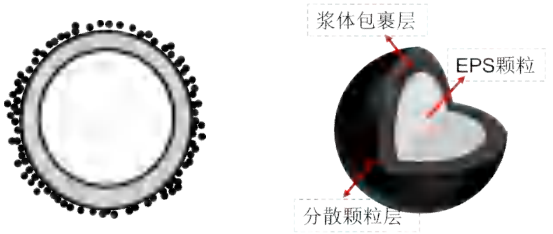

(a) “芝麻团子状”的颗粒　　(b) 颗粒结构

图 1 裹浆复合二次裹颗粒预处理 EPS 颗粒结构

2.2 包裹浆体流动度对包裹层厚度影响

通过调整环氧树脂掺量和减水剂掺量，获得具有不同流动度的浆体，研究浆体的流动度对再生 EPS 包裹层厚度的影响，结果如图 2 和图 3 所示。从图中可以看出，包裹浆体流动度对包裹层厚度有着较大的影响。浆体流动度较大，包裹层厚度较小，如图 2 中Ⅲ区域所示，浆体的流动度超过 180mm，包裹层厚度小于 0.11mm，流动度较大的水泥浆在搅拌时容易沿着 EPS 颗粒间的缝隙下沉至底部，导致 EPS 颗粒的包裹效果较差，因此包裹层比较薄，如图 3(d)所示。浆体流动度小于 120mm 时，如图 2 中Ⅰ区域所示，出现两种情况：第一种是包裹层厚度薄，小于 0.07mm，包裹后的 EPS 会泛白，即露

(C)1994-2023 China Academic Journal Electronic Publishing House. All rights reserved.　http://www.cnki.net

出 EPS 颗粒原本的颜色，同时会有大量的 EPS 与水泥浆体的团聚体产生，如图 3(b)所示；另一种是包裹层厚度较厚，超过 0.18mm，同样会伴有部分 EPS 颗粒泛白的现象，如图 3(a)所示。当浆体的流动度 120-180mm 时，如图 2 中 II 区域所示，流动度比较适宜，EPS 颗粒的包裹效果好，团聚程度小，包裹效果如图 3(c)所示。综合分析浆体流动度与包裹层厚度和团聚程度关系，调控水灰比、减水剂掺量、环氧树脂掺量等，使水泥基材料浆体流动度在 120-180mm，EPS 颗粒包裹层厚度约为 0.12-0.16mm，包裹效果较佳。

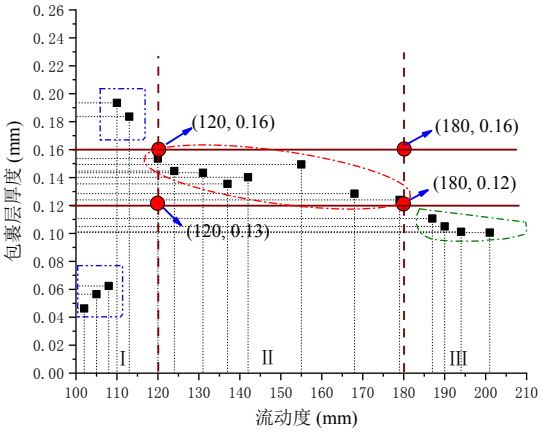

图 2 流动度对包裹层厚度影响

(a) (b)

流动度：<120

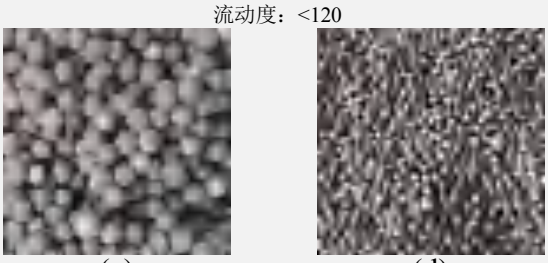

(c) (d)

流动度：120-180mm 流动度：>180mm

图 3 不同流动度对再生 EPS 的包裹状态

2.3 分散颗粒的优选

选用粉煤灰颗粒与再生 EPS 体积比分别为 1:22、1:18、1:15，探讨分散颗粒掺量对双层包裹 EPS 颗粒水泥基材料抗压强度的影响。如图 4 所示，分散颗粒掺量对预包裹 EPS 颗粒水泥基材料抗压强度影响较大，相比未包裹的再生 EPS，分散颗粒与再生 EPS 体积比为 1:22 和 1:15，对双层包裹 EPS 颗粒水泥基材料抗压强度提升幅度较小，粉煤灰与 EPS 颗粒体积比为 1:18 时，试样的 3d、7d、28d 抗压强度都是最高的，其中，环氧树脂掺量为 1%～2%时，包裹层厚度较适宜，对抗压强度提升最明显。

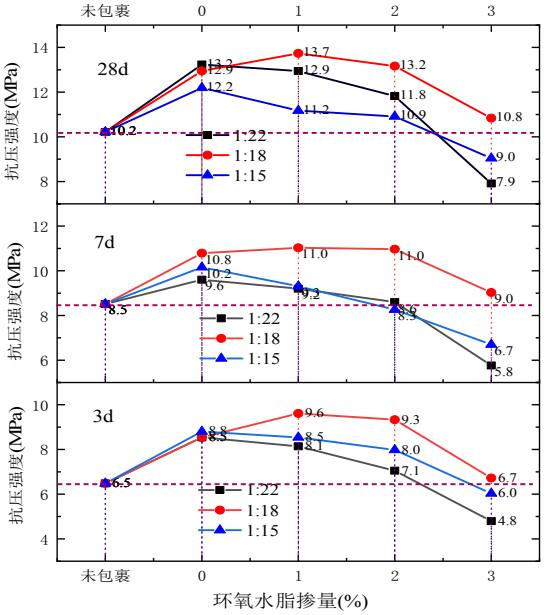

图 4 不同分散颗粒掺量的预包裹 EPS 颗粒对抗压强度影响

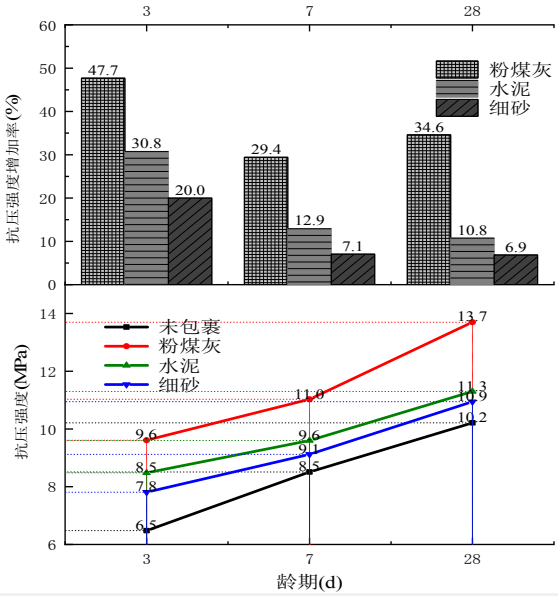

图 5 不同类型分散颗粒预包裹的 EPS 颗粒对抗压强度影响

选用粉煤灰、水泥、细石英砂作为分散颗粒，探讨不同类型分散颗粒对双层包裹 EPS 颗粒水泥基材料抗压强度的影响。如图 5 所示，相比掺未包裹的再生 EPS，采用粉煤灰颗粒分散的预包裹 EPS 的试样抗压强度可提升 30%以上，效果最好，水泥次之，而细砂作为分散颗粒的提升效果最差。粉煤灰是表面光滑玻璃体颗粒，能在水泥颗粒间起到滚珠的效果，减小了浆体内部构造的粘度和颗粒之间的扩散阻力，改善料浆的流变性。

(C)1994-2023 China Academic Journal Electronic Publishing House. All rights reserved. http://www.cnki.net

2.4 裹浆复合二次裹颗粒预处理 EPS 颗粒微观形貌

裹浆复合二次裹颗粒预处理EPS颗粒的包裹层与 EPS 颗粒界面过渡区能比较直观反映包裹的效果。采用扫描电镜观察 EPS 颗粒与不同环氧树脂掺量的包裹层界面过渡区的微观形貌如图 6 所示，分散颗粒都是粉煤灰，分散颗粒与 EPS 的体积比为 1:18。由扫描电镜图可以看出，掺有环氧树脂的包裹层与 EPS 的界面粘接好于纯水泥浆体的包裹层。未掺环氧树脂的包裹层出现了开裂（图 6(a)），由于包裹层为纯水泥料浆，包裹层厚度较薄且强度不高，受力易发生脆性破坏，而 EPS 为柔性材料，作用在 EPS 上的力减小或撤消后会产生弹性回复力，导致包裹层开裂。而掺环氧树脂的包裹层具有较好的韧性和粘性[12]，未出现包裹层开裂的现象，说明掺入环氧树脂能改善包裹层性能和界面过渡区的结合状况。

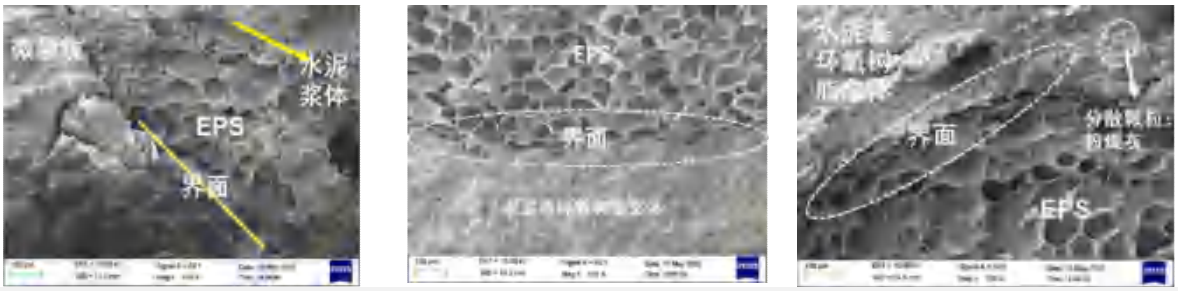

(a) 未掺环氧树脂　(b) 掺 1%环氧树脂　(c) 掺 2%环氧树脂

图 6 包裹层与 EPS 颗粒界面

3 结论

（1）采用裹浆复合二次裹颗粒法预处理再生 EPS 颗粒，可以形成由内层再生 EPS 颗粒、中间层水泥环氧浆体、外层分散粒的多层结构；调控环氧树脂掺量为 1%-2%、料浆流动度在 120-180mm、包裹层厚度在 0.12-0.16mm 时具有较佳的包裹效果。

（2）相比未包裹的再生 EPS 颗粒，粉煤灰为分散颗粒、分散颗粒与再生 EPS 体积比为 1:18 的裹浆复合二次裹颗粒法处理EPS颗粒可以提升抗压强度30%以上；包裹层与再生 EPS 颗粒间界面过渡区结合紧密。

参考文献

[1] 王益民.废聚苯乙烯泡沫塑料的回收利用［J］.中国资源综合利用,2000,18(10):39-43.

[2] BABU D,BABU K G,WANG T H.Effect of Polystyrene Aggregate Size on Strength and Moisture Migration Characteristics of Lightweight Concrete [J].Cement and Concrete Composites,2006,28(6):520-527.

[3] 蔡丽朋.用再生聚苯颗粒生产新型墙体材料的研究[J].新型建筑材料,2014,41(3):78-80.

[4] 程从密,张传镁,焦楚杰,等.EPS 轻集料混凝土研究进展[J].广东建材,2009(1):12-16.

[5] SADRMOMTAZI A,SOBHANI J,MIRGOZAR M A.Properties of Multi -strength Grade EPS Concrete Containing Silica Fume and Rice Husk Ash [J].Construction and Building Materials,2012,35:211-219.

[6] LIU N,CHEN B.Experimental Study of the Influence of EPS Particle Size on the Mechanical Properties of EPS Lightweight Concrete [J].Construction and Building Materials,2014,68(4):227-232.

[7] 杨飞,孙晓敏.EPS 掺量对混凝土力学和保温隔热性能的影响研究[J].新型建筑材料,2020,47(06):117-120+143.

[8] 严捍东,欧小燕,陈秀峰.聚苯乙烯掺量对石渣粉混凝土性能的影响[J].华侨大学学报(自然科学版),2009,30(03):326-330.

[9] Assaad, J.J., El Mir, A.,. Durability of polymer-modified lightweight flowable concrete made using expanded polystyrene[J]. Construction and Building Materials,2020, 249: 118764-118764.

[10] Chung, S.-Y., Abd Elrahman, M., Stephan, D.,. Effects of expanded polystyrene (EPS) sizes and arrangements on the properties of lightweight concrete[J]. Materials and Structures,2018, 51 (3):57-68.

[11] 李政奎.基于氯氧镁水泥制备的 EPS 保温砂浆研究[J].广东建材,2021,37(7):20-22.

[12] 梁学杰.环氧树脂改性水泥混凝土的制备及耐久性实验分析[J].功能材料,2023,54(3):3217-3223.

(C)1994-2023 China Academic Journal Electronic Publishing House. All rights reserved.　http://www.cnki.net

Engineering Structures 318 (2024) 118793

Contents lists available at ScienceDirect

Engineering Structures

journal homepage: www.elsevier.com/locate/engstruct

Experimental study on seismic performance of two-story two-bay. Precast concrete frame with UHPC-based connections

Yanghui Li, Weichen Xue *, Jiafei Jiang

Department of Structural Engineering, Tongji University, Shanghai 200092, China

ARTICLE INFO

Keywords:
Precast concrete frame
UHPC
Cycle loading
Load-carrying capacity
Energy dissipation
Displacement ductility

ABSTRACT

The UHPC-based connections, utilizing Ultra-high performance concrete (UHPC) to connect rebars within precast concrete structures, present the advantages of short splice length, simplified construction, and low cost due to the excellent bond property between UHPC and rebars. This investigation focuses on seismic performance of precast concrete frame (PCF) with UHPC-based connections. The UHPC-based connections were arranged strategically to the beam-column joints and column bases in PCF to connect longitudinal rebars of beams and columns, respectively. Two half-scale, two-story, two-bay reinforced concrete frames, including PCF and a monolithic concrete frame (MCF) for reference, were tested under cycle loading with axial compression ratios of 0.33 in the middle columns and 0.22 in the side columns. The results revealed that PCF exhibited a beam sway mechanism, with all beam hinges developed prior to column hinges, while MCF displayed a mixed sway mechanism, with part of beam hinges developed prior to column hinges. The hysteresis curves of the two frames were globally stable with minimal pinching, and PCF displayed greater energy dissipation compared to MCF. The load-carrying capacity of PCF was 9 % higher than that of MCF. The displacement ductility of PCF was 4.14, exceeding that of MCF by 10 %. The two frames showed similar laws of stiffness degradation. Overall, the precast concrete frame with the UHPC-based connections exhibited better seismic performance in comparison with the monolithic counterpart.

1. Introduction

Precast concrete structures originated in England with a history of over 140 years [1,2]. As a vital precast concrete structure, precast concrete frame structure has been widely employed in civil engineering in seismic regions for decades due to its flexible space arrangement, rapid construction, structural integrity, and notable economic benefits. However, historical earthquake disasters have exposed that seismic resistance of precast concrete frame was heavily dependent on connection reliability of longitudinal reinforcements of precast concrete beam and column components [3,4].

Currently, the primary types of rebar connections involve grouted sleeve connection [5,6], grouted corrugated conduit connection [7,8], bolted connector connection [9,10], and UHPC-based connection [11–13]. The extensively used grouted sleeve connection exhibits stable and reliable connection behavior, but it poses high requirement of rebar positioning and complex grouting process. In addition, the economical grouted corrugated conduit connection requires a quite long lap length of rebar, and its application in dynamic loading and large diameter rebar is restricted [14]. Besides, the bolted connector connection reduces on-site support, but it is costly and presents difficulties in positioning rebar and controlling the tightness degree of the bolt connectors. Table 1 compares the properties of the aforementioned four connections in terms of workability on site, connection reliability, and cost, which are sharp focus in projects. Accordingly, the UHPC-based connection holds a comprehensive advantage in comparison with the rest of connections.

In general, Ultra-high performance concrete (UHPC) presents excellent mechanical properties, including high bond strength with steel rebar (35 MPa-45 MPa) [15], ultra-high strength (compressive strength: 150 MPa-250 MPa, axial tensile strength: $\geq$ 6 MPa) [16,17], tensile hardening [18], and great durability [19,20]. These properties provide a significant benefit in employing UHPC to connect longitudinal reinforcements of precast concrete components [21,22], resulting in reliable connection performance, simplified configuration, easy construction process, and extended service life of the connections. In fact, in 2020 and 2023, approximately 10 thousand $m^3$and 20 thousand m^3 of UHPC were used to connect precast concrete components in China [23], respectively. Even better, for UHPC material, with the

* Corresponding author.
E-mail address: xuewc@tongji.edu.cn (W. Xue).

https://doi.org/10.1016/j.engstruct.2024.118793
Received 17 June 2024; Received in revised form 3 August 2024; Accepted 12 August 2024
Available online 16 August 2024
0141-0296/© 2024 Elsevier Ltd. All rights are reserved, including those for text and data mining, AI training, and similar technologies.

Table 1
Comparisons of rebar connections of precast beams and columns.

Connection identification	Connected length of rebars	Construction complexity	Connection reliability	Cost
Grouted sleeve (WC)	Short	High	High	Moderate
Grouted corrugated conduit (WC)	Long	Low	Moderate	Low
Bolted connector (DC)	Short	Moderate	High	High
UHPC-Based (WC)	Short	Low	High	Moderate

Note: The WC is the wet connection featured by much cast-in-place concrete on site, while the DC is the dry connection featured by little cast-in-place concrete on site.

advancement in material research and widespread promotion of various commercial products (e.g., DUCTAL®, BSI®, and CEMTEC-multiscale®), its cost has subsequently been reduced. For instance, between 2010 and 2024, the price of UHPC has significantly decreased from about \$2200/m^3 to around \$1000/m^3 [24,25].

In the prior studies [26–31], the bond behavior of rebar within UHPC surpassed that within normal concrete. Thanks to the superior tensile properties of UHPC, the high grip stress between UHPC and rebar could prevent UHPC cover cracking by hoop pressure. Generally, for rebars with yield strength of 400–600 MPa, a lap length of 6*d*-8*d* (*d* denotes the rebar diameter) ensured rebar yield for diameters less than 25 mm, while a lap length of 8*d*-10*d* was sufficient for diameters of 25–32 mm.

For decades, cyclic tests have been conducted on precast concrete columns and beam-column joints with UHPC-based connections. Xue [32] tested the precast columns with a splice length of 15*d* (l_s =15*d*, *d*=32 mm) within UHPC. It illustrated that the bearing capacity of precast columns with axial compression ratios (ACR) of 0.24 and 0.48 was 21 % and 10 % higher than that of monolithic columns, respectively. Xue [33] presented that the precast joints (ACR=0.48) displayed beam flexural failure. Besides, the differences in bearing capacity between the precast joints and monolithic joints were within 7 %. Note that the column reinforcements (l_s =15*d*, *d*=32 mm) and beam reinforcements (l_s =15*d*, *d*=25 mm) were connected within UHPC at column bases and joints, respectively. Maya [34] revealed that the precast joints (ACR=0) appeared beam flexural failure. Herein, the beam reinforcements (l_s =15*d*, *d*=20 mm) were connected within UHPC at beam ends when the columns were monolithic. Deng [35] showed that the precast joint (ACR=0.12) exhibited beam flexural failure with a displacement ductility factor of 6.24. Herein, both the column reinforcements (l_s =15*d*, *d*=20 mm) and beam reinforcements (l_s =11*d*, *d*=18 mm) were connected within UHPC in joint. Xiong [36] demonstrated that the precast pretensioned prestressed joint (ACR=0.03) exhibited beam flexural failure and displayed a displacement ductility of 3.36. Note that both the column reinforcements (l_s =16*d*, *d*=25 mm) and beam reinforcements (l_s =20*d*, *d*=14 mm) were connected within UHPC in joint.

Overall, the adequate studies have demonstrated that both precast concrete columns and joints with UHPC-based connections could achieve comparable seismic performance to monolithic contenders. Furthermore, the diameters of beam and column reinforcements basically ranged from 20 mm to 32 mm, and a commonly used 15*d* lap length within UHPC was sufficient to prevent bond failure. However, the following points can be identified from the above review:

a) The study on seismic performance of precast concrete frames with the UHPC-based connections was absent. Additionally, the precast concrete slab was frequently neglected, even though its influence on structural behavior ought not to be overlooked.

b) In most previous works, connecting both beam reinforcements and column reinforcements in joints led to plenty of rebars in joints, increased on-site supports and caused inconvenient assembly, necessitating the optimization of the UHPC-based connection.

c) ACI 318–19 [37], EN 1992–1-1 [38], and NZS 3101: 2006 [39] also lacked related design provisions for precast concrete frame with UHPC-based connections, emphasizing the importance of the related test results for specification preparation.

This study conducted cycle tests on a half-scale, two-story, two-bay precast concrete frame (PCF) with UHPC-based connections, along with a monolithic concrete frame for reference. Considering the monotonic test adopted in most bond behavior studies and for engineering reliability, a 15*d* development length to connect beam reinforcements within UHPC in joints and a 15*d* splice length to connect column reinforcements within UHPC at column bases were employed in PCF, which were also adopted in our previous cycle tests [32,33]. Besides, the axial compression ratios (0.33 in middle columns and 0.22 in side columns) and concrete slabs were considered to simulate high-rise precast concrete frame structures in earthquake zones.

2. Test program

2.1. Test specimens

The experimental model for the reinforced concrete frame was extracted from the two bottom stories of an 18-story student dormitory, situated in a moderate seismic region in Shanghai. Due to the limited experimental space, two half-scale, two-story, two-bay reinforced concrete frame specimens were designed following the principle of geometric similarity. A precast concrete frame (PCF) with UHPC-based connections and a monolithic concrete frame (MCF) were prepared, and both complied with the design regulations of GB 50010–2010 [40] and ACI 318–19. Fig. 1 presents the geometric dimensions and reinforcement particulars of PCF.

PCF consisted of concrete composite beams, precast concrete columns, and concrete composite slabs. The composite beams and precast columns were connected by joints, where the top longitudinal reinforcements of beams passed through. The bottom longitudinal reinforcements of the composite beams were securely anchored within UHPC in joints with an anchorage length of 15*d* (*d* denotes the diameter of beam rebar). Since the UHPC cover for the bottom longitudinal reinforcements of beams was 3*d*, the UHPC in joints attained a height of 115 mm. Meanwhile, the longitudinal reinforcements of the precast columns were connected firmly within UHPC at column bases with a lap length of 15*d* (*d* denotes the diameter of column rebar). The height of UHPC at column bases was 395 mm. Note that the use of the localized UHPC in joint and wedge-shaped configuration at column base reduced UHPC usage by 62 % and by 28 % compared to full pouring, respectively. In addition, the thickness of the precast layer and cast-in-place layer of concrete slabs were 40 mm and 35 mm, respectively.

2.2. Specimens fabrication

Fig. 2 delineates the primary construction processes of PCF. The same construction procedure was employed for both the first and second story of PCF, with a concise description of the first-story process provided as follows: (a) Casting of Precast components, including precast columns, precast beams, precast slabs, and ground beam. (b) Lifting and positioning sequentially of precast columns, precast beams, and precast slabs. (c) Assembling reinforcements sequentially of the joints, precast beams, and precast slabs, along with the installation of the formworks. (d) Casting of UHPC at column bases. (e) Casting of UHPC in joints. (f) Casting of cast-in-place (CIP) concrete.

2.3. Material characterization

The C50 normal concrete, with a nominal cubic compressive strength of 50 MPa and a maximum aggregate size not exceeding 15 mm, was

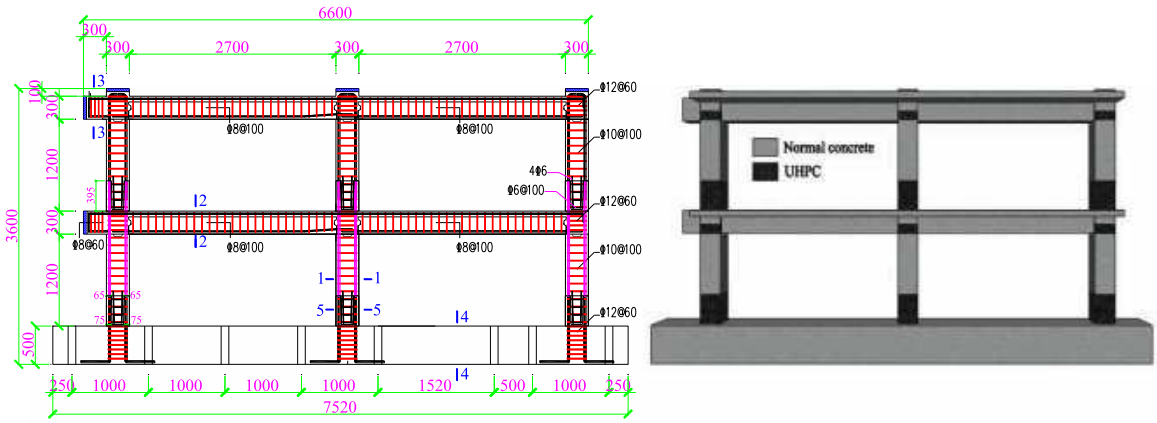

(a) Overall layout

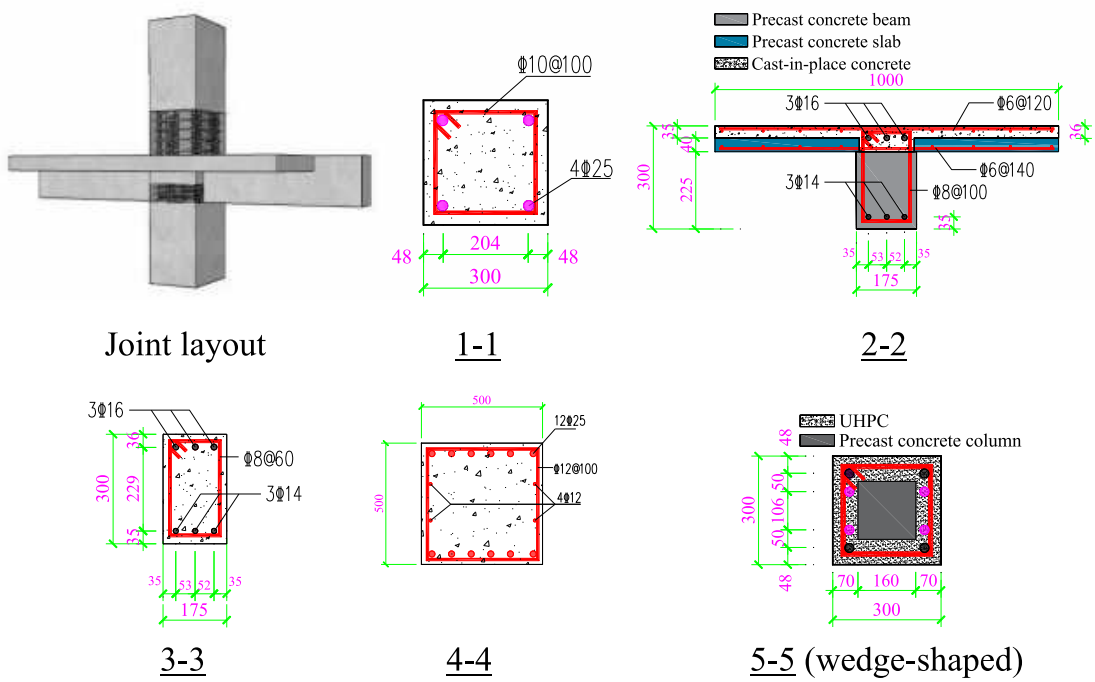

(b) Dimensions and reinforcement details of PCF

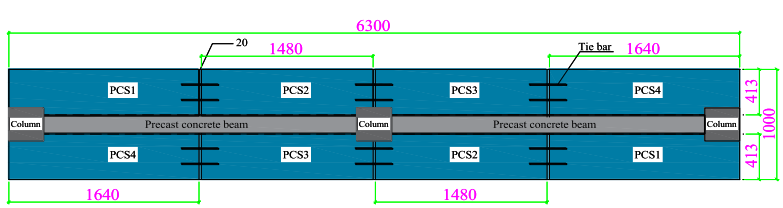

(c) Floor assembly layout (PCS: precast concrete slab)

Fig. 1. Details of PCF (unit: mm).

prepared for both precast concrete and CIP concrete in the two specimens. Mechanical properties testing for the C50 normal concrete followed the specification GB/T 50081–2016 [41], with the measured results listed in Table 2. Meanwhile, a commercial UHPC product from Huaxin Cement Co., LTD., containing 3 % volume ratio of smooth steel fiber with 13 mm in length, 0.2 mm in diameter and 2000 MPa in tensile strength, was utilized to the UHPC-based connection zones of PCF. Mechanical properties testing for the UHPC adhered to the specifications GB/T 31387–2015 [42] and SIA 2052, with the test samples shown in Fig. 3 and the measured results presented in Table 3. In addition, the HRB 400E deformed rebars (yielding strengths ≥ 400 MPa), were utilized as the transverse and longitudinal reinforcements. The mechanical properties of HRB 400E rebars were tested according to the specification GB/T 228.1–2010 [43] and are presented in Table 4.

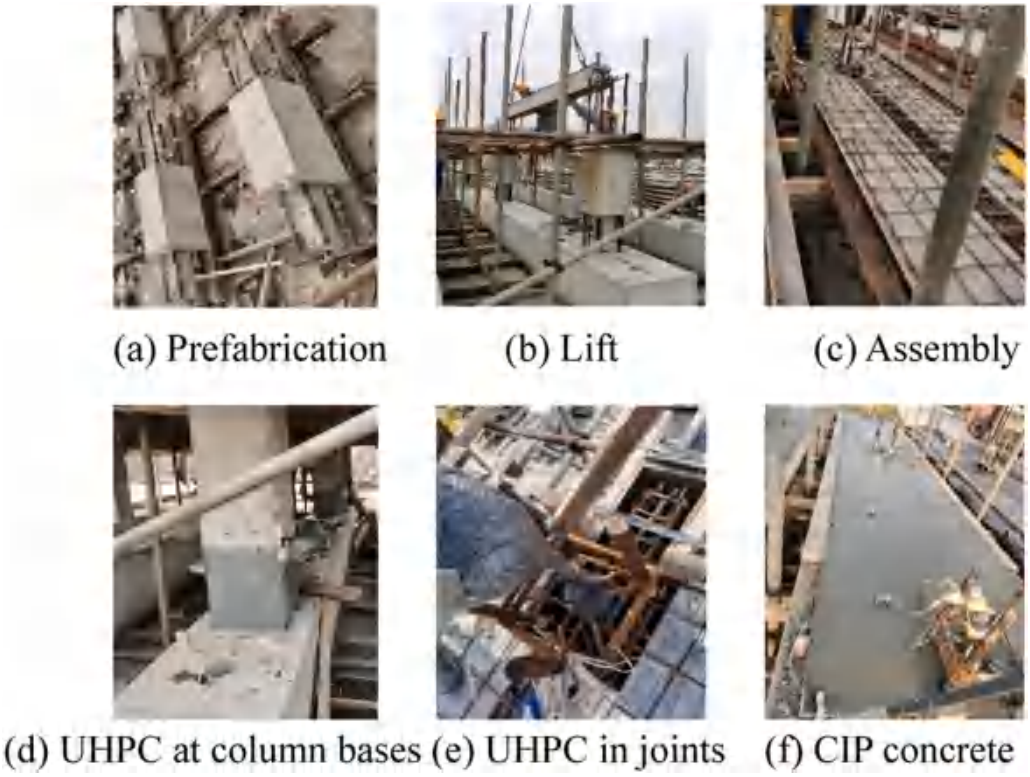

Fig. 2. Primary construction processes of PCF.

Table 2
Mechanical properties of normal concrete.

Specimen		Cubic strength, f_{cu}/MPa	Prism strength, f_c/MPa	Splitting strength, f_t/MPa	Elastic modulus, E_c/× 10^4 MPa
PCF	Precast part	54.3	36.3	2.3	3.3
	CIP part	57.5	38.5	2.4	3.4
MCF		57.5	38.5	2.4	3.4

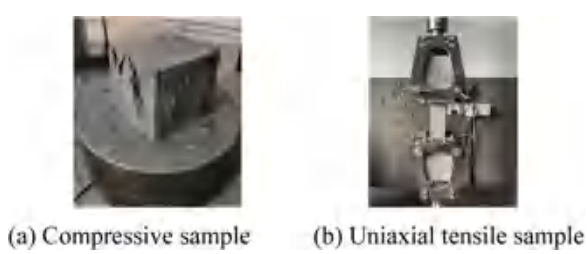

Fig. 3. Test samples of UHPC.

Table 3
Mechanical properties of UHPC.

Specimen	Compressive strength, f_c/MPa	Uniaxial tensile strength, f_t/MPa	Strain of peak compressive strength, ε_{c0}	Elastic modulus, E_c/× 10^4 MPa
PCF	171.1	8.9	0.0033	5.2

Table 4
Mechanical properties of reinforcements.

Item	Diameter/mm	Yielding strength, f_y/MPa	Ultimate strength, f_u/MPa	Elastic modulus, E_s/× 10^5 MPa	Elongation/%
D6	6	445	605	2.0	29.5
D8	8	460	630	2.0	30.0
D10	10	465	635	1.9	29.8
D12	12	435	610	1.9	29.5
D14	14	450	645	2.0	29.1
D16	16	445	635	2.0	29.5
D25	25	440	645	2.0	29.0

2.4. Test setup and loading protocol

Fig. 4 shows the experimental setup for reversed cyclic loading test on the two specimens. The multi-function testing system (MFTS), with a loading capacity of 10000 kN, was utilized to the test in Structural Engineering Laboratory of Tongji University. To provide fixed support boundary, the frame specimen was anchored firmly to the rigid ground by eight ground anchors and further secured by two 500 kN jacks at the ground beam ends. Three constant vertical forces, one with an axial compression ratio of 0.33 (1143.5 kN) for middle column and two with an axial compression ratio of 0.22 (762.3 kN) for side columns, were applied by three 2000 kN jacks to simulate the upper axial forces experienced in the original 18-story structure. Meanwhile, three sliding cars were positioned between the 2000 kN jacks and the steel girder to keep the vertical forces tracing the top of columns during test, thus reflecting the P-Delta effect. Additionally, a spreader steel beam, connected to the frame by a screw system, was used to apply the horizontal cycle loading. And, to simulate the actual response of the two bottom stories in prototype, the horizontal loading center was placed at two-thirds of the floor height to realize a 2:1 loading ratio between the second and first stories.

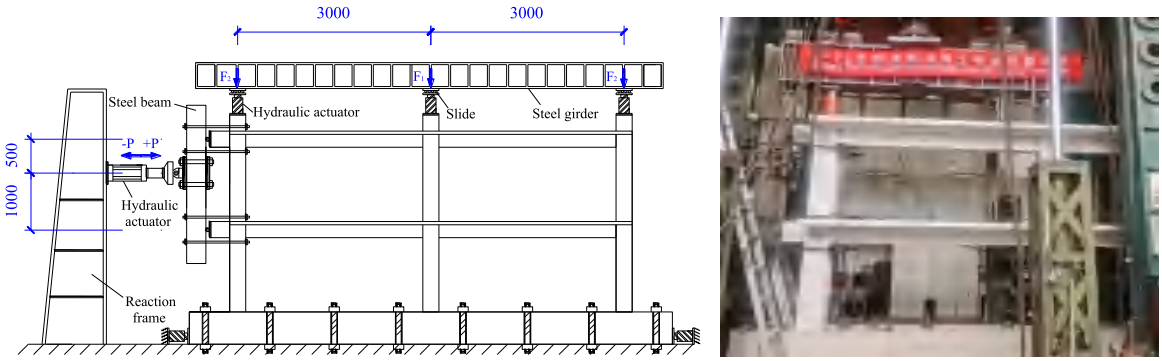

(a) Boundary conditions (b) Loading device

Fig. 4. Experimental setup.

To begin the test, three constant vertical forces were applied to the centers of the top of the three columns and then maintained invariably during the test. Then the horizontal cyclic loading was subjected to a hybrid load-displacement history in JGJ/T 101–2015 [44], as presented in Fig. 5. Herein, note that the displacement incrementally applied by multiples of the drift Δ (Δ = 1/200) of the roof (the center of the second-story beam), and each displacement level was performed three cycles. For convenience, it defined that the positive (negative) loading was to push (pull) the frame.

The test data were automatically recorded using the Solartron Instrument system, and the primary measurements included: a) Horizontal and vertical loads. b) Horizontal displacements of the roof (the center of the second-story beam) and the first floor (the center of the first-story beam), as well as the slips of the ground beams. c) Beams-columns relative rotation angles. d) Longitudinal rebars strains at beam ends and columns ends, as well as the stirrups strains at joints. Fig. 6 depicts the primary measurement arrangements of PCF.

3. Test results

3.1. Test observations and damage pattern

The structural response for both PCF and MCF could be distinguished into four stages with respect to cracking, yielding, ultimate, and failure under cycle loading. Meanwhile, the crack load P_{cr}, yield load P_y, peak load P_{peak} and, ultimate load P_u and corresponding crack drift D_{cr}, yield drift D_y, peak drift D_{peak}, and ultimate drift D_u were obtained during test. Note that the yield displacement was determined by the energy method [45], and the ultimate load dropped to 85 % of the peak load.

In the cracking stage, an initial crack appeared at the first-story beam end for both specimens. Afterward, the two specimens experienced the yielding stage during 1Δ-2Δ. Next, PCF experienced the ultimate stage during 3Δ-4Δ. The positive (negative) P_{peak} of PCF was 885.2 (−681.7) kN, and the positive (negative) D_{peak} of the roof was 1.56 % (−2.04 %). However, MCF experienced the ultimate stage during 3Δ. The positive (negative) P_{peak} of MCF was 787.5 (−649.2) kN, and the positive (negative) D_{peak} of the roof was 1.54 % (−1.48 %).

PCF experienced the failure stage during 5Δ-8Δ, characterized by crushing of concrete and fracturing of the partially longitudinal reinforcements at the bottom of the beam ends. Eventually, when to apply the positive roof drifts of 4.00 % and negative roof drifts of −4.00 %, the loads on PCF decreased to 77 % and 75 % of the P_{peak}, respectively. Meanwhile, the test concluded with the fracture of all the longitudinal reinforcements at the bottom of the beam ends and massive cracks on the UHPC at column bases (with a maximum crack width of 1.1 mm). However, MCF experienced the failure stage during 4Δ-7Δ, characterized by crushing of concrete at a height range of 500 mm at the first-story column bases, along with buckling of the partially longitudinal reinforcements of the first-story beam ends. Eventually, when to apply the positive roof drifts of 3.50 % and negative roof drifts of −3.50 %, the loads on MCF decreased to 70 % and 58 % of the P_{peak}, respectively. Meanwhile, the test concluded with buckling of the longitudinal reinforcements at column bases and fracture of the longitudinal reinforcements at the bottom of the beam ends in the first story.

Fig. 7 shows the global and detailed damage patterns of the specimens in the end of the test. In general, both specimens exhibited more serious damage in the beams and columns of the first story than those of the second story, which was consistent with the distribution of internal forces in frames under the applied loads. In addition, it was observed that the bottom of beams suffered more significant damage than the top in both specimens due to the slab effect. Compared to the significant damage happened to the beams and columns in the first story in MCF, PCF was primarily damaged at the beams in two stories and moderately damaged for all columns. These suggested that UHPC at column bases could avoid severe damage to the first-story columns.

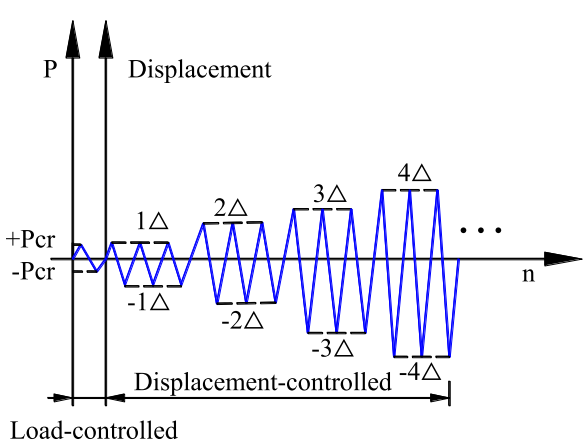

Fig. 5. Load-displacement history.

3.2. Failure mechanism

Failure mechanisms for reinforced concrete frames subjected to seismic loading include beam sway mechanism (all beam hinges form preceding column hinges), mixed sway mechanism (part of beam hinges form preceding column hinges), and story sway mechanism (only column hinges form) [46,47]. The beam mechanism allows for full utilization of plastic deformation capacity of beam ends to maximize energy absorption during earthquakes, achieving a frame structure with superior seismic performance. Hence, it is considered an acceptable failure mechanism in AIJ 1994 and ACI 318–19. However, this ideal failure mechanism was hard to achieve in projects. The complex and high forces

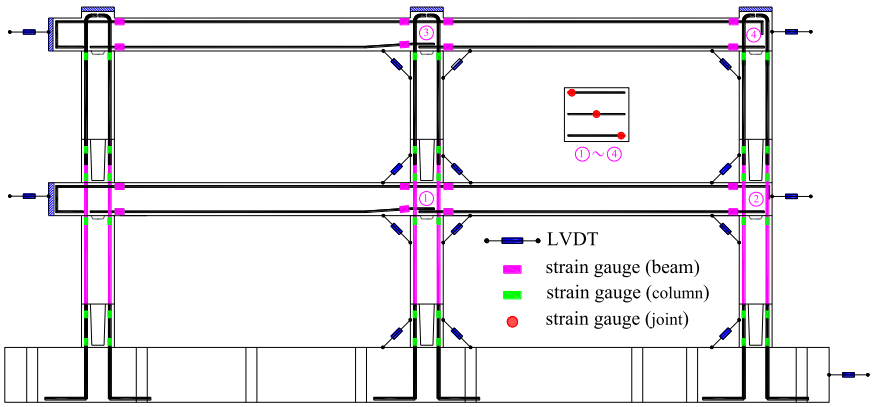

Fig. 6. LVDTs and strain gauges arrangements of PCF.

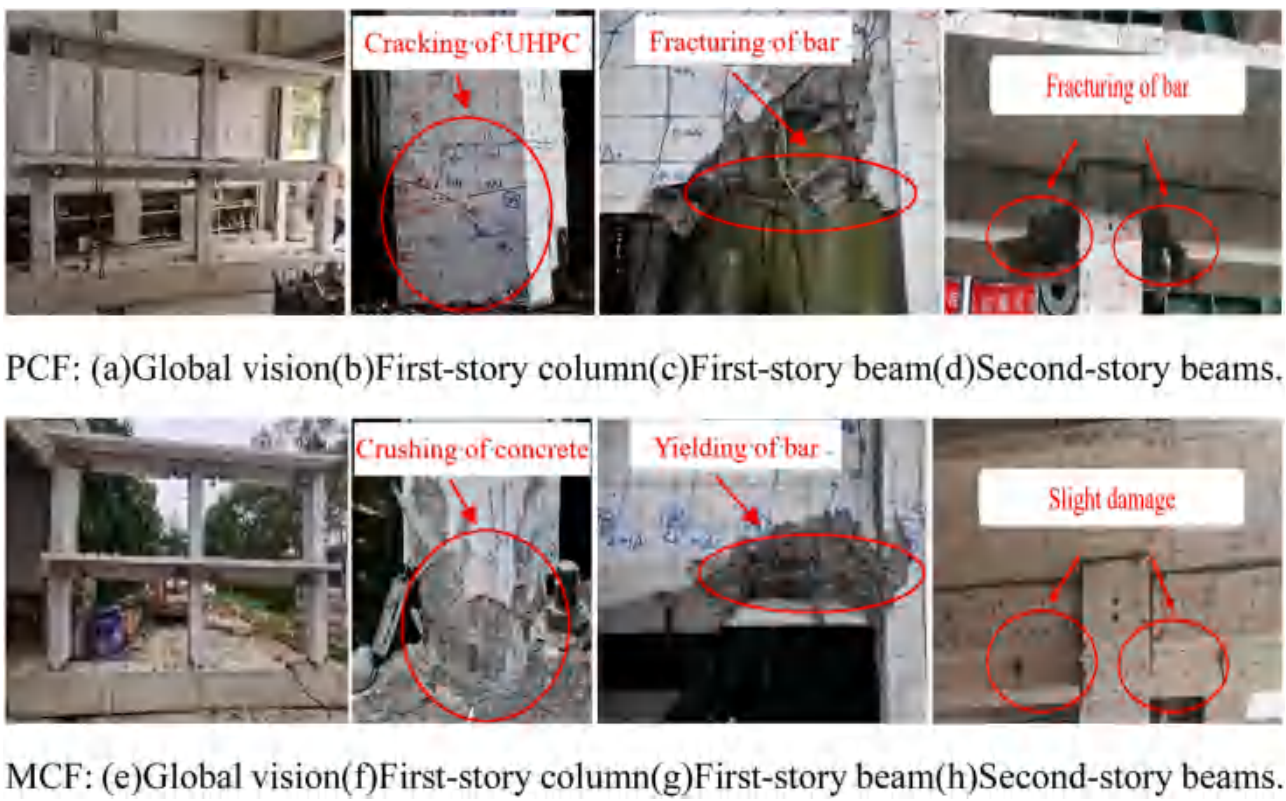

Fig. 7. Damage patterns for specimens.

experienced by the first-story column bases during earthquakes led to premature plastic hinges at the first-story column bases rather than at beam ends [48]. This issue was particularly significant in frame structures with high axial compression ratios, as the P-Delta effect accelerated the damage to the first-story column bases [49].

To prevent premature damage to column bases and achieve the beam mechanism, PCF maintained the same column reinforcements (4D25: four rebars of 25 mm diameter) as MCF, resulting in a long strong zone at column bases due to the long connection length within UHPC. Prior to test, finite element analysis results indicated that PCF achieved the beam mechanism while MCF missed, as depicted in Fig. 8. Note that the friction contact was used to consider the behavior of interface between precast concrete and cast-in-place concrete, and the rebars were embedded into UHPC due to the excellent bond properties between rebars and UHPC [33].

Fig. 9 illustrates the measured development of plastic hinges for the specimens in the test. For PCF, plastic hinges emerged firstly at the first-story beam end, then emerged randomly at the first-story and second-story beam ends, and finally emerged at the first-story column bases. However, for MCF, plastic hinges emerged early at the first-story beam ends, then emerged at the first-story medium column base, and later emerged randomly at other beam ends and first-story column bases. Therefore, similar to the finite element analysis results, PCF achieved the beam mechanism, whereas MCF achieved the mixed mechanism. Furthermore, it was worth noting that PCF may generate the similar failure mechanism to MCF if the diameter of the column longitudinal rebars was reduced following the principle of equal strength, for instance, to 6D20 or 8D18.

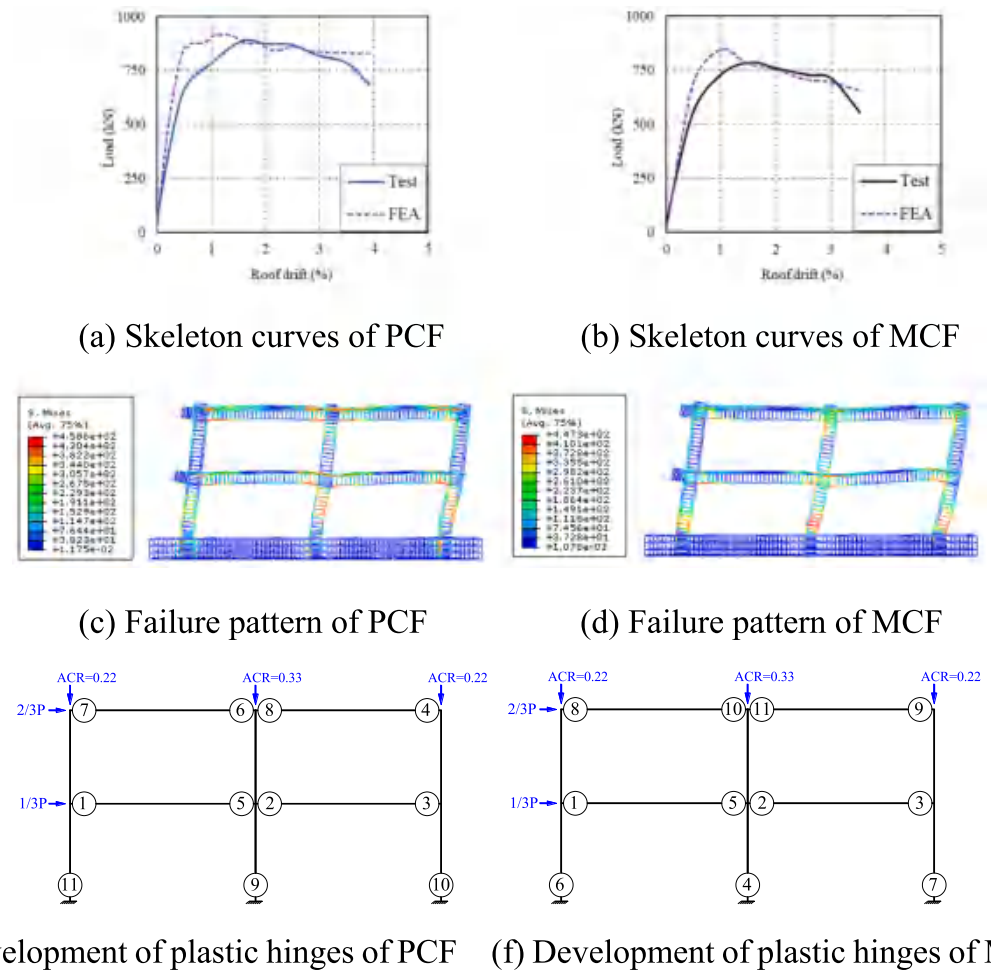

(a) Skeleton curves of PCF (b) Skeleton curves of MCF

(c) Failure pattern of PCF (d) Failure pattern of MCF

(e) Development of plastic hinges of PCF (f) Development of plastic hinges of MCF

Fig. 8. Results of finite element analysis.

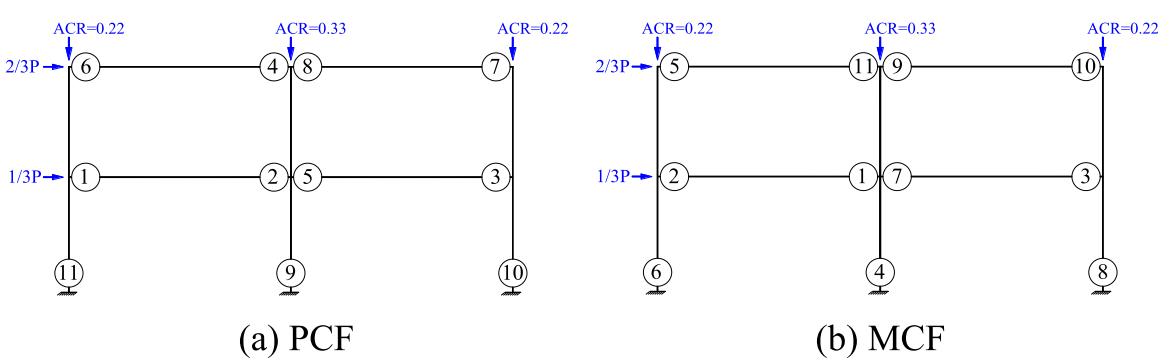

(a) PCF (b) MCF

Fig. 9. Development of plastic hinges in test (ACR: axial compression ratio).

3.3. Hysteresis response

3.3.1. Load-displacement curve

The load-displacement hysteresis curves comprehensively expose the seismic performance of the concrete frames, as illustrated in Fig. 10. Both PCF and MCF exhibited full hysteresis curves, suggesting that the two specimens displayed good seismic performance. Additionally, the first interstory hysteresis curves for both specimens exhibited a similar shape to those of the second interstory, indicating consistent seismic performance between the two stories.

In the cracking stage, both specimens were mainly in elastic state and the hysteresis curves were fairly narrow for both positive and negative loadings. With the increase of displacement, both specimens translated to plastic state, and the areas of hysteresis loops markedly elevated. Finally, the loads achieved the ultimate load P_u, and the hysteresis curves became more pinched. This pinched phenomenon was primarily attributed to the cumulative damage to specimens under high axial compression, including concrete crushing, reinforcement yielding, and bond slippage between the reinforcements and concrete.

When applying a specific displacement level, the hysteresis curves for both specimens followed the previous displacement level path to reach the previous endpoint, and then followed a new low broken line to reach the endpoint of the current displacement level. The decreased slope of the new broken line signified a reduction in frame's stiffness,

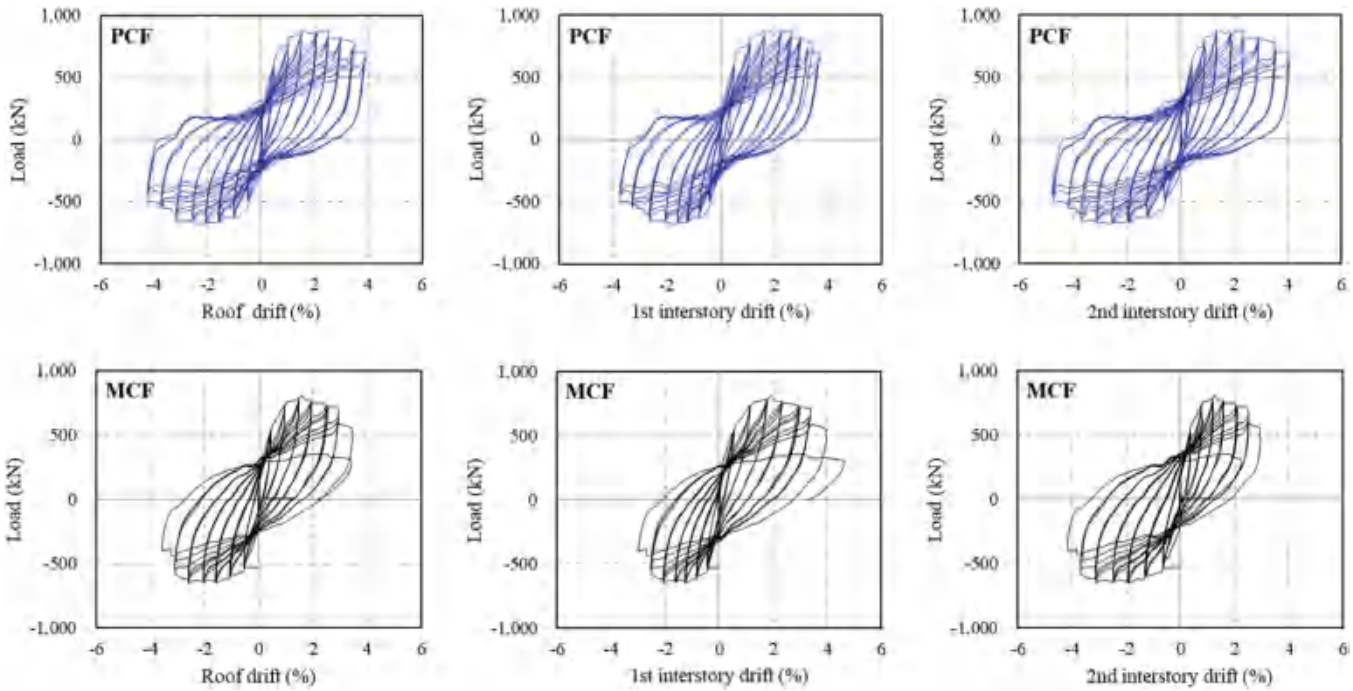

Fig. 10. Load-displacement hysteretic curves of specimens.

mainly resulting from the new damage occurring at current level. Meanwhile, the overlapping points existed in the hysteresis curves for both specimens, potentially related to the elastic behavior of the specimens.

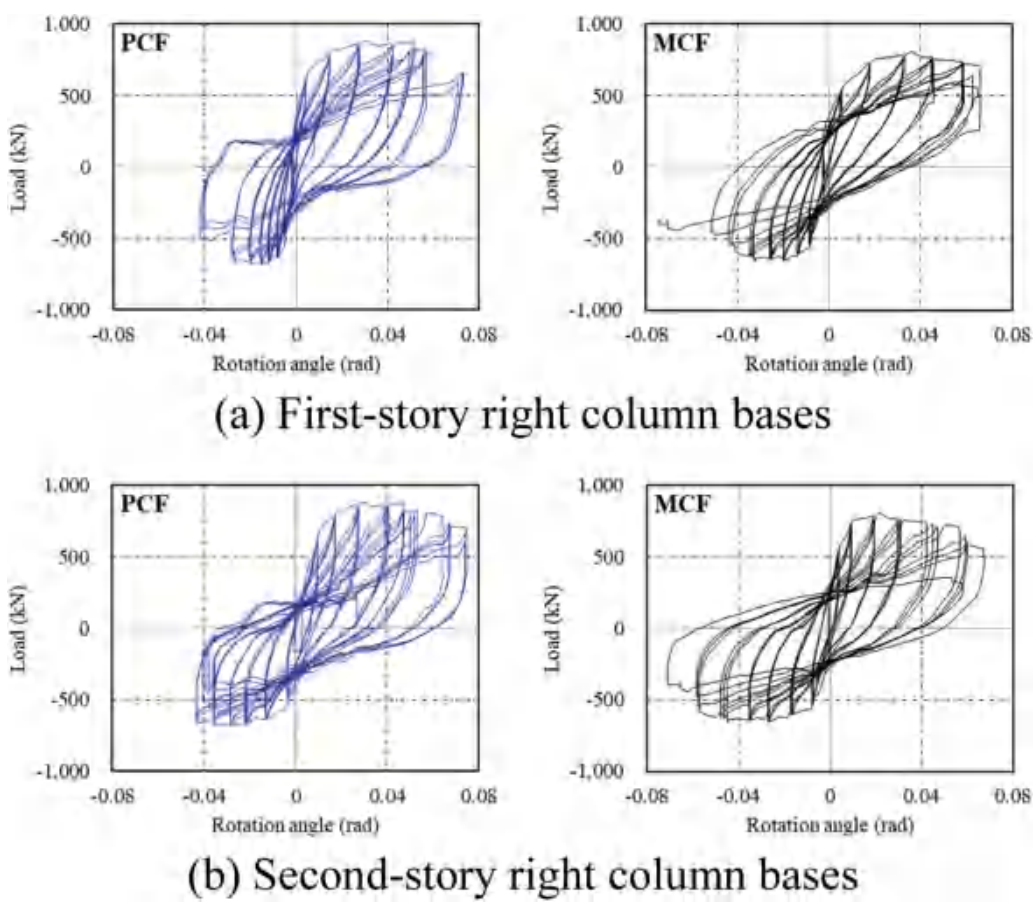

Fig. 11. Rotation angles of beams and columns.

3.3.2. Beam-column relative rotation angle curve

Beam-column relative rotation angles represent the rotational deformation performance of beams and columns and are the basis of nonlinear analysis. The typical beam-column relative rotation angles for both specimens manifested a hysteretic characteristic with the increase of displacement levels, as shown in Fig. 11. There were no distinct differences on the curves of beam-column relative rotation angles between PCF and MCF, signifying similar rotational deformation performance of the beams and columns between the two specimens. It is noteworthy that the beam-column relative rotation angles for both specimens remained within 5°, indicating that the rotation angles of beams and columns were almost the same, and the beams and columns basically maintained a vertical position.

3.4. Skeleton curve

The skeleton curves represent the envelope of the load-displacement hysteresis curves of the specimens, as depicted in Fig. 12. The skeleton curves of PCF and MCF were close, indicating the similar mechanical behavior for both specimens. For each specimen, the skeleton curves of the two stories were also close, indicating a uniform mechanical behavior between the two stories and no existence of a weak story.

In the cracking stage, both specimens remained in the elastic state, and skeleton curves exhibited linearity with nearly identical initial stiffness. When to yielding stage, both specimens were in the elastic-plastic state, and skeleton curves became nonlinear with the reduced stiffness. In the ultimate stage, the skeleton curves gradually rose to the peak load. When to the failure stage, the skeleton curves declined obviously until the specimens failed, resulting from a significant P-Delta effect under high axial compression.

The positive and negative peak load P_{peak} of PCF exceeded those of MCF by 12 % and 5 %, respectively, indicating that the UHPC-based connections could improve the bearing capacity of PCF. Note that the positive P_{peak} was 22 % higher than the negative P_{peak} for PCF, and it was 17 % for MCF, potentially due to the adverse effect of damage accumulation to frames in positive loading and axial tension in beams in negative loading. From the Fig. 12, when the drift reaches 3.5 %, the positive and negative loads for PCF decrease to 89 % and 82 % of P_{peak}, respectively, meeting the requirement of ACI 374.1–05 [50], which specifies that the loads should not fall below 75 % of P_{peak} at drift of 3.5 %.

3.5. Ductility and deformation capacity

Table 5 compares the characteristic loads and displacement ductility factors μ of PCF and MCF, where the μ stands for the value of ultimate drift D_u to yield drift D_y [46], i.e. $\mu = D_u/D_y$. In this section, the focus was on the mean displacement ductility factors μ. The μ of the roof, first story, and second story of MCF were 3.75, 3.68, and 3.78, respectively, while those of PCF were 4.14, 3.96, and 4.41, respectively, exhibiting improvements of 10 %, 7 %, and 17 %, respectively. In comparison with the first story, the second interstory μ of both specimens were higher, possibly attributed to the strong ground beam better realizing the fixed support boundary for the first story.

EN 1998–1: 2004(E) [51] and ASCE 41–06 [52] classify displacement ductility factors of 2.0–4.0 and 4.0–6.5 as medium ductility frames (DCM) and high ductility frames (DCH), respectively. Since the roof displacement ductility factors were 4.14 for PCF and 3.75 for MCF in this test, PCF was categorized as DCH, while MCF was categorized as DCM. Given that neither EN 1998–1: 2004(E) nor ASCE 41–06 overlooked the impact of axial compression, the ductility behavior for PCF with high axial compression ratios was certainly underestimated.

The ultimate drifts D_u of the roof, first story, and second story of MCF were 3.1 %, 3.0 %, and 3.2 %, respectively, while those of PCF were 3.6 %, 3.3 %, and 3.9 %, respectively, displaying a better deformation capacity for PCF. In addition, both specimens had high values of D_y/D_{cr}, demonstrating large safety margins for the service limit state.

3.6. Stiffness degradation

Fig. 13 displays the stiffness degradation curves of the two specimens. Herein, the stiffness K was calculated as the ratio of the load of each cycle under displacement levels to the corresponding displacement [53], i.e. $K = P/\Delta$. The mean stiffness K of three cycles was discussed. The stiffness degradation curves of the two specimens were nearly close, suggesting a similarity in the degradation stiffness laws. Furthermore, the first interstory stiffness degradation curve was similar to that of the second story for each specimen, suggesting a uniform distribution of stiffness between the two stories.

The stiffness of both specimens degraded gradually as the displacement levels expanded. Both specimens showed significant stiffness reduction in the cracking and yielding stages and slight stiffness reduction in the ultimate and failure stages, which were caused by the most cracks and yielding of rebars in early stages in the test. Specifically, when to reach the yield load P_y of the frames, the average stiffness reduction of the roof, first story, and second story of PCF were 83 %, 84 %, and 81 %, respectively, while those of MCF were 86 %, 86 %, and 85 %, respectively.

3.7. Energy dissipation capacity

The energy dissipation capacity reflects the seismic performance of frames and is quantified to the area enclosed by the hysteresis curve [54]. The cumulative dissipated energy of the specimen is the total of the mean dissipated energy of three cycles of each displacement level, as shown in Fig. 14. The energy dissipation curves of PCF and MCF displayed a high degree of similarity, particularly for the roof's, indicating comparable energy dissipation law between the two specimens.

In the cracking stage, energy dissipation for both specimens was small. From the yielding stage to the failure stage, energy dissipation for

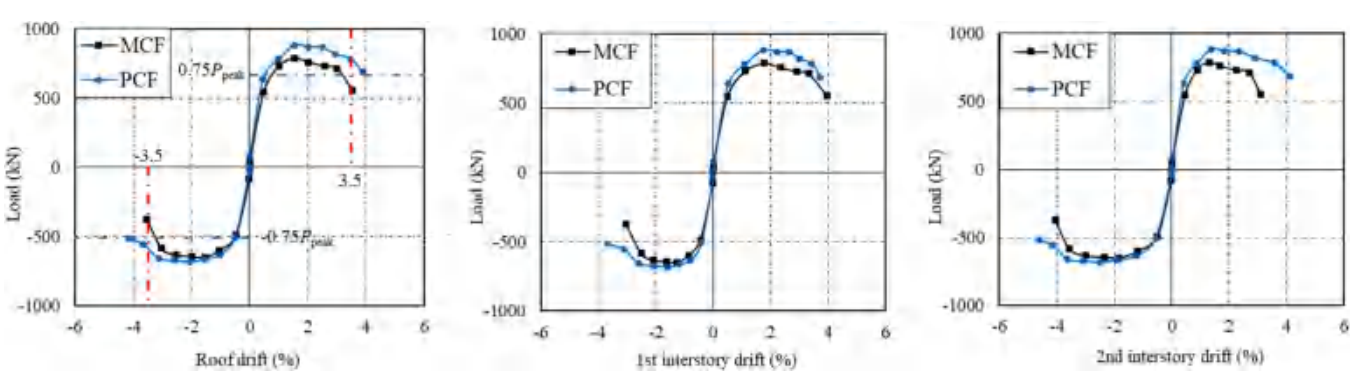

Fig. 12. Skeleton curves of specimens.

Table 5
Comparison of characteristic loads and displacements.

Item		MCF			PCF		
		Roof	First story	Second story	Roof	First story	Second story
P_{cr}/kN	Pos.	40.0	40.0	40.0	80.0	80.0	80.0
	Neg.	80.0	80.0	80.0	40.0	40.0	40.0
D_{cr}/%	Pos.	0.01	0.01	0.01	0.02	0.01	0.02
	Neg.	0.01	0.01	0.01	0.01	0.01	0.01
P_y/kN	Pos.	681.6	675.6	690.5	747.9	748.5	747.2
	Neg.	556.5	562.8	552.8	594.3	600.4	590.9
D_y/%	Pos.	0.87	0.93	0.80	0.87	0.97	0.77
	Neg.	0.81	0.72	0.89	0.86	0.70	1.01
P_{peak}/kN	Pos.	787.5	787.5	787.5	885.2	885.2	885.2
	Neg.	649.2	649.2	647.6	681.7	681.7	681.7
D_{peak}/%	Pos.	1.54	1.77	1.31	1.56	1.75	1.37
	Neg.	1.48	1.76	1.19	2.04	1.58	2.50
P_u/kN	Pos.	669.4	669.4	669.4	752.4	752.4	752.4
	Neg.	551.8	551.8	550.5	579.5	579.5	579.5
D_u/%	Pos.	3.15	3.51	2.80	3.63	3.52	3.73
	Neg.	3.10	2.58	3.63	3.52	2.99	4.05
D_y/D_{cr}	Pos.	87.0	93.0	80.0	43.5	97.0	38.5
	Neg.	81.0	72.0	89.0	86.0	70.0	101.0
	Avg.	84.0	82.5	84.5	64.8	83.5	69.8
μ	Pos.	3.64	3.76	3.51	4.15	3.63	4.82
	Neg.	3.85	3.60	4.06	4.12	4.28	4.00
	Avg.	3.75	3.68	3.78	4.14	3.96	4.41

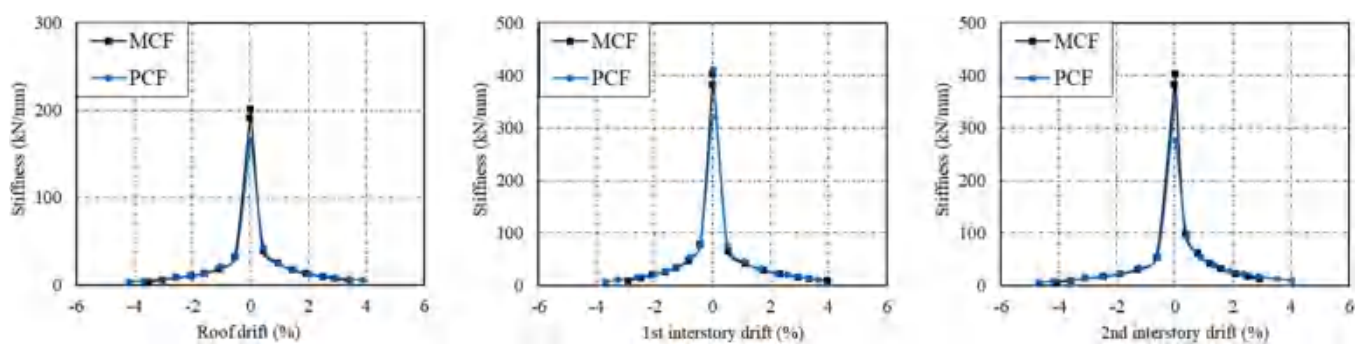

Fig. 13. Stiffness degradation.

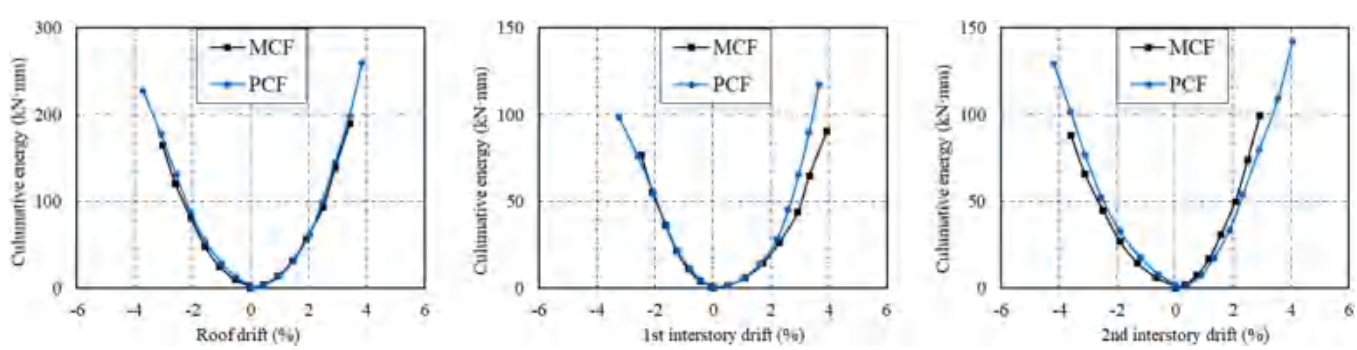

Fig. 14. Energy dissipation.

both specimens increased gradually, transitioning from an energy dissipation pattern dominated by concrete cracking and reinforcement yielding to one dominated by concrete crushing and reinforcement fracture. Compared to MCF, PCF exhibited higher cumulative energy dissipation of the roof, first story, and second story by 37 %, 29 %, and 45 %, respectively. These results demonstrated that the UHPC-based connections employed in PCF significantly enhanced the energy dissipation capacity of frame.

3.8. Rebar strain

Fig. 15 illustrates the typical rebar strains of the column bases, beam ends, and joints for the two specimens. The longitudinal bar strains of the first-story middle column bases for both specimens reached the measured yield strain of 2200 με. However, this strain of PCF was smaller than that of MCF, suggesting that the UHPC at column bases mitigated the damage to column bases. Besides, for PCF, the bottom longitudinal rebar strain of the left beam right end in the second story reached the measured yield strain of 2250 με, while in MCF, it did not.

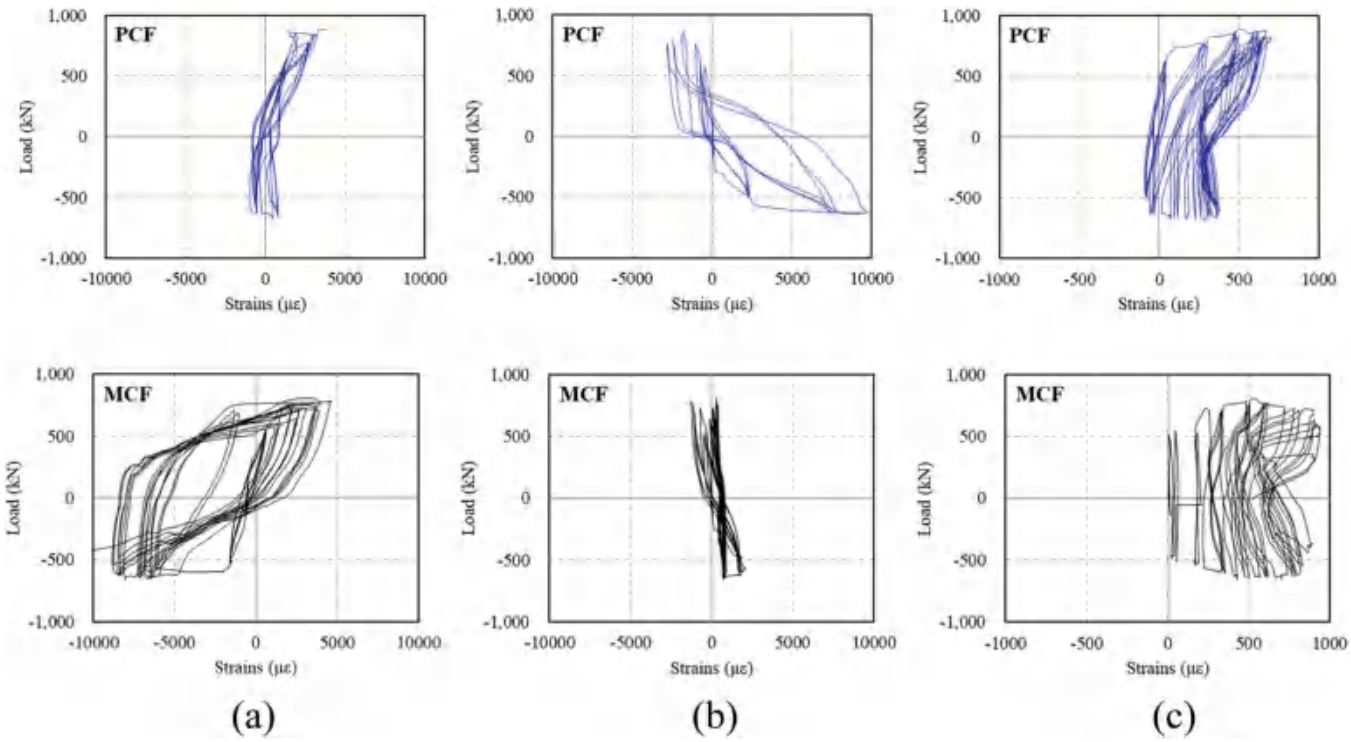

Fig. 15. Strains of rebars: (a) First-story middle column bases. (b) Second-story left beam right ends. (c) Second-story interior joints.

This indicated that the plastic hinges at the second-story beams of PCF were fully developed, whereas in MCF, these were underdeveloped. Additionally, stirrup strains in the second-story interior joints for both specimens were much smaller than the measured yield strains of 2290 με, indicating both specimens meet the design philosophy of strong joint-weak component. Furthermore, the stirrup strain in PCF was relatively smaller than that of MCF, suggesting that the UHPC in joints contributed to the function of stirrups.

4. Conclusions

Seismic performance of the precast concrete frame with UHPC-based connections was systematically investigated in terms of damage pattern, failure mechanism, hysteretic response, ductility, stiffness degradation, and energy dissipation. Based on the test results, the following conclusions could be drawn:

i. The precast concrete frame exhibited a damage pattern of concrete crushing and longitudinal reinforcements fracture at all beam ends of two stories. However, the monolithic concrete frame displayed a damage pattern of significant damage to beam ends and column bases of the first story. And, no destructive cracks were observed at joints for both frames.
ii. While the precast concrete frame exhibited beam mechanism and the monolithic concrete frame exhibited mixed mechanism, the precast concrete frame avoided the premature plastic hinges at the first-story column bases and achieved developed beam plastic hinges.
iii. The full-shaped hysteresis curves of the two frames demonstrated their excellent seismic performance. While both frames displayed a similar law of stage energy dissipation, the precast concrete frame exhibited higher cumulative energy dissipation than the monolithic concrete frame by 37 %.
iv. The load-carrying capacity of the precast concrete frame and monolithic concrete frame was 783.5 kN and 718.4 kN, respectively, with an improvement of 9 % for the precast concrete frame.
v. The displacement ductility factors of the roof, first story, and second story of the precast concrete frame were 4.14, 3.96, and 4.41, respectively, exceeding those of the monolithic concrete frame by 10 %, 7 %, and 17 %, respectively. The ultimate drifts of the two stories of the precast concrete frame were more than 3.3 %, showing a good deformation capacity.
vi. The two frames had a similar law of stiffness degradation, characterized by significant stiffness reduction in cracking and yielding stages, and slight stiffness reduction in ultimate and failure stages.

Overall, compared to the monolithic concrete frame, the precast concrete frame with UHPC-based connections exhibited a better seismic performance, particularly with respect to the load-carrying capacity, ductility, and energy dissipation capacity. In fact, these study results relating to UHPC-based connection has been incorporated into the Chinese specification DG/TJ 08–2154-2022.

CRediT authorship contribution statement

Weichen Xue: Supervision, Methodology, Funding acquisition, Conceptualization. **Yanghui Li:** Writing – original draft, Visualization, Methodology, Formal analysis. **Jiafei Jiang:** Supervision, Investigation.

Declaration of Competing Interest

The authors declare that they have no known competing financial interests or personal relationships that could have appeared to influence the work reported in this paper.

Data availability

Data will be made available on request.

Acknowledgments

This work was supported by Key Technologies Research and Development Program (Grant No.2022YFC3801400); the National Natural Science Foundation of China (Grant No. 52130806); Science and Technology Innovation Plan of Shanghai Science and Technology Commission (Grant No. 22dz1203100); Research and Demonstration of Integrated Structural-Insulation Technology in Ultra-low Energy Buildings (Grant No. 2023TDA3–2).

References

[1] Morris, A.E.J. Precast Concrete in Architecture. London: George Godwin Limited, 1978.
[2] Huber Bachmann, Alfred Steinle. Precast Concrete Structures. Berlin: Ernst & Sohn, A Wiley Company, 2011 . .
[3] Korkmaz HH, Tankut T. Performance of a precast concrete beam-to-beam connection subject to reversed cyclic loading. Eng Struct 2005;27:1392–407.
[4] FIB 43. Structural connections for precast concrete buildings. Fédération internationale du béton, Lausanne, Switzerland, 2008.
[5] Shicai Chen, Weiming Yan, Wenming Wang, et al. Seismic behavior of exterior beam to column joints with layered slab of large precast concrete structures. J Build Struct 2011;32(6) (in Chinese).
[6] Weijing Zhang, Guijie Wang, Chencheng Zhang, et al. Experimental study and finite element analysis on seismic behavior of assembled frames with rebars spliced by mechanical connection. China Civ Eng J 2019;52(5) (in Chinese).
[7] Zheng LX. Grouted precast concrete column connections under reversed cyclic bending and compression. Acids Struct J 1996;93(3):247–56.
[8] Kuttab A, Dougill JW. Grouted and doweled jointed precast concrete columns: behavior in combined bending and compression. Mag Concr Res 1988;40(144): 131–42.
[9] Weichen Xue, Haoyang Bai, Lingjie Dai, et al. Seismic behavior of precast concrete beam-column connections with bolt connectors in columns. Struct Concr 2020;22 (3):1–18.
[10] Palmieri L, Saqan E, French C, et al. Ductile connections for precast concrete frame systems. Acids Spec Publ 1996:162.
[11] Hu Xinyu, Xue Weichen, Yanheng Lv. Seismic behavior of a new type of precast concrete shear wall using UHPC connections at boundary elements. Eng Struct 2024;302:117468.
[12] Hu Rui, Fang Zhi, Shi Caijun. A review on seismic behavior of ultra-high performance concrete members. Adv Struct Eng 2021;24(5):1054–69.
[13] Hung Chung-Chan, Sherif El-Tawil PE, Shih-Ho Chao. A review of developments and challenges for uhpc in structural engineering: behavior. Anal, Des J Struct Eng 2021;147(9). 03121001.
[14] GB/T 51231-2016. Technical standard for assembled buildings with concrete structure. Beijing: China Building Industry Press; 2016.
[15] SIA 2052. Ultra-High Performance Fibre Reinforced Cement-based composites (UHPFRC): Construction material, dimensioning and application. MCS-EPFL Lausanne, Switzerland, 2016.
[16] NFP 18–710. Design of Concrete Structures: Specific Rules for Ultra-High Performance Fibre-Reinforced Concrete (UHPFRC). La Plaine Saint-Denis, France: AFNOR, 2016.
[17] Aaleti S, Petersen B, Sritharan S. Design guide for precast UHPC waffle deck panel system, including connections. FHWA-HIF-13-032. Washington, DC: USDOT,; 2013.
[18] Wille K, El-Tawil S, Naaman AE. Properties of strain hardening ultra high performance fiber reinforced concrete (UHP-FRC) under direct tensile loading. Cem Concr Compos 2014;48:53–66.
[19] Ahlborn TTM, Harris DK, Misson DL, Peuse EJ. Characterization of strength and durability of ultra-high-performance concrete under variable curing conditions. Transp Res Rec 2011;2251(1):68–75.
[20] Li Junquan, Wu Zemei, Shi Caijun, Yuan Qiang, Zhang Zuhua. Durability of ultra-high performance concrete-A review. Constr Build Mater 2020;255:1–13.
[21] Peter Buitelaar. Ultra High Performance Concrete: Developments and Applications during 25 years. Plenary Session International Symposium on UHPC, 2004, Kassel, Germany.
[22] Mari Bøhnsdalen Eide, Jorun-Marie Hisdal. Ultra High Performance Fibre Reinforced Concrete (UHPFRC) - State of the art. COIN Project report no 44, SINTEF Building and Infrastructure, Norwegian, 2012.
[23] 2023 report on the technology and application development of Ultra High Performance Concrete (UHPC) in China. Beijing: China Concrete & Cement-based Products Association.
[24] Amran Mugahed, Murali G, Makul Natt, et al. Sustainable development of eco-friendly ultra-high performance concrete(UHPC): cost, carbon emission, and structural ductility. Constr Build Mater 2023;398:132477.
[25] Jiansheng Fan, Ran Ding. Development on ultra-high performance concrete in building structures. J Chin Ceram Soc 2023;51(5):1246–58 (in Chinese).
[26] Xinyu Hu, Weichen Xue, et al. Bond properties between lapped steel rebars and UHPC under direct tension. Constr Build Mater 2023;408:1–12.
[27] Xinyu Hu, Weichen Xue, Yanheng Lv. Experimental investigations of bond behavior of double-row spliced rebars in Ultra-High Performance Concrete (UHPC). Eng Struct 2023;284:1–11.
[28] Ronanki VS, Aaleti S, Valentim DB. Experimental investigation of bond behavior of mild steel reinforcement in UHPC. Eng Struct 2018;176:707–18.
[29] Yuan J, Graybeal B. Bond of reinforcement in ultra-high-performance concrete. Acids Struct J 2015;112(6).
[30] Lagier F, Massicotte B, Charron JP. Experimental investigation of bond stress distribution and bond strength in unconfined UHPFRC lap splices under direct tension. Cem Concr Compos 2016;74:26–38.
[31] Hu X, Xue W, Xue W, et al. Bond strength of sand-coated deformed GFRP bars in UHPC, HPC, and NC. Constr Build Mater 2023;403:133175.
[32] Hu X, Xue W, Song J, et al. Experimental investigations of precast concrete column with spliced connections based on ultrahigh-performance fiber-reinforced concrete. Struct Concr 2023;24(3):3708–26.
[33] Xue W, Hu X, Song J. Experimental study on seismic behavior of precast concrete beam-column joints using UHPC-based connections. Structures 2021;34:4867–81.
[34] Maya LF, Zanuy C, Albajar L, et al. Experimental assessment of connections for precast concrete frames using ultra high performance fiber reinforced concrete. Constr Build Mat Constr Build Mater 2013;48(19):173–86.
[35] Ma F, Deng M, Ma Y, et al. Experimental study on interior precast concrete beam-column connections with lap-spliced steel bars in field-cast RPC. Eng Struct 2021; 228:111481.
[36] Xiong X, Xie Y, Yao G, et al. Experimental study on seismic performance of precast pretensioned prestressed concrete beam-column interior joints using UHPC for connection. Materials 2022;15(16):5791.
[37] ACI 318-19. Building Code Requirements for Structural Concrete. Farmington Hills, MI, USA: American Concrete Institute; 2019.
[38] EN 1992–1-1: 2023(E). Eurocode 2-Design of Concrete Structures-Part 1–1. European Union: Comité Européen de Normalisation; Brussels, 2023.
[39] NZS 3101: 2006. The Design of Concrete Structures. Wellington: Standards Association of New Zealand; 2006.
[40] GB 50010–2010. Code for design of concrete structures. Beijing: China Building Industry Press; 2010.
[41] GB/T 50081–2016. Standard for test methods of concrete physical and mechanical properties. Beijing: China Building Industry Press; 2016.
[42] GB/T 31387–2015. Reactive powder concrete. Beijing: China Standards Press; 2015.
[43] GB/T 228.1–2010. Metallic Materials-Tensile testing Part 1: Method of test at room temperature. Beijing: China Standards Press; 2010.
[44] JGJ/T 101–2015. Specification for seismic test of buildings. Beijing: China Building Industry Press; 2015.
[45] Park R, Paulay T. Reinforced concrete structures. New York: John Wiley & Sons; 1975.
[46] Paulay T, Priestley MJN. Seismic design of reinforced concrete and masonry buildings. New York: John Wiley & Sons. Ltd,; 1992.
[47] AIJ Structural Guidelines for Reinforced Concrete Buildings. Tokyo, Japan: Architectural Institute of Japan; 1994.
[48] Haoyu Zhang Tao Wang, Lin Xuchuan, et al. Typical seismic damage and discussion of reinforced concrete frames during Nepal's 8.1 magnitude earthquake. Eng Mech 2016;33(9):59–68 (in Chinese).
[49] Xue Weichen, Yang Xinlei. Tests on half-scale, two-story, two-bay, moment-resisting hybrid concrete frames. Acids Struct J 2009;106(5):627–35.
[50] ACI. 374.1-05. Acceptance Criteria for Moment Frames Based on Structural Testing and Commentary. Farmington Hills, MI: American Concrete Institute,; 2005.
[51] EN 1998–1: 2004(E). Eurocode 8: Design of structures for earthquake resistance -Part 1. European Union: Comité Européen de Normalisation; Brussels, 2004.
[52] ASCE/SEI 41–06. Seismic Rehabilitation of Existing Buildings. American Society of Civil Engineering; Virginia, 2007.
[53] Xu Shenchun, Wu Chengqing, Liu Zhongxian, et al. Experimental investigation of seismic behavior of ultra-high performance steel fiber reinforced concrete columns. Eng Struct 2017;152:129–48.
[54] Xue Weichen, Hu Xinyu, Ren Dongsheng, Hu Xiang. Seismic behavior of precast 100 MPa grade HSC frames under reversed cyclic loading. Eng Struct 2021;243: 1–13.

Received: 7 August 2023 | Revised: 18 June 2024 | Accepted: 11 July 2024

DOI: 10.1002/suco.202300619

ARTICLE

Out-of-plane response of prefabricated concrete shear walls connected via grouted sleeves

Weichen Xue | Qian Huang | Zhijun Xu | Jiayin Yu | Ya Li

Department of Structural Engineering, Tongji University, Shanghai, China

Correspondence
Weichen Xue, Department of Structural Engineering, Tongji University, Shanghai, China.
Email: xuewc@tongji.edu.cn

Funding information
National Key R&D Program of China, Grant/Award Number: 2022YFC3801400; Science and Technology Innovation Plan of Shanghai Science and Technology Commission, Grant/Award Number: 22dz1203100; Program Fund of Non-Metallic Excellence and Innovation Center for Building Materials, Grant/Award Number: 2023TDA3-2

Abstract

The out-of-plane response of prefabricated (precast) concrete shear walls (PWs) are usually neglected in the structural designs. However, because of the relatively low stiffness and inevitable deformation of slabs, the out-of-plane behavior of PWs could influence the in-plane response by causing premature failure or stability problems and affect the overall structural performance. This issue becomes significant when single-row connections are employed because the neutral axial is shifted toward the compression side and the out-of-plane capacity is altered accordingly. In this study, PWs with grouted steel sleeve splices were tested under reciprocating cyclic loading. Both single-row and paired connections were considered in test program. It was shown that all PWs suffered bending failure dominated by yielding of reinforcement at the bottom, and their load-carrying capacity, stiffness degeneration trends were similar to the monolithic (cast-in-place) reference walls. Under the normalized compression of 0.12, the ductility of the prefabricated walls was 2.62 and 3.07, which was comparable to that of the reference cast-in-place wall (2.72). For the case that axial compression was not applied, the hysteresis curve of the PW with single-row connection exhibited significant pinching. Nonetheless, the load-carrying capacity of these walls did not exhibit significant drop at the end of the tests due to the lower axial compression, exhibiting high level of deformability. For both load cases, PWs with paired connection exhibited higher energy dissipation than the single-row connected specimens.

KEYWORDS

cyclic loading, displacement ductility, grouted steel sleeves, precast concrete shear walls, single-row connection

1 | INTRODUCTION

The precast concrete structures have drawn global attention in the past few decades, because of their superior advantages in engineering practice including speedy construction, minimized environmental pollution, guaranteed quality and lowered labor and material expenses on site compared to their counterpart conventional monolithic (cast-in-place) concrete structures.[1,2] The precast concrete shear walls (PWs) usually serve as main load carrier in residential buildings, especially in intensive earthquake areas, due to their high lateral stiffness and strength.[3]

In practice, the PWs are commonly manufactured in factories in advance, followed by erection and assembly on the construction sites. Thus, the structural behavior of

FIGURE 1 Schematic sketch of PWs with GS connection.

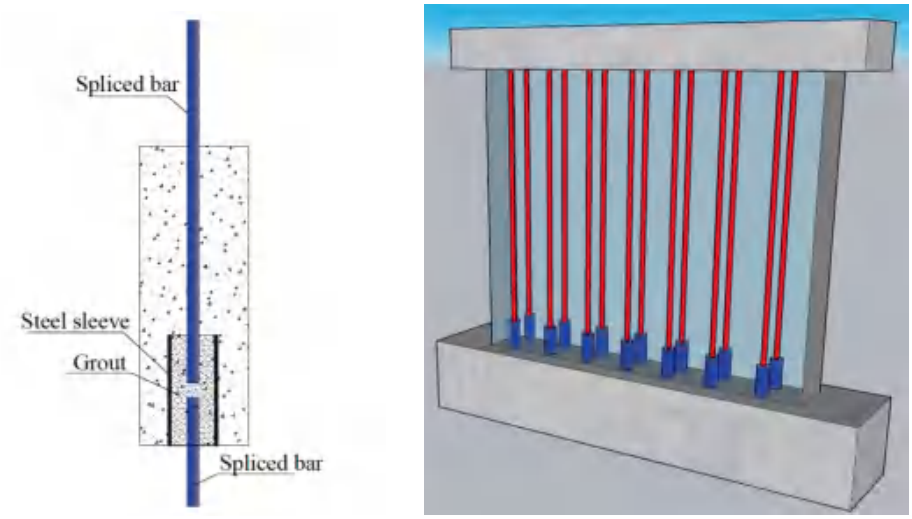

(a) Splicing detail (b) Application in walls

PWs in service are significantly related to their vertical (upper and lower storey) connections.[4–6] Nowadays, the grouted steel sleeve splice (GS) is the most commonly utilized connecting approach for PWs (see Figure 1). The GS is implemented by grouting the splicing bars in the steel sleeves, forming butt-to-butt connections. Current applications and related research works have shown that the PWs with GS could achieve satisfactory in-plane structural performance compared with the monolithic concrete shear walls.[7–10]

At present, because the lateral (in-plane) stiffness of the shear walls is dramatically greater than their transverse (out-of-plane) stiffness, engineering practitioners mainly concerns the in-plane performance of shear walls and neglect their out-of-plane behavior.[11,12] However, shear walls are also subjected to transverse bending moments transferred from upper beams or superstructure, and these bending moments could cause unexpected out-of-plane deflections or even concrete damage because of low stiffness. In addition, current structural designs mainly adopt a "rigid slab" hypothesis, however, the slabs do exhibit elastic behavior in practice under service loads, which also leads to subsequent out-of-plane deformation of the walls.[13] As a result, the concrete damage and nonuniform deflection is able to furtherly lead to tortional deformation of the shear walls or even deteriorate their in-plane performance.[14] In addition, PW applications mostly use paired connections (both sides of the reinforcements in the wall panels are connected with the bottom) in practice, this method could time-consuming and involves a high level of expenses. Thus, a number of studies proposed the single-row connection and verified their in-plane performance by conducting reversed cyclic loading tests. However, since the single-row connection is normally installed at the centerline of the section of walls, this connection layout could shift the neutral axis toward the compression side, and furtherly alter the out-of-plane load bearing capacity.[15,16] The single-row connecting method is timely and economically attractive in practice, however their wide-use still requires a thorough investigation of their the out-of-plane behavior.

The related studies on the out-of-plane behavior of PWs are very limited. Su and Wong[17] investigated the response of slender reinforced concrete shear walls under in-plane seismic actions. It was found that high axial load could induce abrupt out-of-plane failure of the shear walls due to nonuniform distortion of the shear walls with severe cracking and crushing, which led to significant drop in the in-plane load carrying capacity. Similar results were reported in Robazza et al.,[14] Singhal et al.,[18] Rosso et al.,[19,20] and Dashti et al.[21] Gu et al.[22] studied the behavior of double-face superposed concrete shear walls under out-of-plane actions, considering different vertical connections including direct lap splice, additional lap splice and confined additional lap splice connections. The test results showed that the horizontal connection of the shear walls affects the cracking development. The shear walls with vertical connections displayed improved structural response than the corresponding monolithic specimen, and the shear wall with direct lap splice connection exhibited the highest peak strength and displacement ductility. However, only paired connection was considered, and the behavior of single-row connections was not studied.

Previous research works and engineering practices have shown that the deformation of the slabs could lead to out-of-plane deflection of PWs with relatively low

17517648, 2024, 5, Downloaded from https://onlinelibrary.wiley.com/doi/10.1002/suco.202300619 by Tsinghua University Library, Wiley Online Library on [23/01/2025]. See the Terms and Conditions (https://onlinelibrary.wiley.com/terms-and-conditions) on Wiley Online Library for rules of use; OA articles are governed by the applicable Creative Commons License

TABLE 1 List of shear wall specimens.

Group	Walls	Type	Splices	Connection	Normalized compression
I	RW1	Cast-in-place	–	Paired	0.12
	PW1	Precast	GS	Paired	
	PW2	Precast		Single-row	
II	RW2	Cast-in-place	–	Paired	0
	PW3	Precast	GS	Paired	
	PW4	Precast		Single-row	

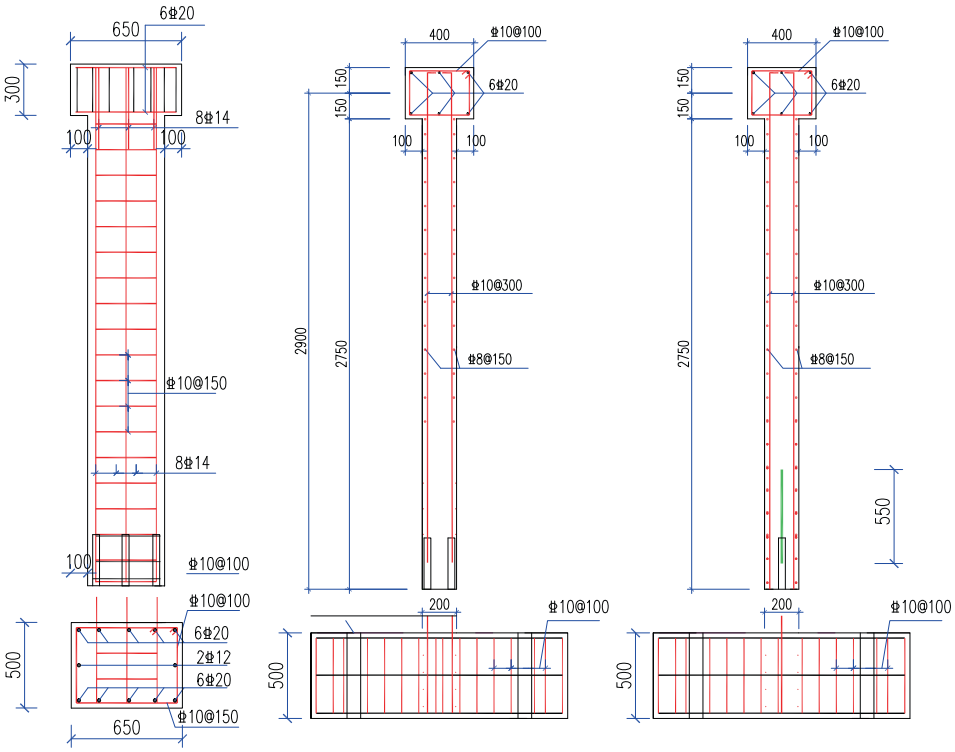

FIGURE 2 Geometric configurations of PWs (PW1&3, PW2&4).

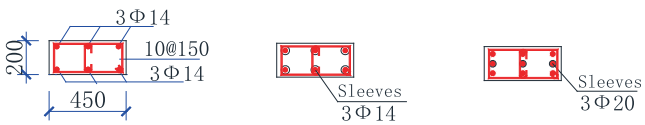

FIGURE 3 Cross sections of PWs (monolithic, paired, and single-row).

stiffness, while current studies only concern the in-plane performance of shear walls. For the vertical connections in PWs, single-row connections could shift the neutral axis and result in altered out-of-plane stiffness and load carrying capacity of PWs. Therefore, the out-of-plane behavior of PWs with sleeve connections are investigated in this study. An experimental program on the cyclic response of six full-scale shear walls comparison was conducted, considering different splicing layouts and axial compressions. The out-of-plane responses of the shear walls under cyclic actions are studied and discussed.

2 | EXPERIMENTAL PROGRAM

2.1 | Shear wall specimens

Six full-scale shear walls, including two cast-in-place concrete shear walls (RW1 and RW2) and four PWs (PW1–PW4) were designed and loaded under reciprocating cyclic actions. Only the boundary elements are considered, because the boundary elements are the main load carriers due to significantly denser reinforcements. Thus, the wall specimens might seem like flat columns. The reinforcement arrangements of the walls were designed based on the international building standards for seismic-resistant structures.[23–25]

Paired and single-row GS connections were considered and separately employed in the precast walls. The test matrix of the specimens can be found in Table 1.

17517648, 2024, 5, Downloaded from https://onlinelibrary.wiley.com/doi/10.1002/suco.202300619 by Tsinghua University Library, Wiley Online Library on [23/01/2025]. See the Terms and Conditions (https://onlinelibrary.wiley.com/terms-and-conditions) on Wiley Online Library for rules of use; OA articles are governed by the applicable Creative Commons License

FIGURE 4 Precast parts.

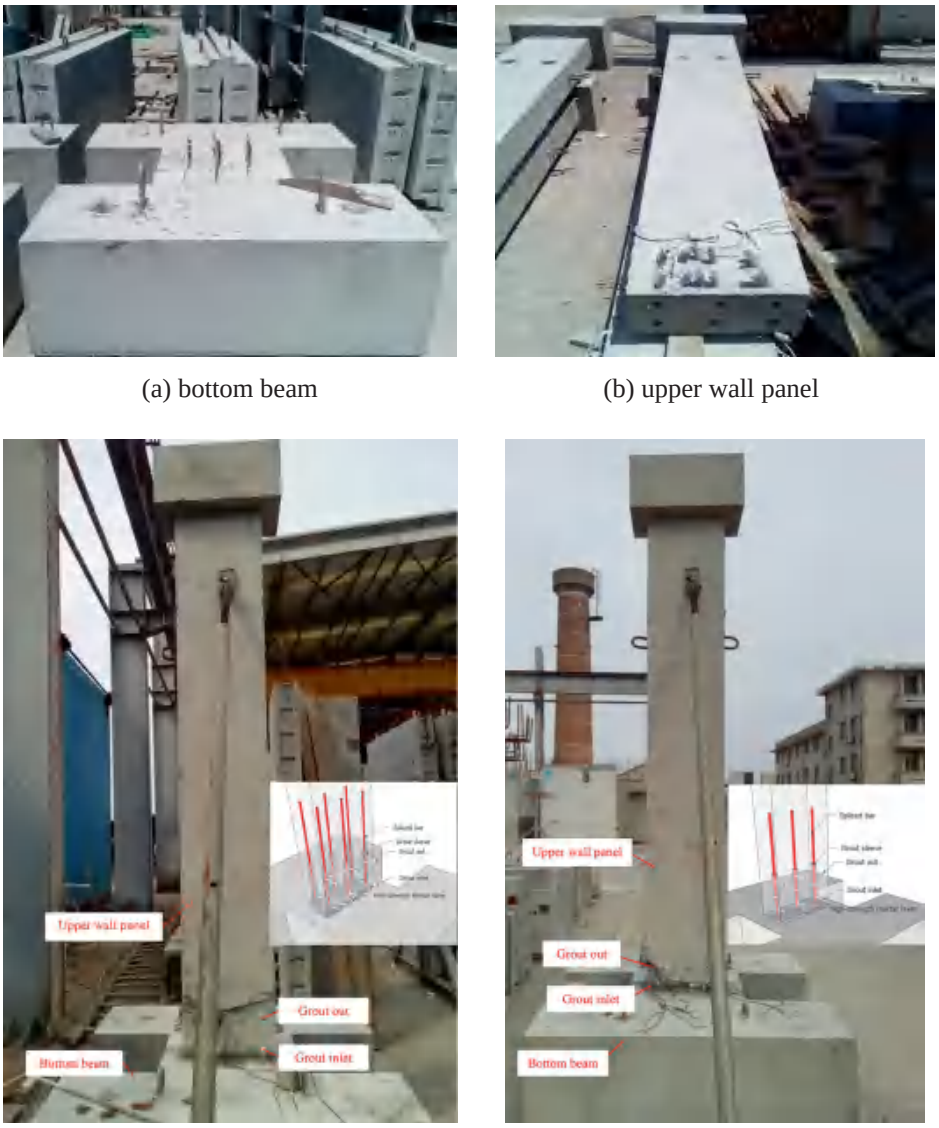

(a) bottom beam (b) upper wall panel

(c) (d)

The monolithic walls and the precast walls were all 2900 mm (height) × 450 mm (width) × 200 mm (thickness) in geometric dimension. The vertical bars were 14 mm in diameter and the stirrups were made with 10 mm bars.

Figures 2 and 3 display the reinforcement layouts and the cross-section of the specimens at the region of connection. The paired connection is the common practice by connecting the vertical reinforcements. The single-row connection is implemented by splicing the extra rebars at the middle-line of wall cross-section, leaving the vertical bars on both sides unconnected. Please note that the paired and single-row connection use different splicing layouts, but the total reinforcement ratio of the connecting rebars were equivalent. Concentric axial load ratios (normalized compression) were 0.12 and 0 for Group I and II, respectively.

For the GS connection, determination of the anchorage depth of the rebars was followed the design guide from the supplier, as the splicing strength must not be lower than the strength of the steel bars under direct tensile tests. For 14 and 20 mm splicing bars, the embedding length of the splicing bars in the sleeves were 120 and 160 mm.

2.2 | Cast of specimens

Preparation of the precast shear walls started from prefabricating the bottom foundations and the upper wall panels in industrial plants (see Figure 4). The steel sleeves were embedded in the upper walls, and the connecting rebars were extended from the lower foundation for further connection. After standard moisture or steam

17517648, 2024, 5, Downloaded from https://onlinelibrary.wiley.com/doi/10.1002/suco.202300619 by Tsinghua University Library, Wiley Online Library on [23/01/2025]. See the Terms and Conditions (https://onlinelibrary.wiley.com/terms-and-conditions) on Wiley Online Library for rules of use; OA articles are governed by the applicable Creative Commons License

TABLE 2 Physical properties of rebars.

Bars	f_y (MPa)	f_u (MPa)	E_s (GPa)
20 mm	412	595	195
16 mm	417	610	199
14 mm	440	627	195
12 mm	443	599	192
10 mm	461	652	210
8 mm	437	628	207

TABLE 3 Physical properties of concrete.

Specimen	f_{cu} (MPa)	f_c (MPa)	f_t (MPa)	E_c (GPa)
RW1	42.6	31.5	3.21	32.7
PW1	44.1	33.2	3.29	33.2
PW2	41.3	32.8	3.30	33.8
RW2	42.9	31.3	3.18	3.14
PW3	42.5	33.6	3.32	33.4
PW4	41.2	32.8	3.31	33.7

curing, the precast parts were sent for assembly. The upper walls were hoisted upright and the splicing bars from the foundation were embedded in the sleeves (see Figure 4). The walls were finished after grouting the sleeves using high-strength, non-shrink mortar with characteristic compressive strength of 80 MPa.

2.3 | Physical properties of materials

Commercial concrete with characteristic cubic compressive strength of 30 MPa were used for the shear walls, and these walls were all reinforced employing 400 MPa steel rebars. When casting the wall specimens, 150 mm × 150 mm × 150 mm concrete cubes, 100 mm × 100 mm × 300 mm, and steel bar segments were also prepared using the same batch. The strengths and moduli of rebars and concrete were tested and are presented in Tables 2 and 3, where f_y, f_u, and E_s refer to the yielding stress, ultimate strength, and Young's modulus of steel rebars and f_{cu}, f_c, f_t, and E_c are the cubic strength, prism strength, tensile strength, and elastic modulus of concrete. The strength of the sleeves is measured as 618 MPa.

2.4 | Test setup

The cyclic tests were performed in the key laboratory for engineering structures in Tongji University. The specimens were seated and positioned on the ground via the used of four anchor bolts, in order to form a fixed constraint at the bottom of the walls. In Group I, the axial compressions were directly applied on the top via a hydraulic jack and a spreader beam before the lateral load was enforced, and the compression ratio (0.12) was the fraction of the vertical action and the characteristic axial load-bearing strength of the walls. Please note that the vertical actuator is actively mobilized, as it will automatically move along with the walls by tracing the applied lateral displacements. In Group II, no axial compression was considered. The horizontal actions were evenly applied to the top beam, resulting in a clear height of 2900 mm. The applied vertical and horizontal loads were not only read by the loading system, but also via load cells attached to the loading surfaces. The deflections of the walls were measured by displacement sensors and the stains of concrete and steel rebars were recorded by strain gauges glued on the concrete and rebar surfaces. The test setup is shown in Figure 5.

After applying the vertical compression, the horizontal loads were enforced via a hybrid load–displacement control. The load-control approach was used at a slow pace for detecting the cracking loads. And the displacement-control method was used afterwards, consisting of 3 reciprocating cycles per drift level (increased by 1.00% drift per level). The loading drift was calculated via dividing the applied displacement by the clear height of the walls (2900 mm). The loading sequence is shown in Figure 6 following the provisions provided in JGJ/T 101-2015.[26] The test was continued till the load-bearing capacity of specimens dropped 15% or the applied displacements reached the stroke of the actuator.

3 | OBSERVATIONS AND DISCUSSIONS

3.1 | Structural behavior and failure

The general structural behavior and failure of the precast specimens resembled with that of the monolithic reference specimens under reversed cyclic loading for both groups. Given the test set up, representative distribution of cracks of the specimens can be seen in Figure 7a, as the cracks were horizontal and parallelly patterned, indicating that all specimens suffered flexual failure (Figure 7b). The failure of the specimens was dominated by yielding of vertical reinforcement at the bottom part of the walls. The stirrups in the specimens were in elastic state throughout the entire loading process, because stain gauges read that all peak strains were all lower than 800 με (yielding of the rebars was above 2250 με). The strength of the specimens in Group I were 15.7, 13.2, and 15.8 kN for RW1, PW1, and PW2,

17517648, 2024, 5, Downloaded from https://onlinelibrary.wiley.com/doi/10.1002/suco.202300619 by Tsinghua University Library, Wiley Online Library on [23/01/2025]. See the Terms and Conditions (https://onlinelibrary.wiley.com/terms-and-conditions) on Wiley Online Library for rules of use; OA articles are governed by the applicable Creative Commons License

FIGURE 5 Test setup.

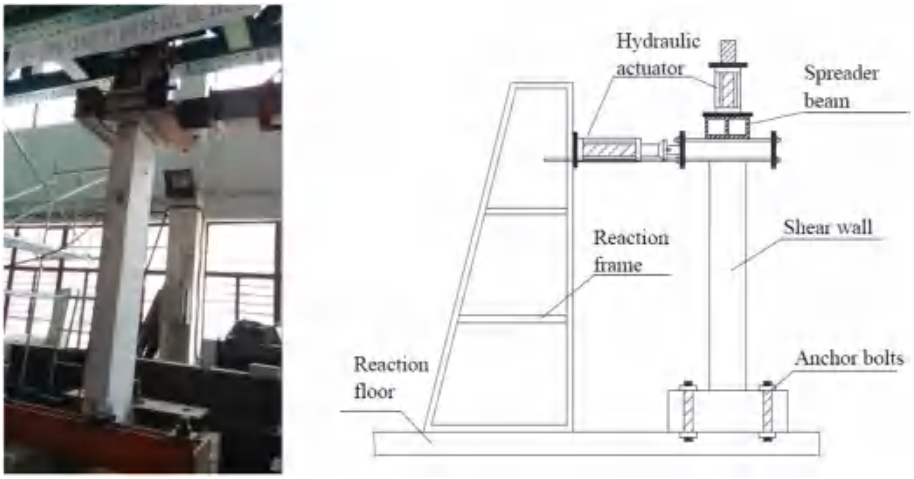

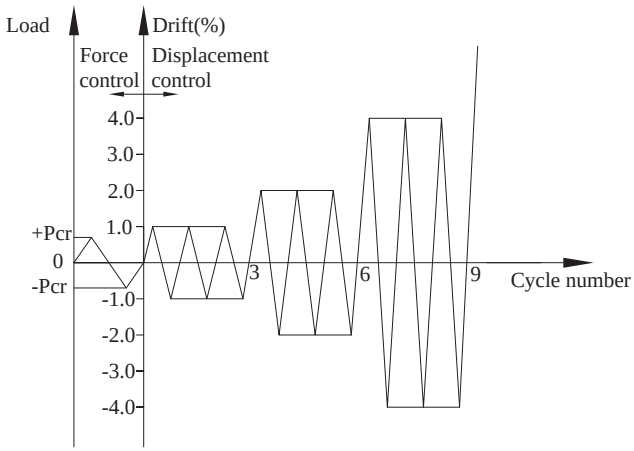

FIGURE 6 Loading history.

respectively. For the case without axial compression, the strength of the walls slightly reduced, and were 12.9, 11.4, and 13.0 kN.

The detailed response of the shear walls is described as follows:

1. Cracking: horizontal cracks appeared when the lateral drift reached 0.25%–0.4% drift near the wall panel-bottom beam interface (approximately 8 kN for Group I and 2 kN for Group II). Shear walls with single-row connection are more prone to cracking due to the reinforcement arranged in the center of the wall. The first crack was approximately 0.02 mm wide. More parallel cracks were observed with the increase of the lateral load and they gradually extended to the two side faces of the walls.
2. Reinforcement yielding: The vertical rebars in PW1, PW2, and RW1 started to yield in tension at the drift from 0.46% to 0.51% (approximately 12 kN for Group I). The vertical rebars in PW3, PW4, and RW2 started to yield in tension at the drift ratio of about 2.95% (approximately 10 kN for Group II). More vertical rebars were found yielded afterwards. Few new cracks appeared after this stage. The cracks slightly opened up to 1.08 mm.
3. Peak Strength: The shear walls achieved their peak strengths from 13.2 to 15.8 kN for Group I and from 11.4 to 13.0 kN for Group II. At the peak loads, slight crushing of was observed at the bottom interface (Figure 7b). The crack widths largened up to 1.2 mm (Figure 7a). The test of specimens in Group II was terminated when the actuator reached its stroke length of 174 mm because the loads did not show any significant decline.
4. Failure: when the load-carrying capacity of the shear wall in Group I dropped 15%, the walls were considered to fail. At failure, severer crushing of concrete was noticed, and the interface of the wall-bottom foundation were slightly lifted due to the slip of the connecting rebars in the sleeves (see Figure 7d). The lifting of the walls at the edge with single-row connection (about 5.9 mm for PW2 and 14.4 mm for PW4) were higher than that of the wall using double-row splicing bars (about 5.0 mm for PW1 and 10.5 mm for PW3). This is mainly because the reinforcement of single-row splices connected wall were arranged in center of the cross sections. In addition, the lifting of RW1 and RW2 were 5.3mm and 10.2mm, respectively.

Generally, the responses of the precast walls with different splicing layouts in Group I were very similar, because the axial compression increased the friction at the wall-bottom interfaces and restrained the slip of the splicing bars, which passively improved the structural integrity. However, in Group II, the behavior of the prefabricated walls was slightly weaker compared with those cast-in-place ones, because the deformation of the walls led to wall rocking, especially for the wall with single-row connection.

17517648, 2024, 5, Downloaded from https://onlinelibrary.wiley.com/doi/10.1002/suco.202300619 by Tsinghua University Library, Wiley Online Library on [23/01/2025]. See the Terms and Conditions (https://onlinelibrary.wiley.com/terms-and-conditions) on Wiley Online Library for rules of use; OA articles are governed by the applicable Creative Commons License

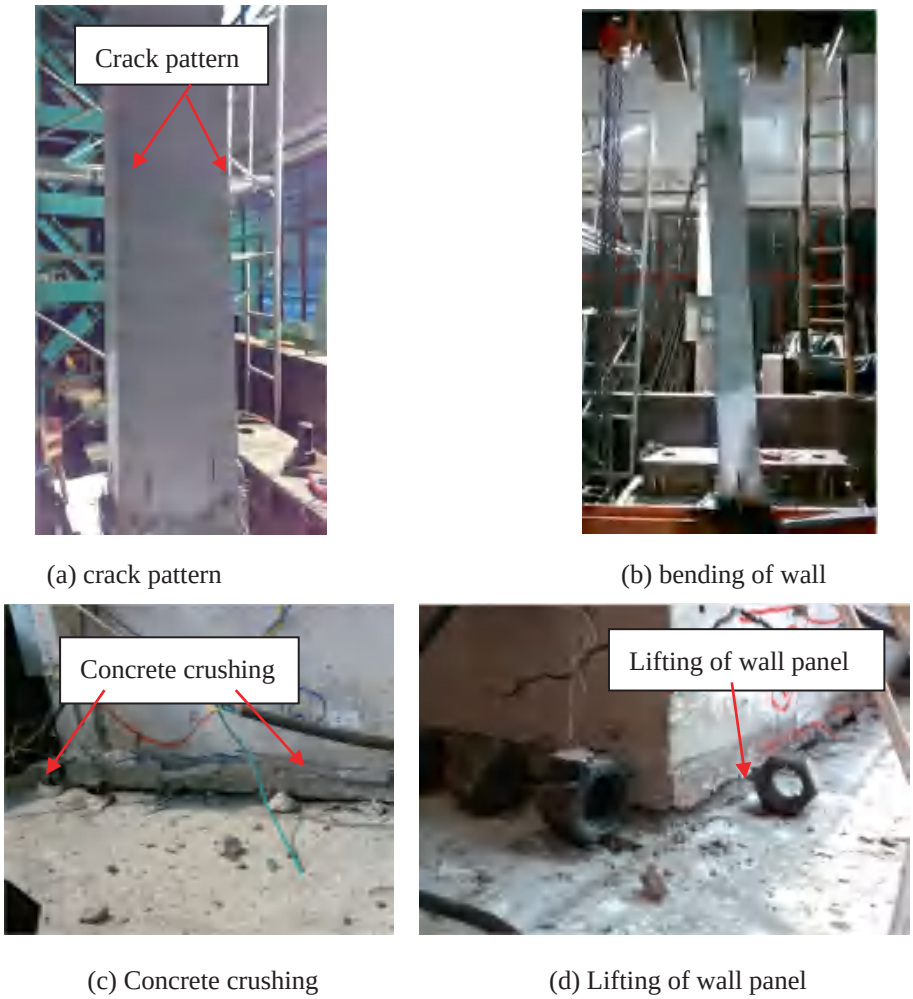

(a) crack pattern (b) bending of wall

(c) Concrete crushing (d) Lifting of wall panel

FIGURE 7 Response of PWs.

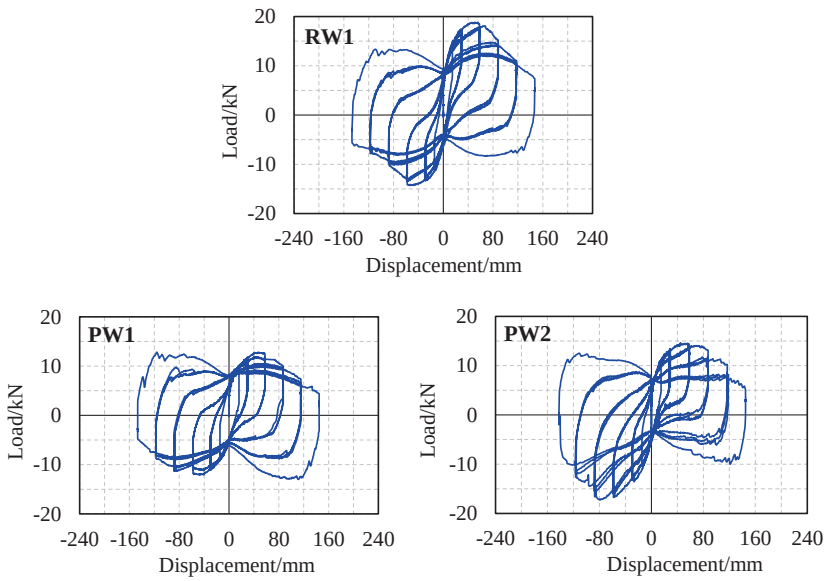

FIGURE 8 Hysteresis curves of specimen under normalized compression of 0.12.

3.2 | Hysteresis curves

The hysteresis curves show the relationship between the load exerted on the structural member and its corresponding lateral displacement under the reversed cyclic loading, which reflects the deformation characteristics and energy dissipation of the structural member during the entire progress of the test, and give a

17517648, 2024, 5, Downloaded from https://onlinelibrary.wiley.com/doi/10.1002/suco.202300619 by Tsinghua University Library, Wiley Online Library on [23/01/2025]. See the Terms and Conditions (https://onlinelibrary.wiley.com/terms-and-conditions) on Wiley Online Library for rules of use; OA articles are governed by the applicable Creative Commons License

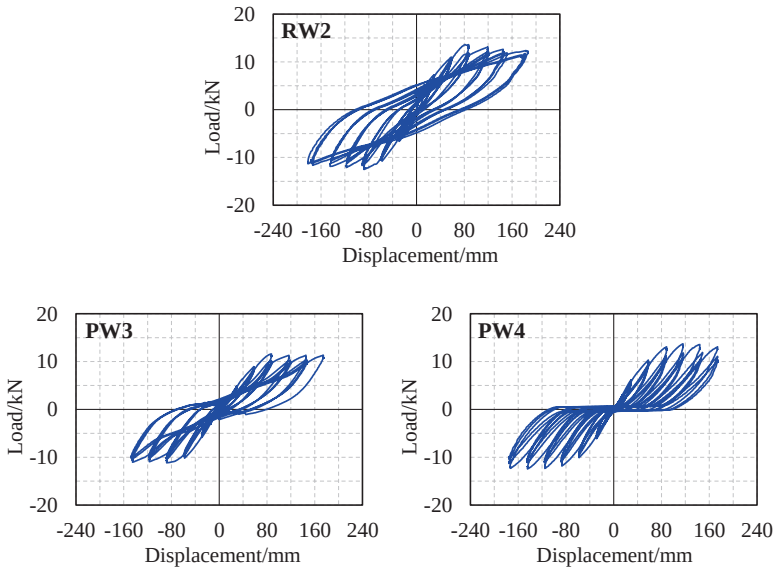

FIGURE 9 Hysteresis curves of specimen under normalized compression of 0.

comprehensive understanding of the seismic performance of the member. The hysteresis curves also provide basis for determining the restoring force model and conducting nonlinear seismic response analysis.

The hysteretic loops of the specimens under the axial load ratio of 0.12 (RW1, PW1, and PW2) are shown in Figure 8. It is found that at small lateral drifts, the area enclosed by the hysteresis curves was negligible, and the area gradually enlarged with the increase of lateral displacements. The loops show some pinching at later loading stages, which could be attributed to yielding and buckling of vertical rebars, concrete crushing and slight bond-slip of splicing rebars. The prefabricated shear walls had the similar shape and same number of hysteretic curves compared with the cast-in-place wall. All specimens demonstrated substantial residual displacements during unloading, resulting in large amount of dissipated energy.

For the specimens without axial compression (Group II; Figure 9), noting that the when applied lateral displacements at the top of the walls reached the maximum stroke of the hydraulic jack, there was no indication of any drop in the bearing capacity of the specimens. The termination of the tests could not reflect the final failure of the shear walls. The hysteresis curves of the shear walls are significantly different from the ones in Group I. It can be seen that the monolithic shear wall RW2 had relatively wide loops, showing a shuttle-like shape. The precast walls, on the other hand, exhibited significantly narrower loops, the wall using single-row splices (PW4) in particular. The narrower curves of the wall with paired connection (PW3) could be caused by the bond-slip of the splicing bars in the sleeves. The shape of the curve of PW4 was mainly attributed to the wall rocking after continuous concrete spalling and the steel yielding.

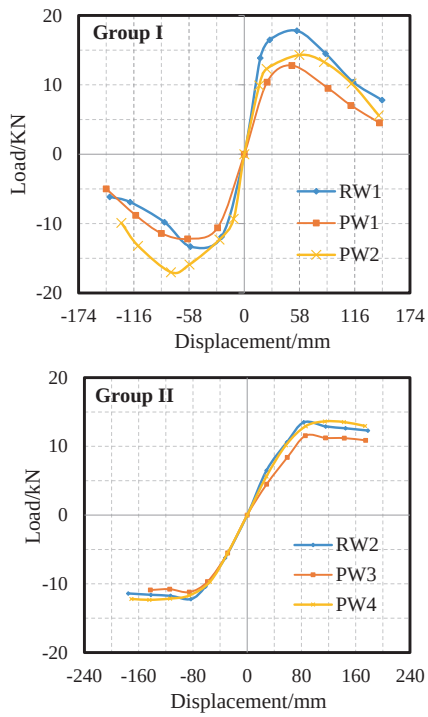

FIGURE 10 Backbone curves of specimens.

3.3 | Backbone curves

The backbone curves are obtained by connecting the peak points in the hysteresis loops of structural members. The backbone curves are the locus of the maximum loads with respect to applied lateral displacements, which reflects the strength, deformability, and the structural rigidity at different phases. The backbone curves are shown in Figure 10 and the critical points on the curves are summarized in Table 4. where P_{cr}, P_y, P_{max}, and P_u

17517648, 2024, 5, Downloaded from https://onlinelibrary.wiley.com/doi/10.1002/suco.202300619 by Tsinghua University Library, Wiley Online Library on [23/01/2025]. See the Terms and Conditions (https://onlinelibrary.wiley.com/terms-and-conditions) on Wiley Online Library for rules of use; OA articles are governed by the applicable Creative Commons License

TABLE 4 Characteristic values of the envelop curves.

Specimen		P_{cr} (kN)	Δ_{cr} (mm)	P_y (kN)	Δ_y (mm)	P_{max} (kN)	Δ_{max} (mm)	P_u (kN)	Δ_u (mm)	Δ_u/Δ_y	Avg.
RW1	POS	11	6.38	17	13.4	17.8	55.3	15.13	80.2	2.52	2.72
	NEG	8.5	5.50	12.3	14.1	13.6	47	11.56	71.6	2.92	
PW1	POS	8	9.36	11.7	12.8	12.8	50	10.88	74.8	2.47	2.62
	NEG	7	7.58	11.9	16.5	13.5	64.6	11.475	91.5	2.77	
PW2	POS	8	14.85	12.69	12.7	14.3	61.3	12.155	95.2	3.46	3.07
	NEG	10	4.53	14.66	13.7	17.2	70.6	14.62	100.4	2.69	
RW2	POS	2	4.08	–	–	13.5	–	–	175	–	–
	NEG	2	4.95	–	–	12.2	–	–	175	–	
PW3	POS	1.5	11.42	–	–	11.6	–	–	175	–	–
	NEG	1	5.64	–	–	11.2	–	–	175	–	
PW4	POS	1	5.33	–	–	13.6	–	–	175	–	–
	NEG	1	5.41	–	–	12.3	–	–	175	–	

refer to the lateral loads at first cracking, specimens yielding, peak load, and the final failure. $\triangle_{cr}$, $\triangle_y$, $\triangle_{max}$, and $\triangle_u$ represent the corresponding lateral displacements. The yielding here is not the load of reinforcement yielding, but calculated based on the equivalent energy model introduced by Park,[27] indicating a significant change of structural behavior and the ultimate load is the load when sudden structural failure happened. The test of specimens in Group II was terminated when the actuator reached its stroke length of 174 mm, which indicated greater deformability of specimens.

Figure 10 shows that, for the specimens with normalized compression of 0.12 (RW1 as well as PW1 and PW2), the structural response under cyclic loading went through four stages: cracking, yielding, peak strength and final failure. Prior to cracking, the load and displacement basically exhibited a linearly positive correlation, and after cracking, the stiffness of the specimens degraded gradually. After yielding, the tangent stiffnesses of the specimens decreased continuously with the increase of displacement and became negative in the post-peak stage. It can be seen that the averaged strength of the shear wall with single-row GS connection (PW2) is higher than that of PW1, which could be contributed to the installation of extra splicing bars, resulting in a higher reinforcement ratio at the bottom part of the wall panel.

For the specimens with axial compression ratio of 0 (RW2, PW3, and PW4), the shear walls without axial compression here behaved similarly to cantilever reinforced beams. The applied loads were found to stay on a relatively stable and did not show any significant drop till the end of the tests. The load–displacement curve of the specimens became approximately flat after specimen yielding and the tangent stiffness approaches zero. The shear wall with paired GS connection (PW3) also showed slightly lower strength, even with shifted neutral axis.

3.4 | Displacement ductility

Ductility is an important metric that reflects the deformability of a structural member, and often expressed by ductility coefficients. The ductility coefficients are calculated by dividing ultimate displacement by the yielding displacement. The ductility of all shear wall in Group I is shown in Table 4. Because the failure displacement of the walls in Group II was not captured in the test, the ductility of these walls is not presented.

It is found the displacement ductility of walls in Group I vary with the change of vertical connections. It is found that PW1 with paired connections exhibited similar ductility to the monolithic one, with a minor difference of only 3%. On the contrary, the wall with single-row connection exhibited better ductility than PW1 and the counterpart monolithic wall, mainly due to the extra splicing bars installed at the center of the section, leading to a slower decline in load-carrying capacity and a significantly higher ultimate failure displacement.

3.5 | Stiffness degeneration

Stiffness degeneration refers to the descending of structural stiffness of a structural member under reciprocating loads. The decline in stiffness could be caused by reinforcement yielding, concrete crushing and cracking, bond-slips of splicing rebars and other structural deterioration. The reduction of the secant stiffness K_j is

17517648, 2024, 5, Downloaded from https://onlinelibrary.wiley.com/doi/10.1002/suco.202300619 by Tsinghua University Library, Wiley Online Library on [23/01/2025]. See the Terms and Conditions (https://onlinelibrary.wiley.com/terms-and-conditions) on Wiley Online Library for rules of use; OA articles are governed by the applicable Creative Commons License

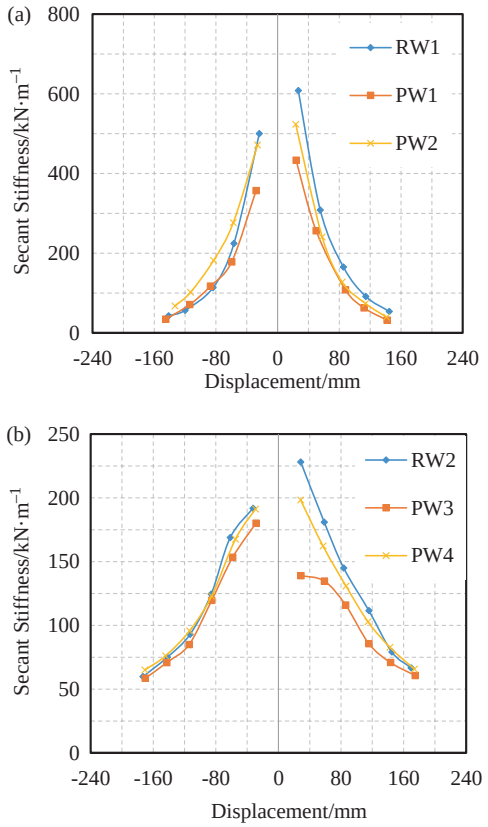

FIGURE 11 Stiffness degeneration: (a) Group I; (b) Group II.

commonly used to describe the stiffness degeneration and is defined as

$$K_j = \frac{\sum_{i=1}^{k} P_j^i}{\sum_{i=1}^{k} \Delta_j^i}, \tag{1}$$

where P_j^i is the horizontal force of ith cycle at the jth drift, Δ_j^i is the corresponding displacement at P_j^i, and k represents the quantity of cycles. The stiffness degenerations of the specimens are calculated and shown in Figure 11.

Figure 11 indicate that at cracking, the secant stiffnesses of the specimens are different, and the stiffnesses of precast specimens are generally lower than that of the monolithic specimens. However, with the increase of lateral displacements, the secant stiffnesses of the specimens decreased and gradually approaches to the same level.

Generally, the stiffness degeneration laws of precast specimens and monolithic reference specimens exhibit very similar trends. During the entire cyclic loading test, the stiffness decline of the specimens was shape after

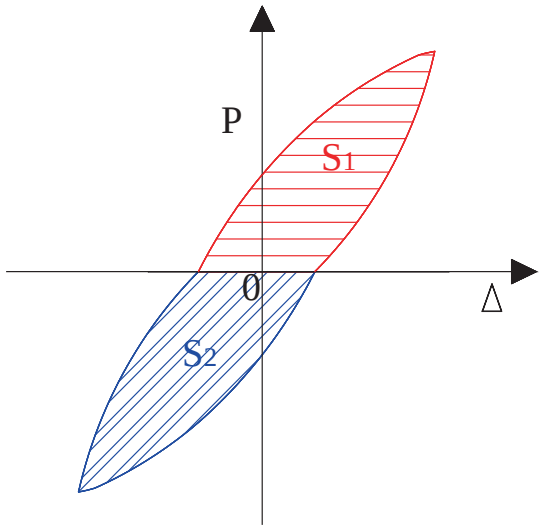

FIGURE 12 Calculation of dissipated energy.

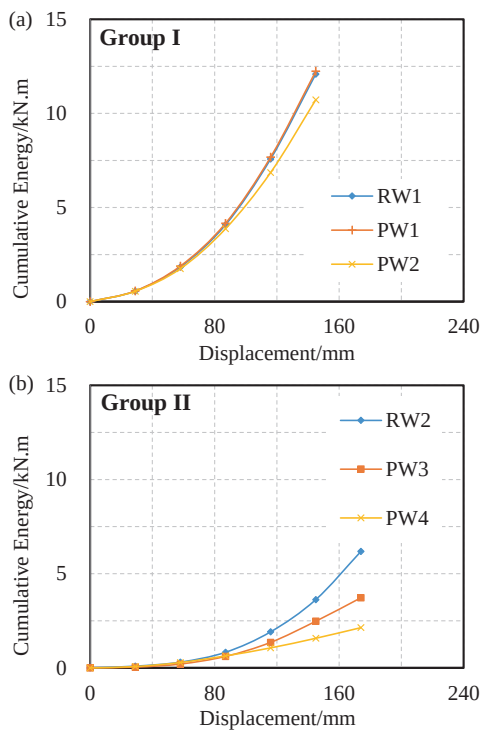

FIGURE 13 Accumulative dissipated energy: (a) Group I; (b) Group II.

cracking and became gentler after reaching the yielding stage, indicating that significant structural deterioration occurred between the cracking and yielding phases as indicated in Section 3.1. This is consistent with observations described in Section 3.1 as development concrete cracking mainly happened before specimen yielding. It is also found that the stiffness of each specimen is higher in the positive direction than in the negative direction, which is attributed to the loading sequence. The lateral

17517648, 2024, 5, Downloaded from https://onlinelibrary.wiley.com/doi/10.1002/suco.202300619 by Tsinghua University Library, Wiley Online Library on [23/01/2025]. See the Terms and Conditions (https://onlinelibrary.wiley.com/terms-and-conditions) on Wiley Online Library for rules of use; OA articles are governed by the applicable Creative Commons License

TABLE 5 Comparison between tested specimens and requirements in Ref.[28]

Categories		Axial load ratio = 0.12			No axial load			Criteria
		RW1	PW1	PW2	RW1	PW3	PW4	
P_{max}/E_{nt}	Pos.	1.19	1.19	1.21	1.06	0.97	1.04	0.90–1.20
	Neg.	1.15	1.14	1.18	1.02	0.97	0.93	
Energy dissipation ratio		0.24	0.25	0.24	0.21	0.23	0.10	≥0.125
K_f/K_i	Pos.	0.18	0.16	0.17	0.16	0.17	0.06	≥0.1
	Neg.	0.17	0.14	0.17	0.14	0.16	0.05	

Note: E_{nt} is the load-carrying capacity determined by ACI 318.[25]
K_f and K_i and are the secant stiffness between ±0.10% maximum drift.

load in positive direction was implemented prior to that in the opposite in each loading cycle, which already caused accumulated structural damage and crippled the subsequent behavior.

3.6 | Energy dissipation

Based on the hysteresis curve of the specimens, the energy dissipation in the elastic and elasto-plastic deformation stages can be studied and analyzed, which is calculated by summing up the area enclosed by the hysteresis loops at each level (as shown in Figure 12). As indicated in Figure 12, the energy dissipation of the specimens during loading and unloading can be expressed by the areas S1 and S2, and the sum of S1 and S2 is the total energy dissipation in one loading cycle.

From Figure 13, it can be seen that when the out-of-plane displacements of the specimen was small, the specimens were behaving in elastic state, and the cumulative energy consumption was minor. With the increase of the lateral displacement and the loading cycles, the specimen gradually exhibited the material nonlinearity, and the cumulative energy dissipation continuously accelerated.

In Group I (axial compression 0.12), the cumulative energy consumption of prefabricated specimens PW1 with paired connections is about 12 kN·m, which is comparable to that of the monolithic reference specimen RW1. On the other hand, the cumulative energy consumption of specimens PW2 with single-row connection of longitudinal bars is 10.8% lower.

In Group II (no axial compression), the energy dissipation capacity of precast specimens was lower than RW2, especially for the one with single-row connection (PW4). This is mainly because of the occurrence of bond-slips of splicing bars, and a plastic hinge was formed in PW4, which significantly reduced the structural stiffness when the specimens were subjected to plastic deformation. Both the results from Group I and II indicate that using single-rows connection somewhat weakens the energy dissipation capability of the specimens.

3.7 | Discussion

The vertical connection of shear walls acts crucially in the behavior of prefabricated walls in service, as it not only significantly affects the structural integrity and determines the tensile, shear, moment capacity of the walls. At present, because the lateral (in-plane) stiffness of the shear walls is dramatically greater than their transverse (out-of-plane) stiffness, engineering practitioners mainly concerns the in-plane performance of shear walls and neglect their out-of-plane behavior. However, shear walls in service are also subjected to out-of-plane flexure due to the bending moments transferred from superstructure and the deformation of adjacent slabs. These bending moments could lead to severe deflections or unexposed concrete damage on account of the low stiffness, which degenerates the in-plane performance of the shear walls. On the other hand, PWs with single-row connections increases the risk of out-of-plane deteriorations, which triggers need of this study.

Based on the observations in the tests, the precast and monolithic shear walls were found to underwent bending failure, regardless of the pattern of connections. The averaged strengths of the precast specimens were relatively close to that of the monolithic walls. The PWs with single-row connections showed higher displacement ductility but lower energy dissipation capacity due to wall rocking.

The hysteresis performance of the tested PWs, is examined via the use of the requirements specified in NEHRP.[28] The specimens that fit all requirements could be considered as emulative structures. The results are summarized in Table 5. It could be seen that PWs in Group I all stay within the requirements. However, in Group II, the energy dissipation and stiffness of PW4 do not satisfy the targets.

17517648, 2024, 5, Downloaded from https://onlinelibrary.wiley.com/doi/10.1002/suco.202300619 by Tsinghua University Library, Wiley Online Library on [23/01/2025]. See the Terms and Conditions (https://onlinelibrary.wiley.com/terms-and-conditions) on Wiley Online Library for rules of use; OA articles are governed by the applicable Creative Commons License

4 | CONCLUSIONS

The out-of-plane behavior of PWs with sleeve connections are investigated in this study, considering both paired and single-row connection layouts. An experimental program on the cyclic response of four full-scale PWs two corresponding monolithic shear walls for comparison was carried out. The axial load ratios were 0.12 and 0. The hysteretic response, backbone curves, ductility coefficients, stiffness degeneration and energy dissipation capability of the walls were studied. The conclusions are drawn as:

1. The prefabricated walls and the cast-in-place walls all exhibited bending failure. The failure was illustrated via crushing, spalling of concrete and yielding of rebars in the connection region.
2. For Group I (axial compression ratio as 0.12), the hysteretic curves of the PWs had comparable shapes and loop numbers, compared with the monolithic specimen. Pinching effect of the curves could be contributed to slight bond-slips of the splicing rebars. The single-row connected walls exhibited slightly higher strength and displacement ductility, revealing that the addition of splicing bar at the centerline of the cross section.
3. For Group II (axial compression ratio as 0), the lateral loads did not drop till the end of the tests (the actuator has reached its maximum stroke), for which the final load-carry capacity and ductility of the PWs could not be directly determined. However, the results also reveal that the specimens have a high level of deformability associated with the wall rocking here. In the hysteretic curve of PW4 (single-row connection), the pinching effect was notable due to the reinforcement arranged in the center of cross sections which resulting in large wall rocking. As a result, the energy dissipation capability of PW4 was marginally lower than others.
4. The PWs with paired GS connections all indicated acceptable cyclic responses and they could be considered to be emulative designs considering both of their in-plane and out-of-plane behavior. The shear walls with single-row connections exhibited worse seismic performance for the case without axial compression. Thus, the authors recommend special considerations or structural enhancement for single-row connected PWs especially when the axial compression is low.

ACKNOWLEDGMENTS

The experimental work presented in this study has been carried out with the financial support from the National Key R&D Program of China (No. 2022YFC3801400), and the Science and Technology Innovation Plan of Shanghai Science and Technology Commission (No. 22dz1203100), and the Program Fund of Non-Metallic Excellence and Innovation Center for Building Materials (No. 2023TDA3-2). The supports are gratefully appreciated.

DATA AVAILABILITY STATEMENT

The data that support the findings of this study are available from the corresponding author upon reasonable request.

ORCID

Weichen Xue https://orcid.org/0000-0002-9779-5676

REFERENCES

1. Steinle A, Bachmann H, Tillmann M. Precast concrete structures. Germany: John Wiley & Sons; 2019.
2. Kurama YC, Sritharan S, Fleischman RB, Restrepo JI, Henry RS, Cleland NM, et al. Seismic-resistant precast concrete structures: state of the art. J Struct Eng. 2018;144(4):03118001.
3. Smith BJ, Kurama YC, McGinnis MJ. Behavior of precast concrete shear walls for seismic regions: comparison of hybrid and emulative specimens. J Struct Eng. 2013;139(11):1917–27.
4. Singhal S, Chourasia A, Chellappa S, Parashar J. Precast reinforced concrete shear walls: state of the art review. Struct Concr. 2019;20(3):886–98.
5. Soudki KA, West JS, Rizkalla SH, Blackett B. Horizontal connections for precast concrete shear wall panels under cyclic shear loading. PCI J. 1996;41(3):64–80.
6. Jiang J, Luo J, Xue W, Hu X, Qin D. Seismic performance of precast concrete double skin shear walls with different vertical connection types[J]. Eng. Struct, 2021, 245: 112911.
7. Einea A, Yamane T, Tadros MK. Grout-filled pipe splices for precast concrete construction. PCI J. 1995;40(1):82–93.
8. Zheng G, Kuang Z, Xiao J, Pan Z. Mechanical performance for defective and repaired grouted sleeve connections under uniaxial and cyclic loadings. Construct Build Mater. 2020;233: 117233.
9. Peng Y, Qian J, Wang Y. Cyclic performance of precast concrete shear walls with a mortar–sleeve connection for longitudinal steel bars. Mater Struct. 2016;49(6):2455–69.
10. Li S, Liu X, Ma Y, Zhang L, Feng H. Influence of grouted sleeve and concrete strength of fabricated shear wall on acoustic emission detection method for sleeve compactness. J Build Eng. 2021;43:102541.
11. Jin L, Xia M, Zhang R, Lin M, Du X. Computational modeling and dynamic response of reinforced concrete shear wall under out-of-plane impact loading. Int J Impact Eng. 2023;172: 104425.
12. Wang W, Luo Q, Sun Z, Wang B, Xu S. Relation analysis between out-of-plane and in-plane failure of corrugated steel plate shear wall. Structure. 2021;29:1522–36.
13. Pecce M, Ceroni F, Maddaloni G, Iannuzzella V. Assessment of the in-plane deformability of RC floors with traditional and innovative lightening elements in RC framed and wall structures. Bull Earthq Eng. 2017;15(7):3125–49.
14. Robazza BR, Brzev S, Yang TY, Elwood KJ, Anderson DL, McEwen B. Out-of-plane behavior of slender reinforced

17517648, 2024, 5, Downloaded from https://onlinelibrary.wiley.com/doi/10.1002/suco.202300619 by Tsinghua University Library, Wiley Online Library on [23/01/2025]. See the Terms and Conditions (https://onlinelibrary.wiley.com/terms-and-conditions) on Wiley Online Library for rules of use; OA articles are governed by the applicable Creative Commons License

masonry shear walls under in-plane loading: experimental investigation. J Struct Eng. 2018;144(3):04018008.
15. Xue W, Huang Q, Li Y. Experimental study of precast concrete shear walls with spiral-confined lap connections under cyclic loads. J Build Eng. 2022;52:104467.
16. Cao Z, Li Q. Effect of connection deficiency on seismic performance of precast concrete shear wall-frame structures. J Earthq Tsunami. 2019;13:1940005.
17. Su RK, Wong SM. Seismic behaviour of slender reinforced concrete shear walls under high axial load ratio. Eng Struct. 2007; 29(8):1957–65.
18. Singhal V, Rai DC. In-plane and out-of-plane behavior of confined masonry walls for various toothing and openings details and prediction of their strength and stiffness. Earthq Eng Struct Dyn. 2016;45(15):2551–69.
19. Rosso A, Almeida JP, Beyer K. Stability of thin reinforced concrete walls under cyclic loads: state-of-the-art and new experimental findings. Bull Earthq Eng. 2016;14(2):455–84.
20. Rosso A, Jiménez-Roa LA, De Almeida JP, Zuniga AP, Blandón CA, Bonett RL, et al. Cyclic tensile-compressive tests on thin concrete boundary elements with a single layer of reinforcement prone to out-of-plane instability. Bull Earthq Eng. 2018;16(2):859–87.
21. Dashti F, Dhakal RP, Pampanin S. Validation of a numerical model for prediction of out-of-plane instability in ductile structural walls under concentric in-plane cyclic loading. J Struct Eng. 2018;144(6):04018039.
22. Gu Q, Deng Q, Tan Y, Tian S, Wang X. Research on the out-of-plane mechanical performance of double-face superposed shear walls with different horizontal connections. J Build Eng. 2022;59:105157.
23. GB 50011-2010. Code for seismic design of buildings. Beijing: China Architecture and Building Press; 2016.
24. GB/T 51231-2016. Technical code for assembled buildings with concrete structure. Beijing: China Architecture & Building Press; 2016.
25. American Concrete Institute. Building code requirements for structural concrete. ACI Committee 318, Farmington Hills 2019, ACI 318R-19.
26. JGJ 101-2015. Specification of test methods for earthquake resistant building. Beijing, China: Ministry of Housing and Urban – Rural Development; 2015.
27. Park R. Evaluation of ductility of structures and structural assemblages from laboratory testing. Bull N Z Natl Soc Earthq Eng. 1989;22(3):55–166.
28. National Earthquake Hazards Reduction Program (NEHRP). Recommended seismic provisions for new buildings and other structures. Washington, DC: Building Seismic Safety Council; 2020.

AUTHOR BIOGRAPHIES

Weichen Xue, Department of Structural Engineering, Tongji University, Shanghai, China.
Email: xuewc@tongji.edu.cn.

Qian Huang, Department of Structural Engineering, Tongji University, Shanghai, China.
Email: qianhuang@tongji.edu.cn.

Zhijun Xu, Department of Structural Engineering, Tongji University, Shanghai, China.
Email: 1332795@tongji.edu.cn.

Jiayin Yu, Department of Structural Engineering, Tongji University, Shanghai, China.
Email: 2111026@tongji.edu.cn.

Ya Li, Department of Structural Engineering, Tongji University, Shanghai, China.
Email: tj_liya@163.com.

How to cite this article: Xue W, Huang Q, Xu Z, Yu J, Li Y. Out-of-plane response of prefabricated concrete shear walls connected via grouted sleeves. Structural Concrete. 2024;25(5):3570–82. https://doi.org/10.1002/suco.202300619

17517648, 2024, 5, Downloaded from https://onlinelibrary.wiley.com/doi/10.1002/suco.202300619 by Tsinghua University Library, Wiley Online Library on [23/01/2025]. See the Terms and Conditions (https://onlinelibrary.wiley.com/terms-and-conditions) on Wiley Online Library for rules of use; OA articles are governed by the applicable Creative Commons License

[文章编号] 1002-8528(2025)04-0110-06　　DOI: 10.13614/j.cnki.11-1962/tu.2025.04.14

带肋复合保温外墙板传热系数计算方法

徐传阳,李君妮,李　昕,史天祥
(中国建筑标准设计研究院有限公司,北京 100044)

[摘　要] 带肋复合保温外墙板作为 1 种外挂墙板,在装配式框架结构的外围护体系中有广阔的应用前景。本文介绍了带肋复合保温外墙板的构造做法及材料选用,提出了带肋复合外墙板的传热分析有限元模型建立方法,并采用理论计算及已报道的试验数据开展了模型验证,分析了带肋复合外墙板的传热特点,研究了保温层厚度、保温锚固件布置方式及密肋层厚度对墙板传热性能的影响,最后提出了带肋复合外墙板传热修正系数的计算方法。

[关键词] 外挂墙板; 复合墙板; 热工性能; 数值计算; 传热系数
[中图分类号] TU111.19　　[文献标识码] A

Calculation Method for Heat Transfer Coefficient of Ribbed Composite Insulated Exterior Wall Panels

XU Chuanyang, LI Junni, LI Xin, SHI Tianxiang
(*China Building Standard Design & Research Institute Co., Ltd., Beijing* 100044, *China*)

Abstract: As a precast concrete facade panel, ribbed composite insulated external wall panels have broad application prospects in the outer envelope system of prefabricated frame structures. This paper described the construction methods and material selection for such ribbed composite insulated external wall panels. A finite element model for heat transfer analysis of ribbed composite external wall panels was established and validated through theoretical calculation with reported test data, to illustrate their heat transfer characteristics, study the influence of insulation layer thickness, layout of insulation retaining anchors, and thickness of the rib layer on the heat transfer performance of wall panels. Finally, this paper put forward a method for calculating the correction factor of the heat transfer coefficient for ribbed composite external wall panels.

Keywords: precast concrete facade panels, composite wall panel, thermal performance, numerical calculation, heat transfer coefficient

0　引　言

装配式建筑通过构件工厂预制、现场拼装的方式,改变了我国传统建筑施工中现场大量施工的工作模式,提高了现场施工效率,显著缩短了施工时间,减少了环境污染。近年来受政策引导及市场需求的影响,装配式建造已经成为我国建设领域重要的建造技术。

随着“双碳”目标的提出,建筑业减碳是目前建筑业的重要发展方向。2022 年 3 月,住建部发布《“十四五”建筑节能与绿色建筑发展规划》,在文件中要求“到 2025 年,建设超低能耗、近零能耗建筑 0.5 亿 m^2 以上”。据统计,在建筑围护系统中,外墙热损失占比高达 70%~80%[1]。因此,为实现装配式建筑的节能及减碳目标,关键途径在于提高建筑中外墙的保温隔热性能,其中结构保温一体化技术由于其具有提高建筑质量、简化施工流程、降低维护成本、提高防火及耐久性等优势,有较为广阔的发展空间。

结构保温一体化技术根据其构造形式,可以分为夹心保温现浇混凝土一体化技术(夹心内模体系)、免拆模复合保温外模板类一体化技术(外模体

[收稿日期] 2024-05-31　　[修回日期] 2024-07-26
[基金项目] “十四五”国家重点研发计划“多功能一体化水泥基围护结构体系”(2022YFC3801400);非金属材料创新中心创新基金“超低能耗建筑保温与结构一体化技术研究与示范”(2023TDA3-2)
[作者简介] 徐传阳(1995-),男,工学博士,高级工程师
[编辑部收稿邮箱] bjb365@126.com; bjb365@vip.126.com

中国知网　https://www.cnki.net

系)、装配式预制墙体一体化技术、自保温砌体一体化技术。预制混凝土夹心外挂墙板作为 1 种典型的装配式预制墙体类一体化产品,适用于装配式框架结构。超低能耗公共建筑多采用框架结构,采用传统预制混凝土夹心保温外挂墙板时,存在保温层超厚、连接件要求高、墙板自重大及综合成本高等问题。为解决上述问题,本文提出 1 种带肋复合保温外墙板,本墙板以混凝土密肋板作为承受面内及面外荷载的主体,在密肋层两侧布置保温板,在保温板外侧布置轻质饰面层,复合成为一体化外挂墙板,具有面密度低、热工性能好等优点。

现阶段针对多层材料复合形成外围护墙板已有一定研究[2-8],主要研究方向包括外围护墙板新型构造研发[2]、力学性能[3]、热工性能[4-7]和抗火性能[8]等。其中热工性能方向的研究主要集中于考虑热桥作用的墙体传热系数的计算,可通过试验检测或数值模拟计算,这两种方法可较为准确地研究不同材料及锚固件布置方式对墙板传热系数的影响。在工程实践中,主要采用传热系数修正系数对夹心保温墙板进行简化计算,如北京市地方标准 DB11/T 2128—2023《预制混凝土夹心保温外墙板应用技术规程》[9],规程针对不同保温材料、保温锚固件型式和保温层的厚度,给出了墙体传热系数修正系数,该系数范围为 1.05~1.30。

本文基于带肋复合保温外墙板构造方法,采用仿真软件 COMSOL Multiphysics 建立精细化有限元模型,分析各参数对墙板传热特性的影响,最后建议了墙体传热系数修正系数的取值。

1　墙体构造

带肋复合保温外墙板构造示意如图 1 所示,该墙板由室内到室外共分为轻质内饰面、内部保温层、密肋层、外部保温层及外饰面层,其中钢筋混凝土密肋层代替传统钢筋混凝土板作为外挂夹心墙板受力主体,大幅降低外挂墙板自重;在密肋层两侧设置保温层消除混凝土肋引起的热桥,同时降低单层保温层厚度;在两侧保温层外侧分别设置室外装饰面层和室内装饰面层,室外装饰面层和室内装饰面层通过贯穿保温层的金属塑料组合锚固件附着于密肋层。轻质内饰面可选用硅酸钙板或水泥纤维板等,内外 2 层保温层可选用常见有机保温材料,包括模塑聚苯板、挤塑聚苯板和硬泡聚氨酯板等,外饰面层可选用超高性能混凝土板或装饰砂浆。

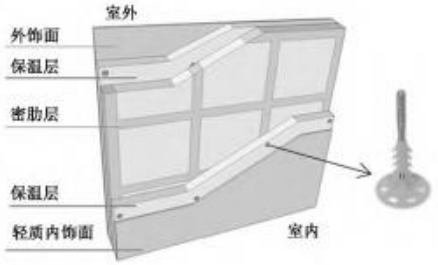

图 1　带肋复合保温外墙板构造示意

本墙板的保温锚固件的设计参照上海市工程建设规范 DG/TJ 08-2433A—2023《外墙保温一体化系统应用技术标准(预制混凝土反打保温外墙)》[10],该标准对金属塑料组合锚固件及保温板的布置方式提出了要求,具体包括保温锚固件的规格、锚固深度、间距等,该构造要求适用于保温厚度为 50~100 mm 的情况,采用带肋复合墙板构造方式,可将此种连接方式下的墙板保温层厚度扩大应用至 100~200 mm,可促进其在热工性能要求更高的建筑或其他气候区的推广应用。基于上述标准,本文对不带窗口和带窗口的 2 个典型墙板进行了初步设计,布置方案如图 2 所示,该保温锚固件为由塑料圆盘和不锈钢杆身构成,可保证不同层间的有效拉结。

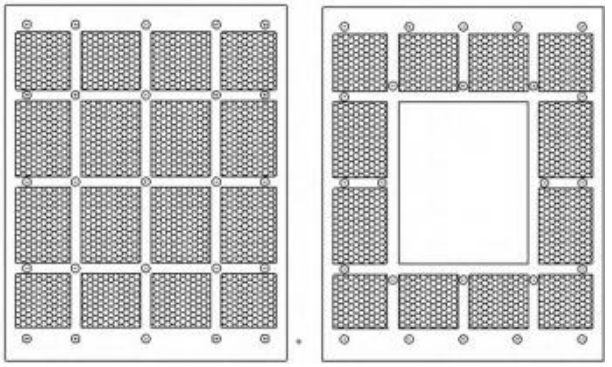

图 2　锚固件布置方案示意

2　墙板传热有限元分析

2.1　模型建立

基于 COMSOL Multiphysics 多物理场仿真软件,建立典型带肋复合保温外墙板的传热分析模型。墙体尺寸参照某实际工程取为 2 600 mm×3 280 mm,保温锚固件按上海市工程建设规范 DG/TJ 08-

中国知网　https://www.cnki.net

2433A-2023《外墙保温一体化系统应用技术标准(预制混凝土反打保温外墙)》[10] 相关要求均匀布置。

图3给出了典型算例的有限元模型构造示意,模型考虑了不同构造层的复合及锚固件与各构造层的锚固,简化锚固件为棒状,不考虑其尾盘的几何形状。图3b给出了网格划分示意。各层材料和锚固件均为常物性,不考虑湿度、温度、压力等因素对各种材料导热系数带来的变化影响,并假设墙体各层材料以及与锚固件之间均为紧密完全接触,无接触热阻。

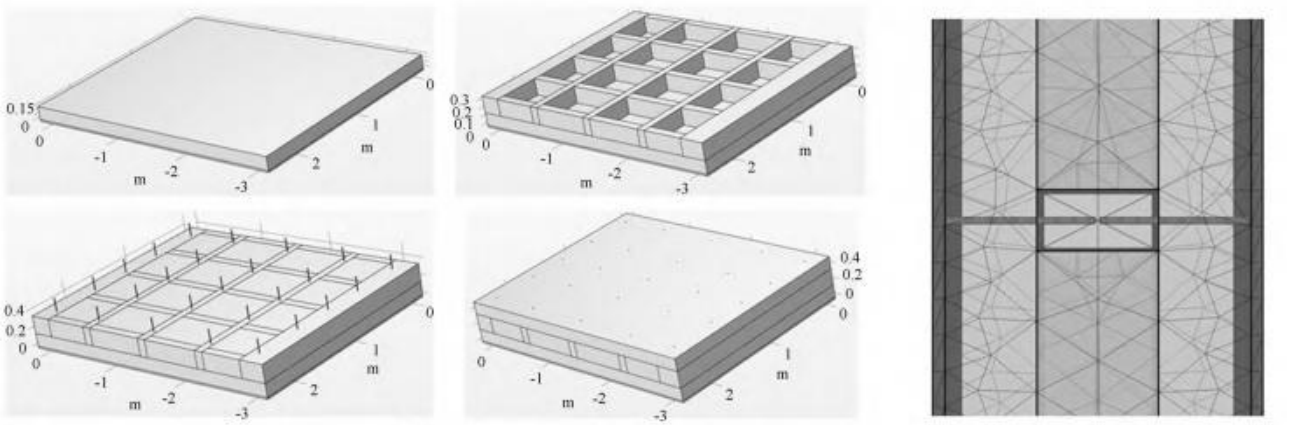

a 分层构造示意　　b 网格划分示意

图3　有限元模型构造示意

模型中假设带肋复合保温外墙板内外表面温度分别为20 ℃及-10 ℃,其他表面设为绝热边界。不同材料的热工参数根据现行国家标准GB 50176—2016《民用建筑热工设计规范》[11] 确定,如表1所示,并取内表面换热阻 R_i 及外表面换热阻 R_e 分别为0.11和0.04 ($m^2 \cdot K$)/W,保温锚固件的导热系数取为0.06 W/(m·K)。

表1　材料热工参数汇总表

材料类型	钢筋混凝土	挤塑聚苯板	硬泡聚氨酯	真空绝热板
导热系数/(W/(m·K))	1.74	0.030	0.024	0.008
密度/(kg/m³)	2 500	20	35	1 800
比热容/(kJ/(kg·K))	0.92	1.38	1.38	1.26

根据上述计算参数,基于软件稳态固体传热物理场,可以得到带肋复合保温外墙板的温度分布,并积分计算内/外表面热通量(W),结合墙板内/外表面面积及室内外温差,计算得到墙体的传热系数 K_f。

2.2　模型验证

为验证本文采用建立的COMSOL Multiphysics建立的热传递分析模型的合理性,本小节采用理论计算结果和Yu等[12] 报道的试验结果对模型进行验证。

考虑2层不同导热系数材料的复合工作的无热桥工况,即为实际应用中保温板材与混凝土墙体组合使用的理想简化。由于模型中仅考虑混凝土、保温材料的导热系数和内、外表面的换热阻,无热桥影响。因此,可通过平壁传热计算公式对系统的整体传热系数进行理论计算。同时,建立本工况下的有限元计算模型,可以通过稳态下热流密度计算得到系统的传热系数。为验证有限元模型的合理性,建立了系列典型模型,模型中混凝土墙板厚度为200 mm,保温层厚度分别为90、160、230、300 mm,保温材料考虑硬泡聚氨酯与挤塑聚苯板。分别采用理论计算与有限元模拟的方法计算得到了系统的平均传热系数,计算结果如表2所示,典型模型的稳态下温度分布图如图4a所示。可见有限元模拟值与理论计算值一致,采用本文提出的建模方法可以合理地考虑不同保温材料复合使用情况下导热系数、保温层厚度和表面换热阻对传热系统的影响。

为进一步验证本文提出的建模方法在考虑热桥影响的情况下,对系统传热系数模拟值计算的合理性,本文采用了Yu等[12] 报道的试验对建模方法进

中国知网 https://www.cnki.net

行验证。在该试验中对 6 个含有保温连接件的预制混凝土夹心保温剪力墙进行了热工性能测试,获得了墙体系统的传热系数实测值。试件的内叶墙厚度为 160 mm,外叶墙厚度为 60 mm,保温材料选用了挤塑聚苯板,试验中参数保温层厚度(30/60/90 mm)、连接件材质[不锈钢、纤维增强复合材料(Fiber Reinforced Plastic, FRP)]、连接件型式(不锈钢 U 型、不锈钢 I 型)及连接件布置个数(4/16 个)。基于试验试件的设计参数,采用本文给出的建模方法建立了相应的有限元计算模型,模型中表面换热系数、初始温度、材料的导热系数均按文献[12]中给出的实测值设定。计算结果如表 3 所示,典型温度分布如图 4b 所示,可见整体上传热系数实测值与模拟计算结果吻合良好,最大偏差为 4.47%。模拟结果可以较好地反应传热系数受热桥影响的规律: 保温层厚度固定的情况下,当热桥影响区域变小(2#、4#),系统的传热系数相应降低; 当连接件由不锈钢材料转化为 FRP 材料时(2#、5#),单个连接件的热桥效应影响变小,系统的传热系数相应降低。

通过采用上述 2 类工况下理论计算数据与试验数据对本文建模方法的验证,可见本文给出的有限元建模方法可以合理地对考虑局部热桥影响的不同导热系数材料组合的系统开展传热系数模拟计算。

表 2　无热桥影响的传热系数计算值与模拟值对比

保温层厚度/mm	硬泡聚氨酯		挤塑聚苯板	
	计算值/(W/(m²·K))	模拟值/(W/(m²·K))	计算值/(W/(m²·K))	模拟值/(W/(m²·K))
90	0.237	0.237	0.330	0.330
160	0.138	0.138	0.194	0.194
230	0.097	0.097	0.138	0.138
300	0.075	0.074	0.107	0.107

表 3　有热桥影响的传热系数实测值与模拟值对比

试件编号	保温层厚度/mm	连接件布置	传热系数实测值/(W/(m²·K))	传热系数模拟值/(W/(m²·K))
1#	30	不锈钢 U 型 16 个	0.949	0.960
2#	60	不锈钢 U 型 16 个	0.537	0.513
3#	90	不锈钢 U 型 16 个	0.365	0.352
4#	60	不锈钢 U 型 4 个	0.481	0.469
5#	60	FRP I 型 16 个	0.479	0.468
6#	60	不锈钢 L 型 16 个	0.555	0.542

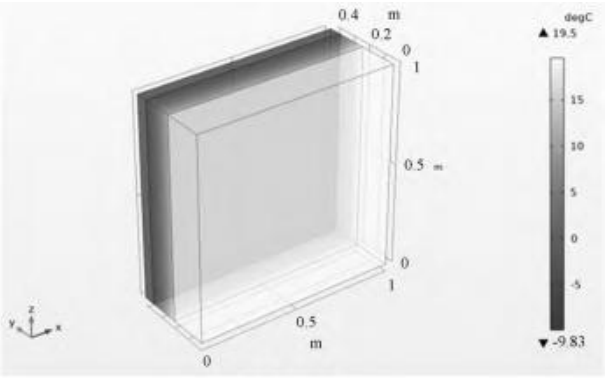

a 无热桥工况

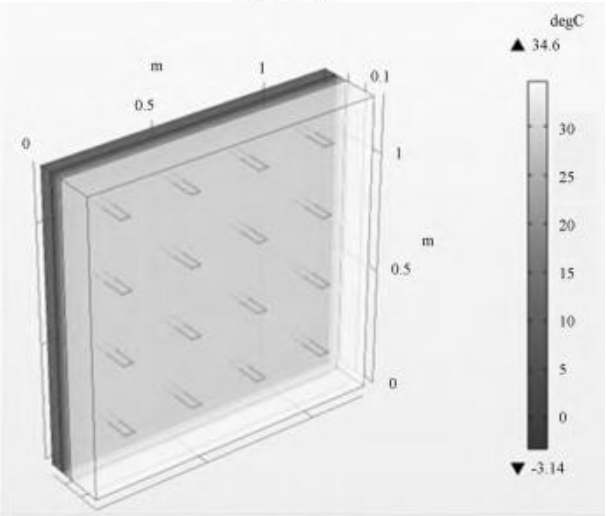

b 有热桥工况

图 4　典型算例温度分布

2.3　墙板传热分析

典型算例中,密肋层厚度为 200 mm,保温层为 150 mm 厚的硬泡聚聚氨酯保温板。

图 5 给出了典型算例的内外表面的温度分布,可见内外表面均存在温度梯度,温差约为 0.1 ℃。在内表面,温度较低的位置对应于混凝土肋布设位置; 在外表面,温度较高的位置对应混凝土肋布设位置,说明热流传递在混凝土肋布设位置传递密度较高,其对热流分布的影响不局限于混凝土肋对应位置,扩散至贯穿保温层贯穿位置,引起了较为明显的热桥效应。另一方面,保温锚固件由于其导热系数与保温材料接近,且截面较小,对墙体传热影响较小。

在工程实践中,常采用平壁传热模型以计算不同材料逐层复合后的整体传热系数 K_{c0},在本案例中,根据平壁传热模型,则复合墙板的传热系数可由式(1)计算。

中国知网　https://www.cnki.net

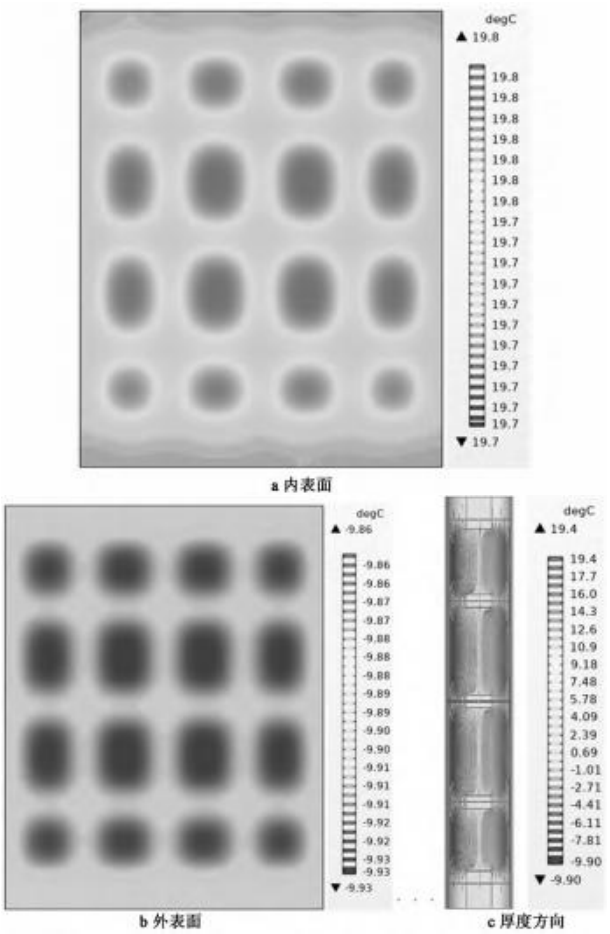

图5 典型算例温度分布

$$K_{c0} = \frac{1}{\frac{h_1}{\lambda_1} + \frac{h_2}{\lambda_2} + \frac{h_3}{\lambda_3} + \frac{h_4}{\lambda_4} + \frac{h_5}{\lambda_5} + R_i + R_e} \quad (1)$$

式中：K_{c0}为平壁传热模型计算得到的整体传热系数，W/(m²·K)；R_i 为内表面换热阻，(m²·K)/W；R_e 为外表面换热阻，(m²·K)/W；内饰面层、内保温层、密肋层、外保温层、外饰面层厚度分别设为 h_1、h_2、h_3、h_4、h_5，mm；各层导热系数分别为 λ_1、λ_2、λ_3、λ_4、λ_5，W/(m·K)。

可根据式(1)分别计算出假设密肋层为单一混凝土材料和保温材料时的墙体传热系数，根据材料面积比确定权重后采用加权法得到墙体计算传热系数 K_c。对典型算例，K_c 和 K_f 分别为 0.065 W/(m²·K) 和 0.076 W/(m²·K)，可见采用加权法计算得到墙体传热系数小于数值模拟计算值，这与上文中对密肋层引起的热桥效应分析结论一致，热桥将放大局部高导热系数材料对墙体整体传热系数的不利影响。因此，在实际工程应用中，为提高工程人员计算效率，需提出对本墙板的传热系数修正系数，如式(2)所示：

$$\zeta = K_f / K_c \quad (2)$$

式中：ζ 为传热系数修正系数；K_c 为采用加权法计算得到墙体传热系数，W/(m²·K)；K_f 为采用数值模拟方法计算的墙体传热系数，W/(m²·K)。

3 参数分析

为研究保温材料、密肋层厚度及保温层厚度对墙体传热系数的影响，本小节开展了针对性参数分析，计算得到的墙体传热系数数值模拟结果及计算值汇总于表4。

表4 墙体传热系数数值模拟计算值 单位：W/(m²·K)

保温层厚度/mm	挤塑聚苯板		硬泡聚氨酯		真空绝热板	
	密肋层厚度/mm					
	150	200	150	200	150	200
50	0.222	0.213	0.188	0.180	0.062	0.060
100	0.130	0.126	0.109	0.106	0.036	0.035
150	0.093	0.091	0.078	0.076	0.025	0.025

对保温材料，墙体的传热系数随保温材料的导热系数的降低而降低。在密肋层厚度150 mm、保温层厚度50 mm的条件下，当保温材料的导热系数由0.030 W/(m·K)降低至0.024和0.008 W/(m·K)时，墙体传热系数由0.222依次降低至0.188和0.062 W/(m²·K)，最大降低比例达72.07%。

对保温层厚度，墙体的传热系数随保温层厚度的提高而降低。在密肋层厚度150 mm并采用挤塑聚苯板保温材料的条件下，当保温厚度由50 mm依次提升至100和150 mm时，墙体的传热系数由0.222 W/(m²·K)依次降低至0.130和0.093 W/(m²·K)，降低比例达58.11%。

对密肋层厚度，墙体的传热系数随密肋层厚度的增加而略有降低，且降低幅度随着两侧保温材料热阻的提高而降低。当采用150 mm厚度的真空绝热板作为保温层材料时，密肋厚度由150 mm增加至200 mm时，墙体的传热系数几乎不受影响。

基于以上参数分析算例，根据式(2)计算得到墙体传热系数修正系数，汇总于表5，在参数范围内，ζ 的范围为1.10~1.37。

对保温材料，墙体的传热系数修正系数(ζ)随保温材料的导热系数的降低而降低。在密肋层厚度

中国知网 https://www.cnki.net

150 mm、保温层厚度 50 mm 的条件下，当保温材料由挤塑聚苯板依次调整为硬泡聚氨酯和真空绝热板时，修正系数由 1.27 依次降低至 1.25 和 1.18，降低比例分别为 1.57%和 7.09%。

对保温层厚度，墙体的传热系数修正系数（ζ）随保温层厚度的提高而降低。在密肋层厚度 150 mm 并采用挤塑聚苯板保温材料的条件下，当保温厚度由 50 mm 依次提升至 100 和 150 mm 时，修正系数由 1.27 依次降低至 1.16 和 1.12，降低比例分别为 8.66%和 11.81%。

对密肋层厚度，墙体的传热系数修正系数（ζ）随密肋层厚度的增加而增加，且增加幅度随着两侧保温材料热阻的提高而降低。当采用 150 mm 厚度的真空绝热板作为保温层材料时，密肋厚度由 150 mm 增加至 200 mm 时，修正系数由 1.10 增加至 1.14。

整体上，复合墙板中保温层热阻可以通过厚度的提高和材料传热系数的提高而提高，该层热阻的提高可以降低密肋热桥和保温锚固件的修正系数。因此对本墙体的构造形式，在保温层厚度 50～150 mm、密肋层厚度 150～200 mm 范围内，对保温层分别选取挤塑聚苯板、硬泡聚氨酯和真空绝热板材时，可偏于保守的将设计修正系数选择 1.40、1.40 和 1.30。

表 5　墙体传热系数修正系数

保温层厚度/mm	挤塑聚苯板		硬泡聚氨酯		真空绝热板	
	密肋层厚度/mm					
	150	200	150	200	150	200
50	1.27	1.37	1.25	1.35	1.18	1.24
100	1.16	1.23	1.16	1.22	1.13	1.17
150	1.12	1.17	1.12	1.17	1.10	1.14

根据协会标准 T/CECS 742—2020《装配式混凝土结构超低能耗居住建筑技术规程》[13]，可确定不同气候区居住类超低能耗建筑的外围护墙体的传热系数要求，对严寒、寒冷、夏热冬冷地区分别按照 0.10、0.15 和 0.20 W/（m^2·K）取值。进一步，考虑不同气候区保温材料的导热系数修正系数，其中挤塑聚苯板和硬泡聚氨酯保温材料在不同气候区的修正系数按现行国家标准 GB 50176-2016《民用建筑热工设计规范》[11] 确定，由于真空绝热板的导热系数受板材平均板缝宽度影响较大，按现行行业标准 JGJ/T 416-2017《建筑用真空绝热板应用技术规程》[14] 建议各气候区材料导热系数修正系数均按照 1.1 取值。通过不同保温层厚度下的模型试算，在典型设计条件下（密肋层厚度 150 mm、肋梁与肋柱宽度 150 mm，肋间距 500 mm）计算出带肋复合保温外墙板的保温层建议厚度，作为工程设计参考，计算结果汇总如表 6。

表 6　保温层厚度建议值

气候区	挤塑聚苯板厚度/mm	硬泡聚氨酯厚度/mm	真空绝热板厚度/mm
严寒	130	110	25
寒冷	80	60	15
夏热冬冷	50	40	10

4　结　论

本文提出了 1 种带肋复合保温外墙板的一体化外墙板构造方法，开展了热工性能计算，阐述了墙体的传热特性，结论汇总如下：

1）带肋复合保温外墙板通过密肋层作为受力主体，两侧保温层降低密肋层热桥影响，可作为不同气候区外挂墙板的备选形式。

2）墙板密肋层中混凝土肋在传热过程中存在较为明显的热桥效应，对墙体的传热系数存在显著影响。

3）可通过降低保温材料导热系数、提高保温层厚度、降低密肋层厚度的途径降低墙板整体传热系数，其中密肋层厚度对墙体传热系数的影响相对较小。

4）参数范围内（保温层厚度 50～150 mm，密肋层厚度 150～200 mm，肋梁与肋柱宽度 150 mm，肋间距 500～700 mm），墙体传热系数的修正系数范围为 1.10～1.37，并提出了带肋复合保温外墙板应用于各气候区居住类超低能耗建筑时保温层厚度的建议值。

参考文献

[1]　张泽平，李珠，董彦莉.建筑保温节能墙体的发展现状与展望[J].工程力学，2007，（S2）：121-128

[2]　冯俊，马昕煦，葛杰，等.围护结构与功能材料一体化外墙板的研究与应用[J].建筑结构，2021，（S2）：51

[3]　欧阳璐，罗家豪，黄宗贵，等.带实心区域预制混凝土夹心外挂板的力学与热工性能[J].建筑节能（中英文），2007，（7）：111-115

（下转第 147 页）

中国知网　https://www.cnki.net

科学，2017，33（2）：83-88

[3] 陈思豪，陈柳. 低温驱动双转轮除湿空调系统研究[J]. 建筑科学，2019，35（08）：89-94+117

[4] 贾钊颖，王赞社，魏彤，等. 冷凝除湿机运行分析与调控策略研究——以西安地区为例[J]. 建筑科学，2023，39（2）：80-88

[5] Niu R P，Jia X T，Geng L Z. Study on the effect of porosity of hollow fiber membrane on humidification performance [J]. Scientific Reports，2022，12：4134

[6] Chen Z，Zhu J，Bai H Y. Performance assessment of a membrane liquid desiccant dehumidification cooling system based on experimental investigations [J]. Energy and Buildings，2017，139：665-679

[7] 赵伟杰，张立志，裴丽霞. 新型除湿技术的研究进展[J]. 化工进展，2008，27（11）：1710-1718

[8] Min J C，Duan J F. Comparison of various methods for evaluating the membrane-type total heat exchanger performance [J]. International Journal of Heat and Mass Transfer，2016，100：758-766

[9] Qi R H，Dong C S，Zhang L-Z. A review of liquid desiccant air dehumidification：From system to material manipulations [J]. Energy and Buildings，2020，215：109897

[10] Xiao L H，Yang M L，Yuan W-Z，et al. Performance characteristics of a novel internally-cooled plate membrane liquid desiccant air dehumidification system [J]. Applied Thermal Engineering，2020，172：115193

[11] Huang S-M，Qiu D，Huang W H，et al. Laminar flow and heat transfer in a quasi-counter flow parallel-plate membrane channel in the solution side with cooling tubes [J]. International Journal of Heat and Mass Transfer，2017，105：769-780

[12] Huang S-M，Zhong Z，Yang M L. Conjugate heat and mass transfer in an internally-cooled membrane-based liquid desiccant dehumidifier（IMLDD）[J]. Journal of Membrane Science，2016，508：73-83

[13] Qiu D，Wu Z H，Huang S-M，et al. Laminar flow and heat transfer in an internally-cooled hexagonal parallel-plate membrane channel（IHPMC）[J]. Applied Thermal Engineering，2017，124：767-780

[14] 黄斯珉. 膜式热泵与空气湿度调节膜操作原理[M]. 北京：科学出版社，2017

（上接第 115 页）

[4] 赵志刚，吕安安，杨思忠，等.超低能耗预制混凝土夹心保温墙板拉结件热工性能分析[J].混凝土与水泥制品，2021，（2）：87-90

[5] 魏燕丽，朱文祥，许锦峰，等.预制混凝土夹心墙板热工性能试验研究[J].江苏建筑，2018，（S1）：59-61

[6] 续璐，丁勇.夏热冬冷地区不同构造形式外墙动态传热特性分析[J].暖通空调，2021，51（6）：21-28

[7] 张相勇，陈华周，高占祥，等.严寒地区装配式钢结构框架-ALC 外墙传热性能有限元分析[J].建筑钢结构进展，2023，25（7）：95-107

[8] 盛学庆，曾聪，潘胜军，等.钢结构装配式变电站一体化围护结构抗火性能研究[J].建筑结构，2023，53（5）：98-102

[9] 北京市住房和城乡建设委员会. DB11/T 2128—2023 预制混凝土夹心保温外墙板应用技术规程[S].北京：中国标准出版社，2023：15-16

[10] 上海市住房和城乡建设委员会. DG/TJ 08-2433A—2023 预制混凝土夹心保温外墙板应用技术规程[S].上海：同济大学出版社。2023：21-22

[11] 中华人民共和国住房和城乡建设部. GB/T 50176—2016 民用建筑热工设计规范[S].北京：中国建筑工业出版社，2016：77-90

[12] Yu S，Liu Y，Wang D，et al. Theoretical，experimental and numerical study on the influence of connectors on the thermal performance of precast concrete sandwich walls [J]. Journal of Building Engineering，2022，57：104886

[13] 中国工程建设标准化协会. T/CECS 742—2020 装配式混凝土结构超低能耗居住建筑技术规程[S].北京：中国建筑工业出版社，2020：6-7

[14] 中华人民共和国住房和城乡建设部. GJ/T 416—2017 建筑用真空绝热板应用技术规程[S].北京：中国建筑工业出版社，2017：4-5

中国知网 https://www.cnki.net

预制夹心保温墙板用新型保温拉结件抗剪性能试验研究*

徐小童[1]，肖　明[1]，王　赞[1]，蒋安维[1]，谷　洋[2]，李　薇[1]

（1 中国建筑标准设计研究院有限公司，北京 100048；2 北京中海地产有限公司，北京 100073）

摘要：为研究新型 FRP 片状、筒状拉结件以及新型不锈钢拉结件在混凝土中的剪切性能，完成了 11 个抗剪试件的静力推出试验，试验主要参数包括混凝土强度、拉结件形式、拉结件组合方式等，通过试件破坏模式及荷载—滑移曲线分析新型拉结件的力学性能。研究表明，新型 FRP 片状与不锈钢针状拉结件、FRP 筒状与不锈钢针状拉结件组合形式均可实现延性破坏模式，可在实际工程中应用推广。在 FRP 片状或筒状拉结件破坏前，剪切荷载主要由 FRP 片状或筒状拉结件承担，不锈钢针状拉结件承担的剪力极小；片状或筒状拉结件破坏后，位移急剧增加，不锈钢拉结件承担的荷载迅速增加，最终实现延性破坏。

关键词：预制夹心保温墙板；拉结件；力学性能；双剪试验；抗剪性能

中图分类号：TU375　　**文献标志码：**A　　**文章编号：**1002-848X(2024)S1-0851-07

Experimental research on shearing behavior of connectors in precast sandwich insulation wall panel

XU Xiaotong[1], XIAO Ming[1], WANG Zan[1], JIANG Anwei[1], GU Yang[2], LI Wei[1]

(1 China Institute of Building Standard Design & Research, Beijing100048, China;
2 China Overseas Development Group Co., Ltd., Beijing 100073, China)

Abstract: To investigate the shear performance of new FRP plate connectors, FRP cylindrical connectors and stainless steel connectors in precast sandwich insulation wall panel, eleven monotonic loading pull-outtests on shear specimens were conducted. The experimental parameters includeconcrete strength, the form and the composition of connectors. The mechanical properties of the new connectorswere analyzedby failure mode and load-slip relationship. Mechanical analysis indicated that the ductile failure mode of FRP plate connectors, FRP cylindrical connectors, as well as the combination of FRP and stainless steel connectors, could meet the application in practical engineering. Before the specimen lost its bearing capacity, FRP plate and cylindrical connectorsbore the shear load, and the stainless steel pin connector provided minimal shear bearing capacity. After the failure of FRP plate and cylindrical connectors, the displacement of the specimenincreased rapidly. The steel pin connectorsbore the load until the specimen produced an expected ductile failure mode.

Keywords: precast sandwich insulation wall panel; connector; mechanical property; double-shear test; shear behavior

0　概述

目前用于预制夹心保温墙板的连接件产品主要分为金属连接件和非金属连接件两大类，金属连接件主要有钢筋桁架、桶状、板状等，非金属连接件主要有板式、针式等。近年来，国内外学者对于不同拉结件的力学性能进行了大量试验研究。同济大学与万科集团等单位合作研发出夹心保温墙体板式 FRP 连接件，并开展连接件材料的受力性能、设计方法及工程应用等研究[1]。杨佳林等人研究了板式纤维增强复合筋的力学性能，试验表明复合筋能满足工程设计要求，具有较大安全储备[2-4]。薛伟辰等人对 FRP 连接件加速老化后的抗拉性能进行试验研究，发现侵蚀后 FRP 连接件劣化区域内的纤维不断被腐蚀，与周围树脂间出现明显脱离现象[5-6]。刘才华对 BFRP 拉结件双剪试件的抗剪性能开展了试验研究，试验研究表明，双剪试件抗剪承载力较高，能够满足设计荷载要求[7]。德国 Kaiserslautern 大学开展了带有棒式碳纤维连接件夹心墙板的试验研究[8]，试验结果表明，连接件最终发生的是弯曲破坏，而

* 国家重点研发计划(2022YFC3801403)，非金属材料创新中心创新基金(2023TDA3-2)，中国建设科技集团科技创新基金项目(Z2017J12)。
第一作者：徐小童，硕士，工程师，主要从事装配式混凝土结构设计及研究工作，Email: hmlfxt@126.com。
通信作者：肖明，硕士，教授级高级工程师，主要从事装配式建筑领域科研、标准编制和工程应用等工作，Email: xiaom1982@qq.com。

中国知网　https://www.cnki.net

整个墙体破坏并不明显。同年，该大学继续开展了棒式 FRP 连接件的抗拔与抗剪的试验，试验结果表明，连接件最终的破坏形式为断裂破坏[9]。Greg Woltman 等人研究了三种类型的 GFRP 连接件的抗剪强度，结果表明改变连接件的尺寸、间距、横截面形状或端部处理对其强度影响不大[10]。Clay Naito 对 14 种不同的抗剪连接类型进行了研究，对其破坏模式和响应进行了量化，并给出了每个连接件简化的多线性强度曲线供设计选用[11]。David C 等人针对格构式 FRP 连接件开展了足尺夹芯保温墙体静力试验，结果表明，连接件具有足够的抗剪性能，能满足组合式墙体的受力要求[12]。

本文针对研发的新型 FRP 片状、FRP 筒状、FRP 片状与不锈钢针状组合形式以及 FRP 筒状与不锈钢针状拉结件组合形式 4 种抗剪试件，进行单向抗剪试验，试验目的是研究新型拉结件的抗剪承载力，得到以上 4 种类型的拉结件的抗剪承载力及破坏模式。

1 试验概况

1.1 试件设计

基于新型 FRP 片状拉结件的单排及双排孔洞两种形式，设计了 3 种 5 个试件，试验主要研究参数包括 FRP 片状拉结件类型、锚固混凝土强度等级。试件设计及构造参数见表 1。

表 1 新型 FRP 片状抗剪试件设计参数

试件编号	片状拉结件形式	后插钢筋形式	混凝土强度/MPa	后插钢筋参数
FPSH6a/c	FPS20C4（单排孔洞）	2 弯 2 直	15	HRB400 级
FPSHa/b	FPS20C4（单排孔洞）	2 弯 2 直	60	直径 6mm
FPDHb	FPD20D4（双排孔洞）	4 弯 4 直	60	长度 400mm

新型 FRP 片状拉结件抗剪试件几何尺寸及构造形式，见图 1。

基于 FRP 片状与不锈钢针状拉结件组合形式设计了 3 种试件，其中包括：单排片状拉结件与一侧为三角形、另一侧为三折段波浪形的不锈钢拉结件组合形式，以及单排片状拉结件与哈芬针状拉结件组合形式。研究参数为不锈钢拉结件形式、锚固混凝土强度等级，见表 2。

新型 FRP 片状与不锈钢针状组合抗剪试件几何尺寸及构造见图 2。

基于新型 FRP 筒状拉结件设计 1 个试件，其中孔洞后插钢筋为 4 根（水平、竖直方向各 2 根）。新型 FRP 筒状拉结件设计参数见表 3。

新型 FRP 筒状拉结件抗剪试件几何尺寸及构造见图 3。

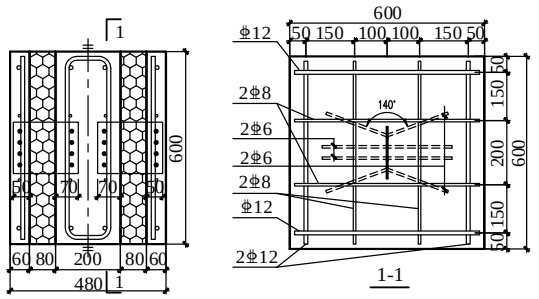

(a) FPSH6a、FPSHa/b

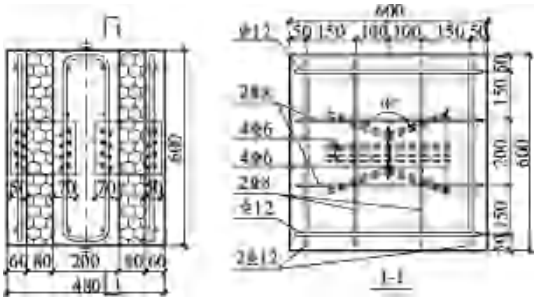

(b) FDSHa/b

图 1 FRP 片状拉结件抗剪试件设计

表 2 新型片状与针状拉结件组合抗剪试件设计参数

试件编号	不锈钢拉结件形式	混凝土强度/MPa	后插钢筋参数
SS+FPa/b	哈芬针状	60	HRB400 级直径 6mm
SS+FPc	一侧弯钩、另一侧三折段波浪形	15	长度 400mm

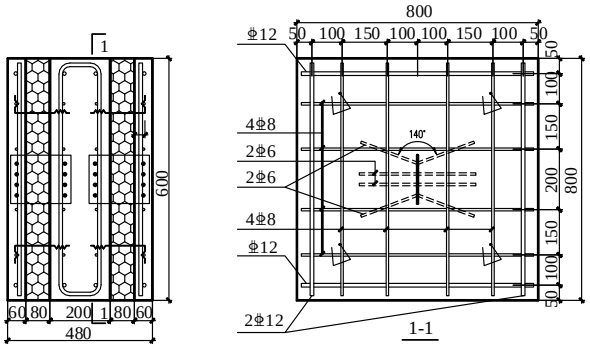

图 2 FRP 片状与不锈钢针状组合抗剪试件设计

表 3 新型 FRP 筒状抗剪试件设计参数

试件编号	后插钢筋形式	混凝土强度/MPa	后插钢筋参数
FTSH6c	水平、竖直方向各 2 根	15	HRB400 级直径 6mm 长度 500mm

基于新型 FRP 筒状拉结件与不锈钢针状拉结件组合抗剪试件设计 2 个试件，主要研究不锈钢针状拉结件形式：一侧为三角形、另一侧为弯钩或弯折三波段，筒状拉结件后插钢筋为 4 根（水平、竖直方向各 2 根）。组合抗剪试件设计参数见表 4。

中国知网 https://www.cnki.net

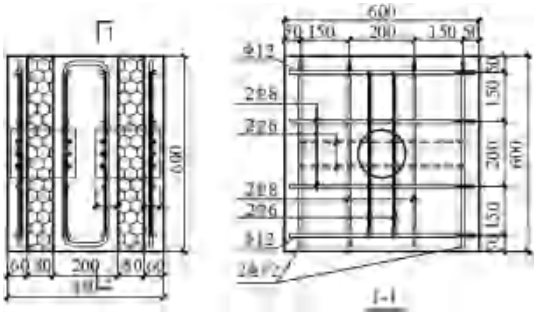

图 3　FRP 筒状拉结件抗剪试件设计

表 4　新型筒状与针状拉结件组合抗剪试件设计参数

试件编号	后插钢筋形式	不锈钢拉结件形式	混凝土强度/MPa	后插钢筋参数
SS+FTa/b	水平、竖直方向各 2 根	一侧三角形、另一侧为弯钩或弯折三波段	15	HRB400 级直径 6mm 长度 500mm

新型 FRP 筒状与不锈钢针状组合抗剪试件几何尺寸及构造见图 4。

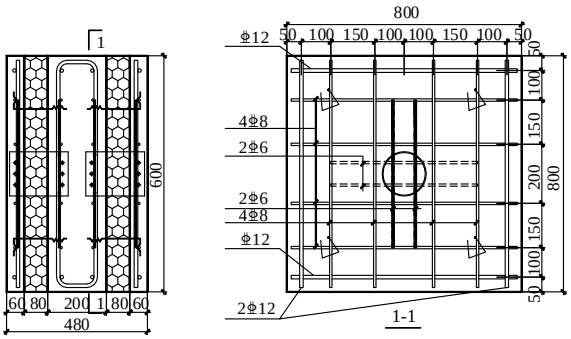

图 4　FRP 筒状与不锈钢针状组合抗剪试件设计

1.2　材料性能

拉结件抗剪性能试验试件采用两批浇筑，FPDHa/b、FPSHa/b 以及 SS+FPa/b 为第一批浇筑试件；FPSH6a、FTSH6c、SS+FPc 以及 SS+FTa/b 为第二批浇筑试件，见图 5。

第一批、第二批试件混凝土立方体抗压强度平均值 $f_{cu,m}$（即试验值）分别为 60.2、15MPa。

2　加载及量测方案

2.1　加载方案

拉结件抗剪试验采用千斤顶进行加载，加载装置示意图及现场照片见图 6。加载过程采用力控制，拉结件抗剪试件的加载速率为 5kN/min。

2.2　测量方案

试验量测内容包括施加于试件上的压力 F、相对剪切位移。每个试件设置四个位移计，以测量拉结件在抗剪试验过程中产生的相对剪切滑移，位移计分别测定左侧与中部、右侧与中部锚

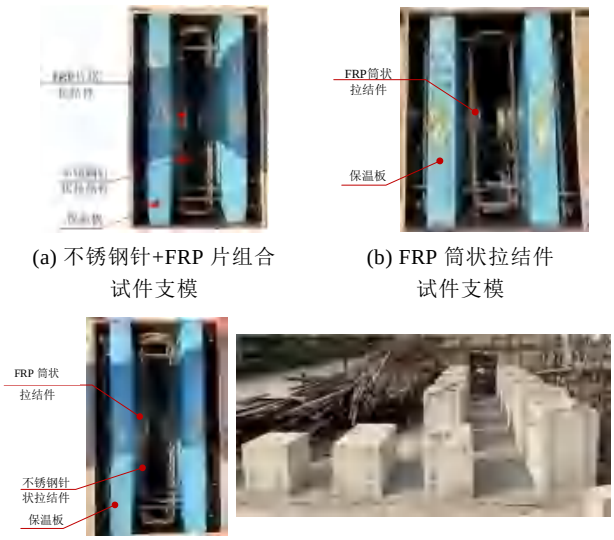

(a) 不锈钢针+FRP 片组合试件支模　(b) FRP 筒状拉结件试件支模

(c) 不锈钢针+FRP 筒组合试件支模　(d) 养护完成

图 5　试件加工图

(a) 加载示意图　(b) 试验现场照片

图 6　拉结件抗剪试件加载装置

固混凝土之间的相对滑移。为消除偏心影响，位移计架设在试件前后对应位置，后期数据处理滑移量分别取各侧两个位移计读数的均值。位移计布置位置如图 7 所示。

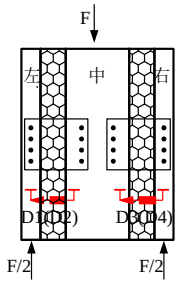

图 7　位移测点图

3　试验结果分析

3.1　FRP 片状拉结件抗剪试件

本节以 FPSH、FPDH 系列抗剪试验结果为例，进行试验结果分析。共 3 个试件，其破坏形态见图 8，试验特征值见表 5。

中国知网　https://www.cnki.net

(a) FPSHa/b

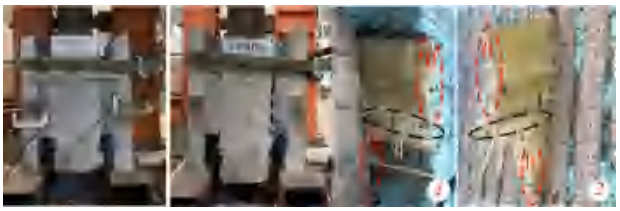

(b) FPDHb

图 8　FRP 片状拉结件试件破坏形态

试件破坏模式介绍：1）试验的破坏模式均为 FRP 片状拉结件中部纤维被拉断；2）受压侧混凝土未发生破坏；3）两组试件破坏模式相同，承载力发展过程及峰值承载力相近。

表 5　FRP 片状拉结件试件试验结果

试件编号	峰值点			平均值	
	F_u/kN	Δ_u^W/mm	Δ_u^E/mm	F/kN	Δ/mm
FPSHa	42.08	5.32	5.11	41.39	5.51
FPSHb	40.69	5.34	6.25		
FPDHb	45.75	6.17	9.11	—	—

结合图 9 试件的荷载–滑移曲线可以将试件的破坏过程大致分为 5 个阶段：

第一阶段：从开始加载到 A 点过程中，拉结件荷载—位移曲线基本呈线性关系。

第二阶段：继续加载至峰值荷载 F_u 过程中，AB 段荷载—位移曲线呈非线性关系，此时 FRP 片状拉结件的部分纤维及树脂发生破坏。

第三阶段：峰值荷载后，拉结件中部区域 I 树脂完全分层剥落，纵向纤维被拉断、横向纤维拔出并发生部分拉断，对应的 BC 段荷载–位移曲线猛降。

第四阶段：CD 段荷载–位移曲线呈屈服段，该阶段拉结件在区域 I 的损伤逐步发展至区域 II，区域 II 逐步发生纤维断裂，位移迅速增加。

第五阶段：区域 II 纵向纤维完全断裂，承载力急剧下降至 E 点，试验结束。

3.2　FRP 片状与不锈钢针状拉结件组合抗剪试件

本节进行 SS+FPa/b、SS+FPc 两组剪切试验结果分析。共 3 个试件，差别在于混凝土强度等级，试件破坏形态见图 10，试验特征值见表 6。

试件破坏模式介绍：1）SS+FPa/b 试件破坏

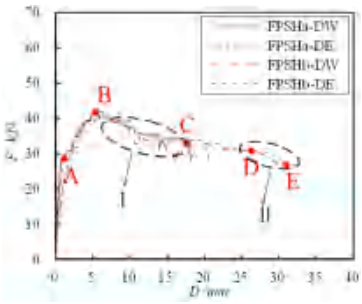

(a) 试件 FPSHa/b

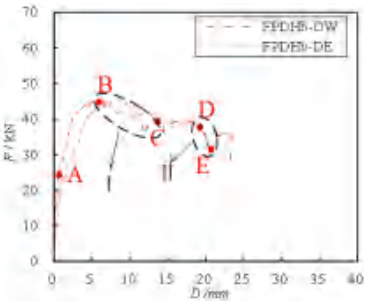

(b) 试件 FPDHb

图 9　FRP 片状与不锈钢针状拉结件试件荷载–滑移曲线

(a) SS+FPa/b

(b) SS+FPc

图 10　FRP 片状与不锈钢针状拉结件试件破坏形态

模式为 FRP 片状拉结件纤维被拉断，不锈钢针状拉结件出现锚固破坏，针状拉结件端部连带分布钢筋被拔出，混凝土出现椎体破坏；2）SS+FPc 试件破坏模式为锚固端受压区混凝土被压碎，FRP 片状拉结件纤维被拉断，不锈钢针状拉结件被拉断；3）试件 SS+FPc 峰值承载力高于 SS+FPa/b，试件 SS+FPc 在峰值承载力下的变形大于 SS+FPa/b，由于试件 SS+FPc 的不锈钢拉结件最终被拉断，而试件 SS+FPa/b 发生端部混凝土锚固破坏，试件 SS+FPc 的延性远高于 SS+FPa/b，达到峰值承载力时，不锈钢拉结件对试件 SS+FPc

中国知网　https://www.cnki.net

表 6　FRP 片状与不锈钢针状拉结件试件试验结果

试件编号	峰值点			平均值	
	F_u/kN	Δ_u^W/mm	Δ_u^E/mm	F/kN	Δ/mm
SS+FPa	50.94	9.81	9.27	53.54	9.90
SS+FPb	55.13	10.03	10.50		
SS+FPc	74.54	45.56	45.62	—	—

的抗剪承载力的贡献较大。

结合图 11 试件的荷载–滑移曲线可以将试件的破坏过程大致分为 4 个阶段：

第一阶段：从开始加载到 A_1 点过程中，拉结件荷载—位移曲线基本呈线性关系。

第二阶段：继续加载至 B_1 过程中，A_1B_1 段荷载—位移曲线呈非线性关系，此时 FRP 片状拉结件部分纤维及树脂发生破坏。

第三阶段：加载至峰值荷载 F_u（荷载–位移曲线 F 点），此阶段不锈钢拉结件开始发挥作用，其在抗剪方向上的分力为试件提供了抗剪承载力，此阶段试件 SS+FPc 的不锈钢拉结件提供了较好的延性。

对于试件 SS+FPa/b，此阶段以不锈钢拉结件开始发挥作用，伴随着 FRP 片状拉结件区域Ⅰ破坏逐渐转移至区域Ⅱ。

对于试件 SS+FPc，此阶段不锈钢拉结件变形较大，为试件提供了较好的延性，伴随着区域Ⅱ的纤维发生断裂。

第四阶段：对于试件 SS+FPa/b，FG 阶段为区域Ⅱ纤维被完全拉断，不锈钢拉结件发生混凝土锚固破坏，与不锈钢拉结件搭接的钢筋网片被逐渐带出，承载力下降至 G 点，试验结束。

对于试件 SS+FPc，到达峰值点 F 时，FRP 片状拉结件完全破坏，不锈钢拉结件被拉断，承载力急剧降至 G 点，试验结束。

3.3　FRP 筒状拉结件抗剪试件

本节进行 FTSH6c 剪切试验结果分析，试件破坏形态见图 12，试验特征值见表 7。

试件破坏模式介绍：1）FRP 筒状拉结件区域Ⅰ沿纵向被撕裂成数条纤维带，沿着锚固混凝土根部横向纤维断裂；2）区域Ⅱ部分没有后插钢筋的部分，被完全拔出，孔洞内部残留混凝土。

结合图 13 试件的荷载–滑移曲线可以将试件的破坏过程大致分为 5 个阶段：

第一阶段：从开始加载到 A 点过程中，拉结件荷载—位移曲线基本呈线性关系。

第二阶段：继续加载至峰值荷载 F_u 过程中，

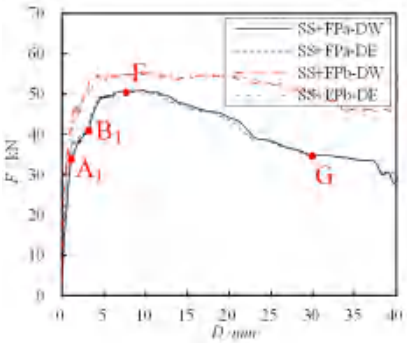

(a) 试件 SS+FPa/b

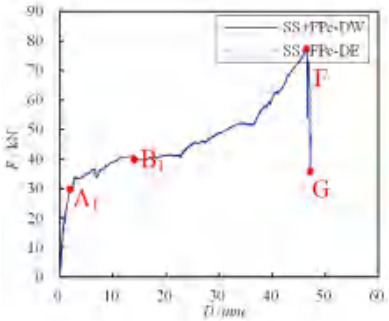

(b) 试件 SS+FPc

图 11　FRP 筒状拉结件试件荷载–滑移曲线

图 12　FRP 筒状拉结件试件破坏形态

表 7　FRP 筒状拉结件试件试验结果

试件编号	峰值点			平均值	
	F_u/kN	Δ_u^W/mm	Δ_u^E/mm	F/kN	Δ/mm
FTSH6c	83.74	6.90	5.73	—	6.32

AB 段荷载–位移曲线呈非线性关系，此时 FRP 筒状拉结件的部分纤维及树脂发生破坏。

第三阶段：峰值荷载后，拉结件区域Ⅰ部分沿纵向被撕裂成数条纤维带，并沿锚固混凝土根部横向纤维被拉断，对应为 BC 段荷载–位移曲线猛降。

第四阶段：CD 段荷载–位移曲线呈屈服段，该阶段拉结件在区域Ⅰ的损伤逐步发展至区域Ⅱ，区域Ⅱ未连接后插钢筋的孔洞部分逐渐发生锚固破坏。

第五阶段：区域Ⅱ部分被完全拔出，承载力从 D 点急剧下降至 E 点，试验结束。

中国知网　https://www.cnki.net

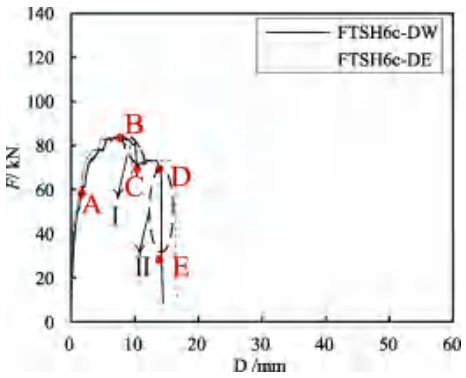

图 13　FRP 筒状拉结件试件荷载–滑移曲线

3.4　FRP 筒状与不锈钢针状拉结件组合抗剪试件

本节为 SS+FT 系列剪切试验结果分析。共 2 个试件，破坏形态见图 14，试验特征值见表 8。

图 14　FRP 筒状与不锈钢针状拉结件试件破坏形态

试件破坏模式介绍：1）SS+FTa/b 试件破坏模式为 FRP 筒状拉结件区域 I 部分沿纵向被撕裂成数条纤维带，并沿锚固混凝土根部，横向纤维发生断裂；2）不锈钢拉结件变形较大，最终发生断裂，不锈钢拉结件在剪切方向的承载力贡献较大。

表 8　FRP 筒状与不锈钢针状拉结件试件试验结果

试件编号	峰值点			平均值	
	F_u/kN	Δ_u^W/mm	Δ_u^E/mm	F/kN	Δ/mm
SS+FTa	110.98	35.70	37.91	105.83	39.85
SS+FTb	100.67	42.85	42.94		

结合图 15 试件的荷载–滑移曲线将试件 SS+FTa/b 的破坏过程大致分为 5 个阶段：

第一阶段：从开始加载到 A_1 点过程中，拉结件荷载—位移曲线基本呈线性关系，试件 SS+FTa/b 的 A_1 点承载力与 FTSH6c 的 A 点承载力几乎相同。

第二阶段：继续加载至 B_1 过程中，A_1B_1 段荷载–位移曲线呈非线性关系，此时 FRP 筒状拉结件发生部分纤维破坏，试件 SS+FTa/b 的 B_1 点承载力与 FTSH6c 的 B 点承载力几乎相同。

第三阶段：峰值荷载后，拉结件区域 I 部分沿纵向被撕裂成数条纤维带，并沿锚固混凝土根部横向纤维被拉断，对应为 B_1C_1 段荷载–位移曲线猛降，试件 SS+FTa/b 的 B_1C_1 段与试件 FTSH6c 的 BC 段荷载–位移曲线趋势相同。

第四阶段：C_1 点加载至峰值荷载 F_u（荷载–位移曲线 F 点），此阶段不锈钢拉结件开始发挥作用，其在抗剪方向上的分力为试件提供了抗剪承载力，此阶段组合拉结件剪切变形增速较快，不锈钢拉结件提供了较好的延性；伴随着 FRP 筒状拉结件区域 I 破坏逐渐转移至区域 II 。

第五阶段：FG 阶段不锈钢拉结件被拉断，区域 II 未连接钢筋部分发生混凝土锚固破坏，承载力下降至 G 点，试验结束。

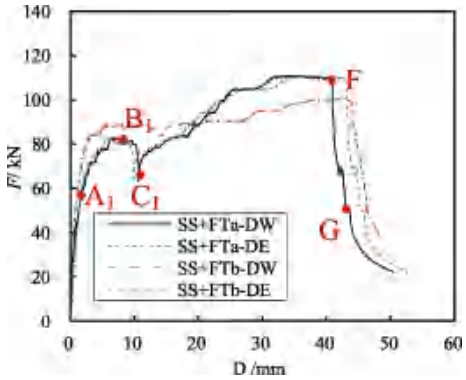

图 15　FRP 筒状与不锈钢针状拉结件试件荷载–滑移曲线

4　试验结论

4.1　FRP 片状拉结件抗剪试验

本文研究了 FRP 片状拉结件单独抗剪试验以及与不锈钢拉结件的组合抗剪试验，试件发展模式如图 16 所示。OA 线性段开展后，FRP 片材树脂及纤维逐渐发生破坏，进入 AB 非线性段；A、B 两点对于 FRP 单片及组合抗剪相同，B 点后承载力发展趋势为：

（1）FRP 单片抗剪：区域 I 范围树脂分层并开裂，纵向纤维逐渐拉断、横向纤维被拔出，承

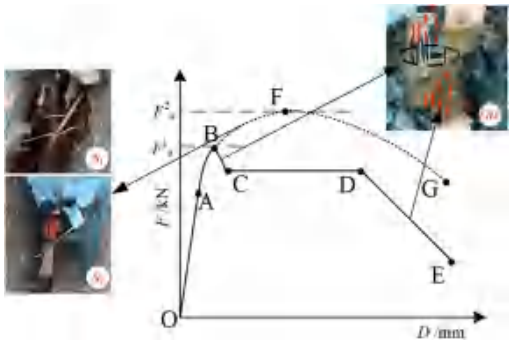

图 16　FRP 片状拉结件抗剪试件荷载–位移曲线

中国知网　https://www.cnki.net

载力进入 BC 下降段；破坏逐渐从区域Ⅰ扩展至区域Ⅱ，承载力进入 CD 屈服阶段；最终区域Ⅱ纵向纤维被拉断，承载力出现 DE 段陡降，试验结束。

（2）FRP 片及不锈钢拉结件组合抗剪：伴随着 FRP 片材纤维断裂、树脂分层压碎，不锈钢拉结件开始提供承载力，随后 FRP 片材破坏逐渐从区域Ⅰ转移至区域Ⅱ，承载力进入 BF 段；当不锈钢拉结件出现混凝土锚固或不锈钢断裂时，承载力进入 FG 阶段，当承载力降至 G 点时，试验结束。

综上所述试验结论如下：

（1）当仅采用片状拉结件时，无论发生材料的剪切破坏还是混凝土的锥体破坏，均为脆性破坏，破坏后承载力迅速下降。

（2）当采用片状拉结件和不锈钢针状拉结件组合时，到片状拉结件破坏前，剪切荷载主要由片状拉结件承担，不锈钢针状拉结件承担的剪力极小；片状拉结件破坏后，位移急剧增加，不锈钢拉结件承担的荷载迅速增加，为延性破坏。

4.2 FRP 筒状拉结件抗剪试验

本文研究了 FRP 筒状拉结件单独抗剪试验以及与不锈钢拉结件的组合抗剪试验，试件发展模式如图 17 所示。OA 线性段开展后，FRP 筒材树脂及纤维逐渐发生破坏，进入 AB 非线性段；区域Ⅰ范围沿纵向撕裂成数条纤维带，承载力进入 BC 下降段；A、B、C 三点对于 FRP 单筒及组合抗剪相同，C 点后承载力发展趋势为：

（1）FRP 单筒抗剪：破坏逐渐从区域Ⅰ范围转移至区域Ⅱ，附加钢筋孔洞范围内纵向纤维逐渐拉断，承载力进入 CD 屈服阶段；最终区域Ⅱ未附加钢筋部分被拔出，承载力出现 DE 段陡降，试验结束。

（2）FRP 筒及不锈钢拉结件组合抗剪：不锈钢拉结件开始提供承载力，伴随 FRP 筒损伤逐渐从区域Ⅰ转移至区域Ⅱ，承载力进入 CF 段；当 FRP 筒锚固端头被拔出、不锈钢拉结件被拉断时，承载力进入 FG 下降阶段，试验结束。

综上所述试验结论如下：

（1）筒状拉结件的破坏模式为筒纤维分区域断裂，破坏承载力较高，不采用缠绕拉挤法进行加工也可完全满足承载力要求。

（2）采用筒状拉结件和不锈钢针状拉结件组合时，到筒状拉结件破坏前，剪切荷载主要由筒状拉结件承担，不锈钢针状拉结件承担的剪力极小；筒状拉结件破坏后，位移急剧增加，不锈钢拉结件承担的荷载迅速增加，为延性破坏。

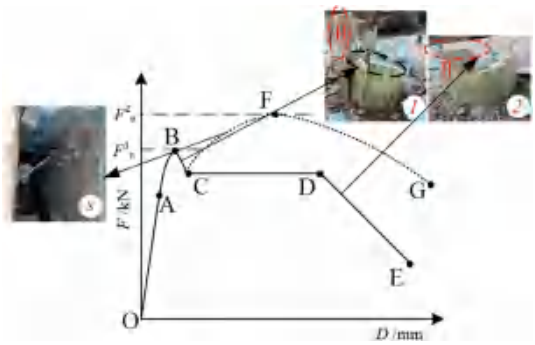

图 17　FRP 筒状拉结件抗剪试件荷载–位移曲线

参　考　文　献

[1] 杨佳林, 秦桁, 刘国权, 等. 板式纤维塑料连接件力学性能试验研究[J]. 塑料工业, 2012, 40(8): 69-72.

[2] 杨佳林, 薛伟辰, 栗新. 预制夹芯保温墙体 FRP 连接件的力学性能试验[J]. 江苏大学学报(自然科学版), 2013, 34(6): 723-729.

[3] 杨佳林, 薛伟辰. 预制夹芯保温墙体 FRP 连接件应用进展[J]. 低温建筑技术, 2012, 34(8): 139-142.

[4] 薛伟辰, 杨佳林, 王君若. 预制夹芯保温墙体 FRP 连接件抗拔性能试验研究[J]. 复合材料科学与工程, 2012(4): 55-59.

[5] 薛伟辰, 付凯, 秦珩. 预制夹芯保温墙体 FRP 连接件抗拉强度加速老化试验研究[J]. 建筑材料学报, 2014, 17(3): 420-424.

[6] 薛伟辰, 付凯, 李向民. 预制夹芯保温墙体 FRP 连接件抗剪性能加速老化试验研究[J]. 建筑结构, 2012, 42(7): 106-108, 118.

[7] 刘才华. BFRP 棒状拉结件预制混凝土夹心保温外墙板力学性能研究[D]. 合肥: 合肥工业大学, 2016.

[8] RAMM W. Report concerning stress tests under dynamic load with regard to an anchoring of three-layered facade panels according to the DEHA-TM System(in German) [R]. University of Kaiserslautern, 1992.

[9] RAMM W. Report concerning stress and shear tests with static load concerning anchoring of three-layered facade panels according to the thermomass building system (in German)[R]. University of Kaiserslautern, 1991.

[10] WOLTMAN G, TOMLINSOND, FAM A. Investigation of various GFRP shear connectors for insulated precast concrete sandwich wall panels[J]. Journal of Composites for Construction, 2013, 17(5): 711-721.

[11] NAITO C, HOEMANNJ, BEACRAFT M, et al. Performance and characterization of shear ties for use in insulated precast concrete sandwich wall panels[J]. Journal of Structural Engineering, 2012, 138(1): 52-61.

[12] EINEA A, SALMON D C, FOGARASI G J, et al. State-of-the-art of precast concrete sandwich panels[J]. PCI Journal, 1991, 36(6): 78-98.

中国知网 https://www.cnki.net

预制夹心保温墙板用新型保温拉结件锚固性能试验研究*

卜凡杰[1]，徐小童[1]，肖　明[1]，王　赞[1]，蒋安维[1]，谷　洋[2]，李　薇[1]

（1 中国建筑标准设计研究院有限公司，北京 100048；2 北京中海地产有限公司，北京 100073）

摘要：为研究新型 FRP 棒状、片状及筒状拉结件，新型不锈钢拉结件在混凝土中的锚固性能，完成了 55 个静力拉拔试验，试验主要参数包括锚固端头形式、锚固长度、后插钢筋构造、纤维强度、混凝土强度等，通过试件破坏模式及荷载—滑移曲线分析新型拉结件的力学性能。研究表明，斜边自端头向内侧倾斜的内凹三角形以及 T 型 FRP 棒状拉结件、三折段或弯钩形式的不锈钢拉结件锚固性能可以满足工程应用要求；FRP 片状拉结件建议采用纵向和斜向纤维布置形式，锚固端头采用单排开孔形式，每个孔道均穿设锚固钢筋以保证其锚固性能及延性；纵向纤维采用拉挤工艺、横向布置纤维毡的 FRP 筒状拉结件，端部孔洞穿设一定锚固长度的附加钢筋后，有效提升其锚固性能及变形能力。

关键词：预制夹心保温墙板；拉结件；拉拔强度；锚固性能

中图分类号：TU375　　**文献标志码：**A　　**文章编号：**1002-848X(2024)S1-0858-09

Experimental research on anchoring performance of connectors in precast sandwich insulation wall panel

BU Fanjie[1], XU Xiaotong[1], XIAO Ming[1], WANG Zan[1], JIANG Anwei[1], GU Yang[2], LI Wei[1]

(1 China Institute of Building Standard Design & Research, Beijing 100048, China;
2 China Overseas Development Group Co., Ltd., Beijing 100073, China)

Abstract: To investigate the anchoring performance of new kinds of FRP rod, plate, and cylindrical connectors, as well as rod-like stainless steel connector in concrete, 55 static pull-out specimens were fully studied. The experimental parameters include anchorage end shapes, anchorage length, post-inserted steel reinforcement arrangement, fiber strength and concrete strength. The mechanical behavior of new connectors were analyzed through the failure patterns and the load-slip curves. The results show that the anchoring performance of concave triangular shapes inclined inward from the end, as well as T-shaped FRP rod connector, and rod-like stainless steel connector with the end of three bends or bent hooks, could meet the application in practical engineering. For FRP plate connector, it is recommended to use the combination of longitudinal and diagonal fiber arrangement. The anchorage end shape should adopt single row of holes with anchored steel reinforcement in each hole to satisfythe pull-out capacity and ductile failure mode. A FRP cylindrical connector designed bylongitudinal pultrusion fibers, horizontal fiber felt, and post-inserted steel reinforcementwith aapplicable anchorage length, can effectively enhance the anchoring and deformation performance.

Keywords: precast sandwich insulation wall panel; connector; pull-out strength; anchoring performance

0　概述

目前国家正在全面推进绿色建筑和建筑工业化战略措施，而装配式建筑是实现住宅产业化的必然途径[1-4]。预制夹心保温墙板具有功能集成度高、装配程度高、制作工业化程度高等优点，成为研究的热点问题，而保温拉结件是预制夹心保温墙板的关键部品部件。近年来，国内外对拉结件的力学性能进行了大量的研究。孟宪宏等人研究了 3 种不同形式玻璃纤维筋连接件的弯锚锚固与抗拉等力学性能，结果表明玻璃纤维筋具有很高的抗拉强度和锚固性能，可用于预制夹心保温外挂墙板内部的连接件[5]。雷义雄等人对 5 组不同温度下的 18 个 BFRP 中心拔出试件进行拉拔试验[6]，结果表明中心拔出试件破坏形态为锥体—黏结复合型破坏。刘明等人进行了 L 型塑料钢筋拉结件灰缝试件试验模拟，结果表明 L 型塑料钢

* 国家重点研发计划(2022YFC3801403)，非金属材料创新中心创新基金(2023TDA3-2)，中国建设科技集团科技创新基金项目(Z2017J12)。
第一作者：卜凡杰，硕士，高级工程师，主要从事装配式混凝土结构设计及研究工作，Email: 68252915@qq.com。
通信作者：徐小童，硕士，工程师，主要从事装配式混凝土结构设计及研究工作，Email: hmlfxt@126.com。

中国知网　https://www.cnki.net

筋拉结件的粘结锚固强度可以满足夹心墙用拉结件的使用要求，有比普通钢筋拉结件更好的延性和变形能力[7]。刘鑫等人设计了一种塑料钢筋拉结件，并对其进行在砂浆和混凝土试件中的粘结性能试验，研究表明塑料钢筋拉结件应采用机械锚固，以满足较高锚固承载力[8]。Shohoko S 等[9]针对日本旭硝子株式会社开发的棒状 FRP 连接件开展了热工性能试验，研究表明采用该连接件的墙板导热系数满足日本保温墙体有关热工参数的规定。Kurama 等[10]通过抗震试验，研究了采用格构式 FRP 连接件的预制夹心外墙板的抗震性能，并给出了墙体抗震设计建议。A. Benayoune 等[11]对采用格构式 FRP 连接件的预制夹心墙板进行了受弯性能试验研究。

本文针对新型 FRP 棒状、不锈钢针状、FRP 片状以及 FRP 筒状拉结件进行锚固单向拉拔试验，试验目的是研究新型拉结件的锚固性能，得到以上四种类型拉结件的锚固承载力及破坏模式。

1 试验概况

1.1 试件设计

基于新型 FRP 棒状拉结件设计了 21 个试验试件，其中截面形式包括圆形、六边形、内凹三角形以及 T 形 4 种，试件参数包括截面形式、锚固端凹槽形式、凹槽端距；同时设计 3 个 Thermomass 拉结件作为对比试件。新型 FRP 试件设计参数及几何尺寸，见表 1。

表 1 新型 FRP 拉结件试件设计参数

试件编号	截面形式	凹槽边距/mm	锚固深度/mm
FBC9a/b/c	圆形	9	40
FBC14a/b/c	圆形	14	40
FBP9a/b/c	六边形	9	40
FBP14a/b/c	六边形	14	40
FBTR11a/b/c	内凹三角形	11	40
FBTR16a/b/c	内凹三角形	16	40
FBT11a/b/c	T 形	11	40
FBTHa/b/c	Thermomass	—	38

以 FBTR 拉结件为例，棒状拉结件加工图、成品图、试件几何尺寸及构造，见图 1。

基于新型不锈钢针状拉结件设计了 12 个试件，其中锚固端头形式为三角形、两折段波浪形、三折段波浪形、弯钩形 4 种，试件参数包括锚固端弯折形式、锚固长度；同时设计 3 个 Halfen 不锈钢针状拉结件作为对比试件。新型不锈钢针状拉结件设计参数及几何尺寸，见表 2。

(a) 加工图　　(b) 成品图

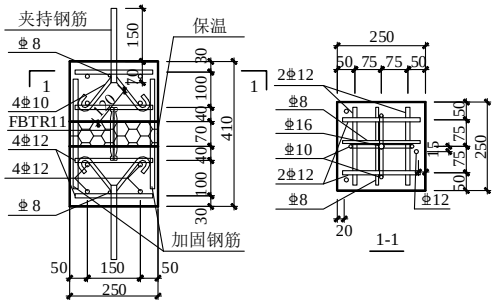

(c) 试件几何尺寸及构造

图 1 FBTR 拉结件试件设计

表 2 新型不锈钢针状拉结件试件设计参数

试件编号	弯折形式	适用范围	锚固长度/mm
STR35a/b/c	三角形	外叶板	35
SW65a/b/c	两折段波浪形	内叶板	65
SW85a/b/c	三折段波浪形	内叶板	85
SHK65a/b/c	弯钩形	内叶板	65
SHALFa/b/c	SPA-A	—	35/85

以 STR+SW 拉结件为例，不锈钢拉结件加工图、成品图、试件几何尺寸及构造，见图 2。

基于新型片状 FRP 拉结件设计了 21 个试件，其中端头开孔形式为单排孔洞（孔边距为 20mm）、双排孔洞（均用于后插钢筋）以及双排孔洞（仅第二排用于后插钢筋，孔边距为 25mm）3 种，试件参数包括开孔形式及孔边距、后插钢筋数量、后插钢筋形式；同时设计 3 个 Halfen 不锈钢片状拉结件作为对比试件。新型 FRP 片状拉结件设计参数及几何尺寸，见表 3。

以 FPD20C4 拉结件为例，FRP 片状拉结件加工图、成品图、试件几何尺寸及构造，见图 3。

基于新型筒状 FRP 拉结件设计了 1 个试件，主要研究后插钢筋为 4 根（双向后插钢筋，各为 2 根），后插钢筋长度为 500mm 的情况。新型 FRP 筒状拉结件设计参数及几何尺寸，见表 4。

中国知网 https://www.cnki.net

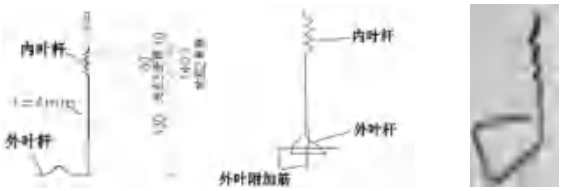

(a) 加工图　　(b) 成品图

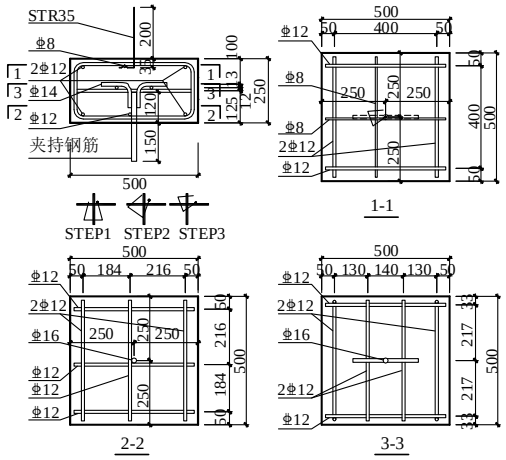

(c) 试件几何尺寸及构造

图 2　STR+SW 拉结件试件设计

表 3　新型 FRP 片状拉结件试件设计参数

试件编号	孔洞形式	孔洞边距/mm	后插钢筋数量	后插钢筋形式	横向纤维强度
FPS20a/b/c	单排	20	—	—	低
FPS20A4a/b/c	单排	20	2	2 直	低
FPS25A4a/b/c	单排	20	2	2 直	高
FPS20C4a/b/c	单排	20	4	2 弯 2 直	低
FPS25C4a/b/c	单排	20	4	2 弯 2 直	高
FPD20C4-1a/b/c	双排	15/30	4	2 弯 2 直	低
FPD20C4-2a/b/c	双排	15/30	4	2 弯 2 直	高
FPD20D4a/b/c	双排	15/30	8	4 弯 4 直	低
FPDD25	双排*	25	—	—	低
FPDD25A4	双排*	25	2	2 直	低
FPDD25B4	双排*	25	4	4 直	低
FPDD25C4a/b/c	双排*	25	4	2 弯 2 直	低
HFP6a/b/c	双排	SP-FA-1-2 00-160	4	2 弯 2 直	低

注：*表示双排孔洞中，仅第二排孔洞用于附加后插钢筋。

FRP 筒状拉结件加工图、成品图、试件几何尺寸及构造，见图 4。

1.2　材料性能

拉结件锚固性能试验试件采用两批浇筑，除 FPS25A4、FPS25C4、FPD20C4-2 与 FT20A 系列外，均为第一批浇筑试件，见图 5。

第一批试件 FRP 棒状拉结件、不锈钢针状拉结件的试件混凝土立方体抗压强度平均值 $f_{cu,m}$（即试验值）为 30.2MPa；FRP（Halfen 不锈钢）片状拉结件的试件混凝土立方体抗压强度平均值 $f_{cu,m}$（即试验值）为 33.0MPa；第二批试件混凝土立方体抗压强度平均值 $f_{cu,m}$（即试验值）为 60.2MPa。

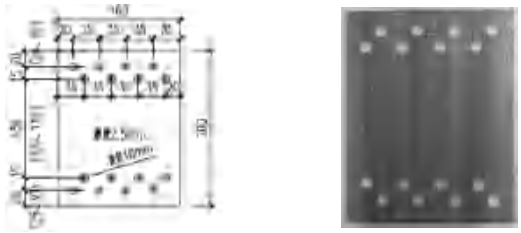

(a) 加工图　　(b) 成品图

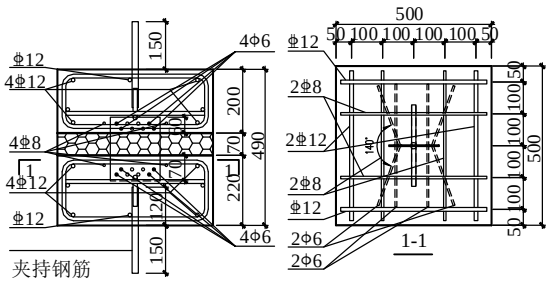

（c）试件几何尺寸及构造

图 3　FPD20C4 拉结件试件设计

表 4　新型 FRP 筒状拉结件试件设计参数

试件编号	孔洞形式	孔洞边距/mm	后插钢筋数量	后插钢筋形式	混凝土强度等级
FT20A	双排、双向	20/30	4	双向各 2 根	C60

(a) 加工图　　(b) 成品图

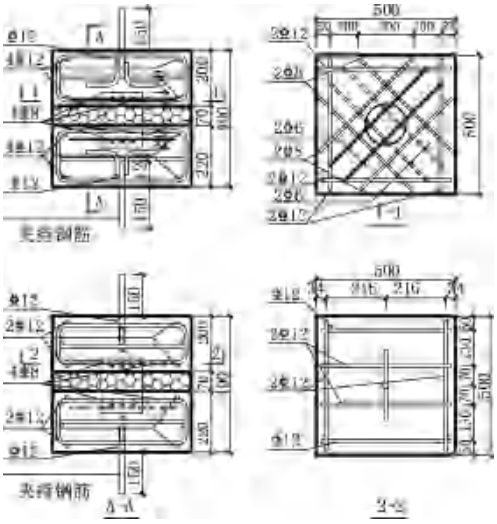

(c) 试件几何尺寸及构造

图 4　筒状拉结件试件设计

中国知网　https://www.cnki.net

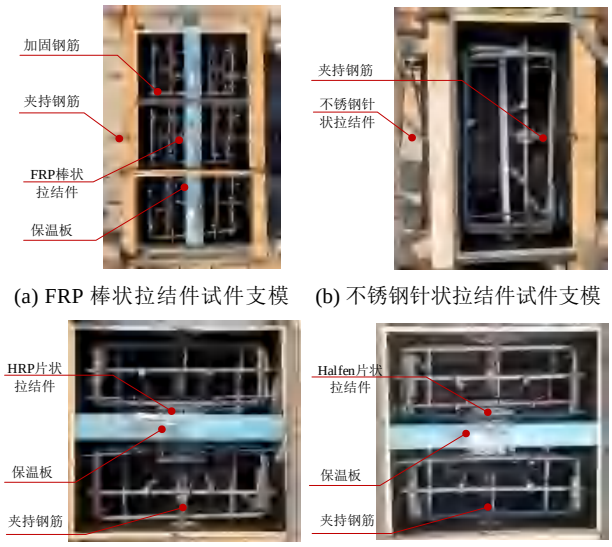

(a) FRP 棒状拉结件试件支模　(b) 不锈钢针状拉结件试件支模

(c) FRP 片状拉结件试件支模　(d) Halfen 片状拉结件试件支模

图 5　试件加工图

FRP 材性试验分别沿 FRP 片状拉结件的水平、垂直以及 45 度方向取样，由于用于采样的试件尺寸限制，上述三类材性试验试件尺寸分别为 160mm×15mm×2.5mm、200mm×20mm×2.5mm 以及 200mm×20mm×2.5mm，材性试验试件两端分别粘贴铝板；试件编号分别为 H1～5、V1～5 以及 S1～5，其中 V1～5 两侧粘贴铝板滑脱，其余材性试验结果见表 5，破坏形式见图 6。

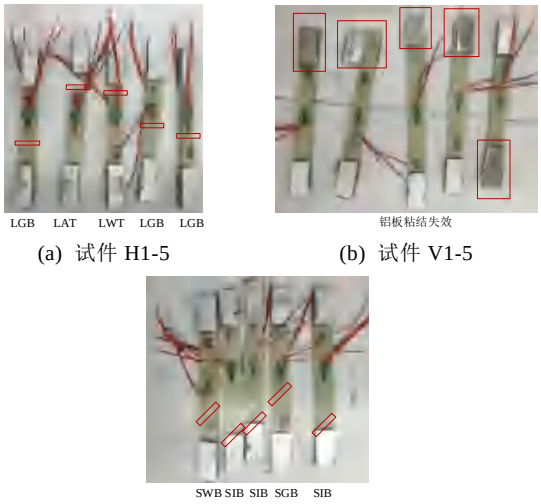

(a) 试件 H1-5　(b) 试件 V1-5

(c) 试件 S1-5

图 6　FRP 材性试验试件破坏模式

破坏模式采用三个字母表示，首字母“L”表示横向破坏、“S”表示斜向 45 度破坏；中间字母“I”表示在夹持/加强片内部破坏、“A”表示在夹持根部或加强片根部破坏、“W”表示在距离夹持/加强片小于 1 倍宽度处破坏、“G”表示在工作段破坏；尾字母“B”表示上部破坏，“T”表示下部破坏。

表 5　FRP 材料拉伸强度实测值/MPa

试件编号	单个试样	平均
H-1	38.11	
H-2	52.51	
H-3	46.67	50.24
H-4	64.37	
H-5	49.55	
S-1	95.88	
S-2	72.02	
S-3	73.46	81.00
S-4	78.10	
S-5	85.52	

2　加载及量测方案

2.1　加载方案

拉结件锚固拉拔试验采用 MTS 试验机进行加载，加载装置示意图及现场照片见图 7、8。加载过程采用位移控制，FRP 棒状拉结件加载速率为 0.5mm/min，不锈钢、FRP 片状拉结件加载速率为 5mm/min。

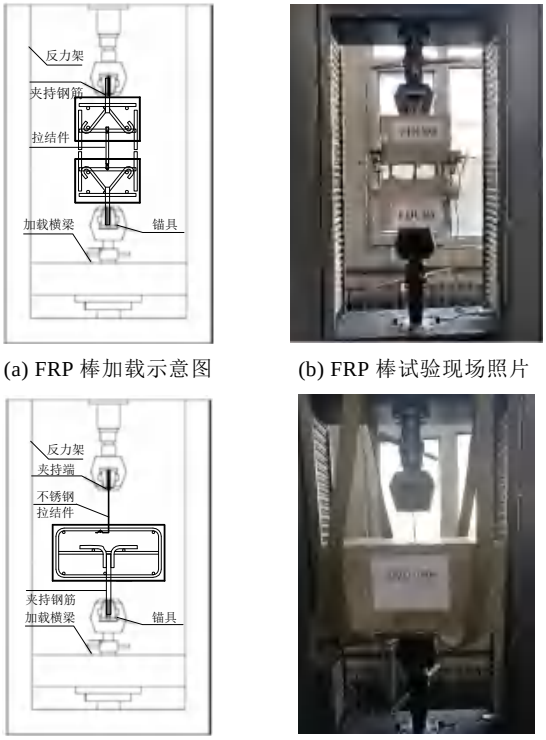

(a) FRP 棒加载示意图　(b) FRP 棒试验现场照片

(c) 不锈钢针加载示意图　(d) 不锈钢针试验现场照片

图 7　FRP 棒、不锈钢针拉结件加载装置

2.2　测量方案

试验量测内容包括施加于试件上的拉力、位

中国知网　https://www.cnki.net

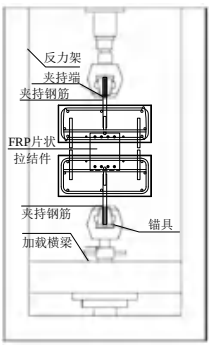

(a) FRP 片加载示意图

(b) FRP 片试验现场照片

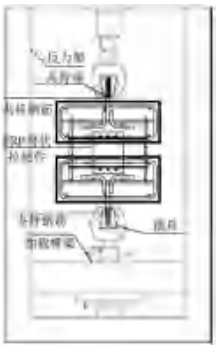

(c) FRP 筒加载示意图

(d) FRP 筒试验现场照片

图 8　FRP 片、筒拉结件加载装置

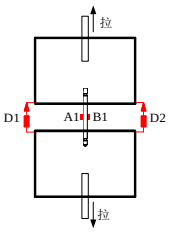

(a) 试件 FBC9/14、FBT11

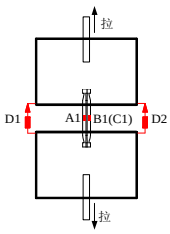

(b) 试件 FBTR11/16

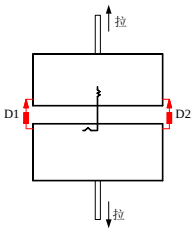

(c) 试件 SHALF

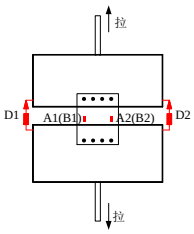

(d) 试件 FPS20、FPS20A4/C4、FPS25A4/C4、FPD20 系列、FPDD25 系列、HFP6

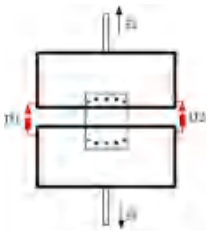

(e) 试件 FT20A

图 9　位移及应变测点图

移和应变。每个试件设置两个位移计，以测量上下锚固端混凝土之间的相对滑移，新型不锈钢针状拉结件夹持端与夹具间无相对滑移，故直接采用 MTS 横梁位移。为消除偏心影响，位移计架设在试件左右对应位置，后期数据处理滑移量取两个位移计读数的均值。

根据 FRP 棒状拉结件形状的差异，在棒体对应位置布置 2～3 个应变片，量测拉结件关键位置的应变；FRP 片状拉结件在片的左右前后对应位置布置 4 个应变片，量测片状拉结件正中部的应变；FRP 筒状拉结件未设置应变片。位移计及应变布置位置如图 9 所示。

3　试验结果分析

3.1　FRP 棒状拉结件

本节以 FBT11 锚固拉拔试验结果为例，进行试验结果分析。本组共 3 个试件，其三角形凹槽为斜边自端头至内部逐渐向内侧倾斜，试件破坏形态见图 10，试验特征值见表 6。

试件破坏模式介绍：1）试验的破坏模式均为混凝土椎体破坏，拉结件表面无纤维断裂或树脂裂缝；2）试件峰值荷载为 14.37kN，离散性较小，混凝土椎体破坏的极限承载力较为稳定；3）试件在峰值荷载下的滑移量为 5.51mm，拉结件根部混凝土几乎完全剥落，峰值荷载处滑移较大。

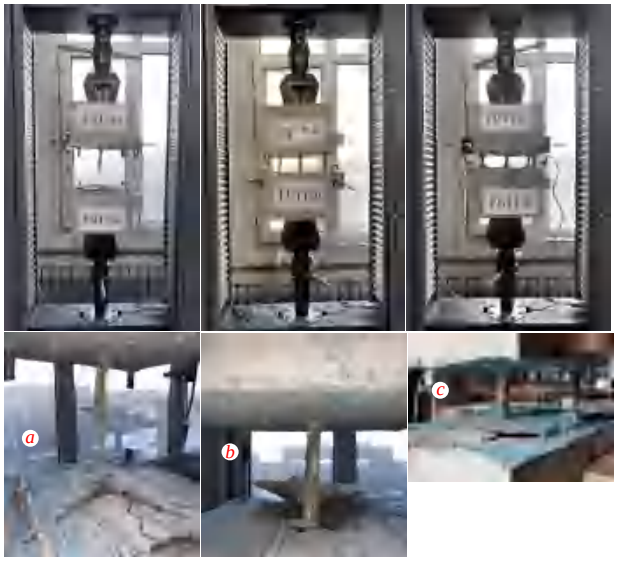

图 10　FRP 棒状拉结件试件破坏形态

表 6　FRP 棒状拉结件试件试验结果

试件编号	峰值点		平均值	
	F_u/kN	Δ_u/mm	F/kN	Δ/mm
FBT11a	14.43	6.09	14.37	5.51
FBT11b	13.81	5.03		
FBT11c	14.88	5.40		

中国知网　https://www.cnki.net

结合图 11 试件的荷载–滑移曲线可以将试件的破坏过程大致分为 3 个阶段：

第一阶段：从开始加载到 0.3～0.4F_u 时，拉结件荷载–位移曲线基本呈线性分布，拉结件与混凝土间滑移在 1.5～2.5mm 之间，拉拔力主要由 FRP 与周围混凝土介质之间的胶结力和机械咬合力承担。

第二阶段：继续加载至峰值荷载过程中，滑移量增大至 1.0～3.0mm，FRP 与混凝土介质间的胶结力丧失，独特的三角形凹槽斜向外侧挤压内嵌混凝土，拉结件根部混凝土逐渐出现裂缝，此阶段锚固承载力主要由 FRP 凹槽与混凝土之间的机械咬合作用承担，滑移量增长速度加快，荷载–位移曲线呈非线性增长。

第三阶段：达到峰值荷载后，拉结件根部混凝土呈椎体破坏，被拉结件连根带起，混凝土表面被挤碎，荷载–滑移曲线急速下降。

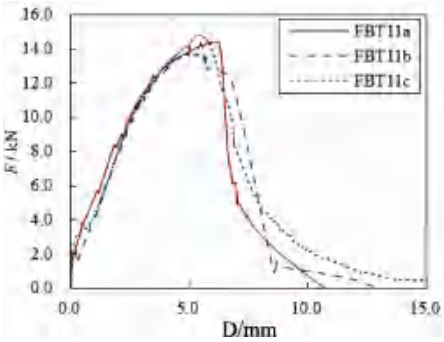

图 11　FRP 棒状拉结件试件荷载–滑移曲线

3.2　不锈钢针状拉结件

本节以 SW85 锚固拉拔试验结果为例，进行试验结果分析。本组共 3 个试件，锚固形式为三折段波浪形，该种锚固形式主要用于内叶板，试件破坏形态见图 12，试验特征值见表 7。

图 12　不锈钢针状拉结件试件破坏形态

试件破坏模式介绍：1）试件的破坏模式均为不锈钢被拉断，拉结件根部混凝土出现椎体破坏；2）试件峰值荷载为 10.75kN，峰值荷载下的滑移量为 12.23mm，承载力离散性较小，试件均在弯折处发生断裂，因此峰值承载力取决于加弯折段过程中对不锈钢的损伤程度。

表 7　不锈钢针状拉结件试件试验结果

试件编号	峰值点		平均值	
	F_u/kN	Δ_u/mm	F/kN	Δ/mm
SW85a	11.26	11.94	10.75	12.23
SW85b	11.08	11.09		
SW85c	9.92	13.67		

结合图 13 试件的荷载–滑移曲线可以将试件的破坏过程大致分为 3 个阶段：

第一阶段：从开始加载到 0.7～0.9F_u 时，拉结件荷载—位移曲线基本呈线性分布，拉结件与混凝土间滑移在 3.0～5.0mm 之间，拉拔力主要由两折段锚固端与周围混凝土介质之间的胶结力承担。

第二阶段：继续加载至峰值荷载过程中，滑移量增大至 11～14mm，三折段锚固端与混凝土介质间的胶结力丧失，弯折段向外侧挤压内嵌混凝土，拉结件根部混凝土出现裂缝并有局部混凝土被压碎，在弯折处不锈钢发生颈缩，荷载–位移曲线呈非线性增长。

第三阶段：达到峰值荷载后，根部混凝土出现椎体破坏，不锈钢于弯折薄弱处被拉断，荷载–滑移曲线急速下降。

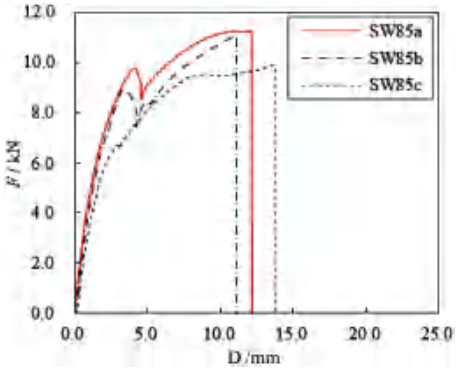

图 13　不锈钢针状拉结件试件荷载–滑移曲线

3.3　FRP 片状拉结件

本节以片状 FRP 拉结件 FPS20C4 系列及 FPS25C4 系列锚固拉拔试验结果为例，进行试验结果分析。本组共 6 个试件，试件为单排孔洞、后插钢筋为 4 根，孔洞直径为 10mm、边距为 20mm，试件破坏形态见图 14，试验特征值见表 8。

试件破坏模式介绍：1）试件在试验结束时，后插钢筋的孔洞均呈现与孔洞同宽的垂直纵向断裂面；2）FPS20C4 系列试件峰值荷载为 25.59kN，

中国知网　https://www.cnki.net

(a) FPS20C4 系列

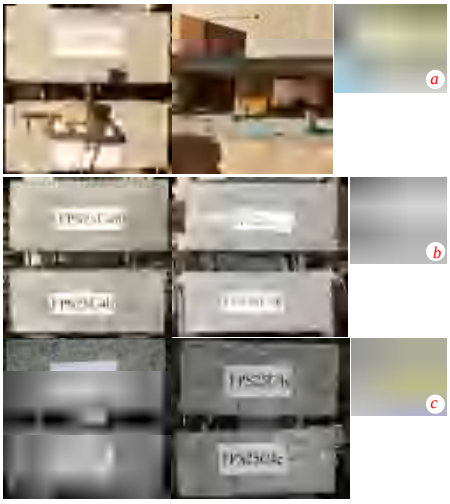

(b) FPS25C4 系列

图 14　FRP 片状拉结件试件破坏形态

峰值荷载下的滑移量为 2.66mm；FPS25C4 系列试件峰值荷载为 47.86kN，峰值荷载下的滑移量为 1.74mm，承载力呈分阶段上升、下降趋势。

表 8　FRP 片状拉结件试件试验结果

试件编号	峰值点		平均值	
	F_u/kN	Δ_u/mm	F/kN	Δ/mm
FPS20C4a	29.26	1.82	25.59	2.66
FPS20C4b	27.72	0.98		
FPS20C4c	19.80	5.17		
FPS25C4a	40.70	1.89	47.86	1.74
FPS25C4b	53.02	1.77		
FPS25C4c	49.86	1.55		

结合图 15 试件的荷载–滑移曲线可以将试件的破坏过程大致分为 3～4 个阶段，以 FPS20C4c 为例：

第一阶段：从开始加载到 c1 峰值点，承载力主要由混凝土与片状 FRP 拉结件之间的胶结力提供；同时，后插钢筋受拉、孔壁受压；当其中一个孔洞发生冲切破坏时，出现第一峰值点 c1。

第二阶段：承载力随后下降，然后进入平台段 c2，当第二孔洞发生冲切破坏时，承载力进入下降段，以此类推。

第三阶段：当孔洞全部发生冲切破坏后，承载力下降至 6kN 左右，试验结束。

类似地，其余试件会出现各别承载力发展阶段合并的情况，例如 FPS25C4c 试件中，出现 c1 峰值点，c2、c3 阶段承载力发展过程与 FPS20C4c 试件的 c2、c3、c4 阶段类似，其余不再赘述。

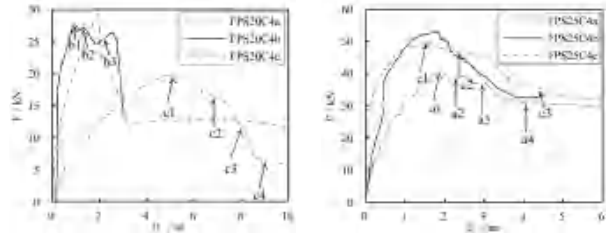

(a) 荷载–位移曲线

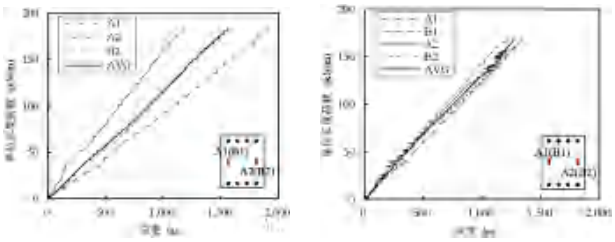

(b) FPS20C4a　　(c) FPS20C4b

图 15　FRP 片状拉结件试件荷载–滑移曲线

3.4　FRP 筒状拉结件

本节为 FRP 筒状拉结件锚固拉拔试验结果分析。锚固端后插钢筋为 4 根（每方向各 2 根），试件破坏形态见图 16，试验特征值见表 9。

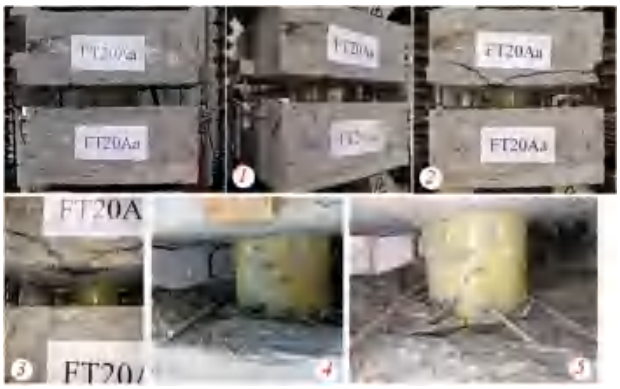

图 16　FRP 筒状拉结件试件破坏形态

试件破坏模式介绍：1）试件破坏模式均为混凝土劈裂，裂缝分布及开展范围广，出现明显剥落，附加钢筋屈服并拔出；2）试件的承载力峰值为 95.5kN，承载力离散程度较小，峰值点对应的位移为 0.50mm。

结合图 17 试件的荷载–滑移曲线将试件

中国知网　https://www.cnki.net

表 9　FPR 筒状拉结件试件峰值点试验结果

试件编号	F_u/kN	Δ_u/mm
FT20Aa	95.5	0.50

FT20Aa 的承载力发展及试件破坏过程总结如下：1）开始加载至 60kN 过程中，拉结件荷载–位移曲线基本呈线性分布，拉结件与混凝土间滑移在 0.2～0.5mm 之间，随后，混凝土与连接件接触的位置开始出现裂缝；2）裂缝从连接件的周边向混凝土试件四角延伸，逐渐明显；随着荷载逐渐增大至 80kN 左右，伴随着混凝土的开裂声，连接件两侧混凝土出现明显的开裂、鼓包，周围混凝土开始剥落；3）随着荷载逐渐达到峰值荷载，混凝土被拉结件及后插钢筋带起，后插钢筋被拔出并逐渐屈服，荷载出现回落，位移增长速度增大，荷载下降至 40kN 以下，试验终止。

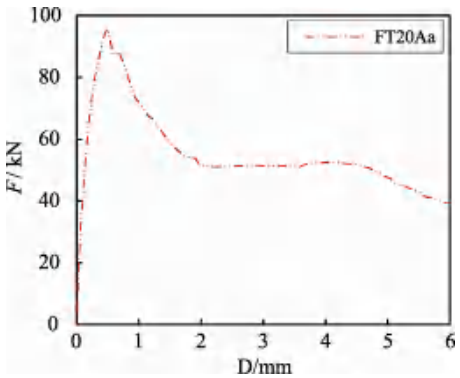

图 17　FPR 筒状拉结件试件荷载–滑移曲线

4　试验结论

4.1　FRP 棒状拉结件锚固试验

本文研究了 FRP 棒状拉结件不同开槽形式、槽口深度、槽口边距对锚固拉拔破坏模式及承载力的影响，主要结论如下：

（1）FBC、FBP 型拉结件破坏模式均为拉结件被拔出，槽口内部残留混凝土，槽口边距对锚固承载力影响不大；FBTR 型拉结件破坏模式为端部槽口 FRP 三个切角被剪断，混凝土未发生椎体破坏，槽口边距增大提高了锚固承载力及变形能力；FBT 型拉结件破坏模式为锚固端部混凝土劈裂，劈裂裂缝沿锚固混凝土对角线延伸至边部；FBTH 型拉结件破坏模式为锚固端部混凝土发生小椎体破坏，端部槽口 FRP 纤维被剪断。

（2）综合三种开槽形式，呈三角形但其斜边自端头至内部逐渐向内侧倾斜的凹槽承载力最高，建议采用。

（3）对于不同截面形式，内凹三角形和 T 形加工较方便，制作墙板时可充分搅动混凝土，建议采用此两类截面形式。

（4）FBT 拉结件的承载力比 FBTH 型拉结件的承载力提高约一倍，且破坏为混凝土破坏，即混凝土强度提高时承载力还可继续提高，该类产品为推荐的 FB 类拉结件形式形式。

综上，建议采用的 FRP 棒状拉结件产品类型以内凹三角形和 T 型为主，呈三角形但其斜边自端头至内部逐渐向内侧倾斜的凹槽形式。

4.2　不锈钢针状拉结件锚固试验

本文研究了不锈钢针状拉结件不同端头弯折形式、锚固深度对锚固拉拔破坏模式及承载力的影响，主要结论如下：

（1）STR 型拉结件端头锚固于外叶板，端头与分布钢筋拉结，锚固深度为 35mm 时破坏模式为根部混凝土椎体破坏，分布钢筋屈服并被拉出；SW 型拉结件端头锚固于内叶板，锚固破坏模式及承载力与端头锚固深度及弯折形式有关；SHK 型拉结件端头锚固于内叶板，端头勾住分布钢筋，破坏模式为不锈钢在夹具压痕处被拉断。

（2）不锈钢针状拉结件的锚固承载力取决于内、外叶板承载力的较小值，随着混凝土强度的提高，当外叶板混凝土劈裂承载力高于不锈钢的断裂承载力时，不锈钢拉结件承载力发挥至最大。

（3）两折段波浪形拉结件的主要破坏模式为端部拔出，破坏为脆性破坏；三折段波浪形拉结件的破坏均为不锈钢拉断，延性较好；弯钩形不锈钢拉结件延性最好，破坏均为不锈钢屈服后拉断，承载力最高，但墙板制作时安装性能略差。

（4）外叶板锚固端形式为弯折三角形，该锚固方式的最终破坏为混凝土劈裂破坏，且承载力最高时位移较大。

综上，内叶锚固段建议根据具体应用需求选择三折段或弯钩形锚固形式，外叶锚固段建议增加抗劈裂钢筋。

4.3　FRP 片状拉结件锚固试验

本文研究了 FRP 片状拉结件不同横向纤维强度、混凝土强度、拉结件开孔形式及孔边距、后插钢筋数量对片状拉结件锚固破坏模式及承载力的影响，主要结论如下：

（1）采用斜向纤维更有利于提高 FRP 拉结件的受拉承载力。采用横向纤维时，强度提高到纵向 80%，承载力提高并不明显，这主要是因为孔洞边的拉力线为斜向；如采用斜向纤维，纤维与主应力方向相同，可提高纤维的使用效果。

中国知网　https://www.cnki.net

（2）相比不穿锚固钢筋或少穿锚固钢筋的 FRP 板，穿锚固钢筋的 FRP 板的承载力和延性都大大提高。穿锚固钢筋数量增加后，各孔洞的 FRP 荷载相应减少，提高了 FRP 板的抗拉承载力；发生混凝土劈裂破坏后，随着变形逐渐增加，钢筋逐渐受拉并提供拉力，对后期延性的提高起到较大的作用。

（3）双排孔的 FRP 板受拉承载力高于单排孔的 FRP 板受拉承载力，但劈裂承载力低于单排孔的劈裂承载力。双排孔 FRP 板，由于其靠内一侧孔的边距较大，因此其 FRP 材料可承担的拉力提高，但此时钢筋距离混凝土表面的最小厚度减少，因此其抗混凝土劈裂承载力有所下降。

综上，片状拉结件建议采用纵向和斜向布置纤维，尽量采用单排孔，每个孔均穿设锚固钢筋。

4.4 FRP 筒状拉结件锚固试验

本文研究了 FRP 筒状拉结件采用纵向纤维拉挤工艺，横向布置纤维毡，附加钢筋为双向各两根 C6、长度为 600mm 条件下，其破坏模式及承载力，主要结论如下：

（1）FRP 筒状拉结件的材料受拉承载力较高，为满足工程应用需求，需保证 FRP 筒状拉结件的破坏模式为混凝土劈裂破坏。混凝土抗劈裂能力与截面面积相关，而 FRP 筒状拉结件的材料受拉承载力与截面周长相关。

（2）FRP 筒状拉结件的每个孔洞均建议穿设钢筋，且应保证每侧钢筋的锚固长度。根据试验结果，混凝土劈裂破坏后，随着变形逐渐增加，钢筋逐渐受拉并提供一定的拉力，对后期承载力和延性具有提高作用。

参 考 文 献

[1] 张季超, 楚先锋, 邱剑辉, 等. 高效、节能、环保预制钢筋混凝土结构住宅体系及其产业化[J]. 工程力学, 2008, 25(S2): 123-133, 138.

[2] 陈敖宜, 张肇毅, 王卉, 等. 建筑工业化及绿色模块建筑[J]. 工业建筑, 2014, 44(6): 108-111.

[3] 黄炜, 张敏, 江永涛, 等. 装配式混凝土墙抗震性能试验研究[J]. 建筑结构学报, 2015, 36(10): 88-95.

[4] 刘才华, 蒋庆, 种迅, 等. BFRP 拉结件预制混凝土夹心保温外墙板抗弯性能试验研究[J]. 工程力学, 2017, 34(S1): 111-115.

[5] 孟宪宏, 周阿龙, 刘海成, 等. 夹心保温外墙板连接件力学性能试验[J]. 沈阳建筑大学学报(自然科学版), 2014, 30(2): 227-234.

[6] 雷义雄, 叶献国, 孙政, 等. 预制混凝土夹芯墙板玄武岩纤维筋拉结件承载性能研究[J]. 工业建筑, 2017, 47(7): 46-51.

[7] 刘明, 李立东, 张延年, 等. L 型塑料钢筋拉结件锚固性能试验[J]. 沈阳建筑大学学报(自然科学版), 2009, 25(5): 925-929.

[8] 刘鑫, 王鑫. 塑料钢筋拉结件粘结试验研究[J]. 建筑技术, 2017, 48(5): 535-537.

[9] SHOHOKO S. Expert’s report on the ACG-Connector system(in Janpanese)[R]. 1997.

[10] KURAMA Y, PESSIKI S, SAUSE R, et al. Seismic behavior and design of unbonded post-tensioned precast concrete walls[J]. PCI Journal, 1999, 44(3): 72-89.

[11] BERAYOUNE A, SAMAD AA ABDUL. Flexural behavior of precast concrete sandwich composite panel experimental and theoretical investigations[J]. Construction and Building Materials, 2007(12): 677-685.

中国知网 https://www.cnki.net

预制混凝土密肋夹心保温外挂墙板受力性能有限元分析

史天祥[1],冯　博[2],肖　明[1],吕晚晴[1,*],韩文龙[1]
(1.中国建筑标准设计研究院有限公司,北京 100044;2.中铁房地产集团北方有限公司,北京 102400)

摘　要:采用 ABAQUS 软件建立了预制混凝土密肋夹心保温外挂墙板模型,分析了其在垂直板面荷载作用下的全过程受力性能,研究了密肋高度、宽度和排布方式、外饰面层厚度对试件承载力和刚度的影响。结果表明:随着密肋高度、宽度的增加,试件的承载力和初始刚度均增大;随着密肋间距的减小,试件的承载力和初始刚度均增大;随着外饰面层厚度的增加,试件的承载力增大,刚度变化较小。

关键词:预制混凝土密肋夹心保温外挂墙板;承载力;刚度;有限元分析;构造参数
中图分类号:TU375.2　　**文献标识码**:A　　doi:10.19761/j.1000-4637.2025.06.058.06

Finite element analysis of stress performance of precast conerete multi-ribbed sandwich insulation facade panels

SHI Tianxiang[1], *FENG Bo*[2], *XIAO Ming*[1], *LYU Wanqing*[1,*], *HAN Wenlong*[1]
(1.China Institute of Building Standard Design & Research Co., Ltd., Beijing 100044, China; 2.China Railway Construction Real Estate Group North Co., Ltd., Beijing 102400, China)

Abstract: A model for precast conerete multi-ribbed sandwich insulation facade panel was established by using ABAQUS software, and its full-process stress performance under vertical plate load was analyzed. The effects of rib height, rib width, rib arrangement, and decorative layer thickness on the bearing capacity and stiffness of the specimens were studied. The results show that with the increase of rib height and rib width, the bearing capacity and initial stiffness of the specimen both increase. As the rib spacing decreases, the bearing capacity and initial stiffness of the specimen increase. As the decorative layer thickness increases, the bearing capacity of the specimen increases, and the stiffness change is relatively small.

Keywords: Precast conerete multi-ribbed sandwich insulation facade panel; Bearing capacity; Stiffness; Finite element analysis; Structural parameter

0　引言

长期以来,建筑能耗和建筑碳排放在我国总能耗与总碳排放中的占比较大[1]。发展推广超低能耗建筑是实现我国建筑节能和“双碳”目标的重要途径之一。已有研究[2]表明,提升外墙的保温隔热性能是降低建筑能耗的关键。传统预制混凝土夹心保温外挂墙板(以下简称传统外挂墙板)在装配式框架结构公共建筑中应用广泛,但其常存在墙板超重、连接节点设计复杂、热桥影响大等问题[3-19]。为此,本文在传统外挂墙板的基础上进行优化,提出了一种预制混凝土密肋夹心保温外挂墙板(以下简称密肋外挂墙板)构造。

密肋外挂墙板从室内向室外由内饰面、内保温层、钢筋混凝土密肋层(以下简称密肋层)、外保温层和外饰面层构成,并通过保温连接件进行可靠连接,可实现结构保温一体化,可为新型工业化背景下装配式框架结构围护体系的设计提供有效解决方案。与传统外挂墙板相比,密肋层替代实心钢筋混凝土墙板可有效降低墙板自重,解决墙板超重问题。同时,在密肋层两侧及肋间区格中填充保温材料,可有效减轻密肋层的热桥影响,并降低单层保温层厚度,便于施工。但是,目前关于密肋外挂墙板的研究相对较少[20];另外,JGJ/T 275—2013《密肋复合板结构技术规程》[21] 虽然对采用密肋构造的剪

基金项目:“十四五”国家重点研发计划项目(2022YFC3801400);非金属材料创新中心创新基金项目(2023TDA3-2)。

力墙墙板给出了相关设计规定,但缺乏密肋构造外挂墙板的设计方法。

综上,本文采用 ABAQUS 软件建立密肋外挂墙板的精细化有限元模型,分析其在垂直板面荷载作用下的全过程受力性能,并以密肋的高度、宽度和排布方式、外饰面层厚度为主要参数,开展典型受力分析,以期为密肋外挂墙板的构造设计和推广应用提供参考。

1　密肋外挂墙板的构造

本文设计的密肋外挂墙板的构造示意图如图 1 所示。其中,外饰面层采用耐久性能好的超高性能混凝土(Ultra-high performance concrete,以下简称 UHPC),密肋层混凝土强度等级为 C30,钢筋采用 HRB400 钢筋,外保温层采用挤塑聚苯乙烯保温板(以下简称 XPS 保温板),保温连接件为不锈钢材质。密肋层承担大部分垂直板面荷载作用,内、外饰面层与保温层通过保温连接件传递面外荷载。

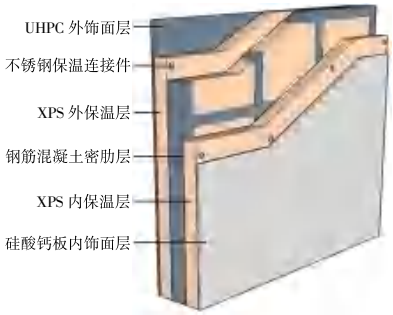

图 1　密肋外挂墙板示意图

Figure 1　Schematic diagram of multi-ribbed facade panel

2　有限元分析模型

2.1　模型建立

本文采用 ABAQUS 软件建立四点支撑平移式密肋外挂墙板有限元模型,宽度为3 500 mm,高度为 2 900 mm,见图 2(a),网格密度为 50 mm。另外,为提高计算模型的收敛性,在单侧风荷载或地震荷载作用下,仅考虑 UHPC 外饰面层、外保温层、保温连接件与密肋层的相互作用,忽略内饰面层与内保温层刚度的影响。因此,本模型共设置 5 道横肋与 6 道纵肋,肋宽与肋高均为 150 mm,外饰面层厚度为 20 mm,外保温层厚度根据 GB/T 51350—2019《近零能耗建筑技术标准》对夏热冬冷地区传热系数的要求取为 40 mm,密肋层布置双层 Ø8@200 mm 钢筋网,保温连接件布置在混凝土横、纵肋轴线交点处,见图 2(b)。

本模型中,钢筋采用 T3D2 桁架单元进行模拟,其余部分均采用 C3D8R 实体单元进行模拟。UHPC 与 C30 混凝土采用塑性损伤模型,其受压、受拉应

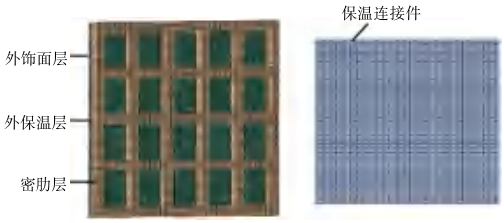

(a)构造　　(b)保温连接件

图 2　密肋外挂墙板模型

Figure 2　Model of multi-ribbed facade panel

力-应变关系按 GB 50010—2010《混凝土结构设计标准(2024 年版)》[22]进行选取。UHPC 抗压强度取 120 MPa,抗拉强度取 7 MPa;钢筋采用理想弹塑性模型,屈服强度、弹性模量分别为 400 MPa、200 GPa;XPS 保温板和不锈钢保温连接件均按弹性考虑,弹性模量分别为 200 MPa 和 200 GPa。外饰面层、外保温层和密肋层间的界面法向行为均采用 ABAQUS 软件中的硬接触定义,界面切向行为采用“罚摩擦”函数定义,摩擦系数取 0.1,钢筋网与保温连接件均嵌入至模型内。

密肋外挂墙板模型的约束条件如图 3 所示,在密肋层 4 个角部设置相应边界条件。在 UHPC 外饰面层施加均布荷载,至跨中挠度为 100 mm 时停止加载[23]。

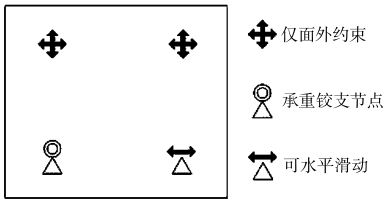

图 3　模型的约束条件

Figure 3　Constraints of the model

2.2　模型验证

本文选取沈蒲生等[25]设计的双向密肋楼板,采用上述模型建模,通过对比试验和有限元计算结果来验证本文所建模型的准确性。图 4 和图 5 分别为试件的裂缝分布形态和均布荷载-跨中挠度曲线,其中,有限元计算得到的裂缝分布情况通过混凝土受拉损伤情况间接表示。

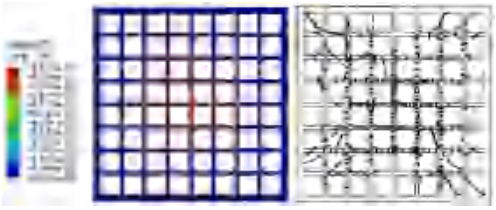

(a)模拟结果　　(b)试验结果[25]

图 4　裂缝分布情况

Figure 4　Distribution of cracks

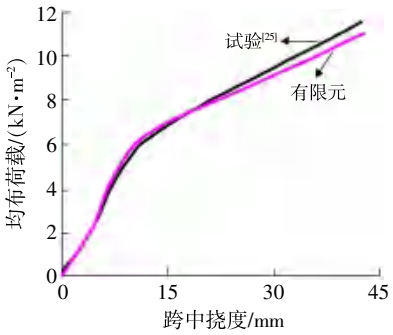

图 5　均布荷载-跨中挠度曲线

Figure 5　Even load-mid span deflection curves

由图 4 和图 5 可知,有限元计算结果与试验结果整体吻合较好，说明本文所建模型的准确度较高,可用于后续分析。

3　有限元结果与分析

3.1　均布荷载-跨中挠度曲线

图 6 为密肋外挂墙板的均布荷载-跨中挠度曲线。其中,对于持久设计状况、地震设计状况下墙板承载力极限状态对应的均布荷载取值，根据 JGJ/T 458—2018《预制混凝土外挂墙板应用技术标准》[24]选取最不利组合计算得到,见表 1。

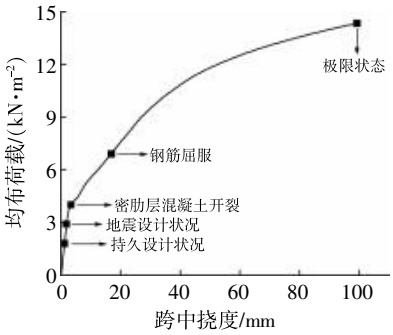

图 6　密肋外挂墙板的均布荷载-跨中挠度曲线

Figure 6　Even load-deflection curves of multi-ribbed facade panel

表 1　不同设计状况下的均布荷载取值

Table 1　Even load values under various design conditions

设计状况	验算内容	荷载类型	作用形式	荷载/(kN·m⁻²)
持久	面外变形	风荷载	均布荷载	1.8
	裂缝宽度	风荷载	均布荷载	1.8
地震	面外承载力	风荷载 地震荷载	均布荷载	2.9

由图 6 可知,当均布荷载达到持久设计状况、地震设计状况的设计承载力(1.8 kN/m²、2.9 kN/m²)时,试件跨中挠度分别为 1.15 mm、1.85 mm，均未达到开裂荷载,钢筋与混凝土均处于弹性状态,设计安全冗余度较高。当均布荷载增至 4.0 kN/m² 时,密肋层受拉侧混凝土开裂，试件面外刚度明显下降,曲线呈非线性特征,此时对应的跨中挠度为 3.38 mm。当均布荷载增至 6.9 kN/m² 时，部分钢筋开始进入屈服阶段,此时跨中挠度达 16.91 mm。随着钢筋发生塑性变形,试件刚度进一步下降,曲线的非线性特征更明显。

3.2　混凝土应变分布

图 7 为密肋层混凝土的应变分布情况。

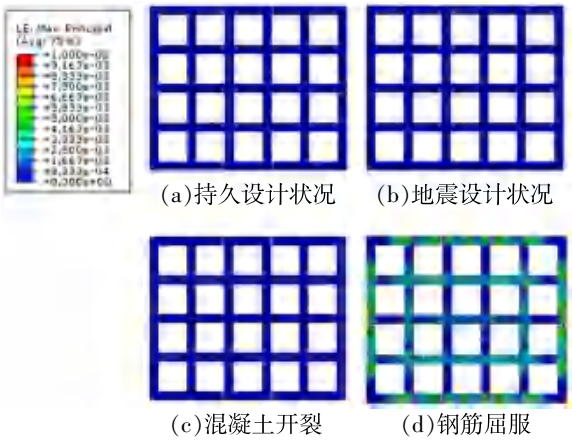

图 7　密肋层混凝土的应变分布

Figure 7　Strain distribution of multi-ribbed concrete

由图 7 可知:持久设计状况、地震设计状况下,密肋层混凝土的最大拉应变分别为 100με、300με,均未达到开裂应变(1 000με);当密肋层混凝土达到开裂应变时,裂缝首先出现在板顶和板底横向肋跨中与竖向肋相交处;当钢筋屈服时,受拉层密肋混凝土出现大面积裂缝,且裂缝处混凝土应变远大于开裂应变。

另外,在有限元分析过程中发现,当试件跨中挠度达到 100 mm 时,UHPC 外饰面层无裂缝出现,应变为 400με。

3.3　钢筋应力分布

图 8 为密肋层钢筋的应力分布情况。

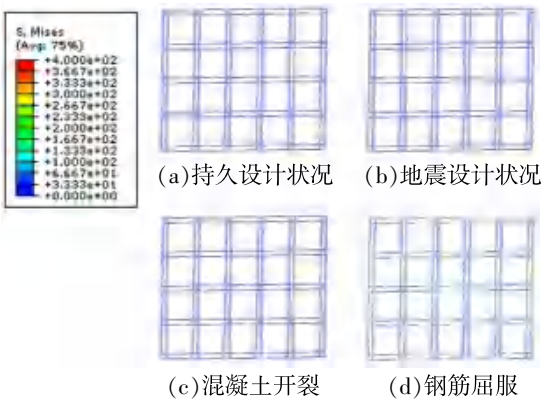

图 8　密肋层钢筋的应力分布

Figure 8　Stress distribution of multi-ribbed steel bars

由图 8 可知:持久设计状况、地震设计状况下,钢筋均处于弹性阶段, 最大应力分别为 16.1 MPa、35.6 MPa;当密肋层混凝土开裂时,钢筋最大应力达到 124.3 MPa,仍处于弹性阶段;此后,随着加载的继续,钢筋应力发展较快,受拉钢筋初次屈服位置与混凝土初次开裂位置较接近,基本也在板顶和板底跨中横肋与纵肋交界处。整体而言,钢筋应力分布呈双向受力特征,由于密肋外挂墙板的宽度大于高度,其长边方向横肋承担的荷载较纵肋有所增大。

4　参数分析

4.1　参数设置

基于上述研究结果,本文控制密肋外挂墙板的尺寸(宽 3 500 mm、高2 900 mm)不变,进一步探究密肋的高度、宽度和排布方式、外饰面层厚度对密肋外挂墙板受力性能的影响,具体参数设计见表 2。其中,ML01 为基准组。

表 2　参数设置

Table 2　Parameter settings

试件编号	外饰面层厚度/mm	密肋高度/mm	密肋宽度/mm	密肋排布
ML01	20	150	150	5 道横肋+6 道纵肋
ML02	20	100	150	5 道横肋+6 道纵肋
ML03	20	200	150	5 道横肋+6 道纵肋
ML04	20	150	100	5 道横肋+6 道纵肋
ML05	20	150	200	5 道横肋+6 道纵肋
ML06	30	150	150	5 道横肋+6 道纵肋
ML07	40	150	150	5 道横肋+6 道纵肋
ML08	20	150	150	4 道横肋+5 道纵肋
ML09	20	150	150	6 道横肋+7 道纵肋

4.2　结果分析

图 9 为不同参数条件下, 试件的均布荷载-跨中挠度曲线。表 3 为试件的开裂荷载与极限荷载。

由图 9 可知, 各试件的均布荷载-跨中挠度曲线发展规律基本一致, 加载初期试件刚度较大,直至密肋层受拉侧混凝土开裂。此后,由于混凝土开裂退出工作,拉力由受拉侧钢筋承担,试件刚度明显降低。随着受拉钢筋在加载过程中不断屈服,试件的刚度进一步降低。

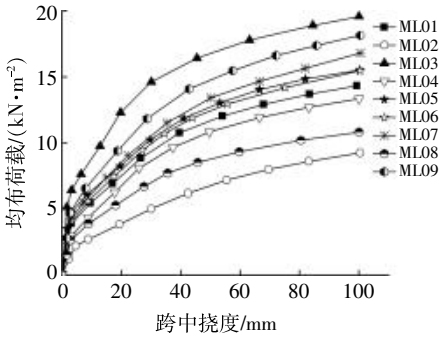

图 9　不同参数条件下的试件均布荷载-跨中挠度曲线

Figure 9　Even load-deflection curves of specimens under various parameter conditions

表 3　试件的开裂荷载与极限荷载

Table 3　Cracking load and ultimate load of specimens　kN/m²

试件编号	ML01	ML02	ML03	ML04	ML05
开裂荷载	3.8	2.1	5.8	3.1	4.7
极限荷载	14.3	9.3	19.6	13.4	15.6
试件编号	ML06	ML07	ML08	ML09	
开裂荷载	4.1	4.4	2.6	4.9	—
极限荷载	15.6	16.8	10.9	18.2	—

一般而言,混凝土开裂前的试件刚度可定义为初始刚度。另外, 由图 9 可知, 在跨中挠度接近 40.00 mm 时,各试件的刚度均明显下降。因此,本文定义跨中挠度 40.00 mm 时对应的刚度为二次刚度,并定义停止加载时的刚度为试件最终刚度。据此,各试件不同阶段的刚度大小见图 10。

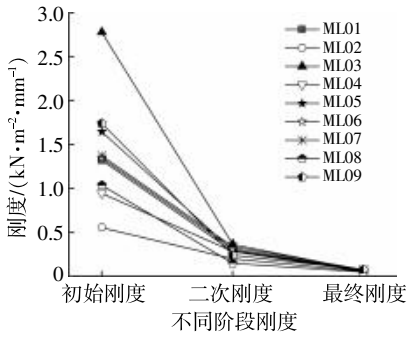

图 10　试件不同阶段的刚度

Figure 10　Stiffness of specimens at different stages

4.2.1　密肋高度的影响

本文选取 ML01 (肋高 150 mm)、ML02 (肋高 100 mm)和 ML03(肋高 200 mm)分析密肋高度对试件受力性能的影响。

由表 3 可知:随着密肋高度的增加,试件的开裂荷载、极限荷载均增大;ML02 试件的开裂荷载、极限荷载分别为 2.1 kN/m²、9.3 kN/m², 较基准组 ML01 试件分别降低了 44.7%、35.0%;ML03 试件的开裂荷载、极限荷载分别为 5.8 kN/m²、19.6 kN/m², 较 ML01 试件分别提高了 52.6%、37.1%。

由图 10 可知,随着密肋高度的增加,试件的初始刚度增大,二次刚度增幅相对较小,最终刚度基本一致。与 ML01 试件相比,ML02 试件的初始刚度降低了 30.8%,ML03 试件的初始刚度提高了 115.4%。

综上,密肋外挂墙板的承载力和初始刚度受密肋高度影响较大,与密肋高度成正比,这与钢筋混凝土梁的受弯性能相似。

4.2.2　密肋宽度的影响

本文选取 ML01（肋宽 150 mm)、ML04（肋宽 100 mm)和 ML05(肋宽 200 mm)分析密肋宽度对试件受力性能的影响。

由表 3 和图 10 可知,当密肋宽度由 150 mm 减小至 100 mm 时，与 ML01 试件相比,ML04 试件的开裂荷载、极限荷载和初始刚度分别降低了 18.4%、6.3%和 30.8%。当密肋宽度由 150 mm 增至 200 mm 时,与 ML01 试件相比,ML05 试件的开裂荷载、极限荷载和初始刚度分别提高了 23.7%、9.1%和 23.1%。

综上,密肋宽度对密肋外挂墙板的承载力和初始刚度有一定影响,随着密肋宽度的增加,试件的承载力和初始刚度均增大。另外,与密肋高度相比,密肋宽度对密肋外挂墙板受力性能的影响相对较小。

4.2.3　密肋间距的影响

本文选取 ML01(5 道横肋+6 道纵肋)、ML08(4 道横肋+5 道纵肋)和 ML09(6 道横肋+7 道纵肋)分析密肋间距对试件受力性能的影响。

由表 3 可知,ML08、ML09 试件的开裂荷载分别为 2.6 kN/m^2、4.9 kN/m^2,极限荷载分别为 10.9 kN/m^2、18.2 kN/m^2。可见,相较于 ML01 试件,减少 1 道横肋与纵肋，试件的开裂荷载、极限荷载分别降低了 31.6%、23.8%,而增加 1 道横肋与纵肋,试件的开裂荷载、极限荷载分别提高了 28.9%、27.3%。

由图 10 可知,ML08、ML09 试件的初始刚度分别与 ML04、ML05 试件相近,这是由于改变密肋间距与改变密肋宽度的原理相似,均改变了受弯构件的宽度,故改变密肋间距与改变密肋宽度对密肋外挂墙板刚度的影响规律相似。

综上,适当减小密肋间距能有效提高密肋外挂墙板的承载力和初始刚度。

4.2.4　外饰面层厚度的影响

本文选取 ML01(外饰面层厚度 20 mm)、ML06(外饰面层厚度 30 mm)和 ML07(外饰面层厚度 40 mm)分析外饰面层厚度对试件受力性能的影响。

由表 3 可知，与 ML01 试件相比,ML06 试件的开裂荷载、极限荷载分别提高了 7.9%、9.1%,ML07 试件的开裂荷载、极限荷载分别提高了 15.8%、17.5%。可见,随着外饰面层厚度的增加,试件的开裂荷载与极限荷载均增大,另外,与极限荷载相比,开裂荷载提升相对较小。原因分析:密肋外挂墙板从开始加荷至受拉区混凝土开裂前，整个截面参与受力,而混凝土开裂瞬间,裂缝处受拉区混凝土退出工作,拉力由钢筋承担,受压区混凝土的抗压能力得到充分发挥,故密肋外挂墙板的开裂荷载提升较小,而极限荷载提升较明显。

由图 10 可知,ML06、ML07 试件的初始刚度与 ML01 试件的初始刚度相近，均为 1.3 kN/(m^2·mm)左右。密肋外挂墙板的初始刚度与混凝土受拉侧强度密切相关,外饰面层位于混凝土受压层,增大外饰面厚度不会改变混凝土受拉侧的强度,故外饰面层厚度对刚度的影响较小。

5　结论

(1)本文提出的密肋外挂墙板适用于装配式框架结构,可有效降低墙板自重和热桥影响,实现结构保温一体化。

(2)持久设计状况与地震设计状况下,混凝土与钢筋均处于弹性阶段，设计安全冗余度较高;UHPC 外饰面层在加载全过程中未开裂。

(3)适当增大密肋高度和宽度均可有效提高密肋外挂墙板的承载力与初始刚度,其中,密肋高度的影响相对更明显;减小密肋间距对密肋外挂墙板受力性能的影响与增大密肋宽度相似;适当增大外饰面层厚度可以提高密肋外挂墙板的承载力,但对刚度影响较小。

参考文献:

[1] 赵彦革,孙倩,韦婉,等.建筑结构类型及方案对碳排放的影响研究[J].建筑结构,2023,53(17):14-18.

[2] 程欣欣.装配式外围护技术在超低能耗建筑中的应用[J].建筑结构,2022,52(增刊 1):1920-1925.

[3] TOMLINSON D,FAM A.Axial load -bending moment interaction diagram of partially composite precast concrete sandwich panels[J].ACI Structural Journal,2018,115(6):1515-1528.

[4] 张鹏.预应力混凝土外挂墙板及其连接节点受力性能研究[J].建筑结构,2023,53(增刊 1):1685-1690.

[5] 肖力光,杜永鸿.预制混凝土夹心保温外挂墙板的研究进展[J].混凝土,2022(8):133-140.

[6] 胡晨,李涛,陈安英,等.点式连接预制混凝土夹心保温外挂墙板抗弯性能研究[J].混凝土,2021(3):116-120,124.

[7] BENAYOUNE A,SAMAD A A A,TRIKHA D N,et al. Structural behaviour of eccentrically loaded precast sandwich panels[J].Construction and Building Materials,2006,20(9):713-724.

[8] 张书航,王大伟,杨新磊.足尺夹心保温外挂墙板拟静力试验研究[J].施工技术,2020,49(5):110-113.

[9] 熊峰,边钰,刘烨,等.预制混凝土夹心保温墙板结构性能研究综述[J].建筑结构,2022,52(23):26-34,125.

[10] 管文.高层装配式建筑预制轻骨料混凝土夹心保温外挂墙板研究[J].施工技术,2018,47(12):100-104.
[11] 朱文祥,许锦峰,吴志敏,等.预制混凝土夹心保温墙板热工性能优化设计建议[J].混凝土,2021(1):132-134.
[12] JOUDI A,SVEDUNG H,RONNELID M.Energy efficient surfaces on building sandwich panels—A dynamic simulation model[J].Energy and Buildings,2011(43):2462-2467.
[13] 石建华,赵学斐,张凡,等.平移式预制混凝土外挂墙板框架足尺低周往复试验研究[J].东南大学学报(自然科学版),2023,53(5):803-811.
[14] 陈忠,李迪,贾伟朋,等.平移式预制混凝土外挂墙板设计与应用[J].施工技术(中英文),2023,52(3):118-124.
[15] 江韩,赵学斐,苗宏恩.平移式预制混凝土外挂墙板连接节点设计方法及受力性能分析[J].建筑结构,2021,51(5):41-47.
[16] 薛伟辰,姜伟庆,宋佳峥,等.预制混凝土夹心保温外挂墙体桁架式不锈钢连接件抗拔与抗剪性能试验研究[J].施工技术,2018,47(12):95-99.
[17] DUTTA D,JAWDHARI A,FAM A.A new studded precast concrete sandwich wall with embedded glass-fiber reinforced polymer channel sections: Part 1, experimental study [J].PCI Journal,2020(4):51-70.
[18] XUE W C,LI Y,FU K,et al.Accelerated ageing test and durability prediction model for mechanical properties of GFRP connectors in precast concrete sandwich panels[J].Construction and Building Materials,2020,237:117632.
[19] JIANG H Z,GUO Z X,LIU J B.Composite behavior of sandwich panels with w-shaped SGFRP connectors[J].Structure Engineering,2018,22(5):1889-1899.
[20] 曹计栓,张虎峰,苏磊,等.钢结构住宅 UHPC 外挂墙板研究及施工技术[J].施工技术(中英文),2024,53(2):79-86.
[21] 中华人民共和国住房和城乡建设部.密肋复合板结构技术规程:JGJ/T 275—2013[S].北京:中国建筑工业出版社,2013.
[22] 中华人民共和国住房和城乡建设部.混凝土结构设计标准(2024 年版):GB 50010—2010[S].北京:中国建筑工业出版社,2010.
[23] 张莉亚.轻钢龙骨混凝土组合外挂墙板优化设计及力学性能研究[D].南京:东南大学,2018.
[24] 中华人民共和国住房和城乡建设部.预制混凝土外挂墙板应用技术标准:JGJ/T 458—2018[S].北京:中国建筑工业出版社,2018.
[25] 沈蒲生,朱建华.四边简支钢筋混凝土双向密肋楼盖极限荷载与挠度计算方法的理论与试验研究[J].土木工程学报,2003(8):7-11.

收稿日期:2024-08-16
第一作者:史天祥(1998—),硕士,工程师。
E-mail:2837585875@qq.com
通信作者:吕晚晴(1994—),博士,工程师。
通信地址:北京市海淀区首体南路 9 号主语国际 2 号楼
E-mail:798693782@qq.com

(上接第 57 页)

design method for precast concrete splice slabs with welded junction plates[J].Structural Concrete,2024,25(6):4480-4497.
[13] ZHANG W B,FENG Y,ZENG X Q,et al.Flexural performances of novel wet joints with sleeve connections in precast composite floor system[J]. Buildings,2024,14(3):822.
[14] CHEN Y,SHI H R,WANG C L,et al.Flexural mechanism and design method of novel precast concrete slabs with crossed bent-up rebar [J].Journal of Building Engineering,2022,50:104216.
[15] 聂鑫,杨悦,聂建国.一种混凝土预制板板端取消胡子筋的构造及施工方法:CN107246107A[P].2017-10-13.
[16] 章雪峰,郑曙光,单玉川,等.四边不出筋密拼连接叠合双向板原位加载对比试验研究[J].建筑结构,2019,49(23):113-117.
[17] 肖宇.预制底板不出筋的混凝土叠合板的受弯性能研究[D].徐州:中国矿业大学,2020.
[18] 陈宝春,季韬,黄卿维,等.超高性能混凝土研究综述[J].建筑科学与工程学报,2014,31(3):1-24.
[19] 钟蕴为,吴永魁,文许高媛,等.超高性能混凝土(UHPC)基本性能研究综述[J].混凝土与水泥制品,2021(9):1-4.
[20] 聂建国,陈必磊,陈戈,等.钢筋混凝土叠合板的试验研究[J].工业建筑,2003,33(12):43-46.
[21] 刘立新,于春,栾文彬,等.预制混凝土叠合板的无筋叠合面抗剪性能试验研究[J].建筑施工,2013,35(1):80-82.

收稿日期:2024-08-20
第一作者:于泽(1995—),男,工程师。
通信作者:朱张峰(1985—),男,博士,副教授。
通信地址: 江苏省南京市浦口区浦珠南路 30 号南京工业大学土木工程学院
E-mail:zzfking2210@163.com

RSC Advances

REVIEW

View Article Online
View Journal | View Issue

Open Access Article. Published on 05 November 2025. Downloaded on 11/6/2025 7:42:05 AM.
This article is licensed under a Creative Commons Attribution-NonCommercial 3.0 Unported Licence.

Check for updates

Cite this: RSC Adv., 2025, 15, 43095

Hydrophobic phenolic/silica aerogel composites with high fire safety and strength for efficient thermal insulation

Zhixin Wang,[a] Yong Kong, *[ab] Mengcheng Nie,[a] Kuo Liu,[c] Qinghua Liu[c] and Xiaodong Shen *[ab]

Received 22nd September 2025
Accepted 21st October 2025

DOI: 10.1039/d5ra07166f

rsc.li/rsc-advances

To develop a polymer-based aerogel composite with excellent fire safety and strength for efficient building insulation, hydrophobic phenolic/silica aerogel composites (PSACs) were synthesized using a facile, self-catalyzed sol–gel process based on co-condensation of resorcinol (R), formaldehyde (F), and 3-(aminopropyl)triethoxysilane (A). The hydrophobicity was achieved via the gas-phase modification of the aerogels. The hydrophobicity and thermal conductivity of the PSACs are governed by the R/A ratio and aerogel density, respectively. A glass fiber paper-reinforced PSAC with an R/A ratio of 2 and an aerogel density around 0.10 g cm^{-3} (GP/RA21-10) exhibits a high water contact angle of 138°, a low thermal conductivity of 0.021 W m^{-1} K^{-1}, and a high strength (1.67 MPa of compression strength, 2.54 MPa of tensile strength, and 1.65 MPa of flexural strength). GP/RA21-10 exhibits significantly superior thermal insulation properties compared to commercially available insulation materials, including thermosetting polystyrene board, silica aerogel coating board, and rock wool. GP/RA21-10 is flame-retardant and high-temperature resistant and demonstrates superior fire safety during building insulation. The design presented here offers important guidelines for the advancement of high-performance building insulation materials.

1 Introduction

The consumption of energy and its related carbon emissions during the operation of a building accounted for over 55% of the total building lifecycle emissions, according to the statistics from the China Association of Building Energy Efficiency. Enhancing building thermal insulation performance is a critical measure to reduce carbon emissions during building operation.[1–6] Characterized by their nanoporous structures with high specific surface areas and high nanopore volumes, silica aerogel composites exhibit much lower thermal conductivity than traditional insulation materials such as thermosetting polystyrene board, rock wool, glass wool, and ceramic fiber felt.[7–13] Therefore, silica aerogel composites have been widely applied in many demanding scenarios such as aerospace, electric vehicles, and for energy saving in industrial operations. However, poor mechanical properties limit the application of silica aerogel composites in buildings.[11,14–18]

Polymer aerogels, such as phenolic aerogel, polyimide aerogel, polyurethane aerogel, cellulose aerogel and so on, have better mechanical properties than silica aerogels, and have been studied extensively.[19–32] Phenolic aerogel in particular exhibits both low thermal conductivity and outstanding mechanical performance.[23–32] Pekala et al. revealed that phenolic aerogels with densities ranging from 0.1 to 0.2 g cm^{-3} exhibit compressive strengths of 0.1 to 0.2 MPa, much higher than those of silica aerogels (~0.01 MPa).[24] However, phenolic aerogels suffer from poor thermal stability including flammability and poor fire safety.[33] Doping inorganic components into phenolic aerogels is an effective method to enhance their thermal stability and can improve their insulation and mechanical properties significantly.[25–39]

Generally, in situ co-polymerization of the phenolic and silica precursors is conducted to develop phenolic/silica composite aerogels with high temperature resistance. Jin et al. developed a phenolic/silica aerogel composite, via multiple impregnation and ambient pressure drying (APD) steps, from methyltrimethoxysilane (MTMS) and phenolic resin precursors and a quartz fiber reinforcement.[29] The composite had a density of 0.3 g cm^{-3} and a thermal conductivity of 0.044 W m^{-1} K^{-1}. Compared to phenolic aerogel composites without organic components, the addition of silica increased the strength by 40% and reduced the line ablation rate at a heat flux of 0.4 MW m^{-2} by 60%. Wang et al. developed a carbon fiber reinforced

[a]College of Materials Science and Engineering, State Key Laboratory of Materials-Oriented Chemical Engineering, Nanjing Tech University, Nanjing 211816, PR China. E-mail: ykong@njtech.edu.cn; xdshen@njtech.edu.cn

[b]Jiangsu Collaborative Innovation Center for Advanced Inorganic Function Composites, Nanjing, 211816, China

[c]Department of Infrastructure, Nanjing Tech University, Nanjing 211816, PR China

© 2025 The Author(s). Published by the Royal Society of Chemistry

Open Access Article. Published on 05 November 2025. Downloaded on 11/6/2025 7:42:05 AM.
This article is licensed under a Creative Commons Attribution-NonCommercial 3.0 Unported Licence.

phenolic/silica aerogel composite via a multi-step sol–gel method and APD, in which the silica solution was dropped into the phenolic solution and stirred at 40 °C until it became homogeneous. Then, the mixed solution underwent a gel-drying process at 80 °C.[30] The resulting aerogel composite exhibited a density of 0.26 g cm^{-3} and a thermal conductivity of 0.055 W m^{-1} K^{-1}. The incorporation of silica led to a 50% enhancement in the maximum fracture strain and a 30% reduction in the line ablation rate under oxyacetylene ablation conditions. Ye et al. developed a thermal protection phenolic/silica aerogel via a complex sol–gel process and APD, using dimethyldimethoxysilane, MTMS, resorcinol and formaldehyde as precursors, and isocyanate-propyltrimethoxysilane as a coupling agent.[40] The aerogel had a density of 0.12 g cm^{-3} and a thermal conductivity of 0.032 W m^{-1} K^{-1}.

These studies reveal that the thermal stability of phenolic aerogels can be improved by introducing silica. However, the synthesis process is complicated and time-consuming, and the thermal conductivity is still too high for use as high-performance thermal insulation materials. More importantly, the resulting phenolic/silica aerogel composites are hydrophilic, restricting their use in humid environments. In this study, phenolic/silica aerogel composites (PSACs) were developed via a facile, self-catalyzed sol–gel process followed by gel drying and aerogel gas-phase modification. The effects of precursor ratio, density, fiber type, and drying method on the architecture and characteristics of the PSACs were explored comprehensively. With low thermal conductivity of 0.021 W m^{-1} K^{-1}, high thermal stability up to 1200 °C, superior hydrophobicity with a water contact angle of 138°, and superior mechanical properties, the PSAC has promise for applications in the domain of building insulation.

2 Experimental

2.1 Materials

Ceramic fiber paper felt (CP, 300 × 300 × 2.50 mm, 0.18 g cm^{-3}) was purchased from Nanjing Gaogeya Fiberglass Development Co., Ltd. Glass fiber paper felt (GP, 300 × 300 × 3.80 mm, 0.16 g cm^{-3}) was purchased from Jiangsu Dali Energy-Saving Technology Co., Ltd. Pre-oxidized PAN fiber needled felt (PANNF, 300 × 300 × 5.00 mm, 0.12 g cm^{-3}) was purchased from Changshu Juge Fiber Products Co., Ltd. Polypropylene fiber felt (PP, 300 × 300 × 5.00 mm, 0.10 g cm^{-3}) was purchased from Xiaoguang Textile Factory. Polyethylene terephthalate felt (PET, 300 × 300 × 5.00 mm, 0.10 g cm^{-3}) was purchased from Guangzhou Hengrui Non-woven Fabric Co., Ltd. Polyethylene felt (PE, 300 × 300 × 1.80 mm, 0.14 g cm^{-3}) was purchased from Hubei Jiateng Textile Co., Ltd. Melamine foam (MF, 300 × 300 × 5.00 mm, 0.05 g cm^{-3}) was purchased from Zhenmo New Material Co., Ltd. 3-(Aminopropyl)triethoxysilane (APTES or A, 98%), formaldehyde (F, 37%), resorcinol (R), and hexamethyldisiloxane (HMDS, 99%) were purchased from Shanghai Aladdin Biochemical Technology Co., Ltd. Ethanol (EtOH, 99.7%) and deionized water (W) were purchased from Nanjing Wanqing Chemical Glassware and Instrument Co., Ltd. All the chemicals were used as received without further purification.

Several commercial insulation materials were used as control samples. Thermosetting polystyrene board (TPSB, 0.20 g cm^{-3}) and extruded polystyrene board (XPSB, 0.04 g cm^{-3}, 0.034 W m^{-1} K^{-1}) were purchased from Xinye Building Materials Business Department. Silica aerogel coating board (SACB, 0.13 g cm^{-3}) was purchased from Shanghai Zhongnan Building Materials Co., Ltd. Rock wool (RW, 0.08 g cm^{-3}) was purchased from Xinlexiang Energy-saving Technology (Shanghai) Co., Ltd.

2.2 Synthesis of hydrophobic PSACs

The synthesis procedure is illustrated in Fig. 1a. R, F, EtOH, and W were combined in a beaker at room temperature with agitation until the R was fully dissolved. APTES was subsequently added to the mixture and stirred for 10 min to prepare the phenolic/silica solution. The fiber felts were impregnated with the phenolic/silica solution with an equal volume. After gelation at 60 °C for 24 h, the wet gels were submerged in ethanol for 48 h to conduct solvent exchange. The alcogels were dried by supercritical drying (SCD) or APD to obtain the PSACs. The hydrophobic modification of the PSACs was conducted using a gas-phase modification at 110 °C for 10 h in a vessel filled with HMDS vapor. As shown in Table S1, PSACs with different R/A molar ratios and densities were prepared, denoted as Z/RAX-Y, where X is the molar ratio of R/A, Y is the theoretical density of the pure aerogel (r_t), and Z is the type of fiber felt.

2.3 Characterization

The apparent density of the PSACs (r_{ac}) was computed based on the weights and physical dimensions of five subsamples. The theoretical density of the pure aerogel (r_t) was calculated by assuming that all the reagents react with each other in stoichiometric ratios (eqn (S1)). The chemical architecture was characterized using Fourier-transform infrared spectroscopy (IR-Sprit). The hydrophobic performance was tested using a water contact angle instrument (MIT-100S). The microstructure was observed using scanning electron microscopy (Regulus 8100). The mechanical properties (compressive, tensile, and flexural) were tested with CMT-4204 at a loading rate of 2 mm min^{-1}. The pore structure was characterized on a Belsorp mini X porosimeter. The thermal conductivity (at 25 °C) was tested with a plate heat flow method using an HFM446. Five subsamples of each sample were tested, and the results were averaged. Thermal insulation performance was measured by a back temperature test at a heat source temperature of 70 °C, which was performed using a constant temperature machine (BILON-W-1009S). The flame-retardant performance was examined by using a butane torch flame for a period of 4 minutes and by combusting on an alcohol lamp for 30 s. The weather resistance was tested by outdoor exposure and under a constant environment of 85 °C and 85% relative humidity (BPS-100CH). The building insulation application was tested using heating tapes with the same outside surface temperature (70 °C).

 © 2025 The Author(s). Published by the Royal Society of Chemistry

Open Access Article. Published on 05 November 2025. Downloaded on 11/6/2025 7:42:05 AM.
This article is licensed under a Creative Commons Attribution-NonCommercial 3.0 Unported Licence.

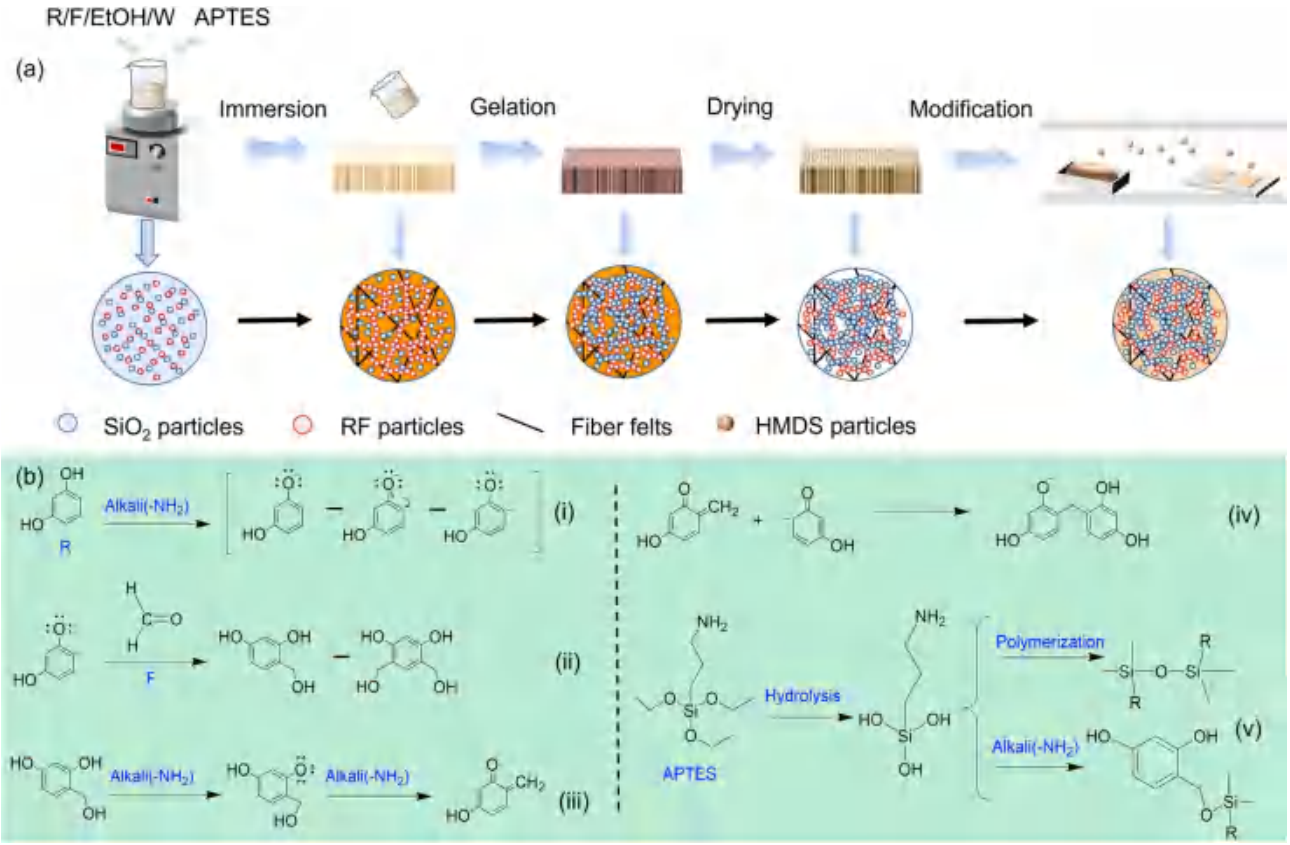

Fig. 1 (a) Preparation of the hydrophobic PSACs and (b) reaction mechanisms that occur during the sol–gel process.

3 Results and discussion

3.1 Sol-gel reaction mechanisms

It is widely recognized that traditional silica aerogels are synthesized via a multi-step sol–gel process based on the catalysis of acids and bases.[7-9] In a solution of R/F/A/EtOH/W, a gel can be formed without adding an acid or base catalyst owing to the Lewis base moieties (-NH_2) in the APTES.[28] The reaction mechanisms that occur during the sol–gel processes used to make the PSACs are shown in Fig. 1b. The polymerization of R and F is a reaction catalyzed by a Lewis base. First, an R anion is formed through deprotonation Fig. 1b(i). Then, an increase in electron density at the 4 or 6 position of R leads to the hydroxymethylation of the positively charged hydroxyl carbon on F (forming a -CH_2OH group) Fig. 1b(ii). The base catalyst will cause R to generate highly active intermediates (o-quinone methyl ether) Fig. 1b(iii), which can react with another molecule of R to form stable methylene bonds Fig. 1b(iv).[41,42] APTES is hydrolyzed to form a Si–OH species, which forms Si–O–Si structures by dehydration condensation. In addition, the Si–OH groups can react with hydroxymethylated R to form Si–O–C linkages Fig. 1b(v).[43,44] The phenolic and Si–O–Si frameworks are mutually interpenetrating, forming a phenolic/silica network with organic and inorganic moieties uniformly hybridized on a molecular scale.

3.2 Effect of the R/A molar ratio and density on the physical properties of the PSACs

The physical properties of the PSACs with different R/A molar ratios and densities are shown in Table S2. All the samples were prepared with CP as the reinforcement using SCD as the drying method. The tiny difference in thickness between the CP and PSACs verifies that there is no obvious volume shrinkage during the synthesis of the PSACs. The apparent densities of the pure aerogels (r_a) are calculated by subtracting the contribution of the fiber felt from the apparent densities of the PSACs (r_{ac}). It is noted that the values of r_a are higher than those of r_t, which is attributed to the fact that the reaction does not reach 100% completion.

The FTIR spectra of the PSACs with different R/A molar ratios and the same theoretical density of pure aerogel (0.10 g cm^{-3}) are shown in Fig. 2a. The chemical structure is hardly affected by the R/A molar ratio. The bands around 1150 cm^{-1} are assigned to the Si–O–Si stretching vibrations.[45,53] The bands at 1600 cm^{-1} could be the result of aromatic C] C vibrations or the bending vibration of the -NH_2 groups.[38,46] The bands at 850 cm^{-1} are attributed to the Si–C bonds that arise from the formation of a phenolic/silica hybrid network within the PSACs.[47,48] The bands at 2950, 2930, 1450 and 1250 cm^{-1} are assigned to the C–H stretching and deformation vibrations.[49,54]

At a constant theoretical density of pure aerogel (0.10 g cm^{-3}), the water contact angle of the PSACs initially

Open Access Article. Published on 05 November 2025. Downloaded on 11/6/2025 7:42:05 AM.
This article is licensed under a Creative Commons Attribution-NonCommercial 3.0 Unported Licence.

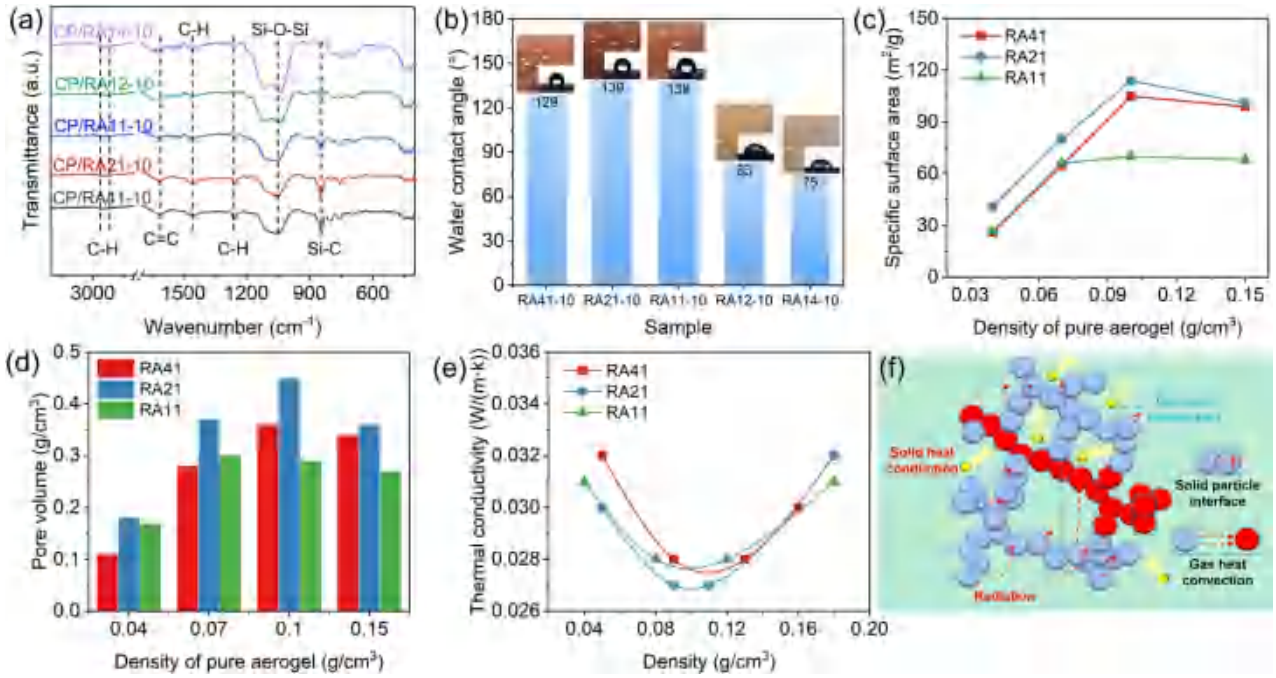

Fig. 2 (a) FTIR spectra of the PSACs with different R/A molar ratios and same theoretical density; (b) water contact angles of the PSACs with different R/A molar ratios; (c) specific surface areas of the PSACs; (d) pore volumes of the PSACs; (e) thermal conductivities of the PSACs with different pure aerogel densities; and (f) thermal insulation mechanism of the PSACs.

increases as the APTES content increases, before starting to decrease as the APTES content continues to rise (Fig. 2b). The highest water contact angle achieved by CP/RA21-10 is 139°. The hydrophobicity is achieved by grafting HMDS on Si–OH species that derive from APTES. However, the APTES contains a strong hydrophilic aminopropyl group. Therefore, the highest water contact angle is obtained with a moderate R/A ratio of 2 : 1. To ensure good hydrophobicity of the PSACs, the R/A molar ratio should not be lower than 1. The influence of the density on the water contact angle of PSACs is weak (Fig. S1).

The pore structure features in the PSACs with different R/A molar ratios and densities are shown in Fig. S2. All samples show type IV isotherms and H2 hysteresis loops without a saturation plateau, indicating the presence of features relating to meso–macroporosity. There is no obvious difference in pore size distribution for the different PSAC samples, and all exhibit a wide pore size distribution in the range of 1–100 nm. It is noted that most pores concentrate in the range of 10–50 nm. The specific surface areas and pore volumes are shown in Fig. 2c and d. The highest specific surface area and pore volume are achieved with a moderate density of 0.10 g cm^{-3}, irrespective of the R/A molar ratio. This is because both higher and lower densities lead to more faults in terms of large voids. For the same theoretical density, a moderate R/A molar ratio of 2 : 1 leads to the highest specific surface area (114 m^2 g^{-1}) and pore volume (0.45 cm^3 g^{-1}).

The relationship between the thermal conductivity (25 °C) and apparent density of the pure aerogel in the PSACs is shown in Fig. 2e. For the PSACs with different R/A molar ratios, all the lowest thermal conductivities are obtained with a moderate density of around 0.10 g cm^{-3} as it leads to the highest specific surface area and pore volume. The PSAC with a R/A molar ratio of 2 exhibits the lowest thermal conductivity of 0.027 W m^{-1} K^{-1}. This is understandable when the thermal transfer mechanism of the aerogel is considered (Fig. 2f). The thermal transfer is mainly composed of solid thermal conduction, gas thermal conduction, gas thermal convection, and thermal radiation. At constant temperature, the effect of gas thermal conduction and thermal radiation is negligible. The solid thermal conduction is suppressed by reducing the contact area of the nanoparticles in the solid framework, or rather by improving the specific surface area. Gas thermal convection can be restrained by reducing the number of macropores and large voids, or rather by improving the pore volume, as determined via a N_2 adsorption test.

3.3 Effect of the fiber felt and drying method on the physical properties of the PSACs

Fiber reinforcement has an important influence on the mechanical properties, insulation performance and thermal stability. Seven fiber felts including CP, GP, PANNF, PP, PET, PE and MF were selected for use in the preparation of the PSACs, and the aerogels were prepared with a R/A molar ratio of 2 and a theoretical pure aerogel density of 0.10 g cm^{-3} (RA21-10). Photographs of the PSACs prepared with different reinforcement materials and using different drying methods are shown in Fig. 3a and b. The PSACs made using SCD exhibit an intact and smooth morphology. However, APD leads to obvious volume shrinkage and deformation, especially for the PSAC that has soft MF as a reinforcement material. Consequently, the densities of the PSACs fabricated using APD are higher than those prepared using SCD (Fig. 3c). Moreover, the thermal conductivities of the PSACs synthesized using APD are much

 © 2025 The Author(s). Published by the Royal Society of Chemistry

Open Access Article. Published on 05 November 2025. Downloaded on 11/6/2025 7:42:05 AM.
This article is licensed under a Creative Commons Attribution-NonCommercial 3.0 Unported Licence.

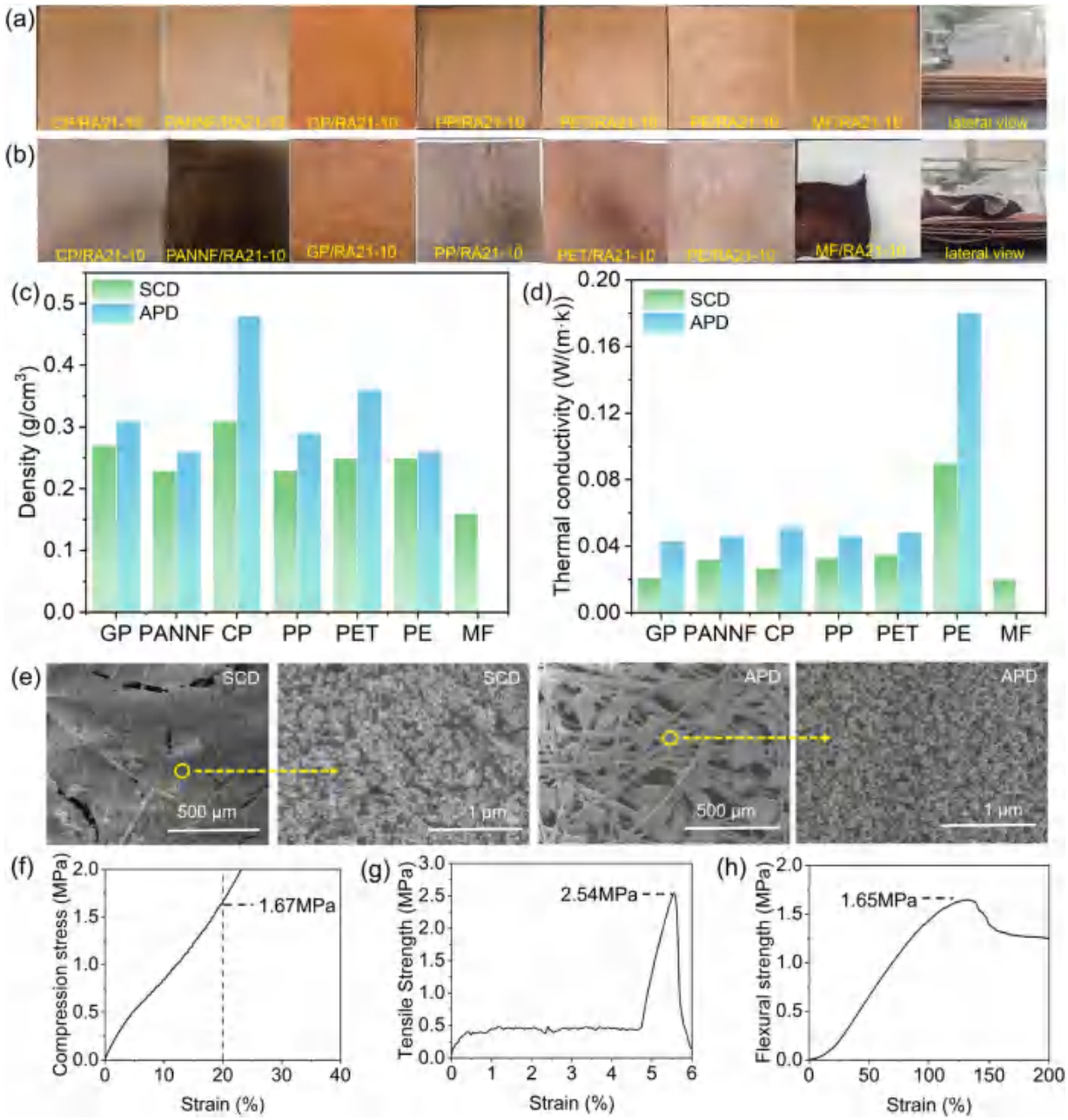

Fig. 3 (a and b) Photographs of PSACs made with different reinforcement materials under (a) SCD and (b) APD; (c) apparent densities of the PSACs made with different reinforcement materials and drying methods; (d) thermal conductivities of the PSACs made with different reinforcement materials and drying methods; (e) SEM images of GP/RA21-10 made using SCD and APD; and (f–h) stress–strain curves of GP/RA21-10: (f) compressive; (g) tensile; and (h) flexural.

higher than those of the PSACs prepared using SCD (Fig. 3d). This finding is attributed to the generation of large voids and the aggregation of nanoparticles during APD, which result from the damage to the porous structure caused by capillary force (Fig. 3e and S3). These findings indicate that SCD is necessary to obtain high-performance PSACs for thermal insulation.

During SCD, the thermal conductivities of the PSACs reinforced with different fiber reinforcement materials including GP, CP, PANNF, PP, PET, PE and MF are 0.021, 0.027, 0.032, 0.033, 0.035, 0.090 and 0.020 W m^{-1} K^{-1}, respectively. The effect of reinforcement on thermal conductivity is attributed to the microstructure of the reinforcement materials, as shown in Fig. S4. CP, PANNF, PP, PE and PET exhibit disorderly and close stacking of their fibers. However, MF and GP exhibit uniform porous frameworks with fine skeletons or fibers. The uniform microstructure favors the impregnation of phenolic/silica sol and the suppression of solid thermal conduction. Hence, the PSACs reinforced with GP and MF (GP/RA21-10 and MF/RA21-10) exhibit lower thermal conductivity than the other samples. However, the hydrophobicity of the PSACs is hardly affected by the fiber type (Fig. S5). It should be noted that MF/RA21-10 is flammable and is not suitable for thermal insulation in

Open Access Article. Published on 05 November 2025. Downloaded on 11/6/2025 7:42:05 AM.
This article is licensed under a Creative Commons Attribution-NonCommercial 3.0 Unported Licence.

buildings. GP/RA21-10 is optimal for insulation in buildings. Furthermore, GP/RA21-10 exhibits much higher compression strength than the other PSAC samples (Fig. S6). The Young's modulus of GP/RA21-10 is 65.3 MPa, and the compression strength is 1.67 MPa at 20% strain (Fig. 3f). As shown in Fig. 3g, the tensile strength of GP/RA21-10 is 2.54 MPa with a failure strain of 5.5%. Fig. 3h demonstrates that GP/RA21-10 has high bending deformation, and the failure bending strain and strength are 105% and 1.65 MPa, respectively. The strength of GP/RA21-10 is much higher than typical silica aerogel composites, which exhibit a compression strength of 0.18 MPa.[50,51]

3.4 Thermal insulation performance

The thermal conductivity of GP/RA21-10 and its state-of-the-art counterparts including other reported polymer/silica aerogels and commercial insulation materials are shown in Fig. 4a. GP/RA21-10 has a much lower thermal conductivity than other phenolic/silica aerogel composites (OPSACs),[30,31,52] a polyimide/silica aerogel composite (PISAC),[22] a polyvinyl alcohol/silica aerogel composite (PVASAC),[11] and commercial insulation materials including TPSB, SACB, and RW.

The insulation performance under practical building insulation conditions is determined on a hot plate apparatus (Fig. 4b). With thermal insulation materials fixed on a 70 °C plate, the temperatures of the cold side (back temperatures) were collected. The back temperatures of samples of GP/RA21-10, TPSB, SACB and RW with the same thickness (40 mm) are shown in Fig. 4c. After 8 h, the stabilized back temperatures of GP/RA21-10, TPSB, SACB and RW were 27.3, 33.4, 32.3 and 33.0 °C, respectively. To achieve the same insulation performance with a back temperature of 33 ± 1 °C on a hot plate of 70 °C, the thicknesses of GP/RA21-10, TPSB, SACB, and RW required were 20, 40, 40, and 50 mm, respectively (Fig. 4d). The insulation performance of GP/RA21-10 is superior to that of other commercial insulation materials.

3.5 Flame-retardant performance

TPSB is widely used for building insulation in China as it can achieve a fire rating of A2. The flammability of GP/RA21-10 (5 mm) and TPSB (5 mm) was compared by combustion with an

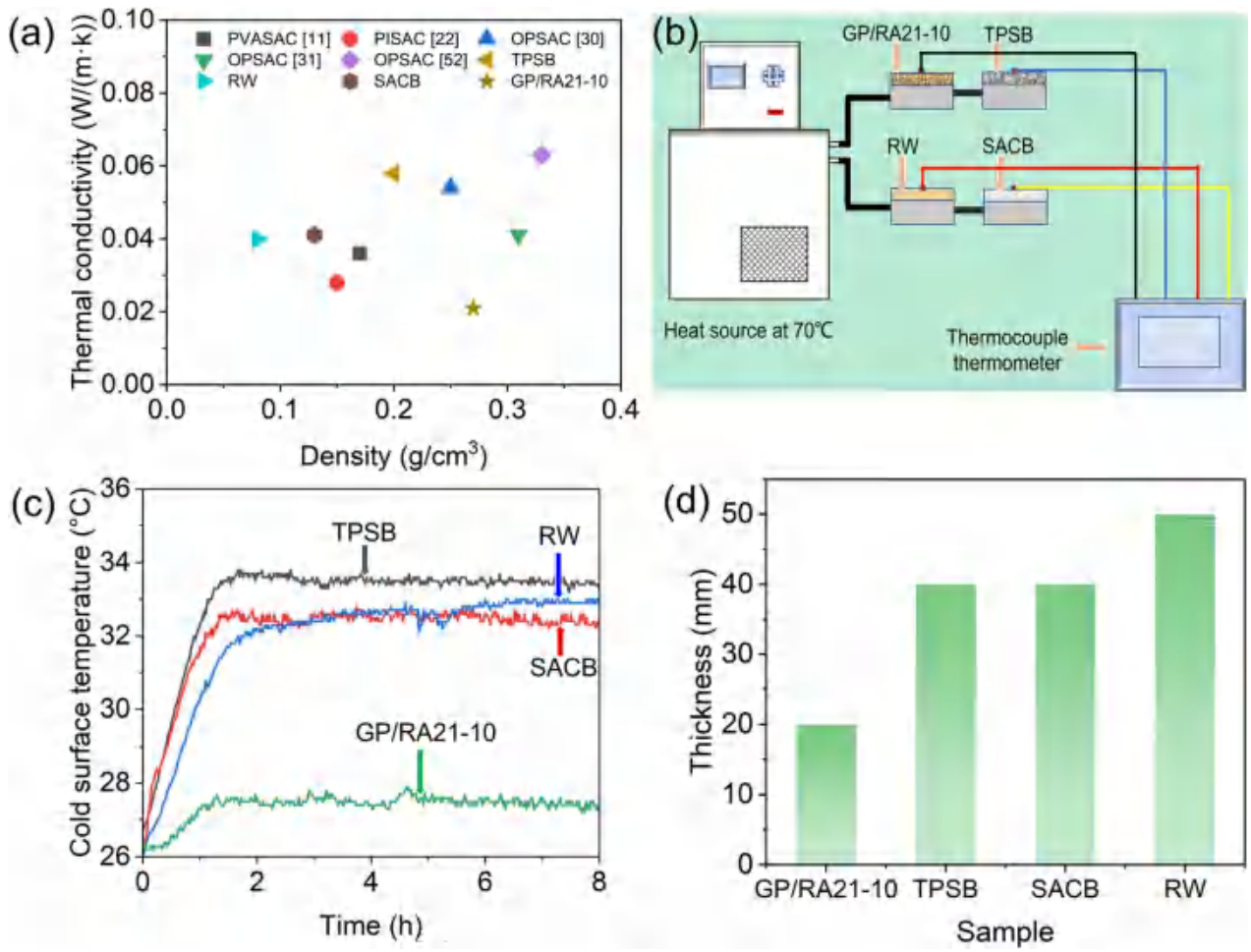

Fig. 4 (a) Thermal conductivities of GP/RA21-10 and its state-of-the-art counterparts (data of the commercial materials were measured together with GP/RA21-10); (b) hot plate apparatus used to estimate the insulation performance; (c) back temperatures of samples of GP/RA21-10, TPSB, SACB, and RW with same thickness (40 mm); and (d) thicknesses of GP/RA21-10, TPSB, SACB, and RW required to achieve same insulation performance with a back temperature of 33 ± 1 °C.

© 2025 The Author(s). Published by the Royal Society of Chemistry

Open Access Article. Published on 05 November 2025. Downloaded on 11/6/2025 7:42:05 AM.
This article is licensed under a Creative Commons Attribution-NonCommercial 3.0 Unported Licence.

alcohol lamp for 30 s (Fig. 5a, b and Video S1). Both GP/RA21-10 and TPSB are flame-retardant and self-extinguish after removing the flame. However, the polymer component in TPSB is burnt off gradually. The thermal shock resistance of GP/RA21-10 (20 mm) and TPSB (40 mm) was investigated under a butane torch flame with a temperature of up to 1200 °C, and the back temperatures were recorded using a thermocouple (Fig. 5c and Video S2). The back temperatures of GP/RA21-10 and TPSB were 34 and 39 °C at 4 min, respectively. Initially, both GP/RA21-10 and TPSB demonstrated superior insulation performance. However, the insulation performance of TPSB degraded remarkably with time as the polymer component was burnt off (Fig. 5c).

GP/RA21-10, after ablation, is divided into the ablative layer, the carbonized layer and the original material (Fig. 5d). The flame-retardant mechanism of GP/RA21-10 relies on the dual

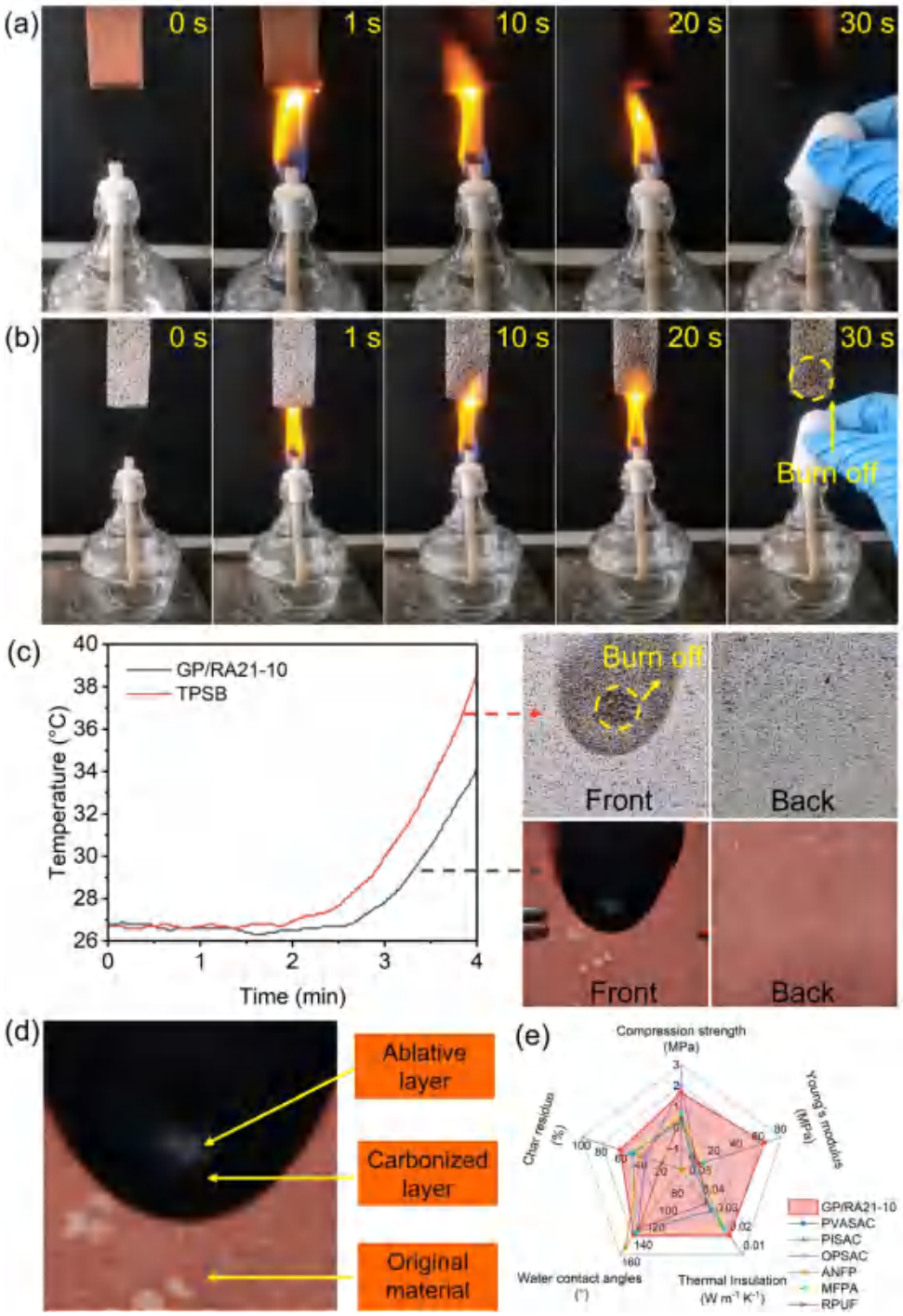

Fig. 5 (a and b) Photographs of GP/RA21-10 (a) and TPSB (b) when subjected to combustion with an alcohol lamp (sample thickness: 5 mm); (c) back temperatures and photographs of GP/RA21-10 (20 mm) and TPSB (40 mm) under a butane torch flame; (d) photograph of GP/RA21-10 after ablation; and (e) comparison of the performance of GP/RA21-10 with other reported insulation aerogels.

Open Access Article. Published on 05 November 2025. Downloaded on 11/6/2025 7:42:05 AM.
This article is licensed under a Creative Commons Attribution-NonCommercial 3.0 Unported Licence.

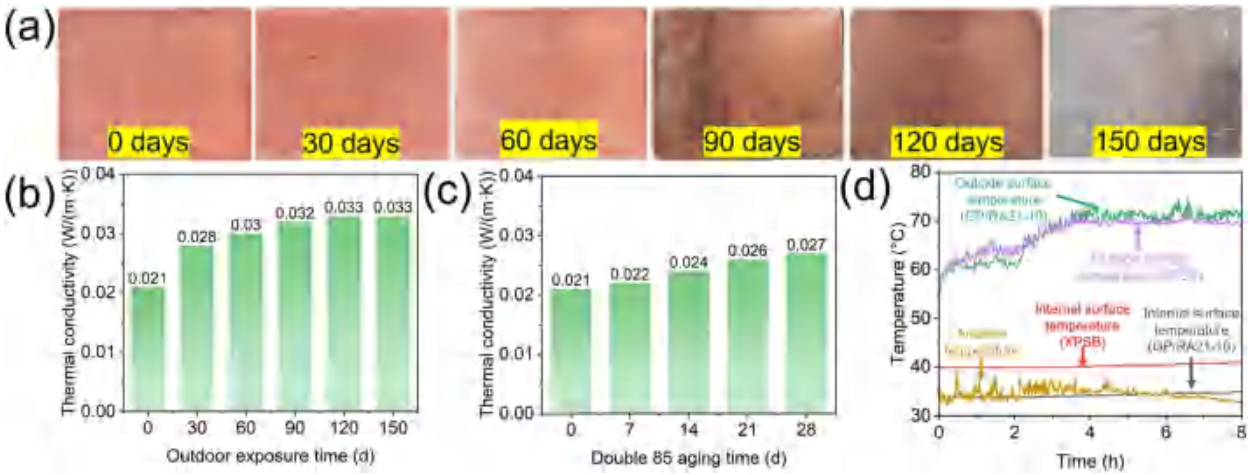

Fig. 6 (a) Photographs of GP/RA21-10 after outdoor exposure for 150 d; (b) thermal conductivities of GP/RA21-10 after outdoor exposure for different time periods; (c) thermal conductivities of GP/RA21-10 after double 85 aging for different time periods; and (d) external building wall insulation performances of GP/RA21-10 and XPSB.

synergy of the organic–inorganic phases and glass fiber-matrix. The pyrolysis of the organic components in the composite takes away most of the heat. Meanwhile, the inorganic components transform into SiO_2 at elevated temperatures, leading to the formation of a dense layer.[26,30] This dense layer adheres to the surface of the aerogel, inhibiting the transfer of heat and oxygen. In addition, the glass fiber skeleton effectively maintains the structural stability of the aerogel, further lessening the impact of the flames and reducing heat transfer, thereby protecting the deeper layers of the base material.[52] Fig. 5e compares the performance of GP/RA-10 and other reported insulation aerogels in terms of compression strength, Young's modulus, thermal insulation, water contact angle and char residue. Details of these properties are included in Table S3. The results indicate that the as-prepared aerogel composite has a better fire safety profile, especially under the effects of a long-term fire atmosphere.

3.6 Weather resistance and application in building insulation

To evaluate the weather resistance of GP/RA21-10, the material was directly placed on the roof to conduct an outdoor exposure test for 150 days (from December to May in Jiangsu, China). The color of GP/RA21-10 darkens gradually within 120 d, and the surface exhibits obvious damage after 150 d (Fig. 6a). This finding is attributed to the decomposition of phenolic components by ultraviolet radiation. The thermal conductivity of GP/RA21-10 increases gradually within 120 d and stabilizes at 0.033 W m^{-1} K^{-1} (Fig. 6b). Alternatively, an accelerated aging test was conducted under constant environmental conditions of 85 °C and 85% relative humidity (double 85 test) to further understand the weather resistance. The thermal conductivities of GP/RA21-10 after double 85 aging for different times are shown in Fig. 6c, and the thermal conductivity gradually increases with aging time due to the moisture-induced damage of the porous structure.

GP/RA21-10 products with a thickness of 20 mm were applied in buildings as external wall insulation materials, and their actual performance was compared with a commercial insulation material, XPSB, with a thickness of 20 mm. When exposed to an outside external wall surface temperature of 70 °C, the internal surface temperature of the GP/RA21-10 insulation material was 6 °C lower than that of XPSB, the insulation material (Fig. 6d). The results indicate that GP/RA21-10 has much better insulation performance than traditional insulation materials.

4 Conclusions

PSACs were synthesized via a facile, self-catalyzed sol–gel process followed by drying of the gels and gas-phase modification of the aerogels. The sol–gel reaction occurs via the self-catalysis of APTES, leading to a phenolic/silica network with organic and inorganic components hybridized uniformly at the molecular level. To ensure good hydrophobicity of the PSACs, the R/A molar ratio should not be lower than 1, whilst the highest water contact angle is achieved with a moderate R/A molar ratio of 2 : 1. For the PSACs with different R/A molar ratios, the lowest thermal conductivities are obtained with a moderate aerogel density around 0.10 g cm^{-3} as this leads to the highest specific surface area and pore volume. The PSACs made using SCD exhibit a more intact and smoother morphology compared to those made using APD, thus leading to materials with lower density and thermal conductivity. The effect of the fiber reinforcement material on hydrophobicity is minor, but its effect on thermal conductivity is significant. Here, MF and GP with uniform porous frameworks with fine skeletons or fibers lead to low thermal conductivity. However, GP/RA21-10 offers significant advantages in terms of hydrophobicity, fire safety, thermal insulation, and strength, whilst reducing the use of building insulation materials by half and lowering the overall cost. Therefore the MF-based PSAC is

 © 2025 The Author(s). Published by the Royal Society of Chemistry

Open Access Article. Published on 05 November 2025. Downloaded on 11/6/2025 7:42:05 AM. This article is licensed under a Creative Commons Attribution-NonCommercial 3.0 Unported Licence.

flammable and is not suitable for building insulation. As a result, a GP-reinforced PSAC with an R/A ratio of 2 : 1 and an aerogel density around 0.10 g cm^{-3} (GP/RA21-10) exhibits a high water contact angle of 138° and a low thermal conductivity of 0.021 W m^{-1} K^{-1}. Moreover, GP/RA21-10 has a high compression strength of 1.67 MPa, a tensile strength of 2.54 MPa, and a flexural strength of 1.65 MPa. The thermal conductivity of GP/RA21-10 is much lower than other phenolic/silica aerogel composites, exhibiting significantly superior thermal insulation properties and fire safety compared to commercially available insulation materials, GP/RA21-10 has great promise as an efficient building insulation material.

Author contributions

Zhixin Wang: investigation, data curation, and writing-original draft. Yong Kong: writing-review and editing, methodology, funding acquisition, and administration. Mengcheng Nie: validation and supervision. Kuo Liu: supervision. Qinghua Liu: supervision. Xiaodong Shen: supervision and funding acquisition.

Conflicts of interest

The authors declare that they have no known competing financial interests or personal relationships that could have appeared to influence the work reported in this paper.

Data availability

Data will be made available on request.

Supplementary information is available. See DOI: https://doi.org/10.1039/d5ra07166f.

Acknowledgements

The authors acknowledge the financial support from the Program Fund of the Non-Metallic Excellence and Innovation Center for Building Materials (24TDA-2) and the Priority Academic Program Development of Jiangsu Higher Education Institution (PAPD).

References

1 X. Jiang, Y. Kong, Z. Y. Zhao and X. D. Shen, Spherical amine grafted silica aerogels for CO_2 capture, RSC Adv., 2020, 10(43), 25911–25917.
2 M. Di Luigi, Z. P. Guo, L. An, J. N. Armstrong, C. Zhou and S. Q. Ren, Manufacturing silica aerogel and cryogel through ambient pressure and freeze drying, RSC Adv., 2022, 12(33), 21213–21222.
3 Y. J. Dai, Y. Q. He, D. D. Yu, J. B. Dai, Y. G. Wang and F. Bai, Study on the effect of semi-transparency on thermal insulation performance of silica aerogel composites, Case Stud. Therm. Eng., 2024, 54, 104010.
4 Q. An, M. Bagheritabar, A. Basem, A. A. Ghabra, Y. Q. Li, M. Tang, L. S. Sabri and R. Sabetvand, The effect of size of copper oxide nanoparticles on the thermal behavior of silica aerogel/paraffin nanostructure in a duct using molecular dynamics simulation, Case Stud. Therm. Eng., 2024, 60, 104666.
5 S. B. Jadhav, A. Makki, D. Hajjar and P. B. Sarawade, Synthesis of light weight recron fiber-reinforced sodium silicate based silica aerogel blankets at an ambient pressure, J. Porous Mater., 2022, 29, 957–969.
6 S. Jadhav and P. Sarawade, Recent advances and prospective of reinforced silica aerogel nanocomposites and their applications, Eur. Polym. J., 2024, 206, 112766T.
7 T. Zhang, D. P. Yu, F. H. Xu, Y. Kong and X. D. Shen, Flexible silica aerogel composites for thermal insulation under high-temperature and thermal-force coupling conditions, ACS Appl. Nano Mater., 2024, 7(6), 6326–6338.
8 D. P. Yu, M. Liu, F. H. Xu, Y. Kong and X. D. Shen, Structure tailoring and thermal performances of water glass-derived silica aerogel composite with high specific surface area and enhanced thermal stability, J. Non-Cryst. Solids, 2024, 630, 122889.
9 Q. Liu, W. J. Zhu, Y. Kong, C. Chu and X. D. Shen, New insights into the resistance of hydrophobic silica aerogel composite to water, moisture, temperature and heat-stress coupling, Ceram. Int., 2024, 50(20), 38189–38199.
10 Q. Liu, Y. Kong, Z. Q. Sun, Z. Y. Liu and X. D. Shen, Facile synthesis of amine hybrid silica aerogel globule via wet casting assisted self-catalysed sol-gel process for CO_2 capture including direct air capture, J. Environ. Chem. Eng., 2024, 12(3), 112913.
11 D. Duan, X. D. Gao, Y. B. Dong, X. M. Qi, X. X. Zhang, M. D. Z. Islam, Y. Q. Wu, X. Zhao and X. M. Li, Green preparation of thermal-insulative, flame retardant, and hydrophobic silica aerogel reinforced poly(vinyl alcohol) composites, ACS Appl. Polym. Mater., 2022, 4(10), 7352–7362.
12 M. Liu, Y. L. Huang, C. Xu, S. J. Yao, G. X. Long, Q. Liu, C. G. Fang and X. X. Wu, Realizing balanced thermal safety and heat insulation in hydrophobic silica aerogel composites, Polym. Degrad. Stab., 2025, 236, 111294.
13 G. Marceau, L. Bertrand and C. Jean-Philippe, Insulation materials for building: dealing with climate change along with other challenges yet to come, IOP Conf. Ser. Earth Environ. Sci., 2024, 1402(1), 012052.
14 Y. H. Wang, X. N. Luo, Q. Li, W. L. Wang, Q. L. Du, H. Yang, L. J. Qiu, Z. Zhang and J. Shen, Industrial application of SiO_2 aerogel prepared by supercritical ethanol (SCE) drying technique as cold and heat insulation materials, J. Sol-Gel Sci. Technol., 2023, 106(2), 341–348.
15 J. Ren, Z. Y. Zhao, Y. Kong, K. M. Zhu, W. Jiang, M. Yuan, J. Q. Tang and X. D. Shen, General approach to the synthesis of metal hybrid carbon/titania aerogel for the oxygen reduction reaction, Energy Fuels, 2024, 38(9), 8262–8276.
16 Q. Liu, Y. Kong and X. D. Shen, Regulating the hydrophobicity and pore structure of silica aerogel for thermal insulation under humid and high temperature conditions, J. Porous Mater., 2024, 32(1), 171–180.

Open Access Article. Published on 05 November 2025. Downloaded on 11/6/2025 7:42:05 AM.
This article is licensed under a Creative Commons Attribution-NonCommercial 3.0 Unported Licence.

17 M. Liu, Y. Kong, B. Q. Zhang and X. D. Shen, New insights into the resistance of silica aerogel to temperature up to 1200 °C, Mater. Lett., 2024, 372, 13705.
18 J. Tang, H. W. Sang, J. H. Chen, H. H. Min, X. Y. Wu, W. D. Zang, J. C. Liu, X. M. Liu, Y. Kong, X. D. Shen, H. Yang, Y. Q. Bu and H. H. Zhang, The use of thin aerogel sheets to suppress the thermal runaway propagation of high energy density cells ($LiNi_{0.8}Co_{0.1}Mn_{0.1}O_2$/Si-C) based module, Process Saf. Environ. Prot., 2024, 186, 1087–1096.
19 X. Y. Zhao, F. Yang, Z. C. Wang, P. M. Ma, W. F. Dong, H. Q. Hou, W. Fan and T. X. Liu, Mechanically strong and thermally insulating polyimide aerogels by homogeneity reinforcement of electrospun nanofibers, Composites, Part B, 2020, 182, 107624.
20 H. Wang, M. Cao, H. B. Zhao, J. X. Liu, C. Z. Geng and Y. Z. Wang, Double-cross-linked aerogels towards ultrahigh mechanical properties and thermal insulation at extreme environment, Chem. Eng. J., 2020, 399, 125698.
21 J. Y. Xue, R. N. Han, Y. M. Li, J. X. Zhang, J. X. Liu and Y. Yang, Advances in multiple reinforcement strategies and applications for silica aerogel, J. Mater. Sci., 2023, 58(36), 14255–14283.
22 Z. F. Fei, Z. C. Yang, G. B. Chen, K. F. Li, S. Zhao and G. H. Su, Preparation and characterization of glass fiber/polyimide/SiO_2 composite aerogels with high specific surface area, J. Mater. Sci., 2018, 53, 12885–12893.
23 C. F. Yuan, D. G. Wang, Y. J. Zhang, K. Li and J. Ding, Research progress on preparation, modification, and application of phenolic aerogel, Nanotechnol. Rev., 2023, 12(1), 39.
24 R. W. Pekala and J. D. LeMay, Organic aerogels: microstructural dependence of mechanical properties in compression, J. Non-Cryst. Solids, 1990, 125, 67–75.
25 T. Liu, W. H. Jiang, H. Q. Qian, X. R. Shi, J. X. Chen, Q. Y. Cao, N. Li, Y. D. Huang and B. Jiang, Nitrogen-Coordinated borate esters induced entangled heterointerface toward multifunctional silicone/phenolic binary aerogel composites, Chem. Eng. J., 2024, 482, 149061.
26 C. Wu, L. M. Wang, X. J. Yan, H. Huang, Y. W. Pan, H. B. Wang, W. Wang, S. Yuan, J. H. Fan, X. Y. Jin, C. Q. Hong and X. H. Zhang, Environmental-friendly and fast production of ultra-strong phenolic aerogel composite with superior thermal insulation and ablative-resistance, Compos. Sci. Technol., 2024, 256, 110776.
27 H. D. Fu, Y. Qin, Z. W. Peng, J. P. Dou and Z. X. Huang, A novel co-continuous Si-Zr hybrid phenolic aerogel composite with excellent antioxidant ablation enabled by sea-island-like ceramic structure at high temperature, Ceram. Int., 2024, 50(12), 21008–21019.
28 J. Ren, T. Zhang, Y. Kong, Z. Y. Zhao, K. M. Zhu, X. Q. Zhang and X. D. Shen, Facile synthesis of phenolic-reinforced silica aerogel composites for thermal insulation under thermal-force coupling conditions, Ceram. Int., 2023, 49(18), 29820–29828.
29 X. Y. Jin, J. G. Xu, Y. W. Pan, H. B. Wang, B. Ma, F. Liu, X. J. Yan, C. Wu, H. Huang, H. M. Cheng, C. Q. Hong and X. H. Zhang, Lightweight and multiscale needle quartz fiber felt reinforced silicon oxycarbide modified phenolic aerogel nanocomposite with enhanced mechanical, insulative and flame-resistant properties, Compos. Sci. Technol., 2021, 217, 109100.
30 W. K. Wang, W. J. Xu, X. F. Jia, F. H. Zhang, Y. P. Cao, C. Ma, J. T. Wang, W. M. Qiao and L. C. Ling, A facile in-situ strategy to fabricate lightweight carbon fiber/silicone-phenolic aerogel composites with superior toughness and ablation performance, J. Mater. Sci., 2024, 59(39), 18488–18498.
31 R. X. Liu, H. B. Wang, C. Q. Hong, X. Y. Jin, Y. W. Pan and X. H. Zhang, Mechanical and dual-stage wind tunnel ablative behavior of ceramic fiber-tile reinforced phenolic aerogel, Compos. Commun., 2022, 36, 101386.
32 L. Wang, X. M. Hu, R. Huang, M. T. Huang, X. Liu, Z. M. Zhou, P. J. Guo, Z. L. Mao, X. S. Xu and X. Wang, Elastic, antiflaming phenolic aerogels for advanced thermal protection at extreme environments, Compos. Commun., 2024, 48, 101889.
33 H. B. Wang, X. J. Yan, X. Y. Jin, Y. W. Pan, C. Wu, H. Huang, C. Q. Hong and X. H. Zhang, Mechanical and thermal ablative behavior of ceramic-modified lightweight quartz felt reinforced phenolic aerogel, Compos. Commun., 2022, 35, 101285.
34 Q. You, G. Liu, Y. Zhong, H. H. Xu, X. F. Zhang, S. S. Shang, M. Yuan, S. Cui and X. D. Shen, Mechanical properties and oxidative ablation behaviors of polysilazane-modified phenolic resin aerogel/carbon fiber fabric composites, Polym. Compos., 2023, 45(1), 1.
35 H. Huang, Y. H. Lv, X. Y. Jin, H. B. Wang, C. Wu, Y. W. Pan, X. J. Yan, C. Q. Hong, W. B. Han and X. H. Zhang, Bifunctional silicone triggered long-range crosslinking phenolic aerogels with flexibility and thermal insulation for thermal regulation, Chem. Eng. J., 2023, 470, 144413.
36 F. Z. Li, J. B. Song, Y. T. Niu, H. W. Zhang, M. Niederberger and W. Cheng, Superelastic cobalt silicate@resorcinol formaldehyde resin core-shell nanobelt aerogel monoliths with outstanding fire retardant and thermal insulating capability, Small, 2023, 19(50), e2302724.
37 Y. L. Cheng, J. W. Zhang, C. Ren, S. P. Zhao, X. D. Zhang and J. P. Fan, Facile preparation of high-strength SiC/C aerogels from pre-reacted resorcinol-formaldehyde and siloxane, J. Ind. Eng. Chem., 2023, 134, 75–83.
38 F. H. Xu, Y. X. Wang, F. C. Tang, X. L. Dai, Z. Y. Zhao, Y. Kong, X. D. Shen and G. F. Shao, Synergistic enhancement of structure and function in carbonaceous SiC aerogels for improved microwave absorption, Carbon, 2025, 233, 119854.
39 X. Y. Jin, C. Liu, H. Huang, R. Q. Pan, C. Wu, X. J. Yan, H. B. Wang, Y. W. Pan, C. Q. Hong and X. H. Zhang, Multiscale, elastic, and low-density carbon fibre/silicon oxycarbide-phenolic interpenetrating aerogel nanocomposite for ablative thermal protection, Composites, Part B, 2022, 245, 110212.
40 D. N. Ye, H. L. Lv, Z. R. Zheng and L. J. Luo, Preparation and properties of flexible phenolic silicone hybrid aerogels for thermal insulation, Molecules, 2024, 29(20), 4942.

 © 2025 The Author(s). Published by the Royal Society of Chemistry

Open Access Article. Published on 05 November 2025. Downloaded on 11/6/2025 7:42:05 AM.
This article is licensed under a Creative Commons Attribution-NonCommercial 3.0 Unported Licence.

41 Y. Kong, J. Y. Zhang, Z. Y. Zhao, X. Jiang and X. D. Shen, Monolithic silicon nitride-based aerogels with large specific surface area and low thermal conductivity, Ceram. Int., 2019, 45(13), 16331–16337.

42 Y. Kong, J. Y. Zhang and X. D. Shen, One-pot sol–gel synthesis of amine hybrid titania/silsesquioxane composite aerogel for CO_2 capture, J. Sol-Gel Sci. Technol., 2017, 84(3), 422–431.

43 B. F. Sandrine, H. Claudia, I. Pierre, J. Edward and T. Salvatore, Evaluation of lightweight and flexible insulating aerogel blankets based on resorcinol-formaldehyde-silica for space applications, Eur. Polym. J., 2017, 93, 403–416.

44 B. X. Liu, W. Ju, J. Zhang, H. L. Fan, Q. C. Wang, X. B. Yi, Z. C. Yu and X. Q. Wang, Improvement of mechanical strength of ultralight resorcinol-formaldehyde/silica aerogel by addition of zirconia, J. Sol-Gel Sci. Technol., 2017, 83(1), 100–108.

45 J. Yan, M. X. Kuang, Y. L. Zhu, Y. K. Chen, C. H. Zhang, H. L. Ma, X. Q. Zhang and L. Kong, Facile, tunable, and environmental friendly synthesis of silica/resorcinol-formaldehyde hybrid xerogels with ultra-low shrinkage using a cationic polyelectrolyte as a soft template, J. Porous Mater., 2023, 30(1), 103–113.

46 Z. Y. Zhao, Y. Cui, Y. Kong, J. Ren, X. Jiang, W. Q. Yan, M. Y. Li, J. Q. Tang, X. Q. Liu and X. D. Shen, Thermal and mechanical performances of the superflexible, hydrophobic, silica-based aerogel for thermal insulation at ultralow temperature, ACS Appl. Mater. Interfaces, 2021, 13(18), 21286–21298.

47 B. L. Shi, Z. L. Zhou, Y. Chen, X. Q. Wang and B. S. Xu, Preparation and properties of hydrophobic and highly transparent SiO_2 aerogels, Ceram. Int., 2023, 49(16), 27597–27603.

48 H. K. Zhao, H. Y. Wang, L. Chen, L. L. Wang and X. Zhao, Preparation of low-cost silica aerogels by high-pressure carbon dioxide methods, J. Non-Cryst. Solids, 2025, 656, 123474.

49 J. Wei, X. T. Li, Y. Wang, B. Chen, M. J. Zhang and C. M. Qin, Photoluminescence property of inexpensive flexible SiC nanowires membrane by electrospinning and carbothermal reduction, J. Am. Ceram. Soc., 2020, 103(11), 6187–6197.

50 J. Y. Xue, L. P. Liu, Y. L. Meng, Z. Chen and Y. Yang, Constructing powerful interface between glass fiber and silica aerogel via an interfacial molecular bridge allows for excellent acoustic-thermal insulation composites, Constr. Build. Mater., 2025, 465, 140260.

51 E. Haq, S. F. A. Zaidi, M. Zubair, M. R. A. Karim, S. K. Padmanabhan and A. Licciulli, Hydrophobic silica aerogel glass-fibre composite with higher strength and thermal insulation based on methyltrimethoxysilane (MTMS) precursor, Energy Build., 2017, 151(1), 494–500.

52 X. Y. Jin, C. Wu, H. B. Wang, Y. W. Pan, H. Huang, W. Wang, J. H. Fan, X. J. Yan, C. Q. Hong and X. H. Zhang, Synergistic reinforcement and multiscaled design of lightweight heat protection and insulation integrated composite with outstanding high-temperature resistance up to 2500 °C, Compos. Sci. Technol., 2023, 232, 109878.

53 F. H. Y, P. F. Jia, L. Song, Y. Hu, B. B. Wang and R. Y. Wu, Multifunctional fabrics based on copper sulfide with excellent electromagnetic interference shielding performance for medical electronics and physical therapy, Chem. Eng. J., 2023, 472, 145091.

54 F. H. Yu, P. F. Jia, B. B. Wang, L. Song and Y. Hu, Unlocking a dual-mode thermal regulation and electromagnetic protection strategy under extreme conditions via bidirectional Janus design, J. Mater. Chem. A, 2025, 13, 23547.

http://pmse.scu.edu.cn

无机杂化酚醛气凝胶研究进展

王智鑫[1]，孔勇[1,2]，沈晓冬[1,2]

（1. 南京工业大学 材料科学与工程学院，江苏 南京 211816；2. 南京工业大学 材料化学工程国家重点实验室，江苏 南京 211816)

摘要: 酚醛气凝胶具有良好的力学性能，可解决氧化硅气凝胶力学性差这一限制应用的难题。然而，抗氧化和抗烧蚀性差限制了酚醛气凝胶在高温隔热领域的应用。无机成分杂化是提升酚醛气凝胶耐温性的有效措施，同时可提高隔热和力学性能，近年来受到研究人员广泛关注。本文综述了无机杂化酚醛气凝胶的最新研究进展，从不同角度对制备方法和无机成分对性能的影响进行了归纳总结。首先，从酚醛来源的角度，结合原位聚合、粉体掺杂和后改性等不同无机成分引入方式阐述了无机杂化酚醛气凝胶的制备方法。然后，分析了无机成分的引入方式和含量、增强纤维对无机杂化酚醛气凝胶隔热、耐温和力学等性能的影响。最后，展望了无机杂化酚醛气凝胶在隔热领域应用前景和发展趋势。

关键词: 无机杂化；酚醛气凝胶；防火阻燃；耐高温；隔热

氧化硅气凝胶具有纳米颗粒构成的三维纳米多孔网络结构，具有低密度、高比表面积、大纳米孔体积等结构特性，表现出优异的高温隔热性能，在航空航天、国防装备、工业和建筑节能以及新能源领域有广泛应用[1]。但力学性能差极大地限制了氧化硅气凝胶的应用推广[2]。聚合物具有长链或交联结构，赋予其良好力学性能，是解决氧化硅气凝胶力学性能差的有效措施。1989 年，Pekala 等[3]以间苯二酚(R)和甲醛(F)为单体首次合成了酚醛(RF)气凝胶，其抗压强度(0.1~0.2MPa)显著高于氧化硅气凝胶(~0.01MPa)，同时具有良好隔热性能。然而，抗氧化和抗烧蚀性差限制了酚醛气凝胶在高温隔热领域的应用，无机成分杂化是提升其耐温性的有效措施，同时可提高绝热性能、阻燃性能和力学性能[4,5]。本文综述了无机杂化酚醛气凝胶的研究进展，从不同角度对其制备方法进行了归纳，总结了无机成分的引入方式、种类和含量以及增强纤维对性能的影响，展望了其在隔热领域的应用前景。

1 无机杂化酚醛气凝胶制备方法概述

气凝胶制备主要包括溶胶-凝胶(凝胶制备)和凝胶干燥两大过程，其中还涉及凝胶的老化和溶剂置换。干燥通常采用常压干燥(APD)和超临界干燥(SCD)。虽然常压干燥设备投入低，但得到的气凝胶比表面积低、导热系数高；超临界干燥可充分保留凝胶网络结构，获得高比表面积、低导热系数的气凝胶[6~9]。超临界干燥工艺已在生产中广泛应用，并表现出良好的技术经济性。

根据酚醛来源，无机杂化酚醛气凝胶通过两种策略制备，一是酚和醛类单体聚合制备，二是线性酚醛树脂(PR)交联固化。考虑无机成分的引入方式，无机杂化酚醛气凝胶制备策略有原位聚合、粉体掺杂和酚醛气凝胶后改性三种。原位聚合法是将无机成分的前驱体与酚醛树脂或高分子单体混

doi: 10.16865/j.cnki.1000-7555.2025.0227
收稿日期：2024-11-27
基金项目：非金属材料创新中心创新基金资助（24TDA-2）
第一作者；王智鑫，E-mail: wangzhixin@njtech.edu.cn
通讯联系人：孔勇，主要从事气凝胶绝热和气体净化材料的制备与应用研究，E-mail: ykong@njtech.edu.cn

合后共同经历溶胶-凝胶过程，无机成分前驱体在酚醛凝胶形成过程发生水解、聚合反应，杂化在酚醛骨架中或与酚醛骨架形成互穿网络结构，是制备无机杂化酚醛气凝胶的主要方法[4~44]。粉体掺杂法是在酚醛气凝胶的前驱体溶液中加入无机粉体，把无机成分物理地分散在酚醛气凝胶骨架中[45, 46]。后改性法是通过与无机前驱体蒸汽与固体骨架的固-气反应实现无机成分在酚醛气凝胶骨架表面的杂化[47]。

2 单体聚合制备无机杂化酚醛气凝胶

2.1 基于多步溶胶-凝胶的原位聚合

由于有机和无机前驱体对溶胶-凝胶条件要求不一致，大多采用多步溶胶-凝胶工艺制备无机杂化酚醛气凝胶，其实现方法有两种：一是分别配制有机和无机溶胶后再混合的有机/无机溶胶混合法；二是原料分多步混合以协调不同前驱体反应动力学的原料逐步混合法。两种方法主要涉及酚醛/氧化硅杂化气凝胶，另有酚醛/氧化铝杂化气凝胶和酚醛/氧化锆杂化气凝胶(Tab.1)。

Tab. 1 Inorganic hybrid phenolic aerogels synthesized by multi-step sol-gel

Monomer	Precursor	Solvent	Drying method	Density (g/cm^3)	Pore volume (cm^3/g)	Specific surface area (m^2/g)	Ref.
R-F	TEOS	$EtOH/H_2O$	SCD	0.110	2.37	513	[7], [19]
R-F	TEOS	H_2O	SCD	0.173	——	554	[15]
R-F	TEOS	$EtOH/H_2O$	APD	0.367	0.40	198	[6]
R-F	TEOS-MTES	H_2O	APD	0.250	——	26	[18]
R-F	DMDMS-MTMS	$EtOH/H_2O$	APD	0.118	——	——	[16]
R-F	$AlCl_3·6H_2O$	$EtOH/H_2O$	SCD	0.112	——	478	[8], [10], [11]
P-F	$ZrOCl_2·8H_2O$	EtOH	APD	——	——	——	[17]

2.1.1 有机/无机溶胶混合法：SiO_2 溶胶通常通过盐酸催化使前驱体在乙醇/水($EtOH/H_2O$)体系中水解-缩合制备；酚醛溶胶通过无水碳酸钠催化使 R 和 F 在水中反应形成。SiO_2 溶胶配制一般在室温~40℃下进行应。常温下 R 和 F 聚合反应动力学速率很低，因此酚醛溶胶配制在 50~85℃下进行。混合溶胶采用氨水调节 pH 值以实现酚醛和 SiO_2 组分的协同凝胶。Kong[7, 19]等使酚醛和 SiO_2 前驱体分别反应 30min 制备溶胶，混合溶胶用氨水调节 pH 至 9.4 进行溶胶-凝胶反应得到湿凝胶，经过超临界干燥制备出密度 $0.11g/cm^3$、孔体积 $2.37cm^3/g$、比表面积 $513m^2/g$ 的酚醛/氧化硅杂化气凝胶。Yan[18]等将酚醛溶胶和 SiO_2 溶胶混合，用氨水调节 PH 值 1~3 制备湿凝胶，常压干燥得到比表面积 $26m^2/g$ 的酚醛/氧化硅杂化气凝胶。

Zhong 等[8, 10, 11]用 $AlCl_3·6H_2O$ 为铝源、环氧丙烷为质子吸附剂，结合超临界干燥得到比表面积 $478m^2/g$ 的酚醛/氧化铝杂化气凝胶。Liu 等[17]以苯酚(P)和 F 为单体在氢氧化钠催化下制备酚醛溶胶、$ZrOCl_2·8H_2O$ 为锆源在双氧水催化下制备 ZrO_2 溶胶，溶胶混合后在 90℃下反应 2h 得到的湿凝胶经常压干燥获得酚醛/氧化锆杂化气凝胶。

2.1.2 原料逐步混合法：Chen 等[15]在室温下将 R、F、乙腈和盐酸搅拌 30min 后加入 TEOS、乙腈、

水、氢氟酸(HF)，然后于 80℃反应得到湿凝胶，湿凝胶经老化和置换后超临界干燥得到比表面积 554m^2/g 的酚醛/氧化硅杂化气凝胶。Xu 等[6]将 TEOS、乙醇和水加入到预制好的酚醛溶液中搅拌 30min，使用氨水调节 pH 值到 6，在 60℃下反应 30min 的得到湿凝胶，湿凝胶经 70℃老化数天、丙酮溶剂置换和常压干燥后得到比表面积 198m^2/g 的酚醛/氧化硅杂化气凝胶。Ye 等[16]在乙醇、十六烷基三甲基溴化铵(CTAC)、尿素、冰醋酸混合溶液中加入 DMDMS 和 MTMS 搅拌 45min，再加入异氰酸酯-丙基三甲氧基硅烷搅拌 30min 至溶液为中性，最后加入 R 和 F 搅拌 30min 后在 90℃下反应得到湿凝胶，湿凝胶常压干燥制备疏水酚醛/氧化硅杂化气凝胶。与分别配制有机和无机溶胶不同的是，原料多步混合制备无机杂化酚醛气凝胶的工艺过程更复杂繁琐，有时需要采用乙腈和 HF 等非温和试剂。

2.2 基于一步溶胶-凝胶的原位聚合

一步溶胶-凝胶法是直接将单体和前驱体混合在一起进行溶胶-凝胶反应制备无机杂化酚醛气凝胶，涉及酚醛/氧化硅杂化气凝胶(Tab.2)。Kong 等[13, 38]以 R、F 为单体，APTES 为前驱体，乙醇和水为溶剂，室温下将上述原料混合搅拌后进行溶胶-凝胶反应得到湿凝胶，湿凝胶经老化和溶剂置换得到醇凝胶，醇凝胶通过常压干燥和超临界干燥制备酚醛/氧化硅杂化气凝胶。其中，超临界干燥和常压干燥制备出的酚醛/氧化硅杂化气凝胶的比表面积分别为 445m^2/g 和 126m^2/g。APTES 中的氨丙基会占据部分孔隙，导致比表面积和孔体积下降，因此 Kong 等[12]通过 TEOS 替代 APTES 将酚醛/氧化硅杂化气凝胶比表面积提升至 946m^2/g。采用相似的方法，Wu 等[39]以邻苯二酚(C)替换 R 制备出比表面积 171m^2/g 的酚醛/氧化硅杂化气凝胶，Yun 等[40, 41]以 AEAPTES 替代 APTES、同时加入 MTMS 制备出比表面积 340m^2/g 的疏水酚醛/氧化硅杂化气凝胶。

Tab. 2 Inorganic hybrid phenolic aerogels synthesized by one-step sol-gel

Monomer	Precursor	Solvent	Drying method	Density (g/cm^3)	Pore volume (cm^3/g)	Specific surface area (m^2/g)	Ref.
R-F	APTES	EtOH/H_2O	SCD	0.164	1.21	445	[13]
R-F	TEOS-APTES	EtOH/H_2O	SCD	——	2.77	946	[12]
R-F	APTES	EtOH/H_2O	APD	0.160	0.48	126	[38]
C-F	APTES	EtOH/H_2O	SCD	0.218	0.88	171	[39]
R-F	AEAPTES-MTMS	EtOH/H_2O	APD	0.140	0.46	340	[40], [41]

APTES 和 AEAPTES 作为一种路易斯碱，使 R 转变为阴离子活性中间体促进 R 和 F 聚合反应，与典型 RF 凝胶合成机理类似；其上的氨丙基对硅烷亲核活化促进硅烷的水解，如 Fig.1。因此，上述一步法不需催化剂，借助硅烷的自催化实现溶胶-凝胶反应，相对于多步溶胶-凝胶法，工艺过程简单、温和、环境友好。

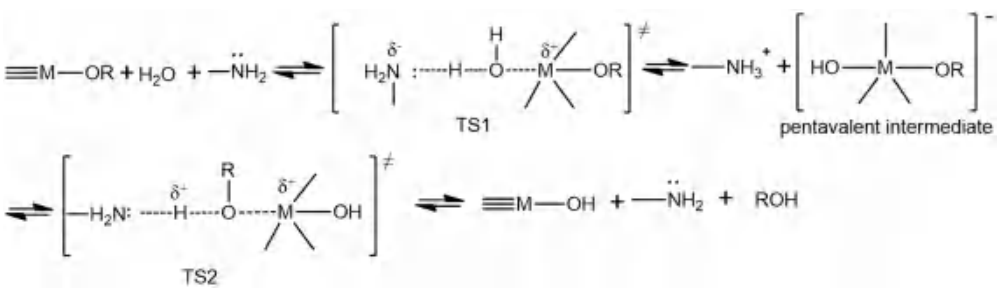

Fig. 1 Hydrolysis mechanism based on the self-catalysis of APTES[7]

2.3 酚醛气凝胶后改性

Wang 等[47]以 P 和 F 为单体，与 2-氨基苯并咪唑和 CTAC 在 60℃下搅拌制备酚醛溶胶，200℃老化和常压干燥制备酚醛气凝胶。酚醛气凝胶于 TEOS/氨水混合蒸气中改性制备酚醛/氧化硅杂化气凝胶(Fig.2)。该方法基于有机硅烷蒸气与气凝胶骨架的气-固反应，具有良好的普适性，但难实现有机和无机组分均一杂化，不利于力学和隔热等性能的协同提升。

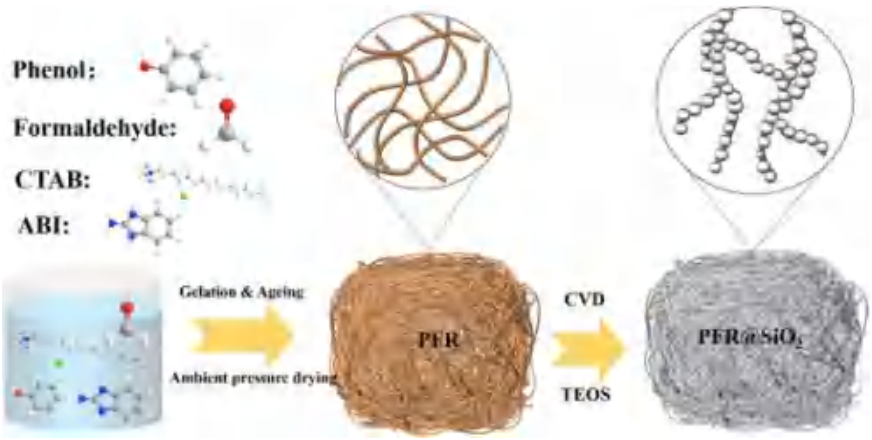

Fig. 2　Synthesis of inorganic hybrid phenolic aerogel via post-modification [47]

3 酚醛树脂交联固化制备无机杂化酚醛气凝胶

PR 成本低，被广泛用于无机杂化酚醛气凝胶的制备，具体工艺是将 PR 溶液与无机前混合，在六亚甲基四胺(HMTA)的交联作用下使 PR 转变为交联网络实现固化/凝胶。PR 室温下交联反应速率相对低，通常在高温(120~180℃)下进行交联反应，而且反应周期相对于单体聚合法更长。该方法常与常压干燥结合制备无机杂化酚醛气凝胶。根据前驱体中有无甲基可得到亲水和疏水无机杂化酚醛气凝胶。PR 交联制备机杂化酚醛气凝胶可通过基于多步和一步溶胶-凝胶的原位聚合实现，另有粉体掺杂法。

3.1 基于多步溶胶-凝胶的原位聚合

3.1.1 有机/无机溶胶混合法：Mohamad 等[30]将 TEOS 和 MTES 制备的 SiO_2 溶胶倒入 PR 异丙醇溶液中于 120℃反应 20h 获得湿凝胶，湿凝胶常压干燥制备出密度 0.092g/cm^3 的疏水酚醛/氧化硅杂化气凝胶。师建军等[20]在 TEOS 制备的 SiO_2 溶胶中加入 PR/乙醇溶液，在 140℃下反应 6h、80℃下老化 80h 获得湿凝胶，湿凝胶常压干燥获得比表面积 35m^2/g 的酚醛/氧化硅杂化气凝胶，比表面积与酚醛气凝胶比提高 45%。Ren[4]等以正丙醇锆和乙酸混合制备 ZrO_2 溶胶，与 PR 溶液混合制备酚醛/氧化锆杂化气凝胶。Fu 等[22]以 MTMS、MTES 和 DMDES 在醋酸催化下反应 1h 制备 SiO_2 溶胶，以丙酸锆、乙酰丙酮、水和异丙醇反应 1h 制备 ZrO_2 溶胶，在 SiO_2 溶胶中依次加入 PR 溶液和 ZrO_2 溶胶，100℃下溶胶-凝胶反应 24h 制备酚醛/氧化硅/氧化锆杂化气凝胶。

3.1.2 多次浸渍法：多次浸渍法先通过浸渍、凝胶、常压干燥把无机成分复合在纤维增强体中，再经过PR浸渍、固化、常压干燥制备无机杂化酚醛气凝胶复合材料。Jin 等[5, 27, 28, 35]将 MTMS 和 DMDES 溶液浸渍纤维毡，经 70℃溶胶-凝胶、常压干燥制得 SiO_2 修饰纤维；再将修饰纤维真空浸渍 PR 溶液，在 120-180℃反应 3h 制得酚醛/氧化硅杂化湿凝胶，干燥后得到疏水酚醛/氧化硅杂化气凝胶复合材料(Fig.3)。

Fig. 3　Fabrication procedure of QCF/SPA composites[28]

3.2 基于一步溶胶-凝胶得到原位聚合

Wang 等[31, 42] 40℃下将 APTES 溶液缓慢滴加至 PR/异丙醇溶液中，在 80℃下溶胶-凝胶反应 3 天制备酚醛/氧化硅杂化气凝胶。Wu 等[32]将 PR、γ-(2,3-环氧丙氧基)丙基三甲氧基硅烷(KH-560)、十二烷基硫酸钠(SDS)和水混合，在 80-180℃下反应制备酚醛/氧化硅杂化气凝胶。Liu 等[29, 37]将硼改性后的 PR 与 HMTA 在 80-120℃下反应 10h 制备出酚醛/氧化硼杂化气凝胶。除了借助含氨基硅烷实现凝胶化[31, 32, 42]，还可利用 HMTA 分解生成的氨为反应体系提供弱碱环境，促进无机前驱体凝胶化[33, 35, 43]。Yin 等[33, 43]将 MTMS 溶液与 PR/乙醇溶液混合，加入 HMTA 后在 120-180℃下反应 8h 制得比表面积 123m^2/g 的酚醛/氧化硅杂化气凝胶，比表面积比同条件下的酚醛气凝胶提高 112%。采用类似方法，Yang 等[35]以 DMDMS 为硅源在制备疏水酚醛/氧化硅杂化气凝胶。值得注意的是，使用 HMTA 分解生成的氨诱导硅基前驱体凝胶化制备酚醛/氧化硅杂化气凝胶周期短，但会残余未反应有机溶剂，需要长时间溶剂置换。

3.3 粉体掺杂法

田志广等[45, 46]在 70℃下把 SiO_2 气凝胶粉末与 PR/乙醇溶液混合，经过固化和干燥制备比表面积为 2.59m^2/g 的酚醛/氧化硅杂化气凝胶。在前驱体溶液/溶胶中掺杂粉体制备无机杂化酚醛气凝胶工艺简单，但难以获得高性能气凝胶。

4　无机成分对酚醛气凝胶性能的影响

Mohamad 等[30]以 TEOS 和 MTES 两种硅基前驱体、PR 为有机原料，采取多步溶胶-凝胶法制备疏水酚醛/氧化硅杂化气凝胶。尽管当 MTES 比例增加带来接触角变大(Fig.4)，但过高的无机前驱体会造成酚醛和氧化硅组分相分离，从而无法凝胶。Cheng 等[19]发现，随着 SiO_2 含量增加，酚醛/氧化硅杂化气凝胶的隔热性能大幅提升，但力学性能变差，这是由于 SiO_2 前驱体形成的纳米多网络减少了热传导路径，同时使骨架变脆弱。Yin 等[43]发现，SiO_2 含量增加对酚醛/氧化硅杂化气凝胶的力学和耐高温性能有显著提升，SiO_2 含量从 0 增加至 0.08mol，抗压强度由 2.5MPa 升至 4.08MPa，烧蚀速率降至 0.073mm/s。然而，导热系数由 0.518W/(m·K)增加至 0.687W/(m·K)，隔热性能变差，这是因为 SiO_2 含量增加，密度随之增加，提供了更多的固体传热通道。可见，合成方法导致的微观结构差异对杂化气凝胶的隔热性能影响较大。

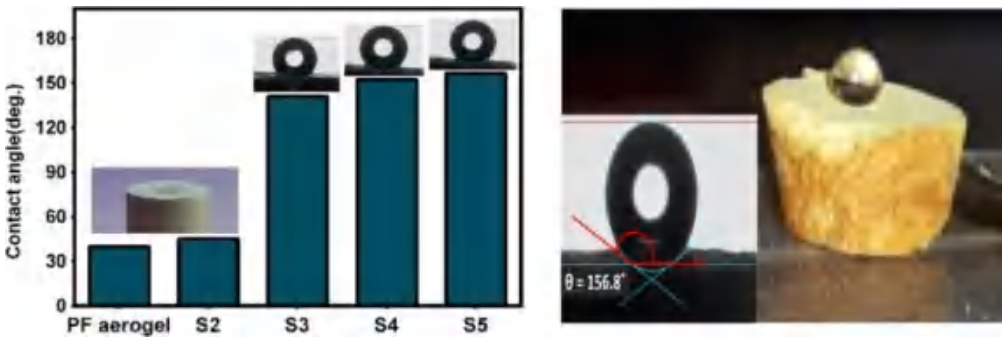

Fig. 4　Water contact angle of silica hybrid phenolic aerogel with different MTMS contents[30]

为了进一步提高酚醛气凝胶的力学、抗氧化、阻燃等性能，研究人员使用无机纤维复合制备其气凝胶复合材料(Tab.3)。Ren 等[38]以陶瓷纤维(CF)为增强材料制备的酚醛/氧化硅杂化气凝胶复合材料导热系数低至 0.024W/(m·K)，且可抵挡 1200℃火焰冲击。Wang 等[31]制备的碳纤维(C)增强酚醛/氧化硅杂化气凝胶复合材料质量烧蚀率和线性烧蚀速率仅 0.0227g/s 和 0.249 mm/s。Wu 等[32]制备的玻璃纤维(GF)增强酚醛/氧化硅杂化气凝胶复合材料在 1200℃下烧蚀半小时后，可保持 56.07℃的冷面温度而不发生任何形状变化。Jin 等[34]制备了石英纤维(QF)增强酚醛/氧化硅杂化气凝胶，与酚醛气凝胶复合材料相比，SiO_2 的引入使抗压强度提高 40%、1200℃残重提高 6.3%。Cheng 等[28, 42]以碳/石英纤维(C/QF)为增强材料制备酚醛/氧化硅杂化气凝胶复合材料，提出一种“双硅双碳多重协同机制”的烧蚀机理。其中“双硅”为 SiO_2 气凝胶和石英纤维，“双碳”为酚醛气凝胶和碳纤维。“双硅”在烧蚀表面形成 SiO_2 薄膜隔离氧气，“双碳”增加 SiO_2 薄膜层的粘度和流动性，以支持其免受气动剥离。

Tab. 3　Properties of inorganic hybrid phenolic aerogels prepared with different fibers

Fiber	Density (g/cm^3)	Compressive strength (MPa)	Thermal conductivity (W/(m·K))	Mass loss rate in TG (%)	Linear ablation rate (mm/s)	Mass ablation rate (g / s)	Ablative condition	Ref.
CF	0.31	2.9	0.024	25.62	——	——	——	[5], [38]
C/QF	0.5	5.96	0. 112	39.21	0. 017	0. 011	2000℃ 300s	[28], [42]
QF	0.3	4.2	0.044	17.3	0.023	0.0065	1.8 MW/m^2 120s	[34]
C	0.26	0.8	0.055	34.05	0.249	0.0227	3000℃ 20s	[31], [42]
GF	0.42	1.7	0.0541	28	0.00261	0.00071	1200℃ 30min	[32]

5　结语与展望

无机杂化酚醛气凝胶不仅继承了酚醛气凝胶材料低密度、低热导率、大比表面积等诸多优点，而且具有更加优异的耐高温和力学性能。无机杂化酚醛气凝胶通过单体聚合和酚醛树脂交联两大策略实现。单体聚合法周期短、反应温度低，气凝胶的比表面积高、导热系数低，因此大多配合超临界干燥工艺。酚醛树脂交联法成本低、工艺简单，但周期长反应温度高，且得到的气凝胶比表面积低、导热系数高，多采用常压干燥工艺。在酚醛气凝胶中引入无机成分可通过原位聚合、粉体掺杂和酚醛气凝胶后改性三种方法实现。其中，原位聚合法可以实现有机和无机成分在分子尺度上的杂化，对气凝胶孔结构影响小，是制备高性能酚醛气凝胶绝热材料的优选。在实际应用中，无机杂化酚醛气凝胶通常与纤维增强材料复合，以进一步提高力学性能。作为一种轻质、高强、耐高温绝热材料，无机

杂化酚醛气凝胶在航空航天、国防装备、工业与建筑节能、新能源汽车等领域具有良好的应用前景。目前的研究主要集中在材料合成及性能研究方面，要实现工程应用，还需突破简单可靠、绿色环保的低成本规模化生产技术，验证典型服役条件下的耐久性和隔热性能。

参考文献：

[1] 赵志扬，孔勇，江幸，等. 具有可逆形变的弹性气凝胶研究进展 [J]. 高分子材料科学与工程，2020，36(5): 175-184.

Zhao Z Y, Kong Y, Jiang X, et al. Recent advances in flexible aerogels [J]. Polymer Materials Science & Engineering, 2020, 36(5): 175-184.

[2] 李婧，黄洁，章伊婷，等. 负载相变微胶囊的三聚氰胺/二氧化硅柔性气凝胶 [J]. 高分子材料科学与工程，2022，38(8): 122-128.

Li J, Huang J, Zhang Y T, et al. Structure and properties of melamine/silicon dioxide flexible aerogels loaded with phase transition microcapsules [J]. Polymer Materials Science & Engineering, 2022, 38(8): 122-128.

[3] Pekala R W. Organic aerogels from the polycondensation of resorcinol with formaldehyde[J]. Journal of Materials Science, 1989, 24: 3221-3227.

[4] Ren S, Hu L, Li X T, et al. Preparation and characterization of organic-inorganic hybrid ZrOC/PF aerogel used as high-temperature insulator[J]. Ceramics International, 2020, 46: 6326-6332.

[5] Liu R X, Wang H B, Hong C Q, et al. Mechanical and dual-stage wind tunnel ablative behavior of ceramic fiber-tile reinforced phenolic aerogel[J]. Composites Communications, 2022, 36: 101386.

[6] Xu H F, Zhang H J, Huang Y D, et al. Porous carbon/silica composite monoliths derived from resorcinol–formaldehyde/TEOS[J]. Journal of Non-Crystalline Solids, 2010, 356: 971-976.

[7] Kong Y, Zhang J Y, Shen X D. One-pot sol–gel synthesis of amine hybrid titania/silsesquioxane composite aerogel for CO_2 capture[J]. Journal of Sol-Gel Science and Technology, 2017, 84: 422-431.

[8] Wu X D, Zhong Y, Kong Y, et al. Preparation and characterization of C/Al_2O_3 composite aerogel with high compressive strength and low thermal conductivity[J]. Journal of Porous Materials, 2015, 22: 1235-1243.

[9] 范佳敏，秦岩，傅华东，等. 有机硅改性酚醛气凝胶的制备及隔热疏水性能[J]. 高分子材料科学与工程，2023，39(10): 29-39.

Fan J M, Qing Y, Fu H D, et al. Preparation, thermal insulation and hydrophobic properties of silicone-modified phenolic aerogel[J]. Polymer Materials Science & Engineering, 2023, 39(10): 29-39.

[10] Zhong Y, Kong Y, Zhang J J, et al. Facile synthesis of monolithic carbon/alumina composite aerogels with high compressive strength using different inorganic aluminium salts[J]. Journal of Porous Materials, 2014, 21: 653-658.

[11] Zhong Y, Shao G F, Wu X D, et al. Robust monolithic polymer(resorcinol-formaldehyde) reinforced alumina aerogel composites with mutually interpenetrating networks[J]. RSC Advances, 2019, 9: 22942-22949.

[12] Kong Y, Zhong Y, Shen X D, et al. Effect of silica sources on nanostructures of resorcinol-formaldehyde/silica and carbon/silicon carbide composite aerogels[J]. Microporous and Mesoporous Materials, 2014, 197: 77-82.

[13] Kong Y, Zhong Y, Shen X D, et al. Synthesis of monolithic mesoporous silicon carbide from resorcinol-formaldehyde/silica composites[J]. Materials Letters, 2013, 99: 108-110.

[14] 王瑞杰，郭建业，宋寒，等. 酚醛气凝胶多功能复合材料的设计与性能[J]. 材料导报，2021，35(A1): 548-551.

Wang R J, Guo J Y, Song H, et al. Design and properties of multifunctional phenolic aerogel composites[J]. Materials Reports, 2021, 35(A1): 548-551.

[15] Chen K, Bao Z H, Du A, et al. Synthesis of resorcinol-formaldehyde/silica composite aerogels and their low-temperature conversion to mesoporous silicon carbide[J]. Microporous and Mesoporous Materials, 2011, 149: 16-24.

[16] Ye D N, Lv H L, Zheng Z R, et al. Preparation and properties of flexible phenolic silicone hybrid aerogels for thermal insulation[J]. Molecules, 2024, 29: 4942.

[17] Liu C Q, Li K Z, Li H J, et al. The effect of zirconium incorporation on the thermal stability and carbonized product of phenol–formaldehyde resin[J]. Polymer Degradation and Stability, 2014, 102: 180-185.

[18] Yan J, Kuang M X, Zhu Y L, et al. Facile, tunable, and environmental friendly synthesis of silica/resorcinol–formaldehyde hybrid xerogels with ultra-low shrinkage using a cationic polyelectrolyte as a soft template[J]. Journal of Porous Materials, 2023, 30: 103-113.

[19] Cheng Y L, Zhang J W, Ren C, et al. Facile preparation of high-strength SiC/C aerogels from pre-reacted

resorcinol–formaldehyde and siloxane[J]. Journal of Industrial and Engineering Chemistry, 2023, 134: 75-83.

[20] 师建军，孔磊，左小彪，等. 酚醛/SiO_2双体系凝胶网络结构杂化气凝胶的制备与性能[J]. 高分子学报, 2018(10): 1307-1314.

Shi J J, Kong L, Zuo X B, et al. Preparation of PR/SiO_2 hybrid phenolic aerogel with Bi-component gel networks[J]. Acta Polymerica Sinica, 2018(10): 1307-1314.

[21] 宋寒，徐春晓，王湘宁，等. 不同树脂前驱体配比对无机酚醛气凝胶隔热复合材料性能的影响研究[J]. 材料导报, 2020, 34(A2): 1525-1527, 54.

Song H, Xu C X, Wang X N, et al. Effects of different resin precursor ratios on properties of inorganic phenolic aerogel insulation composites[J]. Materials Reports, 2020, 34(A2): 1525-1527.

[22] Fu H D, Qin Y, Peng Z W, et al. A novel co-continuous Si–Zr hybrid phenolic aerogel composite with excellent antioxidant ablation enabled by sea-island-like ceramic structure at high temperature[J]. Ceramics International, 2024, 50: 21008-21019.

[23] Gao W, Wang Z Y, Zhang Y Z, et al. High-energy B-O bonds enable the phenolic aerogel with enhanced thermal stability and low thermal conductivity[J]. Applied Surface Science, 2024, 669: 160459.

[24] Huang H, Hong C Q, Jin X Y, et al. Facile fabrication of superflexible and thermal insulating phenolic aerogels backboned by silicone networks[J]. Composites Part A: Applied Science and Manufacturing, 2023, 164: 107270.

[25] Huang H, Lv Y H, Jin X Y, et al. Bifunctional silicone triggered long-range crosslinking phenolic aerogels with flexibility and thermal insulation for thermal regulation[J]. Chemical Engineering Journal, 2023, 470: 144413.

[26] Xiao J, Fang G D, Jin X G, et al. A comprehensive study of pyrolysis characteristics of silicone-modified phenolic aerogel matrix nanocomposites: kinetic analysis, ReaxFF MD simulations, and ANN prediction[J]. Chemical Engineering Journal, 2023, 472: 145049.

[27] Jin X Y, Liu C, Huang H, et al. Multiscale, elastic, and low-density carbon fibre/siliconoxycarbide-phenolic interpenetrating aerogel nanocomposite for ablative thermal protection[J]. Composites Part B: Engineering, 2022, 245: 110212.

[28] Jin X Y, Wu C, Wang H B, et al. Synergistic reinforcement and multiscaled design of lightweight heat protection and insulation integrated composite with outstanding high-temperature resistance up to 2500 °C[J]. Composites Science and Technology, 2023, 232: 1-10.

[29] Liu H L, Wang P, Zhang B, et al. Morphology controlled carbon aerogel with enhanced thermal insulation and mechanical properties: a simple route for the regulated synthesis[J]. Journal of Non-Crystalline Solids, 2021, 564: 120828.

[30] Mohamad M S, Ghasem S, Jamal D, et al. The effect of high temperature sol-gel polymerization parameters on the microstructure and properties of hydrophobic phenol-formaldehyde/silica hybrid aerogels[J]. Journal of Colloid and Interface Science, 2017, 493: 103-110.

[31] Wang W K, Xu W J, Jia X F, et al. A facile in-situ strategy to fabricate lightweight carbon fiber/silicone-phenolic aerogel composites with superior toughness and ablation performance[J]. Journal of Materials Science, 2024, 59: 18488-18498.

[32] Wu C, Wang L M, Yan X J, et al. Environmental-friendly and fast production of ultra-strong phenolic aerogel composite with superior thermal insulation and ablative-resistance[J]. Composites Science and Technology, 2024, 256: 110776.

[33] Wu K D, Zhou Q, Cao J X, et al. Ultrahigh-strength carbon aerogels for high temperature thermal insulation[J]. Journal of Colloid and Interface Science, 2022, 609: 667-675.

[34] Jin X Y, Xu J G, Pan Y W, et al. Lightweight and multiscale needle quartz fiber felt reinforced siliconoxycarbide modified phenolic aerogel nanocomposite with enhanced mechanical, insulative and flame-resistant properties[J]. Composites Science and Technology, 2021, 217: 109100.

[35] Yang D D, Dong S, Xin J Q, et al. Robust and thermostable C/SiOC composite aerogel for efficient microwave absorption, thermal insulation and flame retardancy[J]. Chemical Engineering Journal, 2023, 469: 143851.

[36] You Q, Liu G, Zhong Y, et al. Mechanical properties and oxidative ablation behaviors of polysilazane-modified phenolic resin aerogel/carbon fiber fabric composites[J]. Polymer Composites, 2023, 45: 1.

[37] He H, Geng L Y, Liu F, et al. Facile preparation of a phenolic aerogel with excellent flexibility for thermal insulation[J]. European Polymer Journal, 2022, 163: 110905.

[38] Ren J, Zhang T, Kong Y, et al. Facile synthesis of phenolic-reinforced silica aerogel composites for thermal insulation under thermal-force coupling conditions[J]. Ceramics International, 2023, 49: 29820-29828.

[39] Wu X D, Shao G F, Shen X D, et al. Evolution of the novel C/SiO_2/SiC ternary aerogel with high specific surface area

and improved oxidation resistance[J]. Chemical Engineering Journal, 2017, 330: 1022-1034.

[40] Yun S, Guo T, Zhu X F, et al. Effects of carbonization temperature on structure and mechanical properties of monolithic C/SiO_2 aerogels based on ambient pressure dried superhydrophobic resorcinol–formaldehyde/SiO_2 aerogels[J]. Journal of Porous Materials, 2018, 25: 1825-1830.

[41] Yun S, Luo H J, Gao Y F. Ambient-pressure drying synthesis of large resorcinol-formaldehyde-reinforced silica aerogels with enhanced mechanical strength and superhydrophobicity[J]. Journal of Materials Chemistry A, 2014, 2: 14542-14549.

[42] Cheng H M, Fan Z H, Hong C Q, et al. Lightweight multiscale hybrid carbon-quartz fiber fabric reinforced phenolic-silica aerogel nanocomposite for high temperature thermal protection[J]. Composites Part A: Applied Science and Manufacturing, 2021, 143: 106313.

[43] Yin R Y, Cheng H M, Hong C Q, et al. Synthesis and characterization of novel phenolic resin/silicone hybrid aerogel composites with enhanced thermal, mechanical and ablative properties[J]. Composites Part A: Applied Science and Manufacturing, 2017, 101: 500-510.

[44] Xu F H, Wang Y X, Tang F C, et al. Synergistic enhancement of structure and function in carbonaceous SiC aerogels for improved microwave absorption[J]. Carbon, 2025, 233: 119854.

[45] 郭俊卿，田志广，陈拂晓. SiO_2 气凝胶/环氧树脂/酚醛树脂复合材料性能研究[J]. 化工新型材料，2024，52(6): 253-258.

Guo J Q, Tian Z G, Chen F X. Research on the properties of SiO_2 aerogel/epoxy resin/phenolic resin composite materials[J]. New Chemical Materials, 2024, 52(6): 253-258.

[46] 田志广，郭俊卿，陈拂晓. SiO_2 气凝胶/酚醛树脂复合材料隔热性能研究[J]. 化工新型材料, 2024, 52(7): 162-166.

Tian Z G, Guo J Q, Chen F X. Study on thermal insulation properties of SiO_2 aerogel/phenolic resin composites[J]. New Chemical Materials, 2024, 52(7): 162-166.

[47] Wang L, Hu X M, Huang R, et al. Elastic, antiflaming phenolic aerogels for advanced thermal protection at extreme environments[J]. Composites Communications, 2024, 48: 101889.

Advances in Inorganic Hybrid Phenolic Aerogels

Zhixin Wang[1], Yong Kong[1,2], Xiaodong Shen[1,2]

(1. *College of Materials Science and Engineering, Nanjing Tech University, Nanjing 211816, China;* 2. *State Key Laboratory of Materials-Oriented Chemical Engineering, Nanjing Tech University, Nanjing 211816, China*)

ABSTRACT: Phenolic aerogels have excellent mechanical properties, which can overcome shortcoming of silica aerogel in terms of poor mechanical properties. However, the poor oxidation and ablative resistance limit the application of phenolic aerogel in high-temperature insulation. Hybridization of inorganic components is an effective way to improve the high temperature resistance of phenolic aerogel, as well as thermal insulation and mechanical performance. In this paper, the latest researches of inorganic hybrid phenolic aerogels were reviewed, the preparation method and effects of inorganic components on the performance were summarized from different perspectives. Firstly, the preparation method of inorganic hybrid phenolic aerogels was introduced from the point of phenolic source and introduction way of inorganic component including in situ polymerization, powder doping and post-modification. Then, the effects of the introduction way and content of inorganic component and fiber reinforcement on thermal insulation, high temperature resistance and mechanical property of inorganic hybrid phenolic aerogels were analyzed. Finally, the application prospect and development trend of inorganic hybrid phenolic aerogels in the field of thermal insulation were outlooked.

Keywords: inorganic hybrid; phenolic aerogels; fire resistance; high-temperature resistance; thermal insulation

DOI: 10.12164/j.issn.1003-8965.2024.06.017

薄抹灰外墙外保温系统(ETICS)供应商认证制度探索

张金成[1]，孙诗兵[2]，金晓冬[2]，郭红斌[1]，曾春燕[1]，武薇[1]，韩云鹏[1]
(1.中国国检测试控股集团股份有限公司，北京 100024；
2.北京工业大学 材料科学与工程学院，北京 100124)

摘要：薄抹灰外墙外保温系统(ETICS)在我国规模化推广应用已有20余年，陆续暴露出火灾、脱落、开裂、渗水等问题，一些地区已开始限制其应用，如何加强ETICS质量控制和管理成为业内关注的焦点。我国ETICS的相关产品标准和试验方法均基于EOTA的ETAG 004建立，但并未建立基于系统供应商概念的认证制度，存在质量管理和控制的漏洞。ETICS系统供应商认证制度的建立，是弥补质量管理和控制漏洞的重要手段，从技术和管理的双重角度，使薄抹灰外墙外保温行业更加专业化、标准化、规范化，在双碳战略背景下，有助于ETICS质量提高和风险溯源管控，对于我国建筑节能产业发展有积极意义。

关键词：ETICS；系统供应商；认证；建筑节能
中图分类号：TU504 **文献标志码：**A **文章编号：**1003-8965(2024)06-0079-04

External thermal insulation composite systems (ETICS) supplier and its certification method

ZHANG Jincheng[1], SUN Shibing[2], JIN Xiaodong[2], GUO Hongbin[1], ZENG Chunyan[1], WU Wei[1], HAN Yunpeng[1]
(1. China Testing & Certification International Group Co., Ltd., Beijing 100024;
2. College of Materials Science and Engineering, Beijing University of Technology, Beijing 100124)

Abstract: External thermal insulation composites system (ETICS) has been widely applied in China over two decades, and has gradually exposed prominent problems such as fire, peeling, cracking, and water seepage. The restriction of using ETICS has been published in some regions. Therefore, the quality control and management of ETICS has drawn increasing interests. The relevant product standards and experimental methods of ETICS in China are built based on ETAG 004 of EOTA, but there is no certification based on the concept of system suppliers, which has loopholes in quality management and control. The establishment of ETICS system suppliers certification is an important means to fill the gaps in quality management and control. From the dual perspectives of technology and management, it can make the building exterior wall insulation industry more specialized, standardized, and regulated. In the context of "dual carbon" strategy, it is conducive to the continuous improvement and risk traceability control of ETICS quality, which has a positive significance for promoting the development of China's building energy-saving industry.

Keywords: ETICS; system supplier; certification; building energy saving

1 薄抹灰外墙外保温系统(ETICS)现状

自2020年9月我国宣布"碳达峰、碳中和"目标以来，"双碳"战略成为社会发展的关注点之一[1-3]。根据住房和城乡建设部统计，我国建筑在建造和使用过程中直接能耗超过全社会总能耗的25%，并将逐步增加至1/3以上[4]。因此，降低建筑能耗、实现建筑节能是实现"双碳"战略的重要途经和方法之一。

建筑物外立面在建筑围护结构中占比最大，外立面的隔热保温性能对整个建筑能耗有决定性影响。薄抹灰外墙外保温系统(ETICS)凭借其保温效果好、防结露性能好、施工方便等特点，成为我国建筑墙体保温的主要构造形式(构造如图1(a)所示)[5-7]。ETICS在我国规模化推广应用有20余年历史，随着时间的推移，ETICS陆续暴露出保温系统火灾(图1(b))、东西立面脱落(图1(c))、南北立面渗水(图1(d))等突出问题[8-9]。自2020年起，上海市住建委发布《上海市禁止或者限制生产和使用的用于建设工程的材料目录(第五批)》，禁止采用胶结剂或锚栓及两种方式组合的施工工艺外墙外保温系统[10]，打响了禁用ETICS系统的"第一枪"。随后，河北、新疆、重庆等地均出台了相关政策，禁止或限制ETICS的应用，在行业内引起轰动。

回顾ETICS系统应用的示范起点，龙潭路建设部示范工程(1999年建造，天津，图2(a))、北京卧龙小区项目(1994年建造，北京，图2(b))等工程依然保持稳定运行状态，保

基金项目：非金属材料创新中心创新基金项目(24TDA-5)；北京市教育委员会科研计划项目(KM202410005008)。
第一作者：张金成(1980-)，高级工程师/项目负责人/全国绝热材料标准化技术委员会委员，曾参与制定多部保温节能行业标准。

中国知网 https://www.cnki.net

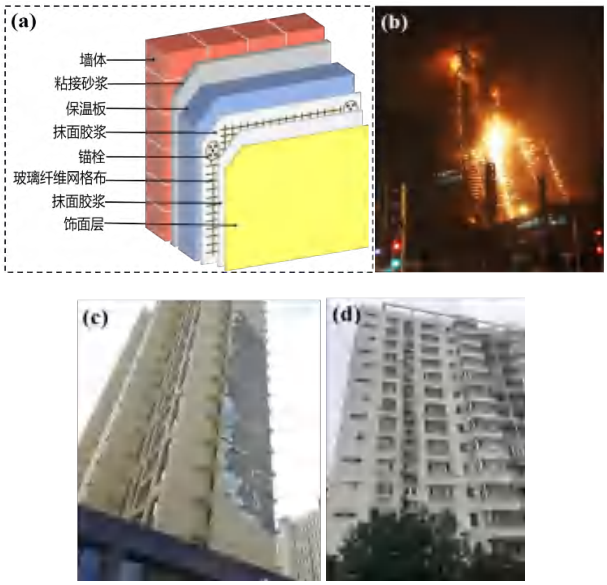

图1　(a)ETICS构造;(b)ETICS火灾案例;(c)ETICS脱落案例;(d)ETICS渗水案例

Fig.1　(a) ETICS construction; (b) ETICS fire case; (c) ETICS detachment case; (d) ETICS water seepage case

温效果良好,未出现破损、开裂、渗水等影响保温效果或观感质量的现象。可见,从严把关的ETICS系统可以经受时间考验。只是在近30余年的市场竞争中,该系统陆续暴露出了设计、施工、材料供应等多方问题。与之相对应,部分地区大力推广的保温系统(装配式建筑结构保温一体化等),并未经过长时间验证,未来风险更加不可控。

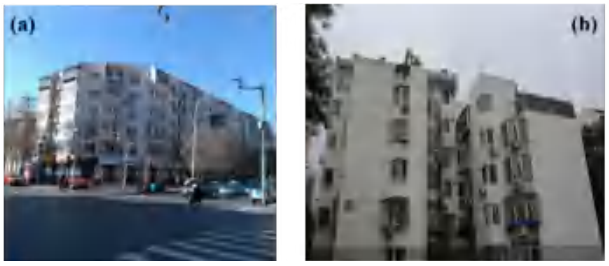

图2　(a)龙潭路建设部示范工程;(b)北京卧龙小区项目

Fig.2　(a) Demonstration project of Longtan Road; (b) Beijing Wolong community project

因此,如何加强ETICS质量控制和管理成为业内关注的焦点。ETICS是由一系列材料和构件组成的、按照特定构造组合的,以实现保温性能、水密性能、抗冲击性能、耐候性等多功能的特殊产品[11]。该产品的提供者,即系统供应商,应具有集成系统材料、研究验证系统可靠性的能力、必要的检验检测能力、必要的专业人员指导系统施工的能力等。但在我国的标准和规范中,强调必须系统材料成套供应,而成套供应的主要依据是提供系统耐候性为主的检测报告。例如,GB 50411–2019《建筑节能工程施工质量验收标准》规定,外墙外保温工程应采用预制构件、定型产品或成套技术,并应由同一供应商提供配套的组成材料和型式检验报告[12]。也即,提供系统检测报告就是系统供应商。这就造成了不具有系统开发能力或能力不足的单位,“拼盘”供应系统的现象,从材料供应这个源头环节就带来了工程质量隐患和管理风险。

2　ETICS系统供应商的能力

我国ETICS系统是借鉴欧美而发展来的,相关产品标准和试验方法也是基于European Organization for Technical Approvals (EOTA)的ETAG 004《欧洲技术认证准则–带抹面的外墙外保温系统(ETICS)》及相关标准建立(欧洲外墙外保温标准体系如表1所示)。在欧洲标准中,明确了ETICS的产品属性,如EN 13499 “Thermal insulation products for buildings – External thermal insulation composite systems (ETICS) based on expanded polystyrene – Specification” 指出,“本标准规定了建筑保温用的、全套交付的、基于模塑聚苯板的、工厂制造的外墙外保温系统的要求”,“阐明了产品的特点及检测、标志、标识的程序”[13]。ETAG 004作为认证准则,明确指出,系统各组成部分应由认证申请人或供应商在工厂生产。系统组成部分均由认证申请人指定,并由认证申请人对其负责。而我国ETICS标准化虽然借鉴欧标,但并未明确提出系统供应商的概念,提供型式检验报告即认定为供应商,但是,供应商是否可以持续、稳定供应?供应商的规模如何?供应商是否具有后期运维、赔付能力?供应商能否根据不同工程应用提出针对性施工指导?由此可见,仅凭型式检验报告无法确保系统及组成材料供应的可靠性。

表1　欧洲外墙外保温标准体系

Tab.1　European external wall insulation standard system

材料标准	系统标准	设计	施工
EN 13163 (EPS) EN 13162 (岩棉) EN 13164 (XPS) EN 13165 (PUR) EN 13166 (PF)	EN 13499 (EPS) EN 13500 (岩棉)	ETAG 004 ETAG 014 (锚固)	European guideline for the application of ETICS
欧洲标准	欧洲标准	欧洲技术认可组织	欧洲薄抹灰外墙外保温协会

综合考虑,ETICS系统供应商应具备如下属性或能力,从而确保ETICS系统的可靠供应。

1)一定的企业规模

ETICS系统供应商承担着材料供应的责任,可以是材料生产商(如保温材料、砂浆生产商),也可以不具备生产能力,但要具备一定的企业规模,而企业规模是其承担责任的基本体现。具有一定规模的企业更注重企业的品牌或长远发展,以此为门槛,可以从根本上规避一定的市场低价、不合理竞争,规避不合格ETICS产品流入市场和应用到工程中,给外保温工程带来隐患。

一定的企业规模不单指生产工厂、库房的面积足够使用,还要有一定数量的管理者、技术人员、客服人员等,有生产能力的系统供应商还要有一定数量的熟练的生产工人。管理者及各岗位员工各司其职,从生产、检验、储存、运输、施工应用等所有环节保证供应产品的合格性,产品

中国知网　https://www.cnki.net

要能准确地应用到工程中，并能对工程进行持续跟踪。

2)必要的检测、系统集成能力

ETICS系统由多种材料复合而成，系统各组成材料的相容性和集成能力是系统供应商最基本的能力之一。因此，无论系统供应商是否某个系统组成材料的生产者，均应建立相应的管理制度，设置相应岗位，由专人负责，严格过程控制，进行材料检测及系统集成，确保材料生产及采购环节质量可控。最终目的是组成材料性能合格，各组成材料性能具有相容性，组合成的系统是合格的产品。

3)工程服务能力

外保温系统依附于建筑主体存在，不同主体结构对外保温系统的安装或固定方式(粘结面积、锚固件数量等)有不同要求。不同的建筑形式以及不同的地区对保温层的厚度的要求也不同，这会对外保温的安装或固定方式提出不同要求。这些决定了系统供应商要针对不同的工程有一定的设计能力，包括热工计算、风荷载计算和承载力计算等。

外保温系统施工前要先对基层墙体的平整度、抗拉强度进行检测，只有在基层墙体满足要求的前提下才能进行外保温施工。据此，系统供应商要具备现场检测的能力，包括墙面的抗拉强度检测、锚栓抗拉承载力检测等。

由于各个工程的保温层厚度、粘结面积、锚固件数量情况不尽相同，这就要求系统供应商可依据工程的实际情况，提供不同的外保温系统施工技术方案。同时，系统供应商要有能力为施工方提供施工技术指导，确保外保温系统按照施工技术方案的要求施工。

4)完整的服务周期

ETICS系统谁供应，谁负责，系统供应商对材料供应负主体责任。同时，系统供应商还应对其所供应的系统进行跟踪，吸取工程实际应用过程中的经验教训，不断提升系统的匹配性和可靠性。

图3 ETICS系统供应商具有的能力

Fig.3 The capabilities possessed by ETICS system suppliers

3 系统供应商认证制度的关键问题

建立ETICS系统供应商认证制度，是要解决当下ETICS系统面临的实际问题，包括工程应用过程中合格材料的供应问题、各组成材料的配套及相容问题、系统及组成材料的工程适用性问题、合理施工问题以及工程质保和维护问题等。为了确保建立的系统供应商认证制度的有效性，需要解决认证体系的科学性、认证规则的合理性和认证体系运行的可靠性三个关键问题。

1)认证体系的科学性

ETICS核心要求是保温的有效性、构造和防火的安全性、系统的耐久性。国内外保温行业围绕这些要求建立了庞大的标准体系，包括国家标准、行业标准、团体标准和地方标准等，在工程应用中，取舍时往往无所适从。依据国内标准体系和国内ETICS实际应用情况建立科学的认证技术体系，是建立认证体系的关键和技术难点。

2)认证规则的合理性

系统供应商认证的过程，要合理识别合格的供应商，确保经认证的系统供应商具备集成系统材料、研究验证系统可靠性的能力、必要的检验检测能力、必要的专业人员指导系统施工等能力。这样的系统供应商能确保为工程供应合格的系统及组成材料，并有能力及主观意愿确保系统的合理应用。所以，认证规则的合理性，有效识别系统供应商的能力，是认证规则制定的关键和难点。

3)认证体系运行的可靠性

认证体系存在的意义不仅是识别具有能力的系统供应商，还要确保系统供应商能力的持续性，并能促使供应商对所提供ETICS产品质量及其技术能力和管理能力不断改进提高。这就要求认证体系中的首次认证和复评监督能持续可靠运行，对供应商起到持续监督作用，这是认证体系运行的技术关键和重点。

4 ETICS系统供应商认证制度产生的效益

1)经济效益

住房和城乡建设部印发的《“十四五”建筑节能与绿色建筑发展规划》提出，到2025年完成3.5亿平方米既有建筑的节能改造以及0.5亿平方米超低能耗、近零能耗建筑的建设，外墙保温施工价格在100~300元/平米之间，直接影响经济效益1000亿元左右，加上外墙外保温在新建建筑上的使用，经济效益还会更高。同时，外墙外保温系统的应用会带动相关产业的发展，包括保温材料、粘结抹面砂浆、增强网格布、锚栓等生产企业、成套系统产品供应企业、施工企业等。ETICS系统供应商认证制度能给外墙保温行业质量带来显著的提升和促进作用，产生不可忽视的经济价值。

2)社会效益

ETICS认证体系能提高建筑的质量和安全性，增强建筑的耐久性和稳定性，增进居民体验，提供更舒适、安全的居住环境。尤其在外墙外保温因“拼盘”问题而导致一系列质量问题而被质疑和限制的当下，ETICS系统供应商认证体系可以提高建筑行业的施工质量和管理水平，使建筑行业更加专业化、标准化、规范化，提升建筑行业的竞争力和公信力，提高建筑行业的整体技术水平。材料源头管控的增强，也有助于重建公众对建筑外墙外保温行业的信任。

3)环境效益

随着全球气候变暖和资源紧张问题日益严峻，建筑节能成为我国当前应对气候变化和促进可持续发展的重要举措之一。ETICS系统是建筑节能的重要组成部分，是实现近零能耗建筑、绿色建筑的重要技术手段，可以有效减少建筑物的热量损失，提高建筑物的隔热保温性能，减少能源消耗，从而减少对环境的污染和破坏，有利于实现节能减排的目标。外墙外保温系统可以提高建筑物的耐久性和

中国知网 https://www.cnki.net

安全性，延长建筑物的使用寿命，减少建筑垃圾的产生和对环境的影响。

5　结语

ETICS系统涉及保温材料、粘结剂、玻纤网格布、锚栓及饰面材料等，ETICS工程包括设计、施工、验收、运维等环节。在该系统性、集成性体系中，ETICS系统供应商认证制度的建立，可以在技术上明确ETICS系统及材料技术要求及其验证评价建设，在管理上明确系统供应商技术能力及质量保障水平建设。建立认证评价标准，确立可表征、可评价的技术要求，确立可识别、可追溯、可改进提升的机制，双管齐下，以“1(技术)+1(管理)”模式，才能确保ETICS认证体系持续可靠运行。

参考文献

[1]郁聪. 建筑运行能耗实现碳达峰碳中和的挑战与对策[J]. 中国能源,2021(9):25–31.

[2]何锦丛. 我国公共建筑碳达峰碳中和推进路径初探[J]. 上海节能,2021(9):938–940.

[3]孙文君,史立强,贾昕. 装配式建筑碳达峰碳中和实施路径研究[J]. 城市情报,2023(12):142–144.

[4]杨海全,朱灿银,曹静. 外墙薄抹灰外保温系统的质量控制浅析[J]. 建筑节能,2019(9):26–28+68.

[5]刘建志,刘驰宇,陈现景,等. 可燃级保温材料薄抹灰外墙保温系统建筑防火性能研究[J]. 工业建筑,2023(S02):732–735.

[6]JACEK M. External thermal insulation composite systems (ETICS) from industry and academia perspective[J]. Sustainability, 2021,13:13705–13722.

[7]王伟. 建筑外墙外保温做法对结构安全性影响分析[J]. 门窗,2023(6):214–216.

[8]毛学墙. 挤塑聚苯板薄抹灰外保温工程案例分析[J]. 建筑,2023(4):137–139.

[9]苟浩军. 建筑外墙外保温系统保温板脱落原因及防治措施[J]. 建材世界,2020(3):58–59+72.

[10]胡永东. 双碳目标背景下建筑外墙保温系统的逐劣升级探析[J]. 安徽建筑,2022(6):79–80.

[11]REZAI S H, ALLARD F, ABELÉ C, et al. Evaluating external thermal insulation composite systems (ETICS) regarding the building’s global performance[J]. Energy procedia, 2015,78:1562–1567.

[12]GB 50411–2019,建筑节能工程施工质量验收标准[S].

[13]ETAG 004, Guideline for European technical approval of external thermal insulation composite systems with rendering[S].

(上接第101页)

3　结论

经过分析水下玻纤套筒加固系统工程应用中存在的问题，并对其检测标准进行梳理，得到以下结论：

1)采用控制玻璃纤维复合材料板的高度和分段灌浆的方式，可解决灌注中出现的离壳和套筒被胀破漏浆问题；在水下玻纤套筒加固系统中引入增强材料，可解决其不能提高待加固物承载力的问题，碳纤维网格因具有可塑性，与灌浆料的浸润性好，具有较好的应用前景。

2)从材料、设计、施工和质量评定4个方面对水下玻纤套筒加固系统的检测标准进行了梳理，分析了T/CSTM 00339–2021和DB41/T 2244–2022的差异和不足，为相关人员、企业了解和掌握标准提供参考，可供设计、施工及验收参考。

参考文献

[1]殷任宏,张延. 公路桥梁水中桩基基础加固设计研究[J]. 交通世界,2024(16):132–134.

[2]陈学健. 外包钢筋混凝土在桥梁水中桩基病害处置的应用[J]. 福建交通科技,2022(9):86–90.

[3]吴靖宇. 水下墩柱玻纤套筒加固技术[J]. 黑龙江科技信息,2014(29):217.

[4]李鹏飞,李志伟,等. 水下墩身玻纤套筒加固关键技术研究[J]. 石家庄铁路职业技术学院学报,2023(3):48–52.

[5]孙永文,陈华. 桥梁涉水桩基玻纤复合材料加固系统应用研究[J]. 交通科技与管理,2024(15):114–116.

[6]肖勇辉. 水下玻纤套筒加固技术研究[J]. 城市道桥与防洪,2017(7):148–149.

[7]段红伟. CFRP网格增强玻纤套筒加固箍筋锈蚀RC柱轴压力学性能[D]. 南昌:华东交通大学,2023.

[8]梁富春,高剑平,段红伟,等. 碳纤维复材网格增强玻璃纤维复材套筒加固箍筋锈蚀钢筋混凝土短柱轴压性能[J]. 工业建筑,2024(6):100–107.

[9]张晋豪,陈龙,张晋滔. 方桩玻纤套筒加护局部施工缺陷分析与建议[J]. 河南科技,2021(36):80–82.

[10]陈还钊. 浅谈传统钢护筒增大截面法加固与水下玻纤套筒加固法对比[J]. 科技展望,2016(17):176.

中国知网　https://www.cnki.net

DOI:10.26936/j.cnki.1003-8965.2025.05.012

薄抹灰外墙外保温系统(ETICS)相容性指标影响因素研究

金晓冬[1]，张浩浩[1]，孙诗兵[1]，张金成[2*]，郭红斌[2]，曾春燕[2]，武薇[2]
(1.北京工业大学 材料科学与工程学院，北京 100124；
2.中国国检测试控股集团股份有限公司，北京 100024)

摘要：薄抹灰外墙外保温系统(ETICS)是由保温材料、粘结砂浆、抹面胶浆等材料组合而成。其中，保温材料与粘结砂浆或抹面胶浆的匹配性至关重要。本文以模塑聚苯乙烯(EPS)和石墨聚苯乙烯(SEPS)为研究对象，探究了保温材料尺寸分别为50×50mm和100×100mm情况下的保温材料垂直于板面抗拉强度、粘结砂浆界面原强度/保温材料以及抹面胶浆界面原强度/保温材料，并以此为依据计算界面“相容性”系数。结果表明，当相容性系数大于1时，破坏模式主要集中在保温板本体，表明界面结合良好；当相容性系数介于0.7~1之间时，破坏多发生于板材与胶粘剂之间，显示界面连接存在一定弱点；而相容性系数小于0.7时，界面破坏尤为严重，揭示出材料间不良的匹配关系。

关键词：EPS；SEPS；粘结强度；界面处理；相容性
中图分类号：TU761 **文献标志码：**A **文章编号：**1003-8965(2025)05-0068-06

Research on the influencing factors of the compatibility index of the exterior insulation system (ETICS) of the thin plastered exterior wall

JIN Xiaodong[1], ZHANG Haohao[1], SUN Shibing[1], ZHANG Jincheng[2], GUO Hongbin[2], ZENG Chunyan[2], WU Wei[2]*
(1. College of Materials Science and Engineering, Beijing University of Technology, Beijing, 100124;
2. China Testing & Certification International Group Co., Ltd., Beijing 100024)

Abstract: The External Thermal Insulation Composite System (ETICS) consists of materials such as thermal insulation materials, bonding mortars, and finishing plasters. Among them, the compatibility between the insulation material and the bonding mortar or finishing plaster is crucial. This study focuses on Expanded Polystyrene (EPS) and Graphite-Enhanced Polystyrene (SEPS), with insulation material sizes of 50×50 mm and 100×100 mm. The study investigates the tensile strength of the insulation material perpendicular to the panel surface, the initial bond strength between the bonding mortar and insulation material, and the initial bond strength between the finishing plaster and insulation material. Based on these results, the “compatibility” coefficient at the interface is calculated. The findings show that when the compatibility coefficient is greater than 1, the failure mode is mainly concentrated in the insulation board itself, indicating a good interface bond. When the compatibility coefficient is between 0.7 and 1, failure predominantly occurs at the interface between the panel and adhesive, suggesting some weakness in the interface connection. When the compatibility coefficient is less than 0.7, the interface failure is particularly severe, indicating poor compatibility between the materials.

Keywords: EPS; SEPS; bonding strength; interface treatment; compatibility

0 引言

薄抹灰外墙外保温系统(ETICS)由保温层、胶粘剂(也称粘结砂浆)、抹面胶浆、耐碱玻璃纤维网格布、锚栓等材料组合而成，具有保温效果好、防凝露性能好、施工方便等特点，是国内外普遍应用的建筑墙体保温构造形式[1-2]，可应用于砖墙、水泥砌块墙、石砌体墙或混凝土基材[3]。由于其良好的施工适应性、优越的热工性能与居住舒适性，ETICS系统在建筑行业中得到了广泛应用[4-5]。我国ETICS系统陆续出现了脱落、火灾等事故，引起了全社会的极大关注[6]。在政府层面，中华人民共和国国务院也于2025年2月发布公告，在全国范围内开展“建筑保温材料安全隐患”专项整治工作[7]。可见，对于ETICS系统的安全性研究具有显著的现实意义。

基金项目：非金属材料创新中心创新基金资助项目(编号：24TDA-5)；北京市教育委员会科研计划项目(编号：KM202410005008)
第一作者：金晓冬(1990-)，男，博士，副教授，研究领域包括阻燃高分子材料、建筑保温材料以及有机无机复合材料。
通讯作者：张金成(1980-)，男，本科，高级工程师，从事建筑节能、保温相关检测及科研工作。

中国知网 https://www.cnki.net

从材料的角度而言，保温材料与粘结砂浆或抹面胶浆界面不相容，是导致ETICS系统脱落的根本原因[8]。针对ETICS系统脱落的问题，学术界也开展了大量的研究工作。如张林峰等从粘结砂浆主要成分入手，探讨其粘结机理、破坏模式及其对粘结强度的影响[9]。王业中则分析了不同齿槽形态的模塑聚苯板及不同养护条件下的粘结强度变化，并研究了粘结与锚栓联合固定的协同效应[10]。杨少龙则关注粘结面积与厚度等参数对挤塑聚苯板与基体粘结强度的影响规律[11]。

尽管业界对保温材料/砂浆粘结安全性进行了较为全面的研究，但ETICS系统的脱落事故依然时有发生。可见，现有标准体系种的指标无法完全体现ETICS系统的安全性。在复合材料或层状结构中，界面的效能通常通过比较界面强度与相邻材料(尤其是较弱一方)的强度来评估。理想的界面设计是使其强度至少不低于较弱基体的强度，以确保载荷有效传递且破坏发生在基体内部而非界面[12-13]。与复合材料载荷传递类似，ETICS中保温材料一面涂抹粘结砂浆以固定上墙，另一面涂抹抹面胶浆加以保护，由此组成了双层砂浆夹心保温材料的复合体系。当这一复合体系受力时，理想的失效方式是保温材料的内部断裂，而非界面剥离。这要求界面粘结强度至少不低于保温材料自身的强度。否则，界面将成为薄弱环节，极易发生脱粘失效。为此，本文提出了ETICS系统“相容性”的概念。“相容性”是指粘结砂浆或抹面胶浆与保温材料的拉伸粘结强度同保温材料垂直于板面方向的抗拉强度的比值(式1)。这种无量纲的比值，更可以直观表达这种“谁强谁弱”以及“强多少倍/弱多少倍”的相对关系。比值越贴近于1，说明粘结效果越好，粘结越可靠，其断裂方式更趋向于保温材料内部断裂。现有标准(如JGJ 144-2019[14])中强制要求“破坏发生在保温板内”的规定，本质上隐含了对保温材料与砂浆粘结界面相容性趋于1的追求。但同时，追求过高相容性会显著增加砂浆成本，本文也将着重探讨相容性的取值范围。

$$\text{相容性}=\frac{\text{粘结砂浆或抹面胶浆与保温材料的拉伸粘结强度}}{\text{保温材料垂直于板面方向的抗拉强度}} \quad (1)$$

值得注意的是，现有标准体系中关于拉伸粘结强度与垂直于板面的抗拉强度测试样品的尺寸并不一致。如JGJ 144-2019《外墙外保温工程技术标准》中规定，拉伸粘结强度的样品尺寸为50mm×50mm或者为直径为50mm；保温材料抗拉强度测试的样品尺寸为100mm×100mm。样品尺寸越大，则形成界面缺陷的可能性越大。综上所述，本文以目前主要的保温材料——模塑聚苯乙烯(EPS)和石墨聚苯乙烯(SEPS)为研究对象，在现有标准体系的基础上提出了相容性概念，并探究了不同样品尺寸情况下的相容性取值可行性。

1　材料与试验方法

1.1　原材料

1)砂浆：本实验所用砂浆符合GB/T 17671《水泥胶砂强度检验方法》要求。

2)EPS、SEPS保温材料：本文所用EPS及SPES来自9家企业供应，保温材料的密度为18-22kg/m^3，保温材料的厚度为其原始厚度(均大于40mm)。具体编号规则如表1所示。

表1　样品编号规则说明

Tab.1　Explanation of sample numbering rules

编号形式	含义说明
0X[注]	第 0X 家企业生产的保温材料（EPS，SEPS）
Z0X	第 0X 家企业生产的保温材料，测试粘结砂浆界面强度
M0X	第 0X 家企业生产的保温材料，测试抹面胶浆界面强度

注：如01对应于第一家企业生产的保温材料，以此类推。

1.2　试验方法

粘结砂浆或抹面胶浆与保温材料的拉伸粘结强度、保温材料垂直于板面方向的抗拉强度均参照GB/T 29906-2013《模塑聚苯板薄抹灰外墙外保温系统材料》进行。进行养护时，养护温度为(23±2)℃，养护湿度为(50±5)%，养护龄期为28天。测试时，实验室的环境温度为(23±5)℃，环境湿度为(50±10)%。

2　实验结果

2.1　垂直于板面方向的抗拉强度

对九家企业生产的EPS和SEPS在50×50mm与100×100mm两个规格下的保温材料抗拉强度进行了测试，其结果如图1所示。

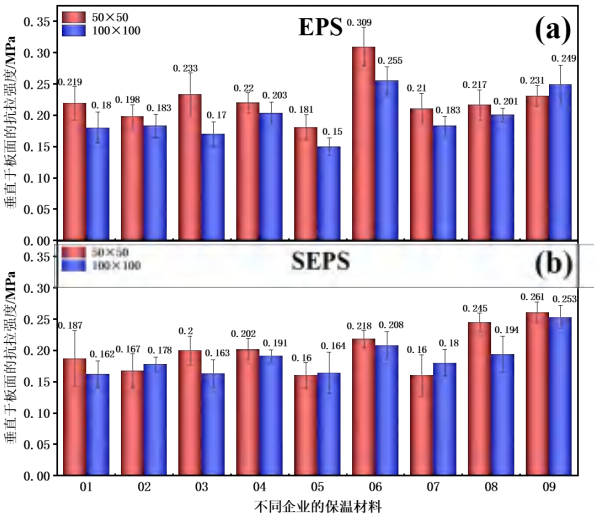

图1　不同尺寸(50×50mm和100×100mm)下EPS(a)和SEPS(b)垂直于板面的抗拉强度

Fig.1　Tensile strength perpendicular to the surface of EPS (a) and SEPS (b) boards with different sizes (50×50mm and 100×100mm)

小尺寸试件往往在拉拔强度测试中表现出高于大尺寸的强度，主要原因可以从缺陷统计分布和界面破坏机理来

中国知网　https://www.cnki.net

理解。试件体积或面积越大，包含临界缺陷(孔隙、不均匀区域等)的概率越高，因此在拉拔过程中更容易在大尺寸区域形成并扩展裂纹，导致强度降低；相反，小尺寸试件“有效体积”较小，遇到足以致裂的缺陷概率下降，表现出较高的强度。其次，界面拉拔试验中特有的应力分布和边界效应也会放大尺寸影响：较大面积的界面更难保证砂浆或胶层在整个区域内均匀浸润与固化，可能产生应力集中区或不连续界面，从而降低整体粘结强度；小面积试件更容易实现均匀施工和控制边缘效应，破坏时裂纹也更可能局限，不易迅速扩展至大面积区域。此外，不同材料改性(如SEPS)可能改变表面粗糙度和浸润行为，使尺寸效应表现相较EPS更稳定一些，但总体趋势仍是面积增大会带来更多潜在缺陷。

2.2　拉伸粘结强度对比

2.2.1　粘结砂浆与保温材料的拉伸粘结强度对比

图2汇总了9家企业在原始状态下，EPS与SEPS与粘结砂浆的拉伸粘结强度对比。实验结果表明，在50×50 mm试件中，共有编号为01–05的EPS样品与粘结砂浆的拉伸粘结强度优于SEPS。而编号为06–09的SEPS强度值更佳。特别是06和08号样品，SEPS/粘结砂浆的拉伸粘结强度可达到0.242 MPa和0.278 MPa。

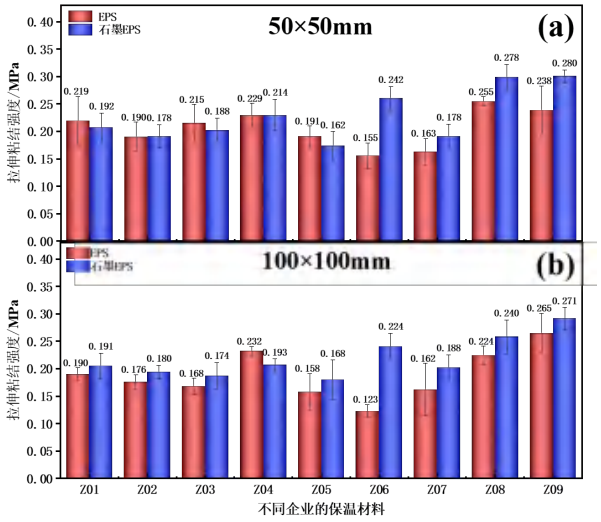

图2　50mm×50mm(a)和100mm×100mm(b)尺寸下EPS和SEPS与粘结砂浆的拉伸粘结强度对比

Fig.2　Tensile bond strength between EPS and SEPS and adhesive mortar at different sizes (50×50mm (a) and 100×100mm (b))

而在样品规格为100×100 mm的试件中，SEPS表现出与粘结砂浆更高的拉伸粘结强度(04号样品除外)，说明尺寸增大时，SEPS与粘结砂浆界面适配性更佳。这一现象也与SEPS的密度略高、骨架结构更紧密等材料特性相关，在试件尺寸增大时，SEPS与砂浆界面的有效接触面积和局部界面强度提升更为明显。综合来看，试件尺寸变化引发的界面应力分布和砂浆界面填充密实性，是导致SEPS在大尺寸条件下界面粘结性能超越EPS的关键因素。

2.2.2　抹面胶浆与保温材料的拉伸粘结强度对比

图3汇总了9家企业EPS板与SEPS板的抹面胶浆原强度。SEPS板的抹面胶浆原强度在多数企业中表现优于对应EPS板。具体而言，50×50 mm试件中，EPS板的抹面胶浆原强度范围为0.125–0.236MPa，最高值出现在企业04(0.236 MPa)；SEPS板的抹面胶浆原强度则在0.174–0.242MPa之间，最高值出现在企业05(0.242MPa)。在100×100 mm试件中，EPS板的抹面胶浆原强度范围为0.166–0.214MPa，其中企业04到0.214MPa的峰值；SEPS板的抹面胶浆原强度在0.166–0.227 MPa之间，最高值由企业06的SEPS板取得(0.227MPa)。

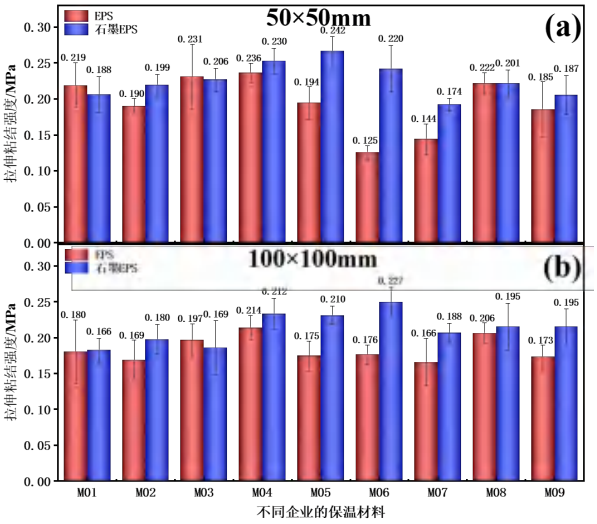

图3　50mm×50mm(a)和100mm×100mm(b)尺寸下EPS和SEPS与抹面胶浆的拉伸粘结强度对比

Fig.3　Tensile bond strength between EPS and SEPS and rendering mortar at different sizes (50×50mm (a) and 100×100mm (b))

通过比较可见，SEPS板在50×50 mm和100×100 mm两个尺寸下均普遍高于EPS板，表现出更好的界面适配性。SEPS板表面较为疏水，起始粘结力较弱，但抹面胶浆中所含短纤维在硬化过程中可形成有效的增强结构，在界面处起到“桥接”微裂缝、抑制应力集中发展的作用，从而显著提高其粘结强度[15]。同时，SEPS板通常具有更高的干密度和致密的表层结构，使得胶浆能在其表面形成更加均匀、紧密的粘结层，有利于承载过程中应力的分散，进一步增强界面稳定性。因此，即使在未改性的情况下，短纤维的抗裂和增韧效应在SEPS板界面上表现更为明显，从而使其粘结性能超过普通EPS板。此外，尺寸效应依然显著：50×50 mm试件的抹面胶浆原强度整体略高于100×100 mm试件，可能与小尺寸样本在拉拔过程中应力集中更显著、界面更易达到破坏状态有关。综合来看，抹面胶浆显著提升了SEPS板的界面粘结性能，尤其在小尺寸条件下效果更为突出。

2.3　粘结系统的相容性

在外墙外保温系统中，保温板与基层之间的拉伸粘结

中国知网　https://www.cnki.net

强度由粘结界面强度、有效粘结面积及材料本体强度共同决定。当体系受到外力拉拔作用时，通常可根据破坏部位划分为四种破坏模式：保温板本体破坏、EPS板与胶粘剂界面破坏、胶粘剂与基层界面破坏及基层破坏，这些模式是衡量界面相容性和系统整体性能的重要依据[16-17]。

保温材料的相容性如图4所示，相容性系数与界面破坏模式呈现出明显的对应关系，可与外墙外保温系统常见的四种破坏类型相匹配。

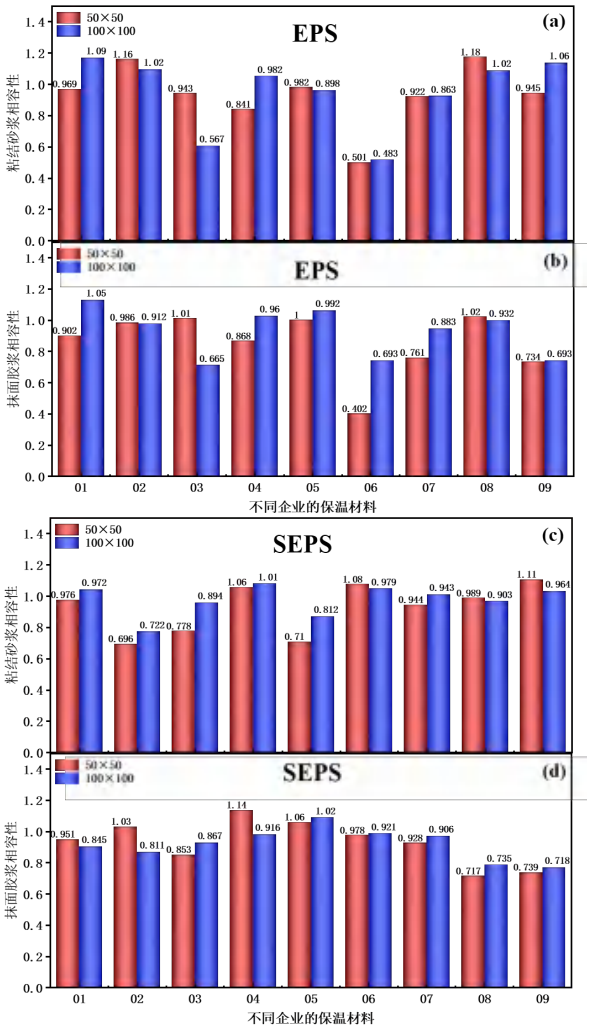

图4　粘结强度相容性

Fig.4　Compatibility of bond strength

具体分析如下：当相容性系数大于1时，试件破坏主要发生在保温板本体(第一类破坏)，如图5所示，泡沫板发生整体断裂，断面多为EPS或SEPS本体结构，界面强度已超过材料本体强度，砂浆层与基层未见破坏，这表明砂浆与泡沫界面形成了稳定的粘结力传递，系统整体相容性良好。当相容性系数在0.7～1之间时，破坏方式如图6所示，主要集中在EPS板与胶粘剂界面(第二类破坏)，断面有部分砂浆附着，但明显可见部分泡沫颗粒脱落或残留，界面连接力不足以达到材料本体强度，呈现部分界面剥离和胶粘剂粘结破坏。当相容性系数小于0.7时，断裂面多在砂浆层表面，表现为砂浆表面脱落或只有极少数泡沫颗粒残留(第三类破坏)，如图7所示，界面粘结力无法有效传递外力，界面相容性差，砂浆层与基层间或砂浆本体破坏最为明显。

图5　相容性大于1破坏示意图

Fig.5　Failure mode for compatibility ratio > 1

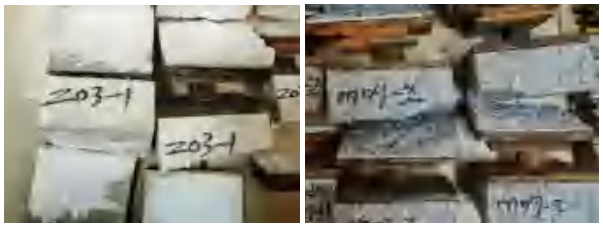

图6　相容性介于0.7～1破坏示意图

Fig.6　Failure mode for compatibility ratio 0.7~1

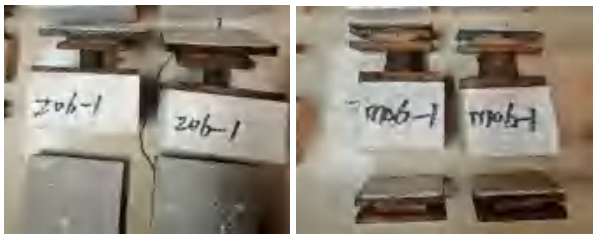

图7　相容性小于0.7破坏示意图

Fig.7　Failure mode for compatibility ratio < 0.7

综上所述，相容性系数不仅是界面匹配性的定量指标，也可直观反映界面力学适配状态。高相容性界面对应保温板本体或基层破坏，显示界面整体匹配良好；低相容性界面则多表现为界面破坏，揭示体系薄弱环节所在。

2.4　网格划分计算面积探究

如图8所示，采用1mm边长网格纸拓印断裂面并计算面积时，测得的面积通常大于用尺子测量得到的近似值，导致按网格面积计算的强度(力/面积)普遍低于尺子法计算结果。这主要源于两方面原因：一方面，普遍的测量方式通常基于对断裂面外廓的简化近似(如近似矩形或多边形)，忽略了表面微小凹凸和边缘波动，因而低估真实面积；另一方面，网格拓印法能通过墨水精确描绘断裂面轮廓，捕捉更多不规则特征，计算出的面积更接近真实值，但因使用1mm网格，其分辨率为1mm²，仍存在有限精度，但相较传统方法更精细。但应注意，由于网格纸拓印依赖人工，存在轻微的描画误差；同时，网格大小(1mm)也决定了面积分辨率。因此可以认为网格法在计算强度时具有一定意义，能更可靠地反映出更真实的面积。

中国知网　https://www.cnki.net

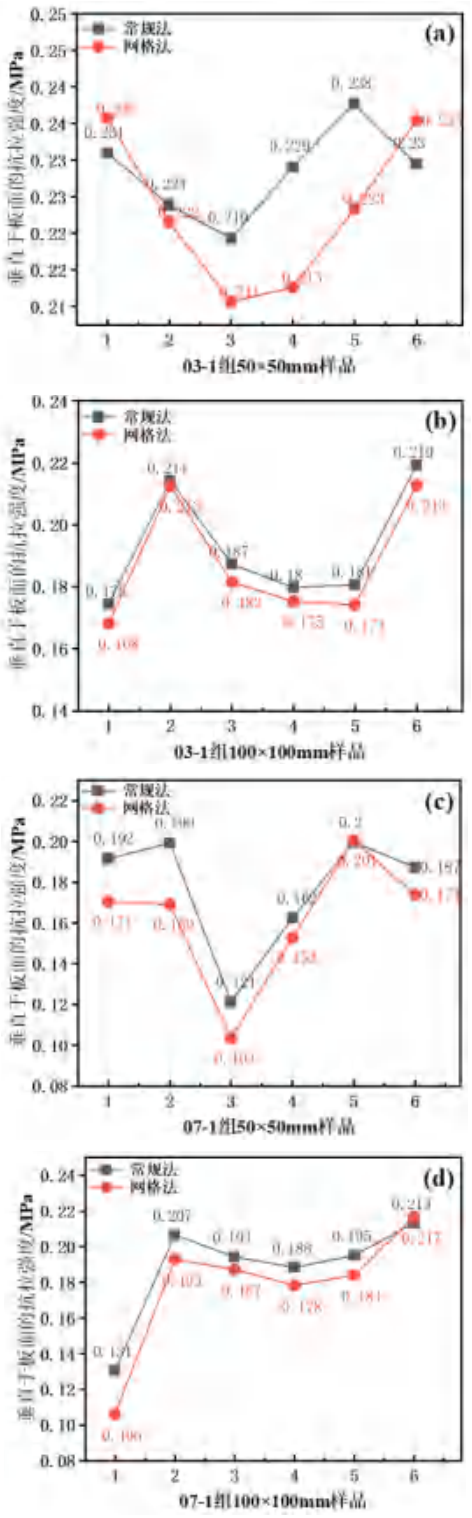

图8　网格面积强度对比

Fig.8　Comparison of strength per grid area

3　结论

本文系统研究了EPS板和SEPS板在不同处理条件下的砂浆粘结性能及其影响因素，选取了9家企业生产的EPS板和SEPS板，依据GB/T 29906–2013标准进行了泡沫本身强度、砂浆粘结强度及抹面胶浆原强度的拉拔试验，结果显示板材类型、界面处理方式及试件尺寸对砂浆粘结性能均具有显著影响。试件尺寸对界面粘结性能影响明显，50×50 mm试件中EPS板界面粘结性能普遍优于SEPS板，砂浆在EPS板表面更易形成稳定的物理嵌合，而在100×100 mm试件中SEPS板粘结强度在部分企业中超过EPS板，说明SEPS板在大尺寸条件下界面适配性更好。试件尺寸增大引起的界面应力分布变化及砂浆流动性增强，使SEPS板密度和骨架结构优势在界面更充分体现，提升了界面有效接触面积和局部强度。抹面胶浆对SEPS板粘结性能的提升尤为明显。界面相容性系数分析结果进一步揭示不同界面处理条件下体系的粘结适配性，相容性系数大于1时破坏主要发生在保温板本体，砂浆界面强度超越材料本体强度，体系相容性良好；相容性系数在0.7~1之间时破坏多集中在EPS板与胶粘剂界面，界面匹配性仍具提升空间；相容性系数低于0.7时破坏主要发生在砂浆层表面，界面粘结力不足，体系力学传递能力受限，这一规律为界面粘结性能的判断和界面优化提供了直观依据和理论支撑。

参考文献

[1]祁俊峰. EPS板薄抹灰外墙外保温系统施工技术的应用[J]. 内蒙古科技与经济, 2018(06): 88–89.

[2]薛一冰, 杨秀燕. EPS薄抹灰外墙外保温系统改进与分析[J]. 建筑节能, 2011, 39(10): 62–65+80.

[3]EOTA. Guideline for European Technical Approval of External Thermal Insulation Composite Systems with Rendering, Edition March 2000 [R]. Brüssel: European Organisation for Technical Approvals, 2000.

[4]GÁLVEZ–MARTOS J L, STYLES D, SCHOENBERGER H, et al. Construction and demolition waste best management practice in Europe [J]. Resources, conservation and recycling, 2018, 136: 166–178.

[5]M. C. GUEDES, L. MATIAS, et al. Thermal comfort criteria and building design: Field work in Portugal [J]. Renewable energy, 2009, 34(11): 2357–2361.

[6]张金成, 孙诗兵, 金晓冬, 等. 薄抹灰外墙外保温系统(ETICS)供应商认证制度探索[J]. 中国建材科技, 2024(06): 79–82.

[7]肖方. 国务院安委办部署推进人员密集场所动火作业和建筑保温材料安全隐患专项整治工作[J]. 中国消防, 2025(2): 6.

[8]S. MALANHO, M. R. VEIGA. Bond strength between layers of ETICS – Influence of the characteristics of mortars and insulation materials [J]. Journal of building engineering ,2020, 28: 101021.

[9]张林峰. 外保温外墙保温层的粘结分析[D]. 天津: 天津大学, 2004.

[10]王业中. 建筑外墙与外保温层联接的试验研究[D]. 青岛: 青岛理工大学, 2008.

[11]杨少龙. XPS保温板与结构层粘结性能试验研究[D]. 武汉: 武汉理工大学, 2011.

中国知网　https://www.cnki.net

[12]秦昌凯, 秦鸿根, 张云升, 等. 浅析外墙外保温界面砂浆粘结强度的试验方法[J]. 建材技术与应用, 2012(05): 9–12.

[13]李雨珊, 尹世平, 徐世烺, 等. 工程水泥基复合材料与发泡式聚苯乙烯保温板的界面粘结性能[J]. 复合材料学报, 2022, 39(11): 5251–5263.

[14]中华人民共和国住房和城乡建设部. 外墙外保温工程技术标准: JGJ 144–2019[S]. 北京: 中国建筑工业出版社, 2019.

[15]T. KANDA, V. C. LI. Effect of fiber strength and fiber–matrix interface on crack bridging in cement composites [J]. J. of engineering mechanics–asce, 1999, 125: 290–299.

[16]陈杨. EPS外墙外保温系统变幅荷载粘贴疲劳试验研究[D]. 济南: 山东建筑大学, 2023.

[17]张玉峰. EPS板外墙外保温系统粘结疲劳性能试验研究[D]. 济南: 山东建筑大学, 2022.

(上接第67页)

2.3 混凝土抗压强度测试

为了解不同配合比混凝土的抗压强度发展规律, 对养护至7d、28d和56d的立方体试件进行抗压强度测试, 测试结果如下表所示:

表4 混凝土抗压强度(MPa)

Tab.4 Concrete compressive strength (MPa)

配合比	7d 抗压强度	28d 抗压强度	56d 抗压强度
配合比 A	32.5	45.8	50.2
配合比 B	30.2	43.5	48.6
配合比 C	28.8	41.2	46.8
配合比 D	31.5	44.2	49.0

从表4可以看出, 随着矿渣和粉煤灰掺量的减少, 混凝土的抗压强度在不同龄期均呈降低趋势。是因为矿渣和粉煤灰具有独特的火山灰活性, 在混凝土水化过程中, 能与水泥水化产物发生二次水化反应, 生成具有胶凝性的水化产物。这些水化产物能填充混凝土内部的孔隙, 增强混凝土的密实性, 提高混凝土的强度。

2.4 实验结果分析

综合上述测试结果看出, 配合比A在各方面表现相对较为出色, 展现出良好的均衡性。虽然配比C在工作性能方面表现最优, 具有较大的坍落度和较好的流动性, 但其力学性能低于其他配合比, 无法满足结构对强度的要求。配合比B和D的性能介于A和C之间, 但在综合性能上不如配合比A均衡。分析配合比A的优势, 其钢渣、矿渣和粉煤灰的掺量相对较为合理。这种合理的掺量设计既充分利用工业废料, 实现资源的循环利用, 又保证混凝土具有良好的工作性能和较高的力学性能。因此, 确定配合比A为最佳配比, 即每立方米胶凝材料中, 钢渣用量为22kg/m³, 矿渣用量为44kg/m³, 粉煤灰用量为44kg/m³。在此配比下, 混凝土不仅具有良好的工作性能, 便于施工操作, 而且具备较高的力学性能, 能满足结构的安全性和耐久性要求, 实现工业废料的有效利用和混凝土性能的优化, 为类似工程提供参考和借鉴。

3 结论

本实验得出的钢渣–矿渣–粉煤灰三元复合固废胶凝材料混凝土最优配合比为A。在实际工程中, 按照该配合比制备钢渣–矿渣–粉煤灰三元复合固废胶凝材料混凝土, 能保证混凝土具备良好的力学性能, 满足工程需求。

参考文献

[1]王忠勇, 张江涛, 张金成, 等. 全固废基固化剂对高含水率淤泥土性能的影响研究[J]. 中国建材科技, 2024, 33(04): 42–46.

[2]常小龙, 王玲玲. 矿物掺合料及纳米SiO_2对煤矸石混凝土基本性能影响研究[J]. 中国建材科技, 2025, 34(01): 13–17+37.

[3]李彦苍, 张子鹤, 张春元, 等. 基于正交试验和超声波波速的水库底泥透水混凝土性能研究[J]. 中国农村水利水电, 2024(1): 156–164.

[4]王进文, 李振宝, 臧金源, 等. 关于机制砂絮凝剂残留值对混凝土性能影响以及其测定和处置方法的研究[J]. 混凝土, 2024(4): 183–186.

[5]黄飞衡, 辛扬帆, 姜葱葱, 等. 固废基掺合料的调制及其对复合胶凝材料抗氯性能的影响[J]. 硅酸盐通报, 2025, 44(3): 1050–1056.

[6]李悦, 谢东, 林辉. 基于响应面法设计与制备磷石膏矿渣基复合胶凝材料[J]. 混凝土, 2024(7): 149–152.

[7]朱增超, 刘贤平, 水中和, 等. 固废基复合胶凝材料配比优化设计及协同效应研究[J]. 硅酸盐通报, 2023, 42(12): 4368–4377.

[8]张喻, 杨建宇, 杨伟军. 硫酸盐–碳化耦合下高性能喷射混凝土耐久性研究[J]. 中国建材科技, 2025, 34(02): 19–23.

[9]余舟, 何兆益, 唐亮, 等. 典型硫酸盐固废复合胶凝材料制备与微观特性研究[J]. 无机盐工业, 2024, 56(4): 90–97.

[10]于延忠, 李冬娜. 固废基胶凝材料对水泥和混凝土性能的影响及机理分析[J]. 混凝土与水泥制品, 2025(07): 102–105+109.

中国知网 https://www.cnki.net

Chemical Engineering Journal 494 (2024) 153285

Contents lists available at ScienceDirect

Chemical Engineering Journal

journal homepage: www.elsevier.com/locate/cej

Self-assembled coatings with durable flame retardancy for EPS foam

Xiaodong Jin [a], Xinyi Wu [a], Wufei Tang [b,*], Zheni Tan [b], Wanfu Wang [a], Shibing Sun [a,*]

[a] College of Materials Science and Engineering, Beijing University of Technology, Beijing 100124, China
[b] Hunan Engineering Technology Research Center for Comprehensive Development and Utilization of Biomass Resources, Hunan University of Science and Engineering, Yongzhou 425199, China

ARTICLE INFO

Keywords:
Expandable Polystyrene
Self-assembly
Ultraviolet curing
Flame retardant durability
Mechanism

ABSTRACT

Layer by layer (LBL) self-assembly coatings upon expandable polystyrene (EPS) surface play an important role in improving its flame retardancy. However, a large number of layers is needed to achieve a satisfied fire performance, and the coatings are difficult to adhere on the inert EPS surface, resulting in the poor durability. In this work, the surface of EPS was activated by ultraviolet ozone (UVO) with the appearance of oxygen contained groups, then a LBL coating with only two bilayers (branched polyethyleneimine (BPEI)-kaolinite (kaol)-BPEI-diethylene triamine penta (methylene phosphonic acid)) was covalently connected on the EPS surface. Compared with neat EPS, the obtained E-K_5D_{30} sample increased the value of limiting oxygen index (LOI) from 18.8 % to 37.7 %, improved the ignition time from 59 s to 95 s, reduced the peak heat release rate (pHRR) value from 282.0 kW/m^2 to 220.9 kW/m^2, and enhanced the char residues from 6.3 % to 32.3 % after the combustion. Moreover, an ultraviolet (UV) curing layer with P/N elements was prepared upon E-K_5D_{30} sample to maximize the flame retardant durability. A novel amino-intercalated kaol was used to play a smoke suppression role. The results showed that E-$K^*_5D_{30}$-P_8N_3 sample further increased the LOI to 39.2 %. Even after 12 h washing, the E-$K^*_5D_{30}$-P_8N_3 sample exhibited a slight LOI reduction to 37.8 %, and fire performance index (FPI) value of 0.405 m^2·s/kW, showing the successful construction of coatings with good fire safety and flame retardant durability.

1. Introduction

Expandable polystyrene (EPS) foam with cellular and porous structures is widely used for its lightweight performance and excellent thermal insulation. However, as a type of organic materials, EPS foam has serious fire hazards [1,2]. While ensuring a good thermal insulation performance and reducing the energy consumption of buildings, finding an efficient and convenient flame retardant modification method to EPS foam is the focus of current research.

Up to now, the surface modification, which can maintain the original properties of substrates, is a useful method to enhance the fire safety for polymeric foams (such as EPS) [3]. The coatings with flame retardancy can be constructed quickly by many post-treatment techniques. Among these methods, layer by layer (LBL) is a universal technology, which relies on the electrostatic interactions between each layers [4]. The LBL coatings are produced by alternately depositing positive and negative components. These layers are adhered by the weak connections such as Van der waals' force or hydrogen bonds [5]. Wang et al [6] used chitosan (CS) as the positive layer and alginate (AL) as the negative layer to construct the LBL coatings on the surface of polyurethane (PU) foams. It proved that the ten sets of CS-AL bilayers (10 BL) reduced the peak heat release rate (pHRR) of PU sample by 66 %. Liu et al [7] modified cotton fabrics by LBL method with 3-aminopropyl triethoxysilane (APTES) and sodium phytate to enhance the flame retardancy of matrix. The peak smoke production rate (pSPR) and total heat release (THR) values of the modified fabric with 15 BL coatings (APTES-sodium phytate) were reduced by 15.4 % and 16.7 % compared with those of uncoated samples, respectively. Zhang et al [8] deposited multilayer coating containing polyallylamine hydrochloride (PAH) and ammonium polyphosphate (APP) onto the surface of cotton blend fibers by LBL assembly. With 10 BL of PAH-APP coatings, the limiting oxygen index (LOI) value was improved from 20.1 % of uncoated fiber to 26.3 %. Zilke et al [9] used phytic acid (PA) and polyvinylamine (PVAm) as the oppositely charged electrolyte to improve the flame retardant of cotton by LBL approach. Vertical flame tests revealed a flame retardant behavior with no afterflame and afterglow time for a PA-PVAm coating with 15 BL.

Currently, LBL technology is primarily applied in PU foam and cotton fabrics to obtain good flame retardancy. However, there is fewer researches on EPS foam using LBL method. This is primarily because

* Corresponding authors.
E-mail addresses: buctfiresafetytwf@163.com (W. Tang), sunshibing@bjut.edu.cn (S. Sun).

https://doi.org/10.1016/j.cej.2024.153285
Received 12 March 2024; Received in revised form 10 May 2024; Accepted 17 June 2024
Available online 18 June 2024
1385-8947/© 2024 Elsevier B.V. All rights are reserved, including those for text and data mining, AI training, and similar technologies.

numerous layers need to be assembled in traditional LBL technology to reach the appropriate flame retardancy, which has serious impacts on the thickness and thermal insulation performance of EPS. Furthermore, the smooth and inert surface of EPS makes it difficult to prepare a flame retardant coating in the beginning, resulting in a weak bonding of the self-assembled coating with the substrate and a poor flame retardant durability.

The present methods for increasing the flame retardancy durability are main as follows: the preparation of covalent bonds or crosslinking networks, the formation of hydrophobic coatings, or introduction of flame retardants [10]. In our previous work [11–13], the ultraviolet ozone (UVO) method was used to activate the surface of extruded polystyrene (XPS) foam. The oxygen content on the XPS surface was significantly increased after the activation. These oxygen contained groups (such as hydroxyl and carboxyl groups) could provide reactive sites for the consequent reactions. Meanwhile, ultraviolet (UV) curing can be considered for producing covalent bonds or crosslinking networks to improve the durability of self-assembled coatings. Carosio et al [14] deposited 3 BL coatings consisting of APP, anionic UV-curable resin and CS on cotton fabrics. The results proved that the modified cotton could be self-extinguished in horizontal burning even after 1 h washing at 65 °C. In addition, the using of inorganic clay in self-assembled coatings can further improve the flame retardancy of the matrix. Alongi [15] et al produced an organic–inorganic hybrid coatings on polyester-cotton blends (PET-CO) composed of APP, CH and silica by LBL assembly method. The results showed that the sample deposited 5 quadlayers (silica/silica/CH/APP) coatings reduced the THR value from 5.0 MJ/m^2 to 4.4 MJ/m^2 and delayed the ignition time (TTI) from 22 s to 26 s. Grunlan et al [16] formed a LBL system by using CH and montmorillonite (MMT). The presence of 10 BL (CH/MMT) reduced the pHRR value of PU matrix by 52 %. Although UV curing has good application potential in improving the flame retardant of coatings, the content of ester groups in UV curing resin is relatively high, which has a negative impact on the release of smoke. Huang [17] prepared the flame retardant RPU samples by the construction of UV curable coatings on the surface. The presence of UV layer did reduce the THR value of RPU samples by 10 %, but the TSR value was enhanced from 897.7 m^2/kg of neat RPU sample to 1098.3 m^2/kg of flame retardant ones. Kaolinite (kaol), with a predominantly plate-like structure, has attracted more attention in the field of fire science because of its inexpensive cost and shielding function. Our previous works have proven [18–22] that the intercalation and exfoliation of kaol improved its dispersion within coatings, which is useful in improving the flame retardancy and smoke suppression of the produced composites.

Overall, this work constructs the organic–inorganic hybrid LBL coating with only two bilayers, combining both the UVO irradiation to activate the surface of EPS and UV curable layers to improve the flame retardant durability. UVO irradiation promotes the appearance of reactive groups contained oxygen which are further covalently connected with self-assembly coatings to consolidate the bonding strength between EPS and LBL coating. In addition, UV curing method is used to build a crosslinking network outside the self-assembly coating, so as to improve the water resistance and flame retardant durability of the surface coating. Moreover, a new kind of amino-intercalated kaol with good dispersivity is prepared to further play an important role in smoke suppression and alleviate the smoke release disadvantages of the UV curing coating with good flame retardant durability.

2. Experimental

2.1. Materials

EPS foam was bought from Qindao Yingkai Thermal Insulation Materials Co., Ltd. The thermal conductivity of EPS is 0.037 W/(m·K) and the density is 20 kg/m^3. Branched polyethyleneimine (BPEI) with the concentration of 50 % was bought from Shanghai Yuanye Co., Ltd. Diethylene triamine penta (methylene phosphonic acid) (DTPMPA) with a concentration of 50 % and analytical polyvinyl alcohol (PVOH) were acquired from Aladdin Bio-Chem Technology Co., Ltd (Shanghai). Kaol was from Shijiazhuang Xingyi mineral products factory. Dimethyl sulfoxide (DMSO), potassium acetate (KAc) and L-serine were produced in Shanghai Macklin Biochemical Co., Ltd. Polyurethane acrylate (PUA), 2-hydroxyethyl methacrylate phosphate (PM-2), triallyl isocyanurate (TAIC) and 2-hydroxy-2-methylpropiophenone (HMPP) were used for the preparation of UV curing coatings. All of the reagents above were analytical and respectively purchased from Chengdu Sicheng Optoelectronic Materials Co., Ltd., Shanghai Yinchang New Materials Co., Ltd., Shanghai Macklin Bio-Chem Co., Ltd. and Shanghai Aladdin Biochemical Technology Co., Ltd.

2.2. Pre-activation treatment of EPS surfaces

The inert EPS surface was irradiated by the UVO lamp (with a wavelength of 148.9 and 253.7 nm, BZS250GF-TC, Shenzhen Huiwo technology Co., Ltd.) in order to improve the chemical activity of surfaces and facilitate the construction of self-assembly coatings. During the UVO activation process, the EPS samples were exposed to a continuous radiation of 25 mW/cm^2 for 5 min with a distance of 10 cm.

2.3. Preparation of amino-intercalated kaol

The preparation of amino-intercalated kaol contained three steps. First, kaol (4 g) was dispersed in the mixed solution of DMSO (40 mL) and deionized water (4.5 mL) for 15 min. The suspension was heated at 60 °C for 24 h. After three times washing with deionized water and filtering, the reacted mixture was dried for 12 h at 60 °C. The obtained products were named as D-kaol. Second, 60 mL of saturated KAc solution was combined with the D-kaol (2 g) and stirred at 60 °C for 24 h in an oil bath. The obtained products after washing and drying were marked as K-kaol. Finally, K-kaol (2 g) was dispersed in 40 mL saturated L-serine solution (2 mol/L) with stirring at 60 °C for 24 h. After three times washing with ethanol, the products were filtered and dried for 12 h at 60 °C. Then the amino-intercalated kaol was obtained and marked as k*aol. The preparation of k*aol was shown in Fig. 1a, and the structural analysis of kaol and k*aol were shown in Fig. S1.

2.4. Preparation of LBL self-assembly flame retardant coatings

Kaol (or k*aol) particles or DTPMPA solutions were added in 8 % PVOH solution with ultrasonic dispersion for 1.5 h at room temperature to prepare 5 % and 30 % homogeneous solutions, respectively. EPS samples were firstly immersed in the 1.0 % BPEI solution for 10 min to obtain the positive surface. Then the treated EPS samples were successively immersed in the solutions of kaol (or k*aol) (negative), BPEI (positive), and DTPMPA (negative) for 10 min. Each dipping was followed by a rinse in deionized water to get rid of the unattached compounds from the previous stage. One BL film was built up by a BPEI and a kaol (or k*aol) single-layer. The other BL was deposited by a BPEI and a DTPMPA single-layer. When the organic inorganic hybrid coatings of 2 BL were achieved, the samples (E-K_5D_{30}) were dried at 60 °C for 24 h. The LBL self-assembly process was shown in Fig. 1b.

2.5. Preparation of the UV curing flame retardant coatings

The monomers (PUA, TAIC, PM-2) and photoinitiator (4 % HMPP) were mixed at room temperature to form a clear solution for preparing UV curing flame retardant coatings. This solution was further coated on the E-K_5D_{30} surfaces by using the 100 μm wire-gauged bar applicator. Then the samples were cured by the UV lamp (with a wavelength of 365 nm, HUV800, Shenzhen Huiwo technology Co., Ltd.) for 30 s. The formulations of obtained EPS samples are given in Table 1.

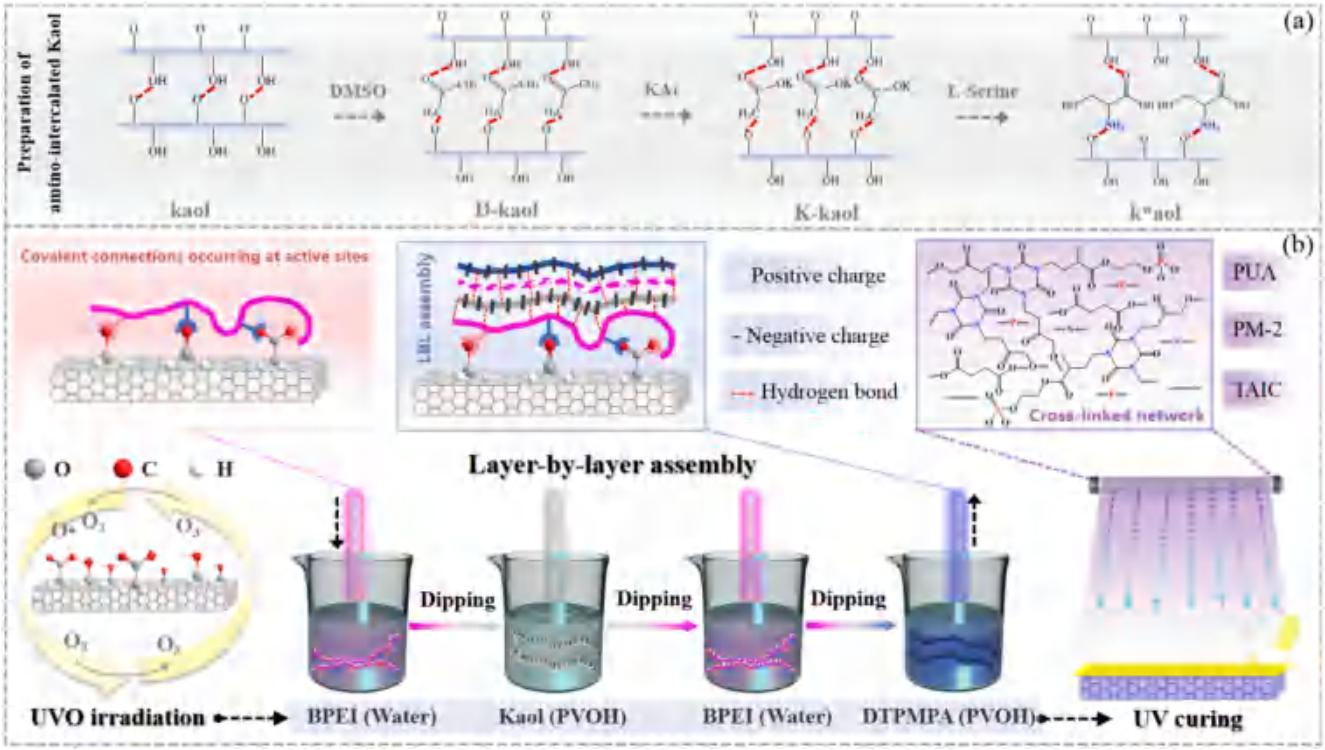

Fig. 1. The preparation process of k*aol (a) and EPS samples (b).

Table 1
The formulations of different EPS samples.

Sample	LBL assembly				UV curing		
	BPEI (%)	kaol [a] (%)	BPEI (%)	DTPMPA (%)	PUA (%)	PM-2 (%)	TAIC (%)
E-Neat	0	0	0	0	0	0	0
E-K_5D_{30}	1	5	1	30	0	0	0
E-K_5D_{30}-P_8N_3	1	5	1	30	10	80	10
E-$K^*_5D_{30}$-P_8N_3	1	5-k*aol	1	30	10	80	10

a: The obtained amino-intercalated kaol is marked as k*aol.

2.6. Measurements

The weight gain rate of samples (weight gain) after coating and the weight loss rate of samples (weight loss) after washing were calculated according to the following equation: Weight gain (or weight loss) = $|W-W_0|/W_0 \times 100$ %, that W_0 and W are the weight of the uncoated (before washing) and coated (after washing) samples.

The contact angles (CA) to water of neat and modified EPS samples were conducted by a Dataphysics-TP50 apparatus (Shanghai Zhongchen Digital Technic Co., Ltd.).

The characteristic spectra of EPS samples were recorded by Spectrum II Fourier Transform Infrared Spectroscopy (FTIR) spectrometer (Perkin Elmer Instruments Co., Ltd. USA) in the region of 4000 ~ 400 cm^{-1} using 32 scans.

The X-ray diffraction (XRD) was tested with the Bruker D8 apparatus (Bruker Instruments Co., Ltd. Germany). CuKα source was used with the λ of 0.154 nm at 40 kV and 20 mA.

The chemical structures of EPS samples were tested by ESCALAB 250 X-ray photoelectron spectroscopy (XPS) instrument (Thermo Fisher Scientific Co., Ltd. USA). The Al Ka X-rays was used and the pass energy was set of 12 kV and 15 mA.

The morphology of coatings and char residues were observed by Gemini 300 scanning electronic microscope (SEM) instrument (Shanghai Carl Zeiss Co., Ltd. China) under 20 kV. The content and distribution of elements were simultaneously analysed by an energy-dispersive spectrometer (EDS).

The thermogravimetric analysis (TGA) was measured in Q50 apparatus from TA Instruments Co., Ltd. The temperature was set from room temperature to 800 °C with the rate of 10 °C /min under N_2 atmosphere.

The Frontier spectrometer (TG-IR) tests were performed on the STA6000 thermogravimetric analyzer outfitted to collect the data of E-Neat and E-$K^*_5D_{30}$-P_8N_3 samples. The spectra were recorded in the frequency region of 4000 ~ 400 cm^{-1} with a resolution of 4 cm^{-1} under N_2 atmosphere. The temperature was set from 30 °C to 800 °C at a rate of 10 °C/min and with a volume flow rate of 50 mL/min.

According to ISO 4589–2, the LOI test was carried out for samples (130 × 10 × 10 mm^3) by using the JF-3 apparatus (Jiangning Nanjing Analytical Instrument Co., Ltd. China).

The vertical burning test (UL-94) were performed according with ASTM D 3801–2010 on a CFZ-3 apparatus (Jiangning Nanjing Analytical Instrument Co., Ltd. China). The dimensions of each sample were 130 × 13 × 10 mm^3.

The combustion test (CONE) in a cone calorimeter (Suzhou Yangyi Instrument Co., Ltd. China) was performed according to ISO 5660 method. The samples (100 × 100 × 10 mm^3) were tested three times under heat radiant flux density of 25 kW/m^2.

To investigate the flame retardant durability of coatings on EPS surfaces, the washing procedure for the coated samples were performed

at room temperature. The EPS samples were weighed and immersed in deionized water for 30 min or 12 h, and then dried under vacuum at 60 °C for 12 h. Finally, the weight of dried samples was measured to calculate the weight loss of coatings according to the above equation. In the washing procedure, five parallel experiments for each sample were performed, and results were averaged after removing the extreme values.

The bonding strength (BS) between EPS samples with surface coating and mortar was tested by a LBY-VI pull-off tensile testing instrument (Beijing Tianyu Technology, Co., Ltd.) according to GB/T 29906–2013. The dimension of EPS samples was 50 mm × 50 mm × 50 mm. First, the fresh mortar with 3 mm thickness was coated upon the surface of EPS samples. Then the obtained EPS/mortar composites were placed at 20 °C and 50 % relative humidity for 7 days. Following that, the EPS side was attached to a cement substrate (200 mm × 200 mm × 100 mm) while the mortar side was attached to a pull head plate (50 mm × 50 mm). After firm adhesion, the BS values collected by pull-off tests at rate of 5 mm/min. In order to evaluate the mechanical durability of samples, pull-off tests of EPS (after aging at 60 °C for 5 days)/mortar composites are further conducted according to GB/T 29906–2013. For the credibility of test results, each formulation was performed 6 times and the standard error was calculated accordingly. The BS values of EPS or aged EPS with mortar were given in the "Supporting Information".

Results and discussion

2.7. Chemical composition and morphology of EPS surface

The FTIR spectra of relevant EPS samples and CA results of E-Neat and E-UVO samples are displayed in Fig. 2. For the control EPS (E-Neat) sample, it mainly presents three peaks (1500 ~ 1240 cm^{-1} (C-H), 3000 ~ 2750 cm^{-1} (CH_2) and 1554 cm^{-1} (C=C)) [23,24]. Additional oxygen-contained groups are found in the FTIR spectrum of UVO-activated (E-UVO) sample, such as C=O (1800 ~ 1700 cm^{-1}) [25]. The appearance of oxygen-contained groups can improve the wettability of EPS surface (the CA value is reduced from 111.7° of E-Neat to 62.4°) and act as reactive groups to further react with BPEI solution. From the spectrum of E-BPEI sample, a new peak at 1593 cm^{-1} is represented by the C=N bond produced by the Schiff based reaction between $–NH_2$ in BPEI and C=O in activated EPS surface, and the peak at 1652 cm^{-1} is assigned to the –CO-NH- reacted from the $–NH_2$ and RO-C=O [26]. At the same time, the peaks ascribe to $–NH_2$ and C-N bonds in BPEI structure are found at 801 cm^{-1} and 1293 cm^{-1} respectively [27,28], verifying the first cationic layer (BPEI) is successfully attached to the EPS surface through chemical bonds during the LBL process.

On the surface of self-assembly E-K_5D_{30} sample, hydroxyl groups are found at 3371 cm^{-1} and 3363 cm^{-1}, corresponding to the crosslinking between PVOH in layers. The hydrogen bonds are stronger compared to the conventional electrostatic force in the self-assembly process. Meanwhile, some new P-contained peaks appear. The peaks of O=P-O appear at 2610 cm^{-1} and 2622 cm^{-1}, the peaks at 2253 cm^{-1} and 2291 cm^{-1} are attributed to P-H bonds, the peaks at 1050 cm^{-1} and 785 cm^{-1} corresponds to P-O-C, and the peak at 1152 cm^{-1} stands for P=O [29,30]. Above analyses preliminarily indicate the construction of E-K_5D_3 coating on the EPS surface. A UV curing coating with P/N flame retardant elements is constructed on the surface of E-K_5D_{30} sample, and the FTIR spectrum of the obtained E-K_5D_{30}-P_8N_3 sample is shown in Fig. 2. The peaks at 1635 cm^{-1} and 810 cm^{-1} (C=C) are not obvious. Instead, the apparent C=O peaks are found at 1730 cm^{-1}, which proves the effective cross-linking of the monomers after UV curing. Some additional groups are also discovered, such as C-N (1293 cm^{-1}), P=O (1152 cm^{-1}) and P-O-C (981 cm^{-1} and 750 cm^{-1}), suggesting the successful construction of P/N rich crosslinking network (E-K_5D_{30}-P_8N_3 sample) [27,29].

Element composition and chemical structure of different EPS samples are analyzed by XPS, and the corresponding results are exhibited in Fig. 3. In E-Neat, the fundamental C-C peaks are found at 284.2 eV and 285.0 eV. The peak at 291.0 eV represents the shake-up satellite [31,32]. For the E-UVO sample, the extra peaks at 286.3 eV (C-O), 287.7 eV (C=O) and 289.2 eV (RO-C=O) come from the activation of EPS after UVO irradiation [32,33]. Meanwhile, the peak intensity of O1s for E-UVO is higher than that of E-Neat (Fig. 3e). Above oxygen-contained groups can also be found in the O1s spectrum of E-UVO sample from Fig. 3f, while the O-C bonds (533.4 eV) are dominant. For the E-BPEI sample, a new peak at 285.7 eV (C=N) [34] is obtained by the reaction between C=O on E-UVO surface and amidogen in BPEI solution through Schiff based reaction. The peak intensity at 289.2 eV (RO-C=O) is lower and at 284.2 eV (C-C/C-N) is higher than those of E-UVO sample, which is due to the reaction of RO-C=O from activated EPS surface and $–NH_2$

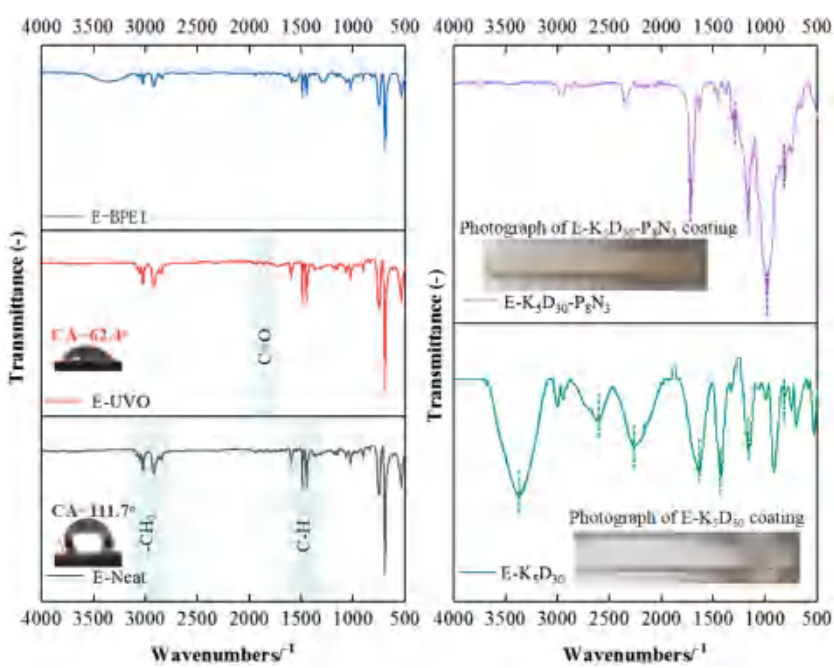

Fig. 2. FTIR spectra and their corresponding CA results of different EPS samples.

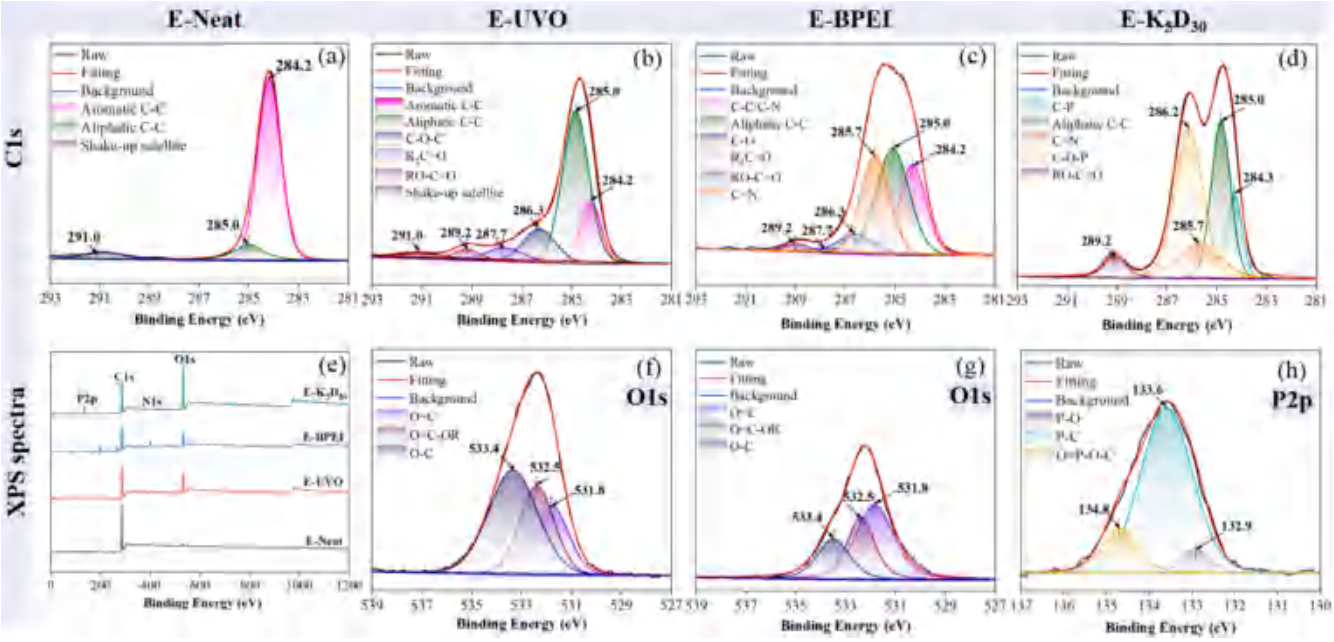

Fig. 3. The XPS spectra of C1s for E-Neat (a), E-UVO (b), E-BPEI (c) and E-K_5D_{30} sample (d), the XPS spectrum for different samples (e), the O1s spectra for E-UVO (f) and E-BPEI sample (g), and the P2p spectra for E-K_5D_{30} sample (h).

from BPEI solution with a new bond appearing (–CO-NH-) [35]. Correspondingly, the peaks intensity of oxygen-contained groups in O1s spectra of E-BPEI sample decreases in Fig. 3g. As a result, chemical bonding between the activated E-UVO surface and the cationic BPEI solution is successfully demonstrated.

In the C1s spectra of E-K_5D_{30} sample (Fig. 3d), some P-contained groups are found. The peaks of C-P and C-O-P locate at 284.3 eV and 286.2 eV, respectively [36,37]. Thus a cross-linked self-assembly coating with rich P element is successfully constructed.

The morphology of EPS samples is observed by SEM as shown in Fig. 4. E-Neat sample has a regularly cellular and porous structure. After the UVO irradiation, the surface of E-UVO sample still keeps regular structure without melting and deformation compared with that of E-Neat sample. Therefore, the effective activation can be realized without damaging the morphology of EPS surfaces by UVO irradiation. The surface morphology of E-K_5D_{30} samples is shown in Fig. 4c-d. The smooth and uniform coating with the thickness around 30 μm can be observed. The morphology of E-K_5D_{30}-P_8N_3 sample is shown in Fig. 4e-f. The surface is dense and smooth due to the high crosslinking degree after UV curing, and the thickness of E-K_5D_{30}-P_8N_3 coating is maintained at 100 μm. The compact surface of E-K_5D_{30}-P_8N_3 without any holes and tiny cracks can ensure the durability of the coating after washing procedure.

The above analysis has confirmed the successful preparation of E-K_5D_{30} and E-K_5D_{30}-P_8N_3 coatings with chemical connections between the activated EPS surface and cationic BPEI solution.

2.8. Flame retardancy and burning behavior of EPS samples

In order to analyze the burning behavior of neat EPS and modified EPS samples with their corresponding weight gain, LOI and UL-94 tests are carried out and the results (including weight growth) are given in Table 2. The digital images of samples during UL-94 tests are shown in Fig. 5.

According to the results, the LOI value of E-Neat is only 18.8 % and disabled to pass any ratings in UL-94 test with obvious molten dripping phenomenon during burning, presenting severe fire hazards. The LOI value of E-K_5D_{30} sample increases to 37.7 % with the LBL self-assembly coating. After the first and second ignition, the sample achieves self-extinguish rapidly and passes V-0 grade in UL-94 test, indicating a

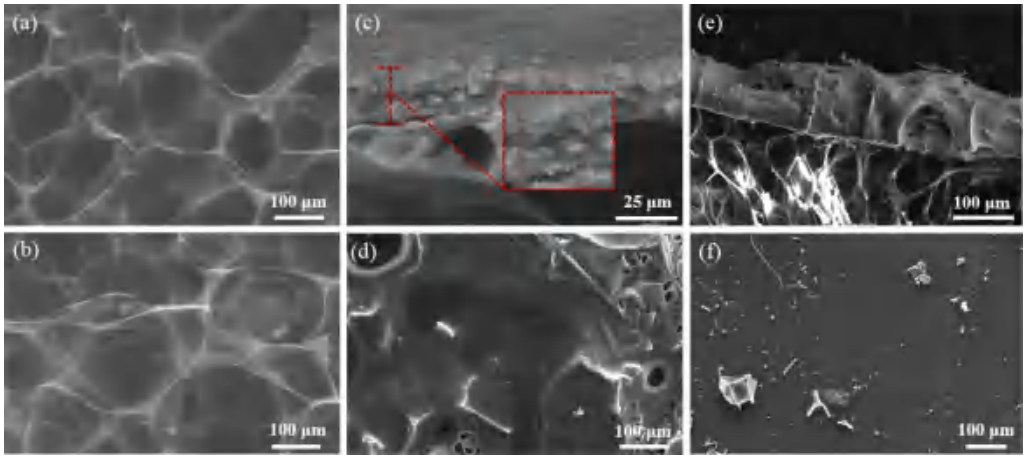

Fig. 4. SEM images of E-Neat (a) and E-UVO sample (b), sectional morphology and SEM images of E-K_5D_{30} (c, d) and E-K_5D_{30}-P_8N_3 sample (e, f).

Table 2
The weight gain, LOI and UL-94 results for EPS samples.

Samples	Weight gain (%)	LOI (%)	UL-94			
			t_1/t_2 (s)	Dripping [a]	Ignition of cotton	Rating
E-Neat	0	18.8 ± 0.5	Burn out	Yes	Yes	NR [b]
E-K_5D_{30}	218.6 ± 3.7	37.7 ± 0.4	0.1/ 0.1	No	No	V-0
E-K_5D_{30}-P_8N_3	360.6 ± 3.0	39.1 ± 0.6	0.1/ 0.1	No	No	V-0
E-K*$_5D_{30}$-P_8N_3	383.5 ± 5.6	39.2 ± 0.4	0.1/ 0.1	No	No	V-0

a: The results were obtained by averaging five parallel tests.
b: NR means the sample that has no grades in UL-94 test.

clear flame retardant effect. The introduction of UV curing coating with P/N elements (E-K_5D_{30}-P_8N_3 sample) further increases the LOI value to 39.1 %. Although there is no significant increase in the LOI value of E-K*$_5D_{30}$-P_8N_3 sample with the use of k*aol, both E-K_5D_{30}-P_8N_3 and E-K*$_5D_{30}$-P_8N_3 samples are immediately extinguished once the ignitor is removed. Meanwhile, good flame retardancy of samples is ensured by the adequate attachment of coatings. According to the weight gain results in Table 2, the weight gain rate of E-K_5D_{30} sample with LBL coating is 218.6 %, and it is further increased to 360.6 % and 383.5 % of E-K_5D_{30}-P_8N_3 and E-K*$_5D_{30}$-P_8N_3 samples with the UV curing coating. Sufficient P/N elements are introduced into the crosslinking network to provide better flame retardancy.

To investigate the effects of flame retardant coatings on the combustion behavior and smoke release of EPS samples, CONE tests are conducted as given in Fig. 6 and Table 3.

When exposed to heat radiation, neat EPS sample deforms rapidly and then burns with the TTI of 59 s. The pHRR and THR values of E-Neat are 282.0 kW/m^2 and 7.7 MJ/m^2, respectively. With the presence of K_5D_{30} coating, the TTI is significantly delayed to 95 s and the pHRR value is decreased to 220.9 kW/m^2. The rapid formation of char layer through carbonization of flame retardants in LBL coating delays the ignition time and prevents the combustion of EPS matrix. In practical application, the fire safety of EPS foam is assessed by the fire performance index (FPI) which represents as the ratio of TTI and pHRR. Higher FPI value of EPS samples can be achieved by the increase of TTI and reduction of pHRR values. While the extension of TTI improves the escape time in the actual fire. The FPI value of E-K_5D_{30} sample is 0.430 m^2·s/kW while that of control EPS is only 0.209 m^2·s/kW, suggesting good fire safety performance of K_5D_{30} coating. However, the THR value of the E-K_5D_{30} sample is slightly increased to 8.5 MJ/m^2 compared with that of E-Neat sample, which is owing to the initial decomposition of DTPMPA and PVOH. After the CONE test, the E-K_5D_{30} sample shows a char residue of 32.3 % as shown in Fig. 6f. With the construction of UV curing coating, the pHRR value of E-K_5D_{30}-P_8N_3 sample is further restricted to 183.7 kW/m^2, and the TTI value is further delayed to 106 s. The introduction of P and N rich monomers in UV curable layers is beneficial to the char formation during combustion. The prolonged TTI value of EPS sample demonstrates a longer escape time in the actual fire. The THR value of E-K_5D_{30}-P_8N_3 sample (10.0 MJ/m^2) is higher than that of control EPS (7.7 MJ/m^2) and E-K_5D_{30} sample (8.5 MJ/m^2), which is attributed to the combustion of ester groups in the curing coating. The char yield of E-K_5D_{30}-P_8N_3 sample is slightly increased to 37.3 %, with the higher FPI value of 0.577 m^2·s/kW. The above results prove the UV curing coating contained P/N elements effectively prevents the spread of flame/heat and further improves the fire safety performance of EPS. With the using of k*aol, the pHRR value of E-K*$_5D_{30}$-P_8N_3 sample is reduced to 150.3 kW/m^2. Although the TTI value of E-K*$_5D_{30}$-P_8N_3 sample is not delayed (96 s), the FPI value (0.639 m^2·s/kW) is the highest among all samples.

Except for TTI and heat release, the smoke release is also a crucial

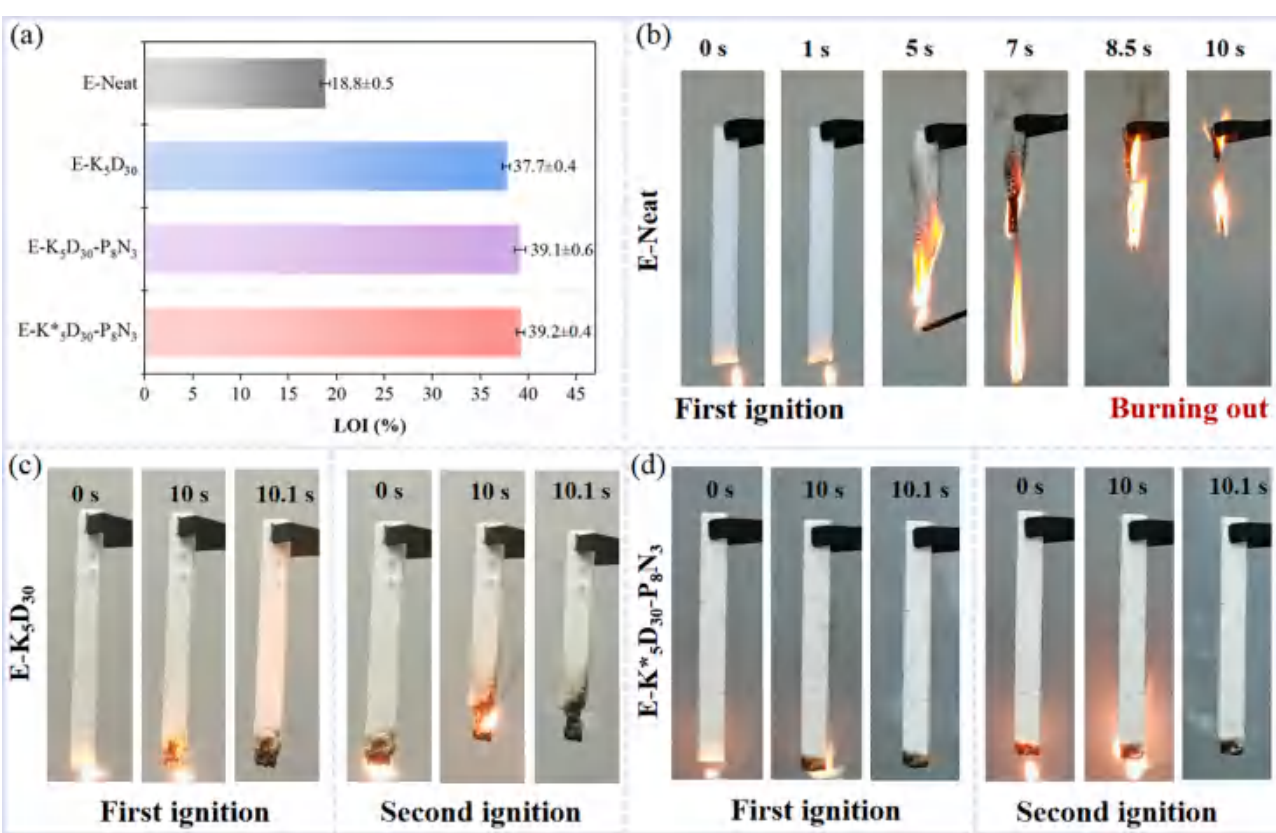

Fig. 5. The results of LOI values (a) and UL-94 test (b-d) of EPS samples.

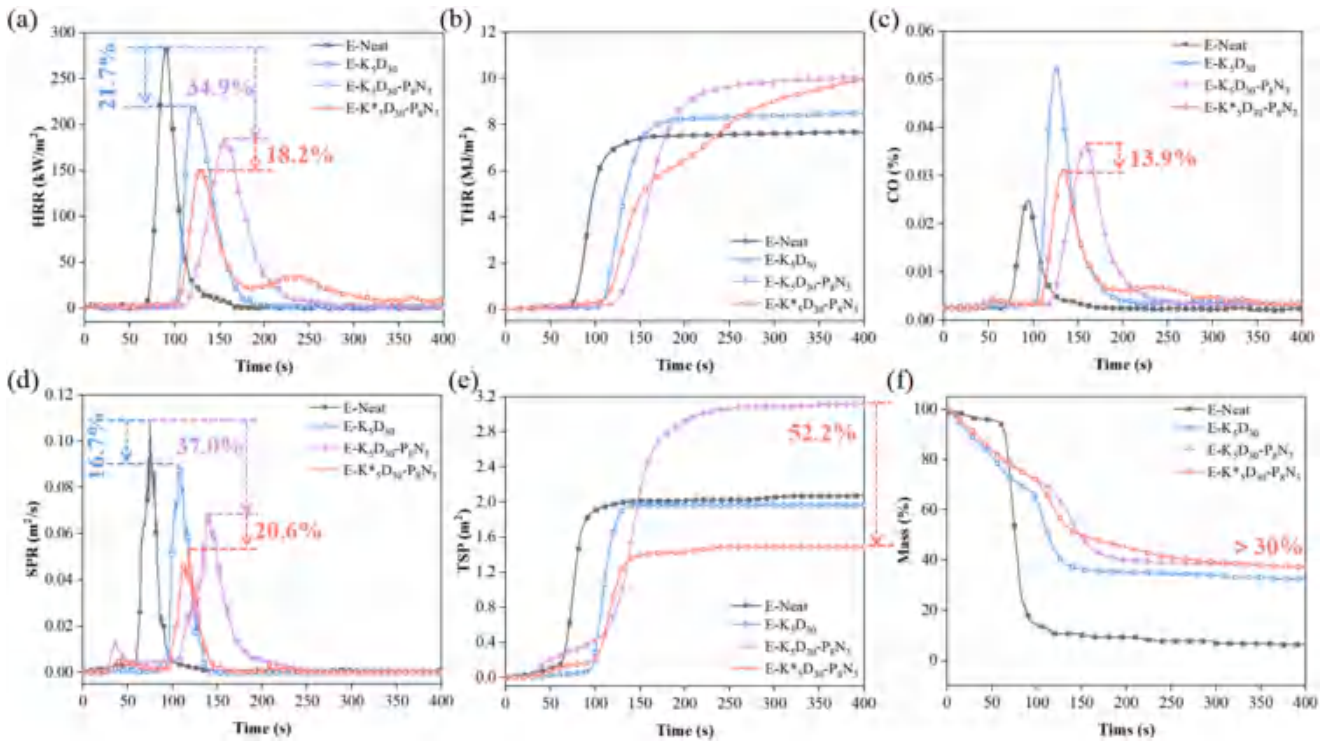

Fig. 6. The CONE test data of EPS samples.

Table 3
Some key results of CONE test for EPS samples.

Sample	Weight gain (%)	TTI (s)	pHRR (kW/m^2)	THR (MJ/m^2)	pSPR (m^2/s)	TSP (m^2)	pCO (%)	Char (%)	FPI (m^2·s/kW)
E-Neat	0	59 ± 3	282.0 ± 14	7.7 ± 3	0.108 ± 0.002	2.08 ± 0.8	0.025 ± 0.003	6.3 ± 0.9	0.209
E-K$_5$D$_{30}$	271.0 ± 5	95 ± 5	220.9 ± 12 (↓ 21.7) [a]	8.5 ± 3	0.090 ± 0.002 (↓ 16.7) [a]	1.96 ± 0.5	0.052 ± 0.005	32.3 ± 1.5	0.430
E-K$_5$D$_{30}$-P$_8$N$_3$	422.4 ± 3	106 ± 5	183.7 ± 9 (↓ 34.9) [a]	10.0 ± 4	0.068 ± 0.004 (↓ 37.0) [a]	3.12 ± 0.4	0.036 ± 0.002	37.3 ± 1.0	0.577
E-K*$_5$D$_{30}$-P$_8$N$_3$	434.5 ± 3	96 ± 2	150.3 ± 13 (↓ 18.2) [b]	10.0 ± 2	0.054 ± 0.002 (↓ 20.6) [b]	1.49 ± 0.4 (↓ 52.2) [b]	0.031 ± 0.004 (↓ 13.9) [b]	37.2 ± 1.3	0.639

a: The reduction rate compared to the E-Neat sample.
b: The reduction rate compared to the E-K$_5$D$_{30}$-P$_8$N$_3$ sample.

index to estimate the flame retardancy of EPS. During CONE, control EPS burns sufficiently and releases less smoke (total smoke production (TSP) = 2.08 m^2) or CO (CO production (pCO) = 0.025 %), as exhibited in Fig. 6c-e. As for E-K$_5$D$_{30}$ sample, the TSP value is decreased to 1.96 m^2 by 5.8 % due to the formation of the crosslinked char layer. As for E-K$_5$D$_{30}$-P$_8$N$_3$ sample, the TSP value is increased to 3.12 m^2. This is due to the insufficient combustion of underlying substrates caused by the barrier effect to oxygen of char layers. Consequently, the production of CO for E-K$_5$D$_{30}$-P$_8$N$_3$ sample is also increased to 0.036 %. The insufficient combustion phenomenon brought by flame retardant coatings is the representation of good char-forming ability [38]. Then, the high-quality char layer formed act as a barrier to prevent the transmission of heat and O$_2$, reducing the pSPR values of E-K$_5$D$_{30}$ and E-K$_5$D$_{30}$-P$_8$N$_3$ samples from 0.108 m^2/s of E-Neat to 0.090 m^2/s and 0.068 m^2/s, respectively.

By contrast, k*aol effectively inhibits the smoke and CO release. The pSPR and TSP values of E-K*$_5$D$_{30}$-P$_8$N$_3$ are 20.6 % and 52.2 % lower than those of E-K$_5$D$_{30}$-P$_8$N$_3$. The value of pCO is further reduced from 0.036 % (E-K$_5$D$_{30}$-P$_8$N$_3$ sample) to 0.031 %. The k*aol with higher layer spacing and specific surface area has better dispersion behavior in coatings and leads to easy exposure of surface groups, contributing to more efficient crosslinking with other degradation products. The char forming process is strengthened, thus playing the physical barrier and smoke suppression effects [17,20]. Moreover, the amino groups inserted into the layer of k*aol also produce non-combustion gases (NH$_3$/H$_2$O), improving the flame retardancy of samples by diluting the fuel in the gas phase.

In summary, the above analysis shows that E-K$_5$D$_{30}$ and E-K$_5$D$_{30}$-P$_8$N$_3$ both have the obvious flame retardant functions which reduce the heat release and increase char yield. Although the insufficient combustion of substrates leads to an increase in the smoke release, the addition of modified kaol effectively reduces the smoke production. The E-K*$_5$D$_{30}$-P$_8$N$_3$ sample plays the more comprehensive flame retardant effects and maximizes the fire safety of EPS foam.

2.9. Thermal stability analysis

The TGA and derivative thermogravimetry (DTG) results under N$_2$ atmosphere of EPS samples are shown in Fig. 7, and some key data are summarized in Table 4.

The pyrolysis of E-Neat sample mainly marches in the range of 400 to 500 °C with a low char residue of 0.8 %, presenting the obvious one-step thermal degradation. The temperature of 5 % weight loss (T$_{5\%}$) of E-Neat sample is 378.4 °C and the temperature of maximal weight loss rate

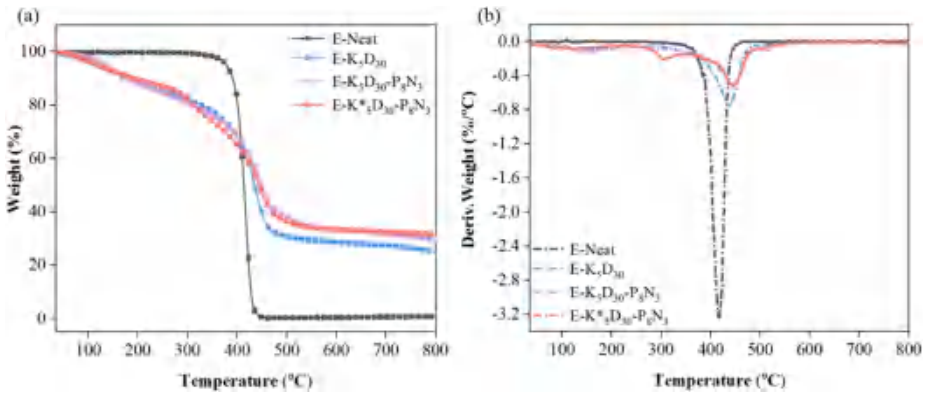

Fig. 7. TGA (a) and DTG (b) results of EPS samples.

Table 4
TGA data of EPS samples under N_2 atmosphere.

Samples	$T_{5\%}$ (°C)	T_{max} (°C)	Residues at 800 °C (%)
E-Neat	378.4	417.3	0.8
E-K_5D_{30}	121.5	437.1	25.1
E-K_5D_{30}-P_8N_3	134.5	444.5	29.5
E-$K^*_5D_{30}$-P_8N_3	118.9	446.8	31.7

(T_{max}) is 417.3 °C. By the presence of surface coatings, the degradations of E-K_5D_{30}, E-K_5D_{30}-P_8N_3 and E-$K^*_5D_{30}$-P_8N_3 samples show three regions which represent the early pyrolysis of coatings, thermal degradation of EPS matrix and dehydration decomposition of kaol/k*aol, respectively. The $T_{5\%}$ value of E-K_5D_{30} is decreased to 121.5 °C, which is ascribed to the dehydration of PVOH and phosphate groups in LBL coating. The decomposition of LBL coating in front of EPS matrix produces H_2O as discussed in the section 3.6. Meanwhile, the crosslinking of pyrolysis products promotes the formation of dense char layer that acts as the physical barrier to delay the T_{max} value to 437.1 °C and increase the residues of 25.1 %. For E-K_5D_{30}-P_8N_3 sample, the $T_{5\%}$ value is further advanced to 134.5 °C, while the T_{max} value is delayed to 444.5 °C with a higher residue of 29.5 %. The above results indicate that the UV curing coating contained P/N elements delays the degradation of EPS matrix, and the existence of phosphate groups in the crosslinking network further promotes the formation of char layer, improving the thermal stability of EPS foam. Moreover, the degradation tends of E-$K^*_5D_{30}$-P_8N_3 and E-K_5D_{30}-P_8N_3 samples are basically consistent, with only a slight delay at the last thermal degradation region for E-$K^*_5D_{30}$-P_8N_3 (the thermal degradation peak at 305 °C is caused by the influence of water). This proves that the modified kaol with higher specific surface area presents better thermal stability.

In general, the thermal stability of EPS foam and char yields are enhanced by the addition of self-assembly and UV curing coatings.

2.10. Flame retardant durability analysis

For the flame retardant coatings applied on EPS foam, the durability is also critical to meet humidity environments in using process. In

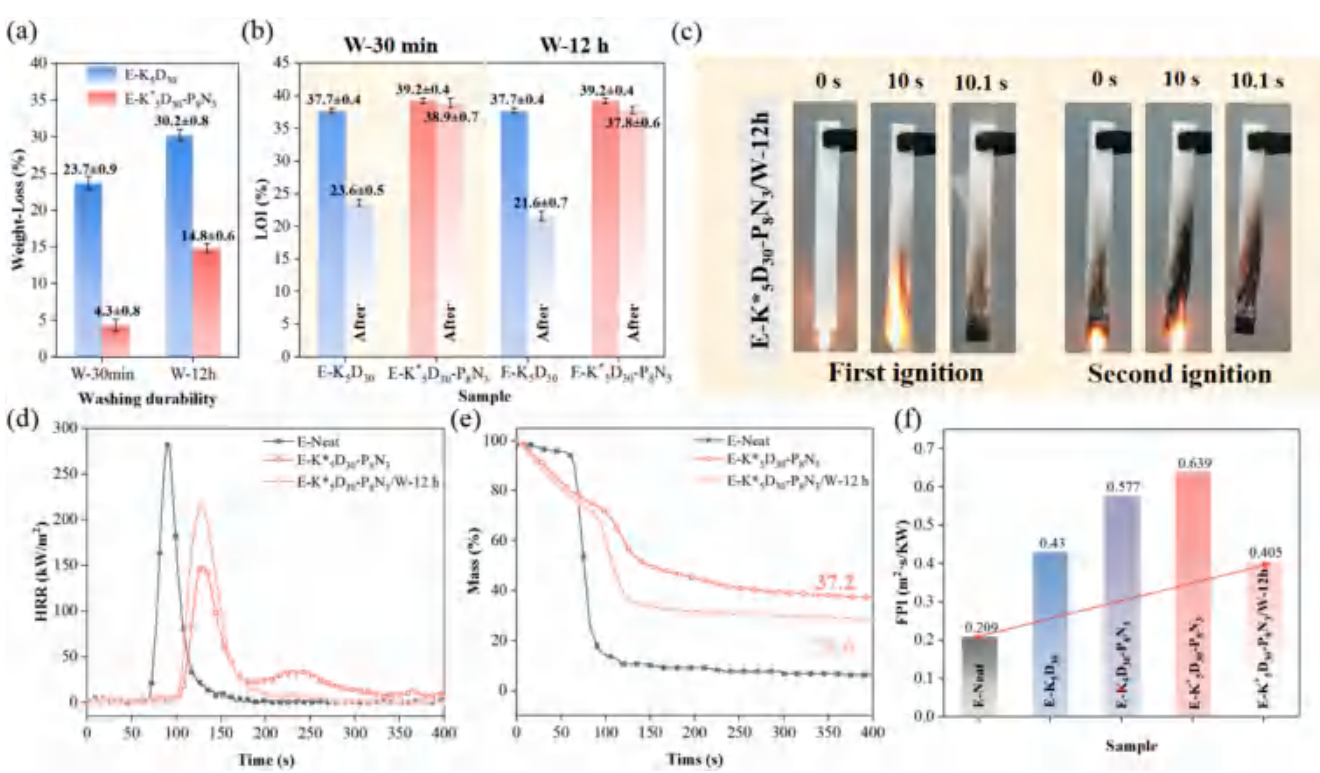

Fig. 8. Weight-loss (a), LOI (b), vertical burning test results (c) and CONE test data (d-f) of EPS samples after washing.

traditional LBL self-assembly method relied on electrostatic power, the combinations between layers are weak, resulting in poor flame retardant durability of coatings. To compare the flame retardant durability of self-assembled and UV curing coatings, E-K_5D_{30} and E-$K^*_5D_{30}$-P_8N_3 samples are soaked in water for 30 min and 12 h respectively. The weight loss and the damage of flame retardant performance for coatings are analyzed, and the corresponding results are given in Fig. 8 and Table 5.

After 30 min washing, the weight loss of E-K_5D_{30} and E-$K^*_5D_{30}$-P_8N_3 samples are 23.7 % and 4.3 %. With the increase of washing duration (12 h), the weight loss of the two samples is further increased to 30.2 % and 14.8 %, which is mainly due to the loss of hydrophilic flame retardants in the coatings. Noteworthy, E-$K^*_5D_{30}$-P_8N_3 sample shows the better resistance to water, maintaining the lower weight loss and adhering most of the flame retardants firmly. This is mainly due to the blocking effect of the dense crosslinking network produced by UV curing that fixes the hydrophilic phosphate groups in the coatings. E-K_5D_{30} and E-$K^*_5D_{30}$-P_8N_3 samples also show tremendous differences in flame retardancy after washing. With 30 min washing, the LOI value of E-K_5D_{30} sample decreases from 37.7 % to 23.6 %, and only reduces from 39.2 % to 38.9 % for E-$K^*_5D_{30}$-P_8N_3 sample. After 12 h washing, the LOI values of E-K_5D_{30} and E-$K^*_5D_{30}$-P_8N_3 samples are further decreased to 21.6 % and 37.8 % respectively, indicating the much lower decrease of LOI for E-$K^*_5D_{30}$-P_8N_3 sample than that for E-K_5D_{30} sample. Moreover, E-$K^*_5D_{30}$-P_8N_3 sample can still self-extinguish and pass V-0 rate during UL-94 test even after the 12 h washing as shown in Fig. 8c. It is therefore can be concluded that UV curing method in our work significantly improved the flame retardant durability.

To further confirm the flame retardant durability of E-$K^*_5D_{30}$-P_8N_3 sample, CONE tests are carried out on the E-Neat, E-$K^*_5D_{30}$-P_8N_3 and E-$K^*_5D_{30}$-P_8N_3/W-12 h samples as shown in Fig. 8d-f. The key data are given in Table 6. The results show that the THR value of E-$K^*_5D_{30}$-P_8N_3/W-12 h sample with 12 h washing is decreased from 10.0 MJ/m^2 (before washing) to 9.3 MJ/m^2, which is primarily because the loss of combustion ester groups in UV curing coating. However, due to the damage of coating and the loss of flame retardants after washing, the flame retardant performance of E-$K^*_5D_{30}$-P_8N_3/W-12 h are disabled to some extent. As shown in Fig. 8d-e, the pHRR of E-$K^*_5D_{30}$-P_8N_3/W-12 h sample has been increased from 150.3 kW/m^2 to 217.1 kW/m^2 compared with the sample before washing, the amount of char residue has been reduced to 28.6 % (but the pHRR value is still lower than control EPS, and a high char yield is maintained). Although the flame retardancy of E-$K^*_5D_{30}$-P_8N_3/W-12 h is reduced to a certain extent, the FPI value remains at 0.405 m^2·s/kW, which is higher than that of E-Neat sample. It demonstrates that the flame retardant E-$K^*_5D_{30}$-P_8N_3 sample maintains high fire safety even under the washing for a long time.

Moreover, a comprehensive comparison on the fire safety performance and flame retardant durability of LBL coating with E-$K^*_5D_{30}$-P_8N_3 sample in our work has been made as shown in Fig. 9 [39–46,6,14]. The results of Fig. 9 and above analysis both show that the E-$K^*_5D_{30}$-P_8N_3 sample (with higher LOI and less layer numbers of the coating) prepared by LBL self-assembly achieves better flame retardancy and maintains the good flame retardancy durability thanks to the external UV curing layer.

Table 5
The weight loss and reduction in LOI for E-K_5D_{30} and E-$K^*_5D_{30}$-P_8N_3 samples after 30 min and 12 h washing.

Sample	30 min washing		12 h washing	
	Weight loss (%)	Reduction in LOI (%)	Weight loss (%)	Reduction in LOI (%)
E-K_5D_{30}	23.7 ± 0.9	37.4	30.2 ± 0.8	42.7
E-$K^*_5D_{30}$-P_8N_3	4.3 ± 0.8	0.8	14.8 ± 0.6	3.6

Table 6
Some key results of CONE test for E-$K^*_5D_{30}$-P_8N_3 sample after 12 h washing.

Sample	TTI (s)	pHRR (kW/m^2)	THR (MJ/m^2)	pSPR (m^2/s)	Char (%)	FPI (m^2·s/kW)
E-Neat	59 ± 3	282.0 ± 14	7.7 ± 3	0.108 ± 0.002	6.3 ± 0.9	0.209
E-$K^*_5D_{30}$-P_8N_3	96 ± 2	150.3 ± 13	10.0 ± 2	0.054 ± 0.002	37.2 ± 1.3	0.639
E-$K^*_5D_{30}$-P_8N_3/W-12h	88 ± 2	217.1 ± 12	9.3 ± 3	0.103 ± 0.004	28.6 ± 2	0.405

2.11. Char residual analysis

The outer and inner char residues for E-K_5D_{30}, E-K_5D_{30}-P_8N_3 and E-$K^*_5D_{30}$-P_8N_3 samples are observed by SEM images, EDS results and EDS-mapping images as shown in Fig. 10.

As exhibited in Fig. 10, the outer and inner residues of E-K_5D_{30} are relatively continuous with some small voids. In terms of the existence of UV curing network, the outer and inner char layers of E-K_5D_{30}-P_8N_3 and E-$K^*_5D_{30}$-P_8N_3 samples are roughly the same, which are dense with fewer visible voids. The protective barrier is essential for suppressing smoke and reducing heat release. Meanwhile, EDS-mapping of E-$K^*_5D_{30}$-P_8N_3 demonstrates that C, N, O, P and Si elements are consisted in char layers as shown in Fig. 10.

Besides, the element composition and content of outer and inner char residues for E-K_5D_{30}, E-K_5D_{30}-P_8N_3 and E-$K^*_5D_{30}$-P_8N_3 are recorded by EDS as shown in Fig. 10. One can see that C element has a clear advantage in the external char residues, while the P/N contents in inner char is higher compared with that in the outer char layer. It indicates that more char is kept in the outer condensed phase to improve the density of char layer, and the more P/N and kaol in the inner condensed phase can enhance the quality of char layer and reduce the heat release and flame spread [47]. For E-$K^*_5D_{30}$-P_8N_3 sample, most C (32.2 %) and P (24.5 %) elements appear in the outer and inner char residues. This shows that the presence of UV curing network and modified kaol further improve the quality of char layers and fix more flame retardant elements in the internal char layers.

In order to analyses the chemical structures of the external and internal char residues for EPS samples, the XPS of the char are conducted as shown in Fig. 11.

In Fig. 11, the external and internal char residues of E-K_5D_{30}, E-K_5D_{30}-P_8N_3 and E-$K^*_5D_{30}$-P_8N_3 samples after CONE tests have the same chemical bonds. The peaks in C1s spectra at 284.3 eV, 284.8 eV, 286.1 eV, 287.2 eV and 288.8 eV belong to C-P, C-C/C-N, C-O/C-O-P, C-O-C and C=O bonds, respectively [48,49]. Correspondingly, the bonds of P-C, P-O and O=P-O-C are found in the P2p spectra at 133.6 eV, 134.2 eV and 134.8 eV, respectively [50–53]. The formation of C-O-P bonds is caused by the dehydration and carbonization of PVOH and UV curing network which are promoted by phosphorus-contained acids released from DTPMPA and PM-2 during burning. The appearance of P-O is due to the dehydration of P-OH groups in the pyrolysis products [54]. Moreover, the appearance of C-N bond indicates that N elements also participate in char formation.

For E-K_5D_{30} sample, the peak intensity of C-C (43.0 %) in the external char and C-P (50.5 %) in the internal char is higher than those of other peaks, indicating that the presence of flame retardants in the self-assembly coating react with PVOH to form cross-linked network, which is helpful to promote the formation of char layers and maintain more flame retardant elements (such as P) in the condensed phase.

Meanwhile, most C-C/C-N bonds (59.2 %) are found for the outer char residues in the E-$K^*_5D_{30}$-P_8N_3 compared with those in other samples. More content of C-C confirms the existence of aromatic char layers, which owns a stable structure and a higher quality. Moreover, the internal char residue (in Fig. 11) of E-$K^*_5D_{30}$-P_8N_3 has higher peak

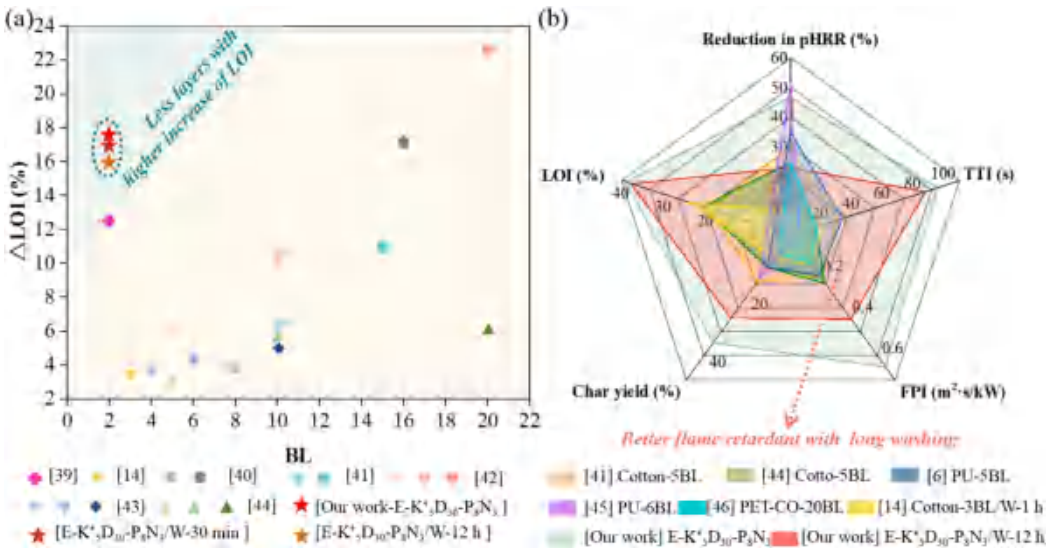

Fig. 9. The comparison of our work with the published flame retardant samples in LOI values (a) and fire safety performance (b).

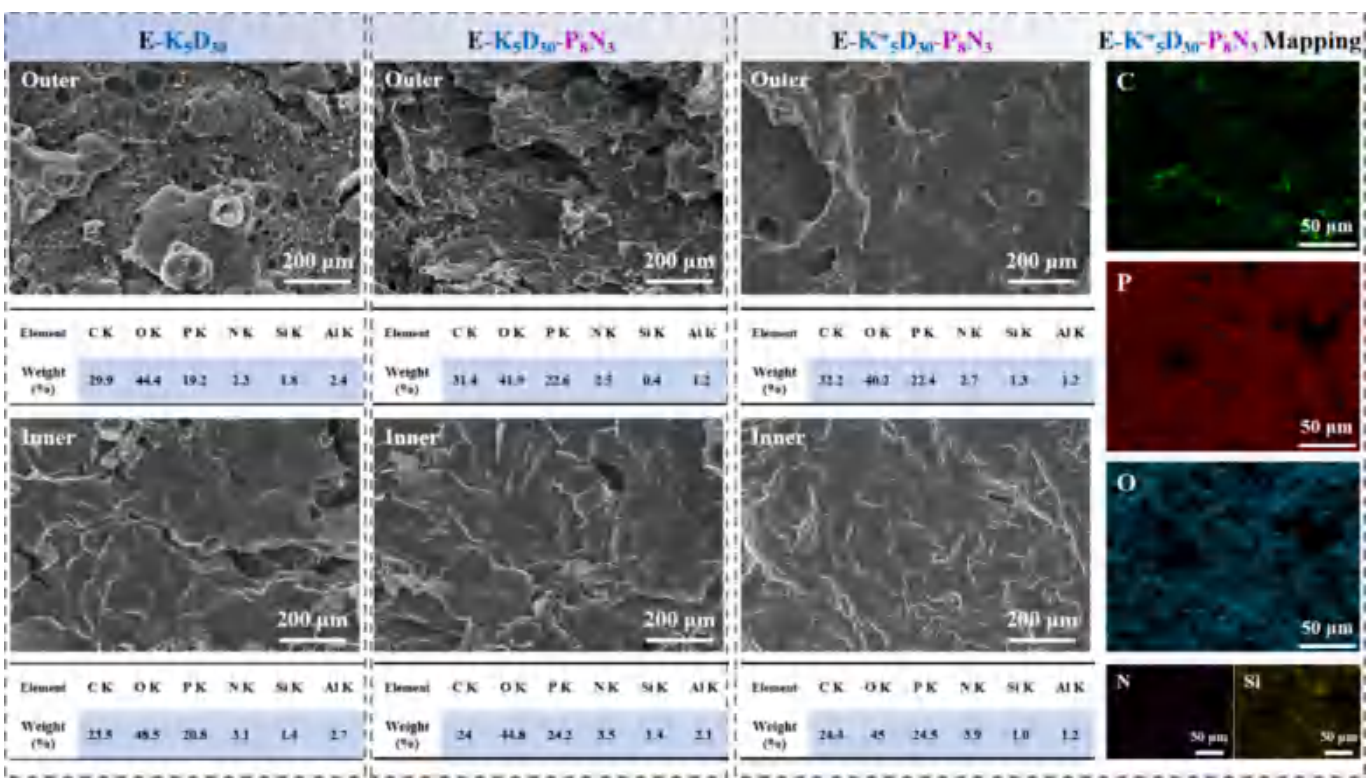

Fig. 10. The SEM images of the outer/inner char residues and EDS results of EPS samples, and EDS-mapping of char residues of E-K*$_5$D$_{30}$-P$_8$N$_3$ after CONE tests.

intensity of P-C and O=P-O-C in comparison with those of E-K$_5$D$_{30}$ sample. The increased amount of P-O-C suggests that the P/N rich UV curable network can promote the production of char layers rather than the mere dehydration and condensation between acid sources.

2.12. Flame retardant mechanism analysis

The TG-IR test is performed to analyze the gaseous pyrolysis products from E-Neat and E-K*$_5$D$_{30}$-P$_8$N$_3$ samples, and the results are shown in Fig. 12. For the E-Neat in Fig. 12a, the peaks at 3000 ~ 2800 cm^{-1}/670 cm^{-1} (C-H), 2361 cm^{-1}/1263 cm^{-1} (CO_2), 1753 cm^{-1} (C=O compounds) and 1088 cm^{-1} (C-O-C) represent the main gaseous products [55–57]. Moreover, the peak intensities of flammable volatiles (C-H, C=O, and C-O-C compounds) for E-K*$_5$D$_{30}$-P$_8$N$_3$ are much lower than those of E-Neat. It indicates that the E-K*$_5$D$_{30}$-P$_8$N$_3$ tends to form dense char layer which reduces the generation of flammable volatiles. Besides, the TG-TR results of E-K*$_5$D$_{30}$-P$_8$N$_3$ show a new peak for N-H at 967 cm^{-1}. And a new peak at 4000 ~ 3500 cm^{-1} represented H_2O appears in the early combustion. The above analysis indicates that the gaseous pyrolysis products of E-K*$_5$D$_{30}$-P$_8$N$_3$ dilute combustible gases by the release of ammonia and H_2O. However, no P signal is detected in the gas phase, suggesting that the phosphate contained groups mainly act in the condensed phase.

Based on the above analyses, the flame retardant mechanism of E-

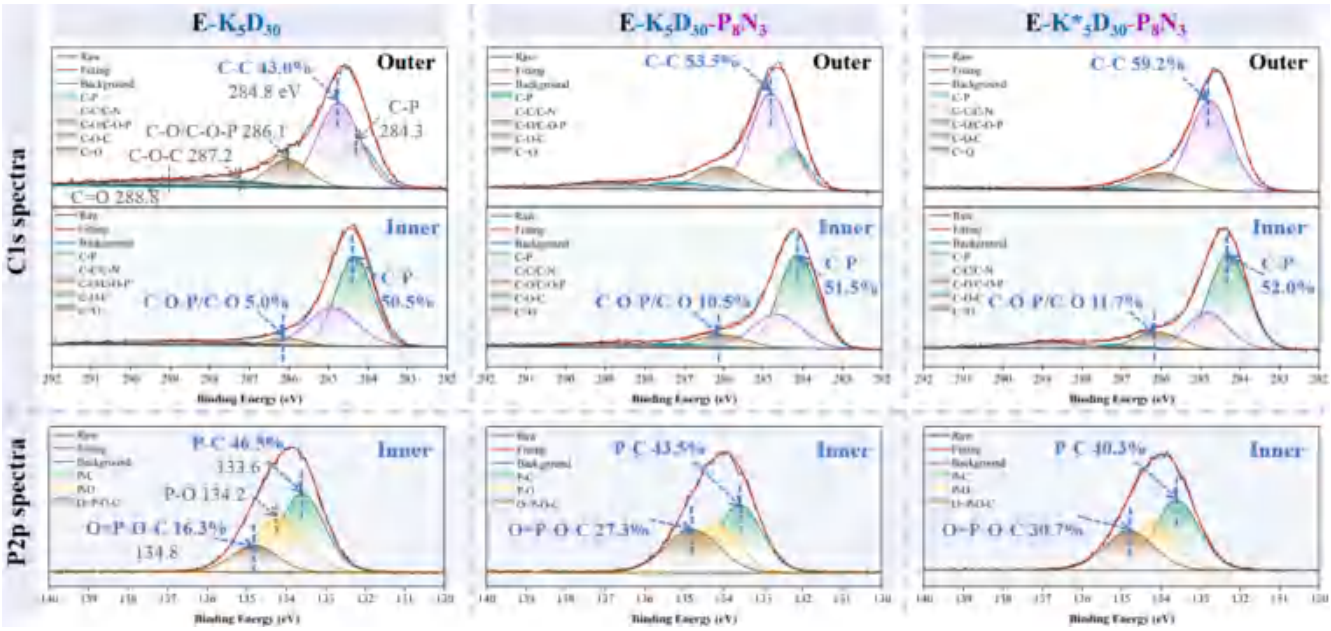

Fig. 11. The XPS spectra of outer/inner char residues of surface coated EPS samples.

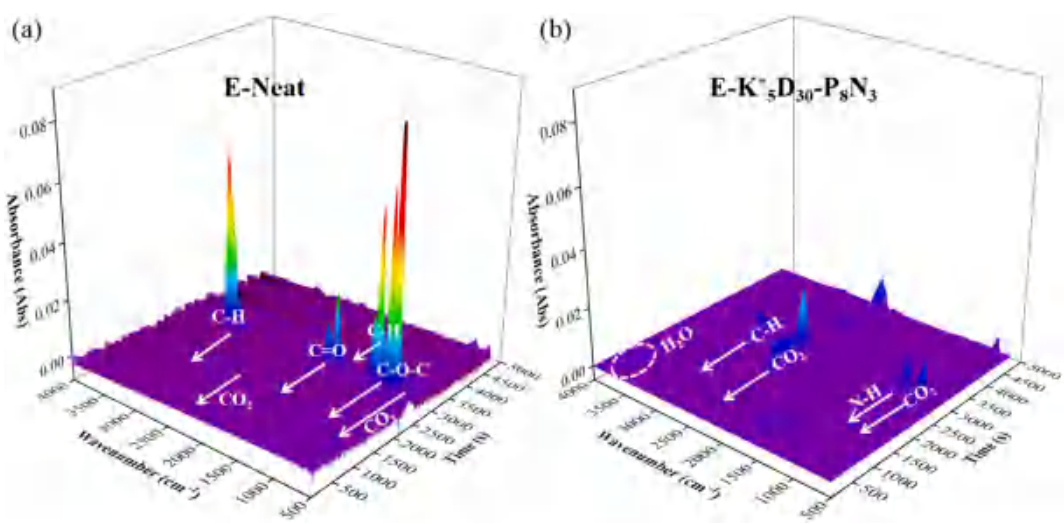

Fig. 12. The 3D TG-IR images of E-Neat (a) and E-K*$_5$D$_{30}$-P$_8$N$_3$ (b).

K$_5$D$_{30}$ and E-K*$_5$D$_{30}$-P$_8$N$_3$ samples are proposed, as illustrated in Fig. 13.

After heating, PVOH and DTPMPA in E-K$_5$D$_{30}$ coating decompose in front of EPS matrix, with the appearance of polyhydroxy groups and pyrolytic products (phosphate/pyrophosphate). The dehydration and crosslinking reactions are catalyzed by the pyrolytic products to generate the crosslinked bonds (such as C-C, C-O-P and C-O) with the formation of dense char layer [48,49]. The high-quality char layer with crosslinking networks inhibits the spread of heat/O$_2$ to EPS matrix. At the same time, the lamellar kaol distributed in the self-assembly coating are evenly attached to the surface of the char layer. This special organic–inorganic hybrid coating can well prevent gas transferring and protect the EPS substrate [58].

For E-K$_5$D$_{30}$-P$_8$N$_3$ sample with UV curing coating, the pyrolysis reactions of the coating occur and the pyrolysis products (hypophosphate ester or phosphate derivatives) appear at the initial combustion. The degradation products catalyze the dehydrated and carbonized process to promote the formation of thermally stable aromatic char [59]. The protective char layer with highly cross-linked suppresses the transmission of heat and O$_2$. In addition, the k*aol with amino groups produces some non-combustible gases (NH$_3$ and H$_2$O) during burning process, reducing the concentration of O$_2$ and combustible gas [17,21]. At the same time, the k*aol with higher specific surface area strengthens the oxidation-crosslinking-carbonization process, dispersing evenly in the dense char layer and adsorbing harmful gases [47,48]. Therefore, the UV curing coating with durability plays the flame retardant role both in the condensed and the gas phase.

3. Conclusions

In our work, two types of organic–inorganic hybrid coatings with the addition of amino-intercalated k*aol were created by LBL self-assembly (only with 2BL) and UV curing methods to improve the flame retardant and its durability of EPS foam. The EPS surface was first activated by UVO irradiation to build the covalent connections between the self-assembly coating and EPS matrix. The obtained E-K$_5$D$_{30}$ sample showed the LOI value of 37.7 %, and the pHRR and pSPR values of

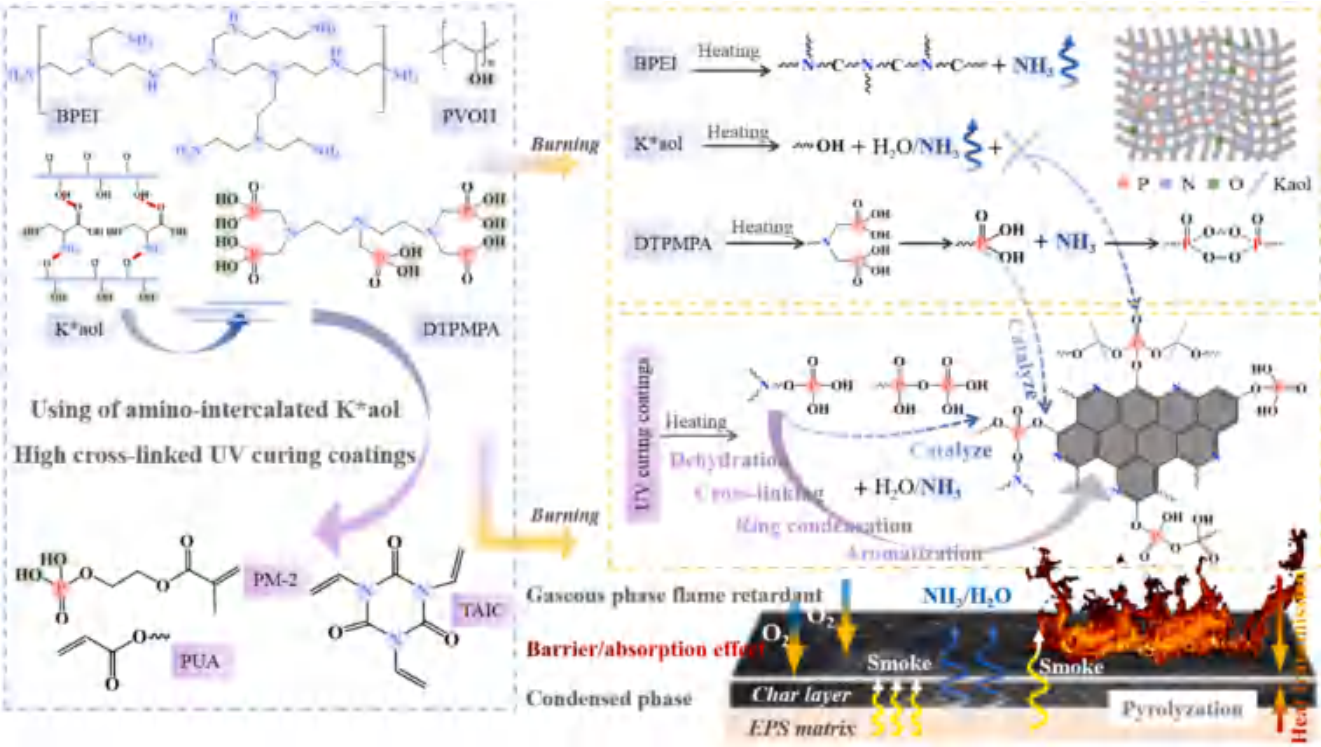

Fig. 13. Proposed flame retardant mechanism of EPS samples containing self-assembly and UV curing coatings.

220.9 kW/m^2 and 0.090 m^2/s (a reduction of 21.7 % and 16.8 % compared with those of control EPS).

The UV curing coating with high crosslinking network fixed more P/N elements in the coating to develop better flame retardant performance. The E-K_5D_{30}-P_8N_3 sample owned higher LOI value of 39.1 %, and was able to delay the TTI (from 59 s of control EPS to 106 s). The values of pHRR (183.7 kW/m^2) and char residues were decreased by 34.9 % and increased to 37.3 % in comparison with those of the control EPS. The smoke release of UV curing coating was further reduced by the using of k*aol. Moreover, the E-K*$_5D_{30}$-P_8N_3 sample showed good flame retardant durability, exhibiting the minimal weight loss of coating (14.8 %), the negligible reduction in LOI (3.6 %), and the FPI value of 0.405 m^2·s/kW after 12 h washing.

CRediT authorship contribution statement

Xiaodong Jin: Writing – original draft, Data curation, Conceptualization. **Xinyi Wu:** Visualization, Data curation. **Wufei Tang:** Resources, Methodology. **Zheni Tan:** Investigation. **Wanfu Wang:** Writing – review & editing, Supervision. **Shibing Sun:** Writing – review & editing, Supervision, Resources.

Declaration of competing interest

The authors declare that they have no known competing financial interests or personal relationships that could have appeared to influence the work reported in this paper.

Data availability

Data will be made available on request.

Acknowledgement

The current work was financially supported by National Natural Science Foundation of China (grant numbers 51903007), the Science and Technology Innovation Program of Hunan Province (2023RC3189) and the program fund of Nonmetallic Excellence and Innovation Center for Building Materials (24PHD-3).

Appendix A. Supplementary data

Supplementary data to this article can be found online at https://doi.org/10.1016/j.cej.2024.153285.

References

[1] J.C. Liu, Y.B. Zhang, Z.L. Yu, W.Y. Yang, J. Luo, B.J. Pan, C. Lu, Enhancement of organoclay on thermal and flame retardant properties of polystyrene/magnesium hydroxide composite, Polym. Composite. 37 (2016) 746–755, https://doi.org/10.1002/pc.23231.

[2] W.F. Ji, D. Wang, J. Guo, B. Fei, X.Y. Gu, H.Y. Li, J. Sun, S. Zhang, The preparation of starch derivatives reacted with urea-phosphoric acid and effects on fire performance of expandable polystyrene foams, Carbohyd. Polym. 233 (2020) 115841, https://doi.org/10.1016/j.carbpol.2020.115841.

[3] Y.P. Bai, C. Zhang, M.R. Li, W.W. Liu, Graft modification of chlorinated polypropylene and coating performance promotion for polypropylene, Int. J. Adhes. 48 (2014) 231–237, https://doi.org/10.1016/j.ijadhadh.2013.09.037.

[4] X.Q. Qiu, Z.W. Li, X.H. Li, Z.J. Zhang, Flame retardant coatings prepared by layer by layer assembly: a review, Chem. Eng. J. 334 (2017) 108–122, https://doi.org/10.1016/j.cej.2017.09.194.

[5] A.L. Davesne, M. Jimenez, F. Samyn, S. Bourbigot, Thin coatings for fire protection: An overview of the existing strategies, with an emphasis on layer-by-layer surface treatments and promising new solutions, Prog. Org. Coat. 154 (2021) 106217, https://doi.org/10.1016/j.porgcoat.2021.106217.

[6] X. Wang, Y.T. Pan, J.T. Wan, D.Y. Wang, An eco-friendly way to fire retardant flexible polyurethane foam: layer-by-layer assembly of fully bio-based substances, RSC. Adv. 4 (2014) 46164–46169, https://doi.org/10.1039/c4ra07972h.

[7] Z.F. Li, C.J. Zhang, L. Cui, P. Zhu, C. Yan, Y. Liu, Fire retardant and thermal degradation properties of cotton fabrics based on APTES and sodium phytate through layer-by-layer assembly, J. Anal. Appl. Pyrol. 123 (2020) 216–223, https://doi.org/10.1016/j.jaap.2016.11.026.

[8] X.D. Liu, X.W. Meng, J. Sun, W.F. Tang, S. Chen, X.H. Peng, X.Y. Gu, B. Fei, S. Bourbigot, S. Zhang, Improving the flame retardant properties of polyester cotton blend fabrics by introducing an intumescent coating via layer by layer assembly, Appl. Polym. Sci. 137 (2020) 49253, https://doi.org/10.1002/app.49253.

[9] O. Zilke, D. Plohl, K. Opwis, T. Mayer-Gall, J.S. Gutmann, A flame-retardant phytic-acid-based LbL-coating for cotton using polyvinylamine, Polym. 12 (2020) 1202, https://doi.org/3390/polym12051202.

[10] P. Qi, F. Chen, Y.C. Li, H.F. Li, X.Y. Gu, J. Sun, S. Zhang, A review of durable flame-retardant fabrics by finishing: fabrication strategies and challenges, Adv. Fiber Mater. 5 (2023) 731–763, https://doi.org/10.1007/s42765-023-00255-x.
[11] X.D. Jin, S.P. Cui, Y. Zhang, X.X. Zhao, F. Lv, S.B. Sun, Y.L. Tian, Z.Y. Zhao, D. H. Liu, Covalent bonding of the extruded polystyrene foams to mortar through ultraviolet-ozone irradiation, Constr. Build. Mater. 325 (2022) 126801, https://doi.org/10.1016/j.conbuildmat.2022.126801.
[12] X.D. Jin, X.Y. Wu, S.P. Cui, W.F. Wang, Y. Zhang, S.B. Sun, D.W. Sun, A robust adhesion between extruded polystyrene foam and mortar through different chemical linkages under ultraviolet-ozone irradiation, Constr. Build. Mater. 345 (2022) 128414, https://doi.org/10.1016/j.conbuildmat.2022.128414.
[13] D.O.H. Teare, N. Emmison, C. Ton-That, R.H. Bradley, Effects of serum on the kinetics of CHO attachment to ultraviolet-ozone modified polystyrene surfaces, J. Colloid. Interf. Sci. 234 (2001) 84–89, https://doi.org/10.1006/jcis.2000.7282.
[14] J. Alongi, A.D. Blasio, F. Carosio, G. Malucelli, UV-cured hybrid organic-inorganic Layer by Layer assemblies: Effect on the flame retardancy of polycarbonate films, Polym. Degrad. Stabil. 107 (2014) 74–81, https://doi.org/10.1016/j.polymdegradstab.2014.05.
[15] J. Alongi, F. Carosio, G. Malucelli, Layer by layer complex architectures based on ammonium polyphosphate, chitosan and silica on polyester-cotton blends: flammability and combustior behaviour, Cellulose. 19 (2012) 1041–1050, https://doi.org/10.1007/s10570-012-9682-8.
[16] G. Laufer, C. Kirkland, A.A. Cain, J.C. Grunlan, Clay-chitosan nanobrick walls: completely renewable gas barrier and flame-retardant nanocoatings, ACS. Appl. Mater. Inte. 4 (2012) 1643–1649, https://doi.org/10.1021/am2017915.
[17] Y.B. Huang, S.H. Jiang, R.C. Liang, Z.W. Liao, G.X. You, A green highly-effective surface flame-retardant strategy for rigid polyurethane foam: Transforming UV-cured coating into intumescent self-extinguishing layer, Compos. Part A-Appl. s. 125 (2019) 105534, https://doi.org/10.1016/j.compositesa. 2019.105534.
[18] W.F. Tang, H.M. Zhang, T. Liu, X.L. Li, H. Yang, W.Z. Huang, Y.H. Liao, X.Y. Gu, S. Zhang, Improving the flame retardancy and smoke suppression of ethylene vinyl acetate composites by introducing the hybrid material of Zn/TiO_2@AKaol, Polym. Degrad. Stabil. 221 (2024) 110673, https://doi.org/10.1016/j.polymdegradstab.2024.110673.
[19] W.F. Tang, Z.D. Qin, F. Liu, S.F. Gong, C. Peng, X.Y. Gu, S. Zhang, X. Wang, X. D. Jin, S. Bourbigot, Influence of two kinds of low dimensional nano-sized silicate clay on the flame retardancy of polypropylene, Mater. Chem. Phys. 256 (2020) 123743, https://doi.org/10.1016/j.matchemphys.2020.123743.
[20] W.F. Tang, L.X. Song, F. Liu, W. Dessie, Z.D. Qin, S. Zhang, X.Y. Gu, Improving the flame retardancy and thermal stability of polypropylene composites via introducing glycine intercalated kaolinite compounds, Appl. Clay. Sci. 217 (2022) 106411, https://doi.org/10.1016/j.clay.2022.106411.
[21] H.Z. Fan, X.Y. Gu, S. Zhang, F. Liu, Y.H. Liao, W.F. Tang, Synergistic effect between novel triazine-based charring agent and modified kaolinite: An efficient system for fire hazard and aging suppression of epoxy resin, Polym. Degrad. Stabil. 204 (2022) 110109, https://doi.org/10.1016/j.polymdegradstab.2022.110109.
[22] W.F. Tang, H.Z. Fan, F. Liu, Y.H. Liao, Q. Xiao, J. Yan, S. Zhang, X.Y. Gu, MoS_2 supported on acid activated kaolinite used in the kaolinite-epoxy resin composites for suppressing smoke toxicity and degradation, Appl. Clay. Sci. 233 (2023) 106822, https://doi.org/10.1016/j.clay.2023.106822.
[23] R. Li, J. Liu, A. Shi, X. Luo, J. Lin, R. Zheng, H. Fan, S.V. Selasie, H. Lin, A facile method to modify polypropylene membrane by polydopamine coating via inkjet printing technique for superior performance, J. Colloid. Interface. Sci. 552 (2019) 719–727, https://doi.org/10.1016/j.jcis.2019.05.108.
[24] T. Gou, X. Wu, Q. Zhao, S. Chang, P. Wang, Novel phosphorus/nitrogen-rich oligomer with numerous reactive groups for durable flame-retardant cotton fabric, Cellulose. 28 (2021) 7405–7419, https://doi.org/10.1007/s10570-021-03980-x.
[25] Y.L. Dou, X.F. Li, K.Y. Zheng, J.W. Liu, J.Z. Hou, Study on curing and flammability properties of UV-curable flame-retardant coating on jute/polypropylene composites surface, J. Therm. Anal. Calorim. 147 (2021) 4597–4610, https://doi.org/10.1007/s10973-021-10864-6.
[26] S. Qiu, Y. Li, P. Qi, D. Meng, J. Sun, H. Li, Z. Cui, X. Gu, S. Zhang, Improving the flame retardancy and accelerating the degradation of poly (lactic acid) in soil by introducing fully bio-based additives, Int. J. Biol. Macromol. 193 (2021) 44–52, https://doi.org/10.1016/j.ijbiomac.2021.10.119.
[27] W. Cheng, Y. Zhang, Y. Tao, J. Lu, J. Liu, B. Wang, L. Song, G. Jie, Y. Hu, Durable electromagnetic interference (EMI) shielding ramie fabric with excellent flame retardancy and Self-healing performance, J. Colloid. Interface. Sci. 602 (2021) 810–821, https://doi.org/10.1016/j.jcis.2021.05.159.
[28] T. Zhu, G. Liu, D. Chen, J. Chen, P. Qi, J. Sun, X. Gu, S. Zhang, Constructing flame-retardant gel polymer electrolytes via multiscale free radical annihilating agents for Ni-rich lithium batteries, Energy. Storag. Mater. 50 (2022) 495–504, https://doi.org/10.1016/j.ensm.2022.05.051.
[29] J. Tu, T. Mao, S. Xie, J. Guan, H. Xiao, P. Wang, Environmentally benign flame-retardant cotton fabric with superior anti-wrinkle performance and restorable flame retardancy, Ind. Crop. Prod. 189 (2022) 115856, https://doi.org/10.1016/j.polymdegradstab.2018.02.020.
[30] T. Gou, X. Wu, Q. Zhao, S. Chang, P. Wang, Novel phosphorus/nitrogen-rich oligomer with numerous reactive groups for durable flame-retardant cotton fabric, Cellulose. 28 (2021) 7405–7419, https://doi.org/10.1007/s10570-021-03980-x.
[31] C. Girardeaux, J.J. Pireaux, Analysis of polystyrene (PS) by XPS, Surf. Sci Spectra. 4 (1996) 130–133, https://doi.org/10.1116/1.1247812.
[32] K. Zarmeena, J. Fahed, S. Zufishan, H. Ainy, F. Tahir, A. Ambreen, B.Z. William, R. Fahad, Current developments in esterification reaction: A review on process and parameters, J. Ind. Eng. Chem. 103 (2021) 80–101, https://doi.org/10.1016/j.jiec.2021.07.018.
[33] D. Xing, B.T. Guan, G.X. Cai, Z. Fang, L.P. Yang, Z.J. Shi, Gold(I)-catalyzed oxidative cleavage of a C-C double bond in water, Org. Lett. 8 (2006) 693–696, https://doi.org/10.1002/chin.201152070.
[34] P. Qi, Y.C. Li, Y. Yao, J. Sun, L. Li, J. Liu, X.Y. Gu, H.F. Li, S. Zhang, Ultra washing durable flame retardant coating for cotton fabric by the covalent bonding and interface polymerization, Chem. Eng. J. 452 (2023), https://doi.org/10.1016/j.cej.2022.139453.
[35] S. Ortelli, G. Malucelli, M. Blosi, I. Zanoni, A.L. Costa, NanoTiO_2@DNA complex: a novel eco, durable, fire retardant design strategy for cotton textiles, J. Colloid. Interface. Sci. 546 (2019) 174–183, https://doi.org/10.1016/j.jcis.2019.03. 055.
[36] W. Xie, Q. Bao, Y. Liu, H. Wen, Q. Wang, Hydrogen bond association to prepare flame retardant polyvinyl alcohol film with high performance, ACS. Appl. Mater. Interfaces. 13 (2021) 5508–5517, https://doi.org/10.1021/acsami.0c19093.
[37] S. Qiu, Y. Li, P. Qi, D. Meng, J. Sun, H. Li, Z. Cui, X.Y. Gu, S. Zhang, Improving the flame retardancy and accelerating the degradation of poly (lactic acid) in soil by introducing fully bio-based additives, Int. J. Biol. Macromol. 193 (2021) 44–52, https://doi.org/10.1016/j.ijbiomac.2021.10.119.
[38] F. Chen, P. Qi, J. Liu, G. Xia, B. Fei, J. Sun, H.X. John, S. Zhang, Rationally designed lentinan outer layer to improve the comprehensive performance of flame-retardant cotton fabrics, Chem. Eng. J. 476 (2023), https://doi.org/10.1016/J.CEJ.2023.146427, 146427.
[39] J.C. Yang, Z.J. Cao, Y.Z. Wang, D.A. Schiraldi, Ammonium polyphosphate-based nanocoating for melamine foam towards high flame retardancy and anti-shrinkage in fire, Polym. 66 (2015) 86–93, https://doi.org/10.1016/j.polymer.2015.04.022.
[40] S.S. Uğur, M. Sarıışık, A.H. Aktas, Nano-Al_2O_3 multilayer film deposition on cotton fabrics by layer-by-layer deposition method, Mater. Res. Bull. 46 (2011) 1202–1206, https://doi.org/10.1016/j.materresbull.2011.04.00.
[41] Y. Liu, Q.Q. Wang, Z.M. Jianga, C.J. Zhang, Z.F. Li, H.Q. Chen, P. Zhu, Effect of chitosan on the fire retardancy and thermal degradation properties of coated cotton fabrics with sodium phytate and APTES by LBL assembly, J. Anal. App. Pyroly. 135 (2018) 289–298, https://doi.org/10.1016/j.jaap.2018.08.024.
[42] F. Fang, X. Zhang, Y.D. Meng, X. Ding, C. Bao, S.Y. Li, H. Zhang, X.Y. Tian, Boron-containing intumescent multilayer nanocoating for extinguishing flame on cotton fabric, Cellulose. 23 (2016) 2161–2172, https://doi.org/10.1007/s10570-016-0928-8.
[43] F. Carosio, A.D. Blasio, F. Cuttica, J. Alongi, G. Malucelli, Self-assembled hybrid nanoarchitectures deposited on poly(urethane) foams capable of chemically adapting to extreme heat, RSC. Ad. 4 (2014) 16674, https://doi.org/10.1039/c4ra01343c.
[44] F. Carosio, A.D. Blasio, J. Alongi, G. Malucelli, Green DNA-based flame retardant coatings assembled through Layer by Layer, Polym. 54 (2013) 5148–5153, https://doi.org/10.1016/j.polymer.2013.07.029.
[45] G. Laufer, C. Kirkland, A.B. Morgan, J.C. Grunlan, Exceptionally flame retardant sulfur-based multilayer nanocoating for polyurethane prepared from aqueous polyelectrolyte solutions, ACS. Macro. Lett. 2 (2013) 361–365, https://doi.org/10.1021/mz400105e.
[46] F. Carosio, J. Alongi, G. Malucelli, Layer by Layer ammonium polyphosphate-based coatings for flame retardancy of polyester-cotton blends, Carbohydr. Polym. 88 (2012) 1460–1469, https://doi.org/10.1016/j.carbpol. 2012.02.049.
[47] X.G. Wang, S.H. Wang, W.J. Wang, H.F. Li, X.D. Liu, X.Y. Gu, S. Bourbigot, Z. W. Wang, J. Sun, S. Zhang, The flammability and mechanical properties of poly (lactic acid) composites containing Ni-MOF nanosheets with polyhydroxy groups, Comp. B. Eng. (2019) 107568, https://doi.org/10.1016/j.compositesb.2019.107568.
[48] J. Tu, T. Mao, S. Xie, J. Guan, H. Xiao, P. Wang, Environmentally benign flame-retardant cotton fabric with superior anti-wrinkle performance and restorable flame retardancy, Ind. Crop. Prod. 189 (2022) 115856, https://doi.org/10.1016/j.indcrop.2022.115856.
[49] T. Gou, X. Wu, Q. Zhao, S. Chang, P. Wang, Novel phosphorus/nitrogen-rich oligomer with numerous reactive groups for durable flame-retardant cotton fabric, Cellulose. 28 (2021) 7405–7419, https://doi.org/10.1007/s10570-021-03980-x.
[50] L. Zhang, Z. Li, Y. Pan, A. Yanez, S. Hu, X. Zhang, Polydopamine induced natural fiber surface functionalization: a way towards flame retardancy of flax/poly(lactic acid) biocomposites, Compos. B. Eng. 154 (2018) 56–63, https://doi.org/10.1016/j.compositesb.2018.07.037.
[51] C. Feng, M. Liang, J. Jiang, J. Huang, H. Liu, Flame retardant properties and mechanism of an efficient intumescent flame retardant PLA composites, Polym. Adv. Technol. 27 (2016) 693–700, https://doi.org/10.1002/pat.3743.
[52] C. Ke, J. Li, K. Fang, Q. Zhu, J. Zhu, Q. Yan, Synergistic effect between a novel hyperbranched charring agent and ammonium polyphosphate on the flame retardant and anti-dripping properties of polylactide, Polym. Degrad. Stab. 95 (2010) 763–770, https://doi.org/10.1016/j.polymdegradstab.2010.02.011.
[53] X.D. Jin, S.P. Cui, S.B. Sun, X.Y. Gu, H.F. Li, X.D. Liu, W.F. Tang, J. Sun, S. Bourbigot, S. Zhang, The preparation of a bio-polyelectrolytes based core-shell structure and its application in flame retardant polylactic acid composites, Compos. Part. a. Appl. Sci. 124 (2019) 105485, https://doi.org/10.1016/j.compositesa. 2019.105485.
[54] W. Liu, R. Shi, X. Ge, H. Huang, X. Chen, M. Mu, A bio-based flame retardant coating used for polyamide 66 fabric, Prog. Org. Coat. 156 (2021) 106271, https://doi.org/10.1016/j.porgcoat.2021.106271.
[55] P. Li, B. Wang, Y. Liu, Y. Xu, Z. Jiang, C. Dong, L. Zhang, Y. Liu, P. Zhu, Fully bio-based coating from chitosan and phytate for fire-safety and antibacterial cotton fabrics, Carbohydr. Polym. 237 (2020) 116173, https://doi.org/10.1016/j.carbpol.2020.116173.
[56] F. Liang, Y. Xu, S. Chen, Y. Zhu, Y. Huang, B. Fei, W. Guo, Fabrication of highly efficient flame-retardant and fluorine-free superhydrophobic cotton fabric by

constructing multielement-containing POSS@ZIF-67@PDMS micro-nano hierarchical coatings, ACS. Appl. Mater. Inter. 14 (2022) 56027–56045, https://doi.org/10.1021/acsami.2c14709.

[57] Y. Chen, Y. Liao, C. Wan, G. Zhang, F. Zhang, Synthesis of a novel P-N reactive ammonium phosphate-based flame retardant for durable finishing of cotton fabric, Colloid. Surf. a. 634 (2022) 127967, https://doi.org/10.1016/j.colsurfa.2021.127967.

[58] D. Rigotti, A. Pegoretti, A. Miotello, R. Checchetto, Interfaces in biopolymer nanocomposites: their role in the gas barrier properties and kinetics of residual solvent desorption, Appl. Surf. Sci. 507 (2020) 145066, https://doi.org/10.1016/j.apsusc. 2019.145066.

[59] S. Wang, D. Kong, H. Chen, Z. Wang, Z. Lu, Construction of a novel B/N/Si synergistic flame retardant system and its application on cotton fabric, Ind. Crop. Prod. 178 (2022) 114574, https://doi.org/10.1016/j.indcrop.2022.114574.

Polymer Degradation and Stability 242 (2025) 111671

Contents lists available at ScienceDirect

Polymer Degradation and Stability

journal homepage: www.journals.elsevier.com/polymer-degradation-and-stability

Recycling of wind turbine blade powder into HDPE wood-plastic composites: Enhanced mechanical and flame-retardant properties via interfacial modification

YiChen Chen [a,1], Wufei Tang [b,1], Zhaozhen Zhang [a], Peixin Li [c], Shibing Sun [a], Wanfu Wang [a,d,*], Xiaodong Jin [a,*]

[a] College of Materials Science and Engineering, Beijing University of Technology, Beijing 100124, China
[b] Hunan Engineering Technology Research Center for Comprehensive Development and Utilization of Biomass Resources, Hunan University of Science and Engineering, Yongzhou 425199, China
[c] Guodian United Power Technology Co.Ltd, Beijing 100039, China
[d] School of New Materials and Chemical Engineering, Tangshan University, Tangshan 063000, China

ARTICLE INFO

Keywords:
Wind turbine blades
Wood-plastic composites
Interfacial modification
Flame retardant

ABSTRACT

To fully recycle the wasted wind turbine blades (rWTB) powder, its major components (glass fiber reinforced plastic (GFRP) and balsa wood (BW)) was incorporated into high-density polyethylene (HDPE) to prepare wood-plastic composites (WPC) with maleic anhydride grafted polyethylene (MAPE) as the compatibilizer. By varying the mass ratio of GFRP to BW, the mechanical properties, interfacial morphology and water absorption of rWTB/HDPE composites were systematically investigated. With the combination of 30 % GFPR and 10 %BW, the obtained H/30G10B composites exhibited the highest the tensile strength (27.73 MPa) and increased impact strength (21.85 KJ/m^2) with the presence of 3 % MAPE. Scanning electron microscopy (SEM) images showed that MAPE improved the interfacial bonding between the filler and the HDPE matrix. To improve the fire resistance of HDPE composites, ammonium polyphosphate (APP) was further incorporated into H/30G10B sample. With the addition of 22 % APP, the best sample could reach a limiting oxygen index (LOI) of 36.8 %, V-0 rating in UL-94 and a decreased heat release in cone calorimetry. In summary, this paper provides a new method for resource utilization of rWTB, which can improve the performance of composites and avoid environmental pollution.

1. Introduction

Recycled wind turbine blade powder (rWTB) is obtained from crushing retired wind turbine blades. The wind power industry is projected to grow rapidly over the next 40 years, driven by the transition to clean energy and sustainable development practices. However, the service life of wind turbine blades is only 20 to 25 years. According to recent projections, China is anticipated to retire over 30,000 wind turbines by 2030, escalating to 90,000 units by 2035 [1]. Current recycling methods, including pyrolysis and mechanical grinding [2–4], struggle with cost efficiency and effective material recovery, especially for glass fiber-reinforced plastic (GFRP) components. These approaches often require high energy input and complex processing steps, which increase economic cost and limit their large-scale application [5,6].

Using rWTB powder directly in wood-plastic composites (WPCs) offers a promising alternative; however, the incompatibility between hydrophilic fillers (e.g., balsa wood (BW)) and hydrophobic matrices (e.g., high-density polyethylene (HDPE)) remains a significant challenge [7]. Retired wind turbine blades, composed mainly GFRP, BW and adhesives, present significant recycling challenges. Nevertheless, direct incorporation of rWTB into polymer composites avoids extensive separation procedures, thereby improving resource utilization efficiency and simplifying processing. More importantly, effective recycling not only mitigates secondary pollution but also promotes circular use of composite waste materials, generating clear environmental and sustainability benefits [8–11]. Current methods of recycling include physical,

* Corresponding authors.
E-mail addresses: 15530581685@163.com (W. Wang), jinxiaodong@bjut.edu.cn (X. Jin).
[1] Yichen Chen and Wufei Tang contributed equally to this work.

https://doi.org/10.1016/j.polymdegradstab.2025.111671
Received 25 July 2025; Received in revised form 14 September 2025; Accepted 15 September 2025
Available online 15 September 2025
0141-3910/© 2025 Elsevier Ltd. All rights are reserved, including those for text and data mining, AI training, and similar technologies.

chemical, and thermal processes.

Wood-Plastic Composites are a type of composite material made by blending thermoplastic matrices with fillers such as wood powder or plant fibers [12,13]. WPCs are increasingly popular due to their excellent dimensional stability, low cost, and wood-like appearance, with applications spanning aerospace, construction, outdoor furniture, automotive interiors, and packaging [14–16]. To improve the mechanical properties of WPC, various reinforcement methods have been explored, including the addition of rigid particles and reinforcing fibers, as well as enhancing the interfacial compatibility between fillers and plastic matrices [17–24].

In this context, the recycled GFRP in rWTB provides lightweight, high-strength, and corrosion-resistant properties, making it an ideal reinforcement material for WPC [16]. Additionally, the BW component of rWTB can serve as a filler and carbon source in WPC. To summary, this work enables the full recycling of rWTB without separating the BW, and enhances the flame retardancy, mechanical properties of WPC while simultaneously addressing recycling cost, efficiency, and sustainability concerns.

Due to the flammability of both plastics and wood fibers, WPCs face limitations in potential applications. Therefore, studying the flame-retardant properties of WPC is critical. Common flame retardants used in WPC include halogenated, nitrogen-phosphorus, aluminum-magnesium, intumescent, and emerging nano-flame retardants. Halogenated flame retardants, while inexpensive, release toxic smoke and corrosive gases, posing environmental and health risks [25]. As a result, halogen-free flame retardants, such as ammonium polyphosphate (APP), have gained wider acceptance. APP promotes the formation of a protective char layer that inhibits heat and flame diffusion, thereby enhancing the flame retardancy of the composite [26–34].

In this study, we aim to identify the optimal ratio of glass fiber reinforced polymer (GFRP) and biomass waste (BW) for developing high-performance recycled wood thermoplastic composites (rWTB/HDPE), thereby streamlining the rWTB sorting process and reducing recycling costs. A comprehensive evaluation was conducted on the mechanical properties, micromorphology, thermal stability, processing performance, water absorption, and density of rWTB/HDPE wood-plastic composites (WPCs) with varying GFRP/BW ratios. Furthermore, the flame retardancy of the composites was investigated both with and without the addition of ammonium polyphosphate (APP). This innovative approach enables both material reinforcement and flame retardancy, simplifying the recycling process while enhancing sustainability. Specifically, APP facilitates the formation of a stable intumescent char layer, while BW provides carbonaceous residues and GFRP reinforces the physical integrity of the protective barrier. The multi-component synergistic effect significantly enhances fire resistance beyond the performance achievable by APP alone.

2. Experimental

2.1. Materials

High-density polyethylene (HDPE) was provided by China Petroleum & Chemical Corporation Maoming Branch (China). Recycled wind turbine blades (rWTB), was provided by Hebei Anjulangqing Environmental Protection Equipment Co. Ltd, (China). Maleic anhydride grafted polyethylene (MAPE) with the grafting rate 1.2 % and melt index of 190°C/2.16kg was provided by Anhui Zesheng Technology Co., Ltd, (China). Ammonium polyphosphate (APP) with degree of polymerization ≥ 1000 was provided by Beijing Mairenda Technology Co. Ltd.

2.2. Measurements

In accordance with the standard ISO 527-1:2012 on the desktop tensile machine (CH-9005A) for tensile strength testing, tensile rate of 50 mm / min, the sample size of 150 mm × 10 mm × 4 mm.

In accordance with the standard ISO 178:2019 in the desktop tensile machine (CH-9005A) on the bending performance testing, compression rate of 20 mm / min, the sample size of 80 mm × 10 mm × 4 mm.

The unnotched impact performance test is carried out on the cantilever beam impact tester (WJ-CJ-12) according to standard ISO 180:2019, and the impact sample size is 80 mm × 10 mm × 4 mm.

The water absorption (WA) test was carried out according to the standard ASTM D1037:2020, the sample size was 25 mm × 25 mm × 4 mm, the sample was immersed in distilled water for 24 h at room temperature, the weight change of the sample before and after the water immersion was calculated as a percentage of the weight of the sample before the water immersion, and the data obtained was the water absorption rate of the sample. The number of test samples for each of the above experiments was 5, and the test results were averaged.

For micro-morphological analysis using an environmental scanning electron microscope (SEM), the sample surface needs to be coated with gold once before testing, and the operating voltage is set to 10 kV.

Fourier infrared spectrometer (FTIR) analysis (Spectrum II type) infrared analysis of samples was conducted. The number of scans is set to 32 times, the scanning range of 4000 ~ 400 cm^{-1}, optical resolution of 8 cm^{-1}.

The rheological properties of the experimental samples were analyzed using Haake's torque rheometer (Rheomix 600P) with a processing temperature of 175 °C and a rotational speed of 40 rpm, and a processing time of about 7 min.

Vertical combustion (UL-94) performance was tested in accordance with the national standard ASTM D3801 in the Jiangning Vertical Combustion Tester (CFZ-5), and the tested. The shape of the samples is 130 mm × 13 mm × 3 mm, at least 5 samples are tested in each group, and the average value of the test results is taken.

Oxygen index (LOI) according to the national standard ASTM D2863-23 in Jiangning oxygen index tester (JT-30) for the test, the sample size of 100 mm × 6.5 mm × 3 mm.

Cone calorimetry (CONE) test in accordance with the ISO 5600 test standards to use the British FFT cone calorimeter on the specimen combustion performance of the characterization of the specimen, the sample size 100 mm × 100 mm × 3 mm, the intensity of the heater radiation was 35 kW/m, and the air flow was 24 L/s.

The heat loss (TG) behavior of the material was tested using a thermogravimetric analyzer (TG209F1, Netzsch, Germany) under the conditions of nitrogen atmosphere with the temperature range of 30 ~ 700°C and the temperature increase rate of 10 °C/min.

2.3. Preparation of rWTB

Firstly, rWTB was initially cut to remove BW, and then crushed, pulverized and sieved to obtain 80-mesh GFRP; the trimmings of BW required for making wind turbine blades were pulverized and sieved to obtain 80-mesh pure BW, and the specific process is shown in Figs. 1 and 2.

2.4. Preparation of WPC

The required raw materials were first dried in a vacuum oven at 80 °C for 12 h. The raw materials were weighed based on the ratios specified in Table 1. The raw materials were melt-compounded using a torque rheometer at 175 °C with a rotor speed of 40 rpm for 7 min. The homogeneous mixture was subsequently compression-molded at 190 °C under 10 MPa for 9 min, followed by cooling at 25 °C for 3 min to obtain standard test specimens. The material was placed in a mold, hot pressed at 190 °C for 9 min under 10 MPa, and subsequently cold pressed for 3 min to form the test sample strip. Finally, the sample strips were tested for different properties according to the test standards.

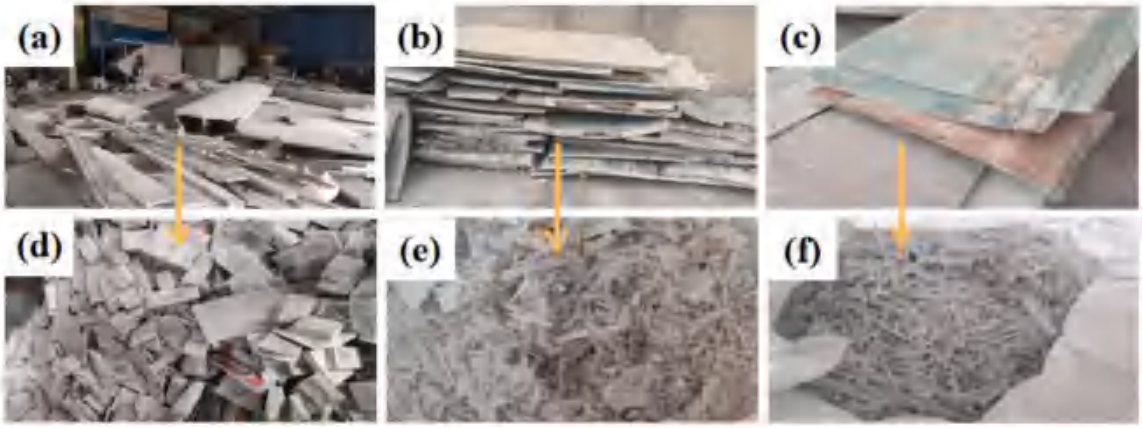

Fig. 1. Preliminary crushing and pulverizing material of rWTB: **(a)** Primary cut stock, **(b)** Secondary cut stock, **(c)** Cut stock with BW removed, **(d)** Primary crushed stock, **(e)** Primary pulverized stock mixed with BW, **(f)** Primary pulverized stock with BW removed.

Fig. 2. Preparation process of BW.

3. Results and discussion

3.1. Basic properties of rWTB

Fig. 3a and 3b illustrate the microscopic morphology of BW and GFRP within rWTB. The crushed and sieved BW exhibits long, strip-like structures with distinct and uniform outer contours, whereas GFRP consists of glass fibers with consistent diameters, interspersed with a small amount of resin adhering to the fiber surfaces. The particle sizes of both materials range from a few micrometers to several hundred micrometers.

To analyze the elemental composition of rWTB, EDS spot scanning was conducted, with the results shown in Fig. 3c. The analysis reveals that the primary elements in the glass fibers are Si and Ca, which together account for over 32 % of the total mass. The resin is predominantly composed of C, which constitutes more than 83 %, followed by O at 13 %. BW is mainly composed of carbon and oxygen, with carbon content reaching 68 %, and oxygen exceeding that of the resin, comprising more than 30 %.

The TG curve of rWTB is presented in Fig. 3d. The curve indicates that the weight loss of GFRP in rWTB begins around 348°C, with a maximum peak at 365°C, stabilizing around 400°C. The total weight loss is approximately 20 %, primarily due to the thermal decomposition of the resin, which corresponds to the resin content in GFRP. For BW, weight loss occurs between 270°C and 380°C, primarily due to the thermal degradation of the wood powder, resulting in a total weight loss of 63 %, with an ash residue of approximately 37 %. Based on these results, GFRP is estimated to contain 80 % glass fibers and 20 % epoxy resin. The thermal decomposition of BW begins at temperatures above 270°C.

Fig. 3e shows the FTIR spectra of GFRP and BW in rWTB. Notable absorption peaks include a -OH at 3340 cm^{-1}, a C-H bond stretch at 2920 cm^{-1}, and a C=O stretch at 1740 cm^{-1}. Additionally, a weak absorption peak for the unsaturated C=C bond in the benzene ring appears at 1508 cm^{-1}. The spectra also reveal characteristic absorption peaks for the C-O stretch at 1037 cm^{-1} and 1026 cm^{-1}, as well as a Si-O bending vibration peak at 921 cm^{-1} [35].

3.2. Mechanical properties

The mechanical performance of rWTB/HDPE composites was systematically investigated by integrating the analysis of BW/GFRP hybrid fillers with the subsequent effect of APP addition. This unified discussion provides a clearer view of the reinforcement mechanism and the property trade-offs associated with flame-retardant incorporation.

3.2.1. Effect of rWTB hybrid fillers (BW and GFRP)

The influence of the GFRP:BW ratio on composite properties was first examined while keeping the HDPE content at 57 % and MAPE at 3 %. As shown in Fig. 4a, the tensile strength of the composites increased with initial GFRP incorporation, reaching a maximum at a GFRP:BW ratio of 3:1, where the tensile strength achieved 27.73 MPa, representing a 41.9 % increase compared to BW-only composites. This enhancement is attributed to the high stiffness of glass fibers, which effectively bear the applied load and transfer stress to the HDPE matrix. However, further increase in GFRP fraction led to a decline in tensile strength, due to poor dispersion and the formation of micro-defects.

In contrast, impact strength (Fig. 4b) exhibited a monotonic increase with increasing GFRP fraction, peaking at 21.85 kJ/m^2 for the 3:1 ratio. The reinforcing effect of GFRP, combined with the energy absorption capability of BW, created a synergistic toughening mechanism. Flexural strength also followed a similar trend, reaching optimal values at the same ratio. Taken together, these results indicate that the 3:1 GFRP:BW ratio achieves a balance between stiffness and toughness, in agreement

Table 1
Formulations of WPC.

Sample		HDPE (%)	BW (%)	GFRP (%)	MAPE (%)	APP (%)
RH	H[a]	100	0	0	0	0
	H/0G40B[b]	57	40	0	3	0
	H/10G30B	57	30	10	3	0
	H/20G20B	57	20	20	3	0
	H/30G10B	57	10	30	3	0
	H/40G0B	57	0	40	3	0
RHM[f]	W[c]	60	10	30	0	0
	W/1M[d]	59	10	30	1	0
	W/2M	58	10	30	2	0
	W/3M	57	10	30	3	0
	W/4M	56	10	30	4	0
	W/5M	55	10	30	5	0
RHMR[g]	H/0G40B/22APP[e]	35	40	0	3	22
	H/10G30B/22APP	35	30	10	3	22
	H/20G20B/22APP	35	20	20	3	22
	H/30G10B/22APP	35	10	30	3	22
	H/30G10B/24APP	33	10	30	3	24
	H/30G10B/26APP	31	10	30	3	26
	H/30G10B/28APP	29	10	30	3	28

[a] H means the sample was pure HDPE;
[b] H/0G40B means the loading of BW is 40 % and the loading of GFRP is 0;
[c] W means the loading of BW is 10 %;
[d] W/1M means the loading of BW is 10 % and the loading of MAPE is 1 %;
[e] H/0G40B/22APP means the loading of BW is 40 % and the loading of APP is 22 %;
[f] RHM means that interface modifier MAPE has been added to the composite material;
[g] RHMR means that flame retardant APP has been added to the composite material;

with prior literature on hybrid natural–synthetic fiber composites [36–39].

MAPE addition further improved the interfacial adhesion between hydrophilic BW, inorganic glass fibers, and the hydrophobic HDPE matrix. At 3 wt% MAPE, tensile and impact strengths were maximized, confirming the compatibilizer's role in stress transfer. Higher MAPE contents, however, resulted in diminishing returns, likely due to excessive low-molecular-weight segments interfering with the HDPE crystalline structure [40–42].

3.2.2. *Effect of APP incorporation*

The addition of APP (Table 2) introduced noticeable changes to mechanical behavior. Tensile strength decreased by up to 23.0 % and impact strength by 60.7 % compared to APP-free composites, while flexural strength showed a slight improvement. These reductions are attributed to four factors: (1) the intrinsic brittleness of APP particles; (2) their tendency to agglomerate, producing stress concentration sites; (3) weakened interfacial bonding between APP and the HDPE matrix compared with BW and GFRP; and (4) the introduction of micro-voids and structural defects during processing. Together, these effects weaken filler-matrix interactions and limit efficient stress transfer.

Despite the loss in toughness, APP incorporation is essential for flame retardancy. The slight improvement in flexural strength suggests that APP also contributes to rigidity, which could be advantageous in structural applications where stiffness is prioritized. Importantly, the observed property reduction aligns with prior studies on APP-filled WPCs, supporting the reliability of the results.

3.2.3. *Integrated discussion and comparison with neat HDPE*

When compared to neat HDPE (literature values: tensile strength ≈ 20-22 MPa; impact strength ≈ 8-10 kJ/m^2), rWTB-filled composites exhibit significantly higher strength and toughness, demonstrating the reinforcing effect of recycled fillers. The introduction of APP, while reducing impact resistance, still yields composites with competitive mechanical properties relative to neat HDPE [41,42].

Overall, these findings highlight the synergistic role of BW and GFRP in enhancing mechanical performance, the critical function of MAPE in compatibilization, and the property trade-offs introduced by APP addition. Such integrated analysis provides a more realistic assessment of the final composite system, balancing reinforcement and flame-retardant requirements for sustainable material design [40]. In particular, the reduction in toughness after APP incorporation can be explained by its intrinsic brittleness, particle agglomeration, weakened interfacial bonding with HDPE, and the introduction of micro-voids and structural defects during processing.

3.3. *Impact section microscopic morphology*

Morphological Analysis of Impact Sections

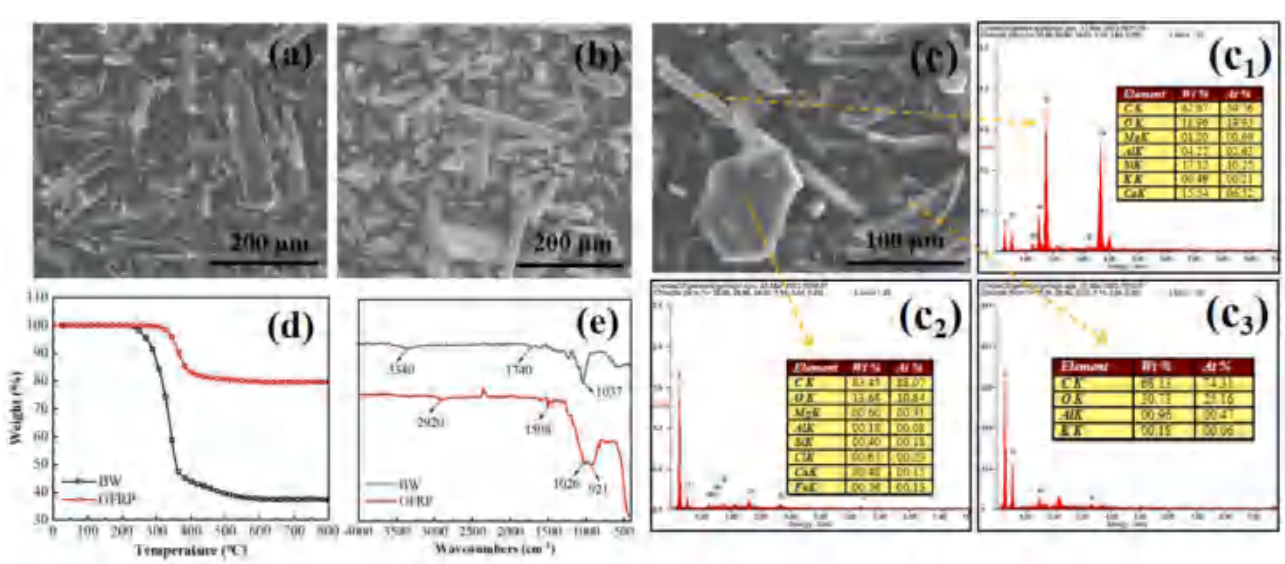

Fig. 3. The basic properties of the rWTB.

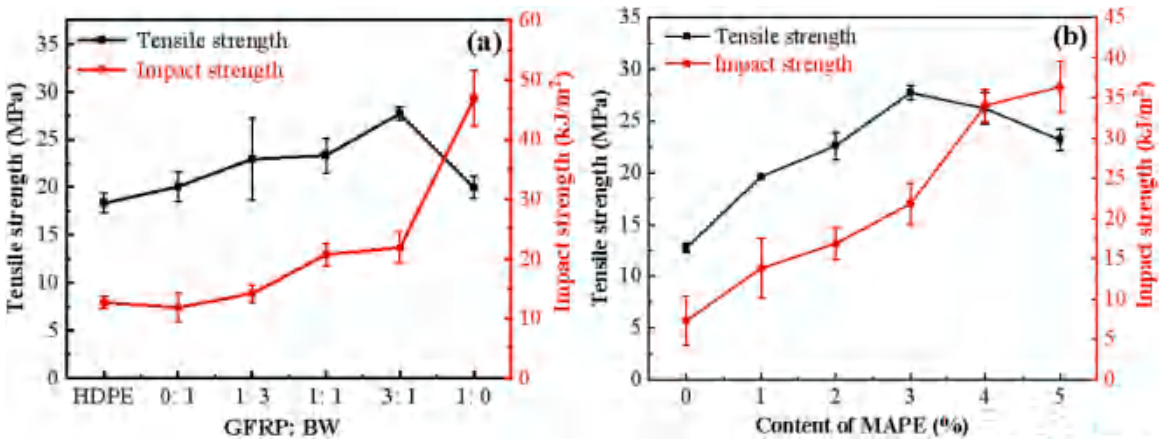

Fig. 4. Mechanical properties of rWTB/HDPE composites: (a) Tensile and impact strength as a function of GFRP:BW ratio; (b) Effect of MAPE content on mechanical performance.

Table 2
rWTB/APP/HDPE mechanical properties results.

Sample	Tensile strength (MPa)	Flexural strength (MPa)	Impact strength (kJ/m^2)
H	18.32	18.48	22.64(Notched)
H/0G40B	20.06	35.21	11.81
H/30G10B	27.73	34.06	21.85
H/20G20B	22.48	38.70	7.63
H/0G40B/ 22APP	19.29	35.71	9.60
H/30G10B/ 28APP	21.35	34.79	8.58

The cross-sectional morphology of the composites was examined by SEM to assess the dispersion of rWTB within the HDPE matrix. As shown in Fig. 5a-c, BW exhibited a certain degree of orientation and uniform dispersion in the matrix. Nevertheless, distinct interfacial boundaries between BW and HDPE were observed, indicating weak interfacial adhesion. Consequently, under external loading, crack propagation tended to follow these interfaces. At low GFRP:BW ratios, BW served as the dominant reinforcing phase, leading to pronounced fiber pull-out and relatively smooth fracture surfaces.

With increasing GFRP content and decreasing BW, the combination of stiff GFRP and energy-absorbing BW improved filler infiltration, dispersion, and compatibility within the HDPE matrix. This synergy promoted stronger filler-matrix interactions with fewer visible defects such as voids and cracks, accompanied by numerous pulled-out glass fibers. However, when the GFRP fraction became excessively high (Fig. 5d), fiber orientation diminished, and the primary failure modes shifted to glass fiber fracture and interfacial debonding (fiber pull-out) [43]. Such conditions disrupted the molding process and promoted internal defects. Under impact loading, these defects served as crack initiation sites, leading to rapid propagation under tensile stress and ultimately reducing tensile strength.

The influence of interfacial modifiers is illustrated in Fig. 5e and 5f. In the absence of MAPE, obvious gaps were observed between the fillers and the HDPE matrix. Fillers were only partially embedded, leaving smooth exposed surfaces that signified poor interfacial bonding. This

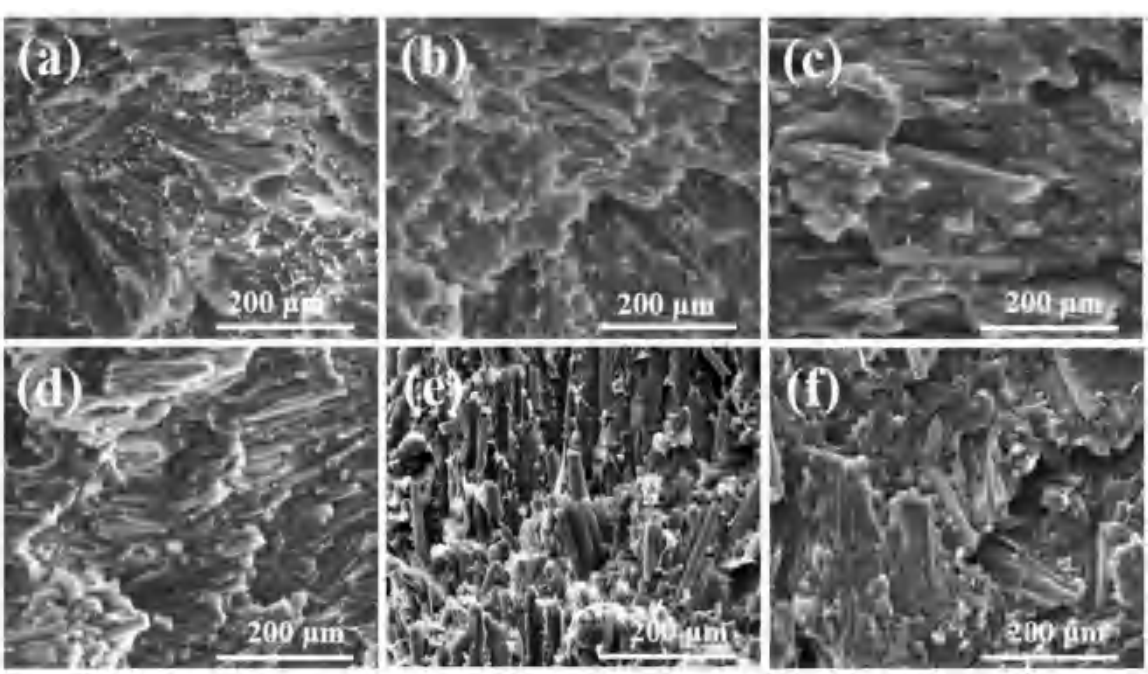

Fig. 5. SEM pictures of rWTB/HDPE impact sections: (a) H/0G40B; (b) H/10G30B;(c) H/30G10B; (d) H/40G0B; (e) W; (f) W/5M.

weak adhesion limited stress transfer to the reinforcing fibers, resulting in fiber debonding, cavities, and compromised composite strength. In contrast, after MAPE modification, HDPE chains entangled with glass fibers, while BW adhered closely to the resin, eliminating visible interfaces and cavities. The cross-section appeared dense and uniform, indicating that MAPE significantly enhanced interfacial adhesion. Consequently, rWTB formed a robust physical interlocking network within the HDPE matrix, enabling efficient stress transfer and improved mechanical performance.

Fig. 6 presents the EDS analysis of the composite with a GFRP:BW ratio of 3:1. The results confirm that glass fibers were tightly embedded and uniformly distributed within the HDPE matrix, with numerous pulled-out fibers visible on the fracture surface. This uniform dispersion further corroborates the excellent mechanical properties achieved at this ratio.

3.4. Flammability

3.4.1. LOI and UL-94 testing

Table 3 presents the LOI and UL-94 test results for HDPE and composites with varying percentages of GFRP and BW. HDPE is highly flammable, with an LOI of only 18.8 %, a short burn time, and significant melt dripping, failing to attain the flammability standards. The addition of 40 % BW increases the LOI to 23.9 %, but it still does not achieve a UL-94 rating, and the melt drop phenomenon remains prominent. This can be attributed to the low thermal conductivity of BW, which inhibits heat transfer and slows the rate of flame propagation [44]. In contrast, when 30 % GFRP and 10 % BW are added (H/30G10B), the LOI decreases slightly to 23.2 %. The presence of epoxy resin in GFRP increases the resin content in the WPC, reducing the wood flour content. Additionally, when heated or ignited, molten HDPE wets the GFRP, spreading rapidly along its surface and releasing combustible gases, which fuel continuous combustion. The GFRP also induces a "candle wick" effect, further promoting combustion [45,46].

To enhance the flame-retardant properties, 22 % APP was incorporated into the composite. With the addition of only 40 % BW (H/0G40B/22APP), the LOI increased to 36.8 %, achieving a V-0 rating in the UL-94 test, with no melt drops. However, when the GFRP to BW ratio was 3:1 (H/10G30B/22APP), the LOI decreased to 35.1 %, failing to achieve a UL-94 rating. Further addition of APP to 28 % resulted in the H/30G10B/28APP sample, which exhibited an LOI of 36.0 % and attained a V-0 rating in the UL-94 test, with no melt drops.

The experimental results also demonstrated that APP significantly thickened the char layer during combustion, effectively suppressing further combustion. BW, containing cellulose, lignin, and hemicellulose, along with the hydroxyl groups in both GFRP and BW, acts as a charcoal-forming agent. APP, as an efficient acid source, thermally decomposes to produce phosphoric acid and meta-phosphoric acid, which enhance dehydration and the charcoal-forming effects in the composite. Moreover, non-combustible gases are generated, diluting the oxygen concentration, forming a swelling flame-retardant system with the wood powder, and improving the composite's overall flame-retardant performance.

Table 3
LOI and UL-94 test results of rWTB/HDPE composite.

Sample	LOI (%)	t_1/t_2[a] (s)	Dripping	Rating
H	18.8	Burn out	Yes	NR
H/0G40B	23.9	Burn out	Yes	NR
H/30G10B	23.2	Burn out	Yes	NR
H/0G40B/22APP	36.8	0/1	No	V-0
H/10G30B/22APP	35.9	0/1	No	V-0
H/20G20B/22APP	35.5	0/5	No	V-0
H/30G10B/22APP	35.1	Burn out	Yes	NR
H/30G10B/24APP	35.6	Burn out	Yes	NR
H/30G10B/26APP	35.8	0/70	No	V-1
H/30G10B/28APP	36.0	0/1	No	V-0

[a] t_1, t_2 represent the after-flame time after the first and second 10 s flame application

3.4.2. CONE analysis

Fig. 7 illustrates the heat release rate (HRR) and total heat release (THR) curves for rWTB/HDPE composites, with detailed data summarized in Table 3. Pure HDPE exhibits a sharp HRR peak (993.2 kW/m^2), indicative of rapid combustion. Upon incorporating 40 % BW (wood flour), the composite demonstrates markedly improved flame retardancy: the pHRR decreases by 50.4 % (493.2 W/m^2), while THR decreases by 14 % (109.3 MJ/m^2). The HRR curve transitions from a sharp peak to a broader, flattened profile, reflecting slowed combustion kinetics due to BW's inherent carbonization capability. This carbon-rich char layer acts as a physical barrier, effectively inhibiting heat and mass transfer. Notably, the addition of GFRP introduces flammable organic resins, leading to a moderate increase in pHRR and THR compared to BW-only composites. However, compared to pure HDPE, the pHRR remains 31.9 % lower

Upon the addition of APP, both heat release rate (HRR) and total heat release rate (THR) of rWTB/HDPE composites are significantly reduced. Compared to the samples without flame retardant, the peak HRR (pHRR) decreases by 63.7 % for the 40 % BW composite (H/0G40B/22APP) and by 70.2 % for the GFRP to BW composite with a 3:1 ratio (H/30G10B/28APP). The THR decreases by 50.3 % and 52.3 %, respectively. The addition of the APP also effectively suppressed the combustion of resin in GFRP, and the difference between H/0G40B/22APP and H/20G20B/22APP was widened significantly, both in terms of HRR and THR values. These results are consistent with the observed fire retardation during the UL-94 test. The smoke production behavior of

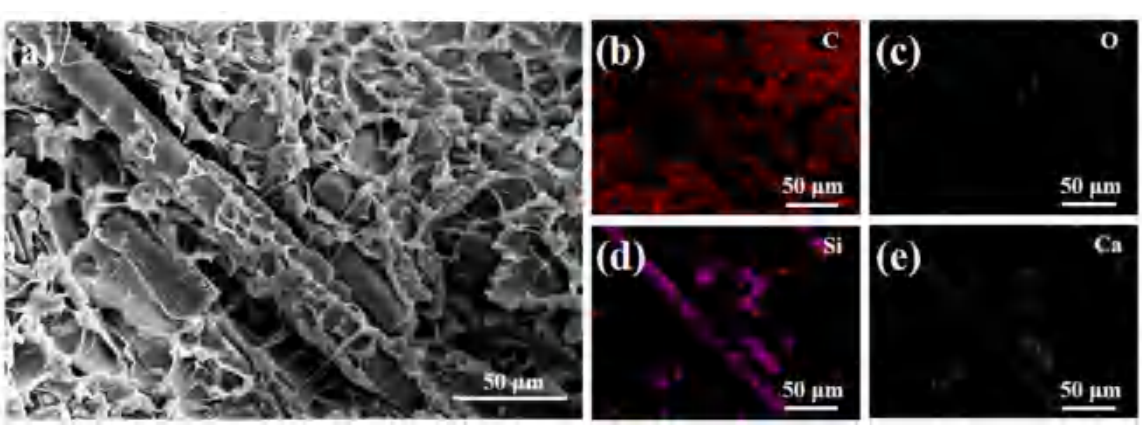

Fig. 6. EDS analysis of the rWTB/HDPE impact section.

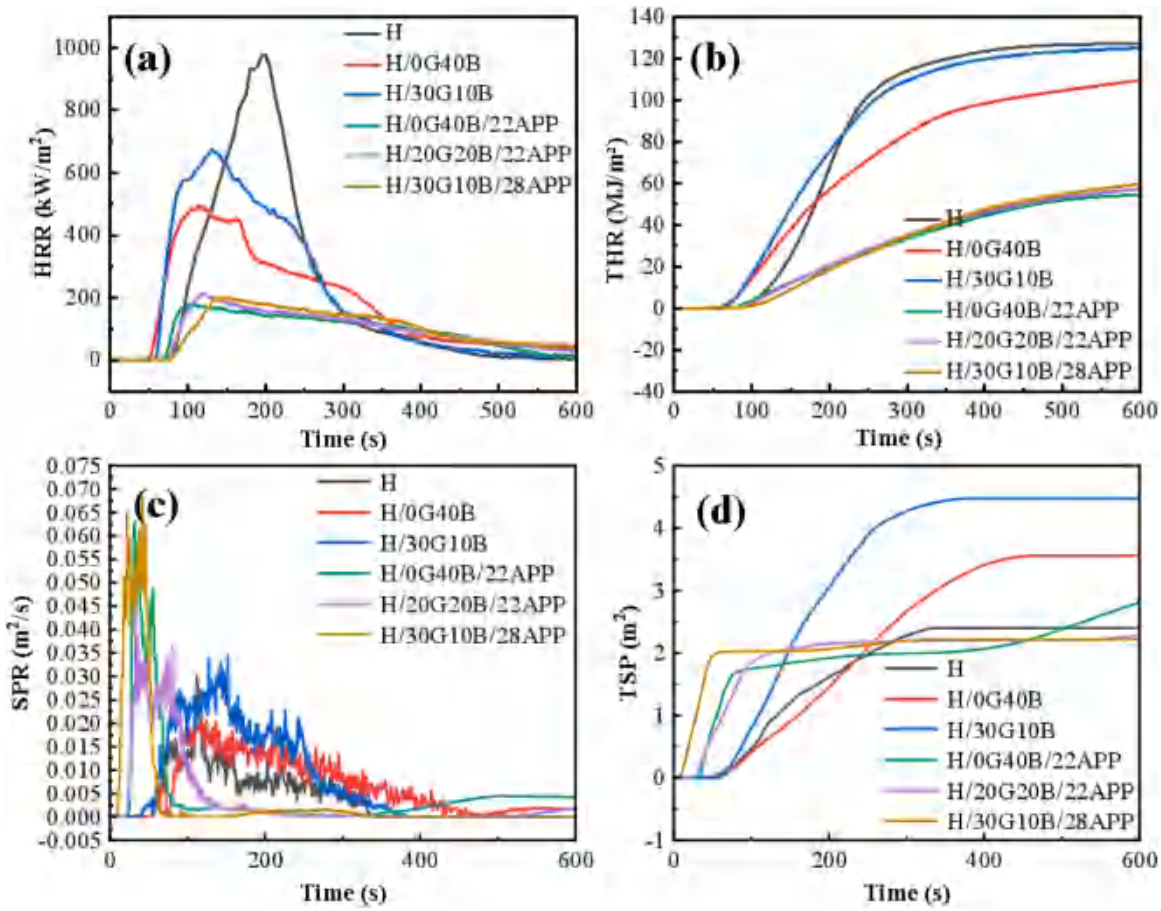

Fig. 7. CONE results of rWTB/APP/HDPE composites: **(a)**HRR; **(b)**THR;**(c)** SPR; **(d)** TSP.

the composites was further evaluated through smoke production rate (SPR) and total smoke production (TSP) analysis (Fig. 7c, d and Table 3). Pure HDPE exhibited relatively low smoke release (SPR=0.030 m^2/s, TSP=2.40 m^2). The incorporation of rWTB alone (H/0G40B and H/30G10B) significantly increased TSP values to 3.55 and 4.47 m^2, respectively, indicating that the degradation of BW and GFRP generated additional volatile products and promoted smoke release. In contrast, the addition of APP effectively suppressed total smoke generation. For example, TSP decreased from 4.47 m^2 (H/30G10B) to 2.21 m^2 (H/30G10B/28APP), and from 3.55 m^2 (H/0G40B) to 2.78 m^2 (H/0G40B/22APP). Although the SPR values of APP-containing composites were slightly higher than those of APP-free systems, their TSP values were markedly reduced. This suggests that APP promotes the formation of a more stable char layer, which delays volatile release and restricts smoke accumulation. The combination of APP with rWTB therefore provides a synergistic effect, simultaneously improving flame retardancy and suppressing overall smoke generation.

Fig. 8 presents the post-combustion char residues of the composites following cone calorimetry. Pure HDPE exhibits negligible char formation (<2 wt%), consistent with its inherent flammability. The incorporation of GFRP and BW moderately increases char residue to 12.5 wt%, forming a discontinuous, fragile carbonaceous layer with visible cracks

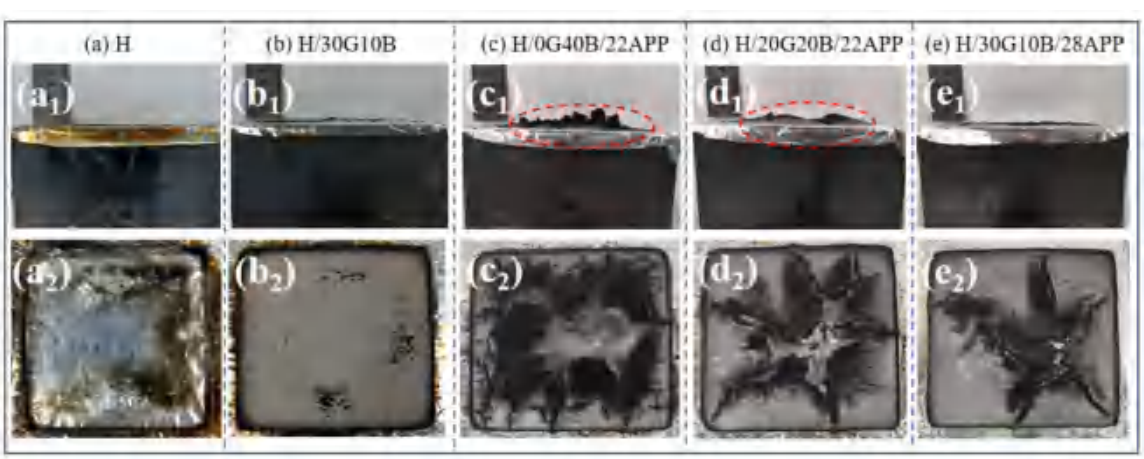

Fig. 8. Photograph of residual ash after CONE test.

(Fig. 8b), indicative of limited barrier functionality. In stark contrast, the APP-containing composite demonstrates a robust, coherent char layer (28.7 wt% residue) characterized by a compact, multi-cellular structure (Fig. 8c). This enhancement is attributed to APP's dual role: (1) as an acid source, it catalyzes phosphorylation of the HDPE matrix and BW-derived polysaccharides, promoting cross-linked aromatic char formation via esterification and etherification reactions; (2) the released NH_3 and H_2O gases from APP decomposition induce foaming, creating a thermally insulating porous architecture and the glass fibers in GFRP act as a skeletal reinforcement within the char matrix, mitigating crack propagation through mechanical interlocking, while the resin component participates in APP-driven cross-linking networks. This synergistic interaction between APP, BW, and GFRP components results in a 35 % increase in char layer density compared to APP-free systems.

3.4.3. TG analysis

The TG curves of rWTB/APP/HDPE composites are shown in Fig. 9b and 9c, with the corresponding data presented in Table 4. From the graphs, it can be observed that the addition of GFRP results in a slight increase in both the onset decomposition temperature and the temperature at 10 % weight loss of the composites. This is attributed to the high thermal resistance of the glass fibers in GFRP. On the other hand, the addition of APP causes a small decrease in both the onset decomposition temperature and the temperature at 10 % weight loss, due to the fact that APP decomposes at lower temperatures.

Despite this decrease in the decomposition temperature, the decomposition of APP generates substances that promote the formation of a char layer. As a result, the residual char rate of the composites with 30 % GFRP increases to 45.1 %, significantly improving the char formation performance Table 5.

Table 4
key data of rWTB/HDPE composites collected from CONE tests.

Sample	TTI (s)	pHRR (kW/m^2)	THR (MJ/m^2)	SPR (m^2/s)	TSP (m^2)
H	74	993.2	127.1	0.030	2.40
H/0G40B	49	493.2	109.3	0.023	3.55
H/30G10B	56	676.7	124.9	0.034	4.47
H/0G40B/22APP	68	179.2	54.3	0.054	2.78
H/20G20B/22APP	71	212.7	66.2	0.063	2.28
H/30G10B/28APP	75	201.4	59.6	0.068	2.21

3.4.4. Flame retardant mechanism

The morphology and composition of the residual char layer were further investigated using SEM and FTIR, as shown in Figs. 9 and 10, respectively. Without APP, the composite primarily converted into powdery ash after combustion. When only BW was added, a sparse char layer with numerous pores and poor continuity formed, resulting in a weak structure that was easily destroyed. The incorporation of 20 %

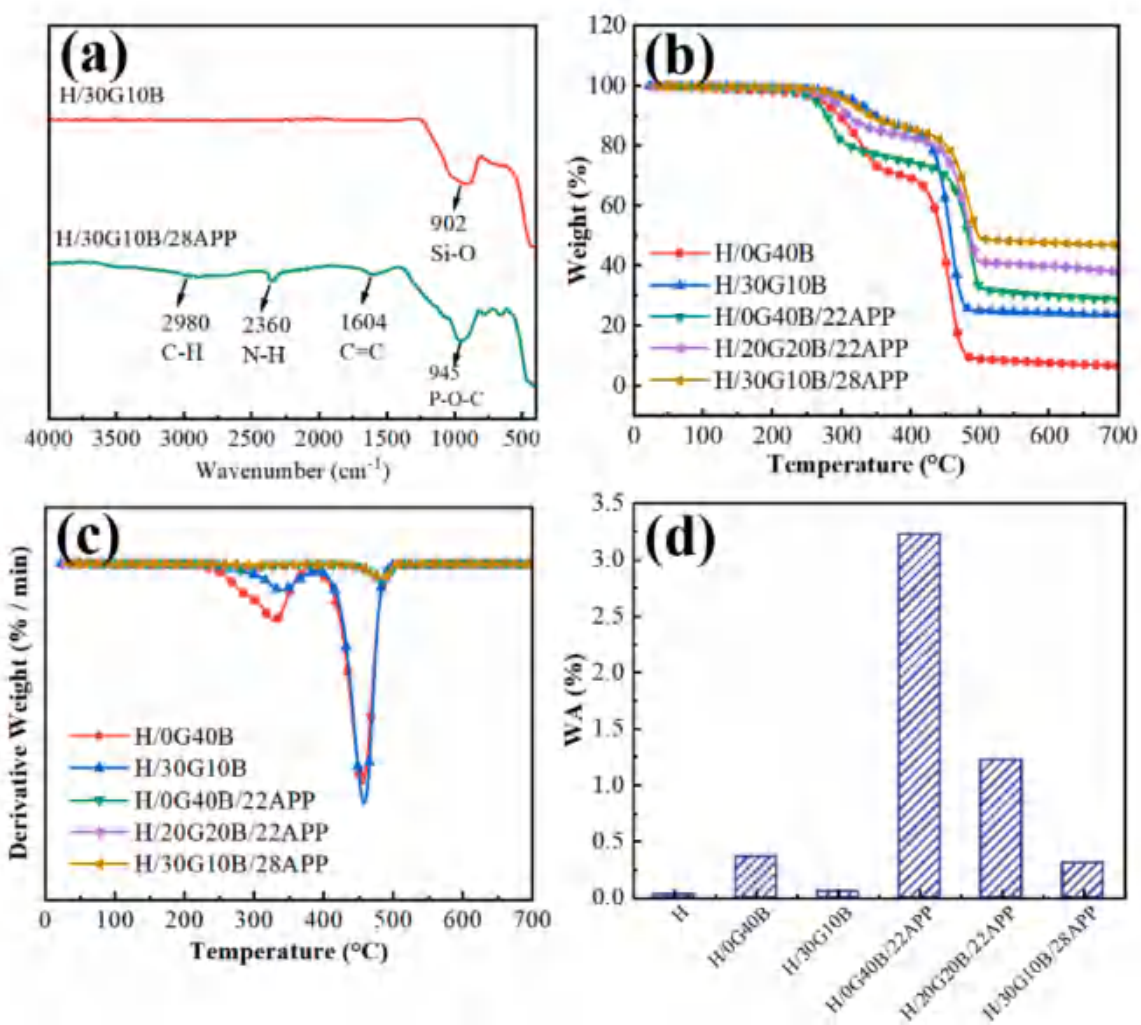

Fig. 9. a) is the infrared curve, b), c) is the TG curve and d) is the 24-hour water absorption test results of the rWTB / APP / HDPE composites.

Table 5
TG data of rWTB/APP/HDPE composites.

Sample	$T_{5\,\%}$ /°C	$T_{10\,\%}$ /°C	T_{max} /°C	Residue/wt %
H/0G40B	271.9	297.1	455.3	6.7
H/30G10B	319.7	349.8	457.8	23.8
H/0G40B/22APP	262.0	278.9	487.2	24.9
H/20G20B/22APP	288.7	310.3	483.5	33.3
H/30G10B/28APP	309.4	342.0	483.8	45.1

GFRP improved the densification of the char layer, enhancing its continuity and reducing pore defects. This increased the char layer strength, effectively hindering heat and oxygen transfer. However, further increasing the GFRP content adversely affected flame-retardant performance. On one hand, the higher resin content promoted heat transfer, accelerating flame propagation. On the other hand, as shown in Fig. 10d_1 and d_2, glass fibers exhibited a "candle wick effect," where softened HDPE flowed along fiber surfaces into the flame zone, facilitating combustion [40]. This phenomenon was confirmed by EDS analysis of the glass fiber surface after combustion (Table 6), which showed significant amounts of C and O. Therefore, GFRP content should not exceed an optimal limit to maintain effective flame retardancy.

FTIR analysis provided further insight into the chemical structure of the residual char. The H/30G10B sample exhibited only the Si-O stretching vibration at 902 cm^{-1}, indicating predominantly inorganic residues, consistent with its appearance as off-white powder after calcination (Fig. 8). In contrast, the H/30G10B/28APP sample displayed characteristic C=C and P-O-C peaks at 1604 cm^{-1} and 945 cm^{-1}, respectively, suggesting that APP reacted with rWTB to form P-O-C structures [17]. Additional -CH (2980 cm^{-1}) and N-H (2360 cm^{-1}) vibrations indicated enhanced char formation. Digital photographs confirmed that the residual char was dense and mechanically robust.

The flame-retardant mechanism of the composites is illustrated in Fig. 11. In systems containing GFRP and BW but without APP, the residual ash content increases after combustion, and no coherent char layer forms. With APP, a continuous carbon layer is produced. The density of this layer increases with GFRP content, likely due to APP decomposition generating polyphosphoric acid and other strong dehydrating agents, which promote the dehydration and carbonization of HDPE, BW, and other materials. The high thermal stability of glass fibers also contributes to the formation of a tightly bonded, dense char layer. During combustion, APP undergoes thermal expansion and embeds into the polymer surface, isolating heat and oxygen. Additionally, the phosphorus and nitrogen in APP release non-combustible gases upon decomposition, diluting oxygen and further inhibiting flame propagation, thereby improving the flame-retardant performance of the composites.

3.5. Water absorption analysis

The water absorption (WA) test is crucial for evaluating the stability of materials, particularly when WPCs are exposed to humid environments for extended periods. Excessive water absorption can lead to deterioration in the dimensional stability of the material, which in turn negatively impacts its physical, mechanical, and other properties, limiting its broader applications.

The results show that adding 40 % BW alone increases the water absorption of the composites. However, incorporating 30 % GFRP and 10 % BW significantly reduces water absorption. The addition of APP increases the water absorption slightly, but overall, the water absorption of the composite remains low.

The primary cause of water absorption in WPCs is the presence of hydrogen bonding and hydroxyl groups in BW, as well as the gaps between the HDPE matrix and the filler, including voids. On the other hand, glass fibers in GFRP, along with the epoxy resin, have low water absorption. As GFRP content increases and BW content decreases, the water absorption of the composite decreases as well, despite the overall mass of the composites remaining unchanged. Moreover, the physical interlocking network structure formed by GFRP and BW enhances the interfacial bonding with the HDPE resin matrix, reducing voids and gaps, which further decreases water absorption.

The addition of APP, however, increases the water absorption of the WPC. This is due to the high water absorption properties of APP, which makes it more prone to absorbing moisture.

4. Conclusions

This study demonstrates that rWTB serves as an effective functional filler in HDPE-based WPCs. Incorporation of 3 wt% MAPE compatibilizer enhances interfacial adhesion between HDPE and rWTB components (GFRP and BW), with optimal mechanical properties achieved at a

Table 6
EDS analysis of GF surface after combustion.

Elemental	C	O	Mg	Al	Si	P	Ca
Content (%)	22.78	51.2	0.51	2.32	2.79	14.59	5.81

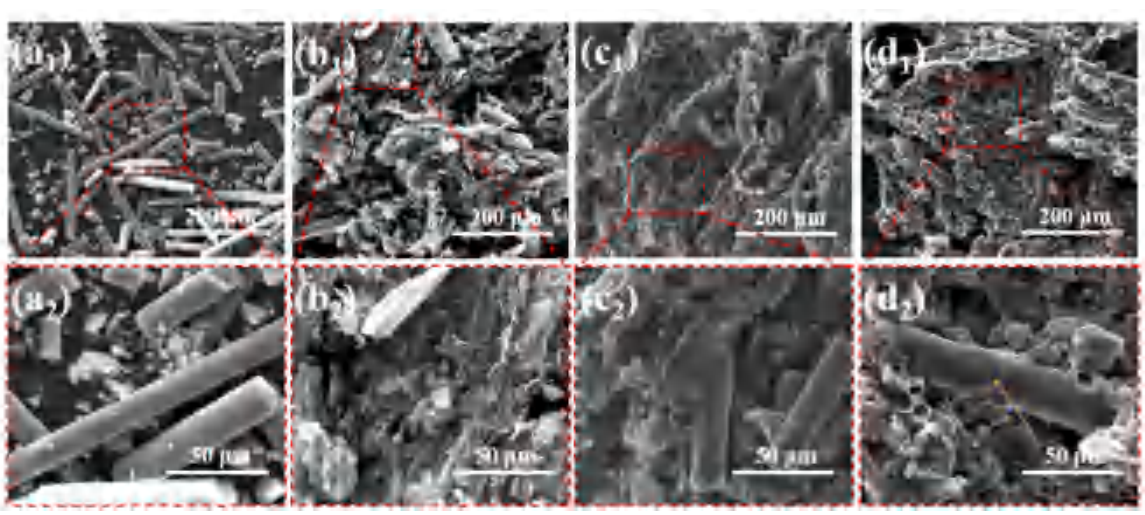

Fig. 10. SEM image of carbon layer of rWTB/APP/HDPE composite: (a_1) H/30G10B (500×); (a_2) H/30G10B (2000×); (b_1) H/0G40B/22APP (500×); (b_2) H/0G40B/22APP (2000×); (c_1) H/20G20B/22APP (500×); (c_2) H/20G20B/22APP (2000×) (d_1) H/30G10B/28APP (500×); (d_2) H/30G10B/28APP (2000×).

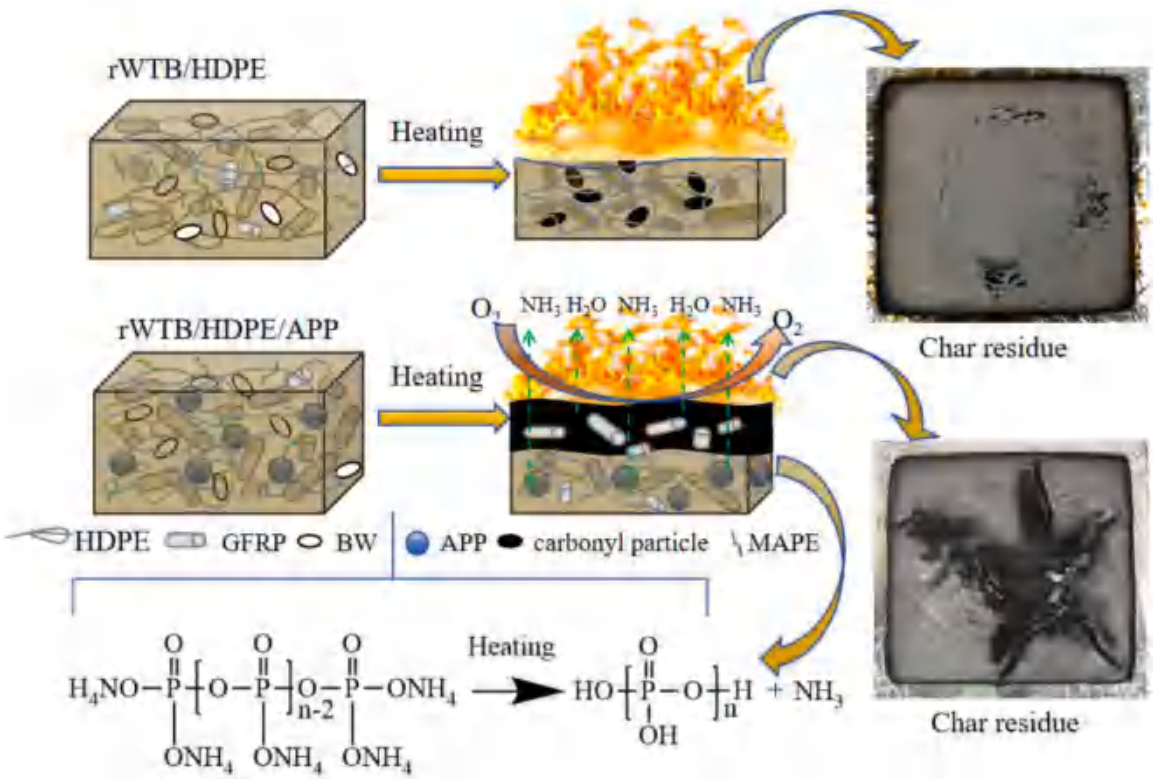

Fig. 11. Flame-retardant Mechanism of rWTB/APP/WPC composites.

GFRP:BW ratio of 3:1, resulting in substantial increases in tensile strength (27.73 MPa, +117.7 %) and impact strength (21.85 kJ/m^2, +197.7 %). The composite's flame retardancy is significantly improved via the synergistic effect of the multi-component system, achieving UL-94 V-0 and LOI values of 35.1-36.8 %, where GFRP reinforces char layer continuity, BW contributes carbonaceous residues, and APP facilitates intumescent char formation. Additionally, rWTB enhances dimensional stability by reducing water absorption. These findings provide insights for designing sustainable, high-performance WPCs with balanced mechanical and flame-retardant properties, while highlighting the need to optimize APP dispersion to minimize trade-offs in mechanical performance.

CRediT authorship contribution statement

YiChen Chen: Writing – original draft, Investigation, Data curation, Conceptualization. **Wufei Tang:** Investigation, Data curation. **Zhaozhen Zhang:** Investigation, Data curation, Conceptualization. **Peixin Li:** Investigation, Data curation. **Shibing Sun:** Data curation. **Wanfu Wang:** Validation, Resources, Methodology. **Xiaodong Jin:** Writing – review & editing, Supervision, Resources, Project administration.

Declaration of competing interest

The authors declare that they have no known competing financial interests or personal relationships that could have appeared to influence the work reported in this paper.

Acknowledgments

This work was supported by the program fund of Nonmetallic Excellence and Innovation Center for Building Materials (24PHD-3) and R&D Program of Beijing Municipal Education Commission (KM202410005008).

Data availability

Data will be made available on request.

References

[1] S. Zeng, Z. Feng, X. Bai, Q. Ma, Z. An, A novel wind turbine blade life extension assessment model considering stiffness degradation, J. Fail. Anal. Prev. 24 (2024) 2006–2013, https://doi.org/10.1007/s11668-024-01986-8.
[2] L. Mishnaevsky, K. Branner, H. Petersen, J. Beauson, M. McGugan, B. Sørensen, Materials for wind turbine blades: an overview, Materials 10 (2017) 1285, https://doi.org/10.3390/ma10111285.
[3] X. Xue, S.Y. Liu, Z.Y. Zhang, Q.Z. Wang, C.Z. Xiao, A technology review of recycling methods for fiber-reinforced thermosets, J. Reinf. Plast. Compos. 41 (2022) 459–480, https://doi.org/10.1177/07316844211055208.
[4] K. Ramirez-Tejeda, D.A. Turcotte, S. Pike, Unsustainable wind turbine blade disposal practices in the United States, J. Environ. Occup. Health. Polic. 26 (2017) 581–598, https://doi.org/10.1177/1048291116676098.
[5] M. Overcash, J. Twomey, E. Asmatulu, E. Vozzola, E. Griffing, Thermoset composite recycling – driving forces, development, and evolution of new opportunities, J. Compos. Mater. 52 (2018) 1033–1043, https://doi.org/10.1177/0021998317720000.
[6] R.S. Ginder, S. Ozcan, Recycling of commercial e-glass reinforced thermoset composites via two temperature step pyrolysis to improve recovered fiber tensile strength and failure strain, Recycling 4 (2019) 24, https://doi.org/10.3390/recycling4020024.
[7] R. Fonte, G. Xydis, Wind turbine blade recycling: an evaluation of the European market potential for recycled composite materials, J. Env. Manage. 287 (2021) 112269, https://doi.org/10.1016/j.jenvman.2021.112269.
[8] A. Nouigues, E.Le Gal La Salle, J.L. Bailleul, Thermo-mechanical characterization of unsaturated polyester/glass fiber composites for recycling, Int. J. Mater. Form. 14 (2021) 153–174, https://doi.org/10.1007/s12289-020-01559-8.
[9] S.R. Naqvi, H.M. Prabhakara, E.A. Bramer, W. Dierkes, R. Akkerman, G. Brem, A critical review on recycling of end-of-life carbon fibre/glass fibre reinforced composites waste using pyrolysis towards a circular economy, Resour. Conserv. Recycl. 136 (2018) 118–129, https://doi.org/10.1016/j.resconrec.2018.04.013.
[10] L. Jiang, C.A. Ulven, D. Gutschmidt, M. Anderson, S. Balo, M. Lee, J. Vigness, Recycling carbon fiber composites using microwave irradiation: reinforcement study of the recycled fiber in new composites, J. Appl. Polym. Sci. 132 (2015), https://doi.org/10.1002/app.42658.
[11] A.M. Nzioka, Y.J. Kim, Surface analysis of glass fibres using XPS and AFM: case study of glass fibres recovered from the glass fibre reinforced polymer using chemical recycling, J. Phys. Conf. Ser. 953 (2018) 012012, https://doi.org/10.1088/1742-6596/953/1/012012.

[12] L. Teuber, V.S. Osburg, W. Toporowski, H. Militz, A. Krause, Wood polymer composites and their contribution to cascading utilisation, J. Clean. Prod. 110 (2016) 9–15, https://doi.org/10.1016/j.jclepro.2015.04.009.
[13] S. Migneault, A. Koubaa, F. Erchiqui, A. Chaala, K. Englund, M.P. Wolcott, Effects of processing method and fiber size on the structure and properties of wood–plastic composites, Compos. Appl. Sci. Manuf. 40 (2009) 80–85, https://doi.org/10.1016/j.compositesa.2008.10.004.
[14] X. Gao, Q. Li, W. Cheng, G. Han, L. Xuan, Effects of moisture content, wood species, and form of raw materials on fiber morphology and mechanical properties of wood fiber-HDPE composites, Polym. Compos. 39 (2018) 3236–3246, https://doi.org/10.1002/pc.24336.
[15] D.J. Gardner, Y. Han, L. Wang, Wood–plastic composite technology, Curr. For. Rep. 1 (2015) 139–150, https://doi.org/10.1007/s40725-015-0016-6.
[16] S.N. Monteiro, F.P.D. Lopes, A.S. Ferreira, D.C.O. Nascimento, Natural-fiber polymer-matrix composites: cheaper, tougher, and environmentally friendly, JOM 61 (2009) 17–22, https://doi.org/10.1007/s11837-009-0004-z.
[17] A. Zolfaghari, A.H. Behravesh, A. Adli, M.T. Sarabi, Continuous glass fiber reinforced wood plastic composite in extrusion process: feasibility and processing, J. Reinf. Plast. Compos. 32 (2013) 52–60, https://doi.org/10.1177/0731684412461461.
[18] K. Wang, C. Yu, W. Liu, R. Huo, H. Fang, X. Chen, Study on flexural property of glass fiber-reinforced polymer reinforced wood–plastic composite panels, Wood. Mater. Sci. Eng. 20 (2025) 478–487, https://doi.org/10.1080/17480272.2024.2355554.
[19] G. Guo, C. Kethineni, Direct injection molding of hybrid polypropylene/wood-fiber composites reinforced with glass fiber and carbon fiber, Int. J. Adv. Manuf. Technol. 106 (2020) 201–209, https://doi.org/10.1007/s00170-019-04572-7.
[20] G.S. Oporto, D.J. Gardner, G. Bernhardt, D.J. Neivandt, Forced air plasma treatment (FAPT) of hybrid wood plastic composite (WPC)–fiber reinforced plastic (FRP) surfaces, Compos. Interfaces. 16 (2009) 847–867, https://doi.org/10.1163/092764409x12477463089116.
[21] S. Durmaz, U. Aras, E. Avci, F. Mengeloğlu, İ. Atar, The effect of chopped glass and carbon fiber reinforcement on physical, mechanical, and fire performance of wood plastic composites, drewno. prace naukowe, doniesienia, komunikaty = wood, Res. Pap. Rep. Announc. 66 (2023), https://doi.org/10.53502/wood-177638.
[22] L. Fang, X. Xiong, X. Wang, H. Chen, X. Mo, Effects of surface modification methods on mechanical and interfacial properties of high-density polyethylene-bonded wood veneer composites, J. Wood. Sci. 63 (2017) 65–73, https://doi.org/10.1007/s10086-016-1589-9.
[23] Y.H. Cui, X.X. Wang, Q. Xu, Z.Z. Xia, Research on moisture absorption behavior of recycled polypropylene matrix wood plastic composites, J. Thermoplast. Compos. Mater. 24 (2011) 65–82, https://doi.org/10.1177/0892705710376470.
[24] A. Dorieh, P.P. Selakjani, M.H. Shahavi, A. Pizzi, S. Ghafari Movahed, M. Farajollah Pour, R. Aghaei, Recent developments in the performance of micro/nanoparticle-modified urea-formaldehyde resins used as wood-based composite binders: a review, Int. J. Adhes. Adhes. 114 (2022) 103106, https://doi.org/10.1016/j.ijadhadh.2022.103106.
[25] T.C. Mokhena, E.R. Sadiku, M.J. Mochane, S.S. Ray, Mechanical properties of fire retardant wood-plastic composites: a review, Express. Polym. Lett. 15 (2021) 744–780, https://doi.org/10.3144/expresspolymlett.2021.61.
[26] D.J. Irvine, J.A. McCluskey, I.M. Robinson, Fire hazards and some common polymers, Polym. Degrad. Stab. 67 (2000) 383–396, https://doi.org/10.1016/S0141-3910(99)00127-5.
[27] L. Liu, M. Qian, P. Song, G. Huang, Y. Yu, S. Fu, Fabrication of green lignin-based flame retardants for enhancing the thermal and fire retardancy properties of polypropylene/wood composites, ACS. Sustain. Chem. Eng. 4 (2016) 2422–2431, https://doi.org/10.1021/acssuschemeng.6b00112.
[28] J.G. Gwon, S.Y. Lee, J.H. Kim, Thermal degradation behavior of polypropylene base wood plastic composites hybridized with metal (aluminum, magnesium) hydroxides, J. Appl. Polym. Sci. 131 (2014), https://doi.org/10.1002/app.40120.
[29] D. Wang, P. Jiang, Z. Chen, J. Sun, H. Li, X. Gu, S. Zhang, Flame retardant research on innovative lightweight wood-plastic composites, J. Appl. Polym. Sci. 140 (2023), https://doi.org/10.1002/app.53965.
[30] G. Bai, C. Guo, L. Li, Synergistic effect of intumescent flame retardant and expandable graphite on mechanical and flame-retardant properties of wood flour-polypropylene composites, Constr. Build. Mater. 50 (2014) 148–153, https://doi.org/10.1016/j.conbuildmat.2013.09.028.
[31] A. Samariha, B. Bazyar, Effect of nanosilica and aluminum hydroxide on thermal, flammability, and morphology properties of nanocomposite made of recycled high-density polyethylene and OCC flour, Bioresources 15 (2020) 3382–3393, https://doi.org/10.15376/biores.15.2.3382-3393.
[32] W. Wang, H. Chen, J. Li, Effects of maleic anhydride grafted polypropylene on the physical, mechanical and flammability properties of wood-flour/polypropylene/ammonium polyphosphate composites, Fibers. Polym. 22 (2021) 1137–1144, https://doi.org/10.1007/s12221-021-0202-z.
[33] Z. Huang, B. Ruan, J. Wu, N. Ma, T. Jiang, F. Tsai, <scp>High-efficiency</scp>ammonium polyphosphate intumescent encapsulated polypropylene flame retardant, J. Appl. Polym. Sci. 138 (2021), https://doi.org/10.1002/app.50413.
[34] H. Hong, H. Liu, H. Zhang, H. He, T. Liu, D. Jia, Flame retarded polyethylene/wood flour composites with high performances: satisfying both sides with intumescent flame retardants and synergistic compatibilizers, respectively, Polym. Compos. 39 (2018) 569–579, https://doi.org/10.1002/pc.23970.
[35] B. Dai, R. Huo, K. Wang, Z. Ma, H. Fang, Study on bending creep performance of GFRP-reinforced PVC-based wood-plastic composite panels, Polymers 14 (2022) 4789, https://doi.org/10.3390/polym14224789.
[36] S. Tungjitpornkull, K. Chaochanchaikul, N. Sombatsompop, Mechanical characterization of E-chopped strand glass fiber reinforced Wood/PVC composites, J. Thermoplast. Compos. Mater. 20 (2007) 535–550, https://doi.org/10.1177/0892705707084541.
[37] N.G. Karsli, C. Ozkan, A. Aytac, V. Deniz, Effects of sizing materials on the properties of carbon fiber-reinforced polyamide 6,6 composites, Polym. Compos. 34 (2013) 1583–1590, https://doi.org/10.1002/pc.22556.
[38] B. Fernández, A. Arbelaiz, A. Valea, F. Mujika, I. Mondragon, A comparative study on the influence of epoxy sizings on the mechanical performance of woven carbon fiber-epoxy composites, Polym. Compos. 25 (2004) 319–330, https://doi.org/10.1002/pc.20026.
[39] K.B. Adhikary, S. Pang, M.P. Staiger, Dimensional stability and mechanical behaviour of wood–plastic composites based on recycled and virgin high-density polyethylene (HDPE), Compos. B. Eng. 39 (2008) 807–815, https://doi.org/10.1016/j.compositesb.2007.10.005.
[40] C. Dolçà, E. Fages, E. Gonga, D. Garcia-Sanoguera, R. Balart, L. Quiles-Carrillo, The effect of varying the amount of short hemp fibers on mechanical and thermal properties of wood–plastic composites from biobased polyethylene processed by injection molding, Polymers 14 (2021) 138, https://doi.org/10.3390/polym14010138.
[41] M.del C. Morcillo, R. Tejada, D. Lascano, D. Garcia-Garcia, D. Garcia-Sanoguera, Manufacturing and characterization of environmentally friendly wood plastic composites using pinecone as a filler into a bio-based high-density polyethylene matrix, Polymer 13 (2021) 4462, https://doi.org/10.3390/polym13244462.
[42] R.M. Bajracharya, A.C. Manalo, W. Karunasena, K. Lau, An overview of mechanical properties and durability of glass-fibre reinforced recycled mixed plastic waste composites, Mater. Des. 62 (1980-2015) (2014) 98–112, https://doi.org/10.1016/j.matdes.2014.04.081.
[43] S. Durmaz, Y.Z. Erdil, E. Avci, Improvement of technological properties of wood plastic composites reinforced with glass and carbon fibre fabric, Polym. Polym. Compos. 29 (2021) S1457–S1465, https://doi.org/10.1177/09673911211054266.
[44] A.U.R. Shah, A. Jalil, A. Sadiq, M. Alzaid, M.S. Naseem, R. Alanazi, S. Alanazi, A. O. Alanzy, I.H. Alsohaimi, R.A. Malik, Effect of rice husk and wood flour on the structural, mechanical, and fire-retardant characteristics of recycled high-density polyethylene, Polymers 15 (2023) 4031, https://doi.org/10.3390/polym15194031.
[45] C.Yargici Kovanci, M. Nofar, A. Ghanbari, Synergistic enhancement of flame retardancy behavior of glass-fiber reinforced polylactide composites through using phosphorus-based flame retardants and chain modifiers, Polymers 14 (2022) 5324, https://doi.org/10.3390/polym14235324.
[46] Z. Hu, T. Shi, Application of a piperazine pyrophosphate intumescent flame retardant in thin-walled glass fiber-reinforced polypropylene materials, J. Appl. Polym. Sci. 140 (2023) 1–13, https://doi.org/10.1002/app.54498.